Cover Picture

Emanuel Vogel,* Martin Michels, Lars Zander, Johann Lex, Nurcan S. Tuzun, and Kendall N. Houk*



The "figure-eight" cyclooctapyrrole octaphyrin-(1.1.1.0.1.1.1.0), a compound susceptible to versatile functionalization, opens a pathway to the first dispirodiporphyrinoid obtained as a binuclear nickel complex. The stage for this transformation is set by the regioselective oxidation of octaphyrin to give the diketo derivative shown in the background. Nickel ions initiate a reaction cascade with the diketone, which leads to the nickel complex of spirodicorrole. For more information see the communication by E. Vogel and K. N. Houk et al. on page 2857ff.

Contents

Obituary

Dieter Sellmann (1941 – 2003) —— **2816** | Coordination Chemistry of N_2 Fixation | *Karl Wieghardt*

Books

Cation Binding by Humic Substances —— **2817** | Edward Tipping | *reviewed by A. Knöchel*

On-line LC-NMR and Related Techniques —— **2817** | Klaus Albert | *reviewed by J.-L. Wolfender*

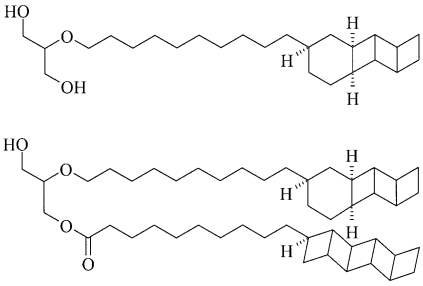
The Chemistry of Medical and Dental Materials —— **2818** | John W. Nicholson | *reviewed by M. Epple*

Highlights

Molecular Ladders

H. Hopf* —— **2822 – 2825**

Step by Step—From Nonnatural to Biological Molecular Ladders



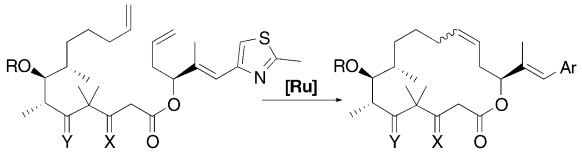
Ladderanes were identified recently as membrane lipids (see structural formulas) in two ammonium-oxidizing bacteria, which is an astonishing observation considering the unusual structural motif and the nontrivial synthesis of this class of compounds.

Minireviews

Macrocycles with (*E*)-Alkenes

J. Prunet* —— **2826 – 2830**

Recent Methods for the Synthesis of (*E*)-Alkene Units in Macrocyclic Natural Products



1a X = α-OTBS/β-H, Y = O, R = TBS
1b X = α-H/β-OH, Y = α-OTPS, R = TBS

2a 86%, *E*/*Z* = 1:1.7
2b 81%, *E*/*Z* = 9:1

Ring-closing metathesis is one of the best methods for the synthesis of macrocycles containing C–C double bonds. Unfortunately, the *E*/*Z* selectivity of the bond formed depends on a number of factors, as the ring-closing reactions in the syntheses of epothilones A and B (**2a** and **2b**) demonstrated (see scheme). [Ru] = Grubbs' catalyst, TBS = *tert*-butyldimethylsilyl, TPS = triphenylsilyl.

Reviews

Catalyst Screening

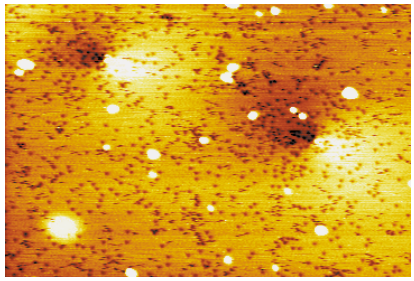
P. Chen* —— **2832 – 2847**

Electrospray Ionization Tandem Mass Spectrometry in High-Throughput Screening of Homogeneous Catalysts

Fishing for catalysts: A method for high-throughput screening for homogeneous catalysts is discussed conceptually and illustrated with several examples of real catalytic systems. Implementation of the strategy, using electrospray ionization tandem mass spectrometry, gives the high-throughput method a very high information content.

Communications

NO can't take the strain: NO molecules are observed to preferentially dissociate near edge dislocations which originate in the bulk phase and intersect the metal surface. The effect is caused by lattice strain, a phenomenon in heterogeneous catalysis, which has been postulated for a long time and is demonstrated here on the atomic scale by calculations and STM images (see picture of two edge dislocations; black points: N atoms).

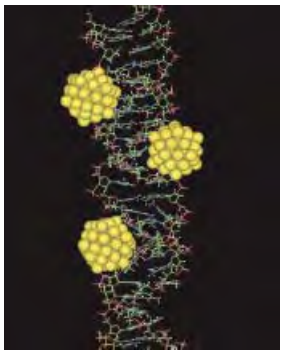


Watching NO Activation on a Surface

J. Wintterlin,* T. Zambelli, J. Trost, J. Greeley, M. Mavrikakis* — **2850 – 2853**

Atomic-Scale Evidence for an Enhanced Catalytic Reactivity of Stretched Surfaces

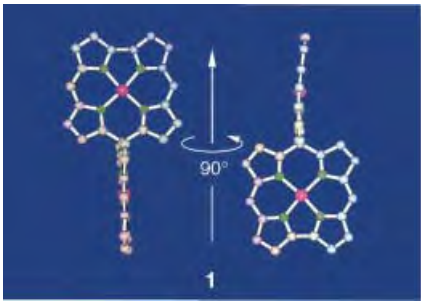
Making 13 from 55: Au_{55} nanoclusters that interact with the major groove of B-DNA (see energy-minimized structure), are broken down into Au_{13} clusters by the transformation of B-DNA into A-DNA, during which the major groove shrinks dramatically. This transformation, which results in the formation of Au_{13} wires, is initiated by the dehydration of the B-DNA under the conditions required for electron microscopy.



DNA/Gold-Cluster Interactions

Y. Liu, W. Meyer-Zaika, S. Franzka, G. Schmid,* M. Tsoli, H. Kuhn — **2853 – 2857**

Gold-Cluster Degradation by the Transition of B-DNA into A-DNA and the Formation of Nanowires



Figures of eight correlate with corrolates: The surprising formation of the spirodicorrole dinickel complex **1**, the first spirodiporphyrin as a metal complex, is the result of the varied chemistry of the "figure-eight" cyclooctapyrrole octaphyrin-(1.1.1.0.1.1.1.0). The conversion of the cyclooctapyrrole into **1** is brought about by a sequence of oxidation and a nickel(II) acetate induced cascade of rearrangement reactions. In structural respects, **1** stands out because of the orthogonal arrangement of the two nickelcorrolate chromophores linked through a common spiro carbon atom.

Spirodiporphyrin Complexes

E. Vogel,* M. Michels, L. Zander, J. Lex, N. S. Tuzun, K. N. Houk* — **2857 – 2862**

Spirodiporphyrins—As Binuclear Metal Complexes

For the USA and Canada:
ANGEWANDTE CHEMIE International Edition (ISSN 1433-7851) is published weekly by Wiley-VCH PO Box 191161, D 69451 Weinheim, Germany. Air freight and mailing in the USA by Publications Expediting Inc. 200 Meacham Ave., Elmont, NY 11003. Periodicals postage paid at Jamaica NY 11431. US POSTMASTER: send address changes to *Angewandte Chemie*, Wiley-VCH, 111 River Street, Hoboken, NJ 07030. Annual institutional subscription price for institutions: Europe € 2998.00/3148.00. Outside Europe US$ 3718.00/3904.00 (valid for print or electronic/print and electronic delivery); for individuals who are personal members of a national chemical society, or whose institution already subscribes, or who are retired or self-employed consultants, print only (including postage and handling charges): Europe € 248.00/Outside Europe US$ 348.00.

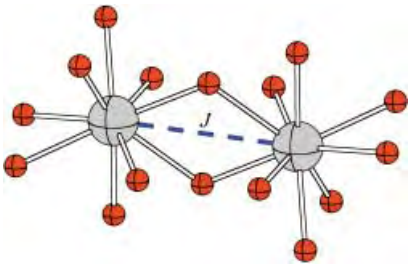
 © 2003 Wiley-VCH Verlag GmbH & Co. KGaA, Weinheim

Contents

Molecular Ferromagnetism

S. T. Hatscher, W. Urland* — **2862 – 2864**

Unexpected Appearance of Molecular Ferromagnetism in the Ordinary Acetate $[\{Gd(OAc)_3(H_2O)_2\}_2]\cdot 4\,H_2O$



Breaking the law: Whereas antiferromagnetic interactions in crystalline carboxylates of lanthanides are often observed, ferromagnetism is unknown. The first example of a ferromagnetic interaction is observed for a crystalline sample of the gadolinium compound $[\{Gd(OAc)_3(H_2O)_2\}_2]\cdot 4\,H_2O$ (see picture Gd: gray, O: red).

Biosynthesis of Orellanine

P. Spiteller, M. Spiteller, W. Steglich* — **2864 – 2867**

Occurrence of the Fungal Toxin Orellanine as a Diglucoside and Investigation of Its Biosynthesis

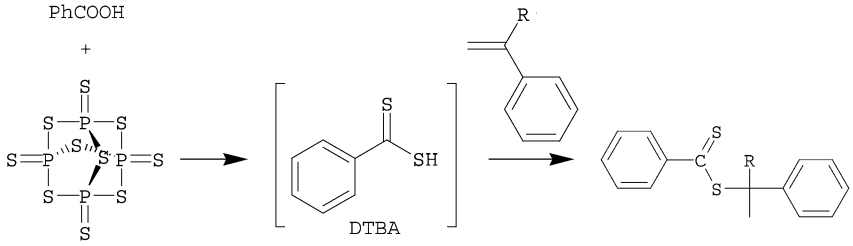


Poisonous mushrooms. The deadly toxin orellanine is present in the toadstools *Cortinarius orellanus* and *C. rubellus* (see photo) as the water-soluble 4,4′-diglucoside. Its biosynthesis starts from anthranilic acid as has been shown by application of $^{15}N/^{14}N$ isotope ratio mass spectrometry.

Controlled Radical Polymerization

A. Duréault, Y. Gnanou,* D. Taton,* M. Destarac, F. Leising — **2869 – 2872**

Reaction of Cyclic Tetrathiophosphates with Carboxylic Acids as a Means to Generate Dithioesters and Control Radical Polymerization By RAFT

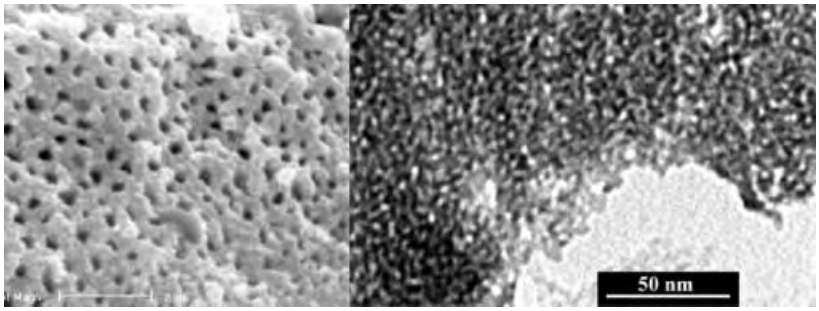


Radical control: Controlled free-radical polymerization of styrene and methyl (meth)acrylate is achieved by using Davy reagents or P_4S_{10} in conjunction with benzoic acid, which leads to in situ formation of dithioesters that act as chain-transfer agents and thus control the reaction. In the case of P_4S_{10}/PhCOOH, dithiobenzoic acid is the key intermediate in this process (see scheme).

Meso-Macroporous Metal Oxides

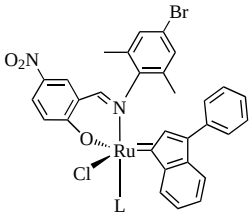
J.-L. Blin, A. Léonard, Z.-Y. Yuan, L. Gigot, A. Vantomme, A. K. Cheetham, B.-L. Su* — **2872 – 2875**

Hierarchically Mesoporous/Macroporous Metal Oxides Templated from Polyethylene Oxide Surfactant Assemblies

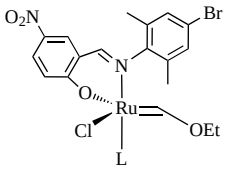


Wormhole-like mesoporous walls are observed within macroporous metal oxides that were synthesized in one step using nonionic alkyl-PEO surfactants as templates. The uniform macropores have a funnel-like shape (tapered towards the center) and are arranged parallel to each other and perpendicular to the tangent of the particle surface (see micrographs). The mesochannels are interconnected with funnel-like macrochannels.

 © 2003 Wiley-VCH Verlag GmbH & Co. KGaA, Weinheim



1



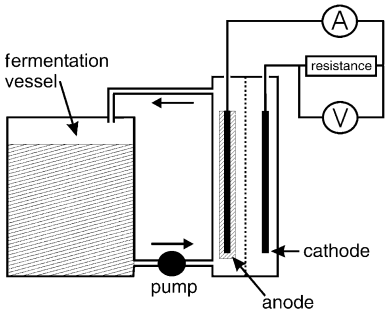
2

Two catalysts for the price of one: Air-stable ruthenium complexes **1** and **2** (L = PCy, 1,3-dimesityl-4,5-dihydroimidazol-2-ylidene) are catalyst precursors for the atom-transfer radical polymerization of vinyl monomers. The catalytic activity is increased when the analogous cationic 14-electron complexes are used. Unusually, these complexes also show a very high activity for the ring-opening-metathesis polymerization of low-strain cyclic olefins.

Schiff Base Based Catalysts

T. Opstal, F. Verpoort* ____ **2876 – 2879**

Synthesis of Highly Active Ruthenium Indenylidene Complexes for Atom-Transfer Radical Polymerization and Ring-Opening-Metathesis Polymerization



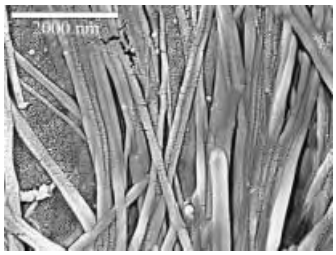
Ever-ready microbes: A microbial fuel cell (depicted) that continuously generates a current output more than one order of magnitude greater than known microbial fuel cells (up to 1.5 $mA\,cm^{-2}$) is reported. The novel fuel cell concept uses polymer-modified catalytically active anodes that shuttle electrons from the bacterial suspension to the anode.

A Microbial Fuel Cell

U. Schröder,* J. Nießen, F. Scholz ____ **2880 – 2883**

A Generation of Microbial Fuel Cells with Current Outputs Boosted by More Than One Order of Magnitude

A self-inducing template-growth approach to the production of nanofibers of 1,3-diphenyl-2-pyrazoline (DP) in the presence of cetyltrimethylammonium bromide (CTAB) in an aqueous phase is discussed (see picture). Not only the surfactant CTAB molecules assume the role of surface-active colloidal stabilizers; but also the rodlike CTAB micelles, which are induced by DP molecules dissolved in spherical CTAB micelles, further direct the growth of cylindrical DP nanofibers like templates. It is found that the crystal-

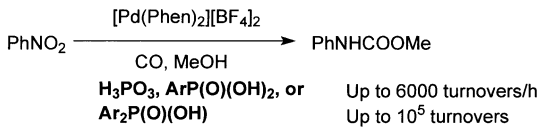


packing forces drive the DP molecules to self-assemble as J-type aggregates in nanofibers.

Micelle-Induced Nanofibers

H. Fu, D. Xiao, J. Yao,* G. Yang ____ **2883 – 2886**

Nanofibers of 1,3-Diphenyl-2-pyrazoline Induced by Cetyltrimethylammonium Bromide Micelles



Phenomenal! The activity of the palladium–phenanthroline catalytic system for the carbonylation of nitrobenzene to methyl phenylcarbamate is greatly enhanced by the addition of phosphorus acids. Of those that were studied, the best promoter is the very cheap, easily separable, and nontoxic phosphoric acid.

Phosphorus Acid-Promoted Catalysis

F. Ragaini,* C. Cognolato, M. Gasperini, S. Cenini ____ **2886 – 2889**

The Carbonylation Reaction of Nitrobenzene to Methyl Phenylcarbamate: Highly Efficient Promoters for the Palladium–Phenanthroline Catalytic System Based on Phosphorus Acids

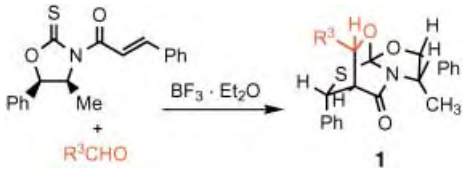
 © 2003 Wiley-VCH Verlag GmbH & Co. KGaA, Weinheim

Contents

Tandem Michael–Aldol Reaction

T. Kataoka,* H. Kinoshita, S. Kinoshita, T. Osamura, S.-i. Watanabe, T. Iwamura, O. Muraoka, G. Tanabe ____ **2889 – 2891**

Asymmetric Induction of Three Consecutive Chiral Centers by Reactions of *N*-Enoylthioamides with Aldehydes

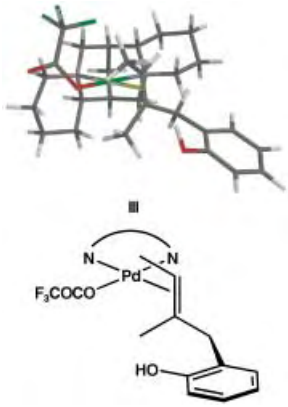


Wrap it up and put on a bow! The reaction of *N*-cinnamoyl-1,3-oxazoline-2-thione with aromatic aldehydes in the presence of $BF_3{\cdot}Et_2O$ diastereoselectively gave adducts **1**, which contain three consecutive asymmetric centers and a chiral bridgehead bound to four heteroatoms.

Pd-Catalyzed Wacker Cyclizations

R. M. Trend, Y. K. Ramtohul, E. M. Ferreira, B. M. Stoltz* ____ **2892 – 2895**

Palladium-Catalyzed Oxidative Wacker Cyclizations in Nonpolar Organic Solvents with Molecular Oxygen: A Stepping Stone to Asymmetric Aerobic Cyclizations

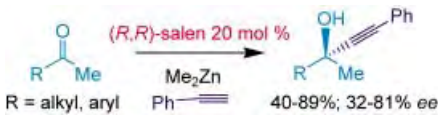


A variety of Pd-catalyzed oxidative nucleophile/alkene cyclizations proceeds in excellent yield under simple aerobic conditions in nonpolar media (Pd catalyst, pyridine, and O_2 in toluene). Nucleophiles for these cyclizations include phenols, carboxylic acids, amides, and primary alcohols. Additionally, enantioselective catalysis is feasible with a Pd-sparteine system (see picture). Enantioselectivities of up to 90% *ee* are observed for simple phenol/alkene cyclizations.

Asymmetric Addition to Ketones

P. G. Cozzi* ____ **2895 – 2898**

Enantioselective Alkynylation of Ketones Catalyzed by Zn(Salen) Complexes



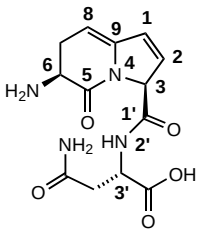
The new frontier in asymmetric catalysis is the selective formation of quaternary stereocenters. The enantioselective addition of nucleophiles to ketones is a particular challenge. Readily prepared Zn(salen) complexes promote the straightforward synthesis of tertiary alcohols from commercially available starting materials (see scheme), thus allowing the preparation of functionalizable chiral building blocks in a catalytic enantioselective procedure that shows broad scope.

Antibiotic Structure Determination

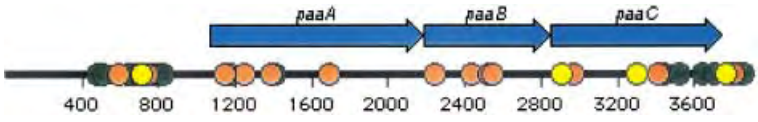
M. Jin, L. Liu, S. A. I. Wright, S. V. Beer, J. Clardy* ____ **2898 – 2901**

Structural and Functional Analysis of Pantocin A: An Antibiotic from *Pantoea agglomerans* Discovered by Heterologous Expression of Cloned Genes

Small-molecule chemistry and biochemical techniques have been used to determine the structure and mode of function of pantocin A (see structure), a naturally occurring antibiotic. Pantocin A functions as an inhibitor of histidine biosynthesis, as shown by its ability to inhibit the action of L-histidinol phosphate aminotransferase, which converts imidazole acetol phosphate to L-histidinol phosphate in *Escherichia coli*.



 © 2003 Wiley-VCH Verlag GmbH & Co. KGaA, Weinheim

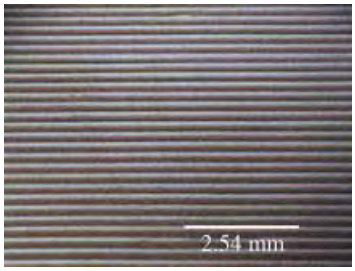


Peptide origins: Feeding experiments carried out with ^{14}C-labeled amino acids have demonstrated that the bicyclic core of pantocin A is derived from glutamate or glutamine residues. Sequencing and transposon mutagenesis of the 3.5 kb stretch of DNA that enables an *Escherichia coli* strain to produce pantocin A has identified three major open-reading frames (*paaA*, *paaB*, and *paaC*) responsible for its construction, and the resistance mechanism (see picture red: inactive, green: active, yellow: reduced activity positions).

Antibiotic Discovery

M. Jin, S. A. I. Wright, S. V. Beer, J. Clardy* ——— **2902 – 2905**

The Biosynthetic Gene Cluster of Pantocin A Provides Insights into Biosynthesis and a Tool for Screening

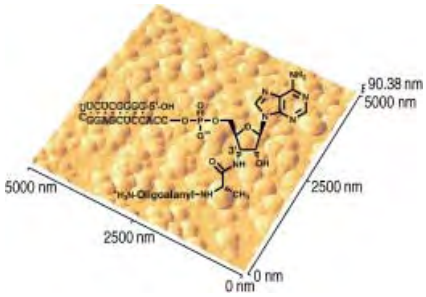


Reading between the lines: Films of manganese oxide nanoparticles can be prepared from immersion into a colloidal solution of tetramethylammonium manganese oxide, followed by solvent evaporation. The resultant films exhibit a series of parallel lines (see picture), which themselves are comprised of many smaller lines. Ion-exchange processes with potassium ions can be accomplished without a loss of structural integrity.

Mn Oxide Nanoparticle Assemblies

O. Giraldo, J. P. Durand, H. Ramanan, K. Laubernds, S. L. Suib,* M. Tsapatsis, S. L. Brock, M. Marquez ——— **2905 – 2909**

Dynamic Organization of Inorganic Nanoparticles into Periodic Micrometer-Scale Patterns

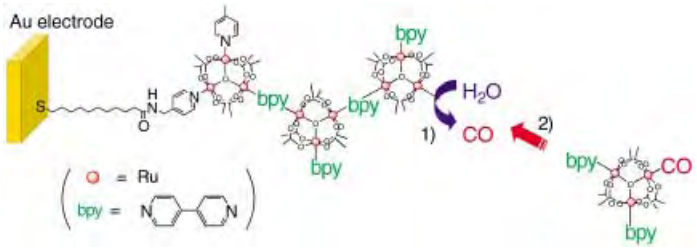


Highly amphiphilic fragments of hydrolytically stable 3′-peptidyl transfer RNA analogues are stepwise assembled on solid support. Their secondary structure and thermal denaturation are studied by using CD and UV spectroscopy, their supramolecular assemblage by using AFM and DLS (see picture).

Synthetic Peptidyl–tRNA Analogues

S. Terenzi, E. Biała, N. Q. Nguyen-Trung, P. Strazewski* ——— **2909 – 2912**

Amphiphilic 3′-Peptidyl-RNA Conjugates



Layer-by-layer metal-cluster molecular multilayers are fabricated onto preorganized self-assembled monolayers on Au electrode surfaces. The molecular building block, $[Ru_3(\mu_3\text{-}O)(\mu\text{-}CH_3COO)_6(bpy)_2(CO)]$ (bpy = 4,4′-bipyridine), is applied by displacing the water ligand on the cluster core (see picture), which is precisely controlled through the electrode potential. The series of multilayers transport electrons across the molecularly linked backbone.

Clusters Layered on Au Surfaces

M. Abe,* T. Michi, A. Sato, T. Kondo, W. Zhou, S. Ye, K. Uosaki,* Y. Sasaki* ——— **2912 – 2915**

Electrochemically Controlled Layer-by-Layer Deposition of Metal-Cluster Molecular Multilayers on Gold

 © 2003 Wiley-VCH Verlag GmbH & Co. KGaA, Weinheim

Contents

Communications labeled with this symbol have been judged by two referees as being "very important papers".

The publication of Communications labeled with this symbol has been accelerated because of their topical or highly competitive nature.

The issues for June 2003 appeared online on the following dates
Issue 21: May 28 · Issue 22: June 5 · Issue 23: June 12 · Issue 24: June 17

Sources

Product and Company Directory

You can start the entry for your company in "Sources" in any issue of *Angewandte Chemie*.

If you would like more information, please do not hesitate to contact us.

Wiley-VCH Verlag – Advertising Department
Tel.: 0 62 01 - 60 65 65
Fax: 0 62 01 - 60 65 50
E-Mail: MSchulz@wiley-vch.de

Service

Keywords ____ 2916

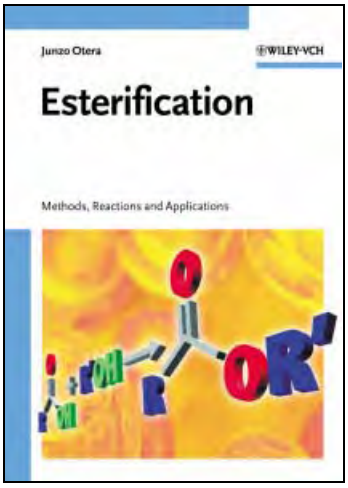
Authors ____ 2917

Events ____ 2815

Vacancies ____ A35

Preview ____ 2919

Just a Must for Organic Chemists



ISBN 3-527-30490-8
*Approx *€ 139,- / sFr 205,-*

**The Euro price is only valid for germany.*

JUNZO OTERA, Okayama University of Science, Japan

Esterification
Methods, Reactions and Applications

2003. Approx XV, 435pp Hbk.

Here, Professor J. Otera brings together for the first time the combined knowledge about this elementary yet multifaceted reaction. Starting from the methodical basics right up to practical applications, this book represents a comprehensive overview of this type of reaction, saving readers time-consuming research among the literature – and not just in practical matters.

- First book bringing together widely spread knowledge about this important reaction
- Written by one of the leading chemists in the field of Esterification
- **All set to become a standard reference for every organic chemist**

Wiley-VCH Verlag
Fax: +49 (0)62 01 - 60 61 84
e-Mail: service@wiley-vch.de
www.wiley-vch.de

Register now for the free
WILEY-VCH Newsletter!
www.wiley-vch.de/home/pas

WILEY-VCH

50613032_kn



Dieter Sellmann (1941–2003): Coordination Chemistry of N_2 Fixation

Dieter Sellmann died unexpectedly on 6 May 2003, at the age of 62. He was an outstanding coordination chemist. His innovative contributions to the modeling of enzymatic nitrogen fixation, that is, the conversion of inert dinitrogen into ammonia under homogeneous catalysis and mild reaction conditions, have made him well known internationally, and have been an inspiration to many of his fellow scientists time and time again. Dieter was an exceptionally gifted synthetic chemist. Over a period of more than 30 years he synthesized interesting, unusual, and esthetically beautiful molecules, with an impressively large number of students.

Dieter Sellmann entered the public scientific scene in 1972 at the Chemiedozententagung (German meeting of junior chemistry lecturers) in Heidelberg with a bang. Unforgettable for all of those present was the masterful, confident way in which he presented his first ground-breaking results in artificial N_2 fixation: the dinuclear diimine complex *trans*-[(μ-N_2H_2){CpMn(CO)$_2$}$_2$][1] and its oxidized dinitrogen product [CpMn(CO)$_2$N$_2$].[2] In 1989 followed the biomimetic complex [(μ-N_2H_2){Fe("N_HS_4")}$_2$], which has many structural and electronic properties that are important in nitrogenase.[3] The synthesis of this complex led him to formulate his much debated mechanism for catalytic N_2 fixation in nature.[4]

The scientist Dieter Sellmann was strict—occasionally remorseless—toward others, but always toward himself as well, when it came to the question of "true" N_2 fixation (under *mild* conditions). He did not accept elemental Li or Na to be *mild* reagents (not even in a disguised form). The reaction should occur under the same conditions as the natural process: in water, at 20 °C, under a pressure of 1 atm, and with a physiological redox potential.

To realize his scientific dream, Dieter had to learn and develop a great deal of organic sulfur chemistry. After taking up an appointment at the University of Paderborn in 1976, he went on to design and synthesize novel sulfur-containing ligands, which are still used today by chemists around the world. Many of his compounds or ideas have been used willingly by others (also by this author) in their chemistry. Dieter was very generous.

From 1980, then at the University of Erlangen, a large variety of thiolate and thioether ligands were synthesized, and their coordination chemistry and efficiency in N_2 fixation was studied—with success: In 2001, N_2 fixation under mild conditions at a Ru center was observed.[5] Dieter was particularly motivated and excited over the last two years; he believed he was near his life's goal and that what he had dreamed of was really possible.

He was an excellent teacher, who shared his enthusiasm for chemistry with his students in clear, concise, often elegant language. He was convinced that only difficult problems were worth working on and ambitious goals worth setting. He traveled a lot and lectured both in Germany and abroad, but relatively reluctantly. During a big conference he once observed, while he stood with a glass of cognac in his hand, as the sun set over the Pacific: "I would much rather be sitting next to my wife on the sofa in Erlangen right now." And he really meant just that.

Dieter was a stimulating speaker in discussions, both when he was asking and when he was replying to questions. He asked and answered questions in his inimitable manner: sometimes downright arrogant, but always precise. In this way he could explain the ins and outs of catalysis to a very renowned colleague in just a few minutes.

Dieter was dedicated to the University of Erlangen and to his field, inorganic chemistry, to an exceptional degree. His rectors loved him, but sometimes also feared him, if he spoke out on matters of principle: for example, to assert that a chemistry laboratory course must have enough money and qualified staff, regardless of the current general financial situation. He fought with wit, carefully chosen words, and his sharp analytical mind against intellectual "nonsense" in committees and in science. One could have glorious arguments with him!

Inorganic chemistry has lost a great scientist and an outstanding personality. We will miss his scientific ideas and his laughter.

Karl Wieghardt
MPI für Bioanorganische Chemie,
Mülheim an der Ruhr (Germany)

[1] a) D. Sellmann, *J. Organomet. Chem.* **1972**, *44*, C46; b) D. Sellmann, *Chem. unserer Zeit* **1973**, *7*, 163.
[2] D. Sellmann, *Angew. Chem.* **1971**, *83*, 1017; *Angew. Chem. Int. Ed. Engl.* **1971**, *10*, 919.
[3] D. Sellmann, W. Soglowek, F. Knoch, M. Moll, *Angew. Chem.* **1989**, *101*, 1244; *Angew. Chem. Int. Ed. Engl.* **1989**, *28*, 1271.
[4] a) D. Sellmann, J. Sutter, *Acc. Chem. Res.* **1997**, *30*, 460, b) D. Sellmann, J. Utz, N. Blum, F. W. Heinemann, *Coord. Chem. Rev.* **1999**, *190–192*, 607.
[5] D. Sellmann, B. Hantsch, A. Rösler, F. W. Heinemann, *Angew. Chem.* **2001**, *113*, 1553; *Angew. Chem. Int. Ed. Engl.* **2001**, *40*, 1505.

 © 2003 Wiley-VCH Verlag GmbH & Co. KGaA, Weinheim

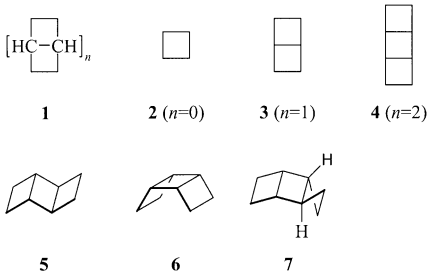
Molecular Ladders

Step by Step—From Nonnatural to Biological Molecular Ladders

*Henning Hopf**

Keywords:
annulations · cycloadditions · ladderanes · polycycles · strained molecules · strained molecules

The molecular analogue of a ladder can be represented by the structure **1**. When

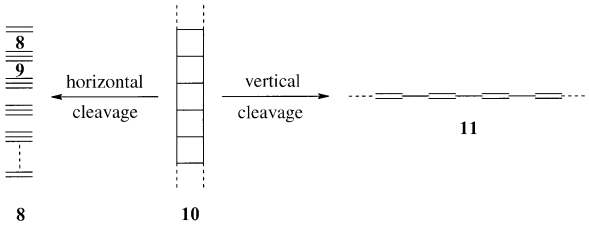


$n=0$ this structure reduces to cyclobutane (**2**), which nobody would consider a ladder-type molecule, and when $n=1$ bicyclo[2.2.0]hexane (**3**) results. But starting with the "four-runged" tricyclo[4.2.0.0^{2,5}]octane (**4**) on, the analogy between the macroscopic and the molecular object is quite evident. Molecules like **1** and **4** are referred to as ladderanes.[1]

In fact, the ladder image is somewhat limited for **1**, since as the number of rungs increases, the stereochemistry quickly becomes more and more complex. Hydrocarbon **4** can form two diastereomers, *anti*- and *syn*-**4**, which are depicted as **5** and **6**, respectively. And even this is a restriction, since the ring junction could in priniciple also have *trans* stereochemistry, as illustrated in **7**. Presumably compounds of this type would be very highly strained, especially if the ladderane would contain more than one *trans* junction. In the following discussion we will consider only *cis*-annelated ladderanes, and even then the number of diastereomers still grows quickly. For a polycyclic hydrocarbon containing four *cis*-fused cyclobutane rings (a pterodactylane, see below) there are three diastereomers, for **1** with $n=4$ there are five possibilities, and with $n=5$ the number of possible arrangements is ten.

How can these molecules be prepared? And, once they have been obtained, how could they be of interest? Retrosynthetically a ladderane **10** can be cleaved either horizontally or vertically (Scheme 1). Horizonal cleavage would lead ultimately to alkenes (**8**, first and last rung of the ladder) and alkynes (**9**, all other rungs). Vertical cleavage would generate the conjugated polyene **11**. If the ends of the molecular ladder are unsaturated, then, in principle, this structure could be built up solely from alkynes. Although the simplicity of these starting materials can hardly be surpassed, their actual conversion into ladder-type stuctures is more difficult and in general fails. For example, it has been known since the days of Reppe that acetylene derivatives may be oligomerized, but the resulting products are usually cyclic unsaturated oligomers—benzene derivatives and other arenes, cyclooctatetraenes—not ladder or stair structures. The conversion of **11** into a ladderane would require more or less parallel alignment of the two polyene strands and a separation of 3 to 4 Å, an entropically rather unlikely situation. It is well known that short conjugated polyene chains cyclize preferably to give cyclobutenes, cyclohexadienes, etc. on photochemical or thermal activation, and do not form ladderanes intermolecularly. Clearly either specialized buildings blocks are required or the polyene chains must be held in parallel orientation by a suitable linker unit.

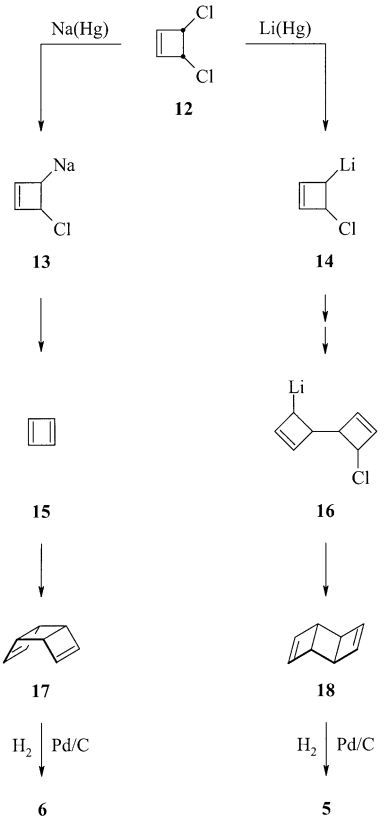
One such "specialized" building block is cyclobutadiene (**15**, Scheme 2). In their pionieering studies on [4*n*]annulenes Nenitzescu and co-workers showed that **15** can be generated by treatment of cyclobutene dichloride **12** with sodium amalgam.[2] The highly reactive antiaromatic intermediate dimerizes under the reaction conditions and yields the *syn* dimer **17**, which on hydrogenation over palladium on charcoal furnishes the *syn*-[3]ladderane **6**. Interestingly, when **12** is treated with lithium amalgam a completely different process takes place (Scheme 2). The resulting *anti* diene **18** is formed in a



Scheme 1. Retrosynthetic analysis of ladderanes.

[*] Prof. Dr. H. Hopf
Universität Braunschweig
Institut für Organische Chemie
Hagenring 30
38106 Braunschweig (Germany)
Fax: (+49) 531-391-5388
E-mail: h.hopf@tu-bs.de

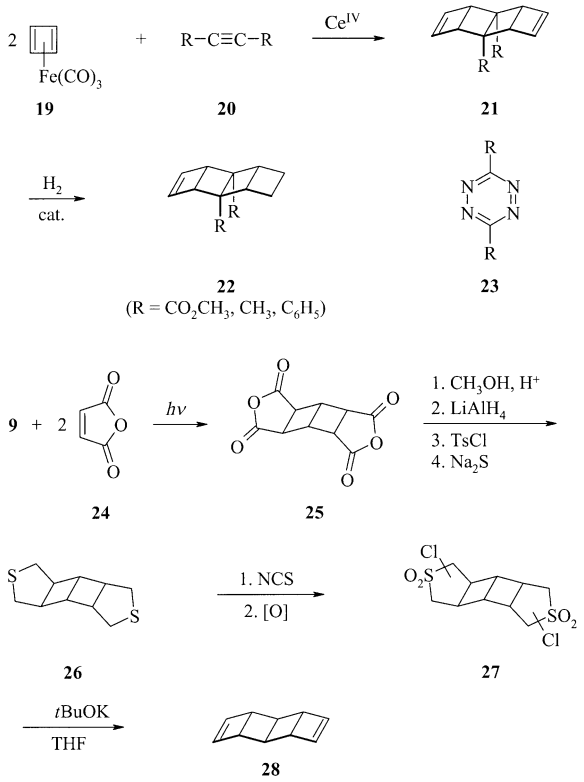
 © 2003 Wiley-VCH Verlag GmbH & Co. KGaA, Weinheim DOI: 10.1002/anie.200301650



Scheme 2. Reaction sequence for the synthesis of **5** and **6** starting from cyclobutene dichloride (**12**).

stepwise sequence via the lithium derivative **14**, which undergoes C–C coupling reactions to give the open dimeric structure **16**, the immediate precursor of **18**. Hydrogenation of **18** yields the expected *anti* isomer **5**.

Cyclobutadienes were, in fact, also shown to be the intermediates of choice in the synthesis of higher analogues of **5** and **6** (Scheme 3). When cyclobutadiene is liberated from its stored form, metal complex **19**, by cerium(IV) oxidation in the presence of the substituted alkyne **20**, double addition and formation of the 2:1 adduct **21**, which contains four annelated cyclobutane rings, results. Hydrogenation converts these dienes—called pterodactyladienes because of their resemblance to the extinct flying reptiles *Pterodactyla*—to the tetracyclic products **22**.[3] Although other substrates such as Dewar benzenes[4] and *s*-tetrazines **23**[5] can replace **20** in cyclobutadiene additions of this type, for the synthesis of the parent hydrocarbon **28** Martin and co-workers had to develop a much more elaborate synthetic sequence (Scheme 3).[6] Thus photochemical addition of maleic anhydride (**24**) to acetylene (**9**) provided the bisadduct **25**.

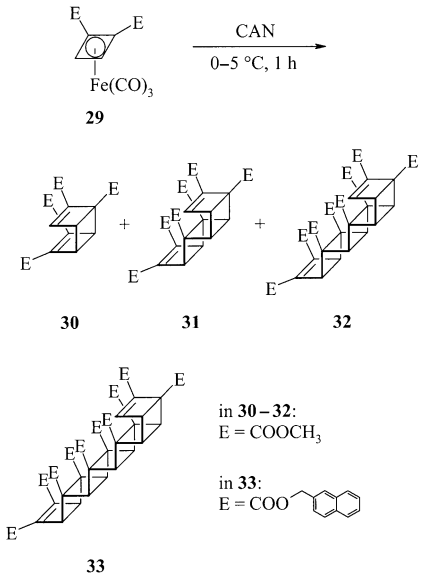


Scheme 3. General approach to the ladderanes and the synthesis of the parent hydrocarbon **28** according to Martin et al.[6]

Conventional procedures were used to convert **25** into the bisthioether **26**, which after chlorination with *N*-chlorosuccinimide (NCS) and oxidation gave the bissulfone **27** as a mixture of isomers. A final Ramburg–Bäcklund ring contraction yielded pterodactyladiene **28**.

Considering the high reactivity of cyclobutadienes, it should in principle be possible to prepare still higher ladderanes by omitting a second addition partner altogether, that is, by letting cyclobutadienes react with themselves. This strategy was first demonstrated by Mehta and co-workers, who on oxidation of diester **29** obtained a product mixture in acceptable yield (55%) containing the ladderane derivatives **30**–**32** in a 3:2:1 ratio (Scheme 4).[7] Later this approach was extended to the preparation of [9]- to [13]ladderane derivatives[8] as well other esters such as **33**.[9]

The parent reaction for the polyene route to ladderanes (**11**→**10**, Scheme 1) is the solid-state photodimerization of cinnamic acid, a process investigated thoroughly by Schmidt and co-workers.[10] In this well-known photodimerization, topochemical control is practically built in since the process only takes place when the distance between the reacting (parallel) double bonds does not exceed ca. 3.5 to 4 Å. This critical distance is provided and main-



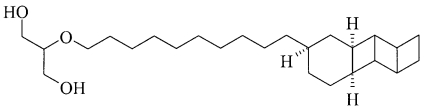
Scheme 4. Synthesis of higher ladderanes starting from iron cyclobutadiene complexes. CAN = ceric ammonium nitrate.

 © 2003 Wiley-VCH Verlag GmbH & Co. KGaA, Weinheim

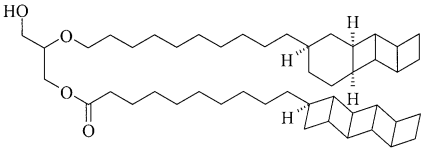
tained in the crystal lattice but breaks down in solution. Hence cinnamic acids do not undergo [2+2]photodimerization in solution. On the other hand, if a rigid spacer is used to hold appropriate functional groups in correct orientation, high-yield photoaddition should also be possible in solution. Such a spacer is provided by the "layered" [2.2]paracyclophane system, in which the distance between the aromatic rings is roughly 3.1 Å. Indeed, when "cinnamic acid dimer" **34** is irradiated in ethanol, the cyclobutane derivative **35** is formed quantitatively, with the highest quantum yield ever measured for such a process (Scheme 5).[11]

The bisvinylogous diester **36** could be obtained readily from **34** in good yield in a few simple steps, and subsequent irradiation gave the [3]ladderane **37**, again in excellent yield. Even at this point the controlling influence of the [2.2]paracyclophane unit has not yet been exhausted; irradiation of the still further extended hexaene diester **38** provides the [5]ladderane derivative **39** (Scheme 5).[12]

The ladderanes discussed here have all been all typical "nonnatural" or "designed" compounds. However, it was recently discovered that ladderanes also occur as the dominant membrane lipids of two anaerobic ammonium-oxidizing (anammox) bacteria.[13] These lipids are found in the anammoxosome, the dedicated intracytoplasmic compartment where anammox catabolism takes place. These naturally occurring "ladderane lipids", with structures such as **40**



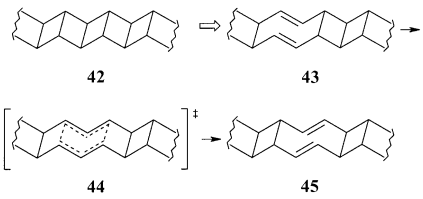
40



41

and **41**, generate an exceptionally dense membrane, helping to contain toxic intermediates such as hydrazine and hydroxylamine. The (unknown) biosynthesis of these biomolecules certainly requires a unique set of enzymes and—considering the high strain energy of a even single cyclobutane ring—very likely has a high energetic cost.

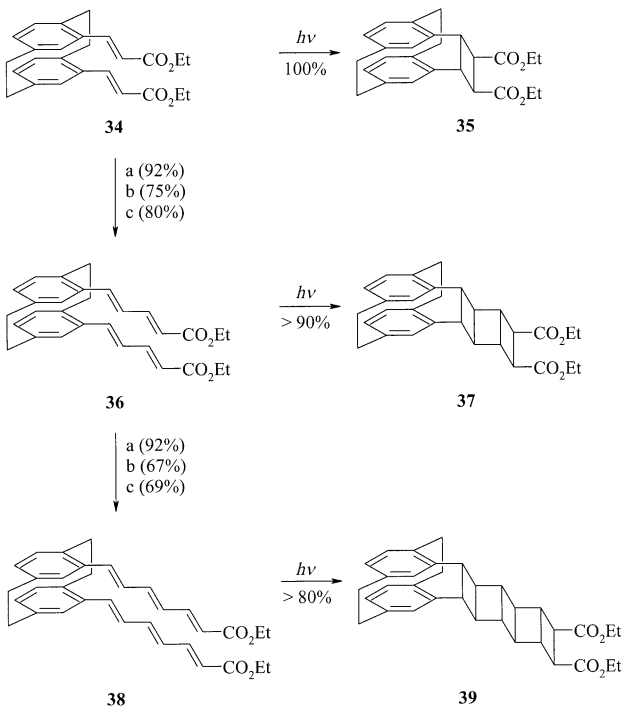
Another recent development concerns the study of acyclic and cyclic sigmatropic "shiftamers" derived from [*n*]ladderanes. Hoffmann and Tantillo have suggested that a formal [2+2]cycloreversion in ladderane **42** would give rise to compound **43**, which has a local "defect" consisting of two parallel double bonds.[14] Diene **43** could isomerize via the boatlike transition state **44** to **45**, which, of course, for the parent systems would be equivalent to **43**.



42 **43** **44** **45**

If this process would be continued along the parallel chains "to infinity", it would lead to a pair of double bonds zipping down the polymer chain. Indeed, B3LYP6-31G(d) calculations suggest that the barrier to the Cope rearrangement is low enough to make the shiftamer **43** fluxional at room temperature. Shiftamers do not necessarily have linear structures. All-*cis* fusion of the cyclobutane rings of a ladderane would eventually generate cyclic molecules in which the moving double bonds would "run around in circles".

The ladderane motif—until recently not more than an idea—has gained interest as a spacer unit allowing large variations in rigidity, three-dimensional structure, and intermolecular distances. Not only could ladderanes lead to novel materials with unusual electronic and bonding properties but they also occur in nature. Having access to reliable synthetic methods to prepare these unusual ladders, we might now expect to climb them quickly and gain interesting perspectives on new preparative transformations, materials, and compounds of biological interest.



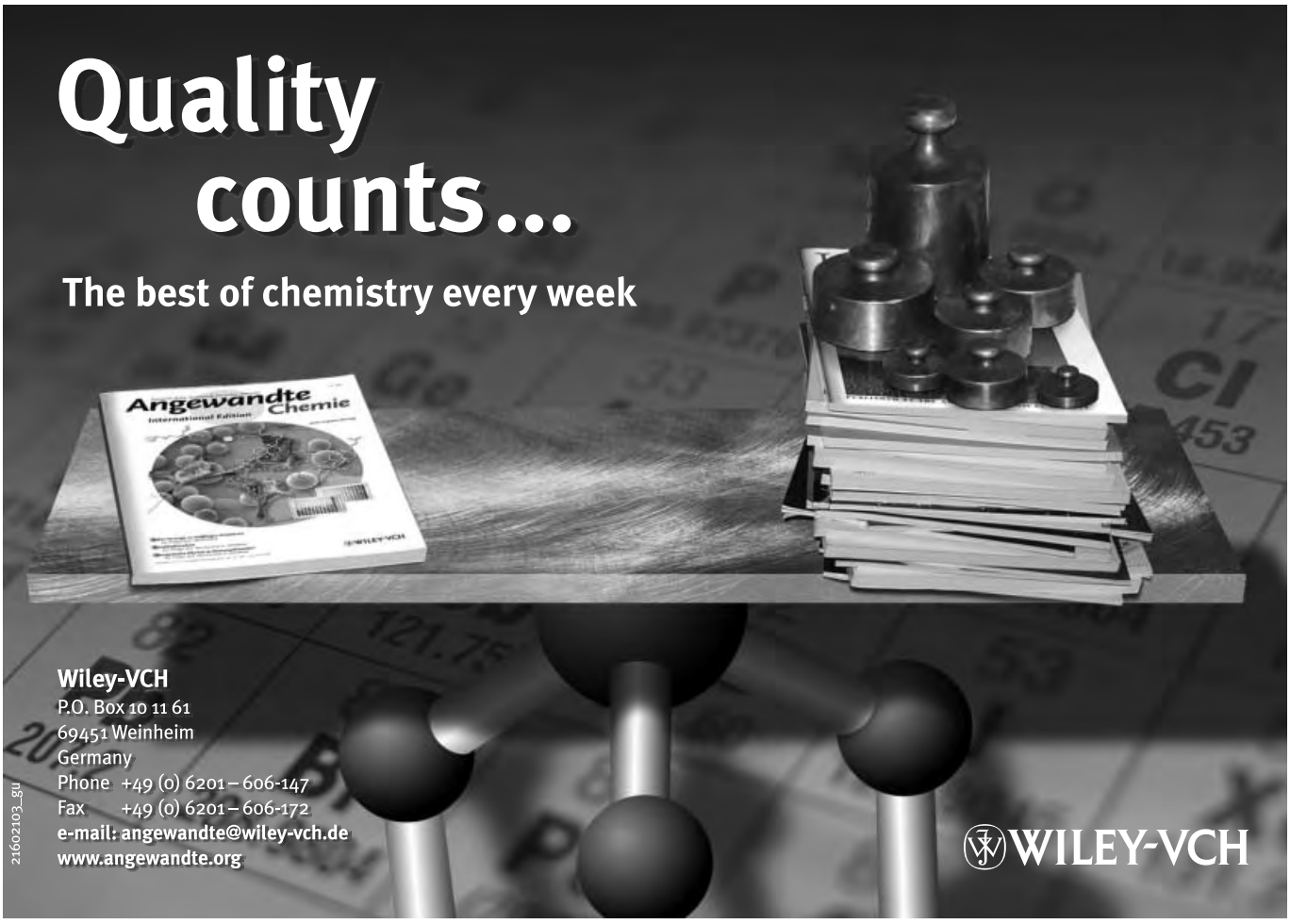
Scheme 5. Spacer-directed ladderanes synthesis. a) Diisobutylaluminum hydride, Et_2O, N_2, −80→0°C; b) MnO_2, CH_2Cl_2, N_2, room temperature; c) NaH, $(EtO)_2P(O)CH_2COOEt$, THF, N_2, room temperature.

[1] H. Hopf, *Classics in Hydrocarbon Chemistry*, Wiley-VCH, Weinheim, **2000**.

[2] M. Avram, I. G. Dinulescu, E. Marcia, G. Mateescu, E. Sliam, C. D. Nenitzescu, *Chem. Ber.* **1964**, *97*, 382–389.

 © 2003 Wiley-VCH Verlag GmbH & Co. KGaA, Weinheim

[3] R. Petit, C. F. Emerson, L. W. Watts, J. D. Fitzpatrick, *Chem. Eng. News* **1965**, *43*, 38; cf. A. Nickon, E. F. Silversmith, *Organic Chemistry–The Name Game*, Pergamon, New York, NY, **1987**, pp. 13 – 15.
[4] H.-D. Martin, M. Hekman, *Angew. Chem.* **1973**, *85*, 615 – 616; *Angew. Chem. Int. Ed. Engl.* **1973**, *12*, 572 – 573.
[5] H.-D. Martin, M. Hekman, *Chimia* **1974**, *28*, 12 – 15; H.-D. Martin, M. Hekman, *Tetrahedron Lett.* **1978**, 1183 – 1186.
[6] H.-D. Martin, B. Mayer, M. Pütter, H. Höchstetter, *Angew. Chem.* **1981**, *93*, 695 – 696; *Angew. Chem. Int. Ed. Engl.* **1981**, *20*, 677 – 678.
[7] G. Mehta, M. B. Viswanath, G. N. Sastry, E. D. Jemmis, D. S. K. Reddy, A. C. Kunwar, *Angew. Chem.* **1992**, *104*, 1557 – 1558; *Angew. Chem. Int. Ed. Engl.* **1992**, *31*, 1488 – 1498.
[8] G. Mehta, M. B. Viswanath, A. C. Kunwar, *J. Org. Chem.* **1994**, *59*, 6131 – 6132.
[9] W. Li, M. A. Fox, *J. Am. Chem. Soc.* **1996**, *118*, 11752 – 11758.
[10] For a summary see G. M. J. Schmidt, *Monogr. Mod. Chem.* **1976**, *76* ("Solid-State Photochemistry").
[11] H. Hopf, H. Greiving, P. G. Jones, J.-P. Desvergne, H. Bouas-Laurent, *J. Chem. Soc. Chem. Commun.* **1994**, 1075 – 1076.
[12] H. Hopf, H. Greiving, P. G. Jones, P. Bubenitschek, *Angew. Chem.* **1995**, *107*, 742 – 744; *Angew. Chem. Int. Ed. Engl.* **1995**, *34*, 685 – 687.
[13] J. S. Sinninghe Damsté, M. Strous, W. I. C. Rijpstra, E. C. Hopmans, J. A. J. Geenevasen, A. C. T. van Duin, L. A. van Niftrik, M. S. M. Jetten, *Nature* **2002**, *419*, 708 – 712.
[14] D. J. Tantillo, R. Hoffmann, *Angew. Chem.* **2002**, *114*, 1075 – 1078; *Angew. Chem. Int. Ed.* **2002**, *41*, 1033 – 1036.



 © 2003 Wiley-VCH Verlag GmbH & Co. KGaA, Weinheim

Macrocycles with (E)-Alkenes

Recent Methods for the Synthesis of (*E*)-Alkene Units in Macrocyclic Natural Products**

*Joëlle Prunet**

Keywords:
alkenes · cyclization · macrocycles · McMurry reactions · metathesis

(E)*-Alkene units are frequently found in macrocyclic natural products. Among the reactions that form the double bond during the cyclization, the classical Horner–Emmons coupling is still frequently used with success. During the last decade, ring-closing metathesis has emerged as a very powerful tool for the synthesis of large rings, but the* E/Z *selectivity, which is rarely predictable, depends on many factors which will be discussed in this review. The best solution might be a two-step procedure involving ring-closing alkyne metathesis (RCAM) followed by stereoselective reduction of the macrocyclic alkyne unit to the corresponding* E *double bond.*

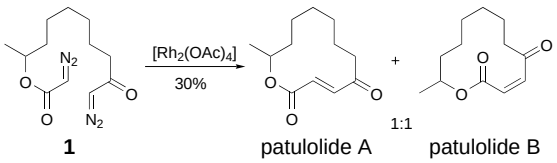
1. Methods for the Synthesis of Macrocyclic Natural Products Containing (E)-Alkene Units

Numerous macrocyclic natural products contain an (*E*)-alkene function.[1] Among the diverse syntheses of this type of molecule, macrolactonization and intramolecular Stille coupling have been the most common cyclization procedures.[2] Of course, these reactions can only be employed to form macrocyclic lactones or dienes. Another recent example of cross-coupling reaction utilized for forming a macrocyclic olefinic natural product is the Suzuki–Miyaura reaction.[3] This minireview will focus on the recently reported reactions that form the *E* double bond during the cyclization.

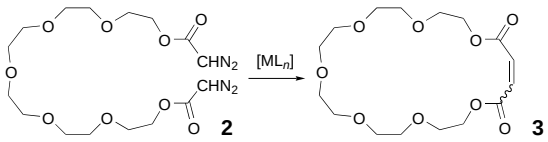
A classical way of making linear or cyclic (*E*)-alkenes conjugated to a ketone or a carboxylic derivative is the Horner–Emmons reaction. It was used in the past few years for the synthesis of rhizoxin D (16-membered ring),[4] lankacyclinol (17-membered ring),[5] zampanolide[6] and dactylolide(18-membered rings), [7] filipin III (28-membered ring),[8] and dermostatin A (36-membered ring).[9] In all cases, the reaction is very stereoselective, leading exclusively to the *E* double bond.

Doyle et al. reported the synthesis of patulolides A and B by catalytic formation of a carbene dimer.[10] They applied this process, well-known for the intermolecular coupling of diazo ketones, to bisdiazo ketone **1**, which produced the (*E*)- and (*Z*)-alkenes in equal amounts when treated with rhodium acetate catalyst (Scheme 1). The yield is moderate and the reaction is not selective in this case, but the authors also described in the same paper the cyclization of the bisdiazoacetate of hexaethyleneglycol **2**. By judicious selection of the catalyst, either the macrocyclic (*E*)- or (*Z*)-alkene **3** can be obtained as the major product (Scheme 2).

The McMurry reaction has also been used in the last few years to form macrocylic alkenes in the cases of cyclic diterpenes sarcophytols A and B[11] and epoxydihydrocembrenes C[12] (Scheme 3). The double bond is formed very



Scheme 1. Synthesis of patulolides A and B.



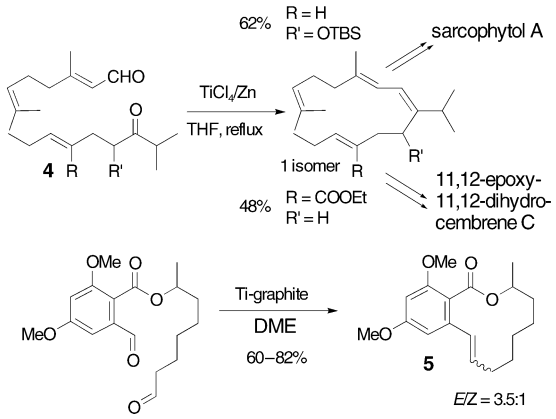
[Cu(MeCN)4]PF6 73%, *E*/Z = 82:18
[Rh2(5*R*-MEPY)4] 75%, *E*/Z = 26:74

Scheme 2. Cyclization of the hexaethyleneglycol derivative **2**. MEPY = Methyl 2-pyrrolidinone-5(*R*)-carboxylate.

[*] Dr. J. Prunet
Laboratoire de Synthèse Organique, UMR CNRS 7652
Ecole Polytechnique, DCSO
91128 Palaiseau Cedex, France
Fax: (+33) 1-69-33-38-51
E-mail: Joelle.Prunet@polytechnique.fr

[**] The CNRS (UMR 7652) and the Ecole Polytechnique are acknowledged for financial support. I thank Dr. Laurence Grimaud for helpful discussions.

 © 2003 Wiley-VCH Verlag GmbH & Co. KGaA, Weinheim DOI: 10.1002/anie.200301628



Scheme 3. McMurry cyclizations in natural product syntheses. DME = 1,2-dimethoxyethane, TBS = *tert*-butyldimethylsilyl.

selectively during the cyclization of compounds **4**. Fürstner et al. described the formation of **5** (a direct precursor of lasiodiplodin), in which the (*E*)-alkene was the major product (Scheme 3).[13]

2. Formation of Macrocycles by Ring-Closing Metathesis

Ring-closing metathesis (RCM) of alkenes has become a powerful tool in organic synthesis, since it involves non-functionalized olefins, which usually are unreactive towards classical reagents, and is compatible with diverse functional groups.[14] The most common RCM catalysts are shown in Figure 1: Grubbs' ruthenium catalysts **6**[15] and **7**,[16] Fürstner's catalyst **8**,[17] Schrock's molybdenum catalyst **9**,[18] and also the second-generation complexes **10**[19] and **11**.[20] The molybdenum carbene complex **9**, which is very air- and moisture-sensitive, tends to be abandoned in favor of air-stable catalysts **10** and **11**, which proved of similar or superior activity. Compound **5** (Scheme 3) was also prepared in 69% yield by RCM with catalyst **10** in toluene at 80 °C.[13] In this case the *E* selectivity is total, illustrating the superiority of the RCM reaction over the McMurry coupling, whose yield is somewhat variable (60–82%).



Joëlle Prunet worked with Prof. Marc Julia in 1986 on the synthesis of avermectin during her undergraduate studies at the Ecole Normale Supérieure (Paris). She obtained her PhD in 1993 with Prof. David A. Evans at Harvard University, where she contributed to the total synthesis of bryostatin. In 1993 she joined the CNRS at the Ecole Polytechnique (Palaiseau), where she also has had a teaching position since 1998. Her research interests include total synthesis of natural products (taxol, dolabelide, FR182877, and bafilomycin) and development of new methodologies for organic synthesis.

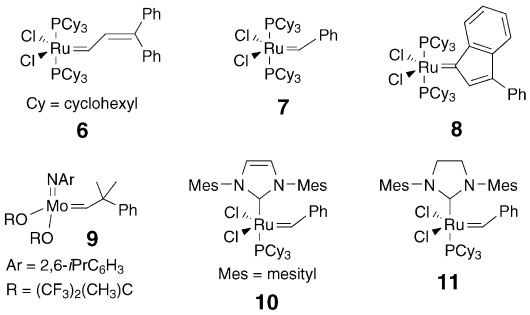
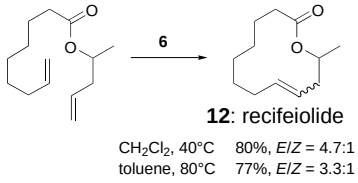


Figure 1. Catalysts for ring-closing metathesis (RCM).

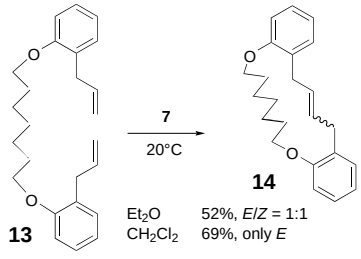
2.1. Effect of Temperature and Solvent on E/Z Selectivity

The synthesis of large rings by olefin metathesis is usually very efficient,[21] but the selectivity of the alkene formation is not always excellent. Moreover, it is not easy to predict the major isomer of the reaction, which is very sensitive to multiple factors. For example, Nakagawa et al. reported a variation of the *E*/*Z* ratio with the reaction temperature during the formation of azacycloundecenes in the presence of catalyst **7**. At 20 °C the *E*/*Z* ratio is 12.5:1, but at 50 °C it is 5.2:1.[22] The key step of the synthesis of recifeiolide (**12**) with catalyst **6** proceeds in good yield, but the *E*/*Z* ratio is modest and also depends on the reaction temperature (Scheme 4).[21]



Scheme 4. Synthesis of recifeiolide (**12**). Influence of the temperature on the selectivity of the RCM.

In the latter reaction, the selectivity might also depend on the solvent, as is the case in the cyclization of diether **13** using catalyst **7** (Scheme 5). In ether, the 17-membered macrocyclic alkene is obtained as a 1:1 mixture of *E* and *Z* olefins, and in dichloromethane, the *E* isomer of **14** is produced exclusively.[23] No rational explanation is given for the solvent or the temperature effect.

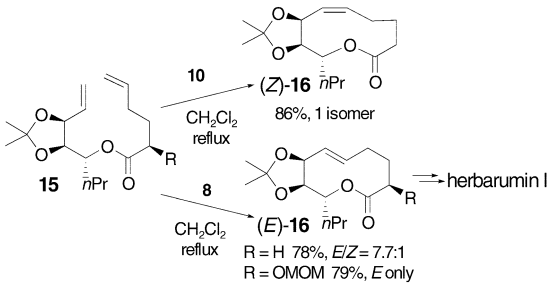


Scheme 5. Influence of the solvent on the selectivity of the RCM.

DOI: 10.1002/anie.200301628
© 2003 Wiley-VCH Verlag GmbH & Co. KGaA, Weinheim

2.2. Effect of the Catalyst

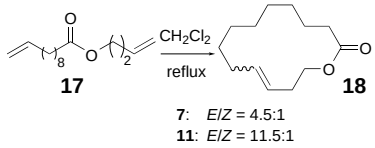
The RCM reaction is generally under thermodynamic control. However, in some cases the catalyst is not active enough to equilibrate the kinetic product, and a less stable cycloalkene can be produced. Fürstner et al. nicely illustrated this trend in their synthesis of herbarumin I[24] (Scheme 6).



Scheme 6. Kinetic or thermodynamic control during RCM, depending on the catalyst. MOM = methoxymethyl.

Semiempirical calculations showed that model lactone (*Z*)-**16** is ca. 3.5 kcal mol^{-1} more stable than the corresponding lactone (*E*)-**16** (R = H), suggesting that thermodynamic control would likely give the undesired isomer for the synthesis of the target molecule. This prediction was verified when compound **15** was submitted to catalyst **8**, whose activity is comparable to the standard Grubbs catalyst **7**. The *E* isomer was obtained as the major product. The *E*/*Z* ratio does not change with time, proving that the reaction is under kinetic control with this catalyst. When the more active second-generation complex **10** was employed, the more stable (*Z*)-**16** lactone was produced as the only isomer. Herbarumin I precursor (*E*)-**16** (R = OMOM) was synthesized with an excellent selectivity with **8**.

The influence of the nature of the catalyst on the RCM selectivity was also observed by Grubbs et al. (Scheme 7).[25] By submitting **17** to a more active catalyst, a higher

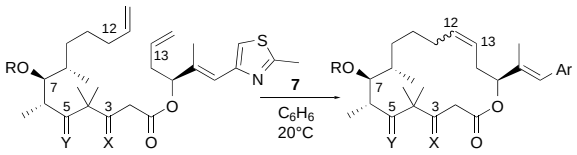


Scheme 7. Influence of the nature of the catalyst on the *E*/*Z* ratio.

proportion of the *E* isomer of lactone **18** was produced. The *E*/*Z* ratio does not significantly change with time when catalyst **7** is used, but it increases from 4.8:1 at 20% conversion to 11.5:1 at 100% conversion with **10**. This increase may be due to secondary metathical isomerization with the more active catalyst. The authors also reported that a 4:1 mixture of *E*/*Z* isomers of lactone **18** could be transformed to a 12:1 mixture with catalyst **10**, while the ratio did not change in the presence of **7**.

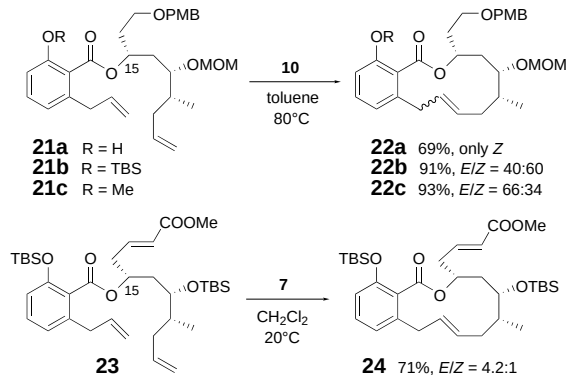
2.3. Effect of Substrate Substituents

Precursors of epothilone A (with a *Z* 12,13-double bond which will lead to the required *cis* 12,13-epoxide) figure among the most highly functionalized macrocycles formed by RCM. In the synthesis described by Nicolaou et al. the best proportion of *Z* isomer was 1:1.[26] In a similar approach towards this natural product, Danishefsky et al. showed that substituents remote from the reaction site (at C3, C5, or the C7 hydroxyl protecting group) had a profound influence on the selectivity of the alkene formation (Scheme 8).[27] The best result in view of the epothilone synthesis was a 1:1.7 *E*/*Z* ratio in the case of **20a**, which was eventually converted into the target molecule. For **20b**, which is epimeric at C3 and possesses a protected alcohol instead of a ketone at C5, the *E*/*Z* ratio switches to 9:1. Once again, there is no reliable method to predict the outcome of the RCM reaction. A better strategy for this total synthesis includes the formation of the (*Z*)-alkene on a linear precursor, and a macrolactonization to close the 16-membered ring.[28]



Scheme 8. Influence of remote substituents on the *E*/*Z* ratio. TPS = triphenylsilyl, TES = triethylsilyl.

Another study concerning the influence of remote substituents was reported by Fürstner et al. in the course of their approach towards the synthesis of salicylihalamides A and B (Scheme 9).[29] The free phenol **21a**, in the presence of catalyst **10** in toluene at 80 °C, furnished the *Z* isomer of **22a** exclusively. With a TBS or a methyl protecting group, the selectivity was rather modest, slightly favoring the (*Z*)-alkene **22b** or the (*E*)-alkene **22c**. Snider et al. obtained a 4.2:1 ratio



Scheme 9. Synthesis of precursors of salicylihalamides A and B. PG = protecting group, PMB = *para*-methoxybenzyl.

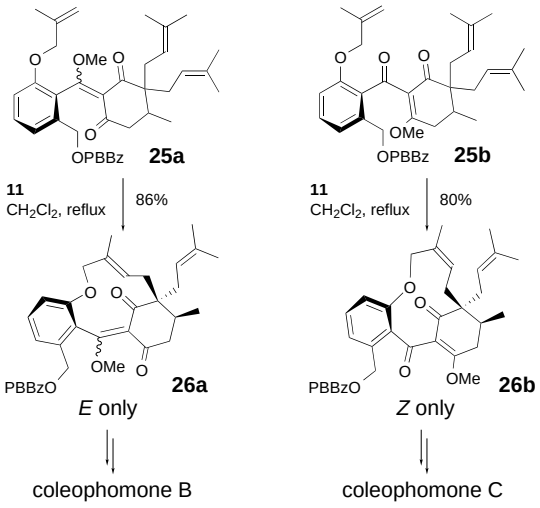
 © 2003 Wiley-VCH Verlag GmbH & Co. KGaA, Weinheim

of (*E*)-**24**/(*Z*)-**24** when treating compound **23** with carbene **7** in dichloromethane;[30] in the case of the fully desilylated **23**, the *Z* isomer is the major product. These results are consistent with Fürstner's observations, although the *E* selectivity of the RCM with the TBS-protected compounds is better in the latter case. On the other hand, De Brabander et al. obtained a 10:1 ratio of (*E*)-**22c**/(*Z*)-**22c** when they exposed **21c** to catalyst **7** in dichloromethane,[31] and Labrecque et al. also observed a 9:1 *E* selectivity for the formation of a nearly identical product with **7**.[32] These results are surprising in the light of Fürstner's result with **21c**, and might be explained by the nature of the RCM catalyst.

2.4. Syntheses of Further Macrocycles by RCM

RCM was the key step in the synthesis of many additional macrocycles with various selectivities: brefeldin A (13-membered ring, $E/Z = 2.2{:}1$),[33] ricinelaidic acid lactone (13-membered ring, *E* only),[34] zearalenone (14-membered ring, *E* only),[13] 14-, 15-, 16-, 18-, and 21-membered ring lactones that are perfume ingredients ($E/Z = 1.4{:}1$ to $7.0{:}1$),[21] aspicillin (18-membered ring, $E/Z = 3{:}1$),[35] a precursor of nonylprodigiosin (18-membered ring, *E* only),[36] griseoviridin (20-membered ring, *E* only),[37] a precursor of 4α-hydroxygermacra-1(10),5-diene (10-membered ring, $E/Z = 5.9{:}1$ for one diastereomer, *E* only for the other),[38] and this list is not exhaustive.

Finally, Nicolaou et al. reported an elegant synthesis of coleophomones B and C (Scheme 10).[39] Regioisomeric enol ethers **25a** and **25b**, obtained from the same tricarbonyl



Scheme 10. Synthesis of coleophomones B and C. PBBz = *para*-bromobenzoate.

precursor, furnished very selectively macrocycles **26a** and **26b** with total selectivity (*E* for **26a**, *Z* for **26b**), which were converted to coleophomones B and C, respectively. Once more, the outcome of the RCM could not be predicted.

3. Outlook

Olefin metathesis is at present the most powerful method for synthesizing large rings containing (*E*)-alkenes, but the *E*/*Z* selectivity is variable and rarely predictable. The answer might lie in an indirect methodology recently reported by Fürstner et al.[40] Macrocyclic alkynes, prepared by ring-closing alkyne metathesis (RCAM), can be reduced in a two-step fashion (*E*-selective Ru-catalyzed hydrosilylation followed by desilylation with AgF) to furnish (*E*)-cycloalkenes with selectivities ranging from 90:10 to >98:2. Fürstner had already reported a complementary approach (RCAM followed by catalytic hydrogenation) for the selective preparation of (*Z*)-cycloalkenes.[41]

Received: January 7, 2003 [M1628]

[1] For a review on polyene macrolide antibiotics, see: S. D. Rychnovsky, *Chem. Rev.* **1995**, *95*, 2021 – 2040.
[2] Recent examples of a) macrolactonization: J. S. Panek, P. Liu, *J. Am. Chem. Soc.* **2000**, *122*, 11090 – 11097; b) intramolecular Stille coupling: I. S. Mitchell, G. Pattenden, J. P. Stonehouse, *Tetrahedron Lett.* **2002**, *43*, 493 – 497.
[3] N. C. Kallan, R. L. Halcomb, *Org. Lett.* **2000**, *2*, 2687 – 2690; see also: S. R. Chemier, S. D. Danishefsky, *Org. Lett.* **2000**, *2*, 2695 – 2698.
[4] a) G. E. Keck, C. A. Wager, T. T. Wager, K. A. Savin, J. A. Covel, M. D. McLaws, D. Krishnamurthy, V. J. Cee, *Angew. Chem.* **2001**, *113*, 237 – 240; *Angew. Chem. Int. Ed.* **2001**, *40*, 231 – 234; b) J. A. Lafontaine, D. P. Provencal, C. Gardelli, J. W. Leahy, *Tetrahedron Lett.* **1999**, *40*, 4145 – 4148.
[5] D. R. Williams, G. S. Cortez, S. L. Bogen, C. M. Rojas, *Angew. Chem.* **2000**, *112*, 4750 – 4753; *Angew. Chem. Int. Ed.* **2000**, *39*, 4612 – 4615.
[6] A. B. Smith III, I. G. Safonov, R. M. Corbett, *J. Am. Chem. Soc.* **2001**, *123*, 12426 – 12427.
[7] A. B. Smith III, I. G. Safonov, *Org. Lett.* **2002**, *4*, 635 – 637.
[8] T. I. Richardson, S. D. Rychnovsky, *Tetrahedron* **1999**, *55*, 8977 – 8996.
[9] C. J. Sinz, S. D. Rychnovsky, *Angew. Chem.* **2001**, *113*, 3324 – 3327; *Angew. Chem. Int. Ed.* **2001**, *40*, 3224 – 3227.
[10] M. P. Doyle, W. Hu, I. M. Philips, *Org. Lett.* **2000**, *2*, 1777 – 1779.
[11] W.-D. Z. Li, Y. Li, Y. Li, *Tetrahedron Lett.* **1999**, *40*, 965 – 968.
[12] Z. Liu, W. Z. Li, L. Peng, Y. Li, Y. Li, *J. Chem. Soc. Perkin Trans. 1* **2000**, 4250 – 4257.
[13] A. Fürstner, O. R. Thiel, N. Kindler, B. Bartkwoska, *J. Org. Chem.* **2000**, *65*, 7990 – 7995.
[14] For recent reviews on RCM, see: a) M. Schuster, S. Blechert, *Angew. Chem.* **1997**, *109*, 2124 – 2145; *Angew. Chem. Int. Ed. Engl.* **1997**, *36*, 2036 – 2056; b) A. Fürstner, *Top. Catal.* **1997**, *4*, 285 – 299; c) S. K. Armstrong, *J. Chem. Soc. Perkin Trans. 1* **1998**, 371 – 388; d) R. H. Grubbs, S. Chang, *Tetrahedron* **1998**, *54*, 4413 – 4450; e) A. Fürstner, *Angew. Chem.* **2000**, *112*, 3140 – 3172; *Angew. Chem. Int. Ed.* **2000**, *39*, 3012 – 3043; f) M. E. Maier, *Angew. Chem.* **2000**, *112*, 2153 – 2157; *Angew. Chem. Int. Ed.* **2000**, *39*, 2073 – 2077.
[15] S. T. Nguyen, R. H. Grubbs, *J. Am. Chem. Soc.* **1993**, *115*, 9858 – 9859.
[16] a) P. Schwab, M. B. France, J. W. Ziller, R. H. Grubbs, *Angew. Chem.* **1995**, *107*, 2179 – 2181; *Angew. Chem. Int. Ed. Engl.* **1995**, *34*, 2039 – 2041; b) P. Schwab, R. H. Grubbs, J. W. Ziller, *J. Am. Chem. Soc.* **1996**, *118*, 100 – 110.
[17] a) A. Fürstner, A. F. Hill, M. Liebl, J. D. E. T. Wilton-Ely, *Chem. Commun.* **1999**, 601 – 602; b) A. Fürstner, J. Grabowski, C. W.

 © 2003 Wiley-VCH Verlag GmbH & Co. KGaA, Weinheim

Lehman, *J. Org. Chem.* **1999**, *64*, 8275 – 8280; c) A. Fürstner, O. Guth, A. Düffels, G. Seidel, M. Liebl, B. Gabor, R. Mynott, *Chem. Eur. J.* **2001**, *7*, 4811 – 4820.
[18] R. R. Schrock, J. S. Murdzek, G. C. Bazan, J. Robbins, M. DiMare, M. O'Regan, *J. Am. Chem. Soc.* **1990**, *112*, 3875 – 3886.
[19] a) J. Huang, E. D. Stevens, S. P. Nolan, J. L. Petersen, *J. Am. Chem. Soc.* **1999**, *121*, 2674 – 2678; b) M. Scholl, T. M. Trnka, J. P. Morgan, R. H. Grubbs, *Tetrahedron Lett.* **1999**, *40*, 2247 – 2250; c) L. Jafarpour, A. C. Hillier, S. P. Nolan, *Organometallics* **2002**, *21*, 442 – 444.
[20] M. Scholl, S. Ding, C. W. Lee, R. H. Grubbs, *Org. Lett.* **1999**, *1*, 953 – 956.
[21] A. Fürstner, K. Langemann, *Synthesis* **1997**, 792 – 803.
[22] M. Arisawa, C. Kato, H. Kaneko, A. Nishida, M. Nakagawa, *J. Chem. Soc. Perkin Trans. 1* **2000**, 1873 – 1876.
[23] K. Nakashima, R. Ito, M. Sono, M. Tori, *Heterocycles* **2000**, *53*, 301 – 314.
[24] a) A. Fürstner, K. Radkowski, *Chem. Commun.* **2001**, 671 – 672; b) A. Fürstner, K. Radkowski, C. Wirtz, R. Goddard, C. Lehmann, R. Mynott, *J. Am. Chem. Soc.* **2002**, *124*, 7061 – 7069; for a similar catalyst effect in the synthesis of microcarpalide, see: J. Murga, E. Falomir, J. Garcia-Fortanet, M. Carda, J. Alberto Marco, *Org. Lett.* **2002**, *4*, 3447 – 3449.
[25] C. W. Lee, R. H. Grubbs, *Org. Lett.* **2000**, *2*, 2145 – 2147.
[26] K. C. Nicolaou, Y. He, D. Vourloumis, H. Vallberg, F. Roschangar, F. Sarabia, S. Ninkovic, Z. Yang, J. I. Trujillo, *J. Am. Chem. Soc.* **1997**, *119*, 7960 – 7973.
[27] D. Meng, D.-S. Su, A. Balog, P. Bertinato, A. J. Sorensen, S. J. Danishefsky, Y.-H. Zheng, T.-C. Chou, L. He, S. B. Horwitz, *J. Am. Chem. Soc.* **1997**, *119*, 2733 – 2734.
[28] K. C. Nicolaou, S. Ninkovic, F. Sarabia, D. Vourloumis, Y. He, H. Vallberg, M. R. V. Finlay, Z. Yang, *J. Am. Chem. Soc.* **1997**, *119*, 7974 – 7991.
[29] A. Fürstner, O. Thiel, G. Blanda, *Org. Lett.* **2000**, *2*, 3731 – 3734.
[30] B. S. Snider, F. Song, *Org. Lett.* **2001**, *3*, 1817 – 1820.
[31] Y. Wu, L. Esser, J. K. De Brabander, *Angew. Chem.* **2000**, *112*, 4478 – 4480; *Angew. Chem. Int. Ed.* **2000**, *39*, 4308 – 4310.
[32] The side-chain at C15 has an extra methylene unit, and the primary alcohol function is protected as a benzyl ether: D. Labrecque, S. Charron, R. Rej, C. Blais, S. Lamothe, *Tetrahedron Lett.* **2001**, *42*, 2645 – 2648.
[33] D. Kim, J. Lee, P. J. Shim, J. I. Lim, T. Doi, S. Kim, *J. Org. Chem.* **2002**, *67*, 772 – 781.
[34] A. Fürstner, K. Langemann, *J. Am. Chem. Soc.* **1997**, *119*, 9130 – 9136.
[35] M. Banwell, K. J. McRae, *Org. Lett.* **2000**, *2*, 3583 – 3586.
[36] A. Fürstner, J. Grabowski, C. Lehmann, *J. Org. Chem.* **1999**, *64*, 8275 – 8280.
[37] C. A. Dvorak, W. D. Schmitz, D. J. Poon, D. C. Pryde, J. P. Lawson, R. A. Amos, A. I. Meyers, *Angew. Chem.* **2000**, *112*, 1730 – 1732; *Angew. Chem. Int. Ed.* **2000**, *39*, 1664 – 1666.
[38] M. Nevelainen, A. M. P. Koskinen, *Angew. Chem.* **2001**, *113*, 4184 – 4186; *Angew. Chem. Int. Ed.* **2001**, *40*, 4060 – 4062.
[39] K. C. Nicolaou, G. Vassilikogiannakis, T. Montagnon, *Angew. Chem.* **2002**, *114*, 3410 – 3415; *Angew. Chem. Int. Ed.* **2002**, *41*, 3276 – 3281.
[40] A. Fürstner, K. Radkowski, *Chem. Commun.* **2002**, 2182 – 2183.
[41] References 4–10 in reference [4].

 © 2003 Wiley-VCH Verlag GmbH & Co. KGaA, Weinheim

Catalyst Screening

Electrospray Ionization Tandem Mass Spectrometry in High-Throughput Screening of Homogeneous Catalysts

*Peter Chen**

Keywords:
combinatorial chemistry · high-throughput screening · homogeneous catalysis · mass spectrometry · organometallic chemistry



© 2003 Wiley-VCH Verlag GmbH & Co. KGaA, Weinheim
DOI: 10.1002/anie.200200560

The frontispiece shows an illustration by John Tenniel and an excerpt from the 1865 edition of Lewis Carroll's "Alice in Wonderland". Because everything in Wonderland runs counter to logic, the Queen of Hearts declares in Alice's trial "Sentence first—verdict afterwards". High-throughput screening of catalysts, as it is conventionally practiced, does "Synthesis first—screening afterwards" which, as is argued in this review, also backwards. Given the particular constraints present in organometallic complexes, it is more efficient to develop a selective synthesis only when it has already been determined that a structure is likely to be better. The consequence is that screening methods must be able to handle ill-defined mixtures. Electrospray ionization tandem mass spectrometry is presented as a technical solution to this problem.

From the Contents

1. Introduction 2833
2. What is Wrong with High-Throughput Screening of Catalysts as Currently Practiced? 2833
3. What Technical Requirement does Screening before Synthesis Impose? 2835
4. Electrospray Ionization Tandem Mass Spectrometry as a Tool for Catalyst Screening 2835
5. Case Study: Fishing for Catalysts in a Solution-Phase Polymerization 2838
6. Case Study: Olefin Metathesis and ROMP with Hofmann Carbenes 2839
7. Case Study: Single-Site Ziegler–Natta Catalysts 2841
8. Conclusion 2846

1. Introduction

In recent years, high-throughput methods based on the screening of libraries of compounds have spread from their origins in biology and medicinal chemistry to other fields which range from catalysis to materials science. In each case, the new technologies were introduced to speed up both the discovery and the optimization of new chemical entities. Applications in homogenous and heterogeneous catalysis[1] present great opportunities for the acceleration of the discovery and optimization process as can be illustrated by a simple comparison of three technology-based industries: microelectronics, pharmaceuticals, and non-pharmaceutical chemistry. Intel, the market leader in microprocessors, derived 85% of its sales in 1987 from products introduced in the same calendar year.[2] For pharmaceutical products introduced since 1960, one sees that the time between introduction of a blockbuster drug and the appearance of the first product from a competitor dropped from almost a decade to less than one year.[3] In both industries, a rapid pace of innovation has become the norm. In the mainstream chemicals business, a comparable acceleration is only now beginning. With over 90% of new processes in the chemical industry involving catalysis, and a typical research and development (R&D) phase of three-to-five years before a process moves to piloting,[4] a more efficient and systematic method for the discovery and optimization of catalysts promises considerable benefits. Moreover, with the paucity of reliable predictive models for organometallic catalysis, high-throughput methods give researchers the ability to more rapidly, and importantly, more broadly search parameter space around a lead structure to probe and refine mechanistic concepts. With the large potential benefits and the substantial research activity in the last five years, the impact of high-throughput screening for catalysts has been surprisingly modest. In this review both the philosophy as well as the technology of high-throughput screening, as applied to catalysis, are discussed and an attempt is made to define the technical requirements needed to achieve significant acceleration of the discovery and optimization process for industrially viable catalysts.

High-throughput screening for catalysts, as it is currently practiced, is usually done with parallel synthesis and screening of candidates using a one-compound-on-one-bead, one-compound-in-one-reactor, or one-compound-in-one-well strategy.[5] One purpose of this review is to show that the unique challenges presented by organometallic catalysts favor an alternative screening strategy that works for pooled libraries, that is, mixtures, if a suitable method for technical implementation can be conceived.

2. What is Wrong with High-Throughput Screening of Catalysts as Currently Practiced?

Screening for catalysts is nothing new. Between 1909 and 1912, Alwin Mittasch and co-workers screened 2500 formulations in 6500 experiments to find the optimum catalyst for

[*] Prof. Dr. P. Chen
Laboratorium für Organische Chemie
ETH Zürich
8093 Zürich (Switzerland)
Fax: (+41) 1-632-1280
E-mail: chen@org.chem.ethz.ch
and
Thales Technologies AG
Technoparkstrasse 1, 8005 Zürich (Switzerland)

 DOI: 10.1002/anie.200200560 © 2003 Wiley-VCH Verlag GmbH & Co. KGaA, Weinheim

the Haber–Bosch ammonia synthesis.[6] Their successful search through variations in composition and reaction conditions found a system which is still used today in only slightly changed form, which indicates that their search was broadly enough conceived to find a global optimum. Modern catalyst research has benefited from better analytical tools and improved chemical understanding, but the basic strategy has remained unchanged: potential catalysts are synthesized and then tested for activity, selectivity, lifetime, or any other of the many figures-of-merit. The transfer of the present generation of high-throughput techniques—such as, combinatorial libraries, split-pool synthesis, miniaturization, robotics—from the pharmaceuticals field promised to accelerate the discovery process, but the basic approach is nevertheless the same: synthesis of defined compounds (or compositions) precedes screening. To understand the argument, consider the individual components of a generalized process:

- The individual members of a compound library must be synthesized. The preparative work can be done conventionally, that is, one compound at a time, or by split-pool methods in the case that a catalyst can be made by sequential assembly. Whereas, a chemist can synthesize approximately one compound per week (assuming the typical complexity of a pharmaceutical intermediate or simple catalyst) at a cost of $7500 per compound, available robotic equipment with combinatorial techniques (and the same chemist) can prepare 800 compounds per week at a cost of $12 per compound.[7] Of course, the presupposition is that the compounds can be prepared by these methods at all.
- The identity of each compound must be encoded. The overwhelming majority of methods encode the identity of compounds spatially.[5] In other words, the compounds are segregated so that, at each location, only one compound is represented. More concretely, there is only one potential catalyst in each well of a microtiter plate, one potential catalyst in each microreactor, or only one potential catalyst on each bead.
- An analytical method must be applied to measure some figure-of-merit for each member of the library. The approach derives from the pharmaceutical industry where such methods are well-established. As an indication of the magnitude of the technical problem—the sheer numbers—one can consider an example from that industry. A library of 37 791 360 hexapeptides was screened for growth inhibition of five Gram-positive bacteria lines. From the library, 41 hits (defined as $IC_{50} < 50\ \mu g\,mL^{-1}$) were found for further development as potential antibiotics.[8] Miniaturization and automation have reduced the time needed to perform a measurement sufficiently so that, in principle, thousands of samples can be processed in a day. Robotics works, however, only for relatively simple measurements, which means that the information content of the screen can be quite limited. This has led to the division of screening into primary and secondary stages, with more sophisticated tests being applied to a small subset of the compound library in the second stage. A few examples use other approaches to signal catalytic turnover. Mass spectrometric[9] or fluorescence-based[10] methods in which the product of a catalyzed reaction incorporates a marker from the catalyst have been demonstrated, but they represent special cases.



Peter Chen was born in Salt Lake City in 1960. In 1987, He earned his Ph.D. from Yale University under the joint supervision of Professors J. A. Berson, S. D. Colson, and W. A. Chupka, with dissertion on the laser spectroscopy of organic radicals. After a postdoctoral appointment with Prof. J. B. Fenn also at Yale, he was appointed Assistant Professor of Chemistry, and subsequently Associate Professor, at Harvard University. Since 1994, he has been Professor for Physical Organic Chemistry at the ETH in Zürich. He is the recipient of numerous awards and honors, including the Camille and Henry Dreyfus Teacher-Scholar Award and the Alfred P. Sloan Fellowship. In 1999 he founded the company Thales Technologies.

In practical terms, the available screening methods themselves impose severe limits on the libraries. Especially because of the miniscule amounts of catalysts in a typical screen—a few milligrams or less—the analytical methods in high-throughput screens usually detect a *product* of the catalyzed reaction, that is, either the chemical product itself or a physical property, such as heat, the magnitude of which is proportional to turnover. The strategy is sensible because the multiple turnovers that define catalysis as such amplify the signal by (perhaps) orders-of-magnitude over a comparable signal based on observation of the catalyst itself. From this basic experimental design, the limitations necessarily follow. If a screen is built on product detection, then the catalysts in a library must be spatially segregated from each other because each member of a library potentially produces the same product. The resulting one-compound-in-one-reactor or one-compound-on-one-bead approach then requires that each individual potential catalyst in a library be synthesized in advance, and importantly, in pure form, to achieve the necessary spatial segregation. For organometallic compounds, the usual preparative problems associated with lability and air- or moisture-sensitivity are augmented by the absence of general, robust synthetic routes to even simple organometallic structures. With complex formation often being reversible and driven to completion by precipitation of the least soluble component, a synthesis that works for one member of a library cannot be assured to work for even close homologues. While these problems also occur in the synthesis of small-molecule libraries that are screened for potential pharmacological activity, they are considerably more extreme in the case of organometallic compounds. Nevertheless, even in the screening of small-molecule drug candidates in the pharmaceutical industry, the bottleneck is not the screen, but rather the synthesis. The investment of the time and manpower needed for development and optimization of a targeted, specific synthesis for an entire substance class of potential catalysts is hard to justify when one knows in advance that few, if any, of the compounds will show any activity. Moreover, the syntheses themselves are hobbled by further constraints. In a multistep synthesis by an automated station,

 © 2003 Wiley-VCH Verlag GmbH & Co. KGaA, Weinheim

purification of intermediate products is technologically problematic. Typically, the one-compound-in-one-reactor or one-compound-on-one-bead approach can be implemented only if each individual step in a multistep synthesis is clean and quantitative. Perhaps it is no surprise that the best examples in which novel catalytic activity have been discovered involve peptidic systems[11] for which four decades of prior optimization have produced coupling reactions that meet the stringent constraints imposed on the preparative chemistry. Unfortunately, general ligand synthesis and organometallic chemistry contains no comparably general synthetic methodology.

The constraints on preparative methods introduces yet another restriction which limits the usefulness of high-throughput screening as usually practiced. In most cases, industrially used catalytic systems are not, in fact, well-characterized complexes. They are rather catalytic formulations, in situ prepared catalysts, or simply unseparated mixtures of components. The patent literature may be regarded as a rich repository of catalytic activity for which the actual catalytic species remain to be identified. Similarly, the catalytic formulations themselves represent not only pooled libraries, but targeted, pooled libraries in that the components in the mixture are typically variations on a single or a few structural themes. These libraries, however, cannot be screened sensibly using parallel methods. Without knowledge of the composition, let alone the structure of the catalytically active species, the design and construction of a complete and exclusive library would be exceedingly difficult, even when some activity is already shown to be present. It is furthermore doubtful that primary screens with low information content can deliver useful results when applied to empirically prepared catalytic formulations of unknown composition.

The balance of constraints renders high-throughput screening of catalysts less useful than the concept would otherwise be expected to be. Knowing this, the question may be posed: What technical innovation would be needed to relax the constraints?

3. What Technical Requirement does "Screening before Synthesis" Impose?

The requirement that each potential catalyst be synthesized in a pure form in advance would be relaxed if the screening method could determine a figure-of-merit for a catalyst within a mixture. In other words, a method for screening a "pooled" as opposed to "parallel" library of catalysts would enable much simpler preparative procedures. Ironically, the principal difficulties in the targeted synthesis of single compounds become advantages. The difficulty in organometallic synthesis comes because 1) there are a large number of energetically similar reaction pathways, and 2) reactions are very often reversible and proceed to thermodynamic equilibrium. Combined with relatively poor separation techniques (in comparison to those available for ordinary organic compounds), these unfortunate facts make multistep organometallic syntheses difficult. However, if one can work with equilibrium mixtures at the level of the screen, these same unfortunate features makes the generation of molecular diversity simple. Facile ligand exchange under mild conditions makes "one-pot" syntheses of mixtures almost trivial. Moreover, the multicomponent catalytic formulations that currently defy high-throughput screening methods become natural starting points; they are by definition pooled libraries of potential catalysts from which interesting new structures can be discovered. One need only recall that these catalytic formulations already show activity; only the specific structures are unknown.

Of course, the need for a targeted synthesis of a pure compound is not altogether eliminated by a pooled screening technique. The specific synthesis is pushed back, however, so that it need only be carried out after the screen has identified likely candidates. The effort to develop a clean synthesis need only be invested once the target has already been shown to be good. The new approach—"screening before synthesis"—means that the number of compounds to be individually synthesized can be drastically reduced relative to that for a comparable parallel screen. The aim of this review is to demonstrate that this approach is not only possible, but holds further advantages over conventional thinking. It is perhaps appropriate at this point to mention that screening of pooled libraries or mixtures is in fact closer to the original concept of screening in biological applications. For example, the screening of cDNA libraries, the identification of ligand–receptor interactions by affinity chromatography or various forms of affinity labeling with fluorescent or radioactive probes,[12] and the more recent identification of useful mutant enzymes by directed evolution all represent in one form or another the screening of pooled libraries.[13]

4. Electrospray Ionization Tandem Mass Spectrometry as a Tool for Catalyst Screening

The particular embodiment of the "screening-before-synthesis" approach covered in this review uses electrospray ionization tandem mass spectrometry to fulfill the technical requirement of screening of multicomponent formulations, pooled libraries, or simply mixtures. There are in principle other variations of this method, but the present example is well-documented by recent work from our group[14–18] on the use of the method for mechanistic studies in organometallic chemistry.[19–23] Electrospray ionization (ESI),[24] which originated in the paint and coatings industry, was first applied to mass spectrometry by Fenn and co-workers[25] who used the method for the mass spectrometry of biomolecules, for example, peptides and proteins, work for which the Nobel Prize was awarded in 2002. Electrospray transfers intact molecular ions from a dilute solution directly to the gas phase by a complicated process involving charged droplet formation, fission, and field desorption.[26] Important for the application in organometallic chemistry is the gentleness by which ions are formed; proteins can be ionized without denaturation and nonconvalent receptor–ligand complexes remain intact. Working directly from dilute solution is also a major advantage for catalysis in that the active species often exist only under these conditions. While ESI for biomolecules

 © 2003 Wiley-VCH Verlag GmbH & Co. KGaA, Weinheim

is usually carried out with aqueous or alcoholic solutions, any polar solvent is also suitable. We have used acetonitrile, acetone, THF, dichloromethane, chloroform, chlorobenzene, or mixtures of these solvents with normally "unsprayable" nonpolar solvents, such as toluene. The typical concentration range for which ESI works well, 0.001–10 mM, also corresponds to the concentration of many catalysts under realistic conditions. For example, take a catalyst which works on a concentrated (for example, 1M) solution of substrate. A realistic catalyst productivity for commercial application corresponds to a substrate-to-catalyst ratio[27] of ≥ 10000, which would mean catalyst concentrations ≤ 0.1 mM. This concentration sits right in the middle of the optimal range for electrospray. Flow rates from nanoliters per minute to microliters per minute mean that direct sampling from a reactor is also possible.

Examination of a block diagram for the ESI mass spectrometer (Figure 1) shows the principal features that enable the technical solution to screening mixtures. The ions produced in the electrospray source are transmitted through a

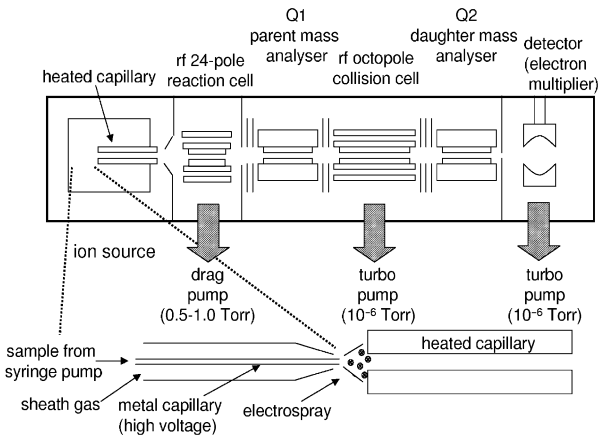


Figure 1. Schematic representation of the modified Finnigan MAT TSQ-700 ESI tandem mass spectrometer. Catalyst ions are sprayed from dilute solution in the ion source, desolvated, and transferred into the vacuum system through the heated capillary, after which the final desolvation or fragmentation occurs at the skimmer. The two radio-frequency (rf) multipoles serve as reaction "vessels" for collisions of the ions with neutral gaseous reagents. After each stage of reaction, product identification and/or selection is carried out in a quadrupole mass analyzer.

heated capillary into the mass spectrometer. Desolvation of the ions occurs in part in the high-pressure region, in part in the capillary, and lastly, in front of the "skimmer" where the ions can collide with background gas. The skimmer potential is an adjustable parameter that controls the extent of desolvation as well as further fragmentation. Setting the potential high gives the user the opportunity to generate coordinatively unsaturated complexes by removal of the most weakly bound ligand and is therefore useful for reactivity studies. The ions pass into the radio-frequency (rf) 24-pole reaction cell where they are thermalized or optionally treated with reagent gases at pressures of approximately 0.1 Torr. The 24-pole serves as an ion guide which confines the ions in the radial direction—a slight longitudinal field from the space-charge drives ions gently through. The ion–molecule reactions occur under thermal conditions, typically 70 °C, with up to 10^5 collisions occurring in the 24-pole. Ions pass then into the first quadrupole in which the reaction products can be selected and separated for a subsequent reaction. The mass-selected ions are then passed into a rf octopole where they can react again with neutral reagent gases, and then mass-analyzed in the second quadrupole. The 24-pole, in contrast to a quadrupole or the original octopole, ensures a Boltzmann distribution for the ion energies. Exchange of energy between the rf field and the ions can occur during an ion–molecule collision, which creates a high-energy tail in the distribution of kinetic energies.[28] Experimentally, we found the translational-energy distribution of ions in the 24-pole to be indistinguishable from a Boltzmann distribution.

Residence time, collision number, and absolute reaction efficiency for either the 24-pole or the octopole can be determined by a combination of experiment and numerical modeling.[23] The Monte Carlo modeling of ion motion in a gas-filled rf multipole ion guide was performed as follows. The differential equations for the ion motion in an ideal multipole field were solved numerically without recourse to the effective potential approximation using a fourth-order Runge-Kutta numerical integration. Collisions were handled in a simplified manner. The probability of a collision between the ion and a buffer gas molecule during a single integration time-step was treated using Langevin theory [Eq. (1)] where $P =$ collision probability, $n =$ gas number density, $v =$ relative velocity, $\sigma =$ Langevin collision cross-section, $p =$ gas pressure, $e =$ elementary charge, $\mu =$ reduced mass, $\varepsilon_0 =$ electrical permittivity of vacuum, $\alpha_e =$ polarizability, $k =$ Boltzmann's constant, $T =$ absolute temperature.

$$P = n\,v\,\sigma = \frac{e}{2\,\varepsilon_0}\sqrt{\frac{\alpha_e}{\mu}}\,\frac{p}{k\,T} \qquad (1)$$

The application of Langevin theory for the collision cross-section greatly simplifies the calculation because, at this level of approximation, the collision probability during a time-step is independent of the relative velocities of the collision partners in the center-of-mass frame.

The velocity of the collision partner is taken from a Boltzmann distribution with a random direction in the laboratory frame-of-reference. For a collision the new direction of the ion is chosen at random in the center-of-mass frame-of-reference and then transformed back to the laboratory frame. This is equivalent to having chosen a random impact parameter for the collision. In Figure 2, the results of the simulation for three pressures and a range of incident kinetic energies (laboratory frame) in the octopole are depicted. A test as to whether or not the simulation gave realistic results was done by sending an ion of a given mass through the first quadrupole, the octopole, and the second quadrupole. The two quadrupoles were scanned with a variable time delay between them. By measuring the transmitted ion intensity as a function of the delay between the two quadrupoles, the mean retention time in the octopole could be determined. It was found to agree within a factor of two with the simulation. Absolute reaction yields for a test

 © 2003 Wiley-VCH Verlag GmbH & Co. KGaA, Weinheim

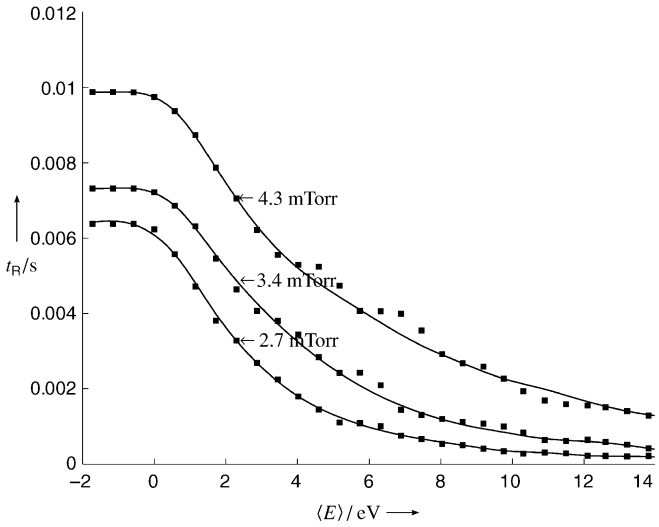


Figure 2. Simulation of the mean ion retention time in the gas-filled octopole collision cell (t_R) as a function of incident ion energy and gas pressure for the reaction of a ruthenium carbene complex with 1-butene. The results at nominally negative incident-ion energies come from the high-energy tail of the ion kinetic-energy distribution. Comparison of the simulated retention times with experimentally measured values shows good agreement, validating the model.

reaction at the same incident ion energies and reagent pressures could also be measured (Figure 3). Because the Monte Carlo simulation realistically reproduces the experimentally determined retention time of the ions in the gas-filled octopole, the absolute collision number from the simulation, approximately 5000 collisions per ion, can be taken as reliable. The number of collisions in the 24-pole, which can handle a 100-fold higher pressure of the reagent gases, is correspondingly higher. Furthermore, because the curves in Figures 2 and 3 are approximately parallel, one can reduce the measured product yield to a reaction probability of

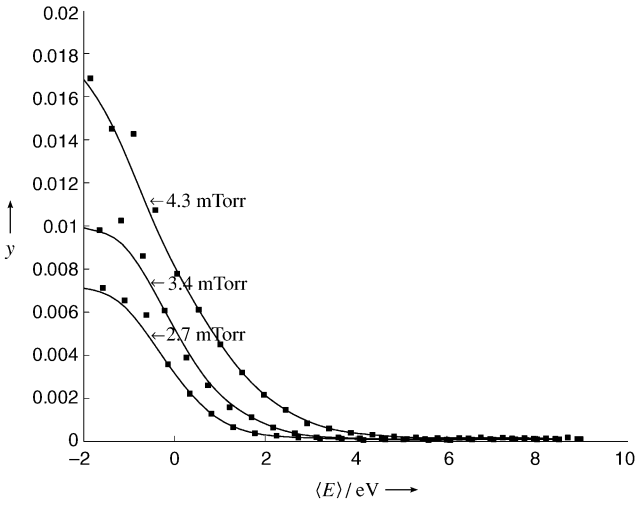


Figure 3. Absolute product yields y for the metathesis reaction of a ruthenium carbene complex and 1-butene as a function of the incident kinetic energy of the incoming ion (laboratory frame) and the pressure of 1-butene in the octopole collision cell.

between 10^{-4} and 10^{-5} per collision, which is typical for many of the organometallic ion–molecule reactions examined in this study. While the absolute reaction efficiency would be regarded as high[22,23] by organometallic chemists, they are very low by the standards of ion–molecule reactions.[29] Nevertheless, the long rf multipoles provide enough collisions for reaction to be observed.

One may question the extent to which gas-phase techniques, even when applied to complexes identical to those in solution, apply as a measure of solution-phase reactivity. After some years of work in the field, we find two answers to this justifiably raised question. First, for the reactions carried out by our group have examined (C–H activation with Ir^{III} [19] or Pt^{II} complexes,[30] catalytic hydrogenation with Rh[20] or Ru complexes[31], olefin metathesis,[21,23] catalytic epoxidation with [Mn(salen)] and an oxidant,[32] aldehyde olefination with high-valent Re compounds,[33] and Ziegler–Natta polymerization with single-site catalysts,[22] have shown that the gross reactivity in the gas phase resembled that in the solution-phase despite initial expectations to the contrary. Often, the relative reactivities, that is, branching ratios, were surprisingly similar to those for the corresponding reaction under more conventional conditions. While one cannot discount coincidence, the preponderance of empirical evidence suggests that the gas-phase ion–molecule chemistry of electrosprayed organometallic complexes provides at least a qualitative guide to their solution-phase reactions. A rough explanation for the similarity—a detailed mechanistic proof remains outstanding—can be proposed. For the earlier generations of gas-phase ion–molecule reactions in organic chemistry,[34] the objects of study were polar reactions, such as nucleophilic substitution or carbonyl addition reactions. The S_N2 reaction probably illustrates the problems most graphically.[35] In solution, the substitution proceeds along a simple reaction coordinate; in the gas phase, there is, on the other hand, the classical double-well potential for ion–molecule reactions. The minima before and after the transition state—they be up to 10 kcal mol^{-1} deep relative to the incoming or outgoing asymptote—are completely general because they result from the attractive electrostatic ion–dipole or ion-induced dipole interaction that arises between any ion and any molecule in the gas phase. Precisely these electrostatic interactions are screened in the condensed phase by the dielectric continuum. The transition from the unsolvated to the solvated case has been examined for simple substitution reactions and it is clear that a large number of solvent molecules must be involved before the electrostatic interactions are significantly screened. While the electrostatic potential creates some differences, perhaps the larger problem comes because of the large magnitude of the free energy of solvation for ions. With absolute magnitudes up to 300 kcal mol^{-1}, a few percent differential solvation along the reaction coordinate is enough to lead to large changes in phenomenological reactivity. The basicity of amines[36] or the acidity of alcohols[37] are among the most salient examples. Facing this background, we naturally began with the expectation that only a limited extrapolation of the results from gas-phase chemistry to solution-phase chemistry would be possible. When experiment after experiment showed other-

 © 2003 Wiley-VCH Verlag GmbH & Co. KGaA, Weinheim

wise, it became necessary to suggest some explanations. One possibility is that the molecules under study have become large enough to provide an intramolecular equivalent of solvation. Such a phenomenon has been proposed for larger carbocations in which the close quantitative analogy between gas-phase stability order and that in nonaqueous solution was rationalized in this way.[38] A second, more likely, explanation relies on the reactions themselves. Whereas nucleophilic substitution or carbonyl addition reactions are inherently polar reactions in which the charge distribution, and hence polar solvation, changes dramatically on going from starting material, to transition state, to product, typical organometallic reactions, such as π complexation, oxidative addition, or reductive elimination, are largely nonpolar reactions in which the charge plays only a spectator role. Mechanistically, these organometallic reactions resemble pericyclic reactions more than carbonyl additions. Experimentally and computationally, a Diels–Alder reaction has a similar activation energy in both the gas phase and in nonpolar to moderately polar solution,[39] so perhaps it should not have been so surprising to find that oxidative addition reactions do as well. The residual electrostatic effects, as well as the absence of counterion effects, accelerates gas-phase reactions in general,[22,23] but, as mentioned above, the effect is common to all ion–molecule reactions so branching ratios are not affected.

The second answer to the question concerning extrapolation of gas-phase chemistry is that the question is, in part, irrelevant. As will be seen in the Ziegler–Natta case below, at least some of the screening can be done with reactions in solution. In other words, the gas-phase ion–molecule chemistry is nothing more than an analytical method applied to reactions under conditions not too different from those in the real process.

It should be emphasized that the new approach to catalyst screening is not specifically dependent on ESI mass spectrometry. Any analytical method which allows screening of a mixture is, in principle, suitable. The particular technical solution in the case of ESI tandem mass spectrometry is the implementation of a method that detects catalyst-bound substrate or catalyst-bound product, rather than the product itself. While challenging from the point-of-view of detection limits, dynamic range of detection, and lability of the target species, the advantages in terms of screening make the development worthwhile.

The work in the cases below was performed using modified triple-quad mass spectrometers. Triple quads, and similarly sector instruments, have lost ground in recent years to Paul traps[40] and FT-ICR (Fourier transform ion cyclotron resonance) spectrometers[41] for applications in the analysis of biological samples, for example, proteomics. At the low-end of the market, the Paul traps provide a more cost-effective LC-MS (LC = liquid chromatography) detector; the high-end of the market is dominated by FT-ICR because of the wide mass range and high resolution possible with these instruments. These two instruments share the feature that they are ion-trap methods, as opposed to transmission devices, such as linear quadrupole, sector, and time-of-flight (TOF) instruments. While it cannot be excluded that at least some of the experiments in the area of homogeneous organometallic catalysis can be carried out in an ion trap, both the Paul traps and the FT-ICR suffer from distinct disadvantages that could limit their utility. In both trap technologies, the number of ions held in the trap is limited (generally between 100 and 10000 ions, with the upper bound set by space-charge effects) which produces problems with counting statistics when ions must represent all possible species deriving from a library of catalysts. Secondly, any technique which stores ions is inherently more sensitive to decomposition of the parent ions. The reasonably large organometallic ions encountered in catalytic applications show a substantial kinetic shift[42] in their dissociation thresholds, which complicates threshold measurements, but, on the other hand, facilitates the observation and handling of labile species. The FT-ICR methods suffer from having a lower dynamic range in comparison to any of the transmission methods, which is crucial if one species is to be found at low concentration in the presence of other, much more abundant complexes. Ions in an FT-ICR have moreover a very low collision rate—there may just be a few collisions per second—in contrast to the collision rate in our rf multipoles of up to $10^6\ s^{-1}$, which means that chemical activation dominates the reactions in the FT-ICR[43] while the reactions in the rf multipole[22] much more closely resemble those in solution under thermal conditions. Among the transmission devices, the triple-quad is to be preferred over both the sector and TOF because of the dynamics of ion–molecule collisions in the various instruments. Ion–molecule collisions at high kinetic energies tend to sample predominantly the repulsive inner wall of the intermolecular potential, meaning that the collision is largely elastic. A low-energy collision, on the other hand, samples the attractive electrostatic well in the intermolecular potential, which means that the collision complex is likely to be longer-lived. Experimentally, the cross-section for reactive collisions falls off rapidly as the kinetic energy is increased.[44] For the typical triple-quad instrument, ion kinetic energies are in the range of zero to a few eV in the laboratory frame, in contrast to the keV energies that are encountered in sector and TOF machines. Accordingly, while other instruments may be ideal for other applications, the triple-quad is the machine of choice for the kind of work on catalysis covered in this review.

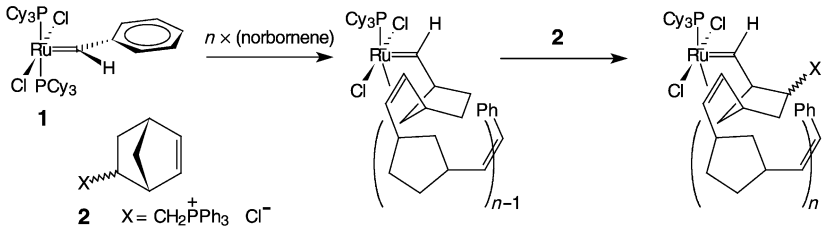
5. Case Study: Fishing for Catalysts in a Solution-Phase Polymerization

In the first case study, the resting-state species in a solution-phase ring-opening metathesis polymerization (ROMP) reaction is "fished out" by using a covalently modified substrate molecule. While the ROMP reaction, being a living polymerization, represents an ideal case for the method, the technique is suitable for more difficult systems with appropriate modifications. The experiment relies on the fact that electrospray detects charged species, that is, ions. If a molecule is uncharged, it cannot be electrosprayed unless a charge is somehow attached. In the case of protein mass spectrometry, neutral proteins can become charged by coordination of a proton or alkali-metal cation. Such proc-

 © 2003 Wiley-VCH Verlag GmbH & Co. KGaA, Weinheim

esses are much less common for the nonprotic solvents in which the typical organometallic catalyst works; in any case, mass spectrometric signal intensities for species that are charged by virtue of noncovalent binding of adventitious cations are typically orders-of-magnitude weaker than the signals from species bearing permanent charge. An uncharged catalyst molecule in a mixture with other uncharged compounds becomes visible in the electrospray mass spectrum when a charged substrate becomes attached.

In the particular experiment[17] depicted in Scheme 1, norbornene with a pendant prosthetic ammonium or phosphonium cation is added, together with ordinary norbornene,



Scheme 1. Derivitization of ruthenium catalysts with cationic norborene species enables detection by ESI-MS.

to the otherwise neutral $[(Cy_3P)_2(Cl)_2Ru{=}CHPh]$ (Cy = cyclohexyl) catalyst in solution. After a short time, the electrospray mass spectrum (Figure 4) shows those ruthenium species which incorporated the charged substrate. While the ruthenium catalyst represents an easy case, even this "trivial" example contains information, not only in what is seen, but also in what is absent. The intramolecular π complex, rather than the bisphosphane complex, is seen as the resting state in the catalytic cycle. In the hypothetical case, in which there were several metathesis-active complexes at work, each would yield its own series, with the mass of the catalytic "headgroup" distinguishing one series from the others. Moreover, anything that was not able to incorporate the charged substrate would simply remain invisible. One must keep one caveat in mind, though. In a catalytic cycle at steady-state, each step may have a different rate constant but they must all have the same rate. Since rate is the rate constant multiplied by one or more concentrations, the most abundant species will be that species prior to the reaction for which the rate constant (times the concentration of the other involved reagents in the case of bimolecular reactions) is smallest.

The observed species—the resting state of the cycle—is not necessarily the most important intermediate in the cycle. It is simply the lowest-energy species among several that could occur. ESI-MS, like any other in situ technique, detects the resting state. In principle, one could vary concentrations of other reagents to vary the resting state, but that requires a substantial knowledge of the catalytic cycle in advance.

This experiment bears a very close methodological relationship to affinity labeling in the screening for a receptor, for example, in biological applications.[12] In that case, a substrate molecule is labeled with either a fluorescent tag or a radioactive marker. The substrate is chosen as one that, upon binding to the target, subsequently covalently functionalizes the target, labeling the target with an easily observable property. The libraries in most biological applications are also inherently mixtures of components. The analogy to the present case of catalysts is not accidental.

6. Case Study: Olefin Metathesis and ROMP with Hofmann Carbenes

Ring-opening metathesis polymerization (ROMP) catalysts are the object of the second case study as well.[18] The catalytic cycle follows the accepted Chauvin mechanism[45] (Scheme 2).

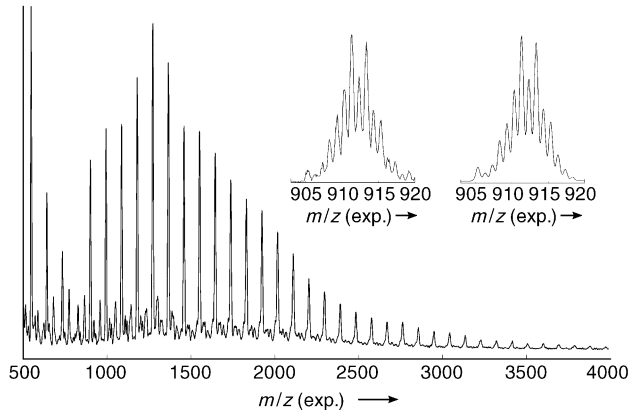
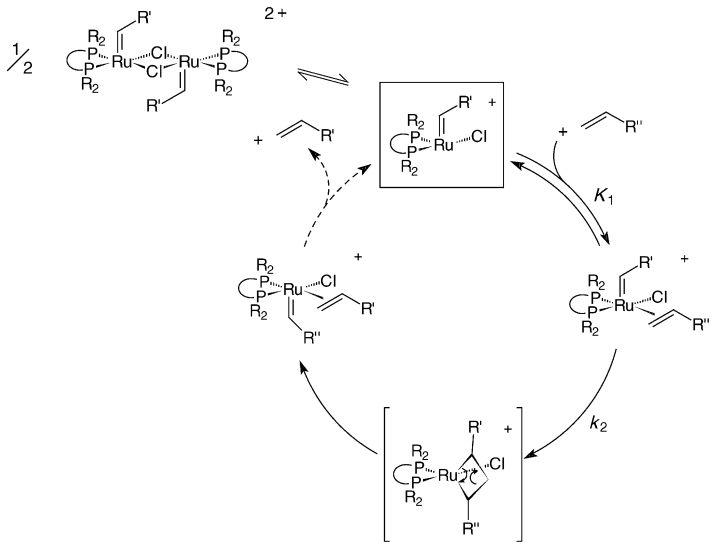


Figure 4. ESI-MS of the catalyst-bound ROMP oligomers obtained by reaction of $[(Cy_3P)_2Cl_2Ru{=}CHPh]$ with norbornene and a covalently functionalized norbornene derivative. Complexes that incorporated the functionalized norbornene are visible in the ESI-MS. The inset compares the isotope pattern of one oligomer against a computed distribution.



Scheme 2. Chauvin mechanism for catalytic ROMP.

© 2003 Wiley-VCH Verlag GmbH & Co. KGaA, Weinheim

In this screen, solution-phase synthesis of the library is followed by electrospray of the mixture, gas-phase selection of each member of the library, and then gas-phase reaction to establish a figure-of-merit. The screen relies on the empirically observed parallel between gas-phase and solution-phase reactions for electrosprayed organometallic complexes. While we have an approximate rationalization for this parallel behavior, it should be emphasized here that the parallel is based on experimental observation of a large number of reaction systems and not a derivation based on first principles. Finally, the top candidate from the gas-phase screen is compared to reference systems in a conventional solution-phase assay to confirm the result. To jump to the conclusion, the successful screen identified the best catalyst, as confirmed in a conventional solution-phase assay, through the performance of 180 reactions in two weeks. Each reaction was repeated independently ten times to ensure statistical significance. Each one of the ten repetitions of the 180 reactions consisted of approximately 60 measurements.

The test system (Scheme 3) was the ruthenium metathesis catalyst prepared by Hofmann and co-workers.[46] It was chosen because it provides a ready access to a high degree of molecular diversity through simple ligand exchanges in solution. Each of the catalysts in the library is potentially accessible through the same, *single* synthesis, although, in cases where the compound was available (through collaboration with the Hofmann group) the separately synthesized compound could be used as well. Note that the measured reactions of separately synthesized compounds and compounds synthesized in situ were found to be identical. Commercially available $[(PCy_3)_2(Cl)_2Ru{=}CHPh]$ was treated, in a few mL of a suitable solvent, with one or more chelating diphosphanes, one or more tetrabutylammonium halide salts, and one or more styrene derivatives to generate in a few minutes all possible combinations of phosphane, halide, and carbene substitutions of the lead structure. For a large number of complexes with an M–X bond (M = metal center), there is a small amount of heterolysis of the metal–halide bond at equilibrium when the solvent is polar enough. This feature is exploited in that the *mixture* of ruthenium complexes, upon electrospray, produces the active species directly in the gas phase. Reaction of isolated active species, selected from among other species according to its m/z ratio, in the rf octopole, leads then to a figure-of-merit for the specific structure.

In this particular case, the basic metathesis activity could be probed by reaction with vinyl ethers. The extent of reaction during the finite residence time in the octopole is a measure of relative rate. Moreover, given that the octopole, which operates under "high pressure", acts more like an ion-drift tube than a collision cell, equilibrium constants for substrate binding could also be determined. A sample spectrum is shown in Figure 5. Reaction with norbornene instead of vinyl ethers gave direct access to ROMP efficiency because the multiple addition of norbornene units could be directly observed.

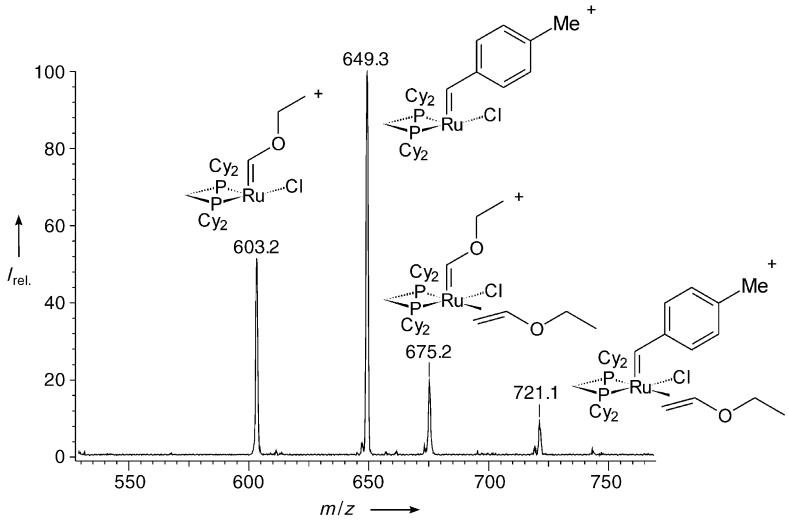
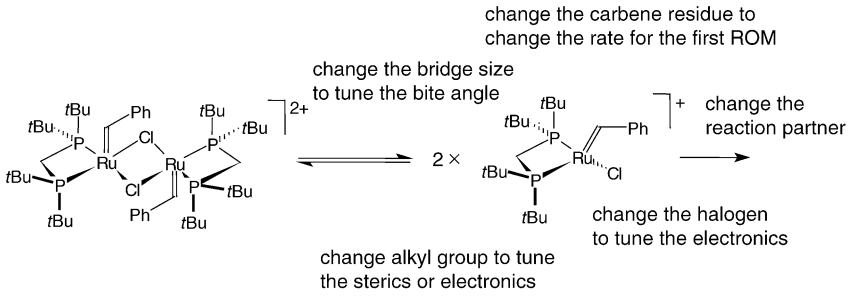
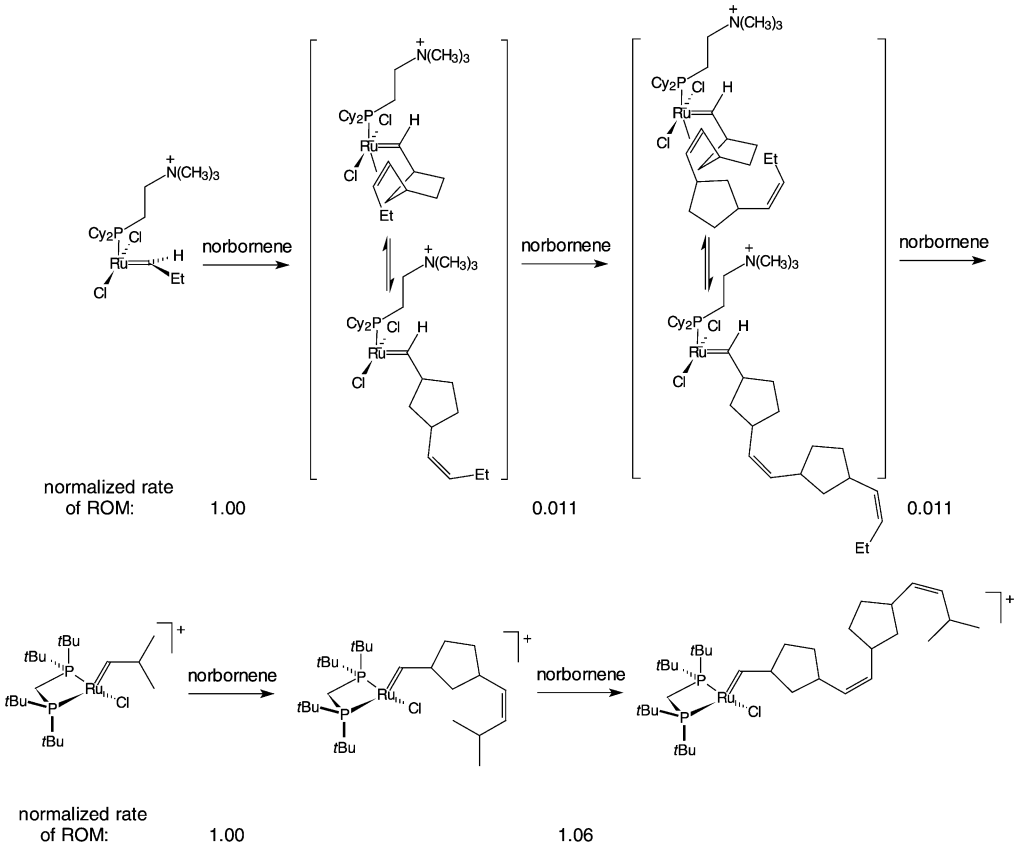


Figure 5. Representative mass spectrum from the reaction of a Hofmann carbene complex with ethyl vinyl ether in the gas phase. One isotopomer of the starting complex, preselected by mass, appears at m/z 649. The adduct mass at m/z 721 is assigned as the π complex; the signal at m/z 603 is the metathesis product. Coordination of another substrate gives m/z 675.

The crudest interpretation of the norbornene addition data would be simply to take the catalyst which makes the longest chains in the gas-phase as the best catalyst. However, a more detailed examination of the relative intensities, modeled with a simple kinetic model, allows the determination of the relative rates for addition of the first norbornene unit versus all subsequent norbornene units (Scheme 4). The significance of the determination was shown in earlier work from our group[23] in which it was demonstrated that the ratio of these rates is a measure of the extent to which intramolecular olefin π complexation (backbiting) occurs. The reversible backbiting introduces a preequilibrium prior to insertion of the next unit of monomer, which manifests itself kinetically as a reduction in the propagation rate relative to the



Scheme 3. Possible modifications of the ruthenium metathesis catalysis of Hofmann et al.



Scheme 4. Kinetic models for calculating the relative rate of addition of the first norborene unit and the subsequent addition steps.

first insertion, for which backbiting is not possible. Complexes which backbite significantly are moreover ideal for ring-closing metathesis (RCM)—the favored method for macrocyclizations in the synthesis of fine chemicals—while those that backbite the least should be best for ROMP. Moreover, the ratio of rates is an important determinant for the polydispersity of the resultant ROMP polymer. When the first addition is much faster than subsequent additions, a narrow polydispersity is expected, and visa versa. These conclusions illustrate the extent to which even decidedly modest mechanistic considerations can lead to highly informative screens by construction of what the pharmaceutical industry calls "surrogate markers" that are more easily measurable than the actual property of interest.

Of course the final proof of the gas-phase screen is the conventional assay in solution (see Figure 6). In the present example, **5** was synthesized and compared to **1**, **3**, and **4** in the ROMP of cyclooctene. As is apparent from the solution-phase data, **5** is not only better than the structurally related **4**, as predicted by the gas-phase data, but also superior to both the first- and second-generation Grubbs ruthenium catalysts.[47]

7. Case Study: Single-Site Ziegler–Natta Catalysts

The application of the new approach in screening to single-site Ziegler–Natta catalysts[48] illustrates another aspect of the methodology. In this example, all of the reaction chemistry involving catalyzed reactions is performed in solution—the gas-phase work enters only as a selective "filter" to screen the solution-phase reactions. In this way, there is no need to assume that solution-phase and gas-phase reactions function in an analogous fashion. The reaction to be screened is the formation of polyolefin—in this case polyethylene from ethylene. A simplified catalytic cycle is depicted in Scheme 5, in which the major events in the polymerization reaction are shown. Depending on the metal–ligand moiety, denoted [M], the turnover-limiting step can be either π complexation or insertion. The former occurs for metallocenes while with late-transition-metal catalysts often, but not always, insertion is the turnover-limiting step. Three distinct experiments comprise the present example. First, a single catalyst is quantitatively assayed using a mechanistic/kinetic model.[15] Second, a pooled library of catalysts is qualitatively assayed in a competition experiment.[14] Third, the two experiments are combined so that quantitative data can be extracted from a pooled library without prior isolation of any of the individual members of that library.[16]

For a quantitative assay of catalyst formation, we chose a palladium complex rather than the more usually employed metallocenes (although a variation of the screen has also been implemented for metallocenes, see below) because 1) the ligand system of the Pd catalyst is combinatorially accessible while that of a metallocene is not, 2) Brookhart's catalysts[49] have been extensively characterized by kinetic techniques.

 © 2003 Wiley-VCH Verlag GmbH & Co. KGaA, Weinheim

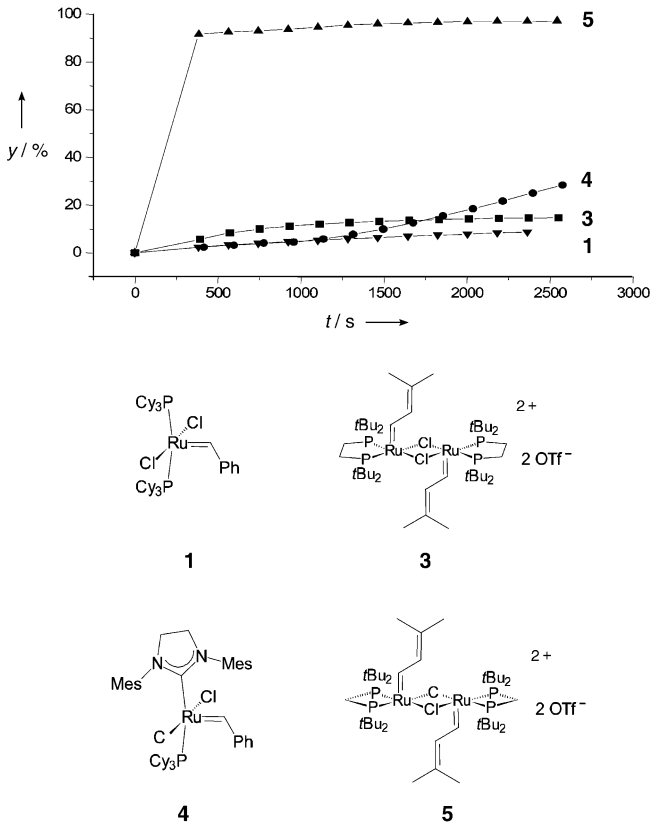
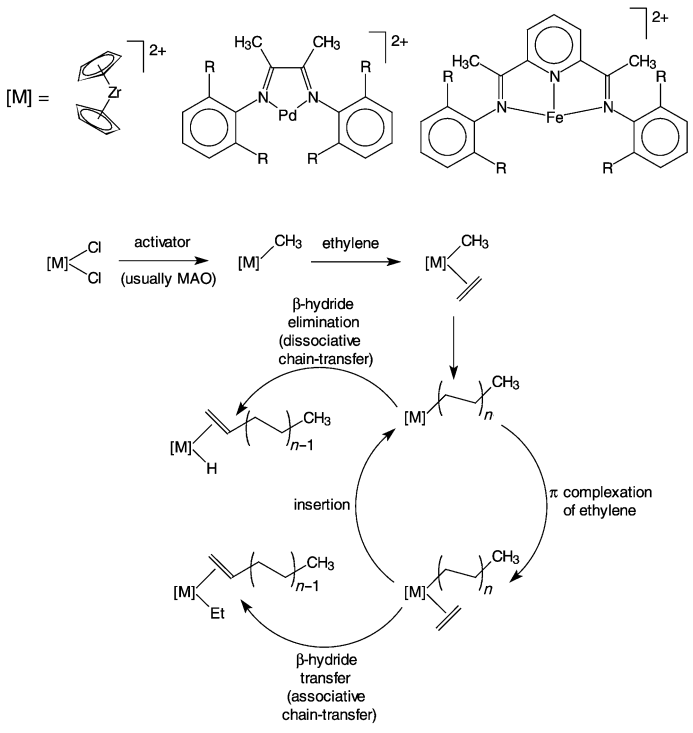


Figure 6. Solution-phase ROMP of cyclooctene by a selection of metathesis catalysts. Complex **5** had shown itself to be the best catalyst in the gas-phase screens.



Scheme 5. Symplified catalytic cycle for polyethylene synthesis.

The latter point is important for the validation of the quantitative values that the present screen produces. As a comparison, a typical laboratory-scale assay of catalyst productivity and polymer molecular weight involves synthesis of enough catalyst to charge a 2 liter autoclave—for a catalyst concentration of 10^{-3} M, the amount is on the order of one gram. Toluene, ethylene, and importantly, activator, for example, methylalumoxane (MAO) in up to several-hundred-fold molar excess with respect to catalyst, are allowed to react over several hours to generate solid polymer on the kilogram scale, which is removed mechanically from the autoclave and then analyzed by, for example, gel permeation chromatography (GPC), for molecular weight. If a different set of process conditions is needed, then the entire procedure is repeated, which requires on the order of one-to-several days. The assay in this example requires 2 mg of catalyst and is complete in approximately 30 minutes. The catalyst is dissolved in 5 mL solvent in a thermostatted pressure cell, placed under a defined pressure of ethylene, and then activated, for example, with MAO. After the reaction has proceeded for a short time, ranging from a few minutes up to half an hour, a good, neutral two-electron donor ligand—the quencher—is added. The quencher coordinates to the active site of the catalyst, deactivating it to further reaction. In principle, the quencher is nothing more than a catalyst poison. In solution, there is now a mixture of free oligomer and polymer chains, which, being uncharged, are invisible to electrospray. Catalyst-bound oligomers, on the other hand, are cationic because the quencher is a neutral ligand, and the "head group" on the catalyst-bound oligomers is cationic. These species are detectable by electrospray. It should be noted that the time for quenching is chosen so as to be long enough for complete mixing after activation, but short enough so that polymer does not precipitate from solution and the viscosity does not change appreciably.

These conditions are needed to ensure that the kinetics reflect the chemical events and not mass transport phenomena. Mass spectra (e.g. Figure 7) show catalyst-bound oligomer chains containing either an even or odd number of carbon atoms, depending on whether or not the oligomers have undergone chain transfer. By fitting the oligomer distributions to the integrated differential equations representing the mechanism of the polymerization, separate values for the initiation, propagation, and chain transfer are obtained. The characteristic shape of the distributions depends on the rates of each of these elementary processes: initiation, propagation, and chain transfer. Furthermore, each of the elementary rates depends on temperature, and, according to the mechanism, also (parametrically) on other process variables, such as pressure. The qualitative magnitudes of each process are easily seen in the distributions shown in Figure 8.

Quantitative values can be obtained by fitting. For the example in Figure 9, the fit is good, which indicates that the mechanism is adequate. By varying the temperature, Arrhenius parameters from the rates are obtained. The activation energies for propagation and chain transfer (18.9 and 21.4 kcal mol^{-1}) agree with those determined conventionally by Brookhart et al. for the closely related systems.[49] More

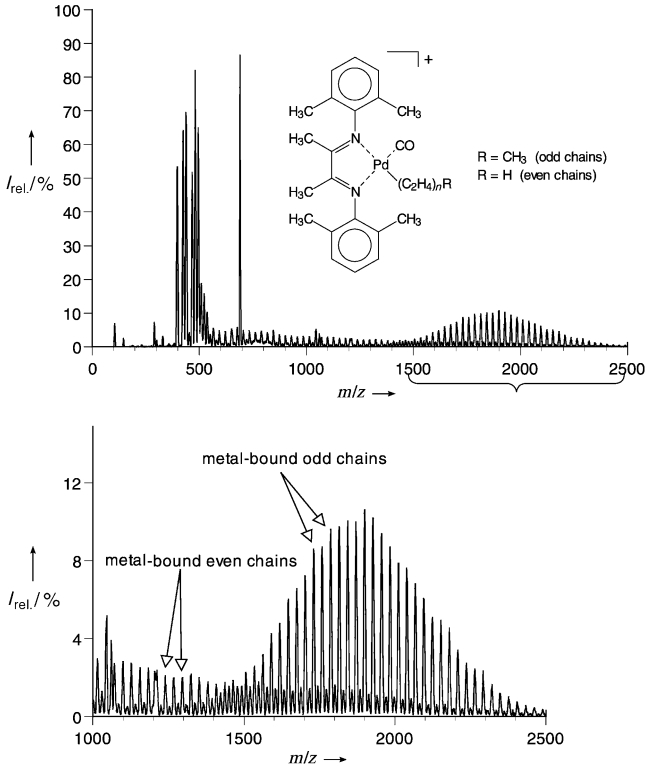


Figure 7. ESI-MS of the catalyst-bound oligomers obtained by polymerization of ethylene with Brookhart's catalyst, followed by quenching with a neutral two-electron donor. The metal-bound odd chains are oligomers built at a metal center which have not yet undergone chain transfer. The even chains have undergone chain transfer at least once.

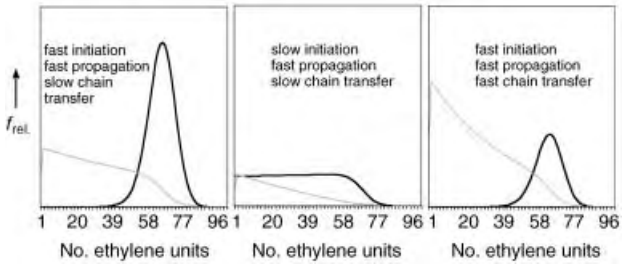


Figure 8. Sample simulation of the odd-chain and even-chain distributions for three possible combinations of initiation, propagation, and chain-transfer rates. The propagation rate were identical in each case; $f_{rel.}$ = relative frequency.

importantly, the measured rates from the fit, or alternatively from the Arrhenius parameters, can be reintroduced into the differential equations describing the mechanism, and then used to compute the rate of ethylene uptake and the molecular weight of polymer. The weight-average molecular weight, computed in this fashion, is a figure-of-merit for the particular catalyst. Moreover, the present assay did not require the actual production of any polymer.

The kinetic parameters can furthermore be used to compute the polymer properties at conditions other than those used for any particular measurement, which means that a finite number of measurements can be used to predict

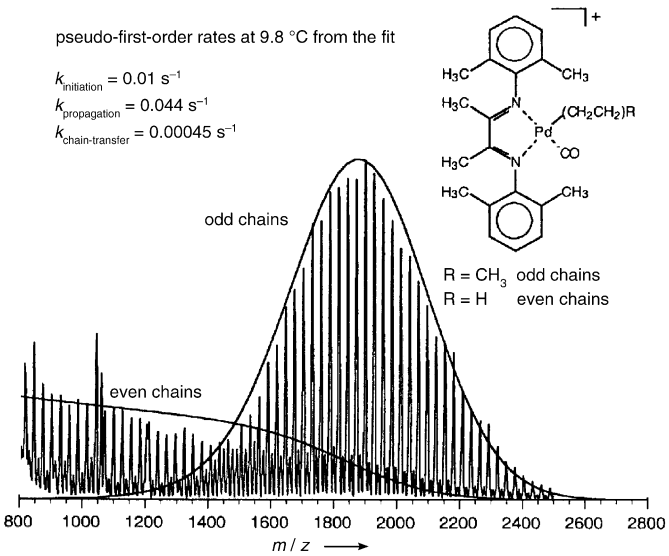


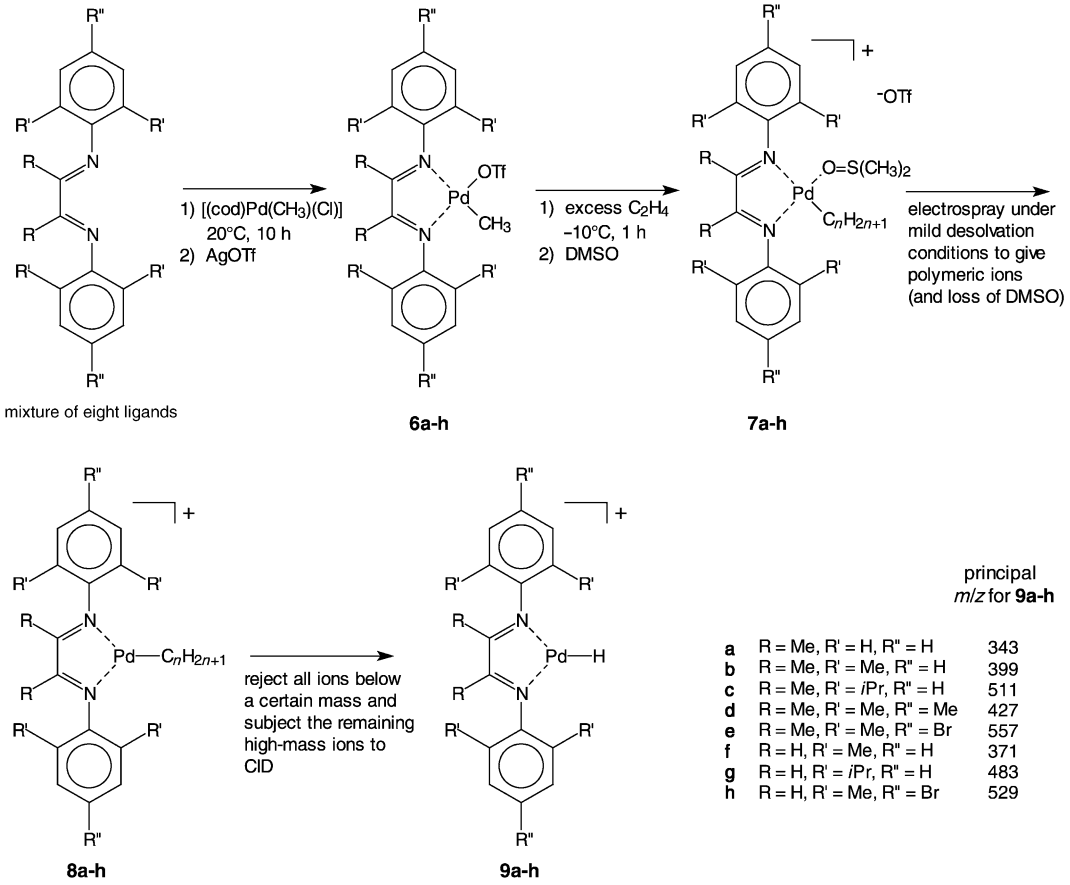
Figure 9. Fit of the odd- and even-chain distributions to initiation, propagation, and chain-transfer rates. Arrhenius analysis of the rates for three temperatures give the activation energies. The absolute values of the rates contains, in addition to chemical kinetics, information on the reactor and concentrations. These, however, contribute to the Arrhenius preexponential factor and not the activation energy.

product properties for an infinite number of process conditions.

While the methodology described above requires only mg amounts of catalyst and a short time, it is still a method that tests catalysts one-at-a-time. A pooled library of catalysts can be simultaneously tested by using a more refined mass-spectrometric experiment.[14] Take a library of eight catalysts—the example works equally well for one hundred at a time—in solution. The catalysts can be mixed together, or more advantageously, prepared in situ by addition of ligands and an appropriate metal source. Using again the Brookhart palladium diimine complexes **6**, such a library was prepared and activated in the presence of ethylene, as shown Scheme 6. Quenching with a neutral two-electron-donor ligand then produces a mixture of metal-bound oligomers, with each of the catalysts in the library producing its own set of distributions. Even with only eight catalysts, the overlapping distributions in the mass spectrum make a direct readout of any single distribution essentially impossible. There are overlapping isotope distributions. Moreover, bearing in mind that, for a fixed total concentration of catalyst in solution, the number of ions corresponding to any single metal-bound oligomer for any one of the catalysts decreases, one recognizes that there is a signal-to-noise problem for larger libraries.

Electrospray of the mixture, selection of only the high-mass ions, and then β-hydride elimination (Scheme 6) produces the clear signal arising from **9c**, the best catalyst (Figure 10). By collapsing all selected catalyst-bound oligomers into a single peak from the hydride species **9c**, the signal-to-noise problem is neatly solved. Again, it should be emphasized that the number of laboratory operations needed to implement the method is approximately independent of the size of the library, in stark contrast to the situation

 © 2003 Wiley-VCH Verlag GmbH & Co. KGaA, Weinheim



Scheme 6. Preparation and activation of a pool library of eight catalysts in the presence of ethylene for simultaneous tests; cod = cyclooctadiene, DMSO = dimethylsulfoxide, CID = collision induced dissociation.

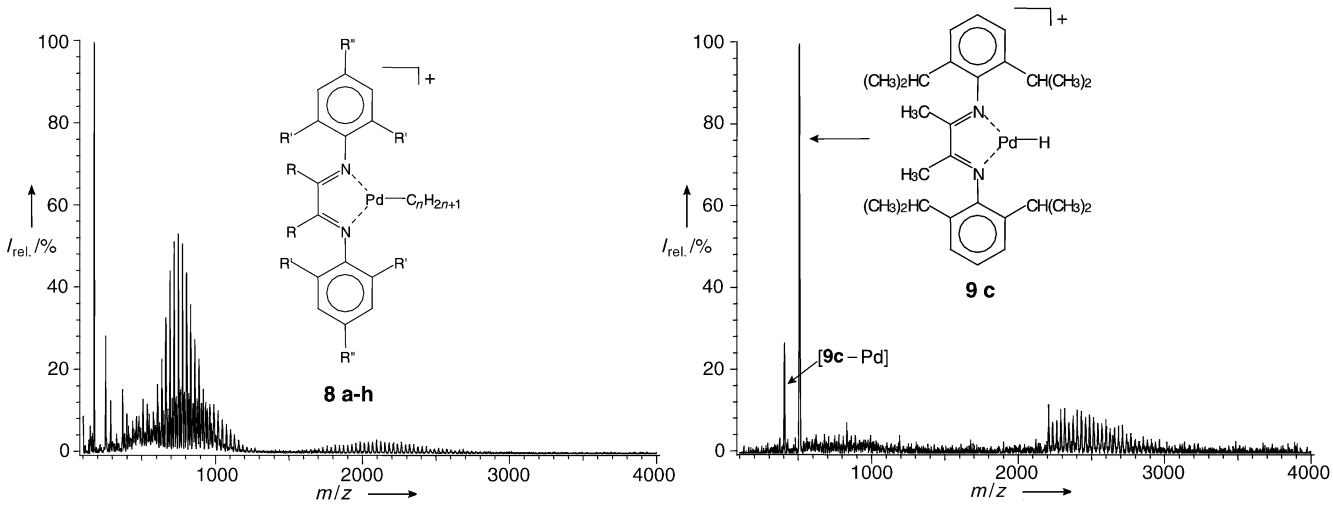


Figure 10. ESI-MS of the quenched mixture of eight catalysts (left) and the result when the ions with m/z > 2200 are chosen and then subjected to β-hydride elimination (right). The clean signal arising from **9c** indicates that this catalyst was responsible for the highest molecular-weight component of the oligomers in the mixture.

with parallel screening. Moreover, while this library was constructed from known components, the experiment is a prototype for screening libraries of unknown substances in a catalytic formulation.

The final experiment combines the quantitative kinetics of the one-catalyst example with the pooled library of the screening case.[16] This experiment shows the power of two-dimensional, or double-selection, mass-spectrometric methods in screening pooled libraries of catalysts.

The experiment uses a so-called "parent-ion scan" in which the second quadrupole in a tandem mass spectrometer is set to detect a product of a reaction—a daughter ion—while

 © 2003 Wiley-VCH Verlag GmbH & Co. KGaA, Weinheim

the first quadrupole is swept. The mass spectrum for the case where the library of eight members (see Scheme 6) is electrosprayed, and the collision-induced β-hydride elimination is used as the filtering reaction, a parent-ion scan for the hydride product ion carrying the same ligand as in the single catalyst study of Figure 9 is shown in Figure 11. The parent ions correspond to those species in the pooled library (a mixture) that, upon undergoing β-hydride elimination, generate the selected palladium hydride. Accordingly, the parent scan produces the same oligomer distributions that would have been obtained had each catalyst been assayed individually. The difference, of course, is that the catalyst-bound oligomer distributions can be obtained from a pooled library without isolating the individual members of the library in advance. The distributions can be fitted to the kinetic scheme as shown above, which means that the final metal-free polymer molecular weights, for example, can be calculated for each catalyst without having to isolate either the catalyst or the polymer in advance.

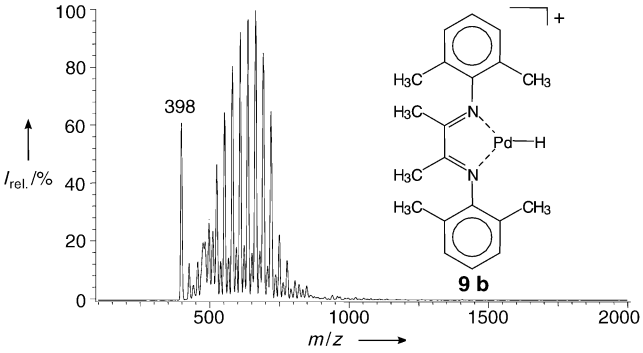
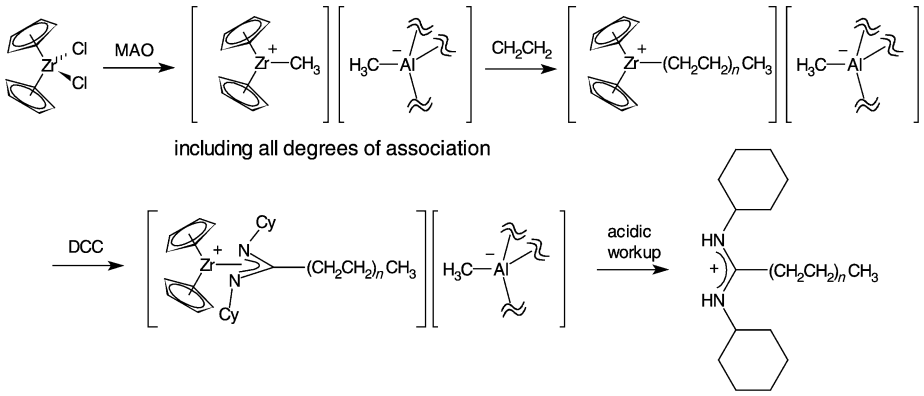


Figure 11. Parent-ion scan of **9b** at *m*/*z* 398, taken by scanning for parent ions, which upon β-hydride elimination, form **9b**. The odd-chain and even-chain distributions are visible and can be used to derive rates.

Palladium is usually considered to be a well-behaved metal, and appears in a large number of homogeneous catalysts. Systems with more labile or more reactive metal–carbon bonds, such as metallocene single-site catalysts, are not necessarily addressable by the same techniques. Modification of the general procedure developed for late-transition-metal systems can adapt the methods, at least in part, to the much more difficult early transition-metal catalysts. One particular modification is shown in Scheme 7. The mass spectrum in Figure 12 represents the reaction of dichlorozirconocene with methylalumoxane (MAO), in excess, treatment with ethylene, quenching with *N*,*N*′-dicyclohexylcarbodiimide (DCC), followed by acidic workup.[50] The metal-bound oligomer chains, both of odd and even chain length, that contain the kinetic information are trapped as long-chain



Scheme 7. DCC-quenshed ethylene polymerization with MAO activated [Cp_2ZrCl_2] (Cp = C_5H_5; see ESI-MS spectrum in Figure 12).

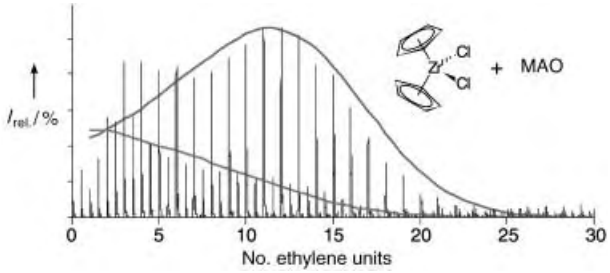


Figure 12. ESI-MS of a DCC-quenched polymerization of ethylene by MAO-activated [Cp_2ZrCl_2] after acidic workup (see Scheme 7). The odd- and even-chain distributions are clearly seen.

aliphatic amidinium ions, that is, the quenching reaction covalently labels metal-bound oligomers with a part of the quench reagent that renders them detectable by ESI-MS. The quenched species, in principle, zirconocenium amidate cations, may be detectable as such, but are much more easily treated by acidic workup and detection as the protonated amidine.

The concept of using a reactive quencher as opposed to simple coordinative quenchers provides the necessary extension of the mass-spectrometric techniques to early transition metals. In effect, by choice of appropriate quencher, the problem of chemical reactivity in more sensitive catalysts can be solved. Similar methodology works for late-transition-metal systems that are more labile than the original palladium complexes, as illustrated in Figure 13.

High-activity catalysts, such as metallocenes or iron-based systems from Brookhart et al.[51] and Gibson et al.,[52] present special challenges. The rate of ethylene incorporation, and the accompanying heat—ethylene insertion is exothermic—is several orders-of-magnitude higher than for the palladium systems. The extremely small amounts of catalysts that would be used in a miniaturized reactor and the large amount of heat evolution pose problems. The former problem makes reagent and solvent purity especially critical; the latter poses challenges for kinetics because the temperature must nevertheless be held constant. Both issues can be addressed by appropriate experimental design.[50]

 © 2003 Wiley-VCH Verlag GmbH & Co. KGaA, Weinheim

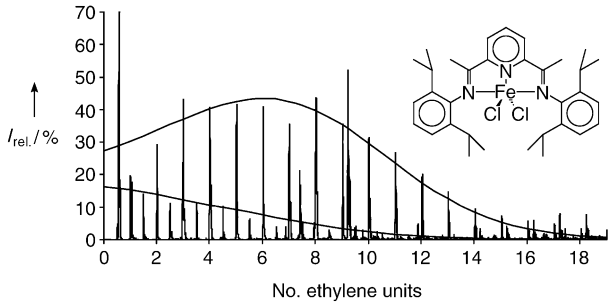


Figure 13. ESI-MS of a DCC-quenched polymerization of ethylene by a MAO-activated Fe-based catalyst after acidic workup. The odd- and even-chain distributions are clearly seen.

8. Conclusion

The goal of this review was to demonstrate a new approach to the screening of catalysts that is perhaps more faithful to the original combinatorial ideal as exemplified in screening in biological contexts. The technical requirement for an implementation of the approach was the development of methods suitable for the screening of pooled libraries and mixtures. Electrospray ionization tandem mass spectrometry meets the technical requirement for the implementation, and provides for significant advantages over the more conventional parallel screening approach. The hallmark of the pooled screening approach is a profoundly mechanistic basis for the screen. One can take the simple adage, "There is no such thing as a free lunch!" to mean in this context that a screen only gives as much information out as is put in. In the present examples, the information put in is mechanistic in nature; the information extracted is performance data for the catalyst or product of catalysis. The examples in this review are by no means exhaustive. In fact, the greatest promise of the present strategy—the screening of catalytic formulations that are themselves not well-defined compounds but rather mixtures prepared in situ—remains to be carried out. Further developments, both on the chemical side and on the instrumental side are ongoing and should lead to further cases in heterogeneous and supported catalysts, and also catalyst systems outside of the area of polymer synthesis.

Received: October 2, 2002 [A560]

[1] K. Burgess, H.-J. Lim, A. M. Porte, G. A. Sulikowski, *Angew. Chem.* **1996**, *108*, 192; *Angew. Chem. Int. Ed. Engl.* **1996**, *35*, 220; S. J. Taylor, J. P. Morken, *Science* **1998**, *280*, 267; M. T. Reetz, M. H. Becker, K. M. Kühling, A. Holzwarth, *Angew. Chem.* **1998**, *110*, 2792; *Angew. Chem. Int. Ed.* **1998**, *37*, 2647; A. C. Cooper, L. H. McAlexander, D. H. Lee, M. T. Torres, R. H. Crabtree, *J. Am. Chem. Soc.* **1998**, *120*, 9971; S. M. Senkan, *Nature* **1998**, *394*, 350; B. M. Cole, K. D. Shimizu, C. A. Krueger, J. P. A. Harrity, M. L. Snapper, A. H. Hoveyda, *Angew. Chem.* **1996**, *108*, 1776; *Angew. Chem. Int. Ed. Engl.* **1996**, *35*, 1668; T. R. Boussie, C. Coutard, H. Turner, V. Murphy, T. S. Powers, *Angew. Chem.* **1998**, *110*, 3472; *Angew. Chem. Int. Ed.* **1998**, *37*, 3272.
[2] D. Hicks, *Res. Technol. Manage.* **2000**, *43*, 34.
[3] *The Economist* **1997**, 20. September, p. 68.
[4] R. Bloksberg-Fireovid, J. Hewes, *Catalysis and Biocatalysis Technologies*, ATP White Paper, **1998**.
[5] B. Jandeleit, H. W. Turner, T. Uno, J. A. M. van Beck, W. H. Weinberg, *CATTECH* **1998**, *2*, 101.
[6] G. Ertl, *Angew. Chem.* **1990**, *102*, 1258; *Angew. Chem. Int. Ed. Engl.* **1990**, *29*, 1219.
[7] P. P. Pescarmona, J. C. van der Waal, I. E. Maxwell, T. Maschmeyer, *Catal. Lett.* **1999**, *63*, 1.
[8] J. M. Ostresh, G. M. Husar, S. E. Blondelle, B. Dörner, P. A. Weber, R. A. Houghton, *Proc. Natl. Acad. Sci. USA* **1994**, *91*, 11138.
[9] J. W. Szewczyk, R. L. Zuckerman, R. G. Bergman, J. A. Ellman, *Angew. Chem.* **2001**, *113*, 222; *Angew. Chem. Int. Ed.* **2001**, *40*, 216.
[10] A. C. Cooper, L. H. McAlexander, D. H. Lee, M. T. Torres, R. H. Crabtree, *J. Am. Chem. Soc.* **1998**, *120*, 9971; K. H. Shaughnessy, P. Kim, J. F. Hartwig, *J. Am. Chem. Soc.* **1999**, *121*, 2123; J. P. Stambuli, S. R. Stauffer, K. H. Shaughnessy, J. F. Hartwig, *J. Am. Chem. Soc.* **2001**, *123*, 2677; S. R. Stauffer, N. A. Beare, J. P. Stambuli, J. F. Hartwig, *J. Am. Chem. Soc.* **2001**, *123*, 4641.
[11] M. B. Francis, E. N. Jacobsen, *Angew. Chem.* **1999**, *111*, 987; *Angew. Chem. Int. Ed.* **1999**, *38*, 937.
[12] L. Stryer, *Biochemistry*, Freeman, New York, **1995**.
[13] S. V. Taylor, P. Kast, D. Hilvert, *Angew. Chem.* **2001**, *113*, 3408; *Angew. Chem. Int. Ed.* **2001**, *40*, 3310; M. T. Reetz, *Angew. Chem.* **2001**, *113*, 292; *Angew. Chem. Int. Ed.* **2001**, *40*, 284.
[14] C. Hinderling, P. Chen, *Angew. Chem.* **1999**, *111*, 2393; *Angew. Chem. Int. Ed.* **1999**, *38*, 2253.
[15] C. Hinderling, P. Chen, *Int. J. Mass Spectrom. Ion Processes* **2000**, *195–196*, 377.
[16] C. Hinderling, C. Adlhart, P. Chen, *Chimia* **2000**, *54*, 232.
[17] C. Adlhart, P. Chen, *Helv. Chim. Acta* **2000**, *83*, 2192.
[18] M. A. O. Volland, C. Adlhart, C. A. Kiener, P. Chen, P. Hofmann, *Chem. Eur. J.* **2001**, *7*, 4621.
[19] C. Hinderling, D. A. Plattner, P. Chen, *Angew. Chem.* **1997**, *109*, 272; *Angew. Chem. Int. Ed. Engl.* **1997**, *36*, 243; C. Hinderling, D. Feichtinger, D. A. Plattner, P. Chen, *J. Am. Chem. Soc.* **1997**, *119*, 10793.
[20] Y. M. Kim, P. Chen, *Int. J. Mass Spectrom. Ion Processes* **1999**, *185–187*, 871; Y. M. Kim, P. Chen, *Int. J. Mass Spectrom. Ion Processes* **2000**, *202*, 1.
[21] C. Adlhart, M. A. O. Volland, P. Hofmann, P. Chen, *Helv. Chim. Acta* **2000**, *83*, 3306.
[22] D. Feichtinger, D. A. Plattner, P. Chen, *J. Am. Chem. Soc.* **1998**, *120*, 7125.
[23] C. Hinderling, C. Adlhart, P. Chen, *Angew. Chem.* **1998**, *110*, 2831; *Angew. Chem. Int. Ed.* **1998**, *37*, 2685; C. Adlhart, C. Hinderling, H. Baumann, P. Chen, *J. Am. Chem. Soc.* **2000**, *122*, 8204.
[24] For a complete monograph on this technology: *Electrospray Ionization Mass Spectrometry* (Ed.: R. D. Cole), Wiley, New York, **1997**.
[25] C. M. Whitehouse, R. N. Dreyer, M. Yamashita, J. B. Fenn, *Anal. Chem.* **1985**, *57*, 675.
[26] J. V. Iribarne, B. A. Thomson, *J. Chem. Phys.* **1976**, *64*, 2287; B. A. Thomson, J. V. Iribarne, *J. Chem. Phys.* **1979**, *71*, 4451.
[27] H. U. Blaser, F. Spindler, M. Studer, *Appl. Catal. A* **2001**, *221*, 119.
[28] D. Gerlich, *Adv. Chem. Phys.* **1992**, *82*, 1.
[29] M. T. Bowers, *Gas Phase Ion Chemistry, Vol. 1–3*, Academic Press, New York, **1979–1984**.
[30] G. Gerdes, P. Chen, unpublished results.
[31] R. Hartmann, P. Chen, unpublished results.
[32] D. Feichtinger, D. A. Plattner, *Angew. Chem.* **1997**, *109*, 1796; *Angew. Chem. Int. Ed. Engl.* **1997**, *36*, 1718; D. A. Plattner, D. Feichtinger, J. El-Bahraoui, O. Wiest, *Int. J. Mass Spectrom.*

2000, *195–196*, 351; D. Feichtinger, D. A. Plattner, *J. Chem. Soc. Perkin Trans. 2* **2000**, 1023; D. Feichtinger, D. A. Plattner, *Chem. Eur. J.* **2001**, *7*, 591; D. A. Plattner, *Int. J. Mass Spectrom.* **2001**, *207*, 125.

[33] X. Zhang, P. Chen, unpublished results.

[34] W. E. Farneth, J. I. Brauman, *J. Am. Chem. Soc.* **1976**, *98*, 7891; W. N. Olmstead, J. I. Brauman, *J. Am. Chem. Soc.* **1977**, *99*, 4219; O. I. Asubiojo, J. I. Brauman, *J. Am. Chem. Soc.* **1979**, *101*, 3715; M. J. Pellerite, J. I. Brauman, *J. Am. Chem. Soc.* **1980**, *102*, 5993; S. Sharma, P. Kebarle, *J. Am. Chem. Soc.* **1982**, *104*, 19; G. Caldwell, T. F. Magnera, P. Kebarle, *J. Am. Chem. Soc.* **1984**, *106*, 959; T. B. McMahon, T. Heinis, G. Nicol, J. K. Hovey, P. Kebarle, *J. Am. Chem. Soc.* **1988**, *110*, 7591.

[35] D. K. Bohme, G. I. MacKay, *J. Am. Chem. Soc.* **1981**, *103*, 978.

[36] D. H. Aue, H. M. Webb, M. T. Bowers, *J. Am. Chem. Soc.* **1976**, *98*, 311.

[37] J. E. Bartmess, J. A. Scott, R. T. McIver, Jr., *J. Am. Chem. Soc.* **1979**, *101*, 6046.

[38] J. F. Wolf, P. G. Harch, R. W. Taft, *J. Am. Chem. Soc.* **1975**, *97*, 2904; R. H. Staley, R. D. Wieting, J. L. Beauchamp, *J. Am. Chem. Soc.* **1977**, *99*, 5964; E. M. Arnett, N. J. Peinta, *J. Am. Chem. Soc.* **1980**, *102*, 3329.

[39] J. F. Blake, W. L. Jorgensen *J. Am. Chem. Soc.* **1991**, *113*, 7430; J. Chandrasekhar, S. Shariffskul, W. L. Jorgensen *J. Phys. Chem. B* **2002**, *106*, 8078.

[40] G. Stafford, Jr., *J. Am. Soc. Mass Spectrom.* **2002**, *13*, 589.

[41] A. G. Marshall, C. L. Hendrickson, G. S. Jackson, *Mass Spectrom. Rev.* **1998**, *17*, 1.

[42] The kinetic shift can be claculated with the program CRUNCH: P. Armentrout, N. F. Dalleska, K. Honna, P. B. Armentrout, *J. Chem. Phys.* **1989**, *90*, 5466; N. F. Dalleska, K. Honna, P. B. Armentrout, *J. Am. Chem. Soc.* **1993**, *115*, 12125.

[43] C. S. Christ, J. R. Eyler, D. E. Richardson, *J. Am. Chem. Soc.* **1988**, *110*, 4038; C. S. Christ, J. R. Eyler, D. E. Richardson, *J. Am. Chem. Soc.* **1990**, *112*, 596; N. G. Alameddin, M. F. Ryan, J. R. Eyler, A. R. Siedle, D. E. Richardson, *Organometallics* **1995**, *14*, 5005; D. E. Richardson, N. G. Alameddin, M. F. Ryan, T. Hayes, J. R. Eyler, A. R. Siedle, *J. Am. Chem. Soc.* **1996**, *118*, 11244.

[44] G. Gioumousis, D. P. Stevenson, *J. Chem. Phys.* **1958**, *29*, 294.

[45] J. L. Herrison, Y. Chauvin, *Makromol. Chem.* **1970**, *141*, 161.

[46] S. M. Hansen, F. Rominger, M. Metz, P. Hofmann, *Chem. Eur. J.* **1999**, *5*, 557; S. M. Hansen, M. A. O. Volland, F. Rominger, F. Eisenträger, P. Hofmann, *Angew. Chem.* **1999**, *111*, 1360; *Angew. Chem. Int. Ed.* **1999**, *38*, 1273; P. Hofmann, M. A. O. Volland, S. M. Hansen, F. Eisenträger, J. H. Gross, K. Stengel, *J. Organomet. Chem.* **2000**, *606*, 88.

[47] T. M. Trnka, R. H. Grubbs, *Acc. Chem. Res.* **2001**, *34*, 18.

[48] G. J. P. Britovsek, V. C. Gibson, D. F. Wass, *Angew. Chem.* **1999**, *111*, 448; *Angew. Chem. Int. Ed.* **1999**, *38*, 428.

[49] L. K. Johnson, C. M. Killian, M. Brookhart, *J. Am. Chem. Soc.* **1995**, *117*, 6414; D. J. Tempel, L. K. Johnson, R. L. Huff, P. S. White, M. Brookhart, *J. Am. Chem. Soc.* **2000**, *122*, 6686.

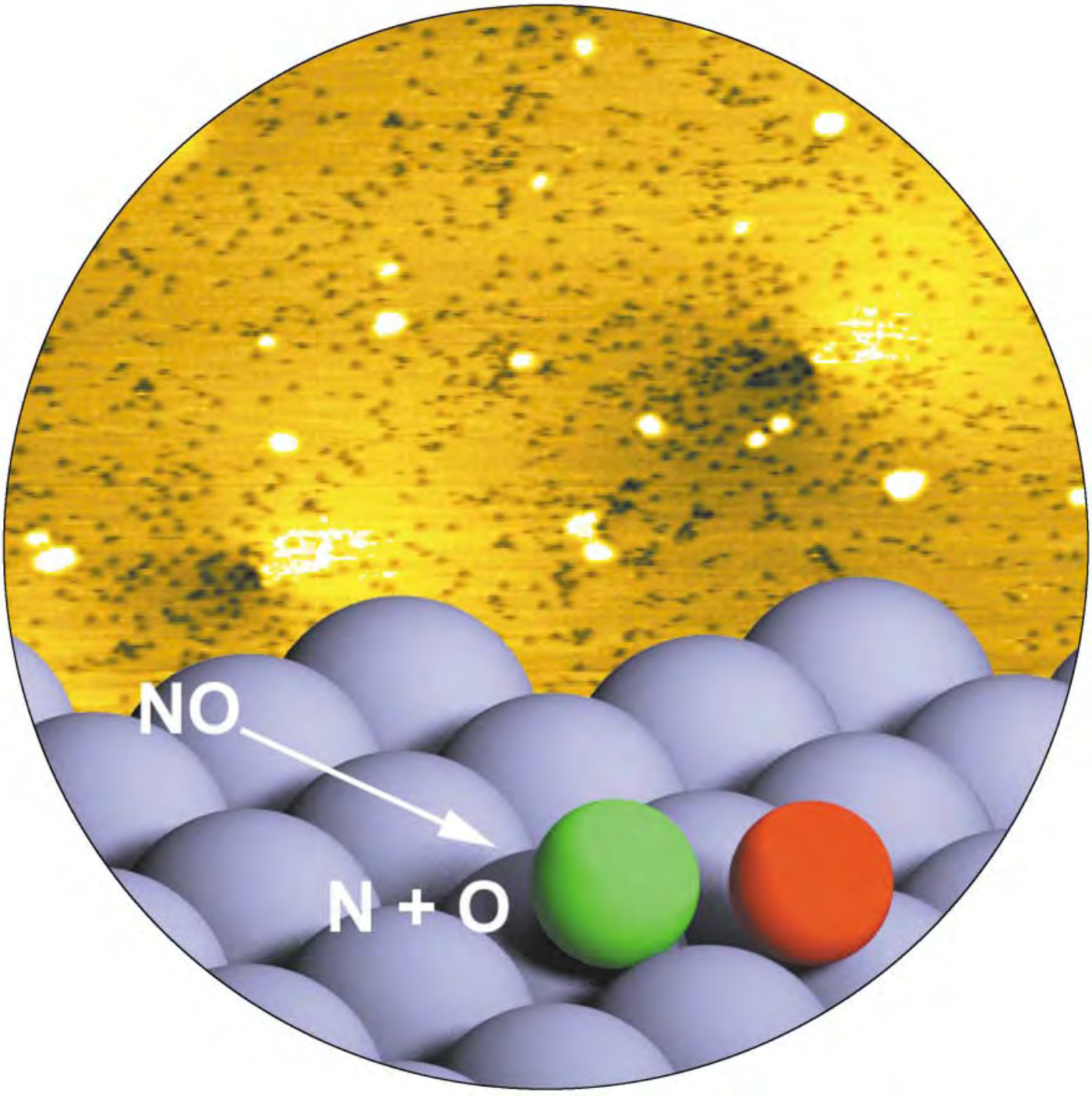
[50] Data from Thales Technologies AG, Zürich (Switzerland).

[51] B. L. Small, M. Brookhart, A. M. A. Bennett, *J. Am. Chem. Soc.* **1998**, *120*, 4049.

[52] G. J. P. Britovsek, V. C. Gibson, B. S. Kimberley, P. J. Maddox, S. J. McTavish, G. A. Solan, A. J. P. White, D. J. Williams, *Chem. Commun.* **1998**, 849; G. J. P. Britovsek, M. Bruce, V. C. Gibson, B. S. Kimberley, P. J. Maddox, S. Mastroianni, S. J. McTavish, C. Redshaw, G. A. Solan, S. Stromberg, A. J. P. White, D. J. Williams, *J. Am. Chem. Soc.* **1999**, *121*, 8728.

 © 2003 Wiley-VCH Verlag GmbH & Co. KGaA, Weinheim

Communications



NO molecules adsorbed on an Ru surface dissociate preferentially at edge dislocations. This long-discussed effect was demonstrated with the aid of scanning tunneling microscope images which show a higher concentration of nitrogen molecules near such defects. For more information see the communication by M. Mavrikakis and J. Wintterlin et al. on the following pages.

DOI: 10.1002/anie.200250845
© 2003 Wiley-VCH Verlag GmbH & Co. KGaA, Weinheim

Watching NO Activation on a Surface

Atomic-Scale Evidence for an Enhanced Catalytic Reactivity of Stretched Surfaces**

Joost Wintterlin, Tomaso Zambelli, J. Trost, Jeffrey Greeley, and Manos Mavrikakis**

It has recently been predicted that the catalytic activity of transition metals will be modified by lattice strain.[1] Changes of the lattice constant alter the d-band width, causing the d-band center (with respect to the Fermi level) to move up or down in energy to keep the d-occupancy constant, which consequently modifies the chemical activity.[2] The effect could be of far-reaching importance for heterogeneous catalysis, because supported catalysts used in industrial processes probably always exhibit some lattice strain, caused, for example, by lattice defects or by interactions with the support material.

Several experimental observations have suggested that such strain effects actually exist. Older investigations found that metals treated by cold-working formed dislocations and displayed an enhanced catalytic activity,[3,4] and recently a correlation between activity and strain in small Cu particles of a Cu/ZnO catalyst was found.[5,6] In all of these cases it was unclear if a lattice expansion or compression was responsible for the reactivity changes or which elementary reaction step was affected. A further observation was an enhanced dissociation probability for oxygen on a heteroepitaxial metal film,[7] although in a bimetallic system the strain effect from the lattice mismatch is convoluted with electronic interactions between film and substrate. The dissociative sticking coefficient of O_2 was also enhanced for a mechanically stretched Cu single crystal.[8] However, strain achieved by this method was very limited because plastic deformations had to be avoided, and the dissociative sticking coefficient varied by only approximately 10%. To play a role in catalysis, strain must be large, which is probably the case only in the immediate neighborhood of defects. The only microscopic observation to date of a strain effect on adsorbates was that O atoms adsorbed on a Ru surface were attracted to defects at which the lattice was locally stretched.[9] This confirmed an important aspect of the predicted strain effect, an influence on the binding energy of adsorbates, but no chemical reaction was involved.

Herein we present what we believe is the first microscopic evidence for a strain effect on the chemical reactivity of a molecule. By means of scanning tunneling microscopy (STM) data we show that the dissociation probability of NO molecules is significantly enhanced near the intersection points of edge-dislocations with an Ru surface. The effect is large and could be relevant for real catalytic reactions. The behavior is in full agreement with results from density functional theory (DFT) calculations.

The experiments were performed in an ultrahigh vacuum chamber, in which also the surface of the (0001) oriented Ru sample was cleaned.[10] In addition to monoatomic steps, the sample surface displayed another type of structural defect (Figure 1). The hexagonal pattern in Figure 1 is the (2×2)O structure that was prepared by dosing the Ru surface with oxygen. The atomic resolution of this ordered structure allows one to construct a Burgers loop around the central defect. A nonvanishing Burgers vector is found, which indicates that at the image center an edge dislocation from the bulk intersects the surface.[11]

The important effect for the present purpose is that around each of these defects the lattice is deformed. On the one side of each dislocation, where the additional half plane is, the lattice is compressed (upper right in Figure 1), and on the opposite side it is stretched (lower left in Figure 1). This deformation primarily represents horizontal strain, parallel to the surface. There is also a small vertical lattice deformation that, because of the extreme vertical resolution power of STM, becomes visible on higher magnification scans (Figure 2). On these scales it becomes apparent that each of the defects is surrounded by two extended regions, one of which appears brighter than the surrounding surface, and the other of which appears darker. These areas extend about 100 Å into the undisturbed surface. The brightness variations represent vertical deformations, where, at the bright side, the surface protrudes approximately 0.2 Å above the level of the undisturbed lattice, and on the dark side it is approximately 0.2 Å lower. These vertical deformations reflect a tendency of the surface to try to relax some of the horizontal strain. On the (horizontally) compressed side of each dislocation, the top lattice layers bulge up a little bit (appearing brighter), and on the stretched side they bend inward (appearing darker). This relaxation is much smaller than the horizontal strain (which is of the order of the Burgers vector $\boldsymbol{b}$), but it can be seen as a marker of the range of the horizontal deformation field around each dislocation.

Dosing of NO on Ru(0001) (without the (2×2)O phase) at 300 K leads to dissociation into N and O atoms.[12] Upon adsorption, the NO molecules can diffuse across the surface until they dissociate, mainly at defects (for example, at atomic steps),[13] which indicates that the dissociation is an activated process. The resulting N atoms are easily resolved by the STM

[*] Prof. Dr. J. Wintterlin,[+] Dr. T. Zambelli, Dr. J. Trost
Fritz-Haber-Institut
Max-Planck-Gesellschaft
14195 Berlin (Germany)
E-mail: wintterlin@cup.uni-muenchen.de
Prof. M. Mavrikakis, J. Greeley
Department of Chemical Engineering
University of Wisconsin
Madison, WI 53706-1691 (USA)
Fax: (+1) 608-262-5434
E-mail: manos@engr.wisc.edu
[+] Current address:
Department Chemie
Univerisität München
81377 München (Germany)
Fax: (+49) 89-2180-77598

[**] T.Z. thanks the DAAD for financial support. M.M. thanks a NSF-CAREER award (CTS-0134561), and NSF-NPACI and DOE-NERSC for supercomputing time. We thank Lars Grabow for help with the graphics.

 © 2003 Wiley-VCH Verlag GmbH & Co. KGaA, Weinheim DOI: 10.1002/anie.200250845

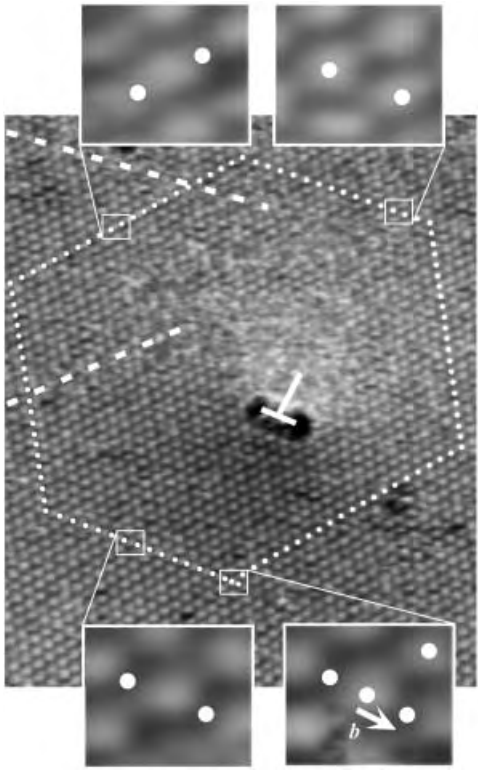


Figure 1. STM image of the Ru(0001) surface (180 Å × 240 Å), covered with a (2×2)O structure (hexagonal pattern). The Burgers loop around the central defect (white dots, the length unit is the lattice constant of the (2×2) structure) has an open end, which indicates that an edge dislocation intersects the surface at the position of the defect. The Burgers vector ***b*** is half a (2×2) lattice constant long, that is, one lattice constant of the substrate (inset lower right). The Burgers loop crosses two domain boundaries in the (2×2) phase (broken lines), where the dot markers switch positions relative to the O atoms of the overlayer (see insets). This observation results from the fact that for an edge dislocation in the (1×1) bulk the (2×2) overlayer has to develop domain boundaries. The blurred area above the dislocation is caused by fluctuations in the oxygen layer, which has a lower binding energy on the compressed side of the dislocation..

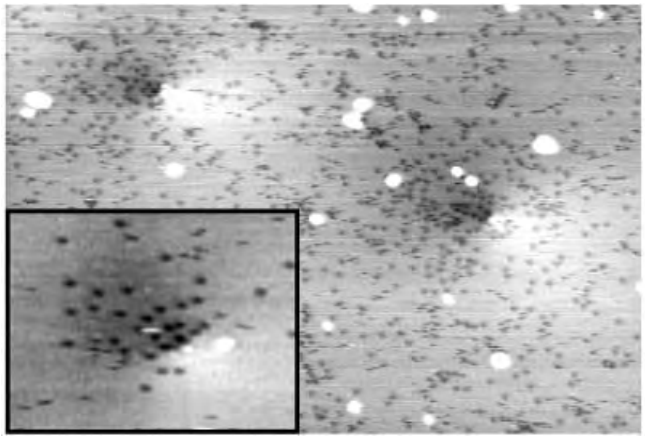


Figure 2. STM image of two edge dislocations, after exposure of 0.3 L of NO on the clean Ru(0001) surface at 300 K (1 L = 1.33×10^{-6} mbar s). The small dark dots are N atoms. (440 Å × 320 Å). Inset: Edge dislocation from a different experiment, after exposure of 0.1 L of NO (70 Å × 50 Å). At the dark, stretched parts near the dislocations concentrations of N atoms are enhanced by factors of 7 in the main image and 18 in the inset.

as almost stationary dark dots, whereas O atoms are more difficult to see at low coverages because of their greater mobility.[14,15] STM images of the edge dislocations, recorded after exposure of small amounts of NO on the Ru surface (Figure 2), reveal much larger concentrations of N atoms at the dark, stretched sides than on the bright, compressed sides or on defect-free terraces. The N and O atoms are easily differentiated from each other based on their different imaging by STM,[10] which allows the atoms on the dark areas to be clearly identified as N atoms. Because of the low mobility of the N atoms,[14] their distribution marks the reaction area for the NO molecules. We conclude that the NO dissociation probability is significantly enhanced on the stretched part of the strain field of edge dislocations.

The magnitude of the horizontal lattice stretch responsible for the observed effect can be estimated from the diameter of the vertically deformed area. A horizontal distortion of the size ***b*** (2.70 Å) has to be distributed over the diameter of the strained core region (half width $\approx$ 100 Å), which gives an average lattice strain of approximately 3% with respect to the unstrained Ru. This value is a lower limit, because the NO molecules may in fact have dissociated closer to the edge dislocation, where the strain is larger. Because of the time delay between NO adsorption and the recording of the STM images, the finite mobility of the N atoms may have already changed the N distribution somewhat. Theoretical models of edge dislocations in the bulk reveal core half widths of a few lattice constants, which correspond to distortions of $\geq 10\%$.[16,17] The lattice distortions mentioned above, which are caused by subsurface "bubbles" of Ar[9] did not exhibit an enhanced activity for NO dissociation. The lattice stretch of 2–3% associated with such distortions is thus below the limit for an enhanced reactivity.

To explain the observed enhanced reactivity of NO in the vicinity of edge dislocations, we performed self-consistent periodic DFT calculations.[18] A three-layer Ru(0001) slab, periodically repeated in a super cell geometry with 5.25 equivalent layers of vacuum between any two successive metal slabs, was used. Adsorption of N, O, and NO, and dissociation of NO were treated using a (4×2) unit cell, a suitable choice to probe the low-coverage behavior of NO on the Ru(0001) surface (computational details are given in the Theoretical Section).

We examined the effect of changing the lattice constant parallel to the surface of the Ru(0001) slab on the thermochemistry and reaction barrier for the dissociation of NO. The calculated lattice constant (d_{eq}) for bulk Ru was found to be 2.74 Å, in reasonable agreement with the experimental value of 2.70 Å. The equilibrium value for c/a of 1.582 was used. The lattice constant (d) was varied between 2.60 and 2.88 Å, which corresponds to a maximum absolute value of relative strain ($\Delta d/d_{eq}$) of approximately 5%. All the metal atoms were kept fixed in their bulk positions. Allowing for relaxation of the topmost metal layer or including more than three metal layers in the slab had a negligible effect on the results. As in previous

 © 2003 Wiley-VCH Verlag GmbH & Co. KGaA, Weinheim

studies on similar systems, we followed the reaction paths by varying the N–O bond length with simultaneous relaxation of all the other molecular degrees of freedom.[1,19]

Figure 3 shows the calculated effect of strain on the adsorption strength of all the species involved in this study. Data in the top and middle panels suggest that atomic oxygen, atomic nitrogen, and molecular NO all bind more strongly to

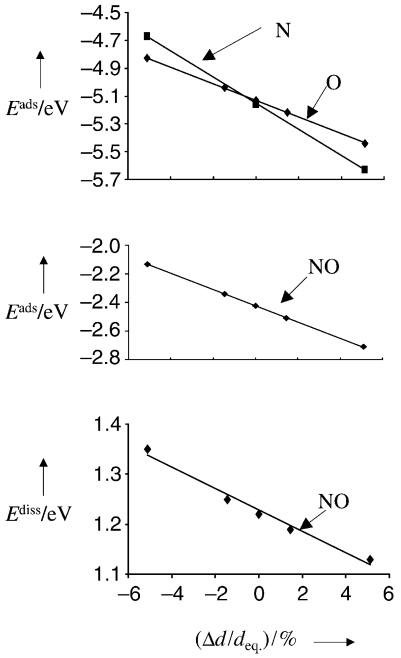


Figure 3. Top: The effect of a relative change in the lattice constant $\Delta d/d_{eq}$ of an Ru(0001) surface on the binding energy of atomic nitrogen (E_N^{ads}) and oxygen (E_O^{ads}; referenced to the clean surface plus the appropriate gas-phase atomic species), middle: the binding energy of molecular NO (E_{NO}^{ads}; referenced to the clean surface plus a gas-phase NO molecule), and bottom: the NO dissociation barrier (E_{NO}^{diss}; referenced to the initial state of the dissociation).

the stretched regions of the surface. The bottom panel of Figure 3 shows that stretched surfaces substantially decrease the barrier for NO dissociation, thereby strongly favoring the dissociation of NO molecules at the stretched regions of the surface.

Figure 4 provides further details for the NO dissociation path on Ru(0001) for three different lattice constants. Strain did not change the preferred adsorption site for any of the adsorbates: atomic nitrogen and oxygen, as well as NO molecules, all prefer hcp sites. The transition-state geometry was found to be of the bridge–bridge type, regardless of the degree of strain, and in good agreement with previous studies for the dissociation of small molecules on metal surfaces.[1,20] Because of the varying degree of electronic coupling between the adsorbate and the surface, along the reaction path, the energy differences arising from lattice strain increase on going from the initial to the transition state to the final state. In all cases though, strain stabilizes the corresponding states. Therefore, on stretched regions of the surface both the adsorption and the dissociation of NO are favored. Finally,

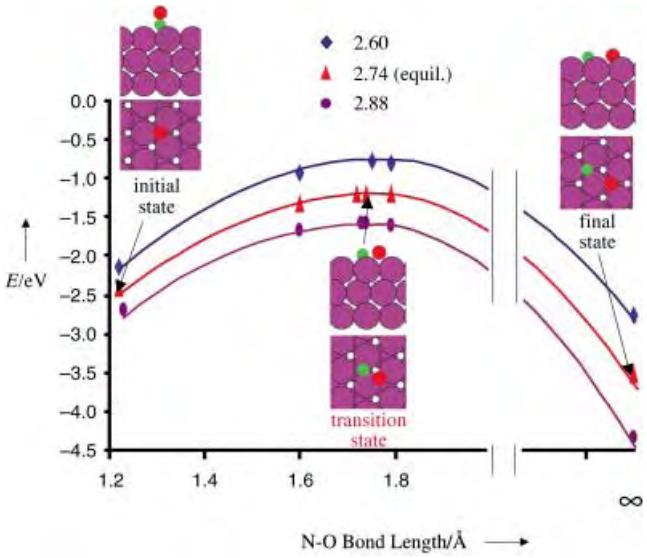


Figure 4. Calculated energy along the reaction coordinate of the N–O bond length during NO dissociation. Continuous lines represent the best fits through the calculated data points. The difference in energy between the highest point and the initial point on each curve is taken as the respective dissociation barrier, shown in the bottom panel of Figure 3. The zero of the energy scale corresponds to the clean surface plus a gas-phase NO molecule. N atoms: green circles, O atoms: red circles, Ru atoms: purple circles.

because of the enhanced adsorption energy of atomic nitrogen and oxygen, it might be expected that both atomic products of the dissociation should be found on the stretched regions of the defects. The experiment, however, only showed N atoms. We suggest that because the O atoms are much more mobile than the N atoms,[14,15] they move away from the reactive site faster. It is therefore expected that the O atoms have been spread evenly over the entire surface by the time the STM images were recorded.

The increased reactivity of stretched surfaces has been attributed to the shift of the d-band center to higher energy that results from the stretching of the surface.[1] The work presented here offers the first microscopic experimental evidence for the effect of strain on reaction kinetics. The implications for catalysis are clear. Almost all catalytic reactions are preceded by bond-activation dissociation steps, which are often rate limiting, and lattice strain is probably present in most applications involving supported catalysts.

Theoretical Section

Adsorption was allowed on only one of the two surfaces exposed and the electrostatic potential was adjusted accordingly.[21] Ionic cores were described by ultrasoft pseudopotentials,[22] and the Kohn–Sham one-electron valence states were expanded in a basis of plane waves with kinetic energies below 25 Ry. The surface Brillouin zone was sampled at eight special k points. The exchange-correlation energy and potential were described by the generalized gradient approximation (PW91).[23,24]

Received: December 27, 2002 [Z50845]

 © 2003 Wiley-VCH Verlag GmbH & Co. KGaA, Weinheim

Keywords: chemisorption · density functional calculations · heterogeneous catalysis · scanning probe microscopy · surface chemistry

[1] M. Mavrikakis, B. Hammer, J. K. Nørskov, *Phys. Rev. Lett.* **1998**, *81*, 2819.
[2] J. Greeley, J. K. Nørskov, M. Mavrikakis, *Annu. Rev. Phys. Chem.* **2002**, *53*, 319.
[3] J. Eckell, *Z. Elektrochem.* **1933**, *39*, 433.
[4] I. Uhara, S. Kishimoto, Y. Yoshida, T. Hikino, *J. Phys. Chem.* **1965**, *69*, 880.
[5] M. M. Günter, T. Ressler, B. Bems, C. Büscher, T. Genger, O. Hinrichsen, M. Muhler, R. Schlögl, *Catal. Lett.* **2001**, *71*, 37.
[6] M. M. Günter, T. Ressler, R. E. Jentoft, B. Bems, *J. Catal.* **2001**, *203*, 133.
[7] S.-K. Shi, H.-I. Lee, J. M. White, *Surf. Sci.* **1981**, *102*, 56.
[8] Y. Uesugi-Saitow, M. Yata, *Phys. Rev. Lett.* **2002**, *88*, 256104-1.
[9] M. Gsell, P. Jakob, D. Menzel, *Science* **1998**, *280*, 717.
[10] J. Trost, T. Zambelli, J. Wintterlin, G. Ertl, *Phys. Rev. B* **1996**, *54*, 17850.
[11] The length of the Burgers vector is one half of a (2×2)O lattice constant, that is, one lattice constant of the Ru substrate, and it points into the close-packed direction of the Ru basal plane ($\boldsymbol{b} = {}^{1}/_{3}\langle\bar{1}2\bar{1}0\rangle$). Such a Burgers vector corresponds to an added half plane intersecting the surface as indicated by the "T"-shaped marker. If we assume that the dislocation is perpendicular to the surface, the corresponding glide plane, spanned by the dislocation and the Burgers vector, would be a $(10\bar{1}0)$ plane, which is precisely the known glide plane of Ru: D. W. Rhys, *J. Less-Common Met.* **1959**, *1*, 269.
[12] H. Conrad, R. Scala, W. Stenzel, R. Unwin, *Surf. Sci.* **1984**, *145*, 1.
[13] T. Zambelli, J. Wintterlin, J. Trost, G. Ertl, *Science* **1996**, *273*, 1688.
[14] T. Zambelli, J. Trost, J. Wintterlin, G. Ertl, *Phys. Rev. Lett.* **1996**, *76*, 795.
[15] J. Wintterlin, J. Trost, S. Renisch, R. Schuster, T. Zambelli, G. Ertl, *Surf. Sci.* **1997**, *394*, 159.
[16] Y. Minonishi, S. Ishioka, M. Koiwa, S. Morozumi, M. Yamaguchi, *Philos. Mag. A* **1981**, *43*, 1017.
[17] Q. F. Fang, R. Wang, *Phys. Rev. B* **2000**, *62*, 9317.
[18] B. Hammer, L. B. Hansen, J. K. Nørskov, *Phys. Rev. B* **1999**, *59*, 7413.
[19] S. Dahl, A. Logadottir, R. C. Egeberg, J. H. Larsen, I. Chorkendorff, E. Törnqvist, J. K. Nørskov, *Phys. Rev. Lett.* **1999**, *83*, 1814.
[20] Y. Xu, M. Mavrikakis, *Surf. Sci.* **2001**, *494*, 131.
[21] J. Neugebauer, M. Scheffler, *Phys. Rev. B* **1992**, *46*, 16067.
[22] D. Vanderbilt, *Phys. Rev. B* **1990**, *41*, 7892.
[23] J. P. Perdew, J. A. Chevary, S. H. Vosko, K. A. Jackson, M. R. Pederson, D. J. Singh, C. Fiolhais, *Phys. Rev. B* **1992**, *46*, 6671.
[24] J. A. White, D. M. Bird, *Phys. Rev. B* **1994**, *50*, 4954.

 © 2003 Wiley-VCH Verlag GmbH & Co. KGaA, Weinheim

DNA/Gold-Cluster Interactions

Gold-Cluster Degradation by the Transition of B-DNA into A-DNA and the Formation of Nanowires**

Yunping Liu, Wolfgang Meyer-Zaika, Steffen Franzka, Günter Schmid, Maria Tsoli, and Hubert Kuhn*

Interactions between metals and biomacromolecules including proteins, polysaccharides, and nucleic acids are important since they can be essential for a number of natural and industrial phenomena. These range from interactions of highly specific metal cofactors with particular proteins[1] to biosorption of heavy metals by polysaccharide hydrogels.[2] The unique features of DNA have been exploited in the development of novel materials, especially in the areas of medicine and nanotechnology. Classical research concerning antitumor drugs has focussed on the interactions of platinum- or ruthenium-containing compounds with the major or minor grooves of polynucleotides.[3–6] There is a tremendous interest in the use of DNA in nanotechnology as a positioning template for the immobilization of metal nanoclusters with view to future applications in the construction of nanoelectronic devices.[7–11] Herein we report the interaction of Au_{55} nanoclusters with the major grooves of B-DNA. The Au_{55} clusters are degraded to Au_{13} clusters by the transition of B-DNA into A-DNA in ultrahigh vacuum, and the resulting shrinkage of the major grooves. We have performed molecular-dynamics simulations and provided further information on the mechanism by which wires of Au_{13} clusters form, and attempt to explain the interwire separation of 0.5 nm.

The interaction of metal nanoparticles with DNA is a well known phenomenon.[12–15] Usually single or double-stranded DNA is decorated by the metal particles which can easily be imaged by transmission electron microscopy (TEM). As an example, Figure 1 shows a piece of λ-DNA, decorated with ligand-stabilized approximately 2-nm Pt particles. The ligand shell consists of (−)cinchonidin and acetic acid.[16]

The shell of clusters around the double-stranded DNA is rather thick, up to 10–15 nm. However, when $[Au_{55}(Ph_2PC_6H_4SO_3H)_{12}Cl_6]$[17] which consists of a 1.4-nm gold core and a 0.4-nm thick ligand shell, is combined with λ-DNA in aqueous solution hybrid structures with a much more distinct habit are formed. Figure 2 shows a typical example of

[*] Prof. Dr. G. Schmid, Dr. Y. Liu, Dr. W. Meyer-Zaika, Dr. S. Franzka
Institut für Anorganische Chemie
Universität Essen
45117 Essen (Germany)
Fax: (+49) 201-183-4195
E-mail: guenter.schmid@uni-essen.de
M. Tsoli, Dr. H. Kuhn
Institut für Physikalische Chemie, Universität Essen
45117 Essen (Germany)

[**] We acknowledge financial support from the Deutsche Forschungsgemeinschaft (DFG) (Graduiertenkolleg 689/1) and from the Fonds der Chemischen Industrie.

 DOI: 10.1002/anie.200250235 © 2003 Wiley-VCH Verlag GmbH & Co. KGaA, Weinheim

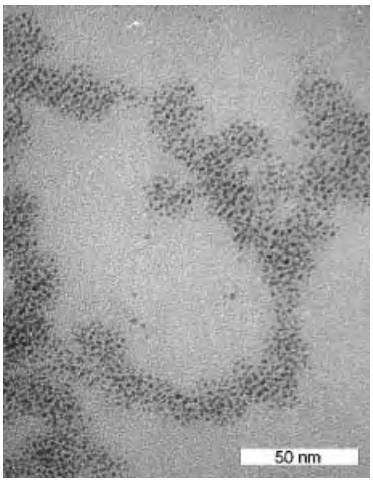


Figure 1. TEM image of λ-DNA pieces, covered with 2-nm Pt nanoparticles.

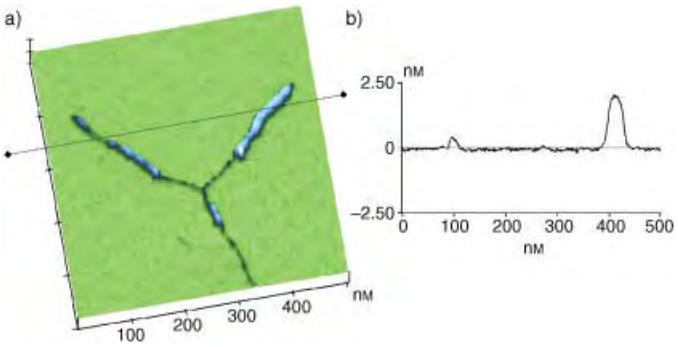


Figure 2. a) AFM image of λ-DNA, partially linked with Au_{55} clusters. b) Height profile of both the bare DNA and a decorated part.

such a sample, imaged by atomic force microscopy (AFM) under air.[18]

This example was selected because parts of the DNA are still bare so that the difference to the cluster-covered section can be observed. The bare parts of the DNA have a height of approximately 0.5–0.6 nm, in agreement with literature data.[19,20] However, larger values for the DNA height, up to about 2 nm are also known.[21,22] It seems that the experimental conditions decisively influence the height. Tapping mode gives smaller values than non-tapping mode. The covered parts have heights of 2.05 ± 0.2 nm. This is considerably less than could be expected if the 2.1–2.3-nm-thick ligand-protected clusters are simply added to the DNA surface. However, if the bare Au_{55} clusters are embedded into the major groves, as is shown below in Figure 5 and discussed below, a total diameter of about 2 nm is very reasonable.

AFM does not usually give as high resolution as TEM so that individual Au_{55} clusters cannot be observed in Figure 2a. That is why we continued characterization of the cluster/DNA combinations by means of TEM. Ligand-stabilized Au_{55} clusters can easily be imaged by TEM with sufficient resolution, as is shown by one typical image (Figure 3) with

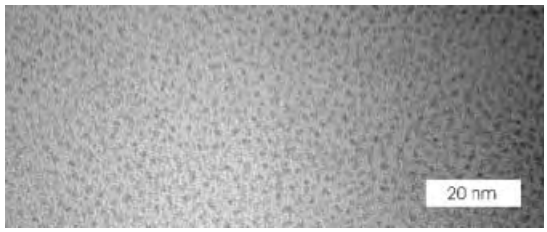


Figure 3. $[Au_{55}(Ph_2PC_6H_4SO_3H)_{12}Cl_6]$ clusters without DNA, deposited on the TEM grid from solution.

randomly oriented 1.4-nm particles, deposited from solution on the carbon-coated copper grid.

If the DNA and the clusters are combined in solution and are then transferred to a carbon-coated copper grid for TEM to be investigated under ultrahigh vacuum conditions, roughly equidistant wires of small gold particles can be imaged, the size of which corresponds approximately to that of Au_{13} clusters, namely 0.6–0.7 nm. Figure 4a shows a typical TEM image of these gold cluster wires. From the magnified section it can be seen that the wires consist of individual particles (Figure 4a, right). Another feature is the highly constant distance of 0.5 nm between the wires. They are rather

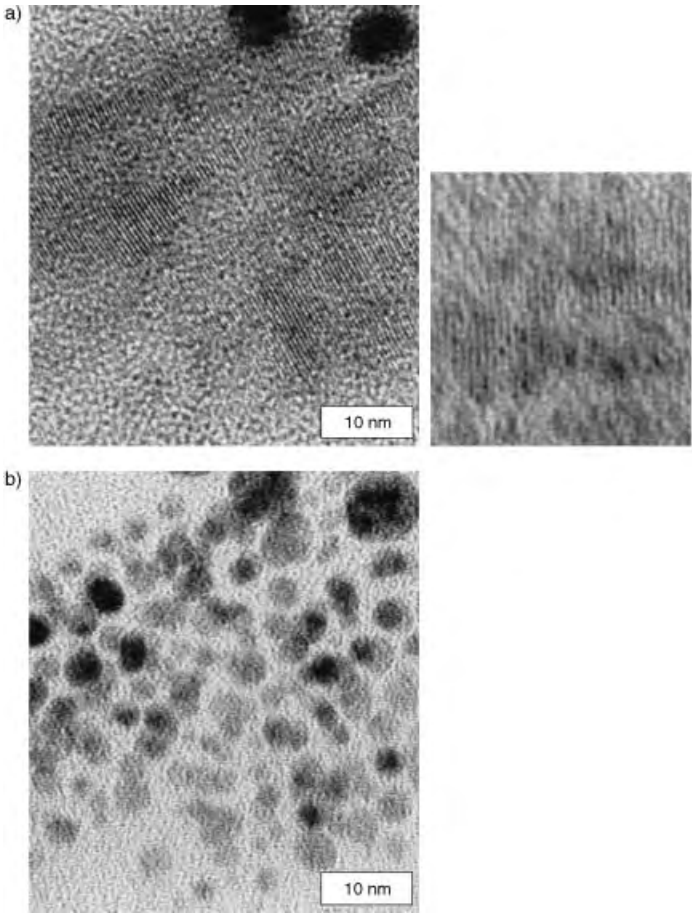


Figure 4. a) TEM image of gold wires consisting of 0.6–0.7-nm particles. b) Micrograph obtained from the same probe after further exposure to the electron beam.

 © 2003 Wiley-VCH Verlag GmbH & Co. KGaA, Weinheim

unstable under the electron-beam irradiation, as can be seen from Figure 4b, taken a few seconds after imaging the wires shown in Figure 4a. Large gold colloids have formed which are not present in normal Au_{55} arrays, such as those shown in Figure 3.

Owing to the interaction of $[Au_{55}(Ph_2PC_6H_4SO_3H)_{12}Cl_6]$ with DNA we believe that some of the phosphane ligands are removed and are substituted by the DNA phosphate groups, which act as a polydentate and chelating ligand sphere towards the gold clusters, trapping them in the major grooves of the B-DNA in the aqueous system.

As will be shown below, the naked cuboctahedrally shaped Au_{55} clusters, 1.4 nm in diameter, fit perfectly into the major grooves of B-DNA. At conditions of relatively high humidity, the minor groove of B-DNA appears to have a "spine-like" aqueous sheath in which the water molecules form highly ordered layers; however, the majority of the water molecules in the major grooves seem to be disordered.[23] During progressive dehydration, this spine of hydration on the minor grooves of B-DNA is disrupted, the integrity of the B-DNA structure is destroyed, and the transition into the A-form occurs. Under vacuum conditions, typical for TEM, the majority of the water molecules bound to the B-DNA are removed, thereby distorting the structure unless it is somehow stabilized by molecules other than water, specifically those capable of bridging opposing phosphates. In this case, given their appropriate dimensions, Au_{13} clusters can replace the water bridges along the major grooves. Consequently, the shrinking process which occurs during the B-DNA to A-DNA transition leads to peeling of the outer 42 gold atoms of Au_{55} and the encapsulation of the inner cluster core, consisting of Au_{13} clusters.

In the TEM images, large gold particles can be observed (see Figure 4a) which have been formed by aggregation of the gold atoms removed from the Au_{55} clusters. So many and such large gold assemblies are not observed when only Au_{55} clusters are imaged by TEM (see Figure 3). Degradation of Au_{55} clusters to Au_{13} clusters has been observed before, although, under completely different conditions.[24] It is surprising that the change of the conformation of a molecule results in such tremendous damage to the metal nanoparticles.

The B-form of DNA has been considered to be the DNA typical of physiological conditions, that is, in aqueous solution with common counterions. It forms two distinct helical grooves, the major and the minor groove. The A-DNA is described as the dehydrated form.[25] The groove geometry consists of deep and narrow major grooves and very shallow and wide minor grooves. It is still unknown whether A-DNA is present under certain physiological conditions. Generally, at low relative humidity or in the presence of 75% ethanol, the transition from B-DNA to A-DNA can take place.[25] Molecular-modeling studies of the interactions of DNA molecules and metal ions or anticancer compounds have provided much useful information concerning the specific and nonspecific binding sites for metal ions and ligand molecules on DNA, the structural changes of DNA upon binding, and the overall distribution of metal ions along the DNA helix.[26–28]

Of the two types of gold clusters used in this simulation study, only the interactions of the Au_{13} cluster with the major grooves on the A-DNA molecule[29] were investigated because, as explained above, this structure is consistent with experimental observations. Four Au_{13} clusters were positioned along the phosphate residues. For B-DNA,[30] both Au_{13} and Au_{55} were studied separately to assess any interactions with the major grooves of the B-DNA. Three Au_{55} clusters were arranged along the phosphate backbone of B-DNA, four Au_{13} clusters were arranged in the major grooves throughout the helix of the B-DNA molecule.

The B-DNA used for these simulations is 7.74 nm long with major grooves 0.9 nm in depth and 1.43 nm in length, coinciding perfectly with the cluster dimension of 1.4 nm. The minor grooves are 0.75–0.85 nm long and 0.67 nm deep. The A-DNA is 6.0 nm long. The major grooves are 1.33 nm deep and 0.74 nm long, whereas the minor groove has a depth of only 0.2 nm, but a length of 1.5 nm. These results are in good agreement with the values reported in the literature.[25] Au_{13} clusters are about 0.60–0.65 nm in diameter and so can be included ideally into these grooves. In addition, the phosphate groups along the major grooves are oriented towards the groove and can hold the Au_{13} clusters tightly. The interaction between B-DNA and Au_{55} clusters is shown in Figure 5. Both DNA and Au_{55} are energy minimized. The clusters interact with the negatively charged oxygen atoms of the phosphate groups, thereby causing a slight distortion in the structural geometry of the B-DNA, that is, the opposing phosphate groups are brought slightly closer together. Consequently, the helix appears to be shorter. In Figure 6 the interaction between the energy-minimized A-DNA structure and Au_{13} clusters is shown. In the projection, each cluster is about 0.5–0.6 nm from the other, in agreement with the experimental findings.

Interactions of Au_{13} clusters with B-DNA do not effect the major-groove geometry, since the clusters are too small to

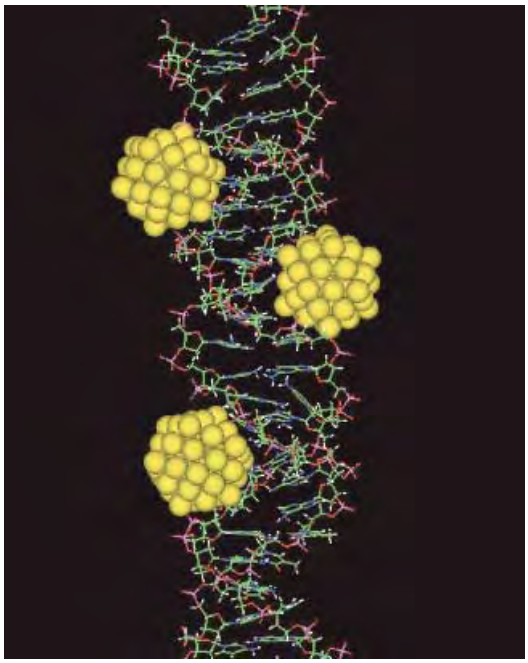


Figure 5. Energy-minimized structure of the B-DNA with Au_{55} clusters arranged along the phosphate backbone of the DNA major grooves.

 © 2003 Wiley-VCH Verlag GmbH & Co. KGaA, Weinheim

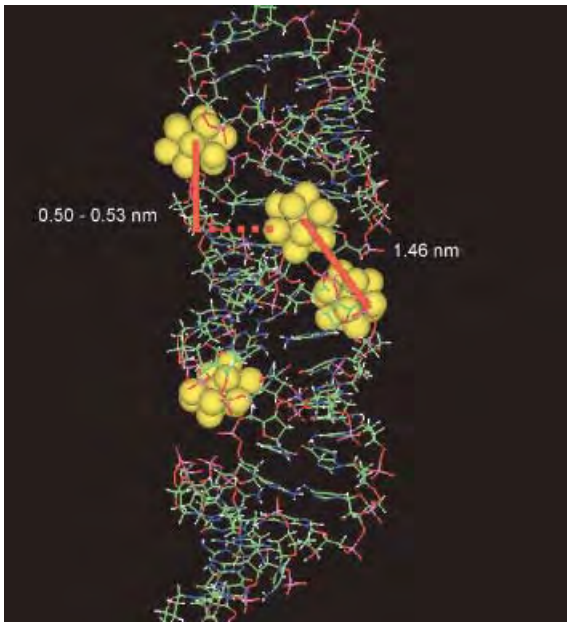


Figure 6. Energy-minimized structure of A-DNA with Au_{13} clusters located along the phosphate backbone of the DNA major grooves. The projection distance between two Au_{13} clusters is shown as a red line.

interact strongly with phosphate groups on the opposing DNA strands. Figure 7 shows a projection of an A-form DNA–Au_{13} system under periodic boundary conditions. The formation of Au_{13} wires is clearly observed. The majority of the Au_{13} clusters are separated from one another by 0.47–0.68 nm; however, there are two clusters that are about 0.8 nm apart and another two that have almost aggregated. The detailed study of the TEM pictures indicates repeated "defects" in the wire structure and so is in good agreement with the result of the simulations.

We calculated the difference in potential energy (stabilization energy, ΔE^{stab}) between the potential energy of the single DNA structure with one Au_{13} cluster ($E^{P}_{DNA\text{-}AU13}$), the potential energy of a single DNA structure (E^{P}_{DNA}), and the potential energy of a single Au_{13} cluster (E^{P}_{AU13}) according to Equation (1).

$$\Delta E^{stab} = (E^{P}_{DNA} + E^{P}_{AU13}) - (E^{P}_{DNA\text{-}AU13}) \quad (1)$$

Corresponding calculations have been performed for Au_{55}. The results are as follows: the stabilization energy of Au_{55} in the major grooves in B-DNA is $-286\ kcal\,mol^{-1}$, but $+75\ kcal\,mol^{-1}$ in A-DNA. For Au_{13}, the stabilization energy with B-DNA is $-22\ kcal\,mol^{-1}$ and $-28\ kcal\,mol^{-1}$ with A-DNA, supporting what has been mentioned above, namely when Au_{13} clusters insert into the major grooves of B-DNA weaker interactions result. Calculations which consider the minor grooves, result only in positive stabilization energies for all cluster and DNA combinations.[31]

Ligand-stabilized Au_{55} clusters can be degraded to Au_{13} clusters by the change of the dimensions of the major grooves in B-DNA, that is, transition to A-DNA. The compression of the length of the groove from 1.43 nm in B-DNA to 0.73 nm in A-DNA corresponds with the change of the cluster diameter from 1.4 to 0.6 nm. This dramatic process is initiated by dehydration under the electron-microscopy conditions. Furthermore the organization of DNA molecules in rows results in the formation of Au_{13} wires 0.5 nm apart, the length of which depends on the number of consecutive, cluster-decorated DNA molecules, and therefore can vary from only a few up to 20 or more nanometers.

Finally, the capability of gold clusters to interact with DNA molecules could one day be exploited for the development of new metal-based anticancer drugs. Preliminary studies have shown that Au_{55} clusters exhibit in vitro cytotoxic potency towards cervical cancer cells as well as cisplatin-resistant and -sensitive lung cancer cells.

Received: September 25, 2002
Revised: March 31, 2003 [Z50235]

Keywords: antitumor agents · DNA structures · electron microscopy · gold · metal–DNA interactions

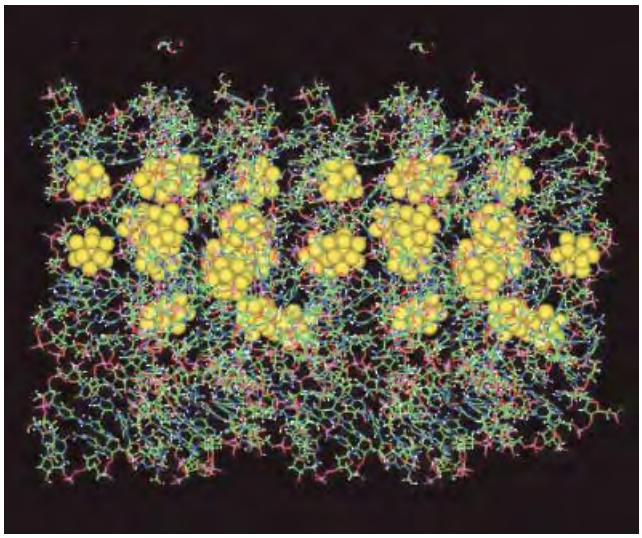


Figure 7. Combination of eight A-DNA sequences with Au_{13} clusters forming wirelike structures.

[1] D. Andersson, P. Hammarstrom, U. Carlsson, *Biochemistry* **2001**, *40*, 2653–2661.
[2] T. Simizu, A. Takada, *Polym. Networks* **1997**, *5*, 267–283.
[3] U. Pindur, G. Fischer, *Curr. Med. Chem.* **1996**, *3*, 379–406.
[4] B. P. Hudson, J. K. Barton, *J. Am. Chem. Soc.* **1998**, *120*, 6877–6888.
[5] X. L. Yang, A. H. Wang, *Pharmacol. Ther.* **1999**, *83*, 181–215.
[6] T. W. Hambley, A. R. Jones, *Coord. Chem. Rev.* **2001**, *212*, 35–59.
[7] R. Bashir, *Superlattices Microstruct.* **2001**, *29*, 1–16.
[8] I. L. Garzón, E. Artacho, M. R. Beltrán, A. García, J. Junquera, K. Michaelian, P. Ordejón, C. Rovira, D. Sánchez-Portal, J. M. Soler, *Nanotechnology* **2001**, *12*, 126–131.
[9] F. Patolsky, Y. Weizmann, O. Lioubashevski, I. Willner, *Angew. Chem.* **2002**, *114*, 2429–2433; *Angew. Chem. Int. Ed.* **2002**, *41*, 2323–2327.
[10] C. A. Mirkin, *Inorg. Chem.* **2000**, *39*, 2258–2272.

 © 2003 Wiley-VCH Verlag GmbH & Co. KGaA, Weinheim

[11] E. Braun, Y. Eichen, U. Sivan, G. Ben-Yoseph, *Nature* **1998**, *391*, 775 – 778.
[12] W. E. Ford, O. Harnack, A. Yasuda, J. M. Wessels, *Adv. Mater.* **2001**, *13*, 1793 – 1797.
[13] J. Richter, R. Seidel, R. Kirsch, M. Mertig, W. Pompe, J. Plaschke, H. K. Schackert, *Adv. Mater.* **2000**, *12*, 507 – 510.
[14] D. Zanchet, C. M. Micheel, W. J. Parak, D. Gerion, A. P. Alivisatos, *Nano Lett.* **2001**, *1*, 32 – 35.
[15] A. Kumar, M. Pattarkine, M. Bhadbhade, A. B. Mandale, K. N. Ganesh, S. S. Datar, C. V. Dharmadhikari, M. Sastry, *Adv. Mater.* **2001**, *13*, 341 – 344.
[16] N. Beyer, PhD thesis, University of Essen, **2000**.
[17] G. Schmid, N. Klein, L. Korste, U. Kreibig, D. Schönauer, *Polyhedron* **1988**, *7*, 605 – 608.
[18] The samples for AFM measurement were prepared in solution by mixing DNA and cluster. A drop of solution was then placed onto a mica surface and dried in air. The measurements were performed with a Nanoscope IIIA, Multi Mode in the tapping mode.
[19] B. Geisler, PhD thesis, University of Marburg **1999**.
[20] M. Antognozzi, M. D. Szczelkun, A. N. Round, M. J. Miles, *Single Mol.* **2002**, *3*, 105 – 110.
[21] M. Kato, C. J. McAllister, S. Hokabe, N. Shimizu, Y. L. Lynbchenko, *Eur. J. Biochem.* **2002**, *269*, 3632 – 3636.
[22] A. Wu, Z. Li, H. Wang, E. Wang, *Anal. Sci.* **2001**, *17*, 582 – 584.
[23] H. R. Drew, R. E. Dickerson, *J. Mol. Biol.* **1981**, *151*, 535 – 556.
[24] G. Schmid, N. Klein, *Angew. Chem.* **1986**, *98*, 910 – 912; *Angew. Chem. Int. Ed. Engl.* **1986**, *25*, 922 – 923.
[25] *Oxford Handbook of Nucleic Acid Structure* (Ed.: S. Neidle), Oxford University Press, New York, **1999**.
[26] J. V. Burda, J. Šponer, J. Leszczynski, P. Hobza, *J. Phys. Chem. B* **1997**, *101*, 9670 – 9677.
[27] B. Lippert, *Coord. Chem. Rev.* **2000**, *200*, 487 – 516.
[28] J. Šponer, M. Sabat, L. Gorb, J. Leszczynski, B. Lippert, P. Hobza, *J. Phys. Chem. B* **2000**, *104*, 7535 – 7544.
[29] N. Verdaguer, J. Aymami, D. Fernández-Former, I. Fita, M. Coll, T. Huynh-Dinh, J. Igolen, J. A. Subirana, *J. Mol. Biol.* **1991**, *221*, 623 – 635.
[30] R. Wing, H. Drew, T. Tsunehiro, C. Broka, S. Tanaka, K. Itakura, R. E. Dickerson, *Nature* **1980**, *287*, 755 – 758.
[31] The crystal structures of dodecameric A-DNA[25] and B-DNA[26] were obtained from the Protein Data Bank (PDP). Two copies of each crystal structure were joined by phosphodiester bonds to form a 24-A-DNA and 24-B-DNA molecules, respectively. Both conformations of DNA in the presence and absence of gold clusters were energy minimized using the Conjugate Gradient Polak–Ribiere method. Minimization was performed to obtain configurations with the lowest possible energy before performing any molecular-dynamic simulations. The atom types and partial charges were assigned according to the PCFF force field.[32,33] The PCFF force field is a second-generation force field which is appropriate for simulations performed on nucleic acids, carbohydrates, and lipids, and contains interaction parameters for many metals including Au.
[32] J. R. Maple, M.-J. Hwang, T. P. Stockfisch, U. Dinur, M. Waldman, C. S. Ewig, A. T. Hagler, *J. Comput. Chem.* **1994**, *15*, 162 – 182.
[33] H. Sun, S. J. Mumby, J. R. Maple, A. T. Hagler, *J. Am. Chem. Soc.* **1994**, *116*, 2978 – 2987.

 © 2003 Wiley-VCH Verlag GmbH & Co. KGaA, Weinheim

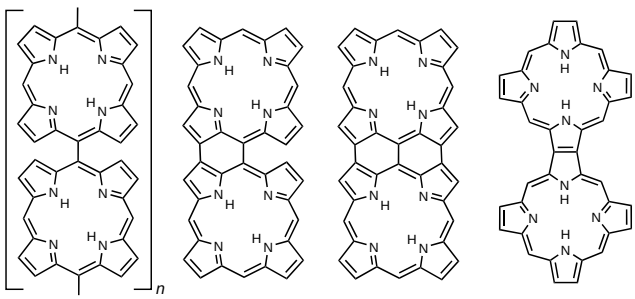
Spirodiporphyrin Complexes

Spirodiporphyrins—As Binuclear Metal Complexes

Emanuel Vogel, Martin Michels, Lars Zander, Johann Lex, Nurcan S. Tuzun, and Kendall N. Houk**

Dedicated to Professor Ronald Breslow

Porphyrin supermolecules constructed from multiple porphyrin moieties that are linked covalently[1] or coordinatively[2] by spacers have developed as an important line of research in porphyrin chemistry (with potential applications as electronic or optical functional units, sensors, and artificial photosynthetic devices). In contrast to these porphyrin supermolecules, the no less intriguing di- and oligoporphyrins devoid of spacers, that is, *meso-meso*-, β-β- or *meso*-β-linked porphyrins, have only recently attracted attention (Scheme 1).



1 **2** **3** **4**

Scheme 1. Diporphyrins **1**–**4** (representative examples).

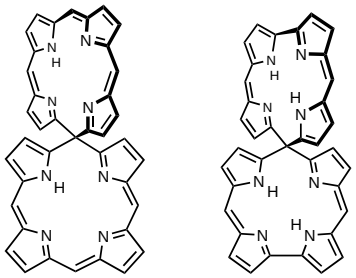
Among the diporphyrins of this type, the *meso-meso*-diporphyrin **1** ($n=1$)[3]—formally corresponding to biphenyl—takes a key position, since not only is it the building block of the fascinating rod molecules **1** ($n>1$) of Osuka et al.[4] but also provides an access through oxidative processes to the multiply linked diporphyrins **2** and **3**.[5] *meso*-β-Diporphyrins, complementary to **1**, are available from suitable metalloporphyrins by electrochemical oxidation[6] and open a pathway to doubly *meso*-β-linked diporphyrins.[7,8] While singly β-β-linked diporphyrins have been known for

[*] Prof. Dr. E. Vogel, Dr. M. Michels, Dr. L. Zander, Dr. J. Lex
Institut für Organische Chemie
Universität zu Köln
Greinstrasse 4, 50939 Köln (Germany)
Fax: (+49) 221-470-5057
E-mail: emanuel.vogel@uni-koeln.de
Prof. K. N. Houk, Dr. N. S. Tuzun
Department of Chemistry & Biochemistry
University of California
405 Hilgard Avenue, Los Angeles, CA 90095-1569 (USA)
Fax: (+1) 310-206-1843
E-mail: houk@chem.ucla.edu

 DOI: 10.1002/anie.200250690 © 2003 Wiley-VCH Verlag GmbH & Co. KGaA, Weinheim

some time,[9] expedient syntheses of such compounds are fairly recent.[10] In addition to the diporphyrins mentioned above, the diporphyrin **4**,[11] in which two porphyrin molecules share a β-β-pyrrole bond has also been described.

To our knowledge, a type of diporphyrins that is still elusive are the *meso*-spirodiporphyrins, represented by spirodiporphyrin **5** and spirodicorrole **6** (Scheme 2; the porphyrin and corrole moieties in **5** and **6**, respectively, exist as isoforms). Compounds **5** and **6** have special appeal because of

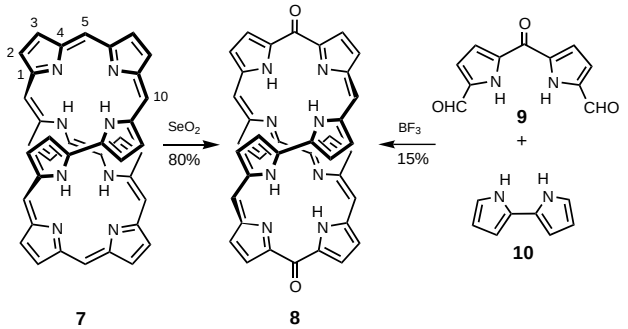


5 **6**

Scheme 2. Spirodiporphyrin (**5**) and spirodicorrole (**6**).

the possibility that they might exhibit spiroconjugation,[12] that is, a homoconjugative interaction between the π systems of the two halves of the molecule separated by the tetragonal spiro center. Although metal-free spirodiporphyrin ligands remain to be synthesized, we have now prepared the binuclear nickel complex **13** of spirodicorrole (as the hexadecaethyl derivative). This complex turned out to be extraordinarily resistant towards demetalation. In addition, the binuclear palladium complex **17** of a very unusual cross-linked figure-eight spirodiporphyrin was obtained.

The nickel complex **13** was encountered in our pursuit of the chemistry of the figure-eight cyclooctapyrrole **7**[13] as a product of a reaction cascade that is to date not fully explained. Apart from its capability to form an entire spectrum of metal complexes,[14a] this cyclooctapyrrole (octaphyrin-(1.1.1.0.1.1.1.0)) is amenable to functionalization in the ring skeleton. Oxidation of **7** with selenium dioxide in chloroform regioselectively furnishes the dioxo derivative **8** in 80% yield (Scheme 3, Table 1). Alternatively, **8** is obtained directly, if only in 15% yield,[14b] by a [2+2] condensation of **9**



Scheme 3. Syntheses of the dioxocyclooctapyrrole **8** (ethyl groups are omitted for clarity).

Table 1: Selected physical data for compounds **8**, **12**, **13**, **16**/**17** (for assignment of numbers to atoms, see Scheme 3 and 4).

8: Golden needles (hexane/dichloromethane), decomp. >300°C; ^{1}H NMR (300 MHz, [D$_8$]toluene, 298 K): δ = 12.40 (s, 4H, N-H), 6.80 ppm (s, 4H, H-10,19,29,38), 4 ABX$_3$ systems: δ = 2.98/2.16/0.71 (m, 20H, H-13a,b,16a,b,32a,b,35a,b), 3.06/3.00/1.43 (m, 20H, H-3a,b,7a,b,22a,b,26a,b), 2.63/2.56/1.23 (m, 20H, H-2a,b,8a,b,21a,b, 27a,b), 2.45/1.08 ppm (m, 20H, H-12a,b,17a,b,31a,b,36a,b); ^{13}C NMR (75.5 MHz, [D$_8$]toluene, 298 K): δ = 179.68, 150.38, 148.62, 141.91, 141.66, 140.81, 139.39, 137.80, 135.67, 117.68, 19.30, 18.16, 18.10, 17.74, 17.54, 16.95, 15.86, 15.36 ppm; IR (KBr): $\tilde{\nu}$ = 3232 (N–H), 2964, 2930, 2869, 1671 (C=O), 1595 (exocycl. C=C), 1279, 1100, 1009 cm^{-1}; UV/Vis (CH_2Cl_2): $\lambda_{max}(\varepsilon)$ = 544 (70000 L mol^{-1} cm^{-1}); MS (FAB): *m*/*z* (%): 1073 (100) $[M+H]^{+\bullet}$; elemental analysis (%) calcd: C 78.32, H 8.26, N 10.44; found: C 78.27, H 8.13, N 10.33

12: Black-golden rods (acetonitrile/dichloromethane), decomp. >300°C; ^{1}H NMR (300 MHz, [D$_8$]toluene, 298 K): δ = 6.63 ppm (s, 4H, H-10,19,29,38), 4 ABX$_3$ systems: δ = 7.24/3.34/1.00 (m, 20H, H-13a,b,16a,b,32a,b,35a,b), 3.03/2.93/1.32 (m, 20H, H-3a,b,7a,b,22a,b, 26a,b), 2.55/2.45/1.16 (m, 20H, H-2a,b,8a,b,21a,b,27a,b), 2.39/ 1.07 ppm (m, 20H, H-12a,b,17a,b,31a,b,36a,b); ^{13}C NMR (75.5 MHz, [D$_8$]toluene, 298 K): δ = 177.07, 162.29, 147.01, 144.30, 143.78, 141.57, 138.38, 137.97, 136.09, 121.22, 21.16, 19.67, 18.24, 17.88, 17.76, 16.64, 16.09, 15.67 ppm; IR (KBr): $\tilde{\nu}$ = 2963, 2929, 2869, 1623 (C=O), 1592 (C=C), 1526, 1265, 1211, 1097, 1011 cm^{-1}; UV/Vis (CH_2Cl_2): $\lambda_{max}(\varepsilon)$ = 551 (61200 L mol^{-1} cm^{-1}); MS (FAB): *m*/*z* (%): 1185 (80) $[M+H]^{+\bullet}$; elemental analysis (%) calcd: C 70.84, H 7.13, N 9.44; found: C 70.84, H 7.04, N 9.37.

13: Bluish-black rhombohedra (methanol/dichloromethane), decomp. >300°C; ^{1}H NMR (300 MHz, [D$_8$]toluene, 298 K): δ = 6.64 ppm (s, 4H, H-5,5′,15,15′), 4 A$_2$X$_3$ systems: δ = 3.25/0.77 (20H, H-8a,b,8a′,b′,12a,b, 12a′,b′), 2.55/1.10 (20H, H-2a,b,2a′,b′,18a,b,18a′,b′), 2.42/1.13 (20H, H-3a,b,3a′,b′,17a,b,17a′,b′), 2.20/0.97 ppm (20H, H-7a,b,7a′,b′,13a,b, 13a′,b′); ^{13}C NMR (75.5 MHz, [D$_8$]toluene, 298 K): δ = 152.41, 147.46, 142.49, 142.05, 139.76, 134.27, 130.38, 130.19, 117.30, 51.33 (C-10), 18.99, 18.91, 18.13, 17.89, 17.55, 17.47, 17.29, 14.10 ppm; IR (KBr): $\tilde{\nu}$ = 2963, 2929, 2869, 1599 (C=C), 1545, 1399, 1274, 1199, 1009, 957 cm^{-1}; UV/Vis (CH_2Cl_2): $\lambda_{max}(\varepsilon)$ = 468 (64200), 668 (79200 L mol^{-1} cm^{-1}); MS (FAB): *m*/*z* (%): 1140 (100) $[M]^{+\bullet}$; elemental analysis (%) calcd C 72.52, H 7.41, N 9.80, Ni 10.27; found: C 72.37, H 7.31, N 9.60, Ni 10.12

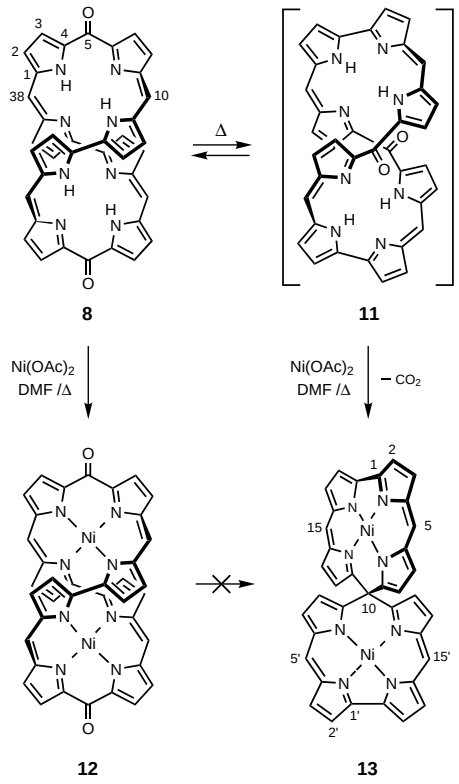
16/**17**: ^{1}H NMR (**16**, 500 MHz, [D$_8$]toluene, 298 K): δ = 7.24 (s, 2H, H-5,24), 6.64 ppm (s, 4H, H-10,19,29,38), 4 ABX$_3$ systems: δ = 4.28/1.80/ 0.43 (m, 20H, H-13a,b,16a,b,32a,b,35a,b), 2.79/1.32 (m, 20H, H-3a,b,7a,b,22a,b,26a,b), 2.73/1.28 (m, 20H, H-2a,b,8a,b,21a,b, 27a,b), 2.25/0.89 ppm (m, 20H, H-12a,b,17a,b,31a,b,36a,b); (**17**, 300 MHz, [D$_8$]toluene, 298 K): δ = 6.22 (s, 2H, H-5,24), 6.50 (s, 2H, H-10,29), 5.50 ppm (s, 2H, H-19,38), 8 ABX$_3$ systems: δ = 4.29/2.83/1.01 (m, 10H, H-16a,b,35a,b), 3.25/2.50/0.85 (m, 10H, H-13a,b,32a,b), 2.41/1.06 (m, 10H, H-3a,b,22a,b), 2.33/1.09 (m, 10H, H-7a,b,26a,b), 2.42/1.21 (m, 10H, H-2a,b,21a,b), 2.32/0.96 (m, 10H, H-8a,b,27a,b), 2.31/2.21/ 0.98 (m, 10H, H-12a,b,31a,b), 2.25/2.11/1.13 ppm (m, 10H, H-17a,b,36a,b); ^{13}C NMR (**16**, 125 MHz, [D$_8$]toluene, 298 K): δ = 153.16, 142.88, 142.00, 141.06, 139.96, 139.69, 138.57, 134.03, 102.05, 101.51, 19.46, 18.73, 18.67, 18.34, 17.06, 17.06, 16.64, 15.20 ppm; (**17**, 75.5 MHz, [D$_8$]toluene, 298 K): δ = 160.71, 156.02, 152.42, 147.21, 145.79, 144.93, 144.76, 143.51, 140.74, 139.88, 138.70, 135.43, 135.32, 133.51, 131.92, 119.96, 100.01, 90.50 (C-14,33), 86.37, 22.76, 20.40, 18.41, 18.34, 18.21, 18.05, 18.01, 18.01, 17.85, 17.10, 16.40, 16.16, 16.11, 15.85, 14.91, 13.99 ppm; IR (CsI) (**17**): $\tilde{\nu}$ = 2963, 2930, 2869, 1613, 1559, 1493, 1268, 1216, 1011, 999 cm^{-1}; UV/Vis (CH_2Cl_2): $\lambda_{max}(\varepsilon)$ = 432 (62800, **17**), 658 (70000 L mol^{-1} cm^{-1}, **16**) (The ε values refer to the quantitative ratio of **16** and **17** in the equilibrium mixture at room temperature); MS (FAB): *m*/*z* (%): 1251 (100) $[M+H]^{+\bullet}$; elemental analysis (%) calcd : C 67.03, H 7.07, N 8.93; found: C 67.19, H 6.94, N 8.61.

 © 2003 Wiley-VCH Verlag GmbH & Co. KGaA, Weinheim

with tetraethylbipyrrole **10** mediated by boron trifluoride/etherate. The regioselectivity of the SeO_2 oxidation of **7** is understandable because **8** should be favored energetically as a result of the presence of four nearly planar dipyrrin substructures. In its properties, the dioxo compound is related to 5,15-dioxo-5,15-dihydroporphyrin (as octaethyl derivative).[15]

The tendency of **8** to undergo metal complexation was tested employing Ni^{II} and Cu^{II} as metal ions. Treatment of **8** with copper(II)acetate in chloroform/methanol gave rise to the formation of a complex even at ambient temperature (complete conversion after 3 h), assumed to be the expected helical dicopper complex. By contrast, incorporation of Ni^{II} into **8** required heating of the ligand with nickel(II)acetate tetrahydrate in DMF under reflux (36 h). Surprisingly, the product obtained on nickel complexation consisted of two binuclear complexes that could be separated by chromatography on alumina (first with toluene/hexane then with toluene) into an olive-green fraction followed by a violet main fraction.

The complex isolated from the main fraction is the dinickel complex **12**, which retains the ring skeleton of **8**, (yield 40%, Scheme 4, Table 1). The ^1H NMR spectrum of **12**, which has only one signal for the *meso* protons, along with four ABX_3 spin systems for the ethyl groups, is indicative of D_2 molecular symmetry. According to an X-ray crystallographic analysis of **12** (Figure 1)[16] the changes of the ring skeleton with respect to **8** are similar to those occurring on nickel complexation of **7**.[14a] Each of the two nickel ions in **12** are thus chelated by two practically planar dipyrrin units.



Scheme 4. Synthesis of the spirodicorrole dinickel complex **13**.

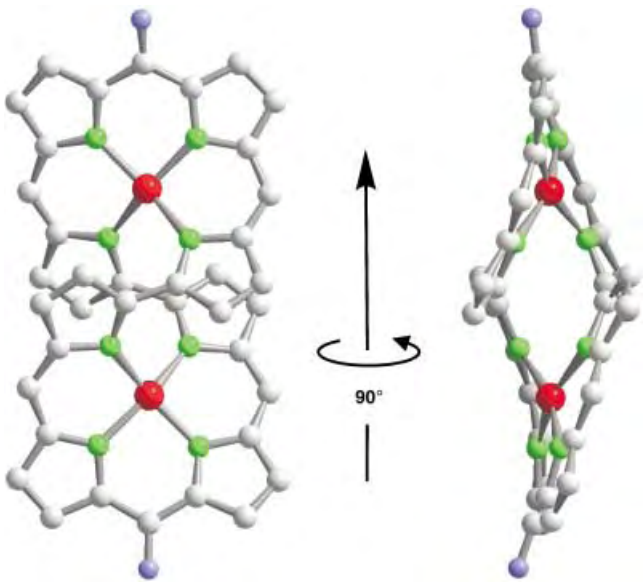


Figure 1. Crystal structure of dioxocyclooctapyrrole as the dinickel complex **12** (ethyl groups omitted for clarity). Left: view of **12**. Right: view of **12** after 90° rotation of the molecule around its longitudinal axis.

The dinickel complex obtained from the olive-green fraction is without precedent, since, to our surprise, it turned out to be the complex **13** of spirodicorrole mentioned in the introduction (yield 9%, Table 1). The elemental analysis, combined with the FAB mass spectrum and the absence of carbonyl bands in the IR spectrum made it clear that the new complex must have originated from a deep-seated skeletal rearrangement of **8**—accompanied by an elimination of carbon dioxide! In light of these observations, the relatively simple ^1H NMR spectrum of the complex, consisting only of a singlet at $\delta = 6.64$ ppm (*meso* protons) and, indicative of loss of chirality, four A_2X_3 spin systems (protons of four different ethyl substituents), can only be rationalized in terms of structure **13**. The final structural verification of **13** was provided by an X-ray analysis (Figure 2),[16] in which the characteristic feature of the complex, two orthogonally oriented nickel corrolates (both as isoforms) linked through a common spiro carbon atom, became visible. The UV/Vis spectrum of **13** (Table 1) attracts special interest because of the possible homoconjugative interaction of the two nickel corrolate chromophores across the spiro center. A full analysis of the spectrum involving a comparison with a suitable reference compound will be reported in a forthcoming publication.[17]

The unusual reaction cascade leading from **8** to **13** appears to be dependent on DMF as a solvent and on Ni^{II} as the metal ion.[18] Further studies are needed to substantiate the nature of the proposed intermediates and to gain deeper insight into the mechanism of the individual reaction steps. It seems reasonable to assume that the skeletal rearrangement accompanied by extrusion of carbon dioxide is preceded by the establishment of the thermal conformational equilibrium **8**⇔**11** through which the remote carbonyl groups are brought into close proximity. Semiempirical PM3(tm) calculations carried out on the two dioxo conformers (with methyl instead

 © 2003 Wiley-VCH Verlag GmbH & Co. KGaA, Weinheim

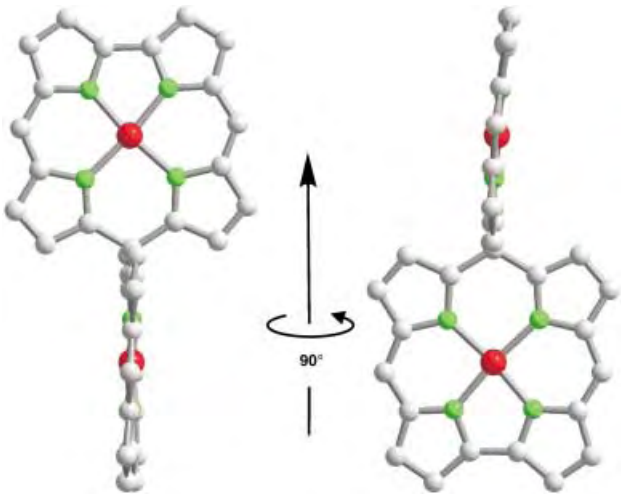
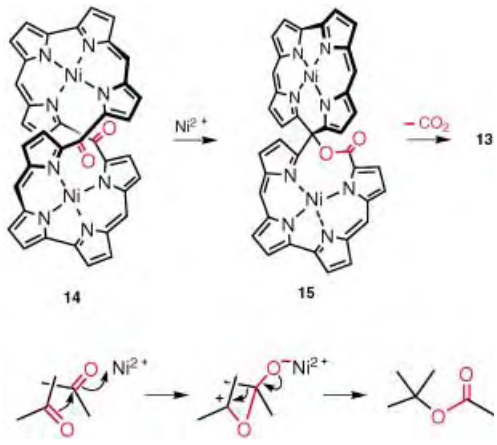


Figure 2. Crystal structure of spirodicorrole as the dinickel complex **13**. Left: view of **13**. Right: view of **13** after 90° rotation of the molecule around its longitudinal axis.

of ethyl groups) lead to the conclusion that **8** and **11** are comparable in energy, while analogous examples[19] suggest that only a low activation barrier separates **8** from **11**. Calculations show that the incorporation of Ni^{II} into **11**, either to form **14** (arbitrarily assumed here) or to give a mononuclear nickel complex, brings the carbonyl groups even closer together and induces strain into the molecule. Therefore, it seems justified to consider the di- or monometalation of **11** as the first reaction step.

The actual skeletal rearrangement is initiated by a kind of neighboring-group effect of the carbonyl groups,[20] set off by an electrophilic attack of the nickel ion (or of a proton) at one of the carbonyl oxygen atoms of **14**. As a consequence, **14** is converted into a carbenium ion with concomitant formation of an oxygen bridge (Scheme 5). The carbenium ion thus generated undergoes a Wagner–Meerwein type rearrangement (1,3-shift) to give, after liberation of the electrophile, the lactone **15**, the strategic intermediate of the reaction cascade.[21] This lactone is expected to undergo a radical or ionic cleavage of the C_{spiro}–O bond relatively easily; subsequent loss of CO_2 from the diradical/zwitterionic species formed in this way provides **13**.



Scheme 5. Top: Rearrangement of the nickel complex **14** into the lactone nickel complex **15** which is assumed to be an intermediate (followed by the thermal decarboxylation of **15**). Bottom: Postulated mechanism for the rearrangement of **14** into **15**.

To support the presumed course of the conversion of **8** into **13**, the enthalpies of formation of the postulated intermediates (for simplification, without ethyl groups) were calculated semiempirically [PM3(tm)] for the gas-phase reaction with simulation of the electrophilic attack by a nickel ion by that of a proton. The enthalpy values obtained were found to be compatible with the mechanism proposed, in particular with respect to the assumption that the lactone **15** is likely to be a stable intermediate at room temperature.

It was in the course of our studies on the metal complexation of the cyclooctapyrrole **7** that we came across yet another spirodiporphyrin, this time as a binuclear palladium complex. When **7** is treated with palladium(II)acetate in boiling DMF (0.5 h) the expected binuclear complex **16** with a helical figure-eight conformation and D_2 symmetry was produced, but this was accompanied by a second complex that was recognized as a constitutional isomer of **16**. According to an X-ray analysis (Figure 3),[16] this isomer, which can be isolated in pure state on slow crystallization from a

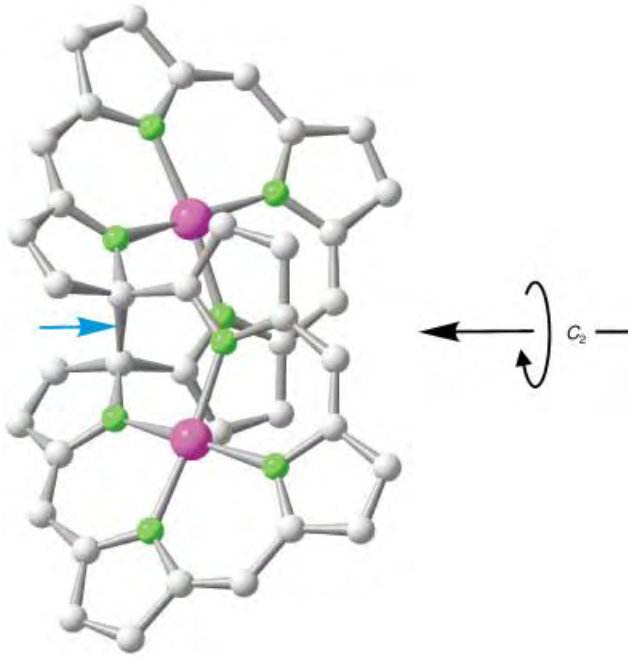
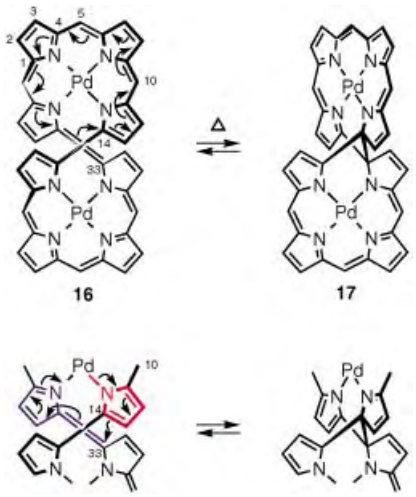


Figure 3. Crystal structure of **17**.

solution of the mixture of complexes in dichloromethane/acetonitrile, is the bisspirodiporphyrin complex **17** (Table 1). As deduced from the structural analysis, **17** can be formed from **16** by a transannular C–C linkage of the α-pyrrolic positions C-14 and C-33 (Scheme 6). The free ligand based on **17**, which so far has defied release from the metal complex consists of two identical tetrapyrrolic ring systems annelated along the newly formed C–C bond. As a C_2-symmetric molecule, its twofold rotational axis orthogonal to the new

 © 2003 Wiley-VCH Verlag GmbH & Co. KGaA, Weinheim



Scheme 6. Top: Thermal equilibrium between the binuclear palladium complex **16** and its bisspirodiporphyrin constitutional isomer **17** (formal 18-π-electrocyclic process). Bottom: Postulated mechanism for the reversible isomerization of **16** to **17**.

bond, **17** retains chirality, a feature corroborated by the ^{1}H NMR spectrum by the presence of eight ABX_3 spin systems for the ethyl substituents.

The measurements of the temperature dependence of the ^{1}H NMR spectrum (in [D$_8$]toluene) reveals that the palladium complex **16** and its spiro isomer **17** exist in a reversible thermal equilibrium, in which, at room temperature, **17** predominates: $K = [\mathbf{17}]/[\mathbf{16}] = 2.3$. A kinetic evaluation of the isomerization of **16** was made possible by the observation that the equilibrium **16**⇄**17** can be displaced photochemically towards the starting compound **16**. Samples of isomer **16**, generated by intensive irradiation of the isomer mixture by means of a halogen lamp (500 W, $\lambda_{max} = 350$ nm), underwent reestablishment of the original thermal equilibrium that could be monitored by NMR spectroscopy at different temperatures, in the dark, through integration of the corresponding signals of **16** and **17**. As deduced from the temperature dependence of the equilibrium constant K ($\ln K$ versus T^{-1}, seven data points, $289\,\mathrm{K} \le T \le 327\,\mathrm{K}$), the isomerization of **16**→**17** is exothermic ($\Delta H = -3.4 \pm 0.1$ kcal mol^{-1}, $\Delta S = -9.8 \pm 0.4$ cal K^{-1} mol^{-1}) and possesses an activation energy $E_a = 23.6 \pm 0.5$ kcal mol^{-1}.

The thermal isomerization of **16** to **17** that constitutes a transannular ring closure is clearly tied to metal coordination since the free ligand **7** shows no tendency to undergo this kind of rearrangement. That **16** undergoes the skeletal rearrangement in question with remarkable ease must be because the incorporation of palladium substantially reduces the distance between the reaction centers C-14 and C-33, from 4.10 Å in **7** to only 2.99 Å (PM3(tm) calculations) and induces strain that is relieved by bond formation. The transannular ring closure as observed for the binuclear palladium complex **16**, is also found with the mixed palladium–platinum complex but seems to be suppressed in the other binuclear metal complexes of **7**.

As far as the mechanism of the isomerization of **16** is concerned, the presence of a conjugated 18-π-electron system in each of the tetrapyrrolic loops suggests that an electrocyclic process is operative. The thermal 18-π-electron electrocyclization would have to follow a disrotatory course to be allowed by the Woodward–Hoffmann rules.[22] However, since the geometry of **16** only permits a conrotatory electrocyclization, it is expedient to consider other mechanisms. A reaction path that can be regarded as an attractive alternative to a symmetry forbidden electrocyclic process is outlined in Scheme 6 (bottom). In this mechanism the transannular ring closure is interpreted as a type of intramolecular Michael addition, in which an electrophilic azafulvene unit (in blue) serves as the acceptor whereas a nucleophilic pyrrole anion coordinated to palladium (in red) functions as the donor. Strong support for this mechanism derives from the recent isolation of an azafulvene (as a bis(azafulvene)) and from the observation that this species spontaneously reacts with bipyrrole in accordance with Scheme 6.[23]

Received: December 3, 2002 [Z50690]

Keywords: chelate · nickel · palladium · porphyrinoids · spiro compounds

[1] Review: J.-H. Chou, M. E. Kosal, H. S. Nalwa, N. A. Rakow, K. S. Suslick in *The Porphyrin Handbook, Vol. 6* (Eds.: K. M. Kadish, K. M. Smith, R. Guilard), Academic Press, San Diego, CA, **2000**, pp. 43–131.

[2] Review: J.-C. Chambron, V. Heitz, J.-P. Sauvage in *The Porphyrin Handbook, Vol. 6* (Eds.: K. M. Kadish, K. M. Smith, R. Guilard), Academic Press, San Diego, CA, **2000**, pp. 1–42.

[3] K. Susumu, T. Shimidzu, K. Tanaka, H. Segawa, *Tetrahedron Lett.* **1996**, *37*, 8399–8402; R. G. Khoury, L. Jaquinod, K. M. Smith, *Chem. Commun.* **1997**, 1057–1058; A. Osuka, H. Shimidzu, *Angew. Chem.* **1997**, *109*, 93–95; *Angew. Chem. Int. Ed. Engl.* **1997**, *36*, 135–137; N. Yoshida, H. Shimidzu, A. Osuka, *Chem. Lett.* **1998**, 55–56.

[4] N. Aratani, A. Osuka, Y. H. Kim, D. H. Jeong, D. Kim, *Angew. Chem.* **2000**, *112,* 1517–1521; *Angew. Chem. Int. Ed.* **2000**, *39*, 1458–1462; D. Kim, A. Osuka, *Second International Conference on Porphyrins and Phthalocyanines (ICPP-2)*, Kyoto (Japan), **2002**, Abstract S-110.

[5] A. Tsuda, A. Nakano, H. Furuta, A. Osuka, *First International Conference on Porphyrins and Phthalocyanines (ICPP-1)*, Dijon, **2000**, Poster 594.

[6] T. Ogawa, Y. Nishimoto, N. Yoshida, N. Ono, A. Osuka, *Angew. Chem.* **1999**, *111*, 140–142; *Angew. Chem. Int. Ed.* **1999**, *38*, 176–179.

[7] A. Tsuda, A. Nakano, H. Furuta, H. Yamochi, A. Osuka, *Angew. Chem.* **2000**, *112*, 572–575; *Angew. Chem. Int. Ed.* **2000**, *39*, 558–561.

[8] Doubly *meso*-β-linked diporphyrins, also described as [2]porphyracenes, were first reported by K. Sugiura, T. Matsumoto, S. Ohkouchi, Y. Naitoh, T. Kawai, Y. Takai, K. Ushiroda, Y. Sakata, *Chem. Commun.* **1999**, 1957–1958.

[9] J. B. Paine III, D. Dolphin, *Can. J. Chem.* **1978**, *56*, 1710–1712.

[10] Y. Deng, C. K. Chang, D. G. Nocera, *Angew. Chem.* **2000**, *112*, 1108–1110; *Angew. Chem. Int. Ed.* **2000**, *39*, 1066–1068.

[11] L. Jaquinod, O. Siri, R. G. Khoury, K. M. Smith, *Chem. Commun.* **1998**, 1261–1262.

[12] H. E. Simmons, T. Fukunaga, *J. Am. Chem. Soc.* **1967**, *89*, 5208–5215; H. Hopf, *Classics in Hydrocarbon Chemistry*, Wiley-VCH, Weinheim, **2000**, pp. 407–410.

[13] E. Vogel, M. Bröring, J. Fink, D. Rosen, H. Schmickler, J. Lex, K. W. K. Chan, Y.-D. Wu, M. Nendel, D. A. Plattner, K. N.

 © 2003 Wiley-VCH Verlag GmbH & Co. KGaA, Weinheim

Houk, *Angew. Chem.* **1995**, *107*, 2705 – 2709; *Angew. Chem. Int. Ed. Engl.* **1995**, *34*, 2511 – 2514. The first cyclopolypyrrole with a figure-eight conformation, a cyclodecapyrrole named turcasarin, was reported by J. L. Sessler, S. J. Weghorn, V. Lynch, M. R. Johnson *Angew. Chem.* **1994**, *106*, 1572 – 1575; *Angew. Chem. Int. Ed. Engl.* **1994**, *33*, 1509 – 1512.

[14] a) M. Michels, PhD thesis, University of Cologne, **1999**; b) L. Zander, PhD thesis, University of Cologne, **1998**.

[15] G. H. Barnett, B. Evans, K. M. Smith, *Tetrahedron* **1975**, *31*, 2711 – 2717; J.-H. Fuhrhop, S. Besecke, J. Subramanian, C. Mengersen, D. Riesner, *J. Am. Chem. Soc.* **1975**, *97*, 7141 – 7152; R. Bonnett, B. D. Chaney, *J. Chem. Soc. Perkin Trans. 1* **1987**, 1063 – 1067; T. Benninghaus, PhD thesis, University of Cologne, **1992**. In connection with the synthesis of **8** the remarkable regioselectivity observed on oxidation of face to face biscorroles to bisoxocorroles should be noted, F. Jérôme, J.-M. Barbe, C. P. Gros, R. Guilard, J. Fischer, R. Weiss, *New J. Chem.* **2001**, *25*, 93 – 101.

[16] Crystal structure data for **12**: $C_{70}H_{84}N_8O_2Ni_2$; $M_r = 1186.87\ g\,mol^{-1}$; crystals from dichloromethane/acetonitrile; triclinic, space group $P\bar{1}$, $a = 13.352(1)$, $b = 14.452(1)$, $c = 19.332(1)$ Å, $\alpha = 79.38(1)$, $\beta = 72.41(2)$, $\gamma = 65.10(1)°$, $V = 3218.4(4)$ Å^3; $Z = 2$, $\rho_{calcd} = 1.225\ g\,cm^{-3}$; $F(000) = 1264$; $\mu_{Mo} = 0.635\ mm^{-1}$; 27111 measured, 13965 independent, 9130 observed reflections ($F_o^2 > 2\sigma F_o^2$); $\Theta_{max} = 27.0°$; $R1 = 0.060$, $wR2 = 0.124$. Crystal structure data for **13**: $C_{69}H_{84}N_8Ni_2$; $M_r = 1142.9\ g\,mol^{-1}$; crystals from methanol/dichloromethane; triclinic, space group $P\bar{1}$, $a = 10.964(1)$, $b = 12.072(1)$, $c = 24.039(1)$ Å, $\alpha = 81.90(1)$, $\beta = 87.32(1)$, $\gamma = 69.64(1)°$, $V = 2953.2(4)$ Å^3; $Z = 2$, $\rho_{calcd} = 1.285\ g\,cm^{-3}$; $F(000) = 1220$; $\mu_{Mo} = 0.687\ mm^{-1}$; 24438 measured, 12735 independent, 6256 observed reflections ($F_o^2 > 2\sigma F_o^2$); $\Theta_{max} = 27°$; $R1 = 0.065$, $wR2 = 0.109$. Crystal structure data for **17**: $C_{70}H_{86}N_8Pd_2$; $M_r = 1252.27\ g\,mol^{-1}$; crystals from dichloromethane/acetonitrile; triclinic, space group $P\bar{1}$, $a = 12.240(1)$, $b = 13.479(1)$, $c = 22.392(1)$ Å, $\alpha = 80.90(1)$, $\beta = 89.62(1)$, $\gamma = 63.74(1)°$, $V = 3263.0(4)$ Å^3; $Z = 2$, $\rho_{calcd} = 1.275\ g\,cm^{-3}$; $F(000) = 1308$; $\mu_{Mo} = 0.597\ mm^{-1}$; 34639 measured, 18300 independent, 10801 observed reflections ($F_o^2 > 2\sigma F_o^2$); $\Theta_{max} = 30.5°$; $R1 = 0.046$, $wR2 = 0.113$. Nonius Kappa CCD diffractometer, room temperature, $Mo_{K\alpha}$ radiation ($\lambda = 0.71073$ Å); the structures were determined by direct methods and refined against F^2 for all independent reflections (heavy atoms with anisotropic temperature factors, H atoms with isotropic temperature factors); $wR2 = [\Sigma w(F_o^2 - F_c^2)^2/\Sigma w(F_o^2)^2]^{1/2}$. Programs used: G. M. Sheldrick, SHELXS-97, program for structure determination, University of Göttingen, Göttingen (Germany), **1997**, G. M. Sheldrick, SHELXL-97, program for refinement, University of Göttingen, Göttingen (Germany), **1997**, and E. Keller, SCHAKAL 99, graphic program, University of Freiburg (Germany), **1999**. Calculations were carried out on the data processing systems of the regional computer center, University of Cologne. CCDC-194718 (**12**), CCDC-194719 (**13**), CCDC-194720 (**17**) contain the supplementary crystallographic data for this paper. These data can be obtained free of charge via www.ccdc.cam.ac.uk/conts/retrieving.html (or from the Cambridge Crystallographic Data Centre, 12 Union Road, Cambridge CB2 1EZ, UK; fax: (+44) 1223-336-033; or deposit@ccdc.cam.ac.uk).

[17] G. Hohlneicher, D. Bremm, J. Wytko, J. Bley-Escrich, J.-P. Gisselbrecht, M. Gross, M. Michels, J. Lex, E. Vogel, unpublished results.

[18] Other divalent metal ions, such as Pd^{II}, Pt^{II}, Cu^{II}, and Zn^{II}, did not give rise to the formation of analogous spirodicorrole metal complexes. PM3(tm) calculations support the hypothesis that the ring closure initiating the reaction cascade is favored by Ni^{II} coordination. The reason for this must be that the ionic radius of Ni^{II} is noticeably smaller than the radii of the other ions tested (Ni^{II}: 0.58 Å versus Pd^{II}: 0.64 Å).

[19] J. A. Wytko, M. Michels, L. Zander, J. Lex, H. Schmickler, E. Vogel, *J. Org. Chem.* **2000**, *65*, 8709 – 8714.

[20] A noteworthy example for a neighboring-group effect involving carbonyl groups—a [2+2] cycloaddition with formation of a 1,2-dioxetane—is represented by the course of the thermolysis of *syn*-15,16-dioxo-1,6:8,13-bismethano[14]annulene, E. Vogel, G. Markowitz, L. Schmalstieg, S. Itô, R. Breuckmann, W. R. Roth, *Angew. Chem.* **1984**, *96*, 719 – 720; *Angew. Chem. Int. Ed. Engl.* **1984**, *23*, 719 – 720.

[21] As the reaction cascade of **8**–**13** is dependent on DMF as a solvent an alternative mechanism for the formation of the hypothetical lactone intermediate **15** must be taken into consideration. If DMF should experience a creeping elimination of dimethylamine at the relatively high reaction temperature, then **15** might arise from a nucleophilic addition of the amine to one of the carbonyl groups of **14** followed by a kind of a benzil–benzilic acid rearrangement of the adduct. Apart from dimethylamine, acetate ion and water (from nickel(II)acetate tetrahydrate) must also be considered as nucleophiles.

[22] R. B. Woodward, R. Hoffmann, *Die Erhaltung der Orbitalsymmetrie*, Verlag Chemie, Weinheim, **1970**. For orbital-symmetry controlled pericyclic reactions in porphyrin chemistry, see: R. B. Woodward, *Spec. Publ. Chem. Soc.* **1967**, *21*, 217 – 249; Y. Yamada, D. Miljkovic, P. Wehrli, B. Golding, P. Löliger, R. Keese, K. Müller, A. Eschenmoser, *Angew. Chem.* **1969**, *81*, 301 – 306; *Angew. Chem. Int. Ed. Engl.* **1969**, *8*, 343 – 348; P. S. Clezy, *Aust. J. Chem.* **1991**, *44*, 1163 – 1193.

[23] J. Setsune, S. Maeda, *J. Am. Chem. Soc.* **2000**, *122*, 12405 – 12406.

 © 2003 Wiley-VCH Verlag GmbH & Co. KGaA, Weinheim

Molecular Ferromagnetism

Unexpected Appearance of Molecular Ferromagnetism in the Ordinary Acetate $[\{Gd(OAc)_3(H_2O)_2\}_2]\cdot 4H_2O$**

*Stephan T. Hatscher and Werner Urland**

The number of publications on molecular magnetic materials has recently increased dramatically.[1] The focus lies on the synthesis of compounds with numerous paramagnetic centers which can be to coupled together to form large spin systems. Another aim is to achieve ferro- or ferrimagnetic coupling, as the more commonly observed antiferromagnetic interactions are of less interest. Therefore the natural choice seems to be compounds containing lanthanide ions as these have large

[*] Prof. Dr. W. Urland, S. T. Hatscher
Institut für Anorganische Chemie
Universität Hannover
Callinstrasse 9, 30167 Hannover (Germany)
Fax: (+49) 511-762-19032
E-mail: urland@acc.uni-hannover.de

[**] S.T.H. expresses his gratitude to Prof. Dante Gatteschi and his group for fruitful discussions and the possibility to perform experiments in Florence with a Marie Curie scholarship.

 © 2003 Wiley-VCH Verlag GmbH & Co. KGaA, Weinheim DOI: 10.1002/anie.200250738

spin moments. The Kanamori–Goodenough rules[2] give an explanation for the occurrence of ferro- or antiferromagnetic exchange for d-block elements, however, to date there is no such concept for f-block elements. In these systems the mostly small exchange coupling constants are problematic. The influence of the ligand field is hard to predict and can easily be misinterpreted as an antiferromagnetic interaction. With this in mind, the Gd^{3+} center with a $^8S_{7/2}$ ground state has a simple spin system as the influence of the ligand field can be neglected.

To date, the main focus was centered on the coupling of lanthanides with radicals,[3–6] Cu^{2+},[7,8] Co^{2+}, Co^{3+}[9] or VO^{2+} ions.[10] Recently ferromagnetic interactions between two Gd^{3+} ions were reported for an amorphous salycylate.[11] The composition of the sample was given by elementary analysis, the dimeric structure was detected by WAXS ("wide-angle X-ray scattering").

Herein, we report the magnetic properties of gadolinium acetate tetrahydrate, $[\{Gd(OAc)_3(H_2O)_2\}_2]\cdot 4H_2O$, whose structure was solved by single-crystal X-ray analysis in 1980.[12] Surprisingly, magnetic susceptibility measurements show that the acetate that crystallizes out of aqueous solution has a ferromagnetic $S=7$ ground state. Such magnetic behavior has not been observed before for such a well characterized compound.

The molecular structure of the acetate is shown in Figure 1 and is dominated by the presence of the dinuclear $[\{Gd(OAc)_3(H_2O)_2\}_2]\cdot 4H_2O$ entity. Two of the six chelating

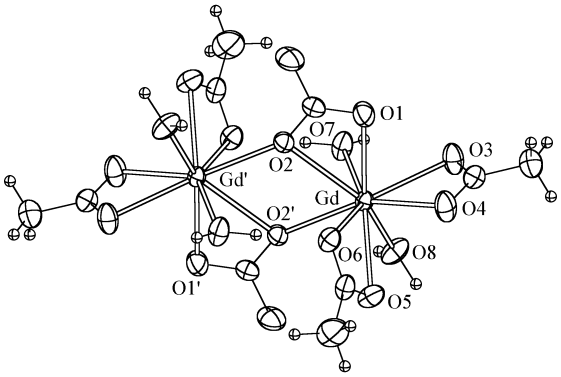


Figure 1. Molecular structure of the dimeric $Gd^{3+}\cdots Gd^{3+}$ entity in $[\{Gd(OAc)_3(H_2O)_2\}_2]\cdot 4H_2O$.

carboxylate units bridge the dimeric centers in a μ_2*O2*;κ^2*O1*,*O2* manner. The oxygen atoms O1 and O1′ are bonded to only one of the two paramagnetic Gd^{3+} ions, whereas O2 and O2′ are bridging atoms bound to both. Additionally two other acetate ions and two water molecules coordinate each Gd^{3+} center. The distance between the two gadolinium ions within this dinuclear unit is 4.206 Å, the smallest intermolecular separation is 6.249 Å.

The dependence of the magnetic moment μ on temperature in a magnetic field of $H=19.9\,kA\,m^{-1}$ (0.25 kOe) is given in Figure 2. At about 120 K the magnetic moment reaches a level of 7.9 μ_B, which, according to Hund's formula, corresponds to the expected value for two non-interacting

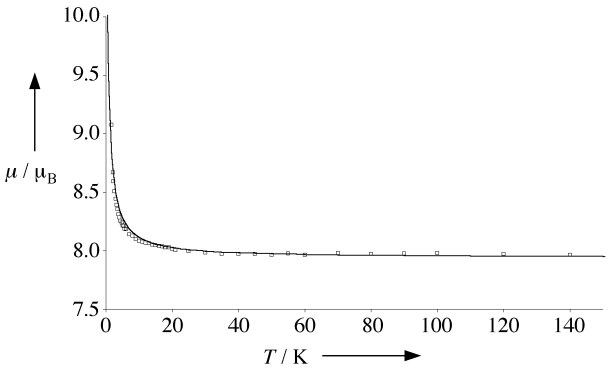


Figure 2. Comparison of measured (□, $H=19.9\,kA\,m^{-1}$) and calculated (——) magnetic moments moments μ of Gd^{3+} in $[\{Gd(OAc)_3(H_2O)_2\}_2]\cdot 4H_2O$.

centers with $S=7/2$ and $g=2.0$. With decreasing temperature the magnetic moment increases, until it reaches 9.07 μ_B at a temperature of 1.74 K.

The magnetic behavior is interpreted with an isotropic spin Hamiltonian of the type $\mathcal{H}=-2J\hat{S}_1\hat{S}_2$, where J represents the exchange coupling constant[13,14] and has a value, after fitting with $g=2$, of 0.03 cm^{-1}. This J value is therefore comparable to the one reported for the Gd^{3+} salycylate $J=0.05\,cm^{-1}$ with a g-value of 1.98.[11] To date, for homodinuclear complexes of gadolinium antiferromagnetic coupling constants J of -0.05 to $-0.21\,cm^{-1}$ have been found.[15]

Also the magnetization curve (Figure 3) supports the ferromagnetic interaction in this compound. The measurement at 1.5 K in fields between 0 and 6 T show a compromise between the calculated curves according to the Brillouin functions for 1) two isolated centers with $S=7/2$, $g=2$, and 2) one system with $S=7$, $g=2$. In the low-field regime the measured values follow calculated curve 2 for the ferromagnetic ground state. In the high-field regime single-ion behavior is observed (curve 1) because of magnetic decoupling.

Possibly the presence of the ferromagnetic ground state depends on the bridging angles of the carboxylate ligands in $[\{Gd(OAc)_3(H_2O)_2\}_2]\cdot 4H_2O$. The Gd-O2-Gd′ angle is 115.5°.

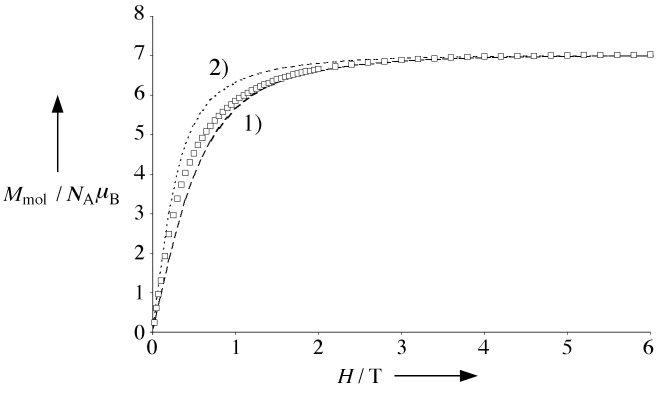


Figure 3. Comparison of the observed (□; $T=1.5$ K) and calculated (– – –) magnetization for $[\{Gd(OAc)_3(H_2O)_2\}_2]\cdot 4H_2O$.

 © 2003 Wiley-VCH Verlag GmbH & Co. KGaA, Weinheim

Further experiments on other carboxylates of lanthanides with different bridging structures are in progress.

Experimental Section

Gd_2O_3 (250 mg, 0.63 mmol; Strem Chemicals, purity 99.9%) was added to acetic acid (2 M; 10 mL; Fluka), slurried, and left for 12 h. The resulting clear solution was concentrated. After another 12 h colorless single crystals of $[\{Gd(OAc)_3(H_2O)_2\}_2]\cdot 4H_2O$ suitable for X-ray structure refinement were obtained.

The magnetic susceptibility measurements were performed with a vibrating sample magnetometer (Oxford Instruments ITC503 MagLabVSM). To prepare the samples single crystals of $[\{Gd(OAc)_3(H_2O)_2\}_2]\cdot 4H_2O$ were finely ground and wrapped in teflon foil. The purity of the sample was checked by X-ray powder measurements. The diamagnetic correction of the measured values was performed using Pascal's increments.[16] The magnetic moment μ was calculated according to Curie's law using the susceptibility values.

Received: December 10, 2002 [Z50738]

Keywords: carboxylate ligands · gadolinium · lanthanides · magnetic properties

[1] see, for example: a) A. L. Barras, A. Caneschi, A. Cornia, F. Fabrizi de Biani, D. Gatteschi, C. Sangregorio, R. Sessoli, L. Sorace, *J. Am. Chem. Soc.* **1999**, *121*, 5302; b) D. J. Price, S. R. Butten, B. Moubaraki, K. S. Murray, *Chem. Commun.* **2002**, 762; c) F. Bellouard, M. Clement-León, E. Coronado, J. R. Galán-Mascarós, C. J. Gómez-García, F. Romero, K. R. Dunbar, *Eur. J. Inorg. Chem.* **2002**, 1603; d) T. Kajiwara, A. Kamiyama, T. Ito, *Chem. Commun.* **2002**, 1256; e) L. Gutierrez, G. Alzuet, J. A. Real, J. Cano, J. Barrás, A. Castiñeiras, *Eur. J. Inorg. Chem.* **2002**, 2094; f) S. Youngme, G. A. van Albada, H. Kooijman, O. Roubeau, W. Somjitsripunya, A. L. Spek, C. Pakawatchai, J. Reedijk, *Eur. J. Inorg. Chem.* **2002**, 2367.

[2] O. Kahn, *Molecular Magnetism*, VCH, New York, **1993**.

[3] C. Benelli, A. Caneschi, D. Gatteschi, L. Pardi, P. Rey, *Inorg. Chem.* **1990**, *29*, 4223.

[4] C. Lescop, D. Luneau, E. Belorisky, P. Fries, M. Guillot, P. Rey, *Inorg. Chem.* **1999**, *38*, 5472.

[5] A. Caneschi, A. Dei, D. Gatteschi, L. Sorace, K. Vostrikova, *Angew. Chem.* **2000**, *112*, 252; *Angew. Chem. Int. Ed.* **2000**, *39*, 249.

[6] J. W. Raebiger, J. S. Miller, *Inorg. Chem.* **2002**, *41*, 3308.

[7] J.-P. Costes, F. Dahan, A. Dupuis, J.-P. Laurent, *Inorg. Chem.* **1996**, *35*, 2400.

[8] I. Ramade, O. Kahn, Y. Jeannin, F. Robert, *Inorg. Chem.* **1997**, *36*, 930.

[9] J.-P. Costes, F. Dahan, J. García-Tojal, *Chem. Eur. J.* **2002**, *8*, 5430.

[10] J.-P. Costes, F. Dahan, B. Donnadieu, J. Garcia-Tojal, J. P. Laurent, *Eur. J. Inorg. Chem.* **2001**, 363.

[11] J.-P. Costes, J. M. Clemente-Juan, F. Dahan, F. Nicodème, M. Verelst, *Angew. Chem.* **2002**, *114*, 333; *Angew. Chem. Int. Ed.* **2002**, *41*, 323.

[12] M. C. Favas, D. L. Kepert, B. W. Skelton, A. H. White, *J. Chem. Soc. Dalton Trans.* **1980**, 454.

[13] J. H. Van Vleck, *The Theory of Electric and Magnetic Susceptibilities*, Oxford University Press, Oxford, **1932**.

[14] H. Lueken, *Magnetochemie*, Teubner, Stuttgart, **1999**

[15] a) P. Guerriero, S. Tamburini, P. A. Vigato, C. Benelli, *Inorg. Chim. Acta* **1991**, *189*, 19; b) S. Liu, L. Gelmini, S. J. Rettig, R. C. Thompson, C. Orvig, *J. Am. Chem. Soc.* **1992**, *114*, 6081; c) A. Panagiotopoulos, T. F. Zafiropoulos, S. P. Perlepes, E. Bakalbassis, I. Masson-Ramade, O. Kahn, A. Terzis, C. P. Raptopoulou, *Inorg. Chem.* **1995**, *34*, 4918, and references therein; d) R. Hedinger, M. Ghisletta, K. Hegetschweiler, E. Toth, A. E. Merbach, R. Sessoli, D. Gatteschi, V. Gramlich, *Inorg. Chem.* **1998**, *37*, 6698; e) J.-P. Costes, F. Dahan, F. Nicodème, *Inorg. Chem.* **2001**, *40*, 5285.

[16] P. Pascal, *Ann. Chim. Phys.* **1910**, *19*, 5.

 © 2003 Wiley-VCH Verlag GmbH & Co. KGaA, Weinheim

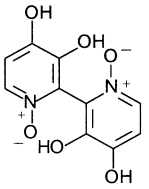
Biosynthesis of Orellanine

Occurrence of the Fungal Toxin Orellanine as a Diglucoside and Investigation of Its Biosynthesis**

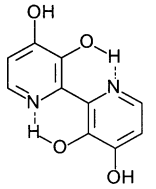
*Peter Spiteller, Michael Spiteller, and Wolfgang Steglich**

Dedicated to Professor Meinhart H. Zenk on the occasion of his 70th birthday

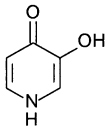
The deadly poisonous toadstool *Cortinarius orellanus* (Fr.) Fr.[1] causes an irreversible loss of kidney function within one to two weeks after ingestion.[2] The toxicity of this fungus was recognized nearly 50 years ago after a tragic mass poisoning in Poland, which caused several deaths.[3] The responsible toxin, orellanine,[4] was assigned the structure 2,2′-bipyridine-3,3′,4,4′-tetrol-1,1′-dioxide (**1**),[5] which has been confirmed by several syntheses[6] and a crystal structure analysis.[7] In this communication we report initial investigations on the biosynthesis of orellanine and the discovery that the toxin occurs mainly as the water-soluble 4,4′-diglucopyranoside **5**.



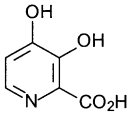
1



2



3



4

[*] Prof. Dr. W. Steglich, Dr. P. Spiteller
Department Chemie
Ludwig-Maximilians-Universität München
Butenandtstrasse 5–13, Haus F, 81377 München (Germany)
Fax: (+49) 89-2180-77756
E-mail: wos@cup.uni-muenchen.de
Prof. Dr. M. Spiteller
Institut für Umweltforschung
Universität Dortmund
Otto-Hahn-Strasse 6, 44227 Dortmund (Germany)

[**] We thank Dr. N. Arnold for his assistance and valuable mycological hints, H. Avak and J. Oeßelmann (Themo Finnigan) for the IR-MS measurements, and Dr. F. Hampson for linguistic help. This work was supported by the Deutsche Forschungsgemeinschaft (SFB 369).

 © 2003 Wiley-VCH Verlag GmbH & Co. KGaA, Weinheim DOI: 10.1002/anie.200351066

It is tempting to speculate from the symmetric structure of orellanine (**1**) that it is generated from two molecules of 3-hydroxy-1*H*-pyridine-4-one (**3**). Oxidative 2,2′-dimerization would yield orelline (**2**), which is then converted into **1** by two consecutive N-oxidations. This assumption is supported by the detection of **3** in the acidified methanolic extract of *C. orellanus* together with 3,4-dihydroxypyridine-2-carboxylic acid (**4**), a further potential precursor of orellanine. Both compounds have been identified by a GC-MS comparison with synthetic samples. Compound **3** is already known to be a degradation product of mimosine and is present in dried leaves of *Leucaena leucocephala*.[8]

Several routes must be considered for the biosynthesis of simple pyridine derivatives. As in mimosine, the pyridine ring could be formed from lysine.[9] Alternatively, 3-hydroxy-1*H*-pyridine-4-one might be generated from ammonia and 3-hydroxy-4*H*-pyran-4-one, which in turn could, like maltol,[10] be derived from carbohydrates. In addition, anthranilic acid and tryptophan are also possible precursors. Both are transformed via 3-hydroxyanthranilic acid into nicotinic acid in animals and yeasts,[11] whereas in bacteria and higher plants nicotinic acid is built up from aspartic acid and dihydroxyacetone phosphate.[12]

Feeding experiments were carried out with toadstools in the natural environment in order to clarify the biosynthesis of orellanine. *C. orellanus* is very rare in Germany. For this reason *C. rubellus* Cooke (*C. speciosissimus* Kühn. Romagn.), which is more common and produces the same toxin, was used instead.[13] After injection of an aqueous solution of the labeled precursor into 5–20 fruit bodies of *C. rubellus*, the toadstools were left in the forest for 5 to 12 days. Then they were collected and the orellanine was isolated. Feeding experiments with [U-^{13}C]glucose or a mixture of U-^{13}C-labeled amino acids showed, according to the NMR analysis, no significant ^{13}C enrichment, which would rule out a direct biosynthetic origin from glucose or lysine. A feeding experiment with [U-^{13}C]glycerol was similarly negative.

In contrast, when [^{15}N]anthranilic acid was applied to the toadstool, ^{15}N NMR measurements indicated a minor incorporation in orellanine. However, the result was not conclusive on account of the very low rate of incorporation, which was approximately 0.1–0.2%. For this reason, the incorporation was determined by using highly sensitive ^{15}N/^{14}N isotope ratio mass spectrometry (IR-MS),[14] a method that was adapted from ^{13}C/^{12}C mass ratio measurements only a couple of years ago.[15] The ^{15}N enrichments obtained after feeding experiments with [^{15}N]anthranilic acid are given in Table 1.

The ^{15}N enrichment of approximately 30% unambiguously confirms the incorporation of [^{15}N]anthranilic acid into orellanine. By application of this method the detection limit for an enrichment is below 0.1%. When [*ring*-^{15}N]tryptophan was applied, the enrichment was only approximately 7%. This result suggests that anthranilic acid is converted directly into 3-hydroxyanthranilic acid, while the kynurenine pathway commencing from tryptophan obviously plays only a minor role. In order to exclude the possibility that the incorporation is due to degradation of anthranilic acid and an unspecific dissemination of ^{15}N in the fungi, $^{15}NH_4{}^{15}NO_3$ was fed in high doses (50 mg per fruit body) to *C. rubellus*, which led to a ^{15}N enrichment of only 13%.

Table 1: ^{15}N enrichment experiments with ^{15}N-labeled compounds fed to *C. rubellus*.

Substance fed	^{15}N/^{14}N ratio [%][a]	^{15}N enrichment [%][a]	Incorporation rate [%]
water (blank)	0.36705	0.20	0.00075
[^{15}N]anthranilic acid (sample 1)	0.46010	25.62	0.0938
[^{15}N]anthranilic acid (sample 2)	0.48497	32.40	0.1187
[*ring*-^{15}N]-DL-Trp	0.39323	7.35	0.0269
$^{15}NH_4{}^{15}NO_3$	0.41544	13.42	0.0491

[a] The ^{15}N enrichments refer to the natural ^{15}N/^{14}N ratio of 0.36630% in nitrogen from air (international standard).

The yield of orellanine was always considerably higher when the methanolic crude extract was acidified with some drops of 2N HCl during the workup procedure from *C. orellanus* and *C. rubellus*. It turned out that the neutral methanolic extract also contains two very polar compounds, which are converted to orellanine by acidification. The liquid chromatography mass spectra (LC-MS) suggest that these compounds are a mono- and a diglycoside of orellanine. The major component could be separated from accompanying carbohydrates by carefully performing HPLC on an amino phase. It was identified by one- and two-dimensional NMR spectroscopy to be orellanine-4,4′-di-β-D-glucopyranoside (**5**).[16] This conclusion is consistent with the fact that feeding *C. rubellus* with [U-^{13}C]glucose leads to high incorporation rates of up to 10% in the sugar moieties of **5**. The incorporation can be detected in the LC-MS by a mass shift of 6 or of 12 units, respectively, and the fragmentation pattern in the LC-MSMS (loss of m/z 168 ($^{13}C_6H_4O_5$)). The position of the glucose units has been proven by the HMBC correlations shown in Figure 1. The occurrence of orellanine in the form of a diglucoside that is soluble in water explains the contradictory reports in the literature on the solubility of this toxin.[17]

Based on the results outlined above we propose the following hypothetical pathway depicted in Scheme 1. However, the order of some steps remains arbitrary. The biosynthesis starts with anthranilic acid (**6**), which is converted via 3-hydroxyanthranilic acid (**7**) into 3,6-dihydroxyanthranilic acid

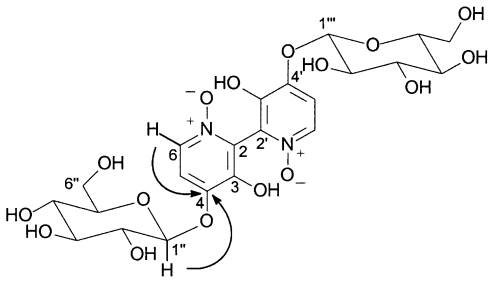
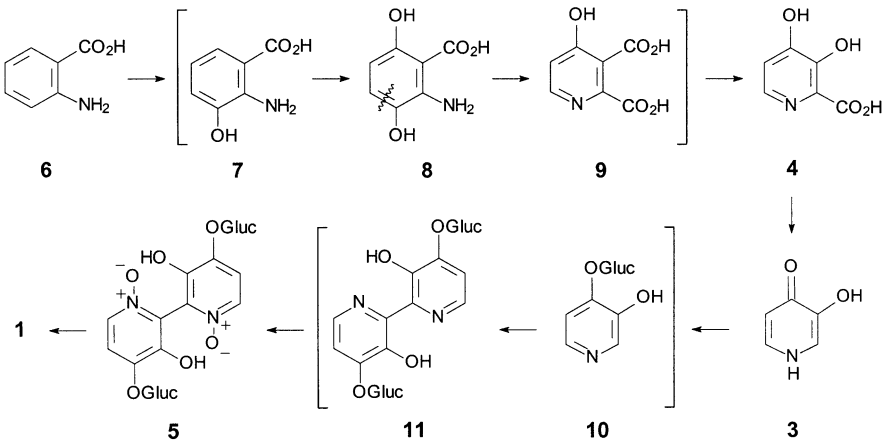


Figure 1. Orellanine-4,4′-diglucopyranoside (**5**) with selected HMBC correlations.

 © 2003 Wiley-VCH Verlag GmbH & Co. KGaA, Weinheim



Scheme 1. Hypothetical biosynthesis of orellanine (**1**) from anthranilic acid. Intermediates in brackets have not yet been identified in the toadstool.

(**8**). Recently, **8** has been recognized by us as a building block of the toadstool pigment blennione.[18] After oxidative ring opening and a new ring closure, 4-hydroxypyridine-2,3-dicarboxylic acid (**9**) could be generated from **8** and then converted by oxidative decarboxylation into 3,4-dihydroxypyridine-2-carboxylic acid (**4**), the precursor of 3-hydroxy-1*H*-pyridine-4-one (**3**). At the latest, at this stage formation of the 4-*O*-glucoside **10** should take place, which enables the regioselective coupling to orelline-4,4′-di-β-D-glucopyranoside (**11**) by generation of a phenoxy radical in position 2.[19] Twofold N-oxidation could finally lead to orellanine-4,4′-di-β-D-glucopyranoside (**5**). Orellanine (**1**) itself is generated by hydrolysis of the diglucoside **5** via the monoglucoside.

The result of a $^{18}O/^{16}O$ IR-MS experiment is in agreement with the proposed route.[20] It indicates that all oxygen atoms of orellanine originate from atmospheric oxygen, since a value of 11‰ was measured for $\Delta^{18}O$. This value is estimated to be approximately 30‰ for oxygen originating from water,[21] excluding precursors from carbohydrate metabolism.

Orellanine is another example for the involvement of anthranilic acid in the biosynthesis of the secondary metabolites of toadstools. In addition, 2-aminobenzaldehyde, the fragrance from *Hebeloma sacchariolens*,[22] the chromoalkaloid necatorone[23] from *Lactarius necator*, and the aminobenzoquinone pigments blennione[18] and lilacinone[24] from some *Lactarius* species are also derived from it.

Experimental Section

Feeding experiments with *C. rubellus* were performed from July to September in the years 1998 to 2001 in moist coniferous forests near Penzberg and Leutstetten in southern Bavaria (Germany). Typically, 5–20 fruit bodies were used for a single experiment. Each fruit body received 20 mg of the potential precursor dissolved in 20 mL of water, which was applied with a syringe. The treated fruit bodies were collected after 5–10 days and frozen at −20 °C.

Isolation of **1**: The frozen fruit bodies (10 g) were extracted with MeOH (3 × 100 mL) in a beaker for 30 min at 25 °C. The combined extracts were filtered and treated with 2 N HCl (10 mL). After evaporation of the solvent at 60 °C in vacuo, the residue was dissolved in 1 mL MeOH prepurified by passage through an RP18 cartridge. Compound **1** was isolated by preparative HPLC, $t_R = 23.5$ min (column: Nucleosil 100 C-18, 7 μm, 20 × 250 mm (Knauer); gradient: 100 % H_2O linear to 100 % MeOH in 40 min; flow rate: 6 mL min^{-1}; detection: UV at $\lambda = 280$ nm). Yield: 12 mg (0.12 % based on the fresh weight). ^{15}N NMR (61 MHz, [D_6]DMSO, reference: DMF $\delta = 77.7$ ppm): $\delta = 207.8$ ppm. LC/ESI-MS: $t_R = 16.4$ min (column: Nucleosil 100 C-18, 5 μm, 250 × 2 mm (Macherey-Nagel); gradient: 5 min isocratic with 100 % H_2O, then linear from 100 % H_2O to 100 % MeCN in 30 min, flow rate: 0.25 mL min^{-1}; detection: UV at $\lambda = 300$ nm); *m/z*: 253 $[M+H]^+$.

Isolation of **5**: The crude extract was prepared as described above for the isolation of **1**, except that the addition of acid was omitted and 50 g of frozen toadstool material was used. Compound **5** was isolated by HPLC from the extract. $t_R = 7$–12 min (column: Nucleosil 100 NH_2, 5 μm, 25 cm × 4.6 mm (Macherey-Nagel); solvent: MeCN/H_2O (1:1), isocratic; flow rate: 2 mL min^{-1}; detection: UV at $\lambda =$ 330 nm). Yield: 12 mg (0.024 % based on the fresh weight),[16] colorless solid. UV/Vis (H_2O): λ_{max} (lg ε) = 237 (3.68), 262 (sh, 3.14), 318 nm (3.15). CD (H_2O): λ_{max} ($\Delta\varepsilon$) = 220 (−1.5), 237 (−16.5), 257 (sh, −5.1), 284 (0.1), 314 (−5.6), 344 (0.9), 360 (−0.1), 373 nm (0.7). ^1H NMR (600 MHz, D_2O): $\delta = 3.43$ (dd, $^3J = 9.0$, 8.4 Hz, 2 H, 4″/4‴-H), 3.53 (dd, $^3J = 9.4$, 9.0 Hz, 2 H, 3″/3‴-H), 3.58 (dd, $^3J = 9.4$, 7.5 Hz, 2 H, 2″/2‴-H), 3.63 (dd, $^3J = 8.4$, 5.5 Hz, 2 H, 5″/5‴-H), 3.68 (dd, $^2J =$ 12.6, $^3J = 5.5$ Hz, 2 H, 6″/6‴-H), 3.84 (dd, $^2J = 12.6$, $^3J = 1.8$ Hz, 2 H, 6″/6‴-H), 5.07 (dd, $^3J = 7.5$, $^4J = 1.6$ Hz, 2 H, 1″/1‴-H), 7.01 (d, $^3J =$ 6.8 Hz, 2 H, 5/5′-H), 7.53 ppm (d, $^3J = 6.8$ Hz, 2 H, 6/6′-H). ^{13}C NMR (151 MHz, D_2O): $\delta = 61.1$ (C-6″/6‴), 69.9 (C-4″/4‴), 73.2 (C-2″/2‴), 75.7 (C-3″/3‴), 76.9 (C-5″/5‴), 100.9 (C-1″/1‴), 111.0 (C-5/5′), 126.3 (C-6/6′), 132.7 (C-2/2′), 151.5 (C-4/4′), 154.5 ppm (C-3/3′). LC/ESI-MS: $t_R = 13.1$ min (same program and column as described for the isolation of **1**), *m/z*: 577 $[M+H]^+$. LC/ESI-MS/MS (parent ion: *m/z* = 577, 25 eV) *m/z* (%): 577 (24) $[M+H]^+$, 415 (65) $[M+H-C_6H_{10}O_5]^+$, 253 (100) $[[M+H-(2\times C_6H_{10}O_5)]^+$.

Identification of **3** and **4** by GC-MS: Frozen fruit bodies (2 g) from *C. rubellus* and from *C. orellanus* were extracted with MeOH (2 × 20 mL). The combined extracts were filtered, 2 N HCl (2 mL) added, and the solvents removed in vacuo at 50 °C. The residue was dissolved in MeOH (2 mL), and carbohydrates were removed by preparative HPLC (RP-18 phase). The fractions containing the pyridine compounds were dried and treated with *N*-methyl-(trimethylsilyl)trifluoroacetamide (100 μL) for 2 h at 40 °C. GC-MS comparison was made by coinjection with corresponding authentic derivatives, which had been synthesized by literature methods[6e].

3,4-Bis(trimethylsilyloxy)pyridine: GC-MS (column: DB5 ms, 30 m × 0.25 mm, 0.25 μm, program: 2 min isotherm at 50 °C, then with 10 K min^{-1} linear to 300 °C): $R_i = 1430$; EI-MS: *m/z* (%): 255 (76), 240 (100), 182 (1), 168 (17), 147 (21), 152 (7), 75 (23), 73 (77), 45 (8).

3,4-Bis(trimethylsilyloxy)pyridine-2-carboxylic acid trimethylsilyl ester: GC-MS (measurement conditions as above): $R_i = 1820$; EI-MS: *m/z* (%): 371 (4), 356 (100), 298 (9), 254 (4), 194 (3), 147 (2), 73 (15).

Received: January 30, 2003 [Z51066]

Keywords: anthranilic acid · biosynthesis · mass spectrometry · natural products · orellanine

[1] H. Besl, A. Bresinsky, *Colour Atlas of Poisonous Fungi*, CRC, Boca Raton, FL, **1990**.

[2] Examples: a) J. F. Marichal, F. Trilby, J. L. Wiederkehr, R. Carbiener, *Nouv. Presse Med.* **1977**, *6*, 2973–2975; b) R. Flammer, *Schweiz. Med. Wochenschr.* **1982**, *112*, 1181–1184; c) T. Schumacher, K. Høiland, *Arch. Toxicol.* **1983**, *53*, 87–106; d) J.-M. Richard, J. Louis, D. Cantin, *Arch. Toxicol.* **1988**, *62*, 242–245; e) H. Prast, E. R. Werner, W. Pfaller, M. Moser, *Arch. Toxicol.* **1988**, *62*, 81–88; f) N. Delpech, S. Rapior, P. Donnadieu, A. P. Cozette, J. P. Ortiz, G. Huchard, *Nephrologie* **1991**, *12*, 63–66.
[3] S. Grzymala, *Z. Pilzkd.* **1957**, *23*, 139–142.
[4] S. Grzymala, *Bull. Trimest. Soc. Mycol. Fr.* **1962**, *78*, 394–404.
[5] W. Z. Antkowiak, W. P. Gessner, *Tetrahedron Lett.* **1979**, 1931–1934.
[6] a) E. V. Dehmlow, H.-J. Schulz, *Tetrahedron Lett.* **1985**, *26*, 4903–4906; b) M. Tiecco, M. Tingoli, L. Testaferri, D. Chianelli, E. Wenkert, *Tetrahedron* **1986**, *42*, 1475–1485; c) E. V. Dehmlow, H.-J. Schulz, *Liebigs Ann. Chem.* **1987**, 857–861; d) H. A. Hasseberg, H. Gerlach, *Helv. Chim. Acta* **1988**, *71*, 957–963; e) F. Trécourt, M. Mallet, O. Mongin, B. Gervais, G. Quéguiner, *Tetrahedron* **1993**, *49*, 8373–8380.
[7] M. Kubicki, T. Borowiak, W. Z. Antkowiak, *J. Crystallogr. Spectrosc. Res.* **1991**, *21*, 401–405.
[8] T. Acamovic, J. P. F. D'Mello, K. W. Fraser, *J. Chromatogr.* **1982**, *236*, 169–179, and references therein.
[9] a) J. W. Hylin, *Phytochemistry* **1964**, *3*, 161–164; b) H. P. Tiwari, W. R. Penrose, I. D. Spenser, *Phytochemistry* **1967**, *6*, 1245–1248.
[10] H. Chen, G. Agnihotri, Z. Guo, N. L. S. Que, X. H. Chen, H.-W. Liu, *J. Am. Chem. Soc.* **1999**, *121*, 8124–8125.
[11] Reviews: a) G. Magni, A. Amici, M. Emanuelli, N. Raffaelli, S. Ruggieri, *Adv. Enzymol. Relat. Areas Mol. Biol.* **1999**, *73*, 135–182; b) T. P. Begley, C. Kinsland, R. A. Mehl, A. Osterman, P. Dorrestein, *Vitam. Horm.* **2001**, *61*, 103–119.
[12] Review: R. F. Dawson, D. R. Christman, R. U. Bjerrum, *Methods Enzymol.* **1971**, *18B*, 90–113.
[13] G. E. B. Koller, K. Høiland, K. Janak, F. C. Stormer, *Mycologia* **2002**, *94*, 752–756. We also could detect the simple pyridine derivatives **3** and **4** in *C. rubellus.*
[14] W. A. Brand, *J. Mass Spectrom.* **1996**, *31*, 125–235.
[15] R. A. Werner, B. A. Bruch, W. A. Brand, *Rapid Commun. Mass Spectrom.* **1999**, *13*, 1237–1241.
[16] The yield of the diglucoside varies and depends on the age and the condition of the toadstools. In addition, major losses occur due to high sensitivity of **5** to hydrolysis and strong adsorption to the amino phase.
[17] H. Kürnsteiner, M. Moser, *Mycopathologia* **1981**, *74*, 65–72.
[18] P. Spiteller, W. Steglich, *J. Nat. Prod.* **2002**, *65*, 725–727.
[19] It cannot be excluded that the carboxylic acid **4** is coupled directly to the orelline diglucoside **11**, after its glucosylation. We are grateful to one of the reviewers for pointing this out.
[20] H.-L. Schmidt, R. A. Werner, A. Roßmann, *Phytochemistry* **2001**, *58*, 9–32.
[21] J. Koziet, *J. Mass Spectrom.* **1997**, *32*, 103–108.
[22] F. v. Nussbaum, W. Spahl, W. Steglich, *Phytochemistry* **1997**, *46*, 261–264.
[23] a) J. D. Klamann, B. Fugmann, W. Steglich, *Phytochemistry* **1989**, *28*, 3519–3522; b) "Bioactive Compounds from Plants": W. Steglich, B. Steffan, T. Eizenhöfer, B. Fugmann, R. Herrmann, J.-D. Klamann, *Ciba Found. Symp.* **1990**, *154*, 56–65.
[24] P. Spiteller, N. Arnold, W. Steglich, *J. Nat. Prod.*, submitted.

 © 2003 Wiley-VCH Verlag GmbH & Co. KGaA, Weinheim

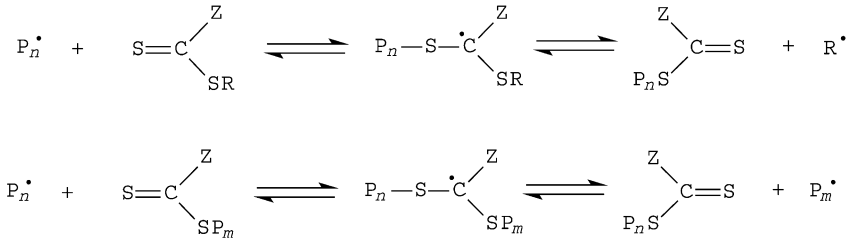
Controlled Radical Polymerization

Reaction of Cyclic Tetrathiophosphates with Carboxylic Acids as a Means to Generate Dithioesters and Control Radical Polymerization By RAFT**

Alex Duréault, Yves Gnanou, Daniel Taton,* Mathias Destarac, and Frédéric Leising*

Substantial research has been devoted in recent years to controlled radical polymerization (CRP).[1] The CRP methods combine the advantages of truly "living" systems with regard the quality of the polymers formed with the inherent ease of radical processes.[1] Among the CRP systems, nitroxide-mediated polymerization (NMP),[2] atom-transfer radical polymerization (ATRP),[3] and reversible addition fragmentation chain transfer (RAFT)[4] have been extensively investigated. However, all of these methods have drawbacks that limit their industrial development. For example, NMP often requires elevated temperatures and is only applicable to a limited number of monomers,[2] and ATRP, though very powerful, is ineffective for monomers that can poison the catalyst (e.g., acrylic acid, acrylamide); moreover, the removal of metal ions from polymers is an unresolved issue on the industrial scale.[3] As to the RAFT process, the preparation of the corresponding chain-transfer agents suffers from drawbacks, such as the use of carbon disulfide or iodine, two toxic reagents.[4] This situation shows the necessity to improve CRP methods before they can be implemented in industry.

Herein we describe the preparation of dithioesters by reaction of Davy reagents or P_4S_{10} with benzoic acid. These dithioesters serve to control in situ the free-radical polymerization of styrene and alkyl (meth)acrylates. Davy reagents and P_4S_{10} are commercially available cyclic tetrathiophosphates that are widely employed for the thionation of carbonyl groups and the preparation of thioamides, thiopeptides, thiolactams, and dithioesters.[5–9] Our aim is to provide an efficient, single-step procedure to access well-defined polymers by generating RAFT agents in situ. A major advantage of our approach is that polymerization can be initiated and controlled by chain-to-chain transfer of ω-thiocarbonylthio groups (Scheme 1)[4] without isolating any intermediates.



Scheme 1. Z = alkyl or aryl, OR, NR^2R^3, SR^4.

Styrene was first polymerized in the bulk at 110 °C in the presence of P_4S_{10} and PhCOOH in a one-pot procedure. After 50 h this afforded a polystyrene (PS) sample with M_n = 5800 g mol^{-1} and a polydispersity index (PDI) of 1.4 (34 % conversion). A similar reaction involving styrene, P_4S_{10}, and PhCOOH was also performed at 60 °C with azobis(isobutyronitrile) (AIBN), as a radical source. This vastly improved control over the polymerization: a PS sample with M_n = 3300 g mol^{-1} and PDI = 1.11 was obtained after 16 h (19 % conversion). To explain these differences, we hypothesized that the reaction between PhCOOH and P_4S_{10} generated dithiobenzoic acid (DTBA) as an intermediate (Scheme 2). Dithiobenzoic acid is usually prepared by reaction of bromobenzene with magnesium and subsequent treatment with CS_2 and aqueous HCl.[10,11] Dithioic acids, such as DTBA, add to substituted alkenes to form dithioesters. Depending on the electron density of the alkene, the addition can either result in a Michael-type reaction (path B) or follow a Markownikoff-type mechanism (path A).[12,13] Therefore, it is likely that the reaction between PhCOOH and P_4S_{10} first generated DTBA, which subsequently added to styrene to give phenylethyl dithiobenzoate (path A in Scheme 2). Such a dithioester, formed in situ, then acted as a chain-transfer agent (CTA) and controlled the RAFT polymerization of styrene.

Next, P_4S_{10} and PhCOOH were heated together in toluene, and the product formed was treated with NaH and bromopropionyl bromide. Propionyl dithiobenzoate was formed (path D in Scheme 2).

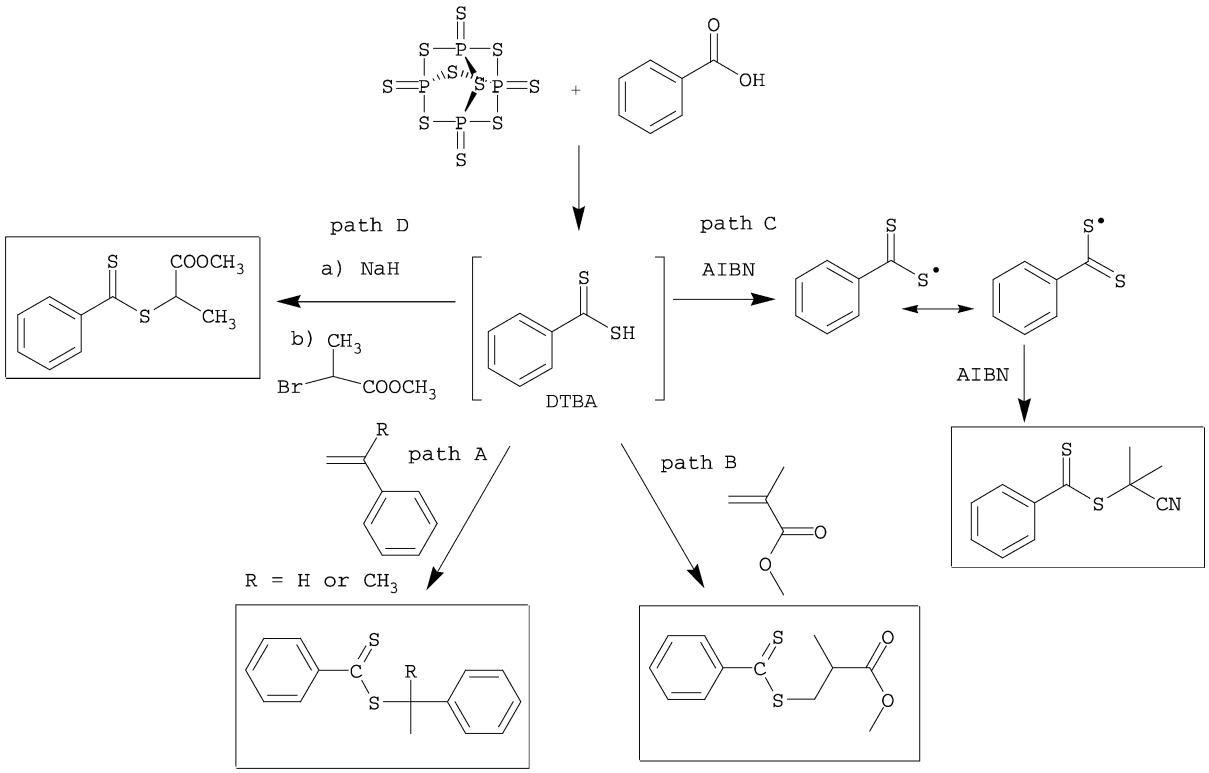
To account for the role of AIBN in the polymerization carried out at 60 °C, a mixture of PhCOOH, P_4S_{10}, and AIBN was heated in toluene at 110 °C (no monomer was added). After workup, cyanopropan-2-yl dithiobenzoate was recovered, as demonstrated by ^{1}H NMR spectroscopy. This dithioester was formed by the radical path C in Scheme 2.[14,15] Cyanopropan-2-yl dithiobenzoate being generated under these conditions methyl methacrylate (MMA) was added, and its polymerization was initiated with AIBN at 60 °C (Table 1). Figure 1 shows size exclusion chromatography (SEC) traces of samples at different reaction times: the molar mass of poly(methyl methacrylate) (PMMA) evolved linearly with increasing monomer conversion, and PDI values remained below 1.3, indicating a controlled polymerization.

Styrene was also polymerized in the presence of Davy-R reagents (Davy reagents carrying an R alkyl group) in

[*] Dr. Y. Gnanou, Dr. D. Taton, Dr. A. Duréault
Laboratoire de Chimie des Polymères Organiques
ENSCPB - Université Bordeaux 1
16 Avenue Pey-Berland, 33607 Pessac (France)
Fax: (+33) 5-5684-8487
E-mail: gnanou@enscpb.fr
taton@enscpb.fr
Dr. D. Taton, Dr. M. Destarac, Dr. F. Leising
RHODIA, Centre de Recherches d'Aubervilliers
52 rue de la Haie Coq, 93 308 Aubervilliers cedex (France)

[**] Financial support by Rhodia is gratefully acknowledged. RAFT = reversible addition fragmentation chain transfer.

 DOI: 10.1002/anie.200250770 © 2003 Wiley-VCH Verlag GmbH & Co. KGaA, Weinheim



Scheme 2.

Table 1: Polymerization of MMA in toluene at 60 °C with P_4S_{10}, PhCOOH, and AIBN.[a]

t [h]	Conversion [%]	M_n [g mol^{-1}]	PDI
0.62	11.2	6300	1.3
1.25	18.2	9200	1.25
2.25	32.3	14900	1.2
3.17	42.5	18700	1.19
17.17	100	42700	1.25

[a] [PhCOOH] = 0.06 mol L^{-1}; [AIBN] = 0.0135 mol L^{-1}; [MMA] = 5.82 mol L^{-1}.

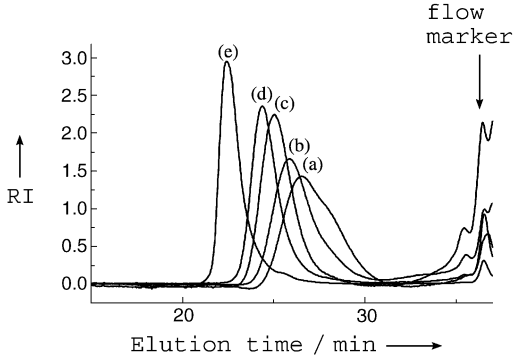
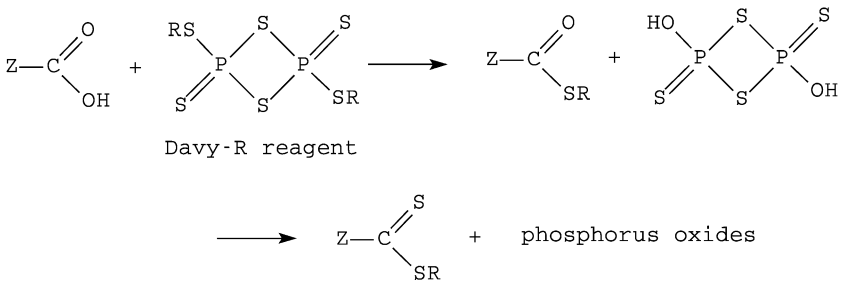


Figure 1. SEC traces (RI) of samples obtained by polymerizing MMA in toluene at 60 °C with P_4S_{10}, AIBN, and PhCOOH, see Table 1; a) *t* = 0.62 h, b *t* = 1.25 h, c) *t* = 2.25 h, d) *t* = 3.17 h, e) *t* = 17.17 h.

conjunction with PhCOOH. It was first verified that the reaction of a Davy-R reagent with PhCOOH effectively yields the dithioester PhC(=S)SR (Scheme 3).[7–11] Afterwards, styrene and AIBN were added to a medium containing benzyl dithiobenzoate formed in situ, and the mixture was heated to 60 °C (Table 2). A continuous increase in molar mass with increasing monomer conversion was observed by SEC. This indicates that methyl, phenyl, and benzyl dithiobenzoates formed in situ controlled the polymerization of styrene. The PDI of the PS samples decreased in the following order: R = benzyl > R = phenyl > R = methyl, which is related to the rate of fragmentation of the homolytic group R.[4] We also noted that the M_n



Scheme 3.

 © 2003 Wiley-VCH Verlag GmbH & Co. KGaA, Weinheim

Table 2: Polymerization of styrene in toluene at 60 °C with Davy-R reagents and PhCOOH.

R	*t* [h]	Conversion [%]	M_n [g mol^{-1}]	PDI
CH_3	17.83	7	2600	1.14
	118	50	15 000	1.72
Ph	44.5	17.5	2450	1.25
	141.5	37.5	2740	1.53
CH_2Ph	7.5	22	1200	1.1
	23	45	4000	1.05

values did not match those expected from the ratio of [monomer] to [PhCOOH] used. This result was attributed to incomplete formation of the dithioester from the reaction of Davy-R reagents with PhCOOH. However, all experiments were reproducible.

Finally, this method was applied to the synthesis of block copolymers. Figure 2 shows the SEC trace of a poly(methyl acrylate) (PMA) precursor synthesized by generating benzyl dithiobenzoate in situ and the subsequently formed PMA-*b*-PS diblock copolymer.

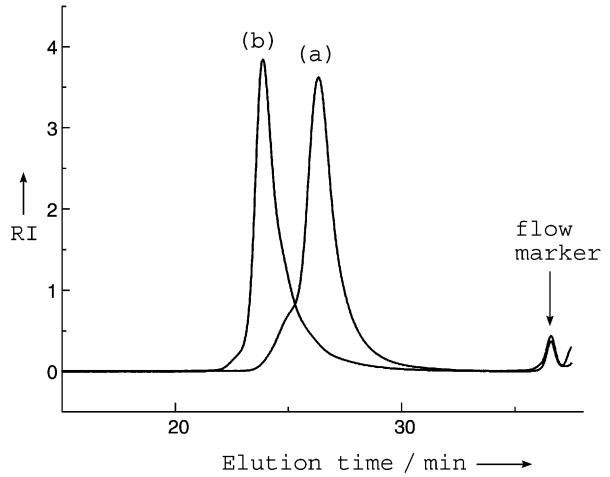


Figure 2. SEC traces (RI) of a PMA obtained by polymerizing MA in toluene at 60 °C with Davy-benzyl reagent and PhCOOH (a) and PMA-*b*-PS diblock copolymer after chain extension (b).

In summary, the use of P_4S_{10} or Davy reagents in conjunction with PhCOOH proved versatile in controlling the free-radical polymerization of styrene and (meth)acrylates under simple conditions. Dithioesters are generated in situ and serve as CTAs in a RAFT process. Dithiobenzoic acid formed by reaction of P_4S_{10} with PhCOOH is the key intermediate in the synthesis of dithioesters. Work is in progress to apply this simple method to the preparation of star polymers.

Experimental Section

AIBN was recrystallized from methanol. P_4S_{10}, Davy-R reagent (R = Me, Ph), benzyl thiol, benzoic acid, and methyl 2-bromopropionate (Aldrich) were used as received. Toluene, styrene, methyl methacrylate, and methyl acrylate (Aldrich) were distilled from CaH_2. The Davy-benzyl reagent was prepared as previously reported in ref. [1617] Polymerization reactions were performed after degassing by freeze–thaw cycles. NMR spectra were recorded on a Bruker AC200 NMR spectrometer. SEC was performed in THF at 25 °C (flow rate 1 mL min^{-1}) on a Varian apparatus equipped with refractive index (Varian)/UV dual detection and fitted with TSK column pack (G3,000HXL, G4,000HXL, G2,000HXL) or on a fast SEC column (PSS SDV linear M 5µ 8 × 300 mm). Calibration was performed with linear PS standards.

Synthesis of cyanoisopropyl dithiobenzoate (Scheme 2, path C): P_4S_{10} (580 mg, 1.3×10^{-3} mol), PhCOOH (670 mg, 5.5×10^{-3} mol), AIBN (2.5 g, 1.5×10^{-2} mol), and toluene (30 mL) were heated at 110 °C for 1 h. The mixture was poured into cyclohexane and the filtrate was purified by chromatography (silica gel in CH_2Cl_2 and alumina with hexane/diethyl ether 9/1). ^{1}H NMR (200 mHz, $CDCl_3$): $\delta = 1.9$ (6 H, s, $2 \times CH_3$), 7.4 (2 H, dd, *m*-ArH), 7.6 (1 H, dd, *p*-ArH), 7.9 ppm (2 H, d, *o*-ArH); ^{13}C NMR (50 mHz, $CDCl_3$): $\delta = 27$ (CH_3), 42.3 (C(CN)), 120.6 (CN), 127.3, 129.2, 133.5, 145.1 (ArC), 223.75 ppm (C=S); MS: *m*/*z* (%): 221 (11), 153 (16), 121 (85), 105 (68), 77 (100).

Synthesis of propionyl dithiobenzoate (Scheme 2, Path D): P_4S_{10} (7.3 g, 1.64×10^{-2} mol), PhCOOH (2 g, 1.64×10^{-2} mol), and toluene (30 mL) were heated at 110 °C for 1 h. The mixture was washed with water at pH 10. After washing with diethyl ether, the aqueous phase was reacidified. After addition of acetonitrile, the solution was treated with NaH. Methyl 2-bromopropionate bromide was added to this suspension and the mixture stirred for 20 h at room temperature. After concentration, the solution was washed with water and the product purified by column chromatography on silica gel in CH_2Cl_2/heptane (9/1). ^{1}H NMR (200 mHz, $CDCl_3$): $\delta = 1.67$ (3 H, d, CH_3), 3.76 (3 H, s, $COOCH_3$), 4.77 (1 H, q, $CSSCHCH_3$), 7.2–8.1 ppm (5 H, m, Ph); ^{13}C NMR (50 mHz, $CDCl_3$): $\delta = 127$–145 (Ar), 224 ppm (C=S); MS: *m*/*z* (%): 240 (8), 207 (7), 121 (100), 77 (31). Polymerization of MMA with P_4S_{10} and PhCOOH (Table 1): PhCOOH (67 mg, 5.5×10^{-4} mol), P_4S_{10} (58 mg, 1.31×10^{-4} mol), and AIBN (250 mg, 1.52×10^{-3} mol) were stirred at 110 °C in toluene (3 mL) for 1 h. After cooling to 60 °C, MMA (6 mL, 5.24×10^{-2} mol) and AIBN (20 mg, 1.22×10^{-4} mol) were added. The mixture was stirred for 24 h. The product was analyzed by SEC after removal of MMA by evaporation (Table 2).

Synthesis of benzyl dithiobenzoate (Scheme 3) and its use to control the polymerization of styrene (Table 2): Davy-benzyl reagent (370 mg, 8.25×10^{-4} mol), PhCOOH (207 mg, 1.65×10^{-3} mol), and toluene (15 mL) were heated at 110 °C for 1 h. Two-thirds of this mixture was withdrawn for analysis after purification by chromatography on silica gel (CH_2Cl_2). ^{1}H NMR (200 mHz, $CDCl_3$): $\delta = 4.62$ (2 H, s, CSS–CH_2Ph), 7.2–8.1 ppm (10 H, m, Ph); ^{13}C NMR (50 mHz, $CDCl_3$): $\delta = 42.88$ (SCH_2Ph), 127–145 (Ar), 224 ppm (C=S); MS: *m*/*z* (%): 244 (13), 228 (25), 121 (22), 105 (100), 91 (37), 77 (38). The remaining third of the mixture was cooled to 60 °C and then styrene (6 mL, 5.24×10^{-2} mol) and AIBN (17.2 mg, 1.05×10^{-4} mol) were added. The solution was analyzed by SEC after removal of styrene by evaporation.

Received: December 13, 2002
Revised: February 12, 2003 [Z50770]

Keywords: block copolymers · phosphorus · polymerization · radical reactions · sulfur

[1] *Handbook of Radical Polymerization* (Eds.: K. Matyjazsewski, T. Davis), Wiley, New York, **2002**.
[2] C. J. Hawker, A. W. Bosman, E. Harth, *Chem. Rev.* **2001**, *101*, 3661.
[3] K. Matyjaszewski, J. Xia, *Chem. Rev.* **2001**, *101*, 2921.

 © 2003 Wiley-VCH Verlag GmbH & Co. KGaA, Weinheim

[4] G. Moad, J. Chiefari, B. Y. K. Chong, J. Krstina, R. T. A. Mayadune, A. Postma, E. Rizzardo, S. H. Thang, *Polym. Int.* **2000**, *33*, 993.
[5] M. Yokoyama, Y. Masegawa, H. Hatanaka, Y. Kawazoe, T. Imamoto, *Synthesis* **1984**, 827.
[6] H. J. Davy, *J. Chem. Soc. Chem. Commun.*. **1982**, 457.
[7] H. Davy, P. Metzner, *Chem. Ind.* **1985**, 824.
[8] G. Tabak, T. N. Pham, G. Levesque, *Polymer* **1998**, *39*, 5561.
[9] A. Sudalai, S. Kanagasabapathy, B. C. Benicewicz, *Org. Lett.* **2000**, *2*, 3213.
[10] R. Jayalakshmi, S. R. Ramadas, C. N. Pillai, *Org. Prep. Proced. Int.* **1981**, *13*, 71.
[11] R. U. Bai, Y. Z. You, C. Y. Pan, *Polym. Int.* **2000**, *49*, 898.
[12] S. Oae, T. Yagihara, T. Okabe, *Tetrahedron* **1972**, *28*, 3203 – 3216.
[13] G. Levesque, G. Tabak, F. Outurquin, J. C. Gressier, *Bull. Soc. Chim. Fr.* **1976**, *7–8*, 1156.
[14] G. Bouhadir, N. Legrand, B. Quiclet-Sire, S. Z. Zard, *Tetrahedron Lett.* **1999**, *40*, 277 – 280.
[15] S. H. Thang, B. Y. K. Chong, R. T. A. Mayadunne, G. Moad, E. Rizzardo, *Tetrahedron Lett.* **1999**, *40*, 2435 – 2438.
[16] H. Davy, *Sulfur Lett.* **1985**, *3*, 39
[17] G. Ohms, U. Fleischer, V. Kaiser, *J. Chem. Soc. Dalton Trans.* **1995**, 1297.

 © 2003 Wiley-VCH Verlag GmbH & Co. KGaA, Weinheim

Meso-Macroporous Metal Oxides

Hierarchically Mesoporous/Macroporous Metal Oxides Templated from Polyethylene Oxide Surfactant Assemblies**

*Jean-Luc Blin, Alexandre Léonard, Zhong-Yong Yuan, Laurent Gigot, Aurélien Vantomme, Anthony K. Cheetham, and Bao-Lian Su**

Surfactant templating techniques based on electrostatic, hydrogen-bonding, covalent, and van der Waals interactions between organic and inorganic species have been developed for the synthesis of materials with a narrow mesopore size distribution and controlled pore structure.[1,2] The use of block copolymers was recently shown to extend the pore sizes of ordered mesoporous oxides up to ten nanometers.[3,4] In addition, macroporous materials with pore sizes ranging from 100 nm to 1 μm can be obtained using latex spheres as templating agents.[5–8] The fabrication of hierarchically ordered structures at multiple length scales has attracted much interest from both a fundamental and practical viewpoint.[9,10] The combination of surfactant and colloidal crystal templating methods, together with microfabrication techniques allows the construction of hierarchical micro/meso/macroporous architectures.[10–15] In this report, hierarchical mesoporous metal oxides with a novel macroporous architecture were synthesized in one step by single-surfactant templating without the need for polymeric spheres to act as a template that generates the macroporous structure. Polyethylene oxide (PEO) surfactants were used, which have been shown to efficiently organize mesoporous materials with structures of disordered wormhole-like MSU-type[16–18] and ordered SBA-*n*[19] and CMI-1[20] materials.

The occurrence of pores with a bimodal pore-size distribution in mesoporous materials is important and useful for both catalysis and the engineering of pore systems.[21] Mesoporous metal-oxide molecular sieves with macroporous structures are of interest as potential catalysts and sorbents, partly because the textural mesopores and intrinsic interconnected pore systems of macrostructures should efficiently transport guest species to framework binding sites. Biomimetic vesicular structures can be formed when the ionic strength of the nonionic surfactant solution is raised from that of the pure aqueous solution through the modification of PEO–H_2O hydrogen bonding; one kind of bimodal mesoporous silica has been synthesized by adding dilute electrolytes during PEO-templating.[22] Spongelike silica membranes with three-dimensional meso-macrostructures (that is, materials composed of mesopores of 2–50 nm in diameter, and macropores with diameters of between 50 nm and several micrometers) were synthesized from an electrolyte phase of a block copolymer/silica system, though inorganic salt crystals inevitably grew together with the silica membrane.[23] Meso-macroporous niobium oxides have also been prepared by adding NaCl to a ligand-assisted templating mixture of niobium ethoxide and amine surfactants; the salt was emphasized as being necessary for macropore (vesicle) formation.[24] We have used a simple method to prepare mesoporous metal oxides, such as TiO_2 and ZrO_2, with macroporous hierarchical structure by the cooperative assembly of nonionic alkyl-PEO surfactants and inorganic precursors derived from metal alkoxides. The synthesized materials exhibit both wormhole-like mesochannels and a funnel-like macrostructure with more accessible pores and a very high internal surface area, which should be significant in processes involving large molecules.

$C_{16}(EO)_{10}$ and $C_{13}(EO)_6$ surfactants were employed as structure-directing agents, and zirconium *n*-propoxide and titanium isopropoxide were used as inorganic precursors. Hydrothermal treatment was performed in a teflon-lined autoclave at 60–80 °C for one to two days. Almost all of the surfactant species in the product channels could be removed by ethanol extraction (as confirmed by IR measurements),

[*] Prof. Dr. B.-L. Su, Dr. J.-L. Blin, A. Léonard, Dr. Z.-Y. Yuan, L. Gigot, A. Vantomme
Laboratory of Inorganic Materials Chemistry
Institute of Studies in Interface Sciences
The University of Namur (FUNDP)
61 rue de Bruxelles, 5000 Namur (Belgium)
Fax: (+32) 81-725-414
E-mail: bao-lian.su@fundp.ac.be
Prof. Dr. A. K. Cheetham
Materials Research Laboratory
University of California
Santa Barbara, CA 93106 (USA)

[**] This work has been carried out within the framework of the Belgian Federal Government PAI-IUAP-5/01 project. A.L. is a FRIA fellow. Z.Y.Y. is a PAI-IUAP research fellow. A.K.C. is the International Francqui Chair holder of Belgium (2000–2002).

Supporting information for this article is available on the WWW under http://www.angewandte.org or from the author.

 © 2003 Wiley-VCH Verlag GmbH & Co. KGaA, Weinheim DOI: 10.1002/anie.200250816

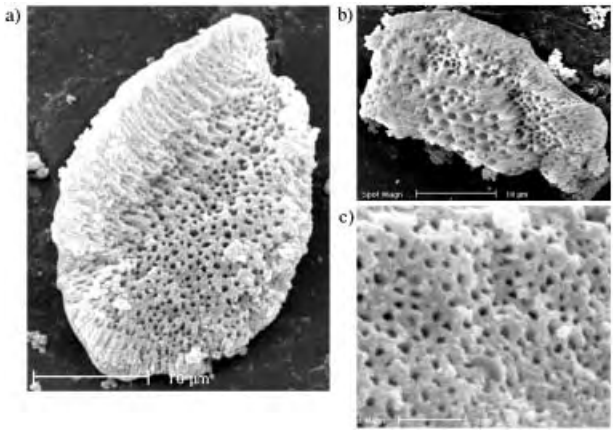


Figure 1. Representative SEM images of mesoporous zirconium oxides showing a novel macroporous structure.

which avoids possible structural collapse caused during high-temperature calcination to free the pores. Figure 1 shows several representative scanning electron microscopy (SEM) images of the synthesized macro-mesoporous zirconia materials, while Figure 2 displays transmission electron microscopy (TEM) images of the zirconia meso-macrostructures viewed along various directions of the macropores. Almost all of the obtained zirconia particles exhibit macroscopic network structures with relatively homogenous macropores of 300–600 nm in dimension, revealed by both SEM and TEM micrographs. A closer observation (Figure 2a) shows some regularity in the macropore array of the oxides formed using single-surfactant templating. Moreover, the macrochannels are arranged parallel to each other and perpendicular to the tangent of the surface of the particle; the pores are funnel-like

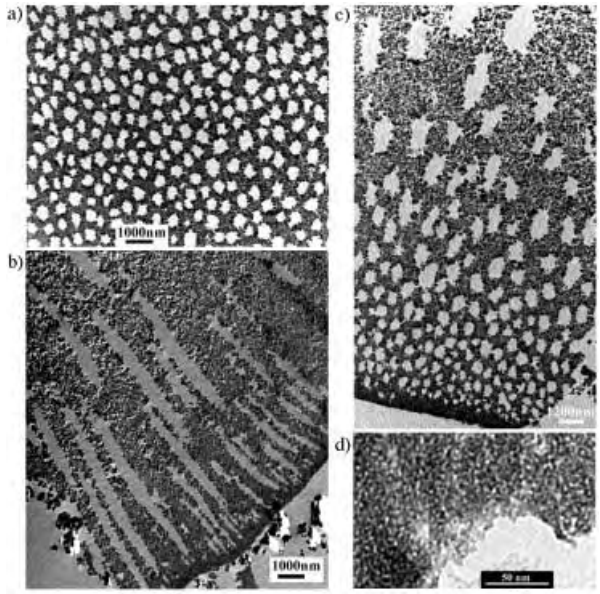


Figure 2. TEM images of ultrathin sections of the macro-mesoporous zirconias. a–c) Low-magnification images of the macropores viewed parallel, perpendicular, and side-on to the pores, respectively; d) a higher magnification image of the macropore walls showing the wormhole-like mesophase.

(tapered towards the center) in shape. TEM images also revealed that the oxide macroporous framework is composed of accessible mesochannels with a wormhole-like array (Figure 2d).

X-ray diffraction shows that the zirconia frameworks possess amorphous walls. One diffraction peak is present in the small-angle region, which is indicative of a disordered mesostructure (see Figure S1 of the Supporting Information). Representative nitrogen adsorption–desorption isotherms and the corresponding Barrett–Joyner–Halenda (BJH) pore-size distributions (obtained from an analysis of the adsorption branch of the isotherm) are shown in Figure 3. A strong uptake of N_2 as a result of capillary condensation is

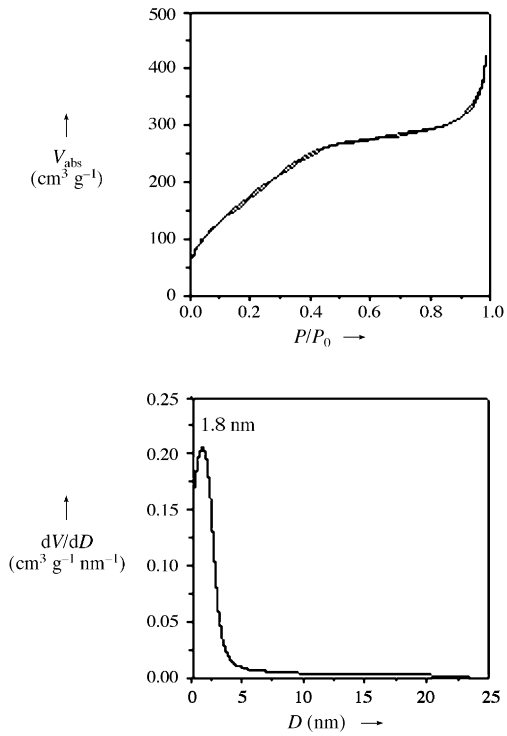


Figure 3. N_2 adsorption–desorption isotherm (left) and the corresponding BJH pore-size distribution curve (right) of macro-mesoporous zirconia. The pore-size distribution was determined from the adsorption branch of the isotherm.

observed in a relative pressure (P/P_0) range of 0.14–0.40 and reaches a plateau at 0.80. This kind of isotherm indicates that the final materials belong to the mesoporous family, with pore sizes close to 2.0 nm. The analysis of pore-size distributions confirms this tendency; the maximum in the BJH pore-size distribution curve is centered at about 1.8 nm. The existence of openings with a pore-diameter distribution located in this range can also be displayed using the Horvath–Kawazoe (HK) method. For relative pressures greater than 0.85, the adsorbed volume of nitrogen increased significantly, rather than remaining constant, because of saturation, which suggests that the material contains an appreciable amount of secondary porosity. Therefore, TEM and SEM observation and N_2 adsorption analysis have revealed that the materials

 © 2003 Wiley-VCH Verlag GmbH & Co. KGaA, Weinheim

exhibit a bimodal pore-size distribution, and are truly meso-macroporous systems. A very high surface area of 550–700 $m^2 g^{-1}$ can be obtained from these materials when synthesized with different surfactant to zirconium ratios. An increase in mesopore size up to 2.6 nm could arise from the increase of hydrothermal temperature or time, though no evident change was observed on the macroporous structure.

Synthesis was carried out at surfactant weight percentages that, according to the phase diagram, afford the existence of micelles in solution (for instance, 10 wt% $C_{16}(EO)_{10}$). The surfactant micellar solution reacted with the metal-oxide species hydrolyzed from the transition-metal alkoxide precursors. Mesostructured surfactant/metal oxide compounds were formed by a well-known neutral surfactant-templating pathway[16,17] through cooperative assembly of hydrolyzed inorganic species and amphiphilic PEO-surfactants. The condensation rates of metal alkoxides in aqueous solutions are normally faster than those of silicon alkoxides, while for zirconium *n*-propoxide, the precipitation rate is very fast when the ratio between the concentration of water and zirconium is higher than four.[25] In this study, the ratio of water to zirconium is located in a range from 20 to 300. Thus, hydrolysis and condensation occurred as soon as $[Zr(OC_3H_7)_4]$ was added to the micellar solution, and the mesostructured surfactant/zirconia nanoparticles are formed with a large number of surface hydroxyl groups, as a result of incomplete condensation. These particle surfaces can be regarded as hydrophilic or polar.

Those surfactant molecules that are not consumed in solution can generally be adsorbed onto hydrophilic solid surfaces, and can then self-assemble at the solid/solution interface following a two-step mechanism.[26–30] Firstly, single molecules are bound through head-group adsorbent interactions. Further adsorption is then strongly promoted by hydrophobic interactions between the tail groups. As a result of the fixation at the solid substrate, the process of surface aggregation takes place at critical aggregate concentrations much lower than the bulk-phase critical micelle concentration. This indicates that the aggregates are truly self-assembled on the surface, and that they are not micelles that are formed in the bulk which then get adsorbed on the surface. An aggregative adsorption process appears to be a cooperative process involving strong lateral interactions between surfactants and weak interactions with the solid surface. Amphiphilic self-assembled aggregates can have a variety of geometrical shapes.[31] Nonionic PEO-surfactants have been observed to form either globular aggregates or continuous bilayer structures on hydrophilic silica.[29] In the present work, the adsorption and self-assembly of surfactant molecules on the external surfaces of zirconia/surfactant nanocomposites occurs to form surface aggregates (otherwise known as "hemi-micelles"[32]) during the formation of internal mesostructures. These primary aggregates can attract more individual surfactant micelles to form "supermicelles". Hydrothermal treatment may play an important role in the formation of supramicellar aggregates, since temperature has a significant effect on the supramolecular organization of surface-active species in aqueous solution.[33] Under static autoclaving, the aggregates may develop following the defined direction (which is perpendicular to the external surface of monolith particles) through micellar coalescence, which generates threadlike (or conical) supermicellar aggregates with the lengths in the micrometer range and diameters in the submicrometer range. Thus, hierarchical monolithic particles form during the aggregation of surfactant/zirconia nanocomposites and these supermicelles should interlink successfully with the surfactant micelles in mesochannels. The removal of the surfactant by ethanol extraction results in the presence of hierarchical mesoporous–macroporous structures with conical (tapered towards the center) parallel macropores. Figure 4 illustrates the proposed formation mechanism

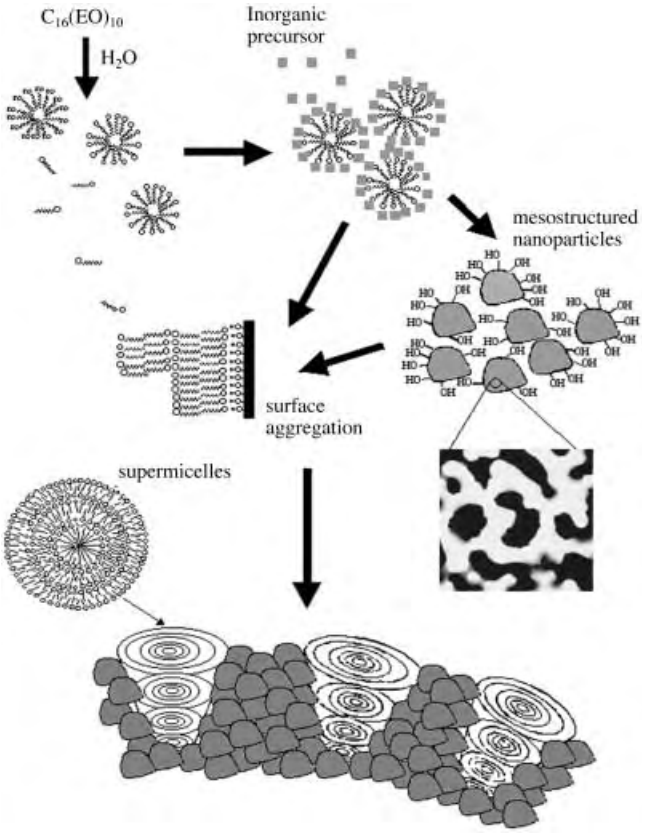


Figure 4. Proposed mechanistic scheme for the formation of macro-mesostructured metal oxides.

of such an architecture. The meso-macrostructured oxide network with open and accessible pores can be successfully preserved after calcination at 500 °C, which indicates a high thermal stability (see Supporting Information). It is expected that meso-macrostructured materials with different macropore shapes could be synthesized by tuning the morphology of supermicelles by varying the experimental parameters, such as pH value, surfactant concentration, hydrothermal temperature, and reaction time.

It is known that the microemulsion droplets induced by stirring can be used to template the macropores. However, these macropores are generally nonuniform or spherical, whereas the macroporous structure in our materials is ordered, regular, and shaped, which compares favorably

 © 2003 Wiley-VCH Verlag GmbH & Co. KGaA, Weinheim

with the well-known liquid-crystal phase behavior of surfactant micelles. Moreover, it was found that the stirring rate did not affect the formation of the macropore structure, and the macropores were even found to be present in the zirconia particles. These were synthesized without stirring the mixture of the Zr precursor and surfactant solution, in which emulsified droplets were not present. A significant amount of C_3H_7OH is generated during the condensation process, and one might expect that this is related to macropore formation. However, further study has shown that propanol has no significant effect on the macropore formation.

The macroporous structure of mesoporous titania has also been obtained by this simple surfactant-templating method. The structure is similar to that of the zirconia materials, but has a larger macropore size (up to about 5 μm) and wormhole-like mesopores of 5 nm dimensions (see Supporting Information). This synthetic strategy can be successfully applied to other metal oxides, such as Nb_2O_5, Ta_2O_5, Al_2O_3, and CeO_2, to prepare macroporous–mesoporous hierarchical structures. The experimental results indicate that the present method is versatile and can be generalized for the formation of macro-mesostructured metal oxides.

In summary, one kind of novel mesoporous metal oxide with funnel-like macroporous structures has been synthesized by a simple surfactant-templating process, which has important implications for use in catalysis, molecular separations, and biological-cell encapsulation. This kind of material can be employed to design inorganic membranes that may be applied in various domains such as process filtration, cell culture, or laboratory filtration. Functionalization of these materials by chemical modifications of their internal pore surface may lead to more practical applications. Additionally, these three-dimensional open structures can also be used as templating materials for the inverted synthesis of new advanced porous materials.

Experimental Section

A micellar solution (5–30 wt%) of decaoxyethylene cetyl ether ($C_{16}(EO)_{10}$) or of polyoxyethylene(6)tridecyl ether ($C_{13}(EO)_6$) was prepared by dissolving the surfactant at room temperature in an aqueous solution for 3 h. Zirconium *n*-propoxide ($[Zr(OC_3H_7)_4]$, 70 wt% in 1-propanol) or titanium isopropoxide ($[Ti(OC_3H_7)_4]$, 97%) was added dropwise to the above medium, followed by further stirring for 3 h at room temperature. The obtained mixture was then transferred to a teflon-lined autoclave and heated under static conditions at 60 °C for 48 h for zirconia, or 80 °C for 24 h for titania. The product was filtered and washed by soxhlet extraction over ethanol for 48 h to remove the surfactant species. X-ray diffraction was carried out on a Philips PW1820 diffractometer using $Cu_{K\alpha}$ radiation. N_2 adsorption and desorption isotherms were determined on a Micromeritics ASAP 2010 sorptometer at −196 °C. Scanning electron microscopy and transmission electron microscopy were carried out on Philips XL-20 (15 keV) and Philips TECNAI-10 (100 kV) microscopes, respectively. The specimen for TEM observation was prepared by epoxy-imbedded microsection and by being mounted on a copper grid.

Received: December 20, 2002
Revised: April 9, 2003 [Z50816]

Keywords: macroporous materials · mesoporous materials · self-assembly · titanium · zirconium

[1] A. Sayari, P. Liu, *Microporous Mater.* **1997**, *12*, 149.
[2] J. Y. Ying, C. P. Mehnert, M. S. Wong, *Angew. Chem.* **1999**, *111*, 58; *Angew. Chem. Int. Ed.* **1999**, *38*, 56.
[3] D. Zhao, J. Feng, Q. Huo, N. Melosh, G. H. Fredrickson, B. F. Chmelka, G. D. Stucky, *Science* **1998**, *279*, 548.
[4] P. Yang, D. Zhao, D. I. Margolese, B. F. Chmelka, G. D. Stucky, *Nature* **1998**, *396*, 152.
[5] B. T. Holland, C. F. Blanford, A. Stein, *Science* **1998**, *281*, 538.
[6] S. H. Park, Y. Xia, *Adv. Mater.* **1998**, *10*, 1045.
[7] C. F. Blanford, H. Yan, R. C. Schroden, M. Al-Daous, A. Stein, *Adv. Mater.* **2001**, *13*, 401.
[8] O. D. Velev, T. A. Jede, R. F. Lobo, A. M. Lenhoff, *Chem. Mater.* **1998**, *10*, 3597.
[9] I. Soten, G. A. Ozin, *Curr. Opin. Colloid Interface Sci.* **1999**, *4*, 325.
[10] P. Yang, T. Deng, D. Zhao, P. Feng, D. Pine, B. F. Chmelka, G. M. Whitesides, G. D. Stucky, *Science* **1998**, *282*, 2244.
[11] B. T. Holland, L. Abrams, A. Stein, *J. Am. Chem. Soc.* **1999**, *121*, 4308.
[12] B. J. Zhang, S. A. Davis, S. Mann, *Chem. Mater.* **2002**, *14*, 1369.
[13] M. Antonietti, B. Berton, C. Göltner, H. Hentze, *Adv. Mater.* **1998**, *10*, 154.
[14] B. Lebeau, C. E. Fowler, S. Mann, C. Farcet, B. Charleux, C. Sanchez, *J. Mater. Chem.* **2000**, *10*, 2105.
[15] R. A. Caruso, M. Antonietti, *Adv. Funct. Mater.* **2002**, *12*, 307.
[16] S. A. Bagshaw, E. Prouzet, T. J. Pinnavaia, *Science* **1995**, *269*, 1242.
[17] S. A. Bagshaw, T. J. Pinnavaia, *Angew. Chem.* **1996**, *108*, 1180; *Angew. Chem. Int. Ed. Engl.* **1996**, *35*, 1102.
[18] E. Prouzet, T. J. Pinnavaia, *Angew. Chem.* **1997**, *109*, 533; *Angew. Chem. Int. Ed. Engl.* **1997**, *36*, 516.
[19] D. Zhao, Q. Huo, J. Feng, B. F. Chmelka, G. D. Stucky, *J. Am. Chem. Soc.* **1998**, *120*, 6024.
[20] J. L. Blin, A. Léonard, B. L. Su, *Chem. Mater.* **2001**, *13*, 3542.
[21] Z. Y. Yuan, J. L. Blin, B. L. Su, *Chem. Commun.* **2002**, 504.
[22] S. A. Bagshaw, *Chem. Commun.* **1999**, 1785.
[23] D. Zhao, P. Yang, B. F. Chmelka, G. D. Stucky, *Chem. Mater.* **1999**, *11*, 1174.
[24] D. M. Antonelli, *Microporous Mesoporous Mater.* **1999**, *33*, 209.
[25] L. Davies, L. Daza, P. Grange, *J. Mater. Sci.* **1995**, *30*, 5087.
[26] H. Lippold, K. Quitzsch, *Colloids Surf. A* **2000**, *172*, 1.
[27] G. G. Warr, *Curr. Opin. Colloid Interface Sci.* **2000**, *5*, 88.
[28] S. Manne, H. E. Gaub, *Science* **1995**, *270*, 1480.
[29] L. M. Grant, F. Tiberg, W. A. Ducker, *J. Phys. Chem. B* **1998**, *102*, 4288.
[30] P. Levitz, H. van Damme, *J. Phys. Chem.* **1984**, *88*, 2228.
[31] J. Israelachvili, *Intermolecular and Surface Forces*, Academic Press, New York, **1992**.
[32] A. M. Gaido, D. W. Fuerstenau, *Trans. Am. Inst. Min. Metall. Pet. Eng.* **1955**, *202*, 958.
[33] K. Toerne, R. Rogers, R. von Wandruszka, *Langmuir* **2001**, *17*, 6119.

 © 2003 Wiley-VCH Verlag GmbH & Co. KGaA, Weinheim

Schiff Base Based Catalysts

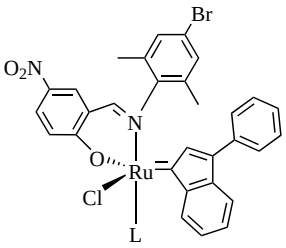
Synthesis of Highly Active Ruthenium Indenylidene Complexes for Atom-Transfer Radical Polymerization and Ring-Opening-Metathesis Polymerization**

*Tom Opstal and Francis Verpoort**

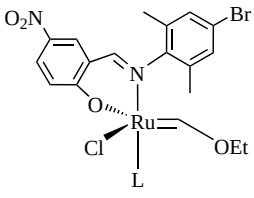
During the last few years ruthenium-based alkylidene complexes bearing N-heterocyclic carbene ligands (NHC) have provided a rush of highly active catalysts for olefin metathesis.[1] Soon thereafter it was recognized that these complexes have more to offer than first thought since they can be successfully introduced in controlled radical reactions, such as atom-transfer radical addition (ATRA)[2] and atom-transfer radical polymerization (ATRP).[3] This trump card opens up vistas for elegant processes that can ultimately streamline multistep sequences and enable diverse post-metathesis functionalizations.

ATRP has developed into one of the most robust synthetic tools available among controlled radical polymerization reactions and it has opened new synthetic routes to a variety of polymeric materials.[4–6] These reactions combine the robustness (functional-group tolerance, an almost no sensitivity to moisture) and the possibility for scale up of a radical polymerization with the absence of the termination and transfer reactions of a living process. The basis of ATRP is the reversible transfer of a (pseudo)halogen atom from a monomeric or polymeric alkyl halide to a transition-metal complex in a lower oxidation state, thus forming an organic radical and a metal complex in a higher oxidation state. Since this equilibrium is shifted to the side of the dormant species, the number of radicals remains very low. Furthermore the exchange between oxidized catalyst and organic radical is very fast which results in an uniform growth of the polymer chains. A strategy that has proven to be very successful in olefin metathesis is the combination of a strongly binding NHC ligand and a rather labile group, such as a phosphane,[1c,d] pyridine,[7] or readily dissociating metal fragments.[8] Another approach that has been pursued, is the use of so-called "dangling ligands".[9] Especially the last variant gives access to robust and stable catalysts at room temperature but highly active systems at slightly elevated temperatures. Sometimes it is necessary to mix monomer and catalyst at room temperature, put them in an appropriate mould, and heat the mixture to start the reaction. In this context we have successfully implemented Schiff base ligands of the salicylaldiminato type as dangling ligands in both olefin metathesis[10] and enol–ester synthesis with alkylidene, indenylidene, and vinylidene fragments.[11] The two donor atoms of this ligand have opposing natures, the phenolate oxygen atom is a hard donor and is known to stabilize the higher oxidation states of ruthenium,[12] whereas the imine nitrogen atom is in comparison soft and is a stabilizer of the lower oxidation states.[13] This ligand fulfils the strict requirements necessary to establish the atom-transfer equilibrium in ATRA and ATRP.[14] Following on from these investigations, we recognized that combining an N-heterocyclic carbene ligand with a bidentate salicylaldimine ligand in the same compound should lead to superior performance because: 1) the strong electron-donating ability of the imidazol-2-ylidene-type ligand can facilitate the decoordination of one side of the bidentate ligand plus it can stabilize the generated intermediate;[15] 2) the bulky mesitylene groups protect the carbene species and prevent bimolecular decomposition;[16] 3) with a phosphane-free catalyst P–C decomposition reactions are avoided.[17]

We synthesized four mixed-ligand ruthenium–(3-phenyl-1-indenylidene) Schiff base complexes **1**–**4**, and found that the reactivities of these species bear comparison with the most active ruthenium-based systems reported to date. These easily accessible and air-stable catalysts combine high activity with a very long catalyst life-time.



1 (L = PCy_3)
2 (L = 1,3-dimesityl-4,5-dihydroimidazol-2-ylidene



3 (L = PCy_3)
4 (L = 1,3-dimesityl-4,5-dihydroimidazol-2-ylidene

Methyl methacrylate (MMA) was chosen as a representative monomer and the polymerization was initiated by ethyl-2-bromo-2-methylpropionate at 85 °C. From the results summarized in Table 1, it appears that the neutral indenylidene complex **1** is moderately active for the conversion of MMA, but the polymer is produced in a well-controlled manner and possesses a very narrow molecular-weight distribution (MWD) ($M_w/M_n = 1.19$).

The molecular weight agrees with the calculated one as indicated by the high initiator efficiency ($f = 0.92$). To increase the activity of the ruthenium–indenylidene systems, a potentially more active 14-electron complex was generated in situ by treating the neutral complex with $AgBF_4$. In this way the chloride was abstracted at room temperature before the monomer and initiator were added.

The active species generated in this way is a cationic ruthenium complex where BF_4^- acts as a counterion. With this cationic species, we studied the possibility to perform

[*] Prof. Dr. F. Verpoort, T. Opstal
Department of Inorganic and Physical Chemistry
Laboratory of Organometallic Chemistry and Catalysis
Ghent University
Krijgslaan 281 (S-3), 9000 Ghent (Belgium)
Fax: (+32) 9-264-4983
E-mail: francis.verpoort@rug.ac.be

[**] We thank the FWO-Flanders and the Research found (BOF) of Ghent University for financial support.

 © 2003 Wiley-VCH Verlag GmbH & Co. KGaA, Weinheim DOI: 10.1002/anie.200250840

Table 1: Ruthenium-catalyzed controlled atom-transfer radical polymerization of MMA.[a]

Conditions	Catalyst	Conversion [%]	M_n[b] [$\times 10^3$]	M_w/M_n	f[c]
neutral[d]	**1**	54	23.5	1.19	0.92
cationic[e]	**1**	73	37.6	1.30	0.78
toluene/water[f]	**1**	82	46.9	1.25	0.74
neutral[d]	**2**	95	39.0	1.21	0.98
cationic[e]	**2**	97	40.0	1.31	1.00
toluene/water[f]	**2**	100	41.9	1.30	0.96
neutral[d]	**3**	74	28.9	1.22	1.0
cationic[e]	**3**	90	45.3	1.43	0.80
toluene/water[f]	**3**	99	64.3	1.57	0.62
neutral[d]	**4**	99	41.4	1.30	0.97
cationic[e]	**4**	100	45.2	1.28	0.89
toluene/water[f]	**4**	100	49.1	1.40	0.82

[a] $[MMA]_0:[initiator]_0:[Ru]_0 = 800:2:1$ (see Experimental Section). [b] Determined with size exclusion chromatography (SEC) with PMMA calibration. [c] Initiation efficiency $f = M_{n,calcd}/M_{n,exp.}$ with $M_{n,calcd} = ([MMA]_0/[initiator]_0) \times M_{w,MMA} \times$ conversion. [d] Neutral complex at 85 °C, 16 h, solvent: toluene (1 mL). [e] Cationic complex at 85 °C, 16 h, solvent: toluene (1 mL). [f] Cationic complex at 85 °C, 16 h, solvent: toluene (1 mL), water (1.5 mL).

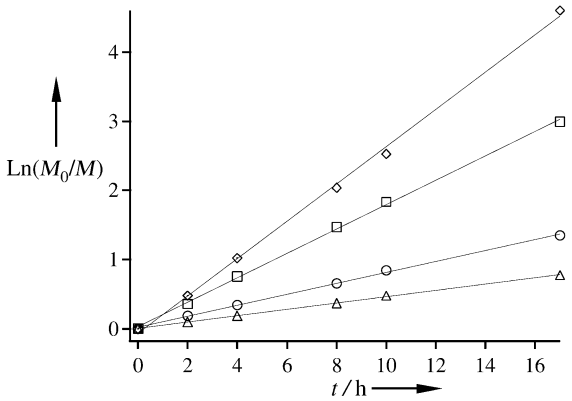


Figure 1. Time dependence of $\ln([M]_0/[M])$ at 85 °C where $[M]_0$ and $[M]$ are the MMA concentrations at times 0 and t. Catalyst **1** (△): $y = 0.0459x + 0.0038$; $r = 0.999$; catalyst **2** (□): $y = 0.1769x + 0.0262$; $r = 0.999$; catalyst **3** (○): $y = 0.0798x + 0.0215$; $r = 0.998$; catalyst **4** (◇): $y = 0.2696x - 0.064$; $r = 0.998$.

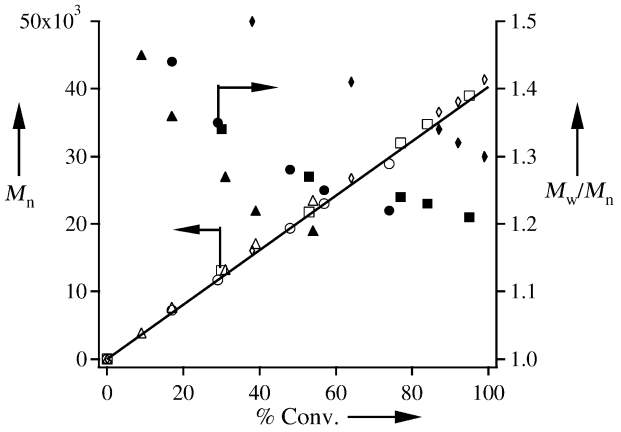


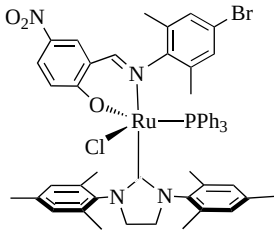
Figure 2. Plot of the molecular weight M_n and M_w/M_n versus the MMA conversion. Catalyst **1** (△, ▲): $y = 434.64x + 29.62$; $r = 0.999$; catalyst **2** (□, ■): $y = 392.15x + 306.89$; $r = 0.999$; catalyst **3** (○, ●): $y = 409.68x + 291.23$; $r = 0.999$; catalyst **4** (◇, ◆): $y = 0.2696x - 0.064$; $r = 0.998$; —— = calculated M_n

ATRP under "suspension" conditions (for instance, with pure toluene as solvent (monomer/toluene = 40/60 v/v %) or in a mixture toluene/water (monomer/toluene/water = 25/37.5/37.5 v/v %)). Unlike conventional suspension or dispersion polymerizations, no dispersants or surfactants were added to the reaction mixture. A pronounced increase in monomer conversion is observed with the cationic species (73 %), yet this is also accompanied with a slight broadening of the MWD ($M_w/M_n = 1.30$) and a decrease in initiator efficiency is observed ($f = 0.78$). This tendency is even more conspicuous in the case of the suspension polymerization (82 %, $M_w/M_n = 1.25$, $f = 0.74$). From the kinetic experiments the apparent propagation constants in the three above mentioned situations can be calculated: $k_{app,1} = 1.28 \times 10^{-5}\ s^{-1}$ (neutral **1**), $k_{app,2} = 2.16 \times 10^{-5}\ s^{-1}$ (cationic **1**), $k_{app,3} = 3.2 \times 10^{-5}\ s^{-1}$ (toluene/water). Under all these experimental conditions all the criteria of a living polymerization are fulfilled as indicated by a linear time dependence of $\ln([M]_0/[M])$ and a linear increase of the molecular weight versus the MMA conversion (e.g. catalyst **1** in Figure 1 and Figure 2).

The linear relation between time and $\ln([M]_0/[M])$ indicates that the number of active species remains constant during polymerization (Figure 1), while a lack of transfer reactions is supported by the linearity of M_n versus conversion (Figure 2). The presence of radical intermediates was demonstrated by the total inhibition of the polymerization after addition of 5 equivalents of galvinoxyl. Furthermore, ^{13}C NMR spectroscopy showed that the poly(methyl methacrylate) (PMMA) obtained in this way is very similar to the PMMA that was radically prepared using AIBN (AIBN = 2,2′-azobis[(2-methyl)propanenitrile] as the initiator in toluene at 85 °C (tacticity: $rr:rm:mm = 58:37:5.2$, $\rho = 0.98$).[18] When the phosphane moiety is replaced in **1** by a more σ-donating imidazol-2-ylidene ligand (**2**) the catalytic activity increased dramatically ($k_{app} = 4.9 \times 10^{-5}\ s^{-1}$ Figure 1). The cationic analogue is highly active (> 95 % conversion) and polymers with predetermined molecular weights and narrow polydispersities are obtained ($M_w/M_n < 1.31$). To elaborate the influence of the ruthenium carbene unit, a modification of the indenylidene entity was performed. The most straightforward route to achieve this transformation is to apply a metathesis step with vinyl ether derivatives. Such compounds can rapidly and selectively react in an irreversible way with the ruthenium carbene fragment to generate the corresponding alkoxycarbene derivative.[19] On this basis the Fischer homologues (**3** and **4**) were generated in situ and tested for the ATRP of MMA. Our results show that catalyst **4** belongs to the most active ruthenium–carbene systems known to date with an almost quantitative conversion, giving polymer with a polydispersity index of 1.30 and an initiation efficiency of 0.97. Furthermore, the cationic congeners are very active (100 % conversion) in pure toluene and in water/toluene

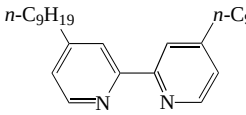
 © 2003 Wiley-VCH Verlag GmbH & Co. KGaA, Weinheim

mixture and in both cases the observed molecular-weight distribution remains narrow (M_w/M_n = 1.28 and 1.4). The exact role of the carbene entity is not unambiguously clear and needs further investigations. We believe that the active ATRP species is derived from the carbene fragment. This is strongly indicated by the fact that the phosphane-containing system, **5**, is not active for ATRP. The results obtained with the best performing systems (**4**) can compete with well-established copper systems for the polymerization of MMA. At present the most active copper system is CuBr/Me_6TREN (TREN = tris(2-(dimethylamino)ethyl)amine). Although it is generally very active for acrylates its activity for MMA polymerization is lower.[20] In Table 2 we compare three copper systems that are very active for the polymerization of methacrylates.[21–23] Ligands **6**–**8** are used in these systems. From Table 2 it is clear that complex **4** and more specific its cationic congener (**4**$^+$) bear comparison with the copper-based systems in terms of activity. However, the copper-based systems still have a better control over the polymers formed which is indicated by the very small molecular-weight distribution combined with a high initiator efficiency.

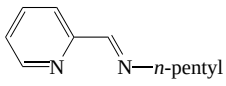


5

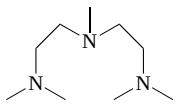
Complexes **1** and **2** were also tested for the ring-opening-metathesis polymerization (ROMP) of some typical low-strain cyclic olefins namely cyclooctene (CyO) and cyclopentene (Cyp; Table 3).



6



7



8

Table 3: ROMP of low-strain cyclic olefins using catalysts **1**–**2**.[a]

Catalyst	Monomer	Monomer/Cat.	t	Conversion [%]	M_n[b] [$\times 10^4$]	M_w/M_n[b]	f[c]
1	CyO	10000	17 h	53	88.5	1.79	0.66
2	CyO	10000	< 15 min	100	121	1.60	0.91
1	Cyp	5000	17 h	41	20	1.78	0.70
2	Cyp	5000	17 h	78	31.6	1.55	0.84

[a] solvent: toluene, room temperature. [b] Determined with size exclusion chromatography (SEC) with PMMA calibration. [c] Initiation efficiency $f = M_{n,calcd}/M_{n,exp.}$ with $M_{n,calcd} = ([Mon]_0/[initiator]_0)\, M_{w,mon}$ · conversion.

From these results it is clear that complex **1** but especially complex **2** are highly active catalysts for the ROMP of cyclopentene and cyclooctene. The phosphane-free system seems to be the best performing one, as a quantitative CyO conversion is obtained at room temperature in less than 15 min. With a turnover frequency of 667 min^{-1} at room temperature for the polymerization of cyclooctene, complex **2** is an alternative to the second-generation Grubbs-type catalysts (for which when monomer/cat. = 10000, conversion is complete in 30 min, no gel permeation chromatography (GPC) data are reported)[24] what is more it gave access to well controlled high-molecular-weight polymers that are soluble in chloroform which is not the case for the system reported by Grubbs and Bielawski.[24] The contribution of transfer reactions is suppressed as the initiator efficiencies are all lower than unity. Cyclopentene, a more challenging monomer to polymerize by ROMP, is also converted in 78% yield after 17 h with a molecular weight that almost fits the theoretical predicted one.

Since the ruthenium–benzylidene analogues are also highly active in all kind of metathesis reactions and they are more readily accessible than other highly active systems, these types of catalyst have great potential.[25,26]

In conclusion we have succeeded in synthesizing a new type of ruthenium indenylidene complex bearing a bidentate Schiff base and/or N-heterocyclic carbene ligands which show a pronounced activity for the controlled radical polymerization of methyl methacrylate. Further fine-tuning of the catalyst into a cationic variant or transforming the indenylidene entity into a Fischer-type carbene improves the activity and give access to well-controlled polymers with a narrow polydispersity. These systems are also highly active for the ROMP of low-strain cyclic olefins. We believe that this system has the highest dual activity in ROMP and ATRP.

Table 2: Comparison of Ru catalyst **4** with the first generation Grubbs catalyst and some conventional Cu catalysts.

Catalyst	Monomer/Cat.	t [h]	Conversion [%]	M_n [$\times 10^3$]	M_w/M_n	f	k_{app} [s^{-1}]
4	800	16	99	41.4	1.30	0.97	4.9×10^{-5}
4$^+$	800	16	100	45.2	1.28	0.89	15.7×10^{-5}
CuCl/**6**[a]	445	20	95	19.8	1.09	1.10	4.2×10^{-5}
CuBr/**7**[b]	100	4	85	8.9	1.23	0.95	12.6×10^{-5}
CuBr/**8**[c]	200	8.5	76	15.2	1.16	0.82	–

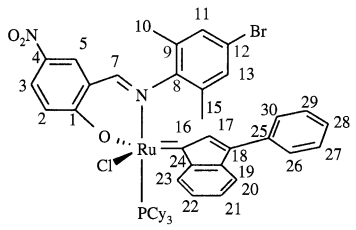
[a][Cu]:[initiator]:[**6**] = 1:2:2, initiator = $MePhSO_2Cl$, T = 90°C, 4.67 M in diphenyl ether.[20] [b] [Cu]:[initiator]:[**7**] = 1:1:2, initiator = ethyl-2-bromo-2-methylpropionate, T = 90°C, 50 v/v% in toluene.[21] [c] [Cu]:[initiator]:[**8**] = 1:1:2, initiator = ethyl-2-bromo-2-methylpropionate, T = 90°C, bulk.[22]

Experimental Section

All reagents and solvents were dried, distilled, and stored under nitrogen by using conventional techniques. Catalyst **1** was made as described in ref. [11b].

Analytical data for **1** (see Figure 3): dark brown solid (yield 80%), ^{1}H NMR (299.89 MHz, [D_6]Benzene, 25°C, TMS): δ = 8.29 (d, 1H, H7), 8.22 (dd, J(H,H) = 6.9 Hz, 1H, H23), 7.74 (d, J(H,H) = 4.6 Hz, 2H, H26), 7.57 (d, 1H, H5), 7.05 (d, J(H,H) = 9.4 Hz,

 © 2003 Wiley-VCH Verlag GmbH & Co. KGaA, Weinheim



1

Figure 3. Numbering scheme for **1**.

H3), 7.49 (d, J(H,H) = 5.5 Hz, 1H, H28), 7.46 (dd, J(H,H) = 6.3, 2.6 Hz, 2H, H27), 7.42 (s, 1H, H17), 7.32 (td, J(H20 ,H21) = J(H21, H22) = 7.0 Hz, 1H, H21), 7.30 (td, J(H21, H22) = J(H22, H23) = 7.5 Hz, 1H, H22), 7.23 (dd, J(H,H) = 7.0 Hz, H20), 6.98 (s, 2H, H11), 6.74 (d, J(H,H) = 9.3 Hz, 1H, H2), 2.42 (q, J(H,H) = 12 Hz, 3H, PCy_3), 2.39 (s, 3H, H10), 1.92–1.56 (m, 20H, CH_2 of PCy_3), 1.42 (d, J(H,H) = 6.7 Hz, 3H, H15), 1.17 ppm (m, 10H, CH_2 of PCy_3); ^{13}C NMR (75.41 MHz, [D_6]Benzene, 25 °C, TMS): δ = 292.04 (s, J(P,C) = 7.8 Hz, C16), 166.00 (s, C7), 165.70 (s, C1), 142.97 (s, C8), 142.50 (s, C24), 140.08 (s, C19), 138.66 (s, C18), 137.75 (d, J(C,H) = 172 Hz, C17), 135.00 (s, C25), 133.6 (s, C4), 132.22 (d, J(C,H) = 162 Hz, C23), 131.38 (s, C9), 130.8 (d, C22), 128.22 (s, C11), 127.93 (d, C21), 127.82 (d, C3), 127.78 (s, C5), 127,00 (d, C28), 126.7 (d, C26, C30), 120.2 (d, C4), 119.1 (s, C6), 118.5 (d, J(C,H) = 155 Hz, C20), 35.0 (CH), 33.4, 31.5, 29.3, 28.6, 24.5 (CH_2 of PCy_3), 18.08 ppm (q, J(C,H) = 124.9 Hz, C10, C16). ^{31}P NMR (121,40 MHz, [D_6]benzene, 25 °C, H_3PO_4): δ = 48.40 ppm (s). Elemental analysis calcd (%) for $C_{48}H_{55}BrClN_2O_3PRu$: C 60.35, H 5.80, N 2.93; found: C 60.97, H 6.34, N 3.17. Complex **2** was synthesized according to literature procedures.[21,27]

Polymerization of MMA: Ruthenium complex (0.0117 mmol) was added to a glass vial that contained toluene (1 mL) and a magnetic stirring bar. The vessel was purged with argon before the monomer (9.35 mmol) and the initiator (0.0234 mmol, 465 μL of a 0.05 M stock solution) was added. The reaction mixture was heated for a set time in a thermostated oil bath at 85 °C. After cooling the mixture it was dissolved in chloroform and the product was precipitated in *n*-octane. The cationic complexes were generated by adding ruthenium complex (0.0117 mmol) to toluene (1 mL) and subsequently adding a 0.2 M $AgBF_4$ stock solution (56 μL) in toluene. After stirring for 20 min, a turbidity of AgCl was detected and the monomer and initiator were then added. In the case of the suspension polymerization at this stage distilled water (1.5 mL) was added. The ethoxy Fischer carbene complex was also obtained in situ by adding 10 equiv of vinyl ether to the catalyst solution (**1** or **2**) and subsequently stirring for 30 min at room temperature. The cationic variants were also generated by adding $AgBF_4$ to the ethoxy ruthenium–carbene solution.

A typical ROMP experiment: catalyst solution (100 μL; 0.1M) was added to a purged glass vessel containing a magnetic stirrer, toluene (5 mL) and monomer (13 mL CyO, 4.4 mL Cyp). The reaction was thermostated at the appropriate temperature and after 17 h the reaction mixture was transferred into a beaker containing $CHCl_3$ (10 mL), ethyl vinyl ether (0.1 mmol), and 2,6-di-*tert*-butyl-4-methylphenol (1 mmol). The resulting solutions were stirred for 1 h and after filtration through a short silica gel columns, precipitated into vigorously stirred methanol. The white, sticky polymer obtained in this way was collected by filtration, washed with methanol, and dried under vacuum.

Received: December 23, 2002
Revised: January 31, 2003 [Z50840]

Keywords: carbene ligands · homogeneous catalysis · polymerization · ruthenium · Schiff bases

[1] a) T. Weskamp, W. C. Schattenmann, M. Spiegler, W. A. Herrmann, *Angew. Chem.* **1998**, *110*, 2631; *Angew. Chem. Int. Ed.* **1998**, *37*, 2490; b) L. Ackermann, A. Fürstner, T. Weskamp, F. J. Kohl, W. A. Herrmann, *Tetrahedron Lett.* **1999**, *40*, 4787; c) M. Scholl, T. M. Trnka, J. P. Morgan, R. H. Grubbs, *Tetrahedron Lett.* **1999**, *40*, 2247; d) J. Huang, H. Z. Schanz, E. D. Stevens, S. P. Nolan, *Organometallics* **1999**, *18*, 5375.
[2] a) J. A. Tallarico, L. M. Malnick, M. L. Snapper, *J. Org. Chem.* **1999**, *64*, 344; b) F. Simal, A. Demonceau, A. F. Noels, *Tetrahedron Lett.* **1999**, *40*, 5689.
[3] a) F. Simal, L. Delaude, D. Jan, A. Demonceau, A. F. Noels, *Polym. Prepr. Am. Chem. Soc. Div. Polym. Chem.* **1999**, *40*, 336; b) F. Simal, A. Demonceau, A. F. Noels, *Recent Res. Dev. Org. Chem.* **1999**, *3*, 455; c) F. Simal, S. Delfosse, A. Demonceau, A. F. Noels, K. Denk, F. J. Kohl, T. Westkamp, W. A. Herrmann, *Chem. Eur. J.* **2000**, *6*, 3047.
[4] K. Matyjaszewski, *Chem. Eur. J.* **1999**, *5*, 3095.
[5] K. Matyjaszewski, J. Xia, *Chem. Rev.* **2001**, *101*, 2921.
[6] M. Kamigaito, T. Ando, M. Sawamoto, *Chem. Rev.* **2001**, *101*, 3689.
[7] M. S. Sanford, J. A. Love, R. H. Grubbs, *Organometallics* **2001**, *20*, 5314.
[8] T. Weskamp, F. J. Kohl, W. Heiringer, D. Gleich, W. A. Herrmann, *Angew. Chem.* **1999**, *111*, 2573; *Angew. Chem. Int. Ed.* **1999**, *38*, 2416.
[9] a) K. Denk, J. Fridgen, W. A. Herrmann, *Adv. Synth. Catal.* **2002**, *344*, 666; b) S. B. Garber, J. S. Kingsbury, B. L. Gray, A. H. Hoveyda, *J. Am. Chem. Soc.* **2000**, *122*, 8168.
[10] B. De Clercq, F. Verpoort, *Adv. Synth. Catal.* **2002**, *344*, 639.
[11] a) T. Opstal, F. Verpoort, *Tetrahedron Lett.* **2002**, *43*, 9259; b) T. Opstal, F. Verpoort, *Synlett* **2002**, *6*, 935.
[12] S. Bhattacharya, S. R. Boone, G. K. Fox, C. G. Pierpont, *J. Am. Chem. Soc.* **1990**, *112*, 1088.
[13] S. Goswami, A. R. Chakravarty, A. Chakravorty, *Inorg. Chem.* **1981**, *20*, 2246.
[14] B. De Clercq, F. Verpoort, *Macromolecules* **2002**, *35*, 8943.
[15] J. Huang, J. H. Schanz, E. D. Stevens, S. P. Nolan, *Organometallics* **1999**, *18*, 2370.
[16] M. Ulman, R. H. Grubbs, *J. Org. Chem.* **1999**, *64*, 7202.
[17] P. Schwab, R. H. Grubbs, J. W. Ziller, *J. Am. Chem. Soc.* **1996**, *118*, 100.
[18] D. M. Haddleton, D. J. Duncalf, D. Kukulj, A. M. Heming, A. J. Shooter, A. J. Clark, *J. Chem. Mater.* **1998**, *8*, 1525.
[19] J. Louie, R. H. Grubbs, *Organometallics* **2002**, *21*, 2153.
[20] T. Grimaud, K. Matyjaszewski, *Macromolecules* **1997**, *30*, 2216.
[21] D. M. Haddleton, M. C. Crossman, B. H. Dana, D. J. Duncalf, A. M. Heming, D. Kukulj, A. J. Shooter, *Macromolecules* **1999**, *32*, 2110.
[22] J. Queffelec, S. G. Gaynor, K. Matyjaszewski, *Macromolecules* **2000**, *33*, 8629.
[23] K. Matyjaszewski, B. Göbelt, H. J. Paik, C. P. Horwitz, *Macromolecules* **2001**, *34*, 430.
[24] C. W. Bielawski, R. H. Grubbs, *Angew. Chem.* **2000**, *112*, 3025; *Angew. Chem. Int. Ed.* **2000**, *39*, 2903.
[25] B. De Clercq, F. Verpoort, *Tetrahedron Lett.* **2002**, *43*, 9101.
[26] H. Wakamatsu, S. Blechert, *Angew. Chem.* **2002**, *114*, 832; *Angew. Chem. Int. Ed.* **2002**, *41*, 794.
[27] L. Jafarpour, H. J. Schanz, E. D. Stevens, S. P. Nolan, *Organometallics* **1999**, *18*, 5416.

 © 2003 Wiley-VCH Verlag GmbH & Co. KGaA, Weinheim

A Microbial Fuel Cell

A Generation of Microbial Fuel Cells with Current Outputs Boosted by More Than One Order of Magnitude**

Uwe Schröder, Juliane Nießen, and Fritz Scholz*

The concept of employing microbial catabolic activity to directly generate electricity from the degradation of organic matter provides access to cheap and environmentally friendly energy sources. The energy conversion can be achieved with the help of microbial fuel cells, in which mostly fermentative microorganisms serve as biocatalysts and from which electrons are diverted and transferred to an electrode to generate electricity. Finding an efficient way to "wire" the microbial activity to an electrode is the key to the success of microbial fuel cells.[1] Hitherto, electricity generation was limited to current densities of about 20 $\mu A\,cm^{-2}$ achieved by the use of dissolved artificial redox mediators[2] and 120 $\mu A\,cm^{-2}$ by using the oxidation of metabolic products at platinum black anodes.[3] Herein we report a microbial fuel cell that continuously generates a current output more than one order of magnitude larger than the known microbial fuel cells (up to 1.5 $mA\,cm^{-2}$). The novel fuel cell concept uses polymer-modified catalytically active anodes which shuttle electrons from the bacterial suspension to the anode.

Until now three concepts have been proposed to wire microbial catabolic activity to electrodes for in situ electricity generation. The differences in these concepts is found at the stage at which electrons are diverted from the microbial catabolic path, and consequently in the way that the electrons are captured: 1) Dissolved artificial redox mediators serve as electron shuttles that penetrate the bacterial cells, divert electrons from the respiration chain and from internal metabolites, and transfer electrons to the fuel cell anode.[4] Current densities of between 5–20 $\mu A\,cm^{-2}$ were reported.[5] However, the low current output, environmental and cost concerns disfavor this concept. 2) Metal-reducing bacteria, such as *Shewanella putrefaciens* that have special cytochromes bound to their outer membrane, can pass electrons directly to an electrode, which mimics the presence of metal ions as the terminal electron acceptors making the presence of artificial electron mediators obsolete.[6] However, the current and power output are rather low. Recently, Park and Zeikus could increase the current output to 16 $\mu A\,cm^{-2}$ by using resting cells of *Shewanella putrefaciens* and enhancing the electron transfer to the anode by using Mn^{4+} ions or neutral red modified anode materials.[7] 3) Fermentation products like hydrogen, methanol, or ethanol have been used for in situ electricity generation. In this case, platinum black electrodes were used as electrocatalytically active anode materials; one such example, a microbial fuel cell based on the hydrogen evolution by immobilized cells of *Clostridium butyricum* was reported.[3] Short circuit currents of 120 $\mu A\,cm^{-2}$ were reached by using lactate as the substrate. The fuel cell concept reported herein overcomes the problems of the previous microbial fuel cells. Central parts of the concept are a novel layered multifunctional anode consisting of a metallic electrocatalyst (present in the form of platinum or platinized carbon cloth electrodes) covered by an electrocatalytic conductive polymer (e.g., polyaniline, poly(neutral red), poly(methylene blue)) and a regenerative-potential program applied to maintain the long-term electrode activity.

The cyclic voltammograms of a polyaniline modified platinum electrode immersed in a stirred anaerobic culture of *Escherichia coli* K12 (Figure 1) demonstrate the electrocatalytic behavior of the electrode material at different stages of the bacterial growth and fermentation. Under fermentative conditions the electrode has a high electrocatalytic activity that is practically constant in the potential range between −0.1 and +0.6 V. The decrease of the activity at more positive potentials is well known for Pt. It is caused by the formation of a PtO layer at the Pt surface. Figure 2 A shows the current measured at the electrode immersed in a freshly inoculated glucose medium when a constant potential of 0.2 V was applied to mimic the presence of a fuel cell cathode. As expected, the current increases as the bacteria pass from the lag phase into the phase of exponential growth. At unmodified carbon electrodes and even at blank platinum electrodes no significant currents were measured. However, the current decreases before the bacterial growth reaches the stationary phase. It does not reach the values obtained in the cyclic

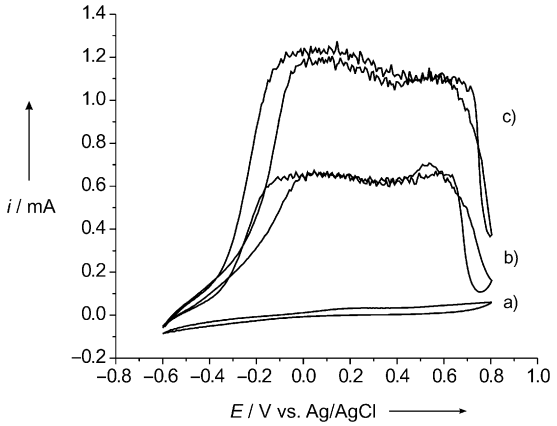


Figure 1. Cyclic voltammograms of a polyaniline-modified platinum electrode (1 cm^2 surface area) placed in a stirred anaerobic culture of *Escherichia coli* K12 in a standard glucose medium ($c_{glucose} = 0.55\ mmol\,L^{-1}$). The experiment was carried out at 37 °C; scan rate 5 $mV\,s^{-1}$. The voltammograms were recorded at different stages of the bacterial growth: a) sterile medium; b) during the exponential growth; c) during the stationary phase of the bacterial growth.

[*] Dr. U. Schröder, J. Nießen, Prof. Dr. F. Scholz
Institut für Chemie und Biochemie
Ernst Moritz Arndt Universität
Soldmannstrasse 16, 17489 Greifswald (Germany)
Fax: (+49) 3834-864-451
E-mail: uweschr@uni-greifswald.de

[**] U.S. gratefully acknowledges support by the Office of Naval Research (ONR project N00014-03-1-0431) and by thee Fonds der Chemischen Industie.

 © 2003 Wiley-VCH Verlag GmbH & Co. KGaA, Weinheim DOI: 10.1002/anie.200350918

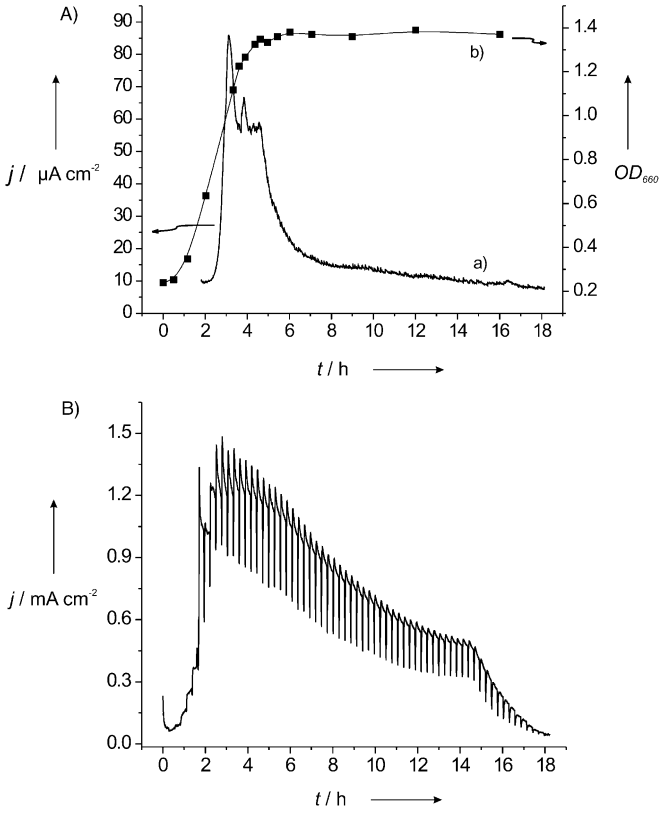


Figure 2. A) Curve a): Chronoamperometric plot of a polyaniline modified platinum electrode placed in a stirred anaerobic culture of *Escherichia coli* K12 in a standard glucose medium ($c_{glucose} = 0.55$ mmol L^{-1}). The potential applied to the electrode was 0.2 V. Curve b): Optical density of the bacterial suspension determined at the wavelength of 660 nm throughout the chronoamperometric experiment. The experiment was carried out at 37 °C. B) Chronoamperometric plot of the modified platinum electrode under the same conditions as those of 2A). Additionally, in an interval of 1000 s potential pulses of 1 V, 5 s were applied to prevent the diminution of the electrode activity. During the potential pulsing the current recording was interrupted.

voltammetric experiment (Figure 1). This phenomenon is the consequence of a diminution of the electrocatalytic activity of the working electrode caused by microbial catabolic by-products and products of the electrocatalytic oxidation and is presumably similar to the deactivation known from direct methanol fuel cells, which is caused by the incomplete oxidation of methanol to form carbon monoxide as an adsorbed layer at the surface of the platinum electrode. In comparison to the unmodified platinum electrode, which was found to be fully blocked, the polymer layer slows down the deactivation but cannot fully prevent it. However, the anode deactivation can be reversed, the performance can be greatly enhanced, and the long-time stability of the electrodes can be maintained with the help of a regenerative-potential program, which can be conveniently performed in situ, that is, within the bacterial medium. A procedure that proved to be most effective is to regularly apply short oxidative-potential pulses to the anode. During the potential pulses, chemisorbed species are presumably oxidized and stripped off from the electrode surface, which reactivates the surface of the metallic electrocatalyst.[8] This procedure prevents the rapid diminution of the anodic currents and increases the current densities to the expected values of 1–1.5 mA cm^{-2} (Figure 2B), which represents an immense progress and offers new prospects for microbial electricity generation.

The importance of the polymer layer for an efficient and sustained electrode activity, as well as for the stability of the electrode function, can be derived from Figure 3. As expected, at the unmodified carbon cloth no microbiologically induced current flow is observed (curve a). A comparison of the platinized only carbon electrode (curve b) and the additionally polyaniline-modified electrode (curve c) shows that whereas the polyaniline-modified electrode gives a stable current flow with a high current density the values for the unprotected electrode lie about 50% below those of the polymer modified electrode. The segments between the individual regeneration pulses show a strong current decrease leading to the pronounced sawtooth structure of the plot. It is caused by a fast deactivation of the unprotected platinum layer.

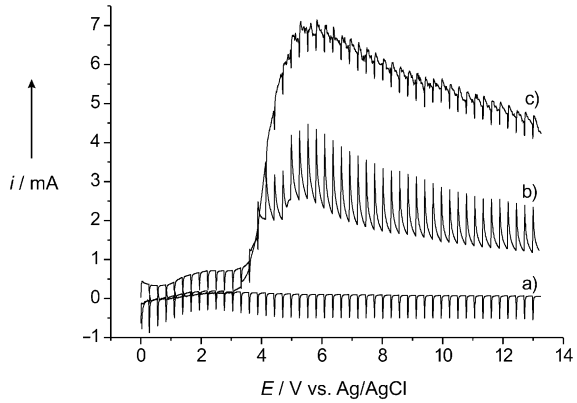


Figure 3. Chronoamperometric plots of differently modified carbon cloth electrodes (25 × 25 mm sized, 0.045 g weight) placed in a stirred anaerobic culture of *Escherichia coli* K12 in a standard glucose medium ($c_{glucose} = 0.55$ mmol L^{-1}). The potential applied to the electrode was 0.2 V. In an interval of 1000 s potential pulses of 1 V, 5 s were applied. Curve a): unmodified carbon cloth; b) platinized carbon cloth, and c) platinized carbon cloth with an overlay of polyaniline. During the potential pulsing the current recording was interrupted. The regular negative current peaks, seen in curve a) and b), are caused by the relaxation of the system after the application of the positive potential pulse.

The conductive polymer has not only a protective function but also directly contributes to the current flow. As presented in Table 1 at purely polyaniline-modified carbon electrodes

Table 1: Mean current densities at differently modified pyrolytic carbon. The electrode was placed in a stirred anaerobic culture of *Escherichia coli* K12 in a standard glucose medium ($c_{glucose} = 0.55$ mmol L^{-1}). The potential applied to the electrode was 0.2 V.

Electrode modification	Current density [$mA^{-1}\,cm^{-2}$]
Polyaniline	0.29
platinum black	0.84
platinum black + polyaniline overlay	1.45

 © 2003 Wiley-VCH Verlag GmbH & Co. KGaA, Weinheim

current densities of 0.29 mA cm^{-2} can be achieved. This result means that whereas the platinum black accesses the oxidation of metabolites, the conductive polymer layer fulfils a multitude of tasks. Consisting of molecular units similar to the conventionally used redox mediators, the polymers form a redox active biocompatible layer that takes the function of the dissolved mediators, thus banishing these artificial compounds from the bacterial medium. Because of their reversible redox behavior and electronic conductivity, the polymers are also involved in the oxidation of excreted metabolites. Additionally to these functions, the polymer layers serve as a barrier allowing metabolic products like H_2, one of the major electroactive products, to diffuse to the electrocatalytically active electrode surface but blocking large molecules from accessing the electrode surface and therewith preserving the underlying electrocatalyst from becoming poisoned. Similar protective effects have been observed for platinum–polymer composites, used for the oxidation of methanol.[9]

The performance of the novel fuel-cell anodes was tested in a model fuel-cell system (Figure 4A) that consisted of a reactor containing an anaerobically growing suspension of

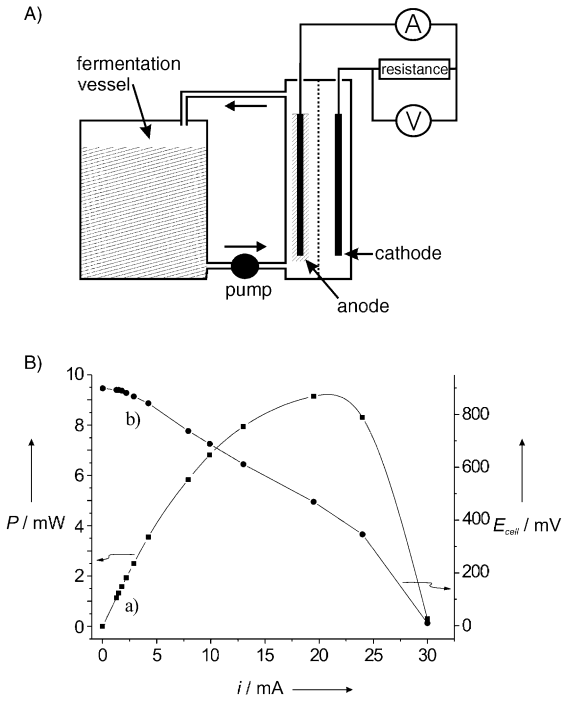


Figure 4. A) Schematic drawing of the novel microbial fuel cell; B) Polarization curves of the model fuel cell. Curve a: Power output P [mW], and curve b: cell voltage, E_{cell}, as a function of the current output i of the fuel cell.

Escherichia coli K12 in a standard glucose medium (55 mM glucose), and the fuel cell consisting of an anode compartment through which the bacterial medium was pumped and a cathode compartment through which the catholyte was pumped. The anode and cathode compartments were separated by a Nafion proton conducting membrane. The anode was a woven graphite cloth, 30 × 25 mm sized, with a weight of 0.05 g, which was platinized and subsequently polyaniline modified. The cathode was unmodified woven graphite and the catholyte was a 50 mM ferricyanide solution in a phosphate buffer identical to the buffer in the bacterial medium. The ferricyanide catholyte was chosen for these experiments as it is easier to handle than an oxygen electrode. For practical applications the ferricyanide electrode will be replaced by an oxygen electrode. The open circuit potential of the fuel cell was 895 mV. Under short circuit conditions the steady state current was 30 mA, and maximum currents of 150 mA were measured. Figure 4B shows the polarization curve of the fuel-cell system as a function of the measured steady-state currents. The maximum power output was 9 mW, which corresponds to a current of 19.5 mA at a cell potential $E_{cell} = 469$ mV. The power output was sufficient to operate continuously a ventilator driven by a 0.4 V motor.

With this concept for a microbial fuel cell, we have raised the limits of microbial electricity generation by more than one order of magnitude. Thanks to a combination of a novel anode design and the applied in situ electrode-generation procedure, a high current and power output can be achieved. As the use of dissolved artificial redox mediators is unnecessary, the operation costs are low and the fuel cell works at a low emission level.

Experimental Section

Electrochemical instrumentation: All systematic electrochemical investigations of the new anode materials were carried out under potentiostatic control by using a three electrode arrangement consisting of the working electrode, a saturated Ag/AgCl reference electrode, and a platinum wire serving as the counter electrode. The counter electrode was separated from the working electrode by a Nafion 117 perfluorinated membrane. The experiments were conducted with a μ-Autolab II and with a PGSTAT 30 Autolab system (Ecochemie, Netherlands). Current and potential measurements at the model fuel-cell system were carried out by using digital multimeters (Keithley 2700). For the determination of the power output a variable resistance (10–1 kΩ) was used as external load. Electrode preparation: For the anode preparation the electrode base material was first platinized by electrochemical reductive deposition from a 50 mmol L^{-1} H_2PtCl_6 solution, then an overlay of a conduction polymer was deposited. The deposition of the conducting polymers was carried out by electrochemical polymerization from the respective monomer solutions by following standard literature procedures, such as the deposition of polyaniline by potential cycling between −0.1 and 1.2 V from a solution containing 0.1 mol L^{-1} H_2SO_4 and 0.1 mol L^{-1} aniline.[10]

Bacterial growths: *Escherichia coli* K12 was grown aerobically at 37 °C for 12–24 h in a standard medium containing 10 g glucose, 5 g yeast extract, 10 g $NaHCO_3$ and 8.5 g NaH_2PO_4 per litre. The same medium served as the anolyte solution in the chronoamperometric and the fuel cell experiments. For experiments 1 mL of an overnight culture were inoculated into fresh medium. By blocking the access of oxygen the bacteria were now cultivated under anaerobic, fermentative conditions.

Received: January 9, 2003 [Z50918]

Keywords: electrochemistry · energy conversion · fuel cells · microbial fuel cells · polymers

 © 2003 Wiley-VCH Verlag GmbH & Co. KGaA, Weinheim

[1] D. Sell in *Biotechnology, Vol. 10* (Ed.: H.-J. Rehm), Wiley-VCH, New York, **2001**, pp. 5 – 23.
[2] D. H. Park, J. G. Zeikus, *Appl. Environ. Microbiol.* **2000**, *66*, 1292 – 1297.
[3] I. Karube, T. Matsunaga, S. Tsuru, S. Suzuki, *Biotechnol. Bioeng.* **1977**, *19*, 1727 – 1733.
[4] S. Wilkinson, *Auton Robot*s **2000**, *9*, 99 – 111.
[5] E. Katz, http://chem.ch.huji.ac.il/~eugeniik/biofuel/biofuel_-cells2_3.html.
[6] a) D. R. Bond, D. E. Holmes, L. M. Tender, D. R. Lovley, *Science* **2002**, *295*, 483 – 485; b) H. J. Kim, H. S. Park, M. S. Hyun, I. S. Chang, M. Kim, B. H. Kim, *Enzyme Microb. Technol.* **2002**, *30*, 145 – 152.
[7] D. H. Park, J. G. Zeikus, *Appl. Microbiol. Biotechnol.* **2002**, *59*, 58 – 61.
[8] K. Bouzek, K.-M. Mangold, K. Jüttner, *J. Appl. Electrochem.* **2001**, *31*, 501 – 507.
[9] K. M. Kost, D. E. Bartak, B. Kazee, T. Kuwana, *Anal. Chem.* **1988**, *60*, 2379 – 2384.
[10] G. Zotti, S. Cattarin, N. Comisso, *J. Electroanal. Chem. Interfacial Electrochem.* **1987**, *235*, 259 – 273.

 © 2003 Wiley-VCH Verlag GmbH & Co. KGaA, Weinheim

Micelle-Induced Nanofibers

Nanofibers of 1,3-Diphenyl-2-pyrazoline Induced by Cetyltrimethylammonium Bromide Micelles**

Hongbing Fu, Debao Xiao, Jiannian Yao, and Guoqiang Yang*

In recent years, organic nanoparticles (ONPs) of low-molecular-weight (MW) active compounds[1–7] have increasingly become of interest in view of the extensive studies with inorganic colloidal crystals.[8–10] The electronic and optical properties of ONPs are fundamentally different from those of inorganic nanoparticles, because of the presence of van der Waals intermolecular interactions.[11] Furthermore, the orientation of building units in inorganic crystals is identical since atoms can be regarded as hard spheres; in contrast, the stacking mode of organic molecules plays an important role in the properties of ONPs.[4b,6] As far as the application is concerned, the modification of optical and electro-optical properties in ONPs, which are achievable only with particle sizes in the middle or lower nanometer range (50–500 nm), allows much more variability and flexibility in both material synthesis and nanoparticle preparation.[1–7]

Investigations of ONPs, however, are only at their initial stages. Until now, the challenge of synthetically controlling the shape of ONPs has been met with limited success.[5] Herein, we report a self-inducing template growth to produce nanofibers of 1,3-diphenyl-2-pyrazoline (DP) in the presence of cetyltrimethylammonium bromide (CTAB) molecules in an aqueous phase. Firstly, the solubilization of DP molecules into the hydrocarbon core of spherical CTAB micelles induces the sphere-to-rod transition of CTAB micelles; then the induced rodlike CTAB micelles direct the growth of cylindrical DP nanofibers like templates. It is found that the crystal packing forces drive DP molecules self-assembling as J-type aggregates in nanofibers. The concomitant property changes upon the formation of J-type aggregates as well as the natural path to carrier mobility through the fiberlike shape may be explored to enhance device performance in many fields.

Stable DP nanoparticles were prepared by injecting a stock DP/ethanol solution (100 μL, 5.0 mM) to an aqueous micellar solution of CTAB (5 mL) and stirred for 5 minutes. The dispersions of DP nanoparticles into water exhibited an off-white turbidity because of the light scattering of the particles. Interestingly, the morphology of DP particles strongly depends on the concentration of CTAB (C_{CTAB}). Without CTAB molecules in the aqueous phase or C_{CTAB} is less than the first critical micelle concentration (CMC, 0.9 mM), DP molecules would deposit quickly. To elucidate the role played by CTAB molecules, five samples, labeled as **1**–**5**, with $C_{CTAB} = 5.4$, 4.0, 2.7, 1.8 and 0.9 mM, respectively, were used in our experiments.

A first insight into the microscopic structure of DP particles was obtained by field emission scanning electron microscopy (FESEM). Figure 1 illustrates the morphology evolution of DP particles with decreasing C_{CTAB}. At $C_{CTAB} = 5.4$ mM (Figure 1a), only the filter pores are observed, that is, no particles above the pore size exist in sample **1**. At $C_{CTAB} = 4.0$ mM, 20–30 nm particles appear on the millipore filter surface, and partially block the filter pores thus reducing the pore size (Figure 1b). Apparent fiberlike shapes with a width of about 110 nm are identified from the junction between the vaguely seen particles in Figure 1c; moreover, the clearly observed filter pores in this image suggest that almost all particles join in the formation of nanofibers. As the C_{CTAB} decreased further, perfect DP nanofibers form with a diameter of 140 nm at $C_{CTAB} = 1.8$ mM (Figure 1d) and of 225 nm at $C_{CTAB} = 0.9$ mM in (Figure 1e), respectively, while the length of fibers adds up to tens of μm in both cases. Noteworthy, the long rodlike CTAB micelles are observed occasionally by FESEM (the inset in Figure 1a) in the samples with C_{CTAB} about 4.5 mM. This observation provides a clue for us to understand the mechanism of the formation of DP nanofibers, and is discussed below.

Only irregularly deposited CTAB films were observed in the FESEM measurements if we directly dropped and dried

[*] Prof. Dr. J. Yao, Dr. H. Fu, D. Xiao, G. Yang
Center for Molecular Science
Institute of Chemistry
Chinese Academy of Sciences
Beijing 100080 (P.R. China)
Fax: (+86) 10-8261-7315
E-mail: jnyao@mail.iccas.ac.cn

[**] This research was supported in part by the National Natural Foundation of China, the National Research Fund for Fundamental Key Projects No.973 (G19990330) and the Chinese Academy of Sciences.

Supporting information for this article is available on the WWW under http://www.angewandte.org or from the author.

 DOI: 10.1002/anie.200350961 © 2003 Wiley-VCH Verlag GmbH & Co. KGaA, Weinheim

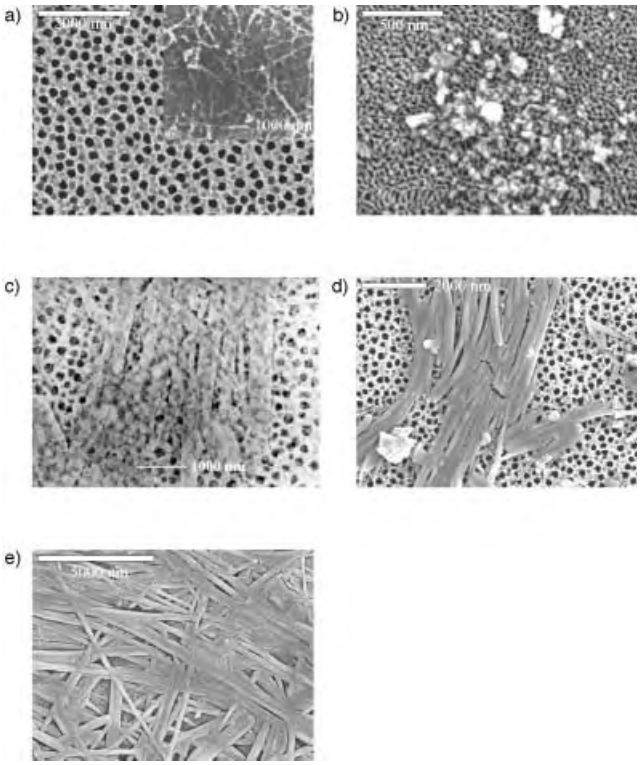


Figure 1. FESEM photographs of DP nanoparticles measured while samples **1**–**5** (image a–e) were filtered on the surface of a millipore filter (pore size 0.02 μm). A gold layer was sputtered onto the surface to increase the conductivity.

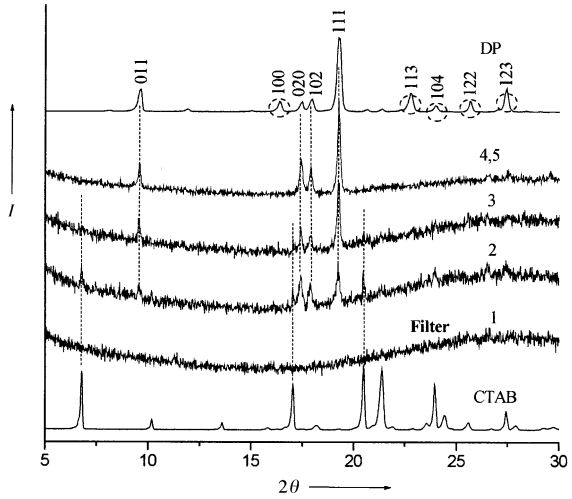


Figure 2. XRD patterns of DP nanoparticles measured while samples **1**–**5** were filtered on the surface of a millipore filter. The top and bottom traces are the spectrum for the pure DP and CTAB powder, I = relative intensity.

the samples on a substrate. Under these conditions, we investigated the DP particles by the means of confocal microscopy based on the strong fluorescence of pyrazoline compounds (see Supporting Information). The fiberlike shapes emerging into the irregular CTAB films were observed while the sample was excited by using a UV light. According to our experiments, these fiberlike DP particles can be reintroduced into water within five to ten minutes under ultrasonic treatment provided we dry the samples under vacuum at $<25\,^{\circ}C$ beforehand. The stability and the facility to redisperse the DP nanofibers account for the thermodynamic stabilization of the colloidal particles by surfactant CTAB molecules.

We also probed the internal structure of DP particles by XRD measurements (Figure 2). Specifically, DP crystallites are in the monoclinic space group $P2_1/c$ with the unit cell dimensions $a=5.404$, $b=10.162$, $c=21.683$ Å, $\beta=92.85°$, $U=1189.3$ Å^3, and with $Z=4$.[12] The characteristic peaks of CTAB attenuate from spectra 2 to 3 and vanish in 5 (Figure 2). This means that the fiberlike particles mainly consist of DP molecules. The intensity ratios between DP characteristic peaks of [111] and [011], $I_{[111]}/I_{[011]}$, are equal to 2.88, 3.14 and 3.74 in the spectra 2, 3 and 4 (or 5), respectively, and is 3.40 in the powder pattern. The concomitant increase of [111] with the growth of nanofibers indicates that DP molecules prefer to arrange themselves along the [111] in the nanofibers. Moreover, peaks of [100], [113], [104], [122] and [123], which are clearly resolved in the DP powder pattern, are not observed in the patterns for the nanofibers. This results from the predominant growth along the [111] plane or the parallel of the incident light to nanofibers placed on the surface of a millipore filter.

Spectroscopic studies, when correlated with the FESEM observations, further clarify the formation process of the fiberlike DP particles. Sample **1** presents a similar absorption spectrum to that of the monomers, including three resolved bands with a maximum at 240 nm arising from the phenyl ring (B_{phenyl}; B = band) and at 302 and 355 nm from the pyrazoline n–π* ($B_{n-\pi^*}$) and π–π* ($B_{\pi-\pi^*}$) transitions,[13] respectively (Figure 3a). We observed the growth of a new band (B_J) at about 425 nm besides the red-shifted B_{phenyl}, $B_{n-\pi^*}$ and $B_{\pi-\pi^*}$ upon going from spectra 2–5 (Figure 3a). This new band of B_J is not detectable in the monomeric solution and is thus expected to originate from the aggregation of DP molecules. The gradual appearance of B_J reflects the formation of DP nanoparticles. To explore the nature of DP aggregates, we also measured the fluorescence emission spectra (Figure 3b). Sample **1** shares the same emission feature of a broad asymmetric band centered at 465 nm with the monomeric solution. From spectra 2 to 5, as the DP molecules aggregate to form nanoparticles, the emission widths gradually become narrower and the emission positions slightly blue shift from 460 to 450 nm. Moreover, the emissions of samples **1**–**5** show a faster fluorescence decay ($\tau=3.7\pm0.3$, 3.4 ± 0.3, 3.1 ± 0.3, 2.5 ± 0.3 and 1.3 ± 0.2 ns, respectively) than that of monomer emission ($\tau=4.2\pm0.3$ ns).

It is known that rodlike CTAB micelles are widely used as templates in the synthesis of inorganic nanorods or nanowires.[8–10] In these cases, C_{CTAB} above the second CMC (100 mM) and/or the introduction of an additional rod-inducing cosurfactant are necessary for the formation of templates of rodlike micelles. Moreover, the diameter of inorganic nanorods or nanowires is determined by the diameter of the rod micelles at the tens-of-nanometer scale. In our experiment, the diameter of DP nanofibers amounts to

 © 2003 Wiley-VCH Verlag GmbH & Co. KGaA, Weinheim

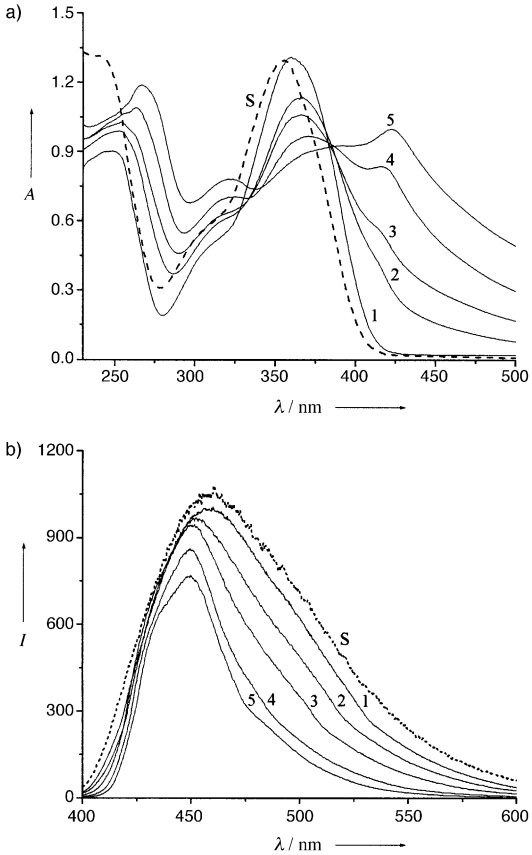


Figure 3. Absorption (a) and emission (b) spectra of samples **1–5** (line 1–5) as compared with the spectrum of 0.1 mM DP/ethanol solution (line S; A = absorbance). Emission spectra were obtained with an excitation wavelength of 360 nm (I = intensity, arbitrary units).

hundreds of nanometer larger than that expected for a rodlike CTAB micelle, and can be tuned easily even at C_{CTAB} within the concentration range of spherical micelles.

CTAB molecules form spherical micelles with a diameter of 6 nm and an aggregation number of 90 within the concentration range from 0.9 to 100 mM.[14] We calculated the molar ratios (N) between DP molecules and CTAB spherical micelles in samples **1–5**, $N = 1.7$, 2.3, 3.3, 5.0 and 10.0, respectively. Analysis of FESEM and spectroscopic data on the parameter N sheds light on the mechanistic basis behind this unusual formation of DP nanofibers.[15] We have identified three distinctive stages in the nanofiber formation (Figure 4). At $N < 2.0$, hyrophobic DP molecules dissolve in the spherical CTAB micelles because of a process called solubilization.[16] In Figure 3, the optical absorption and emission of sample **1** ($N = 1.7$) is similar to that of the monomer. That is, DP molecules which dissolve into spherical CTAB micelles are separated from each other by the CTAB alkyl chains, and therefore in a monomeric state. Importantly, DP molecules, which dissolve into spherical CTAB micelles, induce the sphere-to-rod transition of CTAB micelles like a rod-inducing reagent, such as sodium salicylate[17] and aromatic hydrocarbons.[18] Indeed, such rodlike CTAB micelles were observed by FESEM (Figure 1a inset and Supporting Information). The sphere-to-rod transition of CTAB micelles occurs in our systems at $N \approx 2.0$. At this molar ration, each spherical CTAB micelle will dissolve more than two DP molecules, the strong π–π interactions between DP molecules are likely to drive them to aggregate with each other. Furthermore, the formed rodlike micelles act as templates directing the growth of DP nanofibers. The layer of CTAB molecules surrounding the core of DP provides excellent colloidal stability of the nanofibers. The diameter of DP nanofibers could be easily tuned by changing the value of N.

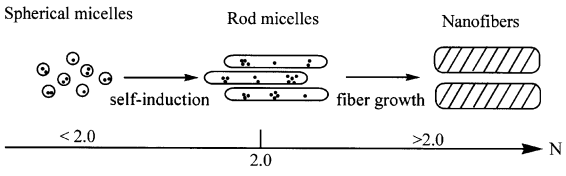


Figure 4. Cartoon representation of self-inducing templates growth for DP nanofibers.

The spectral characteristics observed for DP nanoparticles as compared with those of monomers, that is, the red-shifted absorption, the smaller Stokes shift, and the fast fluorescence decay, are quite different from our previous study on spherical nanoparticles of 1-phenyl-3-((dimethylamino)styryl)-5-((dimethylamino)phenyl)-2-pyrazoline (PDDP),[4a] in which the nanoparticle emission shifts to a lower energy and decays slower than PDDP monomer emission does. In fact, the optical features of DP aggregates are consistent with a picture of J aggregation.[19] According to the molecular exciton model,[19c] the stacking angle, α, which defines the angle between the transition dipole and the molecular axis of the aggregate, is 54.7° or less in a J-type aggregate. As there is no substituent at the 5-position the DP molecules are planar, which leads to a closely packed crystal structure in $P21/c$.[12] The stacking angle between the transition dipole of the DP molecule and the crystallographic a axis is calculated to be 50.7°,[20] which is less than 54.7° and also consistent with the model of J aggregate.[19] The perpendicular distance between two adjacent molecules along the crystallographic a axis is about 3.6 Å.[12] As confirmed by XRD measurements, DP molecules prefer to grow along the [111] plane in nanofibers. Therefore, it is the crystal packing forces that drive theself-assembly of DP molecules as J-type aggregates in DP nanofibers.

In summary, we have developed a simple solution method, self-inducing template growth, for the preparation of stable DP nanofibers in the presence of CTAB in aqueous phase. On the one hand, the surfactant CTAB molecules assume the role of surface-active colloidal stabilizers. On the other hand, those DP molecules dissolved in spherical CTAB micelles induce the formation of rodlike CTAB micelles, and then the as formed rod micelles direct the growth of cylindrical DP nanofibers like templates. It is found that DP nanofibers predominantly grow along the [111], and the crystal packing forces drive DP molecules self-assembling as J-type aggregates in nanofibers.

Received: January 17, 2003 [Z50961]

 © 2003 Wiley-VCH Verlag GmbH & Co. KGaA, Weinheim

Keywords: aggregation · micelles · nanostructures · photochemistry · pi interactions

[1] H. Kasai, H. S. Nalwa, H. Oikawa, S. Okada, H. Matsuda, N. Minami, A. Kakuta, K. Ono, A. Mukoh, H. Nakanishi, *Jpn. J. Appl. Phys. Part 2* **1992**, *31*, L1132.
[2] A. Ibanez, S. Maximov, A. Guiu, C. Chaillout, P. L. Baldeck, *Adv. Mater.* **1998**, *10*, 1540.
[3] D. Horn, J. Rieger, *Angew. Chem.* **2001**, *113*, 4460; *Angew. Chem. Int. Ed.* **2001**, *40*, 4331.
[4] a) H. B. Fu, J. N. Yao, *J. Am. Chem. Soc.* **2001**, *123*, 1434; b) H. B. Fu, B. H. Loo, D. B. Xiao, R. M. Xie, X. H. Ji, J. N. Yao, B. W. Zhang, L. Q. Zhang, *Angew. Chem.* **2002**, *114*, 1004; *Angew. Chem. Int. Ed.* **2002**, *41*, 962; c) R. M. Xie, D. B. Xiao, H. B. Fu, X. H. Ji, W. S. Yang, J. N. Yao, *New J. Chem.* **2001**, *25*, 1362.
[5] J. K. Lee, W. K. Koh, W. S. Chae, Y. R. Kim, *Chem. Commun.* **2002**, 138.
[6] B. K. An, S. K. Kwon, S. D. Jung, S. Y. Park, *J. Am. Chem. Soc.* **2002**, *124*, 14410.
[7] X. C. Gong, T. Milic, C. Xu, J. D. Batteas, C. M. Drain, *J. Am. Chem. Soc.* **2002**, *124*, 14290.
[8] X. G. Peng, L. Manna, W. D. Yang, J. Wichham, E. Scher, A. Kadavanich, A. P. Alivisatos, *Nature* **2000**, *404*, 59.
[9] a) Y. Y. Yu, S. S. Chang, C. L. Lee, C. R. C. Wang, *J. Phys. Chem. B* **1997**, *101*, 6661; b) S. Link, M. B. Mohamed, M. A. El-Sayed, *J. Phys. Chem. B* **1999**, *103*, 3073.
[10] a) N. R. Jana, C. J. Murphy, *Chem. Commun.* **2001**, 617; b) C. J. Murphy, N. R. Jana, *Adv. Mater.* **2002**, *14*, 80.
[11] a) Silinsh, E. A. *Organic Molecular Crystals: Their Electronic States*; Springer-Verlag: Berlin, **1980**; b) M. Pope, C. E. Swenberg, *Electronic Processes in Organic Crystals*; Oxford Univ. Press: Oxford, **1982**.
[12] B. Duffin, *Acta Crystallogr. Sect. B* **1968**, *24*, 1256.
[13] F. Wilkinson, G. P. Kelly, C. Michael, *J. Photochem. Photobiol. A* **1990**, *52*, 309.
[14] T. Imae, R. Kamiya, S. Ikeda, *J. Colloid Interface Sci.* **1985**, *108*, 215.
[15] Tuning the value of *N* by varying the injected quantity of DP/ethanol stock solution could obtain the same results. Moreover, stepwise injection also produced nanofibers.
[16] *Solubilization in Surfactant Aggregates* (Eds.: S. D. Christian, F. F. Scamehorn), Marcel Dekker, New York, **1995**.
[17] T. Shikata, H. Hirata, T. Kotaka, *Langmuir* **1988**, *4*, 354.
[18] P. Lianos, J. Lang, C. Strazielle, R. Zana, *J. Phys. Chem.* **1982**, *86*, 1019.
[19] a) S. Özçelik, D. L. Akins, *J. Phys. Chem. B* **1999**, *103*, 8926–8929; b) E. S. Emerson, M. A. Conlin, A. E. Rosenoff, K. S. Norland, H. Rodriguez, D. Chin, G. R. Bird, *J. Phys. Chem.* **1967**, *71*, 2396; c) M. Kasha, H. R. Rawls, M. A. El-Bayoumi, *Pure Appl. Chem.* **1965**, *11*, 371.
[20] The angle between the pyrazoline plane and the crystallographic *a* axis is calculated to be 53.52°.[12] Thus, $\alpha = 53.52° - (\beta - 90°) \approx 50.7°$.

 © 2003 Wiley-VCH Verlag GmbH & Co. KGaA, Weinheim

Phosphorus Acid-Promoted Catalysis

The Carbonylation Reaction of Nitrobenzene to Methyl Phenylcarbamate: Highly Efficient Promoters for the Palladium–Phenanthroline Catalytic System Based on Phosphorus Acids**

Fabio Ragaini, Carlo Cognolato, Michela Gasperini, and Sergio Cenini*

Carbonylation of nitroarenes to carbamates according to Equation (1) offers a possible alternative to the current

$$ArNO_2 + ROH + 3\,CO \xrightarrow{cat.} ArNHCOOR + 2\,CO_2 \quad (1)$$

technology, which employs the toxic phosgene.[1–3] If the isocyanate is the desired product, this can be obtained by thermal cracking of the carbamate.

Despite intense effort from both industrial and academic laboratories, there is yet to be developed a process that can compete from an economical point of view with the established technology. This is mostly due to the insufficient turnover numbers (TONs) that even the most efficient catalysts can achieve, thus making recycling the catalyst too expensive. In recent years the catalytic system based on palladium–phenanthroline complexes has emerged as the most promising for possible industrial applications.[4–20] Several groups have reported that the addition of acidic cocatalysts (carboxylic acids[8,9,12,14] or phenanthrolinium salts[16–18,20]) markedly improves both the rate and selectivity of the carbonylation of nitroarenes to give isocyanates or carbamates. We were intrigued by the observation by van Leeuwen et al.[12] that there was no correlation between the acidity of the carboxylic acid employed as promoter and the increase in reaction rate. This suggested to us that a bifunctional activation process may be operative, thus as a working hypothesis, we decided to investigate the promoting activity of a series of substances that may have a superior bifunctional activation ability than carboxylic acids. It should be noted that there is presently only some preliminary mechanistic data to indicate that bifunctional activation is

[*] Prof. Dr. F. Ragaini, Dipl.-Chem. C. Cognolato, Dipl.-Chem. M. Gasperini, Prof. Dr. S. Cenini
Dipartimento di Chimica Inorganica Metallorganica e Analitica, ISTM–CNR
and
INSTM, UdR Milano, via Venezian 21, 20133 Milano (Italy)
Fax: (+39) 02-5031-4405
E-mail: fabio.ragaini@unimi.it

[**] Publication of this paper was delayed to allow for patenting: F. Ragaini, S. Cenini, C. Querci, *Ital. Pat. Appl.* MI2000A 000548, **2000** (to Enitecnologie S.p.a., now property of Dow Poliuretani Italia). We thank Enichem for financial support and The Dow Chemical Company for the permission to publish these results. We also thank Dr. C. Querci (Polimeri Europa, Istituto Donegani) for helpful discussions.

Supporting information for this article is available on the WWW under http://www.angewandte.org or from the author.

 © 2003 Wiley-VCH Verlag GmbH & Co. KGaA, Weinheim DOI: 10.1002/anie.200351004

indeed occurring, however, this working hypothesis has proved fruitful in allowing a marked improvement in the efficiency of the catalytic system, in terms of both reaction rate and catalyst lifetime.

As candidates for the promotion of bifunctional activation, we initially investigated 2-hydroxypyridine,[21] which had previously been shown by us to act as a promoter for the reaction in Equation 1 when $[Rh(CO)_4]^-$ was employed as the catalyst,[22] its 5-chloro analogue, and a phosphorus acid:-diphenylphosphinic acid.[21,23] Van Leeuwen and co-workers have reported on the promoting efficiency of carboxylic acids in conjunction with $[Pd(phen)_2][TfO]_2$ (phen = 1,10-phenanthroline; $TfO^- = CF_3SO_3^-$) as a catalyst at 135 °C.[12,14] However, in another paper,[11] the same authors reported that the related $[Pd(phen)_2][BF_4]_2$ complex affords better results. We have compared both of these complexes in the presence of the aforementioned promoters, also including benzoic acid and [phenH][PF_6] for a comparison, and in a broader range of temperatures. The results are reported in Table S1 (see Supporting Information). The main conclusions that can be drawn from the data reported are the following:

1) We confirm that benzoic acid increases both conversion and selectivity when employed at 135 °C with $[Pd(phen)_2][TfO]_2$ as catalyst. However, with the more active tetrafluoborate catalyst, no effect on conversion is observed at either 135 or 150 °C, although an increase in selectivity is still observed. A positive effect on the reaction rate is only observed at 170 °C with $[Pd(phen)_2][BF_4]_2$.
2) 2-Hydroxypyridine and its chlorinated analogue show some promoting effects but, at least for the triflate catalyst, the effect is smaller than that of benzoic acid and thus they were not investigated further.
3) Mestroni's promoter[16–18,20] ([phenH][PF_6]) is also effective with the tetrafluoborate catalyst, in accordance with the literature. Under these conditions it affords better conversions, but lower selectivities with respect to benzoic acid.
4) Diphenylphosphinic acid is clearly the best promoter, and increases rate and selectivity with both catalysts at all temperatures.

Working under a pressure of CO (60 bar), the reaction temperature and the amounts of phen and diphenylphosphinic acid were optimized. During the optimization study it was realized that, in accordance with data reported in the literature,[16–20] the addition of a small amount of 2,2-dimethoxypropane as an internal drying agent has a beneficial effect on the selectivity. This optimization of the conditions allowed us to work at the unprecedented catalytic ratio $PhNO_2$:Pd = 10^4. Under these conditions, the reaction shows an induction time of about one hour, after which it proceeds with a zero-order reaction rate with respect to $PhNO_2$ without showing any rate decrease due to possible decomposition of the catalytic system (Figure 1). The reaction is 5.4 times slower during the first hour than at any following time. It should be noted that the autoclave takes about 15 min to reach the final temperature when immersed in the preheated oil bath (see Experimental Section), but the reaction certainly starts well before full equilibration has been achieved. However, a delay of 15 min in the first hour would, by itself, cause the reaction to be only 1.3 times slower in the first hour than in the following time.

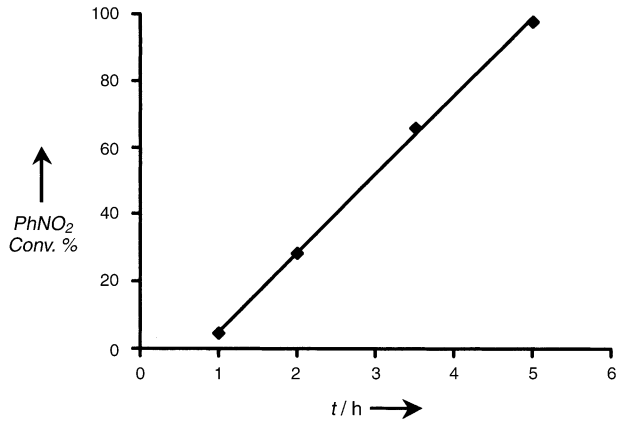


Figure 1. Dependence of $PhNO_2$ conversion on reaction time. Experimental conditions: $[Pd(phen)_2][BF_4]_2$ (2.8 mg, 4.4×10^{-3} mmol) in methanol (30 mL) and 2,2-dimethoxypropane (1.0 mL); molar ratios Pd/phen/Ph_2POOH/$PhNO_2$ = 1:100:682:10000; T = 170 °C; P_{CO} = 60 bar. The linear regression affords a line with the equation: Conv. % = 23.49t − 18.56 (R^2 = 0.999).

Since aniline is known to be formed as an intermediate in several catalytic carbonylation reactions of nitroarenes,[1–3,15] we investigated the effect of its addition from the beginning of such reactions. As shown in Table S2 (see Supporting Information), the addition of aniline (4% with respect to the starting nitrobenzene) accelerates the reaction in the first hour by a factor of approximately four. Thus it is clear that the induction time is, for the most part, due to the required generation of aniline, which is slow in the dry solvent employed. The addition of an equimolar amount of aniline with respect to nitrobenzene has been previously reported to accelerate the rate of the reaction with a palladium–phenanthroline catalyst,[13] but in the presence of such an high amount of aniline the selectivity of the reaction is much decreased and large amounts of azoxybenzene were formed.

At this stage other phosphorus acids were tested. A comparison of the data in Table 1 shows that the introduction of an electron-donating group on the phenyl rings of diphenylphosphinic acid has a small positive effect, but the electron-withdrawing chloride is not tolerated. Phenylphosphonic acid and its substituted analogues are a better class of promoters, but phenylphosphinic acid, which can act as a reductant towards palladium, completely deactivated the catalytic system, apparently because of the fast formation of inactive palladium metal. Even the more acidic dithiodiphenylphosphinic acid was not a suitable promoter, and it is noted that this acid is known not to be a good bifunctional catalyst.[21] However, it was very interesting to observe that the best conversion was obtained with commercial 85% phosphoric acid! This is an ideal promoter in terms of cost, absence of toxicity, and ease of separation from the reaction products. The 1:1 mixture of mono- and dimethylphosphate, obtained by reaction of P_4O_{10} with the stoichiometric amount of methanol, was less efficient, but still retained a high promoting efficiency, which shows that a partial esterification of the acid does not block catalytic activity. Such esterification

 © 2003 Wiley-VCH Verlag GmbH & Co. KGaA, Weinheim

Table 1: Comparison of different phosphorus promoters.[a]

Promoter	Promoter/Pd molar ratio	$PhNO_2$ conv. %[b]	$PhNHCO_2Me$ selectivity [%][c]	$PhNH_2$ selectivity [%][c]	PhN(O)=NPh selectivity [%][c]
–	–	4.6	13.7 (11.0)[d]	–[d]	51.0
Ph_2POOH	682	37.0	89.5 (87.9)[d]	–[d]	1.8
$(4\text{-}MeC_6H_4)_2POOH$	682	37.8	93.3 (91.7)[d]	–[d]	1.9
$(4\text{-}ClC_6H_4)_2POOH$	682	7.7	64.0 (60.3)[d]	–[d]	–
$PhPO(OH)_2$	682	42.5	86.8	< 0.1	1.6
$4\text{-}MeC_6H_4PO(OH)_2$	682	49.2	90.3	0.4	1.6
$4\text{-}ClC_6H_4PO(OH)_2$	682	34.6	86.4	0.7	2.1
Ph_2PSSH	682	–	–	–	–
PhPH(O)OH	682	–	–	–	–
H_3PO_4 (100%)	682	42.6	93.5	2.8	–
H_3PO_4 (100%)	753	47.9	89.0	0.9	–
H_3PO_4 (85%)	682	55.1	87.1	3.0	1.7
$OP(OMe)(OH)_2$/ $OP(OMe)_2(OH)$ 1:1	682	33.4	85.4 (84.0)[d]	–[d]	< 1
PhCOOH	682	17.1	83.6 (77.3)[d]	–[d]	18.6
[phenH][PF_6]	227	10.6	83.8 (81.3)[d]	–[d]	–

[a] Experimental conditions: $[Pd(phen)_2][BF_4]_2$ (1.4 mg, 2.2×10^{-3} mmol) in methanol (15 mL) and 2,2-dimethoxypropane (0.5 mL) for 1.5 h; molar ratio $Pd/phen/PhNH_2/PhNO_2 = 1:100:200:7500$; $P_{CO} = 60$ bar. [b] Calculated with respect to the starting amount of $PhNO_2$. [c] Calculated with respect to the converted $PhNO_2$. Aniline selectivity is calculated considering only the excess amount of aniline compared with the initial quantity. Most of the remaining mass balance is due to diphenylurea, which was observed, but not quantified by GC. Azobenzene was below or very close to the detection limit (0.1%). [d] Less aniline was found at the end of the reaction, as compared with the initial amount. The values in parentheses refer to the selectivity in terms of the total $PhNO_2$ and $PhNH_2$ that had reacted.

does indeed occur during the reaction, but to a small extent. Under the conditions described in Table 1, but for a longer time (6 h), 32% of the added phenylphosphonic acid was transformed into the monomethyl ester and no diester was detectable by ^{31}P NMR spectroscopy. The esterification is a purely organic transformation and essentially the same amount of monoester (30%) is obtained under similar conditions in the absence of the metal and nitrobenzene.

The influence of CO was investigated employing 85% phosphoric acid as the promoter. The reaction is clearly first order with respect to CO pressure (Figure 2). Because of technical limits, we could not investigate initial pressures higher than 100 bar, but these should afford even better results. By working at the conditions described in Table 1, but at 100 bar, we obtained a 81.2% conversion (with a 87.5% selectivity), corresponding to a turnover frequency (TOF) of almost 6000 h^{-1}. The highest value previously reported in the literature for the carbonylation reaction of nitrobenzene to afford methyl phenylcarbamate is 960 h^{-1}.[19] The catalytic system is very stable, and by decreasing the amount of palladium we could obtain an unprecedented 10^5 turnovers in 24 h, albeit with a somewhat lower selectivity (77.5%),[24] which approaches the limit for which a commercial application can be considered.

In conclusion, we have found an improved catalytic system for the carbonylation of nitrobenzene that for the first time yields activities and catalyst lifetimes in the range necessary for industrial applications. Preliminary results indicate that the improved features also apply to the economically very important dinitrotoluenes. Optimization of the experimental conditions with these substrates is in progress.

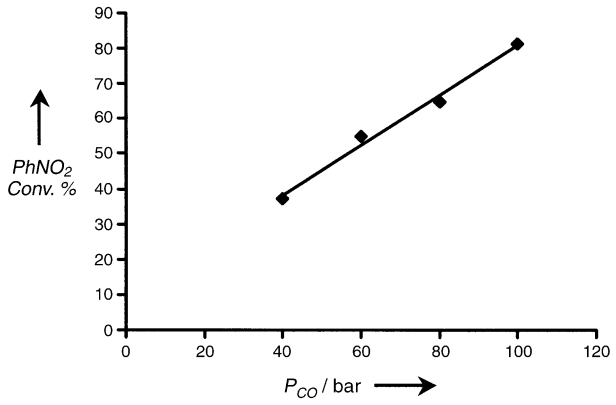


Figure 2. Influence of CO pressure on $PhNO_2$ conversion. Experimental conditions: $[Pd(phen)_2][BF_4]_2$ (1.4 mg, 2.2×10^{-3} mmol) in methanol (15 mL) and 2,2-dimethoxypropane (0.5 mL) for 1 h; molar ratio $Pd/phen/H_3PO_4/PhNH_2/PhNO_2 = 1:100:682:200:7500$; $T = 170\,^{\circ}C$. The linear regression affords a line with the equation: Conv.% $= 0.713\,P_{CO} + 9.69$ ($R^2 = 0.989$).

Experimental Section

In a typical catalytic reaction the catalyst, phen, $PhNO_2$, $PhNH_2$, and the acidic promoter were weighed in a glass liner. The liner was placed inside a Schlenk tube with a wide neck under dinitrogen, which was then cooled to $-78\,^{\circ}C$, evacuated, and filled with dinitrogen, after which the solvent was added. After the solvent was also frozen, the liner was closed with a screw cap that contained glass wool that allows gaseous reagents to exchange. The flask was rapidly transferred to a 200 mL stainless steel autoclave with a magnetic stirrer. The autoclave was then evacuated and filled with dinitrogen three times. CO was then charged at room temperature at the required pressure and the autoclave was immersed in an oil bath preheated to the required temperature; the autoclave took about 15 min to fully equilibrate at the final temperature. Other experimental conditions are reported in the legends of the tables and figures. At the end of the reaction the autoclave was cooled with an ice bath, vented, and the products were analyzed by gas chromatography (with naphthalene as an internal standard).

Received: January 23, 2003 [Z51004]

Keywords: carbamates · carbonylation · homogeneous catalysis · nitroarenes · palladium

 © 2003 Wiley-VCH Verlag GmbH & Co. KGaA, Weinheim

[1] S. Cenini, F. Ragaini, *Catalytic Reductive Carbonylation of Organic Nitro Compounds*, Kluwer Academic Press, Dordrecht, **1997**, and references therein.
[2] F. Paul, *Coord. Chem. Rev.* **2000**, *20*, 269 – 323, and references therein.
[3] A. M. Tafesh, J. Weiguny, *Chem. Rev.* **1996**, *96*, 2035 – 2052, and references therein.
[4] E. Drent, P. W. N. M. Van Leeuwen, US 4,474,978, **1984** (*Eur. Pat. Appl.* EP 86,281, **1983** [*Chem. Abstr.* **1984**, *100*, 6109x]).
[5] E. Drent, Eur. Pat. Appl. EP 231,045, **1987** [*Chem. Abstr.* **1988**, *109*, 128605n].
[6] A. Bontempi, E. Alessio, G. Chanos, G. Mestroni, *J. Mol. Catal.* **1987**, *42*, 67 – 80.
[7] E. Alessio, G. Mestroni, *J. Organomet. Chem.* **1985**, *291*, 117 – 127.
[8] S. Cenini, F. Ragaini, M. Pizzotti, F. Porta, G. Mestroni, E. Alessio, *J. Mol. Catal.* **1991**, *64*, 179 – 190.
[9] P. Leconte, F. Metz, Eur. Pat. Appl. EP 330,591, **1989** [*Chem. Abstr.* **1990**, *112*, 78160c].
[10] P. Wehman, G. C. Dol, E. R. Moorman, P. C. J. Kamer, P. W. N. M. van Leeuwen, J. Fraanje, K. Goubitz, *Organometallics* **1994**, *13*, 4856 – 4869.
[11] P. Wehman, V. E. Kaasjager, W. G. J. de Lange, F. Hartl, P. C. J. Kamer, P. W. N. M. van Leeuwen, J. Fraanje, K. Goubitz, *Organometallics* **1995**, *14*, 3751 – 3761.
[12] P. Wehman, L. Borst, P. C. J. Kamer, P. W. N. M. van Leeuwen, *J. Mol. Catal. A* **1996**, *112*, 23 – 36.
[13] P. Wehman, L. Borst, P. C. J. Kamer, P. W. N. M. van Leeuwen, *Chem. Ber.* **1997**, *130*, 13 – 21.
[14] P. Wehman, P. C. J. Kamer, P. W. N. M. van Leeuwen, *Chem. Commun.* **1996**, 217 – 218.
[15] F. Ragaini, S. Cenini, *J. Mol. Catal. A* **1996**, *109*, 1 – 25, and references therein.
[16] R. Santi, A. M. Romano, P. Panella, G. Mestroni, It. Pat. Appl. MI96A 002071, **1996**.
[17] R. Santi, A. M. Romano, P. Panella, G. Mestroni, It. Pat. Appl. MI96A 002072, **1996**.
[18] R. Santi, A. M. Romano, R. Garrone, P. Panella, It. Pat. Appl. MI97A 000433, **1997**.
[19] R. Santi, A. M. Romano, P. Panella, C. Santini, *J. Mol. Catal. A* **1997**, *127*, 95 – 99.
[20] R. Santi, A. M. Romano, P. Panella, G. Mestroni, A. Sessanta O Santi, *J. Mol. Catal. A* **1999**, *144*, 41 – 45.
[21] L. M. Litvinenko, N. M. Oleinik, *Russ. Chem. Rev.* **1978**, *47*, 401 – 415; *Usp. Khim.* **1978**, *47*, 777 – 803.
[22] F. Ragaini, E. Gallo, S. Cenini, *J. Organomet. Chem.* **2000**, *593–594*, 109 – 118.
[23] a) A. P. Kozlov, S. S. Sazhnev, G. A. Kozlova, Yu. S. Andreiichikov, *Russ. J. Org. Chem.* **1996**, *32*, 1523 – 1528; *Zh. Org. Khim.* **1996**, *32*, 1573 – 1578; b) G. V. Semenyuk, N. G. Razumova, *J. Org. Chem. USSR* **1986**, *22*, 996 – 997; *Zh. Org. Khim.* **1986**, *22*, 1109 – 1110.
[24] The absolute amounts of all the other reagents (including phen and phosphoric acid) have been kept constant and equal to those reported in Table 1, except for the CO pressure (100 bar). Nitrobenzene conversion was complete in this experiment; thus even higher TONs should be possible.

 © 2003 Wiley-VCH Verlag GmbH & Co. KGaA, Weinheim

Tandem Michael–Aldol Reaction

Asymmetric Induction of Three Consecutive Chiral Centers by Reactions of *N*-Enoylthioamides with Aldehydes**

Tadashi Kataoka, Hironori Kinoshita, Sayaka Kinoshita, Takashi Osamura, Shinichi Watanabe, Tatsunori Iwamura, Osamu Muraoka, and Genzoh Tanabe*

Recently we developed a chalcogenide/$TiCl_4$-mediated reaction, which consists of the Michael addition of a chloride ion generated from a chalcogenide/$TiCl_4$ complex to an enone, followed by an aldol reaction with an aldehyde to give an α-chloromethyl aldol, which can be transformed into an α-methylene aldol (the Morita–Baylis–Hillman adduct).[1,2] This reaction is completed much faster than the Morita–Baylis–Hillman reaction[3] and, therefore, can be utilized advantageously in several reactions which do not give good results under Morita–Baylis–Hillman reaction conditions.[4–8] We further studied the tandem Michael–aldol reaction initiated by the intramolecular Michael cyclization of a chalcogenide group to an enone moiety.[9–11] Goodman et al. reported a similar intermolecular example.[12]

While investigating the chalcogenide catalyst, we found that a thioketone acted as a nucleophile toward an enone[13] and a thiourea was also useful for the tandem Michael–aldol reaction.[14] Recently, it was reported that a thiourea moiety added intramolecularly to an enone moiety to form a thiazine ring.[15,16] These reports prompted us to examine the tandem Michael–aldol reaction of *N*-propenoyl cyclic thioamides with aldehydes. We now report the asymmetric tandem Michael–aldol reaction of chiral *N*-cinnamoyl-1,3-thiazolidine-2-thione and its 1,3-oxazolidine congener with aldehydes in the presence of $BF_3{\cdot}Et_2O$.

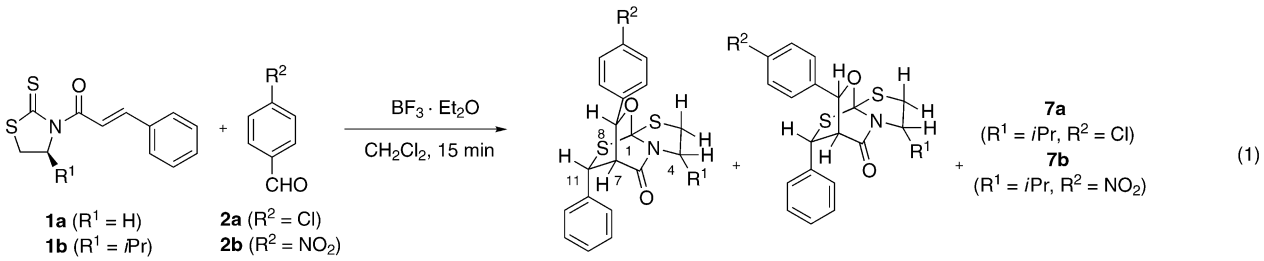
The reaction of *N*-cinnamoyl-1,3-thiazolidine-2-thione (**1a**) with *p*-chlorobenzaldehyde (**2a**) was conducted for the first time [Eq. (1)]. The results are shown in Table 1. Various molar ratios of the starting compounds and the Lewis acid were tested, and the best result was obtained from the reaction of **1a** (2 equiv) with **2a** (1 equiv) in the presence of 3 equiv $BF_3{\cdot}Et_2O$ (Table 1, entry 1). This reaction was quite fast and was completed within 15 minutes at room temper-

[*] Prof. T. Kataoka, H. Kinoshita, S. Kinoshita, T. Osamura, Dr. S. Watanabe, Dr. T. Iwamura
Gifu Pharmaceutical University
6-1 Mitahora-higashi 5-chome, Gifu 502-8585 (Japan)
Fax: (+81) 58-237-5979
E-mail: kataoka@gifu-pu.ac.jp
Prof. O. Muraoka, Dr. G. Tanabe
Faculty of Pharmaceutical Sciences
Kinki University
3-4-1 Kowakae, Higashi-Osaka 577-8502 (Japan)

[**] This work was supported in part by a Grant-in-Aid (No. 3824) from the Japan Society for the Promotion of Science.

Supporting information for this article is available on the WWW under http://www.angewandte.org or from the author.

 DOI: 10.1002/anie.200351106 © 2003 Wiley-VCH Verlag GmbH & Co. KGaA, Weinheim



(1)

Table 1: Representative results for the screening of reaction conditions for the diastereoselective tandem Michael–aldol reactions of *N*-cinnamoyl-1,3-thiazolidine-2-thiones **1a**,**b** with aldehydes **2a**,**b**.

Entry	Enone (equiv)	Aldehyde (equiv)	$BF_3{\cdot}Et_2O$ [equiv]	*T*	Products[a] (% yield)
1	**1a** (2)	**2a** (1)	3	RT	**3a** (58), **4a** (31)
2	**1a** (2)	**2a** (1)	2	RT	**3a** (50), **4a** (33)
3	**1a** (1)	**2a** (2)	3	RT	**3a** (48), **4a** (30)
4	**1b** (2)	**2a** (1)	3	0 °C	**5a** (54), **6a** (28), **7a** (4)
5	**1b** (2)	**2b** (1)	3	0 °C	**5b** (43), **6b** (41), **7b** (4)

[a] Minor products **7a** and **7b** have the same molecular weights and composition formulas, $C_{22}H_{22}ClNO_2S_2$ and $C_{22}H_{22}N_2O_4S_2$, as **5a**, **6a** and **5b**, **6b**, respectively, but the amounts of **7a** and **7b** are so small that their stereostructures could not yet be determined.

ature. The structures of products **3a** and **4a** were determined by comparing the their ^1H and ^{13}C NMR data with those of **5a**, whose structure was elucidated by X-ray analysis (vide infra).

We obtained the three diastereomeric products **5**–**7** from the reactions of chiral thioamide **1b**, which has a 4*S* configuration, with aldehydes **2a**,**b**. X-ray analysis revealed that the major product **5a** ($R^1 = i$Pr, $R^2 = Cl$) has a tricyclic ring system, in which a chiral bridgehead carbon is bound to four heteroatoms (Figure 1). The configuration of the four chiral centers is 1*R*,4*S*,7*R*,8*S*,11*R*.[17] The structure of product **6a**, in which the ClC_6H_4 group is on the same side as H-11, was determined by comparing its ^1H and ^{13}C NMR spectra with those of **5a**. The absolute configuration of the 8-position is 8*R*, opposite to that of **5a**.

Palomo et al. reported that a chiral thioamide can undergo an asymmetric Michael addition to an intramolecular enone moiety with high diastereoselectivity.[16] Based on their findings and ours, we anticipated that the stereoselective formation of the four chiral centers involving three consecutive chiral carbons could be achieved if the aldol reaction of an enolate with an aldehyde could be stereocontrolled. Hence, we selected 4,5-disubstituted oxazolidine-2-thione as a chiral auxiliary and carried out reactions of *N*-cinnamoyl-4*S*-methyl-5*R*-phenyloxazolidinethione (**1c**) with various aldehydes [Eq. (2)] (Table 2).

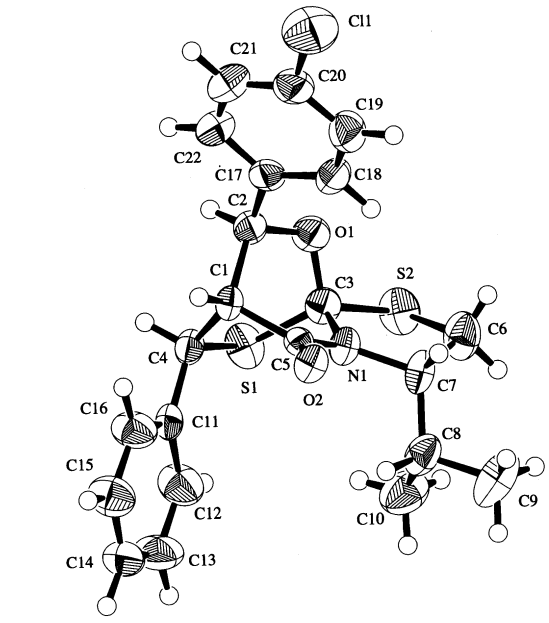
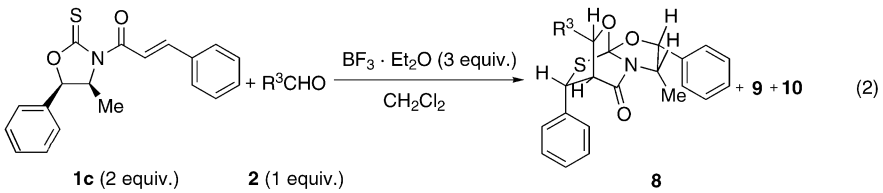


Figure 1. X-ray crystal structure of **5a** (ORTEP drawing).



(2)

The best molar ratio of enone **1** and aldehyde **2** from Table 1 was applied to the reaction of **1c** and **2b**, and the reaction temperature and time were examined. The reaction at −78 °C for 25 h gave **8b** in 27 % yield (Table 2, entry 1). When the reaction was conducted at −40 °C, the chemical yield increased but a small amount of diastereomer **9b** formed (entry 2). The best result was obtained for the reaction at −40 °C for 24 h (entry 3). The stereostructure of

 © 2003 Wiley-VCH Verlag GmbH & Co. KGaA, Weinheim

Table 2: Diastereoselective tandem Michael–aldol reactions of *N*-cinnamoyl-1,3-oxazolidine-2-thione **1c** with aldehydes **2a**–**e**.

Entry	Aldehyde (R^3)	Conditions	Yield [%][a]	**8**:**9**:**10**[b]
1	**2b** (*p*-$NO_2C_6H_4$)	−78 °C, 25 h	27	100:0:0
2	**2b** (*p*-$NO_2C_6H_4$)	−40 °C, 5 h	77	94:6:0
3	**2b** (*p*-$NO_2C_6H_4$)	−40 °C, 24 h	93	95:5:0
4	**2c** (*m*-$NO_2C_6H_4$)	−40 °C, 24 h	85	95:5:0
5	**2a** (*p*-ClC_6H_4)	−40 °C, 24 h	71	86:7:7
6	**2d** (Ph)	0 °C, 1 h	69	69:3:28
7	**2e** (*p*-MeC_6H_4)	0 °C, 1 h	59	92:0:8

[a] Mixture of diastereoisomers. [b] HRMS data indicate that products **9** and **10** have the same molecular formulas as product **8**, but their sterostructures could not be determined because of the small amounts.

the major product **8b** corresponds to that of **6b,** which has a 4-isopropylthiazolidine moiety. Diastereomer ratios of the products were determined from ^{1}H NMR spectra of the crude products. Reactions with *p*-chloro- (**2a**) and *m*-nitrobenzaldehyde (**2c**) were conducted similarly and gave products **8a** and **8c** in good yields together with isomers **9a**,**c** and **10a** (entries 4 and 5). The reaction with benzaldehyde was slow and was conducted at 0 °C, but the diasteromer ratio was decreased (entry 6). Reaction with *p*-tolualdehyde (**2e**) gave the products in a moderate chemical yield (entry 7). The reaction with *o*-nitrobenzaldehyde was very slow because of the steric hindrance, and the reaction with dihydrocinnamaldehyde gave a mixture of products with a low diastereomer ratio.

In conclusion, we have developed a novel tandem Michael–aldol reaction of chiral thioamide-enones with aldehydes, which induces four chiral centers simultaneously. This method is easy to use and gives unusual heterotricyclic compounds with three consecutive chiral centers and a chiral carbon center bound to four heteroatoms. If the products can be converted into polyfunctionalized chiral carboxylic acids, aldehydes, amides or alcohols, they can be widely utilized for organic synthesis. This is the subject of current investigation.

Experimental Section

General procedure: To a stirred solution of (4*S*,5*R*)-4-methyl-5-phenyl-3-[(*E*)-3-phenylprop-2-enoyl]-1,3-oxazolidine-2-thione (**1c**)(323 mg, 1.0 mmol) and *p*-nitrobenzaldehyde (**2b**)(76 mg, 0.5 mmol) in dry CH_2Cl_2 (1.6 mL) was added dropwise a solution of $BF_3{\cdot}Et_2O$ (190 μL, 1.5 mmol) at −40 °C. The mixture was stirred at the same temperature for 24 h, poured into $NaHCO_3$ solution, and extracted with CH_2Cl_2. The combined organic layers were dried over $MgSO_4$ and concentrated under reduced pressure. The residue was purified by recycling preparative HPLC, eluting with chloroform to give **8b** and **9b**.

Received: February 5, 2003 [Z51106]

Keywords: aldol reactions · asymmetric synthesis · C–C coupling · Michael addition · thiocarbonyl compounds

[1] a) T. Kataoka, T. Iwama, S. Tsujiyama, *Chem. Commun.* **1998**, 197–198; b) T. Kataoka, T. Iwama, S. Tsujiyama, T. Iwamura, S. Watanabe, *Tetrahedron* **1998**, *54*, 11813–11824.

[2] T. Kataoka, H. Kinoshita, T. Iwama, S. Tsujiyama, T. Iwamura, S. Watanabe, O. Muraoka, G. Tanabe, *Tetrahedron* **2000**, *56*, 4725–4731.

[3] For reviews of the Morita–Baylis–Hillman reaction: a) S. E. Drewes, G. H. P. Roos, *Tetrahedron* **1988**, *44*, 4653–4670; b) D. Basavaiah, P. D. Rao, R. S. Hyma, *Tetrahedron* **1996**, *52*, 8001–8062; c) E. Ciganek in *Organic Reactions, Vol. 51* (Ed.: L. A. Paquette), Wiley, New York, **1997**, pp. 201–350; d) P. Langer, *Angew. Chem.* **2000**, *112*, 3177–3180; *Angew. Chem. Int. Ed.* **2000**, *39*, 3049–3052; e) D. Basavaiah, A. J. Rao, T. Satyanarayana, *Chem. Rev.* **2003**, *103*, 811–891.

[4] a) T. Kataoka, T. Iwama, H. Kinoshita, S. Tsujiyama, Y. Tsurukami, T. Iwamura, S. Watanabe, *Synlett* **1999**, 197–198; b) T. Kataoka, T. Iwama, H. Kinoshita, Y. Tsurukami, S. Tsujiyama, M. Fujita, E. Honda, T. Iwamura, S. Watanabe, *J. Organomet. Chem.* **2000**, *611*, 455–462.

[5] D. Basavaiah, K. Muthukumaran, B. Sreenivasulu, *Synlett* **1999**, 1249–1250.

[6] T. Bauer, J. Tarasiuk, *Tetrahedron: Asymmetry* **2001**, *12*, 1741–1745.

[7] R. Pathak, A. K. Shaw, A. P. Bhaduri, *Tetrahedron* **2002**, *58*, 3535–3541.

[8] T. Kataoka, H. Kinoshita, S. Kinoshita, T. Iwamura, S. Watanabe, *Angew. Chem.* **2000**, *112*, 2448–2450; *Angew. Chem. Int. Ed.* **2000**, *39*, 2358–2360.

[9] T. Kataoka, S. Kinoshita, H. Kinoshita, M. Fujita, T. Iwamura, S. Watanabe, *Chem. Commun.* **2001**, 1958–1959.

[10] T. Kataoka, H. Kinoshita, S. Kinoshita, T. Iwamura, *J. Chem. Soc. Perkin Trans. 1* **2002**, 2043–2045.

[11] T. Kataoka, H. Kinoshita, S. Kinoshita, T. Iwamura, *Tetrahedron Lett.* **2002**, *43*, 7039–7041.

[12] L. M. Walsh, C. L. Winn, J. M. Goodman, *Tetrahedron Lett.* **2002**, *43*, 8219–8222.

[13] T. Iwama, H. Kinoshita, T. Kataoka, *Tetrahedron Lett.* **1999**, *40*, 3741–3744.

[14] S. Kinoshita, H. Kinoshita, T. Iwamura, S. Watanabe, T. Kataoka, *Chem. Eur. J.* **2003**, *9*, 1496–1502.

[15] A. Hari, B. L. Miller, *Org. Lett.* **2000**, *2*, 3667–3670.

[16] a) C. Palomo, M. Oiarbide, F. Dias, A. Ortiz, A. Linden, *J. Am. Chem. Soc.* **2001**, *123*, 5602–5603; b) A. Ortiz, L. Quintero, H. Hernández, S. Maldonado, G. Mendoza, S. Bernès, *Tetrahedron Lett.* **2003**, *44*, 1129–1132.

[17] Crystal structure data for **5a**: $C_{22}H_{22}ClNO_2S_2$, $M_r = 431.99$, prismatic, space group $P2_12_12_1$, $a = 11.636(2)$, $b = 18.035(2)$, $c = 9.947(2)$ Å, $V = 2087.4(5)$ Å^3, $T = 296$ K, $Z = 4$, $\rho_{calcd} = 1.375$ g cm^{-3}, $\mu(Mo_{K\alpha}) = 4.01$ cm^{-1}, $R = 0.0243$, $R_w = 0.061$. CCDC-200264 contains the supplementary crystallographic data for this paper. These data can be obtained free of charge via www.ccdc.cam.ac.uk/conts/retrieving.html (or from the Cambridge Crystallographic Data Centre, 12 Union Road, Cambridge CB21EZ, UK; fax: (+44) 1223-336-033; or deposit@ccdc.cam.ac.uk).

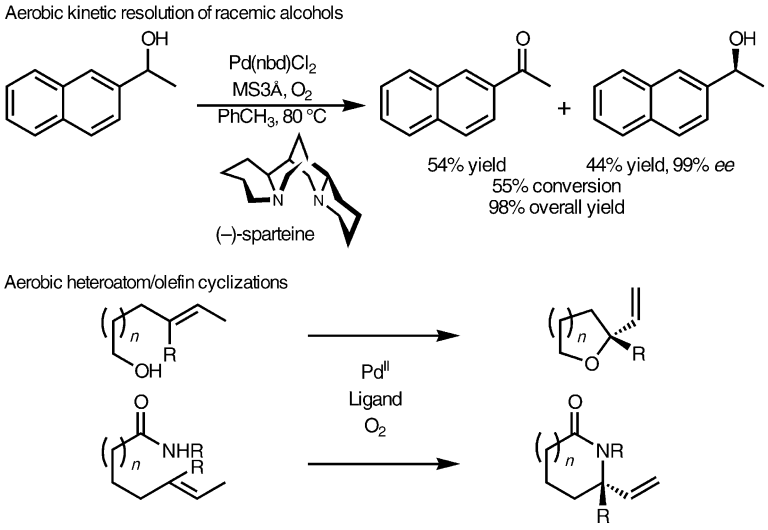
 © 2003 Wiley-VCH Verlag GmbH & Co. KGaA, Weinheim

Pd-Catalyzed Wacker Cyclizations

Palladium-Catalyzed Oxidative Wacker Cyclizations in Nonpolar Organic Solvents with Molecular Oxygen: A Stepping Stone to Asymmetric Aerobic Cyclizations**

*Raissa M. Trend, Yeeman K. Ramtohul, Eric M. Ferreira, and Brian M. Stoltz**

Catalytic asymmetric oxidation-chemistry involving heteroatom transfer from a reagent to a substrate is perhaps unparalleled in synthetic utility for the construction of enantioenriched materials.[1] Conversely, there is a significant deficiency of asymmetric two-electron oxidations that do not involve heteroatom transfer. Some potentially valuable reactions of this type include the oxidation of secondary alcohols and oxidative heterocyclizations (Scheme 1). The design of efficient processes of this nature requires an abundant, inexpensive, and effective stoichiometric oxidant, and a solvent that is amenable to asymmetric catalysis. To begin to address this general synthetic problem, we recently developed a Pd-catalyzed oxidative kinetic resolution of secondary alcohols in toluene that uses molecular oxygen as the terminal oxidant (Scheme 1).[2,3] Herein we demonstrate the utility of this simple system (Pd catalyst, ligand, $PhCH_3$, O_2) for the construction of a range of heterocycles by catalytic oxidative cyclization. We also demonstrate for the first time that aerobic cyclizations of this type are amenable to asymmetric catalysis, and thereby establish a critical proof of concept for the further development of catalytic asymmetric oxidative cyclizations that use molecular oxygen as the sole stoichiometric oxidant.



Scheme 1. Some aerobic oxidation reactions.

Palladium-catalyzed bond-forming constructions have become indispensable in organic chemistry.[4] A favorable property of palladium is that it can serve as both a nucleophile (i.e., Pd^0) and an electrophile (i.e., Pd^{II}), which produces many opportunities for catalysis. Although both modes are prevalent, electrophilic oxidative catalysis by Pd^{II} has garnered less attention in the asymmetric arena. Adding to the disparity is the fact that until recently, cocatalysts (e.g., copper salts) or organic oxidants (e.g., benzoquinone) were necessary for the reoxidation of Pd^0 to Pd^{II}, thus creating a nearly intractable situation for asymmetric catalysis. For example, the use of the traditional copper/O_2 reoxidation system introduces a secondary catalytic cycle, while the benzoquinone system requires the removal of stoichiometric quantities of organic compounds at the end of the reaction. In contrast, reactions that proceed under direct dioxygen coupled catalysis produce H_2O as the sole byproduct. Despite the difficulties of the traditional systems, seminal works by Hosokawa and Murahashi,[5] Hayashi,[6] Sasai,[7] and Bäckvall[8] have established the potential for enantioselective Pd^{II}-catalyzed oxidative cyclizations and dialkoxylations.[9] To the best of our knowledge, however, there were no examples of direct dioxygen-coupled enantioselective Pd^{II}-catalyzed cyclizations prior to this report. In fact, the work on the enantioselective oxidation of secondary alcohols stands as the benchmark for copper-free aerobic asymmetric palladium catalysis.[2,3]

To address this general problem in asymmetric catalysis, we needed to establish the feasibility of aerobic cyclizations under conditions that would eventually be amenable to the introduction of chiral ligands for palladium. Thus, we began our investigation of aerobic oxidative cyclizations with $Pd(OAc)_2$, pyridine, O_2, and MS3Å in $PhCH_3$ at 80 °C (Table 1).[10] We intentionally avoided the more common DMSO-based conditions because of the highly donating nature of DMSO as a ligand for palladium and its use as solvent in such reactions.[11] This would preclude the use of chiral ligands and thus prevent a general entry into asymmetric catalysis.

Treatment of phenol **1** under a range of aerobic oxidation conditions in $PhCH_3$ led to the discovery that the electron-deficient $Pd(TFA)_2$ in conjunction with Na_2CO_3 as a stoichiometric base rapidly produces dihydrobenzofuran **2** in excellent yield (entry 5). Similar to the reactivity observed in the oxidation of secondary alcohols,[9a,c] the absence of pyridine causes a pronounced rate deceleration, and reactions typically proceed to low conversion (entry 6).

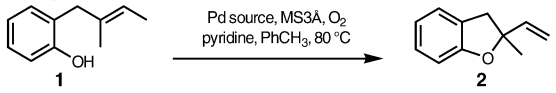
[*] Prof. B. M. Stoltz, R. M. Trend, Dr. Y. K. Ramtohul, E. M. Ferreira
The Arnold and Mabel Beckman Laboratories of Chemical Synthesis
Division of Chemistry and Chemical Engineering
California Institute of Technology
1200 E. California Blvd., MC 164-30, Pasadena, CA 91125 (USA)
Fax: (+1) 626–564–9297
E-mail: stoltz@caltech.edu

[**] The authors wish to thank the NIH-NIGMS (R01 GM65961-01), the University of California TRDRP (postdoctoral fellowship to YKR), the NSF (predoctoral fellowship to EMF), the Dreyfus Foundation, Merck Research Laboratories, Research Corporation, and Abbott Laboratories for generous financial support. Dr. Richmond Sarpong and Mr. Julius Su are gratefully acknowledged for molecular modeling assistance.

Supporting information for this article is available on the WWW under http://www.angewandte.org or from the author.

 © 2003 Wiley-VCH Verlag GmbH & Co. KGaA, Weinheim DOI: 10.1002/anie.200351196

Table 1: Optimization studies.[a]



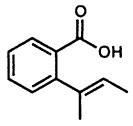
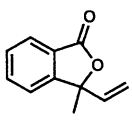
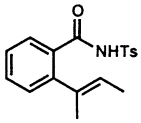
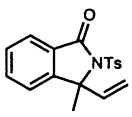
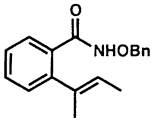
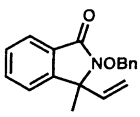
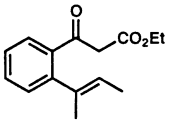
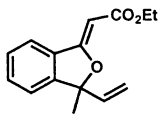
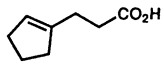
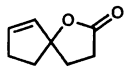
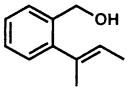
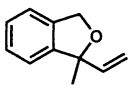
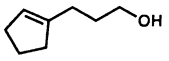
Entry	Pd source	Additive	Time	Yield
1	$Pd(nbd)Cl_2$	None	24 h	7%
2	$PdCl_2$	None	24 h	27%
3	$Pd(OAc)_2$	None	24 h	76%
4	$Pd(TFA)_2$	None	60 min	87%
5	$Pd(TFA)_2$	Na_2CO_3 (2 equiv)	20 min	95%
6	$Pd(TFA)_2$	Na_2CO_3 (2 equiv), no pyridine	24 h	39%

[a] All reactions were carried out with 0.25 mmol of **1**, 5 mol% Pd (0.0125 mmol), 20 mol% pyridine (0.05 mmol), 0.5 mmol additive, 125 mg MS3Å (500 mg mmol^{-1} substrate), and 1 atm O_2 in 2.5 mL $PhCH_3$ (0.1 M in substrate). All yields are based on the isolated product.

Under our optimized conditions, oxidative cyclization of a variety of substituted phenols occurs readily (Table 2). Cyclizations of electron rich phenols are particularly facile, and provide the isolated products with high yields in under 30 min (entries 2–4 and 6–9). Electron deficient phenols serve as excellent substrates as well, although they react more slowly (entry 5). Additionally, dihydropyran systems are accessible under identical conditions (entry 11). Finally, high yields and reasonable rates persist with reduced catalyst loading (2 mol%, entry 12).

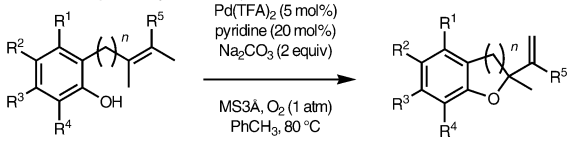
In addition to phenols, we have investigated a number of other nucleophile/alkene oxidative cyclizations. For carboxylic acid derivatives, the addition of stoichiometric amounts of an external base was found to be unnecessary, and exposure simply to $Pd(TFA)_2$, O_2, pyridine, and MS3Å, in $PhCH_3$ at 80 °C leads to a variety of oxidatively cyclized products (Table 3). Importantly, the scope of the cyclization is not limited to benzoic acid derivatives (entries 4 and 5). Moreover, we have shown that oxidative cyclization of primary alcohols is feasible and appears to proceed without significant oxidation to the aldehyde under the optimal conditions (entries 6 and 7).

Table 3: Aerobic oxidative heteroatom/alkene cyclizations.[a]

Entry	Substrate	Product	Time, yield
1[b]			8 h, 90% yield
2[b]			8 h, 88% yield
3[b]			4 h, 82% yield
4[b]			48 h, 63% yield[c,d]
5			48 h, 62% yield[e]
6[b]			3 h, 87% yield[f]
7			10 h, 93% yield[f]

[a] Unless noted, reactions were carried out using 0.25 mmol of starting material, 5 mol% $Pd(TFA)_2$ (0.0125 mmol), 20 mol% pyridine (0.05 mmol), 0.5 mmol additive, 125 mg MS3Å (500 mg mmol^{-1} substrate), and 1 atm O_2 in 1.0 mL (entries 1–5) or 2.5 mL (entries 6–7) $PhCH_3$ at 80 °C. All yields are based on isolated product. [b] The starting material was used as a mixture of *E* and *Z* alkenes. [c] 10 mol% $Pd(TFA)_2$, 40 mol% pyridine, 2 equiv LiOAc. [d] 3:1 *Z*:*E*. [e] 10 mol% $Pd(TFA)_2$, 40 mol% pyridine. [f] 2 equiv Na_2CO_3 were added.

Table 2: Pd-catalyzed aerobic phenol/alkene cyclizations.[a]



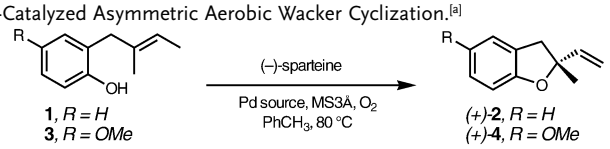
Entry	R^1	R^2	R^3	R^4	R^5	*n*	Time, yield
1	H	H	H	H	H	1	20 min, 95% yield
2	H	Me	H	H	H	1	20 min, 99% yield
3	H	*t*Bu	H	H	H	1	25 min, 90% yield
4	H	OMe	H	H	H	1	15 min, 89% yield
5	H	$COCH_3$	H	H	H	1	25 h, 93% yield
6	H	Me	H	Me	H	1	20 min, 85% yield
7	H	H	H	H	Me	1	25 min, 80% yield
8	OMe	OMe	OMe	H	H	1	10 min, 86% yield
9	H	OMe	H	OMe	H	1	40 min, 80% yield
10	H	OMe	H		H	1	2 h, 93% yield
11[b]	H	H	H	H	H	2	75 min, 85% yield
12[c]	H	H	H	H	H	1	14 h, 86% yield

[a] Unless noted, reactions were carried out with 0.25 mmol of starting material, 5 mol% Pd (0.0125 mmol), 20 mol% pyridine (0.05 mmol), 0.5 mmol additive, 125 mg MS3Å (500 mg mmol^{-1} substrate), and 1 atm O_2 in 2.5 mL $PhCH_3$ (0.1 M in substrate). All yields are based on isolated product. [b] The starting material was used as a 3.6:1 mixture of alkene isomers. [c] 2 mol% $Pd(TFA)_2$, 8 mol% pyridine.

With the success of the racemic aerobic oxidative cyclizations described above, we could then investigate the feasibility of the asymmetric counterpart as a proof of concept that such aerobic cyclizations are amenable to asymmetric catalysis. Thus, we chose to explore the cyclization of phenols, similar to those reported by Hayashi and co-workers,[6] as a test for our catalytic system. Table 4 shows some of the results we have obtained for the asymmetric oxidation of phenols **1** and **3** to ethers

 © 2003 Wiley-VCH Verlag GmbH & Co. KGaA, Weinheim

Table 4: The Pd-Catalyzed Asymmetric Aerobic Wacker Cyclization.[a]



1, *R* = *H*
3, *R* = *OMe*

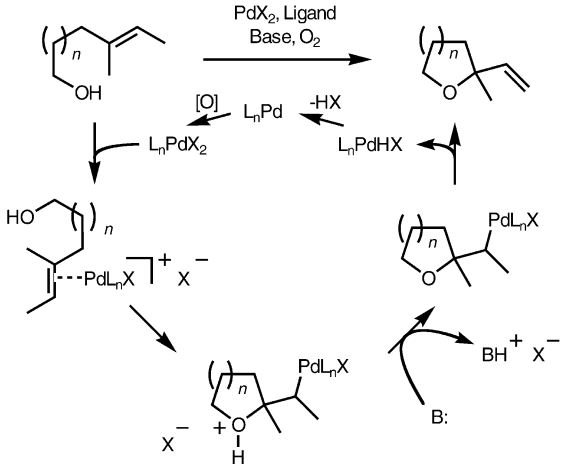
(+)-**2**, *R* = *H*
(+)-**4**, *R* = *OMe*

Entry	Compd	Pd source	Additive	Time	Yield[b]	*ee*
1	**1**	$Pd(nbd)Cl_2$[c]	None	36 h	68%	12%
2	**1**	$PdBr_2$	None	36 h	32%	8%
3	**1**	$PdCl_2$	None	36 h	2%	12%
4	**1**	$Pd(CH_3CN)_2Cl_2$	None	36 h	53%	12%
5	**1**	$Pd(OAc)_2$	None	36 h	18%	51%
6	**1**	$Pd(TFA)_2$	None	36 h	72%	76%
7	**1**	$(sp)Pd(TFA)_2$[d]	None[e]	36 h	83%	77%
8	**1**	$(sp)Pd(TFA)_2$	Na_2CO_3 (2 equiv)[f]	36 h	53%	76%
9	**1**	$(sp)Pd(TFA)_2$	$Ca(OH)_2$ (2 equiv)[f]	36 h	87%[g]	81%
10	**3**	$(sp)Pd(TFA)_2$	$Ca(OH)_2$ (2 equiv)[f]	24 h	64%[g,h]	88%
11	**3**	$(sp)Pd(TFA)_2$	$Ca(OH)_2$ (2 equiv)[f]	60 h@55 °C	57%[g,h]	90%

[a] Entries 1–8 were carried out by using 0.10 mmol of starting material, 10 mol% Pd (0.01 mmol), 40 mol% sparteine (0.04 mmol), 50 mg MS3Å (500 mg mmol^{-1} substrate), and 1 atm O_2 in 1.0 mL $PhCH_3$ (0.1 M in substrate) at 80 °C. Entries 9–11 were carried out using 0.25 mmol of starting material, 10 mol% $(sp)Pd(TFA)_2$ (0.025 mmol), 0.50 mmol $Ca(OH)_2$, 125 mg MS3Å (500 mg mmol^{-1} substrate), and 1 atm O_2 in 2.5 mL $PhCH_3$ (0.1 M in substrate) at 80 °C. [b] Measured by GC. [c] nbd = norbornadiene. [d] sp = (−)-sparteine. [e] 30 mol% (−)-sparteine. [f] 100 mol% (−)-sparteine. [g] Isolated yield. [h] Produced with a dimeric byproduct, see Supporting Information.

(+)-**2** and (+)-**4**, respectively. There is a great deal of disparity in enantioselectivity among palladium sources and additives, as all of the results presented in Table 4 use (−)-sparteine as the sole chiral ligand. Simply changing from $Pd(nbd)Cl_2$ to $Pd(TFA)_2$ results in an increase from 12% *ee* to 76% *ee* (entries 1 and 6). A significant counterion dependence was also observed in our work on the oxidative kinetic resolution of secondary alcohols[2] and points to exceedingly subtle reasons for the general reactivity and enantioselectivity of intermediates in these catalytic reactions. As in the racemic series, we have found that addition of certain bases can accentuate the catalytic activity. Finally, the use of excess (−)-sparteine results in highly enantioselective cyclizations that reach 90% *ee* (entries 8–11).

A plausible mechanism for the aerobic oxidative cyclizations presented herein is outlined in Scheme 2. Initial alkene binding to the electron deficient $L_nPd(TFA)_2$ serves to activate the alkene toward intramolecular nucleophilic attack. Deprotonation of the oxonium ion is facilitated by stoichiometric quantities of the base or by pyridine (or sparteine) through a proton shuttle-type mechanism. In either case, this mechanism accounts for the base-mediated acceleration that is observed in both the racemic and asymmetric cyclizations. Subsequent β-hydride elimination produces $L_nPd(H)X$ that eliminates acid (HX) and L_nPd^0, which, after oxidation by molecular oxygen, reenters the catalytic cycle. Details of the reoxidation steps have been elegantly worked out by Stahl and coworkers.[12]



Scheme 2. Potential mechanism for the Pd-catalyzed aerobic oxidative Cyclizations.

In conclusion, we have demonstrated that several Pd-catalyzed oxidative cyclizations proceed in excellent yield under simple aerobic conditions. Importantly, this system provided entry into enantioselective catalysis with a readily available Pd-sparteine system similar to that used in the previously reported enantioselective alcohol dehydrogenation.[2,3] Although our asymmetric results are somewhat limited in scope at this juncture, we have established for the first time that aerobic cyclizations of this kind are feasible with high levels of enantioselectivity. With this proof of principle established, efforts to expand the scope of and further understand these non-heteroatom-transfer asymmetric aerobic oxidations are ongoing.

Received: February 17, 2003 [Z51196]

Keywords: asymmetric catalysis · homogeneous catalysis · oxidation · oxygen · palladium

[1] a) R. A. Johnson, K. B. Sharpless in *Catalytic Asymmetric Synthesis* (Ed.: I. Ojima), Wiley, New York, **2000**, pp. 231–280; b) T. Katsuki in *Catalytic Asymmetric Synthesis* (Ed.: I. Ojima), Wiley, New York, **2000**, pp. 287–325; c) E. N. Jacobsen in *Comprehensive Asymmetric Catalysis, Vol. 2* (Eds.: E. N. Jacobsen, A. Pfaltz, H. Yamamoto), Springer, Berlin, **1999**, pp. 607–618.

[2] a) E. M. Ferreira, B. M. Stoltz, *J. Am. Chem. Soc.* **2001**, *123*, 7725–7726; b) J. T. Bagdanoff, E. M. Ferreira, B. M. Stoltz, *Org. Lett.* **2003**, *5*, 835–837.

[3] For a similar system, see: D. R. Jensen, J. S. Pugsley, M. S. Sigman, *J. Am. Chem. Soc.* **2001**, *123*, 7475–7476.

[4] For outstanding reviews on Pd-catalyzed reactions, see: a) L. S. Hegedus, *Tetrahedron* **1984**, *40*, 2415–2434; b) M. F. Semmelhack, C. Kim, N. Zhang, C. Bodurow, M. Sanner, W. Dobler, M. Meier, *Pure Appl. Chem.* **1990**, *62*, 2035–2040; c) B. M. Trost, *Acc. Chem. Res.* **1990**, *23*, 34–42; d) J. Tsuji, *Palladium Reagents and Catalysts*, Wiley, Chichester, UK, **1995**, pp. 125–527.

[5] a) T. Hosokawa, T. Uno, S. Inui, S. Murahashi, *J. Am. Chem. Soc.* **1981**, *103*, 2318–2323; b) T. Hosokawa, C. Okuda, S. Murahashi, *J. Org. Chem.* **1985**, *50*, 1282–1287.

[6] a) Y. Uozumi, K. Kato, T. Hayashi, *J. Am. Chem. Soc.* **1997**, *119*, 5063–5064; b) Y. Uozumi, K. Kato, T. Hayashi, *J. Org. Chem.* **1998**, *63*, 5071–5075.

[7] M. A. Arai, M. Kuraishi, T. Arai, H. Sasai, *J. Am. Chem. Soc.* **2001**, *123*, 2907 – 2908.
[8] a) A. Thorarensen, A. Palmgren, K. Itami, J.-E. Bäckvall, *Tetrahedron Lett.* **1997**, *38*, 8541 – 8544; b) K. Itami, A. Palmgren, A. Thorarensen, J.-E. Bäckvall, *J. Org. Chem.* **1998**, *63*, 6466 – 6471; c) H. K. Cotton, R. C. Verboom, L. Johansson, B. J. Plietker, J.-E. Bäckvall, *Organometallics* **2002**, *21*, 3367 – 3375.
[9] For examples of non-oxidative palladium(II)-mediated enantioselective catalysis, see: a) A. Fujii, E. Hagiwara, M. Sodeoka, *J. Am. Chem. Soc.* **1999**, *121*, 5450 – 5458; b) A. El-Qisairi, O. Hamed, P. M. Henry, *J. Org. Chem.* **1998**, *63*, 2790 – 2791; c) Q. Zhang, X. Lu, *J. Am. Chem. Soc.* **2000**, *122*, 7604 – 7605; d) L. E. Overman, T. P. Remarchuk, *J. Am. Chem. Soc.* **2002**, *124*, 12 – 13.
[10] a) These conditions are modeled on the Uemura oxidation conditions, which we used as a launchpad for our oxidative kinetic resolution, see: T. Nishimura, T. Onoue, K. Ohe, S. Uemura, *J. Org. Chem.* **1999**, *64*, 6750 – 6755; b) Uemura has used similar conditions for the ring cleavage of *tert*-cyclobutanols, see: T. Nishimura, K. Ohe, S. Uemura, *J. Am. Chem. Soc.* **1999**, *121*, 2645 – 2646; c) A similar cyclization of sulfonamides was recently reported, see: S. R. Fix, J. L. Brice, S. S. Stahl, *Angew. Chem.* **2002**, *114*, 172 – 174; *Angew. Chem. Int. Ed.* **2002**, *41*, 164 – 166.
[11] For leading references on Pd-mediated oxidative cyclizations using Pd^{II} and O_2 in DMSO, see: a) R. C. Larock, T. R. Hightower, *J. Org. Chem.* **1993**, *58*, 5298 – 5300; b) M. Rönn, J.-E. Bäckvall, P. G. Andersson, *Tetrahedron Lett.* **1995**, *36*, 7749 – 7752; c) R. C. Larock, T. R. Hightower, L. A. Hasvold, K. P. Peterson, *J. Org. Chem.* **1996**, *61*, 3584 – 3585.
[12] a) B. A. Steinhoff, S. S. Stahl, *Org. Lett.* **2002**, *4*, 4179 – 4181; b) B. A. Steinhoff, S. R. Fix, S. S. Stahl, *J. Am. Chem. Soc.* **2002**, *124*, 766 – 767; c) S. S. Stahl, J. L. Thorman, R. C. Nelson, M. A. Kozee, *J. Am. Chem. Soc.* **2001**, *123*, 7188 – 7189.

 © 2003 Wiley-VCH Verlag GmbH & Co. KGaA, Weinheim

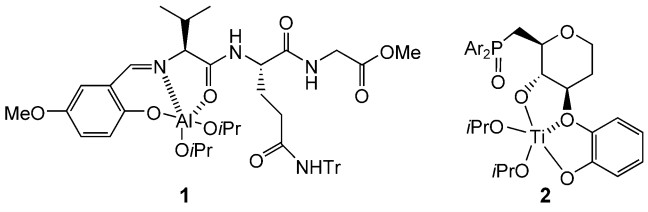
Asymmetric Addition to Ketones

Enantioselective Alkynylation of Ketones Catalyzed by Zn(Salen) Complexes**

*Pier Giorgio Cozzi**

In recent years asymmetric catalysis has reached an impressive level of complexity.[1] However, there are still open challenges in the area of asymmetric catalysis, such as the development of environmentally safe methodologies and the use of substrates until now regarded as unreactive. In particular, ketones remain a great challenge for the state of the art of asymmetric methodologies.[2] Although effective methods have been described for the catalytic enantioselective reduction of ketones, few catalytic enantioselective C–C bond-forming reactions with ketones are known. Ketones are difficult substrates because of their low reactivity and because of the difficulty in controlling facial stereoselectivity.

Recently, pioneering studies were published on the enantioselective addition of allylstannane and diethylzinc to ketones.[2,3] To overcome the low reactivity of the substrate some important catalytic methodologies involve the concept of double activation. The substrate and the nucleophile are brought into close proximity by a system that is able to assemble them in an ordinate transition state.[4] Hoveyda and co-workers[5] and Shibasaki and co-workers[6] described the metal complexes **1** and **2**, respectively, in which the ligand is



able to direct the nucleophile onto the coordinated electrophile, as in an artificial enzyme. A catalytic amount of the metal complexes **1** and **2** was used to promote the addition of cyanide to ketones with the formation of a quaternary stereocenter with high enantioselectivity.

Salen complexes have remarkable properties and are able to act in a cooperative manner.[7] Moreover, a salen–metal complex can behave as a bifunctional Lewis acid–Lewis base catalyst (Figure 1).[8] As a result of efforts toward the development of new catalytic reactions with challenging substrates through the use of salen–metal complexes, herein the first general, facile, and effective method for the catalytic enantioselective addition of alkynes to ketones is reported.[9]

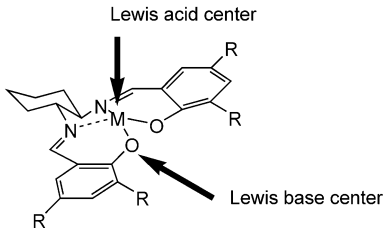


Figure 1. M(salen) as a bifunctional complex.

The addition of terminal alkynes to aldeydes and ketones through the formation of a zinc alkynide in situ has been described by Carreira and co-workers.[10] Impressive enantiomeric excesses were observed in the addition of alkynes to aldehydes in the presence of a substoichiometric amount of the inexpensive chiral ligand *N*-methylephedrine. The reaction appears to be general for substituted alkynes, although

[*] Prof. Dr. P. G. Cozzi
Dipartimento di Chimica "G. Ciamician", Università di Bologna
Via Selmi, 2, 40126 Bologna (Italy)
Fax: (+39) 051-209-9456
E-mail: pgcozzi@ciam.unibo.it

[**] P. G. Cozzi thanks the CNR (Rome), M.I.U.R. (Rome) "Progetto Stereoselezione in Chimica Organica. Metodologie ed Applicazioni", and University of Bologna (funds for selected research topics) for financial support of this research, and Professor Carsten Bolm for a helpful discussion.

Supporting information for this article is available on the WWW under http://www.angewandte.org or from the author.

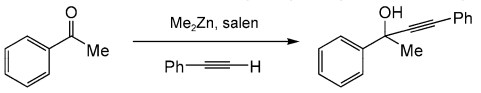
 DOI: 10.1002/anie.200351230 © 2003 Wiley-VCH Verlag GmbH & Co. KGaA, Weinheim

the use of aromatic aldehydes results in lower conversion. Remarkable results with reactive ketones (α-ketoesters) were reported by Jiang et al., who used a different chiral amine.[11] In an alternative method for the formation of the zinc alkynides, Chan and co-workers and Pu and co-workers used dialkyl zinc reagents, and carried out the enantioselective addition of phenylacetylene to aromatic and aliphatic aldehydes in the presence of binol (1,1′-binaphthalene-2,2′-diol), $Ti(OiPr)_4$, and a variety of additives.[12] In our attempts to use these methodologies, low reactivity and low enantioselectivity was observed in the case of acetophenone.

It was reasoned that Zn(salen)[8a,13] (M = Zn, Figure 1) could act as a bifunctional catalyst to enhance the reactivity of ketones toward the attack of zinc alkynides and were delighted to find that the salen complex promoted the addition of phenylacetylene to acetophenone. The model reaction of phenylacetylene with acetophenone was optimized by varying parameters such as solvent, temperature, mode of addition, preparation of the zinc alkynide, and quantity of salen added. The optimized protocol is very straightforward and uses commercially available starting materials. No particular conditions appear to be necessary for the formation of the active complex, and commercial anhydrous toluene was used for all the reactions. The zinc alkynide was prepared by stirring Me_2Zn and phenylacetylene for 1 hour at room temperature in toluene, then the salen was added to the reaction mixture.[14] Finally the ketone was added and the reaction mixture was stirred for several hours at room temperature (Table 1).

As indicated in Table 1, 20 mol% of the salen was required to guarantee sufficient reactivity, while 3 equivalents of the zinc phenylacetylide were used with respect to the ketone. The use of low temperatures slowed the reaction down considerably, and at −15 °C the reaction did not proceed at all. Upon increasing the reaction temperature to 50 °C, fast conversion was observed, but the enantioselectivity was inferior to that observed in other cases. A range of salen ligands were tested with the optimized protocol to increase the enantioselectivity of the reaction (see Supporting Infor-

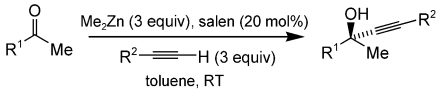
Table 1: Enantioselective addition of phenylacetylene to acetophenone.[a]

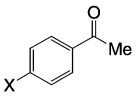
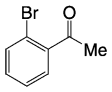
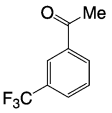
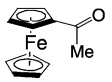
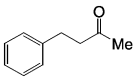


Entry	Salen [mol%]	Additive[b]	Yield [%][c]	*ee* [%][d]
1	10		40	62
2	20		72	61
3	20[e]		n.d.	51
4	20[f]		n.d.	50
5	20[g]		n.d.	53
6	20[h]		85	31
7	10	(*R*,*R*)-indanol	n.d.	39
8	10	(*R*,*R*)-binol	n.d.	30
9	10	dabco	n.d.	53
10	10	2,6-lutidine	n.d.	44
11	20[i]		0	–
12	20[j]		n.d.	42

[a] All the reactions, unless otherwise stated, were carried out in toluene for 96 h at room temperature with the zinc alkynide (3 equiv; prepared by mixing phenylacetylene and Me_2Zn). [b] The additive (10 mol%) was added after the salen to the reaction mixture. [c] Yield after chromatographic purification; n.d. = not determined. [d] The enantiomeric excess was determined by chiral HPLC analysis; see Supporting Information for details. [e] The reaction was performed in Et_2O. [f] The reaction was performed in CH_2Cl_2. [g] The reaction was performed in hexane. [h] The reaction was performed at 50 °C for 48 h. [i] The reaction was performed at −15 °C for 96 h. [j] The zinc alkynide was prepared according to Pu and co-workers; see reference [12c]. dabco = 1,4-diazabicyclo[2.2.2]octane.

Table 2: Enantioselective addition of substituted alkynes to aliphatic and aromatic ketones.[a]



Entry	Ketone	Alkyne	Yield [%][b]	*ee* [%][c]
				
1	X = F	≡—Ph	53	57
2	X = Cl	≡—Ph	55	53
3	X = Br	≡—Ph	78	53
4	X = NO_2	≡—Ph	75	53
5	X = *t*Bu	≡—Ph	45	66
6		≡—Ph	50	70
7		≡—Ph	81	61
8		≡—Ph	40	62
9		≡—Ph	89	32
10		≡—Ph	40	50
11		≡—Ph	84	57
12		≡—Ph	89	80
13		≡—Ph	52	69
14		≡—$SiMe_3$	75	64
15		≡—$SiMe_3$	40[d]	81
16		≡—Cl	40	80

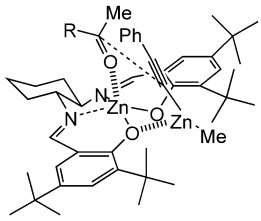
[a] All the reactions were carried out for 36 h for aliphatic ketones and 96 h for aromatic ketones. [b] Yield of isolated product. [c] The enantiomeric excess was determined by GC or HPLC; see Supporting Information for details. [d] Volatile compound.

 © 2003 Wiley-VCH Verlag GmbH & Co. KGaA, Weinheim

mation). In common with many other reactions promoted by salen–metal complexes, the commercially available compound (*R*,*R*)-(−)*N*,*N*′-bis(3,5-di-*tert*-butylsalicilidene)-1,2-cyclohexanediamine (Figure 1, R = *t*Bu) appears to be the most suitable chiral ligand for this reaction. A variety of additives, such as bases, amino alcohols, alcohols, phenols, and other chiral ligands, such as binol, taddol (1,1,4,4-tetraphenyl-2,3-*O*-isopropylidene-L-threitol), and binap (2,2′-bis(diphenylphosphino)-1,1′-binaphthyl) were also added in varying amounts to the reaction mixture, but with no improvement in the enantiomeric excess of the product.[15]

The optimized protocol was used for a range of aromatic and aliphatic ketones (Table 2).[16] The reactions showed good functional-group compatibility and strong deactivating groups such as NO_2 could be present.[17] In general, aromatic ketones proved less reactive than aliphatic ketones, and aromatic ketones that bear an electron-donating group reacted slowly with phenylacetylene. The enantiomeric excess of the product seems to depend on how sterically hindered the ketone is, whereas electronic effects play only a minor role. For all aromatic ketones studied that bear substituents in the 2-, 3-, or 4-position, the enantiomeric excess of the product was in the range 53–70%. The reaction demonstrates a useful level of selectivity with hindered ketones. For all substituted alkynes used in the reaction with *tert*-butyl methyl ketone, the enantiomeric excess of the isolated product was 80–81%. The absolute configuration of the compounds obtained from the addition of trimethylsilylacetylene to aliphatic ketones was established as *S* by comparison of optical rotation values with that reported for a known compound.[18] As there is no reason to believe that the other alkynes react differently, the addition of alkynes is assumed to occur to the *Re* face of the ketones.

Although the mechanism of this reaction has not yet been studied, the correlation between enantioselectivity and the enantiomeric excess of the ligand (nonlinear effect) provided some useful information about the catalyst system. The addition of phenylacetylene to *tert*-butyl methyl ketone was studied with salen of varying enantiomeric purity.[19] Within the limits of experimental error, a linear correlation was found between the enantiomeric excess of the salen ligand and that of the product (Figure 2). This correlation strongly indicates that only one molecule of the salen catalyst is involved in the enantiodifferentiating step, thus suggesting that a Lewis acid–Lewis base double activation promoted by a single salen molecule takes place in the transition state, as proposed in **3**.[20]



3

In summary, the first general catalytic enantioselective addition of terminal alkynes to ketones in the presence of a commercially available chiral ligand was described. Further studies to improve the selectivity and applicability of this methodology through the design of more selective salen ligands are underway.

Received: February 19, 2003 [Z51230]

Keywords: alkynes · asymmetric catalysis · ketones · salen · tertiary alcohols

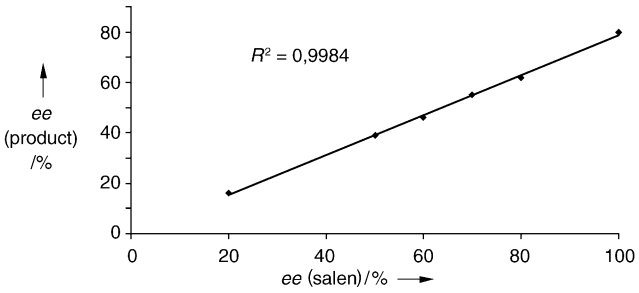


Figure 2. Absence of nonlinear effect in the Zn(salen)-mediated addition of phenylacetylene to *tert*-butyl methyl ketone. *R* = correlation coefficient.

[1] J. Mulzer in *Comprehensive Asymmetric Catalysis, Vol. 1* (Eds.: E. N. Jacobsen, A. Pfaltz, H. Yamamoto), Springer, Heidelberg, **1999**, pp. 35–97.

[2] Only four systems for the catalytic enantioselective addition of alkyl groups to ketones have been reported: Ph_2Zn: a) P. I. Dosa, G. C. Fu, *J. Am. Chem. Soc.* **1998**, *120*, 445–446; Me_2Zn and Et_2Zn: b) D. J. Ramón, M. Yus, *Tetrahedron* **1998**, *54*, 5651–5666; c) C. Garcia, L. K. LaRochelle, P. J. Walsh, *J. Am. Chem. Soc.* **2002**, *124*, 10970–10971; d) E. F. DiMauro, M. C. Kozlowski, *J. Am. Chem. Soc.* **2002**, *124*, 12668–12669.

[3] a) S. Casolari, D. D'Addario, E. Tagliavini, *Org. Lett.* **1999**, *1*, 1061–1063; b) H. Hanawa, S. Kii, K. Maruoka, *Adv. Synth. Catal.* **2001**, *343*, 57–60; c) A. Cunningham, S. Woodward, *Synlett* **2002**, 43–44; d) K. M. Waltz, J. Gavenonis, P. J. Walsh, *Angew. Chem.* ***2002****, 114*, 3849–3852; *Angew. Chem. Int. Ed.* **2002**, *41*, 3697–3699.

[4] For a recent review, see: G. J. Rowlands, *Tetrahedron* **2001**, *57*, 1865–1882.

[5] H. Deng, M. P. Isler, M. L. Snapper, A. H. Hoveyda, *Angew. Chem.* **2002**, *114*, 1051–1054; *Angew. Chem. Int. Ed.* **2002**, *41*, 1009–1012.

[6] Y. Hamashima, M. Kanai, M. Shibasaki, *J. Am. Chem. Soc.* **2000**, *122*, 7412–7413.

[7] a) K. B. Hansen, J. L. Leighton, N. E. Jacobsen, *J. Am. Chem. Soc.* **1996**, *118*, 10924–10925; b) R. G. Konsler, J. Karl, N. E. Jacobsen, *J. Am. Chem. Soc.* **1998**, *120*, 10780–10781; c) D. A. Annis, N. E. Jacobsen, *J. Am. Chem. Soc.* **1999**, *121*, 4147–4154; d) J. M. Ready, N. E. Jacobsen, *J. Am. Chem. Soc.* **2001**, *123*, 2687–2688; e) Y. N. Belokon', S. Caveda-Cepas, B. Green, N. S. Ikonnikov, V. N. Krustalev, V. S. Larichev, M. A. Moscalenko, M. North, L. Orizu, V. I. Tararov, M. Tasinazzo, G. I. Timofeeva, V. Yashkina, *J. Am. Chem. Soc.* **1999**, *121*, 3968–3973.

[8] a) P. G. Cozzi, A. Papa, A. Umani-Ronchi, *Tetrahedron Lett.* **1996**, *37*, 4613–4616; b) E. DiMauro, M. Kozlowski, *Org. Lett.* **2002**, *4*, 3781–3784.

 © 2003 Wiley-VCH Verlag GmbH & Co. KGaA, Weinheim

[9] For the highly enantioselective alkynylation of a ketone used in the synthesis of efavirenz, see: L. Tan, C. Chen, R. D. Tillyer, E. J. J. Grabowski, P. J. Reider, *Angew. Chem.* **1999**, *111*, 724 – 727; *Angew. Chem. Int. Ed.* **1999**, *38*, 711 – 713.
[10] a) D. E. Frantz, R. Fässler, E. M. Carreira, *J. Am. Chem. Soc.* **2000**, *122*, 1806 – 1807; b) D. Boyall, F. López, H. Sasaki, D. E. Frantz, E. M. Carreira, *Org. Lett.* **2000**, *2*, 4233 – 4236; c) D. E. Frantz, R Fässler, C. S. Tomooka, E. M. Carreira, *Acc. Chem. Res.* **2000**, *33*, 373 – 381; d) J. W. Bode, E. M. Carreira, *J. Am. Chem. Soc.* **2001**, *123*, 3611 – 3612; e) N. K. Anad, E. M. Carreira, *J. Am. Chem. Soc.* **2001**, *123*, 9687 – 9688.
[11] B. Jiang, Z. Chen, X. Tang, *Org. Lett.* **2002**, *4*, 3451 – 3453.
[12] a) G. Lu, X. Li, W. L. Chan, A. S. C. Chan, *Chem. Commun.* **2002**, 172 – 173; b) X. Li, G. Lu, W. H. Kwok, A. S. C. Chan, *J. Am. Chem. Soc.* **2002**, *124*, 12636 – 12637; c) G. Gao, D. Moore, R.-G. Xie, L. Pu, *Org. Lett.* **2002**, *4*, 4143 – 4146; d) M.-H. Xu, L. Pu, *Org. Lett.* **2002**, *4*, 4555 – 4557.
[13] a) G. A. Morris, H. Zhou, C. L. Stern, S. T. Nguyen, *Inorg. Chem.* **2001**, *40*, 3222 – 3227; b) E. F. DiMauro, M. C. Kozlowski, *Org. Lett.* **2001**, *3*, 3053 – 3056.
[14] The direct use of a Zn(salen) complex, preprepared according to reference [13a], afforded the same result in the addition of phenylacetylene to acetophenone.
[15] Self-assembled Zn–binol catalysts, prepared in the presence of additives, promote the addition of Et_2Zn to aldehydes with high enantioselectivity; see: a) K. Mikami, R. Angelaud, K. Ding, A. Ishii, A. Tanaka, N. Sawada, K. Kudo, M. Senda, *Eur. J. Org. Chem.* **2001**, *7*, 730 – 737; b) K. Ding, A. Ishii, K. Mikami, *Angew. Chem.* **1999**, *111*, 519 – 523; *Angew. Chem. Int. Ed.* **1999**, *38*, 497 – 501; unfortunately this approach was unsuccessful in our case.
[16] The reaction of chalcone gave a mixture of the 1,2- and the 1,4-adducts.
[17] Methyl and phenyl pyruvate reacted smoothly in our catalytic system without by-product formation and the corresponding product was isolated in high yield (85–90%), although unfortunately as a racemic mixture.
[18] M. Bertrand, J.-P. Dulcere, G. Gil, *Tetrahedron Lett.* **1980**, *21*, 1945 – 1948.
[19] H. B. Kagan, *Adv. Synth. Catal.* **2001**, *343*, 227 – 233.
[20] For crystal data on the coordination of metals to the oxygen atoms of Schiff bases of this type, see: a) J. P. Corden, W. Errington, P. Moore, M. G. H. Wallbridge, *Chem. Commun.* **1999**, 323 – 324; b) E. Gallo, E. Solari, C. Floriani, A. Chiesi-Villa, C. Rizzoli, *Inorg. Chem.* **1997**, *36*, 2178 – 2186; c) D. Cunningham, P. McArdle, M. Mitchell, N. Ní Chonchubhair, M. O'Gara, F. Franceschi, C. Floriani, *Inorg. Chem.* **2000**, *39*, 1639 – 1649; d) B. Cashin, D. Cunningham, P. Daly, P. McArdle, M. Munroe, N. Ní Chonchubhair, *Inorg. Chem.* **2002**, *41*, 773 – 782.

 © 2003 Wiley-VCH Verlag GmbH & Co. KGaA, Weinheim

Antibiotic Structure Determination

Structural and Functional Analysis of Pantocin A: An Antibiotic from *Pantoea agglomerans* Discovered by Heterologous Expression of Cloned Genes**

*Mi Jin, Liang Liu, Sandra A. I. Wright, Steven V. Beer, and Jon Clardy**

The epiphytic bacterium *Erwinia amylovora* causes fire blight, a devastating disease of rosaceous plants such as apple and pear.[1] The closely related but nonpathogenic bacterium *Pantoea agglomerans* (formerly *E. herbicola*), which usually accompanies *E. amylovora* in the wild,[2] produces a family of antibiotics that inhibit *E. amylovora* in a poorly understood strain-dependent fashion.[3,4] The numerous members of this antibiotic family constitute a source of biocontrol agents for fire blight, a pool of new and potentially useful antibiotics against human bacterial pathogens, and a model of nature's ability to produce a "library" of biologically active molecules. The complexity of antibiotic production, especially the multiple antibiotics produced by a given strain and low production in liquid culture, has hampered chemical investigations. We have taken a genomic approach to deconvolute the multiple antibiotics and to address the production problems by a particular strain. Heterologous expression of a genomic DNA library from *P. agglomerans* in *Escherichia coli* provides access to the small-molecule antibiotics. Since both *P. agglomerans* and *E. coli* are members of the widely distributed *Enterobacteriacea*, *E. coli* should be a suitable host for heterologous expression of *P. agglomerans* genes that encode antibiotics. Herein we report the isolation and structure determination of pantocin A, a new peptide-derived antibiotic, and its molecular target.

A genomic library of *P. agglomerans* strain Eh318 was constructed in *E. coli* strain DH5α.[5] Two distinct antibiotic-

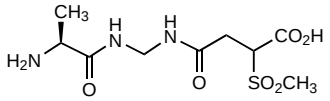
[*] Prof. J. Clardy,[++] M. Jin, L. Liu
Department of Chemistry and Chemical Biology
Cornell University
Ithaca, NY 14853-1301 (USA)
E-mail: jon_clardy@hms.harvard.edu
Prof. S. A. I. Wright,[+] Prof. S. V. Beer
Department of Plant Pathology
Cornell University
Ithaca, NY 14853 (USA)
[+] Current address:
Plant Pathology and Biocontrol Unit
SLU, 750 07 Uppsala (Sweden)
[++] Current address:
Department of Biological Chemistry and Molecular Pharmacology
Harvard Medical School
Boston, MA (USA)
Fax: (+1) 617-432-3702

[**] This work was supported by the National Institutes of Health (National Cancer Institute, R01-CA24487).

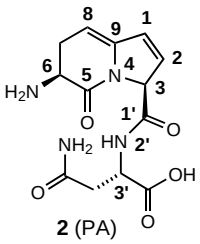
Supporting information for this article is available on the WWW under http://www.angewandte.org or from the author.

 © 2003 Wiley-VCH Verlag GmbH & Co. KGaA, Weinheim DOI: 10.1002/anie.200351053

producing cosmid clones, pCPP702 and pCPP719, were identified, and the two antibiotics they produced were trivially named pantocin A and B, respectively. One indication that the two antibiotics were different came from studies which showed that arginine suppresses the antibiotic activity of pantocin B while histidine suppresses the antibiotic activity of pantocin A. In previous work, pantocin B (PB, **1**) was structurally characterized, and its ability to potently inhibit *N*-



1 (PB)



2 (PA)

acetylornithine transaminase, which catalyzes a committed step in arginine biosynthesis, was established.[6–8] The characterization of pantocin A (PA, **2**) was plagued by inconsistent and low levels of production in liquid culture, together with its acid, base, and thermal lability. Significant reproducible production was eventually achieved by culturing *E. coli* XL2Blue harboring a 3.5 kb subclone of pCPP702 in the high copy number plasmid pUC19 (pUC449).

Isolation of **2** was guided by antibiotic activity against the *E. amylovora* strain Ea273 ($IC_{50} = 200$ nM). Pantocin A (**2**) was purified from large-scale fermentation of *E. coli* XL2Blue-pUC449 by four chromatographic separations using anion-exchange, reverse-phase, and hydrophilic interactions. This compound is an optically active small molecule, and its structure was established by spectroscopic methods and synthesis of a hydrogenated derivative.

PA (**2**) has a molecular formula of $C_{13}H_{16}N_4O_5$ as determined from HRFAB-MS studies. The ^{13}C NMR (Table 1) and DEPT spectra indicate four carbonyl, four olefinic, three methine, and two methylene carbon atoms. Three vinylic, a highly deshielded methine, two Cα amino acid, four Cβ amino acid, and three exchangeable protons could be characterized from ^1H and ^1H-^{13}C HMQC NMR spectra recorded in D_2O and [D_6]DMSO. A loss of $m/z = 132$ in the tandem ESI-MS study suggested the presence of an asparagine residue, which was confirmed by 2D NMR studies. Two spin systems (H6/H7a,b/H8 and H1/H2/H3) identified by COSY experiments coupled with HMBC correlations (H6/C5, H8/C9, H1/C9, and H3/C1′) established a continuous nine-carbon chain (C5 to C1′) containing the non-asparagine carbon atoms in **2**. Two additional HMBC correlations (2′NH/C1′ and H3′/C1′) showed that the C_9 and asparagine fragments must be connected by an amide bond.

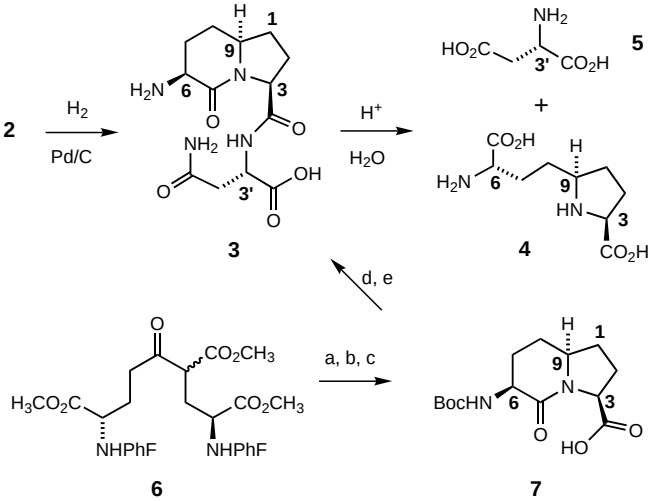
^{15}N NMR experiments on ^{15}N-labeled **2**, which was made using ^{15}N ammonium sulfate in minimal culture media, revealed the nitrogen connectivity. A highly downfield shifted ^{15}N resonance ($\delta = 145.1$ ppm) with correlations to H1, H2, H3, H6, and H8 required N4 to be connected to C3, C5, and C9. A ^{15}N resonance at $\delta = 36.5$ ppm, typical of an amine, and its HMBC correlations with H6 and H7 required an amino group at C6, thus completing the planar structure of **2**.

Table 1: NMR data for **2**.

Atom No.	^{13}C[a]	^1H[b]	^{15}N[c]
1	126.3	6.35 (1H, dd, 6.0, 2.0)	
2	131.5	6.15 (1H, dd, 6.0, 1.7)	
3	66.4	5.21 (1H, brs)	
4-N			145.1 (s)
5	167.9		
6	50.2	3.58 (1H, dd, 13.6, 7.2)	
6-NH_2			36.5 (s)
7	28.6	2.57 (1H, m)	
		2.33 (1H, m)	
8	95.5	5.12 (1H, dd, 6.0, 2.4)	
9	143.3		
1′	166.2		
2′-NH		8.27 (1H, d, 7.5)	126.0 (d, 93.0)
3′	49.8	4.29 (1H, m)	
4′	37.9	2.50 (1H, dd, 15.2, 7.0)	
		2.39 (1H, dd, 15.2, 5.7)	
5′	171.6		
5′-NH_2		6.84, 7.72 (2H, brs)	113.6 (t, 90.0)
6′	172.6		

[a] ^{13}C NMR (100 MHz, 25 °C, [D_6]DMSO). [b] ^1H NMR (500 MHz, 25 °C, [D_6]DMSO) assignments based on ^1H-^{13}C HMQC. [c] ^{15}N NMR (40.5 MHz, 25 °C, D_2O). The ^{15}N chemical shift was calibrated indirectly based on the gyromagnetic ratio of ^{15}N and ^1H according to reference [12].

The stereocenters at C3′, C3, and C6 were defined by the hydrogenation of **2**, NOESY experiments, and synthesis. Hydrogenation of **2** gave **3** as a single diastereomer, and NOESY correlations between H3/H9 and H6/H9 require H3 and H6 to be on the same face (Scheme 1). Hydrolysis of **3** gave **4** and L-aspartic acid (**5**), which set the absolute configuration at C3′ as *S*. Both **3** and its 3(*R*),6(*R*),9(*R*) diastereomer were prepared from **6**, which was synthesized from

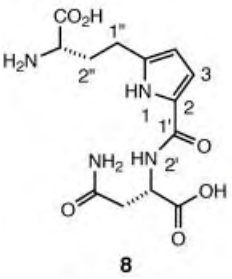


Scheme 1. a) NaOH/dioxane; CH_3I/K_2CO_3/DMSO; b) H_2/Pd-C; c) $(Boc)_2O$/TEA/DMF; NaOH/CH_3OH-H_2O; d) H-Asn-O*t*Bu·HCl, EDC/NMM/DMF; e) TFA/CH_2Cl_2. Boc = *tert*-butoxycarbonyl, TEA = triethylamine, EDC = 3-(3-dimethylaminopropyl)-1-ethylcarbodiimide, NMM = *N*-methylmorpholine, TFA = trifluoroacetic acid.

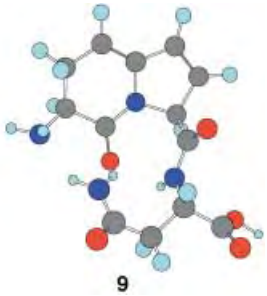
 © 2003 Wiley-VCH Verlag GmbH & Co. KGaA, Weinheim

L- or D-Glu(OMe)-OMe following a literature procedure[9] (Scheme 1). HPLC analysis of synthetic **3** and **3** derived from **2** indicated that the absolute configuration of **3** was 3(*S*),6(*S*). Thus, C3, C6, and C3′ all have the absolute configuration corresponding to an L-amino acid, and the absolute stereostructure of **2** is as shown.

Perhaps the most striking feature of **2**, which to the best of our knowledge has no precedents in reported natural or synthetic compounds, is its very existence given the apparent ease with which it could aromatize to a pyrrole. Removal of a proton from C3, which is α to the carbonyl group at C1′, followed by reprotonation at C8 would generate a pyrrole, and this process likely underlies the lability of **2**. A minor inactive compound was also recovered on isolating **2**, and this was characterized as **8**. Compound **8** arises from the aromatization and hydrolysis of the bicyclic amide bond. No



8

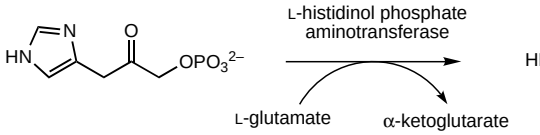


9

material representing aromatization unaccompanied by hydrolysis was isolated—an observation consistent with the known rapid hydrolysis of *N*-acylpyrroles.[10] While **2** is sensitive to acid, base, and elevated temperatures, it survives for days at room temperature in aqueous solution under neutral pH conditions. Two structural features of **2** undoubtedly contribute to its modest persistence: the C3–H bond is shown in energy-minimized structures of **2** not to be aligned with the π bond of the C1′ carbonyl group, and this lack of conjugation creates a kinetic barrier to proton removal (see structure **9**). The out of conjugation conformation is at least partially enforced by hydrogen bonds from asparagine-derived NH groups to the C5 carbonyl oxygen atom. The electron-withdrawing effect of the C5 carbonyl group also diminishes the thermodynamic benefit of aromatization, and this electron-withdrawing effect is enhanced by the same hydrogen bonds.

With the structure of **2** established, we addressed how such a polar molecule gains entry into *E. amylovora* cells and the nature of its molecular target.[11] Addition of the synthetic tripeptide Ala-Gly-Gly to the test medium, in amounts exceeding three times that of **2**, suppresses the antibiotic activity of **2**. Thus, **2** likely gains entry through the tripeptide transporter, and the added tripeptide monopolizes the transporter thereby limiting cellular entry of **2**.[6,11]

Since addition of histidine suppresses the activity of **2**, the cellular target was sought on the histidine biosynthetic pathway.[11] The common strategy of feeding intermediates along a biosynthetic pathway has limited applicability in histidine biosynthesis since many of the intermediates are ionized phosphate esters that have poor cellular access. Using the well-characterized histidine biosynthetic enzymes of *E. coli*, the step catalyzed by L-histidinol phosphate aminotransferase, which converts imidazole acetol phosphate to L-histidinol phosphate [Eq. (1)], was identified as the target of **2**.[11]



L-histidinol phosphate aminotransferase is a pyridoxal-5′-phosphate (PLP) dependent enzyme that couples the reductive amination of imidazole acetol phosphate with the conversion of L-glutamate into α-ketoglutarate.

Pantocin A and B share a close functional relationship that is not apparent from their structures. Both gain access to their cells via the tripeptide transporter and inhibit transaminase-catalyzed amino acid biosynthetic steps that introduce nitrogen functionality.[6,11] Whereas **1** inhibits arginine biosynthesis, **2** inhibits histidine biosynthesis. This functional similarity is unsurprising since they have the common goal of suppressing the growth of bacterial competitors in a nitrogen-poor environment—an environment where import by tripeptide transporters and amino acid biosynthesis are essential.

The structural and functional analysis of **2** (PA) reported here used techniques of small-molecule chemistry and biochemical analysis. The cosmid library/heterologous expression approach provides ready access to the DNA conferring production of **2** on *E. coli* XL2Blue-pUC449. Analysis of this DNA provides insights into the biosynthesis of **2** and identifies strains producing antibiotics related to **2** as discussed in the following communication.

Experimental Section

Cultivation and isolation: *E. coli* XL2Blue-pUC449 was grown in a shaker maintained at 30 °C for 24 h in minimal media supplemented with 100 μg mL^{-1} ampicillin.[5] The culture supernatant was applied to a Dowex 1X8-200 (HCO_3^-) anion-exchange column and eluted with CO_2-saturated H_2O. The active fractions were lyophilized, then applied to a C18 solid-phase extraction column and eluted with H_2O/CH_3CN (100/0 to 90/10). Further fractionation by HPLC, first with a reverse-phase column (Vydac, 218TP510) using H_2O/0.1 M NH_4OAc/CH_3CN (94/5/1), then with a polyhydroxyethyl A column (Poly LC, Inc.) using H_2O/0.1 M NH_4OAc/CH_3CN (20/5/75) gave compounds **2** and **8** in yields of approximately 1 mg L^{-1} and 0.2 mg L^{-1}, respectively.

Cloning of *E. coli*-pUC449: Pantocin A producing cosmid clone pCPP702 was subcloned to generate pCPP1051, from which a XbaI-HindIII fragment was further subcloned into pBluescript to yield plasmid pCPP717.[5] The cloned insert was sequenced (GenBank accession No. U81376). A 3.5 kb DNA fragment was then amplified by a polymerase chain reaction from pCPP717 using primer (5′-CCGCATCTAGAGTAGGTATGAC-3′) and primer (5′-ATACTCTGCAGAGTTGGTGCTCCA-3′), and ligated into pUC19 at the *XbaI* and *PstI* sites. Recombinants were selected

 © 2003 Wiley-VCH Verlag GmbH & Co. KGaA, Weinheim

from transformed *E. coli* XL2 Blue cells on Luria–Bertani plates supplemented with ampicillin at 100 μg mL^{-1}, to yield clone *E. coli* XL2 Blue-pUC449.

2: $[\alpha]_D^{25} = -291.1°$ ($c = 1.8$, H_2O); IR (KBr): $\tilde{\nu}_{max} = 3700–2400$ (br), 1676, 1578, 1402 cm^{-1}; UV (H_2O): λ_{max} (ε) = 200 (12089), 272 nm (5447); HRFAB-MS: *m/z*: 331.1018 [*M*+Na]$^+$, calcd *m/z*: 331.1018 for $C_{13}H_{16}N_4O_5Na$; ESI-MS/MS: *m/z*: 309 [*M*+H]$^+$, 177, 159, 151, 149.

8: ^{1}H NMR (500 MHz, D_2O, 25 °C): $\delta = 6.81$ (1 H,d, $J = 3.7$ Hz, H3), 6.12 (1 H, d, $J = 3.7$ Hz, H4), 4.66 (1 H, dd, $J = 9.0$, 4.5 Hz, H3′(Asn αH)), 3.75 (1 H, t, $J = 6.5$ Hz, H3″), 2.85 (1 H, dd, $J = 15.0$, 4.5 Hz, H4′a), 2.80–2.69 (3 H, m, H1″ and H4′b), 2.25–2.10 ppm (2 H, m, H2″); ^{13}C NMR (100 MHz, 5 % CD_3OD in D_2O, 25 °C): $\delta = 178.6$ (C6′, COOH), 177.0 (C5′, $CONH_2$), 175.4 (C4″) 163.4 (C1′), 137.4 (C5), 125.0 (C2), 113.5 (C3), 108.6 (C4), 55.3 (C3″), 52.9 (C3′), 39.1 (C4′), 31.5 (C2″), 23.8 ppm (C1″); ESI-MS/MS/MS: *m/z*: 327 [*M*+H]$^+$, 310, 195, 177, 149, 132, 106; UV (H_2O): λ_{max} (ε) = 200 (6438), 220 (2994, sh), 275 nm (10887); IR (thin film): $\tilde{\nu}_{max} = 3700–2400$ (br), 1668, 1604, 1533, 1404 cm^{-1}.

Preparation of **3** from **2:** A solution of **2** (2.4 mg) in deionized H_2O (300 μL) was treated with Pd/C (10 wt %, 0.66 mg) and stirred under hydrogen at room temperature for 8 h. The reaction mixture was filtered over celite, washed with deionized H_2O (2 mL), and the combined aqueous fractions were dried to give 1.7 mg of **3**. ^{1}H NMR (500 MHz, D_2O, 25 °C): $\delta = 4.46$ (1 H, d, $J = 9.0$ Hz, H3), 4.40 (1 H, dd, $J = 8.0$, 5.0 Hz, H3′), 3.93 (1 H, t, $J = 8.5$ Hz, H6), 3.74 (1 H, m, H9), 2.76 (1 H, dd, $J = 15.0$, 5.0 Hz, H4′a), 2.65 (1 H, dd, $J = 15.0$, 8.0 Hz, H4′b), 2.35 (1 H, m, H7a), 2.25–2.10 (4 H, m, H2a, 1a, 8a, 2b), 1.91 (1 H, m, H7b), 1.67 (1 H, m, H8b), 1.64 ppm (1 H, m, H1b); ^{13}C NMR (100 MHz, D_2O + 5 % CD_3OD, 25 °C): $\delta = 177.8$ (C6′), 176.6 (C5′), 173.6 (C1′), 169.5 (C5), 61.0 (C3), 59.2 (C9), 53.2 (C3′), 49.6 (C6), 38.6 (C4′), 32.3 (C1), 30.2 (C2), 26.2 (C8), 25.6 (C7); $[\alpha]_D^{25} = -57.8°$ (c = 0.16, H_2O); UV (H_2O): λ_{max} (ε) = 200 nm (2200); IR (thin film): $\tilde{\nu}_{max}$ = 3700–2400 (br), 2954 (sh), 1668, 1529 (sh), 1448, 1392, 1342 cm^{-1}; ESI-MS/MS: *m/z*: 313 [*M*+H]$^+$, 181, 153, 125.

Chiral TLC**:** Chiral TLC analyses were performed on CHIRALPLATE (Macherey-Nagel) using solvent A ($CH_3OH/H_2O/CH_3CN$, 5/5/20) or B (acetone/H_2O/CH_3OH, 10/2/2). **3** (0.15 mg, 0.5 μmol) was heated in 6 M HCl (300 μL) at 85 °C for 19 h to give **4** and **5**. Authentic D- and L- Asn were also treated in the same manner. Compound **5** migrated the same distance as treated L-Asn ($R_f = 0.47$ in A, 0.66 in B), which was easily distinguishable from treated D-Asn ($R_f = 0.40$ in A, 0.58 in B)

3: As shown in Scheme 1, *N*-(PhF) L-or D-dimethyl glutamate was used in a Claisen condensation, reductive amination, and lactam-cyclization sequence to give enantiopure (3*S*,6*S*,9*S*)-**7** or (3*R*,6*R*,9*R*)-**7** following the procedure of Lombart and Lubell.[9] Coupling with *tert*-butyl-L-asparagine ester followed by removal of protecting groups then gave (3*S*,6*S*,9*S*)-**3** or (3*R*,6*R*,9*R*)-**3** in 7 % overall yield.

(3*S*,6*S*,9*S*)-**3**: $[\alpha]_D^{25} = -50.7°$ ($c = 1.01$, H_2O); ^{1}H NMR (500 MHz, D_2O, 25 °C): $\delta = 4.61$ (1 H,dd, $J = 6.0$, 7.0 Hz), 4.51 (1 H, d, $J = 8.8$ Hz), 4.06 (1 H, t, $J = 8.5$ Hz), 3.78 (1 H, m), 2.87–2.77 (2 H, m), 2.42 (1 H, m), 2.31–2.18 (3 H, m), 2.13 (1 H, m), 1.97 (1 H, m), 1.73–1.63 ppm (2 H, m). (The small differences in δ values between (3*S*,6*S*,9*S*)-**3** and **3** derived from **2** are the result of differences in pH values and concentration. Mixing two samples resulted in overlapping peaks). ^{13}C NMR (100 MHz, D_2O + 10 % CD_3OD, 25 °C): $\delta = 175.9$, 175.6, 174.0, 168.0, 60.8, 59.1, 51.1, 49.4, 37.5, 32.3, 30.2, 26.3, 25.0 ppm; IR (thin film): $\tilde{\nu}_{max} = 3700–2400$ (br), 2956 (sh), 1670, 1530 (sh), 1448, 1390, 1340 cm^{-1}; ESI-MS/MS: *m/z*: 313 [*M*+H]$^+$, 181, 153, 125.

(3*R*,6*R*,9*R*)-**3**: $[\alpha]_D^{25} = +45.7°$ ($c = 0.98$, H_2O); ^{1}H NMR (500 MHz, D_2O, 25 °C): $\delta = 4.62$ (1 H, dd, $J = 8.0$, 5.0 Hz), 4.53 (1 H, d, $J = 8.8$ Hz), 4.06 (1 H, t, $J = 8.5$ Hz), 3.78 (1 H, m), 2.84 (1 H, dd, J = 15.5, 5.0 Hz), 2.71 (1 H, dd, J = 15.5, 8.0 Hz), 2.42 (1 H, m), 2.30–2.17 (3 H, m), 2.05 (1 H, m), 1.96 (1 H, m), 1.75–1.64 ppm (2 H, m); ^{13}C NMR (100 MHz, D_2O + 10 % CD_3OD, 25 °C): $\delta = 175.9$, 175.3, 173.9, 168.1, 60.8, 59.1, 50.9, 49.5, 37.6, 32.3, 30.6, 26.3, 25.0 ppm; IR (KBr): $\tilde{\nu}_{max} = 3700–2400$ (br), 2955 (sh), 1671, 1528, 1447 cm^{-1}; ESI-MS/MS: *m/z*: 313 [*M*+H]$^+$, 181, 153, 125.

HPLC analysis was performed on an Aqua C18 column (250 × 4.6 mm, 5 μ, 125 Å, Phenomenex) with a mobile phase of H_2O(0.1 % TFA)/CH_3CN(0.1 % TFA) with a gradient of 100/0 (0–5 min); 100/0 to 85/15 (5–20 min) at 1 mL min^{-1}. (3*R*,6*R*,9*R*)-**3** and (3*S*,6*S*,9*S*)-**3** showed base-line separation with retention times of 15.6 and 15.9 min, respectively. **3** derived from **2** co-migrated with (3*S*,6*S*,9*S*)-**3** but not (3*R*,6*R*,9*R*)-**3**.

Received: January 29, 2003 [Z51053]

Keywords: antibiotics · gene expression · natural products · structure elucidation

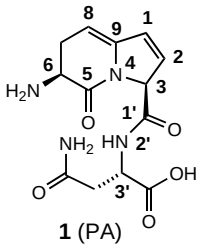
[1] H. S. Aldwinckle, S. V. Beer, *Hortic. Rev.* **1979**, *1*, 423.
[2] J. M. Erskine, L. E. Lopatecki, *Can. J. Microbiol.* **1975**, *21*, 35.
[3] R. S. Wodzinski, J. P. Paulin, *J. Appl. Bacteriol.* **1994**, *76*, 603.
[4] C. A. Ishimaru, E. J. Klos, R. R. Brubaker, *Phytopathology* **1988**, *78*, 746.
[5] S. A. I. Wright, C. H. Zumoff, L. Schneider, S. V. Beer, *Appl. Environ. Microbiol.* **2001**, *67*, 284.
[6] S. F. Brady, S. A. Wright, J. C. Lee, A. E. Sutton, C. H. Zumoff, R. S. Wodzinski, S. V. Beer, J. Clardy, *J. Am. Chem. Soc.* **1999**, *121*, 11912.
[7] A. E. Sutton, J. Clardy, *Org. Lett.* **2000**, *2*, 319.
[8] A. E. Sutton, J. Clardy, *J. Am. Chem. Soc.* **2001**, *123*, 9935.
[9] H.-G. Lombart, W. D. Lubell, *J. Org. Chem.* **1996**, *61*, 9437.
[10] F. M. Menger, J. A. Donohue, *J. Am. Chem. Soc.* **1973**, *95*, 432.
[11] M. Jin, Ph.D. thesis, Cornell University (Ithaca), **2003**.
[12] J. Cavanagh, W. J. Fairbrother, A. G. Palmer III, N. J. Skelton, *Protein NMR Spectroscopy: Principles and Practice*, Academic Press, New York, **1995**.

 © 2003 Wiley-VCH Verlag GmbH & Co. KGaA, Weinheim

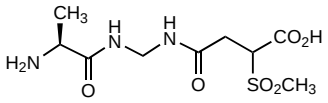
Antibiotic Discovery

The Biosynthetic Gene Cluster of Pantocin A Provides Insights into Biosynthesis and a Tool for Screening**

*Mi Jin, Sandra A. I. Wright, Steven V. Beer, and Jon Clardy**



1 (PA)



2 (PB)

The preceding communication described the isolation and structural characterization of pantocin A (PA, **1**), a member of the diverse family of antibiotics produced by *Pantoea agglomerans*, and its ability to block histidine biosynthesis by inhibiting L-histidinol phosphate aminotransferase. The unusual structure of pantocin A, especially its labile bicyclic core, suggested a previously uncharacterized biosynthetic pathway. Pantocin A (**1**) was discovered through the heterologous expression of a cosmid library, derived from the genomic DNA of *P. agglomerans* strain Eh318, in *Escherichia coli* XL2Blue.[1] This DNA-based approach to the discovery of biologically active small molecules, which facilitated the characterization of the Eh318 antibiotics pantocin A (**1**) and B (**2**),[2] also expedites the identification of the DNA involved in their production. Subcloning of the original cosmid clone pCPP702 resulted in a 3.5 kb DNA fragment that enables *E. coli* XL2Blue-pUC449 to produce **1**. Herein, we report a preliminary analysis of this 3.5-kb sequence that identifies the peptide precursor of **1**, two proteins responsible for its construction, and the resistance (self-immunity) mechanism. This analysis also provides the information needed to identify other strains producing antibiotics related to **1**.

Sequencing of the 3.5 kb insert revealed three major open reading frames (ORFs), which were named *paaA*, *paaB*, and *paaC* (Figure 1 a).[3] Transposon mutagenesis indicated that *paaA* and *paaB* are required for the production of **1** and that disruption of *paaC* leads to reduced production of **1** and poor growth (Figure 1 a).

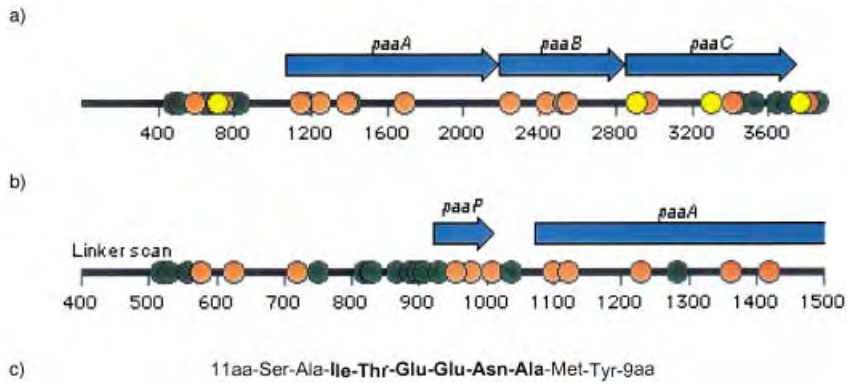


Figure 1. a) Transposon mutagenesis of pUC449. Circles indicate the position of transposon insertion and are color coded for anti-Ea273 activity: inactive: red, active: green, reduced activity: yellow. b) Linker-scan of pUC449 (region 449–1500). Circles indicate the position of a 15-bp linker insertion. c) Pantocin A precursor peptide. Bold symbols represent residues involved in the biosynthesis of **1** and molecules similar to **1**.

The structure of **1**, especially its asparagine side chain and the functionality and absolute configurations at C3 and C6, suggests a peptide origin. Feeding experiments with ^{14}C-labeled Glu and Gln were carried out with *E. coli* XL2Blue-pUC449 in minimal media to determine whether the N4–C9 fragment could arise from a cyclized glutamate or glutamine residue. Feeding with either ^{14}C-labeled Glu or Gln led to the production of ^{14}C-labeled **1** while control feeding with ^{14}C-labeled Leu did not. Uniformly ^{13}C-labeled Glu was fed to determine the labeling pattern of **1**, and ^{13}C NMR analysis revealed that all the carbon atoms in the bicyclic core (C1–C3 and C5–C9) were labeled to a similar extent, while significantly less incorporation was seen in the asparagine carbon atoms. Since Glu can serve as a general carbon source through its conversion into 2-oxoglutarate in the tricarboxylic acid cycle, the observed incorporation pattern likely reflects the partial conversion of Glu into Asn. Thus, **1** originates from two Glu/Gln residues and one Asp/Asn residue.

Two lines of evidence indicate that modification of a ribosomally assembled peptide[4,5] with the general structure -Glu/Gln-Glu/Gln-Asp/Asn- gives rise to **1**. First, the 3.5 kb

[*] Prof. J. Clardy,[++] M. Jin
Department of Chemistry and Chemical Biology
Cornell University
Ithaca, NY 14853-1301 (USA)
E-mail: jon_clardy@hms.harvard.edu
Prof. S. A. I. Wright,[+] Prof. S. V. Beer
Department of Plant Pathology
Cornell University
Ithaca, NY 14853 (USA)
[+] Current address:
Plant Pathology and Biocontrol Unit
SLU, 750 07 Uppsala (Sweden)
[++] Current address:
Department of Biological Chemistry and Molecular Pharmacology
Harvard Medical School
Boston, MA (USA)
Fax: (+1) 617-432-3702

[**] This work was supported by the National Institutes of Health (National Cancer Institute, R01-CA24487).

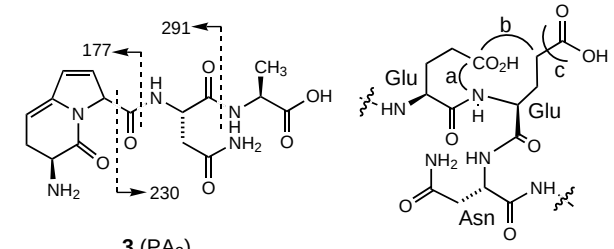
Supporting information for this article is available on the WWW under http://www.angewandte.org or from the author.

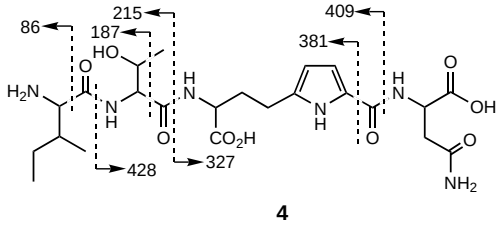
 © 2003 Wiley-VCH Verlag GmbH & Co. KGaA, Weinheim DOI: 10.1002/anie.200351054

insert is too small to encompass the well-known nonribosomal peptide synthesis pathway with its multiple modules.[6] Second, cloning *paaA*, *paaB*, and *paaC* into a pET11a vector and expressing it under the control of a T7 promoter in *E. coli* strain BL21(DE3) did not produce a single clone with PA activity, which indicates that *paaABC* by itself is not sufficient for the biosynthesis of **1**.

We looked for the gene encoding the prepeptide upstream of *paaA* using a transposon-linker scan experiment with a 15-bp oligonucleotide insertion to saturate the 0.6 kb region upstream of the predicted start codon of *paaA* (Figure 1b). This approach revealed an additional small ORF, *paaP*, which is required for the production of **1**. The first indication for a *paaP* requirement came from a frame shift mutant of *paaP* that lost activity. In addition, four other linker insertions upstream of *paaP* abolished the activity of **1**, and these insertions are all in the vicinity of a predicted promoter region[7] (Figure 1b). Evidence for the gain of function was provided by cloning *paaPABC* into expression vector pET11b to transform *E. coli* strain BL21(DE3) gold and observing activity of **1** on Ea273-GA agar assay plates. *PaaP* encodes a 30-residue peptide with the sequence -Glu-Glu-Asn- near its midpoint (Figure 1c).

Chemical evidence coupled with site-directed mutagenesis also implicated *paaP* in the biosynthesis of **1**. Large-scale fermentations of clones producing **1** uncovered a minor metabolite, pantocin A_2 (**3**, PA_2), which is produced along with **1**. PA_2 (**3**) has the same UV spectrum as **1**, the same level





of antibiotic activity against *E. amylovora* test strain Ea273, and a different HPLC retention time. Combined ESI-MS/MS and NMR analyses revealed that **3** is in fact **1** modified by the addition of a C-terminal alanine group. An alanine in this position is encoded by *paaP* (Figure 1c).

In an attempt to produce modified PA-type molecules by altering *paaP*, site-directed mutagenesis of Ala to Val was used to produce clone *E. coli*-pUC449AtV. This clone has reduced antibiotic activity in its culture supernatant. Characterization of all the compounds produced by this mutant clone proved difficult because of low production levels and lability problems, but a stable inactive compound (**4**) was isolated and characterized by NMR spectroscopy and ESI-MS/MS. Compound **4** is the hydrolysis product of the core of **1** bearing additional Ile and Thr residues at the N-terminus, and these N-terminal residues are also predicted by *paaP*. These combined experiments implicate six consecutive residues in the center of the *paaP* gene product with production of **1**. A predicted stem-loop structure follows *paaP*, and the production of the *paaP* gene product might not be tightly coupled to the production of the *paaA–C* gene products.

PaaC is the resistance gene. Transposon insertions in *paaC* do not completely abolish production of **1**,[3] but clones with such insertions grow poorly. Cloning *paaC* into a PA-susceptible *E. coli* strain confers resistance to **1** (Figure 2). *PaaC* is predicted to be a transmembrane protein with 46% sequence similarity to a known *E. coli* efflux pump[9] (accession no. BAB35563) for intermediates on the cysteine biosynthetic pathway. Thus, resistance is based on the transport of **1** out of the producing cell.



Figure 2. Left: *E. coli* BL21(DE3)-pMR102.[8] Right: *E. coli* BL21(DE3)-pMR102*PaaC* showing resistance to **1**.

The roles of the *paaA* and *paaB* gene products are not well-defined, but they must carry out the series of transformations schematically indicated in **5**: a) formation of the C9–N4 bond, b) formation of the C9–C1 bond, and c) oxidative cleavage of the carboxylate bond at C1. The predicted *paaA* gene product, PaaA, has significant sequence similarity to the bacterial ThiF/MoeB family of proteins (37 to 43% identity). ThiF[10] and MoeB[11,12] both adenylate carboxyl groups to activate them for an addition–elimination sequence, and PaaA has the conserved ATP-binding site found in ThiF and MoeB. Thus PaaA is the likely candidate to perform the cyclization shown in **5** (a). BLAST searches on PaaB have shown only low sequence similarities to proteins of unknown function. A Pfam search identified a domain match ($E = 0.025$) in PaaB to the 2OG-Fe^{II} oxygenase superfamily (pfam03171). Since the formation of **1** from the precursor peptide requires an oxidation, this similarity to Pfam might be significant.

The instructions for conferring the ability to both synthesize and resist the remarkable antibiotic **1** in an *E. coli* host are encoded on a 3.5 kb stretch of DNA. The 30 residue peptide precursor of **1** is the product of gene *paaP*; this peptide is modified by PaaA, PaaB, and possibly by unidentified host proteases, which convert the precursor peptide into **1**. The producing organism avoids the toxic effects of **1** by pumping it into the extracellular environment with PaaC where it presumably confers a selective advantage to the producing organism.[13]

 © 2003 Wiley-VCH Verlag GmbH & Co. KGaA, Weinheim

This preliminary understanding of the biosynthesis of **1** also provided a tool for establishing the occurrence of the same or related pathways in other *P. agglomerans* strains. Since the *paaB* gene has the least similarity with other reported genes, it was used to generate a digoxigenin-labeled probe for southern blotting of 88 antibiotic-producing *P. agglomerans* strains.[13] A total of 61 strains hybridized with *paaB*, and these strains were the ones most effective in suppressing *E. amylovora* in tests on immature pears and in apple orchards. Like Eh318, most of the strains hybridizing with *paaB* have histidine-suppressible antibiotic activity, but a few produced antibiotics that were not histidine-suppressible.[13] These strains are likely to produce small molecule antibiotics that differ from **1**. Studies on the structure and mechanism of PaaA and PaaB are underway, as are attempts to characterize new antibiotics related to **1**.

Experimental Section

Transposon mutagenesis: Transposon mutagenesis was performed on pUC449 plasmid DNA using the GPS-1 genome priming system following the manufacturer's protocol (New England Biolabs, Inc.). Either pGPS1.1 or pGPS5 were used as the transprimer donor plasmid, and *E. coli* XL2-blue or DH5α cells were used for transformation. Mutants were selected on Luria–Bertani plates supplemented with 30 μg mL^{-1} kanamycin. Anti-Ea273 activity was tested using a soft agar overlay assay.[3] The positions and orientations of transposon insertions were identified by sequencing. The gene sequence of **1** has GenBank accession no. U81376.

Linker scanning experiment: The GPS-LS linker scanning system was used according to the manufacturer's protocol (New England BioLabs, Inc.). pGPS5 transposon mutants were pooled for plasmid extraction. Plasmid DNA was digested with restriction enzymes XbaI and XcmI. A 2.7-kb DNA fragment was purified on gel from the digestion mixture and ligated into a 5.1-kb XbaI-XcmI fragment from plasmid pUC449. The ligated plasmid DNA was amplified once by transformation into *E. coli* and plasmid extraction on pooled colonies. The derived plasmid DNA was digested with PmeI, religated, and used to transform *E. coli* XL1-blue cells. The resulting mutant clones were assayed for anti-Ea273 activity and sequenced to identify positions of linker insertion.

Cloning of *E. coli*-pUC449AtV: Plasmid pUC449 was amplified using the following primer pair to generate an Ala to Val point mutation: 5′-CTGCTATCACTGAAGAAAATG**T**TATGTATACCAAAGGT CAGG-3′ and 5′-CCTGACCTTTGGTATACATA**A**CATTTTCTTCAGTGA TAGCAG-3′.The PCR product was digested with the restriction enzyme DpnI, and the digested product was used to transform *E. coli* strain XL1-Blue to give *E. coli*-pUC449AtV. The mutant plasmid was sequenced to confirm the site of mutation.

3: Compound **3** was isolated from *E. coli*-pUC449 minimal medium culture, by using the same isolation procedure as that for **1**, in a yield of around 0.2 mg L^{-1}. HRFAB-MS: *m*/*z*: 418.1130 [*M*+K]$^+$, calcd *m*/*z*: 418.1129 for $C_{16}H_{21}N_5O_6K$. ^{1}H NMR (D_2O, 500 MHz, 25 °C): $\delta = 6.44$ (1H, dd, $J = 6.4$, 2.0 Hz, H1), 6.22 (1H, br d, $J = 6.4$ Hz, H2), 5.34 (1H, m, H-8), 5.33 (1H, br s, H3), 4.71 (1H, dd, $J = 8.5$, 5.0 Hz, H3′), 4.25 (1H, dd, $J = 14.5$, 8.0 Hz, H6), 4.08 (1H, q, $J = 7.3$ Hz, H8′), 2.90–2.76 (2H, m, H7), 2.84 (1H, dd, $J = 15.5$, 5.0 Hz, H4′a), 2.72 (1H, dd, $J = 15.5$, 8.5 Hz, H4′b), 1.29 ppm (3H, d, $J = 7.3$ Hz, H9′); ^{13}C NMR (D_2O + 5% CD_3OD, 100 MHz, 25 °C): $\delta =$ 180.6 (C10′ COOH), 175.6 (C6′ CO), 171.8 (C5′, $CONH_2$), 170.6 (C5), 165.8 (C1′), 143.7 (C9), 131.0 (C2), 128.4 (C1), 97.6 (C8), 68.0 (C3), 52.2 (C8′), 51.8 (C3′), 50.2 (C6), 37.3 (C4′), 26.3 (C7), 18.6 ppm (C9′); IR (KBr): $\tilde{\nu} =$ 3700–2400, 1676, 1588, 1404 cm^{-1}; UV (H_2O): λ_{max} (ε) = 201 (9547), 273 (4039); $[\alpha]_D^{25} = -202°$, ($c = 0.5$, H_2O); ESI-MS/MS: *m*/*z*: 380 [*M*+H]$^+$, 291 [*M*−Ala]$^+$, 263, 230, 184, 177 [*M*−Ala−Asn]$^+$, 151. To determine the absolute configuration of the C-terminal alanine, 1 mg of **3** was hydrolyzed in 6 M HCl at 90 °C for 20 h, then dried. The resulting compounds were resolved on a CHIRALPLATE (Macherey–Nagel) using the solvent mixture acetone:H_2O:CH_3OH (10:2:2) and compared with authentic samples of L- and D-Ala treated in the same manner. Ala derived from **3** migrated the same as L-Ala ($R_f = 0.57$) and was readily distinguished from control D-Ala ($R_f = 0.52$).

4: ^{1}H NMR (D_2O, 500 MHz, 25 °C): $\delta = 6.78$ (1H, d, $J = 3.5$ Hz, H3), 6.03 (1H, d, $J = 3.5$ Hz, H4), 4.64 (1H, dd, $J = 8.5$, 5.0 Hz, H3′), 4.35 (1H, d, $J = 7.0$ Hz, Thr αH), 4.19 (1H, dd, $J = 8.0$, 4.0 Hz, H3″), 4.10 (1H, m, Thr βH), 3.94(1H, d, $J = 6.0$ Hz, Ile αH), 2.83 (1H, dd, $J = 15.0$, 5.0 Hz, H4′a), 2.70 (1H, dd, $J = 15.0$, 8.5 Hz, H4′b), 2.67(2H, t, $J = 7.5$ Hz, H1″), 2.11–1.90 (2H, m, H2″), 1.42 (1H, m, Ile βH), 1.23 (3H, d, $J = 6.0$ Hz, Thr γH), 1.20–1.14 (2H, m, Ile γCH_2), 0.94 (3H, d, $J = 7.0$ Hz, Ile γCH_3), 0.84 ppm (3H, t, $J = 7.0$ Hz, Ile δCH_3); ^{13}C NMR (D_2O, externally referenced with 5% CD_3OD in D_2O, 100 MHz, 25 °C): $\delta = 179.1$ (C4″, COOH), 178.6 (Asn COOH), 177.1 (Asn $CONH_2$), 171.5 and 170.6 (Ile and Thr CO) 163.4 (C1′), 138.5 (C5), 124.7 (C2), 113.4 (C3), 108.6 (C4), 68.1 (Thr βCH), 60.7 (Thr αCH), 58.8 (Ile αCH), 55.7 (C3″), 53.0 (Asn αCH), 39.2 (Asn βCH_2), 37.6 (Ile βCH), 32.4 (C2″), 25.1 (Ile γCH_2), 24.3 (C1″), 20.0 (Thr γCH_3), 15.2 (Ile γCH_3), 11.6 ppm (Ile δCH_3); ESI-MS/MS: *m*/*z*: 541 [*M*+H]$^+$, 524, 428 [*M*−N-terminal Ile]$^+$, 409 [*M*−C-terminal Asn]$^+$, 391, 381, 327, 296, 278, 252, 234, 215 [*M*−N-terminal Ile-Thr]$^+$, 209, 195, 187, 169, 86. Compound **4** was isolated from *E. coli*-pUC449AtV minimal media culture in a yield of 0.1 mg L^{-1}.

Southern blot experiments: A nylon membrane (Pall Biodyne B) from Nalge Nunc International and a DIG-high prime DNA labeling and detection starter kit I from Roche Applied Bioscience were used. All test strains were inoculated on a nylon membrane placed on top of an LB agar plate. Eh318 and Ea273 were included as positive and negative controls, respectively. Colonies were grown to at least 2 mm in diameter, then the cells were lysed, and the DNA denatured using 0.4 M NaOH solution. After neutralization with tris(hydroxymethyl)-aminomethane-HCl (tris-HCl) buffer (0.5 M, pH 7.0) and washing (2 × saline sodium citrate solution), the DNA was cross-linked with UV light to the membrane. The *paaB* gene (ca. 800 bp) was amplified by a polymerase chain reaction using primer pair 5′-ATGAGCATTGATAG TATTACCTTTAACGACAAAG-3′ and 5′-CATGAATCTAGAGAACCCGC CATTC-3′, and purified on gel. The amplified *paaB* fragment (1 μg, 16 μL) was denatured and used to generate the DIG-labeled probes at 37 °C for 16 h. Southern blotting was performed according to the manufacturer's protocol. Hybridization was performed using 2.6 μL of denatured probes in 8.5 mL of solution at 45 °C for 16 h. Stringency washes (2x15 m) were performed at 65 °C using 0.5 × saline sodium citrate.

Received: January 29, 2003 [Z51054]

Keywords: amino acids · antibiotics · isotopic labeling

[1] S. A. I. Wright, C. H. Zumoff, L. Schneider, S. V. Beer, *Appl. Environ. Microbiol.* **2001**, *67*, 284.
[2] S. F. Brady, S. A. Wright, J. C. Lee, A. E. Sutton, C. H. Zumoff, R. S. Wodzinski, S. V. Beer, J. Clardy, *J. Am. Chem. Soc.* **1999**, *121*, 11912.
[3] S. A. Wright, Ph.D. thesis, Cornell University (Ithaca), **1997**.
[4] R. Kolter, F. Moreno, *Annu. Rev. Microbiol.* **1992**, *46*, 141.
[5] J. E. Gonzalez-Pastor, J. L. San Millan, F. Moreno, *Nature* **1994**, *369*, 281.
[6] M. A. Marahiel, T. Stachelhaus, H. D. Mootz, *Chem. Rev.* **1997**, *97*, 2651.
[7] BDGP neural network promoter prediction (**1998** version). M. G. Reese, N. L. Harris, F. H. Eeckman, *Biocomputing:*

 © 2003 Wiley-VCH Verlag GmbH & Co. KGaA, Weinheim

Proceedings of the 1996 Pacific Symposium (Ed.: L. Hunter, T. E. Klein), World Scientific Publishing Co, Singapore, **1996**.
[8] M. Munson, P. F. Predki, L. Regan, *Gene* **1994**, *144*, 59.
[9] T. Dassler, T. Maier, C. Winterhalter, A. Bock, *Mol. Microbiol.* **2000**, *36*, 1101.
[10] S. V. Taylor, N. L. Kelleher, C. Kinsland, H. J. Chiu, C. A. Costello, A. D. Backstrom, F. W. McLafferty, T. P. Begley, *J. Biol. Chem.* **1998**, *273*, 16555.
[11] M. W. Lake, M. M. Weubbens, K. V. Rajagopalan, H. Schindelin, *Nature* **2001**, *414*, 325.
[12] S. Leimkuhler, M. M. Wuebbens, K. V. Rajagopalan, *J. Biol. Chem.* **2001**, *276*, 34695.
[13] M. Jin, Ph.D. thesis, Cornell University (Ithaca), **2003**.

 © 2003 Wiley-VCH Verlag GmbH & Co. KGaA, Weinheim

Mn Oxide Nanoparticle Assemblies

Dynamic Organization of Inorganic Nanoparticles into Periodic Micrometer-Scale Patterns**

Oscar Giraldo, Jason P. Durand, Harikrishnan Ramanan, Kate Laubernds, Steven L. Suib, Michael Tsapatsis, Stephanie L. Brock, and Manuel Marquez*

Pattern formation, oscillations, and traveling fronts are widely found in nature.[1,2] Oscillatory phenomena in chemical and biochemical systems include carbon monoxide oxidation on single crystals of platinum,[3] seashell patterns,[4] aggregating slime molds,[5] banding textures in minerals,[6,7] and spiral waves in cardiac arrhythmias[8] and retinal tissue.[9] There has been an interest in the pattern formation of particles formed by self-assembly,[10–12] particularly those driven by physical factors, such as surface tension in evaporating colloidal solutions.[13–15] Herein, we present a study of oscillatory phenomena, in which inorganic nanoparticles are organized with a high degree of periodicity; these phenomena are exhibited in a similar fashion to Liesegang precipitation bands or rings,[16–18] or patterns of colloidal origin, which are formed in ionic or other precipitation–diffusion systems.

A simple synthesis of manganese oxide colloids has been developed.[19] Transmission electron microscopy (TEM) and small-angle neutron scattering (SANS) data show that the colloidal particles are of the order of 2–8 nm in diameter, with a disklike shape, and are dispersed in solution.[19] X-ray absorption spectroscopy indicates that the particles have a layered structure consisting of edge-shared MnO_6 octahedra; the Mn centers exhibiting an average oxidation state of 3.7.[20] These colloids can be organized[21–23] into structures and materials with multiscale ordering. Herein, the formation of inorganic films consisting of regular micrometer-sized parallel lines is reported. The composition and phase of the manganese oxide lines can be altered by ion-exchange or thermal treatment.

Micropatterns of mixed-valent manganese oxide colloids were self-assembled from dilute sols of tetramethylammonium (TMA) manganese oxide. A glass microscope slide was immersed vertically into a colloidal solution and was then placed into a preheated oven held at 85 °C until complete evaporation of the solvent had occurred (Figure 1a). The procedure results in a film composed of parallel lines (Figure 1b). Removal of the hydroxyl groups by silynation from the glass surface or using other types of hydrophobic

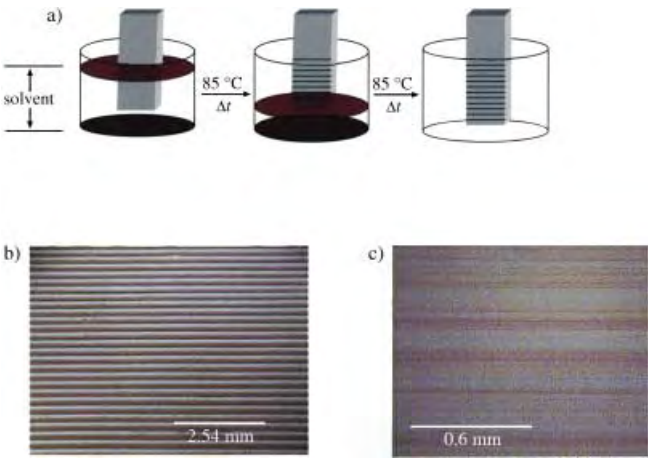


Figure 1. Tetramethylammonium manganese oxide sols form micropatterns of mixed-valent manganese oxide colloids. a) Schematic diagram of the pattern formation; b) self-assembled manganese oxide particles on a glass substrate composed of well-ordered parallel lines, obtained from hydrothermal treatment of a colloid solution; c) a continuous film found near the bottom of the substrate, which results from collapsed lines.

[*] Prof. S. L. Suib, J. P. Durand, K. Laubernds, S. L. Brock,[++] M. Marquez
Department of Chemistry, U-3060, University of Connecticut
55 North Eagleville Rd., Storrs, CT 06269-3060 (USA)
Fax: (+1) 860-486-2981
E-mail: suib@uconnvm.uconn.edu

O. Giraldo[+ ++]
Departamento de Química
Universidad Nacional de Colombia, Bogotá (Colombia)

H. Ramanan, M. Tsapatsis
Department of Chemical Engineering
159 Goessmann Laboratory, University of Massachusetts
Amherst, Massachusetts 01003-3110 (USA)

Prof. S. L. Suib
Department of Chemical Engineering, and Institute of Materials Science
University of Connecticut, Storrs, Connecticut 06269 (USA)

[+] Present address:
Departamento de Física y Química
Universidad Nacional de Colombia, Manizales (Colombia)

[++] Present address:
Department of Chemistry, Wayne State University
5101 Cass Avenue, Detroit, Michigan 48202

[**] We acknowledge Dr. Jim Romanow for helping to collect field emission electron microscopy data and the Institute of Materials Science at the University of Connecticut for use of the microscopy facilities for some of the TEM images. This work was made possible with the support of the Geosciences and Biosciences Division of the Office of Basic Energy Sciences, Office of Science, US Department of Energy.

 DOI: 10.1002/anie.200250712 © 2003 Wiley-VCH Verlag GmbH & Co. KGaA, Weinheim

surfaces, such as teflon, does not allow formation of patterns or any kind of film, which suggests that these patterns can only be assembled on hydrophilic surfaces. The measurements of average line width versus line number shows an increasing trend in the width of material deposition from top to bottom. Figure 2a shows the measurements of the line widths for films prepared with a molar Mn concentration of 10^{-3} M. All lines exhibit the trend seen in Figure 2a with the

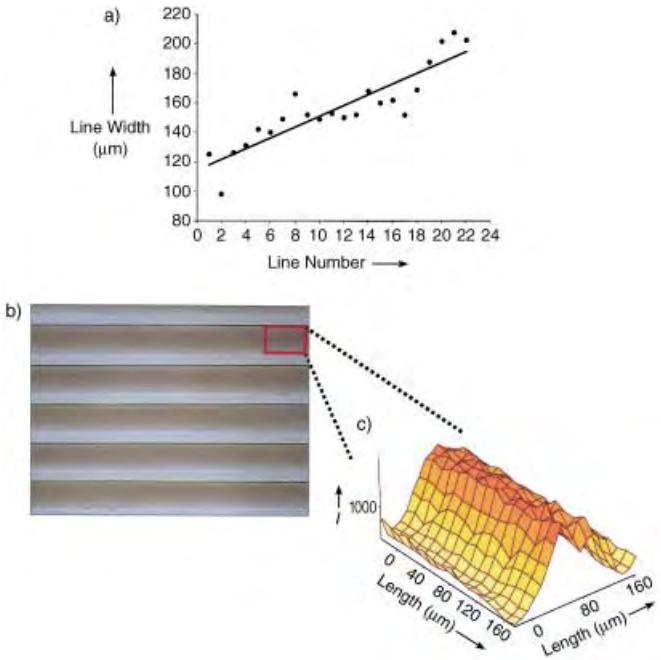


Figure 2. Methods of measuring lines deposited on to a substrate. a) The trend in line width observed in a specific sample while proceeding down the substrate; b) Mn X-ray fluorescence signal from the lines; c) 3D representation of the Mn X-ray fluorescence signal from a line.

relative rate of the increase of width varying, until they collapse at the bottom part of the substrate forming a continuous film (Figure 1c). Figure 2c is a three-dimensional (3D) view of the intensity of the Mn signal obtained by X-ray fluorescence spectroscopy within a line (Figure 2b) that was produced from a 10^{-3} M colloidal TMA manganese oxide solution; the highest concentration of Mn appears to be near the center of the line.

Tapping-mode atomic force microscopy (TM-AFM) was used to measure the topography of the surface. Pronounced surface topography variations can be observed in the cross-sectional perspective (Figure 3a). Red arrows indicate height variations of 34.7 nm while the green ones indicate a variation of 14.7 nm. Surface topography variations are observed to run parallel to each other, which leads to the formation of lines, as shown in the 2D image (Figure 3b). Polarized optical microscopy shows that each line is formed of many thin lines, which are arranged in a stacked fashion (Figure 4a). The curved lines that are observed are caused by disturbances in the system during the formation processes that cause vibrations at the surface of the fluid. Figure 3c shows a 40 μm TM-AFM

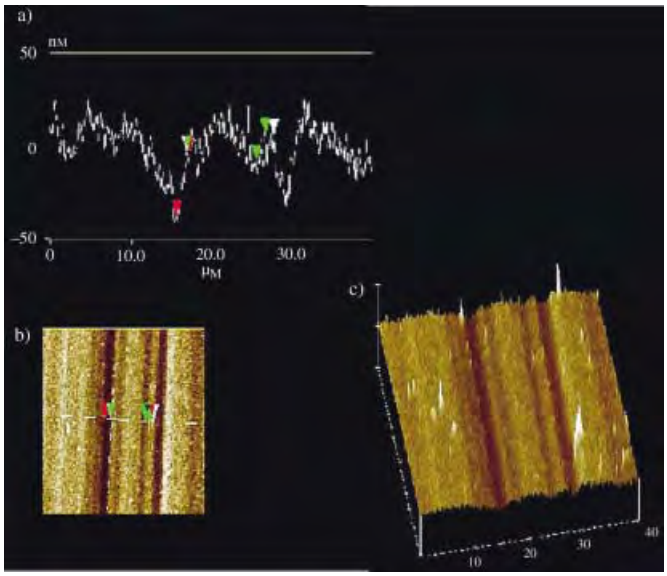


Figure 3. Tapping-mode atomic force microscopy data. a) Cross-sectional view of the surface topography over a 40 μm scan; b) 2D image of the topography, viewed from above the surface; c) 3D image of the 40 μm scan. I = intensity (counts s^{-1})

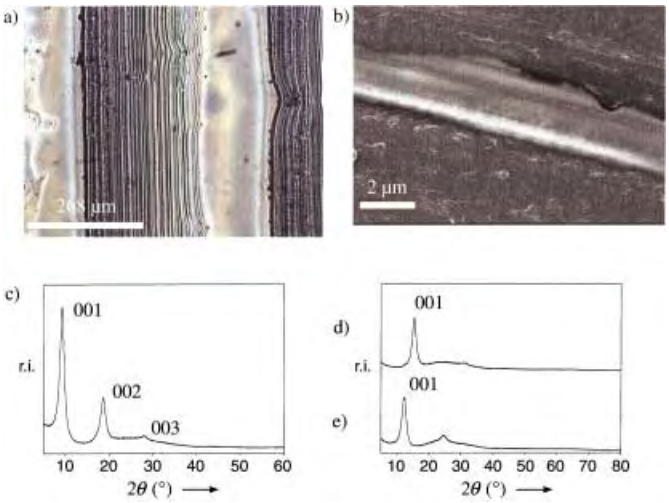


Figure 4. Structural and morphological studies of the manganese oxide micropatterns. a) Reflective optical micrograph indicating that each microline is comprised of many other smaller stacked lines; b) SEM image showing that the film is composed of an agglomeration of manganese oxide particles; c) XRD pattern showing the (00l) reflections of a layered phase, with the largest d spacing (9.8 Å (001)) corresponding to the interlayer separation; d) XRD pattern of a sample on which the lines had undergone ion-exchange with K^+ to remove TMA^+; e) XRD pattern of the same sample after calcination at 500 °C. r.i. = relative intensity.

3D image that illustrates the fine structure of the film. The film is composed of small agglomerations of material, with a broad particle-size distribution from several nanometers to micrometer size. Scanning electron microscopy (SEM) shows a film composed of agglomerations of material with particles of no defined morphology and a wide range of particle size (Figure 4b).

 © 2003 Wiley-VCH Verlag GmbH & Co. KGaA, Weinheim

X-ray diffraction (XRD) studies highlighted the occurrence of mesostructural order in the micropatterns (Figure 4c). Three evenly spaced reflections are observed which can be indexed to the (00*l*) reflections of a layered phase with the largest *d* spacing (0.98 nm; (001)) corresponding to the interlayer spacing. The XRD pattern is consistent with a structure composed of layers of edge-shared manganese oxide octahedra, analogous to the CdI_2 structure,[24] with the TMA cations between the MnO_x layers, without an effective hydration layer. XRD analysis of the deposit does not show the distinct (100) and (110) reflections that are expected.[25]

Complete removal of the organic cation (TMA^+) from the micropatterns can be achieved by ion-exchange using potassium, and leads to the formation of a layered phase corresponding to synthetic birnessite (OL-1) with an interlayer spacing of 0.72 nm (Figure 4d).[25] This phase features an effective hydration sheet with one metal cation residing between the manganese oxide layers. Calcination of the K-ion-exchanged micropatterns (K-OL-1) at 500 °C produced a new phase with an interlayer spacing of 0.57 nm (Figure 4e). This material corresponds to a dehydrated K-OL-1 phase that is also obtained with regular powdered materials under similar conditions.[26] The broad reflection between 15 and 40° (2θ) is an artifact from the glass slide.

TEM was used to examine the materials. Multiple analyses of the deposit shows that the layered material is mostly formed of large platelets (Figure 5a). A magnified view of the circled area in Figure 5a shows strands of a fiberlike structure that reveal the 1 nm layered spacing of the material (Figure 5b). As a result of the preferred orientation of the deposit, with layers assembled parallel to the glass slide (and therefore parallel to the TEM grid in the microtomed sample), the fiberlike structures are noticeable in very limited regions of the sample. The (001) spacing of 0.98 nm, determined by XRD, is in agreement with the 1 nm layered spacing observed by TEM imaging. The preferred orientation of the layers prevents the observation of the intralayer spacings by XRD. The electron diffraction (ED) pattern from the platelet shown in Figure 5c reveals the intralayer structure of the deposit (Figure 5d). The ED pattern is the [001] projection using an orthorhombic crystal geometry ($a = 1.04$, $b = 5.68$ nm). Based on both ED and XRD analysis, we determine that the crystal structure of the layered TMA manganese oxide has an orthorhombic unit cell.

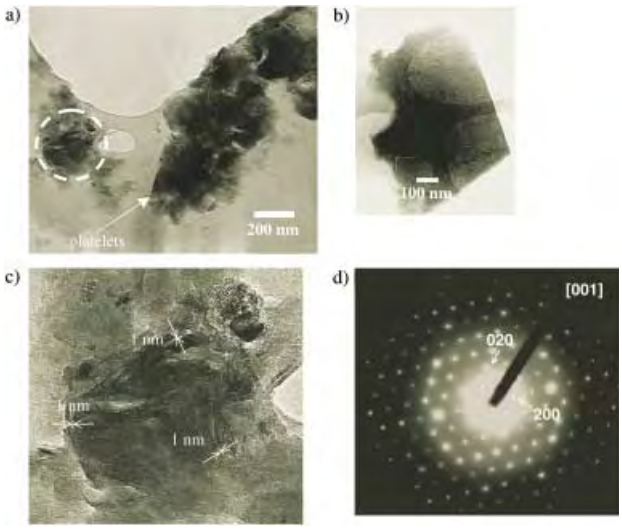


Figure 5. HR-TEM images of tetramethylammonium manganese oxide lines. a) Within the microscale line patterns, platelets are observed; b) a magnified image of the circular region in a), which shows strands and fibers observed with a 1 nm layered spacing; c) an individual platelet, which may correspond to the intralayer structure of the deposit; d) the electron diffraction pattern of the platelet c), indexed as the [001] projection using an orthorhombic crystal geometry ($a = 1.04$ nm, $b = 5.68$ nm).

Previous studies have confirmed the complex nature of the various crystal structures formed by layered manganese oxides.[27] Synthetic Na manganates exist as elongated platelets that give a pseudohexagonal symmetric ED pattern,[28] similar to that which is observed here. The wide range of unit cell dimensions deduced from the structural studies of various synthetic ion-exchanged layered manganese oxides confirms the flexibility of the framework structure.[27] Our TEM results are consistent with earlier studies of synthetic oxides that show ordered layers of MnO_6 octahedra with spacings of 0.96–1.01 nm.[29]

The assembly of the inorganic nanoparticles on a hydrophilic substrate to form well-organized micrometer-scale patterns depends on factors such as surface tension, convection, crystal growth, and particle–particle and particle–substrate interactions. The colloidal solution wets the substrate in a capillary-rise geometry to which the contact line (air/fluid/substrate interface) climbs out of the reservoir forming a meniscus. Since the assembly is carried out at 85 °C, there is a continuous evaporation of the solvent[24,19] at the surface of the fluid, as well as convection from the bottom to the top.

The primary particles (2–8 nm in diameter) start to grow in the bulk of the solution as a consequence of the temperature, and have been observed by SANS data and UV/Vis spectroscopy.[19] Figure 6 shows that the particles initially agglomerate into clusters and these form larger particles that have an elliptical shape. These particles grow by an Ostwald ripening mechanism,[30] in which the growth of the large particles occurs at the expense of the smaller ones. Finally, the elliptical particles associate to form large platelike particles (Figure 6b).

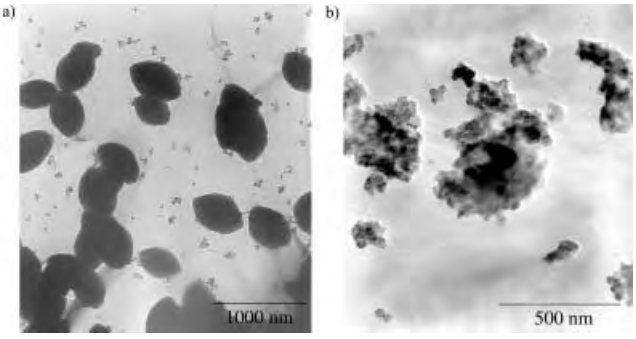


Figure 6. TEM images of a tetramethylammonium manganese oxide colloidal solution. a) Particles agglomerating into clusters; b) larger particles formed over time exhibit an elliptical shape.

 © 2003 Wiley-VCH Verlag GmbH & Co. KGaA, Weinheim

As particle growth proceeds, the particles move, driven by convection, and when they reach the surface of the fluid they rapidly propagate in a horizontal mode driven by the Marangoni effect,[31] which is a surface-tension driven convection effect induced by a temperature gradient and evaporation. When the nanoparticles reach the contact line, they interact strongly with the substrate and precipitate. Large particles will interact more with the substrate and will induce the adhesion of more material. The fact that assembly only occurs at a hydrophilic surface indicates that the substrate–particle interaction may result from hydrogen bonding through hydroxy groups.

The concentration of nanoparticles in the meniscus should be greater than in the bulk,[32] which will result in a faster crystal growth at the drying line, with respect to the bulk. The periodicity that is observed is directly related to variations in the concentration of the large nanoparticles in the meniscus that are continuously fed with the nanoparticles that diffuse from the bulk. As the solvent evaporates there is less fluid left, so that the distance through which the particles have to diffuse is shorter, and the feeding rate at the meniscus increases, which results in greater deposition of material at the substrate. This is experimentally observed as an increase in the line width. The periodic precipitation phenomena might have a close analogy with Liesegang rings, however they are distinct in that precipitation takes place at a drying front rather than in a gel.[33]

These results demonstrate that as a result of time, interaction with a glass surface, surface tension, and crystal growth, these nanoparticles undergo self-assembly from a dissociated colloid. An ordered microarray of lines is composed of nanoparticles that have increased in size relative to those in the original solution and which have a layered structure. These lamellar inorganic micropatterns can undergo ion-exchange reactions with retention of the layered structure. New generations of materials with wide ranges of composition could be readily prepared by ion-exchange methods. These materials can be thermally modified to produce other phases, and therefore may provide templates for a variety of applications. The unique features of these systems include the unusual periodicity, morphology, simple preparation, ease of ion-exchange, and transformations to alternate structures, while preserving the morphology.

Experimental Section

A colloidal solution of lamellar manganese oxide (0.1 M, with respect to Mn) was prepared by adding $((CH_3)_4N)MnO_4$ (10 mmol) to a stirred mixture of distilled deionized water (100 mL) and 2-butanol (30 mL) at room temperature. After 30 min, a dark red-brown solution was formed in the lower aqueous layer. This aqueous solution was isolated from the upper organic layer with a separating funnel and then either used as obtained, or diluted (to 10^{-3} M, with respect to Mn).

The Advanced Photon Source at Argonne National Laboratories was used to study the manganese concentration in $(TMA)_yMnO_x$ lines. TM-AFM images were collected with a NanoScope MultiMode scanning probe microscope (Nanoscope III system controller) from Digital Instruments. Optical microscopy data were obtained on a Kramer video microscopy system with a JVC CCD color video camera.

The $(TMA)_yMnO_x$ lines were ion-exchanged with K^+ ions for preparation of synthetic birnessite (K-OL-1). The ion-exchange reaction was carried out at room temperature by immersing the films in an aqueous solution of KNO_3 (0.1 M), followed by an extensive washing step with deionized water. Finally, the samples were dried in air at room temperature.

High-resolution transmission electron microscopy (HR-TEM) studies of the TMA–manganese oxide lines on glass slides were carried out using a JEOL 3010 microscope operated at 300 kV. Samples of the lines were prepared by transferring small amounts of the deposit from the slides into curing molds and pouring a few drops of epoxy resin over them. To ensure the curing was hard enough for microtoming, the samples were allowed to cure for 3–5 h at 45 °C. The surface was then microtomed (at room temperature conditions, 25 °C) to obtain thin sections on sample grids (Carbon holey film grids, Ted Pella, Inc.) for TEM analysis. Some samples were also prepared from dilute suspensions of the crushed deposit in deionized water. Similar observations were obtained from samples prepared by either of the methods. For TEM analysis of the colloidal suspension, the solution was dropped onto a holey carbon 300 mesh copper grid (SPI). HR-SEM was performed on a Zeiss DSM 982 Gemini field-emission scanning electron microscope.

Received: December 6, 2002
Revised: April 8, 2003 [Z50712]

Keywords: colloids · manganese · nanomaterials · oxides · self-assembly

[1] S. Scott, *Oscillations, Waves and Chaos in Chemical Kinetics*, Oxford Universtiy Press, Oxford, **1995**.
[2] P. Ball, *The Self-Made Tapestry: Pattern Formation in Nature*, Oxford Universtiy Press, Oxford, **1999**.
[3] S. Jakubith, H. H. Rotermund, W. Engel, A. von Oertzen, G. Ertl, *Phys. Rev. Lett.* **1990**, *65*, 3013.
[4] H. Meinhardt, *The Algorithmic Beauty of Sea Shells*, Springer, Berlin, **1995**.
[5] F. Siegert, C. J. Weijer, *Cell Sci.* **1989**, *93*, 325.
[6] R. F. Cooper, J. B. Fanselow, J. K. R. Weber, D. R. Merkley, D. B. Poker, *Science* **1996**, *274*, 1173.
[7] C. Frondel, *Am. Mineral.* **1978**, *63*, 17.
[8] J. M. Davidenko, A. V. Pertsov, R. Salomonsz, W. Baxter, J. Jalife, *Nature* **1992**, *355*, 349.
[9] N. L. Gorelova, J. Bures, *J. Neurobiol.* **1983**, *14*, 353.
[10] A. N. Shipway, E. Katz, I. Willner, *ChemPhysChem* **2000**, *1*, 18.
[11] Y. Xia, J. A. Rogers, K. E. Paul, G. M. Whitesides, *Chem. Rev.* **1999**, *99*, 1823.
[12] H. H. Wickman, J. N. Korley, *Nature* **1998**, *393*, 445.
[13] P. C. Ohara, J. R. Heath, W. M. Gelbart, *Angew. Chem.* **1997**, *109*, 1120; *Angew. Chem. Int. Ed. Engl.* **1997**, *36*, 1078.
[14] M. Maillard, L. Motte, A. T. Ngo, M. P. Pileni, *J. Phys. Chem. B* **2000**, *104*, 11871.
[15] H. Wang, Z. Wang, L. Huang, A. Mitra, Y. Yan, *Langmuir* **2001**, *17*, 2572.
[16] H. K. Henisch, *Crystals in Gels and Liesegang Rings*, Cambridge Universtiy Press, New York, **1988**.
[17] K. F. Mueller, *Science* **1984**, *225*, 1021.
[18] M. Tsapatsis, D. G. Vlachos, S. Kim, H. Ramanan, G. R. Gavalas, *J. Am. Chem. Soc.* **2000**, *122*, 12864.
[19] S. L. Brock, M. Sanabria, S. L. Suib, V. Urban, P. Thijyagarajan, D. Potter, *J. Phys. Chem. B* **1999**, *103*, 7416.
[20] T. Ressler, S. L. Brock, J. Wong, S. L. Suib, *J. Phys. Chem. B* **1999**, *103*, 6407.
[21] O. Giraldo, S. L. Brock, M. Marquez, S. L. Suib, H. Hillhouse, M. Tsapatsis, *Nature* **2000**, *405*, 38.

 © 2003 Wiley-VCH Verlag GmbH & Co. KGaA, Weinheim

[22] O. Giraldo, S. L. Brock, M. Marquez, S. L. Suib, H. Hillhouse, M. Tsapatsis, *J. Am. Chem. Soc.* **2000**, *122*, 12158.
[23] M. Marquez, J. Robinson, V. Van Nostrand, D. Schaefer, L. Ryzhkov, W. Lowe, S. L. Suib, *Chem. Mater.* **2002**, *14*, 1493.
[24] E. Silvester, A. Manceau, V. A. Drits, *Am. Mineral.* **1997**, *82*, 962–978.
[25] R. N. DeGuzman, Y. F. Shen, S. L. Suib, B. R. Shaw, C. L. O'Young, *Chem. Mater.* **1993**, *5*, 1395.
[26] J. Luo, Q. Zhang, A. Huang, O. Giraldo, S. L. Suib, *Inorg. Chem.* **1999**, *38*, 6106.
[27] K. Kuma, A. Usui, W. Paplawsky, B. Gedulin, G. Arrhenius, *Mineral. Mag.* **1994**, *58*, 425.
[28] R. Giovanoli, E. Stahli, W. Feitknecht, *Helv. Chim. Acta* **1970**, *53*, 209.
[29] R. Giovanoli, in *Geology and Geochemistry of Manganese, Vol. 1* (Eds.: I. M. Varentsov, G. Grasselly), Akad. Kiado, Budapest, **1980**, pp. 159–202.
[30] A. Baldan, *J. Mater. Sci.* **2002**, *37*, 2171.
[31] X. Fanton, A. M. Cazabat, *Langmuir* **1998**, *14*, 2554.
[32] Y. Lu, R. Ganguli, C. A. Drewien, M. T. Anderson, C. J. Brinker, W. Gong, Y. Guo, H. Soyez, B. Dunn, M. H. Huang, J. I. Zink, *Nature* **1997**, *389*, 365.
[33] R. E. Liesegang, *Naturwissenschaften* **1896**, *11*, 353.

 © 2003 Wiley-VCH Verlag GmbH & Co. KGaA, Weinheim

Synthetic Peptidyl–tRNA Analogues

Amphiphilic 3′-Peptidyl-RNA Conjugates**

*Silvia Terenzi, Ewa Biała, Nhat Quang Nguyen-Trung, and Peter Strazewski**

The crystal structure of the large ribosomal subunit at nearly atomic resolution determined by Steitz and co-workers constitutes a milestone for the elucidation of the molecular basis of protein synthesis.[1] So far, only analogues of aminoacyl-tRNAs[1b,2] and in vitro-synthesized peptidyl-tRNAs[3,4] have been used in X-ray crystallographic, chemical footprinting, and cryo-electron microscopic structural investigations.

Herein we describe the synthesis and characterization of the first synthetic peptidyl–tRNA analogues, whose structural features should render them suitable for a cocrystallization with the large ribosomal subunit. In contrast to native peptidyl-tRNAs bearing a readily hydrolysable ester linkage between the nascent peptide and the tRNA, we have designed analogues in which the peptide is linked through a stable amide bond.

Our immediate goal, however, is to study the supramolecular aggregation properties of amphiphilic peptidyl-RNA conjugates that are likely to have played an important role at the origin of RNA-controlled peptide synthesis. Largely lipophilic peptides with a well defined secondary structure and appropriate length[5] might have been advantageous in a hypothetical "RNA world", as they could have served as molecular "anchoring devices" that would enable their RNA carriers to be transiently immobilized, compartmentalized, and thus highly concentrated on or in spheroidal lipidic bilayer vesicles, as proposed in the literature.[6] It seems to us of particular interest to investigate such systems experimentally by using synthetic, well-defined model systems, to test, for instance, if and how one could control the direction of RNA insertion into lipidic bilayer vesicles ("RNA-outside" versus "RNA-inside"). Besides, highly amphiphilic macromolecules bear the potential of unexpected material properties that could be exploited in various ways.

The RNA part of our conjugates consists of a 22-mer oligoribonucleotide hairpin mimicking the acceptor stem of *Escherichia coli* $tRNA^{Ala}$ closed by a stable UUCG tetraloop and peptidylated at its 3′-terminal single-stranded overhang, the so-called CCA terminus of tRNAs (Figure 1).

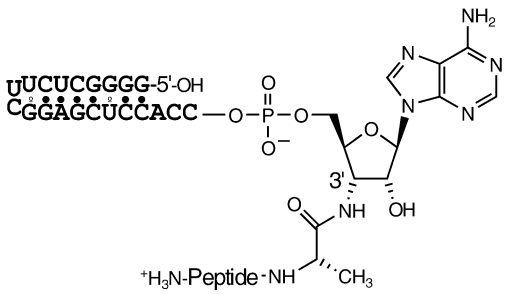


Figure 1. General structure of our 3′-peptidyl-RNA conjugates mimicking the acceptor stem peptidyl-$tRNA^{Ala}$.

Alanine and glutamic acid residues—early prebiotic amino acids—were chosen as the constituents of the oligopeptides. The length of the oligoalanine-based peptides—some with interdispersed or *N*-terminal glutamate residues to modulate their lipophilicity—varies between 8 and 22 amino acids (an α-helix of approximatively 20 amino acids suffices to span a lipidic bilayer). Their sequences are listed in Table 1.

[*] Prof. Dr. P. Strazewski
Laboratoire de Synthèse de Biomolécules
Bâtiment Eugène Chevreul (5ème étage)
Univerisité Claude Bernard - Lyon 1
Domaine Scientifique de la Doua
43 boulevard du 11 novembre 1918, 69622 Villeurbanne Cedex (France)
Fax: (+33) 4-7243-1323
E-mail: peter.strazewski@unibas.ch
S. Terenzi, N. Q. Nguyen-Trung
Institute of Organic Chemistry
University Basel
St. Johanns-Ring 19, 4056 Basel (Switzerland)
Dr. E. Biała
Institute of Bioorganic Chemistry
Polish Academy of Sciences
Noskowskiego 12/14, 61-704 Poznań (Poland)

[**] This work was supported by the Swiss National Science Foundation and the Novartis Foundation. We thank Profs. Paul Jenö and Thomas Kiefhaber, Biocentre, University of Basel, for making available their, respectively, MALDI-ToF and CD spectrometer facilities. We thank Drs. Anthony Coleman and Patrick Shahgaldian, Institut de Biologie et Chimie de Proteines (IBCP), Lyon, for carrying out and analyzing the DLS and AFM measurements.

Supporting information for this article is available on the WWW under http://www.angewandte.org or from the author.

 DOI: 10.1002/anie.200350926 © 2003 Wiley-VCH Verlag GmbH & Co. KGaA, Weinheim

Table 1: Peptide sequences of 3′-peptidyl-RNA.

Conjugate	Sequence
4a	$^{-}O_3PO$-5′-RNA-3′-$(Ala)_8$
4b	HO-5′- RNA-3′-$(Ala)_{16}$
4c	HO-5′- RNA-3′-$(Ala)_{10}$Glu
4d[a]	HO-5′- RNA-3′-$(Ala)_{18}(Glu)_2$pGlu
4e	HO-5′- RNA-3′-$(Ala)_7Glu(Ala)_7Glu(Ala)_4(Glu)_2$
4f	HO-5′- RNA-3′-$(Ala)_{20-22}$

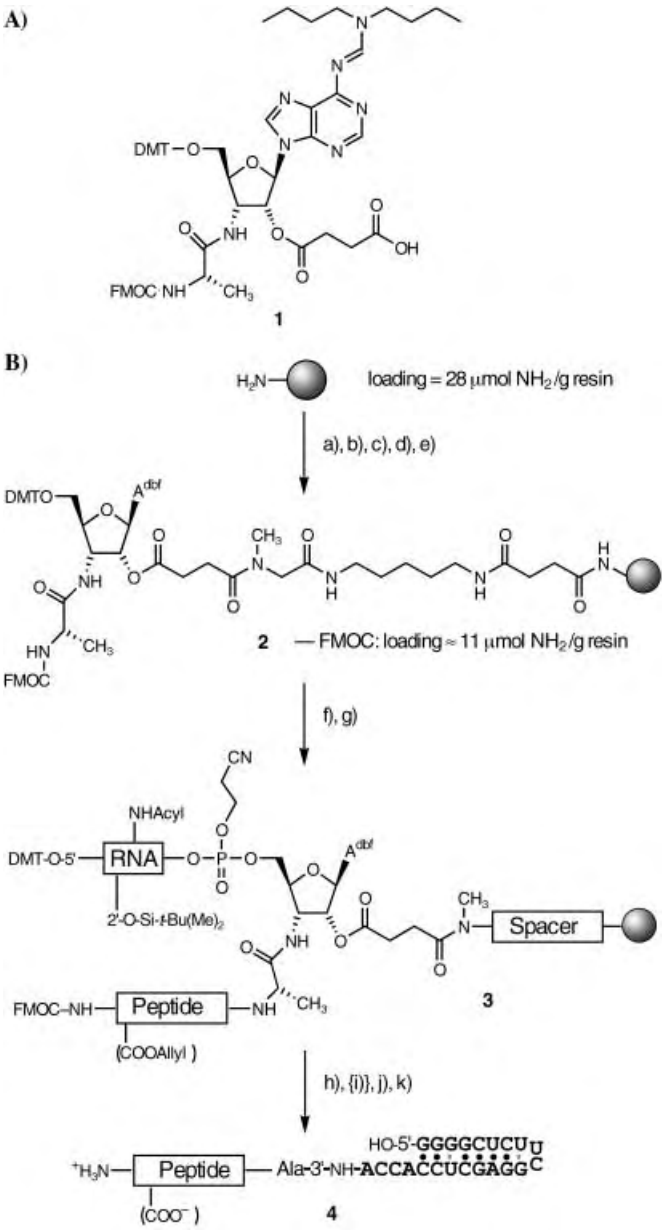
[a] The amino-terminal pyroglutamate was probably formed during the purification steps.

The first building block was the orthogonally protected derivative **1** of 3′-alanylamino-3′-deoxyadenosine[7] immobilized on a suitable resin (Scheme 1). A relatively low loading of the resin was anticipated in view of the fact that we wished to synthesize long oligoalanine stretches that are in danger of aggregating at too high loadings[8] (in situ β-sheet formation), which could jeopardize the overall yields. To avoid undesired ester aminolyses of glutamate side chains that, during the final deprotection with methyl amine, might have generated N^{δ}-methyl glutamines, the glutamic acid side chains were protected as allyl esters, which were cleaved on the solid support before treatment with methyl amine.[9] After completion of the stepwise oligopeptide and then oligoribonucleotide synthesis, the crude conjugates were deprotected and detached from the solid support (by using methyl amine), desilylated, purified by HPLC, and identified by MALDI-ToF mass spectrometry.

The secondary structures of the RNA hairpin and the peptidic moieties were studied by CD spectroscopy at 0, 25, and 60 °C. Under the conditions used the peptide-free RNA hairpin exhibits a T_m value of 87.6 °C and is completely folded (stable A_{260} baseline) up to ≈60 °C.[10] CD spectra at 0 °C (Figure 2; 25 and 60 °C: see Supporting Information) show a strong positive Cotton effect between 245 and 295 nm that originates from the nucleotidic part only. All the conjugates analyzed show a more intense signal at Θ_{270} as compared to the hairpin alone (**4a:** +13%, **4d**: +42%), thus indicating that the single-stranded CCA-terminus of the hairpin, quite free to move when no peptide is present, is rigidified when a peptide is bonded to it. Moreover, the rigidification seems to roughly correlate with the degree of the predicted helicity of the peptide (AGADIR[11]).

The peptidic part induces an additional negative Cotton Effect in the region between 200 and 240 nm. The difference spectra between the peptide-free RNA hairpin and the conjugates (Figure 3) give evidence for the conformation adopted by the RNA-bound peptides in solution.

The negative bands at ≈208 and ≈222 nm are characteristic of α-helical peptides. A helical secondary structure is clearly adopted by **4b**, **4d** and **4e**, whereas **4a**, which has only eight alanines and thus should be predominantly random-coil, does not show the two bands. The degrees of helicity of the peptides were not quantified from the difference spectra because minor contributions to the negative Cotton effect arising from the differential changes originating from the RNA part of the conjugates (with a minimum at 211 nm) can neither be excluded nor determined.



Scheme 1. A) Building block for the synthesis of 3′-peptidyl-RNA. B) Synthesis of the conjugates: a) 1. aminomethyl polystyrene 50% crosslinked with *p*-divinyl benzene, succinic anhydride, DMAP; 2. Ac_2O, pyridine, NMI, DMF; b) 1. Oxalyl chloride, CH_2Cl_2; 2. 1,6-diaminohexane, DMAP, CH_2Cl_2; c) BOC-Sarcosine, HBTU, NMM, DMF; d) 1. TFA/CH_2Cl_2; 2. Et_3N/DMF; e) 1. Building block **1**, HATU, NMM, DMF; 2. Ac_2O, pyridine, NMI, DMF. The loadings were determined by using the quantitative ninhydrin test. f) FMOC-based peptide synthesis, FMOC-amino acid + DEPBT; g) phosphoramidite-based RNA synthesis; h) 3% TCA in CH_2Cl_2; i) 1. $Pd(PPh_3)_4$, $PhSiH_3$, CH_2Cl_2; 2. $NH_4^+Et_2NCS_2^-$/DMF}; j) 38% CH_3NH_2 in EtOH/H_2O (1:1), 2 h, RT; k) $Et_3N{\cdot}3HF$, DMF, 1.5 h, 65 °C; *n*-butanol, −20 °C; SAX- and RP-HPLC. Abbrev.: BOC = *tert*-butoxycarbonyl; dbf = *N*,*N*-di-n-butylformamidine; DEPBT = 3-(diethoxyphosphoryloxy)-1,2,3-benzotriazin-4(3*H*)-one; DMT = *p*,*p*-dimethoxytriphenylmethyl ("dimethoxytrityl"); FMOC = 9-fluorenylmethoxycarbonyl; HATU = *O*-(7-azabenzotriazol-1-yl)-*N*,*N*,*N*′,*N*′-tetramethyluronium hexafluorophosphate; HBTU = *O*-(benzotriazol-1-yl)-*N*,*N*,*N*′,*N*′-tetramethyluronium hexafluorophosphate; NMI = *N*-methylimidazole; NMM = *N*-methylmorpholine; TCA = trichloroacetic acid; TFA = trifluoroacetic acid.

 © 2003 Wiley-VCH Verlag GmbH & Co. KGaA, Weinheim

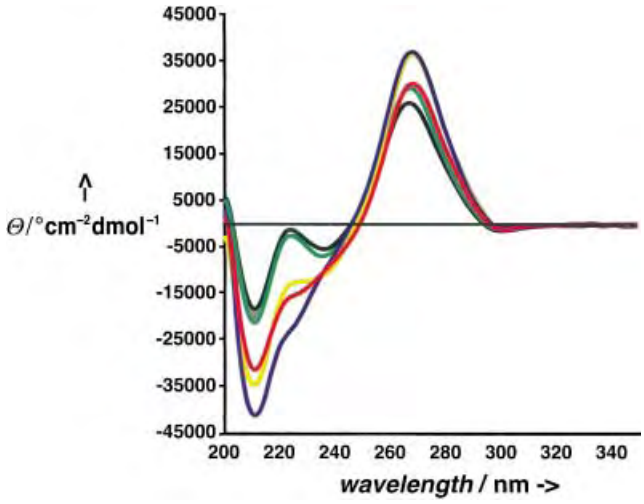


Figure 2. CD spectra of a ≈2.4 μM solution ($A_{260nm,25°C} \approx 0.35$, $\varepsilon_{260,calcd} = 145\,100\ M^{-1}cm^{-1}$, 100 mM NaCl, 10 mM $Na_xH_yPO_4$, pH 7.5) of the conjugates **4a** (green), **4b** (yellow), **4d** (blue), **4e** (red) and the unpeptidylated RNA hairpin × (black) taken at 0°C and normalized for the number of nucleotide residues. A strong and a weak negative Cotton Effect at 211 nm and 236 nm, respectively, and a positive one at 266 nm (black line) are typical for the A conformation of double-stranded RNA.

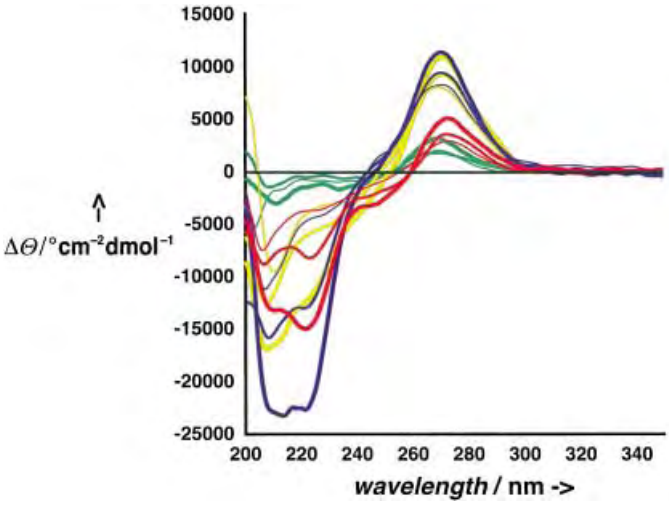


Figure 3. Difference CD spectra (**4a**,**b**,**d**,**e** minus x; see legend of Figure 2 for color scheme) at 0 (thick lines), 25 (normal lines) and 60°C (thin lines), normalized as in Figure 2. Note how the nucleobase region $\Theta_{245-295}$ withstands heat denaturation more than the peptide region $\Theta_{200-240}$, and that Θ_{222} denatures more readily than Θ_{208} at elevated temperatures.[15]

Furthermore, we measured the thermal denaturation profiles of the conjugates **4a–e** between 20 and 102°C at 260 nm (only RNA denaturation observed) and compared them to those of the parent unpeptidylated RNA hairpin, the RNA hairpin bearing a 5′-phosphate, a 3′-alanine, or both. The profiles and corresponding full thermodynamic parameters are shown in the Supporting Information. Briefly, no major influence on the thermodynamic stability of the RNA hairpins is observed in any of the examined conjugates (T_m values: 87.7–88.8°C). However, the presence of a peptide renders the RNA hairpin transition significantly shallower, a statistical effect and strong indication for a higher molecularity of the melting process.[12] Denaturation molecularities higher than one, in turn, are a first indication that our amphiphilic conjugates do show a tendency to aggregate in diluted aqueous solutions, a property that is not observed at all in the denaturation profiles of the unpeptidylated RNA hairpins.

Preliminary dynamic light scattering (DLS) and atomic force microscopy (AFM) studies confirm the above conclusion. Conjugate **4f** forms highly polydisperse aggregates in aqueous solution (size distribution between 80 nm and 1 μm with an abundance peak at 428 nm and an abundance shoulder at around 150 nm, as determined by DLS) which, when deposited on a glass surface and air-dried, form nanovesicles of a much narrower size distribution (Figure 4). DLS and AFM control experiments showed that

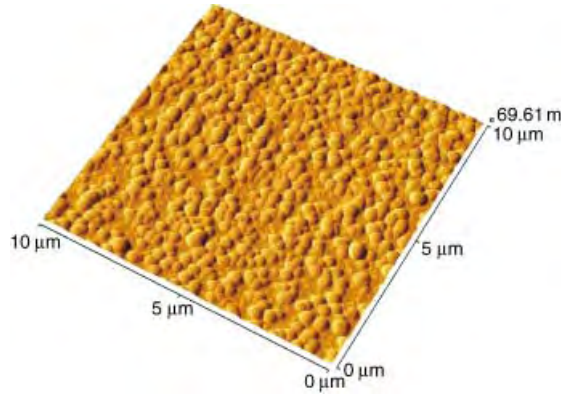


Figure 4. AFM scan over an air-dried solution of conjugate **4f** on a glass plate. Average size of the vesicles (50 vesicles analyzed): $h\varnothing = 13 \times 204$ nm. Polydispersity: $h\varnothing = 2 \times 102–36 \times 380$ nm. Height-diameter ratios: $100h/\varnothing = 2.0–9.5\,\%$, average 5.8%.

the unpeptidylated RNA hairpin, as expected, does not self-assemble in solution, nor does it form vesicles on a surface; when a highly concentrated RNA-hairpin solution was air-dried on a glass plate it instead formed microcrystals of 10–40 μm length (not shown). These observations confirm that amphiphilic constructs containing a hydrophilic RNA hairpin and a hydrophobic α-helical oligopeptide moiety of similar lengths, estimated to be together 9–10 nm long and ≤0.2 nm thick, indeed bear the potential of spontaneous self-assemblage into higher-order structures, even in the absence of lipids.

In conclusion, we have demonstrated the synthetic feasibility of amphiphilic conjugates mimicking peptidyl-tRNA. In the literature many examples of the synthesis of oligo(nucleotide-peptide) conjugates are present that follow two different synthetic strategies: fragment coupling[13] or the stepwise total-synthesis approach.[14] Our conjugates have been synthesized by following the second approach and, to the best of our knowledge, these are the only examples with an oligopeptide directly bonded in a biomimetic (and spacer-free) way to the 3′ terminus of an oligoribonucleotide. We believe that the methodology presented herein is powerful

 © 2003 Wiley-VCH Verlag GmbH & Co. KGaA, Weinheim

and versatile and should be applicable to the stepwise synthesis of many different oligo(ribonucleotide-peptide) conjugates. Our conjugates could open the way to new constructs which might be able to form higher-order assemblies with unexpected properties.

Received: January 13, 2003
Revised: March 24, 2003 [Z50926]

Keywords: amphiphiles · bioorganic chemistry · nucleotides · peptides · self-assembly

[1] a) N. Ban, P. Nissen, J. Hansen, P. B. Moore, T. A. Steitz, *Science* **2000**, *289*, 905; b) P. Nissen, N. Ban, J. Hansen, P. B. Moore, T. A. Steitz, *Science* **2000**, *289*, 920.
[2] a) R. K. Agrawal, A. B. Heagle, P. Penczek, R. A. Grassucci, J. Frank, *Nat. Struct. Biol.* **1999**, *6*, 643; b) H. Stark, M. V. Rodnina, H.-J. Wieden, M. van Heel, W. Wintermeyer, *Cell* **2000**, *100*, 301.
[3] a) K. Stade, S. Riens, D. Bochkariov, R. Brimacombe, *Nucleic Acids Res.* **1994**, *22*, 1394; b) K. M. Choi, R. Brimacombe, *Nucleic Acids Res.* **1998**, *26*, 887.
[4] R. Beckmann, C. M. T. Spahn, N. Eswar, J. Helmers, P. A. Penczek, A. Sali, J. Frank, G. Blobel, *Cell* **2001**, *107*, 361.
[5] A. Percot, X. X. Zhu, M. Lafleur, *Biopolymers* **1999**, *50*, 647.
[6] T. Cavalier-Smith, *J. Mol. Evol.* **2001**, *53*, 555.
[7] a) O. Botta, P. Strazewski, *Nucleosides Nucleotides* **1999**, *18*, 721; b) N. Q. Nguyen-Trung, O. Botta, S. Terenzi, P. Strazewski, *J. Org. Chem.* **2003**, *68*, 2038.
[8] R. Warras, J.-M. Wieruszeski, C. Boutillon, G. Lippens, *J. Am. Chem. Soc.* **2000**, *122*, 1789.
[9] a) Y. Hayakawa, S. Wakabayashi, H. Kato, R. Noyori, *J. Am. Chem. Soc.* **1990**, *112*, 1691; b) N. Thieret, F. Guibé, F. Albericio, *Org. Lett.* **2000**, *2*, 1815.
[10] a) P. Strazewski, E. Biała, K. Gabriel, W. H. McClain, *RNA* **1999**, *5*, 1490; b) E. Biała, P. Strazewski, *J. Am. Chem. Soc.* **2002**, *124*, 3540.
[11] V. Muñoz, L. Serrano *J. Mol. Biol.* **1994**, *245*, 275: http://www.embl-heidelberg.de/Services/serrano/agadir/agadir-start.html.
[12] A. Dorenbeck, M. Scheffler, M. Wüstefeld, G. von Kiedrowski, *Angew. Chem./Angew. Chem. Int. Ed.* **2003**, in press.
[13] a) T. S. Zatsepin, D. A. Stetsenko, A. A. Arzumanov, E. A. Romanova, M. J. Gait, T. S. Oretskaya, *Bioconjugate Chem.* **2002**, *13*, 822; b) D. Forget, D. Boturyn, E. Defrancq, J. Lhomme, P. Dumy, *Chem. Eur. J.* **2001**, *7*, 3976; c) D. A. Stetsenko, M. J. Gait, *J. Org. Chem.* **2000**, *65*, 4900; d) M. McPherson, M. C. Wright, P. A. Lohse, *Synlett* **1999**, 978; e) D. L. McMinn, M. M. Greenberg, *J. Am. Chem. Soc.* **1998**, *120*, 3289; f) S. Soukchareun, J. Haralambidis, G. Tregear, *Bioconjugate Chem.* **1998**, *9*, 466; g) J. G. Harrison, S. Balasubramanian, *Nucleic Acids Res.* **1998**, *26*, 3136.
[14] a) Z. J. Gartner, M. W. Kanan, D. R. Liu, *J. Am. Chem. Soc.* **2002**, *124*, 10304; b) M. Antopolsky, E. Azhayeva, U. Tengvall, A. Azhayev, *Tetrahedron Lett.* **2002**, *43*, 527; c) D. A. Stetsenko, M. J. Gait, *Bioconjugate Chem.* **2001**, *12*, 576; d) M. de Champdoré, L. De Napoli, G. Di Fabio, A. Messere, D. Montesarchio, G. Piccialli, *Chem. Commun.* **2001**, 2598; e) V. Marchán, C. Rodríguez-Tanty, M. Estrada, E. Pedroso, A. Grandas, *Eur. J. Org. Chem.* **2000**, 2495; f) B. García de la Torre, F. Albericio, E. Saison-Behmoaras, A. Bachi, R. Eritja, *Bioconjugate Chem.* **1999**, *10*, 1005; g) I. Schwope, C. F. Bleczinski, C. Richert, *J. Org. Chem.* **1999**, *64*, 4749; h) F. Bergmann, W. Bannwarth, *Tetrahedron Lett.* **1995**, *36*, 1839.
[15] P. Wallimann, R. J. Kennedy, J. S. Miller, W. Shalongo, D. S. Kemp, *J. Am. Chem. Soc.* **2003**, *125*, 1203.

 © 2003 Wiley-VCH Verlag GmbH & Co. KGaA, Weinheim

Clusters Layered on Au Surfaces

Electrochemically Controlled Layer-by-Layer Deposition of Metal-Cluster Molecular Multilayers on Gold**

Masaaki Abe, Takayuki Michi, Akira Sato, Toshihiro Kondo, Wei Zhou, Shen Ye, Kohei Uosaki,* and Yoichi Sasaki**

The ordered and controlled location of molecular compounds on electrode surfaces is essential for the nanometer-scale design of electrochemical interfaces in view of fundamental electron-transfer studies and several lines of applications, such as molecular electronic devices, optical devices, and sensors.[1] Furthermore, layer-by-layer deposition of molecular units onto preorganized self-assembled monolayers (SAMs) has proven to be useful in preparing layered architectures with enhanced properties.[2] Although a significant progress has been made for atomic-scale depositions (such as underpotential deposition and atomic layer epitaxy)[3] or molecular 2D assembly,[4] an "electrochemical-control strategy" to prepare layer-by-layer 3D structures from molecular building blocks is currently unavailable. Herein we report on the successful construction of layer-by-layer nanostructures on a gold electrode by using a redox-active metal-cluster molecule,[5] in which the electrode potential modulation precisely controls the multilayer growth. We show that the series of multilayers display extensive electronic coupling between the linked molecular units, thus allowing facile multielectron transport to occur at interfaces.

[*] Dr. M. Abe, Prof. Dr. K. Uosaki, Prof. Dr. Y. Sasaki, T. Michi, A. Sato, Prof. Dr. T. Kondo[+]
Division of Chemistry, Graduate School of Science, Hokkaido University, Kita-ku, Sapporo 060-0810 (Japan)
Fax: (+81) 11-706-3447
E-mail: mabe@sci.hokudai.ac.jp
uosaki@pcl.sci.hokudai.ac.jp
ysasaki@sci.hokudai.ac.jp
W. Zhou, Prof. Dr. S. Ye[++]
Catalysis Research Center, Hokkaido University
Kita-ku, Sapporo 060-0811 (Japan)
[+] Department of Chemistry, Faculty of Science
Ochanomizu University, 2-1-1, Otsuka, Bunkyo-ku, Tokyo 112-8610 (Japan)
[++] Present address:
PRESTO, Japan Science and Technology Corporation (JST) (Japan)

[**] This work was supported by Grant-in-Aids for Scientific Research on Priority Area of "Electrochemistry of Ordered Interfaces" (Nos. 09554037 and 09237106) and No. 09740483 from the Ministry of Education, Science, Sports and Culture, Japan. Financial support from the Sasakawa Scientific Research Grant from the Japan Science Society (to M.A.) and PRESTO, Japan Science and Technology Corporation (JST) (to S.Y.) is gratefully acknowledged. We thank Prof. M. Osawa (Catalysis Research Center, Hokkaido University) for valuable discussions.

Supporting information for this article is available on the WWW under http://www.angewandte.org or from the author.

 © 2003 Wiley-VCH Verlag GmbH & Co. KGaA, Weinheim DOI: 10.1002/anie.200351334

Our synthetic approach is outlined in Figure 1 and the detailed procedures are provided in the Experimental Section. In the approach, we use a trinuclear ruthenium complex $[Ru_3(\mu_3\text{-}O)(\mu\text{-}CH_3COO)_6(bpy)_2(CO)]$ (**1**, bpy = 4,4′-bipyridine; Figure 1)[6] as a molecular building block. The Ru_3 core of **1** formally contains two Ru^{III} sites and one Ru^{II} site, in which the CO ligand occupies the latter position.[7,8] This class of molecular clusters is known to have well-defined redox processes in solution, and the character of the terminal-ligand displacement is precisely controlled by the redox state of the core of the $Ru_3(\mu_3\text{-}O)$ cluster.[9]

With the aim of constructing molecular multilayers, we prepared close-packed SAMs of a CO-bound Ru_3 complex on an Au(111) electrode[10] (Figure 1a) as described previously.[11] The terminal CO is eliminated when the attached Ru^{II} center is electrochemically oxidized to Ru^{III}, and the monolayer containing a kinetically-labile water molecule shown in Figure 1b is formed (step 1).[11] Immersion of the monolayers shown in Figure 1b into a solution of **1** results in the coordination of **1** to the monolayer binding site through a single Ru^{III}–N(bpy) bond to afford CO-terminated bilayers shown in Figure 1c (step 2). We have successfully prepared molecular multilayers up to five layers, by repeating interfacial reactions (steps 1 and 2) alternately (Figure 1). The bpy- and pyrazine-bridged extended structures that have been characterized[12–14] are relevant to the expected molecular structures in our multilayers.

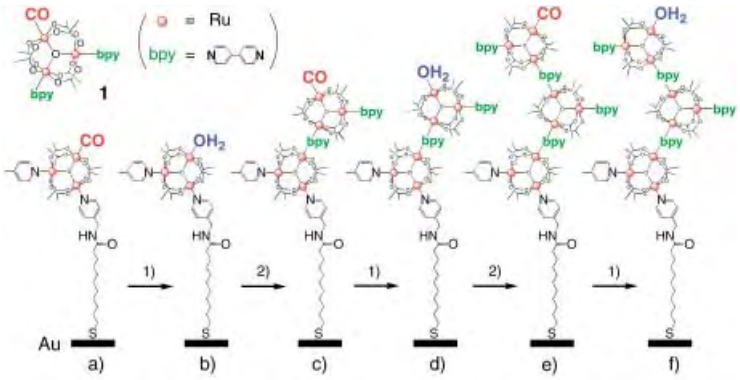


Figure 1. Schematic representation of sequential growth of layer-by-layer multilayers on an Au surface. Only a single molecule attached to Au is shown. Inset: trinuclear ruthenium complex **1**, used as a redox-active molecular building block. Conditions: Step 1: Electrolysis at +0.80 V versus Ag/AgCl for 45 minutes or less, 0.1 M $HClO_4$, 298 K; Step 2: Immersion into an aqueous solution of **1** (0.2 mM), in dark, 4 days, 298 K.

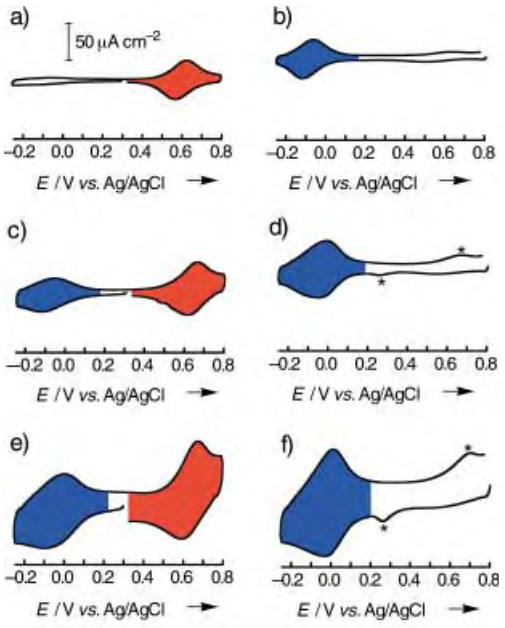


Figure 2. Cyclic voltammograms, recorded in an aqueous solution of 0.1 M $HClO_4$, of monolayers and multilayers sequentially prepared on an Au electrode: a) CO-terminated monolayers; b) water-terminated monolayers; c) CO-terminated bilayers d) water-terminated bilayers; e) CO-terminated trilayers; f) water-terminated trilayers. Red and blue waves correspond to redox couples from the Ru_3 cores with CO and those without CO, respectively. Scan rate = 0.5 $V s^{-1}$.

Cyclic voltammetry was used to follow the multilayer-formation processes. As the redox potentials are substantially different between the "CO-bound" and "CO-free" cluster molecules,[7,8] the surface species were quantitatively evaluated by cyclic voltammetry. A series of cyclic voltammograms (CVs) obtained for the monolayers, bilayers, and trilayers with and without CO, which were sequentially prepared on an Au electrode are depicted in Figure 2a–f. As established previously,[11] the close packed CO-terminated monolayers (the surface coverage $\Gamma = 1.4 \times 10^{-10}$ mol cm^{-2}) result in a $Ru^{II/III}$ couple at the half-wave potential ($E_{1/2}$) of +0.59 V versus Ag/AgCl in contact with an aqueous solution of 0.1 M $HClO_4$ (Figure 2a, red wave). This couple is ascribed to the site at which CO is bonded. When electrolysis is conducted at +0.80 V so that the Ru^{III} redox state is generated, CO dissociation proceeds from the monolayer which gives rise to a redox couple at $E_{1/2} = -0.09$ V (Figure 2b, blue wave). The CO-terminated bilayers (Figure 2c) show a redox wave at $E_{1/2} = +0.64$ V ($\Gamma = 2.0 \times 10^{-10}$ mol cm^{-2}) from **1** coordinatively introduced as a second layer.[15] Complex **1** dissolved in 0.1 M $(C_4H_9)_4NPF_6$-CH_3CN exhibits a reversible redox wave at +0.68 V. An additional wave observed at $E_{1/2} = -0.09$ V ($\Gamma = 1.1 \times 10^{-10}$ mol cm^{-2}) is ascribed to the $Ru^{II}Ru^{III}_2/Ru^{III}_3$ process arising from the underlayer, which is free from CO.[11] Upon subsequent electrolysis (+0.80 V), the CV (Figure 2d) shows evidence of losing CO from the top layer. The increase in charge and the presence of two waves (shaded waves in Figure 2c and d) accompanied with an electrochemical release of CO, provides evidence of clean ligand transformation while maintaining the structural integrity at the surface. It should be noted that unlike CO-free multilayers, the CO-terminated multilayers completely block the coordination of **1** under identical conditions. The CO dissociation from the monolayer and multilayers all obey first-order kinetics with rate constants similar to each other, ranging from 1.2×10^{-2} s^{-1} for the monolayer to 2.0–7.2 × 10^{-2} s^{-1} for the multilayers at 298 K.[16] The negligible

 © 2003 Wiley-VCH Verlag GmbH & Co. KGaA, Weinheim

dependence of the CO-dissociation character on the multilayer generation is important in effectively extending the nanostructures on surfaces.

Figure 3 shows a plot of charge (Q) from the CVs of the water-terminated mono- and multilayers against the number of layers (n). The linear correlation with the slope $Q/n = 1.4 \times 10^{-10}$ mol cm^{-2}, which is consistent with the monolayer coverage used here, is in full accordance with the picture of quantitative generation of multilayers. Each molecular backbone, in principle, is flexible with respect to the rotation around the Ru–N coordination bonds to form the disordered morphology of the film. On the basis of the quantitative-growth feature observed here, however, we rationalize that this effect is minimized because of extensive lateral interactions as a result of the close-packed molecular assembly present in this case.

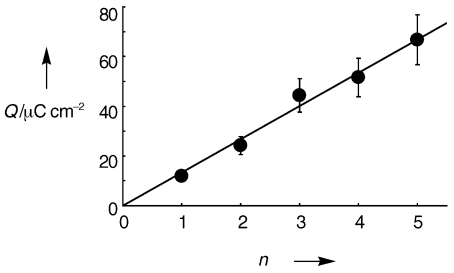


Figure 3. A linear correlation of charge (Q), obtained from the redox wave around −0.1 V, against the number of layers (n) for the series of water-terminated monolayer ($n = 1$) and multilayers ($n = 2$–5).

Fourier transform infrared reflection absorption (FTIRRA) spectroscopy measurements further support the quantitative generation of the molecular multilayers.[17] For the CO-terminated multilayers, the acetate band intensities along with aromatic ring vibration bands arising from bpy ligands (1700–1500 cm^{-1}) increase as the deposition cycle of **1**[18] is increased, while the intensity of the ν(CO) band remains virtually constant (see Supporting Information). The band area was used to evaluate the multilayer growth. We find that the relative intensity ratio $I\{\nu_s(COO)\}/I\{\nu(CO)\}$ linearly increases as the deposition cycle is increased (Figure S1).[19] If we assume that the infrared intensity is not significantly affected by the distance between the surface-confined molecular units and the surface, the trend observed in this case does illustrate the quantitative growth character of our system. Further characterizations, including ellipsometric measurements, are now in progress.

The electron transport behavior of the pentalayer without the top CO is shown in Figure 4. A series of CVs recorded at varying scan rates involve a single redox process ($E_{1/2} = +0.01$ V), which is ascribed to the (0/+1) redox change for each Ru_3 unit, corresponding to the (0/+5) redox change for the entire molecule; ClO_4^- anions balance the charge during the redox cycle.[20] It appears that anodic and cathodic current intensities linearly increase with the increase of scan rates, consistent with the feature of surface-confined redox centers.[21] The separation between the anodic and cathodic peak potentials (ΔE_p) for the pentalayer (0.03 V) is quite small (Figure 4), thus indicating that the electron transport across the large distance molecular wires is substantially facile, because of a significant degree of electronic conjugation between the cluster units through bpy. The rather broad redox wave (full-width at half-maximum, $\Delta E_{1/2} = 0.21$ V) may be attributed to significant lateral interactions and/or the presence of electronic communications between linked Ru_3 cluster cores through bpy. We note that multiple redox cycling for the series of CO-free multilayers does not alter the redox response, and they are stable for days in aqueous electrolyte solution and under atmospheric conditions.

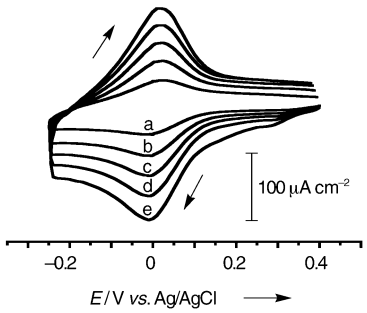


Figure 4. Scan rate dependence of redox waves for the water-terminated pentalayer. Scan rate: a = 0.1, b = 0.2, c = 0.3, d = 0.4, and e = 0.5 V s^{-1}.

In conclusion, we present herein a new method to prepare molecular multilayers with high redox activity, in which layer-by-layer nanostructural growth is controlled by the electrode potential applied. Since our approach can be applied, in principle, to other redox molecules, it will open significant possibilities for the design of new 3D molecular architectures on surfaces, which will be of considerable use in molecular electronics and electrocatalysts.

Experimental Section

Electrochemistry and FTIRRA spectroscopy: Cyclic voltammetry and electrolysis experiments were performed by using Hokuto Denko HA-301 electrochemical systems with an Au(111) electrode ($S = 0.082$ cm^2) covered with monolayers or multilayers as a working electrode, a Pt coil as a counter electrode, and an Ag/AgCl (saturated NaCl) as a reference electrode. An aqueous solution of 0.1 M $HClO_4$ was used as an electrolyte. FTIRRA spectra of monolayers and multilayers were recorded at 298 K in dry air on a Bio-Rad FTS-60A/896 spectrometer equipped with an MCT detector and a Harrick grazing angle reflection accessory.[22] The samples for FTIRRA measurements were prepared on an evaporated Au substrate (thickness, ~200 nm) developed on a Ti-coated (~20 nm) glass plate.

Multilayer preparation procedures: Preparation of CO-terminated monolayers on an Au(111) electrode (Figure 1a) and subsequent conversion to water-terminated monolayers (Figure 1b; step 1) were reported previously.[11] To form bpy-linked CO-terminated bilayers (Figure 1c), the Au electrode covered with the water-terminated monolayer was immersed into an aqueous solution of **1** (0.2 mM, prepared just before use) in the dark at 298 K without potential control (step 2). After four days, it was removed from the solution and rinsed copiously with Milli-Q water. The bilayer formation on the Au electrode was then confirmed by recording CV (only a single cycle) in contact with 0.1 M $HClO_4$ at 0.5 V s^{-1} in the potential range between +0.80 and −0.25 V and scanning from

 © 2003 Wiley-VCH Verlag GmbH & Co. KGaA, Weinheim

+0.30 V (rest potential to the negative direction). To form water-bound bilayers (Figure 1d), the electrode potential was held at +0.80 V, while keeping the same electrochemical setup in which the oxidation state $\{Ru^{III}Ru^{III}(Ru^{III}\text{-}CO)\}$ was generated (step 1). During the electrolysis experiment, CVs were recorded at certain time intervals (10–300 s), as in the case of monolayers,[11] to monitor the CO dissociation process; complete ligand transformation (step 1) typically required 45 min of electrolysis. Alternate procedures were continued to extend the multilayer generation.

Received: March 5, 2003 [Z51334]

Keywords: cluster compounds · electron transport · multilayers · nanotechnology · surface chemistry

[1] *Interfacial Electrochemistry: Theory, Experiment, and Applications* (Ed.: A. Wieckowski), Marcel Dekker, New York, **1999**.

[2] a) A. N. Shipway, E. Katz, I. Willner, *ChemPhysChem* **2000**, *1*, 18; b) A. Hatzor, T. Moav, H. Cohen, S. Matlis, J. Libman, A. Vaskevich, A. Shanzer, I. Rubinstein, *J. Am. Chem. Soc.* **1998**, *120*, 13469; c) D. L. Thomsen III, T. Phely-Bobin, F. Papadimitrakopoulos, *J. Am. Chem. Soc.* **1998**, *120*, 6177; d) V. Huc, J. P. Bourgoin, C. Bureau, F. Valin, G. Zalczer, S. Palacin, *J. Phys. Chem. B* **1999**, *103*, 10489; e) S. B. Bakiamoh, G. J. Blanchard, *Langmuir* **1999**, *15*, 6379; f) V. Huc, F. Armand, J. P. Bourgoin, S. Palacin, *Langmuir* **2001**, *17*, 1928.

[3] a) D. M. Kolb, *Angew. Chem.* **2001**, *113*, 1198; *Angew. Chem. Int. Ed.* **2001**, *40*, 1162; b) T. L. Wade, T. A. Sorenson, J. L. Stickney, *Interfacial Electrochemistry: Theory, Experiment, and Applications* (Ed.: A. Wieckowski), Marcel Dekker, New York, **1999**, p. 757.

[4] a) K. Itaya, *Prog. Surf. Sci.* **1998**, *58*, 121; b) Y. He, T. Ye, E. Borguet, *J. Am. Chem. Soc.* **2002**, *124*, 11964.

[5] For selected references on multilayers prepared from metal complexes, see: a) M. Maskus, H. D. Abruña, *Langmuir* **1996**, *12*, 4455; b) D. A. Offord, S. B. Sachs, M. S. Ennis, T. A. Eberspacher, J. H. Griffin, C. E. D. Chidsey, J. P. Collman, *J. Am. Chem. Soc.* **1998**, *120*, 4478; c) S. Bharathi, M. Nogami, S. Ikeda, *Langmuir* **2001**, *17*, 7468; d) C. Lin, C. R. Kagan, *J. Am. Chem. Soc.* **2003**, *125*, 336.

[6] Complex **1** was prepared by the method similar to that of $[Ru_3(\mu_3\text{-}O)(\mu\text{-}CH_3COO)_6(CO)(py)_2]$ (py = pyridine)[8] by using bpy instead of py. Synthetic details and full characterization data are provided in Supporting Information.

[7] a) S. Ye, H. Akutagawa, K. Uosaki, Y. Sasaki, *Inorg. Chem.* **1995**, *34*, 4527; b) M. Abe, Y. Sasaki, Y. Yamada, K. Tsukahara, S. Yano, T. Yamaguchi, M. Tominaga, I. Taniguchi, T. Ito, *Inorg. Chem.* **1996**, *35*, 6724.

[8] J. A. Baumann, D. J. Salmon, S. T. Wilson, T. J. Meyer, W. E. Hatfield, *Inorg. Chem.* **1978**, *17*, 3342.

[9] M. Abe, Y. Sasaki, A. Nagasawa, T. Ito, *Bull. Chem. Soc. Jpn.* **1992**, *65*, 1411.

[10] a) K. Uosaki, S. Ye, T. Kondo, *J. Phys. Chem.* **1995**, *99*, 14117; b) T. Kondo, S. Horiuchi, I. Yagi, S. Ye, K. Uosaki, *J. Am. Chem. Soc.* **1999**, *121*, 391.

[11] A. Sato, M. Abe, T. Inomata, T. Kondo, S. Ye, K. Uosaki, Y. Sasaki, *Phys. Chem. Chem. Phys.* **2001**, *3*, 3420.

[12] H. E. Toma, K. Araki, A. D. P. Alexiou, S. Nikolaou, S. Dovidauskas, *Coord. Chem. Rev.* **2001**, *219–221*, 187.

[13] a) T. Ito, T. Hamaguchi, H. Nagino, T. Yamaguchi, J. Washington, C. P. Kubiak, *Science* **1997**, *277*, 660; b) T. Yamaguchi, N. Imai, T. Ito, C. P. Kubiak, *Bull. Chem. Soc. Jpn.* **2000**, *73*, 1205; c) C. H. Londergan, J. C. Salsman, S. Ronco, L. M. Dolkas, C. P. Kubiak, *J. Am. Chem. Soc.* **2002**, *124*, 6236.

[14] a) J. A. Baumann, S. T. Wilson, D. J. Salmon, P. L. Hood, T. J. Meyer, *J. Am. Chem. Soc.* **1979**, *101*, 2916; b) H. Kido, H. Nagino, T. Ito, *Chem. Lett.* **1996**, 745.

[15] A larger amount of charge of the CO-bound cluster relative to the CO-free cluster (here the 1:1 stoichiometry is expected) arises from physical adsorption of **1**, which was not removed from the surface by rinsing with water. This situation is also encountered for the following CO-terminated multilayers.

[16] The kinetic aspect of the CO dissociation from the multilayers will be detailed in our future publication.

[17] The CO-terminated monolayer (prepared on an evaporated Au substrate) shows a ν(CO) band at 1948(s) cm^{-1}, ν_{as}(COO) bands at 1613(s) and 1574(m) cm^{-1}, and ν_s(COO) band at 1431(s) cm^{-1}. All these infrared spectroscopic features are similar to the triruthenium derivatives[23a] as well as their monolayers prepared on Au.[23b] Upon electrolysis, the intensity of the ν(CO) band decreases significantly.

[18] Selected IR data of **1** (KBr pellet): 1942(s) [ν(CO)], 1609(s) and 1568(m) [ν_{as}(COO)], and 1420(s) cm^{-1} [ν_s(COO)].

[19] The relative intensity ratio of the two peaks is examined rather than their absolute intensity, because desorption of Au from the Au substrate surface was apparent during the immersion process for deposition, which directly affects the intensity of the infrared band.

[20] We confirm that by using the trilayer without CO the replacement of the electrolyte solution from 0.1 M $HClO_4$ to 0.1 M H_2SO_4 results in a positive shift of $E_{1/2}$ by 0.05 V.

[21] A. J. Bard, L. R. Faulkner, *Electrochemical Methods: Fundamentals and Applications*, 2nd ed., Wiley, New York, **2001**.

[22] A. Miki, S. Ye, M. Osawa, *Chem. Commun.* **2002**, 1500.

[23] a) A. Ohto, A. Tokiwa-Yamamoto, M. Abe, T. Ito, Y. Sasaki, K. Umakoshi, R. D. Cannon, *Chem. Lett.* **1995**, 97; b) M. Abe, S. Ye, T. Kondo, K. Uosaki, Y. Sasaki, *Electrochemistry* **1999**, *67*, 1162.

 © 2003 Wiley-VCH Verlag GmbH & Co. KGaA, Weinheim

Cover Picture

Michael Ruck,* Vitaly Dubenskyy, and Tilo Söhnel



Endohedral clusters are more common in chemistry than expected, such as the inclusion compounds of fullerene (e.g., $He@C_{60}$, left) and the recently discovered $W@Au_{12}$ icosahedron (right). In the Communication by M. Ruck et al. on page 2978 ff., the $Pd@[Bi_{10}]^{4+}$ polycation (above) is presented, which has a pentagonal antiprismatic structure, a semiregular polyhedron first described by Archimedes. The relative weakness of the interaction between the Pd center and the *arachno*-$[Bi_{10}]^{4+}$ unit is discussed.

Contents

Angewandte EarlyView

The following articles are available online (in Wiley Interscience). You can find them at www.angewandte.org under Full text, Forthcoming articles.

R. R. Davda, J. A. Dumesic:*
Catalytic Reforming of Oxygenated Hydrocarbons for Hydrogen with Low Levels of Carbon Monoxide
DOI: 10.1002/anie.200351664
Published online: June 18, 2003

C. J. Matthews, S. T. Onions, G. Morata, L. J. Davis, S. L. Heath, D. J. Price:*
A Self-Assembled Tetracopper Triple-Stranded Helicate: Towards the Controlled Synthesis of Finite One-Dimensional Magnetic Chains
DOI: 10.1002/anie.200251634
Published online: June 23, 2003

Articles judged by the referees or the editior as being either very important or very urgent are immediately edited, proof-read, and electronically published once the manuscript has arrived in the editiorial office in final form. As long as there is no page number available these articles should be cited in the following manner:

Author(s) *Angew. Chem. Int. Ed.*, online publication date, DOI.

Obituary

Günther Otto Schenk (1913–2003) — **2932–2933** — A Pioneer of Radiation Chemistry — *K. Schaffner*

Books

Mapping the Spectrum — **2934** — Klaus Hentschel — *reviewed by C. Reinhardt*

Broadening Electrochemical Horizons — **2934** — Alan M. Bond — *reviewed by R. Holze*

Solvent Mixtures — **2935** — Yizhak Marcus — *reviewed by J. Catalán*

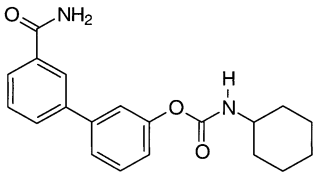
Highlights

Cannabinoid-Receptor Agonists

M. Wendeler, T. Kolter* — **2938–2941**

Inhibitors of Endocannabinoid Degradation: Potential Therapeutics for Neurological Disorders

Joint benefits: Selective inhibitors of endocannabinoid degradation have been developed, among them the shown carbamate, which exhibit anxiolytic and analgesic properties in laboratory animals.

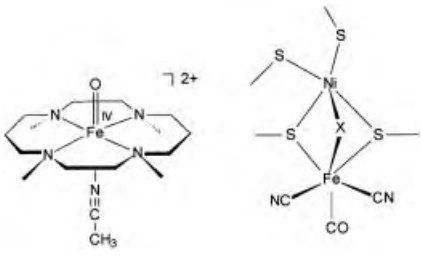


Biological Role of Iron Complexes

L. D. Slep, F. Neese* — **2942–2945**

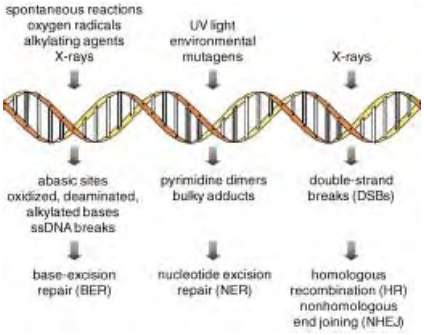
Bioinorganic Reaction Mechanisms: From High-Valent Iron to Bioorganometallic Chemistry

Important aspects of the mechanisms of fundamental bioinorganic reactions have been revealed in recent studies, which have shed light on the structure and properties of high-valent nonheme Fe centers (left structure) as well as on the biosynthetic formation of the Fe–CN bond in Ni–Fe hydrogenases (right).



Reviews

First aid: Several pathways for DNA repair protect the genome from internal and external damaging agents and conditions. Our current understanding of the more important mechanisms is discussed, with an emphasis on the molecular basis of damage recognition/repair and on chemical approaches that have been used to study these processes.



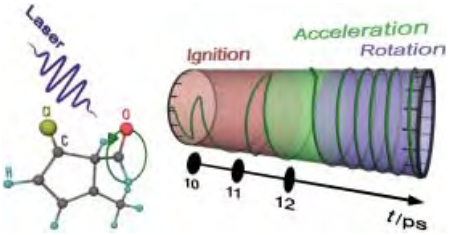
Mechanisms of DNA Repair

O. D. Schärer* ——— **2946 – 2974**

Chemistry and Biology of DNA Repair

Communications

A turn for the better? The unidirectional rotation of chiral molecular motors, driven by a nonhelical laser pulse, can be explained by both quantum and classical mechanical calculations. The aldehyde group of the molecule is the rotor engine. The motor dynamics consists of three regimes: ignition, acceleration, and rotation. The results serve as a guiding principle for the control of molecular motors, such as braking and gears, by using pulsed lasers.

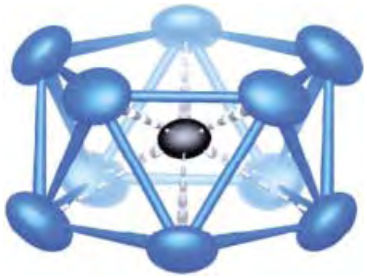


Molecular Motors

K. Hoki, M. Yamaki,
Y. Fujimura* ——— **2976 – 2978**

Chiral Molecular Motors Driven by a Nonhelical Laser Pulse

$Pd@[Bi_{10}]^{4+}$ is the appropriate representation of the first heteronuclear polycation of bismuth and a transition element. The pentagonal Archimedean antiprism $[PdBi_{10}]^{4+}$ (see picture) is a transition-metal-containing variant of the predicted *arachno*-cluster $[Bi_{10}]^{4+}$, in which there are almost no observed host–guest interactions.

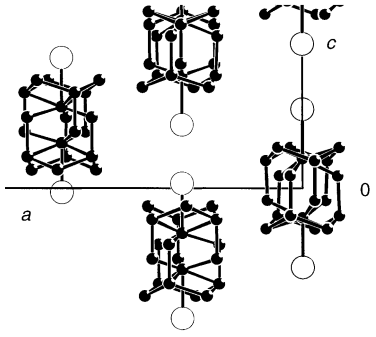


Pd/Bi Polycationic Clusters

M. Ruck,* V. Dubenskyy,
T. Söhnel ——— **2978 – 2982**

Structure and Bonding of $Pd@[Bi_{10}]^{4+}$ in the Subbromide $Bi_{14}PdBr_{16}$

A new molecular material—the 1-bromoadamantane/thiourea inclusion compound (the guest substructure of which is depicted)—has been designed as a dichroic filter for X-ray polarization analysis, based on theoretical predictions of the required structural characteristics. Measurements of X-ray linear dichroism show that this material exhibits essentially optimal performance in such applications.



Filter for X-ray Polarization Analysis

M.-H. Chao, B. M. Kariuki,
K. D. M. Harris,* S. P. Collins,
D. Laundy ——— **2982 – 2985**

Design of a Solid Inclusion Compound with Optimal Properties as a Linear Dichroic Filter for X-ray Polarization Analysis

For the USA and Canada:
ANGEWANDTE CHEMIE International Edition (ISSN 1433-7851) is published weekly by Wiley-VCH PO Box 191161, D 69451 Weinheim, Germany. Air freight and mailing in the USA by Publications Expediting Inc. 200 Meacham Ave., Elmont, NY 11003. Periodicals postage paid at Jamaica NY 11431. US POSTMASTER: send address changes to *Angewandte Chemie*, Wiley-VCH, 111 River Street, Hoboken, NJ 07030. Annual institutional subscription price for institutions: Europe € 2998.00/3148.00. Outside Europe US$ 3718.00/3904.00 (valid for print or electronic/print and electronic delivery); for individuals who are personal members of a national chemical society, or whose institution already subscribes, or who are retired or self-employed consultants, print only (including postage and handling charges): Europe € 248.00/Outside Europe US$ 348.00.

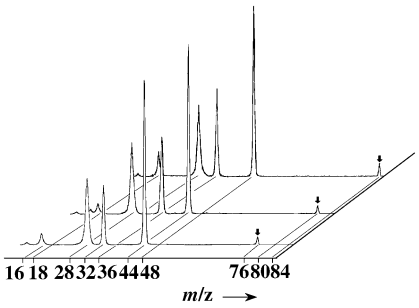
 © 2003 Wiley-VCH Verlag GmbH & Co. KGaA, Weinheim

Contents

CO_4: An MS and Theoretical Study

F. Cacace,* G. de Petris,* M. Rosi, A. Troiani ——— **2985 – 2990**

Carbon Tetraoxide: Theoretically Predicted and Experimentally Detected



CO_4, the proof: Although theoretically predicted to be detectable, CO_4 has proved so far experimentally elusive. We report its discovery as a result of a mass spectrometric and theoretical study showing that CO_4 does exist as a metastable molecule in the gas phase, with a lifetime = 1 μs (see picture showing the neutralization–reionization MS of CO_4^+ with arrows indicating the recovery peaks).

Methane Sulfonation

S. Mukhopadhyay, A. T. Bell* ——— **2990 – 2993**

A High-Yield Approach to the Sulfonation of Methane to Methanesulfonic Acid Initiated by H_2O_2 and a Metal Chloride

$$CH_4 + SO_3 \xrightarrow[\text{MCl, 65–75°C, 3 h}]{\text{urea/}H_2O_2,\ H_2SO_4} CH_3SO_3H \quad (1)$$

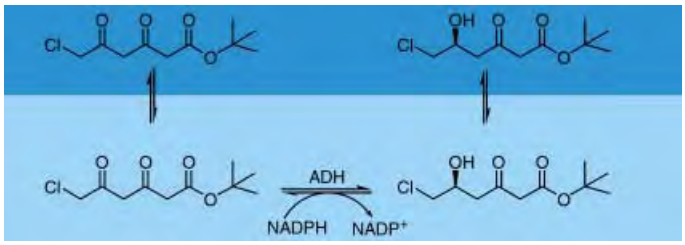
CH_4 conv., 36%
sel. to MSA, 99%

Low temperatures and low pressures suffice for the sulfonation of methane with a suitable free-radical initiator and promoter [Eq. (1)]. Since the $RhCl_3$ promoter can be recycled, and the initiator complex is stable and easy to handle, development of this reaction into an industrial process is promising. MSA = methanesulfonic acid.

Biphasic Enzyme-Catalyzed Reactions

M. Villela Filho, T. Stillger, M. Müller, A. Liese, C. Wandrey* ——— **2993 – 2996**

Is log *P* a Convenient Criterion to Guide the Choice of Solvents for Biphasic Enzymatic Reactions?

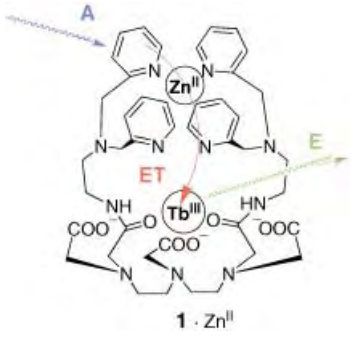


It depends on the choice. The conciliation of the high chemo- and enantioselectivity of the alcohol dehydrogenase(ADH)-catalyzed reduction of ketones and the poor water solubility of substrates can be achieved in aqueous–organic biphasic systems (see picture). But how should the organic phase be chosen?

Zn Sensitive Luminescent Sensors

K. Hanaoka, K. Kikuchi, H. Kojima, Y. Urano, T. Nagano* ——— **2996 – 2999**

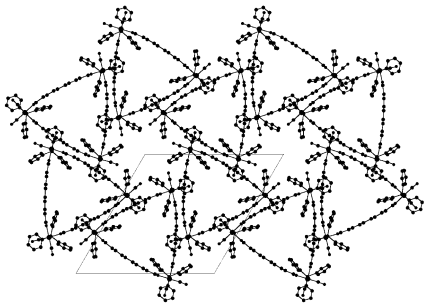
Selective Detection of Zinc Ions with Novel Luminescent Lanthanide Probes



A remarkable enhancement of luminescence is observed in a solution of the Tb^{III} complex **1** upon adding Zn^{II} ions (see picture). Complex **1** has a high selectivity for Zn^{II} and a long luminescence lifetime of the order of milliseconds, thus is an excellent lead compound for the development of Zn^{II}-sensitive luminescent chemosensors with long luminescence lifetimes. A = light absorption, ET = energy transfer, E = light emission.

 © 2003 Wiley-VCH Verlag GmbH & Co. KGaA, Weinheim

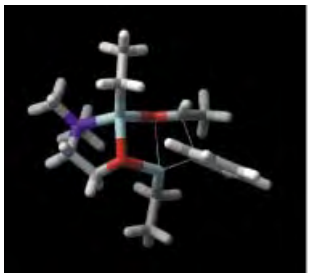
Letting out the guests: The hexagonal closest packing of discrete triangular-tube-shaped organometallic supermolecules of eclipsed-$[\{Ru_2(CO)_4(PPh_3)_2\}(\mu\text{-}4,4'\text{-}O_2CC_6H_4C_6H_4CO_2)]_3$ in the solid state (see picture) permits the production of a microporous material that is not only thermally stable up to 181 °C, but also allows diffusion at room temperature of molecular guests without the framework collapsing.

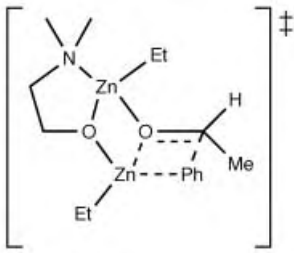


Ru_6 Triangular Molecular Assembly

K.-B. Shiu,* H.-C. Lee, G.-H. Lee, B.-T. Ko, Y. Wang, C.-C. Lin ——— **2999 – 3001**

Solid-State Supramolecular Organization of Supermolecules into a Truly Molecular Zeolite





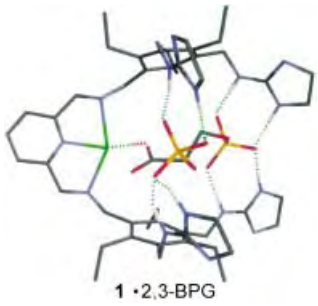
Organozinc Additions: A DFT Study

J. Rudolph, T. Rasmussen, C. Bolm, P.-O. Norrby* ——— **3002 – 3005**

Phenyl versus Ethyl Transfer in the Addition of Organozinc Reagents to Aldehydes: A Theoretical Study

The dramatic improvement in diphenylzinc addition to aldehydes that is obtained by adding diethylzinc was investigated by DFT methods. The strong preference for phenyl over ethyl transfer can be understood in terms of overlap with the phenyl π system in the transition state (see picture). Reasons for the high *ee* value in the presence of Et_2Zn are discussed.

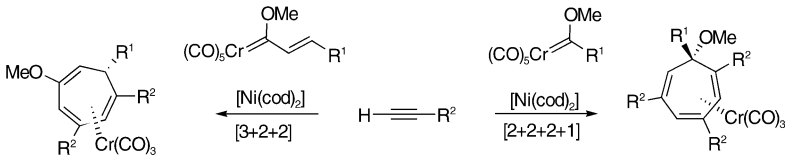
A designed synthetic receptor (**1**), which has guanidinium groups and a Cu^{II} center, is highly effective and selective for binding 2,3-bisphosphoglycerate (2,3-BPG) in physiological media (see picture). The affinity is high enough that the receptor can deprive hemoglobin of available 2,3-BPG, and thus control the active level of 2,3-BPG and the related oxygenation level of hemoglobin. Cu = Green, N = blue, C = gray, P = yellow, O = red.



Receptor for Biological Biphosphate

Z. Zhong, E. V. Anslyn* ——— **3005 – 3008**

Controlling the Oxygenation Level of Hemoglobin by Using a Synthetic Receptor for 2,3-Bisphosphoglycerate



Fischer Carbene Cyclizations

J. Barluenga,* P. Barrio, L. A. López, M. Tomás, S. García-Granda, C. Alvarez-Rúa ——— **3008 – 3011**

Nickel(0)-Mediated [3+2+2] and [2+2+2+1] Cyclization Reactions of Chromium Fischer Carbene Complexes and Alkynes

Dramatic changes in Fischer carbene reactivity occur in the presence of $[Ni(cod)_2]$. Thus, instead of Dötz [3+2+1] benzannulation giving substituted phenols, alkenyl carbene complexes incorporate two equivalents of alkyne in a [3+2+2] cyclization, while simple chromium carbene complexes undergo a [2+2+2+1] cyclization (see scheme). These cyclizations are regio- and diastereoselective.
cod = 1,5-cyclooctadiene.

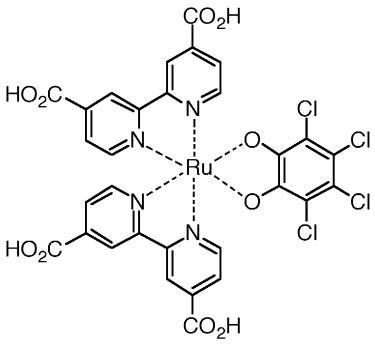
 © 2003 Wiley-VCH Verlag GmbH & Co. KGaA, Weinheim

Contents

Near-Infrared Electrochromic Window

J. García-Cañadas, A. P. Meacham, L. M. Peter,* M. D. Ward* — **3011 – 3014**

A Near-Infrared Electrochromic Window Based on an Sb-Doped SnO_2 Electrode Modified with a Ru–Dioxolene Complex



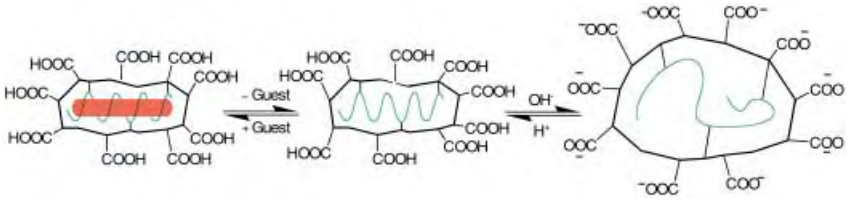
1

A window of opportunity: The ligand-centred redox activity of complex **1** (depicted) is exploited to make an electrochromic window, which demonstrates rapid and reversible changes in optical transmission at 940 nm. The window is made by adsorbing **1** onto a nanocrystalline Sb-doped SnO_2 film attached to a transparent conducting substrate and cycling the applied potential through the catecholate/semiquinone redox couple.

Molecularly Imprinted Polymers

Y. Kanekiyo, R. Naganawa, H. Tao* — **3014 – 3016**

pH-Responsive Molecularly Imprinted Polymers

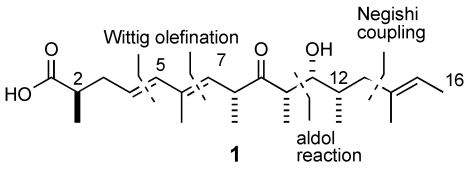


The molecular-recognition ability of molecularly imprinted polymers (MIPs) changes in response to solution acidity (see scheme). The MIPs are created by the copolymerization of an acryloylamylose-template inclusion complex with acrylic acid.

Total Synthesis

I. R. Corrêa, Jr., R. A. Pilli* — **3017 – 3020**

Total Synthesis and Structural Elucidation of (−)-Delactonmycin



1

The key steps in the total synthesis of delactonmycin (**1**) involved a Wittig olefination, a Negishi coupling, and an aldol reaction. The polyketide, which was isolated from *Streptomyces* sp., displays potent inhibitory activity of the nucleocytoplasmic translocation of the HIV-1 regulatory protein Rev.

Self-Assembling Peptide Fibers

M. G. Ryadnov, D. N. Woolfson* — **3021 – 3023**

Introducing Branches into a Self-Assembling Peptide Fiber



The special branch: The design of novel T-shaped peptides that coassemble with linear peptides to produce branched fibers is described (see picture). The bottom-up assembly of peptide-based nanostructures of this type holds promise for the development of novel scaffolds for applications in nanobiotechnology.

 © 2003 Wiley-VCH Verlag GmbH & Co. KGaA, Weinheim



Pole-to-pole: Cyclopropanediesters when treated with nitrones in the presence of catalytic ytterbium triflate undergo a dipolar homo [3+2] cycloaddition to form tetrahydro-1,2-oxazines diastereoselectively (see scheme). This new process has been used in a two-step preparation of the tricyclic core of FR-900482.

1,3-Dipolar Cycloadditions

I. S. Young, M. A. Kerr* ____ **3023 – 3026**

A Homo [3+2] Dipolar Cycloaddition: The Reaction of Nitrones with Cyclopropanes

---

Magic bubbles: ZnSe semiconductor microspheres aggregated from nanocrystals of tunable size have been successfully synthesized for the first time by use of gas bubbles. Based on the interior nanocrystal size and structure, the as-obtained samples exhibit different colors.

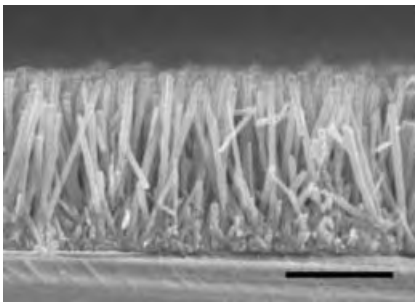


Tunable Semiconductor Microspheres

Q. Peng, Y. Dong, Y. Li* ____ **3027 – 3030**

ZnSe Semiconductor Hollow Microspheres

Homogeneous and dense arrays of ZnO nanowires were synthesized on silicon wafers (and many other substrates) using a mild solution process at 90 °C. Uniform ZnO nanocrystals were deposited to act as seeds for subsequent hydrothermal nanowire growth, which yielded single-crystalline ZnO nanowires grown along the [0001] direction and oriented perpendicular to the wafer surface (see picture; scale bar = 1 μm). The photoluminescence and lasing behavior of the arrays has been studied as a function of annealing treatment conditions.

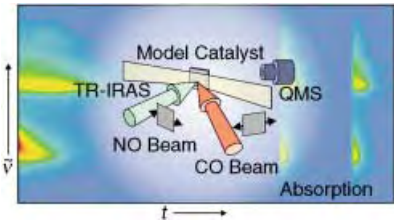


Zinc Oxide Nanowires

L. E. Greene, M. Law, J. Goldberger, F. Kim, J. C. Johnson, Y. Zhang, R. J. Saykally, P. Yang* ____ **3031 – 3034**

Low-Temperature Wafer-Scale Production of ZnO Nanowire Arrays

---



On the edge? The distribution of reactants and products over regular and edge sites of well-shaped palladium nanocrystallites is monitored during catalytic NO decomposition by using a combination of molecular beam techniques and in situ vibrational spectroscopy (see scheme, TR-IRAS = time-resolved IR reflection absorption spectroscopy, QMS = quadrupole mass spectrometer). Atomic nitrogen and oxygen species preferentially occupy edge sites on the catalyst particles. The presence of these co-adsorbates controls the NO dissociation activity.

NO Dissociation on Surfaces

V. Johánek, S. Schauermann, M. Laurin, J. Libuda,* H.-J. Freund ____ **3035 – 3038**

Site Occupation and Activity of Catalyst Nanoparticles Monitored by In Situ Vibrational Spectroscopy

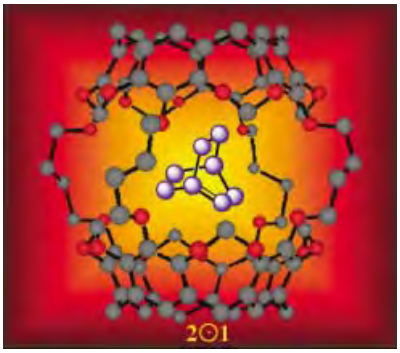
 © 2003 Wiley-VCH Verlag GmbH & Co. KGaA, Weinheim

Contents

anti-Bredt Bridgehead Olefin

P. Roach, R. Warmuth* ____ **3039 – 3042**

The Room-Temperature Stabilization of Bicyclo[2.2.2]oct-1-ene and Bicyclo[3.2.1]oct-1-ene

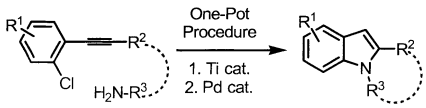


Retardation through incarceration: The highly strained anti-Bredt bridgehead olefin bicyclo[2.2.2]oct-1-ene (**1**) is remarkably stable at 60 °C, if generated photochemically inside the hemicarcerand **2** (see picture). The surrounding host not only prevents the dimerization of **1**, but also retards strongly its intramolecular retro-Diels–Alder reaction by several orders of magnitude.

Catalytic Indol Synthesis

H. Siebeneicher, I. Bytschkov, S. Doye* ____ **3042 – 3044**

A Flexible and Catalytic One-Pot Procedure for the Synthesis of Indoles



One pot, two bonds, three rings: A clever combination of a [Cp_2TiMe_2]-catalyzed hydroamination of alkynes with a Pd-catalyzed N-arylation of imines results in a new and general method for the synthesis of indoles. Impressively, two new C–N bonds are formed during the one-pot procedure (see scheme).

Communications labeled with this symbol have been judged by two referees as being "very important papers".

The publication of Communications labeled with this symbol has been accelerated because of their topical or highly competitive nature.

Sources

Product and Company Directory

You can start the entry for your company in "Sources" in any issue of *Angewandte Chemie*.

If you would like more information, please do not hesitate to contact us.

Wiley-VCH Verlag – Advertising Department
Tel.: 0 62 01 - 60 65 65
Fax: 0 62 01 - 60 65 50
E-Mail: MSchulz@wiley-vch.de

Service

Keywords ____ **3046**

Authors ____ **3047**

Angewandte's Sister Journals ____ **3048 – 3049**

Vacancies ____ **3045**

Preview ____ **3051**

Apology

In the Communication "Direct Liquid-Phase Sulfonation of Methane to Methanesulfonic Acid by SO_3 in the Presence of a Metal Peroxide" by S. Mukhopadhyay and A. T. Bell (*Angew. Chem.* **2003**, *115*, 1049 – 1051; *Angew. Chem. Int. Ed.* **2003**, *42*, 1019 – 1021), the authors missed a cross-reference to their thematically related but independent Communication "Direct Sulfonation of Methane to Methanesulfonic Acid with SO_2 Using Ca Salts as Promoters" (S. Mukhopadhyay und A. T. Bell, *J. Am. Chem. Soc.* **2003**, *125*, 4406 – 4407), and vice versa. The authors apologize for the oversight.

Günther Otto Schenck (1913–2003): A Pioneer of Radiation Chemistry

Günther O. Schenck died on March 25, 2003, in Mülheim an der Ruhr, shortly before his 90th birthday. As a spontaneous response to the sad news, I received numerous expressions in appreciation of Schenck as a scientist, notably also from younger colleagues, who as striving young scientists often used to argue emphatically against Schenck's "Strahlenchemie" (radiation chemistry), particularly when issues such as triplet versus Schenck mechanisms of photosensitization were under debate. Let me cite just three: Samir Farid (Eastman Kodak, Rochester, USA), a former Ph.D. student in Mülheim, wrote: "Schenck will be remembered as a man who influenced the field of photochemistry at a critical time. We owe him a lot of gratitude." Angelo A. Lamola and Nicholas J. Turro, both students of George S. Hammond, one of Schenck's prominent rivals in photochemistry, also expressed their respect. Lamola: "I feel sad because it marks, perhaps, the start of the passing of a great moment in the history of chemistry. … In my discussions and arguments with him, I admired his brilliance and tenacity, and he taught me the value of suspending conclusions while there are possibilities to think about." Finally, Turro: "He was quite a guy!" And this from someone who 30 years ago wrote, "Typically, he has addressed central problems in important areas years before other chemists 'saw the light' and then made use of his anticipative thinking."



Günther O. Schenck

These words refer to the Founding Director (1958) of the "Selbständige Abteilung für Strahlenchemie im Max-Planck-Institut für Kohlenforschung" (Autonomous Department of Radiation Chemistry at the Max Planck Institute of Coal Research) in Mülheim an der Ruhr (Germany), later (1981) to become the Max-Planck-Institut für Strahlenchemie, a center which was soon to be recognized worldwide as a leading multidisciplinary institution in its field, and which was to set standards for Europe. For a rapidly expanding community of photochemists and radiation chemists worldwide, Schenck's "Strahlenchemie" and Mülheim soon became geographical synonyms.

Who was Günther O. Schenck? Born on May 14, 1913, in Lörrach (Germany, just across the border from Basel), he obtained his secondary school diploma (Abitur) in 1932 in Heidelberg. After a short interlude as an apprentice in precision mechanics in Mannheim, he started studying physics at the University of Heidelberg, and subsequently changed to chemistry and physiology. As a chemistry undergraduate and student of Ernst Müller in inorganic chemistry at Freudenberg's institute, he met Hans Kautsky, who taught inorganic chemistry, and who enjoyed discussing his fascinating ideas on luminescence, photosensitized reactions with oxygen, and complex formation of excited states with the young and enthusiastic student. In this period, Schenck also had his first opportunity to meet Karl Ziegler, whose scientific achievements and qualities as a teacher greatly impressed him. After graduating in chemistry (1937), Schenck joined Ziegler, by that time a Full Professor of Chemistry at the University of Halle-Wittenberg (Germany), to take up a Ph.D. project directed toward the synthesis of cantharidin-like compounds. In rapid succession in 1939, he was awarded his Ph.D., married Christel Frommhold, was called to serve for two months in the army upon the outbreak of World War II, and returned to university to finish the first synthesis of the natural product cantharidin. This task was completed by Schenck's first Ph.D. student, E. W. Krockow, in 1941.[1]

The years in Halle proved particularly fruitful scientifically. Schenck was gifted with an extraordinary capacity to unify concepts and information from seemingly unrelated fields and thus derive useful working hypotheses. In this way, based on contemporary insight into photobiology and on Kautsky's theory of oxygen activation, he postulated that molecules such as chlorophyll should be efficient photosensitizers and effect selective oxidation reactions. This concept was promptly demonstrated by an elegant synthesis of the natural endoperoxide ascaridol, through the sensitized photooxidation of α-terpinene, which involved the cycloaddition of oxygen to a diene by using sunlight and spinach leaves (1944).[2] The Schenck reaction, a photosensitized ene reaction with oxygen that affords allylic hydroperoxides, was developed during the same period.[3] In his habilitation thesis (1943), Schenck presented a mechanistic theory for the sensitized photooxidation, which included a hypothetical oxidizing intermediate, $sens^{rad}O_2$. Albeit not entirely correct in the case of the reaction under discussion at the time, the Schenck mechanism of a chemical relay, which accounts for the transfer of an acceptor onto a substrate via a sensitizer–acceptor complex (1948)[4] and was advanced as a visionary general concept prior to the discovery of exciplexes, later proved to be applicable to many physical and chemical processes.

Shortly after the war and before the Russians occupied Halle, a group of scientists including Ziegler and Schenck were rounded up by the US military command and moved to western Germany as part of so-called "Action Paperclip". Schenck stayed with his wife and two children in the home of his mother-in-law in Ziegelhausen near Heidelberg. Until his move in 1949/50 to the University of Göttingen as an Associate Professor, he supported his family by performing first as an accordion soloist, and later as a full-time saxophonist and clarinetist in the "big band" of an old friend and concentration camp survivor, in American clubs. He eventually earned enough money to build a private laboratory and an open-air solar-irradiation pilot plant for the production of ascaridol (see photo on the next page), a drug urgently needed at that time to fight ascaris infections in humans.

The Göttingen period was characterized by continued development of the theory of photosensitization and by a large output of novel photoreactions and their application in synthesis. One such example, which has become a milestone in organic photochemistry, was the sensitized addition of maleic anhydride to benzene.[5] Schenck's unconventional approach to science, his unconditional commitment and forceful argumentation, were respected and accepted by some, and a controversial topic of debate for others. Schenck's

 © 2003 Wiley-VCH Verlag GmbH & Co. KGaA, Weinheim



Schenck's solar irradiation setup for the pilot-scale production of ascaridol by methylene-blue-sensitized photooxidation of α-terpinene in isopropanol, in his garden in Heidelberg (1949).

relationship with his teacher, colleague, and life-long supporter Ziegler was that of a personal and professional friendship between two strong-minded characters, which outlasted many a storm throughout three decades. Research funding in Göttingen by the Deutsche Forschungsgemeinschaft (DFG) became available only after a critical and very skeptical Georg Wittig, upon a visit to the applicant's laboratory in Göttingen in his function as a DFG referee, could be convinced of the scientific significance of the grant proposal. In fact, Wittig—with indirect support also from Karl Freudenberg and Wilhelm Klemm—then helped personally to find the optimal formulations! Success with the DFG was thus finally guaranteed, and followed by additional important support from the Fraunhofer Gesellschaft.

In 1958, Schenck moved to Mülheim an der Ruhr, to take up an appointment that had been proposed to the Max Planck Society by Ziegler. He was thus offered the unique opportunity to build up and organize an institute, known as the "Strahlenchemie", for integrated comparative photochemistry and radiation chemistry, with the additional bonus of a symbiosis with the Max Planck Institute of Coal Research, which could be anticipated to be scientifically and economically fruitful for both institutions. And indeed, there Schenck managed to enlarge the experimental pool of novel photochemical reactions and applications thereof even further, started research in radiation chemistry with pulsed Van de Graaff electron accelerators and with a powerful ^{60}Co source of continuous ionizing radiation, and further elaborated on his mechanistic concepts of the chemistry of electronically excited states and of their subsequent ground-state processes.

However, in the middle of the rapid development experienced in radiation-chemistry research, its leader had to slow down and eventually bring to a halt his energetic activities, because of a serious rare autoimmune disease, Hashimoto thyreoiditis. After spending much of 1967 as a Visiting Professor at the Radiation Laboratory of the University of Notre Dame (Indiana, USA), followed by an extended scientific tour in Japan in 1968, he was granted sick leave, and he could not return actively to work at all before his retirement in 1981. Oskar E. Polansky, designated in 1967 as a second Scientific Member at the Strahlenchemie, took office prematurely to ensure the continuous direction of the institute. Fortunately, Schenck recovered sufficiently to resume work in his office at home and, true to his nature, he threw himself into numerous science-related activities until the last year of his life. He concerned himself with philosophical questions ("How certain do we have to be before we accept a theory?") and environmental issues, which led to his involvement in the technical development of water-disinfecting methods by UV irradiation, his unconventional but realistic views on the relative merits of ecology (such as the detrimental influence of flue-gas-dust scrubbing on the state of forest health; "Can ecological protection harm environmental hygiene?"[6]), and his recommendation that CO_2 emissions from the combustion of fossil fuels be reduced by replacement of the latter with charcoal as a carbon dioxide neutral fuel.

Günther O. Schenck's heritage is of lasting value to chemistry and to a large community of former students and coworkers, many of whom have made their own imprint on chemistry, in academia and in industry. Let me end by reiterating the first of the above citations: "We owe him a lot of gratitude!"

Kurt Schaffner
Mülheim an der Ruhr (Germany)

[1] K. Ziegler, G. O. Schenck, E. W. Krokow, *Naturwiss.* **1941**, *29*, 390.
[2] G. O. Schenck, K. Ziegler, *Naturwiss.* **1944**, *32*, 157.
[3] G. O. Schenck, Deutsches Patent Nr. DE-933925, **1955**.
[4] a) G. O. Schenck, *Naturwiss.* **1948**, *5*, 28; b) G. O. Schenck, *Z. Naturforsch. B.* **1948**, *3*, 59.
[5] R. Steinmetz, *Fortschr. Chem. Forsch.* **1967**, *7*, 445.
[6] G. O. Schenck, *Naturwiss. Rundschau* **1990**, *3*, 93.

 © 2003 Wiley-VCH Verlag GmbH & Co. KGaA, Weinheim

Cannabinoid-Receptor Agonists

Inhibitors of Endocannabinoid Degradation: Potential Therapeutics for Neurological Disorders

*Michaela Wendeler and Thomas Kolter**

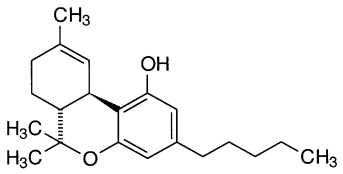
Keywords:
cannabinoids · drug design · lipids · medical chemistry · neurochemistry

Introduction

For a long time, *Cannabis sativa* preparations have been used as drugs for medicinal and recreational purposes. Its dried blossom tips are known as marijuana, and the dried resin as hashish. For 60 years, chemical and physiological effects of cannabinoids have been investigated. Recently, this research has focused on cannabinoid receptors in the human body and their endogenous lipid ligands. Evidence is accumulating that interference with endocannabinoid metabolism offers novel prospects for the treatment of a multitude of disorders such as pain, cancer, epilepsy, and multiple sclerosis. Recently, a series of highly potent inhibitors of endocannabinoid degradation has been described, which promises the development of new strategies for the treatment of anxiety and neurological disorders.[1]

Cannabinoids and Their Receptors

The consumption of cannabinoids leads to a highly complex spectrum of pharmacological effects, which could be of therapeutic benefit for a variety of disorders. They exhibit sedative and mood-altering properties, reduce pain sensation, alleviate nausea and vomiting, stimulate the appetite, alleviate cramps, and relax vascular muscles. At the same time, however, they impair cognitive and motor functions and interfere with sensory perception and short-term memory.[2] The underlying causes of the effects of cannabinoids have only been explored partially. In 1964, after about 20 years of research, the structure of the main psychoactive ingredient of marijuana, (−)-Δ^9-tetrahydrocannabinol (**1**) was finally determined.[3] This laid the foundation for the chemical synthesis of high-affinity cannabinoid derivatives, which in turn led to the identification of the first cannabinoid receptor, CB1, in the central nervous system.[4]



1

Another receptor, CB2, was discovered in 1993.[5] Both receptors are glycoproteins with seven transmembrane helices. Their stimulation leads to the activation of G proteins belonging to the $G_{i/o}$ family, thereby inhibiting the production of adenylyl cyclase and cAMP (cyclic adenosine-3′,5′-monophosphate) and thus regulating numerous signal-transduction pathways.[6] In addition, CB1 receptors are known to inhibit voltage-gated calcium channels and to activate potassium channels. Whereas CB1 is expressed predominantly in the central nervous system and represents one of the most abundant neuromodulatory receptors in the brain, CB2 occurs mainly on immune cells where it contributes to the mediation of the immunosuppressive effect of cannabinoids.[5]

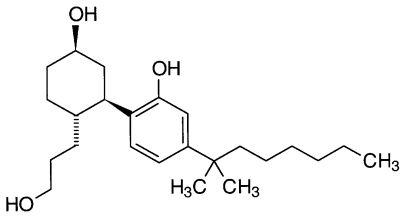
Ligands for Cannabinoid Receptors

Cannabinoid-receptor agonists can be assigned to different classes of compounds. Tetrahydrocannabinol (**1**) belongs to a family of over 60 bi- and tricyclic secondary metabolites that are biosynthetically derived from geranyl pyrophosphate and the polyketide olivetol. Known under the name of marinol, **1** is employed for the alleviation of nausea in cancer patients undergoing chemotherapy and for the treatment of anorexia in patients with AIDS. Structural variations of the cannabinoid backbone led to the synthesis and pharmacological characterization of over 300 compounds.[6] Many of them bind to both receptors, CB1 and CB2, but some ligands with high selectivity for one or the other receptor type have been described.[6]

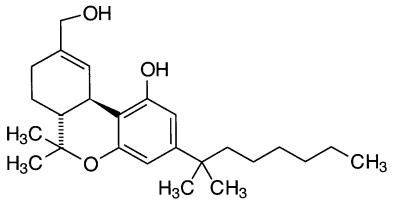
Synthetic analogues are, for example, CP-55,940 (**2**), a full agonist for both receptors that is 4-50 times as potent as **1**. The radio-labeled form of **2** allowed the identification of the first cannabinoid receptor.[7] Another derivative, HU-210 (**3**), is currently one of the most potent cannabinoids.[8] Agonists with aminoalkylindole structure, such as WIN-55,212–2 (**4**),[9] as well as selective antagonists of the CB1 receptor, for example, SR141716A (**5**),[10] have proven to be valuable pharmacological tools.

[*] Priv.-Doz. Dr. T. Kolter,
Dipl.-Chem. M. Wendeler
Kekulé-Institut für Organische Chemie und Biochemie
Universität Bonn
Gerhard-Domagk Strasse 1
53121 Bonn (Germany)
Fax: (+49) 228-73-7778
E-mail: tkolter@uni-bonn.de

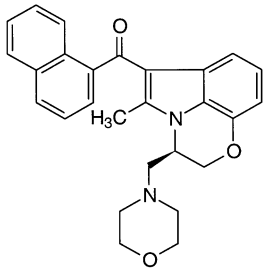
 © 2003 Wiley-VCH Verlag GmbH & Co. KGaA, Weinheim DOI: 10.1002/anie.200301641



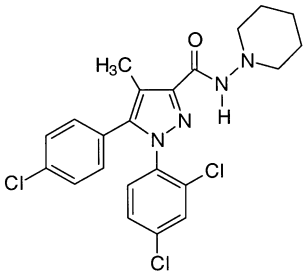
2



3



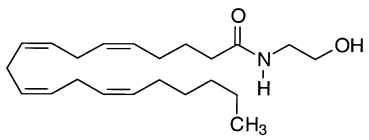
4



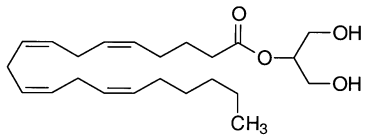
5

Endogenous Cannabinoids

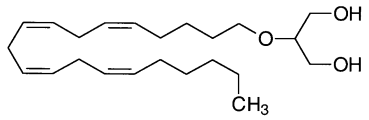
Several endogenous lipids present in mammalian brain tissue have been identified as cannabinoid-receptor agonists. They mimic the pharmacological effects of synthetic or plant-derived cannabinoids, but are metabolically less stable. The first endocannabinoid to be identified was *N*-arachidonoylethanolamine (anandamide, **6**).[11] Later, 2-arachidonoylglycerol (**7**),[12,13] and 2-arachidonylglycerylether (**8**) were found.[14] In contrast to classical neurotransmitters, they



6



7



8

are not stored in synaptic vesicles, but are rapidly synthesized in neurons in response to membrane depolarization and calcium influx.[15] Compounds **6**[16,17] and **7**[18] are biosynthetically derived from different membrane lipids. In the case of anandamide **6,** a transacylase transfers arachidonic acid from the *sn*1-position of phosphatidylcholine to the amino group of phosphatidylethanolamine. Subsequently, **6** is released by the action of a phospholipase D.

Another peculiarity of endocannabinoids is that they act as retrograde synaptic messengers: They are released by postsynaptic neurons, diffuse across the synaptic cleft, and activate the CB1 receptors on presynaptic nerve cells.[19] Endocannabinoid action is terminated within several minutes[20] through intracellular degradation: Endocannabinoids are transported across the cell membrane by a protein-mediated,[21] bidirectional process,[22] then anandamide **6** and related substances are degraded by an enzyme, fatty acid amide hydrolase (FAAH).[23]

Fatty Acid Amide Hydrolase

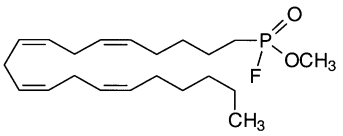
The concentration and signaling duration of several endogenous cannabinoids is regulated primarily by FAAH, a membrane protein that is predominantly expressed in brain and liver. Genetically engineered mice that lack FAAH show significantly elevated levels of anandamide and related fatty acid amides in the brain.[24] If these animals are intraperitoneally treated with anandamide, they show an array of CB1-dependent responses such as hypomotility, catalepsy, and hypothermia. Remarkably, these animals display a lower pain perception, an effect that can be eliminated by the CB1 antagonist **5**. These results conclusively indicate that FAAH plays a key role in the regulation of anandamide action and that the latter modulates pain sensation. Therefore, together with FAAH and with the CB1 receptor, two protein members of the endocannabinoid system are targets for the development of novel analgesics.[25]

FAAH is an integral membrane protein, a homodimer composed of two 63-kD subunits and was previously crystallized in the presence of the irreversible active-site-directed inhibitor methoxy arachidonyl fluorophosphonate **9**.[26] The crystal structure reveals that the active site is accessible from both the cytosolic leaflet of the membrane, and from the aqueous phase of the cytosol. The nucleophilic side chain of Ser241 is part of an unusual Ser-Ser-Lys catalytic triad. The structure of the enzyme suggests that fatty acid amides destined for degradation can directly reach the active site from the membrane and need not be transported through the aqueous phase.

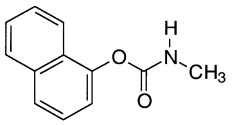
Inhibitors of Fatty Acid Amide Hydrolase

During the last few years, research concentrated on FAAH inhibitors with the aim of developing drugs that amplify the pharmacologically useful effects of endogenous cannabinoids by inhibiting their degradation. These substances would have the advantage of avoiding the unwanted psychotropic effects displayed by Δ^9-THC and other direct-acting exogenous cannabinoid agonists.[27] Previously described FAAH inhibitors, however, did not show the required target selectivity or bioavailability,[28–30] or were not sufficiently investigated with respect to their biological effects.[31]

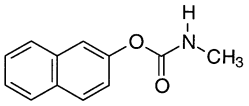
 © 2003 Wiley-VCH Verlag GmbH & Co. KGaA, Weinheim



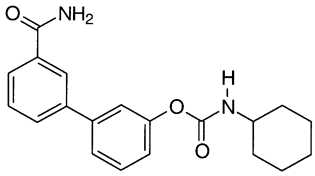
9



10



11



12

Piomelli and co-workers recently reported the discovery of a novel series of selective FAAH inhibitors with carbamate structure.[1] Carbamates are known as covalent inhibitors of serine esterases. In this way, for example, the alkaloid of the calabar bean physostigmin inhibits acetylcholinesterase activity.[32] The cholinesterase inhibitor carbaryl **10** was employed as a lead structure for inhibitor design. Even though this compound proved to be inactive, its positional isomer **11** displayed a weak inhibitory effect ($IC_{50} = 18.6$ μM), which could be enhanced by replacing the *N*-methyl group with an *N*-cyclohexyl substituent. Further optimization of the lead structure resulted in URB597 (**12**), which proved to be the most potent FAAH inhibitor in this series of compounds with an IC_{50}-value of 4 nM in membrane preparations and 0.5 nM in intact neurons.

Kinetic analyses suggest that a nucleophilic attack of the serine residue of the active site at the carbamate irreversibly inactivates the enzyme. Most notably, other serine hydrolases are not inhibited by this compound. In experiments with mice, intraperitoneal injections of **12** resulted in a strong, dose-dependent inhibition of FAAH activity in the brain and a significant increase in the levels of anandamide and other fatty acid ethanolamides in the brain. This was accompanied by anxiolytic and mild analgesic effects, which could be reversed by the CB1 receptor antagonist **5**. These studies demonstrate that the endocannabinoid system plays a major role in the modulation of emotional states.

Future Prospects

In spite of their promising properties,[2] the unwanted psychotropic side effects of cannabinoids prevent their broad clinical application. The increase in endocannabinoid concentration by selective inhibition of their degradation promises to circumvent these disadvantages, but the complexity of the endocannabinoid system must be considered prior to clinical application of inhibitors: Not only anandamide **6**, but also a series of related fatty acid amides such as palmitoylethanolamine, oleamide, and the sleep-inducing *N*-oleoylethanolamine, are degraded by FAAH and might compete together with oxygenated metabolites for the endocannabinoid transporter. Receptors for these bioactive lipids have not yet been identified, but it is likely that inhibition of FAAH might also affect other cellular signal-transduction pathways. In addition to CB1 and CB2 receptors, anandamide also binds to the vanilloid receptor with partly opposing cellular effects. Moreover, some data suggest the existence of nonclassical cannabinoid receptors,[6] whose influence on signal transduction and cell fate is largely unknown.

Apart from the potential treatment of neurological disorders, endocannabinoids promise new concepts in cancer therapy. In the same way as their exogenous analogues, endocannabinoids show significant antitumour effects on some cell lines in vitro through selective inhibition of growth-factor-dependent cell proliferation or the induction of apoptosis.[33] In this respect, metabolically stable analogues that can be administered in very low, nonpsychotropic concentrations, or derivatives that cannot pass the blood–brain barrier, are particularly important.

A better knowledge of the endocannabinoid system will reveal the full therapeutic potential of its modulation and will facilitate the rational design of potent inhibitors with improved biological properties.

[1] S. Kathuria, S. Gaetani, D. Fegley, F. Valino, A. Duranti, A. Tontini, M. Mor, G. Tarzia, G. L. Rana, A. Calignano, A. Giustino, M. Tattoli, M. Palmery, V. Cuomo, D. Piomelli, *Nat. Med.* **2003**, *9*, 76–81.

[2] B. R. Martin, *J. Pharmacol. Exp. Ther.* **2002**, *301*, 790–796.

[3] Y. Gaoni, R. Mechoulam, *J. Am. Chem. Soc.* **1964**, *86*, 1646–1647.

[4] L. A. Matsuda, S. J. Lolait, M. J. Brownstein, A. C. Young, T. I. Bonner, *Nature* **1990**, *346*,561–564.

[5] S. Munro, K. L. Thomas, M. Abu-Shaar, *Nature* **1993**, *365*, 61–65.

[6] A. C. Howlett, F. Barth, T. I. Bonner, G. Cabral, P. Casellas, W. A. Devane, C. C. Felder, M. Herkenham, K. Mackie, B. R. Martin, R. Mechoulam, R. G. Pertwee, *Pharmacol. Rev.* **2002**, *54*, 161–202.

[7] W. A. Devane, F. A. Dysarz, M. R. Johnson, L. S. Melvin, A. C. Howlett, *Mol. Pharmacol.* **1988**, *34*, 605–613.

[8] C. C. Felder, K. E. Joyce, E. M. Briley, J. Mansouri, K. Mackie, O. Blond, Y. Lai, A. L. Ma, R. L. Mitchell, *Mol. Pharmacol.* **1995**, *48*, 443–450.

[9] M. Pacheco, S. R. Childers, R. Arnold, F. Casiano, S. J. Ward, *J. Pharmacol. Exp. Ther.* **1991**, *257*, 170–183.

[10] M. Rinaldi-Carmona, F. Barth, M. Héaulme, D. Shire, B. Calandra, C. Congy, S. Martinez, J. Maurani, G. Neliat, D. Caput, P. Ferrara, P. Soubrié, J. C. Breliere, G. Le Fur, *FEBS Lett.* **1994**, *350*, 240–244.

[11] W. A. Devane, L. Hanus, A. Breuer, R. G. Pertwee, L. A. Stevenson, G. Griffin, D. Gibson, A. Mandelbaum, A. Etinger, R. Mechoulam, *Science* **1992**, *258*, 1946–1949.

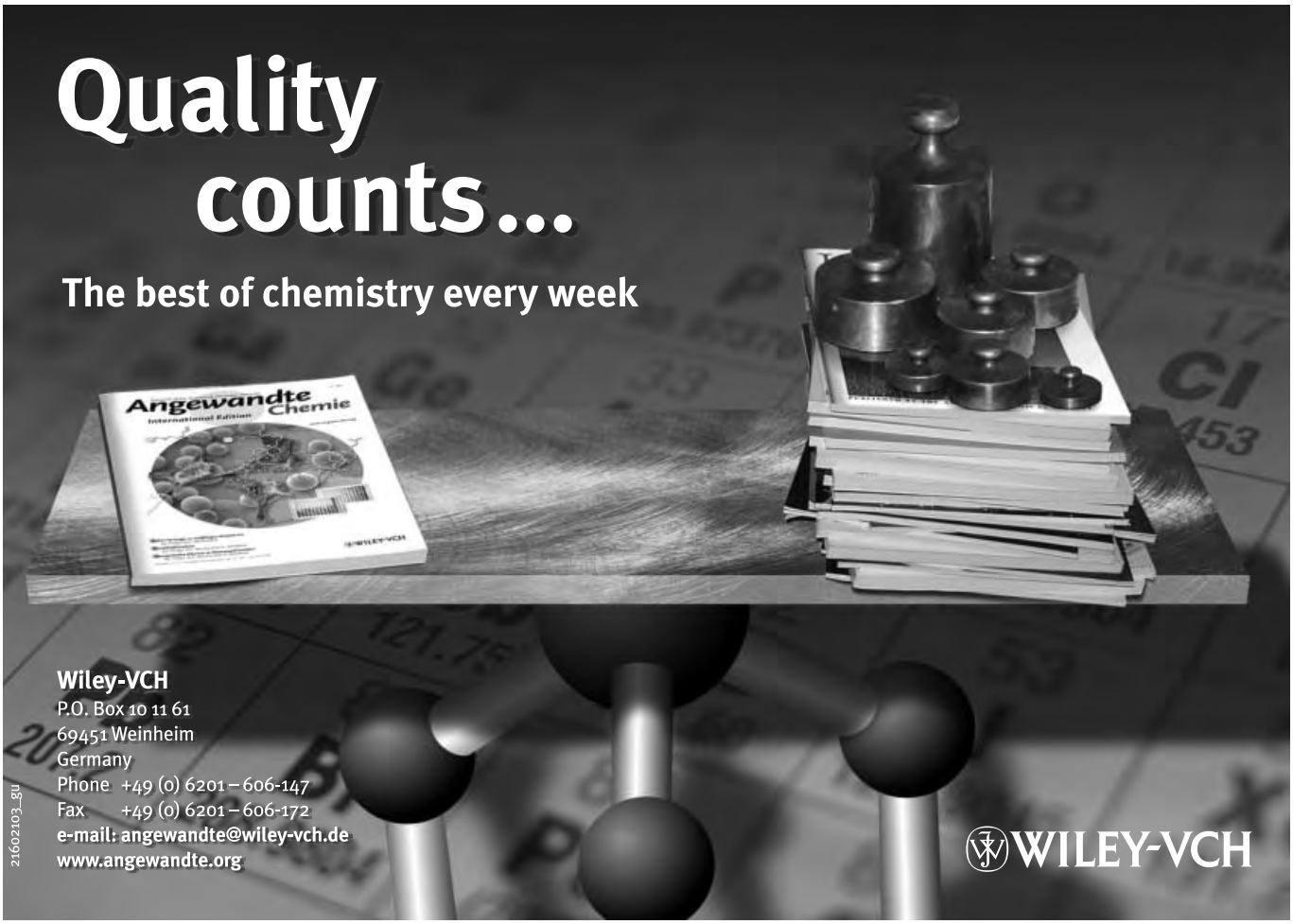
[12] R. Mechoulam, S. Ben-Shabat, L. Hanus, M. Ligumsky, N. E. Kaminski, A. R. Schatz, A. Gopher, S. Almog, B. R. Martin, D. R. Compton, R. G. Pertwee, G. Griffin, M. Bayewitch, J. Barg, Z. Vogel, *Biochem. Pharmacol.* **1995**, *50*, 83–90.

[13] T. Sugiura, S. Kondo, A. Sukagawa, S. Nakane, A. Shinoda, K. Itoh, A. Yamashita, K. Waku, *Biochem. Biophys. Res. Commun.* **1995**, *215*, 89–97.

[14] L. Hanus, S. Abu-Lafi, E. Fride, A. Breuer, Z. Vogel, D. E. Shalev, I. Kus-

 © 2003 Wiley-VCH Verlag GmbH & Co. KGaA, Weinheim

tanovich, R. Mechoulam, *Proc. Natl. Acad. Sci. USA* **2001**, *98,* 3662 – 3665.
[15] V. Di Marzo, L. De Petrocellis, T. Bisogno, D. Melck, *Lipids* **1999**, *34*, 319 – 325.
[16] V. Di Marzo, A. Fontana, H. Cadas, S. Schinelli, G. Cimino, J. C. Schwartz, D. Piomelli, *Nature* **1994**, *372*, 686 – 691.
[17] H. Cadas, S. Gaillet, M. Beltramo, L. Venance, D. Piomelli, *J. Neurosci.* **1996**, *16*, 3934 – 3942.
[18] T. Bisogno, N. Sepe, D. Melck, S. Maurelli, L. De Petrocellis, V. Di Marzo, *Biochem. J.* **1997**, *322*, 671 – 677.
[19] R. I. Wilson, R. A. Nicoll, *Science* **2002**, *296*, 678 – 682.
[20] K. A. Willoughby, S. F. Moore, B. R. Martin, E. F. Ellis, *J. Pharmacol. Exp. Ther.* **1997**, *282*, 243 – 247.
[21] M. Beltramo, N. Stella, A. Calignano, S. Y. Lin, A. Mariyannis, D. Piomelli, *Science* **1997**, *277*,1094 – 1097.
[22] C. J. Hillard, A. Jarrahian, *Chem. Phys. Lipids* **2000**, *108*, 123 – 134.
[23] V. Di Marzo, A. Fontana, H. Cadas, S. Schinelli, G. Cimino, J. C. Schwartz, D. Piomelli, *Nature* **1994**, *372*, 686 – 691.
[24] B. F. Cravatt, K. Demarest, M. P. Patricelli, M. H. Bracey, D. K. Giang, B. R. Martin, A. H. Lichtman, *Proc. Natl. Acad. Sci. USA* **2001**, *98*, 9371 – 9376.
[25] D. Gurwitz, A. Weizman, *Drug Discovery Today* **2002**, *7*, 403 – 406.
[26] M. H. Bracey, M. A. Hanson, K. R. Masuda, R. C. Stevens, B. F. Cravatt, *Science* **2002**, *298*, 1793 – 1796.
[27] W. Hall, N. Solowij, *Lancet* **1998**, *352*, 1611 – 1616.
[28] B. Koutek, G. D. Prestwich, A. C. Howlett, S. A. Chin, D. Salehani, N. Akhavan, D. G. Deutsch, *J. Biol. Chem.* **1994**, *269*, 22 937 – 22 940.
[29] M. Beltramo, E. di Tomaso, D. Piomelli, *FEBS Lett.* **1997**, *403*, 263 – 267.
[30] L. de Petrocellis, D. Melck, N. Ueda, S. Maurelli, Y. Kurahashi, S. Yamamoto, G. Marino, V. Di Marzo, *Biochem. Biophys. Res. Commun.* **1997**, *231*, 82 – 88.
[31] D. L. Boger, H. Sato, R. A. Lerner, M. P. Hedrick, R. A. Fecik, H. Miyauchi, G. D. Wilkie, B. J. Austin, M. P. Patricelli, B. F. Cravatt, *Proc. Natl. Acad. Sci. USA* **2000**, *97*, 5044 – 5049.
[32] G. L. Patrick, *An Introduction to Medicinal Chemistry*, 2nd ed., Oxford University Press, Oxford, **2001**, pp. 473 – 477.
[33] M. Bifulco, V. Di Marzo, *Nat. Med.* **2002**, *8*, 547 – 550.



Biological Role of Iron Complexes

Bioinorganic Reaction Mechanisms: From High-Valent Iron to Bioorganometallic Chemistry

*Leonardo D. Slep and Frank Neese**

Keywords:
bioinorganic chemistry · cyanide ligands · iron complexes · metalloproteins · oxygen activation

A large number of enzymes contain transition-metal ions in their active center. Such enzymes efficiently catalyze a wide range of chemical reactions including those that involve activation of small molecules in a selective way and under extremely mild conditions. Unraveling the underlying structural and electronic features of these fascinating reactions is at the heart of bioinorganic chemistry. The past few years have witnessed significant progress in our understanding of many of these reactions as a result of detailed structural and spectroscopic studies as well as advanced theoretical techniques and kinetic analysis. The preparation of low-molecular-weight model complexes, although often synthetically challenging, is important to help understanding the features of a metalloprotein that are essential to its function. Moreover, the model studies may provide a chemical precedent for a hitherto unknown chemical species or postulated reaction intermediate.

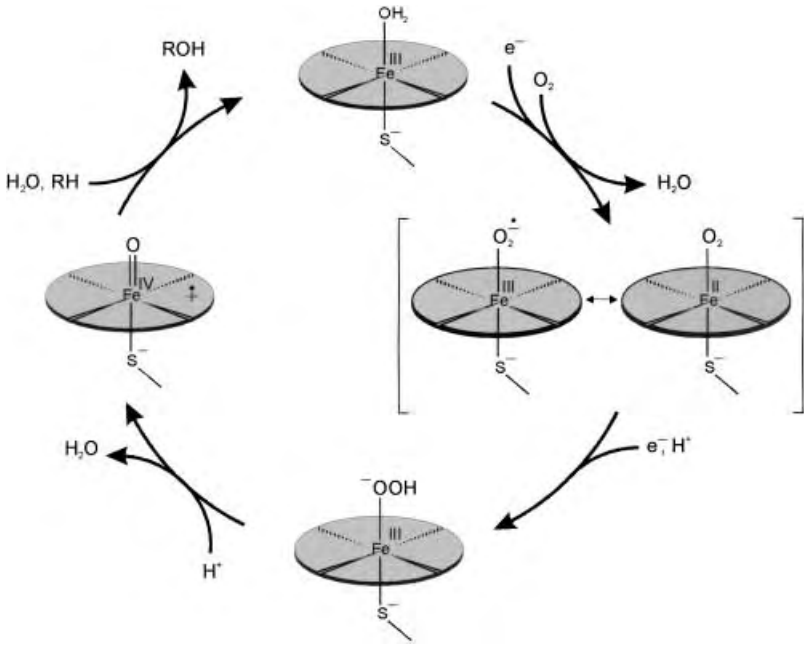
In a recent issue of *Science* two remarkable achievements in bioinorganic chemistry were reported by Münck, Nam, Que and co-workers[1] and by Böck and co-workers,[2] illustrating on how synthetic inorganic chemistry, biochemistry, and spectroscopy complement each other to answer fundamental questions in the field of metalloproteins.

[*] Priv.-Doz. Dr. F. Neese, Dr. L. D. Slep
Max-Planck Institut für Strahlenchemie
Stiftstrasse 34–36
45470 Mülheim an der Ruhr (Germany)
Fax: (+49) 208-306-3951
E-mail: neese@mpi-muelheim.mpg.de

Oxygen Activation in Nonheme Iron Enzymes

The interaction of molecular oxygen with iron in the active sites of proteins must be finely tuned to achieve either reversible O_2 binding in oxygen transport (e.g. in the oxygen-carrier proteins hemoglobin and hemerythrin) or to activate O_2 for further reactivity (e.g. cytochrome P450 (CYP450), mononuclear nonheme iron proteins (NHI), methane monoxygenase (MMO)). It is well known that the activation of O_2 by aqueous Fe^{II} can yield a cascade of radical reactions (Fenton and Haber–Weiss reactions), which involve aggressive reactive species such as $OH^{\bullet}$, $O_2^{\bullet-}$, or H_2O_2, all of which are deleterious to biological systems. The way in which oxygen-activating iron enzymes control this hazardous chemistry and turn it constructively into specific and selective biochemical reactions has fascinated chemists for decades.

The most widespread example of oxygen activation is the hemoprotein cytochrome $P450_{CAM}$, which catalyzes the hydroxylation of camphor with O_2 as the oxygen source. The mechanism of this reaction has been the focus of intense research efforts for more than three decades, the results of which are summarized in Scheme 1. The catalytic cycle starts with the coordination of a molecule of O_2 to the active Fe^{II} site to produce an intermediate that may be considered as a Fe^{III}–superoxide or ferrous–O_2 complex. Subsequent one-electron reduction yields a Fe^{III}–hydroper-

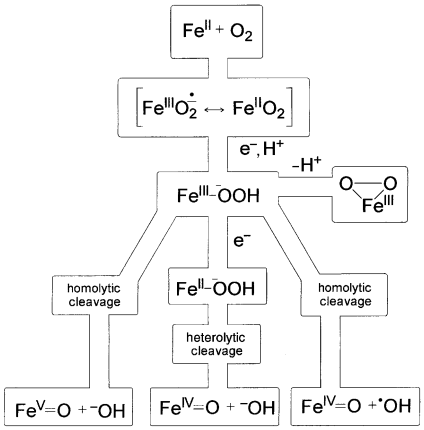


Scheme 1. Important intermediates and steps in the catalytic cycle of CYP_{450}.

 © 2003 Wiley-VCH Verlag GmbH & Co. KGaA, Weinheim DOI: 10.1002/anie.200301649

oxide species. This is followed by heterolytic cleavage of the O–O bond, producing the elusive intermediate known as "compound I", formally an Fe^{V} species. The latter behaves as an extremely powerful oxidant with a redox potential probably exceeding +1 V. It has been proposed to react directly with the substrate in a fast rebound mechanism to yield the hydroxylated product and regenerate the Fe^{III} active site. However, chemical modeling as well as studies on related enzymes such as catalases and peroxidases suggest that these species feature a high-valent $[FeO]^{2+}$ core bound to a porphyrin radical cation rather than a genuine Fe^{V} moiety. Fascinating recent developments in the chemistry of $CYP450_{CAM}$ include the crystallographic characterization of several of the intermediates in the reaction cycle[3a] as well as the quantum-mechanical study of the reaction cycle with explicit inclusion of the protein environment.[3b]

Recently, attention has been focused on mononuclear NHI proteins, which have proven to be as versatile as hemoproteins in oxygen-activation processes.[4] However, a significant point of concern is whether the NHI enzymes could produce high-valent-iron intermediates in the absence of a porphyrin ring acting as an electron reservoir. The existence of compound I-like intermediates has been challenged on the basis of crystallographic studies which have shown that the iron centers in NHI enzymes are always coordinated to "innocent" ligands that presumably can not be ionized at the biologically relevant redox potential window. An attractive alternative to the production of high-valent intermediates is the direct reaction of Fe^{III}–hydroperoxides to yield hydroxylated or epoxidized products (Scheme 2). Recent studies have shown that low-spin and high-spin Fe^{III} hydroperoxides are activated for homolytic O–O and Fe–O bond cleavage, respectively.[5] The deprotonated form, O_2^{2-}, is found in side-on-bound high-spin η^2-Fe^{III}–peroxo complexes, which do not appear to be activated for direct reaction with substrates.[6] The direct reaction of low-spin Fe^{III}–hydroperoxide complexes is, therefore, an alternative mechanism and has been proposed to occur, for instance, in the oxidation of



Scheme 2. Important intermediates in the reactions of NHI enzymes.

DNA by the anticancer drug bleomycin.[7] Fe^{IV} (or even Fe^{V}) intermediates have been frequently proposed in NHI enzyme mechanisms, but have not been detected experimentally. This has inspired synthetic chemists to attempt to prepare high-valent iron model complexes, leading to the first spectroscopic characterization of complexes featuring the terminal $[FeO]^{2+}$ and $[FeN]^{2+}$ moieties[8]

The article by Münck, Nam, Que, and co-workers is a significant advancement towards the preparation and characterization of mononuclear high-valent nonheme iron centers.[1] In this study, they provide complete structural and spectroscopic characterization of the $[FeO]^{2+}$ core in a nonheme environment. The synthesis involved the reaction of the precursor $[Fe(tmc)(OTf)_2]$ (**1**; tmc = 1,4,8,11-tetramethyl-1,4,8,11-tetraazacyclotetradecane, OTf = CF_3SO_3)

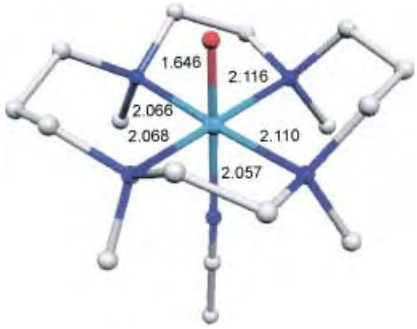


Figure 1. Molecular structure of the $[Fe(tmc)(O)(CH_3CN)]^{2+}$ dication, derived from X-ray crystallography. The given values indicate bond lengths in Å. Hydrogen atoms are omitted for clarity.

with iodosylbenzene (PhIO, an oxygen-atom-transfer reagent) in acetonitrile at −40 °C to yield $[Fe(tmc)(O)(CH_3CN)]^{2+}$ (**2**). This species was characterized by absorption, FT IR, and Mössbauer spectroscopy, as well as by mass spectrometry. Crystallization from CH_3CN/Et_2O at −40 °C yielded the triflate salt **2**·$(OTf)_2$. Its structure consists of a mononuclear iron center in a distorted octahedral environment with a short terminal Fe–O bond (1.646(3) Å, Figure 1). This bond is much shorter than those in bridging oxo ions in dinuclear complexes featuring Fe^{IV} (1.805 Å),[9] or the terminal Fe–O bond in a recently characterized complex featuring the $[FeO]^{+}$ fragment (1.813 Å),[10] and is indicative of increased π-bonding within the terminal $[FeO]^{2+}$ moiety. The short Fe–O bond length is similar to those deduced from EXAFS (extended X-ray absorption fine structure) spectroscopic measurements on high-valent porphyrins and also resembles the values based on the X-ray structural analysis of hemoproteins featuring the $[FeO]^{2+}$ core.[11]

This remarkable results of Münck, Nam, Que, and co-workers provides a well-characterized model complex necessary for evaluating the feasibility of high-valent iron–oxo species in the reaction pathways of NHI enzymes. In addition, these results allow studying the spectroscopic properties of the high-valent NHI oxo unit in the absence of impurities or other chromophores. This provides a sound structural basis for future spectroscopic assignments of this structural motif and an in-depth understanding of the relationship between electronic structure, spectroscopy, and reactivity in these systems.

Biosynthesis of the Fe–CN Bond in Ni–Fe Hydrogenases

Hydrogen gas is an essential nutrient in virtually all forms of life that inhabit anaerobic environments, such as deep-sea hydrothermal vent sites, lake sediments, and the intestines of animals. H_2 is produced by fermentative organisms in the oxidation of sugars and other organic molecules. The liberated electrons are transferred to protons through an electron-transport chain reaction (which involves, among others, the Fe–

 © 2003 Wiley-VCH Verlag GmbH & Co. KGaA, Weinheim

S protein ferredoxin) to produce H_2 gas. This final key step is catalyzed by a family of enzymes that are collectively known as hydrogenases. Hydrogen gas is recycled by other organisms in the same habitat. These bacteria also contain hydrogenases that catalyze the reverse reaction, that is, the oxidation of H_2.

Although several different classes of hydrogenases are known, the most common of these enzymes contain both Ni and Fe ions in their active center (NiFe-H_2ase). The crystal structure of the NiFe-H_2ase from *Desulfovibrio gigas* was solved in 1995[12] and showed that the active site contains a heterodinuclear NiFe site with two terminal cysteine ligands at the Ni end (Figure 2). In addition, there are two bridging cysteine fragments and an unidentified ligand (probably OH^-), which bridge to a nearby Fe center. Recently, a detailed spectroscopic study has provided insight into the electronic structure of the active center and of the reaction intermediates.[13]

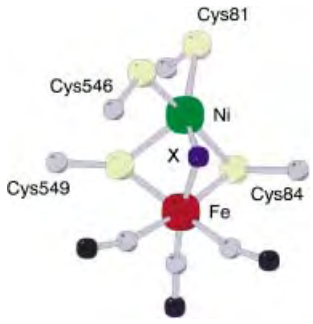
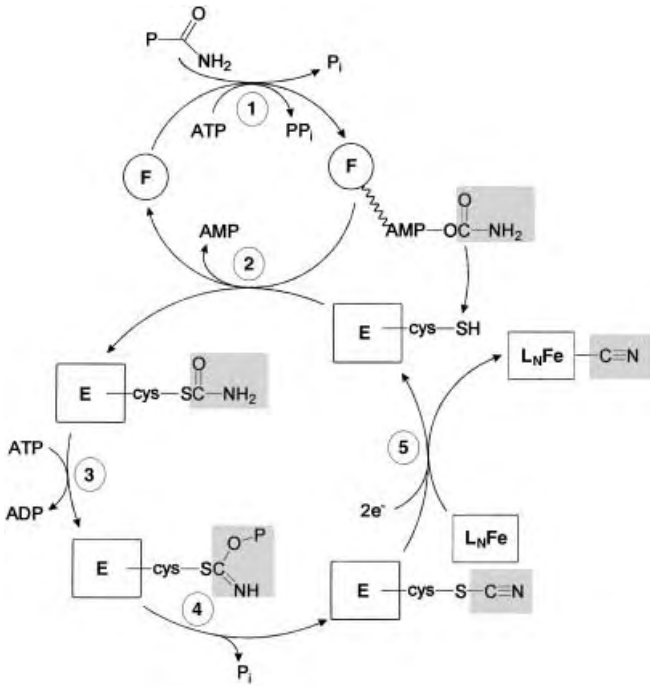


Figure 2. Schematic representation of the active site of the NiFe-H_2ase from *D. vulgaris* obtained by X-ray crystallography of the oxidized protein. The fragment X identifies the third bridging ligand, which has not been identified but is most probably an OH^- group. PDB code 2FRV.

The most striking structural feature of the NiFe-H_2ases involves the three terminal diatomic molecules coordinated to the Fe center (Figure 2). These diatomic species were identified by FTIR spectroscopy as being one CO and two CN^- ligands.[14] This result was quite surprising as both CO and CN^- are highly toxic for biological systems because of their high affinity for the active sites of many metalloenzymes (e.g. hemoproteins involved in cell respiration). CN^- and CO were also found in the active sites of other hydrogenases. It has been proposed that this highly unusual arrangement helps to keep the Fe center in a low-spin low-valent state, which may be relevant to the function of H_2ases.

The identification of CN^- and CO ligands in the active site of metalloproteins subsequently prompted the question of how these toxic species are delivered to the active sites of the enzymes during the biosynthesis, as CO and CN^- are not freely available in biological systems. Böck and co-workers have provided an explanation for this process in the NiFe-H_2ases.[2] Using a combination of radio isotope labeling and mass spectrometry, they showed that organic thiocyanates are a source of CN^-. These thiocyanates are formed as a result of the interaction of two (HypF and HypE) out of seven proteins involved in the maturation of the NiFe active site. A detailed mechanism is outlined in (Scheme 3): The first step of the biosynthesis involves the formation of a carbamoyl adenylate intermediate by the reaction between carbamoyl phosphate (CP, a known intermediate in biosythetic pathways, e.g., the urea cycle) and ATP on the HypF protein. The $CONH_2$ group is subsequently transferred to the thiol group of the C-terminal cysteine residue on the second protein HypE. This protein then performs a complex set of unprecedented reactions: it provides the site for dehydration of the carboxamido moiety in an ATP-dependent step to yield the cyanated cysteine (thiocyanate). This intermediate presumably carries the SCN residue to the active site and finally transfers the electrophilic CN moiety to a nucleophilic iron center to form the Fe–CN unit.

Böck and co-workers explored this mechanism further with a series of elegant model experiments to probe the key steps described above. They showed that the dehydration of *S*-(*n*-decyl)thiocarbamate assisted by ethyl polyphosphate proceeds under mild conditions and yields the corresponding thiocyanate species in a way that resem-



Scheme 3. Biosynthesis of the cyanide ligand in NiFe-H_2ases: 1) formation of the carbamoyl adenylate on the HypF protein (F) involving an ATP–PP_i exchange reaction; 2) the $CONH_2$ group is transferred to the C-terminal cysteine of the HypE protein (E); 3) and 4) ATP-assisted dehydration involving an intermediate phosphorylation of the carbonyl oxygen atom followed by dephosphorylation to yield a thiocyanate; 5) chemical transfer of the CN group to the active center of the NiFe-H_2ase protein (L_N represents the coordination sphere of the active site). ATP = adenosine triphosphate, ADP = adenosine diphosphate, AMP = adenosine monophosphate, P_i = phosphate, PP_i = pyrophosphate.

 © 2003 Wiley-VCH Verlag GmbH & Co. KGaA, Weinheim

bles the natural system. By treating phenyl thiocyanate with $[(\eta^5\text{-}C_5H_5)Fe(CO)_2Br]$ (FpBr) to generate $[(\eta^5\text{-}C_5H_5)Fe(CO)_2CN]$ (FpCN) in good yield, they showed that organic thiocyanates could directly deliver CN to low-valent Fe centers under mild conditions.

The combination of experiments on the natural protein system and on organometallic model compounds have shed light on a remarkable biosynthetic pathway. It was clearly demonstrated that metal–CN units can be formed under biological conditions in the absence of free CN^-. A viable mechanism for the origin of these unusual ligands in the active site of hydrogenases has thus been provided.

Conclusion

The two studies by Münck, Nam, Que, and co-workers[1] and Böck and co-workers[2] are clear examples of how the chemical principles underlying complicated biochemical reactions can be clarified with the use of synthetic model compounds. Furthermore, they demonstrate how potentially toxic intermediates are controlled and/or avoided in biological systems.

[1] J. U. Rohde, J. H. In, M. H. Lim, W. W. Brennessel, M. R. Bukowski, A. Stubna, E. Münck, W. Nam, L. Que, Jr., *Science* **2003**, *299*, 1037.

[2] S. Reissmann, E. Hochleitner, H. Wang, A. Paschos, F. Lottspeich, R. S. Glass, A. Böck, *Science* **2003**, *299*, 1067.

[3] a) I. Schlichting, J. Berendzen, K. Chu, A. M. Stock, S. A. Maves, D. E. Benson, B. M. Sweet, D. Ringe, G. A. Petsko, S. G. Sligar, *Science* **2000**, *287*, 1615; b) J. C. Schöneboom, H. Lin, N. Reuter, W. Thiel, S. Cohen, F. Ogliaro, S. Shaik, *J. Am. Chem. Soc.* **2002**, *124*, 8142.

[4] E. I. Solomon, T. C. Brunold, M. I. Davis, J. N. Kemsley, S. K. Lee, N. Lehnert, F. Neese, A. J. Skulan, Y. S. Yang, J. Zhou, *Chem. Rev.* **2000**, *100*, 235.

[5] a) N. Lehnert, F. Neese, R. Y. N. Ho, L. Que, Jr., E. I. Solomon, *J. Am. Chem. Soc.* **2002**, *124*, 10810; b) N. Lehnert, R. Y. N. Ho, L. Que, Jr., E. I. Solomon, *J. Am. Chem. Soc.* **2001**, *123*, 12802.

[6] F. Neese, E. I. Solomon, *J. Am. Chem. Soc.* **1998**, *120*, 12829.

[7] a) F. Neese, J. M. Zaleski, K. L. Zaleski, E. I. Solomon, *J. Am. Chem. Soc.* **2000**, *122*, 11703; b) E. I. Solomon, A. Decker, N. Lehnert, *Proc. Natl. Acad. Sci. USA* **2003**, *100*, 3589.

[8] a) K. Meyer, E. Bill, B. Mienert, T. Weyhermüller, K. Wieghardt, *J. Am. Chem. Soc.* **1999**, *121*, 4859; b) C. A. Grapperhaus, B. Mienert, E. Bill, T. Weyhermüller, K. Wieghardt, *Inorg. Chem.* **2000**, *39*, 5306.

[9] a) M. Costas, J. U. Rohde, A. Stubna, R. Y. N. Ho, L. Quaroni, E. Münck, L. Que, Jr., *J. Am. Chem. Soc.* **2001**, *123*, 12931; b) H. F. Hsu, Y. H. Dong, L. J. Shu, V. G. Young, L. Que, Jr., *J. Am. Chem. Soc.* **1999**, *121*, 5230.

[10] C. E. MacBeth, A. P. Golombek, V. G. Young, C. Yang, K. Kuczera, M. P. Hendrich, A. S. Borovik, *Science* **2000**, *289*, 938.

[11] a) J. E. Penner-Hahn, K. S. Eble, T. J. McMurry, M. Renner, A. L. Balch, J. T. Groves, J. H. Dawson, K. O. Hodgson, *J. Am. Chem. Soc.* **1986**, *108*, 7819; b) T. Wolter, W. Meyer-Klaucke, M. Muther, D. Mandon, H. Winkler, A. X. Trautwein, R. Weiss, *J. Inorg. Biochem.* **2000**, *78*, 117.

[12] A. Volbeda, M.-H. Charon, C. Piras, E. C. Hatchikian, M. Frey, J. C. Fontecilla-Camps, *Nature* **1995**, *373*, 580.

[13] S. Foerster, M. Stein, M. Brecht, H. Ogata, Y. Higuchi, W. Lubitz, *J. Am. Chem. Soc.* **2003**, *125*, 83.

[14] K. A. Bagley, E. C. Duin, W. Roseboom, S. P. J. Albracht, W. H. Woodruff, *Biochemistry* **1995**, *34*, 5527.

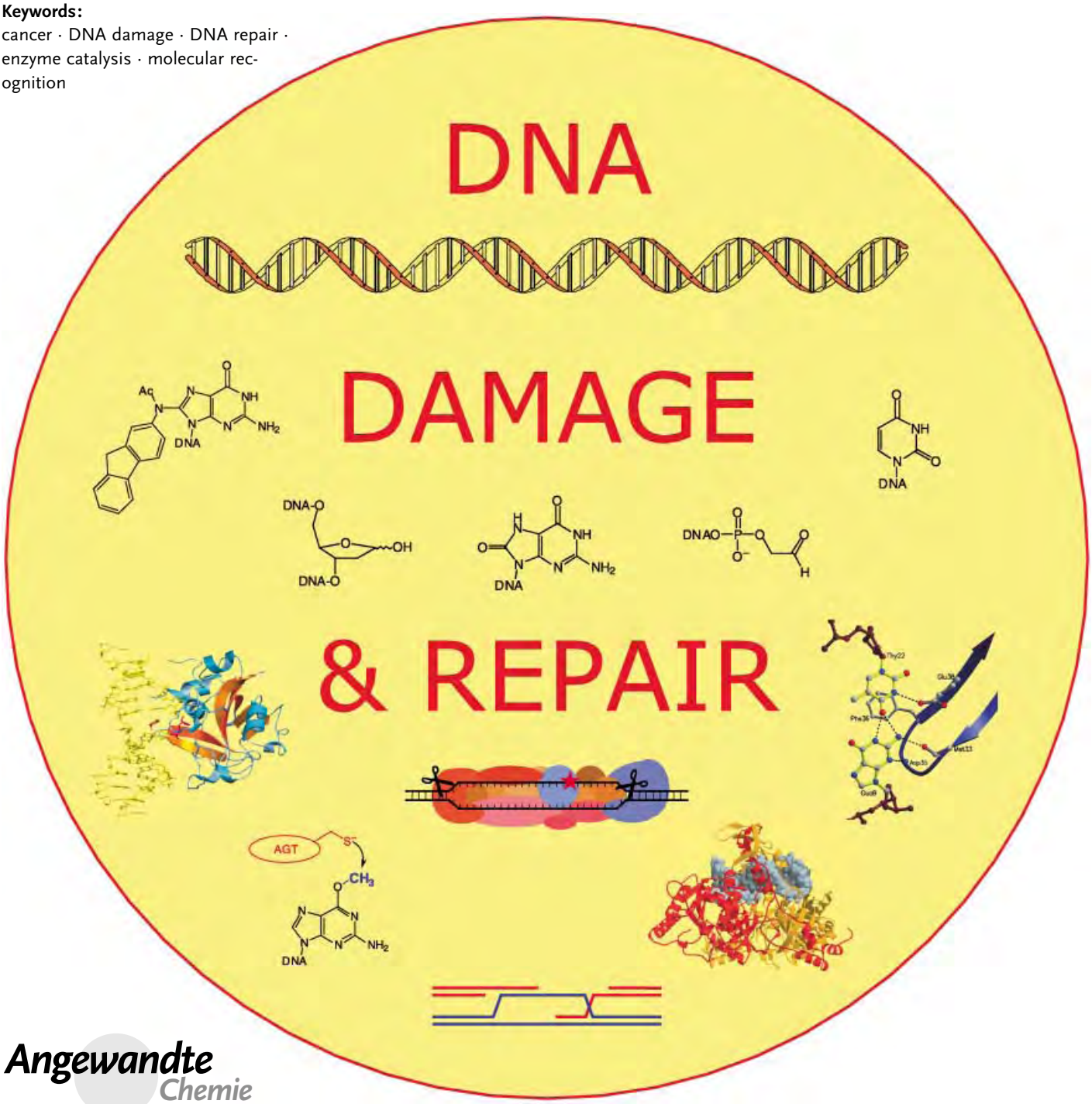
 © 2003 Wiley-VCH Verlag GmbH & Co. KGaA, Weinheim

Mechanisms of DNA Repair

Chemistry and Biology of DNA Repair

*Orlando D. Schärer**

Keywords:
cancer · DNA damage · DNA repair · enzyme catalysis · molecular recognition



© 2003 Wiley-VCH Verlag GmbH & Co. KGaA, Weinheim
DOI: 10.1002/anie.200200523

Numerous agents of endogenous and exogenous origin damage DNA in our genome. There are several DNA-repair pathways that recognize lesions in DNA and remove them through a number of diverse reaction sequences. Defects in DNA-repair proteins are associated with several human hereditary syndromes, which show a marked predisposition to cancer. Although DNA repair is essential for a healthy cell, DNA-repair enzymes counteract the efficiency of a number of important antitumor agents that exert their cytotoxic effects by damaging DNA. DNA-repair enzymes are therefore also targets for drug design. DNA-repair processes differ greatly in their nature and complexity. Whereas some pathways only require a single enzyme to restore the original DNA sequence, others operate through the coordinated action of 30 or more proteins. Our understanding of the genetic, biochemical, and structural basis of DNA repair and related processes has increased dramatically over the past decade. This review summarizes the latest developments in this field.

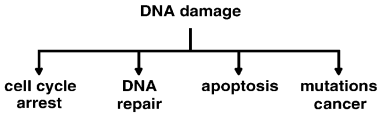
From the Contents

1. Introduction 2947
2. DNA Damage and Responses in Human Cells 2948
3. Repair by Direct Reversal of Damage 2950
4. Base-Excision Repair 2951
5. Nucleotide-Excision Repair 2956
6. Mismatch Repair 2959
7. Repair of Double-Strand Breaks 2961
8. Summary and Outlook 2966

1. Introduction

The maintenance of the genomic integrity is of crucial importance for all organisms. Damage to the DNA that makes up our genes is constantly inflicted by a large number of agents and can have severe effects if it persists. Modifications of DNA can lead to mutations, which alter the coding sequence of DNA and can lead to cancer in mammals. Other DNA lesions interfere with normal cellular transactions, such as DNA replication or transcription, and are deleterious to the cell. Cells have evolved several ways to counteract these adverse effects of damaged DNA. There are various DNA-repair pathways that can remove lesions from DNA. The importance of DNA repair is underscored by several human syndromes that are caused by defects in DNA-repair genes. A hallmark feature of these diseases is a dramatically increased predisposition to cancer. Damage to DNA leads to a number of responses in the cell, which are tightly coordinated with DNA repair (Scheme 1). The cell cycle is arrested in response to DNA damage to allow time for repair before replication and cell division.[1,2] If the damage load is too large for a cell to be repaired, the cell may undergo programmed cell death (apoptosis) to avoid the propagation of highly defective cells.[3] Furthermore, some specialized DNA polymerases tolerate damage during replication and bypass a lesion in a process that either give an accurate replication product or a mutation. The biological roles of these unusual DNA polymerases are not yet clear.[4,5]

The purpose of this review is to provide a comprehensive overview of DNA-repair processes in mammalian cells with an emphasis on the chemical processes involved. Over 100 reviews dealing with different aspects of DNA repair appear every year (e.g., see references [6–8] for recent landmark reviews), but the area has never been comprehensively reviewed from a chemical perspective (e.g., see references [9–13] for chemically oriented reviews dealing with individual pathways). Aside from the clear importance for biology and medicine, there are many reasons why DNA-repair processes should be of interest to the chemical community: 1) The intrinsic reactivity of the many functional groups in DNA is responsible for the generation of damaged DNA. It is therefore important that we understand the chemistry underlying DNA damage. 2) DNA-repair enzymes face a formidable challenge in molecular recognition that we would like to understand: they specifically need to find structurally minor alterations in DNA among the 3 billion base pairs in the human genome. 3) A central goal of molecular and chemical biology is to understand the molecular basis employed by multiprotein systems (or "big protein machines") to catalyze reactions and complex transformations.[14] DNA-repair pathways represent such systems and are experimentally accessible. 4) Most clinically used antitumor agents, for example, ionizing radiation, cisplatin, alkylating agents, and mitomycin C, exert their cytotoxicity by damaging DNA and are counteracted by DNA-repair enzymes. Thus, whereas intact DNA repair is essential for a healthy organism, the selective inhibition of DNA repair in cancerous cells may greatly improve antitumor therapy. DNA-repair enzymes are therefore targets for drug design.



Scheme 1. Responses to and consequences of DNA damage.

[*] Dr. O. D. Schärer
Institute of Molecular Cancer Research
University of Zürich
August Forel Strasse 7, 8008 Zürich (Switzerland)
Fax: (+41) 1-634-8904
E-mail: scharer@imr.unizh.ch

 DOI: 10.1002/anie.200200523 © 2003 Wiley-VCH Verlag GmbH & Co. KGaA, Weinheim

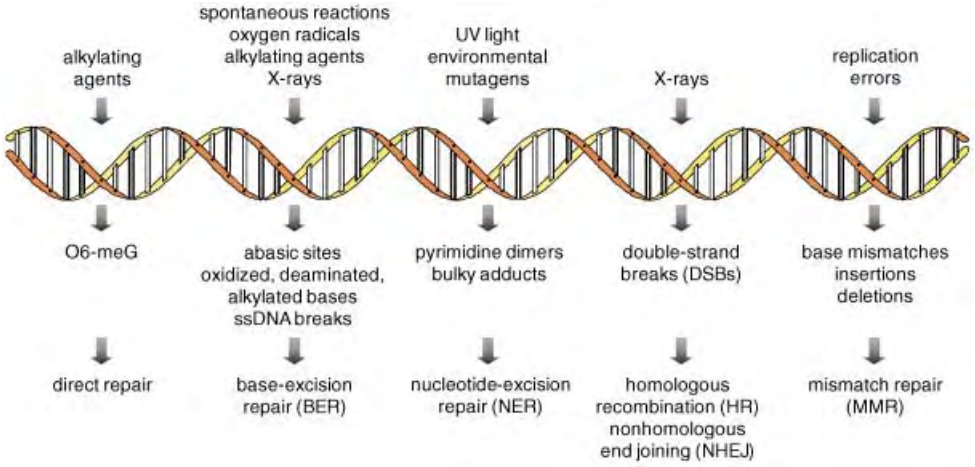


Figure 1. Most common DNA-damaging agents, lesions, and repair pathways.

In the following chapters, the various known forms of DNA damage and the biochemical and structural basis as well as the biological and medical relevance of mammalian-DNA-repair pathways are discussed. The goal is to provide a general overview of the known DNA-repair pathways in mammals and to place special emphasis on two aspects: 1) the specific recognition of damaged sites in DNA by DNA repair enzymes, and 2) chemical approaches that have been used to study DNA repair.

2. DNA Damage and Responses in Human Cells

DNA is not indefinitely stable in aqueous solution and numerous sources of damaging agents of endogenous and exogenous origins additionally contribute to the decay and instability of DNA.[15] Crude estimates of the number of DNA-damage events in a single human cell range from 10^4–10^6 per day, requiring therefore in an adult human (10^{12} cells) about 10^{16}–10^{18} repair events per day.[6] Since alterations in only a small number of base pairs in the genome are in principle sufficient for the induction of cancer, it is clear that DNA-repair systems effectively counteract this threat. Figure 1 provides an overview of the most important agents that cause DNA damage, the lesions formed, and the repair pathways employed to remove these lesions from DNA.



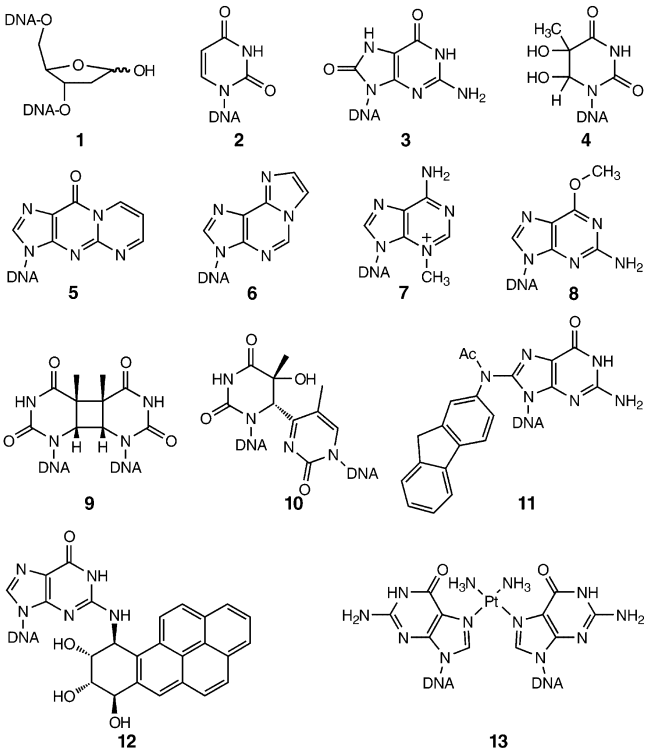
Orlando Schärer was born in Zürich, Switzerland, where he studied Chemistry at the ETH Zürich. In 1996 he completed his PhD thesis with Greg Verdine at Harvard University, Cambridge, USA, and then joined the group of Roland Kanaar and Jan Hoeijmakers at Erasmus University, Rotterdam, The Netherlands. Since 1999 he has been a START fellow of the Swiss National Science Foundation and an EMBO Young Investigator at the University of Zürich. His present research interests span the chemistry and biology of mammalian DNA repair and the related development of approaches to antitumor and gene therapy.

2.1. Damage to the Nucleobases of DNA

The simplest reaction that is potentially harmful to DNA is hydrolysis.[15] The glycosidic bond of purine nucleotides is rather prone to acid-catalyzed hydrolysis. Abasic sites (**1**, Scheme 2), which are the products of depurination, have lost the genetic coding information and can thus lead to mutations during replication.[16] Recent studies, in which a highly sensitive probe for the aldehyde group of abasic sites was used, led to an estimate of the spontaneous generation of almost 10000 abasic sites per human cell per day.[17] Abasic sites are very base-labile and can also spontaneously further fragment to form cytotoxic single-strand beaks. A second hydrolytic reaction can occur at the exocyclic amine groups of C, 5-MeC, A, and G, leading to the bases uracil, thymine, hypoxanthine, and xanthine, respectively.[15] These deaminations can lead to alterations in the coding sequence. The formation of uracil (**2**) from cytidine is the most important of these lesions and has been estimated to occur 100–500 times per day in a human cell.[18]

In addition to water, many reactive species that can modify DNA are generated as a consequence of normal cellular metabolism. Reactive oxygen species (ROS) such as superoxide radical anions, hydrogen peroxide, or hydroxyl radicals are formed as by-products of oxygen metabolism and can react with DNA to give rise to one of over 100 oxidative modifications in DNA found to date.[19,20] The most prominent oxidative base adducts include 8-oxoguanine (**3**), which is mutagenic and can block transcription, and thymine glycol (**4**), which is only mildly mutagenic but blocks DNA replication and transcription.[21,22] Modification of DNA bases by ROS can also occur in an indirect fashion. Polyunsaturated fatty acids, for example, are readily oxidized to form bifunctional electrophiles such as malondialdehyde, which can lead to the formation of the pyrimidinopurinone

 © 2003 Wiley-VCH Verlag GmbH & Co. KGaA, Weinheim



Scheme 2. Examples of common lesions to DNA. Abasic sites (**1**) and uracil (**2**) are induced by hydrolysis; oxidative damage results in the direct formation of 8-oxoguanine (**3**) and thymine glycol (**4**) and indirectly produces M_1G (**5**) and 1,N^6-ethenoadenine (**6**); endogenous and exogenous methylating agents form, among others, 3-methyladenine (**7**) and O^6-methylguanine (**8**). UV radiation induces the formation of photoadducts of adjacent pyrimidines such as the cyclobutane pyrimidine dimers (CPD, **9**) and (6-4) photoadducts (**10**). Aromatic amines or nitro compounds and aromatic hydrocarbons are metabolized in the cells to reactive intermediates that generate adducts of the type **11** or **12** upon reaction with DNA. Many antitumor agents form DNA adducts (e.g. cisplatin forms intra- and interstrand DNA crosslinks by linking two guanine bases in close proximity (**13**)).

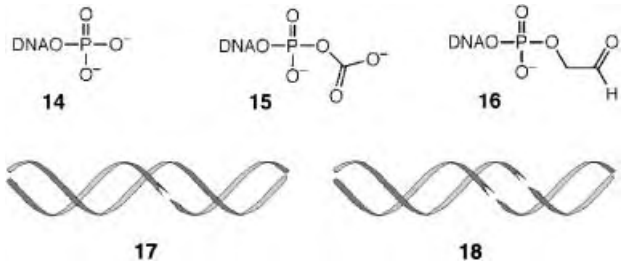
adduct M_1G (**5**) or epoxidation products of acrolein, which form exocyclic etheno modifications of A (**6**), C, and G.[23]

Cofactors of enzymatic reactions, such as *S*-adenosylmethionine (SAM), a methyl-group donor, can accidentally methylate DNA to form 7-methylguanine, a relatively harmless lesion, and 3-methyladenine (**7**), which is highly cytotoxic as a result of its ability to block DNA replication.[24] That relatively rare lesions can be very important is illustrated by various methyl adducts in DNA. In contrast to the rather harmless 7-methylguanine, O^6-methylguanine (**8**) is only a minor product of methylation, but because it is mutagenic and cytotoxic, it is apparently important enough that a separate repair pathway has evolved to deal with this lesion.[25] Base-excision repair and, in the case of O^6-methylguanine, direct repair are the main pathways involved in the repair of spontaneous damage to DNA caused by normal cellular metabolism.[7,15,26]

In addition to these sources of DNA damage from normal cellular metabolism, there are numerous exogenous sources of damage. Some of these, for example, UV radiation from sunlight, are of natural origin and cannot be avoided, whereas others, such as genotoxic compounds found in cigarette smoke, are manmade, and the extent to which they contribute to DNA damage in an individual is dependent on his or her lifestyle. UV radiation leads to the formation of photoadducts between adjacent pyrimidine residues in DNA, principally cyclobutane dimers **9** and (6-4) photoadducts **10**.[27] There are numerous additional examples of adducts of genotoxic compounds, for example, those formed by environmental mutagens such as aromatic amines **11** and aromatic hydrocarbons **12**, and by antitumor agents such as cisplatin (**13**); these compouds are referred to as bulky adducts.[28] Bulky adducts lead to strong local distortion of the DNA double helix and block transcription and DNA replication. These bulky adducts are removed by nucleotide-excision repair (NER) in mammals.[7,29] The ability of NER to remove a large number of structurally diverse lesions from DNA may have evolved specifically to deal with lesions that are sporadically formed by environmental mutagens. Whereas mammals only remove pyrimidine dimers by NER, lower eukaryotes, plants, and bacteria also remove these adducts by photolyases, which transform the dimers back into two monopyrimidines, and in some cases through base-excision DNA repair.

2.2. Damage to the DNA Backbone and Double-Strand Breaks

Damage to the backbone of DNA occurs mostly through oxidation of the deoxyribose sugar, which has several positions that are highly reactive toward oxygen radical species.[20,30,31] Oxidative degradation of the sugar moieties leads to a number of adducts, for example, oligonucleotides with 3′-phosphate (**14**), 3′-phosphoglycolate (**15**), or 3′-phosphoglycaldehyde (**16**) ends, in addition to the complementary fragmented sugars. (See reference [31] for a complete discussion of sugar-fragmentation pathways.) The pattern of adducts formed depends on the position of the hydrogen abstraction in the sugar. All these oxidative reactions lead to the formation DNA breaks. In addition to reactive oxygen species, ionizing radiation and radiomimetic drugs such as bleomycin or neocarzinostatin are known to lead to strand breaks. The primary break products are single-stand breaks (Scheme 3, **17**), which are addressed by a variant of BER. In contrast to oxidative DNA-damaging agents discussed so far,



Scheme 3. Oxygen radical species, ionizing radiation, and radiomimetic drugs such as bleomycin are among the agents that fragment deoxyribose moieties in DNA, eventually yielding DNA with phosphate (**14**), 3-phosphoglycolate (**15**), and 3-phosphoglycaldehyde (**16**) end groups. These fragmentations lead to the formation of single- (**17**) or double-strand breaks (**18**) by damage to the sugar moieties of DNA.

 © 2003 Wiley-VCH Verlag GmbH & Co. KGaA, Weinheim

ionizing radiation and radiomimetic drugs induce multiple damaged sites in close proximity in DNA and thus lead to the formation of double-strand breaks (DSBs) (**18**).[32] DSBs are also formed during replication, either by the replication of a single-strand break or by the collapse of a replication fork.[33] DSBs are obligatory intermediates in other cellular processes such as meiosis or V(D)J recombination, which contribute to genetic diversity in reproduction and the maturation of the immune system, respectively.[34] DSBs are particularly severe lesions because they can lead to gross chromosomal aberrations, and it has been shown that a single DSB left unrepaired in a yeast cell can lead to cell death.[35] DSBs pose a special challenge to the repair machinery, because in contrast to the lesions discussed previously, both DNA strands are damaged and a partner strand is not available as a template for repair. Eukaryotes use two principle pathways to deal with DSBs: homologous recombination (HR) and nonhomologous end joining (NHEJ). Both routes are involved in the repair of DSBs and also include specialized repair functions.[34,36]

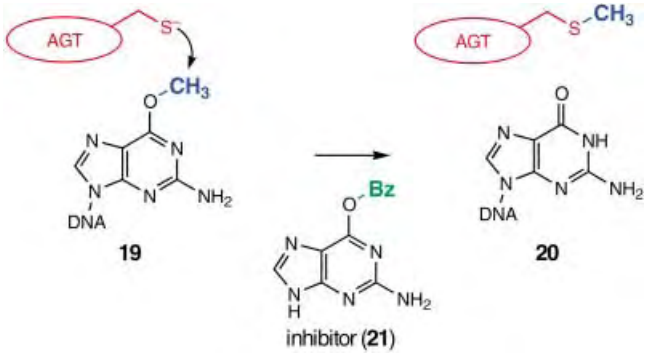
2.3. DNA Interstrand Crosslinks

Another class of lesions in which both DNA strands are damaged are interstrand crosslinks (ICLs) formed by a covalent connection of two DNA bases on opposite strands of DNA. ICLs are highly cytotoxic because they block all transactions that necessitate the separation of the two DNA strands, for example, DNA replication and transcription. Although there is evidence that ICLs occur naturally, for example, through the reaction of DNA with bifunctional electrophilic products of lipid peroxidation, they are expected to be rare.[37] Psoralen, a bifunctional photoreactive aromatic molecule used in photochemotherapy, has frequently been used to assess the biological effects of ICLs.[38] Interestingly, a large number of antitumor drugs, such as the chloroethyl nitroso ureas, nitrogen mustards, mitomycins, and cisplatin, form ICLs; although these adducts are not the major products, they are clinically very relevant.[39] There are indications that the repair of ICLs proceeds through the formation of a DSB, which is then repaired by homologous recombination, but the details of ICL repair are not yet understood.[40]

3. Repair by Direct Reversal of Damage

UV-induced pyrimidine dimers and O^6-alkylguanine adducts can be repaired by direct reversal of damage by photolyases[13,41] and alkylguanine transferases, respectively, in bacteria and lower eukaryotes. In mammals, only O^6-alkylguanine adducts are repaired in this way.[213]

O^6-alkylguanine transferase (AGT) activity is found in most living organisms and counteracts the mutagenic effects of O^6-methylguanine.[42] AGT reverses O^6-alkylguanine to guanine by transferring the alkyl group from DNA to a reactive cysteine group of the protein in an irreversible reaction (Scheme 4). This covalent attachment of the alkyl group to the cysteine residue inactivates the enzyme. AGT is thus a suicide enzyme that is targeted for proteolytic degradation after a single turnover. Structure studies revealed that the active site of AGT is located it the interior of the protein, some distance away from the DNA-binding surface.[43] The protein is thought to employ a nucleotide-flipping



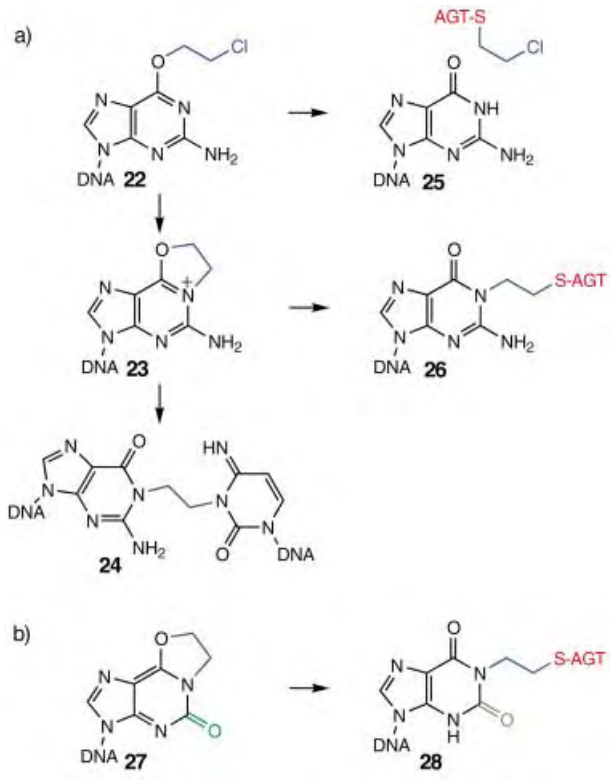
Scheme 4. Mechanisms of repair by O^6-alkylguanine transferase AGT. AGT restores a guanine residue in DNA by transferring the methyl group from O^6-methylguanine (**19**) to a reactive cysteine residue of the protein in an irreversible reaction. O^6-Benzylguanine (**21**) is a potent inhibitor of AGT that is in clinical development for antitumor therapy.

mechanism to bring the substrate base and AGT active-site nucleophile into close proximity (see Section 4.2.2 for a more detailed discussion of base flipping).

The importance of AGT in protecting mammals from toxic and mutagenic effects of alkylating agents has been demonstrated in mice. Transgenic mice that overexpress AGT develop significantly fewer tumors in response to the methylating agent *N*-methyl-*N*-nitrosourea, whereas mice that are deficient in AGT are much more susceptible to the tumor-inducing and toxic effects of this agent than wild-type mice.[44] AGT is an important enzyme in antitumor therapy since it counteracts the cytotoxic effects of antitumor agents of the chloroethyl nitroso urea (CENU) class, for example, BCNU (*N*,*N*-bis(2-chloroethyl) *N*-nitroso urea) or temozolomide. The levels of AGT present in tumors have been shown to be a major determinant for the success of antitumor therapy with CENUs.[42] CENUs initially react with the O^6 carbonyl group of guanine to form adduct **22**, which is subsequently converted into the 1,O^6-ethanoguanine adduct **23**. The adduct **23** rearranges over several hours to the physiologically active ICL **24** (Scheme 5).[45] AGT counteracts the formation of **24** by reacting with **22** or **23** to restore the guanine base or to form the protein–DNA adduct **26**. Evidence for the formation of adduct **26** has been obtained, but it has only been isolated in quantities too small to allow its detailed characterization.[46a] Noll and Clarke addressed this problem with a chemical biological approach and introduced 1,O^6-ethanoxanthine **27**, a stable analogue of **23**, into DNA (Scheme 5).[46b] Ethanoxanthine **27** reacts with AGT to form the stable protein–DNA adduct **28**. This approach should allow the generation of the covalent AGT–DNA adduct **28** in large amounts, which may be used to solve the first structure of AGT bound to DNA.

The interference of AGT with alkylation therapy has led to a search for inhibitors of AGT that may be use in cancer

 © 2003 Wiley-VCH Verlag GmbH & Co. KGaA, Weinheim



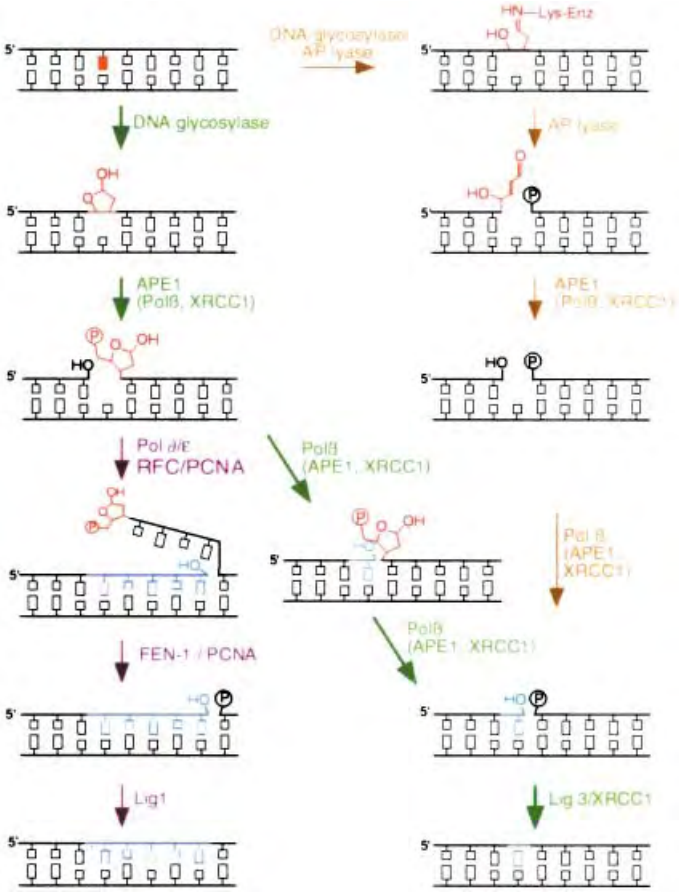
Scheme 5. AGT counteracts the effects of antitumor agents. a) Chloroethyl nitroso ureas react with guanine residues in DNA to form adduct **22**. The latter rearranges to N^1,O^6-ethanoguanine (**23**), which reacts with the cytidine residue located opposite to it to form a DNA interstrand crosslink **24**. AGT can react with **22** and **23** and prevent the formation of the crosslink. b) N^1,O^6-ethanoxanthine (**27**) is a stable analogue of **23** that has been incorporated into DNA synthetically and reacts with AGT to form the protein–DNA crosslink **28**.

therapy in conjunction with alkylating agents. To date, designed inhibitors are principally guanine derivatives with substituents at the O^6 positions. O^6-Benzylguanine (**21**, Scheme 4) has emerged as the standard AGT inhibitor against which new molecules are compared.[47] The efficacy of O^6-BzG in potentiating the cytotoxicity of the CENUs has been demonstrated in animal models, and clinical trials for this combination treatment are underway.[48] A limiting factor of this therapeutic approach is the toxicity to healthy organs, particularly to the bone marrow. Several groups are aiming to circumvent that problem by generating AGT variants that are resistant to inhibition by O^6-BzG that could be used to protect the bone marrow by gene transfer.[49]

4. Base-Excision Repair

4.1. Overview

Damage to DNA bases resulting from deamination, oxidation, and alkylation is mainly repaired by base-excision repair.[7,10,15,26,50] BER is initiated by DNA glycosylases, which recognize damaged bases and excise them from DNA by hydrolyzing the *N*-glycosidic bond between the base and the sugar phosphate backbone of DNA to generate an abasic site (Scheme 6). Nine different human DNA glycosylases have been cloned and characterized, each one with unique substrate specificity (Table 1). Three glycosylases additionally have AP lyase activity, which enables them to cleave the bond between the sugar and the phosphate 3′ to the damaged site (Schemes 6 and 7). AP endonuclease APE1 (also called HAP-1 or Ref-1) is the second enzyme in the pathway and hydrolyzes the phosphodiester bond 5′ to the abasic site to generate a nick. In the main BER pathway, that is, the short-patch repair (designated by green arrows in Scheme 6), polymerase β (Polβ) incorporates a single nucleotide and removes the abasic site by virtue of its AP lyase activity. If



Scheme 6. Overview of base excision repair (BER). The predominant short-patch BER pathway is indicated by green arrows. The enzymes that catalyze each step are indicated and their interacting partners are shown in parenthesis. DNA glycosylases initiate BER by excising damaged bases from DNA and generating abasic sites. APE1 hydrolyzes the phosphate bond 5′ to the abasic site. Polymerase β (Polβ) introduces one nucleotide past the abasic site and then excises the abasic site by virtue of its AP lyase activity. DNA ligase III finally seals the nick and restores the original DNA sequence. If BER is initiated by a bifunctional DNA glycosylase/AP lyase, the pathway demarcated with brown arrows is followed. After excising the base, the AP lyase hydrolyzes the bond 3′ to the abasic site. APE1, Polβ, and DNA ligase III then complete the repair, although the AP lyase activity of Polβ may not be required. In long-patch BER (purple arrows), Polδ/ε and associated factors introduce two to six nucleotides past the abasic site. The resulting overhang is excised by Fen-1 endonuclease and the nick is sealed by DNA ligase I.

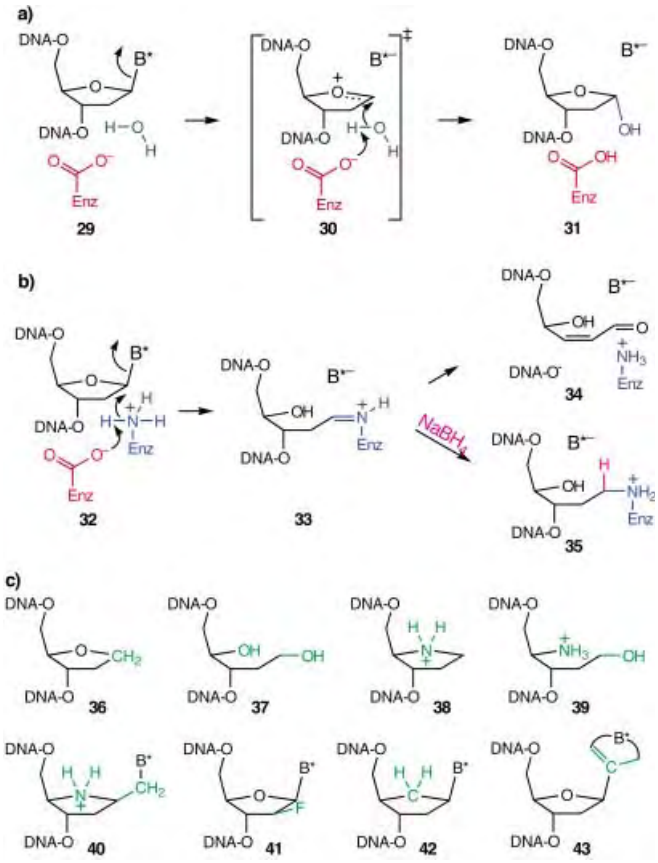
 © 2003 Wiley-VCH Verlag GmbH & Co. KGaA, Weinheim

Table 1: Human DNA glycosylases

Enzyme	Most important substrate	AP lyase
UNG	U, 5-OH-U in ss/dsDNA	no
SMUG1	U, 5-OH-U in ss/dsDNA	no
TDG	U:G, T:G, εC	no
MBD4	U:G, T:G	no
OGG1	8-oxoG:C, fapy	yes
MYH	A:8-oxoG	no
NTH1	ox. pyrimidine, fapy	yes
NEI1	ox. pyrimidine, fapy	yes
AAG (MPG)	3-MeA, 7-MeG, εA, Hx	no

BER is initiated by a bifunctional DNA glycosylase/AP lyase, this AP lyase activity of Polβ may not be required (brown arrows in Scheme 6). The biological significance of the AP lyase activity of DNA glycosylases is still a matter of debate and some studies suggest that it may actually not be used in BER.[51,52] The nick in DNA is sealed by DNA ligase III, which interacts with Polβ through XRCC1 (X-ray repair cross-complementing group 1). Although individual enzymes mediate each step in BER, the process is highly coordinated to ensure smooth repair of the abasic site and strand-break intermediates, which are by themselves highly toxic lesions. DNA glycosylases show high affinity for their products, abasic sites, and likely remain bound to them until APE-1 acts on them. So far no direct interaction between DNA glycosylases and APE-1 has been observed, but APE-1 has been shown to stimulate the reactions catalyzed by various DNA glycosylases. It has been suggested that this occurs by a passive process, in which APE-1 rapidly acts on abasic sites released by DNA glycosylases.[51,53] A recent study has demonstrated that sumoylation (a ubiquitin-like post-translational modification) of the DNA glycosylase TDG increases its turnover rate, providing a possible mechanism for regulation of its binding activity to abasic sites.[54] Whether other DNA glycosylases can also be regulated in this way remains to be seen. The subsequent processing of abasic sites is coordinated by specific protein–protein interactions. APE-1 interacts directly with Polβ and XRCC1, and Polβ interacts with ligaseIII through XRCC1.[55] Whereas the complex between XRCC1 and ligase III is constitutive, the interactions between the other proteins appear to be transient in nature.

A second, minor pathway for the repair of abasic sites in BER, the long-patch repair, has been described (purple arrows in Scheme 6). Long-patch BER relies on polymerase δ/ε and associated replication factors to introduce 2–6 nucleotides after the abasic site, the flap endonuclease Fen-1 to excise the short oligonucleotide overhang generated, and DNA ligase I to seal the nick.[56]



Scheme 7. Reaction mechanism and inhibitors of DNA glycosylases. a) Reaction catalyzed by a monofunctional DNA glycosylase: A water molecule in the active site is deprotonated by a conserved carboxylate side chain of the enzyme and positioned to replace the damaged base at the anomeric position. In the case of UDG, the transition state has been shown to be dissociative based on kinetic isotope-effect measurements. For other DNA glycosylases it has not yet been determined whether the reaction occurs through a dissociative or associative mechanism. It is likely that substantial positive charge accumulates in the transition state of either mechanism. b) Reaction mechanism of bifunctional DNA glycosylase/AP lyases: The first step of the reaction is similar to the reaction catalyzed by monofunctional DNA glycosylases, except that a lysine residue of the enzyme is used as a nucleophile. This leads to the formation of the Schiff base adduct **33**, which undergoes base-catalyzed β elimination, leading to cleavage of the C3′—O bond and strand scission. The Schiff base intermediate **33** can be intercepted by sodium borohydride, resulting in the irreversible formation of the protein–DNA adduct **35**. c) Synthetic inhibitors of DNA glycosylases: Analogues of abasic sites (**36**, **37**) bind DNA glycosylases because most of these enzymes are inhibited by the end product. In inhibitors **38**–**40**, the oxygen atom in the ribose ring is replaced by a nitrogen atom, resulting in a positively charged sugar moiety designed to mimic the transition state. Compounds **41**–**43** contain a stabilized glycosidic bond and are bound, but not processed, by DNA glycosylases.

4.2. DNA Glycosylases

4.2.1. Substrate Specificities of DNA Glycosylases

Four of the known human DNA glycosylases, UDG, SMUG1, TDG, and MBD4 show activity against bases that arise through deamination of C (uracil); TDG and MBD4 are also active against deaminated 5-MeC residues (thymine) (Table 1). UDG is the most efficient DNA glycosylase and is responsible for the removal of most U residues from DNA. UDG interacts with components of the replication machinery and appears to function in clearing the genome of U immediately following replication.[57] On the other hand, SMUG1 appears to function throughout the cell cycle and may therefore be a constitutive backup system for UDG.[58] UDG and SMUG1 are the only DNA glycosylases that act

 © 2003 Wiley-VCH Verlag GmbH & Co. KGaA, Weinheim

both on single-strand DNA (ssDNA) and double-strand DNA (dsDNA), whereas all other enzymes require dsDNA for activity. TDG and MBD4 both have a preference for T and U paired with G residues and might therefore have a specific role in maintaining genomic stability in the context of methylated CpG sequences.[59] Methylation of C residues occurs exclusively in CpG sequences in mammalian genomes and is of great importance for gene silencing and the regulation of transcription. Some studies suggest that TDG has roles in the regulation of transcription and active demethylation as well as to DNA repair.[60] Whether TDG and MBD4 function mainly as DNA-repair enzymes or whether their main roles lie elsewhere remains to be established.

Two enzymes address the mutagenic effects of 8-oxoguanine, one of the most frequent and mutagenic lesions in DNA (Table 1): 1) OGG1 excises 8-oxoG specifically when paired with C. These 8-oxoG residues arise through oxidation of G in dsDNA. OGG1 therefore prevents 8-oxoG from mispairing with A in subsequent rounds of replication.[61] 2) MYH (MutY homologue) glycosylase removes misincorporated A residues paired with 8-oxoG residues (such A-8-oxoG pairs arise during replication).[62] Together with the 8-oxodGTP phosphatase MTH (MutT homologue), which hydrolyzes 8-oxodGTP and removes it from the nucleotide pool, these two DNA glycosylases form a highly coordinated three-stage system to counteract the deleterious effects of 8-oxoG in DNA and in the nucleotide pool.[63]

Oxidized pyrimidines such as thymine glycols are excised by the hNTH1 and hNEI1 glycosylases. Both enzymes have a rather wide substrate specificity and have the ability to excise a variety of oxidized pyrimidines as well as certain oxidized purines from DNA. An unusual feature of the hNTH1 enzyme is that it is stimulated by the XPG protein, which mainly functions in NER (see Section 5.3).[64] The hNEI1 glycosylase was the most recent human DNA glycosylase found and was discovered through database searches after completion of the human genome project.[65] Interestingly, two additional homologues of hNEI1 are present in the human genome, but these have not yet been characterized.

The main function of AAG (also called MPG or ANPG) is likely the repair of alkylated purine residues in DNA, but the enzyme has a remarkably broad substrate specificity, which includes 3-methyladenine, 7-methylguanine, 1,N^6-ethenoadenine, and hypoxanthine.[66] Interestingly, AAG has also been shown to have weak activity on unmodified DNA bases.[67] Consistent with this observation, overexpression of the yeast 3-methyladenine DNA glycosylase Mag (which has properties similar to those of AAG) leads to a strong mutator phenotype, which demonstrates that the tight regulation of BER is important to avoid mutagenic effects of abasic sites.[68]

Although it is not clear whether additional DNA glycosylases exist in the human genome, the recent, and somewhat unexpected, discoveries of SMUG1 and NEI1-3 raises the possibility that additional human DNA glycosylases exist.[65,69] It is worth mentioning that SMUG1 was isolated through a chemical biological approach by using an expression-cloning screen to identify enzymes that bind to generic synthetic inhibitors of DNA glycosylases.[69] Because of the redundancy of enzymes that act on U, SMUG1 may not have been easily discovered by using traditional biochemical and genetic approaches. Perhaps chemical biological approaches such as that used for SMUG1 will lead to the discovery of additional DNA glycosylases.

4.2.2. Mechanism and Inhibitors of DNA Glycosylases

DNA glycosylases fall into two mechanistic classes:[70] 1) Monofunctional DNA glycosylases use a water molecule as a nucleophile to cleave the *N*-glycosidic bond and thus generate abasic sites (Scheme 7a). 2) Bifunctional glycosylases/AP lyases use an amino group of the enzyme as a nucleophile to generate a Schiff base intermediate, which can undergo base-catalyzed β elimination thus leading to scission of the C3−O bond between the abasic site and the sugar phosphate (Scheme 7b). OGG1, NTH1, and NEI1 are the only mammalian glycosylases that exhibit AP lyase activity. The AP lyase has been instrumental in the isolation and characterization of OGG1 and hNTH1. The Schiff base intermediate **33** of the reaction can be reduced to an amine, resulting in the stable covalent protein–DNA complex **35** (Scheme 7b). The formation of this complex is highly specific and is readily formed between an appropriate substrate oligonucleotide and a DNA glycosylase in a crude cell extract.[71,72]

The reaction catalyzed by DNA glycosylases is formally related to enzymes such as glycosidases or nucleoside hydrolases.[73] Mechanistic models were originally based on this analogy, and the reaction catalyzed by DNA glycosylases has been suggested to proceed by a mixed S_N1/S_N2 mechanism with substantial positive charge accumulated in the ribose ring, especially at C1′ and O1′. Whether the transition state of the DNA-glycosylase-catalyzed reaction has more dissociative or associative character has thus far only been addressed directly for UDG (see below).[74] This enzyme appears to function by a dissociative mechanism. In the absence of detailed mechanistic information, inhibitors of DNA glycosylases were designed either based on the importance of the positive charge in the transition state or based on the fact that most DNA glycoyslases are inhibited by their products, abasic sites (Scheme 7c).[9,10]

The simplest inhibitors of DNA glycosylases are stable abasic site derivatives such as **36** and **37**.[71,75,76] A second class of inhibitors (e.g. **38**–**40**) were designed to mimic the positive charge in the transition state.[69,76,77] For this purpose, the oxygen in the ribose ring was replaced with a positively charged ammonium group. A third class of inhibitors, **41**–**43**, contain stabilized glycosidic bonds as a result of the modification of the ribose ring or the base, which makes them resistant to DNA glycosylases.[78] These inhibitors have been exceedingly useful for structure studies of DNA glycosylases bound to DNA and for the isolation of novel DNA glycosylases.

4.2.3. Structure and Mechanism Studies of DNA Glycosylases

In recent years, several high-resolution crystal structures of DNA glycosylases bound to their substrates, substrate

 © 2003 Wiley-VCH Verlag GmbH & Co. KGaA, Weinheim

analogues, or products have been solved. DNA glycosylases are therefore the best-understood DNA-repair enzymes in terms of damage recognition and catalysis, and several reviews covering this topic have appeared recently.[10,79] This Review is restricted to the discussion of what we have learned from structural and biochemical studies of three human enzymes, UDG, OGG1, and AAG. Studies of these three DNA glycosylases have been particularly instructive in establishing the principles of the mode of action of this class of enzymes.

Many features are common to all DNA glycosylases: All enzymes employ a nucleotide-flipping mechanism in which the target nucleotide is extruded out of the DNA double helix and into the active site of the enzyme, where catalysis takes place (Figure 2a, Figure 3a). Nucleotide flipping is an ingenious way for enzymes that catalyze reactions on DNA to gain access to bonds that are buried in the major or minor groove of DNA, which otherwise present inaccessible reaction trajectories for enzyme catalysis. The principle of base flipping was initially observed for DNA methyltransferase enzymes[80] and has since been shown to be employed by all DNA glycosylases. Extrusion of the target nucleotide involves local distortion of DNA and is accomplished by rotation around the phosphodiester bonds flanking the target nucleotide. A bulky hydrophobic or aromatic residue is usually inserted into the DNA helix to take the position of the displaced base. For UDG, a pinch-push-pull mechanism has been proposed to lead to the nucleotide flipping. The first step rapid (nonspecific) scanning of the DNA backbone by compression of two adjacent phosphodiester bonds (pinching). This is followed by full kinking of the backbone and insertion of a loop containing the residue to fill the void left by the extruded nucleotide into the minor groove (pushing). Finally, binding of the uracil base in a specific binding pocket (pull) occurs.[81] The binding of the damaged bases in the active site of the enzyme is accomplished through π stacking, hydrophobic interactions, and hydrogen bonding. Interestingly, certain DNA glycosylases (e.g. UDG) have a highly specific binding pocket, whereas others (e.g. AAG) have much broader substrate specificity.[10] The reaction rates of certain glycosylases (e.g. OGG1) are furthermore strongly dependent on the base opposite the damage.

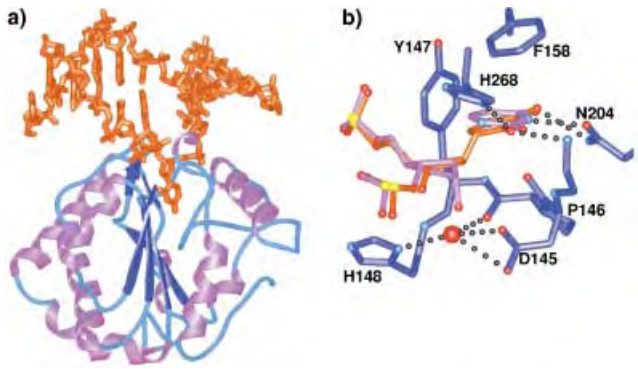


Figure 2. Cocrystal structure of UDG bound to an uncleavable substrate analogue. a) Overall structure of UDG bound to a deoxypseudouridine-containing oligonucleotide. The target nucleotide is flipped out of the DNA double helix into the active site of the enzyme (orange = DNA, blue = UDG β-sheets, purple = UDG α-helices). b) Active site of UDG with the uracil-binding pocket. The structures of the uncleaved substrate (orange) and product (pink) complex derived from two different structures are superimposed. Amino acids that are important for catalysis (D145, H148, H268) and those that form the uracil binding pocket (Y147, F158, N204) are shown. Reprinted with permission of the National Academy of Sciences 2000.[86]

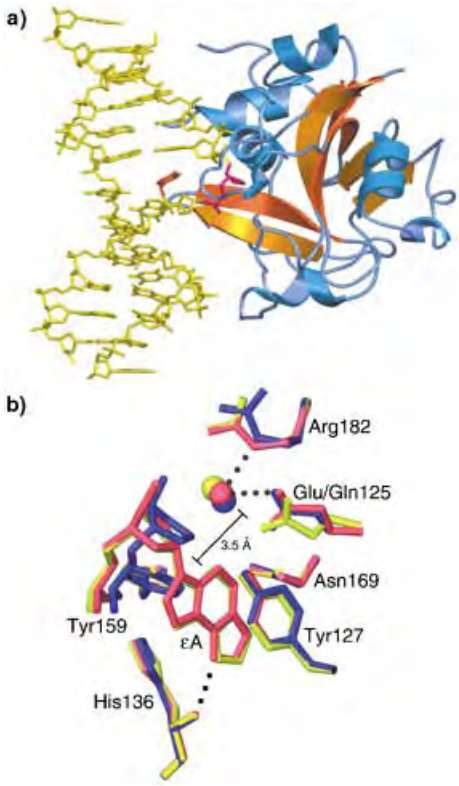


Figure 3. Structure of AAG bound to DNA. a) Overview of the crystal structure of AAG complexed to DNA that contains a pyrrolidine inhibitor. AAG binds in the minor groove of DNA and expels the pyrrolidine (pink) into the active site of the enzyme. Tyr162 (orange) intercalates in the space vacated by the flipped nucleotide (yellow = DNA, blue = protein (α-helices and turns), orange = proteins (β-sheets)). Reprinted with permission of Elsevier Science 2000.[91] b) Structure of the active site of AAG. Superposition of the active sites of the wild-type pyrrolidine–DNA (blue), E125Q/εA–DNA (yellow), and wild-type εA–DNA (red) complexes shows that the different DNA substrates are bound in similar orientations. The water molecule between Glu/Gln125 and the anomeric carbon center is conserved in all three structures and likely serves as the nucleophile in the reaction. The base-binding pocket is lined with aromatic residues (Tyr127, His136). The amide in the main chain of His136 forms a hydrogen bond with εA at N^6, providing specificity against A. Reprinted with permission of the National Academy of Sciences 2000.[92]

UDG is not only the most specific, but also the most efficient of all known DNA glycosylases. It exhibits rate accelerations in the order of 10^{12}, about five orders of magnitude higher than typical rate enhancements observed for other DNA glycosylases.[12] Structural and biochemical studies of UDG from various organisms (human, *E. coli*, herpes simplex virus) have been carried out, and these will be discussed here with reference to the human enzyme. Early structural studies of UDG bound to its product base U

 © 2003 Wiley-VCH Verlag GmbH & Co. KGaA, Weinheim

revealed a tight binding pocket that provides specificity for U over all other bases.[82] The specificity is provided by a bifurcate hydrogen bond to O4 and HN3 of U by Asn204, which excludes binding of cytosine and purine bases, and the tight packing of the aromatic group of Tyr147 against C5, which leaves no room for the methyl group in T (Figure 2b). In agreement with structural data, a Tyr147Ala mutant of UDG has the ability to excise T, while the Asn204Asp mutant can excise C.[83] Subsequent cocrystal structures of mutant UDG bound to a product complex and wild-type UDG to a stable C-nucleoside analogue of U confirmed these observations and showed that Leu272 is responsible for replacing the damaged nucleotide in the double helix.[84–86] The Leu272Ala mutant has a significantly lower catalytic rate, which can be restored to wild-type levels by placing a bulky pyrene base opposite U that leads to extrahelical preorganization of the target base.[87] The cocrystal structures revealed a role of Asp145 in catalysis through activation of a water molecule as a nucleophile for base displacement (Figure 2b) and an interaction between His268 and O^2 of U leading to the activation of U as a leaving group.[84,86]

UDG from *E. coli* is the only glycosylase that has been studied thoroughly in terms of mechanistic enzymology. Kinetic isotope measurements revealed that UDG proceeds through a transition state with dissociative character and implied an oxocarbenium ion as an intermediate.[74] It will be interesting to see whether other DNA glycosylases proceed through transition states with the same amount of dissociative character. NMR and raman spectroscopic studies revealed that N^1 of U has a much decreased pK_a value in the UDG active site and can thus be present as an anion in the reaction and interact favorably with the carbenium ion in the transition state.[88] A neutral short hydrogen bond between His187 (His268 in the human enzyme, Figure 2b) and O^2 of U appears to be crucial for the formation of this anion.[89] The dissociative nature of the transition state has recently been supported by computational studies.[90] These studies further implied that a large fraction of the stabilization energy of the transition state is not provided by the enzyme, but rather by substrate autocatalysis through interactions between the negatively charged phosphate bonds of the substrate and the carbenium ion. The extensive structural, spectroscopic, and kinetic studies of UDG together with the synthesis of substrate analogues have provided much insight into the mechanism of this efficient enzyme.

A striking characteristic of the AAG DNA glycosylase is its wide substrate specificity, which includes 3-methyladenine, 7-methylguanine, hypoxanthine, and 1,N^6-ethenoadenine.[66] How AAG is able to specifically recognize such diverse lesions that have no clear common structural motif is puzzling. Structures of AAG bound to DNA illustrate how nucleotide flipping is accomplished by insertion of a tyrosine residue on the tip of a loop of AAG through the minor groove into the position of the displaced base (Figure 3a).[91,92] The structure of an active-site mutant of AAG bound to an εA residue shows how the damaged base is bound through stacking interactions with aromatic residues in the protein. A specific hydrogen bond from the amide of the main chain of His136 to the N^6 position discriminates against an unmodified A residue (Figure 3b).[92] Although the recognition of hypoxanthine and 3-methyladenine can be reconciled from this structure, it does not explain the specificity for 7-methylguanine. This clearly shows how different structures of DNA glycosylases bound to various substrates and mutational analyses are necessary to understand damaged-base recognition fully. Insight into the mechanism of the catalytic hydrolysis of glycosidic bonds was obtained from the structure of the active-site mutant bound to the εA substrate and the structure of wild-type AAG bound to a pyrrolidine inhibitor (**35** in Scheme 7).[91,92] In both structures, a water molecule between the anomeric carbon atom and the catalytically essential Glu125 residue is clearly visible (Figure 3b). This water molecule is ideally positioned to displace the damaged base in an inline displacement. Whether the transition state of this reaction has more associative or dissociative character remains to be seen.

Structures of the 8-oxoguanine DNA glycosylase OGG1 bound to DNA provided the first look at a bifunctional mammalian DNA glycosylase/AP lyase and showed how this enzyme specifically recognizes the base that is paired with 8-oxoG. OGG1 inserts a loop that contains an asparagine residue to extrude the substrate base from the DNA helix into the active-site binding pocket.[93] Preferential binding of 8-oxoG over G arises because of a specific hydrogen bond to the H-N^7 group and an overall geometry of the binding pocket that ensures preferential binding of 8-oxoG (Figure 4a). The cytosine base paired with 8-oxoG interacts through hydrogen bonds with Asn149 as well as with Arg154 and Arg204 (Figure 4b). These interactions are physiologically relevant as the excision of 8-oxoG that is paired with bases other than C can constitute a mutagenic event (see Section 2.2.1.). Interestingly, a mutation was found in OGG1 from a cancer cell line in which Arg154 was replaced by His. The resulting enzyme has a much broader substrate specificity with respect to the base paired with 8-oxoG and might therefore contribute to mutagenesis rather than repair.

The examples of UDG, AAG, and OGG1 illustrate how much progress has been made in understanding the molecular basis of damaged-base recognition by DNA glycosylases. Several issues and details however remain to be elucidated. In particular, it is not understood how the damaged bases are specifically recognized before they are flipped out into the active-site binding pocket. Is every single base flipped out of the DNA helix in a processive manner or are specific features of damaged base pairs in reDNA recognized?[94,95] Progress in this area has recently been achieved by studying the binding of OGG1 to damaged (8-oxoG) and undamaged sites in DNA using atomic force microscopic imaging of single molecules.[96] Consistent with the results from crystal structures of OGG1 bound to DNA, OGG1 introduced a sharp bend at damaged sites. At undamaged sites, OGG1 bound either with no bending or with a bending angle equivalent to those found for damaged sites. These observations suggest a two-step model by which OGG1 searches for damage: The DNA glycosylases first interact weakly with DNA. In a second step, a structural transition involves flipping of undamaged sites into the active-site pocket, where it is probed for its structural integrity and only excised if it is recognized as a suitable substrate. This

 © 2003 Wiley-VCH Verlag GmbH & Co. KGaA, Weinheim

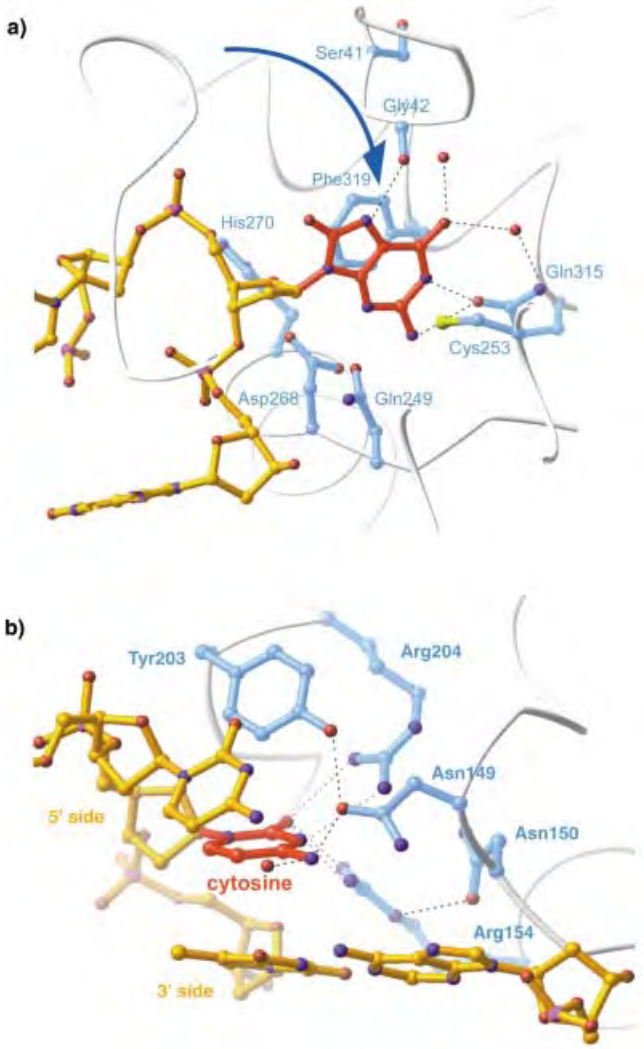


Figure 4. Recognition of 8oxoG and C by OGG1 (light blue = protein residues, red = 8oxoG and C bases, yellow = bulk DNA). a) Ball-and-stick representation of the active site of the enzyme. Cys 253, Gln 315, and Phe 319 line the binding pocket. A hydrogen bond from the amide carbonyl group of Gly 42 to N^7-H is crucial for the preferential binding of 8oxoG over G. b) The recognition pocket of the estranged C. The Watson–Crick face of C interacts with Arg 154, Asn 149, and Arg 204 through specific hydrogen bonds, thus favoring C over other bases. Reprinted with permission of Cold Spring Harbor Laboratory Press 2000.[95]

biphasic mode of searching for damage is consistent with kinetic measurements of nucleotide flipping by UDG.[97] Further developments in atomic force microscopy in solution or single-molecule fluorescence measurements should provide new possibilities for this intriguing question to be pursued.

4.3. Biological Significance of BER Defects

In contrast to NER and MMR defects, no deficiencies in BER enzymes have been found in humans to date.[214] This implies that defects in BER are either lethal or of no severe consequence, so that any defect in a particular gene would go unnoticed. As BER acts on DNA lesions that are produced in normal cellular metabolism, BER is expected to be an essential process. The first knock-out-mouse model with defects in BER proteins were of those downstream of DNA glycosylases, namely APE-1, Polβ, and XRCC1. Mice that were deficient in these genes all died at the embryonic stage, thus indicating that these genes are essential for mammals.[98] In contrast, and unexpectedly, it was found that mice deficient in the DNA glycosylases AAG, OGG1, UDG, NTH1, and MYH did not display any overt phenotype abnormalities nor a significant increase in spontaneous carcinogenesis.[99–101] These observations can be interpreted in three ways: 1) A defect in a single DNA glycosylase may not have a significant impact, whereas the accumulation of abasic-site intermediates arising from all eight known DNA glycosylases may have severe consequences. 2) The critical lesion that leads to mortality in mice deficient in enzymes downstream of DNA glycosylases may not be damaged bases, but rather AP sites that are formed spontaneously by depurination. 3) There may be backup pathways to repair damage that is usually repaired by DNA glycosylases. Such backup functions may be assumed by other DNA glycosylases, as in the case of the four DNA glycosylases that act on uracil. Alternatively, the damage may be repaired through other pathways, for example, the processing of oxidative damage through NER (see Section 5). Notably, UNG(−/−) mice have higher steady-state levels of U in their genome, but without any apparent consequence.[100] Mice with defects in multiple DNA glycosylases or DNA-repair pathways should help to clarify these questions.

5. Nucleotide-Excision Repair

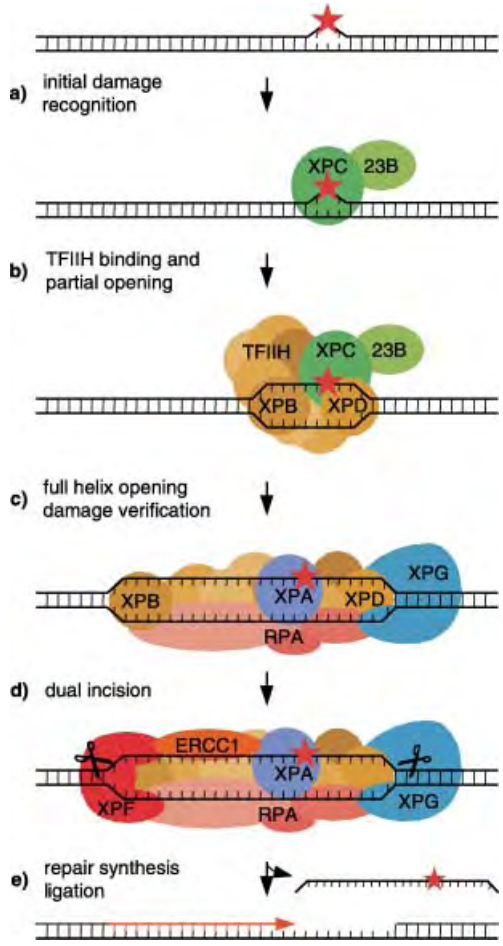
5.1. Overview

Nucleotide-excision repair is the pathway that removes bulky base adducts (such as those formed by UV light, various environmental mutagens, and certain chemotherapeutic agents) from DNA.[29] Although its main biological role is likely to deal with UV damage to DNA, NER is remarkable in its broad substrate specificity. NER might therefore allow an organism to deal with unexpected environmental DNA-damaging agents. The efficiency of repair of a given lesion can vary over several orders of magnitude and there appears to be a general correlation between the efficiency with which a given lesion is repaired and the amount of helical distortion it causes.[102] Simple mismatches or bubbles are, however, not substrates for NER, which indicates that distortion of the DNA backbone alone is not sufficient to qualify as an NER substrate. A bipartite model for recognition has been proposed that involves recognition of a helical distortion followed by localization and verification of the chemically modified base. This two-step process results in the excision of the damaged oligonucleotide.[103] The core NER reaction has been reconstituted with purified proteins, which has led to considerable progress in our understanding of the biochemical basis of the pathway.[104] The steps involved in NER are the recognition of damaged residues and bubble formation,

 © 2003 Wiley-VCH Verlag GmbH & Co. KGaA, Weinheim

dual incision of the damaged DNA strand 5′ and 3′ to the lesion, release of an oligonucleotide 24–32 nucleotides in length containing the damage, and repair synthesis and ligation of the resulting gap (Scheme 8).

About 30 proteins contribute to NER: XPC-hHR23B, the nine subunits of TFIIH, XPA, the trimeric ssDNA-binding protein RPA, and XPG are involved in damage recognition and bubble formation, the two endonucleases XPG and ERCC1-XPF make the incision 3′ and 5′ to the damage, and the polymerases Polδ and Polε, the sliding clamp PCNA, the pentameric clamp loader RFC, and DNA ligase I are involved in the repair synthesis and ligation steps. Additional factors have been shown to contribute to NER, but are not required for the core reaction in vitro. The pathway described in the previous paragraph applies to repair of nontranscribed DNA, which makes up the bulk of genomic DNA. This is also referred to as global genome repair (GGR). In actively transcribed genes, damage in the transcribed strand is repaired more efficiently by a specialized NER pathway called transcription-coupled repair (TCR).[105] TCR was initially discovered based on observations that lesions that can block RNA polymerases are repaired more rapidly in actively transcribed regions of the genome.[106] TCR is an important system to ensure that lesions are repaired efficiently in active regions of the genome. With the exception of XPC-hHR23B, all the genes involved in NER are also required for TCR. TCR requires additional genes, including CSA and CSB genes, which are not required for GGR. Although the dual incision and repair synthesis steps are likely the same in TCR and GGR, initial damage recognition in TCR is probably mediated by a stalled RNA polymerase, but is not yet understood at the biochemical level.



Scheme 8. Nucleotide excision repair (NER): a) A DNA lesion that causes helical distortion (red star) is initially recognized by XPC/hHR23B. b) XPC/hHR23B recruits TFIIH to the lesion and the two helicase subunits of TFIIH, XPB, and XPD cause partial opening of the DNA around the lesion. c) TFIIH attracts XPG and XPA/RPA to the lesion, further DNA opening takes places, and a bubble of about 25 base pairs is formed. XPC is probably no longer part of the complex at this point. d) XPA and RPA verify the damage and ensure the proper positioning of the two endonucleases, XPG and ERCC1/XPF. XPG makes the incision 3′ to, ERCC1/XPF 5′ to the damage and an oligonucleotide of about 25–32 nucleotides in length is released. e) The replication machinery fills in the gap and DNA ligase I seals the nick.

5.2. Mechanism of Damage Recognition and Incision in NER

The mechanism of damage recognition in GGR has been a matter of much debate and controversy over the past decade.[107] This controversy was caused by the fact that none of the factors involved in NER display a high enough specificity for damaged DNA to be a convincing candidate for the initial damage-recognition protein. XPA, XPC, TFIIH, and RPA all display moderate specificity for damaged over undamaged DNA, which at first glance seems to be insufficient to find individual damaged residues against the enormous background of unmodified DNA. High-resolution structural studies of XPA and RPA and low-resolution structures of TFIIH have so far failed to provide any clear information on how these proteins might display selectivity for damaged DNA.[108] Competition experiments aimed at determining the order in which NER proteins interact with the damaged DNA and experiments probing the requirements for unwinding DNA in NER suggested that XPC-hR23B is the initial damage-recognition protein.[109,110] Other studies have challenged this hypothesis and suggest that XPA together with RPA act as the initial recognition factor.[111,112] The hypothesis that XPC is the initial recognition factor has prevailed in light of recent experiments to determine the order of assembly of NER proteins in living cells. This study used spatially defined UV irradiation of cells to generate locally damaged DNA.[113] After UV irradiation and fixing of the cells, probing with monoclonal antibodies against UV-damaged DNA and NER proteins revealed that UV adducts and NER proteins accumulated together in the irradiated compartments of the cells. When this experiment was carried out in cells deficient in various NER factors it was found that XPC was required for the assembly of all other proteins and the XPB subunit of TFIIH was required for all proteins except XPC. Localization of XPF-ERCC1 additionally required the presence of XPA, whereas accumulation of XPG required TFIIH but not XPA. This in vivo study is consistent with the model for NER shown in Scheme 8 and is supported by results from biochemical investigations: XPC-hHR23B binds the damaged DNA and recruits TFIIH to the damaged site.[109,110,114] The helicase subunits of TFIIH, XPB,

 © 2003 Wiley-VCH Verlag GmbH & Co. KGaA, Weinheim

and XPD cause partial unwinding of the DNA around the damaged area; further unwinding and recruitment of XPA, RPA, and XPG results in the formation of the fully opened structure.[110] TFIIH has been shown to interact with XPG and XPA and is hence probably responsible for attracting these two proteins to the site of the lesion.[115] Interestingly, it appears that XPC-hHR23B is no longer part of the NER preincision complex once XPG is bound, and it is likely that XPA is bound to the lesion in this phase.[111,116] XPA in turn interacts with RPA and ERCC1-XPF and is thus responsible for completing the assembly of the NER complex.[117] XPA and RPA appear to play a special role in damage verification and in the correct positioning of the two endonucleases, XPG and XPF-ERCC1, prior to incision.[116,118] The incision 3′ to the lesion is then carried out by XPG, the 5′ incision by XPF-ERCC1; the latter requires the structural presence but not the catalytic activity of XPG.[119–121] XPG is a member of the FEN-1 family of structure-specific nucleases and shows nuclease activity against substrates with ss/dsDNA junctions with a 5′-ssDNA overhang.[120,122] XPF-ERCC1 has a polarity opposite to that of XPG and cleaves 3′ ssDNA overhangs at ss/dsDNA junctions.[119,123] The XPF subunit of the heterodimer contains a conserved nuclease motif that is responsible for catalyzing the incision.[124] Whether ERCC1 has additional roles other than stabilizing XPF and providing a link to the NER machinery through interaction with XPA is presently unknown.

Additional factors have been implicated in NER, although these are not required for the core reaction in vitro. Most prominent among those is DDB (damaged-DNA-binding protein), a heterodimer consisting of p125 (DDB1) and p48 (DDB2). The latter is not present in XPE cells. The role of DDB has remained enigmatic for a long time, but recent data support the notion that it may be required for the repair of certain lesions. XPE has been found at the site of UV damage in living cells and has been shown to specifically stimulate NER of cyclobutane dimers, but not (6-4)photoproducts.[125] These observations suggest that the repair of certain lesions may require proteins in addition to the core NER factors. On the other hand it has also been demonstrated that certain strong helix-deforming lesions can be repaired independently of XPC.[126]

An exciting new area in the study of NER pathways has been the development of new approaches to observe the NER reactions in living cells. NER proteins were fused to the green fluorescent protein (GFP) and expressed in cells deficient in the corresponding wild-type NER protein. Remarkably, attachment of the 30-kDa GFP to native proteins does not impair their NER proficiency in most cases. The mobility of the NER–GFP fusion proteins was observed in real time in vivo by using advanced fluorescent microscopic techniques such as FRAP (fluorescence redistribution after photobleaching). These studies have revealed that NER proteins diffuse freely through the nucleus, become transiently immobilized after UV irradiation, and are released after the damage has been repaired.[127] Further development of such approaches will allow the observation of the NER reaction in more detail in vivo, and will represent a big step toward validating observations from in vitro biochemical experiments.

5.3. Biological Significance of NER

Three rare autosomal recessive disorders are associated with a defect in NER: xeroderma pigmentosum (XP), Cockayne syndrome (CS), and trichothiodystrophy (TTD).[128–130] The three conditions display pleiotropic phenotypes and share an extreme sensitivity to sunlight. XP patients have a partial or total defect in GGR and, with the exception of XPC and XPE patients, also TCR, while CS and TTD patients are only deficient in TCR. XP patients display symptoms that are consistent with a defect in the repair of DNA damage induced by UV light, including a 1000-fold higher predisposition to skin cancer and progressive degenerative alteration of skin and eyes. These symptoms can be explained by sensitivity to UV light and are in some cases accompanied by neurological abnormalities. Neurological abnormalities are only found in patients with severe NER defects and have been attributed to the accumulation of certain forms of oxidative damage in neurons.

Apart from the extreme photosensitivity, the symptoms displayed by CS patients on the other hand are at first glance not as clearly related to a DNA-repair defect. CSB patients, for example, do not show a clear predisposition to cancer, which indicates that they do not accumulate the same amount of damage that can lead to mutations as do XP patients. Many other symptoms displayed by CS patients are difficult to explain by a defect in TCR alone, especially considering that GGR- and TCR-deficient XP patients do not display such symptoms. These symptoms include severe neurological abnormalities, short stature, birdlike faces, tooth decay, and cataracts. The mean life expectancy of CS patients is 12.5 years. Indeed, it has been suggested that CSA and CSB have a more general role in transcription, and that some of the features of CS could be a result of a partial defect in transcription.[131] In addition to having a defect in transcription-coupled NER, CSB cells are defective in a more recently discovered phenomenon termed transcription-coupled base-excision repair (TC-BER) of oxidative damage. This process is not yet well-understood, but in analogy to transcription-coupled NER appears to involve the preferential repair of oxidative lesions in transcribed genes by using BER machinery. How BER enzymes are directed to damage in transcribed genes is not yet understood. The process involves CSB, TFIIH, and XPG, but not other NER factors.[22,132] To what extend TC-BER contributes to the characteristics of CS is not yet clear.

TTD patients show many symptoms of the CS patients and additionally show characteristic sulfur-deficient, brittle hair and scaling of the skin. The symptoms of TTD have been attributed to lower levels of TFIIH. NER (both GGR and TCR) appear to require higher levels of TFIIH than transcription, arguing against a dramatic defect of transcription in TTD patients. Low amounts of TFIIH could, however, be a rate-limiting factor in the transcription of certain genes and could explain the specific symptoms of the TTD patients.[130,133] A very unusual feature was recently observed in a subset of TTD patients: During fever episodes, these patients lost their hair and their general condition worsened. The patients fully recovered when their fever had subsided.

 © 2003 Wiley-VCH Verlag GmbH & Co. KGaA, Weinheim

Analysis of their cells revealed that they contain a mutation in XPD that renders TFIIH temperature-sensitive.[134] This is a rare case of an allele that results in a temperature-sensitive phenotype in humans; such alleles are typically only found (or purposely generated) in lower organisms.

The importance of the XP, CS, and TTD syndromes (together with the existence of UV-sensitive hamster cells with defects in NER) in the elucidation of the NER process cannot be overstated. The availability of cells with mutations in almost all NER genes, the knowledge of the phenotypes caused by these deficiencies, the establishment of complementation groups and assays to assess NER proficiency in living cells have provided powerful tools for the elucidation of NER and TCR.[128] Conversely, it has been possible to pinpoint the complex phenotypes displayed by XP, CS, and TTD to specific events in a biochemical pathway and specific mutations in a gene.

In the past decade, mouse models with defects in most NER genes have been generated, and in most cases have yielded phenotypes closely related to those displayed by the corresponding human patients.[101,129] In some cases, they have also yielded additional insight into the physiological importance of NER. For example, no human patients with a defect in ERCC1 have been found to date and patients with mutations in XPF usually display a very mild phenotype. The generation of ERCC1 mice revealed that these mice display a phenotype that is more severe than those found in mice displaying the classical XP phenotype;[135] depending on the genetic background, these mice die in utero or a few months after birth. ERCC1(−/−) mice are much smaller that their wild-type littermates, suffer from liver and kidney abnormalities, and show cellular senescence, which leads to premature ageing.

How can we explain these observations? Previous observations in yeast and hamster cells have demonstrated that ERCC1 and XPF are involved in homologous recombination and interstrand-crosslink repair. Defects in these additional functions of ERCC1 outside NER therefore make important contributions to the observed phenotype. The mild phenotype of the human XPF patients is likely a result of only partial inactivation of the protein by specific XPF mutations.

6. Mismatch Repair

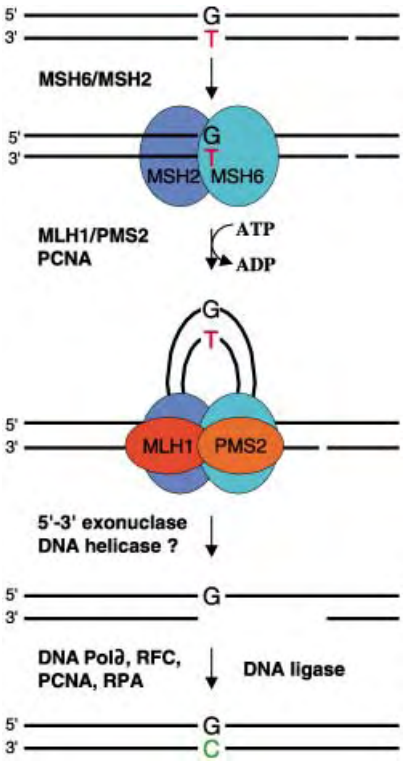
6.1. Overview

DNA replication is a highly complex and accurate process with an overall error rate of only 1 in 10^{10}.[136] Replication polymerases introduce about one erroneous nucleotide per 10^5 nucleotide, and the 3′→5′-proofreading activity associated with polymerases contributes another factor of 100 to the replication fidelity by excising mispaired nucleotides before they are further extended by the polymerase. The remaining factor of 10^3 is contributed by the mismatch repair (MMR) system, which eliminates base–base mismatches as well as nucleotide deletions and insertions introduced by polymerases. MMR is in essence conserved from bacteria to humans, although there are important differences among various organisms. MMR is unique among the DNA repair pathways in that MMR enzymes face the task of identifying one of two chemically unaltered bases in a mispair or loop as aberrant. The manner in which this strand discrimination takes place is one of the most important differences in the MMR systems of prokaryotes and eukaryotes. In *E. coli*, this discrimination is made possible by methylation of specific sequences of the genomic DNA.[137,138] Immediately following replication, only the parental strands, not the daughter strands, are methylated and MMR occurs before methylation of the daughter strand by methyltransferase enzymes. The MMR machinery uses the partially methylated status of the DNA to discriminate between the original template strand and the newly synthesized one. In this situation, the nonmethylated strand is, by definition, the strand carrying the erroneous information and excision always occurs on this strand. Eukaryotes do not have such a straightforward mechanism to discriminate between new and old strands after replication, and the basis for strand discrimination in MMR in eukaryotes is presently unknown. Current models suggest that the MMR machinery is tightly coupled to the replication apparatus and that this connection serves to identify the newly synthesized strand through a replication memory.[139]

Much of what we know about MMR was originally discovered in bacteria, and similarities and differences in higher systems were subsequently discovered. The basic features of MMR have been reconstituted in vitro with purified proteins from *E. coli*.[137,138,140] The initiator of MMR is the MutS homodimer, which binds to mismatches and insertion/deletion loops. The affinity of MutS for a given mismatch or loop is to a first approximation proportional to the overall repair rate.[141] After binding to the mismatch, MutS triggers ATP-dependent assembly of the repairosome, during which MutS moves away from the mismatch and the MutL homodimer is recruited. MutL is thought to serve as a bridging factor between MutL and MutH, which upon encountering a partially methylated GATC site nicks the newly synthesized strand 5′ of the nonmethylated GATC sequence.[142] This nick serves as an entry point for helicase II (UvrD) and one of several endonucleases (Exo VII, RecJ, or ExoI), which degrade the nicked strand past the mismatch.[142] The ssDNA thus generated is protected by the single-strand-binding protein (SSB), and the gap is filled by DNA polymerase III, while DNA ligase repairs the nick.

Consistent with the differing mechanism of strand discrimination, no MutH homologues have been found in eukaryotes. In contrast, three homologues each of MutS (MSH2, MSH3, and MSH6) and MutL (MLH1, MLH3, and PMS2) are involved in MMR in eukaryotes. (PMS2 = post meiotic segregation, named after the phenotype of an MMR-deficient yeast strain.)[143] The homodimeric MutS initiates bacterial MMR, whereas one of two heterodimers, hMutSα (consisting of MSH2 and MSH6) or MutSβ (consisting of MSH3 and MSH6), initiates MMR in eukaryotes (Scheme 9).[139,144] MutSα binds to single mismatches and to small insertion/deletion loops, whereas MutSβ only binds to insertion/deletion loops of various sizes.[145] As is the case in the bacterial system, MutS dimers trigger the assembly of the MMR machinery. The ATPase activity of the MutS complexes is crucial in this

 © 2003 Wiley-VCH Verlag GmbH & Co. KGaA, Weinheim



Scheme 9. Human mismatch repair pathway. The nicked strand contains the erroneous base. A base/base mismatch resulting from faulty replication is recognized by the MSH6–MSH2 heterodimer (MutSα). ATP drives the bidirectional threading of DNA through MutSα. Recruitment of MLH1/PMS2 (MutLα) and PCNA leads to the formation of a loop structure with the MMR proteins at the base and mismatch in the loop. One or several exonucleases and helicases are then recruited to degrade the error-containing strand. The gap is subsequently filled by the replication machinery, and DNA ligase I seals the nick.

process, although its precise role is still a matter of controversy.[146] A conformational change in MutSα converts the heterodimer into a sliding clamp that translocates along the DNA away from the mismatch. Assembly of the MMR repairosome requires the MutL homologues MLH1/PMS2 (MutLα), if MMR is initiated by MutSα and MLH1/PMS2 (MutLα), or MLH1/MLH3 (MutLβ) in the case of initiation by MutSβ. In analogy to bacterial MMR, it has been proposed that a so-called α or Ω loop is formed (Scheme 9) with MutS and MutL proteins at the base of the loops and the mismatch in the loop.[147] The subsequent steps involve degradation of the error-containing strand by exonucleases and, perhaps, helicases. Exo1 has been shown to be involved in MMR, but other nucleases or helicases have not yet been identified.[148] The repair synthesis is carried out by the replication machinery. A direct link between the replication machinery and MMR is provided by PCNA, the processivity factor in replication, which has been found to interact with the eukaryotic MutS and MutL homologues.[149]

6.2. Damage Recognition in MMR

Two recent high-resolution crystal structures of the bacterial MutS homodimer bound to a mismatch and to an unpaired base have provided insight into the mechanism of damage recognition in MMR.[150,151] The overall structure of the complex has been compared to a pair of praying hands, with the DNA held between the thumbs and fingers (Figure 5a). One of the most remarkable features revealed by this structure is that two identical polypeptides of the MutS dimer bind to the mismatch in an asymmetrical fashion. The nominal homodimer thus interacts with the damaged site as a functional heterodimer, in which both subunits contact the DNA, but only one of the subunits interacts with the mismatch. Interestingly, the binding mode of MutS to DNA containing a mismatched or looped-out base is very similar. The bound DNA is mostly a B-form structure, with a strong local kink of about 60° toward the major groove at the mismatched or looped-out nucleotide (Figure 5b). The thymine base in the mismatch is displaced toward the minor groove and pairs with the G unit located opposite with a hydrogen-bond pairing pattern that is different from a G–T mismatch in solution (Figure 5c). The T base interacts with a highly conserved Phe-X-Glu motif. The Phe of this motif interacts with the mismatched or looped-out base through π-stacking interactions. Photocrosslinking experiments with 5-iodouracil and mutational analysis are consistent with a direct role in base binding of this residue. Interestingly, mutation of the corresponding Phe residue in MSH6, but not MSH2, eliminates MMR activity, confirming that MSH6 is the subunit of MutSα that interacts with the mismatch.[152] The glutamate residue of the Phe-X-Glu motif forms a hydrogen bond to the N3-H position of the mismatched or looped-out thymine. Mutation of the Glu residue does not significantly diminish the mismatch-binding activity of MutS, but yields an MMR-deficient phenotype in vivo. Substitution of the T residue with the isosteric difluorotoluene, which is unable to form hydrogen bonds, also showed little effect on the binding activity.[153] The hydrogen bond between Glu and T may therefore ultimately be responsible for mismatch discrimination in a step following damage recognition. The mismatch-binding mode found in these structures suggests that MutS may scan the genome for weakened Watson–Crick hydrogen bonding and stacking interactions to recognize mismatched or looped-out bases.

Although these studies provided insight into the mechanisms of damage recognition by the MutS proteins, a different central question in MMR, the role of the ATPase activity of MutS, remained unanswered. A composite ATP-binding site was found at the opposite end of the DNA-binding domain and was occupied by ADP in the two structures. Perhaps a structure of MutS bound to a nonhydrolyzable ATP analogue could provide some insight into the differences between the ADP- and ATP-bound states of MutS.

6.3. Biological Significance of MMR Defects

Defects in MMR are associated with hereditary nonpolyposis colon cancer (HNPCC), a familial form of early-onset colon cancer.[154] The discovery that defects in MMR directly lead to increased cancer incidence was one of the main breakthroughs that led to a boom in research related to

 © 2003 Wiley-VCH Verlag GmbH & Co. KGaA, Weinheim

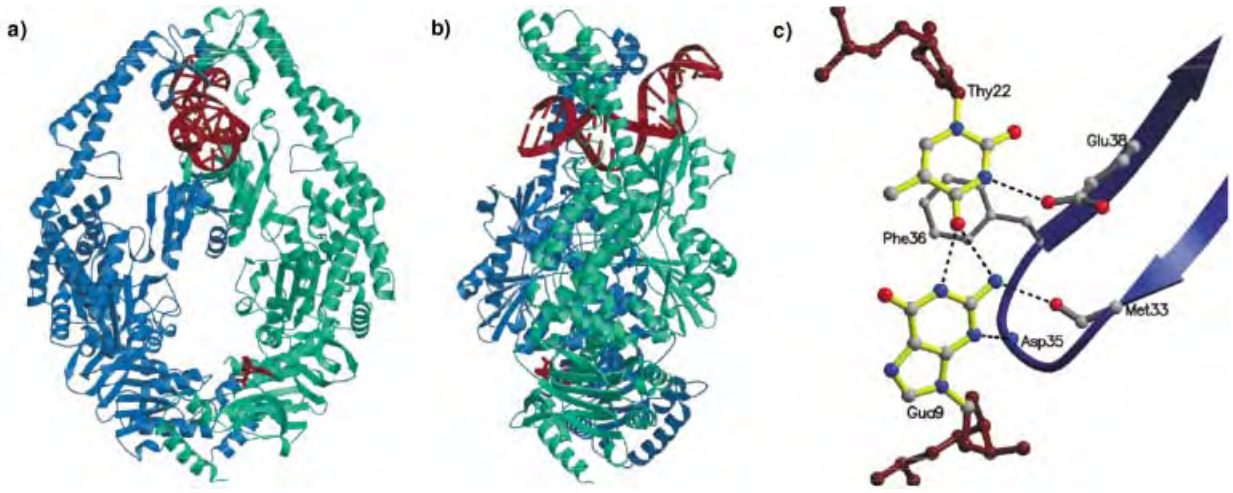


Figure 5. Crystal structure of the MutS–DNA complex. a) Overview of the structure of the MutS homodimer bound to an oligonucleotide containing a G/T mismatch (red = DNA and ADP). Only one of the subunits of MutS (green) interacts with the mismatch, the second monomer (blue) binds to the DNA, but not to the mismatch. The two identical subunits of MutS thus interact with the mismatch as a functional heterodimer. b) Side view of a) rotated by 80°. The DNA is kinked by about 60° at the site of the mismatch. c) Interaction site of MutS with the mismatched T. The G–T mispair has a different structure from a G–T wobble pair in free DNA, which has hydrogen bonds between guanine O^6 and thymine N^3 and guanine N^1 and thyimine O^2. Phe36 is essential for MutS binding and MMR and stacks against the thymine. The hydrogen bond from Glu38 to thymine is essential for MMR, but not for MutS binding. Reprinted with permission of Macmillan Magazines Ltd 2000.[150]

DNA repair in the past decade.[155] Why defects in MMR primarily result in cancers of the colon, endometrium, and ovaries, but not in other tissues is not understood. Consistent with our understanding of the mechanism of MMR, HNPCC is mainly brought about by mutations in the two nonredundant genes of the pathway, MLH1 (60% of all cases) or MSH2 (35% of all cases). Cells mutated in MSH6 also display a mutator phenotype as a result of their inability to repair single-base mismatches.[156] In humans, this defect is apparently normally not severe enough to bring about the "classical" HNPCC manifestations, although germline mutations in MSH6 that result in late-onset HNPCC have been described.[154]

Mice with deficiencies in MMR genes have been generated and these have allowed a more detailed analysis of the effects of individual genes on carcinogenesis. Just one study that compared the tumor formation in MSH2-, MSH3-, and MSH6-deficient mice will be mentioned here: MSH3(−/−) mice were tumor-free, MSH6(−/−) mice showed some tumor incidence, and MSH2(−/−) mice showed a very significant predisposition to tumors.[157] Double-mutant MSH6(−/−)–MSH3(−/−) mice, however, developed tumors at the level of MSH2(−/−) animals, which demonstrates that inactivation of both MSH3 and MSH6 genes is equivalent to inactivation of MSH2. This example demonstrates the synergy of biochemical and genetic approaches in the study of DNA-repair pathways. Thanks to recent progress in our understanding of the genetics and biochemistry of MMR, it is now possible to make genotype/phenotype predictions of how a given mutation in a MMR gene might manifest itself in HNPCC. These advances will provide opportunities for surveillance of HNPCC families and will allow early medical intervention in individuals predisposed to colon cancer.

A second aspect of MMR that is important for cancer therapy is related to a role of MMR proteins in signaling the presence of DNA damage to the apoptotic machinery. Although the details of this signaling process are not yet understood, it has been shown that cells deficient in MMR are resistant to many agents used in antitumor therapy, presumably because of lack of induction of apoptosis in response to MMR-mediated damage processing. The knowledge of the MMR status of a tumor cell may therefore have a strong predictive value in the outcome of a chemotherapeutic regime used to treat a given set of tumor cells.[158]

7. Repair of Double-Strand Breaks

DSBs can be induced by a number of endogenous and exogenous sources and are necessary or accidental intermediates in a number of cellular transactions (see Section 2.2). Although DSBs are formed much less frequently than other forms of endogenous damage, the consequences of DSBs can be very severe. In line with the severity of this form of damage, two independent pathways for the repair of DSBs have evolved.[34,36] One of these, homologous recombination (HR), is an intrinsically accurate repair pathway that uses extensive regions of DNA homology as coding information. The homologous DNA is usually the sister chromatid (an identical copy of the chromosome generated in replication and present before cell division) and may also be the homologous chromosome (second, nonidentical copy of a chromosome present in the cell). Nonhomologous end joining, on the other hand involves the relatively simple coordinated rejoining of the broken DNA ends and uses no or extremely limited regions of homology as a template for repair. This process is not necessarily accurate and deletions of a few nucleotides are often introduced at the site of the DSB. Based on the availability of radiation sensitive mutants in higher and lower eukaryotes, it was initially thought that

 © 2003 Wiley-VCH Verlag GmbH & Co. KGaA, Weinheim

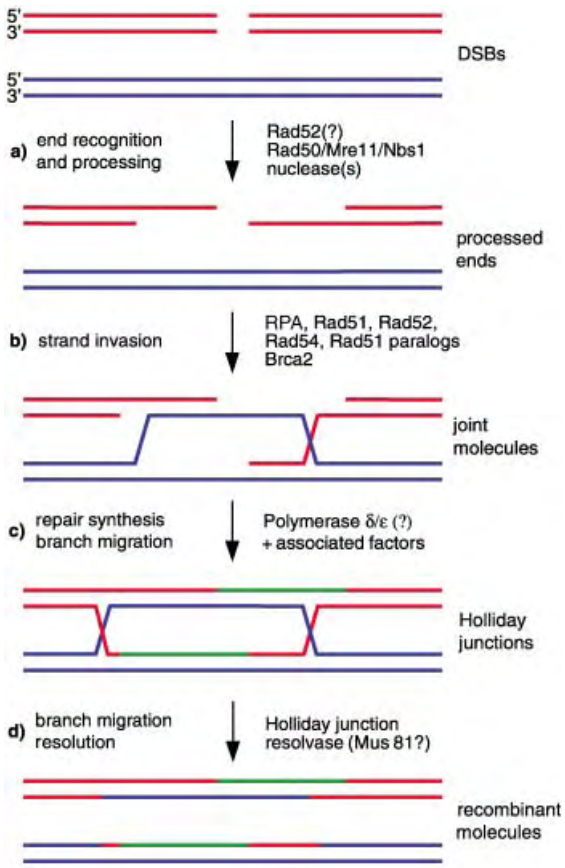
NHEJ is the predominant or perhaps exclusive pathway for repair of DSBs in higher eukaryotes, including humans, and that HR was predominant in lower eukaryotes, such as the yeast *S. cerevisiae*. This view has changed somewhat in recent years and it has become apparent that both pathways are important for all eukaryotes. In general, HR is important for rapidly dividing cells and is particularly important in the S and G2 phases of the cell cycle, during which a sister chromatid is available as a template for HR. NHEJ appears to be more important in quiescent or terminally differentiated cells and in the stages of the cell cycle such as G1 during which a sister chromatid is not available. The two pathways also fulfill specialized roles in the repair of DSBs. HR is important for meiosis or the repair of DNA interstrand crosslinks, whereas NHEJ is required for the joining of DNA fragments in the generation of diversity in the immune system in V(D)J recombination and telomere maintenance.

7.1. Repair of DSBs by Homologous Recombination

HR is a highly complex pathway that uses an intact homologous DNA molecule as a template to repair a DSB accurately. The first step in DSB repair by HR is the processing of the ends of the break to generate 3′ single-stranded tails (Scheme 10).[35,159,160] These single-stranded tails are then used in the search for a homologous template and in the formation of joint molecules, the central recognition steps in HR. The joint molecules provide a template for repair synthesis. Sealing of the nick following successful synthesis leads to the formation of branched DNA structures called Holliday junctions, in which the two parent DNA duplexes are linked together. The Holliday junctions can migrate along the joined DNA (a process called branch migration) and finally undergo resolution at an appropriate location in the DNA to regenerate two intact copies of duplex DNA. The biochemistry of HR has been studied in some detail in bacteria.[159,161] Most of what we know about HR in eukaryotes originated from the identification of genes involved in the process using yeast genetics.[35,162] These studies revealed the existence of the RAD52 group of genes that play a central role in HR. Of these, RAD50, MRE11, and XRS2 were shown to be involved in the initial processing of DSBs to form 3′ single-stranded ends, whereas RAD51, RAD52, RAD54, RAD55, RAD57, and RAD59 were shown to play a role in the homologous pairing and the strand-invasion step (Scheme 10). HR in higher eukaryotes is mediated by homologues of the yeast RAD52 group of genes, although some additional genes are present. Reconstitution of homologous recombination in eukaryotes has not yet been achieved, but the biochemical roles of some of the proteins involved are emerging and will be discussed here in the order of the steps involved.

7.1.1. End Binding and Processing

Biochemical and electron-microscopy studies have shown that Rad52 preferentially binds to the ends of DSBs, especially to ends with ssDNA overhangs.[163] Although



Scheme 10. Double-strand break (DSB) repair by homologous recombination. The damaged DNA is shown in red, the undamaged homologous template in blue, and sequences introduced by repair synthesis in green. a) Initial recognition of a DSB may involve binding of the Rad52 protein. Nucleolytic processing of the DNA ends to form 3′-ssDNA overhangs involves the Rad50/Mre11/Nbs1 complex, probably in conjunction with another nuclease. b) The ssDNA ends are bound by the ssDNA-binding protein RPA and with the help of Rad52 and the Rad51 paralogs (Rad51B, C, D and XRCC2, 3), Rad51 is loaded onto the ssDNA to form a nucleoprotein filament. The BRCA2 protein has a role in regulating Rad51 activity and may directly stimulate the formation of the nucleoprotein filament. This nucleoprotein filament searches for homologous duplex DNA, and a strand-exchange reaction generates a joint molecule between the damaged and undamaged DNA, a step stimulated by Rad54. c) In a process that is not well-understood, DNA polymerases and their associated factors carry out repair synthesis and Holliday junctions are formed. d) Holliday junctions are resolved by endonucleolytic cleavage and rejoining in a reaction that may involve the Mus81 protein and in which two intact DNA molecules are formed.

genetic evidence for this role of RAD52 has not yet been obtained, these results suggest that Rad52 may serve as an initial DSB-binding factor and as such may play a role in channeling breaks into the HR rather than the NHEJ pathways.

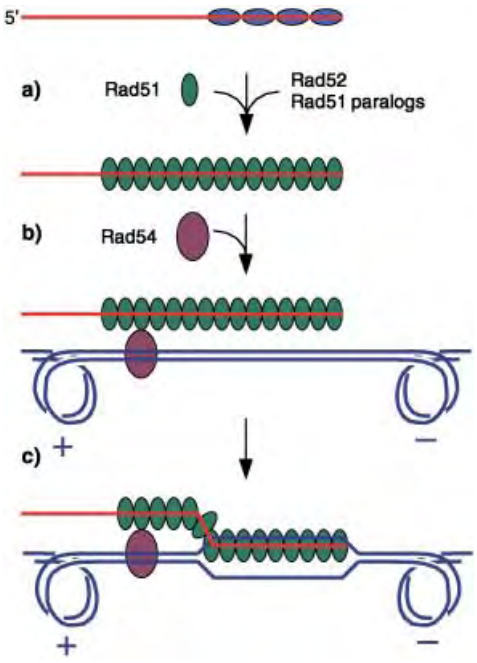
DSBs are subsequently processed by a 5′→3′ exonuclease to generate 3′ ssDNA overhangs. This step involves a trimeric complex composed of Rad50, Mre11, and Nbs1 (RMN complex) in humans and of Rad50, Mre11, and Xrs2 (RMX complex) in yeast cells. Biochemical analysis of the RMN and RMX complex revealed that Mre11 has nuclease activity, although it has the wrong (3′→5′) polarity required to

 © 2003 Wiley-VCH Verlag GmbH & Co. KGaA, Weinheim

generate 3′ ssDNA overhangs.[164] That the nuclease activity of Mre11 may therefore not be required for HR is supported by the genetic analysis that certain nuclease-deficient mutants of Mre11 display no evident defects in recombination.[165] It is therefore likely that the RMN complex acts in conjunction with other factors that posses the required 5′→3′ exonuclease activity.[166] Rad50/Mre11/Nbs1 is the only known factor that is important for both HR and NHEJ (see Section 7.2) and plays an additional role in DNA-damage signaling.

7.1.2. Homologous Pairing and Strand Exchange

The central step in HR is the homologous pairing and strand-exchange reaction that brings the broken DNA ends in contact with the donor template for repair synthesis (Scheme 11). The central protein in this step in eukaryotes



Scheme 11. Homologous pairing and strand-exchange reaction. a) 3′-ssDNA overhangs are bound by the RPA protein. Efficient loading of the Rad51 protein onto the ssDNA to form the nucleoprotein filament in the presence of RPA is stimulated by Rad52 and the Rad51 paralogs (Rad51B, C, D and XRCC2, 3). b) Rad51 in the nucleoprotein filament interacts with Rad54. c) The invasion of the target dsDNA by the nucleoprotein filament is stimulated by the Rad54 protein, which induces superhelical torsion in the target dsDNA, thereby facilitating strand invasion. Rad54 may also facilitate access to the dsDNA by removing histone proteins in the nucleosome.

is the Rad51 protein, which shows many similarities to its well-studied bacterial homologue, the RecA protein. Rad51 and RecA both polymerize on ssDNA to form so-called nucleoprotein filaments on ssDNA (right-handed superhelical structures, which have been visualized by electron microscopy) with a protein monomer/nucleotide stoichiometry of 1:3. These nucleoprotein filaments are the active species in the search for homology in the donor-template molecule and the strand-exchange reaction.[167] RecA is more efficient at catalyzing strand-exchange reactions than Rad51, which can only form nucleoprotein filaments efficiently with the help of additional factors such as RPA, Rad52, and a number of proteins with homology to Rad51. RPA, the single-stranded-DNA-binding protein, binds to the ssDNA overhangs to remove secondary structures of ssDNA. Rad52, which can anneal complementary ssDNA strands and bind to DNA ends, has been shown to stimulate the strand-exchange reaction by facilitating binding of Rad51 to ssDNA in the presence of RPA.[168] A similar role in stimulating the strand-exchange reaction has been demonstrated for the yeast Rad51 homologues Rad55 and Rad57, which form a stable heterodimer.[169] Intriguingly, mammals have five additional Rad51-like proteins (Xrcc2, Xrcc3, Rad51B, Rad51C, and Rad51D).[170] Although it is becoming evident that these five proteins are involved in homologous recombination and are essential for the maintenance of genomic stability,[171] their biochemical characterization is still in its infancy. In the same way as Rad55/57 in yeast, these proteins appear to form heteromultimer complexes that can stimulate the strand-exchange reactions.[172] Whether any of the Rad51 paralogs are able to mediate strand-exchange reactions in the absence of Rad51 at a significant level and whether such an activity could be important in any additional role of homologous recombination such as interstrand-crosslink repair remains to be elucidated. Rad54 has also been shown to interact with Rad51 and to stimulate the Rad51-catalyzed strand-exchange reaction.[173] It likely does so by facilitating joint molecule formation between the nucleoprotein filament of ssDNA and Rad51 and the dsDNA. The Rad54 protein is a member of the Swi2/Snf2 family of dsDNA-dependent ATPases, which are involved in various aspects of DNA metabolism, such as chromatin remodeling.[174] Rad54 can modify the topology of DNA and present models suggest that a change of topology induced in the dsDNA target could facilitate the strand-exchange reaction (Scheme 11c).[175] Additional roles for Rad54 have been proposed, for example, as a factor to facilitate access to the dsDNA target by removing nucleosomal proteins.[176]

7.1.3. Repair Synthesis, Branch Migration, and Resolution

The later steps in HR, branch migration and Holliday-junction resolution, have been reconstituted in bacteria, in which the RuvA and RuvB proteins mediate branch migration and RuvC catalyzes the resolution of Holliday junctions.[177] These steps have remained obscure in eukaryotes, but two important recent discoveries mark the beginning of the elucidation of these steps. First, a complex of unknown constitution with branch-migration activity and Holliday-junction-resolution activity very similar to that of RuvABC has been isolated from human-cell extracts, indicating that the basic mechanism of the late steps may be similar in bacteria and eukaryotes.[178] Second, the Mus81 protein, which is conserved in all eukaryotes, has been shown to cleave Holliday junctions; the Mus81 is complexed with the Eme1 protein in yeast *S. pombe* and is part of a complex with yet unidentified additional factors in human cells.[179] The cleavage pattern observed for Mus81 is somewhat different from

 © 2003 Wiley-VCH Verlag GmbH & Co. KGaA, Weinheim

that found in cell extracts, and very recent studies have shown that the two activities are not identical.[180] The exact function of the two enzyme complexes remain to be elucidated.

7.1.4. Regulation of Homologous Recombination

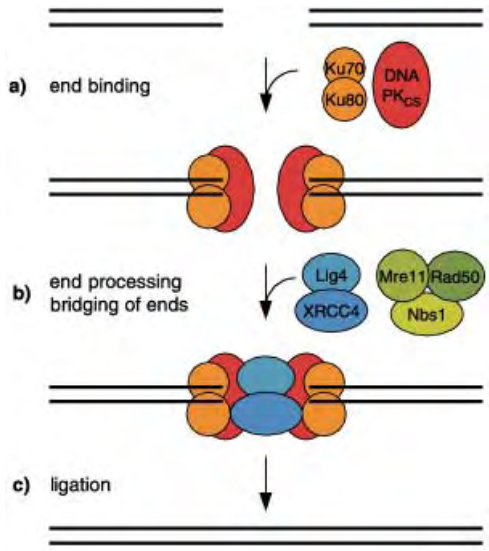
Homologous recombination is a tightly regulated process and several factors directly affect the function of the proteins involved.[2,181] Just one example will be used to illustrate this point here: the control of Rad51 by the breast cancer susceptibility gene BRCA2. Germline mutations in the BRCA1 and BRCA2 genes lead to a predisposition to breast cancer. A possible role of BRCA1/2 in homologous recombination has been suggested by the direct interaction of Rad51 and BRCA1/2 and a defect in the repair of DSBs in BRCA1/2-deficient cells.[182] Recent studies using fragments of BRCA2 have provided some insight into how the protein may regulate the activities of Rad51. The crystal structure of the C-terminal of BRCA2 revealed that the protein contains domains involved in ssDNA and dsDNA binding. This fragment has furthermore been shown to stimulate the strand-exchange reaction mediated by Rad51.[183]

Short peptides that mimic a different part of BRCA2, the Brc domains, which interact with Rad51, inhibit polymerization of Rad51, and thereby prevent its ability to form a nucleoprotein filament and mediate strand-exchange reactions.[184] Structural studies have revealed that Brc peptides mimic a motif in Rad51 that is responsible for Rad51 oligomerization.[185] As different domains of BRCA2 have the ability to stimulate or inhibit Rad51, BRCA2 possibly has two functions: suppressing inappropriate HR and stimulating it when necessary. Further insight into how BRCA2 regulates Rad51 and HR might be revealed through biochemical studies of the entire protein. BRCA2 and BRCA1 have many additional roles in the regulation of cellular responses to DNA damage that are beyond the scope of this review.[186]

7.2. Nonhomologous End Joining

In contrast to HR, NHEJ is a conceptually simple pathway that involves the religation of broken ends and does not require a homologous template. As the DNA ends may be damaged, this mode of repair is not necessarily accurate and can involve the loss of a few nucleotides. The genetic requirements for NHEJ were originally elucidated in radiosensitive hamster cell lines and revealed the involvement of at least two complexes, the DNA protein kinase (DNA-PK), which consists of the three components DNA protein kinase catalytic subunit (DNA-PK_{CS}), Ku70, and Ku80, and the complex between the XRCC4 protein and DNA ligase IV.[187] Subsequent genetic studies in yeast further implicated the Mre11/Rad50/Xrs2 complex in NHEJ and an equivalent role has been suggested for the human Mre11/Rad50/Nbs1 complex.[188]

NHEJ is initiated by the Ku70/Ku80 heterodimer, which selectively binds to DNA ends and recruits DNA-PK_{CS} (Scheme 12).[189] DNA-PK_{CS} is a protein kinase that can phosphorylate a number of proteins, including the Ku proteins, Xrcc4, p53, and itself. While the kinase activity of DNA-PK_{CS} is important for NHEJ, it is not yet clear what the relevant target for phosphorylation is. The bridging of the two DNA ends requires the Rad50/Mre11/Nbs1 and Xrcc4/DNA ligase IV complexes, and consequently components of both complexes interact with the Ku proteins.[190,191] Both XRCC4 and Rad50 consist of a globular domain and long helical domains that can form multimers in an intra- or intermolecular fashion, and these interactions are probably important for bridging the DNA ends.[190,192,193] DSBs formed by damaging agents usually contain fragmented ribose residues and can therefore not be re-ligated directly. Some form of end processing must therefore occur before the ends can be sealed. Genetic evidence suggests that the presence, but not the nuclease activity of Mre11, is required for trimming the DNA ends. Candidate genes responsible for processing DNA ends in NHEJ include the flap endonuclease FEN-1 and a recently identified gene, termed Artemis.[194] This gene shares homology with the metallo-β-lactamase family and was isolated from the radiosensitive phenotype caused by its own inactivation. The Xrcc4/DNA ligase IV complex is responsible for catalyzing the ligation step (Scheme 12c).[195]



Scheme 12. DSB repair by nonhomologous end joining (NHEJ). a) DSBs are recognized by the Ku70 and Ku80 proteins, which specifically bind to DNA ends and form a complex with the DNA-dependent protein kinase catalytic subunit (DNA-PK_{CS}). b) The ends of the break may be processed in a step involving Rad50/Mre11/Nbs1 and a further nuclease; a few base pairs may be removed in this step. The Rad50/Mre11/Nbs1 and Xrcc4/DNA ligase IV complexes have structural features that suggest that they are involved in the bridging of the DNA ends. c) The two ends are ligated by Xrcc4/DNA ligase IV to restore a continuous DNA molecule. NHEJ is not intrinsically error-free and may result in the loss of a few nucleotides.

7.2.1. Recognition of DNA Ends by Ku70/Ku80

Recently the structure of the Ku70/80 heterodimer bound to a DNA substrate designed to have only a single dsDNA end has been solved.[196] Although Ku70 and Ku80 share only very limited sequence homology, the two polypeptides share a common topology and bind to the DNA as a pseudohomo-

 © 2003 Wiley-VCH Verlag GmbH & Co. KGaA, Weinheim

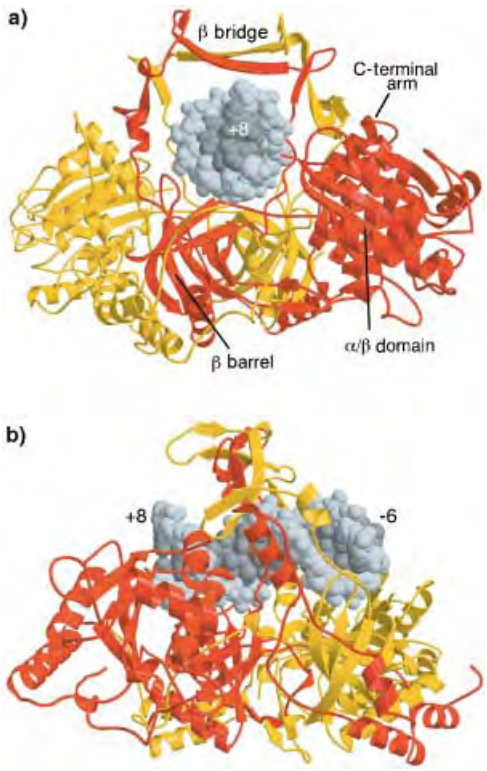


Figure 6. Structure of the Ku70/Ku80 complex bound to DNA (red = Ku70, yellow = Ku80, light gray = DNA backbone, dark gray = DNA bases). a) View down the DNA helix. Although Ku70 and Ku80 only share very limited homology, their overall structures are very similar and they bind DNA as an asymmetric pseudodimer. Ku70/Ku80 encircles the DNA with a globular β-barrel domain on one side and a narrow β-bridge on the other. b) Side view of a). The top of the DNA (position −6) is accessible to solvent, hence allowing the interaction of the DNA end with other proteins in NHEJ. Reprinted with the permission of Macmillan Magazines Ltd 2001.[196]

dimer. The complex has a ringlike shape with the DNA threaded through the opening (Figure 6). One face of the DNA is bound by the globular β-barrel domain, which covers about two helical turns, and the other face is covered by the narrow β-bridge, which is made up of only two β-strands, one from each subunit of Ku. The Ku proteins do not make direct contact with the DNA bases and interact only with a few sites of the sugar–phosphate backbone. The shape of the ring is remarkably complementary to the DNA helix. The ringlike structure explains why Ku70/Ku80 preferentially binds to DNA ends rather than to closed circular structures and how it can slide into the interior of the helix after initial binding with the ends. Consistent with biochemical data, the Ku complex binds DNA asymmetrically, with Ku70 located closer to the end.[197] Since the Ku proteins bind toward the interior of the helix, the end is accessible for interaction with additional proteins.

7.3. Biological Consequences of Deficiencies in DSB Repair

An important manifestation of defective DSB repair is chromosomal instability, which is characterized by gross rearrangement of chromosomes. In contrast to mutational instability displayed, for example, by defects in MMR or NER, which typically affect a single gene at a time, chromosomal instability can lead to loss of entire parts of chromosomes with very severe effects.[34] Several human syndromes that are associated with defects in DSB repair have been described. Most of these do not stem from direct defects in HR or NHEJ, but rather from defective regulation of DSB repair. Three related conditions are ataxia telangiectasia (AT, resulting from a defect in the ATM gene), an AT-like disorder (resulting from a defect in MRE11), and Nijmegen breakage syndrome (resulting from a defect in NBS1).[198] Among the complicated phenotypes of these conditions, predisposition to cancer, immunodeficiency, and hypersensitivity to ionizing radiation stand out as features associated with defective DSB repair. Cells from these patients show increased levels of chromosomal translocations and failure to activate specific cell-cycle checkpoints. The mutations in MRE11 and NBS that lead to those syndromes do not result in an overall DNA-repair defect, but appear to hamper the ability to activate cell-cycle checkpoints. Notably, null mutations in MRE11 or RAD50 in mice are lethal, even at the cellular level, suggesting that their role in DNA repair is essential.[199] The predisposition of individuals with mutations in the BRCA1/BRCA2 genes to breast and ovarian cancer may be viewed along similar lines. Null mutations in these genes leads to early embryonic lethality, whereas partial defects are not life-threatening, but lead to chromosomal instability and eventually cancer.[186]

That defects in NHEJ lead to the sensitivity to ionizing radiation was known early on from the study of several mutant Chinese hamster ovary cells with deficiencies in the KU70, KU80, and XRCC4 genes.[187] The subsequent generation of mice that are deficient in the NHEJ components KU70, KU80, DNA-PK_{CS}, XRCC4, and DNA ligase IV have allowed the further analysis of the consequences of NHEJ deficiency.[34,200] The common phenotypes of such mice include radiosensitivity, predisposition to cancer, and immune deficiency as a result of defects in V(D)J recombination. These effects can be explained readily by a defect in NHEJ. The severity of the phenotypes displayed by NHEJ-deficient mice ranges from embryonic lethality (XRCC4 and DNA ligase IV), to growth retardation (KU70 and KU80), to no overt manifestations of growth retardation or cellular senescence (DNA-PK_{CS}). Further analysis of mice that are deficient in KU70 and KU80 revealed frequent spontaneous chromosome breaks resulting from defective DSB repair.[201] The severe phenotype of XRCC4 and DNA-ligase IV-deficient mice was found to be caused by a defect in the neurons, which undergo massive apoptosis in the developing brain.[202] This apoptotic response can be suppressed if induction of apoptosis is suppressed by additional disruption of the p53 or ATM genes. A handful of patients with a deficiency in DNA ligase IV have been found to date; these patients suffer from marked radiosensitivity and, in some cases, from immunodeficiency and developmental and growth delay. These defects are caused by point mutation in the gene and therefore do not result in a complete defect in DNA ligase IV.[203]

The biological role of HR has been addressed by the generation of knockout mice and chicken DT40 cell lines with

 © 2003 Wiley-VCH Verlag GmbH & Co. KGaA, Weinheim

deficiencies in various genes. Mice and cells deficient in strand-exchange protein RAD51 are not viable, pointing to an essential function of the gene.[204] A direct role for RAD51 in maintaining genomic stability has been demonstrated in chicken cell lines in which ablation of RAD51 could be conditionally induced. Analysis of these cells revealed that after repression of RAD51 expression, the cells stop dividing and display a large number of chromatid breaks.[205] Three mouse models with deficiencies in RAD51 paralogs (XRCC2, RAD51B, and RAD51D) have been generated and defects in these genes also result in early embryonic lethality.[206] Cells deficient in any one of the five RAD51 paralogs are, however, viable, and analysis of the knockout cells have demonstrated a role in homologous recombination and maintenance of chromosomal stability.[171] In contrast, ablation of mouse or chicken RAD52 is almost inconsequential. These animals are perfectly healthy, and the only cellular phenotype is a slight decrease in HR.[207] This is in sharp contrast to studies of yeast cells, in which mutation of RAD52 leads to the most severe consequences of all HR-deficiency mutations observed.[35] It has been shown that RAD52 and the RAD51 paralog, XRCC3, have partially redundant functions in chicken DT40 cells, an observation that may explain the difference in yeast cells.[208] There is also the possibility that there is a functional redundancy and that mammals possess additional (functional) homologues of RAD52. RAD54-deficient mice provided the only viable mammalian animal model with a real defect in recombination so far. Embryonic RAD54 stem cells were sensitive to ionizing radiation and to the DNA interstrand-crosslinking agent mitomycin C, whereas adult RAD54(−/−) mice only showed sensitivity to mitomycin C, but not to ionizing radiation.[209] Together with data showing that mice deficient in both RAD54 and KU70 were more sensitive to ionizing radiation than singly deficient animals, these observation show that the two pathways are synergistic, and that HR is more important for DSB repair early in development in stem cells than in adult cells.[210]

8. Summary and Outlook

The main DNA repair pathways in humans—direct repair (DR), base excision repair (BER), nucleotide excision repair (NER), mismatch repair (MMR), homologous recombination (HR), and nonhomologous end joining (NHEJ)—fulfill essential roles in maintaining genomic integrity. Defects in many of these pathways are associated with hereditary syndromes in humans and lead to predisposition to cancer. Our understanding of the molecular basis underlying DNA repair has markedly increased in the past decade. DR and BER represent rather simple pathways in molecular terms and the mechanisms of damage recognition and catalysis have been elucidated in some detail. These insights were made possible by the combination of biochemical, structural, and chemical approaches that have enabled the resolution of high-resolution structures of repair enzymes bound to their DNA targets. The more complex DNA repair pathways, NER, MMR, HR, and NHEJ are not yet understood at the same detailed level, which is not surprising considering that these processes require the coordinated action of up to 30 polypeptides. We can expect that our understanding of these pathways will dramatically increase in the near future. Chemical biology should make major contributions in the elucidation of the mechanisms of damage recognition and catalysis in these complex systems.

This review has focused on DNA repair pathways in the strictest sense, namely pathways that are known to involve the active removal of damage from DNA and the restoration the original DNA sequence. Several additional human hereditary disorders are known that feature genomic instability and predisposition to cancer as a hallmark feature and that result from defects in genes other than those described so far. Among these are the Bloom, Werner, and Rothmund–Thomson syndromes. These diseases are related to a deficiency in the BLM, WRN, and RECQ4 genes, respectively, which encode proteins with helicase or helicase/endonuclease activity.[211] These helicases interact, among others, with proteins involved in NHEJ and DNA replication, and their role is likely to resolve unusual DNA intermediates in DNA repair and replication processes. Patients affected by these conditions also show overt signs of premature aging. Fanconi anemia (FA) is another syndrome with spontaneous chromosomal instability as a hallmark feature.[212] FA can be caused by deficiency in one of at least eight FA genes; at the cellular level, FA cells display a marked specificity to DNA interstrand-crosslinking agents. Whether the FA genes are directly involved in a pathway of interstrand-crosslink repair or whether they have signaling or regulatory functions is not yet known.

Progress in understanding the traditional DNA-repair pathways as well as the elucidation of other pathways involved in maintaining genome stability are areas that can immensely benefit from chemical biological approaches. Hopefully this Review will further stimulate the interest of the chemical community in studying the basis of the many pathways involved in maintaining genomic stability.

Glossary

AGT	Alkylguanine transferase. DNA-repair enzymes that directly transform O^6-alkylguanine adducts into guanine residues by transferring the alkyl group onto an cysteine residue of the enzyme.
AP endonuclease	Enzymes involved in base-excision repair that hydrolyzes the phosphodiester bond 5′ to an abasic site.
AP lyase	Enzymatic activity present in certain DNA glycosylases and polymerase β that catalyzes the cleavage of the bond between an abasic site and the phosphate group in the 3′ direction.
BRCA1/2	Genes that likely play a role in the regulation of the HR process. Defects in BRCA1/2 lead to a pre-

 © 2003 Wiley-VCH Verlag GmbH & Co. KGaA, Weinheim

	disposition to breast cancer in humans.
Bulky DNA adducts	Sterically demanding adducts with DNA bases that locally distort the DNA double helix and are caused, for example, by UV light or environmental mutagens.
CSA	Gene involved in TCR. Contains 5-WD repeats, which are normally involved in protein–protein interactions, but its precise function is not yet known.
CSB	DNA-dependent ATPase with homology to chromatin-remodeling factors. Involved in TCR and present in elongating complex of RNA polymerase II.
DNA glycosylase	Enzymes that initiate base-excision repair by recognizing damaged bases in DNA and cleave the glycosidic bond between the base and the sugar–phosphate backbone.
DNA ligase III	DNA ligase with specialized role in sealing nicks in the final step of base-excision repair.
DNA ligase IV	DNA ligase involved in sealing DSBs in NHEJ.
DNA-PK	DNA-dependent protein kinase. Complex of Ku70, Ku80, and DNA-PK_{CS}. Plays a role in the regulation of NHEJ.
DNA-PK_{CS}	DNA-dependent protein kinase catalytic subunit. Large protein kinase that forms DNA-PK with Ku70 and Ku80. Involved in the phosphorylation of various proteins.
ERCC1/XPF	heterodimeric structure-specific endonuclease that makes the 5′ incision in NER. ERCC1 interacts with XPA.
Flap endonuclease Fen-1	Structure-specific endonuclease involved in the processing of lagging strands in replication. Has additional roles in processing DNA flap structures in BER.
GGR	Global genome repair. NER that takes place anywhere in the genome, except in actively transcribed genes.
Holliday Junction	Four-stranded DNA molecules named after their discoverer Robin Holliday. In these molecules, the repair template and the damaged strand that contained the DSB are linked following the repair process. Holliday junctions are eventually resolved to restore the two original dsDNA molecules.
HR23B	Stabilizes XPC and contains ubiquitin-like domains that are probably involved in the regulation of NER.
ICLs	Interstrand crosslinks. Highly cytotoxic DNA modification in which the two strands of DNA are held together by a covalent linkage.
Joint molecule	During HR the ends of a DSB are linked to the repair template following strand invasion to form a joint molecule.
Ku70/80	Heterodimeric protein involved in NHEJ. Initiates the process by binding to DNA ends. Forms a tight complex with DNA-PK_{CS} in vivo.
Long-patch repair	Minor subpathway of BER in which two to six nucleotides are introduced in place of the damaged base.
MLH1	MutL homologue 1. Forms heterodimers MutLα with PMS2 and MutLβ with MLH3.
MLH3	MutL homologue 3. Forms heterodimer MutLβ with MLH1.
Mre11	Metal-dependent exonuclease that is part of the RMN complex with Rad50 and Nbs1. Involved in HR and NHEJ.
MSH3	MutS homologue 3. Forms heterodimer MutSβ (coupled with MSH2), which is involved in the initiation of MMR of insertion/deletion loops.
MSH6	MutS homologue 6. Forms heterodimer MutSα (with MSH2), which is involved in the initiation of MMR of mismatches and small insertion/deletion loops.
Nbs1	Forms RMN complex with Rad50 and Mre11 that is involved in NR and NHEJ.
Nucleoprotein filament	Rad51 (and RecA) form superhelical structures with ssDNA. Active species in the strand-invasion step in HR.
Nucleotide flipping	Rotation of specific, single nucleotides out of the double helix into the active site of the enzyme, where a chemical reaction is catalyzed.
Photolyase	Flavin-dependent repair enzymes that directly revert pyrimidine dimers generated by UV irradiation into their corresponding monomers.
Polymerase β	Polymerase involved in BER, specialized in the repair of short patches. This enzyme exhibits AP lyase activity in addition to polymerase activity.
Polymerase δ/ε	The main polymerases involved in DNA replication. These are also involved in the repair synthesis steps of long-patch BER, NER, mismatch repair, and HR.

 © 2003 Wiley-VCH Verlag GmbH & Co. KGaA, Weinheim

Rad50	Protein that forms the RMN complex with Mre11 and Nbs1. Involved in HR and NHEJ.
Rad51	Main eukaryotic strand-exchange protein that mediates strand exchange and homologous pairing reaction. The Rad51-mediated reaction is stimulated by Rad52, RPA, Rad54, and Rad51 paralogs.
Rad51 Paralogs	A paralog is a gene that is homologous to another gene in the same genome. Mammals have five paralogs of Rad51 (Rad51B,C,D and XRCC2,3), which are also involved in homologous recombination.
Rad52	Protein with DNA-end-binding and ssDNA-annealing activities in vitro. Stimulates formation of nucleoprotein filaments by Rad51.
Rad54	DNA-dependent ATPase with similarities to proteins involved in chromatin remodeling. Can induce changes in DNA topology. Rad54 interacts with and stimulates Rad51.
RecA	Bacterial protein that mediates strand exchange and homologous pairing reactions.
ROS	Reactive oxygen species. Various oxygen-containing radicals that occur naturally as part of oxidative metabolism and cause damage to various biomolecules, including DNA and proteins.
RPA	ssDNA-binding protein involved in replication, recombination, nucleotide-excision repair, and mismatch repair. Interacts with numerous proteins involved in DNA replication and repair.
Short-patch repair	Main subpathway of BER in which a single nucleotide is introduced in the repair synthesis step in place of the damaged base.
TCR	Transcription-coupled repair. Specialized NER pathway responsible for the accelerated repair of adducts in actively transcribed genes.
TFIIH	Factor consisting of nine subunits involved in NER and basal transcription. Contains the XPB and XPD helicases, which are responsible for opening the DNA around the lesion in NER.
V(D)J recombination	Specialized site-specific recombination process active in the maturation of the immune system to generate diversity in immunoglobulins and T-cell receptors.
XPA	Protein that binds specifically to damaged DNA and interacts with RPA, TFIIH, and ERCC1. Likely involved in damage verification in NER following initial recognition.
XPC	Damage-recognition protein in GGR. Forms a stable complex with hHR23B and is dispensable for transcription-coupled repair.
XPE/DDB1/2	Protein heterodimer of p48(DDB2)/p125(DDB1) that binds specifically to damaged DNA. Not required for the core NER reaction in vitro. May be required for the repair of certain lesions.
XPG	Structure-specific endonuclease that makes the 3′ incision in NER.
XRCC1	X-ray repair cross complementing group 1 protein involved in BER by bridging polymerase β and DNA ligase III.
Xrcc4	Protein involved in NHEJ that forms a heterodimeric complex with DNA ligase IV and may be involved in bridging DNA ends.

I am very grateful to Rolf Buff for translating the manuscript into German. Furthermore, I would like to thank Steve Bruner, Greg Verdine, Tom Ellenberger, Brian Chapados, John Tainer, Titia Sixma, and Jonathan Goldberg for figures, Greg Verdine and Roland Kanaar for communicating data prior to publication, and Primo Schär and Josef Jiricny for comments on the manuscript. Research on DNA repair in the author's lab is supported by the Swiss National Science Foundation, the Human Frontier Science Programme, the European Commission, the Association for International Cancer Research, the Krebsliga des Kantons Zürich, and the Sassella Stiftung. O.D.S. is a START fellow of the Swiss National Science Foundation and an EMBO Young Investigator.

Received: March 11, 2002 [A523]

[1] B. B. Zhou, S. J. Elledge, *Nature* **2000**, *408*, 433.
[2] J. Rouse, S. P. Jackson, *Science* **2002**, *297*, 547.
[3] T. Rich, R. L. Allen, A. H. Wyllie, *Nature* **2000**, *407*, 777.
[4] E. C. Friedberg, R. Wagner, M. Radman, *Science* **2002**, *296*, 1627.
[5] P. M. J. Burgers, E. V. Koonin, E. Bruford, L. Blanco, K. C. Burtis, M. F. Christman, W. C. Copeland, E. C. Friedberg, F. Hanaoka, D. C. Hinkle, C. W. Lawrence, M. Nakanishi, H. Ohmori, L. Prakash, S. Prakash, C.-A. Reynaud, A. Sugino, T. Todo, Z. Wang, J.-C. Weill, R. Woodgate, *J. Biol. Chem.* **2001**, *276*, 43487; M. F. Goodman, B. Tippin, *Nat. Rev. Mol. Cell Biol.* **2000**, *1*, 101; R. Woodgate, *Genes Dev.* **1999**, *13*, 2191.
[6] E. C. Friedberg, G. C. Walker, W. Siede, *DNA Repair and Mutagenesis*, American Society for Microbiology, Washington, **1995**.
[7] T. Lindahl, R. D. Wood, *Science* **1999**, *286*, 1897.
[8] J. H. Hoeijmakers, *Nature* **2001**, *411*, 366.
[9] O. D. Schärer, L. Deng, G. L. Verdine, *Curr. Opin. Chem. Biol.* **1997**, *1*, 526; S. S. David, S. D. Williams, *Chem. Rev.* **1998**, *98*, 1221.

 © 2003 Wiley-VCH Verlag GmbH & Co. KGaA, Weinheim

[10] O. D. Schärer, J. Jiricny, *Bioessays* **2001**, *23*, 270.
[11] O. D. Schärer, *Chimia* **2001**, *55*, 340.
[12] J. T. Stivers, A. C. Drohat, *Arch. Biochem. Biophys.* **2001**, *396*, 1.
[13] T. Carell, L. T. Burgdorf, L. M. Kundu, M. Cichon, *Curr. Opin. Chem. Biol.* **2001**, *5*, 491.
[14] B. Alberts, *Cell* **1998**, *92*, 291.
[15] T. Lindahl, *Nature* **1993**, *362*, 709.
[16] L. A. Loeb, B. D. Preston, *Annu. Rev. Genet.* **1986**, *20*, 201.
[17] J. Nakamura, V. E. Walker, P. B. Upton, S. Y. Chiang, Y. W. Kow, J. A. Swenberg, *Cancer Res.* **1998**, *58*, 222.
[18] L. A. Frederico, T. A. Kunkel, B. R. Shaw, *Biochemistry* **1990**, *29*, 2532; J. C. Shen, W. M. Rideout III, P. A. Jones, *Nucleic Acids Res.* **1994**, *22*, 972.
[19] K. B. Beckman, B. N. Ames, *J. Biol. Chem.* **1997**, *272*, 19633; J. Cadet, C. D'Ham, T. Douki, J. P. Pouget, J. L. Ravanat, S. Sauvaigo, *Free Radical Res.* **1998**, *29*, 541; J. Cadet, T. Delatour, T. Douki, D. Gasparutto, J. P. Pouget, J. L. Ravanat, S. Sauvaigo, *Mutat. Res.* **1999**, *424*, 9.
[20] C. J. Burrows, J. G. Muller, *Chem. Rev.* **1998**, *98*, 1109.
[21] D. Wang, D. A. Kreutzer, J. M. Essigmann, *Mutat. Res.* **1998**, *400*, 99.
[22] F. Le Page, E. E. Kwoh, A. Avrutskaya, A. Gentil, S. A. Leadon, A. Sarasin, P. K. Cooper, *Cell* **2000**, *101*, 159.
[23] L. J. Marnett, *Carcinogenesis* **2000**, *21*, 361; L. J. Marnett, J. P. Plastaras, *Trends Genet.* **2001**, *17*, 214.
[24] B. Rydberg, T. Lindahl, *EMBO J.* **1982**, *1*, 211; L. R. Barrows, P. N. Magee, *Carcinogenesis* **1982**, *3*, 349; R. Saffhill, G. P. Margison, P. J. O'Connor, *Biochim. Biophys. Acta* **1985**, *823*, 111.
[25] M. Bignami, M. O'Driscoll, G. Aquilina, P. Karran, *Mutat. Res.* **2000**, *462*, 71.
[26] H. Nilsen, H. E. Krokan, *Carcinogenesis* **2001**, *22*, 987.
[27] J. L. Ravanat, T. Douki, J. Cadet, *J. Photochem. Photobiol. B* **2001**, *63*, 88.
[28] V. Purohit, A. K. Basu, *Chem. Res. Toxicol.* **2000**, *13*, 673; J. Szeliga, A. Dipple, *Chem. Res. Toxicol.* **1998**, *11*, 1; E. R. Jamieson, S. J. Lippard, *Chem. Rev.* **1999**, *99*, 2467.
[29] A. Sancar, *Annu. Rev. Biochem.* **1996**, *65*, 43; R. D. Wood, *J. Biol. Chem.* **1997**, *272*, 23465; W. L. de Laat, N. G. Jaspers, J. H. Hoeijmakers, *Genes Dev.* **1999**, *13*, 768.
[30] B. Giese, *Chimia* **2001**, *55*, 275; M. M. Greenberg, *Chem. Res. Toxicol.* **1998**, *11*, 1235.
[31] W. K. Pogozelski, T. D. Tullius, *Chem. Rev.* **1998**, *98*.
[32] S. S. Wallace, *Radiat. Res.* **1998**, *150*, S60; B. M. Sutherland, P. V. Bennett, O. Sidorkina, J. Laval, *Proc. Natl. Acad. Sci. USA* **2000**, *97*, 103.
[33] M. M. Cox, M. F. Goodman, K. N. Kreuzer, D. J. Sherratt, S. J. Sandler, K. J. Marians, *Nature* **2000**, *404*, 37; S. C. Kowalczykowski, *Trends Biochem. Sci.* **2000**, *25*, 156.
[34] D. C. van Gent, J. H. Hoeijmakers, R. Kanaar, *Nat. Rev. Genet.* **2001**, *2*, 196.
[35] F. Paques, J. E. Haber, *Microbiol. Mol. Biol. Rev.* **1999**, *63*, 349.
[36] K. K. Khanna, S. P. Jackson, *Nat. Genet.* **2001**, *27*, 247.
[37] L. J. Niedernhofer, M. Riley, N. Schnetz-Boutaud, G. Sanduwaran, A. K. Chaudhary, G. R. Reddy, L. J. Marnett, *Chem. Res. Toxicol.* **1997**, *10*, 556.
[38] J. E. Hearst, *Chem. Res. Toxicol.* **1989**, *2*, 69; F. P. Gasparro, A. Felli, I. M. Schmitt, *Recent Results Cancer Res.* **1997**, *143*, 101.
[39] P. D. Lawley, D. H. Phillips, *Mutat. Res.* **1996**, *355*, 13; S. R. Rajski, R. M. Williams, *Chem. Rev.* **1998**, *98*, 2723.
[40] M. L. Dronkert, R. Kanaar, *Mutat. Res.* **2001**, *486*, 217; P. J. McHugh, V. J. Spanswick, J. A. Hartley, *Lancet Oncol.* **2001**, *2*, 483.
[41] G. B. Sancar, *Mutat. Res.* **2000**, *451*, 25.
[42] A. E. Pegg, *Mutat. Res.* **2000**, *462*, 83.
[43] D. S. Daniels, C. D. Mol, A. S. Arvai, S. Kanugula, A. E. Pegg, J. A. Tainer, *EMBO J.* **2000**, *19*, 1719; J. E. Wibley, A. E. Pegg, P. C. Moody, *Nucleic Acids Res.* **2000**, *28*, 393.
[44] L. L. Dumenco, E. Allay, K. Norton, S. L. Gerson, *Science* **1993**, *259*, 219; T. Tsuzuki, K. Sakumi, A. Shiraishi, H. Kawate, H. Igarashi, T. Iwakuma, Y. Tominaga, S. Zhang, S. Shimizu, T. Ishikawa, *Carcinogenesis* **1996**, *17*, 1215; H. Kawate, K. Sakumi, T. Tsuzuki, Y. Nakatsuru, T. Ishikawa, S. Takahashi, H. Takano, T. Noda, M. Sekiguchi, *Proc. Natl. Acad. Sci. USA* **1998**, *95*, 5116.
[45] D. B. Ludlum, *Cancer Invest.* **1997**, *15*, 588.
[46] a) T. P. Brent, J. S. Remack, D. G. Smith, *Cancer Res.* **1987**, *47*, 6185; T. P. Brent, J. S. Remack, *Nucleic Acids Res.* **1988**, *16*, 6779; P. E. Gonzaga, L. Harris, G. P. Margison, T. P. Brent, *Nucleic Acids Res.* **1990**, *18*, 3961; P. E. Gonzaga, P. M. Potter, T. Q. Niu, D. Yu, D. B. Ludlum, J. A. Rafferty, G. P. Margison, T. P. Brent, *Cancer Res.* **1992**, *52*, 6052; b) D. M. Noll, N. D. Clarke, *Nucleic Acids Res.* **2001**, *29*, 4025.
[47] M. E. Dolan, R. C. Moschel, A. E. Pegg, *Proc. Natl. Acad. Sci. USA* **1990**, *87*, 5368; R. C. Moschel, M. G. McDougall, M. E. Dolan, L. Stine, A. E. Pegg, *J. Med. Chem.* **1992**, *35*, 4486; M. E. Dolan, A. E. Pegg, *Clin. Cancer Res.* **1997**, *3*, 837; R. S. McElhinney, D. J. Donnelly, J. E. McCormick, J. Kelly, A. J. Watson, J. A. Rafferty, R. H. Elder, M. R. Middleton, M. A. Willington, T. B. H. McMurry, G. P. Margison, *J. Med. Chem.* **1998**, *41*, 5265.
[48] H. S. Friedman, J. Pluda, J. A. Quinn, R. B. Ewesuedo, L. Long, A. H. Friedman, I. Cokgor, O. M. Colvin, M. M. Haglund, D. M. Ashley, J. N. Rich, J. Sampson, A. E. Pegg, R. C. Moschel, R. E. McLendon, J. M. Provenzale, E. S. Stewart, S. Tourt-Uhlig, A. M. Garcia-Turner, J. E. Herndon II, D. D. Bigner, M. E. Dolan. *J. Clin. Oncol.* **2000**, *18*, 3522; R. L. Schilsky, M. E. Dolan, D. Bertucci, R. B. Ewesuedo, N. J. Vogelzang, S. Mani, L. R. Wilson, M. J. Ratain, *Clin. Cancer Res.* **2000**, *6*, 3025; H. S. Friedman, *Clin. Cancer Res.* **2000**, *6*, 2967.
[49] R. B. Roth, L. D. Samson, *Mutat. Res.* **2000**, *462*, 107; L. P. Encell, D. M. Landis, L. A. Loeb, *Nat. Biotechnol.* **1999**, *17*, 143; K. Kleibl, G. P. Margison, *Neoplasma* **1998**, *45*, 181.
[50] E. Seeberg, L. Eide, M. Bjoras, *Trends Biochem. Sci.* **1995**, *20*, 391; H. E. Krokan, R. Standal, G. Slupphaug, *Biochem. J.* **1997**, *325*, 1; H. E. Krokan, H. Nilsen, F. Skorpen, M. Otterlei, G. Slupphaug, *FEBS Lett.* **2000**, *476*, 73.
[51] A. E. Vidal, I. D. Hickson, S. Boiteux, J. P. Radicella, *Nucleic Acids Res.* **2001**, *29*, 1285.
[52] S. L. Allinson, I. I. Dianova, G. L. Dianov, *EMBO J.* **2001**, *20*, 6919.
[53] T. R. Waters, P. Gallinari, J. Jiricny, P. F. Swann, *J. Biol. Chem.* **1999**, *274*, 67; C. D. Mol, T. Izumi, S. Mitra, J. A. Tainer, *Nature* **2000**, *403*, 451.
[54] U. Hardeland, R. Steinacher, J. Jiricny, P. Schär, *EMBO J.* **2002**, *21*, 1456.
[55] Y. Kubota, R. A. Nash, A. Klungland, P. Schär, D. E. Barnes, T. Lindahl, *EMBO J.* **1996**, *15*, 6662; R. A. Bennett, D. M. Wilson III, D. Wong, B. Demple, *Proc. Natl. Acad. Sci. USA* **1997**, *94*, 7166; A. E. Vidal, S. Boiteux, I. D. Hickson, J. P. Radicella, *EMBO J.* **2001**, *20*, 6530.
[56] B. Pascucci, M. Stucki, Z. O. Jonsson, E. Dogliotti, U. Hubscher, *J. Biol. Chem.* **1999**, *274*, 33696; Y. Matsumoto, K. Kim, J. Hurwitz, R. Gary, D. S. Levin, A. E. Tomkinson, M. S. Park, *J. Biol. Chem.* **1999**, *274*, 33703.
[57] M. Otterlei, E. Warbrick, T. A. Nagelhus, T. Haug, G. Slupphaug, M. Akbari, P. A. Aas, K. Steinsbekk, O. Bakke, H. E. Krokan, *EMBO J.* **1999**, *18*, 3834.
[58] H. Nilsen, K. A. Haushalter, P. Robins, D. E. Barnes, G. L. Verdine, T. Lindahl, *EMBO J.* **2001**, *20*, 4278.

 © 2003 Wiley-VCH Verlag GmbH & Co. KGaA, Weinheim

[59] B. Hendrich, U. Hardeland, H. H. Ng, J. Jiricny, A. Bird, *Nature* **1999**, *401*, 301; U. Hardeland, M. Bentele, T. Lettieri, R. Steinacher, J. Jiricny, P. Schär, *Prog. Nucleic Acid Res. Mol. Biol.* **2001**, *68*, 235.
[60] S. Um, M. Harbers, A. Benecke, B. Pierrat, R. Losson, P. Chambon, *J. Biol. Chem.* **1998**, *273*, 20728; B. Zhu, Y. Zheng, D. Hess, H. Angliker, S. Schwarz, M. Siegmann, S. Thiry, J. P. Jost, *Proc. Natl. Acad. Sci. USA* **2000**, *97*, 5135.
[61] S. Boiteux, J. P. Radicella, *Biochimie* **1999**, *81*, 59.
[62] M. M. Slupska, W. M. Luther, J. H. Chiang, H. Yang, J. H. Miller, *J. Bacteriol.* **1999**, *181*, 6210.
[63] M. L. Michaels, C. Cruz, A. P. Grollman, J. H. Miller, *Proc. Natl. Acad. Sci. USA* **1992**, *89*, 7022; A. P. Grollman, M. Moriya, *Trends Genet.* **1993**, *9*, 246.
[64] A. Klungland, M. Hoss, D. Gunz, A. Constantinou, S. G. Clarkson, P. W. Doetsch, P. H. Bolton, R. D. Wood, T. Lindahl, *Mol. Cell* **1999**, *3*, 33; T. Bessho, *Nucleic Acids Res.* **1999**, *27*, 979.
[65] T. K. Hazra, T. Izumi, I. Boldogh, B. Imhoff, Y. W. Kow, P. Jaruga, M. Dizdaroglu, S. Mitra, *Proc. Natl. Acad. Sci. USA* **2002**, *99*, 3523; V. Bandaru, S. Sunkara, S. S. Wallace, J. P. Bond, *DNA Repair* **2002**, *1*.
[66] M. D. Wyatt, J. M. Allan, A. Y. Lau, T. E. Ellenberger, L. D. Samson, *Bioessays* **1999**, *21*, 668.
[67] K. G. Berdal, R. F. Johansen, E. Seeberg, *EMBO J.* **1998**, *17*, 363.
[68] B. J. Glassner, L. J. Rasmussen, M. T. Najarian, L. M. Posnick, L. D. Samson, *Proc. Natl. Acad. Sci. USA* **1998**, *95*, 9997.
[69] K. A. Haushalter, M. W. Todd Stukenberg, M. W. Kirschner, G. L. Verdine, *Curr. Biol.* **1999**, *9*, 174.
[70] M. L. Dodson, M. L. Michaels, R. S. Lloyd, *J. Biol. Chem.* **1994**, *269*, 32709.
[71] H. M. Nash, S. D. Bruner, O. D. Schärer, T. Kawate, T. A. Addona, E. Spooner, W. S. Lane, G. L. Verdine, *Curr. Biol.* **1996**, *6*, 968.
[72] T. P. Hilbert, R. J. Boorstein, H. C. Kung, P. H. Bolton, D. Xing, R. P. Cunningham, G. W. Teebor, *Biochemistry* **1996**, *35*, 2505.
[73] V. L. Schramm, B. A. Horenstein, P. C. Kline, *J. Biol. Chem.* **1994**, *269*, 18259; T. D. Heightman, A. T. Vasella, *Angew. Chem.* **1999**, *111*, 794; *Angew. Chem. Int. Ed.* **1999**, *38*, 750; D. L. Zechel, S. G. Withers, *Acc. Chem. Res.* **2000**, *33*, 11.
[74] R. M. Werner, J. T. Stivers, *Biochemistry* **2000**, *39*, 14054.
[75] B. Castaing, S. Boiteux, C. Zelwer, *Nucleic Acids Res.* **1992**, *20*, 389; B. Castaing, J. L. Fourrey, N. Hervouet, M. Thomas, S. Boiteux, C. Zelwer, *Nucleic Acids Res.* **1999**, *27*, 608.
[76] O. D. Schärer, H. M. Nash, J. Jiricny, J. Laval, G. L. Verdine, *J. Biol. Chem.* **1998**, *273*, 8592.
[77] O. D. Schärer, J.-Y. Ortholand, A. Ganesan, K. Ezaz-Nikpay, G. L. Verdine, *J. Am. Chem. Soc.* **1995**, *117*, 6623; L. Deng, O. D. Schärer, G. L. Verdine, *J. Am. Chem. Soc.* **1997**, *119*, 7865.
[78] O. D. Schärer, G. L. Verdine, *J. Am. Chem. Soc.* **1995**, *117*, 10781; O. D. Schärer, T. Kawate, P. Gallinari, J. Jiricny, G. L. Verdine, *Proc. Natl. Acad. Sci. USA* **1997**, *94*, 4878; S. L. Porello, S. D. Williams, H. Kuhn, M. L. Michels, S. S. David, *J. Am. Chem. Soc.* **1996**, *118*, 10684; C. L. Chepanoske, S. L. Porello, T. Fujiwara, H. Sugiyama, S. S. David, *Nucleic Acids Res.* **1999**, *27*, 3197.
[79] C. D. Mol, S. S. Parikh, C. D. Putnam, T. P. Lo, J. A. Tainer, *Annu. Rev. Biophys. Biomol. Struct.* **1999**, *28*, 101; A. K. McCullough, M. L. Dodson, R. S. Lloyd, *Annu. Rev. Biochem.* **1999**, *68*, 255; T. Hollis, A. Lau, T. Ellenberger, *Mutat. Res.* **2000**, *460*, 201; L. H. Pearl, *Mutat. Res.* **2000**, *460*, 165; T. Hollis, A. Lau, T. Ellenberger, *Prog. Nucleic Acid Res. Mol. Biol.* **2001**, *68*, 305; D. J. Hosfield, D. S. Daniels, C. D. Mol, C. D. Putnam, S. S. Parikh, J. A. Tainer, *Prog. Nucleic Acid Res. Mol. Biol.* **2001**, *68*, 315.
[80] S. Klimasauskas, S. Kumar, R. J. Roberts, X. Cheng, *Cell* **1994**, *76*, 357; K. M. Reinisch, L. Chen, G. L. Verdine, W. N. Lipscomb, *Cell* **1995**, *82*, 143.
[81] S. S. Parikh, C. D. Putnam, J. A. Tainer, *Mutat. Res.* **2000**, *460*, 183.
[82] R. Savva, K. McAuley-Hecht, T. Brown, L. Pearl, *Nature* **1995**, *373*, 487; C. D. Mol, A. S. Arvai, G. Slupphaug, B. Kavli, I. Alseth, H. E. Krokan, J. A. Tainer, *Cell* **1995**, *80*, 869.
[83] B. Kavli, G. Slupphaug, C. D. Mol, A. S. Arvai, S. B. Peterson, J. A. Tainer, H. E. Krokan, *EMBO J.* **1996**, *15*, 3442.
[84] G. Slupphaug, C. D. Mol, B. Kavli, A. S. Arvai, H. E. Krokan, J. A. Tainer, *Nature* **1996**, *384*, 87.
[85] S. S. Parikh, C. D. Mol, G. Slupphaug, S. Bharati, H. E. Krokan, J. A. Tainer, *EMBO J.* **1998**, *17*, 5214.
[86] S. S. Parikh, G. Walcher, G. D. Jones, G. Slupphaug, H. E. Krokan, G. M. Blackburn, J. A. Tainer, *Proc. Natl. Acad. Sci. USA* **2000**, *97*, 5083.
[87] Y. L. Jiang, K. Kwon, J. T. Stivers, *J. Biol. Chem.* **2001**, *276*, 42347.
[88] A. C. Drohat, J. T. Stivers, *J. Am. Chem. Soc.* **2000**, *122*, 1840.
[89] A. C. Drohat, J. T. Stivers, *Biochemistry* **2000**, *39*, 11865.
[90] A. R. Dinner, G. M. Blackburn, M. Karplus, *Nature* **2001**, *413*, 752.
[91] A. Y. Lau, O. D. Schärer, L. Samson, G. L. Verdine, T. Ellenberger, *Cell* **1998**, *95*, 249.
[92] A. Y. Lau, M. D. Wyatt, B. J. Glassner, L. D. Samson, T. Ellenberger, *Proc. Natl. Acad. Sci. USA* **2000**, *97*, 13573.
[93] S. D. Bruner, D. P. Norman, G. L. Verdine, *Nature* **2000**, *403*, 859.
[94] G. L. Verdine, S. D. Bruner, *Chem. Biol.* **1997**, *4*, 329.
[95] S. D. Bruner, D. P. G. Norman, J. C. Fromme, G. L. Verdine, *Cold Spring Harbor Symp. Quant. Biol.* **2000**, *65*, 103.
[96] L. Chen, K. A. Haushalter, C. M. Lieber, G. L. Verdine, *Chem. Biol.* **2002**, *9*, 345.
[97] J. Dong, A. C. Drohat, J. T. Stivers, K. W. Pankiewicz, P. R. Carey, *Biochemistry* **2000**, *39*, 13241; J. T. Stivers, K. W. Pankiewicz, K. A. Watanabe, *Biochemistry* **1999**, *38*, 952.
[98] D. M. Wilson III, L. H. Thompson, *Proc. Natl. Acad. Sci. USA* **1997**, *94*, 12754; S. Xanthoudakis, R. J. Smeyne, J. D. Wallace, T. Curran, *Proc. Natl. Acad. Sci. USA* **1996**, *93*, 8919; H. Gu, J. D. Marth, P. C. Orban, H. Mossmann, K. Rajewsky, *Science* **1994**, *265*, 103; R. S. Tebbs, M. L. Flannery, J. J. Meneses, A. Hartmann, J. D. Tucker, L. H. Thompson, J. E. Cleaver, R. A. Pedersen, *Dev. Biol.* **1999**, *208*, 513.
[99] B. P. Engelward, G. Weeda, M. D. Wyatt, J. L. Broekhof, J. de Wit, I. Donker, J. M. Allan, B. Gold, J. H. Hoeijmakers, L. D. Samson, *Proc. Natl. Acad. Sci. USA* **1997**, *94*, 13087; B. Hang, B. Singer, G. P. Margison, R. H. Elder, *Proc. Natl. Acad. Sci. USA* **1997**, *94*, 12869; A. Klungland, I. Rosewell, S. Hollenbach, E. Larsen, G. Daly, B. Epe, E. Seeberg, T. Lindahl, D. E. Barnes, *Proc. Natl. Acad. Sci. USA* **1999**, *96*, 13300; O. Minowa, T. Arai, M. Hirano, Y. Monden, S. Nakai, M. Fukuda, M. Itoh, H. Takano, Y. Hippou, H. Aburatani, K. Masumura, T. Nohmi, S. Nishimura, T. Noda, *Proc. Natl. Acad. Sci. USA* **2000**, *97*, 4156; M. Takao, S. Kanno, T. Shiromoto, R. Hasegawa, H. Ide, S. Ikeda, A. H. Sarker, S. Seki, J. Z. Xing, X. C. Le, M. Weinfeld, K. Kobayashi, J. Miyazaki, M. Muijtjens, J. H. J. Hoeijmakers, G. van der Horst, A. Yasui, *EMBO J.* **2002**, *21*, 3486; M. T. Ocampo, W. Chaung, D. R. Marenstein, M. K. Chan, A. Altamirano, A. K. Basu, R. J. Boorstein, R. P. Cunningham, G. W. Teebor, *Mol. Cell. Biol.* **2002**, *22*, 6111.
[100] H. Nilsen, I. Rosewell, P. Robins, C. F. Skjelbred, S. Andersen, G. Slupphaug, G. Daly, H. E. Krokan, T. Lindahl, D. E. Barnes, *Mol. Cell* **2000**, *5*, 1059.
[101] E. C. Friedberg, L. B. Meira, *Mutat. Res.* **2000**, *459*, 243.
[102] D. Gunz, M. T. Hess, H. Naegeli, *J. Biol. Chem.* **1996**, *271*, 25089.

 © 2003 Wiley-VCH Verlag GmbH & Co. KGaA, Weinheim

[103] M. T. Hess, U. Schwitter, M. Petretta, B. Giese, H. Naegeli, *Proc. Natl. Acad. Sci. USA* **1997**, *94*, 6664; K. Sugasawa, T. Okamoto, Y. Shimizu, C. Masutani, S. Iwai, F. Hanaoka, *Genes Dev.* **2001**, *15*, 507.

[104] A. Aboussekhra, M. Biggerstaff, M. K. Shivji, J. A. Vilpo, V. Moncollin, V. N. Podust, M. Protic, U. Hubscher, J. M. Egly, R. D. Wood, *Cell* **1995**, *80*, 859; D. Mu, C. H. Park, T. Matsunaga, D. S. Hsu, J. T. Reardon, A. Sancar, *J. Biol. Chem.* **1995**, *270*, 2415; S. J. Araujo, F. Tirode, F. Coin, H. Pospiech, J. E. Syvaoja, M. Stucki, U. Hübscher, J. M. Egly, R. D. Wood, *Genes Dev.* **2000**, *14*, 349; M. Araki, C. Masutani, T. Maekawa, Y. Watanabe, A. Yamada, R. Kusumoto, D. Sakai, K. Sugasawa, Y. Ohkuma, F. Hanaoka, *Mutat. Res.* **2000**, *459*, 147.

[105] J. Q. Svejstrup, *Nat. Rev. Mol. Cell Biol.* **2002**, *3*, 21.

[106] V. A. Bohr, C. A. Smith, D. S. Okumoto, P. C. Hanawalt, *Cell* **1985**, *40*, 359; I. Mellon, G. Spivak, P. C. Hanawalt, *Cell* **1987**, *51*, 241.

[107] D. P. Batty, R. D. Wood, *Gene* **2000**, *241*, 193.

[108] T. Ikegami, I. Kuraoka, M. Saijo, N. Kodo, Y. Kyogoku, K. Morikawa, K. Tanaka, M. Shirakawa, *Nat. Struct. Biol.* **1998**, *5*, 701; G. W. Buchko, S. Ni, B. D. Thrall, M. A. Kennedy, *Nucleic Acids Res.* **1998**, *26*, 2779; G. W. Buchko, C. S. Tung, K. McAteer, N. G. Isern, L. D. Spicer, M. A. Kennedy, *Nucleic Acids Res.* **2001**, *29*, 2635; A. Bochkarev, R. A. Pfuetzner, A. M. Edwards, L. Frappier, *Nature* **1997**, *385*, 176; A. Bochkarev, E. Bochkareva, L. Frappier, A. M. Edwards, *EMBO J.* **1999**, *18*, 4498; E. Bochkareva, V. Belegu, S. Korolev, A. Bochkarev, *EMBO J.* **2001**, *20*, 612; P. Schultz, S. Fribourg, A. Poterszman, V. Mallouh, D. Moras, J. M. Egly, *Cell* **2000**, *102*, 599; W. H. Chang, R. D. Kornberg, *Cell* **2000**, *102*, 609.

[109] K. Sugasawa, J. M. Ng, C. Masutani, S. Iwai, P. J. van der Spek, A. P. Eker, F. Hanaoka, D. Bootsma, J. H. Hoeijmakers, *Mol. Cell* **1998**, *2*, 223.

[110] E. Evans, J. G. Moggs, J. R. Hwang, J. M. Egly, R. D. Wood, *EMBO J.* **1997**, *16*, 6559.

[111] M. Wakasugi, A. Sancar, *Proc. Natl. Acad. Sci. USA* **1998**, *95*, 6669.

[112] M. Wakasugi, A. Sancar, *J. Biol. Chem.* **1999**, *274*, 18759.

[113] M. Volker, M. J. Mone, P. Karmakar, A. van Hoffen, W. Schul, W. Vermeulen, J. H. Hoeijmakers, R. van Driel, A. A. van Zeeland, L. H. Mullenders, *Mol. Cell* **2001**, *8*, 213.

[114] M. Yokoi, C. Masutani, T. Maekawa, K. Sugasawa, Y. Ohkuma, F. Hanaoka, *J. Biol. Chem.* **2000**, *275*, 9870.

[115] N. Iyer, M. S. Reagan, K. J. Wu, B. Canagarajah, E. C. Friedberg, *Biochemistry* **1996**, *35*, 2157; S. Nocentini, F. Coin, M. Saijo, K. Tanaka, J. M. Egly, *J. Biol. Chem.* **1997**, *272*, 22991; S. J. Araujo, E. A. Nigg, R. D. Wood, *Mol. Cell. Biol.* **2001**, *21*, 2281.

[116] M. Missura, T. Buterin, R. Hindges, U. Hübscher, J. Kasparkova, V. Brabec, H. Naegeli, *EMBO J.* **2001**, *20*, 3554.

[117] L. Li, S. J. Elledge, C. A. Peterson, E. S. Bales, R. J. Legerski, *Proc. Natl. Acad. Sci. USA* **1994**, *91*, 5012; L. Li, C. A. Peterson, X. Lu, R. J. Legerski, *Mol. Cell. Biol.* **1995**, *15*, 1993; C. H. Park, A. Sancar, *Proc. Natl. Acad. Sci. USA* **1994**, *91*, 5017; M. Saijo, I. Kuraoka, C. Masutani, F. Hanaoka, K. Tanaka, *Nucleic Acids Res.* **1996**, *24*, 4719.

[118] Z. He, L. A. Henricksen, M. S. Wold, C. J. Ingles, *Nature* **1995**, *374*, 566; W. L. de Laat, E. Appeldoorn, K. Sugasawa, E. Weterings, N. G. Jaspers, J. H. Hoeijmakers, *Genes Dev.* **1998**, *12*, 2598.

[119] A. M. Sijbers, W. L. de Laat, R. R. Ariza, M. Biggerstaff, Y.-F. Wei, J. G. Moggs, K. C. Carter, B. K. Shell, E. Evans, M. C. de Jong, S. Rademakers, J. de Rooij, N. G. J. Jaspers, J. H. J. Hoeijmakers, R. D. Wood, *Cell* **1996**, *86*, 811.

[120] A. O'Donovan, A. A. Davies, J. G. Moggs, S. C. West, R. D. Wood, *Nature* **1994**, *371*, 432.

[121] T. Matsunaga, D. Mu, C. H. Park, J. T. Reardon, A. Sancar, *J. Biol. Chem.* **1995**, *270*, 20862; M. Wakasugi, J. T. Reardon, A. Sancar, *J. Biol. Chem.* **1997**, *272*, 16030.

[122] E. Evans, J. Fellows, A. Coffer, R. D. Wood, *EMBO J.* **1997**, *16*, 625; M. R. Lieber, *Bioessays* **1997**, *19*, 233; A. Constantinou, D. Gunz, E. Evans, P. Lalle, P. A. Bates, R. D. Wood, S. G. Clarkson, *J. Biol. Chem.* **1999**, *274*, 5637.

[123] W. L. de Laat, E. Appeldoorn, N. G. J. Jaspers, J. H. J. Hoeijmakers, *J. Biol. Chem.* **1998**, *273*, 7835.

[124] J. H. Enzlin, O. D. Schärer, *EMBO J.* **2002**, *21*, 2045.

[125] J. Y. Tang, B. J. Hwang, J. M. Ford, P. C. Hanawalt, G. Chu, *Mol. Cell* **2000**, *5*, 737; M. Wakasugi, M. Shimizu, H. Morioka, S. Linn, O. Nikaido, T. Matsunaga, *J. Biol. Chem.* **2001**, *276*, 15434; M. Wakasugi, A. Kawashima, H. Morioka, S. Linn, A. Sancar, T. Mori, O. Nikaido, T. Matsunaga, *J. Biol. Chem.* **2002**, *277*, 1637.

[126] D. Mu, D. S. Hsu, A. Sancar, *J. Biol. Chem.* **1996**, *271*, 8285; D. Mu, A. Sancar, *J. Biol. Chem.* **1997**, *272*, 7570.

[127] A. B. Houtsmuller, S. Rademakers, A. L. Nigg, D. Hoogstraten, J. H. Hoeijmakers, W. Vermeulen, *Science* **1999**, *284*, 958.

[128] D. Bootsma, K. H. Kraemer, J. E. Cleaver, J. H. J Hoeijmakers in *The Genetic Basis of Cancer* (Eds.: B. Vogelstein, K. W. Kinzler), McGraw-Hill, New York, **1998**, p. 245.

[129] J. de Boer, J. H. Hoeijmakers, *Carcinogenesis* **2000**, *21*, 453.

[130] E. Bergmann, J. M. Egly, *Trends Genet.* **2001**, *17*, 279.

[131] A. J. van Gool, G. T. van der Horst, E. Citterio, J. H. Hoeijmakers, *EMBO J.* **1997**, *16*, 4155.

[132] P. K. Cooper, T. Nouspikel, S. G. Clarkson, S. A. Leadon, *Science* **1997**, *275*, 990.

[133] W. Vermeulen, E. Bergmann, J. Auriol, S. Rademakers, P. Frit, E. Appeldoorn, J. H. Hoeijmakers, J. M. Egly, *Nat. Genet.* **2000**, *26*, 307.

[134] W. Vermeulen, S. Rademakers, N. G. Jaspers, E. Appeldoorn, A. Raams, B. Klein, W. J. Kleijer, L. K. Hansen, J. H. Hoeijmakers, *Nat. Genet.* **2001**, *27*, 299.

[135] J. McWhir, J. Selfridge, D. J. Harrison, S. Squires, D. W. Melton, *Nat. Genet.* **1993**, *5*, 217; G. Weeda, I. Donker, J. de Wit, H. Morreau, R. Janssens, C. J. Vissers, A. Nigg, H. van Steeg, D. Bootsma, J. H. J. Hoeijmakers, *Curr. Biol.* **1997**, *7*, 427.

[136] T. A. Kunkel, *J. Biol. Chem.* **1992**, *267*, 18251.

[137] P. Modrich, *Annu. Rev. Genet.* **1991**, *25*, 229.

[138] P. Modrich, R. Lahue, *Annu. Rev. Biochem.* **1996**, *65*, 101.

[139] J. Jiricny, *EMBO J.* **1998**, *17*, 6427.

[140] R. S. Lahue, K. G. Au, P. Modrich, *Science* **1989**, *245*, 160.

[141] S. S. Su, R. S. Lahue, K. G. Au, P. Modrich, *J. Biol. Chem.* **1988**, *263*, 6829.

[142] K. M. Welsh, A. L. Lu, S. Clark, P. Modrich, *J. Biol. Chem.* **1987**, *262*, 15624; K. G. Au, K. Welsh, P. Modrich, *J. Biol. Chem.* **1992**, *267*, 12142.

[143] B. D. Harfe, S. Jinks-Robertson, *Annu. Rev. Genet.* **2000**, *34*, 359.

[144] P. Hsieh, *Mutat. Res.* **2001**, *486*, 71.

[145] I. Iaccarino, G. Marra, F. Palombo, J. Jiricny, *EMBO J.* **1998**, *17*, 2677; I. Iaccarino, F. Palombo, J. Drummond, N. F. Totty, J. J. Hsuan, P. Modrich, J. Jiricny, *Curr. Biol.* **1996**, *6*, 484; F. Palombo, I. Iaccarino, E. Nakajima, M. Ikejima, T. Shimada, J. Jiricny, *Curr. Biol.* **1996**, *6*, 1181; S. Acharya, T. Wilson, S. Gradia, M. F. Kane, S. Guerrette, G. T. Marsischky, R. Kolodner, R. Fishel, *Proc. Natl. Acad. Sci. USA* **1996**, *93*, 13629; J. Genschel, S. J. Littman, J. T. Drummond, P. Modrich, *J. Biol. Chem.* **1998**, *273*, 19895.

[146] L. J. Blackwell, D. Martik, K. P. Bjornson, E. S. Bjornson, P. Modrich, *J. Biol. Chem.* **1998**, *273*, 32055; L. J. Blackwell, K. P. Bjornson, D. J. Allen, P. Modrich, *J. Biol. Chem.* **2001**, *276*, 34339; S. Gradia, D. Subramanian, T. Wilson, S. Acharya, A. Makhov, J. Griffith, R. Fishel, *Mol. Cell* **1999**, *3*, 255; I.

 © 2003 Wiley-VCH Verlag GmbH & Co. KGaA, Weinheim

Iaccarino, G. Marra, P. Dufner, J. Jiricny, *J. Biol. Chem.* **2000**, *275*, 2080.
[147] D. J. Allen, A. Makhov, M. Grilley, J. Taylor, R. Thresher, P. Modrich, J. D. Griffith, *EMBO J.* **1997**, *16*, 4467.
[148] P. Szankasi, G. R. Smith, *Science* **1995**, *267*, 1166; D. X. Tishkoff, N. Filosi, G. M. Gaida, R. D. Kolodner, *Cell* **1997**, *88*, 253; P. T. Tran, J. A. Simon, R. M. Liskay, *Proc. Natl. Acad. Sci. USA* **2001**, *98*, 9760.
[149] A. Umar, A. B. Buermeyer, J. A. Simon, D. C. Thomas, A. B. Clark, R. M. Liskay, T. A. Kunkel, *Cell* **1996**, *87*, 65; R. E. Johnson, G. K. Kovvali, S. N. Guzder, N. S. Amin, C. Holm, Y. Habraken, P. Sung, L. Prakash, S. Prakash, *J. Biol. Chem.* **1996**, *271*, 27987; J. C. Eissenberg, R. Ayyagari, X. V. Gomes, P. M. Burgers, *Mol. Cell. Biol.* **1997**, *17*, 6367; H. E. Kleczkowska, G. Marra, T. Lettieri, J. Jiricny, *Genes Dev.* **2001**, *15*, 724.
[150] M. H. Lamers, A. Perrakis, J. H. Enzlin, H. H. Winterwerp, N. de Wind, T. K. Sixma, *Nature* **2000**, *407*, 711.
[151] G. Obmolova, C. Ban, P. Hsieh, W. Yang, *Nature* **2000**, *407*, 703.
[152] V. A. Malkov, I. Biswas, R. D. Camerini-Otero, P. Hsieh, *J. Biol. Chem.* **1997**, *272*, 23811; J. Bowers, T. Sokolsky, T. Quach, E. Alani, *J. Biol. Chem.* **1999**, *274*, 16115; P. Dufner, G. Marra, M. Raschle, J. Jiricny, *J. Biol. Chem.* **2000**, *275*, 36550; R. Das Gupta, R. D. Kolodner, *Nat. Genet.* **2000**, *24*, 53.
[153] M. J. Schofield, F. E. Brownewell, S. Nayak, C. Du, E. T. Kool, P. Hsieh, *J. Biol. Chem.* **2001**, *276*, 45505; K. Drotschmann, W. Yang, F. E. Brownewell, E. T. Kool, T. A. Kunkel, *J. Biol. Chem.* **2001**, *276*, 46225.
[154] J. Jiricny, M. Nystrom-Lahti, *Curr. Opin. Genet. Dev.* **2000**, *10*, 157.
[155] R. Fishel, M. K. Lescoe, M. R. Rao, N. G. Copeland, N. A. Jenkins, J. Garber, M. Kane, R. Kolodner, *Cell* **1993**, *75*, 1027; F. S. Leach, N. C. Nicolaides, N. Papadopoulos, B. Liu, J. Jen, R. Parsons, P. Peltomaki, P. Sistonen, L. A. Aaltonen, M. Nystrom-Lahti, *Cell* **1993**, *75*, 1215; R. Parsons, G. M. Li, M. J. Longley, W. H. Fang, N. Papadopoulos, J. Jen, A. de la Chapelle, K. W. Kinzler, B. Vogelstein, P. Modrich, *Cell* **1993**, *75*, 1227; C. E. Bronner, S. M. Baker, P. T. Morrison, G. Warren, L. G. Smith, M. K. Lescoe, M. Kane, C. Earabino, J. Lipford, A. Lindblom, P. Tannergård, R. J. Bollag, A. R. Godwin, D. C. Ward, M. Nordenskjøld, R. Fishel, R. Kolodner, R. M. Liskay, *Nature* **1994**, *368*, 258; N. Papadopoulos, N. C. Nicolaides, Y.-F. Wei, S. M. Ruben, K. C. Carter, C. A. Rosen, W. A. Haseltine, R. D. Fleischmann, C. M. Fraser, M. D. Adams, J. C. Venter, S. R. Hamilton, G. M. Petersen, P. Watson, H. T. Lynch, P. Peltomaki, J.-P. Mecklin, A. de la Chapelle, K. W. Kinzler, B. Vogelstein, *Science* **1994**, *263*, 1625; N. C. Nicolaides, N. Papadopoulos, B. Liu, Y. F. Wei, K. C. Carter, S. M. Ruben, C. A. Rosen, W. A. Haseltine, R. D. Fleischmann, C. M. Fraser, M. D. Adams, J. C. Venter, M. G. Dunlop, S. R. Hamilton, G. M. Petersen, A. de la Chapelle, B. Vogelstein, K. W. Kinzler, *Nature* **1994**, *371*, 75; N. Papadopoulos, N. C. Nicolaides, B. Liu, R. Parsons, C. Lengauer, F. Palombo, A. D'Arrigo, S. Markowitz, J. K. Willson, K. W. Kinzler, J. Jiricny, B. Vogelstein, *Science* **1995**, *268*, 1915.
[156] W. Edelmann, K. Yang, A. Umar, J. Heyer, K. Lau, K. Fan, W. Liedtke, P. E. Cohen, M. F. Kane, J. R. Lipford, N. Yu, G. F. Crouse, J. W. Pollard, T. Kunkel, M. Lipkin, R. Kolodner, R. Kucherlapati, *Cell* **1997**, *91*, 467.
[157] N. de Wind, M. Dekker, N. Claij, L. Jansen, Y. van Klink, M. Radman, G. Riggins, M. van der Valk, K. van't Wout, H. te Riele, *Nat. Genet.* **1999**, *23*, 359.
[158] G. M. Li, *Oncol. Res.* **1999**, *11*, 393.
[159] S. C. Kowalczykowski, D. A. Dixon, A. K. Eggleston, S. D. Lauder, W. M. Rehrauer, *Microbiol. Rev.* **1994**, *58*, 401.
[160] G. A. Cromie, J. C. Connelly, D. R. Leach, *Mol. Cell.* **2001**, *8*, 1163; M. Modesti, R. Kanaar, *Genome Biol.* **2001**, *2*.
[161] S. C. West, *Annu. Rev. Genet.* **1997**, *31*, 213.
[162] J. C. Game, *Semin. Cancer Biol.* **1993**, *4*, 73.
[163] E. Van Dyck, A. Z. Stasiak, A. Stasiak, S. C. West, *Nature* **1999**, *398*, 728; C. A. Parsons, P. Baumann, E. Van Dyck, S. C. West, *EMBO J.* **2000**, *19*, 4175; A. Z. Stasiak, E. Larquet, A. Stasiak, S. Muller, A. Engel, E. Van Dyck, S. C. West, E. H. Egelman, *Curr. Biol.* **2000**, *10*, 337.
[164] K. M. Trujillo, S. S. Yuan, E. Y. Lee, P. Sung, *J. Biol. Chem.* **1998**, *273*, 21447; T. T. Paull, M. Gellert, *Mol. Cell* **1998**, *1*, 969.
[165] D. A. Bressan, B. K. Baxter, J. H. Petrini, *Mol. Cell. Biol.* **1999**, *19*, 7681.
[166] H. Tsubouchi, H. Ogawa, *Mol. Biol. Cell* **2000**, *11*, 2221; S. Moreau, E. A. Morgan, L. S. Symington, *Genetics* **2001**, *159*, 1423.
[167] T. Ogawa, X. Yu, A. Shinohara, E. H. Egelman, *Science* **1993**, *259*, 1896; P. Sung, *Science* **1994**, *265*, 1241; P. Baumann, F. E. Benson, S. C. West, *Cell* **1996**, *87*, 757; R. C. Gupta, L. R. Bazemore, E. I. Golub, C. M. Radding, *Proc. Natl. Acad. Sci. USA* **1997**, *94*, 463; P. Baumann, S. C. West, *Trends Biochem. Sci.* **1998**, *23*, 247.
[168] F. E. Benson, P. Baumann, S. C. West, *Nature* **1998**, *391*, 401; J. H. New, T. Sugiyama, E. Zaitseva, S. C. Kowalczykowski, *Nature* **1998**, *391*, 407; A. Shinohara, T. Ogawa, *Nature* **1998**, *391*, 404; P. Sung, *J. Biol. Chem.* **1997**, *272*, 28194.
[169] P. Sung, *Genes Dev.* **1997**, *11*, 1111.
[170] J. Thacker, *Trends Genet.* **1999**, *15*, 166; L. H. Thompson, D. Schild, *Mutat. Res.* **2001**, *477*, 131.
[171] N. Liu, J. E. Lamerdin, R. S. Tebbs, D. Schild, J. D. Tucker, M. R. Shen, K. W. Brookman, M. J. Siciliano, C. A. Walter, W. Fan, L. S. Narayana, Z.-Q. Zhou, A. W. Adamson, K. J. Sorensen, D. J. Chen, N. J. Jones, L. H. Thompson, *Mol. Cell* **1998**, *1*, 783; R. D. Johnson, N. Liu, M. Jasin, *Nature* **1999**, *401*, 397; A. J. Pierce, R. D. Johnson, L. H. Thompson, M. Jasin, *Genes Dev.* **1999**, *13*, 2633; M. Takata, M. S. Sasaki, E. Sonoda, T. Fukushima, C. Morrison, J. S. Albala, S. M. Swagemakers, R. Kanaar, L. H. Thompson, S. Takeda, *Mol. Cell. Biol.* **2000**, *20*, 6476; M. Takata, M. S. Sasaki, S. Tachiiri, T. Fukushima, E. Sonoda, D. Schild, L. H. Thompson, S. Takeda, *Mol. Cell. Biol.* **2001**, *21*, 2858.
[172] J. P. Braybrooke, K. G. Spink, J. Thacker, I. D. Hickson, *J. Biol. Chem.* **2000**, *275*, 29100; D. Schild, Y. Lio, D. W. Collins, T. Tsomondo, D. J. Chen, *J. Biol. Chem.* **2000**, *275*, 16443; K. A. Miller, D. M. Yoshikawa, I. R. McConnell, R. Clark, D. Schild, J. S. Albala, *J. Biol. Chem.* **2001**, *13*, 13; H. Kurumizaka, S. Ikawa, M. Nakada, K. Eda, W. Kagawa, M. Takata, S. Takeda, S. Yokoyama, T. Shibata, *Proc. Natl. Acad. Sci. USA* **2001**, *98*, 5538; J. Y. Masson, M. C. Tarsounas, A. Z. Stasiak, A. Stasiak, R. Shah, M. J. McIlwraith, F. E. Benson, S. C. West, *Genes Dev.* **2001**, *15*, 3296; S. Sigurdsson, S. Van Komen, W. Bussen, D. Schild, J. S. Albala, P. Sung, *Genes Dev.* **2001**, *15*, 3308; N. Liu, D. Schild, M. P. Thelen, L. H. Thompson, *Nucleic Acids Res.* **2002**, *30*, 1009; C. Wiese, D. W. Collins, J. S. Albala, L. H. Thompson, A. Kronenberg, D. Schild, *Nucleic Acids Res.* **2002**, *30*, 1001; H. Kurumizaka, S. Ikawa, M. Nakada, R. Enomoto, W. Kagawa, T. Kinebuchi, M. Yamazoe, S. Yokoyama, T. Shibata, *J. Biol. Chem.* **2002**, *277*, 14315.
[173] H. Jiang, Y. Xie, P. Houston, K. Stemke-Hale, U. H. Mortensen, R. Rothstein, T. Kodadek, *J. Biol. Chem.* **1996**, *271*, 33181; B. Clever, H. Interthal, J. Schmuckli-Maurer, J. King, M. Sigrist, W. D. Heyer, *EMBO J.* **1997**, *16*, 2535; T. L. Tan, J. Essers, E. Citterio, S. M. Swagemakers, J. de Wit, F. E. Benson, J. H. Hoeijmakers, R. Kanaar, *Curr. Biol.* **1999**, *9*, 325; G. Petukhova, S. Stratton, P. Sung, *Nature* **1998**, *393*, 91.
[174] S. M. Swagemakers, J. Essers, J. de Wit, J. H. Hoeijmakers, R. Kanaar, *J. Biol. Chem.* **1998**, *273*, 28292.
[175] J. Essers, R. W. Hendriks, J. Wesoly, C. E. Beerens, B. Smit, J. H. Hoeijmakers, C. Wyman, M. L. Dronkert, R. Kanaar, *DNA Repair* **2002**, *1*, 779.

 © 2003 Wiley-VCH Verlag GmbH & Co. KGaA, Weinheim

[176] D. Ristic, C. Wyman, C. Paulusma, R. Kanaar, *Proc. Natl. Acad. Sci. USA* **2001**, *98*, 8454; S. Van Komen, G. Petukhova, S. Sigurdsson, S. Stratton, P. Sung, *Mol. Cell* **2000**, *6*, 563.
[177] A. K. Eggleston, A. H. Mitchell, S. C. West, *Cell* **1997**, *89*, 607.
[178] A. Constantinou, A. A. Davies, S. C. West, *Cell* **2001**, *104*, 259.
[179] M. N. Boddy, P.-H. L. Gaillard, W. H. McDonald, P. Shanahan, J. R. Yates III, P. Russell, *Cell* **2001**, *107*, 537; X.-B. Chen, R. Melchionna, C.-M. Denis, P.-H. Gaillard, A. Blasina, I. Van de Weyer, M. N. Boddy, P. Russell, J. Vialard, C. H. McGowan, *Mol. Cell* **2001**, *8*, 1117.
[180] A. Constantinou, X. B. Chen, C. H. McGowan, S. C. West, *EMBO J.* **2002**, *21*, 5577.
[181] S. P. Jackson, *Carcinogenesis* **2002**, *23*, 687.
[182] J. N. Snouwaert, L. C. Gowen, A. M. Latour, A. R. Mohn, A. Xiao, L. DiBiase, B. H. Koller, *Oncogene* **1999**, *18*, 7900; M. E. Moynahan, J. W. Chiu, B. H. Koller, M. Jasin, *Mol. Cell* **1999**, *4*, 511; M. E. Moynahan, A. J. Pierce, M. Jasin, *Mol. Cell* **2001**, *7*, 263.
[183] H. Yang, P. D. Jeffrey, J. Miller, E. Kinnucan, Y. Sun, N. H. Thoma, N. Zheng, P. L. Chen, W. H. Lee, N. P. Pavletich, *Science* **2002**, *297*, 1837.
[184] A. A. Davies, J. Y. Masson, M. J. McIlwraith, A. Z. Stasiak, A. Stasiak, A. R. Venkitaraman, S. C. West, *Mol. Cell* **2001**, *7*, 273.
[185] L. Pellegrini, D. S. Yu, T. Lo, S. Anand, M. Lee, T. L. Blundell, A. R. Venkitaraman, *Nature* **2002**, *420*, 287.
[186] A. R. Venkitaraman, *Cell* **2002**, *108*, 171.
[187] P. A. Jeggo, *Radiat. Res.* **1998**, *150*, S80.
[188] S. E. Critchlow, S. P. Jackson, *Trends Biochem. Sci.* **1998**, *23*, 394; J. E. Haber, *Trends Genet.* **2000**, *16*, 259.
[189] W. S. Dynan, S. Yoo, *Nucleic Acids Res.* **1998**, *26*, 1551; G. C. Smith, S. P. Jackson, *Genes Dev.* **1999**, *13*, 916.
[190] L. Chen, K. Trujillo, W. Ramos, P. Sung, A. E. Tomkinson, *Mol. Cell* **2001**, *8*, 1105.
[191] J. Huang, W. S. Dynan, *Nucleic Acids Res.* **2002**, *30*, 667; W. Goedecke, M. Eijpe, H. H. Offenberg, M. van Aalderen, C. Heyting, *Nat. Genet.* **1999**, *23*, 194; S. A. Nick McElhinny, C. M. Snowden, J. McCarville, D. A. Ramsden, *Mol. Cell. Biol.* **2000**, *20*, 2996.
[192] M. S. Junop, M. Modesti, A. Guarne, R. Ghirlando, M. Gellert, W. Yang, *EMBO J.* **2000**, *19*, 5962; B. L. Sibanda, S. E. Critchlow, J. Begun, X. Y. Pei, S. P. Jackson, T. L. Blundell, L. Pellegrini, *Nat. Struct. Biol.* **2001**, *8*, 1015; K. P. Hopfner, A. Karcher, L. Craig, T. T. Woo, J. P. Carney, J. A. Tainer, *Cell* **2001**, *105*, 473; K. P. Hopfner, A. Karcher, D. S. Shin, L. Craig, L. M. Arthur, J. P. Carney, J. A. Tainer, *Cell* **2000**, *101*, 789.
[193] M. de Jager, J. van Noort, D. C. van Gent, C. Dekker, R. Kanaar, C. Wyman, *Mol. Cell* **2001**, *8*, 1129.
[194] D. Moshous, I. Callebaut, R. de Chasseval, B. Corneo, M. Cavazzana-Calvo, F. Le Deist, I. Tezcan, O. Sanal, Y. Bertrand, N. Philippe, A. Fischer, J.-P. de Villartay, *Cell* **2001**, *105*, 177; Y. Ma, U. Pannicke, K. Schwarz, M. R. Lieber, *Cell* **2002**, *108*, 781; X. Wu, T. E. Wilson, M. R. Lieber, *Proc. Natl. Acad. Sci. USA* **1999**, *96*, 1303.
[195] U. Grawunder, M. Wilm, X. Wu, P. Kulesza, T. E. Wilson, M. Mann, M. R. Lieber, *Nature* **1997**, *388*, 492; S. E. Critchlow, R. P. Bowater, S. P. Jackson, *Curr. Biol.* **1997**, *7*, 588; G. Herrmann, T. Lindahl, P. Schär, *EMBO J.* **1998**, *17*, 4188; S. H. Teo, S. P. Jackson, *Curr. Biol.* **2000**, *10*, 165.
[196] J. R. Walker, R. A. Corpina, J. Goldberg, *Nature* **2001**, *412*, 607.
[197] S. Yoo, A. Kimzey, W. S. Dynan, *J. Biol. Chem.* **1999**, *274*, 20034.
[198] Y. Shiloh, *Annu. Rev. Genet.* **1997**, *31*, 635; J. P. Carney, R. S. Maser, H. Olivares, E. M. Davis, M. Le Beau, J. R. Yates III, L. Hays, W. F. Morgan, J. H. Petrini, *Cell* **1998**, *93*, 477; R. Varon, C. Vissinga, M. Platzer, K. M. Cerosaletti, K. H. Chrzanowska, K. Saar, G. Beckmann, E. Seemanova, P. R. Cooper, N. J. Nowak, M. Stumm, C. M. R. Weemaes, R. A. Gatti, R. K. Wilson, M. Digweed, A. Rosenthal, K. Sperling, P. Concannon, A. Reis, *Cell* **1998**, *93*, 467; G. S. Stewart, R. S. Maser, T. Stankovic, D. A. Bressan, M. I. Kaplan, N. G. Jaspers, A. Raams, P. J. Byrd, J. H. Petrini, A. M. Taylor, *Cell* **1999**, *99*, 577; M. B. Kastan, D. S. Lim, *Nat. Rev. Mol. Cell Biol.* **2000**, *1*, 179.
[199] Y. Xiao, D. T. Weaver, *Nucleic Acids Res.* **1997**, *25*, 2985; G. Luo, M. S. Yao, C. F. Bender, M. Mills, A. R. Bladl, A. Bradley, J. H. Petrini, *Proc. Natl. Acad. Sci. USA* **1999**, *96*, 7376.
[200] D. O. Ferguson, F. W. Alt, *Oncogene* **2001**, *20*, 5572; A. J. Pierce, J. M. Stark, F. D. Araujo, M. E. Moynahan, M. Berwick, M. Jasin, *Trends Cell Biol.* **2001**, *11*, S52.
[201] D. O. Ferguson, J. M. Sekiguchi, S. Chang, K. M. Frank, Y. Gao, R. A. DePinho, F. W. Alt, *Proc. Natl. Acad. Sci. USA* **2000**, *97*, 6630; M. J. Difilippantonio, J. Zhu, H. T. Chen, E. Meffre, M. C. Nussenzweig, E. E. Max, T. Ried, A. Nussenzweig, *Nature* **2000**, *404*, 510; Z. E. Karanjawala, U. Grawunder, C. L. Hsieh, M. R. Lieber, *Curr. Biol.* **1999**, *9*, 1501.
[202] K. M. Frank, N. E. Sharpless, Y. Gao, J. M. Sekiguchi, D. O. Ferguson, C. Zhu, J. P. Manis, J. Horner, R. A. DePinho, F. W. Alt, *Mol. Cell* **2000**, *5*, 993; Y. Gao, D. O. Ferguson, W. Xie, J. P. Manis, J. Sekiguchi, K. M. Frank, J. Chaudhuri, J. Horner, R. A. DePinho, F. W. Alt, *Nature* **2000**, *404*, 897; Y. Lee, D. E. Barnes, T. Lindahl, P. J. McKinnon, *Genes Dev.* **2000**, *14*, 2576.
[203] E. Riballo, S. E. Critchlow, S. H. Teo, A. J. Doherty, A. Priestley, B. Broughton, B. Kysela, H. Beamish, N. Plowman, C. F. Arlett, A. R. Lehmann, S. P. Jackson, P. A. Jeggo, *Curr. Biol.* **1999**, *9*, 699; E. Riballo, A. J. Doherty, Y. Dai, T. Stiff, M. A. Oettinger, P. A. Jeggo, B. Kysela, *J. Biol. Chem.* **2001**, *276*, 31124; M. O'Driscoll, K. M. Cerosaletti, P. M. Girard, Y. Dai, M. Stumm, B. Kysela, B. Hirsch, A. Gennery, S. E. Palmer, J. Seidel, R. A. Gatti, R. Varon, M. A. Oettinger, H. Neitzel, P. A. Jeggo, P. Concannon, *Mol. Cell* **2001**, *8*, 1175.
[204] D. S. Lim, P. Hasty, *Mol. Cell. Biol.* **1996**, *16*, 7133; T. Tsuzuki, Y. Fujii, K. Sakumi, Y. Tominaga, K. Nakao, M. Sekiguchi, A. Matsushiro, Y. Yoshimura, T. Morita, *Proc. Natl. Acad. Sci. USA* **1996**, *93*, 6236.
[205] E. Sonoda, M. S. Sasaki, J. M. Buerstedde, O. Bezzubova, A. Shinohara, H. Ogawa, M. Takata, Y. Yamaguchi-Iwai, S. Takeda, *EMBO J.* **1998**, *17*, 598.
[206] Z. Shu, S. Smith, L. Wang, M. C. Rice, E. B. Kmiec, *Mol. Cell. Biol.* **1999**, *19*, 8686; B. Deans, C. S. Griffin, M. Maconochie, J. Thacker, *EMBO J.* **2000**, *19*, 6675; D. L. Pittman, J. C. Schimenti, *Genesis* **2000**, *26*, 167.
[207] T. Rijkers, J. Van Den Ouweland, B. Morolli, A. G. Rolink, W. M. Baarends, P. P. Van Sloun, P. H. Lohman, A. Pastink, *Mol. Cell. Biol.* **1998**, *18*, 6423; Y. Yamaguchi-Iwai, E. Sonoda, J. M. Buerstedde, O. Bezzubova, C. Morrison, M. Takata, A. Shinohara, S. Takeda, *Mol. Cell. Biol.* **1998**, *18*, 6430.
[208] A. Fujimori, S. Tachiiri, E. Sonoda, L. H. Thompson, P. K. Dhar, M. Hiraoka, S. Takeda, Y. Zhang, M. Reth, M. Takata, *EMBO J.* **2001**, *20*, 5513.
[209] J. Essers, R. W. Hendriks, S. M. Swagemakers, C. Troelstra, J. de Wit, D. Bootsma, J. H. Hoeijmakers, R. Kanaar, *Cell* **1997**, *89*, 195.
[210] J. Essers, H. van Steeg, J. de Wit, S. M. Swagemakers, M. Vermeij, J. H. Hoeijmakers, R. Kanaar, *EMBO J.* **2000**, *19*, 1703; M. Takata, M. S. Sasaki, E. Sonoda, C. Morrison, M. Hashimoto, H. Utsumi, Y. Yamaguchi-Iwai, A. Shinohara, S. Takeda, *EMBO J.* **1998**, *17*, 5497.
[211] P. Mohaghegh, I. D. Hickson, *Hum. Mol. Genet.* **2001**, *10*, 741; J. Shen, L. A. Loeb, *Mech. Ageing Dev.* **2001**, *122*, 921; R. M. Brosh, V. A. Bohr, *Exp. Gerontol.* **2002**, *37*, 491.
[212] H. Joenje, K. J. Patel, *Nat. Rev. Genet.* **2001**, *2*, 446; M. Grompe, A. D'Andrea, *Hum. Mol. Genet.* **2001**, *10*, 2253.
[213] Note added in proof: A series of recent studies have revealed the existence of another direct repair pathway that is conserved

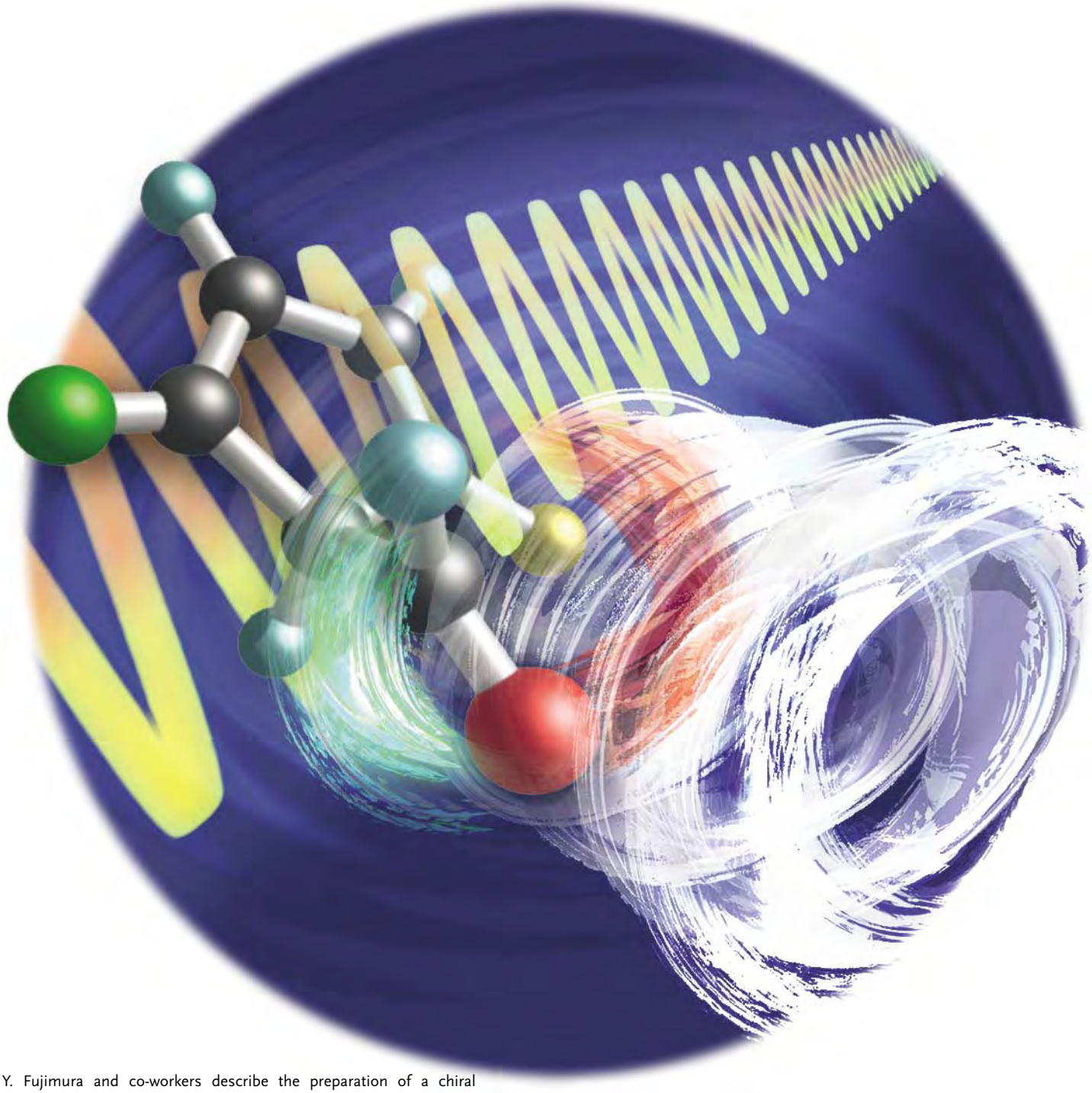
 © 2003 Wiley-VCH Verlag GmbH & Co. KGaA, Weinheim

from bacteria to man: This involves the oxidative demethylation of 1-methyladenine and 3-methylcytosine by the AlkB protein: S. C. Trewick, T. F. Henshaw, R. P. Hausinger, T. Lindahl, B. Sedgwick, *Nature* **2002**, *419*, 174; P. Ø Falnes, R. F. Johansen, E. Seeberg, *Nature* **2002**, *419*, 178; T. Duncan, S. C. Trewick, P. Koivisto, P. A. Bates, T. Lindahl, B. Sedgwick, *Proc. Natl. Acad. Sci. USA* **2002**, *99*, 16660; P. A. Aas, M. Otterlei, P. Ø Falnes, C. B. Vågbø, F. Skorpen, M. Akbari, O. Sundheim, M. Bjørås, G. Slupphaug, E. Seeberg, H. E. Krokan, *Nature* **2003**, *421*, 859.

[214] Note added in Proof: Recent studies have linked defects in the MYH gene to familial colorectal adenomas: N. Al-Tassan, N. H. Chmiel, J. Maynard, N. Fleming, A. L. Livingston, G. T. Williams, A. K. Hodges, D. R. Davies, S. S. David, J. R. Sampson, J. P. Cheadle, *Nat. Genet.* **2002**, *30*, 227; S. Jones, P. Emmerson, J. Maynard, J. M. Best, S. Jordan, G. T. Williams, J. R. Sampson, J. P. Cheadle, *Hum. Mol. Genet.* **2002**, *11*, 2961.

 © 2003 Wiley-VCH Verlag GmbH & Co. KGaA, Weinheim

Communications



Y. Fujimura and co-workers describe the preparation of a chiral molecular motor on page 2975 ff. The unidirectional rotation of the motor, which is driven by the coherent properties of the electromagnetic field that exists due to a nonhelical laser pulse, has been explained by calculations that are based on both classical and quantum mechanics.

DOI: 10.1002/anie.200250872
© 2003 Wiley-VCH Verlag GmbH & Co. KGaA, Weinheim

Molecular Motors

Chiral Molecular Motors Driven by a Nonhelical Laser Pulse**

*Kunihito Hoki, Masahiro Yamaki, and Yuichi Fujimura**

The field of molecular motors and machines is one of the most rapidly advancing research areas in applied chemistry.[1–4] It is expected that this area will play an important role in the advent of nanoscience and nanotechnology. Most of the molecular motors reported to date have been made from chiral molecules that have asymmetric potentials. Furthermore, these motors are driven by concentration gradients that are created by thermal and chemical forces, or by the time-correlated forces of electromagnetic radiation.[5–9] Light-driven molecular motors are particularly interesting because their rotational directions, as well as their torque, can be controlled by utilizing the properties of light, such as photon polarization, frequency, and pulse shape.[10,11] For example, a grid-mounted molecular dipolar rotor, driven by a circularly polarized electric field, has been theoretically studied on the basis of classical molecular dynamics.[6] It should be noted that if helical light fields, such as circularly polarized lasers are used, the chirality of the molecular motors is unnecessary.[12] Interesting experiments regarding nonhelical-light-driven chiral molecular motors have recently been reported;[8,9] such motors consist of an alkene with two chiral centers. *cis–trans* Isomerization that is induced by linearly polarized visible or UV light generates repetitive unidirectional rotation around a central carbon–carbon double bond, which is followed by thermally induced *cis–trans* isomerization; the latter blocks reverse rotation. In those experiments, the rate-determining step of the motor action is the thermally controlled isomerization, which is an incoherent process.[8,9] To the best of our knowledge, there are only a few reports on molecular motors driven by using the coherent properties of radiation fields. Investigation of molecular motors driven by the coherent properties of electromagnetic fields is therefore required.

In this communication, on the basis of both quantum and classical mechanical calculations, we explain how a chiral molecular motor is unidirectionally driven by a nonhelical coherent light pulse. For this purpose, 2-chloro-5-methylcyclopenta-2,4-dienecarbaldehyde was chosen (Figure 1), which is a simple, chiral molecular motor. In this communication, chiral molecules with an *R* formation are called (*R*)-motors, and those with an *S* formation are termed (*S*)-motors. The dihedral angle α between the O^1–C^2–C^3 and C^2–C^3–H^4 planes is set to be variable of the internal rotation of the CHO group around the C^2–C^3 bond.

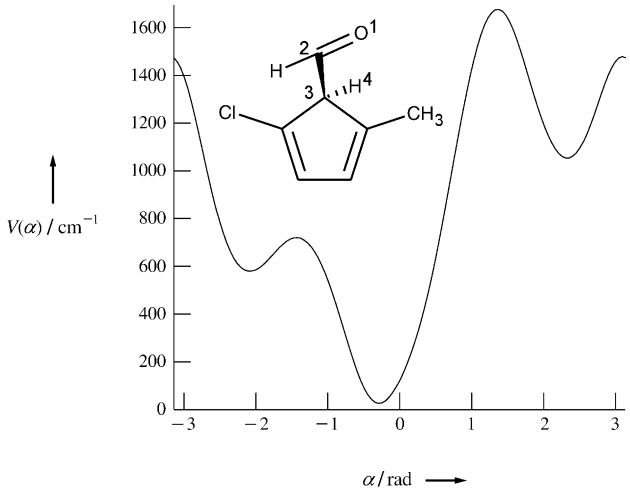


Figure 1. The potential energy of an (*R*)-motor as a function of the internal rotation coordinate α. The (*R*)-motor is also shown. The CHO group around the C^2–C^3 bond is considered as the engine of the motor, which is driven by a linearly polarized laser pulse.

Figure 1 shows the potential energy of the (*R*)-motor as a function of α. This chiral molecule has several properties that are essential for a molecular motor. First, the potential energy $V(\alpha)$ is asymmetric, as shown in Figure 1. The potential is most stable at $\alpha = -0.26$ rad. The potential slope is gentle between $\alpha = -0.26$ and -1.3 rad, and in contrast is steep between $\alpha = -0.26$ and 1.3 rad.

Secondly, the components of the dipole moment vector $\boldsymbol{\mu}(\alpha)$ vary greatly with different values of α because of the electronegativity of the O^1 atom. The difference between the maximum and minimum of the components of the dipole moment vector is nearly 4 D.[12] Dipole interactions with electric fields of a few GV m^{-1} compare to a potential barrier height of 1600 cm^{-1}. The values of $V(\alpha)$ and $\boldsymbol{\mu}(\alpha)$ were calculated using an ab initio MO method.[13]

Thirdly, the rotational constants are 1.97, 1.16, and 0.79 GHz. Thus, the effects of molecular rotation with periods of a few hundred picoseconds can be safely ignored, since the molecular-motor dynamics of interest occur within several tens of picoseconds.

The Hamiltonian of the molecular motor in a laser field $\boldsymbol{E}(t)$ is expressed as:

$$\mathscr{H}(t) = -\frac{\hbar^2}{2I}\frac{\partial^2}{\partial\alpha^2} + V(\alpha, t) \quad (1)$$

Here, I is the moment of inertia of internal rotation. The total potential including the molecule–radiation field interaction $V(\alpha,t)$ is expressed within the dipole approximation as:

$$V(\alpha, t) = V(\alpha) - \mu(\alpha) \cdot \boldsymbol{E}(t) \quad (2)$$

[*] Prof. Y. Fujimura, K. Hoki, M. Yamaki
Department of Chemistry
Graduate School of Science, Tohoku University
Sendai 980-8578 (Japan)
Fax: (+81) 22-217-7715
E-mail: fujimura@mcl.chem.tohoku.ac.jp

[**] This work was partly supported by Grant-in-Aid for Scientific Research on Priority Areas, "Control of Molecules in Intense Laser Fields" (Area No. 419) from the Ministry of Education, Science and Culture, Japan. One of the authors (K.H.) acknowledges support from a Research Fellowship of the JSPS (No. 6254).

 © 2003 Wiley-VCH Verlag GmbH & Co. KGaA, Weinheim DOI: 10.1002/anie.200250872

The time evolution of the molecular state, $\Psi(t)$, is estimated by solving the time-dependent Schrödinger equation:

$$i\hbar\frac{\partial}{\partial t}\Psi(t) = \mathscr{H}(t)\,\Psi(t) \tag{3}$$

As a measure of molecular-motor action, we introduce a quantum mechanical expectation value of the angular momentum operator of the internal rotation, $\langle \ell(t)\rangle$, defined as:

$$\langle \ell(t)\rangle = \int_0^{2\pi} \mathrm{d}\alpha\, \Psi(t)^*\left(-i\hbar\frac{\partial}{\partial\alpha}\right)\Psi(t) \tag{4}$$

Here, the sign and absolute quantity of the expectation value correspond to the direction of the angular momentum and its magnitude, respectively.

Figure 2b shows values for $\langle \ell(t)\rangle$ calculated for an (*R*)-motor driven by a linearly polarized laser pulse in the *Z* direction at the low-temperature limit.[14] The envelope of the electric field of the pulse used is shown in Figure 2a. For simplicity, the body of the molecular motor was fixed at a space: the direction of the C^2–C^3 bond is parallel to the *z* axis, and the angle between the C^3–H^4 bond, projected onto the *yz* plane and the *z* axis is 0.1π, at which angle the laser pulse strongly interacts with the motor. Figure 2b shows that the direction of rotation is unidirectional, as suggested by the gentle slope of the potential shown in Figure 1. Furthermore,

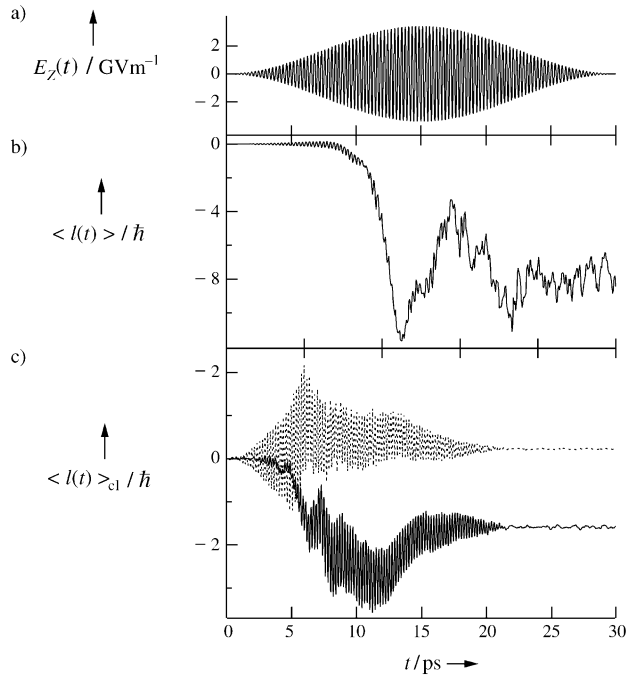


Figure 2. a) The electric field of a laser pulse that is linearly polarized to the *z* axis $E_z(t) = E_0 \sin^2(\pi t/t_f)\cos(\omega t)$ for $0 < t < t_f$ and $E_z(t) = 0$ for $t_f < t$. Here, $t_f = 30$ ps, $E_0 = 3.4$ GVm^{-1}, and $\omega = 124$ cm^{-1}; b) temporal behavior of the quantum-mechanically averaged angular momentum, $\langle \ell(t)\rangle$; c) temporal behavior of the averaged angular momentum based on classical mechanics, $\langle \ell(t)\rangle_{cl}$. The solid line shows the angular momentum of an (*R*)-motor, and the dotted line shows that of an analogous achiral molecule.

Figure 2b shows that the temporal behavior of the motor can be divided into three regimes: ignition, acceleration, and free rotation. In the ignition regime, the dynamics of the motor are characterized by the large amplitude vibration of a pendulum motion. In the second regime, the motor begins rotating unidirectionally and is accelerated by the applied laser pulse. The magnitude of $\langle \ell(t)\rangle$ follows the pulse envelope, as is qualitatively shown by comparing Figure 2a and b. Between the second and third regimes, such relationships start to break down. In the third regime, in which the driving laser pulse decreases in intensity and is eventually turned off, $\langle \ell(t)\rangle$ becomes a constant value (with some fluctuation) and the motor is in a steady state.

So far only the (*R*)-motor has been discussed. The (*S*)-motor can be considered similarly, as the potential energies of the (*S*)- and (*R*)-motors are mirror images of each other, with respect to a reflection plane located at $\alpha = 0$. The unidirectional motions of the (*S*)- and (*R*)-motors are opposite to each other. We obtained a value for $\langle \ell(t)\rangle$ of 9.4×10^{11} rad s^{-1} after the laser pulse ($t_f < t$).

To clarify the origin of the unidirectional motion shown in Figure 2b, the results can be presented based on Newton's laws of motion.[15] The initial ensemble was set to be a canonical ensemble at $T = 150$ K. In Figure 2c, the solid line shows the ensemble-averaged angular momentum, $\langle \ell(t)\rangle_{cl}$. The temporal behavior of $\langle \ell(t)\rangle_{cl}$ is similar to that shown in Figure 2b, except for its smaller magnitude, which arises mainly a result of temperature effects. To highlight the important role of the asymmetric shape of the potential, the dotted line in Figure 2c shows $\langle \ell(t)\rangle_{cl}$ for an achiral molecule, where a chlorine atom is substituted for the methyl group of the chiral molecule. In the case of the achiral molecule, unidirectional internal rotation is not created after the laser pulse is turned off. This indicates that the unidirectional internal rotation of the molecule driven by a linearly polarized laser pulse originates from molecular chirality. Figure 3 shows one of the classical trajectories of the molecular motor. Here, the values for $\alpha(0)$ (−0.27 rad) and the angular momentum $\ell(0)$ (7.1 $\hbar$) were set as initial conditions. Figure 3 shows that the motor dynamics consist again of three regimes (ignition, acceleration, and rotation), and that the motor begins moving unidirectionally toward negative values of the asymmetric potential, $\alpha(t)$, with a gentle slope near 13 ps, followed by a pendulum motion. The

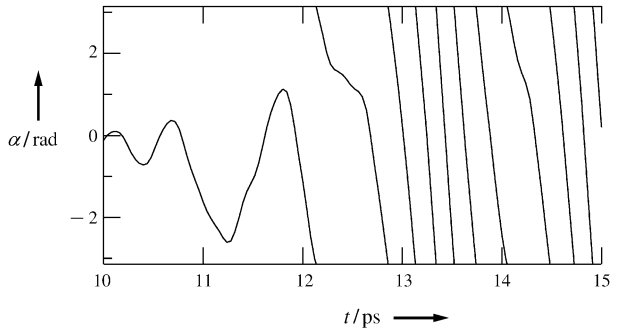


Figure 3. The classical trajectory of a chiral molecular motor, driven by a linearly polarized laser pulse.

 © 2003 Wiley-VCH Verlag GmbH & Co. KGaA, Weinheim

shoulder appearing between 12 and 13 ps originates from climbing the "potential hump" located near $\alpha = 1.3$ rad.

In conclusion, the unidirectional rotation of chiral molecular motors driven by a nonhelical laser pulse has been explained on the basis of both quantum mechanical and classical mechanical calculations. The origin of the unidirectional rotation lies in both the asymmetric potential of chiral molecules and time-correlated forces created by laser–molecule interactions.[16] The results obtained in this study serve as a theoretical basis for the control of molecular motors with pulsed lasers. A further study of molecular motors taking into account damping effects will be presented elsewhere.

Received: December 30, 2002 [Z50872]

Keywords: chirality · laser chemistry · molecular dynamics · molecular motors · nanotechnology

[1] C. Joachim, J. K. Gimzewski in *Molecular Machines and Motors* (Ed.: J.-P. Sauvage), Springer, Berlin, **2001**, pp. 1–18; T. R. Kelly, J. P. Sestelo in *Molecular Machines and Motors* (Ed.: J.-P. Sauvage), Springer, Berlin, **2001**, pp. 19–53; L. Raehm, J.-P. Sauvage in *Molecular Machines and Motors* (Ed.: J.-P. Sauvage), Springer, Berlin, **2001**, pp. 55–78.
[2] J. K. Gimzewsky, C. Joachim, R. R. Schittler, V. Langlais, H. Tang, I. Johannesen, *Science* **1988**, *281*, 531–533.
[3] R. E. Tuzun, D. W. Niod, B. G. Sumpter, *Nanotechnology* **1995**, *6*, 52–63.
[4] V. Balzani, M. Gómez-López, J. F. Stoddart, *Acc. Chem. Res.* **1998**, *31*, 405–414.
[5] J.-P. Sauvage, *Acc. Chem. Res.* **1998**, *31*, 611–619.
[6] J. Vacek, J. Michl, *Proc. Natl. Acad. Sci. USA* **2001**, 98, 5481–5486.
[7] B. Space, H. Rabitz, A. Lörincz, P. Moore, *J. Chem. Phys.* **1996**, *105*, 9515–9524.
[8] N. Koumura, R. W. J. Zijlstra, R. A. van Delden, N. Harada, B. L. Feringa, *Nature* **1999**, *401*, 152–155.
[9] B. L. Feringa, N. Koumura, R. A. van Delden, M. K. J. Ter Wiel, *Appl. Phys. A* **2002**,75, 301–308.
[10] A. Assion, T. Baumert, M. Bergt, T. Brixner, B. Kiefer, V. Seyfried, M. Strehle, G. Gerber, *Science* **1998**, *282*, 919–922.
[11] T. Brixner, G. Gerber, *Opt. Lett.* **2001**, 26, 557–559.
[12] K. Hoki, M. Yamaki, S. Koseki, Y. Fujimura, *J. Chem. Phys.* **2003**, *118*, 497–504.
[13] Gaussian 98 (Revision A.7), M. J. Frisch, G. W. Trucks, H. B. Schlegel, G. E. Scuseria, M. A. Robb, J. R. Cheeseman, V. G. Zakrzewski, J. A. Montgomery, R. E. Stratmann, J. C. Burant, S. Dapprich, J. M. Millam, A. D. Daniels, K. N. Kudin, M. C. Strain, O. Farkas, J. Tomasi, V. Barone, M. Cossi, R. Cammi, B. Mennucci, C. Pomelli, C. Adamo, S. Clifford, J. Ochterski, G. A. Petersson, P. Y. Ayala, Q. Cui, K. Morokuma, D. K. Malick, A. D. Rabuck, K. Raghavachari, J. B. Foresman, J. Cioslowski, J. V. Ortiz, B. B. Stefanov, G. Liu, A. Liashenko, P. Piskorz, I. Komaromi, R. Gomperts, R. L. Martin, D. J. Fox, T. Keith, M. A. Al-Laham, C. Y. Peng, A. Nanayakkara, C. Gonzalez, M. Challacombe, P. M. W. Gill, B. G. Johnson, W. Chen, M. W. Wong, J. L. Andres, M. Head-Gordon, E. S. Replogle, J. A. Pople, Gaussian, Inc., Pittsburgh, PA, **1998**. The 6-31G(d) basis set and the MP2 method were used.
[14] See Ref. [12] for details of the calculations.
[15] The classically averaged angular momentum was obtained by using a Monte Carlo integration method with 10^6 trajectories.
[16] K. Hoki, M. Yamaki, S. Koseki, Y. Fujimura, unpublished results.

 © 2003 Wiley-VCH Verlag GmbH & Co. KGaA, Weinheim

Pd/Bi Polycationic Clusters

Structure and Bonding of Pd@$[Bi_{10}]^{4+}$ in the Subbromide $Bi_{14}PdBr_{16}$**

Michael Ruck, Vitaly Dubenskyy, and Tilo Söhnel*

Dedicated to Prof. Hubert Langbein on the occasion of his 60th birthday

The number of compounds that contain polycations is tiny compared with the huge variety that contain polyanions. Most of the hitherto known polycations are formed by the heavy and electron-rich elements of the p block of the periodic table,[1] particularly selenium,[2] tellurium,[2] and bismuth.[3] Besides homonuclear polycations such as $[Te_8]^{2+}$[4] and $[Bi_9]^{5+}$,[5] mixed species of these elements are also accessible, as the example $[Bi_4Te_4]^{4+}$[6] illustrates. Here we present the first heteronuclear polycation of bismuth and a transition element, which combines theoretically predicted features with some unexpected findings.

The title compound $Bi_{14}PdBr_{16}$ is a comparatively halogen-rich member of a series of ternary bismuth subhalides[7] that ranges from the intermetallic compounds Bi_nM (M = Ru, Rh, Ir, Ni, Pd, Pt; $n \geq 1$) to the binary bismuth subhalides, for example, BiI,[8] BiBr,[9] Bi_6Br_7,[9] and Bi_6Cl_7[5]. Within this sequence the character of the species changes as a result of the progressive expansion of regions of electronic localization. The weakly oxidized subhalides, such as $Bi_{12}Rh_3Br_2$[10] or $Bi_{5.6}Ni_5I$[11] are three-dimensional metallic frameworks with an inclusion of halide anions. Further increase of the halogen content leads to a significant reduction in the degree of metallic conductivity. Accordingly, the subiodides $Bi_{13}Pt_3I_7$[12] and $Bi_{12}Ni_4I_3$[13] consist of alternating metallic and semiconducting layers (two-dimensional metals), while only metallic rods remain embedded within isolating matrices in the structures of $Bi_9Ir_2I_3$[14] and $Bi_{6.86}Ni_2Br_5$[7] (one-dimensional metals). Passing through the intermediate steps of the semiconducting columnar structures, such as Bi_4RuX_2 (X = Br, I)[15] and their oligomeric fragments, for example, $Bi_{24}Ru_3Br_{20}$[16], the "halogen-rich" end-members of the series, that is, ionic cluster salts such as $Bi_{14}Si_2MI_{12}$ (M = Rh, Ir)[17] or $Bi_{6+x}MX_{12+y}$ (M = Rh, Ir, Pt; X = Cl, Br),[18] as well as the molecular cluster compound Bi_7RhBr_8[19], are reached.

The transition-metal content of the new subbromide $Bi_{14}PdBr_{16}$ is the lowest of the entire series. Subdividing the formula of $Bi_{14}PdBr_{16}$ into $14\,BiBr{\cdot}PdBr_2$ illustrates the proximity to the monobromide BiBr.[9] However, determina-

[*] Prof. Dr. M. Ruck, Dr. V. Dubenskyy, Dr. T. Söhnel
Institut für Anorganische Chemie
Technische Universität Dresden
01062 Dresden (Germany)
Fax: (+49) 351-463-37287
E-mail: Michael.Ruck@chemie.tu-dresden.de

[**] This work was supported by the DAAD and the Fonds der Chemischen Industrie. We thank Dr. O. Rademacher and J. Krug for experimental assistance.

 © 2003 Wiley-VCH Verlag GmbH & Co. KGaA, Weinheim DOI: 10.1002/anie.200250801

tion of the structure by single-crystal X-ray diffraction reveals that $Bi_{14}PdBr_{16}$ possesses no constitutional relationship with either BiBr or $PdBr_2$. Instead it is a complex salt that consists of cluster cations $[PdBi_{10}]^{4+}$ and anionic octahedra chains $^1_\infty[Bi_4Br_{16}^{4-}]$ (Figure 1).

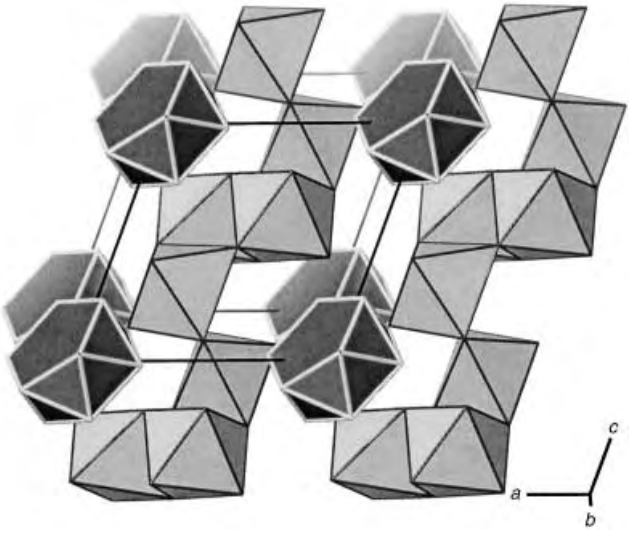


Figure 1. Crystal structure of $Bi_{14}PdBr_{16}$ containing $[PdBi_{10}]^{4+}$ Archimedean antiprisms and $^1_\infty[(BiBr_{2/1}Br_{4/2}^{-})_4]$ zigzag chains.

The eye-catching building block in the triclinic crystal structure is the cationic cluster $[PdBi_{10}]^{4+}$, a pentagonal antiprism of ten Bi atoms with a Pd atom at their center (Figure 2). The only crystallographic symmetry of the $[PdBi_{10}]^{4+}$ polycation is the center of inversion; nonetheless the D_{5d} symmetry of the pentagonal antiprism is almost perfectly observed: The maximum deviation from a plane of the Bi atoms in a pentagon is less than 2 pm, the bond angles in the ring are $108 \pm 0.6°$, and the rotation angle between the two rings is about 42°. Furthermore, the interatomic distances within the five-membered ring (313–319 pm) and between the two pentagons (311–318 pm) are equivalent. The Pd–Bi bonds range from 297 to 302 pm in length, with an average of 300 pm, and the Bi-Pd-Bi angle for neighboring Bi atoms is about 63.4°, and is independent of whether the Bi atoms belong to one or other pentagons. Thus, the $[PdBi_{10}]^{4+}$ polycation is a semiregular or Archimedean polyhedron.

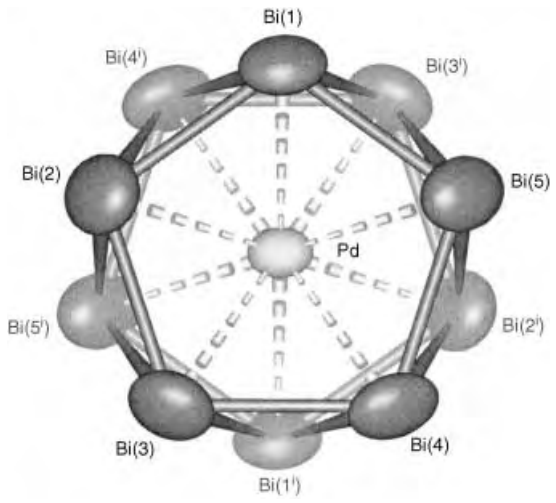


Figure 2. $[PdBi_{10}]^{4+}$ cluster in the crystal structure of $Bi_{14}PdBr_{16}$ (the ellipsoids represent 90% probability). Selected bond lengths [pm] and angles [°]: Pd-Bi(1) 301.9(2), Pd-Bi(2) 296.9(1), Pd-Bi(3) 298.7(2), Pd-Bi(4) 301.4(2), Pd-Bi(5) 301.0(1), Bi(1)-Bi(2) 315.3(2), Bi(2)-Bi(3) 317.4(2), Bi(3)-Bi(4) 313.5(1), Bi(4)-Bi(5) 318.8(2), Bi(5)-Bi(1) 312.8(1), Bi(1)-Bi(3') 314.2(2), Bi(1)-Bi(4') 318.1(2); Bi(1)-Pd-Bi(2) 63.53(4), Bi(1)-Pd-Bi(3') 63.09(4), Bi(1)-Bi(2)-Bi(3) 108.03(4). Symmetry code: (i) $-x, -y, -z$.

Electronic neutrality is maintained by polymeric bromobismuthate(III) anions, $^1_\infty[BiBr_4^{-}]$. Despite their simple composition, the constitution of the anions is rather complex: Six Br atoms surround each of the Bi atoms Bi(6) and Bi(7) in a distorted octahedral coordination (Figure 3). The $[Bi^{III}Br_6]$ octahedra are paired by sharing common edges while the

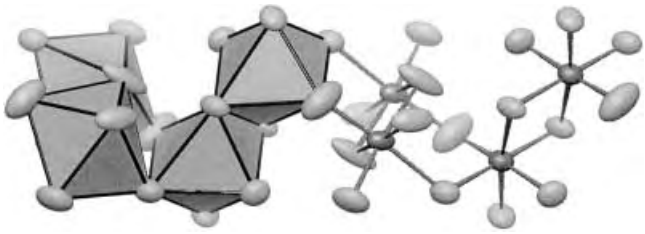


Figure 3. Concatenation of $[BiBr_6]$ octahedra in the anionic bromobismuthate(III) polymer $^1_\infty[(BiBr_{2/1}Br_{4/2}^{-})_4]$ (the ellipsoids represent 90% probability).

octahedra pairs are linked by common corners to form the infinite zigzag chain $^1_\infty[(BiBr_{2/1}Br_{4/2}^{-})_4]$. The separation of the polycations from the anionic chains is evident: The Bi–Br bond lengths in the bromobismuthate(III) chain range from 272 to 325 pm, with an average of 291 pm; the shortest separation between a Bi atom of the $[PdBi_{10}]^{4+}$ polycation and a Br atom is 345 pm.

Until now all bismuth polycations have proved to have an optimized electron count,[20] while the halogenobismuthate(III) anions provide a seemingly infinite number of possibilities in adjusting their constitution, conformation, and charge in order to meet the dominant spatial, electronic, and electrostatic requirements of the diverse polycations.[7] Thus any discussion about the chemical bonding in $Bi_{14}PdBr_{16}$ must focus on the $[PdBi_{10}]^{4+}$ cluster.

Only a few ten-coordinated polyhedra with high symmetry exist. Among them, only the pentagonal prism and antiprism provide symmetry equivalence of all vertices. If the interligand distance, as well as the separation between the ligands and the central atom remain constant, the rotation of the two pentagons from the eclipsed to the staggered conformation is the only remaining conformational degree of freedom that can be used to optimize the interactions between the rings.

In order to gain a deeper understanding of the bonding character, quantum mechanical calculations for the solid (relativistic density functional theory (DFT) and extended Hückel (EH) calculations) and the isolated cluster cation (EH) were performed. Independent of the method used in the

 © 2003 Wiley-VCH Verlag GmbH & Co. KGaA, Weinheim

calculations, the band structure of $Bi_{14}PdBr_{16}$ displays only moderate dispersions for all bands, which is indicative of highly localized electrons and predominantly ionic interactions (Figure 4). The calculated band gap of approximately 1 eV corresponds with the black color of the powder.

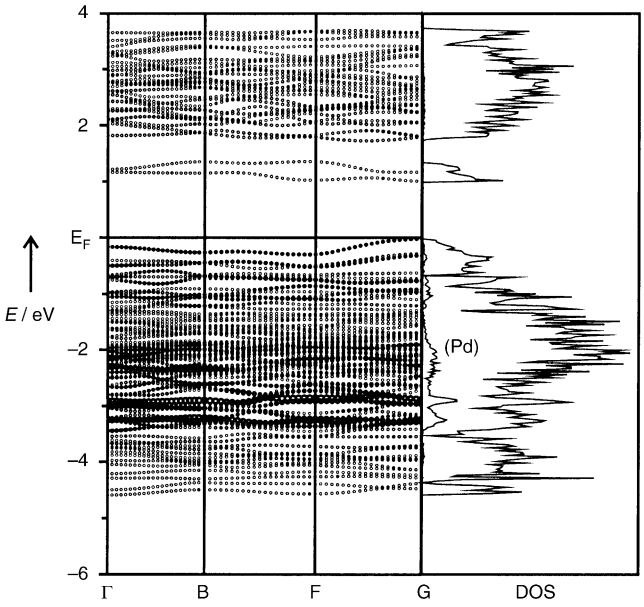


Figure 4. Electronic band structure and density of states (DOS) of $Bi_{14}PdBr_{16}$ from relativistic DFT calculations.

The crystal orbital overlap population (COOP) derived from the EH band-structure calculations demonstrates only a slight orbital overlap, especially between Bi and Pd (Figure 5), which is in agreement with the small dispersion of the Pd bands in the DFT band structure ("fat bands" in Figure 4). Although some states near the Fermi level are antibonding, the sum of the COOP(Bi–Pd) up to the Fermi level is still a small positive number, that is, the Bi–Pd interactions are weakly bonding. The weakness of the interaction between the central transition-metal atom and the surrounding Bi atoms represents an essential difference to the known, filled bismuth clusters, such as $[MBi_6X_{12}]$[17,18] or $[RhBi_7Br_8]$.[19]

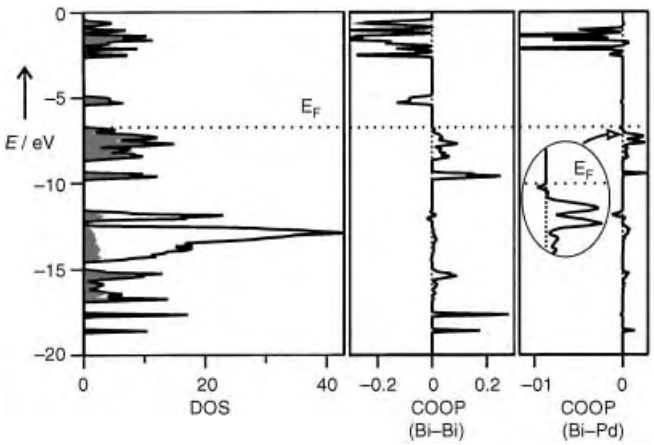


Figure 5. Total DOS and projected DOS of the Bi and Pd atoms (highlighted) in $Bi_{14}PdBr_{16}$, as well as overlap populations (COOP) for Bi–Bi and Bi–Pd interactions, as derived from EH calculations.

For the Bi–Bi interactions in the polycation, the Fermi level neatly separates the bonding from the antibonding states, that is to say the cluster shell has the optimum number of electrons. The almost identical COOP for the Bi–Bi interactions, both within the five-membered rings and between them, confirms a uniform bonding in the equilateral triangles of the pentagonal antiprism. Consequently, and in contrast to well-known bis(η^5-cyclopentadienyl) complexes of transition metals such as ferrocene, the inter-ring interaction is not predominantly steric but covalent. The $[PdBi_{10}]^{4+}$ polycation is a filled cluster, not a complex. Recently it has been predicted from ab initio (DFT-B3LYP) calculations that the hypothetical empty $[Bi_{10}]^{4+}$ polycation should have the shape of a D_{5d} pentagonal antiprism with Bi–Bi interactions of 324 pm within the rings, and 322 pm between them.[20] Actually the bonding situation, and even the shapes of the HOMO and LUMO, are nearly the same for the $[Bi_{10}]^{4+}$ shell of the $[PdBi_{10}]^{4+}$ cluster as for the empty $[Bi_{10}]^{4+}$ polycation. Disregarding the 6s electrons, which do not contribute because of their stabilization by relativistic effects, the $[Bi_{10}]^{4+}$ polyhedron with $10\times3-4=26$ electrons in the skeleton fulfills the expectations for an *arachno*-cluster of 10 atoms ($2\times n + 6 = 26$ electrons for bonding within the cluster).

All of these details imply that the positive charge of the $[PdBi_{10}]^{4+}$ cation is located on the Bi shell and the Pd atom is essentially uncharged. The closed-shell behavior ($4d^{10}5s^0$) of the Pd atom is even more evident in the corresponding MO scheme (Figure 6): The 4d orbitals of the Pd atom, filled with 10 electrons, are almost unaffected by the inclusion in the $[Bi_{10}]^{4+}$ antiprism, while the 5s orbital of the Pd atom undergoes a repulsion, which shifts it to energies high above the Fermi level. Regarding the weak interaction between the closed Pd^0 shell and the electron-precise *arachno*-cluster $[Bi_{10}]^{4+}$, the appropriate formulation for the $[PdBi_{10}]^{4+}$ polycation is $Pd@[Bi_{10}]^{4+}$, an endohedral inclusion compound comparable to $He@C_{60}$,[21] or in some aspects to the recently discovered $W@Au_{12}$ and $Mo@Au_{12}$ molecules.[22]

In this light, experimental observations have further meaning: All attempts to synthesize bismuth palladium subbromides directly from the elements have failed because of the precipitation of $PdBr_2$ and the formation of $[Bi_9]^{5+}$ polycations (crystallizing as Bi_6Br_7). However, the high-temperature reaction of the intermetallic phase Bi_2Pd with additional bismuth and bromine yields gray lustrous platelets of $Bi_{14}PdBr_{16}$. Thus, we argue that the synthetic clue is to hide the palladium center from the oxidizing halogen atoms by initially "wrapping" it in bismuth atoms through the preformation of the intermetallic phase, and to use it at the same time as a template for the arrangement of the entropically less favorable $[Bi_{10}]^{4+}$ polycation.

Experimental Section

Synthesis: Prior to its use in synthesis, Bi shot (99.9%, Riedel-de Haën) was reduced with hydrogen at 490 K to remove any oxide

 © 2003 Wiley-VCH Verlag GmbH & Co. KGaA, Weinheim

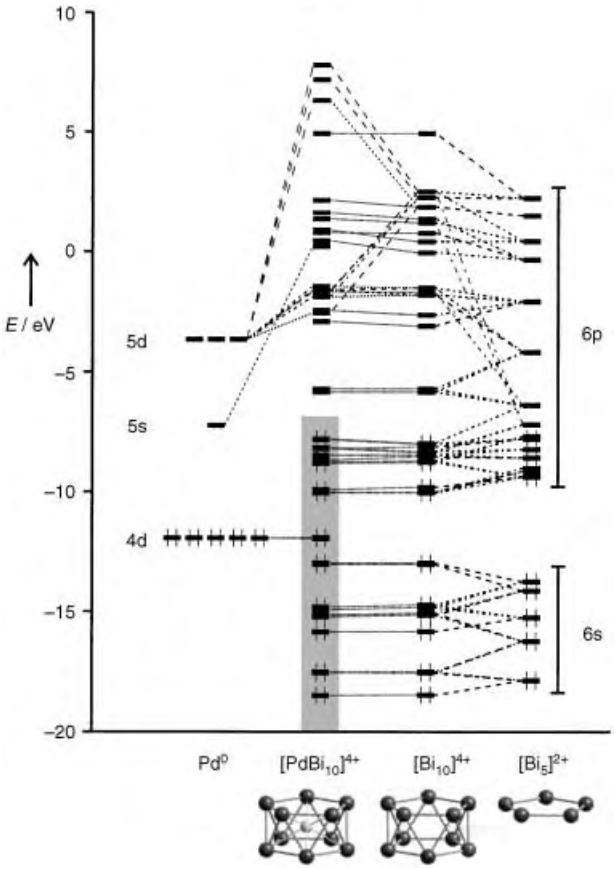


Figure 6. Evolution of the MO diagram of $[PdBi_{10}]^{4+}$ (point group C_i) based on EH calculations (filled MOs are highlighted).

from the surface. Then, Bi and Pd powder (99.99%, Degussa) were reacted in an evacuated quartz ampoule to give the intermetallic phase Bi_2Pd (m.p. 758 K).[23] To synthesise $Bi_{14}PdBr_{16}$, the starting materials Bi_2Pd (5 mmol), Bi (18 mmol), and Br_2 (20 mmol, 99.5%, Riedel-de Haën) were heated to 1270 K in an evacuated quartz ampoule. After two days the sample was cooled to 670 K over a period of a further four days. Any residual $BiBr_3$ was sublimed from the solid product while the temperature was reduced from 600 K to room temperature. Gray lustrous platelets of $Bi_{14}PdBr_{16}$ can be removed easily from unavoidable by-products, such as Bi_6Br_7 (black needles); pure $Bi_{14}PdBr_{16}$ can be left in the air without any visible decomposition. The energy-dispersive X-ray (EDX) analysis of a single crystal that had previously been checked by precession photography for a crystallographic match with $Bi_{14}PdBr_{16}$ gave the atomic ratio Bi:Pd:Br = 47:7:46; EDX is only a semiquantitative technique, which in this case overestimates the Pd content somewhat.

Crystal-structure determination of $Bi_{14}PdBr_{16}$: four-circle diffractometer CAD4 (Enraf Nonius), $Mo_{K\alpha}$ radiation, $\lambda = 71.073$ pm, ω/θ-scan, $2\theta_{max} = 60°$, $T = 293(2)$ K; crystal dimensions $0.45 \times 0.15 \times 0.05$ mm^3, triclinic, space group $P\bar{1}$ (No. 2), lattice parameters from 75 reflections of a powder diffraction diagram (Stadi P, $Cu_{K\alpha}$ radiation, 293(2) K): $a = 1084.8(7)$, $b = 1103.0(6)$, $c = 1115.7(4)$ pm, $\alpha = 118.15(3)$, $\beta = 108.82(3)$, $\gamma = 91.94(3)°$, $V = 1086.1 \times 10^6$ pm^3, $Z = 1$, $\rho_{calcd} = 6.591$ g cm^{-1}, $\mu(Mo_{K\alpha}) = 716$ cm^{-1}, numerical absorption correction (X-RED), crystal description optimized using 17 ψ-scans (X-SHAPE), transmission factors 0.136 to 0.003, structure solution with direct methods (SHELXS), full-matrix least-squares refinement on F_o^2 (SHELXL[24]), 11 183 reflections, 6070 unique, 142 parameters, anisotropic displacement parameters, $R1(3478\,F_o > 4\sigma(F_o)) = 0.035$, $wR2 = 0.043$, residual electron density $+2.17$ to -1.96×10^{-6} pm^{-3}. Graphical representation: DIAMOND. Further details on the crystal structure investigation may be obtained from the Fachinformationszentrum Karlsruhe, 76344 Eggenstein-Leopoldshafen, Germany (fax: (+49) 7247-808-666; e-mail: crysdata@fiz-karlsruhe.de), on quoting the depository number CSD-412895.

Theoretical calculations: DFT calculations were performed with the WIEN97[25] code using the linearized augmented plane wave (LAPW) method. The muffin-tin radii were chosen to be 2.6 au for Pd, 2.6 au for Bi, and 2.4 au for Br. RKMAX and GMAX were taken to be 10 and 12 au^{-1}, respectively. The local-density functional LDA[26] was used as the exchange-correlation functional. The Brillouin-zone integration was performed using a tetrahedron method[27] using 64 inequivalent k points corresponding to 150 k points throughout the whole Brillouin zone within the SCF cycles. 90 inequivalent k points (250 k points in the Brillouin zone) were used for the calculation of the density of states (DOS). The extended Hückel calculations were performed using the YAeHMOP program[28] with the following parameters: orbital energies H_{ij} [eV] (coefficient ζ1); Bi: 6s −15.19 (2.56), 6p −7.790 (2.07); Br: 4s −22.08 (2.59), 4p −13.10 (2.13); Pd 5s −7.32 (2.19), 5p −3.75 (2.15), 4d −12.02 (5.98); double ζ-functions for Pd: 0.5535, 2.6130, 0.6701.

Received: December 19, 2002 [Z50801]

Keywords: bismuth · cluster compounds · palladium · polycations · subvalent compounds

[1] H. G. von Schnering, *Angew. Chem.* **1981**, *93*, 44–63; *Angew. Chem. Int. Ed. Engl.* **1981**, *20*, 33–50.
[2] J. Beck, *Coord. Chem. Rev.* **1997**, *163*, 55–70.
[3] M. Ruck, *Angew. Chem.* **2001**, *113*, 1222–1234; *Angew. Chem. Int. Ed.* **2001**, *40*, 1182–1193.
[4] a) J. Beck, K. Müller-Buschbaum, *Z. Anorg. Allg. Chem.* **1997**, *623*, 409–413; b) A. Baumann, J. Beck, T. Hilbert, *Z. Naturforsch. B* **1999**, *54*, 1253–1259; c) J. Beck, A. Fischer, *Z. Anorg. Allg. Chem.* **2002**, *628*, 369–372.
[5] $[Bi_9]^{5+}$ in Bi_6Cl_7: a) A. Hershaft, J. D. Corbett, *Inorg. Chem.* **1963**, *2*, 979–985; b) R. M. Friedman, J. D. Corbett, *Inorg. Chim. Acta* **1973**, *7*, 525–527; c) J. Beck, C. J. Brendel, L. Bengtsson-Kloo, B. Krebs, M. Mummert, A. Stankowski, S. Ulvenlund, *Chem. Ber.* **1996**, *129*, 1219–1226; $[Bi_9]^{5+}$ in $Bi_{10}M_3X_{18}$ (M = Zr, Hf; X = Cl, Br): d) R. M. Friedman, J. D. Corbett, *Inorg. Chem.* **1973**, *12*, 1134–1139; e) A. N. Kuznetsov, A. V. Shevel'kov, S. I. Troyanov, B. A. Popovkin, *Zh. Neorg. Khim.* **1996**, *41*, 958–961; *Russ. J. Inorg. Chem.* **1996**, *41*, 920–923; f) A. N. Kuznetsov, A. V. Shevel'kov, B. A. Popovkin, *Koord. Khim.* **1998**, *24*, 919–924; *Russ. J. Coord. Chem.* **1998**, *24*, 861–866; $[Bi_9]^{5+}$ in $Bi_{37}InBr_{48}$: g) M. Ruck, V. Dubenskyy, S. Paul, *Z. Anorg. Allg. Chem.* **2003**, *629*, 375–380.
[6] J. Beck, M. Dolg, S. Schlüter, *Angew. Chem.* **2001**, *113*, 2347–2350; *Angew. Chem. Int. Ed.* **2001**, *40*, 2287–2290.
[7] M. Ruck, *Angew. Chem.* **2001**, *113*, 1222–1234; *Angew. Chem. Int. Ed.* **2001**, *40*, 1182–1193.
[8] H. G. von Schnering, H. von Benda, C. Kalveram, *Z. Anorg. Allg. Chem.* **1978**, *438*, 37–52.
[9] H. von Benda, A. Simon, W. Bauhofer, *Z. Anorg. Allg. Chem.* **1978**, *438*, 53–67.
[10] M. Ruck, *Solid State Sci.*, **2001**, *3*, 369–376.
[11] M. Ruck, *Z. Anorg. Allg. Chem.* **1995**, *621*, 2034–2042.
[12] M. Ruck, *Z. Anorg. Allg. Chem.* **1997**, *623*, 1535–1541.
[13] M. Ruck, *Z. Anorg. Allg. Chem.* **1997**, *623*, 243–249.
[14] M. Ruck, R. M. Heich, *Z. Anorg. Allg. Chem.* **2000**, *626*, 2449–2456.
[15] M. Ruck, *Z. Anorg. Allg. Chem.* **1997**, *623*, 1583–1590.
[16] M. Ruck, *Z. Anorg. Allg. Chem.* **1997**, *623*, 1591–1598.
[17] M. Ruck, *Z. Anorg. Allg. Chem.* **2000**, *626*, 14–22.

 © 2003 Wiley-VCH Verlag GmbH & Co. KGaA, Weinheim

[18] a) M. Ruck, *Z. Anorg. Allg. Chem.* **1998**, *624*, 521 – 528; b) S. Hampel, M. Ruck, *Z. Kristallogr. Suppl.* **2001**, *18*, 143.
[19] a) M. Ruck, *Angew. Chem.* **1997**, *109*, 2059 – 2062; *Angew. Chem. Int. Ed. Engl.* **1997**, *36*, 1971 – 1973; b) Z. Xu, Z. Lin, *Angew. Chem.* **1998**, *110*, 1815 – 1818; *Angew. Chem. Int. Ed.* **1998**, *37*, 1686 – 1689.
[20] A. N. Kuznetsov, L. Kloo, M. Lindsjö, J. Rosdahl, H. Stoll, *Chem. Eur. J.* **2001**, *7*, 2821 – 2828.
[21] a) T. Weiske, D. K. Böhme, J. Hrušák, W. Krätschmer, H. Schwarz, *Angew. Chem.* **1991**, *103*, 898 – 900; *Angew. Chem. Int. Ed. Engl.* **1991**, *30*, 884 – 886; b) Y. Rubin, *Top. Curr. Chem.* **1999**, *199*, 67 – 91.
[22] X. Li, B. Kiran, J. Li, H.-J. Zhai, L. S. Wang, *Angew. Chem.* **2002**, *114*, 4980 – 4983; *Angew. Chem. Int. Ed.* **2002**, *41*, 4786 – 4789.
[23] H. Okamoto in *Binary Alloy Phase Diagrams*, 2nd ed. (Ed.: T. B. Masalski), ASM International, Materials Park, OH, **1990**, p. 772 – 775.
[24] G. M. Sheldrick, SHELXL-97, Program for Crystal Structure Determination, University of Göttingen, Göttingen (Germany), **1997**.
[25] P. Blaha, K. Schwarz, J. Luitz, WIEN97, A Full Potential Linearized Augumented Plane Wave Package for Calculating Crystal Properties, Vienna University of Technology, Vienna (Austria), **1999**.
[26] J. P. Perdew, Y. Wang, *Phys. Rev. B* **1992**, *45*, 13244.
[27] P. E. Blöchl, O. Jepsen, O. K. Andersen, *Phys. Rev. B* **1994**, *49*, 16223.
[28] G. Landrum, YAeHMOP, Yet Another extended Hückel Molecular Orbital Package, Cornell University, Ithaca (USA), **1997**.

Filter for X-ray Polarization Analysis

Design of a Solid Inclusion Compound with Optimal Properties as a Linear Dichroic Filter for X-ray Polarization Analysis**

Mao-Hsun Chao, Benson M. Kariuki, Kenneth D. M. Harris, Steven P. Collins, and David Laundy*

In the case of visible light, studies of polarization are dominated by the use of dichroic filters (e.g. the Polaroid sheet[1]), for which photons with polarization parallel to a certain axis in the material are preferentially attenuated over those with polarization perpendicular to this axis. In principle, materials analogous to the Polaroid sheet may be developed for applications as dichroic filters in other regions of the electromagnetic spectrum, and in the present paper we focus on the analysis of polarized X-ray radiation (produced, for example, from a synchrotron source). A suitable dichroic filter would be a crystal for which the absorption of polarized X-rays depends significantly on the orientation of the crystal. Such materials have considerable potential in a range of applications, for example in the field of magnetic X-ray scattering.[2]

While linear dichroism at X-ray absorption edges is well documented,[4] the exploitation of this effect in a filter material for X-ray polarization analysis was demonstrated for the first time only very recently.[5] This work explored the bromine K edge linear dichroism of the 1,10-dibromodecane/urea inclusion compound, in which 1,10-dibromodecane guest molecules are included within tunnels in the urea host structure.[6–9] This material exhibits a strongly dichroic resonance close to the absorption edge, with the ratio of absorption coefficients[10] attaining a value of $R_\gamma = 0.65$ (i.e. the attenuation is higher by a factor of about 3/2 for the crystal orientation with the tunnel axis parallel to the direction of incident X-ray polarization than the crystal orientation with the tunnel axis perpendicular). The 1,10-dibromodecane/urea material is thus effective for X-ray polarization analysis, and has indeed been tested successfully in the first dichroic polarization analysis of magnetic diffraction,[5] involving a study of antiferromagnetic holmium.

In spite of this success, however, the efficiency of 1,10-dibromodecane/urea as a dichroic filter is limited by the fact that the C–Br bonds undergo reorientation[11,12] around the tunnel axis at ambient temperature and are oriented at $\approx 35°$ to this axis.[5] Theoretical considerations, elaborated elsewhere,[5] suggest that a material in which all C–Br bonds are aligned parallel to the tunnel would be significantly more effective than 1,10-dibromodecane/urea (corresponding to a reduction in R_γ by a factor of about 2). In this paper, we describe a new molecular material—the 1-bromoadamantane/thiourea inclusion compound—that has been *designed* specifically to give optimal properties as a dichroic filter for X-ray polarization analysis.

The main features of our design strategy were: 1) to have a guest molecule with only one C–Br bond (thus, by constraining all molecules to have the same orientation, all C–Br bonds would implicitly be aligned parallel to each other), 2) to constrain the orientation of the guest within the host structure such that the C–Br bonds of all guest molecules are parallel and do not undergo dynamic reorientation (at the temperature of the intended operation of the analyzer, ideally room temperature), and 3) to ensure that the direction of the C–Br bonds bears a straightforward relationship to the crystal morphology, such that the analyzer crystal(s) could be aligned readily during polarization analysis.

These requirements are most readily satisfied for a material in which all guest molecules are oriented such that their C–Br bonds are parallel to the host tunnel. As described above, it is difficult to envisage a material based on the urea tunnel structure that can satisfy requirements 1) and 2), and

[*] Prof. K. D. M. Harris, M.-H. Chao, Dr. B. M. Kariuki
School of Chemical Sciences, University of Birmingham, Edgbaston, Birmingham B15 2TT (UK)
Fax: (+44) 121-414-7473
E-mail: K.D.M.Harris@bham.ac.uk
Dr. S. P. Collins, Dr. D. Laundy
Daresbury Laboratory, Warrington
Cheshire WA4 4AD (UK)

[**] We are grateful to EPSRC (grant to KDMH) for financial support, and to CLRC for the award of beamtime on Station 16.3 at Daresbury Laboratory.

Supporting information for this article is available on the WWW under http://www.angewandte.org or from the author.

 © 2003 Wiley-VCH Verlag GmbH & Co. KGaA, Weinheim DOI: 10.1002/anie.200350891

thiourea inclusion compounds provide a better opportunity for achieving the desired orientational characteristics of the guest molecules. While the urea tunnel is essentially cylindrical, the tunnel in conventional thiourea-inclusion compounds[9] may be considered to comprise "cages" (diameter ≈ 7.1 Å) connected by narrower "windows" (diameter ≈ 5.8 Å). Our design of the 1-bromoadamantane/thiourea inclusion compound was based on the rationale that the adamantane moiety would essentially fill the cage, with the C–Br bond constrained to project into the narrower window region between adjacent cages and thus oriented essentially parallel to the tunnel axis. It is already known[13] that adamantane forms an inclusion compound with thiourea in which the adamantane guest molecules efficiently fill the cages in the conventional thiourea tunnel structure. Furthermore, thiourea inclusion compounds usually have a needle morphology, with the host tunnel parallel to the needle axis, which would allow straightforward alignment of the crystal in polarization analysis. Herein, we describe the preparation and structural characterization of 1-bromoadamantane/thiourea, and assess the performance of this material as a dichroic filter for X-ray polarization analysis. To our knowledge, the formation of the 1-bromoadamantane/thiourea inclusion compound has not been reported previously.

The 1-bromoadamantane/thiourea inclusion compound was prepared by using standard crystallization procedures for thiourea inclusion compounds, by slowly cooling a solution containing the guest (1-bromoadamantane) and thiourea dissolved in methanol. Comparatively large needle-shaped crystals (typical dimensions $1 \times 1 \times 10\ \mathrm{mm}^3$) were obtained. Structural properties of 1-bromoadamantane/thiourea were determined from single crystal X-ray diffraction data recorded at 200 K.[14] Differential scanning calorimetry indicates that the material does not undergo any phase transitions between this temperature and ambient temperature. Full structural details will be presented elsewhere[17] and only the salient features are discussed here. As expected, the thiourea molecules form a tunnel host structure (Figure 1a), constructed from N–H···S hydrogen bonding between the thiourea molecules. This structure differs to some extent from the conventional thiourea host structure (it is well known[9] that the host structure in thiourea inclusion compounds can exhibit variations depending on the guest molecule). Within the repeat unit (24.75 Å) along the tunnel, there are three crystallographically independent 1-bromoadamantane guest molecule sites (Figure 1b), corresponding[18] to a thiourea/guest molar ratio of 4:1. Importantly, the C–Br bond of each guest molecule lies parallel to

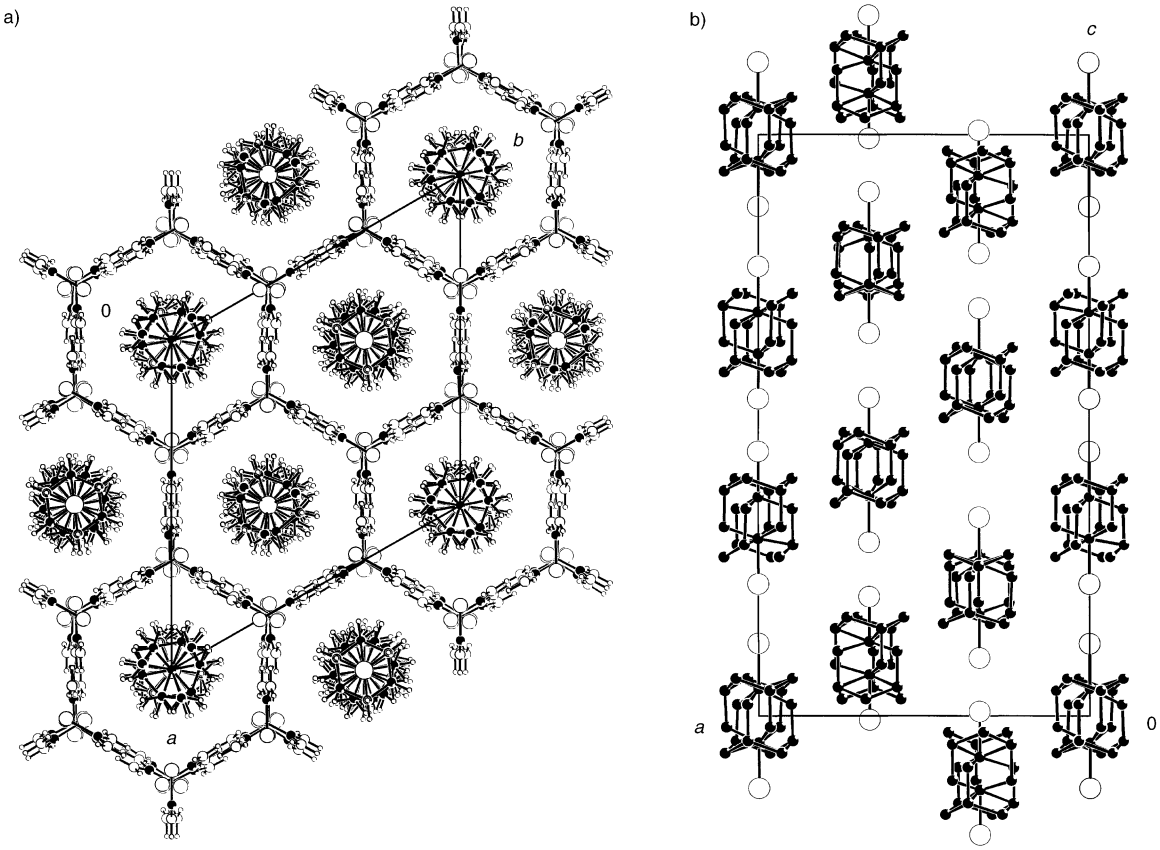


Figure 1. a) Crystal structure of 1-bromoadamantane/thiourea at 200 K viewed along the tunnel axis (*c* axis) of the thiourea host structure. In each tunnel, there are three crystallographically independent 1-bromoadamantane guest molecules, each of which is disordered between two orientations. b) The guest substructure in 1-bromoadamantane/thiourea (thiourea molecules omitted for clarity) viewed perpendicular to the tunnel axis, which is vertical. Note that the C–Br bonds of all guest molecules lie parallel to the tunnel axis. The disorder is discussed in the text. Hydrogen atoms are omitted for clarity.

 © 2003 Wiley-VCH Verlag GmbH & Co. KGaA, Weinheim

the thiourea host tunnel, as required in our design strategy for an X-ray polarization analyzer. For each guest molecule, there is disorder between two orientations (with essentially equal occupancies) in which the C–Br bond lies along the positive *c* axis or the negative *c* axis. Given the spatial constraints imposed by the host tunnel, it is unlikely that the guest molecules undergo dynamic interconversion between the two orientations, and this disorder is presumably "locked in" during crystal growth.[19] Importantly, in each orientation, the C–Br bond lies parallel to the tunnel axis, and therefore the performance as a polarization analyzer should be unaffected by this disorder. Clearly (as seen in Figure 1b), the positions of the carbon atoms of the adamantane moiety are different for each orientation of the molecule.

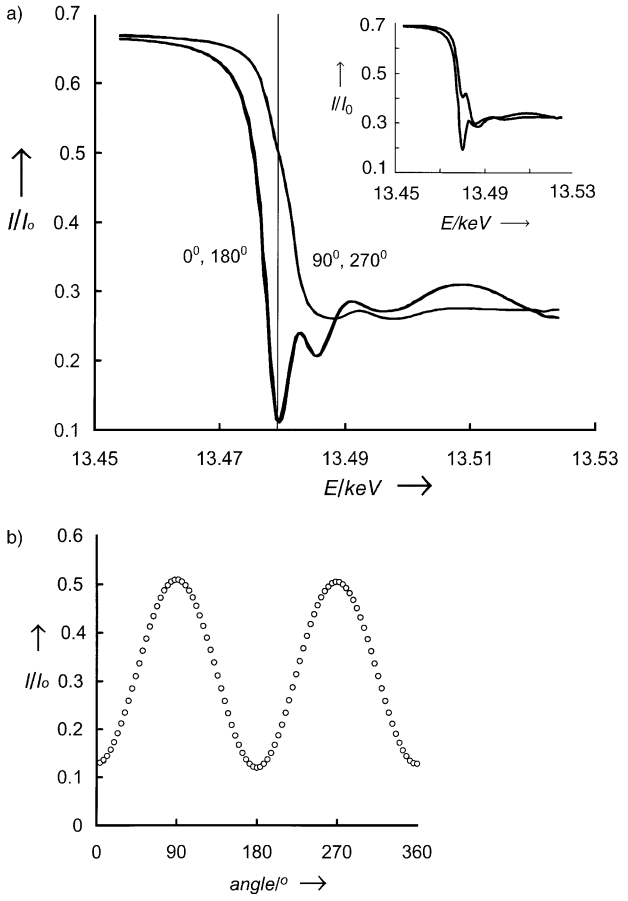


Figure 2. a) X-ray transmittance[10] (I/I_o) through a crystal of 1-bromoadamantane/thiourea as a function of energy (E) close to the Br K-edge, with the X-ray polarization parallel (0° and 180°) and perpendicular (90° and 270°) to the crystal *c* axis. The vertical line is at 13.479 keV (see text). The insert shows the corresponding data for 1,10-dibromodecane/urea.[5] One notable difference between the data for the two materials is the complete absence of a resonance at 13.479 keV for 1-bromoadamantane/thiourea when the X-ray polarization is perpendicular to the *c* axis and therefore perpendicular to the C–Br bonds. b) X-ray transmittance (I/I_o) as a function of the orientation of a crystal of 1-bromoadamantane/thiourea (defined as the angle between the tunnel axis of the crystal and the electric vector of the polarized incident X-ray beam) at the value of energy (13.479 keV) at which the ratio of absorption coefficients R_γ is minimum.

To assess the performance of 1-bromoadamantane/thiourea as a dichroic filter for polarized X-rays, dichroism spectra were measured for a single crystal on Station 16.3, at the Synchrotron Radiation Source, Daresbury Laboratory.[21,22] Figure 2a shows the X-ray transmittance[10] as a function of X-ray energy (close to the bromine K edge, 13.474 keV) for both the parallel and perpendicular orientations of the crystal, and Figure 2b shows the X-ray transmittance as a function of crystal orientation at 13.479 keV. Close to the absorption edge, the transmission of polarized X-rays through the crystal shows a very significant dependence on crystal orientation. The maximum dependence is at 13.479 keV, and corresponds to $R_\gamma = 0.32$. This represents an improvement in performance of 1-bromoadamantane/thiourea, in comparison to 1,10-dibromodecane/urea, by a factor of 2, and the value of R_γ for 1-bromoadamantane/thiourea is very close to the minimum attainable value predicted theoretically[5] (on the assumption that the only factor influencing the difference in performance of the two materials arises from the different C–Br bond orientations).

In summary, we have demonstrated the successful implementation of a crystal-design strategy to produce a material, the 1-bromoadamantane/thiourea-inclusion compound, which exhibits essentially optimal performance as a dichroic filter for X-ray polarization analysis. This material will be valuable in a range of X-ray measurements, at wavelengths close to the bromine K-edge, most notably in studies of nonresonant magnetic scattering. Investigations to assess the stability of this material[23] with respect to time and radiation exposure are in progress, and strategies for producing large platelike samples with suitable dimensions and orientational characteristics for practical applications as polarization analyzers are under development.

Received: January 7, 2003
Revised: February 7, 2003 [Z50891]

Keywords: host–guest systems · inclusion compounds · X-ray diffraction · X-ray polarization analysis

[1] E. H. Land, *J. Opt. Soc. Am.* **1951**, *41*, 957.
[2] For a magnetic material, spin and orbital magnetism lead to a very weak scattering signal for which the polarization dependence is very different from classical "charge" scattering, and provides a signature of the relative contributions from spin and orbital magnetic moments.[3] The ability to determine separate spin and orbital densities in magnetic crystals is unique to nonresonant X-ray diffraction, and information of this type is vital for understanding the origin of fundamental materials properties, such as magnetic anisotropy. One reason that progress in this field has been slow is that conventional X-ray polarization analyzers are diffraction-based, tend to have low efficiency, and suffer from systematic errors arising from variations in beam divergence, analyzer crystal uniformity, and misalignment.
[3] D. Gibbs, G. Grübel, D. R. Harshman, E. D. Isaacs, D. B. McWhan, D. Mills, C. Vettier, *Phys. Rev. B* **1991**, *43*, 5663.
[4] C. Brouder, *J. Phys. Condens. Matter* **1990**, *2*, 701.
[5] S. P. Collins, D. Laundy, K. D. M. Harris, B. M. Kariuki, C. L. Bauer, S. D. Brown, P. Thompson, *J. Phys. Condens. Matter* **2002**, *14*, 123.

 © 2003 Wiley-VCH Verlag GmbH & Co. KGaA, Weinheim

[6] A. E. Smith, *Acta Crystallogr.* **1952**, *5*, 224.
[7] K. D. M. Harris, J. M. Thomas, *J. Chem. Soc. Faraday Trans.* **1990**, *86*, 2985.
[8] K. D. M. Harris, S. P. Smart, M. D. Hollingsworth, *J. Chem. Soc. Faraday Trans.* **1991**, *87*, 3423.
[9] M. D. Hollingsworth, K. D. M. Harris, in *Comprehensive Supramolecular Chemistry, Vol. 6* (Ed.: D. D. MacNicol, F. Toda, R. Bishop), Pergamon, Oxford, **1996**, p. 177.
[10] The ratio R_γ is defined as $\gamma_{min}/\gamma_{max}$, where γ_{min} and γ_{max} are the values of the linear absorption coefficients for the crystal orientations with lowest and highest attenuation respectively. For the materials studied here, γ_{min} and γ_{max} arise, respectively, for crystal orientations with the tunnel axis essentially perpendicular and parallel to the electric vector of the polarized incident X-ray beam. The linear absorption coefficient γ is related from the ratio of the transmitted (I) and incident (I_o) X-ray intensities as follows: $I/I_o = \exp(-\gamma t)$, where t is the sample thickness. X-ray transmittance (see Figure 2) refers to the measured ratio I/I_o.
[11] F. Guillaume, S. P. Smart, K. D. M. Harris, A. J. Dianoux, *J. Phys. Condens. Matter* **1994**, *6*, 2169.
[12] A. E. Aliev, S. P. Smart, I. J. Shannon, K. D. M. Harris, *J. Chem. Soc. Faraday Trans.* **1996**, *92*, 2179.
[13] R. Gopal, B. E. Robertson, J. S. Rutherford, *Acta Crystallogr. Sect. C* **1989**, *45*, 257.
[14] Single-crystal X-ray-diffraction data were recorded on a Bruker SMART 6000 diffractometer with a graphite-monochromated $Cu_{K\alpha 1}$ source and CCD area detector: $[SC(NH_2)_2]_{12}[C_{10}H_{15}Br]_3$; crystal size $0.32 \times 0.40 \times 0.22\ mm^3$; $T = 200$ K; $\lambda = 1.54178$ Å; Trigonal, $P321$; $a = 16.1112(1)$ Å, $c = 24.7533(2)$ Å; $V = 5564.41(7)$ Å^3; $Z = 3$. The structure was solved by using SHELXS86[15] and refined by using SHELXL 97[16] ($R_1 = 11.99\%$; w$R_2 = 32.95\%$). Note that the crystal used for the X-ray diffraction study was not needlelike, and was considerably smaller than typical crystals of this material. Powder X-ray diffraction confirms that the structure determined from this crystal is representative of the bulk material.
[15] G. M. Sheldrick, SHELXS 86, Program for the Solution of Crystal Structures, University of Göttingen (Germany), **1986**.
[16] G. M. Sheldrick, SHELXL 97, Program for the Refinement of Crystal Structures, University of Göttingen, (Germany), **1993**.
[17] M.-H. Chao, B. M. Kariuki, K. D. M. Harris, unpublished results.
[18] The thiourea/guest molar ratio of 4:1 was confirmed from the results of elemental analysis. This stoichiometry of 1-bromoadamantane/thiourea differs from that of conventional thiourea-inclusion compounds,[9] for which there are typically two guest molecules per 12 Å along the tunnel and the thiourea/guest molar ratio is 3:1.
[19] Analysis of the single-crystal diffraction data cannot distinguish whether this disorder represents (1) disorder in the orientations of individual molecules within a given tunnel, or (2) an ordered arrangement of the C–Br bond vectors within each tunnel, with the disorder in the average crystal structure arising from different tunnels having different orientations of the (ordered) C–Br bond directions. Interpretation of our disorder model in terms of situation (1) would correspond to unfavourable local interactions between Br atoms (Br···Br separations as short as 2.14–2.75 Å), and therefore we believe that situation (2) is more plausible. For comparison, the Br···Br separation for two Br atoms in van der Waals contact is ≈ 3.7 Å.[20] Bromine K-edge EXAFS spectroscopy would be informative for directly determining the Br···Br separations between neighbouring guest molecules in this structure.
[20] A. Bondi, *J. Phys. Chem.* **1964**, *68*, 441.
[21] S. P. Collins, B. M. Murphy, C. C. Tang, M. C. Miller, G. Oszlanyi, *J. Phys. D* **1999**, *32*, A81.
[22] Linear polarization of incident X-ray beam $\approx 95\%$.
[23] From the investigations that we have carried out so far, the 1-bromoadamantane/thiourea inclusion compound does not undergo any thermal decomposition (e.g. by loss of the guest component) at ambient temperature, and no beam damage was observed during the X-ray studies described in this paper. The 1,10-dibromodecane/urea inclusion compound studied previously[5] also exhibited suitable characteristics with regard to stability for applications in X-ray polarization analysis.

 © 2003 Wiley-VCH Verlag GmbH & Co. KGaA, Weinheim

CO_4: An MS and Theoretical Study

Carbon Tetraoxide: Theoretically Predicted and Experimentally Detected**

Fulvio Cacace, Giulia de Petris,* Marzio Rosi, and Anna Troiani*

The current interest in CO_n ($n > 2$) oxides reflects the growing recognition of their role in different research areas. First, CO_n species are key intermediates in the reactions of atomic and molecular oxygen with the lower oxides of carbon, hydrocarbons, and other organic molecules.[1] Furthermore, CO_n oxides and their ions are relevant to the chemistry of the terrestrial[2] and planetary[3] atmospheres. More importantly, members of the CO_n family are potential high-energy density materials (HEDM), the next generation of environmentally benign propellants and explosives.[4] CO_4 is of special interest, since ab initio MP2, QCISD and MP2/6-31G* calculations[5–7] have identified a CO_4 D_{2d} $^1A_1$ singlet as a metastable species that releases from 80 to 93 kcal mol^{-1} upon dissociation into CO_2 ($X\ ^1\Sigma^+$) and O_2 ($a^1\Delta$). Another isomer of C_{2v} symmetry has been identified on the potential energy surface (PES) of the lowest $^1A_1$ singlet state, and two local C_{2v} minima have been located on the low-lying, excited triplet PES.[7] In summary, the available theoretical results identify two singlets of D_{2d} and C_{2v} symmetry as the lowest energy CO_4

[*] Prof. Dr. F. Cacace, Prof. Dr. G. de Petris, Dr. A. Troiani
Dipartimento di Studi di Chimica e Tecnologia delle Sostanze Biologicamente Attive
Università di Roma "La Sapienza"
P.le Aldo Moro 5, 00185 Roma, (Italy)
Fax: (+39) 6-4991-3602
E-mail: julio.cacace@uniroma1.it
giulia.depetris@uniroma1.it

Prof. M. Rosi
Dipartimento di Ingegneria Civile ed Ambientale Sezione Tecnologie Chimiche e Materiali per L'Ingegneria
Università di Perugia
Via Duranti, 06131 Perugia (Italy)

[**] This work has been supported by the Rome University "La Sapienza", the Perugia University, the Consiglio Nazionale delle Ricerche (CNR) and the Ministero dell'Istruzione, Università e Ricerca (MIUR).

Supporting information for this article is available on the WWW under http://www.angewandte.org or from the author.

 DOI: 10.1002/anie.200350936 © 2003 Wiley-VCH Verlag GmbH & Co. KGaA, Weinheim

isomers and suggest that these molecules, albeit metastable, might be detectable. So far, however, CO_4 has been experimentally elusive, the only species observed being a weakly bonded $CO\cdots O_3$ van der Waals complex formed by codeposition of CO and O_3 in an Ar matrix, stable only below 10 K, as at higher temperatures its monomers react yielding CO_2.[8]

We report herein the experimental discovery of CO_4, a metastable molecule sufficiently long-lived to allow its positive detection as an isolated species in the gas state. We utilized a well-established technique, neutralization–reionization mass spectrometry (NRMS),[9] implemented on a highly sensitive instrument previously used for the detection of other elusive molecules, including N_4, O_4, HO_3, and the $[H_2O^+O_2^-]$ CT complex.[10,11]

First, a population containing, among other ions, a CO_4^+ precursor amenable to neutralization was prepared. Next, the structure of the mass-selected CO_4^+ ions was assayed by collision techniques. In the third step, the actual neutralization–reionization sequence was performed, which detected a significant CO_4 "recovery" peak. Confirmatory experiments were carried out with ^{18}O-labeled reagents to rule out the conceivable interference from isobaric contaminants. Finally, the results of NRMS experiments were compared with those of the computational study of the $CO_4^{+/0}$ system at the B3LYP and CCSD(T) level of theory.

The CO_4^+ cation, m/z 76, was obtained from two reactions that involved the ionization of CO_2/O_2 and CO_2/O_3 mixtures by 70 eV electrons. The first route, that conceivably involves two distinct processes [Eq. (1a), (1b)]

$$O_2^+ + CO_2 \xrightarrow{M} CO_4^+ \quad (1a)$$

$$CO_2^+ + O_2 \xrightarrow{M} CO_4^+ \quad (1b)$$

requires association of the reagents, and therefore was studied by chemical ionization (CI) at sufficiently high pressures as to ensure partial collisional stabilization of the adduct. The second reaction

$$O_3^+ + CO_2 \rightarrow CO_4^+ + O \quad (2)$$

was studied also in the low-pressure range, accessible to Fourier-transform ion cyclotron resonance (FTICR) spectrometry. This technique allowed us to unambiguously identify the charged reagent and to positively assign the charged product of m/z 76 as $^{12}C^{16}O_4^+$ by accurate mass measurements, consistent with the shift from m/z 76 to 80 of the charged product noted in CI experiments, in which $^{16}O_2$ is replaced by $^{18}O_2$ (Figure 1).

Irrespective of the preparation method, the CO_4^+ populations probed by collisionally activated dissociation (CAD) and multistage mass-spectrometry (MS^3) techniques show the same collisional fragmentation pattern, whose salient features can be summarized as follows: the CAD spectra display signals arising from the O_2^+ ion as the major fragment, together with less intense signals from CO_2^+, CO^+ and O^+ ions, and weak signals ($<1\,\%$) from O_3^+ and CO_3^+ ions (Figure 2). The CAD spectra of the $C^{16}O_2{}^{18}O_2^+$ population obtained from reactions (1a)/(1b) when using $^{18}O_2$ display signals from $^{18}O_2^+$ ions as the most abundant fragment, together with signals from $C^{16}O_2^+$, $C^{16}O^+$, $^{16}O^+$, $^{18}O^+$ ions and

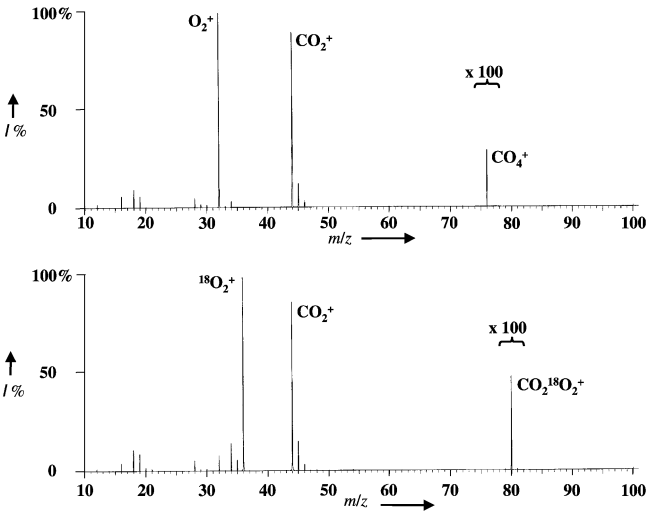


Figure 1. CI spectra of(top) $CO_2/^{16}O_2$, (bottom) $CO_2/^{18}O_2$ mixtures.

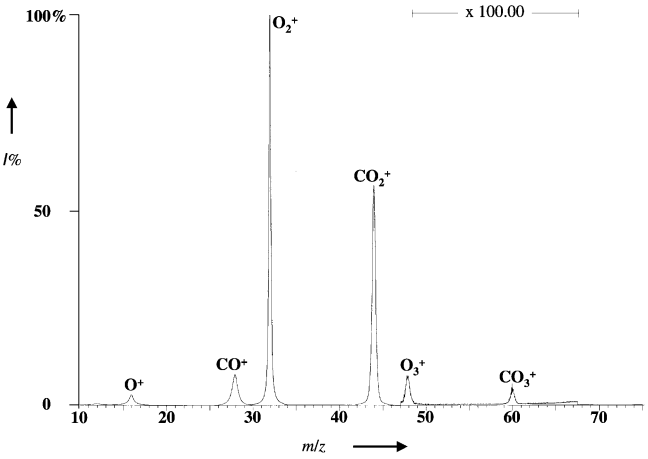


Figure 2. CAD spectra of the CO_4^+ population, see text.

weak signals from the $C^{16}O_2{}^{18}O^+$ and $C^{16}O^{18}O_2^+$ isotopomers and from the $^{16}O^{18}O_2^+$ ion.

NRMS of CO_4^+, performed by using CH_4 and O_2 as the collision gases in the neutralization and reionization cell, respectively, gives a significant "recovery" peak of $m/z = 76$ (Figure 3). To rule out conceivable interferences from isobaric adventitious contaminants, the NR spectra of $^{12}C^{18}O_4^+$ (from $^{12}C^{18}O_2$ and $^{18}O_2$), and of $^{12}C^{16}O_2{}^{18}O_2^+$ (from $^{12}C^{16}O_2$ and $^{18}O_2$) were recorded (Figure 3). Invariably, the m/z ratio of the "recovery" peak undergoes the shift expected for the specific isotopomer used, thus confirming that neutral CO_4 does exist in the gas state, with a lifetime exceeding the flight time from the neutralization to the reionization cell, namely about 1 μs.

Figure 4 illustrates the geometries and relative energies of the CO_4^+ ion and CO_4 species identified. On the doublet PES the most stable species is the $C_s{}^2A''$ ion **1**, in essence a cluster formed by CO_2 and O_2 units joined by electrostatic forces and characterized by a large separation of the monomers. The $C_s{}^2A'$ ion **2** and the $C_{2v}{}^2A_2$ doublet **3** lie at considerably higher energies (some 4 eV). Another cluster, the $C_s{}^4A''$ species **4,** was identified on the quartet PES.

 © 2003 Wiley-VCH Verlag GmbH & Co. KGaA, Weinheim

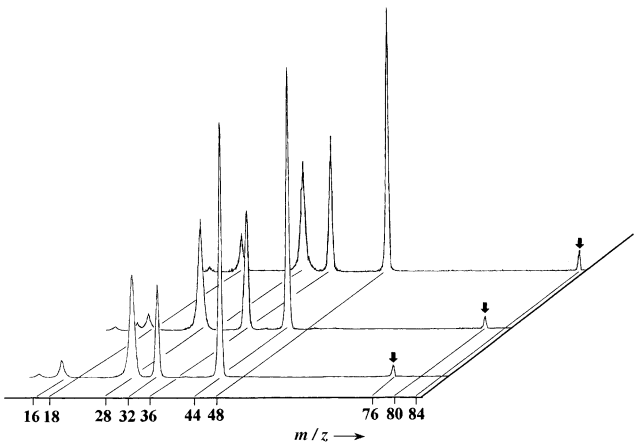


Figure 3. NR spectra of $^{12}C^{16}O_4^+$, *m/z* 76 (bottom trace), $^{12}C^{16}O_2{}^{18}O_2^+$, *m/z* 80 (middle trace) and $^{12}C^{18}O_4^+$, *m/z* 84 (top trace). The arrows indicate the "recovery" peaks at the appropriate *m/z* ratios.

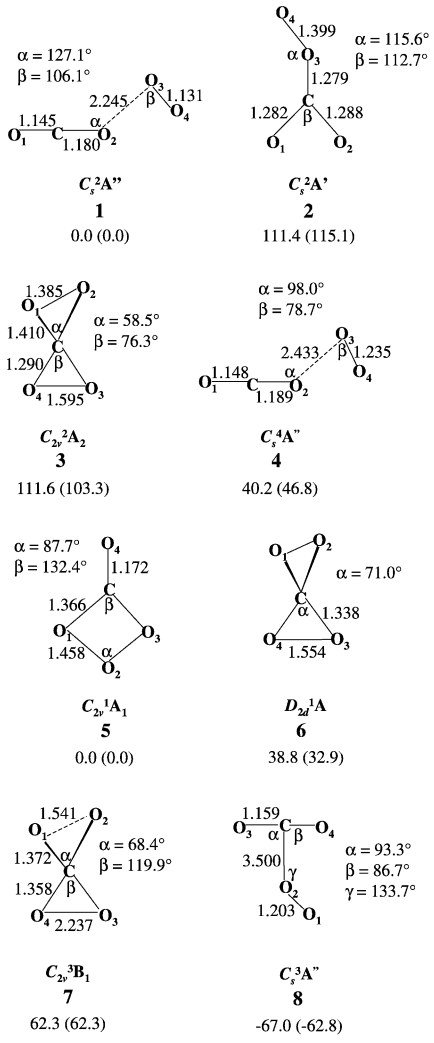


Figure 4. Optimized geometries and relative energies of the CO_4^+ and CO_4 species calculated at the B3LYP and the CCSD(T) (in parentheses) level.

With regards to neutral CO_4, the most stable species on the singlet PES is the $C_{2v}{}^1A_1$ molecule **5,** which is unstable with respect to the spin forbidden dissociation into CO_2 and O_2 in their ground states by 67.5 and 62.7 kcal mol^{-1} at the B3LYP and CCSD(T) level, respectively. By using higher energy calculations (38.8 and 32.9 kcal mol^{-1} at the B3LYP and the CCSD(T) level, respectively) we localized **6**, a singlet of D_{2d} symmetry. Based on the experimental separation between $O_2(^3\Sigma_g^-)$ and $O_2(^1\Delta_g)$, 22.64 kcal mol^{-1},[22] **5** is also unstable towards dissociation into ground-state CO_2 and singlet O_2. On the triplet PES we localized the weakly bound cluster **8,** which is unstable against dissociation once the zero point energy correction is included. Both processes (1a) and (1b) can contribute to the formation of CO_4^+ ions in a O_2/CO_2 mixture ionized by electron impact. Indeed, despite the higher ionization energy (IE) of CO_2, primary CO_2^+ ions are not efficiently depleted by the remarkably slow, $k_3 = 5.5 \times 10^{-11}$ cm^3 s^{-1} charge exchange [Eq. (3)].[23]

$$CO_2^+ + O_2 \rightarrow CO_2 + O_2^+ \qquad (3)$$

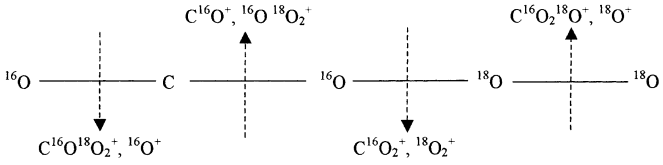
Thus, two processes, different with respect to the charged reagent and the energetics, contribute to the formation of CO_4^+ ions in the EI of O_2/CO_2 mixtures. As to process (1a), association of a ground-state O_2^+ ($^2\prod_g$) with CO_2 is known to yield a $[O_2^+ CO_2]$ cluster, characterized by a binding energy (BE) of the monomers estimated as 0.48 eV,[24] $\geq$0.46 eV,[25] and 0.4 ± 0.05 eV.[26] Another source of CO_4^+ ions is process (1b), as discussed above. Furthermore, CO_4^+ ions of unknown structure and stability can arise from excited precursors. Indeed, under conditions similar to those prevailing in this study, $CO_2{}^{*+}$[27] and $O_2{}^{*+}$ ions[27c,28] are known to be formed in excited states, for example, $O_2^+(^4\prod_u)$, which is sufficiently long-lived to promote processes energetically inaccessible to ground-state reagents.[29] We conclude that reactions promoted by excited species can yield CO_4^+ ions, of unknown structure and stability, other than those arising from ground-state reagents. This view is supported by the results of photoexcitation studies, which show that irradiation of the $[O_2^+(X^2\prod)\ CO_2(X^1\Sigma)]$ adduct with 375–590 nm photons causes its dissociation into $CO_2^+(X^2\prod)$ and O_2 $(X^3\Sigma)$,[25,26,30] rather than into O_2^+ and CO_2, despite the large (1.7 eV) energetic bias in favor of the latter process. Of particular interest to the present discussion, 10% to 25% of the photoexcited CO_4^+ species are estimated to be formed in a *bound* state, and subsequently undergo predissociation, eventually yielding $CO_2(X^2\prod)$ and $O_2(a^1\Delta)$.[26] In summary, EI of an O_2/CO_2 mixture is expected to yield a complex population of CO_4^+ ions of different stability, structure and lifetime.

The structural information on the composition of the CO_4^+ population provided by CAD and MS^3 spectrometry is hardly conclusive. Let's consider the cluster(s) of O-C-O-O-O connectivity formed by O_2 and CO_2 units joined by essentially electrostatic forces, in which the bond between the monomers is considerably longer and weaker than the O–C–O and O–O bonds. The cluster is probably the most abundant component of the CO_4^+ population sampled, and its predominant fragmentation channel gives back the CO_2 and O_2 monomers,

 © 2003 Wiley-VCH Verlag GmbH & Co. KGaA, Weinheim

with the charge mainly located on the latter one, characterized by the lower IE.

Furthermore, all signals from the fragments displayed by the CAD spectra of $C^{16}O_4^+$ ion, and its $C^{16}O_2{}^{18}O_2^+$ isotopomer, can in principle be accounted for by the fission of one bond of the cluster, for example, in the case of the $C^{16}O_2{}^{18}O_2^+$ ion.



However, the CAD and MS/MS results do not exclude the presence of CO_4^+ ions other than the cluster of O-C-O-O-O connectivity. Apart from the possibility that several of the charged fragments may arise from other isomers, the mixed character of the CO_4^+ population is suggested by certain experimental observations, for example, the intensity ratio of the $C^{16}O_2{}^{18}O^+$ and $C^{16}O^{18}O_2^+$ fragments from the $C^{16}O_2{}^{18}O_2^+$ isotopomer shows large variations (from 1:1 to 1:3), well above those noted for other fragments. Despite the low absolute intensity of the peaks from $C^{16}O_2{}^{18}O^+$ and $C^{16}O^{18}O_2^+$ ions, this suggests that the two isotopomers arise from the fragmentation of different CO_4^+ species, whose relative abundances are critically affected by small changes in the experimental conditions in the ion source.

The results of the NR experiments conclusively show that neutral CO_4 does exist in the gas phase with a lifetime in excess of about 1 μs, a long time on the molecular scale, being sufficient for an exhaustive exploration of the entire rotovibrational manifold. It is natural, at this point, to inquire as to the structure of the CO_4 species detected. Although a rigorous assignment is impossible, a reasonable hypothesis can be based on the available theoretical results and the specific features of NR experiments. As neutralization is a vertical process, the parent ion and the neutral molecule must be structurally alike to ensure sufficiently favorable Franck–Condon overlap of the transition. The theoretically predicted CO_4 species include the singlets **5** and **6**, the triplet **7** and the van der Waals complex **8.** Complex **8** will not be discussed further, because the low binding energy of its monomers would not allow its survival in the neutralization step. Indeed, the neutral species must reside in a sufficiently deep energy well to be detectable by NRMS.[31] As to triplet **7**, its exothermic dissociation into $CO_2(X^1\Sigma^+)$ and $O_2(X^3\Sigma^-)$ is expected to be very fast, as no *kinetic* barrier could be identified, and hence **7** is not detectable in NR experiments. Thus, one is left with singlets **5** and **6**, whose dissociation into $CO_2(X^1\Sigma^+)$ and $O_2(a^1\Delta)$ is also exothermic, and hence their detectability depends on the existence of sizable kinetic barriers to dissociation. This rules out **5**, as no such a barrier could be identified, thus restricting the choice to singlet **6**, whose dissociation into $CO_2(X^1\Sigma_g^+)$ and $O_2(a^1\Delta_g)$ is forbidden by orbital symmetry rules[5,7] and hence can be expected to have a significant barrier,[32] in addition to that presumably arising from steric factors.[7] However, an indirect route to dissociation could involve fast nonradiative singlet–triplet decay of **6** into **7**, prone to dissociation into $CO_2(X^1\Sigma_g^+)$ and O_2 $(X^3\Sigma_g^-)$. Fortunately, the barrier to the nonradiative decay of **6** into **7**, and hence the barrier to dissociation of **6**, has been investigated in details by Averyanov, Khait and Puzanov,[7] whose estimate sets the barrier height in the range from 15.0 to 27.3 kcal mol^{-1}. Among the ionic precursors of **6** in our NR experiments, only **3** has the same connectivity as **6**, whereas its geometry is similar but not identical to that of the neutral molecule. Consequently, **6** formed from the vertical neutralization process is expected to contain excess energy (the Franck-Condon energy), that we have calculated to amount to 15.5 and 17.0 kcal mol^{-1} at to B3LYP and the CCSD(T) levels of theory, respectively. These results show that following neutralization of **3,** the D_{2d} $^1A^1$ singlet should survive dissociation, and hence it represents the most likely (indeed, the only) candidate, although a more rigorous assignment requires additional studies, in particular a more detailed theoretical analysis of the difficult CO_4 system.

In conclusion, the present results demonstrate the existence of a metastable CO_4 molecule with a lifetime exceeding 1 μs in the isolate gas state, whose structure can tentatively by assigned as a D_{2d} $^1A_1$ singlet, based on the available experimental and theoretical evidence.

Apart from its intrinsic interest, the discovery of CO_4, long theoretically predicted but so far experimentally elusive, may be significant to atmospheric chemistry and especially to the high energy density materials (HEDM) field, in that the CO_4 isomer detected, that is, the D_{2d} singlet, is a metastable species calculated to release more than 80 kcal mol^{-1} upon dissociation into CO_2 and O_2.[7]

Experimental Section

The experiments were performed by using a modified ZABSpec oa-TOF instrument (VG Micromass) of EBE-TOF configuration, where E, B stand for electric and magnetic sectors and TOF for orthogonal time-of-flight mass spectrometer. The instrument was fitted with EI and CI ion sources, a gas cell located in the first field free region and two pairs of gas cells located after the magnet along the beam path. Typical operating conditions of the CI source were as follows: source temperature: 373 K, repeller voltage: 0 V, emission current 1 mA, nominal electron energy: 50 eV. Typical EI source conditions were: source temperature: 373 K, trap current: 200 μA, electron energy: 50 eV. The ions from the source were accelerated to 6–8 kV and their CAD and NR spectra recorded, by using the first of the collision cells pair, located between the magnet and the second E sector. The target gas used in the CAD experiments was He, which was admitted into the first cell at a pressure adjusted to obtain a 80% transmittance. In the NR experiments CH_4, used as the neutralizing gas, was also admitted into the first of the cells pair at such a pressure to obtain a beam transmittance of 80%. All ions were then removed by a pair of high voltage ($\pm$0.8 kV) deflecting electrodes, and the beam of fast neutral species entered the second cell, in which reionization was achieved by using O_2 as the stationary collider. The NR spectra were averaged over 100 acquisitions to improve the signal-to-noise ratio. The following MS^3 (multi-stage mass spectrometry) experiments were performed: 1) The selected precursor ion underwent decomposition by collision with He in one of the cells located in the second field free region, and the energy-selected daughter ions were structurally analyzed by CAD-TOF in the cell located in the TOF mass spectrometer; 2) The same experiment was performed by selecting the charged fragments formed by collisions occurring in the cell

 © 2003 Wiley-VCH Verlag GmbH & Co. KGaA, Weinheim

located in the first field free region. An Apex 47e spectrometer, (Bruker Spectrospin AG), equipped with an external CI/EI ion source and a cylindrical infinity cell[33] was used in FTICR experiments. The ions generated in the source and driven into the resonance cell, were mass-selected by soft ejection techniques and allowed to react with the neutral species at pressures ranging from 10^{-8} to 10^{-7} Torr. Accurate mass analyses were performed to unambiguously identify the charged products. The gases, research-grade products with a stated purity in excess of 99.95 mol%, were used as such without further purification. Ozone was prepared by passing UHP oxygen through a commercial ozonizer, collected over silica in a trap cooled to 77 K, and released by gradual warming of the trap. The $^{18}O_2$ (99 ^{18}O atom%) and the $C^{18}O_2$ (98.7 ^{18}O atom%) samples were obtained from Ikon Stable Isotopes, Inc.

Computational Methods: Density functional theory, by using the hybrid[12] B3LYP functional,[13] was used to localize the stationary points of the investigated systems and to evaluate the vibrational frequencies. Although it is well know that density functional methods that use nonhybrid functionals sometimes tend to overestimate bond lengths,[14] hybrid functionals as B3LYP usually provide geometrical parameters in excellent agreement with experiment.[15] Single point energy calculations at the optimized geometries were performed using the coupled-cluster single and double excitation method[16] with a perturbational estimate of the triple excitations [CCSD(T) approach][17] in order to include extensively correlated contributions.[18] Transition states were located by using the synchronous transit-guided quasi-Newton method reported by Schlegel and coworkers.[19] The 6-311+G(3df) basis set[20] was used. Zero point energy corrections evaluated at the B3LYP6-311+(3df) level were added to the CCSD(T) energies. The 0 K total energies of the species of interest were corrected to 298 K by adding translational, rotational and vibrational contributions. The absolute entropies were calculated by using standard statistical-mechanical procedures from scaled harmonic frequencies and moments of inertia relative to B3LYP6-311+G(3df) optimised geometries. All calculations were performed using Gaussian 98.[21]

Received: January 14, 2003
Revised: February 28, 2003 [Z50936]

Keywords: atmospheric chemistry · computer chemistry · density functional calculations · mass spectrometry

[1] J. M. Parnis, L. E. Hoover, T. D. Fridgen, R. D. Lafleur, *J. Phys. Chem.* **1993**, *97*, 10708.
[2] a) R. S. Narcisi, A. D. Bailey, L. Della Lucca, C. Sherman, D. M. Thomas, *J. Atmos. Terr. Phys.* **1971**, *33*, 1147; b) F. Arnold, A. A. Viggiano, E. E. Ferguson, *Planet. Space Sci.* **1982**, *30*, 1317; c) J. Wisemberg, G. Kockarts, *J. Geophys. Res.* **1980**, *85*, 4642; d) L. Thomas, M. R. Bowman, J. *Atmos. Terr. Phys.* **1985**, *47*, 547; e) A. A. Viggiano, R. A. Morris, J. F. Paulson, *J. Chem. Phys.* **1989**, *91*, 5855; f) M. K. Dymek, *Adv. Space Explor.* **1980**, *8*, 115; g) R. P. Wayne, *Chemistry of Atmospheres*, Oxford University Press, Oxford, **2000**.
[3] a) (Ed.: G. M. Keating) *Adv. Space Res.* **1990**, *10*, No 5; b) J. L. Fox, *Icarus* **1982**, *51*, 248; c) G. L. Hashimoto, Y. Abe, S. Sasaki, *Geophys. Res. Lett.* **1997**, *24*, 289.
[4] a) H. Shields, A. L. S. Smith, *Appl. Phys.* **1978**, *16*, 111; b)W. B. Scott, *Aviat. Week Space Technol.* **1988**, *21*, 19; c) T. M. Klapötke, G. Holl, *Green Chem.* **2001**, *3*, G75.
[5] A. S. Averyanov, Yu. G. Khait, Yu. V. Puzanov, *J. Mol. Struct. (THEOCHEM)* **1996**, *367*, 87.
[6] a) J. Song, Yu. G. Khait, M. R. Hoffmann, *J. Phys. Chem. A* **1999**, *103*, 521; b) A. A. Korkin, P. v. R. Schleyer, R. J. Boyd, *Chem. Phys. Lett.* **1994**, *227*, 312.
[7] A. S. Averyanov, Yu. G. Khait, Yu. V. Puzanov, *J. Mol. Struct. (THEOCHEM)* **1999**, *459*, 95.
[8] V. Raducu, D. Jasmin, R. Dahoo, P. Brosslet, B. Gauthier-Roy, L. Abouaf-Marguin, *J. Chem. Phys.* **1994**, *101*, 1878.
[9] a) R. Lavertu, M. Catte, A. Pontenero, D. Le Goff, *C. R. Seances Acad. Sci. Ser. C* **1996**, *263*, 1099; b) J. K. Terlouw, H. Schwarz, *Angew. Chem.* **1987**, *99*, 829; *Angew. Chem. Int. Ed. Engl.* **1987**, *26*, 805; c) D. Suelzle, H. Schwarz, *Chem. Ber.* **1989**, *122*, 1803; d) D. Schröder, D. Suelzle, J. Hrusák, D. K. Boehme, H. Schwarz, *Int. J. Mass Spectrom. Ion Processes* **1991**, *110*, 145; e) G. I. Gellene, R. F. Porter, *Acc. Chem. Res.* **1983**, *16*, 200; f) C. Wesdemiotis, F. W. McLafferty, *Chem. Rev.* **1987**, *87*, 485; g) N. Goldberg, H. Schwarz, *Acc. Chem. Res.*, **1994**, *27*, 347; h) C. A. Schalley, G. Hornung, D. Schröder, H. Schwarz, *Chem. Soc. Rev.* **1998**, *27*, 91; i) C. A. Schalley, G. Hornung, D. Schröder, H. Schwarz, *Int. J. Mass Spectrom. Ion Processes* **1998**, *172*, 181.
[10] a) F. Cacace, G. de Petris, F. Pepi, A. Troiani, *Science* **1999**, *285*, 81; b) F. Cacace, G. de Petris, F. Pepi, A. Troiani, *Angew. Chem.* **2000**, *112*, 375; *Angew. Chem. Int. Ed.* **2000**, *39*, 367; c) F. Cacace, G. de Petris, A. Troiani, *Angew. Chem.* **2001**, *113*, 4186; *Angew. Chem. Int. Ed.* **2001**, *40*, 4062.
[11] F. Cacace, G. de Petris, A. Troiani, *Science* **2002**, *295*, 480.
[12] A. D. Becke, *J. Chem. Phys.* **1993**, *98*, 5648.
[13] P. J. Stevens, F. J. Devlin, C. F. Chablowski, M. J. Frisch, *J. Phys. Chem.* **1994**, *98*, 11623.
[14] B. Mannfors, J. T. Koskinen, L.-O. Pietilä, L. Ahjopalo, *J. Molec. Struct. (THEOCHEM)* **1997**, *39*, 393.
[15] C. W. Bauschlicher, A. Ricca, H. Partridge, S. R. Langhoff in *Recent Advances in Density Functional Theory, Part II* (Ed.: D. P. Chong), World Scientific Publishing Co., Singapore, **1997**.
[16] R. J. Bartlett, *Annu. Rev. Phys. Chem.* **1981**, *32*, 359.
[17] K. Raghavachari, G. W. Trucks, J. A. Pople, M. Head-Gordon, *Chem. Phys. Lett.* **1989**, *157*, 479.
[18] J. Olsen, P. Jorgensen, H. Koch, A. Balkova, R. J. Bartlett, *J. Chem. Phys.* **1996**, *104*, 8007.
[19] a) C. Peng, H. B. Schlegel, *Isr. J. Chem.* **1994**, *33*, 449; b) C. Peng, P. Y. Ayala, H. B. Schlegel, M. J. Frisch, *J. Comput. Chem.* **1996**, *17*, 49.
[20] a) R. Krishnan, J. S. Binkley, R. Seeger, J. A. Pople, *J. Chem. Phys.* **1980**, *72*, 650; b) A. D. McLean, G. S. Chandler, *J. Chem. Phys.* **1980**, *72*, 5639; c) T. Clark, J. Chandrasekhar, G. W. Spitznagel, P. von R. Schleyer, *J. Comput. Chem.* **1983**, *4*, 294; d) M. J. Frisch, J. A. Pople, J. S. Binkley, *J. Chem. Phys.* **1984**, *80*, 3265.
[21] Gaussian 98 (Revision A.7), M. J. Frisch, G. W. Trucks, H. B. Schlegel, G. E. Scuseria, M. A. Robb, J. R. Cheeseman, V. G. Zakrzewski, J. A. Montgomery, R. E. Stratmann, J. C. Burant, S. Dapprich, J. M. Millam, A. D. Daniels, K. N. Kudin, M. C. Strain, O. Farkas, J. Tomasi, V. Barone, M. Cossi, R. Cammi, B. Mennucci, C. Pomelli, C. Adamo, S. Clifford, J. Ochterski, G. A. Petersson, P. Y. Ayala, Q. Cui, K. Morokuma, D. K. Malick, A. D. Rabuck, K. Raghavachari, J. B. Foresman, J. Cioslowski, J. V. Ortiz, B. B. Stefanov, G. Liu, A. Liashenko, P. Piskorz, I. Komaromi, R. Gomperts, R. L. Martin, D. J. Fox, T. Keith, M. A. Al-Laham, C. Y. Peng, A. Nanayakkara, C. Gonzalez, M. Challacombe, P. M. W. Gill, B. G. Johnson, W. Chen, M. W. Wong, J. L. Andres, M. Head-Gordon, E. S. Replogle, J. A. Pople, Gaussian, Inc., Pittsburgh, PA, **1998**.
[22] M. K. P. Huber, G. Herzberg, *Constants of Diatomic Molecules*, Van Nostrand, New York, **1978**.
[23] V. G. Anicich, *J. Phys. Chem. Ref. Data* **1993**, *22*, 1550.
[24] K. Hiraoka, *Progress Report of the Atomic Collisional Research, Vol. 11* in Japan Society for Atomic Collision Research, Wakoshi, Japan, **1985**, p. 183.
[25] R. A. Beyer, J. A. Vanderoff, *J. Chem. Phys.* **1976**, *65*, 2313.
[26] H.-S. Kim, C.-H. Kuo, M. T. Bowers, *J. Chem. Phys.* **1987**, *87*, 2667.

 © 2003 Wiley-VCH Verlag GmbH & Co. KGaA, Weinheim

[27] a) B. Wannberg, H. Veenhuizen, L. Mattsson, K. E. Norell, L. Karlson, K. Siegbahn, *J. Phys. B* **1984**, *17*, L259, and references therein; b) T. Baer, P.M Guyon, *J. Chem. Phys.* **1986**, *85*, 4765; c) P. H. Krupenil, *J. Phys. Chem. Ref. Dataa* **1972**, *1*, 423.
[28] a) V. Cermak, Z. Herman, *Collect. Czech. Chem. Commun.* **1962**, *27*, 1493; b) K. S. Griffith, G. I. Gellene, *J. Chem. Phys.* **1992**, *96*, 4403.
[29] F. Cacace, G. de Petris, M. Rosi, A. Troiani, *Chem. Eur. J.* **2002**, *8*, 3653, and references therein.
[30] G. P. Smith, L. C. Lee, *J. Chem. Phys.* **1978**, *69*, 5393.
[31] The barrier to dissociation required for the detection of the neutral is generally estimated $\geq$8–10 kcal mol^{-1}. However, appreciably lower barriers have been reported for certain systems, see: D. Schröder, C. A. Schalley, N. Goldberg, J. Hrusák, H. Schwarz, *Chem. Eur. J.* **1996**, *2*, 1235. In any case, the well deepth required for detection in NR experiments largely exceeds that of the neutral $CO_2 \cdots O_2$ complex and, as a matter of fact, van der Waals complexes are hardly detectable by NRMS.
[32] P. R. Bunker, *Molecular Symmetry and Spectroscopy*, Academic Press, New York, **1979**.
[33] P. Caravatti, M. Alleman, *Org. Mass Spectrom.* **1991**, *26*, 514.

 © 2003 Wiley-VCH Verlag GmbH & Co. KGaA, Weinheim

Methane Sulfonation

A High-Yield Approach to the Sulfonation of Methane to Methanesulfonic Acid Initiated by H_2O_2 and a Metal Chloride**

*Sudip Mukhopadhyay and Alexis T. Bell**

Methane is abundant and relatively inexpensive, making it an attractive feedstock for producing bulk chemicals. However, the low reactivity of methane makes it difficult to develop commercially viable processes for methane conversion.[1] Because of favorable thermodynamics, many authors have investigated the oxidation and oxidative carbonylation of methane.[2] By contrast, the sulfonation of methane to give methanesulfonic acid has not received as much attention despite its commercial importance.[3] The current commercial process for the synthesis of methanesulfonic acid (MSA) relies on the chlorine-oxidation of thiomethane.[4] While this process is highly productive, it produces six moles of HCl per mole of MSA, resulting in a coupling of the demand for the primary product and the by-product. It has been shown[5] that $K_2S_2O_8$ can be used as a free-radical initiator to sulfonate methane with SO_3 in fuming sulfuric acid under very high methane pressure. The conversion of methane to MSA is reported to be 3–6% under 1000 psig methane pressure (1 psig = 6.895×10^3 Pa).[5] We recently have shown that metal peroxides can be used as an effective radical initiator for methane activation in sulfuric acid solvent.[6] However, once the metal peroxides have activated methane they are converted into the metal sulfate salts, which cannot be recycled back to the metal peroxide. The economics of producing and handling safely the necessary amounts of metal peroxide must also be considered if a practical process is to be developed. Thus, there is considerable incentive to look for a way to generate metal peroxo species in situ from a cheap source such as H_2O_2.

In this communication we show that methane will undergo liquid-phase sulfonation to MSA with SO_3 in sulfuric acid. A small amount of urea/H_2O_2 is used as a free-radical initiator and a small amount of a metal chloride salt, particularly $RhCl_3$, is used as a promoter [Eq. (1)].

$$CH_4 + SO_3 \xrightarrow[\text{MCl, } 65-75^{\circ}C,\ 3\,h]{\text{urea}/H_2O_2,\ H_2SO_4} CH_3SO_3H \qquad (1)$$

In a typical reaction[7] methane was treated with 30-wt.% SO_3 in H_2SO_4 to form MSA in the presence of small amounts of urea/H_2O_2 (Aldrich) and a metal chloride salt. Reactions were carried out in a high-pressure, glass-lined Parr autoclave. The MSA thus formed was identified and quantified by ^{1}H NMR spectroscopy.[5] Unless otherwise noted, no other sulfur-containing products were detected in either the gas or the liquid phase. Analysis of the product formed from SO_3 and $^{13}CH_4$ by ^{13}C NMR spectroscopy indicates that $^{13}CH_3SO_3H$ is formed exclusively from $^{13}CH_4$. Only a small amount of ethane was observed in the gas phase in the absence of SO_3 when 100% H_2SO_4 was used as the solvent. Since this product was absent when the autoclave was not pressurized with methane, the appearance of ethane is attributed to the coupling of methyl radicals.

Table 1 shows the effect of different promoters on the sulfonation of methane. The conversion of SO_3, the limiting reagent, is defined as the ratio of the moles of SO_3 converted into MSA to the total moles of SO_3 in to the autoclave. When urea/H_2O_2 served as the initiator, and in the absence of any promoter, the conversion of SO_3 to MSA was 23% (Table 1, entry 1). When the reaction was carried out in the presence of $CaCl_2$, $BaCl_2$, $FeCl_3$, and $NbCl_5$ there was a moderate increase in the conversion of SO_3 to MSA (entries 2–5). $TaCl_5$, $AlCl_3$, $HgCl_2$, and AgCl are even more effective as promoters (entries 6–9). The most effective promoter, though, is $RhCl_3$ (entry 10). KCl, $RuCl_3$, $[Rh(CO)_2Cl)]_2$, $NiCl_2$, $PdCl_2$, $PtCl_2$, $CuCl_2$, and $VOCl_3$ had a negative effect on MSA synthesis relative to what was observed without the addition of a promoter (entries 11–18).

Table 2 shows the effect of different process parameters when urea/H_2O_2 and $RhCl_3$ were used as the initiator and the promoter, respectively. The conversion of SO_3 to MSA was 42% after 26 h of reaction when the initial methane pressure was 100 psig. The conversion of SO_3 to MSA increased monotonically with increasing methane pressure (Table 2, entries 1–4), reaching a level of 86% for an initial methane pressure of 650 psig. It is noted that the conversion of

[*] Prof. A. T. Bell, S. Mukhopadhyay
Department of Chemical Engineering
University of California
Berkeley, CA 94720-1462 (USA)
Fax: (+1) 510-642-4778
E-mail: bell@cchem.berkeley.edu

[**] This work was supported by Atofina Chemicals Inc., North America.

 © 2003 Wiley-VCH Verlag GmbH & Co. KGaA, Weinheim DOI: 10.1002/anie.200350976

Table 1: Effect of different metal chloride salts on the rate of methane sulfonation with SO_3.[a]

Entry	Promoter [mmol]	MSA [mmol]	Conv. of SO_3 [%][b]	Sel. to MSA [%]
1	none, 0	4.9	23	100
2	$CaCl_2$, 0.33	7.2	34	100
3	$BaCl_2$, 0.33	6.8	32	100
4	$FeCl_3$, 0.33	6.4	30	100
5	$NbCl_5$, 0.33	6.2	29	99.8
6	$TaCl_5$, 0.33	11.5	54	99.3
7	$AlCl_3$, 0.33	11.9	56	99.3
8	$HgCl_2$, 0.33	12.5	59	99
9	AgCl, 0.33	13	61	99.6
10	$RhCl_3$, 0.33	18.3	86	99.9
11	KCl, 0.33	4.3	20	100
12	$RuCl_3$, 0.37	0.64	3	80
13	$[Rh(CO)_2Cl]_2$, 0.4	0.21	1	100
14	$NiCl_2{\cdot}6H_2O$, 0.36	0	0	0
15	$PdCl_2$, 0.33	0.06	0.27	8
16	$PtCl_2$, 0.33	0.64	3	10
17	$CuCl_2$, 0.33	0	0	0
18	$VOCl_{3,\ 0.33}$	0	0	0

[a] Reaction conditions: 650 psig (179 mmol) methane, 1.7 g (21.26 mmol) SO_3 (mol ratio methane:SO_3 = 8.4), 0.74 mmol urea/H_2O_2, 5.67 g fuming sulfuric acid (30 wt% SO_3), 3 h, 65 °C. [b] Ratio of the moles of SO_3 converted to MSA to the total moles of SO_3 taken initially in the reaction mixture.

Table 2: Effect of process parameters on the sulfonation of methane.[a]

Entry	CH_4 [psig], (mmol)	t [h]	Initiator [mmol]	$RhCl_3$ [mmol]	T [°C]	MSA [mmol]	SO_3 conv. [%],[b] (CH_4 conv. [%])[c]
1	100(31)	26	urea/H_2O_2,0.74	0.33	65	8.9	42(29)
2	200(58)	14	urea/H_2O_2,0.74	0.33	65	9.8	46(17)
3	450(125)	3	urea/H_2O_2,0.74	0.33	65	16.8	79(13)
4	650(179)	3	urea/H_2O_2,0.74	0.33	65	18.2	86(10)
5	650(179)	3	none, 0	0.33	65	0.06	0.3(–)
6	650(179)	3	urea/H_2O_2,0.16	0.33	65	14.5	68(8)
7	650(179)	3	urea/H_2O_2,0.46	0.33	65	17.6	83(10)
8	650(179)	3	urea/H_2O_2,0.96	0.33	65	13.2	62(7)
9	650(179)	3	urea/H_2O_2,0.74	0	65	4.9	23(3)
10	650(179)	3	urea/H_2O_2,0.74	0.05	65	14.7	69(8)
11	650(179)	3	urea/H_2O_2,0.74	0.14	65	20.2	95(11)
12	650(179)	3	urea/H_2O_2,0.74	0.24	65	19.1	90(10)
13	650(179)	3	urea/H_2O_2,0.74	0.33	75	19.3	91(11)
14	650(179)	3	urea/H_2O_2,0.74	0.33	85	11.5	54(6)
15	200(58)	3	urea/H_2O_2,0.74	0.33	130	4.6	22(20)
16	200(58)	3	urea/H_2O_2,0.74	0.33	160	0.5	2(24)
17	100(31)	72	urea/H_2O_2,0.65	0.30	85	11.1	52(36)
18[d]	650(179)	3	urea/H_2O_2,0.85	0.24	65	32	75(18)
19	650(179)	3	$K_2S_2O_8$, 0.74	0.33	65	3.6	17(2)
20	650(179)	3	$K_4P_2O_8$, 0.74	0.33	65	3.4	16(2)
21	650(179)	3	CaO_2, 0.74	0.33	65	13.3	63(7)
22	650(179)	3	Br_2, 0.74	0.33	65	1.9	9(2)
23	650(179)	3	Cl_2, 0.74	0.33	65	0.8	4(1)
24	650(179)	3	I_2, 0.74	0.33	65	0	0(0.5)

[a] Reaction conditions: SO_3 (1.7 g, 21.26 mmol), urea/H_2O_2 as radical initiator, $RhCl_3$ as promoter, solvent, fuming sulfuric acid (30 wt% SO_3, 5.67 g) as solvent. [b] Moles of SO_3 converted to MSA/total moles of SO_3 in the autoclave. [c] Moles of methane converted/moles of methane in the autoclave. [d] Amount of fuming sulfuric acid used, 11.34 g (initial SO_3 amount, 42.52 mmol).

methane, shown in parentheses, decreases with increasing methane pressure, since the number of moles of methane in the autoclave increases, whereas the number of moles of SO_3 remains constant.

The amount of free-radical initiator, urea/H_2O_2, was varied from 0 mmol to 0.96 mmol, while the amount of the promoter, $RhCl_3$, was kept constant at 0.33 mmol. It was observed that with an increase in the amount of initiator from 0 mmol to 0.16 mmol, the conversion of SO_3 to MSA increased from 0.3 to 68%. A maximum conversion of 86% was achieved with 0.74 mmol of the promoter (Table 2, entries 5–8). The reaction can also be initiated by using 50-wt% H_2O_2 solution as the initiator. An excess of SO_3 was used to remove the water ($H_2O + SO_3 \rightarrow H_2SO_4$) associated with the H_2O_2 solution. For these circumstances, the conversion of SO_3 to MSA was only 16% after 3 h of reaction in the presence of $RhCl_3$. Consequently, for all subsequent reactions, H_2O_2 was introduced as anhydrous urea/H_2O_2.

 © 2003 Wiley-VCH Verlag GmbH & Co. KGaA, Weinheim

The reaction was studied with different amounts of $RhCl_3$ (Table 2, entries 9–12). With an increase in the amount of $RhCl_3$, the conversion of SO_3 to MSA increased marginally. A maximum SO_3 conversion of 95% was achieved with 0.14 mmol $RhCl_3$ for a methane pressure of 650 psig. The conversion of methane to MSA under this reaction condition was 11%.

The conversion of SO_3 to MSA increased from 86 to 91% (3 h reaction time) when the temperature was increased from 65 to 75°C. However, with a further increase in temperature to 85°C, the conversion decreased to 54% (Table 2, entries 4, 13, and 14) and a small amount of CH_3OSO_3H appeared as a product. When the reaction temperature was increased to 130°C, CH_3OSO_3H became the major product. At 160°C, the total conversion of methane was 24%, of which 0.86% was to MSA, 1.26% to CO_2, 1.2% to methanedisulfonic acid, and the balance to CH_3OSO_3H (entries 15 and 16).

The highest conversion of methane to MSA, 36% (Table 2, entry 17), was obtained after 72 h of reaction. In this case the initial methane pressure was 100 psig, the temperature was 85°C, the amount of urea/H_2O_2 was 0.65 mmol, and the amount of $RhCl_3$ was 0.3 mmol. Since the selectivity to MSA was 99.99%, the overall yield of MSA was 36% based on methane. Comparison of entries 12 and 18 in Table 2 shows that the conversion of methane to MSA can be raised by increasing the initial amount of fuming sulfuric acid. When the amount was doubled, the methane conversion increased from 10% to 18%.

The effectiveness of $K_2S_2O_8$, $K_4P_2O_8$, CaO_2, Br_2, Cl_2, and I_2 as initiators was examined in the presence of $RhCl_3$. It was found that the combination of $RhCl_3$ and urea/H_2O_2 was the most effective combination of promoter and initiator under the reaction conditions used (Table 2, entries 19–23). The order of reactivity of the initiators in the presence of $RhCl_3$ as the promoter was urea/H_2O_2 > CaO_2 > $K_2S_2O_8$ > $K_4P_2O_8$ > Br_2 > Cl_2. With iodine as the initiator, 3% of the SO_3 in the reactor was converted to CH_3OSO_3H but no MSA was detected (Table 2, entry 24), which is consistent with recent reports.[8]

The mechanism by which H_2O_2 either alone or in combination with $RhCl_3$ promotes the sulfonation of methane is not understood. In previous studies[5,6] of methane sulfonation utilizing inorganic peroxide initiators, e.g., $K_2S_2O_8$, K_4P_2O8, CaO_2, it was suggested that decomposition of the initiator produces methyl radicals, which then react with SO_3 to form $CH_3SO_3^{\bullet}$ radicals and then CH_3SO_3H. Inhibition of the reaction by O_2 together with the appearance of small amounts of ethane in the gas phase suggest that a free-radical mechanism may be operative in the systems investigated in this study. The initiating species in the present case could be $OH^{\bullet}$ radicals formed by decomposition of H_2O_2, or $RhClO_2$ or $RhCl_2OOH$ formed from the reaction of H_2O_2 with $RhCl_3$.

The increase in the conversion of SO_3 from 23% to 86% (after 3 h reaction time) when a small amount of $RhCl_3$ is added to the synthesis mixture together with urea/H_2O_2 strongly suggests that the activation of methane is initiated not only by H_2O_2 but also by a metal–peroxo or metal–hydroperoxo species[9] produced in situ by the reversible reaction between urea/H_2O_2 and $RhCl_3$. Consistent with this logic, Table 2 shows that the maximum conversion of SO_3 to MSA (86–95%) is obtained when the molar ratio of urea/H_2O_2 to $RhCl_3$ is between 2.24 and 5.28. Furthermore, when a fresh amount of urea/H_2O_2, methane, and SO_3 was added to the reaction mixture after 3 h, the reaction proceeded in the same way as the initial reaction with fresh reaction mixture. This strongly suggests that the promoter, $RhCl_3$, is recycled in situ in the acidic solution. The importance of $RhCl_3$ is further supported by an experiment in which a fresh batch of urea/H_2O_2, methane, and SO_3 was added to a reaction mixture after 3 h, but one to which $RhCl_3$ had not been added. In this case, no additional reaction was observed.

When the reaction mixture is cooled to 0°C, most of the Rh salt can be separated from the reaction mixture by precipitation. The separation of MSA from the reaction mixture is straightforward, as MSA can be used as a solvent instead of H_2SO_4.

In conclusion, we have developed a highly effective, low-temperature reaction protocol for sulfonating methane to give methanesulfonic acid at low methane pressures. For a methane pressure of 100 psig, the conversion of methane to MSA is 29–36% and the selectivity to MSA is 99.9%. $RhCl_3$ enhances the initiation of the reaction by urea/H_2O_2, presumably through the formation of a metal–peroxo or metal–hydroperoxo species in situ. Most of the $RhCl_3$ can be recovered from the reaction mixture by precipitation at 0°C. The separation of MSA from the reaction mixture is straightforward as MSA can be used as a solvent instead of H_2SO_4. At higher temperatures (160–170°C) the same reaction scheme can be extended to synthesize CH_3OSO_3H, which can be easily hydrolyzed to methanol.

Received: January 20, 2003 [Z50976]

Keywords: C–H activation · homogeneous catalysis · methane · sulfonation

[1] a) C. L. Hill, *Activation and Functionalization of Alkanes*, Wiley, New York, **1989**; b) M. G. Axelrod, A. M. Gaffney, R. Pitchai, J. A. Sofranko, *Natural Gas Conversion II*, Elsevier, Amsterdam, **1994**, p. 93; c) C. Starr, M. F. Searl, S. Alpert, *Science* **1992**, *256*, 981; d) A. E. Shilov, G. B. Shul'pin, *Activation and Catalytic Reactions of Saturated Hydrocarbons in the Presence of Metal Complexes,* Kluwer Academic Publishers, Dordrecht, **2000**; e) G. A. Olah, A. Molnar, *Hydrocarbon Chemistry*, Wiley, New York, **1995**; f) B. A. Arndtsen, R. G. Bergman, *Science* **1995**, *270*, 1970; g) S. E. Bromberg, H. Yang, M. C. Asplund, T. Lian, B. K. McNamara, K. T. Kotz, J. S. Yeston, M. Wilkens, H. Frei, R. G. Bergman, C. B. Harris, *Science* **1997**, *278*, 260; h) M. Lin, A. Sen, *Nature* **1994**, *368*, 613; i) A. Sen, *Acc. Chem. Res.* **1998**, *31*, 550; j) J. A. Labinger, *Fuel Process. Technol.* **1995**, *42*, 325; k) R. H. Crabtree, *Chem. Rev.* **1995**, *95*, 987; l) A. E. Shilov, G. B. Shul'pin, *Chem. Rev.* **1997**, *97,* 2879; m) G. Dyker, *Angew. Chem.* **1999**, *111,* 1808; *Angew. Chem. Int. Ed.* **1999**, *38,* 1698; n) H. D. Gesser, N. R. Hunter, *Catal. Today* **1998**, *42*, 183; o) J. H. Lunsford, *Catal. Today* **2000**, *63*, 165; p) J. T. Golden, R. A. Andersen, R. G. Bergman, *J. Am. Chem. Soc.* **2001**, *123*, 5837; q) J. A. Labinger, J. E. Bercaw, *Nature* **2002**, *417*, 507; r) M. Muehlhofer, T. Strassner, W. A. Herrmann, *Angew. Chem.* **2002**, *114,* 1817; *Angew. Chem. Int. Ed.* **2002**, *41,* 1745.

 © 2003 Wiley-VCH Verlag GmbH & Co. KGaA, Weinheim

[2] a) T. Nishiguchi, K. Nakata, K. Takaki, Y. Fujiwara, *Chem. Lett.* **1992**, *7*, 1141; b) E. G. Chepaikin, A. P. Bezruchenko, A. A. Leshcheva, G. N. Boyko, I. V. Kuzmenkov, E. H. Grigoryan, A. E. Shilov, *J. Mol. Catal. A* **2001**, *169*, 89; c) R. A. Periana, D. J. Taube, E. R. Evitt, D. G. Loffer, P. R. Wentrcek, G. Voss, T. Masuda, *Science* **1993**, *259*, 340; d) R. A. Periana, D. J. Taube, S. Gamble, H. Taube, T. Satoh, H. Fujii, *Science* **1998**, *280*, 560.

[3] a) *Ullmann's Encyclopedia of Industrial Chemistry, Vol. A25,* VCH, Weinheim, **1994**, pp. 503 – 506; b) F. M. Beringer, R. A. Falk, *J. Am. Chem. Soc.* **1959**, *81*, 2997; c) H. A. Young, *J. Am. Chem. Soc.* **1937**, *59*, 811; d) R. C. Murray, *J. Chem. Soc.* **1933**, 739.

[4] a) J. I. Kroschwitz, M. Howe-Grant, *Kirk Othmer Encyclopedia of Chemical Technology*, Wiley, New York, **1991**; b) R. Guertin, US-A 3626004 **1971**.

[5] a) N. Basickes, T. E. Hogan, A. Sen, *J. Am. Chem. Soc.* **1996**, *118*, 13111; b) L. J. Lobree, A. T. Bell, *Ind. Eng. Chem. Res.* **2001**, *40*, 736; c) S. Mukhopadhyay, A. T. Bell, *Ind. Eng. Chem. Res.* **2002**, *41*, 5901; d) S. Mukhopadhyay, A. T. Bell, *Org. Proc. Res. Dev.* **2003**, in press; e) S. Mukhopadhyay, A. T. Bell, *J. Am. Chem. Soc.* **2003**, in press.

[6] S. Mukhopadhyay, A. T. Bell, *Angew. Chem.* **2003**, *115*, 1049; *Angew. Chem. Int. Ed.* **2003**, *42*, 1019.

[7] A 100-mL glass-lined high-pressure Parr autoclave reactor equipped with a small Teflon-coated magnetic stir bar was charged with urea/H_2O_2 (0.74 mmol), $RhCl_3$ (0.33 mmol), and fuming H_2SO_4 (5.69 g; 1.707 g of SO_3 in 3.983 g H_2SO_4). The reactor was purged with N_2 to expel the air from the system and then pressurized with methane (650 psig) from the adjacent connecting cylinders. The reaction mixture was stirred and heated to 65 °C for 3 h. After the stipulated period of time, the reactor was cooled with ice, vented, and opened. The reaction mixture was then added slowly to 0.5 g of water and then taken for ^{1}H NMR analysis. D_2O and methanol were used in a capillary as the lock references. The corresponding ^{1}H NMR chemical shifts for MSA were between 2.87 ppm and 3.02 ppm, depending on the concentration of MSA in the mixture.

[8] R. A. Periana, O. Mirinov, D. J. Taube, S. Gamble, *Chem. Commun.* **2002**, 2376.

[9] For the activation of methane with a Ca–peroxo species in the presence of a stoichiometric amount of $K_2S_2O_8$ see, a) M. Asadullah, T. Kitamura, Y. Fujiwara, *Angew. Chem.* **2000**, *112*, 2609; *Angew. Chem. Int. Ed.* **2000**, *39*, 2475; b) For the use of oxovanadium(v)peroxo complexes in methane activation, see G. V. Nizova, G. Siiss-Fank, G. B. Shul'pin, *Chem. Commun.* **1997**, 397; However, with this V – peroxo complex, no conversion of SO_3 to MSA is observed under our reaction conditions.

 © 2003 Wiley-VCH Verlag GmbH & Co. KGaA, Weinheim

Biphasic Enzyme-Catalyzed Reactions

Is log *P* a Convenient Criterion to Guide the Choice of Solvents for Biphasic Enzymatic Reactions?**

*Murillo Villela Filho, Thomas Stillger, Michael Müller, Andreas Liese, and Christian Wandrey**

The high chemo- and enantioselectivity of enzyme-catalyzed hydrogen transfer are well documented in the literature.[1] Recent articles compared the biocatalytic methods for the reduction of ketones with classical chemical reactions.[2] The advantages of the former were summarized by Faber and co-workers.[3] Although a vast variety of ketones are reduced enantioselectively by commercially available enzymes under mild conditions, isolated alcohol dehydrogenases (ADH) are in comparison seldom used as catalysts in daily chemical laboratory work. The major reason for this discrepancy is the incompatibility of the required reaction conditions for the enzyme with most substrates.[4] Enzymes usually require aqueous environments in which the organic substrates are poorly soluble and in some cases even unstable. A straightforward solution to this problem is the application of biphasic systems.[5] In these systems, the enzyme and the cofactor are dissolved in the aqueous phase, while the hydrophobic substrate is present in a high concentration in the organic phase. As the occurrence of a liquid–liquid interface and presence of residual amounts of organic solvent in water can lead to deactivation of the biocatalyst, methods to guide the choice of the proper solvent have been proposed, such as that reported by Brink and Tramper.[6] Laane et al. suggested using the polarity of solvents, expressed by the log *P* value,[7] as the main criterion for optimizing organic solvents in multi-liquid-phase biocatalysis.[8] This concept has since had a widespread influence on the choice of organic solvents used as the second phase in enzymatic transformations and was assumed to be valid for cofactor-requiring enzymes.[1c,9] Attempts to use ADH under liquid–liquid biphasic conditions employing solvents with a high log *P* afforded unsatisfactory results,[10] which led to the conclusion that alcohol dehydrogenases were not stable in biphasic systems.[11]

Herein we present results guiding the choice of organic solvents suitable for use as the second phase in ADH-catalyzed reactions and their application in the reduction of poorly soluble ketones.

[*] Prof. Dr. C. Wandrey, Dipl.-Chem. M. Villela Filho, Dipl.-Chem. T. Stillger, Dr. M. Müller, Dr. A. Liese
Institut für Biotechnologie 2
Forschungszentrum Jülich GmbH
52425 Jülich (Germany)
Fax (+49) 2461-61-3870
E-mail: c.wandrey@fz-juelich.de

[**] The authors would like to express their gratitude to Dr. Werner Hummel for sharing his insights and for supplying LBADH.

Supporting information for this article is available on the WWW under http://www.angewandte.org or from the author.

 DOI: 10.1002/anie.200351089 © 2003 Wiley-VCH Verlag GmbH & Co. KGaA, Weinheim

Because there are some examples of enzymatic reactions for which no correlation between activity retention and log *P* were found,[12] we assumed that a new method of searching for a water-immiscible organic solvent for use as the second phase in ADH-catalyzed reductions should be developed. Mozhaev et al. noticed that log *P* should only be used to compare solvents of the same functionality (e.g. alcohols) and that it is not a convenient parameter for the comparison of solvents of different functionality.[13] Therefore, we decided to test the stability of three different commercially available ADH (from horse liver, HLADH, from *Thermoanaerobium brockii*, TBADH, and from *Lactobacillus brevis*, LBADH) in the presence of water-immiscible organic solvents of different functionality, regardless of their log *P*.[14] Thus, nonane was used as a representative example of unbranched alkanes, cyclohexane of cyclic alkanes, toluene of aromatic compounds, dichloromethane of halogenated solvents, *tert*-butyl methyl ether (MTBE) of ethers, and ethyl acetate of esters. Though soluble in water, *tert*-butanol was also tested as a model to study the effect of tertiary alcohols on the enzymes activity, as these alcohols cannot be accepted as substrates. The corresponding log *P* values were calculated according to the fragmentation method of Crippen (Figure 1).[15]

Samples of the enzymes were dissolved in phosphate buffer and an equal amount of an organic solvent was added.[16] The system was stirred continuously to maintain an emulsion during the whole experiment. To ensure that the observed loss of activity can be mainly attributed to the presence of the organic solvent and is not caused by thermal deactivation, the emulsion was kept at 4 °C. Samples were taken periodically and the activity was measured under standard assay conditions.[17]

For all three enzymes the measured residual activity (A_t) can be described by considering the contributions of instantaneous inhibition (I) and time-dependent deactivation ($k'_{dea}t$) [Eq. (1)].

$$A_t = A_0\, I\, e^{-k'_{dea}t} \qquad (1)$$

I was determined by comparing the enzyme activity in the water phase before and five minutes after the addition of the organic solvent. Its magnitude depends on the specific interaction between organic solvent and enzyme and no general tendency can be observed.[18] Surprisingly, an increase in activity after the addition of the solvent was observed in some cases.

The observed time-dependent deactivation of all three enzymes can be described as a first-order exponential decay of the activity.

This model allows the calculation of the apparent rate constant of deactivation (k'_{dea}) and the half-life for every combination of enzyme and solvent.[19] To evaluate the importance of the hydrophobicity of the solvent for the retention of enzyme stability in multiliquid systems, histograms showing the calculated half-life were ordered according to increasing log *P*-values (Figure 1). The enzyme stability shows no dependence on the solvent hydrophobicity.

A comparison of the three graphs reveals great similarity concerning the stability pattern of the three enzymes in the presence of organic solvents. While unsatisfactory results were obtained with aromatic, aliphatic hydrocarbons, or halogenated solvents, all three enzymes have the highest stability in the presence of MTBE. This finding is consistent with the assumption that the solvent functionality would be of greater significance for enzyme deactivation than the frequently mentioned log *P*. To test this hypothesis, the stability of the enzymes in the presence of another three short-chained ethers (diethyl ether, diisopropyl ether and di-*n*-butyl ether) was studied. In the case of diethyl ether and diisopropyl ether the stabilities observed were again higher than those in the presence of aromatic and aliphatic hydrocarbons, and halogenated solvents, thus strengthening our assumption. For di-*n*-butyl ether the results obtained were less satisfactory and comparable with those of other solvents. Thus, it was established that log *P* was not an adequate parameter to describe the trend of enzyme tolerance to organic solvents, even while comparing ethers. Rather, a trend of higher stability of the enzymes in the presence of ethers with short-chained aliphatic residues was observed.

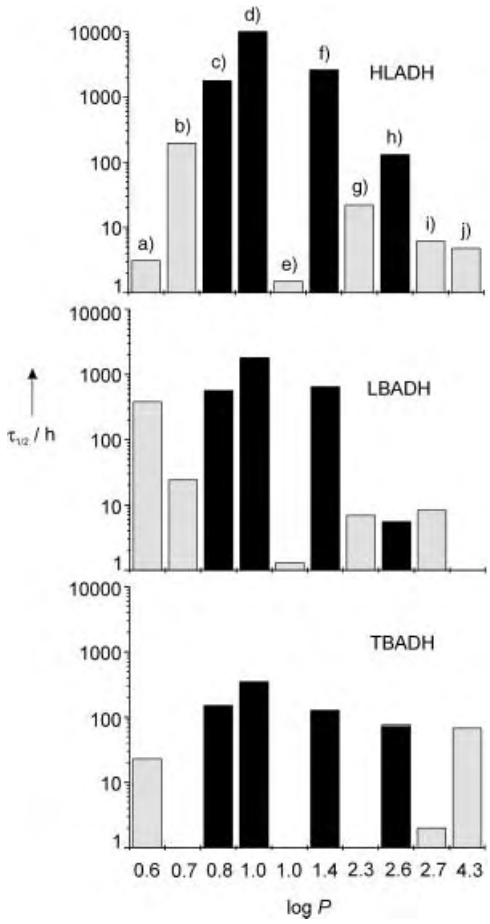


Figure 1. Logarithmic plot of the half-lives of HLADH, LBADH and TBADH at 4 °C in biphasic systems (aqueous/organic solvent 50:50, v/v): a) *tert*-butanol (log *P* = 0.6), b) ethyl acetate (log *P* = 0.7), c) diethyl ether (log *P* = 0.8), d) *tert*-butyl methyl ether (log *P* = 1.0), e) dichloromethane (log *P* = 1.0), f) di*iso*propyl ether (log *P* = 1.4), g) toluene (log *P* = 2.3), h) di-*n*-butyl ether (log *P* = 2.6), i) cyclohexane (log *P* = 2.7), j) nonane (log *P* = 4.3).

 © 2003 Wiley-VCH Verlag GmbH & Co. KGaA, Weinheim

Further studies were carried out with MTBE because of the good results obtained and the absence of peroxide formation. LBADH was arbitrarily chosen as the enzyme to be used in the biphasic biotransformation studies.

The feasibility of the biphasic biotransformation was confirmed by reducing acetophenone to (*R*)-phenylethanol. A solution containing LBADH and the reduced cofactor NADPH was mixed with a solution of 1.0 mM acetophenone in MTBE in a repetitive batch mode (Figure 2).[20] In this way,

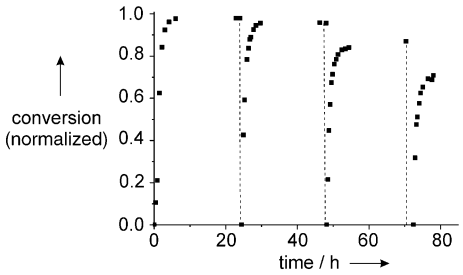
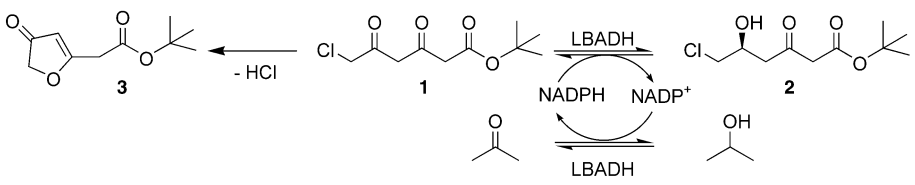


Figure 2. First four repetitive batches of the LBADH-catalyzed reduction of acetophenone in MTBE/water 50:50, v/v biphasic system at 20 °C (enzyme concentration = 0.4 U mL^{-1}).

the productivity of enzyme and cofactor was enhanced. The simple distillation of the solvent allows a facile workup. This procedure was repeated for 1400 h since the half-life of LBADH at room temperature under these conditions is 480 h. The obtained (*R*)-phenylethanol is optically pure (*ee* > 99 %, GC-analysis), thus confirming that the enantioselectivity of the enzyme is not altered by the presence of an organic phase.[21] NADPH is regenerated in situ by the addition of 2-propanol to the emulsion in a concentration of 1.5 M.[22] The acetone accumulation caused a progressive limitation of the achievable conversion.[23]

The utility of the biphasic approach was demonstrated by its application in the reduction of *tert*-butyl 6-chloro-3,5-dioxohexanoate (**1**) to *tert*-butyl (*S*)-6-chloro-5-hydroxy-3-oxohexanoate (**2**) by LBADH.[24] This reaction is of practical interest because the product is an advanced building block in the synthesis of HMG-CoA reductase inhibitors.[25] The substrate is poorly soluble and also unstable in water. Through the elimination of HCl the corresponding furanone **3** is formed (Scheme 1). In an MTBE/water biphasic system ten times the amount of **1** could be converted in one single batch than would have been possible in pure water. A 210 mM solution of **1** in the organic solvent was used, thus increasing the productivity of enzyme and cofactor. Moreover, the undesired degradation of the substrate could be discriminated; high conversion (98 %) and selectivity (70 %) were achieved. Once again, the enantioselectivity of the enzymatic reduction was not affected (*ee* > 99.5 %). For the regeneration of the cofactor 2-propanol was used as a reducing agent.[26]



Scheme 1. Enzymatic reduction of *tert*-butyl 6-chloro-3,5-dioxohexanoate with substrate-coupled cofactor regeneration and the undesired formation of furanone **3**.

In conclusion, we have shown that the log *P* concept is not satisfactory to guide the choice of an organic solvent serving as the second phase in ADH-catalyzed reactions. The biphasic enzymatic reduction of ketones is possible if short-chained aliphatic ethers are employed. This suggests that a single physicochemical parameter is incapable of satisfactorily predicting the biocompatibility of organic solvents, given the complexity of the enzyme deactivation in biphasic systems.[27] Rather a set of properties is necessary to guide the solvent choice. Based on our results, we propose that the set of properties inherent in the chemical functionality (e.g. ether) give rise to the compatibility of solvents with alcohol dehydrogenases.[28] Therefore, we recommend that instead of the hydrophobicity of the solvent (log *P*) its functionality should be considered when screening for a solvent. The identification of the same pattern of stability in the presence of solvents for benzaldehyde lyase from *Pseudomonas fluorescens* Biovar I,[29] and the report that an *S*-hydroxynitrile lyase from *Hevea brasiliensis* is stable in the presence of MTBE encourages the application of this idea for other enzymes which are active in the bulk of the aqueous phase.[30]

The tolerance of ADH towards organic solvents described herein increases the compatibility of the enantio- and regioselectivity of the enzymes with hydrophobic nonnatural substrates. Moreover, the presence of a water-immiscible solvent facilitates the use of ADH in continuous operations.

Received: February 3, 2003
Revised: April 7, 2003 [Z51089]

Keywords: asymmetric catalysis · biphasic catalysis · lyases · medium engineering · oxidoreductases

[1] a) C.-H. Wong, G. M. Whitesides, *Enzymes in synthetic organic chemistry*, Elsevier Science, New York, **1994**; b) K. Faber, *Biotransformations in organic chemistry*, Springer, Berlin, **1997**; c) M.-R. Kula, U. Kragl, in *Stereoselective Biocatalysis* (Ed.: R. N. Patel), Marcel Dekker, New York, **2000**, pp. 839–866; d) A. Liese, K. Seelbach, C. Wandrey, *Industrial Biotransformations,* Wiley-VCH, Weinheim, **2000**.

[2] a) E. Schmidt, H. U. Blaser, P. F. Fauquex, G. Sedelmeier, F. Spindler in *Microbial reagents in organic synthesis* (Ed.: S. Servi), Kluver Academic Publishers, Dordrecht, **1992**, pp. 377–388; b) B. Bachmann, D. Seebach, *Helv. Chim. Acta* **1998**, *81*, 2430–2461; c) S. Rissom, J. Beliczey, G. Giffels, U. Kragl, C. Wandrey, *Tetrahedron: Asymmetry* **1999**, *10*, 923–928; d) A. Hage, D. Petra, J. Field, D. Schipper, J. Wijnberg, P. Kamer, J. Reek, P. van Leeuwen, R. Wever, H. Schoemaker, *Tetrahedron: Asymmetry* **2001**, *12*, 1025–1034; e) S. Laue, L. Greiner, J. Wöltinger, A. Liese, *Adv. Synth. Catal.* **2001**, *343*, 711–720.

[3] W. Stampfer, B. Kosjek, C. Moitzi, W. Kroutil, K. Faber, *Angew. Chem.* **2002**, *114*, 1056–1059; *Angew. Chem. Int. Ed.* **2002**, *41*, 1014–1017.

[4] a) A. Klibanov, *Nature* **2001**, *409*, 241–246; b) A. Schmid, J. S. Dordick, B. Hauer, A. Kiener, M.

 © 2003 Wiley-VCH Verlag GmbH & Co. KGaA, Weinheim

Wubbolts, B. Witholt, *Nature* **2001**, *409*, 258 – 268; c) A. Liese, T. Zelinski, M.-R. Kula, H. Kierkels, M. Karutz, U. Kragl, C. Wandrey, *J. Mol. Catal. B* **1998**, *4*, 91 – 99.
[5] a) G. Carrea, *Trends Biotechnol.* **1984**, *2*, 102 – 106; b) N. Kizaki, Y. Yasohara, J. Hasegawa, M. Wada, M. Kataoka, S. Shimizu, *Appl. Microbiol. Biotechnol.* **2001**, *55*, 590 – 595; c) H. Gröger, W. Hummel, S. Buchholz, K. Drauz, T. V. Nguyen, C. Rollmann, H. Hüsken, K. Abokitse, *Org. Lett.* **2003**, *5*, 173 – 176.
[6] L. E. S. Brink, J. Tramper, *Biotechnol. Bioeng.* **1985**, *27*, 1258 – 1269.
[7] Logarithm of the partition coefficient of a given compound in the standard *n*-octanol/water two-phase system.
[8] C. Laane, S. Boeren, K. Vos, *Trends Biotechnol.* **1985**, *3*, 251 – 252.
[9] S. Kise, M. Hayashida, *J. Biotechnol.* **1990**, *14*, 221 – 228.
[10] Either high amounts of enzyme were needed, for example: J. R. Matos, C.-H. Wong, *J. Org. Chem.* **1986**, *51*, 2388 – 2389; or fast deactivation was detected for example: M. Wolberg, Dissertation, Universität Oldenburg, **2001**.
[11] a) J. Peters in *Biotechnology, Vol. 8a*, 2nd ed. (Eds.: H.-J. Rehm, G. Reed), Wiley-VCH, Weinheim, **1998**, pp. 391 – 474; b) S.-I. Suye, K. Kamiya, T. Kawamoto, A. Tanaka, *Biocatal. Biotransform.* **2002**, *20*, 23 – 28; c) W. Kruse, W. Hummel, U. Kragl, *Recl. Trav. Chim. Pays-Bas* **1996**, *115*, 239 – 243.
[12] M. H. Vermuë, J. Tramper, *Pure Appl. Chem.* **1995**, *67*, 345 – 373.
[13] V. Y. Mozhaev, Y. L. Khmelnitsky, M. V. Sergeeva, A. B. Belova, N. L. Klyachko, A. V. Levashov, K. Martinek, *Eur. J. Biochem.* **1989**, *184*, 597 – 602.
[14] HLADH requires NADH as cofactor, TBADH and LBADH require NADPH as cofactor. The LBADH used in this work was overexpressed in a recombinant *Escherichia coli* strain and used in the form of crude cell extract, see: B. Riebel, Dissertation, Universität Düsseldorf, **1996**.
[15] A. K. Ghose, G. M. Crippen, *J. Chem. Inf. Comput. Sci.* **1987**, *27*, 21 – 35.
[16] To minimize changes in the phase volumes, the organic solvent was previously saturated with water. The reaction mixture was shaken vigorously for one minute resulting in the saturation of the aqueous phase with the organic solvent.
[17] Protocol for the standard assays are available as Supporting Information.
[18] Neither the nature (competitive, uncompetitive or noncompetitive) nor the cause of this instantaneous inhibition was further investigated; the values are available as supporting information.
[19] Half-lives are calculated as $\tau_{1/2} = \ln 2/k'_{dea}$.
[20] After the equilibrium conversion had been reached, the organic phase containing the product was removed and replaced by a fresh solution of acetophenone in MTBE, so that conversion could take place anew.
[21] See: a) P. A. Fitzpatrick, A. M. Klibanov, *J. Am. Chem. Soc.* **1991**, *113*, 3166 – 3171; b) A. Jönsson, E. Wehtje, P. Adlercreutz, B. Mattiasson, *Biochim. Biophys. Acta* **1999**, *1430*, 313 – 322.
[22] a) W. Hummel, M.-R. Kula, *Eur. J. Biochem.* **1989**, *184*, 1 – 13; b) T. Schubert, W. Hummel, M. Müller, *Angew. Chem.* **2002**, *114*, 656 – 659; *Angew. Chem. Int. Ed.* **2002**, *41*, 634 – 637.
[23] T. Stillger, M. Bönitz, M. Villela Filho, A. Liese, *Chem. Ing. Tech.* **2002**, *74*, 1035 – 1039.
[24] a) M. Wolberg, W. Hummel, C. Wandrey, M. Müller, *Angew. Chem.* **2000**, *112*, 4476 – 4478; *Angew. Chem. Int. Ed.* **2000**, *39*, 4306 – 4308; b) M. Wolberg, W. Hummel, M. Müller, *Chem. Eur. J.* **2001**, *7*, 4562 – 4571.
[25] J. K. Thottahil, Y. Pendri, W. S. Li, D. R. Kronenthal, (Squibb& Sons, Inc.), US 5278313, **1994** [*Chem. Abstr.* **1994**, *120*, 217699r].
[26] To improve the stability of the cofactor it was necessary to increase the aqueous pH-value to 7.0 (5.5 in reference [24]), consequently enhancing the rate of the side reaction. Under this condition the total turnover number of the cofactor (defined as the amount of product per amount of cofactor) was 2500.
[27] Cf. A. Ghatorae, G. Bell, P. Halling, *Biotechnol. Bioeng.* **1994**, *13*, 331 – 336.
[28] Chemical functionality is a pragmatic label for a set of molecular properties, such as the presence of certain heteroatoms and residues, the absence of others, molecular geometry, electronic density distribution and frontier orbitals, and consequent macroscopic properties of solvents, such as surface tension, solubility, solvatation energy.
[29] See Supporting Information.
[30] M. Bauer, H. Griengl, W. Steiner, *Enzyme Microb. Technol.* **1999**, *24*, 514 – 522.

 © 2003 Wiley-VCH Verlag GmbH & Co. KGaA, Weinheim

Zn Sensitive Luminescent Sensors

Selective Detection of Zinc Ions with Novel Luminescent Lanthanide Probes**

*Kenjiro Hanaoka, Kazuya Kikuchi, Hirotatsu Kojima, Yasuteru Urano, and Tetsuo Nagano**

The zinc ion (Zn^{II}) is the second most abundant heavy metal ion, after iron, in the human body and plays important roles in various biological systems. For example, it is an essential component of many enzymes, transcription factors, and synaptic vesicles in excitatory nerve terminals.[1,2] Zinc is also an important factor in regulating synaptic transmission and cell death.[3]

So far, several Zn^{II}-selective fluorescent sensor molecules have been reported.[4] However, there are still few reports about long-lifetime fluorescent sensors for Zn^{II} ions. The fluorescence lifetimes of typical organic compounds, including common zinc-selective fluorescent sensor molecules, are in the nanosecond region. On the other hand, luminescent lanthanide complexes, in particular Tb^{III} and Eu^{III} complexes, have large Stokes shifts and long luminescence lifetimes in the

[*] Prof. Dr. T. Nagano, K. Hanaoka, Dr. K. Kikuchi,[+] Dr. H. Kojima, Dr. Y. Urano
Graduate School of Pharmaceutical Sciences
The University of Tokyo
7-3-1 Hongo, Bunkyo-ku, Tokyo 113-0033 (Japan)
Fax: (+81) 3-5841-4855
E-mail: tlong@mol.f.u-tokyo.ac.jp

[+] Additional address:
Presto, JST Corporation, Kawaguchi, Saitama (Japan)

[**] This study was supported in part by the Ministry of Education, Culture, Sports, Science and Technology, the Japanese Government (the Advanced and Innovational Research Program in Life Sciences, and grants 13024217, 13558078, 1367232 & 14045210 to K.K.), and also by Takeda Science Foundation, by Nagase Science and Technology Foundation, and by Sankyo Foundation.

Supporting information for this article is available on the WWW under http://www.angewandte.org or from the author.

 © 2003 Wiley-VCH Verlag GmbH & Co. KGaA, Weinheim DOI: 10.1002/anie.200351122

order of milliseconds.[5] These long-lived luminescent compounds have the advantage that short-lived background fluorescence and scattered light decay to negligible levels when a pulse of excitation light is applied and the emitted light is collected after an appropriate delay time.

Herein we report novel sensitive luminescent sensors for Zn^{II} ions, that is, Tb^{III} and Eu^{III} diethylenetriaminepentaacetic acid (DTPA)-bisamide complexes, [Tb$\mathbf{L_1}$] and [Eu$\mathbf{L_1}$] (Figure 1). It is known that *N*,*N*,*N*′,*N*′-tetrakis(2-pyridylmethyl)ethylenediamine (TPEN) complexes readily with Zn^{II} ions, but hardly at all with Ca^{II} and Mg^{II} ions.[6] In the characterization of the new compound [Tb$\mathbf{L_1}$], we observed that the time-resolved emission intensity of Tb^{III} ions increased upon addition of Zn^{II} ions between 0 and 1 equiv in 100 mM HEPES buffer at pH 7.4 (Figure 2). The luminescence emission showed three bands at 490 nm, 546 nm, and 587 nm arising from transitions from the $^5D_4$ excited state to the $^7F_6$, $^7F_5$ and $^7F_4$ ground manifold, respectively.[7] The emission intensity of [Eu$\mathbf{L_1}$] upon adding Zn^{II} ions changed in a similar way to that of [Tb$\mathbf{L_1}$], but with only a sixth of the intensity. The luminescence emission data also revealed very high selectivity for Zn^{II} ions compared with Ca^{II} and Mg^{II} ions. The luminescence emission enhancement in 100 mM HEPES buffer (pH 7.4) containing 5 mM Ca^{II} or Mg^{II} ions showed that these ions had no effect in the presence or absence of Zn^{II} ions (Figure 3). The complex [Tb$\mathbf{L_1}$] also showed high selectivity for Zn^{II} compared with heavy metal ions (Fe^{II}, Fe^{III}, Cu^{II}, Ni^{II}, Co^{II}, Mn^{II}) and some anions (Cl^-, carbonate, and phosphate). The luminescent intensities of [Tb$\mathbf{L_1}$] in 100 mM HEPES buffer (pH 7.4) were not increased by the addition of any of the above heavy metal ions (1 equiv to [Tb$\mathbf{L_1}$]) or other anions (100 mM Cl^-, 10 mM carbonate, and 10 mM phosphate; see Supporting Information). We also added one equivalent of Cu^{II} ions to the solution of [Tb$\mathbf{L_1}$] (100 mM HEPES buffer; pH 7.4) containing one equivalent of Zn^{II} ions. In this experiment, the luminescence emission intensity decreased to a fifth of the emission enhancement upon adding one equivalent of Zn^{II} ions only. The emission lifetime of [Tb$\mathbf{L_1}$] after the addition of 1.0 equivalent of Zn^{II} ions was measured in 100 mM HEPES buffer (pH 7.4). The emission signal showed a single exponential decay with a lifetime of 1.45 ms. The compound [Tb$\mathbf{L_1}$] showed an apparent dissociation constant for Zn^{II} of 2.6 nM (pH 7.4, 295 K). Furthermore, at the excitation wavelength of 260 nm with the emission wavelength of 545 nm, the correlation between the Zn^{II} ion concentration and the emission intensity was determined and was found to be linear in the range from 0 to 1.0×10^{-4} M. The detection limit (3σ) in 100 mM HEPES buffer (pH 7.4) by using 100 μM of [Tb$\mathbf{L_1}$] was calculated (see Supporting Information), and found to be 4.8×10^{-6} M.

We examined the absorption spectra of a solution of [Tb$\mathbf{L_1}$] in the presence of various concentrations of Zn^{II} ions (Figure 4). The absorbance between 230 and 300 nm changed linearly with an increase in the concentration of Zn^{II} ions up to a molar ratio of 1:1 Zn^{II}/[Tb$\mathbf{L_1}$], and remained at a plateau upon adding more Zn^{II} ions. The Job plot of the luminescence

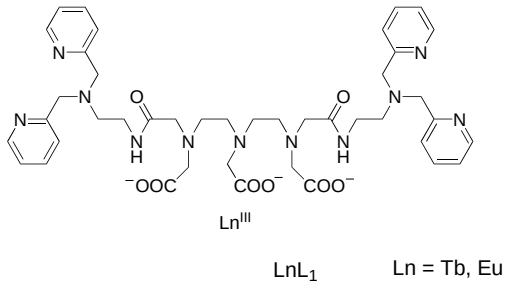


Figure 1. Structures of Tb^{III} and Eu^{III} DTPA-bisamide complexes, [Tb$\mathbf{L_1}$] and [Eu$\mathbf{L_1}$].

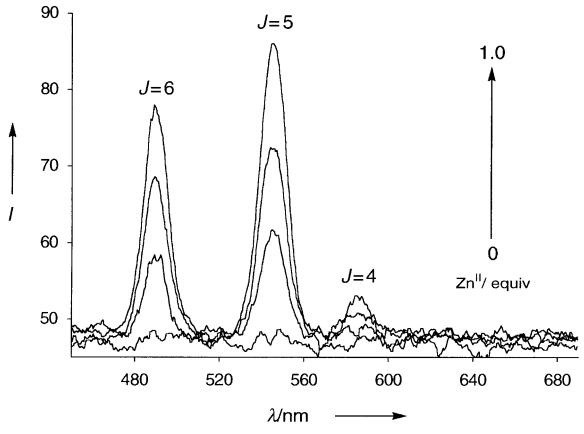


Figure 2. Emission spectra (excitation at 260 nm) of [Tb$\mathbf{L_1}$] (100 μM) in the presence of various concentrations of Zn^{II} ions: 0–1.0 equivalents Zn^{II} ions with respect to [Tb$\mathbf{L_1}$]. These spectra were measured at pH 7.4 (100 mM HEPES buffer) and 22 °C by using a delay time of 0.05 ms and a gate time of 1.00 ms. The bands arise from $^5D_4\rightarrow{}^7F_J$ transitions; the *J* values of the bands are labeled. *I* = Intensity (arbitrary units).

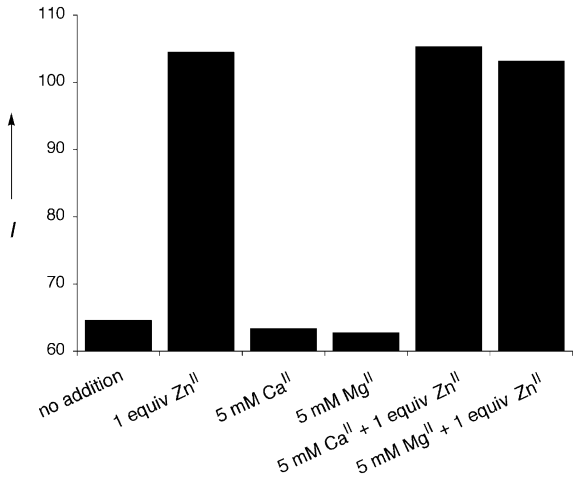


Figure 3. The luminescence intensity of [Tb$\mathbf{L_1}$] (100 μM) at 545 nm upon the addition of Zn^{II}, Ca^{II} or Mg^{II} ions (excitation at 260 nm) in 100 mM HEPES buffer (pH 7.4) at 22 °C. Cations were added as $ZnCl_2$ (1 equiv to [Tb$\mathbf{L_1}$]), $CaCl_2$ or $MgCl_2$ (5 mM). *I* = Intensity (arbitrary units).

 © 2003 Wiley-VCH Verlag GmbH & Co. KGaA, Weinheim

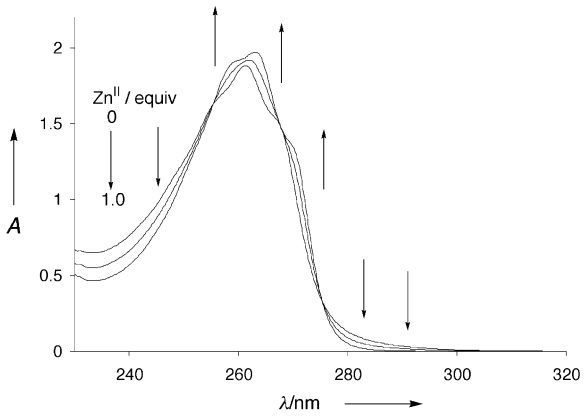


Figure 4. UV/Vis absorption spectra of [Tb**L**$_1$] (150 μM) in HEPES buffer (100 mM; pH 7.4) in the presence of various concentrations of Zn^{II} ions: 0, 0.5, 1.0 equiv On the addition of between 1.0 and 3.0 equivalents of Zn^{II} ions, the absorption spectra hardly changed. *A* = Absorbance.

emission intensity of Tb^{III} for complexation between [Tb**L**$_1$] and Zn^{II} has a maximum at a mole fraction of 0.5, thus indicative of the formation of a 1:1 complex.[8] Figure 5 shows the proposed conformational change of the structure in the presence of Zn^{II}. The light-conversion process of absorption to emission by energy transfer in [Tb**L**$_1$] is also shown (Figure 5).[9,10] The previously reported Zn^{II}-sensitive luminescent lanthanide probe operates through a PET (photoinduced electron transfer) process.[10a] We investigated the mechanism of luminescence increase of our probes by measuring the effects of D_2O and pH. We measured the luminescence emission spectra of [Tb**L**$_1$] in D_2O solution at pD 7.40 (100 mM HEPES buffer) in the presence of various concentrations of Zn^{II} ions. The emission spectra in D_2O solution changed in the same manner as those in H_2O solution. It can be considered from this result that the increase of the emission intensity upon addition of Zn^{II} does not mainly because of a change in the direct interaction of water molecules with the Tb^{III} ion.[10b,11] Further, there was no effect of H^+ ions on the emission spectra of [Tb**L**$_1$] between pH 3.0 and 10.0 in the absence of Zn^{II} ions. The $\log K_A$ values of TPEN are 7.12, 4.81, 3.30 and 2.88.[12] Therefore, it is unlikely that the increase of the emission intensity of [Tb**L**$_1$] generated by the addition of Zn^{II} ions can be ascribed to the cessation of the PET process, which occurs from the tertiary amine of the TPEN moiety to a pyridyl group. From these results, the enhancement of the emission intensity of our probes upon Zn^{II}-binding appears to be the result of efficient intramolecular energy transfer from the pyridyl group to the Tb^{III} ion. Further investigations are underway to establish the mechanism of the luminescence enhancement.

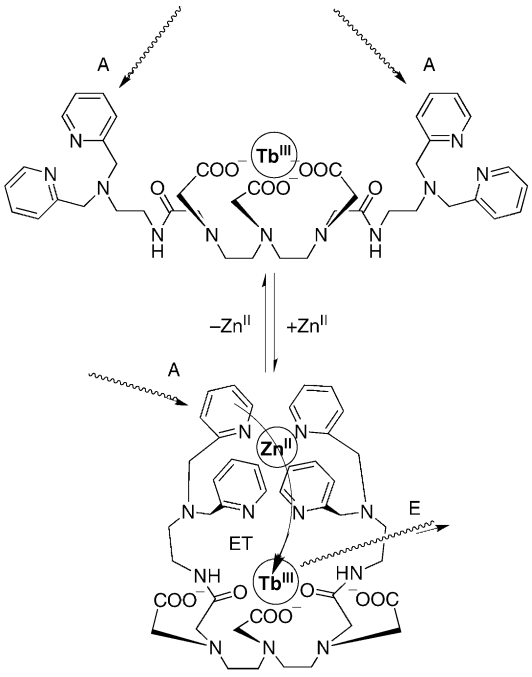


Figure 5. Schematic of [Tb**L**$_1$] representing the proposed conformational alteration of the structure in the presence and absence of Zn^{II} ions. The light-conversion process of absorption-energy transfer-emission, A-ET-E, performed by [Tb**L**$_1$], is also represented.

In summary, the novel Zn^{II}-ion-sensitive luminescent probe [Tb**L**$_1$] showed a remarkable increase in the luminescence emission of Tb^{III} ion upon the addition of Zn^{II} ions, with a long emission lifetime in the order of milliseconds. The novel probes described herein should be excellent lead complexes for the further development of highly selective, Zn^{II}-ion-sensitive luminescent chemosensors with long luminescence lifetimes and a remarkable "on-off" switching of emission.

Received: February 6, 2003
Revised: March 20, 2003 [Z51122]

Keywords: lanthanides · luminescence · terbium · time-resolved spectroscopy · zinc

[1] a) B. L. Vallee, K. H. Falchuk, *Physiol. Rev.* **1993**, *73*, 79–118; b) J. M. Berg, Y. Shi, *Science* **1996**, *271*, 1081–1085.
[2] C. J. Frederickson, *Int. Rev. Neurobiol.* **1989**, *31*, 145–238.
[3] D. W. Choi, J. Y. Koh, *Annu. Rev. Neurosci.* **1998**, *21*, 347–375.
[4] a) C. J. Frederickson, E. J. Kasarskis, D. Ringo, R. E. Frederickson, *J. Neurosci. Methods* **1987**, *20*, 91–103; b) P. D. Zalewski, I. J. Forbes, W. H. Betts, *Biochem. J.* **1993**, *296*, 403–408; c) T. Hirano, K. Kikuchi, Y. Urano, T. Higuchi, T. Nagano, *J. Am. Chem. Soc.* **2000**, *122*, 12399–12400; d) G. K. Walkup, S. C. Burdette, S. J. Lippard, R. Y. Tsien, *J. Am. Chem. Soc.* **2000**, *122*, 5644–5645; e) R. P. Haugland, *Handbook of Fluorescent Probes and Research Chemicals*, 6th ed., Molecular Probes, Eugene, OR, **1996**, pp. 531–540.
[5] a) D. Parker, J. A. G. Williams, *J. Chem. Soc. Dalton Trans.* **1996**, 3613–3628; b) M. Li, P. R. Selvin, *J. Am. Chem. Soc.* **1995**, *117*, 8132–8138.
[6] L. G. Sillén, A. E. Martell, *Stability Constants of Metal-Ion Complexes: Special Publication No. 17*, The Chemical Society, Burlington House, London, **1964**.
[7] T. Gunnlaugsson, D. A. Mac Dónail, D. Parker, *Chem. Commun.* **2000**, 93–94.
[8] T. Nabeshima, N. Tsukada, K. Nishijima, H. Ohshiro, Y. Yano, *J. Org. Chem.* **1996**, *61*, 4342–4350.
[9] D. Parker, P. K. Senanayake, J. A. G. Williams, *J. Chem. Soc. Perkin Trans. 2* **1998**, 2129–2139.

 © 2003 Wiley-VCH Verlag GmbH & Co. KGaA, Weinheim

[10] a) O. Reany, T. Gunnlaugsson, D. Parker, *Chem. Commun.* **2000**, 473 – 474; b) M. P. Lowe, D. Parker, *Chem. Commun.* **2000**, 707 – 708; c) T. Gunnlaugsson, D. Parker, *Chem. Commun.* **1998**, 511 – 512; d) D. Parker, J. A. G. Williams, *Chem. Commun.* **1998**, 245 – 246; e) D. Parker, K. Senanayake, J. A. G. Williams, *Chem. Commun.* **1997**, 1777 – 1778; f) S. Aime, A. Barge, M. Botta, J. A. K. Howard, R. Kataky, M. P. Lowe, J. M. Moloney, D. Parker, A. S. de Sousa, *Chem. Commun.* **1999**, 1047 – 1048.

[11] W. H. Li, G. Parigi, M. Fragai, C. Luchinat, T. J. Meade, *Inorg. Chem.* **2002**, *41*,4018 – 4024.

[12] A. E. Martell, R. M. Smith, NIST Critically Selected Stability Constants of Metal Complexes: NIST Standard Reference Database 46, Version 6.0, **2001**.

 © 2003 Wiley-VCH Verlag GmbH & Co. KGaA, Weinheim

Ru_6 Triangular Molecular Assembly

Solid-State Supramolecular Organization of Supermolecules into a Truly Molecular Zeolite**

Kom-Bei Shiu, Hong-Chan Lee, Gene-Hsiang Lee, Bao-Tsan Ko, Yu Wang, and Chu-Chieh Lin*

Both inorganic zeolites and organic zeolitelike solids are attracting intense interest currently because of their functional properties.[1] However, in contrast to many network porous materials with permanent porosity after partial or total removal of guests,[2] zero-dimensional (i.e. discrete) analogues are scarce in the literature.[3] The inherent difficulty in stabilizing such a material arises from the lack of structural rigidity, from its low thermal stability, and from the close-packing requirement of the molecular entities to minimize the Gibbs free energy by filling the voids in the structure.[4] Herein, we present a truly molecular zeolite with both structural rigidity and suitable thermal stability. The formation of this solid through cooperative self-assembly of unique triangular-tube organometallic supermolecules in both solution and the solid state is apparently driven positively by the close packing requirement in the molecular crystals. This material contains two types of 1D channels that are filled with solvent guests. However, the rigid nature of the solid architecture not only allows the complete removal of the molecular guests at ambient temperature without collapse of framework, but also has high thermal stability. Interestingly, the water molecules adsorbed into the microporous material also increase its thermal stability.

The treatment of $[Ru_3(CO)_{12}]$ with 4,4′-biphenyldicarboxylic acid, followed by the addition of PPh_3, produced eclipsed-$[\{Ru_2(CO)_4(PPh_3)_2\}(\mu\text{-}4,4'\text{-}O_2CC_6H_4C_6H_4CO_2)]_3$ (**1**).[5] Complex **1** is air-stable when solid and readily soluble in acetone and CH_2Cl_2, indicative of molecular aggregates in the solid state. Indeed, as determined by single-crystal X-ray crystallography at 150 K, the crystal structure of **1** consists of discrete molecules in a shape of an equilateral-triangle shaped tube (Figure 1). The single crystals, grown from CH_2Cl_2/MeOH, were found to contain many solvent guests are present (Figure 2). The six bonded phosphane ligands, which are situated on the rims of two tube openings, do not close the tube but allow guests to move in and out. The triangle edge, which has a length of 15.340(1) Å, is defined by the midpoints of the Ru–Ru bonds, whereas the depth of the tube is determined approximately by the Ru–Ru bond length (about 2.7 Å).

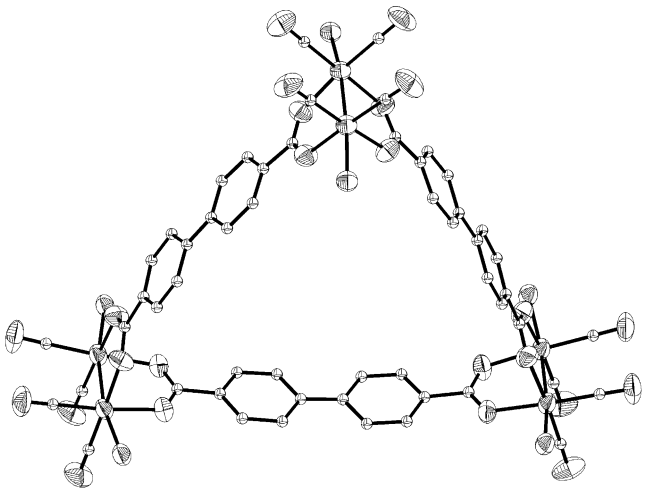


Figure 1. Triangular-tube supermolecule, **1** (ORTEP plot, thermal ellipsoids at the 50% probability level). All phenyl groups and hydrogen atoms are omitted for clarity.

Molecules of **1** were packed in a hexagonal closest packing (hcp) arrangement with alternating ABAB layers. Except for the guest molecules, each lattice contains two molecular units: one unit in the A layer is symmetrically related by a screw 6_3 axis to another in the B layer (Figure 2 and 3). A noncovalent association between the phenyl groups of the phosphane, attracted through edge-to-face π–π stacking interactions[6] can also be observed (Figure 3). Interestingly, apart from

[*] Prof. Dr. K.-B. Shiu, H.-C. Lee
Department of Chemistry
National Cheng Kung University
Tainan City 701 (Taiwan)
Fax: (+886) 6-274-0552
E-mail: kbshiu@mail.ncku.edu.tw
G.-H. Lee, Prof. Dr. Y. Wang
Instrument Center
National Taiwan University
Taipei 106 (Taiwan)
B.-T. Ko, Prof. Dr. C.-C. Lin
Instrument Center
National Chung-Hsing University
Taichung 402 (Taiwan)

[**] This work was supported by the National Science Council of the Republic of China for financial support of this research (Contract No. NSC89-2113-M006-019 and NSC90-2113-M006-021). We thank Prof. Dr. H. Teng of Chemical Engineering Department of National Cheng Kung University for measuring the BET area of the molecular zeolite.

Supporting information for this article is available on the WWW under http://www.angewandte.org or from the author.

 DOI: 10.1002/anie.200351149 © 2003 Wiley-VCH Verlag GmbH & Co. KGaA, Weinheim

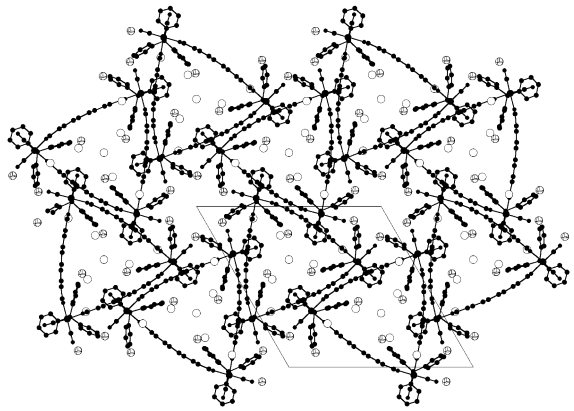


Figure 2. Packed structure of solvated **1** in the solid state along [001] with filled spheres for nonhydrogen atoms of molecule **1**, hollow spheres for CH_2Cl_2, and octant-shaded spheres for MeOH. The central hollow sphere inside the trigonal channel contains two disordered CH_2Cl_2 molecules at two different depths. All the hydrogen atoms of **1** have been omitted for clarity.

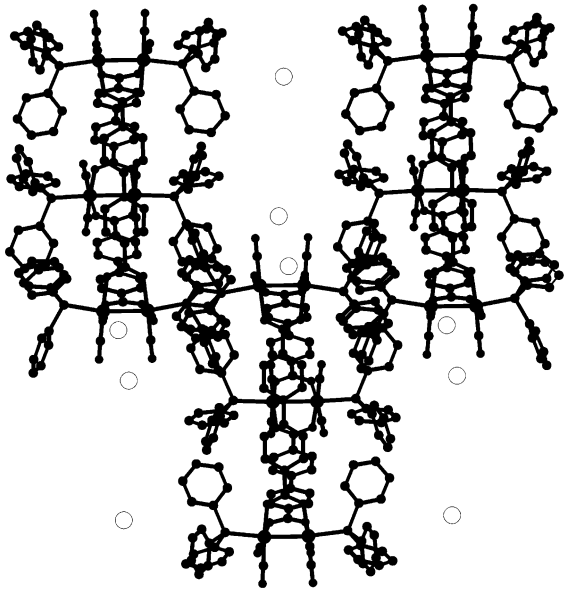


Figure 3. The clefts between two triangular-tube molecules with each cleft containing three CH_2Cl_2 molecules shown as hollow spheres.

the intrinsic 1D trigonal channels (Figure 1), the interstices in **1** also form another 1D "trigonal" channel, which has three MeOH located within, but viewed as a 1D "hexagonal" channel has six hexagonally distributed MeOH molecules in the projection plot (Figure 2). Each hexagonal opening has an edge length of about 13.12(1) Å. Two separate locations within the trigonal channel were found to accept solvent guests: five CH_2Cl_2 and three MeOH molecules are located inside the triangular tube and three CH_2Cl_2 molecules (each at an average position of two disordered sites) are in the clefts between two triangular tubes and close to the three rims of the molecular triangle (Figure 2 and 3).

After one day, all solvated crystals remain transparent when viewed with an optical microscope. However, after the crystals were exposed to air at ambient temperature for several hours, the solvent guests evaporated, while the crystals absorbed moisture from the atmosphere. A thermal gravimetric analysis (TGA) of some of these crystals showed a 0.04 % weight loss at 81.8 °C, which corresponds to the loss of 0.1 H_2O molecules per formula unit. Decomposition of the compound occurred at 203.8 °C with another weight loss of 2.46 %, which corresponds to the loss of 2.5 CO molecules per formula unit (Figure 4 a). The release of water at 81.8 °C was

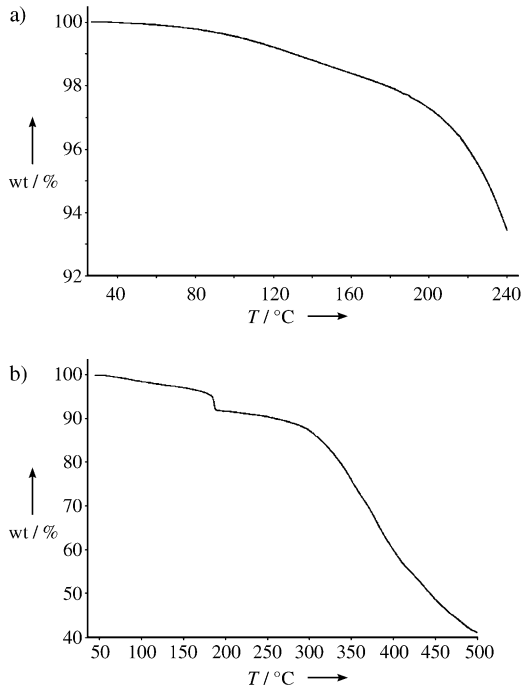


Figure 4. Thermal gravimetric analyses for a) solvated- and b) desolvated-crystals of **1**. Wt = residual weight fraction.

also confirmed by a ^1H NMR study of the product. Interestingly, TGA of some desolvated crystals, obtained after carefully pumping off the solvents, showed that the thermal decomposition occurs at a lower temperature, 181.1 °C (Figure 4 b). Hence, it is evident that the adsorbed water molecules increase the thermal stability of the molecular framework in **1**.

To understand the framework rigidity and the increased thermal stability of **1** during the drying process, the single-crystal X-ray analysis of an air-dried crystal at 293 K was carried out. Both solvated and air-dried single crystals of **1** maintain an identical space group, $P6_3/m$, but with slightly longer unit-cell lengths and a larger volume ($a = b =$ 23.8883(18), $c = 20.202(2)$ Å, and $V = 9984.0(15)$ Å^3) in the air-dried crystal relative to the solvated one ($a = b =$ 23.5248(5), $c = 20.0767(5)$ Å, and $V = 9622.2(4)$ Å^3), probably arising from thermal expansion, which is further supported by the similarity observed in most bond lengths, but not bond angles. Differential scanning calorimetry (DSC) of some typical air-dried crystals showed water desorption, but no apparent phase change up to 175 °C. The framework of **1** remains rigid through noncovalent interactions between 150 and 448 K.

 © 2003 Wiley-VCH Verlag GmbH & Co. KGaA, Weinheim

From the Fourier difference maps of the air-dried structure **1** (Figure 5), the location of the water molecules in each lattice were assigned on the basis of three residual electron peaks (between 1.1 and 1.3 e Å^{-3}).[5a] Coincidentally, the locations of six water molecules in the air-dried crystal are

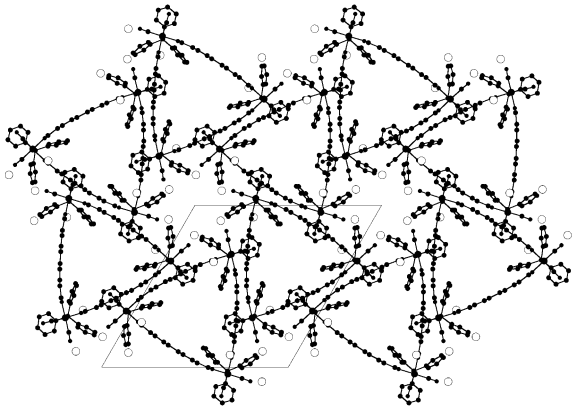


Figure 5. Packing structure of air-dried **1** in the solid state along [001]. All hydrogen atoms are omitted for clarity. Water molecules are shown as hollow spheres.

close to those of MeOH guests in the hexagonal channels of the solvated crystal, and the locations of six other water molecules are also close to those of CH_2Cl_2 guests inside the clefts (compare Figure 2 with Figure 5). It appears that the dipole–dipole attractive interactions between the polar surface of the porous adsorbent, **1**, and the water adsorbates direct site-selective adsorption. However, it is still a physisorption rather than chemisorption, as the closest distances between any water oxygen atom and any other nearby atom, hydrogen or nonhydrogen, are all longer than 3.6 Å. Apparently, the hydrophilic water molecules push the nearby hydrophobic phenyl groups of the phosphane ligands closer together through edge-to-face π–π stacking interactions,[6] thus increasing both the rigidity and thermal stability of the framework and raising the decomposition temperature from 181.1 °C for the desolvated crystals, to 203.8 °C for the air-dried crystals. The hydrophilic MeOH molecules, used as one of two crystallization solvents for **1**, may also exert similar hydrophobic–hydrophilic interactions, thus facilitating the preorganization of **1**, through intermolecular noncovalent association of phenyl groups of the phosphane ligands, into the porous material. Based on the van der Waals volumes of CH_2Cl_2 and MeOH,[7] we find that in the solvated **1**, the guest molecules—16 CH_2Cl_2 and 12 MeOH—have a volume of 1.354 Å^3, which is 14 % of the unit cell volume. A sorption experiment with an adsorbate, N_2, and **1** as the adsorbent at 77.35 K was also carried out. An apparent BET surface area of 16.12 m^2 g^{-1} with a corresponding pore volume of 0.049 cm^3 cm^{-3} was obtained.

The results presented herein reveal that a truly molecular zeolite with suitable thermal stability and structural rigidity can be readily synthesized by using tetracarbonyl- and diphosphane-ligated diruthenium as building blocks and dicarboxylates as links. Future investigations will focus on the synthesis and characterization of similar porous materials with larger pores, elongated triangular tubes, and/or chiral channels by using suitable dicarboxylate links.

Received: February 10, 2003
Revised: April 28, 2003 [Z51149]

Keywords: microporous materials · noncovalent interactions · self-assembly · supramolecular chemistry · zeolite analogues

[1] I. W. C. E. Arends, R. A. Sheldon, M. Wallau, U. Schuchardt, *Angew. Chem.* **1997**, *109*, 1190; *Angew. Chem. Int. Ed. Engl.* **1997**, *36*, 1144, and references therein.

[2] a) H. Li, M. Eddaoudi, T. L. Groy, O. M. Yaghi, *J. Am. Chem. Soc.* **1998**, *120*, 8571; b) H. Li, M. Eddaoudi, M. O'Keeffe, O. M. Yaghi, *Nature* **1999**, *402*, 276; c) S. S. Y. Chui, S. M. F. Lo, J. P. H. Charmant, A. G. Orpen, I. D. Williams, *Science* **1999**, *283*, 1148; d) C. J. Kepert, M. J. Rosseinsky, *Chem. Commun.* **1999**, 375–376; e) K. Biradha, Y. Hongo, M. Fujita, *Angew. Chem.* **2000**, *112*, 4001–4003; *Angew. Chem. Int. Ed.* **2000**, *39*, 3843–3845; f) M. Eddaoudi, H. Li, O. M. Yaghi, *J. Am. Chem. Soc.* **2000**, *122*, 1391; g) B. Chen, M. Eddaoudi, T. M. Reineke, J. W. Kampf, M. O'Keeffe, O. M. Yaghi, *J. Am. Chem. Soc.* **2000**, *122*, 11559–11560; h) M. Kondon, M. Shimamura, S. Noro, S. Minakoshi, A. Asami, K. Seki, S. Kitagawa, *Chem. Mater.* **2000**, *12*, 1288; i) K. Seki, *Chem. Commun.* **2001**, 1496; j) G. Papaefstathiou, L. R. MacGillivray, *Angew. Chem.* **2002**, *114*, 2174–2177; *Angew. Chem. Int. Ed.* **2002**, *41*, 2070–2073.

[3] G. A. Mines, B.-C. Tzeng, K. J. Stevenson, J. Li, J. T. Hupp, *Angew. Chem.* **2002**, *114*, 162–165; *Angew. Chem. Int. Ed.* **2002**, *41*, 154–157.

[4] a) A. I. Kitaigorodsky, *Molecular Crystals and Molecules*, Academic Press, New York, **1973**; b) A. Gavezzotti, *Acc. Chem. Res.* **1994**, *27*, 309; c) M. U. Schmidt, U. Englert, *J. Chem. Soc. Dalton Trans.* **1996**, 2077.

[5] a) See Supporting Information for details of synthesis and characterization, crystal data for solvated and air-dried structures of **1**, and the assignment for the adsorbed water locations in air-dried **1**. b) CCDC-192219 (solvated **1**) and 192221 (air-dried **1**) contain the supplementary crystallographic data for this paper. These data can be obtained free of charge via www.ccdc.cam.ac.uk/conts/retrieving.html (or from the Cambridge Crystallographic Data Centre, 12 Union Road, Cambridge CB2 1EZ, UK; fax: (+44) 1223-336-033; or deposit@ccdc.cam.ac.uk).

[6] J. W. Steed, J. L. Atwood, *Supramolecular Chemistry*, Wiley, New York, **2000**, p. 26.

[7] Y. Marcus, *The Properties of Solvents*, Wiley, New York, **1998**.

 © 2003 Wiley-VCH Verlag GmbH & Co. KGaA, Weinheim

Organozinc Additions: A DFT Study

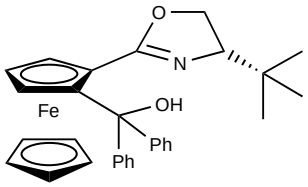
Phenyl versus Ethyl Transfer in the Addition of Organozinc Reagents to Aldehydes: A Theoretical Study**

*Jens Rudolph, Torben Rasmussen, Carsten Bolm, and Per-Ola Norrby**

The discovery of the amino-alcohol-catalyzed enantioselective alkyl transfer to aldehydes by Oguni and Omi in 1984 initiated the ever-growing interest in the development of new and highly selective chiral ligands for the asymmetric synthesis of secondary and tertiary alcohols.[1] In line with the initial use of (*S*)-leucinol, most new ligands are based on β-amino alcohols or their derivatives.[2] Significant developments in the addition of organozinc compounds to aldehydes have led to tremendous progress in terms of the variety of ligand structures and available transferable moieties. Among the latter, enantioselective aryl transfer to aromatic aldehydes is interesting in that it gives access to chiral diarylmethanols, important precursors for pharmacologically and biologically active compounds.[3] In the organozinc route to diarylmethanols, enantioselectivity is achieved by differentiation between an aryl group and a hydrogen atom, whereas alternative routes, such as asymmetric reduction of diarylketones, rely on differentiation between two similar aryl groups, a task which can be successful in isolated instances[4] but cannot easily be generalized. Initially, the organozinc route relied on the use of pure diphenylzinc or mixed phenylzinc reagents prepared in situ,[2,5–7] but has recently been extended to a general method for asymmetric aryl transfer utilizing aryl boronic acids.[8]

Several features distinguish the reactivity of diarylzinc reagents from the related dialkylzinc compounds. First, the background reaction rate is substantially higher: Ph_2Zn adds to aldehydes at room temperature even in the absence of ligand. However, the reaction is still ligand-accelerated,[9] and a substantially faster reaction and moderate-to-good enantioselectivity are obtained in the presence of a chiral ligand.[6]

A remarkable result is obtained by using a mixture of Et_2Zn and Ph_2Zn as phenyl source. The reaction is slightly slower than with Ph_2Zn alone,[10] but shows substantially higher enantioselectivity (up to 98% *ee* with ligand **1**) for a wide variety of aldehydes, and is completely selective for Ph transfer.[6] Under optimized conditions[6b–e,10] (1.3 equiv Et_2Zn and 0.65 equiv Ph_2Zn), the Et/Ph ratio at full conversion is approximately eight, and still no ethyl transfer is observed; that is, phenyl transfer is orders of magnitude faster. This interesting result promted us to undertake a theoretical study to probe the underlying causes for the difference in reactivity.



1

The mechanism for the addition of Et_2Zn to aldehydes has been the subject of intense research.[11] Noyori et al. proposed a convincing mechanism based on a combination of experimental and theoretical investigations.[12,13] Several groups have extended and validated the computational model for a large range of systems.[14,15] A concensus on the source of selectivity is depicted in Figure 1. Generally, the major

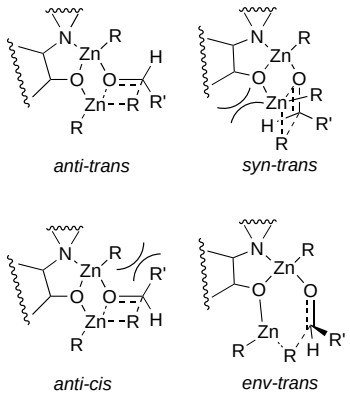


Figure 1. Proposed transition states for the addition of R_2Zn to aldehydes.

enantiomer is produced from the *anti-trans* path, in which the aldehyde coordinates to the catalytic Zn center through the *trans* lone pair, and the R group *anti* to the ligand is transferring. The minor enantiomer can arise from several sources: The *inv* path (not shown), in which imperfect blocking by the ligand allows coordination to the opposite face of the catalytic Zn center; the *anti-cis* path, in which the aldehyde has inverted and coordinates with the *cis* lone pair; the *syn-trans* path, in which the *syn* R group is transferring; and the *env-trans* path, in which the *syn-trans* transition state

[*] Prof. Dr. P.-O. Norrby
Department of Chemistry
Technical University of Denmark
Building 201, Kemitorvet, 2800 Kgs. Lyngby (Denmark)
Fax: (+45) 45933968
E-mail: pon@kemi.dtu.dk

Dipl.-Chem. J. Rudolph, Prof. Dr. C. Bolm
Institut für Organische Chemie der RWTH Aachen
Professor Pirlet Str. 1, 52074 Aachen (Germany)

Dr. T. Rasmussen
Department of Theoretical Chemistry, Lund University
Chemical Center, P.O. Box 124, 22100 Lund (Sweden)

[**] Support from the Danish Natural Sciences Research Council and the Carlsberg Foundation is gratefully acknowledged. C.B. and J.R. are grateful to the Fonds der Chemischen Industrie and to the Deutsche Forschungsgemeinschaft (DFG) within the Collaborative Research Center (SFB) 380 and the Graduiertenkolleg 440 for financial support.

Supporting information for this article is available on the WWW under http://www.angewandte.org or from the author.

 © 2003 Wiley-VCH Verlag GmbH & Co. KGaA, Weinheim DOI: 10.1002/anie.200351150

(TS) opens to give a six-membered cyclic TS in an envelope conformation.[15] For unhindered aliphatic aldehydes, the *anti-cis* path is generally only slightly disfavored, and it leads to low selectivity, whereas aromatic aldehydes experience a severe steric clash due to the strong conjugation in the TS.[13b,15b] When a ligand capable of blocking one face of the catalytic Zn center is used in combination with a conjugated aldehyde, the minor enantiomer usually arises from the *syn-trans* path, which is inherently disfavored by about 10–15 kJ mol^{-1} for alkyl transfer.[13,15]

Here we present a DFT investigation of reaction paths for Ph_2Zn in the presence and absence of Et_2Zn, and addressing the reactivity pattern and plausible causes for selectivity in phenyl transfer.

All calculations were performed at the B3LYP/LACVP* level (Hay–Wadt double-ζ valence + ECP for Zn,[16] 6-31G* for other atoms) in Jaguar 4.2 from Schrödinger Inc.[17] Stationary points were verified by analytical normal-mode analysis. The model system employed here is based on our previous study:[15a] a β-dimethylaminoethanol ligand, acetaldehyde (R′ = Me), and alkyl substituents R (Figure 2). For

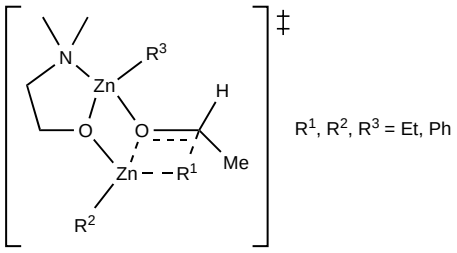
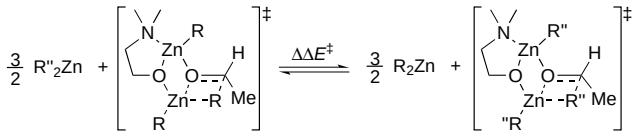


Figure 2. Computational model system, exemplified by an *anti-trans* transition state.

the last-named, we tested all eight combinations of Et and Ph in the *anti-trans* TS. For the all-Ph combination we also located the *syn-trans*, *anti-cis*, and *env-trans* TSs depicted in Figure 1. All calculated structures are available as Supporting Information. Relative activation energies calculated from the isodesmic comparison depicted in Scheme 1 are given in Table 1.



Scheme 1. Example of an isodesmic equilibrium for calculating relative activation energies.

The data in Table 1 clearly show the higher reactivity for Ph compared to Et transfer. The best TS for Et transfer (entry 4) is 40 kJ mol^{-1} higher in energy than the best TS for Ph transfer (entry 8). The difference can be understood from a detailed analysis of the TS structures. For both moieties, the TS geometry is reminiscent of the free anion, with the filled lobe pointing between the Zn atom and the carbonyl C atom (Figure 3); the TS is the point of minimum overlap of the

Table 1: Calculated relative activation energies $\Delta\Delta E^{\neq}$ [kJ mol^{-1}] (Scheme 1), with R^1–R^3 as defined in Figure 2.

Entry	$R^1R^2R^3$	TS type	$\Delta\Delta E^{\neq}$ [kJ mol^{-1}]
1	EtEtEt	*anti-trans*	50
2	EtEtPh	*anti-trans*	41
3	EtPhEt	*anti-trans*	47
4	EtPhPh	*anti-trans*	40
5	PhEtEt	*anti-trans*	18
6	PhEtPh	*anti-trans*	10
7	PhPhEt	*anti-trans*	9
8	PhPhPh	*anti-trans*	0
9	PhPhPh	*syn-trans*	27
10	PhPhPh	*env-trans*	19
11	PhPhPh	*anti-cis*	2

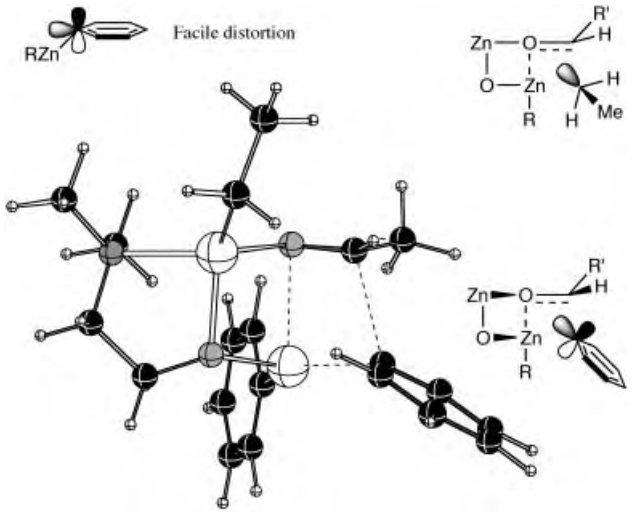


Figure 3. Comparison of Et and Ph transfer, and the transition state for entry 7, Table 1.

anion with an electron acceptor. However, for the Ph moiety the filled aromatic π orbital (illustrated by a p orbital in Figure 3) is overlapping with the electron-poor Zn and C atoms, and this provides additional stabilization. Calculations on simple organozinc reagents show that the overlap with the π system of the phenyl group is also possible in the reagent itself, as seen in the crystal structure of the Ph_2Zn dimer.[18] The phenyl group easily bends to expose the anionic lobe (Figure 3), whereas the corresponding distortion for the ethyl moiety is a high-energy process. Thus, even in the presence of a 10- or even 100-fold excess of ethyl reagent, clean phenyl transfer would be expected. This is in good agreement with the observations of Bolm et al.[6b–e,10]

The transition states are formed from combination of R_2Zn with the aldehyde and the actual catalyst, an RZn–ligand complex.[13] The availability of the combinations of R groups required for the paths in Table 1 was investigated by calculating the equilibrium $Ph_2Zn + Et_2Zn \rightleftarrows 2\,PhEtZn$, which was found to be virtually thermoneutral ($\Delta E = 0.2$ kJ mol^{-1}). Thus, all three R_2Zn complexes will be present in the reaction mixture, in agreement with the observation by NMR spectroscopy of formation of an additional Ph–Zn moiety on addition

 © 2003 Wiley-VCH Verlag GmbH & Co. KGaA, Weinheim

of Et_2Zn to Ph_2Zn.[10] Fast exchange of R groups is expected from the crystal structure of the Ph_2Zn dimer,[18] so that R_2Zn can be assumed to be present as a statistical mixture (Curtin–Hammett conditions).[19]

Looking more closely at the possible paths for the reagent mixture reveals that the highest reactivity is obtained with the pure phenyl system, in perfect agreement with the observation of higher reactivity in the absence of Et_2Zn.[6b–e,10] Replacing one spectator phenyl with an ethyl group increases the activation energy by 9–10 kJ mol^{-1} (Table 1, entries 6 and 7). The effect is additive; replacing both spectator groups causes an increase in activation energy of 18 kJ mol^{-1} (Table 1, entry 5). The more electronegative phenyl group increases the Lewis acidity of Zn, and thus increases the reactivity of the coordinated aldehyde. As a consistent trend, replacing an ethyl with a phenyl group causes a slight increase in the Mulliken charge at the directly bonded Zn atom. Furthermore, the bystander phenyl group can also stabilize the hypovalent, three-coordinate Zn atom in the product by π bonding. By coincidence, the magnitudes of these effects add to give similar numerical values for both bystander groups.

From earlier studies on ethyl transfer at the same level of theory as the current study,[15a] we know that the *anti-cis* TS is only slightly higher in energy than the *anti-trans* TS, and hence low selectivities result for unencumbered aliphatic aldehydes unless the ligand has a geometry that specifically disfavors the *anti-cis* pathway.[15b] For conjugated aldehydes, the *anti-cis* path is selectively disfavored by a steric clash with the bystander alkyl group on the catalytic Zn center, and can generally be ignored.[15b] Thus, for aromatic aldehydes, the minor enantiomer is mostly produced by the *syn-trans* and possibly the *env-trans* pathway. Interestingly, these two paths (especially *syn-trans*) are highly disfavored for Ph transfer (Table 1, entries 9 and 10). The *syn-trans* path is 27 kJ mol^{-1} higher in energy than the *anti-trans* path in the all-Ph case, as opposed to a difference of about 15 kJ mol^{-1} for alkyl transfer.[15a] On the other hand, it is not a priori certain that the *anti-cis* path is also prohibited for aryl transfer to aromatic aldehydes; phenyl–phenyl interactions can stabilize transition states if the geometry is suitable.[20] A full computational analysis of the selectivity should include both the aromatic aldehyde and ligand **1** in the calculation. However, such an analysis at the DFT level is still beyond our computational resources. We plan to address the selectivity issue further by Q2MM[20,21] or QM/MM[14c–e] calculations.

With regard to the selectivity, we know from experimental studies that for most aldehydes, the *ee* values obtained with only Ph_2Zn and ligand **1** is lower than when the Ph_2Zn/Et_2Zn mixture is employed. There can be two reasons for such a difference: either addition of Et_2Zn opens up a new, faster, and more selective path, or it suppresses the nonselective path by depleting the concentration of the required components. Both experiment and theory indicate that the latter explanation is operative here. The activation barriers are not lowered by the introduction of ethyl groups (Table 1), and the observed reaction rate does not increase.[10] Furthermore, the computational results for the reagent pre-equilibrium, as well as tentative NMR spectroscopic assignment of the same equilibrium in THF,[10] indicates that Ph_2Zn (required for the all-Ph path, Table 1, entry 8, and also for the background reaction) is still present in the reaction mixture after addition of a twofold excess of Et_2Zn. This leaves us with the last component of the reaction, the catalyst formed from deprotonated ligand **1** and RZn. The size of the ligand has so far precluded a DFT investigation, but it is reasonable to assume that the bulk of the system would disfavor the phenyl group. If most of the catalyst is present as EtZn·**1**, only paths with R^3 = Et would contribute to product formation. This could also rationalize the higher selectivity in the presence of Et_2Zn. For phenyl transfer, we expect most of the minor enantiomer to arise from the *anti-cis* path (Table 1, entries 9–11), and we know from previous studies that R^3 = Et selectively disfavors this path for aromatic aldehydes,[15b] whereas preliminary calculations indicate that the phenyl–phenyl interaction in systems with R^3 = Ph is less repulsive. Thus, a depletion of the concentration of PhZn·**1** in favor of EtZn·**1** upon addition of Et_2Zn rationalizes the experimental observations, and also clarifies why ligand **1** in combination with the Ph_2Zn/Et_2Zn mixture generally gives high *ee* values, whereas other ligand systems for phenyl transfer seem to be very dependent on the exact reaction conditions.

Received: February 10, 2003 [Z51150]

Keywords: alkylation · density functional calculations · transition states · zinc

[1] N. Oguni, T. Omi, *Tetrahedron Lett.* **1984**, *25*, 2823–2824.
[2] Reviews: a) K. Soai, S. Niwa, *Chem. Rev.* **1992**, *92*, 833–856; b) L. Pu, H.-B. Yu, *Chem. Rev.* **2001**, *101*, 757–824.
[3] a) K. Meguro, M. Aizawa, T. Sohda, Y. Kawamatsu, A. Nagaoka, *Chem. Pharm. Bull.* **1985**, *33*, 3787–3797; b) F. Toda, K. Tanaka, K. Koshiro, *Tetrahedron: Asymmetry* **1991**, *2*, 873–874; c) S. Stanchev, R. Rakovska, N. Berova, G. Snatzke, *Tetrahedron: Asymmetry* **1995**, *6*, 183–198; d) M. Botta, V. Summa, F. Corelli, G. Di Pietro, P. Lombardi, *Tetrahedron: Asymmetry* **1996**, *7*, 1263–1266.
[4] a) E. J. Corey, R. K. Bakshi, S. J. Shibata, *J. Am. Chem. Soc.* **1987**, *109*, 5551–5553; b) E. J. Corey, R. K. Bakshi, S. J. Shibata, C.-P. Chen, V. K. Singh, *J. Am. Chem. Soc.* **1987**, *109*, 7925–7926; c) E. J. Corey, S. J. Shibata, R. K. Bakshi, *J. Org. Chem.* **1988**, *53*, 2861–2863; d) E. J. Corey, J. O. Link, R. K. Bakshi, *Tetrahedron Lett.* **1992**, *33*, 7107–7110; e) T. Ohkuma, M. Koizumi, H. Ikehira, T. Yokozawa, R. Noyori, *Org. Lett.* **2000**, *2*, 659–662. For reviews, see f) E. J. Corey, C. J. Helal, *Angew. Chem.* **1998**, *110*, 2092–2118; *Angew. Chem. Int. Ed.* **1998**, *37*, 1986–2012; g) R. Noyori, T. Ohkuma, *Angew. Chem.* **2001**, *113*, 40–75; *Angew. Chem. Int. Ed.* **2001**, *40*, 40–73.
[5] a) P. I. Dosa, J. C. Ruble, G. C. Fu, *J. Org. Chem.* **1997**, *62*, 444–445; b) W.-S. Huang, Q.-S. Hu, L. Pu, *J. Org. Chem.* **1999**, *64*, 7940–7956; c) W.-S. Huang, L. Pu, *Tetrahedron Lett.* **2000**, *41*, 145–149.
[6] a) C. Bolm, K. Muñiz, *Chem. Commun.* **1999**, 1295–1296; b) C. Bolm, N. Hermanns, J. P. Hildebrand, K. Muñiz, *Angew. Chem.* **2000**, *112*, 3607–3609; *Angew. Chem. Int. Ed.* **2000**, *39*, 3465–3467; c) C. Bolm, M. Kesselgruber, N. Hermanns, J. P. Hildebrand, *Angew. Chem.* **2001**, *113*, 1536–1538; *Angew. Chem. Int. Ed.* **2001**, *40*, 1488–1490; d) C. Bolm, M. Kesselgruber, A. Grenz, N. Hermanns, J. P. Hildebrand, *New J. Chem.* **2001**, *25*, 13–15; e) C. Bolm, N. Hermanns, M. Kesselgruber, J. P.

 © 2003 Wiley-VCH Verlag GmbH & Co. KGaA, Weinheim

Hildebrand, *J. Organomet. Chem.* **2001**, *624*, 157 – 161; f) For a recent review on catalyzed asymmetric arylation reactions, see C. Bolm, J. P. Hildebrand, K. Muñiz, N. Hermanns, *Angew. Chem.* **2001**, *113*, 3382 – 3407; *Angew. Chem. Int. Ed.* **2001**, *40*, 3284 – 3308.

[7] a) G. Zhao, X.-G. Li, X.-R. Wang, *Tetrahedron: Asymmetry* **2001**, *12*, 399 – 403; b) D.-H. Ko, K. H. Kim, D.-C. Ha, *Org. Lett.* **2002**, *4*, 3759 – 3762.

[8] C. Bolm, J. Rudolph, *J. Am. Chem. Soc.* **2002**, *124*, 14850 – 14851.

[9] D. J. Berrisford, C. Bolm, K. B. Sharpless, *Angew. Chem.* **1995**, *107*, 1159 – 1171; *Angew. Chem. Int. Ed. Engl.* **1995**, *34*, 1050 – 1064.

[10] C. Bolm, N. Hermanns, M. Kesselgruber, K. Wenz, J. Rudolph, K. Muñiz, J. P. Hildebrand, unpublished results.

[11] a) M. Kitamura, S. Suga, K. Kawai, R. Noyori, *J. Am. Chem. Soc.* **1986**, *108*, 6071 – 6072; b) S. Itsuno, J. M. J. Fréchet, *J. Org. Chem.* **1987**, *52*, 4140 – 4142; c) A. A. Smaardijk, H. Wynberg, *J. Org. Chem.* **1987**, *52*, 135 – 137; d) D. A. Evans, *Science* **1988**, *240*, 420 – 426; e) E. J. Corey, P.-W. Yuen, F. J. Hannon, D. A. Wierda, *J. Org. Chem.* **1990**, *55*, 784 – 786; f) R. Noyori, M. Kitamura, *Angew. Chem.* **1991**, *103*, 34 – 55; *Angew. Chem. Int. Ed. Engl.* **1991**, *30*, 49 – 69; g) R. Noyori, *Asymmetric Catalysis in Organic Synthesis*, Wiley, New York, **1994**; h) H. Steinhagen, G. Helmchen, *Angew. Chem.* **1996**, *108*, 2489 – 2492; *Angew. Chem. Int. Ed. Engl.* **1996**, *35*, 2339 – 2342.

[12] a) M. Kitamura, S. Okada, S. Suga, R. Noyori, *J. Am. Chem. Soc.* **1989**, *111*, 4028 – 4038; b) M. Kitamura, S. Suga, M. Niwa, R. Noyori, *J. Am. Chem. Soc.* **1995**, *117*, 4832 – 4842; c) M. Kitamura, S. Suga, H. Oka, R. Noyori, *J. Am. Chem. Soc.* **1998**, *120*, 9800 – 9809; d) M. Kitamura, H. Oka, R. Noyori, *Tetrahedron* **1999**, *55*, 3605 – 3614.

[13] a) M. Yamakawa, R. Noyori, *J. Am. Chem. Soc.* **1995**, *117*, 6327 – 6335; b) M. Yamakawa, R. Noyori, *Organometallics* **1999**, *18*, 128 – 133.

[14] a) A. Vidal-Ferran, A. Moyano, M. A. Pericàs, A. Riera, *Tetrahedron Lett.* **1997**, *38*, 8773 – 8776; b) B. Goldfuss, K. N. Houk, *J. Org. Chem.* **1998**, *63*, 8998 – 9006; c) B. Goldfuss, M. Steigelmann, S. I. Khan, K. N. Houk, *J. Org. Chem.* **2000**, *65*, 77 – 82; d) J. Vázquez, M. A. Pericàs, F. Maseras, A. Lledós, *J. Org. Chem.* **2000**, *65*, 7303 – 7309; e) B. Goldfuss, M. Steigelmann, F. Rominger, *Eur. J. Org. Chem.* **2000**, 1785 – 1792; f) T. J. Davis, J. Balsells, P. J. Carroll, P. J. Walsh, *Org. Lett.* **2001**, *3*, 699 – 702.

[15] a) T. Rasmussen, P.-O. Norrby, *J. Am. Chem. Soc.* **2001**, *123*, 2464 – 2465; b) T. Rasmussen, P.-O. Norrby, *J. Am. Chem. Soc.* **2003**, 125, 5130 – 5138.

[16] P. J. Hay, W. R. Wadt, *J. Chem. Phys.* **1985**, *82*, 270 – 283.

[17] http://www.schrodinger.com

[18] P. R. Markies, G. Schat, O. S. Akkerman, F. Bickelhaupt, *Organometallics* **1990**, *9*, 2243 – 2247.

[19] H. Maskill, *The Physical Basis of Organic Compounds*; Oxford University Press, Oxford, **1985**, pp. 293 – 295.

[20] P.-O. Norrby, T. Rasmussen, J. Haller, T. Strassner, K. N. Houk, *J. Am. Chem. Soc.* **1999**, *121*, 10186 – 10192.

[21] P.-O. Norrby, *J. Mol. Struct. (THEOCHEM.)*. **2000**, *506*, 9 – 16.

 © 2003 Wiley-VCH Verlag GmbH & Co. KGaA, Weinheim

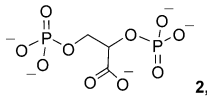
Receptor for Biological Biphosphate

Controlling the Oxygenation Level of Hemoglobin by Using a Synthetic Receptor for 2,3-Bisphosphoglycerate**

*Zhenlin Zhong and Eric V. Anslyn**

2,3-Bisphosphoglycerate (2,3-BPG) is an allosteric effector that modulates the oxygenation level of hemoglobin. It is present in human and most other mammalian erythrocytes, normally in an approximately equimolar concentration to that of hemoglobins. It is a glycolytic intermediate resulting from the interconversion between 1,3-phosphoglycerate and 3-phosphoglycerate catalyzed by phosphoglycerate mutase.[1] As an allosteric effector, 2,3-BPG regulates the oxygen binding and releasing ability of hemoglobin[2] by binding to a central cavity created by the spatial arrangement of the four heme proteins. Specifically, the docking of 2,3-BPG to this cavity decreases the oxygen affinity of hemoglobin, because 2,3-BPG preferentially binds to deoxyhemoglobin.[3,4]

Various inherited diseases lead to abnormal concentrations of 2,3-BPG and altered levels of oxygen transport.[5] Increased levels of 2,3-BPG are present in patients suffering from hypoxemia and anemia, because this facilitates the oxygen release of oxyhemoglobin into tissue.[6] In contrast, high 2,3-BPG levels in individuals with sickle cell anemia are harmful, because 2,3-BPG favors sickling by facilitating the polymerization of sickle hemoglobin.[7–9] Controlling the physiological concentration of 2,3-BPG could yield a treatment for these diseases. Our goal was to create a receptor[10] that would have a sufficiently high affinity and selectivity for 2,3-BPG to effectively modulate its concentration in physiological media, and thereby control hemoglobin oxygenation.



2,3-BPG

Herein, we describe a rationally designed synthetic receptor (**1**) that has a highly preorganized cavity composed of a Cu^{II} center and four guanidinium groups that serve as binding sites. The receptor displays high affinity and good selectivity for 2,3-BPG. We further show that this receptor will strip the 2,3-BPG from horse hemolyzate, and therefore modulate the oxygenation level of the horse hemoglobin. The

[*] Prof. Dr. E. V. Anslyn, Dr. Z. Zhong
Department of Chemistry and Biochemistry
The University of Texas at Austin
Austin, TX 78712 (USA)
Fax: (+1) 512-471-7791
E-mail: anslyn@ccwf.cc.utexas.edu

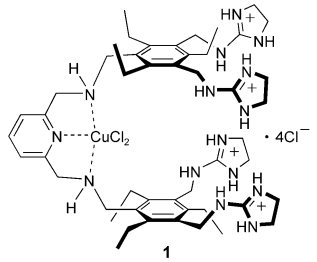
[**] This work was in part funded by the National Institutes of Health (GM57306), an ARO-MURI grant, and the Welch Foundation.

Supporting information for this article is available on the WWW under http://www.angewandte.org or from the author.

 DOI: 10.1002/anie.200351165 © 2003 Wiley-VCH Verlag GmbH & Co. KGaA, Weinheim

strategy of sequestering a biological effector with a small synthetic compound is an intriguing approach to controlling physiological function, and represents an alternative to the standard approach of creating small molecules that bind to biological macromolecules, thereby modulating their activity.

2,3-BPG is a highly anionic molecule that is strongly hydrated in water. Hence, several molecular-recognition contacts are required in a receptor to successfully compete with the solvation of this target. Nature competes with solvation by forming several salt bridges between 2,3-BPG and the cationic side chains of lysine and histidine in deoxyhemoglobin.[4] Based upon this precedent, receptor **1** was designed. This receptor contains guanidinium groups rather than ammonium and imidazolium groups as with the natural receptor, because molecular recognition entities of guanidiniums are well known to bind phosphates in both biological and synthetic receptors.[11,12] Furthermore, receptor **1** has a single Cu^{II} binding site, designed to complex the carboxylate or phosphate group of 2,3-BPG. The molecular recognition entities converge creating a clam-shell-shaped cavity. The clam shell is organized upon metal binding. Lastly, the hexa substitution of the two benzene rings in **1** imparts a thermodynamic preference for adjacent groups to be in an up and down pattern,[13] thereby imparting convergence of the guanidinium groups prior to binding 2,3-BPG.



1

Molecular modeling[14] shows that **1** has a cavity complementary in size, shape, and charge to 2,3-BPG (Figure 1). The guest slips in between the clam shells, and fits tightly with a large number of binding interactions. The modeling reveals eight hydrogen bonds and five pairs of cation–anion interactions between 2,3-BPG and **1**. Specifically, the carboxylate of 2,3-BPG binds to the Cu^{II} center while the phosphates of 2,3-BPG are flanked from above and below by the guanidinium groups.

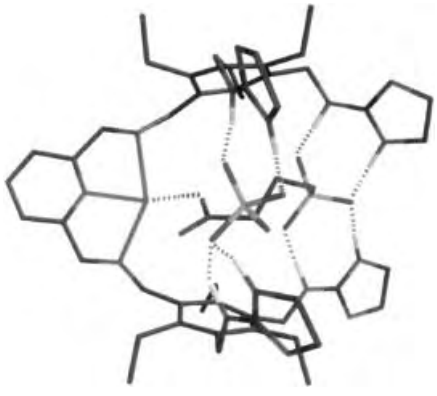
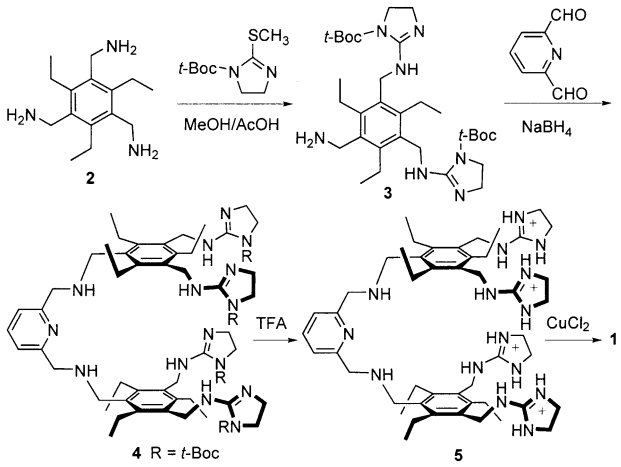


Figure 1. A proposed structure of the complex of **1** and 2,3-BPG.

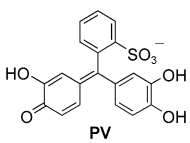
The synthesis of the receptor is shown in Scheme 1 (see Supporting Information). Triaminomethyltriethylbenzene (**2**)[15] was allowed to react with two equivalents of *N*-*t*Boc-2-methylthio-2-imidazoline[16] in MeOH/AcOH, thus giving the bis(*t*Boc-guanidine)-monoamino-containing structure **3** with a yield of 33%. Reductive amination of pyridine-2,6-dicarboxaldehyde with **3** by using sodium borohydride gave the *t*Boc-protected ligand **4** in 76% yield, which was deprotected in TFA/CH_2Cl_2 giving the free ligand **5** quantitatively. Finally, the complexation of **5** with one equivalent of $CuCl_2$ gave the receptor **1**.[17]



Scheme 1. Synthesis of receptor **1**.

The molecular recognition behavior of **1** with 2,3-BPG and its analogues was studied with an indicator displacement assay[18] by using pyrocatechol violet (PV) in a 1:1 water/methanol solution buffered with 10 mM HEPES at pH 7.4. Figure 2a and 2b show the UV/Vis spectroscopic change of the indicator upon complexation with **1** and displacement from **1** by 2,3-BPG respectively. The binding of PV to **1** causes an absorbance decrease at the λ_{max} of 445 nm and an increase at a new λ_{max} of 590 nm with an isosbestic point at 490 nm (Figure 2a), thus yielding a visual change from yellow to blue. The titration data fits well to a typical 1:1 binding algorithm[19] with a binding constant of $1.4 \times 10^6\,M^{-1}$. The addition of 2,3-BPG to a solution of the complex between **1** and PV causes a reversal of the spectral response, thus giving an increase at 445 nm and a decrease at 590 nm, and a color change back to yellow. This implies that the indicator was cleanly displaced from the binding cavity of receptor **1** by 2,3-BPG (Figure 2b). This colorimetric response yields a visual response and a quantitative sensing ensemble for 2,3-BPG.

An independent UV/Vis titration of **1** directly with 2,3-BPG in water buffered with 10 mM HEPES at pH 7.4 also shows a 1:1 binding, which changes the Cu^{II} d–d absorption. While free **1** has a maximum absorbance at 678 nm with a $\varepsilon =$



PV

 © 2003 Wiley-VCH Verlag GmbH & Co. KGaA, Weinheim

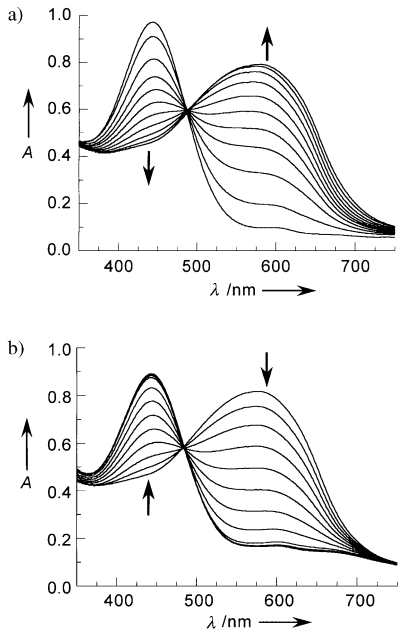


Figure 2. UV/Vis absorbance spectra of a) 0.054 mM solution of PV in the presence of 0–1.1 equivalents of **1** and b) 0.06 mM **1** and 0.054 mM PV solution in the presence of 0–0.08 mM of 2,3-BPG. Conditions: 1:1 MeOH/H_2O, 10 mM HEPES buffer, pH 7.4, 25 °C.

$210\,M^{-1}cm^{-1}$, its 2,3-BPG complex has a maximum absorbance at 660 nm with a $\varepsilon = 170\,M^{-1}cm^{-1}$. These results indicate that the copper center plays an important role in the binding. Because the binding is very strong, an accurate binding constant was not obtained from this direct titration.

Alternatively, the binding constant of **1** with 2,3-BPG in 1:1 water/methanol (v/v) was calculated to be $8.0\times10^8\,M^{-1}$ by using the competitive spectrophotometric method[19] on the basis of the spectrum changes shown in Figure 2b. Similarly, the binding constants for analogues of 2,3-BPG in the same solvent mixture were measured (Table 1). There is good

Table 1: Binding constants with receptor **1** in 1:1 water/methanol at pH 7.4, 25 °C.

Analyte (as sodium salt)	Binding constant [M^{-1}]
2,3-BPG	8×10^8 (4×10^{7}[a])
Phospho(enol)pyruvate	1.3×10^7
2-Phosphoglycerate	1.1×10^7
3-Phosphoglycerate	4.7×10^6
β-Glycerophosphate	6×10^4
Acetate	7×10^3

[a] in water at pH 6.8, 25 °C.

selectivity for binding with **1**. For example, the binding constants for the analogues of 2,3-BPG that have one less phosphate are 80 to 180 times lower than that of 2,3-BPG, while the binding constants for simple phosphates and carboxylates are four to five orders of magnitude lower. Apparently, the selectivity is related to the numbers of ion pairs. A binding constant relevant to the use of **1** in blood was desirable for the ultimate goal of this study. However, displacement of the indicator PV from **1** does not show a perfectly clean isosbestic point in pure water at pH 7.4, possibly because of a small amount of aggregation. To avoid this problem, a slight adjustment of the pH was necessary. At pH 6.8,[20] a clean isosbestic point was found, and the binding constant between **1** and 2,3-BPG in water was determined to be $4\times10^7\,M^{-1}$. A drop in the binding constant of only 20-fold occurs upon going to pure water from 50% methanol. Yet, at pH 6.8 the phosphates of 2,3-BPG are protonated to a greater extent than at pH 7.4. Although this binding constant is quite high, it is actually slightly lower than it would be at pH 7.4.

The influence of receptor **1** on the oxygenation levels of hemoglobin was studied spectrophotometrically with a tonometer by using the method of Benesch.[21] Figure 3 shows the

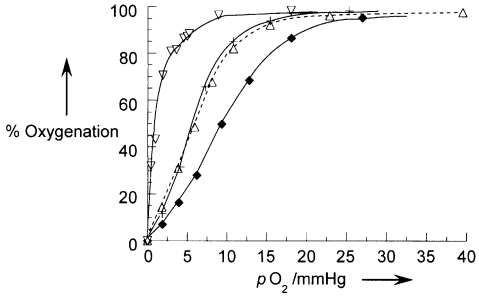


Figure 3. Oxygenation curves of hemoglobin in diluted hemolyzate of horse red cells (0.04 mM hemoglobin, 10 mM phosphate buffer, pH 7.2, 25 °C). (+) Original hemolyzate, (▽) hemolyzate with 0.16 mM **1**, (◆) hemolyzate with 0.16 mM additional 2,3-BPG, (△) hemolyzate with 0.16 mM additional 2,3-BPG and 0.16 mM **1**.

oxygenation curves of hemoglobin in horse red-cell hemolyzate diluted in 10 mM phosphate buffer solution at pH 7.2. The curve for native hemolyzate (+) has the classic shape found in introductory biochemistry textbooks.[22] We first studied the effect of just **1** on the horse hemolyzate. The addition of **1** to the diluted hemolyzate causes the curve to move to lower oxygen pressure (Figure 3▽), thus indicating an increase of the oxygen affinity of hemoglobin. Therefore, as anticipated, the addition of **1** leads to the stripping of the natural 2,3-BPG from hemoglobin. Next, the addition of 2,3-BPG to horse hemolyzate was studied to show that the hemoglobin was responding to 2,3-BPG as it should. Addition of 2,3-BPG was found to decrease the oxygen affinity (◆), as expected. Lastly, the addition of an equivalent of **1** counteracted the added 2,3-BPG, thus revealing that the additional 2,3-BPG was captured by the receptor (△).

All these results are in accordance with the binding affinity we determined for **1**. Because the binding constant of receptor **1** with 2,3-BPG (near $10^7\,M^{-1}$) is significantly higher than that of hemoglobin with 2,3-BPG (on the order of 10^4 to $10^5\,M^{-1}$),[3,23,24] the receptor depletes the 2,3-BPG from the hemoglobin complex and thereby increases the oxygenation level to that of striped hemoglobin.

In conclusion, we have created a designed synthetic receptor that is highly effective and selective for binding 2,3-BPG, even in physiological media. The affinity is high enough that the receptor can deprive hemoglobin of available 2,3-

 © 2003 Wiley-VCH Verlag GmbH & Co. KGaA, Weinheim

BPG, and thus control the active level of 2,3-BPG and the related oxygenation level of hemoglobin. The use of a small organic receptor to bind and regulate the levels of a biological effector, and thereby control a physiological function, represents a rarely explored means towards the development of a pharmaceutical agent.[25] Traditionally, small organic molecules are used to bind large biomolecules, and thereby regulate biological function. We believe that the sequestering of small effectors, agonists, and antagonists, by synthetic receptors could play an alternative or complementary role.

Experimental Section

Preparation and analysis of hemolyzate: Fresh defibrinated horse blood (0.6 mL) was centrifuged at 4000 rpm for 5 minutes to isolate the red cells. The supernatant was removed, and the cells were washed four times with 0.9% sodium chloride (1.5 mL each time) in the centrifuge tube. The isolated and washed red cells were hemolyzed by adding distilled water (ca. 1.2 mL). Toluene (ca. 0.3 mL) was added and mixed with the hemolyzate by shaking vigorously. After centrifugation of the sample at 12000 rpm for 10 minutes, the lower clear red layer was transferred by using a pipette to a new centrifuge tube. The toluene-treatment procedure was repeated twice until the interface between the toluene layer and the hemolyzate layer was clear. The hemolyzate was stored in a refrigerator and used within three days. Figure 3 was generated by using the method of Benesch.[21]

Received: February 12, 2003
Revised: April 29, 2003 [Z51165]

Keywords: bioinorganic chemistry · drug design · heme proteins · host–guest systems · receptors

[1] S. I. Winn, H. C. Watson, R. N. Harkins, L. A. Fothergill, *Philos. Trans. R. Soc. London Ser. B* **1981**, *293*, 121 – 130.
[2] R. Benesch, R. E. Benesch, *Nature* **1969**, *221*, 618 – 621.
[3] A. Arnone, *Nature* **1972**, *237*, 146 – 149.
[4] R. Benesch, R. E. Benesch, C. I. Yu, *Proc. Natl. Acad. Sci. USA* **1968**, *59*, 526 – 532.
[5] M. Delivoria-Papadopoulos, F. A. Oski, A. J. Gottlieb, *Science* **1969**, *165*, 601 – 602.
[6] R. Juel, *CRC Crit. Rev. Clin. Lab. Sci.* **1979**, *10*, 113 – 146.
[7] W. N. Poillon, B. C. Kim, O. Castro, *Blood* **1998**, *91*, 1777 – 1783.
[8] W. N. Poillon, B. C. Kim, R. J. Labotka, C. U. Hicks, J. A. Kark, *Blood* **1995**, *85*, 3289 – 3296.
[9] M.-C. Garel, N. Arous, M. C. Calvin, C. T. Craescu, J. Rosa, R. Rosa, *Proc. Natl. Acad. Sci. USA* **1994**, *91*, 3593 – 3597.
[10] For a previous receptor from our group for 2,3-BPG, see M. D. Best, E. V. Anslyn, *Chem. Eur. J.* **2003**, *9*, 51 – 57.
[11] S. Tobey, E. V. Anslyn in *Kluwer-Plenum Symposium Series on Anion-Recognition*, in press.
[12] C. L. Hannon, E. V. Anslyn in *Bioorganic Chemistry Frontiers III* (Ed.: H. Dugas), Springer, Heidelberg, **1993**, pp. 193 – 256.
[13] D. J. Iverson, G. Hunter, J. F. Blount, J. R. Damewood, K. Mislow, *J. Am. Chem. Soc.* **1981**, *103*, 6073 – 6083.
[14] Molecular modeling was performed with MacSpartan Pro (Wavefunction, Inc.). The structure was energy-minimized by Merck Molecular Force Field in gas phase.
[15] L. A. Cabell, M. D. Best, J. J. Lavigne, S. E. Schneider, D. M. Perreault, M.-K. Monahan, E. V. Anslyn, *J. Chem. Soc. Perkin Trans. 2* **2001**, 315 – 323.
[16] S. R. Mundla, L. J. Wilson, S. R. Klopfenstein, W. L. Seibel, N. N. Nikolaides, *Tetrahedron Lett.* **2000**, *41*, 6563 – 6566.
[17] The stoichiometry of the complex of ligand **5** with $CuCl_2$ was determined to be 1:1 by the mole-ratio method by monitoring the UV/Vis absorbance at 670 nm.
[18] S. L. Wiskur, H. Ait-Haddou, J. J. Lavigne, E. V. Anslyn, *Acc. Chem. Res.* **2001**, *34*, 963 – 972.
[19] K. A. Connors, *Binding Constants, The Measurement of Molecular Complex Stability*, Wiley, New York, **1987**.
[20] At the adjusted pH, the phenols are essentially completely protonated. E. Chiacchierini, R. Gocchieri, L. Sommer, *Collect. Czech. Chem. Commun.* **1973**, *38*, 1478 – 1496.
[21] R. Benesch, G. Macduff, R. E. Benesch, *Anal. Biochem.* **1965**, *11*, 81 – 87.
[22] C. K. Mathews, K. E. Van Holde, *Biochemistry*, 2nd ed., Benjamin-Cummings, **1996**, p. 233.
[23] M. K. Hobish, D. A. Powers, *Proteins Struct. Funct. Genet.* **1986**, *1*, 164 – 175.
[24] N. Hamasaki, Z. B. Rose, *J. Biol. Chem.* **1974**, *249*, 7896 – 7901.
[25] For another example, see: C. C. Huval, S. R. Holmes-Farley, G. M. Whitesides (Geltex Pharmaceticals, Inc.), WO 0038664, **2000**.

 © 2003 Wiley-VCH Verlag GmbH & Co. KGaA, Weinheim

Fischer Carbene Cyclizations

Nickel(0)-Mediated [3+2+2] and [2+2+2+1] Cyclization Reactions of Chromium Fischer Carbene Complexes and Alkynes**

José Barluenga, Pablo Barrio, Luis A. López, Miguel Tomás, Santiago García-Granda, and Carmen Alvarez-Rúa*

Although Fischer carbene complexes of Group 6 metals have demonstrated great potential in synthetic organic chemistry,[1] such complexes of late transition metals are almost unknown. Wilke et al.[2] and Pinhas and Simunic[3] reported the complexes $[L_2Ni{=}C(NR_2)Ph]$ and $[(CO)_3Ni{=}C(OSiMe_3)Bu]$, respectively.[4] The feasibility of the transmetalation reaction

[*] Prof. Dr. J. Barluenga, P. Barrio, Dr. L. A. López, Prof. Dr. M. Tomás
Instituto Universitario de Química Organometálica "E. Moles"
Unidad Asociada al CSIC, Universidad de Oviedo
Julián Clavería 8, 33071 Oviedo (Spain)
Fax: (+34) 98-510-3450
E-mail: barluenga@sauron.quimica.uniovi.es
Dr. S. García-Granda,[+] Dr. C. Alvarez-Rúa[+]
Departamento de Química Física y Analítica, Universidad de Oviedo
Julián Clavería 8, 33071 Oviedo (Spain)

[+] X-ray crystal structure analysis.

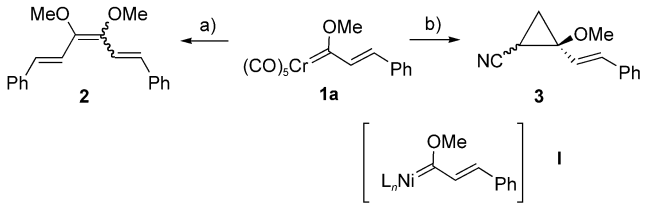
[**] Financial support for this work is acknowledged (BQU2001-3853 and PR-01-GE-9). P.B. thanks the Principado de Asturias for a predoctoral fellowship.

Supporting information for this article is available on the WWW under http://www.angewandte.org or from the author, and includes experimental procedures, spectral and analytical data for all products, and X-ray data for compounds **5b** and **8e**.

 © 2003 Wiley-VCH Verlag GmbH & Co. KGaA, Weinheim DOI: 10.1002/anie.200351216

as a route to these carbene complexes has been studied by us[5] and others.[6–8] Because of our interest in this area, as well as the importance of nickel carbene complexes as catalysts in carbon–carbon bond formation,[9] we explored the reactivity of chromium Fischer carbene complexes toward alkynes in the presence of Ni^0 complexes, which allowed us to discover a new synthetic potential for chromium carbene complexes.

First, the active role of nickel was seen (Scheme 1) in the formation of dimer **2** (1:1 *Z/E* mixture, 90%) from complex **1a** and [Ni(cod)$_2$] (cod = 1,5-cyclooctadiene; 10 mol%, THF, 2 h), and of cyclopropane **3** (1:1 *cis*/*trans* mixture, 85%) from **1a**, acrylonitrile, and [Ni(cod)$_2$] (10 mol%, MeCN, 25 °C, 3 h). Neither reaction occurs in the absence of nickel catalyst. On the basis of previous reports[5,10] we realized that some nickel alkoxycarbene species **I** might act as the active nickel intermediate.[11]

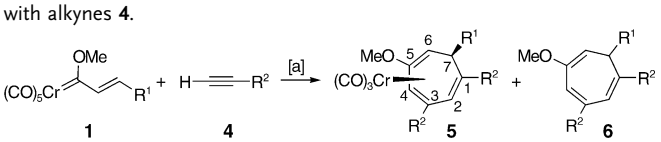


Scheme 1. Ni^0-catalyzed dimerization and cyclopropanation of chromium carbene complex **1a**. Reagents and conditions: a) [Ni(cod)$_2$] (10 mol%), THF, 25 °C, 2 h, 90%; b) acrylonitrile, [Ni(cod)$_2$] (10 mol%), MeCN, 25 °C, 3 h, 85%.

Therefore, we decided to investigate whether the hypothetical alkoxycarbene complex **I** might display a new type of carbene reactivity. Among a number of unsaturated substrates, we selected alkynes since their thermal reaction with chromium carbene complexes to give substituted phenols—the so-called benzannulation or Dötz reaction—is the most emblematic reaction of Fischer carbene complexes.[12] Thus, alkenyl carbene complexes **1** were mixed with terminal alkynes **4** at −10 °C in acetonitrile in the presence of a stoichiometric amount of [Ni(cod)$_2$]. The reaction mixture was allowed to warm to 20 °C over 2 h. Removal of the solvent and column chromatography of the residue afforded cycloheptatriene tricarbonyl chromium(0) complexes **5** in good yields (Table 1, entries 1–6). In the case of phenylacetylene (entry 7), a mixture of **5g** (30% yield) and decomplexed cycloheptatriene **6g** (40% yield) was formed. This nickel-mediated [3+2+2] cyclization of Fischer carbene complexes and alkynes takes place with complete regio- and stereoselectivity, the *endo* isomer being solely formed. Electron-poor alkynes also undergo this cyclization; for example, methyl propynoate affords the functionalized cycloheptatriene **6h** (entry 8). Phenol derivatives arising from the Dötz reaction were usually detected in less than 5% yield, while no higher oligomerization products were observed in the crude reaction mixtures.

The *endo* configuration of compounds **5** is based on the $^3J_{H6,H7}$ coupling constant (3.3–4.4 Hz),[13] and the unambiguous structure of **5b** was determined by an X-ray analysis (Figure 1).[14]

Table 1: [3+2+2] cyclization of chromium alkenyl carbene complexes **1** with alkynes **4**.



entry	R^1	R^2	**5** [%][b]	**6** [%][b]
1	Ph	*n*Pr	**5a** (86)	–
2	ferrocenyl	*n*Pr	**5b** (73)	–
3	2-furyl	*n*Pr	**5c** (76)	–
4	*n*Pr	*n*Pr	**5d** (62)	–
5	Ph	Me_3Si	**5e** (80)	–
6	Ph	$(CH_2)_3CN$	**5f** (78)	–
7	2-furyl	Ph	**5g** (30)	**6g** (40)
8	Ph	CO_2Me	–	**6h** (75)

[a] MeCN, **1**:**4**:[Ni(cod)$_2$] 1:3:1.1, −10 to 20 °C, 2 h. [b] Yields of isolated products.

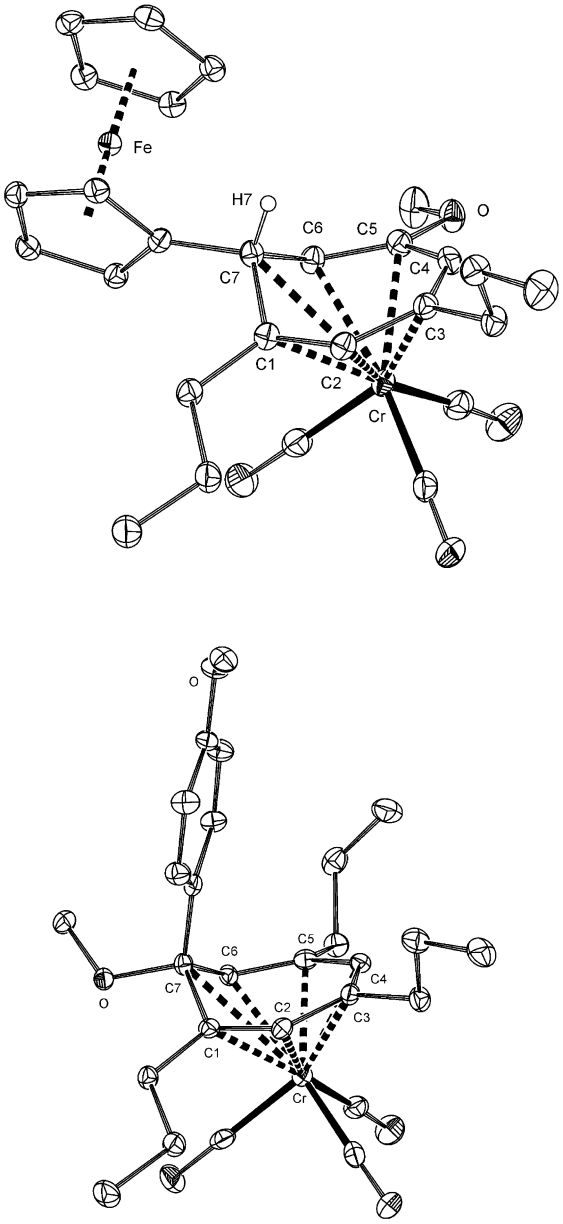
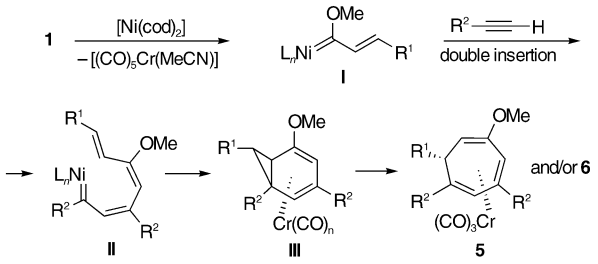


Figure 1. Top: ORTEP plot (30% ellipsoids) for **5b**; bottom: ORTEP plot (30% ellipsoids) for **8e**.

 © 2003 Wiley-VCH Verlag GmbH & Co. KGaA, Weinheim

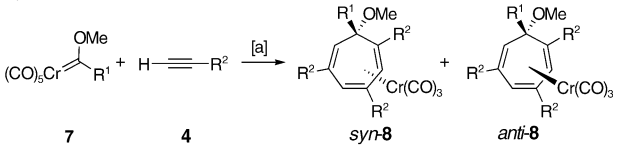


Scheme 2. Proposed mechanism for the formation of **5** and **6**.

A possible pathway for the formation of **5** is depicted in Scheme 2. First, chromium–nickel exchange forms the nickel species **I** (where L denotes cod, MeCN, or alkyne).[15] Formation of the pentacarbonyl(acetonitrile)chromium(0) complex is expected to facilitate metal exchange.[5] The nickel complex **I** undergoes a double regioselective alkyne insertion[16] to produce the new nickel carbene complex **II**, which then cyclizes to give **5** and/or **6**. This cyclization probably proceeds by intramolecular cyclopropanation (see Scheme 1) to form the norcaradiene species **III**, which isomerizes to the cycloheptatriene ring.[17]

We were further intrigued whether 1-nickela-1,3,5,7-octatetraenes of type **II** might also be available by assembling simple chromium carbene complexes **7** and three alkyne units. This goal was achieved by using terminal alkynes **4** and $[Ni(cod)_2]$ (1.1 equiv), which, under the reaction conditions given above, gave complexes **8** in high yields (Table 2). In this

Table 2: [2+2+2+1] cyclization of chromium carbene complexes **7** with alkynes **4**.



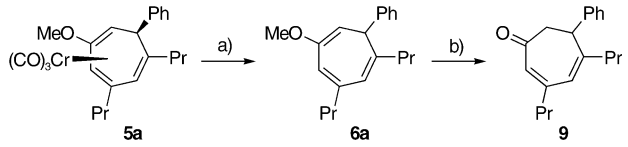
7 **4** *syn*-**8** *anti*-**8**

entry	R^1	R^2	**8** [%][b]	*syn*:*anti*[c]
1	Me	*n*Pr	**8a** (92)	>98:2
2	Me	Me_3Si	**8b** (65)	>98:2
3	Me	$(CH_2)_3CN$	**8c** (96)	>98:2
4	c-C_3H_5	*n*Pr	**8d** (75)	>98:2
5	*p*-$MeOC_6H_4$	*n*Pr	**8e** (83)	>98:2
6	2-furyl	*n*Pr	**8f** (86)	90:10
7	Ph	*n*Pr	**8g** (68)	60:40

[a] MeCN, **7**:**4**:$[Ni(cod)_2]$ 1:4:1.1, −10 to 20 °C, 2 h. [b] Yields of isolated products. [c] ^{1}H NMR spectroscopy (300 MHz) on the crude reaction mixture.

novel [2+2+2+1] cyclization three consecutive alkyne insertion reactions are efficiently accomplished in a regioselective manner. The *syn* isomer was found to be the sole (entries 1–5) or the major isomer (entries 6 and 7).The structural assignment of *syn*-**8a–d** was based on NMR spectroscopic data. Moreover, an X-ray analysis was performed on compound **8e** (Figure 1).[14]

Apart from the synthetic importance of the cycloheptatriene chromium complexes,[18] the corresponding metal-free



Scheme 3. Decomplexation of **5a** and hydrolysis of **6a**. Reagents and conditions: a) CO (35 bar), MeCN, 25 °C, 48 h, quantitative; b) 1 N HCl, THF, 25 °C, 2 h, 95 %.

systems are readily accessible by CO exchange (Scheme 3). For instance, cycloadduct **5a** was demetalated under CO pressure (35 bar, MeCN, 25 °C, 48 h) to provide **6a** quantitatively, which was in turn hydrolyzed (1N HCl, THF, 25 °C, 2 h) to give ketone **9** (95 % yield).

In conclusion, we have reported a novel reactivity pattern for chromium Fischer carbene complexes. Specifically, [3+2+2] and [2+2+2+1] cyclization reactions, which are rarely found in the literature,[19,20] between these complexes and alkynes are very efficient in the presence of Ni^0. These reactions are based on a facile chromium–nickel exchange and on the particular reactivity of the assumed nickel carbene species. In this context, some points are noteworthy: 1) the new Fischer alkoxycarbene complexes of nickel(0) readily undergo consecutive alkyne insertion reactions, 2) the first cyclopropanation reaction of nickel carbene complexes is reported here, and 3) no heptannulation reactions mediated or catalyzed by nickel carbene species have been hitherto reported.[16a]

Thus, the reactivity of Fischer carbene complexes can be modified not only in a quantitative way,[8] but also in a qualitative manner. The synthetic potential of Fischer carbene complexes should be expandable by combination with appropriate transition metals. Further work to develop a catalytic process[21] and to design an asymmetric version of the reaction is underway.

Received: February 18, 2003 [Z51216]

Keywords: alkynes · carbene ligands · chromium · cyclization · nickel

[1] W. D. Wulff in *Comprehensive Organometallic Chemistry II, Vol. 12* (Eds.: E. W. Abel, F. G. A., Stone, G. Wilkinson), Pergamon, New York, **1995**, p. 469.
[2] B. Gabor, C. Krüger, B. Marczinke, R. Mynott, G. Wilke, *Angew. Chem.* **1991**, *103*, 1711; *Angew. Chem. Int. Ed. Engl.* **1991**, *30*, 1666.
[3] a) L. Simunic, A. R. Pinhas, *Organometallics* **1987**, *6*, 1358; b) L. Simunic, A. R. Pinhas, *Inorg. Chem.* **1989**, *28*, 2400.
[4] For a Pd^{II} aminocarbene complex, see A. C. Albéniz, P. Espinet, R. Manrique, A. Pérez-Mateo, *Angew. Chem.* **2002**, *114*, 2469; *Angew. Chem. Int. Ed.* **2002**, *41*, 2363.
[5] J. Barluenga, L. A. López, O. Löber, M. Tomás, S. García-Granda, C. Alvarez-Rúa, J. Borge, *Angew. Chem.* **2001**, *113*, 3495; *Angew. Chem. Int. Ed.* **2001**, *40*, 3392.
[6] a) T. Liu, K. R. Reddy, *Chem. Soc. Rev.* **1999**, *28*, 315; b) R.-Z. Ku, J.-C. Huang, J.-Y. Cho, F.-M. Kiang, K. R. Reddy, Y.-C. Chen, K.-J. Lee, J.-H. Lee, G.-H. Lee, S.-M. Peng, S.-T. Liu, *Organometallics* **1999**, *18*, 2145.

 © 2003 Wiley-VCH Verlag GmbH & Co. KGaA, Weinheim

[7] a) For [Mo{=CPh(OMe)}(CO)(Cp)(NO)] with [Fe(CO)$_5$], see E. O. Fischer, H.-J. Beck, C. G. Kreiter, J. Lynch, J. Müller, E. Winkler, *Chem. Ber.* **1972**, *105*, 162; b) For [W{=CPh(OMe)}(CO)$_5$] with H[AuCl$_4$], see R. Aumann, E. O. Fischer, *Chem. Ber.* **1981**, *114*, 1853; c) For [W{=CPh(OMe)}(CO)$_5$] and [W{=CPh(NEt$_2$)}(CO)$_5$] with [PdBr(C$_6$F$_5$)(MeCN)$_2$], see ref. [4].

[8] In several papers Sierra et al. have proposed palladium biscarbene complexes as the active intermediates in the palladium-catalyzed dimerization of chromium(0) alkoxycarbene complexes: a) M. A. Sierra, M. J. Mancheño, E. Sáez, J. C. del Amo, *J. Am. Chem. Soc.* **1998**, *120*, 6812; b) M. A. Sierra, J. C. del Amo, M. J. Mancheño, M. Gómez-Gallego, *J. Am. Chem. Soc.* **2001**, *123*, 851; c) M. A. Sierra, J. C. del Amo, M. J. Mancheño, M. Gómez-Gallego, M. R. Torres, *Chem. Commun.* **2002**, 1842. Other carbene species of Rh, Cu, and Pd have been proposed as intermediates: d) I. Göttker-Schnetmann, R. Aumann, *Organometallics* **2001**, *20*, 346; e) I. Göttker-Schnetmann, R. Aumann, K. Bergander, *Organometallics* **2001**, *20*, 3574; f) R. Aumann, I. Göttker-Schnetmann, R. Fröhlich, O. Meyer, *Eur. J. Org. Chem.* **1999**, 2545; g) H. Sakurai, K. Tanabe, K. Narasaka, *Chem. Lett.* **1999**, 75.

[9] a) C. P. Kubiak in *Comprehensive Organometallic Chemistry II, Vol. 9* (Eds.: E. W. Abel, F. G. A. Stone, G. Wilkinson), Pergamon, New York, **1995**, p. 1. Selected references: b) V. P. W. Böhm, C. W. K. Gstöttmayr, T. Weskamp, W. A. Herrmann, *Angew. Chem.* **2001**, *113*, 3500; *Angew. Chem. Int. Ed.* **2001**, *40*, 3387; c) Y. Sato, M. Takimoto, M. Mori, *J. Am. Chem. Soc.* **2000**, *122*, 1624.

[10] Complexes [Ni{=CBu(OSiMe$_3$)}(CO)$_3$] and [Ni{=CBu(O-Li)}(CO)$_3$] dimerize rapidly at room temperature and at low temperature, respectively. See ref. [3b].

[11] a) The preparation of *N*-heterocyclic carbenes of Ni^0 was first reported by Arduengo et al.: A. J. Arduengo III, S. F. Gamper, J. C. Calabrese, F. Davidson, *J. Am. Chem. Soc.* **1994**, *116*, 4391; b) For the preparation and X-ray structure of a diphenylcarbene complex of Ni^0, see D. J. Mindiola, G. L. Hillhouse, *J. Am. Chem. Soc.* **2002**, *124*, 9976.

[12] K. H. Dötz, *Angew. Chem.* **1984**, *96*, 573; *Angew. Chem. Int. Ed. Engl.* **1984**, *23*, 587.

[13] It was found for related complexes that the coupling constant between H6 and H7 is about 8 Hz for the *exo* isomer and about 2 Hz for the *endo* isomer: S. D. Reynolds, T. A. Albright, *Organometallics* **1985**, *4*, 980.

[14] See Supporting Information for crystal data of **5b** and **8e**.

[15] The corresponding nickel(0) biscarbene complex is very unlikely to be formed, because 1) no dimerization occurs, and 2) when 0.5 equiv of [Ni(cod)$_2$] is used the yield of **5a** drops to 45% and about half of the carbene complex **1a** is recovered.

[16] a) The insertion of alkynes into nickel carbene complexes was demonstrated by Eisch et al. in the cross-oligomerization of alkynes with carbene sources to give substituted cyclopentadienes: J. J. Eisch, A. A. Aradi, M. A. Lucarelli, Y. Qian, *Tetrahedron* **1998**, *54*, 1169; b) The insertion of carbonyl and sulfur substrates into a diphenylcarbene nickel(0) complex has been just reported (ref. [11b]).

[17] a) For a related formation of oxepines by alkyne insertion into a rhodium(I) carbene complex, see A. Padwa, S. L. Xu, *J. Am. Chem. Soc.* **1992**, *114*, 5881; b) For the norcaradiene–cycloheptatriene equilibrium, see A. A. Jarzecki, J. Gajewski, E. R. Davidson, *J. Am. Chem. Soc.* **1999**, *121*, 6928.

[18] R. H. Rigby, *Tetrahedron* **1999**, *55*, 4521.

[19] a) For an elegant allyl/alkyne [3+2+2] cycloaddition mediated by cobalt, see N. Etkin, T. L. Dzwiniel, K. E. Schweibert, J. M. Stryker, *J. Am. Chem. Soc.* **1998**, *120*, 9702; b) For the carbonylative cyclization of enediynes, see I. Ojima, S.-Y. Lee, *J. Am. Chem. Soc.* **2000**, *122*, 2385.

[20] The [2+2+1+1] cyclization of simple Fischer carbene complexes and alkynes has been reported: W. D. Wulf, R. W. Kaesler, G. A. Peterson, P.-C. Tang, *J. Am. Chem. Soc.* **1985**, *107*, 1060.

[21] Significantly, we found that the cyclization of the carbene complex **1** (R^1 = Ph) and methyl propiolate to produce **6g** (Table 1, entry 8) also takes place in the presence of 10 mol% of [Ni(cod)$_2$], albeit in somewhat lower yield than with 1.1 equivalents (55 versus 75%).

 © 2003 Wiley-VCH Verlag GmbH & Co. KGaA, Weinheim

Near-Infrared Electrochromic Window

A Near-Infrared Electrochromic Window Based on an Sb-Doped SnO_2 Electrode Modified with a Ru–Dioxolene Complex**

Jorge García-Cañadas, Andrew P. Meacham, Laurence M. Peter, and Michael D. Ward**

Candidate materials for electrochromic devices (e.g. viologens, conducting polymers, metallopolymers, metal oxides), generally exhibit redox states with distinctly different electronic UV/Vis absorption spectra.[1] Compounds that exhibit electrochromism in the near-infrared (NIR) region of the spectrum are much less well-known, despite the considerable technological importance of this region of the spectrum for uses as diverse as medicine (photodynamic therapy), telecommunications (silica-based fiber-optic devices operate in the 1300–1500 nm window), and even applications to aerospace and military camouflage.[2,3] Some conducting polymers have been shown to exhibit NIR electrochromism.[3] The well-known reversible redox activity of transition metal complexes makes them excellent candidates for use as electrochromic materials, although this activity is usually confined to the visible region of the spectrum.[4] We recently described extensive series of both ruthenium-dioxolene and oxo–Mo^{V}–

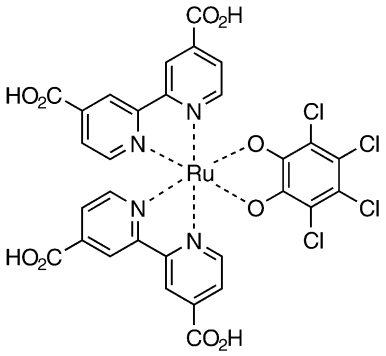
[*] Prof. L. M. Peter
Department of Chemistry
University of Bath
Bath BA2 7AY (UK)
Fax: (+44) 1225-385-802
E-mail: l.m.peter@bath.ac.uk
Prof. M. D. Ward, A. P. Meacham
School of Chemistry
University of Bristol
Cantock's Close, Bristol BS8 1TS (UK)
Fax: (+44) 117-929-0509
E-mail: mike.ward@bristol.ac.uk
J. García-Cañadas
Departamento de Química
Universidad Autónoma de Madrid
28049 Madrid (Spain)

[**] We thank Johnson Matthey and the EPSRC for financial support, and Dr. Upul Wijayantha for help in the fabrication of the tin oxide electrodes.

 DOI: 10.1002/anie.200351338 © 2003 Wiley-VCH Verlag GmbH & Co. KGaA, Weinheim

phenolate complexes whose redox activity is associated with the appearance/disappearance of intense NIR charge-transfer transitions.[5] In the case of the Ru–dioxolene systems, the electrochromism is based on the redox activity of the dioxolene ligand: oxidation of this ligand (from its catecholate form to the semiquinone and then quinone forms) results in the appearance of strong MLCT transitions in the NIR region,[5] as first demonstrated by Lever and co-workers.[6] To turn this behavior into a useful device, the electrochromic dyes need to be attached to a solid support for fast switching.

Herein, we describe the preparation and characterization of a NIR electrochromic window based on a conducting glass electrode coated with a thin nanocrystalline film of Sb-doped SnO_2, which is modified with the complex bis(2,2′-bipyridine-4,4′-dicarboxylic acid) (tetrachlorocatecholato)ruthenium(II), complex **1**. This complex is a derivative of $[Ru(bpy)_2(Cl_4cat)]$



1

(cat = catecholate), known to show NIR electrochromism,[6] but contains appended carboxylate groups to anchor the complex to a metal oxide surface. Nanocrystalline antimony-doped tin oxide (SnO_2:Sb) electrodes were chosen because they are highly conducting and electrons can tunnel easily in either direction between the adsorbed electroactive species and the SnO_2 conduction band.[7] Compared with TiO_2, SnO_2 is a better electron acceptor as its conduction band is about 0.5 V lower in energy.[8] The behavior of the electrochromic electrode was studied by cyclic voltammetry and spectroelectrochemical methods.

Complex **1** was prepared by the treatment of tetrachlorocatechol with $[Ru(dcbpy)_2Cl_2]$ (dcbpy = 2,2′-bipyridine-4,4′-dicarboxylic acid) in aqueous methanol at reflux, and purified by chromatography on Sephadex-G25 with MeOH.[9,10] The cyclic voltammogram in MeOH/KOH (Figure 1a) shows a chemically reversible catecholate/semiquinone couple at +0.18 V versus SCE, followed at higher potential (+0.94 V) by an irreversible semiquinone/quinone couple. The Ru^{II}/Ru^{III} couple, which is expected at a still more positive potential, was not observed within the accessible potential window.[6] In Figure 1b are the results of a spectroelectrochemical study in water which show the electronic spectra of **1** (no NIR absorption) and electrochemically-generated $[\mathbf{1}]^+$ (showing a transition at 940 nm arising from a $Ru^{II} \rightarrow$semiquinone MLCT transition following oxidation of the dioxolene ligand). These spectroscopic properties are similar to those observed for the noncarboxylated parent complex $[Ru(bpy)_2(Cl_4cat)]$.[6] This complex was then adsorbed from a MeOH/EtOH solution onto an electrode prepared from a layer of nanocrystalline Sb-doped SnO_2 on a transparent, conducting substrate.[11,12]

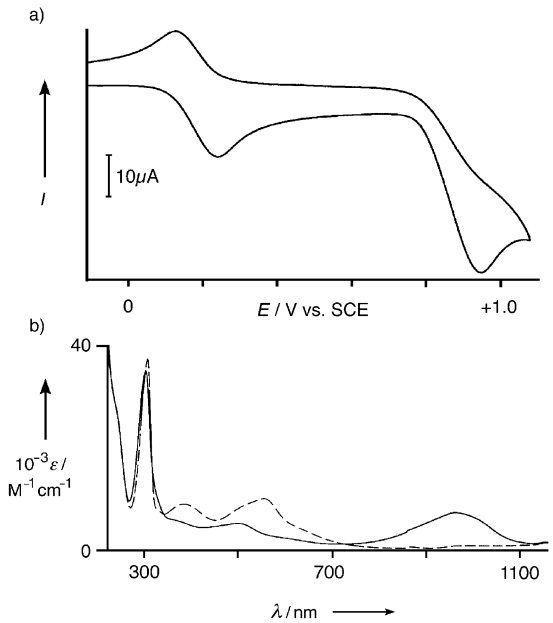


Figure 1. a) Cyclic voltammogram of **1** in MeOH containing 0.01 M KOH at a Pt-bead working electrode (scan rate 0.1 V sec^{-1}). b) Electronic spectra of **1** (•••••) and $[\mathbf{1}]^+$ (——) in water/0.1 M $NaClO_4$ from a spectroelectrochemistry experiment in an OTTLE cell at 293 K.

Figure 2 shows a cyclic voltammogram of the modified electrode recorded at a sweep rate of 10 mV s^{-1}. When the experiment was performed in the absence of the adsorbed dye, only the featureless background charging current typical of highly doped SnO_2:Sb electrodes[13] was observed. It follows that the peaks seen in Figure 2 arise from the oxidation and reduction of the catecholate/semiquinone couple. The electrode is initially blue-gray (catecholate

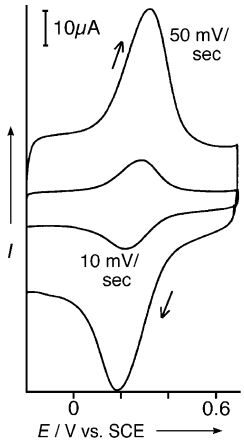


Figure 2. Cyclic voltammograms at 10 mV sec^{-1} and 50 mV sec^{-1} of a porous nanocrystalline Sb-doped SnO_2 film modified with complex **1**; recorded in acetonitrile containing 0.1 M Bu_4NPF_6.

 © 2003 Wiley-VCH Verlag GmbH & Co. KGaA, Weinheim

form), changes to pink (semiquinone form) during oxidation, and returns to blue-gray during the reverse sweep. The two peaks observed in the voltammogram are almost symmetric as expected for the case of a thermodynamically ideal surface-attached redox system; the small separation between the two peak potentials may arise from interactions between the species in the densely populated substrate,[14] as well as from the ohmic potential drop in the system.

The changes in the optical transmittance of the film (at two different wavelengths) as a function of applied potential (scanned at 10 $mV\,s^{-1}$) are shown in Figure 3. At 630 nm, the

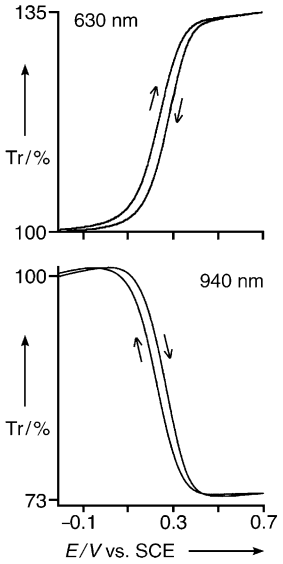


Figure 3. Changes in optical transmittance at 630 and 940 nm of a Sb-doped SnO_2 film modified with complex **1**; recorded with acetonitrile containing 0.1 M Bu_4NPF_6. Sweep rate was 10 mV sec^{-1}. The values have been normalized to the initial transmission at the beginning of the voltage sweep (i.e. in the reduced catecholate form of the dye) in each case.

transmittance increases on oxidation, and decreases (returning to its initial value) on reduction, thus indicating the reversible behavior of the system. The small hysteresis demonstrates the reversibility of the electrochromic couple. At 940 nm, the transmittance of the electrode decreases on the oxidation sweep due to the appearance of the MLCT transition, and decreases (returning to its initial value) during the reductive sweep. The same small hysteresis effect already mentioned was observed. Background optical transmittance experiments at the three wavelengths without the presence of adsorbed **1** showed no significant change of transmittance. In all cases, the changes in transmittance are in agreement with what would be expected on the basis of the spectroelectrochemical properties (Figure 1). It is clear from these results that the reversible ligand-based redox process of **1** provides a good basis for electrochromic systems operating both in the visible and NIR. The extensive redox activity and substantial NIR electrochromism of related dinuclear and trinuclear Ru–dioxolene complexes means that they are very promising candidates for NIR electrochromic windows.

The optical switching speed of the electrochromic layer is determined by the rate of the oxidation/reduction process. The current that flows to the porous electrode is required not only to effect the redox switching but also to charge the electrical double layer of the nanocrystalline SnO_2 support, which has a high surface area, thus resulting in a high background current (Figure 2). The magnitude of the background current indicates that the internal surface area of the porous oxide film is at least 500 times larger than the geometric area. Based on this internal surface area, the charge under the voltammetric peaks can be used to estimate the coverage of the internal surface with the complex as of the order of 10^{13} molecules cm^{-2}, which is consistent with monolayer coverage.[15]

The dynamic electrical and optical properties of the electrochromic layer were also characterized by using a small sinusoidal modulation of the electrode potential. The low-frequency spectroelectrochemical response of the modified electrode could be modeled by a single time constant with a value of about 0.5 s, which means that the window should switch almost completely (98%) in 1.5 seconds. This switching time will be susceptible to improvement, as the time constant is determined predominantly by the series resistance of the conducting glass electrode and the electrolyte solution (80Ω total) and is not determined by the properties of **1**. Consequently, the use of electrode and cell designs that give lower values of series resistance will improve the response time of the electrochromic window.

Received: March 6, 2003 [Z51338]

Keywords: cyclic voltammetry · electrochemistry · electrochromism · near infrared · ruthenium

[1] a) R. J. Mortimer, *Electrochim. Acta*, **1999**, *44*, 2971; b) R. J. Mortimer, *Chem. Soc. Rev.* **1997**, *26*, 147; c) D. R. Rosseinsky, R. J. Mortimer, *Adv. Mater.* **2001**, *13*, 783.

[2] a) *Integrated Optical Circuits and Components: Design and Applications* (Ed.: E. J. Murphy), Marcel Dekker, New York, **1999**; b) M. Emmelius, G. Pawlowski, H. W. Vollmann, *Angew. Chem. Int. Ed. Engl.* **1989**, *28*, 1445; c) J. Fabian, R. Zahradnik, *Angew. Chem. Int. Ed. Engl.* **1989**, *28*, 677; d) J. Fabian, H. Nakazumi, M. Matsuoka, *Chem. Rev.* **1992**, *92*, 1197.

[3] a) P. Chandrasekhar, B. J. Zay, D. Ross, T. McQueeney, G. C. Birur, T. Swanson, L. Kauder, D. Douglas, *Abstr. Pap. Am. Chem. Soc.* **2002**, *223*, 287; b) P. Chandrasekhar, B. J. Zay, G. C. Birur, S. Rawal, E. A Pierson, L. Kauder, T. Swanson, *Adv. Funct. Mater.* **2002**, *12*, 95; c) P. Topart, P. Hourquebie, *Thin Solid Films* **1999**, *352*, 243.

[4] a) M. Kaneko, S. Teratani, K. Harashima, *J. Electroanal. Chem.* **1992**, *325*, 325; b) T. Onikubo, R. J. Lin, M. Kaneko, *J. Electroanal. Chem.* **1993**, *361*, 143; c) T. R. I. Cataldi, G. E. de Benedetto, C. Campa, *J. Electroanal. Chem.* **1997**, *437*, 93; d) M. Yagi, S. Umemiya, *J. Phys. Chem. B* **2002**, *106*, 6355.

[5] M. D. Ward, J. A. McCleverty, *J. Chem. Soc. Dalton Trans.* **2002**, 275.

[6] M. Haga, E. S. Dodsworth, A. B. P. Lever, *Inorg. Chem.* **1986**, *25*, 447.

[7] G. Boschloo, D. Fitzmaurice, *J. Phys. Chem. B* **1999**, *103*, 3093.

[8] I. Bedja, S. Hotchandani, P. V. Kamat, *J. Phys. Chem.* **1994**, *98*, 4133.

 © 2003 Wiley-VCH Verlag GmbH & Co. KGaA, Weinheim

[9] A mixture of $[Ru(dcbpy)_2Cl_2]$ (ref. [10]) (50 mg, 75 μmol), tetrachlorocatechol (25 mg, 160 μmol, excess) and KOH (0.1 g in MeOH/water (1:1, 50 cm^3) was heated to reflux for 5 h. After the removal of the solvent in vacuo the residue was dissolved in the minimum volume of MeOH and purified by repeated chromatography on Sephadex-G25, elution with MeOH followed by recrystallisation from MeOH/diethyl ether (yield: ca. 20%). Negative-ion ESMS: *m/z* 416 $\{M - 4K^+ + 2H^+\}^{2+}$. The elemental analysis consistently indicated the presence of several molecules of water of crystallization. A typical example is given. Elemental analysis calcd(%) for $\mathbf{1}\cdot 7H_2O$: C 32.4, H 2.4, N 5.0% found (%): C 32.2, H 2.2, N 5.0.

[10] M. K. Nazeeruddin, S. M. Zakeeruddin, R. Humphry-Baker, M. Jirousek, P. Liska, N. Vlachopoulos, V. Shklover, C.-H. Fischer, M. Grätzel, *Inorg. Chem.* **1999**, *38*, 6298.

[11] The conductive glass substrate (Libby Owens Ford, F^--doped SnO_2) was cleaned by brushing with Decon 5% solution, rinsing with milli-Q water, immersion for 30 minutes in boiling 2-propanol, rinsing again with milli-Q water and drying in an air stream. The Sb-doped SnO_2 (15% in H_2O colloidal dispersion, Alfa Aesar) was spread over the cleaned glass substrate with a glass rod by using adhesive tape spacers. The geometric area of the film was 1.5 cm^2. The plate was then fired at 450°C for 30 minutes in air. This process was repeated four times to get four layers of SnO_2 and so increase the thickness of the film to around 2–3 microns. The SnO_2 film was then modified by chemisorption of the Ru complex **1** from a MeOH/EtOH solution (3×10^{-4} M) over 20 h, then removed and placed in a horizontal position for homogeneous drying for a few minutes prior to use. Measurements by using this modified electrode were carried out under dinitrogen at room temperature in a three-electrode cell. Pt wire was used as a counter electrode and Ag wire as the reference electrode. The electrolytic solution was dry acetonitrile containing 0.1 M Bu_4NPF_6. A small amount of ferrocene was added to the solution after the measurements and used as an internal standard; the conversion of potential values to the SCE scale was carried out by using published values. (ref. [12]) Optical measurements were performed by illuminating the cell from the substrate side with a light emitting diode at 940 or 630 nm and collecting the transmitted light with a silicon photodetector in a Faraday dark box while taking care to eliminate stray light. The output of the photodetector was connected with a current amplifier. Frequency-resolved measurements were performed at fixed dc potential by using a Solartron 1250 frequency-response analyser. The potential amplitude was 10 mV root mean square in all cases.

[12] N. G. Connelly, W. E. Geiger, *Chem. Rev.* **1996**, *96*, 877.

[13] U. zum Felde, M. Haase, H. Weller, *J. Phys. Chem. B* **2000**, *104*, 9388.

[14] A. J. Bard, L. R. Faulkner, *Electrochemical Methods: Fundamentals and applications, 2nd ed.*, Wiley, New York **2001**.

[15] The surface coverage of complex **1** was calculated from the faradaic charge in the cyclic voltammogram. The charge (2 mC) is divided by the estimated internal surface area (500 cm^2) to obtain a charge per unit area of 4 μC cm^{-2}. This corresponds to 4×10^{-11} mol cm^{-2} or 2.4×10^{13} molecules cm^{-2}. This is equivalent to a monolayer if one assumes an area per molecule of 4×10^{-14} cm^2. This is an order of magnitude estimate only as the orientation of the adsorbed molecules is not known; however, the figures look reasonable for monolayer coverage.

 © 2003 Wiley-VCH Verlag GmbH & Co. KGaA, Weinheim

Molecularly Imprinted Polymers

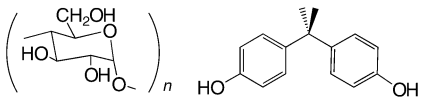
pH-Responsive Molecularly Imprinted Polymers

*Yasumasa Kanekiyo, Ryuichi Naganawa, and Hiroaki Tao**

Molecular imprinting is a powerful tool for the creation of molecular recognition materials having excellent molecular recognition ability.[1] In general, molecularly imprinted polymers (MIPs) are synthesized by the copolymerization of a functional monomer–template complex with a crosslinker. To create binding sites complementary to the shape of a template molecule, a high fraction of crosslinker is usually used, so that the binding sites are rigidly retained in the crosslinked polymer network. Accordingly, it is difficult to deform the binding sites for the sake of controlling binding characteristics. This is a significant drawback of MIP technique, and the development of a new type of MIP having flexible binding sites is desired.[2]

Recently, new types of MIPs that respond to stimuli are emerging. Alvarez-Lorenzo et al. have reported MIPs that change their rebinding abilities towards metal ions[3] and anionic molecules[4] in response to the temperature of the solution. In these systems, functional groups are dispersed in loosely crosslinked *N*-isopropylacrylamide (NIPA) polymer. Since NIPA polymer undergoes a reversible swelling–shrinking cycle in response to the external temperature, the rebinding ability is controllable by changing the solution temperature, which leads to a change in the structure of the binding sites.

Our group recently established a novel molecular imprinting strategy using amylose as a host matrix.[5] This method consists of helical inclusion-complex formation between

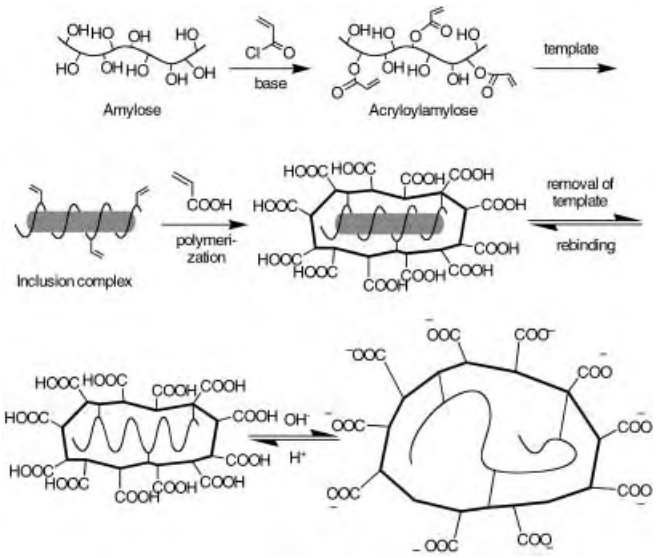


Amylose Bisphenol-A

amylose modified with acryloyl groups (acryloylamylose) and a template molecule in aqueous solution followed by radical copolymerization with a crosslinker (*N*,*N*′-methylenebisacrylamide). The resultant polymer retains a hydrophobic cavity that is complementary to the molecular shape of the template. It occurred to us that if acryloylamylose is copolymerized with a monomer having ionizable units such as carboxyl group, and the crosslinking density is appropriately tuned, the imprinted binding site should reversibly

[*] Dr. H. Tao, Dr. Y. Kanekiyo, Dr. R. Naganawa
National Institute of Advanced Industrial Science and Technology (AIST)
16-1 Onogawa, 305-8569 Tsukuba (Japan)
Fax: (+81) 29-861-8308
E-mail: hiro-tao@aist.go.jp

 © 2003 Wiley-VCH Verlag GmbH & Co. KGaA, Weinheim DOI: 10.1002/anie.200351381



Scheme 1. Synthesis of amylose-based imprinted polymer and its pH-responsive structural change.

change its structure depending on the pH of the solution (Scheme 1).

Synthesis of acryloylamylose and the subsequent inclusion-complex formation with bisphenol-A as a template were conducted by the method already reported.[5] To control the crosslinking density of the imprinted polymers, the degree of substitution (DS)[6] of acryloylamylose was varied between 0.15 and 0.22. The higher DS results in the creation of more crosslinking points in the imprinted polymers. The stoichiometry of the complex between acryloylamylose and bisphenol-A was assessed by measuring the solubility difference of bisphenol-A in pure water and in aqueous acryloylamylose solution (Table 1). Acryloylamylose with DS = 0.22 shows a

Table 1: Complexation between Acryloylamylose and Bisphenol-A

DS[a]	solubility of bisphenol-A in water [mM]	in acryloylamylose solution[b] [mM]	[glucose unit]/ [complexed bisphenol-A]
0.15	1.12	6.38	27.5
0.22	1.12	5.84	30.7

[a] For the definition of DS, see Ref. [6]. [b] Concentration of acryloylamylose: 25 g L^{-1}.

10% lower complexation ability than the case of acryloylamylose with DS = 0.15. It is known that the intramolecular hydrogen bonding between hydroxyl groups plays an important role in stabilizing the helical conformation of amylose.[7] Hence, the modification of hydroxyl groups in amylose could disrupt the intramolecular hydrogen bonding and lower the complexation ability. In the present system, however, the difference in the complexation ability between the two acryloylamylose is relatively small.

After the formation of the inclusion complex, polymerization was carried out as follows: acrylic acid (10 mg) and 2,2′-azobis(2-amidinopropane) dihydrochloride (initiator, 1.6 mg) were added to an aqueous solution (2 mL) containing acryloylamylose (50 mg) and bisphenol-A (saturated). Bisphenol-A was excluded from the preparation of nonimprinted polymer. The stirring solution was irradiated by UV light (365 nm) at 25 °C for 3 h. The resultant polymer was copiously washed with acetone and methanol. Complete removal of bisphenol-A from the imprinted polymer was confirmed by HPLC analysis of the washing solvent. The reference polymer, which does not have ionizable units was also synthesized according to the same procedure mentioned above, except that acrylic acid was replaced with the same weight of acrylamide. These polymers were obtained as white powders, which were easily dispersible in aqueous solutions without any processing, such as grinding.

For the measurement of the rebinding ability, the imprinted polymer or nonimprinted polymer (5 mg) was dispersed in an aqueous solution of bisphenol-A (25 μM, 1 mL) and stirred at 25 °C for 3 h. After the reaction mixture was subject to centrifugation (90 000 rpm, 5 min) the amount of bound bisphenol-A was determined by HPLC analysis of the supernatant solution. Figure 1 shows the pH dependence

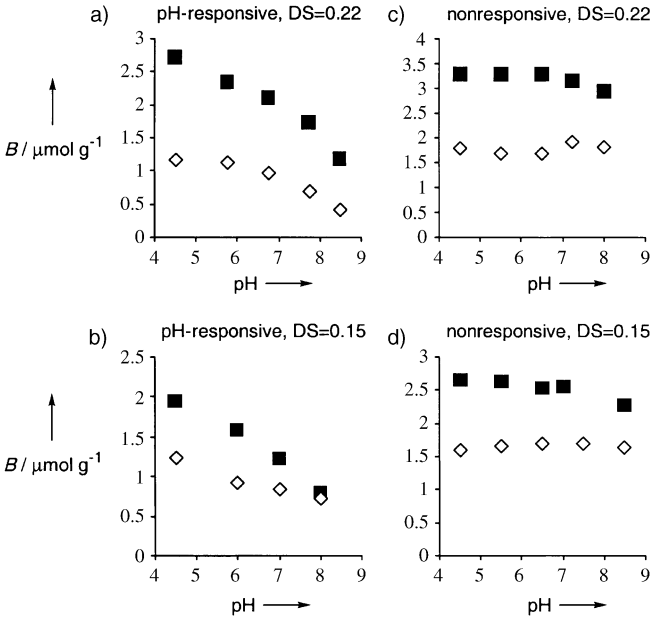


Figure 1. Rebinding abilities of imprinted polymers toward bisphenol-A at various values of pH: (■) imprinted, (◇) nonimprinted. pH-responsive polymers were copolymerized with acrylic acid, whereas nonresponsive polymers were copolymerized with acrylamide. *B* = binding ability.

of the rebinding abilities for the polymers. The polymers copolymerized with acrylic acid gradually decrease their rebinding abilities with increasing pH of the solution (Figure 1a and b). On the other hand, the polymers copolymerized with acrylamide show virtually no response toward pH variation (Figure 1c and d).[8] Deprotonation from the hydroxyl group in bisphenol-A is negligible in the measurement conditions as the pK_a value is 9.8.[9] Thus, we have verified that the introduction of carboxyl groups into the polymer matrix is essential for the creation of pH responsiveness.

 © 2003 Wiley-VCH Verlag GmbH & Co. KGaA, Weinheim

The imprinted polymer synthesized from acryloylamylose with DS = 0.22 shows a higher rebinding ability than the case in which acryloylamylose with DS = 0.15 is used. For acryloylamylose with DS = 0.15, at higher values of pH the difference in the rebinding ability between the imprinted polymer and the nonimprinted polymer almost disappears, whereas for acryloylamylose with DS = 0.22 the difference still exists. These observations clearly support the view that the binding cavity created through the imprinting process is disrupted by a conformational change in amylose chain arising from the electrostatic repulsion between anionic carboxylate groups. It is understandable that the higher the crosslinking density, the better the rebinding ability because the imprinted binding site is rigidly retained. On the other hand, the recognition ability of the more rigid polymer is more difficult to erase.

We also examined the reversibility of the erasing and regeneration process for the molecular memory. While successively changing the acidity of an aqueous bisphenol-A solution, the rebinding abilities of the imprinted polymer that is copolymerized with acrylic acid were measured. The rebinding ability, as shown in Figure 2, reversibly decreases and increases by changing the conditions from acidic to basic and vice versa.[10]

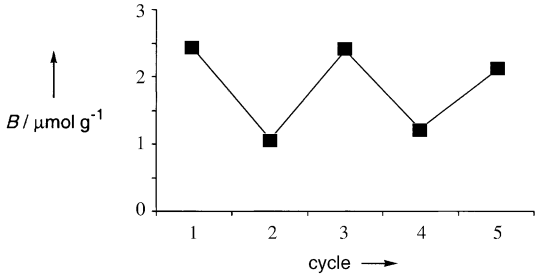


Figure 2. Reversible erasing and regeneration of molecular memory. The imprinted polymer copolymerized with acrylic acid was consecutively immersed in acidic (pH ≈ 4.5, odd cycles) and basic (pH ≈ 8.5, even cycles) solutions containing 25 μM of bisphenol-A. Acryloylamylose with DS = 0.21 was used for imprinting.

In conclusion, the work presented herein has demonstrated for the first time a novel strategy to create pH-responsive molecularly imprinted polymers using amylose as the host matrix. It is confirmed that changing acidity of the solution reversibly controls the rebinding ability toward bisphenol-A. We expect that the present system is expandable to the imprinting of other hydrophobic molecules. The system may have metal responsiveness arising from the complex formation with carboxylate groups, which is currently under investigation in our laboratory. Notably, the present system mainly consists of a naturally occurring product, which is abundantly obtained from common food products, such as wheat, potato, and rice. We thus believe that the present methodology is a promising way to develop environment-friendly separation materials, human-body-friendly drug delivery systems, etc. in the near future.

Received: March 12, 2003 [Z51381]

Keywords: copolymerization · host–guest systems · inclusion compounds · molecular imprinting · nanostructures

[1] a) *Molecular and Ionic Recognition with Imprinted Polymers* (Eds.: R. A. Bartsch, M. Maeda), American Chemical Society, Washington, DC, **1997**; b) *Molecularly Imprinted Polymers* (Ed.: B. Sellergren), Elsevier, Amsterdam, **2001**; c) *Molecular Imprinting-from Fundamentals to Applications* (Eds.: M. Komiyama, T. Takeuchi, T. Mukawa, H. Asanuma), VCH, Weinheim, **2002**; d) *Molecularly Imprinted Materials-Sensors and Other Devices* (Eds.: K. J. Shea, M. J. Roberts, M. Yan), The Materials Research Society, Warrendale, **2002**.

[2] M. E. Byrne, K. Park, N. A. Peppas, *Adv. Drug Delivery Rev.* **2002**, *54*, 149 – 161.

[3] a) C. Alvarez-Lorenzo, O. Guney, T. Oya, Y. Sakai, M. Kobayashi, T. Enoki, Y. Takeoka, T. Ishibashi, K. Kuroda, K. Tanaka, G. Wang, A. Y. Grosberg, S. Masamune, T. Tanaka, *Macromolecules* **2000**, *33*, 8693 – 8697; b) C. Alvarez-Lorenzo, O. Guney, T. Oya, Y. Sakai, M. Kobayashi, T. Enoki, Y. Takeoka, T. Ishibashi, K. Kuroda, K. Tanaka, G. Wang, A. Y. Grosberg, S. Masamune, T. Tanaka, *J. Chem. Phys.* **2001**, *114*, 2812 – 2816; c) H. Hiratani, C. Alvarez-Lorenzo, J. Chung, O. Guney, A. Y. Grosberg, T. Tanaka, *Langmuir* **2001**, *17*, 4431 – 4436.

[4] T. Moritani, C. Alvarez-Lorenzo, *Macromolecules* **2001**, *34*, 7796 – 7803.

[5] Y. Kanekiyo, R. Naganawa, H. Tao, *Chem. Commun.* **2002**, 2698 – 2699.

[6] The DS value is defined as the average number of acryloyl groups per anhydroglucose unit.

[7] a) Y. Hui, Y. Gai, *Makromol. Chem.* **1988**, *189*, 683 – 690; b) Y. Hui, Y. Gai, *Makromol. Chem.* **1988**, *189*, 1287 – 1294.

[8] A slight decrease in the rebinding ability at higher values of pH can be attributed to the existence of small amount of carboxylate groups derived from the hydrolysis of amide moieties.

[9] M. del Olmo, A. Zafra, A. Gonzalez-Casado, J. L. Vilchez, *Int. J. Environ. Anal. Chem.* **1998**, *69*, 99 – 110.

[10] The reversibility is gradually decreased with increasing acid–base cycles, which can be attributed to the hydrolysis of the ester bonds connecting amylose chain with crosslinking matrix.

 © 2003 Wiley-VCH Verlag GmbH & Co. KGaA, Weinheim

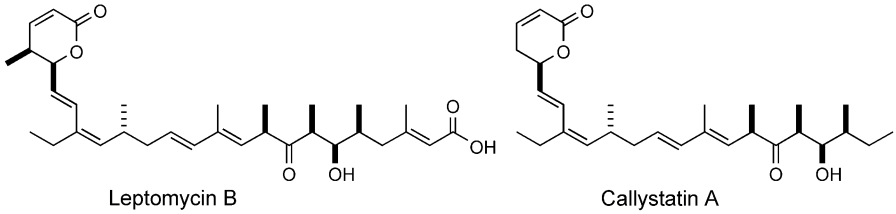
Total Synthesis

Total Synthesis and Structural Elucidation of (−)-Delactonmycin**

*Ivan R. Corrêa, Jr. and Ronaldo A. Pilli**

Dedicated to Professor Albert J. Kascheres on the occasion of his 60th birthday

In recent years, a number of highly cytotoxic polyketides with similar chemical structures, including the leptomycins, kazusamycins, anguinomycins, and leptolstatins, were isolated as secondary metabolites from *Streptomyces* strains.[1] In 1997, Wang et al. identified two novel polyketides, named delactonmycin and dilactonmycin, in the extracts from *Streptomyces* strain A92-308902 with very potent inhibitory activity of the nucleo-cytoplasmic translocation of the HIV-1 regulatory protein Rev.[2] The planar structure of delactonmycin was established by spectroscopic methods, but its relative as well as its absolute configuration remained unknown. In our synthetic studies towards the elucidation of the relative configuration of delactonmycin (**1**), we were led to presume that it is the same as that of leptomycin B and callystatin A—a structurally related polyketide isolated from the marine sponge *Callyspongia truncata*[3]—whose relative and absolute configurations were established by spectroscopic methods and total synthesis.[4,5]



Our interest in the synthesis of delactonmycin stemmed from its greater structural simplicity relative to that of other members of this class, which renders it an interesting model compound for structure–activity studies.[6] Additionally, the implementation of a successful approach to **1** would pave the way to the total synthesis of other polyketides whose structures have not yet been confirmed by total synthesis. Herein, we disclose our approach and results toward the first total synthesis and structural elucidation of (−)-delactonmycin (**1**, Scheme 1).

The installation of the C4–C5 bond through *E*-selective Wittig olefination between aldehyde **2** and phosphonium bromide **3** was left to a late stage of the synthesis in our retrosynthetic analysis. In turn, **3** could be obtained from a Wittig olefination of aldehyde **4** with ethyl triphenylphosphoranylidene propionate. It was envisaged that aldehyde **4** could be prepared from the *syn* aldol adduct obtained from the reaction between ethyl ketone **5** and γ,δ-unsaturated aldehyde **6**. The fragments **2**, **5**, and **6** are available from the methyl (*R*)- and (*S*)-3-hydroxy-2-methylpropionates, which we have already used in the total synthesis of the aglycon of the macrolide antibiotic 10-deoxymethymycin.[7]

Aldehyde **6** was readily obtained through the sequence shown in Scheme 2. A palladium-catalyzed cross-coupling reaction between the chiral zinc homoenolate **8**[8,9] and *cis*-2-bromo-2-butene (both commercially available) led to the formation of **11**, which was carefully reduced with diisobutylaluminum hydride at −90 °C to afford **6** in 86% overall yield. Ketone **5** was prepared as described by Paterson et al.[10] in three steps and 57% overall yield. Conversion of (*R*)-**7** into the Weinreb amide **9** was followed by protection as its *p*-methoxybenzyl ether **10**. Subsequent addition of ethyl magnesium bromide provided ethyl ketone **5**. Treatment of **5** with stannous triflate and Et_3N at −78 °C in CH_2Cl_2 generated the corresponding *Z* enolate, which reacted with the γ,δ-unsaturated aldehyde **6** to afford the *syn* aldol adduct **12** in 75% yield (92% based on consumed starting material) and 96:4 diastereomeric ratio. The stereochemical control observed in the formation of **12** is ultimately derived from the tin(II) enolate of ketone **5**.[11]

As depicted in Scheme 1, we planned to postpone the installation of the ketone at C9 to a late stage in our synthetic sequence in order to carry out the requisite functional-group manipulation and chain extension. The stereoselective formation of 1,3-diol **13** was explored using metal-chelation control and intermolecular hydride transfer. The best 1,3-*syn* diastereofacial selectivity (d.r. 95:5) was achieved in the reduction of β-hydroxyketone **12** with DIBAL-H at −78 °C (Scheme 3).[12] The diastereomeric ratio was determined by GC/MS analysis of acetonide **14**.

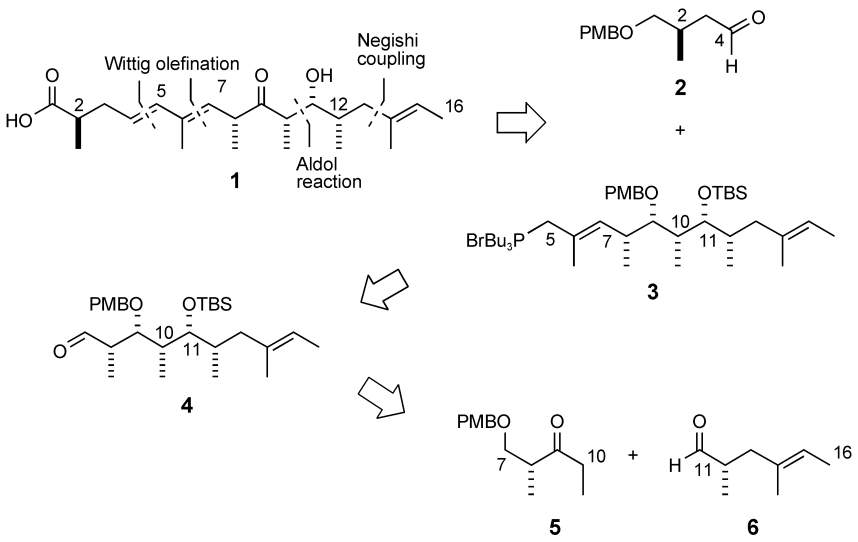
Having secured the diastereoselective preparation of *syn*-diol **13**, we proceeded to its oxidative conversion with DDQ

[*] Prof. R. A. Pilli, I. R. Corrêa, Jr.
Instituto de Química
Universidade Estadual de Campinas – UNICAMP
Campinas, SP – C.P. 6154, 13084-971 (Brazil)
Fax: (+55) 19-3788-3023
E-mail: pilli@iqm.unicamp.br

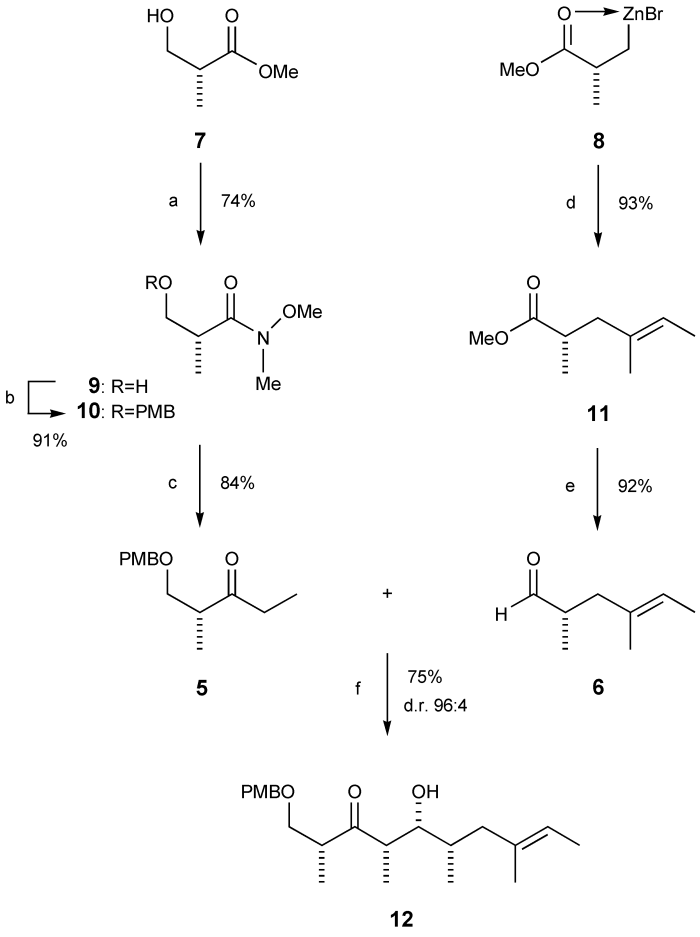
[**] This work was supported by the Fundação de Amparo à Pesquisa do Estado de São Paulo (FAPESP) and the Conselho Nacional para o Desenvolvimento Científico e Tecnológico (CNPq). We are grateful to Dr. Y. Wang, Novartis Pharma for providing us with ^1H and ^{13}C NMR spectra of natural delactonmycin and to Prof. Dr. A. de Meijere, Georg-August Universität, Göttingen for critical reading of the manuscript.

Supporting information for this article is available on the WWW under http://www.angewandte.org or from the author (spectroscopic and analytical data for compounds (−)-**13**, (−)-**20**, and (−)-**1**, including a CD curve for (−)-**1**).

 DOI: 10.1002/anie.200351347 © 2003 Wiley-VCH Verlag GmbH & Co. KGaA, Weinheim



Scheme 1. Retrosynthetic analysis of the putative stereostructure of delactonmycin.



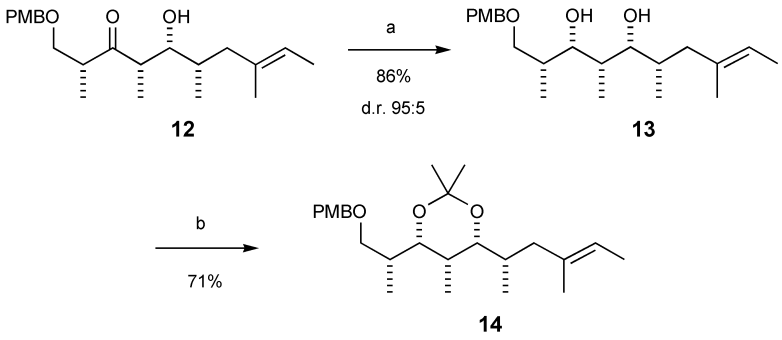
Scheme 2. Synthesis of **12**. Reagents and conditions: a) MeONHMe·HCl, $AlMe_3$, CH_2Cl_2, 0 °C→RT, 18 h; b) PMBOC(=NH)CCl_3, CSA, CH_2Cl_2, room temperature, 18 h; c) EtMgBr, Et_2O, 0 °C, 1 h; d) *cis*-2-bromo-2-butene, [$PdCl_2(PPh_3)_2$], THF, 0 °C→RT, 24 h; e) DIBAL-H, hexane, −90 °C, 1 h; f) $Sn(OTf)_2$, Et_3N, CH_2Cl_2, −78 °C; then **5**, 2 h; then **6**, −78 °C, 2 h and −50 °C, 1 h. PMB = *p*-methoxybenzyl, CSA = camphor-10-sulfonic acid, Tf = trifluoromethanesulfonyl. DIBAL-H = diisobutylaluminium hydride.

into the corresponding *p*-methoxybenzylidene acetal **15** under anhydrous conditions[14] and protection of the secondary hydroxy group at C11 as the *tert*-butyldimethylsilyl ether **16** (Scheme 4). Regioselective cleavage of the PMP acetal[14] efficiently provided the primary alcohol **17**, and its subsequent oxidation with Dess–Martin periodinane led to the aldehyde **4**. An *E*-selective Wittig olefination of **4** with $Ph_3P{=}C(Me)CO_2Et$ in toluene afforded α,β-unsaturated ester **18** as the only product. Reduction of the ester moiety in **18** with DIBAL-H provided the allylic alcohol **19**, which was converted with CBr_4 and PPh_3 in the presence of 2,6-lutidine into the corresponding bromide **20** in 31% overall yield from β-hydroxyketone **12**. The *all-syn* configuration in bromide **20** was established after analysis of the ^1H and ^{13}C NMR spectra and NOESY experiments carried out with acetonide **14** and *p*-methoxybenzylidene acetal **15** (Figure 1).

At this stage, a final Wittig olefination was used to join the known aldehyde **2**[15] and the tributylphosphonium salt derived from allylic bromide **20** (Scheme 5). The coupling was carried out under the conditions described by Tamura et al.[16] to provide **21** (d.r. *E*/*Z* 8:1). Next we sought the chemoselective deprotection of the PMB ethers at C1 and C9. Attempts to deprotect **21** with DDQ invariably gave complex reaction mixtures.[17] In fact, closer inspection of the literature revealed that several authors have been unable to remove methoxybenzyl groups in the presence of conjugated dienes.[18] Several alternative methods (hydrogenolysis, reduction with dissolved metal, as well as Lewis acid conditions)[19,20] were investigated for model compounds without much success. After extensive experimentation, the PMB group of **21** was selectively cleaved with TFA in CH_2Cl_2 to give diol **22**, albeit in low yield.[21]

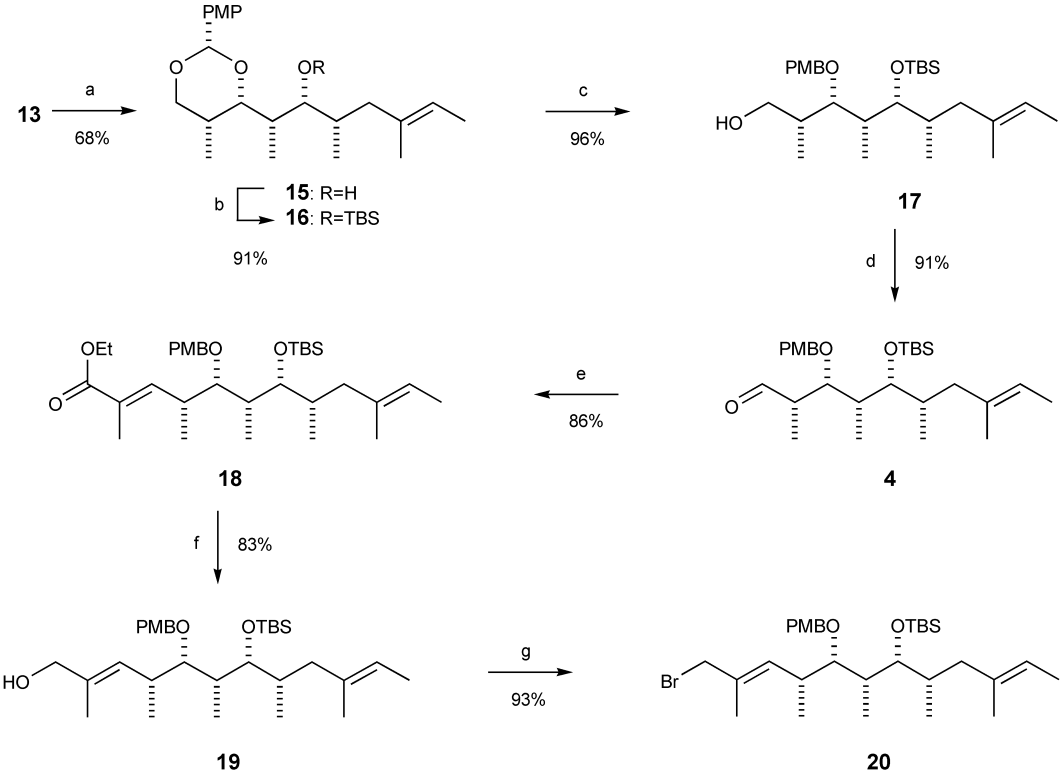
The synthesis was completed with the double oxidation of **22** (oxidation with Dess–Martin periodinane[22] followed by Pinnick oxidation to the carboxylic acid[23]) and deprotection of the secondary TBS ether with HF/pyridine complex in THF. The spectroscopic data of the synthetic (−)-delac-

 © 2003 Wiley-VCH Verlag GmbH & Co. KGaA, Weinheim



Scheme 3. Synthesis of **13** and determination of its d.r. Reagents and conditions: a) DIBAL-H, THF, −78 °C, 3 h; b) $Me_2C(OMe)_2$, PTSA, CH_2Cl_2, room temperature, 12 h. PTSA = *p*-toluenesulfonic acid.

tonmycin (**1**) (IR, HRMS, ^1H and ^{13}C NMR) nicely matched those reported for the natural product,[2] thus allowing us to confirm their identity and unambiguously establish its relative configuration. Unfortunately, the lack of a sample of natural delactonmycin (**1**) or its chiroptical data precluded the determination of its absolute configuration at this point. Studies directed towards the total synthesis of other members of this family of polyketides are now underway in our laboratory and will be reported in due course.



Scheme 4. Synthesis of **20**. Reagents and conditions: a) DDQ, molecular sieves (3 Å), CH_2Cl_2, room temperature, 30 min; b) TBSOTf, 2,6-lutidine, 0 °C → RT, 1 h; c) DIBAL-H, CH_2Cl_2, 0 °C → RT, 2 h; d) Dess–Martin periodinane, CH_2Cl_2/H_2O, room temperature, 15 min; e) $Ph_3P{=}C(Me)CO_2Et$, toluene, room temperature, 36 h; f) DIBAL-H, CH_2Cl_2, −78 °C, 1 h; g) CBr_4, PPh_3, 2,6-lutidine, CH_3CN, room temperature, 15 min. DDQ = 2,3-dichloro-5,6-dicyanobenzoquinone, TBS = *tert*-butyldimethylsilyl, PMP = *p*-methoxyphenyl.

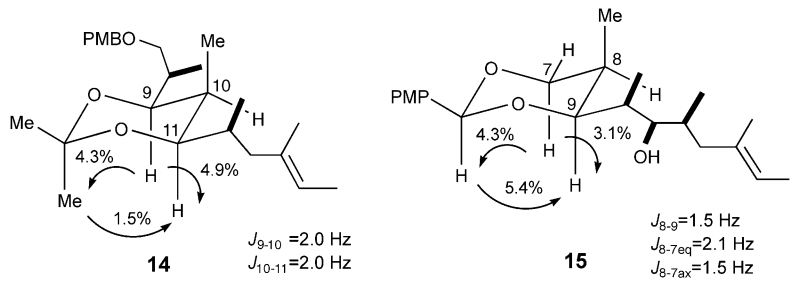
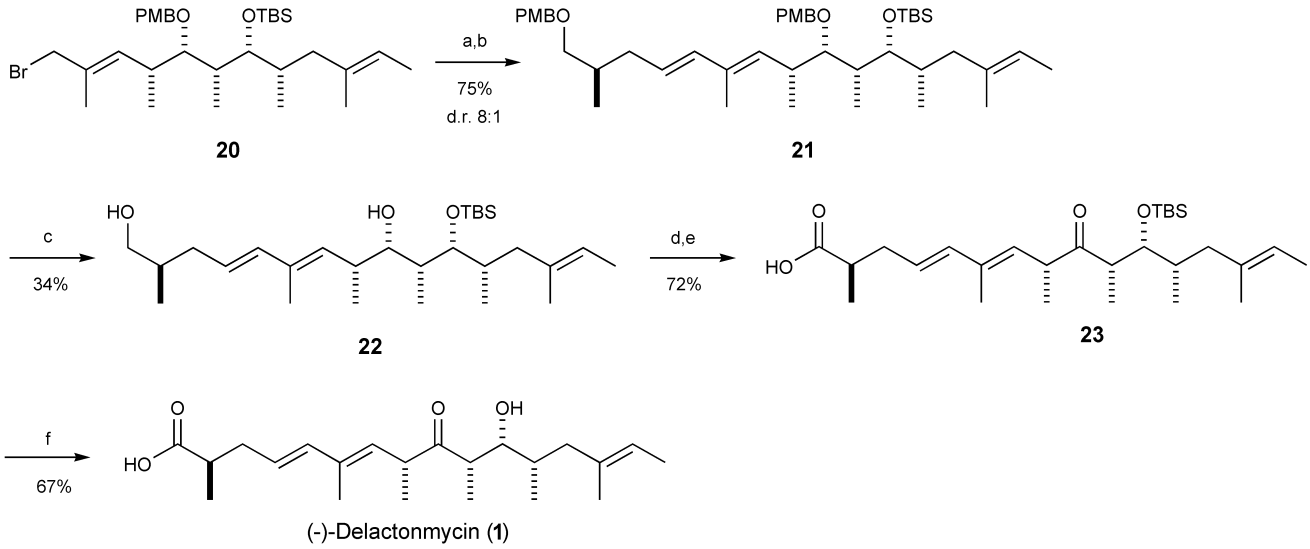


Figure 1. Configurational assignment of acetonide **14** and *p*-methoxybenzylidene acetal **15**.

Received: March 7, 2003 [Z51347]

Keywords: antiviral agents · natural products · structure elucidation · total synthesis · Wittig reactions

 © 2003 Wiley-VCH Verlag GmbH & Co. KGaA, Weinheim



Scheme 5. Completion of **1**. Reagents and conditions: a) PBu_3, MeCN, room temperature, 2 h; b) **2**, KO*t*Bu, toluene, 0 °C, 2 h; c) TFA, CH_2Cl_2, room temperature, 20 min; d) Dess–Martin periodinane, CH_2Cl_2/H_2O, room temperature, 30 min; e) $NaClO_2$, NaH_2PO_4, 2-methyl-2-butene, *t*BuOH/H_2O, room temperature, 2 h; f) HF·pyridine, THF, room temperature, 64 h. TFA = trifluoroacetic acid.

[1] M. Kalesse, M. Christmann, *Synthesis* **2002**, 981 – 1003, and references therein.

[2] Y. Wang, M. Ponelle, J.-J. Sanglier, B. Wolff, *Helv. Chim. Acta* **1997**, *80*, 2157 – 2167.

[3] a) N. Murakami, W. Wang, M. Aoki, Y. Tsutsui, K. Higuchi, S. Aoki, M. Kobayashi, *Tetrahedron Lett.* **1997**, *38*, 5533 – 5536; b) M. Kobayashi, K. Higuchi, N. Murakami, H. Tajima, S. Aoki, *Tetrahedron Lett.* **1998**, *39*, 2859 – 2862.

[4] For the total synthesis of leptomycin B, see: M. Kobayashi, W. Wang, Y. Tsutsui, M. Sugimoto, N. Murakami, *Tetrahedron Lett.* **1998**, *39*, 8291 – 8294.

[5] For total syntheses of callystatin A, see: a) N. Murakami, W. Wang, M. Aoki, Y. Tsutsui, M. Sugimoto, M. Kobayashi, *Tetrahedron Lett.* **1998**, *39*, 2349 – 2352; b) M. T. Crimmins, B. W. King, *J. Am. Chem. Soc.* **1998**, *120*, 9084 – 9085; c) A. B. Smith III, B. M. Brandt, *Org. Lett.* **2001**, *3*, 1685 – 1688; d) M. Kalesse, M. Quitschalle, C. P. Khandavalli, A. Saeed, *Org. Lett.* **2001**, *3*, 3107 – 3109; e) J. A. Marshall, M. P. Bourbeau, *J. Org. Chem.* **2002**, *67*, 2751 – 2754; f) J. L. Vicario, A. Job, M. Wolberg, M. Müller, D. Enders, *Org. Lett.* **2002**, *4*, 1023 – 1026; g) D. Enders, J. L. Vicario, A. Job, M. Wolberg, M. Müller, *Chem. Eur. J.* **2002**, *8*, 4272 – 4284; h) M. Lautens, T. A. Stammers, *Synthesis* **2002**, 1993 – 2012.

[6] a) N. Murakami, M. Sugimoto, M. Kobayashi, *Bioorg. Med. Chem.* **2001**, *9*, 557 – 567; b) N. Murakami, M. Sugimoto, T. Nakajima, M. Kawanishi, Y. Tsutsui, M. Kobayashi, *Bioorg. Med. Chem.* **2000**, *8*, 2651 – 2661.

[7] R. A. Pilli, C. K. Z. de Andrade, C. R. O. Souto, A. de Meijere, *J. Org. Chem.* **1998**, *63*, 7811 – 7819.

[8] E. Nakamura, K. Sekiya, I. Kuwajima, *Tetrahedron Lett.* **1987**, *28*, 337 – 340.

[9] Y. Tamaru, H. Ochiai, T. Nakamura, K. Tsubaki, Z. Yoshida, *Tetrahedron Lett.* **1985**, *26*, 5559 – 5562.

[10] I. Paterson, E. A. Arnott, *Tetrahedron Lett.* **1998**, *39*, 7185 – 7188.

[11] I. Paterson, R. D. Tillyer, *Tetrahedron Lett.* **1992**, *33*, 4233 – 4236.

[12] S.-i. Kiyooka, H. Kuroda, Y. Shimasaki, *Tetrahedron Lett.* **1986**, *27*, 3009 – 3012.

[13] Y. Oikawa, T. Yoshioka, O. Yonemitsu, *Tetrahedron Lett.* **1982**, *23*, 889 – 892.

[14] S. Takano, M. Akiyama, S. Sato, K. Ogasawara, *Chem. Lett.* **1983**, 1593 – 1596.

[15] Aldehyde **2** was prepared in five steps from (*S*)-**7** in 56 % overall yield: J. Mulzer, M. Hanbauer, *Tetrahedron Lett.* **2000**, *41*, 33 – 36.

[16] R. Tamura, K. Saegusa, M. Kakihana, D. Oda, *J. Org. Chem.* **1988**, *53*, 2723 – 2728.

[17] K. Horita, T. Yoshioka, T. Tanaka, Y. Oikawa, O. Yonemitsu, *Tetrahedron* **1986**, *42*, 3021 – 3028.

[18] a) T. Onoda, R. Shirai, S. Iwasaki, *Tetrahedron Lett.* **1997**, *38*, 1443 – 1446; b) S. M. Bauer, R. W. Armstrong, *J. Am. Chem. Soc.* **1999**, *121*, 6355 – 6366; c) K. A. Scheidt, T. D. Bannister, A. Tasaka, M. D. Wendt, B. M. Savall, G. J. Fegley, W. R. Roush, *J. Am. Chem. Soc.* **2002**, *124*, 6981.

[19] T. W. Greene, P. G. M. Wuts, *Protective Groups in Organic Synthesis*, 3rd ed., Wiley, New York, **1999**.

[20] K. Jarowicki, P. Kocienski, *J. Chem. Soc. Perkin Trans. 1* **2001**, 2109 – 2135, and references therein.

[21] a) J. D. White, J. C. Amedio, *J. Org. Chem.* **1989**, *54*, 736 – 738; b) L. Yan, D. Kahne, *Synlett* **1995**, 523 – 524.

[22] a) B. D. Dess, J. C. Martin, *J. Am. Chem. Soc.* **1991**, *113*, 7277 – 7287; b) B. D. Dess, J. C. Martin, *J. Org. Chem.* **1983**, *48*, 4155 – 4156.

[23] B. S. Bal, W. E. Childers, H. W. Pinnick, *Tetrahedron* **1981**, *37*, 2091 – 2096.

 © 2003 Wiley-VCH Verlag GmbH & Co. KGaA, Weinheim

Self-Assembling Peptide Fibers

Introducing Branches into a Self-Assembling Peptide Fiber**

*Maxim G. Ryadnov and Derek N. Woolfson**

There is a growing interest in employing peptides as building blocks in the self-assembly of supramolecular structures.[1] Such assemblies have potential as novel scaffolds for functionalizing surfaces and in tissue engineering.[2] Elsewhere,[3] we described a self-assembling fiber (SAF) system comprising two designed peptides (**1** and **2**, also known as SAF-p1 and SAF-2a, Figure 1). These sequences are based on established

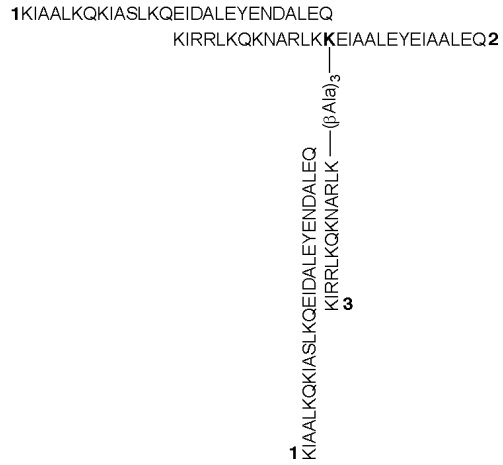


Figure 1. SAF and T-SAF peptide building blocks of linear and branched fibers. Lysine 14 of **2** is highlighted in bold.

design principles for leucine-zipper motifs.[4] However, unlike all other leucine zippers, which are blunt ended, the SAF peptides are designed to assemble with sticky ends that facilitate fibrillogenesis (Figure 1, see also Supporting Information). Like other systems,[1a,c,f] the SAF peptides are linear and form exclusively linear and nonbranching fibers when mixed; note, **2** is a slight redesign of the previously described SAF-p2,[3] this new design combines with **1** to give more-stable and better-ordered linear fibers (see Supporting Information). Natural protein fibers, such as those formed by actin, collagen, and fibrin form branches. We set out to design special units to complement the standard SAF building blocks and, so, engineer branched fibers de novo. Herein we report T-shaped peptides, T-SAFs, that coassemble with the standard SAF peptides to give branched self-assembling fibers. In T-SAFs the "bar" of the "T" is the complete SAF peptide **2** and the "stem" (peptide **3**) is the *N*-terminal half of **2**; the stem and the bar are joined through a linker, typically of three β-alanine (βALA) units, between the *C*-terminus of peptide **3** and the ε-amino group of the central lysine (lysine 14) of peptide **2** (Figure 1). In principle, when combined with peptides **1** and **2**, T-SAFs should promote assembly of orthogonally conjoined fibers.

We applied different approaches[5] to synthesize T-SAFs (supporting information), however, only two gave the desired product in reasonable yields: a) punctuated solid phase synthesis, in which the bar peptide was synthesized, followed by synthesis of the stem from the side chain of selectively deprotected lysine 14; b) chemoselective ligation by using deprotected bar and stem peptides, in which lysine 14 was activated as bromoacetyl to accept a *C*-terminal cysteine engineered into **3**. In both methods it was essential to extend the side chain of lysine 14 of the bar peptide with β-alanine or ε-aminohexanoic acid units before coupling it to the stem peptide.

We tested coassembly of T-SAF with **1** and **2** under our standard conditions (100 μM each of **1** and **2,** 10 mM 3-(N-morpholino)propanesulfonic acid (MOPS) pH 7, 20 °C, overnight). For **1** and **2** alone, transmission and scanning electron microscopy (TEM and SEM) revealed linear structures ≈ 50 nm thick that extend for many microns without deviation, junctions or branches (Supporting Information). However, with 0.01 to 100 μM T-SAF branches were visible

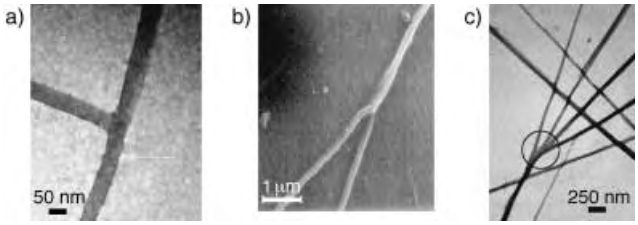


Figure 2. TEM (a and c) and SEM (b) images of fibers formed in the presence of T-SAF peptide. Peptides **1**, **2** and T-SAF were at 100 μM.

(Figure 2, see also Supporting Information). The highest density of the branched fibers was observed at equimolar ratios of T-SAF and SAF peptides — 100 μM in each of peptides **1**, **2** and the T-SAF — in which ≈ 30 % of the fibers had branches. Otherwise, the appearance of these fibers was similar to that of the straight fibers.

Most of the branched fibers had just one branch; multiply branched fibers were also present (circled in Figure 2c), but these were less frequent. This is perhaps surprising given that, apart from the additions to lysine 14, the bar of the T-SAF was identical to **2**. Thus, incorporation of T-SAFs into fibers might have been expected to occur at a similar rate to peptide **2**, which would have resulted in multiply branched fibers and possibly cross-linked networks. However, the samples did not gel as might have been expected in this case. Thus, for the current design incorporation of T-SAFs and subsequent branching is not quantitative and has to be assessed empirically as a function of T-SAF concentration.

[*] Dr. D. N. Woolfson, Dr. M. G. Ryadnov
Centre for Biomolecular Design and Drug Development
School of Biological Sciences
University of Sussex
Falmer BN1 9QG (UK)
Fax: (+44) 1273-678-433
E-mail: dek@biols.susx.ac.uk

[**] We thank Dave Randall for recording the SEM images, members of the DNW group for discussions and the BBSRC of the UK for financial support (grant E13753).

Supporting information for this article is available on the WWW under http://www.angewandte.org or from the author.

 DOI: 10.1002/anie.200351418 © 2003 Wiley-VCH Verlag GmbH & Co. KGaA, Weinheim

We used circular dichroism (CD) spectroscopy to investigate further the effect of T-SAF on the coassembly of peptides **1** and **2**. CD spectroscopy allows the rate and extent of fiber assembly to be gauged in solution.[3] In isolation, peptides **1** and **2** were unfolded, but when mixed they coassembled to form α-helical fibers with a distinctive CD spectrum (Figure 3a). CD spectra recorded at intervals after

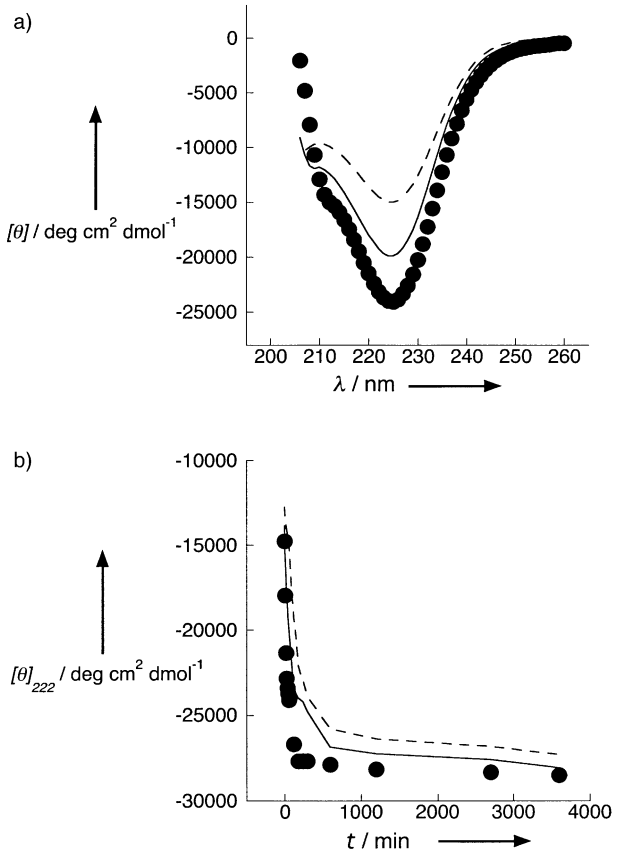


Figure 3. CD measurements following the assembly of peptides **1** and **2** in the absence and presence of T-SAF. a) CD spectra for a mixture of peptides **1** and **2** (black discs); representative spectra for mixtures with T-SAF at 0.1 μM (solid line) and 10 μM T-SAF (broken line). b) Build up of the CD signal at 222 nm for the various mixtures. Key: as in (a). Conditions: 100 μM in peptides 1 and 2, 10 mM MOPS, pH 7, 20 °C.

mixing showed the buildup of the α-helical structure, which was complete within several hours at 20 °C, at which point the fibers are "mature". In contrast, 1:1 mixtures of peptide **1** and T-SAF failed to yield CD spectra or electron micrographs indicative of fiber formation. Thus, T-SAF did not substitute completely for peptide **2** in fiber assembly. Figure 3a shows representative CD spectra recorded 1 hour after mixing peptides **1** and **2** in the presence of 0.01 to 100 μM T-SAF. Essentially, higher concentrations of T-SAF reduced α-helix formation in this time. T-SAF at a concentration of 1 μM provided an interesting cutoff: at this concentration and above the helical content was ≈50% of that for a pure peptide **1** + **2** mixture (Figure 3a). Furthermore, TEM images recorded for these samples showed no visible linear or branched fibers, and further incubations of 2 hours were required to observe these. At the lower T-SAF concentrations, the higher helical signals were achieved (Figure 3a), and fibers were observed by TEM. At all concentrations of T-SAF, the final helical signal did plateau. However, the time taken to achieve this increased with increasing concentration of T-SAF; for instance, with 100 μM of each of peptides **1** and **2** and T-SAF maturation took 2–3 days. Interestingly, the kinetics of fiber assembly in the presence of T-SAF also grouped with T-SAF concentration above and below 1 μM (Figure 3b). TEM images recorded for all of the matured samples revealed both linear and branched fibers.

A model consistent with the CD data, and the low density of branching observed by EM, is that **2** and T-SAF compete for **1** during fiber assembly with **2** being the preferred partner. What causes this preference? First, the mature fibers are multistranded and many peptide units thick.[3] Thus, appendages to the peptide building blocks, such as those in T-SAF, probably interrupt thickening and are not fully tolerated in fiber assembly. Second, fibers comprising purely **1** and **2** show considerable internal order; the leucine zippers are hexagonally packed and aligned along the long fiber axis.[7] This order is also likely to limit the inclusion of peptides other than **1** and **2** into the fibers, as these would effectively be imperfections. HPLC analysis of matured fibers confirmed that T-SAF incorporated into fibers at the expense of **2**. The incorporation increased and saturated with increasing T-SAF: at 1 μM T-SAF virtually all the peptide was incorporated (≈0.7% of the total peptide in the fibers), but only ≈ten times more incorporation was achieved at 100 μM T-SAF (Table S1, Supporting Information).

Further evidence for direct incorporation of T-SAF came from the following control. We made a T-terminator peptide (see Supporting Information) in which the stem was the *C*-terminal half of peptide **2** rather than its *N*-terminal half. This construction should not propagate orthogonal fibers as shown in Figure 1. Indeed, this was observed: in combination with peptides **1** and **2**, the T-terminator yielded short (< 1 μm), thin (< 20 nm) and unbranched structures at up to 1 μM, and completely inhibited fiber assembly above this concentration.

Peptides that form amyloid and amyloidlike structures also branch.[1g,6] In this case, the peptides form protofibrils that wrap around each other in a ropelike fashion to form the matured fibers, and some unfinished ends of the protofibrils produce branches. The assembly of our structures is different: first, the SAFs appear to be rigid rods that are unlikely to wrap around one another; second, we introduce the notion of rationally designed branching into a synthetic self-assembling fiber. We have demonstrated this through the coassembly of novel T-shaped peptides with linear building blocks. The bottom-up assembly of peptide-based nanostructures of this type holds promise for the development of novel scaffolds for applications in nanobiotechnology.[2]

Experimental Section

Peptide synthesis: Peptides were synthesized by using standard Fmoc protocols, purified by reversed-phase HPLC, and analyzed by MALDI-Tof mass spectrometry (supporting information).

 © 2003 Wiley-VCH Verlag GmbH & Co. KGaA, Weinheim

Fiber assembly: All samples of fibers were prepared with peptide **1** and peptide **2** (each at 100 μM) with the designated amounts of T-SAF peptides, and incubated for 1–120 h at 20 °C in filtered 10 mM MOPS, pH 7.

CD spectroscopy: All peptide samples were prepared as above. CD Measurements were made in 1 mm quartz cuvettes. Data points for CD spectra were recorded at 1 nm intervals by using a 1 nm bandwidth and 4–16 s response times. After baseline correction, ellipticities in mdeg were converted to molar ellipticities ($[\theta]$, deg cm^2 dmol res^{-1}) by normalizing for the concentration of peptide bonds. The concentration of peptide bonds was taken as 54 μM ($2 \times (28-1)) \times$ 100 μM) for all spectra. This neglected any contribution to the CD from the T-SAFs. Time course measurements were made at 222 nm recording spectra every 10 min during first 60 min period and every 60 min after. The signals were converted to molar ellipticities ($[\theta]_{222}$) neglecting the concentrations of the T-SAF peptides.

HPLC analysis of incorporation of T-SAF peptides into fibers: 300 μL of fiber-forming mixtures (100 μM in peptides **1** and **2** SAF, 10 mM MOPS, pH 7) were incubated at room temperature for $\approx$30 h with different concentrations of T-SAF (100 and 1 μM). After incubation each sample was centrifuged to pellet the fibers. The pellets obtained from three or six samples containing the same starting concentration of T-SAF were combined, washed with the buffer and dissolved in 20 μL of HPLC buffer A for analytical reversed-phase HPLC. Peptide fractions were identified by MALDI-TOF, and collected, lyophilized and dissolved in 200 μL of water. The concentrations of peptides in these fractions were calculated based on the absorbance at 280 nm. This procedure was repeated three times for each measurement. The results are summarized in the Supporting Information.

EM visualization and analysis: Fiber suspensions were dried onto carbon-coated copper specimen grids and stained with uranyl acetate (all at 20 °C) for electron microscopy as described elsewhere.[3] The numbers of branched fibers present were measured over 200–250 fibers. Standard deviations on the measurements were 0.01 (for SAF/T-SAF, 100: $\leq$0.1 μM) and 0.15 (for SAF/T-SAF, 100: $\geq$1 μM). Additional TEM and SEM images are found in the Supporting Information.

Received: March 17, 2003 [Z51418]

Keywords: fibrous proteins · nanostructures · peptides · protein design · self-assembly

[1] a) S. G. Zhang, T. Holmes, C. Lockshin, A. Rich, *Proc. Natl. Acad. Sci. USA* **1993**, *90*, 3334–3338; b) M. R. Ghadiri, J. R. Granja, R. A. Milligan, D. E. McRee, N. Khazanovich, *Nature* **1993**, *366*, 324–327; c) A. Aggeli, M. Bell, N. Boden, J. N. Keen, P. F. Knowles, T. C. B. McLeish, M. Pitkeathly, S. E. Radford, *Nature* **1997**, *386*, 259–262; d) C. E. MacPhee, C. M. Dobson, *J. Am. Chem. Soc.* **2000**, *122*, 12707–12713; e) J. E. Padilla, C. Colovos, T. O. Yeates, *Proc. Natl. Acad. Sci. USA* **2001**, *98*, 2217–2221; f) S. A. Potekhin, T. N. Melnik, V. Popov, N. F. Lanina, A. A. Vazina, P. Rigler, A. S. Verdini, G. Corradin, A. V. Kajava, *Chem. Biol.* **2001**, *8*, 1025–1032; g) A. Aggeli, I. A. Nyrkova, M. Bell, R. Harding, L. Carrick, T. C. McLeish, A. N. Semenov, N. Boden, *Proc. Natl. Acad. Sci. USA* **2001**, *9*, 11857–11862.

[2] a) T. C. Holmes, *Trends Biotechnol.* **2002**, *20*, 16–21; b) T. O. Yeates, J. E. Padilla, *Curr Opin Struct Biol* **2002**, *12*, 464–470.

[3] M. J. Pandya, G. M. Spooner, M. Sunde, J. R. Thorpe, A. Rodger, D. N. Woolfson, *Biochemistry* **2000**, *39*, 8728–8734.

[4] a) P. B. Harbury, T. Zhang, P. S. Kim, T. Alber, *Science* **1993**, *262*, 1401–1407; b) A. Lupas, *Contrib. Gynecol. Obstet.* **1996**, *21*, 375–382; c) D. N. Woolfson, T. Alber, *Protein Sci.* **1995**, *4*, 1596–1607.

[5] a) A. Aletras, K. Barlos, D. Gatos, S. Koutsogianni, P. Mamos, *Int. Enamelist* **1995**, *45*, 488–496; b) J. A. Borgia, G. B. Fields, *Trends Biotechnol.* **2000**, *18*, 243–251; c) P. E. Dawson, S. B. H. Kent, *J. Am. Chem. Soc.* **1993**, *115*, 7263–7266; d) S. A. Kates, S. B. Daniels, F. Albericio, *Anal. Biochem.* **1993**, *212*, 303–310; e) M. Mutter, S. Vuilleumier, *Angew. Chem. Int. Ed. Engl.* **1989**, *28*, 535–554; f) J. P. Tam, *Proc. Natl. Acad. Sci. USA* **1988**, *85*, 5409–5413.

[6] J. D. Harper, C. M. Lieber, P. T. Lansbury, Jr., *Chem. Biol.* **1997**, *4*, 951–959.

[7] A. M Smith, D. N. Woolfson, unpublished results.

 © 2003 Wiley-VCH Verlag GmbH & Co. KGaA, Weinheim

1,3-Dipolar Cycloadditions

A Homo [3+2] Dipolar Cycloaddition: The Reaction of Nitrones with Cyclopropanes**

*Ian S. Young and Michael A. Kerr**

Cycloadditions are among the most trusted of chemical transformations available to the synthetic chemist. The predictability of the transition state based on steric and electronic considerations allows for the strategic construction of complex molecular assemblies. While the Diels–Alder reaction has received the most attention, 1,3-dipolar cycloadditions have also maintained a place of prominence in the toolbox of the synthetic chemist.[1]

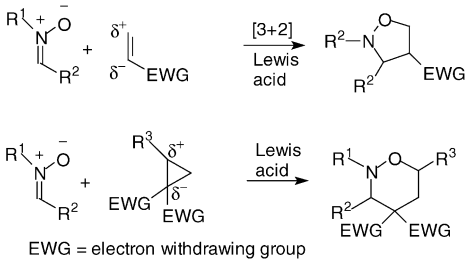
During recent studies of the synthetic reactions of cyclopropanediesters,[2] we were struck by the fact that simple 1,1-cyclopropane diesters behaved very much like α,β-unsaturated carbonyl compounds in their ability to react with nucleophiles in what could be considered a homo-Michael addition (an observation not unnoticed by others).[3,4] The strained bonds in the cyclopropane ring have long been considered to have a significant π character[5] and in 1,1-cyclopropane diesters this bond can be polarized and further weakened by coordination of a Lewis acid to one or both of the ester moieties. This reactivity suggests that such compounds are one-carbon homologues of electron-deficient olefins, and led us to investigate their reactions with nitrones in what is naively a dipolar homo [3+2] cycloaddition[6] (Scheme 1) resulting in the formation of tetrahydro-1,2-oxazines.[7] In this communication we disclose the first reaction of a nitrone with a cyclopropane to produce a

[*] Prof. Dr. M. A. Kerr, I. S. Young
Department of Chemistry
The University of Western Ontario
London, Ontario N6A 5B7 (Canada)
Fax: (+1) 519-661-3022
E-mail: makerr@uwo.ca

[**] We thank the Natural Sciences and Engineering Research Council (NSERC) for funding. I.Y. is the recipient of an NSERC postgraduate scholarship.

Supporting information for this article is available on the WWW under http://www.angewandte.org or from the author.

 DOI: 10.1002/anie.200351573 © 2003 Wiley-VCH Verlag GmbH & Co. KGaA, Weinheim



Scheme 1. The homo [3 + 2] cycloaddition of nitrones with cyclopropanes.

tetrahydro-1,2-oxazine and the application of this "cycloaddition" to the synthesis of the [3.3.1] bicyclic core of FR-900482 and related compounds.[8]

In the initial experiment we combined the *N*-*p*-tolyl nitrone (**1a**) with dimethyl-2-phenyl-1,1-cyclopropanedicarboxylate (**2b**) in the presence of 5 mol% $Yb(OTf)_3$ in dichloromethane. The mixture was stirred overnight, and yielded the expected cycloadduct in 94% yield (see Table 1). To probe the generality of this reaction, a number of nitrones[9] **1a–d** were treated with several readily prepared cyclopropanes **2a–d**.[10] The results are shown in Table 1. A brief survey of a series of common Lewis acids ($BF_3{\cdot}OEt_2$, $Cu(OTf)_2$, $Sc(OTf)_3$, $TiCl_4$, $SnCl_4$, and $AlCl_3$) failed to identify a catalyst superior to $Yb(OTf)_3$.[11] The nitrones bearing a *p*-tolyl group on the nitrogen atom were significantly more reactive than those bearing a methyl group and proceeded to give the products in generally better yields. The presence of a phenyl, styryl, or vinyl substituent vicinal to the diester moiety on the cyclopropane unit greatly reduced the reaction times and for the phenyl and styryl cases, resulted in excellent yields. The modest yields observed with the vinyl cyclopropane may be due to some polymerization under the Lewis acid conditions. In all cases the sole regioisomer isolated had the oxygen atom of the nitrone distal to the geminal diester moiety. This regioselectivity, as well as the increased reaction rates with a π system vicinal to the diester moiety, is explained by considering that the cyclopropane likely undergoes a significant degree of charge separation in the presence of a Lewis acid such as $Yb(OTf)_3$ (Figure 1). Such a charge

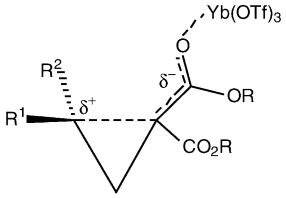


Figure 1. Lewis acid induced polarization of 1,1-cyclopropanediesters.

separation would be enhanced by the presence of a carbocation-stabilizing group on the cyclopropane unit (R^1 or R^2 = phenyl or vinyl). In every case examined the reactions produced, as a single diastereomer, the product in which the substituents at C3 and C6 bore a *cis* relationship. This was confirmed by analysis of the coupling constants in the ^1H NMR spectra and by single-crystal X-ray analysis in the case of compounds **3b**, **c**, and **f** (entries 2, 3, and 6).

While it is convenient to label this reaction as a cycloaddition based on the formation of a ring structure and by analogy to the reaction of a nitrone with an alkene, the transformation may proceed in a number of ways. Figure 2

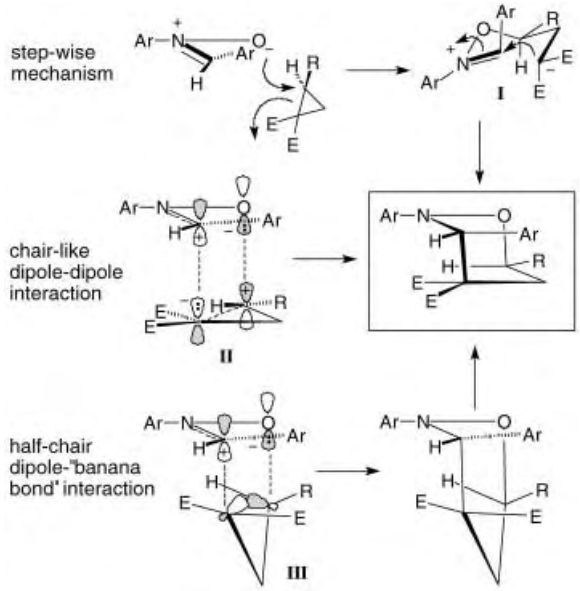
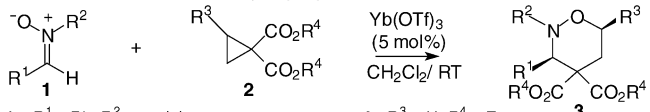


Figure 2. Possible reaction modes for nitrones with cyclopropane diesters.

shows three models for the reaction course: 1) A stepwise annulation mechanism involving an initial attack of the nitrone oxygen atom onto the cyclopropane followed by the attack of the resulting malonate onto the imminium species **I** via a chair conformation, 2) a concerted reaction in which the transition state has the cyclopropane largely ring-opened to a 1,3-dipolar species and reacting with the 1,3-dipolar nitrone **II**, and 3) a fully concerted [3 + 2] cycloaddition in which the transition state has the nitrone reacting with the strained σ bond in a half-chair conformation (**III**). In each case the most favorable conformation would result in the observed *cis* relationship between the substituents at C3 and C6 on the newly formed tetrahydro-1,2-oxazine. The fact that the reactions are entirely stereoselective and yield what is most likely to be the kinetic product (an axial/equatorial relationship between the C3 and C6 substituents) implies a concerted process although a stepwise process (via species **I**), in which there is no bond rotation before ring closure cannot be ruled out. It is conceivable that in cases where the substituent on the cyclopropane unit can stabilize a developing carbocation, the process may resemble a transition state such as **II** (substantial charge separation in the cyclopropane) whereas in the case of the unsubstituted cyclopropane **2a** there would be much less charge separation prior to reaction with the nitrone and transition state **III** may be a more accurate description. Efforts are in progress to perform computer-modeling experiments at a high level of theory to gain insight into a possible course of reaction.

 © 2003 Wiley-VCH Verlag GmbH & Co. KGaA, Weinheim

Table 1: The reaction of nitrones with 1,1-cyclopropanediesters.



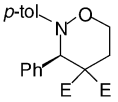
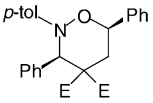
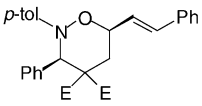
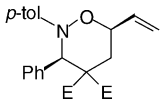
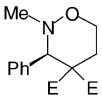
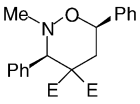
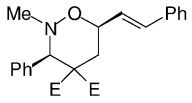
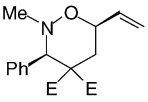
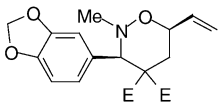
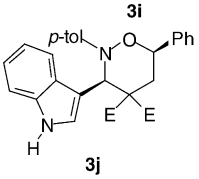
1

1a R^1 = Ph, R^2 = *p*-tolyl
1b R^1 = Ph, R^2 = Me
1c R^1 = 3,4-methylenedioxyphenyl, R^2 = Me
1d R^1 = 3-indolyl, R^2 = *p*-tolyl

2

2a R^3 = H, R^4 = Et
2b R^3 = Ph, R^4 = Me
2c R^3 = styryl, R^4 = Me
2d R^3 = vinyl, R^4 = Et

3

Entry	Nitrone	Cyclopropane	*t* [h]	Product (**3**)[c]	Yield
1	**1a**	**2a**	18[a]	 **3a**	77%
2	**1a**	**2b**	18	 **3b**	94%
3	**1a**	**2c**	5	 **3c**	95%
4	**1a**	**2d**	42	 **3d**	73%
5	**1b**	**2a**	18[b]	 **3e**	76%
6	**1b**	**2b**	42	 **3f**	84%
7	**1b**	**2c**	36	 **3g**	74%
8	**1b**	**2d**	18[b]	 **3h**	52%
9	**1c**	**2c**	42	 **3i**	50%
10	**1d**	**2b**	3[d]	 **3j**	96%

[a] $Yb(OTf)_3$ (20 mol%) was used. [b] The reaction was performed in refluxing 1,2-dichloroethane. [c] E = methyl or ethyl ester. [d] CH_3CN was used as solvent.

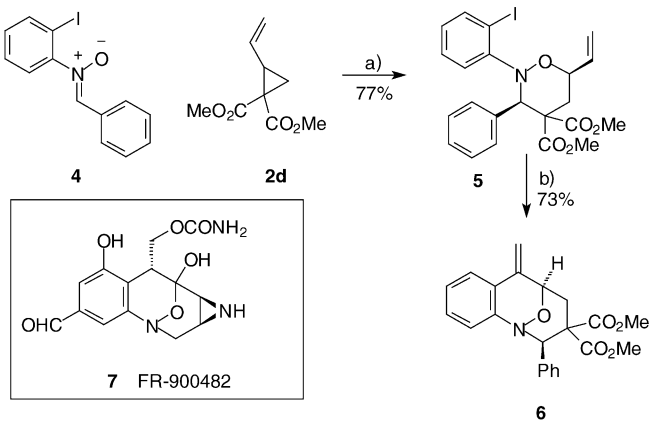
Recently there have been several total syntheses of the antitumor antibiotic FR-900482 (**7**, Scheme 2), a compound that bears the tetrahydro-1,2-oxazine ring as a key structural element.[12] A significant portion of the synthetic efforts were aimed at the preparation of the [3.3.1] bicyclic core, a task that is well suited to the reactions described above. The synthesis of the tricyclic ring system present in FR-900482 commences with the treatment of nitrone **4** with cyclopropane **2d** under the influence of catalytic $Yb(OTf)_3$, which yields 1,2-oxazine **5** in 77% yield. Heck cyclization (in the style of Danishefsky[12b]), produced the desired target compound **6** in 73% yield, and 56% over the two steps.

In conclusion, we have presented a new mode of chemical reactivity for cyclopropanediesters and nitrones, which has resulted in a valuable, high-yielding, and stereoselective synthetic protocol. This reaction represents the first example of a dipolar homo [3+2] cycloaddition. The utility of the reaction was demonstrated in a two-step preparation of the tricyclic skeleton of FR-900482 with its unusual tetrahydro-1,2-oxazine core. Our future and ongoing efforts in this regard include the investigation of a Kobayashi-type chiral ytterbium catalyst[13] to generate adducts as a single antipode, an investigation of the mechanistic nature of the reaction, the application of this transformation to the chemical synthesis of FR-900482, and the chemical transformations of the adducts to yield useful intermediates for chemical synthesis.

Experimental Section

3: $Yb(OTf)_3 \cdot xH_2O$ (5 mol%) was added to a solution of cyclopropane **2** (0.5 mmol) and nitrone **1** (0.6 mmol) in CH_2Cl_2 (4 mL) or 1,2-dichloroethane. Reactions in CH_2Cl_2 were performed at room temperature, while reactions in 1,2-dichloroethane were refluxed for the time indicated in Table 1. The reaction mixture was then preadsorbed onto silica gel and the pure product was obtained after flash column chromatog-

 © 2003 Wiley-VCH Verlag GmbH & Co. KGaA, Weinheim



Scheme 2. Synthesis of the FR-900482 skeleton. a) $Yb(OTf)_3$, CH_2Cl_2, 25 °C, 18 h; b) $[Pd(PPh_3)_4]$ (20 mol%), Et_3N, 80 °C, 18 h.

raphy on silica gel (elution with 2% ethyl acetate in hexanes). Samples could be recrystallized from CH_2Cl_2/hexanes if desired.

Physical properties for **3c**: m.p. 141–142 °C, colorless needles. $R_f = 0.36$ (20% ethyl acetate in hexanes); ^{1}H NMR (400 MHz, $CDCl_3$): $\delta = 7.58$–7.55 (m, 2H), 7.51–7.49 (m, 2H), 7.40–7.36 (m, 2H), 7.33–7.28 (m, 1H), 7.22–7.19 (m, 3H), 7.02–6.95 (m, 4H), 6.83 (d, $^3J = 16.4$ Hz, 1H), 6.43 (dd, $^3J = 16.4$, 6.4 Hz, 1H), 5.68 (s, 1H), 4.71–4.66 (m, 1H), 3.92 (s, 3H), 3.48 (s, 3H), 2.74–2.65 (m, 2H), 2.19 ppm (s, 3H). ^{13}C NMR (100 MHz, $CDCl_3$) $\delta = 170.0$, 168.3, 146.2, 136.6, 135.0, 132.5, 131.0, 130.5, 129.0, 128.6, 128.0, 128.0, 127.9, 127.0, 126.6, 116.1, 77.1, 59.1, 53.4, 52.6, 30.6, 20.5 ppm.; IR (thin film): $\tilde{\nu} =$ 3057, 3026, 2951, 2928, 1741, 1612, 1508, 1438, 1239, 1200, 1075, 965, 816, 747, 698 cm^{-1}.; HRMS (70 eV) calcd for $C_{29}H_{29}O_5N = 471.2047$, found 471.2034.

Received: April 4, 2003 [Z51573]

Keywords: cycloaddition · cycloalkanes · heterocycles · nitrones

[1] a) *1,3-Dipolar Cycloaddition Chemistry, Vol. 1* (Ed. A. Padwa), Wiley, New York, **1984**; b) R. Huisgen in *Advances in Cycloaddition, Vol. 1*, (Ed.: D. P. Curran), JAI Press Inc., Greenwich, **1988**, pp. 1–32; c) P. Deshong, S. W. Lander, Jr., J. M. Leginus, C. M. Dicken in *Advances in Cycloaddition, Vol. 1*, (Ed.: D. P. Curran), JAI Press Inc., Greenwich, **1988**, pp. 87–128; d) A. Padwa in *Advances in Cycloaddition, Vol. 2*, (Ed.: D. P. Curran), JAI Press Inc., Greenwich, **1990**, pp. 1–91; e) W. Carruthers, *Cycloaddition Reactions in Organic Synthesis*, Pergamon, Oxford, **1990**; f) A. Padwa in *Comprehensive Organic Synthesis, Vol. 4* (Eds.: B. M. Trost, I. Flemming), Wiley, New York, **1991**; g) P. A. Wade in *Comprehensive Organic Synthesis, Vol. 4* (Eds.: B. M. Trost, I. Flemming), Wiley, New York, **1991**; h) R. Huisgen in *1,3-Dipolar Cycloaddition Chemistry, Vol. 1* (Ed.: A. Padwa), Wiley, New York, **1984**, pp. 1–176; i) K. V. Gothelf, K. A. Jorgensen. *Chem. Rev.* **1998**, *98*, 863; j) S. Kanemasa, *Synlett* **2002**, 1371; k) K. V. Gothelf in *Cycloaddition Reactions in Organic Synthesis* (Eds.: S. Kobayashi and K. A. Jorgensen), Wiley-VCH, Weinheim, **2002**,pp. 211–248; l) S. Kanemasa in *Cycloaddition Reactions in Organic Synthesis* (Eds.: S. Kobayashi and K. A. Jorgensen), Wiley-VCH, Weinheim, **2002**, pp. 249–300.

[2] a) P. E. Harrington, M. A. Kerr, *Tetrahedron Lett.* **1997**, *38,* 5949; b) M. A. Kerr, R. G. Keddy, *Tetrahedron Lett.* **1999**, 5671; c) D. B. England, T. D. O. Kuss, R. G. Keddy, *J. Org. Chem.* **2001**, *66*, 4704; d) D. B. England, T. K. Woo, M. A. Kerr, *Can. J. Chem.* **2001**, *79*, 992.

[3] For a review see: a) S. J. Danishefsky, *Accts. Chem. Res.* **1979**, *12*, 66. For more recent examples see: b) H. Kotsuki, K. Arimura, T. Maruzawa, R. Ohshima, *Synlett* **1999**, 650; c) E. J. Corey, T. Gant, *Tetrahedron Lett.* **1994**, *35,* 5373.

[4] For an excellent review of the chemistry of related cyclopropanes see: H.-U. Reissig, R. Zimmer, *Chem. Rev.* **2003**, *103*, 1151.

[5] T. T. Tidwell in *The Chemistry of the Cyclopropyl Group, part 1*, (Ed.: Z. Rappoport), Wiley, New York, **1987**.

[6] It may be tempting to refer to this process as a [3+3] cycloaddition reaction, however since a methylene unit of the reacting cyclopropane is not electronically involved in the reaction, we prefer the designation "homo [3+2] cycloaddition".

[7] The Reissig group has elegantly prepared 1,2-oxazines by the reaction of nitrones with lithiated allenes. See: R. Pulz, S. Cicchi, A. Brandi, H.-U. Reissig, *Eur. J. Org. Chem.* **2003**, 1153, and references therein.

[8] a) M. Iwani, S. Kiyoto, H. Terano, M. Kohsaka, H. Aoki, H. Imanaka, *J. Antibiot.* **1987**, *40*, 589; b) S. Kiyoto, T. Shibata, M. Yamashita, T. Komori, M. Okuharq, H. Terano, M. Kohsaka, H. Aoki, H. Imanaka, *J. Antibiot.* **1987**, *40*, 594; c) I. Uchida, S. Takase, H. Kayakiri, S. Kiyoto, M. Hashimoto, *J. Am. Chem. Soc.* **1987**, *109*, 4108.

[9] V. Gautheron-Chapoulaud, S. U. Pandya, P. Cividino, G. Masson, S. Py, Y. Vallee, *Synlett* **2001**, 1281.

[10] E. J. Corey, M. Chaykovsky, *J. Am. Chem. Soc.* **1965**, *87*, 1353.

[11] Ytterbium triflate has emerged as an excellent catalyst for a wide variety of synthetic transformations. For general references see a) S. Kobayashi in *Lanthanides: Chemistry and Use in Organic Synthesis* (Ed.: S. Kobayashi), Springer, New York, **1999**, pp. 63–118; b) S. Kobayashi, M. Sugiura, H. Kitagawa, W. W. L. Lam, *Chem. Rev.* **2002**, *102*, 2227; c) R. W. Marshman, *Aldrichimica Acta*, **1995**, *28*, 77.

[12] Racemic total syntheses: a) T. Fukuyama, L. Xu, S. Goto, *J. Am. Chem. Soc.* **1992**, *114*, 383; b) J. M. Schkeryantz, S. J. Danishefsky, *J. Am. Chem. Soc.* **1995**, *117*, 4722; enantioselective total syntheses: c) T. Kato, E. Itoh, T. Yoshino, S. Terashima, *Tetrahedron* **1997**, *53*, 10229; d) T. C. Judd, R. M. Williams, *Angew. Chem.* **2002**, *114*, 4877; *Angew. Chem. Int. Ed.* **2002**, *41*, 4683; e) M. Suzuki, J. Kambe, H. Tokuyama, T. Fukuyama, *Angew. Chem.* **2002**, *114*, 4880; *Angew. Chem. Int. Ed.* **2002**, *41*, 4686; for a synthesis of related racemic FR-66979 see: f) R. Ducray, M. A. Ciufolini, *Angew. Chem.* **2002**, *114*, 4882; *Angew. Chem. Int. Ed.* **2002**, *41*, 4688.

[13] S. Kobayashi, M. Kawamura, *J. Am. Chem. Soc.* **1998**, *120*, 5841.

 © 2003 Wiley-VCH Verlag GmbH & Co. KGaA, Weinheim

Tunable Semiconductor Microspheres

ZnSe Semiconductor Hollow Microspheres**

*Qing Peng, Yajie Dong, and Yadong Li**

Colloidal microspheres have been of continuous research interest ever since the beginning of the 20th century.[1–3] Traditionally, these systems have been regarded as ideal theoretical and practical objects of research because their intrinsic properties might be finely tuned by simply changing parameters, such as the diameter, the chemical composition, the bulk structure, and the crystallinity.[1–2] Recently, monodispersed silica and some polymer microspheres (e.g., polystyrene and poly(methyl methacrylate) have been employed as fundamental building blocks in the fabrication of photonic bandgap (PBG) crystals,[3–7] 3D macroporous materials[8,9] and 3D crystalline arrays as optical sensors.[10] Although recent progress in this field has mostly concentrated on their potential optical application, the employed microspheres themselves do not exhibit any particularly interesting optical, nonlinear optical or electro-optical functionality.[3] To introduce particular optical properties into these systems, semiconductors[11] or metals[12] have been incorporated into silica or polymer colloids during the synthetic step, or coated onto polymer sphere templates to prepare TiO_2, SnO_2,[13] and ZnS[14] hollow spheres or core–shell structures.[15] However, until now, a simple template-free method to prepare semiconductor microspheres with intrinsic optical properties is much needed.

As an important group II–VI semiconductor with a room temperature bulk band gap of 2.67 eV (460 nm), ZnSe has long been a material of choice for blue diode lasers and photovoltaic solar cells. Efforts in the preparation of ZnSe usually focused on the synthesis of ZnSe nanocrystals with luminescent properties from single molecular precursors.[16–19] However, with a relatively high refractive index of 2.4 (at 300 K), ZnSe might also be ideal building blocks for materials with 3D PBG properties, but monodispersed ZnSe microspheres have not yet been reported. Recently, we reported the syntheses of a series of metal chalcogenides such as cubic α-MnSe, $MnSe_2$ microcrystals,[20] and CdSe[21] nanorods. Herein, we report a novel and controllable method developed to prepare monodispersed ZnSe semiconductor microspheres. These microspheres were found to form through the aggregation of small ZnSe nanocrystals sizes, which could be finely tuned by temperature control. Optical characterization showed that the microspheres have interesting photonic properties.

Salts of ZnO_2^{2-} and SeO_3^{2-} ions were chosen as the source of Zn^{2+} and Se^{2-} ions, respectively. The reaction process can be formulated as shown in Equation (1). After tuning the

$$2\,SeO_3^{2-} + 2\,ZnO_2^{2-} + 3\,N_2H_4 \rightarrow 2\,ZnSe + 3\,N_2 + 2\,H_2O + 8\,OH^- \quad (1)$$

reaction temperature from 100 °C to 180 °C, and the products **1** (100 °C), **2** (140 °C), **3** (180 °C) were obtained.

For comparison, control experiment has also been carried out under 180 °C [Eq. (2)] and product **4** was thus obtained.

$$2\,SeO_3^{2-} + 2\,ZnO^{2+} + 3\,N_2H_4 \rightarrow 2\,ZnSe + 3\,N_2 + 6\,H_2O \quad (2)$$

It is interesting to note two features of these products: First, they display gradient evolution in color from yellow to green from **1** to **4** (Figure 1), which implies that the intrinsic optical properties have changed. Secondly, upon aging, product **1** slowly changed from yellow to dark red (1, 1′, 1″ in Figure 1), while all the others remained unchanged, which suggests a different stability in **1** compared with the other products.

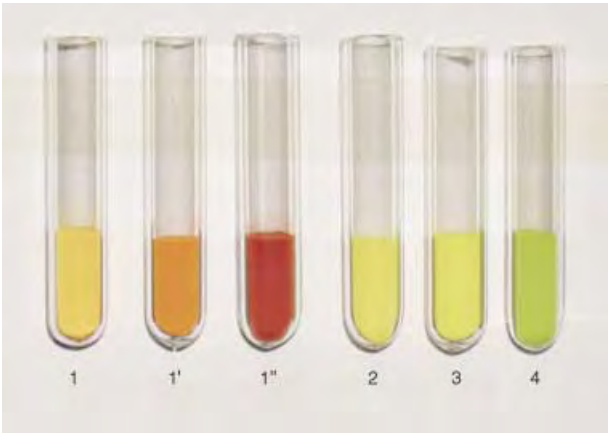


Figure 1. Color evolution of the as-obtained ZnSe products. Products **1**, **2**, and **3** are prepared by the route shown Equation (1) at 100 °C, 140 °C, and 180 °C respectively. Product **4** is prepared through the route shown in Equation (2) at 180 °C. Upon aging, the color of product **1** slowly changed from yellow to dark red (form **1** to **1**′, two weeks later, and finally to **1**″, one month later).

The structures and morphologies of products were investigated by powder X-ray diffractometery (XRD) and scanning electron microscopy (SEM). Figure 2 shows the evolution of the XRD patterns from **1** to **4**. From this figure, it is clear that all these products are pure-phase cubic ZnSe. With elevated reaction temperatures (100 °C, 140 °C, 180 °C), the crystallinity of products becomes high, and the **4** obtained through Equation (2) shows the highest crystallinity. Based on the half-peak breadth of ZnSe(111) diffraction peak, the mean size of the products was calculated from the Scherrer equation and listed in Table 1. It is interesting to note that the color of ZnSe products is strongly dependent on their sizes.

[*] Prof. Dr. Y. Li, Q. Peng, Y. Dong
Department of Chemistry
The Key Laboratory of Atomic & Molecular Nanosciences (Ministry of Education)
Tsinghua University
Beijing, 100084 (China)
Fax: (+86) 10-6278-8765
E-mail: ydli@tsinghua.edu.cn.

[**] This work was supported by the NSFC (20025102, 50028201,20151001), the Foundation for the Author of National Excellent Doctoral Dissertation of P.R. China, and the State Key Project of Fundamental Research for nanomaterials and nanostructures.

 DOI: 10.1002/anie.200250695 © 2003 Wiley-VCH Verlag GmbH & Co. KGaA, Weinheim

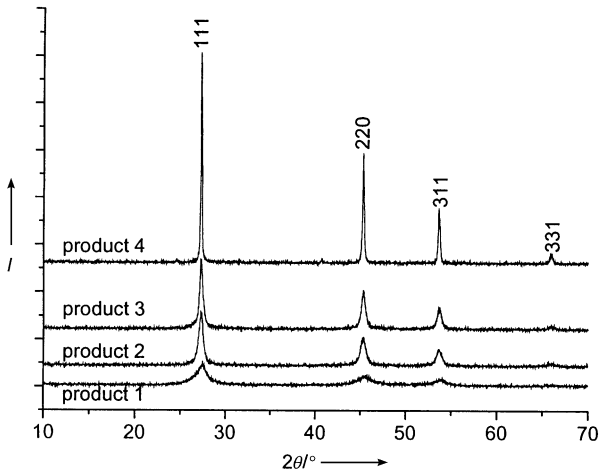


Figure 2. XRD patterns of products **1** (100 °C), **2** (140 °C), **3** (180 °C). *I* = intensity, arbitrary units.

Table 1: Size of the interior nanocrystals in microspheres evaluated by XRD and TEM or HRTEM.

Reaction	Temperature	XRD (size)	TEM or HRTEM (size)
Eq. (1)	100 °C	5.8 nm	5–6 nm
	140 °C	14.2 nm	~15 nm
	180 °C	19.1 nm	~20 nm
Eq. (2)	180 °C	–	~100 nm

SEM images (Figure 3a–c) show that these products are all microspheres with diameters of about 3 μm. These microspheres are well dispersed with good monodispersity (Figure 3a and b), although a little portion of them have discrepant diameters. Product **1** to **3** through Equation (1) are usually of smooth surface (inset of Figure 3a, Figure 3b), whereas the surface of product **4** (Figure 3c) is relatively rough. The inset of Figure 3c shows that this sphere was aggregated from small nanocrystals of about 100 nm. To

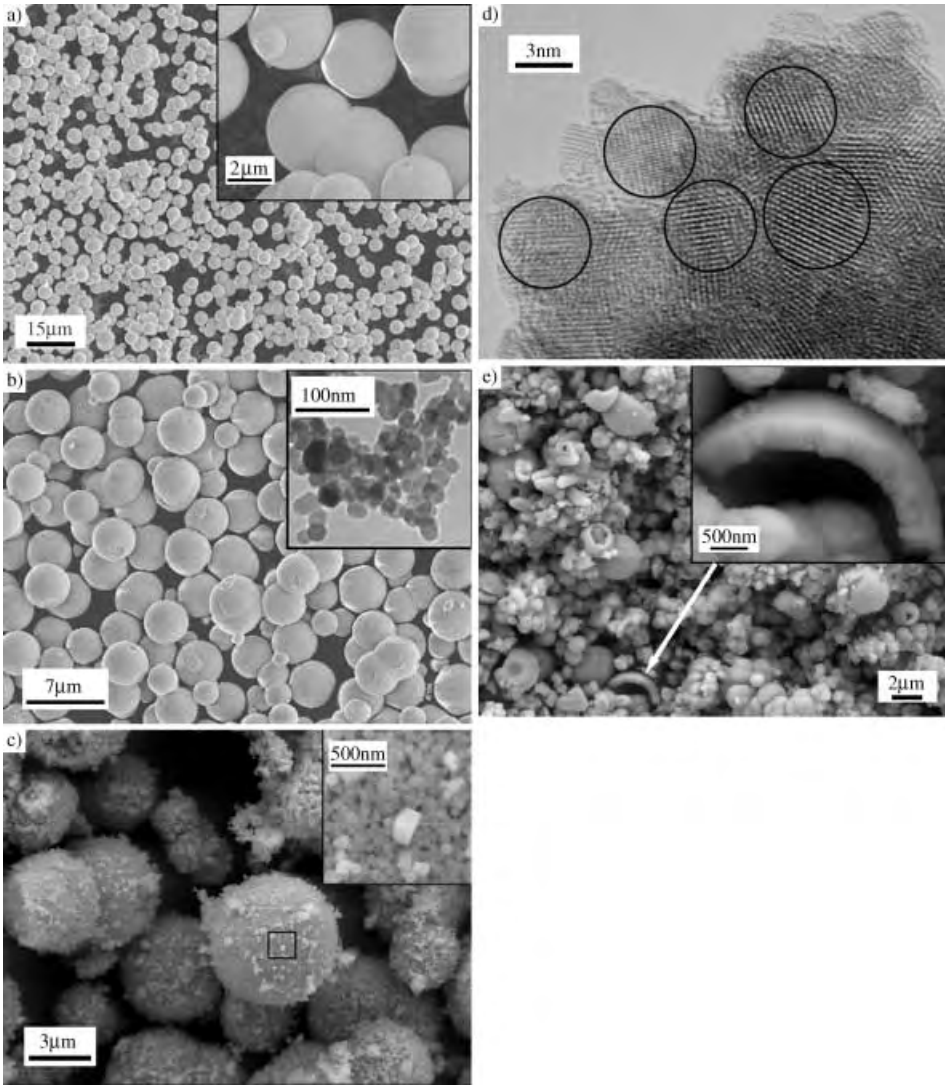


Figure 3. From a) to c): SEM images of ZnSe microspheres, a) product 1, b) product **3**, c) product **4**. Inset of a) is the high magnification image of product **1**. Inset of b) shows the interior small nanocrystals of product **3** after grinding. The size of them is about 20 nm. Inset of c) is the high magnification image taken from the highlighted section in c; d): HRTEM image of product **1** after grinding, which indicates that the microspheres are the aggregation of small nanocrystals with the size of about 5–6 nm. e) SEM image of the broken ZnSe microspheres (from product **3**). Inset shows an individual broken shell, which indicates that these microspheres are hollow inside.

 © 2003 Wiley-VCH Verlag GmbH & Co. KGaA, Weinheim

further investigate the interior structure of those smooth spheres, they were ground, dispersed in ethanol, dipped onto copper grids and characterized by transmission electron microscopy (TEM), and high resolution transmission electron microscopy (HRTEM). Figure 3d and the inset of Figure 3b show that they were also aggregated from nanocrystals of smaller size but better monodispersity. The sizes of the nanocrystals measured from TEM, HRTEM are also listed in Table 1 and they agree with the XRD results very well. Acid treatment (3M citric acid solution was used, heating for 10–20 minutes) was also employed to break these spheres (see SEM image, Figure 3e). Most of the spheres have been destroyed, but there still many broken spheres present, which clearly show that they are hollow inside. The inset of Figure 3e shows an individual broken shell of one sphere and the shell thickness of the microsphere is about 300 nm.

Based on these observations, an aggregation mechanism to form ZnSe hollow microspheres is proposed, with reference to the preparation of monodispersed SiO_2 or TiO_2 microspheres.[22] In our reactions, the SeO_3^{2-} ions are reduced first by hydrazine to Se atoms, which are further reduced or disproportionate in the alkaline solution to generate Se^{2-} ions,[20,21] and these ions react with ZnO_2^{2-} [Eq. (1)] or Zn^{2+} ions [Eq. (2)] to form ZnSe monomers. As illustrated in Figure 4, after the initial nucleation, the monomers will grow

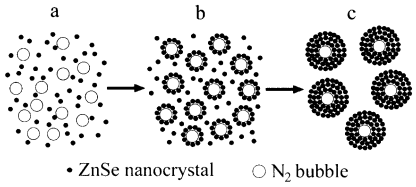


Figure 4. Schematic representation of the formation mechanism of ZnSe microspheres.

into nanocrystals (step a). These nanocrystals have a tendency to aggregate, and at the same time, lots of microbubbles of N_2 produced in the reaction provide the aggregation center (step b). Driven by the minimization of interfacial energy, small ZnSe nanocrystals may aggregate around the gas–liquid interface between N_2 and water (step b) and finally hollow ZnSe microspheres form (step c). In comparison, the direct reaction of Zn and Se under similar hydrothermal conditions, in which no microbubbles were introduced into the system, only led to ZnSe nanocrystals.[23,24]

The use of gas bubbles produced during the reaction to provide aggregation centers is a novel and effective method to fabricate hollow microspheres. Compared to the other template-synthetic methods, this soft-template method is very simple, convenient and avoids the introduction of impurities, and is therefore suitable for modern chemical synthesis. This idea might be extended to other solution systems in which easily aggregated monodispersed nanocrystals are produced during the reaction. The gas bubbles will help these nanocrystals to aggregate to form hollow microspheres. Our continuing studies are focusing on the development of improved techniques for improved control of the spheres, such as the sphere size, shell thickness, and homogeneity of the spheres.

To further investigate the color change of ZnSe microspheres and their intrinsic optical properties, optical characterizations were carried out by optical diffuse reflectance and photoluminescence spectra. Based on the procedure described in the literature,[25,26] optical diffuse-reflectance spectra can be used to estimate the bandgap (e_g) of semiconductors. The Kubelka–Munk function,[27] which is the ratio between the absorption and scattering factors, is used to plot the absorbance. In Figure 5, an absorption edge at 2.63 eV

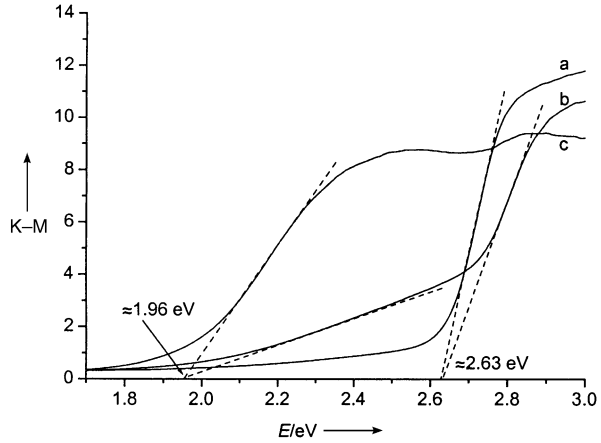


Figure 5. Optical diffuse reflectance spectra (UV/Vis) of the products. a) A typical curve of stable samples (product **2**, **3**, and **4**), which show an absorption edge at about 2.63 eV. b) Two absorption edges at 2.63 eV and 1.96 eV are observed in product **1**′ (two weeks later). c) Only the absorption edge of 1.96 eV can be observed in product **1**″ (one month later). K–M = Kubelka–Munk function.

(trace a) is found for stable products (**2**, **3**, and **4**), which coincides very well with the e_g of bulk ZnSe. Trace b and c are from product 1′ and 1″ respectively. Two absorption edges are observed at 2.63 eV and 1.96 eV (e_g of bulk selenium) in trace b, and only one absorption edge can be found at 1.96 eV in trace c. Further investigation suggests that this is because the Se^{2-} ion on the surface of spheres in product **1** was oxidized in the air to amorphous Se and thus a ZnSe/Se core–shell structure was formed. Detailed study of this heterostructure will be presented in another report. On the basis of above results (see also Table 1), it can be found that the colloidal stability of ZnSe microspheres is strongly depended on the size of interior nanocrystals. Because of the high surface effect, ZnSe nanocrystals with size of about 5–6 nm are not stable in the air.

Figure 6 shows the photoluminescence spectra ($\lambda_{exc.}$ = 290 nm) of ZnSe microspheres. An emission maximum at 2.57 eV is found for product **2**–**4**, which corresponds to the e_g of ZnSe. While for product 1′, two emission peaks at 2.57 eV and 2.71 eV are observed. This may also be caused by the formation of core–shell structure of the sample. The little red shift (~0.05 eV) of photoluminescence peak (2.57 eV) with respect to the absorption spectrum (2.63 eV, Figure 5a) is caused by the Stokes shift, which is attributed to emission from a "dark exciton".[19]

 © 2003 Wiley-VCH Verlag GmbH & Co. KGaA, Weinheim

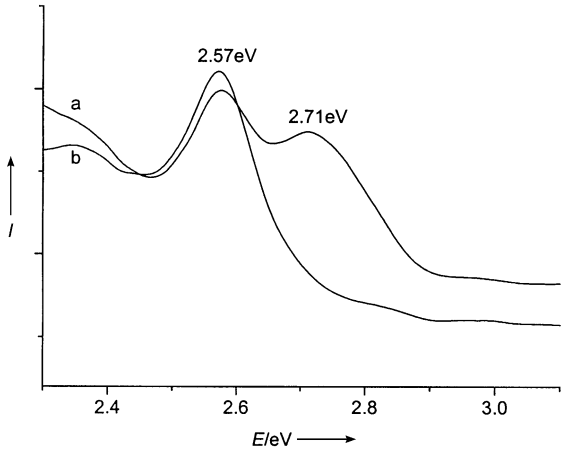


Figure 6. Photoluminescence spectra of as-obtained products. a) product 1′ (two weeks later); b) stable samples (product 2, 3, and 4). I = intensity, arbitrary units.

In conclusion, ZnSe semiconductor microspheres have been successfully synthesized for the first time. The hollow nature together with the tunable interior nanocrystal size of these microspheres make them ideal entity for inter incorporation or surface modification, which might bring novel optical, electronic and magnetic properties.

Experimental Section

For products **1**–**3** [Eq. (1)], analytical-grade $ZnSO_4{\cdot}7H_2O$ (0.29 g, 0.001 mol) and Na_2SeO_3 (0.17 g, 0.001 mol) were dissolved in NaOH (1M, 20 mL) and H_2O (10 mL) respectively to form clear solutions. These solutions were mixed together in a 50 mL Teflon-lined autoclave of and $N_2H_4{\cdot}H_2O$ (10 mL) was added into the mixture. After the mixture was stirred for five min, the autoclave was sealed and heated at one of three different temperatures: 100 °C, 140 °C, 180 °C for 2 h. The system was then allowed to cool to room temperature. The final product was collected by filtration, and washed with deionized water to remove any possible ionic remnants, then dried at 60 °C. For product **4** [Eq. (2)], no NaOH was added and all the other steps are the same as that of Equation (1).

The samples were characterized on a Bruker D8-advance X-ray powder diffractometer with $Cu_{K\alpha}$ radiation ($\lambda = 1.5418$ Å). The size and morphology of the ZnSe microspheres was determined at 20 kV by a JEOL JSM-6301F scanning electron microscope and at 200 kV by an Hitachi H-800 transmission electron microscope (TEM) and a JEOL JEM-2010F high-resolution transmission electron microscope. Optical diffuse reflectance of the samples was recorded on a Shimadzu UV-2100S spectrophotometer. Photoluminescence experiments were conducted in air on a Perkin-Elmer LS-50B fluorescence spectrophotometer.

Received: December 4, 2002
Revised: February 17, 2003 [Z50695]

Keywords: microspheres · nanostructures · selenium · semiconductors · zinc

[1] a) E. Matijevic, *Acc. Chem. Res.* **1981**, *14*, 22; b) E. Matijevic, *Langmuir* **1994**, *10*, 8.
[2] G. Mie, *Ann. Phys.* **1908**, *25*, 377.
[3] a) Y. N. Xia, B. Gates, Y. D. Yin, Y. Lu, *Adv. Mater.* **2000**,*12*, 693, and references therein; b) Y. N. Xia, B. Gates, Y. D. Yin, *Aust. J. Chem.* **2001**, *54*, 287.
[4] J. E. G. J. Wijnhoven, W. L. Vos, *Science* **1998**, *281*, 802.
[5] A. Blanco, E. Chomski, S. Grabtchak, M. Ibisate, S. John, S. W. Leonard, C. Lopez, F. Meseguer, H. Miguez, J. P. Mondia, G. A. Ozin, O. Toader, H. M. van Driel, *Nature* **2000**, *405*, 437.
[6] D. J. Norris, Y. A. Vlasov, *Adv. Mater.* **2001**, *13*, 371.
[7] A. D. Dinsmore, J. C. Crocker, A. G. Yodh, *Curr. Opin. Colloid Interface Sci.* **1998**, *3*, 5.
[8] a) B. T. Holland, C. F. Blanford, A. Stein, *Science* **1998**, *281*, 538; b) A. Stein, R. C. Schroden, *Curr. Opin. Solid State Mater. Sci.* **2001**, *5*, 553.
[9] S. A. Johnson, P. J. Ollivier, T. E. Mallouk, *Science* **1999**, *283*, 963.
[10] J. H. Holtz, S. A. Asher, *Nature* **1997**, *389* , 829.
[11] S. Y. Chang, L. Liu, S. A. Asher, *J. Am. Chem. Soc.* **1994**, *116*, 6745.
[12] a) K. Kulbaba, R. Resendes, A. Cheng, A. Bartole, A. Safa-Sefat, N. Coombs, H. D. H. Stover, J. E. Greedan, G. A. Ozin, I. Manners, *Adv. Mater.* **2001**, *13*, 732; b) K. Kulbaba, A. Cheng, A. Bartole, S. Greenberg, R. Resendes, N. Coombs, A. Safa-Sefat, J. E. Greedan, H. D. H. Stover, G. A. Ozin, I. Manners, *J. Am. Chem. Soc.* **2002**, *124*, 12522.
[13] Z. Y. Zhong, Y. D. Yin, B. Gates, Y. N. Xia, *Adv. Mater.* **2000**, *12*, 206.
[14] M. L. Breen, A. D. Dinsmore, R. H. Pink, S. B. Qadri, B. R. Ratna, *Langmuir* **2001**, *17* , 903.
[15] F. Caruso, *Adv. Mater.* **2001**, *13*, 11.
[16] M. A. Hines, P. Guyot-Sionnest, *J. Phys. Chem. B* **1998**, *102*, 3655.
[17] Y. W. Jun, J. E. Koo, J. Cheon, *Chem. Commun.* **2000**, 1243.
[18] F. T. Quinlan, J. Kuther, W. Tremel, W. Knoll, S. Risbud, P. Stroeve, *Langmuir* **2000**, *16*, 4049.
[19] M. A. Malik, N. Revaprasadu, P. O'Brien, *Chem. Mater.* **2001**, *13*, 913.
[20] Q. Peng, Y. J. Dong, Z. X. Deng, H. Z. Kou, S. Gao, Y. D. Li, *J. Phys. Chem. B* **2002**, *106*, 9261.
[21] Q. Peng, Y. J. Dong, Z. X. Deng, Y. D. Li, *Inorg. Chem.* **2002**, *41*, 5249.
[22] M. Ocana, R. Rodriguez-Clemente, C. J. SERNA, *Adv. Mater.* **1995**, *7*, 212.
[23] C. Wang, W. X. Zhang, X. F. Qian, X. M. Zhang, Y. Xie, Y. T. Qian, *Mater. Chem. Phys.* **1999**, *2409*, 1–4.
[24] Q. Peng, Y. J. Dong, Z. X. Deng, X. M. Sun, Y. D. Li, *Inorg. Chem.* **2001**, *40*, 3840.
[25] J. Li, Z. Chen, X. X. Wang, D. M. Proserpio, *J. Alloys Compd.* **1997**, *262*, 28.
[26] A. A. Patel, F. X. Wu, J. Z. Zhang, *J. Phys. Chem. B* **2000**, 104, 11598.
[27] G. Kortum, *Reflectance Spectroscopy: Principles, Methods, Applications*, Springer, Berlin, **1969**.

 © 2003 Wiley-VCH Verlag GmbH & Co. KGaA, Weinheim

Zinc Oxide Nanowires

Low-Temperature Wafer-Scale Production of ZnO Nanowire Arrays**

*Lori E. Greene, Matt Law, Joshua Goldberger, Franklin Kim, Justin C. Johnson, Yanfeng Zhang, Richard J. Saykally, and Peidong Yang**

Since the first report of ultraviolet lasing from ZnO nanowires,[1] substantial effort has been devoted to the development of synthetic methodologies for one-dimensional ZnO nanostructures. Among the various techniques described in the literature, evaporation and condensation processes are favored for their simplicity and high-quality products, but these gas-phase approaches generally require economically prohibitive temperatures of 800–900 °C.[2] Despite recent MOCVD schemes that reduced the deposition temperature to 450 °C by using organometallic zinc precursors,[3] the commercial potential of gas-phase-grown ZnO nanowires remains constrained by the expensive and/or insulating (for example, Al_2O_3) substrates required for oriented growth, as well as the size and cost of the vapor deposition systems. A low-temperature, large-scale, and versatile synthetic process is needed before ZnO nanowire arrays find realistic applications in solar energy conversion, light emission, and other promising areas.

Solution approaches to ZnO nanowires are appealing because of their low growth temperatures and good potential for scale-up. In this regard, Vayssieres et al. developed a hydrothermal process for producing arrays of ZnO microrods and nanorods on conducting glass substrates at 95 °C.[4,5] Recently, a seeded growth process was used to make helical ZnO rods and columns at a similar temperature.[6] Here we expand on these synthetic methods to produce homogeneous and dense arrays of ZnO nanowires that can be grown on arbitrary substrates under mild aqueous conditions. We present data for arrays on four-inch (ca. 10 cm) silicon wafers and two-inch plastic substrates, which demonstrate the ease of commercial scale-up. The simple two-step procedure yields oriented nanowire films with the largest surface area yet reported for nanowire arrays. The growth process ensures that a majority of the nanowires in the array are in direct contact with the substrate and provide a continuous pathway for carrier transport, an important feature for future electronic devices based on these materials.

Well-aligned ZnO nanowire arrays were grown using a simple two-step process. In the first step, ZnO nanocrystals (5–10 nm in diameter) were spin-cast several times onto a four-inch Si(100) wafer to form a 50–200-nm thick film of crystal seeds. Between coatings, the wafer was annealed at 150 °C to ensure particle adhesion to the wafer surface. The ZnO nanocrystals were prepared according to the method of Pacholski.[7] A NaOH solution in methanol (0.03 M) was added slowly to a solution of zinc acetate dihydrate (0.01 M) in methanol at 60 °C and stirred for two hours. The resulting nanoparticles are spherical and stable for at least two weeks in solution. After uniformly coating the silicon wafer with ZnO nanocrystals, hydrothermal ZnO growth was carried out by suspending the wafer upside-down in an open crystallizing dish filled with an aqueous solution of zinc nitrate hydrate (0.025 M) and methenamine or diethylenetriamine (0.025 M) at 90 °C. Reaction times spanned from 0.5 to 6 h. The wafer was then removed from solution, rinsed with deionized water, and dried. A field-emission scanning electron microscope (FESEM) was used to examine the morphology of the nanowire array across the entire wafer, while single nanowires were characterized by transmission electron microscopy (TEM). Nanowire crystallinity and growth direction were analyzed by X-ray diffraction and electron diffraction techniques.

SEM images taken of several four-inch samples showed that the entire wafer was coated with a highly uniform and densely packed array of ZnO nanowires (Figure 1). X-ray diffraction (not shown) gave a wurtzite ZnO pattern with an enhanced (002) peak resulting from the vertical orientation of the nanowires. A typical synthesis (1.5 h) yielded wires with diameters ranging between 40–80 nm and lengths of 1.5–2 μm.

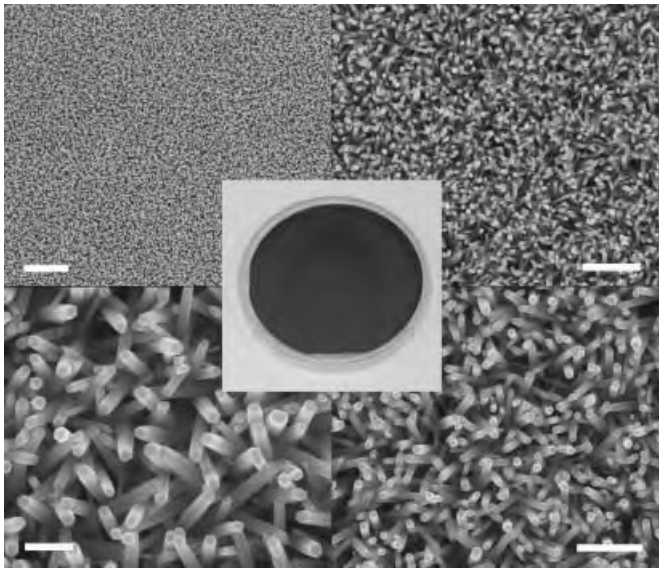


Figure 1. ZnO nanowire array on a four-inch (ca. 10 cm) silicon wafer. At the center is a photograph of a coated wafer, surrounded by SEM images of the array at different locations and magnifications. These images are representative of the entire surface. Scale bars, clockwise from upper left: 2 μm, 1 μm. 500 nm, and 200 nm.

[*] Prof. P. Yang, L. E. Greene,[+] M. Law,[+] J. Goldberger, F. Kim, J. C. Johnson, Y. Zhang, Prof. R. J. Saykally
Department of Chemistry
Lawrence Berkeley National Laboratory
University of California, Berkeley, CA 94720 (USA)
E-mail: p_yang@uclink.berkeley.edu

[+] These authors have contributed equally to this work.

[**] This work was supported by the Department of Energy. P.Y. is an Alfred P. Sloan Research Fellow. Work at the Lawrence Berkeley National Laboratory was supported by the Office of Science, Basic Energy Sciences, Division of Materials Science of the U.S. Department of Energy. We thank the National Center for Electron Microscopy for the use of their facilities.

 DOI: 10.1002/anie.200351461 © 2003 Wiley-VCH Verlag GmbH & Co. KGaA, Weinheim

With a measured nanowire number density on the order of 10^{10} cm^{-2}, these arrays have a ZnO surface area of, conservatively, at least 50 cm^2 per cm^2 of substrate (~ 10 m^2 g^{-1}). The average size of the nanowires increased with longer reaction time, up to 200–300 nm wide by 3 μm long for a 6-h experiment (Figure 2a). High-magnification SEM imaging of a sample grown for 6 h (Figure 2b) reveals that the surfaces of these solution-grown wires are rough compared to the gas-phase nanowire arrays produced in our laboratory, which might be expected for crystallization in a solution environment. Also, a substantial percentage of the nanowires fuse together after longer reaction times.

Cross-sectional SEM views of the arrays (Figure 2c) suggest that the ZnO nanowires grow nearly vertically and penetrate a thin (~ 100 nm) layer of nanocrystals. It is desirable for electronic applications to make the nanoparticle layer as thin and continuous as possible, ideally a few particle diameters in extent. No effort has been made here to optimize the deposition of the nanoparticle film. In the future, improved nanoparticle spin-coating or Langmuir–Blodgett techniques will be used to address this issue.

TEM characterization of individual nanowires removed from the arrays indicates that they are single-crystalline and grow in the [0001] direction (Figure 2d). The cluster morphology shown in the image is fairly common and suggests that multiple nanowires often grow from a single aggregate of ZnO nanoparticles attached to the substrate. We would like to point out that the initial deposition of the nanocrystals is critical for the formation of the current arrays of nanowires with thin diameters. Otherwise, microrod arrays would be obtained, as has been reported earlier.[4] Further investigation is needed to better understand the detailed mechanism of this nanowire growth process. In addition, unlike previous reports[4] where crystal growth occurs within enclosed flasks, the current process is carried out in open vessels, which points to the possibility of large-scale reel-to-reel production of such nanowire arrays.

This low-temperature hydrothermal method is substrate-independent and produces high-quality nanowire arrays on ITO glass, sapphire, titanium foil, and polymer surfaces. Figure 3 shows the growth of a nanowire array on a flexible two-inch polydimethylsiloxane (PDMS) substrate. This array is identical to those grown on silicon except for a network of microscale cracks (Figure 3c) that form because of the inflexibility of the ZnO nanowire film.

The ultraviolet and visible photoluminescence (PL) of as-grown nanowire arrays was measured in the temperature range $4.5 \leq T \leq 300$ K using a low-power, unfocused 325 nm

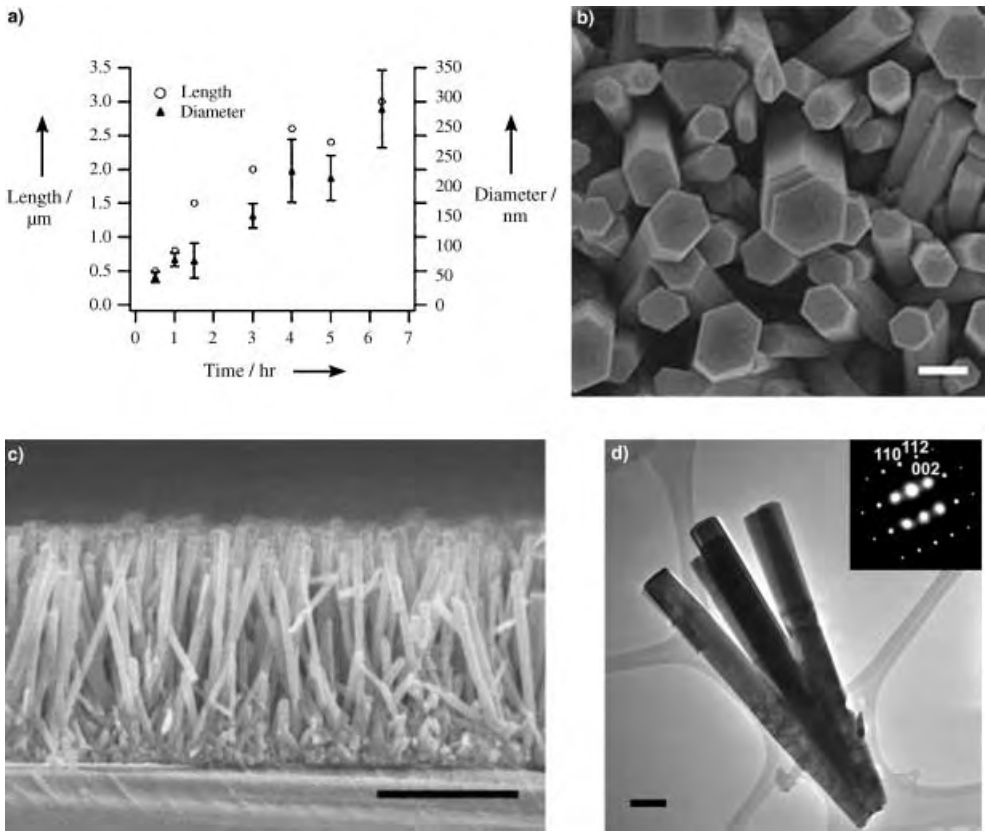


Figure 2. a) Plot showing the average length and diameter of array nanowires as a function of growth time. Each diameter data point was determined using 100 nanowires, with error bars indicating the standard deviation; b) SEM image of an array grown over 6 h showing the relatively rough surfaces of the nanowires (scale bar = 200 nm); c) cross-sectional SEM image of an array grown over 1.5 h on a silicon wafer (scale bar = 1 μm); d) transmission electron micrograph of a cluster of ZnO nanowires removed from an array grown over 1.5 h (scale bar = 90 nm). The inset shows the [100] electron diffraction pattern of an isolated, single nanowire from a different region of the sample. The growth axis is along the [001] direction.

 © 2003 Wiley-VCH Verlag GmbH & Co. KGaA, Weinheim

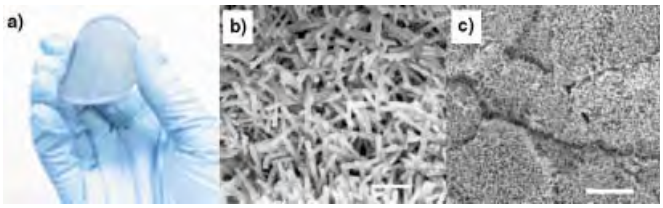


Figure 3. ZnO nanowire array on a two-inch (ca. 5 cm) PDMS substrate. a) Photograph of the flexed array on PDMS; b) SEM image showing the array morphology (scale bar = 1 μm); c) Low-magnification SEM image of the cracks formed in the array after handling (scale bar = 5 μm).

line of a He–Cd laser as the excitation source. Room-temperature spectra of as-grown samples show a weak band-edge emission at 378 nm (3.29 eV) resulting from free-exciton annihilation, and a very strong and broad yellow-orange emission that is fit well by two Gaussians, with a major peak centered at 605 nm (2.05 eV) and a shoulder at 730 nm (1.70 eV). The three peaks grow more intense with decreasing temperature as a result of the freeze-out of phonons and quenching of nonradiative recombination processes (Figure 4). A 90 meV blue shift of the band-edge emission over this temperature range (Figure 4 inset) is caused by the thermal contraction of the lattice and changing electron–phonon interactions.[8] The temperature dependence of the orange (2.05 eV) PL intensity can be expressed by a simple thermal activation model of the form,[9]

$$I = I_O/(1 + A\exp(-E_A/k_B T)). \quad (1)$$

By fitting the experimental data (Figure 4 inset) we obtain an activation energy $E_A = 71$ meV for the nonradiative mechanisms responsible for quenching the orange luminescence. This value is comparable to the energy reported in a previous study of single-crystal and powder samples.[10]

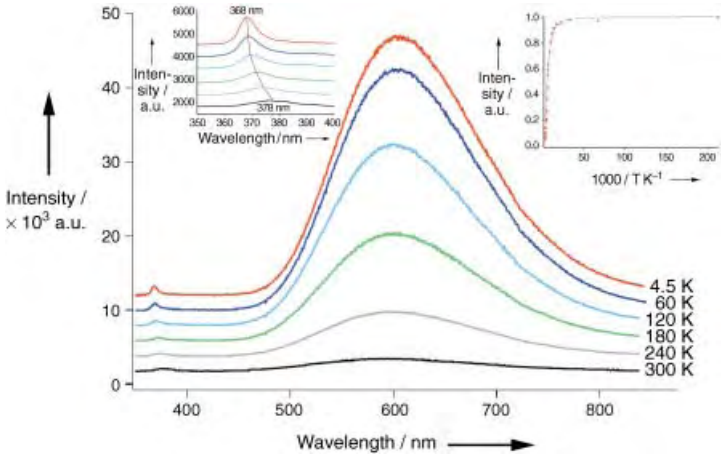


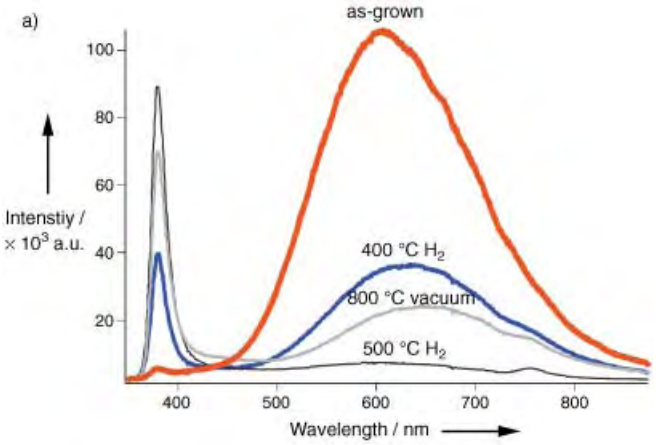
Figure 4. Temperature-dependent photoluminescence of a ZnO nanowire array on a silicon substrate; spectra are offset for clarity. The left inset is a magnification of the band-edge emission showing a 90 meV blue shift (3.29 to 3.38 eV) as the temperature was lowered from 300 to 4.5 K. The right inset is the normalized intensity of the orange emission plotted as a function of inverse temperature. The solid line is a theoretical fit to the data as described in the text.

It is known that pure ZnO can show green and/or orange visible luminescence depending on the growth temperature and availability of oxygen during sample preparation.[11] The green emission results from the recombination of electrons with holes trapped in singly ionized oxygen vacancies (V_O^+) and is commonly seen in ZnO materials synthesized under oxygen-deficient conditions, such as the gas-phase nanowires produced in this laboratory.[12] The orange emission is less commonly reported and its origin, although not fully understood, seems to involve interstitial oxygen ions (O_i^-).[13] Orange PL has been seen in ZnO grown electrochemically,[14] hydrothermally,[15] and by pulsed laser deposition[16] and spray pyrolysis.[17] The strong orange PL and complete absence of green emission from the nanowire arrays grown under aqueous conditions presented in this work is consistent with the above assignments. Regardless of the exact origin of the orange emission, the large ratio of orange PL intensity to band-edge PL intensity indicates that the as-grown nanowires are rich in atomic defects.

PL and lasing measurements were combined with a series of annealing treatments to investigate the nature of the orange emission. Three samples were collected from arrays prepared in both 1.5-h and 3-h experiments on silicon, and then annealed in one of three environments; either 400 °C in 10 % H_2/90 % Ar for 15 min, 500 °C in 10 % H_2/90 % Ar for 15 min, or 800 °C at 5×10^{-6} Torr for 2 h. One sample from each wafer was left untreated as a control. Post-anneal SEM imaging of each sample confirmed that the nanowires survived visibly undamaged, except for a slight surface etching seen in the 500 °C H_2 treatments. Room-temperature PL spectra of samples prepared over 1.5 h show a progressive quenching of the orange emission with a simultaneous increase of the band-edge PL intensity (Figure 5). The marked weakening of the orange emission after vacuum annealing is consistent with the involvement of oxygen interstitials in the luminescence. The 500 °C H_2 treatment causes a nearly complete quenching of the orange PL and results in a spectrum that is dominated by band-edge emission. It is interesting that the green PL feature, which should develop in response to sufficiently reducing treatments,[17] was not observed even in an array sample that was exposed to hydrogen at 600 °C and appeared heavily etched in SEM.

The lasing behavior of the eight array samples was investigated by far-field PL imaging using an experimental setup described previously.[18] We found that neither of the as-grown samples showed lasing at sub-ablation pumping intensities. Lasing of array nanowires on the annealed 1.5-h samples was observed in only a small fraction of the wires, most likely those at the upper limit of the diameter distribution, which have a sufficient cavity finesse to support a single lasing mode. The annealed 3-h samples (average diameter $d = 125$ nm, length 2 μm) showed lasing in roughly ten times the number of wires as the 1.5-h arrays (average diameter 60 nm, length 1.5 μm), which is reasonable

 © 2003 Wiley-VCH Verlag GmbH & Co. KGaA, Weinheim



c)

Sample	Treatment	Threshold / μJ cm⁻²
3-hour solution no.1	none	> 15
3-hour solution no.2	800°C vacuum	6.1
3-hour solution no.3	400°C H_2 / Ar	3.9
3-hour solution no.4	500°C H_2 / Ar	2.9
Gas phase	none	0.50

Figure 5. Photoluminescence spectra of four arrays (a) grown over 1.5 h after annealing treatments. Samples prepared over 3 h (b) showed qualitatively identical behavior; (c) Average lasing thresholds for active wires.

as less diffraction loss would be expected for larger wires. A typical PL spectrum of a solution array prepared over 3 h and pumped above threshold (Figure 5b) shows several relatively sharp lasing peaks superimposed on a broad PL background. However, the percentage of lasing wires in the 3-h arrays remained low, probably because their short wire lengths lead to high gain thresholds. A comparison of the average lasing thresholds for the active wires on the three annealed solution-grown arrays and a gas-phase array (Figure 5c) illustrates that the threshold tends to decrease as the ratio of ultraviolet PL to visible PL increases, with the gas-phase array lasing at one fifth of the threshold of the most reduced 3-h sample. A more detailed analysis of the optical properties of the various ZnO nanowire arrays is forthcoming.

Dense arrays of ZnO nanowires with high surface area can be grown on arbitrary substrates of any size using the mild solution process described in this study. The use of small, homogeneous ZnO nanocrystals as a seed layer helps produce nanowires of relatively small diameter. The nanowires are well-oriented and most are in intimate contact with the substrate. Annealing as-grown arrays in reducing atmospheres quenches the intense orange emission and lowers the lasing threshold of the larger nanowires to values similar to gas-phase samples. With further improvements, these ZnO nanowire arrays should find applications in solar cells, light emission, and other devices.

Received: March 24, 2003 [Z51461]

Keywords: electron microscopy · nanowires · oxides · photoluminescence · zinc

[1] a) M. H. Huang, S. Mao, H. Feick, H. Yan, Y. Wu, H. Kind, E. Weber, R. Russo, P. Yang, *Science* **2001**, *292*, 1897; b) J. Johnson, H. Yan, R. Schaller, L. Haber, R. Saykally, P. Yang, *J. Phys. Chem. B* **2001**, *105*, 11387.
[2] a) P. Yang, H. Yan, S. Mao, R. Russo, J. Johnson, R. Saykally, N. Morris, J. Pham, R. He, H. Choi, *Adv. Funct. Mater.* **2002**, *12*, 323; b) B. D. Yao, Y. F. Chan, N. Wang, *Appl. Phys. Lett.* **2002**, *81*, 757.
[3] W. I. Park, G. Yi, M. Kim, S. L. Pennycook, *Adv. Mater.* **2002**, *14*, 1841.
[4] L. Vayssieres, K. Keis, A. Hagfeldt, S. Lindquist, *Chem. Mater.* **2001**, *13*, 4395.
[5] L. Vayssieres, *Adv. Mater.* **2003**, *15*, 464.
[6] Z. R. Tian, J. A. Voigt, J. Liu, B. Mckenzie, M. J. Mcdermott, *J. Am. Chem. Soc.* **2002**, *124*, 12954.
[7] C. Pacholski, A. Kornowski, H. Weller, *Angew. Chem.* **2002**, *114*, 1234; *Angew. Chem. Int. Ed.* **2002**, *41*, 1188.
[8] X. T. Zhang, Y. C. Liu, Z. Z. Zhi, J. Y. Zhang, Y. M. Lu, D. Z. Shen, W. Xu, X. W. Fan, X. G. Kong, *J. Lumin.* **2002**, *99*, 149.
[9] D. S. Jiang, H. Jung, K. Ploog, *J. Appl. Phys.* **1988**, *64*, 1371.
[10] R. B. Lauer, *J. Phys. Chem. Solids* **1973**, *34*, 249.
[11] a) Y. Zelikin, A. P. Zhukovskii, *Opt. Spektrosk.* **1961**, *11*, 397; b) S. Bhushan, R. P. Asare, *Indian J. Pure Appl. Phys.* **1981**, *19*, 694.
[12] A. van Dijken, E. A. Meulenkamp, D. Vanmaekelbergh, A. Meijerink, *J. Lumin.* **2000**, *90*, 123.
[13] M. Liu, A. H. Kitai, P. Mascher, *J. Lumin.* **1992**, *54*, 35.
[14] M. J. Zheng, L. D. Zhang, G. H. Li, W. Z. Shen, *Chem. Phys. Lett.* **2002**, *363*, 123.
[15] T. Sekiguchi, S. Miyashita, K. Obara, T. Shishido, N. Sakagami, *J. Cryst. Growth* **2000**, *214*/215, 72.
[16] X. L. Wu, G. G. Siu, C. L. Fu, H. C. Ong, *Appl. Phys. Lett.* **2001**, *78*, 2285.
[17] S. A. Studenikin, N. Golego, M. Cocivera, *J. Appl. Phys.* **1998**, *84*, 2287.
[18] a) J. Johnson, H. J. Choi, K. P. Knutsen, R. D. Schaller, P. Yang, R. J. Saykally, *Nat. Mater.* **2002**, *1*, 101; c) H. Yan, R. He, M. Law, J. Johnson, R. Saykally, P. Yang, *J. Am. Chem. Soc.* **2003**, *125*, 4728.

 © 2003 Wiley-VCH Verlag GmbH & Co. KGaA, Weinheim

NO Dissociation on Surfaces

Site Occupation and Activity of Catalyst Nanoparticles Monitored by In Situ Vibrational Spectroscopy**

Viktor Johánek, Swetlana Schauermann, Mathias Laurin, Jörg Libuda, and Hans-Joachim Freund*

In many cases, the performance of heterogeneous catalysts sensitively depends on the structural properties of their surfaces. Often, size and structure of the nanometer-sized active catalyst particles are optimized empirically to provide a distribution of adsorption and reaction sites which maximizes selectivity and activity for the reaction system of interest. But how do the ensembles of different sites on a catalyst particle control the microscopic reaction kinetics and lead to size and structure dependencies? In spite of the large industrial and economical impact of this question, there is hardly any detailed understanding of the molecular origins of such effects (e.g. refs. [1,2]). This lack of detailed knowledge is related to both serious experimental problems in studies on real catalyst and the enormous complexity of their surfaces. To overcome these difficulties, we have recently started to combine two experimental approaches: 1) using supported model catalysts with a reduced level of complexity and 2) molecular-beam techniques, which provide detailed kinetic data under most well-controlled conditions.[3]

A key problem in kinetic studies on catalyst surfaces, which remains unsolved in most cases, is the spectroscopic identification of the different particle sites and the possibility to examine in situ their occupation by reactant and product species under normal reaction conditions. Herein, we present results of the NO dissociation on Pd/Al_2O_3, for which it was possible to monitor the reactant distribution on the catalyst nanoparticles and the related reaction kinetics under reaction conditions. We investigate adsorbed NO by TR-IRAS (time-resolved IR reflection absorption spectroscopy) and from this data draw conclusions on the distribution of dissociation products on the catalyst particles.

Recently, we investigated the decomposition of methanol on Pd nanocrystallites and were able to show how selectivity in a system of two competing decomposition reactions, C–H and C–O bond scission, is controlled by the presence of specific sites on the particles.[4] This was achieved using adsorbed CO as a sensitive probe molecule for the site occupation. However, the adsorbate distribution could not be monitored under reaction conditions, but had to be investigated at lower sample temperature after terminating the reaction.

Herein, we focus on the NO dissociation and reduction, which is of scientific and industrial interest in environmental catalysis.[5] On Pd surfaces, the reaction has a pronounced structure dependence. Whereas on Pd(111) NO remains intact up to high temperatures, Pd(100) and stepped Pd surfaces have much higher activity towards NO dissociation (see e.g. refs. [6–10] and references therein). Consequently, prominent structure and size effects are expected for supported Pd catalysts and have been observed experimentally.[11,12] Most importantly, however, the products of NO dissociation, atomic nitrogen and oxygen, play a key role for the reaction kinetics, for example, in the case of the CO–NO reaction.[13] Thus, the distribution of NO dissociation products on the particles, under reaction conditions, and their influence on the dissociation activity is a critical but still open question.

Combining molecular-beam methods and in situ TR-IRAS we show that under conditions of NO dissociation on alumina supported Pd crystallites, the dissociation products, atomic oxygen and nitrogen, preferentially occupy edge and defect sites on the particles. After selectively removing oxygen strongly bound nitrogen species remain and lead to reduced NO adsorption at the particle edges. Simultaneously, the rate of NO dissociation is found to be strongly enhanced.

The model catalyst used in this study is based on a well ordered Al_2O_3 film on a NiAl(110) single crystal and has been characterized in detail.[14,15] Briefly, Pd particles are grown under well-controlled conditions in UHV (ultrahigh vacuum) with particle size, shape, and density being controlled by the deposition conditions. An STM image of the particles is displayed in Figure 1a (from ref. [14]), a schematic model is shown in Figure 1b. The majority of aggregates are found to have the morphology of well-shaped crystallites with an average size of approximately 6 nm, predominantly exposing (111) facets and a very small number of (100) facets. After preparation, the particles are stabilized by extended oxygen exposure as described elsewhere.[14,16] Subsequently, the surface oxygen is removed by a pulse of CO. This procedure has no major influence on the particle morphology.[14]

Figure 1c shows IRAS spectra, which were recorded of the pristine model surface immediately after switching on the NO molecular beam. No NO adsorption is observed for the clean alumina film at 300 K. For the Pd particles, three main absorption features in the N–O stretching-frequency range are observed: 1) an absorption band, which shifts from $\tilde{\nu} = 1595\ cm^{-1}$ at a sample temperature of 300 K to $\tilde{\nu} = 1548\ cm^{-1}$ at 475 K, 2) a band between $\tilde{\nu} = 1656\ cm^{-1}$ (300 K) and $\tilde{\nu} = 1628\ cm^{-1}$ (475 K) and 3) a strong absorption band at $\tilde{\nu} = 1735\ cm^{-1}$ (300 K), which vanishes at sample temperatures exceeding 400 K.

Based on single-crystal experiments on Pd(111) (ref [17] and references therein) and theoretical calculations,[18,19] bands 1 and 3 can be attributed to NO adsorbed at threefold hollow sites (1) and at on-top sites (3) on (111) facets. For absorption band 2 there are in principle two possible assign-

[*] Dr. J. Libuda, Dr. V. Johánek, Dipl.-Chem. S. Schauermann, Dipl.-Chem. M. Laurin, Prof. Dr. H.-J. Freund
Fritz-Haber-Institut der
Max-Planck-Gesellschaft
Faradayweg 4–6, 14195 Berlin (Germany)
Fax: (+49) 30-8413-4139
E-mail: libuda@fhi-berlin.mpg.de

[**] We acknowledge financial support of this project by the Volkswagen Foundation (Partnerschaftsprogramm "The Mechanism and Kinetics of NO Reduction Reactions on Noble Metal Surfaces—From Single Crystal Surfaces to Supported Model Catalysts") and thank Dr. C. S. Gopinath for many helpful discussions.

 DOI: 10.1002/anie.200351228 © 2003 Wiley-VCH Verlag GmbH & Co. KGaA, Weinheim

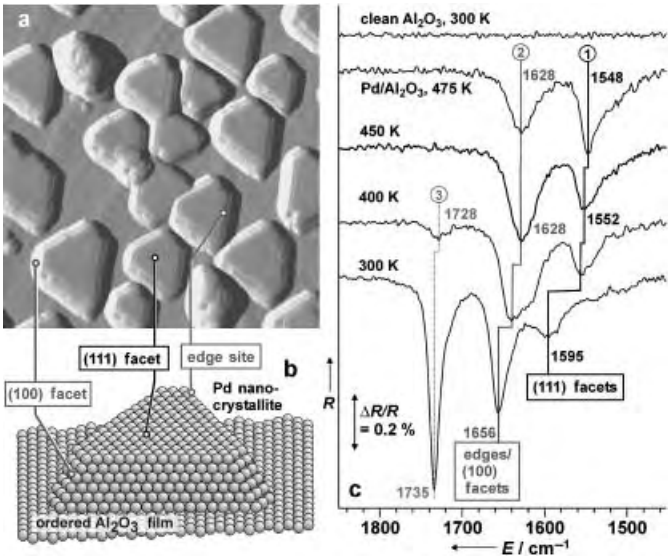


Figure 1. a) STM image of the Pd particles supported on Al_2O_3/NiAl(110) (40 nm × 40 nm; reproduced from ref. [14]), b) schematic representation of the Pd crystallites in (a), c) IR spectra (N–O stretching-frequency region) of the clean alumina film and the Pd particles supported on the film acquired immediately after admission of the NO beam, showing bands 1, 2, and 3; R = reflectivity.

ments. First, there is a large number of edge sites available (e.g. more than 30 % of the top facet atoms are located at the particle edge, see Figure 1 b). To some extent, this situation is comparable to NO adsorption at stepped Pd surfaces. For Pd(112) for example, Ramsier et al. found an absorption feature at temperatures above room temperature between $\tilde{\nu} = 1655$ and 1670 cm^{-1}.[6] In addition to the edge sites, a contribution from the (100) facets is possible. At high coverage on Pd(100) single crystals, bridge-bonded NO gives rise to a characteristic absorption feature between approximately $\tilde{\nu} = 1630$ and 1670 cm^{-1}.[20,21] Based on the morphology of the particles, however, we can conclude that the contribution of the (100) facets is minor. In addition, the large tilting angle of the (100) facets leads to a suppression of the IR absorption as a result of the metal surface-selection rule, which—because of the small thickness of the oxide film—also applies for the present model surface.[22] Consequently, we assign band 2 to NO species predominately located at particle edges and a minor contribution from (100) facets. However, an exact quantification of the relative population of the different states is complicated because of dipole coupling effects, which may lead to some degree of intensity transfer between the bands.[23] Hence, we restrict ourselves to qualitative conclusions in the following discussion of site occupation.

We monitored the kinetics of NO decomposition at 450 K. For this purpose IR spectra are recorded continuously during exposure of the probe to the NO beam (see Figure 2). The integral intensity of the two absorption features 1 and 2 is displayed in Figure 2 b. The on-top sites which give rise to band 3 are not populated at this sample temperature. From the data it is clear that initially absorption band 2 decreases in intensity, then band 1. By sufficiently long exposure times both NO absorption features vanish completely.

The loss of NO adsorption capacity can be attributed to the accumulation of dissociation products (atomic nitrogen and oxygen) on the surface of the particles. The preferential loss of the absorption feature 2, mainly NO at particle edges, indicates that adsorption of the product species at these sites is favorable (note that in the beginning there is a slight increase in intensity of band 1, which accordingly can be assigned to reduced intensity transfer to the high frequency band 2 with decreasing NO population at particle edges). This observation is consistent with a recent STM study of oxygen adsorption on the same Pd model catalyst, which showed preferential adsorption of oxygen at the particle edges.[24] Note that from the desorption behavior of oxygen on Pd single-crystal surfaces (desorption occurs between approximately 700 K and 1000 K, e.g. refs [9,25]), suggests that the rate of oxygen desorption is negligible under the reaction conditions applied in this work. Nitrogen, however, can leave the surface via formation of N_2 or N_2O,[9,10] with the ratio of both products sensitively depending on the reaction conditions and surface structure. In addition, strongly adsorbed nitrogen species have been observed both on single-crystal surfaces and on supported particles[10,13] (leading to high-temperature N_2 desorption features between 500 and 650 K). These findings suggest that a fraction of the atomic nitrogen

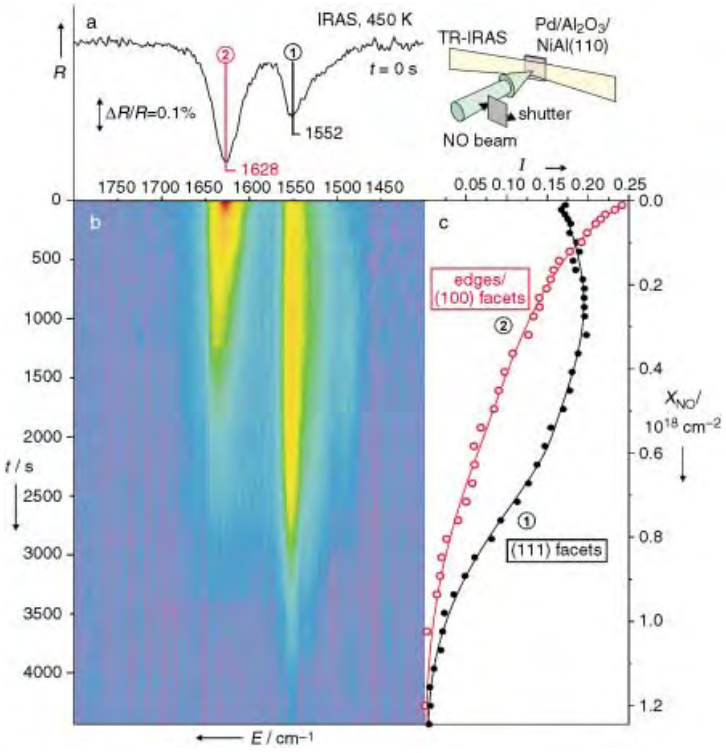


Figure 2. a) IR spectrum (N–O stretching-frequency region) of a Pd model catalyst, taken immediately after admission of the NO beam, b) time-resolved IRAS experiment showing the development of the absorption bands 1 and 2 as a function of time and exposure (X_{NO}), c) integral intensity (I) of the two absorption bands in the N–O stretching-frequency region.

 © 2003 Wiley-VCH Verlag GmbH & Co. KGaA, Weinheim

may remain on the particles under the reaction conditions applied here.

To investigate the role of adsorbed nitrogen and its influence on the dissociation kinetics, a CO titration experiment was performed (Figure 3). Again, the pristine catalyst is exposed to a continuous NO beam and the kinetic data for the NO decomposition are recorded by TR-IRAS (Figure 3a). The integral intensity of both absorption features is shown in Figure 3b. At specific times a CO pulse is applied to the sample by a second beam source. The CO efficiently removes all the adsorbed oxygen from the surface through oxidation to CO_2 (see ref. [3] and references therein). The corresponding CO_2 quadrupole mass spectrometer signal (Figure 3c) provides a measure for the oxygen coverage of the sample. Carbon contamination resulting from CO dissociation or disproportionation can be excluded under these conditions.[3,26]

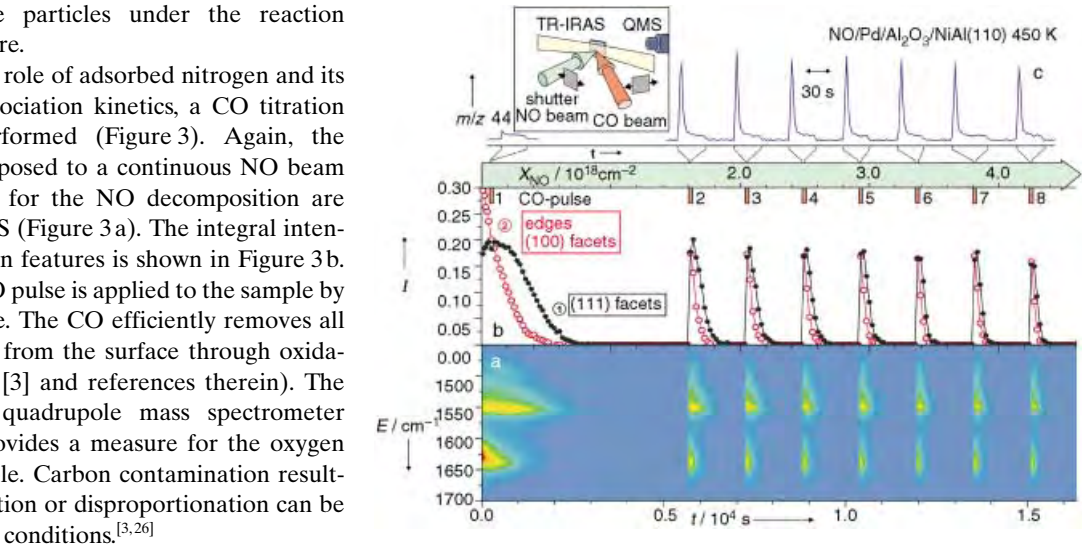


Figure 3. a) Time resolved IRAS experiment showing the development of the NO absorption bands 1 and 2 as a function of NO exposure (X_{NO}) and CO pulsing, b) integral intensity (I) of the two absorption bands in the N–O stretching-frequency region, c) CO_2 mass spectrometer signal recorded during CO pulsing.

As discussed above, the intensity of absorption band 2 (edges) immediately decreases upon NO exposure, whereas the (111) facet sites (band 1) are affected later. A first CO pulse applied at low NO exposures yields the expected low CO_2 signal, which indicates that initially the surface is oxygen free. In addition, the CO pulse has a negligible effect on the rate of NO decomposition (the slight decrease in the intensity of band 1 during the CO pulse arises from a small amount of co-adsorbed CO, present only during the CO exposure. In addition, compared with the reaction presented in Figure 2, a weak acceleration of the reaction is noticed, which is a result of same kinetic effect as that of oxygen removal, see below).

A second CO pulse is applied after the surface is completely covered by the dissociation products. The substantial CO_2 signal indicates a high oxygen coverage of the catalyst. After removal of the surface oxygen, IR NO absorption band 1 is fully restored, whereas absorption band 2 is only restored to about 60% of its original intensity and remains blue-shifted by approximately 8 cm^{-1} (Figure 4a). From this observation we conclude that strongly bound nitrogen species remain preferentially adsorbed in the vicinity of edge sites on the particles and modify the adsorption properties of these sites.

It is remarkable that a constant CO_2 yield is found for subsequent CO titration experiments (Figure 3c and 4a). It follows that the NO dissociation capacity is constant, that is, there is no further accumulation of nitrogen beyond the well-defined level formed in the initial exposure.

Another striking result from this experiment is that after initial oxygen removal, the rate at which the surface is covered by dissociation products increases greatly. As shown by CO titration the same amount of NO dissociates in each cycle. Thus this difference must be due to an increased dissociation rate and not to a loss in adsorption capacity. Quantitatively, the effect is illustrated in Figure 4b, which shows the exposure which is required to reduce the IR band intensities to half of their original value. From this data and the structural data for the model catalyst we can derive an estimate of the absolute NO dissociation probability (Figure 4c). On the partially nitrogen-covered particles, an increase in the dissociation probability by a factor of approximately five is found with respect to the pristine surface.

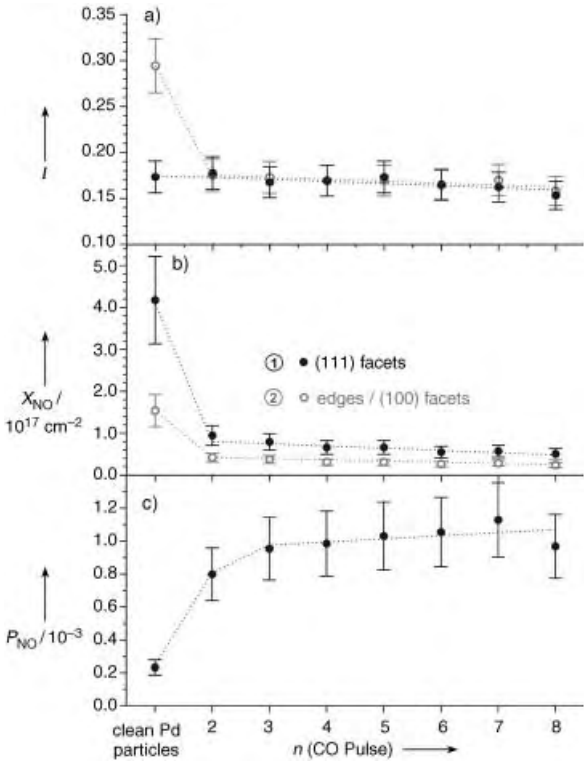


Figure 4. a) Integral intensity (I) of the two IR absorption bands 1 and 2 in the N–O stretching-frequency region for the pristine Pd particles and immediately after surface-oxygen removal by CO pulsing (n corresponds to the number of the CO pulses in Figure 3), b) NO (X_{NO}) exposure required to reduce the intensity of the individual NO bands to half of their original value, c) absolute NO dissociation probability (P_{NO}).

 © 2003 Wiley-VCH Verlag GmbH & Co. KGaA, Weinheim

These observations suggest that atomic adsorbate species that are preferentially bound in vicinity of particle edges critically control the dissociation activity. Specifically, there are two effects which could contribute to the increase in the dissociation rate. Firstly, the presence of strongly bound nitrogen may lead to a reduced NO coverage at the active sites and thus to reduced blocking of these sites and hence faster NO dissociation. Secondly, atomic nitrogen and oxygen species co-adsorbed in the vicinity of the active sites may have different effects on the activation barrier for dissociation. Thus, a possible scenario would be that during the first pulse (starting from N- and O-free particles) a large fraction of the dissociation sites is decorated with atomic oxygen whereas in subsequent pulses (after removing the atomic oxygen) there is preferential decoration by atomic nitrogen. Future theoretical calculations may help to identify the exact role of these effects for the dissociation kinetics. The implications of the current results for the catalytically important CO–NO co-adsorption and reaction system will be discussed elsewhere.[27]

In conclusion, under normal reaction conditions we have monitored the distribution of NO and its dissociation products, over different types of adsorption sites present on nanometer-sized Pd crystallites of a supported model catalyst. Molecular beam methods and in situ time-resolved IR reflection absorption spectroscopy were combined to obtain simultaneous information on the site-occupation and reaction rate. It was shown that the NO dissociation products preferentially occupy edge and (100) facets sites rather than the (111) facets which form the majority of the sites. After selectively removing oxygen by a CO pulse, a well-defined coverage of strongly adsorbed nitrogen remains and modifies the adsorption properties of the particle edges. The presence of nitrogen and oxygen adsorbates at the edge sites critically controls the NO dissociation activity.

Experimental Section

All experiments were performed in a UHV molecular-beam apparatus at the Fritz-Haber-Institute (Berlin) which allows up to three beams to be crossed on the sample surface.[28] The NO beam (Messer Griesheim, 99.5%) and the CO beam (Linde, 99.997%) are generated by doubly differentially pumped effusive multichannel array sources after purification of the gases by cold traps and filters (Mykrolis). Adsorption studies and spectroscopy at sample temperatures between 100–300 K were performed on both the pristine alumina film and the Pd particles to exclude any influence of contaminants, such as NO_2. For all the experiments the NO beam intensity was 2.8×10^{14} molecules $cm^{-2} s^{-1}$ and the CO beam intensity was 2.9×10^{14} molecules $cm^{-2} s^{-1}$ (duration of CO pulses ca. 30 s). For reaction-rate measurements, an automated quadrupole mass spectrometer system (ABB Extrel) was employed. IR spectra were acquired using a vacuum FT-IR spectrometer (Bruker IFS 66v/S) at a spectral resolution of 2 cm^{-1} and the spectral features were quantified by integrating between the peak onset and the spectral minimum. The spectra in Figure 1 were recorded at NO exposures not exceeding 2.2×10^{16} molecules cm^{-2}. The alumina film was prepared by sputtering and annealing of an NiAl(110) single crystal, followed by an oxidation and annealing procedure, the details of which are given elsewhere.[29] Cleanliness and quality of the oxide film were checked by LEED (low-energy electron diffraction) and AES (Auger electron spectroscopy). Before the experiment, Pd (>99.9%) was deposited by using a commercial evaporator (Focus, EFM 3; Pd coverage: 2.7×10^{15} atoms cm^{-2}, sample temperature: 300 K). The evaporator flux was calibrated by a quartz microbalance prior to use. To avoid damage by ion bombardment, the sample was biased during Pd evaporation. After preparation the Pd particles were stabilized by extended exposure to oxygen (2.7×10^{14} molecules $cm^{-2} s^{-1}$, 2400 s, sample temperature 495 K) and subsequent by surface-oxygen removal by CO.[14,16] Dissociation probabilities were estimated based on the rate of decrease of the total absorption in the N–O stretching-frequency region using a Pd surface atom density of 5.4×10^{14} atoms cm^{-2} [14,26] and assuming a surface-oxygen saturation coverage of 0.25.[30]

Received: February 19, 2003 [Z51228]

Keywords: heterogeneous catalysis · kinetics · nitrogen oxide · supported catalysts · surface chemistry

[1] V. P. Zhdanov, B. Kasemo, *Surf. Sci. Rep.* **2000**, *39*, 25.
[2] C. R. Henry, *Surf. Sci. Rep.* **1998**, *31*, 231.
[3] J. Libuda, H.-J. Freund, *J. Phys. Chem. B* **2002**, *106*, 4901.
[4] S. Schauermann, J. Hoffmann, V. Johánek, J. Hartmann, J. Libuda, H.-J. Freund, *Angew. Chem.* **2002**, *114*, 2643; *Angew. Chem. Int. Ed.* **2002**, *41*, 2532.
[5] R. J. Farrauto, R. M. Heck, *Catal. Today* **2000**, *55*, 179.
[6] R. D. Ramsier, Q. Gao, H. Neergaard Waltenburg, K.-W. Lee, O. W. Nooij, L. Lefferts, J. T. Yates, Jr., *Surf. Sci.* **1994**, *320*, 209.
[7] R. D. Ramsier, Q. Gao, H. Neergaard Waltenburg, J. T. Yates, Jr., *J. Chem. Phys.* **1994**, *100*, 6837.
[8] S. Sugai, H. Watanabe, T. Kioka, H. Miki, K. Kawasaki, *Surf. Sci.* **1991**, *259*, 109.
[9] R. G. Sharpe, M. Bowker, *Surf. Sci.* **1996**, *360*, 21.
[10] M. Hirsimaki, M. Valden, *J. Chem. Phys.* **2001**, *114*, 2345.
[11] L. Piccolo, C. R. Henry, *Appl. Surf. Sci.* **2000**, *162–163*, 670.
[12] G. Prevot, C. R. Henry, *J. Phys. Chem. B* **2002**, *106*, 12191.
[13] D. R. Rainer, S. M. Vesecky, M. Koranne, W. S. Oh, D. W. Goodman, *J. Catal.* **1997**, *167*, 234.
[14] I. Meusel, J. Hoffmann, J. Hartmann, M. Heemeier, M. Bäumer, J. Libuda, H.-J. Freund, *Catal. Lett.* **2001**, *71*, 5.
[15] M. Bäumer, H.-J. Freund, *Prog. Surf. Sci.* **1999**, *61*, 127.
[16] S. Shaikhutdinov, M. Heemeier, J. Hoffmann, I. Meusel, B. Richter, M. Bäumer, H. Kuhlenbeck, J. Libuda, H.-J. Freund, R. Oldman, S. D. Jackson, C. Konvicka, M. Schmid, P. Varga, *Surf. Sci.* **2002**, *501*, 270.
[17] W. S. Brown, D. A. King, *J. Phys. Chem. B* **2000**, *104*, 2578.
[18] D. Loffreda, D. Simon, P. Sautet, *Chem. Phys. Lett.* **1998**, *291*, 15.
[19] D. Loffreda, D. Simon, P. Sautet, *J. Chem. Phys.* **1998**, *108*, 6447.
[20] C. Nyberg, P. Uvdal, *Surf. Sci.* **1988**, *204*, 517.
[21] X. Xu, P. Chen, D. W. Goodman, *J. Phys. Chem.* **1994**, *98*, 9242.
[22] F. M. Hoffmann, *Surf. Sci. Rep.* **1983**, *3*, 107.
[23] P. Hollins, *Surf. Sci. Rep.* **1992**, *16*, 51.
[24] K. H. Hansen, Z. Sljivancanin, E. Laegsgaard, F. Besenbacher, I. Stensgaard, *Surf. Sci.* **2002**, *505*, 25.
[25] H. Conrad, G. Ertl, J. Küppers, E. E. Latta, *Surf. Sci.* **1977**, *65*, 235.
[26] J. Libuda, I. Meusel, J. Hoffmann, J. Hartmann, L. Piccolo, C. R. Henry, H.-J. Freund, *J. Chem. Phys.* **2001**, *114*, 4669.
[27] S. Schauermann, V. Johánek, J. Hoffmann, M. Laurin, J. Libuda, H.-J. Freund, unpublished results.
[28] J. Libuda, I. Meusel, J. Hartmann, H.-J. Freund, *Rev. Sci. Instrum.* **2000**, *71*, 4395.
[29] J. Libuda, F. Winkelmann, M. Bäumer, H.-J. Freund, T. Bertrams, H. Neddermeyer, K. Müller, *Surf. Sci.* **1994**, *318*, 61.
[30] F. P. Leisenberger, G. Koller, M. Sock, S. Surnev, M. G. Ramsey, F. P. Netzer, B. Klötzer, K. Hayek, *Surf. Sci.* **2000**, *445*, 380.

 © 2003 Wiley-VCH Verlag GmbH & Co. KGaA, Weinheim

anti-Bredt Bridgehead Olefin

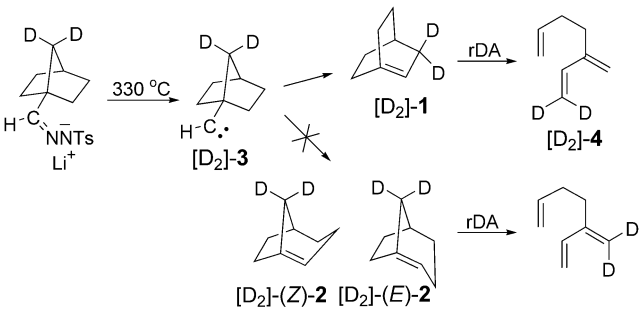
The Room-Temperature Stabilization of Bicyclo[2.2.2]oct-1-ene and Bicyclo[3.2.1]oct-1-ene**

*Paul Roach and Ralf Warmuth**

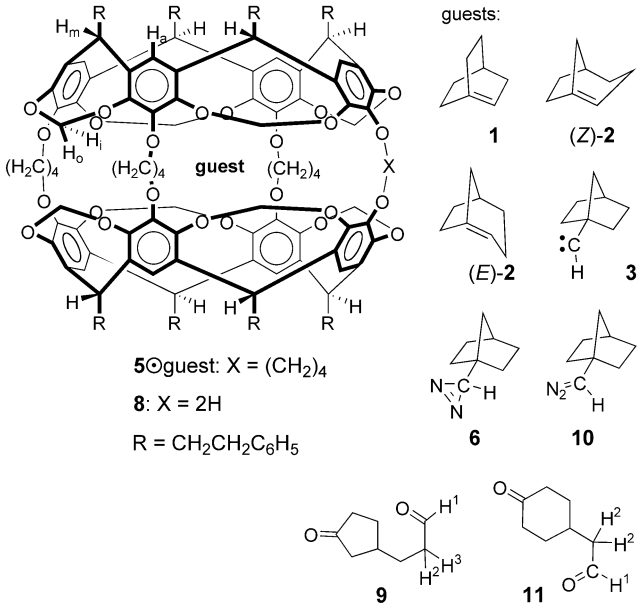
Dedicated to Professor Kendall N. Houk on the occasion of his 60th birthday

Ever since Julius Bredt noted that C=C bonds in pinene and camphene derivatives avoid the bridgehead position, a phenomenon now known as Bredt's rule,[1] the generation and investigation of anti-Bredt molecules that violate this rule has become an attractive and important subfield of hydrocarbon chemistry.[2] Based on the concept of olefinic strain (OS),[3] anti-Bredt olefins are classified as isolable ($OS \leq 17$ kcal mol^{-1}), observable ($17 \leq OS \leq 21$ kcal mol^{-1}),[4] or unstable ($OS \geq 21$ kcal mol^{-1}). The investigation of unstable anti-Bredt molecules that are closest to the borderline between olefin and 1,2-diradical, is important for structural organic chemistry but also a challenging task requiring the use of either bulky protecting groups,[5] matrix-isolation techniques, or ultra-fast spectroscopic methods.[5b,6] We are very interested in the three highly strained bridgehead olefins bicyclo[2.2.2]oct-1-ene (**1**), (*E*)- and (*Z*)-bicyclo[3.2.1]oct-1-ene ((*E*)-**2** and (*Z*)-**2**), which have predicted OS of 40.4, 42.2, and 28.6 kcal mol^{-1}, respectively.[3] Thirty years ago, Wolf and Jones, Jr. introduced the carbene route towards these bridgehead olefins, which are potential ring-expansion products of 1-bicyclo[2.2.1]heptyl carbene **3**.[7a] Even though high-level calculations predict preferred insertion into a two-carbon bridge leading to (*E*)-**2**,[8] thermolysis or photolysis of suitable carbene precursors gave only **1**,[7] which underwent a retro-Diels–Alder (rDA) reaction to **4** or dimerized prior to its detection (Scheme 1).

The reason for this discrepancy is not fully clear, but might be due to the participation of excited precursors. This and the possibility to generate three highly strained bridgehead olefins from one carbene precursor prompted us to investigate the chemistry of **3** inside a hemicarcerand and we are pleased to report herein the room temperature stabilization of both **1** and (*Z*)-**2** in the inner phase of **5** (Scheme 2).[9–11]



Scheme 1. The carbene route to bicyclo[2.2.2]oct-1-ene (**1**).[7a]



Scheme 2. Complexes of **5** with guest molecules.

We choose 1-bicyclo[2.2.1]heptyldiazirine (**6**) as the carbene precursor, which we prepared from 1-bicyclo[2.2.1]-heptylcarboxaldehyde (**7**) according to a general procedure published by Platz and co-workers.[12,13] Reacting diol **8** with $MsO(CH_2)_4OMs$ ($Ms = SO_2Me$), Cs_2CO_3, and excess **6** in hexamethyl phosphoramide (HMPA) gave hemicarceplex **5** ⊙ **6** in 36 % yield. Photolysis of **5** ⊙ **6** in degassed $CDCl_3$ ($\lambda >$ 300 nm; 0 °C) produced a new hemicarceplex **A** in 64 % yield together with various unidentified compounds, which we tentatively assign to innermolecular addition/insertion products between transient **3** and **5** (Figure 1 a, b).

Based on its NMR spectroscopic properties and its reaction with oxygen, we assign **A** to the (*Z*)-bicyclo[3.2.1]oct-1-ene hemicarceplex **5** ⊙ (*Z*)-**2**.[14] In the ^{1}H NMR spectrum, the vinylic proton H^1 appears as a doublet of doublets at $\delta = 4.41$ ppm, which served as starting point for the sequential assignment of all other protons from the DQCOSY, TOCSY, and ROESY spectra of the photolysis mixture (Scheme 3, right).

Especially, a NOE effect between H^1 and H^{10} at $\delta = -0.41$ ppm is consistent with the guest being (*Z*)-**2** rather

[*] Dr. R. Warmuth
Department of Chemistry and Chemical Biology
Rutgers, The State University of New Jersey
Piscataway, NJ 08854–8087 (USA)
Fax: (+1) 732-445-5312
E-mail: warmuth@rutchem.rutgers.edu
P. Roach
Department of Chemistry
The Nottingham Trent University
Nottingham, NG11 8NS (UK)

[**] This work was carried out at Kansas State University. P.R. is an undergraduate student participant. We thank the National Science Foundation (Grant CHE-0075749) for generous support of our research.

Supporting information for this article is available on the WWW under http://www.angewandte.org or from the author.

 DOI: 10.1002/anie.200351120 © 2003 Wiley-VCH Verlag GmbH & Co. KGaA, Weinheim

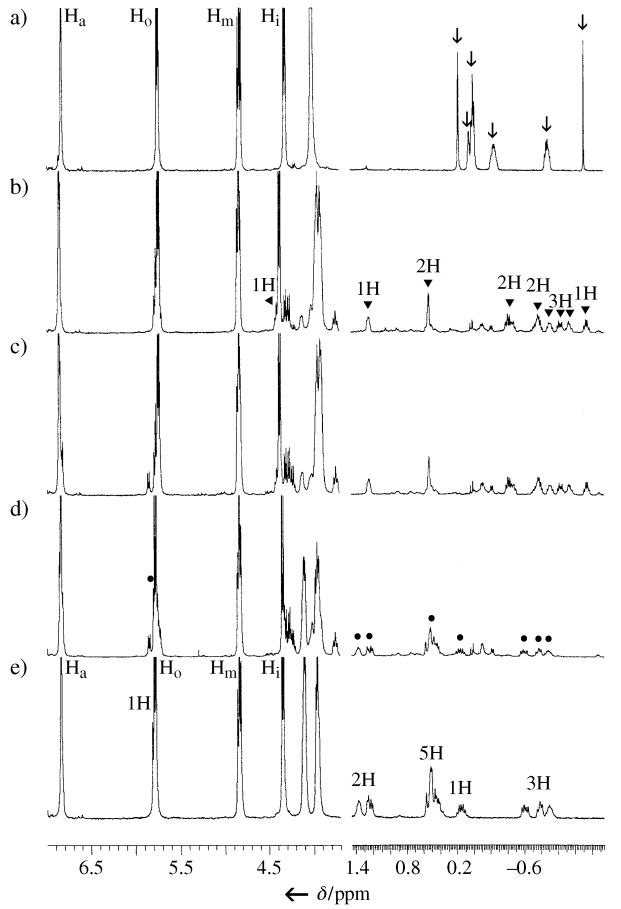
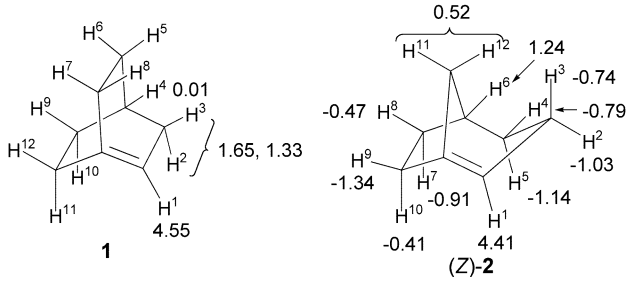


Figure 1. Section of the ^{1}H NMR spectra (400 MHz, 23 °C, $CDCl_3$) of **5** ⊙ **6** (a–d) and of **5** ⊙ **9** (e). a) Before and b) after irradiation ($\lambda > 300$ nm, 0 °C, 2 h) in the absence of oxygen. c) Same solution as b) after heating at 95 °C for one week. d) Same solution as c) after the solid photoproducts had been heated at 60 °C in the presence of oxygen for 48 h. Signals assigned to protons of incarcerated **6** (↓), (*Z*)-**2** (▼), and **9** (●). For the assignment of the hemicarcerand protons H_a, H_o, H_m, and H_i see Scheme 2.



Scheme 3. Comparison of the ^{1}H NMR spectroscopic data of incarcerated **1** and (*Z*)-**2**.

than (*E*)-**2**. Whereas **5** ⊙ (*Z*)-**2** is thermally very stable in the absence of O_2 and showed no detectable decomposition if heated for one week to 95 °C (Figure 1c), it reacted quantitatively with O_2 (60 °C, 2 days) to an oxidation product the elemental analysis, FAB-MS, FT-IR, and ^{1}H NMR spectrum of which are consistent with the ketoaldehyde hemicarceplex **5** ⊙ **9** (Figure 1d, e; Scheme 2).[5b,c,15] The ^{1}H NMR spectrum of **5** ⊙ **9** shows a characteristic singlet at $\delta = 5.81$ ppm (1H), which we assign to H^1 of **9** and which shows a weak cross-correlation to the adjacent methylene proton H^2 at $\delta =$ 0.48 ppm in the TOCSY spectrum.

When we briefly photolyzed **5** ⊙ **6** (4 min) under the same conditions as above, the ^{1}H NMR spectrum indicated formation of two further hemicarceplexes **B** (23 %) and **C** (18 %) in addition to **5** ⊙ (*Z*)-**2** (29 %) and **5** ⊙ **6** (23 %). **B** and **C** decomposed upon further photolysis. We assign **B** to the diazomethane hemicarceplex **5** ⊙ **10**,[14] the formation of which is expected and supported by the appearance of a characteristic absorption band at $\tilde{\nu}_{CNN} = 2056.2$ cm^{-1} in the FT-IR spectrum.[10e,g,16] We assign **C** to the anti-Bredt olefin hemicarceplex **5** ⊙ **1**,[14] based on its ^{1}H NMR spectrum, its photo and thermal chemistry and its reaction with O_2. Whereas **5** ⊙ **10** is photo-labile above 335 nm, **5** ⊙ **1** is stable under these conditions,[17] and photolysis of **5** ⊙ **6** above 335 nm gave **5** ⊙ **1** (yield ≤ 23 %). A section of the ^{1}H NMR spectrum of **5** ⊙ **1** is shown in Figure 2a. The doublet of doublets at $\delta = 4.55$ ppm ($^3J = 8.0$, 9.8 Hz), which we assign to the vinylic proton H^1 of **1** and which cross-correlates to protons H^2 and H^3 at $\delta = 1.65$ and 1.33 ppm in the DQCOSY, is very characteristic (Scheme 3, left). The remaining protons

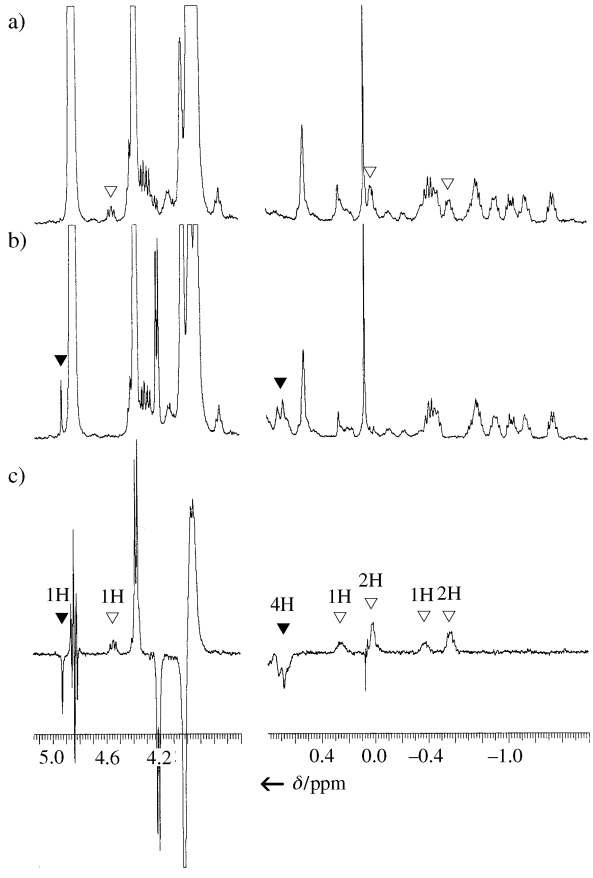


Figure 2. Section of the ^{1}H NMR spectra (400 MHz, 23 °C, $CDCl_3$) of **5** ⊙ **6**. a) After irradiation ($\lambda > 335$ nm, 0 °C, 2 h) in the absence of oxygen. b) Same solution as a) after exposure to atmospheric oxygen (15 min, 23 °C). c) difference spectrum (a) − (b). Signals assigned to protons of incarcerated **1** (▽) and **11** (▼).

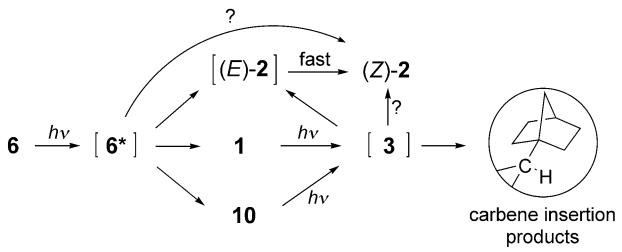
 © 2003 Wiley-VCH Verlag GmbH & Co. KGaA, Weinheim

of **1** are assigned to multiplets at $\delta = 0.01$ (H^4), 1.58, 0.97, 0.01, −0.57 (H^5, H^6, H^9, H^{10}), 0.27, 0.91, −0.38, and −0.59 ppm (H^7, H^8, H^{11}, H^{12}).

When exposed to atmospheric O_2, **5**⊙**1** oxidized rapidly affording the ketoaldehyde hemicarceplex **5**⊙**11** ($k = 1.3 \times 10^{-3}\,sec^{-1}$).[5b,c,15] Formation of **5**⊙**11** is supported by elemental analysis, FAB mass spectrometry, FT-IR ($\tilde{\nu}$(C=O) at 1726 cm^{-1} and 1721 cm^{-1}), and NMR spectroscopy (Figure 2b and c). The ^1H NMR spectrum shows a characteristic singlet at $\delta = 4.92$ ppm for the aldehyde proton H^1 of **11**. From the delayed formation of **5**⊙**11** ($k_{formation} \approx 3 \times 10^{-3}\,sec^{-1}$), we conclude that oxidation of **1** is stepwise via an intermediate dioxetane.[15] Spectroscopic evidence for incarcerated (*E*)-**2** could not be obtained. However, formation of small amounts of **5**⊙**9** during the photolysis of **5**⊙**6** under aerobic conditions supports that **5**⊙(*E*)-**2** indeed formed and isomerized to **5**⊙(*Z*)-**2** before it could be detected.[18]

The thermal stability of **5**⊙**1** is remarkable. At 61.7 °C, the rate constant for the retro-Diels–Alder reaction of incarcerated **1** is $k = 2.2 \times 10^{-5}\,sec^{-1}$, from which we calculate a free activation enthalpy of $\Delta G^{\ddagger}_{335K} = 26.8\,kcal\,mol^{-1}$. Ruck and Jones, Jr. showed that **3**, which they generated photochemically from a non-nitrogen precursor, gives **4** in 25% yield via **1** together with various dimers at 60 °C and gives **4** quantitatively at 100 °C.[7c] Hence, the lifetime of free **1** at 61.7 °C cannot be more than a minute and the retro-Diels–Alder reaction of incarcerated **1** must be more than 2000-fold retarded by the surrounding host. The increased internal stability of incarcerated **1** cannot be a result of a partial reversibility of the reaction **1**→**4**,[19] but must be due to steric interactions that build up inside **5** as the transition state is reached. Concerted Diels–Alder and retro-Diels–Alder reactions have negative activation volumes.[20] Thus, our observation is consistent with a stepwise mechanism, not surprisingly, since any strain in a cyclohexene ring will lower the activation barrier more for a step-wise than for a concerted retro-Diels–Alder pathway.

Further analysis of the photo and thermal chemistry of **5**⊙**6** gave insight into the mechanism of the ring-expansion reactions (Scheme 4). At the initial stage of the photolysis of



Scheme 4. Photochemistry of incarcerated **6**.

5⊙**6** only **5**⊙**1**, **5**⊙(*Z*)-**2**, **5**⊙**10**, but no carbene insertion products were detected by ^1H NMR spectroscopy. The amount of **5**⊙**1** increased until all the **5**⊙**6** had been consumed. Irradiation of **5**⊙**10** or **5**⊙**1** yielded **5**⊙(*Z*)-**2** and carbene insertion products. Thermolysis of **5**⊙**6** (71–100 °C) gave **5**⊙**1** and **5**⊙(*Z*)-**2** in a 1:3 ratio and only trace amounts of carbene insertion products.[21] Compound **5**⊙**10** is an intermediate in the thermolysis. Thus, a) **1** and (*Z*)-**2** and/or (*E*)-**2** (initial ratio[**1**]/[(*Z*)-**2**] and/or [(*E*)-**2**] = 1.1:1) are formed directly from the photochemically excited **6*** and b) incarcerated **3** rearranges to (*Z*)-**2** and/or (*E*)-**2** and not to **1** as theory predicts but contrary to the experiments by Ruck and Jones, Jr. (Scheme 4).[7c,22] This situation underlines the influence of encapsulation on the conformational space and intramolecular chemistry of carbenes.[11b]

In summary, we have stabilized at room temperature two highly strained anti-Bredt bridgehead olefins containing a *trans*-cyclohexene or a *trans*-cycloheptene ring by incarceration, which suppresses inter- and intramolecular reaction channels. Remarkable is the high barrier for the retro-Diels–Alder reaction of incarcerated **1**, which, if added to its olefin strain energy (OS), exceeds the π-bond strength of a C=C bond. Thus, the determination of the enantiomerization barrier of **1** might be possible and would give a direct measure for the p orbital overlap energy. A lower limit of this barrier ($\Delta G^{\ddagger}_{295K} > 14\,kcal\,mol^{-1}$) can be estimated from the chemical shift difference of the diastereotopic protons H^2 and H^3 of **1** ($\Delta\delta = 128$ Hz).

Received: February 6, 2003 [Z51120]

Keywords: carbenes · hemicarcerands · host–guest systems · ring expansion · strained molecules

[1] J. Bredt, H. Thouet, L. Schmitz, *Justus Liebigs Ann. Chem.* **1924**, *437*, 1.
[2] a) P. M. Warner, *Chem. Rev.* **1989**, *89*, 1067; b) H. Hopf, *Classics in Hydrocarbon Chemistry*, Wiley-VCH, Weinheim, **2000**, p. 122.
[3] W. F. Maier, P. von R. Schleyer, *J. Am. Chem. Soc.* **1981**, *103*, 1891.
[4] a) J. R. Wiseman, J. A. Chong, *J. Am. Chem. Soc.* **1969**, *91*, 7775; b) M. S. Gudipati, J. G. Radziszewski, P. Kaszynski, J. Michl, *J. Org. Chem.* **1993**, *58*, 3668.
[5] a) S. F. Sellers, T. C. Klebach, F. Hollywood, M. Jones, Jr., *J. Am. Chem. Soc.* **1982**, *104*, 7075; b) K. Hirai, H. Tomioka, T. Okazaki, K. Tokunaga, T. Kitagawa, K. Takeuchi, *J. Phys. Org. Chem.* **1999**, *12*, 165; c) M. Ohno, M. Itoh, M. Umeda, R. Furuta, K. Kondo, S. Equchi, *J. Am. Chem. Soc.* **1996**, *118*, 4981.
[6] E. L. Tae, Z. Zhu, M. S. Platz, *J. Phys. Chem. A* **2001**, *105*, 3803.
[7] a) A. D. Wolf, M. Jones, Jr., *J. Am. Chem. Soc.* **1973**, *95*, 8209; b) N. Bian, M. Jones, Jr., *Tetrahedron Lett.* **1993**, *34*, 3967; c) R. T. Ruck, M. Jones, Jr., *Tetrahedron Lett.* **1998**, *39*, 4433.
[8] C. M. Geise, C. M. Hadad, *J. Am. Chem. Soc.* **2000**, *122*, 5861.
[9] a) D. J. Cram, J. M. Cram, *Container Molecules and Their Guests* (Ed.: J. F. Stoddart), The Royal Society of Chemistry, Cambridge, UK, **1994**; b) A. Jasat, J. C. Sherman, *Chem. Rev.* **1999**, *99*, 931.
[10] a) D. J. Cram, M. E. Tanner, R. Thomas, *Angew. Chem.* **1991**, *103*, 1048; *Angew. Chem. Int. Ed. Engl.* **1991**, *30*, 1024; b) R. Warmuth, *Angew. Chem.* **1997**, *109*, 1406; *Angew. Chem. Int. Ed. Engl.* **1997**, *36*, 1347; c) R. Warmuth, *J. Chem. Soc. Chem. Commun.* **1998**, 59; d) R. Warmuth, M. A. Marvel, *Angew. Chem.* **2000**, *112*, 1168; *Angew. Chem. Int. Ed.* **2000**, *39*, 1117; e) R. Warmuth, M. A. Marvel, *Chem. Eur. J.* **2001**, *7*, 1209; f) R. Warmuth, *J. Am. Chem. Soc.* **2001**, *123*, 6955; g) J.-L. Kerdelhué, K. J. Langenwalter, R. Warmuth, *J. Am. Chem. Soc.* **2003**, *125*, 973.
[11] For related reactions inside cyclodextrins, see: a) U. H. Brinker, R. Buchkremer, M. G. Rosenberg, M. D. Poliks, M. Orlando,

 © 2003 Wiley-VCH Verlag GmbH & Co. KGaA, Weinheim

M. L. Gross, *Angew. Chem.* **1993**, *105*, 1427; *Angew. Chem. Int. Ed. Engl.* **1993**, *32*, 1344; b) U. H. Brinker, M. G. Rosenberg in *Advances in Carbene Chemistry, Vol. 2* (Ed.: U. H. Brinker), Jai, London, **1998**, p. 29.
[12] K. Kostova, V. Dimitrov, *Synth. Commun.* **1995**, *25*, 1575.
[13] I. R. Likhotvorik, E. L. Tae, C. Ventre, M. S. Platz, *Tetrahedron Lett.* **2000**, *41*, 795.
[14] This hemicarceplex was not isolated. Its yield was estimated from the ^{1}H NMR spectrum of the product mixture.
[15] H. O. House, R. J. Outcalt, J. L. Haack, D. van der Veer, *J. Org. Chem.* **1983**, *48*, 1654.
[16] M. T. H. Liu, *Chem. Soc. Rev.* **1982**, *11*, 127.
[17] Based on the photochemistry of 1-adamantene,[6] which has an OS of 39.4 kcal mol^{-1} and which shows a $\lambda_{max} = 310$ nm, the photosensitivity of **1** below 335 nm is not surprising.
[18] The life-time of *trans*-1-phenylcyclohexene is 9 μs at room temperature: L. Bonneau, J. Joussot-Dubien, L. Salem, A. J. Yarwood, *J. Am. Chem. Soc.* **1976**, *98*, 4329.
[19] a) A. M. A. van Wageningen, P. Timmerman, J. P. M. van Duynhoven, W. Verboom, F. C. J. M. van Veggel, D. N. Reinhoudt, *Chem. Eur. J.* **1997**, *3*, 639; b) S. K. Körner, F. C. Tucci, D. M. Rudkevich, T. Heinz, J. Rebek, Jr., *Chem. Eur. J.* **2000**, *6*, 188.
[20] a) G. Jenner, J. Rimmelin, *Tetrahedron Lett.* **1980**, *21*, 3039; b) R. van Eldik, T. Asano, W. J. LeNoble, *Chem. Rev.* **1989**, *89*, 549.
[21] The amount of **5** ⊙ **1** was determined from the amount of free **4**, which formed under these conditions by the retro-Diels–Alder reaction of **1** followed by the dissociation of **5** ⊙ **4**.
[22] The precursor to **4** in the experiments by Ruck and Jones, Jr., must be **1** and cannot be (*E*)-**2**.[7c] The latter would isomerize to (*Z*)-**2** prior to its retro-Diels–Alder reaction. (*Z*)-**2** is a thermodynamic sink under these conditions and is unlikely to rearrange to **4** (life-time of **5** ⊙ (*Z*)-**2** = 4.4 h at 197 °C).

 © 2003 Wiley-VCH Verlag GmbH & Co. KGaA, Weinheim

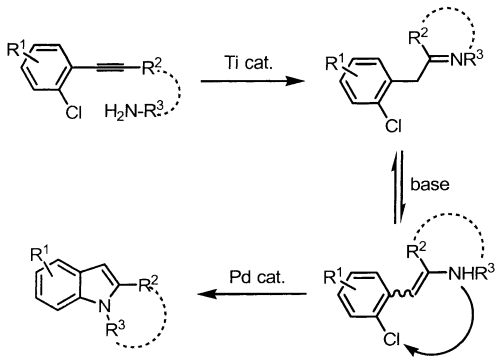
Catalytic Indol Synthesis

A Flexible and Catalytic One-Pot Procedure for the Synthesis of Indoles**

*Holger Siebeneicher, Igor Bytschkov, and Sven Doye**

Initiated by improved screening methods, a steadily increasing demand for highly flexible synthetic procedures has evolved during the last couple of years. The major purpose of these synthetic methods is the fast generation of various derivatives of a certain class of substances. In the past, we have repeatedly shown that the titanium-catalyzed hydroamination of alkynes[1] is a versatile tool for the highly flexible synthesis of biologically interesting compounds.[2] Expanding these studies, we now present a highly flexible and catalytic one-pot procedure for the synthesis of indoles[3] employing *ortho*-chloro-substituted 1-phenyl-2-alkyl alkynes or phenyl-(aminoalkyl)alkynes as starting materials.

The general principle of the one-pot procedure is shown in Scheme 1. The major expectation is that under basic conditions, the imines, which are regioselectively formed during



Scheme 1. Outline of a flexible and catalytic one-pot procedure for the synthesis of indoles.

the hydroamination in the presence of the Ti catalyst $[Cp_2TiMe_2]$ ($Cp = C_5H_5$)[4], will be in equilibrium with the corresponding enamines. In addition, an *ortho*-chloro-substituent in the benzene ring, should offer the possibility to convert the enamines into indoles by a Pd-catalyzed N-arylation/cyclization (Buchwald–Hartwig reaction).[5] Since the enamines are removed from the equilibrium during this cyclization step it should be possible to convert the imines completely into indoles. However, to our knowledge, corresponding N-arylations of N-substituted imines under basic conditions in the presence of Pd-catalysts have not been reported.[6]

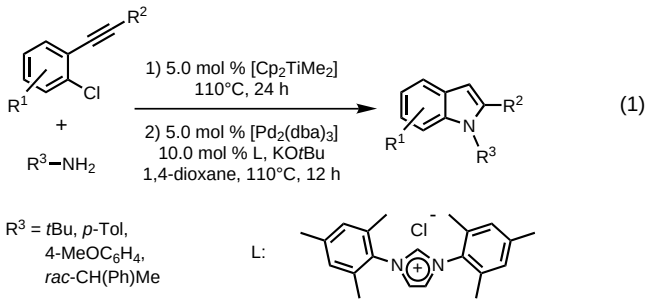
To investigate the scope of the suggested synthetic strategy, which includes two C–N bond-forming steps, we synthesized a number of *ortho*-chloro-substituted 1-phenyl-2-alkyl alkynes (**1**–**10**, Table 1) by Sonogashira couplings[7] starting from simple 1-chloro-2-iodobenzenes and terminal alkynes.[2c] The alkynes **1**–**10**, which could be isolated in high yields, were then used for the one-pot procedure. For this purpose, the alkynes were first hydroaminated with an arbitrary primary amine in the presence of 5 mol% $[Cp_2TiMe_2]$. Subsequently, 5 mol% $[Pd_2(dba)_3]$ (dba = dibenzylideneacetone, 10 mol% 1,3-bis(2,4,6-trimethylphenyl)imidazolium chloride, and KO*t*Bu were added directly to the reaction mixture. After heating the resulting mixture to 110 °C, most of the 1,2-, 1,2,5-, and 1,2,6-substituted indoles **11**–**20** could be isolated in good yields [Eq. (1), Table 1]. However, the reaction of **4** and *tert*-butylamine gave the corresponding indole **14** in only 39% yield. This modest result is because the regioselectivity of the $[Cp_2TiMe_2]$-catalyzed hydroamination of 1-phenyl-2-alkenyl alkynes is worse than that of 1-phenyl-2-alkyl alkynes.[2b]

[*] Dr. S. Doye, Dipl.-Chem. H. Siebeneicher, Dr. I. Bytschkov
Institut für Organische Chemie
Universität Hannover
Schneiderberg 1B, 30167 Hannover (Germany)
Fax: (+49) 511-762-30-11
E-mail: sven.doye@oci.uni-hannover.de

[**] This work was supported by the Deutsche Forschungsgemeinschaft, the Fonds der Chemischen Industrie, and the Dr. Otto Röhm Gedächtnisstiftung, Darmstadt. We further thank Professor E. Winterfeldt for his generous support of our research.

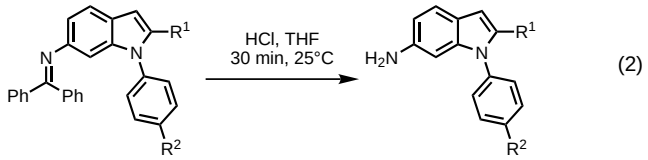
Supporting information for this article is available on the WWW under http://www.angewandte.org or from the author.

 © 2003 Wiley-VCH Verlag GmbH & Co. KGaA, Weinheim DOI: 10.1002/anie.200351345



(1)

As can be seen from Table 1, methyl and benzyl ethers (entries 2, 5–7, 10), CF_3 groups (entry 8), and diphenylimine groups (entries 9, 10) are functional groups that are tolerated under the reaction conditions. However, from a synthetic point of view the successful transformations of the imine-functionalized alkynes **9** and **10** into the indoles **19** and **20** are especially interesting because these products can be easily converted into the 6-aminoindoles **21** and **22** under acidic conditions [Eq. (2)].[6a]



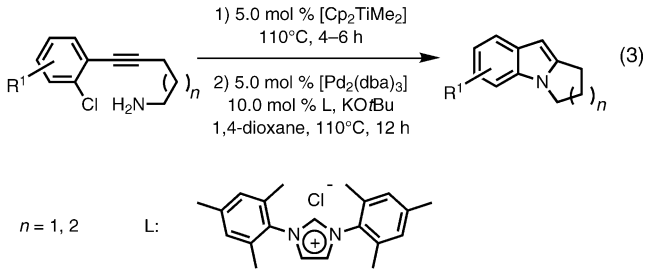
(2)

19 R^1 = *c*Pr, R^2 = Me
20 R^1 = *n*Bu, R^2 = OMe

21 R^1 = *c*Pr, R^2 = Me (86%)
22 R^1 = *n*Bu, R^2 = OMe (85%)

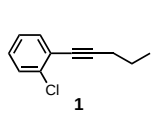
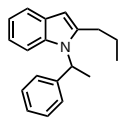
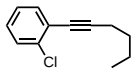
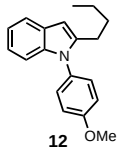
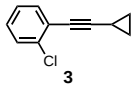
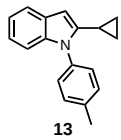
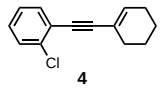
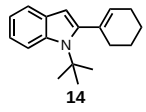
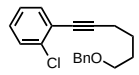
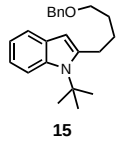
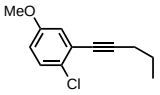
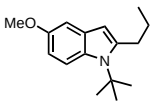
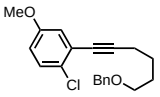
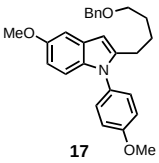
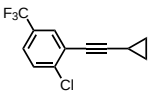
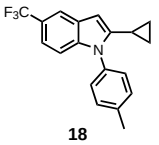
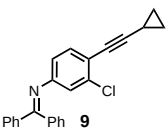
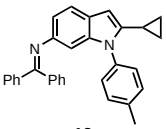
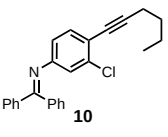
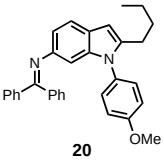
The products **11**, **12**, **17**, and **20** have potentially removable protecting groups at the indole N atom. In addition, the O groups located in the side chains of **15** and **17** offer various possibilities for further synthetic transformations (e.g. cyclization to the carbazole skeleton).

For completeness, we also synthesized some *ortho*-chloro-substituted 1-phenyl-2-(aminoalkyl)alkynes **23**–**30** by Sonogashira couplings[8] and used them as substrates for the described one-pot procedure [Eq. (3), Table 2]. During this study, we recognized that the hydroamination reactions employing **23** and **25**–**30** went to completion within 4–6 h while the sterically demanding δ-aminoalkyne **24** needed 48 h to reach 100 % conversion. However, after the second part of the one-pot procedure (the Pd-catalyzed cyclization reaction) only the piperidine derivatives **31**–**34** could be obtained easily and in reasonable yields (53–77 %, entries 1–4). Starting from the related γ-aminoalkynes **27**–**30**, only **28** could be converted into the corresponding indole **36** (53 % yield). Clearly,



(3)

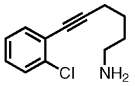
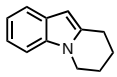
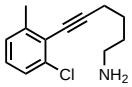
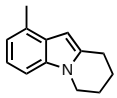
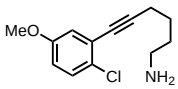
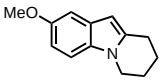
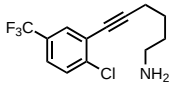
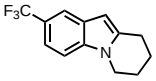
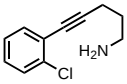
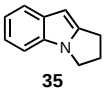
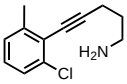
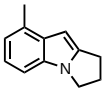
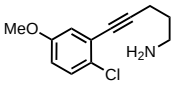
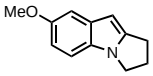
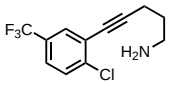
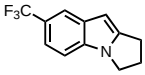
Table 1: One-pot procedure for the synthesis of indoles from *ortho*-chloro-substituted 1-phenyl-2-alkyl alkynes and primary amines.

Entry	Alkyne	Product	Yield [%][a]
1	 **1**	 **11**	65[b]
2	 **2**	 **12**	78
3	 **3**	 **13**	77
4	 **4**	 **14**	39
5	 **5**	 **15**	70
6	 **6**	 **16**	65
7	 **7**	 **17**	81
8	 **8**	 **18**	68
9	 **9**	 **19**	75
10	 **10**	 **20**	64

[a] Reaction conditions: 1) alkyne (2.0 mmol), amine (2.0 mmol), $[Cp_2TiMe_2]$ (0.48 mol L^{-1} in toluene, 0.1 mmol, 5.0 mol %), 110 °C, 24 h; 2) $[Pd_2(dba)_3]$ (0.1 mmol, 5.0 mol %), 1,3-bis(2,4,6-trimethylphenyl)imidazolium chloride (0.2 mmol, 10.0 mol %), KO*t*Bu (3.0 mmol), 1,4-dioxane, 110 °C, 12 h. [b] 10.0 mol % $[Cp_2TiMe_2]$ and amine (3.0 mmol) were used.

 © 2003 Wiley-VCH Verlag GmbH & Co. KGaA, Weinheim

Table 2: One-pot procedure for the synthesis of indoles from *ortho*-chloro-substituted 1-phenyl-2-(aminoalkyl)alkynes.

Entry	Aminoalkyne	Product	Yield [%][a]
1	 **23**	 **31**	68
2	 **24**	 **32**	53[b]
3	 **25**	 **33**	75
4	 **26**	 **34**	77
5	 **27**	 **35**	–[c]
6	 **28**	 **36**	53
7	 **29**	 **37**	–[c]
8	 **30**	 **38**	–[c]

[a] Reaction conditions: 1) aminoalkyne (1.0 mmol), [Cp_2TiMe_2] (0.48 mol L^{-1} in toluene, 0.05 mmol, 5.0 mol%), 110°C, 4–6 h; 2) [$Pd_2(dba)_3$] (0.05 mmol, 5.0 mol%), 1,3-bis(2,4,6-trimethylphenyl)-imidazolium chloride (0.1 mmol, 10.0 mol%), KO*t*Bu (1.5 mmol), 1,4-dioxane, 110°C, 12 h. [b] The reaction time of the hydroamination step was 48 h. [c] After a successful hydroamination reaction, no cyclization product could be isolated.

cyclization reactions that result in the formation of two annulated five-membered rings are disfavored by the increased ring-strain. However, the reasonable results obtained with substrates **24** and **28** prove that our one-pot procedure can also be applied successfully for the synthesis of 4-substituted indoles (**32**, **36**).

In summary, we have shown that a clever combination of a [Cp_2TiMe_2]-catalyzed hydroamination of alkynes with a Pd-catalyzed N-arylation of imines results in a new and general method for the synthesis of indoles, in which two new C–N bonds are formed during the one-pot procedure. Since the starting materials employed are easily accessible from 1-chloro-2-iodobenzenes and terminal alkynes by Sonogashira coupling reactions this procedure offers a great deal of synthetic flexibility.

Experimental Section

A Schlenk tube equipped with a Teflon stopcock and a magnetic stirring bar was charged with amine (2.0 mmol), alkyne (2.0 mmol), and a solution of [Cp_2TiMe_2] (0.21 mL, 0.48 M in toluene, 0.1 mmol, 5.0 mol%). The mixture was heated under argon to 110°C for 24 h (thin-layer chromatography (TLC) monitoring). After the resulting brown liquid had cooled to room temperature, [$Pd_2(dba)_3$] (92 mg, 0.1 mmol, 5.0 mol%), 1,3-bis(2,4,6-trimethylphenyl)imidazolium chloride (68 mg, 0.2 mmol, 10.0 mol%), KO*t*Bu (337 mg, 3.0 mmol), and 1,4-dioxane (5.0 mL) were added. The mixture was heated to 110°C for further 12 h (TLC monitoring) and then filtered through SiO_2. After the SiO_2 had been washed with CH_2Cl_2, the organic layer was concentrated under vacuum. The residue was purified by flash chromatography (SiO_2).

Received: March 6, 2003 [Z51345]

Keywords: alkynes · homogeneous catalysis · hydroamination · palladium · titanium

[1] For reviews, see: a) F. Pohlki, S. Doye, *Chem. Soc. Rev.* **2003**, *32*, 104–114; b) I. Bytschkov, S. Doye, *Eur. J. Org. Chem.* **2003**, 935–946.

[2] a) E. Haak, I. Bytschkov, S. Doye, *Eur. J. Org. Chem.* **2002**, 457–463; b) H. Siebeneicher, S. Doye, *Eur. J. Org. Chem.* **2002**, 1213–1220; c) I. Bytschkov, H. Siebeneicher, S. Doye, *Eur. J. Org. Chem.* **2003**, in press.

[3] For a summary of recently published methods for the synthesis of indoles, see: a) T. L. Gilchrist, *J. Chem. Soc. Perkin Trans. 1* **2001**, 2491–2515; a new method for the synthesis of highly substituted indoles was published recently. This publication includes further references for the synthesis of indoles: b) J. L. Rutherford, M. P. Rainka, S. L. Buchwald, *J. Am. Chem. Soc.* **2002**, *124*, 15168–15169.

[4] a) N. A. Petasis in *Encyclopedia of Reagents for Organic Synthesis, Vol. 1* (Ed.: L. A. Paquette), Wiley, New York, **1995**, pp. 470–473; b) H. Siebeneicher, S. Doye, *J. Prakt. Chem.* **2000**, *342*, 102–106.

[5] For reviews, see: a) J. P. Wolfe, S. Wagaw, J.-F. Marcoux, S. L. Buchwald, *Acc. Chem. Res.* **1998**, *31*, 805–818; b) B. H. Yang, S. L. Buchwald, *J. Organomet. Chem.* **1999**, *576*, 125–146; c) A. R. Muci, S. L. Buchwald, *Top. Curr. Chem.* **2002**, *219*, 131–209; d) J. F. Hartwig, *Synlett* **1997**, 329–340; e) J. F. Hartwig, *Angew. Chem.* **1998**, *110*, 2154–2177; *Angew. Chem. Int. Ed.* **1998**, *37*, 2046–2067.

[6] The Pd-catalyzed N-arylation of benzophenone imine has been described: a) J. P. Wolfe, J. Åhman, J. P. Sadighi, R. A. Singer, S. L. Buchwald, *Tetrahedron Lett.* **1997**, *38*, 6367–6370; The Pd-catalyzed N-arylation of N,N-disubstituted hydrazones has been described by: b) M. Watanabe, T. Yamamoto, M. Nishiyama, *Angew. Chem.* **2000**, *112*, 2620–2623; *Angew. Chem. Int. Ed.* **2000**, *39*, 2501–2504.

[7] a) K. Sonogashira, Y. Tohda, N. Hagihara, *Tetrahedron Lett.* **1975**, *16*, 4467–4470; b) K. Sonogashira in *Comprehensive Organic Synthesis, Vol. 3* (Eds.: B. M. Trost, I. A. Fleming), Pergamon, Oxford, **1991**, pp. 521–549.

[8] a) M. R. Gagné, C. L. Stern, T. J. Marks, *J. Am. Chem. Soc.* **1992**, *114*, 275–294; b) I. Bytschkov, S. Doye, *Tetrahedron Lett.* **2002**, *43*, 3715–3718; c) I. Bytschkov, PhD thesis, University of Hannover, **2002**.

 © 2003 Wiley-VCH Verlag GmbH & Co. KGaA, Weinheim

Cover Picture

Marcel Mayor* and Claudia Didschies

As a circular path for electrons a giant macrocycle with a periphery consisting of exclusively conjugation-active units has been designed. With a diameter of 12 nm it is probably the largest synthesized, shape-persistent, and monodisperse cyclic structure to date. In addition, the front wheel of a bicycle is shown, the 16-fold symmetry of which inspired the design of the molecule. For more information on this molecule see the Communication by M. Mayor and C. Didschies on page 3176 ff.



Contents

Angewandte EarlyView

The following articles are available online (in Wiley Interscience). You can find them at www.angewandte.org, under Full Text, Forthcoming Articles.

F. Würthner, S. Yao, U. Beginn:*
Highly Ordered Merocyanine Dye Assemblies by Supramolecular Polymerization and Hierarchical Self-Organization
DOI: 10.1002/anie.200351414
Published online: July 3, 2003

R. R. Davda, J. A. Dumesic:*
Catalytic Reforming of Oxygenated Hydrocarbons for Hydrogen with Low Levels of Carbon Monoxide
DOI: 10.1002/anie.200351664
Published online: June 18, 2003

Articles judged by the referees or the editior as being either very important or very urgent are immediately edited, proof-read, and electronically published once the manuscript has arrived in the editiorial office in final form. As long as there is no page number available these articles should be cited in the following manner:

Author(s) *Angew. Chem. Int. Ed.*, online publication date, DOI.

News

Physical Chemistry: Prizes for Ertl ____ **3064**

Inorganic Chemistry: Oro Recognized ____ **3064**

Organic Chemistry: Bürgenstock Brief ____ **3064**

Web Sites

http://www.rna.icmb.utexas.edu ____ **3065** — Evolution of the Ribosome — *Burkhard Luy*

Books

Cohesion ____ **3066** — John S. Rowlinson — *reviewed by Ralf Ludwig*

Organic Synthetic Methods ____ **3067** — James R. Hanson — *reviewed by A. Stephen K. Hashmi*

Highlights

Biosynthesis of Fungal Alkaloids

F. von Nussbaum* ____ **3068 – 3071**

Stephacidin B—A New Stage of Complexity within Prenylated Indole Alkaloids from Fungi



stephacidin B

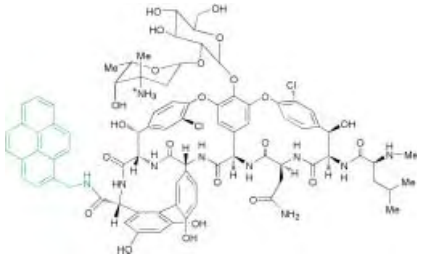
With its 15 rings, stephacidin B (see structure) is one of the most complex indole alkaloids to be isolated from fungi. The pseudosymmetric structure indicates that a new type of dimerization takes place at a late stage of the biosynthesis.

Bioactive Hydrogelators

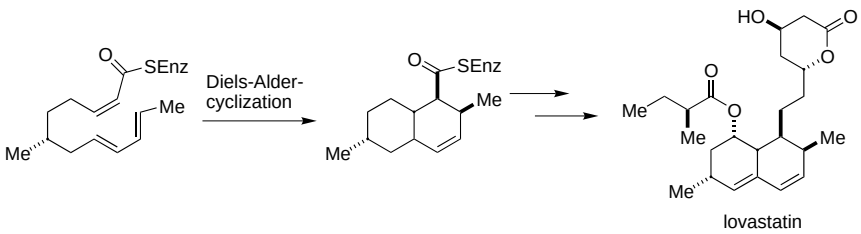
J. C. Tiller* ____ **3072 – 3075**

Increasing the Local Concentration of Drugs by Hydrogel Formation

Drugs that gel: The first hydrogel-forming drug, a pyrene-derivatized form of the antibiotic vancomycin (see structure), exhibits an 11-fold higher antimicrobial activity than vancomycin itself. A possible mechanism for this effect and its influence on future drug design are discussed.



Reviews



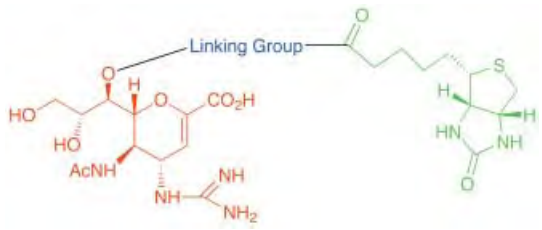
Do they or don't they? A Diels–Alder cycloaddition has been assumed to occur in the biosynthesis of numerous natural products, for example, lovastatin (see scheme). The existence of enzymes that catalyze these reactions (Diels–Alderases) was until recently not know for certainty, even when biosynthetic investigations and the biommetic total syntheses in some cases suggested it to be so.

Biosynthetic Diels–Alder Reactions

E. M. Stocking,
R. M. Williams* ——— **3078 – 3115**

Chemistry and Biology of Biosynthetic Diels–Alder Reactions

Communications

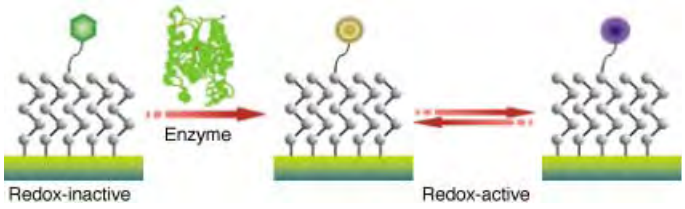


Catching flu: The influenza virus neuraminidase inhibitor zanamivir (red) is functionalized at the 7-position to give derivatives that retain a high affinity for the enzyme. When conjugated to biotin (green) or onto microspheres, such derivatives can be used to capture or aggregate influenza virus particles.

Towards Influenza Detection

J. L. McKimm-Breschkin,* P. M. Colman, B. Jin, G. Y. Krippner, M. McDonald, P. A. Reece, S. P. Tucker, L. Waddington, K. G. Watson,* W.-Y. Wu ——— **3118 – 3121**

Tethered Neuraminidase Inhibitors That Bind an Influenza Virus: A First Step Towards a Diagnostic Method for Influenza



A dynamic substrate that transduces a biological activity into an electrical signal has been developed (see scheme). The enzymatic conversion of a redox-inactive substrate presented at a self-assembled monolayer produced a redox-active product that is monitored electrochemically in real time.

Electrochemical Transduction

W.-S. Yeo, M. Mrksich* ——— **3121 – 3124**

Self-Assembled Monolayers That Transduce Enzymatic Activities to Electrical Signals

For the USA and Canada:
ANGEWANDTE CHEMIE International Edition (ISSN 1433-7851) is published weekly by Wiley-VCH PO Box 191161, D 69451 Weinheim, Germany. Air freight and mailing in the USA by Publications Expediting Inc. 200 Meacham Ave., Elmont, NY 11003. Periodicals postage paid at Jamaica NY 11431. US POSTMASTER: send address changes to *Angewandte Chemie*, Wiley-VCH, 111 River Street, Hoboken, NJ 07030. Annual institutional subscription price for institutions: Europe € 2998.00/3148.00. Outside Europe US$ 3718.00/3904.00 (valid for print or electronic/print and electronic delivery); for individuals who are personal members of a national chemical society, or whose institution already subscribes, or who are retired or self-employed consultants, print only (including postage and handling charges): Europe € 248.00/Outside Europe US$ 348.00.

 © 2003 Wiley-VCH Verlag GmbH & Co. KGaA, Weinheim

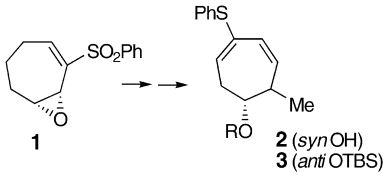
Contents

Polypropionate Synthesis

E. Torres, Y. Chen, I. C. Kim, P. L. Fuchs* ——— 3124 – 3131

Functionality Propagation by Alkylative Oxidation of Cross-Conjugated Cycloheptadienyl Sulfones

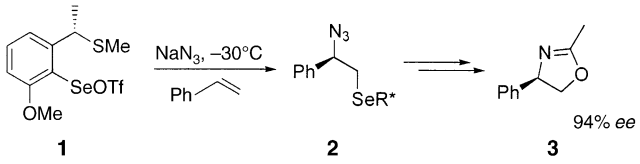
Getting the most out of sulfur. Enantiopure epoxyvinyl sulfone **1** is transformed to *syn*- and *anti*-dienyl sulfones **2** and **3**, respectively, by means of a nucleophilic methylation/sulfenylation/directed elimination reaction sequence. Compound **2** has been converted into termini-differentiated seven-carbon polypropionate segments found in five biologically significant natural products.



Asymmetric Azidoselenenylation

M. Tiecco,* L. Testaferri, C. Santi, C. Tomassini, F. Marini, L. Bagnoli, A. Temperini ——— 3131 – 3133

Asymmetric Azidoselenenylation of Alkenes: A Key Step for the Synthesis of Enantiomerically Enriched Nitrogen-Containing Compounds



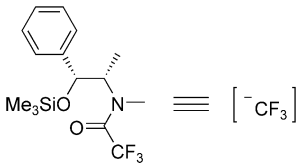
Chiral, nonracemic azidoselenides such as **2** are useful intermediates for the synthesis of enantiomerically enriched nitrogen-containing compounds (e.g. **3**). The asymmetric electrophilic azidoselenenylation of a variety of alkenes with the sulfur-containing chiral selenenyl triflate **1** and sodium azide occurred with high facial selectivity to provide an array of azidoselenides, which were further elaborated.

Trifluoromethylation

J. Joubert, S. Roussel, C. Christophe, T. Billard,* B. R. Langlois,* T. Vidal ——— 3133 – 3136

Trifluoroacetamides from Amino Alcohols as Nucleophilic Trifluoromethylating Reagents

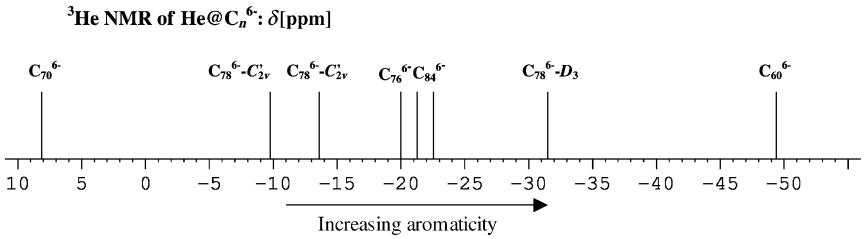
Both non-enolizable and enolizable carbonyl compounds underwent nucleophilic trifluoromethylation by a new family of cheap and efficient trifluoroacetamide reagents derived from *vic*-amino alcohols (see picture). From an ecological and an economic viewpoint these represent a promising alternative to other known trifluoromethylation reagents.



Probing Fullerene Aromaticity

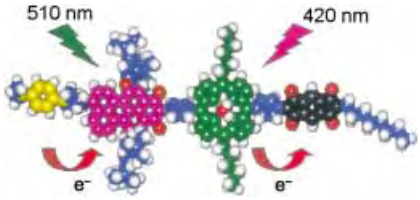
T. Sternfeld, M. Saunders, R. J. Cross, M. Rabinovitz* ——— 3136 – 3139

The Inside Story of Fullerene Anions: A ^{3}He NMR Aromaticity Probe



Fullerene anions with helium atoms contained inside the cage exhibit degrees of aromaticity that can be predicted through the measurement of ^{3}He chemical shifts (see picture). These chemical shifts help to demonstrate that the magnetic properties of fullerenes, and their anions, are not simply related to the number of carbon atoms or the number of electrons in the π system.

 © 2003 Wiley-VCH Verlag GmbH & Co. KGaA, Weinheim

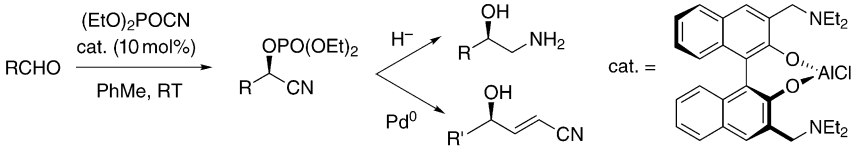


A fast switch: A covalent molecular tetrad (see picture), consisting of two electron donor/acceptor pairs acts as a high-speed molecular AND gate when it is sequentially excited using laser pulses having two different wavelengths. This system of using two sequential photodriven electron transfers is analogous to photosystems I and II in green plants which act in series to separate charge for long periods of time.

Logic Gates

M. Andersson, L. E. Sinks, R. T. Hayes, Y. Zhao, M. R. Wasielewski* **3139 – 3143**

Bio-Inspired Optically Controlled Ultrafast Molecular AND Gate



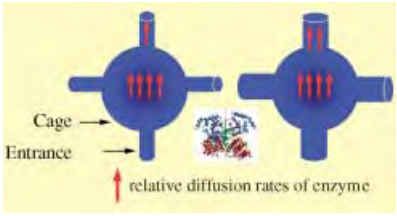
(*R*)- and (*S*)-binolam–AlCl complexes act as bifunctional catalysts to mediate the enantioselective cyanophosphorylation of aldehydes at room temperature. The resulting chiral cyanohydrin *O*-phosphates can be reduced to β-aminoalcohols or, when suitably substituted, can be transformed into γ-cyanoallylic alcohols through palladium-catalyzed allylic substitution, without loss of enantiomeric excess (see scheme).

Asymmetric Cyanophosphorylation

A. Baeza, J. Casas, C. Nájera,* J. M. Sansano, J. M. Saá* **3143 – 3146**

Enantioselective Synthesis of Cyanohydrin *O*-Phosphates Mediated by the Bifunctional Catalyst Binolam–AlCl

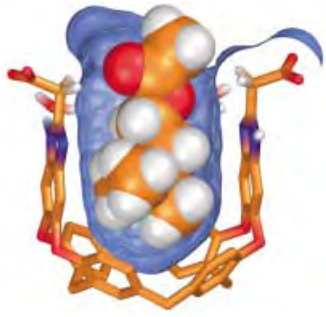
Large cavities (≈10–12.3 nm) of cubic (*Fm-3m*) mesoporous silica without intergrowth are synthesized in the presence of block copolymer templates. The entrance sizes of these cavities can be adjusted in the range of ≈4–9 nm as confirmed by nitrogen sorption studies and an examination of the negative gold replicas. The 3D open mesostructures facilitate the transportation of biomolecules (see picture), as well as the replication of a large-pore (9 nm) cubic mesoporous carbon.



Mesoporous Silica with Large Entrances

J. Fan, C. Yu,* F. Gao, J. Lei, B. Tian, L. Wang, Q. Luo, B. Tu, W. Zhou, D. Zhao* **3146 – 3150**

Cubic Mesoporous Silica with Large Controllable Entrance Sizes and Advanced Adsorption Properties



Four negative charges at the entrance of a deep pocket, lined with aromatic residues are the features of a synthetic receptor which shows high affinity for acetylcholine (see picture) and choline in water. The size, shape, and charge recognition elements featured in the natural enzyme acetylcholinesterase are reproduced by the synthetic receptor.

Choline Recognition in Water

F. Hof, L. Trembleau, E. C. Ullrich, J. Rebek, Jr.* **3150 – 3153**

Acetylcholine Recognition by a Deep, Biomimetic Pocket

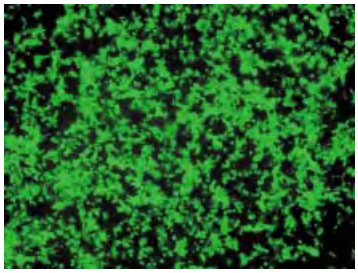
 © 2003 Wiley-VCH Verlag GmbH & Co. KGaA, Weinheim

Contents

Gene Delivery Proteins

D. G. Anderson, D. M. Lynn, R. Langer* ——— 3153 – 3158

Semi-Automated Synthesis and Screening of a Large Library of Degradable Cationic Polymers for Gene Delivery

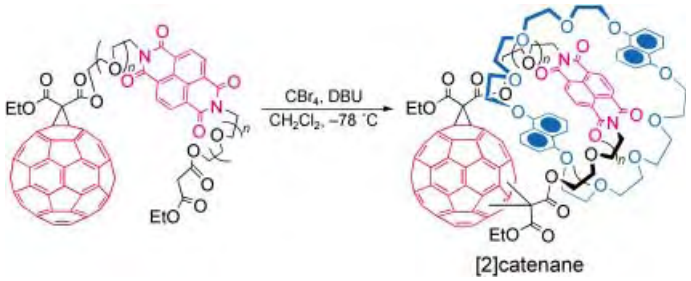


Higher delivery efficiency than conventional nonviral systems (such as poly(ethyleneimine)) have been identified in 46 polymers through cell-based screening of a large, 2350-member library by a high-throughput, semi-automated process. The transfection potential of the polymers was assessed by testing their ability to deliver luciferase expressing plasmid and green fluorescent protein plasmid (see picture) to a monkey kidney fibroblast cell line.

Fullerene-Based Catenanes/Rotaxanes

Y. Nakamura, S. Minami, K. Iizuka, J. Nishimura* ——— 3158 – 3162

Preparation of Neutral [60]Fullerene-Based [2]Catenanes and [2]Rotaxanes Bearing an Electron-Deficient Aromatic Diimide Moiety



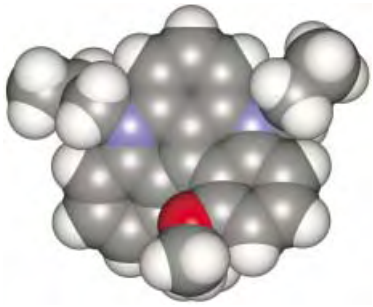
Crowning glory: An unprecedented [2]catenane that exhibits a donor–acceptor–donor–acceptor stacking motif was obtained through intramolecular Bingel reactions of [60]fullerene monoadducts that bear a naphthalenetetracarboxylic diimide moiety, in the presence of 1,5-dinaphtho[38]crown-10 ether at −78 °C (see scheme; DBU = 1,8-diazabicyclo[5.4.0]undec-7-ene).

Heterohelicene Derivatives

C. Herse, D. Bas, F. C. Krebs, T. Bürgi, J. Weber, T. Wesolowski, B. W. Laursen,* J. Lacour* ——— 3162 – 3166

A Highly Configurationally Stable [4]Heterohelicenium Cation

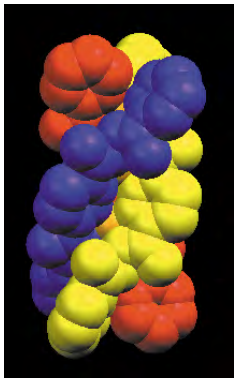
A [4](hetero)helicenium cation was resolved using the hexacoordinated phosphorus-containing binphat anion (see picture: N, blue; O, red; C, gray). Its absolute configuration was determined by vibrational circular dichroism spectroscopy. The barrier of interconversion of its enantiomers is higher than that of [6]helicene.



Triple-Stranded Helicates

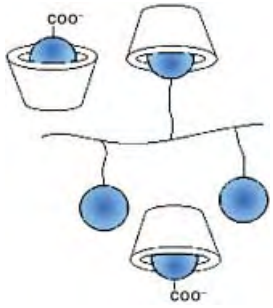
C. J. Matthews,* S. T. Onions, G. Morata, L. J. Davis, S. L. Heath, D. J. Price ——— 3166 – 3169

A Self-Assembled Tetracopper Triple-Stranded Helicate: Towards the Controlled Synthesis of Finite One-Dimensional Magnetic Chains



Spiraling into control: A finite linear arrangement of four magnetically coupled copper(II) centers has been generated within a triple-stranded helical motif that was formed through a strict self-assembly process between a single octadentate ligand and Cu^{II} ions (see picture). This approach opens the way to constructing finite one-dimensional magnetic chains in a controlled manner.

 © 2003 Wiley-VCH Verlag GmbH & Co. KGaA, Weinheim

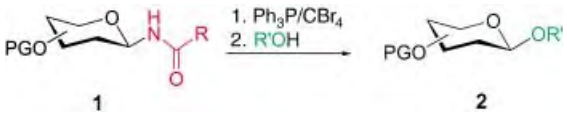


Parting the clouds: A supramolecular recognition reaction of cyclodexdrins with polymers—adamantyl derivative *N*-isopropylacrylamide copolymers—with inverse phase behavior is described. The turbidity of the polymer solutions depends upon the cyclodextrin concentration. Competition reactions with potassium-1-adamantylcarboxylate show that the inclusion-complex formation is reversible (see scheme).

Thermoreversible Polymers

H. Ritter,* O. Sadowski, E. Tepper ——— **3171 – 3173**

Influence of Cyclodextrin Molecules on the Synthesis and the Thermoresponsive Solution Behavior of *N*-Isopropylacrylamide Copolymers with Adamantyl Groups in the Side-Chains



1 2

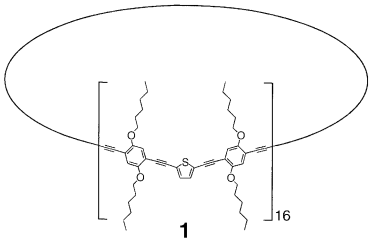
Reactivity upon demand: Because of their stability towards acids, bases, and many oxidizing and reducing agents, *N*-glycosyl amides **1** (see scheme) can be used as anomerically protected carbohydrates. The amide function can be cleaved under mild conditions with Ph_3P/CBr_4 and the carbohydrate activated for the synthesis of N- and O-glycosides **2**. PG = protecting group.

Anomeric Protecting Groups

N. Pleuss, H. Kunz* ——— **3174 – 3176**

N-Glycosyl Amides: Removal of the Anomeric Protecting Group and Conversion into Glycosyl Donors

Ever increasing circles? The giant cycle **1** has a diameter of 12 nm making it the largest, shape persistent and monodisperse cyclic molecular structure designed and synthesized to date. A modular approach consisting of a series of subsequent dimerization steps made **1** accessible.



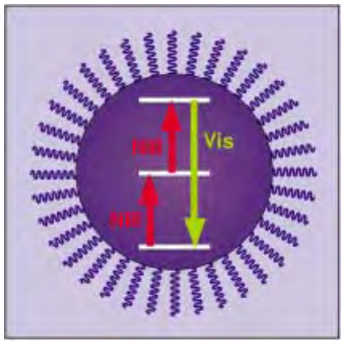
1

Shape Persistent Organic Ring

M. Mayor,* C. Didschies ——— **3176 – 3179**

A Giant Conjugated Molecular Ring

Light converter: The emission of visible light (Vis) upon excitation in the near-infrared (NIR) has been observed for the first time in a transparent solution. Excitation at 975 nm (marked red in the picture) of optically clear colloidal solutions of $LuPO_4:Yb^{3+}$, Tm^{3+}, and $YbPO_4:Er^{3+}$ nanocrystals in chloroform leads to visible upconversion luminescence in the blue, green, or red spectral regions.



Upconversion of Photons

S. Heer, O. Lehmann, M. Haase, H.-U. Güdel* ——— **3179 – 3182**

Blue, Green, and Red Upconversion Emission from Lanthanide-Doped $LuPO_4$ and $YbPO_4$ Nanocrystals in a Transparent Colloidal Solution

VIP Communications labeled with this symbol have been judged by two referees as being "very important papers".

The publication of Communications labeled with this symbol has been accelerated because of their topical or highly competitive nature.

 © 2003 Wiley-VCH Verlag GmbH & Co. KGaA, Weinheim

Sources

Product and Company Directory

You can start the entry for your company in "Sources" in any issue of *Angewandte Chemie*.

If you would like more information, please do not hesitate to contact us.

Wiley-VCH Verlag – Advertising Department
Tel.: 0 62 01 - 60 65 65
Fax: 0 62 01 - 60 65 50
E-Mail: MSchulz@wiley-vch.de

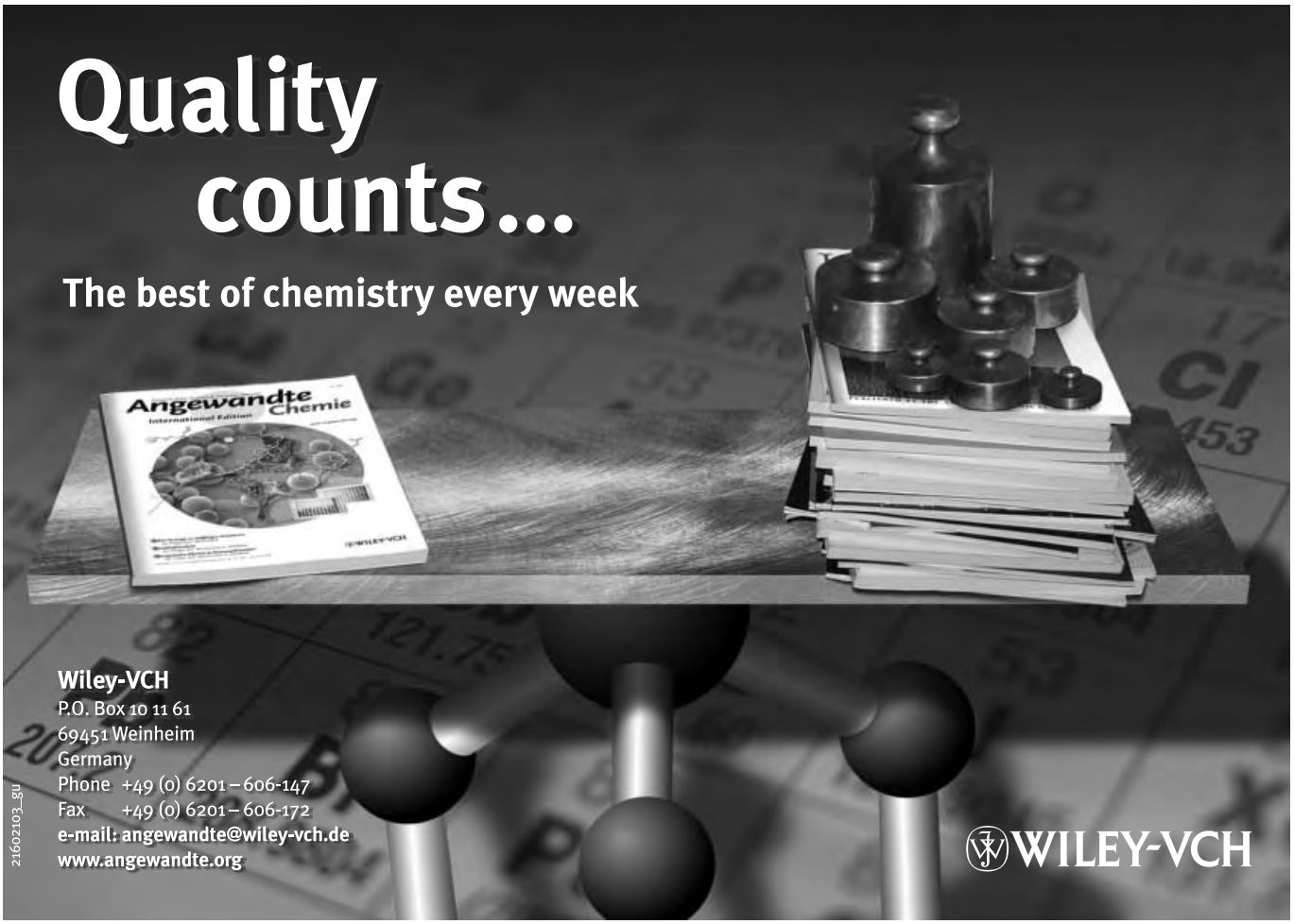
Service

Keywords ____ *3184*

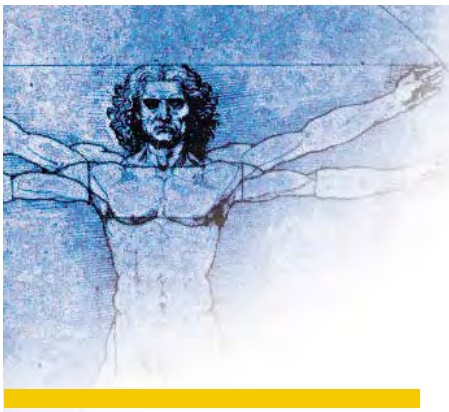
Authors ____ *3185*

Angewandte's Sister Journals ____ *3186*

Preview ____ *3187*



 © 2003 Wiley-VCH Verlag GmbH & Co. KGaA, Weinheim



Numerous Awards to G. Ertl

Gerhard Ertl, Director of the Fritz-Haber-Institut of the Max-Planck-Gesellschaft in Berlin, has again been recognized with several awards for his achievements in the fields of surface chemistry and heterogeneous catalysis. He recently received honorary doctorates from the Catholic University Leuven (Belgium) and Chalmers University of Technology in Göteborg (Sweden). Furthermore, he held the Karl Ziegler Lecture at the Max-Planck-Institut für Kohlenforschung (Mülheim an der Ruhr, Germany) on the topic "Reactions at Surfaces: from Atoms to Complexes" and the FMC Lecture Series at Princeton University (New Jersey, USA).



G. Ertl

Ertl studied physics at the Universität Stuttgart and received his Ph.D. in electrochemistry in 1965 from the Technische Universität München under the guidance of Heinz Gerischer. In 1968 he was appointed as a Professor of Physical Chemistry at the Universität Hannover. In 1973 he went on to the Universität München and in 1986 succeeded his Ph.D. supervisor as Director of the Fritz-Haber-Institut. He has received numerous awards, the most important of which are the Wolf Prize in Chemistry in 1998 and the Japan Prize of the Science and Technology Foundation of Japan in 1992. Ertl is a member of the Editorial Advisory Board of *ChemPhysChem* and *Chemistry—A European Journal*, and was a member of the Editorial Board of *Angewandte Chemie* from 1991 to 2000.

The work of Ertl's research group[1] is focused on the structure, dynamics, and reactivity of solid surfaces in contact with liquid or gas phases. Single-crystal materials play a role in this research, as do clusters, colloids, thin layers, and "real" catalysts. They recently published a Communication on "Surface Coordination Chemistry: Dihydrogen versus Hydride Complexes on $RuO_2(110)$".[2]

L. Oro Receives Sacconi Medal

Luis A. Oro (Zaragoza, Spain) received the Sacconi Medal of the Società Chimica Italiana in recognition of his work on organometallic coordination chemistry. His prize lecture is entitled "Hydrido Iridium Triisopropylphosphine Complexes".



L. Oro

Oro received his Ph.D. in 1970 from the University of Zaragoza. After a period of postdoctoral research in Cambridge (UK), he held positions at the Universities of Zaragoza, Madrid Complutense, and Santander, before returning to Zaragoza in 1982 as a Professor of Inorganic Chemistry. Oro is President of the Real Sociedad Española de Química and coeditor of a multivolume handbook on metal clusters.[3] The most recent Communication by his research group is entitled "A Hexanuclear Iridium Chain".[4]

Stimulating Discussions at Bürgenstock

The legendary "Bürgenstock Conference" on stereochemistry, which is a ESF/EUChem conference, was held successfully in April on Bürgenstock in Switzerland. This year Jan-E. Bäckvall (Stockholm; Chairman of the Editorial Board of *Chemistry—A European Journal*) officiated as President. The following lectures were held:

- Anthony G. M. Barrett: An obsession with macrocyclic compounds
- T. V. RajanBabu: Stereochemical control in inter- and intramolecular reactions of olefins and acetylenes
- Manfred T. Reetz: Evolutionary and combinatorial methods in enantioselective (bio)catalysis
- Klaas Martinus Pos: On the structure and function of bacterial pumps and bacterial protein glycosylation
- Jeffery W. Kelly: The chemistry and biology of misfolding diseases
- Ari Helenius: Quality control during protein folding
- Karl Anker Jørgensen: A failed reaction leading to new catalytic asymmetric transformations
- David W. C. MacMillan: Development of new catalysis concepts of broad utility to chemical synthesis
- Pher G. Andersson: Development and application of a new class of chiral ligands
- Masahiro Murakami: The stereochemistry of electrocyclic reactions dominated by hyperconjugation rather than sterics
- Chris A. Hunter: Quantitative approaches to molecular recognition
- David A. Leigh: Tooling up for nanoworld: hydrogen bond assembled 'molecular machinery'
- Takashi Kato: Nanostructured liquid crystals: supramolecular self-assembly of soft materials
- Timothy M. Swager: Polymer electronics for ultra-sensitive chemical and biological sensors

The Presidents for the next two years will be Herbert Waldmann (Dortmund, Germany) and Alain Krief (Namur, Belgien). The next conference will take place from 17 to 23 April 2004 in the usual place.

[1] a) G. Ertl, *Angew. Chem.* **1976**, *88*, 423; *Angew. Chem. Int. Ed. Engl.* **1976**, *15*, 391, b) G. Ertl, *Angew. Chem.* **1990**, *102*, 1258; *Angew. Chem. Int. Ed. Engl.* **1990**, *29*, 1219.

[2] J. Wang, C.-Y. Fan, Q. Sun, K. Reuter, K. Jacobi, M. Scheffler, G. Ertl, *Angew. Chem.* **2003**, *115*, 2201; *Angew. Chem. Int. Ed.* **2003**, *42*, 2151.

[3] *Metal Clusters in Chemistry* (Eds.: P. Braunstein, L. A. Oro, P. R. Raithby), Wiley-VCH, Weinheim, **1999**.

[4] C. Tejel, M. A. Ciriano, B. E. Villarroya, J. A. López, F. J. Lahoz, L. A. Oro, *Angew. Chem.* **2003**, *115*, 547; *Angew. Chem. Int. Ed.* **2003**, *42*, 529.

 © 2003 Wiley-VCH Verlag GmbH & Co. KGaA, Weinheim

Biosynthesis of Fungal Alkaloids

Stephacidin B—A New Stage of Complexity within Prenylated Indole Alkaloids from Fungi**

*Franz von Nussbaum**

Keywords:
alkaloids · amino acids · biosynthesis · natural products · structure elucidation

Dedicated to Professor Samuel J. Danishefsky

Introduction

Though counting is not as easy as expected in the age of international databases, it is estimated that about 20000 alkaloids are known.[1,2] So far the widespread nonuniform use of the term "alkaloid" has hampered the development of a consistent categorization system. Instead, an orthogonal (and thereby unfortunately overlapping) subclassification related to the structure (e.g. β-carboline alkaloids) or the origin (e.g. Strychnos alkaloids) has been favored.

Traditionally, alkaloids have been isolated from plants and to a minor extent from animals. Isoquinoline and indole alkaloids have turned out to be the most prominent structural classes. However, the screening of microorganisms for new antibiotics and the analysis of toadstools in the study of their toxicity[3] as well as of their pigmentation[4] has shown that alkaloid chemistry is not limited to plants and animals. A large number of alkaloids—especially compounds biosynthetically derived from tryptophan—were isolated from fungi.

Stephacidin B: An Exciting Structure with Promising Biological Activity

Recently, a group from the Bristol-Myers Squibb Pharmaceutical Research Institute[5] described stephacidin B (**2**) as a new antibiotic with cellular antitumor activity (Scheme 1). The unprecedented structural architecture of stephacidin B (**2**) provides a new level of complexity within prenylated indole alkaloids from fungi (Figure 1). Both indole moieties are present in rare oxidation states. Whereas *N*-methoxyindole alkaloids have been isolated sporadically, only very few *N*-hydroxyindoles[6] and indole nitrones have thus far been isolated from natural sources.

Stephacidin A (**1**) and stephacidin B (**2**) were obtained by fermentation of *Aspergillus ochraceus* WC76466. Unfortunately, the complete relative stereochemistry has not been established for stephacidin A, although extensive NMR spectroscopic experiments have been performed. Stephacidin A and B showed in vitro cytotoxicity against a panel of human tumor cell lines. Where-

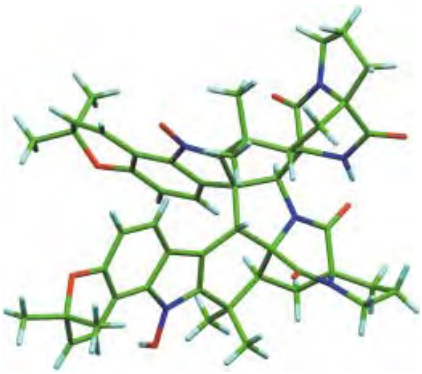
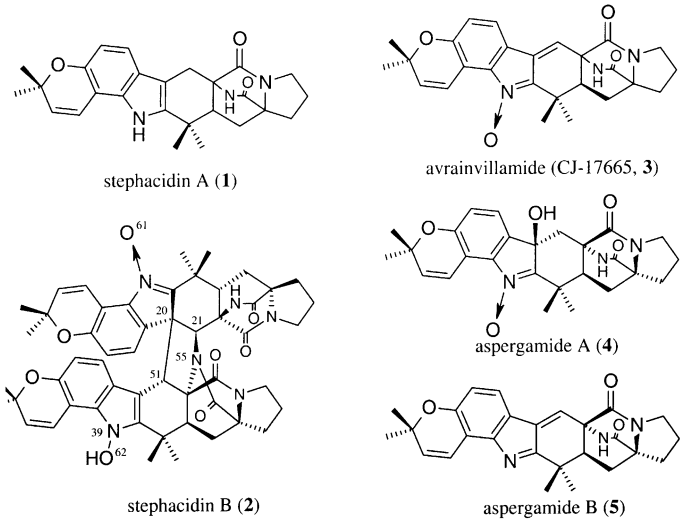


Figure 1. Crystal structure of stephacidin B (**2**)[5] (stick representation,[16] relative stereochemistry).



Scheme 1. Stephacidin B (**2**)[5] and related alkaloids[14,15] from *Aspergillus ochraceus* (relative stereochemistry).

[*] Dr. F. von Nussbaum
Medicinal Chemistry
Pharma Research, Bayer AG
42096 Wuppertal (Germany)
Fax: (+49) 202-36-969-4797
E-mail:
franz.vonnussbaum.fv@bayer-ag.de

[**] I am indebted to my colleagues Dr. Nils Griebenow and Dr. Robert Velten for valuable discussions.

 © 2003 Wiley-VCH Verlag GmbH & Co. KGaA, Weinheim DOI: 10.1002/anie.200301646

as the observed IC_{50} values for stephacidin A (**1**) were basically in the one-digit micromolar range for ovarian, colon, breast, and lung cancer cell lines, the more complex stephacidin B (**2**) showed a five to thirtyfold higher activity. The strongest cytotoxicity for **1** and **2** was observed with testosterone-dependent prostate LNCaP cancer cells. The Bristol-Myers-Squibb group suggested (see below) that a new mode of action might play a role here. Unfortunately, no detailed data were provided that supports this promising assessment. With functional genomics at hand, the stephacidins could become a further example showing that bioactive natural products should not only be considered as lead structures for new pharmacophores or toxophores but also as possible hints at novel biological targets and/or modes of action that might be addressed later on by drugs with completely different structures (cf. chemical genomics).

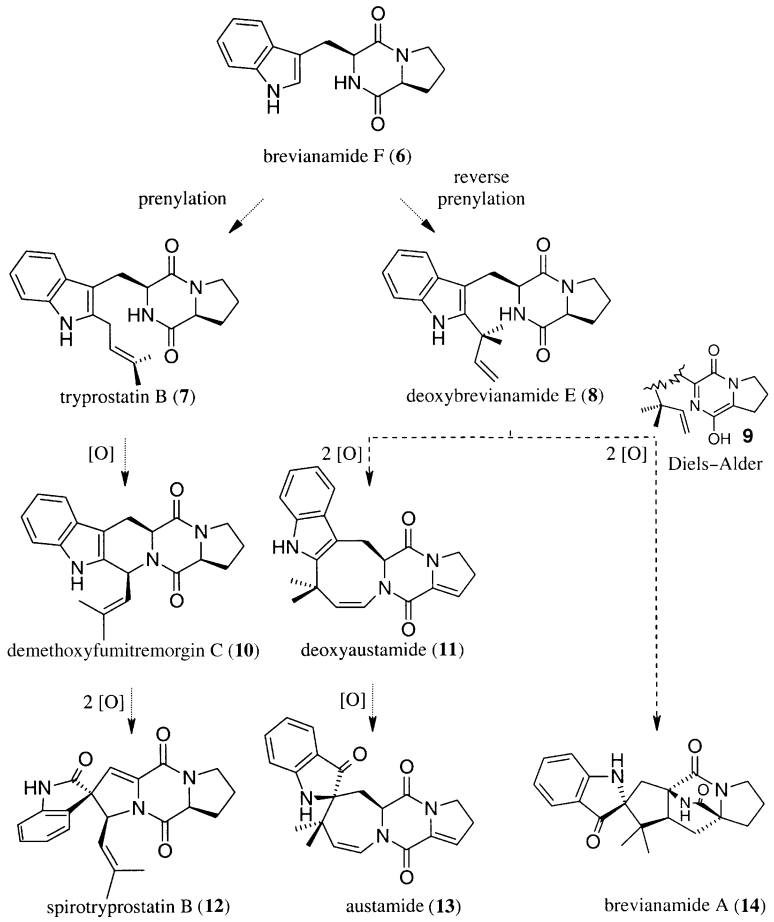
Biosynthesis of Stephacidin B: A Lesson for Combinatorial Chemistry

Prenylated tryptophan-derived alkaloids isolated from fungi are a good example of Nature's impressive ability to build "compound libraries" of high structural diversity from only a limited panel of "starting materials" that are structurally not diverse at all. Enzyme-catalyzed selective C–H-oxidation reactions are powerful tools in the assembly of complex carbon skeletons. In alkaloid biogenesis, this combinatorial redox chemistry is complemented by a diverse condensation chemistry that exploits the ambivalent reactivity of heteroatom-rich building blocks such as tryptophan, tyrosine, or dopa (3,4-dihydroxyphenylalanine). The range of possible condensation modes is often increased by an electronic modulation of the polar chemical functionalities by redox processes (e.g. phenols⇄quinones) as well as by the intermediate coordination of Lewis acids (e.g. protons, methylation⇄demethylation).

These trends within the biogenesis of alkaloids may well be illustrated by a multifaceted group of fungal metabolites that are derived only from a single entity of tryptophan, proline, and isoprene (Scheme 2).[7,8] The stephacidins are closely related to this series and accordingly should have a corresponding biosynthetic origin, even though they bear additional isoprene units at their indole moieties (as encountered in various paraherquamides and marcfortines). Starting from *cyclo*-Trp-Pro (**6**), a pure condensation product, prenylation or reverse prenylation leads to tryprostatin B (**7**)[9] or deoxybrevianamide E (**8**), respectively (Scheme 2). From here on, the structural complexity increases with every oxidation step in the proceeding biosynthetic cascades. Often the last oxidative "degree of freedom" is the conversion of the indole systems into the corresponding spiroxindole or spiro-ψ-indoxyl systems (e.g. demethoxyfumitremorgin C (**10**) to spirotryprostatin B (**12**),[10] or deoxyaustamide (**11**) to austamide (**13**)). The characteristic diazabicyclo[2.2.2] ring system of the stephacidins is well-known from various brevianamides, paraherquamides, and marcfortines.[8] An intriguing intramolecular Diels–Alder step has been proposed by Birch[11] and by Porter and Sammes[12] as a key step in the biosynthesis of these systems (Scheme 2). Although mechanistic details of this remarkable transformation (**8**→**14**) remain the issue of ongoing investigations,[8] it can be recognized as a formal oxidation of the inner diketopiperazine ring (**8**→**9**) that triggers the following Diels-Alder-type conversion (**9**→**14**). Contemporary research regarding the biosynthesis and synthesis of brevianamide- and paraherquamide-type alkaloids is dominated by the group of Williams.[8]

Is Stephacidin B a Michael–Michael Dimerization Product?

Structurally closely related to stephacidin A (**1**) is avrainvillamide (**3**)[13]



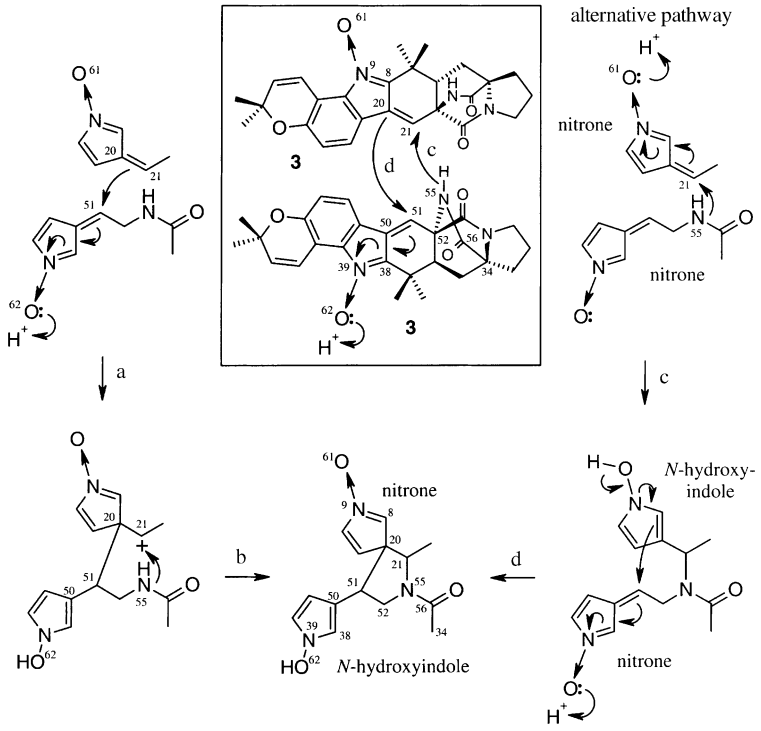
Scheme 2. Representative tryptophan- and proline-derived monoprenylated alkaloids isolated from fungi. Arrangement according to the (hypothetical) biosynthetic processing level.

 © 2003 Wiley-VCH Verlag GmbH & Co. KGaA, Weinheim

(CJ-17665),[14] which has also been isolated from the fermentation broth of two *Aspergillus* strains. These strains were independently obtained from a green alga sample (*Avrainvillae* sp.) collected in the Bahamas (marine habitat) and from a soil sample collected in Venezuela (terrestrial habitat). As in the case of stephacidina A and B, avrainvillamide (**3**) also showed cellular anticancer activity. Moreover, **3** exhibited antibacterial activity against some multidrug-resistant Gram-positive cocci. The unusual nitrone functionality present in **2** and **3** was also encountered in aspergamide A (**4**),[15] a further fermentation product of the same organism *Aspergillus ochraceus*. In addition to nitrone **4**, Zeeck and co-workers also obtained its anhydrodeoxy congener aspergamide B (**5**).

The Bristol-Myers Squibb group has already pointed out that stephacidin B (**2**) might be a dimer of avrainvillamide (**3**), which itself could be a biosynthetic oxidation product of stephacidin A (**1**). The manner in which the two avrainvillamide units are linked (C20–C51, C21–N55) strongly indicates a dimerization mode that has not yet been described for indole alkaloids. Qian-Cutrone et al. suggested an initial protonation of the "lower" monomeric unit at O62, which would initiate an electrophilic attack of C51 at the C20–C21 double bond of the "upper" unit and thereby generate a (secondary) carbocation at C21 (stephacidin B numbering, Scheme 3, step a). Final attack by the "lower" amidic N55 at C21 would close the central five-membered ring (step b).

Clearly, a late-stage biosynthesis of stephacidin B (**2**) that involves "monomeric" intermediates of type **3** appears reasonable as all five metabolites **1–5** have been isolated from the same species *A. ochraceus*. However, at this juncture an alternative reaction pathway shall be suggested that avoids the secondary carbocation as an intermediate (Scheme 3): Dimerization of avrainvillamide (**3**) can be initiated by a nucleophilic attack of the "lower" amidic N55 at the "upper" nitrone Michael acceptor (step c). This C21–N55-bond formation would be accompanied by a switch of the electrophilic "upper" nitrone system to a nucleophilic *N*-hydroxyindole system (step c). Subsequent attack of the "upper" donor at the "lower" nitrone Michael acceptor would generate the spiro center at C20 (step d) and thereby conclude the dimerization. Notably, this biosynthetic transformation hints at a type of Michael addition that has not yet been described. Although 1,4-additions of amide nitrogen atoms to carbonyl Michael systems are known, related Michael reactivity for 2-vinyl nitrones (formally nitrone Michael acceptors) could not be found in the literature.



Scheme 3. An alternative proposal for the late-stage biosynthesis of stephacidin B (**2**) through a Michael–Michael dimerization.

Conclusion

Natural products that present novel structural features often raise many questions regarding their biosynthesis and their possible total synthesis. With 15 rings, stephacidin B (**2**) is one of the most complex indole alkaloids isolated from fungi. Two tryptophan subunits are connected in a way that implicates an unusual dimerization within the late-stage biosynthesis. This natural transformation is an interesting model for a conceivable (biomimetic) partial synthesis of stephacidin B (**2**) starting from natural avrainvillamide (**3**). Furthermore, the biosynthesis of stephacidin B might also be of interest for organic synthetic methodology as it hints at a potential Michael-type reactivity of 2-vinyl nitrones. Further investigations should clarify whether the final dimerization (or pseudodimerization) requires enzymatic catalysis.

The promising in vitro cytotoxicity of **2** against testosterone-dependent prostate LNCaP cancer cells not only qualifies this indole alkaloid as a potential chemical lead structure but also highlights the general importance of distinctive natural products as valuable clues to new biological targets and/or modes of action.

[1] *Dictionary of Natural Products* (CD-ROM), Chapman & Hall/CRC, **1982–2003**.
[2] *Römpp Encyclopedia. Natural Products* (Eds.: W. Steglich, B. Fugmann, S. Lang-Fugmann), Thieme, Stuttgart, **2000**.
[3] "Alkaloids from Mushrooms": R. Antikowiak, W. Z. Antikowiak, *Alkaloids* **1991**, *40*, 189–340.
[4] a) "Pigments of Fungi (Macromycetes)": M. Gill, W. Steglich, *Prog. Chem. Org. Nat. Prod.* **1987**, *51*, 1–317; b) M. Gill, *Nat. Prod. Rep.* **1999**, *16*, 301–317.

 © 2003 Wiley-VCH Verlag GmbH & Co. KGaA, Weinheim

[5] a) J. Qian-Cutrone, S. Huang, Y.-Z. Shu, D. Vyas, C. Fairchild, A. Menendez, K. Krampitz, R. Dalterio, S. E. Klohr, Q. Gao, *J. Am. Chem. Soc.* **2002**, *124*, 14556 – 14557; b) J. Qian-Cutrone, K. D. Krampitz, Y.-Z. Shu, L.-P. Chang, S. E. Lowe, U.S. Patent 6,291,461, **2001** [*Chem. Abstr.* **2001**, *135*, 236411].
[6] M. Somei, *Adv. Heterocycl. Chem.* **2002**, *82*, 101 – 155.
[7] A. J. Birch, J. J. Wright, *Tetrahedron* **1970**, *26*, 2329 – 2344.
[8] a) R. M. Williams, E. M. Stocking, J. F. Sanz-Cervera, *Top. Curr. Chem.* **2000**, *209*, 97 – 173; b) R. M. Williams, *Chem. Pharm. Bull.* **2002**, *50*, 711 – 740; c) R. M. Williams, R. J. Cox, *Acc. Chem. Res.* **2003**, *36*, 127 – 139.
[9] Isolation: a) C.-B. Cui, H. Kakeya, G. Okada, R. Onose, M. Ubukata, I. Takahashi, K. Isono, H. Osada, *J. Antibiot.* **1995**, *48*, 1382 – 1384; synthesis: b) K. M. Depew, S. J. Danishefsky, N. Rosen, L. Sepp-Lorenzino, *J. Am. Chem. Soc.* **1996**, *118*, 12463 – 12464.
[10] Isolation: a) C.-B. Cui, H. Kakeya, H. Osada, *Tetrahedron* **1996**, *52*, 12651 – 12666; stereochemistry: b) F. von Nussbaum, S. J. Danishefsky, *Angew. Chem.* **2000**, *112*, 2259 – 2262; *Angew. Chem. Int. Ed.* **2000**, *39*, 2175 – 2178.
[11] A. J. Birch, *J. Agric. Food Chem.* **1971**, *19*, 1088 – 1092.
[12] A. E. A. Porter, P. G. Sammes, *J. Chem. Soc. Chem. Commun.* **1970**, 1103.
[13] W. Fenical, P. R. Jensen, X. C. Cheng, U.S. Patent 6,066,635, **2000** [*Chem. Abstr.* **2000**, *132*, 346709].
[14] Y. Sugie, H. Hirai, T. Inagaki, M. Ishiguro, Y.-J. Kim, Y. Kojima, T. Sakakibara, S. Sakemi, A. Sugiura, Y. Suzuki, L. Brennan, J. Duignan, L. H. Huang, J. Sutcliffe, N. Kojima, *J. Antibiot.* **2001**, *54*, 911 – 916.
[15] a) J. Fuchser, PhD Thesis, University of Göttingen, **1995**; stereochemistry: b) A. Zeeck, personal communication, **2003**.
[16] Cambridge Crystallographic Data Centre, Mercury 1.1.2.

 © 2003 Wiley-VCH Verlag GmbH & Co. KGaA, Weinheim

Bioactive Hydrogelators

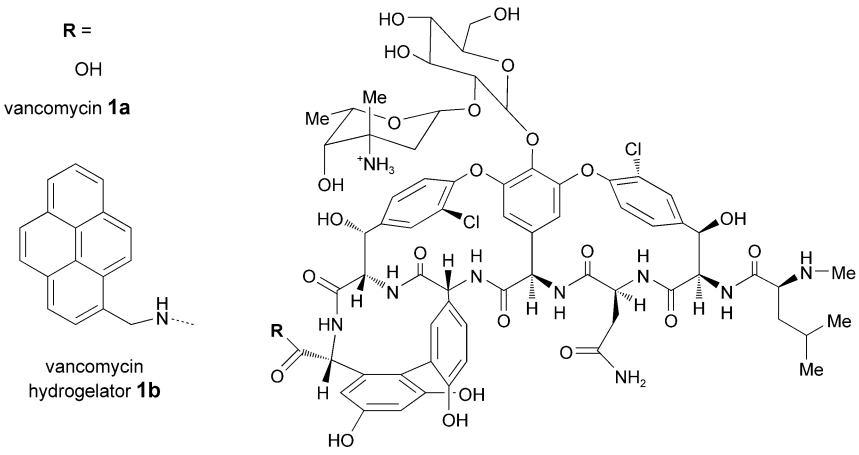
Increasing the Local Concentration of Drugs by Hydrogel Formation**

*Joerg C. Tiller**

Keywords:
antibiotics · drug design · gels · hydrogelators · vancomycin

During the last decade the development of drugs and other bioactive agents for medicine, agriculture, infection control, and biotechnology has been greatly sped up particularly by using combinatorial approaches as well as computer modeling.[1] Although specificity and activity of new agents could be improved, most still show severe side effects. Therefore, an important consideration is that the agents must be directed to the target site with sufficient but nontoxic concentrations. A solution to this problem can be an increased local concentration of agents on the surfaces of cells and in organs or other tissue. The concentration drugs on surfaces of synthetic materials, such as catheters, implants, and even water pipes, is of great interest too. The immobilization of low- and high-molecular-weight agents, coating with drug-loaded gels, and the application of bioadhesive polymer–drug conjugates are commonly used approaches to obtain increased local drug concentrations.[2] A very recent approach is the local concentration of bioactive agents by hydrogel formation.

The first example of converting an agent into its analogous hydrogelators by means of chemical modification was recently reported by Xing et al.[3] The authors derivatized the antibiotic vancomycin (**1a**) with a pyrene group to form **1b**. Already 0.36 wt% of **1b** dissolved in water led to the formation of a gel without additional heating. The gel is composed of interconnected helical fibers, as verified by analysis by CD and fluorescence spectroscopy and transmission electron microscopy. Remarkably, the modified vancomycin **1b** exhibits up to 11-fold higher activity than **1a** against different bacteria.



The authors suggested that this effect might originate from the local concentration of the antibiotic analogue **1b** on the bacterial surfaces. Two different mechanisms are possible. In the first, it is possible that the drug forms a gel locally on bacterial surfaces, even though the concentration in the solution used was up to 30 times lower than the minimal gelation concentration (MGC). The process would start with the specific adhesion of **1b** to a surface, in the case of vancomycin by formation of hydrogen bonds between the Lys-D-Ala-D-Ala peptide backbone of the drug to compatible domains on the bacterial surface.[4] (Vancomycin acts by specific binding to the bacterial cell surface and thereby inhibiting the formation of a new cell wall.) The adhered hydrogel-forming drug, which is now concentrated on the surface (eventually above MGC), starts to self-assemble. The resulting organized structure attracts more drug molecules from the surrounding solution, which leads to the amplification of the concentration of the drug on the surface (Figure 1).

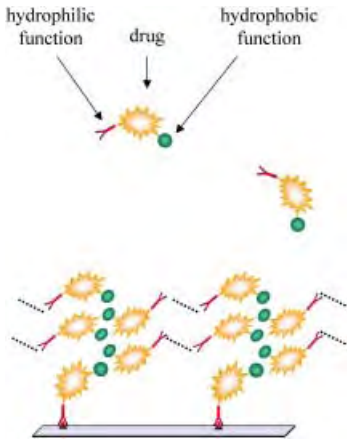


Figure 1. Idealized structure of a bioactive hydrogelator that has formed a gel on a surface.

[*] Dr. J. C. Tiller
Freiburger Materialforschungszentrum
Albert-Ludwigs-Universität Freiburg
Stefan-Meier-Strasse 21
79104 Freiburg (Germany)
Fax: (+49) 761-203-4700
E-mail: joerg.tiller@fmf.uni-freiburg.de

[**] The author thanks the Deutsche Forschungsgemeinschaft (Emmy-Noether-Programm) and the Fonds der Chemischen Industrie for financial support.

 © 2003 Wiley-VCH Verlag GmbH & Co. KGaA, Weinheim DOI: 10.1002/anie.200301647

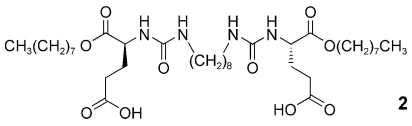
The second possible mechanism involves the adhesion of fiberlike structures of the hydrogel-forming drug, which are formed in the surrounding solution. In both cases, the concentration of the gelating antibiotic at the surface would be significantly higher than that of the analogous nongelating agent. If this concept can be further proven, it might be the basis of a new method to enhance the activity of numerous drugs and to coat surfaces such as catheters or wounds with bioactive agents.

To investigate the proposed principle, it would be useful to find a model system that could also provide information on the functions that can be used for modifying other bioactive agents. As **1b** is a low-molecular-weight hydrogelator, other reported molecules of this kind that could serve as model systems will be briefly reviewed in the following section. The basis of the increased activity of a hydrogel-forming bioactive agent seems to be:

- no significant decrease in biological activity relative to the original agent;
- a low MGC and formation of a stable solution below the MGC;
- a specific affinity for the target site or surface.

In contrast to organogelators, the number of low-molecular-weight hydrogelators is rather limited. The structure of 3D networks of these gelators consists of helical fiberlike, rodlike, or micellar shapes, which are interconnected, for example, by hydrogen bonds. Most of the described hydrogelators form gels only in the presence of 1–10% of an organic solvent such as dimethyl sulfoxide or methanol.[5] These compounds can hardly be used as models for biological systems. There are only a few low-molecular-weight hydrogelators that form gels in plain water or aqueous buffer without additional solvents.

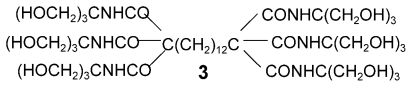
Estroff and Hamilton have reported low-molecular-weight hydrogelators based on bisurea dicarboxylic acid.[6] A series of these compounds showed a strongly pH-dependent gel formation in water at very low concentrations (0.3 wt%). For example, a mixture of **2** with phosphate buffer was a homogeneous solution at pH 7.9, whereas it became a rigid gel at pH 6.7. Scanning



2

electron microscope pictures of the hydrogel revealed the same fibrous structure described for the above-mentioned hydrogelating vancomycin derivative. Gel formation only occurred after heating the solutions.

Readily water-soluble, gel-forming, low-molecular-weight, dendritic bolaamphiphiles, so-called [9]-*n*-[9] arborols, were described by Newkome et al.[7] The gels were formed by heating aqueous solutions of this substance (2–8 wt%) at 80°C, which is the phase-transition temperature of such systems, and cooling them to room temperature. Compound **3** formed gels over a wide

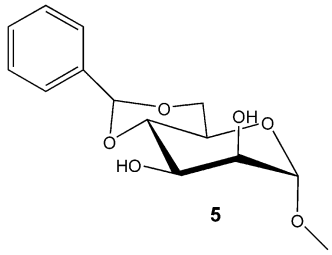


3

range of pH values (2–11) in buffers of varying ionic strengths.

Recently, water-soluble hydrogelators based on lysine derivatized with fatty acids (with neutral and positively charged end groups) were reported to have an MGC of less than 0.3 wt%.[8] In contrast to other hydrogelators, **4**, for example, is soluble in water and need not be boiled or sonicated as it readily dissolves at 40°C and forms a clear hydrogel with a nanoscale fibrous structure upon cooling to room temperature.

Glycolipids are a large group of gelators for organic solvents and, in a few cases, for water. Fuhrhop et al. as well as Pfannemüller and Welte investigated hydrogels of *n*-octylgluconamides, which were formed by cooling the boiling aqueous solutions to room temperature (typical for saccharide-based hydrogelators or glycolipids).[9] It was shown that only pure stereoisomers form gels (GMC ≈ 0.5 wt%), but not racemic mixtures. Dilution of the solutions or gels below 0.5 wt% led to precipitation. Shinkai and co-workers investigated benzylidene derivatives of monosaccharides as water-soluble hydrogelators and showed that the stereochemistry of the gelator has a strong influence on the gel-forming potential of the derivatives.[10] Whereas the D-mannose-based structure **5** forms a strong



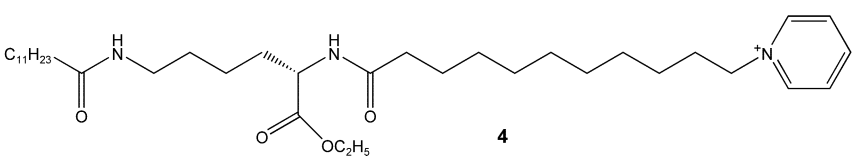
5

hydrogel, compounds based on D-glucose or D-galactose do not. Shinkai and co-workers found a similar effect for the gelation of glucose- and galactose-derivatized azo dyes.[11] In this case, only the glucose derivative formed a hydrogel.

Kiyonaka et al. described the first combinatorial approach for the screening of hydrogelators.[12] The authors derivatized *N*-acetylgalactosamine with various amino acids on solid supports. The compounds prepared in this way are mostly water-soluble, and some form hydrogels at concentrations of 4 mM that surprisingly shrink with increasing temperature.

Hamada et al. synthesized a number of azo dyes that form hydrogels in water without further heating.[13] These compounds are intensely colored and exhibit a high GMC value of about 5 wt%.

Pang and Zhu reported that the partially fluorinated fatty acid $CF_3(CF_2)_5CH_2COOH$ forms a hydrogel in water at a concentration of about 8 wt%.[14] The gel was formed by sonicating the suspension of the insoluble compound in water. Owing to the high MGC and the insolubility of the semi-fluorinated acids, however, such com-



4

 © 2003 Wiley-VCH Verlag GmbH & Co. KGaA, Weinheim

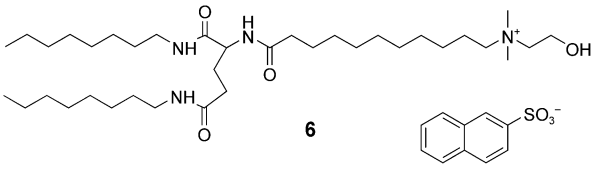
pounds do not fulfill the required conditions for a model system for hydrogelating drugs.

Besides of the synthetic hydrogelators, a number of relatively small peptides (11–20 amino acid residues) can act as hydrogelators.[15] For hydrogelation, the peptides must form β sheets in water. Although these compounds are water-soluble, exhibit GMC values of 1 wt % and lower, and form gels without additional heating, they can hardly be used for the modification of drugs as the complex structure will most likely inhibit the biological activity of the drug.

Another problem in medicine is the local concentration of bioactive agents, which is of particular interest in the field of cancer therapy, because most cytostatics unfortunately still have many side-effects. This drug concentration is possible by spontaneous local gel formation, during which the drug is trapped. To ensure that gelation occurs at the right place and time, it should be triggered by a specific parameter such as a change in temperature.

Westhaus and Messersmith recently reported a thermally triggered gel-forming system, which allows the formation of hydrogels with entrapped agents when the temperature is increased from room to body temperature.[16] This system, illustrated in Figure 2, is based on two-compound hydrogelators (calcium ions and alginates). To separate the calcium ions from the alginate, the metal ions were trapped as $CaCl_2$ within temperature-sensitive bilayer lipid vesicles (90 % dipalmitoylphosphatidylcholine and 10 % dimyristoylphosphatidylcholine). An aqueous solution of such vesicles, alginate, and a drug is stable at room temperature. Upon injection into the body, the lipid vesicles disintegrate as a result of the rise in temperature and the calcium ions were released, thus causing a spontaneous gelation of the alginates with concomitant trapping of the bioactive drug.

As injection of a nondegradable polymer into body tissue is a problem, the application of degradable polymers would be ideal.[17] However, only a few are available, and these are not suited to hydrogel formation. A good alternative would be low-molecular-weight hydrogelators instead of polymers. Recently reported low-molecular-weight two-component systems could have the same gel-forming properties as the Ca alginate system. Kimizuka and Nakashima described the gel formation of cationic glutamate amphiphiles **6** with anions such as naphthylsulfonate.[18] After the addition of the anionic compounds to stable aqueous solutions of the cations, clear hydrogels were formed within a few minutes. Huc and co-workers used so-called gemini surfactants for a water-gelling system.[19] The gel-forming mixture consists of *N,N′*-dicetyl-*N,N,N′,N′*-tetramethylethylenediamine dichloride and tartrates. An aqueous solution of these compounds forms a gel at room temperature at concentrations as low as 1 mM.



6

The synthesis of the first hydrogel-forming bioactive agent could open a new field of drug design based on the transformation of effective bioactive agents into their hydrogelator analogues. The challenge is the modification of the drug without affecting its biological activity. Furthermore, all compounds must be nontoxic. The basis for this field will be the development of a larger number of low-molecular-weight hydrogelators to obtain a variety of structural motifs, which can be use either as model systems or as functional groups for drug modification. The use of combinatorial synthesis will be helpful for this purpose. The same is true for two-component hydrogelating systems, which need to be optimized, particularly with respect to rapid gel formation and biocompatibility.

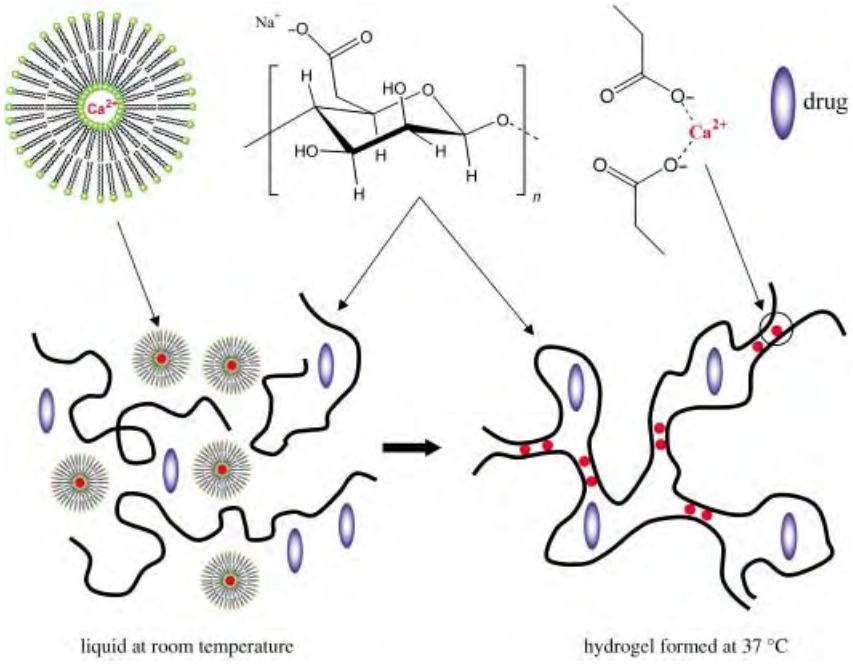


Figure 2. Thermally triggered formation of an alginate drug hydrogel.

[1] D. Gorse, A. Rees, M. Kaczorek, R. Lahana, *Drug Discovery Today* **1999**, *4*, 257–264.

[2] a) V. P. Torchilin, *Eur. J. Pharm. Sci.* **2000**, 11, S81–S91; b) A. D. Woolfson, R. K. Malcolm, P. A. McCarron, D. S. Jones in *Polymeric Biomaterials*, (Ed.: S. Dumitriu), Marcel Dekker, New York, **2002**, pp. 1063–1081.

[3] B. Xing, C.-W. Yu, K.-H. Chow, P.-L. Ho, D. Fu, B. Xu, *J. Am. Chem. Soc.* **2002**, *124*, 14846–14847.

[4] D. H. Williams, A. J. Masguire, W. Tsuzuki, M. S. Westwell, *Science* **1998**, *280*, 711–714.

[5] a) Jong, G. John, M. Masuda, K. Yoshida, S. Shinkai, T. Shimizu, *Langmuir* **2001**, *17*, 7229–7232; b) F. M. Menger, K. L. Caran, *J. Am. Chem. Soc.* **2000**,

 © 2003 Wiley-VCH Verlag GmbH & Co. KGaA, Weinheim

122, 11659 – 11691; c) S. Bhattacharya, S. N. G. Acharya, *Chem. Mater.* **1999**, *11*, 3504 – 3511; d) U. Maitra, S. Mukhopadhyay, A. Sarkar, P. Rao, S. S. Indi, *Angew. Chem.* **2001**, *113*, 2341 – 2343; *Angew. Chem. Int. Ed.* **2001**, *40*, 2281 – 2283.

[6] L. A. Estroff, A. D. Hamilton, *Angew. Chem.* **2000**, *112*, 3589 – 3592, *Angew. Chem. Int. Ed.* **2000**, *39*, 3477 – 3450.

[7] G. R. Newkome, G. R. Baker, S. Arai, M. J. Saunders, P. S. Rosso, K. J. Theriot, C. N. Moorefield, L. E. Rogers, J. E. Miller, T. R. Lieus, M. E. Murray, B. Phillips, L. Pascal, *J. Am. Chem. Soc.* **1990**, *112*, 8458 – 8465.

[8] M. Suzuki, M. Yumoto, M. Kimura, H. Shirai, K. Hanabusa, Kenji, *Chem. Eur. J.* **2003**, *9*, 348 – 354.

[9] a) J.-H. Fuhrhop, P. Schnieder, J. Rosenberg, E. Boekema, *J. Am. Chem. Soc.* **1987**, *109*, 3387 – 3390; b) B. Pfannemüller, W. Welte, *Chem. Phys. Lipids* **1985**, *37*, 227 – 240.

[10] K. Yoza, Y. Ono, K. Yoshihaa, T. Akao, H. Shinmori, M. Takeuchi, S. Shinkai, D. N. Reinhoudt, *Chem. Commun.* **1998**, 907 – 908.

[11] M. Amaike, H. Kobayashi, S. Shinkai, *Chem. Lett.* **2001**, 620 – 621.

[12] S. Kiyonaka, K. Sugiyasu, S. Shinkai, I. Hamachi, *J. Am. Chem. Soc.* **2002**, *124*, 10954 – 10955.

[13] K. Hamada, K. Yamada, M. Mitsuishi, M. Ohira, K. Miyazaki, *J. Chem. Soc. Chem. Commun.* **1992**, 544 – 545.

[14] S. Pang, D. Zhu, *Chem. Phys. Lett.* **2002**, *358*, 479 – 483.

[15] a) J. P. Schneider, D. J. Pochan, B. Ozbas, K. Rajagopal, L. Pakstis, J. Kretsinger, *J. Am. Chem. Soc.* **2002**, *124*, 15030 – 15037; b) J. H. Collier, B.-H. Hu, J. W. Ruberti, J. Zhang, P. Shum, D. H. Thompson, P. B. Messersmith, *J. Am. Chem. Soc.* **2001**, *123*, 9463 – 9464; c) A. Aggeli, M. Bell, N. Boden, J. N. Keen, P. F. Knowles, T. C. B. McLeish, M. Pitkeathly, S. E. Radford, *Nature* **1997**, *386*, 259 – 262.

[16] E. Westhaus, P. B. Messersmith, *Biomaterials* **2001**, *22*, 453 – 462.

[17] K. E. Uhrich, S. M. Cannizzaro, R. S. Langer, K. M Shakesheff, *Chem. Rev.* **1999**, *99,* 3181 – 3198.

[18] T. Nakashima, N. Kimizuka, *Adv. Mater.* **2002**, *14*, 1113 – 1116.

[19] R. Oda, I. Huc, S. J. Candau, *Angew. Chem.* **1998**, *110*, 2835 – 2838, *Angew. Chem. Int. Ed.* **1998**, *37*, 2689 – 2693.

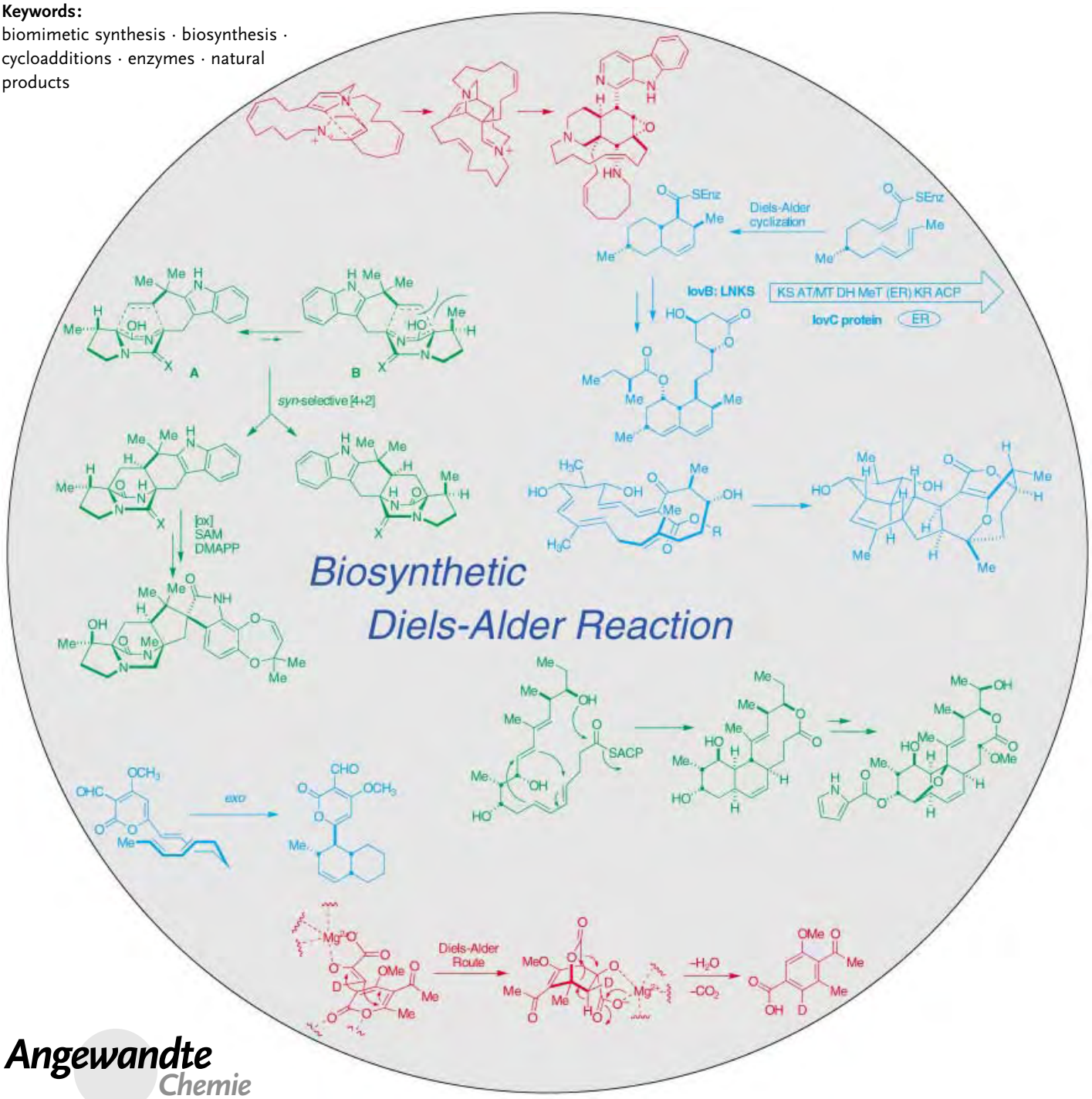
 © 2003 Wiley-VCH Verlag GmbH & Co. KGaA, Weinheim

Biosynthetic Diels–Alder Reactions

Chemistry and Biology of Biosynthetic Diels–Alder Reactions

*Emily M. Stocking and Robert M. Williams**

Keywords:
biomimetic synthesis · biosynthesis · cycloadditions · enzymes · natural products



 © 2003 Wiley-VCH Verlag GmbH & Co. KGaA, Weinheim DOI: 10.1002/anie.200200534

Nature's repertoire of biosynthetic transformations has recently been recognized to include the Diels–Alder cycloaddition reaction. Evidence now exists that there are enzymes that mediate the Diels–Alder reaction in secondary metabolic biosynthetic pathways. 2002 marked the 100th anniversary of Alder's birth and 75 years since the discovery of the Diels–Alder reaction. It would appear that living systems discovered and made use of this ubiquitously useful ring-forming reaction eons ago for the construction of complex natural products. In this Review an overview is given of all of the known classes of natural products (polyketides, isoprenoids, phenylpropanoids, alkaloids) that have been speculated to arise by a biological Diels–Alder reaction.

From the Contents

1. Introduction	3079
2. Polyketides	3080
3. Isoprenoids	3092
4. Phenylpropanoids	3096
5. Alkaloids	3098
6. Addendum	3110
7. Summary	3111

1. Introduction

The Diels–Alder reaction is a powerful reaction for the formation of carbon–carbon bonds in synthetic organic chemistry which allows facile, stereospecific entry into six-membered ring systems.[1] The structures of various secondary metabolites have led to an array of provocative proposals which suggest that nature might also make use of this valuable reaction.[2] An intriguing aspect of many of these biosynthetic proposals involves the possibility of enzymatic catalysis of the [4+2] cycloaddition, which would accommodate the stereochemistry extant in the respective natural product. Enzymes generally catalyze reactions by stabilizing the structure and charge of the developing transition state. For most reactions subject to this stratagem of catalysis, both the starting substrate and the product differ significantly from the transition state with respect to structure. Both the product and the starting substrate must bind to the enzyme less tightly than the transition-state structure for catalysis to occur. The transition state in the Diels–Alder reaction is highly ordered and closely resembles the structure of the product. In other words, an enzyme that was designed to stabilize the transition-state structure for this reaction would be expected to be inhibited by the product (by tight binding) and turnover (thus, catalysis) would be precluded. Alternatively, the free energy of activation can be lowered by raising the ground-state energy of the reactants. This might be accomplished in the Diels–Alder reaction by the introduction of torsional strain into the dienophile or diene components, but it is difficult to find solid precedent for this strategy in the literature. The prospect of discovering a Diels–Alderase is therefore especially enticing to mechanistic enzymologists, since it could represent a new mechanism of catalysis in nature.

Until recently, the existence of a Diels–Alderase has remained elusive, but catalysis of the Diels–Alder cycloaddition reaction by biomolecules has indeed been realized. Hilvert et al. first reported the catalysis of a Diels–Alder reaction by an antibody in 1989.[3] Monoclonal antibodies were raised against hapten **1** (Scheme 1), which resembles the transition state of the Diels–Alder reaction between tetrachlorothiophene dioxide (**3**) and *N*-ethylmaleimide (**4**). The antibody catalyzed the Diels–Alder reaction by binding the diene **3** and dienophile **4** in a reactive conformation, thus lowering the entropy of activation. The problem of product inhibition was overcome by the extrusion of SO_2 from the labile cycloadduct to give a product **5** that did not resemble **1** and, thus, catalyst turnover was not impeded.

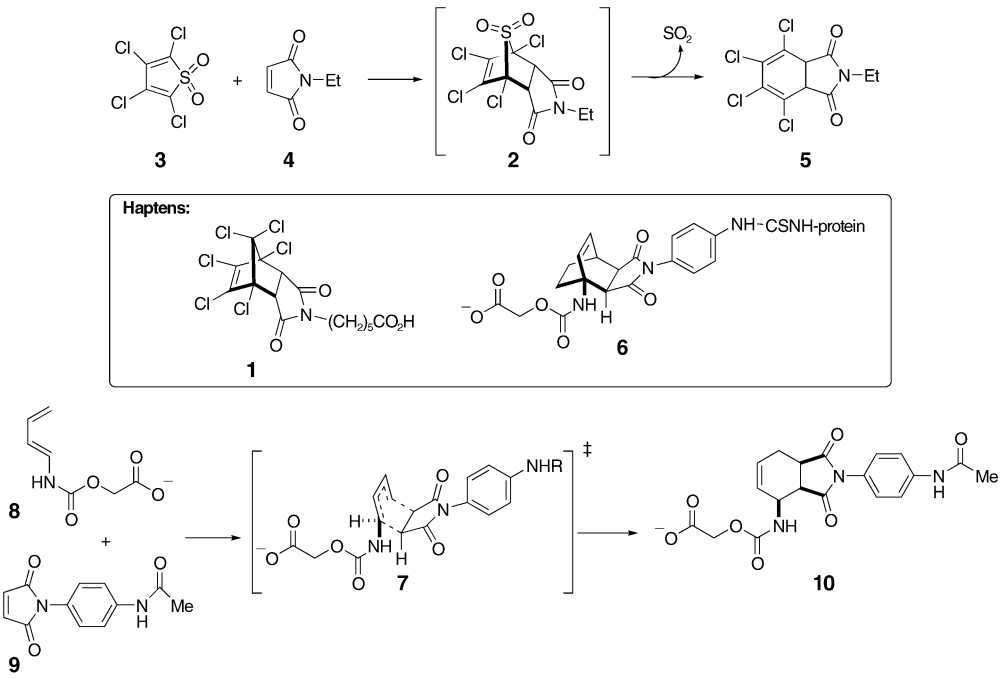
Braisted and Schultz used an alternative approach to overcome the difficulty of product inhibition in Diels–Alder catalysis by an antibody (Scheme 1).[4] They used an ethano bridge to lock the cyclohexene ring of the hapten **6** into a conformation resembling the proposed transition state **7** for the Diels–Alder reaction bewteen the acyclic diene **8** and the dienophile **9**. The authors argue that the product **10** prefers a twisted chair conformation relative to the rigid boat conformation induced by the bicyclo[2.2.2] hapten **6** that allows for release from the antibody combining site. Subsequent structural elucidation of the complex formed between this catalytic antibody and the hapten revealed the presence of 89 van der Waals interactions and two hydrogen bonds between the antibody and its hapten. These interactions apparently activate the dienophile and control the relative geometries of the bound substrates.[5]

Another type of biomolecule used to catalyze the Diels–Alder reaction is ribonucleic acid (RNA).[6] However, the mechanism of catalysis is radically different from that of catalytic antibodies. Since RNA Diels–Alderase activity is reliant on base specificity and the coordination of a transition metal, the mode of catalysis is more likely akin to Lewis acid catalysis of the Diels–Alder reaction.

The role of protein organization in natural systems and the possible mechanism of catalysis has long been a subject of debate, and was rekindled by the recent characterization of two naturally occurring potential Diels–Alderases.[7,8] The isolation of these enzymes also

[*] Professor Dr. R. M. Williams, Dr. E. M. Stocking
Department of Chemistry
Colorado State University
Fort Collins, CO 80523 (USA)
Fax: (+1) 970-491-3944
E-mail: rmw@chem.colostate.edu

 DOI: 10.1002/anie.200200534 © 2003 Wiley-VCH Verlag GmbH & Co. KGaA, Weinheim



Scheme 1. Antibody catalysis of Diels–Alder reactions.[3,4]

establishes the Diels–Alder reaction as a viable biosynthetic transformation.

This Review is intended to provide an overview of the natural products that have been proposed in the literature to be constructed biosynthetically by a Diels–Alder reaction, both catalyzed and uncatalyzed. Where available, the biosynthetic studies pertaining to these substances to probe these questions are summarized. Although there are countless structures that can formally be envisioned to arise by a [4+2] cycloaddition, this Review is limited to those natural products that have been described in the literature as putative Diels–Alder cycloadducts. The Review is organized into classes of compounds based on their biosynthetic derivations: polyketides (acetate), isoprenoids (mevalonate), phenylpropanoids (shikimic acid), and alkaloids (amino acids). In many cases, this segregation is superficial, since many compounds are often of mixed biosynthetic origins (for example, cytochalasans, pycnidione, and brevianamides).

2. Polyketides

Since polyketides are derived from acetate, these compounds are particularly well-suited for isotopic labeling studies. For example, isotopically labeled precursors, such as ^{13}C-acetate, are readily accessible, comparatively cheap, and are often readily incorporated into the corresponding secondary metabolite in feeding experiments. Thus, it is hardly surprising that a large portion of the experimental evidence for the Diels–Alder reaction in nature has been obtained for this class of compounds. In fact, both lovastatin and macrophomic acid, for which reported Diels–Alderase enzymes have been isolated,[7,8] are classified as polyketides.



Robert M. Williams was born in New York in 1953 and attended Syracuse University where he received his B.A. in Chemistry in 1975. He obtained his Ph.D. in 1979 at MIT and was a postdoctoral fellow at Harvard (1979–1980). He joined the faculty at Colorado State University in 1980 and was named a University Distinguished Professor in 2002, his current position. His research interests include the total synthesis of natural products, biosynthetic pathways, studies on antitumor drug–DNA interactions, and the design and synthesis of antibiotics.



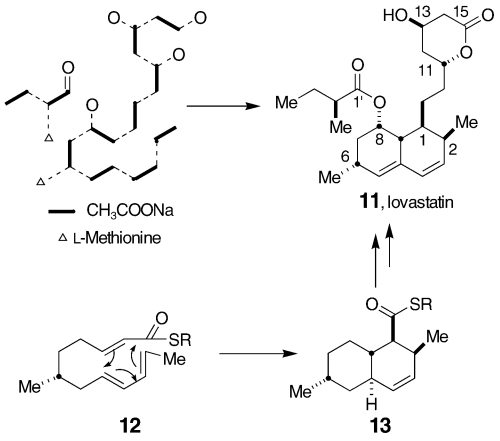
Emily Stocking was born in Oakland, California in 1970. She obtained a B.A.S. in Chemistry and Biology at the University of California at Davis and in 1993 she took a position at the NIH Stable Isotopes Resource at Los Alamos National Laboratory. In 1994 she joined the research group of Professor R. M. Williams at Colorado State University. Her doctoral studies included the total synthesis of the indole alkaloid VM55599 and studies on the biosynthesis of paraherquamide A. Since completion of her degree in 2001, she has worked at Johnson and Johnson Pharmaceutical Research and Development in La Jolla, California.

 © 2003 Wiley-VCH Verlag GmbH & Co. KGaA, Weinheim

2.1. Decalin Polyketides

2.1.1. Lovastatin (Mevinolin)

Lovastatin (**11**), also known as mevinolin, has received significant attention in the literature, since it is a potent inhibitor of cholesterol biosynthesis in humans and has become a clinically useful and very successful drug. Feeding experiments on the producing fungal strain *Aspergillus terreus* (ATCC 20542) with [1-^{13}C], [2-^{13}C]-, [1,2-$^{13}C_2$]-, [1-^{13}C,1-$^{18}O_2$]-, [1-^{13}C,2-$^{2}H_3$]-, and [2-^{13}C,2-$^{2}H_3$]acetates established that lovastatin is comprised of a C_{18} unit and a C_4 unit constructed through the head-to-tail attachment of acetate (Scheme 2).[9]



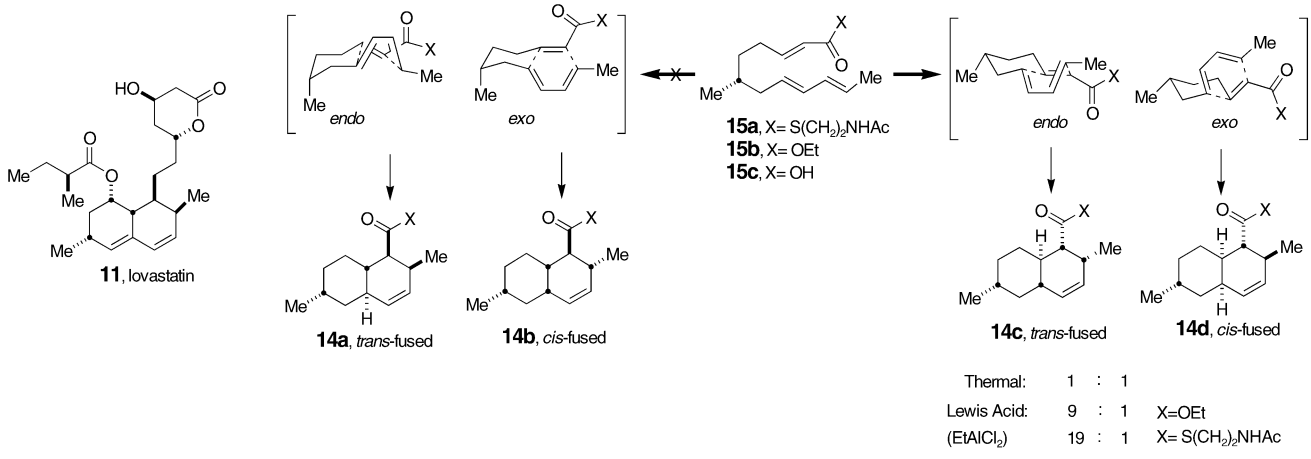
Scheme 2. Origin of the carbon atoms of lovastatin (**11**) and proposed biogenesis.[9,10]

Interestingly, of the five oxygen atoms in lovastatin, only the oxygen atom attached at C11 could definitively be assigned as a derivative of acetate. In addition, it was discovered that the two methyl groups at C2 and C6 are derived from *S*-adenosylmethionine (SAM), as shown by feeding experiments with [$^{13}CH_3$]methionine.

Re-examination of the origin of the oxygen atoms in lovastatin (**11**) was made possible by the subculture selection of a new strain of *Aspergillus terreus* (MF 4845), which increased the production of **11** to 200 mg per litre of culture.[10] Fermentation of *Aspergillus terreus* in the presence of an $^{18}O_2$-enriched atmosphere showed the oxygen atom at C8 was derived from molecular oxygen. A separate feeding experiment with [1-^{13}C,1-$^{18}O_2$]acetate indicated the oxygen atoms at C1′, C11, C13, and C15 are derived from acetate. The results of these feeding experiments as well as the previous experiments led to the biosynthetic hypothesis outlined in Scheme 2.[9,13] Vederas and co-workers speculated that the enzymes involved in the biosynthesis of lovastatin (**11**) are similar to those involved in the biosynthesis of fatty acids.[9] They proposed that condensation of acetate units (from malonate) could produce a triene **12** that would undergo an *endo*-selective Diels–Alder cycloadditon to the decalin **13**.

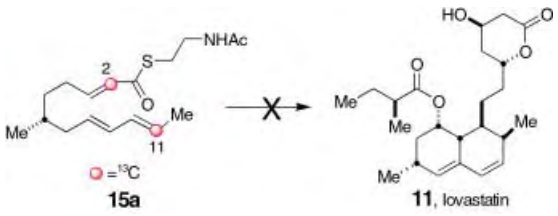
The first test of this hypothesis was a synthesis of the analogue **14** through laboratory Diels–Alder cyclizations of the thioester **15a**, ethyl ester **15b**, and acid **15c** both thermally and with a Lewis acid catalyst (Scheme 3).[11] There was a 1:1 ratio of the *endo*(**14c**):*exo*(**14d**) products in the thermal cyclization, presumably through a chairlike transition state with the methyl side chain disposed in a pseudo-equatorial manner. However, no *endo* product **14a** corresponding to the stereochemistry of **11** was observed (with a pseudo-axial methyl side chain in the transition state). The Lewis acid catalyzed Diels–Alder reaction gave the same two products as the thermal reaction but in a 9:1 *endo*:*exo* ratio for **15b** and a 19:1 ratio for **15a**. The absence of product **14a** in the laboratory cyclizaton suggests that the Diels–Alder cyclization in the biogenesis of **11** could be enzymatic.

Feeding experiments were performed under a variety of conditions on *Aspergillus terreus* (MF4845) with **15a** doubly labeled with ^{13}C at C2 and C11 to test for Diels–Alder activity in vivo (Scheme 4).[11] This doubly labeled precursor readily degrades by β oxidation to smaller building blocks (for example, acetate). Incorporation of the intact precursor would lead to adjacent ^{13}C labels, which would be perceived as carbon–carbon coupling in the ^{13}C NMR spectrum. However, feeding experiments with [2,11-$^{13}C_2$]-**15a** did not reveal detectable ^{13}C–^{13}C coupling in the ^{13}C NMR spectra. Appa-



Scheme 3. Synthesis of the decalin **14** though an in vitro Diels–Alder cyclization of triene **15**. Thermally: toluene, 160 °C, 4 days; Lewis acid catalyzed: 0.9 equiv $EtAlCl_2$, RT, 3 h.[11]

 © 2003 Wiley-VCH Verlag GmbH & Co. KGaA, Weinheim

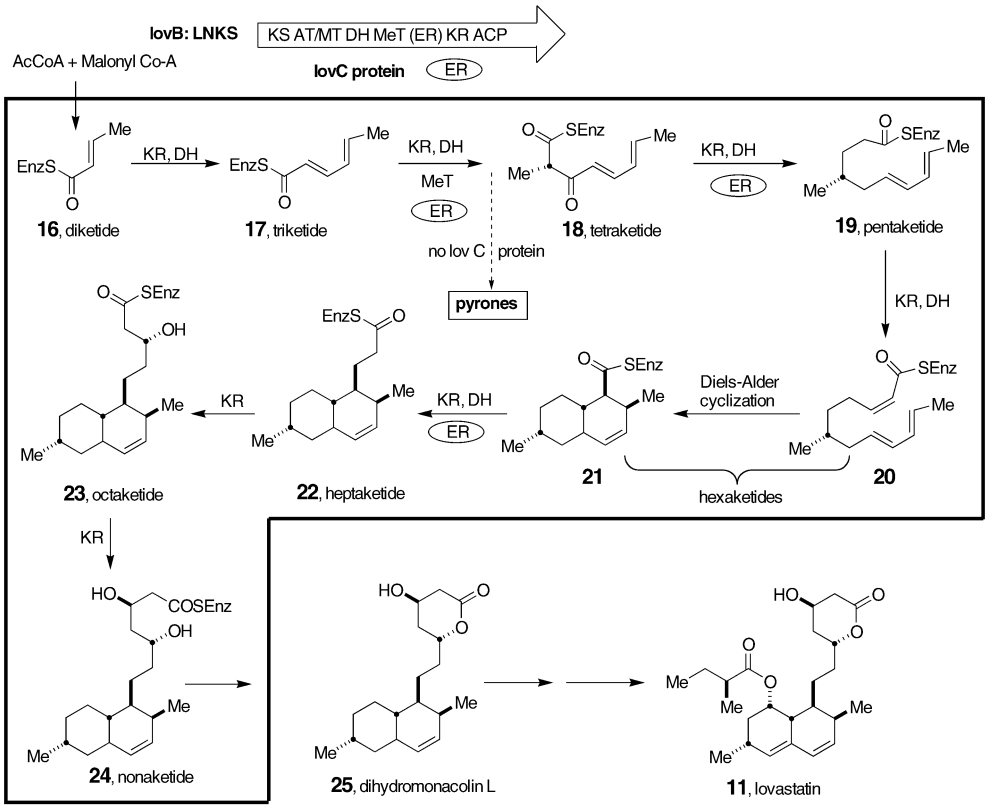


Scheme 4. Feeding experiment with [2,11-$^{13}C_2$]-**15a** in the investigation of the Diels–Alder activity of *A. terreus* (MF4845).[11]

rently, **15a** was catabolized before it could undergo cycloaddition.

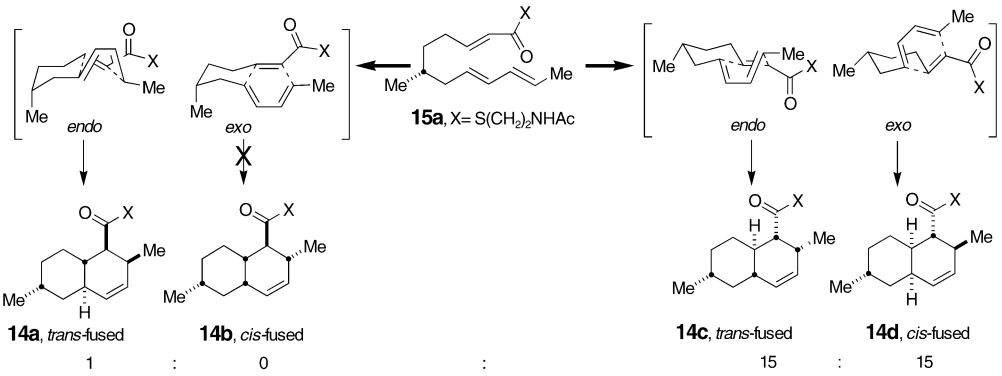
A complete outline of the proposed biosynthesis of **11** including the role of the *lovB* and *lovC* genes is shown in Scheme 5. Vederas, Hutchinson, and co-workers demonstrated that dihydromonacolin L (**25**), an established intermediate in the biosynthesis of lovastatin (**11**),[12] was formed in a heterologous host, *Aspergillus nidulans*, containing the *lovB* and *lovC* genes from *Aspergillus terreus*.[13] In addition, expression of the lovB protein (lovastatin nonaketide synthase, LNKS) in the absence of lovC protein led to truncated pyrones because of the inefficient enoyl reduction at the tetraketide stage. These results were interpreted as supporting the notion of catalytic Diels–Alder activity for LNKS.[7,13]

The enzymatic activity of LNKS was tested on **15a**, the analogue of the proposed cycloaddition precursor. The *N*-acetylcysteamine (NAC) ester **15a** (Scheme 6) was added to an aqueous buffered solution containing pure homogenous LNKS protein.[7] The *endo*-Diels–Alder product **14a**, which had the same stereochemistry observed in **11**, was obtained along with the non-enzymatic products **14c** and **14d** (**14a**:**14c**:**14d** = 1:15:15). The *cis*-fused *exo*-product **14b** was not observed under any conditions. When **15a** was added to thermally denatured LNKS, adducts **14c** and **14d** were formed, but **14a** was not detected. Cycloadducts **14c** and **14d** result from a transition state with the C6 methyl group in a sterically favored pseudo-equatorial arrangement. However, the transition state leading to **14a** requires a more crowded pseudo-axial disposition of the methyl group at C6. Thus, it seems the function of LNKS is to bind the substrate in a conformation that resembles the *endo* transition state that leads to **14a** (analogous to the mode of action of catalytic antibodies). In addition, hydrogen bonding of the carbonyl oxygen atom within the active site of LNKS would make the dienophile more electron deficient, thus resembling Lewis acid catalysis of laboratory Diels–Alder reactions. Since the product **14a** was not obtained in the presence of denatured LNKS, the asymmetric induction of the Diels–Alder reaction cannot be caused by nonspecific binding of a chiral protein.[14] Therefore, LNKS represents the first naturally occurring Diels–Alderase enzyme to be purified to homogeneity.[7]



Scheme 5. Proposed biosynthetic pathway for lovastatin (**11**). The boxed region shows reactions catalyzed with LNKS and the lovC protein. The domains for the LNKS and the lovC protein were assigned from sequence homology to other polyketide synthase (PKS) proteins.[7] KR = keto reductase, DH = dehydratase, MeT = methyltransferase, ER = enoyl reductase, KS = β-ketoacyl synthase, ACP = acyl carrier protein, AT/MT = acetyl/malonyltransferase.

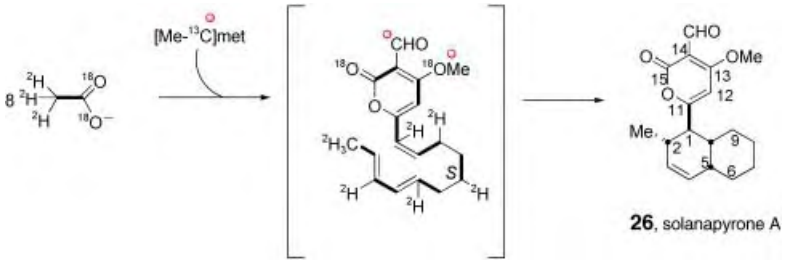
 © 2003 Wiley-VCH Verlag GmbH & Co. KGaA, Weinheim



Scheme 6. Synthesis of **14** though an in vitro enzymatic Diels–Alder cyclization.[7]

2.1.2. *Solanapyrones*

Another decalin polyketide thought to arise through a [4+2] cycloaddition is solanapyrone, a phytotoxin produced by the pathogenic fungus, *Alternaria solani*.[15] A series of feeding experiments with singly and multiply labeled acetate and [$^{13}CH_3$]methionine revealed the origin of all the carbon atoms in solanapyrone A (**26**).[16] The results are summarized in Scheme 7. An upfield shift of the C13 and C15 signals in the ^{13}C NMR spectra after feeding experiments with [1-^{13}C,1-^{18}O]acetate excluded the possibility that the polyketide is derived by oxidative scission of a longer precursor and indicates that C15 is the terminal carbon atom of the polyketide. Feeding experiments with [1-^{13}C,2-$^{2}H_3$]- and [2-^{13}C,2-$^{2}H_3$]acetate established the fate of the hydrogen atoms and proved that the *pro-S* hydrogen atom is retained by the enoyl reductase. The stereochemistry at C1, C2, C5, and C10, the location of the double bond, and the stereochemistry at C5 and C7 with the acetate deuterium atoms are consistent with a Diels–Alder construction of the decalin ring system.



Scheme 7. Incorporation of labeled acetate and methionine into solanapyrone A (**26**).[16]

The isolation of the minor metabolite solanapyrone D (**27**), a diastereomer of **26**, provided additional support for the Diels–Alder reaction in the biosynthetic pathway.[17] Rotation about the C5–C6 bond in the Diels–Alder reaction could give rise to either the *exo*- or *endo*-cycloaddition products (Scheme 8). Dreiding models indicate a similar stability of the two transition states **28** and **29**, but a biomimetic synthesis of **26** provided a 2:1 product ratio in favor of the *endo* adduct **27**.[18] Since the *exo* product is the major isomer observed in the natural system, this was the first indication that the reaction might be enzyme-mediated.

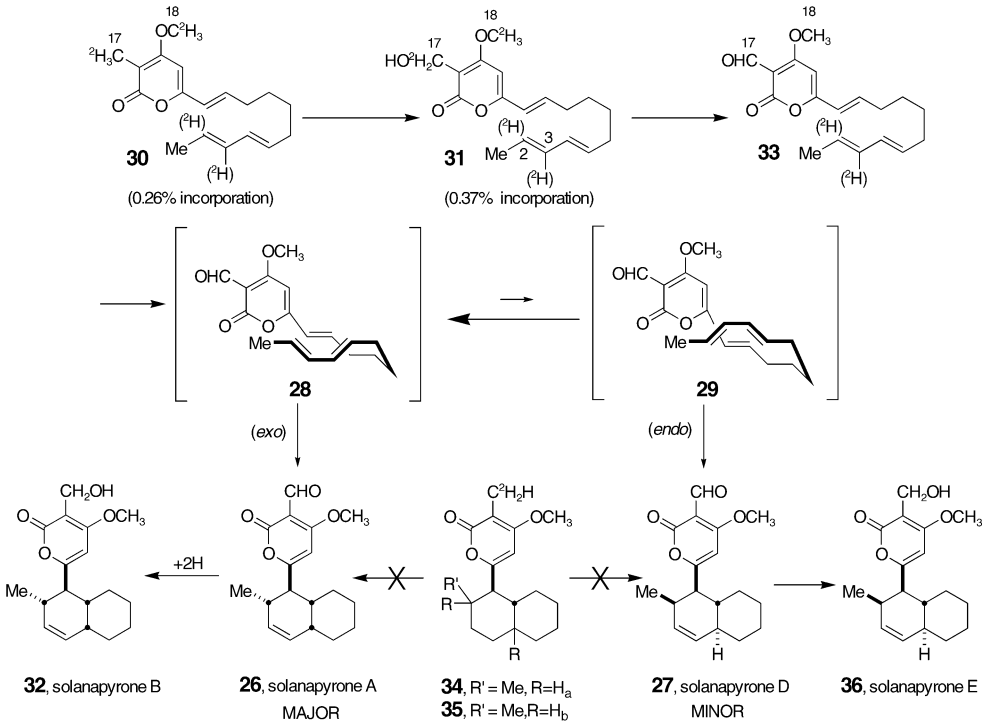
Evidence for the biosynthetic Diels–Alder reaction in the biosynthesis of solanapyrone was obtained when the achiral deuterated trienes **30** and **31** were incorporated in vivo into **26** and **32**.[19,20] Incorporation of the precursor **30** indicated loss of deuterium at C17. The ratio of the integration for the signals of deuterium at C17 to deuterium at C18 in the ^{2}H NMR spectrum changed from 2:3 in **30** to a ratio of 1:4.3 for **26** and 1:5.1 for **32**. Observation of the same deuterium ratio for **26** and **32** indicates that **26** is reduced to **32** and that the two triene precursors **30** and **31** are oxidized to the same intermediate, presumably the C17 aldehyde prosolanopyrone II (**33**). Feeding experiments could not be performed with **33** because it was so reactive and underwent spontaneous *endo* cyclization in aqueous conditions.

The reactivity of the aldehyde **33** makes it a likely candidate as a direct substrate for the Diels–Alder cyclization (Scheme 8). Incorporation of the [$^{2}H_7$]-**31** with an essentially unchanged deuterium ratio demonstrated that the diene/dienophile precursor was incorporated intact. Additionally, the labeled compounds **34** and **35** were not incorporated into **26** or **27**, which indicates that the Diels–Alder reaction probably occurs after oxidation.

Enzymatic activity was found in a cell-free extract of *Alternaria solani*, which catalyzed the conversion of **33** into solanapyrones A (**26**) and D (**27**) in 25% yield with a ratio of the *exo* to *endo* cycloadduct of 53:47 .[21] A control experiment with denatured enzyme provided a 3:97 ratio of the *exo* to *endo* cycloadducts with only 10% consumption of starting material. The observed stereoselectivity in the cell-free extract was interpreted as being indicative of enzymatic activity.

Conversion of **31** with the crude enzyme preparation was accomplished in 25% yield (19% **26** and **27**, 6% **33**) with an *exo*/ *endo*-cycloaddition ratio of 85:15 and an optical purity (for **26**) of 99% *ee*. The optical purity of **26** produced from **33** was 92% *ee*. Since this value is lower than that obtained from **31**, it seems that a single enzyme catalyzing the oxidation and cycloaddition is responsible for producing the optically pure solanapyrones found in the natural system. Further proof of

 © 2003 Wiley-VCH Verlag GmbH & Co. KGaA, Weinheim



Scheme 8. Incorporation of deuterated trienes into solanapyrones A (**26**) and D (**27**). The thioacetal of **27** is the major product (2:1) in the laboratory synthesis.[19,20]

this sequence of events was obtained when the enzymatic cycloaddition reaction of **31** was suppressed in the absence of oxygen (argon atmosphere).

2.1.3. *Nargenicin*

Nargenicin (**37**), a polyketide antibiotic isolated from *Nocardia argentinensis*, contains a macrocyclic lactone fused to a *cis*-octahydronaphthaline (octalin) ring system that is derived biosynthetically from five acetate and four propionate units.[22] Feeding experiments with [1-$^{18}O_2$,1-^{13}C]acetate and [1-$^{18}O_2$,1-^{13}C]propionate indicated that the oxygen atoms at C1 and C11 were derived from acetate while the oxygen atoms at C9 and C17 were derived from propionate (Scheme 9, inset). In accord with these results, incubation of *N. argentinensis* with ^{13}C-labeled acetate and propionate in an $^{18}O_2$-enriched atmosphere indicated that the two ether oxygen atoms at C2 and at C13 and the hydroxy group at C18 are derived from molecular oxygen.[23]

Since the oxygen atom at C13 is not derived from propionate, this implies that the C4–C13 bond is not formed by an aldol-type condensation. Instead, a Diels–Alder cyclization was invoked through the intermediacy of the triene **38** (Scheme 9). By the incorporation of the ^{13}C- and/or ^{2}H-labeled NAC esters of the precursors **40**, **41**, **42**, and **44** (Scheme 9), Cane et al. demonstrated that the stereochemistry and level of oxidation are set prior to chain elongation.[24] The incorporation of [$^{13}C_2$]-**44** also further supports the notion that the *cis*-octalin ring system is generated through a Diels–Alder cycloaddition.[24]

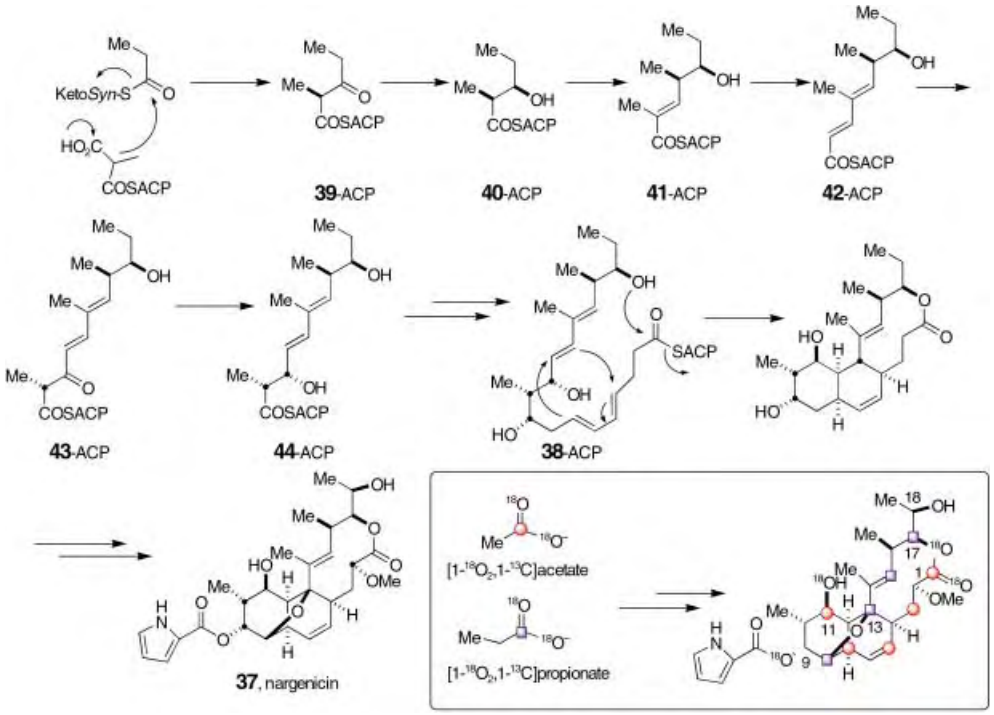
2.1.4. *Betaenone B*

Betaenone B (**45**) is a phytotoxin from *Phoma betae* (a fungus) that causes a leaf spot disease on sugar beet. Feeding experiments with [1-^{13}C,1-$^{18}O_2$]acetate indicated that only the oxygen atom at C16 of **45** is derived from acetate (Scheme 10).[25] The absence of an ^{18}O-induced isotopic shift in the signal corresponding to C18 could indicate that the oxygen atom is derived from molecular oxygen or it could indicate a "washing out" of the label by exchange with water.

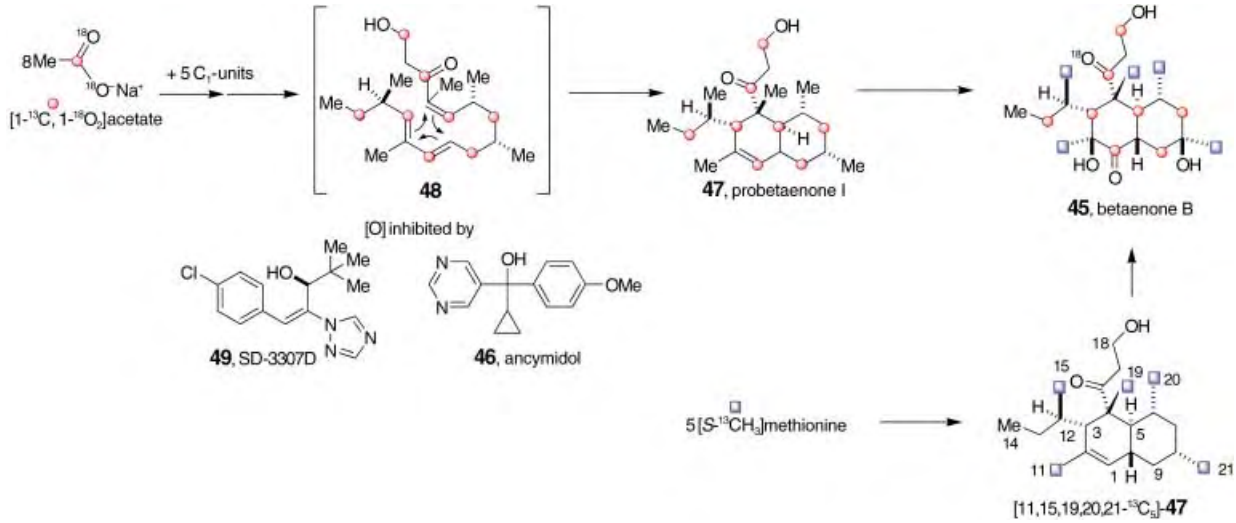
When a P450 inhibitor, ancymidol (**46**), was added to cultures of *P. betae*, the production of betaenone B (**45**) was suppressed in proportion to the amount of inhibitor added. In addition, a new deoxygenated metabolite, probetaenone I (**47**), was isolated which was proposed to be a biosynthetic precursor of **45** through the intramolecular Diels–Alder reaction of the projected intermediate **48**.[25]

Probetaenone I (**47**) was later proven to be a precursor to **45** (Scheme 10). Separate feeding experiments of *Phoma betae* with [1-^{14}C]acetate, [1,2-$^{13}C_2$]acetate, and [*S*-$^{13}CH_3$]methionine in the presence of the P450 inhibitor SD-3307D (**49**) provided labeled **47**. Subsequent feeding experiments with each labeled probetaenone I (**47**) displayed incorporation into **45** (6.02% incorporation from [1-^{14}C]acetate, 19.1% enrichment from [1,2-$^{13}C_2$]acetate, and 9.6% enrichment from [*S*-$^{13}CH_3$]methionine).[26] Synthesis of **47** through an intramolecular Diels–Alder reaction confirmed the structure and provided credence for the proposed biosynthetic pathway.[27]

 © 2003 Wiley-VCH Verlag GmbH & Co. KGaA, Weinheim



Scheme 9. Proposed biosynthesis of nargenicin (**37**).[23,24d]

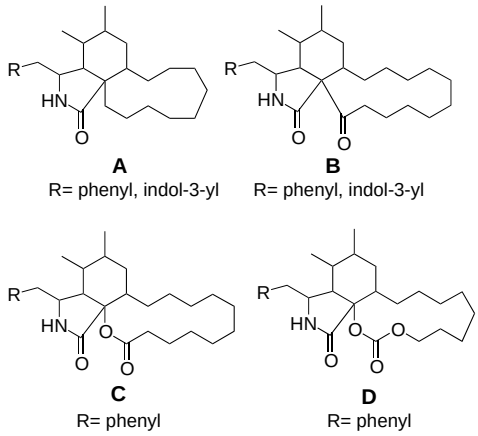


Scheme 10. Biosynthetic studies on betaenone B (**45**).[25,26]

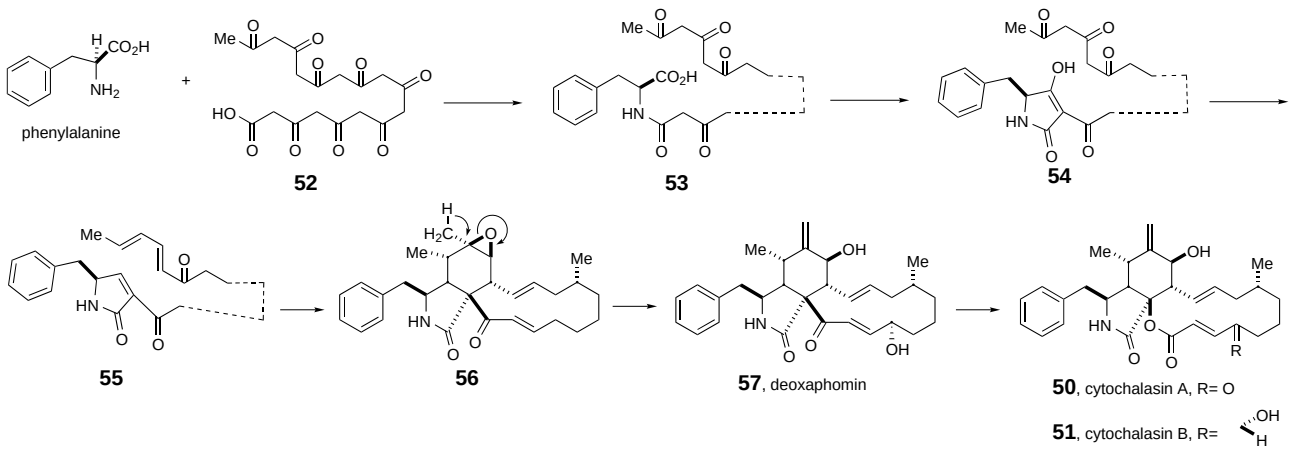
2.2. Macrocyclic Polyketides

2.2.1. Cytochalasans

The cytochalasans are a large family of macrocyclic polyketides that possess cytostatic activity.[28] To date, approximately 60 natural products belonging to this class of mycotoxins have been isolated.[29] Structurally, the cytochalasans are characterized by a highly substituted perhydroisoindole group fused to a macrocyclic ring to give the four basic skeletal structures **A**–**D**. The majority of the macrocycles are carbocyclic, but the macrocycle can also be a lactone or cyclic carbonate.



 © 2003 Wiley-VCH Verlag GmbH & Co. KGaA, Weinheim



Scheme 11. Proposed biosynthesis of cytochalasins A (**50**) and B (**51**).[28]

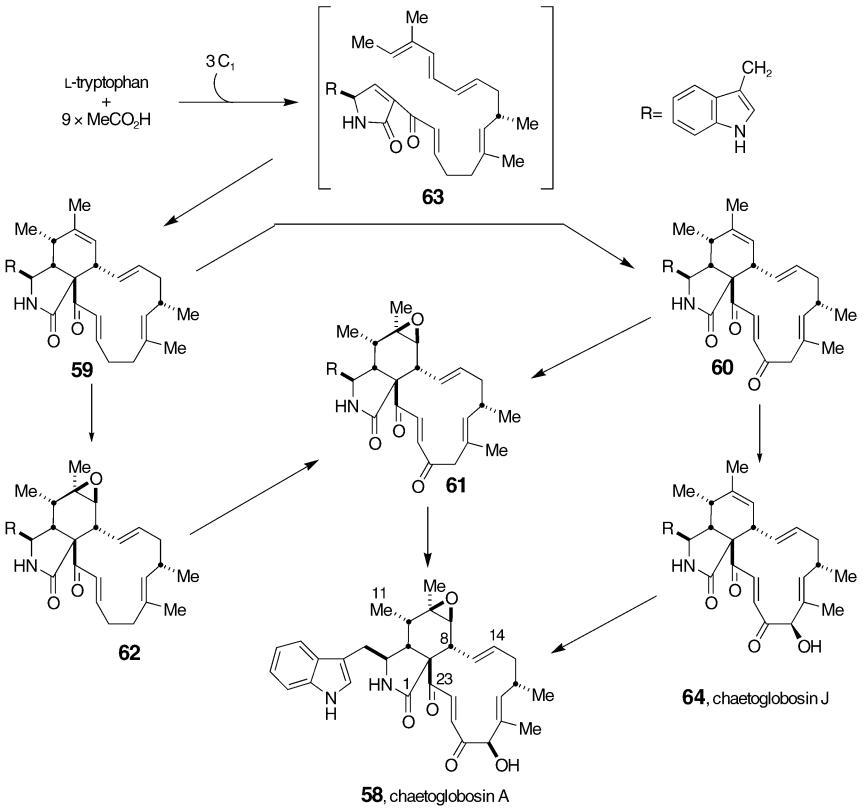
Feeding experiments have established acetate,[30,31] propionate,[30,31] methionine,[31,32] phenylalanine,[33] and tryptophan[31] as biosynthetic precursors to the cytochalasans. The perhydroisoindole group of cytochalasin A (**50**) and B (**51**) is thought to arise through an *endo*-selective intramolecular Diels–Alder reaction (Scheme 11).[28] Incorporation of deoxaphomin (**57**) into **51** indicates that oxidation to the macrolide occurs after the putative Diels–Alder cyclization and implies there is a common biosynthetic pathway for the cytochalasans.[34]

Indirect evidence for the Diels–Alder-mediated biosynthesis of the cytochalasins was obtained by feeding[35] and inhibition[36] experiments with *Chaetomium subaffine*, which produces chaetoglobosin A (**58**, Scheme 12). A feeding experiment with [1-^{13}C,2-$^{2}H_3$]acetate showed retention of the deuterium labels at C11, C8, and C14.[35] Retention of deuterium at C8 and C14 precludes formation of the perhydroisoindole and macrocycle through a proposed formation of a carbon–carbon bond in which a carbonyl group is located at C14.[28] A feeding experiment with [1-^{13}C,1-$^{18}O_2$]acetate established that the oxygen atoms at C1 and C23 originate from the acetate, while incubation in an $^{18}O_2$-enriched atmosphere displayed an upfield shift of the C6, C7, and C20 signals in the NMR spectrum.[35] An inhibition experiment with the cytochrome P450 inhibitor metapyrone led to the formation of the metabolites **59**–**62** (with **59** as the major product).[36] These results led to the biosynthetic proposal for the formation of **58** outlined in Scheme 12. An intramolecular Diels–Alder reaction of the putative hexaene **63** would provide **59**, which could then undergo a stepwise oxidation to provide **58**.

The possibility for enzymatic involvement in the proposed Diels–Alder cyclization of the cytochalasans was evidenced by the retro-Diels–Alder reaction of **59** (Scheme 13). Instead of forming the expected triene **63**, pyrolysis (180 °C, sealed tube) of **59** produced equal amounts of starting material and the diastereomer **65**.[35] The lack of stereoselectivity in the thermal Diels–Alder reaction supports the hypothesis that an enzyme preorganizes the substrate conformation to favor the *endo*-transition state in the biological system, which results in exclusive formation of **59**.

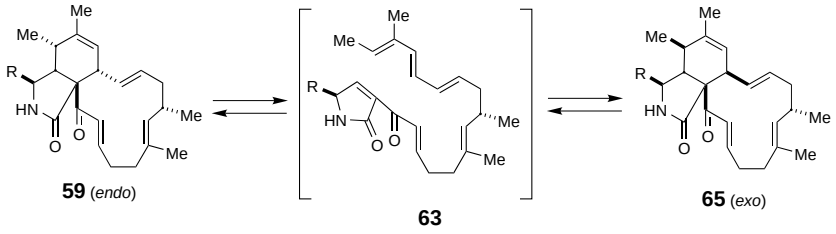
2.2.2. *Cochleamycins*

The polyketide origin of cochleamycins A (**66**) and B (**67**), produced by *Streptomyces* sp. strain DT136, was determined from feeding experiments with [1-^{13}C]acetate, [2-^{13}C]acetate,

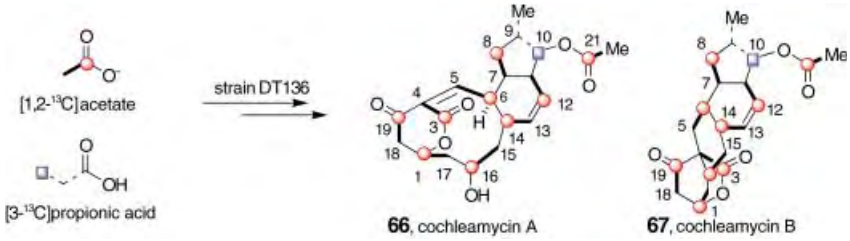


Scheme 12. Proposed biosynthesis of chaetoglobosin A (**58**).[35]

 © 2003 Wiley-VCH Verlag GmbH & Co. KGaA, Weinheim



Scheme 13. Retro-Diels–Alder reaction of the chaetoglobosin A precursor **59**.[35]



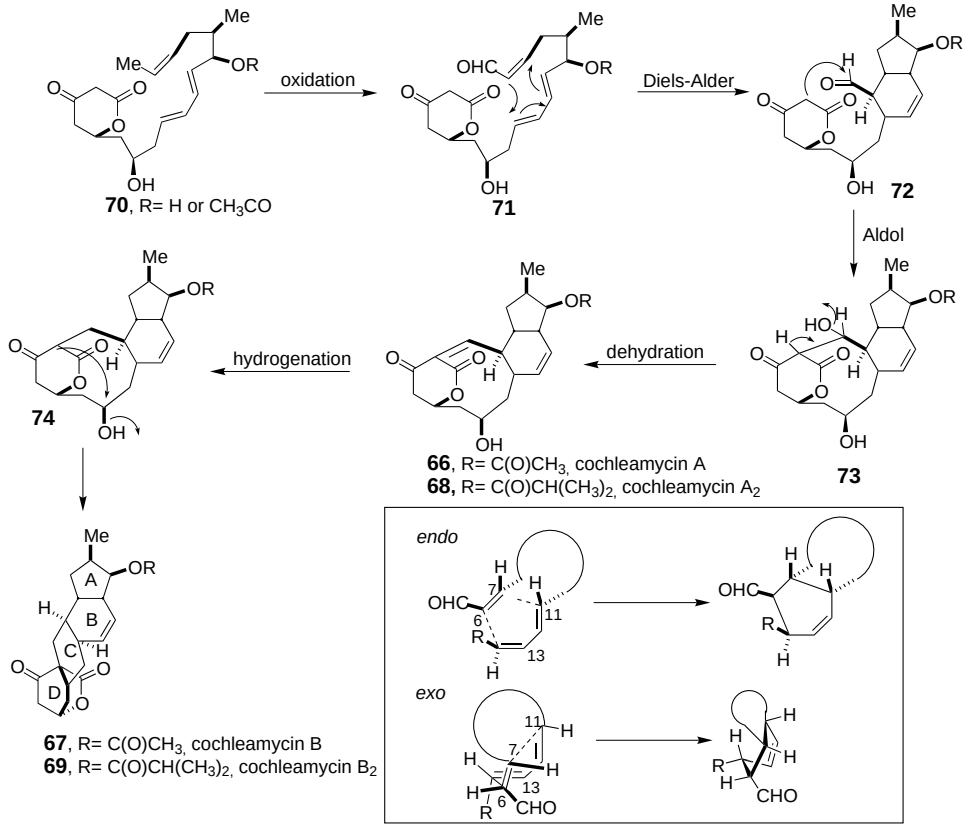
Scheme 14. Incorporation of acetate and propionic acid into cochleamycin A (**66**) and B (**67**).[37]

[1,2-$^{13}C_2$]acetate, and [3-^{13}C]propionic acid (Scheme 14).[37] Based on these results, the biosynthesis shown in Scheme 15 was proposed.

Oxidation of the allylic methyl group in the proposed intermediate **70** followed by an intramolecular Diels–Alder reaction and aldol condensation could lead to the formation of **66**. Formation of **67** is thought to arise from reductive transannular cyclization at the C4- and C16-positions of **66** accompanied by elimination of the hydroxy group at C16. The desired stereochemistry for the intramolecular Diels–Alder reaction at the AB- and BC-ring junctures can be obtained by *endo* addition of the *trans*-olefin at the C6-position to the 11-*trans*-13-*cis*-diene, or by the *exo* addition of the *trans* olefin to the 11-*cis*,13-*trans*-diene (Scheme 15, inset).

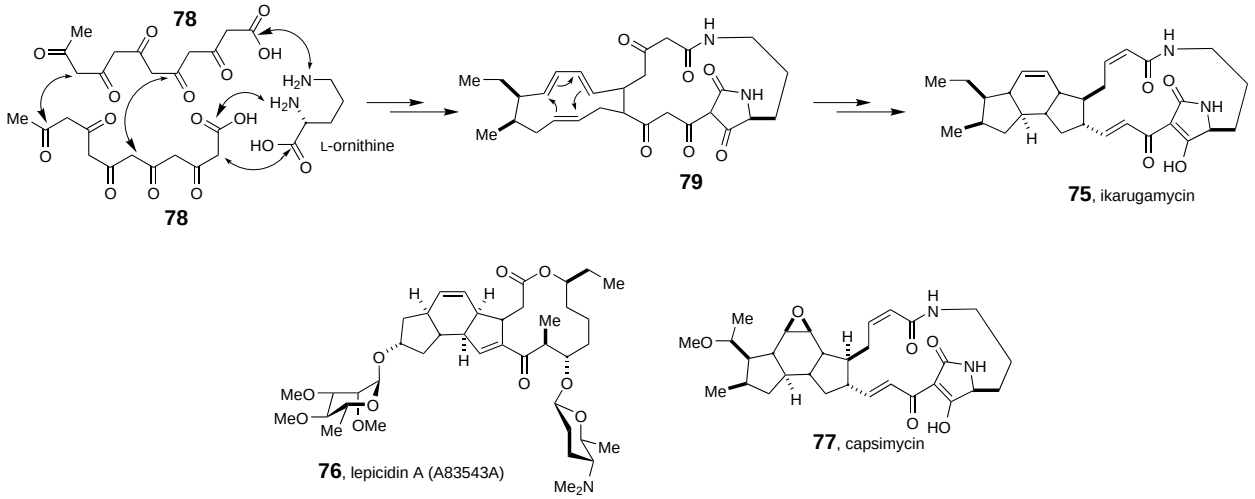
2.2.3. *Ikarugamycin*

Ikarugamycin (**75**)[38] is a member of a small family of macrocyclic antibiotics produced by *Streptomyces phaeochromogenes* var. *ikaruganensis* Sakai, which possess an unusual perhydro-*as*-indacene ring system. Other members of this family include lepicidin A (**76**, A83543A)[39] and capsimycin (**77**).[40] The structure and stereochemistry of ikarugamycin were determined by Ito and Hirata in 1972.[38a,b] They proposed that ikarugamycin was biosynthesized from two hexaacetate units **78** and L-ornithine, and that the decahydroindacene skeleton



Scheme 15. Proposed biosynthetic pathway of cochleamycins A (**66**) and B (**67**).[37]

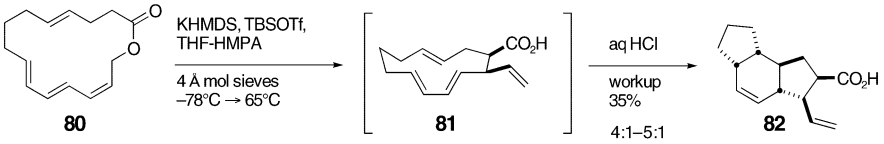
 © 2003 Wiley-VCH Verlag GmbH & Co. KGaA, Weinheim



Scheme 16. Proposed biosynthesis of ikarugamycin (**75**) and structures of related natural products lepicidin A (**76**) and capsimycin (**77**).[38–40]

was synthesized through a transannular Diels–Alder reaction of **79** (Scheme 16).

Roush and Works modeled this system with a functionalized cyclododecatriene **81** (Scheme 17).[41] Stereoselective enolate Claisen ring contraction of lactone **80** provided the desired triene **81** in situ. Heating the reaction mixture to 65 °C overnight provided a mixture of the Diels–Alder cycloadducts **82** and a second diastereomer (4:1–5:1). Evans and Black pursued an alternate route for the synthesis of the decahydro-*as*-indacene skeleton of **76**, in which they utilized an intramolecular Diels–Alder reaction in conjuction with an aldol reaction.[42] Additional biosynthetic studies on this interesting family of natural products have not yet appeared.



Scheme 17. Biomimetic synthesis of the perhydro-*as*-indacene ring system of **75**. KHMDS = potassium hexamethyldisilazide, TBS = tributylsily, Tf = trifluoromethanesulfonyl, HMPA = hexamethyl phosphoramide.[41]

2.3. Perhydroindane Polyketides

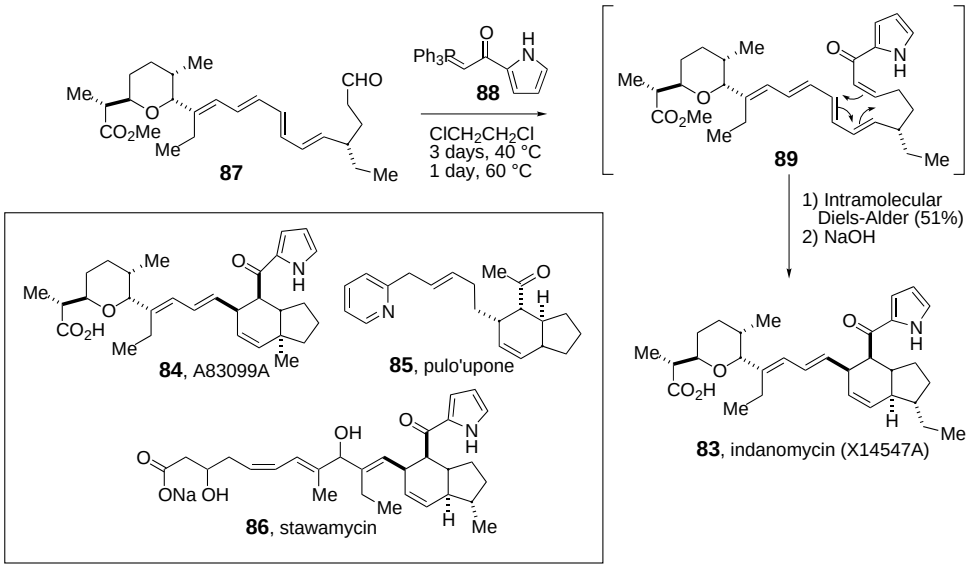
Indanomycin (**83**, X14547A)[43] is a member of a small family of polyketides produced by *Streptomyces antibioticus* which contain a perhydroindane skeleton. Other members of this family include the antibiotic A83099A (**84**), which is produced by *Streptomyces setonii*,[44] the marine natural product pulo'upone (**85**), which is produced by the mollusk *Philinopsis speciosa*,[45] and stawamycin (**86**), produced by a *Streptomyces* sp. Tularik 8349.[46] Roush et al. hypothesized that the biosynthesis of **83** might involve an intramolecular Diels–Alder reaction via a pentaene intermediate such as **89**.[47] Based on this hypothesis, the total synthesis of indanomycin was completed by using an intramolecular [4+2] cycloaddition of **89** as the key step (Scheme 18).[47c] The isomerically pure product was obtained in 51 % yield with 5 % of a mixture of *cis*-fused products and 5 % of the C10,C11-*Z* isomer.

2.4. Other Polyketides

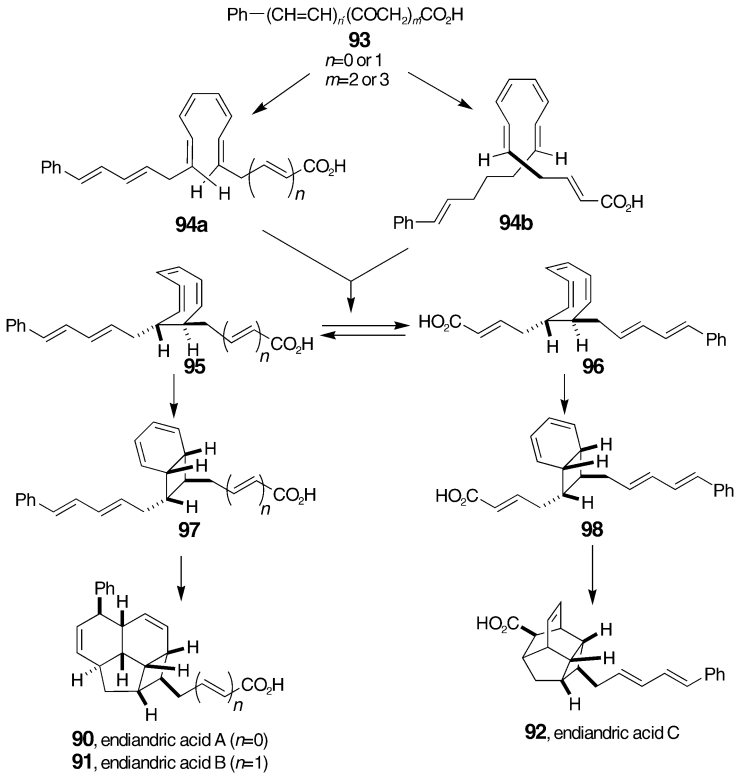
2.4.1. Endiandric Acids

The endiandric acids are isolates from the leaves of the Australian plant *Endiandra introrsa* (*Lauraceae*).[48] Since endiandric acid A (**90**) and B (**91**) occur together with endiandric acid C (**92**), and as these compounds are isolated in racemic form, Bandaranayake et al. postulated there was a unified biogenesis involving a series of electrocyclizations from an achiral precursor (Scheme 19).[49] They proposed that a polyketide of type **93** might lead to a phenylpolyene acid with a central conjugated tetraene unit. An 8π conrotatory electrocyclization of the all-*cis* tetraene **94a** or the *trans*,*cis*,*cis*,*trans* isomer **94b**, followed by a 6π disrotatory electrocyclization and finally an intramolecular Diels–Alder (4πs+2πs) cycloaddition would provide **90** and **91** or **92**, respectively.

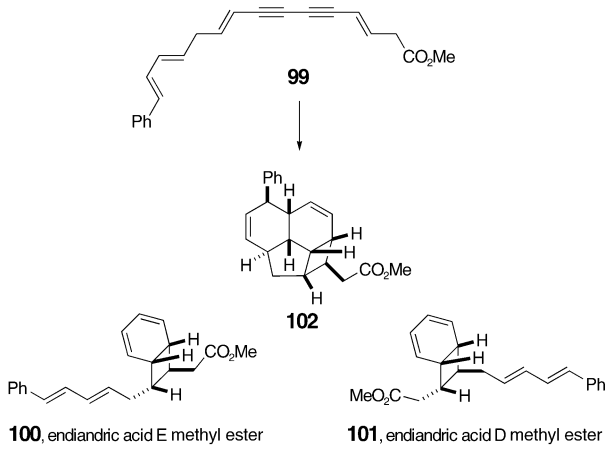
Nicolaou et al. explored the feasibility of the proposed pathway though a biomimetic synthesis. Stepwise stereocontrolled syntheses of endiandric acids A–D (**90**–**92**, **101**) were first completed to determine if the proposed sequence of events was viable.[50] Next, they completed a one-pot electrocyclic cascade reaction.[51] Hydrogenation of the acyclic precursor **99** (Scheme 20) with Lindlar's catalyst provided the methyl esters of endiandric acids E and D (**100** and **101**), while brief heating of the reaction provided the methyl ester (**102**) of endiandric acid A. An analogue of **99** with an elongated chain was used to synthesize **91** and **92** along with



Scheme 18. Biomimetic total synthesis of indanomycin (**83**).[47c] The inset shows the structures of related natural products A83099A (**84**),[44] pulo'upone (**85**),[45] and stawamycin (**86**).[46]



Scheme 19. Proposed biosynthesis of endiandric acids A–C (**90**–**92**).[49]



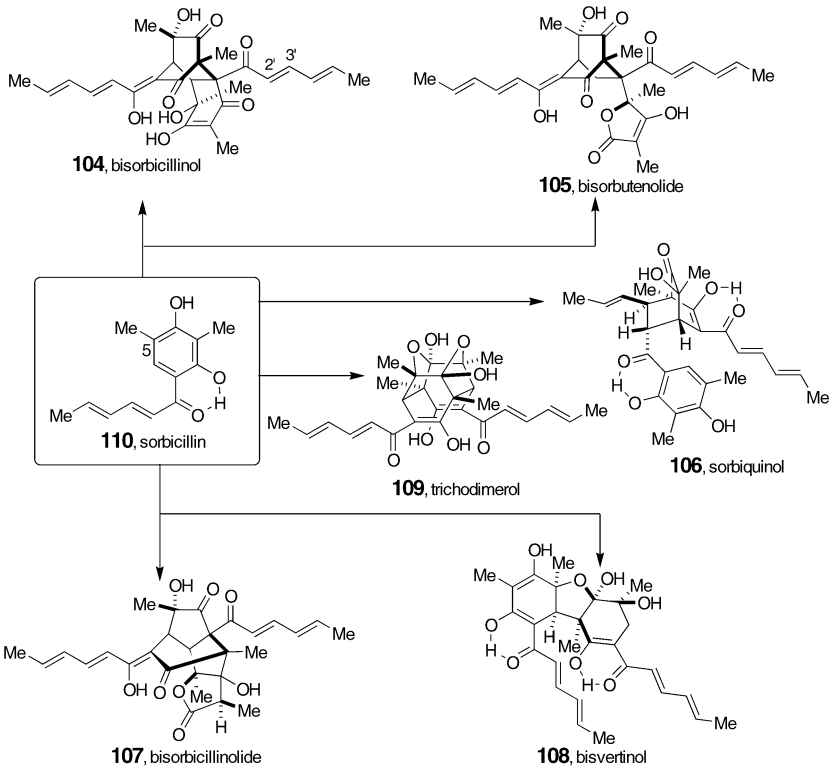
Scheme 20. Biomimetic synthesis of the endiandric acids.[51]

the unnatural endiandric acids G–F. These syntheses validate the biosynthetic hypothesis of Bandaranayake et al. and indicate that these electrocyclic reactions are not enzymatically catalyzed. In addition, the syntheses of the unnatural endiandric acids E–G may help in the identification of these compounds in the natural system.

2.4.2. *Bisorbicillinoids*

The bisorbicillinoids (**103**–**109**) are a growing family of mycotoxins that are proposed to arise from a common biosynthetic precursor, sorbicillin (**110**, Scheme 21). The 2′,3′-dihydro derivative of biscorbicillinol (**104**), the first member of the bisvertinoquinol (**103**) class of compounds to be isolated, was postulated to be a Diels–Alder adduct of two different quinols derived from the the co-metabolites **110** and 2′,3′-dihydrosorbicillin through enantioselective oxidation of C5.[52] This route was postulated because the structure of **103** is consistent with a spontaneous *endo*-selective Diels–Alder reaction. However, the variations in the sorbyl and dehydrosorbyl side chains mean that four Diels–Alder adducts are possible. Only one optically active bisvertinoquinol-type product was observed in the cultures, which

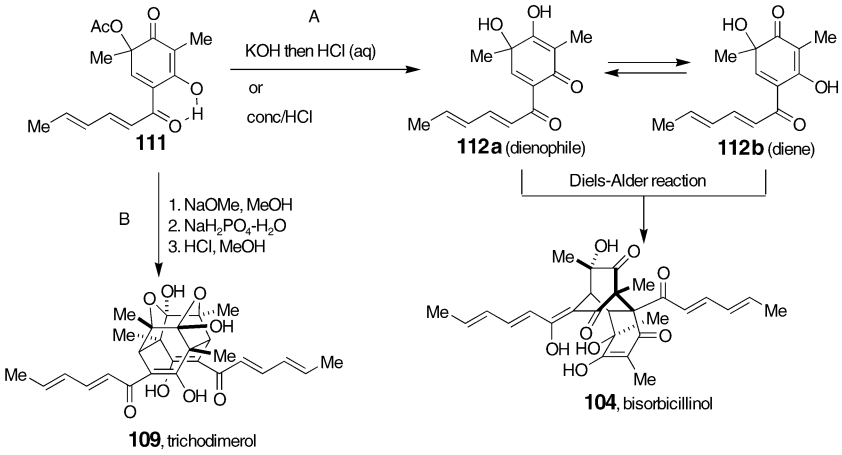
 © 2003 Wiley-VCH Verlag GmbH & Co. KGaA, Weinheim



Scheme 21. Biomimetic total syntheses of bisorbicillinol mycotoxins from the same precursor **110**.[55]

suggests that chain differentiation occurs after the Diels–Alder reaction and that **103** is not an artifact of isolation.

A similar biosynthetic Diels–Alder proposal has been made by Abe, Murata, and Hirota for bisorbicillinol (**104**), which could form bisorbutenolide (**105**) through an anionic casade reaction.[53] Sorbiquinol (**106**) has also been postulated to arise from a [4+2] cycloaddition. However, for **106**, the Diels–Alder reaction would occur between the C2′–C3′ double bond of the sorbicillin (**110**) side chain as the dienophile and enantioselectively oxidized sorbicillin as the diene.[54] Alternatively, the biosyntheses of bisorbicillinolide (**107**) and trichodimerol (**109**) can be rationalized as products of an oxidation-Michael-ketalization cascade.[55]



Scheme 22. Biomimetic total syntheses of bisorbicillinol (**104**) by Nicolaou et al. (Path A)[55a,b] and of trichlorodimerol (**109**) by Barnes–Seeman and Corey (Path B).[55c]

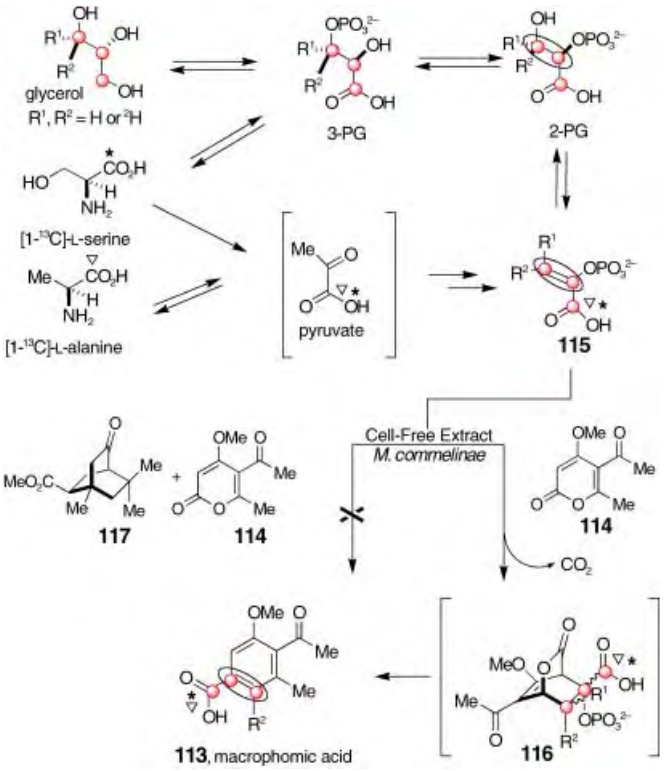
In support of the proposed biosynthetic pathways, two research groups independently and concomitantly completed the biomimetic total syntheses of bisorbicillinol (**104**) and trichodimerol (**109**, Scheme 22).[55] Nicolaou et al. reported that basic or acidic hydrolysis of the acetoxy functionality of **111** provided the quinols **112a** and **112b** which spontaneously formed the Diels–Alder cycloadduct **104** (path A in Scheme 22)[55a,b] Four stereogenic centers were created in the Diels–Alder reaction with complete regio- and diastereocontrol. Additionally, the quinol intermediate **112b** has recently been identified as a metabolite of the bisorbicillinoid producing fungus *Trichoderma* sp. USF-2690.[56]

Barnes–Seeman and Corey used the same acetoxydiene as the Nicolaou lab, but instead found that careful neutralization of the methoxide hydrolysis of **111** with NaH_2PO_4 (Path B in Scheme 22) followed by treatment with methanolic HCl provided trichodimerol (**109**) in 10% yield.[55c]

2.4.3. *Macrophomic Acid*

Macrophomic acid (**113**) is a fungal metabolite isolated from *Macrophoma commelinae*. Sakurai et al. established that macrophomic acid is derived from an unidentified C3 unit and the 2-pyrone **114** with loss of CO_2 and an unidentified C_3 unit.[57] Subsequent work on the biosynthesis of macrophomic acid revealed incorporation of [1-^{13}C]-L-alanine, [1-^{13}C]-L-serine, [U-^{13}C]glycerol, (1*RS*,2*S*)-[1-^{2}H]glycerol, and (1*RS*,2*R*)-[1-^{2}H]glycerol.[58] Based on these experiments, Oikawa et al. proposed the biosynthetic pathway outlined in Scheme 23 with phosphoenolpyruvate (**115**) as the C_3 unit. In practice, incubation of a cell-free extract of *M. commelinae* with **114** and **115** led to the enzymatic formation of **113**.[58]

The proposed biosynthetic pathway for macrophomic acid entails an inverse-electron-demand Diels–Alder reaction of **114** and the dienophile **115**. The intermediate **116** is transformed to **113** by successive retro-Diels–Alder reaction and *syn* elimination of phosphoric acid. To test this hypothesis, an analogue **117** of the putative bicyclic intermediate **116** was synthesized and incubated with the cell-free extract of



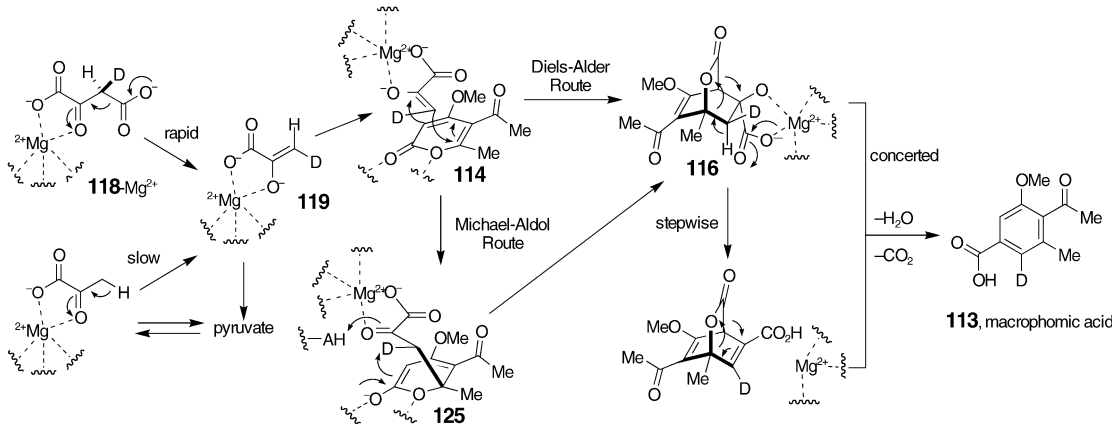
Scheme 23. Original biosynthetic proposal for macrophomic acid (**113**).[58] 3-PG = glycerin-3-phosphate.

M. commelinae, **114**, and **115**. The analogue **117** inhibited the formation of **113** (IC_{50} value 200 μM).[58]

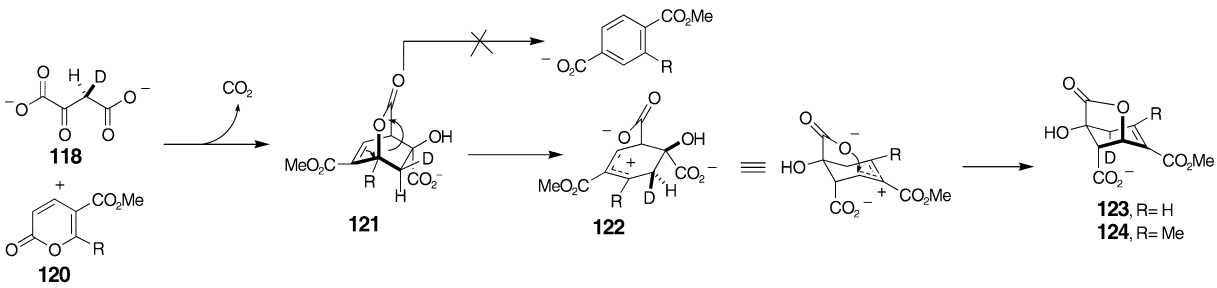
A recent re-examination of the origin of the C_3 unit led to the discovery that oxaloacetate (**118**) is a more efficient and direct precursor to **113**. The Mg^{2+}-dependent enzyme macrophomate synthase was isolated and purified by using oxaloacetate as the sole substrate for the C3 unit.[59,60] This single enzyme, a homodimer of a 36-kDa protein, was found to catalyze a five-step transformation involving two decarboxylations, two C–C bond-forming reactions, and a dehydration.[8]

Oikawa and co-workers speculate that the C3 unit might still be an enol pyruvate (**119**), the product of oxaloacetate decarboxylation. To test this, macrophomate synthase was incubated with **118** in the absence of **114** in a lactate dehydrogenase coupled assay.[8] Rapid formation of pyruvate was observed. However, in a competition experiment, **114** was found to inhibit the conversion of **118** into pyruvate. This observation indicates that the enzymatic product of oxaloacetate decarboxylation is not hydrolyzed and undergoes further reaction with **114** (Scheme 24).

Incubation of macrophomate synthase with oxaloacetate (**118**) and 2-pyrones lacking a C4 substituent, such as methyl coumalate (**120**), result in the formation of aberrant bicyclic compounds such as **123** and **124** (Scheme 25).[8,61] The location of the double bond and absence of an oxygen functionality at C5 suggests that the proposed intermediate **121** undergoes allylic rearrangement and subsequent re-lactonization. The aberrant cycloadduct **123** may be formed instead of the



Scheme 24. Revised proposal for the biosynthesis of **113**.[8]



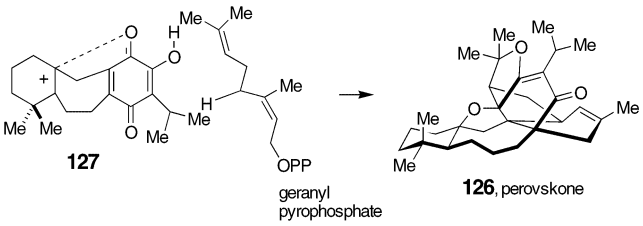
Scheme 25. Proposed mechanism for the formation of side products by a cycloaddition catalyzed by macrophomate synthase.[8]

 © 2003 Wiley-VCH Verlag GmbH & Co. KGaA, Weinheim

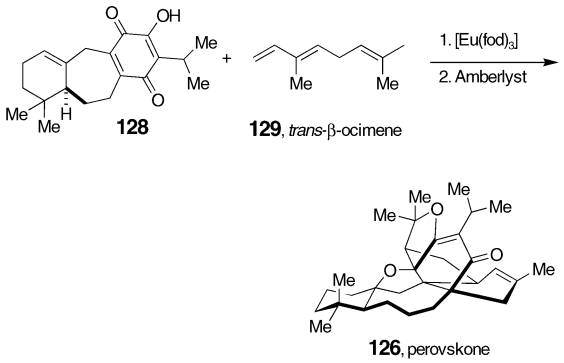
benzoate because the lack of a C4 substituent causes improper interaction between the catalytic residue and the elimination groups or because the C4 substituent interrupts attack of the carboxylate group on the carbocation. In either case, the driving force for the rearrangement is probably the release of steric strain of **121**. Deuterium labeling experiments revealed the pro-*R* position of adduct **124** is retained, which indicates that the first decarboxyation step provides the *Z* enolate.[8] The stereochemistry of the decarboxylation reaction is consistent with the known enzyme, phosphoenolpyruvate carboxylase.

Two possible routes, a stepwise Michael–aldol reaction or a concerted Diels–Alder reaction, can account for C–C bond formation by macrophomate synthase (Scheme 24).[8] In the Michael–aldol reaction, attack of the enolate on **114** would provide the first C–C bond and stabilize the negative charge on the 2-pyrone. Subsequently, the enolate could attack the newly formed carbonyl group to afford the bicyclic intermediate **116**. However, an intermediate in which only a single C–C bond has been formed, such as **125**, has not been observed for reactions catalyzed by macrophomate synthase. In the second case, a Diels–Alder cyclization may resemble an antibody-catalyzed Diels–Alder reaction. The bicyclic intermediate **116** in the macrophomate synthase catalyzed reaction could be stabilized by the groups used for recognition of the enolate and **114**.

Support for the Diels–Alder proposal was proffered from a known example of a [4+2] cycloaddition of a 2-pyrone and an equivalent of pyruvate enolate.[62] Oikawa and co-workers interpreted the high stereospecificity observed in aberrant cyclization products from the macrophomate synthase catalyzed cyclization as being consistent with a concerted mechanism. However, since the "normal" reaction products from the synthase are achiral, this is highly speculative. Nevertheless, more information will be needed to determine if the C–C bond-forming reactions of macrophomate synthase indeed arise from a concerted Diels–Alder reaction that is enzyme-mediated.



Scheme 26. Early biosynthetic proposal for perovskone (**126**).[63]



Scheme 27. Biomimetic total synthesis of perovskone (**126**).[64] fod = 1,1,1,2,2,3,3-heptafluoro-7,7-dimethyl-4,6-octandionate.

3. Isoprenoids

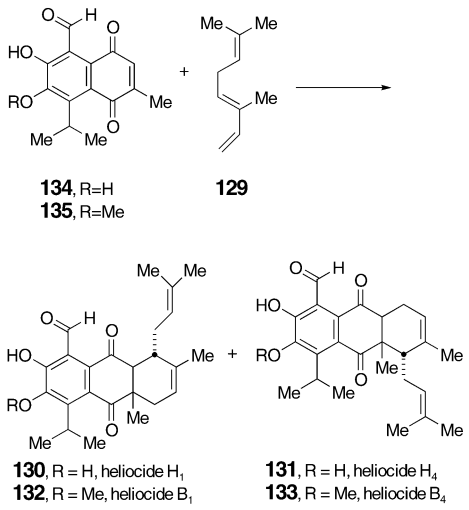
3.1. Derivatives of Myrcene and trans-β-Ocimene

3.1.1. Perovskone

The terpenes myrcene and *trans*-β-ocimene are often utilized as dienes in the construction of Diels–Alder-derived natural products. Perovskone (**126**) is a triterpene isolated from *Perovskia abrotanoides*. Initially, it was thought that **126** was constructed from an icetexone precursor **127** and geranyl pyrophosphate (Scheme 26).[63] A [4+2] cycloaddition route from **128** and *trans*-β-ocimene **129** was later proposed and this concept was used to complete a biomimetic total synthesis (Scheme 27).[64]

3.1.2. Heliocides

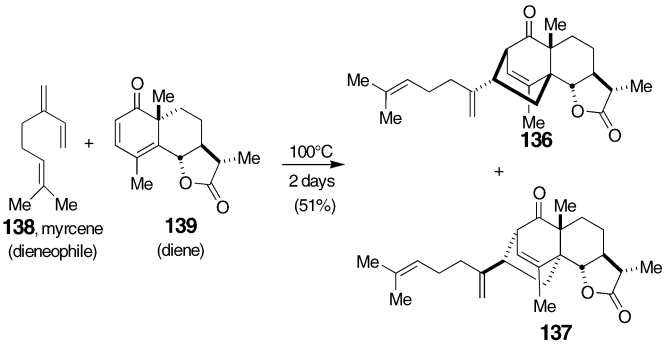
Heliocides H_1 (**130**), H_4 (**131**), B_1 (**132**), and B_4 (**133**) are proposed to be derived from *trans*-β-ocimene (**129**) and hemigossypolone (**134**) or its methyl ether derivative (**135**). Heliocides B_1 (**132**) and B_4 (**133**) were synthesized in a 3:1 ratio by a biomimetic [4+2] cycloaddition; this is the same ratio observed in the isolation of the natural products (Scheme 28).[65] While incorporation studies have not been reported, the biomimetic synthesis shown in Scheme 28 provides indirect, provocative evidence for the postulated biosynthesis.



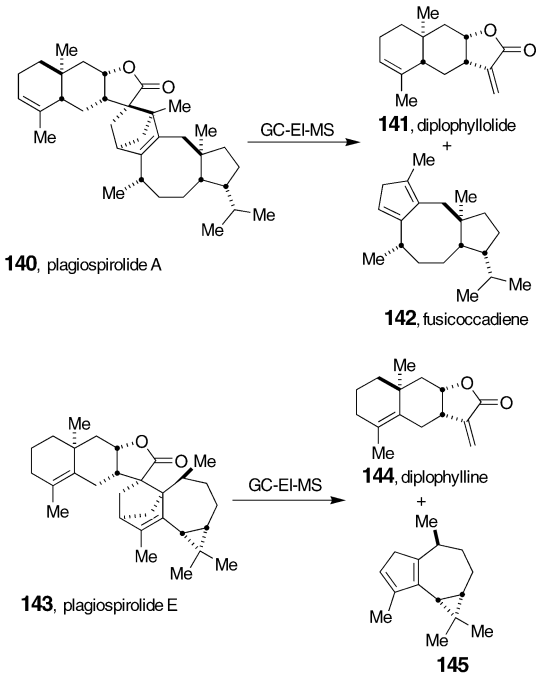
Scheme 28. Biomimetic synthesis of heliocides B_1 (**132**) and B_4 (**133**).[65]

3.1.3. Eudesmanolides

The eudesmanolides **136** and **137** were isolated from the aerial parts of *Artemisia herba-alba*.[66] They are formally derived through an inverse-electron-demand Diels–Alder reaction between myrcene (**138**) as the dienophile and **139** as the dieneone. The synthesis of **136** and **137** was accomplished in a 1:1 ratio by heating **138** and **139** to 100 °C (Scheme 29). Since the conditions required for the synthesis of **136** and **137** are so harsh, it is unlikely that they are artifacts of isolation.



Scheme 29. Biomimetic synthesis of eudesmanolide adducts **136** and **137**.[66]



Scheme 30. Retro-Diels–Alder fragmentation of plagiospirolide A (**140**) and plagiospirolide E (**143**).[67,68]

3.2. α-exo-Methylene-γ-lactones

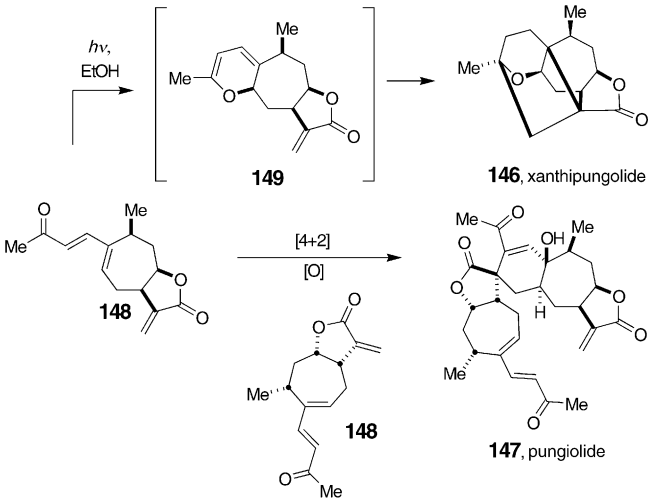
3.2.1. Plagiospirolides

GC-EIMS analysis was carried out on plagiospirolide A (**140**) to enable the structures of the spiroterpenoids isolated from the Panamanian liverwort *Plagiochila moritziana* to be determined. Diplophyllolide (**141**) and fusicoccadiene (**142**) were detected, possibly resulting from a retro-Diels–Alder reaction, and both substances were isolated from extracts of *Plagiochila moritziana*.[67] Further isolations of *Plagiochila moritziana* provided plagiospirolide E (**143**). Again, GC-EIMS provided potential retro-Diels–Alder products—diplophylline (**144**) isolated from *Plagiochila moritziana* and the diene (**145**, Scheme 30).[68]

Since a synthetic Diels–Alder route to the related triterpenes from *Helenium autumnale* required harsh conditions and gave low yields of a mixture of isomers,[69] it is unlikely that **140** is an artifact of isolation. In addition, since no other diastereomers of **140** were found in *P. moritizana* cultures, it is possible that the putative biosynthetic Diels–Alder reaction is enzymatic.

3.2.2. Xanthipungliolide, Pungiolide, and Others

Besides the plagiospirolides, there are a number of putative Diels–Alder adducts derived from α-*exo*-methylene-γ-lactones. The species *Xanthium pungens* produces both xanthipungolide (**146**) and pungiolide (**147**).[70] Both substances were proposed to be biosynthetic derivatives of xanthanolide **148** (Scheme 31). It was proposed that an electrocyclic reaction of **148** forms **149** which is then followed by an intramolecular Diels–Alder reaction in the biogenesis of **146**. This proposal was supported by the synthesis of **146** from **148**, accomplished by irradiation of **148** in ethanol. The biosynthesis of the dimer **147** is thought to arise from an intermolecular Diels–Alder reaction of **148** followed by an oxidation.

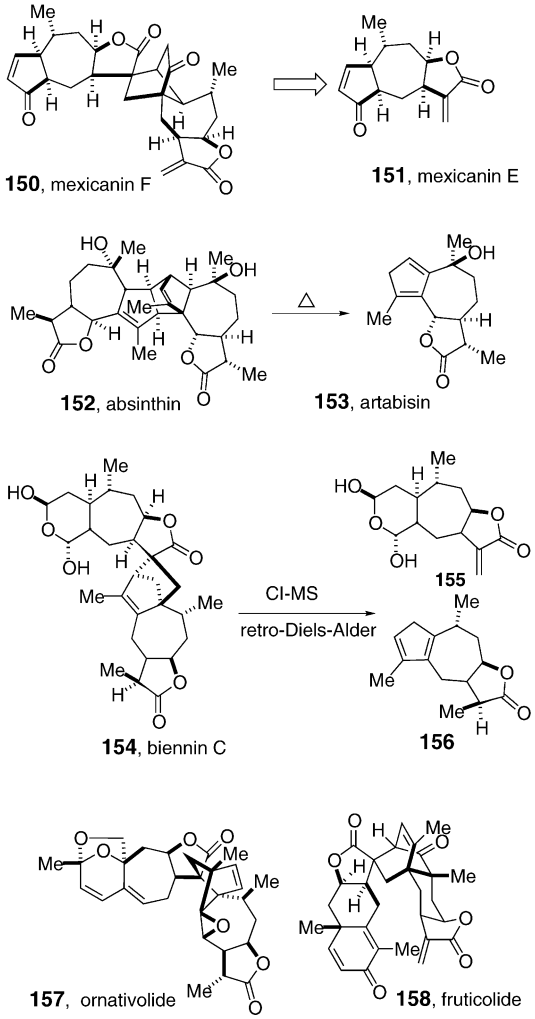


Scheme 31. Proposed biosynthesis of xanthipungolide (**146**) and pungiolide (**147**).[70]

Mexicanin F (**150**), from *Helenium mexicanin*, is thought to arise from the co-metabolite mexicanin E (**151**).[71] Heating the dimeric sesquiterpene lactone absinthin (**152**) gives the

 © 2003 Wiley-VCH Verlag GmbH & Co. KGaA, Weinheim

monomer artabisin (**153**).[72] From its fragmentation pattern in the CI mass spectrum, the biogenesis of biennin C (**154**) was proposed to occur from an intermolecular cycloaddition of the monomers **155** and **156**.[73] Ornativolide A (**157**)[74] and fruticolide (**158**)[75] could also be [4+2] cycloadducts derived from α-*exo*-methylene-γ-lactones (Scheme 32).

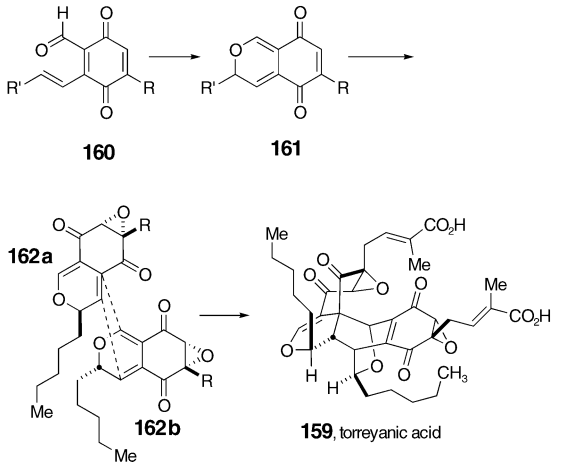


Scheme 32. Diels-Alder cycloadducts derived from α-*exo*-methylene-γ-lactones.[71–75]

3.3. Homodimer Terpenoids

3.3.1. Torreyanic Acid

Torreyanic acid (**159**) is a cytotoxin isolated from the endophytic fungus *Pestalotiopsis microspora*.[76] This substance possesses an unusual dimeric quinone structure that was postulated to arise from a Diels–Alder cycloaddition of two diastereomeric monomers. A proposed biosynthetic pathway might involve the following: a) electrocyclic ring closure of achiral **160** to form racemic **161**; b) enzymatic oxidation to generate the diastereomers **162a** and **162b**; and c) a [4+2] cycloaddition to produce **159** (Scheme 33). A

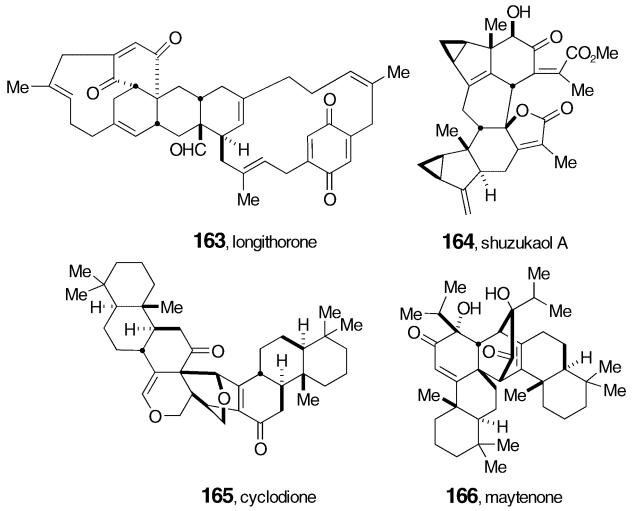


Scheme 33. Proposed biosynthesis of torreyanic acid (**159**).[76] R = $CH_2CH{=}C(CH_3)COOH$, R′ = C_5H_{11}.

biomimetic total synthesis of **159** was recently completed, which employed the [4+2] dimerization of diastereomeric monomers.[77]

3.3.2. Longithorone and Other Homodimer Terpenoids

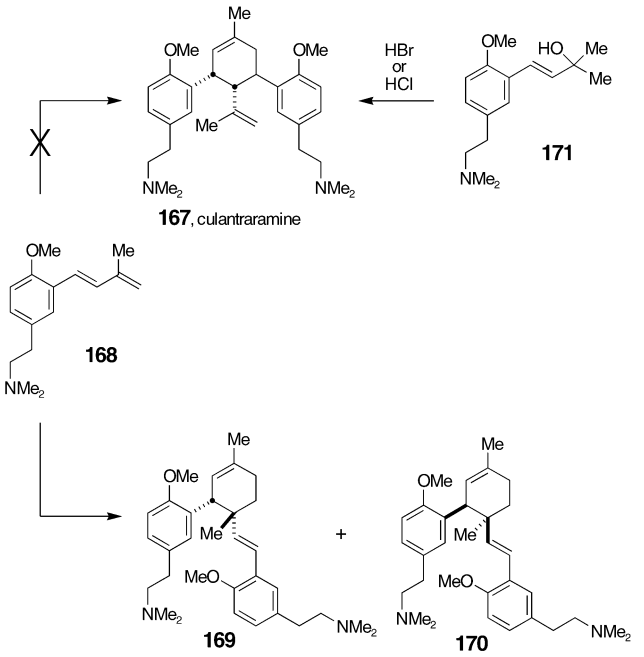
There are a number of examples of terpenoid homodimers that might arise through a [4+2] cycloaddition. A recent example of a Diels–Alder-cyclized quinone dimer is longithorone (**163**), isolated from a marine tunicate.[78] Other examples include shizukaol A (**164**),[79] cyclodione (**165**),[80] and maytenone (**166**; Scheme 34).[81]



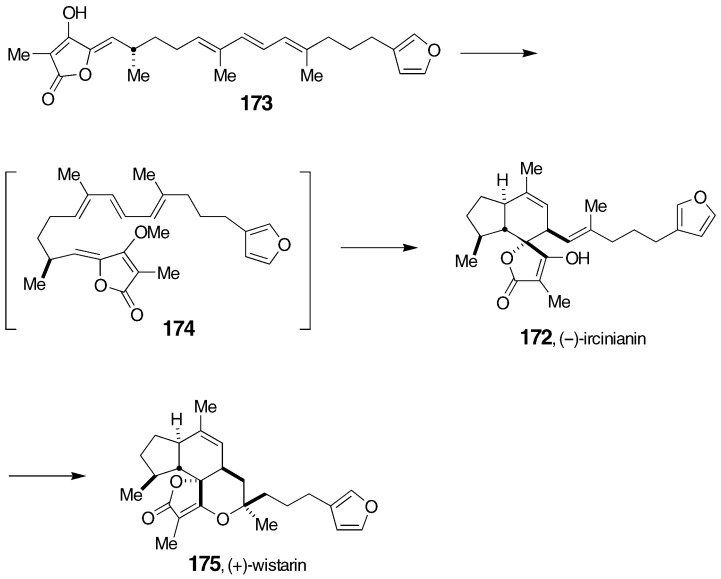
Scheme 34. Homodimeric terpenes as possible Diels–Alder cycloadducts.[78–81]

3.3.3. Culantraramine

Caution needs to be taken when considering the biosynthesis of these dimers; for example, culantraramine (**167**) could be considered as a natural Diels–Alder cycloadduct.[82] However, when the proposed precursor **168** was allowed to



Scheme 35. Biosynthetic studies on culantraramine (**167**).[82]



Scheme 36. Proposed biosynthesis of ircinianin (**172**) and wistarin (**175**).[85]

stand in xylene at room temperature for 10 days, the cycloadducts **169** and **170** were obtained, not the natural product **167** (Scheme 35). On the other hand, when **171** was treated with acid, the product **167** was formed at room temperature within 30 minutes. Thus, it seems that the biosynthesis of **167** does not occur though a "true" Diels–Alder cyclization, but perhaps through a nonsynchronous cation–diene [4+2] cycloaddition.

3.4. Other Isoprenoids

3.4.1. Ircinianin and Wistarin

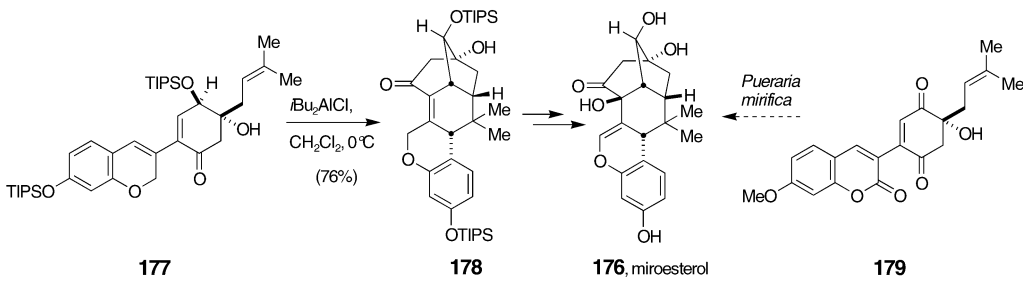
Ircinianin (**172**) is a sesterterpene isolated from the marine sponge *Ircinia wistarii*. It was postulated to arise from a [4+2] cycloaddition of the linear tetraene (**173**).[83] Both the racemate and the (−) isomer of **172** have been synthesized utilizing this approach.[84] Wistarin (**175**) is a tetracyclic isomer of tricyclic **172**. Interestingly, both the (+) and (−) isomers of **175** have been isolated, but only one enantiomer of **172** has been isolated (Scheme 36).[85] This observation could be considered as evidence that the formation of **175** is mediated by enzyme catalysis.

3.4.2. Miroesterol

Miroesterol (**176**) is an estrogenic phenol isolated from the Thai medicinal plant *Pueraria mirifi*ca. A key step in the first total synthesis of this compound by Corey and Wu was the Lewis acid catalyzed cyclization of the tricyclic ketone **177** to form **178** (Scheme 37).[86] This reaction can be regarded as a transannular double cation-olefin cyclization or as a Lewis acid catalyzed, inverse-electron-demand intramolecular Diels–Alder reaction. Interestingly, during the course of the total synthesis of **176**, approximately 1 mg of **179** was also isolated from extracts of *P. mirifi*ca. It is thus possible that **179** is a biosynthetic precursor to **176**, in which case **176** may arise through an inverse-electron-demand Diels–Alder cycloaddition.

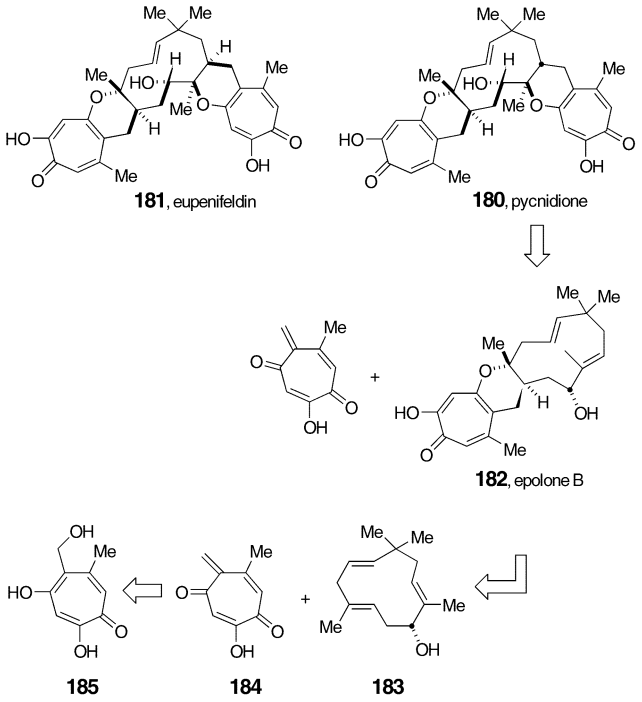
3.4.3. Pycnidione and Others

Pycnidione (**180**),[87] eupenifeldin (**181**),[88] and epolone B (**182**)[89] are a group of recently isolated fungal metabolites that possess identical tropolone rings attached to a sesqui-



Scheme 37. Key step in the total synthesis of miroesterol (**176**).[86] TIPS = triisopropylsilyl.

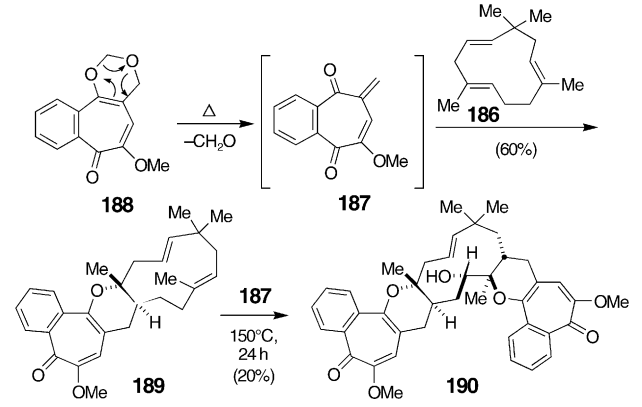
 © 2003 Wiley-VCH Verlag GmbH & Co. KGaA, Weinheim



Scheme 38. Proposed biosynthesis of epolone B (**182**) and pycnidione (**180**).[90]

terpene backbone. Biosynthetically, these compounds are proposed to arise from a hetero-Diels–Alder reaction of the C11-hydroxylated humulene **183** and quinone methide tropolone **184** (Scheme 38). The quinone methide **184** may in turn be generated by dehydration of the trihydroxy species **185**. Cai et al. suggested epolone B (**182**) might be a biosynthetic precursor to pycnidione (**180**) through a second hetero-Diels–Alder reaction.[89]

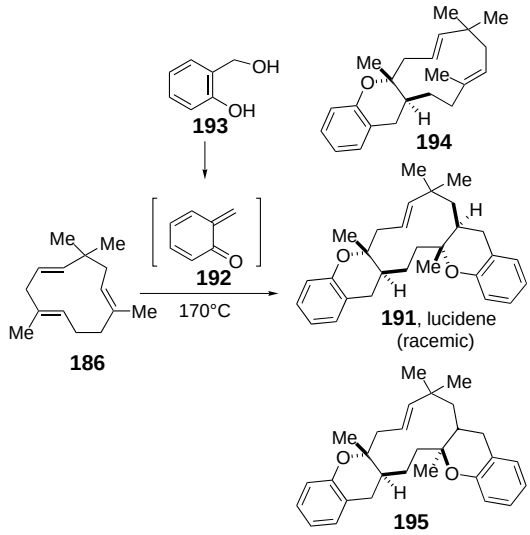
To test this hypothesis, a model study was performed using humulene (**186**) and the benzotropolone **187** (Scheme 39). The benzotropolone **187** was formed from a thermal retro-Diels–Alder reaction of **188**.[90] In situ trapping with humulene (**186**) afforded the Diels–Alder cycloadduct **189**, which is analogous to epolone B (**182**). Addition of an excess of **187** at 150 °C gave **190** as a 1:1 mixture of diastereomers. Since the



Scheme 39. Biomimetic synthesis of an analogue of epolone B **189**[90] and the pycnidione **190**.

naturally occurring Diels–Alder cycloadducts **180**–**182** are enantiomerically pure, there is a possibility that the addition of the tropolone is enzymatically catalyzed in the natural system.

A structurally similar compound, lucidene (**191**), has been isolated in racemic form from the root bark of *Uraria lucida*.[91] It has been proposed as the product of a double [4+2] cycloaddition of *o*-benzoquinone methide (**192**) and α-humulene (**186**), which is also a co-metabolite. A biomimetic synthesis provided the natural product **191** as well as the monoadduct **194** and isolucidene (**195**).[92] Unlike compounds **180**–**182**, lucidene (**191**) is not optically active, thus it most likely arises from a non-enzymatic Diels–Alder reaction (Scheme 40).



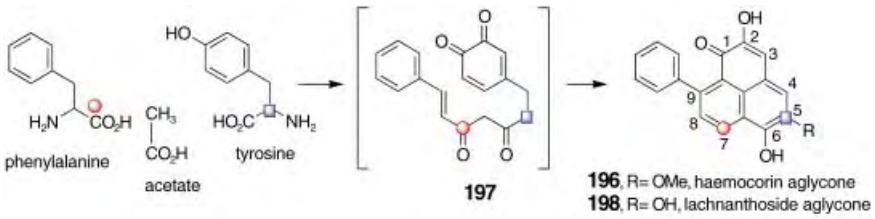
Scheme 40. Biomimetic total synthesis of lucidene (**191**).[92]

4. Phenylpropanoids

4.1. Intramolecular Cycloadducts

4.1.1. Phenylphenalenones

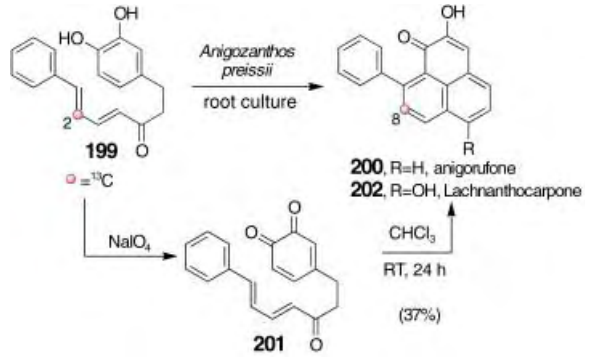
Phenylphenalenones are characteristic pigments found in the monocotyledon family *Tinctoria*. An early study on the biosynthesis of these compounds indicated that [2-^{14}C]tyrosine was incorporated specifically at C5 of the haemocorin aglycone (**196**).[93] A biosynthetic pathway was proposed (Scheme 41) that involves condensation of one molecule each of phenylalanine and tyrosine (or the metabolic equivalent) with one molecule of acetic acid and loss of a carboxy group to provide a diarylheptanoid intermediate **197**. This intermediate could then cyclize, possibly through a Diels–Alder cycloaddition, to provide the phenylphenalenone ring system. Further evidence for this pathway was the specific incorporation of [1-^{13}C]phenylalanine at C7 of the lachnanthoside aglycone (**198**).[94] Although phenylalanine and tyrosine were found to be precursors to the phenylphenalenones, other shikimate-derived phenylpropanoids, such as cinnamic



Scheme 41. Proposed biosynthesis of the phenylphenalenones.[97]

acid and coumaric acid, have also been determined to be precursors.[95,96]

It was not until 1995 that experimental evidence for the intermediacy of a diarylheptanoid in phenylphenalenone biosynthesis was obtained. Höschler and Schneider showed that the Diels–Alder precursor **199** was specifically incorporated into anigorufone (**200**) from feeding experiments with the cultured roots of *Anigozanthos preissii* (Scheme 42).[96] An earlier synthetic study showed that after oxidation with



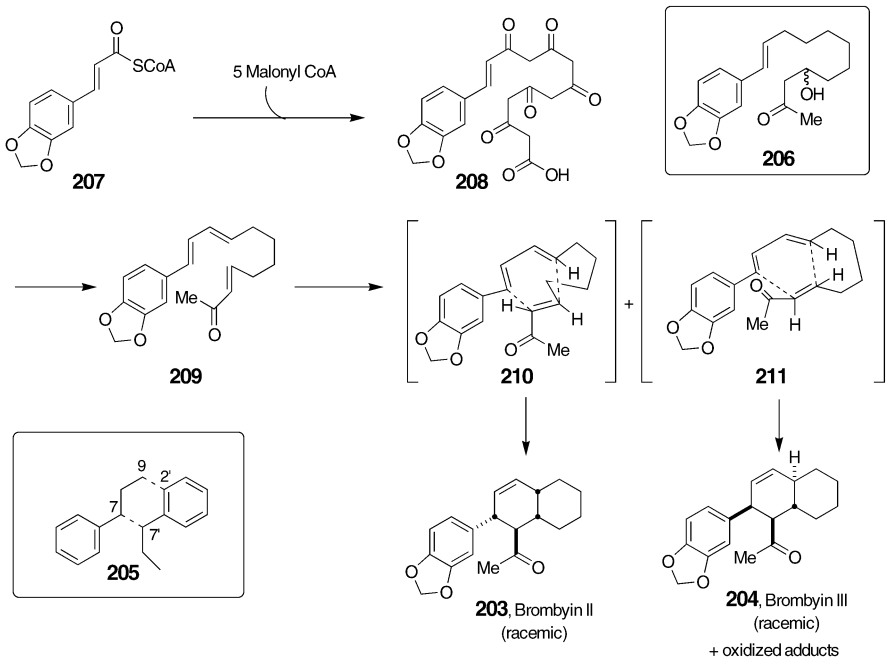
Scheme 42. Synthesis and biosynthesis of phenylphenalenones **200** and **202**.[96,97]

$NaIO_4$, unlabeled **199** was converted into lachnanthocarpone (**202**) spontaneously at room temperature through an intramolecular Diels–Alder cycloaddition.[97] Thus, the Diels–Alder cyclization leading to the phenylphenalenone ring system appears to be nonenzymatic.

4.1.2. Brombyins

The brombyins are novel decalin derivatives from the Australian tree *Brombya platynema* which are produced in nature in racemic form.[98] Although the metabolites **203** and **204** could be biogenetically derived from the oxidative coupling of two cinnamic acid residues (the 9-2′-, 7-7′-positions in **205**, Scheme 43), this seems unlikely because of the perhydrogenated nature of one of the six-membered rings and the lack of optical activity of the natural products.

Instead, the isolation of the intermediate **206** led to the hypothesis of the linkage of a single C_6C_3 moiety **207** with an acetate chain to give an intermediate such as **208** (Scheme 43). A spontaneous intramolecular Diels–Alder cyclization of intermediate **209** could lead to two racemic products corresponding to **203** and **204**.



Scheme 43. Proposed biosynthesis of the brombyins.[98]

4.2. Intermolecular Dimeric Cycloadducts

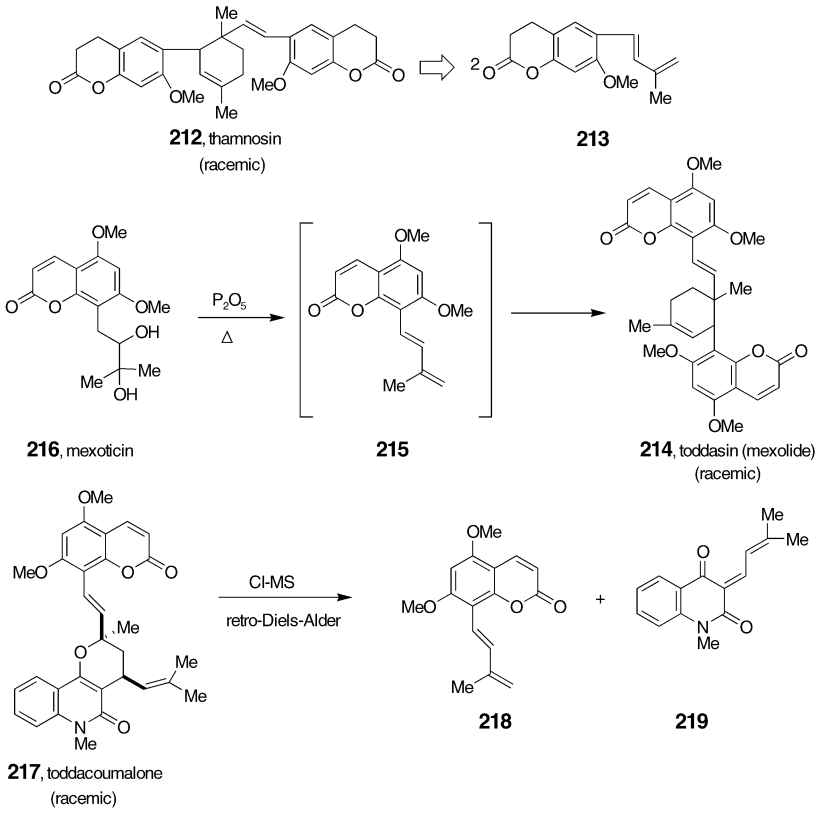
4.2.1. Dimeric Coumarins

Another group of phenylpropanoid Diels–Alder adducts is represented by the dimeric coumarins (Scheme 44). The first dicoumarin discovered, thamnosin (**212**), was postulated to arise from the Diels–Alder cycloaddition of two molecules of the monomer **213**.[99] Later, the dicoumarin toddasin (**214**, mexolide) was isolated from two different sources, *Toddalia asiatica* and *Murraya exotic*a.[100,101] EI mass spectrometry of **214** led to the formation of the retro-Diels–Alder fragment **215**.[100] Treatment of mexoticin (**216**), a co-metabolite of **214** in *Murraya exotica*, with P_2O_5 in refluxing xylenes led to the formation of **214**, presumably through the dehydration product **215**.[101] Toddacoumalone (**217**) was the first example of a mixed coumarin dimer. The CI mass spectrum of **217** showed the presence of protonated ions corresponding to the coumarin **218** and the quinolone **219**.[102]

4.2.2. Kuwanon J and Chalcomoracin

Other phenylpropanoids that are reportedly derived from a biological Diels–Alder cyclization are the metabolites kuwanon J (**220**) and chalcomoracin (**221**) from *Morus alba* L. Selection of callus cultures from *Morus alba* that

 © 2003 Wiley-VCH Verlag GmbH & Co. KGaA, Weinheim



Scheme 44. Diels–Alder cycloaddition to give the coumarin dimers and their fragmentation through a retro-Diels–Alder reaction.[99–102]

efficiently produce Diels–Alder-type adducts (ca. 100 times more of **220** and **221** than the intact plant) allowed biosynthetic studies to be performed on these compounds.[103] Feeding experiments with [1-^{13}C]-, [2-^{13}C]-, and [1,2-$^{13}C_2$]acetate revealed that **220** and **221** are formed from the condensation of two cinnamoylpolyketide-derived skeletons **222** (see Scheme 45).

The arylbenzofuran skeleton of **220** is apparently formed from a novel type of cyclization of the cinnamoylpolyketide **222** followed by decarboxylation to give **223**.[103] Interestingly, [1-^{13}C]-, [2-^{13}C]-, and [1,2-^{13}C]acetate were not incorporated into the prenyl groups of **220** and **221**, thus indicating that the isoprene groups are not derived through the usual mevalonate pathway.[103,104] Incorporation of [3-^{13}C]-L-phenylalanine and [3-^{13}C]-L-tyrosine into both halves of **220** and **221** suggests a common biosynthetic route to the cinnamoylpolyketide skeleton via *p*-coumarate.[105]

Addition of the *O*-methylated chalcone **229** to *Morus alba* cell cultures resulted in the formation of **230** as well as the *O*-methyl derivatives of kuwanon J (**231**) and chalcomoracin (**232**).[106] The structure of **230** indicates that prenylation occurs after aromatization of the cinnamoyl polyketide. Subsequent addition of **230** to *M. alba* cell cultures resulted in the formation of **231** and **232.** This result strongly suggests that, in the natural system, one molecule of the prenylated chalcone is recognized as the dienophile (**225**) while another prenylated chalcone, after dehydrogenation, acts as the diene (**226** or **228**). Compounds **231** and **232** are optically active and possess the same configuration as **220** and **221**, which suggests that the condensation reaction between these partners is enzymatic.[106] Close examination of the Diels–Alder-type adducts after [2-^{13}C]acetate feeding experiments with *M. alba* revealed that the adducts kuwanon V (**233**) and mulberrofuran (**234**) had a higher enrichment factor (24 and 22%, respectively) than either **220** or **221** (4 and 17%, respectively).[107] This result suggests that **220** and **221** are formed by hydroxylation of **233** and **234**.

Biotransformation experiments with *M. alba* cell cultures were also used to determine the structure of the Diels–Alder adduct artonin (**235**, Scheme 46).[108] Since **235** is only a minor metabolite from the root bark of *Artocarpus heterophyllus* (0.7 mg), structure determination was difficult. The co-occurrence of artocarpesin (**236**) in the same plant led to the proposed biogenesis and structure shown in Scheme 46. To confirm this proposal, **236** was added to a *M. alba* cell culture. Work-up provided an aberrant metabolite (8 mg, 3.5×10^{-6}%) that had an identical mass and ^{1}H NMR spectrum as **235**. These results indicate that in *M. alba* cultures, **236** reacted as a diene and **237**, which is produced in the cells, acted as a dienophile in the formation of the putative cycloadduct.

4.2.3. Asatone

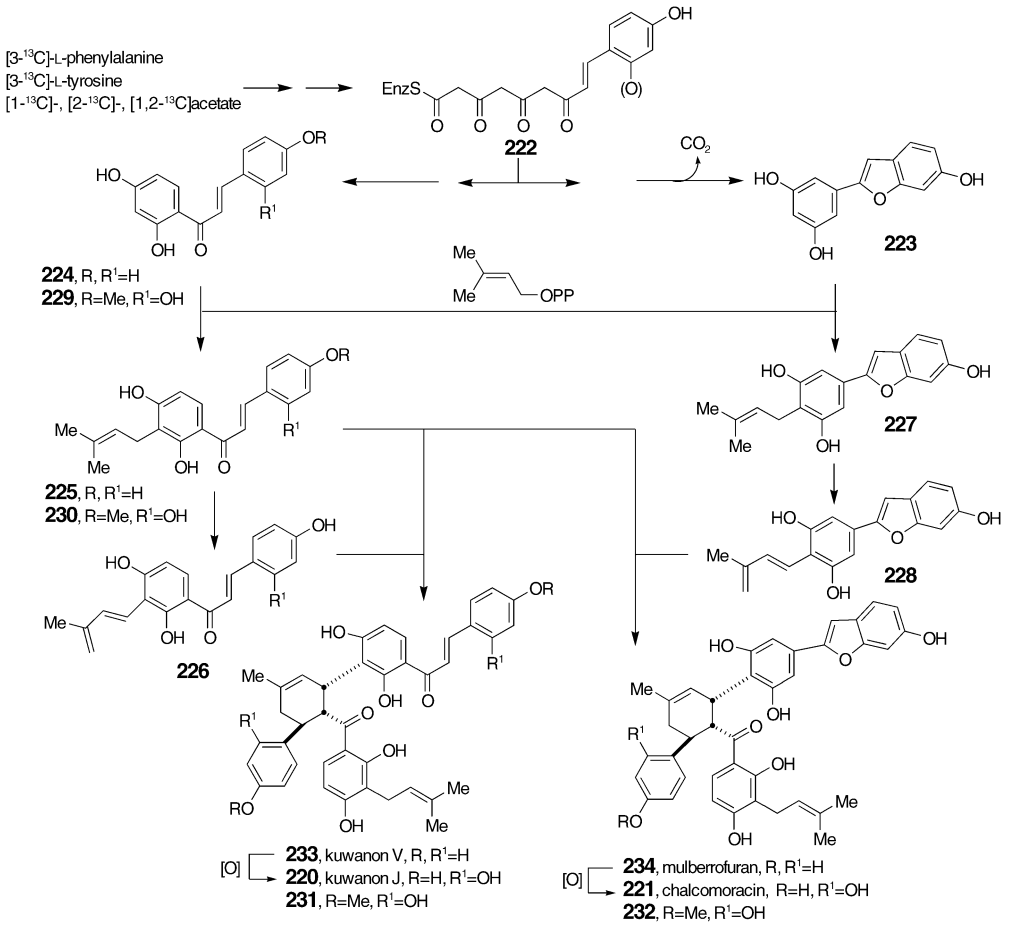
Asatone (**238**) is a neolignan isolated from the stems and rhizomes of *Asarum teitonese* Hayata.[109] The base peak in the mass spectrum of **238** was observed at half the molecular weight, which is consistent with a retro-Diels–Alder fragmentation. The skeleton of **238** is comprised of two C_6C_3 units, which biosynthetically can be envisioned as enzymatically oxidized 4-allyl-2,6-dimethoxyphenol (**239**, Scheme 47). The optically inactive dienone **240** can then dimerize to provide **238** through an intermolecular Diels–Alder reaction. In fact, anodic oxidation of **239** in methanol provided a mixture of **240** and **238**. **240** was quantitatively converted into asatone (**238**) upon standing at room temperature.[110] The related lignans heterotropatrione (**241**) and isoheterotropatrione (**242**) were postulated to be the Diels–Alder adducts of **238** and **240**.[111]

5. Alkaloids

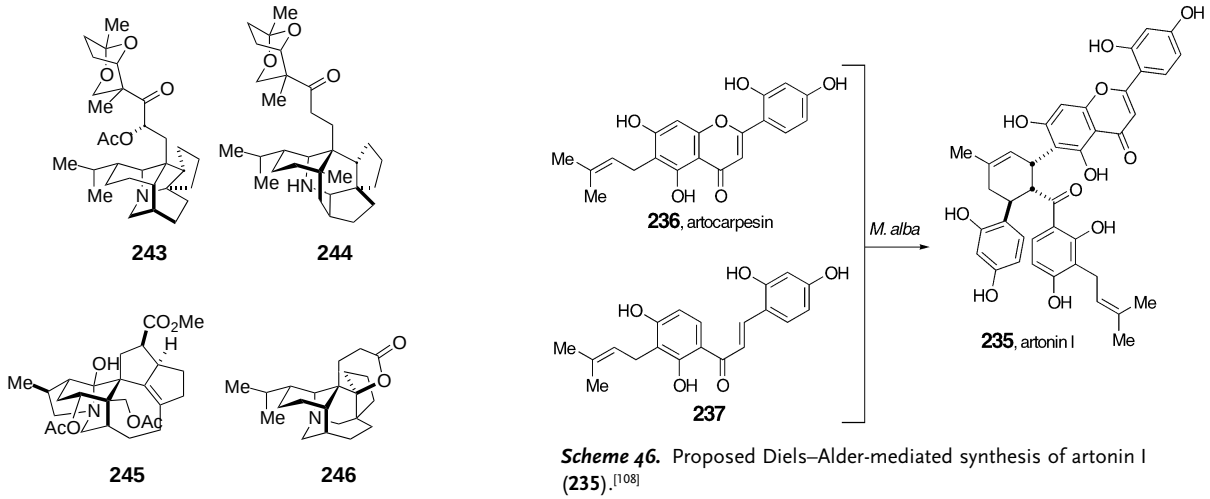
5.1. Daphniphyllum Alkaloids

The daphniphylline alkaloids are a growing class of polycyclic natural products that were first isolated in 1909 from the deciduous tree Yuzurha (*Daphniphyllum macropodum*). The four different skeletal classes of daphniphylline alkaloids are represented by daphnipylline (**243**), secodaphniphylline (**244**), yuzurimine (**245**), and daphnilactone A

 © 2003 Wiley-VCH Verlag GmbH & Co. KGaA, Weinheim



Scheme 45. Proposed biosynthesis of kuwanon J (**220**) and chalcomoracin (**221**).[106]

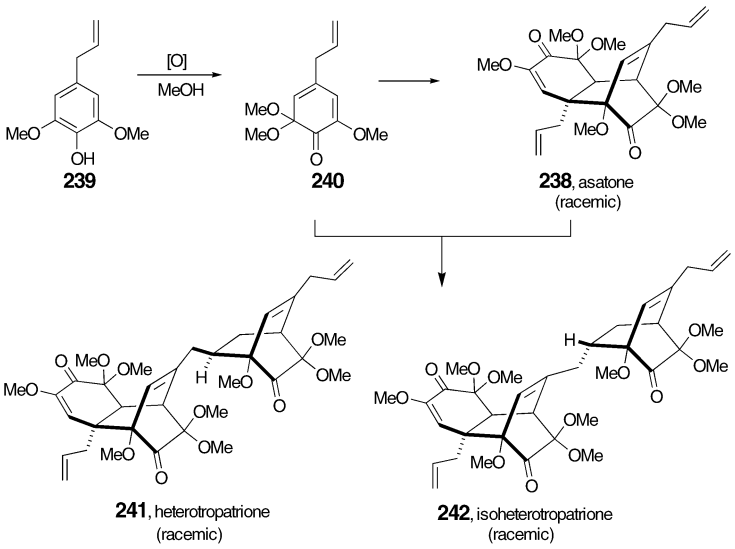


Scheme 46. Proposed Diels–Alder-mediated synthesis of artonin I (**235**).[108]

(**246**). Early work on the biosynthesis of daphniphylline (**243**) established its mevalonate origin via a squalene-like intermediate.[112] Later, Ruggeri and Heathcock devised a biosynthetic proposal for the construction of the complex polycyclic ring systems of the daphniphyllum alkaloids through a hetero-Diels–Alder cyclization (see Scheme 48).[113,114]

They proposed that the squalene-derived dialdehyde **247** might condense with pyridoxamine to provide the azadiene **248**. A prototropic shift in **248** would give **249**, which upon nucleophilic addition of an amine (possibly from lysine) would furnish the enamine **250**. An intramolecular enamine/enal cyclization of **250** would afford a bicyclic dihydropyran dervative **251**. A process of proton-mediated addition and elimination would then provide the dihydropyridine derivative **255**. A catalyzed intramolecular hetero-Diels–Alder reaction of **255** would give the tetrahydropyridine **256**.

 © 2003 Wiley-VCH Verlag GmbH & Co. KGaA, Weinheim



Scheme 47. Biosynthesis of asatone (**238**) and the heterotropatriones **241** and **242**.[110,111]

Subsequent enelike cyclization of **256** would give the pentacyclic compound proto-daphniphylline (**257**), a proposed precursor to daphniphylline.

To explore the proposed biosynthesis, Heathcock et al. completed a biomimetic total synthesis of **257** (see Scheme 49).[115] The synthesis utilizes a one-pot procedure that was also used to synthesize five daphniphyllum alkaloids.[115,116] Oxidation of the 1,5-diol **258** to the dialdehyde **259** was accomplished through a Swern oxidation. The crude reaction mixture was treated with ammonia followed by acetic acid and ammonium acetate to provide the azadiene **261**. An intramolecular Diels–Alder reaction furnished the imine **256**. Heating the acetic acid solution of the imine then facilitated an intramolecular aza–Prins cyclization and gave **257**.

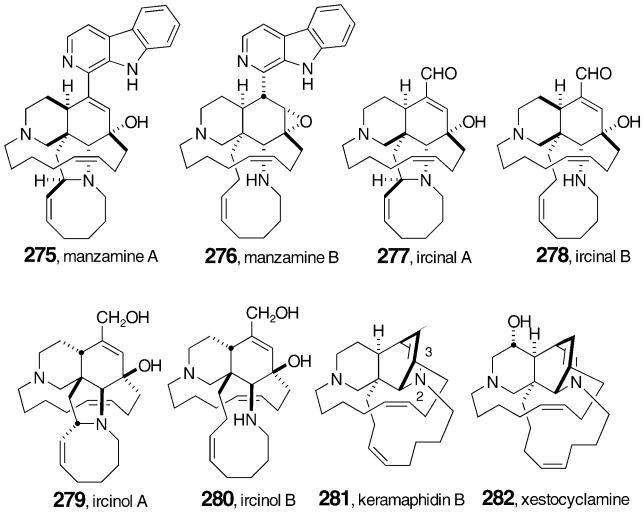
5.2. Indole Alkaloids

5.2.1. Iboga/Aspidosperma Alkaloids

The iboga and aspidosperma alkaloids are perhaps the most well-known examples of natural products potentially arising from a biosynthetic Diels–Alder reaction, and yet there is still no definitive proof for this biosynthetic pathway. By 1970, Scott had elucidated a significant portion of the biosynthetic pathway through hydroponic feeding experiments with *Vinca rosea* shoots.[117] These results along with chronological isolation studies led to the proposed biosynthetic pathway outlined in Scheme 50. The intermediacy of **271** was invoked to explain the incorporation of stemmadenine (**272**) into both catharanthine (**273**, iboga skeleton) and into vindoline (**274**, aspidosperma skeleton). Scott proposed that heterolytic ring opening and concomitant dehydration of stemmadenine (**272**) would lead to the formation of dehydrosecodine (**271**), which could undergo two possible [4+2] cycloadditions. If the 2-dihydropyridine system of **271** behaved as a dienophile, then **274** would be produced. If, on the other hand, the 2-dihydropyridine ring of **271** reacted as a diene, then **273** would be formed. However, with the exception of biomimetic syntheses,[118] no direct biosynthetic evidence for this provocative postulate has been obtained.

5.2.2. Manzamine Alkaloids

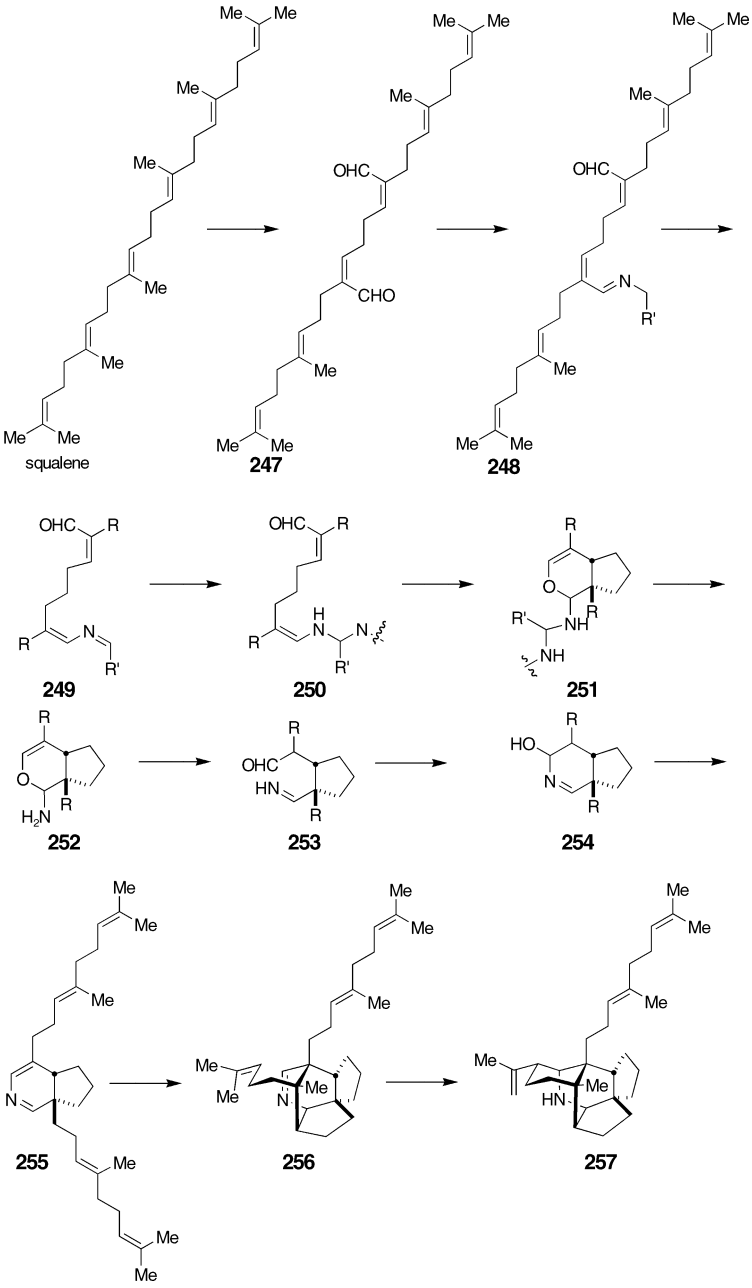
The manzamines are a growing group of cytotoxic marine sponge alkaloids that possess unusual polycyclic diamine skeletons. Among this group are manzamine A (**275**) and B (**276**),[119] ircinal A (**277**) and B (**278**),[120] ircinol A (**279**) and B



(**280**),[121] keramaphidin B (**281**),[122] xestocyclamine (**282**),[123] and ingenamine.[124] The ircinals **277** and **278** were proposed to be biosynthetic precursors to the manzamines **275** and **276**.[120] In fact, **277** was chemically transformed to **275** through a Pictet–Spengler cyclization with tryptamine and subsequent oxidation with 2,3-dichloro-5,6-dicyano-1,4-benzoquinone (DDQ).[120] Ircinols **279** and **280** are antipodes of the alcoholic forms of **277** and **278** and represent the first alkaloids in this class of compounds to possess the opposite absolute configuration to that of the manzamines.[119] Keramaphidin B (**281**) was also postulated as a manzamine biosynthetic precursor through formation of an ircinal from hydrolysis the N2–C3 bond of the imino form of **281**.[122]

In 1992, Baldwin and Whitehead outlined an elegant unified biogenesis for the manzamines (Scheme 51).[125] Manzamine B (**276**) was envisioned to be derived from four building blocks: ammonia, the C_{10} unit **283**, a C_3 unit (acrolein), and tryptophan. The key step for the proposed biogenesis was an intramolecular *endo*-Diels–Alder cycloaddition of a partially reduced bispyridinium species (**284**→**285**→**286**). The intermediacy of **284** was supported by the isolation of the bispyridinium macrocycles cyclostellettamines A–F from the marine sponge *Stelletta maxima*.[126] Later, Baldwin et al. expanded their biosynthetic proposal to include **281**.[127]

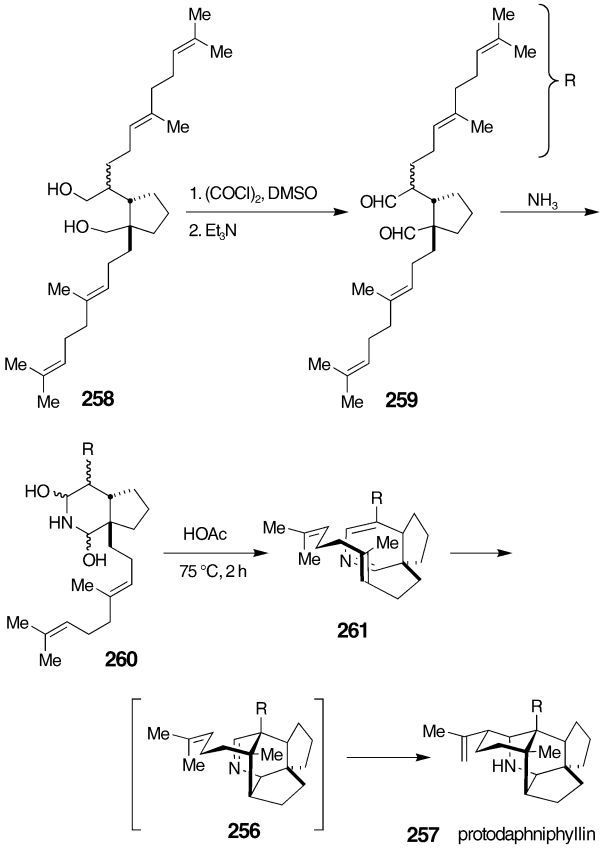
Baldwin, et al., completed a biomimetic total synthesis of keramaphidin B (**281**) by dissolving the proposed intermediate **284** in a methanol/Tris buffer solution followed by



Scheme 48. Proposed biosynthesis of the daphniphyllum alkaloids.[113,114]

reduction with $NaBH_4$ to provide a small amount of **281** (Tris = tris(hydroxymethyl)aminomethane).[128] The low yield of **281** was rationalized as a reflection of the inclination of intermediate **285** to disproportionate. The researchers further argued that in vivo, a Diels–Alderase could limit the conformational mobility of the substrate, which would not only minimize the change in entropy toward the transition state but would also obviate the intrinsic problem of disproportionation.

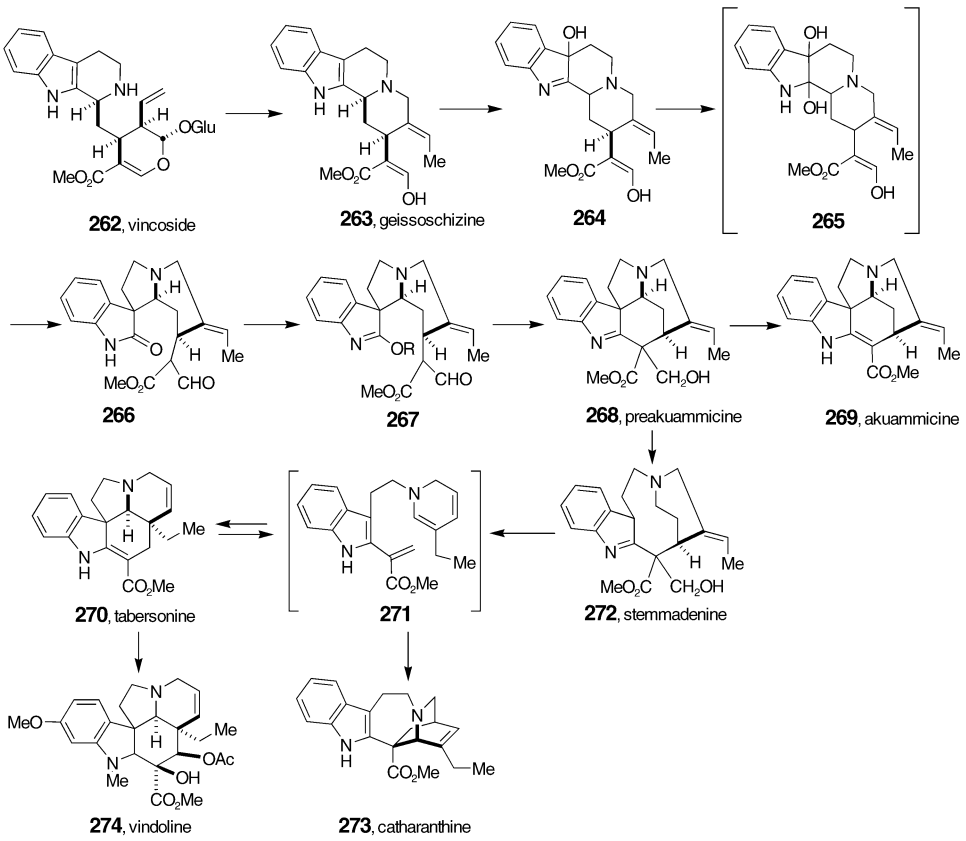
Marazano and co-workers proposed an alternate route for the biosynthesis of the manzamines in 1998.[129] They suggested that the biosynthetic Diels–Alder reaction could involve a substituted 5-amino-2,4-pentadienal as the diene thereby avoiding the problem of disproportionation and implementing less ring strain during the [4+2] cycloadditon. In this proposal, the building blocks of malondialdehyde (instead of acrolein), ammonia, and an appropriate unsaturated dialdehyde would generate the macrocycle **290**. From **290**, two possible routes were proposed (Scheme 52). Analogous to the model of Baldwin et al., reductive cyclization of **290** would lead to the dihydropyridinium species **291**. Diels–Alder cycloaddition followed by reduction of **292** would directly produce the proposed manzamine precursor, aldehyde **288**. Alternatively, direct cyclization of **290** to give intermediate **293**, followed by reduction of the resulting imine functionality and cyclization would provide the enamine **294**, which presumably could lead to manzamine B (**276**). The occurrence of the proposed enamine **294** was justified by the isolation of the manzamine dimer, kauluamine, isolated from an Indonesian sponge.[130]



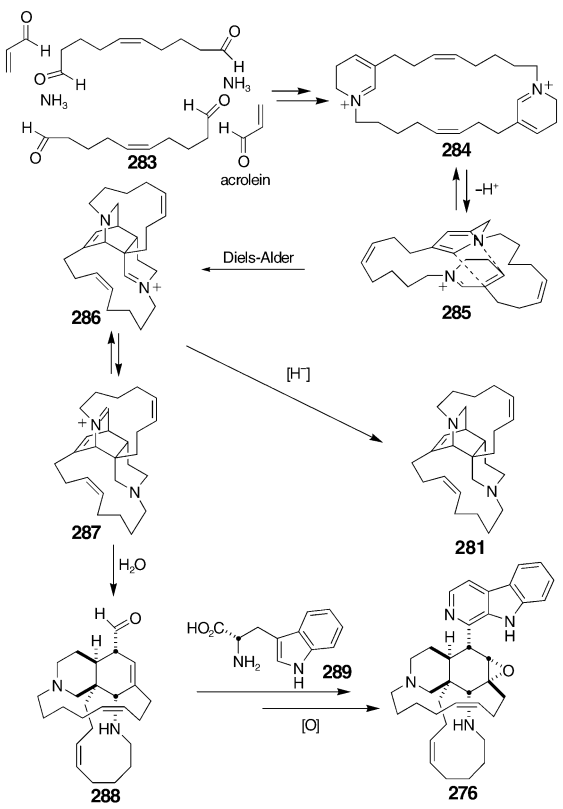
Scheme 49. Biomimetic total synthesis of protodaphniphylline (**257**).[115]

To test the first of these alternate biosynthetic routes, Marazano and co-workers performed a model synthesis as shown in Scheme 53. However, the cycloaddition of the salt **295** with **296** only produced the amino ester **297**. Presumably intramolecular hydride transfer occurred to give **298** followed by hydrolysis of the resultant imine **299**.

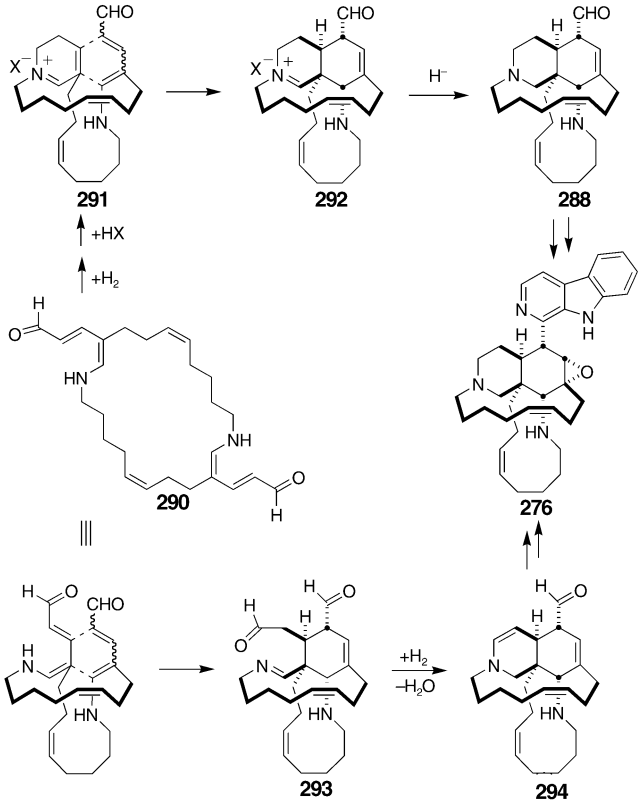
 © 2003 Wiley-VCH Verlag GmbH & Co. KGaA, Weinheim



Scheme 50. Proposed biosynthesis of the iboga and aspidosperma alkaloids.[117]

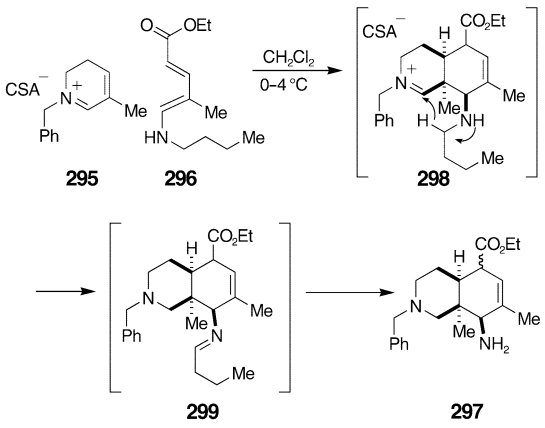


Scheme 51. Proposed biosynthesis by Baldwin et al. of manzamine B (**276**).[127]



Scheme 52. Proposed biosynthesis by Marazano and co-workers of manzamine B (**276**).[129a]

 © 2003 Wiley-VCH Verlag GmbH & Co. KGaA, Weinheim

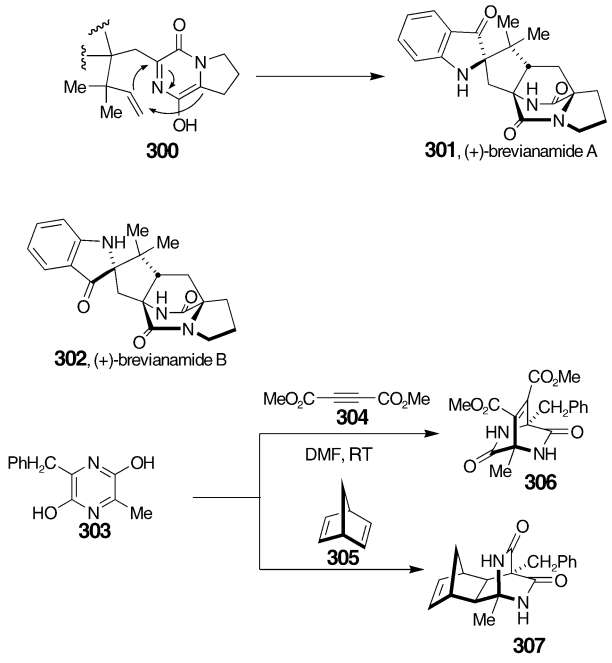


Scheme 53. Model study for the proposed biosynthetic Diels–Alder cycloaddition of the manzamine alkaloids.[129b] CSA = camphorsulfonic acid.

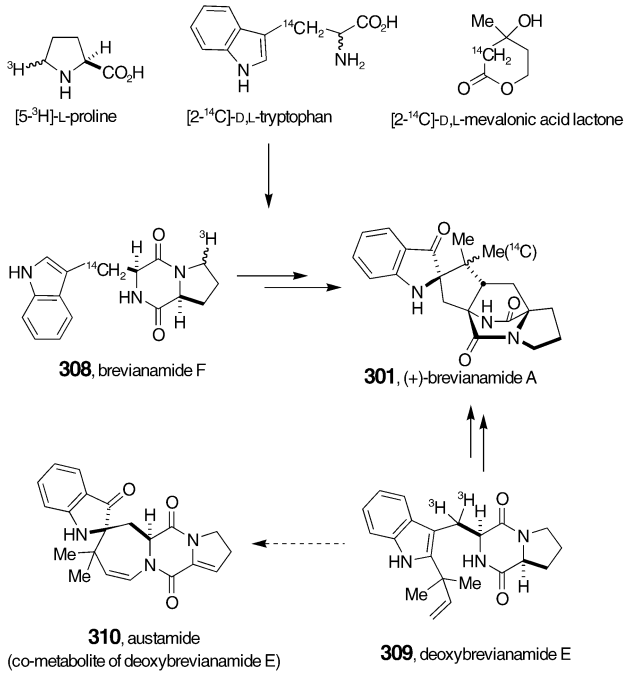
5.2.3. *Brevianamides*

Birch, Wright, and Russel first isolated the fungal metabolite brevianamide A (**301**) from *Penicillium brevicompactum* as well as other minor metabolites including brevianamide B (**302**).[131] In 1970, Sammes proposed that the unique bicyclo[2.2.2]diazaoctan ring system of brevianamide A originated from a hetero-Diels–Alder cycloaddition reaction from **300**.[132] This hypothesis was evaluated experimentally by treating the model dihydroxypyrazine **303** with dimethyl acetylenedicarboxylate (**304**) and with norbornadiene (**305**) to provide the Diels–Alder cycloadducts **306** and **307**, respectively (Scheme 54).

Early radiolabeling and feeding experiments performed by Birch and co-workers indicated that tryptophan, proline, and mevalonic acid were precursors to brevianamide A (Scheme 55).[133] This same study also revealed the incorporation of isotopically labeled brevianamide F (**308**) into **301** in significant radiochemical yield. From these results, it was postulated that the reverse-prenylated intermediate deoxybrevianamide E (**309**) was a biosynthetic precursor. Deoxybrevianamide E (**309**) was isolated from the austamide (**310**) producing fungus, *Aspergillus ustus*, but it has not been detected as a free metabolite from brevianamide-producing cultures. In 1993 Williams and co-workers performed feeding experiments with [8-$^3H_2$]-**309** that provided strong experimental evidence that **309** was a biosynthetic precursor to **301** and **302**.[134]



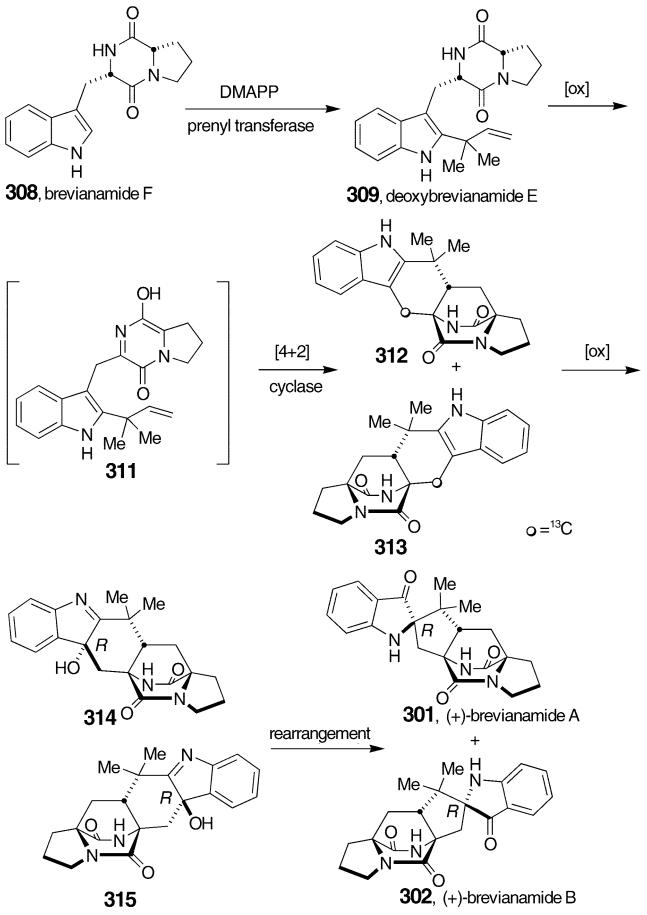
Scheme 54. Proposed and a model study by Porter and Sammes of the biosynthesis of brevianamide A (**301**).[132]



Scheme 55. Biosynthetic studies on the brevianamides.[133,134]

Williams and co-workers completed the first asymmetric total synthesis of (−)-brevianamide B (**302**), which revealed an unusual enantiomorphic relationship between **301** and **302** with respect to the bicyclo[2.2.2]diazaoctan nucleus.[135] Based on these results, the biogenesis outlined in Scheme 56 was postulated. According to this proposal, two-electron oxidation of **309** would yield the azadiene **311**, which would suffer intramolecular hetero-Diels–Alder cycloaddition to form the enantiomeric hexacyclic cycloadducts **312** and **313**. Finally, *R*-selective oxidation of the indole at the 3-position and a pinacol-type rearrangement would provide **301** and **302**. Feeding experiments were performed with *Penicillium brevicompactum* using the proposed synthetic ^{13}C-labeled intermediates **312** and **313**, yet no detectable incorporation was observed.[134] In addition, efforts to identify compounds **312** and **313** as natural metabolites of *Penicillium brevicompactum* failed to produce any evidence for these substances. Although these results do not rigorously exclude the biosynthetic

 © 2003 Wiley-VCH Verlag GmbH & Co. KGaA, Weinheim

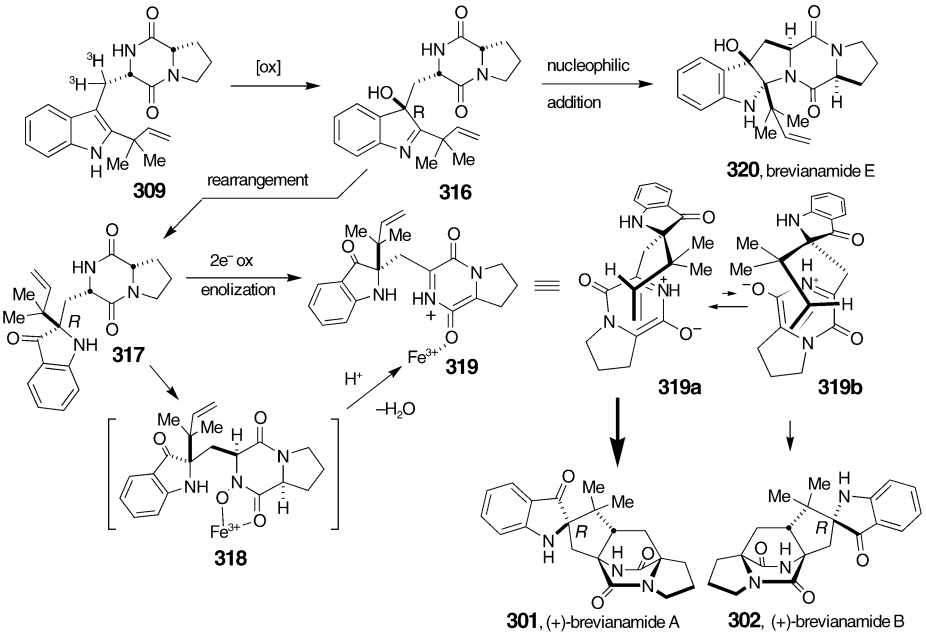


Scheme 56. Initial proposal by Williams et al. for the biosynthesis of brevianamides.[135] DMAPP = allyldimethyl diphosphonate.

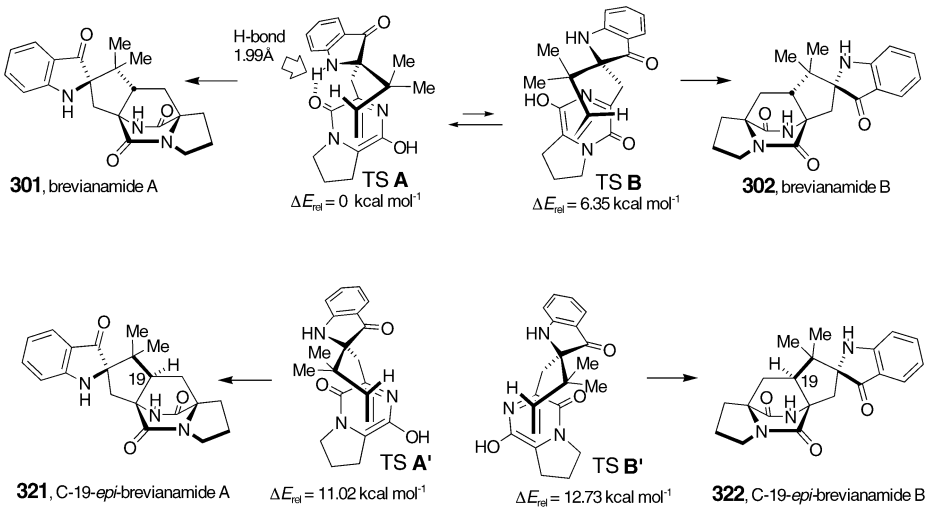
intermediacy of **312** or **313**, it led to the proposal of an alternate biosynthetic pathway as illustrated in Scheme 57.[134]

In the new proposal, **309** was envisaged to undergo oxidation to the hydroxyindolenine **316** and pinacol rearrangement to the indoxyl **317** before forming the requisite azadiene **319** through two-electron oxidation and enolization. The intermediacy of **316** was supported by the isolation of the co-metabolite brevianamide E (**320**), which was shown to be a shunt metabolite formed by irreversible nucleophilic ring closure via **316**. It was demonstrated that [8-$^3H_2$]-**309** was incorporated into **320** in high radiochemical yield (38.5% specific incorporation).[134] However, tritium-labeled **320** when re-fed to cultures of *P. brevicompactum* resulted in no significant radiochemical labeling of either brevianamide A or B, thus indicating that brevianamide E is indeed a shunt metabolite. Based on these findings, it was speculated that the hydroxyindolenine **316** could suffer two fates: 1) irreversible ring closure to brevianamide E or 2) pinacol-type rearrangement to **317** leading ultimately to brevianamides A and B. The natural products **301** and **302** would thus arise from the putative intramolecular hetero-Diels–Alder cycloaddition of the azadiene **319**. For this hypothesis to be valid, **319** must form a major conformer **319a** that results in the formation of **301** and a minor conformer **319b** produces **302**. It is also possible that **316** is oxidized to the corresponding azadiene prior to the pinacol-type rearrangement, wherein the intramolecular Diels–Alder reaction would give the two diastereomeric hydroxyindolenine precursors to **301** and **302**. This possibility has not yet been experimentally tested.

Ab initio calculations were carried out to determine if there was a conformational predilection of the azadiene **319**.[136] The potential energy barriers for the four possible diastereomeric transtion-state structures **A**, **B**, **A′**, and **B′** were calculated (6-31G*/3-21G; Scheme 58). The potential energy barrier for **A** was determined to be 38.68 kcal mol^{-1} and the potential energy barriers for **B**, **A′**, and **B′** were higher by 6.35, 11.02, and 12.73 kcal mol^{-1}, respectively. While the transition-state structures **A** and **B** lead to the observed biosynthetic products **301** and **302**, respectively, the transition-state structures **A′** and **B′** lead to diastereomers **321** and **322**, respectively, which are unknown as natural products. The positioning of the vinyl group in relation to the azadiene system may cause the difference in energy between the four transition states, and the difference between **A** and **B** was rationalized by the capacity of **A** to access an intramolecular hydrogen bond between the indoxylamino group and the oxygen atom of the amide carbonyl group. This ab initio study is consistent with the observed product ratios of **301** and **302**



Scheme 57. Revised biosynthetic proposal for the brevianamides.[134]

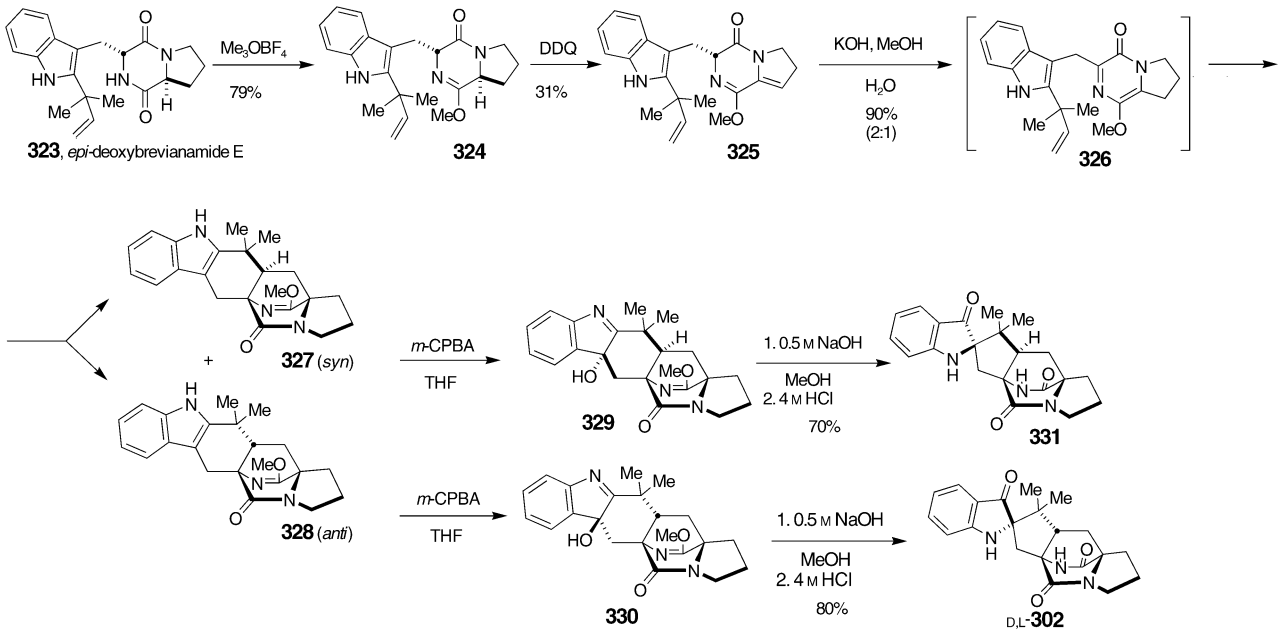


Scheme 58. Calculation of the energy barriers of the four possible transition states (TS) of the Diels–Alder cyclization of the brevianamides.[136]

and supports the proposal of an intramolecular Diels–Alder cycloaddition of the proposed key biosynthetic intermediate **319**. However, the issue of enzymatic catalysis or protein organization of the pretransition state conformers remains unsolved.

Although the biogenesis of the brevianamides was first postulated to occur through a biosynthetic Diels–Alder cycloaddition in 1970 by Porter and Sammes,[132] there was very little published data on the reactivity of such azadienic systems until recently.[137] To expore the feasibility of an intramolecular [4+2] reaction for the construction of the bicyclo[2.2.2]diazaoctan, a biomimetic total synthesis of brevianamide B (**302**) was completed by Williams and coworkers (Scheme 59).[138] Treatment of *epi*-deoxybrevianamide E (**323**) with trimethyloxonium tetrafluoroborate provided the lactim ether **324**. Subsequent oxidation with DDQ gave the azadiene **325**, which cyclized spontaneously upon tautomerization under aqueous basic conditions to furnish the racemic, diastereomeric cycloadducts **327** and **328** in a 2:1 ratio (90% combined yield) favoring the unnatural *syn* product **327**.

Separate diastereoselective oxidations of **327** and **328** with *m*-CPBA provided the hydroxyindolenines **329** and **330**, respectively. Finally, base-catalyzed pinacol-type rearrangements and removal of the lactim ethers provided racemic C19-*epi*-brevianamide A (**331**) and racemic brevianamide B (**302**). This study demonstrated that the core bicyclo[2.2.2]diazaoctane can indeed arise through an intramolecular Diels–Alder cyclization of the unactivated isoprene-derived dienophile and an azadiene system structurally and electronically similar to that proposed for the biosynthesis in water under ambient conditions. However, the stereoselectivity in the biosynthetic system which exclusively favors formation of the *anti* product, was not mirrored in the laboratory cyclization which favored the *syn configuration* at C19. These results raise the possibility of protein organization of the pretransition state conformations of the substrate, but leave uncertainty as to the oxidation state of the indole moiety (indole, hydroxyindolenine, or indoxyl).

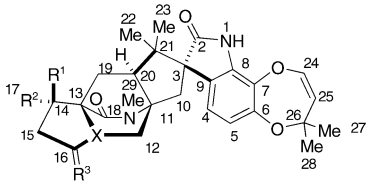


Scheme 59. Biomimetic synthesis of brevianamide B (**302**).[138] DDQ = 2,3-dichloro-5,6-dicyano-1,4-benzoquinone, *m*-CPBA = *m*-chloroperbenzoic acid.

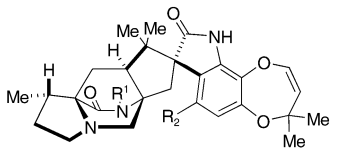
 © 2003 Wiley-VCH Verlag GmbH & Co. KGaA, Weinheim

5.2.4. *Paraherquamides*

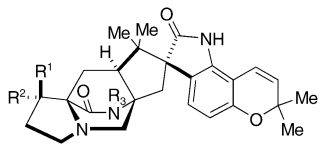
The paraherquamides (**332**–**344**) are a group of heptacyclic mycotoxins isolated from various *Penicillium* sp. and *Aspergillus* sp. Structurally, the paraherquamides are similar to the brevianamides, and vary with respect to the substitution and oxygenation in the proline and the prenylated oxindole rings. The first member of this family of spirooxindoles to be discovered was paraherquamide A (**332**), isolated in 1980 from *Penicillium paraherquei*.[139] Subsequently, paraherquamides A–G (**332**–**335, 338, 341, 342**) were isolated from *Penicillium charlesii* (*fellutanum*).[140] Paraherquamides A (**332**), E (**338**), F (**341**), and G (**342**) were also isolated from a *Penicillium* sp. (IMI332995) found in the soil of Kemer, Turkey. Several related compounds, including VM55595 (**343**), VM55596 (**336**), VM55597 (**337**), and VM55599 (**344**), were also isolated from this strain.[141] VM55599 (**344**) is the only member of the family that contains an indole ring instead of an oxindole ring. The most recent additions to the paraherquamide family are SB203105 (**339**) and SB200437 (**340**), which were isolated in 1998 from an *Aspergillus sp.* (IMI337664).[142]



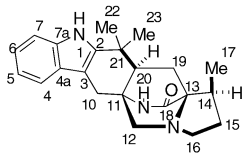
332, (–)-paraherquamide A, R^1 = OH, R^2 = Me, R^3 = H_2, X = N
333, (–)-paraherquamide B, R^1 = H, R^2 = H, R^3 = H_2, X = N
334, (–)-paraherquamide C, R^1 = R^2 = CH_2, R^3 = H_2, X = N
335, (–)-paraherquamide D, R^1 = O, R^2 = CH_2, R^3 = H_2, X = N
336, VM55596, R^1 = OH, R^2 = Me, R^3 = H_2, X = N^+-O^-
337, VM55597, R^1 = OH, R^2 = Me, R^3 = O, X = N



338, paraherquamide E (VM54159), R^1 = Me, R^2 = H
339, SB203105, R^1 = Me, R^2 = OH
340, SB200437, R^1 = H, R^2 = H



341, paraherquamide F (VM55594), R^1 = H, R^2 = Me, R^3 = Me
342, paraherquamide G (VM54158), R^1 = OH, R^2 = Me, R^3 = Me
343, VM55595, R^1 = H, R^2 = Me, R^3 = H



344, VM55599

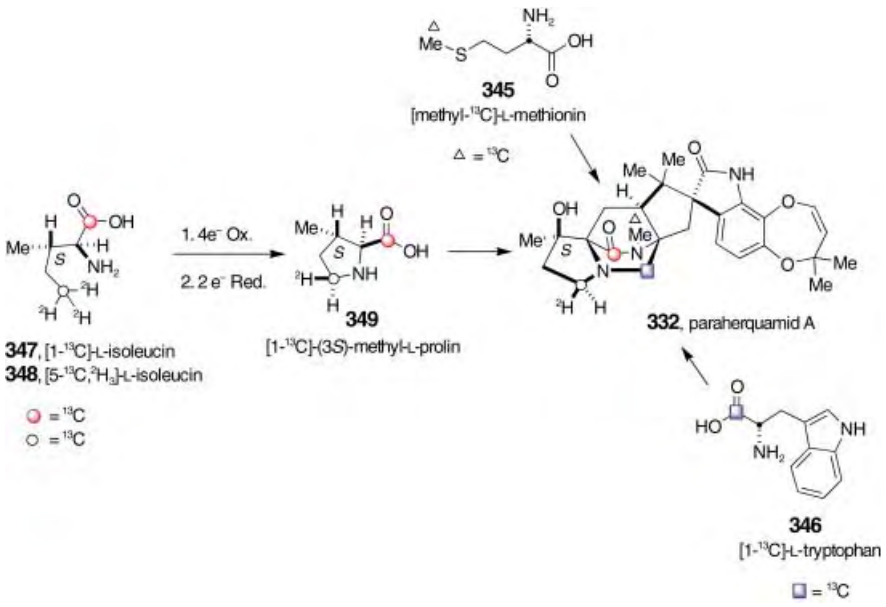
Through feeding experiments, Williams and co-workers determined that L-methionine, L-tryptophan, and L-isoleucine were the proteinogenic amino acid building blocks, which give rise to paraherquamide A (**332**, Scheme 60).[143] Incorporation of isotopically labeled L-isoleucine revealed that it was the source of the unusual nonproteinogenic amino acid β-methylproline (which is later converted into β-methyl-β-hydroxyproline) through a four-electron oxidation/two-electron reduction sequence with retention of the *pro-S* hydrogen atom at C16 (paraherquamide numbering).[143,144] Additional feeding experiments with [$^{13}C_2$]acetate and [$^{13}C_6$]glucose revealed the mevalonate origin of the isoprene moieties (C19–C23 and C24–C28) of **332**.[145]

Interestingly, the feeding experiments indicated that *Penicillium fellutanum* constructs each isoprene-derived quaternary center in **332** by disparate stereochemical pathways. The quaternary center in the dioxepin ring (C24–C28) was found to be formed in a completely stereospecific manner. However, scrambling of the ^{13}C label into both of the *gem*-dimethyl groups was observed in the quaternary center of the bicyclo[2.2.2]diazaoctane portion (C19–C23), thus indicating that the stereochemical integrity of the acetate-derived ^{13}C label in the dimethylallyl pyrophosphate moiety was sacrificed in the construction of this quaternary center.

Williams and co-workers proposed that a "reverse" prenyltransferase catalyzes a nonface-selective intermolecular S_N2'-type addition of the dimethylallyl pyrophosphate moiety to the 2-position of the tryptophan-derived indole ring, thus scrambling the *Z*-^{13}C label in the isoprene moiety (Scheme 61). Analogous to the proposed biosynthesis for the brevianamides, it was anticipated that this reverse-prenylated moiety **351** would undergo a [4+2] cycloaddition reaction across the α carbon atoms of L-tryptophan and (3*S*)-methyl-L-proline and eventually lead to paraherquamide A (**332**).

As in the case of the brevianamides, it was unclear whether oxidation of the tryptophan moiety occurred before or after the putative hetero-Diels–Alder reaction. Isolation of the hexacyclic indolic metabolite VM55599 (**344**) from the paraherquamide-producing *Penicillium* sp. (IMI332995) suggested that the tryptophan oxidations occur after the construction of the bicyclo[2.2.2] ring system. However, the relative stereochemistry of C14 and C20 in **344**, as determined by Everett and co-workers by extensive ^1H NMR NOE data, was found to be opposite to that found in **332**.[141] If the β-methylproline ring of **344** was derived, as in the case of **322**, from (*S*)-isoleucine, then cycloaddition would have to occur from the seemingly more hindered face of the azadiene system (**B** in Scheme 62) with the methyl group of the β-methylproline ring *syn* to the bridging isoprene moiety. If, on the other hand, cycloaddition occurs with the methyl group of the β-methylproline ring *anti* to the bridging isoprene unit (**A** in Scheme 62), then an intermediate would be formed which could lead to all of the paraherquamides containing a β-methylproline moiety. Indirect support for the hypothesis that

 © 2003 Wiley-VCH Verlag GmbH & Co. KGaA, Weinheim

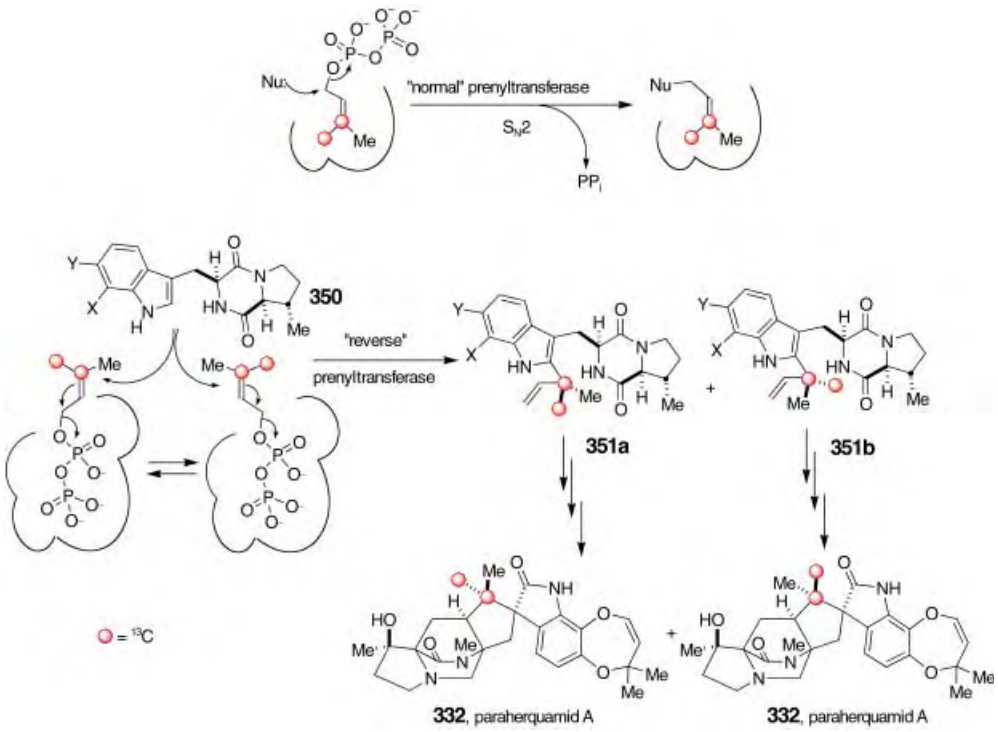


Scheme 60. Incorporation of amino acids into paraherquamide A (**332**).[143]

the major cycloaddition pathway passes through conformer **A** was based on the small amount of **344** isolated from *Penicillium* sp. (IMI332995) cultures (**344**:**332** ca. 1:600).[146]

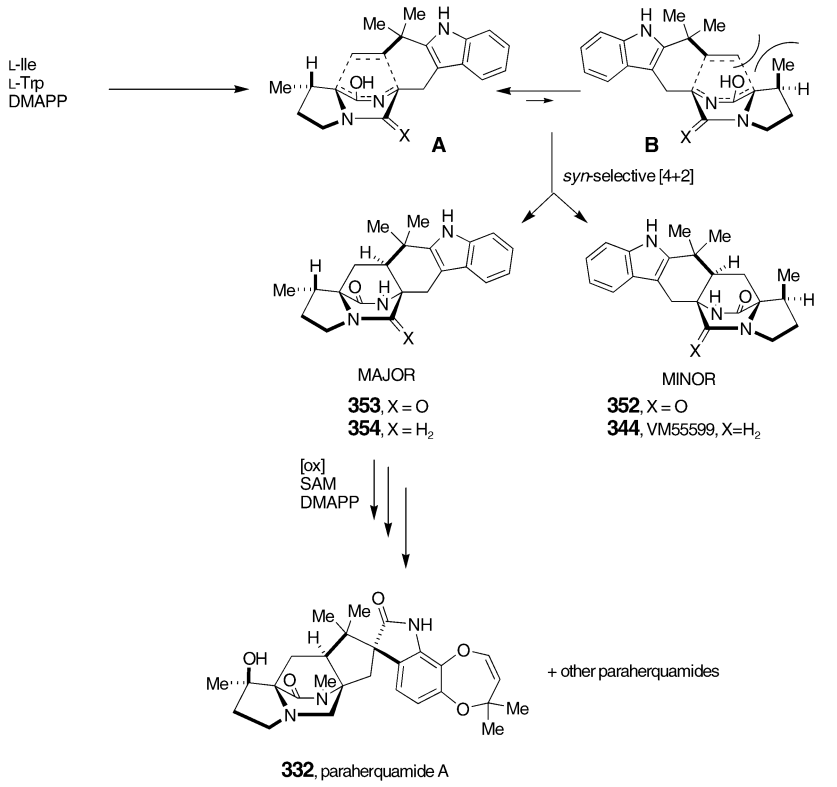
To determine if **344** was an intermediate in the biosynthesis of **332**, as initially postulated by Everett and co-workers, Williams and co-workers prepared [$^{13}C_2$]-(±)-**344**, the oxidized form of [$^{13}C_2$]-(±)-**352** as well as the alleged ^{13}C-labeled paraherquamide progenitors **353** and **354**, and examined these substances as potential pathway metabolites in *Penicillium fellutanum*.[147] Syntheses of these labeled substrates were accomplished through a biomimetic intramolecular Diels–Alder cycloaddition strategy as illustrated in Scheme 63.[146,147] Interestingly, the laboratory cycloaddition slightly favored (1.47:1) the approach of the dienophile from the same face as the methyl group in the β-methyl proline ring, which leads to the relative stereochemistry of **344**. Additionally, the ratio of the *anti* to *syn* isomers at C20 was approximately 1:2.4 in favor of the natural configuration. As in the related cycloaddition reaction of **326** (Scheme 59) the poor facial bias of the laboratory Diels–Alder reaction strongly hints that protein organization of the pretransition state conformers might be operative in the biosynthesis of paraherquamide A.

Feeding experiments with the ^{13}C-labeled cycloadducts revealed no incorporation in (±)-**344**, its oxidized counterpart (±)-**352**, or the diketopiperazine (±)-**353** (Scheme 64). However, significant incorporation of (±)-**354**, the C14 epimer of **344**, into paraherquamide A (**332**) was observed by ^{13}C NMR spectroscopy and from analysis of the electrospray mass spectrum (0.72% incorporation). These results indicate that the formation of the bicyclo[2.2.2]diazaoctane ring system occurs at the stage of the nonoxidized



Scheme 61. Proposed mechanism for the attachment of the C19–C23 segment in paraherquamide A (**332**).[145]

 © 2003 Wiley-VCH Verlag GmbH & Co. KGaA, Weinheim

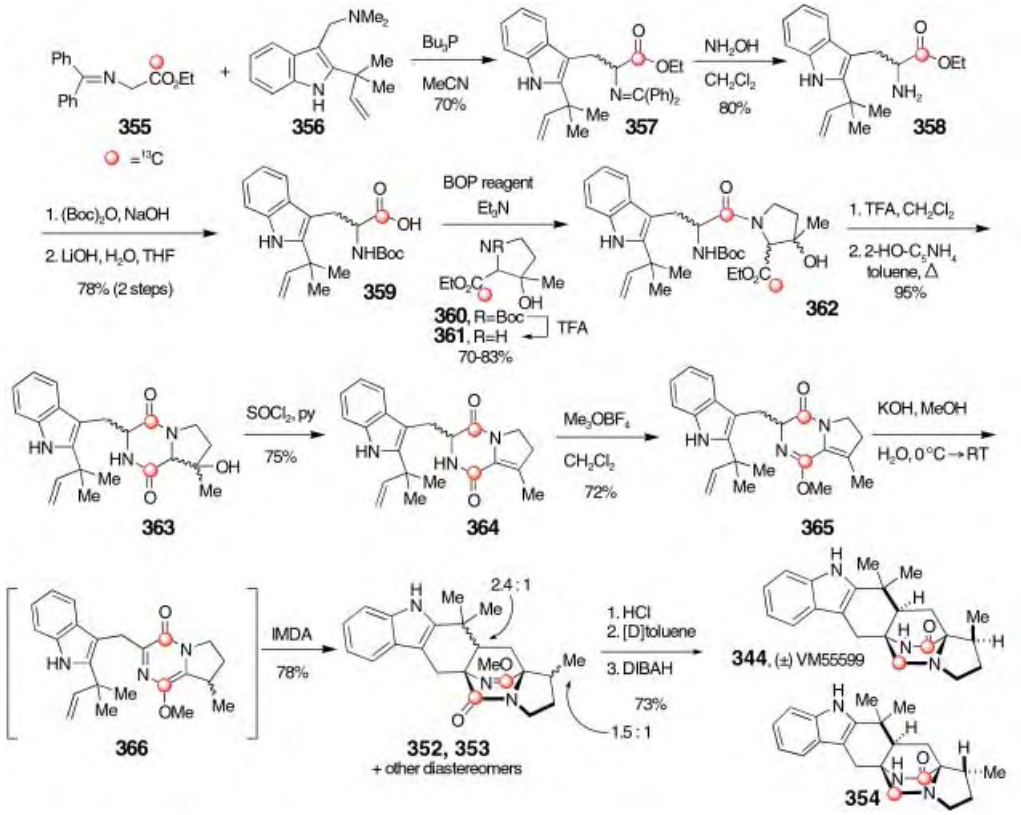


Scheme 62. Proposed unified biogenesis of paraherquamide A (**332**) and VM55599 (**344**).[146]

tryptophanyl moiety (namely, indolyl). These results provide additional evidence that **344** is a minor shunt metabolite of the paraherquamide pathway. Moreover, these results document the intermediacy of an advanced metabolite **354**, potentially formed by an intramolecular hetero-Diels–Alder cycloaddition, which contains the core structural elements of the paraherquamide framework prior to a series of oxygenation reactions.

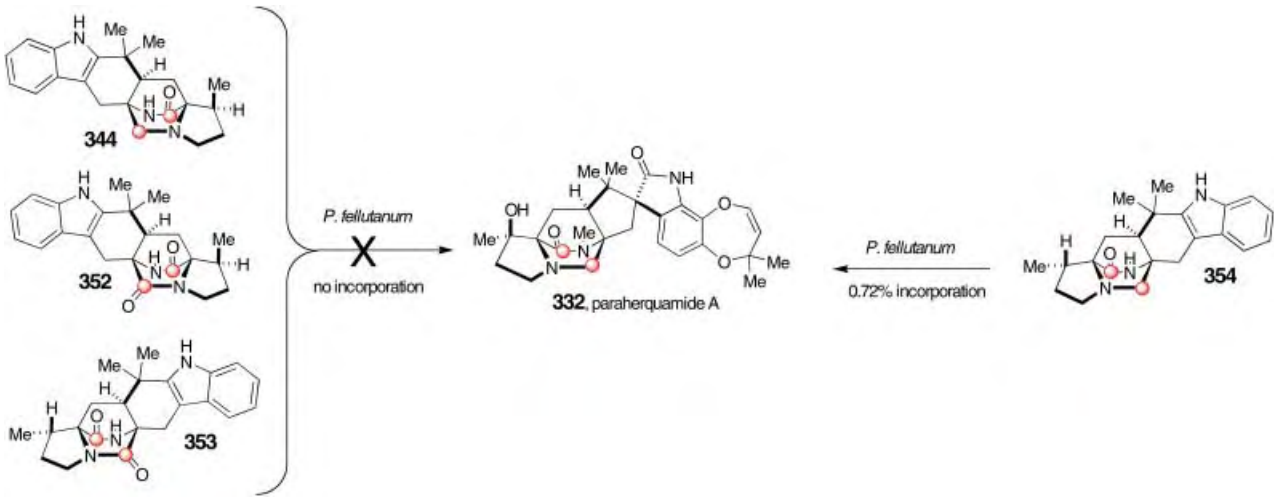
Very recently, Sanz-Cervera and Williams completed an asymmetric biomimetic total synthesis of (−)-**344** that served to unambiguously establish the absolute stereochemistry of this substance (Scheme 65).[148] As predicted by these authors in the unified biogenesis proposal depicted in Scheme 62, **344** retains the (*S*)-Ile stereochemistry in the β-methylproline ring and consequently, has a bicyclo[2.2.2]-diazaoctane ring system that is enantiomorphic to that embedded in the paraherquamides.

It was quite surprising to observe that cycloadduct **353**, which contains the relative and absolute stereochemistry of the

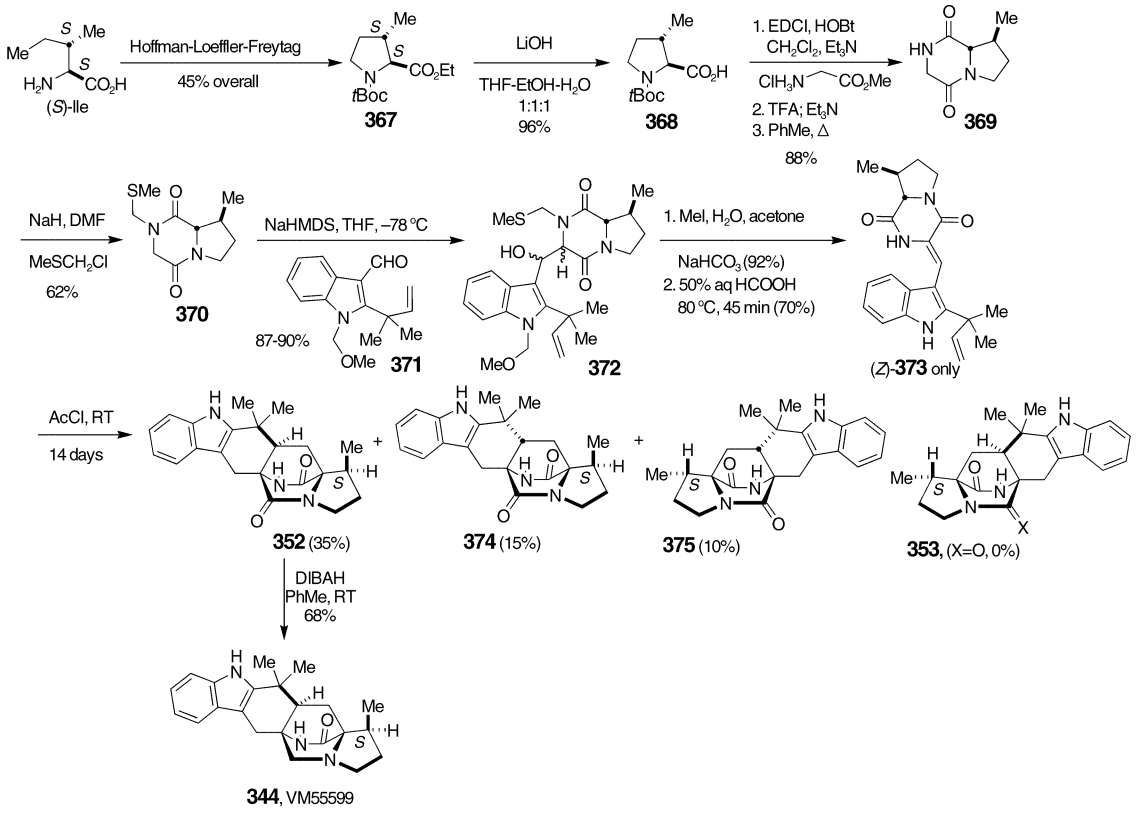


Scheme 63. Biomimetic synthesis of [$^{13}C_2$]-(±)-**344** and other potential intermediates in the biosynthesis of **332**.[146,147] Boc = *tert*-butoxycarbonyl, BOP = benzotriazol-1-yloxytris(dimethylamino)phosphonium hexafluorophosphate, DIBAH = diisobutylaluminum hydride. The numbers 2.4:1 and 1.5:1 on **352**, **353** indicate the *syn*/*anti* relationship between C20 and the cyclic amino acid residue and between the methyl groups that are pointing up and down, respectively.

 © 2003 Wiley-VCH Verlag GmbH & Co. KGaA, Weinheim



Scheme 64. Feeding experiments with ^{13}C-labeled indolic progenitor candidates of paraherquamide A (**332**).[146] EDCI = 3-(3-dimethylaminopropyl)-1-ethylcarbodiimide, HOBt = 1-hydroxy-1*H*-benzotriazole, NaHMDS = sodium hexamethyldisilazanide.

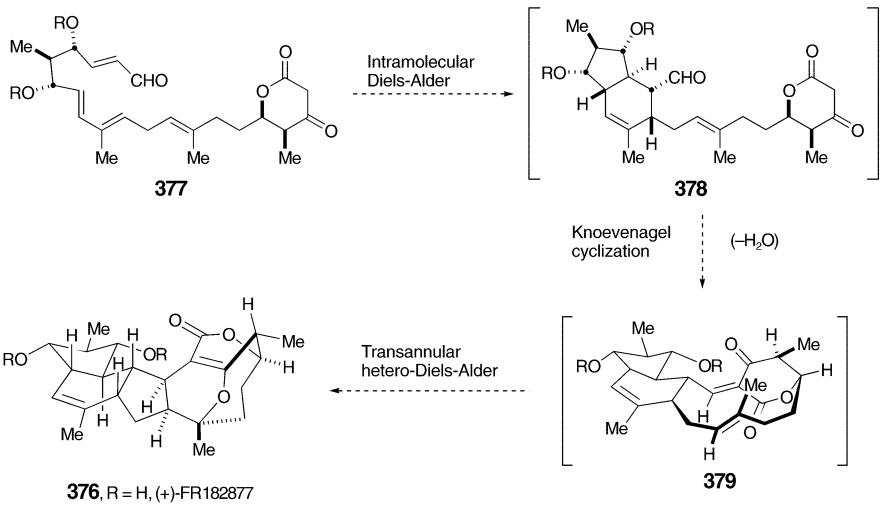


Scheme 65. Asymmetric biomimetic synthesis of **344** and establishment of the absolute stereostructure.[148]

paraherquamides, was not detected from the cycloaddition reaction. The cycloadducts obtained in the previously reported racemic synthesis gave (as lactim ethers) compounds stereochemically corresponding to **352**:**374**:**375**:**353** in a ratio of 3.7:1.6:1:2.6. In the present case, the ratio is 3.5:1.5:1:0. In the biological system, the diastereochemical distribution is expressed as > 600:1 (corresponding to **332**:**344**) as evidenced by the complete lack of natural metabolites that would arise from substances containing the stereochemistry imbedded in either **374** or **375**. The laboratory intramolecular Diels–Alder cycloadditions described in Schemes 63 and 65 again demonstrate an unexpected proclivity for the formation of the relative stereochemistry of **344**. This result is in sharp contradiction to the stereochemical preference expressed in nature. Although the oxidation state of the putative azadiene species (**A**/**B**, X = O or H_2 in Scheme 62) in the biological system currently remains uncertain. The contrast between the two biomimetic laboratory cycloaddition reactions and that

 © 2003 Wiley-VCH Verlag GmbH & Co. KGaA, Weinheim

postulated to occur in the biosynthetic constructions strongly implicates protein organization of the precyclization substrate conformation to greatly favor formation of the paraherquamide stereochemistry.



Scheme 66. Biogenesis of FR182877 (**376**) initially proposed by Sorensen and co-workers.[151a]

6. Addendum

Since submission of this manuscript, several recent papers appeared on the biomimetic total synthesis of FR182877 (**376**) and longithorone (**163**). As these works have significant implications concerning the biosynthesis of these natural products, the key findings will be briefly described.

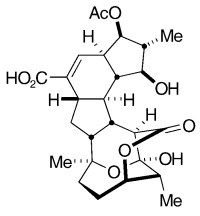
FR182877

Two impressive biomimetic total syntheses of FR182877 (**376**) have appeared[149,150] that provide experimental support for a provocative biogenetic proposal originally suggested by Sorensen and co-workers in 1999.[151] The construction of FR182877 (formerly known as WS9885B) could arise by a cascade of cyclization reactions (Scheme 66) involving: a) an intramolecular Diels–Alder cycloaddition from the polyketide **377** to **378,** b) an intramolecular Knoevenagel cyclization (to **379**), and c) a transannular hetero-Diels–Alder cycloaddition to directly furnish **376**.

In 2001, Sorensen and co-workers suggested a slight revision of this elegant biogenesis wherein the related polyketide substrate **380** would undergo an intramolecular Knoevenagel cyclization (to **381**). Successive transannular Diels–Alder and transannular hetero-Diels–Alder cycloadditions then directly furnished **376** (Scheme 67).[151b]

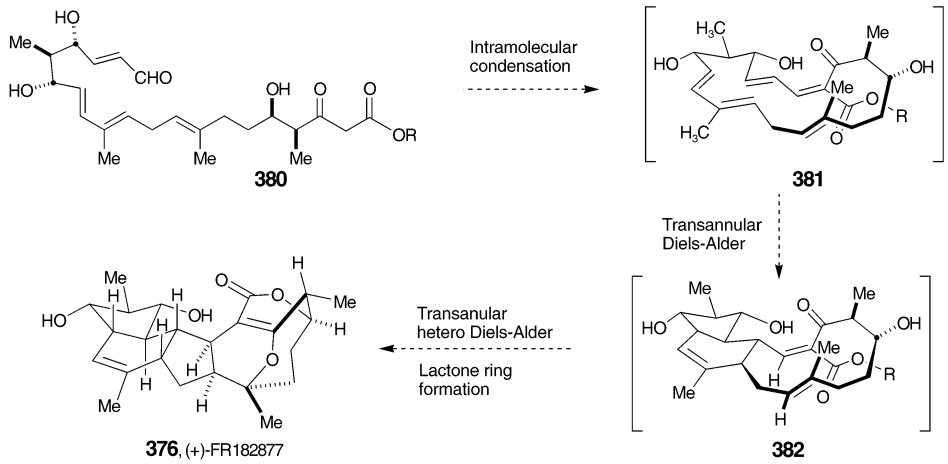
This strategy inspired a biomimetic total syntheses of this natural product[149] that lends strong, albeit indirect, experimental support for the biogenetic hypothesis. The key features of the total synthesis of (+)-FR182877 by Sorensen and co-workers are illustrated in Scheme 68.

Evans and Starr also reported a biomimetic cyclization cascade to (−)-**376** (Scheme 69).[150] This study also confirmed the absolute configuration of this natural product.[152] The biosynthesis of the related natural product hexacyclinic acid (**390**)[153] may arise from an alternative *exo* conformer of a related polyketide-derived macrocycle.

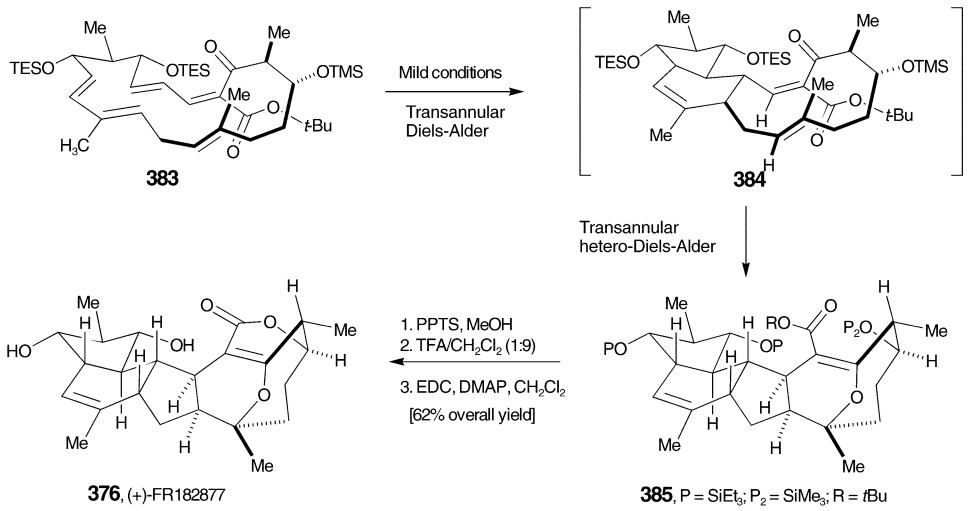


Longithorone

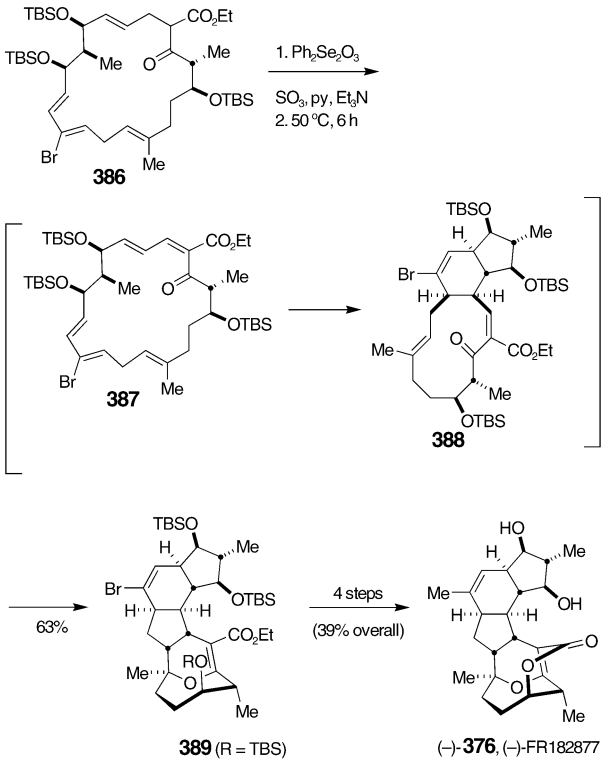
Shair and co-workers recently completed an elegant and impressive biomimetic total synthesis of longithorone (**163**). These researchers exploited an interesting chirality-transfer strategy that involved the use of stereogenic centers to control the atropisomerism followed by removal of the stereogenic centers, and, transfer of the atropisomerism chirality back to the stereogenic centers.



Scheme 67. Revised biogenesis of **376** proposed by Sorensen and co-workers.[151b]

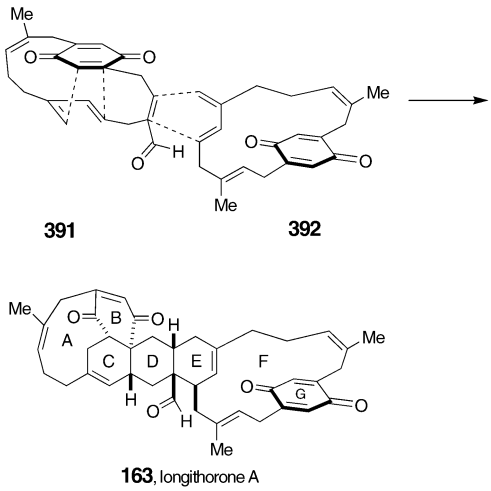


Scheme 68. Biomimetic total synthesis of (+)-**376** by Sorensen and co-workers.[149] DMAP = dimethylaminopyridine, EDC = 1,2-dichloroethane, PPTS = pyridinium *p*-toluenesulfonate, TES = triethylsilyl.



Scheme 69. Biomimetic total synthesis of (−)-**376** by Evans and Starr.[150] TBS = *tert*-butyldimethylsilyl.

Schmitz and co-workers proposed a provocative biogenesis of longithorone wherein an intermolecular Diels–Alder reaction between [12]paracyclophanes **391** and **392** form ring E and a subsequent transannular intramolecular Diels–Alder reaction across **391** forms rings A, C, and D (Scheme 70).[78a] Shair and co-workers have capitalized on this hypothesis in a beautiful total synthesis of (−)-**163** (Scheme 71).[78b]

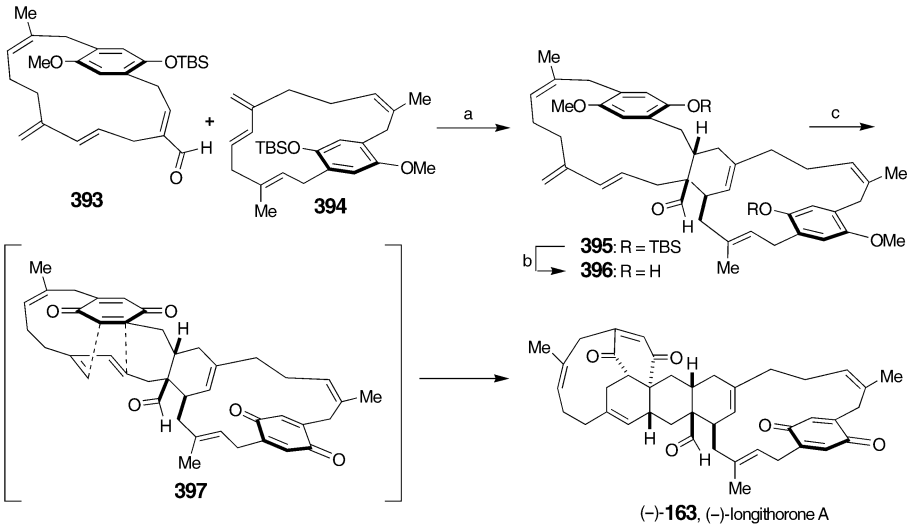


Scheme 70. Biogenesis of longithorone A (**163**) as proposed by Schmitz and co-workers.[78a]

7. Summary

The rapidly accumulating body of literature in this field that has been summarized in this Review suggests that nature indeed utilizes the Diels–Alder construction to generate a complex array of natural products. In many cases, such as in the endiandric acids,[49] lucidene (**191**),[92] and asatone (**238**),[110] current experimental evidence argues that the putative biosynthetic Diels–Alder cyclization reactions are not enzyme-mediated, but occur spontaneously in the producing organism in a stereorandom fashion and give rise to racemic products. For the natural products that are enantiomerically pure, there is growing evidence that the Diels–Alder reactions might be enzyme-mediated. The experimental evidence for enzyme involvement is, however, circumstantial for virtually all of these systems. For example, the biomimetic laboratory cyclizations of the epolone B (**182**)[90] and VM55599 (**344**)[146] systems were not stereoselective,

 © 2003 Wiley-VCH Verlag GmbH & Co. KGaA, Weinheim



Scheme 71. Biomimetic total synthesis of (−)-**163** by Shair and co-workers.[78b] a) Me_2AlCl, CH_2Cl_2, −20 °C (70%, diastereomeric ratio 1:1.4); b) TBAF, THF, 0 °C; c) PhI(O), MeCN-H_2O, 0→25 °C (90%, 2 steps).

which indicates that there may be some protein organization of the pretransition state conformations in the natural system.[154] The three systems in which the strongest and most direct experimental support for the existence of a Diels–Alderase resides are: a) the enzymatic activity observed for cell-free extracts of *Alternaria solani*[21] that leads to the production of solanapyrone A (**11**), b) lovastatin nonaketide synthase[7] that leads to the production of lovastatin, and c) macrophomate synthase[8] that leads to the production of macrophomic acid (**113**). Despite the impressive and difficult experimental work that the authors of these publications have gathered, in the quest for proving the existence of a Diels–Alderase, rigorous proof that the purified or partially purified (in the case of solanapyrone) proteins are catalyzing (that is, accelerating the rates of these reactions relative to the uncatalyzed systems) the pericyclic Diels–Alder reaction remains to be rigorously established. A great deal of difficult biophysical and kinetic work needs to be done on these systems to ascertain if true catalysis occurs, as measured by the classical tests of rate acceleration and stereoselectivity versus the substrate conversions to product in the absence of enzyme.

The authors are grateful to the National Institutes of Health and the National Science Foundation for supporting the portions of their work described in this review. We are also grateful to Prof. John C. Vederas of the University of Alberta and Prof. Hideaki Oikawa of Hokkaido University, for providing preprints of their work. The authors are grateful to Dr. Rhona J. Cox for careful proof reading of the manuscript.

Received: April 30, 2002 [A534]

[1] For excellent recent reviews on the Diels-Alder reaction, see a) E. J. Corey, A. Guzman-Perez, *Angew. Chem.* **1998**, *110*, 402–415; *Angew. Chem. Int. Ed.* **1998**, *37*, 388–401; b) E. J. Corey, *Angew. Chem.* **2002**, *114*, 1724–1741; *Angew. Chem. Int. Ed.* **2002**, *41*, 1650–1667; c) K. C. Nicolaou, S. A. Snyder, T. Montagnon, G. Vassilikogiannakis, *Angew. Chem.* **2002**, *114*, 1742–1773; *Angew. Chem. Int. Ed.* **2002**, *41*, 1668–1698.

[2] a) S. Laschat, *Angew. Chem.* **1996**, *108*, 313–315; *Angew. Chem. Int. Ed. Engl.* **1996**, *35*, 289–291; b) A. Ichihara, H. Oikawa, *Curr. Org. Chem.* **1998**, *2*, 365–394.

[3] D. Hilvert, K. W. Hill, K. D. Nared, M.-T. M. Auditor, *J. Am. Chem. Soc.* **1989**, *111*, 9261–9263.

[4] A. C. Braisted, P. G. Schultz, *J. Am. Chem. Soc.* **1990**, *112*, 7430–7431.

[5] F. E. Romesberg, B. Spiller, P. G. Schultz, R. C. Stevens, *Science* **1998**, *279*, 1929–1933.

[6] a) T. M. Tarasow, B. E. Eaton, *Cell. Mol. Life Sci.* **1999**, *55*, 1463–1472; b) B. Seelig, A. Jäschke, *Chem. Biol.* **1999**, *6*, 167–176; c) B. Seelig, S. Keiper, F. Stuhlmann, A. Jäschke, *Angew. Chem.* **2000**, *112*, 4764–4768; *Angew. Chem. Int. Ed.* **2000**, *39*, 4576–4579.

[7] K. Auclair, A. Sutherland, J. Kennedy, D. J. Witter, J. P. Van den Heever, C. R. Hutchinson, J. C. Vederas, *J. Am. Chem. Soc.* **2000**, *122*, 11519–11520.

[8] K. Watanabe, T. Mie, A. Ichihara, H. Oikawa, M. Honma, *J. Biol. Chem.* **2000**, *275*, 38393–38401.

[9] a) J. K. Chan, R. N. Moore, T. T. Nakashima, J. C. Vederas, *J. Am. Chem. Soc.* **1983**, *105*, 3334–3336; b) R. N. Moore, G. Bigam, J. K. Chan, A. M. Hogg, T. T. Nakashima, J. C. Vederas, *J. Am. Chem. Soc.* **1985**, *107*, 3694–3701.

[10] Y. Yoshizawa, D. J. Witter, Y. Liu, J. C. Vederas, *J. Am. Chem. Soc.* **1994**, *116*, 2693–2694.

[11] D. J. Witter, J. C. Vederas, *J. Org. Chem.* **1996**, *61*, 2613–2623.

[12] a) L. R. Trieber, C. S. Reamer, H. G. Ramjit, *J. Antibiot.* **1989**, *42*, 30–36; b) T. Nakamura, D. Komagata, S. Murakawa, K. Sakai, A. Endo, *J. Antibiot.* **1990**, *43*, 1597–1600.

[13] J. Kennedy, K. Auclair, S. G. Kendrew, C. Park, J. C. Vederas, C. R. Hutchison, *Science* **1999**, *284*, 1368–1372.

[14] S. Colonna, A. Manfredi, R. Annunziata, *Tetrahedron Lett.* **1988**, *29*, 3347–3350.

[15] A. Ichihara, S. Tazaki, S. Sakamura, *Tetrahedron Lett.* **1983**, *24*, 5373–5376.

[16] H. Oikawa, T. Yokota, T. Abe, A. Ichihara, S. Sakamura, Y. Yoshizawa, J. C. Vederas, *J. Chem. Soc. Chem. Commun.* **1989**, 1282–1284.

[17] H. Oikawa, T. Yokota, A. Ichihara, S. Sakamura, *J. Chem. Soc. Chem. Commun.* **1989**, 1284–1285.

[18] A. Ichihara, M. Miki, H. Tazaki, S. Sakamura, *Tetrahedron Lett.* **1987**, *28*, 1175–1178.

[19] H. Oikawa, Y. Suzuki, A. Naya, K. Katayama, A. Ichihara, *J. Am. Chem. Soc.* **1994**, *116*, 3605–3606.

[20] H. Oikawa, Y. Suzuki, K. Katayama, A. Naya, C. Sakano, A. Ichihara, *J. Chem. Soc. Perkin Trans. 1* **1999**, 1225–1232.

[21] H. Oikawa, K. Katayama, Y. Suzuki, A. Ichihara, *J. Chem. Soc. Chem. Commun.* **1995**, 1321–1322.

[22] D. E. Cane, C.-C. Yang, *J. Am. Chem. Soc.* **1984**, *106*, 784–787.

[23] D. E. Cane, C.-C. Yang, *J. Antibiot.* **1985**, *38*, 423–426.

[24] a) D. E. Cane, W. R. Ott, *J. Am. Chem. Soc.* **1988**, *110*, 4840–4841; b) D. E. Cane, P. C. Prabhakaran, W. Tan, W. R. Ott, *Tetrahedron Lett.* **1991**, *32*, 5457–5460; c) D. E. Cane, W. Tan, W. R. Ott, *J. Am. Chem. Soc.* **1993**, *115*, 527–535; d) D. E. Cane, G. Luo, *J. Am. Chem. Soc.* **1995**, *117*, 6633–6634.

 © 2003 Wiley-VCH Verlag GmbH & Co. KGaA, Weinheim

[25] a) H. Oikawa, A. Ichihara, S. Sakamura, *J. Chem. Soc. Chem. Commun.* **1988**, 600 – 602; b) P. H. Harrison, D. E. Cane, *Chemtracts: Org. Chem.* **1988**, **1**, 369 – 371.
[26] H. Oikawa, A. Ichihara, S. Sakamura, *J. Chem. Soc. Chem. Commun.* **1990**, 908 – 909.
[27] S. Miki, Y. Sato, H. Tabuchi, H. Oikawa, A. Ichihara, S. Sakamura, *J. Chem. Soc. Perkin Trans. 1* **1990**, 1228 – 1229.
[28] C. Tamm in *The Biosynthesis of Mycotoxins. A Study in Secondary Metabolism* (Ed.: P. Steyn), Academic Press, New York **1980**, pp. 269 – 299.
[29] A. Hadener, G. Ritter, P. M. Schaeffer in *Bioorganic Chemistry: Highlights and New Aspects* (Eds.: U. Diederichsen, T. K. Lindhorst, B. Westermann, L. A. Wessjohann), Wiley-VCH, New York, **1999**, pp. 89 – 94.
[30] J. C. Vederas, W. Graf, L. David, C. Tamm, *Helv. Chim. Acta* **1975**, *58*, 1886 – 1898.
[31] A. Probst, C. Tamm, *Helv. Chim. Acta* **1981**, *64*, 2065 – 2077.
[32] R. Wyss, C. Tamm, *Croat. Chem. Acta* **1986**, *58*, 537 – 546.
[33] a) J. C. Vederas, C. Tamm, *Helv. Chim. Acta* **1976**, *59*, 558 – 566; b) A. Haedener, P. Roth, C. Tamm, *Z. Naturforsch. C* **1989**, *44,* 19 – 32.
[34] J.-L. Robert, C. Tamm, *Helv. Chim. Acta* **1975**, *58*, 2501 – 2504.
[35] H. Oikawa, Y. Murakami, A. Ichihara, *J. Chem. Soc. Perkin Trans. 1* **1992**, 2955 – 2959.
[36] H. Oikawa, Y. Murakami, A. Ichihara, *J. Chem. Soc. Perkin Trans. 1* **1992**, 2949 – 2953.
[37] K. Shindo, M. Sakakibara, H. Kawai, *J. Antibiot.* **1996**, *49*, 249 – 252.
[38] a) S. Ito, Y. Hirata, *Tetrahedron Lett.* **1972**, 1181 – 1184; b) S. Ito, Y. Hirata, *Tetrahedron Lett.* **1972**, *13*, 1185 – 1188; c) S. Ito, Y. Hirata, *Tetrahedron Lett.* **1972**, *25*, 2557 – 2560; d) S. Ito, Y. Hirata, *Bull. Chem. Soc. Jpn.* **1977**, *50*, 1813 – 1820.
[39] H. A. Kirst, K. H. Michel, J. W. Martin, L. C. Creemer, E. H. Cio, R. C. Yao, W. M. Nakatsukasa, L. D. Boeck, J. L. Occolowitz, J. W. Paschal, J. B. Deeter, N. D. Jones, G. D. Thompson, *Tetrahedron Lett.* **1991**, *32*, 4839 – 4842.
[40] S. Aizawa, H. Akatsu, T. Satomi, T. Nagatsu, R. Taguchi, A. Seino, *J. Antibiot.* **1979**, *32*, 193 – 196; for the related metabolite hexacyclinic acid, see also ref. [153]; for a recent biomimetic synthesis of another related metabolite, FR182877 (**376**), see refs. [149–151].
[41] W. R. Roush, A. B. Works, *Tetrahedron Lett.* **1996**, *37*, 8065 – 8068.
[42] D. A. Evans, W. C. Black, *J. Am. Chem. Soc.* **1993**, *115*, 4497 – 4513.
[43] J. W. Westley, R. H. Evans, Jr., C.-M. Liu, T. Hermann, J. F. Blount, *J. Am. Chem. Soc.* **1978**, *100*, 6784 – 6786.
[44] S. H. Larsen, L. D. Boeck, F. P. Mertz, J. W. Paschal, J. L. Occolowitz, *J. Antibiot.* **1988**, *41*, 1170 – 1177.
[45] S. J. Coval, P. J. Scheuer, *J. Org. Chem.* **1985**, *50*, 3024 – 3025.
[46] S. Miao, M. R. Anstee, V. Baichwal, A. Park, *Tetrahedron Lett.* **1995**, *36*, 5699 – 5702.
[47] a) W. R. Roush, A. G. Myers, *J. Org. Chem.* **1981**, *46*, 1509 – 1511; b) W. R. Roush, S. M. Peseckis, *Tetrahedron Lett.* **1982**, *23*, 4879 – 4882; c) W. R. Roush, S. M. Peseckis, A. E. Walts, *J. Org. Chem.* **1984**, *49*, 3429 – 3432.
[48] W. M. Bandaranayake, J. E. Banfield, D. St. C. Black, G. D. Fallon, B. M. Gatehouse, *J. Chem. Soc. Chem. Commun.* **1980**, 162 – 163.
[49] W. M. Bandaranayake, J. E. Banfield, D. St. C. Black, *J. Chem. Soc. Chem. Commun.* **1980**, 902 – 903.
[50] a) K. C. Nicolaou, N. A. Petasis, R. E. Zipkin, J. Uenishi, *J. Am. Chem. Soc.* **1982**, *104*, 5555 – 5557; b) K. C. Nicolaou, N. A. Petasis, J. Uenishi, R. E. Zipkin, *J. Am. Chem. Soc.* **1982**, *104*, 5557 – 5558.
[51] a) K. C. Nicolaou, R. E. Zipkin, N. A. Petasis, *J. Am. Chem. Soc.* **1982**, *104*, 5558 – 5560; b) K. C. Nicolaou, N. A. Petasis, R. E. Zipkin, *J. Am. Chem. Soc.* **1982**, *104*, 5560 – 5562.
[52] a) L. S. Trifonov, A. S. Dreiding, L. Hoesch, D. M. Rast, *Helv. Chim. Acta* **1981**, *64*, 1843 – 1846; b) L. S. Trifonov, J. H. Bieri, R. Prewo, A. S. Dreiding, L. Hoesch, D. M. Rast, *Tetrahedron* **1983**, *39*, 4243 – 4256.
[53] a) N. Abe, T. Murata, A. Hirota, *Biosci. Biotechnol. Biochem.* **1998**, *62*, 661 – 666; b) N. Abe, T. Murata, A. Hirota, *Biosci. Biotechnol. Biochem.* **1998**, *62*, 2120 – 2126.
[54] R. Andrade, W. A. Ayer, L. S. Trifonov, *Can. J. Chem.* **1996**, *74*, 371 – 379.
[55] a) K. C. Nicolaou, K. B. Simonsen, G. Vassilikogiannakis, P. S. Baran, V. P. Vidali, E. N. Pitsinos, E. A. Couladouros, *Angew. Chem.* **1999**, *111*, 3762 – 3766; *Angew. Chem. Int. Ed.* **1999**, *38*, 3555 – 3559; b) K. C. Nicolaou, G. Vassilikogiannakis, K. B. Simonsen, P. S. Baran, Y.-L. Zhong, V. P. Vidali, E. N. Pitsinos, E. A. Couladouros, *J. Am. Chem. Soc.* **2000**, *122*, 3071 – 3079; c) D. Barnes-Seeman, E. J. Corey, *Org. Lett.* **1999**, *1*, 1503 – 1504.
[56] N. Abe, O. Sugimoto, K. Tanji, A. Hirota, *J. Am. Chem. Soc.* **2000**, *122*, 12 606 – 12 607.
[57] a) I. Sakurai, H. Suzuki, K. Miyaijima, S. Akiyama, S. Simizu, Y. Yamamoto, *Chem. Pharm. Bull.* **1985**, *33*, 5141 – 5143; b) I. Sakurai, H. Suzuki, S. Simizu, Y. Yamamoto, *Chem. Pharm. Bull.* **1988**, *36*, 2003 – 2011.
[58] H. Oikawa, K. Yagi, K. Watanabe, M. Honma, A. Ichihara, *Chem. Commun.* **1997**, 97 – 98.
[59] H. Oikawa, K. Watanabe, K. Yagi, S. Ohashi, T. Mie, A. Ichihara, M. Honma, *Tetrahedron Lett.* **1999**, *40*, 6983 – 6986.
[60] K. Watanabe, H. Oikawa, K. Yagi, S. Ohashi, T. Mie, A. Ichihara, M. Honma, *J. Biochem.* **2000**, *127*, 467 – 473.
[61] K. Watanbe, T, Mie, A. Ichihara, H. Oikawa, M. Honma, *Tetrahedron Lett.* **2000**, *41*, 1443 – 1446.
[62] K. Afarinkia, V. Vinader, T. D. Nelson, G. H. Posner, *Tetrahedron* **1992**, *48*, 9111 – 9171.
[63] A. Parvez, M. I. Choudhary, F. Akhter, M. Noorwala, F. V. Mohammad, N. M. Hasan, T. Zamir, V. U. Ahmad, *J. Org. Chem.* **1992**, *57*, 4339 – 4340.
[64] G. Majetich, Y. Zhang, *J. Am. Chem. Soc.* **1994**, *116*, 4979 – 4980.
[65] A. A. Bell, R. D. Stipanovic, D. H. O'Brien, P. A. Fryxell, *Phytochemistry* **1978**, *17*, 1297 – 1305.
[66] J. A. Marco, J. F. Sanz, E. Falcó, J. Jakupovic, J. Lex, *Tetrahedron* **1990**, *46*, 7941 – 7950.
[67] J. Spörle, H. Becker, M. P. Gupta, M. Veith, V. Huch, *Tetrahedron* **1989**, *45*, 5003 – 5014.
[68] J. Spörle, H. Becker, N. S. Allen, M. P. Gupta, *Phytochemistry* **1991**, *30*, 3043 – 3047.
[69] R. Matusch, H. Haberlein, *Liebigs Ann. Chem.* **1987**, 455 – 457.
[70] A. A. Ahmed, J. Jakupovic, F. Bohlmann, H. A. Regaila, A. M. Ahmed, *Phytochemistry* **1990**, *29*, 2211 – 2215.
[71] A. R. de Vivar, G. Delgado, *Tetrahedron Lett.* **1985**, *26*, 579 – 582.
[72] J. Beauhaire, J. L. Fourrey, M. Vuilhorgne, J. Y. Lallemand, *Tetrahedron Lett.* **1980**, *21*, 3191 – 3194.
[73] F. Gao, H. Wang, T. J. Mabry, *Phytochemistry* **1990**, *29*, 3875 – 3880.
[74] C. Zdero, F. Bohlmann, *Phytochemistry* **1989**, *28*, 3105 – 3120.
[75] J. Jakupovic, A. Schuster, F. Bohlmann, M. O. Dillon, *Phytochemistry* **1988**, *27*, 1113 – 1120.
[76] J. C. Lee, G. A. Strobel, E. Lobkovsky, J. Clardy, *J. Org. Chem.* **1996**, *61*, 3232 – 3233.
[77] C. Li, E. Lobkovsky, J. A. Porco, Jr., *J. Am. Chem. Soc.* **2000**, *122*, 10 484 – 10 485.
[78] a) X. Fu, M. B. Hossain, D. van der Helm, F. J. Schmitz, *J. Am. Chem. Soc.* **1994**, *116*, 12 125 – 12 126; b) for a recent biomimetic

 © 2003 Wiley-VCH Verlag GmbH & Co. KGaA, Weinheim

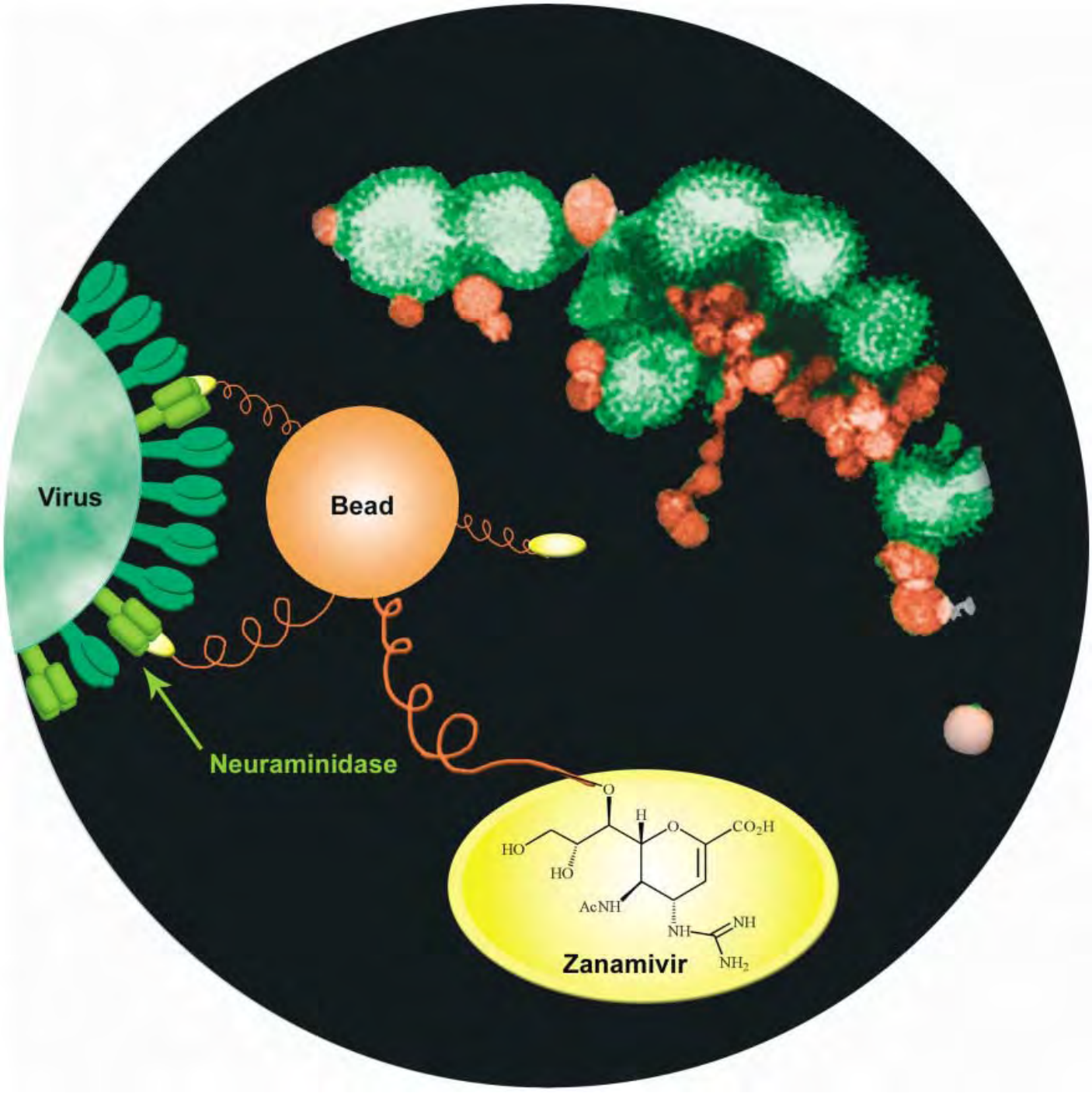
total synthesis of longithorone (see Addendum), see M. E. Layton, C. A. Morales, M. D. Shair, *J. Am. Chem. Soc.* **2002**, *124*, 773 – 775.
[79] J. Kawabata, Y. Fukushi, S. Tahara, J. Mizutani, *Phytochemistry* **1990**, *29*, 2332 – 2334.
[80] P. Tane, K.-E. Bergquist, M. Téné, B. T. Ngadjui, J. F. Ayafor, O. Sterner, *Tetrahedron* **1995**, *51*, 11595 – 11600.
[81] C. P. Falshaw, T. J. King, *J. Chem. Soc. Perkin Trans. 1* **1983**, 1749 – 1752.
[82] D. R. Schroeder, F. R. Stermitz, *Tetrahedron* **1985**, *41*, 4309 – 4320.
[83] W. Hofheinz, P. Schönholzer, *Helv. Chim. Acta* **1977**, *60*, 1367 – 1370.
[84] a) K. Takeda, M. Sato, E. Yoshii, *Tetrahedron Lett.* **1986**, *27*, 3903 – 3906; b) J. Uenishi, R. Kawahama, O. Yonemitsu, *J. Org. Chem.* **1997**, *62*, 1691 – 1701.
[85] A. Fontana, I. Fakhr, E. Mollo, G. Cimino, *Tetrahedron: Asymmetry* **1999**, *10*, 3869 – 3872.
[86] E. J. Corey, L. I. Wu, *J. Am. Chem. Soc.* **1993**, *115*, 9327 – 9328.
[87] G. H. Harris, K. Hoogsteen, K. C. Silverman, S. L. Raghoobar, G. F. Bills, R. B. Lingham, J. L. Smith, H. W. Dougherty, C. Cascales, F. Paláez, *Tetrahedron* **1993**, *49*, 2139 – 2144.
[88] F. Mayerl, Q. Gao, S. Huang, S. E. Klohr, J. A. Matson, D. R. Gustavson, D. M. Pirnik, R. L. Berry, C. Fairchild, W. C. Rose, *J. Antibiot.* **1993**, *46*, 1082 – 1088.
[89] P. Cai, D. Smith, B. Cunningham, S. Brown-Shimer, B. Katz, C. Pearce, D. Venables, D. Houck, *J. Nat. Prod.* **1998**, *61*, 791 – 795.
[90] J. E. Baldwin, A. V. W. Mayweg, K. Neumann, G. J. Pritchard, *Org. Lett.* **1999**, *1*, 1933 – 1935.
[91] H. Weenen, M. H. H. Nkunya, A. A. El-Fadl, S. Harkema, B. Zwanenburg, *J. Org. Chem.* **1990**, *55*, 5107 – 5109.
[92] R. M. Adlington, J. E. Baldwin, G. J. Pritchard, A. J. Williams, D. J. Watkin, *Org. Lett.* **1999**, *1*, 1937 – 1939.
[93] R. Thomas, *Biochem. J.* **1961**, *78*, 807 – 813.
[94] A. D. Harmon, J. M. Edwards, R. J. Highet, *Tetrahedron Lett.* **1977**, 4471 – 4474.
[95] a) B. Schmitt, B. Schneider, *Phytochemistry* **1999**, *52*, 45 – 53; b) B. Schmitt, D. Höschler, B. Schneider, *Phytochemistry* **2000**, *53*, 331 – 337.
[96] D. Höschler, B. Schnieder, *J. Chem. Soc. Chem. Commun.* **1995**, 525 – 526.
[97] a) A. C. Bazan, J. M. Edwards, U. Weiss, *Tetrahedron* **1978**, *34*, 3005 – 3015; b) U. Weiss, *Proc. Indian Acad. Sci. Chem. Sci.* **1984**, *93*, 1159 – 1169.
[98] I. C. Parsons, A. I. Gray, T. G. Hartley, P. G. Waterman, *Phytochemistry* **1993**, *33*, 479 – 482.
[99] J. P. Kutney, T. Inaba, O. L. Dreyer, *Tetrahedron* **1970**, *26*, 3171 – 3184.
[100] P. N. Sharma, A. Shoeb, R. S. Kapil, S. P. Popli, *Phytochemistry* **1980**, *19*, 1258 – 1260.
[101] D. P. Chakraborty, S. Roy, A. Chakraborty, A. K. Mandal, B. K. Chowdhury, *Tetrahedron* **1980**, *36*, 3563 – 3564.
[102] H. Ishii, J.-I. Kobayashi, T. Ishikawa, *Tetrahedron Lett.* **1991**, *32*, 6907 – 6910.
[103] Y. Hano, T. Nomura, S. Ueda, *Chem. Pharm. Bull.* **1989**, *37*, 554 – 556.
[104] a) T. Nomura, Y. Hano, *Nat. Prod. Rep.* **1994**, 205 – 218; b) T. Nomura, *Pure Appl. Chem.* **1999**, *71*, 1115 – 1118.
[105] Y. Hano, T. Nomura, S. Ueda, *Can. J. Chem.* **1994**, *72*, 12 – 14.
[106] Y. Hano, T. Nomura, S. Ueda, *J. Chem. Soc. Chem. Commun.* **1990**, 610 – 613.
[107] Y. Hano, T. Nomura, S. Ueda, *Heterocycles* **1999**, *51*, 231 – 235.
[108] Y. Hano, M. Aida, T. Nomura, S. Ueda, *J. Chem. Soc. Chem. Commun.* **1992**, 1177 – 1178.
[109] S. Yamamura, Y. Terada, Y.-P. Chen, M. Hong, *Bull. Chem. Soc. Jpn.* **1976**, *49*, 1940 – 1948.
[110] a) M. Iguchi, A. Nishiyama, Y. Terada, S. Yamaura, *Tetrahedron Lett.* **1977**, *18*, 4511 – 4514; b) A. Nishiyama, H. Eto, Y. Terada, M. Iguchi, S. Yamamura, *Chem. Pharm. Bull.* **1983**, *13*, 2820 – 2833.
[111] M. Niwa, Y. Terada, M. Nonoyama, S. Yamamura, *Tetrahedron Lett.* **1979**, *20*, 813 – 816.
[112] a) K. T. Suzuki, S. Okuda, H. Niwa, M. Toda, Y. Hirata, S. Yamamura, *Tetrahedron Lett.* **1973**, *14*, 799 – 802; b) H. Niwa, Y. Hirata, K. T. Suzuki, S. Yamamura, *Tetrahedron Lett.* **1973**, *14*, 2129 – 2132.
[113] R. B. Ruggeri, C. H. Heathcock, *Pure Appl. Chem.* **1989**, *61*, 289 – 292.
[114] C. H. Heathcock, *Proc. Natl. Acad. Sci. USA* **1996**, *93*, 14323 – 14327.
[115] C. H. Heathcock, S. Piettre, R. B. Ruggeri, J. A. Ragan, J. C. Kath, *J. Org. Chem.* **1992**, *57*, 2554 – 2566.
[116] a) C. H. Heathcock, J. A. Stafford, *J. Org. Chem.* **1992**, *57*, 2566 – 2574; b) C. H. Heathcock, R. B. Ruggerri, K. F. McClure, *J. Org. Chem.* **1992**, *57*, 2585 – 2594.
[117] A. I. Scott, *Acc. Chem. Res.* **1970**, *3*, 151 – 157.
[118] See, for example, a) W. Carroll, P. A. Grieco, *J. Am. Chem. Soc.* **1993**, *115*, 1164 – 1165; b) M. E. Kuehne, W. G. Bornmann, W. G. Earley, I. Marko, *J. Org. Chem.* **1986**, *51*, 2913 – 2927; c) W. G. Bornmann, M. E. Kuehne, *J. Org. Chem.* **1992**, *57*, 1752 – 1760; d) R. T. Brow, M. Kandasamy, *Tetrahedron Lett.* **2000**, *41*, 3547 – 3550.
[119] a) R. Sakai, T. Higa, C. W. Jefford, G. Bernardinelli, *J. Am. Chem. Soc.* **1986**, *108*, 6404 – 6405; b) H. Nakamura, S. Deng, J. Kobayashi, Y. Ohizumi, Y. Tomotake, T. Matsuzaki, *Tetrahedron Lett.* **1987**, *28*, 621 – 624; c) R. Sakai, S. Kohmoto, T. Higa, C. W. Jefford, G. Bernardinelli, *Tetrahedron Lett.* **1987**, *28*, 5493 – 5496; d) T. Ichiba, R. Sakai, S. Komoto, G. Saucy, T. Higa, *Tetrahedron Lett.* **1988**, *29*, 3083 – 3086.
[120] K. Kondo, H. Shigemori, Y. Kikuchi, M. Ishibashi, T. Sasaki, J. Kobayashi, *J. Org. Chem.* **1992**, *57*, 2480 – 2483.
[121] M. Tsuda, N. Kawasaki, J. Kobayashi, *Tetrahedron* **1994**, *50*, 7957 – 7960.
[122] J. Kobayashi, M. Tsuda, N. Kawasaki, K. Matsumoto, T. Adachi, *Tetrahedron Lett.* **1994**, *35*, 4383 – 4386.
[123] J. Rodríguez, P. Crews, *Tetrahedron Lett.* **1994**, *35*, 4719 – 4722.
[124] F. Kong, R. J. Andersen, T. M. Allen, *Tetrahedron Lett.* **1994**, *35*, 1643 – 1646.
[125] J. E. Baldwin, R. C. Whitehead, *Tetrahedron Lett.* **1992**, *33*, 2059 – 2062.
[126] N. Fusetani, N. Asai, S. Matsunaga, K. Honda, K. Yasumoro, *Tetrahedron Lett.* **1994**, *35*, 3967 – 3970.
[127] J. E. Baldwin, T. D. W. Claridge, A. J. Culshaw, F. A. Heupel, V. Lee, D. R. Spring, R. C. Whitehead, R. J. Boughtflower, I. M. Mutton, R. J. Upton, *Angew. Chem.* **1998**, *110*, 2806 – 2808; *Angew. Chem. Int. Ed.* **1998**, *37*, 2661 – 2663.
[128] a) J. E. Baldwin, T. D. W. Claridge, A. J. Culshaw, F. A. Heupel, S. Smrcková, R. C. Whitehead, *Tetrahedron Lett.* **1996**, *37*, 6919 – 6922; b) J. E. Baldwin, T. D. W. Claridge, A. J. Culshaw, F. A. Heupel, V. Lee, D. R. Spring, R. C. Whitehead, *Chem. Eur. J.* **1999**, *5*, 3154 – 3161.
[129] a) A. Kaiser, X. Billot, A. Gateau-Olesker, C. Marazano, B. C. Das, *J. Am. Chem. Soc.* **1998**, *120*, 8026 – 8034; b) K. Jakubowicz, K. Ben Abdeljelil, M. Herdemann, M.-T. Martin, A. Gateau-Olesker, A. Al Mourabit, C. Marazano, B. C. Das, *J. Org. Chem.* **1999**, *64*, 7381 – 7387.
[130] I. I. Ohtani, T. Ichiba, M. Isobe, M. Kelly-Borges, P. J. Scheuer, *J. Am. Chem. Soc.* **1995**, *117*, 10743 – 10744.
[131] a) A. J. Birch, J. J. Wright, *Chem. Commun.* **1969**, 644 – 645; b) A. J. Birch, J. J. Wright, *Tetrahedron* **1970**, *26*, 2329 – 2344; c) A. J. Birch, R. A. Russel, *Tetrahedron* **1972**, *28*, 2999 – 3008.
[132] A. E. A. Porter, P. G. Sammes, *Chem. Commun.* **1970**, 1103.

 © 2003 Wiley-VCH Verlag GmbH & Co. KGaA, Weinheim

[133] J. Baldas, A. J. Birch, R. A. Russell, *J. Chem. Soc. Perkin Trans. 1* **1974**, 50 – 52.
[134] J. F. Sanz-Cervera, T. Glinka, R. M. Williams, *Tetrahedron* **1993**, *49*, 8471 – 8482.
[135] a) R. M. Williams, E. Kwast, H. Coffman, T. Glinka, *J. Am. Chem. Soc.* **1989**, *111*, 3064 – 3065; b) R. M. Williams, T. Glinka, E. E. Kwast, *J. Am. Chem. Soc.* **1988**, *110*, 5927 – 5929.
[136] L. R. Domingo, J. F. Sanz-Cervera, R. M. Williams, M. T. Picher, J. A. Marco, *J. Org. Chem.* **1997**, *62*, 1662 – 1667.
[137] J. F. Sanz-Cervera, R. M. Williams, J. A. Marco, J. M. López-Sánchez, F. González, M. E. Martínez, F. Sancenón, *Tetrahedron* **2000**, *56*, 6345 – 6358.
[138] a) R. M. Williams, J. F. Sanz-Cervera, F. Sancenón, J. A. Marco, K. Halligan, *J. Am. Chem. Soc.* **1998**, *120*, 1090 – 1091; b) R. M. Williams, J. F. Sanz-Cervera, F. Sancenón, J. A. Marco, K. M. Halligan, *Bioorg. Med. Chem.* **1998**, *6*, 1233 – 1241.
[139] M. Yamazaki, E. Okuyama, M. Kobayashi, H. Inoue, *Tetrahedron Lett.* **1981**, *22*, 135 – 136.
[140] J. G. Ondeyka, R. T. Goegelman, J. M. Schaeffer, L. Kelemen, L. Zitano, *J. Antibiot.* **1990**, *43*, 1375 – 1379.
[141] a) S. E. Blanchflower, R. M. Banks, J. R. Everett, B. R. Manger, C. Reading, *J. Antibiot.* **1991**, *44*, 492 – 497; b) S. E. Blanchflower, R. M. Banks, J. R. Everett, C. Reading, *J. Antibiot.* **1993**, *46*, 1355 – 1363.
[142] R. M. Banks, S. E. Blanchflower, J. R. Everett, B. R. Manger, C. Reading, *J. Antibiot.* **1998**, *50*, 840 – 846.
[143] E. M. Stocking, J. F. Sanz-Cervera, R. M. Williams, C. J. Unkefer, *J. Am. Chem. Soc.* **1996**, *118*, 7008 – 7009.
[144] E. M. Stocking, R. A. Martinez, L. A. Silks, J. F. Sanz-Cervera, R. M. Williams, *J. Am. Chem. Soc.* **2001**, *123*, 3391 – 3392.
[145] a) E. M. Stocking, J. F. Sanz-Cervera, R. M. Williams, *Angew. Chem.* **1999**, *111*, 880 – 883; *Angew. Chem. Int. Ed.* **1999**, *38*, 786 – 789; b) E. M. Stocking, R. M. Williams, J. F. Sanz-Cervera, *J. Am. Chem. Soc.* **2000**, *122*, 9089 – 9098.
[146] E. M. Stocking, J. F. Sanz-Cervera, R. M. Williams, *J. Am. Chem. Soc.* **2000**, *122*, 1675 – 1683.
[147] E. M. Stocking, J. F. Sanz-Cervera, R. M. Williams, *Angew. Chem.* **2001**, *113*, 1336 – 1338; *Angew. Chem. Int. Ed.* **2001**, *40*, 1296 – 1298.
[148] J. F. Sanz-Cervera, R. M. Williams, *J. Am. Chem. Soc.* **2002**, *124*, 2556 – 2559.
[149] D. A. Vosburg, C. D. Vanderwal, E. J. Sorensen, *J. Am. Chem. Soc.* **2002**, *124*, 4552 – 4553.
[150] D. A. Evans, J. T. Starr, *Angew. Chem.* **2002**, *114*, 1865 – 1868; *Angew. Chem. Int. Ed.* **2002**, *41*, 1787 – 1790.
[151] a) C. D. Vanderwal, D. A. Vosburg, S. Weiler, E. J. Sorensen, *Org. Lett.* **1999**, *1*, 645 – 648; b) C. D. Vanderwal, D. A. Vosburg, E. J. Sorensen, *Org. Lett.* **2001**, *3*, 4307 – 4310.
[152] For the isolation and structure determination of FR182877 (**376**), see a) B. Sato, H. Muramatsu, M. Miyauchi, Y. Hori, S. Takase, M. Hino, S. Hashimoto, H. Terano, *J. Antibiot.* **2000**, *53*, 123 – 130; b) B. Sato, H. Nakajima, Y. Hori, M. Hino, S. Hashimoto, H. Terano, *J. Antibiot.* **2000**, *53*, 615 – 622.
[153] R. Höfs, M. Walker, A. Zeeck, *Angew. Chem.* **2000**, *112*, 3400 – 3403; *Angew. Chem. Int. Ed.* **2000**, *39*, 3258 – 3261.
[154] For a recent report on an inverse-electron-demand Diels–Alder reaction in the polyketide biosynthesis of (+)-desoxygaliellalactone in the fungus *Galiella rufa*, see M. Johansson, B. Kopcke, H. Anke, O. Sterner, *Angew. Chem.* **2002**, *114*, 2261 – 2264; *Angew. Chem. Int. Ed.* **2002**, *41*, 2158 – 2160.

 © 2003 Wiley-VCH Verlag GmbH & Co. KGaA, Weinheim

Communications



The transmission electron microscopy image illustrates the capture and aggregation of influenza virions by using microspheres (average diameter 32 nm), which have been coated with a tethered form of zanamivir, a potent neuraminidase inhibitor. For more information see the communication by J. L. McKimm-Breschkin, K. G. Watson et al. on the following pages.

DOI: 10.1002/anie.200250402
© 2003 Wiley-VCH Verlag GmbH & Co. KGaA, Weinheim

Towards Influenza Detection

Tethered Neuraminidase Inhibitors That Bind an Influenza Virus: A First Step Towards a Diagnostic Method for Influenza

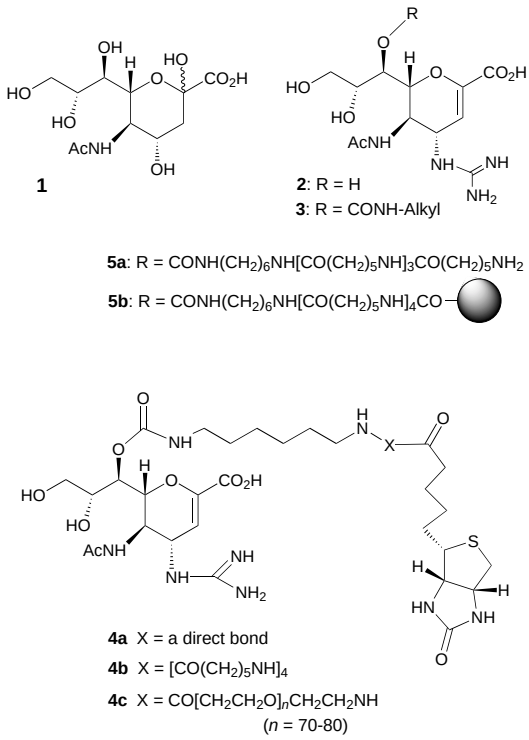
Jennifer L. McKimm-Breschkin, Peter M. Colman, Betty Jin, Guy Y. Krippner, Mandy McDonald, Phillip A. Reece, Simon P. Tucker, Lynne Waddington, Keith G. Watson,* and Wen-Yang Wu*

Influenza viruses are isolated as small (80 to 120 nm diameter), generally spherical particles.[1] The lipid bilayer envelope of the virus is derived from the host cell and protruding from this membrane on the surface of the virus are two virus-encoded glycoproteins, hemagglutinin (HA) and neuraminidase (NA). HA is the major surface antigen of the virus and is responsible for the binding of virions to the receptors of the host cell and for fusion between the virion envelope and the host cell.[2] NA, the minor surface antigen, is a glycosidase that cleaves sialic acid, **1** (*N*-acetylneuraminic acid) from the terminal position of glycoproteins and it is thought to be important for the release of virions from the surface of the host cell, and possibly also enhances infectivity by allowing movement of the virus through the mucins lining the respiratory tract.[3] Herein we describe the synthesis of tethered NA inhibitors, which potentially have a high affinity for all strains of influenza A and B, and can be used to capture influenza virions.

The structure of influenza NA has been extensively studied and found to consist of a tetrameric head that is anchored to the viral membrane by a long stalk.[4] Studies of the X-ray crystal structure of influenza NA bound to sialic acid revealed the location of the enzyme active site[5] and showed that it is lined with about 20 amino acids that are invariant in the NA of all known strains of influenza A and B. On the basis of the X-ray crystallographic structural information for influenza NA, several novel inhibitors were designed and synthesised[6] including 2,3-dehydro-2,4-dideoxy-4-guanidino-*N*-acetyl-neuraminic acid, **2** (4-guanidino-Neu5Ac2en, zanamivir), which has been approved for the treatment of influenza.[7]

The X-ray crystal structure of zanamivir bound to influenza NA indicates that the 7-hydroxy group has no close interactions with the protein, and in fact points directly out and away from the active site.[8] Based on this information, Andrews et al. prepared a series of 7-carbamate derivatives **3** of zanamivir **2** and found that the compounds retain high affinity for influenza NA and many also have good antiviral properties.[9] Importantly, compounds **3** showed a similar affinity for both influenza A and B, in contrast to other derivatives of **2** with altered glycerol side chains.[10]

Seeking an influenza-detection method that is independent of viral strain, we explored the feasibility of using functionalized 7-carbamate derivatives of zanamivir to selectively capture influenza virions. Thus zanamivir-biotin conjugates **4a–c** with different length linkers were prepared (Scheme 1) as outlined in Scheme 2 and their inhibition



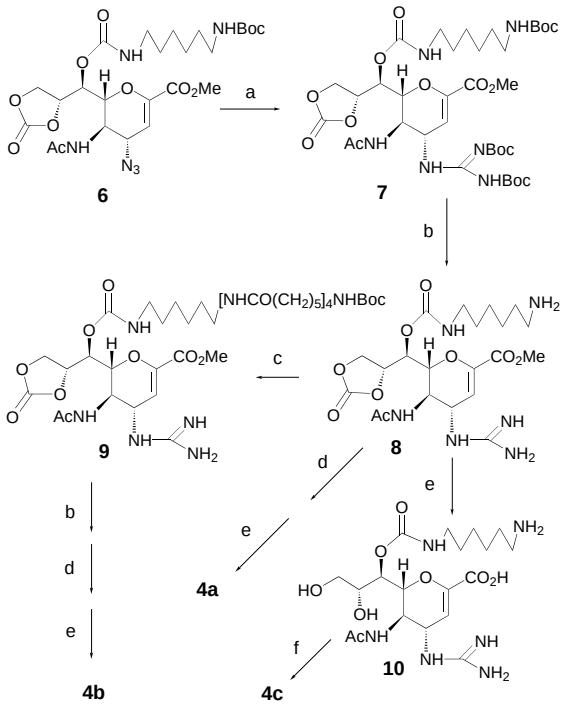
Scheme 1. Structure of sialic acid **1**, zanamivir **2** and 7-carbamate derivatives **3**, **4a–c** and **5a–b.** In the case of microspheres **5b**, there are many **5a** units bound to each bead.

constants for influenza NA were measured in an enzyme assay. The data (Table 1) shows that all three conjugates, although not as active as **2**, are good inhibitors of influenza NA and bind to three representative influenza strains with approximately equal affinity. There is a gradual reduction in binding affinity of zanamivir derivatives **4a–c** as the size of the appended group increases, but even compound **4c**, which has a 3400 dalton polyethylene glycol (PEG) spacer group

[*] Dr. J. L. McKimm-Breschkin,[+] Prof. P. M. Colman,[++] M. McDonald, L. Waddington
Biomolecular Research Institute
343 Royal Parade, Parkville
Victoria 3052 (Australia)
E-mail: jennifer.mckimm-breschkin@csiro.au
Dr. K. G. Watson,[++] B. Jin, Dr. G. Y. Krippner, Dr. P. A. Reece, Dr. S. P. Tucker, Dr. W.-Y. Wu
Biota Holdings, Level 4
616 St Kilda Road, Melbourne, Victoria 3004 (Australia)
E-mail: kwatson@wehi.edu.au
[+] new address:
CSIRO Division of Health Sciences & Nutrition
343 Royal Parade, Parkville, Victoria 3052 (Australia)
Fax: (+61) 3-9662-7101
[++] new address:
Structural Biology Division
Walter & Eliza Hall Institute of Medical Research
1G Royal Parade, Parkville, Victoria 3050 (Australia)
Fax: (+61) 3-9347-0852

Supporting information for this article is available on the WWW under http://www.angewandte.org or from the author.

 © 2003 Wiley-VCH Verlag GmbH & Co. KGaA, Weinheim DOI: 10.1002/anie.200250402



Scheme 2. Synthesis of zanamivir–biotin conjugates **4a–c**. a) H_2, Pd–C, MeOH/Toluene, room temperature, 1 h, then bis-Boc-pyrazole-1-carboxamidine, MeOH, 30 °C, 5 days, 49%; b) TFA, room temperature, 1 h; c) $HO_2C(CH_2)_5[NHCO(CH_2)_5]_3NHBoc$, KO*t*Bu, *i*BuOCOCl, MeOH, 0→20 °C, 32%; d) NHS-biotin, K_2CO_3, H_2O/acetone, room temperature, 3 h; e) Et_3N, H_2O/MeOH, room temperature, 16 h; f) NHS-$COCH_2CH_2$-3400PEG-NH-biotin, pyridine, room temperature, 3 days, 36%.

Table 1: Inhibition of influenza virus NA by **2** and biotin conjugates **4a–c**.

Compound	IC_{50} [nM] on neuraminidase from three influenza types		
	A/NWS/Tokyo/3/67(H1N2)	A/NWS/G70C/75/(H1N9)	B/Victoria/02/87
2	1.3	1.0	2.5
4a	10	4.8	22
4b	30	20	50
4c	180	200	220

(approximately 75 PEG units or 225 atoms in length), still shows submicromolar inhibition (IC_{50} 2×10^{-7} M) of the enzyme.

The ability of the biotinylated compounds **4a–c** to capture influenza particles was tested in an ELISA-based assay. Avidin coated plates were saturated with the conjugates **4a–c**, the plates were washed to remove unbound conjugate, and serial dilutions of influenza virus were added starting with 100 Hemagglutinating units (HAU, 100 HAU is approximately 5×10^6 virus particles). The plates were washed again to remove unbound virus, and the captured influenza was detected by using an anti-HA antiserum–horseradish peroxidase (HRP) conjugate and chromogenic substrate. Initial experiments with compound **4a**, which has only a short 1,6-hexanediamine spacer group between the drug and biotin molecules, failed to show significant capture of the virus (data not shown), whereas experiments with a biotinylated anti-neuraminidase antibody control resulted in a strong signal. In contrast to **4a**, compounds **4b** and **4c** gave rise to strong positive signals, thus indicating the successful capture of the influenza virus, with the longer PEG3400 conjugate **4c** giving rise to a signal that was similar to that from the 1 μg mL^{-1} NA antibody–biotin control NC-10 (Figure 1).

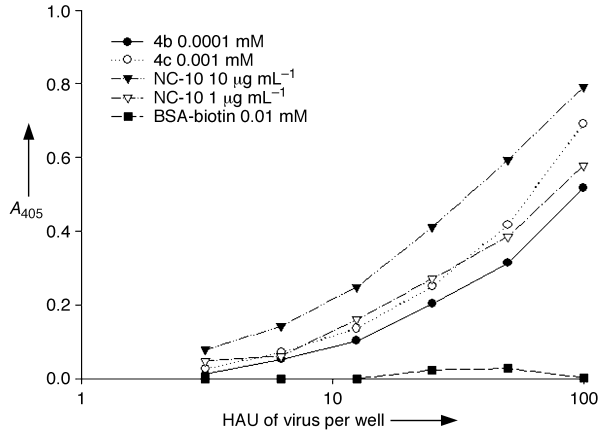


Figure 1. ELISA based detection of influenza A (NWS/G70C) captured with biotinylated compounds **4b–c**, or biotinylated NA–antibody control NC-10, bound to avidin coated microplate wells and detected with a HA–Ab/Ab–HRP enzyme conjugate.

Previous reports have demonstrated the importance of a long spacer group in the application of biotin[11] and antibody[12] conjugates for the capture macromolecules or binding to microspheres. The ability of tethered NA inhibitors **4a–c** to capture influenza may be determined by several steric factors including the numerous HA spikes on the influenza surface, the presence of oligosaccharides on the NA heads,[4] and the fact that the enzyme active site is about 10 Å below the surface of the protein. Based on the calculated root mean square length (end-to-end distance) for PEG3400 in water, the tethered zanamivir in surface-bound conjugate **4c** would be an average distance of about 45 Å from the avidin surface (Figure 2).[13] The slightly superior capture of virus by the

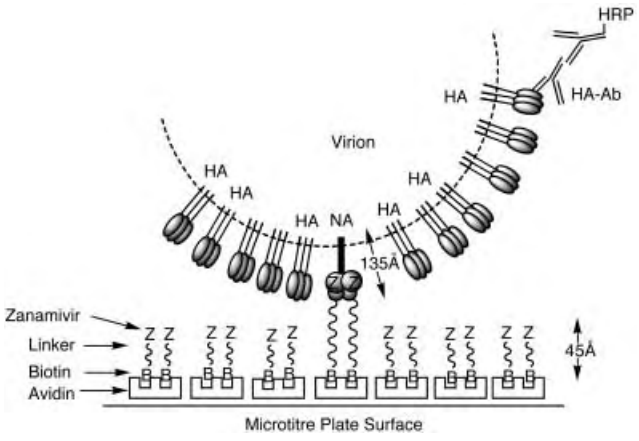


Figure 2. Schematic representation of a captured influenza virion showing the NA, HA, and ELISA detection

 © 2003 Wiley-VCH Verlag GmbH & Co. KGaA, Weinheim

biotinylated NA-antibody control NC-10 (Figure 1) may be due to a combination of factors including the greater affinity ($K_D = 1.3 \times 10^{-8}$ M) of the NA/antibody interaction,[14] and a reduction of surface steric effects resulting from the antibody binding site being held further from the surface by the larger (> 100 Å) framework of the antibody molecule.

To visualize the interaction between influenza virions and tethered zanamivir we prepared microspheres coated with covalently bound zanamivir for examination under transmission electron microscopy (TEM). Thus the zanamivir tetracaproamide derivative **5a** was coupled with carboxylated polystyrene microspheres of average diameter 32 nm to give functionalized beads represented by formula **5b** (Scheme 1). When mixed with influenza and examined by TEM, microspheres **5b** were observed to interact closely with the surface of the virions (Figure 3A). In addition, self-aggregation of the microspheres was commonly seen, along with spheres, which were either decorated with free NA molecules or cross-linked to other spheres by NA molecules or viral membrane fragments containing NA. To confirm the involvement of NA binding in the cross-linking role played by **5b**, excess zanamivir **2** was added, whereupon the previously observed aggregates were almost completely eliminated (Figure 3B). To further exclude the possibility that the association of microspheres **5b** with influenza virus was nonspecific, a second experiment was performed in which Respiratory Syncytial Virus (RSV), a virus that has no NA, was mixed with the influenza virus suspension, and the sample was treated as described above. It was found that while the great majority of influenza virions were closely associated with microspheres, RSV virions were almost always isolated, even when **5b** was present in considerable excess (TEM not shown).

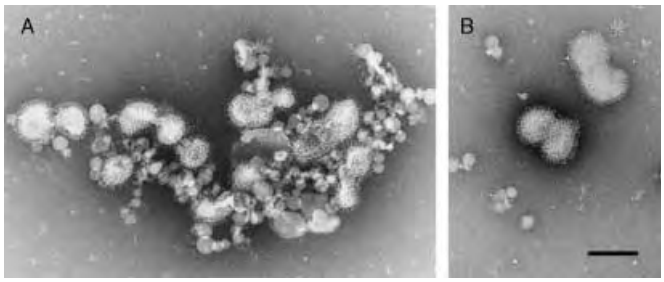


Figure 3. A) TEM images of influenza virus showing 32(±10 nm) microspheres **5b** binding to virions and causing aggregation. Some spheres appear to be decorated or cross-linked by free NA or small fragments of cell membrane containing NA. B) Addition of excess zanamivir **2** prevents virus aggregation by **5b**. Magnification bar 100 nm.

Antibodies to the influenza surface proteins HA or NA, being strain-specific, are not useful for the general detection of influenza and thus the limitation in our present results is the use of a strain-specific anti-HA antibody/enzyme conjugate as the detection reagent. One possible extension of our results would be to employ a nonspecific influenza capture surface and then use a neuraminidase-binding reagent, such as compound **4c**, together with an avidin/enzyme conjugate, for the detection stage. For example, there are various reported methods for the general, nonspecific capture of influenza virus onto a surface including the use of the fetuin (a sialylated glycoprotein),[15] nitrocellulose[16] and nylon membrane.[17]

There is a clear need for more rapid, specific and clinically relevant detection methods for influenza.[18] The results of our experiments indicate that the use of tethered NA inhibitor **4c** or the microspheres **5b** could form the basis for a new detection method for all strains of influenza A and B. We believe this to be the first demonstration that it is possible to take an inhibitor of a viral enzyme, tether it to a surface, and then capture that virus.

Experimental Section

Details of the synthetic methods used for the preparation of compounds **4a–c** are provided in the Supporting Information. Briefly, compounds **4a–c** and **5a** were prepared by starting from the known 4-azido sialic acid derivative **6**[9] as outlined in Scheme 2. Zanamivir coated microspheres **5b** were prepared by coupling 32 nm carboxylated polystyrene beads (Bangs Laboratories) with the tetracaproamide derivative **5a** of zanamivir.

The NA inhibition assay was carried out following the method of Potier et al.[19] by using methylumbelliferone-*N*-acetyl neuraminic acid as substrate. All samples were tested in duplicate and for comparison zanamivir **2** and 2,3-dehydro-2-deoxy *N*-acetyl neuraminic acid (DANA) were included in each assay.

ELISA experiments: PVC 96-well ELISA plates (Dynatech, USA) were coated overnight with avidin, 2 μg mL^{-1} in PBS. Plates were blocked with PBS/Tween 20 (0.1%) and washed with PBS prior to the addition of the biotinylated compounds **4a–c.** A biotinylated anti-NA antibody NC-10[20] (specific to the test strain of influenza) was used as a positive control and a BSA-biotin conjugate provided a negative control. After a 1 hour incubation, the plates were washed to remove unbound compound and then, starting with 100 Hemagglutinating units (HAU) of virus, serial twofold dilutions of the reassortant NWS/G70C (H1N9, obtained from R. Webster[20]) were added and incubated for 1 hour at room temperature. After another wash, captured virus were detected by treatment with a polyclonal anti-HA antiserum, followed by a sheep antirabbit-horseradish peroxidase conjugate and treatment with a chromogenic (ABTS) substrate. Very similar results were obtained with plates coated with 0.1, 0.01 or 0.001 mM of the biotinylated compounds, thus indicating that all concentrations were saturating the available avidin sites.

TEM experiments: Influenza virus was diluted in phosphate-buffered saline (PBS) to a concentration of approximately 10^7 particles mL^{-1}. Mixtures of viral suspension and microspheres **5b** in a variety of ratios were incubated at 4°C for 15 mins. Droplets of the mixture (3 μL) were then applied to glow-discharged, carbon-coated 400-mesh grids for 30 s and were stained with 2% potassium phosphotungstate at a pH of 6.5. The grids were air-dried and examined at 60 kV accelerating voltage in a JEOL 100B transmission electron microscope at magnifications between 40000 and 100000×. Electron micrographs were recorded on Kodak SO-163 film and were developed in Kodak D19 developer. In some experiments excess zanamivir **2** (100 μM) was added to the mixture of virus and microspheres **5b** prior to incubation.

Received: October 21, 2002
Revised: April 24, 2003 [Z50402]

Keywords: antiviral agents · glycoconjugates · hydrolases · influenza viruses · sialic acids

 © 2003 Wiley-VCH Verlag GmbH & Co. KGaA, Weinheim

[1] R. G. Webster, W. J. Beam, O. T. Gorman, T. M. Chambers, Y. Kawaoka, *Microbiol. Rev.* **1992**, *56*, 152.
[2] J. J. Skehel, D. C. Wiley, *Annu. Rev. Biochem.* **2000**, *69*, 531.
[3] C. Liu, M. C. Eichelberger, R. W. Compans, G. M. Air, *J. Virol.* **1995**, *69*, 1099.
[4] J. N. Varghese, P. M. Colman, *J. Mol. Biol.* **1991**, *221*, 473.
[5] J. N. Varghese, J. L. McKimm-Breschkin, J. B. Caldwell, A. A. Kortt, P. M. Colman, *Proteins Struct. Funct. Genet.* **1992**, *14*, 327.
[6] J. C. Dyason, M. von Itzstein, *Aust. J. Chem.* **2001**, *54*, 663, and references therein.
[7] S. M. Cheer, A. J. Wagstaff, *Drugs* **2002**, *62*, 71.
[8] J. N. Varghese, V. C. Epa, P. M. Colman, *Protein Sci.* **1995**, *4*, 1081.
[9] D. M. Andrews, P. C. Cherry, D. C. Humber, P. S. Jones, S. P. Keeling, P. F. Martin, C. D. Shaw, S. Swanson, *Eur. J. Med. Chem.* **1999**, *34*, 563.
[10] P. W. Smith, S. L. Sollis, P. D. Howes, P. C. Cherry, K. N. Cobley, H. Taylor, A. R. Whittington, Scicinski, R. C. Bethell, N. Taylor, T. Skarzynski, A. Cleasby, O. Singh, A. Wonacott, J. Varghese, P. Colman, *Bioorg. Med. Chem. Lett.* **1996**, *6*, 2931.
[11] a) K. E. Meier, A. E. Ruoho, *Methods Enzymol.* **1990**, *184*, 660; b) J. Y. Wong, T. L. Kuhl, J. N. Israelachvili, N. Mullah, S. Zalipsky, *Science* **1997**, *275*, 820.
[12] C. Bieniarz, M. Husain, G. Barnes, C. A. King, C. J. Welch, *Bioconjugate Chem.* **1996**, *7*, 88.
[13] a) C. Sarmoria, D. Blankschtein, *J. Phys. Chem.* **1992**, *96*, 1978; b) S. P. Powers, I. Foo, D. Pinon, U. G. Klueppelberg, J. F. Hedstrom, L. J. Miller, *Biochemistry* **1991**, *30*, 676.
[14] W. R. Tulip, V. R. Harley, R. G. Webster, J. Novotny, *Biochemistry* **1994**, *33*, 7986.
[15] a) A. S. Gambaryan, M. N. Matrosovich, *J. Virol. Methods* **1992**, *39*, 111; b) G. B. Sigal, M. Mammen, G. Dahmann, G. M. Whitesides, *J. Am. Chem. Soc.* **1996**, *118*, 3789.
[16] K. Furuya, S. Noro, T. Yamagishi, N. Sakurada, *J. Virol. Methods* **1984**, *9*, 193.
[17] G. Duverlie, L. Houbart, B. Visse, J.-J. Chomel, J.-C. Manuguerra, C. Hannoun, J. Orfila, *J. Virol. Methods* **1992**, *40*, 193.
[18] A. Linde, *Antiviral Res.* **2001**, *51*, 81.
[19] M. Potier, L. Mameli, M. Belisle, L. Dallaire, S. B. Melancon, *Anal. Biochem.* **1979**, *94*, 287.
[20] R. G. Webster, G. M. Air, D. W. Metzger, P. M. Colman, J. N. Varghese, A. T. Baker, W. G. Laver, *J. Virol.* **1987**, *61*, 2910.

 © 2003 Wiley-VCH Verlag GmbH & Co. KGaA, Weinheim

Electrochemical Transduction

Self-Assembled Monolayers That Transduce Enzymatic Activities to Electrical Signals**

*Woon-Seok Yeo and Milan Mrksich**

The development of chemical methods to control the interactions of materials with proteins, enzymes, and cells is important to fundamental studies in chemical biology and to many applications in biotechnology.[1] A wide range of strategies for immobilizing ligands to materials now allows excellent control over ligand–receptor interactions at an interface. An emerging theme in this field aims to add dynamic control over ligand–receptor interactions to enable the design of active substrates that can manipulate, in real time, the interactions of proteins and cells with a surface. Okano and co-workers, for example, exploited the thermal-phase transition of poly(*N*-isopropylacrylamide) films to demonstrate substrates that could reversibly modulate the adhesion of cells.[2] Willner and co-workers developed a class of monolayer substrates in which the activities of immobilized ligands can be reversibly switched with light.[3] We have developed electroactive substrates that allow discrete ligands to be switched on or off in response to electrical potentials.[4] These advances have provided an unprecedented ability to study and manipulate the adhesion of cells. In this communication, we extend on these early reports by demonstrating an interface that can specifically translate biological activities to electrical signals.[5] This example now establishes the basis for designing electroactive interfaces that not only manipulate but also respond to cellular activities.

Our approach for transducing a biological activity to an electrical signal relies on the enzymatic conversion of a redox-inactive molecule to generate a redox-active product (Figure 1). By tethering the substrate molecule to an electrode, the redox-active product resulting from enzyme action can be efficiently detected. We implement this strategy with the enzyme cutinase[6] and 4-hydroxyphenyl valerate as the substrate. Cutinase is a 22 kDa serine esterase that efficiently removes the acyl group from this substrate, to produce the redox-active hydroquinone.[7]

We prepared a self-assembled monolayer (SAM) containing an alkanethiolate terminated by a 4-hydroxyphenyl valerate moiety [8], and a tri(ethylene glycol)-terminated alkanethiolate in a ratio of 1:2. We used MALDI-TOF mass spectrometry to establish that the interfacial enzymatic

[*] Prof. M. Mrksich, W.-S. Yeo
Department of Chemistry
Institute for Biophysical Dynamics, The University of Chicago
5735 S. Ellis Ave., Chicago, IL 60637 (USA)
Fax: (+1) 773-702-0805
E-mail: mmrksich@midway.uchicago.edu

[**] This work was supported by the National Science Foundation and the Materials Research Science and Engineering Center.

Supporting information for this article is available on the WWW under http://www.angewandte.org or from the author.

 DOI: 10.1002/anie.200250862 © 2003 Wiley-VCH Verlag GmbH & Co. KGaA, Weinheim

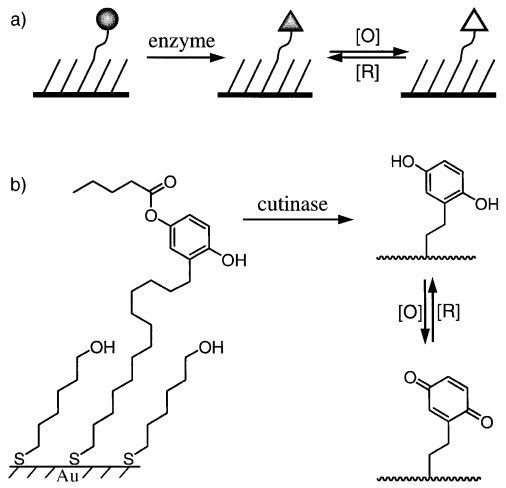


Figure 1. Strategy for designing an interface that transduces a biological activity to an electrical signal. a) A substrate molecule for an enzyme is immobilized to a self-assembled monolayer. The enzymatic reaction converts the substrate into a redox-active product, which can be detected and quantified with cyclic voltammetry; b) this work uses monolayers presenting 4-hydroxyphenyl valerate, which is efficiently hydrolyzed by cutinase, a serine esterase, to afford the hydroquinone. The reversible electrochemical oxidation of the hydroquinone to the corresponding benzoquinone produces an electrical signal.

reaction proceeds to give the intended products. The mass spectrum of the monolayer showed two major peaks at m/z 969.9 and 1246.1 (Figure 2a).[9] The first peak corresponds to the mixed disulfide derived from the two alkanethiolate species, while the second peak results from the symmetric disulfide derived from the 4-hydroxyphenyl valerate terminated alkanethiolate. An identical monolayer was subjected to an enzymatic reaction by applying a solution containing cutinase (10 nM) in phosphate-buffered saline (PBS) at

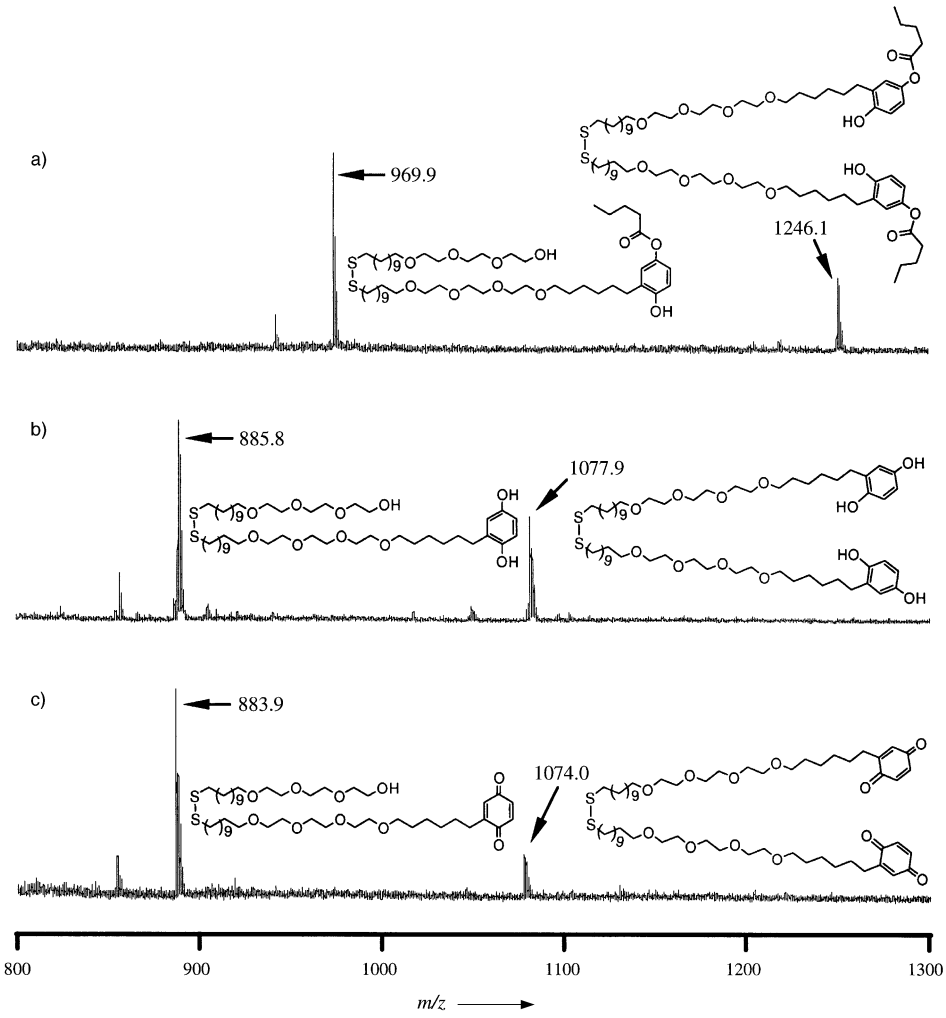


Figure 2. Characterization of the interfacial enzymatic reaction with MALDI-TOF mass spectrometry. All peaks correspond to sodium adducts of disulfides. a) A monolayer containing alkanethiols terminated in 4-hydroxyphenyl valerate and tri(ethylene glycol) groups gave disulfide peaks corresponding to unsymmetric and symmetric disulfides; b) after treatment with cutinase (10 nM in PBS at pH 7.4 for 10 min), the original peaks were absent and gave rise to two new peaks corresponding to the product hydroquinone; c) oxidation of the resulting hydroquinone (10 mM iron(III) chloride in PBS at pH 7.4) afforded the corresponding benzoquinone.

 © 2003 Wiley-VCH Verlag GmbH & Co. KGaA, Weinheim

pH 7.4. The reaction was stopped after 10 min and the monolayer was analyzed by MALDI-TOF. Two new peaks corresponding to disulfides containing the product hydroquinone were observed (Figure 2b). Significantly, the peaks for the parent ester are absent, which shows that the enzymatic reaction proceeded in essentially quantitative yield. Finally, treatment of the monolayer with iron(III) chloride (10 mM in PBS) efficiently converted the hydroquinone groups to the corresponding benzoquinone groups (Figure 2c).

Cyclic voltammetry was then employed to monitor the enzymatic reaction in real time.[10] For these experiments, monolayers were prepared from a mixture of the 4-hydroxyphenyl valerate terminated alkanethiol and 6-mercapto-1-hexanol (Figure 1b).[11] Cyclic voltammetry showed that the monolayer was not electroactive, but displayed only a non-faradaic current that remained constant over 50 consecutive cycles. Upon the addition of cutinase to the medium (10 nM), however, voltammetric waves for both oxidation and reduction appeared and increased smoothly with time until they reached a maximum value (Figure 3).[12] These waves are due to the oxidation of the enzymatically generated hydroquinone

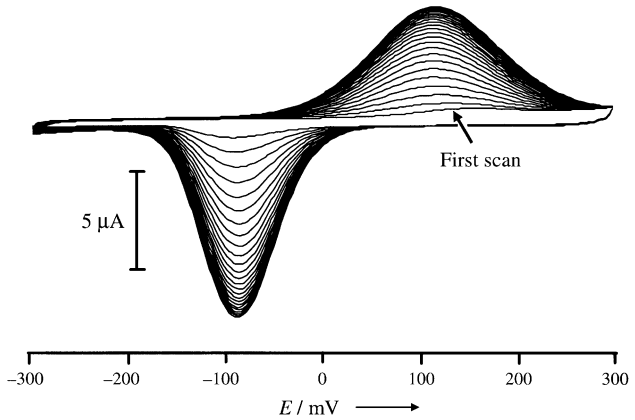


Figure 3. A series of cyclic voltammograms showing the enzymatic cleavage of the 4-hydroxyphenyl valerate group on the monolayer. Prior to cutinase treatment, cyclic voltammetry showed only a non-faradaic current. After cutinase was added to the solution (10 nM), peak currents for both reduction and oxidation appeared and increased with time as the enzymatic reaction generated hydroquinone groups on the monolayer.

group, and the corresponding reduction of the benzoquinone. To provide further evidence that the enzymatic reaction indeed generated the hydroquinone, we treated the resulting monolayer with a tri(ethylene glycol)-substituted cyclopentadiene (5 mM) and found that voltammetric peaks decreased, as expected for a Diels–Alder reaction between the diene and benzoquinone (data not shown).[4a,5] As a final control, we found that cutinase, which was inactivated by a 4-nitrophenyl phosphonate irreversible inhibitor, had no effect on the monolayer.[13]

Finally, we investigated the kinetic profile for cutinase action on the immobilized 4-hydroxyphenyl valerate groups. Figure 4a shows the time-dependent increase in the density of hydroquinone for a series of monolayers that initially present

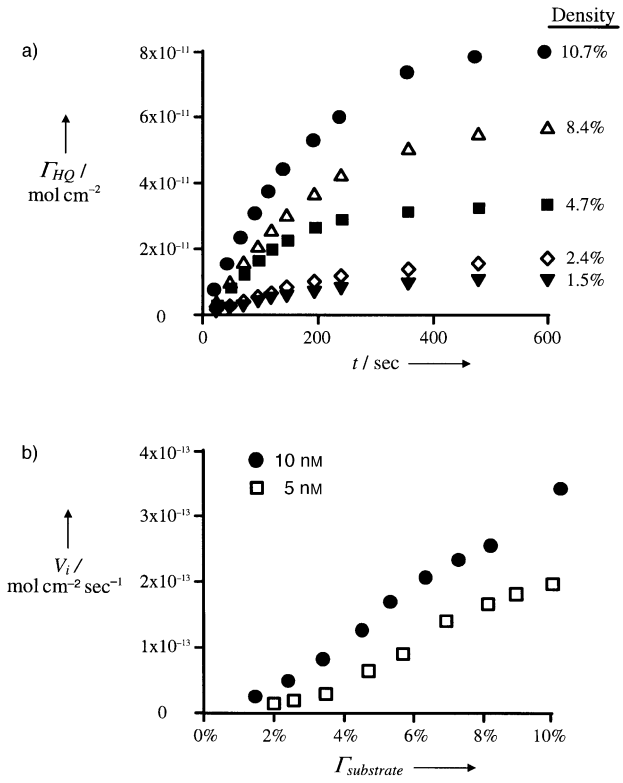


Figure 4. Kinetic profile for the interfacial enzymatic reaction. a) The amount of hydroquinone produced on the monolayer (Γ_{HQ}) was determined by cyclic voltammetry and is plotted versus time for several monolayers presenting 4-hydroxyphenyl valerate at densities ranging from 1.5% to 10.7%; b) the initial rates of the enzymatic reaction (for both 5 nM and 10 nM cutinase) depend linearly on the density of 4-hydroxyphenyl valerate on the monolayers ($\Gamma_{substrate}$).

4-hydroxyphenyl valerate at densities ranging from 1.5% to 10.7%.[14] For each monolayer, the density of hydroquinone initially increased linearly with time, and leveled off at a maximum density that is determined by the initial density of 4-hydroxyphenyl valerate on the monolayer. The initial reaction rates at two different concentrations of cutinase (5 nM and 10 nM) also increased approximately linearly with the density of 4-hydroxyphenyl valerate on the monolayer (Figure 4b). Overall, these results show that this interfacial enzymatic reaction is kinetically well-behaved and that the enzymatic activity can be measured in real time with excellent sensitivity.

This work describes a new strategy for transducing biological activities into electrical signals. The biological and electrical activities are linked by way of a redox-active molecule that results from an enzymatic conversion. This work represents an important advance on previous demonstrations of dynamic substrates that modulate activities of ligands in response to electrical potential. With this new demonstration, it is now possible to design interfaces that transduce biological and electrical signals in both directions across the interface. We believe that this strategy will prove important for fundamental studies of enzymatic activity at interfaces, for mechanistic studies of cellular activity, and for the development of cell-based sensors. For the latter oppor-

 © 2003 Wiley-VCH Verlag GmbH & Co. KGaA, Weinheim

tunity, cells can be engineered with enzymes that induce electrical signals—in analogy to the common use of green fluorescent protein (GFP) as a fluorescent reporter—and give a purely electrical interface for recording cellular dynamics. A further attraction of this methodology is that it can take advantage of many enzyme–substrate pairs and therefore realize multiple channels of electrochemical coupling between cells and electrodes.

Received: December 27, 2002 [Z50862]

Keywords: cyclic voltammetry · enzymes · interfaces · redox chemistry · self-assembly

[1] a) M. Mrksich, G. M. Whitesides, *Annu. Rev. Biophys. Biomol. Struct.* **1996**, *25*, 55; b) A. K. Dillow, M. Tirrell, *Curr. Opin. Solid State Mater. Sci.* **1998**, *3*, 252; c) M. Mrksich, *Chem. Soc. Rev.* **2000**, *29*, 267; d) I. Willner, E. Katz, *Angew. Chem. Int. Ed.* **2000**, *39*, 1180; e) D. R. Jung, R. Kapur, T. Adams, K. A. Giuliano, M. Mrksich, H. G. Craighead, D. L. Taylor, *Crit. Rev. Biotechnol.* **2001**, *21*, 111.

[2] a) T. Okano, N. Yamata, J. Sakai, Y. Sakurai, *Biomaterials* **1995**, *16*, 297–303; b) T. O. Collier, J. M. Anderson, A. Kikuchi, T. Okano, *J. Biomed. Mater. Res.* **2002**, *59*, 136.

[3] a) R. Blonder, E. Katz, I. Willner, V. Wray, A. F. Bückmann, *J. Am. Chem. Soc.* **1997**, *119*, 11747; b) R. Blonder, S. Levi, G. Tao, I. Ben-Dov, I. Willner, *J. Am. Chem. Soc.* **1997**, *119*, 10467.

[4] a) M. N. Yousaf, M. Mrksich, *J. Am. Chem. Soc.* **1999**, *121*, 4286; b) C. D. Hodneland, M. Mrksich, *J. Am. Chem. Soc.* **2000**, *122*, 4235; c) W. -S. Yeo, C. D. Hodneland, M. Mrksich, *ChemBioChem* **2001**, *2*, 590.

[5] a) M. N. Yousaf, B. T. Houseman, M. Mrksich, *Proc. Natl. Acad. Sci. USA* **2001**, *98*, 5992; b) M. N. Yousaf, B. T. Houseman, M. Mrksich, *Angew. Chem. Int. Ed.* **2001**, *40*, 1093.

[6] C. Martinez, P. De Geus, M. Lauwereys, G. Matthyssens, C. Cambilau, *Nature* **1992**, *356*, 6370.

[7] a) Y. Sato, M. Fujita, F. Mizutani, K. Uosaki, *J. Electroanal. Chem.* **1996**, *409*, 145; b) M. N. Yousaf, E. W. L. Chan, M. Mrksich, *Angew. Chem. Int. Ed.* **2000**, *39*, 1943; c) Y. Kwon, M. Mrksich, *J. Am. Chem. Soc.* **2002**, *124*, 806.

[8] The 4-hydroxyphenyl valerate terminated alkanethiol with tri(ethylene glycol) moiety was synthesized in ten steps from commercially available reagents. All intermediates gave satisfactory ^{1}H NMR spectra.

[9] For the mass spectrometry experiments, we used the tri(ethylene glycol)-containing alkanethiols to increase the molecular weight, since ions below *m*/*z* 600 are not easily analyzed due to overlap with signals from the organic matrix. The monolayers were analyzed on a Voyager-DE Biospectroscopy mass spectrometer using 2,5-dihydroxyl benzoic acid (1 μL of a 10 mg mL^{-1} solution in acetonitrile) as a matrix. Sodium adducts of disulfides are the major species that are observed in MALDI spectra of the SAMs of alkanethiolates: see J. Su, M. Mrksich, *Angew. Chem. Int. Ed.* **2002**, *41*, 4715, and J. L. Trevor, K. R. Lykke, M. J. Pellin, L. Hanley, *Langmuir* **1998**, *14*, 1664.

[10] Cyclic voltammetry was performed with a Bioanalytical Systems CV-50W potentiostat using PBS as the electrolyte at pH 7.4, scanning from −300 mV to +300 mV at a rate of 100 mV s^{-1}. All experiments used a custom-designed electrochemical cell with the monolayer as the working electrode, a Pt wire as the counter electrode, and an Ag/AgCl reference electrode.

[11] The 4-hydroxyphenyl valerate terminated alkanethiol was synthesized in eight steps from commercially available reagents. All intermediates gave satisfactory ^{1}H NMR spectra. For the synthetic scheme and experimental details, see Supporting Information.

[12] The density of 4-hydroxyphenyl valerate for this monolayer was approximately 9%, as determined by integration of the area under the redox wave after the enzymatic reaction was completed. This analysis assumes that the 4-hydroxyphenyl valerate was quantitatively converted to hydroquinone.

[13] For the protocols used to prepare cutinase and the inhibitor, see; C. D. Hodneland, Y. S. Lee, D. -H. Min, M. Mrksich, *Proc. Natl. Acad. Sci. USA* **2002**, *99*, 5048.

[14] For each monolayer, the density of hydroquinone on the surface was determined by integration of the areas under the redox waves in the cyclic voltammograms.

 © 2003 Wiley-VCH Verlag GmbH & Co. KGaA, Weinheim

Polypropionate Synthesis

Functionality Propagation by Alkylative Oxidation of Cross-Conjugated Cycloheptadienyl Sulfones**

*Eduardo Torres, Yuzhong Chen, In Chul Kim, and P. L. Fuchs**

Chemists routinely adopt multiply convergent syntheses that combine stereochemically defined, functionality-rich segments. Yet this strategy alone does not guarantee an efficient synthesis. Rather, the selection of easily scaled segments primarily determines the success of a synthetic project. Catalytic processes for the preparation of enantiopure segments have intrinsic advantages over the stoichiometric use of enantiopure auxiliaries or reagents, as these "high-overhead" strategies generate added time and expense. Even successful syntheses that adopt the latter approach may be limited with respect to potential scale-up.

All syntheses that target a single enantiomer must be related ultimately to one or more substances in the chiral pool.[1] Syntheses that generate their asymmetry by means of a chiral catalyst are highly desirable because one molecule of catalyst is responsible for the creation of a multitude of new chiral progeny.

Over the past five years we have been developing cross-conjugated six- and seven-membered dienyl sulfones to

[*] Prof. P. L. Fuchs, E. Torres, Y. Chen, I. C. Kim
Department of Chemistry
Purdue University
West Lafayette, IN 47907 (USA)
Fax: (+1) 765-494-7679
E-mail: pfuchs@purdue.edu

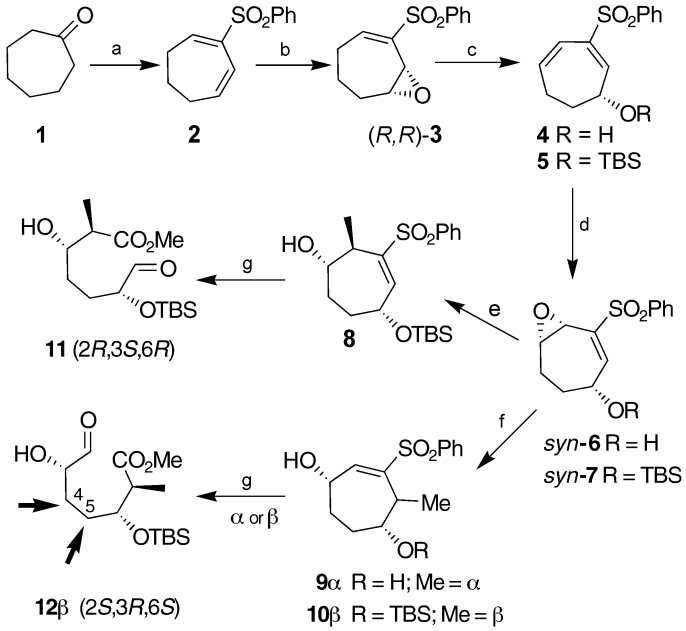
[**] We thank Karl Wood and Arlene Rothwell for MS data and Daniel Lee for elemental analyses. E.T. wishes to thank Pfizer, Inc. for a fellowship.

Supporting information for this article is available on the WWW under http://www.angewandte.org or from the author.

 © 2003 Wiley-VCH Verlag GmbH & Co. KGaA, Weinheim DOI: 10.1002/anie.200350955

generate a collection of termini-differentiated acyclic arrays bearing two to five stereocenters.[2] Jacobsen asymmetric epoxidation of dienyl sulfone **2** with ca. 1% catalyst loading gives either epoxide (*R*,*R*)-**3** or (*S*,*S*)-**3** in >80% yield and >97% *ee* (Scheme 1).[3,4] When the same protocol was applied to **5**, double stereoselection (>12:1) resulted and the individual isomers of **6** and **7** were isolated as crystalline products in >75% yield and >97% *de*.[5,6]

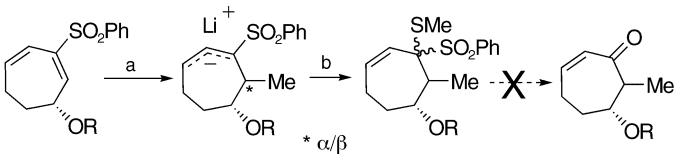
The complementary reactions of trimethylaluminum and dimethylcuprate with silyl ether *syn*-**7** gave alcohols **8** and **10β**, respectively (Scheme 1). Alternatively, when alcohol



Scheme 1. Preparation of acyclic arrays. For reaction conditions, see refs. [3–6]. TBS = *tert*-butyldimethylsilyl.

syn-**6** was treated with methyllithium, methylation occurred on the α-face of the vinyl sulfone, providing product **9α**. While cleavage of the vinyl sulfones **8** and **10β** gave the pseudoenantiomers (enantiomers with protecting group reversal) **11** and **12β**, respectively, it is apparent that further evolution of these compounds in order to access polypropionates with functional groups at C4 and C5 (marked with arrows in compound **12β**, Scheme 1) would not be easily accomplished.

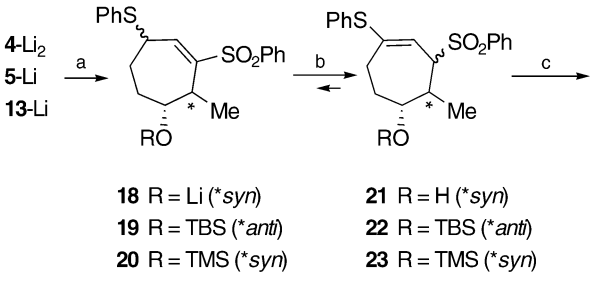
Our new protocol for functionalizing the remaining two centers began by treating compounds **4** and **5** with methyllithium to generate allyl sulfonyl anions **4**-Li_2 and **5**-Li, respectively (Scheme 2). Quenching of these anions at low temperature delivered **14α** and **15β** (as mixtures of sulfone diastereomers) in >85% yield. HPLC analysis revealed that methylation of both intermediates occurred with complementary >10:1 diastereoselectivity. Unfortunately, sulfenylation with dimethyl disulfide or methyl thiolsulfonate gave a complicated mixture of products, which appeared to result from both α- and γ-sulfenylation of the intermediate allylic

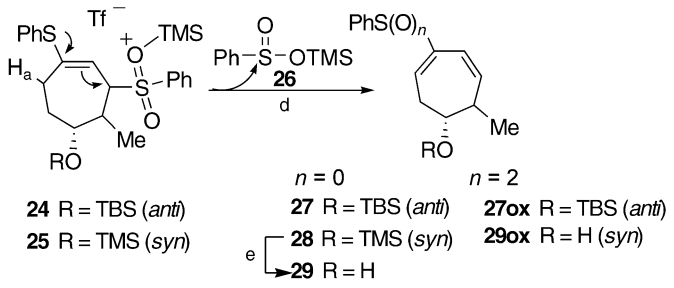


Scheme 2. Initial sulfenylation attempts. a) MeLi, THF, −78°C, b) Me_2S. TMS = trimethylsilyl.

anions. Attempted hydrolysis of these mixtures to enones **16** or **17** was unrewarding.

A subsequent experiment showed that reaction of the allylic anions **4**-Li_2 and **5**-Li with the sterically more demanding diphenyl disulfide suffered regiospecific quenching at the γ-position, initially affording *syn*-**18** and *anti*-**19** as a mixture of sulfide diastereomers (Scheme 3). We monitored the reaction to find that the intermediate vinyl sulfones *syn*-**18** and *anti*-**19** isomerize to allyl sulfones *syn*-**21** and *anti*-**22** under the basic reaction conditions. While ionization of the γ-phenylsulfonyl moiety of acyclic vinyl ethers and vinyl sulfides is known to generate enones and enals, the corresponding reaction for cyclic substrates is far less common.[7,8] After considerable experimentation we found that reaction of allyl sulfones *syn*-**21** and *anti*-**22** with TMS triflate and triethylamine in methylene chloride at reflux effected regiospecific elimination to dienylsulfides *syn*-**29** and *anti*-**27**. This transformation relies upon the unique amphoteric nature of the sulfone moiety.[9] While sulfones are commonly used as electron-withdrawing groups to polarize olefins and inductively stabilize anions, it is the





Scheme 3. γ-Sulfenylation and diene transposition. a) 1. MeLi, THF, −78°C, 2. Ph_2S_2; b) warm to RT, c) TMSOTf, Et_3N, CH_2Cl_2, d) reflux. RT = room temperature, Tf = trifluoromethanesulfonyl.

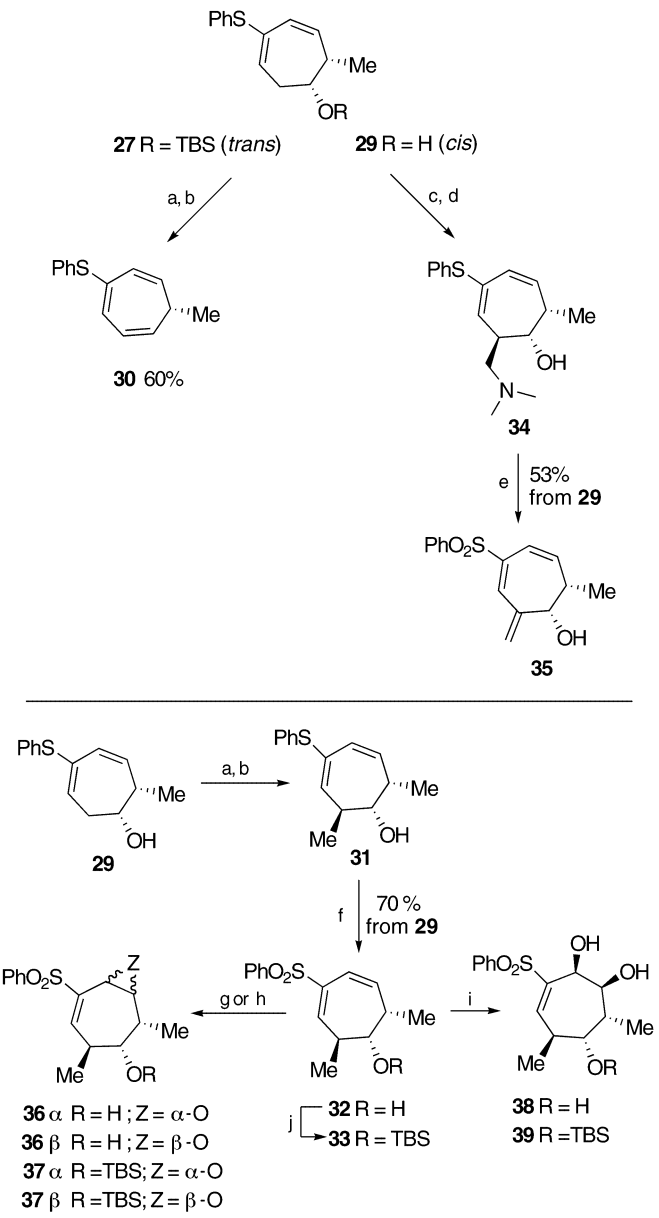
 © 2003 Wiley-VCH Verlag GmbH & Co. KGaA, Weinheim

leaving group ability of phenyl sulfinic acid ($pK_a = 7.1$), which enables the lone pair of phenylvinyl sulfide group to expel sulfinate.[10] Presumably the silyl triflate serves to activate the sulfone moiety by forming silyl ethers **24** and **25** reversibly, thereby also preventing readdition of silyl sulfinate **26** once the vinyl thionium ion loses the proximal proton H_a.[11] Compounds **27** and **29** can be oxidized to the key dienyl sulfones **27ox** and **29ox** simply by addition of *m*CPBA to the crude reaction mixture. This two-operation sequence enables stereoselective methylation with simultaneous establishment of a new, transposed diene (Scheme 3). The enantiopure stereodiads **27** and **29** are obtained in five operations from cycloheptanone **1** (overall yields are >40% on a 40-g scale). These key substrates can serve as progenitors to compounds bearing up to five stereocenters, thereby potentially enabling synthesis of an entire collection of enantiopure diastereomers from catalytically generated epoxide **3** (or *ent*-**3**). Elimination of the sulfone moiety from the TMS ether **13** afforded the unexpected *syn*-**28** (Scheme 3). *syn*-Addition directed by OLi groups has been demonstrated on many occasions, but since the oxygen atom in silyloxy groups is generally not thought to be accessible for coordination, it appeared possible that more subtle conformational effects were involved.[12] Conformational modeling shows that in the preferred conformation of the TMS derivative of **19** the silyl ether function is equatorial, which places the TMS group away from the α-face of the vinyl sulfone, providing unencumbered access for conjugate addition.

To demonstrate the value of enantiopure *anti* and *syn* stereodiads **27** and **29**, we have explored the preparation of a group of termini-differentiated seven-carbon segments projected to be of use in the synthesis of bioactive polypropionate-derived natural products. Initially, the syntheses of the highest priority targets relied on *syn* intermediates **21**, **23**, and **29** as starting materials; however, recent (unpublished) results indicate that the *anti* intermediates **19**, **22**, and **27** are equally useful (Scheme 4). Further functionalization of these substrates gives cycloheptenyl sulfones, which afford termini-differentiated aldehyde segments after oxidative cleavage.[13] For example, direct methylation of the dianion of alcohol **29** produces dienylsulfide **31** (Scheme 4, structure confirmed by X-ray diffraction analysis).[14] Oxidation of **31** provides dienyl sulfone **32** in 70% overall yield from **29**. The necessity of "protecting" the hydroxy group as an oxido anion is apparent from attempted alkylation of **27**, which suffers β-elimination to give trienylsulfide **30**, as expected. Treatment of the dianion of **29** with Eschenmoser's salt ($H_2C{=}N(CH_3)_2I$) gives amine **34**, which undergoes smooth trisoxidation to afford trienylsulfone **35** upon exposure to excess *m*CPBA.[15] Oxidation of dienyl sulfones **32** and **33** with *m*CPBA was unselective, but **36**–**39** could be obtained with high diastereoselectivity when molybdenum, manganese, and osmium complexes were used to catalyze the oxidizations (Scheme 4).

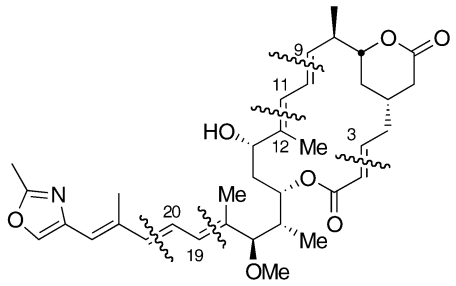
Rhizoxin, the bisepoxide of rhizoxin D (**40**, Scheme 5), was isolated by Okuda et al. from rice seedlings infected with *Rhizopus chinensis*.[16–18] Eight total and/or formal syntheses of rhizoxin (four via rhizoxin D) have been reported.[19]

Our strategy for the synthesis of rhizoxin D (**40**) was to develop a one- or two-pot method for sequentially linking a pair of carbonyl compounds through a two-carbon unit that would be the the C–C single bond in a butadienyl unit in the final compound (Scheme 5). In the event, acylation of *ent*-**21** followed by hydrolysis gave β-sulfonyl ketone **41**, which was then transformed into silyl dienyl ether **42**.[20] Addition of singlet oxygen to **42** effected stereospecific formation of stable bicyclic peroxide **43** (the OTIPS group was necessary for selective addition (>95%) to the β-face).[21] Epoxidation of silyl enol ether **43** with dimethyl dioxirane (DMDO)



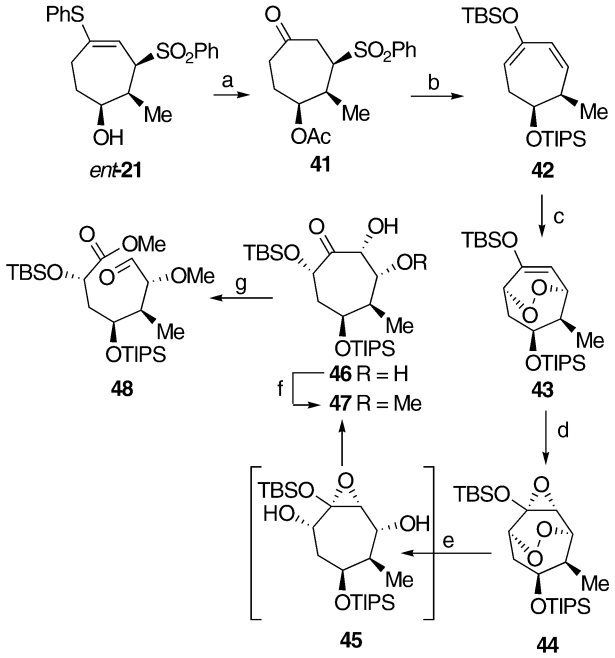
Scheme 4. Preparation of stereopentad progenitors. a) 2.2 equiv *n*BuLi, THF −78°C to −7°C; b) 5 equiv MeI, −90° to −50°C; c) 2.2 equiv *n*BuLi, THF, −78°C to −5°C, 90 min; d) 2.5 equiv $H_2C{=}N(CH_3)_2I$, THF, −70°C to 0°C, 1.5 h; e) 4 equiv *m*CPBA, CH_2Cl_2, 25°C, 1 h; f) 2.2 equiv *m*CPBA, CH_2Cl_2, 25°C, 30 min; g) TBHP, 5%[$Mo(CO)_6$], 88%, >15:1 α/β; h) 10% [(*R*,*R*)-Mn(salen)Cl], H_2O_2, 1 equiv NH_4OAc, 83%, <1:20 α/β; i) cat. OsO_4, >80%, single diastereomer. j) 1.2 equiv TBSOTf, 2 equiv lutidine, CH_2Cl_2, 25°C, 2 h. *m*CPBA = *meta*-chloroperbenzoic acid, TBHP = *tert*-butyl hydroperoxide.

 © 2003 Wiley-VCH Verlag GmbH & Co. KGaA, Weinheim



40: rhizoxin D

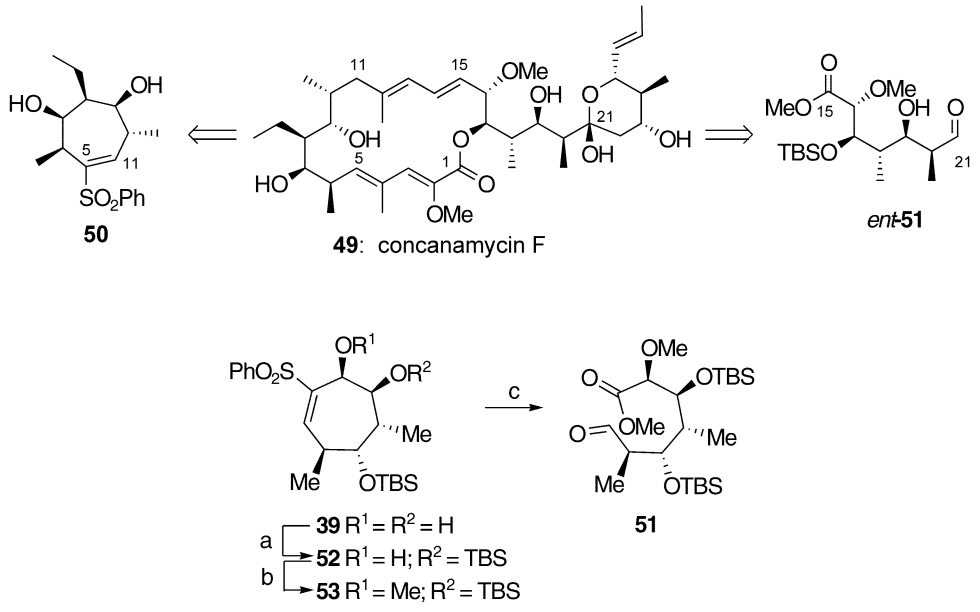
Scheme 5. Synthesis of C12–C18 of rhizoxin D (**40**). a) 1. Ac_2O, Et_3N, DMAP, CH_2Cl_2, RT, 0.5 h, 2. $HgCl_2$, TMSCl, NaI, H_2O, CH_3CN, RT, 16 h, 85% from *ent*-**21**; b) 1. DBU, toluene, RT, 2 h, 2. TBDMSOTf, *i*Pr_2EtN, CH_2Cl_2, RT, 1 h, 3. KOH, MeOH, RT, 10 min, 4. TIPSOTf, Et_3N, CH_2Cl_2, RT, 1 h, 68% overall from **41**; c) $^1O_2$, TPP, CH_2Cl_2, −78 °C, 30 min; d) DMDO, CH_2Cl_2, 0 °C, 2 h; e) H_2, Pd/C, $NaHCO_3$, MeOH, RT, 20 min, 53% from 42; f) cat. Me_2SnCl_2, MeOTf, K_2CO_3, CH_2Cl_2, 17–20 °C, 8 h, 88%; g) $Pb(OAc)_4$, pyridine, MeOH/C_6H_6, 0 °C, 1.5 h, 85%. DMAP = dimethylaminopyridine, DMDO = dimethyldioxirane, TBDMS = *tert*-butyldimethylsilyl, TIPS = triisopropylsilyl, TPP = 5,10,15,20-tetraphenyl-21*H*,23*H*-porphine.



provided the isolable α-epoxysilyl ether **44**.[22] Hydrogenation of **44** proceeded, as desired, with silicon migration to give diol **46** in 83% yield. Methylation of the keto-diol **46** absolutely required the dimethyltin chloride catalyst to effect regiospecific O-methylation at the more electron-rich distal hydroxy group, rapidly providing ketone **47** in high yield. (This is the first example for a 1-keto-2,3-diol).[23] Methylation or silylation without the tin catalyst was very slow and strongly favored functionalization of the opposite hydroxy group. Cleavage of **47** in methanol with lead tetraacetate completed the synthesis of enantiopure aldehyde ester **48** (Scheme 5).[24]

Concanamycin F (**49**), also called concanolide A, is the most intricate parent aglycone of a series of related macrocyclic lactones bearing considerable structural homology (Scheme 6). This family also includes biafilomycin A and hygrolidin.[25–27] Concanamycin F (**49**) has been synthesized by the groups of Paterson in 2000 and Toshima in 2001 in 44 and 53 steps, respectively.[28,29]

Our analysis of concanamycin F (**49**) envisages the construction of a pair of stereopentads derived from vinyl sulfones **50** and **53** (Scheme 6). While synthesis of compound **50** is not yet complete, we have been able to make good use of the diol **39** for generation of stereopentad **51**. Silylation of **39**



Scheme 6. Synthesis of the *ent*-C15–C21 fragment of concanomycin F (**49**). a) TBSOTf, 2,6-lutidine, CH_2Cl_2, −78 °C, 2 h, 99%; b) KOH/MeI/DMSO, 25 °C, 5 min, 94%; c) O_3, CH_2Cl_2/MeOH (1:2), $NaHCO_3$, −78 °C, 15 min, then PPh_3, 92%.

 © 2003 Wiley-VCH Verlag GmbH & Co. KGaA, Weinheim

provided vinyl sulfone **52** in near-quantitative yield, which was directly methylated in DMSO to give vinyl sulfone **53** in 94% yield. Ozonolysis of **53** afforded ester aldehyde **51** in 92% yield. Compound **51** is the enantiomer of the C15–C21 stereopentad of concanamycin F (**49**, Scheme 6).

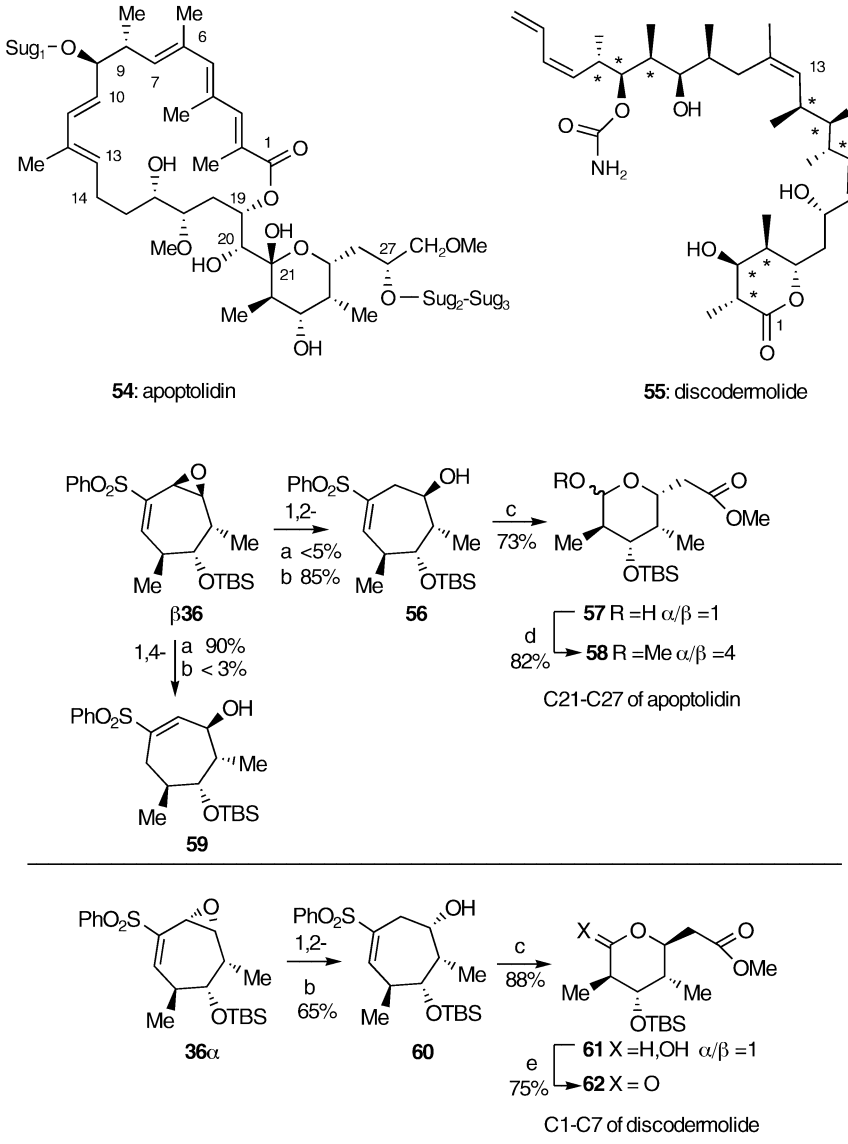
Apoptolidin (**54**) is a 20-membered macrocyclic lactone isolated from *Norcardiopsis* sp. (Scheme 7).[30] "Apoptolidin induced apoptotic cell death in rat gila cells transformed with the E1A oncogene at 11 ng mL^{-1} but did not cause cell death in normal gila cells or fibroblasts at >100 g mL^{-1}."[30f–g,31] The group of K. C. Nicolaou provided the first total synthesis of apoptolidin (**54**) in ca. 90 steps.[30f–g,31]

Discodermolide (**55**), like paclitaxel (taxol), has been shown to stabilize microtubules but is more potent and inhibits the growth of paclitaxel-resistant cells.[32,33] The material is in high demand for clinical trials, and synthesis is the only viable source. Five total syntheses and related synthetic approaches all based on aldol-based stereoselection strategies with acyclic substrates have been reported which begin with enantiopure 3-hydroxy 2-methylpropionate.[34] The second-generation synthesis by Smith et al. utilized a total of 34 steps with a linear supply line of only 24 operations and provided the first gram of (+)-discodermolide (**55**). The overall yield was 6%.[35]

Our approach to apoptolidin (**54**) and discodermolide (**55**) makes use of the central stereotriads **32** and **33** as precursors to the key epoxides **36α** and **36β**, respectively. Preparation of the C21–C27 segment of apoptolidin (**54**) is accomplished from epoxide **36β** beginning with selective 1,2-reduction with DIBAL-H to provide alcohol **56**. The complementary 1,4-reduction to produce alcohol **59** can be achieved selectively with borane–THF. Completing the synthesis of the apoptolidin segment simply requires ozonolysis of **56** to give a δ-hydroxy aldehyde intermediate, which cyclizes to hemiacetal **57**. Protection of **57** as acetal **58** gave a 4:1 mixture of anomers, which can be separated easily by chromatography (Scheme 7). Acetal **58** is also the C20–26 segment of phorboxazole (not shown).[36]

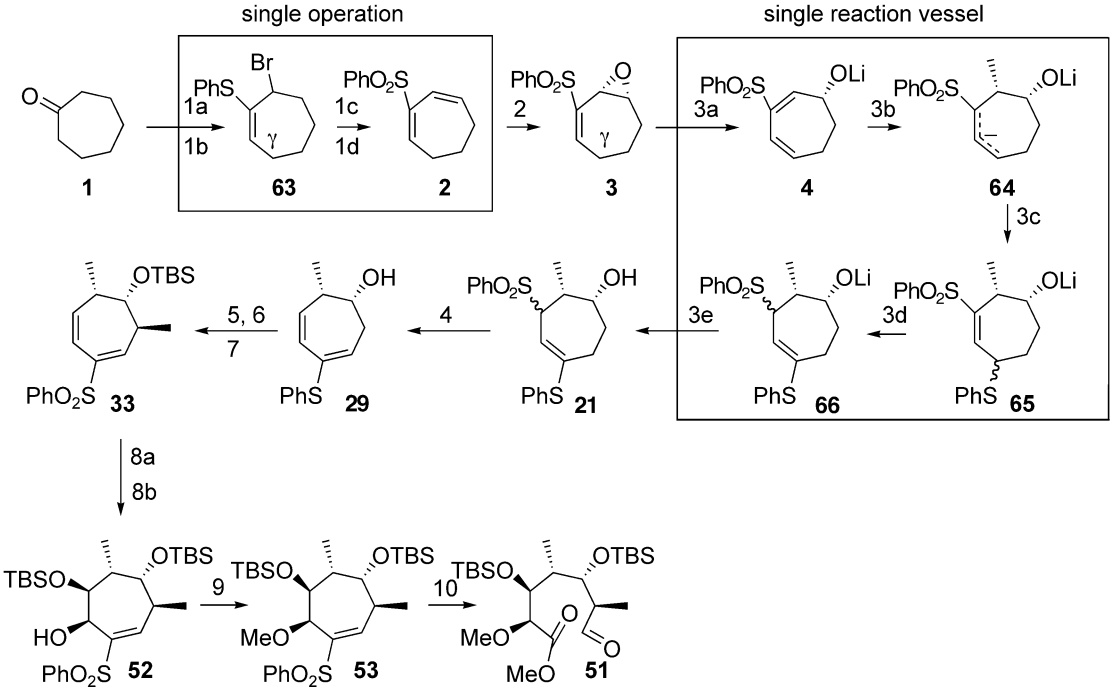
In parallel fashion to the synthesis of **58**, we prepared the C1–C7 segment of discodermolide (**55**) by employing epoxide **36α** for 1,2-reduction with DIBAL-H. This afforded alcohol **60** in 65% yield. Subsequent ozonolysis afforded hemiacetal **61**, which smoothly underwent PDC oxidation to give lactone ester **62** in 75% yield (Scheme 7).

The lessons that Trost is teaching about atom economy prompt questions of the strategic validity of the dienyl sulfone methodology since sulfur is not found in the product.[37] We can address this point by briefly examining our synthesis of segment **51**, which begins with cycloheptanone (**1**) The sulfur atoms used in this strategy are essential for the synthesis (Scheme 8). The initial vinyl sulfide activates the olefin for bromination in operation 1b. The sulfone formed by oxidization (operation 1c) activates the allylic position for base-promoted 1,4-elimination in operation 1d to yield dienyl sulfone **2**. The electrophilic double bond in the cross-conjugated dienyl sulfone **2** is flanked by a sterically demanding sp^3-hybridized sulfone moiety, which has been shown to be crucial for the high enantiomeric excess obtained in the Jacobsen epoxidation (operation 2).[5] Once again, in



Scheme 7. Preparation of C21–C27 of apoptolidin (**54**) and C1–C7 of discodermolide (**55**). a) 1.6 equiv BH_3·THF, THF, 0°C warming to 25°C, 12 h; b) 1.5 equiv DIBAL-H, −78°C; c) O_3, CH_2Cl_2/MeOH (1:2), $NaHCO_3$, −78°C, 15 min; d) Ag_2O, MeI, CH_3CN, reflux, 3 h; e) 5 equiv PDC, CH_2Cl_2, 25°C, 10 h. DIBAL-H = diisobutylaluminum hydride.

 © 2003 Wiley-VCH Verlag GmbH & Co. KGaA, Weinheim



Scheme 8. Evaluation of the contribution of sulfur functional groups in the synthesis of ester aldehyde **51** (for a discussion of the operations refer to the text).

a 1,4-elimination (operation 3a) epoxy vinyl sulfone **3** is transformed into intermediate **4**, which undergoes conjugate addition with methyllithium (operation 3b) to provide the allyl sulfonyl anion **64**, which is directly sulfenylated to **65** (operation 3c). Vinyl sulfone **65** equilibrates to **66** in operation 3d and is finally protonated to **21** in operation 3e. Vinylogous dioxythioacetal **21** undergoes vinyl-sulfide-promoted loss of sulfinic acid in operation 4 to afford cross-conjugated dienyl sulfide **29** after workup. Methylation of the dianion of **29** (operation 5), followed by oxidation of sulfide, and alcohol protection gives **33**. Catalytic substrate-based dihydroxylation followed by regiospecific silylation of the more available hydroxy group generates alcohol **52**, which undergoes O-methylation to **53**, and finally, cleavage of the vinyl sulfone (operation 10) to deliver the target stereopentad **51**.

In the course of this synthesis we have introduced and ultimately removed two sulfur moieties. While this may be negative from the viewpoint of atom economy, the groups are absolutely essential to the chemistry. The synthesis of **51** via a dienyl sulfone exploits a chiral catalyst, and all further stereochemistry is related to the newly created stereocenter(s). This creates less costly "overhead" than a synthesis employing an enantiopure starting material and then twice using either a chiral reagent or a chiral auxiliary. This difference can be especially significant when reactions are scaled up, since the cost of auxiliaries or reagents cost, recycling, and/or disposal all strongly impact production cost.

In conclusion, it has been shown that a new alkylative sulfenylation–desulfonylation reaction efficiently transforms enantiopure epoxyvinyl sulfone **3** to *syn* and *anti* dienylsulfides **29** and **27** in two operations. This reaction permits the stereospecific functionalization of all seven carbons of a cycloheptyl system, ultimately providing seven-carbon termini-differentiated polypropionate stereotetrads and stereopentads appropriate for natural product synthesis.

Received: January 16, 2003 [Z50955]

Keywords: epoxidation · polypropionates · stereoselectivity · sulfones · synthetic methods

[1] P. L. Fuchs, *Tetrahedron* **2001**, *57*, 6855 – 6875.
[2] Synthesis via vinyl sulfones **87**; Chiral Carbon Collection 11.
[3] a) Z. Tong, Y. Chen, M. F. Hentemann, P. L. Fuchs, *Tetrahedron Lett.* **2000**, *41*, 7795 – 7799; b) M. F. Hentemann, P. L. Fuchs, *Org. Lett.* **1999**, *1*, 355 – 357; c) J. Evarts, E. Torres, P. L. Fuchs, *J. Am. Chem. Soc.* **2002**, *124*, 11093 – 11101.
[4] D. Myers, P. L. Fuchs, *J. Org. Chem.* **2002**, *67*, 200 – 204. The 2-phenylsulfonyl-1,3-cycloheptadiene **2** and both enantiomers of **3** will soon be available from Aldrich.
[5] M. F. Hentemann, P. L. Fuchs, *Tetrahedron Lett.* **1997**, *38*, 5615 – 5618.
[6] W. Jiang, D. A. Lantrip, P. L. Fuchs, *Org. Lett.* **2000**, *2*, 2181 – 2184.
[7] a) B. M. Trost, M. R. Ghadiri, *Bull. Soc. Chim. Fr.* **1993**, *130*, 433 – 442; b) D. Craig, C. J. Etheridge, *Tetrahedron Lett.* **1993**, *34*, 7487 – 7488; c) M. Harmata, V. R. Fletcher, R. J. Claassen II, *J. Am. Chem. Soc.* **1991**, *113*, 9861 – 9862.
[8] a) S. H. Kim, Z. Jin, P. L. Fuchs, *Tetrahedron Lett.* **1995**, *36*, 4537 – 4538; b) Z. Jin, P. L. Fuchs, *J. Am. Chem. Soc.* **1995**, *117*, 3022 – 3028; c) Z. Jin, P. L. Fuchs, *J. Am. Chem. Soc.* **1994**, *116*, 5995 – 5996.
[9] Nitriles, phosphonates, and nitro compounds also exhibit this attribute, but the balance between bond strength and pK_a is optimal for the aryl sulfone moiety.

 © 2003 Wiley-VCH Verlag GmbH & Co. KGaA, Weinheim

[10] Phenyl sulfones are about 10^5 times less reactive than chloride as leaving groups. A. K. Colter, R. E. Miller, *J. Org. Chem.* **1971**, *36*, 1898 – 1903. β-Sulfonyl ketones, homoallyl, homopropargyl, and homobenzyl sulfones, having an allylically activated C–H π bond or α-heteroatom-substituted sulfones are competent leaving groups. The reaction shown in Scheme 3 is a vinylogous example of the latter case.

[11] For an example of intramolecular silylation of the oxygen atom of a sulfone, see: P. C. Van Dort, P. L. Fuchs, *J. Am. Chem. Soc.* **1994**, *116*, 5657 – 5661.

[12] For examples in which the siloxy groups appear to direct the reaction, see: J. Clayden, M. Julia, *Synlett* **1995**, 103 – 104.

[13] For alternative ring-cleavage approaches to synthesis of six- and especially seven-carbon sequences bearing multiple stereocenters, see the following leading references: a) M. Lautens, J. T. Colucci, S. Hiebert, N. D. Smith, G. Bouchain, *Org. Lett.* **2002**, *4*, 1879 – 1882; b) O. Arjona, R. Menchaca, J. Plumet, *J. Org. Chem.* **2001**, *66*, 2400 – 2413; c) O. Arjona, R. Menchaca, J. Plumet, *Org. Lett.* **2001**, *3*, 107 – 109; d) P. Vogel, J. Cossy, J. Plumet, O. Arjona, *Tetrahedron* **1999**, *55*, 13521 – 13642; e) P. Vogel, A.-F. Sevin, P. Kernen, M. Bialecki, *Pure. Appl. Chem.* **1996**, *68*, 719 – 722; f) M. Bialecki, P. Vogel, *Helv. Chim. Acta* **1995**, *78*, 325 – 343; g) M. Lautens, *Pure. Appl. Chem.* **1992**, *64*, 1873 – 1882.

[14] X-ray data has been submitted to the Cambridge Crystallographic database.

[15] C. Lehmann, B. Schweizer, C. Leumann, A. Eschenmoser, *Helv. Chim. Acta* **1997**, *80*, 1421 – 1442.

[16] S. Siwasaki, H. Kobayashi, J. Furukawa, M. Namikoshi, S. Okuda, Z. Sato, I. Matsuda, T. Noda, *J. Antibiot.* **1984**, *37*, 354 – 362.

[17] S. Kaplan, A. R. Hanauske, N. Pavlidis, U. Bruntsch, A. Te Velde, J. Wanders, B. Heinrich, J. Verweij, *Br. J. Cancer* **1996**, *73*, 403 – 405.

[18] M. Nakada, *J. Synth. Org. Chem. Jpn.* **1995**, *53*, 122 – 137.

[19] a) M. Nakada, S. Kobayashi, S. Iwasaki, M. Ohno, *Tetrahedron Lett.* **1993**, *34*, 1035 – 1038; b) M. Nakada, S. Kobayashi, M. Shibasaki, S. Iwasaki, M. Ohno, *Tetrahedron Lett.* **1993**, *34*, 1039 – 1042; c) A. V. Rama Rao, G. V. M. Sharma, M. N. Bhanu, *Tetrahedron Lett.* **1992**, *33*, 3907 – 3910; d) A. V. Rama Rao, M. N. Bhanu, G. V. M. Sharma, *Tetrahedron Lett.* **1993**, *34*, 707 – 710; e) G. F. Keck, M. Park, D. Krishnamurthy, *J. Org. Chem.* **1993**, *58*, 3787 – 3788; f) G. E. Keck, K. A. Savin, M. A. Weglarz, E. N. K. Cressman, *Tetrahedron Lett.* **1996**, *37*, 3291 – 3294; g) A. S. Kende, B. E. Blass, J. R. Henry, *Tetrahedron Lett.* **1995**, *36*, 4741 – 4744; h) J. A. Lafontaine, J. W. Leahy, *Tetrahedron Lett.* **1995**, *36*, 6029 – 6032; i) D. Provencal, C. Gardelli, J. A. Lafontaine, J. W. Leahy, *Tetrahedron Lett.* **1995**, *36*, 6033 – 6036; j) J. A. Lafontaine, D. Provencal, C. Gardelli, J. W. Leahy, *Tetrahedron Lett.* **1999**, *40*, 4145 – 4148; k) D. R. Williams, K. M. Werner, B. Feng, *Tetrahedron Lett.* **1997**, *38*, 6825 – 6828.

[20] P. A. Grieco, Y. Dai, *Tetrahedron Lett.* **1998**, *39*, 6997.

[21] C. R. Johnson, A. Golebiowski, D. H. Steensma, M. A. Scialdone, *J. Org. Chem.* **1993**, *58*, 7185 – 7194.

[22] W. Adam, L. Hadjiarapoglou, X. Wang, *Tetrahedron Lett.* **1989**, *30*, 6497 – 6500.

[23] a) T. Maki, F. Iwasaki, Y. Matsumura, *Tetrahedron Lett.* **1998**, *39*, 5601 – 5604; b) A. Gateau-Olesker, J. Clephax, S. D. Gero, *Tetrahedron Lett.* **1986**, *27*, 41 – 44; c) M. J. Martinelli, N. K. Nayyar, E. D. Moher, U. P. Dhokte, J. M. Pawlak, R. Vaidyanathan, *Org. Lett.* **1999**, *1*, 447 – 450.

[24] D. L. Cheney, L. A. Paquette, *J. Org. Chem.* **1989**, *54*, 3334 – 3347.

[25] a) K. Toshima, T. Jyojima, H. Yamaguchi, Y. Noguchi, T. Yoshida, H. Murase, M. Nakata, S. Matsumura, *J. Org. Chem.* **1997**, *62*, 3271 – 3284; b) K. A. Scheidt, A. Tasaka, T. D. Bannister, M. D. Wendt, W. R. Roush, *Angew. Chem.* **1999**, *111*, 1760 – 1762; *Angew. Chem. Int. Ed.* **1999**, *38*, 1652 – 1655; c) D. A. Evans, M. A. Calter, *Tetrahedron Lett.* **1993**, *34*, 6871 – 6874.

[26] a) K. Makino, N. Nakajima, S.-i. Hashimoto, O. Yonemitsu, *Tetrahedron Lett.* **1996**, *37*, 9077 – 9080; b) S. Hanessian, A. Tehim, Q. Meng, K. Granberg, *Tetrahedron Lett.* **1996**, *37*, 9001 – 9004.

[27] S. Gagliardi, P. A. Gatti, P. Belfiore, A. Zocchetti, G. D. Clarke, C. Farina, *J. Med. Chem.* **1998**, *41*, 1883 – 1893.

[28] a) K. Toshima, T. Jyojima, N. Miyamoto, M. Katohno, M. Nakata, S. Matsumura, *J. Org. Chem.* **2001**, *66*, 1708 – 1715; b) T. Jyojima, N. Miyamoto, M. Katohno, M. Nakata, S. Matsumura, K. Toshima, *Tetrahedron Lett.* **1998**, *39*, 6007 – 6010; c) T. Jyojima, M. Katohno, N. Miyamoto, M. Nakata, S. Matsumura, K. Toshima, *Tetrahedron Lett.* **1998**, *39*, 6003 – 6006.

[29] I. Paterson, V. A. Doughty, M. D. McLeod, T. Trieselmann, *Angew. Chem.* **2000**, *112*, 1364 – 1368; *Angew. Chem. Int. Ed.* **2000**, *39*, 1308 – 1312.

[30] a) J. D. Pennington, H. J. Williams, A. R. Salomon, G. A. Sulikowski, *Org. Lett.* **2002**, *4*, 3823 – 3825; b) P. A. Wender, A. V. Gulledge, O. D. Jankowski, H. Seto, *Org. Lett.* **2002**, *4*, 3819 – 3822; c) A. R. Salomon, D. W. Voehringer, L. A. Herzenberg, C. Khosla, *Proc. Natl. Acad. Sci. USA* **2000**, *97*, 14766 – 14771; d) A. R. Salomon, D. W. Voehringer, L. A. Herzenberg, C. Khosla, *Chem. Biol.* **2001**, *8*, 71 – 80; e) J. Schuppan, H. Wehlan, S. Keiper, U. Koert, *Angew. Chem.* **2001**, *113*, 2125 – 2128; *Angew. Chem. Int. Ed.* **2001**, *40*, 2063 – 2066; f) K. C. Nicolaou, Y. Li, K. C. Fylaktakidou, H. J. Mitchell, K. Sugita, *Angew. Chem.* **2001**, *113*, 3968 – 3972; *Angew. Chem. Int. Ed.* **2001**, *40*, 3854 – 3857; ; g) K. C. Nicolaou, Y. Li, K. C. Fylaktakidou, H. J. Mitchell, H.-X. Wei, B. Weyershausen, *Angew. Chem.* **2001**, *113*, 3791 – 3795; *Angew. Chem. Int. Ed.* **2001**, *40*, 3849 – 3854; ; h) A. R. Salomon, Y. Zhang, H. Seto, C. Khosia, *Org. Lett.* **2001**, *3*, 57 – 59; i) G. A. Sulikowski, W.-M. Lee, B. Jin, B. Wu, *Org. Lett.* **2000**, *2*, 1439 – 1442; j) J. Schuppan, B. Ziemer, U. Koert, *Tetrahedron Lett.* **2000**, *41*, 621 – 624; k) K. C. Nicolaou, Y. Li, B. Weyershausen, H.-x. Wei, *Chem. Commun.* **2000**, 307 – 308; l) M. Kinoshita, H. Takami, M. Taniguchi, T. Tamai, *Bull. Chem. Soc. Jpn.* **1987**, *60*, 2151 – 2161; m) Y. Hayakawa, J. W. Kim, H. Adachi, K. Shin-ya, K.-i. Fujita, H. Seto, *J. Am. Chem. Soc.* **1998**, *120*, 3524 – 3525.

[31] K. C. Nicolaou, Y. Li, B. Weyershausen, H. Wei, *Chem. Commun.* **2000**, 307 – 308.

[32] a) S. P. Gunasekera, M. Gunasekera, E. Longley, G. K. Schulte, *J. Org. Chem.* **1990**, *55*, 4912 – 4915; b) R. J. Kowalski, P. Giannakakou, S. P. Gunasekera, R. E. Longley, B. W. Day, E. Hamel, *Mol. Pharmacol.* **1997**, *52*, 613 – 622; c) E. Ter Haar, R. J. Kowalski, E. Hamel, C. M. Lin, R. E. Longley, S. P. Gunasekera, H. S. Rosenkranz, B. W. Day, *Biochemistry* **1996**, *35*, 243 – 250.

[33] a) P. Giannakakou, T. Fojo, *Clin. Cancer Res.* **2000**, *6*, 1613 – 1615; b) L. A. Martello, H. M. McDaid, D. L. Regl, C.-P. H. Yang, D. Meng, T. R. R. Pettus, M. D. Kaufman, H. Arimoto, S. J. Danishefsky, A. B. Smith III, S. B. Horwitz, *Clin. Cancer Res.* **2000**, *6*, 1978 – 1987.

[34] a) I. Paterson, G. J. Florence, K. Gerlach, J. P. Scott, N. Sereinig, *J. Am. Chem. Soc.* **2001**, *123*, 9535 – 9544; b) S. A. Filla, J. J. Song, L. Chen, S. Masamune, *Tetrahedron Lett.* **1999**, *40*, 5449 – 5453; c) J. A. Marshall, B. A. Johns, *J. Org. Chem.* **1998**, *63*, 7885 – 7892; d) J. A. Marshall, Z. Lu, B. A. Johns, *J. Org. Chem.* **1998**, *63*, 817 – 823; e) S. S. Harried, G. Yang, A. Strawn, D. C. Myles, *J. Org. Chem.* **1997**, *62*, 6098 – 6099; f) D. L. Clark, C. H. Heathcock, *J. Org. Chem.* **1993**, *58*, 5878 – 5879; g) I. Paterson, S. P. Wren, *J. Chem. Soc. Chem. Commun.* **1993**, 1790 – 1792; g) I. Paterson, A. Schlapbach, *Synlett* **1995**, 498 – 500; h) G. Yang, D. C. Myles, *Tetrahedron Lett.* **1994**, *35*, 1313 – 1316; i) G. Yang, D. C. Myles, *Tetrahedron Lett.* **1994**, *35*, 2503 – 2504; j) J. M. C. Golec, S. D. Jones, *Tetrahedron Lett.* **1993**, *34*, 8159 – 8162; k) J. M. C. Golec, R. J. Gillespie, *Tetrahedron Lett.* **1993**, *34*,

 © 2003 Wiley-VCH Verlag GmbH & Co. KGaA, Weinheim

8167 – 8168; l) P. L. Evans, J. M. C. Golec, R. J. Gillespie, *Tetrahedron Lett.* **1993**, *34*, 8163 – 8166; m) S. S. Harried, G. Yang, M. A. Strawn, D. C. Myles, *J. Org. Chem.* **1997**, *62*, 6098 – 6099; n) D. T. Hung, J. B. Nerenberg, S. L. Schreiber, *J. Am. Chem. Soc.* **1996**, *118*, 11054 – 11080; o) A. B. Smith III, T. J. Beauchamp, M. J. LaMarche, M. D. Kaufman, Y. Qiu, H. Arimoto, D. R. Jones, K. Kobayashi, *J. Am. Chem. Soc.* **2000**, *122*, 8654 – 8664; p) I. Paterson, S. P. Wren, *J. Chem. Soc. Chem. Commun.* **1993**, 1790 – 1792; q) I. Paterson, A. Schlapbach, *Synlett* **1995**, 498 – 500; r) I. Paterson, G. J. Florence, *Tetrahedron Lett.* **2000**, *41*, 6935 – 6939.

[35] a) A. B. Smith III, T. J. Beauchamp, M. J. LaMarche, M. D. Kaufman, Y. Qiu, H. Arimoto, D. R. Jones, K. Kobayashi, *J. Am. Chem. Soc.* **2000**, *122*, 8654 – 8664; b) M. J. Tomaszewski, *Chem. Eur. J.* **1996**, *2*, 847 – 868; c) G. Godjoian, V. R. Wang, A. M. Ayala, R. V. Martinez, R. Martinez-Bernhardt, C. G. Gutierrez, *Tetrahedron Lett.* **1996**, *37*, 433 – 436; d) P. K. Richter, H. Khatuya, P. Bertinato, R. A. Miller, N. Nagashima, M. Ohno, *Chem. Lett.* **1987**, 141 – 144.

[36] a) T. F. Molinski, *Tetrahedron Lett.* **1996**, *37*, 7879 – 7880; b) P. A. Searle, T. F. Molinski, *J. Am. Chem. Soc.* **1996**, *118*, 9422 – 9423; c) P. A. Searle, T. F. Molinski, *J. Am. Chem. Soc.* **1995**, *117*, 8126 – 8131.

[37] B. M. Trost, *Angew. Chem.* **1995**, *107*, 285; *Angew. Chem. Int. Ed. Engl.* **1995**, *34*, 259 – 281.

 © 2003 Wiley-VCH Verlag GmbH & Co. KGaA, Weinheim

Asymmetric Azidoselenenylation

Asymmetric Azidoselenenylation of Alkenes: A Key Step for the Synthesis of Enantiomerically Enriched Nitrogen-Containing Compounds**

Marcello Tiecco, Lorenzo Testaferri, Claudio Santi, Cristina Tomassini, Francesca Marini, Luana Bagnoli, and Andrea Temperini*

Organic azides are versatile starting materials for the synthesis of a variety of nitrogen-containing compounds. The azido group can react with both nucleophilic and electrophilic reagents and can be used in 1,3-dipolar cycloaddition reactions.[1] One of the most convenient ways to produce organic azides is the electrophilic addition to alkenes of an appropriate reagent, such as hydrazoic acid,[2] mercuric azide,[3] or iodine azide.[4] Considerably improved results were obtained by using organoselenium reagents. The first example of the azidoselenenylation of alkenes was reported by Hassner and Amarasekara.[5] The reaction was effected with PhSeCl and sodium azide in DMSO and proceeded through the formation of a cyclic seleniranium ion intermediate, which then underwent ring opening by nucleophilic attack of the azide anion. The addition products therefore resulted from a stereospecific *trans* addition. However, the reaction was not regiospecific. Similarly, the reaction of exocyclic alkenes with *N*-(phenylseleno)phthalimide and azidotrimethylsilane gave rise to a mixture of regioisomers.[6] More recently we reported that the stereospecific azidoselenenylation of alkenes can be carried out more conveniently with phenylselenenyl triflate and sodium azide in acetonitrile.[7] We have also reported the use of an azido radical to promote the azidoselenenylation of olefins. The reaction is, of course, not stereospecific in this case, and the anti-Markownikoff addition products are formed.[8]

We report the first example of a remarkable asymmetric electrophilic azidoselenenylation of olefins that occurs with a very high level of facial selectivity. This process is made possible by the use of chiral, nonracemic selenium reagents. During the last 10 years several research groups have developed simple and efficient procedures for the preparation of chiral, nonracemic diselenides.[9] These compounds have been employed in various asymmetric reactions, mainly as precursors of electrophilic reagents,[9] but also as catalysts[10] or as a source of chiral selenium anions.[11] A common characteristic of all chiral diselenides studied is the close proximity of a heteroatom (oxygen or nitrogen) that can interact with selenium. We recently described the synthesis of the sulfur-containing diselenides di-2-[(1*S*)-1-(methylthio)-ethyl]phenyl diselenide (**1**)[12] and di-2-methoxy-6-[(1*S*)-1-(methylthio)ethyl]phenyl diselenide (**2**).[13] Electrophilic reagents derived from these diselenides were used to effect asymmetric hydroxyselenenylation,[12,13] methoxyselenenylation,[12,13] and cyclofunctionalization reactions,[14] which proceeded with very high facial selectivity under very mild experimental conditions.

Preliminary experiments on asymmetric azidoselenenylation were carried out on styrene with the chiral diselenides **1**–**5**. Upon treatment with bromine and silver triflate, **1**–**5** were converted into the corresponding electrophilic selenenyl triflate reagents **6**–**10**. These reacted with styrene (**11**) in the presence of 1 equivalent of sodium azide to afford a mixture of the corresponding diastereomeric addition products **12**–**16** (Scheme 1).

The observed diastereomeric ratios and chemical yields are summarized in Table 1. The excellent selectivity observed

Table 1: Asymmetric azidoselenenylation of styrene.

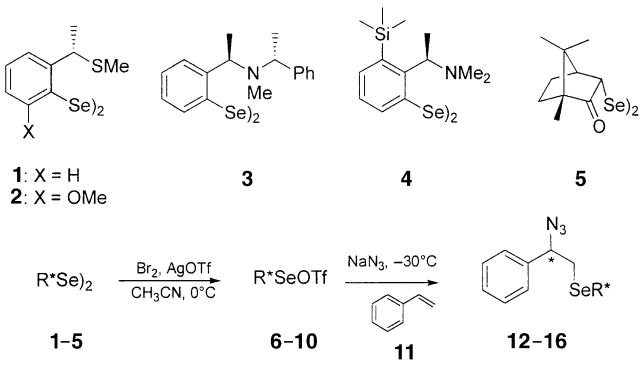
Diselenide	*t* [h]	Yield [%]	d.r.
1	22	90	91:9
2	21	90	97:3
3	20	70	52:48
4	21	10	87:13
5	30	28	75:25

[*] Prof. M. Tiecco, L. Testaferri, C. Santi, C. Tomassini, F. Marini, L. Bagnoli, A. Temperini
Dipartimento di Chimica e Tecnologia del Farmaco
Sezione di Chimica Organica, Università di Perugia
06123-Perugia (Italy)
Fax: (+39) 075-585-5116
E-mail: tiecco@unipg.it

[**] Financial support from MURST, National Project "Stereoselezione in Sintesi Organica. Metodologie ed Applicazioni", the University of Perugia, Progetti di Ateneo, and CNR, Rome is gratefully acknowledged.

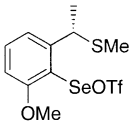
Supporting information for this article is available on the WWW under http://www.angewandte.org or from the author.

 DOI: 10.1002/anie.200351229 © 2003 Wiley-VCH Verlag GmbH & Co. KGaA, Weinheim



Scheme 1. Asymmetric azidoselenenylation of styrene.

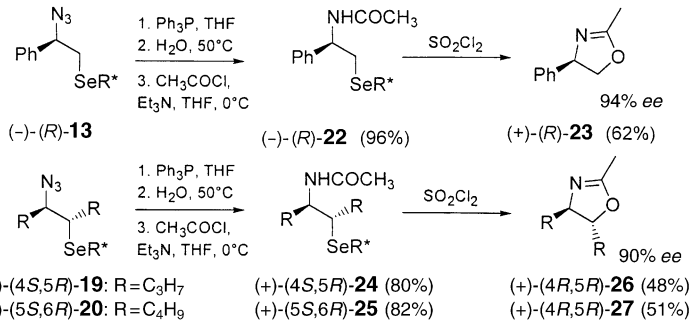
with the diselenides **1** and **2** seems to indicate that the interaction of the selenium atom with the sulfur atom is stronger than its interaction with the other heteroatoms (oxygen or nitrogen) used in previous investigations.



7

On the basis of these results all further reactions were carried out with the diselenide **2** as precursor to the electrophilic arylselenenyl triflate **7**. Experimental conditions, chemical yields, and diastereomeric ratios for the reactions of **7** with a variety of alkenes are reported in Table 2.

The azidoselenenylation products were obtained in every case as an inseparable mixture of the two possible diastereomers. The results reported in Table 2 indicate that this azidoselenenylation reaction is a stereospecific *trans* addition (Table 2, entries 2, 4, and 5) that occurs regioselectively (Table 2, entries 1, 2, 3, and 6) with Markownikoff orientation. The diastereomeric ratios were determined from the ^{1}H NMR spectra of the crude reaction mixtures and confirmed after purification by column chromatography. Excellent levels of diastereoselectivity were obtained in all cases. The major isomers of the azidoselenides **13** and **18**–**20** are depicted in Table 2. In the cases of **13**, **19**, and **20** these were determined after conversion into the known oxazolines[15] **23**, **26**, and **27** (Scheme 2). For this purpose the azides were reduced to the corresponding amines, which were then treated in situ with CH_3COCl at 0 °C. The acetamido selenides **22**, **24**, and **25** thus obtained underwent a stereospecific S_N2 intramolecular deselenenylation upon treatment with SO_2Cl_2 to afford the oxazolines **23**, **26**, and **27**, respectively.[15] The absolute configurations of compounds **17** and **18** were assigned by analogy.

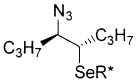
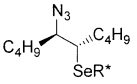
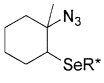


Scheme 2. Conversion of azidoselenides into optically active oxazolines.

To highlight the importance of these compounds as synthetic intermediates, some of the azidoselenides were then transformed into other enantiomerically enriched nitrogen-containing compounds. The benzoyl derivative **28** was prepared from **20** as indicated in Scheme 3. The corresponding selenoxide, obtained by treatment of **28** with *meta*-chloroperbenzoic acid (*m*CPBA),[16] underwent spontaneous deselenenylation to afford the optically active aziridine **29** by an intramolecular nucleophilic substitution, and the α,β-unsaturated amide **30** by an elimination process.

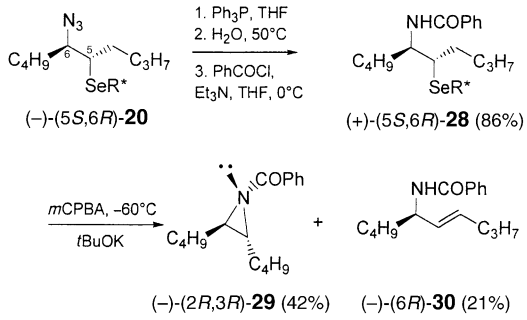
Enantiomerically enriched azides can be also conveniently employed in 1,3-dipolar cycloadditions to allow the synthesis of triazoles.[17] Thus, as indicated in Scheme 4, the azide **13** was treated with dimethyl acetylenedicarboxylate to give the triazole **31**.[17] Deselenenylation of **31** with triphenyltin hydride and AIBN (azobisisobutyronitrile) then afforded the triazole **32**. The enantiomeric excess of **32**

Table 2: Asymmetric azidoselenenylation of alkenes with the diselenide **2**.[a]

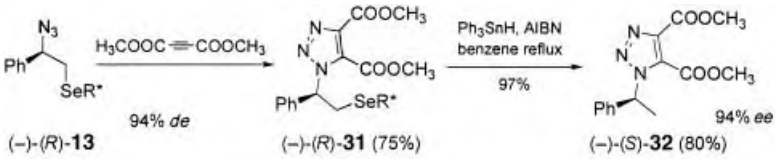
Entry	Alkene	Azidoselenide		*t* [h]	Yield [%]	d.r.
1	styrene (**11**)		**13**	21	90	97:3
2	β-methylstyrene		**17**	20	70	98:2
3	α-methylstyrene		**18**	18	60	99:1
4	(*E*)-4-octene		**19**	24	95	95:5
5	(*E*)-5-decene		**20**	20	95	95:5
6	1-methyl-1-cyclohexene		**21**	20	70	95:5

[a] In a typical experiment, bromine (0.5 mmol) and silver triflate (1.1 mmol) were added to a solution of the diselenide **2** (0.5 mmol) in MeCN (2.5 mL) at 0 °C. After 15 min the mixture was cooled to −30 °C and sodium azide (1.0 mmol) was added. The reaction mixture was stirred for 30 min, then the alkene (1.0 mmol) was added, and the mixture was allowed to warm to room temperature gradually. Upon completion of the reaction (monitored by TLC and GC–MS), the mixture was filtered through anhydrous K_2CO_3, and the filtrate was concentrated under vacuum.

 © 2003 Wiley-VCH Verlag GmbH & Co. KGaA, Weinheim



Scheme 3. Preparation of optically active aziridines.



Scheme 4. Conversion of azidoselenides into optically active triazoles.

was identical to the diastereomeric excess of the starting azide.

In conclusion, we have reported the first example of the highly enantioselective addition of a nitrogen nucleophile to a carbon–carbon double bond, which was made possible by the use of chiral, nonracemic electrophilic selenium reagents. An important aspect of this new reaction lies in the synthetic applications of the resulting azidoselenides. These products can be conveniently used in the synthesis of a variety of nitrogen-containing derivatives of very high optical purity.

Received: February 19, 2003 [Z51229]

Keywords: alkenes · asymmetric synthesis · azides · heterocycles · selenium

[1] T. Sheradsky in *The Chemistry of the Azido Group* (Ed.: S. Patai), Interscience, New York, **1971**, pp. 322–390.
[2] a) J. H. Bayer, *J. Am. Chem. Soc.* **1951**, *73*, 5248–5252; b) A. Hassner, R. Fibiger, D. Andsik, *J. Org. Chem.* **1984**, *49*, 4237–4244; c) G. W. Breton, K. Daus, P. J. Kropp, *J. Org. Chem.* **1992**, *57*, 6646–6648.
[3] J. E. Galle, A. Hassner, *J. Am. Chem. Soc.* **1972**, *94*, 3930–3933.
[4] a) A. Hassner, L. A. Levy, *J. Am. Chem. Soc.* **1965**, *87*, 4203–4204; b) A. Hassner, F. W. Frowler, *J. Org. Chem.* **1968**, *33*, 2686–2691; c) A. Hassner, F. Boerwinkle, L. A. Levy, *J. Am. Chem. Soc.* **1970**, *92*, 4879–4883; d) V. Zhdankin, P. J. Stang, *Chem. Rev.* **2002**, *102*, 2523–2584.
[5] A. Hassner, A. S. Amarasekara, *Tetrahedron Lett.* **1987**, *28*, 5185–5188. Azidoselenides were previously obtained from β-bromoselenides: J. N. Denis, J. Vicens, A. Krief, *Tetrahedron Lett.* **1979**, *29*, 2697–2700.
[6] R. M. Giuliano, F. Duarte, *Synlett* **1991**, 419–421.
[7] M. Tiecco, L. Testaferri, A. Temperini, L. Bagnoli, F. Marini, C. Santi, *Synth. Commun.* **1998**, *28*, 2167–2179.
[8] M. Tingoli, M. Tiecco, D. Chianelli, R. Balducci, A. Temperini, *J. Org. Chem.* **1991**, *56*, 6809–6813.
[9] "Organoselenium Chemistry: Modern Developments in Organic Synthesis": M. Tiecco, *Top. Curr. Chem.* **2000**, 7–54.
[10] a) M. Tiecco, L. Testaferri, C. Santi, C. Tomassini, F. Marini, L. Bagnoli, A. Temperini, *Tetrahedron: Asymmetry* **2000**, *11*, 4645–4650; b) C. Santi, T. Wirth, *Tetrahedron: Asymmetry* **1999**, *10*, 1019–1023.
[11] T. Wirth, *Tetrahedron* **1999**, *55*, 1–28.
[12] M. Tiecco, L. Testaferri, L. Bagnoli, F. Marini, A. Temperini, C. Tomassini, C. Santi, *Tetrahedron Lett.* **2000**, *41*, 3241–3245.
[13] M. Tiecco, L. Testaferri, C. Santi, C. Tomassini, F. Marini, L. Bagnoli, A. Temperini, *Chem. Eur. J.* **2002**, *8*, 1118–1124.
[14] a) M. Tiecco, L. Testaferri, F. Marini, S. Sternativo, A. Temperini, L. Bagnoli, C. Santi, *Tetrahedron: Asymmetry* **2001**, *12*, 1493–1502; b) M. Tiecco, L. Testaferri, L. Bagnoli, V. Purgatorio, A. Temperini, F. Marini, C. Santi, *Tetrahedron: Asymmetry* **2001**, *12*, 3297–3304.
[15] M. Tiecco, L. Testaferri, C. Santi, C. Tomassini, F. Marini, L. Bagnoli, A. Temperini, *Eur. J. Org. Chem.* **2000**, 3451–3457.
[16] V. R. Ward, M. A. Cooper, A. D. Ward, *J. Chem. Soc. Perkin Trans. 1* **2001**, 944–945.
[17] G. Broggini, G. Molteni, G. Zucchi, *Synthesis* **1995**, 647–648.

 © 2003 Wiley-VCH Verlag GmbH & Co. KGaA, Weinheim

Trifluoromethylation

Trifluoroacetamides from Amino Alcohols as Nucleophilic Trifluoromethylating Reagents**

Jérôme Joubert, Solveig Roussel, Carole Christophe, Thierry Billard, Bernard R. Langlois,* and Thierry Vidal*

In memory of Odile Miani

Fluorinated compounds exhibit unique properties,[1] which are of huge interest in a wide range of applications.[2] Consequently, the number of new organofluorine products that appear each year is growing steadily.[3] Trifluoromethyl-substituted compounds constitute a particular class with specific properties, such as the high lipophilicity provided by this group. Thus, such molecules find pharmaceutical applications,[2] as illustrated by two drugs recently introduced for

[*] Dr. T. Billard, Dr. B. R. Langlois, J. Joubert, S. Roussel, C. Christophe
Laboratoire SERCOF, Université Claude Bernard Lyon 1
Bât. Chevreul – 43 Bd du 11 Novembre 1918
69622 Villeurbanne (France)
Fax: (+33) 472431323
E-mail: billard@univ-lyon1.fr
bernard.langlois@univ-lyon1.fr
Dr. T. Vidal
Rhodia Co., Centre de Recherche de Lyon
85, Av. des Frères Perret, 69192 Saint-Fons Cedex (France)

[**] We thank the CNRS and Rhodia Co. for financial support.

Supporting information for this article is available on the WWW under http://www.angewandte.org or from the author.

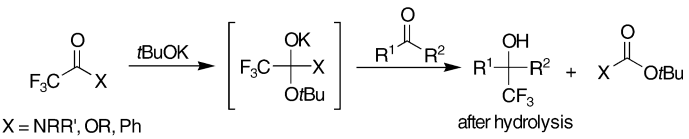
 DOI: 10.1002/anie.200351301 © 2003 Wiley-VCH Verlag GmbH & Co. KGaA, Weinheim

the treatment of human diseases, efavirenz[4] (anti-HIV) and celecoxib[5] (antiarthritic).

In the last two decades, many reliable methods have been reported for the introduction of a CF_3 group into organic compounds,[6] and in recent years, anionic trifluoromethylation has emerged as one of the most powerful strategies. However, these anionic methods suffer from the limited availability of efficient reagents that are able to overcome the high instability of the CF_3 anion, which is known to decompose rapidly and almost irreversibly into a fluoride anion and difluorocarbene.

The most popular reagent for these anionic methods is currently (trifluoromethyl)trimethylsilane (CF_3SiMe_3, Ruppert–Prakash reagent), which is both very powerful for synthetic applications and commercially available.[7] However, its preparation from CF_3Br, the industrial production of which is now restricted for ecological reasons,[8] constitutes a drawback for large-scale applications.

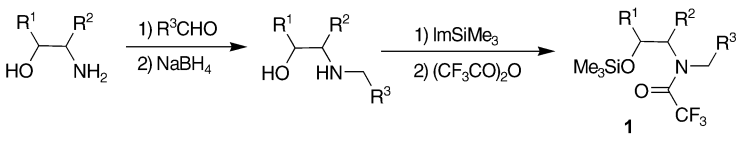
In our quest for new trifluoromethylating reagents, we have recently shown that some hemiaminals of trifluoroacetaldehyde are useful tools for the nucleophilic trifluoromethylation of non-enolizable carbonyl compounds.[9] More recently, we demonstrated that trifluoroacetamides,[10a] trifluoromethanesulfinamides,[10b] and α,α,α-trifluoroacetophenone[10c] also behave as efficient trifluoromethylating reagents under the action of potassium *tert*-butoxide (Scheme 1).



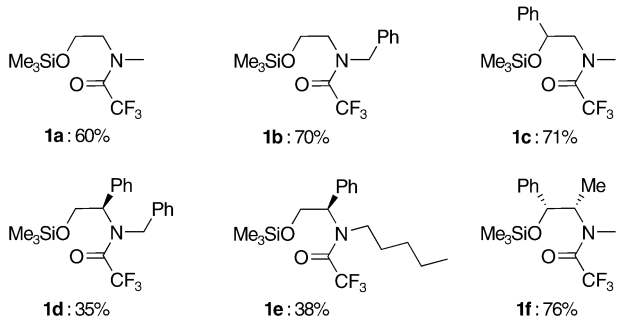
Scheme 1. Trifluoromethylation with trifluoroacetic acid derivatives.

Although trifluoroacetic acid derivatives are economically and ecologically friendly trifluoromethylating agents, the presence of a strong base in these reactions precludes the use of enolizable substrates. To circumvent this drawback, we envisaged a strategy in which slow delivery of the alcoholate would favor nucleophilic attack over deprotonation by this species. This led us to study the reactivity of trifluoroacetamides derived from *O*-silylated *vic*-amino alcohols. These compounds were easily prepared from commercially available amino alcohols (Scheme 2).

A variety of reagents were synthesized by this procedure, as shown in Scheme 3 (overall yields are given for the purified compounds). To access their potential as trifluoromethylating reagents, **1a–f** were desilylated with CsF in 1,2-dimethoxyethane (DME), according to the method used in our previous



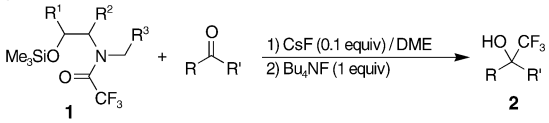
Scheme 2. Synthesis of *N*-trifluoroacetyl *O*-trimethylsilyl *vic*-amino alcohols. $ImSiMe_3$ = *N*-(trimethylsilyl)imidazole.



Scheme 3. *N*-trifluoroacetyl *O*-trimethylsilyl *vic*-amino alcohols.

studies.[9a–b] As models for different types of carbonyl electrophiles, we chose benzophenone (for non-enolizable substrates), benzaldehyde (for aldehyde substrates), and acetophenone (for enolizable substrates). The results are summarized in Table 1.

Table 1: Trifluoromethylation of benzophenone, benzaldehyde, and acetophenone with trifluoroacetamides **1**.



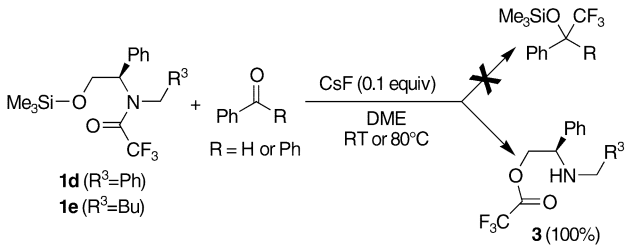
Entry	**1**	*T* [°C]	Yield [%] (*t* [h]) R = R′ = Ph (**2a**)	R = Ph, R′ = H (**2b**)	R = Ph, R′ = CH_3 (**2c**)
1	**a**	[a]	no transfer[b]		
2	**a**	50	59 (24)	no transfer[c]	21 (108)
3	**a**	80	60 (5)	43 (24)	41 (24)
4	**b**	50	50 (30)		
5	**b**	80	50 (24)	52 (24)	28 (24)
6	**c**	50	44 (24)		
7	**c**	80	54 (24)	56 (24)	26 (24)
8	**f**	50	71 (6)	85 (6)	
9	**f**	80	74 (2)		
10	**f**	[a]	76 (24)	89 (24)	58 (120)

[a] Room temperature. [b] 3 days. [c] 24 h.

Table 1 shows that the substitution at the nitrogen atom did not greatly influence the ability of these new reagents to transfer their CF_3 group (entries 1–5). In contrast, the influence of substituents R^1 and R^2 was more important. Indeed, when no substituent was present ($R^1 = R^2 = H$), or when only one substituent was present, and in the α position relative to the oxygen atom, trifluoromethylation occurred under heating at 80 °C (Table 1, entries 3, 5, and 7). However, when a substituent was present in the α position relative to the nitrogen atom (and $R^1 = H$), no CF_3 transfer was observed, and instead migration of the trifluoroacetyl group from the nitrogen atom to the oxygen atom occurred (Scheme 4). On the other hand, when both adjacent carbon centers were substituted, as in the case of **1f**, trifluoromethylation proceeded even at room temperature (Table 1, entries 8–10).

Thus, this new family of reagents allowed the trifluoromethylation of both non-enolizable and enolizable carbonyl

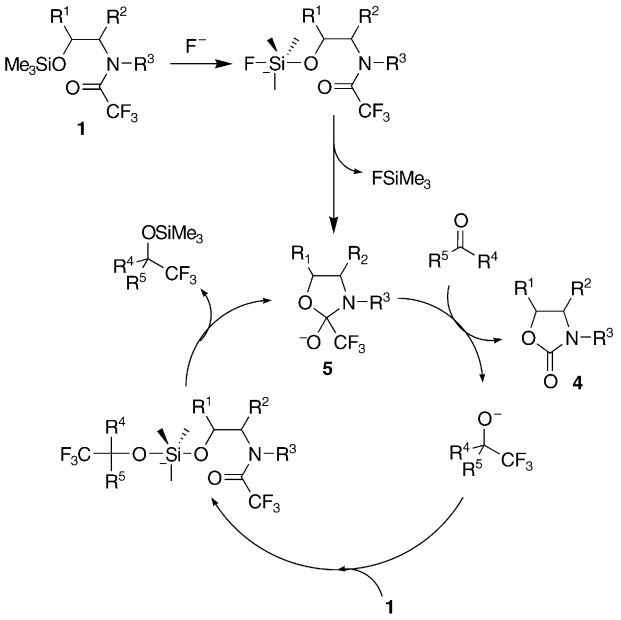
 © 2003 Wiley-VCH Verlag GmbH & Co. KGaA, Weinheim



Scheme 4. Trifluoroacetyl migration with **1d** and **1e**.

compounds. Compound **1f**, derived from cheap and commercially available ephedrine, was the best candidate, as it promoted the formation of the desired products in good yields even at room temperature. Furthermore, **1f** is a stable white solid that can be stored for long periods of time, whereas **1a–c** have a shelf life of less than 48 h. The long reaction time of **1f** with acetophenone led us to use soluble tetrabutylammonium triphenyldifluorosilicate (TBAT)[11] in THF instead of CsF in DME as the desilylating agent. With this reagent a 60% yield of **2c** was observed after 6 h, in contrast to the 5 days required with CsF/DME (Table 1, entry 10).

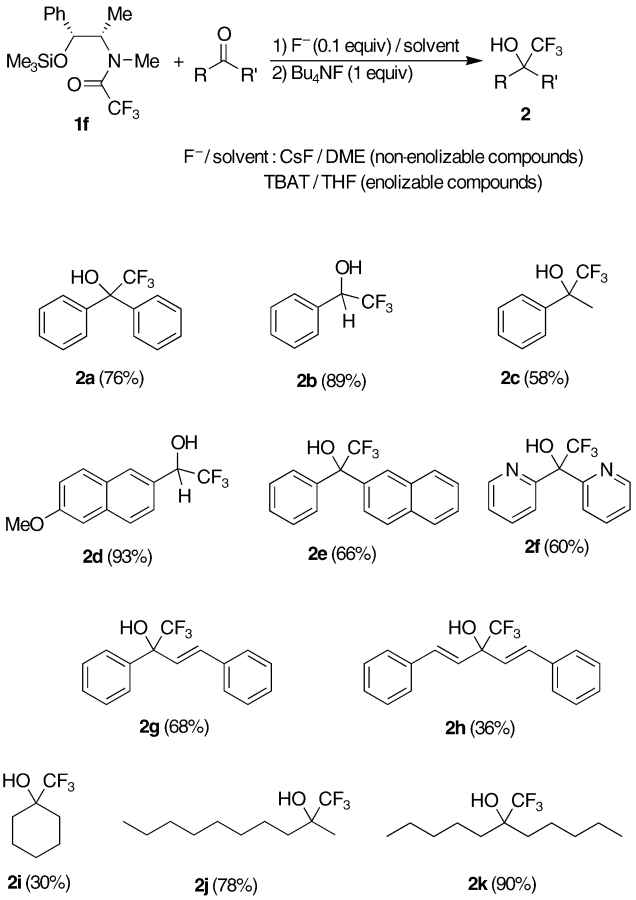
The mechanism shown in Scheme 5 could be proposed, by analogy with previous work.[7a,9a] This proposal was supported by the isolation and characterization of oxazolidinones **4** from



Scheme 5. Mechanism of the trifluoromethylation with **1**.

the reaction. Nevertheless, studies to better understand the role of the various substituents are in progress in our laboratory.

From these preliminary results with simple substrates, compound **1f** appeared to be the most powerful trifluoromethylating reagent of those studied. Consequently, its reactivity toward diverse carbonyl compounds was examined (Scheme 6).



Scheme 6. Reactivity of **1f**.

Thus, a wide range of non-enolizable and enolizable carbonyl compounds (aldehydes, ketones, α,β-unsaturated ketones) were trifluoromethylated with **1f** in satisfactory yields. Although **1f** is a chiral reagent, it did not induce any chirality in the trifluoromethylation of prochiral carbonyl substrates. No enantiomeric excess was observed for any of the products.

In conclusion, we have demonstrated that trifluoroacetamides derived from *O*-silylated *vic*-amino alcohols constitute a new class of nucleophilic trifluoromethylating reagents. The trifluoroacetamide derived from ephedrine is especially promising, as it trifluoromethylates both enolizable and non-enolizable carbonyl compounds in satisfying yields under mild conditions. To our knowledge, this is the first reagent that is likely to provide competition for the Ruppert–Prakash reagent. Our new challenge is to design similar reagents for enantioselective trifluoromethylation. These studies are in progress in our laboratory.

Experimental Section

Typical procedure: **1f**: A flame-dried three-necked vessel was successively charged with ephedrine (6.6 g, 40 mmol) and dichloromethane (40 mL) under nitrogen. The resulting mixture was cooled to 0 °C, then *N*-(trimethylsilyl)imidazole (6 mL, 41 mmol) was added. The reaction mixture was stirred at 0 °C for 40 min, then warmed to

 © 2003 Wiley-VCH Verlag GmbH & Co. KGaA, Weinheim

room temperature and stirred for a further 2 h. After this period, diisopropylethylamine (7.2 mL, 41.4 mmol) was added and the mixture was cooled again to 0 °C. A solution of trifluoroacetic anhydride (5.6 mL, 40 mmol) in CH_2Cl_2 (16 mL) was then added dropwise over 1.5 h, after which the mixture was stirred at 0 °C for 10 min, then at room temperature for 4 h. The reaction mixture was then washed with 6% aqueous $NaHCO_3$ and the organic phase was dried over Na_2SO_4 and concentrated in vacuo. The crude residue was purified by chromatography over silica gel.

Typical trifluoromethylation procedure: A solution of tetrabutylammonium triphenyldifluorosilicate (TBAT; 54 mg, 0.1 equiv) in THF (0.5 mL) was added dropwise over 15 min to a stirred solution of **1f** (1 mmol) and the electrophile (1 mmol) in THF (1 mL). After 6 h, the crude product was desilylated by treatment with TBAF (1M in THF, 1 mL) for 1 h, then the mixture was extracted with pentane and brine. The organic phase was dried over Na_2SO_4 and the solvent was evaporated in vacuo. The crude product was purified by flash chromatography over silica gel.

Received: February 28, 2003 [Z51301]

Keywords: alcohols · amino alcohols · fluorine · nucleophilic addition · trifluoromethylation

[1] a) "Organo-Fluorine Compounds": U. Groß, S. Rüdiger, *Methods Org. Chem. (Houben-Weyl) 4th ed. 1952–*, Vol. E10a, pp. 18–26; b) B. E. Smart, *J. Fluorine Chem.* **2001**, *109*, 3–11.

[2] a) R. Filler, Y. Kobayashi, L. M. Yagulpolskii, *Organofluorine Compounds in Medicinal Chemistry and Biomedical Applications*, Elsevier, Amsterdam, **1993**; b) R. E. Banks, B. E. Smart, J. C. Tatlow, *Organofluorine Chemistry: Principles and Commercial Applications*, Plenum, New York, **1994**; c) J. T. Welch, S. Eswarakrishnan, *Fluorine in Bioorganic Chemistry*, Wiley, New York, **1991**; d) *Fluorine-containing Amino Acids. Synthesis and Properties* (Eds.: V. P. Kukhar, V. A. Soloshonok), Wiley, Chichester, **1995**; e) T. Hiyama, *Organofluorine Compounds: Chemistry and Properties*, Springer, Berlin, **2000**, chap. 5, pp. 137–182; f) A. Becker, *Inventory of Industrial Fluoro-Biochemicals*, Eyrolles, Paris, **1996**.

[3] H. Schofield, *J. Fluorine Chem.* **1999**, *100*, 7–11.

[4] a) J. Ren, J. Milton, K. L. Weaver, S. A. Short, D. I. Stuart, D. K. Stammers, *Structure* **2000**, *8*, 1089–1094; b) O. S. Pedersen, E. B. Pedersen, *Synthesis* **2000**, 479–495.

[5] a) L. M. Jackson, C. J. Hawkey, *Drugs* **2000**, *59*, 1207–1216; b) M. L. P. Price, W. J. Jorgensen, *J. Am. Chem. Soc.* **2000**, *122*, 9455–9466.

[6] M. A. McClinton, D. A. McClinton, *Tetrahedron* **1992**, *48*, 6555–6666.

[7] a) G. K. S. Prakash, A. K. Yudin, *Chem. Rev.* **1997**, *97*, 757–786; b) R. P. Singh, J. M. Shreeve, *Tetrahedron* **2000**, *56*, 7613–7632; c) G. K. S. Prakash, M. Mandal, *J. Fluorine Chem.* **2001**, *112*, 123–131; d) T. Billard, B. R. Langlois, *Tetrahedron Lett.* **1996**, *37*, 6865–6868; e) T. Billard, S. Large, B. R. Langlois, *Tetrahedron Lett.* **1997**, *38*, 65–68.

[8] a) M. Hudlicky, A. E. Pavlath, *Chemistry of Organic Fluorine Compounds II. A Critical Review*, ACS Monograph 187, American Chemical Society, Washington, DC, **1995**, pp. 1092–1100; b) B. D. Key, R. D. Howell, C. S. Criddle, *Environ. Sci. Technol.* **1997**, *31*, 2445–2454.

[9] a) T. Billard, S. Bruns, B. R. Langlois, *Org. Lett.* **2000**, *2*, 2101–2103; b) T. Billard, B. R. Langlois, G. Blond, *Tetrahedron Lett.* **2000**, *41*, 8777–8780; c) T. Billard, B. R. Langlois, G. Blond, *Eur. J. Org. Chem.* **2001**, 1467–1471; d) B. R. Langlois, T. Billard, *Synthesis* **2003**, 185–194.

[10] a) L. Jablonski, J. Joubert, T. Billard, B. R. Langlois, *Synlett* **2003**, *2*, 230–232; b) D. Inschauspe, J.-B. Sortais, T. Billard, B. R. Langlois, *Synlett* **2003**, *2*, 233–235; c) L. Jablonski, T. Billard, B. R. Langlois, *Tetrahedron Lett.* **2003**, *44*, 1055–1057.

[11] C. J. Handy, Y.-F. Lam, P. DeShong, *J. Org. Chem.* **2000**, *65*, 3542–3543.

 © 2003 Wiley-VCH Verlag GmbH & Co. KGaA, Weinheim

Probing Fullerene Aromaticity

The Inside Story of Fullerene Anions: A ^{3}He NMR Aromaticity Probe**

*Tamar Sternfeld, Martin Saunders, R. James Cross, and Mordecai Rabinovitz**

A fundamental chemical question concerning the fullerenes involves their aromatic nature.[1] For many reasons, it is impossible to experimentally obtain anything that is similar to a resonance energy for a fullerene. We must therefore rely on information obtained from magnetic properties. Since fullerenes are borderless polycyclic conjugated systems with internal cavities, it is possible to study the diamagnetism from the inside. Incorporating ^{3}He inside a fullerene cage (endohedral) and measuring its NMR chemical shift compared with the shift of helium outside gives a direct measurement of the shielding of the magnetic field by the fullerene.[2,3] The magnetic field inside the fullerene is a consequence of diamagnetism and is related to the ring currents in the fullerene molecular orbitals.[4]

The aromaticity of C_{60} and C_{70} has been thoroughly investigated theoretically and experimentally. An interesting aspect of these investigations was the observation that the addition of electrons[5] drastically changes the magnetic properties of fullerenes. Reducing these fullerenes to their hexaanions inverted their aromatic character.[1]

^{3}He NMR chemical shifts have clearly shown the extraordinary changes that occur in the aromaticity of C_{60} and C_{70} upon reduction. While the ^{3}He chemical shift of He@C_{60} appears at $\delta = -6.4$ ppm, that of He@C_{60}^{6-} is shifted to an extremely high field ($\delta = -49.5$ ppm), which exemplifies the much higher aromatic character of the C_{60}^{6-} ion. On the other hand, the ^{3}He NMR of He@C_{70}^{6-} is shifted to low field, when compared with the neutral state (δ(He@C_{70}) $= -28.8$; δ(He@

[*] Prof. Dr. M. Rabinovitz, T. Sternfeld
Department of Organic Chemistry
The Hebrew University of Jerusalem
Jerusalem 91904 (Israel)
Fax: (+ 972) 2-652-7547
E-mail: mordecai@vms.huji.ac.il
Prof. Dr. M. Saunders, Prof. Dr. R. J. Cross
Department of Chemistry
Yale University
New Haven, CT 06520–8107 (USA).

[**] This research was supported by the Israel Science Foundation (ISF), grant 147/00.

 © 2003 Wiley-VCH Verlag GmbH & Co. KGaA, Weinheim DOI: 10.1002/anie.200351429

C_{70}^{6-}) = 8.3 ppm), thus pointing a reduction in aromaticity.[6] Fullerenes can also host two endohedral helium atoms,[7] and the ratio of the amounts of $He_2@C_n$ and $He@C_n$ is highly dependent on the fullerene size. The chemical shift of the dihelium species is close to that of the monohelium species, and it can be shifted to either a slightly higher or lower field. The difference between the mono- and dihelium resonances can give an indication about the homogeneity and the direction of the magnetic-field gradient inside the fullerene, since the mono- and dihelium forms exhibit different magnetic properties resulting from a slight difference in the location of the helium atoms. In a previous report, we demonstrated that the reduction of fullerenes can affect the magnetic-field gradient inside the fullerene.[8]

Beside C_{60} and C_{70}, higher fullerenes (C_n, $n > 70$) can also be prepared using the Krätchmer–Huffman procedure.[9] Their separation[10] and characterization are very challenging, because of their relatively similar shape, and the multiplicity of the resulting ^{13}C NMR signals.[11] It has been shown previously that the ^3He NMR chemical shifts of higher fullerenes, $He@C_n$, lie between two extremes, that is, the low-field $^3He@C_{60}$ and the high-field $^3He@C_{70}$, which points to their "intermediate" aromatic character.[3c–d]

The higher fullerenes are able to accept a relatively large number of electrons into their π systems, in a manner similar to that of C_{60} and C_{70}. This behavior was demonstrated by their electrochemistry,[12] and explained by the availability of low-lying unoccupied molecular orbitals,[13] which results in high electron affinities.[14] Calculations suggest that the addition of electrons should change the magnetic properties of the higher fullerenes.[15]

The purpose of this research was to study the magnetic properties of the anions of higher fullerenes by ^3He NMR spectroscopy. The main objectives were: a) Monitoring the changes in the aromaticity of the higher fullerenes on reduction; b) comparing the aromaticity of the anions of higher fullerenes to establish whether it depends on their size and/or their symmetry/topology; c) examination of the chemical shifts of the mono- and dihelium species in higher fullerene anions.

A mixture of ^3He-labeled fullerenes that contained mainly C_{70}, C_{76}, C_{78}, and C_{84} was separated by HPLC, depending on their molecular weight.[16] C_{76} was separated as one isomer,[10a] but C_{78} and C_{84} were separated as mixtures of isomers. The three isomers of C_{78} (C_{2v} (2)[17], C'_{2v} (3)[17] and D_3) were separated into two fractions (C_{78}-A and C_{78}-B), each of which contained a mixture of two isomers in unequal ratios (Figure 1). Unfortunately, a similar separation was not possible for the different isomers of C_{84}. The separation process was followed by measuring the ^3He NMR spectra of the mixture before separation, and those of each fraction obtained. [18] The ^3He chemical shifts of the neutral fullerenes (Table 1) are in good agreement with previously reported results.[3c–d] Most of the fullerenes showed a small ^3He NMR signal which is due to the $^3He_2@C_n$ species, in addition to the major ^3He NMR signal (Table 1).

Each fullerene fraction (2–5 mg) was reduced with lithium metal in [D_8]THF, in the presence of a trace of corannulene[6] and $^3He@C_{60}$ as an internal reference. The reduction process was followed by observing the solution color (up to the point that a green color was observed, which is indicative of the corannulene monoanion), and by measuring ^3He NMR spectra. The ^3He NMR data of all of the fullerene anions ($He@C_{76}^{6-}$, $He@C_{78}^{6-}$, and $He@C_{84}^{6-}$) together with those of $He@C_{60}^{6-}$ and $He@C_{70}^{6-}$ are summarized in Table 1, and compared with the chemical shifts of the neutral species.

The ^3He NMR spectra of the two fractions of C_{78}, together with the ^{13}C NMR spectra, make it possible to assign the ^3He

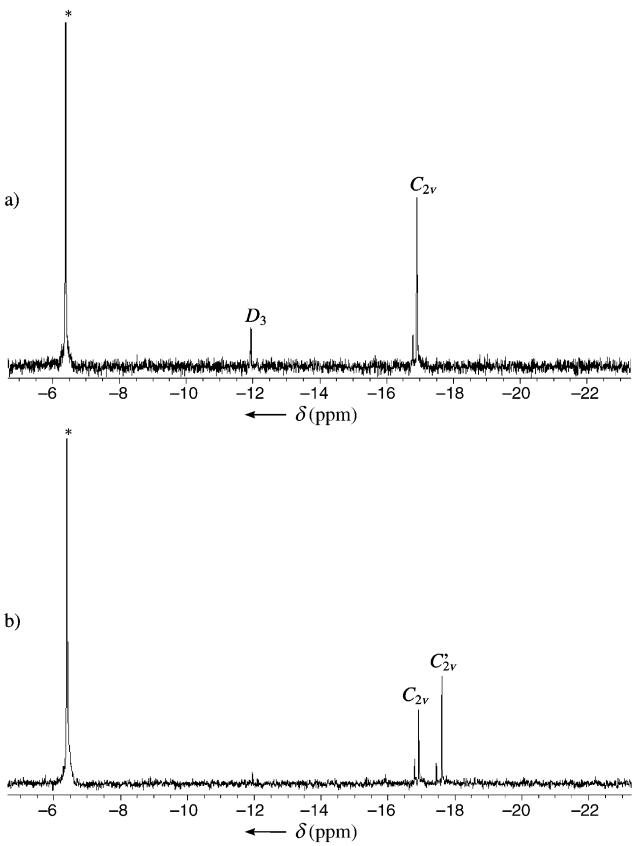


Figure 1. ^3He NMR spectra (methylnaphthalene/CD_2Cl_2) of the two fractions of C_{78} containing the three isomers. a) Fraction C_{78}-A; b) fraction C_{78}-B. * = $^3He@C_{60}$ (internal reference).

Table 1: ^3He NMR chemical shifts (in ppm) of $He@C_n$, $He@C_n^{6-}$ and the dihelium species (in parentheses).

	Neutral[a]	Anion	Δ[d]
$He@C_{60}$	−6.40	−49.27 [b], (−49.17)[c]	−42.87
$He@C_{70}$	−28.82, (−28.81)	+8.20[b], (+8.04)[c]	+37.02
$He@C_{76}$	−18.75, (−18.61)	−20.62, (−20.55)	−1.87
$He@C_{78}$-C_{2v}	−16.91, (−16.79)	−10.02	+6.89
$He@C_{78}$-D_3	−11.94	−32.39, (−32.54)	−20.45
$He@C_{78}$-C'_{2v}	−17.60, (−17.45)	−13.50, (−13.61)	+4.1
$He@C_{84}$ (mixture of isomers)	−7.53, (−7.57), −8.40, (−8.43), −8.99, −9.64, (−9.68)	−22.12, (−22.06), −22.80, (−22.76)	≈−12

[a] Mostly consistent with data reported in refs. [3] and [7a], see text. [b] Taken from ref. [6]. [c] Taken from ref. [8].
[d] $\delta(He@C_n^{6-}) - \delta(He@C_n)$.

 © 2003 Wiley-VCH Verlag GmbH & Co. KGaA, Weinheim

signals of the different isomers. In the first fraction of C_{78}^{6-} (C_{78}-A), two signals were observed in the ^{3}He NMR spectrum; a major peak at −32.39 ppm and a smaller peak at −10.02 ppm (Figure 2). These two peaks were assigned as the anions of the isomers C_{78}-D_3 and C_{78}-C_{2v}, respectively. The

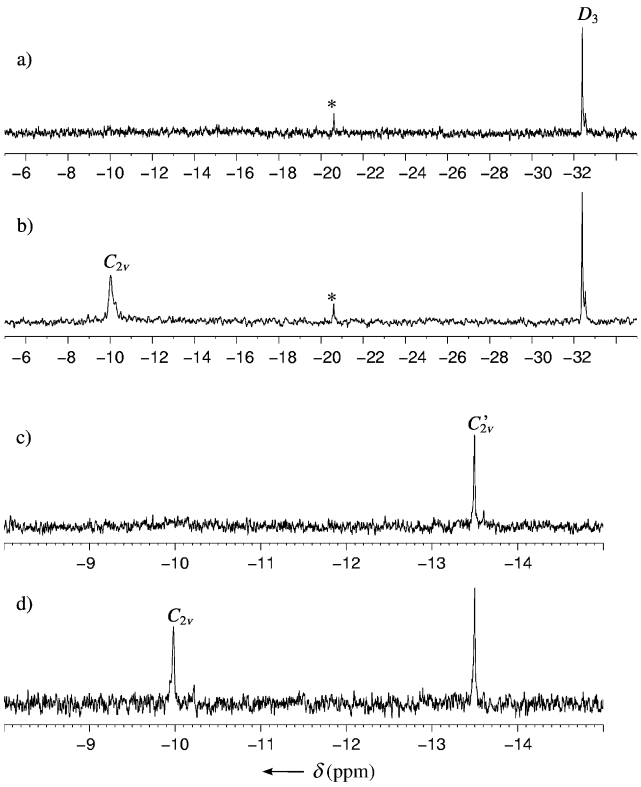


Figure 2. ^{3}He NMR spectra ([D$_8$]THF) of the two fractions of C_{78}^{6-} as a function of reduction time. a) the reduced fraction C_{78}-A; b) the same fraction after an additional 20 min reduction; c) the reduced fraction C_{78}-B; d) the same fraction after an additional 20 min reduction. * = a trace of ^{3}He@C_{76}^{6-}.

signals in the spectrum of fraction C_{78}-B were observed at −10.02 ppm (the same as in fraction C_{78}-A: C_{2v}-isomer) and at −13.5 ppm, which was assigned to the isomer C_{78}-C'_{2v}.

The assignment of the different isomers of C_{78} was based on the ^{13}C NMR spectrum of the reduced fractions. The ^{13}C NMR spectra of the reduced fraction C_{78}-A, was the same (at both 170 K and 298 K) as in our previous study of C_{78}^{6-}, which included the C_{2v} and D_3 isomers.[19] The ^{13}C NMR spectrum of fraction C_{78}-B did not contain the absorption of the D_3 isomer at 298 K, and a different ^{13}C NMR spectrum appeared at 170 K. This led us to conclude that the C'_{2v} isomer is the major form present in this fraction, and that the minor form is the C_{2v} isomer.[20]

By measuring the ^{3}He NMR spectra of both fractions as a function of reduction time, it can be seen that the signal of the C_{2v} isomer appears soon after the two other signals were observed (Figure 2). This means that a longer reduction time is needed for this isomer, even though it constitutes the larger component of the mixture (in fraction C_{78}-A), as was shown from the spectrum of the neutral isomers. This phenomenon was also observed by measuring the ^{13}C NMR spectra.[19]

Two major signals for He@C_{84}^{6-} were observed, one at −22.12 ppm and the other at −22.80 ppm, and one major signal appeared for ^{3}He@C_{76}^{6-} at −20.62 ppm. The ^{3}He NMR chemical shifts of all of the anions of the higher fullerenes are between two extremes: the high-field shift of He@C_{60}^{6-}, and the low-field shift of He@C_{70}^{6-}. Thus, an "aromaticity scale" of the fullerene anions can be suggested: $C_{60}^{6-} > C_{78}^{6-}(D_3) > C_{84}^{6-}$(two isomers) $> C_{76}^{6-} > C_{78}^{6-}(C'_{2v}) > C_{78}^{6-}(C_{2v}) > C_{70}^{6-}$.[21] The magnetic properties of the fullerene anions are in line with the magnetic susceptibility calculations.[15]

Comparison between the ^{3}He NMR chemical shifts of the neutral fullerenes and their anions (Table 1) shows that the changes in the chemical shifts are different from one fullerene to another. While the ^{3}He signals of C_{78}-D_3, C_{84}, and C_{76} are shifted to higher field as a result of their reduction, the two isomers of C_{78}-C_{2v} are shifted to lower field. These changes point to an increase or decrease, respectively, in the aromaticity of the fullerenes. These two opposite trends were observed in the reduction of C_{60} and C_{70}, but in a much more dramatic manner.

The magnetic properties of fullerenes and their anions are not simply related to the number of carbon atoms or the number of electrons in the π system. This is demonstrated by the three C_{78} isomers, which behave quite differently. The aromatic character of C_{78}-D_3 increases, when reduced, thus C_{78}^{6-}-D_3 is highly aromatic. However, the aromaticity of the two C_{2v} isomers decreases as a result of the reduction, and their anions show lower aromatic character than the anion of the D_3 isomer (the C_{2v} isomer shows lower aromaticity than C'_{2v}).

The $He_2@C_n^{6-}$ signal was also observed in most of the ^{3}He NMR spectra. As for the neutral compounds, these minor signals appear at a slightly higher or lower field than the major signals (Table 1). In most of the "highly aromatic" fullerene anions, which show a high-field ^{3}He chemical shift (C_{60}^{6-}, C_{84}^{6-}, C_{76}^{6-}), the $^3He_2@C_n^{6-}$ resonance is shifted to a lower field, compared with the monohelium compound ^{3}He@C_n^{6-}. On the other hand, when the monohelium signal is shifted to a low field (C_{70}^{6-}, C_{78}^{6-}-C_{2v}), the signal for the dihelium compound is shifted to higher field. This can be explained by the direction of the magnetic-field gradient inside the fullerene. In most of the highly aromatic fullerene anions, the aromaticity is at its highest close to the fullerene center (as indicated by the chemical shift of the monohelium compound). An opposite behavior is observed for the "less aromatic" fullerene anions.[8]

The differences in the aromaticity of the isomers of reduced C_{78} are not only visible from the ^{3}He chemical shifts, but are also demonstrated kinetically.[22] The two isomers of C_{78}^{6-}-D_3 and C'_{2v}, which are found to be more aromatic than C_{78}^{6-}-C_{2v}, also have a faster reduction rate.[23] This can indicate the presence of a more stable transition state, which is affected by their aromaticity.[24]

Received: March 18, 2003 [Z51429]

Keywords: anions · aromaticity · fullerenes · helium · NMR spectroscopy

 © 2003 Wiley-VCH Verlag GmbH & Co. KGaA, Weinheim

[1] M. Bühl, A. Hirsch, *Chem. Rev.* **2001**, *101*, 1153, and references therein.

[2] a) M. Bühl, W. Thiel, H. Jiao, P. v. R. Schleyer, M. Saunders, F. A. L. Anet, *J. Am. Chem. Soc.* **1994**, *116*, 6005; b) V. Elser, R. C. Haddon, *Nature* **1987**, *325*, 792; c) A. Pasquarello, M. Schlüter, R. C. Haddon, *Science* **1992**, *257*, 1660; d) Z. Chen, J. Cioslowski, N. Rao, D. Moncrieff, M. Bühl, A. Hirsch, W. Thiel, *Theor. Chem. Acc.* **2001**, *106*, 364.

[3] a) M. Saunders, H. A. Jiménez-Vázquez, R. J. Cross, S. Mroczkowski, D. I. Freedberg, F. A. L. Anet, *Nature* **1994**, *367*, 256; b) A. B. Smith III, R. M. Strongin, L. Brard, W. J. Romanow, M. Saunders, H. A. Jiménez-Vázquez, R. J. Cross, *J. Am. Chem. Soc.* **1994**, *116*, 10831; c) M. Saunders, R. J. Cross, H. A. Jiménez-Vázquez, R. Shimshi, A. Khong, *Science* **1996**, *271*, 1693; d) M. Saunders, H. A. Jiménez-Vázquez, R. J. Cross, S. Mroczkowski, M. L. Gross, D. E. Giblin, R. J. Poreda, *J. Am. Chem. Soc.* **1994**, *116*, 2193; e) M. Saunders, H. A. Jiménez-Vázquez, R. J. Cross, W. E. Billups, C. Gesenberg, A. Gonzalez, W. Luo, R. C. Haddon, F. Diederich, A. Herrmann, *J. Am. Chem. Soc.* **1995**, *117*, 9305.

[4] Even though the relationship between aromatic character and diamagnetism in fullerenes remains the subject of discussion, the endohedral ^{3}He NMR chemical shift has been used extensively as a reliable probe for aromaticity.

[5] C. A. Reed, R. B. Bolskar, *Chem. Rev.* **2000**, *100*, 1075, and references therein.

[6] E. Shabtai, A. Weitz, R. C. Haddon, R. E. Hoffman, M. Rabinovitz, A. Khong, R. J. Cross, M. Saunders, P. C. Cheng, L. T. Scott, *J. Am. Chem. Soc.* **1998**, *120*, 6389.

[7] a) A. Khong, H. A. Jimenez-Vazquez, M. Saunders, R. J. Cross, J. Laskin, T. Peres, C. Lifshitz, R. Strongin, A. B. Smith III, *J. Am. Chem. Soc.* **1998**, *120*, 6380; b) T. Weiske, H. Schwarz, *Angew. Chem. Int. Ed. Engl.* **1992**, *31*, 605.

[8] T. Sternfeld, R. E. Hoffman, M. Saunders, R. J. Cross, M. S. Symala, M. Rabinovitz, *J. Am. Chem. Soc.* **2002**, *124*, 8786.

[9] W. Krätchmer, L. D. Lamb, K. Fostiropoulos, D. R. Huffman, *Nature*, **1990**, *347*, 354.

[10] a) R. Ettl, I. Chao, F. Diederich, R. L. Whetten, *Nature* **1991**, *353*, 149; b) F. Diederich, R. L. Whetten, C. Thilgen, R. Ettl, I. Chao, M. M. Alvarez, *Science* **1991**, *254*, 1768; c) K. Kikuchi, N. Nakahara, T. Wakabayashi, S. Suzuki, H. Shiromaru, Y. Miyake, K. Saito, I. Ikemoto, M. Kainosho, Y. Achiba, *Nature* **1992**, *357*, 142; d) R. Taylor, G. J. Langley, A. G. Avent, T. J. S. Dennis, H. W. Kroto, D. R. M. Walton, *J. Chem. Soc. Perkin Trans. 2* **1993**, 1029; e) T. J. S. Dennis, T. Kai, T. Tomiyama, H. Shinohara, *Chem. Commun.* **1998**, 619; f) T. J. S. Dennis, T. Kai, K. Asato, T. Tomiyama, H. Shinohara, T. Yoshida, Y. Kobayashi, H. Ishiwatari, Y. Miyake, K. Kikuchi, Y. Achiba, *J. Phys. Chem. A* **1999**, *103*, 8747; g) N. Tagmatarchis, A. G. Avent, K. Prassides, T. J. S. Dennis, H. Shinohara, *Chem. Commun.* **1999**, 1023; h) F. H. Hennrich, R. H. Michel, A. Fischer, S. Richard-Schneider, S. Gilb, M. M. Kappes, D. Fuchs, M. Bürk, K. Kobayashi, S. Nagase, *Angew. Chem. Int. Ed. Engl.* **1996**, *35*, 1732; i) C. R. Wang, T. Sugai, T. Kai, T. Tomiyama, H. Shinohara, *Chem. Commun.* **2000**, 557.

[11] a) F. Diederich, R. Ettl, Y. Rubin, R. L. Whetten, R. Beck, M. Alvarez, S. Anz, D. Sensharma, F. Wudl, K. C. Khemani, A. Koch, *Science* **1991**, *252*, 548; b) F. Diederich, R. L. Whetten, *Acc. Chem. Res.* **1992**, *25*, 119, and references therein.

[12] L. Echegoyen, L. E. Echegoyen, *Acc. Chem. Res.* **1998**, *31*, 593 and reference therein.

[13] a) P. W. Fowler, J. Woolrich, *Chem. Phys. Lett.* **1986**, *127*, 78; b) S. Saito, S. Okada, S. Sawada, N. Hamada, *Phys. Rev. Lett.* **1995**, *75*, 685; c) J. A. Azamar-Barrios, T. J. S. Dennis, S. Sadhukan, H. Shinohara, G. E. Scuseria, A. Pénicaud, *J. Phys. Chem. A* **2001**, *105*, 4627; d) R. C. Haddon, L. E. Brus, K. Raghavachari, *Chem. Phys. Lett.* **1986**, *125*, 459.

[14] a) O. V. Boltalina, L. N. A. Sidorov, A. Ya. Borshchevsky, E. V. Sukhanova, E. V. Skokan, *Rapid Commun. Mass Spectrom.* **1993**, *7*, 1009; b) L. N. Sidorov, O. V. Boltalina, A. Ya. Borshchevsky, *Rapid Commun. Mass Spectrom.* **1997**, *11*, 662.

[15] R. C. Haddon, A. Pasquarello, *Phys. Rev. B* **1994**, *50*, 16459.

[16] The mixture of fullerenes was purchased from MER Corporation (Tucson, USA). ^{3}He labeling was achieved under high temperature and pressure (see ref. [3]). The HPLC separation was preformed with a 2-(1-pyrenyl)ethylsilyl (PYE) column (10×250 mm) with toluene as the eluent at a flow rate of 2 mL min^{-1}, and a UV/Vis detector (400 nm).

[17] P. W. Fowler, D. E. Manolopoulos, *An Atlas of Fullerenes*, Oxford University Press, Oxford, **1995**.

[18] The ^{3}He NMR spectra of the neutral fullerenes were recorded at room temperature in a 3:1 methylnaphthalene/CD_2Cl_2 mixture, adding [Cr(acac)$_3$] as a relaxation agent.

[19] T. Sternfeld, C. Thilgen, Z. Chen, S. Siefken, P. v. R. Schleyer, W. Thiel, F. Diederich, M. Rabinovitz, *J. Org. Chem.* **2003**, DOI: 10.1021/JO030106n.

[20] This obvious assignment makes it also possible to assign the ^{3}He NMR chemical shifts of the neutral isomers of He@C_{78}.

[21] The assignment as hexaanions is based on DFT calculations, see ref. [19].

[22] The neutral compounds are not soluble in THF, and the C_{2v} isomer was found in larger quantities than the D_3 isomer.

[23] Such behavior was encountered in the reduction of a series of C_{26} fragments of C_{60}; the more aromatic anion was afforded first: R. Shenhar, R. Beust, S. Hagen, H. E. Bronstein, I. Willner, L. T. Scott, M. Rabinovitz, *J. Chem. Soc. Perkin Trans. 2* **2002**, 449.

[24] The C_{78}^{6-}-C_{2v} signal is broader, which can result from an equilibrium being formed with a triplet state.

 © 2003 Wiley-VCH Verlag GmbH & Co. KGaA, Weinheim

Logic Gates

Bio-Inspired Optically Controlled Ultrafast Molecular AND Gate**

*Mikael Andersson, Louise E. Sinks, Ryan T. Hayes, Yongyu Zhao, and Michael R. Wasielewski**

Photoinduced electron-transfer reactions can occur on a timescale of a hundred femtoseconds, so that in principle, molecular electronic devices based on optically controlled

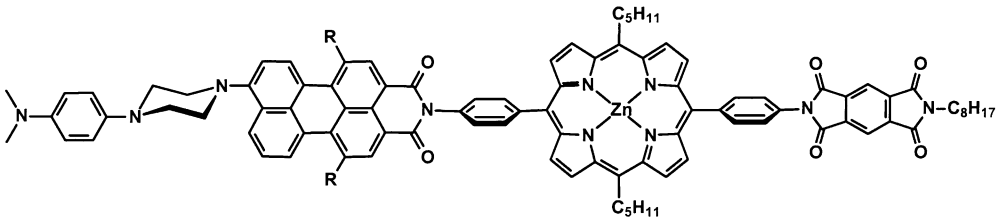
[*] Prof. M. R. Wasielewski, M. Andersson, L. E. Sinks, R. T. Hayes, Y. Zhao
Department of Chemistry
Center for Nanofabrication and Molecular Self-Assembly
Northwestern University
Evanston, IL 60208-3113 (USA)
Fax: (+1) 847-467-1423
E-mail: wasielew@chem.northwestern.edu

[**] M.A. gratefully acknowledges a postdoctoral grant from the Swedish Foundation for International Cooperation in Research and Higher Education. This work was supported by the US National Science Foundation.

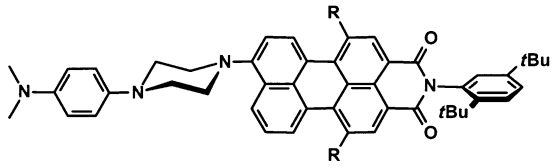
Supporting information for this article is available on the WWW under http://www.angewandte.org or from the author.

 DOI: 10.1002/anie.200351488 © 2003 Wiley-VCH Verlag GmbH & Co. KGaA, Weinheim

electron transfers can function at very high speeds.[1–9] In earlier work we examined a variety of molecular-switch concepts that use two laser pulses to control electron movement within multiple donor–acceptor assemblies.[10–14] While several other research groups have observed logic-gate behavior based on molecular recognition using fluorescent chemosensor materials,[15–19] our goal is to develop systems that switch on an ultrafast time scale using only electron transport. It is well-known that photosynthetic organisms use ultrafast photoinduced electron-transfer reactions to convert solar energy into chemical potential. In particular, photosystems I and II in green plants effectively act in series to separate charge over long distances for long times. We have employed this strategy to produce a covalent molecular tetrad, TMPD-6PMI-ZnP-PI (**1**, Scheme 1), which consists of two electron donor/acceptor pairs, TMPD-6PMI and ZnP-PI,

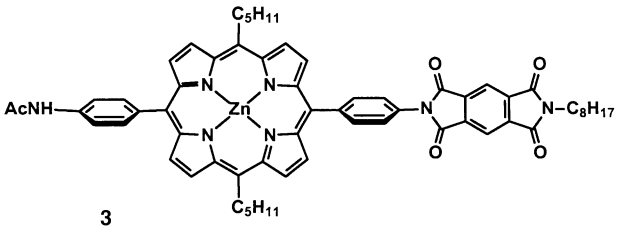


1

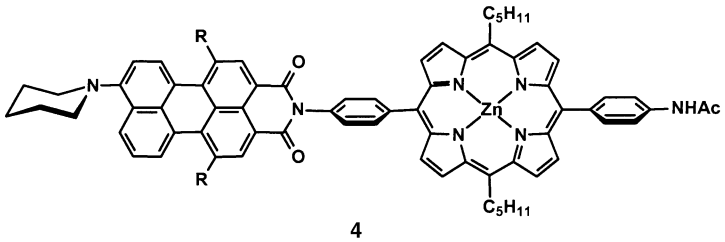


R = 3,5-di-*t*butylphenoxy

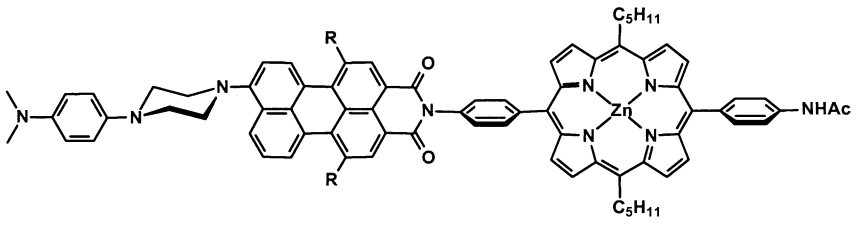
2



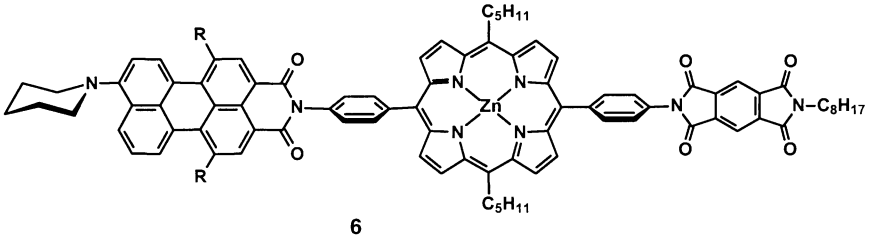
3



4



5



6

Scheme 1. Structures of the molecules used in this study.

 © 2003 Wiley-VCH Verlag GmbH & Co. KGaA, Weinheim

in which each donor–acceptor pair can be selectively excited using different wavelengths of light. Selective excitation of either 6PMI at 540 nm or ZnP at 420 nm leads to formation of $TMPD^{+}$-$6PMI^{-}$ or ZnP^{+}-PI^{-}, respectively, which subsequently undergo rapid charge recombination on a sub-nanosecond time scale, and thus represent a 0 output. However, sequential formation of both ion pairs on a time scale as short as 50 ps, irrespective of which ion pair is produced first, yields $TMPD^{+}$-$6PMI^{-}$-ZnP^{+}-PI^{-}, in which the central ion pair recombines competitively to yield the distal ion pair $TMPD^{+}$-6PMI-ZnP-PI^{-}, which lives for 650 ns, and thus represents a 1 output. Thus, the tetrad exhibits true AND gate behavior using two sequential photodriven electron transfers analogous to photosystems I and II.

The synthesis and characterization of **1**–**6** are described in the Supporting Information. The excited-state energies of 6PMI and ZnP are both 2.07 eV, while those of TMPD and PI are both greater than 3.0 eV.[20] The free energies for the photoinduced charge-separation reactions in toluene were estimated from the expression $\Delta G_{CS} = E^{OX}_{1/2} - E^{RED}_{1/2} - E_S - e^2_0/\varepsilon r + C$, where $E^{OX}_{1/2}$ and $E^{RED}_{1/2}$ are the one-electron redox potentials for oxidation of the donor and reduction of the acceptor in butyronitrile, respectively; E_S is the energy of the lowest excited singlet state; $e^2_0/\varepsilon r$ is the coulomb interaction between the ions; and C corrects for the solvation of the ions in toluene using established methods.[21] All spectroscopic measurements were performed in toluene, where $e^2_0/\varepsilon r + C \cong 0.4$ eV for the ion pairs used in this study.[21] The ZnP and 6PMI chromophores were selectively excited with 100-fs laser pulses at 420 and 510 nm, respectively.[11] Several reference molecules were examined (Scheme 1) to unravel the complex energy- and electron-transfer dynamics possible within **1**. Molecules **2** and **3** were used to determine the rates of electron transfer within the TMPD-6PMI and ZnP-PI pairs, while **4**–**6** were used to ascertain the degree of energy and electron transfer cross-talk between these pairs. The reduction potential of 6PMI is −0.90 V versus the saturated calomel electrode (SCE) and the oxidation potential of TMPD is 0.35 V versus SCE, so that $\Delta G_{CS} \cong -0.4$ eV in toluene. Photoexcitation of 6PMI in **2** with laser pulses with a wavelength of 510 nm (510-nm pulse) results in the charge separation (CS) reaction TMPD-^{1}*6PMI→$TMPD^{+}$-$6PMI^{-}$ with a 1/*e* time of $\tau = 18$ ps followed by the charge recombination (CR) reaction $TMPD^{+}$-$6PMI^{-}$→TMPD-6PMI with $\tau = 55$ ps. The course of the reaction is followed using the absorption of the radical anion of $6PMI^{-}$ at 645 nm.[13,22] The reduction potential of PI is −0.79 V versus SCE and the oxidation potential of ZnP is 0.72 V versus SCE, so that $\Delta G_{CS} \cong -0.2$ eV in toluene. Selective photoexcitation of ZnP in **3** with laser pulses with a wavelength of 420 nm (420-nm pulse) results in the CS reaction ^{1}*ZnP-PI→ZnP^{+}-PI^{-} with $\tau = 55$ ps followed by the CR reaction ZnP^{+}-PI^{-}→ZnP-PI with $\tau = 320$ ps. In this case, the reaction is followed using the absorption of the radical anion of PI^{-} at 720 nm.[23,24]

It was important to determine whether the reactions ^{1}*(6PMI-ZnP)→$6PMI^{-}$-ZnP^{+} and ^{1}*(6PMI-ZnP)→$6PMI^{+}$-ZnP^{-} can occur following photoexcitation of either 6PMI or ZnP. The 6PMI unit undergoes one-electron oxidation at 0.81 V versus SCE, while ZnP is reduced at −1.56 V versus SCE. Thus, the energy levels of $6PMI^{-}$-ZnP^{+} and $6PMI^{+}$-ZnP^{-} in toluene are approximately 2.1 eV and 2.8 eV, respectively, and so formation of these ions from the 2.07 eV excited singlet states of either 6PMI and ZnP should be very slow. However, singlet–singlet energy transfer between 6PMI and ZnP may still occur. Data obtained on **4** using selective photoexcitation of 6PMI with 510-nm pulses shows that the energy-transfer reaction ^{1}*6PMI-ZnP→6PMI-^{1}*ZnP occurs with $\tau = 27$ ps, while selective excitation of ZnP with 420-nm pulses results in singlet energy transfer in the opposite direction, namely, ^{1}*ZnP-6PMI→ZnP-^{1}*6PMI with $\tau = 53$ ps. Thus, the rates of energy transfer between these chromophores are relatively rapid.

Excitation of **6** with 420-nm pulses results in the formation of PI^{-} with $\tau = 63$ ps, while excitation of **6** with 510-nm pulses yields PI^{-} with $\tau = 122$ ps. The observed time constants for the formation of PI^{-} in **6** agree well with a kinetic model using the rate constants measured directly in **2**–**4** that assumes a singlet energy transfer pre-equilibrium occurs between 6PMI and ZnP prior to the formation of ZnP^{+}-PI^{-}. A similar analysis can be performed with triad **5**, in which selective excitation of 6PMI produces $TMPD^{+}$-$6PMI^{-}$-ZnP with $\tau = 14$ ps. The time constants for the individual energy- and electron-transfer processes are summarized in Figure 1.

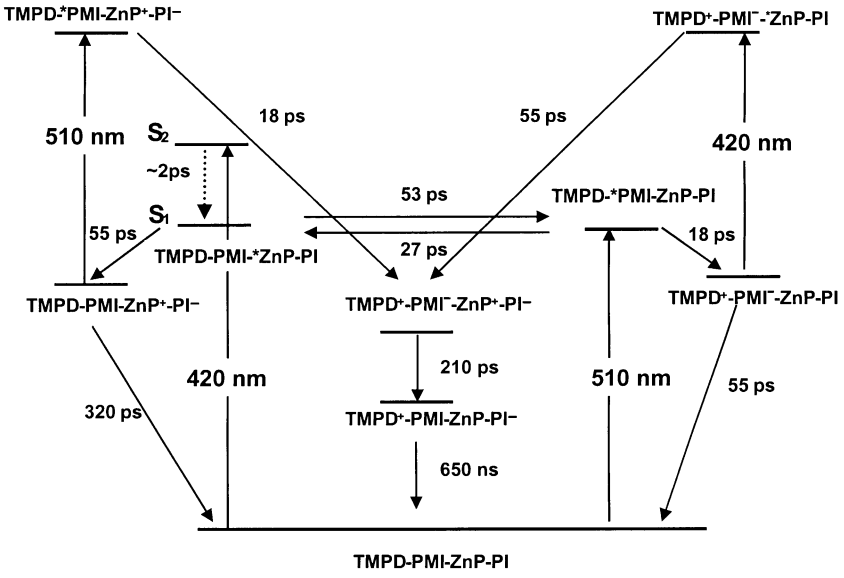


Figure 1. Energy- and electron-transfer pathways and time constants for TMPD-6PMI-ZnP-PI.

The time constants for the formation and decay of ZnP^{+}-PI^{-} in **1** on excitation of ZnP were found to be 41 and 440 ps, respectively, by monitoring the PI^{-} absorption at at 723 nm. Electron transfer from ^{1}*ZnP to PI is competitive with energy transfer from ^{1}*ZnP to 6PMI, so that the quantum yield of ZnP^{+}-PI^{-} is about 0.45. Similarly, selective excitation of 6PMI

 © 2003 Wiley-VCH Verlag GmbH & Co. KGaA, Weinheim

within **1** produces $TMPD^+$-$6PMI^-$ with $\tau = 12$ ps which is in competition with energy transfer from ^{1}*6PMI to ZnP. In the two pulse experiments on **1**,[25] a 420-nm pulse at $t = 0$ generates TMPD-6PMI-ZnP^+-PI^-, which is followed by a second 540-nm pulse at $t = 60$ ps that generates $TMPD^+$-$6PMI^-$-ZnP^+-PI^-. Figure 2 compares the transient absorption

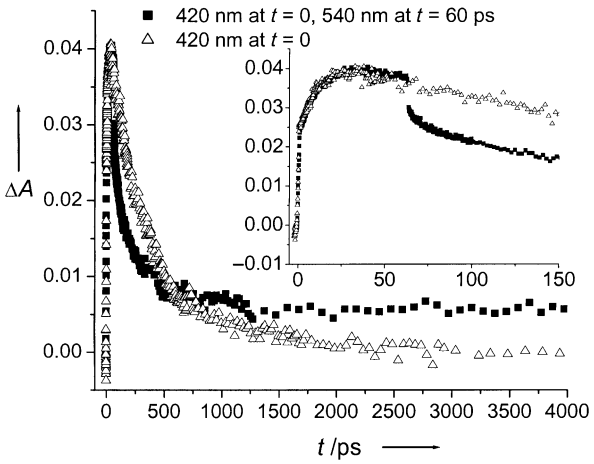


Figure 2. Transient absorption changes at 723 nm after single-pulse excitation at $t = 0$ with light with a wavelength of 420 nm, and after two-pulse excitation with a 420-nm pulse at $t = 0$ and a 540-nm pulse at $t = 60$ ps. Inset: expansion of the time axis in the main figure.

kinetics of **1** at 723 nm following a single 420-nm pulse and following the 420-nm, 540-nm two-pulse sequence. The transient absorption decays to the baseline following single-pulse excitation, while application of the second 540-nm pulse results in the formation of a residual transient absorption with a long lifetime. The transient spectra in Figure 3 show that the long-lived species absorbing at 723 nm is PI^-. Nanosecond flash photolysis[26] using two 7 ns pulses at wavelengths of 416 nm ($t = 0$) and 532 nm ($t = 1$ ns) were used to determine

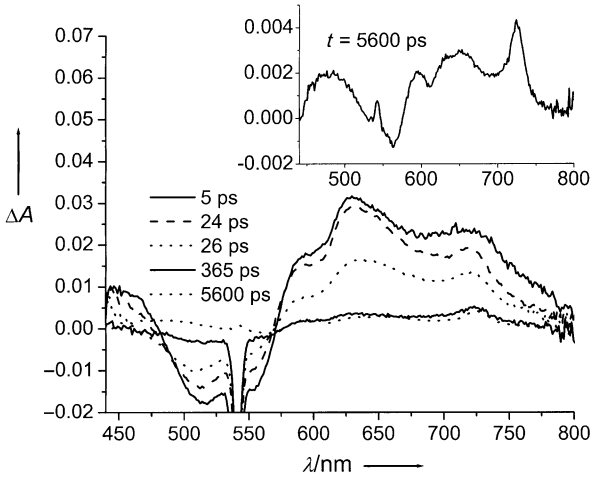


Figure 3. Transient absorption spectra observed at various indicated time delays after excitation at $t = 0$ with a 540-nm laser pulse followed by a second 420-nm pulse at $t = 25$ ps. Inset: the PI^- ion is seen as a peak at 723 nm at long delay times.

that the lifetime of PI^- is 650 ns. Application of either of the nanosecond pulses alone to **1** does not produce a long-lived PI^- signal. We suggest that the long-lived ion pair is $TMPD^+$-6PMI-ZnP-PI^-, which is formed by recombination of the central ion pair in $TMPD^+$-$6PMI^-$-ZnP^+-PI^-. The quantum yield of this ion pair is about 0.16, whereas when the pulse order is reversed, so that 6PMI is excited before ZnP, the long-lived ion pair is formed with a quantum yield of 0.25. These yields are consistent with the rate constants for the competitive ion-pair recombination reactions of $TMPD^+$-$6PMI^-$ and ZnP^+-PI^-.

Achieving logic-gate behavior in electron donor/acceptor molecules requires subtle balancing of the electronic couplings and free energy changes among the various photogenerated ion-pair states. We have demonstrated a supramolecular tetrad in which that reversible formation of a long-lived charge-separated state occurs only when two excitation pulses are applied to it. The rates of the competitive electron-transfer processes within such systems need to be further optimized to increase the efficiency with which the "on" state is formed, as well as to ensure that the tetrad will function in a solid-state environment.

Received: March 26, 2003 [Z51488]

Keywords: · donor–acceptor systems · electron transfer · molecular devices · photochemistry

[1] A. Aviram, M. A. Ratner, *Chem. Phys. Lett.* **1974**, *29*, 277.
[2] J. J. Hopfield, J. N. Onuchic, D. N. Beratan, *Science* **1988**, *241*, 817.
[3] A. P. de Silva, H. Q. N. Gunaratne, T. Gunnlaugsson, A. J. M. Huxley, C. P. McCoy, J. T. Radmacher, T. E. Rice, *Chem. Rev.* **1997**, *97*, 1515.
[4] R. M. Metzger, *Acc. Chem. Res.* **1999**, *32*, 950.
[5] A. S. Lukas, M. R. Wasielewski in *Approaches to an Optically Controlled Molecular Switch, Vol. V* (Ed.: A. P. de Silva), Wiley-VCH, Amsterdam, **2000**, p. 48.
[6] C. P. Collier, G. Matterstei, E. W. Wong, Y. Luo, K. Beverly, J. Sampaio, F. M. Raymo, J. F. Stoddart, J. R. Heath, *Science* **2000**, *289*, 1172.
[7] I. W. Willner, B. Willner, *Pure Appl. Chem.* **2001**, *73*, 535.
[8] A. P. H. J. Schenning, J. van Herrikhuyzen, P. Jonkheijm, Z. Chen, F. Wuerthner, E. W. Meijer, *J. Am. Chem. Soc.* **2002**, *124*, 10252.
[9] M. del Rosario Benites, T. E. Johnson, S. Weghorn, L. Yu, P. D. Rao, J. R. Diers, S. I. Yang, C. Kirmaier, D. F. Bocian, D. Holten, J. S. Lindsey, *J. Mater. Chem.* **2002**, *12*, 65.
[10] D. Gosztola, M. P. Niemczyk, M. R. Wasielewski, *J. Am. Chem. Soc.* **1998**, *120*, 5118.
[11] A. S. Lukas, S. E. Miller, M. R. Wasielewski, *J. Phys. Chem. B* **2000**, *104*, 931.
[12] R. T. Hayes, M. R. Wasielewski, D. Gosztola, *J. Am. Chem. Soc.* **2000**, *122*, 5563.
[13] E. M. Just, M. R. Wasielewski, *Superlattices Microstruct.* **2000**, *28*, 317.
[14] A. S. Lukas, P. J. Bushard, M. R. Wasielewski, *J. Am. Chem. Soc.* **2001**, *123*, 2440.
[15] A. P. de Silva, H. Q. N. Gunaratne, C. P. McCoy, *Nature* **1993**, *364*, 42.
[16] C. R. Cooper, T. D. James, *Chem. Commun.* **1997**, 1419.

 © 2003 Wiley-VCH Verlag GmbH & Co. KGaA, Weinheim

[17] M. Inouye, K. Akamatsu, H. Nakazumi, *J. Am. Chem. Soc.* **1997**, *119*, 9160.
[18] F. Pina, M. Maestri, V. Balzani, *Chem. Commun.* **1999**, 107.
[19] L. Gobbi, P. Seiler, F. Diederich, *Angew. Chem.* **1999**, *111*, 737; *Angew. Chem. Int. Ed.* **1999**, *38*, 674.
[20] S. E. Miller, Y. Zhao, R. Schaller, V. Mulloni, E. M. Just, R. C. Johnson, M. R. Wasielewski, *Chem. Phys.* **2002**, *275*, 167.
[21] S. R. Greenfield, W. A. Svec, D. Gosztola, M. R. Wasielewski, *J. Am. Chem. Soc.* **1996**, *118*, 6767.
[22] D. Gosztola, M. P. Niemczyk, W. Svec, A. S. Lukas, M. R. Wasielewski, *J. Phys. Chem. A* **2000**, *104*, 6545.
[23] S. F. Rak, T. H. Jozefiak, L. L. Miller, *J. Org. Chem.* **1990**, *55*, 4794.
[24] A. Osuka, S. Nakajima, K. Maruyama, N. Mataga, T. Asahi, *Chem. Lett.* **1991**, 1003.
[25] M. P. Debreczeny, W. A. Svec, E. M. Marsh, M. R. Wasielewski, *J. Am. Chem. Soc.* **1996**, *118*, 8174.
[26] A. S. Lukas, P. J. Bushard, M. R. Wasielewski, *J. Phys. Chem. A* **2002**, *106*, 2074.

 © 2003 Wiley-VCH Verlag GmbH & Co. KGaA, Weinheim

Asymmetric Cyanophosphorylation

Enantioselective Synthesis of Cyanohydrin *O*-Phosphates Mediated by the Bifunctional Catalyst Binolam–AlCl**

Alejandro Baeza, Jesús Casas, Carmen Nájera, José M. Sansano, and José M. Saá**

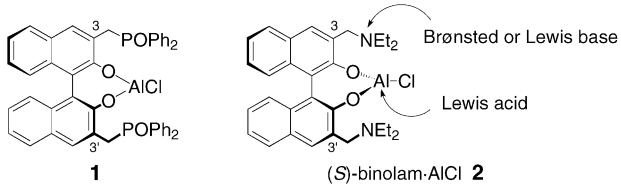
Dedicated to Professor Lutz F. Tietze on the occasion of his 60th birthday

Modern organic chemistry is committed to a number of social demands, including the pressure to develop catalytic, highly efficient processes (in terms of both chemical yield and stereochemical purity), which are not aggressive toward the environment. With this in mind, we carried out a study on the enantioselective synthesis of cyanohydrins and derivatives thereof.

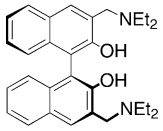
[*] Prof. Dr. C. Nájera, Dipl.-Chem. A. Baeza, Dipl.-Chem. J. Casas, Dr. J. M. Sansano
Departamento de Química Orgánica, Universidad de Alicante
Apartado 99, 03080 Alicante (Spain)
Fax: (+34) 96-590-3549
E-mail: cnajera@ua.es
Prof. Dr. J. M. Saá
Departament de Química, Universitat de les Illes Balears
07071 Palma de Mallorca (Spain)
Fax: (+34) 971-173-426
E-mail: jmsaa@uib.es

[**] This work was supported by the DGES of the Spanish Ministerio de Ciencia y Tecnología (PB97–0123 and BQU2001–0724-C02-) and by Generalitat Valenciana (CTIOIB/2002/320). A.B. also thanks Generalitat Valenciana for a predoctoral fellowship.

Owing to the fact that optically active α-hydroxynitriles (cyanohydrins) are versatile building blocks for the synthesis of biologically active compounds,[1] the search for simple processes for the enantioselective hydrocyanation of carbonyl compounds has occupied organic chemists for a number of years. Enzymatic methods aside,[1b] until recently most of the chiral catalysts designed and developed by chemists for these endeavors have been monofunctional catalysts, such as standard Lewis acids[2] or organocatalysts.[3] For reasons of efficacy, organic chemists are interested in the design of bifunctional and multifunctional catalysts. Recently, C_2-symmetric bifunctional catalysts[4] based on a 2,2′-dihydroxy-1,1′-binaphthalene–aluminum complex with either phosphinoyl or amino arms at C3 and C3′ (**1**[5] and **2**,[6] respectively) were



1 (*S*)-binolam·AlCl **2**



(*S*)-binolam **3**

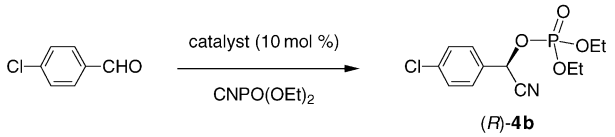
shown to promote the highly enantioselective silylcyanation of aldehydes. The asymmetric cyanation of ketones with trimethylsilyl cyanide in the presence of a peptidic chiral ligand is also promoted by an aluminum complex that acts as a bifunctional catalyst.[7] However, the intrinsic instability of cyanohydrins (and their silyl ethers) has moved researchers to look for new routes to directly access robust, multipurpose *O*-protected cyanohydrins. The asymmetric cyanoformylation of ketones catalyzed by a chiral tertiary amine[8] and of aldehydes by an yttrium–lithium–binol heterobimetallic complex,[9] or by the monometallic aluminum complex **2**,[10] are just recent examples of the upsurge of activity in this area, focused on the enantioselective synthesis of cyanohydrin *O*-carbonates.

In continuation of our search for highly efficient catalytic systems (perfect catalysts, as described by Noyori),[11] we now report the first enantioselective cyanophosphorylation of aldehydes catalyzed by the monometallic bifunctional system **2**. We also describe herein a number of useful applications of the resulting enantiomerically enriched cyanohydrin *O*-phosphates as valuable, previously unknown chiral building blocks in standard modern organic synthesis.[12,13]

In our search for the best catalytic system for the cyanophosphorylation of aldehydes, we examined the reaction of *p*-chlorobenzaldehyde with commercially available diethyl cyanophosphonate in the presence of a series of Lewis acids under a variety of reaction conditions, as shown in Table 1. All catalytic systems were freshly prepared by stirring

 DOI: 10.1002/anie.200351552 © 2003 Wiley-VCH Verlag GmbH & Co. KGaA, Weinheim

Table 1: Cyanophosphorylation of *p*-chlorobenzaldehyde catalyzed by preformed Lewis acid–(*S*)-**3** complexes.[a]

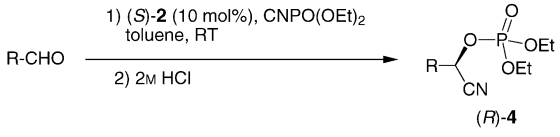


(*R*)-**4b**

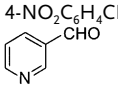
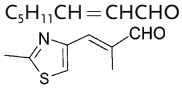
Entry	Lewis acid	Solvent	*t* [h]	Conversion [%][b]	*ee* [%][c]
1	Me_2AlCl	CH_2Cl_2	19	>98	70
2	Me_2AlCl	THF	24	96	98
3	Me_2AlCl	$PhCH_3$	20	>98	96
4	Me_2AlCl[d]	$PhCH_3$	48	<15	–
5	Me_2AlCl[e]	$PhCH_3$	48	–	–
6	Et_2AlCN	$PhCH_3$	7	>98	56
7	Me_2AlOMe	$PhCH_3$	0.6	>98	62
8	$Ti(OiPr)_4$	$PhCH_3$	1	>98	24

[a] Reagents and conditions: catalyst (10 mol%) preformed from (*S*)-**3** and the Lewis acid (1:1), $CNPO(OEt)_2$, solvent, room temperature, then workup with 2 M HCl. [b] Determined by ^{1}H NMR spectroscopic analysis after acidic workup. [c] Determined by HPLC analysis on a chiral phase (Daicel Chiralpak AD). [d] Molecular sieves (4 Å) were added (7.5% water, 50 mg/0.25 mmol; see reference [6]). [e] Triphenylphosphane oxide (20 mol%) was added.

Table 2: Enantioselective synthesis of (*R*)-cyanohydrin *O*-phosphates **4** catalyzed by complex (*S*)-**2**.



(*R*)-**4**

Entry	Aldehyde	*t* [h]	**4**	Yield [%][a]	*ee* [%][b]
1	PhCHO	4	**a**	89	98
2	$4\text{-}ClC_6H_4CHO$	20	**b**	88	96
3	$4\text{-}(MeO)C_6H_4CHO$	10	**c**	87	98
4	$4\text{-}NO_2C_6H_4CHO$	50	**d**	87	26
5		24	**e**	90	4
6	$CH_3CH=CHCHO$	2	**f**	89	88
7	$C_5H_{11}CH=CHCHO$	6	**g**	90	94
8		4	**h**	89	90
9	$C_6H_{13}CHO$	3	**i**	90	98[c]
10	$PhCH_2CH_2CHO$	2	**j**	90	92

[a] Yields of the cyanohydrin *O*-phosphates after acidic hydrolysis and column chromatography. [b] Enantiomeric excesses were determined by HPLC analysis on a chiral phase (Daicel Chiralcel OD-H, and Daicel Chiralpak AD and AS). [c] Determined by GC on a chiral phase (γ-cyclodextrin).

a 1:1 mixture of the ligand (*S*)-binolam (**3**) and the desired Lewis acid at room temperature in the appropriate solvent for 1 h. *p*-Chlorobenzaldehyde and diethyl cyanophosphonate (3 equiv relative to aldehyde) were then added in one portion at room temperature under an argon atmosphere, and the resulting mixture was stirred for the time stated.

As shown (Table 1, entries 2 and 3), the best results were obtained with (*S*)-binolam–AlCl **2** (10 mol%), generated in situ by mixing (*S*)-binolam **3** and commercial diethylaluminum chloride in anhydrous toluene or THF. Although a very high enantiomeric excess was observed when the reaction was performed in THF (Table 1, entry 2), toluene was selected as the solvent for further studies, as its use led to a cleaner reaction (Table 1, entry 3). The reaction became impractically slow at lower temperatures. No important effects analogous to those observed with 4-Å molecular sieves and triphenylphosphane oxide in the cyanosilylation of aldehydes in the presence of complex **2**[6] were observed in this cyanophosphorylation reaction (Table 1, entries 4 and 5). The reaction was accelerated by using the corresponding chiral aluminum methoxide complex, but a lower enantiomeric excess was observed (Table 1, entry 7), even at lower temperatures. Catalytic titanium aggregates also accelerated the addition reaction but did not improve the enantioselectivity of the cyanophosphorylation relative to the aluminum complexes (Table 1, entry 8). A number of aldehydes were subjected to the optimized reaction conditions to assess the scope and limitations of the preparation of (*R*)-cyanohydrin *O*-phosphates **4** (Table 2).

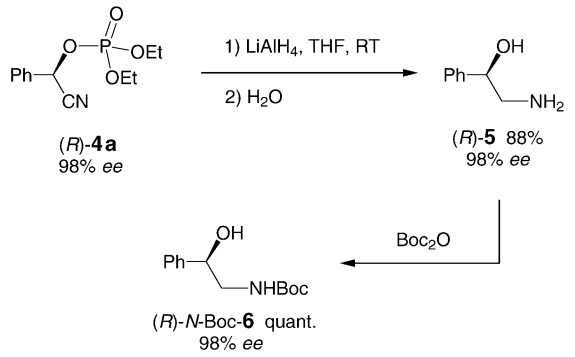
Aromatic, aliphatic, and α,β-unsaturated aldehydes were found to undergo highly efficient enantioselective cyanophosphorylation under these reaction conditions in high yields (Table 2). Aromatic aldehydes with electron-withdrawing substituents reacted somewhat slowly (Table 2, entries 2 and 4). Furthermore, in the case of *p*-nitrobenzaldehyde, enantioselectivity was found to be poor (Table 2, entry 4), which suggests the existence of a competing achiral route as a result of coordination of the nitro group to the aluminum center. It was thought that heteroaromatic aldehydes, or other aldehydes with a basic site to compete with the amino-armed catalyst, would be a challenging substrates. In fact, pyridine-3-carboxaldehyde afforded almost racemic material (Table 2, entry 5). However, the reaction of an aldehyde that bears a thiazole moiety[14] led to **4h** (a possible key intermediate in the synthesis of epothilone A[14,15]) in excellent chemical yield and stereochemical purity (Table 2, entry 8), in accordance with the lower basicity of the thiazole nitrogen atom (pK_a 2.4). As expected, when the aluminum complex (*R*)-**2** was used with the aldehydes in entries 1 and 2 of Table 2, the enantiomeric products (*S*)-**4** were obtained in reliable and reproducible chemical yields and enantiomeric excesses. Most importantly, the valuable chiral ligand **3** was readily extracted from the reaction mixture (93% recovery) after acidic workup, and could be reused without any significant loss of activity. Thus, compound **4a** was again obtained in 98% *ee* (see Table 2, entry 1) with recovered ligand **3**, as reported previously.[6,11]

When we tried to synthesize compounds **4** from the corresponding enantiomerically pure cyanohydrins, to determine the absolute configuration of our cyanophosphorylation products, we observed that partial racemization occurred in the presence of organic bases (triethylamine, pyridine, and *N*-methylimidazole) and with both diethyl chlorophosphate[16] and diethyl cyanophosphonate as phosphorylating agents. Partial racemization was also observed when cyanophosphates **4a** and **4j** were synthesized by treating optically pure cyanohydrins with diethyl chlorophosphite in pyridine, followed by iodine-mediated oxidation.[17] In this reaction the

 © 2003 Wiley-VCH Verlag GmbH & Co. KGaA, Weinheim

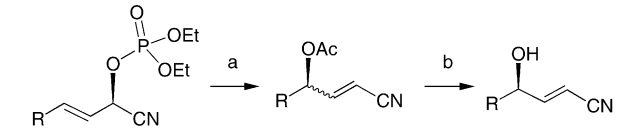
enantiomeric excess is lost in the first step as revealed by the chiral HPLC data of the intermediate cyanohydrin *O*-phosphite. These results clearly enhance the value of this catalytic cyanophosphorylation of aldehydes, which ensures access to enantiomerically enriched compounds **4**.

To demonstrate interesting applications of the chiral cyanohydrin *O*-phosphates **4** obtained, we investigated their reduction to the corresponding aminoalcohols, as well as stereospecific [3,3] sigmatropic chirality transfer. No loss of enantiomeric excess was observed in the reduction of compound (*R*)-**4a** with lithium aluminum hydride to give enantiomerically enriched β-aminoalcohol (*R*)-**5**[18] and, after protection of the amino group, its *N*-Boc derivative **6**,[19] in good chemical yields (Scheme 1). These transformations also served to confirm the absolute configuration already assigned to **4**.



Scheme 1. Reduction of chiral cyanohydrin *O*-phosphate **4a**. Boc = *tert*-butoxycarbonyl.

Palladium-catalyzed allylic displacement of allylic phosphates (*R*)-**4f** and (*R*)-**4g** with sodium acetate as the nucleophile gave the expected γ-acetates **7f** and **7g** as 0.25:1 and 0.2:1 *Z*/*E* mixtures, respectively. Basic hydrolysis of the crude acetates **7**, according to the reported procedure,[20] led to the *R*-configured *E* cyanoallylic alcohols **8f** and **8g** in 75 and 83% yield, respectively. No loss of enantiomeric excess was observed (Scheme 2). These cyanoallylic alcohols are important building blocks for organic synthesis.[20–24] The



(*R*)-**4f** (R = Me) 88% *ee*
(*R*)-**4g** (R = C_5H_{11}) 94% *ee*
(*R*)-**8f** 75%, 88% *ee*
(*R*)-**8g** 83%, 94% *ee*

Scheme 2. Asymmetric palladium-catalyzed allylic substitution of cyanophosphorylation products **4f** and **4g**: a) $Pd(OAc)_2$, PPh_3, NaOAc; b) K_2CO_3, MeOH.

absolute configuration of allylic alcohols **8f**[21] and **8g**,[20] assigned on the basis of the reported $[\alpha]_D$ values, is in accordance with the well-known double inversion described for palladium-catalyzed allylic nucleophilic substitution of chiral allylic phosphates.[25]

A strong nonlinear effect (NLE)[26] was apparent for the enantioselective cyanophosphorylation of aldehydes.[27] This unexpected behavior (to the best of our knowledge it is the first example described in the literature for an aluminum-based catalytic complex) can be assigned to the different stability of dimeric species relative to monomers, according to HF/6-31G* ab initio calculations.[28] Thus, whereas the combinations *R,R* or *S,S* can form unstable dimeric species (relative to monomers) with tetravalent aluminum atoms and nonligating aminomethyl arms, the corresponding *R,S* dimer cannot form a similar species, and this combination gives rise instead to much more stable, weakly bound monomers with internal coordination by one aminomethyl arm.[29]

From a mechanistic viewpoint, we postulate that the enantioselective cyanophosphorylation reaction described above involves the intervention of a bifunctional catalyst (either Lewis acid–Lewis base or Lewis acid–Brønsted base). This is supported by the following observations. First, the reaction promoted by the aluminum derivative of (*S*)-binol, rather than that derived from (*S*)-binolam, led to the racemic cyanohydrin *O*-phosphate in very low conversion (10%) after 48 h. Second, the addition of an external base (triethylamine, 20 mol%) under otherwise standard conditions led to the acceleration of the reaction and induced a dramatic drop in the enantiomeric excess of the product (38% *ee*).

Experimental Section

Dimethylaluminum chloride (1M solution in hexanes, 0.025 mmol, 25 μL) was added to a solution of enantiopure (*S*)-binolam **3**[30] (0.025 mmol, 11.4 mg) in dry toluene (1 mL) under argon, and the resulting suspension was stirred at room temperature for 1 h. The freshly distilled aldehyde (0.25 mmol) and diethyl cyanophosphonate (0.75 mmol, 125 μL) were then added in one portion. The reaction was monitored by ^{1}H NMR spectroscopy and when it was judged complete, aqueous hydrochloric acid (2M, 2 mL) and ethyl acetate (2 mL) were added. The resulting mixture was stirred vigorously for 10 min, then the emulsion was filtered and the organic layer was separated, dried ($MgSO_4$), and concentrated. The residue was purified by flash chromatography to give the pure cyanohydrin *O*-phosphate **4**.

Received: April 2, 2003 [Z51552]

Keywords: aluminum · asymmetric catalysis · homogeneous catalysis · binaphthols · cyanohydrins

[1] a) M. North, *Tetrahedron: Asymmetry* **2003**, *14*, 147–176; b) H. Gröger, *Adv. Synth. Catal.* **2001**, *343*, 547–558; c) R. J. H. Gregory, *Chem. Rev.* **1999**, *99*, 3649–3682; d) F. Effenberger, *Angew. Chem.* **1994**, *106*, 1609–1619; *Angew. Chem. Int. Ed. Engl.* **1994**, *33*, 1555–1564; e) M. North, *Synlett* **1993**, 807–820; f) C. G. Kruse in *Chirality in Industry* (Eds.: A. N. Collins, G. N. Schedrake, J. Crosby), Wiley, Chichester, **1992**, pp. 279–299.

[2] For recent examples, see: a) T. Ooi, T. Miura, K. Takaya, H. Ichikawa, K. Maruoka, *Tetrahedron* **2001**, *57*, 867–873; b) Y. N. Belokon, B. Green, N. S. Ikonnikov, M. North, T. Parsons, V. I. Tararov, *Tetrahedron* **2001**, *57*, 771–779; c) C. Baleizao, B. Gigante, H. García, A. Corma, *Green Chem.* **2002**, *4*, 272–274; d) Z. Yang, Z. Zhou, C. Tang, *Synth. Commun.* **2001**, *31*, 3031–3036.

 © 2003 Wiley-VCH Verlag GmbH & Co. KGaA, Weinheim

[3] For reviews, see: a) E. R. Jarvo, S. J. Miller, *Tetrahedron* **2002**, *58*, 2481 – 2495; b) P. L. Dalko, L. Moisan, *Angew. Chem.* **2001**, *113*, 3840 – 3864; *Angew. Chem. Int. Ed.* **2001**, *40*, 3726 – 3748.

[4] For reviews, see: a) M. Shibasaki, M. Kanai, *Chem. Pharm. Bull.* **2001**, *49*, 511 – 524; b) G. J. Rowlands, *Tetrahedron* **2001**, *57*, 1865 – 1882; c) H. Gröger, *Chem. Eur. J.* **2001**, *7*, 5246 – 5251; d) M. Shibasaki, M. Kanai, K. Funabashi, *Chem. Commun.* **2002**, 1989 – 1999.

[5] a) Y. Hamashima, D. Sawada, M. Kanai, M. Shibasaki, *J. Am. Chem. Soc.* **1999**, *121*, 2641 – 2642; b) Y. Yamashima, D. Sawada, H. Nogami, M. Kanai, M. Shibasaki, *Tetrahedron* **2001**, *57*, 805 – 814.

[6] J. Casas, C. Nájera, J. M. Sansano, J. M. Saá, *Org. Lett.* **2002**, *4*, 2589 – 2592.

[7] H. Deng, M. P. Isler, M. L. Snapper, A. H. Hoveyda, *Angew. Chem.* **2002**, *114*, 1051 – 1054; *Angew. Chem. Int. Ed.* **2002**, *41*, 1009 – 1012.

[8] S. K. Tian, L. Deng, *J. Am. Chem. Soc.* **2001**, *123*, 6195 – 6196.

[9] J. Tian, N. Yamagiwa, S. Matsunaga, M. Shibasaki, *Angew. Chem.* **2002**, *114*, 3788 – 3790; *Angew. Chem. Int. Ed.* **2002**, *41*, 3636 – 3638.

[10] J. Casas, A. Baeza, C. Nájera, J. M. Sansano, J. M. Saá, *Tetrahedron: Asymmetry* **2003**, *14*, 197 – 200.

[11] R. Noyori, *Angew. Chem.* **2002**, *114*, 2108 – 2123; *Angew. Chem. Int. Ed.* **2002**, *41*, 2008 – 2022.

[12] I. Micó, C. Nájera, *Tetrahedron* **1993**, *49*, 4327 – 4332, and references therein.

[13] a) T. Schrader, *Chem. Eur. J.* **1997**, *3*, 1273 – 1282; b) T. Schrader, *Angew. Chem.* **1995**, *107*, 1001 – 1002; *Angew. Chem. Int. Ed. Engl.* **1995**, *34*, 917 – 919.

[14] a) D. Sawada, M. Shibasaki, *Angew. Chem.* **2000**, *112*, 215 – 219; *Angew. Chem. Int. Ed.* **2000**, *39*, 209 – 213; b) D. Sawada, M. Kanai, M. Shibasaki, *J. Am. Chem. Soc.* **2000**, *122*, 10521 – 10532.

[15] a) K. C. Nicolaou, D. Hepworth, N. P. King, M. R. V. Finlay, R. Scarpelli, M. M. A. Pereira, B. Bollbuck, A. Bigot, B. Werschkun, N. Winssinger, *Chem. Eur. J.* **2000**, *6*, 2783 – 2800; b) J. W. Bode, E. M. Carreira, *J. Org. Chem.* **2001**, *66*, 6410 – 6424.

[16] R. L. Letsinger, W. B. Lunsford, *J. Am. Chem. Soc.* **1976**, *98*, 3655 – 3661.

[17] J. W. Perich, P. F. Alewood, R. B. Johns, *Synthesis* **1986**, 572 – 573.

[18] $[\alpha]_D = -48.0$ ($c = 2$, EtOH). For the *S* form $[\alpha]_D = +48.6$ ($c = 2.01$, EtOH). B. T. Cho, S. K. Kang, S. H. Shin, *Tetrahedron: Asymmetry* **2002**, *13*, 1209 – 1217.

[19] $[\alpha]_D = -3.4$ ($c = 1$, EtOH); for the *S* form $[\alpha]_D = +3.5$ ($c = 1$, EtOH); A. Kawamoto, M. Wills, *Tetrahedron: Asymmetry* **2000**, *11*, 3257 – 3261.

[20] D. V. Johnson, H. Griengl, *Tetrahedron* **1997**, *53*, 617 – 624.

[21] M. Tiecco, L. Testaferri, F. Marini, C. Santi, L. Bagnoli, A. Temperini, *Tetrahedron: Asymmetry* **1999**, *10*, 747 – 757.

[22] I. Yamakawa, H. Urabe, Y. Kobayashi, F. Sato, *Tetrahedron Lett.* **1991**, *32*, 2045 – 2048.

[23] H. Abe, H. Nitta, A. Mori, S. Inoue, *Chem. Lett.* **1992**, 2443 – 2446.

[24] Y. Kitano, T. Matsumoto, T. Wakasa, S. Okamoto, T. Shimazaki, Y. Kobayashi, F. Sato, *Tetrahedron Lett.* **1987**, *28*, 6351 – 6354.

[25] J. Tsuji in *Palladium Reagents and Catalysts, Innovation in Organic Synthesis*, Wiley, Chichester, **1995**.

[26] For some recent reviews of the NLE, see: a) H. B. Kagan, *Synlett* **2001**, 888 – 899; b) K. Soai, T. Shibata, I. Sato, *Acc. Chem. Res.* **2000**, *33*, 382 – 390; c) D. Heller, H.-J. Drexler, C. Fischer, H. Buschmann, W. Baumann, B. Heller, *Angew. Chem.* **2000**, *112*, 505 – 509; *Angew. Chem. Int. Ed.* **2000**, *39*, 495 – 499.

[27] A weaker, positive NLE was observed in the enantioselective cyanoformylation reaction of aldehydes; J. Casas, unpublished results.

[28] Gaussian 98 (Revision A.7), M. J. Frisch, G. W. Trucks, H. B. Schlegel, G. E. Scuseria, M. A. Robb, J. R. Cheeseman, V. G. Zakrzewski, J. A. Montgomery, R. E. Stratmann, J. C. Burant, S. Dapprich, J. M. Millam, A. D. Daniels, K. N. Kudin, M. C. Strain, O. Farkas, J. Tomasi, V. Barone, M. Cossi, R. Cammi, B. Mennucci, C. Pomelli, C. Adamo, S. Clifford, J. Ochterski, G. A. Petersson, P. Y. Ayala, Q. Cui, K. Morokuma, D. K. Malick, A. D. Rabuck, K. Raghavachari, J. B. Foresman, J. Cioslowski, J. V. Ortiz, B. B. Stefanov, G. Liu, A. Liashenko, P. Piskorz, I. Komaromi, R. Gomperts, R. L. Martin, D. J. Fox, T. Keith, M. A. Al-Laham, C. Y. Peng, A. Nanayakkara, C. Gonzalez, M. Challacombe, P. M. W. Gill, B. G. Johnson, W. Chen, M. W. Wong, J. L. Andres, M. Head-Gordon, E. S. Replogle, J. A. Pople, Gaussian, Inc., Pittsburgh, PA, **1998**.

[29] a) J. A. Francis, C. N. McMahon, S. G. Bott, A. R. Barron, *Organometallics* **1999**, *18*, 4399 – 4416; b) J. Lewinski, J. Zachara, I. Justyniak, *Organometallics* **1997**, *16*, 4597 – 4605; c) J. Lewinski, J. Zachara, I. Justyniak, *Chem. Commun.* **1997**, 1519 – 1520; d) D. A. Atwood, F. P. Gabbai, J. Lu, M. P. Remington, D. Rutherford, M. P. Sibi, *Organometallics* **1996**, *15*, 2308 – 2313; e) R. Kumar, M. L Sierra, J. P. Oliver, *Organometallics* **1994**, *13*, 4285 – 4293; f) M. L. Sierra, V. Srini, J. de Mel, J. P. Oliver, *Organometallics* **1989**, *8*, 2486 – 2488.

[30] (*S*)- and (*R*)-binolam are commercially available from MEDALCHEMY, S. L.

 © 2003 Wiley-VCH Verlag GmbH & Co. KGaA, Weinheim

Mesoporous Silica with Large Entrances

Cubic Mesoporous Silica with Large Controllable Entrance Sizes and Advanced Adsorption Properties**

Jie Fan, Chengzhong Yu, Feng Gao, Jie Lei, Bozhi Tian, Limin Wang, Qian Luo, Bo Tu, Wuzong Zhou, and Dongyuan Zhao**

Recently, mesoporous materials have attracted much attention because of their emerging applications in catalysis, adsorption, sensors, and separations.[1] It is generally accepted

[*] Dr. C. Yu, Prof. Dr. D. Zhao, J. Fan, F. Gao, J. Lei, B. Tian, L. Wang, Q. Luo, B. Tu
Shanghai Key Laboratory of Molecular Catalysis and Innovative Materials
Department of Chemistry
Fudan University
Shanghai 200433 (P. R. China)
Fax: (+86) 21-6564-1740
E-mail: czyu@fudan.edu.cn
dyzhao@fudan.edu.cn
Dr. W. Zhou
School of Chemistry
University of St. Andrews
St. Andrews, Fife KY16 9ST (UK)

[**] Supported by the National Science Foundation of China (29925309 and 20233030), State Key Research Program (G2000048001 and 2002AA321010), Shanghai Science Committee (0212nm043).

Supporting information for this article is available on the WWW under http://www.angewandte.org or from the author.

 © 2003 Wiley-VCH Verlag GmbH & Co. KGaA, Weinheim DOI: 10.1002/anie.200351027

that mesoporous materials with 3D pore systems exhibit more advantages in mass diffusion and transportation compared with MCM-41 materials[2,3] containing 1D channels. Cubic mesoporous silicas MCM-48 (*Ia-3d*),[2,3] SBA-1 (*Pm-3n*),[4] SBA-16 (*Im-3m*),[5] FDU-1,[6] and SBA-2,[4,7] SBA-12[5,8] with 3D hexagonal structures ($P6_3/mmc$) have been synthesized. FDU-1 was originally reported to have a body-centered cubic structure (*Im-3m*). Very recently it was suggested based on high-resolution transmission electron microscopy (HRTEM) and small-angle X-ray scattering that FDU-1 silica synthesized under typical conditions was a face-centered cubic structure (*Fm-3m*) with 3D hexagonal mesophase intergrowth.[9] Such intergrowth is also common in SBA-2[7] and SBA-12.[8] However, a pure face-centered cubic (*Fm-3m*) mesoporous material without intergrowth has not been reported yet. Except for MCM-48 material with a bicontinuous pore structure and a cubic (*Im-3m*) mesostructure with possible bicontinuous "Plumber's Nightmare" pore morphology,[10] most of these cubic and 3D hexagonal mesoporous materials have cagelike pore structures, in which relatively large cavities are connected by some pore entrances with smaller sizes (also referred to as windows or connectivities in some literatures, see Figure 1). Gas sorption analysis method

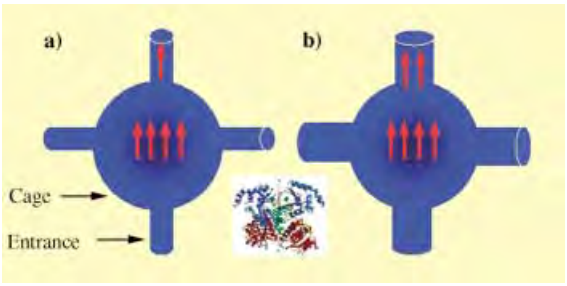


Figure 1. Schematic drawing of the cavity and entrance of a cagelike mesoporous material with similar cavity sizes but different entrance sizes, a) small entrances, b) large entrances. The diffusion rates of enzymes (inset of Figure 1) within the cage and entrance are represented by the number of arrows.

may be applied to well define the sizes of these parameters.[11] TEM techniques have also been developed to solve the structures of both the cavities and the connectivities of mesoporous materials.[8,12]

The pore engineering of mesoporous materials is of great importance for various applications where different sizes of molecules are involved. By choosing structure-directing agents such as block copolymers, by using swelling agents, and by manipulating synthesis conditions, such as the temperature of the hydrothermal treatment, mesoporous materials with desired structures and adjustable pore sizes have been obtained.[5] In the cases of mesoporous materials with cagelike structures, much effort has been devoted to the control of the cavity size, while little work has been carried out to study another important structural parameter, the pore entrance. Jaroniec and co-workers reported the tailoring of entrance sizes in FDU-1 materials by the modification of the silica surface with monofunctional organosilane, thus the entrance sizes may be controlled within a certain range (5.0–1.2 nm).[13] However, such small entrance sizes of mesoporous materials may limit their uses in protein adsorption and separation processes.[14,15] By performing hydrothermal treatment for a sufficiently long time at temperatures below 393 K, Jaroneic and co-workers also showed that the pore-entrance size of FDU-1 silica could be enlarged, but there was evidence that the distribution of the pore-entrance size was quite broad.[9]

Herein, we report our synthesis of a large cavity ($10 \approx 12.3$ nm) cubic (*Fm-3m*) mesoporous silica (denoted as FDU-12) in the presence of block copolymer templates. The size of the entrances may be adjusted in the range of $4 \approx 9$ nm as confirmed by nitrogen-sorption studies and by examining the negative replicas of gold and carbon. Most importantly, it is revealed that the entrance size of mesoporous materials is a key factor for the applications in which mass transportations and diffusions are involved, by the following observations: First, the immobilization of enzymes is facilitated for FDU-12 materials with large entrance sizes (Figure 1). Second, cubic mesoporous carbon replicas with ordered large pores (up to 9.8 nm) have been synthesized by using FDU-12 with widened entrance sizes as the hard templates. These results may add a new understanding to the correlation between structure parameters and the properties of mesoporous materials.

Mesoporous FDU-12 samples were synthesized in acidic solutions by using nonionic block copolymer $EO_{106}PO_{70}EO_{106}$ (EO is poly(ethylene oxide) and PO is poly(propylene oxide)) as a template, 1,3,5-trimethylbenzene (TMB) together with inorganic salts (e.g. KCl), as additives, and tetraethyl orthosilicate (TEOS) as the silica source. Hydrothermal treatment was performed on the resulting silica–surfactant-composite precipitates at different temperatures (designated FDU-12–X, X indicates the temperature of hydrothermal treatment). The synthesized samples were calcined at 823 K for 6 h to obtain mesoporous silica materials.

Powder X-ray diffraction (XRD) patterns of the as-synthesized and calcined FDU-12–373 specimens are shown in Figure 2. Both patterns show five well-resolved peaks, which can be assigned to the (111), (220), (311), (331) and (442) reflections of a face-centered cubic structure. There are several possibilities of the space group for FDU-12 from the extinction condition of XRD patterns, such as *Fm-3m* and *Fm-3c*. The ideal structure of FDU-12 is speculated to have a space group *Fm-3m*, as it has the highest symmetry among all possible space groups. The unit cell parameters calculated from the XRD data are 29.2 and 25.3 nm for the as-synthesized and calcined specimens, respectively. Calcination of the sample gives rise to relatively low shrinkage ($\approx 12\,\%$) and an increase of the diffraction intensity. FDU-12 is quite stable; even after higher temperature hydrothermal treatment (up to 413 K), the corresponding intensive (111) and (311) diffraction peaks for a face-centered cubic mesostructure are still observed.

TEM images of calcined FDU-12–373 materials taken along the [100] and [111] directions are shown in Figure 3a and 3b, respectively. Taken directly from the images, the unit cell parameter *a* is estimated to be 26 nm, which is in good

 © 2003 Wiley-VCH Verlag GmbH & Co. KGaA, Weinheim

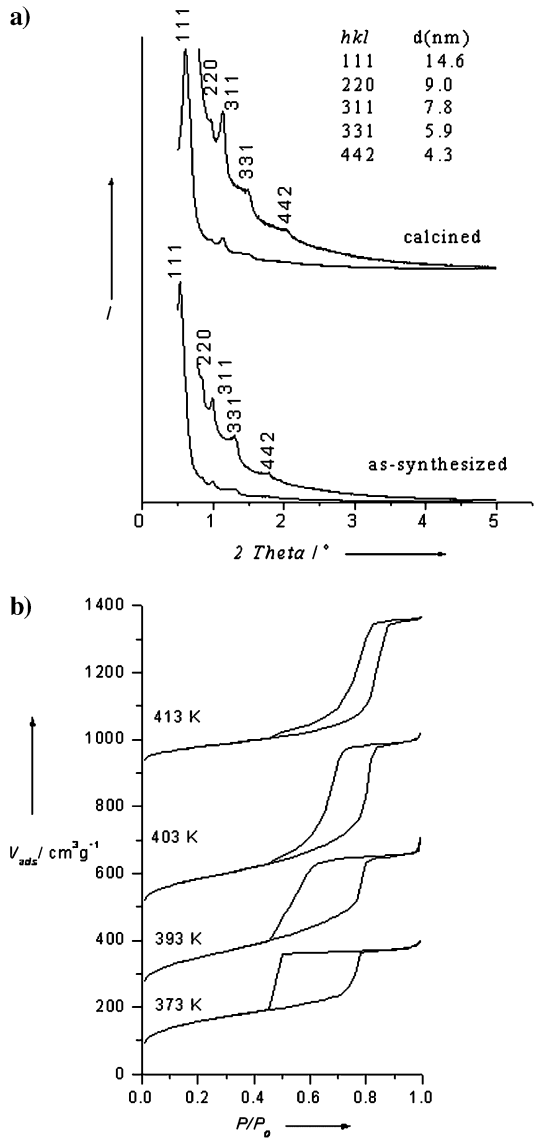


Figure 2. a) XRD patterns (I = intensity) of FDU-12–373 and b) nitrogen sorption isotherms of calcined FDU-12–X samples. The adsorption isotherms for FDU-12–393, –403, and –413 samples are shifted by 200, 450, 900 cm^{3}g^{-1} (STP), respectively.

accordance with the XRD results. The highly ordered lattice array over large domains under the TEM observations suggests that the FDU-12 products have a uniform, well-defined cubic mesostructure (*Fm-3m*) without intergrowth. The diameter of the cages may be directly measured from the thin edge of the particle in Figure 3a (see also Supporting Information) to be about 10.7 nm, in good accordance with the N_2 sorption results (see below). In addition, 1D-like large pores that are formed by the linear combination of many spherical cages can be further observed in the TEM images (see Supporting Information), thus implying that the calcined FDU-12 have large entrances. Scanning electron microscopy (SEM) images of the calcined FDU-12 show mostly spherical morphologies (see Supporting Information). These spherical particles have relatively uniform sizes of 2–3 μm. Different hydrothermal-treatment temperatures (373–413 K) result in little change in particle morphology.

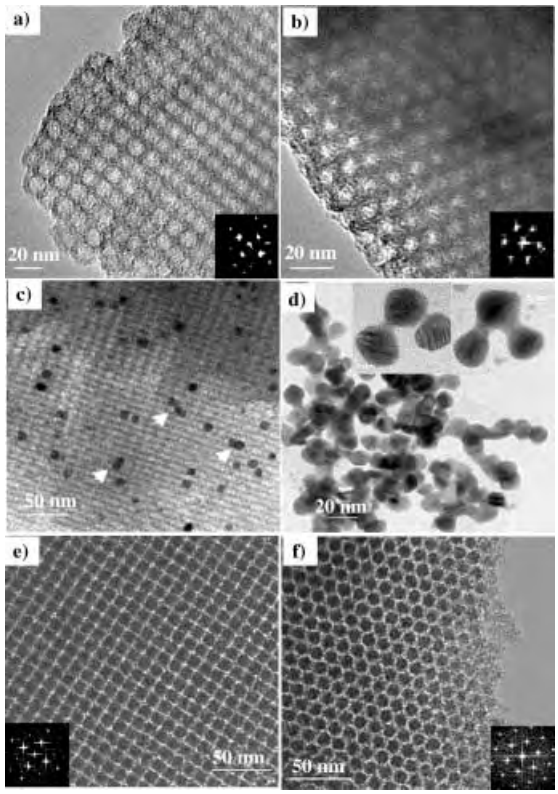


Figure 3. TEM images a) and b) of FDU-12–373 recorded along the [100] and [111] directions (Fourier diffractograms inset), respectively. TEM images c) of Au/FDU-12–403 and d) Au nanocrystals after removal of the silica frameworks. The insets show enlarged TEM images of dumbbell-like Au nanoparticles formed inside FDU-12–373 (left) and FDU-12–403 (right). TEM images e) and f) of C-FDU-12–403 viewed down the [100] and [111] directions (Fourier diffractograms inset), respectively.

Normally, a conventional large pore cagelike mesoporous silica, such as SBA-16[5] or FDU-1,[6] shows a large H_2 hysteresis loop, similar to FDU-12–373 (Figure 2b). On the other hand, no hysteresis loop is observed in SBA-1, SBA-2 and SBA-12 in which the sizes of cavities and entrances are relatively smaller.[4,5] In the case of FDU-12–X materials, it is noteworthy that the hysteresis loops become smaller with increasing temperature of the hydrothermal treatment (373 → 413 K), FDU-12–403 and FDU-12–413 materials even have typical H_1 hysteresis loops. Accordingly, the shift of desorption branches to high relative pressure indicates that the entrance sizes of FDU-12 have been enlarged. It is noteworthy that both the cavity and the entrance size distributions of FDU-12–X materials are quite narrow, as can be seen from the steep change from the adsorption and desorption branches, respectively. The sizes of the cavities and entrances as well as other physical parameters of FDU-12-X are listed in Table 1. When the hydrothermal treatment temperature is increased from 373 to 413 K, the cavity size is increased to a small extent from 10 to 12.3 nm (increasing 23%), while the entrance size is increased much more significantly from ≈4 to 8.9 nm (increasing 123%). These structural features are very important in understanding the properties of the FDU-12–X materials.

 © 2003 Wiley-VCH Verlag GmbH & Co. KGaA, Weinheim

Table 1: Physicochemical properties of calcined mesoporous silica FDU-12-X.

Sample	*a* (nm)	Pore size (nm)	Entrance size (nm)	Pore volume (cm^3g^{-1})	Surface area (m^2g^{-1})
FDU-12–373	25.3	10.0[a]	≈4[b]	0.66	712
FDU-12–393	26.7	11.0[a]	5.3[a]	0.73	569
FDU-12–403	27.3	12.4[a]	7.5[a]	0.86	480
FDU-12–413	27.8	12.3[a]	8.9[a]	0.78	281

[a] Calculated from the desorption branch of the N_2 adsorption/desorption isotherms based on BJH model. [b] Estimated from the corresponding Au nanocrystal images

The cavity and entrance sizes of FDU-12–X materials have also been determined from their negative replicas of dilute Au nanocrystals. Figure 3c shows a TEM image of Au/FDU-12–403 specimen, which shows that all the Au nanoparticles are well confined in the cavities. As the loading amount of Au is quite low (3.0 wt%), it may be observed that occasionally two or three Au nanoparticles are located in neighboring cavities and connected through the entrances (indicated by small arrows). After removal of the silica frameworks, these connected Au nanoparticles show a dumbbell-like morphology (Figure 3d), which directly reveals that two cavities with ≈12 nm in diameter are connected by an entrance of ≈8 nm in size (Figure 3d, inset, right), in accordance with the sorption results. For comparison, the entrance size of FDU-12–373 is about 4 nm estimated from the Au TEM image (Figure 3d, inset, left), smaller than that of FDU-12–403, but still larger than that of conventional SBA-16 materials (≈2.3 nm).[12] It is noted that FDU-12–413 materials have the largest uniform entrance size among all known ordered mesoporous materials with cagelike structures.

By using the same structure-directing agents, cubic mesoporous materials SBA-16 (*Im-3m*) were synthesized by Stucky and co-workers.[5] In our experiments, inorganic salts were employed to increase the interaction of the silicate species with nonionic block copolymers, thus resulting in highly ordered products.[16] A swelling agent, TMB, was used to enlarge the entrance and cavity sizes.[17] The organic TMB may also enter the hydrophobic part of micelles and increase the volume ratio of the hydrophobic core, leading to a phase transformation from the body-centered cubic structure (*Im-3m*) to a more closely packed face-centered cubic structure (*Fm-3m*).[18] The careful manipulating of different synthesis conditions has led to the successful synthesis of FDU-12 mesoporous materials with enlarged pore entrance sizes.

The immobilization of proteins is of great importance for applications such as biosensors and biocatalysis. Recently, mesoporous silica was shown to be a more promising material in bioimmobilization in comparison with conventional sol–gels because of their uniform pore size, large surface area, pore volume and opened pore structures.[19,20] The advantage of widening the size of the pore entrances of mesoporous materials with cubic cagelike structures was reflected in the immobilization of proteins within the FDU-12–X materials. Lysozyme with an average spherical diameter of ≈3.2 nm was used to examine the protein immobilization ability of FDU-12. Over the same period of contact time, lysozyme was adsorbed increasingly into FDU-12 with increasing entrance sizes (Figure 4). Furthermore, the time for lysozyme adsorbed within FDU-12 to reach the equilibrium was also found to depend strongly on the size of the entrances. The fast equilibrium (4 hours) was observed for the FDU-12–413 and FDU-12–403 with large entrances, whereas it took more than three days to reach the equilibrium for FDU-12–373 silica with relatively smaller entrances. For comparison, SBA-16 materials with the smallest entrances[5] have the lowest lysozyme adsorption and longest equilibrium time. As the particle size, pore volume and pore size vary only in a small range for FDU-12–X materials, and the surface area of FDU-12–413 is the smallest among all samples; the observed difference for the immobilization property in parallel experiments may be mostly attributed to the differences of the entrance sizes of the FDU-12–X materials.

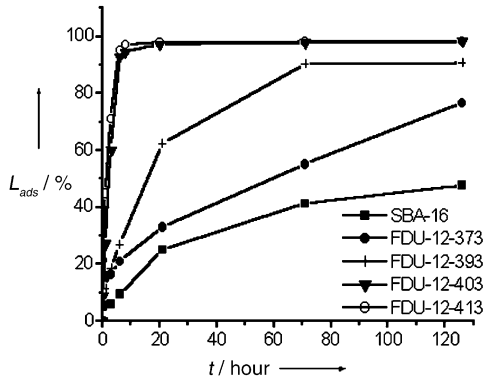


Figure 4. Adsorption of lysozyme within caged mesoporous silicas as a function of contact time. L_{ads} = lysozyme adsorbed amount (W:W).

Mesoporous FDU-12 materials with large entrances are also found to be more suitable hard templates for the synthesis of ordered nanoporous carbon than conventional SBA-16 materials. TEM (Figure 3e and f), XRD and nitrogen sorption results (see Supporting Information) show that the carbon replica, C-FDU-12–403, synthesized from the FDU-12–403 templates have well ordered mesostructures (*Fm-3m*), while the structural order of mesoporous carbon synthesized from the traditional SBA-16 templates with smaller entrances (≈2.3 nm)[12] is quite poor (see Supporting Information). The cell parameter *a* of C-FDU-12–403 calculated from XRD and TEM is 23.9 and 22.7 nm, respectively. The relatively smaller cell parameter of C-FDU-12–403 compared to that of its silica template FDU-12–403 (27.3 nm) may be attributed to the high temperature treatment during the replication process. TEM images of FDU-12–X and the corresponding C-FDU-12–X materials viewed along the same directions show reverse contrast. The pore size of C-FDU-12–X can reach 9.8 nm when FDU-12–373 is applied as the hard template (Supporting Information) calculated by using the BJH method, the largest among all reported cubic ordered

 © 2003 Wiley-VCH Verlag GmbH & Co. KGaA, Weinheim

mesoporous carbon materials. These large-pore mesoporous carbon with interconnected networks is of great importance for various applications including electrodes for supercapacitors, sensors for large biomolecules and the adsorption of bulky pollutants.[21]

In summary, large pore face-centered cubic (*Fm-3m*) mesoporous silicas FDU-12–X without intergrowth with other phases have been synthesized by using nonionic block copolymer templates. The entrance sizes of these materials can be continuously tailored (4–9 nm). Most importantly, this work shows that the entrance size of mesoporous materials with cagelike structures is a key factor for the applications in which mass transportation and diffusion are necessary. Such large pore materials with enlarged entrance sizes have proven to be much useful in protein adsorption and carbon replica processes.

Experimental Section

In a typical synthesis, 2.0 g of triblock copolymers $EO_{106}PO_{70}EO_{106}$ (F127, BASF), 2.0 g of TMB and 5.0 g of KCl were dissolved in 120 mL of 2 M HCl and stirred for 24 h. TEOS (8.3 g) was added to the resulting reaction mixture, which was left to stir for a further 24 h at 313 K before being transferred to an autoclave and heated at the desired temperature for 72 h. The solid product was collected by filtration and dried at room temperature in air. The resulted silica/surfactant composite powder was calcined at 823 K for 6 h to obtain mesoporous silica.

The Au nanocrystals were prepared by using FDU-12–X as the hard templates according to a reported method.[22] Kinetic experiments to determine the amount of lysozyme adsorbed into the mesoporous materials as a function of contact time were conducted by mixing 4 mL of 1.0 mg mL^{-1} protein solution (potassium phosphate as buffer at pH 7.0) with 40 mg of mesoporous silica under stirring at 20 °C in a vessel covered to prevent evaporation. Samples were withdrawn periodically for immediate analysis and then returned to the mixture. Adsorbed amounts were calculated from the difference of concentrations of the enzyme before and after adsorption measured by UV spectroscopy at 280 nm. The synthesis of mesoporous carbon (denoted as C-FDU-12-X) is similar to that reported by Ryoo and co-workers except for difference of silica-to-sucrose ratios.[23]

Received: January 27, 2003
Revised: May 7, 2003 [Z51027]

Keywords: adsorption · carbon · enzymes · mesoporous materials · silica

[1] M. E. Davis, *Nature* **2002**, *417*, 813.
[2] C. T. Kresge, M. E. Leonowicz, W. J. Roth, J. C. Vartuli, J. S. Beck, *Nature* **1992**, *359*, 710.
[3] J. S. Beck, J. C. Vartuli, W. J. Roth, M. E. Leonowicz, C. T. Kresge, K. D. Schmitt, C. T. W. Chu, D. H. Olson, E. W. Sheppard, et al. , *J. Am. Chem. Soc.* **1992**, *114*, 10834.
[4] Q. S. Huo, D. I. Margolese, G. D. Stucky, *Chem. Mater.* **1996**, *8*, 1147.
[5] D. Zhao, Q. Huo, J. Feng, B. F. Chmelka, G. D. Stucky, *J. Am. Chem. Soc.* **1998**, *120*, 6024.
[6] C. Yu, Y. Yu, D. Zhao, *Chem. Commun.* **2000**, 575.
[7] W. Z. Zhou, H. M. A. Hunter, P. A. Wright, Q. F. Ge, J. M. Thomas, *J. Phys. Chem. B* **1998**, *102*, 6933.
[8] Y. Sakamoto, I. Diaz, O. Terasaki, D. Y. Zhao, J. Perez-Pariente, J. M. Kim, G. D. Stucky, *J. Phys. Chem. B* **2002**, *106*, 3118.
[9] J. R. Matos, M. Kruk, L. P. Mercuri, M. Jaroniec, L. Zhao, T. Kamiyama, O. Terasaki, T. J. Pinnavaia, Y. Liu, *J. Am. Chem. Soc.* **2003**, *125,* 821.
[10] A. C. Finnefrock, R. Ulrich, A. Du Chesne, C. C. Honeker, K. Schumacher, K. K. Unger, S. M. Gruner, U. Wiesner, *Angew. Chem.* **2001**, *113,* 1247; *Angew. Chem. Int. Ed.* **2001**, *40*, 1207.
[11] M. Kruk, M. Jaroniec, *Chem. Mater.* **2001**, *13*, 3169.
[12] Y. H. Sakamoto, M. Kaneda, O. Terasaki, D. Y. Zhao, J. M. Kim, G. Stucky, H. J. Shim, R. Ryoo, *Nature* **2000**, *408*, 449.
[13] M. Kruk, V. Antochshuk, J. R. Matos, L. P. Mercuri, M. Jaroniec, *J. Am. Chem. Soc.* **2002**, *124*, 768.
[14] Y. J. Han, G. D. Stucky, A. Butler, *J. Am. Chem. Soc.* **1999**, *121*, 9897.
[15] J. W. Zhao, F. Gao, Y. L. Fu, W. Jin, P. Y. Yang, D. Y. Zhao, *Chem. Commun.* **2002**, 752.
[16] C. Z. Yu, B. Z. Tian, J. Fan, G. D. Stucky, D. Y. Zhao, *J. Am. Chem. Soc.* **2002**, *124*, 4556.
[17] J. Fan, C. Z. Yu, L. M. Wang, B. Tu, D. Y. Zhao, Y. Sakamoto, O. Terasaki, *J. Am. Chem. Soc.* **2001**, *123*, 12113.
[18] J. M. Kim, Y. Sakamoto, Y. K. Hwang, Y. U. Kwon, O. Terasaki, S. E. Park, G. D. Stucky, *J. Phys. Chem. B* **2002**, *106*, 2552.
[19] J. Deere, E. Magner, J. G. Wall, B. K. Hodnett, *Chem. Commun.* **2001**, 465.
[20] J. Deere, E. Magner, J. G. Wall, B. K. Hodnett, *J. Phys. Chem. B* **2002**, *106*, 7340.
[21] J. Lee, K. Sohn, T. Hyeon, *J. Am. Chem. Soc.* **2001**, *123*, 5146.
[22] Y. J. Han, J. M. Kim, G. D. Stucky, *Chem. Mater.* **2000**, *12*, 2068.
[23] S. Jun, S. H. Joo, R. Ryoo, M. Kruk, M. Jaroniec, Z. Liu, T. Ohsuna, O. Terasaki, *J. Am. Chem. Soc.* **2000**, *122*, 10712.

 © 2003 Wiley-VCH Verlag GmbH & Co. KGaA, Weinheim

Choline Recognition in Water

Acetylcholine Recognition by a Deep, Biomimetic Pocket**

*Fraser Hof, Laurent Trembleau, Elke Christine Ullrich, and Julius Rebek, Jr.**

Synthetic receptors for small targets relevant to biology often mimic the molecular recognition features of naturally occurring proteins. For the target molecule acetylcholine (**1**$^+$), X-ray structural information is available for its cognate esterase. Negatively charged Asp and Glu residues on the enzyme

[*] Prof. J. Rebek, Jr., F. Hof,[+] L. Trembleau,[+] E. C. Ullrich
The Department of Chemistry and
the Skaggs Institute for Chemical Biology
The Scripps Research Institute
10550 N. Torrey Pines Rd.
MB-26, La Jolla, CA, 92037 (USA)
Fax: (+1) 858-784-2876
E-mail: jrebek@scripps.edu

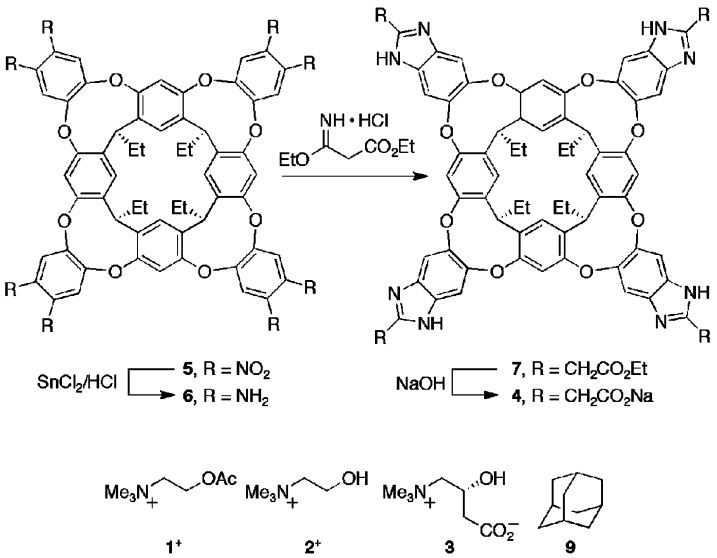
[+] These authors contributed equally to this work.

[**] This research was supported by the Skaggs Institute for Chemical Biology and the NIH (GM 27932). E.C.U. thanks the Deutsche Forschungsgemeinschaft for fellowship support. The authors thank Prof. Pablo Ballester for helpful discussions.

 © 2003 Wiley-VCH Verlag GmbH & Co. KGaA, Weinheim DOI: 10.1002/anie.200351174

surround the mouth of a deep (ca. 20 Å) active-site gorge.[1] Once the substrate enters the gorge it is guided to the active site and there secured almost exclusively by aromatic residues.[2,3] The quaternary ammonium function of acetylcholine does not permit the use of conventional hydrogen bonds or salt bridges; rather, the ion presents a thin layer of positive charge on its surface. These features of the target and enzyme[4] have inspired the synthesis of synthetic receptors for quaternary ammonium ions with negative charges on concave aromatic surfaces. The first examples were cyclophanes appended with polar solubilizing groups.[5–9] Receptors based on clefts,[10–14] porphyrins,[15–17] calixarenes/resocinarenes,[18–23] and metal–ligand clusters[24] have followed, and yielded an assortment of thermodynamically stable host–guest complexes. Examples of good binding selectivity[5,12] and kinetic stability[24] in water remain elusive, but some success has been achieved in organic media.[25] In general, the concavity of these receptors is modest—they surround only a small fraction of the target molecules. We describe here a deep pocket synthetic receptor that binds acetylcholine ($\mathbf{1}^+$) and choline ($\mathbf{2}^+$) in water with high thermodynamic and kinetic stability. Selectivity over L-carnitine (**3**) is established by the positioning of negative charges at the mouth of the deep pocket.

The receptor **4** is prepared from the known octanitrocavitand **5**[26] in three steps (Scheme 1). Reduction of **5** to the octaamine **6** with $SnCl_2$ and subsequent heating in the presence of the appropriate imidate led to the formation of the tetrabenzimidazole tetraester **7** in 62% yield.[27] The ester is hydrolyzed with NaOH to provide cavitand **4** as the tetrasodium salt. The negative charges found on the upper rim of **4** enable its solubility in water at pH/pD 7.8 at levels up to 10 mM.



Scheme 1. Synthesis of receptor **4**, and the structures of some guests that form kinetically stable complexes in water.

A 1 mM sample of **4** in D_2O provides an NMR spectrum that has sharp signals and shows the characteristics and symmetry expected for a time-averaged C_{4v} conformation (Figure 1a). Rapid tautomerization of the benzimidazoles occurs on the NMR time scale, facilitated by the water molecules that complete the seam of hydrogen bonds. These water molecules are known to stabilize the pocketlike conformation of structurally related cavitands in organic solvents.[28] The methine protons are observed at $\delta = 5.5$ ppm, which indicates that the host exists in a vase-shaped conformation.[29] In solution this preformed hydrophobic cavity is

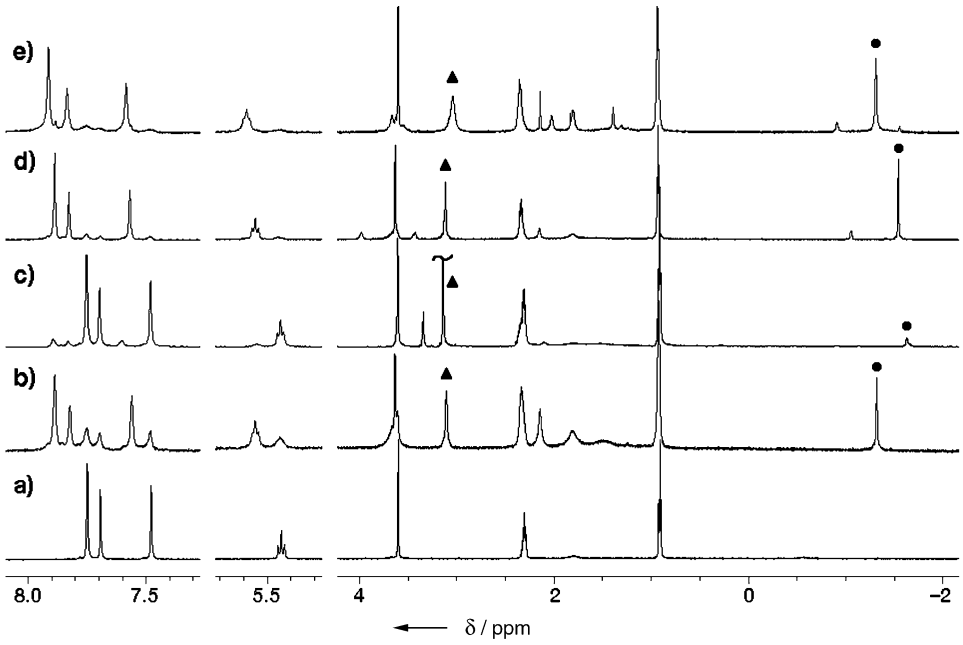


Figure 1. ^{1}H NMR spectra of host **4** at 1 mM in D_2O: a) before the addition of guest, and in the presence of about one equivalent of: b) Me_4NBr, c) L-carnitine, d) choline chloride, and e) acetylcholine chloride. Signals arising from free and bound guest protons are marked with (▲) and (●), respectively.

 © 2003 Wiley-VCH Verlag GmbH & Co. KGaA, Weinheim

occupied by one encapsulated THF molecule, and likely accompanied by an unknown amount of water. The adventitious THF resists removal even when solid **4** is heated at 100 °C under high vacuum. When one equivalent of tetramethylammonium bromide ($\mathbf{8}^+Br^-$) is added to a solution of **4** in D_2O, the THF is released and a separate set of host resonances appears: A new signal corresponding to encapsulated $\mathbf{8}^+$ appears at $\delta = -1.35$ ppm, which is shifted $\delta = 4.4$ ppm upfield of the free guest (Figure 2c). The large anisotropy experienced by the bound guest shows it is included deep within the pocket, surrounded by aromatic walls. NMR titrations provide an association constant of $4300\,M^{-1}$ for $\mathbf{8}^+$ with **4** in D_2O (Table 1). Larger cations such as tetrapropylammonium and tetrabutylammonium show no evidence of complex formation; they cannot fit within the binding pocket. The host also demonstrates functional group selectivity—primary amines (for example, glycine methyl ester hydrochloride) and heterocycles (for example, imidazole, pyridine, and methylpyridinium salts) do not form stable complexes with **4**.

Similar 1:1 host–cation complexes are formed with acetylcholine chloride ($\mathbf{1}^+Cl^-$) and choline chloride ($\mathbf{2}^+Cl^-$), with association constants greater than $10^4\,M^{-1}$ (the limit of the NMR determinations). Direct competition of $\mathbf{1}^+$ with $\mathbf{2}^+$ reveals a slight (5:4) preference for the binding of choline. The structurally related, but zwitterionic guest, L-carnitine (**3**) shows a binding constant of only $140\,M^{-1}$. For $\mathbf{1}^+$, $\mathbf{2}^+$, and **3** the NMR spectra of each host–guest complex indicates that the trimethylammonium residue of each guest is bound deep within the aromatic pocket ($\Delta\delta = 4.4$–4.9 ppm). The binding of L-carnitine in this mode positions the guest's carboxylate group in proximity to the four carboxylate residues that decorate the opening of the host's pocket (Figure 2). The resulting electrostatic repulsion is likely to be responsible for the host's rejection of L-carnitine relative to choline and acetylcholine.

Isothermal titration calorimetry (ITC) was carried out to measure the enthalpy and entropy of complex formation for each guest. In general, the calorimetric data gives K_a values that agree with those obtained by NMR titrations (Table 1). The enthalpy of binding contributes significantly to the thermodynamic stability of each host–guest complex—it is likely that some portion of this enthalpy arises from complementary electrostatic interactions. The complexation of choline shows the most favorable enthalpy of binding, with a compensating unfavorable entropy term. For all other guests the entropy of binding is favorable, and constitutes a significant portion of the free energy of complexation. The binding of guests within the cavity causes the release of ordered THF and water molecules from the preformed cavity—a hydrophobic effect that is expected to be responsible for the favorable entropy of binding. The origins of the unfavorable entropy of complexation for choline are less clear. Additional evidence for a hydrophobic driving force is provided by the study of adamantane (**9**), a neutral hydrocarbon. Sonication of a D_2O solution of **4** in the presence of solid adamantane (**9**) results in the extraction of the insoluble solid into water. ^1H NMR studies show that this uncharged guest forms a 1:1 complex similar to those formed by charged guests (**1**–**3** and **8**).

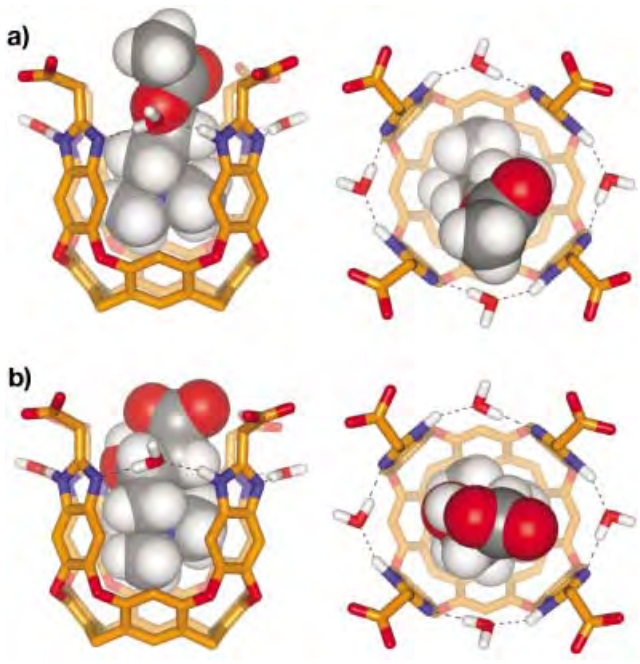


Figure 2. Molecular models of a) acetylcholine and b) L-carnitine complexed with host **4** clearly show the origin of the host's low affinity for the latter: the binding of trimethylammonium groups within the aromatic cavity results in the placement of the carboxylate group of carnitine near the host's negatively charged rim. Only the four water molecules that are thought to form the host's hydrogen bonding seam have been included in the models. Some protons and pendant alkyl groups have been omitted for clarity.

Table 1: Thermodynamic parameters for the binding of guests by **4** in water.[a]

Guest	NMR[b] K_a (M^{-1})	ITC[c] K_a (M^{-1})	$-\Delta H$ (kcal mol^{-1})	ΔS (cal K^{-1} mol^{-1})
Me_4N^+	4300 ± 600	3800 ± 600	2.4 ± 0.1	8.3
choline	$>10^4$	25900 ± 700	9.0 ± 0.1	−10.0
acetylcholine	$>10^4$	14600 ± 1200	4.1 ± 0.1	5.3
L-carnitine	140 ± 10	150 ± 10	2.1 ± 0.1	2.9

[a] pH/pD of each solution is 7.8. [b] NMR titrations were carried out in D_2O at 298 K using a constant host concentration of 1 mM. The limit for accurate determinations using this method is $10^4\,M^{-1}$. [c] Isothermal titration calorimetry was carried out in H_2O at 298 K using starting host concentrations between 0.1 and 5 mM. The enthalpy (ΔH) is directly measured, and values for K_a and ΔS are determined by fitting the data to a binding isotherm. For the fitting procedure the host–guest ratio was constrained between 0.90:1 and 1.10:1, except for choline for which a satisfactory fit was only available using a ratio of 0.63:1.

 © 2003 Wiley-VCH Verlag GmbH & Co. KGaA, Weinheim

In addition to the observed thermodynamic stability, these complexes exhibit unusually high kinetic stability. Previously reported receptors for acetylcholine in water (with association constants as high as $10^5\,\text{M}^{-1}$) do not demonstrate slow exchange of free and bound guest on the NMR time scale.[6,19,22] In contrast, complexes of host **4** and its guests give rise to separate NMR signals for the free and bound species in each case. To further characterize the kinetic stability of this system, the rates of guest exchange were determined from 2D NOESY experiments on the complex of **4** with $\mathbf{8}^+$. Integration of the cross-peaks gives kinetic parameters for the exchange process;[30] the release rate of the guest ion at 298 K is $8.2\,\text{s}^{-1}$, which corresponds to an energy barrier for guest exchange of 16 kcal mol^{-1}.

The similarities between acetylcholinesterase and **4** begin and end with binding—the synthetic host shows no signs of catalytic activity. But the monofunctionalization of related cavitands[31] suggests that catalytically useful groups can eventually be directed into the binding pocket. In the meantime, the synthetic receptor described here represents an unprecedented combination of affinity and kinetic stability for recognition of acetylcholine and choline in water.

Received: February 13, 2003 [Z51174]

Keywords: acetylcholine · cation–pi interactions · host–guest systems · molecular recognition · receptors

[1] J. L. Sussman, M. Harel, F. Frolow, C. Oefner, A. Goldman, L. Toker, I. Silman, *Science* **1991**, *253*, 872.
[2] M. Harel, I. Schalk, L. Ehret-Sabatier, F. Bouet, M. Goeldner, C. Hirth, P. H. Axelsen, I. Silman, J. L. Sussman, *Proc. Natl. Acad. Sci. USA* **1993**, *90*, 9031.
[3] M. Harel, D. M. Quinn, H. K. Nair, I. Silman, J. L. Sussman, *J. Am. Chem. Soc.* **1996**, *118*, 2340.
[4] N. Zacharias, D. A. Dougherty, *Trends Pharmacol. Sci.* **2002**, *23*, 281.
[5] T. H. Webb, H. Suh, C. S. Wilcox, *J. Am. Chem. Soc.* **1991**, *113*, 8554.
[6] R. Meric, J. P. Vigneron, J.-M. Lehn, *J. Chem. Soc. Chem. Commun.* **1993**, 129.
[7] S. M. Ngola, D. A. Dougherty, *J. Org. Chem.* **1998**, *63*, 4566.
[8] S. M. Ngola, P. C. Kearney, S. Mecozzi, K. Russell, D. A. Dougherty, *J. Am. Chem. Soc.* **1999**, *121*, 1192.
[9] K. Kano, T. Kitae, Y. Shimofuri, N. Tanaka, Y. Mineta, *Chem. Eur.J.* **2000**, *6*, 2705.
[10] A. Metzger, V. M. Lynch, E. V. Anslyn, *Angew. Chem.* **1997**, *109*, 911; *Angew. Chem. Int. Ed.* **1997**, *36*, 862.
[11] A. Metzger, E. V. Anslyn, *Angew. Chem.* **1998**, *110*, 682; *Angew. Chem. Int. Ed.* **1998**, *37*, 649.
[12] K. Niikura, A. Metzger, E. V. Anslyn, *J. Am. Chem. Soc.* **1998**, *120*, 8533.
[13] M. Rekharsky, Y. Inoue, S. Tobey, A. Metzger, E. Anslyn, *J. Am. Chem. Soc.* **2002**, *124*, 14959.
[14] T. Grawe, T. Schrader, R. Zadmard, A. Kraft, *J. Org. Chem.* **2002**, *67*, 3755.
[15] M. Sirish, H.-J. Schneider, *Chem. Commun.* **1999**, 907.
[16] R. K. Jain, A. D. Hamilton, *Org. Lett.* **2000**, *2*, 1721.
[17] T. Mizutani, K. Wada, S. Kitagawa, *J. Am. Chem. Soc.* **2001**, *123*, 6459.
[18] J. L. Atwood, L. J. Barbour, P. C. Junk, G. W. Orr, *Supramol. Chem.* **1995**, *5*, 105.
[19] J.-M. Lehn, R. Meric, J.-P. Vigneron, M. Cesario, J. Guilhem, C. Pascard, Z. Asfari, J. Vicens, *Supramol. Chem.* **1995**, *5*, 97.
[20] F. Sansone, S. Barboso, A. Casnati, D. Sciotto, R. Ungaro, *Tetrahedron Lett.* **1999**, *40*, 4741.
[21] G. Arena, A. Contino, T. Fujimoto, D. Sciotto, Y. Aoyama, *Supramol. Chem.* **2000**, *11*, 279.
[22] S. J. Park, J.-I. Hong, *Tetrahedron Lett.* **2000**, *41*, 8311.
[23] M. Lazzarotto, F. Sansone, L. Baldini, A. Casnati, P. Cozzini, R. Ungaro, *Eur. J. Org. Chem.* **2001**, 595.
[24] D. L. Caulder, K. N. Raymond, *Acc. Chem. Res.* **1999**, *32*, 975.
[25] P. Ballester, A. Shivanyuk, A. R. Far, J. Rebek, Jr., *J. Am. Chem. Soc.* **2002**, *124*, 14014.
[26] P. Amrhein, A. Shivanyuk, D. W. Johnson, J. Rebek, Jr., *J. Am. Chem. Soc.* **2002**, *124*, 10349.
[27] T. J. Church, N. S. Cutshall, A. R. Gangloff, T. E. Jenkins, M. S. Linsell, J. Litvak, K. D. Rice, J. R. Spencer, V. R. Wang, in *PCT Int. Appl.*, (Axys Pharmaceuticals Corporation, Wo, USA) **1998**, p. 108.
[28] A. R. Far, A. Shivanyuk, J. Rebek, Jr., *J. Am. Chem. Soc.* **2002**, *124*, 2854.
[29] J. R. Moran, J. L. Ericson, E. Dalcanale, J. A. Bryant, C. B. Knobler, D. J. Cram, *J. Am. Chem. Soc.* **1991**, *113*, 5707.
[30] E. W. Abel, T. P. J. Coston, K. G. Orrell, V. Sik, D. Stephenson, *J. Magn. Reson.* **1986**, *70*, 34.
[31] A. R. Renslo, J. Rebek, Jr., *Angew. Chem.* **2000**, *112*, 3419; *Angew. Chem. Int. Ed.* **2000**, *39*, 3281.

 © 2003 Wiley-VCH Verlag GmbH & Co. KGaA, Weinheim

Gene Delivery Proteins

Semi-Automated Synthesis and Screening of a Large Library of Degradable Cationic Polymers for Gene Delivery**

*Daniel G. Anderson, David M. Lynn, and Robert Langer**

The combinatorial, automated high-throughput synthesis and evaluation of small molecules has revolutionized modern drug discovery. Here we describe the first high-throughput, semi-automated methodology for the synthesis and screening

[*] Prof. R. Langer, D. G. Anderson
Department of Chemical Engineering, Room E25-342
Massachusetts Institute of Technology
Cambridge, Massachusetts 02139 (USA)
Fax: (+1) 617-258-8827
E-mail: rlanger@mit.edu
Prof. D. M. Lynn
Department of Chemical and Biological Engineering
University of Wisconsin—Madison
Madison, WI 53706 (USA)

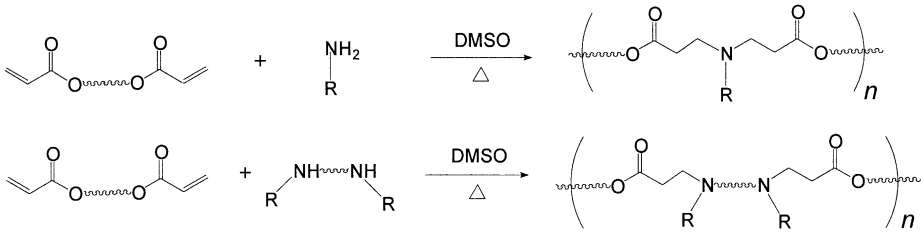
[**] This work was supported by the NSF (through the MIT Biotechnology Process and Engineering Center) and the NIH (Grant No.: EB00244). D.G.A also thanks the NIH for his postdoctoral fellowship. Finally, we would like to thank the many members of the Langer research group for their help, in particular Nashuad Hossain, Akin Akinc, and David Putnam.

 DOI: 10.1002/anie.200351244 © 2003 Wiley-VCH Verlag GmbH & Co. KGaA, Weinheim

of a large library of polymers for gene delivery. A key feature of these methods is that synthesis, storage, and cell-based testing are all performed without removing solvent, thereby allowing high- throughput manipulations using simple, easily automated fluid-handling systems. By using these methods, we synthesized a library of 2350 structurally unique, degradable, cationic polymers. High-throughput, cell-based screening has identified 46 new polymers that transfect with a higher efficiency than conventional nonviral delivery systems such as poly(ethyleneimine).

The major barrier to the success of gene therapy in the clinic remains the lack of safe and efficient DNA-delivery methods. Currently, the majority of clinical trials use modified viruses as delivery vehicles, which, while effective at transferring DNA to cells, suffer from potentially serious toxicity and production problems.[1,2] In contrast, nonviral systems offer a number of potential advantages, including ease of production, stability, low immunogenicity and toxicity, and reduced vector size limitations.[3] Despite these advantages, however, existing nonviral delivery systems are far less efficient than viral vectors.[4] One promising group of nonviral delivery compounds are cationic polymers, which spontaneously bind and condense DNA.[5–12] We have been particularly interested in poly(β-amino ester)s as delivery agents which have been shown to generally possess low cytotoxicity and are easily synthesized by the conjugate addition of a primary amine or bis(secondary amine) to a diacrylate (Scheme 1).[11,12]

The traditional development of new biomedical polymers has been an iterative process: polymers typically are designed one at a time and then individually tested for their properties. More recently, attention has focused on the development of parallel, combinatorial approaches that facilitate the generation of structurally diverse libraries of polymeric biomaterials.[12–15] However, the methods used in all previous studies are still relatively low-throughput, and therefore were not able to generate large amounts of structure–function information.



Scheme 1. Synthesis of poly(β-amino ester)s. Poly(β-amino ester)s were synthesized by the conjugate addition of primary or bis(secondary amines) to diacrylates.

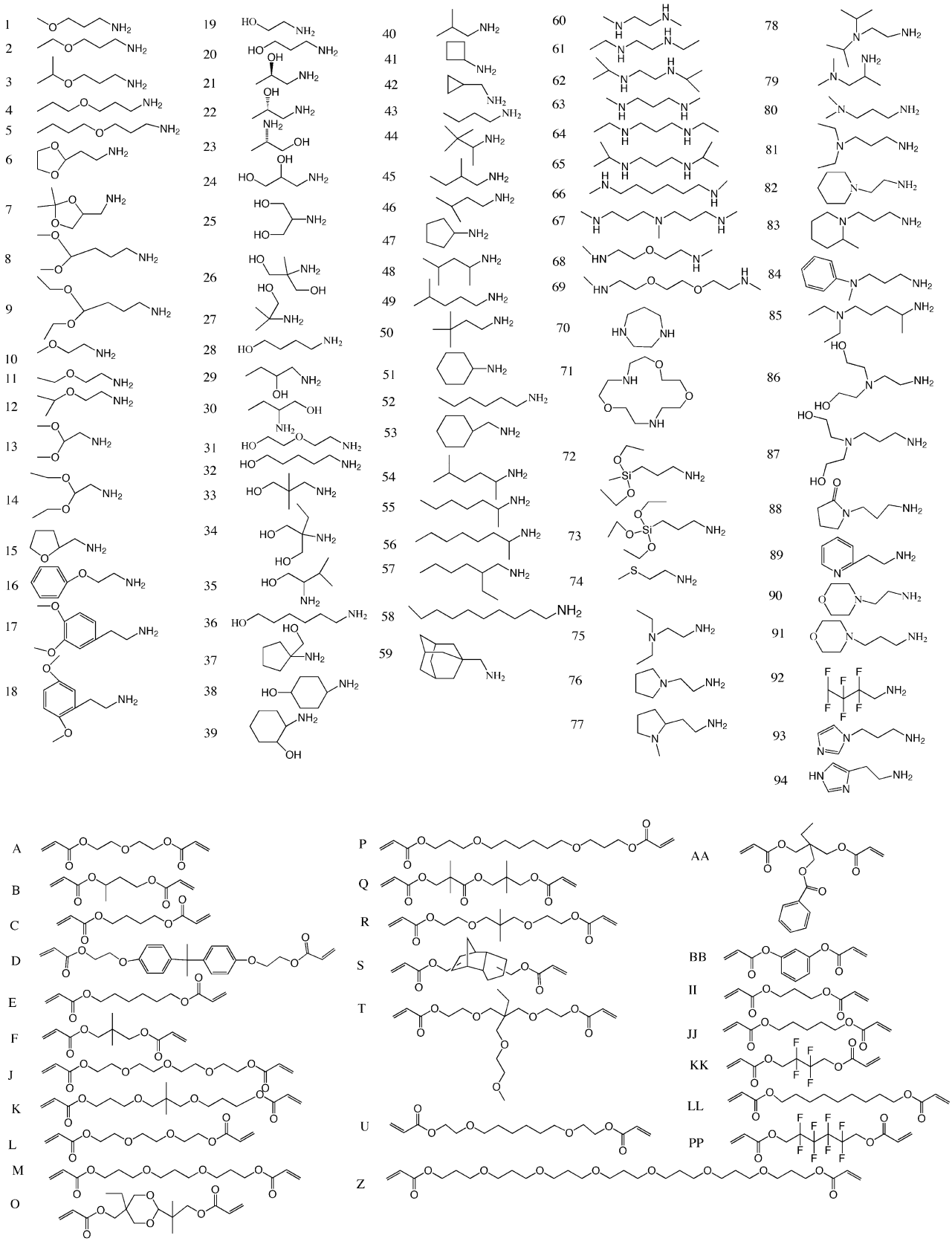
Among the primary factors limiting the throughput and automation of poly(β-amino ester) synthesis and testing was the viscosity of the monomer and polymer solutions, and the difficulty with manipulating the solid polymer products. While automation of liquid handling is straightforward using conventional robotics, the manipulation of solids and viscous liquids on a small scale is not. Therefore, we sought to develop a general procedure with which polymers could be synthesized and screened in cell-based assays without leaving the solution phase. Since this would require the presence of residual solvent in the cell assays, we chose to use a relatively nontoxic solvent: dimethyl sulfoxide (DMSO). DMSO is a widely used solvent in the culturing of cells, and is commonly used when storing frozen stocks of cells. It is miscible with water and is generally well-tolerated.

The first step in preparing for high-throughput synthesis was to identify conditions that would allow for the production of polymer and yet possess a manageable viscosity. Small-scale, pilot experiments showed that polymerizations could be performed effectively at 1.6 M in DMSO at 56 °C for 5 days. Based on this, we prepared a general strategy for synthesis and testing. All monomers (Scheme 2) were diluted to 1.6 M in DMSO, and then using both a fluid-handling robot and a 12-channel micropipetter, we added 150 μL of each amine and diacrylate monomer into a polypropylene, deep-well plate, and sealed it with aluminum foil. These were placed on an orbital shaker and incubated at 56 °C for 5 days. To compensate for the increased viscosity of the polymeric solutions, we added 1 mL of DMSO to each well of the plate and then stored them frozen at 4 °C until ready for use. These synthetic methods greatly increased our throughput, and allowed us to set up all 2350 reactions in a single day. Furthermore, the production and storage of polymers in a 96-well format allowed for an easy transition to an automated 96-well format, cell-based testing of the efficiency of polymer transfection.

Once synthesized, all polymers were tested for their ability to deliver the luciferase expressing plasmid, pCMV-luc, into the monkey kidney fibroblast cell-line COS-7. The large size of the polymer library necessitated the development of a high-throughput method for the cell-based screening of transfection efficiency. Since polymers were stored in 96-well plates, we performed all polymer dilution, DNA complexation, and cell transfections in parallel by directly transferring polymers from plate to plate using a liquid-handling robot. All polymers were synthesized using the same concentration of amine monomer, thus comparison between polymers at a fixed ratio of the amine-containing monomer to DNA phosphate (N:P ratio) was straightforward. While the amine monomers contain either one, two, or three amines per monomer, initial broad-based screens for transfection efficiency were greatly simplified by maintaining a constant monomer concentration in all the wells of a single plate, and therefore a constant volume of polymer solution per reaction (see the Experimental Section).

We selected N:P ratios of 10:1, 20:1, and 40:1 for our initial screens based on our previous experience with these types of polymers. We screened all 2350 polymers at these three ratios with our high-throughput system. Transfection values at the best conditions for each polymer were tabulated into a histogram (Figure 1). These results were compared to three controls: naked DNA (no transfection agent), poly-

 © 2003 Wiley-VCH Verlag GmbH & Co. KGaA, Weinheim



Scheme 2. Amino (numbers) and diacrylate (letters) monomers.

 © 2003 Wiley-VCH Verlag GmbH & Co. KGaA, Weinheim

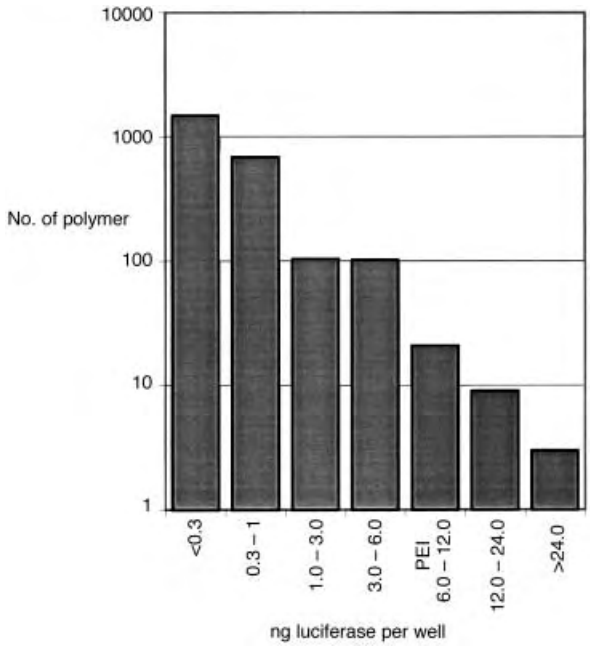


Figure 1. Histogram of polymer transfection efficiencies. In the first screen all 2350 polymers were tested for their ability to deliver pCMV-luc DNA at N:P ratios of 40:1, 20:1, and 10:1 to COS-7 cells. PEI transfection efficiency is shown for reference. COS-7 cells readily take up naked DNA, and in our conditions produce 0.15 ± 0.05 ng of luciferase per well. Under optimized conditions, 1 h transfections with PEI produce 6.0 ± 0.2 ng per well, and the best lipid reagent we have used, lipofectamine 2000, produces 13.5 ± 1.9 ng per well.

(ethyleneimine) (PEI), and lipofectamine 2000. The low, residual levels of DMSO present in the transfection solutions did not affect the transfection efficiency of either naked DNA or PEI. Thirty three of the 2350 polymers were found to be as good or better than PEI in this unoptimized system.

Since cationic polymer transfections tend to be sensitive to the polymer:DNA ratio,[16] we decided to individually optimize the transfection conditions with the best polymers from our preliminary screen. The average transfection efficiencies in the optimized conditions for the best 50 polymers are shown in Figure 2, along with control data. In this experiment, 46 polymers were identified that transfect as good or better than PEI. All 93 of these polymers were also tested for their ability to bind DNA using agarose gel electrophoresis (Figure 2). Interestingly, while almost all of the polymers do bind DNA as expected, two polymers that transfect at high levels do not: M17 and KK89 (Figure 2).

To further examine the transfection properties of these polymers, ten of the best polymers were tested for their ability to deliver the green fluorescent protein plasmid, pCMV-eGFP. Unlike pCMV-luc, pCMV-eGFP provides information concerning what percentage of cells is transfected. High levels of transfection were observed for all ten polymers, and two of the best are shown in Figure 3.

The "hits" identified in the above assays (Figure 2) reveal a surprisingly diverse and unexpected collection of polymers. Particularly surprising is the large collection of polymers containing hydrophobic monomer D. In fact, the diacrylate

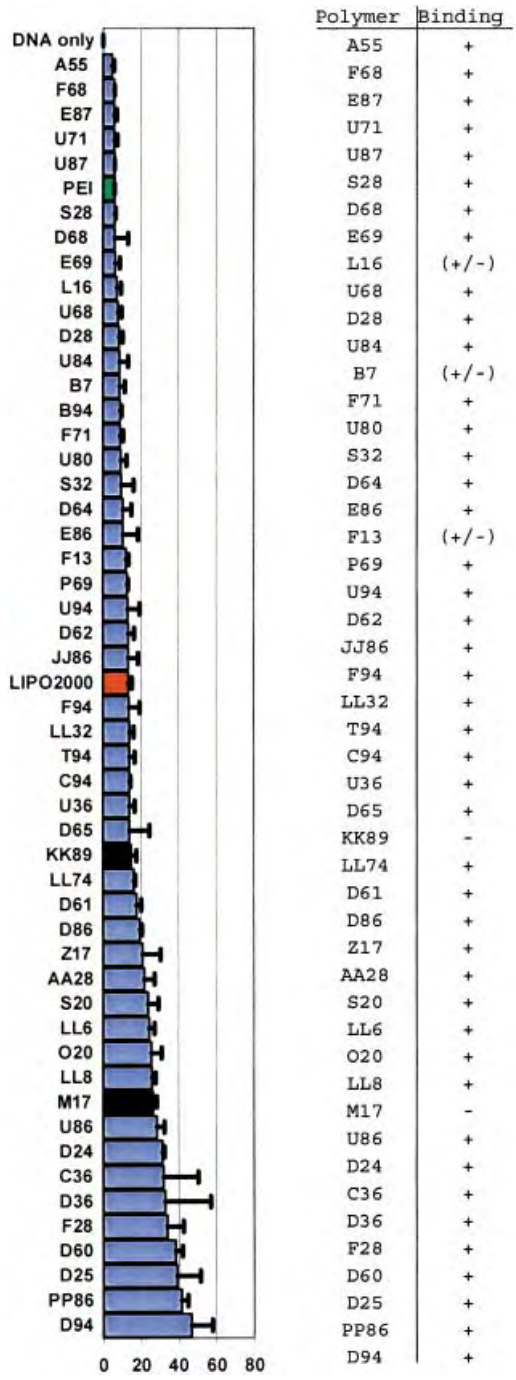


Figure 2. Left) Optimized transfection efficiency of the top 50 polymers relative to PEI and lipofectamine 2000. Polymers were tested as described in the Experimental Section. In the first broad screen N:P ratios of 40:1, 20:1, and 10:1 were tested. The top 93 were rescreened in triplicate at the following N:P ratios: (the optimal N:P ratio from the first screen) $\times 0.5$, 0.75, 1.0, 1.25, 1.5, and 1.75. Control reactions are labeled in red, and polymers that did not bind DNA in a gel electrophoresis assay are shown in black. Right) DNA binding of polymers as determined by agarose gel electrophoresis. The data was tabulated in the following manner: 1) fully shifted DNA is represented by (+), 2) partially shifted DNA is represented by (+/−), 3) unbound DNA is represented by (−).

 © 2003 Wiley-VCH Verlag GmbH & Co. KGaA, Weinheim

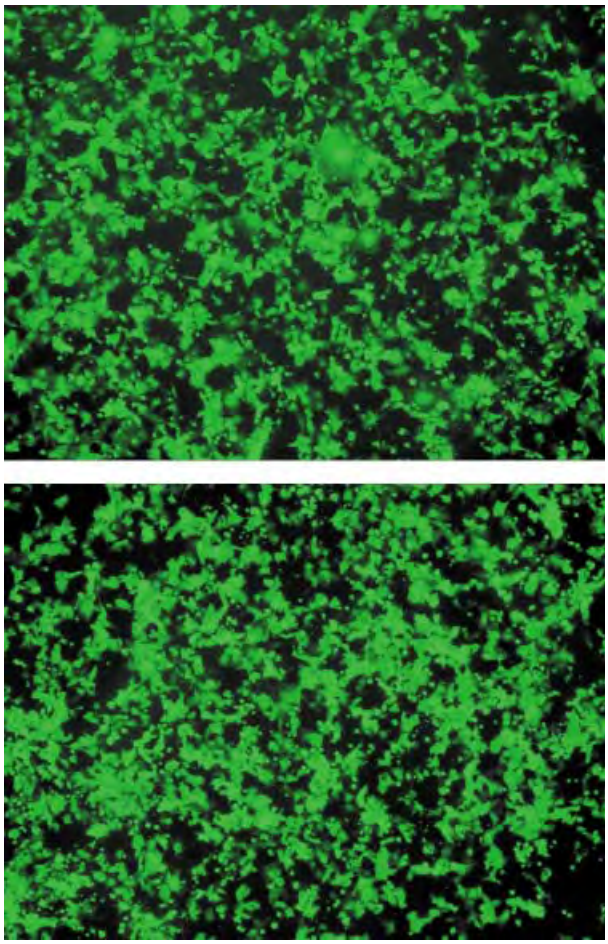


Figure 3. Transfection of COS-7 cells using enhanced green fluorescent protein plasmid. Cells were transfected at an N:P ratio of (optimal N:P from the broad screen) × 1.25 with 600 ng of DNA. Regions of the well showing high transfection are shown for the following polymers: top: C36, bottom: D94.

monomers used to make the 50 best-performing polymers are almost always hydrophobic. Further analysis reveals two more common features of the effective polymers: 1) 12 of the 26 polymers that are better than the best conventional reagent, lipofectamine 2000, have mono- or dialcohol side groups, and 2) linear, bis(secondary amines) are also over represented in the hit structures. Also surprising was the identification of two polymers that transfect at high levels, but do not appear to bind DNA (KK89 and M17). Both are also insoluble at pH 5 and pH 7, and we speculate that their ability to facilitate DNA uptake may be a result of permeabilization of the cellular membrane. While the mechanisms behind the function of these polymers remains unclear at this point, we are developing second-generation DNA delivery polymers using these data as design criteria.

Also important for the function of gene-delivery polymers is length.[17,18] Using these results as a guideline, we are in the process of creating a range of polymer lengths for the most effective DNA-delivery polymers by carefully varying the relative concentration of the monomer. Eventually, in vivo experiments will be critical in determining the safety, efficacy, and ultimate utility of these polymers for gene therapy.

We have described the combinatorial synthesis and testing of 2350 structurally unique poly (β-amino ester)s for their ability to transfect the mammalian cell line, COS-7. We were able to set-up all 2350 synthetic reactions in a single day by using semi-automated methods, and then test the transfection potential of these polymers at a rate of about 1000 per day. The methods we have developed here are not limited to gene-delivery polymers, but can be more broadly applied towards the identification of materials for nucleic acid, protein, and drug delivery, as well as in other areas of medicine.

Experimental Section

Polymer synthesis: Monomers were purchased from Aldrich (Milwaukee, WI), TCI (Portland, OR), Pfaltz & Bauer (Waterbury, CT), Matrix Scientific (Columbia, SC), Acros-Fisher (Pittsburg, PA), Scientific Polymer (Ontario, NY), Polysciences (Warrington, PA), and Dajac monomer-polymer (Feasterville, PA). The monomers were dissolved in DMSO (Aldrich) to a final concentration of 1.6 M. All possible pairwise combinations of amine and diacrylate monomers were added in aliquots (150 μL) to each well of the 96-well polypropylene masterblock deep-well plates (2 ml, Griener America, Longwood, FL). The plates were sealed with aluminum foil, and incubated at 56 °C while rotating them on an orbital shaker. After 5 days, DMSO (1 ml) was added to each well, and the plates were resealed and stored frozen at 4 °C until ready to be used.

Transfection experiments: 14,000 cos-7 cells (ATCC, Manassas, VA) were seeded into each well of a solid white or clear 96-well plate (Corning-Costar, Kennebunk, ME) and allowed to attach overnight in growth medium composed of phenol red free Dulbecco's modified eagle medium (DMEM, 500 mL), heat-inactivated fetal bovine serum (FBS, 50 mL), penicillin/streptomycin (5 mL, Invitrogen, Carlsbad, CA). Each well of a master block 96-well plate was filled with 25 mM sodium acetate at pH 5 (1 ml). The polymer/DMSO solution (40, 20, or 10 μL) was then added. The diluted polymer (25 μL) was added to 60 $\mu g\,mL^{-1}$ pCMV-luc DNA (25 μL; Promega, Madison, WI) or pEGFP-N1 (Invitrogen) in a half-volume 96-well plate. These were incubated for 10 min, and then the polymer-DNA solution (30 μL) was added to optimem (200 μL) containing sodium bicarbonate (Invitrogen) in 96-well polystyrene plates. The medium was removed from the cells using a 12-channel wand (V&P Scientific, San Diego, CA) after which the optimem-polymer-DNA solution (150 μL) was immediately added. The complexes were incubated with the cells for 1 h and then removed using the 12-channel wand and replaced with growth medium (105 μL). Cells were allowed to grow for three days at 37 °C in 5 % CO_2 and then analyzed for luminescence (pCMV-luc) or fluorescence (pEGFP-N1). Control experiments were performed as described above, but using poly(ethyleneimine) $M_r = 25\,000$ (Aldrich) instead of the synthesized polymer, and at polymer:DNA weight ratios of 0.5:1, 0.75:1, 1:1, 1.25:1, 1.5:1, and 2:1. Lipofectamine 2000 (Invitrogen) transfections were performed as described by the vendor, except that complexes were removed after 1 h.

Luminescence was analyzed using bright-glo assay kits (Promega). Briefly, Bright-glo solution (100 μL) was added to each well of the microtiter plate containing media and cells. Luminescence was measured using a Mithras Luminometer (Berthold, Oak Ridge, TN). In some cases a neutral density fliter (Chroma, Brattleboro, VT) was used to prevent saturation of the luminometer. A standard curve for luciferase was generated by titration of luciferase enzyme (Promega) into growth media in white microtiter plates. eGFP expression was examined using a Zeiss Axiovert 200 inverted microscope.

Agarose gel electrophoresis DNA-binding assays were done at an N:P ratio of 40:1, as previously described.[12] All liquid handling was performed using an EDR384S/96S robot (Labcyte, Union City, CA)

 © 2003 Wiley-VCH Verlag GmbH & Co. KGaA, Weinheim

or a 12-channel micropipetter (Thermo Labsystems, Vantaa, Finland), in a laminar flow hood.

Received: February 21, 2003 [Z51244]

Keywords: DNA · gene therapy · high-throughput screening · polycations · polymers

[1] http://www.wiley.co.uk/genetherapy/clinical/2002.
[2] N. Somia, I. M. Verma, *Nat. Rev. Genet.* **2000**, *1*, 91.
[3] F. D. Ledley, *Hum. Gene Ther.* **1995**, *6*, 1129.
[4] D. Luo, W. M. Saltzman, *Nat. Biotechnol.* **2000**, *18*, 33.
[5] J. Fominaya, W. Wels, *J. Biol. Chem.* **1996**, *271*, 10560.
[6] J. J. Schwartz, S. Zhang, *Curr. Opin. Mol. Ther.* **2000**, *2*, 162.
[7] O. Boussif, F. Lezoualch, M. A. Zanta, M. D. Mergny, D. Scherman, B. Demeneix, J. P. Behr, *Proc. Natl. Acad. Sci. USA* **1995**, *92*, 7297.
[8] A. V. Kabanov, P. L. Felgner, L. W. Seymour, *Self-assembling complexes for gene delivery: from laboratory to clinical trial*, Wiley, Chichester, New York, **1998**.
[9] Y. B. Lim, C. H. Kim, K. Kim, S. W. Kim, J. S. Park, *J. Am. Chem. Soc.* **2000**, *122*, 6524.
[10] Y. B. Lim, S. M. Kim, H. Suh, J. S. Park, *Bioconjugate Chem.* **2002**, *13*, 952.
[11] D. M. Lynn, R. Langer, *J. Am. Chem. Soc.* **2000**, *122*, 10761.
[12] D. M. Lynn, D. G. Anderson, D. Putnam, R. Langer, *J. Am. Chem. Soc.* **2001**, *123*, 8155.
[13] S. Brocchini, *Adv. Drug Delivery Rev.* **2001**, *53*, 123.
[14] J. E. Murphy, T. Uno, J. D. Hamer, F. E. Cohen, V. Dwarki, R. N. Zuckermann, *Proc. Natl. Acad. Sci. USA* **1998**, *95*, 1517.
[15] S. Brocchini, K. James, V. Tangpasuthadol, J. Kohn, *J. Am. Chem. Soc.* **1997**, *119*, 4553.
[16] C. L. Gebhart, A. V. Kabanov, *J. Controlled Release* **2001**, *73*, 401.
[17] J. S. Remy, B. Abdallah, M. A. Zanta, O. Boussif, J. P. Behr, B. Demeneix, *Adv. Drug Delivery Rev.* **1998**, *30*, 85.
[18] D. V. Schaffer, N. A. Fidelman, N. Dan, D. A. Lauffenburger, *Biotechnol. Bioeng.* **2000**, *67*, 598.

 © 2003 Wiley-VCH Verlag GmbH & Co. KGaA, Weinheim

Fullerene-Based Catenanes/Rotaxanes

Preparation of Neutral [60]Fullerene-Based [2]Catenanes and [2]Rotaxanes Bearing an Electron-Deficient Aromatic Diimide Moiety**

*Yosuke Nakamura, Satoshi Minami, Kazuki Iizuka, and Jun Nishimura**

Dedicated to Professor Emeritus Dr. Soichi Misumi on the occasion of his 77th birthday

Since [60]fullerene has become available in macroscopic quantities, its covalent functionalization has been widely developed.[1] In parallel with chemical transformations, supramolecular fullerene chemistry has also been explored.[2] The complexation of [60]fullerene itself by π-electron-rich compounds, such as hydroquinone,[3] BEDT-TTF,[4] ferrocene,[5] porphyrins,[6] and macrocyclic receptors including cyclodextrin,[7] cyclotriveratrylene,[8] calixarenes,[9] and related compounds has been extensively investigated. The progress in covalent functionalization of fullerene has led to further development of supramolecular architectures and molecular assemblies incorporating fullerene.[2,10,11]

In the last decade, a variety of molecules, including rotaxanes and catenanes, have been fabricated through noncovalent bonding interactions.[12] These molecular assemblies have attracted much interest because of their fascinating topological features and potential application in molecular devices. The introduction of [60]fullerene into these systems promises further enhancement of the functionality of such molecular assemblies because of its unique electronic properties, especially as a strong electron acceptor.[13]

However, examples that incorporate [60]fullerene into rotaxanes and catenanes,[14–16] which have been constructed by independent synthetic methodologies, are extremely limited. Diederich, Sauvage, et al. have prepared a [2]rotaxane that possesses two fullerene stoppers at the ends of its threadlike component, which takes advantage of the coordination of Cu^+ ions by 1,10-phenanthroline ligands.[14] In addition Diederich, Stoddart, et al. prepared a [60]fullerene-containing [2]catenane that includes a *trans*-4 bisadduct as a building block, based on the charge-transfer (CT) interaction between the π-electron-deficient cyclobis(paraquat-*p*-phenylene) and the π-electron-rich 1,4-dialkoxybenzene moieties.[15] To the best of our knowledge, this is the only example of a [60]fullerene-based [2]catenane, and there has been no

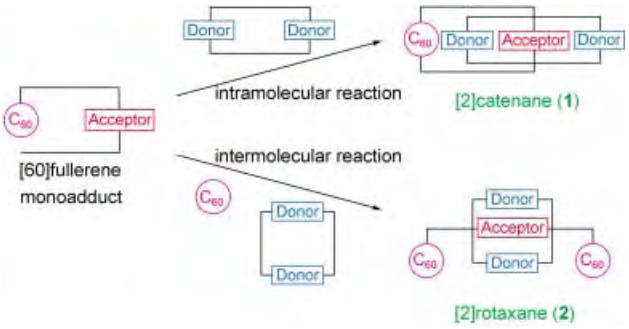
[*] Prof. Dr. J. Nishimura, Dr. Y. Nakamura, S. Minami, K. Iizuka
Department of Nano-Material Systems
Graduate School of Engineering
Gunma University, Tenjin-cho, Kiryu, Gunma 376-8515 (Japan)
Fax: (+81) 277-30-1314
E-mail: nisimura@chem.gunma-u.ac.jp

[**] This work was financially supported by a Grant-in-Aid from the Ministry of Education, Science, Sports and Culture, Japan. The authors are grateful to Prof. Dr. Takayuki Takarada and Dr. Kayoko Morishita (Gunma University) for their assistance with MALDI-TOF mass spectrometry measurements.

 © 2003 Wiley-VCH Verlag GmbH & Co. KGaA, Weinheim DOI: 10.1002/anie.200351411

report of [2]catenanes to date, in which the electron-accepting ability of [60]fullerene is directly involved.

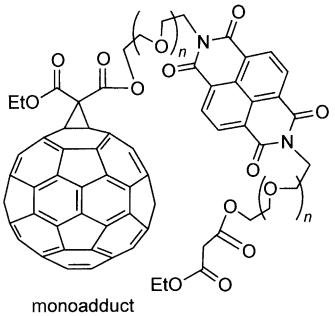
In the present study, we have developed new synthetic strategies to form neutral fullerene-based [2]catenanes **1** and [2]rotaxanes **2**, which consist of a fullerene derivative that carries another electron-acceptor moiety and an electron-donating macrocycle, such as a benzocrown ether, as shown in Scheme 1. In the [2]catenanes **1**, a cyclic fullerene bisadduct



Scheme 1. Synthetic strategies toward fullerene-based [2]catenanes or [2]rotaxanes.

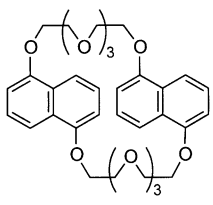
and a benzocrown ether are interlocked. Since fullerene also serves as an electron acceptor, **1** has an intriguing D-A-D-A (D = donor, A = acceptor) stacking structure. In the [2]rotaxanes **2**, a crown ether encircles the acceptor moiety of a dumbbell-shaped molecule, which carries two [60]fullerene groups that act as stoppers at both termini. Their formation is mainly based on the CT interaction between the components. It is noteworthy that they can be prepared from the identical precursor, namely, an acyclic fullerene monoadduct, which exhibits another electron-accepting moiety; for the [2]catenanes, the monoadduct is transformed into a cyclic bisadduct by appropriate intramolecular reactions in the presence of an electron-donating macrocycle, while for the [2]rotaxanes, the monoadduct reacts with another [60]fullerene molecule.

To realize the strategies highlighted in Scheme 1, we designed monoadducts **3a** and **3b**, which incorporate a naphthalenetetracarboxylic diimide moiety as an acceptor, a malonate ester as a reactive site for [60]fullerene, and oligooxyethylene linkages to connect them. Since such a diimide has been suitably employed as a component of



monoadduct

3a: *n* = 2
3b: *n* = 3

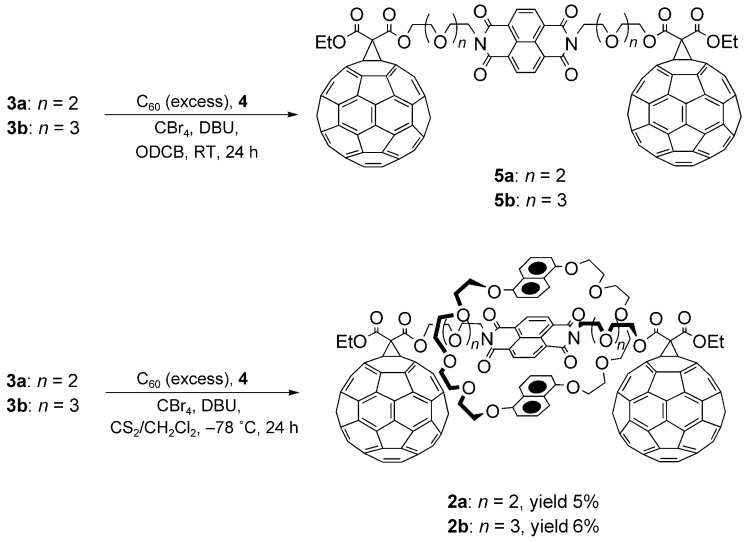


4

catenanes by Sanders et al.,[17] **3a** and **3b** are suitable to perform as the key building blocks outlined in Scheme 1. In practice, we have succeeded in the preparation of both [2]rotaxanes and [2]catenanes.

Monoadducts **3a** and **3b** were prepared using the Bingel reaction[18,19] by treating the corresponding naphthalenetetracarboxylic-diimide-containing bis(ethyl malonate) moiety with [60]fullerene in the presence of CBr_4 and 1,8-diazabicyclo[5.4.0]undec-7-ene (DBU) in toluene at room temperature. Both **3a** and **3b** were isolated by column chromatography followed by GPC, if necessary, and readily characterized by APCI mass spectrometry and ^{1}H NMR spectroscopy.

To prepare the fullerene-based [2]rotaxanes **2**, the Bingel reaction of **3a** or **3b** with an excess of [60]fullerene was first carried out in the presence of 1,5-dinaphtho-[38]crown-10 ether (**4**) in *o*-dichlorobenzene (ODCB) at room temperature. Although the dumbbell-shaped [60]fullerene dimers **5a** and **5b** were produced without incorporating **4**, the desired [2]rotaxane **2** was not detected (Scheme 2). Thus, the Bingel



Scheme 2. Synthesis of fullerene-based [2]rotaxanes **2**.

reactions were carried out in CS_2/CH_2Cl_2 at −78 °C, where the formation of a pseudorotaxane was expected to be more preferable from the viewpoint of entropy. In a remarkable contrast with the reactions at room temperature, the desired [2]rotaxanes **2a** and **2b** were successfully produced and isolated by column chromatography and GPC.

Compounds **2a** and **2b** were characterized by ^{1}H NMR spectroscopy and MALDI-TOF mass spectrometry. As shown in Figure 1, the MALDI-TOF mass spectrum of **2a** clearly indicates the molecular ion peak ($m/z = 2830$). A fragmentation peak at $m/z = 1474$ is also observed, which results from the loss of [60]fullerene and **4** from **2a** by cleavage of the cyclopropane ring (retro-Bingel reaction). In the ^{1}H NMR spectrum of **2a** (Figure 2a), the malonate methylene protons ($\delta = 3.35$ ppm) of **3a** are missing, and the methyl protons of two ethoxycarbonyl groups are observed as a single triplet ($\delta = 1.50$ ppm). These observations indicate that the reaction between **3a** and [60]fullerene had proceeded, since the

 © 2003 Wiley-VCH Verlag GmbH & Co. KGaA, Weinheim

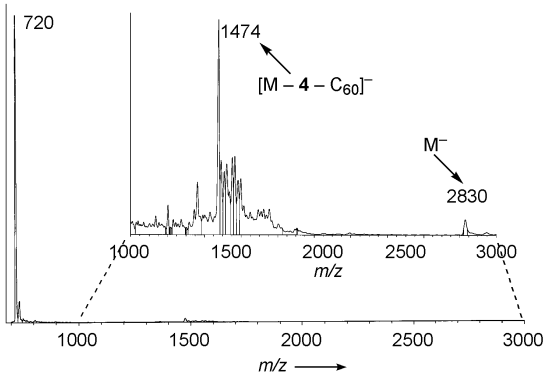


Figure 1. MALDI-TOF mass spectrum of [2]rotaxane **2a**; mode: negative; matrix: dithranol.

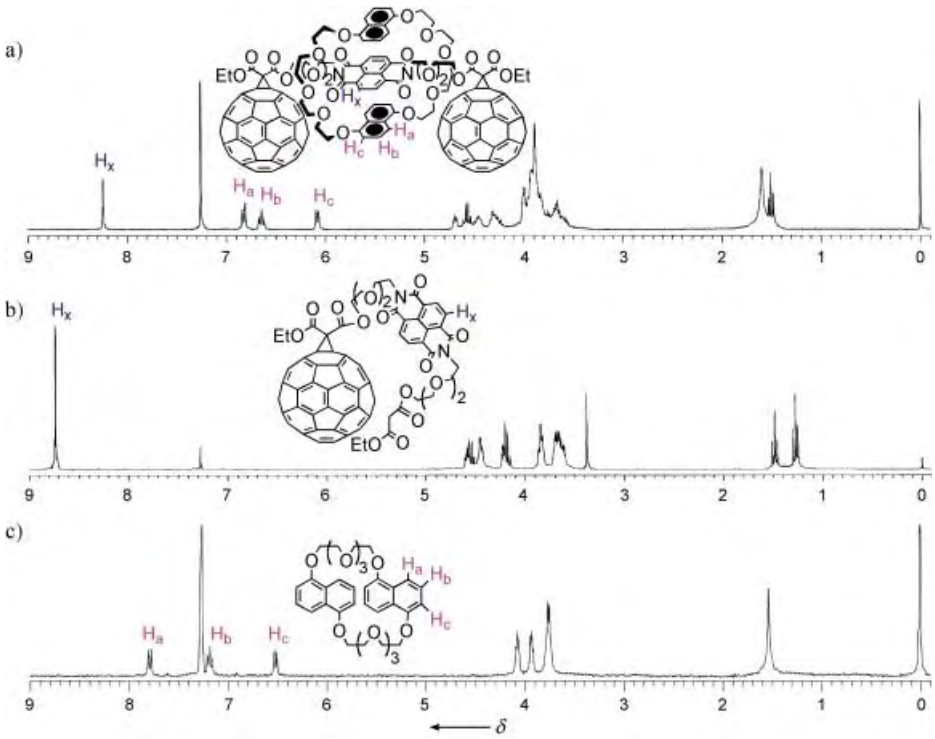
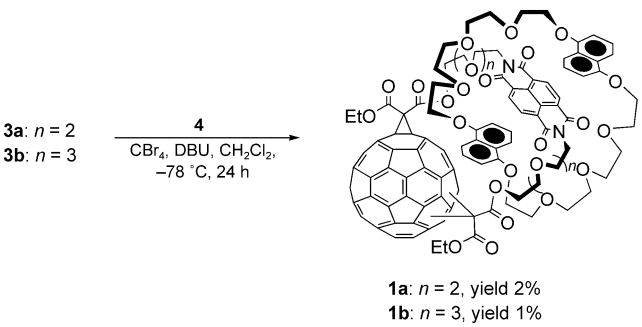


Figure 2. ^{1}H NMR spectra of a) **2a**, b) **3a**, and c) **4** in $CDCl_3$ at room temperature (300 MHz).

methyl protons in **3a** were observed as two sets of nonequivalent triplets. No aromatic proton peaks resulting from pristine **3a** and **4** were detected in **2a** (cf. Figure 2b, and c). Instead, only one set of high-field-shifted aromatic peaks of **3a** and **4** were observed. This high-field shift is ascribed to the shielding effect of the opposite aromatic groups, apparently indicating that **4** encircles the diimide moiety of **3a**, since no high-field shift was observed for the mixed solution containing dimer **5a** and **4**. The stoichiometry of **3a** and **4** was found to be 1:1 based on the integral ratio. Therefore, the data undoubtedly demonstrates that **2a** is a [2]rotaxane composed of **3a**, **4**, and [60]fullerene. [2]Rotaxane **2b** bearing longer linkages showed spectroscopic features similar to those of **2a**.

For the preparation of fullerene-based [2]catenanes **1**, the intramolecular Bingel reactions of the monoadducts **3** were examined in the presence of crown ether **4**. First, **3a** or **3b** was allowed to react with CBr_4 and DBU in the presence of **4** in CH_2Cl_2 at room temperature. However, only bisadducts that did not incorporate **4** were obtained as a regioisomeric mixture. In contrast, the reaction at −78 °C successfully afforded the desired [2]catenanes **1a** and **1b**, similar to the [2]rotaxane formation at this temperature (Scheme 3).

Compounds **1a** and **1b** were isolated and characterized in a similar fashion to **2a** and **2b**. In the MALDI-TOF mass spectrum of **1a**, the molecular-ion peak of catenane **1a** (m/z = 2110) was observed (Figure 3). The fragmentation peak (m/z = 1474) arising from the loss of **4** from cleavage of the cyclopropane ring is also detected. The relative intensity of the molecular-ion peak is much higher than that for the rotaxanes **2a** and **2b**, which suggests that **1a** has much higher stability. This is reasonably explained as follows: **1a** contains a [60]fullerene bisadduct as a building block, in which a fullerene moiety and a diimide moiety are connected through two cyclopropane rings, whereas **2a** and **2b** are both composed of two monoadduct residues possessing a single cyclopropane ring. Furthermore, the D-A-D-A stacking structure enhances the stability of **1a**. In the ^{1}H NMR spectrum of **1a**, no aromatic signals from free **3a** and **4** are detected, and the malonate methylene protons of **3a** are also missing (Figure 4). Only a set of high-field-shifted aromatic peaks of **3a** and **4** are observed. Therefore, **1a** must be a [2]catenane composed of **3a** and **4**. Compared to the ^{1}H NMR spectrum of **2a**, the signals of **1a** are subjected to considerable broadening. This suggests that the two components are tightly interlocked so that the mobility of crown ether **4** is considerably limited. [2]Catenane **1b**



Scheme 3. Synthesis of fullerene-based [2]catenanes **1**.

 © 2003 Wiley-VCH Verlag GmbH & Co. KGaA, Weinheim

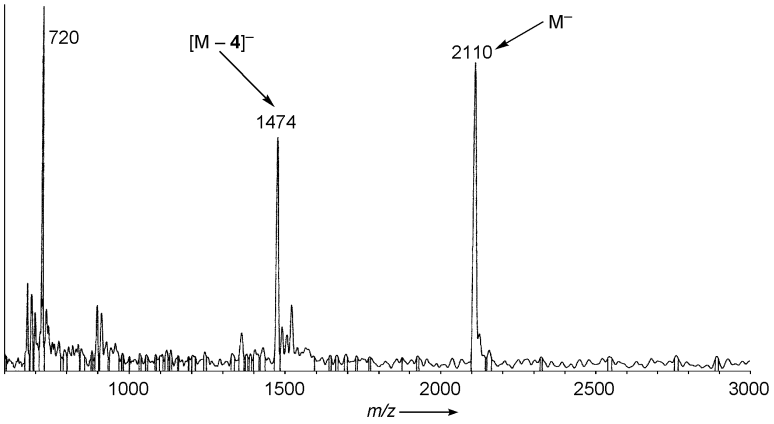


Figure 3. MALDI-TOF mass spectrum of [2]catenane **1a**; mode: negative; matrix: dithranol.

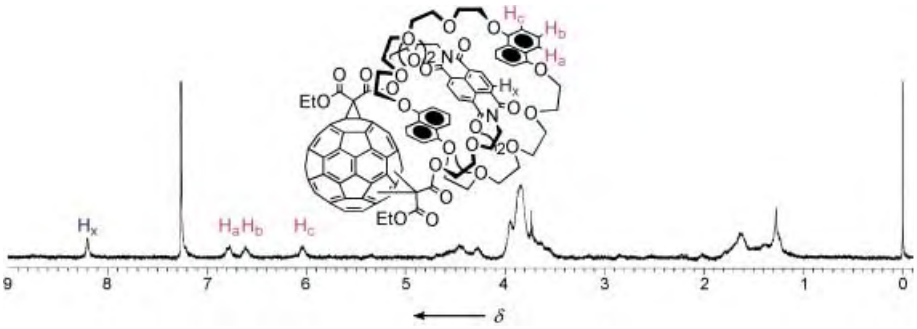


Figure 4. ^{1}H NMR spectra of [2]catenane **1a** in $CDCl_3$ at room temperature (300 MHz).

bearing longer linkages exhibited spectroscopic features similar to those of **1a**.

In summary, the intramolecular Bingel reactions of monoadducts **3a** and **3b** in the presence of **4** at −78 °C successfully afforded novel neutral [2]catenanes **1a** and **1b** with a D-A-D-A stacking structure, while the intermolecular Bingel reactions of **3a** and **3b** with [60]fullerene gave [2]rotaxanes **2a** and **2b**. The lowering of reaction temperature is critical for the formation of the [2]catenanes and [2]rotaxanes. The former is the first example of a [2]catenane in which the electron-accepting ability of [60]fullerene is explicitly involved in the catenane formation and in which [60]fullerene is a part of the cyclic components. It is noteworthy that both interlocked compounds were obtained from the same precursors. An investigation of the electrochemical, electronic, and photophysical properties of the obtained [2]catenanes and [2]rotaxanes is now in progress.

Experimental Section

2a: A solution of **3a** (219.4 mg, 0.149 mmol), **4** (565.4 mg, 0.889 mmol), and CBr_4 (493 mg, 1.49 mmol) in CH_2Cl_2 (20 mL) was added to a solution of C_{60} (1.07 g, 1.49 mmol) in CS_2 (20 mL), and the mixture was cooled down to −78 °C. Subsequently, DBU (226 mg, 1.49 mmol) was added, and then the mixture was stirred at −78 °C for 24 h under a nitrogen atmosphere. Purification of the obtained mixture by column chromatography (SiO_2, toluene/MeOH (1:1)) and GPC ($CHCl_3$) gave 21.0 mg of [2]rotaxane **2a** as a brown solid (yield 5 %). ^{1}H NMR ($CDCl_3$, 300 MHz): $\delta = 1.50$ (t, $J = 7.2$ Hz, 6H), 3.56–4.49 (m, 56H), 4.57 (q, $J = 7.1$ Hz, 4H), 4.69 (t, $J = 4.8$ Hz, 4H), 6.08 (d, $J = 7.5$ Hz, 4H), 6.65 (t, $J = 8.0$ Hz, 4H), 6.82 (d, $J = 8.3$ Hz, 4H), 8.24 ppm (s, 4H). MALDI-TOF-MS: m/z 2830 [M^-], 1474 ([M-**4**-C_{60}]$^-$).

1a: DBU (308.4 mg, 2.03 mmol) was added to a solution of **3a** (598.9 mg, 0.406 mmol), **4** (388.0 mg, 0.610 mmol), and CBr_4 (673.5 mg, 2.03 mmol) in CH_2Cl_2 (40 mL) at −78 °C, and the mixture was stirred for 24 h at the same temperature under a nitrogen atmosphere. Purification of the obtained mixture by column chromatography (SiO_2, toluene/MeOH (1:1)) and GPC ($CHCl_3$) gave 9.37 mg of [2]catenane **1a** as a brown solid (yield 2 %). ^{1}H NMR ($CDCl_3$, 300 MHz): $\delta =$ 3.45–4.69 (m, 60H), 6.03 (br, 4H), 6.61 (br, 4H), 6.77 (br, 4H), 8.20 ppm (s, 4H). MALDI-TOF-MS: m/z 2110 [M^-], 1474 ([M-**4**]$^-$).

Received: March 14, 2003 [Z51411]

Keywords: catenanes · donor–acceptor systems · fullerenes · rotaxanes · supramolecular chemistry

[1] a) A. Hirsch, *The Chemistry of the Fullerenes*, Thieme, Stuttgart, **1994**; b) F. Diederich, C. Thilgen, *Science* **1996**, *271*, 317–323; c) A. Hirsch, *Top. Curr. Chem.* **1999**, *199*, 1–65.

[2] F. Diederich, M. Gómez-López, *Chem. Soc. Rev.* **1999**, *28*, 263–277, and references therein.

[3] O. Ermer, *Helv. Chim. Acta* **1991**, *74*, 1339–1351.

[4] A. Izuoka, T. Tachikawa, T. Sugawara, Y. Suzuki, M. Konno, Y. Saito, H. Shinohara, *J. Chem. Soc. Chem. Commun.* **1992**, 1472–1473.

[5] J. D. Crane, P. B. Hitchcock, H. W. Kroto, R. Taylor, D. R. M. Walton, *J. Chem. Soc. Chem. Commun.* **1992**, 1764–1765.

[6] a) K. Tashiro, Y. Hirabayashi, T. Aida, K. Saigo, K. Fujiwara, K. Komatsu, S. Sakamoto, K. Yamaguchi, *J. Am. Chem. Soc.* **2002**, *124*, 12086–12087; b) M. Ayabe, A. Ikeda, Y. Kubo, M. Takeuchi, S. Shinkai, *Angew. Chem.* **2002**, *114*, 2914–2916; *Angew. Chem. Int. Ed.* **2002**, *41*, 2790–2792; c) J.-Y. Zheng, K. Tashiro, Y. Hirabayashi, K. Kinbara, K. Saigo, T. Aida, S. Sakamoto, K. Yamaguchi, *Angew. Chem.* **2001**, *113*, 1909–1913; *Angew. Chem. Int. Ed.* **2001**, *40*, 1857–1861; d) D. Sun, F. S. Tham, C. A. Reed, L. Chaker, M. Burgess, P. D. W. Boyd, *J. Am. Chem. Soc.* **2000**, *122*, 10704–10705; e) P. D. W. Boyd, M. C. Hodgson, C. E. F. Rickard, A. G. Oliver, L. Chaker, P. J. Brothers, R. D. Bolskar, F. S. Tham, C. A. Reed, *J. Am. Chem. Soc.* **1999**, *121*, 10487–10495; f) K. Tashiro, T. Aida, J.-Y. Zheng, K. Kinbara, K. Saigo, S. Sakamoto, K. Yamaguchi, *J. Am. Chem. Soc.* **1999**, *121*, 9477–9478; g) M. M. Olmstead, D. A. Costa, K. Maitra, B. C. Noll, S. L. Phillips, P. M. V. Calcar, A. L. Balch, *J. Am. Chem. Soc.* **1999**, *121*, 7090–7097.

[7] a) T. Anderson, G. Westman, G. Stenhagen, M. Sundahl, O. Wennerström, *Tetrahedron Lett.* **1995**, *36*, 597–600; b) Z. Yoshida, H. Takekuma, S. Takekuma, Y. Matsubara, *Angew. Chem.* **1994**, *106*, 1658–1660; *Angew. Chem. Int. Ed. Engl.* **1994**,

 © 2003 Wiley-VCH Verlag GmbH & Co. KGaA, Weinheim

33, 1597 – 1599; c) T. Anderson, K. Nilsson, M. Sundahl, G. Westman, O. Wennerström, *J. Chem. Soc. Chem. Commun.* **1992**, 604 – 606.

[8] a) H. Matsubara, S. Oguri, K. Asano, K. Yamamoto, *Chem. Lett.* **1999**, 431 – 432; b) H. Matsubara, T. Shimura, A. Hasegawa, M. Semba, K. Asano, K. Yamamoto, *Chem. Lett.* **1998**, 1099 – 1100; c) H. Matsubara, A. Hasegawa, K. Shiwaku, M. Uno, S. Takahashi, K. Yamamoto, *Chem. Lett.* **1998**, 923 – 924; d) J. L. Atwood, M. J. Barnes, M. G. Gardiner, C. L. Raston, *Chem. Commun.* **1996**, 1449 – 1450; e) J. W. Steed, P. C. Junk, J. L. Atwood, M. J. Barnes, C. L. Raston, R. S. Burkhalter, *J. Am. Chem. Soc.* **1994**, *116*, 10346 – 10347.

[9] a) T. Haino, H. Araki, Y. Fujiwara, Y. Tanimoto, Y. Fukazawa, *Chem. Commun.* **2002**, 2148 – 2149; b) T. Haino, H. Araki, Y. Fukazawa, *Tetrahedron Lett.* **2001**, *42*, 3203 – 3206; c) J. L. Atwood, L. J. Barbour, P. J. Nichols, C. L. Raston, C. A. Sandoval, *Chem. Eur. J.* **1999**, *5*, 990 – 996; d) T. Haino, M. Yanase, Y. Fukazawa, *Angew. Chem.* **1998**, *110*, 1044 – 1046; *Angew. Chem. Int. Ed.* **1998**, *37*, 997 – 998; e) K. Tsubaki, K. Takayoshi, T. Kinoshita, K. Fuji, *Chem. Commun.* **1998**, 895 – 896; f) T. Haino, M. Yanase, Y. Fukazawa, *Tetrahedron Lett.* **1997**, *38*, 3739 – 3742; g) T. Haino, M. Yanase, Y. Fukazawa, *Angew. Chem.* **1997**, *109*, 288 – 290; *Angew. Chem. Int. Ed. Engl.* **1997**, *36*, 259 – 260; h) A. Ikeda, M. Yoshimura, S. Shinkai, *Tetrahedron Lett.* **1997**, *38*, 2107 – 2110; g) N. S. Isaacs, P. J. Nichols, C. L. Raston, C. A. Sandova, D. J. Young, *Chem. Commun.* **1997**, 1839 – 1840; h) J. L. Atwood, G. A. Koutsantonis, C. L. Raston, *Nature* **1994**, *368*, 229 – 231; i) T. Suzuki, K. Nakashima, S. Shinkai, *Chem. Lett.* **1994**, 699 – 702.

[10] a) L. Sánchez, M. T. Rispens, J. C. Hummelen, *Angew. Chem.* **2002**, *114*, 866 – 868; *Angew. Chem. Int. Ed.* **2002**, *41*, 838 – 840; b) J. J. González, S. González, E. M. Priego, C. Luo, D. M. Guldi, J. de Mendoza, N. Martín, *Chem. Commun.* **2001**, 163 – 164; c) A. M. Cassell, W. A. Scrivens, J. M. Tour, *Angew. Chem.* **1998**, *110*, 1670 – 1672; *Angew. Chem. Int. Ed.* **1998**, *37*, 1528 – 1531.

[11] F. Diederich, L. Echegoyen, M. Gómez-López, R. Kessinger, J. F. Stoddart, *J. Chem. Soc. Perkin Trans. 2* **1999**, 1577 – 1586.

[12] a) S. J. Rowan, S. J. Cantrill, G. R. L. Cousins, J. K. M. Sanders, J. F. Stoddart, *Angew. Chem.* **2002**, *114*, 938 – 993; *Angew. Chem. Int. Ed.* **2002**, *41*, 899 – 952; b) *Molecular Catenanes, Rotaxanes and Knots* (Eds.: J.-P. Sauvage, C. Dietrich-Buchecker), Wiley-VCH, Weinheim, **1999**; c) F. Vögtle, T. Dunnwald, T. Schmidt, *Acc. Chem. Res.* **1996**, *29*, 451 – 460; d) D. B. Amabilino, J. F. Stoddart, *Chem. Rev.* **1995**, *95*, 2725 – 2828; e) C. O. Dietrich-Buchecker, J.-P. Sauvage, *Chem. Rev.* **1987**, *87*, 795 – 810.

[13] C. S. Foote, *Top. Curr. Chem.* **1994**, *169*, 347 – 363.

[14] a) F. Diederich, C. Dietrich-Buchecker, J.-F. Nierengarten, J.-P. Sauvage, *J. Chem. Soc. Chem. Commun.* **1995**, 781 – 782; b) N. Armaroli, F. Diederich, C. O. Dietrich-Buchecker, L. Flamigni, G. Marconi, J.-F. Nierengarten, J.-P. Sauvage, *Chem. Eur. J.* **1998**, *4*, 406 – 416.

[15] P. R. Ashton, F. Diederich, M. Gómez-López, J.-F. Nierengarten, J. A. Preece, F. M. Raymo, J. F. Stoddart, *Angew. Chem.* **1997**, *109*, 1611 – 1614; *Angew. Chem. Int. Ed. Engl.* **1997**, *36*, 1448 – 1451.

[16] a) N. Watanabe, N. Kihara, Y. Furusho, T. Takata, Y. Araki, O. Ito, *Angew. Chem.* **2003**, *115*, 705 – 707; *Angew. Chem. Int. Ed.* **2003**, *42*, 681 – 683; b) T. Da Ros, D. M. Guldi, A. F. Morales, D. A. Leigh, M. Prato, R. Turco, *Org. Lett.* **2003**, *5*, 689 – 691.

[17] a) L. Raehm, D. G. Hamilton, J. K. M. Sanders, *Synlett* **2002**, 1743 – 1761; b) D. G. Hamilton, M. Montalti, L. Prodi, M. Fontani, P. Zanello, J. K. M. Sanders, *Chem. Eur. J.* **2000**, *6*, 608 – 617; c) J. G. Hansen, N. Feeder, D. G. Hamilton, M. J. Gunter, J. Becher, J. K. M. Sanders, *Org. Lett.* **2000**, *2*, 449 – 452; d) D. G. Hamilton, L. Prodi, N. Feeder, J. K. M. Sanders, *J. Chem. Soc. Perkin Trans. 1* **1999**, 1057 – 1065; e) D. G. Hamilton, J. K. M. Sanders, *Chem. Commun.* **1998**, 1749 – 1750; f) A. C. Try, M. M. Harding, D. G. Hamilton, J. K. M. Sanders, *Chem. Commun.* **1998**, 723 – 724; g) D. G. Hamilton, N. Feeder, L. Prodi, S. J. Teat, W. Clegg, J. K. M. Sanders, *J. Am. Chem. Soc.* **1998**, *120*, 1096 – 1097; h) D. G. Hamilton, J. K. M. Sanders, J. E. Davies, W. Clegg, S. J. Teat, *Chem. Commun.* **1997**, 897 – 898.

[18] C. Bingel, *Chem. Ber.* **1993**, *126*, 1957 – 1959.

[19] X. Camps, A. Hirsch, *J. Chem. Soc. Perkin Trans. 1* **1997**, 1595 – 1596.

 © 2003 Wiley-VCH Verlag GmbH & Co. KGaA, Weinheim

Heterohelicene Derivatives

A Highly Configurationally Stable [4]Heterohelicenium Cation**

Christelle Herse, Delphine Bas, Frederik C. Krebs, Thomas Bürgi, Jacques Weber, Tomasz Wesolowski, Bo W. Laursen, and Jérôme Lacour**

Helicenes and heterohelicenes, which present fascinating left- or right-handed chiral helical structures (of *M* and *P* configuration respectively), have been intensively studied for their excellent self-assembling, chiroptical, photochromic, and nonlinear optical properties, as well as in asymmetric molecular recognition and synthesis, sensors, and polymer fields.[1,2]

The large helicenes, such as [6]helicene, are configurationally stable at room temperature.[1] The enantiomers can be separated, stored over long periods of time, and used for the above-mentioned applications. The barrier of interconversion between the *M* and *P* enantiomers of smaller [4](hetero)helicene derivatives is however much lower as the racemization takes place rapidly in solution at room

[*] Dr. B. W. Laursen
Nano-Science Center, Department of Chemistry
Universitatesparken 5, 2100 Copenhagen (Denmark)
Fax: (+45) 3532-0460
E-mail: bwl@nano.ku.dk

Prof. J. Lacour, C. Herse, D. Bas, Prof. J. Weber, Dr. T. Wesolowski
Départements de Chimie Organique et de Chimie Physique
Université de Genève
quai Ernest Ansermet 30, 1211 Genève 4 (Switzerland)
Fax: (41) 22-328-73-96
E-mail: jerome.lacour@chiorg.unige.ch

Dr. F. C. Krebs
The Danish Polymer Centre, RISØ National Laboratory
PO Box 49, 4000 Roskilde (Denmark)

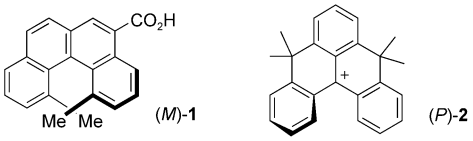
Dr. T. Bürgi
Institute of Chemical and Bioengineering, ETH-Hönggerberg
HCI D127, Wolfgang-Pauli-Strasse 10, 8093 Zürich (Switzerland)

[**] We are grateful for financial support of this work by the Swiss National Science Foundation, the Federal Office for Education and Science, and the Sandoz Family Foundation (J.L.).

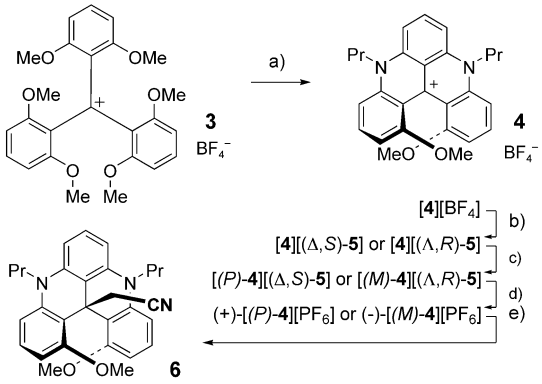
Supporting information for this article is available on the WWW under http://www.angewandte.org or from the author.

 © 2003 Wiley-VCH Verlag GmbH & Co. KGaA, Weinheim DOI: 10.1002/anie.200351443

temperature.[3] Only the 1,12-dimethylbenzo[*c*]phenanthrene derivatives **1** have been reported in a nonracemic form.[4] Newman and Wise have shown that **1** racemizes at rather high temperatures (greater than 250 °C); its enantiomeric purity and absolute configuration are however unknown. Hellwinkel and co-workers recognized that the doubly bridged triaryl carbenium ions **2**, which are charged analogs of [4]helicenes, may exhibit chirality.[5] However, only a few examples of such carbenium ions have been synthesized and investigated in this context, and none of these cationic compounds were resolved. High configurational stability of [4]helicenium compounds is, therefore, unknown and debatable.



Recently, the reactions of primary amines with the readily available salts of the known cation **3** have been described (Scheme 1).[6] Dimethoxyquinacridinium systems (**4**, pre-



Scheme 1. a) *n*PrNH$_2$, NMP, 45 min, 110 °C, 85 %; b) [Me$_2$NH$_2$][(Δ,*S*)-**5**] or [Me$_2$NH$_2$][(Λ,*R*)-**5**] (1.3 equiv), CH$_2$Cl$_2$/acetone, then chromatography (Al$_2$O$_3$, CH$_2$Cl$_2$), 96–97 %, d.r. 1:1; c) precipitation in C$_6$H$_6$/THF (3:1), 30 %, d.r. > 49:1; d) KPF$_6$ (excess), CH$_2$Cl$_2$/H$_2$O (1:1), 97 %, e.r. > 49:1; e) NaH, CH$_3$CN, 20 °C, 55 %. A *P* configuration for **4** and **6** is shown arbitrarily. NMP = *N*-methylpyrrolidone.

pared from *n*-propylamine; Scheme 1, step a) can be isolated in good yields. These compounds are the result of consecutive *ortho* S$_N$Ar reactions of the primary amines with **3**. The molecular framework of the cation contains four *ortho*-condensed aromatic rings. As such, compounds **4** may be regarded as [4](hetero)helicene derivatives. Herein, we report on the resolution, the absolute configuration assignment by vibrational circular dichroism (VCD) spectroscopy, and the very high configurational stability of **4**; this compound, prepared and resolved in only two steps from **3**, and being more stable ($\Delta G^{\neq} = 172.8\ \mathrm{kJ\,mol^{-1}}$ at 200 °C) than the famous [6]helicene.

It appeared to us that strong steric repulsions should exist between the methoxy substituents in positions 1 and 13 of compounds **4**, which would prevent the systems from being planar. These derivatives would thus adopt a twisted helical conformation typical of helicene derivatives. This was confirmed by X-ray diffraction analysis of the [**4**][Ph$_4$B] salt, which crystallized as a racemate with both enantiomers included in the structure (Figure 1).[7]

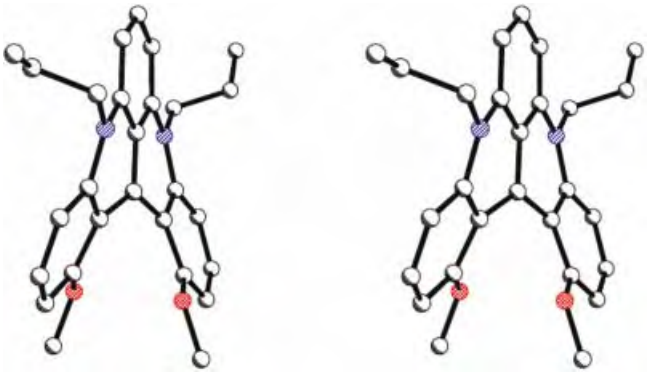
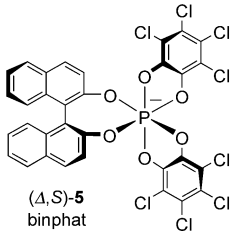


Figure 1. A stereoview showing the molecular geometry of **4** as obtained from the solved X-ray structure of the tetraphenylborate salt. The anion and the hydrogen atoms are omitted for clarity; nitrogen (blue), oxygen (red).

In the molecular structure of **4**, the two oxygen atoms are positioned exactly above one another, and their separation regulates the inner pitch of the helicenium system (2.7 Å). In the case of the carbohelicenes, such as [6]helicene, pitches of 3.2–3.3 Å were found.[1b] In this skeleton the twisting is mainly manifested in the bonds between the central carbon atom and the two methoxy-substituted rings and in the bonds between these rings and the nitrogen bridges.

The chiral nature of dimethoxyquinacridinium ion **4** was ascertained, but the degree of its configurational stability was debatable. As the determination of the racemization barrier of a chiral substance usually requires the physical separation of its enantiomers, a resolution to obtain **4** in an enantiomerically pure form was considered. For the resolution of chiral cations, the most obvious approach is to form diastereomeric salts by pairing the racemic cation with an enantiopure anion, and then attempt to separate the diastereomers through solubility differences.[8] Recently, the synthesis of the chiral hexacoordinated phosphorus-centered binphat anion (**5**) was reported (as Δ or Λ enantiomers).[9] This anion can be prepared following a three-step one-pot protocol using enantiopure binol, tetrachlorocatechol, *o*-chloranil, and P(NMe$_2$)$_3$. With (*S*)-binol, only one of the four possible diastereomers (Δδ) is usually isolated (85 % yield). This anion is an efficient NMR chiral-shift and asymmetry-inducing agent for cationic substances and, in particular, organic derivatives.[9,10]



An anion pairing of the racemic cation **4** and an enantiopure binphat anion ([(Δ,*S*)-**5**] or [(Λ,*R*)-**5**]) was therefore considered. Previously, it has been observed that anion **5** confers to its salts a poor affinity for polar chromatographic phases as they elute rapidly over basic alumina.[10b,c] For the preparation of the diastereomeric salts, solutions of racemic (±)-[**4**][BF$_4$] (1.0 equiv) in CH$_2$Cl$_2$/acetone (1:1) and of

 © 2003 Wiley-VCH Verlag GmbH & Co. KGaA, Weinheim

$[Me_2NH_2][(\Delta,S)$-**5**] or $[Me_2NH_2][(\Lambda,R)$-**5**] (1.3 equiv) in acetone were prepared and mixed together. Preparative column chromatography experiments (Al_2O_3, CH_2Cl_2) afforded salts [**4**][(Δ,*S*)-**5**] or [**4**][(Λ,*R*)-**5**] as the only eluted compounds in good yields (96–97%).

NMR spectroscopic analysis of the isolated salts revealed an efficient NMR enantiodifferentiation of chiral cation **4** by the enantiopure counterion **5**.[10] Two sets of signals were observed in both ^1H and ^{13}C NMR spectra; one for each the *P* and *M* enantiomers of **4**. Integration of the respective signals indicated a 1:1 ratio (Figure 2, spectrum b). The [**4**][(Δ,*S*)-**5**]

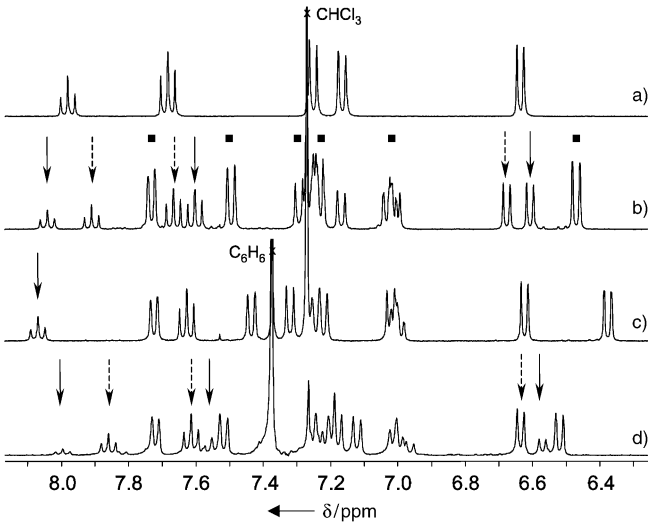


Figure 2. Sections of the ^1H NMR spectra (400 MHz, $CDCl_3$, $\delta = 8.16$–6.25 ppm) of: a) (±)-[**4**][BF_4]; b) [**4**][(Δ,*S*)-**5**], d.r. 1:1; c) [*P*-**4**][(Δ,*S*)-**5**], d.r. > 49:1; d) [**4**][(Δ,*S*)-**5**], d.r. 2.4:1. Plain and dashed arrows indicate some of the signals of [*P*-**4**][(Δ,*S*)-**5**] and [*M*-**4**][(Δ,*S*)-**5**], respectively. ■ represents the signals of anion **5**.

salt was then dissolved in a minimum amount of benzene/THF (3:1) and the resulting solution placed for 24 h at low temperature (−25 °C). After slowly warming up the solution to 20 °C, a green solid was collected by filtration (30%). This compound was analyzed by ^1H NMR spectroscopy ($CDCl_3$) which revealed the presence of a single set of signals (Figure 2, spectrum c), diastereomeric ratio d.r. > 49:1).[11] The mother liquor was concentrated in vacuo and ^1H NMR analysis revealed an excess of the other diastereomeric salt (70%; Figure 2, spectrum d), d.r. 2.4:1). From the [**4**][(Λ,*R*)-**5**] salt, similar results were obtained allowing the isolation of a solid and a mother liquor with analogous yields and selectivities. This physical separation of the diastereomeric salts demonstrated that cation **4** is configurationally stable at room temperature. The isolated diastereomerically pure or enriched fractions were converted into the hexafluorophosphate salts in near quantitative yield (97%) by treatment of the substrates with an excess of KPF_6 in CH_2Cl_2/H_2O. From [**4**][(Δ,*S*)-**5**], the salts (+)-[**4**][PF_6] (enantiomeric ratio e.r. > 49:1)[12,13] and enantioenriched (−)-[**4**][PF_6] were obtained from the solid and the mother liquor, respectively. Enantiopure (−)-[**4**][PF_6] (e.r. > 49:1)[13] was obtained using the solid fraction from [**4**][(Λ,*R*)-**5**].

Unfortunately, X-ray quality crystals of the diastereomerically pure salts could not be obtained. The absolute configuration of the separated enantiomers of **4** was determined by VCD.[14,15] A sample of (+)-[**4**][PF_6] (e.r. > 49:1) was analyzed by this method. As expected, positive and negative signals were measured (Figure 3). Using the molecular structure of **4**

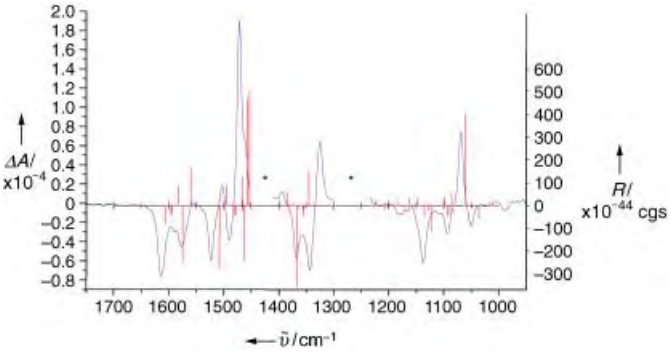


Figure 3. Experimental (blue) vibrational circular dichroism spectrum and theoretical rotational strength (red) of (+)-[(*P*)-**4**][PF_6]. The spectral region marked with asterisks was not accessible because of strong solvent absorption (*R* is the calculated rotational strength and Δ*A* is the experimental differential absorption).

determined by X-ray diffraction analysis, density functional theory (DFT) closed-shell calculations were performed using the Gaussian98 program.[16,17] A geometry was optimized for the *P* enantiomer of cation **4**. The rigidity of the molecule allows us to consider that the geometry of the minimum obtained in the gas phase is not strongly influenced by the presence of a solvent. Infrared and VCD spectra were then calculated and assigned. The simulations reproduced the overall shape of the spectrum with regards to its absorbance and sign patterns (Figure 3). The positions of the bands were quite well reproduced (within 15 cm^{-1}) and the relative intensities compared well with the experiment for the majority of the peaks. Overall, a good agreement between the experimental and theoretical spectra was observed allowing the assignment of a *P* configuration for the carbenium ion in the (+)-[**4**][PF_6] salt. For (−)-[**4**][PF_6], the predominant configuration of **4** corresponds therefore to the *M* helicity. Starting from [**4**][(Λ,*R*)-**5**], the [(*M*)-**4**][(Λ,*R*)-**5**] and [(*P*)-**4**][(Λ,*R*)-**5**] salts are thus obtained predominantly in the solid and mother liquor respectively.

The initial question of the determination of the interconversion barrier between the enantiomers of **4** could then be examined. In the literature, kinetics of the racemization of helicenes have usually involved chiroptical methods.[1a] Accurate measurements of the racemization kinetics were realized using the high rotatory power of these derivatives. Unfortunately, the intense absorption of cation **4** in the visible region limited the use of chiroptical methods.[12] To precisely analyze the racemization kinetics, an accurate chromatographic method to determine the enantiomeric purity of **4** was sought.[18]

Previously, Siegel et al. and Krebs, Laursen, and coworkers have shown that reactive carbanions can attack the center of some structurally related carbenium ions to

 © 2003 Wiley-VCH Verlag GmbH & Co. KGaA, Weinheim

generate rigid neutral molecular cavities.[19] The reactivity of acetonitrile toward [**4**][PF_6] salts was studied in the presence of NaH at room temperature, and the desired product **6**, formed by the addition of CH_2CN, was isolated (Scheme 1). Evidently, the helicity of the [4]helicene skeleton remains after the addition of the central acetonitrile moiety and **6** is therefore chiral. Supposing a high configurational stability for **4**, a similarly high barrier of racemization was foreseen for **6**; the addition of the nucleophile occurring most probably with retention of the absolute sense of the helical configuration.

From (±)-[**4**][PF_6], (−)-(*M*)-[**4**][PF_6], and (+)-(*P*)-[**4**][PF_6],[13] compounds (±)-**6**, (−)-**6**, and (+)-**6** were obtained, respectively. Chiral stationary phase (CSP) HPLC (Chiralpak AD-H, Daicel) analysis of the racemic sample (±)-**6** revealed a baseline-to-baseline separation of two peaks ($t_R = 34.9$ and 35.7 min) integrating in a 1:1 ratio. For sample (−)-**6**, an enantiomeric excess of 96.4% (major enantiomer: $t_R = 34.9$) was determined; this precise value being in full agreement with the enantiomeric purity measured by NMR for the (−)-(*M*)-[**4**][PF_6] salt.[13]

By utilizing this method, the racemization of **4** was studied. Solid samples of (−)-(*M*)-[**4**][PF_6] were heated in a metal bath, removed at given times, and reacted with CH_3CN/NaH at 20 °C to give **6**, which was analyzed by CSP-HPLC. An interconversion between the *M* and *P* enantiomers was only observed at temperatures equal to, or higher than 200 °C. Measurements at four different temperatures (200, 210, 220, and 230 °C) were performed and first-order kinetics observed. From the enantiomeric excesses determined by CSP-HPLC, the kinetic constants (k) and the activation parameters were determined (see the Supporting Information), which are summarized in Table 1. At 200 °C, the free energy of

Table 1: Racemization of (−)-(*M*)-[**4**][PF_6]. T is the experimental temperature, k the kinetic constant, $t_{1/2}$ is the half-life, $\Delta H^{\neq}$, $\Delta S^{\neq}$, and $\Delta G^{\neq}$ are the enthalpy, the entropy, and the free energy of activation, respectively.

T [°C]	k [s^{-1}]	$t_{1/2}$ [h]	$\Delta H^{\neq}$ [a]	$\Delta S^{\neq}$ [b]	$\Delta G^{\neq}$ [a]
200	1.05×10^{-6}	182.7	218.7	97.1	172.8
210	2.89×10^{-6}	66.6	218.6	96.9	171.8
220	9.5×10^{-6}	20.3	218.5	96.7	170.8
230	2.99×10^{-5}	6.4	218.5	96.6	169.9

[a] kJ mol^{-1}. [b] J mol^{-1} K^{-1}.

activation ($\Delta G^{\neq}$) of the racemization is 172.8 kJ mol^{-1} and the half-life ($t_{1/2}$) is 182.7 h. This compares favorably with the [6]helicene at 196 °C ($\Delta G^{\neq} = 154.3$ kJ mol^{-1}, $t_{1/2} =$ 13.4 min).[1a,20]

In conclusion, we have shown that the dimethoxyquinacridinium cations **4** are (hetero)helicenium cations that can be simply prepared and resolved. Kinetic measurements have demonstrated a very high configurational stability for this helical species through the use of accurate chromatography analysis. This study also includes the first application of vibrational circular dichroism in the study of chiral helical derivatives and demonstrates the very high potential of this technique.

Received: March 19, 2003 [Z51443]

Keywords: asymmetric synthesis · carbenium ions · chiral resolution · circular dichroism · helicenes

[1] a) W. H. Laarhoven, W. J. C. Prinsen, *Top. Curr. Chem.* **1984**, *125*, 63 – 130; b) K. P. Meurer, F. Vögtle, *Top. Curr. Chem.* **1985**, *127*, 1 – 76; c) T. J. Katz, *Angew. Chem.* **2000**, *112*, 1997 – 1999; *Angew. Chem. Int. Ed.* **2000**, *39*, 1921 – 1923.

[2] For recent references, see: S. D. Han, A. D. Bond, R. L. Disch, D. Holmes, J. M. Schulman, S. J. Teat, K. P. C. Vollhardt, G. D. Whitener, *Angew. Chem.* **2002**, *114*, 3357 – 3361; *Angew. Chem. Int. Ed.* **2002**, *41*, 3223 – 3227; F. Teply, I. G. Stara, I. Stary, A. Kollarovic, D. Saman, L. Rulisek, P. Fiedler, *J. Am. Chem. Soc.* **2002**, *124*, 9175 – 9180; M. C. Carreno, S. Garcia-Cerrada, A. Urbano, *Chem. Commun.* **2002**, 1412 – 1413; T. Verbiest, S. Sioncke, A. Persoons, L. Vyklicky, T. J. Katz, *Angew. Chem.* **2002**, *114*, 4038 – 4040; *Angew. Chem. Int. Ed.* **2002**, *41*, 3882 – 3884; Y. Kitahara, K. Tanaka, *Chem. Commun.* **2002**, 932 – 933; I. Sato, R. Yamashima, K. Kadowaki, J. Yamamoto, T. Shibata, K. Soai, *Angew. Chem.* **2001**, *113*, 1130 – 1132; *Angew. Chem. Int. Ed.* **2001**, *40*, 1096 – 1098; T. B. Norsten, A. Peters, R. McDonald, M. T. Wang, N. R. Branda, *J. Am. Chem. Soc.* **2001**, *123*, 7447 – 7448; K. E. S. Phillips, T. J. Katz, S. Jockusch, A. J. Lovinger, N. J. Turro, *J. Am. Chem. Soc.* **2001**, *123*, 11 899 – 11 907; M. T. Reetz, S. Sostmann, *Tetrahedron* **2001**, *57*, 2515 – 2520; F. Furche, R. Ahlrichs, C. Wachsmann, E. Weber, A. Sobanski, F. Vögtle, S. Grimme, *J. Am. Chem. Soc.* **2000**, *122*, 1717 – 1724; A. Rajca, H. Wang, M. Pink, S. Rajca, *Angew. Chem.* **2000**, *112*, 4655 – 4657; *Angew. Chem. Int. Ed.* **2000**, *39*, 4481 – 4483; D. J. Weix, S. D. Dreher, T. J. Katz, *J. Am. Chem. Soc.* **2000**, *122*, 10 027 – 10 032; M. T. Reetz, E. W. Beuttenmuller, R. Goddard, *Tetrahedron Lett.* **1997**, *38*, 3211 – 3214; A. Terfort, H. Gorls, H. Brunner, *Synthesis* **1997**, 79 – 86.

[3] S. Grimme, S. D. Peyerimhoff, *Chem. Phys.* **1996**, *204*, 411 – 417; M. K. Lakshman, P. L. Kole, S. Chaturvedi, J. H. Saugier, H. J. C. Yeh, J. P. Glusker, H. L. Carrell, A. K. Katz, C. E. Afshar, W.-M. Dashwood, G. Kenniston, W. M. Baird, *J. Am. Chem. Soc.* **2000**, *122*, 12 629 – 12 636.

[4] M. S. Newman, R. M. Wise, *J. Am. Chem. Soc.* **1956**, *78*, 450 – 454; H. Okubo, M. Yamaguchi, C. Kabuto, *J. Org. Chem.* **1998**, *63*, 9500 – 9509; H. Okubo, M. Yamaguchi, *J. Org. Chem.* **2001**, *66*, 824 – 830.

[5] D. Hellwinkel, G. Aulmich, *Chem. Ber.* **1979**, *112*, 2602 – 2608; D. Hellwinkel, G. Aulmich, W. Warth, *Chem. Ber.* **1980**, *113*, 3275 – 3293; D. Hellwinkel, G. Aulmich, M. Melan, *Chem. Ber.* **1981**, *114*, 86 – 108.

[6] B. W. Laursen, F. C. Krebs, *Angew. Chem.* **2000**, *112*, 3574 – 3576; *Angew. Chem. Int. Ed.* **2000**, *39*, 3432 – 3434; B. W. Laursen, F. C. Krebs, *Chem. Eur. J.* **2001**, *7*, 1773 – 1783.

[7] CCDC-205385 contains the supplementary crystallographic data for this paper. These data can be obtained free of charge via www.ccdc.cam.ac.uk/conts/retrieving.html (or from the Cambridge Crystallographic Data Centre, 12, Union Road, Cambridge CB2 1EZ, UK; fax: (+44) 1223-336-033; or deposit@ccdc.cam.ac.uk).

[8] E. L. Eliel, S. H. Wilen, *Stereochemistry of Organic Compounds,* 1st ed., Wiley, New York, **1994**; J. Jacques, A. Collet, S. H. Wilen, *Enantiomers, Racemates, and Resolutions,* 2nd ed., Krieger, Melbourne, **1994**.

[9] J. Lacour, A. Londez, C. Goujon-Ginglinger, V. Buss, G. Bernardinelli, *Org. Lett.* **2000**, *2*, 4185 – 4188. Note: Δ or Λ corresponds to the configuration of the P center, and δ or λ to the conformational isomerism of the binol ligand.

[10] a) C. Pasquini, V. Desvergnes-Breuil, J. J. Jodry, A. Dalla Cort, J. Lacour, *Tetrahedron Lett.* **2002**, *43*, 423 – 426; b) J. Lacour, L. Vial, C. Herse, *Org. Lett.* **2002**, *4*, 1351 – 1354; c) L. Vial, J.

 © 2003 Wiley-VCH Verlag GmbH & Co. KGaA, Weinheim

Lacour, *Org. Lett.* **2002**, *4*, 3939 – 3942; d) L. Pasquato, C. Herse, J. Lacour, *Tetrahedron Lett.* **2002**, *43*, 5517 – 5520.
[11] The configuration [(*P*)-**4**][(Δ,*S*)-**5**] was assigned in the course of the study (see below).
[12] Cation **4** is an effective dye, absorbing light efficiently in most of the visible region (ref. [6]). Very dilute solutions and restricted wavelengths were required to measure the specific optical rotations.
[13] Enantiomeric ratios determined by ^{1}H NMR spectroscopy using [Bu_4N][(Δ,*S*)-**5**] (ref. [10b]) as a chiral shift agent.
[14] L. A. Nafie, T. A. Keiderling, P. J. Stephens, *J. Am. Chem. Soc.* **1976**, *98*, 2715 – 2723; L. A. Nafie, T. B. Freedman, *Enantiomer* **1998**, *3*, 283 – 297; T. Bürgi, A. Vargas, A. Baiker, *J. Chem. Soc. Perkin Trans. 2* **2002**, 1596 – 1601.
[15] Complex electronic circular dichroism spectra were measured (see the Supporting Information). No attempts have been made to use them to assign the configuration of the [**4**][PF_6] salts. For a recent article describing modern quantum chemical methods to predict electronic circular dichroism spectra, see: C. Diedrich, S. Grimme, *J. Phys. Chem. A* **2003**, *107*, 2524 – 2539.
[16] This theoretical study was carried out applying the BP86 exchange-correlation functional of the Generalized Gradient Approximation (GGA) type with the 6-31G** basis set. See D. Bas, P.-Y. Morgantini, J. Weber, T. A. Wesolowski, *Chimia* **2003**, *57*, 173 – 174; A. D. Becke, *Phys. Rev. A* **1988**, *38*, 3098 – 3100; J. P. Perdew, *Phys. Rev. B* **1986**, *33*, 8822 – 8824.
[17] Gaussian 98 (Revision A.7), M. J. Frisch, G. W. Trucks, H. B. Schlegel, G. E. Scuseria, M. A. Robb, J. R. Cheeseman, V. G. Zakrzewski, J. A. Montgomery, R. E. Stratmann, J. C. Burant, S. Dapprich, J. M. Millam, A. D. Daniels, K. N. Kudin, M. C. Strain, O. Farkas, J. Tomasi, V. Barone, M. Cossi, R. Cammi, B. Mennucci, C. Pomelli, C. Adamo, S. Clifford, J. Ochterski, G. A. Petersson, P. Y. Ayala, Q. Cui, K. Morokuma, D. K. Malick, A. D. Rabuck, K. Raghavachari, J. B. Foresman, J. Cioslowski, J. V. Ortiz, B. B. Stefanov, G. Liu, A. Liashenko, P. Piskorz, I. Komaromi, R. Gomperts, R. L. Martin, D. J. Fox, T. Keith, M. A. Al-Laham, C. Y. Peng, A. Nanayakkara, C. Gonzalez, M. Challacombe, P. M. W. Gill, B. G. Johnson, W. Chen, M. W. Wong, J. L. Andres, M. Head-Gordon, E. S. Replogle, J. A. Pople, Gaussian, Inc., Pittsburgh, PA, **1998**.
[18] CSP-HPLC can be used to resolve helicenes, for example, C. Stammel, R. Frohlich, C. Wolff, H. Wenck, A. de Meijere, J. Mattay, *Eur. J. Org. Chem.* **1999**, 1709 – 1718.
[19] M. Lofthagen, R. V. Clark, K. K. Baldridge, J. S. Siegel, *J. Org. Chem.* **1992**, *57*, 61 – 69; B. W. Laursen, F. C. Krebs, M. F. Nielsen, K. Bechgaard, J. B. Christensen, N. Harrit, *J. Am. Chem. Soc.* **1998**, *120*, 12255 – 12263.
[20] The barrier of racemization for **4** and the nature of the transition state are currently under investigation by DFT calculations. These results will be published in detail elsewhere.

 © 2003 Wiley-VCH Verlag GmbH & Co. KGaA, Weinheim

Triple-Stranded Helicates

A Self-Assembled Tetracopper Triple-Stranded Helicate: Towards the Controlled Synthesis of Finite One-Dimensional Magnetic Chains**

Craig J. Matthews, Stuart T. Onions, Gérald Morata, Lisa J. Davis, Sarah L. Heath, and Daniel J. Price*

The majority of self-assembled metallic helicates contain two metal centers, whilst those containing three or more remain quite rare.[1] The limitation to synthesizing high-nuclearity helicates appears to be the design of the organic ligand, since double- and quadruple-stranded helicates containing five[2] and nine[3] metal centers, respectively, have been reported. This is in contrast to triple-stranded helicates, which have not progressed beyond the inclusion of three metal centers.[4] The apparent lack of high-nuclearity helicates has undoubtedly limited the exploitation of these systems, which is currently driven towards the development of molecular devices having predetermined properties and functions such as chirality,[5] energy transfer,[6] metal–metal bonding,[7] and DNA groove binding.[8] Surprisingly, helicates exhibiting magnetic exchange remain scarce,[9] since the adjacent metal ions are often bridged by long spacers that preclude viable super-exchange pathways. However the preparation of high-nuclearity helicates with adjacent metal centers bridged by a single atom, or groups of atoms, provide an ideal opportunity to study the magnetic exchange between fixed numbers of paramagnetic metal centers in an isolated finite one-dimensional (1D) system. These systems could serve as useful models to provide further insights into the magnetic properties of infinite 1D magnetic-chain compounds,[10] which occupy an intermediate position between zero-dimensional clusters and 3D extended lattices, and as building blocks for future supramolecular devices.[11] Consequently we have embarked upon a program to exploit the helical structural

[*] Dr. C. J. Matthews, S. T. Onions, G. Morata, L. J. Davis
Department of Chemistry and Physics
Nottingham Trent University
Clifton Lane, Nottingham, NG11 8NS (UK)
Fax: (+44) 115-848-6636
E-mail: craig.matthews@ntu.ac.uk

Dr. S. L. Heath
Department of Chemistry
The University of Manchester
Oxford Road, Manchester, M13 9PL (UK)

Dr. D. J. Price
Department of Chemistry
University of Southampton
Highfield, Southampton, SO17 1BJ (UK)

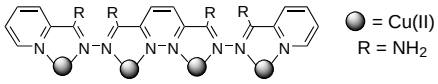
[**] Financial support from The Nottingham Trent University, The Royal Society (University Research Fellowship to S.L.H. and equipment grant to C.J.M.), The Nuffield Foundation (NAL/00237/G), and EPSRC (Advanced Research Fellowship to D.J.P.) is gratefully acknowledged. We thank the EPSRC National Crystallography Service for preliminary structural data.

Supporting information for this article is available on the WWW under http://www.angewandte.org or from the author.

 © 2003 Wiley-VCH Verlag GmbH & Co. KGaA, Weinheim DOI: 10.1002/anie.200351634

motif as a means of producing finite 1D magnetic chains in a controlled manner.

We now report the synthesis, structural characterization, and magnetic properties of the first triple-stranded helicate containing four metal centers $[Cu_4(L)_3](ClO_4)_8 \cdot 14H_2O$ (**1**) that exhibits intramolecular magnetic exchange between metal centers and is formed through the self-assembly of ligand L and $Cu(ClO_4)_2 \cdot 6H_2O$ (the preparation of ligand L is given in the Supporting Information). The design and synthesis of L was adapted from the pd2am ligand (pd2am = *N*-(bis(pyridine-2-amidine)pyridazine-3′,6′-dicaboxyamido)), which has produced a trinuclear nickel(II) triple-stranded helicate[9a] and a dodecanuclear copper(II) 4×4 gridlike assembly[12] that both suffer from incomplete metal-ion coordination. Replacement of the amide linkage within pd2am for a more innocuous amidrazone linkage through the reaction of the imidate ester of 3,6-dicyanopyridazine with pyridine-2-amidrazone in dry MeOH affords the ligand L in 91% yield and presents it with a linear arrangement of alternating sequences of bridging $N{-}N_{diazine}$ and $N{-}N_{pyridazine}$ bidentate binding sites that are capable of coordinating four adjacent metal centers (Scheme 1). This sequencing of



Scheme 1.

flexible and rigid N_2–azine binding sites within the ligand framework provides a route to propagate magnetic exchange between metal centers, as well as providing the subtle steric constraints to favor helical formation as opposed to other oligonuclear species when self-assembled with octahedral metal centers.

Reaction of L with $Cu(ClO_4)_2 \cdot 6H_2O$ (3:4) in aqueous acetonitrile yielded dark-brown crystals (78% yield), which upon standing for three weeks were found suitable for X-ray diffraction. The structure[13] of the cation in **1** (Figure 1) consists of three ligand strands that twist around a pseudo-linear array of four six-coordinate Cu^{II} centers (Cu1-Cu2-Cu3 172.0°; Cu2-Cu3-Cu4 171.6°) that defines the helical axis. The bending of the Cu_4 chain is slight in comparison to the only other known tetranuclear copper(II) chain compound where a marked curvature is observed.[14] The long external dimension of the helicate is approximately 18 Å and the internal Cu1–Cu4 distance is 11.149(1) Å, with adjacent copper–copper separations of Cu1-Cu2 3.743(1), Cu2-Cu3 3.743(1), and Cu3-Cu4 3.730(1) Å. The ligands experience a significant degree of twisting about the flexible $N{-}N_{diazine}$ bonds, which is reflected by the disposition of the pyridine rings that point in approximately opposite directions. The twist experienced by each ligand between adjacent copper centers can be estimated by examining the angles between the least-squares planes of the pyridyl amidrazone (N_{py}-C-C-$N_{diazine}$) and the pyridazyl amidrazone ($N_{diazine}$-C-C-$N_{pyridazine}$) chelating subunits. Angles between adjacent $N{-}N_{diazine}$-bridged Cu centers fall in the range 75–89° and are consistent with the M_2L_3 pyridylimine-based helicates[9c,15] containing methyl or amine side chains, whereas adjacent $N{-}N_{pyridazine}$-bridged Cu centers are essentially coplanar (3–11°), which highlights the rigidity of this bridging group. The four copper centers (Figure 1) have distorted octahedral geometries, which becomes gradually more pronounced from Cu1 through to Cu4, and is manifested through the tapering of the ligands towards the Cu4 end of the helicate. The Cu1 center could be regarded as having a square-based pyramidal geometry (axial: Cu-N13 2.203(2); equatorial: Cu-N 1.997–2.063 Å, with an extremely long Cu-N3 contact of 2.408(7) Å occupying the sixth site. An elongated tetragonal geometry is observed for Cu2 (axial: Cu-N18 2.267(2) Å; Cu-N28 2.247(2) Å; equatorial: Cu-N 1.989–2.088 Å) in comparison to Cu3 and Cu4, which have no obvious axis of elongation but do have a substantial range of bond lengths (Cu3 1.974–2.313 Å; Cu4 2.019–2.225 Å). This type of coordination environment has been observed for a dicopper(II) double-stranded helicate and has been described as a dynamic Jahn–Teller effect.[16] It appears to have arisen in this case as a result of the stereoelectronic preference of the metal ion, rather than being imposed by the disposition of binding sites within the ligand. Examination of a solution of redissolved crystals of **1** in acetonitrile by electrospray mass spectroscopy at various cone voltages displayed four sets of peaks that correspond to the species $[Cu_4L_3(ClO_4)_n]^{8-n}$ ($n = 3$–6) together with their acetonitrile adducts. No other discernible peaks were observed, which indicates that the helical Cu_4L_3 motif is preserved in solution.

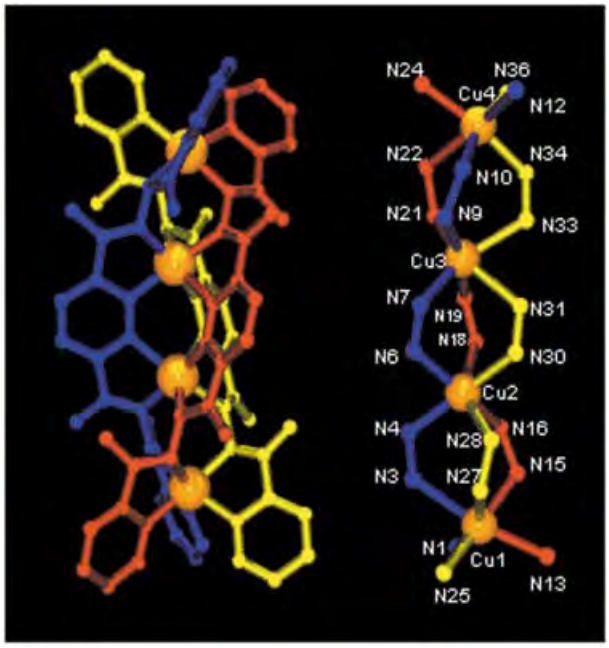


Figure 1. Left: POV-Ray structural representation of the $[Cu_4L_3]^{8+}$ cation in **1** (hydrogen atoms omitted for clarity). Right: tetranuclear core in **1**. Selected bond lengths [Å]. Cu1: N3 2.408(7), N13 2.203(7), N1 2.063(7), N27 2.045(7), N15 2.015(7), N25 1.997(8); Cu2: N18 2.267(8), N28 2.248(7), N30 2.089(7), N16 2.048(7), N6 2.000(6), N4 1.990(8); Cu3: N31 2.312(7), N33 2.178(8), N7 2.151(7), N21 2.045(7), N19 1.988(7), N9 1.974(7); Cu4: N10 2.212(8), N12 2.163(9), N22 2.225(7), N36 2.119(9), N24 2.019(7), N34 2.016(7).

 © 2003 Wiley-VCH Verlag GmbH & Co. KGaA, Weinheim

The magnetic susceptibility of a powdered sample of **1** was measured (Figure 2). The room temperature moment of 1.99(1) μ_B corresponds to an average g value of 2.29 per Cu^{II} center. The sample obeys a Curie–Weiss law over the entire measured thermal range with $C = 0.493(2)$ cm^3 mol^{-1} K

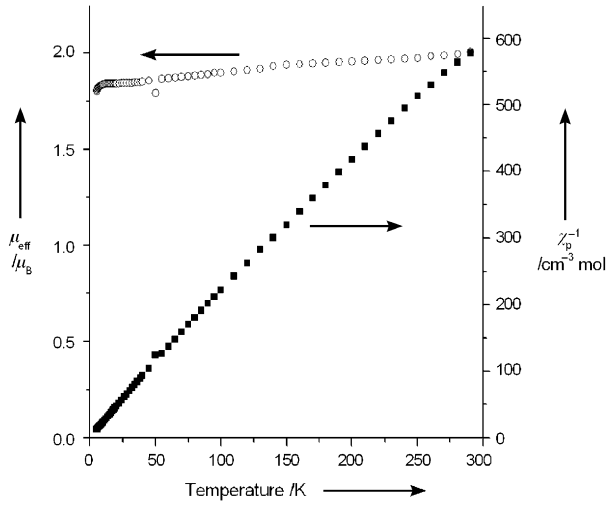


Figure 2. Reciprocal magnetic susceptibility and the effective magnetic moment as a function of temperature. The data reveals the weakness of the interactions between neighboring copper ions in the linear unit.

and $\theta = -4.6(6)$ K per Cu^{II} center, which suggests a lack of significant coupling. Alternatively, the small negative Weiss constant could be equated with a small antiferromagnetic exchange interaction between adjacent Cu^{II} ions. Attempts to extract values for the coupling constants by modeling the data as a tetranuclear system of interacting $S = 1/2$ ions were unsatisfactory. A successful fit of thermal susceptibility data relies on changes in the relative populations of the different states. In this case the very small size of the magnetic interactions (as inferred from the Curie–Weiss behavior) results in all eight magnetic states being closely spaced and at much lower energies, thus throughout the 5 to 280 K experimental range all states are almost equally populated.

Structural considerations can help to explain why the coupling is so small in **1**. While diazine and pyridazine bridges can mediate a significant antiferromagnetic exchange interaction[9c,17] the value of this coupling is very dependant on the copper coordination geometry. This is because the magnetic orbitals are normally $d_{x^2-y^2}$, and the relative geometry of these orbitals on neighboring copper ions is crucial to the sign and magnitude of the coupling constant. In **1** the local xy plane of the Cu1 and Cu2 ions is tilted from one metal ion to the next; more significantly the helical structure of the complex imposes a twist between the local crystal-field x and y axes of neighboring copper ions. The effect of this twist is to reduce the overlap integral responsible for the antiferromagnetic exchange contribution. A twist of 45° between the x and y axes in neighboring copper ions results in strictly orthogonal orbitals and a value of zero for the overlap integral. The corresponding reduction in the antiferromagnetic component to the coupling often allows an underlying ferromagnetic exchange interaction to become dominant. In our case it is likely that the twisted structure results in a near balance between antiferromagnetic and ferromagnetic components to the exchange coupling. The Cu–N bond-length distribution for Cu3 and Cu4 makes it difficult to be sure of the magnetic orbitals on these ions.

In conclusion, this report has demonstrated that a tetranuclear "magnetic" helicate can be generated through a strict self-assembly process between the single octadentate ligand L and Cu^{II} ions. The helicate can be classed as being saturated and homotopic as the coordination algorithm of the four octahedral Cu^{II} centers is exactly matched by the three symmetrical ligands. Efforts are currently being driven in several directions that are centered on examining the coordination properties of L with other metals and increasing the number of metal centers by incorporating additional or alternative diazine-chelating subunits within the ligand framework.

Experimental Section

1: Elemental analysis (%) calcd for $[Cu_4(C_{18}H_{18}N_{12})_3](ClO_4)_8 \cdot 14H_2O$: C 25.9, H 3.3, N 20.1; found (vacuum-dried sample): C 26.1, H 2.9, N 19.8; IR (nujol mull): $\tilde{\nu} = 3584$ (sh; ν_{H_2O}), 3331 (ν_{NH/H_2O}), 1659 (ν_{CN}), 1074 cm^{-1} (ν_{ClO_4}); UV/Vis (nujol mull): $\tilde{\nu} = 785$ nm; (MeCN): 785 nm (60).

Field-cooled magnetization studies were performed on a Quantum Design SQUID magnetometer operating at 0.02 T between 5 and 280 K. The powdered sample was held in an eicosane matrix to prevent reorientational effects. Corrections were made for diamagnetism including the samples inherent contribution estimated from Pascal's constants[10] to be -293×10^{-6} cm^3 mol^{-1} (all molar quantities are given per Cu ion).

Received: April 11, 2003 [Z51634]
Published online: June 23, 2003

Keywords: copper · helical structures · magnetism · N ligands · self-assembly

[1] a) M. Albrecht, *Chem. Rev.* **2001**, *101*, 3457–3497; b) C. Piguet, G. Bernardinelli, G. Hopfgartner, *Chem. Rev.* **1997**, *97*, 2005–2062; c) A. F. Williams, *Chem. Eur. J.* **1997**, *3*, 15–19.
[2] J.-M. Lehn, A. Rigault, *Angew. Chem.* **1988**, *100*, 1099–1100; *Angew. Chem. Int. Ed. Engl.* **1988**, *27*, 1095–1096.
[3] S. M. Peng, C. C. Wang, Y. L. Jang, Y. H. Chen, F. Y. Li, C. Y. Mou, M. K. Leung, *J. Magn. Magn. Mater.* **2000**, *209*, 80–83.
[4] a) R. Kramer, J.-M. Lehn, A. De Cian, J. Fischer, *Angew. Chem.* **1993**, *105*, 764–767; *Angew. Chem. Int. Ed. Engl.* **1993**, *32*, 703–706; b) B. Bocquet, G. Bernardinelli, N. Ouali, S. Floquet, G. Hopfgartner, C. Piguet, *Chem. Commun.* **2002**, 930–931.
[5] a) U. Knof, A. von Zelewsky, *Angew. Chem.* **1999**, *111*, 312–333; *Angew. Chem. Int. Ed.* **1999**, *38*, 302–322; b) M. Albrecht, *Chem. Eur. J.* **2000**, *6*, 3485–3489.
[6] C. Piguet, J.-C. G. Bunzli, *Eur. J. Solid State Inorg. Chem.* **1996**, *33*, 165–174.
[7] F. A. Cotton, L. M. Daniels, C. A. Murillo, X. Wang, *Chem. Commun.* **1999**, 2461–2462.
[8] M. J. Hannon, V. Moreno, M. J. Prieto, E. Moldrheim, E. Sletten, I. Meistermann, C. J. Isaac, K. J. Sanders, A. Rodger, *Angew. Chem.* **2001**, *113*, 903–908; *Angew. Chem. Int. Ed.* **2001**, *40*, 880–884.

 © 2003 Wiley-VCH Verlag GmbH & Co. KGaA, Weinheim

[9] a) L. K. Thompson, C. J. Matthews, L. Zhao, C. Wilson, M. A. Leech, J. A. K. Howard, *J. Chem. Soc. Dalton Trans.* **2001**, 2258 – 2263; b) G. Aromi, P. Carrero Berzal, P. Gamez, O. Roubeau, H. Kooijman, A. L. Spek, W. L. Driessen, J. Reedijk, *Angew. Chem.* **2001**, *113*, 3552 – 3554; *Angew. Chem. Int. Ed.* **2001**, *40*, 3444 – 3446; c) Z. Xu, L. K. Thompson, D. O. Miller, H. J. Clase, J. A. K. Howard, A. E. Goeta, *Inorg. Chem.* **1998**, *37*, 3620 – 3627.

[10] See for example, O. Kahn, *Molecular Magnetism*, VCH, Weinheim, **1993**.

[11] J. K. Bera, K. R. Dunbar, *Angew. Chem.* **2002**, *114*, 4633 – 4637; *Angew. Chem. Int. Ed.* **2002**, *41*, 4453 – 4457.

[12] C. J. Matthews, S. T. Onions, G. Morata, M. Bosch Salvia, M. R. J. Elsegood, D. J. Price, *Chem. Commun.* **2003**, 320 – 321.

[13] Crystal data for **1**: $C_{54}H_{82}N_{36}O_{46}Cl_9Cu_4$, brown plate, $0.10 \times 0.30 \times 0.39$ mm, triclinic, $P\bar{1}$, $a = 12.0630(14)$, $b = 17.4593(20)$, $c = 22.9083(26)$ Å, $\alpha = 89.095(2)$, $\beta = 82.266(2)$, $\gamma = 88.020(2)°$, $V = 4777.7(9)$ Å^3, $Z = 2$, $\rho_{calcd} = 1.769$ g cm^{-1}, $2\theta_{max} = 46.74°$, $\lambda(Mo_{K\alpha}) = 0.71073$ Å, $\mu = 1.243$ mm^{-1} (no absorption correction applied), 39524 reflections were recorded of which 13771 were unique ($R_{int} = 0.0663$) and 8394 had $F > 2\sigma(F)$. The structure was solved by direct methods, all hydrogen atoms were placed in idealized positions, all other atoms were refined anisotropically by a full-matrix least-squares method on F^2 to give $R1 = 0.0691$ (2σ data), $wR2 = 0.2090$, $S = 1.036$ (all data), max./min. residual electron density $+1.578/-1.678$ e Å^{-3}. CCDC-207896 (**1**) contains the supplementary crystallographic data for this paper. These data can be obtained free of charge via www.ccdc.cam.ac.uk/conts/retrieving.html (or from the Cambridge Crystallographic Data Centre, 12, Union Road, Cambridge CB21EZ, UK; fax: (+44) 1223-336-033; or deposit@ccdc.cam.ac.uk). A number of restraints were applied to the model. In particular the bond lengths, bond angles, and thermal parameters of the perchlorate counterions were restrained to be similar. Orientational and positional disorder was observed for many of these anions. In addition, the anisotropic thermal parameters of the terminal pyridyl rings in the ligand have been restrained to a rigid group model.

[14] G. Aromi, P. Gamez, O. Roubeau, H. Kooijman, A. L. Spek, W. L. Driessen, J. Reedijk, *Angew. Chem.* **2002**, *114*, 1216 – 1218; *Angew. Chem. Int. Ed.* **2002**, *41*, 1168 – 1170.

[15] a) G. Dong, P. Ke-liang, D. Chun-ying, H. Cheng, M. Qing-jin, *Inorg. Chem.* **2002**, *41*, 5978 – 5985; b) J. Hamblin, A. Jackson, N. W. Alcock, M. J. Hannon, *J. Chem. Soc. Dalton Trans.* **2002**, 1635 – 1641; c) P. D. W. Boyd, M. Gerloch, G. Sheldrick, *J. Chem. Soc. Dalton Trans.* **1974**, 1097 – 1102.

[16] C. R. Rice, S. Worl, J. C. Jeffery, R. L. Paul, M. D. Ward, *J. Chem. Soc. Dalton Trans.* **2001**, 550 – 559.

[17] a) Z. Xu, L. K. Thompson, C. J. Matthews, D. O. Miller, A. E. Goeta, C. Wilson, J. A. K. Howard, M. Ohba, H. Ōkawa, *J. Chem. Soc. Dalton Trans.* **2000**, 69 – 77.

 © 2003 Wiley-VCH Verlag GmbH & Co. KGaA, Weinheim

Thermoreversible Polymers

Influence of Cyclodextrin Molecules on the Synthesis and the Thermoresponsive Solution Behavior of *N*-Isopropylacrylamide Copolymers with Adamantyl Groups in the Side-Chains

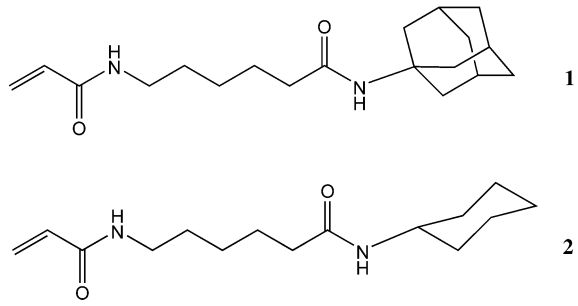
Helmut Ritter, Oleg Sadowski, and Elmar Tepper*

The thermoresponsive effect describes a property of water-soluble, or organic-solvent-soluble polymers that show an inverse phase behavior. These polymers are soluble at low temperature and precipitate spontaneously on heating; a typical example of such a polymer is poly(*N*-isopropylacrylamide).[1] The temperature range in which the phase separation out of water occurs is less than 1 K, this sharp transition can be easily determined by turbidity measurements. The temperature of this transition, which is known as lower critical solution temperature (LCST), is 34 °C in a pure aqueous solution, and is almost independent of the concentration and the molecular weight of the polymers.[2] Nevertheless, the LCST depends on the solvent composition,[3] on the type and quantity at salts or detergents,[4] as well as on the structure of the polymers, which can be varied by installation of comonomers.[5] LCST characteristics of polymers open up various possibilities for their use as, for example, thermally isolable carriers of biologically active reagents[6] or as temperature-sensitive analytical systems for complex material classes.

Herein, the influences of polymer-bound adamantyl and cyclohexyl components on the LCST of the corresponding *N*-isopropylacrylamide copolymers are investigated for the first time. The dominant aspect was the supramolecular effect between the cyclodextrins (CDs) and the adamantyl side chains. Supramolecular effects, such as host–guest interactions, have been studied in detail for polymers.[7] To date there are no examples of the LCST of thermoreversible polymers being controlled through noncovalent interactions with CD additives in water.

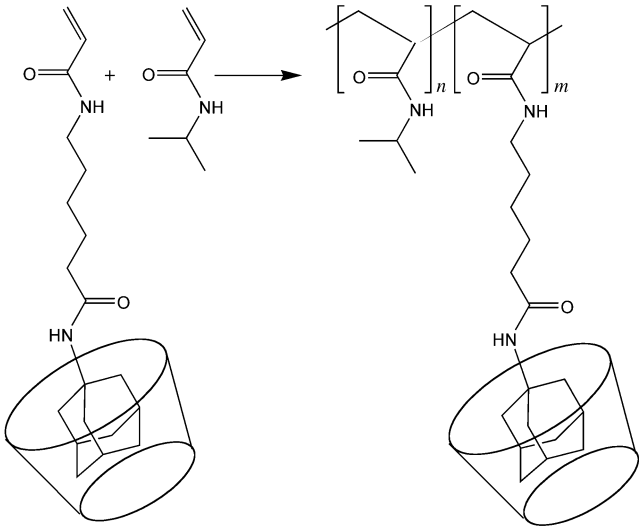
The acrylamide monomer **1** was synthesized,[8] it contains an adamantyl group linked through a short spacer. A second monomer **2**, which contains a cyclohexyl group was also prepared for comparative purposes.[9]

Industrially, vinyl monomers are predominantly polymerized radically in bulk, but also in solution or in aqueous emulsion. In the typical emulsion polymerization, however, only monomers that are water-soluble and liquid are applicable. To overcome these restrictions, we have been examining for some years the polymerization behavior of monomers which form inclusion complexes with CDs.[10] Thus the polymerization reactions were carried out in an aqueous solution of *N*-isopropylacrylamide (NIPAAM) and the inclusion complex formed between monomer **1** and 2,6-dimethyl-β-CD (Me_2-β-CD).[11] Monomer **1**, which is very sparingly soluble in water, spontaneously forms the water-soluble complex **3** on addition of an equimolar quantity of Me_2-β-CD. Complex **3** can be polymerized with a redox initiation system, in water, without any emulsifying agent (Scheme 1).[12]



1

2



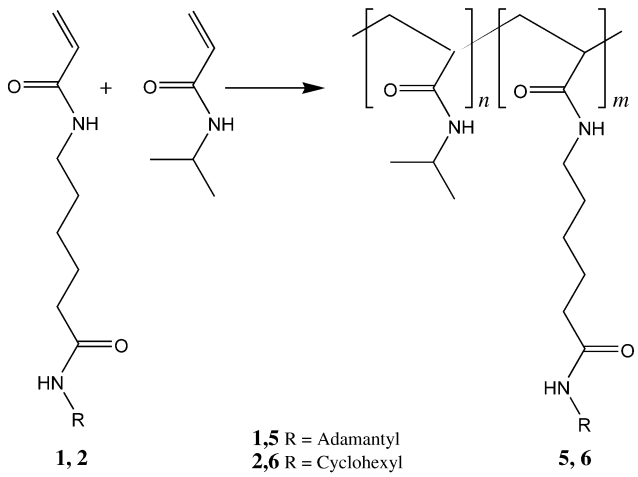
3 **4**

Scheme 1. Radically copolymerization of complex **3** and NIPAAM; $n/m = 20:1$.

After polymerization the aqueous reaction mixture was dialyzed for two days, then freeze dried. Gel-permeation chromatography (GPC)[13] of the resulting adamantyl-containing copolymer **4** showed it to include of the original amount of β-CD, which indicates a high affinity of the polymer **4** to β-CD. Thus the adamantyl side groups in the polymer **4** must form a stable complex with the cyclodextrin during the dialysis, otherwise free cyclodextrin would diffuse through the pores of the dialysis tube. Under the conditions of the GPC (use of DMF as solvent) the cyclodextrin molecules detach and are eluted, corresponding to their molecular weights, after the polymer.

[*] Prof. Dr. H. Ritter
Institut für Organische Chemie und
Makromolekulare Chemie II
Heinrich-Heine-Universität Düsseldorf
Universitätsstrasse 1, 40225 Düsseldorf (Germany)
Fax: (+49) 211-811-5840
E-mail: h.ritter@uni-duesseldorf.de
Dr. O. Sadowski, Dipl.-Chem. E. Tepper
Intitut für Organische Chemie
Johannes-Gutenberg-Universität Mainz
Duesbergweg 10–14, 55099 Mainz (Germany)

 DOI: 10.1002/anie.200250814 © 2003 Wiley-VCH Verlag GmbH & Co. KGaA, Weinheim



Scheme 2. Radical copolymerization of **1** and **2** with NIPAAM in DMF without any host compound; $n/m = 20{:}1$.

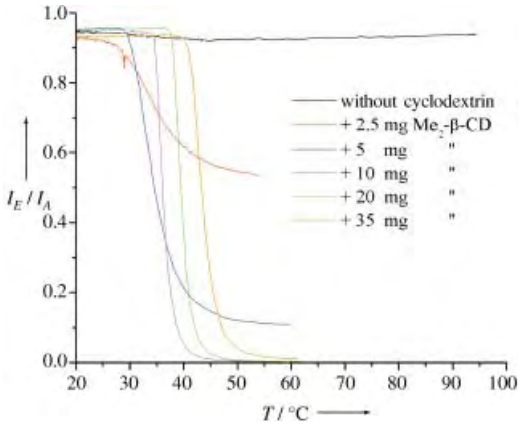


Figure 1. Influence of the Me_2-β-CD amount on the optical turbidity of a solution of copolymer **5** (7.5 mg in 3 mL water) for the determination of LCST; I_E/I_A = transmittance [670 nm].

To examine the dependence of the LCST behavior of these copolymers upon the CD quantity, the radical copolymerization **1** with NIPAAM in a 1:20 ratio, in DMF, without any addition of CD was carried out (Scheme 2).[14] As a comparison, the copolymer **6**, from cyclohexyl monomer **2** and NIPAAM (ratio 1:20), and a NIPAAM homopolymer **7** were prepared by the same method. Optical turbidity measurements[15] showed no LCST for aqueous solutions of **5** up to 95 °C. On the other hand, solutions of **6** have a transition at 31 °C, which is near (4 °C lower than) that of **7** (Table 1). The lower LCST for **6** than **7** is attributed to the

Table 1: The properties of the synthesized copolymers.

Polymer	LCST [°C]	n/m	M_n [g mol^{-1}][a]	M_w/M_n[a]
5	>95	1:20	17400	2.90
6	31	1:20	16100	3.58
7	35	–	71000	6.18

[a] Ref. [13].

hydrophobic effect,[2] which is the decrease of the LCST with increasing numbers of hydrophobic side-chain groups. This effect is essentially the result of the temperature dependent stability of clathrat cages of water molecules, which form around the hydrophobic components, and thus increase water solubility. Because of the presence of the spherical hydrophobic adamantyl groups in **5**, a polymer–polymer interaction is clearly so impeded that phase separation does not occur, although the hydrophobic contribution is as large as in **6**.

Through addition of Me_2-β-CDs[8] to a solution of **5**, the LCST drastically decreases to around 40 °C. In Figure 1, a layout is shown for turbidity curves for different Me_2-β-CD concentrations. The influence of CD concentration on the degree of turbidity up to the value, after which a shift in the LCST to higher temperatures results (after the addition of 20 mg CD), is clearly shown. A comparable effect also appears on addition of native β-cyclodextrin to a solution of **5**. On the other hand, additions of D-glucose to a solution of **5** has no effect on the LCST. Additions of Me_2-β-CD to a solution of pure **7** cause no change in the LCST. This observation is compatible with results from other groups[16] which show that physical mixing of CD and poly(NIPAAM) causes no significant changes to the LCST. On the other hand, a dependence of the LCST of poly(NIPAAM) with CD, is found when these components are "threaded" before polymerization. In contrast to the LCST depression in **5**, cyclodextrin threaded on the main chain of poly(NIPAAM) resulted in an increase of the LCST.[16]

In our case, because of their stabile inclusion in CD-rings, the adamantyl groups support the intermolecular association ability of the polymer strands to the extent that the LCST drastically decreases. In the cyclohexyl-containing copolymer **6**, on the other hand, there is only a slight tendency to form stable inclusion complexes with the CDs.[17]

To investigate the stability of the CD included, polymer-bounded adamantyl groups, an aqueous solution of **5** was mixed with the quantity of Me_2-β-CD (10 mg) that causes the maximum turbidly in the LCST. Subsequently, the solution was treated with increasing amounts of the small molecule potassium-1-adamantylcarboxylate (**8**), which should compete with the polymer-bounded adamantyl groups (Figure 2).



8

As shown in Figure 3, the expected effect could be clearly detected by the loss of turbidity intensity. With two equivalents of potassium-1-adamantylcarboxylate (4 mg), the CD is largely displaced from the polymer.

With the adamantyl containing *N*-isopropylacrylamide copolymers, it could be shown how the LCST behavior can be

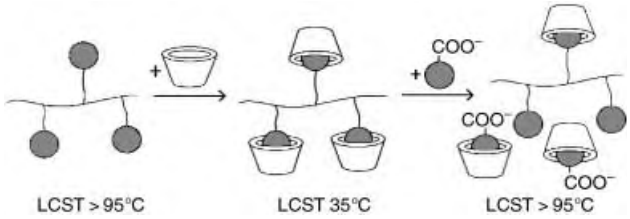


Figure 2. The interaction of **5** with CD and potassium-1-adamantylcarboxylate.

 © 2003 Wiley-VCH Verlag GmbH & Co. KGaA, Weinheim

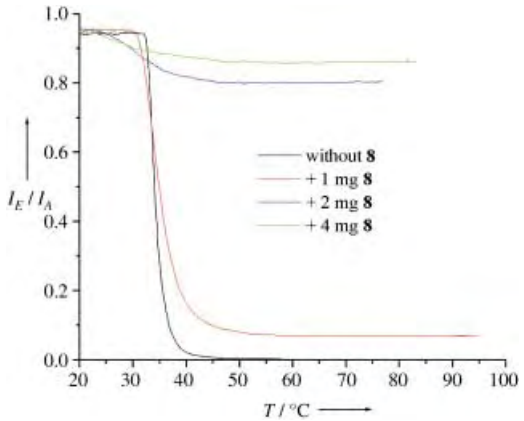


Figure 3. Temperature dependence turbidity curves from Me_2-β-CD-complexed copolymer **5** (7.5 mg polymer in 3 mL water) with different amounts of **8**.

drastically influenced by noncovalent interaction with cyclodextrins. These polymers are a good example for an analytical system based on supramolecular recognition. The new adamantyl-derivatized copolymer **5** is thus an interesting polymer probe that reacts sensitively to the presence of β-cyclodextrins. In addition, this copolymer is fundamentally suitable as a precipitation agent for methyl-type cyclodextrins which can be released again simply by heating the solution.

Received: December 20, 2002 [Z50814]

Keywords: cyclodextrins · host–guest systems · supramolecular recognition · thermoreversible polymers

[1] H. G. Schild, *Prog. Polym. Sci.* **1992**, *17*, 163.
[2] M. Heskins, J. E. Guilett, *J. Macromol. Sci. Chem.* **1969**, *2*, 1441.
[3] F. M. Winnik, H. Ringsdorf, J. Venzmer, *Macromolecules* **1990**, *23*, 2415.
[4] X. J. Wu, R. H. Pelton, K. C. Tam, D. R. Woods, A. E. Hamielec, *J. Polym. Sci. Part A* **1993**, *31*, 957.
[5] F. Seker, A. B. Ellis, *J. Polym. Sci. Part A* **1998**, *36*, 2095.
[6] M. Bayhan, A. Tuncel, *J. Appl. Polym. Sci.* **1998**, *67*, 1127.
[7] a) M. Born, H. Ritter, *Makromol. Chem. Rapid Commun.* **1991**, *12*, 471; b) A. Harada, J. L. M. Kamachi, *Nature* **1992**, *356*, 325; c) M. Weickemeier, G. Wenz, J. Huff, *Macromol. Rapid Commun.* **1997**, *18*, 1117; d) C. Amiel, B. Sebille, *J. Inclusion Phenom. Mol. Recognit. Chem.* **1996**, *25*, 61.
[8] Syntheses of **1**: 6-*N*-Acrylamidohexanoic acid was prepared as in ref. [18]. $(C_2H_5)_3N$ (1.39 mL; 0.01 mol) was added to a solution of 6-*N*-Acrylamidohexanoic acid (1.85 g, 0.01 mol) in THF (50 mL) and cooled to 0 °C. Subsequently ethyl chloroformate (0.96 mL; 0.01 mol) was added under stirring and after 40 min aminoadamantane (1.51 g; 0.01 mol) was added. The reaction mixture was stirred for 2 h at 0 °C and subsequently for 16 h at room temperature. The mixture was diluted with diethyl ether (50 mL) and recrystallized in the refrigerator (at +4 °C) over night. The crude product was then collected and purified by column chromatography (SiO_2, CH_2Cl_2/CH_3OH 95:5). Yield: 47 %. ^{1}H NMR (200 MHz, $CDCl_3$): $\delta = 6.30$ (s br (overlapped), 1 H, N11-H), 6.26 (dd, 1 H, C2-H), 6.10 (dd, 1 H, $J = 9.8$, 2.4 Hz, C1-H_a), 5.56 (dd, 1 H, $J = 17.0$ Hz, C1-H_b), 5.25 (m, 1 H, N4-H) 3.30 (pseudo-q, 2 H, C5-H_2), 2.06 (t, 2 H, $J = 7.3$ Hz, C9-H_2), 2.04 (m, 3 H, C14-H), 1.98 (m, 6 H, C13-H_2) 1.64 (m, 6 H, C15-H_2), 1.16–1.60 ppm (m br, C6–C8-H_2); ^{13}C NMR (50 MHz, $CDCl_3$): $\delta = 172.23$, 165.70, 131.12, 126.09, 51.90, 41.68, 36.36, 37.25, 29.43, 28.85, 26.13, 24.50 ppm; *m*/*z*: 316.2 $[M]^+$; elemental analysis (%) calcd for $C_{19}H_{26}N_2O_2$: C 72.12, H 8:92; found: C 71.96, H 9.12.
[9] Syntheses of **2**: Was carry out analogous to that in ref. [8] except aminocylohexane was used instead of aminoadamantane. Yield: 53 %. ^{1}H NMR (200 MHz, $CDCl_3$): $\delta = 6.26$ (dd, 1 H, C2-H), 6.10 (dd, 1 H, C1-H_a: $J = 16.0$, 2.9 Hz), 6.05 (m, br (overlapped), N4-H), 5.61 (dd, 1 H, $J = 9.8$ Hz, C1-H_b) 5.46 (d, br, 1 H, $J = 7.3$ Hz, N11-H), 3.84–3.63 (m, br, 1 H, C12-H), 3.34 (pseudo-q, 2 H, C5-H_2), 2.12 (t, 2 H, $J = 6.8$ Hz, C9-H_2), 2.00–0.97(m, br, 16 H, C6,7,8-CH_2, C13,14,15- CH_2), 1.40–1.10 ppm (m, 8 H, 4 CH_2); ^{13}C NMR (50 MHz, $CDCl_3$): $\delta = 172.08$, 165.72, 131.o6, 126.06, 48.23, 39.17, 36.53, 33.18, 28.95, 26.22, 25.52, 25.02, 24.88 ppm; *m*/*z*: 266.2 $[M]^+$; elemental analysis (%) calcd for $C_{15}H_{26}N_2O_2$: C 67.63, H 9.84; found: C 67.47, H 9.95.
[10] a) J. Storsberg, H. Ritter, *Macromol. Rapid Commun.* **2000**, *21*, 236–241; b) S. Bernhardt, P. Glöckner, A. Theis, H. Ritter, *Macromolecules* **2001**, *34*, 1647–1649.
[11] Technical 2,6-dimethyl-β-cyclodextrin with a methylation average of 1.8 was applied.
[12] Polymerzation of **4**: **1** (80 mg) and Me_2-β-CD (350 mg) were dissolved in phosphate buffered water (12 mL) and mixed with NIPAAM (600 mg). Under nitrogen potassium peroxodisulfate (5.2 mg) and sodium disulfide (4 mg) were added, and the mixture was stirred at 40 °C until no more monomer could be detected by GPC. Subsequently the aqueous solution was dialyzed in a 8000D dialysis membrane for 48 h against water. The aqueous solution was then filtered through a membrane filter (0.45 μm) and freeze dried.
[13] Die GPC measurements ware carried out in DMF/0.1 % LiCl with HEMA columns (PSS company: 3 × 30 cm, 0.8 cm diameter, 1 × 40, 1 × 100, 1 × 3000 Å), the detection was by UV spectroscopy at 275 nm and with a refractive index detector. The evaluation was with the aid of a computer program (PSS company).
[14] Polymerization of **5** and **6**: The copolymerization was carried out under stirring in DMF (6 mL) at 60 °C for 16 h under nitrogen. As the radical initiator 2,2′-azobis[(2-methyl)propanenitrile] (AIBN; 2.3 mg) was added. Subsequently the reaction mixture was diluted with water (50 mL) and dialyzed in an 8000D dialysis membrane for 24 h. The aqueous solutions were filtered through membrane filters (0.45 μm) and freeze dried.
[15] The turbidity measurements were with a home-made apparatus: a 4-mL autosampler bottle contained in a peltier element thermostated aluminum heating block, the degree of the turbidly was measured by a power-regulated semiconductor laser with a wavelength of 670 nm and a silicon photodiode, the heating rate was 1 °C min^{-1}. The controlling and data recording was with a personal computer.
[16] S. J. Han, M. K. Yoo, Y. K. Sung, Y. M. Lee, C. S. Cho, *Macromol. Rapid Commun.* **1998**, *19*, 403- 407.
[17] M. V. Rekharsky, Y. Inoue, *Chem. Rev.* **1998**, *98*, 1875–1917.
[18] H. Yamada, *Carbohydr. Res.* **1998**, *305*, 443–461.

 © 2003 Wiley-VCH Verlag GmbH & Co. KGaA, Weinheim

Anomeric Protecting Groups

N-Glycosyl Amides: Removal of the Anomeric Protecting Group and Conversion into Glycosyl Donors**

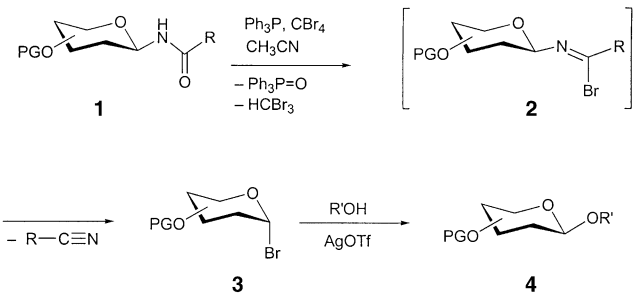
*Norbert Pleuss and Horst Kunz**

Dedicated to Professor Helmut Schwarz on the occasion of his 60th birthday

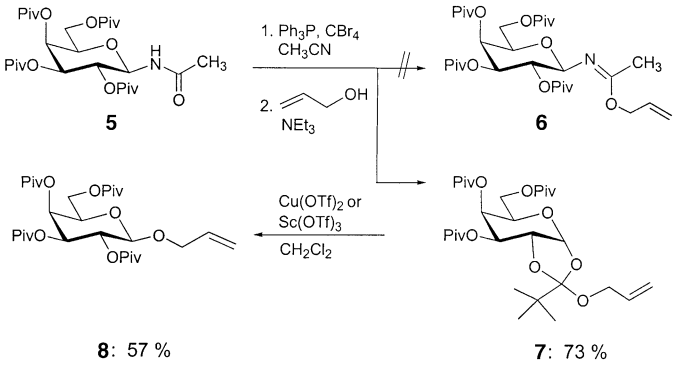
During the past years important functions of the carbohydrates in glycoconjugates have been discovered in biological recognition phenomena.[1,2] Recently developed methods for the synthesis of glycosides and saccharides used as model substances have been crucial to the considerable progress made in this area. Besides modern versions of the Koenigs–Knorr reaction,[3] the trichloroacetimidate method[4] and the activation of thioglycosides with soft thiophilic activators[6] have become increasingly important. Glycosyl donors such as thioglycosides, 4-pentenylglycosides,[7] and to some extent also glycals[8] have the advantage of being stable enough to serve as anomerically protected compounds as long as they are not exposed to electrophiles. They also are not stable under the conditions of hydrogenolysis, for example, during the removal of benzyl protecting groups.

N-Glycosyl amides are stable under acidic as well as under basic conditions and also insensitive towards oxidation and hydrogenation. Because of their resistance to cleavage, *N*-glycosyl amides have not been considered as protecting groups for the anomeric center. In contrast, the inertness of the N^4-glycosylasparagine structure, which is based on the stability of *N*-glycoproteins, has been used for many years in biochemical analyses for differentiation against *O*-glycoproteins.[9]

We describe here a mild method not only for the cleavage of *N*-glycosyl amides as anomeric protecting groups but also for their activation as glycosyl donors in glycoside synthesis. It consists of a retro-Ritter reaction, which is initiated by the treatment of glycosyl amide **1** with the Appel reagent[10] triphenylphosphane/tetrabromomethane (Scheme 1). The reaction was discovered when *N*-(2,3,4,6-tetra-*O*-pivaloyl-β-D-galactopyranosyl)acetamide (**5**) was to be converted into *O*-allyl-imidoester **6** (Scheme 2). Surprisingly, allyl orthoester **7** was isolated instead. Orthoester **7** undergoes rearrangement when treated with copper or scandium triflate catalysts to give allyl glycoside **8**. Apparently the imidoyl bromide intermediate (analogous to **2**, Scheme 1) is so unstable at room temperature that it releases acetonitrile with formation of the glycosyl cation to furnish the acyloxonium ion or the α-glycosyl bromide (analogous to **3**), which in the absence of alcohols can be isolated and identified by NMR spectroscopy. When a base and allyl alcohol are added, orthoester **7** is obtained.

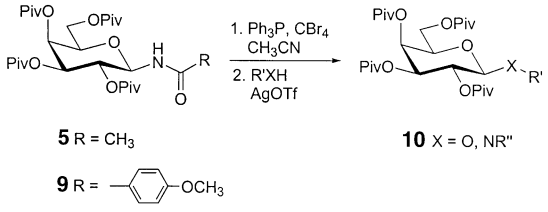


Scheme 1. General reaction scheme for the synthesis of glycosides from *N*-glycosyl amides. PG = protecting group.



Scheme 2. Conversion of *N*-glycosyl acetamide **5** into orthoester **7** and transition-metal-catalyzed rearrangement of orthoester **7** into glycoside **8**.

The unexpected reactivity of imidoyl bromide **2** was utilized to develop a new method for the synthesis of glycosides. First amide **1** was treated with the Appel reagent. Then, instead of the tertiary amine, silver triflate[12] was used with the alcohol to yield glycoside **4**. The electronic features of the amide substituent have a significant effect on the efficiency of this glycoside synthesis, as is shown by the yields of stereoselective glycosylation reactions of *N*-galactosyl amides **5** and **9** with alcohols and amines (Scheme 3, Table 1). *N*-Galactosyl amides **5** and **9** were prepared almost quantitatively from 2,3,4,6-tetra-*O*-pivaloyl-β-D-galactopyranosylamine[13] and the corresponding acid chlorides in the presence of triethylamine in dichloromethane. Under basic conditions the electron-rich anomeric amide **9** is much more stable than **5**, but under acidic conditions they are compara-



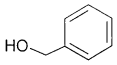
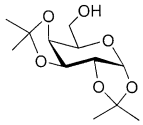
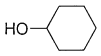
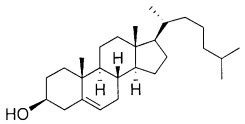
Scheme 3. Glycosylation reactions with *N*-glycosyl acetamide **5** and *N*-glycosyl anisamide **9**.

[*] Prof. Dr. H. Kunz, Dipl.-Chem. N. Pleuss
Institut für Organische Chemie
Universität Mainz
Duesbergweg 10–14, 55128 Mainz (Germany)
Fax: (+49) 6131-392-4786
E-mail: hokunz@uni-mainz.de

[**] This work was supported by the Deutsche Forschungsgemeinschaft and the Fonds der Chemischen Industrie.

 © 2003 Wiley-VCH Verlag GmbH & Co. KGaA, Weinheim DOI: 10.1002/anie.200351351

Table 1: Synthesis of O- and N-glycosides **10** from *N*-glycosyl amides **5** and **9**.

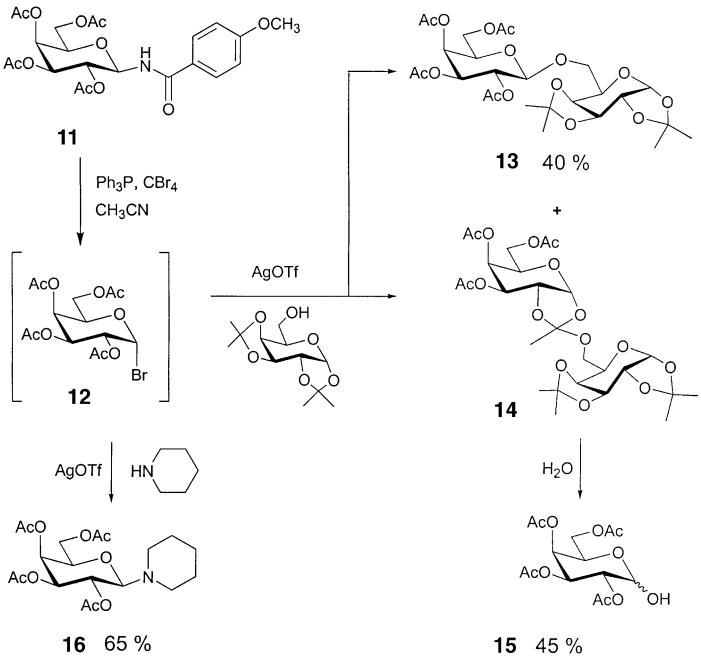
R′-XH	Product	Yield [%] from **5**	Yield [%] from **9**
	**10a**	27	81
	**10b**	38	60
	**10c**	24	69
	**10d**	11	83
	**10e**	–	66
NH_3	**10f**	25	79[13]
	**10g**	45	74

ble. Thus, electronic effects do not affect the capacity of *N*-glycosyl amides as protecting groups.

The results in Table 1 show that the glycosides **10** are obtained in moderate yields from acetamide **5** but in good yields from anisoyl amide **9**, which has higher electron density at the oxygen atom of the carbonyl group. Furthermore, acid-labile structures in the glycosyl acceptor (**10b**) are not affected, and even steroid alcohols like **10e** can be glycosylated. The examples **10f** and **10g** show that *N*-glycosides are also accessible by this method. It should be noted that pivaloyl-protected glycosyl donors, which block the formation of orthoesters by steric hindrance,[14] are generally less reactive. For this reason they are often used in the synthesis of complex oligosaccharides,[15,16] especially since the *O*-acetyl-protected glycosyl bromides undergo undesired side reactions in the presence of silver triflate, resulting mainly the formation of orthoesters and products of their further conversion.[14]

This method for activating *N*-glycosyl amides can be applied to *O*-acetyl-protected compounds like *N*-(tetra-*O*-acetyl-β-D-galactopyranosyl)anisoyl amide (**11**, Scheme 4). The tetra-*O*-galactosyl bromide **12**, which is formed almost quantitatively by treatment with the Appel reagent, reacts with di-*O*-isopropylidene galactopyranose and silver triflate to give galactoside **13** and the corresponding orthoester **14**. During workup orthoester **14** is hydrolyzed to give the anomerically deprotected compound **15**. The total yield of this anomeric activation is high, although glycoside **13** is obtained only in moderate yields due to the side reactions of acetyl-protected glycosyl bromides[14] mentioned above. With water as the nucleophile, compound **15** can be prepared almost quantitatively and used for activation, for example as trichloroacetimidate.[4] When the glycosyl bromide is reacted with an amine, *N*-β-galactosylpiperidine **16** can be isolated in good yield since orthocarboxylic acid derivatives of amines are more acid-labile than orthoesters.

A major requirement for the activation of *N*-glycosyl amides with the Appel reagent is sufficient electron density at



Scheme 4. Reactions of tetra-*O*-acetyl-protected glycosyl bromide **12**.

the amide carbonyl oxygen atom. The *N*-glycosyl trifluoroacetamide analogous to **5** cannot be transformed into a glycosyl donor by this procedure. This example shows that the described glycosylation method employing an amide as the anomeric function and a nitrile as the leaving group is formally an inversion of Schmidt's trichloroacetimidate method,[4] in which a nitrile is introduced for anomeric activation and an amide serves as the leaving group.

In summary glycosylation reactions with *N*-glycosyl amides exhibit a number of advantages. The *N*-glycosyl amides are very stable compounds that can be activated at room temperature under mild and neutral conditions. Labile functional groups in the glycosyl acceptors are not affected, and a variety of alcohols and amines can be glycosylated with high yields.

Experimental Section

General procedure for glycosylation reactions with *N*-glycosyl amide **9**: To a solution of **9** (200 mg, 0.31 mmol) and PPh_3 (162 mg, 0.62 mmol) in anhydrous CH_3CN (15 mL) under an argon atmosphere was added a solution of CBr_4 (306 mg, 0.92 mmol) in dry CH_3CN (5 mL) at room temperature. The reaction mixture was stirred for 4 h, then a solution of the glycosyl acceptor (1.5–3 equiv) and AgOTf (158 mg, 0.62 mmol) in anhydrous CH_3CN (5 mL) was added. The mixture was stirred for 18 h, AgBr was filtered off, anhydrous CH_2Cl_2 (100 mL) was added, and the solution was washed with saturated aqueous NaCl (3 × 30 mL). The organic layer was dried over $MgSO_4$, the solvent removed in vacuo, and the resulting residue purified by chromatography on silica gel (cyclohexane/EtOAc 3:1 to 5:1) to afford O- and N-glycosides.

Received: March 7, 2003 [Z51351]

Keywords: Appel reagent · glycosides · glycosyl amides · protecting groups · retro-Ritter reaction

 © 2003 Wiley-VCH Verlag GmbH & Co. KGaA, Weinheim

[1] Review articles: a) T. D. Butters, R. A. Dwek, F. M. Platt, *Chem. Rev.* **2000**, *100*, 4683; b) A. Varki, *Glycobiology* **1993**, *3*, 97.
[2] A. Helenius, M. Aebi, *Science* **2001**, *291*, 2364.
[3] H. Paulsen, *Angew. Chem.* **1982**, *94*, 184; *Angew. Chem. Int. Ed. Engl.* **1982**, *21*, 155.
[4] a) R. R. Schmidt, J. Michel, *Angew. Chem.* **1980**, *92*, 763; *Angew. Chem. Int. Ed. Engl.* **1980**, *19*, 731; b) R. R. Schmidt, W. Kinzy, *Adv. Carbohydr. Chem. Biochem.* **1994**, *50*, 21.
[5] R. J. Ferrier, R. W. Hay, N. Vethaviyasar, *Carbohydr. Res.* **1973**, *27*, 55.
[6] P. J. Garegg, *Adv. Carbohydr. Chem. Biochem.* **1997**, *52*, 179.
[7] B. Fraser-Reid, U. E. Udong, Z. Wu, H. Ottosson, R. Meritt, C. S. Rao, C. Roberts, R. Madsen, *Synlett* **1992**, 927.
[8] Review article: S. J. Danishefsky, M. Bilodeau, *Angew. Chem.* **1996**, *108*, 1482; *Angew. Chem. Int. Ed. Engl.* **1996**, *35*, 1381.
[9] R. D. Marshall, A. Neuberger, *Adv. Carbohydr. Chem. Biochem.* **1970**, *25*, 407.
[10] Review article: R. Appel, *Angew. Chem.* **1975**, *87*, 863; *Angew. Chem. Int. Ed. Engl.* **1975**, *14*, 801.
[11] P. Allef, H. Kunz, *Tetrahedron: Asymmetry* **2000**, *11*, 375.
[12] S. Hanessian, J. Banoub, *Carbohydr. Res.* **1977**, *53*, C13.
[13] a) H. Kunz, W. Sager, D. Schanzenbach, M. Decker, *Liebigs Ann. Chem.* **1991**, 649; b) H. Kunz, W. Pfrengle, K. Rück, W. Sager, *Synthesis* **1991**, 1039.
[14] A. Harreus, H. Kunz, *Liebigs Ann. Chem.* **1982**, 41.
[15] P. H. Seeberger, M. Eckhardt, C. E. Guttridge, S. J. Danishefsky, *J. Am. Chem. Soc.* **1997**, *119*, 10064.
[16] K. C. Nicolaou, T. Caulfield, H. Kataoka, T. Kumazawa, *J. Am. Chem. Soc.* **1988**, *110*, 7910.

 © 2003 Wiley-VCH Verlag GmbH & Co. KGaA, Weinheim

Shape Persistent Organic Ring

A Giant Conjugated Molecular Ring**

Marcel Mayor and Claudia Didschies*

Very small cyclic metallic structures ($\varnothing \approx 1$ μm) are known to support persistent currents at low temperature by the coherence of electron wavefunctions over the whole ring. For example, non-dissipative persistent currents have been detected in samples consisting of 10^7 identical, parallel and isolated copper rings through the dependence of the magnetic moment on the applied magnetic field. The magnetism of the sample is periodic in the quantized magnetic flux $\Phi_0 = h e^{-1}$ enclosed by each ring (h being Planck's constant and e being the elementary charge).[1] To our knowledge, persistent currents periodic in the enclosed flux have not been observed for organic molecules to date and we intend to demonstrate this effect in a giant molecular ring. This macrocyclic model compound has to fulfill certain requirements in size and conjugation. As the magnetic flux Φ, given by the product of the enclosed surface $r^2\pi$ multiplied by the magnetic field B ($\Phi = r^2 \pi B$), has to be in the order of the magnetic flux quantum ($\Phi_0 = h e^{-1}$) to observe a full oscillation, the radius r needed can be estimated from Equation (1), with B in Tesla.

$$r = \sqrt{\frac{h}{e B \pi}} \tag{1}$$

The largest static magnetic fields currently available are about 30–40 T. The required radius of a molecular ring-structure which may allow the monitoring of a full oscillation of the magnetization in these magnetic fields is according to Equation (1) to be about 6 nm.

Cyclic molecular structures have attained considerable interest as size- and shape-persistent objects.[2] The synthetic strategies are usually based on modular approaches, such as acetylene scaffolding[3,4] and other repetitive reaction sequences, for example, Suzuki coupling steps to give macrocyclic oligophenylenes.[5] Large cyclic molecules, such as the "gigantocycles" from Godt and co-workers,[6] the shape-persistent cyclic oligophenylene rings consisting of 24 phenylene rings with a diameter of about 3 nm from Schüter and co-workers,[5] and the macrocyclic porphyrin hexamer with a diameter of about 4.6 nm from Gossauer and co-workers[7] are known to date. Structures with fully conjugated π systems as the periphery are particularly promising candidates, as persistent currents depend on the coherence of the electron wavefunction over the whole ring. Hence, cycles comprising tectons that interrupt conjugation, such as *meta*-connected-benzene units, are less suited for the purpose. Only few examples of cycles with fully conjugated periphery, such as the cyclic oligothiophenes reported by Bäuerle and co-workers[8] are known to date.

Herein we present the design, synthesis, and characterization of the giant molecular cycle **1**, with a diameter of about 12 nm, and which has a periphery of exclusively conjugation-active subunits, such as acetylene- and diacetylene-connected *para*-thiophene and *para*-benzene rings.

2,5-Diethynylthiophene turned out to be the ideal corner unit: the *para*-connection the two acetylene units guarantees electronic communication and an angle of about 155°.[9] very close to the internal angle of a hexadecagon (157.5°; Figure 1). The small difference of the two angles can easily be compensated by the flexibility of ethinyl and butadiynyl linkers.[10] In addition, a hexadecagon is an ideal target from a synthetic point of view: Oligomers with $16 = 2^4$ units may be prepared by four sequential dimerization steps.

1,4-di(4′-ethynyl-2′,5′-dihexyloxy-benzene)butadiyne, a conjugated rigid-rod-like spacer, was used as the sides of the hexadecagon to enlarge its diameter to the required 12 nm

[*] Dr. M. Mayor, C. Didschies
Institute for Nanotechnology
Forschungszentrum Karlsruhe GmbH
Postfach 3640, 76021 Karlsruhe (Germany)
Fax: (+49) 7247-82-5685
E-mail: marcel.mayor@int.fzk.de

[**] We are grateful to Prof. Dr. Hilbert von Löhneysen for suggesting the synthesis of molecular nanocycles for persistent-current experiments, and Dr. Detlef Beckmann and Dr. Heiko B. Weber for their patience in introducing us to some principles of mesoscopic physics. Financial support from the Strategiefond of the Helmholtz Foundation is gratefully acknowledged.

Supporting information for this article is available on the WWW under http://www.angewandte.org or from the author.

 © 2003 Wiley-VCH Verlag GmbH & Co. KGaA, Weinheim DOI: 10.1002/anie.200250763

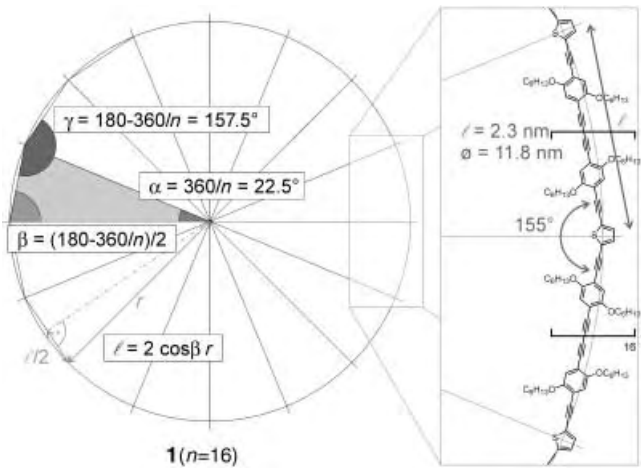
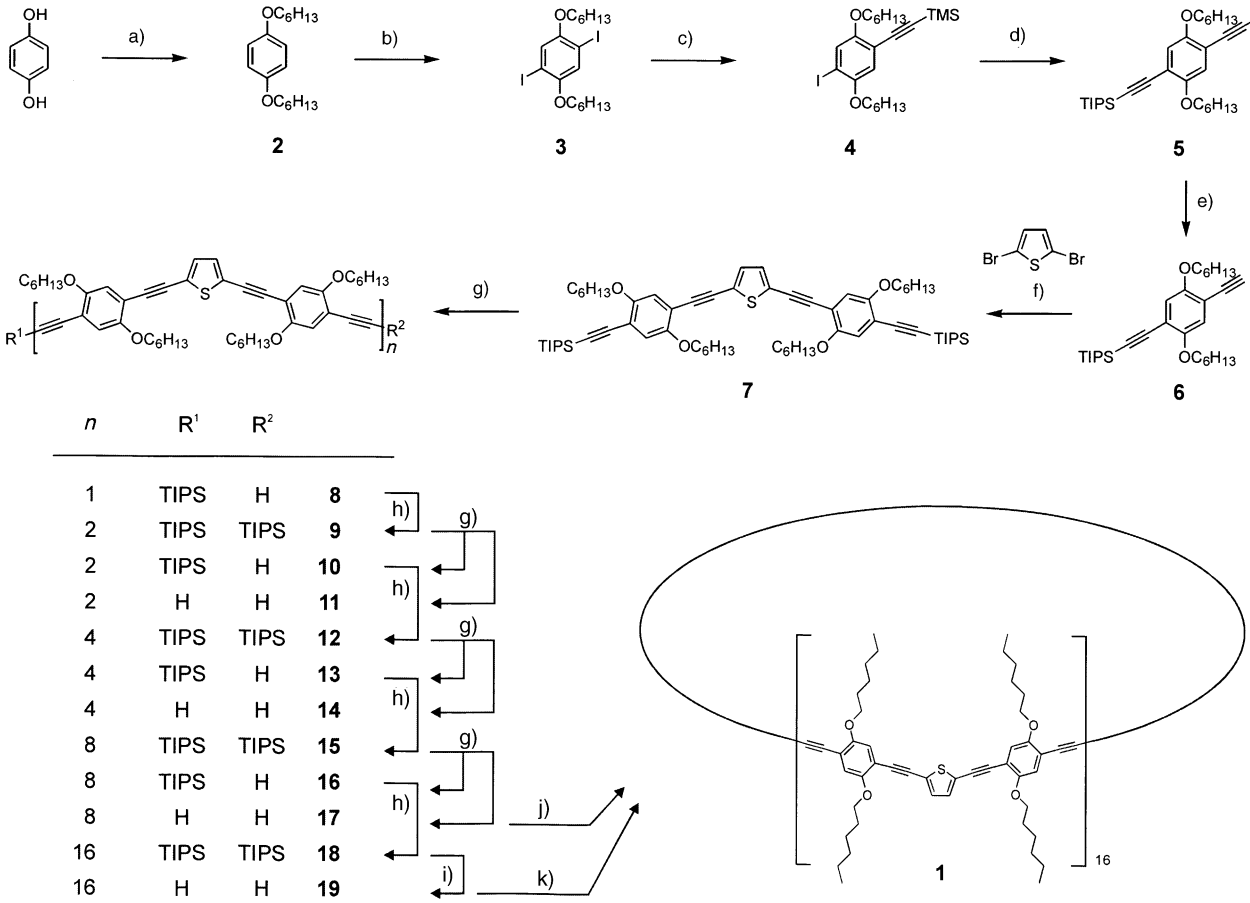


Figure 1. Left: Graphical representation of a hexadecagon. Formulae for a regular polygon to determine the angle opened by each corner and the geometric dependence between diameter ∅ and edge-length ℓ. The given angle-values are calculated for a regular hexadecagon ($n=16$). Right: the designed structure of **1**, a hexadecagon with an edge-length of 2.3 nm, and a diameter of about 11.8 nm.

(Figure 1). Furthermore, the symmetric butadiyne spacer allowed the stepwise synthesis by oxidative acetylene-coupling strategies, which have been used successfully for cyclic structures.[4,8,11]

The synthesis of the huge cycle **1** is displayed in Scheme 1. The spacer unit was build up in a manner similar to a procedure described by Höger and co-workers.[12] Hydroquinone was heated under reflux with hexylbromide in acetonitrile in the presence of potassium carbonate to give the 1,4-dihexyloxybenzene (**2**) in 56% yield. Iodination gave 1,4-diiodo-2,5-dihexyloxybenzene (**3**) in 78% yield as a white solid. Using the Pd^0 and Cu^I catalyzed Sonogashira coupling reaction[13] in piperidine at room temperature one iodine atom of **3** was substituted by a trimethylsilylethynyl (TMSCCH) group (**4**, 52%). With similar reaction conditions the iodine of **4** was replaced by trisisopropylsilylethynyl (TIPSCCH) giving **5** in 92% yield. Selective deprotection of the TMS protecting group gave the acetylene **6** in quantitative yield. Both bromine atoms of 2,5-dibromothiophene were substituted by **6**[14] in a further Sonogashira coupling to give the doubly TIPS-protected parent building block **7** of the cycle (89%). Monodeprotection of **7** with tetrabutylammo-



n	R^1	R^2		
1	TIPS	H	**8**	h)
2	TIPS	TIPS	**9**	g)
2	TIPS	H	**10**	h)
2	H	H	**11**	g)
4	TIPS	TIPS	**12**	h)
4	TIPS	H	**13**	g)
4	H	H	**14**	h)
8	TIPS	TIPS	**15**	g)
8	TIPS	H	**16**	h)
8	H	H	**17**	j)
16	TIPS	TIPS	**18**	i)
16	H	H	**19**	k)

Scheme 1. Synthesis of **1**: a) *n*-$C_6H_{13}Br$, K_2CO_3, CH_3CN, reflux. b) I_2, KIO_3, AcOH, H_2SO_4, reflux. c) TMSCCH, $[Pd(PPh_3)_4]$, CuI, $C_5H_{10}NH$, RT. d) TIPSCCH, $[Pd(PPh_3)_4]$, CuI, $C_5H_{10}NH$, RT. e) NaOH, THF, MeOH, RT. f) $[Pd(PPh_3)_4]$, CuI, *i*Pr_2NH, reflux. g) TBAF, THF, AcOH, RT. h) $CuAc_2$, C_5H_5N, 60–70°C. i) TBAF, THF, RT. j) **17** (2×10^{-4} M), $CuAc_2$ (7 equiv), C_5H_5N, 70°C, 14 h. k) **19** (8.3×10^{-6} M), $CuAc_2$ (150 equiv), C_5H_5N, 85°C, 7 days.

 © 2003 Wiley-VCH Verlag GmbH & Co. KGaA, Weinheim

niumfluoride (TBAF) and a trace of water and acetic acid gave the monoprotected building block **8** (53%). Oxidative acetylene coupling[15] with copper acetate as catalyst gave the doubly protected **9** (88%) in which two connected ring units are already present. Similar deprotection steps as described for **7** transferred **9** into the monoprotected dimer **10** (50%) and into the fully deprotected dimer **11** (32%). The oxidative acetylene coupling of **10** yielded the chainlike tetramer **12** (86%), which was transferred to its mono- and completely deprotected forms **13** (48%) and **14** (30%). Oxidative acetylene coupling of **13** then gave the chainlike octamer **15**. Deprotection of **15** gave the monoprotected octamer **16** (45%) and the terminally bisdeprotected octamer **17** (30%).

Our first attempts to obtain the target structure **1** were based on a high-dilution dimerization reaction of **17**. A 2×10^{-4} M solution of **17** in pyridine with 7 equivalents of copper acetate were kept at 60°C for 14 h. After workup, the crude reaction product was analyzed by means of ^{1}H NMR spectroscopy and MALDI-TOF mass spectrometry. The disappearance of the singlett ($\delta=3.37$ ppm) for the acetylene protons was indicative for successful cyclization. However, the mass spectrum displayed a series of signals that could all be attributed to cyclic oligomers: cycles with 8 (m/z 5848), 16 (**1**, m/z 11697), 24 (m/z 17545), and even 32 units (m/z 23393) could be distinguished. These first investigations demonstrated the existence of the target compound, however, all attempts to isolate specific cyclic products from the reaction mixture failed.

To favor the formation of the cyclic hexadecamer **1**, the cyclization of the chainlike hexadecamer **19** under even more diluted conditions was envisaged. Therefore, the terminally monoprotected octamer **16** was dimerized under oxidative acetylene-coupling conditions to the double protected hexadecamer **18** (86%). Compound **18** was fully deprotected yielding hexadecamer **19**. A 8.3×10^{-6} M solution of **19** in pyridine with 150 equivalents of copper acetate were kept at 85°C for 7 days. The reaction mixture monitored frequently by ^{1}H NMR spectroscopy. The disappearance of the signal for the acetyleneic proton of **19** in the ^{1}H NMR spectrum at $\delta=$ 3.36 ppm pointed to completion of the cyclization reaction. After Workup and column chromatography, **1** was isolated as orange glassy enamel in 38% yield, which was soluble in aprotic organic solvents such as $CHCl_3$, CH_2Cl_2, toluene, and THF.

The ^{1}H and ^{13}C NMR spectra fully agreed with the proposed highly symmetric cyclic structure of **1**. Noteworthy is the lack of acetylenic proton signals in the range between $\delta=3$–3.5 ppm of the ^{1}H NMR spectrum, which clearly indicates the absence of open-chain oligomers. Unexpectedly, the ^{13}C NMR spectrum in $CDCl_3$ displayed only three instead of the expected four signals in the range for acetylenic carbons. However, by changing the solvent to [D$_8$]THF, all four signals were resolved at $\delta=80.28$, 80.54, 88.73, and 92.33 ppm. The MALDI TOF MS spectrum displayed only the signal expected for **1** at m/z 11697 (Figure 2). All the characterization data confirms the identity of the isolated reaction product as the cyclic structure **1**.

Of interest were the UV/Vis spectra of the cycle **1** in comparison with the series of deprotected open-chain

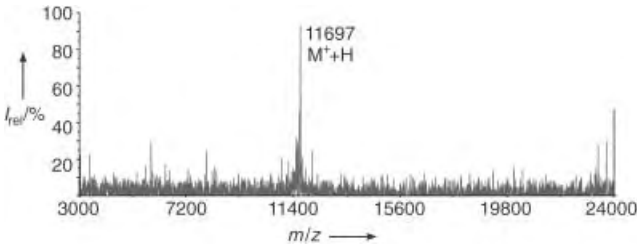


Figure 2. MALDI-TOF-MS of $[\mathbf{1}+H]^+$ ($C_{768}H_{928}O_{64}S_{16}$: m/z 11696).

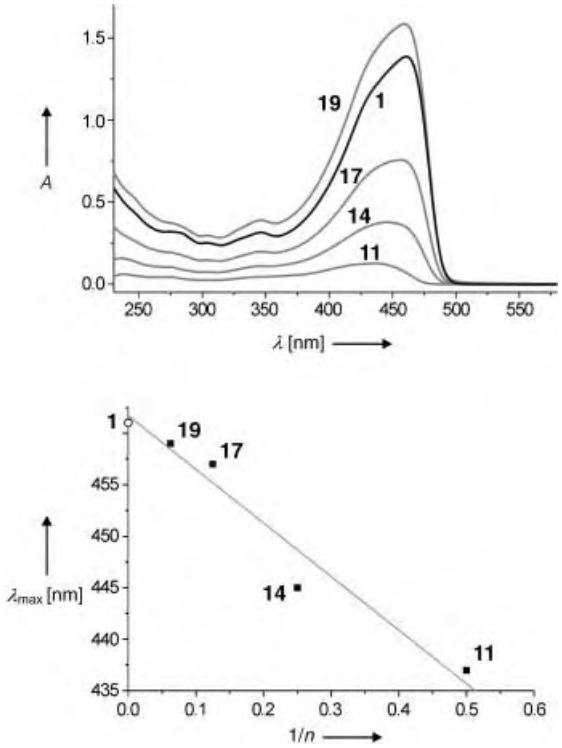


Figure 3. Top: UV/Vis spectra (CH_2Cl_2, $T=298$ K) of **1** and the open-chain oligomers **11**, **14**, **17** and **19**. Bottom: Absorption maxima of oligomers **11**, **14**, **17** and **19** (■) plotted against reciprocal chain-length, and fitted linearly; (○) absorption maxima of **1**.

oligomers **11**, **14**, **17**, and **19** (Figure 3, top) as an indicator for the conjugation in **1**. The longest-wavelength absorption maxima of the compounds **11**, **14**, **17**, and **19** are at 437, 445, 457, and 459 nm, respectively, indicating a continuous bathochromic shift with increasing chain length n. When these values were plotted against the reciprocal chain length $1/n$, linear regression gives a theoretical absorption maxima for infinite chain length at 462 nm (Figure 3, bottom).[16] The value of 461 nm recorded for the cycle **1** is very close to this theoretical value. Thus the optical investigations indicate promising properties of **1**. We are currently investigating the self-organization properties of **1** in the solid state and on surfaces to prepare samples suitable for persistent-current investigations in strong magnetic fields.

Experimental Section

1: Open-chain hexadecamer **19** (36 mg, 3.077 μmol) was dissolved in pyridine (372 mL). Copper acetate monohydrate (92.2 mg,

 © 2003 Wiley-VCH Verlag GmbH & Co. KGaA, Weinheim

461.5 μmol, 150 equiv) was added. The reaction mixture was heated to 85 °C. The course of the cyclization reaction was monitored by ^{1}H NMR spectroscopy. After 7 days, cyclization was complete. The reaction mixture was concentrated and poured onto 0 °C cold 2 N HCl. Extraction with toluene and subsequent column chromatography (1. silica, THF/*n*-hexane 1/2; 2. silica, CH_2Cl_2/*n*-hexane 7/4) yielded **1** (13.7 mg, 1.171 μmol, 38 %) as orange glassy enamel. ^{1}H NMR (300 MHz, $CDCl_3$): $\delta = 7.16$ (s, 32 H), 6.98 (s, 32 H), 6.96 (s, 32 H), 4.00 (m, 128 H), 2.0–1.7 (m, 128 H), 1.65–1.2 (m, 384 H), 1.1–0.75 ppm (m, 192 H); ^{13}C NMR (75 MHz, $CDCl_3$): $\delta = 154.97$, 153.44, 131.92, 124.99, 117.58, 116.43, 114.36, 112.95, 91.00, 88.34, 79.57, 69.78, 69.61, 31.57, 31.55, 29.18, 29.09, 25.70, 25.62, 22.66, 22.63, 14.09 ppm; ^{13}C NMR (75 MHz, [D$_8$]THF): $\delta = 156.16$, 154.73, 133.15, 126.05, 118.22, 117.03, 115.27, 113.85, 92.33, 88.73, 80.54, 80.28, 70.30, 70.17, 32.72, 30.30, 30.22, 26.86, 26.76, 23.78, 23.74, 14.66 ppm; MALDI-TOF-MS: 11697 $[M+H]^+$, $[M]^+$ for $C_{768}H_{928}O_{64}S_{16}$: 11696.

Received: December 13, 2002 [Z50763]

Keywords: alkynes · conjugation · cyclization · macrocycles · oxidative coupling

[1] L. P. Lévy, G. Dolan, J. Dunsmuir, H. Bouchiat, *Phys. Rev. Lett.* **1990**, *64*, 2074 – 2077.
[2] For a review: a) C. Grave, A. D. Schlüter, *Eur. J. Org. Chem.* **2002**, 3075 – 3098; b) V. Prautzsch, S. Ibach, F. Vögtle, *J. Inclusion Phenom. Macrocyclic Chem.* **1999**, *33*, 427 – 457.
[3] a) J. S. Moore, J. Zhang, *Angew. Chem.* **1992**, *104*, 873 – 874; *Angew. Chem. Int. Ed. Engl.* **1992**, *31*, 922 – 924; b) S. Höger, V. Enkelmann, *Angew. Chem.* **1995**, *107*, 2917 – 2919; *Angew. Chem. Int. Ed. Engl.* **1995**, *34*, 2713 – 2716; c) D. W. J. McCallien, J. K. M. Sanders, *J. Am. Chem. Soc.* **1995**, *117*, 6611 – 6612; d) F. Diederich in *Modern Acetylene Chemistry* (Eds.: P. J. Stang, F. Diederich), VCH, Weinheim, **1995**, pp. 443 – 471; e) M. M. Haley, *Synlett* **1998**, 557 – 565; f) Y. Tobe, N. Utsumi, A. Nagano, K. Naemura, *Angew. Chem.* **1998**, *110*, 1347 – 1349; *Angew. Chem. Int. Ed.* **1998**, *37*, 1285 – 1287.
[4] M. Mayor, J.-M. Lehn, *J. Am. Chem. Soc.* **1999**, *121,* 11231 – 11232.
[5] a) V. Hensel, K. Lützow, J. Jakob, K. Gessler, W. Saenger, A. D. Schlüter, *Angew. Chem.* **1997**, *109*, 2768 – 2770; *Angew. Chem. Int. Ed. Engl.* **1997**, *36*, 2654 – 2656; b) V. Hensel, A. D. Schlüter, *Chem. Eur. J.* **1999**, *5*, 421 – 429.
[6] A. Godt, S. Duda, Ö. Ünsal, J. Thiel, A. Härter, M. Ross, C. Tschierske, S. Diele, *Chem. Eur. J.* **2002**, *8*, 5094 – 5106.
[7] a) O. Mongin, A. Schuwey, M.-A. Vallot, A. Gossauer, *Tetrahedron Lett.* **1999**, *40*, 8347 – 8350; b) S. Rucareanu, O. Mongin, A. Schuwey, N. Hoyler, A. Gossauer, *J. Org. Chem.* **2001**, *66*, 4973 – 4988.
[8] J. Krömer, I. Rios-Carreras, G. Fuhrmann, C. Munsch, M. Wunderlin, T. Debaerdemaeker, E. Mena-Osteritz, P. Bäuerle, *Angew. Chem.* **2000**, *112*, 3623 – 3628; *Angew. Chem. Int. Ed.* **2000**, *39*, 3481 – 3486.
[9] The angle made by the two acetylene groups of 155° is determined by MM + calculations on 2,5-di(2′-phenyletynyl)thiophene as a model compound for the corner unit (155°) and from X-ray data for the angle made by the two acetylene groups of the 2,5-bis(ethynylthiophene) tecton (154.3°) in: W. L. Driessen, T. X. Neenan, *Acta Crystallogr. Sect. C* **1996**, *52*, 59 – 61.
[10] J. K. Young, J. S. Moore in *Modern Acetylene Chemistry* (Eds.: P. J. Stang, F. Diederich), VCH, Weinheim, **1995**, pp. 415 – 442.
[11] J. Anthony, A. M. Boldi, C. Boudon, J.-P. Gisselbrecht, M. Gross, P. Seiler, C. B. Knobler, F. Diederich, *Helv. Chim. Acta* **1995**, *78*, 797 – 817.
[12] S. Höger, A.-D. Meckenstock, S. Müller, *Chem. Eur. J.* **1998**, *4*, 2423 – 2434.
[13] K. Sonogashira in *Metal-catalyzed Cross-coupling Reactions* (Eds.: F. Diederich, P. J. Stang), Wiley-VCH, Weinheim, **1998**, pp. 203 – 227.
[14] Acetylene coupling on 2,5-dibromothiophenes: T. X. Neenan, G. M. Whitesides, *J. Org. Chem.* **1988**, *53*, 2489 – 2496.
[15] A. S. Hay, *J. Org. Chem.* **1960**, *25*, 1275 – 1276.
[16] a) Y. Geerts, G. Klärner, K. Müllen in *Electronic Materials: The Oligomer Approach* (Eds.: K. Müllen, G. Wegner), Wiley-VCH, Weinheim, **1998**, pp. 1 – 103; b) P. Bäuerle in *Electronic Materials: The Oligomer Approach* (Eds.: K. Müllen, G. Wegner), Wiley-VCH, Weinheim, **1998**, pp. 105 – 197.

 © 2003 Wiley-VCH Verlag GmbH & Co. KGaA, Weinheim

Upconversion of Photons

Blue, Green, and Red Upconversion Emission from Lanthanide-Doped $LuPO_4$ and $YbPO_4$ Nanocrystals in a Transparent Colloidal Solution**

*Stephan Heer, Olaf Lehmann, Markus Haase, and Hans-Ulrich Güdel**

We report the first observation of photon-upconversion in transparent colloids, that is, the emission of visible (Vis) light from a solution excited in the near-infrared (NIR). The solutions displaying this multiphoton process consist of transparent colloids of lanthanide-doped nanoparticles. Lanthanide-doped crystalline and amorphous materials play an outstanding role in lighting, display, and solid-state laser materials.[1–2] Many of these materials show high luminescence quantum yields and, since usually more than one metastable excited state exists, multiple emissions are observed.

In recent years, several research groups have reported on the doping of nanocrystalline hosts with ions of the f elements.[3–15] Among these, ligand-capped nanoparticles are of particular interest, as they combine the advantage of a rigid crystal environment for the dopant ions with the advantage of

[*] Prof. Dr. H.-U. Güdel, S. Heer
Department of Chemistry and Biochemistry
University of Bern
3000 Bern 9 (Switzerland)
Fax: (+41) 31-631-4399
E-mail: hans-ulrich.guedel@iac.unibe.ch
O. Lehmann, Dr. M. Haase
Institute of Physical Chemistry
University of Hamburg
Bundesstrasse 45, 20146 Hamburg (Germany)

[**] We thank A. Kornowski and S. Bartholdi-Nawrath for the TEM investigations and Dr. K. Kömpe for measuring X-ray powder diffractograms. Part of this work was financially supported by the Swiss National Science Foundation.

 DOI: 10.1002/anie.200351091 © 2003 Wiley-VCH Verlag GmbH & Co. KGaA, Weinheim

high solubility in liquids. We have previously shown that ligand-capped nanocrystals of the lanthanide phosphates can be prepared with narrow particle size distribution.[3–5,15] As colloidal solutions of these materials often display high luminescence quantum yields of the dopant ions,[3, 4,15] these nanocrystalline systems may be considered as active components in future electroluminescent devices, for the labeling of biomolecules, or for the amplification of signals transmitted through fiber cables.[4,15,16]

Further possible applications can be expected to arise from the phenomenon of photon upconversion, that is, the emission of light at shorter wavelength than the excitation. Upconversion emission has been observed and studied in many doped bulk materials, mostly in oxides and halides. The most efficient upconversion phosphors currently known are based on the most frequently used upconversion ions Er^{3+} (for NIR to green) and Tm^{3+} (NIR to blue), often in combination with Yb^{3+} as a sensitizer.[17] Applications range from near-IR (NIR) detection[18] to imaging and lasers.[19] A three-dimensional red-, green-, and blue-emitting display based on upconversion processes in a glass has been demonstrated.[20]

There have been a number of recent reports in the literature about upconversion luminescence in nanomaterials.[21–24] All of these studies, however, have been performed on dried powdered materials. The crucial test is to disperse the particles in a fully transparent colloidal solution and then to induce upconversion in the fluid state. This is a test of the particle quality, but it is also a prerequisite for any imaging or display applications based on the upconversion principle in a fluid. Besides good crystallinity, a reasonable particle size distribution is required, and the particles have to be properly surface modified to ensure colloidal solubility. Herein we use the well-established upconversion couples Yb^{3+}/Tm^{3+} and Yb^{3+}/Er^{3+} to demonstrate the feasibility of inducing and application of upconversion in solution.[17]

Ligand-capped lanthanide phosphate nanoparticles prepared by the method given below are readily soluble in organic solvents and form colloidal solutions of well-separated particles.[3–5,15] Figure 1a displays micrographs of $LuPO_4$:49 % Yb^{3+},1 % Tm^{3+} nanoparticles recorded by transmission electron microscopy (TEM). The sample shows the narrow particle size distribution usually observed for this preparation method as well as a mean particle diameter of about 6–8 nm. Similar to $YbPO_4$:5 % Er^{3+} nanoparticles,[5] the powder X-ray diffraction of $LuPO_4$:49 % Yb^{3+},1 % Tm^{3+} nanoparticles (Figure 1b) display strongly broadened peaks at positions in accord with the tetragonal xenotime phase known from bulk $YbPO_4$ and bulk $LuPO_4$. A mean particle size of about 7 nm is calculated from the peak width at half maximum height by using the Debye–Scherrer formula (shape parameter $K = 1.0$). This value is in accord with the size determined from the TEM images.

Figure 2a shows a survey absorption spectrum of a transparent colloidal solution with 6.7 wt % of $YbPO_4$:5 % Er^{3+} nanocrystals in chloroform. It is dominated by the strong $^2F_{7/2} \rightarrow {}^2F_{5/2}$ absorption band of Yb^{3+} centered at about 10500 cm^{-1} in the NIR region. The weak absorption lines in the visible region are readily assigned to f-f transitions

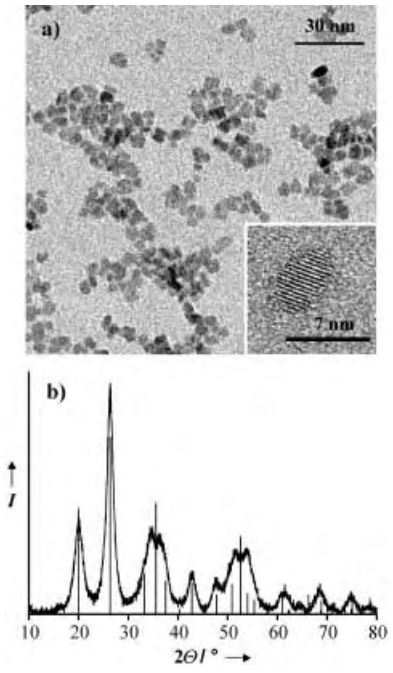


Figure 1. a) TEM micrograph of $LuPO_4$:49 %Yb^{3+},1 %Tm^{3+} nanocrystals. Inset: High-resolution image of a nanocrystal. b) Powder XRD pattern of $LuPO_4$:49 %Yb^{3+},1 %Tm^{3+} nanocrystals. The line spectrum corresponds to the literature data of bulk $LuPO_4$ (PDF No. 84–337 reference pattern, body-centered tetragonal, space group I_{41}/amd).

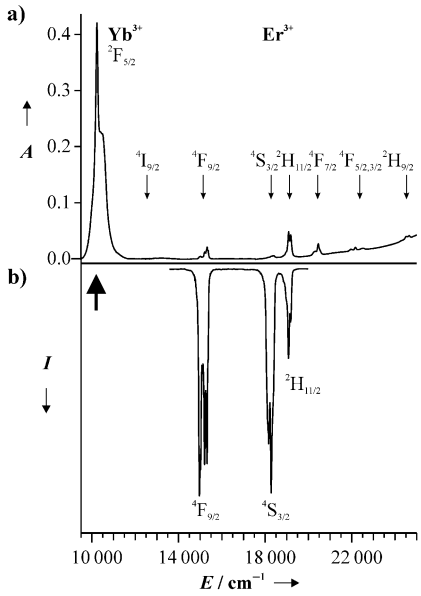


Figure 2. a) Absorption spectrum and assignments of the $YbPO_4$:5 %Er^{3+} colloid. b) Upconversion luminescence spectrum and assignments after excitation at 10230 cm^{-1} (see arrow) with a laser power of 300 mW.

of the Er^{3+} ion as shown in the Figure. Figure 2b shows the upconversion luminescence spectrum of the same solution obtained by exciting into the prominent absorption peak of the Yb^{3+} ion at 10230 cm^{-1} with 300-mW laser power (arrow in Figure 2a). This luminescence is visible to the eye and

 © 2003 Wiley-VCH Verlag GmbH & Co. KGaA, Weinheim

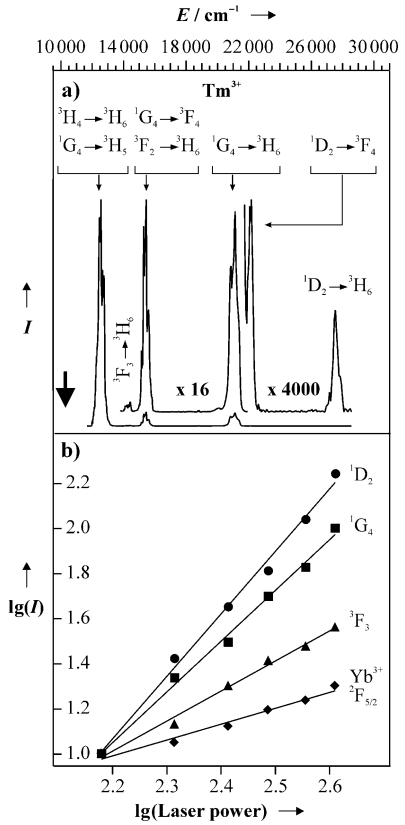


Figure 3. a) As in Figure 2b), but for $LuPO_4$:49%Yb^{3+},1%Tm^{3+}. b) Power dependence of the $LuPO_4$:49%Yb^{3+},1%Tm^{3+} upconversion intensity of the bands at 22000 cm^{-1} (●, $^1D_2 \rightarrow {}^3F_4$), 21000 cm^{-1} (■, $^1G_4 \rightarrow {}^3H_6$), 14000 cm^{-1} (▲, $^3F_3 \rightarrow {}^3F_4$), and 10000 cm^{-1} (◆, Yb^{3+} $^2F_{5/2} \rightarrow {}^2F_{7/2}$ of Yb^{3+}).

appears green. Figure 3a shows the upconversion luminescence spectrum of a transparent colloidal solution with 6.7 wt% of $LuPO_4$:49%Yb^{3+},1%Tm^{3+} nanocrystals in chloroform after 300-mW excitation of the $^2F_{7/2} \rightarrow {}^2F_{5/2}$ transition of the Yb^{3+} ion at 10230 cm^{-1} (arrow in Figure 3a). The upconversion luminecence appears blue and red. The upconversion excitation spectra of both samples were found to correspond to the $^2F_{7/2} \rightarrow {}^2F_{5/2}$ absorption band of the Yb^{3+} ion (Figure 2a).

The remarkable result of this study is the observation—by eye and by spectroscopy—of upconversion luminescence in the fluid state, which to our knowledge is without precedent. Our own attempts to induce upconversion in molecular encapsulation complexes of Er^{3+} and Tm^{3+} in solution have failed.[25] We ascribe the observation of upconversion in our solutions to our nanoparticles having a high crystal quality. Lanthanide ions at the crystal surface are not likely to show upconversion, because of their proximity to the high energy N–H and C–H vibrational oscillators of the dodecylamine protecting layer and the solvent. These vibrational oscillators are very efficient quenchers of the metastable states in molecular complexes of lanthanides. We, therefore, attribute the observed upconversion to Er^{3+} and Tm^{3+} ions replacing Yb^{3+} and Lu^{3+} ions, respectively, inside the nanocrystals.

The observed upconversion spectra in Figures 2a and 3a are similar to the corresponding spectra of solid oxide materials containing Er^{3+} and Tm^{3+} ions, respectively, and we can expect analogous upconversion mechanisms. In our $YbPO_4$:5%Er^{3+} sample the host lattice itself acts as a sensitizer, and the Yb^{3+} excitations can be considered as excitonic. In a first nonradiative energy transfer step an $^2F_{5/2}$ excitation of the Yb^{3+} ion (about 10230 cm^{-1}) is transferred to a Er^{3+} ion to create a $^4I_{11/2}$ excited state. A second NIR photon takes the Er^{3+} ion to a higher energetic state, whose energy lies in the visible region. Emission from $^2H_{11/2}$ and $^4S_{3/2}$ leads to the dominant green luminescence between 18000 cm^{-1} and 19300 cm^{-1}. The red emission centered at 15200 cm^{-1} arises from the $^4F_{9/2} \rightarrow {}^4I_{15/2}$ transition of the Er^{3+} ion. In macrocrystalline Yb^{3+}/Er^{3+} upconversion materials the ratio of green to red emission intensity can be tuned by varying the concentration of the Yb^{3+} and Er^{3+} ions. We would expect similar behavior in nanomaterials.

The $LuPO_4$:49%Yb^3,1%Tm^{3+} system shows a richer upconversion scheme (Figure 4). Up to four $^2F_{5/2}$ excitations of the Yb^{3+} ions (at about 10230 cm^{-1}) can be injected

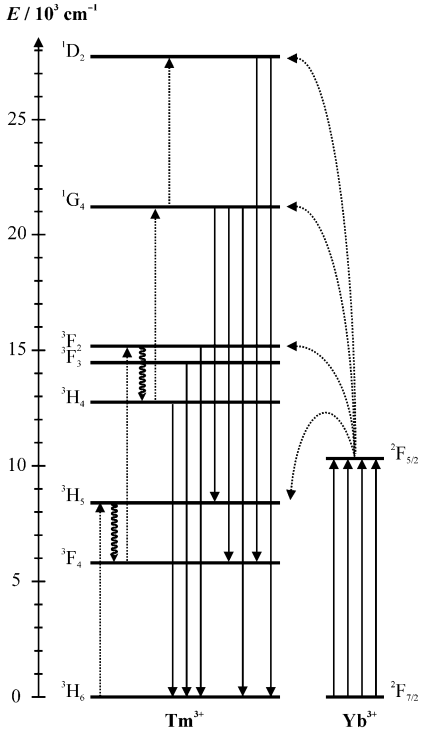


Figure 4. Energy level and upconversion scheme for the $LuPO_4$:49%Yb^{3+},1%Tm^{3+} system. Full, dotted, and curly arrows indicate radiative, nonradiative energy transfer, and multiphonon relaxation processes, respectively.

nonradiatively into the Tm^{3+} ion to excite it up to the $^1D_2$ level in the near-UV region. This result is in good agreement with our experimental results. We observe upconversion emission from four different levels, with the dominant blue band around 21000 cm^{-1} assigned to the $^1G_4 \rightarrow {}^3H_6$ transition of the Tm^{3+} ion. The assignments in Figure 3a, which are spectroscopically straightforward from energy considerations, are nicely confirmed by the experimental power dependencies of the respective upconversion emission

 © 2003 Wiley-VCH Verlag GmbH & Co. KGaA, Weinheim

intensities. Figure 3b shows different power dependences for the various emissions. The slopes of 2.9, 2.2, 1.3, and 0.7 derived from the experimental data in this double logarithmic representation are in good agreement with the 4-, 3-, 2-, and 1-photon excitation processes, respectively, described in Ref. [26] and shown schematically in Figure 4.

We have demonstrated the feasibility of exciting blue, green, and red light emission in transparent colloidal solutions by upconversion excitation in the near-IR region. We consider this work as a first and important step towards the development of materials with considerable application potential for luminescent markers, imaging, and displays in fluid media. Extremely powerful and cheap semiconductor light sources are available for the spectral region around 980 nm, and thus upconversion excitation of visible luminescence would be an elegant alternative for such applications. The overall efficiency of the upconversion processes in our samples is still very poor compared with the best upconversion phosphors in the solid state. There is plenty of scope for improvement, however, and we are engaged in a research program in this direction. One apparent direction is the reduction of the phonon energies of the host lattice to reduce multiphonon relaxation processes and thus increase the lifetimes of the metastable states involved in upconversion. Another direction is the protection of the nanocrystals from high-energy vibrational oscillators by growing a shell of an inert material on the surface of the particles.

Experimental Section

Er^{3+}-doped $LuPO_4$ and $YbPO_4$ nanoparticles were prepared as described recently.[5] Ligand-capped $LuPO_4$:Yb,Tm nanoparticles were synthesized analogously by treating hydrated lutetium chloride (5 mmol), hydrated ytterbium chloride (4.9 mmol), and hydrated thulium chloride (0.1 mmol) with phosphoric acid in a high-boiling mixture of the coordinating solvents tributylphosphate, trihexylamine, and diphenyl ether. The nanoparticles were surface-modified by dissolving $LuPO_4$:49 % Yb^{3+}, 1 % Tm^{3+} or $YbPO_4$:5 % Er^{3+} (500 mg) in dodecylamine (5 g) at 100 °C under nitrogen to increase their solubility in chloroform.[5] After one hour at 100 °C, the solution was allowed to cool to about 50 °C and subsequently mixed with toluene (5–10 mL). The nanoparticles were precipitated from this solution by adding methanol (20–30 mL), the precipitate was separated by centrifugation, washed three times with methanol, and finally dried at room temperature.

Samples used in this study were prepared by dissolving the nanoparticle powder (300 mg) in $CHCl_3$ (3.00 mL, Fluka, $\geq$ 99.5 %). This led to an almost transparent dispersion with a concentration of 6.7 wt %. This was passed through a 0.2 μm filter to give an optically transparent dispersion. Absorption spectra were measured on a Cary 5E (Varian) spectrometer in cuvettes of 1-cm path length (Hellma, QX). Luminescence spectra were measured with the same samples in the same cuvettes as the absorption spectra. They were excited by an Nd:YVO_4 laser (Spectra Physics Millennia XS-FRU, second harmonic) pumped tunable Ti:sapphire laser (Spectra Physics 3900S) in the NIR region. The luminescence was dispersed by a 0.85-m double monochromator (Spex 1402) using gratings with 1200 lines per mm (blaze angle optimal for gratings 500 nm) after detection by a cooled photomultiplyer (Hamamatsu 3310–01) using a photon counting system (Stanford Research SR 400). All the spectra were corrected for the sensitivity of the monochromator and the detection system as well as for the refractive index of air (vacuum correction). They are represented as photon flux versus wavenumbers. In all the experiments the excitation laser was focused with a lens of $f = 53$ mm. X-ray diffraction patterns of powder samples were recorded with a Philips X'pert system. High-resolution electron micrographs of the particles were taken using a Philips CM 300 UT transmission electron microscope equipped with a CCD-camera (Gatan).

Received: February 3, 2003 [Z51091]

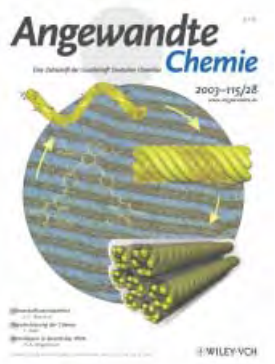
Keywords: colloids · lanthanides · luminescence · nanocrystals · upconversion

[1] A. A. Kaminskii, *Laser Crystals*, Springer, Berlin **1994**.
[2] T. Jüstel, H. Nikol, C. Ronda, *Angew. Chem.* **1998**, *110*, 3250; *Angew. Chem. Int. Ed.* **1998**, *37*, 3084.
[3] H. Meyssamy, K. Riwotzki, A. Kornowski, S. Naused, M. Haase, *J. Phys. Chem. B* **2000**, *104*, 2824.
[4] K. Riwotzki, H. Meyssamy, H. Schnablegger, A. Kornowski, M. Haase, *Angew. Chem.* **2001**, *113*, 574; *Angew. Chem. Int. Ed.* **2001**, *40*, 573.
[5] O. Lehmann, H. Meyssamy, K. Kömpe, H. Schnablegger, M. Haase, *J. Phys. Chem. B*, in press.
[6] M. Yin, W. Zhang, S. Xia; J.-C. Krupa, *J. Lumin.* **1996**, *68*, 335.
[7] G. E. S. Brito, S. J. L. Rebeiro, V. Briois, J. Dexpert-Ghys, C. V. Santilli, S. H. Pulcinelli, *J. Sol-Gel Sci. Technol.* **1997**, *8*, 261.
[8] B. Tissue, *Chem. Mater.* **1998**, *10*, 2837.
[9] K. Riwotzki, M. Haase, *J. Phys. Chem. B* **1998**, *102,* 10129.
[10] Y. L. Soo, S. W. Huang, Z. H. Ming, Y. H. Kao, G. C. Smith, E. Goldburt, R. Hodel, B. Kulkarni, J. V. D. Veliadis, R. N. Bhargava, *J. Appl. Phys.* **1998**, *83*, 5404.
[11] T. Schmidt, G. Müller, L. Spanhel, K. Kerkel, A. Forchel, *Chem. Mater.* **1998**, *10*, 5404.
[12] H. Meyssamy, K. Riwotzki, A. Kornowski, S. Naused, M. Haase, *Adv. Mater.* **1999**, *11*, 840.
[13] A. Huignard, T. Gacoin, J.-P. Boilot, *Chem. Mater.* **2000**, *12*, 1090.
[14] Z. Wie, L. Sun, C. Liao, C. Yan, S. Huang, *Appl. Phys. Lett.* **2002**, *80*, 1447.
[15] G. A. Hebbink, J. W. Stouwdam, D. N. Reinhoudt, F. J. M. van Veggel, *Adv. Mater.* **2002**, *14*, 1147.
[16] P. Schuetz, F. Caruso, *Chem. Mater.* **2002**, *14*, 4509.
[17] "Upconversion Phosphors": M. P. Hehlen, M. L. F. Phillips, N. J. Cockroft, H. U. Güdel, *Encyclopedia of Materials: Science and Technology, Vol. 10*, Pergamon/Elsevier, Oxford **2001**, p. 9456.
[18] N. Bloembergen, *Phys. Rev. Lett.* **1959**, *2*, 84.
[19] W. Lenth, R. M. Mcfarlane, *J. Lumin.* **1990**, *45*, 346–350.
[20] E. Downing, L. Hesselink, J. Ralston, and R. Macfarlane, *Science* **1996**, *273*, 1185.
[21] D. Matsuura, *Appl. Phys. Lett.* **2002**, *81*, 4526.
[22] G. Yi, B. Sun, F. Yang, D. Chen, Y. Zhou, J. Cheng, *Chem. Mater.* **2002**, *14*, 2910.
[23] J. A. Cabobianco, J. C. Boyer, F. Vetrone, A. Speghini, M. Bettinelli, *Chem. Mater.* **2002**, *14*, 2915.
[24] A. Amitava, C. S. Friend, R. Kapoor, P. N. Prasad, *J. Phys. Chem. B.* **2002**, *106*, 1909.
[25] C. Reinhard, H. U. Güdel, *Inorg. Chem.* **2002**, *41*, 1048.
[26] M. Pollnau, D. R. Gamelin, S. R. Lüthi, M. P. Hehlen, H. U. Güdel, *Phys. Rev. B* **2000**, *61*, 3337.

 © 2003 Wiley-VCH Verlag GmbH & Co. KGaA, Weinheim

Cover Picture

Frank Würthner,* Sheng Yao, and Uwe Beginn



Hierarchical self-organization of bis(merocyanins), as shown in the cover picture, lead in the first step to helical polymers (top), which come together to form rod-type aggregates in methylcyclohexane (middle right). These arrange finally at higher concentrations into a hexagonal dense packing (bottom). As F. Würthner et al. describe in their Communication on page 3247 ff., gels and liquid-crystalline films can be generated in this way with unusual textures, as shown in the background.

Contents

Angewandte EarlyView

The following articles are available online (in Wiley Interscience). You can find them at www.angewandte.org, under Full Text, Forthcoming Articles.

I. D. Hills, G. C. Fu:*
Catalytic Enantioselective Synthesis of Oxindoles and Benzofuranones that Bear a Quaternary Stereocenter
DOI: 10.1002/anie.200351666
Published online: July 3, 2003

T. J. Kidd, T. J. A. Loontjens, D. A. Leigh,* J. K. Y. Wong:*
Rotaxane Building Blocks bearing Blocked Isocyanate Stoppers: Polyrotaxanes through Post-Assembly Chain Extension
DOI: 10.1002/anie.200351458
Published online: July 3, 2003

R. R. Davda, J. A. Dumesic:*
Catalytic Reforming of Oxygenated Hydrocarbons for Hydrogen with Low Levels of Carbon Monoxide
DOI: 10.1002/anie.200351664
Published online: June 18, 2003

Articles judged by the referees or the editior as being either very important or very urgent are immediately edited, proof-read, and electronically published once the manuscript has arrived in the editiorial office in its final form. As long as there is no page number available these articles should be cited in the following manner:

Author(s) *Angew. Chem. Int. Ed.*, online publication date, DOI.

News

Materials Science: Whitesides Recognized ——— **3200**

Brédas on the Move ——— **3200**

Books

Medicinal Chemistry ——— **3201** — Frank D. King — *reviewed by G. Adam*

Chemical Analysis in the Laboratory ——— **3202** — I. Mueller-Harvey, R. M. Baker — *reviewed by M. Vogel*

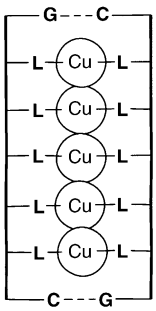
Highlights

Metal Ions in Artificial DNA

H.-A. Wagenknecht* ——— **3204 – 3206**

Metal-Mediated DNA Base Pairing and Metal Arrays in Artificial DNA: Towards New Nanodevices

Inside the helix: In addition to hydrogen bonds and π stacking in natural DNA, metal-ion-mediated base pairing is a third key motif for the interaction between complementary DNA. The introduction of several metal-ion-mediated base pairs adjacent to each other in DNA allows the self-assembled alignment of the metal centers to form a ferromagnetically coupled chain within the DNA-like double helix (see picture).



Essays

Popularization of Chemistry

S. Shaik* ——— **3208 – 3215**

Chemistry—A Central Pillar of Human Culture

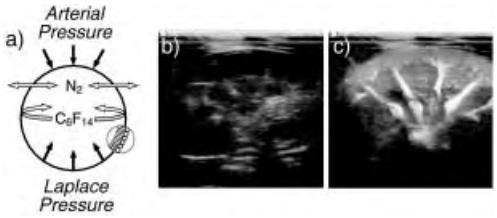
Chemistry is the intellectual adventure of Mankind in his excursion through his own material being. As this journey unfolds, so Mankind discovers the complex connection between matter and its emergent spiritual manifestations. Chemistry defines the limitation of the power over matter, and exemplifies this limitation by, for example, pollution and chemical warfare. Ruling over matter means also mastering the right ways of tinkering with it. These and other aspects of our science are discussed in this essay.

Reviews

Ultrasound Contrast Agents

E. G. Schutt, D. H. Klein, R. M. Mattrey, J. G. Riess* _____ 3218 – 3235

Injectable Microbubbles as Contrast Agents for Diagnostic Ultrasound Imaging: The Key Role of Perfluorochemicals



Perfluorocarbon gases are essential for stabilizing intravenously injectable microbubbles (see diagram; the microbubble (a) is osmotically stabilized with perfluorohexane) that function as reflectors for ultrasound contrast enhancement. The vascular tree of a rabbit kidney (b) "lights up" upon administration of the contrast agent (c). Contrast-specific imaging modes can result in earlier and increased diagnostic and prognostic accuracy, and clinical and economical value.

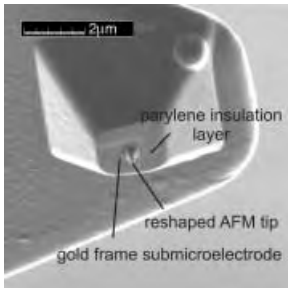
Communications

Imaging Enzyme Activity

A. Kueng, C. Kranz,* A. Lugstein, E. Bertagnolli, B. Mizaikoff _ 3238 – 3240

Integrated AFM–SECM in Tapping Mode: Simultaneous Topographical and Electrochemical Imaging of Enzyme Activity

Microscopically measuring the activity of glucose oxidase (GOD): Microfabricated difunctional AFM–SECM (atomic force microscopy–scanning electrochemical microscopy) tips with integrated micro- and nanoelectrodes (see picture) enable independent, simultaneous investigation of surface topography and enzymatic activity, for example, of the oxidoreductase enzyme GOD, in soft samples in AFM tapping mode.

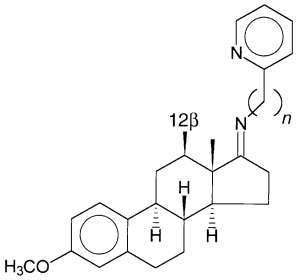


Diastereoselective Hydroxylations

B. Schönecker,* T. Zheldakova, Y. Liu, M. Kötteritzsch, W. Günther, H. Görls _____ 3240 – 3244

Biomimetic Hydroxylation of Non-activated CH_2 Groups with Copper Complexes and Molecular Oxygen

Copper(I) complexes with steroidal ligands (see formula) undergo regio- and stereoselective γ-hydroxylation in the 12β-position of the steroid in the presence of molecular oxygen. After reduction a 17β,12β-amino alcohol is obtained. Under hydrolytic conditions a 12β-hydroxy-17-ketone can be isolated.



n = 1, 2

For the USA and Canada:
ANGEWANDTE CHEMIE International Edition (ISSN 1433-7851) is published weekly by Wiley-VCH PO Box 191161, D 69451 Weinheim, Germany. Air freight and mailing in the USA by Publications Expediting Inc. 200 Meacham Ave., Elmont, NY 11003. Periodicals postage paid at Jamaica NY 11431. US POSTMASTER: send address changes to *Angewandte Chemie*, Wiley-VCH, 111 River Street, Hoboken, NJ 07030. Annual institutional subscription price for institutions: Europe € 2998.00/3148.00. Outside Europe US$ 3718.00/3904.00 (valid for print or electronic/print and electronic delivery); for individuals who are personal members of a national chemical society, or whose institution already subscribes, or who are retired or self-employed consultants, print only (including postage and handling charges): Europe € 248.00/Outside Europe US$ 348.00.

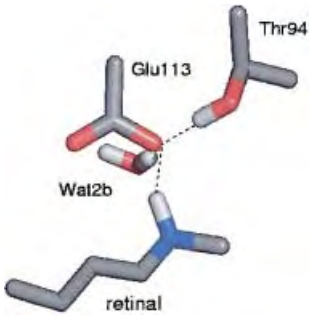
 © 2003 Wiley-VCH Verlag GmbH & Co. KGaA, Weinheim

Contents

The Chemistry of Vision

V. Buss,* M. Sugihara, P. Entel, J. Hafner ——— 3245 – 3247

Thr94 and Wat2b Effect Protonation of the Retinal Chromophore in Rhodopsin

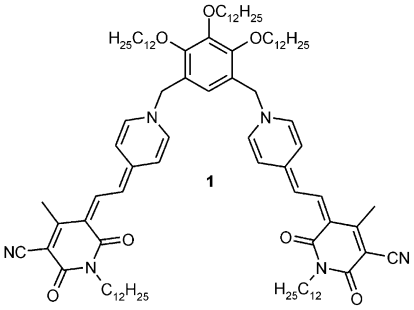


Only with the help from (little) "friends" is it possible for the 11-*cis*-retinal Schiff base to compete successfully against Glu113 for a proton (see picture). A strategically placed amino acid, Thr94, plus a water molecule are sufficient to reduce the basicity of the glutamate and stabilize the protonated chromophore—this is the result of ab initio optimization and molecular-dynamic study of the retinal binding site in rhodopsin.

Self-Organization of Dyes

F. Würthner,* S. Yao, U. Beginn ——— 3247 – 3250

Highly Ordered Merocyanine Dye Assemblies by Supramolecular Polymerization and Hierarchical Self-Organization

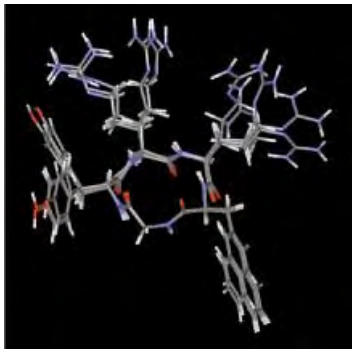


Step by step: Bis(merocyanine) dyes **1** self-assemble in a stepwise manner with increasing concentration to afford supramolecular polymers, organogels, and liquid-crystalline phases. The close contacts between the chromophores within these superstructures enables strong D- and H-type excitonic coupling to be observed.

Rational Drug Design

N. Fujii,* S. Oishi, K. Hiramatsu, T. Araki, S. Ueda, H. Tamamura, A. Otaka, S. Kusano, S. Terakubo, H. Nakashima, J. A. Broach, J. O. Trent, Z.-x. Wang, S. C. Peiper ——— 3251 – 3253

Molecular-Size Reduction of a Potent CXCR4-Chemokine Antagonist Using Orthogonal Combination of Conformation- and Sequence-Based Libraries



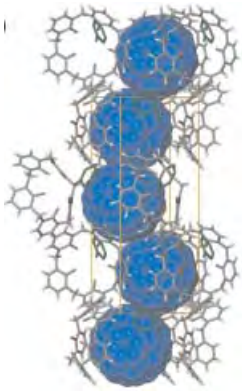
Efficient downsizing of peptides: By combination of two orthogonal "conformation-based" and "sequence-based" libraries, the cyclic pentapeptide *cyclo*-(-L-Nal 1-Gly 2-D-Tyr 3-L-Arg 4-L-Arg 5-) (Nal = L-3-(2-naphthyl)alanine; see overlay of the five lowest energy structures), which exhibited strong CXCR4 antagonism (IC_{50} = 4 nM) comparable to that of a 14-residue lead compound, T140, was discovered.

C_{60}/Calixarene Complex

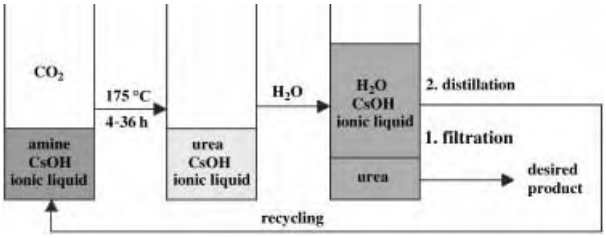
J. L. Atwood,* L. J. Barbour,* M. W. Heaven, C. L. Raston* ——— 3254 – 3257

Controlling van der Waals Contacts in Complexes of Fullerene C_{60}

An impurity aids in the purification of C_{60}. A 1:1 complex of C_{60} and calix[5]arene crystallizes from toluene (see picture) with the fullerenes organized in a one-dimensional zigzag array shrouded by a sheath of calixarenes. The complex forms in the presence of other globular molecules including C_{70}, the major impurity in fullerite.



 © 2003 Wiley-VCH Verlag GmbH & Co. KGaA, Weinheim

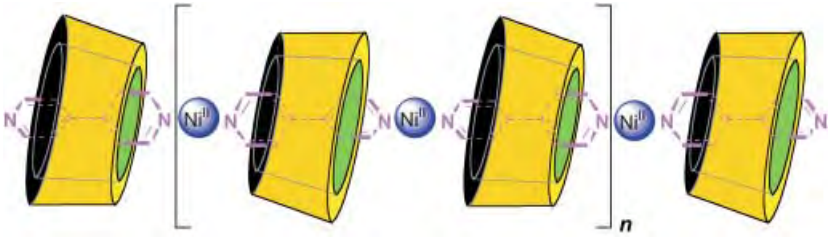


Simple, clean, safe, reproducible, and practical describes the synthesis of disubstituted urea derivatives, which are effectively synthesized from amines and carbon dioxide with a CsOH/ionic-liquid catalyst system. The products are easily separated and the catalytic system can be reused without deactivation (see picture).

CO_2 Activation in an Ionic Liquid

F. Shi, Y. Deng,* T. SiMa, J. Peng, Y. Gu, B. Qiao ——— **3257 – 3260**

Alternatives to Phosgene and Carbon Monoxide: Synthesis of Symmetric Urea Derivatives with Carbon Dioxide in Ionic Liquids

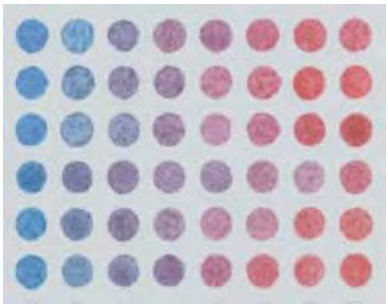


The missing link: Ni^{II} ions have been used to coordinate to 4,4′-dipyridine included within β-cyclodextrin to form a linear polymeric rotaxane (see schematic representation). The binding of the 4,4′-dipyridine within the cyclodextrin has been examined both in solution and in the solid state.

Polymeric Coordination Rotaxane

Y. Liu,* Y.-L. Zhao, H.-Y. Zhang, H.-B. Song ——— **3260 – 3263**

Polymeric Rotaxane Constructed from the Inclusion Complex of β-Cyclodextrin and 4,4′-Dipyridine by Coordination with Nickel(II) Ions

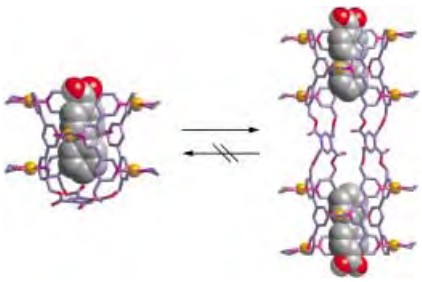


Rugged and sensitive chromatic solid-state materials are obtained by encapsulation of bichromic polydiacetylene-phospholipid liposomes appended with immunoglobulins in hybrid silica–siloxane sol–gel polymers. The resulting composites undergo dramatic and visible blue-to-red color transitions upon exposure to the corresponding antigens (see picture) and have applications as sensors.

Solid-State Sol–Gel Biosensors

I. Gill,* A. Ballesteros ——— **3264 – 3267**

Immunoglobulin–Polydiacetylene Sol–Gel Nanocomposites as Solid-State Chromatic Biosensors



Crystal engineering: A dodecapyridine ligand and six Pd^{II} ions self-assemble to give a mono-end-capped coordination tube that has significant stability, but is converted into a double open tube through crystallization. Once formed, there is no route back to the capped tube (see picture). Despite the labile nature of Pd^{II}–pyridine coordination bonds, both structures are not in a rapid equilibrium and are, therefore, kinetically trapped during self-assembly.

Kinetic Control of Self-Assembly

S. Tashiro, M. Tominaga, T. Kusukawa, M. Kawano, S. Sakamoto, K. Yamaguchi, M. Fujita* ——— **3267 – 3270**

Pd^{II}-Directed Dynamic Assembly of a Dodecapyridine Ligand into End-Capped and Open Tubes: The Importance of Kinetic Control in Self-Assembly

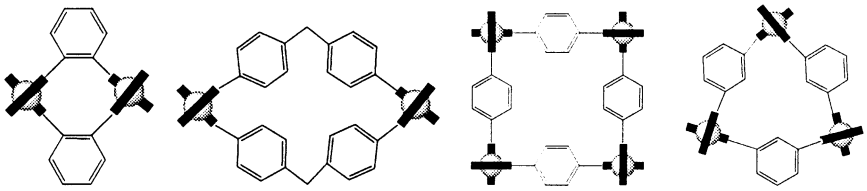
 © 2003 Wiley-VCH Verlag GmbH & Co. KGaA, Weinheim

Contents

Self-Assembly of Pyrrole Derivatives

Z. Wu, Q. Chen, S. Xiong, B. Xin, Z. Zhao, L. Jiang, J. S. Ma* ——— **3271 – 3274**

Double-Stranded Helicates, Triangles, and Squares Formed by the Self-Assembly of Pyrrol-2-ylmethyleneamines and Zn^{II} Ions

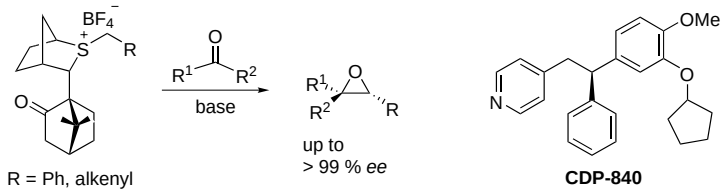


Neutral double-stranded helicates and molecular triangles and squares are formed through the self-assembly of spacer-bridged bis(pyrrol-2-ylmethyleneamine) ligands and Zn^{II} ions (see scheme). The steric requirements of the Zn centers and the size and relative flexibility of the ligands dictate the degree of association, and hence, the geometry of the products.

Asymmetric Synthesis of Epoxides

V. K. Aggarwal,* I. Bae, H.-Y. Lee,* J. Richardson, D. T. Williams ——— **3274 – 3278**

Sulfur-Ylide-Mediated Synthesis of Functionalized and Trisubstituted Epoxides with High Enantioselectivity; Application to the Synthesis of CDP-840

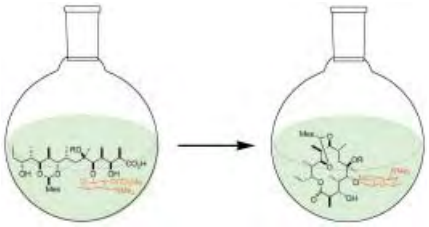


Benzyl and substituted allyl sulfonium salts react with a broad range of simple and functionalized aldehydes and ketones to give epoxides with high diastereoselectivity and high enantioselectivity (see scheme). The process has been applied to a short synthesis of the phosphodiesterase-IV inhibitor CDP-840. R^1, R^2 = hydrogen, alkyl, alkenyl, alkynyl, aryl, or pyridyl.

Natural Product Synthesis

P. J. Hergenrother, A. Hodgson, A. S. Judd, W.-C. Lee, S. F. Martin* —— **3278 – 3281**

An Abiotic Strategy for the Enantioselective Synthesis of Erythromycin B

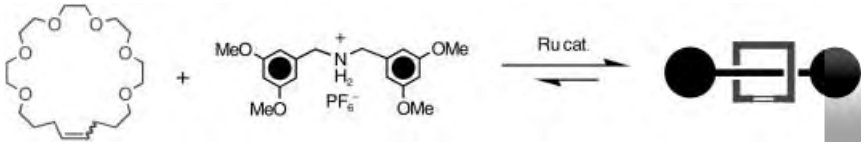


Sweet success: The classical approach to macrolide antibiotics involves a macrocyclization followed by the introduction of the carbohydrate residue(s). Now for the first time, a glycosylated seco-acid (see scheme, left) was cyclized to give an intermediate that was converted into a naturally occurring macrolide, as exemplified by the synthesis of erythromycin B (right).

Reversible Rotaxane Synthesis

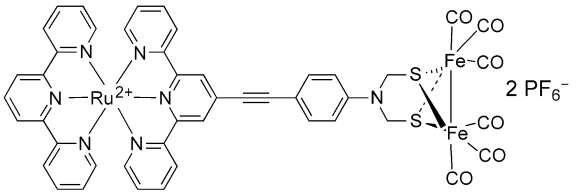
A. F. M. Kilbinger, S. J. Cantrill, A. W. Waltman, M. W. Day, R. H. Grubbs* ——— **3281 – 3285**

Magic Ring Rotaxanes by Olefin Metathesis



Trick or treat? Ruthenium alkylidene catalyzed ring-closing metathesis of crown ether like diene substrates around a dumbbell-shaped secondary ammonium ion affords [2]rotaxanes. The reversible nature of this process has been demonstrated through a "magic ring" synthesis, wherein the preformed olefinic macrocycle and dumbbell-shaped component equilibrate to form the hydrogen-bond-stabilized [2]rotaxane in the presence of a metathesis catalyst (see scheme).

 © 2003 Wiley-VCH Verlag GmbH & Co. KGaA, Weinheim

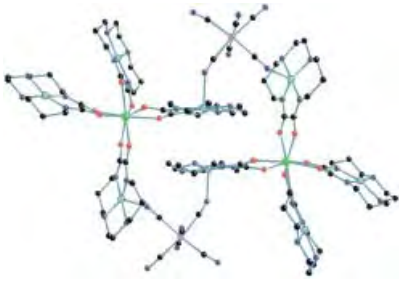


First synthetic steps towards light-driven hydrogen production have been achieved by covalently linking a $[Ru^{II}(terpy)_2]$ (terpy = 2,2′:6′,2″-terpyridine) photosensitizer to a biomimetic model of the iron hydrogenase active site (see picture). The IR data show that there is little electronic communication between the redox-active metal centers in the ground state.

Electron-Transfer Processes

S. Ott, M. Kritikos, B. Åkermark,* L. Sun* ——— **3285 – 3288**

Synthesis and Structure of a Biomimetic Model of the Iron Hydrogenase Active Site Covalently Linked to a Ruthenium Photosensitizer

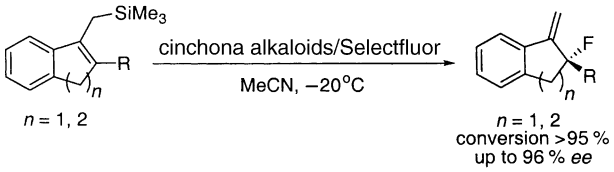


Ion bridge: A unique mixed heterotrimetallic coordination polymer (depicted) with a bridging $[Cr(CN)_6]^{3-}$ ion is synthesized by the slow diffusion of a macrocyclic oxamido-Cu^{II} complex, and gadolinium trichloride into potassium hexacyanochromate(III). Intermetallic ferromagnetic coupling is operative within the 2D layer, giving rise to an $S = 7$ ground state. C = black, Cr = pink, Cu = blue, Gd = green, N = violet, O = red.

A Heterotrimetallic Complex

H.-Z. Kou,* B. C. Zhou, S. Gao, R.-J. Wang ——— **3288 – 3291**

A 2D Cyano- and Oxamidato-Bridged Heterotrimetallic Cr^{III}-Cu^{II}-Gd^{III} Complex



Enantiopure *N*-fluorocinchona alkaloids promoted the electrophilic fluorodesilylation of allyl silanes in a conceptually new approach to the regio- and enantioselective formation of allylic fluorides (see scheme). Excellent conversions were observed in these reactions, which afforded the desired allylic fluorides with up to 96% *ee*.

Chiral Allylic Fluorides

B. Greedy, J.-M. Paris, T. Vidal, V. Gouverneur* ——— **3291 – 3294**

Regio- and Enantioselective Synthesis of Allylic Fluorides by Electrophilic Fluorodesilylation of Allyl Silanes



One ligand, four anions! Four anionic forms of a single ligand bis[*N*-(2,6-diisopropylphenyl)imino]acenaphthene (dpp-bian) were isolated on a preparative scale for the first time and unambiguously characterized by single-crystal X-ray structure analysis. The ligand, dpp-bian, may be easily reduced in diethyl ether by sodium metal to give the mono-, di-, tri-, or tetranion (depicted).

Four Anions of a Diimine Ligand

I. L. Fedushkin,* A. A. Skatova, V. A. Chudakova, G. K. Fukin ——— **3294 – 3298**

Four-Step Reduction of dpp-bian with Sodium Metal: Crystal Structures of the Sodium Salts of the Mono-, Di-, Tri-, and Tetraanions of dpp-bian

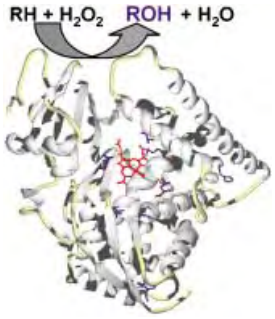
 © 2003 Wiley-VCH Verlag GmbH & Co. KGaA, Weinheim

Contents

Enzyme Engineering

P. C. Cirino, F. H. Arnold* — **3299 – 3301**

A Self-Sufficient Peroxide-Driven Hydroxylation Biocatalyst

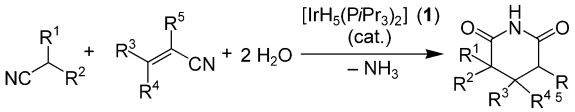


Directed evolution of the heme domain of cytochrome P450 BM-3 has resulted in a versatile, highly active peroxide-driven hydroxylation catalyst (see picture) that requires neither NADPH nor reductase and functions in a cell-free reaction system. This simplified, "biomimetic" catalyst is amenable to further optimization, for example, to improve stability or alter its substrate range.

Ambiphilic Lewis Acid and Base Catalyst

H. Takaya, K. Yoshida, K. Isozaki, H. Terai, S.-I. Murahashi* — **3302 – 3304**

Transition-Metal-Based Lewis Acid and Base Ambiphilic Catalysts of Iridium Hydride Complexes: Multicomponent Synthesis of Glutarimides



Mutual destruction of reagents in acid- and base-promoted reactions in the same container is now avoidable with the iridium polyhydride complex $[IrH_5(PiPr_3)_2]$ (**1**), which is an ambiphilic Lewis acid and base catalyst. By using catalyst **1**, a three-component reaction of nitriles, olefins, and water proceeds efficiently to give glutarimides, which are pharmacologically important (see scheme).

VIP Communications labeled with this symbol have been judged by two referees as being "very important papers".

The publication of Communications labeled with this symbol has been accelerated because of their topical or highly competitive nature.

Sources

Product and Company Directory

You can start the entry for your company in "Sources" in any issue of *Angewandte Chemie*.

If you would like more information, please do not hesitate to contact us.

Wiley-VCH Verlag – Advertising Department
Tel.: 0 62 01 - 60 65 65
Fax: 0 62 01 - 60 65 50
E-Mail: MSchulz@wiley-vch.de

Service

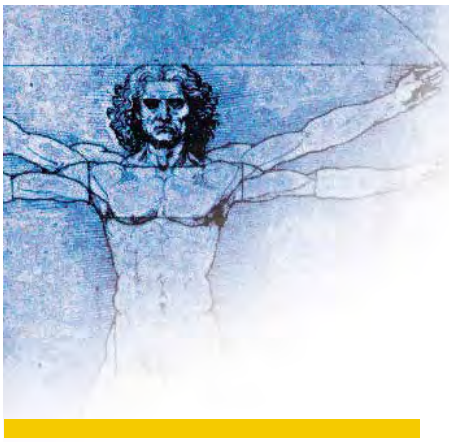
Keywords — *3306*

Authors — *3307*

Angewandte's Sister Journals — *3308*

Vacancies — *3199*

Preview — *3309*



G. Whitesides Receives Kyoto Prize

The Kyoto Prizes are being awarded this year for the 19th time to people active in the arts and in the sciences who have made an outstanding contribution to the further development of their discipline. The Prizes are funded by a Foundation established by Kazuo Inamori, founder of the Japanese technology corporate group Kyocera. George M. Whitesides (Harvard University) is the recipient of the Kyoto Prize in the category Advanced Technology. The other laureates are the astrophysicist Eugene N. Parker from Chicago (Basic Sciences) and Tamao Yoshida, a traditional Japanese puppeteer (Arts and Philosophy).



G. Whitesides

Whitesides is being awarded the Kyoto Prize in recognition of his services to materials science. His work links bio- and nanotechnology, as is nicely illustrated by his recent Communication in *Angewandte Chemie* entitled "Self-Healing Systems Having a Design Stimulated by the Vertebrate Spine".[1] His Review on "Soft Lithography"[2] is among the ten *Angewandte* articles most often downloaded since 2000. A second Review from the same year entitled "Polyvalent Interactions in Biological Systems: Implications for Design and Use of Multivalent Ligands and Inhibitors" shows the breadth of his research interests.[3]

George M. Whitesides did his first degree at Harvard University (Cambridge, MA, USA) and completed his Ph.D. in 1964 at the California Institute of Technology (Pasadena, CA, USA) under the guidance of J. D. Roberts. He was a professor at the Massachusetts Institute of Technology (Boston, MA, USA) from 1963 until 1982. He then moved to the Department of Chemistry at Harvard University, where he was Head of Department from 1986 to 1989. Whitesides is currently Mallinckrodt Professor of Chemistry. Biochemistry, chemistry at interfaces, materials science, molecular virology, optics, molecular self-assembly, bioanalytical chemistry, microelectromechanical systems, microfluidic systems, and nonequilibrium systems all count among his current research interests. He is a member of the International Advisory Board of *Angewandte Chemie*.

J.-L. Brédas: A Bridge over the Atlantic

One foot in Europe, the other in North America: This is nothing new to Jean-Luc Brédas. He remains a professor at the University of Mons-Hainaut (Belgium) and Director of the Center for Molecular Electronics and Photonics there. However, his "foot" in the USA is moving: Brédas is leaving the University of Arizona in Tucson and will take up a position as Professor of Chemistry and Biochemistry at the Georgia Institute of Technology in Atlanta in August. His "bridging" function makes an intensive exchange program for graduate students possible.



J.-L. Brédas

Brédas began his career as an independent researcher in 1977 at the University of Namur (Belgium). In 1988 he took up an appointment at the University of Mons, and in 1999 he took up another in Arizona, while keeping his position in Belgium. At "Georgia Tech", together with colleagues from chemistry and optics, he will set up the Center on Organic Electronics and Photonics, which will bring together researchers from different disciplines and is intended to foster international collaborations in the medium term. A new building should be ready to move into in three years.

The work of Brédas's research group is focused on the structural, optical, and electronic properties of new materials for electronics, photonics, and information technology. They apply methods in quantum chemisty and in the physics of condensed matter in this research. The object of their studies often involves oligomers and polymers with π-conjugated main chains.[4] A recent publication is entitled "Resonant Tunneling Processes along Conjugated Molecular Wires: A Quantum-Chemical Description".[5]

Brédas is the recipient of numerous awards and was President of the Société Royale de Chimie, the chemical society of the French-speaking part of Belgium, from 1997 to 1999. He is a member of the Advisory Boards of the *European Journal of Inorganic Chemistry* and *Advanced Functional Materials*.

[1] M. Boncheva, G. M. Whitesides, *Angew. Chem.* **2003**, *115*, 2748; *Angew. Chem. Int. Ed.* **2003**, *42*, 2644.

[2] Y. Xia, G. M. Whitesides, *Angew. Chem.* **1998**, *110*, 568; *Angew. Chem. Int. Ed.* **1998**, *37*, 550.

[3] M, Mammen, S.-K. Choi, G. M. Whitesides, *Angew. Chem.* **1998**, *110*, 2908; *Angew. Chem. Int. Ed.* **1998**, *37*, 2754.

[4] J. Cornil, D. Beljonne, J.-P. Calbert, J.-L. Brédas, *Adv. Mater.* **2001**, *13*, 1053.

[5] Y. Karzazi, J. Cornil, J.-L. Brédas, *Adv. Func. Mater.* **2002**, *12*, 787.

 © 2003 Wiley-VCH Verlag GmbH & Co. KGaA, Weinheim

Metal Ions in Artificial DNA

Metal-Mediated DNA Base Pairing and Metal Arrays in Artificial DNA: Towards New Nanodevices

*Hans-Achim Wagenknecht**

Keywords:
base pairing · DNA structures · metal–metal interactions · nucleoside mimetics · oligonucleotides

Fifty years after the elucidation of the DNA double-helix structure, the unique properties of the DNA double helix continue to fascinate chemists. The principle of base pairing between two complementary oligonucleotide strands is rather uncomplicated. Essentially, two noncovalent forces mainly stabilize the double-helical structure of DNA: a) the arene–arene π stacking of the planar heterocycles of the DNA bases, and b) the hydrogen bonding between the complementary DNA bases.

Besides the biological importance of DNA as the carrier of genetic information, the regular and canonical structure of duplex DNA can be regarded as a template for the bioinspired generation of new functionalized molecular architectures.[1] Especially the self-assembly and the highly specific interstrand recognition of two complementary oligonucleotides represent the most promising aspects of the DNA framework on the way to new inorganic and bioorganic nanosize devices.[2]

One important strategy for the functionalization of DNA duplexes is the replacement of the natural bases by artificial nucleosides or nucleoside mimics.[3] However, this approach is restricted to molecules with a distinct shape and size that should be comparable to normal base pairs to ensure that the DNA modifications occur highly specifically and site selectively.[3] In the last 2–3 years, a new generation of such nucleoside mimics were reported in which the hydrogen-bonding interactions were replaced by a metal-mediated base pairing.[4–6] The advantage of this modification strategy is that it allows the metal ions to be placed in the interior of the DNA duplex. This represents an important structural prerequisite for the development of new molecular devices based on interacting metal centers. Tor and Weizman coined the term "ligandosides" for suitable metal ion nucleoside chelators, which should fulfill the following requirements:[4]

a) The nucleoside mimics should be compatible with the standard automated DNA synthesis.
b) The chelating part of the nucleoside mimics should have a higher affinity than natural DNA bases towards metal ions.
c) The nucleoside mimics should form planar complexes with metal ions, and their dimensions should be comparable with those of a DNA base pair.

The groups of Tor,[4] Schultz and Meggers,[5] and Shionoya[6] synthesized a few strong chelators that meet the above criteria and incorporated them as artificial DNA bases into oligonucleotides (Figure 1). DNA base pairing resulted from the addition of metal ions such as Cu^{II}, Pd^{II}, or Ag^{I}, which form planar complexes with the nucleoside chelators. The planarity of these artificial DNA base pairs ensures their proper intercalation within the DNA base stack. A remarkable consequence of the insertion of just one artificial metal-ion-mediated base pair is that the thermal stability of the modified DNA duplex is strongly enhanced relative to one with normal hydrogen-bond interactions.

The incorporation of metal complexes as artificial base pairs into the biopolymer DNA represents a third key motif for interactions between the two complementary strands of the biopolymeric DNA. Hence, this modification can be recognized as an extension of the genetic alphabet and, more importantly, is also expected to lead to novel DNA structures and functions. An important milestone towards such new DNA architectures was recently reported by Shionoya and co-workers, who incorporated several metal ions adjacent to each other into an artificial DNA framework. As a result, a self-assembled metal array was formed.[7] Examples of one-dimensional arrays in solution are quite limited and they are mainly investigated in the solid-state.[8] Shionoya and co-workers synthesized a hydroxypyridone nucleobase, which meets all the criteria for a ligandoside.[4] The deprotonated hydroxypyridone chelator forms stable, planar, and electrostatically neutral complexes in the presence of Cu^{II} ions (Scheme 1).[9]

The hydroxypyridone nucleoside was synthetically incorporated through automated phosphoramidite chemistry into short oligonucleotides that contain three to seven nucleotide units. The DNA base sequences were designed in such a way that between one and five Cu^{II}-modified nucleosides were placed adjacent to each other. An important observation was that the modified oligonucleotides do not form stable duplex structures in the absence of Cu^{II} ions. Thus, duplex formation can be attributed solely to the Cu^{II}-mediated alterna-

[*] H.-A. Wagenknecht
Institute for Organic Chemistry
and Biochemistry
Technical University of Munich
Lichtenbergstrasse 4
85747 Garching (Germany)
Fax: (+49) 89-289-13210
E-mail: wagenknecht@ch.tum.de

 © 2003 Wiley-VCH Verlag GmbH & Co. KGaA, Weinheim DOI: 10.1002/anie.200301661

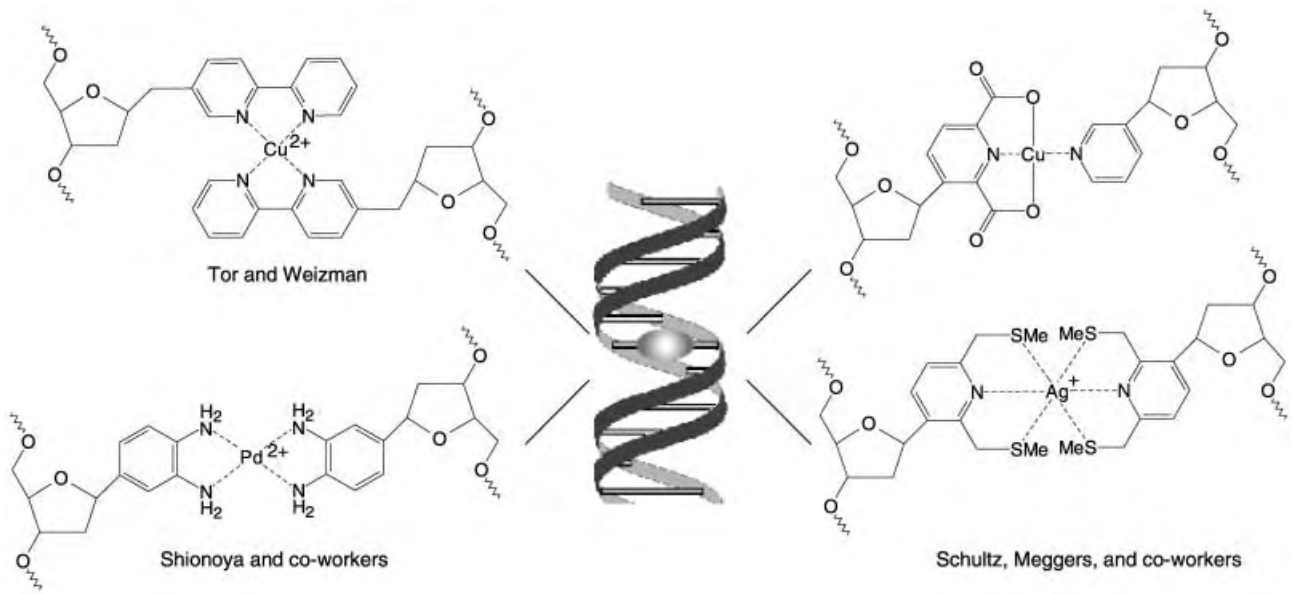
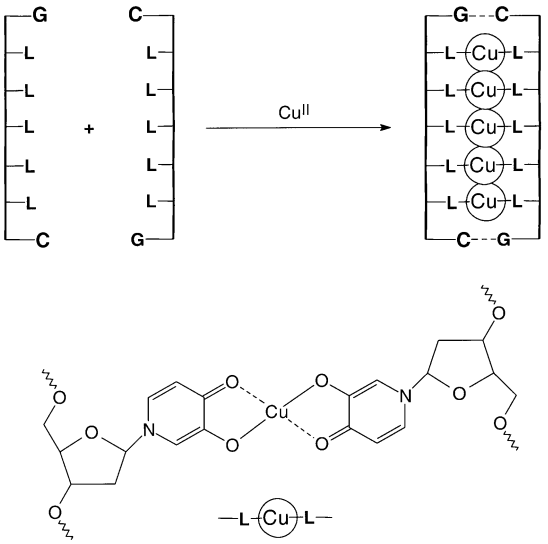


Figure 1. Metal-ion-mediated base pairs replace natural base pairs in DNA duplexes and, as a result, enhance the thermal stability.[4–6]



Scheme 1. Formation of a metal array of hydroxypyridone–Cu^{II} complexes inside a DNA-like duplex through Cu^{II}-mediated self-assembly of two complementary oligonucleotides.

tive base pairing. The successful formation of helical DNA-like duplexes was confirmed spectroscopically:

a) The UV/Vis spectra showed an additional band at 307 nm as a result of Cu^{II} complexation;
b) Electrospray ionization mass spectrometry provided the correct masses for the intermolecular oligonucleotide complexes.
c) Circular dichroism spectra confirmed the right-handed helicity of the duplexes.

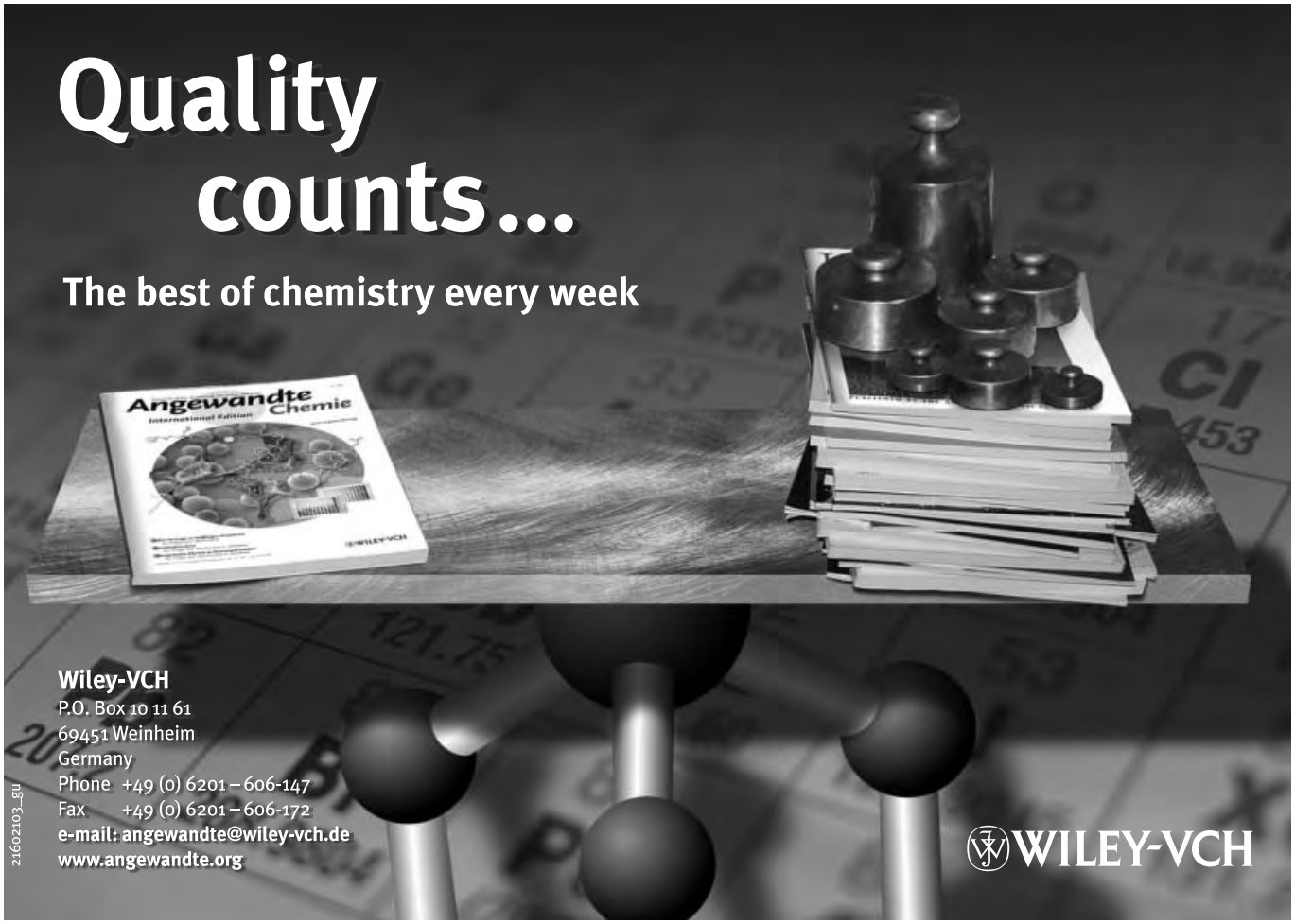
The most important structural feature of this artificial DNA is the alignment of the Cu^{II} ions along the axes inside the duplexes. The canonical helical conformation of these DNA-like duplexes ensure regular Cu^{II}–Cu^{II} distances. EPR spectroscopy was employed to characterize the mode of interaction between the stacked Cu^{II}-mediated base pairs. The EPR spectra were quite different from that of a single Cu^{II}-containing base pair and confirmed a ferromagnetic coupling through the unpaired d electron of each of the Cu^{II} ions ($S = {}^1/_2$). Thus the spectrum of the duplex with n adjacent Cu^{II} centers could be attributed to the spin state $S = n/2$ ($n = 1$–5). Based on the fine splitting of the EPR signals the Cu^{II}–Cu^{II} distance in the artificial DNA duplexes could be estimated to be 3.7 Å, which is remarkably similar to the distance between two adjacent base pairs in natural DNA duplexes (3.4 Å).

In conclusion, the replacement of hydrogen-bonded base pairs with metal complexes represents a promising modification on the way towards new molecular devices based on interacting metal centers. The work of Shionoya and co-workers clearly describes a remarkable example of how this idea can be applied to arrange a discrete one-dimensional metal array in a predictable manner. The DNA serves simply as a structural framework. The formation of a magnetic chain by the self-assembled alignment of metal centers within a DNA-like double helix is of great importance to the field of nanotechnology as it provides the basis for novel nanodevices such as semiconductors, molecular magnets, and wires.

[1] J.-M. Lehn, *Supramolecular Chemistry: Concepts and Perspectives*, Wiley-VCH, Weinheim, **1995**.
[2] a) C. M. Niemeyer, *Angew. Chem.* **2001**, *113*, 4254–4257; *Angew. Chem. Int. Ed.* **2001**, *40*, 4128–4158; b) C. M. Niemeyer, M. Adler, *Angew. Chem.* **2002**, *114*, 3933–3937; *Angew. Chem. Int. Ed.* **2002**, *41*, 3779–3783.
[3] a) E. T. Kool, J. C. Morales, K. M. Guckian, *Angew. Chem.* **2000**, *112*, 1046–1968; *Angew. Chem. Int. Ed.* **2000**, *39*, 990–1009; b) E. T. Kool, *Acc. Chem. Res.* **2002**, *35*, 936–943.
[4] a) H. Weizman, Y. Tor, *Chem. Commun.* **2001**, 453–454; b) H. Weizman, Y. Tor, *J. Am. Chem. Soc.* **2001**, *123*, 3375–3376.
[5] a) E. Meggers, P. L. Holland, William B. Tolman, F. E. Romesberg, P. G. Schultz, *J. Am. Chem. Soc.* **2000**, *122*, 10714–10715; b) S. Atwell, E. Meggers, G. Spraggon, P. G. Schultz, *J. Am. Chem. Soc.* **2001**, *123*, 12364–12367; c) N. Zimmermann,

 © 2003 Wiley-VCH Verlag GmbH & Co. KGaA, Weinheim

E. Meggers, P. G. Schultz, *J. Am. Chem. Soc.* **2002**, *124*, 13684 – 13685.
[6] a) M. Tasaka, K. Tanaka, M. Shiro, M. Shionoya, *Supramol. Chem.* **2001**, *13*, 671 – 675; b) K. Tanaka, M. Tasaka, H. Cao, M. Shionoya, *Supramol. Chem.* **2002**, *14*, 255 – 261; c) K. Tanaka, Y. Yamada, M. Shionoya, *J. Am. Chem. Soc.* **2002**, *124*, 8802 – 8803.
[7] K. Tanaka, A. Tengeiji, T. Kato, N. Toyama, M. Shionoya, *Science* **2003**, *299*, 1212 – 1213.
[8] a) G. M. Finniss, E. Canadell, C. Campana, K. R. Dunbar, *Angew. Chem.* **1996**, *108*, 2946 – 2948; *Angew. Chem. Int. Ed. Engl.* **1996**, *35*, 2772 – 2774; b) R. Palmans, D. B. MacQueen, C. G. Pierpont, A. J. Frank, *J. Am. Chem. Soc.* **1996**, *118*, 12647 – 12653; c) S.-Y. Lai, T.-W. Lin, Y.-H. Chen, C.-C. Wang, G.-H. Lee, M.-h. Yang, M.-k. Leung, S.-M. Peng, *J. Am. Chem. Soc.* **1999**, *121*, 250 – 251.
[9] K. Tanaka, A. Tengeiji, T. Kato, N. Toyama, M. Shiro, M. Shionoya, *J. Am. Chem. Soc.* **2002**, *124*, 12494 – 12498.



Popularization of Chemistry

Chemistry—A Central Pillar of Human Culture**

*Sason Shaik**

Keywords:
chemistry didactic · history of science · popularization of chemistry

Dedicated to my students of the "second culture" who taught me that what is useful is not necessarily also enchanting!

Little seems to have changed in the public image of chemistry and chemists, since Gabriel-François Venel depicted, in 1753, in Diderot's Encyclopedia, the "miserable state of the chemical community" as being "isolated in the midst of the greater people hardly curious of its business".[1] We are all painfully aware of the public image of chemistry,[2] and its status, in the media, as "the forgotten science".[2a] Nevertheless, popularization of chemistry[3] remains scant, and chemists themselves regard such attempts with ambivalence, if not disdain, as if admitting the verdict that there is little in their science that can enchant the layman. While there may be difficulties to enchant the layman with chemistry, popularize we must! We just have to find new ways to tell the story of "the chemical universe" and project the position of chemistry as a central pillar of human culture.

Chemistry is the window given to Mankind to glimpse into its material essence

[*] Prof. S. Shaik
Department of Organic Chemistry and The Lise Meitner-Minerva Center for Computational Quantum Chemistry
Hebrew University
91904, Jerusalem (Israel)
Fax: (+972) 2-658-4680
E-mail: sason@yfaat.ch.huji.ac.il

[**] This Essay is based on a course given to students of the humanities & social sciences, and follows the outline of a public lecture given for the first time in "The Chemistry Year" (1999). Subsequently, it has been given each year to freshmen chemistry students and to audiences of chemists and other scientists. It is an example of a successful experience at popularizing chemistry and is a proposal for a teaching strategy, and a philosophy.

This Essay shares with the readers my own experience of popularizing chemistry by delivering the following universal message of our science, that:

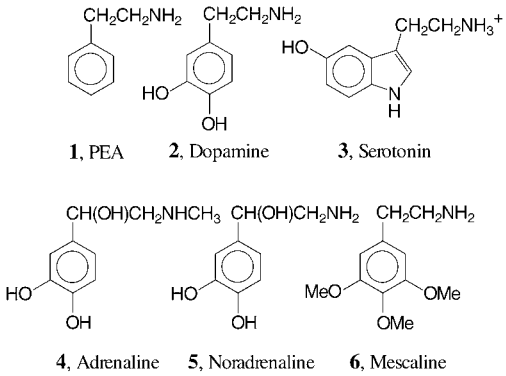
- Chemistry is the window given to Mankind to glimpse into its material essence.

It is through its relation to human characteristics such as love, addiction, sex, dream, and pleasure, that chemistry can be appreciated in its above universal sense. It is this universality that makes chemical knowledge a dictum and an enchanting story for the layman. Once this point is made, it paves the way to the introduction of concepts associated with "chemical matter" and how structure and interactions trigger human traits. Subsequently, a connection is made between the universal message of chemistry, and the system of thought of alchemists who considered that every material entity had also a spiritual manifestation and vice versa. The Essay is constructed along these lines, and its content can serve as an example either for an introductory lecture in freshmen chemistry or a popular-science talk to the general public.

Love, Addiction, Psychological Balance, and More

Pheromones are molecules that control the "love life" and all communicative aspects of insects.[4a] This is true also for higher organisms, such as mammals;[4b] humans do not seem to be an exception. Thus, even though the chemical details of the emotional map are not yet worked out, it has become gradually evident that emotional life is written in an alphabet of genetically determined patterns and coded by specific brain chemicals. For example, a recent discovery[5] reveals that individuals with different forms (alleles) of the gene, which encodes the transporter protein of the brain-chemical serotonin, exhibit different patterns of activity in the brain's emotional center, the amygdala. A hyperactive amygdala is associated with permanent anxiety even in nonthreatening situations.[5] Indeed, our brains are chemically wired.[6] Some of these neurochemicals are neurotransmitters, others are neuromdulators that regulate the action of neurotransmitters, and others include hormones. These neurochemicals act sometimes on their own, other times with neuromodulators and other neurotransmitters, and sometimes by a cascade that leads to secondary molecules, which transduce the signal to the final trigger.[6]

Research suggests that the brain-chemical 2-phenylethylamine (**1**; PEA;[7,8] Scheme 1), is a neurotransmitter and neuromodulator of libido and interpersonal energy;[7a] its administra-



1, PEA **2**, Dopamine **3**, Serotonin

4, Adrenaline **5**, Noradrenaline **6**, Mescaline

Scheme 1. Molecules of emotion.

 © 2003 Wiley-VCH Verlag GmbH & Co. KGaA, Weinheim DOI: 10.1002/anie.200330038

tion increases emotional warmth, affection, sexuality, and the feeling of physical energy. It was even implicated in the "runner's high", which is the feeling of well-being that accompanies physical exertion.[9] While PEA may function together with neurotransmitters (e.g., dopamine (**2**) and serotonin (**3**), Scheme 1), its action in the emotional domain is unique.[7] Recently, it was discovered[8] that PEA has indeed a specific receptor located mainly in the amygdala, the brain's emotional command center. Unique also are the facts that PEA has a very short lifetime (minutes), and is degraded by a specific isoform of the enzyme MAO (monoamine oxygenase), the MAO_B isozyme. The short lifetime suggests that PEA has a special biodynamic role, possibly associated with excitory effects triggered in a short space of time. By contrast, other neuroamines (serotonin (**3**), noradrenaline (**5**), and dopamine (**2**)) have long lifetimes (hours) and are degraded by the other isozyme, MAO_A.

The effects of PEA on human behavior have led to the hypothesis (henceforth the "psychochemical hypothesis") that PEA is associated with the event of "falling in love".[10] Even though this connection is speculative, it is nevertheless interesting to learn of the psychochemical hypothesis, since it might contain some truth considering the role of PEA in regulating affect. Walsh[10a] gives a vivid description of the action of PEA: When we meet someone who attracts us "the whistle blows at the PEA factory". Unlike other mammals where "falling in love" is triggered by scent or touch, in humans the main trigger is sight. A mere glimpse is required to activate the sensation of romantic love. This is how the biblical story of David and Bathsheba begins: "From the roof he saw a woman bathing. The woman was very beautiful…". The synthesis of PEA, in the brain, and its relay into the entire nervous system are implicated in the generation of excitement at the sight of the subject of love, and the great longing when the lover is not around.[10a,11] PEA is also present in chocolate, Nutrasweet (for which the main ingredient is aspartame), and diet soft drinks, and its concentration rises with smoking of marijuana.[10d] However, all these sources of PEA do not produce the kick of the brain-PEA. They fail to do so, in part because of their fast degradation by the enzyme MAO_B. Thus, even though PEA can cross the blood–brain barrier, most of it would by degraded without the addition of MAO_B blockers.[7] Externally administered love potions may exist in Shakespeare's Midsummer-Night's Dream, while in reality our chemical system jealously safeguards the exclusivity of emotional response.

The psychochemical hypothesis[10] assigns roles to other neurotransmitters, which figure in our psychobiological energy. One such family of neurotransmitters is the endorphins produced in the hypothalamus, the brain stem, and the pituitary gland.[12] Endorphins are neuropeptides (β-endorphin, the most potent of the known endorphins, contains 31 residues) that serve as natural painkillers in the body. They act on specific opiate receptors,[12] to produce analgesia and create a sense of well-being. However, according to the psychochemical hypothesis[10d] they also play a major role in maintaining durable relationships. Thus, in the course of time after falling in love, the body requires larger doses of PEA to maintain the same initial kick, and we gradually "fall out of love".[10a–c] Had this been the entire story, love would have consisted of romance alone. Fortunately, the brain being a versatile chemist, also makes endorphins that fix us with durable partnerships. Thus, whenever we see our partner, the brain squirts a dose of endorphin that permeates the entire body,[10d] which in turn gets imbued by a sense of security, calm, and well-being. The sharp, almost physical pain that accompanies the loss of a loved-one is thought to be caused by the sudden arrest of the endorphin mechanism.

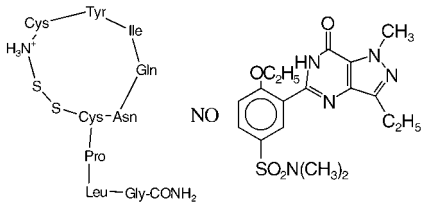
PEA is only one of a few neuroamines that act as molecules of the emotions, which are shown in Scheme 1. The molecule dopamine (**2**) is manufactured from tyrosine in the Ventral tegmental area of the brain and is released in the frontal cortex. This molecule is involved in reward-seeking behavior, learning, drug addiction, and development of dependencies, including trained conditioning and willed control.[6c] According to the psychochemical hypothesis,[10] dopamine regulates the desire to pursue pleasure, to seek danger, and is the motivator to achieve and to desire. With too little dopamine there is little joy of life, little sense of adventure and experience,[10,13] while too large quantities or enhanced dopamine absorption by nerve cells lead to addictive behavior. It appears now that addictive behavior is associated with long-term potentiation (changes) in the synapses between the neurons, much like in memory and learning.[6c]

Serotonin (**3**) is formed (from tryptophan) in the raphe nuclei, deep in the brain stem,[5] and is then transported to the nerve endings. It is the "mood molecule",[10d] responsible for the psychological balance, and is the innate antidepressant. Problems in the serotonin cycle are associated with ailments, such as chronic pain, depression, Alzheimer's diseases, strokes, and Parkinson's disease. Serotonin deficiency is associated with aggression (including sexual), depression, schizophrenia, craving for carbohydrates and sweets. Normal levels cause a balanced personality, while excess is associated with anxiety. Serotonin can be found in bananas, tomatoes, and pasta. But again, this does not mean that eating any one of these foods increases serotonin levels in the brain, because of its fast degradation by the enzyme MAO_A.

Adrenaline (**4**) and noradrenaline (**5**) also known as epinephrine and norepinephrine are shown in Scheme 1). These are the stress hormones, which prepare the body for strenuous activity. Adrenaline, released from the adrenal medulla, acts to raise the level of glucose in the blood and thereby provides the surge of energy needed for performing demanding tasks or facing dangers. Noradrenaline is a neurotransmitter, which is also activated in stressful situations along with adrenaline. However, it is implicated (in conjunction with PEA and dopamine) in maintaining the sensation of vitality and focus. The molecule **6** (Scheme 1) is a hallucinogenic drug known as mescaline. The structural similarity of mescaline to the innate drugs is apparent. It raises thoughts about the "reality" of emotions, independent of their unique chemical motors.

A neuropeptide that figures in the psychochemical hypothesis.[10,14] is oxy-

 © 2003 Wiley-VCH Verlag GmbH & Co. KGaA, Weinheim



7, Oxytocin **8**, Nitric Oxide **9**, Viagra

Scheme 2. Molecules of pleasure and well-being.

tocin (**7**, Scheme 2), a nonapeptide formed in the pituitary gland. Oxytocin was one of the first natural peptides to be synthesized in the laboratory and thereby demonstrated the chemical origins of psychobiological energy flow. In humans, oxytocin induces labor near the end of pregnancy, controls contraction of the uterine muscles, and stimulates the flow of milk during suckling. In laboratory animals, it was established that oxytocin promotes sexual behavior and pair bonding. By extrapolation, it has been proposed[10,14] that oxytocin is one of the molecules responsible for "pair bonding",[14] and is behind the human urge to touch, caress, and assure. One can simply rub the back of one's neck to feel the pleasing sensation caused by oxytocin secretion. The sensation gets much stronger when your partner does it for you, since this is an evolutionary chemical mechanism of seeking and getting addicted to "togetherness". In women, oxytocin is thought to play additional important roles. During nursing, the surge of oxytocin causes pleasure and relaxation and thereby reinforces the mother–child bond. During lovemaking the surge of oxytocin causes the female's orgasm. Oxytocin thus regulates our "chemical commitment" and its consequential well-being.

Male's orgasm is geared towards ejaculation that was recently demonstrated[15] to be chemically triggered and controlled by a population of spinal neurons (lumbar spinothalamic (LSt)) and located in the two segments (L3 and L4) of the lumbar region. These neurons form part of the spino-thalamic tract that relay sensory information from the body to the thalamus area of the brain, which in turn uses a chemical relay that results in ejaculation. However ejaculation requires an initial erection, which is also chemically triggered, by the natural Viagra, nitric oxide (**8**; Scheme 2) which is an important neurotransmitter responsible for the regulation of blood flow.[16] It is so essential, that a special enzyme, called nitric oxide synthase (NOS), exists for the sole purpose of degrading L-arginine amino acid to generate NO in the endothelial cells.[16] The diffusion of NO (and its binding to the heme of the guanylate cyclase) to the smooth muscle cells, in the walls of the penile arteries of the erectable tissue, causes a cascade of chemical events, by the end of which the muscle cells are depleted from Ca^{2+} ions, the muscles then relax and thereby enable a blood flow into the penis and its eventual erection.

Nitric oxide is also involved in the mechanism of long-term memory (long-term potentiation-LTP) in the hippocampus.[6,17] In memory, NO acts as a neuromodulator that helps the L-glutamate receptor, NMDA (*N*-methyl D-aspartate), increase the concentration of Ca^{2+} ions within the cells. This results in repetitive firing patterns of the cell, which is the essence of LTP. One cannot avoid smiling at the recognition that erection and memory require opposite mechanisms of Ca^{2+} ion flow, outwards versus inwards.

The artificial compound sildenafil (**9**) better known under the trade name Viagra (Scheme 2), is simple enough to synthesize that a 2nd year undergraduate student who had completed a laboratory course of chemical synthesis may be able to produce homemade quantities of this molecule. The molecule interferes with the mechanism of the NO-induced Ca^{2+} ion depletion described above. The excitement caused by Viagra has barely subsided, and chemists are already utilizing their understanding of the mechanism of the erection-based NO mechanism to synthesize drugs that are "more than Viagra."[18] The love elixir may well be within the reach of chemistry.

The discovery of the chemical neurotransmission in the late 1950s has led to a paradigm shift from an "electrical brain" to a "chemical brain".[6c,d] Thus, it is the neurotransmitters that carry the information flow between nerve cells, and serve as the means by which the brain commands and receives information from the body and reacts to external stimuli. At any given time 100 billion (100×10^9) nerve cells may be engaged in this "conversation", which is conducted by two prototypical mechanisms—fast ion "firing" and the slow biochemical cascade—and combinations thereof.[6b] Cell communication is an exceedingly rich and fast developing topic that cannot be elaborated in this popularizing essay.[6,19] Perhaps the easiest to illustrate, albeit very briefly, is the mode of cell communication that is triggered by a neurotansmitter molecule and mediated by an electrical impulse ("firing").

At rest, the nerve cells are segregated by gaps, known as synapses.[19] The synaptic gap is the "off" position while the neurotransmitter is responsible for the "on" position by bridging this gap and enabling the transmission of the signal into the cell. The neurotransmitter molecules are stored in sacs in the nerve endings of a pre-synaptic cell. When an electrical signal (for example, a flux of Ca^{2+} ions) reaches the cell, it swells and its sacs release the neurotransmitter molecules that cross the gap and attach themselves to receptors of the next cell, the post-synaptic cell. The receptor is an ion channel, made from a bundle of a few proteins (for example, NMDA, the receptor of L-glutamate contains five proteins,[17] while the receptors of the amine neurotransmitters, in Scheme 1, belong to a special family of G-protein coupled receptors (GPCRs) which include seven helices[20]). The attached neurotransmitter opens the channel by causing a conformational change in the receptor. The opened channel then allows an ion flux that causes another neurotransmitter to cross the synaptic gap, leading another cell to fire (this may also activate intracellular biochemical pathways, e.g., as in LTP where persistent changes are induced in the post synaptic cell).

The neurotransmitter molecules, which completed their job, must then return to their nerve endings (the transporter cells) by recrossing the synaptic gap. Otherwise they generate radicals, by inhibition of superoxide dismutase, that lead to the death of the cell owing to its chemical degradation. In the case of neuroamines, the enzymes $MAO_{A,B}$ degrade any stray neurotransmitter, not on a receptor or inside a sac in a transporter

 © 2003 Wiley-VCH Verlag GmbH & Co. KGaA, Weinheim

cell (neurotransmitters are replenished in the brain by specific biochemical pathways). A recent exciting discovery is associated with the mechanisms of return of serotonin molecules to their pre-synaptic cells.[5] Serotonin is assisted to recross the synaptic gap by transporter proteins, which in turn are encoded by a gene that has two forms (alleles). One of these alleles produces only about half as much of the transporter protein as the other allele, thus resulting in a more frequent neurotransmission by the serotonin molecules.[5] This higher frequency manifests in the brain as a hyperactive amygdala, and is associated with the psychological state of permanent anxiety and fearfulness. This is a striking connection between isoforms of a single gene, transportation efficiency of a single brain chemical, and different patterns of human response to emotion-laden stimuli.

The understanding of the chemical essence of neurotransmission enabled the synthesis of drugs that function by homing in on the neurotransmitter. For example, Prozac (an antidepressant) homes in on serotonin by blocking the transporter cell and causing the small amount of serotonin to go back to the receptor and induce refiring. Redux (an anti-obesity drug that has been recently taken off the market owing to its undesirable side effects) on the other hand, homes in on the sacs of the transporter cell and causes enhanced transportation of the serotonin. L-DOPA can cross the blood–brain barrier and be converted into dopamine, and is used for treatment of Parkinson's patients with dopamine deficiency. Recent results from chemists show that, for example, acetyl choline and serotonin attach their positive ends to the receptor by making a type of a π complex with the aromatic rings of the amino acids, Tyr and Trp.[21] Thus, the interaction of the neurotransmitter with the ion channel of the receptor turns out to be chemically very specific. Eventually we may find that these interactions, and hence also the "emotional" domains of a given neurotransmitter, are coded in a manner akin to DNA or to protein synthesis, though not through hydrogen-bonding interactions.

The above examples, the unfolding universality of the neurotransmission mechanisms in nature, and the recent establishment of a trinity: gene, neurotransmission and brain patterns, personality traits,[5] indicate that despite the biocomplexity, in the basis of the most wondrous human characteristics there lies fundamental simplicity. An information flow between the unconscious (the body) and the conscious (the brain) domains of the biosystem is carried out by molecular triggers through weak interactions and conformational changes. Even learning and behavioral changes in one's own lifetime are the result of chemical reactions.[6a,c] In short, the whole emotional-sensory-intellectual system,[19,22] which we term "human", has a molecular basis. This highlights the following central position of chemistry for the human race:

- Mankind is made of chemical matter, the same matter that constitutes all substances. Mankind is indeed the "salt of the earth".
- Mankind has learnt, and is still learning, the secrets of manipulating and shaping chemical matter. This gnosis is chemistry.
- Chemistry is hence the window that Mankind uses to probe his own material being and come to terms with its limitations.
- It is the ultimate fate and quest of Mankind to widen the window.

Philosophy tends to characterize self-cognition and free choice as human characteristics that form the great divide from the rest of the animal world. I recently read that rats dream about themselves and their whereabouts during the day (running around their laboratory mazes).[23] In this sense, a rat certainly has a form of self-cognition and awareness. In fact, the chemistry of emotions, memory, learning, is universal, much as are the genetic code and the synthesis of proteins. Thus, the great divide between humans and the animal world is not any form of self-cognition and free choice. It is rather the self-cognition gained as Mankind has journeyed through chemical matter in the unconscious process of selfintrospection, we call chemistry. Thus, whereas the details of the above story are certainly simplistic and new facts will replace quite a few of them, the above lesson is with us to stay.

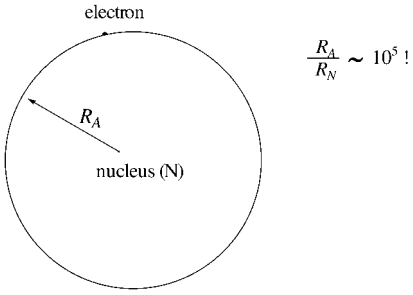
The Chemical Matter

Since Mankind is made of chemical matter, this is a good point to discuss some key features of the chemical matter that may pertain to this identity.

The central paradigms of chemistry are that:

- There exist atoms, which can form chemical bonds.
- The bonds are directed in space and determine the molecular architecture, the reactivity, and interactivity potentials of molecules.
- This in turn holds all the properties of inanimate and animate matter.

The atom is a neutral entity composed of electrons and protons, which are charged particles, and neutrons, which are neutral particles. The electron mass is 1/2000 of those of the proton and neutron. Scheme 3 shows dimensions of



Scheme 3. Dimensions of the atom and the nucleus - All that "matters" resides in a minute space and the electrons "hover over the surface of the deep".

an average atom as a sphere (defined by a 99% probability of locating the electrons), which is occupied in its center by a nucleus that packs together all the massive particles. The radius (R) of the atom is 1 Å. However, the radius of the nucleus is 10^5-times smaller. If we represent the atom as a football field, the nucleus will not even be the football, but rather a speck of dust on a shoe of the player standing in the center of the field. The chemical matter is empty and we, made from it, are sculpted voids.

Why doesn't the void collapse unto itself? The architecture of the void is shaped by the behavior of this tiny, particle/not-particle, entity called the electron. In general, all chemical matter and its various interaction modes abide by the rules of the electron. In this sense,

 © 2003 Wiley-VCH Verlag GmbH & Co. KGaA, Weinheim

chemical matter is unique because the electron is already an elementary particle and hence, chemical patterns cannot be further reduced or constructed from the bottom up (that is, from more elementary constituents). As an elementary particle, a few "laws" govern the electron behavior. The Heisenberg uncertainty principle forbids the electron to be located and have, at the same time, a definite energy (velocity). Therefore the electron is delocalized in space and "hovers" over the nucleus. In brief, the uncertainty principle gauges the size of the void in the atomic entity.

Accepting that atoms do not collapse, why then they do not all combine into a single giant molecule, making all of us pieces of the same material continuum (a material *nirvana*)? Here comes to play the Pauli exclusion principle, which when applied to electrons, imposes upon all atoms a specific connectivity that chemists discovered as early as the 19th Century and called it "valency". It is the exclusion principle that underlies the division of matter into discrete molecules, and this is also the creator of the molecular diversity of the chemical matter.

The outcome of these two laws is that chemistry is a game of Lego with atoms and fragments, which have specified connectivities. The patterns of connecting two fragments form the architecture of the molecule, its electric and magnetic properties, and its modes of interaction, with other molecules and with light, to form new information and emergent properties. This, in a nutshell, is chemical causality. The magnum opus of the chemical matter and its emergent qualities are manifestations of the architecture of the molecule and the movements of its atoms.

Molecular Architecture

Figure 1 shows a demonstration of the transcendental function of architecture using diamond and graphite. Diamond and graphite are both made of carbon atoms. However, they differ in their architecture that is nascent from the degree of freedom in the four-connectivity of carbon. Diamond is hard and translucent, while graphite is opaque and brittle. The different architecture determines the outcome of the interaction of the two compounds with light. But much more than that: Diamond is "beautiful" and expensive while graphite "ugly" and cheap. Some people will murder for diamonds and scheme daring robberies, others will simply eulogize its beauty. No one will devote a single such thought to graphite. The architectural differences of diamond and graphite transcend into social and moral values and into poetry. This is a demonstration how information stored in the architecture of matter is mediated by light through molecular processes of the biosystem to evoke an emotional–mental response. This is an emergent property of the architecture of matter through the information created by its interaction with light, and through the specific evocation mediated by the chemical mechanisms of neurotransmitters and neuromodulators.

"Let there be light"

Indeed, our inner-visual world is shaped by the interaction of a molecule with light and by the ability of one molecule to exist in two definite states. The visual pigment is the rhodopsin receptor, a G-protein coupled receptor (GPCR),[20,24] that contains a chromophore called retinal. The retinal, in Scheme 4, has a *cis* configuration that gives the molecule a shape of a short curve. Upon light absorption, the molecule is isomerized to the *trans* configuration and thereby attains the shape of a lengthened chain. This architectural change modifies the structure of the membrane and activates a G-protein.[20] This event triggers an amplification of the initial signal, which is transmitted as a neural signal and onward to imaging.[24] Subsequently, another event of neurotransmission, yet to be elucidated, takes over and evokes an emotional response (oh diamonds are beautiful!). Our cognition of shape and the innate sense of beauty are outcomes of the interaction of matter with light and of the motions of the atoms of matter. This is reminiscent of the emotional–sensory system that is activated by the chemical mechanisms of the neurotransmitters and neuromodulators.

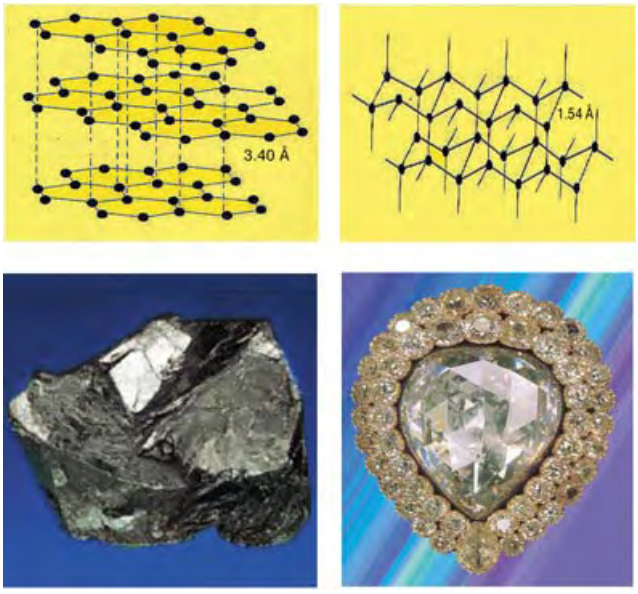
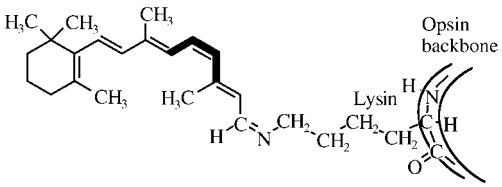


Figure 1. Molecular architecture transcends to social values and poetry. On top, structures of graphite (left) and diamond (right). At the bottom, the real materials, a piece of graphite (left) and the Topkapi diamond (right).



Scheme 4. The light sensitive chromophore of rhodopsin in its resting state, the double bond with *cis* configuration is shown in bold.

 © 2003 Wiley-VCH Verlag GmbH & Co. KGaA, Weinheim

Chemistry and Its Emergent Expressions

Again and again one witnesses the same truism, that in the basis of the human attributes there lies chemical mediation. Molecules, weak molecular interactions and conformational energies harbor information that make us tick. This algorithm is everywhere; from the way "matter recognizes matter" by chirality recognition,[25] or lock-and-key fits, to the genetic code and protein synthesis that are based on the hydrogen-bonding templates. Chemistry provides infinite ways by which a few fundamental mechanisms and the power of numerous combinations can lead to a great variety of emergent qualities. This chemical machinery, its genetic origins, and its emergent emotional-sensory expressions[5] form the "psychophysical connection" (body = chemistry; spirit = thinking, emotions, motivation) that is gradually unfolding.[6c,f,19,26,27]

Dawn and Future

In the dawn of chemistry there was alchemy. The first alchemist was Hermes Trismegistus, shown in Figure 2.[28a,29] This legendary figure gave Mankind the "Hermetic Knowledge of the Divine Art". The phrase Hermetic Knowledge evokes the sense of mysticism and magic, which is brushed off by modern chemists. However, we must recognize that alchemists were trying to do precisely what modern chemists are doing to day. The alchemists investigated matter in order to formulate a world viewpoint–as system of philosophy and cognition. In their system, spirit and matter were entangled;[28b] every material entity had a spiritual manifestation and vice versa.

Alchemists also practiced the manipulation of matter and left behind chemical tools, which are still in contemporary use.[28b] Maria the Jewess is considered to be the first alchemist in the Western world. The tools she invented for gentle warming and separation of matter serve chemistry to this day, and she may thus be credited as being the first to investigate the behavior of matter, something that chemists do to this day. The accumulation of chemical knowledge has taught us, however slowly, that behind the spectrum of human traits there lie chemical mechanisms of molecular motions and mutual interactions of molecules with each other and with the surrounding photonic field. We come full circle, to close a chasm between the old and modern worlds of chemistry. Chemistry is the intellectual adventure of Mankind in his excursion through his own material being. As this journey unfolds, so Mankind discovers the complex connection between matter and its emergent spiritual manifestations.[27]

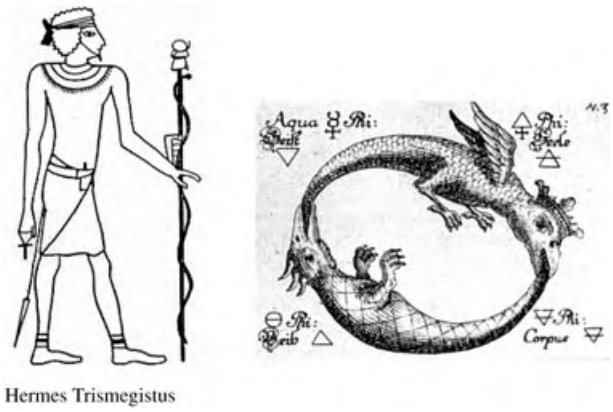


Figure 2. The "first" alchemist (left) and the unification of matter, spirit, and soul (right). Adapted with permission from refs. [28a] and [28b], respectively.

Closing Remarks

Clearly, chemistry is the manifestation of the personal and universal cognition of Mankind of his own material being, and is also the intellectual matchmaker between this material being and Mankind's rule over matter. On the one hand, with knowledge of chemistry we are Matter that possesses self-cognition and gnosis, which have immense importance for progress and well being of Mankind. On the other hand, practicing our control over matter, we are constantly reminded of the warning to Mankind (represented by Cain) in the Old Testament, Genesis 4:7: "Sin is crouching at your door; it desires to have you, but you must master it." Chemistry defines the limitation of the power over matter, and exemplifies this limitation by, for example, pollution and chemical warfare. Ruling over matter means also mastering the right ways of tinkering with it. We are still not there, and our chemistry has yet to fulfill the biblical dictum.

Bringing chemistry closer to the public is the duty of chemists, especially in these times when some of the world's major problems are chemistry-laden. However, imparting knowledge is easy only if the topic is fascinating, which chemistry certainly is. In a way, chemistry is a practical form of introspection—an unconscious introspective analysis that has taken place as Mankind journeyed through Matter. Chemistry brings to life Mankind's internal experience of change, of betterment, and the innate knowledge that changes are brought by the existence of opposites with great affinity. All in all, chemistry touches the human existence, well-being, and commitment to be a benevolent master of matter—our essential constituent. All these features make chemistry a central pillar of human culture.

The author is indebted to D. Avnir, R. Fisch, R. Hoffmann, E. Keinan, D. Milstein, A. D. Mosnaim, C. Nowerstein, D. Porte, R. Rachamimoff, Z. Rappoport, H. Schwarz, A. Stanger, and H. Vancik for helpful discussions and comments. Z. Naor is thanked for making accessible his own material on "chemistry of Love". H. Sabelli has kindly provided ref. [7a]. My daughter Yif'at, helped with the artwork of Figure 1, and S. de Visser and D. Danovich with the rest. Needless to say, none of them should be held responsible for the content of the essay.

[1] "peux curieux de son commerce et n'attendant presque rien de son industrie". For a discussion, see: B. Bensaude-Vincent, *Bull. Hist. Chem.* **1999**, *23*, 1.

[2] See for example, a) R. M. Baum, *Chem. Eng. News* **1995**, *73*(17), 49; b) R. M. Baum, *Chem. Eng. News* **2001**, *79*(36), 5; c) M. Jacobs, *Chem. Eng. News* **2001**, *79*(25), 5; *Chem. Eng. News* **1999**, *77*(15), 5; d) W. Berry, *Life is a Miracle*,

 © 2003 Wiley-VCH Verlag GmbH & Co. KGaA, Weinheim

Counterpoint Press, Boulder, CO, **2000** (chemistry is mentioned once on p. 20 in association with pollution); e) see however, B. Werth, *The Billion-Dollar Molecule,* Simon and Schuster, New York, **1994** (the book creates however a wrong impression that chemistry is only the synthesis part, while the rest, even NMR spectroscopy or molecular modeling, is not).

[3] See for example, a) R. Hoffmann, P. Laszlo, *Angew. Chem.* **2001**, *113*, 1065; *Angew. Chem. Int. Ed.* **2001**, *40*, 1033; b) R. Hoffmann, *The Same and Not the Same,* Columbia University Press, New York, **1995**; c) R. Hoffmann, S. Leibowitz-Schmidt, *Old Wine New Flasks*, W. H. Freeman, New York, **1997**; d) R. Hoffmann, V. Torrence, *Chemistry Imagined*, Smithsonian, Washington, **1993**; e) H. Vancik, *Found. Chem.* **1999**, *1*, 241; f) H. Vancik, *Found. Chem.*, in press; g) A. L. Buchachneko, *Herald Russ. Acad. Sci. (Transl. of Vestn. Ross. Akad. Nauk.)* **2001**, *71*, 311.

[4] a) See for example, A. Shani, *CHEMTECH* **1998**, 30; b) S. Jacob, M. K. McClintock, B. Zelano, C. Ober, *Nat. Genet.* **2002**, *30*, 175. Note that even in humans for women the male odor appears to play a role.

[5] A. R. Hariri, V. S. Mattay, A. Tessitore, B. Kolachana, F. Fera, D. Goldman, M. F. Egan, D. R. Weinberger, *Science* **2002**, *297*, 400.

[6] a) See review and articles in a special issue of *Science* **2001**, *294* from the groups of Greengard, Holden, Helmuth, Carlsson, b) P. Greengard, *Science* **2001**, *294*, 1024. The mechanisms by which nerve cells communicate involve fast and slow synaptic transmissions. The fast mode (1 ms) involves the excitory mechanism of neurotransmission. The slow mode (100 ms to minutes) involves the generation of secondary messengers and a subsequent sequence of biochemical steps. There is interplay between the slow and fast mechanisms (The 2000 Nobel Prize for Medicine was awarded for the investigation of the slow mechanism, see A. Carlsson, *ChemBioChem* **2001**, *2*, 484 – 493 c) On addictive behavior, see: C. Holden, *Science* **2001**, *294*, 980; L. Helmuth, *Science* **2001**, *294*, 982 – 984; C. H. Rankin, *Science* **2002**, *296*, 1624; B. Brembs, F. D. Lorenzetti, F. D. Reyes, D. A. Baxter, J. H. Byrne, *Science* **2002**, *296*, 1706; d) A. Carlsson, *Science* **2001**, *294*, 1021; e) For developments in the science of signal transduction, see the articles by L. B. Ray, S. A. Kliewer et al., A. S. Cashmore et al., C. A. Parent and P. Devreotes and by S. Artavanis-Tsakonas et al. in *Science* **1999**, *284*, 755 – 776 and articles from L. B. Ray and N. .R. Gough, D. V. Goeddel, and H. Wajant, et al. and R. Iyengar, et al. G. A. Koretzky, et al. J. C. Cambier and D. P. McDonnell et al., R. T. Moon, et al L. Attisianno and J.L. Warna, et al., L. E. Elden et al. E. E. Farmer and J. Sheen et al., T. R. Parsons et al., C. M. Horvath and L. C. Cantley et al. in Signal Transduction Knowledge Environment (STKE) from *Science* (*Science* **2002**, *296*, 1632 – 1657 and on the internet site www.stke.org); f) See the articles from P. Stern, S. Cohen-Corey, M. Sheng et al. J. Rettig and E. Neher, M. L. Dustin and D. R. Colman and by D. J. Selkoe on "Neuroscience: A Vibrant Connection" in *Science* **2002**, *298*, 769 – 791.

[7] a) For a most recent review, see: H. Sabelli in *Alternative Medications and the Treatment of Psychiatric Disorders* (Eds.: D. Michoulon, F. Rosenbaum), Lippincott Williams & Willkins, Philadelphia **2002**, pp. 83 – 110; b) H. C. Sabelli, J. I. Javaid, *J. Neuropsychiatry Clin. Neurosci.* **1995**, *7*, 6; c) M. E. Wolf, A. D. Mosnaim, *Clin. Pharmacol.* **1983**, *14*, 385.

[8] B. Borowsky, N. Adham, K. J. Jones, R. Raddatz, R. Artymyshyn, K. L. Ogozalek, M. M. Durkin, P. P. Lkhlani, J. A. Bonini, S. Pathirana, N. Boyle, X. Pu, E. Kouranova, H. Lichtblau, F. Y. Ochoa, T. A. Branchek, C. Gerald, *Proc. Natl. Acad. Sci. USA* **2001**, *98*, 8966.

[9] A. Szabo, E. Billett, J. Turner, *Br. J. Sports Med.* **2001**, *35*, 342.

[10] a) A. Walsh, *The Science of Love,* Prometheus Books, Buffalo, NY, **1991**; b) M. Leibowitz, *The Chemistry of Love*, Berkeley Book, New York, **1983**; c) M. B. Krassner, *Chem. Eng. News* **1983**, *61*(33), 22; d) T. L. Crenshaw, *The Alchemy of Love*, G. P. Putnam, New York, **1996**; e) H. E. Fisher, *Anatomy of Love*, Norton, New York, **1992**.

[11] It was found in a study of medical students that at the early stage of "romantic love" they exhibited changes in serotonin transporter similar to the changes reported in obsessive–compulsive disorder. See: D. Marazziti, H. S. Akiskal, A. Rossi, G. B. Cassano, *Psychol. Med.* **1999**, *29*, 741.

[12] C. B. Pert, *Molecules of Emotion*, Simon & Schuster, **1997**.

[13] a) J. M. Nash, *TIME*, May 26, **1997**, p 43; b) T. Greenfeld, *TIME*, September 6, **1999**, p 55.

[14] a) C. S. Carter, *Psychoneuroendocrinology* **1998**, *23*, 779; b) L. J. Young, M. M. Lim, B. Gingrich, T. R. Insel, *Horm. Behav.* **2001**, *40, 133*.

[15] W. A. Truitt, L. M. Coolen, *Science* **2002**, *297*, 1566.

[16] See the Nobel Lecture, R. F. Furchgott, *Angew. Chem.* **1999**, *111*, 1990; *Angew. Chem. Int. Ed.* **1999**, *38*, 1870.

[17] a) L. R. Squire, E. R. Kandel, *Memory: From Mind to Molecules*, Scientific American Library, New York, **1999**; b) M. D. Lemonick, *TIME*, September 13, **1999**, p 52; c) Y. Kovalchuk, E. Hanse, K. W. Kafitz, A. Konnerth, *Science* **2002**, *295*, 1729.

[18] K. E. Wilson, *Chem. Eng. News* **1998**, *76*(27), 29.

[19] J. LeDoux, *Synaptic Self. How Brains Become Who We Are?*, Viking, New York, **2002**.

[20] These receptors activate guanine nucleotide binding proteins (G-proteins) in the interior of the cells. The G proteins are signaling molecules within the cell and they stimulate ion channel, and cause the synthesis of second messenger molecules. See descriptions and discussions of G proteins in, a) C. A. Parent, P. N. Devreotes, *Science* **1999**, *284*, 765; b) S. P. Neves, P. T. Ram, R. Iyengar, *Science* **2002**, *296*, 765.

[21] W. Zhjong, J. P. Gallivan, Y. Zhang, L. Li, H. A. Lester, D. A. Daugherty, *Proc. Natl. Acad. Sci. USA* **1998**, *95*, 12088; L. Li, W. Zhong, N. Zacharias, C. Gibbs, H. A. Lester, D. A. Daugherty, *Chem. Biol.* **2001**, *8*, 47.

[22] For a discussion of "taste" and "smell", see: C. L. Wilkinson, *Chem. Eng. News* **2000**, *78*(18), 1; P. Zurer, *Chem. Eng. News* **1996**, *74*(41), 5.

[23] *TIME*, February 5, **2001**, p 51.

[24] a) K. Palczewski, T. Kumasaka, T. Hori, C. A. Bhnke, H. Motoshima, B. A. Fox, I. Le Trong, D. C. Teller, T. Okada, R. E. Stenkamp, M. Yamamoto, M. Miyanao, *Science* **2000**, *289*, 739; b) The neurons of the visual system, which respond to different parts of the same object become "fixed" by firing in synchronicity. This synchronicity of neural firing tends to prefer symmetric objects. See, S. H. Lee, R. Blake, *Science* **1999**, *284*, 1165.

[25] A beautiful metaphor for chiral recognition is the "Handshakes in the Dark", described by Hoffmann on p. 40 in ref [3b]. This can become very "handy" in a public talk—shake hands with your audience to illustrate chiral recognition.

[26] The drug "Ecstasy"(3,4-methylenedioxymethamphetamine) was recently shown to cause huge amplification of serotonin neurotransmission. The drain of serotonin causes depression, as well as permanent brain damage and profound dopaminergic toxocity (disruption of the axon of neurons, and vulnerability to Parkinson's desease). See *Science* **2002**, *297*, 2185.

[27] Unlike chemistry that uses a very precise language, neurochemistry has been forced to use a much less precise language, because of the necessity to shift from the level of chemical-mechanical details (neurotransmission, brain re-

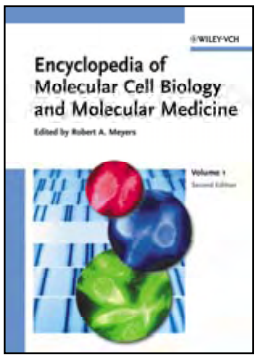
gions, etc) to the level of integrated experience (depression, love, motivation). The chasm between these levels can be likened to the relationship between the letters of alphabet and a poem. The letters are certainly the only constituents of the poem, but not every pile of letters makes a poem. Bridging this language gap in a manner that draws the relation between the whole and its parts is a great challenge that lies ahead. See e.g., "Whole-istic Biology" in *Science* **2002**, *295*, 1661 – 1682.

[28] a) C. J. S. Thompson, *The Lure and Romance of Alchemy*, Senate Press, **1990**; b) R. Patai, *The Jewish Alchemists*, Princeton University Press, Princeton, **1994**, pp. 62, 63, 79, 254.

[29] H. W. Schütt, *Auf der Suche nach dem Stein der Weisen – die Geschichte der Alchemie*, Beck, Munich, **2000**.

In the printed version, the DOI is incorrect. The correct DOI is 10.1002/anie.200330038

The Nucleus of Knowledge



2005. Approx. 10,000 pages.
Hardcover.
ISBN 3-527-30542-4
Prepublication price
approx. € 4144.-
valid until March 31, 2004
thereafter approx. € 4944.-

Publication dates:
volumes 1-5 Jan 2004
volumes 6-10 Aug 2004
volumes 11 –16 May 2005

ROBERT A. MEYERS, Ramtech Ltd., Tarzana, CA, USA (ed.)

Encyclopedia of Molecular Cell Biology and Molecular Medicine

16 Volume Set

"*This series is a classic...*" - Molecular Medicine Today/Trends in Molecular Medicine

The insight of 10 Nobel laureates

The second edition of the bestselling "Encyclopedia of Molecular Biology and Molecular Medicine" provides a one-stop working library of the molecular basis of life, disease diagnosis and therapy with a new focus on the cell level.

It was designed in collaboration with a founding board of 10 Nobel laureates. The encyclopedia is published in 16 volumes containing approximately 425 articles. Each article presents an in-depth treatment accompanied by a key word list with definitions and an extensive bipartite bibliography of primary and secondary papers.

Save € 800,- until March 31st, 2004

http://meyers-emcbmm.de

Register now for the free
WILEY-VCH Newsletter!
www.wiley-vch.de/home/pas

WILEY-VCH • P.O. Box 11 11 61 • D-69451 Weinheim, Germany • Fax: +49 (0) 62 01 - 60 61 84
e-mail: service@wiley-vch.de • www.wiley-vch.de

WILEY-VCH

57503052_kn

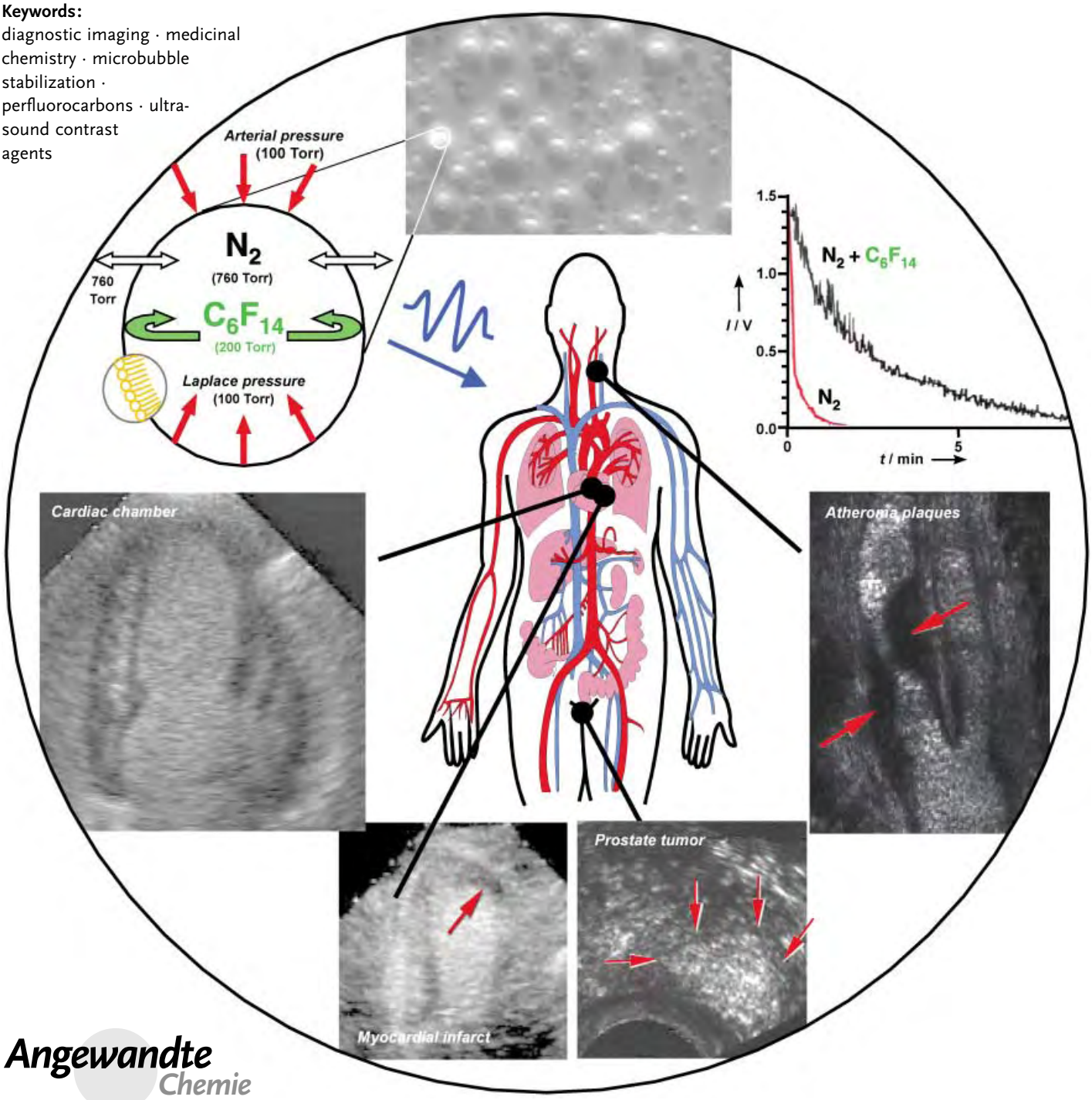
 © 2003 Wiley-VCH Verlag GmbH & Co. KGaA, Weinheim

Ultrasound Contrast Agents

Injectable Microbubbles as Contrast Agents for Diagnostic Ultrasound Imaging: The Key Role of Perfluorochemicals**

*Ernest G. Schutt, David H. Klein, Robert M. Mattrey, and Jean G. Riess**

Keywords:
diagnostic imaging · medicinal chemistry · microbubble stabilization · perfluorocarbons · ultrasound contrast agents



© 2003 Wiley-VCH Verlag GmbH & Co. KGaA, Weinheim
DOI: 10.1002/anie.200200550

Ultrasonography has, until recently, lacked effective contrast-enhancing agents. Micrometer-sized gas bubbles that resonate at a diagnostic frequency are ideal reflectors for ultrasound. However, simple air bubbles, when injected into the blood stream, disappear within seconds through the combined effects of Laplace pressure, blood pressure, and exposure to ultrasound energy. Use of fluorocarbon vapor, by extending the persistence of microbubbles in vivo from seconds to minutes, propelled contrast ultrasonography into clinical practice. Imaging techniques that selectively suppress tissue, but not microbubble signal, further increase image contrast. Approved products consist of C_3F_8 or SF_6 microbubbles, and N_2 microbubbles osmotically stabilized with C_6F_{14}. These agents allow the detection and characterization of cardiovascular abnormalities and solid organ lesions, such as tumors. By providing higher quality images, they improve the accuracy and confidence of disease diagnosis, and can play a decisive role in clinical decision making. New objectives include agents that target specific cells for the molecular imaging of disease, and drug and gene delivery, including ultrasound-triggered delivery.

From the Contents

1. Introduction—The Need for Enhanced Ultrasound Contrast 3219
2. Concepts and Methods 3220
3. Pharmaceutical Products 3225
4. Images of Physiology and Pathology 3228
5. Summary and Outlook 3232

"*A picture is worth a thousand words.*"

1. Introduction—The Need for Enhanced Ultrasound Contrast

Ultrasound is the most widely used imaging technique in the world. For example, there are 75000 ultrasound instruments installed in the United States, compared with only 7000 instruments for computed tomography and 5000 for magnetic resonance imaging. It is a versatile, noninvasive, low risk, low cost, and portable real-time imaging technique. An estimated 100 million ultrasound scans of the heart, vascular system, and abdominal organs are conducted worldwide each year (including over 30 million scans in the United States). However, unlike the other major medical imaging modalities, such as X-ray radiology and magnetic resonance imaging, ultrasound has until recently been limited by the lack of effective contrast agents.

A contrast agent, by definition, alters image contrast in a meaningful way that helps the diagnostician to distinguish between normal and abnormal conditions. This could be by highlighting tissue borders, such as cardiac chamber and ventricular wall, or providing an alteration in the expected time-dependent or geographic distribution patterns in a tissue of interest, such as a tumor in the liver. Visualization of blood and blood flow within an organ is essential for helping to distinguish normal from injured or abnormal tissues. Because the normal liver, spleen, or kidney has similar acoustic properties to many tumors or to a hematoma when these organs are injured, there are fundamental limitations on the ability of ultrasound alone to differentiate between healthy and diseased tissue. While the vascular lumen of large and medium-sized vessels is easily depicted, the lumen of small vessels, particularly when they are inside an organ, is not recognizable from surrounding tissues.

Regardless of the ability of an imaging technique to display structural detail, contrast media are needed to increase the amount of information obtained by the technique. In addition to increasing the contrast between pathologic and background tissues, an agent whose pharmacokinetics are understood will provide meaningful physiologic information as its rate of entry, rate of elimination, and degree of accumulation are monitored over time in a region of interest.

Around 20% of examinations of the heart (echocardiograms) do not provide images of adequate quality to allow the visualization of the inner border of the heart (endocardial border) for accurate diagnosis of ventricular dysfunction. Thus additional non-ultrasound testing procedures are required, which are often more invasive, always more expensive, and sometimes of higher risk. The development of effective ultrasound contrast agents consisting of injectable micrometer-sized gas bubbles that highlight the endocardial border has made contrast echocardiography a clinical reality.[1–5]

When imaging solid organs such as the liver, abnormal areas, such as a blood clot after trauma or a tumor are not visible in nearly 40 to 50% of cases. The ability to see blood flowing into the liver as the microbubbles percolate through

[*] Prof. J. G. Riess
Les Giaines, 06950 Falicon (France)
Fax: (+33) 493-84-98-25
E-mail: jriess@allp.com

E. G. Schutt, Dr. D. H. Klein
Research and Development Department
Alliance Pharmaceutical Corp.
6175 Lusk Blvd, San Diego, 92121 CA (USA)

Prof. J. G. Riess, Prof. R. M. Mattrey
MRI Institute
University of California at San Diego, Medical Center
410 Dickinson St, San Diego, CA 92103-1990 (USA)

[**] The authors are all affiliated with or consult for Alliance Pharmaceutical Corp. However, the opinions expressed here are solely theirs and not necessarily those of the corporation.

 DOI: 10.1002/anie.200200550 © 2003 Wiley-VCH Verlag GmbH & Co. KGaA, Weinheim

its vascular space, and then when all the vascular spaces are filled, allows the diagnostician to recognize the type of pathology that is present. Contrast echosonography is thus expected to contribute substantially to the current global emphasis of achieving earlier, more accurate, more cost-effective diagnoses.

The development of ultrasound contrast agents involves perfluorocarbon (PFC; *F-* represents perfluoro- throughout this Review), surfactant, and colloid chemistry.[6,7] A unique and important characteristic of ultrasound contrast imaging is that the agent interacts with, and is modified by, the imaging beam. This means that contrast agent and imaging technique are intimately interrelated, which offers unique avenues for signal manipulation and contrast improvement. This Review summarizes the principles that underlie, and the technological advances that have led to the commercialization of contrast agents for ultrasound imaging. Only a limited selection of references are cited, but these provide access to a wealth of other papers.

2. Concepts and Methods

An effective ultrasound contrast agent should help to differentiate between tissue types, both normal and pathological, by providing differential backscatter (echoes). This requires that the acoustic impedance (resistance to sound propagation; related to the product of tissue density and sound velocity) between these tissues must be made different. In addition to having a dramatically different acoustic impedance than tissues, microbubbles also resonate with the ultrasound wave, which increases the backscatter of blood by up to ten orders of magnitude more than red blood cells,[8a] which, when combined with contrast specific imaging, allows the detection of a single microbubble.[8b] Contrast agents can provide real-time images of blood flowing through the heart chambers, vessels, and capillary beds. Some agents are then slowed in the circulation of the liver and spleen or are taken up by phagocytic cells, specifically enhancing these organs.[9] Some other agents can be designed to specifically target a receptor system.



Jean G. Riess *received his doctorate from the University of Strasbourg (working with Prof. G. Ourisson), and then spent two years with Prof. J. Van Wazer (Monsanto, USA). In 1968 he was made Professor at the University of Nice, where he founded, directed, and eventually became the honorary director of the Unité de Chimie Moléculaire. His present interests are in fluorocarbons, fluorinated amphiphiles and their colloid chemistry, including fluorocarbon emulsions for in vivo oxygen delivery (so-called "blood substitutes"), fluorocarbon-based contrast agents, fluorinated self-assemblies, and drug delivery systems. He has published about 365 papers and is the holder of 25 patents.*

2.1. Injectable Micrometer-Sized Gas Bubbles for Enhanced, Prolonged Backscatter

The intensity of ultrasound scattered by small (smaller than the wavelength of the ultrasound radiation) spherical particles is proportional to the square of the difference in compressibility and the difference in density of the scatterer and the medium, as shown in Equation (1),[10] where I is the

$$I/I_0 \sim 1/9\, n\, V\, [k^4\, r^6 (\gamma_c + \gamma_d \cos\theta)^2 / d^2] \quad (1)$$

scattered intensity, I_0 is the incident intensity, n is the number density of scattering particles, V is the scattering volume, k is the wave number, r is the radius of the particle, γ_c is the compressibility term ($\gamma_c = (\kappa_s - \kappa_m)/\kappa_m$, κ_s and κ_m are the compressibilities of the scatterer and the medium, respectively), γ_d is the density term ($\gamma_d = (3\rho_s - 3\rho_m)/(2\rho_s + \rho_m)$, ρ_s and ρ_m are the densities of the scatterer and the medium, respectively), θ is the scattering angle (180° for backscattering), and d is the distance from the scatterers (note that when bubbles resonate the scattering efficiency is many times greater than Equation (1) predicts).

The compressibility of gaseous particles (bubbles) is several orders of magnitude higher than that of any liquid or solid, which makes bubbles highly echogenic, that is, gaseous microbubbles provide a high scattering intensity per particle.[8a] Therefore, when a small amount of such an agent is injected intravenously (typically 0.25 mL of injectable agent, a miniscule dose, which contains about 2.5×10^8 microbubbles), blood spaces, including the heart chambers, become bright, which enables blood to be distinguished from surrounding tissues.

Furthermore, when microbubbles are exposed to the compression and expansion force of a sound wave at a critical frequency, they resonate and become transmitters themselves. Fortunately, microbubbles in the micrometer size range resonate in the usual diagnostic ultrasound frequency range (1–3 MHz). The shell that encloses the bubbles can impede the ability of the microbubble to resonate. The extent of this interference depends on the nature of the shell. Also, because microbubbles are such effective reflectors of the transmitted sound, too many microbubbles can impede the penetration of the sound beam deep into the tissue causing what is called "shadowing" of the deep structures.

2.2. The Ideal Gas Bubble for Ultrasound Contrast Imaging

Bubble size is a critical parameter that must be controlled between set limits. The intensity of scattering by nonresonant gas bubbles is proportional to the sixth power of the radius of the bubble [Eq. (1)], hence, the larger the bubble, the better the scattering intensity. However, the acceptable upper size limit for in vivo usage is determined by the need for bubbles to cross capillary beds, and bubbles larger than 6–8 μm are trapped in the lung capillaries. The current accepted sizes are in the range of 1–7 μm, preferably around 3 μm, with as narrow a size distribution as possible. Bubble size needs to be controlled both at the time of injection and throughout the

 © 2003 Wiley-VCH Verlag GmbH & Co. KGaA, Weinheim

circulation lifetime; bubble growth or aggregation in the circulation must be avoided.

As several minutes are needed for an effective and convenient examination of a patient, the bubbles need to be stable enough in the systemic circulation to survive multiple passages through the lung and heart. Therefore, an adequate in vivo bubble half-life is another major requirement.

Additionally, the product should preferably not contain blood-derived proteinaceous components and, to maximize resonance, should have a soft elastic shell. It should be effective at low doses, readily metabolized and/or excreted, and have minimal side-effects. As a drug product, it should be easy to manufacture reproducibly, it should preferably be heat sterilizable, and it should have a shelf life of at least two years, if possible at room temperature. It should be user-friendly and allow well-controlled, consistent dosing. Bubble design may be optimized for specific applications such as harmonic imaging or specific tissue targeting.

2.3. The Issue of In Vivo Bubble Stability: Where Perfluorochemicals Come In

The challenge when using air microbubbles as contrast agents is that, when infused intravenously, the air dissolves very rapidly in the blood and thus bubbles are lost from the circulation before the ultrasound study can be completed. The reason for this is that the gas pressure within the bubbles is the sum of the equilibrium pressure (Henry's law), the Laplace pressure, and the blood pressure, which together exceed the gas pressure in the blood. Additionally, oxygen metabolism also lowers the oxygen tension in the blood, which provides another route for oxygen to leave the bubble. A further factor is that exposure to intense ultrasound energy leads to bubble destruction as rapid bubble contraction and expansion at resonance mechanically stresses and weakens the encapsulating shell.

The Laplace pressure ΔP experienced by a gas bubble is given by Equation (2), in which σ is the air/water interfacial

$$\Delta P = 2\sigma/r \tag{2}$$

tension and r is the radius of the bubble. The surfactant film on the surface of the bubble reduces the air/water interfacial tension σ and thus decreases the Laplace pressure, but does not eliminate it. As gas leaves the bubble, driven by the pressure gradient, the bubble shrinks and the Laplace pressure increases, which accelerates the rate of gas dissolution and the resulting microbubble shrinkage. The rate of bubble shrinkage resulting from the dissolution of the gas into the bloodstream is predicted to follow Equation (3), in which

$$\mathrm{d}r/\mathrm{d}t = -D\,L\,[(p|^* + 2\sigma/r)/(p_{\mathrm{atm}} + 4\sigma/3\,r)][1/r + 1/\sqrt{\pi D t}] \tag{3}$$

D is the diffusivity of the gas in water, L is the partition coefficient of the gas between the gaseous phase and aqueous phase (known, when calculated as the ratio of the solubility of the gas in the liquid to the density of the gas, as the Ostwald coefficient), p_{atm} is the atmospheric pressure, and $\bar{p}^*$ is the excess pressure, which has contributions from the systemic blood pressure and oxygen metabolism. This is also represented in Figure 1.[11]

To slow the rate at which gas bubbles dissolve in the blood, one has to reduce L and, hence, also the water

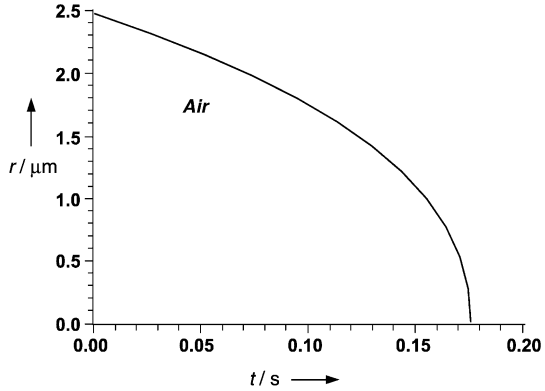


Figure 1. Dissolution of an air bubble in the bloodstream (radius r as a function of time t) as predicted from Equation (3) (initial radius 2.5 μm; excess internal pressure, $\bar{p}^*$ 4300 Pa; interfacial tension 70 mN m^{-1}). Taken from ref. [11].

solubility of the enclosed gases. The lower the Ostwald coefficient L, the longer the bubble exists. This reduction can be achieved by including some PFCs in the bubble, which are the least water-soluble, yet volatile chemicals known (Table 1). Those which have the lowest Ostwald coefficients are most effective. Inclusion of an appropriate PFC can increase the lifetime of an air bubble (approximately 5 μm in diameter) in the bloodstream from seconds to several minutes.

2.4. Controlling the Bubble Size: Perfluorocarbons as Osmotic Bubble Stabilizers

When microbubbles containing only PFC vapor are injected into the circulation, they will take up air from the blood. This process is driven by the concentration gradient between air dissolved in the blood and the zero air concentration within the bubbles. They will swell until the partial pressure of air inside the bubble equals the ambient saturation concentration and the PFC partial pressure equals the combined Laplace and arterial blood pressures (Figure 2). On the other hand, when insufficient PFC is present, the bubble will shrink rapidly and may eventually reach the collapse radius, r_c, which is defined in Equation 4,

$$r_c = 2\sigma/p_{\mathrm{sat}(T)} \tag{4}$$

where $p_{\mathrm{sat}(T)}$ is the saturated vapor pressure of the PFC at temperature T. This underpins the idea of designing bubbles in which the partial pressure of the PFC is set to exactly counterbalance the Laplace and arterial pressures.[11,12] The thermodynamically controlled collapse of microbubbles is then retarded and their growth in vivo is also prevented,

 © 2003 Wiley-VCH Verlag GmbH & Co. KGaA, Weinheim

Table 1: Critical characteristics of perfluorochemicals for microbubble stabilization.[11,15]

Gas	M_r (bp [°C])	Water solubility of compounds (25 °C) [mol m^{-3}]	L ($\times 10^6$)	Saturated vapor pressure (37 °C) [kPa]
N_2	30 (−196)	0.63	14480 (35 °C)	
O_2	32 (−183)	1.32	27730 (35 °C)	
C_2F_6	138 (−73)	1.45	1272	3500
SF_6	146 (−64)	0.27		2530 (27 °C)
n-C_3F_8	188 (−37)	0.19	530	1160
n-C_4F_{10}	238 (−2)	0.021	202	380
n-C_5F_{12}	288 (29)	4×10^{-3}	117	130
n-C_6F_{14}	338 (57)	2.7×10^{-4}	23	48
$CF_3(OCF_2)_3OCF_3$	352 (59)		17 (37 °C)	39
$CF_3(OCF_2CF_2)_2OCF_3$	386 (64)		4 (37 °C)	33
$CF_3(OCF_2)_4OCF_3$	418 (83)		3 (37 °C)	17

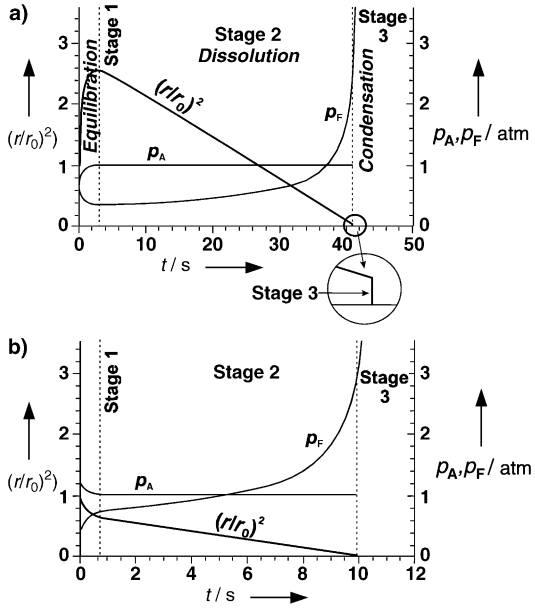


Figure 2. Simulation of the size change $(r/r_0)^2$ over time t of a microbubble in water filled with n-perfluorobutane (F) and air (A). Mole fraction, PFC/(PFC + N_2): a) 1, b) 0.25 (initial radius, $r_0 = 2.5$ μm; excess pressure, $\bar{p}^*$ 4300 Pa; interfacial tension 70 mN m^{-1}; 37 °C). Changes in p_A and p_F, the partial pressures of gases A and F in the bubble, are also represented. Taken from ref. [11].

which allows clinically safe and diagnostically extended circulation times. This stabilization concept requires no mechanical device, such as a hard-shell structure.

2.5. The Dynamics of Bubbles In Vivo

Van Liew et al.[13] and Kabalnov et al.[11] have provided a theoretical analysis of the kinetics of dissolution of microbubbles in the bloodstream for gas mixtures containing a sparingly soluble gas, the latter in the role of an osmotic stabilizing agent. The latter publication also takes into account the possibility that the osmotic agent may condense into a liquid, and provides analytical, rather than purely numerical treatment.

The rate of decrease of the particle radius over time resulting from the dissolution of a gas inside a bubble into water is given by Equation (3). For a given PFC, the rate of dissolution of the bubble in vivo depends primarily on the Laplace pressure. It further depends on the excess pressure $\bar{p}^*$ defined above. In addition, the vapor pressure of the osmotic stabilizing gas at body temperature is also important in determining the longevity of the bubble; if it is too low, the bubble may reach the collapse radius [Eq. (4)]; the sparingly soluble gas may then condense into a liquid.[11]

Three stages have been distinguished for the dissolution of a gas bubble containing air (A) and a sparingly water-soluble stabilizing gas (F) in the bloodstream (Figure 2). First, the bubble adjusts to bloodstream conditions; it rapidly swells or shrinks as O_2, N_2, and CO_2 enter or leave the bubble until their activities are equal inside and outside the bubble. Key parameters include the initial mole fraction of the gas osmotic agent, bubble surface tension, blood pressure, and the level of oxygen metabolism. The equilibrium expression for blood saturated with air at atmospheric pressure is given by Equation (5),[11] where C_F

$$(C_F + C_A)RT = p_A + p_F = 2\sigma/r + p_{blood} + p_{atm} \quad (5)$$

and C_A are the concentrations, and p_A and F are the partial pressures of gases A and F in the bubble, p_{blood} and p_{atm} represent the blood pressure and atmospheric pressure, respectively, $2\sigma/r$ is the Laplace pressure, R is the gas constant and T is the absolute temperature. In the absence of any gas changes owing to metabolism, the partial pressure of the sparingly water-soluble osmotic gas F counterbalances the Laplace pressure and the blood pressure, and Equation (5) simplifies to Equation (6). In the living body, metabolism and

$$p_F = 2\sigma/r + p_{blood} \quad (6)$$

temperature changes shift the partial pressures of O_2, CO_2, and H_2O away from atmospheric saturation by some amounts Δp_{O_2}, Δp_{CO_2}, and Δp_{H_2O}, which are the excess partial pressures of these gases in the bubble, relative to atmospheric saturation values. The pressure of the osmotic gas also supports these shifts, as described in Equation 7[13].

$$p_F = 2\sigma/r + p_{blood} + \Delta p_{O_2} + \Delta p_{CO_2} + \Delta p_{H_2O} \quad (7)$$

In the second stage the sparingly soluble osmotic gas slowly diffuses out of the bubble. This rate is limited by the low blood solubility of the osmotic stabilizing gas. As the radius of the bubble slowly decreases, the partial pressure of the osmotic gas increases to keep up with increasing Laplace pressure.

 © 2003 Wiley-VCH Verlag GmbH & Co. KGaA, Weinheim

In the final stage, the partial pressure of the osmotic agent becomes so high that the agent may condense. The bubble then rapidly turns into a tiny liquid emulsion droplet with a low compressibility that makes it nearly invisible to ultrasound. Reducing the interfacial tension reduces the Laplace pressure and thus shifts condensation to a later time point, but unless the interfacial tension becomes zero, collapse of the bubble can only be delayed, but not prevented.

The simulations shown in Figure 2 illustrate the difference in behavior of a bubble filled only with a PFC gas (a) versus a bubble osmotically stabilized with that PFC (b).[11] In the first case, the diameter of an isolated bubble initially increases rapidly as blood gases are drawn in to reach an equilibrium [Eq. (5)], then slowly decreases (the square of the diameter decreases nearly linearly with time) as the PFC slowly diffuses out. In the second case, the bubble is already roughly equilibrated with the blood gases and so does not exhibit the initial growth spurt, but moves directly into the slowly shrinking mode. As the bubble shrinks through progressive loss of the stabilizing gas, the partial pressure of air in the bubble remains essentially constant at about 1 atm, while the partial pressure of the osmotic agent increases steeply as it keeps up with the increasing Laplace pressure that results from the smaller radius. Eventually, the Laplace pressure causes the PFC to condense into a liquid. This is why the saturated vapor pressure is an important factor in choosing the PFC.

Another mechanism occurs in parallel with the interaction of the PFC within the microbubble and blood. As microbubbles traverse lung capillaries, the PFC comes into contact with air-filled alveoli, causing it to escape the microbubble and enter the alveolus to be subsequently exhaled. This process, which is the normal excretion route for PFCs,[14] decreases the PFC content of the microbubbles and leads to decreased size, increased surface tension, and ultimately collapse. This process also decreases the size of larger microbubbles that could be trapped in the lung; as the diameter decreases to below about 8 μm the microbubble is released into the circulation, acting in some respect as a slow-release mechanism.

2.6. Choosing Perfluorochemicals for Bubble Stabilization

The osmotic agent needs to combine a low Ostwald coefficient value ($< 10^{-4}$) and a relatively high saturated vapor pressure at body temperature ($> 3 \times 10^4$ Pa). Polar gases, the inert gases Ne or Ar, and even hydrocarbons do not meet these requirements; only a few PFCs satisfy them. As a result of extremely low water solubility, the PFC vapor remains in the microbubble, where it dilutes the water-soluble gases present, such that they have a partial pressure of 1 atm (the pressure at which blood is saturated with air in the lungs), even though the total pressure inside the bubble is larger. This sets up an equilibrium where the water-soluble gases diffuse in and out of the bubble while the PFC vapor supports the surface tension and blood pressure forces (Figure 3). The most effective osmotic stabilizers are those found towards the bottom of Table 1.

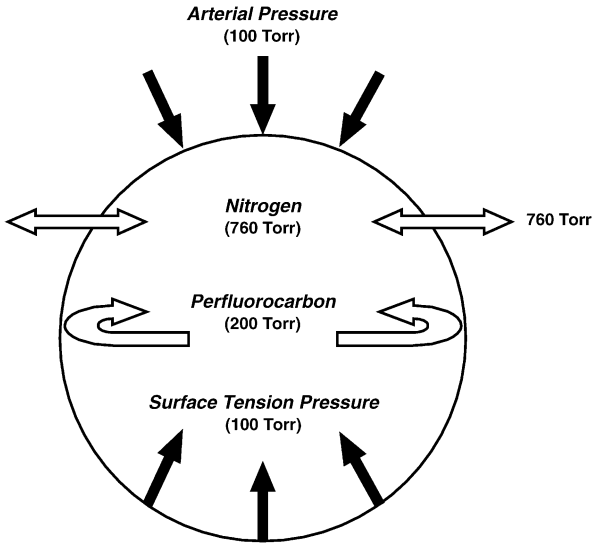


Figure 3. The osmotically stabilized bubble concept: An osmotic equilibrium is set up where the water-soluble gases, whose partial pressure inside the bubble remains essentially constant at 1 atm, diffuse in and out of the bubble while the added partial pressure of the PFC vapor counterbalances the combined forces of blood pressure and Laplace pressure.

Experimental studies support the general trends, bubble dissolution profiles, and strong dependence on the nature and saturated vapor pressure of the PFC predicted by theory. In particular, the effect of the nature of the PFC on the persistence of microbubbles of similar formulations was confirmed in the circulation of rabbits, whether the PFC was used alone or as an osmotic stabilizer in PFC/N_2 mixtures.[15] Bubble persistence increased with molecular weight (decreasing Ostwald coefficient; Figure 4) from approximately 2 min for C_2F_6 to greater than 40 min for *F*-diglyme, $C_6F_{14}O_3$, and then decreased to 8 min for $C_6F_{14}O_5$,

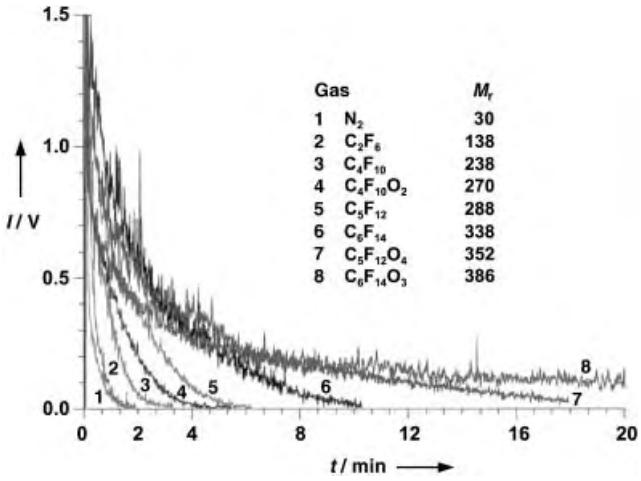


Figure 4. Comparison of the decay of ultrasound signal (Doppler signal intensity *I* over time *t*) observed in rabbits for different osmotic stabilizers; mole fraction (PFC/(PFC + N_2) = 0.1–0.2; dose = 1 mg kg^{-1} body weight). Taken from ref. [15].

 © 2003 Wiley-VCH Verlag GmbH & Co. KGaA, Weinheim

for which the saturated vapor pressure apparently became insufficient, leading to condensation and bubble collapse.

From the strong dependence of signal decay on the nature of the filling gas versus the limited dependence of signal decay on dose, it was also concluded that the intravascular persistence of the microbubbles was probably controlled mainly by dissolution rather than clearance by the reticuloendothelial system (the system that is, among others, in charge of clearing the blood from foreign particulate matter).

However, there were significant quantitative differences between theory and experimental results, in particular where the absolute persistence time of the microbubbles in vivo is concerned, which was underestimated by about a factor of three.[15] This may, in part, be an effect of the mechanical properties of the shells surrounding the bubbles, or it may arise from the numerous assumptions that limit the theoretical models. Theoretical predictions of acoustic backscatter were also somewhat inadequate.[16] Possible changes in shell composition from interaction with surface-active blood components have been suggested as being a factor, as well as altered surface tensions of the shell surfactants under compression while shrinking.

2.7. Bubble-Specific Harmonic Imaging

Microbubbles expand and contract when subjected to ultrasound, and resonate at an incident ultrasound wave frequency that depends primarily on bubble size (for example, at around 3 MHz for a 3 μm bubble). When the ultrasound intensity is sufficient, microbubbles produce not only strong backscattered sound waves at the transmitted frequency, but also a significant amount of super- and subharmonics of the incident sound wave.[17,18] The nonlinear echoes result from asymmetric oscillations of the bubbles in the ultrasound field. Stiff capsules are a priori less desirable, as they will tend to dampen the oscillations that produce nonlinear backscattering.

Harmonic emissions can be used to further improve contrast ultrasound images by suppressing signal (Figure 5). Broadband transducers can typically be made to transmit at between 1.3 and 3 MHz and receive at twice that frequency, that is, between 2.6 and 6 MHz, while filtering the transmitted frequency from the received signal. As echoes from red cells and tissues are a reflection of the transmitted frequency and those from microbubbles are at the second harmonic frequency, signals from non-microbubble reflectors are essentially suppressed. Harmonic ultrasound imaging thus becomes a *microbubble-specific* imaging mode that increases image contrast between microbubble-containing and non-microbubble-containing regions, the latter being poor harmonic resonators. (Figure 6a,b) Harmonic imaging is therefore particularly beneficial for visualizing the blood, even when flow is slow or in very small vessels in tissues where Doppler techniques are severely limited.[19–22]

The resolution and sensitivity of harmonic imaging can be further improved by using pulse-inversion techniques, in which two pulses are delivered in close sequence with one pulse 180° out of phase from the other (Figure 7). When the

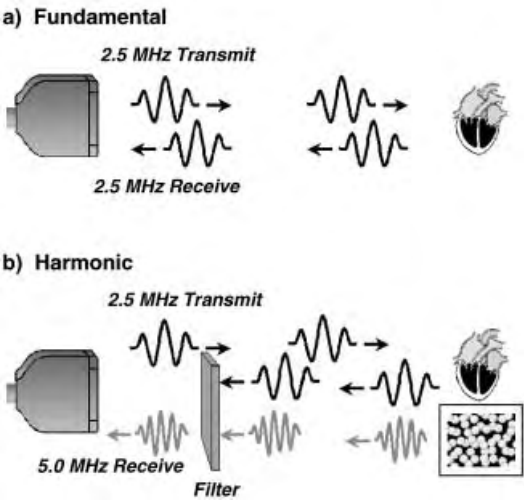


Figure 5. Fundamental (a) and harmonic (b) imaging: In the fundamental imaging mode (the original mode for ultrasound imaging), an ultrasound transducer transmits a narrow-band pulse centered at a given frequency (e.g., 2.5 MHz) into the body. During the receive mode, part of the sound that is reflected from objects in the body is used to create the image (a). Because microbubbles are extremely compressible in comparison to tissues, they not only reflect sound more efficiently than tissues, but they also create distortions (harmonics) in the reflected sound. One of the strongest of these harmonics occurs at twice the transmitted frequency, known as the second harmonic. Early harmonic-imaging instruments used electronic filters to block tissue signal and produce images from the second harmonic signal emanating from the microbubbles (b).

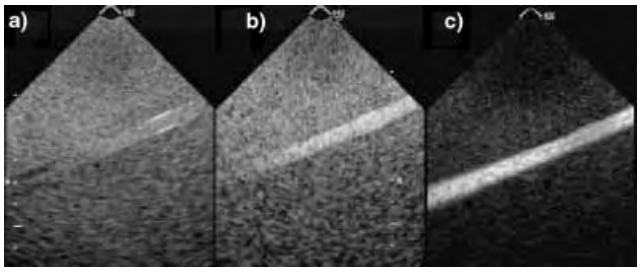


Figure 6. Images of an in vitro "phantom" (model) vessel containing the PFC bubble contrast agent Optison surrounded by tissue-mimicking material. a) A conventional, non-contrasted image; b) a harmonic image with improved contrast between agent and tissue; c) a pulse-inversion harmonic image; contrast is further improved by suppressing linear echoes from tissue. Taken from ref. [3].

received signals from these two pulses are added, linear reflectors (such as red blood cells) produce minimal signal, as their two echoes are equal and opposite, and hence cancel out. Since microbubbles behave differently during the positive and negative pressure of the sound wave (nonlinear reflectors), the two echoes do not cancel, which results in a high-contrast image (Figure 6c).[3] Because the pulses in this scheme can be broadband, images are of higher spatial resolution than second-harmonic-imaging techniques alone. Furthermore, because microbubbles are destroyed by sound waves, particularly at high pressure and at resonance,[23] the first pulse can destroy the microbubble leaving the second pulse unopposed, which results in an even stronger signal.[24] Should the

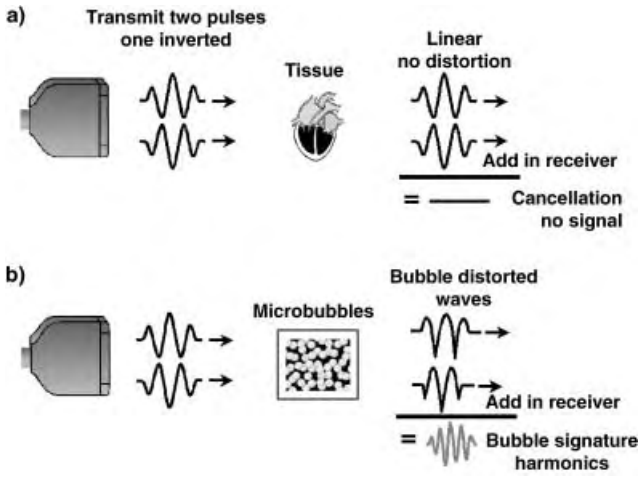


Figure 7. Phase-inversion harmonic low-power imaging: The early second-harmonic-imaging instruments used bandpass filters to generate images from frequencies that were mostly reflected by microbubbles. These images still contained some signal from the tissue. The more efficient pulse-inversion modes use a pulse cancellation technique (see text for details).

microbubble be in motion, as within an artery, the two echoes again will not cancel because the microbubble would have changed position, decreasing signal cancellation.[24] The pulse-inversion technique, also called phase inversion, is a very powerful tool that produces high contrast at high resolution and is particularly effective when imaging blood vessels.[25,26] Its sensitivity is so high that a single microbubble can be monitored.[8b] This contrast-specific imaging technique has become the standard ultrasound imaging technique (Figure 8).

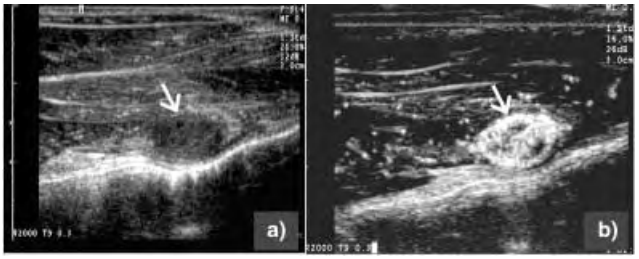


Figure 8. Images of a 6×10 mm Vx2 tumor (arrow) implanted in the thigh of a rabbit before (a) and after (b) the intravenous administration of 0.3 mL of Imagent using phase-inversion techniques at 7 MHz. Because tumors contain more blood and therefore microbubbles than muscle, and the phase-inversion technique suppresses tissue signal but not microbubble signal, the tumor becomes extremely bright relative to muscle, which increases its conspicuity.

Further imaging improvement is continuously being achieved by developing new pulse sequences and new signal processing methods specifically designed for contrast sonography, in other words, by tailoring the instruments to fit the agents.

2.8. Quantifying Blood Flow

Microbubble contrast agents have two unique properties that are not available with agents in use with X-ray or magnetic resonance imaging. First, because microbubbles are larger than 1 μm in diameter they are limited in distribution to the vascular spaces and are true blood pool agents; thus, when a signal is received it is strictly from the vascular space. The second unique property is that the bubbles can be destroyed by the ultrasound wave itself. This property allows "bleaching" studies to be performed, in which the bubbles in a region of interest are first destroyed (bleached) and their reappearance monitored.[17,27,28] Controlled destruction is accomplished by intermittent high-power ultrasound pulses that clear the tissue of microbubbles. Intermittent imaging or low-power imaging following the clearing pulse can monitor the reentry of microbubbles into the field, and provides a unique tool for kinetic studies to estimate tissue blood flow and fractional blood volume.[28–30] The possible consequences of ultrasound-induced microbubble destruction in tissues are also being investigated.[31]

Bleaching experiments are performed in two ways. One method uses intermittent imaging, in which the tissue is cleared from microbubbles with each imaging frame. Once cleared, the brightness of the tissue increases as an exponential curve with a time constant that is inversely proportional to blood flow, and a plateau that is proportional to the fractional blood volume of the tissue (Figure 9a). Image contrast between two tissue regions changes as a function of delay time between two consecutive frames. With a short interval delay (<1 s), differential tissue enhancement or image contrast will reflect differences in blood flow as regions with higher flow will accumulate more microbubbles than regions with slow flow. If, on the other hand, intermittent imaging is performed with a long interval delay (>5 s), differential tissue enhancement or image contrast will reflect differences in fractional blood volume, since microbubbles would have had time to fill the entire vascular space, and tissue brightness will be related to the amount of blood present in the tissue (Figure 9b).

The second type of bleaching experiment involves clearing the tissue from microbubbles with high-power pulses (still within the allowable diagnostic range) and then observing the refilling of the tissue in real time at low power with minimal microbubble destruction, as if a new bolus of contrast was injected. This technique allows the detection of time-dependent perfusion differences within various tissue regions. Of course, this can be performed several times within a single injection so long as a sufficient number of microbubbles are still present in the circulation.

3. Pharmaceutical Products

The development of injectable contrast agents follows the rules and constraints applicable to all pharmaceuticals. Good manufacturing practices, quality control, and quality assurance are required and regulated. Licensure by health authorities demands that both safety and efficacy be demonstrated.

 © 2003 Wiley-VCH Verlag GmbH & Co. KGaA, Weinheim

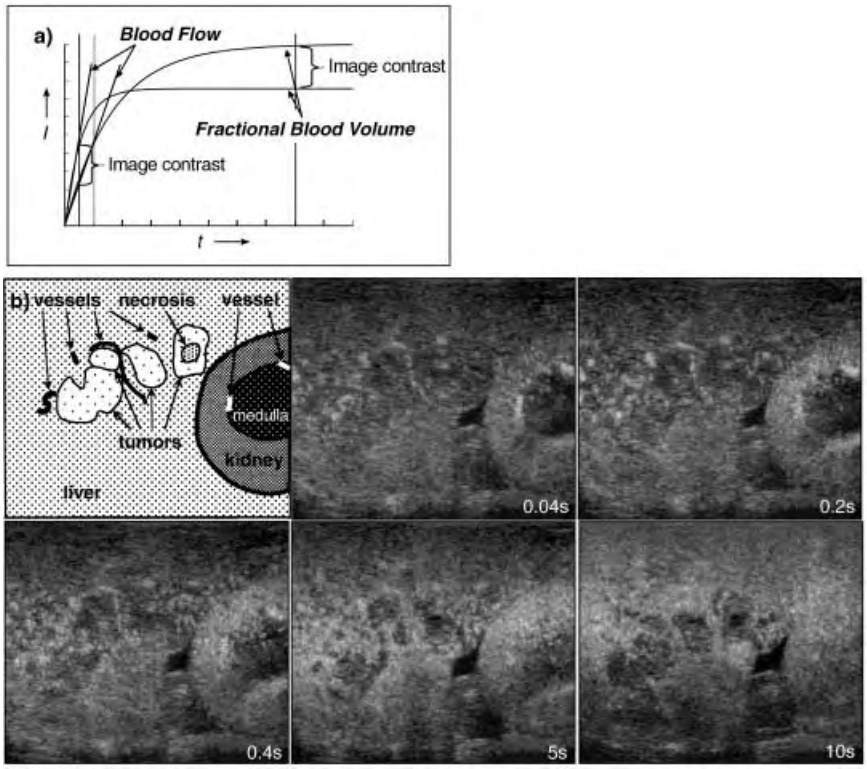


Figure 9. The effect of intermittent imaging on tissue brightness and image contrast: a) Theoretical graph of tissue brightness as a function of delay time between consecutive frames where all microbubbles are cleared with every frame. Two tissues with different blood flow and fractional blood volume are shown. Note that image contrast with a short or long delay time reflects differences in blood flow or fractional blood volume, respectively; tissues with greater flow, or more blood, appear brighter. b) The effect of intermittent imaging of a Vx2 tumor in a rabbit liver during the infusion of Imagent. The schematic describes the visualized anatomy, which is identical on all frames, acquired with 0.04, 0.2, 0.4, 5, and 10 s delay between two consecutive frames. Over the background of the liver, the images include the kidney and tumor nodules implanted in the liver. As the delay increased toward 10 s, improved definition of the tumor nodules and margins was obtained; a small area of necrosis within one nodule was only seen with a 10 s delay. This indicates that the tumors have similar blood flow but a smaller fractional blood volume than the liver. Vessels on the other hand, are best seen with a 0.04 s delay as they have the highest blood flow, which allows the microbubbles to refill the vessels in this very short time interval. Vessels are no longer visible with long delay times. Tissues become brighter with longer delay times as more and more bubbles fill their microcirculation. Taken from ref. [80].

Wide acceptance adds the requirements that both clinical and economic value must be shown. The highly competitive nature of large-market product development limits the availability of specific information about the basic chemistry and manufacturing processes involved in certain products.

3.1. Early Contrast Agents

Ultrasound contrast agents were pioneered by Gramiak and Shah, who observed that strong, but short-lived echoes were generated in the aorta and heart after agitated saline solutions that entrained free air bubbles had been injected into patients through an intra-aortic catheter.[32] Sonicated carbonated water and sodium citrate, dextrose, and renografin (a solution of a 3,5-diacetamino-2,4,6-triiodobenzoic acid salt formulation used as an X-ray contrast agent) solutions were subsequently investigated.[8a] However, the bubbles formed were too large and too unstable. Stabilization of air bubbles by micrometer-sized solid particles was investigated for liver imaging; for example, solid iodipamide ethyl ether particles with air trapped inside.[33] The solid matrix provided some of the stability required for sustained echogenicity, but the echogenicity was less than for a "free" gas bubble.

Encapsulated gas bubbles were then proposed. For example, nitrogen-filled, 7–8 μm-sized DPPC "liposomes" were prepared; however, the circulation half-life was of the order of only one minute.[34] Diverse hard-shell (gelatin, alginate) microcapsules were also investigated, but were too large for intravenous use. Contrast agents based on biodegradable polymeric microballoons (about 3 μm in diameter) were prepared from poly((*tert*-butyloxycarbonylmethyl)glutamate) using an emulsion polymerization process.[35] The polymeric shell was expected to increase bubble resistance to pressure. The use of thick, less gas-permeable shells provides an alternative way of stabilizing microbubbles (or rather microcapsules in this case). However, thick bubbles can substantially reduce the efficiency of ultrasound scattering.

Liquid particles were also assessed, including submicrometer-sized emulsions of *F*-octyl bromide.[36] Liquid PFCs are indeed more compressible and have a lower acoustic velocity than water. The emulsion particles had a long in vivo persistence, which initially allowed blood pool imaging, and later imaging of the liver and spleen. The dose of PFC required for effective imaging was, however, three orders of magnitude larger than with PFC-based gaseous bubbles.

The first commercial products launched in the early 1990s in Europe and the United States, respectively, were Echovist (Schering AG, Germany) and Albunex (Molecular Biosystems Inc., USA). Echovist consists of microcrystalline galactose particles that act as a template providing nidation sites within which air bubbles form when suspended in water,[37] while Albunex consists of air microbubbles inside heat-denatured human albumin shells.[38] These particles were, however, not stable enough to pass the pulmonary capillary bed and reach the left side of the heart when injected intravenously. Their half-life in vivo could be measured in seconds, and thus provided limited utility. Schering subsequently developed Levovist, which also consists of microcrystalline galactose microparticles, but is complemented with palmitic acid, which coats the microbubbles that form after dissolution in water and vigorous agitation, and provides increased stability.[39,40]

 © 2003 Wiley-VCH Verlag GmbH & Co. KGaA, Weinheim

3.2. Perfluorochemical-Based Contrast Agents: The Critical Components

PFCs are, par excellence, the sparingly soluble gases needed for stabilizing air bubbles in the circulation. They are extremely stable, biologically inert, and can be manufactured at very high purity. When injected into the bloodstream, they are excreted intact (that is, nonmetabolized) in the expired air. The pulmonary elimination half-life of the *F*-alkanes used in ultrasound contrast products is of the order of minutes. Extensive toxicity and absorption, distribution, and excretion data exist on neat and emulsified PFCs as a result of intensive research and development efforts on the use of PFCs in blood substitutes,[14,41] liquid ventilation, and drug delivery.[7,42,43]

Current ultrasound contrast products, and those under development, contain a PFC either as the sole component of the gas phase or as one of the components. The choices for the material that makes up the surface of the bubble include denatured (heat-polymerized) human serum albumin, biodegradable synthetic polymers, or a phospholipid membrane. In the latter case, there is a definite analogy, from the colloid chemistry standpoint, between an aqueous microbubble suspension and injectable lipid or PFC emulsions, liposomes, and individual living cells. The phospholipids that are used typically consist of synthetic zwitterionic phosphatidylcholines and ethanolamines, glycerol diesters, and negatively charged fatty acids and phosphatidic acids, although the use of negatively charged components may not be desirable.[44] Other ingredients commonly used in pharmaceutical formulation may include poly(ethylene glycol) or poloxamers, hydroxyethyl starch, buffers, and salts.

Although the injectable bubble suspensions used for diagnosis typically contain several hundred million bubbles per mL, the total dose of finely divided intravenously injected gases needed for the examination of a 70 kg person is less than 250 μL, and that of the PFC can be as little as 20% of that amount. Peak blood concentrations of the PFC are then of the order of 10 ng per mL blood, and most of the PFC is exhaled within minutes.

3.3. A PFC-Based Contrast Agent with an Albumin-Derived Shell

Molecular Biosystems improved the intravascular stability of their first-generation product, Albunex, by replacing air with *F*-propane. The new product, Optison, consists of a ready-to-use suspension of microcapsules of heat-denaturated human albumin filled with *F*-propane.[30,45–47] The agent, which requires refrigerated storage, was introduced in 1998 and is currently being marketed by the Amersham Health Corp. (UK) in Europe and the United States. Numerous experimental studies and clinical reports have demonstrated the efficacy of Optison.[30,45–48]

3.4. A Perfluorocarbon Liquid/Gas-Phase Shift-Based Product

EchoGen (Sonus Pharmaceuticals Inc., USA) consisted of an emulsion of liquid *F*-pentane in water. This PFC converts to a gas (bp 29°C) at body temperature unless there is a nucleation barrier. A fluorinated surfactant was necessary to stabilize the emulsion. Upon injection, the emulsion droplets (ca. 0.3 μm in diameter) were expected to nucleate and convert into gas bubbles of approximately 2–5 μm in size.[49] Preliminary testing suggested that a prolonged efficacy and ability to enhance cardiology and radiology images was obtained.[50,51] The product was tested through Phase III clinical studies, but the company eventually withdrew it from consideration by the United States Food and Drug Administration (FDA).

Among the potential difficulties with such a phase-shift approach is the predicted instability of the emulsion that contains the volatile *F*-pentane. This effect occurs because the rate of particle growth through Ostwald ripening increases sharply as the molecular weight decreases and water solubility increases. In clinical trials, the liquid/gas-phase transition required "activation" in the ultrasound facility prior to injection. The activation step involved the creation and release of a vacuum in the syringe containing the product, which "boils" the emulsion prior to injection. This procedure was instituted to reduce the uncertainties associated with a nucleation barrier to the required phase change,[49b] but was considered to be an inconvenience. There may be a further problem controlling in vivo particle sizes and growth under those conditions (see Section 2.5).

3.5. Lipid Shell-Based Perfluorochemical Gas Microbubbles

Definity, a microbubble contrast agent initially developed by ImaRx (USA) and then by DuPont Pharmaceuticals (USA) is provided as a vial containing the precursor components that, upon "activation", yield a suspension of lipid microspheres that contain *F*-propane. The lipids are a blend of dipalmitoylphosphatidylcholine (DPPC), a methyl-poly(ethylene glycol) dipalmitoylphosphatidylethanolamine (MPEG5000 DPPE) and a small amount of negatively charged dipalmitoylphosphatidic acid (DPPA). These components are stored refrigerated under a headspace of *F*-propane. The final step in preparing the injectable agent is performed by the pharmacist or ultrasonographer. The components are agitated in a calibrated mechanical shaker to produce a suspension of PFC bubbles (1.1–3.3 μm in size) within a lipid shell. Definity was licensed by the FDA in August 2001 and has been launched by Bristol-Myers-Squibb (USA). Papers illustrating the efficacy of the product have been presented.[52,53]

SonoVue, a contrast agent developed by Bracco International (Italy), utilizes sulfur hexafluoride as the perfluorochemical. The product consists of a lyophilized phospholipid/poly(ethylene glycol)/palmitic acid powder, which may consist of lyophilized liposomes, and is stored under SF_6. It has a shelf life of two years at room temperature. Upon the addition of a saline solution, a suspension of microbubbles (ca. 2.5 μm in mean diameter) stabilized by a lipidic monolayer is produced.[54] Most of the SF_6 is exhaled intact within about 10 min. SonoVue has been licensed in Europe and is under review by the FDA in the United States. A number of papers about SonoVue have been presented.[55–57]

 © 2003 Wiley-VCH Verlag GmbH & Co. KGaA, Weinheim

3.6. Microbubbles Osmotically Stabilized with a Perfluorocarbon

Imagent (previously known as Imavist; Alliance Pharmaceutical Corp., USA) is based on the concept of osmotic stabilization. Optimal size control of the bubbles in vivo is achieved using a mixture of nitrogen and the required amount of *F*-hexane needed to osmotically stabilize the bubbles at approximately 3 μm. This amount is about five times less than if a pure PFC were used because osmotic stabilization requires only enough PFC to balance the Laplace pressure and the blood pressure. The product is provided as spray-dried, micrometer-sized hollow and porous spheres (Figure 10a) that are bottled in individual doses under the nitrogen/*F*-hexane mixture, which allows for shipping and extended storage at room temperature. The microsphere formulation includes hydroxyethyl starch (as a water-soluble structure agent that serves as a mold or template for the desired bubbles), dimyristoylphosphatidylcholine (which forms the bubble coating), a poloxamer (as a wetting agent), a phosphate buffer, and sodium chloride, which is used to obtain the correct pH and osmolality conditions. These materials form a spherical shell upon spray-drying which, on the addition of sterile water, dissolves to leave a single-layer phospholipid membrane that encloses the gases to create an isotonic pH-adjusted dispersion of microbubbles that is ready for administration (Figure 10b).

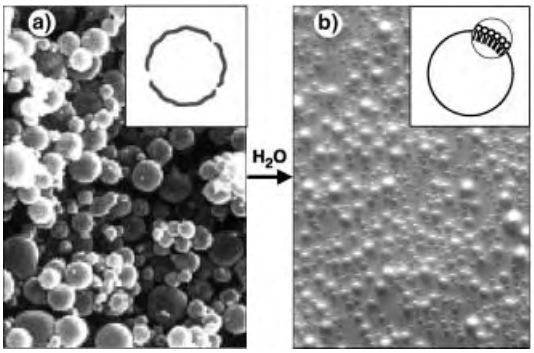


Figure 10. Spray-dried, hollow perforated microspheres viewed by freeze-fracture electron microscopy (a) that upon contact with water convert into lipid-coated microbubbles (b; viewed by optical microscopy). The filling gas is then entrapped within the bubble. Courtesy of the Alliance Pharmaceutical Corp.

The size of the particle is fixed at the time of microbubble constitution by the size of the spray-dried microspheres, and is maintained in vivo by osmotic stabilization; the amount of *F*-hexane having been calculated to ensure that the bubbles cannot grow in vivo. Imagent was approved in the spring of 2002 in the United States. The efficacy of this product has been reported.[21,22,58,59]

3.7. Further Contrast Agents under Investigation

Sonazoid (Amersham Health, UK) is another lipid shell-based agent that uses *F*-butane as the PFC gas;[60,61] however, ist development appears to have been halted. AI-700 (Acusphere, USA) consists of PFC-containing bubbles enclosed in a biodegradable synthetic polymer shell.[62]

Further interesting experimental preparations include *F*-butane-exposed sonicated dextrose albumin (PESDA) microbubbles;[28,63–65] BR14,[66] a lipid-coated *F*-butane-containing microbubble agent that has a longer circulation time than its SF_6-filled analogue; and MP1950 (Mallinckrodt, USA), a *F*-butane microbubble with a phospholipid shell.[67]

4. Images of Physiology and Pathology

Although the field of ultrasound contrast began in the 1960s[68] and entered into clinical application in the late 1980s[69] and the 1990s,[38,70] it did not achieve widespread interest until recent times. Three critical advances in the last few years propelled the field into wider clinical practice: 1) The use of PFC vapor to stabilize microbubbles extended their in vivo survival from seconds to minutes, thus making their use practical; 2) the use of completely digital ultrasound equipment and the adoption of broadband transducers simplified implementation of novel pulsing schemes and signal processing; 3) greater understanding of the microbubble/sound interaction that led to the introduction of harmonic imaging (and took advantage of the fact that microbubbles are destroyed by ultrasound) to allow real-time suppression of tissue signal without affecting bubble signal, dramatically increasing image contrast. Pulse- or phase-inversion technology is now the standard contrast-imaging technique that is offered by all instrument companies. These techniques are extremely sensitive to the presence of microbubbles in the field of view, even allowing for the detection of single microbubbles.[8b]

The present PFC-based microbubble ultrasound contrast agents were primarily designed to remain within the vascular space to image the blood pool. This characteristic is ideal for both contrast echocardiography and vascular imaging, particularly when combined with bubble-specific imaging modes. Restriction of the microbubbles to the vascular space, and their controllable destruction by ultrasound, makes them ideal for imaging solid organs such as the liver or kidneys.

The applications of ultrasound contrast to cardiac, vascular, and solid-organ imaging are highlighted below and are discussed fully elsewhere.[1–5] Since cardiac imaging is typically performed by cardiologists and noncardiac applications are predominantly carried out by radiologists in the United States, and to a somewhat lesser degree in Europe, there has been an arbitrary division of applications as "cardiological" or "radiological" depending on the specialty of the physician involved. This distinction is apparent rather than real because the microbubbles fill all four cardiac chambers and the vascular space, and then percolate through the microcirculation of all tissues, which allows for the imaging of the heart, the vessels and tissues, including the myocardium, liver, spleen, and kidneys.

4.1. Imaging of the Cardiac Chamber

Echocardiography is used extensively to assess ischemic heart disease, the leading cause of death in the Western

 © 2003 Wiley-VCH Verlag GmbH & Co. KGaA, Weinheim

World. Approximately 20% of the examinations do not show all of the key regions of the left ventricle required to assess the three coronary perfusion beds for insufficiency, particularly in the older and more obese patients where the disease is more prevalent. The use of a contrast agent that fills the cardiac chamber with signal highlights the left ventricular cavity and promotes the recognition of the inner border of the left ventricular wall to assess its motion during systolic contraction. Delineation of the left ventricular endocardial border is the first and only indication approved in the United States for the presently available agents that demonstrated superior performance over noncontrasted procedures. Effective delineation of the ventricular border (Figure 11) helps to assess

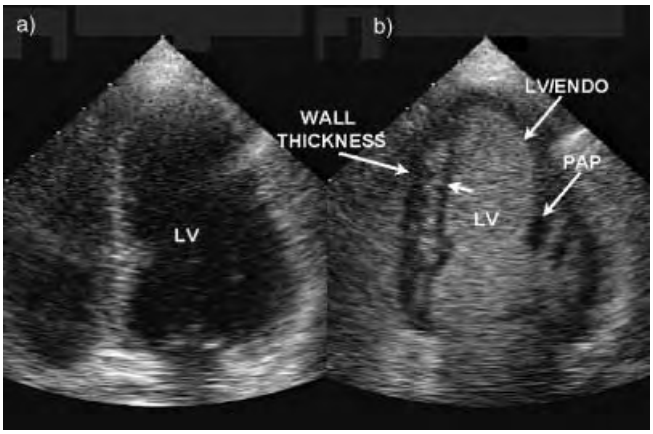


Figure 11. Left ventricular cavity opacification: a) View of the left ventricle of a patient; b) the same view after a bolus injection of Imagent microbubble contrast agent. The left ventricle (LV), endocardial border (LV/ENDO), and papillary muscle (PAP) are clearly seen after addition of contrast agent, which allows myocardial (heart muscle) thickening to be evaluated. When watching the heart in motion, normal functioning heart muscle thickens as it contracts, while abnormal heart muscle moves less and does not thicken. Taken from ref. [101].

global heart function by measuring the ejection fraction (the percentage of the blood in the left ventricle that is ejected during a heart beat), as well as to monitor the wall motion of the perfusion beds of the coronary arteries to detect coronary insufficiency.

Contrast-enhanced cardiac imaging during stress examinations is even more effective than imaging at rest.[2] Since the coronary circulation has a built-in flow reserve, the heart is able to compensate for decreased coronary blood flow at rest. However, during increased demand (stress) induced pharmacologically or by exercise, loss of coronary flow reserve caused by narrowing of the affected artery manifests itself as a regional wall motion abnormality. Of course, in severe coronary artery disease abnormal wall motion will already be present at rest.

Dramatic improvement in image quality was obtained with PFC-based contrast agents, resulting in increased diagnostic accuracy and leading to a reduction in downstream testing, and a possible improvement in patient outcome.[2] The agents have demonstrated substantial value in patients that are difficult to image.[47] By allowing direct visualization of the cardiac chambers to assess regional and global left ventricular function, contrast-specific ultrasound imaging also provides a straightforward means of monitoring the success of surgical or drug interventions.

4.2. Vascular Imaging

The purposes of vascular imaging are: 1) To determine that supply vessels are not occluded; 2) to assess whether arterial wall abnormalities such as atherosclerotic plaques do not exist or, if they do exist, to assess their effect on flow; 3) to determine whether the direction of flow and velocity profile through the cardiac cycle are normal; 4) to acquire an X-ray angiogram-like (the imaging of blood vessels) visualization of the vascular tree within organs. Standard Doppler imaging provides flow velocity data, but it is not reliable at demonstrating structural changes in vessels. Filling the vessel with the signal from contrast media has been shown to be effective at detecting disease with X-ray angiography, and now with contrast-enhanced X-ray-computed tomography and magnetic resonance imaging. The need for contrast in vascular imaging with ultrasound is also important since an acute thrombus (blood clot) is typically difficult to detect, as it assumes a similar appearance to blood, which allows the vessel to look normal when in fact it may be totally occluded. To remedy this limitation and locate a possible clot, compression is applied over the vein; a vein containing a clot fails to compress. This approach has made sonography the imaging technique of choice for the assessment of leg and arm veins; however the technique fails in pelvic or abdominal veins, where compression is impossible. Filling the vein with an ultrasound contrast medium allows for clear visualization of clots and even the tiny tortuous open channels that form as a clot begins to recanalize.[71] These channels are recognizable owing to the ability of ultrasound to detect single microbubbles as they negotiate their way through the clot. This capability will allow sonography to fully and reliably assess abdominal and pelvic veins as well as the veins at the thoracic inlet.

When imaging the extracranial carotid arteries, standard (noncontrast) sonography cannot consistently depict the noncalcified atherosclerotic plaques, nor can it depict plaque ulcerations. Filling the artery with a PFC-based ultrasound contrast agent can accurately display the arterial inner wall, which helps to demonstrate plaques in detail (Figure 12).[59,72a] Even plaque ulceration can be detected. Recognizing that plaques are ulcerated is important since platelet/fibrin clots that develop in the ulcer crater can dislodge to occlude an artery downstream, which can cause transient or permanent ischemia and stroke. When tested in patients undergoing standard carotid X-ray angiography, contrast-enhanced ultrasonography was as accurate as X-ray angiography in directly measuring percent diameter narrowing.[72a] In addition, it was also possible to accurately measure percent area narrowing as contrast-enhanced ultrasound displays both the outer and the inner surfaces of the arterial wall, and because sonography is a cross-sectional technique; such measurements are more predictive of flow restriction.

 © 2003 Wiley-VCH Verlag GmbH & Co. KGaA, Weinheim

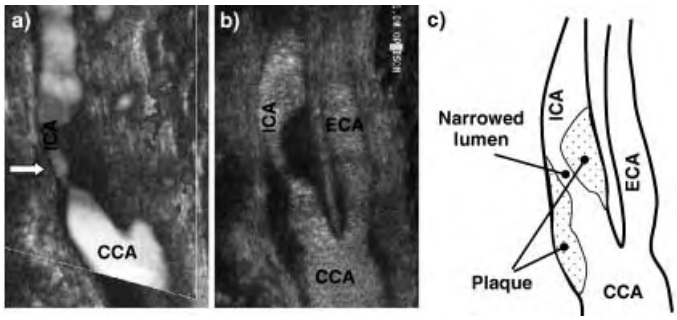


Figure 12. Views of the carotid artery bifurcation using power Doppler imaging taken before administration of the contrast agent (a), and following the intravenous bolus injection of 1.0 mL of Optison (b) using phase-inversion imaging at 7 MHz; c) a schematic to depict the anatomy displayed in b). Although image a) suggests the presence of a narrowed internal carotid artery (ICA, arrow) resulting from plaque formation, the post-contrast grayscale image shows the anatomy in full detail (cf. c); CCA, ICA, and ECA are the common, internal, and external carotid arteries, respectively). The exact configuration of the narrowed lumen and the true thickness and internal architecture of the plaques on the arterial walls are shown. The severity of the stenosis is apparent.

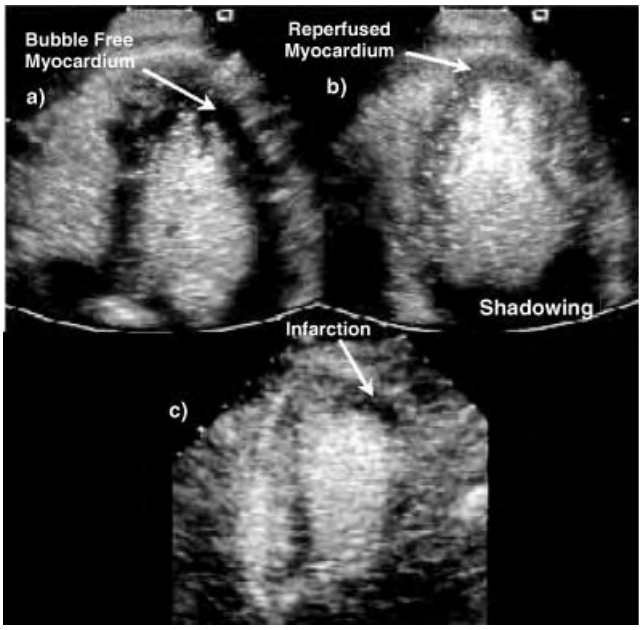


Figure 13. Myocardial perfusion: a) Ultrasound image of the left ventricle of a normal healthy heart directly after a high-power ultrasound pulse has destroyed Imagent microbubbles in the myocardium, which causes the myocardium to appear dark while the ventricular cavity remains bright; b) the brightening of the myocardium occurs as fresh blood, perfusing the muscle, brings new contrast agent into view. The lower part of this image is darker because of shadowing (the concentration of microbubbles is too high for the ultrasound to penetrate this deep); c) an image of an infarcted region (supplied by a blocked blood vessel) visible as a dark area (compare with the healthy myocardium in b)). Courtesy of the Alliance Pharmaceutical Corp.

Imaging the intracranial circulation has remained a challenge because of severe sound attenuation by the skull, which limits the assessment of arterial disease. The use of ultrasound contrast to boost the intracranial Doppler signal has allowed not only improved data collection but also gross visualization of key arteries to significantly shorten the examination.[72b]

4.3. Imaging Tissue Perfusion

The ability to recognize perfused tissues and the pattern of perfusion is critical for the detection of diseased tissues. While standard sonography is capable of demonstrating the tissue architecture of the myocardium and solid organs, it is insensitive to tissue changes caused by ischemia, such as coronary insufficiency, and is even insensitive to tissue changes during the early phase of total vascular occlusion and tissue infarction.[21b]

The use of ultrasound contrast to fill all the vascular spaces in tissues enables the clear depiction of nonperfused regions,[21a] thus allowing the detection of vascular occlusion immediately after it occurs. Observing the pattern of perfusion as microbubbles fill the organ in real time allows the detection of abnormal perfusion patterns, as is observed in tumors.[21a] Performing bleaching experiments (Section 2.8) by destroying microbubbles by ultrasound and observing how quickly one region fills relative to another allows the detection of vascular insufficiency.[29,73]

The assessment of myocardial perfusion is key to diagnosing coronary artery disease and acute myocardial infarction (Figure 13), determining the area at risk of necrosis, measuring tissue flow velocities, and evaluating and even grading stenoses and the success of thrombolytic treatment.[19,45,50,55,74]

Contrast-specific ultrasound imaging of the myocardium may offer results equivalent to perfusion imaging with radiopharmaceuticals, both at rest and with exercise, with the advantage of providing direct, real-time information on both heart function and perfusion.[47] The advantages of using ultrasound contrast are not only the lesser cost of the agent but also elimination of the handling and disposing of radioactive materials, environmental hazard and monitoring, and patient time and convenience. These advantages result in substantial cost savings. Research is also underway to look at brain perfusion.[72d]

Sonography is capable of detecting tumors within organs as they typically alter the appearance of the normal tissue architecture. However, detecting tumors remains difficult, particularly when small (<2 cm), and recognizing benign from malignant solid lesions is even more difficult. The tumor detection rate for sonography of the liver, the most commonly involved solid organ, ranges from 40 to 70% depending on the skill of the sonographer.

By observing the filling pattern and the arterial tree within an organ in real time, contrast-specific ultrasound imaging can not only enable the detection of abnormal regions, but also improve the ability to characterize diseases (that is, to distinguish between infection, infarction, trauma, cancer, and so forth; Figure 14).[75] For example, the vascular supply to malignant tissue is different to that from normal tissue, usually presenting tortuous and disorganized branching, increased microvessel density at the periphery of the tumor,

 © 2003 Wiley-VCH Verlag GmbH & Co. KGaA, Weinheim

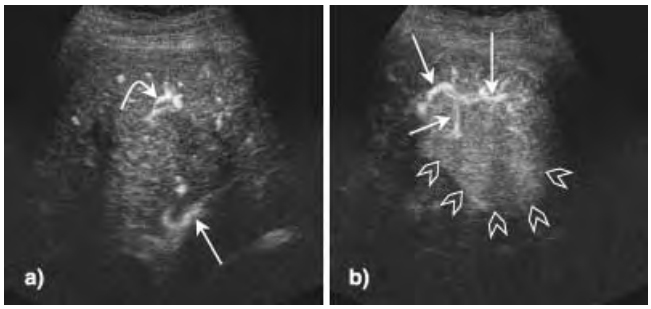


Figure 14. Two selected frames from a real-time imaging series acquired during the bolus injection of Optison into a patient with a liver tumor. a) Early arrival of the contrast agent highlights the tumor-feeding artery (arrow) and the immediate visualization of a central tumor artery (curved arrow) in a region that without contrast appeared like normal liver; b) moments later, the intratumor vascular bed can be seen as vessels supply the tumor with blood from the center outward (arrows). Simultaneously, tumor tissue is markedly enhanced compared with the liver (dark background), clearly delineating the tumor margin (arrowheads). The pattern of enhancement of this lesion assumes a spoke-wheel pattern, and the complete and homogeneous enhancement of the tumor is characteristic of a benign liver tumor, called focal nodular hyperplasia. The ability to see vessels within tumors is only possible with contrast ultrasound.

as well as increased flow to the periphery and slower, decreased, or zero flow to the center.[75] Contrast echosonography allows the quantification of tumor microcirculation and the assessment of angiogenesis consequent to tumor growth.[76] Significant improvement in the detection of disease has been achieved in rabbit models,[77] as well as detection and characterization in humans.[58,75] A clinical investigation of prostate vascularity indicated that contrast may improve the detection of prostatic cancer as a result of selective enhancement of malignant prostatic tissue.[58] Renal cortical blood flow and ischemia could also be assessed.[78] In the case of renal infarction, contrast echosonography visualized the infarcted region that was not visible without a contrast agent, and image contrast and duration were superior with harmonic imaging, which provided exceptional detail.[21a]

Microbubble agents may also be of value for imaging the liver after the bubbles have been taken up by the reticuloendothelial system (RES), or caught within the complex vascular bed of the liver.[79] The visibility of liver lesions, including carcinoma and metastasis, was substantially enhanced when microbubbles were present, which allowed, in particular, the detection of smaller metastases.[79,80]

4.4. Molecular Imaging and Therapeutic Microbubbles

Contrast ultrasonography can be used to guide needle biopsies, for the positioning of radiofrequency electrodes for the thermal ablation of hepatic metastasis, to assess tissue destruction, and to detect residual viable tumor by the evaluation of perfusion. Contrast-enhanced ultrasound images taken at various time points may prove useful in monitoring therapeutic progress and thus may support efficacy claims for the marketing approval of a drug. For example, cardiac function can be monitored before, during, and after a given treatment. Likewise, the functionality of a vessel graft can be confirmed.

Tissue-specific contrast agents can be designed for uptake by the RES, lymph nodes, or other tissues. Incorporation of phosphatidylserine into their lipid shell favors the uptake of microbubbles by leukocytes in areas of inflammation, thus allowing ultrasound imaging of the inflammation.[84] Microbubbles outfitted with a targeting device can be used to seek and mark specific targets, which then become visible during ultrasound imaging. Such detection of the specific molecular signature of a given pathology is referred to as *molecular imaging*.[82] Targeting can be achieved by attachment (covalently through lipophobic interaction or through avidin/biotin coupling) of appropriate ligands including antibodies. Because microbubbles are normally restricted to the vascular system, targeting is essentially limited to pathologies that express specific antigens within the vascular lumen. Privileged target tissues include thrombi, atheroma plaques, areas of inflammation, and tumors. For example, thrombus-specific *F*-butane microbubbles (Aerosome MRX-408; ImaRx) have been prepared by incorporating a surface ligand that targets the GPIIb/IIIa receptor found on activated platelets.[83] Attachment of anti-P-selectin antibodies through an avidin/biotin complex promoted selective accumulation of microbubbles in areas of inflammation and ischemia/reperfusion injury in animals.[85] Targeting of specific receptors on the surface of the endothelium may help to detect active angiogenesis in tumors.[86]

Microbubbles subjected to ultrasound have potential as therapeutic tools. For example, in vivo arterial thrombolysis (clot dissolution) has been achieved in rabbits without a thrombolytic drug, simply by using microbubbles and externally applying ultrasound energy.[65,81] Clot lysis was further improved by combining microbubbles, urokinase treatment, and ultrasound. A rather large-sized (ca. 1.5 μm) phase-shift emulsion made of *F*-pentane and bovine albumin, which vaporizes into large bubbles (75–150 μm) under ultrasound irradiation, was suggested to have potential for occluding blood vessels in cancerous tissue, thus restricting the blood supply to the tumor.[87]

Sonoporation is a technique that uses ultrasound to produce transient, nonlethal perforations in cell membranes and capillaries (capillary permeability enhancement), and facilitates the penetration of active substances (including large molecules), genes, and particles into the cell. This process may be helped by the administration of microbubbles.[88,89] The acoustic power needed to achieve sonoporation appears to be substantially reduced when microbubbles are present.[88] The delivery of colloidal particles and red blood cells across the endothelium to tissues has been achieved through microvessel wall ruptures that were created by targeted microbubble destruction with high-power ultrasound.[88]

Like other fluorinated colloids,[6,7c,43,82c,90] microbubbles can be loaded with therapeutic agents. Taxol, a lipophilic chemotherapeutic drug, showed reduced toxicity when incorporated into lipid-coated *F*-butane microbubbles.[91] However, the cargo space available in the membrane of the bubble

 © 2003 Wiley-VCH Verlag GmbH & Co. KGaA, Weinheim

is usually relatively small, which means that only potent drugs can be considered. Thicker shells can be used, but at the expense of ultrasound scattering efficacy. Some particles closely related to those used as shells in ultrasound contrast agents are being investigated for pulmonary delivery of antibiotics, antiasthmatic drugs, and immunoglobulins.[92–94]

Stabilized microbubbles may prove useful for delivering oxygen and other gases to tissue.[95,96] Microbubbles that can readily swell and shrink as a function of the environment should be particularly appropriate for this application.

The combination of bubble targeting and ultrasound-triggered bubble disruption in the targeted tissue offers further opportunities. Drug- or gene-loaded targeted microbubbles can be made to collapse under ultrasound pressure and project their active content into specific cells. This strategy could help protect normal tissue from toxic drugs. *F*-propane microspheres with a recombinant adenovirus gene vector attached to their surface were infused into the jugular vein of rats and subsequently disrupted by insonation.[97] Expression of the transgene in the myocardium of the animal was increased tenfold over control experiments. Microbubble shells incorporating positively charged lipids would be most adept at taking up plasmid DNA.[98] Targeting ligands may promote the attachment of the microbubble-DNA complexes to specific cells. Ultrasound activation can then propel DNA into surrounding tissues for transfection. Diagnostic ultrasound resulted in enhanced deposition of synthetic antisense oligonucleotides in the insonated kidney after intravenous administration of oligonucleotide-labeled PFC-exposed sonicated dextrose albumin microbubbles.[63]

4.5. Side Effects

With the introduction of Optison, the first PFC-based microbubble agent in the late 1990s, and now the approval of several more PFC-based agents, several million injections have been given clinically and no deaths have been reported that were attributable to the agent. In addition, there have been no reports of clinically significant side effects. The only observed and reproducible clinical effects have been premature ventricular contractions during high-power triggered imaging of the heart while ultrasound contrast is in the circulation.[99] This phenomenon, which is not clearly understood, is likely to be irrelevant given the absence of a negative clinical outcome after millions of doses.

5. Summary and Outlook

Ultrasound, the most widely used diagnostic imaging technique, has until very recently lacked effective contrast-enhancing agents. Gas bubbles in the micrometer size range are a priori ideal reflectors for ultrasound. However, air bubbles, when injected into the bloodstream, dissolve and collapse within seconds because of the combined effects of Laplace pressure, blood pressure, oxygen metabolism, and exposure to ultrasound energy. Perfluorochemicals, because of their extremely low water solubility, have been instrumental in achieving the stability required for thin-shell gaseous microbubbles to be distributed throughout the vascular space and persist in vivo for the duration of an ultrasound examination. Several perfluorochemical-stabilized microbubble concepts have been developed. Some key characteristics include: low water solubility and high vapor pressure of the perfluorochemical, adequate control of bubble size and growth, and preferably a highly deformable elastic shell. Microbubble products that have now assumed medical practice include albumin-coated *F*-propane, lipid monolayer-coated *F*-propane or sulfur hexafluoride, and lipid monolayer-coated nitrogen osmotically stabilized with *F*-hexane.

The capacity for microbubbles to resonate in a nonlinear fashion when exposed to ultrasonic waves leads to the emission of harmonic frequencies that have allowed the development of contrast-specific imaging modes. The interaction of sound with microbubbles and the ability to listen only to microbubble signals is unique to ultrasound imaging and can be regarded as an entirely novel imaging technique in its own right. Concurrently, new ultrasound hardware and software systems have been designed specifically to be used with contrast agents to achieve state-of-the-art images.

Microbubbles can help to visualize the cavities of the heart, as well as the blood flow in vessels and blood perfusion in organs, thereby allowing the detection and characterization of structural and functional cardiovascular abnormalities, organ lesions and tumors. Contrast echocardiology provides a clear delineation of the endocardial wall, improved definition of wall motion and thickening, at rest and during exercise. Enhanced endocardial border definition enables an improved evaluation of cardiac structure and function, which leads to substantial improvements in diagnostic and prognostic accuracy and confidence. It also allows earlier detection and treatment of underlying cardiac pathophysiology.

Accurate assessments of myocardial perfusion and of coronary insufficiency are being refined. The clinical potential for solid-organ imaging is being developed and appears extremely promising.

Further goals of contrast sonography now appear to be within reach. They include providing more simple and more effective methods for imaging blood vessels that should result in improved diagnostic accuracy for a wide range of conditions, such as the detection of plaques or clots in the carotid arteries or abdominal or pelvic veins, the assessment of microcirculatory blood flow (that is, tissue perfusion), quantification of regional ischemia or infarction, enhancement of the accuracy of cancer detection, and characterization and staging tumors in such organs as the liver, breast, and prostate. Tissue targeting, may encourage application-specific bubble design.

The advent of effective ultrasound contrast agents enables the acquisition of higher quality ultrasound images, thus increasing diagnostic performance and confidence while decreasing the time for diagnosis. This should play a decisive role in clinical decision making.

Importantly, by providing accurate and reliable early diagnosis of disease and increased patient management efficacy, contrast sonography could help reduce downstream

 © 2003 Wiley-VCH Verlag GmbH & Co. KGaA, Weinheim

resource use. The reduction of overall healthcare costs justifies incremental examination costs (Figure 15).[47,100] The increased diagnostic accuracy and reliability gained by combining perfluorochemical-based ultrasound contrast agents with improvements in the software of instruments, together with the low cost and portability of this imaging technique (relative to most other modern diagnostic modalities) are likely to further expand the range of the applications of ultrasound imaging. Contrast echosonography may, in particular, offer considerable cost savings over magnetic resonance imaging and nuclear imaging. Given a similar diagnostic accuracy, the increasing cost of healthcare constraints is certain to promote the least expensive modality. Contrast echosonography, by providing similar or improved diagnostic and prognostic accuracy at lower cost is thus likely to emerge as a dominant patient management strategy.[11]

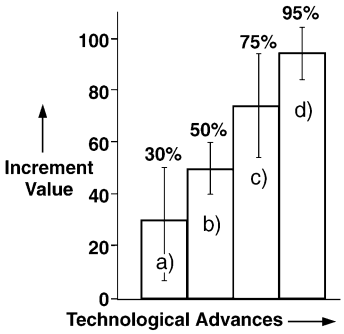


Figure 15. Estimation of the added diagnostic value of ultrasound when using contrast agents and harmonic echocardiographic imaging: a) fundamental imaging; b) harmonic imaging; c) myocardial contrast echocardiography; d) myocardial contrast echocardiography plus harmonic imaging. Taken from ref. [100].

Further medical advances involving microbubbles are likely to emerge that are related to specific tissue tracing and drug, gene, and gas (including oxygen) delivery. This includes ultrasound-induced capillary permeability enhancement, targeted delivery, and ultrasound-triggered targeted delivery. Targeting to specific sites may be achieved by the attachment of ligands that target receptors on the surface of specific cells, which will allow the molecular imaging of inflammation, ischemia/reperfusion injury, atheroma plaques, or sites of angiogenesis, and hence of active tumor growth.

A drug substance can be incorporated into the shell of a bubble or attached to its surface. Bubble/drug circulation and distribution can be monitored by ultrasound imaging. Ultrasound disruption and local release of the active substances can be triggered (and focused) when the microspheres reach the intended target. The combination of bubble targeting and ultrasound-triggered bubble disruption in the targeted tissue could help protect surrounding normal tissue from toxic drugs. Ultrasound could possibly also be used to activate prodrugs. The concepts and technology developed to produce contrast agents may be applied to new drug vector systems, such as microspheres with reduced aerodynamic radii for pulmonary drug delivery.

We would like to thank our colleagues at Alliance for their dedicated research and development efforts.

Received: August 7, 2002 [A550]

[1] *Medical Radiology—Diagnostic Imaging and Radiation Oncology Series* (Eds.: H. S. Thomsen, R. Muller, R. F. Mattrey) Springer, Heidelberg, **1999**.
[2] S. L. Mulvagh, A. N. DeMaria, S. B. Feinstein, P. N. Burns, S. Kaul, J. G. Miller, M. Monaghan, T. R. Porter, L. J. Shaw, F. S. Villanueva, *J. Am. Soc. Echocardiogr.* **2000**, *13*, 331.
[3] H. Becher, P. N. Burns, *Handbook of Contrast Echocardiography—Left Ventricular Function and Myocardial Perfusion*, Springer, Berlin, **2000**.
[4] G. A. Taylor, *Pediatr. Radiol.* **2000**, *30*, 101.
[5] *Ultrasound Contrast Agents—Basic Principles and Clinical Applications*, 2nd ed. (Eds.: B. B. Goldberg, J. S. Raichlen, F. Forsberg), Martin Dunitz, London, **2001**.
[6] J. G. Riess, *Tetrahedron* **2002**, *58*, 4113.
[7] a) J. G. Riess, *J. Fluorine Chem.* **2002**, *114*, 119; b) J. G. Riess, *Curr. Opin. Colloid Interf. Sci.* **2003**, in press; J. G. Riess in *Handbook of Fluorous Chemistry* (Eds.: J. A. Gladysz, D. P. Curran, I. Horváth), Wiley-VCH, Weinheim, in press.
[8] a) J. Ophir, K. J. Parker, *Ultrasound Med. Biol.* **1989**, *15*, 319; b) A. L. Klibanov, P. T. Rasche, M. S. Hughes, J. K. Wojdyla, K. P. Galen, J. H. Wible, G. H. Brandenburger, *Acad. Radiol.* **2002**, *9(Suppl. 2)*, S279.
[9] Y. Kono, G. C. Steinbach, T. Peterson, G. W. Schmid-Schöenbein, R. F. Mattrey, *Radiology* **2002**, *224, 253*.
[10] P. M. Morse, K. U. Ingard, *Theoretical Acoustics*, McGraw Hill, New York **1968**.
[11] A. Kabalnov, D. Klein, T. Pelura, E. Schutt, J. Weers, *Ultrasound Med. Biol.* **1998**, *24*, 739.
[12] E. G. Schutt, T. J. Pelura, R. M. Hopkins, *Acad. Radiol.* **1996**, *35*, S188.
[13] H. D. van Liew, M. E. Burkard, *J. Appl. Physiol.* **1995**, *79*, 1379; H. D. van Liew, S. Raychaudhuri, *J. Appl. Physiol.* **1997**, *82*, 2045.
[14] J. G. Riess, *Chem. Rev.* **2001**, *101*, 2797.
[15] A. Kabalnov, J. Bradley, S. Flaim, D. Klein, T. Pelura, B. Peters, S. Otto, J. Reynolds, E. Schutt, J. Weers, *Ultrasound Med. Biol.* **1998**, *24*, 751.
[16] F. Forsberg, R. Basude, J.-B. Liu, J. Alessandro, W. T. Shi, N. M. Rawool, B. B. Goldberg, M. A. Weatley, *Ultrasound Med. Biol.* **1999**, *25*, 1203.
[17] P. N. Burns, *Clin. Radiol.* **1996**, *51 (Suppl. 1)*, 50.
[18] a) P. D. Krishna, V. L. Newhouse, *Ultrasound Med. Biol.* **1997**, *23*, 453; b) N. de Jong, A. Bouakaz, F. J. Ten Cate, *Ultrasonics* **2002**, *40*, 567.
[19] S. L. Mulvagh, D. A. Foley, B. C. Aeschbacher, K. W. Klarich, J. B. Seward, *J. Am. Coll. Cardiol.* **1996**, *27*, 1519.
[20] M. R. Allen, P. A. Pellikka, H. R. Villarraga, K. W. Klarich, D. A. Foley, S. L. Mulvagh, J. B. Seward, *Int. J. Cardiac Imaging* **1999**, *15*, 215.
[21] a) M. S. Girard, R. F. Mattrey, K. G. Baker, T. Peterson, L. H. Deiranieh, G. C. Steinbach, *J. Ultrasound Med.* **2000**, *19*, 185; b) C. B. Sirlin, M. S. Girard, K. G. Baker, G. C. Steinbach, L. H. Deiranieh, R. F. Mattrey *Ultrasound Med. Biol.* **1999**, *25*, 331.
[22] F. Forsberg, J. B. Liu, H. J. Chiou, N. M. Rawool, L. Parker, B. B. Goldberg, *Ultrasonics* **2000**, *38*, 110.
[23] C. B. Sirlin, T. Pelura, R. F. Mattrey in ref. [1], chap. 28, p. 333.
[24] G. C. Steinbach in *Trends in Contrast Media* (Eds.: H. S. Thomsen, R. Muller, R. F. Mattrey), Springer, Berlin, **1999**, chap. 27, p. 321.
[25] D. Hope Simpson, C. T. Chin, P. N. Burns, *IEEE Trans. Ultras. Ferroelectr. Freq. Control* **1999**, *46*, 372.

 © 2003 Wiley-VCH Verlag GmbH & Co. KGaA, Weinheim

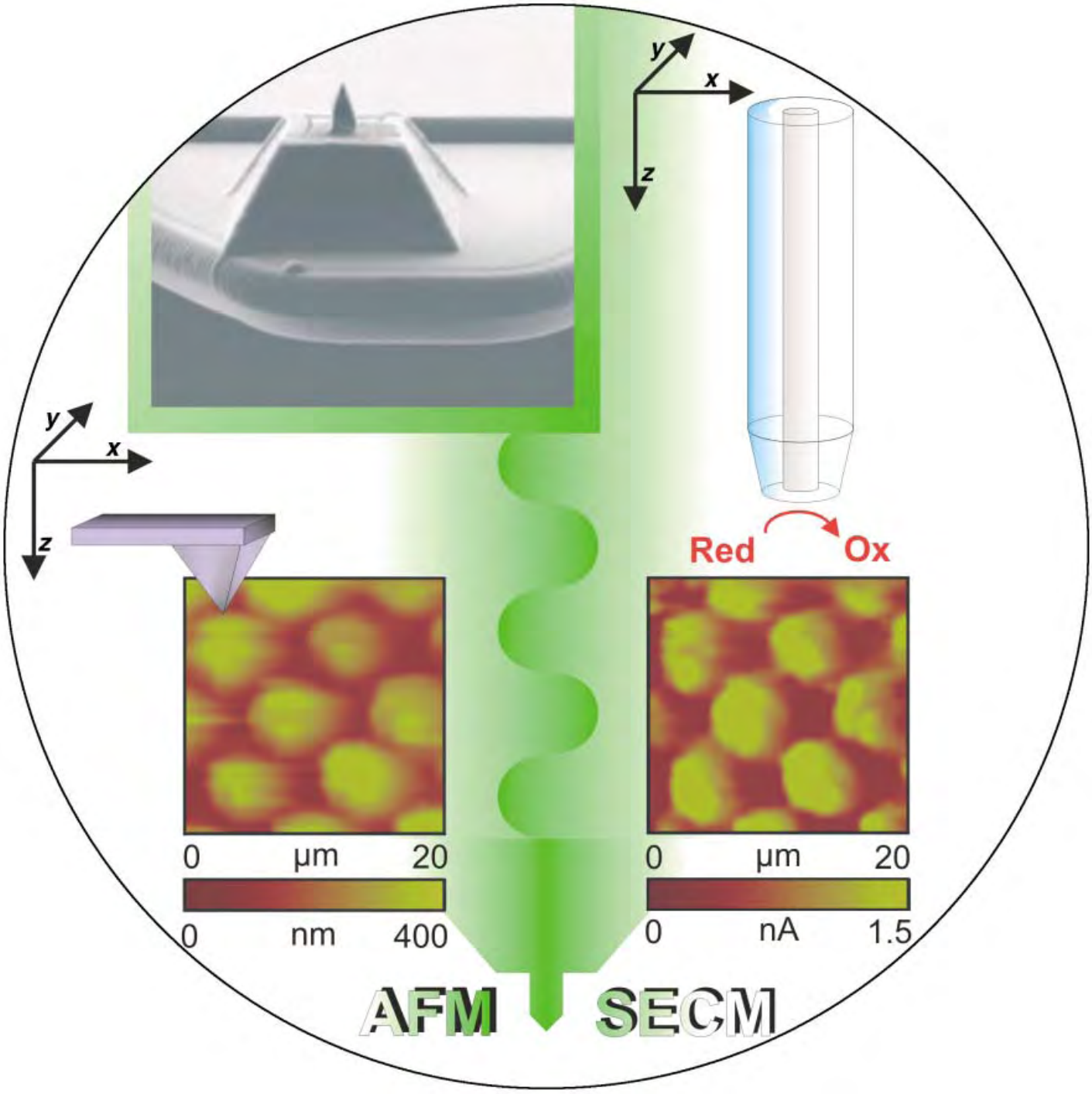
[26] C. B. Sirlin, B. Coley, R. F. Mattrey in ref. [1], chap. 30, p. 355.
[27] T. R. Porter, S. Li, L. Jiang, P. Grayburn, U. Deligonul, *J. Am. Soc. Echocardiogr.* **1999**, *12*, 266.
[28] R. E. Ronderos, M. Boskis, N. Chung, D. B. Corneli, E. M. Escudero, J. W. Ha, C. Charlante, S.-J. Rim, M. Portis, N. Fabris, J. Camilletti, A. A. Mele, F. Otero, T. R. Porter, *Clin. Cardiol.* **2002**, *25*, 103.
[29] K. Wei, A. R. Jayaweera, S. Firoozan, A. Linka, D. M. Skyba, S. Kaul, *Circulation* **1998**, *97*, 473.
[30] a) S. Kaul, R. Senior, H. Dittrich, U. Raval, R. Khattar, A. Lahiri, *Circulation* **1997**, *96*, 785; b) P. N. Burns, S. R. Wilson, D. H. Simpson, *Invest. Radiol.* **2000**, *35*, 58.
[31] a) D. M. Skyba, R. J. Price, A. Z. Linka, T. C. Skalak, S. Kaul, *Circulation* **1998**, *98*, 290; b) T. Ay, X. Havaux, G. Van Kamp, B. Campanelli, G. Gisellu, A. Pasquet, J.-F. Denet, J. Merlin, J.-L. J. Vanoverschelde, *Circulation* **2001**, *104*, 461.
[32] R. Gramiak, P. M. Shah, *Invest. Radiol.* **1968**, *3*, 356.
[33] M. R. Violante, R. B. Baggs, T. Tuthill, P. Dentinger, K. J. Parker, *Invest. Radiol.* **1991**, *26*, S194.
[34] E. C. Unger, D. Shen, T. Fritz, B. Kulik, P. Lund, G.-L. Lu, D. Yellowhair, R. Ramaswami, T. Matsunaga, *Invest. Radiol.* **1994**, *29*, S134.
[35] M. Schneider, P. Bussat, M. B. Barrau, F. Bodino, C. Gotti, E. Hybl, M. L. Pelaprat, F. Yan, *Invest. Radiol.* **1991**, *26*, S190.
[36] R. F. Mattrey, *Artif. Cells Blood Substitutes Immobilization Biotechnol.* **1994**, *22*, 295.
[37] H. von Bibra, F. Hartmann, M. Petrik, R. Schlief, U. Renner, H. Blomer, *Z. Kardiol.* **1989**, *78*, 101.
[38] S. B. Feinstein, J. Cheirif, F. J. Ten Cate, P. R. Silverman, P. A. Heidenreich, C. Dick, R. M. Desir, W. F. Armstrong, M. A. Quinones, P. M. Shah, *J. Am. Coll. Cardiol.* **1990**, *16*, 316.
[39] B. B. Goldberg, J.-B. Liu, P. N. Burns, D. A. Merton, F. Forsberg, *J. Ultrasound Med.* **1993**, *12*, 463.
[40] R. Schurmann, R. Schlief, *Radiol. Med.* **1994**, *87 (Suppl. 1)*, 15.
[41] a) M. P. Krafft, J. G. Riess, J. G. Weers in *Submicronic Emulsions in Drug Targeting and Delivery* (Hrsg.: S. Benita), Harwood, Amsterdam, **1998**, S. 235; b) M. P. Krafft, A. Chittofrati, J. G. Riess, *Curr. Opin. Colloid Interf. Sci.* **2003**, in press.
[42] M. P. Krafft, J. G. Riess, *Biochimie* **1998**, *80*, 489.
[43] M. P. Krafft, *Adv. Drug Delivery Rev.* **2001**, *47*, 209.
[44] N. G. Fisher, J. P. Christiansen, A. Klibanov, R. P. Taylor, S. Kaul, J. R. Lindner, *J. Am. Soc. Echocardiogr.* **2002**, *15*, 479.
[45] a) H. C. Dittrich, G. L. Bales, T. Kuvelas, R. M. Hunt, B. A. McFerran, Y. Greener, *J. Am. Soc. Echocardiogr.* **1995**, *8*, 465; b) J. Hancock, H. Dittrich, D. E. Levitt, M. J. Monaghan, *Heart* **1999**, *81*, 636; c) J. Cwajg, F. Xie, E. O'Leary, D. Kricsfeld, H. Dittrich, T. R. Porter, *Am. Heart J.* **2000**, *139*, 675.
[46] J. L. Cohen, J. Cheirif, D. S. Segar, L. D. Gillam, J. S. Gottdiener, E. Hausnerova, D. E. Bruns, *J. Am. Coll. Cardiol.* **1998**, *32*, 746.
[47] L. J. Shaw, L. Gillam, S. Feinstein, J. Dent, G. Plotnick, *Am. J. Managed Care* **1998**, *4*, SP169.
[48] S. R. Wilson, P. N. Burns, D. Muradali, J. A. Wilson, X. Lai, *Radiology* **2000**, *215*, 153.
[49] a) J.-M. Correas, S. D. Quay, *Clin. Radiol.* **1996**, *51* (Suppl. 1), 11; b) F. Forsberg, R. Roy, D. A. Merton, N. M. Rawool, J. B. Liu, M. Huang, D. Kessler, B. B. Goldberg, *Ultrasound Med. Biol.* **1998**, *24*, 1143; c) J.-M. Correas, A. R. Meuter, E. Singlas, D. R. Kessler, D. Wozak, S. C. Quay, *Ultrasound Med. Biol.* **2001**, *27*, 565.
[50] S. Beppu, H. Matsuda, T. Shishido, M. Matsumura, K. Niyatake, *J. Am. Soc. Echocardiogr.* **1997**, *10*, 11.
[51] P. A. Grayburn, J. Weiss, T. Hack, E. Klodas, J. Raichlen, M. Vannan, A. Klein, D. Kitzman, S. Chrysant, J. Cohen, D. Abrahamson, E. Foster, J. Perez, G. Aurigemma, J. Panza, M. Picard, B. Byrd, D. Segar, S. Jacobson, D. Sahn, A. DeMaria, *J. Am. Coll. Cardiol.* **1998**, *32*, 230.
[52] K. Tiemann, S. Lohmeier, S. Kuntz, J. Köster, C. Pohl, P. Burns, T. R. Porter, N. C. Nanda, B. Lüderitz, H. Becher, *Echocardiography* **1999**, *16*, 799.
[53] H. Maruyama, S. Matsutani, H. Saisho, N. Kamiyama, H. Yuki, K. Miyata, *Ultrasound Med. Biol.* **2000**, *26*, 1429.
[54] M. Schneider, *Echocardiography* **1999**, *16*, 743.
[55] a) D. Rovai, V. Lubrano, C. Vassalle, M. Paterni, C. Marini, M. Kozakova, M. Castellari, L. Taddei, M. G. Trivella, A. Distante, A. N. DeMaria, A. L'Abbate, *J. Am. Soc. Echocardiogr.* **1998**, *11*, 169; b) S. Lafitte, A. Higashiyama, H. Masugata, B. Peters, M. Strachan, O. L. Kwan, A. N. DeMaria, *J. Am. Coll. Cardiol.* **2002**, *39*, 1546.
[56] a) R. Senior, O. Andersson, K. Caidahl, P. Carlens, M. C. Herregods, R. Jenni, A. Kenny, A. Melcher, J. Svedenhag, J. L. Vanoverschelde, B. Wandt, B. R. Widgren, G. Williams, P. Guerret, K. la Rosee, L. Agati, G. Bezante, *Echocardiography* **2000**, *17*, 705; b) D. Bokor, J. B. Chambers, J. P. Rees, T. G. K. Mant, F. Luzzani, A. Spinazzi, *Invest. Radiol.* **2001**, *36*, 104.
[57] H. Madjar, H. J. Prömpeler, C. Del Favero, B. J. Hackelöer, J. B. Llull, *Eur. J. Ultrasound* **2000**, *12*, 123.
[58] E. J. Halpern, L. Verkh, F. Forsberg, L. G. Gomella, R. F. Mattrey, B. B. Goldberg, *Am. J. Roentgenol.* **2000**, *174*, 1575.
[59] C. B. Sirlin, Y. Z. Lee, M. S. Girard, T. M. Peterson, G. C. Steinbach, K. G. Baker, R. F. Mattrey, *Acad. Radiol.* **2001**, *8*, 162.
[60] J.-B. Liu, D. A. Meron, B. B. Goldberg, N. M. Rawool, W. T. Shi, F. Forsberg, *J. Ultrasound Med.* **2002**, *21*, 161.
[61] T. H. Marwick, R. Brunken, N. Meland, E. Brochet, F. M. Baer, T. Binder, F. Flachskampf, O. Kamp, C. Nienaber, P. Nihoyannopoulos, L. Pierard, J.-L. Vanoverschelde, P. van der Wouw, K. Lindvall, *J. Am. Coll. Cardiol.* **1998**, *32*, 1260.
[62] M. Picard, N. Pandian, F. Morcerf, F. Wackers, J. E. Udelson, N. Weissman, P. Grayburn, A. Klein, M. Vannan, J. Yao, R. Fetterman, R. Walovitch, A. DeMaria, *J. Am. Soc. Echocardiogr.* **2001**, *14*, 460.
[63] T. P. Porter, P. L. Iversen, S. Li, F. Xie, *J. Ultrasound Med.* **1996**, *15*, 577.
[64] a) T. R. Porter, S. Li, D. Kricsfeld, R. W. Armbruster, *J. Am. Coll. Cardiol.* **1997**, *29*, 791; b) G. Rocchi, J. D. Kasprzak, T. W. Galema, N. de Jong, F. J. Ten Cate, *Am. J. Cardiol.* **2001**, *87*, 278.
[65] T. R. Porter, R. F. LeVeen, R. Fox, A. Kricsfeld, F. Xie, *Am. Heart J.* **1999**, *132*, 964.
[66] a) R. Leischik, C. Kuhlmann, C. Bruch, A. Jeremias, T. Buck, R. Erbel, *Int. J. Cardiac Imaging* **1997**, *13*, 387; b) N. G. Fisher, J. P. Christiansen, H. Leong-Poi, A. R. Jayaweera, J. R. Lindner, S. Kaul, *J. Am. Coll. Cardiol.* **2002**, *39*, 530;c) G. Seidel, K. Meyer, C. Algermissen, A. Broillet, *Ultrasound Med. Biol.* **2001**, *27*, 915.
[67] P. A. Dayton, J. E. Chomas, A. F. H. Lum, J. S. Allen, J. R. Lindner, S. I. Simon, K. W. Ferrara, *Biophys. J.* **2001**, *80*, 1547.
[68] R. Gramiak, P. M. Shah, D. H. Kramer, *Radiology* **1969**, *92*, 939.
[69] R. F. Mattrey, G. Strich, R. E. Shelton, B. B. Gosink, G. R. Leopold, T. Lee, J. Forsythe, *Radiology* **1987**, *163*, 339.
[70] S. Beckmann, M. Schartl, W. Bocksch, H. Paeprer, *Z. Kardiol.* **1993**, *82*, 317.
[71] B. D. Coley, M. A. Trambert, R. F. Mattrey, *Am. J. Roentgenol.* **1994**, *163*, 961.
[72] a) Y. Kono, S. P. Pinnell, C. B. Sirlin, S. R. Sparks, B. Georgy, W. Wong, R. F. Mattrey, *Radiology*, in press; b) T. Postert, B. Braun, N. Pfundtner, R. Sprengelmeyer, S. Meves, H. Przuntek, T. Buttner, *Ultrasound Med. Biol.* **1998**, *24*, 953; c) G. Seidel, L. Claassen, K. Meyer, M. Vidal-Langwasser, *Ultrasound Med. Biol.* **2001**, 27, 1059;d) G. Seidel, K. Meyer, V. Metzler, D. Toth, M. Vida-Langwasser, T. Aach, *Ultrasound Med. Biol.* **2002**, *28*, 183.

 © 2003 Wiley-VCH Verlag GmbH & Co. KGaA, Weinheim

[73] K. Ohmori, B. Cotter, O. L. Kwan, K. Mitzushige, A. N. DeMaria, *Am. Heart J.* **1997**, *134*, 1066.
[74] J. M. A. Swinburn, A. Lahiri, R. Senior, *J. Am. Coll. Cardiol.* **2001**, *38*, 19.
[75] S. R. Wilson, P. N. Burns, *Semin. Liver Dis.* **2001**, *21*, 147.
[76] D. Strohmeyer, F. Frauscher, A. Klauser, W. Recheis, G. Eibl, W. Horninger, H. Steiner, H. Volgger, G. Bartsch, *Anticancer Res.* **2001**, *21*, 2907.
[77] M. S. Girard, Y. Kono, C. B. Sirlin, K. G. Baker, L. H. Deiranieh, R. F. Mattrey, *Acad. Radiol.* **2001**, *8*, 734.
[78] G. A. Taylor, C. E. Barnewolt, B. H. Adler, P. S. Dunning, *Am. J. Roentgenol.* **1998**, *170*, 417.
[79] M. J. K. Blomley, J. C. Cooke, E. C. Unger, M. J. Monaghan, D. O. Cosgrove, *BMJ Br. Med. J.* **2001**, *322*, 1222.
[80] T. Albrecht, C. W. Hoffmann, S. A. Schmitz, S. Schettler, A. Overberg, C. T. Germer, K. J. Wolf, *Am. J. Roentgenol.* **2001**, *176*, 1191.
[81] a) Y. Birnbaum, H. Luo, T. Nagai, M. C. Fishbein, T. M. Peterson, S. Li, D. Kricsfeld, T. R. Porter, R. J. Siegel, *Circulation* **1998**, *97*, 130; b) T. R. Porter, R. F. LeVeen, R. Fox, A. Kricsfeld, F. Xie, *Am. Heart J.* **1996**, *132*, 964.
[82] a) P. A. Dayton, K. W. Ferrara, *J. Magn. Reson. Imaging* **2002**, *16*, 362; b) A. L. Klibanov, *Top. Curr. Chem.* **2002**, *222*, 73; c) G. M. Lanza, S. A. Wickline, *Prog. Cardiovasc. Dis.* **2001**, *44*, 13; d) J. R. Lindner, *Am. J. Cardiol.* **2002**, *90* (Suppl.), 723.
[83] a) Y. Wu, E. C. Unger, T. P. McCreery, R. H. Sweitzer, D. Shen, G. Wu, M. D. Vielhauer, *Invest. Radiol.* **1998**, *33*, 880; b) P. A. Schumann, J. P. Christiansen, R. M. Quigley, T. P. McCreery, R. H. Schweitzer, E. C. Unger, J. R. Lindner, T. O. Matsunaga, *Invest. Radiol.* **2002**, *37*, 587.
[84] J. R. Lindner, J. Song, F. Xu, A. L. Klibanov, K. Singbartl, K. Ley, S. Kaul, *Circulation* **2000**, *102*, 2745.
[85] J. R. Lindner, J. Song, J. Christiansen, A. L. Klibanov, F. Xu, K. Ley, *Circulation* **2001**, *104*, 2107.
[86] K. W. Ferrara, C. R. Merritt, P. N. Burns, F. S. Foster, R. F. Mattrey, S. A. Wickline, *Acad. Radiol.* **2000**, *7*, 824.
[87] O. D. Kripfgans, J. B. Fowlkes, D. L. Miller, O. P. Eldevik, P. L. Carson, *Ultrasound Med. Biol.* **2000**, *26*, 1177.
[88] R. J. Price, D. M. Skyba, S. Kaul, T. C. Skalak, *Circulation* **1998**, *98*, 1264.
[89] E. C. Unger, E. Hersh, M. Vannan, T. O. Matsunaga, T. McCreery, *Prog. Cardiovasc. Dis.* **2001**, *44*, 45.
[90] J. G. Riess, *J. Drug Targeting* **1994**, *2*, 455.
[91] E. C. Unger, T. P. McCreery, R. H. Sweitzer, V. E. Caldwell, Y. Wu, *Invest. Radiol.* **1998**, *33*, 886.
[92] L. A. Dellamary, T. E. Tarara, D. J. Smith, C. H. Woelk, A. Adractas, M. L. Costello, H. Gill, J. G. Weers, *Pharm. Res.* **2000**, *17*, 168.
[93] D. J. Smith, L. M. Gambone, T. Tarara, D. R. Meays, L. A. Dellamary, C. M. Woods, J. Weers, *Pharm. Res.* **2001**, *18*, 1556.
[94] A. I. Bot, T. E. Tarara, D. J. Smith, S. R. Bot, C. M. Woods, J. G. Weers, *Pharm. Res.* **2000**, *17*, 275.
[95] H. D. van Liew, M. E. Burkard, *Adv. Exp. Med. Biol.* **1997**, *411*, 395.
[96] C. E. G. Lundgren, G. W. Bergoe, I. Tyssebotn, Syllabus, 4th International Symposium on Current Issues in Blood Substitute Research (Stockholm), **2002**, p. 40.
[97] R. V. Shohet, S. Chen, Y.-T. Zhou, Z. Wang, R. S. Meidell, R. H. Unger, P. A. Grayburn, *Circulation* **2000**, *101*, 2554.
[98] M. W. Miller, *Ultrasound Med. Biol.* **2000**, *26* (Suppl. 1), S59.
[99] P. A. van der Wouw, A. C. Brauns, S. E. Bailey, J. E. Powers, A. A. Wilde, *J. Am. Soc. Echocardiogr.* **2000**, *13*, 288.
[100] L. J. Shaw, M. J. Monaghan, P. Nihoyannopoulos, *Heart* **1999**, *82* (Suppl. III), 16.
[101] N. C. Nanda, D. W. Kitzman, L. J. Crouse, H. C. Dittrich, *Echocardiography* **2002**, in press.

 © 2003 Wiley-VCH Verlag GmbH & Co. KGaA, Weinheim

Communications



Surface topography and the enzyme activity of soft bioactive probes can be investigated simultaneously with a new technique. More about this method, a combination of atomic force and scanning electrochemical microscopy, can be found in the following Communication by C. Kranz et al.

DOI: 10.1002/anie.200351111
© 2003 Wiley-VCH Verlag GmbH & Co. KGaA, Weinheim

Imaging Enzyme Activity

Integrated AFM–SECM in Tapping Mode: Simultaneous Topographical and Electrochemical Imaging of Enzyme Activity**

Angelika Kueng, Christine Kranz, Alois Lugstein, Emmerich Bertagnolli, and Boris Mizaikoff*

Since the introduction of atomic force microscopy (AFM) in 1986,[1] AFM has matured to a scanning probe technique regularly applied for investigation of biological samples. AFM in tapping mode operation is particularly useful for imaging soft sample surfaces, such as biological specimens.[2] A significantly reduced tip–sample contact time results in minimized frictional forces avoiding damage.[3] Applications of AFM in this area include the investigation of structural[4] and mechanical properties[5] of individual proteins in physiologically relevant environments and real-time probing of protein–protein interactions.[6] Direct observation of enzyme activity has been described for proteins adsorbed onto mica surfaces by detecting height fluctuations of the cantilever[7] or from measuring force spectra.[8] Despite the superior sensitivity, application of these methods is limited to atomically flat, synthetic samples. To date none of these approaches allowed the specific detection of a molecular product resulting from enzymatic substrate conversion.

Recent instrumental developments in the field of scanning probe microscopy (SPM) are aimed at combined techniques which provide simultaneous information on the surface topography and on the physical and chemical surface properties. As many biochemically relevant processes are based on electrochemical conversion of molecules, techniques gathering laterally resolved information on coupled oxidation–reduction processes are of particular interest. The combination of AFM with scanning electrochemical microscopy (SECM) provides a promising concept to achieve this intriguing task by allowing the position-specific probing of (electro)chemical surface properties by a scanning probe technique.

[*] Dr. C. Kranz, Dr. A. Kueng, Prof. B. Mizaikoff
School of Chemistry and Biochemistry
Georgia Institute of Technology
Atlanta, GA 30332-0400 (USA)
Fax: (+1) 404-894-7452
E-mail: christine.kranz@chemistry.gatech.edu
Dr. A. Lugstein, Prof. E. Bertagnolli
Solid State Electronics Institute
Vienna University of Technology
Floragasse 7, 1040 Vienna (Austria)

[**] This work was supported by the NSF (grant No. 0216368 within the program "Biocomplexity in the Environment"), the Max Kade Foundation, New York, and the "Fonds zur Förderung der wissenschaftlichen Forschung", Austria (grants P14122-CHE and J2230). PCT Patents are granted on this technology (WO2001094877A1 and WO2001094926A1). AFM = atomic force microscopy, SECM = scanning electrochemical microscopy.

SECM is a powerful technique to obtain in situ information on a wide range of (electro)chemical processes occurring at liquid–solid and liquid–liquid interfaces.[9] Signal generation in SECM is based on surface-induced changes of a Faraday current. This current results from hemispherical diffusion of redox-active species to a biased ultra-microelectrode (UME) scanned across the sample surface in the nearfield regime.[10] SECM has been applied successfully to the investigation of biological samples, including localized imaging of enzyme activity[11] and for spatially resolved detection of neurotransmitter release.[12] However, one major drawback of SECM in comparison to AFM and other SPM techniques is the limited lateral resolution as a result of signal-dependent positioning of the UME in common operation modes in which the UME is scanned over the sample at a constant height.[13] Consequently, any progress towards improved lateral resolution in SECM has to address current-independent positioning, particularly the use of nanoelectrodes requires precise control of the distance between the scanning nanoelectrode and the sample surface.

Besides the application of non-electrode tips in SECM using a shear-force based constant-distance mode,[14] the combination of AFM–SECM[15] is a particularly attractive strategy for achieving complementary electrochemical and topographical information with high lateral resolution in a single time- and space-correlated measurement. AFM probes with integrated UMEs promise to be a powerful analytical tool. Microfabrication of nano- and sub-microelectrodes integrated into conventional AFM tips is an elegant and versatile approach combining SECM and AFM.[16] The integration of an electroactive area at an exactly defined distance above the apex of the AFM tip allows the distance between electrode and probe to remain constant, regardless of the surface topography, which enables simultaneous electrochemical and AFM imaging in contact mode and tapping mode operation.[17]

Herein difunctional probes with integrated electrodes (Figure 1) are successfully applied to simultaneously image topographical and electrochemical properties of a biologically active sample in AFM tapping mode. The pores of a periodic micro-structure were filled with a soft polymer matrix in which the oxidoreductase enzyme glucose oxidase (GOD) was immobilized. The enzymatic activity of the GOD was electrochemically imaged during mapping of the topography.

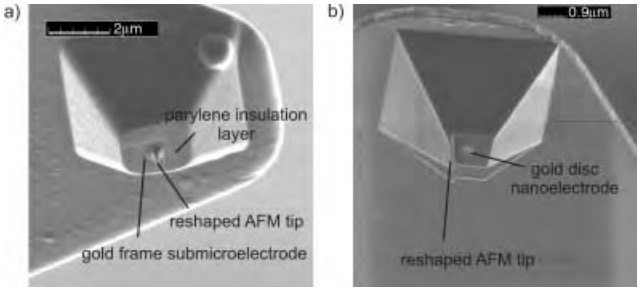


Figure 1. FIB image of a) an integrated frame sub-microelectrode with an edge length of 770 nm and a tip height of 700 nm and b) an integrated disc nanoelectrode with a diameter of 300 nm.

 © 2003 Wiley-VCH Verlag GmbH & Co. KGaA, Weinheim DOI: 10.1002/anie.200351111

For fabrication of integrated AFM-SECM tips conventional Si_3N_4 cantilevers with pyramidal tips are coated with a 100-nm thick gold layer and subsequently insulated with a 700-nm thick layer of xylylene polymer (Parylene C) by chemical vapor deposition polymerization. Three-dimensional focused-ion-beam (FIB) milling enables reproducible exposition of an electroactive area, with defined geometry and dimensions, above the apex of the original AFM tip. Finally, the original AFM tip is shortened with FIB to ensure the optimum working distance between electrode and sample surface. This technique also allows the modification of the modified AFM tip to guarantee optimal image quality (Figure 1). Besides the described design of frame sub-microelectrodes (Figure 1a) disc nanoelectrodes (Figure 1b) can also be integrated. A detailed description of fabrication and characterization processes is given elsewhere.[16,17]

To demonstrate the capability and resolution of microfabricated combined AFM–SECM tips, imaging of various samples was performed in AFM contact mode and SECM feedback mode.[16,17] The topographic image quality of the remodeled tip is comparable to that obtained with non-modified AFM Si_3N_4 cantilevers as shown in previous studies.[18]

Imaging enzyme activity in AFM tapping mode was performed at a micro pattern of isolated enzyme-containing polymer spots (Figure 2). A periodically micropatterned

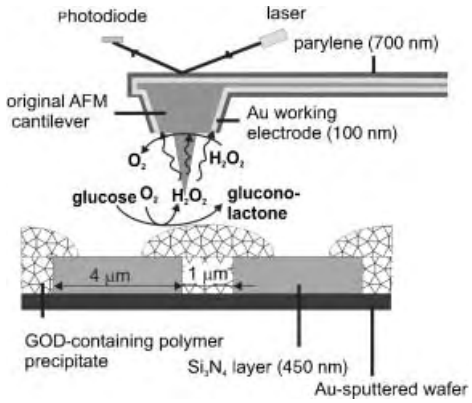


Figure 2. Schematic representation of simultaneous AFM–SECM imaging and the reactions involved at the surface of the micropatterned sample with the integrated electrode operating in generation–collection mode.

silicon nitride layer (450 nm layer thickness) was deposited onto a gold coated silicone wafer. GOD was entrapped inside the conducting holes by electrochemically induced precipitation of a polymer suspension.[19] Simultaneous tapping mode topographical and electrochemical imaging of the enzyme activity was performed with an integrated frame sub-microelectrode shown in Figure 1a. As demonstrated recently, the application of difunctional tips in AFM tapping mode is a prerequisite for successful imaging of soft biological samples or polymers.[20] Electrochemical images recorded in tapping mode reveal a current response and lateral resolution comparable to the electrochemical images of the same probe recorded in contact mode.

For localized detection of GOD activity the generation–collection mode of SECM[21] was applied. In the presence of the substrate glucose, H_2O_2 is locally generated as a byproduct of the enzymatic reaction (see Figure 2). GOD catalyzes the conversion of glucose into gluconolactone. H_2O_2 is directly detected at the integrated electrode, which is biased at a potential of 750 mV (versus Ag/AgCl). A schematic of the involved reactions and the measurement principle is given in Figure 2.

Figure 3 shows simultaneously recorded height (a, d), amplitude (b, e), and current (c, f) images recorded in tapping mode in absence (a–c) and presence (d–f) of glucose. The amplitude images (Figure 3b and e) suppress small variations in topography and emphasize the edges of topographical features for increased contrast.

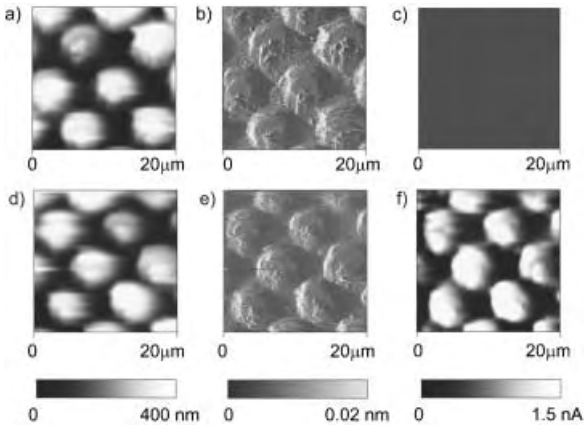


Figure 3. Simultaneously recorded topography of the enzyme-containing periodic polymer structure (height image) and current image of GOD activity in AFM tapping mode with free drive amplitude of 5 V and drive frequency of 32.4 kHz. Height (a and e), corresponding amplitude (b and e), and simultaneously recorded Faraday current (c and f) images recorded in air-saturated phosphate buffer (0.1 mol L^{-1}, pH 7.4) in the absence (a–c) and in the presence (d–f; 50 mmol L^{-1}) of glucose. The tip was held at a potential of 0.75 V (versus Ag/AgCl quasi-reference electrode). Electrode edge length: 770 nm; tip height: 700 nm; scan rate: 3 Hz.

In the absence of glucose in solution there is no enzymatic activity and the current recorded at the electrode during AFM tapping mode imaging of the enzyme-containing polymer spots is negligible and reveals no electrochemical features (Figure 3c). In the presence of glucose there is an increase in the current recorded at the integrated sub-microelectrode as a result of localized production of H_2O_2 when the tip is scanned across the GOD-containing polymer spots (Figure 3f). The periodicity of the polymer pattern in the electrochemical image corresponds well with the topography measured simultaneously by the integrated AFM tip.

These results demonstrate for the first time the feasibility of combined AFM–SECM technology for imaging soft biological samples with enzymatic redox activity in tapping mode. The investigation of complex biological systems and molecular biological interactions, for example, signaling processes at cell surfaces, demands simultaneous information on multiple parameters correlated in space and time. The

 © 2003 Wiley-VCH Verlag GmbH & Co. KGaA, Weinheim

development of bifunctional AFM–SECM probes represents a significant advancement in SPM methodology and is a first step towards improved analytical instrumentation for elucidating complex bioprocesses at a nanoscale. With the described microfabrication technology, integrated frame or ring electrodes with edge lengths or diameters down to 300 nm and disc electrodes with diameters under 100 nm can be realized. Currently achieved electrode dimensions already correspond well with biologically relevant feature sizes and there is considerable scope for using this instrumentation in a variety of ways to probe a whole range of biological substrates and relevant bioprocesses.

Experimental Section

Sample preparation for imaging enzyme activity (Figure 2): An aqueous solution containing GOD (5 mg mL^{-1}) and Canguard polymer suspension (70 μL mL^{-1}) was stored for at least 30 min at 4 °C before usage. For polymer film formation, a potential-pulse profile (2200 mV for 0.2 s, 800 mV for 1 s, and 0 mV for 5 s, versus Ag/AgCl quasi-reference electrode) was applied 12 times leading to the formation of the polymer-entrapped enzyme pattern within the pores of the periodic micropattern (Quantifoil, Germany). The sample was rinsed with water and phosphate buffer (0.1 mol L^{-1}, pH 7.4) and stored for at least 12 h at 4 °C before analysis with AFM–SECM.[19]

All measurements were done with a Nanoscope III AFM (Digital Instruments, Santa Barbara, CA, USA) equipped with a tapping mode liquid cell with inlets used for Pt-counter and Ag/AgCl quasi-reference electrodes. The output signal of the bipotentiostat (CH-Instruments, Austin, TX, USA) was read in at the additional AD channel offered by the AFM instrument. A detailed description of the experimental setup is given elsewhere.[16–18] The current recorded at the integrated electrode is obtained simultaneously with the topographical information provided by the reshaped AFM tip.

Received: February 5, 2003 [Z51111]

Keywords: analytical methods · atomic force microscopy · enzymes · scanning microscopy · tapping mode

[1] G. Binnig, C. F. Quate, C. Gerber, *Phys. Rev. Lett.* **1986**, *56*, 930–933.
[2] P. K. Hansma, J. P. Cleveland, M. Radmacher, D. A. Walters, P. E. Hillner, M. Bezanilla, M. Fritz, D. Vie, H. G. Hansma, C. B. Prater, J. Massie, L. Fukunaga, J. Gurley, V. Elings, *Appl. Phys. Lett.* **1994**, *64*, 1738–1740.
[3] C. A. J. Putman, K. O. van der Werf, B. G. De Grooth, N. F. Van Hulst, J. Greve, *Appl. Phys. Lett.* **1994**, *64*, 2454–2456; C. Le Grimellec, M.-C. Giocondi, R. Pujol, E. Lesniewska, *Single Mol.* **2000**, *1*, 105–107.
[4] D. J. Muller, A. Engel, *J. Mol. Biol.* **1999**, *285*, 1347–1351.
[5] F. Oesterhelt, D. Oesterhelt, M. Pfeiffer, A. Engel, H. E. Gaub, D. J. Müller, *Science* **2000**, *288*, 143–146; M. Rief, M. Gautel, F. Oesterhelt, J. M. Fernadez, H. E. Gaub, *Science* **1997**, *276*, 1109–1112.
[6] M. B. Viani, L. I. , Pietrasanta, J. B. Thompson, A. Chand, I. C. Gebeshuber, J. H. Kindt, M. Richter, H. G. Hansma, P. K. Hansma, *Nat. Struct. Biol.* **2000**, *7*, 644–647.
[7] M. Radmacher, M. Fritz, H. G. Hansma, P. K. Hansma, *Science* **1994**, *265*, 1577–1579.
[8] Z. Yingge, Z. Delu, B. Chunli, W. Chen, *Life Sci.* **1999**, *65*, PL253–PL260.
[9] M. V. Mirkin, B. R. Horrocks, *Anal. Chim. Acta* **2000**, *406*, 119–146.
[10] J. Kwak, A. J. Bard, *Anal. Chem.* **1989**, *61*, 1221–1227.
[11] D. T. Pierce, A. J. Bard, *Anal. Chem.* **1993**, *65*, 3598–3604.
[12] A. Hengstenberg, A. Blöchl, I. D. Dietzel, W. Schuhmann, *Angew. Chem.* **2001**, *113*, 942–946; *Angew. Chem. Int. Ed.* **2001**, *40*, 905–908.
[13] A. J. Bard, F. R. F. Fan, M. V. Mirkin in *Electroanalytical Chemistry, Vol. 18* (Ed.: A. J. Bard), Marcel Dekker, New York, **1994**, pp. 268–293.
[14] A. Hengstenberg, C. Kranz, W. Schuhmann, *Chem. Eur. J.* **2000**, *6*, 1548–1554.
[15] C. E. Gardner, J. V. Macpherson, *Anal. Chem.* **2002**, *74*, 576A–584A; J. V. Macpherson, P. R. Unwin, *Anal. Chem.* **2001**, *73*, 550, and references therein.
[16] C. Kranz, G. Friedbacher, B. Mizaikoff, A. Lugstein, J. Smoliner, E. Bertagnolli, *Anal. Chem.* **2001**, *73*, 2491–2500.
[17] A. Lugstein, E. Bertagnolli, C. Kranz, A. Kueng, B. Mizaikoff, *Appl. Phys. Lett.* **2002**, *81*, 349–351.
[18] C. Kranz, B. Mizaikoff, A. Lugstein, E. Bertagnolli, *ACS Symp. Ser.* **2002**, *811*, 320–336.
[19] C. Kurzawa, A. Hengstenberg, W. Schuhmann, *Anal. Chem.* **2002**, *74*, 355–361.
[20] A. Kueng, C. Kranz, B. Mizaikoff, A. Lugstein, E. Bertagnolli, *Appl. Phys. Lett.* **2003**, *82*, 1592–1594.
[21] G. Wittstock, *Fresenius J. Anal. Chem.* **2001**, *370*, 303–315.

 © 2003 Wiley-VCH Verlag GmbH & Co. KGaA, Weinheim

Diastereoselective Hydroxylations

Biomimetic Hydroxylation of Nonactivated CH_2 Groups with Copper Complexes and Molecular Oxygen**

Bruno Schönecker, Tatjana Zheldakova, Yong Liu, Manuela Kötteritzsch, Wolfgang Günther, and Helmar Görls*

In memory of Kurt Ponsold

Selective hydroxylation with molecular oxygen mediated by copper-containing enzymes (e.g. tyrosinase, dopamine-β-

[*] Prof. Dr. B. Schönecker, Dr. Y. Liu, M. Kötteritzsch, Dr. W. Günther
Institut für Organische Chemie und Makromolekulare Chemie
Friedrich-Schiller-Universität Jena
Lessingstrasse 8, 07743 Jena (Germany)
Fax: (+49) 3641-948292
E-mail: c8scbr@uni-jena.de

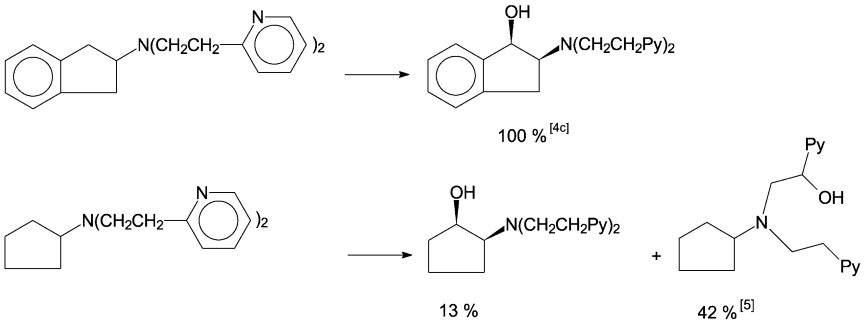
Dr. T. Zheldakova
Institute for Bioorganic Chemistry
Belorussian National Academy of Sciences
Minsk (Belorussia)

Dr. H. Görls
Institut für Anorganische und Analytische Chemie
Friedrich-Schiller-Universität Jena
Lessingstrasse 8, 07743 Jena (Germany)

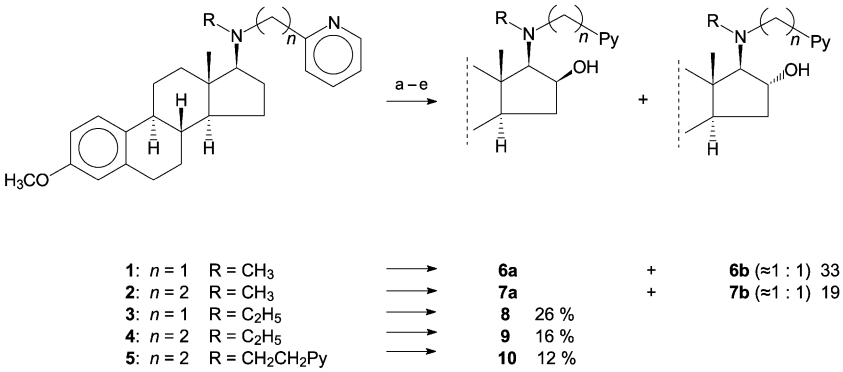
[**] This research was supported by the Deutsche Forschungsgemeinschaft (SFB 436 "Metallvermittelte Reaktionen nach dem Vorbild der Natur"), the Thuringian Ministerium für Wissenschaft, Forschung und Kunst, and the Fonds der Chemischen Industrie. We thank Schering AG, Berlin, and Jenapharm GmbH & Co. KG, Jena, for providing us with steroids.

 © 2003 Wiley-VCH Verlag GmbH & Co. KGaA, Weinheim DOI: 10.1002/anie.200250815

hydroxylase) in living organisms provides a fascinating model for investigating the hydroxylation of organic substrates with simple copper complexes.[1] In spite of rapid progress in this field, which is evident from structural investigations on the copper–oxygen intermediates found in hydroxylation reactions[2] and successful quantitative hydroxylations of aromatic[3] and benzylic ligands,[2g,4] hydroxylation of nonactivated CH_2 groups is still very difficult. Reglier et al. described one of the few known examples, the copper-mediated hydroxylation of propyl and cyclopentyl groups in the β-position to an *N*,*N*-bis[2-(2-pyridyl)ethyl]amino ligand with molecular oxygen.[5] The hydroxylation of the cyclopentyl ring, similar to hydroxylation of the benzyl position in related 2-aminoindanes,[4c] is stereoselective and results in a *cis*-amino alcohol.[5] In contrast to the reaction of the aminoindane variant, which is quantitative, hydroxylation of propyl and cyclopentyl derivatives is considerably less effective with maximum yields of 10% and 13%, respectively. The major products in this case are alcohols resulting from hydroxylation of the CH_2 groups adjacent to the pyridine ring (64% and 42% yield, respectively, Scheme 1).[5]



Scheme 1. Examples of intramolecular hydroxylations of ligands. Py = pyridyl.



Scheme 2. 16-Hydroxylations. a) $Cu(CF_3SO_3)_2$, CH_2Cl_2; b) benzoin, $N(C_2H_5)_3$, Ar; c) O_2; d) NH_4OH, H_2O; e) chromatography on silica gel.

We report here on current progress in diastereoselective hydroxylation reactions. We selected chiral steroidal ligands for our studies owing to their well-defined conformations as well as the possibility of placing copper-complexing N-donor atoms in different spatial environments.[6] Since bidentate pyridylethylamino ligands have been employed successfully for the hydroxylation of benzyl groups in β-positions,[4e] we synthesized 17β-*N*-alkyl-*N*-[2-(2-pyridyl)ethyl]amino ligands as well as the related *N*-[(2-pyridyl)methyl]amino-3-methoxy-estra-1.3.5(10)-trienes **1**–**4** (Scheme 2) with the intent of investigating the hydroxylation of nonactivated CH_2 groups upon complexation with copper(I) ions.

For the hydroxylation reaction itself we employed the method of Itoh and Fukuzumi et al. (see Experimental Section) because of the anticipated good yields.[4b–d] The hydroxylations were carried out at room temperature in anhydrous CH_2Cl_2 under an atmosphere of pure oxygen. After decomplexation by treatment with aqueous ammonia, the reaction mixture was separated by column chromatography on silica gel. In addition to various amounts of recovered starting ligand, polar products in yields of 16% to 33% were isolated in all cases (Scheme 2), which were identified by detailed ^1H and ^{13}C NMR analyses as 16-hydroxylated steroids.

Analogous to the results of Reglier et al.,[4c,5] hydroxylation of the *N*-ethyl compounds **3** and **4** resulted in the expected 16β-alcohols **8** (26%) and **9** (16%), which are the products of a *cis*-β-hydroxylation. Hydroxylation of the *N*-methyl compounds **1** and **2** resulted in the *cis* products **6a** and **7a** as well as, unexpectedly, the diastereomeric *trans* products **6b** and **7b** in approximately equal yields. This is the first reported example of a *trans*-β-hydroxylation. For comparison we then hydroxylated the tridentate ligand **5**. In accord with the results reported by Reglier et al.[5] only the 16β-alcohol **10** was obtained in 12% yield.

The difference in the hydroxylation of the *N*-methyl and the *N*-ethyl compounds shows that small changes in the ligand can greatly alter the diastereoselectivity. In this case steric interactions of the N ligands with the 13β-methyl group probably affect the conformation of the ligand in the metal complexes, thus leading to a *cis* or a *trans* abstraction of the 16β and 16α H atoms. The fact that small changes in the ligand can also lead to different product ratios of the peroxo–oxo complex equilibria has already been demonstrated.[7]

We have, to date, been unable to obtain X-ray structural analyses of copper complexes with the aminoalkyl-2-pyridine ligands or their oxygen adducts; however, the solid-state structure of a bis(μ-hydroxy)dicopper(II) complex (Figure 1) obtained from **1**, $[Cu(CH_3CN)_4ClO_4]$, and oxygen shows a nearly planar orientation of the N, Cu, and O atoms, thus indicating that such a geometry can be assumed for the active oxidating species. Rather unexpectedly, both of the large steroidal residues are located on the same side of the complex (*syn* orientation).[3m]

 © 2003 Wiley-VCH Verlag GmbH & Co. KGaA, Weinheim

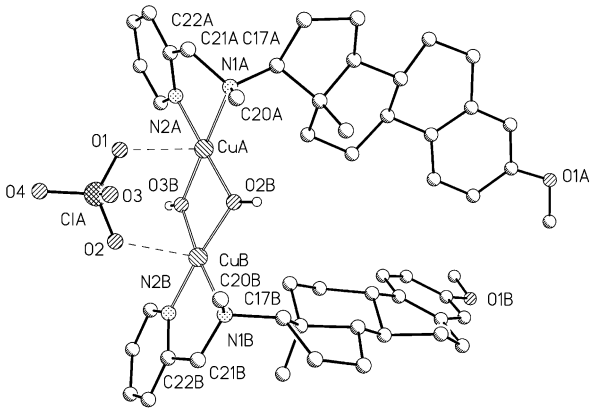
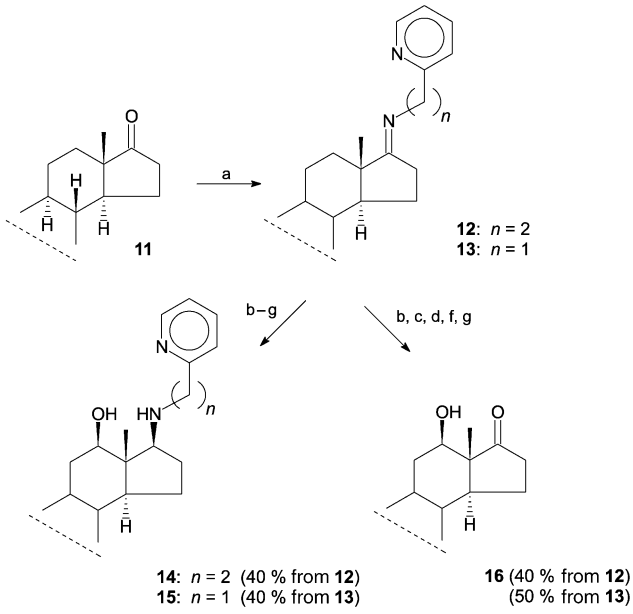


Figure 1. X-ray crystal structure of the bis(μ-hydroxy)dicopper(II) complex.

Our investigations clearly show that nonactivated CH_2 groups can be hydroxylated with easily accessible bidentate pyridylethyl- and pyridylmethylamino ligands. The yields are somewhat better than those with the corresponding tridentate ligands. The yields for the pyridinemethylamino compounds are higher than those for the pyridineethylamino derivatives (Cu,5-ring/Cu,6-ring). The highest diastereoselectivities were obtained with the *N*-ethyl ligands.

If several different conformations of the ligand are possible, the selectivity suffers. We therefore looked for several ligands in which the conformational flexibility has been sterically fixed. The 17-imines **12** and **13** (Scheme 3), which were obtained as intermediates in the synthesis of **1**–**4**, seemed to be ideal for our purposes. Rather than the conformationally mobile complexing amino functionality, imines **12** and **13** have a C–N double bond in an *anti* configuration at C17, which effectively "freezes" the complexing functionality. Due to the sensitivity of the imine, the C=N double bond was reduced with $NaBH_4$ immediately following the hydroxylation of **12**. This resulted in crystals of a polar amino alcohol (40% yield) whose ^1H and ^{13}C NMR spectra clearly indicate that a regio- and stereoselective 12-hydroxylation had taken place to give compound **14**. An X-ray crystal structure analysis showed the product to have the 12β configuration.



Scheme 3. 12β-Hydroxylations. a) $Py(CH_2)_nNH_2$ ($n=1$, 2), refluxing toluene, *p*-toluenesulfonic acid; b) $Cu(CF_3SO_3)_2$, CH_2Cl_2; c) benzoin, $N(C_2H_5)_3$, Ar; d) O_2; e) $NaBH_4$, CH_3OH; f) NH_4OH, H_2O; g) chromatography on silica gel.

In a second experiment the imino group was hydrolyzed in aqueous ammonia solution rather than decomplexed by reduction with $NaBH_4$. This resulted in the previously unknown 12β-hydroxy-17-ketone **16** in 40% yield (Scheme 3). Treatment of **13** under these conditions resulted in **16** (50%) as well as recovered starting ketone **11** (30%).

In contrast to the known α-[8] and β-hydroxylations[4,5] this 12β-hydroxylation represents the first γ-hydroxylation of a nonactivated CH_2 group that, in addition, is regio- and stereoselective. The yields of 50% are the best obtained so far for copper-mediated hydroxylations of nonactivated CH_2 groups and almost suffice for practical synthetic purposes.

Breslow et al. recently reported the stereoselective hydroxylation of steroid derivatives in 6α- and 9α-positions with manganese(III)porphyrin catalysts that were linked by means of spacers to β-cyclodextrin. Phenyliodosobenzene was employed as the oxidation reagent.[9] Similar manganese porphyrins linked to the 3α-hydroxy group of androstane through a spacer have already been employed (Breslow's remote-oxidation reactions[10]) for hydroxylations in position 12. In addition to the 12α-hydroxylation, oxidation to give the 12-ketone as well as additional hydroxylation at the 14α-position occurred.[11]

Copper-mediated γ-hydroxylations have been, to our knowledge, reported only for aromatic compounds in which the hydroxylation usually takes place between two *m*-xylyl spacers bearing N-donor atoms (tyrosinase models).[3a–m] Reglier et al. tried unsuccessfully to induce the γ-hydroxylation of an activated benzyl group in 2-aminotetralin with tridentate ligands.[2g] A 12β-hydroxylation succeeds with simple and easy-to-synthesize bidentate C-iminoethyl- and C-iminomethyl-2-pyridine ligands, which can be removed easily to regenerate the carbonyl group. If desired, the imines can also be reduced to secondary amines. In this manner, biologically interesting 1,3-amino alcohols can be obtained. Up until now, 12β-hydroxy-estra-1.3.5(10)-trienes have been available only through chemical modification of bile acids (multistep synthesis) or through microbial hydroxylation.[12] One should also mention that the 11β-hydroxy group (important for corticoids) can also be introduced in several steps starting from 12-hydroxysteroids.[13]

These and further investigations on hydroxylations should lead to a model in which the spatial requirements for an effective attack of the copper–oxygen complex on the C–H bond can be deduced. It is remarkable that the attack of the oxygen occurs from the β-side of the steroid; when external reagents are employed, this is hindered by the pseudoaxial 13β-CH_3 group (see Figure 2). The solid-state structure of ligand **13** (Figure 2) shows that the distances between the central N atom (N1) and the 12β hydrogen atoms (H12B and

 © 2003 Wiley-VCH Verlag GmbH & Co. KGaA, Weinheim

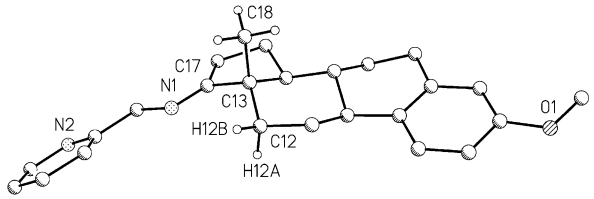


Figure 2. X-ray crystal structure of **13**.

H12A) are equivalent (2.93 Å). However, the C17=N1–C13–12βH functionality lies in the same plane as the nitrogen lone pair. In the active complex the copper and oxygen atoms should also lie in this plane (similar to Figure 1), and an oxygen atom is able to abstract 12βH from the copper- and oxygen-containing seven-membered-ring structure since only C12 sticks out of the ring plane. The 12αH atom cannot be incorporated in such a planar orientation. In a formal sense this mechanism resembles the Barton reaction in which a δ-functionalization (H-atom abstraction) occurs via an alkoxy radical which is part of a six-membered-ring intermediate. (An example would be the 11β-O-radical attack on 18 H).[14]

The intermolecular hydroxylations of nonactivated CH_2 groups in copper–oxygen complexes of bidentate ligands described in this article function better (higher yields) than hydroxylations with tridentate ligands. Only *cis*-hydroxylation in the β-position occurred for *N*-ethylaminoalkylpyridine ligands; additional *trans*-hydroxylation was observed for *N*-methylaminoalkylpyridine ligands. Total yields for the hydroxylation are higher for the *N*-alkyl-2-pyridylmethylamino ligands than for the *N*-alkyl-2-pyridylethylamino derivatives. A regio- and stereoselective γ-hydroxylation with yields sufficient for synthetic applications was obtained with the simple (and easily removable) 2-pyridylalkylimino ligands. As observed above, the yield for the 2-pyridylmethyl compound is higher than for the 2-pyridylethyl derivative. This method has opened up a novel (and chemically easily accessible) method for the synthesis of 12β-hydroxy steroids. We are currently investigating the hydroxylation reactions of further bidentate imines.

Experimental Section

Synthesis of **16**: A solution of **13** (1.0 g, 2.67 mmol) in anhydrous dichloromethane (150 mL) was stirred continually at room temperature, and water-free copper(II)triflate (0.97 g, 2.67 mmol) was added slowly. After 3 h the green solution was degassed with argon. Under an argon atmosphere and with continual stirring, benzoin (1.13 g, 5.34 mmol) and triethylamine (0.74 mL, 5.34 mmol) were added. After 20 h the argon atmosphere was replaced by an O_2 atmosphere. The now yellow-brown solution was stirred a further 3 d, during which it turned dark green. Over a period of 2 h, aqueous ammonia (25% NH_3, 3 × 30 mL) was added under vigorous stirring. The aqueous phase was separated and extracted twice with dichloromethane. The combined organic phases were concentrated and dried over Na_2SO_4, and the solvent was removed by distillation. The residue was separated by chromatography on silica gel (Merck) eluting with dichloromethane. After the benzoin/benzil fraction had been removed, **11** (0.23 g, 30%) was obtained. Elution with CH_2Cl_2/CH_3OH (95:5) resulted in **16** (0.40 g, 50%), m.p. 153–155 °C (CH_3OH). HRMS (ESI): found: 323.16233, calcd for $C_{19}H_{24}NaO_3$ [*M*+Na]: 323.16231.

Synthesis of **14**: A solution of compound **12** (148 mg, 0.38 mmol) in dichloromethane (50 mL) was prepared and treated with the required amounts of reagents and solvents as described in the synthesis of **16**. After the reaction mixture had been stirred for 3 d under an oxygen atmosphere, the solvent was removed by distillation and the residue dissolved in absolute CH_3OH (50 mL). Under continual stirring, $NaBH_4$ (86 mg, 2.27 mmol) was slowly added. After 1 h the solvent was removed by distillation, and the dark, solid residue was dissolved in $CHCl_3$. The solution was washed three times with aqueous ammonia (25% NH_3). The combined aqueous phases were extracted twice with $CHCl_3$. The combined organic phases were dried with Na_2SO_4 and the solvent removed by distillation. The brown residue was purified by column chromatography with silica gel (Merck) eluting with CH_2Cl_2. An aromatic fraction, estradiol-3-methylether, and smaller amounts of nonpolar reaction products were obtained. Elution with CH_2Cl_2/CH_3OH (80:20) yielded **14** (61 mg, 39.5%), m.p. 195–196 °C (CH_3OH). HRMS (ESI): found 407.27045, calcd for $C_{26}H_{35}O_2N$ [*M*+1]: 407.26985.

The X-ray structural analysis and measurement of the reflection intensities was performed at −90 °C with a Nonius KappaCCD-diffractometer with $Mo_{K\alpha}$ radiation ($\lambda = 0.71069$ Å, graphite monochromator). Lorentz and polarization corrections were applied, but a correction for the absorption was not.[15,16] The structure was solved by direct methods (SHELXS[17]). Most of the non-hydrogen atoms could be localized. Difference Fourier transformation located the remainder. The initial structural assignment was improved by a full-matrix least squares routine (anisotrope to F_o^2; SHELXL-97).[18] The hydrogen atoms in the 12-CH_2 group of compound **13** as well as those in the imino and hydroxy groups in **14** could be located by difference Fourier transformations and were refined isotropically. The other hydrogens were calculated (geometrically ideal positions) and included in the refinement with an isotrope temperature factor of 1.2–1.5 for the non-hydrogen atoms.[19] The copper complex $[Cu_2(L1)_2]\cdot 2ClO_4$ crystallized in two (symmetry-independent) molecules that are structurally identical. The absolute configuration of the compounds could be determined from the starting compounds. XP software (Siemens Analytical X-ray Instruments, Inc.) was used for the representation of the structures.

Crystal data for **13**:[19] $C_{25}H_{30}N_2O$, $M_r = 374.51\ g\,mol^{-1}$, colorless cubes, $0.04 \times 0.04 \times 0.04\ mm^3$, monoclinic, space group $P2_1$, $a = 6.0164(1)$, $b = 21.5750(5)$, $c = 8.0533(2)$ Å, $\beta = 97.255(1)°$, $V = 1036.98(4)$ Å^3, $T = -90$ °C, $Z = 2$, $\rho_{calcd} = 1.199\ g\,cm^{-3}$, $\mu(Mo_{K\alpha}) = 0.73\ cm^{-1}$, $F(000) = 404$, a total of 4344 reflections up to $h(-7/7)$, $k(-28/25)$, $l(-10/10)$ measured in a range from $2.55° \le \Theta \le 27.49°$, $\Theta_{max} = 99.6\%$. There are 4344 symmetry-independent reflections, 3635 reflections with $F_o > 4\sigma(F_o)$, 261 parameters, 1 restraint, $R1_{obs} = 0.043$, $wR^2_{obs} = 0.093$, $R1_{all} = 0.057$, $wR^2_{all} = 0.099$, GOF = 1.051, Flack parameter 1(1), differential electron density max/min: 0.174/−0.193 e Å^{-3}.

Crystal data for **14**:[19] $C_{26}H_{34}N_2O_2$, $M_r = 406.55\ g\,mol^{-1}$, colorless cubes, $0.10 \times 0.06 \times 0.05\ mm^3$, monoclinic, space group $P2_1$, $a = 10.8407(7)$, $b = 8.1476(5)$, $c = 12.1883(9)$ Å, $\beta = 94.234(3)°$, $V = 1073.60(12)$ Å^3, $T = -90$ °C, $Z = 2$, $\rho_{calcd} = 1.258\ g\,cm^{-3}$, $\mu(Mo_{K\alpha}) = 0.79\ cm^{-1}$, $F(000) = 440$, a total of 4267 reflections up to $h(-14/14)$, $k(-9/10)$, $l(-15/15)$ measured in a range from $1.88° \le \Theta \le 27.55°$, $\Theta_{max} = 99.1\%$, of these 4267 are symmetry independent reflections, 2967 reflections with $F_o > 4\sigma(F_o)$, 279 parameters, 1 restraint, $R1_{obs} = 0.054$, $wR^2_{obs} = 0.106$, $R1_{all} = 0.093$, $wR^2_{all} = 0.123$, GOF = 1.015, Flack parameter 3(2), differential electron density max/min: 0.187/−0.192 e Å^{-3}.

Crystal data for $[Cu_2(L1)_2]\cdot 2(ClO_4)$: $[C_{52}H_{70}Cu_2N_4O_4]^{+\cdot} 2[ClO_4]^{-}\cdot 1/2\,CH_3OH$, $M_r = 1157.12\ g\,mol^{-1}$, light blue cubes, $0.09 \times 0.07 \times 0.05\ mm^3$, monoclinic, space group $P2_1$, $a = 9.8605(2)$, $b = 35.0026(7)$, $c = 16.5160(4)$ Å, $\beta = 107.002(1)°$, $V = 5451.2(2)$ Å^3, $T = -90$ °C, $Z = 4$, $\rho_{calcd} = 1.410\ g\,cm^{-3}$, $\mu(Mo_{K\alpha}) = 9.43\ cm^{-1}$, $F(000) =$

 © 2003 Wiley-VCH Verlag GmbH & Co. KGaA, Weinheim

2428, a total of 20775 reflections up to $h(-12/12)$, $k(-44/44)$, $l(-21/21)$ measured in a range from $1.74° \le \Theta \le 27.51°$, $\Theta_{max} = 95.2\%$, of these 20775 are symmetry-independent reflections, 15860 reflections with $F_o > 4\sigma(F_o)$, 1307 parameters, 1 restraint, $R1_{obs} = 0.080$, $wR^2_{obs} = 0.189$, $R1_{all} = 0.112$, $wR^2_{all} = 0.210$, GOF = 1.098, Flack parameter 0.04(1), differential electron density max/min: 1.969/−0.703 e Å^{-3}.

Received: December 5, 2003 [Z50815]

Keywords: C–H activation · copper · hydroxylation · O–O activation · steroids

[1] a) N. Kitajima, Y. Morooka, *Chem. Rev.* **1994**, *94*, 737–757; b) W. Kaim, J. Rall, *Angew. Chem.* **1996**, *108*, 47–64; *Angew. Chem. Int. Ed. Engl.* **1996**, *35*, 43–60; c) M. Pascaly, I. Jolk, B. Krebs, *Chem. Unserer Zeit* **1999**, *33*, 334–341.

[2] a) K. D. Karlin, S. Kaderli, A. D. Zuberbühler, *Acc. Chem. Res.* **1997**, *30*, 139–147; b) L. Que, Jr., W. B. Tolman, *Angew. Chem.* **2002**, *114*, 1160–1185; *Angew. Chem. Int. Ed.* **2002**, *41*, 1114–1137; c) R. Than, A. Feldmann, B. Krebs, *Coord. Chem. Rev.* **1999**, *182*, 211–241; d) P. L. Holland, W. P. Tolman, *Coord. Chem. Rev.* **1999**, *190–192*, 855–869; e) S. Schindler, *Eur. J. Inorg. Chem.* **2000**, 2311–2326; f) A. G. Blackman, W. P. Tolman, *Struct. Bonding (Berlin)* **2000**, *97*, 179–211; g) I. Blain, M. Giorgi, I. DeRiggi, M. Reglier, *Eur. J. Inorg. Chem.* **2001**, 205–211.

[3] a) K. D. Karlin, J. C. Hayes, Y. Gultneh, R. W. Cruse, J. W. McKown, J. P. Hutchinson, J. Zubieta, *J. Am. Chem. Soc.* **1984**, *106*, 2121–2128; b) O. J. Gelling, F. van Bolhuis, A. Meetsma, B. L. Feringa, *J. Chem. Soc. Chem. Commun.* **1988**, 552–554; c) L. Casella, M. Gullotti, G. Pallanza, L. Rigoni, *J. Am. Chem. Soc.* **1988**, *110*, 4221–4227; d) R. Menif, A. E. Martell, *J. Chem. Soc. Chem. Commun.* **1989**, 1521–1523; e) O. J. Gelling, B. L. Feringa, *J. Am. Chem. Soc.* **1990**, *112*, 7599–7604; f) R. Menif, A. E. Martell, P. J. Squattrito, A. Clearfield, *Inorg. Chem.* **1990**, *29*, 4723–4729; g) T. N. Sorrell, V. A. Vankai, M. L. Garrity, *Inorg. Chem.* **1991**, *30*, 207–210; h) T. N. Sorrell, M. L. Garrity, *Inorg. Chem.* **1991**, *30*, 210–215; i) M. Becker, S. Schindler, R. van Eldik, *Inorg. Chem.* **1994**, *33*, 5370–5371; j) S. Ryan, H. Adams, D. E. Fenton, M. Becker, S. Schindler, *Inorg. Chem.* **1998**, *37*, 2134–2140; k) M. Becker, S. Schindler, K. D. Karlin, T. A. Kaden, S. Kaderli, T. Palanche, A. D. Zuberbühler, *Inorg. Chem.* **1999**, *38*, 1989–1995; l) E. Pidcock, H. V. Obias, C. X. Zhang, K. D. Karlin, E. I. Solomon, *J. Am. Chem. Soc.* **1998**, *120*, 7841–7847; m) P. L. Holland, K. R. Rodgers, W. B. Tolman, *Angew. Chem.* **1999**, *111*, 1210–1213; *Angew. Chem. Int. Ed.* **1999**, *38*, 1139–1142; n) L. Santagostini, M. Gullotti, E. Monzani, L. Casella, R. Dillinger, F. Tuczek, *Chem. Eur. J.* **2000**, *6*, 519–522; o) S. Itoh, H. Kumei, M. Taki, S. Nagatomo, T. Kitagawa, S. Fukuzumi, *J. Am. Chem. Soc.* **2001**, *123*, 6708–6709.

[4] a) E. Amadei, E. H. Alilou, F. Eydoux, M. Pierrot, M. Reglier, B. Waegell, *J. Chem. Soc. Chem. Commun.* **1992**, 1782–1784; b) S. Itoh, T. Kondo, M. Komatsu, Y. Ohshiro, C. Li, N. Kanehisa, Y. Kai, S. Fukuzumi, *J. Am. Chem. Soc.* **1995**, *117*, 4714–4715; c) I, Blain, P. Bruno, M. Giorgi, E. Lojou, D. Lexa, M. Reglier, *Eur. J. Inorg. Chem.* **1998**, 1297–1304; d) S. Itoh, H. Nakao, L. M. Berreau, T. Kondo, M. Komatsu, S. Fukuzumi, *J. Am. Chem. Soc.* **1998**, *120*, 2890–2899; e) S. Itoh, M. Taki, H. Nakao, P. L. Holland, W. B. Tolman, L. Que, Jr., S. Fukuzumi, *Angew. Chem.* **2000**, *112*, 409–411; *Angew. Chem. Int. Ed.* **2000**, *39*, 398–400.

[5] I. Blain, M. Giorgi, I. De Riggi, M. Reglier, *Eur. J. Inorg. Chem.* **2000**, 393–398.

[6] a) M. Gonschior, M. Kötteritzsch, M. Rost, B. Schönecker, R. Wyrwa, *Tetrahedron: Asymmetry* **2000**, *11*, 2159–2182; b) St. Diekmann, J. Weston, E. Anders, W. Boland, B. Schönecker, T. Hettmann, J. von Langen, S. Erhardt, M. Mauksch, M. Bräuer, C. Beckmann, M. Rost, P. Sperling, E. Heinz, *Rev. Mol. Biotechnol.* **2002**, *90*, 73–94; c) M. Dubs, R. Krieg, H. Görls, B. Schönecker, *Steroids* **2000**, *65*, 305–318; d) R. Krieg, M. Dubs, H. Görls, B. Schönecker, *Chem. Ber.* **1996**, *129*, 1497–1501.

[7] a) K. D. Karlin, D.-H. Lee, S. Kaderli, A. D. Zuberbühler, *Chem. Commun.* **1997**, 475–476; b) V. Mahadevan, M. J. Henson, E. I. Solomon, T. D. P. Stack, *J. Am. Chem. Soc.* **2000**, *122*, 10249–10250; c) H. Hayashi, S. Fujinami, S. Nagatomo, S. Ogo, M. Suzuki, A. Uehara, Y. Watanabe, T. Kitagawa, *J. Am. Chem. Soc.* **2000**, *122*, 2124–2125; d) Y. Shimazaki, T. Nogami, F. Tani, A. Odani, O. Yamauchi, *Angew. Chem.* **2001**, *113*, 3977–3980; *Angew. Chem. Int. Ed.* **2001**, *40*, 3859–3862; e) H.-C. Liang, C. X. Zhang, M. J. Henson, R. D. Sommer, K. R. Hatwell, S. Kaderli, A. D. Zuberbühler, A. L. Rheingold, E. I. Solomon, K. D. Karlin, *J. Am. Chem. Soc.* **2002**, *124*, 4170–4171; f) M. Taki, S. Teramae, S. Nagatomo, Y. Tachi, T. Kitagawa, S. Itoh, S. Fukuzumi, *J. Am. Chem. Soc.* **2002**, *124*, 6367–6377.

[8] S. Mahapatra, J. A. Halfen, W. B. Tolman, *J. Am. Chem. Soc.* **1996**, *118*, 11575–11586.

[9] a) R. Breslow, J. Yan, S. Belvedere, *Tetrahedron Lett.* **2002**, *43*, 363–365; b) R. Breslow, J. Yang, J. Yan, *Tetrahedron* **2002**, *58*, 653–659.

[10] a) R. Breslow, *Acc. Chem. Res.* **1980**, *13*, 170–177; b) R. Breslow, *Chemtracts: Org. Chem.* **1988**, 333–348; c) E. J. Parish, N. Aksara, T. L. Boos, *Lipids* **1997**, *32*, 1325–1330.

[11] P. A. Grieco, T. L. Stuk, *J. Am. Chem. Soc.* **1990**, *112*, 7799–7801.

[12] a) M. M. Coombs, R. H. Roderick, *J. Chem. Soc. C* **1967**, 1819–1821; b) , US Patent 3324153, **1967**.

[13] L. F. Fieser, M. Fieser, *Steroide*, VCH, Weinheim, **1961**, pp. 693–705.

[14] G. Majetich, K. Wheless, *Tetrahedron* **1995**, *51*, 7095–7129.

[15] COLLECT, Data Collection Software, Nonius B.V., Netherlands, **1998**.

[16] "Processing of X-Ray Diffraction Data Collected in Oscillation Mode": Z. Otwinowski, W. Minor, *Methods Enzymol.* **1997**, *276*, 307–326.

[17] G. M. Sheldrick, *Acta Crystallogr. Sect. A* **1990**, *46*, 467–473.

[18] G. M. Sheldrick, SHELXL-97, University of Göttingen, Göttingen (Germany), **1993**.

[19] CCDC-199645, -199646, and -204451 contain the supplementary crystallographic data for this paper. These data can be obtained free of charge via www.ccdc.cam.ac.uk/conts/retrieving.html (or from the Cambridge Crystallographic Data Centre, 12, Union Road, Cambridge CB21EZ, UK; fax: (+44) 1223-336-033; or deposit@ccdc.cam.ac.uk).

 © 2003 Wiley-VCH Verlag GmbH & Co. KGaA, Weinheim

The Chemistry of Vision

Thr94 and Wat2b Effect Protonation of the Retinal Chromophore in Rhodopsin**

Volker Buss, Minoru Sugihara, Peter Entel, and Jürgen Hafner*

Both the extraordinary stability of the protonated retinal Schiff base in rhodopsin, with an estimated apparent pK_a possibly higher than 16,[1] and the swiftness of deprotonation following light absorption as a structural pre-requisite for reaching the signaling state[2] have been the subject of much study. Various models of the binding site, involving Glu113 as the counterion, and water bridging and stabilizing the ion pair, have been proposed.[3] The first X-ray structures of the protein which have become available recently[4,5] offer the opportunity to study the binding site in atomic detail and start to understand the mechanism which nature has developed to switch the protonation state of the chromophore according to the need of the particular intermediate.

We have applied ab initio quantum-mechanics to the protein and find that the peculiar arrangement of the ion pair in the binding pocket is sufficient to establish an energy plateau from which both states, the proton attached either to the Schiff base or to the carboxylate ion, are reversibly accessible. Fine tuning of the plateau is achieved by Thr94 and a water molecule (Wat2b) which we propose form together with Glu113 the complex counterion of the chromophore in rhodopsin.

For modeling the binding site the following components have been considered: the complete retinal chromophore linked to Lys296, the counterion Glu113, Thr94 (which connects by a hydrogen bond to Glu113), and a water molecule. The starting geometry was taken from the rhodopsin coordinates laid down as 1F88 in the protein data bank (PDB)[4] and from a more recent X-ray structure[5] which locates two water molecules (Wat2a and Wat2b) close to the binding site. The atoms of the amino acids involved in peptide bonding were saturated with hydrogen where necessary. Also, these atoms were the only ones which were kept fixed during geometry optimization and the molecular dynamics (MD) study, all other atoms were allowed to move freely without constraints. The theoretical method used for the calculation has been described elsewhere;[6] basically we perform ab initio quantum-mechanical MD simulations based on density functional theory (DFT) using Vanderbilt–Kresse ultrasoft pseudopotentials[7] in a plane-wave expansion of the basis set.[8]

The starting geometry of the binding-site has been energy-minimized and then subjected to an MD with simulated annealing for 200 fs subject only to the constraints listed above. The resulting structure is shown in Figure 1, together with an overlay of the initial 1F88 conformation. It is clear that there is a significant degree of conformity between the structure derived from the electron density map and the calculated structure. Note especially the water molecule which is shifted slightly but does not bridge the Schiff base and the counterion, simply because there is not enough space. Significant differences are observed for Thr94 which rotates about the C_α–C_β bond to orient the hydroxy group towards the carboxylate oxygen atom, and for the retinal chromophore which, as a result of the absence of the protein pocket, becomes planar from N_{16} to C_6. As we have shown elsewhere[9] the highly twisted geometry of the retinal chromophore is caused by interaction with the protein environment.

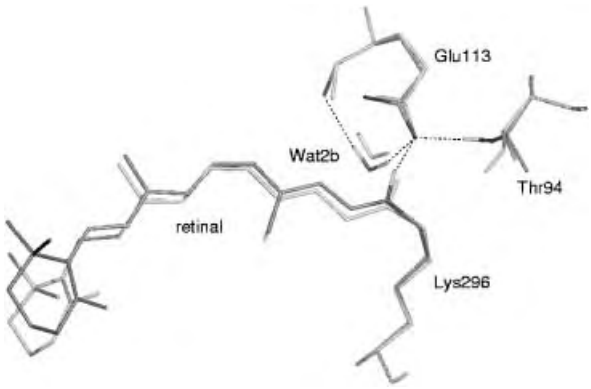


Figure 1. Minimized geometry (in dark gray) of the 11-*cis*-retinal Schiff base attached to Lys296 with the complex counterion consisting of Glu113, Thr94, and a water molecule (Wat2b; broken lines indicate hydrogen bonds). The overlaid structure (in light gray) is the initial 1F88 conformation.

The final structure features a network of hydrogen bonds extending from the central oxygen atom of the carboxylate group to the Schiff base nitrogen atom (distance: 2.60 Å), to the threonine hydroxy group (2.67 Å) and to the water molecule (3.18 Å). The water molecule makes another hydrogen bond to the backbone oxygen atom of Glu113 (3.04 Å). The second oxygen atom of the carboxylate group does not coordinate in this model because there is no ligand nearby.[10] The bridging proton is significantly closer to the Schiff base nitrogen atom (1.10 Å) than to the carboxylate oxygen atom (1.51 Å); from this, and from an analysis of the chromophore (bond lengths and charge distribution) we conclude that the chromophore in this complex is protonated.

[*] Prof. Dr. V. Buss
Institut für Chemie
Universität Duisburg-Essen
47048 Duisburg (Germany)
Fax: (+49) 203-379-2772
E-mail: theobuss@uni-duisburg.de
Dr. M. Sugihara, Prof. Dr. P. Entel
Institut für Theoretische Tieftemperaturphysik
Universität Duisburg-Essen, 47048 Duisburg (Germany)
Prof. Dr. J. Hafner
Institut für Materialphysik
Universität Wien, 1090 Wien (Austria)

[**] This work was supported by the Research Group "Molecular Mechanisms of Retinal Protein Action" by the German Research Council, and the Graduate School "Structure and Dynamics of Heterogeneous System" at the University of Duisburg.

 DOI: 10.1002/anie.200351034 © 2003 Wiley-VCH Verlag GmbH & Co. KGaA, Weinheim

To study the dynamic behavior of the system we performed several MD simulations. A summary of these calculations is presented in Figure 2, where the movement of the bridging proton (in the middle) between the Schiff base

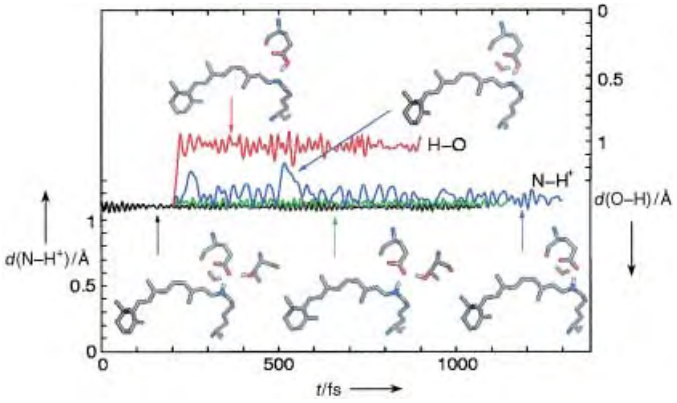


Figure 2. MD simulation of the complex shown in Figure 1 (in black) and the effects of removing components of the complex counterion: removal of Thr 94 (blue), removal of Wat2b (green), removal of Thr 94 and Wat2b (red). Depicted is the N-H^+ separation and the O-H separation, depending on the protonation state. Arrows and structures depict the different complexes and their protonation states.

nitrogen atom (bottom) and the carboxylate oxygen atom (top) is plotted as a function of time. The structure is stable against deprotonation of the chromophore: if the simulation starts with the both the carboxy group and the Schiff base neutral, the carboxy group immediately deprotonates and the proton swings back to the nitrogen atom, apparently without energy barrier. 200 fs into the MD simulation of the complete structure (Figure 2, black) three parallel simulations were started. In one, only the water molecule Wat2b was removed from the complex (green), in the second Thr 94 (blue), and finally both Wat2b and Thr 94 were removed (red). The results can be summarized as follows: The effect of water on the stability of the complex is almost insignificant; the presence of Thr 94 alone is sufficient to keep the chromophore protonated. In contrast, the water molecule alone is hardly able to keep the Schiff base protonated; the bridging proton performs oscillations with large, irregular amplitudes. This situation, and the reduced frequency, indicate that the binding to the Schiff base has become significantly weaker. Finally, without Wat2b and Thr 94 the chromophore deprotonates immediately, with the proton shifting by more than 0.6 Å towards the glutamate oxygen atom.

Central for the mobility of the proton is the short bridge between the Schiff base and the counterion which attests to the strength of the hydrogen bond (Figure 3). The calculated distance from the Glu 113 oxygen atom to the Schiff base nitrogen atom is significantly shorter than the mean length of the N–H···O hydrogen bond of 2.74 Å according to a Cambridge structural database (CSD) search involving 306 entries,[11a] and at the lower limit of distances determined for histidine–carboxylate complexes.[11b] In addition, the almost planar *syn* orientation (deviation from the COO^- plane: 3°) is known to be the optimum geometry for hydrogen

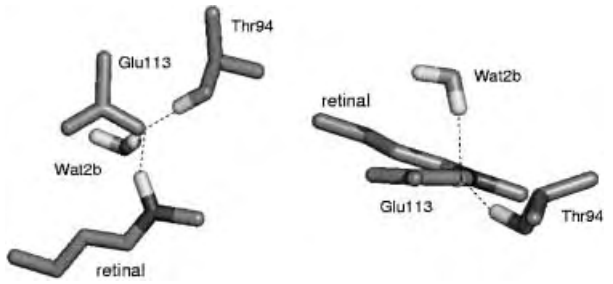


Figure 3. Close-up of the hydrogen-bond network involving the protonated retinal Schiff base and the complex counterion. Left: the Glu 113 carboxy group, right: side view.

bonding involving the carboxylate group.[12] Without an interaction (infinite separation) the neutral glutamatic acid/Schiff base system is 86 kcal mol^{-1} than the charged ion pair made up of glutamate and protonated Schiff base. In the geometry found for the optimized complex this large energy difference is reduced to 4.8 kcal mol^{-1} (B3LYP 6–311G** results; corresponding Hartree–Fock 6-311G** values are 86.5 and 4.6 kcal mol^{-1}). Fine-tuning of the hydrogen bond is then achieved by the very unusual arrangement of the remaining two proton donors at the binding site, Wat2b and Thr 94, and their competition, with the Schiff base, for the lone pair on the carboxylate oxygen atom. The hydroxy group of Thr 94 has a definite advantage (over Wat2b) because of its position closer to the plane of the carboxylate group (deviation 35° versus 77° for Wat2b) and its *anti* orientation at the carboxylate oxygen. This is in stark contrast to the water molecule whose access to the lone-pair electrons of the carboxylate oxygen atom is severely hindered. As a consequence the hydrogen bond between the Thr 94 and the glutamate is stronger and shorter, and is more efficient than the water molecule in stabilizing the protonated Schiff base, as is demonstrated in the MD calculations.

Regulating the protonation state of the retinal chromophore is of crucial importance for the visual process. Protonation transforms the six localized double bonds into a delocalized highly polarizable π system which is required for long-wavelength absorbance and wavelength regulation by the protein environment, though probably not for efficient photoisomerization.[13] Deprotonation on the other hand is required after light absorption for the protein to reach the activated state.[14] Also, deprotonation of the retinal Schiff base has been proposed to lower the barrier for thermal isomerization of the chromophore and thus increase the effects of photoreceptor noise,[15] a proposal which has been questioned elsewhere.[16] Thr 94 may be preferred over water Wat2b to maintain the proper protonation state of the Schiff base because it is locally fixed and more easily controlled than free floating water molecules. The possible involvement of Thr 94 in stabilizing the chromophore binding site has been concluded from point mutations leading to congenital stationary night blindness (CSNB).[17]

Received: January 28, 2003 [Z51034]

 © 2003 Wiley-VCH Verlag GmbH & Co. KGaA, Weinheim

Keywords: hydrogen bonds · molecular dynamics · protonation · rhodopsin · theoretical chemistry

[1] G. Steinberg, M. Ottolenghi, M. Sheves, *Biophys. J.* **1993**, *64*, 1499 – 1502.
[2] a) T. Sakmar, *Prog. Nucleic Acid Res. Mol. Biol.* **1998**, *59*, 1 – 34; b) M. Nakagawa, T. Iwasa, M. Kikkawa, M. Tsuda, T. Ebrey, *Proc. Natl. Acad. Sci. USA* **1999**, *96*, 6189 – 6192.
[3] a) F. I. Harosi, C. Sandorfy, *Photochem. Photobiol.* **1995**, *61*, 510 – 517; b) M. Han, S. O. Smith, *Biochemistry* **1995**, *34*, 1425 – 1432; c) Y. Gat, M. Sheves, *J. Am. Chem. Soc.* **1993**, *115*, 3772 – 3773; d) B. C. Hudson, R. R. Birge, *J. Phys. Chem. A* **1999**, *103*, 2274 – 2281.
[4] K. Palczewski, T. Kumaska, T. Hori, C. A. Behnke, H. Motoshima, B. A. Fox, I. Le Trong, D. C. Teller, T. Okada, R. E. Stenkamp , M. Yamamoto, M. Miyamo, *Science* **2000**, *289*, 739 – 745.
[5] T. Okada, Y. Fujiyoshi, M. Silow, E. Navarro, E. M. Landau, Y. Shichida, *Proc. Natl. Acad. Sci. USA* **2002**, *99*, 5982 – 5987.
[6] G. Kresse, J. Furthmüller, *Phys. Rev. B* **1996**, *54*, 11169 – 11186.
[7] D. Vanderbilt, *Phys. Rev. B* **1990**, *41*, 7892 – 7895.
[8] For the MD calculations we employed a periodic boundary box of $28 \times 24 \times 24$ Å^3 to exclude the interaction with image molecules, and one *k*-point (Γ-point only). The cut-off energy of the plane-wave basis was set at 396 eV. All the calculations were performed in the generalized gradient approximation, microcanonical ensemble, and a time step of 1.0 fs.
[9] M. Sugihara, V. Buss, P. Entel, M. Elstner, T. Frauenheim, *Biochemistry* **2002**, *41*, 15259 – 15266.
[10] According to the 1F88 structure this second oxygen atom of Glu113, hydrogen binds with Cys187. However, the structural changes upon inclusion of Cys187 are insignificant. The four distances listed in the text change to 2.63, 2.66, 3.15, and 3.04 Å and the chromophore is still protonated.
[11] a) Y. Wie, A. C. de Dios, A. E. McDermott, *J. Am. Chem. Soc.* **1999**, *121*, 10389 – 10394; b) D. Braga, L. Maini, F. Grepioni, A. De Cian, O. Felix, J. Fischer, M. W. Hosseini, *New J. Chem.* **2000**, *24*, 547 – 553.
[12] a) M. R. Petersen, I. G. Csizmadia, *J. Am. Chem. Soc.* **1979**, *101*, 1076 – 1079; b) J. P. Glusker, *Top. Curr. Chem.* **1998**, *198*, 1 – 56.
[13] K. Fahmy, T. P. Sakmar, *Biochemistry* **1993**, *32*, 9165 – 9171.
[14] T. Okada, O. P. Ernst, K. Palczewski, K. P. Hofmann, *Trends Biochem. Sci.* **2001**, *26*, 318 – 324.
[15] R. B. Barlow, R. R. Birge, E. Kaplan, J. R. Tallent, *Nature* **1993**, *366*, 64 – 66.
[16] T. G. Ebrey, *Methods Enzymol.* **2000**, *315*, 196 – 207.
[17] a) N. al-Jandal, G. J. Farrar, A. S. Kiang, M. M. Humphries, N. Bannon, J. B. C. Findlay, P. Humphries, P. F. Kenna, *Hum. Mutat.* **1999**, *13*, 75 – 81; b) P. Garriga, J. Manyosa, *FEBS Lett.* **2002**, *528*, 17 – 22.

 © 2003 Wiley-VCH Verlag GmbH & Co. KGaA, Weinheim

Self-Organization of Dyes

Highly Ordered Merocyanine Dye Assemblies by Supramolecular Polymerization and Hierarchical Self-Organization**

Frank Würthner, Sheng Yao, and Uwe Beginn*

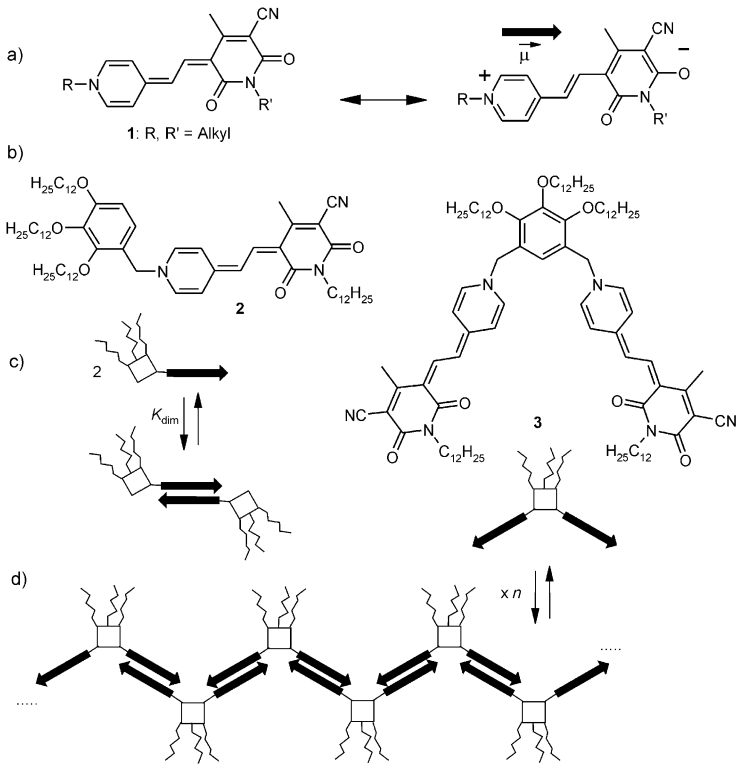
Highly organized dye assemblies are crucial for the energy- and electron-transfer events in natural photosynthesis.[1–3] Dye organization is also considered to be the key to advanced functional organic materials for electronics and photonics.[4] Nevertheless rational control of dye–dye interactions in supramolecular architectures is still a difficult task[5] and most known dye assemblies are constructed as simple one-dimensional stacks through aggregation of their π systems.[6] In special cases, such as the famous J or Scheibe aggregates of cyanine dyes,[7,8] accidental discovery led to more diverse architectures including two-dimensional brick-work and tubular aggregates that found application as sensitizers in silver halide photography.[9] Here we report on highly ordered cylindrical merocyanine dye assemblies that could be obtained in a controlled way by applying the concepts of supramolecular polymerization[10] and hierarchical self-organization.[4,5]

Scheme 1 shows the merocyanines dyes employed in this study. These dyes constitute supramolecular and functional building blocks at the same time. The former property is related to the extremely high dipole moments of 17 D (Scheme 1a) that afford dimerization constants of $K_{dim} > 10^6\,M^{-1}$ in low polar solvents such as dioxane and tetrachloromethane.[11] In our earlier work we showed that this high binding strength arises predominantly from dipolar interactions and that the formation of closely packed centrosymmetric dimers is a general feature of this class of compounds (Scheme 1c).[11] On the other hand, functionality is provided by the highly polarizable π system of this chromophore ($\alpha = 65 \times 10^{-40}\,CV^{-1}m^2$, $\lambda_{max} \approx 570$ nm).[11] Thus, strong excitonic interactions between the dyes and even bandlike transition states are expected if the dyes are organized in proximity.

[*] Prof. Dr. F. Würthner, Dr. S. Yao[+]
Institut für Organische Chemie
Universität Würzburg
Am Hubland, 97074 Würzburg (Germany)
Fax: (+49) 931–888–4756
E-mail: wuerthner@chemie.uni-wuerzburg.de
Dr. U. Beginn
Institut für Technische und Makromolekulare Chemie
RWTH Aachen
Worringerweg 1, 52056 Aachen (Germany)
[+] Present address: Dr. S. Yao
Department of Chemistry
University of Central Florida
Orlando, FL 32816 (USA)

[**] We gratefully acknowledge financial support for this work by the Deutsche Forschungsgemeinschaft (Wu 317/1–3).

 DOI: 10.1002/anie.200351414 © 2003 Wiley-VCH Verlag GmbH & Co. KGaA, Weinheim



Scheme 1. a) Mesomeric structures for highly dipolar merocyanine dyes **1**; b) tridodecyloxybenzyl-substituted merocyanine dye **2** and bis(merocyanine) dye **3**; c) model for the dimerization of dyes **2**; and d) model for the supramolecular polymerization of dyes **3** by dipolar aggregation.

For this current study merocyanine dye **2** and bis(merocyanine) dye **3** were prepared.[12] The presence of the tridodecyloxybenzyl substituents makes these dyes soluble even in the least polar aliphatic solvents, which enables the highest binding strength for electrostatic interactions to be obtained.[11]

The UV/Vis spectra of **2** show simple monomer–dimer ($\lambda_{max} \approx 570$ and 490 nm, respectively) aggregation equilibria in all organic solvents, and accordingly do not differ from those of the unsubstituted parent dyes **1**. The dimerized species remain stable in the least polar aliphatic solvents, even in the most dilute conditions, so that $K_{dim} > 10^8\,\text{M}^{-1}$. In contrast, bis(merocyanine) dye **3** shows a more complex behavior with absorption bands that are related to three different species (Figure 1a): A monomer band (M band) of the nonaggregated dyes at $\lambda_{max} \approx 570$ nm (most intense in the polar solvent dichloromethane), a hypsochromically shifted band of dimerized dyes at $\lambda_{max} \approx 480$ nm (D band, most pronounced in trichloroethylene (TCE)), and an even more hypsochromically shifted sharp H band at $\lambda_{max} = 447$ nm (in the least polar solvents tetrachloromethane and methylcyclohexane (MCH)). It is noteworthy that the observation of a D band already indicates that supramolecular polymerization has occurred through the existence of two receptor sites at each molecule (Scheme 1d).[13] Accordingly, the formation of the H band suggests a further aggregation process of the polymeric strands to form a more stable assembly.

It is remarkable that this H aggregate was so stable in MCH that neither dilution to 10^{-7} M nor heating at 50 °C over several weeks could disrupt it. A fully reversible transition to the D aggregated and monomeric species could, however, be accomplished by increasing the solvent polarity by addition of THF (and vice versa). Figure 1b shows the absorption spectra of **3** in THF/MCH mixtures; two equilibria are evident, each of which is characterized by a quasi-isosbestic point. Thus, between pure THF and 39% MCH (red lines) the transition from the monomeric dye to the D aggregate occurs and at >40% MCH the H aggregate form very abruptly. Full reversibility between the two species could be demonstrated in a 42:58 MCH:THF solution by changing the temperature.

The polymeric properties of **3** were investigated in THF, TCE, and MCH solution by capillary viscosity measurements. Low values of the intrinsic viscosity were measured (15 mL g^{-1} in THF and 30 mL g^{-1} in TCE) in the former two solvents, which suggests the presence of nonaggregated molecules in THF and small oligomeric species in TCE. In contrast, high viscosities were observed in MCH solutions. The Huggins plots of the reduced viscosities ($\eta_{red} = (\eta/\eta_0 - 1)/c$; η = solution viscosity, η_0 = solvent viscosity, c = substance concentration) shown in Figure 2 enable two regions with different slopes to be distinguished. In the concentration range from 0.5 to 2 mM (that is < 3 g L^{-1}) η_{red} values of about 650 mL g^{-1} are obtained, which are typical of macromolec-

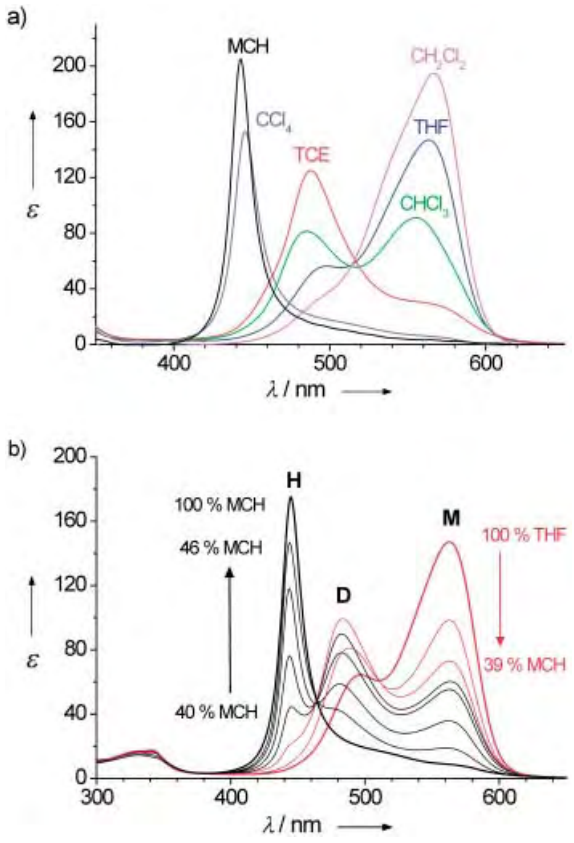


Figure 1. UV/Vis absorption spectra (ε in $10^3\,\text{M}^{-1}\,\text{cm}^{-1}$) of 10^{-5} M solutions of dye **3** at 293 K: a) in pure solvents of different polarity and b) in MCH/THF mixtures.

 © 2003 Wiley-VCH Verlag GmbH & Co. KGaA, Weinheim

ular solutions. Addition of the monotopic dye **2**, which acts as a chain termination unit, results in a significant drop in the viscosity, which again confirms the physical nature of this supramolecular polymer.[10]

The viscosity increases sharply at increasing dye concentrations ($>3\,g\,L^{-1}$ in Figure 2) and results in gelation at about $10\,g\,L^{-1}$ (Figure 3), the formation of a lyotropic mesophase, and eventually a solvent-free film with an unusual liquid-crystalline texture. X-ray diffraction analysis of this film revealed a hexagonal columnar order with a lattice constant of 4.34 nm—a distance that is in good agreement with the size of the rods visualized by magnification in the cryo-TEM study (Figure 3).[14]

Taking all our data into consideration we conclude that a hierarchical growth process for dye **3** occurs which involves the structures shown in Figure 4. At low concentrations and in polar solvents monomeric bis(merocyanine) dyes are present whose dipoles are saturated by the polar solvent molecules (Figure 4a). Upon reducing the solvent polarity, each of the two chromophores of **3** "dimerizes" with another dye in an antiparallel fashion thus minimizing the electrostatic energy (D-aggregated state). The resulting structure of the single elementary fibrils is a random-coil polymeric chain[13] that can easily fold into the helical conformation shown in Figure 4b. Intertwining of six of these polymeric chains affords a densely packed rod that contains each dye in van der Waals distance to two antiparallel-oriented neighboring dyes (H aggregate) and with all the tridodecyloxyphenyl units pointing outwards toward the solvent (Figure 4c). Such an arrangement is considered to be highly favored in aliphatic solvents. The formation of gels and mesophases at higher concentrations are understood according to Figure 4d by means of an entanglement of the alkyl chains, whose interdigitation leads to a shrinkage of the rod diameter from 5.1 nm (our model with extended alkyl chains) to 4.34 nm for the columnar distance in the bulk material.

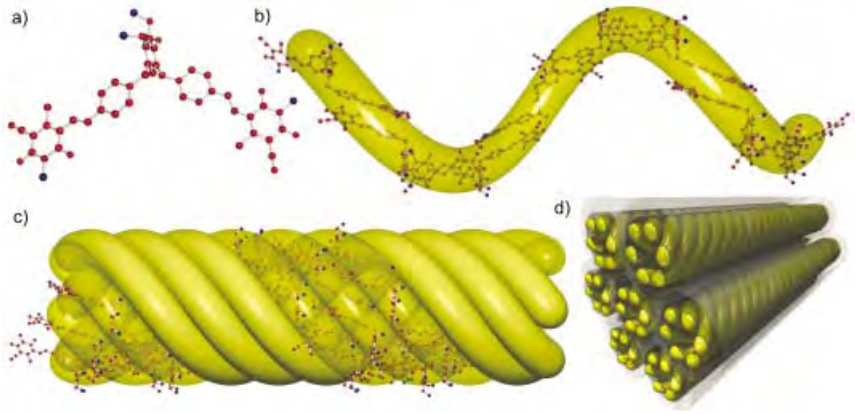


Figure 4. Model for the hierarchical growth of **3** assemblies: a) force-field-optimized molecular structure of **3**; b) helical supramolecular polymer of **3** formed by dipolar aggregation of the merocyanine units; c) rod-type H aggregate formed from six helical polymeric strands; all the tridodecyloxyphenyl chains point to the outside of the rods; d) hexagonal arrangement of the columns. For clarity and ease of calculation, all dodecyl chains have been replaced by methyl groups.

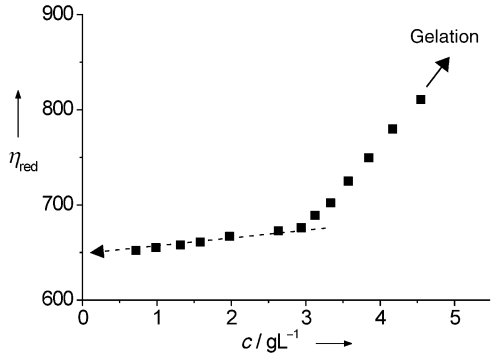


Figure 2. Reduced viscosities of solutions of dye **3** in MCH at 30 °C (η_{red} values are given in $mL\,g^{-1}$).

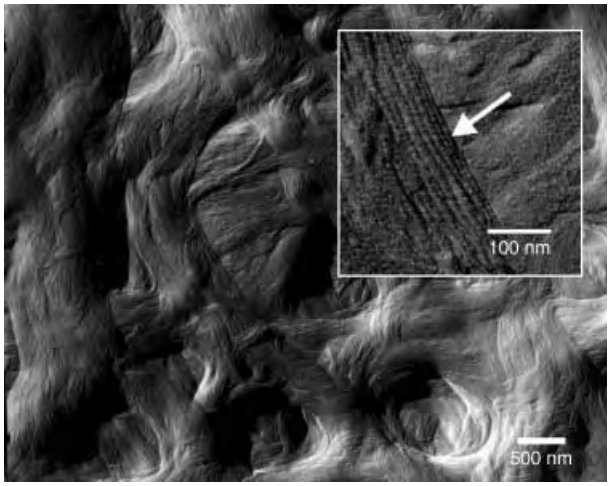


Figure 3. Cryo-TEM picture (negative) of a gel of dye **3** in *n*-hexane at a concentration of 6.5×10^{-3} M. The inset shows a magnification of the rod aggregates.

The self-assembly and the tubular structural feature of these remarkably defined dye aggregates are reminiscent of naturally occurring chlorophyll dye rod elements in the chlorosomes of photosynthetic bacteria.[3] However, synthesis and structural modifications of bis(merocyanine) dyes are much easier to accomplish and their self-organization is feasible in a more reliable manner in organic media. Therefore, a lot of fascinating possibilities might arise for merocyanine dye assemblies, especially if their intermolecular arrangement could be changed to provide J- instead of H-type excitonic coupling.

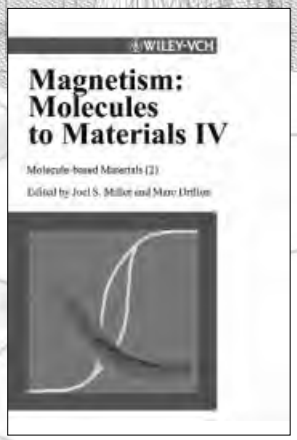
Received: March 17, 2003 [Z51414]
Published online: July 3, 2003

Keywords: aggregation · dyes/pigments · polymethines · self-assembly · supramolecular polymers

 © 2003 Wiley-VCH Verlag GmbH & Co. KGaA, Weinheim

[1] R. Huber, *Angew. Chem.* **1989**, *101*, 849 – 871; *Angew. Chem. Int. Ed. Engl.* **1989**, *28*, 848 – 869.
[2] T. Pullerits, V. Sundström, *Acc. Chem. Res.* **1999**, *29*, 381 – 389.
[3] A. R. Holzwarth, M. Katterle, M. G. Müller, Y.-Z. Ma, V. I. Prokhorenko, *Pure Appl. Chem.* **2001**, *73*, 469 – 474.
[4] a) G. M. Whitesides, J. P. Matthias, C. T. Seto, *Science* **1991**, *254*, 1312 – 1319; b) J.-M. Lehn, *Science* **2002**, *295*, 2400 – 2403; c) O. Ikkala, G. ten Brinke, *Science* **2002**, *295*, 2407 – 2409.
[5] a) H. Engelkamp, S. Middelbeck, R. J. M. Nolte, *Science* **1999**, *284*, 785 – 788; b) F. S. Schoonbeek, J. H. van Esch, B. Wegewijs, D. B. A. Rep, M. P. de Haas, T. M. Klapwijk, R. M. Kellogg, B. L. Feringa, *Angew. Chem.* **1999**, *111*, 1486 – 1490; *Angew. Chem. Int. Ed.* **1999**, *38*, 1393 – 1397; c) F. Würthner, C. Thalacker, A. Sautter, *Adv. Mater.* **1999**, *11*, 754 – 758; d) A. P. H. J. Schenning, P. Jonkheijm, E. Peeters, E. W. Meijer, *J. Am. Chem. Soc.* **2001**, *123*, 409 – 416; e) A. Ajayaghosh, S. J. George, *J. Am. Chem. Soc.* **2001**, *123*, 5148 – 5149.
[6] a) C. F. van Nostrum, *Adv. Mater.* **1996**, *8*, 1027 – 1030; b) J. Vacus, J. Simon, *Adv. Mater.* **1995**, *7*, 797 – 800; c) F. Würthner, C. Thalacker, S. Diele, C. Tschierske, *Chem. Eur. J.* **2001**, *7*, 2245 – 2253.
[7] a) E. Jelley, *Nature* **1936**, *138*, 1009; b) G. Scheibe *Angew. Chem.* **1936**, *49*, 563 – 563; c) D. Möbius, *Adv. Mater.* **1995**, *7*, 437 – 444; d) A. Mishra, R. K. Behera, P. K. Behera, B. K. Mishra, G. B. Behera, *Chem. Rev.* **2000**, *100*, 1973 – 2011; e) A. Pawlik, S. Kirstein, U. De Rossi, S. Dähne, *J. Phys. Chem. B* **1997**, *101*, 5646 – 5651; f) H. von Berlepsch, C. Böttcher, L. Dähne, *J. Phys. Chem. B* **2000**, *104*, 8792 – 8799.
[8] Merocyanine dye aggregates have been observed before in water and on surfaces. However, the structural properties of these aggregates remained unclear and their formation was attributed to a different kind of intermolecular interaction, that is, dispersion forces as for cationic cyanine dye aggregates: M. Kussler, H. Balli, *Helv. Chim. Acta* **1989**, *72*, 17 – 28.
[9] a) F. Dietz, *J. Signalaufzeichnungsmater.* **1973**, *3*, 157 – 180; b) A. H. Herz, *Adv. Colloid and Interface Science* **1977**, *8*, 237 – 298.
[10] L. Brunsveld, B. J. B. Folmer, E. W. Meijer, R. P. Sijbesma, *Chem. Rev.* **2001**, *101*, 4071 – 4097.
[11] F. Würthner, S. Yao, T. Debaerdemaeker, R. Wortmann, *J. Am. Chem. Soc.* **2002**, *124*, 9431 – 9447.
[12] The synthesis follows our earlier procedures (ref. [11]) and will be reported elsewhere. Dyes **2** and **3** have been characterized by ^{1}H NMR spectroscopy, mass spectrometry, and elemental analysis.
[13] The formation of the D band could be also related to the formation of a cyclic oligomeric aggregate that opens to the extended polymeric form upon further self-assembly to the H-aggregated state. For concentration-dependent equilibria between supramolecular polymers and cycles, see a) X. Chi, A. J. Guerin, R. A. Haycock, C. A. Hunter, L. D. Sarson, *J. Chem. Soc. Chem. Commun.* **1995**, 2563 – 2565; b) G. Ercolani, *J. Phys. Chem. B* **1998**, *102*, 5699 – 5703; c) G. Ercolani, M. Ioele, D. Monti, *New. J. Chem.* **2001**, *25*, 783 – 789.
[14] Well-defined X-ray reflections ($Cu_{K\alpha}$ radiation) at $2\Theta = 2.35°$ (100), 4.06° (110), 4.67° (200), 8.04° (220), 7.01° (300), 8.36° (310), and 12.23° (330) provide evidence for an ordered hexagonal lattice composed of rods of 4.34 nm diameter. We note that the resolution of the TEM micrograph provides only an upper limit of 15 nm for these rods.

Magnetism: Molecules to Materials



J.S. MILLER, University of Utah, Salt Lake City, USA; **M. DRILLON**, Inst. de Physique et Chimie des Materiaux de Strasbourg, France (Eds)

As a depository of contemporary knowledge on key topics related to magnetism, this open series of volumes provides a much-needed comprehensive overview of this growing interdisciplinary field. In topical reviews written by foremost scientists trends and recent advances focusing on the correlations between electronic structure and magnetic properties are explained in a clear and detailed way. The balance between theory and experiment within this series will guide advanced students and specialists alike to this research area. It will help evaluate own experimental observations and serve as a base for the design of new magnetic materials. A unique reference work, indispensable for everyone concerned with the phenomena of magnetism!

Reviews for Volume II:
"... presents a good ... current overview of an active and diverse research area."
Journal of the American Chemical Society

NEW: Magnetism: Molecules to Materials IV
Molecule-based Materials (2)
2002. XI, 492 pp. 300 fig. HC
€ 159.-/£ 95.-/US$ 125.-
3-527-30429-0

Magnetism: Molecules to Materials III
Nanosized Magnetic Materials
2001. XV, 388 pp. 209 fig. 14 tab. HC
€ 139.-/£ 80.-/US$ 125.-
3-527-30302-2

Magnetism: Molecules to Materials II
Molecule-Based Materials
2001. XIV, 489 pp. 323 fig. 43 tab. HC
€ 159.-/£ 95.-/US$ 125.-
3-527-30301-4

Magnetism: Molecules to Materials I
Models and Experiments
2001. XVI, 437 pp. 270 fig. 33 tab. HC
€ 139.-/£ 80.-/US$ 125.-
3-527-29772-3

John Wiley & Sons, Ltd.
Baffins Lane Chichester, West Sussex, PO 19 1UD, UK
Fax: +44 (0)1243-775878

WILEY-VCH · P.O. Box 10 11 61 · 69451 Weinheim, Germany · Fax: +49 (0) 62 01-60 61 84 · e-mail: service@wiley-vch.de · http://www.wiley-vch.de

WILEY

WILEY-VCH

14602094.vi

 © 2003 Wiley-VCH Verlag GmbH & Co. KGaA, Weinheim

Rational Drug Design

Molecular-Size Reduction of a Potent CXCR4-Chemokine Antagonist Using Orthogonal Combination of Conformation- and Sequence-Based Libraries**

Nobutaka Fujii, Shinya Oishi, Kenichi Hiramatsu, Takanobu Araki, Satoshi Ueda, Hirokazu Tamamura, Akira Otaka, Shuichi Kusano, Shigemi Terakubo, Hideki Nakashima, James A. Broach, John O. Trent, Zi-xuan Wang, and Stephen C. Peiper*

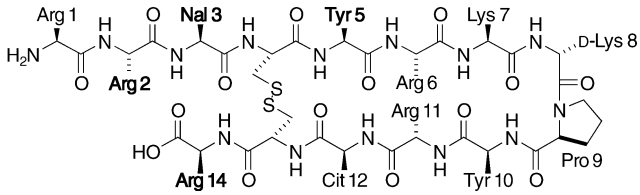
The information available on natural ligands provided by recent advances in genome science is exponentially increasing and amplifies the opportunities for medicinal chemists to develop novel pharmaceuticals.[1] Rational drug design of agonists/antagonists from natural ligands offers one of the most powerful methodologies for drug discovery, while development of innovative methods is required to facilitate the processes. Herein, we report a new strategy for the downsizing of bioactive peptides using two orthogonal small libraries of cyclic peptides, which allowed us to identify a novel CXCR4 antagonist equipotent to the parent peptide.[2]

[*] Prof. N. Fujii, S. Oishi, K. Hiramatsu, T. Araki, S. Ueda, Dr. H. Tamamura, Dr. A. Otaka
Graduate School of Pharmaceutical Sciences
Kyoto University
Sakyo-ku, Kyoto 606-8501 (Japan)
Fax: (+81) 75-753-4570
E-mail: nfujii@pharm.kyoto-u.ac.jp
Dr. S. Kusano, S. Terakubo, Prof. H. Nakashima
St. Marianna University
School of Medicine
Miyamae-ku, Kawasaki 216-8511 (Japan)
Dr. J. A. Broach
Department of Molecular Biology
Princeton University
Princeton, NJ 08544 (USA)
Dr. J. O. Trent
James Graham Brown Cancer Center
University of Louisville
Louisville, KY 40202 (USA)
Dr. Z.-x. Wang, Prof. S. C. Peiper
Department of Pathology
Medical College of Georgia
Augusta, GA 30912 (USA)

[**] The authors thank Dr. Terrence R. Burke, Jr. (NCI, NIH) for reading the manuscript and valuable discussions. We also thank Ms. Akane Omagari, Ms. Kiyomi Hashimoto, and Mr. Akira Matsumura for technical assistance in the preparation of cyclic peptides. This work was supported by Health and Labour Sciences Research Grants (Research on HIV/AIDS) and a Grant-in-Aid for Scientific Research from the Ministry of Education, Culture, Sports, Science, and Technology of Japan. Computation time was provided by the Supercomputer Laboratory, Institute for Chemical Research, Kyoto University. S.O. is grateful for a Research Fellowship from the Japan Society for the Promotion of Science for Young Scientists.

Supporting information for this article is available on the WWW under http://www.angewandte.org or from the author.

We previously reported that T140[3] is a highly potent specific antagonist of the CXCR4-chemokine receptor, which is relevant to HIV-1 infection, cancer metastasis, rheumatoid arthritis, and chronic lymphocytic B-cell leukemia.[4] Our structure–activity relationship studies on T140, which consists of 14 amino acid residues and one disulfide bridge between Cys 4 and Cys 13, have revealed that four indispensable amino acid residues, Arg 2, Nal 3, Tyr 5, and Arg 14, are responsible for its intrinsic bioactivity (Scheme 1).[3a] In addition, NMR



Scheme 1. Structure of T140; bold = indispensable residues, Nal = L-3-(2-naphthyl)alanine, Cit = L-citrulline.

and computational studies on T140 have demonstrated that it adopts an antiparallel β-sheet conformation which is connected by a type II′ β-turn with D-Lys 8-Pro 9 in the $i+1$- and $i+2$-positions. Meanwhile, the three pharmacologically significant residues, Arg 2, Nal 3, and Arg 14, are highly mobile since they are located outside the macrocycle constrained by the disulfide bridge.[3b] We chose cyclic pentapeptides as a molecular template to dispose these four requisite residues in proximity. It was our expectation that these could potentially distribute themselves in coincidence with the topology of the distal pharmacophores in the bioactive conformation of T140. Additionally, potent cyclic peptides obtained in this fashion would enable us to develop low-molecular-weight CXCR4 antagonists through rational design. A possible pentapeptide library included 192 peptides (12 sequences × 16 stereoisomers, Figure 1).[5] Two orthogonal focused libraries containing a limited number of cyclic peptides were utilized to avoid the time-consuming effort required for the synthesis of 192 cyclic peptides.

A distinctive "conformation-based" library (first library) with diverse sequences was initially designed, which included 48 cyclic pentapeptides (12 sequences × 4 stereoisomers). We expected that initial use of this library containing differential sequences could give opportunities to efficiently extract potent compounds from the 192 possible peptides, thus resulting in identification of the required sequence. On the basis of intensive research on cyclic RGD peptides by Kessler et al., in which *cyclo*(-L-Arg-Gly-L-Asp-D-Phe-L-Val-) and *cyclo*(-L-Arg-Gly-L-Asp-L-Phe-D-Val-) exhibited two different βII′/γ-turn arrangements, four well-established arrays were chosen for the library (Scheme 2): *cyclo*(-L-Xaa 1-Gly 2-L-Xaa 3-D-Xaa 4-L-Xaa 5-) **1a–12a** (group I) and *cyclo*(-L-Xaa 1-Gly 2-L-Xaa 3-L-Xaa 4-D-Xaa 5-) **1b–12b** (group II), and their enantiomers, *cyclo*(-D-Xaa 1-Gly 2-D-Xaa 3-L-Xaa 4-D-Xaa 5-) **1c–12c** (group III) and *cyclo*(-D-Xaa 1-Gly 2-D-Xaa 3-D-Xaa 4-L-Xaa 5-) **1d–12d** (group IV). Among these, the D/L-Xaa[4] residue could be in the $i+1$ position of the βII′-turn in groups I and III, while the Gly 2 residue could

 DOI: 10.1002/anie.200351024 © 2003 Wiley-VCH Verlag GmbH & Co. KGaA, Weinheim

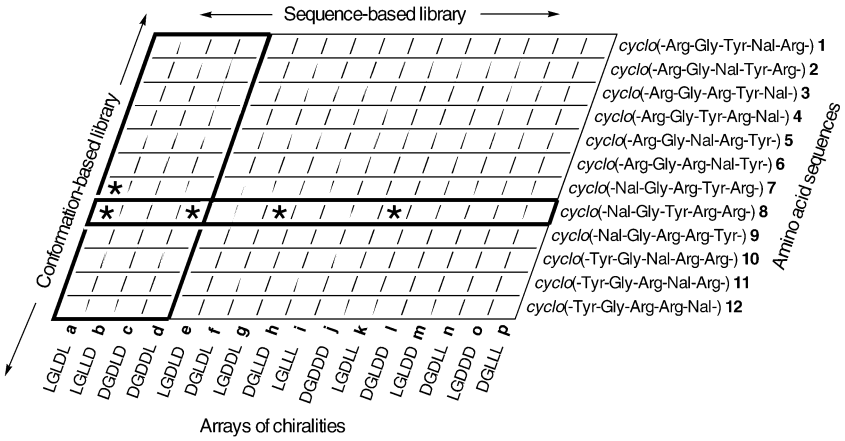
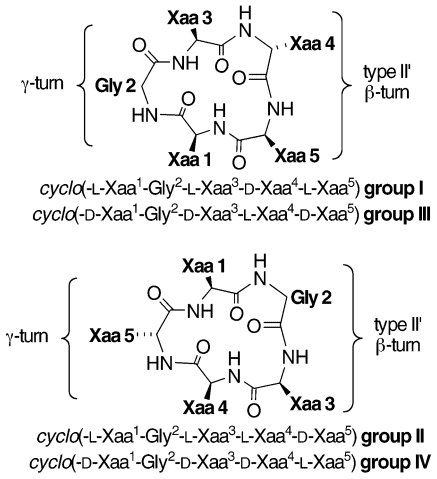


Figure 1. Design of two orthogonal libraries of cyclic peptides; L = L-amino acids, D = D-amino acids, G = glycine.



Scheme 2. Structures of the peptides used in the "conformation-based" library.

occupy the same position in groups II and IV. Parallel synthesis of 48 cyclic peptides followed by evaluation of their biological activities were performed.[6] As a result, we found three compounds, *cyclo*(-L-Nal 1-Gly 2-L-Arg 3-D-Tyr 4-L-Arg 5-) (**7a**), *cyclo*(-L-Nal 1-Gly 2-L-Tyr 3-D-Arg 4-L-Arg 5-) (**8a**), and *cyclo*(-D-Nal 1-Gly 2-D-Tyr 3-D-Arg 4-L-Arg 5-) (**8d**), with moderate CXCR4-antagonistic activity and anti-HIV activity from the "conformation-based" library (see the Supporting Information).[7]

Next, we addressed the two cyclic peptides **8a** and **8d** resulting from the first library that possessed two amino acids with common chirality and functionality in the 4- and 5-positions. This similarity indicated that potent compounds would be obtained from *cyclo*(-D-Nal 1-Gly 2-L-Tyr 3-D-Arg 4-L-Arg 5-) (**8f**) and/or *cyclo*(-L-Nal 1-Gly 2-D-Tyr 3-D-Arg 4-L-Arg 5-) (**8g**), which were Nal 1 and Tyr 3 epimers of **8a** and **8d**. In fact, **8g** was more potent than any other compounds evaluated up to this point (IC_{50} value for CXCR4 = 0.008 μM, EC_{50} value for HIV replication = 0.11 μM). Hence, we designed a "sequence-based" library (second library), wherein diverse chirality arrays of the common amino acid sequence, *cyclo*(-L/D-Nal 1-Gly 2-L/D-Tyr 3-L/D-Arg 4-L/D-Arg 5-), were employed (1 sequence × 16 stereoisomers).[8] In this library *cyclo*(-L-Nal 1-Gly 2-D-Tyr 3-L-Arg 4-L-Arg 5-) (**8k**), which is an epimer of **8g** at Arg 4, exhibited the most potent CXCR4-antagonistic activity (IC_{50} = 0.004 μM) and anti-HIV activity (EC_{50} = 0.038 μM) among all the cyclic pentapeptides (Table 1).

A [^{125}I]SDF-1–CXCR4 (SDF = stromal cell-derived factor) binding inhibition assay showed that the binding affinities of cyclic peptides **8d**, **8g**, and **8k** paralleled their anti-HIV activity. This supported the conclusion that the anti-HIV activities of these cyclic peptides were based on a similar CXCR4 inhibition as that of T140. Peptides, such as **8k**, which have an affinity comparable to that of T140 can be used to evaluate the bioactive conformations of T140. Moreover, these peptides can act as valuable tools to understand the essential pharmacophore topology to CXCR4 antagonism, and thus may facilitate the design of novel nonpeptidic CXCR4 antagonists.

Table 1: Biological activities of T140 and cyclic peptides.

Peptide	IC_{50} [μM][a]	EC_{50} [μM][b]	Peptide	IC_{50} [μM][a]	EC_{50} [μM][b]
T140	0.004	0.060			
8a	0.1–1.0	4.3	**8j**	1.0–10	17
8d	0.016	0.28	**8k**	0.004	0.038
8e	0.1–1.0	20	**8l**	1.0–10	> 200
8f	0.1–1.0	> 200	**8m**	0.1–1.0	11
8g	0.008	0.11	**8n**	0.1–1.0	0.76
8h	> 10	27	**8o**	0.1–1.0	8.2
8i	0.14	2.4	**8p**	0.1–1.0	4.4

[a] IC_{50} values for the cyclic pentapeptides are based on the inhibition of [^{125}I]SDF-1 binding to CXCR4 transfectants of Chinese hamster ovary (CHO) cells. [b] EC_{50} values are based on the inhibition of HIV-induced cytopathogenicity in MT-4 cells.

To confirm the importance of the ring structure as well as the sequence of the cyclic peptides **8d**, **8g**, and **8k** for the anti-HIV activity, the linear peptides **13a–e**, **14a–e**, and **15a–e**, which corresponded to linear products containing the five peptide residues, were synthesized and evaluated (see the Supporting Information). The remarkably reduced activity of the linear peptides (less than 10^{-2} times the activity of the corresponding cyclic congeners) showed that an appropriate ring structure was essential for bioactivity.

The solution conformation of **8k** was estimated by measurement of the ^{1}H NMR spectra in DMSO, according to the previous reports on various cyclic pentapeptides, to estimate its solution conformation.[2] No low temperature coefficients were observed for the chemical shifts of the amide protons. This observation could potentially exclude a reduction in the solvent accessibility as a result of the formation of internal hydrogen bonds. In some cases, pronounced cross-peaks could be observed in NOESY spectra between two amide protons or an amide proton and

 © 2003 Wiley-VCH Verlag GmbH & Co. KGaA, Weinheim

an α-proton of the respective forward residues. Cross-peaks between Gly2 H^N/D-Tyr3 H^N, Arg4 H^N/Arg5 H^N, and Arg5 H^N/Nal1 H^N indicate that these pairs of amide hydrogen atoms may be oriented in the same directions. On the other hand, the strong NOE interactions of Nal1 H^α/Gly2 H^N and D-Tyr3 H^α/Arg4 H^N show that these pairs of protons are in proximity across the peptide bonds. We performed simulated annealing molecular dynamics/energy minimization by using dihedral and distance constraints derived from ^{1}H NMR measurements (Figure 2). The peptide backbones in

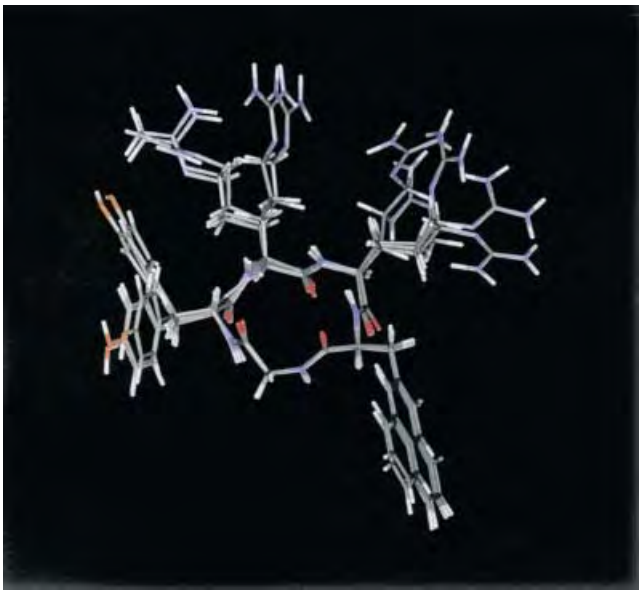


Figure 2. Overlay of five low-energy structures of **8k**.

five energy-minimized structures exhibited nearly symmetrical pentagonal shapes. The carbonyl oxygen atoms in four amide bonds, excluding that between Nal1 and Gly2, were oriented away from the side chains of the respective following residues. This result was consistent with the structures expected from the NOESY spectra. While the exact correlation of the spatial dispositions of each pharmacophore of **8k** with those of T140 are not clear, the calculated structures can provide insight that is applicable to the structure–based design of nonpeptide CXCR4 antagonists.

In summary, we have designed two orthogonal cyclic peptide libraries, which consist of a "conformation-based" library and a "sequence-based" library. The distinctive sequential use of these libraries led to the efficient discovery of new active cyclic peptides **8d**, **8g**, and **8k** that possess bioactivities comparable to T140. This orthogonal strategy may be widely useful for finding new lead compounds from natural/unnatural bioactive peptides and proteins.

Received: January 27, 2003 [Z51024]

Keywords: antagonists · antiviral agents · drug design · high-throughput screening · peptides

[1] For recent reviews of drug discovery from natural/unnatural peptides, see a) V. J. Hruby, P. M. Balse, *Curr. Med. Chem.* **2000**, *7*, 945; b) N. Fujii, H. Tamamura, *Curr. Opin. Invest. Drugs* **2001**, *2*, 1198.

[2] Cyclic oligopeptides, which are relatively constrained by a ring structure, have been successfully employed for designing nonpeptidic agents in medicinal chemistry, see a) T. Fukami, T. Nagase, K. Fujita, T. Hayama, K. Niiyama, T. Mase, S. Nakajima, T. Fukuroda, T. Saeki, M. Nishikibe, M. Ihara, M. Yano, K. Ishikawa, *J. Med. Chem.* **1995**, *38*, 4309; b) R. Haubner, R. Gratias, B. Diefenbach, S. L. Goodman, A. Jonczyk, H. Kessler, *J. Am. Chem. Soc.* **1996**, *118*, 7461; c) A. F. Spatola, Y. Crozet, *J. Med. Chem.* **1996**, *39*, 3842; d) J. Wermuth, S. L. Goodman, A. Jonczyk, H. Kessler, *J. Am. Chem. Soc.* **1997**, *119*, 1328; e) R. Haubner, D. Finsinger, H. Kessler, *Angew. Chem.* **1997**, *109*, 1440; *Angew. Chem. Int. Ed. Engl.* **1997**, *36*, 1374; f) K. Nakayama, H. C. Kawano, H. Inagaki, T. Ohta, *Org. Lett.* **2001**, *3*, 3447; g) H. C. Kawano, K. Nakayama, H. Inagaki, T. Ohta, *Org. Lett.* **2001**, *3*, 3451.

[3] a) H. Tamamura, A. Omagari, S. Oishi, T. Kanamoto, N. Yamamoto, S. C. Peiper, H. Nakashima, A. Otaka, N. Fujii, *Bioorg. Med. Chem. Lett.* **2000**, *10*, 2633; b) H. Tamamura, M. Sugioka, Y. Odagaki, A. Omagari, Y. Kan, S. Oishi, H. Nakashima, N. Yamamoto, S. C. Peiper, N. Hamanaka, A. Otaka, N. Fujii, *Bioorg. Med. Chem. Lett.* **2001**, *11*, 359.

[4] a) J. A. Burger, M. Burger, T. Kipps, *Blood* **1999**, *94*, 3658; b) T. Nanki, K. Hayashida, H. S. EI-Gabalawy, S. Suson, K. Shi, H. J. Girschick, S. Yavuz, P. E. Lipsky, *J. Immunol.* **2000**, *165*, 6590; c) A. Müller, B. Homey, H. Soto, N. Ge, D. Catron, M. E. Buchanan, T. Mcclanahan, E. Murphy, W. Yuan, S. M. Wagner, J. L. Barrera, A. Mohar, E. Verástegui, A. Zlotnik, *Nature* **2001**, *410*, 50; d) M. K. Schwarz, T. N. C. Wells, *Nat. Rev. Drug Discovery* **2002**, *1*, 347.

[5] An additional Gly residue was employed as a spacer to avoid epimerization of a C-terminal residue during cyclization in peptide synthesis.

[6] The synthesis and evaluation of cyclic peptides are described in detail in the Supporting Information.

[7] CXCR4 is known to participate in infection by X4-HIV virus,[9] and in our previous research the affinities of T140 derivatives for CXCR4 have correlated with the anti-HIV activity.

[8] The principal concept of "sequence-based" libraries has been reported as the "spatial-screening" methodology: H. Kessler, B. Kutscher, R. Kerssebaum, A. Klein, J. Lautz in *Peptides: Structures and Function, Proceedings of the Ninth American Peptide Symposium* (Eds.: C. M. Deber, V. J. Hruby, K. Kopple), Pierce Chemical Company, Rockford, **1985**, pp. 83–92; and reference [2b].

[9] Y. Feng, C. C. Broder, P. E. Kennedy, E. A. Berger, *Science* **1996**, *272*, 872.

 © 2003 Wiley-VCH Verlag GmbH & Co. KGaA, Weinheim

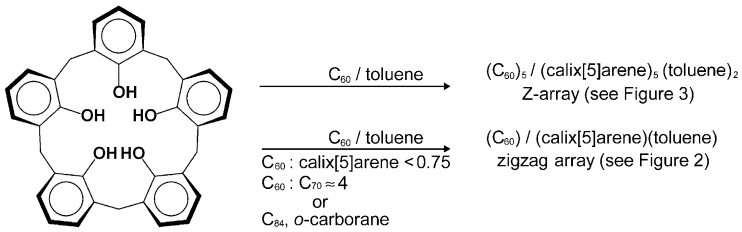
C_{60}/Calixarene Complex

Controlling van der Waals Contacts in Complexes of Fullerene C_{60}**

Jerry L. Atwood, Leonard J. Barbour,* Michael W. Heaven, and Colin L. Raston**

The most common method of generating fullerenes, using an electric arc between two graphite rods, yields C_{60} and C_{70} in a ratio of roughly 19:5. Consequently, the ubiquitous coexistence of C_{70} with C_{60} has been somewhat of a hindrance in the purification of the latter. Viable methods for the purification of fullerenes include supramolecular complexation with calix[*n*]arenes.[1] For example, we have shown that *p-tert*-butylcalix[8]arene binds C_{60} selectively, thus allowing C_{60} to be separated from fullerite with $>99.5\%$ purity.[2] Conceivably, the complex is a micellelike arrangement of three fullerenes surrounded by three double-cone calixarenes.[3] Calix[6]arene also forms a complex with either C_{60} or C_{70}, in which the fullerene is situated in each of the shallow cavities of the double-cone-shaped calixarene. This arrangement yields a 1:2 host–guest complex in which the fullerenes form an extended three-dimensional crisscrossed array of linear strands.[4]

Owing to the C_{5v} cone conformation of calix[5]arene (Scheme 1), its size and curvature are complementary to C_{60} and its principle axis extremities suit C_{70}.[5] Accordingly it has been a popular choice for host–guest studies with these fullerenes. Generally, 1:1 and 2:2 complexes result in which each fullerene is situated in the cavity of a calixarene. Various modified forms of calix[5]arene have also been used to probe the host–guest interaction, including substituted calix[5]-arenes,[6,7] biscalix[5]arenes,[8–10] and calix[5]arenes self-assembled by means of noncovalent metal–ligand interactions.[11] Only recently has the solid-state structure of a C_{60} complex of the unmodified, shallow-cavity calix[5]arene been elucidated.[12] Here the fullerenes assemble in a Z-array, comprising five close-packed columns enshrouded by a sheath of calix[5]arene molecules. Some of the fullerenes are capped by two *trans*-calixarenes, while others are associated with the cavity of only one calixarene, or are not associated with any cavities at all.



Scheme 1. Crystallization of calix[5]arene with C_{60}, C_{70}, and other globular molecules.

[*] Prof. J. L. Atwood, Prof. L. J. Barbour, M. W. Heaven
Department of Chemistry
University of Missouri-Columbia
Columbia, MO 65211 (USA)
Fax: (+1) 573-884-9606
E-mail: atwoodj@missouri.edu
barbourl@missouri.edu
Prof. C. L. Raston
Department of Chemistry
University of Western Australia
Crawley, WA 6009 (Australia)
Fax: (+61) 8-9380-1005
E-mail: clraston@chem.uwa.edu.au

[**] We thank the EPSRC and the NSF for financial support of this work.

In further exploring the chemistry of fullerenes and calix[5]arene, we have now encountered yet another complex with the same units but with the calixarene and fullerene in a simple 1:1 ratio (cf. 4:5 for the Z-array).[12] Initially this new complex formed in the presence of C_{70}, which is remarkable in that, far from being a hindrance, C_{70} actually facilitates the formation of a different complex of calix[5]arene and C_{60}. If the C_{60}:C_{70} molar ratio is varied while the total amount of calix[5]arene is kept constant (i.e. about 1.3:1 calixarene/fullerene) a progression of solid-state structures, from the Z-array to the new C_{60}/calix[5]arene structural motif **1**, and then to a C_{70}/calix[5]arene complex, is obtained.

Calix[5]arene and exclusively C_{70} form a complex isolated as clusters of slender dark-red needles (Figure 1a), which have thus far been unsuitable for single-crystal X-ray analysis. These clusters form in the presence of C_{60} up to a C_{60}:C_{70} molar ratio of ca. 2.3:1 (with 1.4 mol equiv calix[5]arene) (Table 1). When the C_{60}:C_{70} molar ratio is close to ca. 4.5:1 (1.4 mol equiv calix[5]arene), the new complex **1** forms along with the C_{70}/calixarene complex (Figure 1b and c). Complex **1** forms up to a 10:1 molar ratio of C_{60}:C_{70}, while at higher ratios the Z-array results (Figure 1d).[12] The ability of C_{70} to influence the composition of a system in a crystal by mediating the crystallization process is unprecedented. In the absence of C_{70} and with excess calix[5]arene (1.3 mol-equiv) the C_{60}/calix[5]arene Z-array results (Figure 1d).

X-ray diffraction analysis[13] of **1** reveals a simple 1:1:1 complex of C_{60}, calix[5]arene, and toluene (Figure 2). The C_{60} molecules form a slightly helical, zigzag, one-dimensional oligomeric array. It is not surprising that the *exo* cavity surface of two adjacent calix[5]arenes abut close to each C_{60}, considering the electron-deficient nature of the fullerene and the electron-rich oxygen atoms and arene rings of the calix[5]arenes.

To further investigate the role of C_{70} in the formation of **1** we seeded toluene solutions of fullerite (containing ca. 5:1 C_{60}:C_{70}) and calix[5]arene (close to the same molar ratios as above) with crystals of either the Z-array or the zigzag array. In all cases the only complex formed was the new C_{60}/calix[5]arene complex **1**. Moreover, addition of crystals of **1** to a 1:1 solution of C_{60} and calix[5]arene in toluene also results in the formation of **1**. Thus here the crystal is seeding the crystallization of **1** at the expense of the Z-array, as opposed to the C_{70} mediation in the previous experiments. Complex **1** can therefore be regarded as the thermodynamically favored product, at least when the ratio of C_{60} to calix[5]arene is 1:1. The Z-array seed crystals had no effect on the crystallization outcome for solutions of fullerite or C_{60} with calix[5]arene.

 © 2003 Wiley-VCH Verlag GmbH & Co. KGaA, Weinheim DOI: 10.1002/anie.200351033



Figure 1. Photographs of crystals of a) C_{70}/calix[5]arene, b) **1** and C_{70}/calix[5]arene (2:1 C_{60}:C_{70} and calix[5]arene), c) **1** resulting from 4:1 C_{60}:C_{70} and calix[5]arene, and d) Z-array C_{60}/calix[5]arene (tenfold magnification)

Table 1: Crystallizations of calix[5]arene/C_{60}/C_{70} complexes from toluene (ca. 1 mg fullerene mL^{-1} toluene) and resulting complexes; yields ca. $>75\%$.

C_{60}:C_{70}	C_{60}:Calix[5]arene	Crystal type
0–1.2:1	0–3.7:1	C_{70} complex[a]
2.3:1	0.49:1	zigzag array[b]/C_{70} complex
3.5–10.5:1	0.51–0.65:1	zigzag array
	0.07–0.7:1	zigzag array
	0.75–1.0:1	Z-array[c]

[a] C_{70}/calix[5]arene by comparison with X-ray powder diffraction data of C_{70}/calix[5]arene. [b] This paper. [c] Ref. [11].

Adding other globular molecules such as *o*-carborane ($1,2\text{-}C_2B_{10}H_{12}$) or C_{84} in place of C_{70} to toluene solutions of C_{60} and calix[5]arene also results in the formation of **1**, even though the carborane itself is known to form complexes with the calixarene.[14] Thus these additives also mediate the crystallization of the new complex, although their role in the crystallization process is as yet unclear. However, in solutions of C_{60} and bowl-shaped molecules in a 1:1 ratio, aggregation of the fullerenes is proposed to occur by polarization effects,[15–17] and aggregation could then lead to the fullerene-rich Z-array. The other globular molecules could

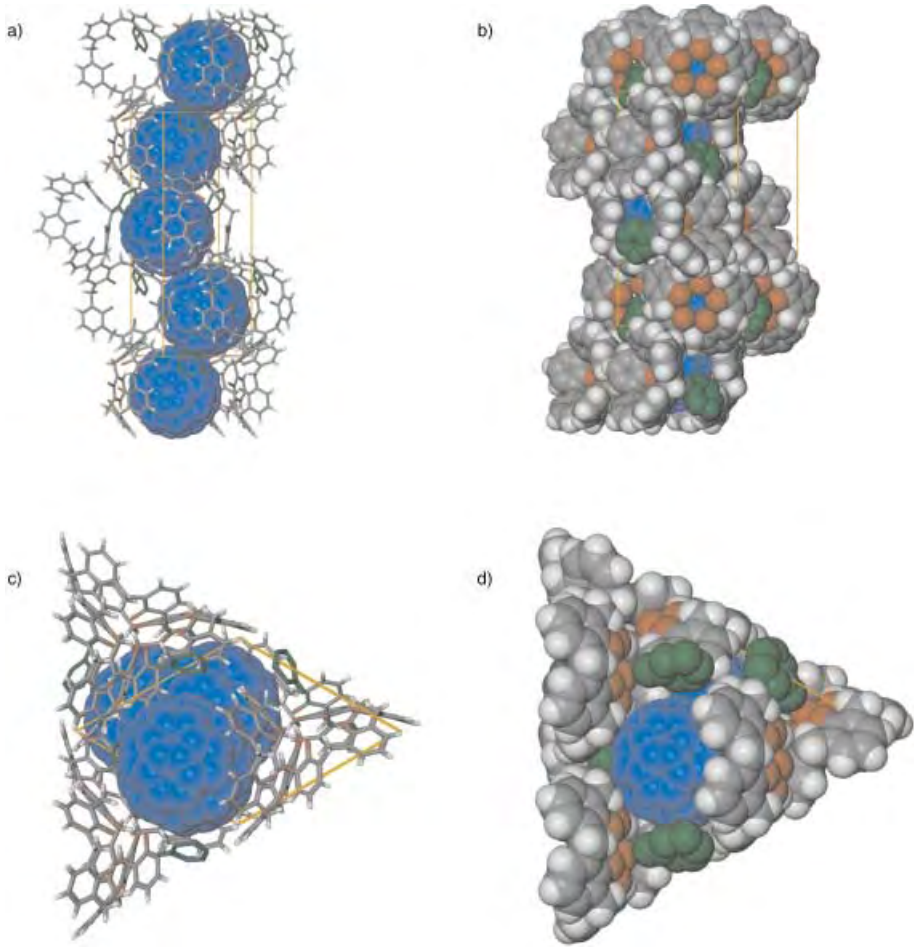


Figure 2. X-ray crystal structure of [(C_{60})(calix[5]arene)]·toluene (**1**) projected at right angles to the zigzag array of fullerenes (a and b), and almost along the array (c and d). Blue = C_{60}, dark and light gray = carbon and hydrogen atoms of the calixarene, red = oxygen atoms, dark green = toluene.

 © 2003 Wiley-VCH Verlag GmbH & Co. KGaA, Weinheim

effectively disrupt the aggregation of C_{60} molecules. Moreover, the presence of an excess of calix[5]arene results in the new zigzag array, which can be rationalized by the dominance of the 1:1 supermolecule in solution, which possibly also minimizes aggregation of the fullerenes.

To confirm that either the Z-shaped or zigzag array **1** were representative of bulk samples, X-ray powder diffraction studies were undertaken. Distinct diffraction patterns were obtained, as was also the case for the C_{70}/calix[5]arene complex; we found no evidence for the presence of mixtures of two or three of the complexes. UV/Vis studies on toluene or chloroform solutions prepared from single crystals of the C_{60} Z-shaped and zigzag arrays, and the ill-defined C_{70} complex were undertaken. Spectra were recorded after a single crystal had been dissolved slowly over a period of one week in either solvent. Complex **1**, crystallized in the presence of C_{70}, showed only traces of the higher fullerene according to HPLC analysis. Both the electronic spectrum and single-crystal data show that the higher fullerene is not an integral part of the solid-state structure.[18,19]

The use of C_{70} as a mediator in crystallizing a new structural motif of C_{60} with calix[5]arene is interesting, since calix[5]arene is one of the few known hosts to complex C_{60} in solution.[1] We believe that the influence of globular additives on the resulting structure can be rationalized by considering how spherical molecules generally prefer to pack. In the fullerene-rich Z-array structure, the C_{60} molecules aggregate into several linear strands that make van der Waals contact with one another. Adjacent strands are staggered with respect to one another such that each C_{60} molecule is in close contact with four to six of its like neighbors. Careful consideration of the individual C_{60} molecules shows that each is in a two-dimensional, pseudohexagonal-close-packed environment. Indeed, each of the molecules of the central strand is surrounded by six nearest neighbors, and this is the preferred arrangement for close-packed spheres. The C_{70}, carborane, or C_{84} molecules are similar in size and shape to C_{60}. However, we postulate that these molecules are sufficiently different that they disrupt the formation of the pseudohexagonal-close-packed arrangement. This allows the C_{60} molecules to adopt the alternative low-energy structure **1**, in which hexagonal packing does not play a role. It is likely that during crystal growth C_{60} molecules in this less constrained structure can be replaced by the globular additives. However, the growth of crystals from solution is a dynamic and reversible process in which the molecules can be deposited as well as removed from the growth boundary of the material. In most cases, this mechanism allows the crystal to "repair" itself by rejecting molecules that might fit but that do not conform to the minimum-energy packing mode.

It is appropriate to summarize the types of structurally authenticated arrays of C_{60} involving large calixarenes and related molecules, and molecules with curved surfaces (Figure 3). Aggregates have been identified and characterized.[3] There are the one-dimensional arrays (linear,[20] zigzag,[15,16] linear double strands,[1] and a linear Z-array of five strands[12]), two-dimensional arrays (hexagonal-close-packed[16] and corrugated sheets[1]), and three-dimensional arrays.[4] Controlling the assembly of fullerenes into zigzag or Z-arrays, depending on the presence of a third component which itself does not form part of the assembly, is an important development in the materials science of fullerenes and promises to expand the structural types possible for C_{60} as well as for C_{70} and higher fullerenes. These results are particular timely with regard to constructing fullerene arrays (at the van der Waals limit or covalently linked) for polymerization.

Received: January 28, 2003 [Z51033]

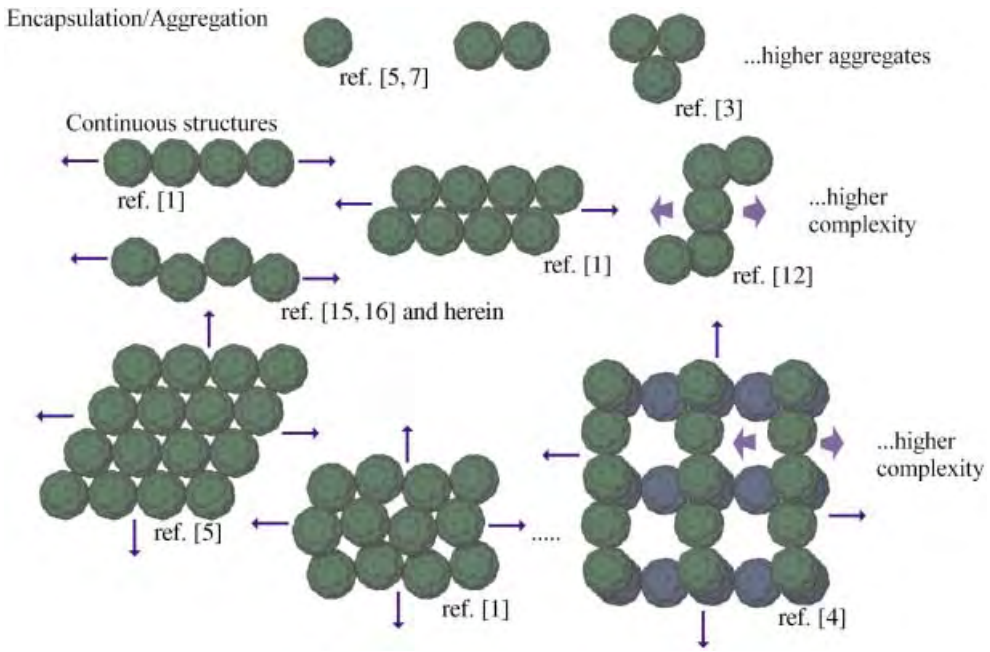


Figure 3. Encapsulation/aggregation and ordering of C_{60} molecules into 1D, 2D, and 3D arrays (host molecules not shown).

 © 2003 Wiley-VCH Verlag GmbH & Co. KGaA, Weinheim

Keywords: aggregation · calixarenes · crystal growth · fullerenes · host–guest systems

[1] R. Taylor, J. P. Hare, A. K. Abdul-Sada, H. W. Kroto, *J. Chem. Soc. Chem. Commun.* **1990**, 1423 – 1425.
[2] J. L. Atwood, G. A. Koutsantonis, C. L. Raston, *Nature* **1994**, *368*, 229 – 312.
[3] C. L. Raston, J. L. Atwood, P. J. Nichols, I. B. N. Sudria, *Chem. Commun.* **1996**, 2615 – 2616.
[4] J. L. Atwood, L. J. Barbour, C. L. Raston, I. B. N. Sudria, *Angew. Chem.* **1998**, *110*, 1029 – 1031; *Angew. Chem. Int. Ed.* **1998**, *37*, 981 – 983.
[5] J. L. Atwood, L. J. Barbour, P. J. Nichols, C. L. Raston, C. A. Sandoval, *Chem. Eur. J.* **1999**, *5*, 990 – 996.
[6] T. Haino, M. Yanase, Y. Fukazawa, *Angew. Chem.* **1997**, *109*, 288 – 289; *Angew. Chem. Int. Ed. Engl.* **1997**, *36*, 259 – 260.
[7] M. Makha, M. J. Hardie, C. L. Raston, *Chem. Commun.* **2002**, 1446 – 1447.
[8] T. Haino, M. Yanase, Y. Fukazawa, *Angew. Chem.* **1998**, *110,* 1044 – 1046; *Angew. Chem. Int. Ed.* **1998**, *37,* 997 – 998.
[9] S. E. Biali, V. Böhmer, I. Columbus, G. Ferguson, C. Grüttner, F. Grynszpan, E. F. Paulus, I. Thondorf, *J. Chem. Soc. Perkin Trans. 2* **1998**, 2261 – 2269.
[10] J. Wang, S. G. Bodige, W. H. Watson, C. D. Gutsche, *J. Org. Chem.* **2000**, *65*, 8260 – 8263.
[11] T. Haino, Y. Yamanaka, H. Araki, Y. Fukazawa, *Chem. Commun.* **2002**, 402 – 403.
[12] J. L. Atwood, L. J. Barbour, C. L. Raston, *Cryst. Growth Des.* **2002**, *2,* 3 – 6.
[13] Crystal data for [(C_{60})(calix[5]arene)]·toluene (**1**): $C_{102}H_{38}O_5$, $M_r = 1343.32$, dark red prism, $0.20 \times 0.20 \times 0.15\ mm^3$, trigonal, space group $P3_2$ (No. 145), $a = b = 13.7630(1)$, $c = 26.9435(3)$ Å, $V = 4419.88(7)$ Å^3, $Z = 3$, $\rho_{calcd} = 1.514\ g\,cm^{-3}$, $F_{000} = 2070$, Nonius KappaCCD area-detector (ω scan mode, $Mo_{K\alpha}$ radiation, $\lambda = 0.71073$ Å), $T = 173(2)$ K, $2\theta_{max} = 55.7°$, 21952 reflections collected, 10980 unique ($R_{int} = 0.0304$). The structure was solved and refined using the SHELX-97 software package and the X-Seed[21] interface. Direct methods yielded all non-hydrogen atoms of the calixarene and toluene molecules of the asymmetric unit. While none of the C_{60} atoms could be located unequivocally, the position of the rotationally disordered fullerene was indicated by a spheroid of difference electron density. Two idealized C_{60} molecules were placed on this position in two different orientations, and each molecule was assigned a site occupancy factor of 50%. This procedure allowed adequate refinement of a rotationally disordered model for C_{60} of known location. The calixarene atoms were refined anisotropically (full-matrix least squares method on F^2). Hydrogen atoms were placed in calculated positions with their isotropic thermal parameters riding on those of their parent atoms. Final GOF = 3.393, $R1 = 0.2557$, $wR2 = 0.6101$, R indices based on 9974 reflections with $I > 2\sigma(I)$ (refinement on F^2), 375 parameters, 626 restraints. Lorentz, polarization, and absorption corrections applied, $\mu = 0.092\ mm^{-1}$. All X-ray structure figures were prepared with X-Seed.[21] CCDC-202602 contains the supplementary crystallographic data for this paper. These data can be obtained free of charge via www.ccdc.cam.ac.uk/conts/retrieving.html (or from the Cambridge Crystallographic Data Centre, 12, Union Road, Cambridge CB2 1EZ, UK; fax: (+44) 1223-336-033; or deposit@ccdc.cam.ac.uk).
[14] M. J. Hardie, C. L. Raston, *Eur. J. Inorg. Chem.* **1999**, 195 – 200.
[15] J. L. Atwood, M. J. Barnes, M. G. Gardiner, C. L. Raston, *Chem. Commun.* **1996**, 1449 – 1450.
[16] A. M. Bond, W. J. Miao, C. L. Raston, T. J. Ness, M. J. Barnes, J. L. Atwood, *J. Phys. Chem. B* **2001**, *105*, 1687 – 1695.
[17] A. Drljaca, C. Kepert, L. Spiccia, C. L. Raston, C. A. Sandoval, T. D. Smith, *Chem. Commun.* **1997**, 195 – 196.
[18] J. P. Hare, H. W. Kroto, R. Taylor, *Chem. Phys. Lett.* **1991**, *177*, 394 – 398.
[19] M. Diack, R. L. Hettich, R. N. Compton, G. Guiochon, *Anal. Chem.* **1992**, *64*, 2143 – 2148.
[20] L. J. Barbour, G. W. Orr, J. L. Atwood, *Chem. Commun.* **1998**, 1901 – 1902.
[21] L. J. Barbour, *J. Supramol. Chem.* **2001**, *1*, 189 – 191.

 © 2003 Wiley-VCH Verlag GmbH & Co. KGaA, Weinheim

CO_2 Activation in an Ionic Liquid

Alternatives to Phosgene and Carbon Monoxide: Synthesis of Symmetric Urea Derivatives with Carbon Dioxide in Ionic Liquids**

Feng Shi, Youquan Deng, Tianlong SiMa, Jiajian Peng, Yanlong Gu, and Botao Qiao*

N-containing compounds such as isocyanates, carbamates, and *N*,*N*′-disubstituted urea derivatives are important chemicals. For example, the world production of isocyanates exceeded 5 megatons in 2001. Currently, these chemicals are mainly manufactured by the phosgenation of amines . The worldwide production of phosgene ranges from 6–8 megatons per year, which have been used mainly (> 85 %) for the synthesis of isocyanates and their derivatives. Therefore, as a first step, the use of an alternative to phosgene in the synthesis of isocyanates should be found to help eliminate the use of phosgene altogether.[1–2]

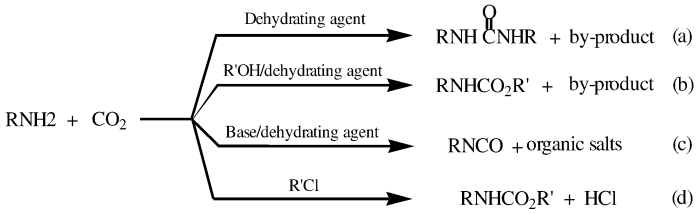
Many strategies for nonphosgene routes, including reductive carbonylation[3] and oxidative carbonylation[4] by using CO as carbonyl source, and the use of Pd,[5] Ru,[6] Rh,[7] Fe,[8] Ni,[9] Co,[10] Mn,[11] Se,[12] Au,[13] and W[14] catalysts, have been extensively studied. The progress in this field of research, however, is relatively slow. Carbon monoxide is also poisonous and the mixing of CO and O_2 for oxidative carbonylation is potentially explosive. As an alternative, the use of dimethyl carbonate or dimethyl sulfate as phosgene substitutes are relatively expensive for commercial applications.[15] Therefore, the most desirable option to avoid phosgene is to replace it with CO_2 directly. Besides the abundance of CO_2 and its environmentally benign nature, a process that uses CO_2 has the benefit of recycling carbon from the atmosphere when its use is linked with other processes that emit CO_2. The detrimental influence of CO_2 as a "green house" gas has

[*] Prof. Y. Deng, Dr. F. Shi, T. SiMa, J. Peng, Y. Gu, B. Qiao
Centre for Green Chemistry and Catalysis
Lanzhou Institute of Chemical Physics
Chinese Academy of Sciences, Lanzhou, 730000 (China)
Fax: (+86) 931-8277088
E-mail: ydeng@ns.lzb.ac.cn

[**] This work was financially supported by the National Natural Science Foundation of China (No.20225309)

 DOI: 10.1002/anie.200351098 © 2003 Wiley-VCH Verlag GmbH & Co. KGaA, Weinheim

received more and more attention, so its use as raw material for basic chemical production is an attractive subject. Until now, the studies of carbonylation reactions of nitrogen containing compounds by using CO_2 are relatively few in comparison with those that make use of CO, probably because of the chemical inertness of CO_2. Nevertheless, only four kinds of carbonylations of N-containing compounds that make use of CO_2 as the carbonyl source have been reported[16] (Scheme 1).



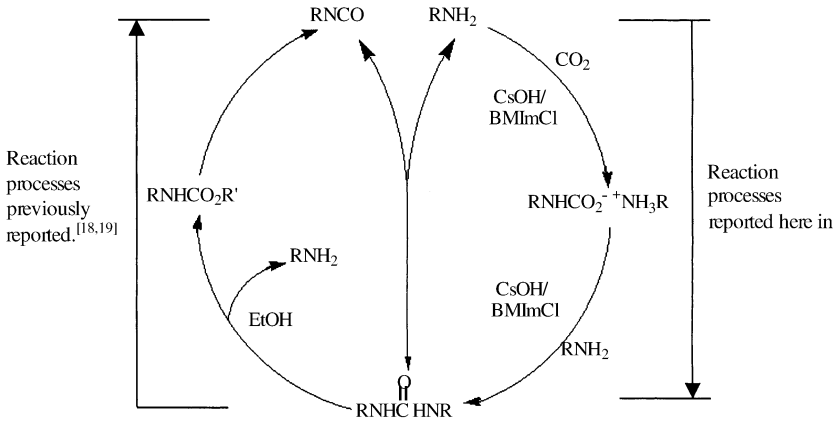
Scheme 1. Carbonylations of N-containing compounds with CO_2 as the carbonyl source.

Although the desired products are obtained in good yields by these routes (ca. 60–90%), large amounts of dehydrating agents, such as PCl_5, $POCl_3$, dicyclohexylcarbodiimide (reactions a, b and c) and/or an appropriate base, such as Et_3N (reaction c), or relatively expensive alkyl chlorides, R′Cl (reaction d) are needed. Furthermore, large amounts of by-products, such as Et_3NHCl, $Et_3NHPOCl$, HCl are inevitably formed. Although CO_2 was used as a carbonyl source as an alternative to phosgene in the synthesis of isocyanate and its derivatives, this route was not only more expensive but also environmentally less friendly.

Recently, room-temperature ionic liquids, a reaction media with very low vapor pressure, peculiar physicochemical properties, and selective solubility towards many organic and inorganic substances, have attracted growing interest. Many catalytic reactions that proceed in ionic liquids were reported, with satisfactory performances in many cases.[17] The combination of ionic liquids as versatile and novel reaction media with a suitable catalyst, such as acid, base, nanostructures, or metal-complex, may result in a more diverse and flexible "platform" to establish a highly effective and easily separable catalytic system.

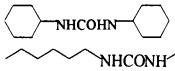
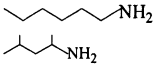
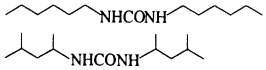
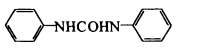
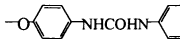
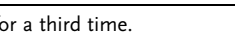
Herein, we report an effective process for the direct synthesis and separation of symmetric urea derivatives in good yield from amines by using CO_2 as the carbonyl source. The recyclable catalytic system consists of an ionic liquid and base and avoids the need for stoichiometric quantities of dehydrating agent. As it was demonstrated that *N*,*N*′-disubstituted urea derivatives could easily be converted into the corresponding carbamates,[18] and the carbamates can be thermally decomposed to form isocyanates,[19] thus, the breakthrough in the synthesis of *N*,*N*′-disubstituted urea derivatives in the absence of stoichiometric quantities of dehydrating agents should imply a breakthrough in the synthesis of isocyanates with CO_2 and amine without the need of stoichiometric quantities dehydrating agent. These processes are illustrated in Scheme 2.

A series of aliphatic amines, and even aromatic amines, react with CO_2 to afford corresponding urea derivatives with moderate to high yields in the presence of the CsOH/ionic-liquid catalyst system (Table 1).[20] The type of cations and anions of the ionic liquids have a strong impact on the



Scheme 2. The transformations between urea, carbamate, and isocyanate derived from amine and CO_2.

Table 1: Results for synthesis of symmetric urea derivatives with carbon dioxide.

Entry	Substrates	Ionic liquid	Catalysts	*t* [h]	Product	Yield [%, isolated]
1		$BMImBF_4$	CsOH	4		84.5
2		$BMImPF_6$	CsOH	4		56.6
3		BMImCl	CsOH	4		98
4[a]		BMImCl	CsOH	4		93
5		CMImCl	CsOH	4		–
6		BMImCl	KOH	4		53.5
7		BMImCl	CsOH	6		93
8		BMImCl	CsOH	6		86
9		BMImCl	CsOH	36		27
10		BMImCl	CsOH	36		33

[a] The catalyst system had been twice recovered and used for a third time.

 © 2003 Wiley-VCH Verlag GmbH & Co. KGaA, Weinheim

formation of urea derivatives when cyclohexylamine is the substrate (Table 1 entries 1–6).[21] If the conversion is sufficiently high, the desired product precipitates on adding about 10 mL water into the reaction mixture as urea is insoluble in water,[22] whereas CsOH and the ionic liquid are water-soluble (Figure 1). The solid product could be recovered by filtration and dried. A yield of 98% was obtained when BMImCl ionic liquid containing CsOH was employed (Table 1 entry 3).

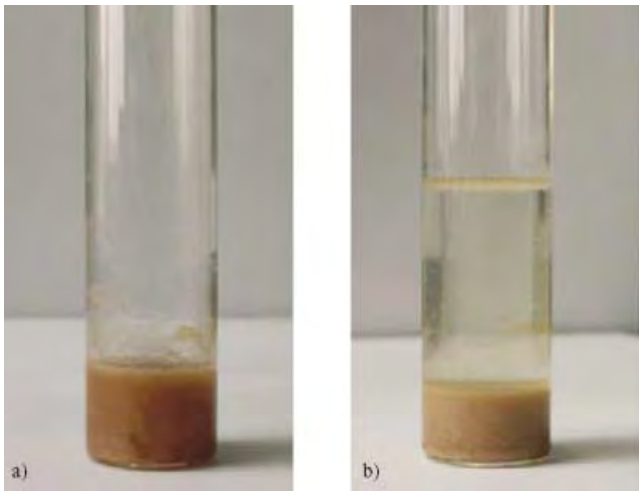


Figure 1. a) The resulting liquid mixture after the reaction of cyclohexylamine with CO_2. b) The reaction mixture with added water, the ionic liquid and base dissolved in the water layer and the crystallized product precipitated.

The use of a weaker base was found to disfavor the formation of urea derivatives; a yield of only 53.5% was obtained when CsOH was replaced with KOH, a relatively weak base. The ionic liquid was indispensable for the formation of the desired product as the yield of dicyclohexyl urea was almost zero in the absence of ionic liquid.

As to primary amines with a linear chain, a longer reaction time was needed to obtain similar yields to those of cyclohexylamine, (Table 1 entries 7, 8).

Surprisingly, good results were also achieved with aromatic amines, which have never been effectively carbonylated directly by carbon dioxide, although longer reaction times were required. Yields of 27% and 33% were obtained with aniline and *p*-methoxylaniline, respectively, (Table 1entries 9, 10). No urea derivative was afforded with *m*-nitroaniline, which may be attributed to the strong electron-withdrawing property of the nitro group.

The recycling of BMImCl/CsOH catalyst system was also tested. Ionic liquid containing CsOH could be recovered and reused after it was distillated to remove water, and a yield of 93% of urea was obtained when CsOH/BMImCl system was used for a third time.

In summary, the organic-solvent- and dehydrating-agent-free process for carbonylation of both aliphatic and aromatic amines with carbon dioxide to afford urea derivatives is simple, clean, safe, reproducible, and even practical. Furthermore, urea derivatives are potential precursors for the phosgene- and carbon monoxide-free synthesis of isocyanates. The concept of reaction and separation has been fulfilled with a simple CsOH/ionic liquid catalyst system that takes advantage of the nonvolatility and selective solubility of the ionic liquid. This concept may be expanded to other catalysis systems.

Received: February 4, 2003 [Z51098]

Keywords: amines · carbon dioxide · carbonylation · green chemistry · ionic liquids

[1] M. Aresta, E. Quaranta, *CHEMTECH* **1997**, 32.
[2] M. Aresta, A. Ciccarese, P. Giannoccaro, E. Quaranta, I. Tommasi, *Gazz. Chim. Ital.* **1995**, *125*, 509.
[3] A. M. Tafesh, J. Weiguny, *Chem. Rev.* **1996**, *96,* 2035.
[4] T. W. leung, B. D. Dombek, *J. Chem. Soc. Chem. Commun.* **1992**, 205.
[5] a) V. L. K. Valli, H. Alper, *J. Am. Chem. Soc.* **1993**, *115,* 3778; b) E. Alessio, G. Mestroni, *J. Organomet. Chem.* **1985**, *291,* 117; c) Y. Izumi, Y. Satoh, H. Kondoh, K. Yrabe, *J. Mol. Catal.* **1992**, *72,* 37; d) Y. Izumi, Y. Satoh, K. Urabe, *Chem. Lett.* **1990**, 795; e) A. A. Kelkar, D. S. Kolhe, S. Kanagasabapathy, R. V. Chaudhari, *Ind. Eng. Chem. Res.* **1992**, *31,* 172; f) P. Wehman, P. C. J. Kamer, P. W. N. M. van Leeuwen, *Chem. Commun.* **1996**, 217; g) I. Pri-Bar, J. Schwartz, *J. Org. Chem.* **1995**, *60,* 8124; h) V. L. K. Valli, H. Alper, *Organometallics* **1995**, *14*, 80; i) P. Wehman, V. E. Kaasjager, W. G. J. de Lange, F. Hartl, P. C. J. Kamer, P. W. N. M. van Leeuwen, *Organometallics* **1995**, *14,* 3751; j) F. Bigi, R. Maggi, G. Sartori, *Green Chem.* **2000**, *2*, 140.
[6] a) S. Cenini, M. Pizzotti, C. Crotti, F. Porta, G. La Monica, *J. Chem. Soc. Chem. Commun.* **1984**, 1286; b) D. K. Mukherjee, B. K. Palit, C. R. Saha, *J. Mol. Catal.* **1994**, *91*, 19.
[7] a) F. Ragaini, S. Cenini, A. Fumagalli, C. Crotti, *J. Organomet. Chem.* **1992**, *428*, 401; b) F. Ragaini, S. Cenini, F. Demartin, *Organometallics* **1994**, *13,* 1178; c) C. V. Rode, S. P. Gupte, R. V. Chaudhari, C. D. Pirozhkov, A. L. Lapidus, *J. Mol. Catal.* **1994**, *91,* 195.
[8] R. Ugo, R. Psaro, M. Pizzotti, P. Nardi, C. Dossi, A. Andreetta, G. Capparella, *J. Organomet. Chem.* **1991**, *417,* 211.
[9] a) H. Hoberg, F. J. Fananas, H. J. Riegel, *J. Organomet. Chem.* **1983**, *254,* 267; b) P. Giannoccaro, C. F. Nobile, P. Mastrorolli, N. Ravasio, *J. Organomet. Chem.* **1991**, *419*, 251.
[10] a) G. Maddinelli, M. Nall, B. Rindone, S. Tollari, *J. Mol. Catal.* **1987**, *39*, 71; b) A. Bassoli, B. Rindone, S. Tollari, *J. Mol. Catal.* **1990**, *60*, 41.
[11] a) F. Calderazzo, *Inorg. Chem.* **1965**, *4*, 293; b) B. D. Dombek, R. J. Angelici, *J. Organomet. Chem.* **1977**, *134*, 203; c) S. C. Srivastava, A. K. Shrimal, A. Sricastava, *J. Organomet. Chem.* **1991**, *414*, 65.
[12] a) N. Sonoda, *Pure Appl. Chem.* **1993**, *65*, 699; b) Y. Yang and S. Liu, *Tetrahedron Lett.* **1999**, *40*, 4845; c) H. S. Kim, Y. J. Kim, H. Lee, S. D. Lee, C. S. Chin, *J. Catal.* **1999**, *184*, 526.
[13] a) F. Shi, Y. Deng, H. Yang, T. SiMa, *Chem. Commun*, **2001**, 345; b) F. Shi, Y. Deng, *Chem. Commun.* **2001**, 432; c) F. Shi, Y. Deng, ***J. Catal.*** **2002**, *211,* 548.
[14] a) J. E. McCusker, K. A. Abboud, L. McElwee-White, *Organometallics* **1997**, *16*, 3863; b) L. Lee, D. Chen, Y. Lin, Y. Lo, C. H. Lin, G. Lee, Y. Wang, *Organometallics* **1997**, *16,* 4636; c) J. E. McCusker, J. Logan, L. McElwee-White, *Organometallics* **1998**, *17*, 4037; d) J. E. McCusker, A. D. Main, K. S. Johnson, C. A. Grasso, L. McElwee-White, *J. Org. Chem.* **2000**, *65,* 5216.
[15] a) Y. Fu, T. Baba, Y. Ono, *J. Catal.* **2001**, *197*, 91; b) R. N. Salvatore, S. I. Shin, A. S. Nagle, K. W. Jung, *J. Org. Chem.* **2001**, *66,* 1035; c) M. Selva, P. Tundo, A. Perosa, *Tetrahedron Lett.* **2002**, *43*, 1217.

 © 2003 Wiley-VCH Verlag GmbH & Co. KGaA, Weinheim

[16] a) J. Fournier, C. Bruneau, P. H. Dixneuf, S. Lecolier, *J. Org. Chem.* **1991**, *56*, 4456; b) M. Aresta, E. Quaranta, *Tetrahedron* **1992**, *48*, 1515; c) F. Minisci, F. Coppa, F. Fontana, *J. Chem. Soc. Chem. Commun.* **1994**, 679; d) T. E. Waldman, W. D. McGhee, *J. Chem. Soc. Chem. Commun.* **1994**, 957; e) M. J. Horvath, D. Saylik, P. S. Elmes, W. R. Jackson, C. G. Lovel, K. Moody, *Tetrahedron Lett.* **1999**, *40*, 363; f) M. Abla, J. Choi, T. Sakakura, *Chem. Commun.* **2001**, 2238.

[17] a) T. Welton, *Chem. Rev.* **1999**, *99,* 2071; b) P. Wasserscheild, W. Keim, *Angew. Chem.* **2000**, *112,* 3926; *Angew. Chem. Int. Ed.* **2000**, *39,* 3772; c) W. Liu, A. G. Fadeev, B. Qi, E. Smela, B. R. Mattes, J. Ding, G. M. Spinks, J. Mazurkiewicz, D. Zhou, G. G. Wallace, D. R. MacFarlane, S. A. Forsyth, M. Forsyth, *Science* **2002**, *297*, 983; d) J. Dupont, R. F. de Souza, P. A. Z. Suarez, *Chem. Rev.* **2002**, *102*, 3667.

[18] S. Cenini, F. Ragaini, *Catalytic reductive carbonylation of organic nitro compounds*, Kluwer Academic Publishers, **1997**, pp. 60–61.

[19] a) T. Okawa, T. Aoki, H. Matsunaga, H. Igarashi, , US Patent, 5502244, **1996**; b) T. Yagii, T. Itokazu, K. Oka, Y. Tanaka, H. Kojima, K. Murata, US Patent, 5914428, **1999**.

[20] The ionic liquids were synthesized according to reported procedures (P. Bonhote, A. P. Dias, N. Papageorgiou, K. Kalyanasundaram, M. Grätzel, *Inorg. Chem.* **1996**, *35*, 1168) with slight modifications. The following ionic liquids were synthesized: 1-*n*-butyl-3-methyl imidazolium tetrafluoroborate ($BMImBF_4$), 1-*n*-butyl-3-methyl imidazolium hexafluorophosphate ($BMImPF_6$), 1-*n*-butyl-3-methyl imidazolium chloride (BMImCl) and 1-*n*-cetic-3-methyl imidazolium chloride (CMImCl). A typical procedure for the carbonylation of amines with CO_2 is as follows. 2 ml (or 2 g) of amine, 3 ml of ionic liquid and 0.05 g of base were put into an autoclave (100 ml) with a magnetic stirring bar. Carbon dioxide (60 atm, purity $>99\%$) was introduced into the reactor, and the reaction was stirred and heated at 170 °C for 4–36 h. Water (10 mL) was added into the resulting reaction mixture, and the desired resulted product precipitated out. The solid product was recovered by filtration, washing and drying. Ionic liquid containing CsOH could also be recovered and reused after the filtrate was distillated to remove water. All products were qualitatively analyzed with a HP 6890/5973 GC–MS and quantitatively analyzed with HP 1790GC (flame ion detector).

[21] When using CsOH/CMImCl, a foamy mixture resulted that could not be separated effectively, although the conversion of cyclohexylamine was analyzed by GC and found to be $>95\%$.

[22] The by-products formed in the reactions were only carbamic salts, which readily dissolved in water.

 © 2003 Wiley-VCH Verlag GmbH & Co. KGaA, Weinheim

Polymeric Coordination Rotaxane

Polymeric Rotaxane Constructed from the Inclusion Complex of β-Cyclodextrin and 4,4′-Dipyridine by Coordination with Nickel(II) Ions**

Yu Liu, Yan-Li Zhao, Heng-Yi Zhang, and Hai-Bin Song*

Nanometer-sized supramolecular assemblies created by the simple inclusion complexation of host cyclodextrins (CDs) and guest molecules have attracted more and more attention in recent years because of their potential to serve as molecular devices and molecular machines, as well as functional materials.[1–4] Indeed, CDs can be threaded on a polymer chain to form a polyrotaxane and extended to molecular tubes through the cross-linking of adjacent CD units in a polyrotaxane.[5] Furthermore, β- and γ-cyclodextrins can also be constructed into nanometer-sized molecular tubes linked by diphenylhexatrienes,[6] and conjugated polyrotaxanes can be used as building blocks to form insulated molecular wires on which α- or β-CDs are threaded.[7] We recently showed that the resulting complex formed from an organoselenium-bridged β-CD dimer and a platinum ion could be fabricated into bis(molecular tube)s through formation of a pesudorotaxane with poly(propylene glycol), and the bridged bis(β-cyclodextrin)s and calix[4]arene derivatives could also form nanometer-sized linear aggregations by simple host–guest inclusion complexation.[8–10] Molecular semiconductors can also be exploited for organic electronics and single molecules can be manipulated and incorporated into nano-engineered devices at a supramolecular level by threading a charge-transport macromolecule.[11–15] However, higher order polymeric rotaxanes fabricated by metal-ion binding to the inclusion complexes formed between CDs and aromatic molecules have not been investigated so far. Dipyridine–metal complexes have very interesting photochemical and other properties, and therefore many studies have been devoted to this topic.[16] Herein we report our investigations on two uncommon supramolecular aggregations: assembly **1**, formed from the reaction of β-CD with 4,4′-dipyridine (DPD), and polymeric rotaxane **2**, which was synthesized by coordination of **1** with Ni^{II} ions. The binding behavior of **1** and **2** was examined, both in solution and in the solid state, by ^1H NMR

[*] Prof. Dr. Y. Liu, Dr. Y.-L. Zhao, Dr. H.-Y. Zhang, Dr. H.-B. Song
Department of Chemistry
State Key Laboratory of Elemento-Organic Chemistry
Nankai University
Tianjin, 300071 (P. R. China)
Fax: (+86) 22-2350-3625 or 2350-4853
E-mail: yuliu@public.tpt.tj.cn

[**] This work was supported by the NSFC (Nos. 29992590-8 and 20272028), the Tianjin Natural Science Foundation (No. 013613511), and the Foundation of Ministry of Education of China. We also thank Professor Yoshihisa Inoue at Osaka University for helpful advice about the polymeric rotaxane.

Supporting information for this article is available on the WWW under http://www.angewandte.org or from the author.

 © 2003 Wiley-VCH Verlag GmbH & Co. KGaA, Weinheim DOI: 10.1002/anie.200351128

spectroscopy, X-ray crystallography, induced circular dichroism, powder X-ray diffraction studies, thermogravimetric (TG) and differential thermal analysis (DTA), scanning tunneling microscopy (STM), and transmission electron microscopy (TEM). The binding behavior of the supramolecular assembly formed by the molecular recognition of the host and guest in solution and in the solid state is of particular interest, since the inclusion complex and the polymeric rotaxane display different photophysical behavior. The present investigations have revealed that the resulting complex of CDs with guest molecules is the first step in the formation of a polymeric rotaxane, which provides access to coordination polymeric supramolecules with CDs, and will serve to further our understanding of this developing, but less investigated, area of electroactive organic materials that contain CDs and a coordination linkage.

The polymeric rotaxane **2** was prepared according to the procedures shown in Figure 1. The 1:1 **1**:Ni^{II} coordination in **2** was confirmed by the results of elemental analyses and UV/Vis titration experiments. Direct evidence for the formation of the supramolecular assembly **1** from β-CD and DPD was

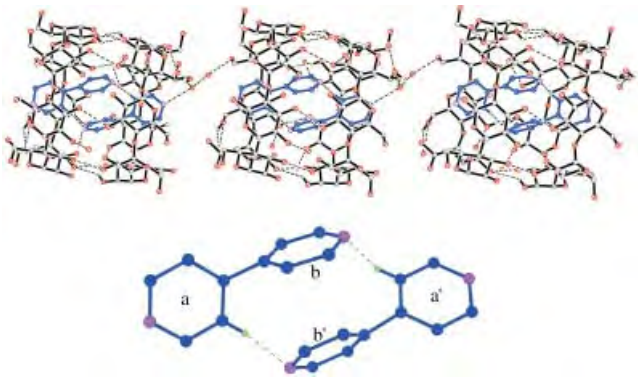


Figure 2. X-ray crystal structure showing the head-to-head channel structure of **1** (top) and the DPD backbones (bottom). The dihedral angles between the plane of the DPD molecular axis and the heptagons composed of seven O atoms of the β-CD are 71.1° and 63.3°, respectively. The DPD molecules are colored by atom type: blue: carbon atoms, pink: nitrogen atoms, and blue: chemical bonds. The CD dimers are also colored by atom type: gray: carbon atoms, red: oxygen atoms, and green: hydrogen atoms involved in hydrogen-bonding interactions.

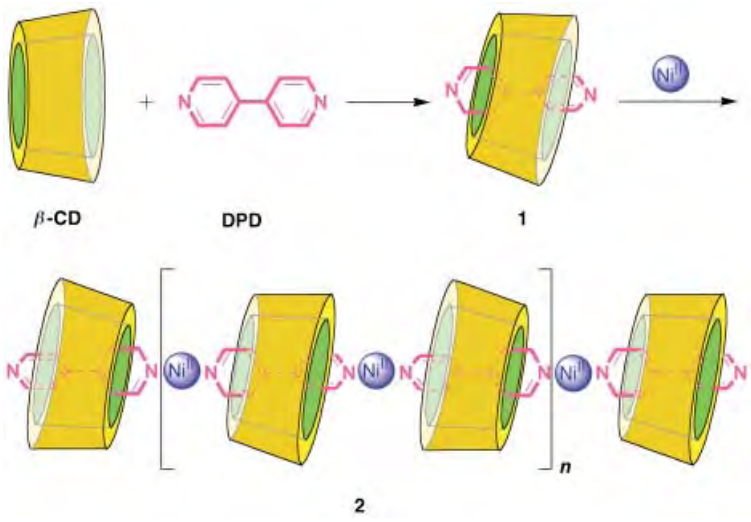


Figure 1. Schematic representation of the formation of **1** and **2**.

obtained in the solid state.[17] As shown in Figure 2, two DPD molecules are embedded into two β-CD cavities in different directions to form a head-to-head dimer arrangement (space group $P\bar{1}$), which is entirely different from the general inclusion complexes formed with β-CD in the solid state.[18] The aromatic ring *a* (or *a*′) of every DPD molecule in the self-assembled dimers is deeply included in a β-CD cavity and another aromatic ring *b* (or *b*′) is only shallowly embedded into the cavity, with a dihedral angel of 94.5° (or 75.6°) between rings *a* (or *a*′) and *b* (or *b*′). This unique assembly behavior is attributed to the cooperative interactions of 13 hydrogen bonds (11 of them come from the hydroxy groups on the secondary sides of the β-CDs and two of them involve a nitrogen atom in the *b* (and *b*′) ring and a *meta*-hydrogen atom in the *a*′ (and *a*) ring) and π-π stacking of two aromatic rings in a face-to-face arrangement (dihedral angel: 42.2°, centroid separation between *b* and *b*′: 3.634 Å) which fix the orientation of the DPD molecules and makes dimer aggregation possible. Interestingly, the head-to-head dimers can further self-assemble to form polymeric supramolecules through formation of hydrogen bonds between dimers using the nitrogen atom in the *a*′ ring.

The binding behavior of **1** and **2** in solution was examined by ^{1}H NMR spectroscopy carried out at 25 °C in D_2O. A change in the chemical shift of all the protons of the DPD molecule is observed in the presence of β-CD relative to a free molecule: the *meta* protons shift upfield (ca. 0.02 ppm) and the *ortho* protons shift downfield (ca. 0.09 ppm), which indicates that a complex has formed between DPD and β-CD. Relative to complex **1**, the *meta* protons in **2** were deshielded by about 0.09 ppm and the *ortho* protons were shielded by about 0.02 ppm in the presence of Ni^{II} ions, thus suggesting that the nitrogen atoms must coordinate to the Ni^{II} ions.[19] The IR spectra of **1** and **2** showed that the C=N stretching vibration in DPD is shifted from 1595 to 1608 cm^{-1}, which could also be ascribed to the coordination of $NiCl_2$.

The induced circular dichroism (ICD) spectra[20] of **1** and **2** were also measured. As can be seen from Figure 3, the circular dichroism spectrum of **1** showed a strong positive Cotton effect, which corresponds to the ^1L_a band at 241 nm ($\Delta\varepsilon = 0.70\ dm^{-3}mol^{-1}cm^{-1}$) and a negative Cotton effect for the ^1L_b band at 269 nm ($\Delta\varepsilon = -0.23\ dm^{-3}mol^{-1}cm^{-1}$). According to the pioneering studies of Kajtár et al.[21] and Harata and Uedaira[22] on the ICD phenomena of cyclodextrin complexes, we can deduce that the DPD moiety of **1** has entered into the β-CD cavity with a slightly acclivitous orientation, which is consistent with that seen in the crystal structure of **1**. Interestingly, the DPD molecule in the β-CD cavity tethered by a Ni^{II} ion gives an opposite ICD signal: a major negative Cotton effect at 232 nm ($\Delta\varepsilon =$

 © 2003 Wiley-VCH Verlag GmbH & Co. KGaA, Weinheim

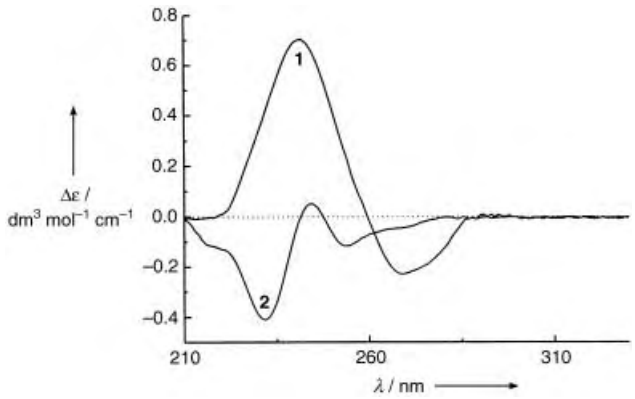


Figure 3. Circular dichroism spectra of **1** (7.9×10^{-5} mol dm^{-3}) and **2** (5.9×10^{-5} mol dm^{-3}) in aqueous solution at 25 °C.

-0.41 dm^{-3}mol^{-1}cm^{-1}) and a moderate negative Cotton effect at 254 nm ($\Delta\varepsilon = -0.12$ dm^{-3}mol^{-1}cm^{-1}) is observed. The opposite ICD signals observed between **1** and **2** indicate that not only do the DPD molecules still lie in the cavity of β-CDs after the formation of **2**, but also that the DPD moiety of **2** may become more acclivitous in the cavity of β-CDs after coordination of Ni^{II} ions.

The powder X-ray diffraction patterns[8,23] of β-CD, DPD, **1**, and **2** were obtained using a Rigaku D/max-2500 diffractometer with CuKα radiation. The diffractogram of β-CDs shows a characteristic reflection at $2\theta = 12.4°$($d = 7.13$ Å) and that of DPD shows a characteristic reflection at $2\theta = 12.5°$($d = 7.06$ Å; see Supporting Information). However, these reflections are changed to $2\theta = 11.8°$ ($d = 7.49$ Å) and $2\theta = 12.1°$ ($d = 7.30$ Å) in the diffractogram of complex **1,** thus indicating that the arrangement of the cyclodextrin in **1** is changed by introduction of DPD. This result is consistent with the arrangement found in the crystal structure. Interestingly, the same characteristic reflection at $2\theta = 12.4°$ ($d = 7.11$ Å) appears again in the diffractogram of **2**, which shows that the coordination of Ni^{II} ions makes the cyclodextrin and DPD reorient upon construction of the polymeric rotaxane **2**.

The thermal stabilities of **1** and **2** were measured by TG and DTA. The TG results showed that the decomposition point of polymeric rotaxane **2** is higher than that of complex **1**. The decomposing temperatures of **1** and **2** are about 244 and 253 °C, respectively, which may be ascribed to the dissociation of β-CD and DPD. The DTA analyses showed an endothermic peak at about 333 °C for **1** and an exothermic peak at about 355 °C for **2**, which represent the temperatures of decomposition of the β-CD. Therefore, these higher thermal dissociation temperatures clearly indicated that the coordination of Ni^{II} ions played a stabilizing role in the molecular aggregation of **2**.

Scanning tunneling microscopy (STM) has become a convenient and widely employed method for the elucidation of the microstructures of supramolecular aggregates.[6,9,10,24,25] The STM image of **2** (Figure 4)[26] shows a regular arrangement of chains of supramolecules on a graphite substrate, which indicates that the polymeric rotaxanes are formed through the coordination of β-CD–DPD complexes with Ni^{II} ions. From the size and shape of the patterns, one bright

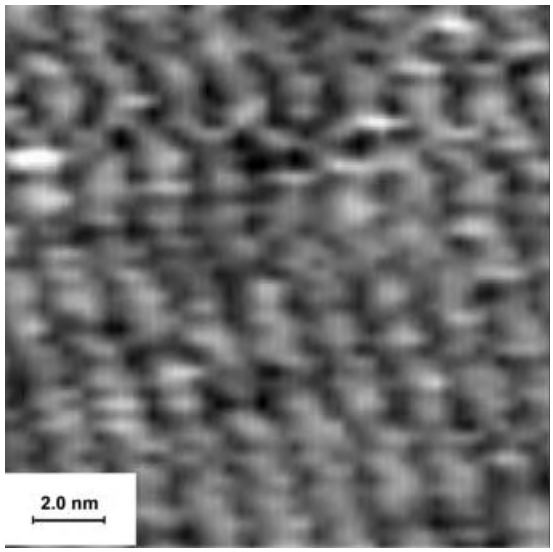


Figure 4. STM image of polymeric rotaxane **2**.

dot corresponds to a β-CD unit, which lies with its longitudinal axis parallel to the surface. The average distance between two adjacent cyclodextrin units in a polymeric rotaxane is about 0.9 nm, while the distance between two adjacent polymeric rotaxanes is roughly 1.9 nm, which results in noticeable topologies.

Transmission electron microscopy (TEM) has also been performed to provide further insight into the size and shape of the aggregates on drying. For visualization by TEM, a sample was prepared by placing one drop of the solution of the polymeric rotaxane **2** onto a carbon-coated copper grid, and then a palladium–iridium alloy was added to thicken the drop and make the images clearer. Thus, the TEM micrographs have only been used to measure the length of the molecular assembly. The detailed TEM micrograph shown in Figure 5 illustrates one of the polymeric rotaxanes **2** with a length of approximately 450 nm.

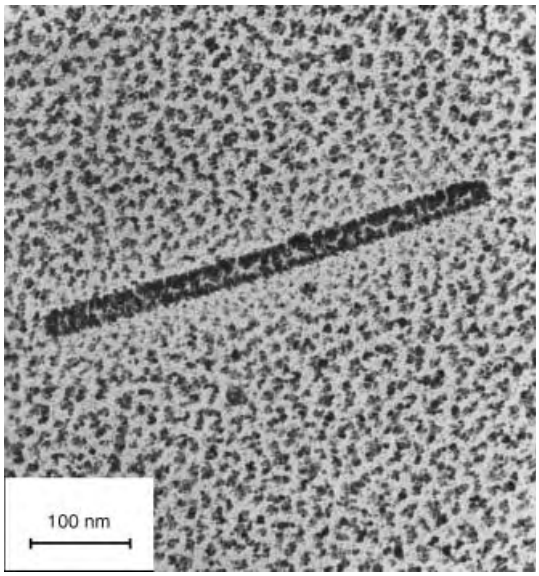


Figure 5. TEM image of polymeric rotaxane **2**.

 © 2003 Wiley-VCH Verlag GmbH & Co. KGaA, Weinheim

In summary, two novel polymeric supramolecules have been synthesized by the inclusion complexation of DPD in β-CD and the subsequent coordination of the complex with nickel ions in aqueous solution. The results obtained further suggested that β-CDs could provide a simple means for linking organic molecules into linear-shaped aggregates, which could be used as connectors for designing novel functional materials and which could possess the potential to serve as molecular devices and molecular machines. Endeavors to explore the application of chain supramolecules are currently in progress.

Experimental Section

1: A mixture of β-cyclodextrin (1 mmol) and 4,4′-dipyridine (DPD, 1 mmol) was allowed to react in aqueous solution (60 mL) with stirring at 30 °C for 5 h. The precipitate formed was filtrated to give a white powder. The crude product was then dissolved in hot water to make a saturated solution, which was cooled to room temperature. After removing the precipitates by filtration, a small amount of water was added to the filtrate. The resultant solution was kept at room temperature for a week. The colorless crystal of **1** that formed was collected along with its mother liquor for X-ray crystallographic analysis; yield 78 %. FTIR (KBr): $\tilde{\nu}$ = 3341, 2929, 1595, 1534, 1414, 1365, 1332, 1299, 1241, 1155, 1080, 1032, 944, 851, 805, 756, 611, 578, 528 cm^{-1}; ^1H NMR (300 MHz, D_2O, tetramethylsilane (TMS)): δ = 3.37–3.69 (m, 42H), 4.88–4.90 (d, 7H), 7.53–7.55 (d, 4H), 8.52–8.54 ppm (d, 4H); elemental analysis calcd for $C_{52}H_{78}O_{35}N_2 \cdot 7H_2O$: C 44.07, H 6.54; N 1.98 %; found: C 43.73, H 6.04, N 2.37 %.

2: An aqueous solution (10 mL) of nickel chloride ($NiCl_2 \cdot 6H_2O$, 0.1 mmol) was added dropwise to an aqueous solution (20 mL) of **1** (0.1 mmol). The resultant mixture was then stirred at 40 °C for 7 h. The solvent was evaporated under a reduced pressure, and the precipitate formed was filtered off to give a green powder. The crude product was recrystallized and purified from water and dried in vacuo to give sample **2**; yield 35 %. FTIR (KBr): $\tilde{\nu}$ = 3358, 2930, 1608, 1535, 1491, 1415, 1332, 1221, 1156, 1079, 1031, 945, 855, 809, 756, 707, 577, 531 cm^{-1}; ^1H NMR (300 MHz, D_2O, TMS): δ = 3.39–3.81 (m, 42H), 4.90–4.91 (d, 7H), 7.62–7.64 (d, 4H), 8.50–8.52 ppm (d, 4H); elemental analysis calcd for $(C_{52}H_{78}O_{35}N_2NiCl_2 \cdot 10H_2O)_n$: C 39.01, H 6.17, N 1.75 %; found: C 39.27, H 6.00, N 1.51 %.

Received: February 7, 2003
Revised: March 19, 2003 [Z51128]

Keywords: coordination modes · cyclodextrins · nickel · polymers · rotaxanes

[1] F. M. Raymo, J. F. Stoddart, *Chem. Rev.* **1999**, *99*, 1643–1663.
[2] A. Harada, *Acc. Chem. Res.* **2001**, *34*, 456–464.
[3] B. H. Hong, S. C. Bae, C.-W. Lee, S. Jeong, K. S. Kim, *Science* **2001**, *294*, 348–351.
[4] D. T. Bong, T. D. Clark, J. R. Granja, M. R. Ghadiri, *Angew. Chem.* **2001**, *113*, 1016–1041; *Angew. Chem. Int. Ed.* **2001**, *40*, 988–1011.
[5] a) A. Harada, J. Li, M. Kamachi, *Nature* **1992**, *356*, 325–327; b) A. Harada, J. Li, M. Kamachi, *Nature* **1993**, *364*, 516–518.
[6] G. Li, L. B. McGown, *Science* **1994**, *264*, 249–251.
[7] a) P. N. Taylor, M. J. O'Connell, L. A. McNeill, M. J. Hall, R. T. Aplin, H. L. Anderson, *Angew. Chem.* **2000**, *112*, 3598–3602; *Angew. Chem. Int. Ed.* **2000**, *39*, 3456–3460; b) F. Cacialli, J. S. Wilson, J. J. Michels, C. Daniel, C. Silva, R. H. Friend, N. Severin, P. Samorì, J. P. Rabe, M. J. O'Connell, P. N. Taylor, H. L. Anderson, *Nat. Mater.* **2002**, *1*, 160–164.
[8] Y. Liu, C.-C. You, H.-Y. Zhang, S.-Z. Kang, C.-F. Zhu, C. Wang, *Nano Lett.* **2001**, *1*, 613–616.
[9] Y. Liu, L. Li, H.-Y. Zhang, Y.-L. Zhao, X. Wu, *Macromolecules* **2002**, *35*, 9934–9938.
[10] Y. Liu, L. Li, Z. Fan, H.-Y. Zhang, X. Wu, S.-X. Liu, X.-D. Guan, *Nano Lett.* **2002**, *2*, 257–261.
[11] C. P. Collier, J. O. Jeppesen, Y. Luo, J. Perkins, E. W. Wong, J. R. Heath, J. F. Stoddart, *J. Am. Chem. Soc.* **2001**, *123*, 12632–12641.
[12] S. A. Nepogodiev, J. F. Stoddart, *Chem. Rev.* **1998**, *98*, 1959–1976.
[13] S. S. Zhu, T. M. Swager, *J. Am. Chem. Soc.* **1997**, *119*, 12568–12577.
[14] M. J. Maclachlan, A. Rose, T. M. Swager, *J. Am. Chem. Soc.* **2001**, *123*, 9180–9181.
[15] A. D. Shukla, H. C. Bajaj, A. Das, *Angew. Chem.* **2001**, *113*, 460–462; *Angew. Chem. Int. Ed.* **2001**, *40*, 446–448.
[16] U. S. Schubert, C. Eschbaumer, *Angew. Chem.* **2002**, *114*, 3016–3050; *Angew. Chem. Int. Ed.* **2002**, *41*, 2892–2926.
[17] The X-ray intensity data of **1** were collected on a standard Siemens SMART CCD area detector system equipped with a normal-focus molybdenum-target X-ray tube (λ = 0.71073 Å) operated at 2.0 kW (50 kV, 40 mA) and a graphite monchromator at T = 298 K. Crystal data for **1**: $C_{104}H_{194}N_4O_{89}$: M_r = 2924.63 (including water molecules); dimensions = 0.36 × 0.34 × 0.30 mm; triclinic; space group: $P\bar{1}$; unit cell dimensions: a = 15.364(3), b = 15.497(3), c = 18.115(3) Å, V = 3705.0(11) $Å^3$; Z = 1; ρ_{calcd} = 1.311 $g\,cm^{-3}$; data/restraints/parameters 15431/39/1649. Final R indices $R1$ = 0.0907, $wR2$ = 0.2432. The structures were solved by using direct methods and refined by employing full-matrix least squares on F^2 (Siemens, SHELXTL, version 5.04). CCDC-203243 contains the supplementary crystallographic data for this paper. These data can be obtained free of charge via www.ccdc.cam.ac.uk/conts/retrieving.html (or from the Cambridge Crystallographic Data Centre, 12 Union Road, Cambridge CB2 1EZ, UK; fax: (+44) 1223-336-033; or deposit@ccdc.cam.ac.uk).
[18] K. Harata, *Chem. Rev.* **1998**, *98*, 1803–1827.
[19] a) R. S. Wylie, D. H. Macartney, *J. Am. Chem. Soc.* **1992**, *114*, 3136–3138; b) Y. Liu, Y. Chen, L. Li, H.-Y. Zhang, S.-X. Liu, X.-D. Guan, *J. Org. Chem.* **2001**, *66*, 8518–8527.
[20] Circular dichroism (CD) and UV/Vis spectra were recorded in a conventional quartz cell (light path 10 nm) on a JASCO J-715S spectropolarimeter or a Shimadzu UV-2401PC spectrophotometer equipped with a PTC-348WI temperature controller to keep the temperature at 25 °C.
[21] M. Kajtár, C. Horvath-Toro, E. Kuthi, J. Szejtli, *Acta Chim. Acad. Sci. Hung.* **1982**, *110*, 327–355.
[22] K. Harata, H. Uedaira, *Bull. Chem. Soc. Jpn.* **1975**, *48*, 375–378.
[23] a) A. Harada, S. Suzuki, M. Okada, M. Kamachi, *Macromolecules* **1996**, *29*, 5611–5614; b) H. Okumura, Y. Kawaguchi, A. Harada, *Macromolecules* **2001**, *34*, 6338–6343.
[24] H. Shigekawa, K. Miyake, J. Sumaoka, A. Harada, M. Komiyama, *J. Am. Chem. Soc.* **2000**, *122*, 5411–5412.
[25] S. De Feyter, A. Gesquiè, M. M. Abdel-Mottaleb, P. C. M. Grim, F. C. De Schryver, C. Meiners, M. Sieffert, S. Valiyaveettil, K. Müllen, *Acc. Chem. Res.* **2000**, *33*, 520–531.
[26] STM experiments were performed by using a DS-89S instrument with a W tip, and were carried out with a sample bias voltage of +300 mV. All images were recorded in the constant-current mode at 2.10 nA. An aqueous solution of sample **2** was prepared at a concentration of 5.5×10^{-5} M and dripped onto a freshly prepared highly ordered pyrolytic graphite surface at room temperature. The sample was then dried in a vacuum for 30 minutes.

 © 2003 Wiley-VCH Verlag GmbH & Co. KGaA, Weinheim

Solid-State Sol–Gel Biosensors

Immunoglobulin–Polydiacetylene Sol–Gel Nanocomposites as Solid-State Chromatic Biosensors

Iqbal Gill and Antonio Ballesteros*

Conjugated polydiacetylenes (PDAs) derived from the polymerization of 1,3-diacetylenic acid derivatives have attracted great interest in the domain of sensors by virtue of the intense bichromatic properties of their conjugated ene-yne backbones and the ease with which molecular recognition platforms can be coupled with PDA-mediated signal transduction to create colorimetric sensors.[1] Thus, bichromic self-assembled PDA structures, such as monolayers, bilayers, and liposomes displaying synthetic and biological receptors, undergo dramatic color changes corresponding to a transition from a highly conjugated "blue form" of the PDA to a less-conjugated "red form" in response to the molecular recognition event, without the requirement for any co-reagents.[1] Indeed, PDA-based systems have proved to be versatile and sensitive sensors for a wide range of analytes including cations, arenes, polyols, microbial toxins, oligopeptides, proteins, antibodies, and even bacteria and viruses.[2] However, most studies have utilized solution-phase sensing, which has necessarily limited the wider application of PDAs, as many sensor and array devices require solid-state materials which are stable, reusable, and amenable to large-scale fabrication.[3] Efforts have been made to achieve this goal by depositing PDA monolayers and bilayers onto glass, quartz, silicon, and polystyrene substrates as well as by entrapping them within silica sol–gels,[2h,j,l,4] but the resultant materials have been compromised by limited stability and processability, or long response times and reduced sensitivity to analytes, and as a result the need for a generic, stable, and fast-response solid-state PDA sensor platform remains.

Herein it is shown that highly responsive solid-state chromatic sensors can be produced by encapsulating PDA–phospholipid vesicles modified with immunoglobulin (IgG) in hybrid sol–gel materials composed of silica and functionalized siloxanes. The materials produced are rugged and processable and can be fabricated as monoliths, thick films, and microarrays, and furnish colorimetric biosensors that are sensitive and show short response times.

[*] Dr. I. Gill
BioSynTech
512 Franklin Avenue, Nutley, NJ 07110 (USA)
Fax: (+1) 973-542-0383
E-mail: iqbalgill@yahoo.com
Prof. Dr. A. Ballesteros
Department of Biocatalysis
CSIC Institute of Catalysis
Campus UAM, Cantoblanco, 28049 Madrid (Spain)

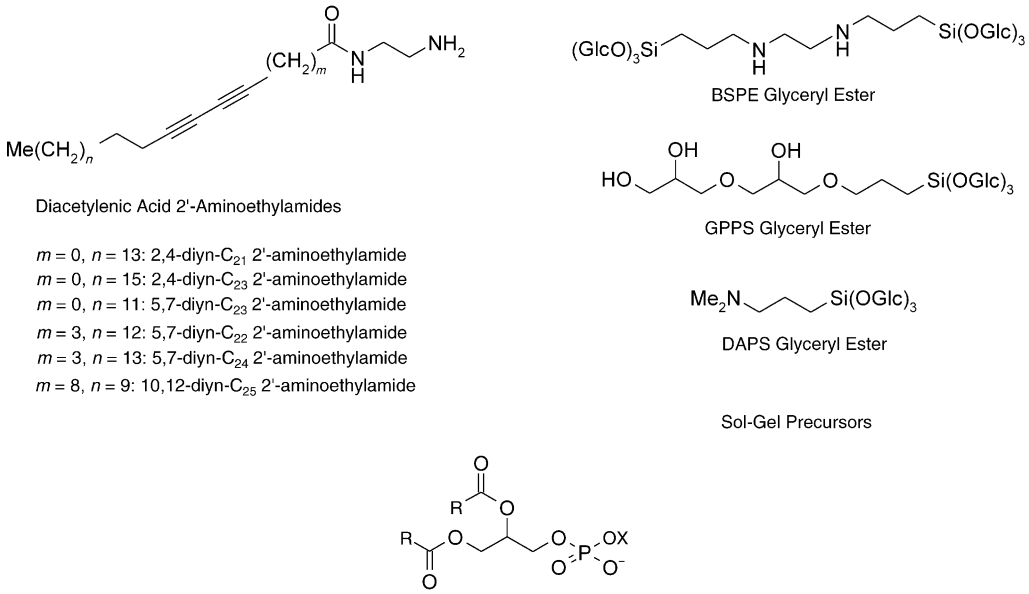
Supporting information for this article is available on the WWW under http://www.angewandte.org or from the author.

In view of the efficient encapsulation of sensitive biological materials in functionalized, hydrophilic siloxane sol–gels,[3a–c,5] we explored whether such polymers could be used for the entrapment of liposomes composed of PDA and biological materials, and whether the trapped conjugates would efficiently undergo the required blue-to-red color transitions upon challenge with the corresponding analytes. For this purpose, IgGs including anti-human α-fetoprotein, anti-*E. coli* β-galactosidase, anti-bovine serum albumin (anti-BSA), and anti-yeast alkaline phosphatase were conjugated (reduced IgGs were coupled using *N*-sulfosuccinimidyl-4-(maleimidomethyl)cyclohexane-1-carboxylate) to liposomes composed of $21{:}2\Delta^{2a,4a}$, $23{:}2\Delta^{2a,4a}$, $22{:}2\Delta^{5a,7a}$, $23{:}2\Delta^{5a,7a}$, $24{:}2\Delta^{5a,7a}$, and $25{:}2\Delta^{2a,4a}$ acid 2′-aminoethylamides and various glyceryl, ethanolamine, and choline phospholipids (Scheme 1). The conjugates were polymerized to furnish blue-form IgG-PDA-phospholipid vesicles, and these were encapsulated in sol–gels composed of silica, 3-(3′-glyceroxy-2′-hydroxyprop-1′-oxy)propylsiloxane (GPPS), *N*,*N*-dimethyl-3-aminopropylsiloxane (DAPS), *N*,*N*′-bis(3-siloxypropyl)ethylenediamine (BSPE), and poly(vinyl alcohol) (PVA; Scheme 1). Silica was chosen for its mechanical rigidity and high encapsulation efficiency, while the functional siloxanes and PVA were selected for their high biocompatibility together with their ability to form highly mesoporous sol–gel polymer frameworks.[5,6]

Encapsulation of the IgG-PDA-phospholipid vesicles provided transparent blue, mesoporous composites which were deposited as thick films onto cellulose, nylon, polycarbonate, alumina, silica, and glass (Figure 1). Only slight color changes (< 7%) were observed upon sol–gel entrapment of the blue-form vesicles (Figure 2a), which indicates that encapsulation did not have a sufficient effect on the vesicle structure so as to trigger switching of the PDA conformation and that the liposomes were largely encapsulated in their native state. More importantly, exposure of the IgG-PDA sol–gels to antigens (α-fetoprotein, β-galactosidase, BSA, and phosphatase) resulted in the blue ($\lambda_{max} = 620$–670 nm) to red ($\lambda_{max} = 510$–560 nm) color changes characteristic of IgG-PDA-phospholipid solutions (Figure 1 and 2a), which demonstrates that both the biomolecular recognition of IgG and structural transition functions of PDA were preserved upon entrapment. In contrast, IgG-free PDA solutions and sol–gels underwent negligible (< 9%) color changes when exposed to antigens.

Libraries of 90–270 compositions were prepared for each immunosensor by varying the type and amount of diacetylene, phospholipid, and sol–gel precursor. These mixtures were then screened for the rate and extent of colorimetric response (CR), where CR is defined as $CR = \frac{(B_0 - B_1)}{B_0}$, in which $B = \frac{A_{Blue}}{(A_{Blue} + A_{Red})}$, B_0 and B_1 are the pre- and postexposure values, and $A_{Blue/Red}$ is the blue/red absorbance.[2m] It should be noted that a CR value of 0.10–0.15 (namely, 10–15% of the maximum possible colorimetric response) was usually readily discernible by the naked eye. Screenings showed that liposomes containing 40–60, 10–30, and 10 mol% of tricosa-2,4-diynoic acid ($23{:}2\Delta^{2a,4a}$) 2′-aminoethylamide, dimyristoylphosphocholine (DMPC), and linoleoylpalmitoylphosphati-

 © 2003 Wiley-VCH Verlag GmbH & Co. KGaA, Weinheim DOI: 10.1002/anie.200351290



Scheme 1. Structures of lipids and sol–gel precursors used for forming IgG–PDA sol–gels.

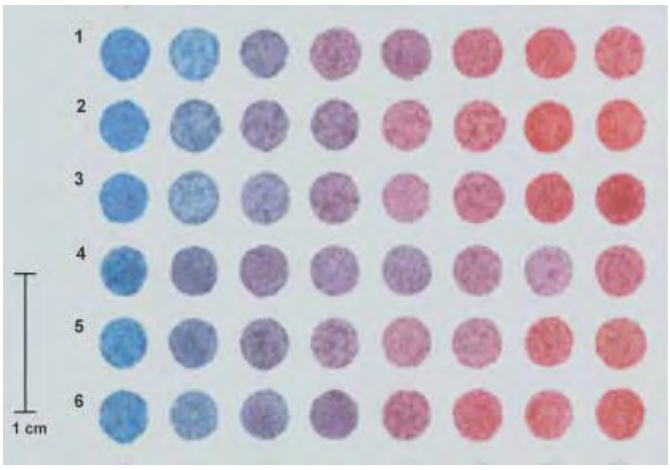


Figure 1. Anti-*E. coli* β-galactosidase IgG-PDA-liposome sol–gel spot array. Lanes 1–6 correspond to composites incorporating PDAs derived from 2,4-diyn-C_{21}, 2,4-diyn-C_{23}, 5,7-diyn-C_{22}, 5,7-diyn-C_{23}, 5,7-diyn-C_{24}, and 10,12-diyn-C_{25} acids, respectively. Vertical lanes (left to right) correspond to antigen concentrations of 0, 10, 20, 30, 40, 50, 70, and 100 ng mL^{-1}. Liposomes were formed from 60:30:10 mol% of diacetylenic 2′-aminoethylamide:DMPC:LPPE and were loaded with about 0.01 mg of IgG per mg of lipid. Liposomes were polymerized (UV, 254 nm, 1–2 min), mixed with sol–gel precursor, then spotted (ca. 100 μL) onto cellulose. The array was aged in a closed container at 4 °C for 40 h, then washed with phosphate buffer (50 mM, pH 7), before exposure to antigen (100 μL per spot) at 20 °C for 10 min. The sol–gels consisted of 40:10:10:30:10 (% w/w) silica-GPPS-DAPS-BSPE-PVA and held 0.78 mg of vesicles and 6.5 μg of IgG per spot.

dylethanolamine (LPPE), respectively, provided the most responsive and stable conjugates, and that a mixture of silica (30–40% w/w), GPPS (20–30% w/w), DAPS (5% w/w), BSPE (10–35% w/w), and PVA (10–15% w/w) gave the best balance of colorimetric response, stability, and mechanical properties for the final composites. The composites provided CR rates that were about two to threefold lower than those of the liposome solutions, which led to a CR value of 0.5 after about 1.1–1.6 min versus 0.5–0.6 min for the liposome solutions, and the maximal responses were about 68–76% compared to 89–92% (Figure 2b and 2c). Thus, encapsulation decreased the response rate as well as the total response, as expected from diffusional limitations and the steric restrictions which inevitably result from entrapment in sol–gel matrices.[5]

Despite encapsulation in a polymer framework, the recognition–transduction responses of the native IgG-PDA-phospholipid liposomes were preserved to a large degree in the composites, and antigens were readily detected down to 200–400 pg mL^{-1} with a corresponding response saturation at 1.0–1.4 ng mL^{-1}. This result compares favorably with the detection level of about 50–100 pg mL^{-1} and response saturation at 0.8–1.0 ng mL^{-1} that were observed for vesicle solutions (Figure 2d). Importantly, the IgG-PDA sol–gel materials showed little cross-reactivity, with CR values of less than 0.1 generally being observed upon challenge with proteins other than the corresponding antigens (Figure 2b and 2d). Also, interestingly, the performances of composites

 © 2003 Wiley-VCH Verlag GmbH & Co. KGaA, Weinheim

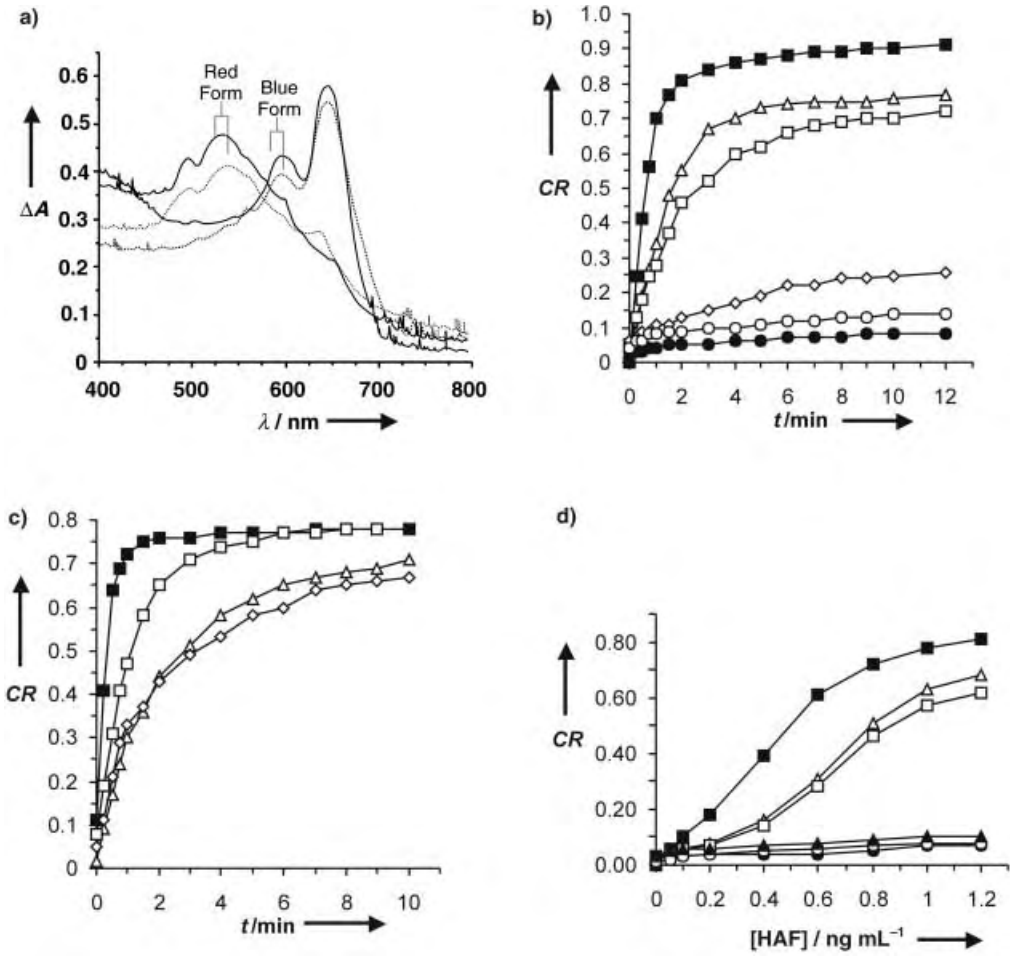


Figure 2. a) UV/Vis spectra of blue- and red-form IgG-poly(2,4-diyn-C_{23}) liposomes: aqueous (upper, solid lines) and sol–gel encapsulated (lower, broken lines). b) Colorimetric responses (*CR*) of aqueous and encapsulated anti-human α-fetoprotein IgG-poly(2,4-diyn-C_{23}) liposomes: ■: aqueous liposomes, exposed to α-fetoprotein at 1.5 ng mL^{-1}; liposomes in aged (closed container, 40 h, 4 °C); △: wet 35:20:5:30:10 (% w/w) silica-GPPS-DAPS-BSPE-PVA sol–gel, exposed to α-fetoprotein at 1.5 ng mL^{-1}; □: liposomes in sol–gels aged and dried (open container, 40 h, 4 °C), exposed to α-fetoprotein at 1.5 ng mL^{-1}; ◇: liposomes in aged, wet pure silica sol–gel, exposed to α-fetoprotein at 1.5 ng mL^{-1}; ○: liposomes in aged, wet 35:20:5:30:10 (% w/w) silica-GPPS-DAPS-BSPE-PVA sol–gel exposed to 15 ng mL^{-1} of BSA; ●: control PDA sol–gel without IgG. c) Colorimetric responses of IgG-poly(2,4-diyn-C_{23}) liposomes encapsulated in aged (closed container, 40 h, 4 °C), wet 35:20:5:30:10 (% w/w) silica-GPPS-DAPS-BSPE-PVA sol–gels: ■: anti-α-fetoprotein IgG-PDA liposomes; □: anti-*E. coli* β-galactosidase IgG-PDA liposomes; △: anti-BSA IgG-PDA liposomes; ◇: anti-alkaline phosphatase IgG-PDA liposomes. The materials were incubated with the corresponding antigens at 10 ng mL^{-1}. d) Colorimetric response of IgG-poly(2,4-diyn-C_{23}) liposomes to α-fetoprotein concentration, after 10 min incubation: ■: aqueous anti-human α-fetoprotein IgG-PDA liposomes; △: aqueous anti-human α-fetoprotein IgG-PDA liposomes in aged (closed container, 40 h, 4 °C), wet 35:20:5:30:10 (% w/w) silica-GPPS-DAPS-BSPE-PVA sol–gel; □: aqueous anti-human α-fetoprotein IgG-PDA liposomes in aged and dried (open container, 40 h, 4 °C) sol–gel; ▲: anti-BSA IgG-PDA in aged, wet 35:20:5:30:10 (% w/w) silica-GPPS-DAPS-BSPE-PVA sol–gel exposed to α-fetoprotein; ○: anti-β-galactosidase IgG-PDA in aged, wet 35:20:5:30:10 (% w/w) silica-GPPS-DAPS-BSPE-PVA sol–gel exposed to α-fetoprotein; ●: control PDA-sol–gel without IgG. Abbreviations: HAF, human α-fetoprotein.

that were aged and dried (at 4 °C, 40 h, ca. 9–14 % w/w water content) were not greatly diminished over those of the aged, wet composites (at 4 °C, 40 h, ca. 35–40 % w/w water content; Figure 2b and 2d). This result indicates the protective influence of the functional siloxane sol–gel network in providing an open hydrophilic framework that enables the efficient ingress and recognition of antigens at the IgG-PDA liposome surface, and also allows for the rapid and extensive structural transition of the PDA polymer to the red form. In contrast, entrapment of the vesicles in aged, wet pure silica sol–gels (aged at 4 °C, 40 h, ca. 40 % w/w water content) resulted in materials which were considerably less responsive, and whose maximal CR values were in the region of 0.2–0.35 (Figure 2b), thus underscoring the importance of the physicochemistry of the sol–gel matrix. It should also be noted that the hybrid composites furnished semi-rigid or flexible solids which were dimensionally stable and mechanically robust and could be cast as monoliths or applied as thick-film coatings on cellulose, nylon, polycarbonate, silica, alumina, and glass.

The successful fabrication of reagentless solid-state IgG-PDA sol–gel biosensors, and their ease of production, together with the availability of novel PDAs,[1c] facile interfacing of receptors with PDAs,[1,2] and recent advances

 © 2003 Wiley-VCH Verlag GmbH & Co. KGaA, Weinheim

in silica–PDA composites[7] and hybrid and templated sol–gel polymers,[8] offers a potentially simple and generic route to solid-state colorimetric sensor and microarray platforms.

Received: February 27, 2003 [Z51290]

Keywords: biosensors · liposomes · nanocomposites · polydiacetylenes · sol–gel processes

[1] a) R. Jelinek, S. Kolusheva, *Biotechnol. Adv.* **2001**, *19*, 109–118; b) R. Jelinek, *Drug Develop. Res.* **2000**, *50*, 497–501; c) A. Sarkar, S. Okada, H. Matsuzawa, H. Matsuda, H. Nakanishi, *J. Mater. Chem.* **2000**, *10*, 819–828; d) S. Okada, S. Peng, W. Spevak, D. H. Charych, *Acc. Chem. Res.* **1998**, *31*, 229–239; e) D. H. Charych, J. O. Nagy, W. Spevak, M. Bednarski, *Science* **1993**, *261*, 585–588.

[2] a) S. Kolusheva, R. Kafri, M. Katz, R. Jelinek, *J. Am. Chem. Soc.* **2001**, *123*, 417–422; b) Z. Ma, J. Li, L. Jiang, *Langmuir* **2000**, *16*, 7801–7804; c) S. Kolusheva, T. Shahal, R. Jelinek, *J. Am. Chem. Soc.* **2000**, *122*, 776–780; d) S. Kolusheva, L. Boyer, R. Jelinek, *Nature Biotechnol.* **2000**, *18*, 225–227; e) S. Kolusheva, T. Shahal, R. Jelinek, *J. Am. Chem. Soc.* **2000**, *122*, 776–780; f) S. Kolusheva, T. Shahal, R. Jelinek, *Biochemistry* **2000**, *39*, 15851–15859; g) S. Y. Okada, R. Jelinek, D. Charych, *Angew. Chem.* **1999**, *111*, 678–682; *Angew. Chem. Int. Ed.* **1999**, *38*, 655–659; h) D. L. Dermody, Y. Lee, T. Kim, R. M. Crooks, *Langmuir* **1999**, *15*, 8435–8440; i) S. Wang, R. M. Leblanc, *Biochim. Biophys. Acta* **1999**, *1419*, 307–312; j) M. Niwa, T. Ishida, T. Kato, N. Higashi, *J. Mater. Chem.* **1998**, *8*, 1697–1701; k) J. J. Pan, D. H. Charych, *Langmuir* **1997**, *13*, 1365–1367; l) Q. Cheng, R. C. Stevens, *Chem. Phys. Lipids* **1997**, *87*, 41–53; m) D. H. Charych, Q. Cheng, A. Reichert, G. Kuzeimko, M. Stroh, J. O. Nagy, W. Spevak, R. C. Stevens, *Chem. Biol.* **1996**, *3*, 113–120; m) W. Spevak, J. O. Nagy, D. H. Charych, *Adv. Mater.* **1995**, *7*, 85–89.

[3] a) I. Gill, A. Ballesteros, *Trends Biotechnol.* **2000**, *18*, 282–296; b) I. Gill, A. Ballesteros, *Trends Biotechnol.* **2000**, *18*, 469–473; c) I. Gill, *Chem. Mater.* **2001**, 13, 3404–3421; d) C. A. Niemeyer, D. Blohm, *Angew. Chem.* **1999**, *111*, 3039–3043; *Angew. Chem. Int. Ed.* **1999**, *38*, 2865–2869; e) H. Zhu, M. Snyder, *Curr. Opin. Chem. Biol.* **2001**, *50*, 40–45; f) T. Kodadek, *Chem. Biol.* **2001**, *8*, 105–115; g) T. Cass, F. S. Ligler, *Immobilized Biomolecules in Analysis*, Oxford University Press, Oxford, **1998**; h) J. R. Woodward, R. Spokane, *Chem. Anal.* **1998**, *148*, 227–235.

[4] a) Y. Jo, T. Inoue, K. Takada, **2001** US Patent 6, 277,652; b) S. A. Yamanaka, D. H. Charych, D. A. Loy, D. Y. Sasaki, *Langmuir* **1997**, *13*, 5049–5053.

[5] I. Gill, A. Ballesteros, *J. Am. Chem. Soc.* **1998**, *120*, 8587–8598.

[6] a) M. S. Rao, B. C. Dave, *Adv. Mater.* **2002**, *14*, 443–447; b) M. S. Rao, B. C. Dave, *J. Am. Chem. Soc.* **1998**, *120*, 13270–13271; c) M. Meyer, A. Fischer, A. Hoffmann, *J. Phys. Chem. B* **2002**, *106*, 1528–1533.

[7] Y. Lu, Y. Yang, A. Sellinger, M. Lu, J. Huang, H. Fan, R. Haddad, G. Lopez, A. R. Burns, D. Y. Sasaki, J. Shelnutt, C. J. Brinker, *Nature* **2001**, *410*, 913–917.

[8] a) J. H. Chang, L. Wang, Y. Shin, B. Jeong, J. C. Birnbaum, G. L. Exarhos, *Adv. Mater.* **2002**, *14*, 382; b) R. A. Caruso, M. Antonietti. *Adv. Func. Mater.* **2002**, *12*, 307–312; c) A. C. Finnefrock, R. Ulrich, A. Du Chesne, C. C. Honeker, K. Schumacher, K. K. Unger, S. M. Gruner, U. Wiesner, *Angew. Chem.* **2001**, *113*, 1248–1251; *Angew. Chem. Int. Ed.* **2001**, *40*, 1208–1212; d) N. A. Melosh, P. Davidson, B. F. Chemelka, *J. Am. Chem. Soc.* **2000**, *122*, 823–829.

 © 2003 Wiley-VCH Verlag GmbH & Co. KGaA, Weinheim

Kinetic Control of Self-Assembly

Pd^{II}-Directed Dynamic Assembly of a Dodecapyridine Ligand into End-Capped and Open Tubes: The Importance of Kinetic Control in Self-Assembly**

*Shohei Tashiro, Masahide Tominaga, Takahiro Kusukawa, Masaki Kawano, Shigeru Sakamoto, Kentaro Yamaguchi, and Makoto Fujita**

Dynamic assembly deals with two or more self-assembled units, which are on a relatively flat potential energy surface and are interconverted into each other by the re-sorting or reorganization of the component species.[1–3] When dynamic structures have a cavity suitable for recognizing a guest, the predominant assembly of one particular host structure is induced by adding an appropriate guest. Such a guest-induced assembly of a specific host framework is often seen in biological events, and has been actively studied in both hydrogen-bonded and coordination assembly systems.[2] Here we report a unique dynamic assembly where, under a set of identical thermodynamic conditions, the same guest induces the formation of two different assemblies depending on whether the assembly process experiences crystallization or not.

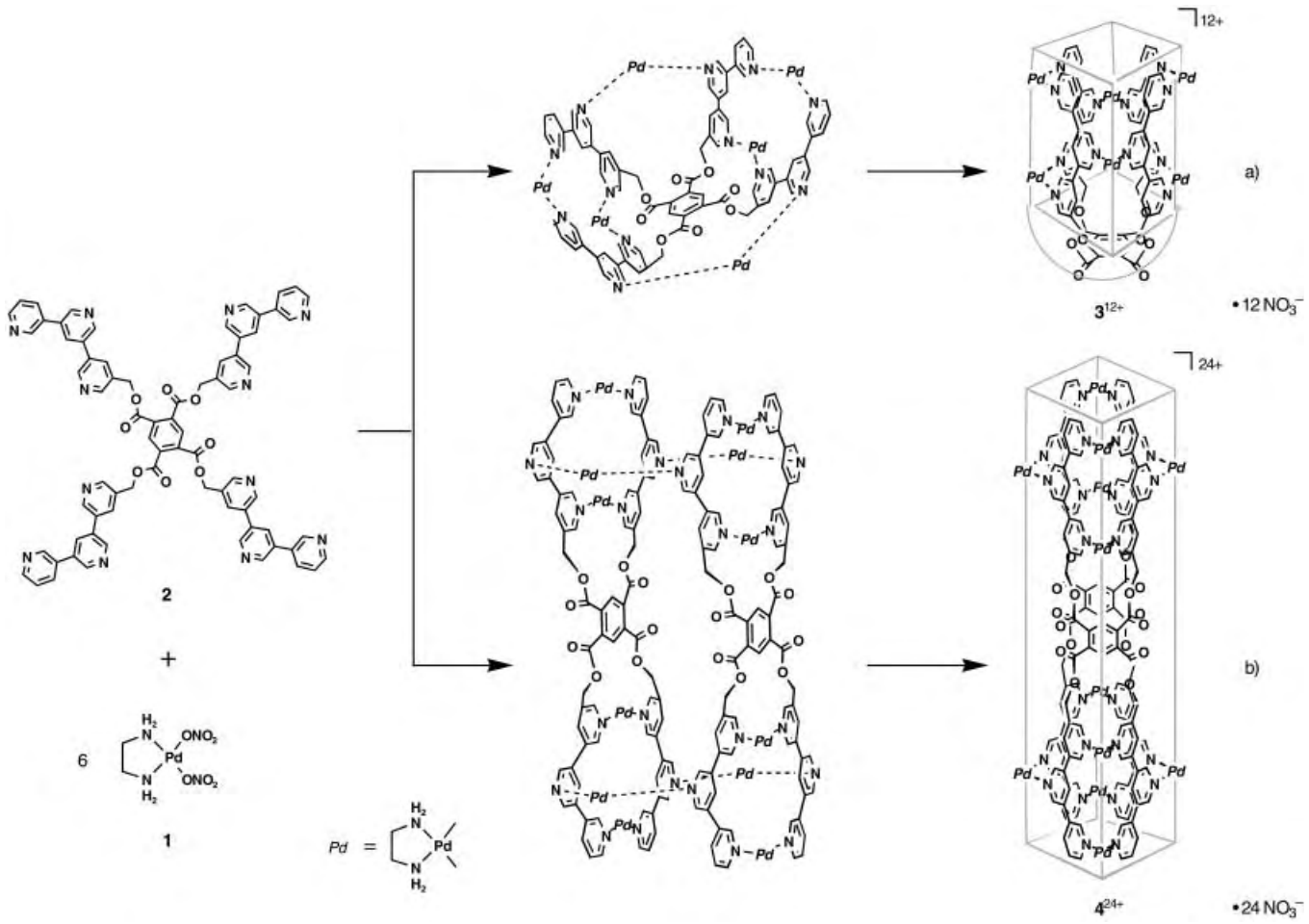
The dynamic assembly discussed here stems from the {(en)Pd^{II}} coordination block **1** (en = 1,2-ethanediamine) and ligand **2**, which has four tripyridine podands on a benzenetetracarboxylate scaffold.[4] In an analogy with the guest-induced assembly of coordination nanotubes obtained from oligo(3,5-pyridine) ligands and Pd units,[5] ligand **2** is expected to yield the mono-end-capped coordination tube $\mathbf{3}^{12+}$ upon complexation with **1** in the presence of an appropriate guest (Scheme 1a).[6] This tube is designed to differentiate between the ends of symmetrical rodlike molecules; namely, the end that is accommodated at the bottom of the tube should show different properties from the other end. We have found that, in addition to expected structure $\mathbf{3}^{12+}$, the complexation of **1** and **2** also gives rise to the double open tube, $\mathbf{4}^{24+}$, in which ligand **2** adopts an extended conformation (Scheme 1b). This open tube is observed only at higher concentrations as a

[*] Prof. Dr. M. Fujita, S. Tashiro, Dr. M. Tominaga, Dr. T. Kusukawa, Dr. M. Kawano
Department of Applied Chemistry, School of Engineering
The University of Tokyo
7-3-1 Hongo, Bunkyo-ku, Tokyo 113-8656 (Japan)
Fax: (+81) 3-5841-7257
E-mail: mfujita@appchem.t.u-tokyo.ac.jp
Dr. S. Sakamoto, Prof. Dr. K. Yamaguchi
Chemical Analysis Center, Chiba University
Yayoi-cho, Inage-ku, Chiba 263-8522 (Japan)

[**] This research was supported by the CREST project of the Japan Science and Technology Corporation (JST), for which M.F. is the principal investigator.

Supporting information for this article is available on the WWW under http://www.angewandte.org or from the author.

 DOI: 10.1002/anie.200351397 © 2003 Wiley-VCH Verlag GmbH & Co. KGaA, Weinheim



Scheme 1. Self-assembly of a) the mono-end-capped tube $\mathbf{3}^{12+}$, and b) the double open tube $\mathbf{4}^{24+}$. The template molecules necessary for the formation of $\mathbf{3}^{12+}$ and $\mathbf{4}^{24+}$ are omitted for clarity.

minor component, but is isolated in a pure form through slow crystallization. Interestingly, once isolated, $\mathbf{4}^{24+}$ is not converted into $\mathbf{3}^{12+}$ at lower concentrations, which indicates that both structures are kinetically trapped at local minima of the potential surface. Accordingly, we discuss here the self-assembly and the host–guest behavior of the end-capped tube $\mathbf{3}^{12+}$ and the open tube $\mathbf{4}^{24+}$, as well as the importance of kinetic effects in their self-assembly processes.

The quantitative assembly of **2** into end-capped tube $\mathbf{3}^{12+}$ was, in fact, accomplished by the template effect of rodlike guests such as 4,4′-dimethylbiphenyl (**5**).[7] Without the template, the complexation of ligand **2** with [(en)Pd(NO_3)$_2$] (**1**) in D_2O resulted in a complex mixture (Figure 1a). The addition of **5** to the solution, however, induced the assembly of a single product within 3 h at 70 °C (Figure 1b). In the tube structure, the side arms of **2** are equivalent whereas the methylene protons on each side arm are diastereotopic and thus observed as an AB quartet. In addition to satisfactory NMR, the formation of complex ion $\mathbf{3}^{12+}$ was strongly supported by cold-spray ionization mass spectrometry (CSI-MS).[8,9]

Observation by ^{1}H NMR spectroscopy yielded some structural aspects of the inclusion complex. As expected, the

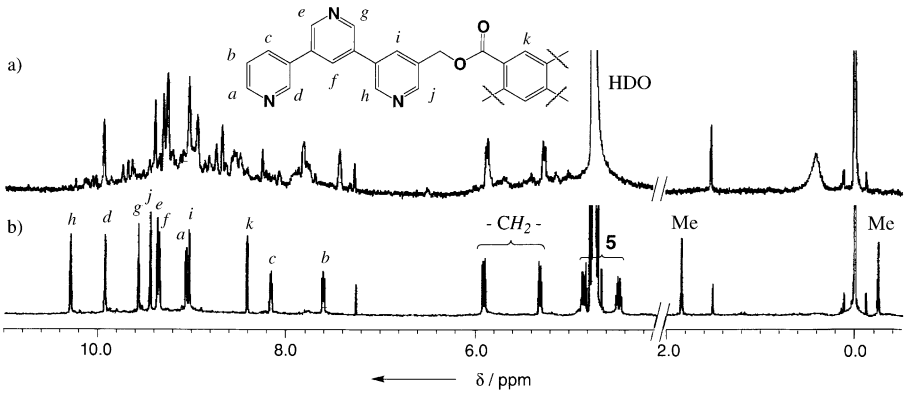


Figure 1. ^{1}H NMR spectroscopic observation of the guest-templated formation of $\mathbf{5}\subset\mathbf{3}^{12+}$ (500 MHz, D_2O, 25 °C, TMS). a) An oligomeric mixture obtained from **2** (1.7 μmol) and [(en)Pd(NO_3)$_2$] (10.2 μmol) in D_2O (0.8 mL); b) the $\mathbf{5}\subset\mathbf{3}^{12+}$ complex assembled after the addition of **5** (1.7 μmol).

 © 2003 Wiley-VCH Verlag GmbH & Co. KGaA, Weinheim

two methyl groups of guest **5** accommodated in $\mathbf{3}^{12+}$ were clearly discriminated, and were observed at $\delta = -0.25$ and 1.83 ppm (Figure 1b). The significant upfield shift of one methyl group (approximately −2.6 ppm shifted from ordinary chemical-shift region) suggests that this methyl group is located on the benzene scaffold and surrounded by four pyridine rings. Below 60 °C, these two methyl resonances did not coalesce, which indicates that the guest is strongly bound within the deep cavity of $\mathbf{3}^{12+}$, and the flipping of the guest along its long axis is suppressed.[10] Aromatic protons of **5** were also shifted upfield, being observed at $\delta = 4.47$–4.86 ppm.

Asymmetric guests, such as sodium biphenylcarboxylate ($Na^+\mathbf{6}^-$) could be efficiently accommodated in a unidirectional fashion.[7] Only one isomer was formed in which the hydrophobic biphenyl group was included deep within the tube and the hydrophilic carboxylate group was exposed outside, as indicated by ^{1}H NMR spectroscopy (Figure 2a). Interestingly, disodium biphenyldicarboxylate ($2Na^+\mathbf{7}^{2-}$), which was bound in an open tube in our previous study,[5] was not included in $\mathbf{3}^{12+}$, which shows that the end-capped site of $\mathbf{3}^{12+}$ provides an efficient hydrophobic pocket that cannot bind the hydrophilic portion of the guest.

The self-assembly of inclusion complex $\mathbf{6}^-\subset\mathbf{3}^{12+}$ was concomitant with the formation of a minor component at high concentrations ($[\mathbf{2}]_0 > 8$ mM; Figure 2b). Fortunately, this minor product was isolated as single crystals by slow evaporation (over more than two weeks) of the solution. X-ray crystallographic analysis showed that this product ($\mathbf{4}^{24+}$) is a double open tube, which consists of two molecules of ligand **2** that are held together by twelve {(en)Pd} units (Figure 3).[7,11] Open tube $\mathbf{4}^{24+}$ accommodates two molecules of $\mathbf{6}^-$, each of which is oriented so that its carboxylate group is exposed outside the tube. An important feature is that the 16-component self-assembled structure (two ligands, twelve metals, and two guests) possesses a 3.0 nm molecular tube, which is one of the longest among those structurally defined by crystallography. The biphenyl moiety is surrounded by a hydrophobic framework through efficient π–π and CH–π interactions. The elemental analysis was consistent with a formula of $(Na\mathbf{6})_2\subset\mathbf{4}(NO_3)_{24}\cdot 45\,H_2O$.

The stability of the isolated $(\mathbf{6}^-)_2\subset\mathbf{4}^{24+}$ complex requires special attention. When crystals of $(\mathbf{6}^-)_2\subset\mathbf{4}^{24+}$ were dissolved in D_2O at room temperature, we observed the $(\mathbf{6}^-)_2\subset\mathbf{4}^{24+}$ complex in a pure form (Figure 2c) although the $\mathbf{6}^-\subset\mathbf{3}^{12+}$ complex was the major product before isolation. More surprisingly, the $(\mathbf{6}^-)_2\subset\mathbf{4}^{24+}$ complex remained unchanged in solution, even after one month. These results clearly show that the $\mathbf{6}^-\subset\mathbf{3}^{12+}$ and $(\mathbf{6}^-)_2\subset\mathbf{4}^{24+}$ complexes are not in equilibrium despite the labile nature of Pd^{II}–pyridine coordination bonds. Slow conversion to the $(\mathbf{6}^-)_2\subset\mathbf{4}^{24+}$ complex only occurs when $\mathbf{6}^-\subset\mathbf{3}^{12+}$ is crystallized at high concentrations.

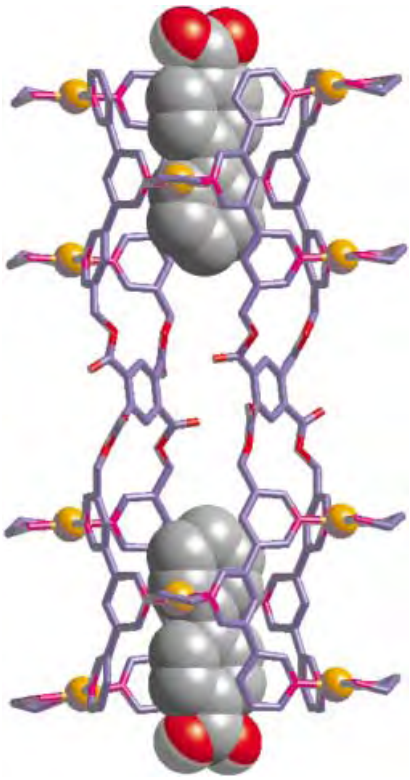


Figure 3. Crystal structure of $(\mathbf{6}^-)_2\subset\mathbf{4}^{24+}$. For clarity, H atoms, water molecules, and NO_3^- ions are omitted.

It is noteworthy that two different assemblies ($\mathbf{6}^-\subset\mathbf{3}^{12+}$ and $(\mathbf{6}^-)_2\subset\mathbf{4}^{24+}$) were obtained under a set of identical thermodynamic conditions, dependent only on whether the assembly process involved crystallization or not. We thus

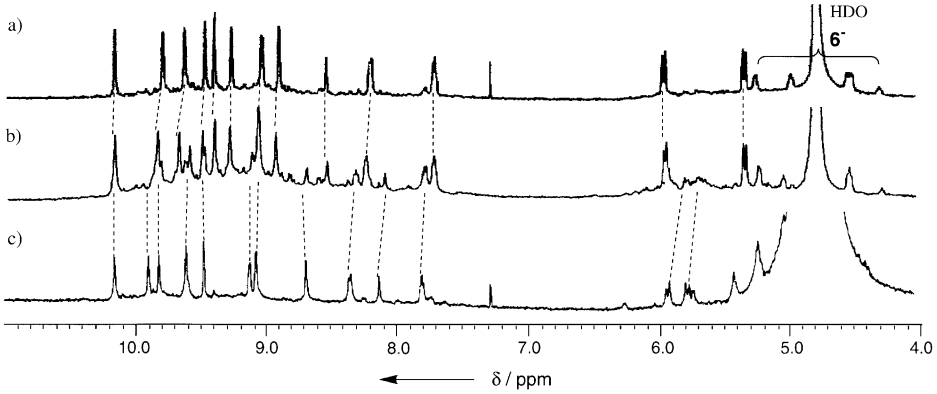


Figure 2. ^{1}H NMR spectra showing the conversion of $\mathbf{6}^-\subset\mathbf{3}^{12+}$ into $(\mathbf{6}^-)_2\subset\mathbf{4}^{24+}$ (500 MHz, D_2O, 25 °C, TMS). a) $[\mathbf{2}]_0 = 2.1$ mM; b) $[\mathbf{2}]_0 = 8.5$ mM; c) complex $(\mathbf{6}^-)_2\subset\mathbf{4}^{24+}$ isolated as crystals.

 © 2003 Wiley-VCH Verlag GmbH & Co. KGaA, Weinheim

suggest the following: a) Complexes $\mathbf{6}^{-}\subset\mathbf{3}^{12+}$ and $(\mathbf{6}^{-})_2\subset\mathbf{4}^{24+}$, which are sustained by 12 and 24 Pd^{II}–pyridine interactions, respectively, are not thermodynamically trapped, but rather kinetically trapped structures; b) complex $\mathbf{6}^{-}\subset\mathbf{3}^{12+}$ is kinetically formed and trapped through intramolecular complexation, although the more stable $(\mathbf{6}^{-})_2\subset\mathbf{4}^{24+}$ complex also exists on a potential energy surface; c) the interconversion of $\mathbf{6}^{-}\subset\mathbf{3}^{12+}$ into $(\mathbf{6}^{-})_2\subset\mathbf{4}^{24+}$ does not occur at low concentrations, but is slowly promoted at high concentrations, and much more strongly facilitated by removing the $(\mathbf{6}^{-})_2\subset\mathbf{4}^{24+}$ complex through crystallization.

Received: March 14, 2003 [Z51397]

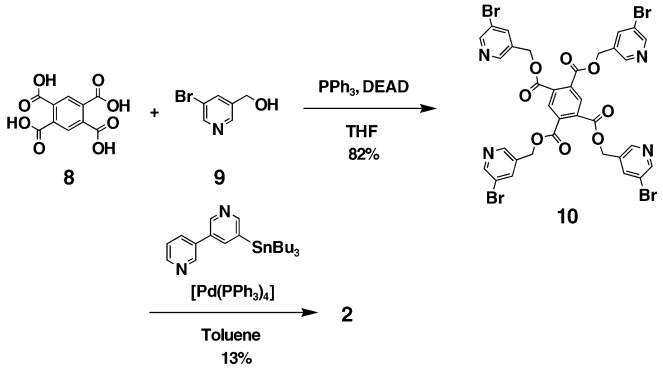
Keywords: coordination modes · molecular recognition · nanotubes · palladium · self-assembly

[1] For reviews: a) I. Huc, J.-M. Lehn, *Proc. Natl. Acad. Sci. USA* **1997**, *94*, 2106–2110; b) J.-M. Lehn, *Chem. Eur. J.* **1999**, *5*, 2455–2463; c) G. R. L. Cousins, S.-A. Poulsen, J. K. M. Sanders, *Curr. Opin. Chem. Biol.* **2000**, *4*, 270–279; d) S. J. Rowan, S. J. Cantrill, G. R. L. Cousins, J. K. M. Sanders, J. F. Stoddart, *Angew. Chem.* **2002**, *114*, 938–993; *Angew. Chem. Int. Ed.* **2002**, *41*, 898–952.

[2] a) M. Fujita, S. Nagao, K. Ogura, *J. Am. Chem. Soc.* **1995**, *117*, 1649–1650; b) B. Hasenknopf, J.-M. Lehn, N. Boumediene, A. Dupont-Gervais, A. V. Dorsselaer, B. Kneisel, D. Fenske, *J. Am. Chem. Soc.* **1997**, *119*, 10956–10962; c) B. Klekota, M. H. Hammond, B. L. Miller, *Tetrahedron Lett.* **1997**, *38*, 8639–8642; d) M. Scherer, D. L. Caulder, D. W. Johnson, K. N. Raymond, *Angew. Chem.* **1999**, *111*, 1690–1694; *Angew. Chem. Int. Ed.* **1999**, *38*, 1588–1592; e) M. Albrecht, O. Blau, R. Fröhlich, *Chem. Eur. J.* **1999**, *5*, 48–56; f) S. Hiraoka, M. Fujita, *J. Am. Chem. Soc.* **1999**, *121*, 10239–10240; g) Y. Kubota, S. Sakamoto, K. Yamaguchi, M. Fujita, *Proc. Natl. Acad. Sci. USA* **2002**, *99*, 4854–4856; h) S. Otto, R. L. E. Furlan, J. K. M. Sanders, *Science* **2002**, *297*, 590–593.

[3] a) G. W. Orr, L. J. Barbour, J. L. Atwood, *Science* **1999**, *285*, 1049–1052; b) M. Ziegler, J. J. Miranda, U. N. Andersen, D. W. Johnson, J. A. Leary, K. N. Raymond, *Angew. Chem.* **2001**, *113*, 755–758; *Angew. Chem. Int. Ed.* **2001**, *40*, 733–736; c) S. Hiraoka, T. Yi, M. Shiro, M. Shionoya, *J. Am. Chem. Soc.* **2002**, *124*, 14510–14511; d) C.-Y. Su, Y.-P. Cai, C.-L. Chen, F. Lissner, B.-S. Kang, W. Kaim, *Angew. Chem.* **2002**, *114*, 3519–3523; *Angew. Chem. Int. Ed.* **2002**, *41*, 3371–3375.

[4] Ligand **2** was synthesized as follows: The Mitsunobu esterification of tetracarboxylic acid **8** with alcohol **9** gave tetrabromide precursor **10** (82%), which is subsequently treated with tributyltin bipyridine under the Stille coupling conditions ($[Pd(PPh_3)_4]$ (10 mol%), toluene, reflux) to give **2** in 13% yield.



[5] a) M. Aoyagi, K. Biradha, M. Fujita, *J. Am. Chem. Soc.* **1999**, *121*, 7457–7458; b) M. Aoyagi, S. Tashiro, M. Tominaga, K. Biradha, M. Fujita, *Chem. Commun.* **2002**, 2036–2037; c) M. Tominaga, S. Tashiro, M. Aoyagi, M. Fujita, *Chem. Commun.* **2002**, 2038–2039.

[6] a) I. Tabushi, K. Shimokawa, N. Shimizu, H. Shirakata, K. Fujita, *J. Am. Chem. Soc.* **1976**, *98*, 7855–7856; b) S. Zhao, J. H. T. Luong, *J. Chem. Soc. Chem. Commun.* **1995**, 663–664; c) D. Whang, J. Heo, J. H. Park, K. Kim, *Angew. Chem.* **1998**, *110*, 83–85; *Angew. Chem. Int. Ed.* **1998**, *37*, 78–80; d) T. Heinz, D. M. Rudkevich, J. Rebek, Jr., *Nature* **1998**, *394*, 764–766; e) S. Saito, C. Nuckolls, J. Rebek, Jr., *J. Am. Chem. Soc.* **2000**, *122*, 9628–9630.

[7] For the physical properties of $\mathbf{5}\subset\mathbf{3}^{12+}$, $\mathbf{6}^{-}\subset\mathbf{3}^{12+}$, and $(\mathbf{6}^{-})_2\subset\mathbf{4}^{24+}$, see the Supporting Information.

[8] a) S. Sakamoto, M. Fujita, K. Kim, K. Yamaguchi, *Tetrahedron* **2000**, *56*, 955–964; b) Y. Yamanoi, Y. Sakamoto, T. Kusukawa, M. Fujita, S. Sakamoto, K. Yamaguchi, *J. Am. Chem. Soc.* **2001**, *123*, 980–981.

[9] Complex $\mathbf{3}^{12+}$ was analyzed by CSI-MS to investigate the accommodation of biphenylcarboxylate or naphthalene as a guest. A series of $[M-(NO_3)_n]^{n+}$ peaks were observed. See Supporting Information.

[10] At 80 °C, broad methyl signals were observed indicating that the coalescence temperature was being approached (see the Supporting Information).

[11] Crystal data for $(\mathbf{6}^{-})_2\subset\mathbf{4}^{24+}$ ($C_{202}H_{218}N_{72}O_{119}Pd_{14}$, $M_w = 7048.08$): crystal dimensions $0.40\times0.20\times0.20\ mm^3$, triclinic, $P\bar{1}$, $a = 16.494(4)$, $b = 16.610(4)$, $c = 31.977(8)$ Å, $\alpha = 78.438(5)$, $\beta = 86.281(5)$, $\gamma = 70.333(4)°$, $V = 8082(3)$ Å^3, $Z = 1$, $\rho_{calcd} = 1.438\ mg\,m^{-3}$, $F(000) = 3482$, radiation: $\lambda(Mo_{K\alpha}) = 0.71073$ Å, $T = 113(2)$ K, reflections collected/unique 51758/35688 ($R_{int} = 0.0585$). The structure was solved by direct methods (SHELXL-97) and refined by full-matrix least-squares methods on F^2 with 1658 parameters. $R_1 = 0.1255$ ($I > 2\sigma(I)$), $wR_2 = 0.3444$, GOF = 1.149, max./min. residual density 3.141/−3.798 e Å^{-3}. Several water molecules, nitrate molecules, and 1,2-ethanediamine ligands are disordered. Guest molecules sit on two positions (1:1 ratio) in the cavity of a host molecule. The thermal temperature factors of some disordered groups were constrained. The bond lengths of severely disordered molecules were chemically restrained. CCDC-204999 contains the supplementary crystallographic data for this paper. These data can be obtained free of charge via www.ccdc.cam.ac.uk/conts/retrieving.html (or from the Cambridge Crystallographic Data Centre, 12, Union Road, Cambridge CB2 1EZ, UK; fax: (+44) 1223-336-033; or deposit@ccdc.cam.ac.uk).

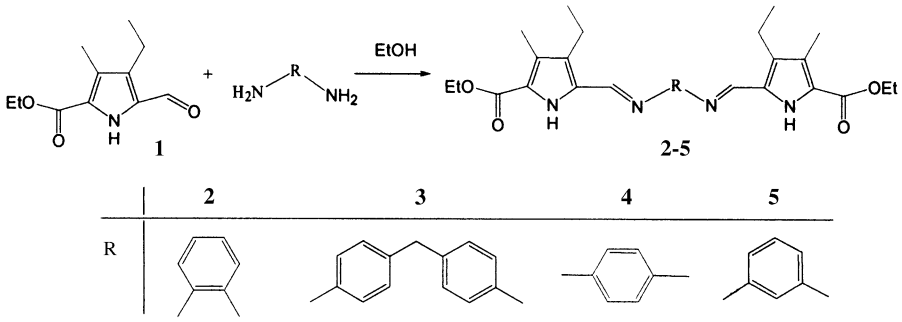
 © 2003 Wiley-VCH Verlag GmbH & Co. KGaA, Weinheim

Self-Assembly of Pyrrole Derivatives

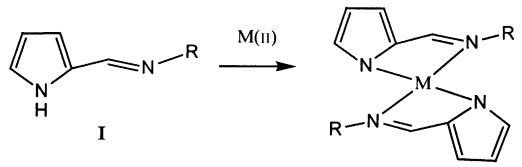
Double-Stranded Helicates, Triangles, and Squares Formed by the Self-Assembly of Pyrrol-2-ylmethyleneamines and Zn^{II} Ions**

*Zhikun Wu, Qingqi Chen, Shaoxiang Xiong, Bin Xin, Zhenwen Zhao, Lijin Jiang, and Jin Shi Ma**

The metal complexes of ligands **I**, a pyrrol-2-yl Schiff base or pyrrol-2-ylmethyleneamine, have been known for a long time.[1–3] Macrocycles containing pyrrol-2-ylmethyleneamine units, such as texaphyrins and expanded porphyrins,[4] have been extensively investigated. Linear-spacer-bridged bis(pyrrol-2-ylmethyleneamine)s and their complexes with metal ions were recently reported,[5–9] which showed that both the preparation of the ligands



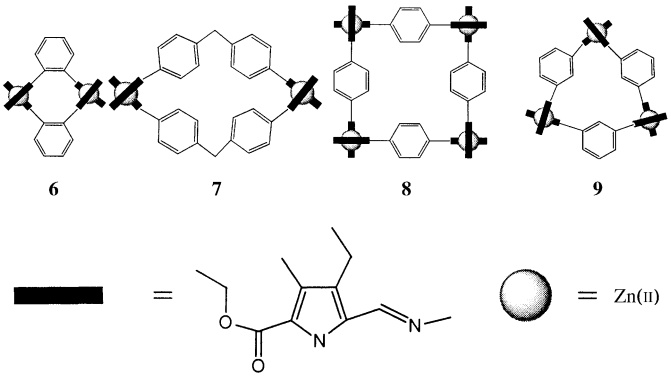
Scheme 1. Synthesis and structure of ligands **2**–**5**.



and the complexes were highly efficient, and the metal complexes formed by pyrrol-2-ylmethyleneamines possessed good solubility in common solvents. These facts encouraged us to explore their use as a building block for supramolecular self-assembly. In this paper we report the neutral double-stranded helicates, trimeric triangles, and tetrameric squares formed through the self-assembly of spacer-bridged bis(pyrrol-2-ylmethyleneamine) ligands with Zn^{II} ions.

Ligands **2**–**5** were prepared in high yields (Scheme 1) by the condensation of diamines with 4-ethyl-5-formyl-3-methyl-1*H*-pyrrole-2-carboxylic acid ethyl ester (**1**) in ethanol. The ligands **2**–**5** were each reacted with zinc(II) acetate dihydrate in THF (Scheme 2), to give the complexes **6**–**9**, respectively, in excellent yields. The complexes, isolated as red (**6** and **8**) or yellow (**7** and **9**) powders, are soluble in most common organic solvents. Crystals were grown by slowly evaporating their solutions in THF/EtOH (**6** and **7**), THF/MeOH (**8**), or THF/di(ethylene glycol) (**9**). All of the crystals are stable in the dark under a nitrogen atmosphere, but decomposed quickly in the air.

Analysis of the complexes, primarily by MALDI-TOF mass spectrometry, showed that the molecular masses of **6** and **7** were 1105 and 1284, respectively, which corresponds to dimeric complexes with two ligands and two zinc centers. However, the molecular masses of **8** and **9** were found to be 2209 and 1675, which corresponds to a tetrameric complex (four ligands and Zn centers) and trimeric complex (three ligands and Zn centers), respectively.



Scheme 2. Schematic representation of complexes **6**–**9**.

The ^1H NMR spectra of the zinc complexes **6**–**9** in $CDCl_3$ show a single set of proton resonances that could be fully assigned, which suggests that they exist as single species in solution. In all cases, the disappearance of the NH protons from the free ligands was observed, which is in agreement

[*] Prof. Dr. J. S. Ma, Z. Wu, Prof. Dr. L. Jiang
Center for Molecular Science, Institute of Chemistry
Chinese Academy of Sciences
Beijing 100080 (China)
Fax: (+86) 10-8261-7315
E-mail: jsma@iccas.ac.cn
Dr. Q. Chen
Biomarin Pharmaceutical, Inc.
46 Galli Drive, Novato, CA 94949 (USA)
Dr. S. Xiong, B. Xin, Z. Zhao
Beijing MS Center, Institute of Chemistry
Chinese Academy of Sciences
Beijing 100080 (China)

[**] This study was supported by the major state basic research development program (G2000078100), NSFC (20172055), and CAS (CMS-CX200205). We thank Ms. S.-H. Zhou (Institute of Biophysics) for NMR spectroscopy, Dr. M. Shi, and Y. Li (Institute of Chemistry) for X-ray analysis.

Supporting information for this article is available on the WWW under http://www.angewandte.org or from the author.

 DOI: 10.1002/anie.200350908 © 2003 Wiley-VCH Verlag GmbH & Co. KGaA, Weinheim

with the double deprotonation of the Schiff bases. In comparison with the corresponding free ligands, complexes **6**–**9** have up-field shifts for most of the protons. Interestingly, the -CH_2- groups in both the ester group and pyrrole ring of complexes **6**, **8**, and **9**, in which there are rigid phenylene spacers, show chiral behavior in solution. In the free ligands, the two protons of the -CH_2- groups of the ethyl ester moieties are identical and give a single quartet, however, they appear as two sets of multiplets in the complexes. Similar behavior was observed for the methylene protons of the ethyl groups in pyrrole ring. These results imply that the strong coordination of the pyrrol-2-ylmethyleneamine with the zinc ion removes the inherent enantiotropic nature of the protons making them diastereotopic and chiral. These observations are very similar to those reported by Bermejo and coworkers.[9] The ^{13}C NMR spectra of complexes **6**–**9** in $CDCl_3$ consist of the expected signals.

X-ray analysis of complexes **6**[10] (Figure 1 a) and **7**[11] (Figure 1 b) indicate that their structures possess a double-stranded helical geometry that results from a severe twist around the phenyl or diphenylmethane bridge. This twist divides the ligand into two pyrrol-2-ylmethyleneamine subunits, each of which is bound to a different Zn^{II} ion. As a result, the Zn^{II} center and its two pyrrol-2-ylmethyleneamine segments have an almost tetrahedral geometry, from which the bond angles and bond lengths have only a small deviation. The two Zn^{II} ions in **6** and **7** are separated by 3.7 Å and 11.0 Å, respectively.

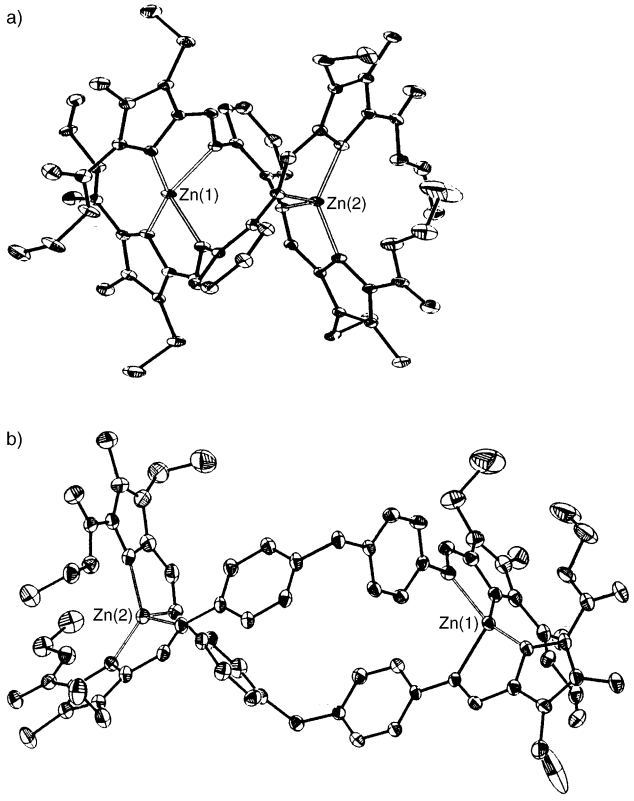


Figure 1. X-ray crystal structures of **6** (a) and **7** (b); H atoms and solvent molecules are omitted for clarity.

The X-ray structure of **8**[12] (Figure 2) displays a tetranuclear distorted square composed of four Zn^{II} ions and four ligands, with inner dimensions of 8.7 × 8.7 Å. All of the benzene units lie almost perpendicular to the square plane

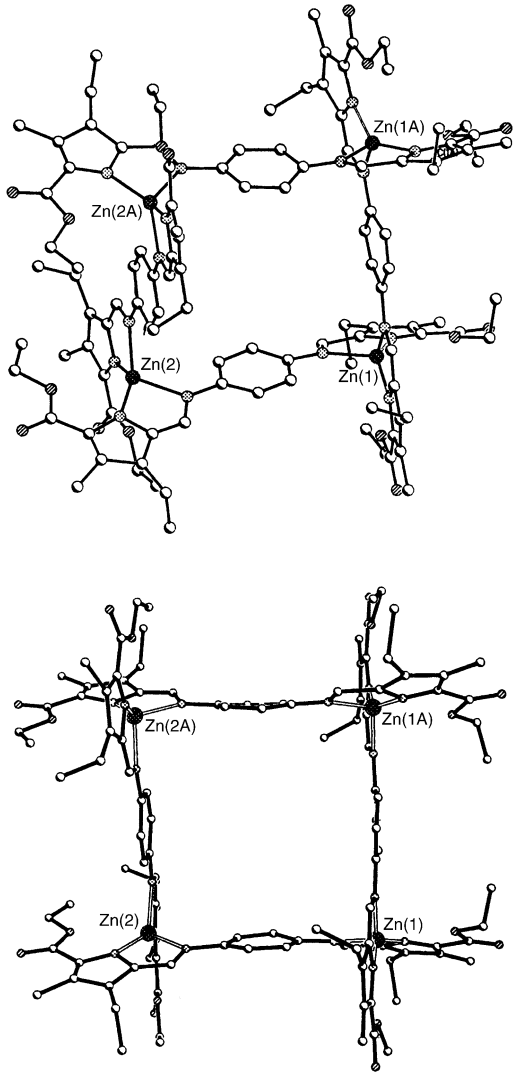


Figure 2. X-ray crystal structure of **8**; two orientations are shown, which emphasize the helical structure (above) and the cavity (below); H atoms and solvent molecules are omitted for clarity.

formed through the Zn centers. At each metal center, one pyrrol-2-ylmethyleneamine unit lies above the molecular plane, while the other unit lies below. The framework of compound **8** possesses D_4 geometry; two pyrrol-2-ylmethyleneamine units adopt a *trans* arrangement, which is similar to the recently reported molecular squares.[13–15] In compound **8**, the plane of the benzene ring in each ligand is slightly deviated from those of the two pyrrol-2-ylmethyleneamine units, with dihedral angles of 22.5° and 18.7°.

The X-ray analysis[16] of complex **9** (Figure 3) shows that it possesses a triangular structure. The ligands bind to the three metal centers so that one Schiff-base unit points up from the molecular plane, while the other points down. This motif is

 © 2003 Wiley-VCH Verlag GmbH & Co. KGaA, Weinheim

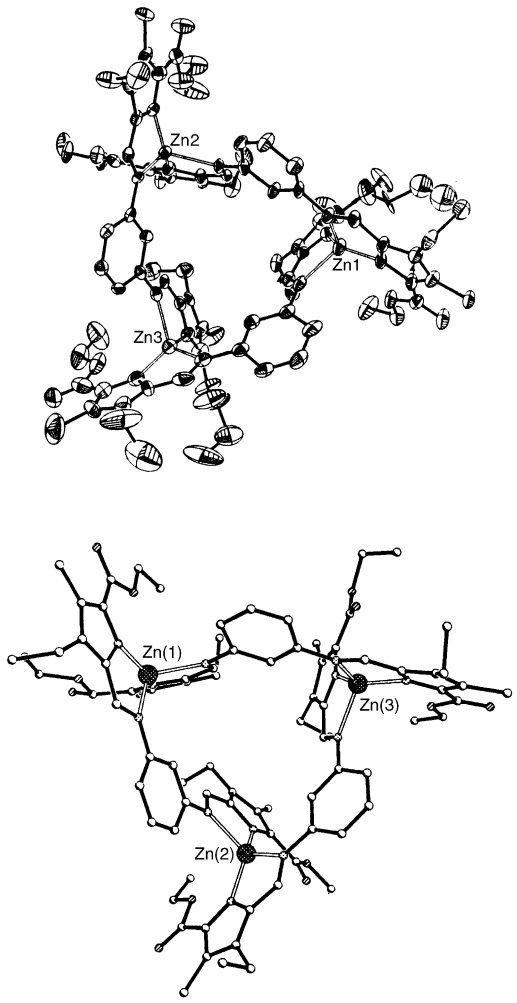


Figure 3. X-ray crystal structure of **9**; two orientations are shown, which emphasize the helical structure (above) and the cavity (below); H atoms and solvent molecules are omitted for clarity.

very similar to other recently reported triangular complexes.[17,18] The separation of the Zn atoms in the near-equilateral-triangular structure is approximately 7.5 Å. However, the overall edges of the triangle in **9** are slightly bent due to a slight deviation of the benzene ring plane from the two Schiff base planes, the dihedral angles of which are 26.3° and 2.0°.

The self-assembly of ligands **2**–**5** reflects the steric demand of the zinc ion and the arrangement of the pyrrol-2-ylmethyleneamine moieties around spacer bridges. The geometric flexibility derived from the phenyl or diphenylmethane bridges in **2**–**5** can allow the ligands to satisfy the steric requirement of the zinc ion. In all cases, a distorted coordination is mainly preferred by the zinc centers, which forces the *trans* arrangement of both halves of the bis(pyrrol-2-ylmethyleneamine) ligands.

In conclusion, we have demonstrated that pyrrol-2-ylmethyleneamine is an ideal building block for supramolecular architecture through self-assembly. It possesses similar coordinate properties to its analogues, such as dipyrrin,[18–20] and excellent solubility in common solvents. By varying the spacer bridges between two pyrrol-2-ylmethyleneamine units, the resulting bis(pyrrol-2-ylmethyleneamine) ligands can self-assemble to form supramolecules with interesting shapes, such as double-stranded helicates, triangles, and squares.

Received: January 7, 2003
Revised: May 6, 2003 [Z50908]

Keywords: pyrroles · Schiff bases · self-assembly · supramolecular chemistry · zinc

[1] A. Chakravorty, R. H. Holm, *Inorg. Chem.* **1964**, *3*, 1521–1524.
[2] J. H. Weber, *Inorg. Chem.* **1967**, *6*, 258–262.
[3] N. A. H. Male, M. Thornton-Pett, M. Bochmann, *J. Chem. Soc. Dalton Trans.* **1997**, 2487–2494.
[4] For reviews see: a) J. L. Sessler, S. J. Weghorn, *Expanded, Contracted, and Ismoeric Porphyrins*, Pergamon Press, Oxford, **1997**; b) A. Jasat, D. Dolphin, *Chem. Rev.* **1997**, *97*, 2267–2340.
[5] N. A. Bailey, A. Barras, D. E. Fenton, M. S. Gonzales, R. Moody, C. O. R. D. Barbarin, *J. Chem. Soc. Dalton Trans.* **1984**, 2741–2746.
[6] S. Brooker, B. M. Carter, *Acta Crystallogr. Sect. C* **1995**, *51*, 1522–1524.
[7] M. Grigora, G. Stoica, I. Cianghe, C. I. Simionescu, *Rev. Roum. Chim.* **1997**, *42*, 993–998.
[8] F. Franceschi, G. Guillemot, E. Solari, C. Floriani, N. Re, H. Birkedal, P. Pattison, *Chem. Eur. J.* **2001**, *7*, 1468–1478.
[9] M. Vazquez, M. Bermejo, M. Fondo, A. Garcia-Deibe, A. M. Gonzalez, R. Pedrido, *Eur. J. Inorg. Chem* **2002**, 465–472.
[10] Crystal structure analyses were measured on a Rigaku R-Axis Rapid IP diffractometer using graphite-monochromated $Mo_{K\alpha}$ radiation ($\lambda = 0.71073$ Å) at 123(2) K. Crystal data for **6**: $C_{60}H_{72}N_8O_9Zn_2$, $M_r = 1180.00$, red crystal, $0.46 \times 0.29 \times 0.23$ mm^3, triclinic, space group $P\bar{1}$, $Z = 2$, $a = 12.4491(2)$, $b = 12.6670(3)$, $c = 20.8710(8)$ Å, $\alpha = 80.375(3)$, $\beta = 85.578(4)$, $\gamma = 61.353(3)°$, $V = 2847.65(14)$ Å^3, $\rho_{calcd} = 1.376$ g cm^{-3}, $F(000) = 1240$. A total of 17723 reflections were measured in the range $1.98 \le \theta \le 27.50$ (*hkl* range indices: $-15 \le h \le 16$, $-16 \le k \le 16$, $-27 \le l \le 27$), 11782 unique reflections (R(int) = 0.0521). The structure was refined on F^2 to $R_w = 0.1204$, $R = 0.0520$ (7232 reflections with $I > 2\sigma(I)$), and GOF = 0.907 on F^2 for 722 refined parameters.
[11] Crystal data for **7**: $C_{80}H_{99}N_8O_{11.5}Zn_2$, $M_r = 1487.41$, yellow crystal, $0.48 \times 0.28 \times 0.20$ mm^3, monoclinic, space group $P2(1)/c$, $Z = 4$, $a = 18.3613(8)$, $b = 14.7764(6)$, $c = 29.1222(13)$ Å, $\beta = 98.1140(10)°$, $V = 7822.2(5)$ Å^3, $\rho_{calcd} = 1.263$ g cm^{-3}, $F(000) = 3148$. A total of 28828 reflections were measured in the range $2.17 \le \theta \le 27.48$ (*hkl* range indices: $-23 \le h \le 23$, $-19 \le k \le 19$, $-37 \le l \le 37$), 17523 unique reflections [R(int) = 0.0553]. The structure was refined on F^2 to $R_w = 0.1500$, $R = 0.0641$ (8243 reflections with $I > 2\sigma(I)$), and GOF = 0.874 on F^2 for 899 refined parameters.
[12] Crystal data for **8**: $C_{113}H_{136}N_{16}O_{23}Zn_4$, $M_r = 2347.86$, red crystal, $0.96 \times 0.26 \times 0.22$ mm^3, tetragonal, space group $I\bar{4}2d$, $Z = 8$, $a = 30.5974(7)$, $b = 30.5974(7)$, $c = 33.0573(8)$ Å, $\alpha = \beta = \gamma = 90°$, $V = 30948.3(13)$ Å^3, $\rho_{calcd} = 1.008$ g cm^{-3}, $F(000) = 9840$. A total of 18119 reflections were measured in the range $2.48 \le \theta \le 27.48$ (*hkl* range indices: $-39 \le h \le 39$, $-28 \le k \le 28$, $-42 \le l \le 42$), 17549 unique reflections [R(int) = 0.0357]. The structure was refined on F^2 to $R_w = 0.1200$, $R = 0.0595$ (2482 reflections with $I > 2\sigma(I)$), and GOF = 0.372 on F^2 for 687 refined parameters.
[13] T. Bark, M. Duggeli, H. Stoeckli-Evans, A. von Zelesky, *Angew. Chem. Int. Ed.* **2001**, *40*, 2848–2851.
[14] C. S. Campos-Fernandez, R. Clerac, K. R. Dunbar, *Angew. Chem. Int. Ed.* **1999**, *38*, 3477–3479.

 © 2003 Wiley-VCH Verlag GmbH & Co. KGaA, Weinheim

[15] X.-H. Bu, H. Morishita, K. Tanaka, K. Biradha, S. Furusho, M. Shionoya, *Chem. Commun.* **2000**, 971 – 972..
[16] Crystal data for **9**: $C_{93}H_{121}N_{12}O_{15}Zn_3$, $M_r = 1843.13$, yellow crystal, $0.79 \times 0.30 \times 0.14\ mm^3$, triclinic, space group $P\bar{1}$, $Z = 2$, $a = 15.2518(14)$, $b = 18.760(3)$, $c = 19.4142(9)$ Å, $\alpha = 74.267(4)$, $\beta = 75.913(5)$, $\gamma = 69.273(5)°$, $V = 4933.2(9)$ Å^3, $\rho_{calcd} = 1.241\ g\,cm^{-3}$, $F(000) = 1946$. A total of 25581 reflections were measured in the range $1.61 \le \theta \le 27.49$ (*hkl* range indices: $-18 \le h \le 19$, $-24 \le k \le 24$, $-25 \le l \le 25$), 18924 unique reflections [R(int) = 0.1206]. The structure was refined on F^2 to $R_w = 0.1530$, $R = 0.0738$ (4351 reflections with $I > 2\sigma(I)$), and GOF = 0.701 on F^2 for 1062 refined parameters.
[17] A. Neels, H. Stoeckli-Evans, *Inorg. Chem.* **1999**, *38,* 6164 – 6170.
[18] A. Thompson, S. J. Rettig, D. Dolphin, *Chem. Commun.* **1999**, 631 – 632.
[19] a) Y. Zhang, A. Thompson, S. J. Rettig, D. Dolphin, *J. Am. Chem. Soc.* **1998**, *120*, 13537 – 13538; b) A. Thompson, D. Dolphin, *Org. Lett.* **2000**, *2*, 1315 – 1318; c) A. Thompson, D. Dolphin, *J. Org. Chem.* **2000**, *65*, 7870 – 7877; d) Q. Chen, Y. Zhang, D. Dolphin, *Tetrahedron Lett.* **2002**, *43*, 8413 – 8416.
[20] a) Y. Zhang, Z. Wang, C. Yan, G. Li, J. S. Ma, *Tetrahedron Lett.* **2000**, *41*, 7717 – 7721; b) Y. Zhang, J. S. Ma, *Org. Prep. Proced. Int.* **2001**, *33,* 81 – 86.
[21] CCDC-199238 (**6**), -199237 (**7**), -199239 (**8**), and -200320 (**9**) contain the supplementary crystallographic data for this paper. These data can be obtained free of charge via www.ccdc.cam.ac.uk/conts/retrieving.html (or from the Cambridge Crystallographic Data Centre, 12, Union Road, Cambridge CB2 1EZ, UK; fax: (+44) 1223-336-033; or deposit@ccdc.cam.ac.uk).

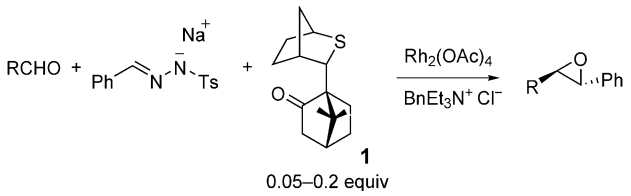
 © 2003 Wiley-VCH Verlag GmbH & Co. KGaA, Weinheim

Asymmetric Synthesis of Epoxides

Sulfur-Ylide-Mediated Synthesis of Functionalized and Trisubstituted Epoxides with High Enantioselectivity; Application to the Synthesis of CDP-840**

Varinder K. Aggarwal, Imhyuck Bae, Hee-Yoon Lee,* Jeffery Richardson, and David T. Williams*

The carbonyl group occupies a position of central importance in organic synthesis as it allows ready functionalization, for example, in the α, β, and γ positions. Direct transformations into other versatile functional groups, such as alkenes and epoxides, further increase the importance of carbonyl groups in synthesis. The ability to conduct such transformations enantioselectively would be extremely useful, and toward this goal we recently reported a practical, catalytic, and asymmetric conversion of aldehydes into epoxides by using the sulfide **1** (Scheme 1).[1] The sulfide **1**, which is readily available in both enantiomeric forms, was obtained in four steps in 48% overall yield from camphorsulfonyl chloride.



Scheme 1. Catalytic and asymmetric epoxidation of aldehydes; conditions: $Rh_2(OAc)_4$ (1 mol%), $BnEt_3N^+Cl^-$ (10 mol%), CH_3CN, 40°C.

However, attempts to apply our catalytic process to the synthesis of CDP-840, through an epoxidation reaction with 4-pyridinecarboxaldehyde, were unsuccessful. In mapping out the scope of the catalytic process we discovered that, as well as the reactions of heteroaromatic aldehydes that bear basic groups, those of *n*-alkyl aliphatic aldehydes, α,β-unsaturated aldehydes, acetylenic aldehydes, and ketones gave either low yields, low diastereomeric ratios, or low enantioselectivities.[2] A further limitation of the catalytic process emerged when we attempted to use α,β-unsaturated hydrazones with the chiral sulfide **1**, as only low yields were observed. As unsaturated epoxides[3] and epoxides that contain a basic nitrogen functionality are difficult to prepare by oxidative methods, we were keen to find a solution to this problem. Indeed, a common limitation in catalytic asymmetric synthesis is substrate specificity and one solution to the problem is to devise a stoichiometric process with good recovery of the chirality-transfer agent. An outstanding example is the Evans auxiliary, which, even though it is used in stoichiometric amounts, is widely employed as a result of its broad applicability, reliability, and recyclability. Although enantioselective epoxidations with stoichiometric quantities of sulfide have been described, their scope is limited. Solladié-Cavallo et al. have only described the reaction of Eliel's oxathiane benzyl sulfonium salt with aromatic,[4] heteroaromatic,[5] and α,β-unsaturated aldehydes.[6] Metzner and coworkers have reported moderate to high enantioselectivities in reactions of *trans*-2,5-dimethylthiolane benzyl sulfonium salt with aromatic and heteroaromatic aldehydes[7] and moderate enantioselectivities in related allyl sulfonium salt reactions.[8] Furthermore, it is not possible to access both enantiomers of these sulfides easily, which further limits their practical applications.

Herein we describe a process for the epoxidation of a very broad range of carbonyl compounds, including ketones, in high yields and with high selectivities. Although stoichiometric quantities of sulfide were required, the resulting high

[*] Prof. Dr. V. K. Aggarwal, J. Richardson, D. T. Williams
School of Chemistry, University of Bristol
Cantock's Close, Bristol BS8 1TS (UK)
Fax: (+44) 117-929-8611
E-mail: v.aggarwal@bristol.ac.uk
Prof. Dr. H.-Y. Lee, I. Bae
Centre for Molecular Design and Synthesis
Department of Chemistry and School of Molecular Science (BK21)
Korea Advanced Institute of Science and Technology
Daejon 305-701 (Republic of Korea)
Fax: (+82) 42-869-2810
E-mail: leehy@kaist.ac.kr

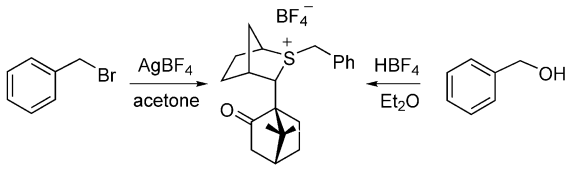
[**] We thank the BBSRC and the EPSRC for studentships (D.T.W. and J.R.), and the Brain Korea-21 project for financial support (I.B.).

Supporting information for this article is available on the WWW under http://www.angewandte.org or from the author.

 © 2003 Wiley-VCH Verlag GmbH & Co. KGaA, Weinheim DOI: 10.1002/anie.200350968

enantioselectivities, diastereoselectivities, and yields, together with the increase in scope, now allow this process to be employed in the synthesis of complex and challenging targets, which is also exemplified herein.

Initial studies were carried out with the benzyl sulfonium salt **2a**. This salt was originally prepared from the sulfide **1**, BnBr, and $AgBF_4$, but we have since found that the reaction of **1** with BnOH in the presence of HBF_4 in Et_2O is also effective. Although the use of ROH/HX has been reported previously for the synthesis of sulfonium salts, a large excess of the sulfide is invariably required.[9] We have found conditions under which the sulfonium salt is formed in high yield in the presence of just 1 equivalent of the sulfide. This process is more economical and gives cleaner products, as the salt simply precipitates from the solution in diethyl ether (Scheme 2).



2a

Scheme 2. Preparation of the chiral sulfonium salt.

Subsequent treatment of the salt with a carbonyl compound and either a phosphazene base[5,10] at low temperature or KOH[11] at room temperature furnished the corresponding epoxides (Table 1). Following an initial reaction with benzaldehyde, in which the corresponding epoxide was produced with very high selectivity (Table 1, entry 1), only substrates that performed poorly in the catalytic reaction were examined. The reactions of pyridine carboxaldehydes (Table 1, entries 2 and 3) gave the desired epoxides in high yields and with high diastereoselectivities and almost perfect (> 99 %) enantioselectivities under both sets of conditions. A series of unsaturated aldehydes were tested (Table 1, entries 5–7) and although reactions with acrolein proceeded in low yields, the use of methacrolein and crotonaldehyde both led to yields of up to 90 %. In all cases the selectivities were exceptionally high. High enantioselectivities were also observed with acetylenic aldehydes (e.g. Table 1, entry 8), although diastereoselectivities were poor. In the cases in which the epoxide was stable to chromatography, the sulfide was recovered in essentially quantitative yield.

Ketones,[12] which have never been employed previously in asymmetric sulfur-ylide-mediated epoxidations, performed remarkably well in this system to furnish epoxides with high enantioselectivities. Cyclohexanone and 4-*tert*-butylcyclohexanone (Table 1, entries 9 and 10) provide dramatic examples of the effectiveness of the epoxidation process. In the latter case the epoxide was obtained as a single diastereomer and a single enantiomer in high yield (Scheme 3). Furthermore, the method was found to be applicable to nonsymmetrical ketones, although in these cases the *cis* diastereomer was formed preferentially (exclusively in the case of *p*-nitroacetophenone) with moderate to high enantioselectivity. The full scope of the reaction with ketones is currently being investigated. These are the first examples of both the desymmetrization of a carbonyl group and the asymmetric synthesis of trisubstituted epoxides with chiral sulfur ylides.

The process was also extended to α,β-unsaturated sulfonium salts, which were prepared either by the reaction of the sulfide with the corresponding alcohol and HBF_4, or by alkylation with the appropriate unsaturated bromide. Although the use of allyl and methallyl sulfonium salts led to moderate yields of the epoxides (perhaps because of competing γ attack), high diastereoselectivities and high enantioselectivities were nevertheless observed. However, with the more substituted substrates **2d** and **2e** high yields were once again observed and the high selectivities maintained. Interestingly, considerably higher diastereoselectivities are observed with α-substituted (d.r. > 99:1) than with α-unsubstituted (d.r. = 91:9) α,β-unsaturated sulfonium salts. Metzner and co-workers made a similar observation.[8] Although α,β-unsaturated sulfonium salts have been employed in epoxidation reactions,[13] it has been reported that [2,3] sigmatropic rearrangements often compete.[14] No such rearrangements were observed in our case, thus indicating that ylide equilibration did not occur.

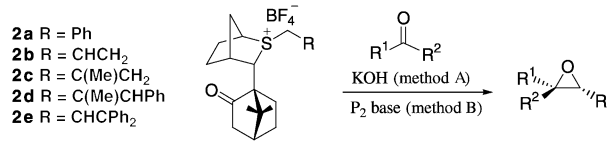
Although in all cases the use of the phosphazene base at low temperature (method B) provided superior results to KOH at room temperature (method A), the fact that high enantioselectivities were also observed under the latter conditions will render this the method of choice for industrial applications in many cases. However, high selectivities could only be obtained by using the phosphazene base at low temperature in some cases (Table 1, entries 4 and 13). As the use of this phosphazene base is undesirable for large-scale operations, a lower cost, lower-molecular-weight base that would perform as effectively was sought. A number of cheap and readily available bases were tested and we discovered that potassium hexamethyldisilazide (KHMDS) was indeed equally effective (method C).

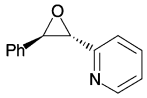
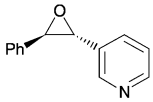
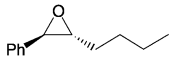
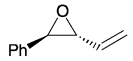
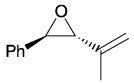
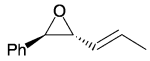
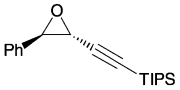
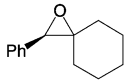
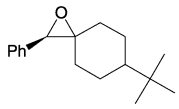
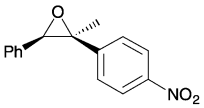
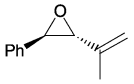
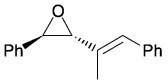
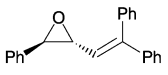
The high yields and selectivities observed, coupled with the recyclable nature of the sulfide, render this process practical for these especially difficult substrates. This feature was demonstrated in a short synthesis of the anti-inflammatory agent CDP-840.[15] We envisaged that CDP-840 could be obtained from the alcohol **3**, which could itself be prepared by a copper-catalyzed regioselective ring opening of the diaryl epoxide **4** with a Grignard reagent (Scheme 4).

As the alcohol was to be removed in the final step, we could tolerate a mixture of *cis* and *trans* epoxides, provided that both were obtained with high enantioselectivity and with the same configuration (*S*) at C3. These requirements led us to consider the coupling of the sulfonium salt **5** with 4-pyridinecarboxaldehyde. The sulfonium salt **5** was prepared by treating the aryl alcohol **6** and *ent*-**1** with HBF_4 in Et_2O. Again, this direct method for sulfonium salt formation was found to be cleaner, higher yielding, and more economical than the standard two-step procedure involving formation of the bromide followed by alkylation in the presence of $AgBF_4$. Subsequent treatment of the salt with the phosphazene base and the aldehyde furnished the epoxide in high yield with

 © 2003 Wiley-VCH Verlag GmbH & Co. KGaA, Weinheim

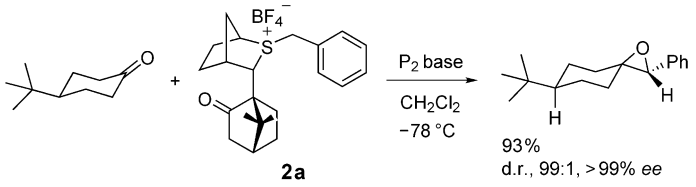
Table 1: Reactions of sulfonium salts with various electrophiles



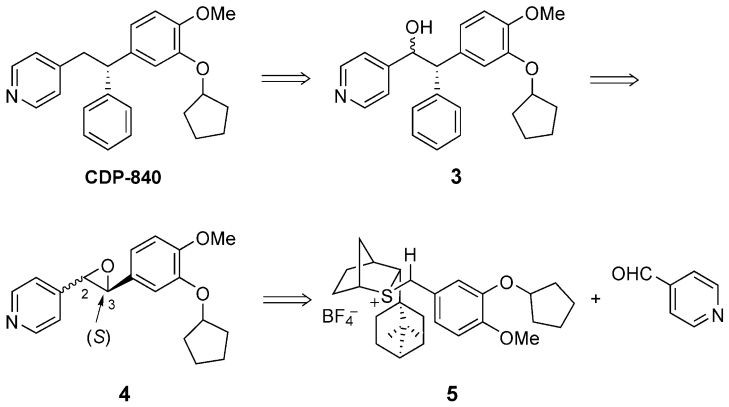
Entry	Salt	Electrophile	Major product	Method[a]	Yield [%][b]	d.r.[c]	*ee*[d]
1	**2a**[e]	benzaldehyde		A	75	98:2	98
2	**2a**	2-pyridine-carboxaldehyde		A B	91 88	91:9 98:2	95 (80[f]) 99
3	**2a**	3-pyridine-carboxaldehyde		A B	74 59	97:3 >99:1	98 >99
4	**2a**	valeraldehyde		A B C	58 64 87	60:40 92:8 90:10	91 97 >99
5	**2a**	acrolein		A B	30[g],[h] 19[g],[h]	90:10 >99:1	97 >99
6	**2a**	methacrolein		A B	51[g] 52[g]	96:4 >99:1	96 99
7	**2a**	crotonaldehyde		A B	72[g] 90[g]	98:2 >99:1	90 95
8	**2a**	TIPS-propargyl aldehyde		A B	50 51	60:40 63:37	95 99
9	**2a**	cyclohexanone		B	85	–	92
10	**2a**	4-*tert*-butyl-cyclohexanone		B	93	99:1	>99
11	**2a**	acetophenone		B	77	33:67	93 (50[f])
12	**2a**	*p*-nitro-acetophenone		B	73	>1:99	71
13	**2b**[e]	benzaldehyde		A B C	33[g] 43[g] 28[g]	71:29 91:9 82:18	84 89 90
14	**2c**[e]	benzaldehyde		A B	37[g] 26[g]	97:3 >99:1	97 97
15	**2d**[i]	benzaldehyde		A B	96[g] 93[g]	96:4 >99:1	90 93
16	**2e**[i],[j]	benzaldehyde		B	69[g]	91:9	90

[a] Method A: carbonyl compound, KOH, MeCN/H_2O (9:1), room temperature; method B: P_2 base, CH_2Cl_2, −78 °C, 10 min, followed by addition of the carbonyl compound; method C: KHMDS (0.5 M in toluene), THF, −78 °C, 2 h, followed by addition of the carbonyl compound. [b] Yield of isolated product. [c] *Trans*/*cis*. [d] In all cases the major enantiomer has the *R* configuration at the benzylic position. [e] Prepared from the alkyl bromide followed by counterion exchange. [f] The *ee* value for the *cis* isomer. [g] The yield was determined by ^{1}H NMR spectroscopy against an internal standard (the epoxide is unstable on silica gel). [h] Aldehyde: 5 equiv. [i] Prepared from the alcohol and HBF_4. [j] We thank Mamta Patel for carrying out this experiment.

 © 2003 Wiley-VCH Verlag GmbH & Co. KGaA, Weinheim



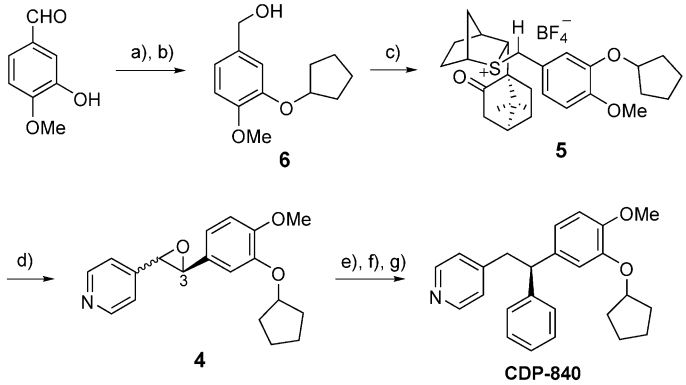
Scheme 3. Desymmetrization of 4-*tert*-butylcyclohexanone. P_2 base = *N*,*N*,*N*′,*N*′-tetramethyl-*N*″-(tris(dimethylamino)phosphoranylidene)phosphoric triamide ethylimine.



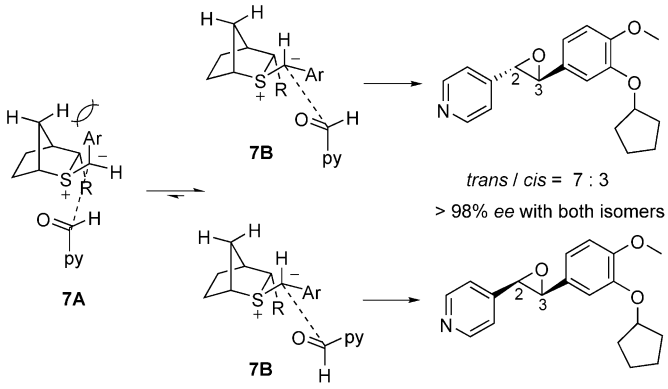
Scheme 4. Retrosynthetic analysis of CDP-840.

essentially complete control of enantioselectivity (Scheme 5). Furthermore, the sulfide was recovered in quantitative yield.

The diastereoselectivity of the epoxidation was low, but as expected this proved inconsequential for our total synthesis. The origin of the enantioselectivity for both diastereomers is explained in Scheme 6.[16] The reaction of the ylide **7** with 4-pyridinecarboxaldehyde to give the intermediate betaine is not reversible as the ylide is destabilized by the *p*-methoxy substituent. The enantioselectivity is therefore determined by the ylide conformation and its face selectivity.[17] The high enantioselectivity observed is a consequence of ylide conformer **7B** being strongly favored over conformer **7A** owing to 1,4-steric interactions and essentially complete preference for *Si*-face attack, as the *Re* face of the ylide is hindered by the bulky camphor moiety. As the aldehyde can approach in different orientations, both betaine diastereomers and thereby the two epoxide diastereomers are formed. The ylide is less stable than a benzyl-substituted ylide and the betaines are formed non-reversibly, which accounts for the low diastereoselectivity observed. Crucially, the epoxide stereocenter at C3 has the *S* configuration in both isomers. To preserve the integrity of the C3 stereogenic center the method of purification of the epoxide turned out to be critical. Purification on silica gel resulted in some decomposition but also changed the diastereomeric ratio from 7:3 to 9:1. Furthermore, the enantiomeric excess of the purified *trans* epoxide was much lower. Presumably silica-gel-promoted ring opening at C3 of the acid-sensitive *cis* epoxide, and following bond rotation and ring closure the *trans* epoxide was obtained with the opposite stereochemistry at C3, thus eroding the enantiomeric excess. However, purification on basic alumina gave the epoxide in high yield and high enantioselectivity, and in the same diastereomeric ratio as observed in the crude reaction mixture, thus indicating that no equilibration had occurred. Ring opening of the epoxide with PhMgBr occurred with complete regioselectivity and with clean inversion of stereochemistry at C3. Finally, removal of the hydroxy group furnished CDP-840 in enantiomerically pure form. Comparison of the optical rotation of our sample of CDP-840 with the literature value[18] not only confirmed its absolute configuration but also lent further weight to our model for the source of the enantioselectivity.



Scheme 5. Synthesis of CDP-840. Reagents and conditions: a) K_2CO_3, cyclopentyl bromide, DMF, 60°C, 12 h, 97%; b) $NaBH_4$, MeOH, room temperature, 1 h, 99%; c) *ent*-**1**, HBF_4, Et_2O, room temperature, 4 h, 80%; d) P_2 base, CH_2Cl_2, −78°C, 15 min, then 4-pyridinecarboxaldehyde, −78°C, 1 h, 89% (*trans*/*cis* = 7:3), >98% *ee*; e) PhMgBr (2.5 equiv), CuI (0.25 equiv), THF, −40°C, 15 h, 85%; f) Et_3N, MsCl, CH_2Cl_2, 0°C, 30 min; g) Zn, AcOH, room temperature, 5 h, 80% (2 steps). DMF = *N*,*N*-dimethylformamide; Ms = methanesulfonyl.



Scheme 6. The origin of the enantioselectivity. py = pyridyl.

In summary, we have described the highly enantio- and diastereoselective reaction of aldehydes and ketones with chiral sulfonium ylides to generate di- and trisubstituted epoxides. The scope of the epoxidation reaction was further

 © 2003 Wiley-VCH Verlag GmbH & Co. KGaA, Weinheim

demonstrated by its application to the synthesis of a target compound (CDP-840) with significant functionality.

Received: January 20, 2003
Revised: April 29, 2003 [Z50968]

Keywords: asymmetric synthesis · epoxidation · sulfur · synthetic methods · ylides

[1] V. K. Aggarwal, E. Alonso, G. Hynd, K. M. Lydon, M. J. Palmer, M. Porcelloni, J. R. Studley, *Angew. Chem.* **2001**, *113*, 1479 – 1482; *Angew. Chem. Int. Ed.* **2001**, *40*, 1430 – 1433.
[2] These studies will be presented in a paper on the scope and limitation of the catalytic sulfur ylide process.
[3] M. Frohn, M. Dalkiewicz, Y. Tu, Z.-X. Wang, Y. Shi, *J. Org. Chem.* **1998**, *63*, 2948 – 2953.
[4] A. Solladié-Cavallo, A. Diep-Vohuule, *Tetrahedron: Asymmetry* **1996**, *7*, 1783 – 1788.
[5] A. Solladié-Cavallo, M. Roje, T. Isarno, V. Sunjic, *Eur. J. Org. Chem.* **2000**, 1077 – 1080.
[6] A. Solladié-Cavallo, L. Bouérat, M. Roje, *Tetrahedron Lett.* **2000**, *41*, 7309 – 7312.
[7] J. Zanardi, C. Leriverend, D. Aubert, K. Julienne, P. Metzner, *J. Org. Chem.* **2001**, *66*, 5620 – 5623.
[8] J. Zanardi, D. Lamazure, S. Miniere, V. Reboul, P. Metzner, *J. Org. Chem.* **2002**, *67*, 9083 – 9086.
[9] a) J. Forrester, R. V. H. Jones, L. Newtons, P. N. Preston, *Tetrahedron* **2001**, *57*, 2871 – 2884; b) S. Zhang, D. Marchall, L. S. Liebeskind, *J. Org. Chem.* **1999**, *64*, 2796 – 2804; c) B. Badet, L. Jacob, M. Julia, *Tetrahedron* **1981**, *37*, 887 – 890.
[10] X. S. Fei, J. G. Verkade, *Heteroat. Chem.* **1999**, *10*, 538 – 540.
[11] K. Julienne, P. Metzner, V. Henryon, *J. Chem. Soc. Perkin Trans. 1* **1999**, 731 – 735.
[12] For an example of a reaction of a chiral sulfimide ylide with a ketone to give a terminal epoxide, see: C. P. Baird, P. C. Tayor, *J. Chem. Soc. Chem. Commun.* **1995**, 893 – 894.
[13] a) Y.-G. Zhou, A.-H. Li, X.-L. Hou, L.-X. Dai, *Chem. Commun.* **1996**, 1353 – 1354; b) M. W. Rowbottom, N. Mathews, T. Gallagher, *J. Chem. Soc. Perkin Trans. 1* **1998**, 3927 – 3929; c) A. Fürstner, T. Gastner, *Org. Lett.* **2000**, *2*, 2467 – 2470.
[14] a) R. W. La Rochelle, B. M. Trost, L. Krepski, *J. Org. Chem.* **1971**, *36*, 1126 – 1136; b) J.-B. Qusset, C. Mioskowski, G. Solladié, *Tetrahedron Lett.* **1983**, *24*, 4419 – 4422; c) A.-H. Li, L.-X. Dai, X.-L. Hou, M.-B. Chen, *J. Org. Chem.* **1996**, *61*, 4641 – 4648; d) S. Ye, Z.-Z. Huang, C.-A. Xia, Y. Tang, L.-X. Dai, *J. Am. Chem. Soc.* **2002**, *124*, 2432 – 2433.
[15] a) R. P. Alexander, G. J. Warrellow, M. A. W. Eaton, E. C. Boyd, J. C. Head, J. R. Porter, J. A. Brown, J. T. Reuberson, B. Hutchinson, P. Turner, B. Boyce, D. Barnes, B. Mason, A. Cannell, R. J. Taylor, A. Zomaya, A. Millican, J. Leonard, R. Morphy, M. Wales, M. Perry, R. A. Allen, N. Gozzard, B. Hughes, G. Higgs, *Bioorg. Med. Chem. Lett.* **2002**, *12*, 1451 – 1456; b) I. N. Houpis, A. Molina, I. Dorziotis, R. A. Reamer, R. P. Volante, P. J. Reider, *Tetrahedron Lett.* **1997**, *38*, 7131 – 7134; c) J. E. Lynch, W.-B. Choi, H. R. O. Churchill, R. P. Volanter, R. A. Reamer, R. G. Ball, *J. Org. Chem.* **1997**, *62*, 9223 – 9228.
[16] This model also applies to the substrates shown in Table 1.
[17] For a full discussion of factors that govern the enantioselectivity, see V. K. Aggarwal, J. Richardson, *Chem. Commun.* **2003**, in press.
[18] Celltech Therapeutics Ltd, US patent No. 5,608,070.

 © 2003 Wiley-VCH Verlag GmbH & Co. KGaA, Weinheim

Natural Product Synthesis

An Abiotic Strategy for the Enantioselective Synthesis of Erythromycin B**

*Paul J. Hergenrother, Anne Hodgson, Andrew S. Judd, Wen-Cherng Lee, and Stephen F. Martin**

Erythromycin A (**1**) and erythromycin B (**2**), which owe their antibiotic activity to their ability to inhibit ribosomal-dependent protein biosynthesis, are arguably the best-known members of the macrolide family of antibiotics.[1] Despite the advent of a myriad of newer antibiotics, **1** continues to be the drug of choice for the clinical treatment of numerous pathogenic bacteria. Consequent to their important antibiotic activity and their complex structures, these natural products have been the objects of synthetic investigations for more than two decades,[2] and a substantial amount of novel and useful chemistry has emerged from these efforts. Indeed, these antibiotics have served as a veritable testing ground for evaluating methods for effecting acyclic stereochemical control. All these advances notwithstanding, it is noteworthy that there has only been a single report of the total synthesis of **1** and of **2**. In an elegant series of studies that culminated in 1981 with the total synthesis of **1**, the Woodward group not only solved problems of stereochemical control and glycosylation of the macrocyclic lactone, but also identified many of the control elements associated with the macrolactonization of seco-acid derivatives.[3] Oishi and co-workers subsequently recorded a formal synthesis of **1**,[4] and the Tatsuta group developed an alternative strategy for glycosylating the macrocyclic aglycone.[5] More recently we reported the total synthesis of **2** through a plan in which the carbohydrate residues were also introduced following the macrolactonization step.[6] Indeed, the synthetic strategy of installing the carbohydrate groups *after* cyclization of a suitable seco-acid derivative follows the general lines of the putative biosynthesis of the macrolide antibiotics.[7,8]

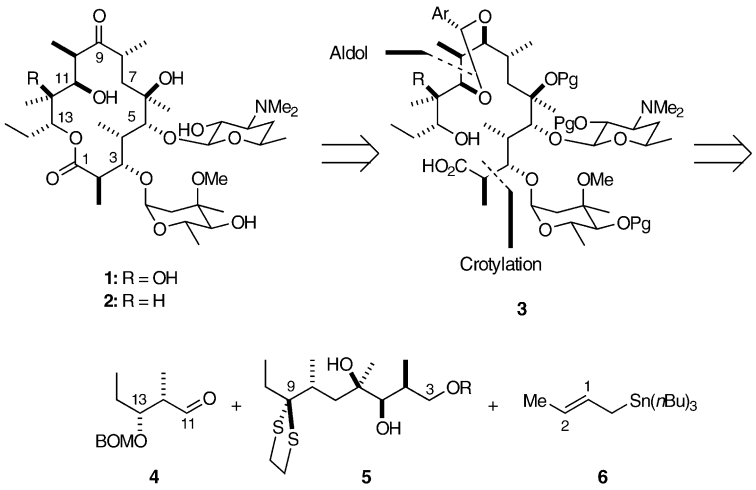
We have long been interested in exploring a different end game for the synthesis of the erythromycin antibiotics in which either one or both of the carbohydrate substituents

[*] Prof. Dr. S. F. Martin, P. J. Hergenrother, Dr. A. Hodgson, Dr. A. S. Judd, W.-C. Lee
Department of Chemistry and Biochemistry, The University of Texas Austin, TX 78712 (USA)
Fax: (+1) 512-471-4180
E-mail: sfmartin@mail.utexas.edu

[**] Taken in part from the PhD Dissertations of W.-C.L, The University of Texas, Austin, 1992, and P.J.H, The University of Texas, Austin, 1999 (present address, Department of Chemistry, University of Illinois, Urbana, IL 61801 (USA)). We thank the NIH (GM 31077), the Robert A. Welch Foundation, Pfizer, Inc, and Merck Research Laboratories for their generous support of this research. A.S.J. is also grateful for an NRSA Postdoctoral Fellowship from the NIH (5F32GM19992). We thank Dr. Paul A. Lartey (Abbott Laboratories) for a generous gift of erythromycin A for use as a source of D-desosamine and L-cladinose, and we are grateful to Dr. Erica Kraynack and Dr. Philippe Breton for conducting exploratory glycosylation studies.

 © 2003 Wiley-VCH Verlag GmbH & Co. KGaA, Weinheim DOI: 10.1002/anie.200351136

would be appended *prior* to the macrolactonization step (Scheme 1). In principle, the carbohydrate residues themselves might serve as protecting groups for the hydroxy functions at C3 and C5, thereby potentially resulting in a more concise route to **2**. This strategy was not without its risks, however, as the Woodward group had nicely defined many of the structural parameters required for the successful cyclization of erythromycin seco-acid derivatives.[3] These studies had clearly revealed the critical importance of rigidifying the seco-acid backbone in the regions spanning the C3–C5 and C8–C12 segments, typically by using cyclic derivatives that incorporated the oxygen substituents at C3, C5, C9, and C11. Hence, to establish the underlying viability of this abiotic approach to the erythromycins, we first established in a key experiment that a derivative of **3** did indeed undergo macrolactonization.[9] We now report the successful implementation of the strategy outlined in Scheme 1 for the synthesis of **2** from subunits **4**–**6**.

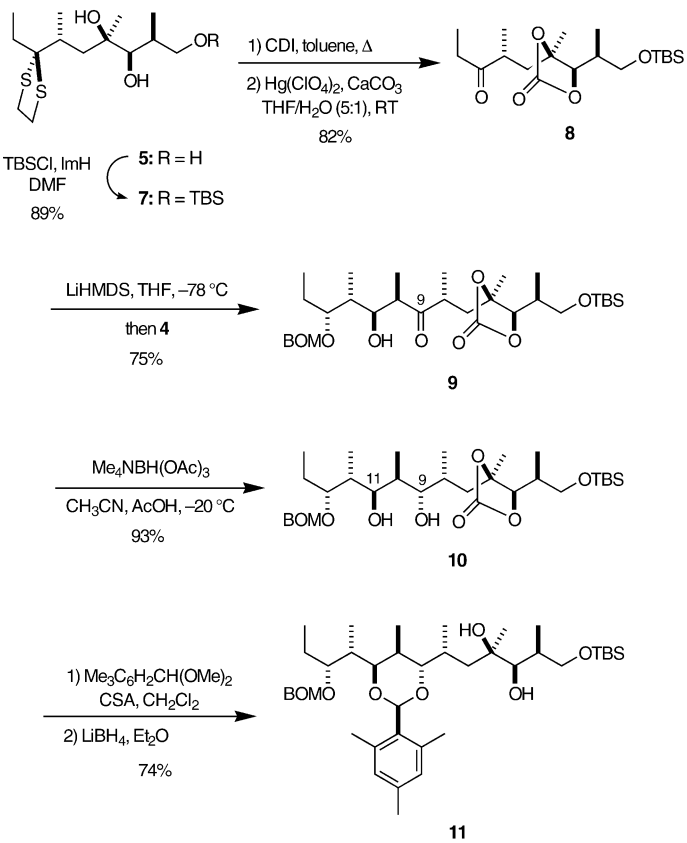


Scheme 1. Retrosynthetic analysis of erythromycin A (**1**) and erythromycin B (**2**). Pg = protecting group, BOM = benzyloxymethyl.

The synthesis commences with selective protection of the primary hydroxy group of the triol **5**, which we had previously prepared in seven steps from ethyl furan,[10] to give **7** (Scheme 2). Conversion of the diol moiety in **7** into a cyclic carbonate followed by removal of the dithiolane protecting group afforded the ketone **8**.[11] The subsequent aldol reaction of the enolate of **8** with the known aldehyde **4**[10] proceeded with high diastereoselectivity (d.r. > 95:5) to give **9**. The C9 ketone function was stereoselectively (d.r. = 98:2) reduced with $Me_4NBH(OAc)_3$ according the Evans protocol to give **10**,[12] thereby setting the *S* configuration at C9 that would be required for the macrolactonization. The C9–C11 *anti* diol moiety was then protected as its cyclic mesitylene (Mes) acetal, and the cyclic carbonate protecting group was removed to furnish the glycosylation substrate **11**, thus completing the first phase of the synthesis.

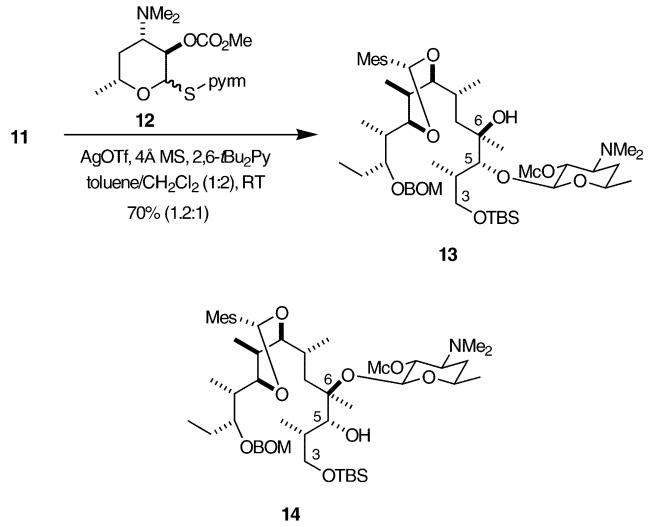
Prior art in the area of introducing desosamine residues onto macrocyclic lactones suggested that **11** should react selectively with a suitable desosamine donor to give **13**.[3,5,6] Much to our surprise, however, we found that the reaction of **11** with **12** under conditions that were defined only after considerable experimentation gave a mixture of **13** and **14** (1.2:1) in a combined yield of 70%, together with 20–25% of recovered **11** (Scheme 3). Glycosylation of the tertiary hydroxy group at C6 of **11** was thus remarkably facile, and **14** was formed in significant quantities, irrespective of numerous variations in the coupling procedure. We also explored the feasibility of protecting the hydroxy group at C6 but were unable to introduce the desosamine subunit on such protected substrates. Ultimately, we had to be content with separating the isomeric C5- and C6-glycosylated products and continuing the synthesis with **13**.

To introduce the remaining three-carbon unit of the erythromycin backbone, it was first necessary to oxidize the alcohol function at C3 to an aldehyde. However, we found that if the hydroxy group at C6 was not protected prior to generating the aldehyde at C3, a five-membered lactol that could not be advanced in the synthesis was unavoidably formed. The most expeditious solution to this problem involved deprotection of the primary alcohol group at C3 of **13** followed by reaction of the resultant diol with TESOTf to give an intermediate 3,5-diprotected diol, which underwent desilylation and Swern oxidation of the hydroxy function at C3 to give **15**

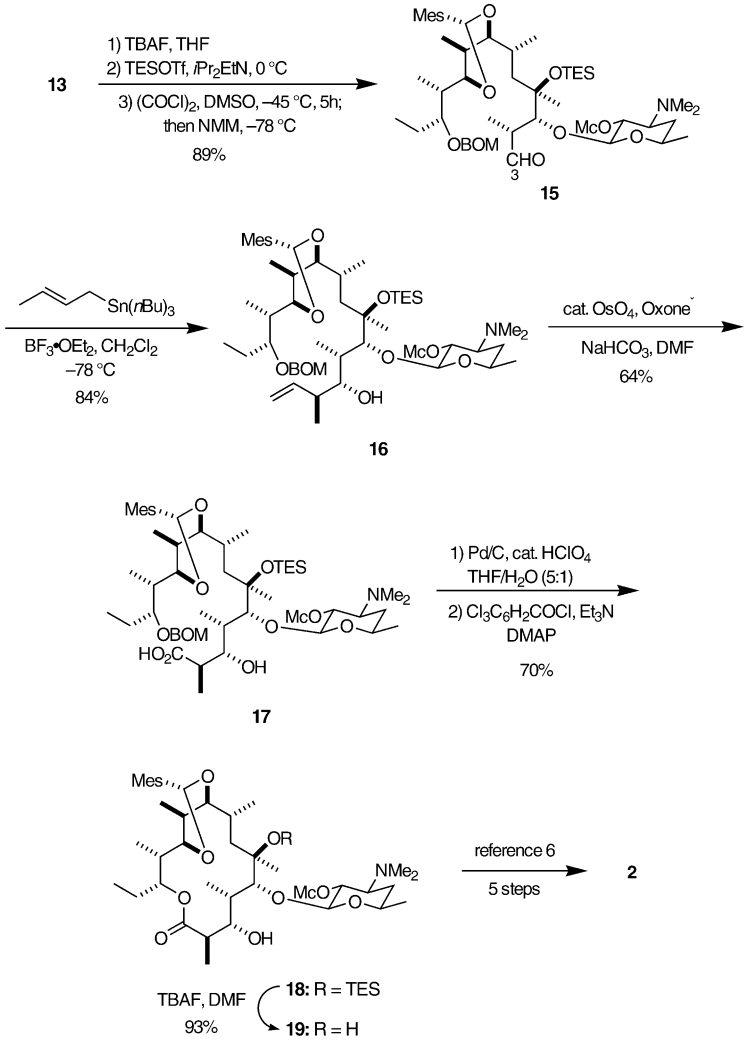


Scheme 2. Synthesis of C3–C15 backbone subunit **11**. TBS = *tert*-butyldimethylsilyl, ImH = imidazole, DMF = *N*,*N*-dimethylformamide, CDI = *N*,*N*-carbonyl diimidazole, HMDS = 1,1,1,3,3,3-hexamethyldisilazane, CSA = (−)-camphorsulfonic acid.

 © 2003 Wiley-VCH Verlag GmbH & Co. KGaA, Weinheim



Scheme 3. Synthesis of glycosylated C3–C15 backbone subunit **13**. pyrm = 2-pyrimidinyl, Tf = trifluoromethanesulfonyl, MS = molecular sieves, Py = pyridine, Mc = methoxycarbonyl.



Scheme 4. Synthesis of erythromycin B (**2**). TBAF = tetrabutylammonium fluoride, TES = triethylsilyl, DMSO = dimethyl sulfoxide, NMM = *N*-methylmorpholine, DMAP = 4-dimethylaminopyridine.

(Scheme 4).[13] The reaction of **15** with crotylstannane in the presence of $BF_3{\cdot}OEt_2$ then furnished **16**[14] in 84% yield, together with about 12% of a mixture of other diastereomeric adducts. We briefly explored the possibility of introducing the remaining carbon atoms into **15** through a number of different aldol reactions,[15] but these efforts did not yield significant quantities of the desired adduct.

It then remained to oxidize the terminal C–C double bond to generate the C1 carboxylic acid. In previous work, we had developed two- and three-step protocols for effecting this transformation,[6,10] but we found that the oxidation of **16** to give **17** by using a recently developed procedure for organometallic ozonolysis provided an efficient one-step alternative.[16] Removal of the protecting group from the C13 hydroxy function by hydrogenolysis under carefully defined conditions gave an unstable hydroxy acid, which was then cyclized according to the Yamaguchi protocol to furnish **18**.[17] Deprotection of the hydroxy group at C6 then delivered **19**, which we had previously converted in five steps into erythromycin B (**2**), thereby completing a synthesis of erythromycin B (**2**).[6]

In conclusion, we have completed a novel synthesis of erythromycin B by using an abiotic strategy in which a key step is the cyclization of a glycosylated seco-acid derivative. As such, this synthesis represents the first time that a naturally occuring macrolide antibiotic has been prepared through an approach in which a sugar residue is appended *prior* to the macrolactonization step. Moreover, the ability to cyclize the hydroxy acid derived from **17** clearly illustrates that more structural flexibility in the backbone can be tolerated in the cyclization step than was previously recognized.[3]

Received: February 7, 2003 [Z51136]

Keywords: asymmetric synthesis · cyclization · glycosylation · macrolactonization · natural products · total synthesis

[1] *Macrolide Antibiotics* (Ed.: S. Omura), Academic Press, Orlando, FL, **1984**.

[2] For leading references and representative synthetic approaches, see: a) E. J. Corey, P. B. Hopkins, S. Kim, S.-E. Yoo, K. P. Nambiar, J. R. Falck, *J. Am. Chem. Soc.* **1979**, *101*, 7131; b) S. Masamune, M. Hirama, S. Mori, S. A. Ali, D. S. Garvey, *J. Am. Chem. Soc.* **1981**, *103*, 1568; c) B. Bernet, P. M. Bishop, M. Caron, T. Kawamata, B. L. Roy, L. Ruest, G. Sauve, P. Soucy, P. Deslongchamps, *Can. J. Chem.* **1985**, *63*, 2810, 2814, 2818; d) G. Stork, S. D. Rychnovsky, *J. Am. Chem. Soc.* **1987**, *109*, 1564, 1565; e) A. R. Chamberlin, M. Dezube, S. H. Reich, D. J. Sall, *J. Am. Chem. Soc.* **1989**, *111*, 6247; f) I. Paterson, D. J. Rawson, *Tetrahedron Lett.* **1989**, *30*, 7463; g) M. Nakata, M. Arai, K. Tomooka, N. Ohsawa, M. Kinoshita, *Bull. Chem. Soc. Jpn.* **1989**, *62*, 2618; h) M. Hikota, H. Tone, K. Horita, O. Yonemitsu, *J. Org. Chem.* **1990**, *55*, 7; i) D. C. Myles, S. J. Danishefsky, G. Schulte, *J. Org. Chem.* **1990**, *55*, 1636; j) M. Hikota, H. Tone, K. Horita, O. Yonemitsu, *Tetrahedron* **1990**, *46*, 4613; k) A. F. Sviridov, V. S. Borodkin, M. S. Ermolenko, D. V. Yashunsky, N. K. Kochetkov, *Tetrahedron* **1991**, *47*, 2291, 2317; l) J. Mulzer, P. A. Mareski, J. Buschmann, P. Luger, *Synthesis* **1992**, 215; m) R. Sturmer, K. Ritter, R. W. Hoffmann, *Angew. Chem.* **1993**, *105*, 112; *Angew. Chem. Int. Ed. Engl.* **1993**, *32*, 101; n) D. A. Evans, A. S. Kim, *Tetrahedron Lett.* **1997**, *38*, 53.

 © 2003 Wiley-VCH Verlag GmbH & Co. KGaA, Weinheim

[3] R. B. Woodward, E. Logusch, K. P. Nambiar, K. Sakan, D. E. Ward, B.-W. Au-Yeung, P. Balaram, L. J. Browne, P. J. Card, C. H. Chen, R. B. Chenevert, A. Fliri, K. Frobel, H. J. Gais, D. G. Garratt, K. Hayakawa, W. Heggie, D. P. Hesson, D. Hoppe, I. Hoppe, J. A. Hyatt, D. Ikeda, P. A. Jacobi, K. S. Kim, Y. Kojima, K. Krowicki, V. J. Lee, T. Leutert, S. Malchenko, J. Martens, R. S. Matthews, B. S. Ong, J. B. Press, T. V. Rajan Babu, G. Rousseau, H. M. Sauter, M. Suzuki, K. Tatsuta, L. M. Tolbert, E. A. Truesdale, I. Uchida, Y. Ueda, T. Uyehara, A. T. Vasella, W. C. Vladuchick, P. A. Wade, R. M. Williams, H. N.-C. Wong, *J. Am. Chem. Soc.* **1981**, *103*, 3210; R. B. Woodward, E. Logusch, K. P. Nambiar, K. Sakan, D. E. Ward, B.-W. Au-Yeung, P. Balaram, L. J. Browne, P. J. Card, C. H. Chen, R. B. Chenevert, A. Fliri, K. Frobel, H. J. Gais, D. G. Garratt, K. Hayakawa, W. Heggie, D. P. Hesson, D. Hoppe, I. Hoppe, J. A. Hyatt, D. Ikeda, P. A. Jacobi, K. S. Kim, Y. Kojima, K. Krowicki, V. J. Lee, T. Leutert, S. Malchenko, J. Martens, R. S. Matthews, B. S. Ong, J. B. Press, T. V. Rajan Babu, G. Rousseau, H. M. Sauter, M. Suzuki, K. Tatsuta, L. M. Tolbert, E. A. Truesdale, I. Uchida, Y. Ueda, T. Uyehara, A. T. Vasella, W. C. Vladuchick, P. A. Wade, R. M. Williams, H. N.-C. Wong, *J. Am. Chem. Soc.* **1981**, *103*, 3213; R. B. Woodward, E. Logusch, K. P. Nambiar, K. Sakan, D. E. Ward, B.-W. Au-Yeung, P. Balaram, L. J. Browne, P. J. Card, C. H. Chen, R. B. Chenevert, A. Fliri, K. Frobel, H. J. Gais, D. G. Garratt, K. Hayakawa, W. Heggie, D. P. Hesson, D. Hoppe, I. Hoppe, J. A. Hyatt, D. Ikeda, P. A. Jacobi, K. S. Kim, Y. Kojima, K. Krowicki, V. J. Lee, T. Leutert, S. Malchenko, J. Martens, R. S. Matthews, B. S. Ong, J. B. Press, T. V. Rajan Babu, G. Rousseau, H. M. Sauter, M. Suzuki, K. Tatsuta, L. M. Tolbert, E. A. Truesdale, I. Uchida, Y. Ueda, T. Uyehara, A. T. Vasella, W. C. Vladuchick, P. A. Wade, R. M. Williams, H. N.-C. Wong, *J. Am. Chem. Soc.* **1981**, *103*, 3215

[4] T. Nakata, M. Fukui, T. Oishi, *Tetrahedron Lett.* **1988**, *29*, 2219; T. Nakata, M. Fukui, T. Oishi, *Tetrahedron Lett.* **1988**, *29*, 2223.

[5] K. Toshima, Y. Nozaki, S. Mukaiyama, T. Tamai, M. Nakata, K. Tatsuta, M. Kinoshita, *J. Am. Chem. Soc.* **1995**, *117*, 3717.

[6] S. F. Martin, T. Hida, P. R. Kym, M. Loft, A. Hodgson, *J. Am. Chem. Soc.* **1997**, *119*, 3193.

[7] J. Staunton, B. Wilkinson, *Chem. Rev.* **1997**, *97*, 2611.

[8] For a critical overview of strategic approaches, see: J. Mulzer, *Angew. Chem.* **1991**, *103*, 1484; *Angew. Chem. Int. Ed. Engl.* **1991**, *30*, 1452.

[9] S. F. Martin, M. Yamashita, *J. Am. Chem. Soc.* **1991**, *113*, 5478.

[10] S. F. Martin W.-C. Lee, G. J. Pacofsky, R. P. Gist, T. A. Mulhern, *J. Am. Chem. Soc.* **1994**, *116*, 4674.

[11] The structure assigned to each compound was in accord with its spectral (^{1}H and ^{13}C NMR, IR, MS) characteristics. Analytical samples of new compounds were obtained by flash chromatography and gave satisfactory identification by high-resolution mass spectrometry. All yields are based on isolated, purified materials that were $\geq 95\,\%$ pure.

[12] D. A. Evans, K. T. Chapman, E. M. Carreira, *J. Am. Chem. Soc.* **1988**, *110*, 3560.

[13] G. A. Tolstikov, M. S. Miftakhov, M. E. Adler, N. G. Komissarova, O. M. Kuznetsov, N. S. Vostrikov, *Synthesis* **1989**, 940.

[14] Preliminary attempts to introduce the cladinose residue to the masked seco-acid **16** were unsuccessful.

[15] a) D. A. Evans, J. V. Nelson, E. Vogel, T. R. Taber, *J. Am. Chem. Soc.* **1981**, *103*, 3099; b) M. T. Crimmins, B. W. King, E. A. Tabet, K. Chaudhary, *J. Org. Chem.* **2001**, *66*, 894; c) M. T. Crimmins, K. Chaudhary, *Org. Lett.* **2000**, *2*, 775.

[16] B. R. Travis, R. S. Narayan, B. Borhan, *J. Am. Chem. Soc.* **2002**, *124*, 3824.

[17] J. Inanaga, K. Hirata, H. Saeki, T. Katsuki, M. Yamaguchi, *Bull. Chem. Soc. Jpn.* **1979**, *52*, 1989.

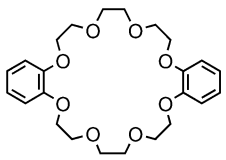
 © 2003 Wiley-VCH Verlag GmbH & Co. KGaA, Weinheim

Reversible Rotaxane Synthesis

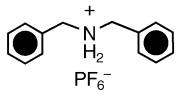
Magic Ring Rotaxanes by Olefin Metathesis**

*Andreas F. M. Kilbinger, Stuart J. Cantrill, Andrew W. Waltman, Michael W. Day, and Robert H. Grubbs**

Rotaxanes[1] are mechanically interlocked molecules composed of a dumbbell-shaped component around which one or more macrocycles are trapped. In some cases, the ability to move—in a controlled fashion—these intimate noncovalently linked components with respect to one another, has led to the creation of molecular switches[2] which have had a significant impact on the emerging field of molecular computing.[3] Although the majority of rotaxane syntheses to date have relied upon kinetic control,[4] that is, employing an irreversible final reaction step, a resurgence in the popularity of dynamic covalent chemistry[5] has spurred an interest in pursuing rotaxane formation under thermodynamic control.[6] Reversible reactions[7] utilized for this purpose include the formation (and subsequent associated cleavage) of functional groups such as imines[8] and disulfides.[9] Olefin metathesis, mediated by functional-group-tolerant ruthenium alkylidene catalysts,[10] has been used in the thermodynamically controlled synthesis of a [2]catenane,[8d,11] and, more recently, has been applied[12] to the anion-templated synthesis of a [2]rotaxane. One of the most established[13] supramolecular synthons employed in the construction of rotaxanes exploits the mutual recognition exhibited by secondary dialkylammonium ($R_2NH_2^+$) ions and suitably sized crown ethers,[14] most notably dibenzo[24]crown-8 (**DB24C8**). Here, we combine



DB24C8



DBA·PF_6

[*] Prof. R. H. Grubbs, Dr. A. F. M. Kilbinger, Dr. S. J. Cantrill, A. W. Waltman
Arnold and Mabel Beckman Laboratory of Chemical Synthesis
Division of Chemistry and Chemical Engineering
Pasadena, CA 91125 (USA)
Fax: (+1) 626–564–9297
E-mail: rhg@caltech.edu
Dr. M. W. Day
Beckman Institute
X-Ray Crystallography Laboratory
California Institute of Technology
Pasadena, CA 91125 (USA)

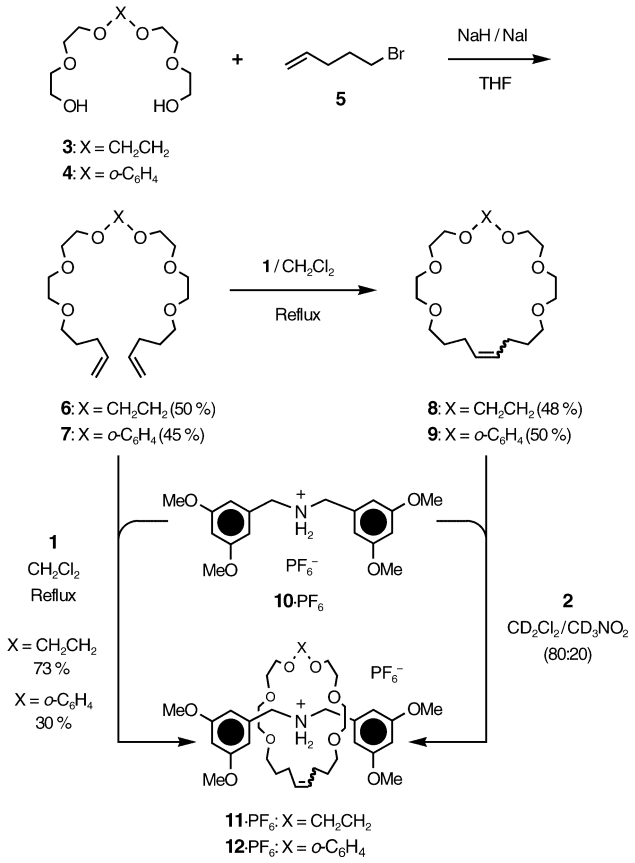
[**] A.F.M.K. thanks the Alexander von Humboldt Foundation for a Feodor–Lynen Research Fellowship. We thank Dr. Mona Shahgholi for performing the mass spectrometric analyses, Dr. Jennifer Love for assisting with initial NMR spectroscopic measurements, and Dr. Steven Goldberg for valuable comments regarding this manuscript.

Supporting information for this article is available on the WWW under http://www.angewandte.org or from the author.

 DOI: 10.1002/anie.200351167 © 2003 Wiley-VCH Verlag GmbH & Co. KGaA, Weinheim

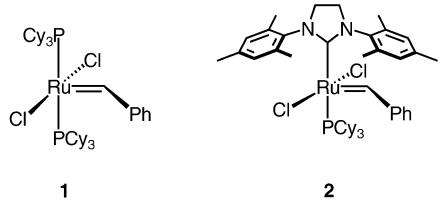
the reliability of this supramolecular synthon with the versatile reversible ring-closing-metathesis (RCM) reaction to form rotaxanes under thermodynamic control.

In an effort to mimic the significant $R_2NH_2^+$ ion binding capability of **DB24C8**, our first target macrocycle was designed such that it retained many of the desirable features of the original crown ether. Pentaethylene glycol (**3**) was bisalkylated with 5-bromo-1-pentene (**5**) to afford (Scheme 1)



Scheme 1. Synthesis of the olefin macrocycles **8** and **9**, via their corresponding diolefin precursors **6** and **7**, respectively. Rotaxane synthesis can be achieved through either a ring-closing-metathesis approach, by utilizing **6** and **7** as starting materials (lower left pathway), or by a magic ring synthesis in which the preformed macrocycles **8** and **9** are employed (lower right pathway).

the terminal diolefin **6** in moderate yield. Treatment of **6** with $(PCy_3)_2(Cl)_2Ru{=}CHPh$ (**1**),[15] under dilute conditions, gave the 24-membered olefinic crown ether analogue **8** as a mixture of *E* and *Z* isomers. The constitution of **8** is strikingly similar in nature to the macrocyclic skeleton of **DB24C8**, thereby satisfying our primary design criterion outlined above. Indeed, subsequent ^{1}H NMR spectroscopic investigations revealed that **8** does interact with dibenzylammonium hexafluorophosphate (**DBA**·PF_6) to form a 1:1 complex with a threaded geometry, that is, a pseudorotaxane. The association constant (K_a)[16] for this process is 100 M^{-1} (CD_3CN, 295 K), which is slightly lower than the value of 320 M^{-1} reported[17] for **DB24C8** under similar conditions. The major contributing factor[18] to this reduced binding affinity arises presumably from the "loss" of two ether oxygen atoms—on going from **DB24C8** to **8**—thereby decreasing the hydrogen-bonding potential between the two components.



Encouraged by these findings, the RCM reaction of the terminal diolefin **6** was repeated (Scheme 1) in the presence of a dumbbell-shaped template containing an ammonium ion, namely bis(3,5-dimethoxybenzyl)ammonium hexafluorophosphate (**10**·PF_6),[19] to afford, in 73 % yield, the corresponding [2]rotaxane **11**·PF_6 as a mixture of *E* and *Z* isomers. The significant templating effect of the $R_2NH_2^+$ ion can be appreciated by comparing this reaction with the untemplated macrocyclization of **6** to form **8**. Whereas the untemplated reaction is carried out at about 5 mM (to avoid oligo/polymerization) and yields only 48 % of the desired macrocycle, the templated reacton can be performed at much higher concentrations (ca. 100 mM in this case) to give 73 % of the ring-closed product, namely the rotaxane. Subsequent characterization by ^{1}H and ^{13}C NMR spectroscopy, mass spectrometry (electrospray), and single-crystal X-ray analysis[20] (Figure 1)

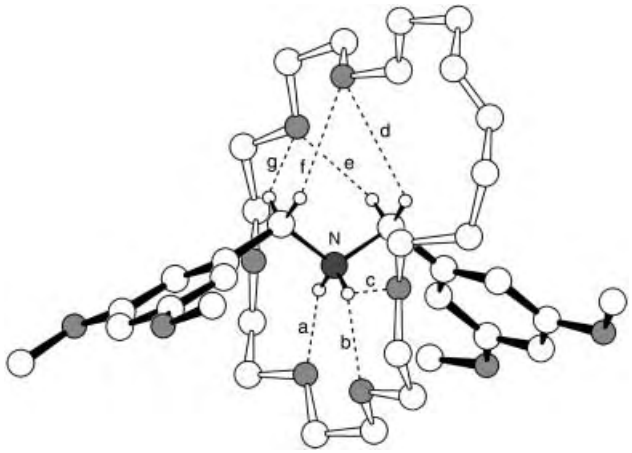


Figure 1. Ball-and-stick representation of the solid-state structure of the [2]rotaxane **11**·PF_6. Hydrogen-bonding geometries [N^+···O], [H···O] [Å], [N^+–H···O] [°]: a) 2.86, 2.04, 156; b) 2.87, 2.08, 142; c) 3.03, 2.27, 137; [C···O], [H···O] [Å], [C–H···O] [°]: d) 3.35, 2.89, 109; e) 3.41, 2.48, 161; f) 3.34, 2.88, 110; g) 3.53, 2.66, 152.

confirmed unambiguously the interlocked nature of **11**·PF_6. The cluster of peaks in the carbon–carbon double bond region of the final difference map, as well as displacement ellipsoids, some anomalous bond lengths, and the high *R* and GOF values indicate a degree of conformational disorder of this hydrocarbon loop and suggest that a mixture of *E* and *Z* isomers are present. No attempt was made to model this disorder. Subsequent hydrogenation (H_2/Pd/C) of **11**·PF_6 gave the saturated rotaxane **13**·PF_6 (see Supporting Information),

 © 2003 Wiley-VCH Verlag GmbH & Co. KGaA, Weinheim

in which the two olefin isomers collapsed into a single species, thereby facilitating the spectroscopic analysis.

Derivatization of the crown ether, to allow for the construction of extended supramolecular arrays,[21] is most easily achieved through a benzo ring that is fused to the parent macrocycle. The benzo analogues of both **6** and **8** were prepared (Scheme 1) in a similar fashion. Alkylation of the known[22] diol **4** afforded the diolefin **7**, which was subsequently converted into the desired benzocrown ether analogue **9** through a RCM reaction mediated by **1**. The K_a value for the interaction between **9** and **DBA**·PF_6 was shown[23] to be about $10\,M^{-1}$ (CD_3CN, 295 K), approximately one order of magnitude lower that that observed for **8**. This decreased affinity for ammonium ion binding can be attributed to the reduced hydrogen-bonding ability of the benzo-substituted macrocycle, namely, two of the oxygen atom donors are now phenolic in nature and are consequently less basic. Nonetheless, the benzo-substituted rotaxane **12**·PF_6 (*E*/*Z* mixture) was obtained (Scheme 1) upon the RCM reaction of **7** in the presence of **10**·PF_6, albeit in a reduced yield (30% instead of 73%). In addition to NMR spectroscopic and mass spectrometric characterization, X-ray quality single crystals[24] of this compound (Figure 2) were obtained upon slow evaporation of an EtOAc solution. The crystal structure of **12**·PF_6 contains both *E* and *Z* isomers, which are present at the same site in an approximately 1:1 ratio. Reasonable geometries in this disordered region were only obtained with a number of restraints. Once again, the *E*/*Z* mixture contributes to the high *R* and GOF values obtained.

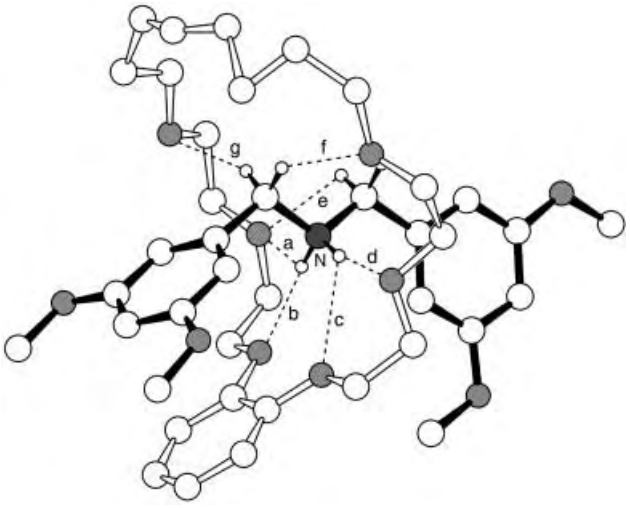


Figure 2. Ball-and-stick representation of the solid-state structure of the benzo-substituted [2]rotaxane **12**·PF_6. Hydrogen-bonding geometries [N^+···O], [H···O] [Å], [N^+–H···O] [°]: a) 3.10, 2.55, 119; b) 3.03, 2.14, 162; c) 3.08, 2.55, 117; d) 2.88, 1.98, 167; [C···O], [H···O] [Å], [C-H···O] [°]: e) 3.14, 2.53, 120; f) 3.41, 2.56, 143; g) 3.48, 2.53, 161.

To demonstrate the inherent reversibility of rotaxane formation by olefin metathesis, a "magic ring"[11a] experiment was performed in which the rotaxane was assembled (Scheme 1) directly from its preformed components, namely, the dumbbell and the macrocycle. A CD_2Cl_2/CD_3NO_2 (80:20) solution[25] containing equimolar quantities of crown ether **8** and the dumbbell-shaped compound **10**·PF_6 was prepared. Prior to the addition of any catalyst, ^{1}H NMR spectroscopic analysis revealed that, as expected, the terminally bulky-substituted secondary ammonium cation $\mathbf{10}^+$ cannot pass through the cavity of the 24-membered macrocyclic ring. Enabling the metathesis pathway, however, upon the addition of $(IMesH_2)(PCy_3)(Cl)_2Ru{=}CHPh$ (**2**)[26] (10 mol%), allows the system to equilibrate to a thermodynamic minimum (a process driven by the creation of N^+–H···O and C–H···O hydrogen bonds), and results in the formation of the [2]rotaxane **11**·PF_6. This transformation was monitored (Figure 3) by ^{1}H NMR spectroscopy, and equilibrium

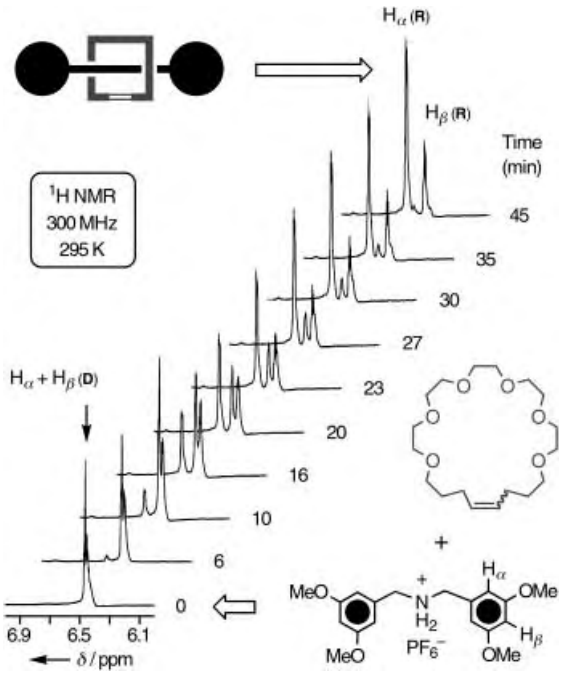


Figure 3. Partial ^{1}H NMR spectra showing the change over time in the environment of H_α and H_β as the dumbbell (**D**) component converts into the rotaxane (**R**) during the magic ring synthesis in which macrocycle **8** and **10**·PF_6 were employed as starting materials.

(> 95% interlocked species) was achieved in 45 minutes. Spectral assignments were made by comparison to an authentic sample of the rotaxane isolated previously in the RCM approach, and mass spectrometric analysis also confirmed that the major component in solution was, indeed, the [2]rotaxane **11**·PF_6.

In an analogous fashion, the magic ring experiment was repeated with the benzo-derivative **9** and resulted (Figure 4) in a similar outcome. In this case, the equilibrium position is reached in less time (ca. 20 min), and affords a smaller proportion of the interlocked species (ca. 85% of the [2]rotaxane **12**·PF_6), which presumably reflects the reduced affinity of this particular macrocycle for secondary dibenzylammonium ions. No decrease of catalyst activity was observed over the duration of the magic ring syntheses described above, as indicated by the undiminished intensity of the carbene (benzylidene) singlet of the catalytic species ($\delta =$

 © 2003 Wiley-VCH Verlag GmbH & Co. KGaA, Weinheim

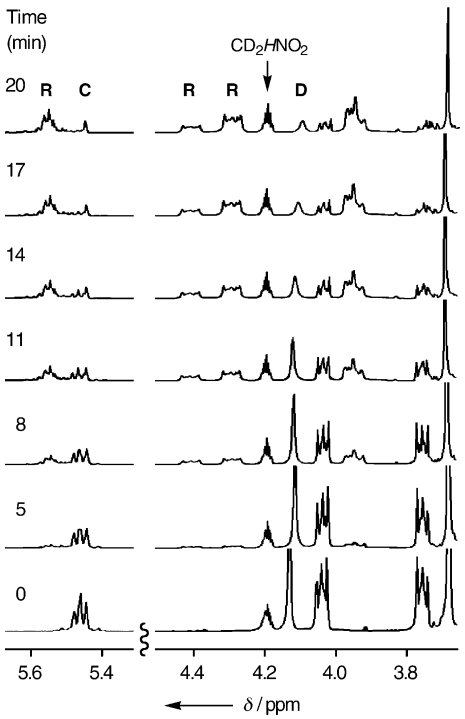


Figure 4. Partial ^{1}H NMR spectra showing the change over time during the magic ring synthesis in which macrocycle **9** and **10**·PF_6 were employed as starting materials. The singlet at $\delta = 4.15$ ppm, which arises from the methylene proton of the free dumbbell (**D**) component, diminishes over time. Conversely, the characteristic multiplets centered around $\delta = 4.27$ and 4.40 ppm indicate the formation of two new interlocked products, namely, the *E* and *Z* isomers, respectively, of the corresponding [2]rotaxane **12**·PF_6 (**R**). Furthermore, the multiplet at $\delta = 5.45$ ppm, corresponding to the olefinic protons of the free crown ether analogue (**C**), also reduces in intensity at the expense of the multiplet just downfield from it—which corresponds to the olefinic resonances of the (*E*/*Z*) rotaxane mixture (**R**).

19.0 ppm) in the ^{1}H NMR spectrum. Furthermore, the magic ring syntheses of the [2]rotaxanes employ the more active metathesis catalyst **2**, and, under this particular set of conditions, the transformations occur with very high yields that approach, in the case of the non-benzo system, quantitative numbers.

In conclusion, diolefin macrocyclic precursors have been shown to cyclize around an appropriately substituted dibenzylammonium salt to produce the corresponding [2]rotaxanes. Exploiting ruthenium carbene mediated olefin metathesis in this "clipping" procedure allows for the assembly process to occur in a reversible fashion, namely, it can operate under thermodynamic control. This dynamic feature can be utilized to synthesize mechanically interlocked molecules under magic ring conditions, whereby preformed components can be exposed to the necessary catalytic agent (**1** or **2** in this case) causing the macrocycle to open and close repeatedly while the system strives to reach a thermodynamic minimum. The successful application of this methodology to the synthesis of simple [2]rotaxanes, has enabled the creation of other, more intricate, interlocked molecular architectures (for example, catenanes,[1] daisy chains,[21] and other interlocked polymeric systems) to be explored. Moreover, the ability to drive these systems to almost quantitative conversion allows for the pursuit of high-molecular-weight polymers with novel interlocked architectures.

Experimental Section

General procedure for "magic ring" experiments: Catalyst **2** (0.8 mg, 10^{-3} mmol) was added under a dry N_2 atmosphere to a solution of unsaturated crown ether **8** or **9** (10 mmol) and **10**·PF_6 (4.6 mg, 10^{-2} mmol) in CD_2Cl_2/CD_3NO_2 (80:20, 1.0 mL). The reaction was followed by ^{1}H NMR spectroscopy under ambient conditions. For all other experimental procedures and characterization data, see the Supporting Information.

Received: February 13, 2003 [Z51167]
Published online: July 3, 2003

Keywords: macrocycles · metathesis · rotaxanes · ruthenium · template synthesis

[1] a) D. B. Amabilino, J. F. Stoddart, *Chem. Rev.* **1995**, *95*, 2725–2828; b) *Molecular Catenanes, Rotaxanes and Knots* (Eds.: J.-P. Sauvage, C. Dietrich-Buchecker), Wiley-VCH, Weinheim, **1999**.
[2] a) V. Bermudez, N. Capron, T. Gase, F. G. Gatti, F. Kajzar, D. A. Leigh, F. Zerbetto, S. W. Zhang, *Nature* **2000**, *406*, 608–611; b) J.-P. Collin, C. Dietrich-Buchecker, P. Gaviña, M. C. Jimenez-Molero, J.-P. Sauvage, *Acc. Chem. Res.* **2001**, *34*, 477–487.
[3] a) A. R. Pease, J. F. Stoddart, *Struct. Bonding (Berlin)* **2001**, *99*, 189–236; b) Y. Luo, C. P. Collier, J. O. Jeppesen, K. A. Nielsen, E. Delonno, G. Ho, J. Perkins, H.-R. Tseng, T. Yamamoto, J. F. Stoddart, J. R. Heath, *ChemPhysChem* **2002**, *3*, 519–525.
[4] For recent examples of kinetically controlled rotaxane syntheses, see a) J. E. H. Buston, F. Marken, H. L. Anderson, *Chem. Commun.* **2001**, 1046–1047; b) S.-H. Chiu, S. J. Rowan, S. J. Cantrill, J. F. Stoddart, A. J. P. White, D. J. Williams, *Chem. Eur. J.* **2002**, *8*, 5170–5183.
[5] a) J.-M. Lehn, *Chem. Eur. J.* **1999**, *5*, 2455–2463; b) S. J. Rowan, S. J. Cantrill, G. R. L. Cousins, J. K. M. Sanders, J. F. Stoddart, *Angew. Chem.* **2002**, *114*, 938–993; *Angew. Chem. Int. Ed.* **2002**, *41*, 898–952.
[6] For the earliest reported examples of a rotaxane synthesis that utilizes reversible formation of a covalent bond, see I. T. Harrison, *J. Chem. Soc. Chem. Commun.* **1972**, 231–232.
[7] Certain kinetically labile metal–ligand interactions have also been exploited, as the reversible "reaction" step, in the formation of dynamic (organometallic) rotaxanes; for a recent example, see C. A. Hunter, C. M. R. Low, M. J. Packer, S. E. Spey, J. G. Vinter, M. O. Vysotsky, C. Zonta, *Angew. Chem.* **2001**, *113*, 2750–2754; *Angew. Chem. Int. Ed.* **2001**, *40*, 2678–2682.
[8] a) S. J. Cantrill, S. J. Rowan, J. F. Stoddart, *Org. Lett.* **1999**, *1*, 1363–1366; b) P. T. Glink, A. I. Olivia, J. F. Stoddart, A. J. P. White, D. J. Williams, *Angew. Chem.* **2001**, *113*, 1922–1927; *Angew. Chem. Int. Ed.* **2001**, *40*, 1870–1875; c) D. A. Leigh, P. J. Lusby, S. J. Teat, A. J. Wilson, J. K. Y. Wong, *Angew. Chem.* **2001**, *113*, 1586–1591; *Angew. Chem. Int. Ed.* **2001**, *40*, 1538–1543.
[9] a) A. G. Kolchinski, N. W. Alcock, R. A. Roesner, D. H. Busch, *Chem. Commun.* **1998**, 1437–1438; b) T. Oku, Y. Furusho, T. Takata, *J. Polym. Sci.* **2003**, *41*, 119–123.
[10] T. M. Trnka, R. H. Grubbs, *Acc. Chem. Res.* **2001**, *34*, 18–29.
[11] a) T. J. Kidd, D. A. Leigh, A. J. Wilson, *J. Am. Chem. Soc.* **1999**, *121*, 1599–1600; for other catenane syntheses employing RCM, see b) D. G. Hamilton, N. Feeder, S. J. Teat, J. K. M. Sanders, *New J. Chem.* **1998**, 1019–1021; c) M. Weck, B. Mohr, J.-P.

 © 2003 Wiley-VCH Verlag GmbH & Co. KGaA, Weinheim

Sauvage, R. H. Grubbs, *J. Org. Chem.* **1999**, *64*, 5463 – 5471, respectively.

[12] J. A. Wisner, P. D. Beer, M. G. B. Drew, M. R. Sambrook, *J. Am. Chem. Soc.* **2002**, *124*, 12469 – 12476. During the course of our investigations, this report of rotaxane formation, by using ring-closing-olefin metathesis, appeared in the literature. Although the authors note that the metathesis reaction is under thermodynamic control, this aspect of the reaction is not investigated further.

[13] a) A. G. Kolchinski, D. H. Busch, N. W. Alcock, *J. Chem. Soc. Chem. Commun.* **1995**, 1289 – 1291; b) S. J. Cantrill, A. R. Pease, J. F. Stoddart, *J. Chem. Soc. Dalton Trans.* **2000**, 3715 – 3734, and references therein.

[14] S. J. Cantrill, D. A. Fulton, A. M. Heiss, A. R. Pease, J. F. Stoddart, A. J. P. White, D. J. Williams, *Chem. Eur. J.* **2000**, *6*, 2274 – 2287.

[15] P. Schwab, R. H. Grubbs, J. W. Ziller, *J. Am. Chem. Soc.* **1996**, *118*, 100 – 110.

[16] The association constant for this slowly equilibrating system was determined using the single-point method, see J. C. Adrian, C. S. Wilcox, *J. Am. Chem. Soc.* **1991**, *113*, 678 – 680. It should be noted that, in this case, the K_a value reflects a total association constant, which combines the contributions from both the *cis* and *trans* isomers of the crown ether present in solution.

[17] P. R. Ashton, R. A. Bartsch, S. J. Cantrill, R. E. Hanes, Jr., S. K. Hickingbottom, J. N. Lowe, J. A. Preece, J. F. Stoddart, V. S. Talanov, Z.-H. Wang, *Tetrahedron Lett.* **1999**, *40*, 3661 – 3664.

[18] Hydrogenation of **8** affords the saturated crown ether **15**, which was shown (by ^{1}H NMR spectroscopy) to bind dibenzylammonium hexafluorophosphate with a K_a value of $90\,M^{-1}$. This value differs only slightly from that observed for **8**, thus suggesting that the carbon–carbon double bond has little effect upon the ability to bind secondary ammonium ions.

[19] S. J. Cantrill, M. C. T. Fyfe, A. M. Heiss, J. F. Stoddart, A. J. P. White, D. J. Williams, *Org. Lett.* **2000**, *2*, 61 – 64.

[20] Crystal data for **11**·PF_6: $[C_{36}H_{58}NO_{10}][PF_6]$; $M_r = 809.80$; $0.19 \times 0.20 \times 0.24$ mm; colorless; monoclinic; spave group $P2_1/n$ (no. 14), $Z = 4$; $a = 13.3814(7)$, $b = 19.3278(10)$, $c = 16.1791(8)$ Å, $\beta = 109.105(1)°$; $V = 3594.0(4)$ Å^3; $\rho_{calcd} = 1.360$ gcm^{-3}; $Mo_{K\alpha}$ radiation ($\lambda = 0.71073$ Å); $2\theta_{max} = 56.8°$; ω-scans on a SMART 1000 ccd; $T = 98$ K; 67646 reflections measured (all 9326 unique used); $-17 \le h \le 17$, $-25 \le k \le 25$, $-21 \le L \le 20$; Lorentz factor but no absorption correction ($\mu = 0.15$ mm^{-1}) applied; structure solved and refined with full-matrix least-squares on F^2 with SHELXL-97[27]; 9326 data, 0 restraints, and 583 parameters; R(6046 reflections $> 2\sigma(I)$, all data) = 0.070, 0.107; R_w(6046 reflections $> 2\sigma(I)$, all data) = 0.109, 0.113; $S = 2.62$; hydrogen atoms on the macrocyle were riding, while those on the cation were unrestrained; greatest final electron density difference excursions of 1.41 e·Å^3 at 1.02 Å from H(11A) and -1.36 e·Å^3 at 0.42 Å from C(12).[28]

[21] S. J. Cantrill, G. J. Youn, J. F. Stoddart, D. J. Williams, *J. Org. Chem.* **2001**, *66*, 6857 – 6872.

[22] B. Colonna, L. Echegoyen, *Chem. Commun.* **2001**, 1104 – 1105.

[23] Hydrogenation of olefin macrocycle **9** affords the saturated analogue **16**, which shows little change in the binding affinity for **DBA**·PF_6 ($K_a \sim 10\,M^{-1}$).

[24] Crystal data for **12**·PF_6: $[C_{40}H_{58}NO_{10}][PF_6]$; $M_r = 857.84$; $0.24 \times 0.31 \times 0.33$ mm; colorless; monoclinic; space group $P2_1/n$ (no. 14), $Z = 4$; $a = 14.3407(6)$, $b = 19.2063(8)$, $c = 15.8720(7)$ Å, $\beta = 107.353(1)°$; $V = 4172.7(3)$ Å^3; $\rho_{calcd} = 1.366$ gcm^{-3}; $Mo_{K\alpha}$ radiation ($\lambda = 0.71073$ Å); $2\theta_{max} = 55.4°$; ω-scans on a SMART 1000 ccd; $T = 98$ K; 83324 reflections measured (all 9644 unique used); $-18 \le h \le 18$, $-25 \le k \le 24$, $-21 \le L \le 21$; Lorentz factor but no absorption correction ($\mu = 0.15$ mm^{-1}) applied; structure solved and refined with full-matrix least-squares on F^2 with SHELXL-97[27]; 9644 data, 235 restraints (distance, planarity, and anisotropic displacement parameter restaints in the macrocylic double bond region which was disordered ca. 1:1 E:Z), and 582 parameters; R(6838 reflections $> 2\sigma(I)$, all data) = 0.063, 0.090; R_w(6838 reflections $> 2\sigma(I)$, all data) = 0.105, 0.107; $S = 3.48$; all hydrogen atoms were riding on attached atoms; greatest final electron density difference excursions of 0.78 e·Å^3 and -0.82 e·Å.[28]

[25] CD_3NO_2 is required to ensure complete dissolution of **10**·PF_6.

[26] $IMesH_2$ = 1,3-dimesityl-4,5-dihydroimidazol-2-ylidene, see M. Scholl, S. Ding, C. W. Lee, R. H. Grubbs, *Org. Lett.* **1999**, *1*, 953 – 956.

[27] G. M. Sheldrick, SHELXL-97, Program for Structure Refinement, University of Göttingen, Göttingen (Germany), **1997**.

[28] CCDC 188147 (**11**·PF_6) and CCDC 188995 (**12**·PF_6) contain the supplementary crystallographic data for this paper. These data can be obtained free of charge via www.ccdc.cam.ac.uk/conts/retrieving.html (or from the Cambridge Crystallographic Data Centre, 12 Union Road, Cambridge CB21EZ, UK; fax: (+44) 1223-336-033; or deposit@ccdc.cam.ac.uk). Structure factors are available from the authors via email:xray@caltech.edu.

 © 2003 Wiley-VCH Verlag GmbH & Co. KGaA, Weinheim

Electron-Transfer Processes

Synthesis and Structure of a Biomimetic Model of the Iron Hydrogenase Active Site Covalently Linked to a Ruthenium Photosensitizer**

Sascha Ott, Mikael Kritikos, Björn Åkermark, and Licheng Sun**

Although known for more than 75 years,[1] sulfur-containing binuclear complexes of iron have recently experienced a renaissance as interesting synthetic targets as they closely resemble the active site of iron hydrogenases (FeH), a naturally occurring class of enzymes which regulate the production and consumption of hydrogen in microorganisms.[2–5] Crystallographic studies revealed the active site of the natural system to consist of two iron(I) cations which are linked by an unusual bridging dithiolate ligand.[6,7] It has been

[*] Prof. Dr. B. Åkermark, Dr. L. Sun, Dr. S. Ott
Department of Organic Chemistry
Arrhenius Laboratory, Stockholm University
10691 Stockholm (Sweden)
Fax: (+46) 8-154-908
E-mail: bjorn.akermark@organ.su.se
licheng.sun@organ.su.se
Dr. M. Kritikos
Department of Structural Chemistry
Arrhenius Laboratory, Stockholm University
10691 Stockholm (Sweden)

[**] The authors thank Dr. Jonas Bergquist and Charlotte Hagman (University of Uppsala) for the measurement of the ESI mass spectrum of **1**. Financial support for this work was provided by the Swedish Energy Agency, the Knut and Alice Wallenberg Foundation, the Swedish Research Council for Natural Science (NFR), and the Swedish Research Council (VR).

 DOI: 10.1002/anie.200351192 © 2003 Wiley-VCH Verlag GmbH & Co. KGaA, Weinheim

suggested that this ligand contains a nitrogen heteroatom and possesses the structure SCH_2NHCH_2S.[8,9] The remaining primary coordination sphere around the dinuclear iron active site is occupied by the diatomic ligands CO and CN^-, as well as by a thiol-linked tetranuclear Fe cluster.[6,7,10–12] In the natural system one coordination site remains vacant to allow for hydride or hydrogen coordination.[10]

Recently, Rauchfuss and co-workers have shown that a biomimetic model of FeH can serve as a catalyst for electrochemical hydrogen production.[13] In the context of our interest in photochemical fuel production[14] we became intrigued by the possibility of covalently linking a biomimetic model of the iron hydrogenase active site to a ruthenium photosensitizer in an attempt to afford hydrogen production by the action of light. The projected process is illustrated in Figure 1. It commences with the absorption of a photon by the ruthenium photosensitizer (step 1, Figure 1). The photoexcited ruthenium complex is oxidatively quenched by the dinuclear iron site, which gives rise to a reduced iron species (step 2, Figure 1). After regeneration of the photosensitizer (by an external electron donor), this process is repeated to afford a doubly reduced diiron species which could then drive the reduction of protons. The possibility of introducing ligands different from CO on to the iron portion of the system is of great importance as the redox properties of the structure can thereby be altered significantly to suit the electronic requirements of this process.

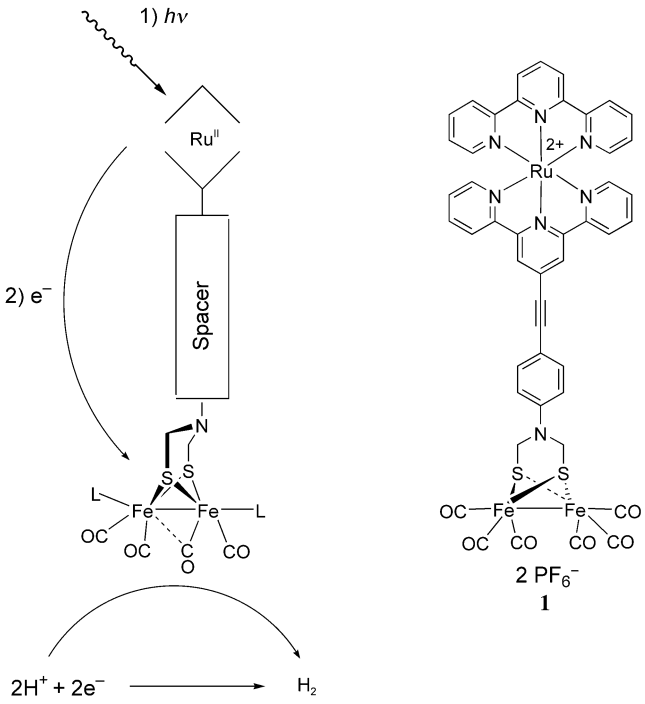
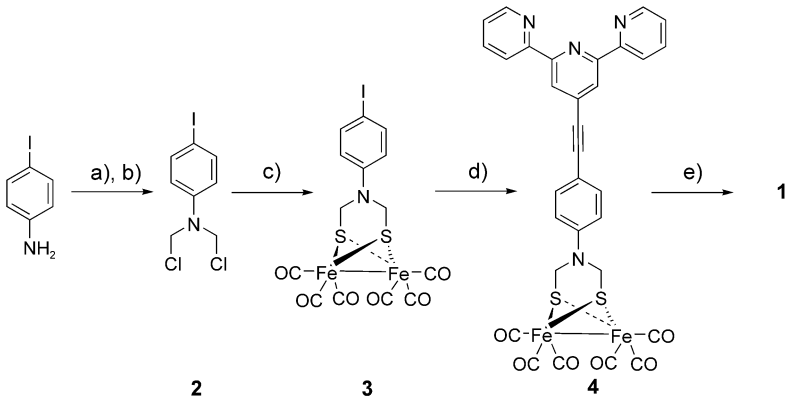


Figure 1. Schematic representation for the projected photoinduced reduction of protons. L = CO, CN^-, PX_3, or thiolates.

We recently prepared a ruthenium(tris)bipyridine type of photosensitizer linked to a diiron complex, in which the iron atoms are connected by a dithiol bridge.[15] Herein we present the synthesis of a novel system in which a 2-aza-1,3-dithiol-bridged dinuclear iron complex is covalently linked to a ruthenium photosensitizer. The system was designed to fulfil various aspects: $[Ru(terpy)_2]^{2+}$ (terpy = 2,2′:6′,2″-terpyridine) was chosen as the photosensitizer because of its geometric advantages over other Ru complexes with didentate ligands.[16] An acetylenic linker between the redox-active termini was selected not only to gain precise control over their spatial separation, but also to prolong the lifetime of the excited state of $[Ru(terpy)_2]^{2+}$[17] so that electron transfer to the iron portion can occur. Finally, the dithiolate bridge in the diiron site was chosen to contain a nitrogen heteroatom, as this arrangement may play an essential role in the production of hydrogen in the natural system.[8,9] With this reasoning, **1** was selected as the target complex.



Scheme 1. a) *p*-CH_2O, CH_2Cl_2, RT, 3 h; b) $SOCl_2$, RT, 30 min; c) $Li_2(SFe(CO)_3)_2$, THF, −78 °C, 5 min, 76%; d) 4′-ethynyl-2,2′:6′,2″-terpyridine, $[PdCl_2(PPh)_2]$, CuI, Et_3N, toluene, 40 °C, 3 h, 57%; e) $[RuCl_2(terpy)]$·DMSO, MeOH, reflux, 4 h, 29%.

The diiron portion was established by applying a recently published procedure for the preparation of some related complexes.[18] Thus, the lithium salt of diironhexacarbonyldisulfide[19] was treated with *N,N*-di(chloromethyl)-4-iodoaniline (**2**), which in turn was synthesized from *p*-iodoaniline in two steps (Scheme 1).[18] Structural analysis of **3** by single-crystal X-ray diffraction[20] (Figure 2) revealed the familiar distorted square-pyramidal arrangement around the iron nuclei. The Fe–Fe bond length of 2.499(1) Å is in good agreement with other crystal structure data of this type of complex.[18,21] The arene substituent resides in an axial position directly above one carbonyl ligand. The π conjugation between the phenyl ring and the nitrogen p orbital is somewhat interrupted in the solid state, as evident from a deviation of the nitrogen atom by 0.164(3) Å from the plane defined by the C7, C8, and C9 atoms. The sum of the C-N-C angles around N1 is 356°. The azadithiolate-bridged diiron species **3** represents the first complex of this kind where the nitrogen atom is linked to an aromatic system.

The iodo functionality in the iron complex **3** could be utilized for further elaboration by reaction of the former complex with 4′-ethynyl-2,2′:6′,2″-terpyridine[22,23] under the cross-coupling conditions used by Sonogashira et al.[24] to

 © 2003 Wiley-VCH Verlag GmbH & Co. KGaA, Weinheim

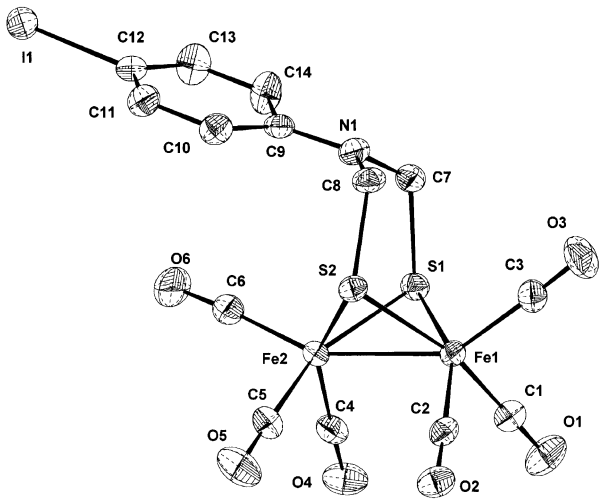


Figure 2. ORTEP (ellipsoids at 30% probability level) view of **3**[20] Selected bond lengths [Å]: Fe1-Fe2 2.4988(8), Fe1-S1 2.2537(10), Fe1-S2 2.2630(10), Fe2-S1 2.2573(10), Fe2-S2 2.2682(10), Fe1-C1 1.798(4), Fe1-C2 1.799(3), Fe1-C3 1.795(4), Fe2-C4 1.778(4), Fe2-C5 1.792(4), Fe2-C6 1.812(4), S1-C7 1.847(4), S2-C8 1.861(4), N1-C7 1.431(5) N1-C8 1.413(5), N1-C9 1.404(5).

afford the terpyridine-coupled dinuclear iron complex **4**. In the solid state, the iron carbonyl portion of **4** is stable towards ligand substitution by the polypyridine unit as unambiguously demonstrated by single-crystal X-ray diffraction studies[20] (Figure 3). Apart from the ethynylterpyridine fragment, the crystal structure of **4** closely resembles that of **3**. The rigidity of the system enables the distance from the nitrogen atom (N2) of the central pyridine ring to the Fe cations to be calculated as 11.892(3) and 13.996(3) Å. The electronic similarities between complexes **3** and **4** are further corroborated by their respective IR spectra, which are alike and

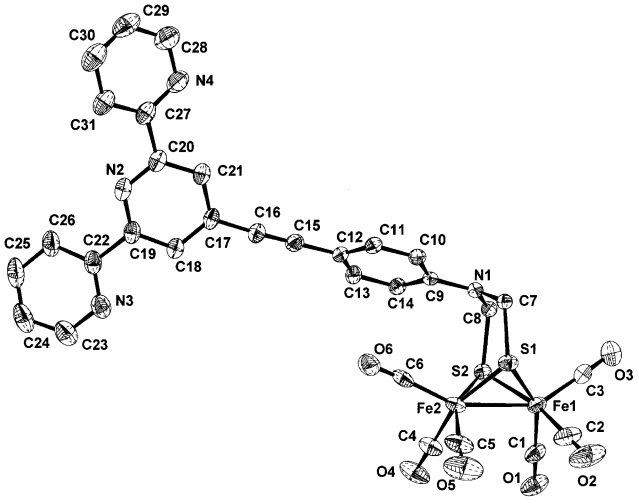


Figure 3. ORTEP (ellipsoids at 30% probability level) view of **4**[20] Selected bond lengths [Å]: Fe1-Fe2 2.5056(7), Fe1-S1 2.2625(9), Fe1-S2 2.2631(9), Fe2-S1 2.2559(9), Fe2-S2 2.2576(8), Fe1-C1 1.778(4), Fe1-C2 1.789(4), Fe1-C3 1.778(4), Fe2-C4 1.784(4), Fe2-C5 1.785(4), Fe2-C6 1.801(4), S1-C7 1.850(3), S2-C8 1.852(3), N1-C7 1.432(4) N1-C8 1.424(4), N1-C9 1.402(4).

exhibit three major bands in the CO region at 2076, 2038, and 2001 cm^{-1}. This resemblance indicates that the iron carbonyl portion is insensitive to the presence of an acetylenic substituent on the aniline as well as to the terpyridine. Solutions of **4** in organic solvents are unstable at room temperature and decompose within minutes upon exposure to light, presumably as a result of light-induced decarbonylation followed by intermolecular terpyridine complexation. However, as a freshly prepared solution in methanol which is kept in the dark, ligand **4** coordinates readily to the {Ru(terpy)} fragment,[25] which gives rise to the desired trinuclear complex **1**. The IR spectrum of a solution of **1** in CH_2Cl_2 shows a pattern in the CO region that is identical to that found for complexes **3** and **4**. This observation indicates there is negligible electronic communication between the redox-active ruthenium center and the iron termini. In contrast to **4**, solutions of **1** are stable and can be stored under ambient conditions for extended periods of time.

Whereas the vast majority of reports in the past have concentrated on ligand-exchange reactions on the Fe-Fe portion,[2–5] this work represents one of the few examples in the literature[26] where chemistry is performed on the organic bridge of an assembled dinuclear iron complex and ultimately leads to a covalent connection to a ruthenium photosensitizer. The preparation of **4** with its free terpyridine metal-binding pocket will enable the incorporation of many different metals, thus offering an insight into electron-transfer processes in a biomimetic model of the active site of FeH. The design of **1** allows the exchange of ligands on the iron portion to facilitate electron transfer from the photoexcited ruthenium complex. Such a modified molecular assembly could promote the light-driven reduction of protons. Experimental efforts in these directions together with in-depth photophysical studies of the system are currently in progress.

Experimental Section

4: $[PdCl_2(PPh_3)_2]$ (18 mg, 0.025 mmol) and CuI (2 mg, 0.01 mmol) were added successively to a degassed solution of iodoarene **3** (150 mg, 0.25 mmol) and 4′-ethynyl-2,2′:6′,2″-terpyridine (73 mg, 0.28 mmol) in triethylamine and toluene (1:1, 20 mL) at 40 °C. After the mixture had been stirred in the dark for 3 h at this temperature, it was concentrated in vacuo and the black residue was subjected to column chromatography, conducted in the dark (Al_2O_3, CH_2Cl_2), to give **4** as a red solid (102 mg, 0.14 mmol, 57%). Elemental analysis (%) calcd for $C_{31}H_{18}Fe_2N_4O_6S_2$: C 51.83, H 2.52, N 7.80; found: C 51.70, H 2.62, N 7.67; ^{1}H NMR (300 MHz, $CDCl_3$): $\delta = 8.71$ (m, 2H), 8.59 (m, 2H), 8.54 (s, 2H), 7.85 (m, 2H), 7.50 (d, $J = 8.7$ Hz, 2H), 7.34 (m, 2H), 6.70 (d, $J = 8.7$ Hz, 2H), 4.30 ppm (s, 4H, NCH_2S); ^{13}C NMR (75 MHz, $CDCl_3$): $\delta = 206.8$, 155.7, 155.4, 149.1, 144.7, 136.9, 133.8, 133.7, 123.9, 122.6, 121.2, 115.3, 113.6, 94.1, 87.0, 49.4 ppm; IR (CH_2Cl_2): $\tilde{\nu} = 2214$ (C≡C), 2076, 2038, 2001 cm^{-1} (C=O).

1: $[RuCl_2(terpy)(DMSO)]$ (67 mg, 0.14 mmol) was added to a degassed solution of **4** (100 mg, 0.14 mmol) in methanol (30 mL). The mixture was refluxed in the dark for 4 h, before the solvent was removed in vacuo. The remaining brown solid was purified by flash chromatography on silica gel (solvent: CH_3CN:H_2O:sat. aq KNO_3 = 90:9:1). After removal of the solvent in vacuo and anion exchange with NH_4PF_6, the red solid was recrystallized from CH_2Cl_2/Et_2O (55 mg, 0.04 mmol, 29%). Elemental analysis (%) calcd for $C_{46}H_{29}F_{12}Fe_2N_7O_6P_2RuS_2$: C 41.21, H 2.18, N 7.31; found: C 41.50, H 2.15, N 7.56; ^{1}H NMR (300 MHz, CD_3CN): $\delta = 8.82$ (s, 2H), 8.75 (d,

 © 2003 Wiley-VCH Verlag GmbH & Co. KGaA, Weinheim

$J = 8.3$ Hz, 2H), 8.49 (m, 4H), 8.42 (t, $J = 8.3$ Hz, 1H), 7.93 (m, 4H), 7.70 (d, $J = 9.0$ Hz, 2H), 7.39 (m, 2H), 7.34 (m, 2H), 7.17 (m, 4H), 6.98 (d, $J = 9.0$ Hz, 2H), 4.50 ppm (s, 4H, NCH_2S); ^{13}C NMR (75 MHz, CD_3CN): $\delta = 209.0$, 159.6, 159.3, 156.9 (2C), 154.2 (2C), 147.6, 139.8 (2C), 137.7, 135.6, 132.3, 129.3, 128.1, 126.5, 126.1 (2C), 125.4, 117.4, 113.0, 99.7, 87.4, 50.8 ppm; IR (CH_2Cl_2): $\tilde{\nu} = 2192$ (C≡C), 2077, 2038, 2001 cm^{-1} (C=O); ESI-MS: Ru-isotopic pattern centered at $m/z = 1197.9$ (100%) $[M-PF_6^-]^+$, calcd for $[M-PF_6^-]^+$: $m/z = 1197.9$.

Received: February 17, 2003
Revised: May 19, 2003 [Z51192]

Keywords: bioinorganic chemistry · enzyme models · iron hydrogenase · ruthenium · structure elucidation

[1] H. Reihlen, A. von Friedolsheim, W. Oswald, *Justus Liebigs Ann. Chem.* **1928**, 72–96.
[2] M. Y. Darensbourg, E. J. Lyon, J. J. Smee, *Coord. Chem. Rev.* **2000**, *206–207*, 533–561.
[3] F. Gloaguen, J. D. Lawrence, M. Schmidt, S. R. Wilson, T. B. Rauchfuss, *J. Am. Chem. Soc.* **2001**, *123*, 12518–12527.
[4] S. J. George, Z. Cui, M. Razavet, C. J. Pickett, *Chem. Eur. J.* **2002**, *8*, 4037–4046.
[5] E. J. Lyon, I. P. Georgakaki, J. H. Reibenspies, M. Y. Darensbourg, *J. Am. Chem. Soc.* **2001**, *123*, 3268–3278.
[6] J. W. Peters, W. N. Lanzilotta, B. J. Lemon, L. C. Seefeldt, *Science* **1998**, *282*, 1853–1858.
[7] Y. Nicolet, C. Piras, P. Legrand, E. C. Hatchikian, J. C. Fontecilla-Camps, *Structure* **1999**, *7*, 13–23.
[8] Y. Nicolet, A. L. De Lacey, X. Vernede, V. M. Fernandez, E. C. Hatchikian, J. C. Fontecilla-Camps, *J. Am. Chem. Soc.* **2001**, *123*, 1596–1602.
[9] H.-J. Fan, M. B. Hall, *J. Am. Chem. Soc.* **2001**, *123*, 3828–3829.
[10] R. Cammack, *Nature* **1999**, *397*, 214–215.
[11] Y. Nicolet, B. J. Lemon, J. C. Fontecilla-Camps, J. W. Peters, *Trends Biochem. Sci.* **2000**, *25*, 138–143.
[12] J. W. Peters, *Curr. Opin. Struct. Biol.* **1999**, *9*, 670–676.
[13] F. Gloaguen, J. D. Lawrence, T. B. Rauchfuss, *J. Am. Chem. Soc.* **2001**, *123,* 9476–9477.
[14] L. Sun, L. Hammarström, B. Åkermark, S. Styring, *Chem. Soc. Rev.* **2001**, *30*, 36–49.
[15] H. Wolpher, M. Borgström, L. Hammarström, J. Bergquist, V. Sundstr̈m, S. Styring, L. Sun, B. Åkermark, *Inorg. Chem. Commun.* **2003**, in press.
[16] L. Hammarström, F. Barigelletti, L. Flamigni, M. T. Indelli, N. Armaroli, G. Calogero, M. Guardigli, A. Sour, J.-P. Collin, J.-P. Sauvage, *J. Phys. Chem. A* **1997**, *101*, 9061–9069.
[17] A. C. Benniston, V. Grosshenny, A. Harriman, R. Ziessel, *Angew. Chem.* **1994**, *106*, 1956–1958; *Angew. Chem. Int. Ed. Engl.* **1994**, *33*, 1884–1885.
[18] J. D. Lawrence, H. Li, T. B. Rauchfuss, *Chem. Commun.* **2001**, 1482–1483.
[19] P. F. Brandt, D. A. Lesch, P. R. Stafford, T. B. Rauchfuss, *Inorg. Synth.* **1997**, *31*, 112–116.
[20] Crystallographic data (excluding structure factors) for the structures reported in this paper have been deposited with the Cambridge Crystallographic Data Centre as supplementary publication nos. CCDC-203101 (**3**) and CCDC-203102 (**4**). Copies of the data can be obtained free of charge via www.ccdc.cam.ac.uk/conts/retrieving.html (or from the Cambridge Crystallographic Data Centre, 12 Union Road, Cambridge CB21EZ, UK; fax: (+44) 1223-336-033; or deposit@ccdc.cam.ac.uk).
[21] J. D. Lawrence, H. Li, T. B. Rauchfuss, M. Benard, M.-M. Rohmer, *Angew. Chem.* **2001**, *113*, 1818–1821; *Angew. Chem. Int. Ed.* **2001**, *40*, 1768–1771.
[22] K. T. Potts, D. Konwar, *J. Org. Chem.* **1991**, *56*, 4815–4816.
[23] V. Grosshenny, F. M. Romero, R. Ziessel, *J. Org. Chem.* **1997**, *62*, 1491–1500.
[24] K. Sonogashira, Y. Tohda, N. Hagihara, *Tetrahedron Lett.* **1975**, *16,* 4467–4470.
[25] T. Norrby, A. Börje, B. Åkermark, L. Hammarström, J. Alsins, K. Lashgari, R. Norrestam, J. Mårtensson, G. Stenhagen, *Inorg. Chem.* **1997**, *36*, 5850–5858.
[26] S. Salyi, M. Kritikos, B. Åkermark, L. Sun, *Chem. Eur. J.* **2003**, *9*, 557–560.

 © 2003 Wiley-VCH Verlag GmbH & Co. KGaA, Weinheim

A Heterotrimetallic Complex

A 2D Cyano- and Oxamidato-Bridged Heterotrimetallic Cr^{III}-Cu^{II}-Gd^{III} Complex**

Hui-Zhong Kou, Bei Chuan Zhou, Song Gao, and Ru-Ji Wang*

Coordination Chemistry provides a powerful tool for the construction of extended or isolated compounds with a particular structure and tunable physical properties.[1] Magnetism of coordination compounds is an active field of research, involving chemistry, physics, biology, and material science.[2]

The ability of the oxamidato group to transmit efficiently magnetic coupling has been well documented.[3] The oxamidato-bridged Gd^{III}–Cu^{II} complexes have been investigated magnetically since the pioneering research by Gatteschi et al., who first found that the Gd^{III}–Cu^{II} exchange is ferromagnetic.[4] Recently, a four-coordinate macrocyclic oxamido–Cu^{II} complex has been used as "the complex ligand" to successfully construct polynuclear Cu_6Nd_2 complexes.[5] It is anticipated that the coordinated CuL group (L = 1,4,8,11-tetraazacyclotradecane-2,3-dione) could accept donor atoms

[*] Dr. H.-Z. Kou, B. C. Zhou, Prof. R.-J. Wang
Department of Chemistry, Tsinghua University
Beijing 100084 (P. R. China)
Fax: (+86) 10-62788765
E-mail: kouhz@mail.tsinghua.edu.cn

Prof. S. Gao
State Key Laboratory of Rare Earth Materials Chemistry and Applications
College of Chemistry & Molecular Engineering
Peking University, Beijing 100871 (P. R. China)

[**] This work was supported by the National Natural Science Foundation of China (project No.: 20201008 & 50272034). K.H.Z. gratefully acknowledges Prof. Yadong Li for providing excellent work conditions.

Supporting information for this article is available on the WWW under http://www.angewandte.org or from the author.

 © 2003 Wiley-VCH Verlag GmbH & Co. KGaA, Weinheim DOI: 10.1002/anie.200351248

at the axial positions giving rise to a five- or six-coordinate environment around the Cu^{2+} ion.

The nitrogen ends of the cyanide ligands of hexacyanometallates are strong donor atoms that could connect two metal ions. Cyanide-bridged transition metal (3d) complexes or 4f–3d complexes have attracted extensive interest because they might be used as magnetic, magneto-optical, porous, or catalytic materials with practical applications.[6–11]

Combining the above two approaches, we have designed a unique 2D mixed bridging-ligand complex $[Gd(CuL)_4Cr(CN)_6{\cdot}5H_2O]_\infty$ (**1**), which contains three different paramagnetic metal ions.

Complex **1** is prepared by the treatment of [CuL],[12] $GdCl_3{\cdot}6H_2O$ with $K_3[Cr(CN)_6]$ in an H_2O/EtOH mixture. Single-crystal X-ray crystallography[13] reveals that **1** consists of a 2D neutral polymer $[Gd(CuL)_4Cr(CN)_6]_\infty$ (Figure 1). The

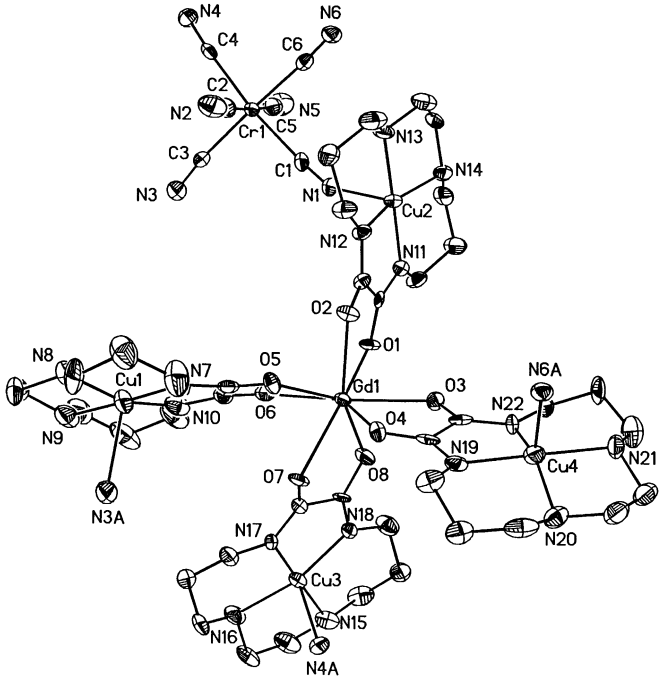


Figure 1. ORTEP plot of the polymeric complex **1** (thermal ellipsoids set at the 30% probability level.

structure comprises a bridging $[Cr(CN)_6]^{3-}$ ion, four macrocyclic Cu^{II} units and one Gd^{III} ion. The Gd^{III} ion is surrounded by eight oxygen atoms from four {CuL} groups, thus yielding a local $[Gd(CuL)_4]$ moiety. Each $[Cr(CN)_6]^{3-}$ ion connects to four different CuL units through four equatorial CN^- bridges with two *trans*-CN^- ligands intact. Therefore, each Cu^{2+} ion of {CuL} is five coordinate with four nitrogen atoms of L located at the equatorial plane and one cyano nitrogen atom of $[Cr(CN)_6]^{3-}$ at the apical position. The $Cu{-}N_{apical}$ bond lengths range from 2.317(11) to 2.548(14) Å. The adjacent metal–metal separations are from 5.145(3) to 5.296(3) Å for Cu–Cr and from 5.704(3) to 5.787(3) Å for Cu···Gd, respectively. The mixed cyanide and oxamidato bridges connect the metal ions generating a nonplanar 2D layer (Figure 2 and Supporting Information). The layer topology can be described as a distorted gridlike molecular structure with two Cr^{III} and two Gd^{III} ions at the vertices and four {CuL} groups at the four sides of each "propeller". The propellers pack in such a way that two different types of holes are formed (Figure 2b, labeled I and II, see also Supporting Information). Within the layer, three pairs (Cu1···Cu1A, Cu2···Cu2B and Cu3···Cu3C) of CuL groups arrange in a face-to-face fashion, with the Cu···Cu distances ranging from 4.629(3) to 5.534(3) Å.[14] The long Cu···Cu separations preclude the interactions between the Cu^{II} ions. The interstitial water molecules are situated between the layers.

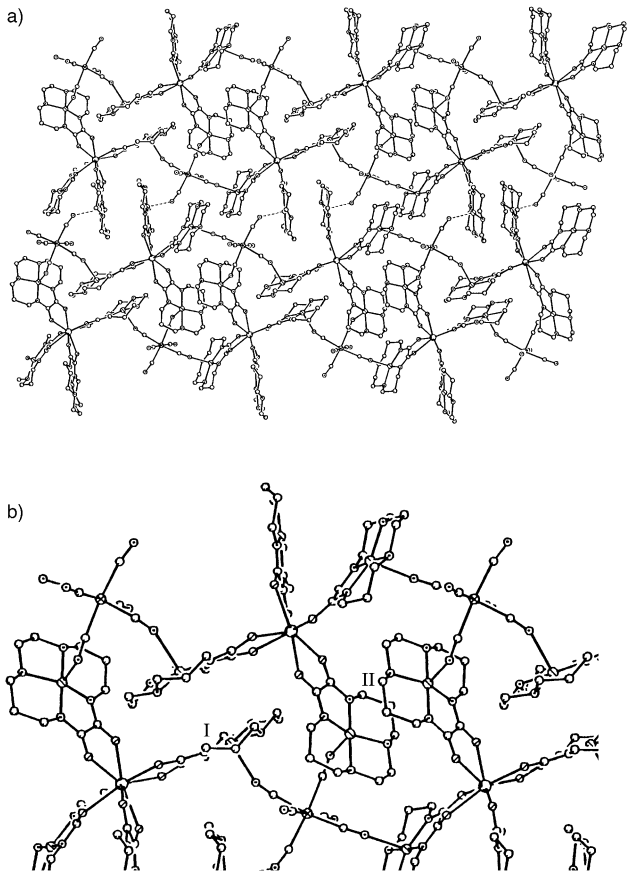


Figure 2. a) Layer structure of **1**. b) Layer structure enlarged to show both types of holes present (labeled I and II).

Figure 3 shows the $\chi_m T$ vs. T plot of **1** measured on a SQUID magnetometer in the temperature range of 5–290 K under 1000 Oe. The room temperature $\chi_m T$ value of 11.0 emu K mol^{-1} is close to the expected spin-only value of 11.25 emu K mol^{-1}. The increase of $\chi_m T$ with a decrease in temperature suggests the presence of global ferromagnetic interactions between adjacent metal ions. The Weiss constant derived from the $\chi_m{}^{-1}$ versus T plot is equal to $+3.8$ K with the Curie constant of 11.0 emu K mol^{-1}, which is consistent with the calculated value of 11.25 emu K mol^{-1} ($g = 2.0$) per $GdCu_4Cr$. As shown in Inset of Figure 3, $\chi_m T$ decreases below 3.2 K (10 kOe data), which can be assigned to the saturation effect. The low field data (≤ 2 kOe) do not show the decrease in $\chi_m T$ below 3 K, which supports the above supposition. The field-cooled magnetization (FCM) curve of **1** measured in a

 © 2003 Wiley-VCH Verlag GmbH & Co. KGaA, Weinheim

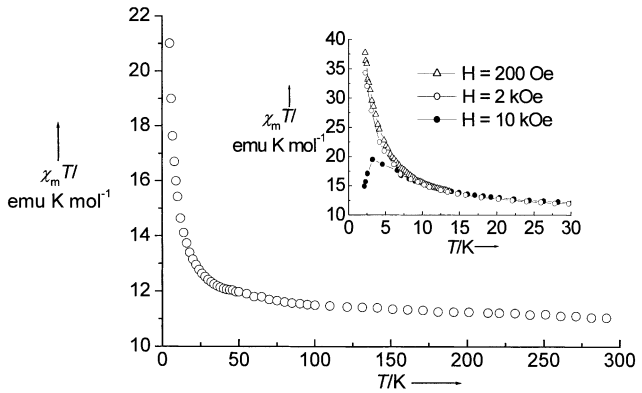


Figure 3. Temperature dependence of $\chi_m T$ for **1** in a 1000 Oe applied field. Inset: Temperature dependences of $\chi_m T$ for **1** in different applied magnetic fields (solid lines are a guide for the eye).

low field of 200 Oe and the zero-static AC magnetization measurements show the absence of spontaneous magnetization down to 1.8 K. The field dependence of the magnetization (0–70 kOe) measured at 1.8 K shows the saturation of the magnetization (Figure 4), reaching 14.6 Nβ at 70 kOe for a

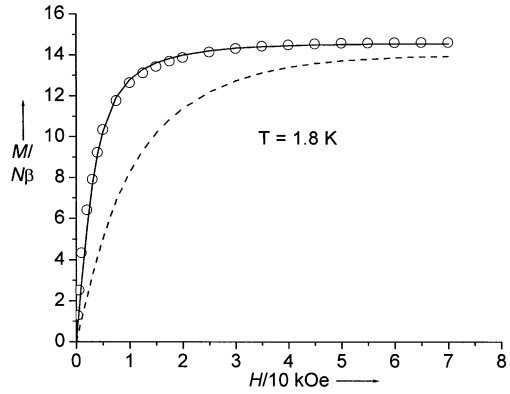


Figure 4. Field dependence of magnetization of **1** at 1.8 K. The lines represent the Brillouin function that corresponds to noninteracting $S = S_{Gd} + 4S_{Cu} + S_{Cr}$ ions (dashed, with $g = 2.0$) and $S = 7$ spin state (solid, with $g = 2.08$).

ferromagnetic Cr^{III}–Cu^{II}–Gd^{III} system with $S_T = 7$. The theoretical Brillouin curve for an $S = 7$ spin state with $g = 2.08$ fits well the experimental curve. The experimental curve lies above that corresponding to noninteracting S_{Gd}, S_{Cr} and four S_{Cu} spins, thus indicating the presence of intermetallic Cu^{II}–Cr^{III} and Cu^{II}–Gd^{III} ferromagnetic coupling.[15] This also shows the absence of Cr^{III}–CN–Gd^{III} linkages, which have been shown to be antiferromagnetic.[16] Future work will be devoted to designing extended species with such linkages that might exhibit magnetic ordering and new bifunctional behavior.

Heterobimetallic or heterotrimetallic complexes with two different spins are often seen, but those with three different spins are rare.[11,17] Complex **1** is the first structurally characterized 2D heterotrimetallic complex with three different spin carriers. This research opens new synthetic pathways for the design of novel and complicated materials with potentially new functional properties.

Experimental Section

1: Platelet violet single crystals of **1** were formed reproducibly by slow diffusion of [CuL] and $GdCl_3 \cdot 6H_2O$ (molar ratio = 4:1) in H_2O into $K_3[Cr(CN)_6]$ in an H_2O/EtOH (2:1) mixture after a few weeks. Yield: 40 %. IR: $\tilde{\nu} = 2122\ cm^{-1}$ (C≡N), $1600\ cm^{-1}$ (C=O).

Magnetic measurements were performed on a few manually selected single crystals (ca. 11.0 mg) by using a MagLab 2000 magnetometer, and the variable-temperature magnetic susceptibility measurements in an applied field of 1000 Oe were performed on a Quantum Design MPMS-7 SQUID magnetometer. Plots of field-cooled magnetization (FCM) and zero-field AC magnetic susceptibilities have been deposited in Supporting Information.

Received: February 21, 2003
Revised: April 16, 2003 [Z51248]

Keywords: bridging ligands · chromium · copper · cyanides · gadolinium · magnetic properties

[1] O. M. Yaghi, M. O'Keeffe, M. Kanatzidis, *J. Solid State Chem.* **2000**, *152*, 1.
[2] O. Kahn, *Molecular Magnetism*, VCH, Weinheim, **1993**.
[3] C. Benelli, A. C. Fabretti, A. Giusti, *J. Chem. Soc. Dalton Trans.* **1993**, 409; J. L. Sanz, R. Ruiz, A. Gleizes, F. Lloret, J. Faus, M. Julve, J. J. Borras-Almenar, Y. Journaux, *Inorg. Chem.* **1996**, *35*, 7384; O. Guillou, P. Bergerat, O. Kahn, E. Bakalbassis, K. Boubekeur, P. Batail, M. Guillot, *Inorg. Chem.* **1992**, *31,* 110; Y. T. Li, Z. H. Jiang, D. Z. Liao, S. P. Yan, S. L. Ma, X. Y. Li, G. L. Wang, *Polyhedron* **1993**, *12*, 2781.
[4] A. Bencini, C. Benelli, A. Caneschi, R. L. Barlin, A. Dei, D. Gatteschi, *J. Am. Chem. Soc.* **1985**, *107*, 8128.
[5] J.-K. Tang, Y.-Z. Li, Q.-L. Wang, E.-Q. Gao, D.-Z. Liao, Z.-H. Jiang, S.-P. Yan, P. Cheng, L.-F. Wang, G.-L. Wang, *Inorg. Chem.* **2002**, *41,* 2188.
[6] S. M. Holmes, G. S. Girolami, *J. Am. Chem. Soc.* **1999**, *121*, 5593; S. Ferlay, T. Mallah, R. Ouahes, P. Veillet, M. Verdaguer, *Nature* **1995**, *378*, 701; O. Sato, T. Iyoda, A. Fujishima, K. Hashimoto, *Science* **1996**, *271*, 49.
[7] M. S. El Fallah, E. Rentschler, A. Caneschi, R. Sessoli and D. Gatteschi, *Angew. Chem.* **1996**, *108*, 2081; *Angew. Chem. Int. Ed. Engl.* **1996**, *35*, 1947; M. Ohba, N. Usuki, N. Fukita, H. Okawa, *Angew. Chem.* **1999**, *111*, 1911; *Angew. Chem. Int. Ed.* **1999**, *38*, 1795; A. Marvilliers, S. Parsons, E. Riviere, J. P. Audiere, T. Mallah, *Chem. Commun.* **1999**, 2217; J. A. Smith, J.-R. Galán-Mascarós, R. Clérac, K. R. Dunbar, *Chem. Commun.* **2000**, 1077; H. Miyasaka, N. Matsumoto, H. Okawa, N. Re, E. Gallo, C. Floriani, *Angew. Chem.* **1995**, *107*, 1565; *Angew. Chem. Int. Ed. Engl.* **1995**, *34*, 1446; S. Ferlay, T. Mallah, J. Vaissermann, F. Bartolome, P. Veillet, M. Verdaguer, *Chem. Commun.* **1996**, 2481; M. P. Shores, J. J. Sokol, J. R. Long, *J. Am. Chem. Soc.* **2002**, *124*, 2279; R. J. Parker, D. C. Hockless, B. Moubaraki, K. S. Murray, L. Spiccia, *Chem. Commun.* **1996**, 2789.
[8] H.-Z. Kou, S. Gao, J. Zhang, G.-H. Wen, G. Su, R. K. Zheng, X. X. Zhang, *J. Am. Chem. Soc.* **2001**, *123*, 11 809; F. Thétiot, S. Triki, J. S. Pala, C. J. Gómez-García, S. Golhen, *Chem. Commun.* **2002**, 1078; M. S. El Fallah, J. Ribas, X. Solans, M. Font-Bardia, *J. Chem. Soc. Dalton Trans.* **2001**, 247; D. G. Fu, J. Chen, X. S. Tan, L. J. Jiang, S. W. Zhang, P. J. Zheng, W. X. Tang, *Inorg. Chem.* **1997**, *36*, 220.

 © 2003 Wiley-VCH Verlag GmbH & Co. KGaA, Weinheim

[9] a) F. Bellouard, M. Clemente-Leon, E. Coronado, J. R. Galan-Mascaros, C. J. Gómez-García, F. Romero, K. R. Dunbar, *Eur. J. Inorg. Chem.* **2002**, 1603; b) K. Inoue, H. Imai, P. S. Ghalsasi, K. Kikuchi, M. Ohba, H. Okawa, J. V. Yakhmi, *Angew. Chem.* **2001**, *113*, 4372; *Angew. Chem. Int. Ed.* **2001**, *40*, 4242.

[10] J. Lu, W. T. A. Harrison, A. J. Jacobson, *Angew. Chem.* **1995**, *107*, 2759; *Angew. Chem. Int. Ed. Engl.* **1995**, *34*, 2557; H. Yuge, Y. Noda, T. Iwamoto, *Inorg. Chem.* **1996**, *35*, 1842; M. J. Scott, R. H. Holm, *J. Am. Chem. Soc.* **1994**, *116*, 11357; L. G. Beauvais, J. R. Long, *J. Am. Chem. Soc.* **2002**, *124*, 12096.

[11] K. E. Vostrikova, D. Luneau, W. Wernsdorfer, P. Rey, M. Verdaguer, *J. Am. Chem. Soc.* **2000**, *122*, 718; A. Marvilliers, Y. Pei, J. C. Boquera, K. E. Vostrikova, C. Paulsen, E. Rivière, J.-P. Audière, T. Mallah, *Chem. Commun.*, **1999**, 1951; A. M. Madalan, H. W. Roesky, M. Andruh, M. Noltemeyer, N. Stanica, *Chem. Commun.* **2002**, 1638.

[12] L. Cronin, A. R. Mount, S. Parsons, N. Robertson, *J. Chem. Soc. Dalton Trans.* **1999**, 1925.

[13] Crystal data: **1** ($C_{46}H_{82}N_{22}O_{13}Cu_4GdCr$), $M_w = 1614.75$, $T = 293$ K, triclinic, space group $P\bar{1}$, $a = 12.892(1)$, $b = 15.965(1)$, $c = 17.471(1)$ Å, $\alpha = 72.902(3)$, $\beta = 81.444(3)$, $\gamma = 77.166(3)°$, $U = 3337.8(7)$ Å^3, $Z = 1$, $\rho_{calcd} = 1.607$ g cm^{-3}, $\mu = 2.734$ mm^{-1}, $2\theta_{max} = 50°$, $\lambda(Mo_{K\alpha}) = 0.71073$ Å, 18880 measured reflections, 11507 unique reflections, 6049 observed reflections ($I > 2\sigma(I)$). The structure was solved by direct methods (SHELXS-97). All nonhydrogen atoms were refined anisotropically (SHELXL-97). All hydrogen atoms were added geometrically and refined by using a riding model. $R1 = 0.0968$, $wR2 = 0.1846$ (all data), GOF = 1.062 based on 802 parameters. CCDC-204380 (**1**) contains the supplementary crystallographic data for this paper. These data can be obtained free of charge via www.ccdc.cam.ac.uk/conts/retrieving.html (or from the Cambridge Crystallographic Data Centre, 12 Union Road, Cambridge CB21EZ, UK; fax: (+44) 1223-336-033; or deposit@ccdc.cam.ac.uk).

[14] Symmetry operations: *A*: $1-x, 1-y, 1-z$; *B*: $1-x, 1-y, z$; *C*: $-x, 2-y, z$.

[15] Previous reports have unambiguously demonstrated that the Cu^{II}–Cr^{III} magnetic coupling through the cyano bridges is ferromagnetic. See Reference [8].

[16] A. Figuerola, C. Diaz, M. S. El Fallah, J. Ribas, M. Maestro, J. E. Mahia, *Chem. Commun.* **2001**, 1204; H.-Z. Kou, S. Gao, B.-W. Sun, J. Zhang, *Chem. Mater.* **2001**, *13*, 1431.

[17] H. O. Stumpf, L. Ouahab, Y. Pei, P. Bergerat, O. Kahn, *J. Am. Chem. Soc.* **1994**, *116*, 3866; G. Ballester, E. Coronado, C. Gimenez-Saiz, F. M. Romero, *Angew. Chem.* **2001**, *113*, 814; *Angew. Chem. Int. Ed.* **2001**, *40*, 792; C. N. Verani, T. Weyhermuller, E. Rentschler, E. Bill, P. Chaudhuri, *Chem. Commun.* **1998**, 2475.

 © 2003 Wiley-VCH Verlag GmbH & Co. KGaA, Weinheim

Chiral Allylic Fluorides

Regio- and Enantioselective Synthesis of Allylic Fluorides by Electrophilic Fluorodesilylation of Allyl Silanes**

*Benjamin Greedy, Jean-Marc Paris, Thierry Vidal, and Véronique Gouverneur**

Organofluorine compounds are extremely rare in nature and it is only recently that a fluorinase enzyme was discovered that catalyzes carbon–fluorine bond formation.[1] However, the chemistry of bioactive fluoroorganic compounds is a rapidly developing area of research because of their importance in biomedical applications.[2] Methodologies for enantioselective fluorination (C–F bond formation) are still in demand despite recent advances in this field, which include the synthesis of new chiral N–F reagents and the development of the first catalytic enantioselective fluorination of β-ketoesters.[3] Most of these studies have been aimed at creating an efficient and general process for the enantioselective preparation of α-fluorocarbonyl compounds. In contrast, methods for the enantioselective preparation of allylic fluorides are rare, and only one protocol that uses electrophilic N–F reagents is known.[4]

The nucleophilic displacement of allylic alcohols with reagents such as (diethylamino)sulfur trifluoride (DAST) has been used to produce allylic fluorides, but this transformation suffers from problems of low stereo- and regioselectivity as a result of allylic transposition.[5] Important exceptions have been reported in the area of sugar chemistry in which anchimeric assistance minimizes these problems, and in transition-metal chemistry, as exemplified by the work of Gree et al.[6] However, the total absence of a strategy based on the use of an enantioselective electrophilic fluorination process prompted us to embark on a study aimed at the development of such a reaction.

The electrophilic cleavage of activated silanes provides the synthetic organic chemist with many opportunities.[7] These reactions take advantage of the β effect of a silicon center and thus require substrates that have adjacent π systems, such as vinyl, aryl, and allyl silanes. With the appearance of electrophilic sources of fluorine, the concept of electrophilic fluorodesilylation emerged,[8] and our group recently reported the first fluorodesilylation reactions of vinyl

[*] Dr. V. Gouverneur, B. Greedy
The Dyson Perrins Laboratory, University of Oxford
South Parks Road, Oxford OX1 3QY (UK)
Fax: (+44) 1865-275-644
E-mail: veronique.gouverneur@chem.ox.ac.uk
Dr. J.-M. Paris, Dr. T. Vidal
Rhodia Recherches, Centre de Recherches de Lyon
85, Avenue des Freres Perret, 69192 Saint-Fons Cedex (France)

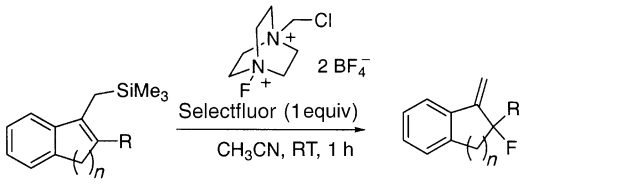
[**] This work was generously supported by Rhodia Organique Fine (full CASE Industrial Studentship to B.G.).

Supporting information for this article is available on the WWW under http://www.angewandte.org or from the author.

 DOI: 10.1002/anie.200351405 © 2003 Wiley-VCH Verlag GmbH & Co. KGaA, Weinheim

silanes with the electrophilic fluorinating reagent Selectfluor (1-chloromethyl-4-fluoro-1,4-diazoniabicyclo[2.2.2]octane bis(tetrafluoroborate)).[9] As an extension of this methodology, we now report a conceptually new approach to chiral nonracemic allylic fluorides, based on the enantioselective electrophilic fluorodesilylation of allyl silanes. We anticipated that we could take advantage of both the β effect of a silicon center and the availability of new enantiopure N–F reagents to address the problems of regio- and enantioselectivity, respectively.

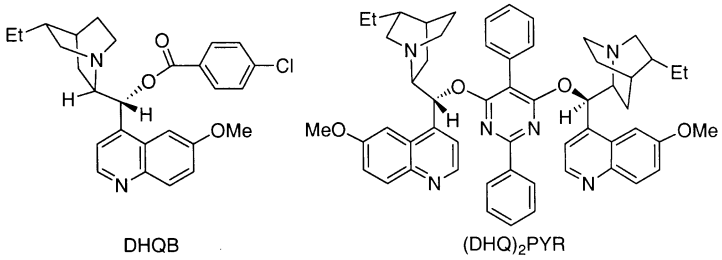
We carried out a preliminary study with the model allyl silanes **1a–f**, all of which were prepared according to literature procedures.[10] A screening of several commercially available N–F compounds revealed Selectfluor to be the best reagent for the electrophilic fluorodesilylation of compound **1a**. All allyl silanes **1a–f** reacted at room temperature in MeCN with 1 equivalent of Selectfluor to afford the corresponding allylic fluorides within just 1 hour. Compounds **2a** and **2c–f** were isolated in yields ranging from 63 to 78%. In the reaction of compound **1b** to give **2b**, 100% conversion was observed. However, the fluorinated product **2b** was unstable to purification and unfortunately no yield can be reported for this compound. These results showed that the electrophilic fluorodesilylation of allyl silanes was feasible, and that it occurred at a vastly accelerated rate relative to the fluorination of vinyl silanes (Scheme 1).[9]



1a $n=1$ R = H — (±)-**2a** $n=1$ R = H 65%
1b $n=1$ R = Me — (±)-**2b** $n=1$ R = Me 100% (conversion)
1c $n=1$ R = Bn — (±)-**2c** $n=1$ R = Bn 74%
1d $n=2$ R = H — (±)-**2d** $n=2$ R = H 71%
1e $n=2$ R = Me — (±)-**2e** $n=2$ R = Me 63%
1f $n=2$ R = Bn — (±)-**2f** $n=2$ R = Bn 78%

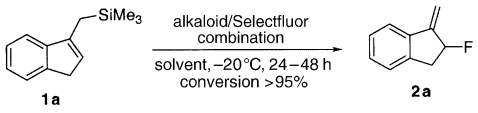
Scheme 1. Electrophilic fluorodesilylation of allyl silanes **1a–f** with Selectfluor.

These preliminary results encouraged us to investigate the use of enantiopure *N*-fluorocinchona alkaloids in an enantioselective version of this new reaction. In recent work by Shibata et al.[11] and Cahard and co-workers[12] on the fluorination of silyl enol ethers with *N*-fluorocinchona alkaloids, α-fluorocarbonyl compounds were prepared with *ee* values of up to 91%. *N*-Fluorocinchona alkaloids have proved to be efficient reagents and are readily prepared from commercially available compounds. We therefore explored the efficiency of this class of reagent for the enantioselective synthesis of allylic fluorides from the corresponding allyl silanes (Scheme 2, Table 1). After a systematic screening of several commercially available cinchona alkaloids used in combination with Selectfluor, we found that the $(DHQ)_2PYR$/Selectfluor combination in MeCN at −20°C effected the enantioselective fluorination of **1a** to furnish



Scheme 2. Representative cinchona alkaloids.

Table 1: Variation of the cinchona alkaloid in the enantioselective fluorination of **1a**.



Entry	Alkaloid[a]	Solvent	*ee* [%]
1	DHQB	CH_3CN	28
2	DHQMQE	CH_3CN	32
3	DHQPE	CH_3CN	48
4	$(DHQ)_2PYR$	CH_3CN	60
5	$(DHQ)_2PYR$	CH_2Cl_2	53

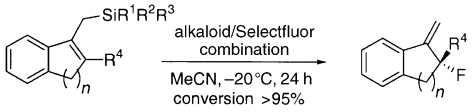
[a] DHQMQE = dihydroquinine 4-methyl-2-quinoyl ether; DHQPE = dihydroquinine 9-phenanthyl ether.

compound **2a** in 24 hours, with excellent conversion (> 95%) and 60% *ee* (Table 1, entry 4). Other systems were less efficient, such as DHQB and DHQPE, which yielded **2a** with *ee* values of 28 and 48%, respectively (Table 1, entries 1 and 3). No beneficial effect was observed upon lowering the temperature of the reaction, which led to longer reaction times with no improvement in the enantioselectivity. The use of CH_2Cl_2 instead of MeCN resulted in a decreased enantiomeric excess (Table 1, entries 4 and 5). Furthermore, we found the use of the fluorinated cinchona alkaloids as isolated reagents to be problematic, as the chemical yields observed were less satisfactory.[12,13] In subsequent studies we therefore used the protocol developed by Shibata et al. for the preparation of these reagents in situ.[11]

We next investigated the effectiveness of our system for the enantioselective fluorination of allyl silanes **1c–h**.[14] As can be seen from the results summarized in Table 2, the corresponding allylic fluorides could be formed with very high conversion (in all cases greater than 95%) and with moderate to excellent *ee* values. Of the substrates tested, the benzyl-substituted allyl silane **1c** gave the best results, as reflected by the very high enantiomeric excess observed (96% *ee*) for the allylic fluoride **2c**. As was also observed in the reactions of **1a**, the best reagent for this transformation was $(DHQ)_2PYR$/Selectfluor, which gave **2c** with 96% *ee*. DHQMQE was also very effective and promoted the formation of **2c** with 93% *ee* (Table 2, entries 2 and 4). For allyl silanes **1d–f**, the *ee* values of the products were usually lower, and $(DHQ)_2PYR$ and DHQPE were the alkaloids of choice (Table 2, entries 5–13). As a general trend, we found that better *ee* values were observed when the substrates had a larger R^4 substituent. Indeed, substrate **1f**, with a benzyl group as the R^4 substitu-

 © 2003 Wiley-VCH Verlag GmbH & Co. KGaA, Weinheim

Table 2: Enantioselective fluorodesilylation of allyl silanes **1c–h**.



Entry	**1**	*n*	R^1	R^2	R^3	R^4	Alkaloid	Product[a]	*ee* [%]
1	**c**	1	Me	Me	Me	CH_2Ph	DHQB	(*R*)-**2c**	85
2	**c**	1	Me	Me	Me	CH_2Ph	$(DHQ)_2PYR$	(*R*)-**2c**	96
3	**c**	1	Me	Me	Me	CH_2Ph	DHQPE	(*R*)-**2c**	84
4	**c**	1	Me	Me	Me	CH_2Ph	DHQMQE	(*R*)-**2c**	93
5	**d**	2	Me	Me	Me	H	DHQB	**2d**	9
6	**d**	2	Me	Me	Me	H	$(DHQ)_2PYR$	**2d**	22
7	**d**	2	Me	Me	Me	H	DHQPE	**2d**	30
8	**e**	2	Me	Me	Me	Me	DHQB	(*R*)-**2e**	8
9	**e**	2	Me	Me	Me	Me	$(DHQ)_2PYR$	(*R*)-**2e**	45
10	**e**	2	Me	Me	Me	Me	DHQPE	(*R*)-**2e**	21
11	**f**	2	Me	Me	Me	CH_2Ph	DHQB	(*S*)-**2f**	53
12	**f**	2	Me	Me	Me	CH_2Ph	$(DHQ)_2PYR$	(*S*)-**2f**	83
13	**f**	2	Me	Me	Me	CH_2Ph	DHQPE	(*S*)-**2f**	64
14	**g**	1	Me	Me	Ph	H	DHQB	**2a**	35
15	**g**	1	Me	Me	Ph	H	DHQMQE	**2a**	35
16	**g**	1	Me	Me	Ph	H	$(DHQ)_2PYR$	**2a**	73
17	**h**	1	Ph	Ph	Ph	H	$(DHQ)_2PYR$	**2a**	87

[a] Absolute configuration not determined for **2a** or **2d**.

ent, was fluorinated in the presence of $(DHQ)_2PYR$ to give **2f** with 83% *ee* (Table 2, entry 12). We then investigated the influence of the silyl substituent on the enantiomeric excess of the product (Table 2, entries 14–17). In the reaction of **1g**, which has a dimethylphenylsilyl substituent instead of the trimethylsilyl group, a slight improvement of the *ee* values of **2a** was observed for most alkaloids with no significant decrease of reactivity, relative to **1a**. The best result was obtained in the presence of $(DHQ)_2PYR$, which allowed the formation of the corresponding allylic fluoride **2a** with 73% *ee* (Table 2, entry 16). By further increasing the steric bulk of the substrate with a triphenylsilyl group, **2a** could be prepared (from **1h**) with 87% *ee* (Table 2, entry 17). It is therefore apparent that the steric bulk of the silyl group itself is important with regard to enantioselectivity. The levels of enantioselectivity observed in the reactions to form the allylic fluorides **2a** and **2c–g** compare favorably with the best *ee* values observed by Shibata et al., and Cahard and coworkers, for fluorinated ketones.[11,12]

To assign the absolute configurations of the products, compounds **2c**, **2e**, and **2f** were prepared by an alternative asymmetric method.[14] We assume that the reactive conformation of the *N*-fluorocinchona alkaloids is similar to the one suggested by Shibata et al., as the reactions described herein were performed under similar conditions to those for the fluorination of analogous silyl enol ethers.[11] However, there might be significant differences in the reactive conformations of the allyl silanes relative to analogous silyl enol ethers, as well as in their approach toward the chiral N–F reagent. The observation that fluorinated products are formed with different *ee* values from allyl silanes than from analogous silyl enol ethers in the presence of the same alkaloid supports this hypothesis. We are currently exploring these mechanistic aspects to better understand this novel enantioselective transformation.

In conclusion, we have described herein the first regio- and enantioselective route to allylic fluorides from the corresponding allyl silanes. The concept of electrophilic fluorodesilylation combined with the use of enantiopure *N*-fluorocinchona alkaloids provided a highly efficient method for the preparation of allylic fluorides with *ee* values of up to 96%. A clearer understanding of the mechanism by which this reagent-controlled enantioselectivity originates will require a more detailed study. Furthermore, the extension of this expeditious route to other allyl silanes is the object of current work in our laboratory.

Received: March 14, 2003 [Z51405]

Keywords: allylic compounds · asymmetric synthesis · cinchona alkaloids · fluorides · silanes

[1] a) D. O'Hagan, D. B. Harper, *Nat. Prod. Rep.* **1994**, *11*, 123–133; b) D. O'Hagan, C. Schaffrath, S. L. Cobb, J. T. G. Hamilton, C. D. Murphy, *Nature* **2002**, *416*, 279; c) C. Schaffrath, S. L. Cobb, D. O'Hagan, *Angew. Chem.* **2002**, *114*, 4069–4071; *Angew. Chem. Int. Ed.* **2002**, *41*, 3913–3915.

[2] "Biomedical Frontiers of Fluorine Chemistry": I. Ojima, J. R. McCarthy, J. T. Welch, *ACS Symp. Ser.* **1996**, 639; "Asymmetric Fluoroorganic Chemistry. Synthesis, Applications and Future Directions": P. V. Ramachandran, *ACS Symp. Ser.* **2000**, 746.

[3] a) K. Muniz, *Angew. Chem.* **2001**, *113*, 1701–1704; *Angew. Chem. Int. Ed.* **2001**, *40*, 1653–1656; b) L. Hintermann, A. Togni, *Angew. Chem.* **2000**, *112*, 4530–4533; *Angew. Chem. Int. Ed.* **2000**, *39*, 4359–4362; c) S. Piana, I. Devillers, A. Togni, U. Rothlisberger, *Angew. Chem.* **2002**, *114*, 1021–1024; *Angew. Chem. Int. Ed.* **2002**, *41*, 979–982; d) D. Y. Kim, E. J. Park, *Org. Lett.* **2002**, *4*, 545–547; e) Y. Hamashima, K. Yagi, H. Takano, L. Tamas, M. Sodeoka, *J. Am. Chem. Soc.* **2002**, *124*, 14530–14531.

[4] F. A. Davis, H. Qi, *Tetrahedron Lett.* **1996**, *37*, 4345–4348.

[5] a) W. J. Middleton, US Patent 3914265, **1975**; b) G. M. Blackburn, D. E. Kent, *J. Chem. Soc. Chem. Commun.* **1981**, 511; c) O. Piva, *Synlett* **1994**, 729.

[6] a) F. Canfarini, A. Giolitti, A. Guidi, F. Pasqui, V. Pestellini, F. Arcamone, *Tetrahedron Lett.* **1993**, *34*, 4697–4700; b) L. S. Jeong, M. C. Nicklaus, C. George, V. E. Marquez, *Tetrahedron Lett.* **1994**, *35*, 7569–7572; c) D. M. Gree, C. J. M. Kermarrec, J. T. Martelli, R. L. Gree, J.-P. Lellouche, L. J. Toupet, *J. Org. Chem.* **1996**, *61*, 1918–1919; d) C. Kermarrec, V. Madiot, D. Gree, A. Meyer, R. Gree, *Tetrahedron Lett.* **1996**, *37*, 5691–5694; e) S. Legoupy, C. Crevisy, J.-C. Guillemin, R. Gree, *J. Fluorine Chem.* **1999**, *93*, 171–173.

[7] For an excellent review on Si chemistry, see: M. A. Brook, *Silicon in Organic, Organometallic, and Polymer Chemistry*, Wiley, Chichester, **2000**, Chaps. 14 and 16.

[8] V. Gouverneur, B. Greedy, *Chem. Eur. J.* **2002**, *8*, 766–771.

[9] B. Greedy, V. Gouverneur, *Chem. Commun.* **2001**, 233–234.

[10] a) R. Leino, F. J. Gomez, A. P. Cole, R. M. Waymouth, *Macromolecules* **2001**, *34*, 2072–2082; b) M. G. Saulnier, J. F. Kadow,

 © 2003 Wiley-VCH Verlag GmbH & Co. KGaA, Weinheim

M. M. Tun, D. R. Langley, D. M. Vyas, *J. Am. Chem. Soc.* **1989**, *111*, 8320 – 8321; for details, see Supporting Information.
[11] a) N. Shibata, E. Suzuki, Y. Takeuchi, *J. Am. Chem. Soc.* **2000**, *122*, 10728 – 10729; b) N. Shibata, E. Suzuki, T. Asahi, M. Shiro, *J. Am. Chem. Soc.* **2001**, *123*, 7001 – 7009; c) N. Shibata, T. Ishimaru, E. Suzuki, K. L. Kirk, *J. Org. Chem.* **2003**, *68*, 2494 – 2497.
[12] a) D. Cahard, C. Audouard, J.-C. Plaquevent, N. Roques, *Org. Lett.* **2000**, *2*, 3699 – 3701; b) D. Cahard, C. Audouard, J.-C. Plaquevent, L. Toupet, N. Roques, *Tetrahedron Lett.* **2001**, *42*, 1867 – 1869; c) C. Baudequin, J.-C. Plaquevent, C. Audouard, D. Cahard, *Green Chemistry*, **2002**, *4*, 584 – 586; d) B. Mohar, J. Baudoux, J.-C. Plaquevent, D. Cahard, *Angew. Chem.* **2001**, *113*, 4339 – 4341; *Angew. Chem. Int. Ed.* **2001**, *40*, 4214 – 4216.
[13] We thank Dr. J.-C. Plaquevent and Dr. D. Cahard for providing samples of the N–F reagents derived from the following alkaloids: cinchonine, cinchonidine, quinine, quinidine, *p*-chlorobenzylhydroquinidine, *p*-chlorobenzylcinchonine, *p*-chlorobenzylquinine, *p*-chlorobenzylquinidine.
[14] For details, see Supporting Information.

 © 2003 Wiley-VCH Verlag GmbH & Co. KGaA, Weinheim

Four Anions of a Diimine Ligand

Four-Step Reduction of dpp-bian with Sodium Metal: Crystal Structures of the Sodium Salts of the Mono-, Di-, Tri- and Tetraanions of dpp-bian**

Igor L. Fedushkin, Alexandra A. Skatova, Valentina A. Chudakova, and Georgy K. Fukin*

Dedicated to Professor Herbert Schumann on the occasion of his 68th birthday.

In the beginning of the 1990 s Elsevier, van Asselt and co-workers introduced the bis(*N*-arylimino)acenaphthene ligand (Ar-bian) into coordination chemistry.[1] Over the past decade transition-metal complexes of this ligand have been studied extensively because of a wide range of possible applications in catalysis, for example, in the hydrogenation of alkynes,[2a] in C–C[2b] and C–Sn[2c] bond formation, and especially in olefin polymerization.[3] The Ar-bian ligands combine both the α,α′-diimine and the naphthalene π systems in a single π system. As complexes of the dianions of α,α′-diimines[4] as well as naphthalene[5] were reported, we suggested that Ar-bian ligands might form stable mono- and di-, and possibly even tri- and tetraanions by electron transfer to their mixed 14-electron imine–naphthalene π system. Despite the extensive current interest in hydrocarbons with high negative charge only a few examples of well-defined tetraanions are reported in the literature. Among them are large conjugated systems, for example, rubrene ($C_{42}H_{28}$),[6a] decacyclene ($C_{36}H_{12}$),[6b] corannulene ($C_{20}H_{15}$),[6c,d] indenocorannulene ($C_{26}H_{19}$),[6e] [5] radialene ($C_{29}H_{62}Si_8$),[6f,g] and fullerene (C_{60}).[6h] One common feature of the aromatic hydrocarbon anions is that they often disproportionate to species oxidized and reduced by one electron, thus not allowing the isolation of some intermediate anions. The disproportionation process is dependent on the nature of both anion and cation. For instance, attempts of the exchange reaction between lithium naphthalenide, $Li^+(C_{10}H_8)^-$ and lanthanide halides in THF lead to the disproportionation of the radical anions of $(C_{10}H_8)^-$ to the dianion $(C_{10}H_8)^{2-}$ and neutral naphthalene, affording solely lanthanide complexes with the naphthalene dianion.[5b–e] Recently, Gambarotta, Budzelaar and co-workers reported the formation and crystal structure of a trianion formed by reduction of α,α′-diiminopyridine with lithium.[7] Again, regardless of the stoichiometric ratio, the reduction afforded only the trianionic species. Herein we report the reduction of Ar-bian with alkali metals to $[Ar\text{-bian}]^{n-}$ ($n = 1$–4). For this study we chose the most commonly used Ar-bian ligand—bis[*N*-(2,6-diisopropylphenyl)imino]acenaphthene, (2,6-*i*Pr$_2$PhNC)$_2$($C_{12}H_6$).

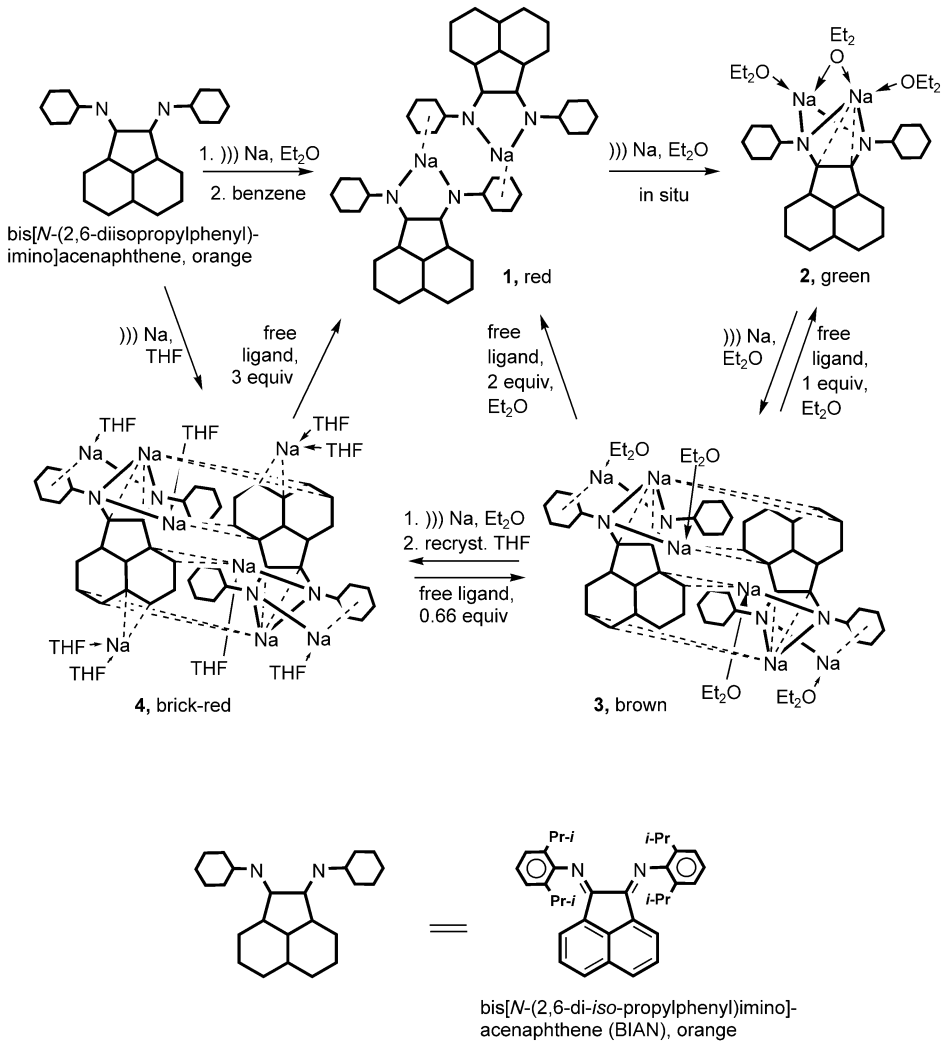
The reduction of (2,6-*i*Pr$_2$PhNC)$_2$($C_{12}H_6$) with sodium in diethyl ether occurred stepwise (Scheme 1) with the consecutive formation of the sodium complexes of the mono-, di-, tri- and tetraanions of the ligand, [{Na(2,6-*i*Pr$_2$PhNC)$_2$-($C_{12}H_6$)}$_2$] (**1**), [Na$_2$(Et$_2$O)$_3$(2,6-*i*Pr$_2$PhNC)$_2$($C_{12}H_6$)] (**2**), [{Na$_3$(Et$_2$O)$_2$(2,6-*i*Pr$_2$PhNC)$_2$($C_{12}H_6$)}$_2$] (**3**) and [{Na$_4$(thf)$_4$-(2,6-*i*Pr$_2$PhNC)$_2$($C_{12}H_6$)}$_2$] (**4**). The formation of **1** and **2** can be easily detected by the color change of the reaction solution. During the reduction the color changes in the following sequence: orange (free ligand), red (radical anion) and deep green (dianion). The complexes **3** and **4** precipitate from the reaction solution as brown and brick-red microcrystalline solids, respectively (Scheme 1). Therefore, it is difficult to separately recognize their formation. Complete conversion of the ligand to the tetraanion is achieved reproducibly by stirring vigorously the ligand and sodium for 5 h. The intermediate complexes **1**, **2** and **3** were obtained by the addition of 3, 2 or 0.66 equivalents, respectively, of the free ligand to complex **4**.

Complexes **1**–**4** are thermally quite stable: no changes were observed when crystalline samples of **1**–**4** were heated up to 246 °C in sealed and evacuated capillaries. Compounds **1** and **3** are paramagnetic. Their magnetic moments at room temperature (**1**, 1.95; **3**, 1.68 BM) correspond to one unpaired electron per ligand in both cases. As anticipated, complexes **2** and **4** are diamagnetic. The isopropyl methyl groups appear as two doublets centerd at 1.41 and 1.33 ppm (^3J(H,H) = 8.0 Hz for both doublets) in the ^{1}H NMR spectrum of **2** in C_6D_6 due to the hindered rotation about the aryl carbon-to-nitrogen bond. The signal for the four *H*-C(CH$_3$)$_2$ protons appears as a septet at 3.85 ppm (^3J(H,H) = 8.0 Hz). The twelve aromatic protons are found in a relatively narrow region (7.32–

[*] Dr. I. L. Fedushkin, Dr. A. A. Skatova, Dr. V. A. Chudakova, Dr. G. K. Fukin
G. A. Razuvaev Institute of Organometallic Chemistry
Russian Academy of Sciences
Tropinina 49, 603950 Nizhny Novgorod GSP-445 (Russia)
Fax: (+7) 8312-661-497
E-mail: igorfed@imoc.sinn.ru

[**] This work was supported by the Russian Foundation for Basic Research (Grant No. 03-03-32246à), dpp-bian = bis[*N*-(2,6-diisopropylphenyl)imino]acenaphthene

 © 2003 Wiley-VCH Verlag GmbH & Co. KGaA, Weinheim DOI: 10.1002/anie.200351408



Scheme 1. Synthesis of complexes **1**–**4**.

6.51 ppm). Despite of the extreme sensitivity of complex **4** towards air and moisture attempts to obtain its ^{1}H NMR spectrum were undertaken. The spectrum obtained in [D_8]-THF revealed the presence of some impurities amounting to about 10%. These narrow signals are attributable to those observed for compound **2** in C_6D_6. The dominant signals in the spectrum are noticeably broadened and high-field shifted and probably are from the aromatic protons of the tetraanion ($\delta = 6.56$, 6.45, 5.83, 4.64, 3.93, 2.83 ppm). The signal corresponding to *H*-C(CH_3)$_2$ protons appears to be partly overlap the THF signal at 3.60 ppm. The isopropyl methyl groups are observed as a broad single signal at 0.91 ppm.

The molecular structures of **1**, **2**, **3** and **4** were determined by single crystal X-ray diffraction. The crystals of **2** and **3** were grown from diethyl ether. The crystals of **1** and **4** were obtained from benzene and THF, respectively. The aggregation of **1** (Figure 1) to the centrosymmetric dimer with arene coordination of the sodium in the solid state is probably a result of the loss of coordinated Et_2O molecules during the crystallization from benzene. The sodium atom deviates from the plane formed with N(1)C(1)C(2)N(2) fragment by only 6.7°. Although there is a significant difference in the sodium to nitrogen bond distances (2.2837(13) and 2.3511(14) Å) in **1**, the similar C(1)-N(1) (1.3239(18) Å) and C(2)-N(2) (1.3326(19) Å) distances indicate a rather symmetrical diimine moiety N=C–C=N. These bonds are elongated compared with those in the neutral ligand in [$CuCl_2$(2,6-*i*Pr_2PhNC)$_2$($C_{12}H_6$)(AcOH)][9] (av 1.287 Å), thus reflecting population of the LUMO which has a high contribution of nitrogen orbitals. In contrast, the C(1)–C(2) bond in **1** is shortened to 1.446 Å compare to that in the copper(II) complex [$CuCl_2$(2,6-*i*Pr_2PhNC)$_2$($C_{12}H_6$)(AcOH)] (1.500 Å).[9] The sodium-to-arene distances in **1** range from 2.7330(19) to 2.972(2) Å (av 2.8571 Å).

The reduction of the radical anion to the dianion causes further elongation of the C–N bonds (1.387(4) and 1.386(4) Å) and shortening of the C(1)-C(2) bond (1.402(4) Å) in the ligand (Figure 2). The second sodium atom in the dianion is situated over the center of the plane formed by the metallacycle -Na(1)N(1)C(1)C(2)N(2). The dihedral angles between planes N(1)Na(1)N(2) and N(1)Na(2)N(2) and the plane formed with enediamido N(1)C(1)C(2)N(2) moiety are 23.9 and 77.0°, respectively. The different positions of the sodium atoms relative to the

 © 2003 Wiley-VCH Verlag GmbH & Co. KGaA, Weinheim

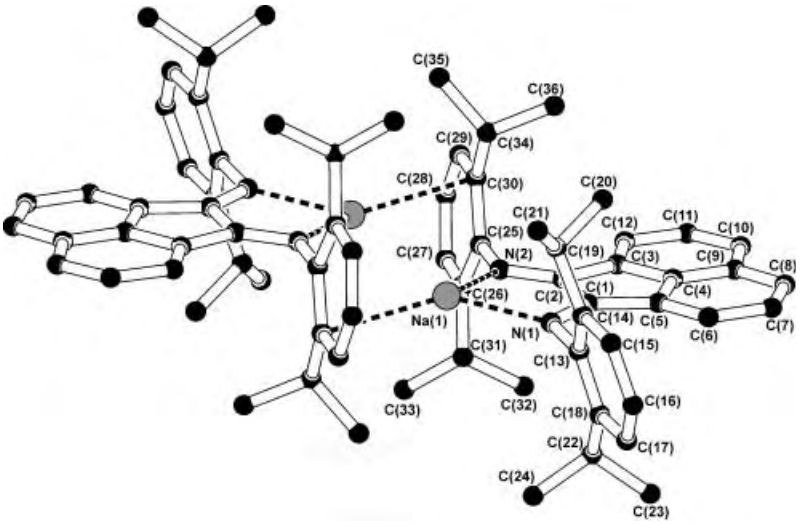


Figure 1. PLATON[8] presentation of the molecular structure of **1**. Selected bond lengths [Å] and angles [°]: Na(1)-N(1) 2.2837(13), Na(1)-N(2) 2.3511(14), Na(1)-C(1) 3.0180(15), Na(1)-C(2) 3.0496(15), Na(1)-C(25) 2.7903(16), Na(1)-C(26) 2.8573(19), Na(1)-C(27) 2.949(2), Na(1)-C(28) 2.972(2), Na(1)-C(29) 2.841(2), Na(1)-C(30) 2.7330(19), N(1)-C(1) 1.3239(18), N(2)-C(2) 1.3326(19), N(1)-C(13) 1.4113(19), N(2)-C(25) 1.406(2), C(1)-C(2) 1.446(2), C(1)-C(5) 1.477(2), C(2)-C(3) 1.475(2), C(3)-C(4) 1.413(2), C(4)-C(5) 1.414(2), C(5)-C(6) 1.376(2), C(3)-C(12) 1.377(2), C(4)-C(9) 1.396(2); C(1)-N(1)-C(13) 118.94(12), C(2)-N(2)-C(25) 117.14(12), N(1)-Na(1)-N(2) 76.04(5), C(1)-Na(1)-C(2) 27.57(4).

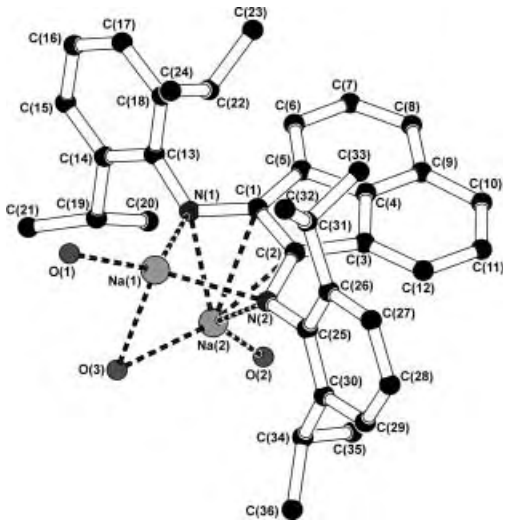


Figure 2. PLATON[8] presentation of the molecular structure of **2**. The carbon atoms of the solvent molecules are omitted. Selected bond lengths [Å] and angles [°]: Na(1)-N(1) 2.343(3), Na(1)-N(2) 2.398(3), Na(1)-O(1) 2.311(3), Na(2)-O(2) 2.289(3), Na(1)-O(3) 2.588(3), Na(2)-O(3) 2.456(3), Na(1)-C(1) 3.053(3), Na(1)-C(2) 3.077(3), Na(2)-N(1) 2.418(3), Na(2)-N(2) 2.465(3), Na(2)-C(1) 2.596(3), Na(2)-C(2) 2.614(3), N(1)-C(1) 1.387(4), N(2)-C(2) 1.386(4), N(1)-C(13) 1.400(4), N(2)-C(25) 1.407(4), C(1)-C(2) 1.402(4), Na(1)-Na(2) 2.9559(18); N(1)-Na(1)-N(2) 75.26(9), C(1)-Na(1)-C(2) 26.45(8), N(1)-Na(2)-N(2) 72.71(9), C(1)-Na(2)-C(2) 31.22(9).

diimine dianion may be explained by different types of bonding of the metal atoms to the −:N:−C=C−:N:− system. The short Na(1)–N(1) (2.343(3) Å) and Na(1)–N(2) (2.398(3) Å) distances may be attributed to σ sodium-to-nitrogen bonding while the longer bonds N(2)–N(1) (2.418(3) Å) and Na(1)–N(2) (2.465(3) Å) may reflect π bonding between Na (2) and enediamido moiety. Each sodium atom in **2** is coordinated by a terminal Et_2O molecule; a third Et_2O molecule bridges the two sodium atoms.

The coordination mode of the metal atoms to the ligand changes significantly on going from **2** to **3** (Figure 3). In the crystal, two $[Na]^+[\{Na(Et_2O)\}^+]_2[(2,6\text{-}i Pr_2PhNC)_2(C_{12}H_6)]^{-3}$ moieties aggregate to form a centrosymmetric dimer of two coplanar acenaphthylene π systems in a head-to-tail arrangement. Four sodium atoms are placed between the two acenaphtylene planes. A similar structure with four lithium cations between the two layers of the dimeric [coronannulene]$^{4-}$ superstructure was deduced from ^{7}Li NMR spectroscopy.[10] Two lithium cations placed between two aromatic systems were recently established by X-ray crystallography for the complex with acenaphthylene dianion, $[Li(Et_2O)_2]_2[@Li]_2[C_{12}H_8]_2$.[11] In **3**, the sodium atom Na(1), which is in a similar position to the Na(1) atoms in molecules **1** and **2**, is coordinated to only one nitrogen atom, N(2). The bonding of Na(2) with the ligand in **3** is similar to that of Na(2) in **2**. An electron pair of N(1), analogous to

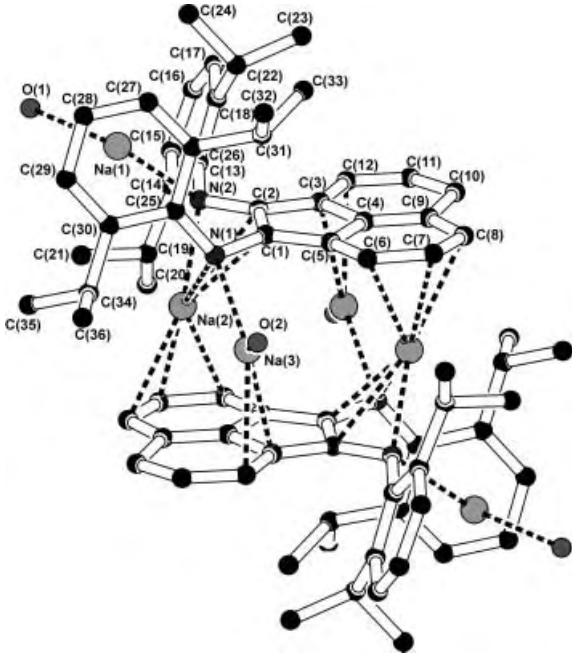


Figure 3. PLATON[8] presentation of the molecular structure of **3**. The carbon atoms of the solvent molecules are omitted. Selected bond lengths [Å] and angles [°]: Na(1)-O(1) 2.329(3), Na(1)-N(2) 2.367(3), Na(1)-C(13) 2.859(4), Na(1)-Na(2) 3.7071(18), Na(2)-N(1) 2.411(3), Na(2)-N(2) 2.402(3), Na(2)-C(1) 2.616(3), Na(2)-C(2) 2.617(3), Na(2)-C(4) 2.963(3), Na(2)-C(5) 2.897(3), Na(2)-C(6) 2.732(3), Na(2)-C(7) 2.656(3), Na(2)-C(8) 2.731(3), Na(2)-C(9) 2.927(3), Na(3)-O(2) 2.347(3), Na(3)-N(1) 2.361(3), Na(3)-C(1) 3.099(3), Na(3)-C(3) 2.714(3), Na(3)-C(4) 3.081(3), Na(3)-C(11) 3.086(4), Na(3)-C(12) 2.688(3), N(1)-C(1) 1.438(4), N(2)-C(2) 1.397(4), C(1)-C(2) 1.424(4), Na(3)-Na(2)′ 4.061(2), Na(2)-Na(3) 3.4814(19); Na(1)-Na(2)-Na(3) 107.65(4), Na(2)-Na(3)-Na(2′) 82.49(4).

 © 2003 Wiley-VCH Verlag GmbH & Co. KGaA, Weinheim

that of N(1) bonded to Na(1) in complex **2** , forms a bond with a third sodium atom Na(3). This atom has two short contacts to two carbon atoms of the naphthalene system of its symmetry equivalent subunit. Furthermore, Na(2) also has short contacts with carbon atoms of one benzene ring of the symmetry equivalent naphthalene subunit. This indicates that the negative charge in $\{(2,6\text{-}i\mathrm{Pr}_2\mathrm{PhNC})_2(\mathrm{C}_{12}\mathrm{H}_6)\}^{-3}$ is delocalised over the whole diimine–naphthalene π system. As in **2**, Na(1) is coordinated in η^6 fashion by the phenyl ring attached to N (1). These Na(1)–C(phenyl) bond distances fall in a narrower (2.788(3)-2.905(2) Å, av 2.846 Å) range compared to those in **1**.

The structural motif of complex **4** (Figure 4) is very similar to that of complex **3**. The additional sodium cations Na(7) and Na(8) are situated over each naphthalene system due to the additional negative charge on the naphthalene part of the ligand. It is interesting to note that the coordination sphere of Na(7) and Na(8) is completed by two thf ligands as well as two *i*Pr groups indicating a kind of agostic interaction between H atoms of the *i*Pr groups and sodium atoms Na(7) and Na(8) with distances as small as 2.0545 Å (Na(8)···H(21C)).

In conclusion, we have established that recently commonly used ligand, dpp-bian, may be easily reduced in diethyl ether by sodium metal to mono-, di-, tri- and tetranions. For the first time four anionic forms of a single ligand have been isolated on a preparative scale and unambiguously characterized by single crystal X-ray structure analysis. The structures indicate that the first two electrons are placed at the diimine subsystem and the other two electrons at the naphthalene part. It would be interesting to investigate whether the electronic isomers of the ligand dianion may exist with both negative charges localized either on the diimine, or on the naphthalene moieties. As seen from the crystal data of **1**–**4**, the four reduced forms of the ligand display a variety of the coordination modes. We plan to carry out exchange reactions of the sodium derivatives **3** and **4** with the halides of tri- and tetravalent metals. This may result in the discovery of new complexes, which may serve as reducing agents in organic substrate transformations.

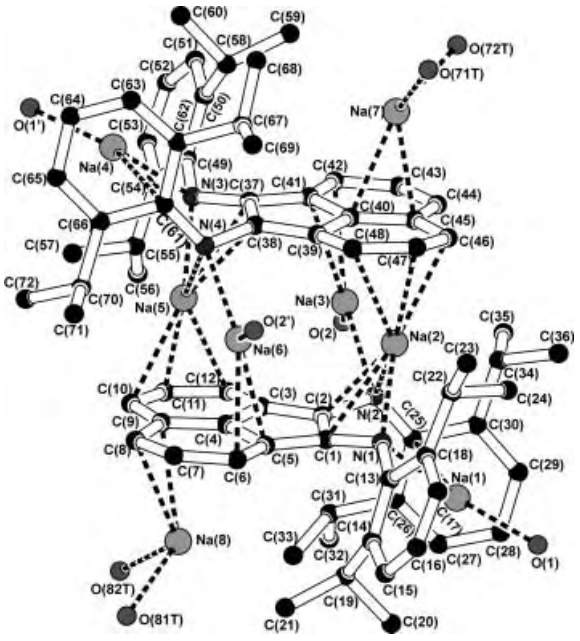


Figure 4. PLATON[8] presentation of the molecular structure of **4**. The carbon atoms of the solvent molecules are omitted. Selected bond lengths [Å] and angles [°]: Na(1)-O(1) 2.248(3), Na(1)-N(1) 2.381(3), Na(2)-N(1) 2.329(4), Na(2)-N(2) 2.398(3), Na(2)-C(1) 2.598(4), Na(2)-C(2) 2.589(3), Na(2)-C(45) 2.927(6), Na(2)-C(46) 2.610(6), Na(2)-C(47) 2.548(5), Na(2)-C(48) 2.733(5), Na(3)-C(40) 2.833(5), Na(3)-C(41) 2.692(5), Na(3)-C(42) 2.684(6), Na(3)-C(43) 2.826(6), Na(8)-O(81T) 2.326(4), Na(8)-O(82T) 2.334(3), Na(8)-C(4) 2.812(4), Na(8)-C(5) 2.923(4), Na(8)-C(6) 2.922(4), Na(8)-C(7) 2.758(4), Na(8)-C(8) 2.584(4), Na(8)-C(9) 2.665(4), Na(8)-C(21) 3.034(5), N(1)-C(1) 1.422(4), N(2)-C(2) 1.441(5), C(1)-C(2) 1.444(5), Na(1)-Na(2) 3.691(2), Na(3)-Na(5) 3.924(3), Na(2)-Na(3) 3.305(3); Na(1)-Na(2)-Na(2) 105.60(6), Na(2)-Na(3)-Na(5) 85.10(6), Na(4)-Na(5)-Na(6) 107.06(5), Na(2)-Na(6)-Na(5) 86.72(6).

Experimental Section

All manipulations were carried out under reduced pressure using Schlenk ampoules. Diethyl ether, THF and benzene were condensed into reaction ampoules from sodium/benzophenon prior to use. The ligand dpp-bian was prepared according to a literature procedure.[9] The ^{1}H NMR spectra were recorded on a Bruker DPX-200 NMR spectrometer. Magnetic moments for **1** and **3** were determined by the Faraday method.

1: A suspension of dpp-bian (0.5 g, 1.0 mmol) in Et_2O (30 mL) was added to an ampoule containing a single piece of sodium (1.15 g, 50 mmol). The mixture was stirred for 4 h, during which the precipitation of a brick-red solid occurred. The suspension of **4** was decanted from the metal and treated in situ with free ligand (1.45 g, 2.9 mmol); the solids dissolved instantly and the mixture turned red. Evaporation of the solvent in vacuo and crystallization from benzene (60 mL) afforded 1.1 g (55 %) of **1** as red crystals. m.p. > 246 °C; Elemental analysis calcd (%) for $C_{72}H_{80}N_4Na_2$ (1047.4): C 82.56, H 7.70; found: C 82.34, H 7.93; $\mu_{eff} = 1.95$ BM. Crystal data for **1**: $C_{72}H_{80}N_4Na_2$, $M_r = 1047.4$, monoclinic, space group P(2)1/n, $a = 12.7883(7)$, $b = 13.1620(7)$, $c = 18.9586(10)$ Å; $\beta = 106.6330(10)°$, $V = 3057.6(3)$ Å^3, $Z = 4$, $T = 183(2)$ K, $F_{000} = 1124$, $\mu = 0.078$ mm^{-1}, $\theta = 1.91–23.29°$, reflection collected 20140, independent reflections 4399 [$R_{int} = 0.0385$], $GOF = 1.005$, $R = 0.0425$, $wR^2 = 0.1033$, largest diff. peak and hole 0.256/-0.212 e Å^{-3}.

2: The dpp-bian ligand (0.5 g, 1.0 mmol) was added to a suspension of **4** (prepared from 0.5 g, 1.0 mmol of dpp-bian prepared in situ as described for **1**). The resulting green solution was concentrated in vacuo (15 mL), and left to stand at 20 °C to give **2** as large dark-red crystals (0.73 g, 48 %). M.p. > 246 °C; elemental anal (%) calcd for $C_{48}H_{70}N_2Na_2O_3$ (769.04): C 74.96, H 9.17; found: C 75.02, H 9.30; ^{1}H NMR (200 MHz, C_6D_6, 20 °C, TMS): $\delta = 7.32–6.51$ (12 H, aromatic), 3.85 (sept, 4 H, C*H*(Me)$_2$), 3.18 (q, 12 H, CH_2), 1.41 (d, 12 H, CH(C*H*$_3$)$_2$, ^3J(H,H) = 8.0 Hz), 1.33 (d, 12 H, CH(C*H*$_3$)$_2$, $^3J = 8.0$ Hz), 1.02 ppm (t, 18 H, CH_3). Crystal data for **2**: $C_{48}H_{70}N_2Na_2O_3$, $M_r = 769.04$, monoclinic, space group P(2)1/n, $a = 12.3158(9)$, $b = 19.3819(14)$, $c = 18.8024(13)$ Å, $\beta = 92.9540(10)°$, $V = 4482.2(6)$ Å^3, $Z = 4$, $T = 100(2)$ K, $F_{000} = 1672$, $\mu = 0.086$ mm^{-1}, $\theta = 1.51–22.00°$, reflection collected 24405, independent reflections 5481 [$R_{int} = 0.0246$], $GOF = 1.090$, $R = 0.0670$, $wR^2 = 0.1903$, largest diff. peak and hole 0.767/−0.330 e Å^{-3}.

3: The ligand dpp-bian (0.17 g, 0.34 mmol) was added to a suspension of **4** (from 0.5 g, 1.0 mmol of the ligand, 20 mL of Et_2O, prepared as described above). The brick-red solid of **4** dissolved partially and the solution became darker. The mixture was centrifuged and the solution was decanted affording 0.11 g (21 %) of compound **3** after drying in vacuo at 20 °C within 2 min. m.p. > 246 °C; $\mu_{eff} = 1.68$ BM. The extreme air-sensitive nature of compounds **3** and **4** prevented any meaningful analytical data being obtained. Crystals of

 © 2003 Wiley-VCH Verlag GmbH & Co. KGaA, Weinheim

3 suitable for X-ray analysis were obtained within two weeks in a flask that was left undisturbed containing sodium metal, dpp-bian, and Et_2O. Crystal data for **3**: $C_{88}H_{120}N_4Na_6O_4{\cdot}C_4H_{10}O$, $M_r = 1510.01$, triclinic, space group P1, $a = 12.792(2)$, $b = 13.034(2)$, $c = 14.323(2)$ Å, $\alpha = 68.204(3)$, $\beta = 85.292(3)$, $\gamma = 79.442(3)°$, $V = 2179.6(6)$ Å^3, $Z = 1$, $T = 183(2)$ K, $F_{000} = 800$, $\mu = 0.094$ mm^{-1}, $\theta = 1.71–23.35°$, reflection collected 12975, independent reflections 6273 [$R_{int} = 0.0362$], GOF = 1.015, $R = 0.0794$, $wR^2 = 0.2182$, largest diff. peak and hole 0.786/−0.459 e Å^{-3}.

4: A suspension of **4** (prepared from 0.5 g, 1.0 mmol of dpp-bian prepared as described above) was decanted from the metal and centrifuged. Decantation of the solution left a brick-red solid which was dried at 20 °C in vacuum for 2 min. Yield 0.52 g (57 %). m.p. > 246 °C. As no acceptable elemental analysis on **4** could be obtained we proved the formation of **4** by the oxidation of the complex with iodine. A solution of iodine (0.51 g, 2.0 mmol) in Et_2O (40 mL) was added dropwise to a suspension of **4**, which was obtained from 0.5 g (1.0 mmol) of the ligand. After addition of 50 % of the I_2 solution the mixture turned green and after 75 % the solution became red. The addition of the remaining iodine caused almost complete discoloration of the mixture. Suitable crystals of compound **4** for X-ray analysis were obtained from THF. Crystal data for **4**: $C_{104}H_{144}N_4Na_8O_8{\cdot}C_4H_8O$, $M_r = 1834.25$, monoclinic, space group P(2)1/n, $a = 26.3483(14)$, $b = 16.4269(9)$, $c = 26.9621(14)$ Å, $\beta = 118.9560(10)°$, $V = 10210.9(9)$ Å^3, $Z = 4$, $T = 150(2)$ K, $F_{000} = 3920$, $\mu = 0.103$ mm^{-1}, $\theta = 0.89–22.00°$, reflection collected 59234, independent reflections 12526 [$R_{int} = 0.0554$], $GOF = 1.173$, $R = 0.0968$, $wR^2 = 0.2682$, largest diff. peak and hole 0.674/−0.634 e Å^{-3}. CCDC-205954 (**1**) CCDC-205955 (**2**) CCDC-205956 (**3**) and CCDC-205957 (**4**) contains the supplementary crystallographic data for this paper. These data can be obtained free of charge at www.ccdc.cam.ac.uk/conts/retrieving.html [or from the Cambridge Crystallographic Data Center, 12, Union Road, Cambridge CB2 1EZ, UK; fax: (internat.) +44–1223/336–033; E-mail: deposit@ccdc.cam.ac.uk].

Received: March 14, 2003 [Z51408]

Keywords: N ligands · polyanions · reduction · sodium · structure elucidation

[1] a) R. van Asselt, K. Vrieze, C. J. Elsevier, *J. Organomet. Chem.* **1994**, *480*, 27; b) R. van Asselt, C. J. Elsevier, W. J. J. Smeets, A. L. Spek, R. Benedix, *Recl. Trav. Chim. Pays-Bas* **1994**, *113*, 88; c) R. van Asselt, C. J. Elsevier, *Organometallics* **1994**, *13*, 1972; d) R. van Asselt, C. J. Elsevier, W. J. J. Smeets, A. L. Spek, *Inorg. Chem.* **1994**, *33*, 1521; e) R. van Asselt, E. Rijnberg, C. J. Elsevier, *Organometallics* **1994**, *13*, 706; f) R. van Asselt, E. E. C. G. Gielens, R. E. Rulke, K. Vrieze, C. J. Elsevier, *J. Am. Chem. Soc.* **1994**, *116*, 977; g) R. van Asselt, E. E. C. G. Gielens, R. E. Rulke, C. J. Elsevier, *J. Chem. Soc. Chem. Commun.* **1993**, 1203.

[2] a) M. W. van Laren, C. J. Elsevier, *Angew. Chem.* **1999**, *111*, 3926; *Angew. Chem. Int. Ed.* **1999**, *38*, 3715; b) R. van Belzen, H. Hoffmann, C. J. Elsevier, *Angew. Chem.* **1997**, *109*, 1823–1825; *Angew. Chem. Int. Ed. Engl.* **1997**, *36*, 1743; c) E. Shirakawa, T. Hiyama, *J. Organomet. Chem.* **2002**, *653*, 114.

[3] a) D. Pappalardo, M. Mazzeo, S. Antinucci, C. Pellecchia, *Macromolecules* **2000**, *33*, 9483; b) D. J. Tempel, L. K. Johnson, R. L. Huff, P. S. White, M. Brookhart, *J. Am. Chem. Soc.* **2000**, *122*, 6686; c) D. P. Gates, S. A. Svejda, E. Onate, Ch. M. Killian, L. K. Johnson, P. S. White, M. Brookhart, *Macromolecules* **2000**, *33*, 2320; d) S. A. Svejda, M. Brookhart, *Organometallics* **1999**, *18*, 65; e) M. Gasperini, F. Ragaini, S. Cenini, *Organometallics* **2002**, *21*, 2950.

[4] a) A. A. Trifonov, L. N. Zakharov, M. N. Bochkarev, Yu. T. Struchkov, *Izv. Akad. Nauk, Izv. Akad. Nauk Ser. Khim.* **1994**, 148; b) H. Görls, B. Neumüller, A. Scholz, J. Scholz, *Angew. Chem.* **1995**, *107*, 732; *Angew. Chem. Int. Ed. Engl.* **1995**, *34*, 673; c) M. Haaf, A. Schmiedl, T. A. Schmedake, D. R. Powell, A. J. Millevolte, M. Denk, R. West, *J. Am. Chem. Soc.* **1998**, *120*, 12714; d) J. Scholz, H. Görls, H. Schumann, R. Weimann, *Organometallics*, **2001**, *20*, 4394; e) H. Bock, J.-M. Lehn, J. Pauls, S. Holl, V. Krenzel, *Angew. Chem. Int. Ed.* **1999**, *38*, 952; f) I. L. Fedushkin, T. V. Petrovskaya, F. Girgsdies, R. D. Köhn, M. N. Bochkarev, H. Schumann, *Angew. Chem.* **1999**, *111*, 2407; *Angew. Chem. Int. Ed.* **1999**, *38*, 2262.

[5] a) J. J. Brooks, W. Rhine, G. D. Stucky, *J. Am. Chem. Soc.* **1972**, *94*, 7346; b) A. V. Protchenko, L. N. Zakharov, M. N. Bochkarev, Yu. T. Struchkov, *J. Organomet. Chem.* **1993**, *447*, 209; c) I. L. Fedushkin, M. N. Bochkarev, H. Schumann, L. Esser, G. Kociok-Kohn, *J. Organomet. Chem.* **1995**, *489*, 145; d) M. N. Bochkarev, I. L. Fedushkin, R. B. Larichev, *Russ. Chem. Bull.* **1996**, *45*, 2443; e) M. N. Bochkarev, I. L. Fedushkin, A. A. Fagin, H. Schumann, J. Demtschuk, *Chem. Commun.* **1997**, 1783.

[6] a) H. Bock, K. Gharagozloo-Hubmann, C. Näther, N. Nagel, Z. Havlas, *Angew. Chem.* **1996**, *108*, 720; *Angew. Chem. Int. Ed. Engl.* **1996**, *35*, 631; b) H. Bock, K. Gharagozloo-Hubmann, S. Holl, M. Sievert, *Z. Naturforsch.* **2000**, *55b*, 1163; c) A. Weitz, M. Rabinovitz, P.-C. Cheng, L. T. Scott, *Synthetic Metals*, **1997**, *86*, 2159; d) E. Shabtai, R. E. Hoffman, P.-C. Cheng, E. Bayrd, D. V. Preda, L. T. Scott, M. Rabinovitz, *J. Chem. Soc. Perkin. Trans.*, **2000**, *2*, 129; e) I. Aprahamian, R. E. Hoffman, T. Sheradsky, D. V. Preda, M. Bancu, L. T. Scott, M. Rabinovitz, *Angew. Chem.* **2002**, *114*, 1788; *Angew. Chem. Int. Ed.* **2002**, *41*, 1712; f) A. Sekiguchi, T. Matsuo, C. Kabuto, *Angew. Chem.*, **1997**, *109*, 2572; *Angew. Chem. Int. Ed. Engl.* **1997**, *36,* 2462; g) T. Matsuo, H. Fure, A. Sekigichi, *J. Chem. Soc. Chem. Commun.*, **1999**, 1981; h) Y. Sun, Ch. A. Reed, *J. Chem. Soc. Chem. Commun.*, **1997**, 747.

[7] D. Enright, S. Gambarotta, G. P. A. Yap, P. H. M. Budzelaar, *Angew. Chem. Int. Ed.* **2002**, *41*, 3873.

[8] A. L. Spek, *PLATON A Multipurpose Crystallographic Tool,* Utrecht University **2000**.

[9] A. A. Paulovicova, U.; El-Ayaan, K. Shibayama, T. Morita, Y. Fukuda, *Eur. J. Inorg. Chem.* **2001**, 2641–2646.

[10] A. Ayalon, A. Sygula, P. C. Cheng, M. Rabinovitz, P. W. Rabideau, L. T. Scott, *Science*, **1994**, *265*, 1065.

[11] I. L. Fedushkin, G. V. Khoroshen′kov, M. N. Bochkarev, S. Mühle, H. Schumann, *Russ. Chem. Bull. Int. Ed.*, in press.

 © 2003 Wiley-VCH Verlag GmbH & Co. KGaA, Weinheim

Enzyme Engineering

A Self-Sufficient Peroxide-Driven Hydroxylation Biocatalyst**

*Patrick C. Cirino and Frances H. Arnold**

Controlled, selective oxidations of unactivated C–H bonds are among the most desired transformations in catalysis.[1] Limitations to chemical oxidation catalysts include low turnover numbers, low or no regioselectivity, poor reaction specificity, their use of environmentally harmful components (for example, heavy metals or halogens), or their requirements for harsh, expensive reaction conditions. Many oxygenase enzymes catalyze the insertion of oxygen into unactivated C–H bonds[2,3] and are superior to synthetic catalysts with regard to selectivity and turnover rate.[4] Enzymes have found numerous industrial applications,[5] and the use of enzymes in industrial biocatalysis is expected to grow significantly.[6] One limitation to the application of oxygenases is their requirement for an expensive cofactor such as NAD(P)H, which precludes their use in vitro without addition of a coupled, cofactor-regenerating system.[7] The need for additional proteins to transfer electrons from the cofactor to the oxygenase presents a further complication. Here we describe a self-sufficient P450 BM-3 variant which utilizes hydrogen peroxide (H_2O_2) to catalyze hydroxylation and epoxidation at high rates.

The cytochromes P450 are heme-containing oxygenases which collectively catalyze a variety of oxidations on a diverse array of substrates.[3,8] The natural P450 catalytic cycle utilizes two electrons from NAD(P)H to activate dioxygen, although P450s are also capable of utilizing peroxides as a source of oxygen through a peroxide "shunt" pathway. In principle, this "peroxygenase" activity offers an opportunity to employ cell-free P450 catalysis without requiring NAD(P)H regeneration, additional proteins, or dioxygen, and eliminates rate-limiting electron-transfer steps.[9] In practice, this non-natural pathway is too inefficient for any practical application.

The soluble P450 BM-3 enzyme catalyzes the hydroxylation of sub-terminal C–H bonds of medium chain (C_{12}–C_{18}) fatty acids and amides[10] with initial rates exceeding 3000 min^{-1}.[11] The activities of P450 BM-3 and its corresponding F87A mutant in reactions driven by H_2O_2 were recently characterized.[12,13] Whereas the wild-type enzyme is inactivated after only a few turnovers, the F87A mutant supports low levels of peroxygenase activity (ca. 70 total turnovers). In a previous study we demonstrated that directed evolution could increase the rate of peroxide-driven naphthalene hydroxylation by cytochrome P450cam.[9] Since then, our efforts have focused on improving the peroxygenase activity of the more active P450 BM-3 as a step towards engineering a "biomimetic" hydroxylation catalyst.

The P450 BM-3 heme domain (BMP)[14] supports peroxygenase activity[12] and is more thermostable than the full-length P450 BM-3 protein (unpublished data). Removal of the reductase domain also results in an approximate fourfold increased molar expression (ca. 70 mg L^{-1} in shake-flask cultures). We used BMP mutant F87A (HF87A) as the starting point (parent) to increase catalyst performance by sequential rounds of random mutagenesis and screening for H_2O_2-driven hydroxylation of 12-*p*-nitrophenoxycarboxylic acid (12-pNCA).[15] Experimental details and a description of the evolutionary path are available in the Supporting Information.

Fifth-generation mutant "21B3" is nearly 20-fold more active than HF87A in 10 mM H_2O_2 using 12-pNCA as the substrate.[16] Figure 1 shows the activities of HF87A and 21B3 at different peroxide concentrations. Activities are reported as initial rates of *p*-nitrophenolate (pNP) formation at room temperature.[17] The peroxygenase reaction follows apparent Michaelis–Menten kinetics. Whereas the apparent K_m value for H_2O_2 in HF87A is about 30 mM, in 21B3 the apparent K_m value is reduced to about 8 mM. Total turnover numbers (TON) of approximately 1000 are achieved.

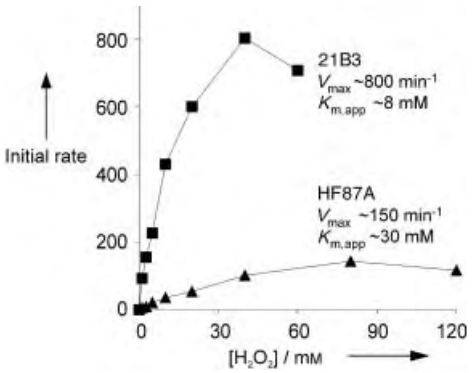


Figure 1. Initial rates ((mol pNP formed) (mol P450)$^{-1}$ min^{-1}) of peroxide-driven 12-pNCA hydroxylation by P450 BMP variants HF87A and 21B3 in different H_2O_2 concentrations. Reactions were performed at room temperature and contained 300 μM 12-pNCA, 6% DMSO, and purified enzyme (0.5 μM HF87A or 0.2 μM 21B3) in 100 mM Tris-HCl, pH 8.2. Tris = tris(hydroxymethyl)aminoethane.

Improved peroxygenase activity also extends to fatty acid substrates, with product distributions that are the same as those from HF87A, as demonstrated in Figure 2 for reactions of HF87A and 21B3 with lauric (dodecanoic) acid and myristic (tetradecanoic) acid. No products other than those shown were identified from these reactions. Using 10 mM H_2O_2, the initial rate of lauric acid hydroxylation, estimated from the amount of product formed in the first minute of

[*] Prof. Dr. F. H. Arnold, P. C. Cirino
Division of Chemistry and Chemical Engineering
California Institute of Technology
Pasadena, CA 91125 (USA)
Fax: (+1) 626-568-8743
E-mail: frances@cheme.caltech.edu

[**] This work was supported by the Biotechnology Research and Development Corporation (Peoria, IL) and an NSF Graduate Research Fellowship awarded to P.C.C. The authors thank Ulrich Schwaneberg for guidance and Denis Shcherbakov for laboratory assistance.

Supporting information for this article is available on the WWW under http://www.angewandte.org or from the author.

 DOI: 10.1002/anie.200351434 © 2003 Wiley-VCH Verlag GmbH & Co. KGaA, Weinheim

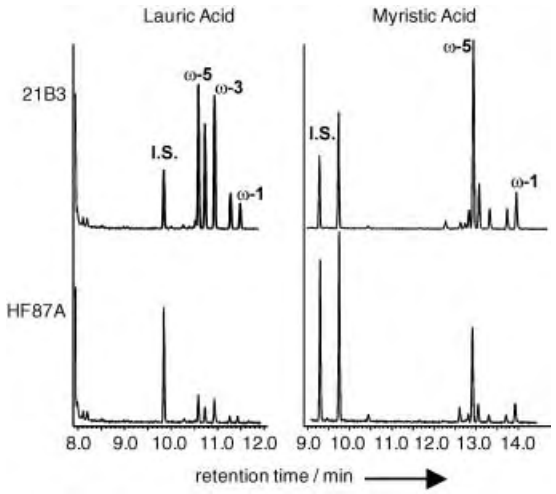


Figure 2. Chromatograms of the trimethylsilyl-derivatized hydroxylated products from H_2O_2-driven reactions of P450 BMP variants HF87A and 21B3 with lauric acid and myristic acid. The reactions contained purified enzyme (1–4 μM) and 1–2 mM substrate in 500 μL 100 mM Tris-HCl, pH 8.2. The reactions were initiated by the addition of 5 mM or 10 mM H_2O_2, carried out at room temperature, and stopped by the addition of 7.5 μL 6 M HCl, as described.[12] I.S. is the internal standard (10-hydroxydecanoic acid), which was added to all samples in an equal amount (30 nmoles) at the end of each reaction so that products could be quantified relative to the area of the I.S. peak.

summarizes the activities of 21B3 compared to HF87A for the various substrates tested.

The major limitation of this system is rapid enzyme inactivation as a result of peroxide-mediated heme degradation, as indicated by a decrease in the heme absorbance peak in the presence of H_2O_2 (not shown). Figure 3 shows the time-courses of pNP formation from reactions of 21B3 on 12-pNCA in 1 mM, 5 mM, and 10 mM H_2O_2. The enzyme is essentially inactive within 5 minutes in 10 mM H_2O_2. Inactivation appears to be turnover-dependent (similar TONs are reached from reactions in 1 mM, 5 mM, and 10 mM H_2O_2), and the ratio of peroxygenase turnovers to heme-degrading turnovers increased with each generation of evolution (half-lives in a given concentration of peroxide did not increase).

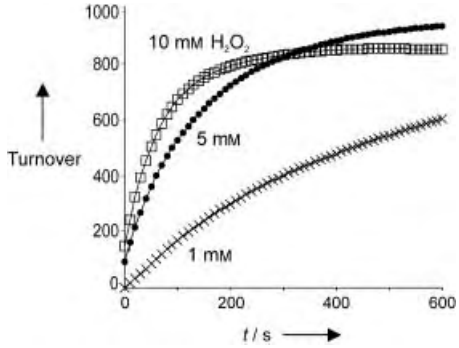


Figure 3. Time-courses of pNP formation for reactions catalyzed by P450 BMP variant 21B3 with 12-pNCA in 1, 5, and 10 mM H_2O_2. Increasing peroxide concentration increases the peroxygenase activity as well as the rate of enzyme inactivation. The reactions were performed at room temperature and contained 250 μM 12-pNCA, 6.3% DMSO, and either 0.94 μM F87A or 0.15 μM 21B3 in 100 mM Tris-HCl, pH 8.2. Turnover is expressed in (mol pNP formed) (mol P450)$^{-1}$.

reaction (see ref. [12] or Supporting Information), is about 50 mol (mol P450)$^{-1}$ min^{-1} for 21B3. The TON for lauric acid in 5 mM H_2O_2 is about 280. Similar results are observed with decanoic (capric) acid.

Oxidation of styrene to styrene oxide is also significantly improved with 21B3. (Relaxed substrate specificity was expected since specificity was not among the selection criteria during screening.) The initial rate of styrene oxide production by 21B3 is 55 mol (mol P450)$^{-1}$ min^{-1} in 10 mM H_2O_2 (estimated from the amount of product formed in the first minute of reaction), with a TON of about 240 in 5 mM H_2O_2. In contrast, the initial rate for HF87A in 10 mM H_2O_2 is approximately 2.4 mol (mol P450)$^{-1}$ min^{-1}, with a TON of only about 10. For comparison, the NADPH-driven styrene oxidation activity of wild-type BM-3 (for which styrene is a poor substrate) is about 30 mol (mol P450)$^{-1}$ min^{-1}. Table 1

Table 1: Summary of peroxygenase activities of P450 BMP variants HF87A and 21B3.

Substrate	Measurement	HF87A	21B3
12-pNCA[a]	initial rate[b]	23	430
12-pNCA[a]	TON[c]	90	980
lauric acid	initial rate	10	50
lauric acid	TON	70	280
styrene[d]	initial rate	2.4	54
styrene[d]	TON	10	240

[a] Activity on 12-pNCA was measured in the presence of 6% DMSO (see ref. [16]). [b] Initial rates were determined in 10 mM H_2O_2 and are reported as (mol product) (mol P450)$^{-1}$ min^{-1}. [c] Total enzyme turnovers. TON values were determined in 5 mM H_2O_2. [d] Styrene oxide is the only product.

Sequence analysis of 21B3 reveals thirteen nucleotide substitutions relative to the HF87A sequence, nine of which result in amino acid substitutions. The BMP crystal structure[18] shows that the mutations are dispersed throughout the protein scaffold. No mutations appear in the active site, substrate binding channel, or F and G helices of the heme domain. There are also no mutations in any β-sheets of the β-sheet-rich region of the structure. Four mutations lie on the protein surface. A list of the amino acid substitutions and information on the positions of these mutations are available in the Supporting Information.

The fungal heme enzyme chloroperoxidase (CPO) has received much attention for its ability to catalyze the H_2O_2-driven, enantioselective epoxidation of alkenes.[19] CPO does not efficiently hydroxylate unactivated C–H bonds,[20] which is the hallmark of P450 chemistry. Furthermore, protein engineering on CPO has been extremely limited, as a result of its lack of functional expression in bacteria or yeast. The P450s SPα (CYP152B1) and BSβ (CYP152A1) are two recently discovered H_2O_2-driven fatty acid α- and β-hydroxylases.[21–23] Their highly specialized catalytic mechanisms[24] limits the substrate range and therefore the applications of these P450s for biotransformations.

 © 2003 Wiley-VCH Verlag GmbH & Co. KGaA, Weinheim

Cytochrome P450 BM-3 is a versatile hydroxylase whose "designability" has been demonstrated[25] and whose biotechnological relevance has been established.[26] Directed evolution allows us to engineer into this enzyme functions not required or permitted in its natural biological context. For example, a P450 BM-3 variant which efficiently hydroxylates alkanes was recently described.[27] An efficient H_2O_2-driven BMP variant allows us to exploit this powerful and versatile hydroxylase in a cell-free reaction system that requires neither NADPH nor reductase. This catalyst is easy to synthesize (high expression levels are achieved in *E. coli*), requires minimal preparation,[28] and is active under mild conditions (namely, 25 °C, 1 atm). The self-sufficiency of the H_2O_2-driven heme domain encourages further protein engineering to explore potential synthetic applications of this catalytic system.

Received: March 18, 2003 [Z51434]

Keywords: biocatalysis · cytochrome P450 · enzymes · oxidation · peroxygenase

[1] a) J. A. Labinger, J. E. Bercaw, *Nature* **2002**, *417*, 507; b) R. H. Crabtree, *J. Chem. Soc. Dalton Trans.* **2001**, 2437; c) Y. Ishii, S. Sakaguchi, T. Iwahama, *Adv. Synth. Catal.* **2001**, *343*, 393; d) M. Costas, K. Chen, L. Que, *Coord. Chem. Rev.* **2000**, *200*, 517; e) G. B. Maravin, M. V. Avdeev, E. I. Bagrii, *Pet. Chem. Ind. Dev. Annu* **2000**, *40*, 1; f) S. S. Stahl, J. A. Labinger, J. E. Bercaw, *Angew. Chem.* **1998**, *110*, 2298; *Angew. Chem. Int. Ed.* **1998**, *37*, 2181; g) A. E. Shilov, G. B. Shul'pin, *Chem. Rev.* **1997**, *97*, 2879.

[2] a) D. A. Kopp, S. J. Lippard, *Curr. Opin. Chem. Biol.* **2002**, *6*, 568; b) T. H. Smits, S. B. Balada, B. Witholt, J. B. van Beilen, *J. Bacteriol.* **2002**, *184*, 1733; c) M. M. Marin, T. H. Smits, J. B. van Beilen, F. Rojo, *J. Bacteriol.* **2001**, *183*, 4202; d) A. Ratajczak, W. Geissdorfer, W. Hillen, *Appl. Environ. Microbiol.* **1998**, *64*, 1175.

[3] P. R. Ortiz de Montellano, *Cytochrome P450: Structure, Mechanism, and Biochemistry*, 2nd ed., Plenum, New York, **1995**.

[4] H. L. Holland, H. K. Weber, *Curr. Opin. Biotechnol.* **2000**, *11*, 547.

[5] a) O. Kirk, T. V. Borchert, C. C. Fuglsang, *Curr. Opin. Biotechnol.* **2002**, *13*, 345; b) A. Liese, K. Seelbach, C. Wandrey, *Industrial Biotransformations*, Wiley-VCH, Weinheim, **2000**.

[6] A. Schmid, J. S. Dordick, B. Hauer, A. Kiener, M. Wubbolts, B. Witholt, *Nature* **2001**, *409*, 258.

[7] a) Z. Li, J. B. van Beilen, W. A. Duetz, A. Schmid, A. de Raadt, H. Griengl, B. Witholt, *Curr. Opin. Chem. Biol.* **2002**, *6*, 136; b) W. A. Duetz, J. B. van Beilen, B. Witholt, *Curr. Opin. Biotechnol.* **2001**, *12*, 419; c) K. M. Koeller, C. H. Wong, *Nature* **2001**, *409*, 232.

[8] D. Mansuy, *Comp. Biochem. Physiol. Part C: Pharmacol. Toxicol. Endocrinol.* **1998**, *121*, 5.

[9] H. Joo, Z. Lin, F. H. Arnold, *Nature* **1999**, *399*, 670.

[10] Y. Miura, A. J. Fulco, *Biochim. Biophys. Acta* **1975**, *388*, 305.

[11] J. H. Capdevila, S. Wei, C. Helvig, J. R. Falck, Y. Belosludtsev, G. Truan, S. E. Graham-Lorence, J. A. Peterson, *J. Biol. Chem.* **1996**, *271*, 22663.

[12] P. C. Cirino, F. H. Arnold, *Adv. Synth. Catal.* **2002**, *344*, 932.

[13] Q. S. Li, J. Ogawa, S. Shimizu, *Biochem. Biophys. Res. Commun.* **2001**, *280*, 1258.

[14] BMP consists of the first 463 amino acids. A 6-His sequence was included at the C-terminus with no notable effect on activity.

[15] U. Schwaneberg, C. Schmidt-Dannert, J. Schmitt, R. D. Schmid, *Anal. Biochem.* **1999**, *269*, 359.

[16] Screening was performed in the presence of DMSO (6.3%) to help solubilize 12-pNCA (see Supporting Information). The initial rate of HF87A with 12-pNCA in 6% DMSO (23 (mol product) (mol P450)$^{-1}$ min^{-1}) is nearly half of that in 1% DMSO (40 (mol product) (mol P450)$^{-1}$ min^{-1}), while similar TONs are reached. As a result of evolution in DMSO, 21B3 activity is not inhibited by DMSO until concentrations exceed 10%.

[17] Both HF87A and 21B3 are approximately 100% selective for the C-12 position of 12-pNCA, and result in nearly complete conversion of hydroxylated products into pNP.

[18] K. G. Ravichandran, S. S. Boddupalli, C. A. Hasermann, J. A. Peterson, J. Deisenhofer, *Science* **1993**, *261*, 731.

[19] F. van Rantwijk, R. A. Sheldon, *Curr. Opin. Biotechnol.* **2000**, *11*, 554.

[20] CPO is reported to oxidize unactivated C–H bonds in the radical probe substrate (*trans*-2-phenyl-1-methylcyclopropane) with a TON of 20, where only 31% of the product was alcohol; see P. H. Toy, M. Newcomb, L. P. Hager, *Chem. Res. Toxicol.* **1998**, *11*, 816.

[21] a) I. Matsunaga, T. Sumimoto, M. Ayata, H. Ogura, *FEBS Lett.* **2002**, *528*, 90; b) I. Matsunaga, N. Yokotani, O. Gotoh, E. Kusunose, M. Yamada, K. Ichihara, *J. Biol. Chem.* **1997**, *272*, 23592.

[22] I. Matsunaga, A. Yamada, D. S. Lee, E. Obayashi, N. Fujiwara, K. Kobayashi, H. Ogura, Y. Shiro, *Biochemistry* **2002**, *41*, 1886.

[23] I. Matsunaga, A. Ueda, T. Sumimoto, K. Ichihara, M. Ayata, H. Ogura, *Arch. Biochem. Biophys.* **2001**, *394*, 45.

[24] These P450s have unique active sites which include an Arg residue (see ref. [22]). Only fatty acids are accepted as substrates, and the carboxylate group of the substrate is positioned into the active site upon substrate binding. It is believed that the carboxylate group and the Arg residue work together to bind peroxide and facilitate O–O bond cleavage (see ref. [21]).

[25] P. C. Cirino, F. H. Arnold, *Curr. Opin. Chem. Biol.* **2002**, *6*, 130.

[26] F. P. Guengerich, *Nat. Rev. Drug Discovery* **2002**, *1*, 359.

[27] A. Glieder, E. T. Farinas, F. H. Arnold, *Nat. Biotechnol.* **2002**, *20*, 1135.

[28] Crude lysate or purified protein can be used.

 © 2003 Wiley-VCH Verlag GmbH & Co. KGaA, Weinheim

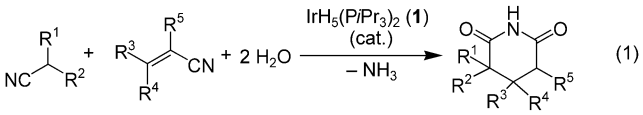
Ambiphilic Lewis Acid and Base Catalyst

Transition-Metal-Based Lewis Acid and Base Ambiphilic Catalysts of Iridium Hydride Complexes: Multicomponent Synthesis of Glutarimides**

*Hikaru Takaya, Kazunori Yoshida, Katsuhiro Isozaki, Hiroki Terai, and Shun-Ichi Murahashi**

The majority of reactions promoted by Lewis acids or bases are stoichiometric. Catalysts based on transition metals instead of conventional Lewis acids and bases might be useful, because the neutralization of reagents would not be necessary, and salts would not form. We found that such transition-metal-based Lewis acid[1–4] and base[1,5] catalysts that have low redox potentials are environmentally benign and useful for organic synthesis. This concept can be extended to ambiphilic catalysts based on transition metals.[6] These catalysts make possible both acid- and base-promoted reactions in a single container without the mutual destruction of reagents by neutralization, and multicomponent catalytic reactions that may be useful for combinatorial chemistry can be constructed.

We report herein that the iridium polyhydride complex $[IrH_5(P\mathit{i}Pr_3)_2]$ **1** is an excellent Lewis acid and base ambiphilic catalyst based on a transition metal, and that a novel three-component reaction of nitriles, olefins, and water occurs in the presence of catalyst **1** to gave glutarimides, which are highly versatile intermediates for synthesis of biologically active compounds [Eq. 1].[7] Iridium complex **1** is important as both

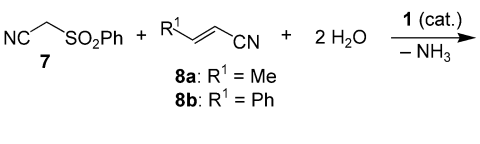


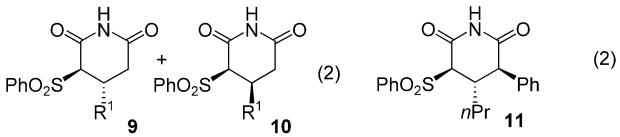
(1)

a redox base and Lewis acid catalyst.[8] The α-C–H activation of nitriles occurs to give a carbanion equivalent species for Michael addition,[5,9] and activation of the C≡N triple bond promotes hydration and amidation of nitriles.[4] In this way, the ambiphilic iridium complex **1** catalyzes the one-pot reaction of a mixture of nitriles, olefins, and water to give glutarimides efficiently.

Glutarimides have recently attracted attention as useful pharmaceuticals with pharmacological effects such as immunomodulatory, neuroplegic, and antitumor activity,[10] and hence methods for the ready synthesis of these compounds are needed. A variety of glutarimides can be prepared by the three-component reaction reported herein. Representative reactions are listed in Table 1. A range of substituents needed for pharmacological activity can be easily introduced into the 2- or 3-position of the glutarimide ring. The reaction of a mixture of α-aryl alkanenitrile, acrylonitrile **2**, and water (1:1:5) gave the corresponding 2-arylglutarimides in a yield of 92% or more (Table 1, entries 1 and 2). The conventional methods for the synthesis of these glutarimides, with Triton B and sulfuric acid used in that order, gave less than a 37% yield.[11] The glutarimide **3** thus obtained is an useful sedative Glutethimide and a precursor of Aminoglutethimide, an anticancer drug. The reaction of methyl 2-cyanopropanoate proceeds efficiently to give the corresponding 2-substituted glutarimide accompanied by removal of the ester group (Table 1, entry 3). The reaction of methyl 3-(4-chlorophenyl)-2-cyanopropanoate gave the corresponding glutarimide **4,** which may be a useful anticonvulsant (Table 1, entry 4).[12] The esterolytic reaction is useful for the synthesis of 3-substituted glutarimides. The treatment of methyl cyanoacetate **5** with β-substituted cyanoolefin in the presence of water gave the corresponding 3-substituted glutarimide **6** (Table 1, entry 5). α,β-Unsaturated esters also can be used as starting substrates. In fact, glutarimide **6** was also obtained from methyl crotonate. Similar three-component reactions of 1,3-dicarbonyl compounds can be carried out by α-C–H activation of the carbonyl group. In this way, 4-methyl-4,6,7,8-tetrahydro-1*H*,3*H*-quinoline-2,5-dione was obtained from 1,3-cyclohexanedione, crotononitrile, and water (Table 1, entry 7).[13]

The efficiency of such reactions is highlighted by the stereoselective synthesis of glutarimides. The reaction of a mixture of (benzenesulfonyl)acetonitrile **7**, cyanoolefin **8a**, and water gave **9a** ($R^1 = Me$) selectively in a 64% yield (**9a**:**10a** = 96:4) [Eq. 2].[14] It is noteworthy that a diastereomer **9b** ($R^1 = Ph$)[14] was obtained exclusively in 52% yield from the reaction of a mixture of **7**, **8b**, and water. The reaction of a mixture of **7** (*Z*)-2-phenyl-2-hexenenitrile, and





[*] Prof. Dr. S.-I. Murahashi,[+] Dr. H. Takaya, K. Yoshida, K. Isozaki, H. Terai
Department of Chemistry
Graduate School of Engineering Science
Osaka University
1–3, Machikaneyama, Toyonaka, Osaka 560-8531 (Japan)
E-mail: murahashi@high.ous.ac.jp

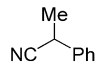
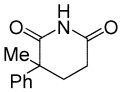
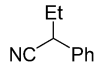
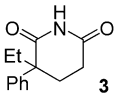
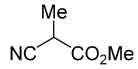
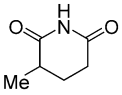
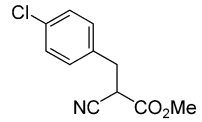
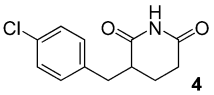
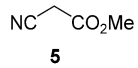
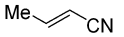
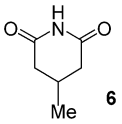
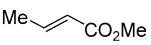
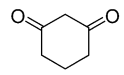
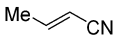
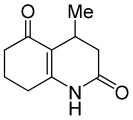
[+] Present address: Department of Chemistry
Faculty of Engineering
Okayama University of Science
1–1, Ridaicho, Okayama 700-0005 (Japan)
Fax: (+81) 86-256-9513

[**] This work was supported by the "Research for the Future Program", The Japan Society for the Promotion of Science, and a Grant-in-Aid for Scientific Research, the Ministry of Education, Culture, Sports, Science, and Technology, Japan.

Supporting information for this article is available on the WWW under http://www.angewandte.org or from the author.

 © 2003 Wiley-VCH Verlag GmbH & Co. KGaA, Weinheim DOI: 10.1002/anie.200351689

Table 1: Iridium-catalyzed three-component reaction.[a]

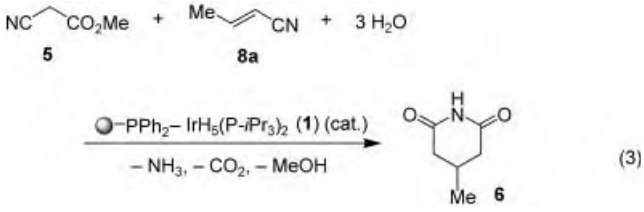
Entry	Pronucleophile	Olefin	Product	Yield[b] (%)
1		 **2**		94
2		**2**	 **3**	92[c]
3		**2**		98
4		**2**	 **4**	90
5	 **5**		 **6**	91
6	**5**		**6**	69
7				68

[a] A mixture of nitriles (1.0 mmol), olefins (1.1 mmol), H_2O (5.0 mmol), and $IrH_5(PiPr_3)_2$ (**1**) (0.10 mmol) in THF (0.25 mL) was stirred in a sealed glass tube at 150 °C for 20 h under an argon atmosphere. [b] Yield of isolated product based on starting pronucleophiles. [c] 2.0 mmol of **2** was added and the reaction was carried out at 180 °C for 30 h.

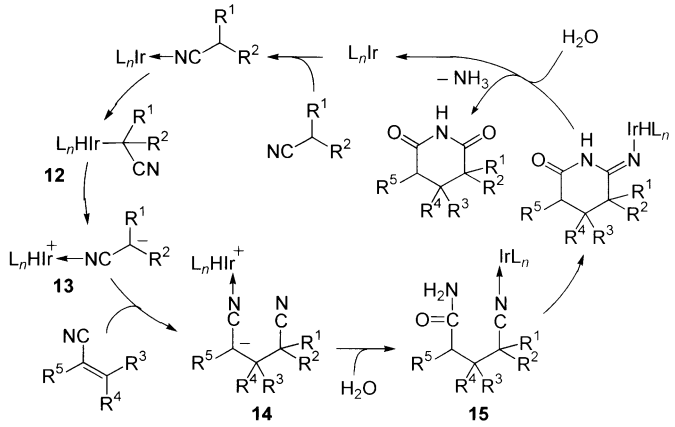
water gave only one diastereomer **11**[15] (yield 30%) among the four possible diastereomers.

This reaction might be explained in terms of the mechanism shown in Scheme 1. The catalytically active species seems to be the coordinatively unsaturated iridium species (L_nIr), formed by the dissociation of molecular hydrogen. The coordination of nitrile to L_nIr and α-C–H activation of nitriles would give the C-bound α-cyanocarbanion complex of iridium **12**. Isomerization of **12** to the corresponding N-bound cyanocarbanion complex **13**[5b,16] would occur, and the addition of **13** to olefin followed by isomerization would give cyanocarbanion intermediate **14**.[17,18] Isomerization of **14** to a ketenimino iridium intermediate[19] followed by the nucleophilic addition of water and proton transfer would give amide complex **15**.[13] The amide intermediate was detected at the earlier stage of the reaction; however, the Michael adduct could not be detected during the reaction. Iridium-promoted intramolecular addition of the amide moiety of **15** to the coordinated nitrile and subsequent hydrolysis[4,20] would afford glutarimide, ammonia, and (L_nIr) to complete the catalytic cycle. The stereoselective formation of glutarimides can be ascribed to the isomerization of **15** by α-C–H activations of the amide and nitrile.[21] In the three-component reaction, the iridium catalyst acts as a base to generate the carbon nucleophile by α-C–H activation and also acts as a Lewis acid to activate and hydrolyze the C≡N triple bonds of nitriles.

We have found that $RuH_2(PPh_3)_4$ is an efficient transition-metal-based-base catalyst and can be used for selective four-component condensation reactions in combinatorial chemistry.[22] Such reactions can lead to the combinatorial synthesis of glutarimides. A polymer-supported iridium catalyst would be an excellent catalyst for the one-pot, three-component synthesis of glutarimides. In the presence of polystyrene-supported **1** (10 mol%), the three-component reaction of **5**, **8a**, and water gave 3-methylglutarimide (**6**) in 69% yield [Eq. 3].



(3)



Scheme 1.

Received: April 17, 2003 [Z51689]

Keywords: ambiphilic catalyst · C-H activation · glutarimide · iridium · multicomponent reactions

[1] a) S.-I. Murahashi, T. Naota, *Bull. Chem. Soc. Jpn.* **1996**, *69*, 1805; b) S.-I. Murahashi, H. Takaya, *Acc. Chem. Res.* **2000**, *33*, 225.
[2] B. Bosnich, *Aldrichimica Acta* **1998**, *31*, 76.
[3] a) J. W. Faller, C. J. Smart, *Tetrahedron Lett.* **1989**, *30*, 1189; b) W. Odenkirk, A. L. Rheingold, B. Bosnich, *J. Am. Chem. Soc.* **1992**, *114*, 6392; c) E. P. Kündig, C. M. Saudan, G. Bernardinelli, *Angew. Chem. Int. Ed.* **1999**, *38*, 1220.
[4] S.-I. Murahashi, T. Naota, E. Saito, *J. Am. Chem. Soc.* **1986**, *108*, 7846.

 © 2003 Wiley-VCH Verlag GmbH & Co. KGaA, Weinheim

[5] a) T. Naota, H. Taki, M. Mizuno, S.-I. Murahashi, *J. Am. Chem. Soc.* **1989**, *111*, 5954; b) S.-I. Murahashi, T. Naota, H. Taki, M. Mizuno, H. Takaya, S. Komiya, Y. Mizuho, N. Oyasato, M. Hiraoka, M. Hirano, A. Fukuoka, *J. Am. Chem. Soc.* **1995**, *117*, 12436.

[6] Our difinition of ambiphilic catalyst is a single redox catalyst used as either a Lewis acid or base under neutral conditions. Such catalyst is different from ambiphilic reagents and intermediates that function alternatively as nucleophiles and electrophiles. See, a) L. S. Hegedus, M. S. Holden, *J. Org. Chem.* **1985**, *50*, 3920; b) B. A. Andersen, H. F. Sleiman, A. K. Chang, L. M. White, *J. Am. Chem. Soc.* **1991**, *113*, 4871; c) T. Kondo, H. Ono, N. Satake, T. Mitsudo, Y. Watanabe, *Organometallics* **1995**, *14*, 1945; d) H. Nakamura, J.-G. Shim, Y. Yamamoto, *J. Am. Chem. Soc.* **1997**, *119*, 8113.

[7] M. Rubiralta, E. Giralt, A. Diez in *Piperidine*, Elsevier, Amsterdam, **1991**, Chap. 9, and references therein.

[8] H. Takaya, T. Naota, S.-I. Murahashi, *J. Am. Chem. Soc.* **1998**, *120*, 4244.

[9] C-H activations by iridium complexes see also, a) B. A. Anderson, R. G. Bergman, T. Mobley, T. H. Peterson, *Acc. Chem. Res.* **1995**, *28*, 154, and references therein; b) H. Chen, S. Schlecht, T. C. Semple, J. F. Hartwig, *Science* **2000**, *287*, 1995; c) F. Liu, E. B. Pak, B. Singh, C. M. Jensen, A. S. Goldman, *J. Am. Chem. Soc.* **1999**, *121*, 4086.

[10] a) D. Michalska, B. Morzyk, D. C. Bienko, W. Wojciechowski, *Med. Hypotheses* **2000**, *54*, 472; b) J. M. Jacobson, *Expert. Opin. Pharmacother.* **2000**, *1*, 849.

[11] R. W. Hartmann, B. Christine, *J. Med. Chem.* **1986**, *29*, 1362.

[12] R. R. Goehring, T. D. Greenwood, G. C. Nwokogu, J. S. Pisipati, T. G. Rogers, J. F. Wolfe, *J. Med. Chem.* **1990**, *33*, 926.

[13] S.-I. Murahashi, S. Sasao, E. Saito, T. Naota, *J. Org. Chem.* **1992**, *57*, 2521.

[14] The stereochemistries of **9a** and **9b** were unequivocally determined by X-ray crystal structure analysis.

[15] The stereochemistry of **11** was determined by NOE and NOESY experiments.

[16] a) T. Naota, A. Tannna, S.-I. Murahashi, *J. Am. Chem. Soc.* **2000**, *122*, 2960; b) T. Naota, A. Tannna, S. Kamuro, S.-I. Murahashi, *J. Am. Chem. Soc.* **2002**, *124*, 6842 and reference therein.

[17] a) Y. Mizuho, N. Kasuga, S. Komiya, *Chem. Lett.* **1991**, 2127; b) M. Hirano, S. Kiyota, M. Imoto, S. Komiya, *Chem. Commun.* **2000**, 1679.

[18] T. Naota, A. Tannna, S.-I. Murahashi, *Chem. Commun.* **2001**, 63.

[19] Stable ketenimino iridium complexes have been isolated. The IR spectra of the complexes show $\tilde{\nu}$(CN) at 2140 cm^{-1} and their ^{13}C NMR chemical shifts shifted to extremely lower magnetic field (about 149 ppm), indicating high reactivity of the C≡N group of iridium complexes towards water.

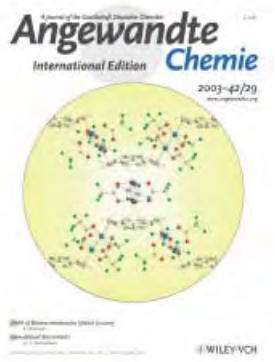
[20] The iridium-catalyzed reaction of 4-cyano-4-phenylpentanamide and water gave 2-methyl-2-phenylglutarimide in 99% yield.

[21] The iridium-catalyzed Michael addition proceeds nonstereoselectively, but the iridium-catalyzed cyclocondensation of 3-methyl-2-(phenylsulfonyl)-pentanedinitrile proceeds with high diastereoselevtivity (**9a**:**10a** = 96:4).

[22] H. Takaya, S.-I. Murahashi, *Synlett*, **2001**, 991.

 © 2003 Wiley-VCH Verlag GmbH & Co. KGaA, Weinheim

Cover Picture



Marina A. Petrukhina,* Kristian W. Andreini, James Mack, and Lawrence T. Scott

Microscale deposition from the vapor phase, as described in the study by M. A. Petrukhina et al. on page 3375 ff., has yielded the first metal complexes of an open geodesic polyarene to have been characterized crystallographically. The $\{Rh_2(CF_3COO)_4\}$ unit shown at the center of the picture (Rh blue, O red, F green, C dark gray, H light gray) is sandwiched between two corannulene molecules. Three metal centers coordinate to corranulene units on both the concave and convex π surfaces.

Angewandte EarlyView

The following articles are available online (in Wiley Interscience). You can find them at www.angewandte.org, under Full Text, Forthcoming Articles.

M. Toganoh, Y. Matsuo, E. Nakamura:*
Rhenium-Templated Regioselective Polyhydrogenation Reaction of [60]Fullerene
DOI: 10.1002/anie.200351722
Published online: July 11, 2003

N. T. Tran, L. F. Dahl:*
Nanosized $[Pd_{69}(CO)_{36}(PEt_3)_{18}]$: Metal-Core Geometry Containing a Linear Assembly of Three Face-Sharing Centered Pd_{33} Icosahedra Inside of a Hexagonal-Shaped Pd_{30} Tube
DOI: 10.1002/anie.200351738
Published online: July 11, 2003

R. R. Davda, J. A. Dumesic:*
Catalytic Reforming of Oxygenated Hydrocarbons for Hydrogen with Low Levels of Carbon Monoxide
DOI: 10.1002/anie.200351664
Published online: June 18, 2003

I. D. Hills, G. C. Fu:*
Catalytic Enantioselective Synthesis of Oxindoles and Benzofuranones that Bear a Quaternary Stereocenter
DOI: 10.1002/anie.200351666
Published online: July 3, 2003

Articles judged by the referees or the editior as being either very important or very urgent are immediately edited, proof-read, and electronically published once the manuscript has arrived in the editiorial office in final form. As long as there is no page number available these articles should be cited in the following manner:

Author(s) *Angew. Chem. Int. Ed.*, online publication date, DOI.

Obituary

Ilya Prigogine (1917–2003) **3324–3325** — Structure Formation far from Equilibrium — *Grégoire Nicolis*

Books

Encyclopedia of Electrochemistry, Vol. 9 **3326** — George S. Wilson — *reviewed by Wolfgang Schumann*

Encyclopedia of Electrochemistry, Vol. 1 **3327** — Eliezer Gileadi, Michael Urbakh — *reviewed by Rudolf Holze*

Correspondence

Bonding and Geometry

R. J. Gillespie,* P. L. A. Popelier **3331–3334**
G. Frenking* **3335**

"Chemical Bonding and Molecular Geometry": Comments on a Book Review and Reply to the Comments of Gillespie and Popelier

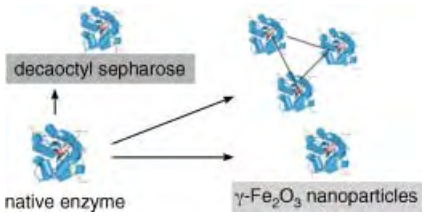
A model debate: The recent review of the book "Chemical Bonding and Molecular Geometry" has led to a discussion between the authors and the reviewer regarding the validity of the models chosen and the conclusions drawn.

Highlights

Immobilized Biocatalysts

U. T. Bornscheuer* **3336–3337**

Immobilizing Enzymes: How to Create More Suitable Biocatalysts



More immobile and more stable: The advantages of the immobilization of biocatalysts, for example, through the formation of aggregates or linking to iron oxide nanoparticles and organic supports (see scheme), include an enhanced stability, simple separation from the reaction mixture, and often an increased activity of the immobilizate.

© 2003 Wiley-VCH Verlag GmbH & Co. KGaA, Weinheim

Contents

Reviews

NMR of Biomacromolecules

K. Wüthrich* ——— **3340 – 3363**

NMR Studies of Structure and Function of Biological Macromolecules (Nobel Lecture)

The structure of proteins (such as that of bovine prion protein, see picture) and further information on the dynamics and structural, thermodynamic, and kinetic aspects of their interactions with other components in solution can be obtained by NMR methods developed by K. Wüthrich and his group. In his Nobel Lecture, Wüthrich delves into the past, present, and future of these techniques, and offers us a glimpse into his life.



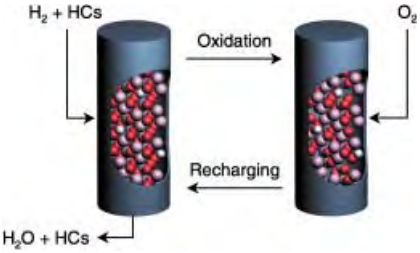
Communications

Clean Hydrogen Oxidation

G. Rothenberg,* E. A. de Graaf, A. Bliek ——— **3366 – 3368**

Solvent-Free Synthesis of Rechargeable Solid Oxygen Reservoirs for Clean Hydrogen Oxidation

Cutting out the coke: The concept of catalytic oxidative dehydrogenation by using solid oxygen exchangers and a solvent-free parallel synthesis of a set of ten bimetallic catalysts is described. The compounds were tested in the selective oxidation of hydrogen in the presence of ethane and ethylene (HCs) at 600 °C. Cerium tungsten oxide was found to be a superb rechargeable "oxygen reservoir" (see picture), with 97% chemoselectivity and negligible coking levels.



Self-Assembling Circuits

M. Boncheva, R. Ferrigno, D. A. Bruzewicz, G. M. Whitesides* ——— **3368 – 3371**

Plasticity in Self-Assembly: Templating Generates Functionally Different Circuits from a Single Precursor

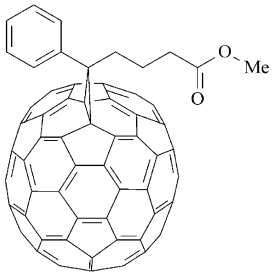
The structures and patterns of electrical connections within 3D self-assembled aggregates can be templated by the geometry of the space in which the self-assembly proceeds. This finding demonstrates that, in principle, multiple functions can be derived from the same set of components by controlling a macroscopic variable (see picture).



For the USA and Canada:
ANGEWANDTE CHEMIE International Edition (ISSN 1433-7851) is published weekly by Wiley-VCH PO Box 191161, D 69451 Weinheim, Germany. Air freight and mailing in the USA by Publications Expediting Inc. 200 Meacham Ave., Elmont, NY 11003. Periodicals postage paid at Jamaica NY 11431. US POSTMASTER: send address changes to *Angewandte Chemie*, Wiley-VCH, 111 River Street, Hoboken, NJ 07030. Annual institutional subscription price for institutions: Europe € 2998.00/3148.00. Outside Europe US$ 3718.00/3904.00 (valid for print or electronic/print and electronic delivery); for individuals who are personal members of a national chemical society, or whose institution already subscribes, or who are retired or self-employed consultants, print only (including postage and handling charges): Europe € 248.00/Outside Europe US$ 348.00.

© 2003 Wiley-VCH Verlag GmbH & Co. KGaA, Weinheim

Owing to their increased absorption of light in the visible region, [70]fullerene derivatives provide a high photocurrent when incorporated as the electron acceptor in thin-film polymer photovoltaic cells. An incident-photon-to-current efficiency of 66% is obtained when [70]PCBM (see picture) is used in combination with a poly(*p*-phenylene vinylene). These high currents originate from an ultrafast charge transfer that occurs upon photoexcitation of either the fullerene or the polymer.



[70]PCBM

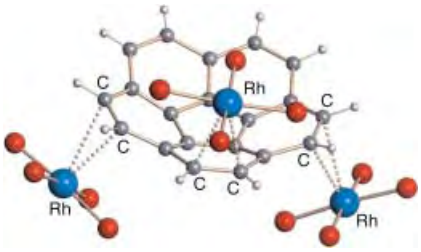
[70]Fullerene-Based Photovoltaics

M. M. Wienk, J. M. Kroon,* W. J. H. Verhees, J. Knol, J. C. Hummelen,* P. A. van Hal, R. A. J. Janssen* _____ **3371 – 3375**

Efficient Methano[70]fullerene/MDMO-PPV Bulk Heterojunction Photovoltaic Cells

---

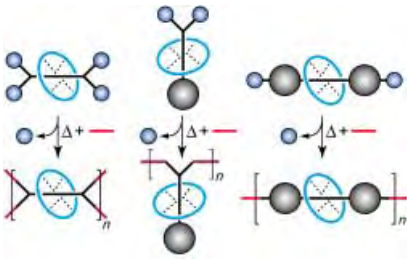
Corannulene, the smallest subunit of C_{60} that retains a curved surface, forms crystalline η^2-coordinated π complexes with dirhodium(II) tetrakis(trifluoroacetate) by using solvent-free gas-phase deposition. As many as three metal atoms coordinate to the double bonds found at the rim of each corannulene, with one such atom always located on the concave surface (see picture).



Corannulene Complexes

M. A. Petrukhina,* K. W. Andreini, J. Mack, L. T. Scott _____ **3375 – 3379**

Transition-Metal Complexes of an Open Geodesic Polyarene



A simple versatile route to polyrotaxanes with a variety of topologies is described through the synthesis and subsequent polymerization of readily accessible and stable rotaxane monomers containing bulky blocked isocyanate stopper groups.

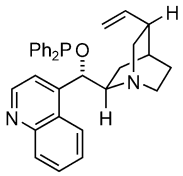
Polyrotaxanes

T. J. Kidd, T. J. A. Loontjens,* D. A. Leigh,* J. K. Y. Wong _____ **3379 – 3383**

Rotaxane Building Blocks bearing Blocked Isocyanate Stoppers: Polyrotaxanes through Post-Assembly Chain Extension

---

An effective catalyst for the asymmetric monobenzoylation of *meso*-1,2-diols was designed—the phosphinite derivative of cinchonine (see formula). In the presence of 30 mol% of this catalyst the monobenzoylated products were obtained with high yields and enantioselectivities.



Desymmetrizing meso-Diols

S. Mizuta, M. Sadamori, T. Fujimoto,* I. Yamamoto _____ **3383 – 3385**

Asymmetric Desymmetrization of *meso*-1,2-Diols by Phosphinite Derivatives of Cinchona Alkaloids

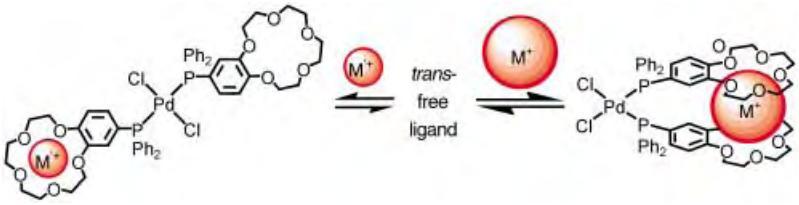
© 2003 Wiley-VCH Verlag GmbH & Co. KGaA, Weinheim

Contents

Metal-Ion Induced Isomerization

V. W.-W. Yam,* X.-X. Lu, C.-C. Ko ——— 3385 – 3388

First Observation of Alkali Metal Ion Induced *Trans–Cis* Isomerization of Palladium(II) Phosphane Complexes Containing Crown Ether Moieties



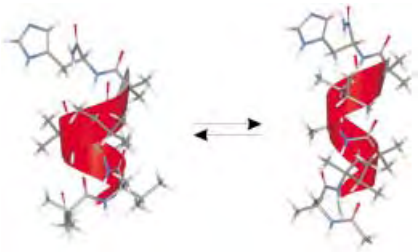
Ion switches: The addition of small metal ions (such as Li^+ and Na^+) to *trans*-palladium(II) complexes of PPh_2-substituted benzo[15]crown-5 and benzo[18]-crown-6 results in the formation of 1:1 *trans* adducts. However, the addition of large alkali ions (such as K^+, Rb^+, and Cs^+) enforces the complexes to undergo a *trans–cis* isomerization to enable formation of intramolecular sandwich adducts (see schematic representation).

Solvent-Driven Helix Equilibria

P. Pengo, L. Pasquato,* S. Moro, A. Brigo, F. Fogolari, Q. B. Broxterman, B. Kaptein, P. Scrimin* ——— 3388 – 3392

Quantitative Correlation of Solvent Polarity with the α-/3_{10}-Helix Equilibrium: A Heptapeptide Behaves as a Solvent-Driven Molecular Spring

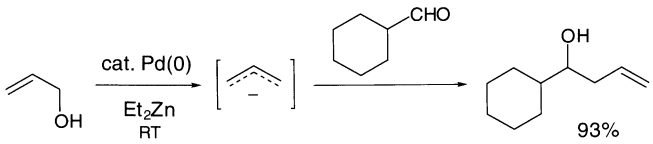
The long and the short of it: Just by changing the polarity of the solvent the highly folded heptapeptide Ac-[Aib-L-(αMe)Val-Aib]$_2$-L-His-NH_2 converts from an α into a 3_{10} helix (see picture). The equilibrium constant between the two conformations correlates with the empirical solvent polarity parameter E_T^N. Molecular dynamics calculations show that the peptide elongates (3_{10} helix) or shortens (α helix) on switching from one conformation to the other.



Allylation of Aliphatic Aldehydes

M. Kimura, M. Shimizu, K. Shibata, M. Tazoe, Y. Tamaru* ——— 3392 – 3395

Pd-Catalyzed Nucleophilic Alkylation of Aliphatic Aldehydes with Allyl Alcohols: Allyl, 2-Tetrahydrofuryl, and 2-Tetrahydropyranyl Ethers as Useful C_3, C_4, and C_5 Sources

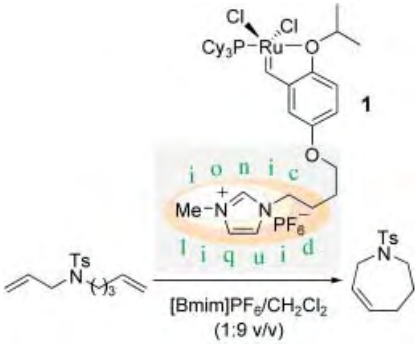


A combination of Pd^0 and Et_2Zn generates an allyl anion species from allyl alcohols which can be used for the allylation of aliphatic aldehydes to provide homoallyl alcohols in good yields (see scheme). The reaction proceeds at room temperature in poor coordination solvents, such as a mixture of toluene and *n*-hexane.

Olefin Metathesis in Ionic Liquids

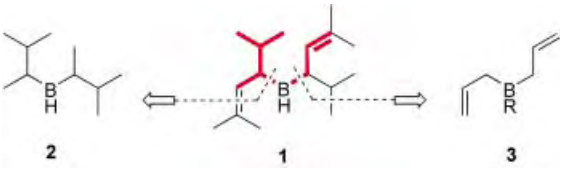
Q. Yao,* Y. Zhang ——— 3395 – 3398

Olefin Metathesis in the Ionic Liquid 1-Butyl-3-methylimidazolium Hexafluorophosphate Using a Recyclable Ru Catalyst: Remarkable Effect of a Designer Ionic Tag



Designer labels: Ruthenium carbene complex **1** bearing an ionic tag was shown to be a highly reactive catalyst for the ring-closing metathesis of various diene and enyne substrates in minimally ionic solvent systems (see scheme; Bmim = 1-butyl-3-methylimidazolium, Ts = toluene-4-sulfonyl). The catalyst can be repeatedly recycled and reused (up to at least 10 cycles) without significant loss of its activity, whereas other catalysts tested exhibited a dramatic diminishment in their activity upon recovery from the ionic layer.

© 2003 Wiley-VCH Verlag GmbH & Co. KGaA, Weinheim

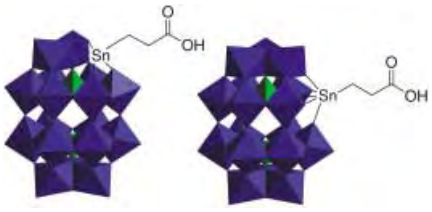


The best of the old: The new hydroboration reagent **1** combines the selectivity of disiamylborane (**2**) with the reactivity towards carbonyls of allyl boranes **3**. Conventional oxidative workup conditions are avoided, as facile hydrolysis in protic media provides the corresponding boronic acids with up to 99% anti-Markovnikov selectivities. A one-pot hydroboration/Suzuki–Miyaura protocol adds to the synthetic value of **1**.

Hydroboration Reagents

A. V. Kalinin, S. Scherer, V. Snieckus* ——— 3399 – 3404

Di(isopropylprenyl)borane: A New Hydroboration Reagent for the Synthesis of Alkyl and Alkenyl Boronic Acids

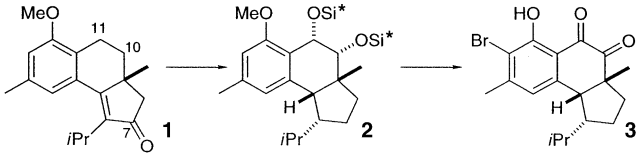


Making derivatives of organic side chains on polyoxometalates is an important prerequisite for their application in biology. Compounds α_1- and α_2-$[P_2W_{17}O_{61}\{Sn(CH_2)_2CO_2H\}]^{7-}$ (depicted) were prepared for the first time and coupled with alcohols and amines, including C-protected amino acids.

Functionalizing Polyoxotungstates

S. Bareyt, S. Piligkos, B. Hasenknopf,* P. Gouzerh, E. Lacôte, S. Thorimbert, M. Malacria* ——— 3404 – 3406

Highly Efficient Peptide Bond Formation to Functionalized Wells-Dawson-Type Polyoxotungstates

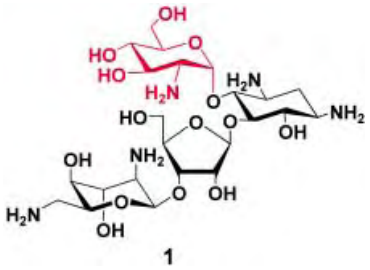


Stereoselective hydrogenation of the tetrasubstituted double bond in enone **1** is possible, provided the keto group at C7 is first removed and the α face is blocked by *tert*-butyldimethylsiloxy groups at positions 10 and 11. The resulting product **2** is easily converted into hamigeran B (**3**), a marine natural product with powerful activity against herpes and polio viruses. Si* = *t*BuMe$_2$Si.

Natural Product Synthesis

D. L. J. Clive,* J. Wang ——— 3406 – 3409

Stereospecific Total Synthesis of the Antiviral Agent Hamigeran B—Use of Large Silyl Groups to Enforce Facial Selectivity and to Suppress Hydrogenolysis

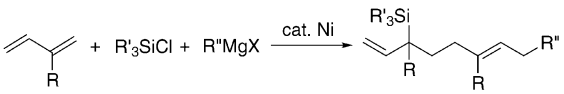


A good starting point for the design of potent bactericidal compounds is the aminoglycoside paromomycin (**1**). The A-ring (shown in red) was replaced with a range of heterocycles. An ESIMS-based RNA-binding assay was used to screen the binding affinities of the products.

Aminoglycoside Mimetics

Y. Ding,* S. A. Hofstadler, E. E. Swayze, L. Risen, R. H. Griffey ——— 3409 – 3412

Design and Synthesis of Paromomycin-Related Heterocycle-Substituted Aminoglycoside Mimetics Based on a Mass Spectrometry RNA-Binding Assay



In a multicomponent coupling reaction, 1,3-butadienes underwent Ni-catalyzed dimerization and carbosilylation in the presence of a chlorosilane and a Grignard reagent at −20 °C (see scheme). The coupling product was obtained regio- and stereoselectively when unsubstituted 1,3-butadiene was used. (R = H, Me, or C_9H_{19}; R′, R″ = hydrocarbon substituent.)

Carbosilylation-Dimerization

J. Terao, A. Oda, A. Ikumi, A. Nakamura, H. Kuniyasu, N. Kambe* ——— 3412 – 3414

Nickel-Catalyzed Dimerization and Carbosilylation of 1,3-Butadienes with Chlorosilanes and Grignard Reagents

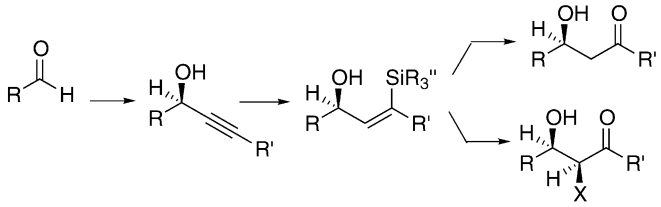
 © 2003 Wiley-VCH Verlag GmbH & Co. KGaA, Weinheim

Contents

Regioselective Hydrosilylation

B. M. Trost,* Z. T. Ball, T. Jöge ——— **3415 – 3418**

Regioselective Hydrosilylation of Propargylic Alcohols: An Aldol Surrogate



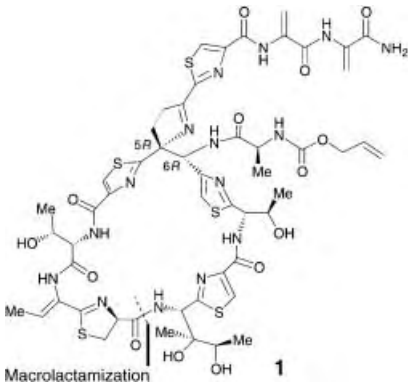
Aldol products from a non-aldol reaction: A one-pot protocol effects hydrosilylation of propargyl alcohols and subsequent oxidative cleavage to yield β-hydroxy ketones in a chemo-, regio-, and enantioselective fashion. Further structural elaboration of the intermediate γ-hydroxyvinylsilane is possible before the carbonyl group is unmasked (see scheme).

Natural Product Analogues

K. C. Nicolaou,* M. Nevalainen, M. Zak, S. Bulat, M. Bella, B. S. Safina ——— **3418 – 3424**

Synthetic Studies on Thiostrepton: Construction of Thiostrepton Analogues with the Thiazoline-Containing Macrocycle

Leading the way: The novel thiostrepton analogue **1** and its 5*S*,6*S* diastereomer were synthesized through macrolactamization reactions. Forays towards the total synthesis of the natural product itself should follow a similar strategy.

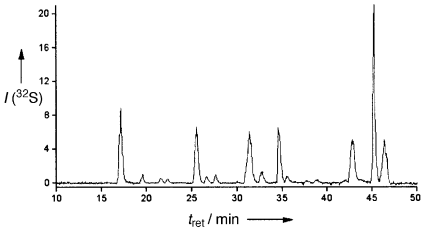


Element Mass Spectrometry

M. Wind, A. Wegener, A. Eisenmenger, R. Kellner, W. D. Lehmann* . **3425 – 3427**

Sulfur as the Key Element for Quantitative Protein Analysis by Capillary Liquid Chromatography Coupled to Element Mass Spectrometry

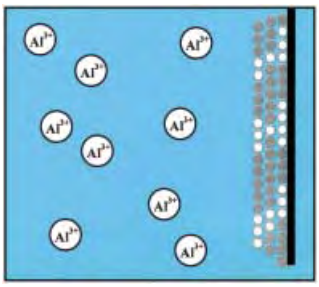
The impact of ^{32}S quantification by capillary chromatography coupled to element mass spectrometry was demonstrated for three areas in proteomic analysis: for absolute quantification of a peptide, for the characterization of a protein digest (see chromatogram), and for the estimation of the efficiency of electrospray ionization.



Electrodeposition of Nanocrystals

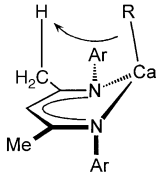
F. Endres,* M. Bukowski, R. Hempelmann,* H. Natter ——— **3428 – 3430**

Electrodeposition of Nanocrystalline Metals and Alloys from Ionic Liquids



Better than water: A method for the electrodeposition of nanocrystalline metals and alloys from ionic liquids has been developed (see schematic representation). This method enables the synthesis of aluminum nanocrystals with average grain sizes of about 10 nm, Al-Mn alloys, as well as Fe and Pd nanocrystals.

A heteroleptic benzylcalcium complex decomposes by means of C–H activation (see picture), a reaction typical for d^0-metal complexes. This finding closes the gap between the chemistry of the heavier alkaline-earth and the early d- and f-block metals. The product, a dimeric calcium complex, was characterized by X-ray crystallography.

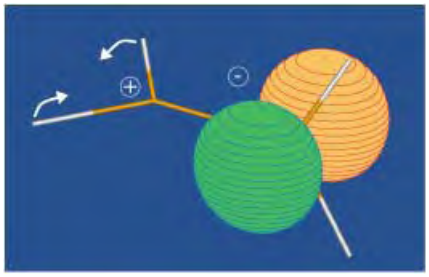


C–H Activation in Ca Complexes

S. Harder* ——— **3430 – 3434**

Intramolecular C–H Activation in Alkaline-Earth Metal Complexes

Surprisingly polar: The single-sided scissoring-induced sudden-polarization effect in D_{2d} ethene is first order (see picture). The important role of this coordinate was until now overlooked, although it was known for a long time that each geometrical distortion that leads to a breakage of the D_{2d} symmetry results in a charge separation.



Sudden-Polarization Effects

A. Viel, R. P. Krawczyk, U. Manthe, W. Domcke* ——— **3434 – 3436**

The Sudden-Polarization Effect and its Role in the Ultrafast Photochemistry of Ethene

VIP Communications labeled with this symbol have been judged by two referees as being "very important papers".

The publication of Communications labeled with this symbol has been accelerated because of their topical or highly competitive nature.

The issues for July 2003 appeared online on the following dates
Issue 25: June 24. · Issue 26: July 2. · Issue 27: July 10. · Issue 28: July 16

Sources

Product and Company Directory

You can start the entry for your company in "Sources" in any issue of *Angewandte Chemie*.

If you would like more information, please do not hesitate to contact us.

Wiley-VCH Verlag – Advertising Department
Tel.: 0 62 01 - 60 65 65
Fax: 0 62 01 - 60 65 50
E-Mail: MSchulz@wiley-vch.de

Service

Keywords ——— *3438*

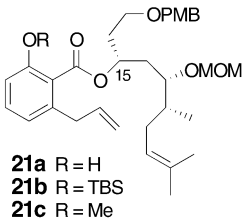
Authors ——— *3439*

Preview ——— *3441*

 © 2003 Wiley-VCH Verlag GmbH & Co. KGaA, Weinheim

Corrigendum

In the minireview "Recent Methods for the Synthesis of (*E*)-Alkene Units in Macrocyclic Natural Products" by **J. Prunet** (*Angew. Chem. Int. Ed.* **2003**, *42*, 2826–2830) an incorrect formula was given in Scheme 9 on p. 2828 for **21a–c**. A methylene group is shown instead of the correct isopropylidene group. The corrected formula is shown on the right.



21a R = H
21b R = TBS
21c R = Me

The text on p. 2829 should read:

On the other hand, De Brabander et al. obtained a 10:1 ratio of (*E*)-**22c**/(*Z*)-**22c** when they exposed a monosubstituted olefin analogue of **21c** to catalyst **7** in dichloromethane,[31] and Labrecque et al. observed a 9:1 *E* selectivity for the formation of a product nearly identical to **7**.[32] These results can be explained by the nature of the RCM catalyst, as shown by De Brabander:[31] With the first-generation catalyst **7** kinetic ratios are obtained, while thermodynamic equilibrium is reached with the more active second-generation catalysts, as it is the case for herbarumin I (Scheme 6).

References [31] and [32] should be completed:

[31] a) Y. Wu, L. Esser, J. K. De Brabander, *Angew. Chem.* **2000**, *112*, 4478–4480; *Angew. Chem. Int. Ed.* **2000**, *39*, 4308–4310; b) Y. Wu, X. Liao, R. Wang, X.-S. Xie, J. De Brabander, *J. Am. Chem. Soc.* **2002**, *124*, 3245–3253.

[32] The side chain at C15 has an extra methylene unit, and the primary hydroxy function is protected as a benzyl ether: D. Labrecque, S. Charron, R. Rej, C. Blais, S. Lamothe, *Tetrahedron Lett.* **2001**, *42*, 2645–2648. Smith and Zheng reported a 10:1 *E* selectivity for the formation of an analogue of **24** (CH_2OPMB instead of COOMe, Me-protected phenol) with catalyst **7**, see: A. B. Smith III, J. Zheng, *Synlett*, **2001**, 1019–1023

 © 2003 Wiley-VCH Verlag GmbH & Co. KGaA, Weinheim

Ilya Prigogine (1917–2003): Structure Formation Far from Equilibrium

Ilya Prigogine, winner of the Nobel Prize for Chemistry in 1977, died on 28 May 2003 in Brussels. He was one of the founders of modern theory of irreversibility and a leading figure in science throughout the last 50 years.


Ilya Prigogine

Prigogine was born in Moscow on 25 January 1917. His family left Russia in 1921 and, after a stay in Germany, settled in Belgium in 1929. Prigogine graduated in chemistry and physics from the Université Libre de Bruxelles, carried out his PhD in chemistry there, and completed his habilitation thesis in 1945. He became a full Professor in the Faculty of Sciences at the same university in 1951 and held this position until his retirement in 1987. From 1959 to 2003 he was Director of the International Solvay Institutes of Physics and Chemistry, founded by the famous Belgian industrialist Ernest Solvay. From 1967 he was a Professor in the Physics Department of the University of Texas at Austin, where he founded the Ilya Prigogine Center for Studies in Statistical Mechanics, Thermodynamics, and Complex Systems.

Prigogine's research touched on an extraordinary variety of subjects, yet throughout his career he consistently worked to bring the constructive role of irreversibility into focus in the understanding of natural phenomena. His driving force was the conviction that irreversibility and the arrow of time are fundamental properties of evolution and complexification, which are ubiquitous in the natural world. He realized that he had to break with prevailing ideas to implement this conviction. At times he also felt that his work touched upon matters that extended beyond the traditional realm of the physical sciences. He then had the courage to draw epistemological, philosophical, and cultural conclusions that were in his view appropriate. Because of this continuity of ideas and this humanistic dimension, Prigogine's impact on science goes further than his individual technical contributions and his well-known books.

Dissipative Structures

Prigogine's investigations into irreversibility started with macroscopic-level approaches. His work contributed to a renaissance of the entire field of thermodynamics. In this regard, he was lucky to have been a student in the 1940s of Theophile De Donder, one of the rare scientists of his time to believe that one could set up a consistent thermodynamic theory that extended beyond the range of equilibrium phenomena and incorporated irreversibility in an explicit manner.

Prigogine built on De Donder's results and in 1945–1949 worked out a general macroscopic theory of systems that operate under constraints that move them away from equilibrium. His work, along with that of Lars Onsager and Josef Meixner, led to a local formulation that culminated in the derivation of an entropy-balance equation, which featured the famous bilinear structure of entropy production. The application of this formalism to the linear range of irreversible processes led him to derive his minimum-entropy-production theorem, in which he asserted that systems under weak nonequilibrium constraint eventually attain a stable state of minimum dissipation. Following this initial success, he and his Brussels colleague Paul Glansdorff tried for almost two decades to extend the result to the entire range of nonequilibrium phenomena, but made no substantial progress. They eventually realized that this lack of success was not of a technical nature, but rather reflected the lack of universal trends in the ways natural systems evolve away from equilibrium.

Interestingly, at about the same time, the groups of Benno Hess[1] in Germany and of Anatol Zhabotinski in Russia were reporting exciting results on oscillatory behavior in biochemical and chemical systems, and provided experimental support of this idea as well as additional motivation for two novel developments: a thermodynamic-stability theory based on the excess entropy generated by the perturbations, and the analysis of prototypical nonlinear kinetic models such as the reversible Lotka–Volterra model and the Brusselator (see Figure 1). This work gradually gave rise to the concept of dissipative structure, which was formulated in 1966–1967 by Prigogine and his colleagues as a state that reflects the ability of a system to utilize energy dissipated out of equilibrium to generate novel phenomena, which arises from the "thermodynamic branch" of equilibrium-like states through an instability. By identifying the universal role of the distance from equilibrium as a source of order, this result provided a unifying framework for the understanding of a host of self-organization phenomena. It also introduced a type of "biological" thinking, which acted as a source of inspiration for many and redefined the relationship between the physical and the life sciences. A very important development that illustrates this synergy between biology, irreversibility, thermodynamics, and nonlinear kinetics is the seminal work of Manfred Eigen and his colleagues on hypercycles[2] and the evolution of biological information carriers, initiated in the late 1960s to early 1970s.

Foundations of Irreversibility

From the very early stages of his career, Prigogine recognized the need to address the microscopic foundations of irreversible phenomena. In a seminal paper published in 1949, he showed by using Boltzmann's kinetic equation that the local formalism of irreversible thermodynamics was valid only if the particle's position–velocity probability distribution deviated slightly from local equilibrium. This work was subsequently extended to include chemically reacting systems and still serves as a reference in understanding the origin of the phenomenological rate laws used in chemical kinetics. It also led to the prediction that deviations from these laws (associated with the appearance of a non-Maxwellian velocity distribution of the particles) are possible under certain conditions, for example, when strongly exothermic steps are present in a reaction sequence. By the mid-1950s, the need to go beyond the assumptions upon which the Boltzmann equation is

 © 2003 Wiley-VCH Verlag GmbH & Co. KGaA, Weinheim

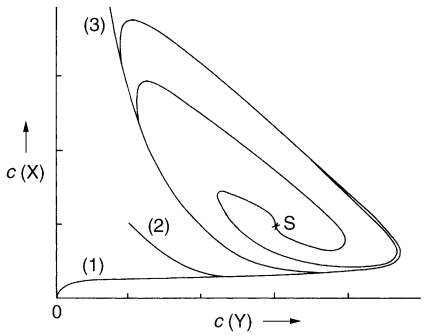


Figure 1. The Brusselator: In the reaction of compounds A and B to give the products D and E by the mechanism $A \rightarrow X$, $2X + Y \rightarrow 3X$, $B + X \rightarrow Y + D$, and $X \rightarrow E$, the same periodic trajectory for the concentrations of X and Y is always observed irrespective of the initial conditions (S: unstable stationary state).

based became Prigogine's central preoccupation. In the late 1950s to early 1960s, by using a systematic perturbative approach to the solution of the Liouville equation, he and his colleagues derived irreversible-transport equations that encompassed large classes of systems, from dense fluids to anharmonic solids and plasmas. In parallel, in collaboration with Robert Herman, Prigogine developed a kinetic theory of traffic flow in which he managed to incorporate terms related to the behavioral trends of the driver.

Following the advent of the concept of dissipative structure in the late 1960s, Prigogine felt that the microscopic basis of irreversibility had to be reassessed. He initiated a new approach that integrated fundamental properties of microscopic-level dynamics from the work of Henri Poincaré and Andrei Kolmogorov, such as nonintegrability and resonance. This allowed him to specify the types of initial configuration that can evolve thermodynamically and to obtain formal but exact probabilistic equations for these configurations. The fundamental role of probability in the understanding of irreversibility as a time-symmetry-breaking phenomenon was thereby identified.

Prigogine's insatiable curiosity pushed him to become involved in an extraordinary variety of activities. He was passionate about literature, philosophy, and art, and one of his favorite pastimes was playing the piano. He attracted a large number of students and associates from all over the world. He also became actively involved in science policy, and made a decisive impact on the development of a coherent European Research Program in the mid-1980s. He insisted on the need to establish flexible mechanisms that would enable the rapid recognition and encouragement of innovative ideas from the scientific community, for which he coined the term "hopeful fluctuations".

Prigogine was one of the most honored scientists of our time. He was a member of the Belgian Royal Academy, the National Academy of Sciences of the USA, and the USSR Academy of Sciences, held honorary degrees from over 40 universities, and received many prestigious scientific awards in addition to the Nobel Prize,[3] such as the Francqui Prize in 1955, the Solvay Prize in 1965, the Cothenius Gold Medal of the Akademie Leopoldina in 1975, the Rumford Gold Medal of the Royal Society in 1976, and the Honda Prize in 1983. Prigogine never really retired. He was working on several projects until the very last days of his life. He authored or co-authored 16 books[4] and a huge number of specialized and review papers as well as articles addressed to the general public.

He is survived by his second wife Marina Prokopowicz and his two sons Yves and Pascal.

Grégoire Nicolis
Université Libre de Bruxelles
Brussels (Belgium)

[1] M. Engelhardt, S. C. Müller, *Angew. Chem.* **2003**, *115*, 2432; *Angew. Chem. Int. Ed.* **2003**, *42*, 2330.
[2] M. Eigen, *Int. J. Quantum Chem.* **1978**, 219.
[3] I. Prigogine, *Angew. Chem.* **1978**, *90*, 704.
[4] For example, a) I. Prigogine, *From Being to Becoming*, W. H. Freeman, San Francisco, **1980**, b) G. Nicolis, I. Prigogine, *Self-Organization in Nonequilibrium Systems: From Dissipative Structures to Order through Fluctuations*, John Wiley and Sons, New York, **1977**; I. Prigogine, I. Stengers, *Entre le temps et l'éternité*, Fayard, Paris, **1988**.

 © 2003 Wiley-VCH Verlag GmbH & Co. KGaA, Weinheim

Bonding and Geometry

"Chemical Bonding and Molecular Geometry": Comments on a Book Review

R. J. Gillespie and P. L. A. Popelier*

Keywords:
bond theory · correspondence · density functional calculations · molecular geometry

In a recent review[1a] of our book "Chemical Bonding and Molecular Geometry"[1b] Frenking praised certain features such as our treatment of the connection between dipole moments and the charge distribution of a molecule as well as the discussion of the Pauli principle as fundamental to the understanding of the electronic structure of molecules. However, he severely criticizes our use of the electron density rather than the wave function approach and our use of the VSEPR and LCP models as a basis for understanding chemical bonding. He cites many statements described as "absurdities" that we show are either incorrect quotations from the book, statements taken out of context, or statements that he has simply misunderstood.

We do not agree with Frenking's claim that chemical bonding and molecular geometry can be understood only in terms of the wave function and not in terms of the electron density. The electron density can not only be obtained directly from the wave function, it can also be obtained by experiment. In one of his early papers Schrodinger[2] states clearly that the quantity of physical interest is $\psi\psi^*$ (from which the density is obtained) and not the wave function ψ, which Frenking himself admits is "too abstract and too elusive for the human imagination to grasp". Nevertheless he states that "it is only the wave function that gives an explanation for the chemical bond, whereas all attempts to explain the chemical bond in terms of the electron density have failed", although he gives no justification for this sweeping statement. Furthermore, in apparent contradiction, he states that the AIM theory, which is based on topological analysis of electron density "has become an important tool among other methods for analyzing the bonding situation in molecules". This is because, in contrast to the wave function which is "too abstract … to grasp", electron density is easily understood and pictured.

Slater[3] has shown that the force that accounts for chemical bonding is the electrostatic force, in particular the electrostatic attraction of the nuclei for the electrons (which is expressible in terms of the electron density) and the repulsions between the electrons and between the nuclei.

There is no "exchange force" nor any force resulting from the "resonance of the wave function". According to Slater,[4] the exchange integral of Heitler and London[5] "can be given a physical interpretation: it rises from the exchange charge which piles up between the atoms, and which is attracted strongly to the nuclei, since it tends to be localized between them". All the points concerning the wave function and the electron density that we have mentioned have been thoroughly discussed in a recent paper by Bader.[6] Finally it should be noted that Frenking's arguments are not, in fact, based on the wave function, but on arbitrary and approximate orbital models and the atomic-centred basis functions used in their expansion, which have no more physical reality than the wave function itself.

Now we deal with some of Frenking's more specific criticisms which are directed mainly at the VSEPR and LCP models. These models, we should note, are independent of any quantum-mechanical arguments and of the electron density, although they are supported by quantum mechanics, particularly, the importance of the Pauli principle in leading to the formation of electron pairs as described in Chapter 4 of our book and by the analysis of the electron density using the AIM theory[7,8] as described in Chapters 6 and 7 of our book. In the following sections the italic headers refer to locations in the review.

Page 144, column 1: With regard to our discussion of dipole moments and charge distribution, Frenking states "This part is well done and worth reading but then on page 39 one finds some statements about the bonding situation in BF_3 and SiF_4 which involve contradictory and selective arguments". Although we stated that in the resonance structures the positive charges at the fluorine atoms do not agree with the large calculated negative charges, we did not give this as a *reason* why the resonance structure description of these molecules involving double bonds is an inadequate description. We merely stated that these formal charges are inconsistent with the real charges. The real reason for the apparently short bonds in these molecules is, as we state clearly on page 39, "because of the (strong) attraction between the atoms due to their (large and opposite) atomic charges" for example, B +2.43, F −0.81. We are well aware that formal charges are not real charges, as we state clearly on page 17.

[*] Prof. Dr. R. J. Gillespie
Department of Chemistry
McMaster University
1280 Main Street West, Hamilton
ONL8S 4M1 (Canada)
Fax: (+1) 905-522-2509
E-mail: gillespi@mcmaster.ca
P. L. A. Popelier
Department of Chemistry
UMIST, Manchester M60 1QD (UK)

DOI: 10.1002/anie.200320066
© 2003 Wiley-VCH Verlag GmbH & Co. KGaA, Weinheim

However, when resonance structures are written to describe bonding, the formal charges *are* then usually regarded as real charges, as, for example, when the polarity of the bond in HF is described by a combination of the two resonance structures H–F and $H^+ F^-$. It is in this sense that we stated that these resonance structures which place positive charges on the fluorine atoms are inconsistent with the calculated charges.

Page 144, column 3: "When finally one reads that the orbital model with σ and π bonds would not predict that the ethylene molecule is planar, it becomes clear that the view point of the authors is biased." We maintain that our viewpoint is not biased and that this statement is correct because the σ–π model is only a *description* of the bonding based on the *known* planarity of the molecule. Indeed this description is in general only valid for planar molecules. The description of the σ bonds as sp^2 is based on the knowledge of the planarity of the molecule. An alternative, but equivalent, orbital description of the bonding in ethylene can be given in terms of sp^3 orbitals and two bent bonds between the carbon atoms, as is clearly explained on pages 76 to 79 of our book. In fact neither of these descriptions of the bonding is exact in that the HCH bond angle in ethylene is 116 and not 120° as is assumed by the sigma–pi description, nor is it 109.5° as assumed by the bent-bond description. A state of hybridization in between sp^2 and sp^3 must be presupposed to give a description that corresponds to the observed bond angle.

Page 144, column 3 (bottom): Frenking criticizes our explanation of the decrease in bond angles with increasing electronegativity difference between the ligand and the central atom on the grounds that bond angles in AH_3 and AF_3 are not always consistent with this explanation. This is because this is one of the cases where ligand–ligand interactions are important and may override the predictions of the VSEPR model. In the case of the hydrides, the small size of the hydrogen atom allows bond angles to be unusually small when the hydrogen ligands are repelled close to each other by a lone pair, as occurs in AH_3 molecules. However, there are many examples where bond angles do decrease consistently with this electronegativity difference, as for example among all the halides listed in Table 4.3 (page 96), where we see, for example, that the bond angles of the fluorides and the chlorides decrease consistently from N to Sb.

We fully realize that there are some exceptions to the VSEPR model, many of which can be accounted for in terms of ligand–ligand interactions, and so we follow the chapter on VSEPR with a chapter on the ligand close packing (LCP) model. It is not to be expected that a qualitative model such as the VSEPR model would be without exceptions, and we do not claim this. Nevertheless, as Frenking states, "the heuristic VSEPR model has become an important standard model for understanding the structures of inorganic molcular compounds". Moreover, as Frenking also states, "the VSEPR model receives a quantum mechanical justification and explanation that is based on the AIM theory". We admit that it has some deficiences but, as we show, they are not nearly as numerous or as serious as Frenking leads readers to believe. Moreover, there are, in most cases, good explanations for these exceptions.

Page 145, column 1: Frenking states that the LCP model "appears rather odd" because "a large number of quantum mechanical calculations show that the bonded distance between two atoms is determined mainly by their direct electronic interactions". The LCP model does not claim that the bonding distance is determined only by packing considerations but claims only that bonds in four-coordinated molecules are longer than in three-coordinated molecules because three ligands can pack more closely than four. In other words, ligand–ligand interactions may affect bond lengths but they are not the primary determining factor. The LCP model provides an alternative explanation to the conventional explanation based on the change in hybridization from sp^2 to sp^3, which, as we have already pointed out, cannot be regarded as a true *explanation* because hybridization is not a physical phenomenon but only provides the basis for a particular *description* of the bonding. Frenking states that the LCP model fails for heavier main-group elements because the A···X distances for A = Al, Si, P, S and X = F, Cl, O become shorter, not longer, as the coordination number increases. However, he quotes only the fact that the P–F bond is longer in PF_3 than in PF_4^+. Here, Frenking ignores two important concepts of the LCP and VSEPR models that are clearly explained in our book and that are widely accepted, namely that lone pairs are regarded as pseudo ligands and contribute to the coordination number, so that both PF_3 and PF_4^+ are four coordinate, and that they lengthen adjacent bonds. In fact, if we consider a series of molecules in which the coordination number does indeed increase and in which there are no lone pairs then we find that bond lengths do increase with coordination number, as is evident in the following examples: AlF_4^- (169.9 pm), AlF_6^{3-} (189.7 pm); SiF_4 (157.0 pm), SiF_6^{2-} (172.9 pm); PF_4^+ (145.7 pm), PF_6^- (158.0 pm). The variation of bond length with coordination number is also discussed and illustrated with other examples on pages 122 and 123.

Page 145, column 3: Frenking states that our assertion that the attraction between the two atoms in a pure covalent bond is due only to the electron density accumulated between their nuclei is "completely wrong". This claim is contrary to the opinion of Slater and, moreover, is in apparent contradiction with Frenking's statement in the previous column that "the bonding line between two atoms is revealed (in the AIM theory) without making more or less arbitrary assumptions", because this bonding line is the line along which the density is larger than in any other direction; in other words, it shows where the density is accumulated between the two nuclei. Since the only forces operative in a molecule are the electrostatic forces between the charge density and the nuclei as well as between the nuclei themselves, it is reasonable to claim that the bonding force between two atoms is due to the electron density accumulated between the two nuclei.

Page 145, column 3: We argue that, because the atomic charges in BF_3 suggest a stronger interatomic charge interaction in BF_3 than in LiF, while at the same time the density at the bond critical point increases from LiF to BF_3, we must conclude that both the ionic character and the covalent character of

 © 2003 Wiley-VCH Verlag GmbH & Co. KGaA, Weinheim

the A–F bond increases from LiF to BF_3. This conclusion contradicts the commonly held view that increasing covalent character is accompanied by decreasing ionic character and vice versa. This view is exemplified by the common description of bond polarity in terms of resonance structures such as H–F and $H^+ F^-$, which assumes that as covalent character increases ionic character decreases, and vice versa. However, we do not agree with this view, although Frenking appears to think that we do, as it is not consistent with the evidence from the electron density that clearly indicates that both covalent character and ionic character increase from LiF to BF_3 in so far as covalent character is measured by the electron density at the bond critical point and ionic character is measured by the atomic charges. Thus, it is as clear to us, as it is to Frenking, that the ionic and covalent contributions may both increase, although we disagree with Frenking that this is also clear to all other chemists. To describe our argument as a "con", thus implying that we have deliberately tried to deceive the reader, is completely unjustified and unscientific.

Page 146, column 1: We see nothing wrong with our laconic or terse statement that "the reasons for the large bond angles in $N(CF_3)_3$ and $N(SCF_3)_3$ are not clear". As we admit, the VSEPR theory cannot be expected to explain every feature of molecular structure. Perhaps Frenking or another reader of our book might be able to provide an explanation. In criticizing our discussion of the relative Lewis acid strengths of BF_3 and BCl_3, Frenking states that the fact that BF_3 is a weaker Lewis acid than BCl_3, despite the atomic charge of boron in BF_3 being larger than that of boron in BCl_3, cannot therefore be explained by the electron density, but he does not explain how he reaches this conclusion. We do not criticise the widely held $p(\pi)$ back-donation explanation simply because it is expressed in terms of orbitals, but because, as we discuss in our book, there is no other evidence for it other than the short length of the B–F bond which can alternatively be accounted for by the large polarity of the B–F bond.

Page 146, column 2: We do not "praise AIM atomic charges as a basis for the nature of the chemical bond" as Frenking claims. They are simply one of the properties of a molecule related to the electron-density distribution that are useful in understanding bonding. Although he states earlier that the AIM theory "has become an important tool … for analyzing the bonding situation in molecules" he nevertheless criticizes the atomic charges, quoting the case of methane for which the atomic charges on hydrogen have a very small negative value of -0.04. In other words, the atomic charges in this molecule are very close to zero. However, his criticism of these charges amounts only to the subjective statement that "everybody who knows about the fundamental difference between the chemical behavior of protic and hydridic hydrogen will be startled by this". Perhaps they will be startled, but this is no evidence that these charges are incorrect. Essentially, the charge transfer is zero as expected, which indicates that CH_4, situated at the boundary between hydridic and protic behavior, shows neither type of behavior.

There follows a criticism of our discussion of the geometry of CF_3O^- in which Frenking states that "the authors fail to justify why they are using the radius of the carbonyl oxygen for the oxygen atom". But nowhere in our discussion do we use, or even mention, the radius of the carbonyl oxygen atom. In general, as we state elsewhere in the book, we do not find covalent (atomic) radii to be a useful concept. Frenking seems to have completely misunderstood our arguments, which can be simply summarized by the statement that Lewis structures may be used to *describe* the bonding in OCF_3^-, but they do not provide an explanation for the geometry which can be understood in terms of the LCP model independently of the Lewis structures used to describe the bonding. To describe our arguments as "deceptive" is both unjustified and unfair. We do not claim, as Frenking states, that the shorter bond in CO compared with CO_2 is consistent with the LCP model. It is clear to anyone that ligand packing is not relevant when there are only one or two ligands. We state only (p. 206) that "molecules in which the carbon is four-coordinated have longer CO bonds than in molecules in which the carbon is three-coordinated which in turn are longer than the bonds in CO_2 and CO". We make no comparison of the bond lengths in CO_2 and CO. Ligand packing places a restraint on the lengths of the bonds when they are close-packed, as in four- and three-coordinated molecules, but this restraint is absent in both CO_2 and CO.

Page 146, column 3: In our discussion of the description of the bonding in SF_6, our aim was to show that the common representation of bond polarity using Lewis structures with ionic bonds is unnecessarily complicated. This type of description does, as we have mentioned before, consider formal charges to be real charges—it would be useless if it did not. To give a description consistent with the atomc charge on sulfur of $+3.55$ it would be necessary to include further structures with more than two ionic bonds as well as those written in accordance with the octet rule structures which give a charge of $+2.0$ on sulfur, thus further complicating the description. If we accept, as Lewis did, that the bonds are polar, and that a bond line can be used to describe a polar bond as well as a nonpolar bond, then the Lewis type structure with six-bond lines is a perfectly acceptable description, and there is no need to use a multitude of Lewis structures incorporating ionic bonds. Once again Frenking has not understood our arguments. We are perfectly aware that formal charges are not real charges, but in describing bond polarity in terms of Lewis structures formal charges are indeed taken to represent real charges, a point that does not seem to have been appreciated by Frenking.

Following this discussion he claims to have found data in the tables that contradict the VSEPR and LCP models. He gives only the example of the lengths of the equatorial bonds in SF_4 (154.5 pm) and in SF_2 (162.5 ppm) and claims that these are not in accordance with the LCP model, which he says predicts that the bonds in SF_4 should be longer than in SF_2. However, he ignores the bond-lengthening effect of the lone pairs, which must also be taken it account since SF_2 has two lone paris whereas SF_4 has only one.

Frenking claims that the reason why the lone electron pair in SeF_6^{2-}, IF_6^-, and XeF_6 "suddenly becomes inactive,

 © 2003 Wiley-VCH Verlag GmbH & Co. KGaA, Weinheim

although it plays an important role in the C_{4v} geometry of IF_5, remains unclear". In fact the lone pair does not suddenly become inactive in these molecules, but it is partially active giving the observed C_{3v} geometries. This, as we explain, is because the space occupied by the six ligands leaves insufficient space for a full lone pair, which therefore partially occupies the valence shell while remaining partially in the region immediately surrounding the core. In IF_5, which has only five ligands, there is plenty of space in the valence shell to accommodate the lone pair. This point has previously been thoroughly discussed in an article in this journal[9] and in a forthcoming article.[10]

We could quote several other examples where Frenking has misrepresented or misunderstood our arguments, but lack of space prevents discussion of them here.

In summary, we may say a) Frenking's detailed criticisms that are leveled mainly at the VSEPR and LCP models, based as they are on his lack of understanding and misinterpretation of our arguments are unjustified. These models are independent of both the wave function of the molecule and the electron density, although they receive support from the analysis of the electron density and from quantum mechanics. b) The question of whether or not the wave function or the electron density is the more fundamental is perhaps open to dispute, but in our opinion the electron density, which is an easily understandable property of a molecule and can be obtained directly from the wave function and by experiment, is much more useful for understanding chemical bonding and molecular geometry than is the wave function, which Frenking states "is too abstract and elusive for the human imagination to grasp". When Frenking refers to the wave function he must surely be referring to approximate orbital models based on the wave function and, as we show, in the case of ethylene for example, these are just descriptions of the bonding that in general are not unique and do not explain geometry. c) We believe that our book does indeed provide a useful introduction to models and theories of chemical bonding and geometry, in particular, to simple orbital models, the VSEPR model, the LCP model, and the AIM analysis of the electron density, which is presented at a level much more accessible to undergraduate students than Bader's original monograph.[7] Moreover, our book shows students that none of these models and theories are perfect, although they all have their uses.

[1] a) G. Frenking, *Angew. Chem.* **2003**, *115*, 152; *Angew. Chem. Int. Ed.* **2003**, *42*, 143; b) *Chemical Bonding and Molecular Geometry* (Eds.: R. J. Gillespie, P. L. A. Poplier), Oxford University Press, New York, **2001**.

[2] E. Schrödinger, *Ann. Phys.* **1926**, *81*, 109.

[3] J. C. Slater in *Quantum Theory of Molecules and Solids*, McGraw Hill , New York, **1963**.

[4] J. C. Slater, *J. Chem. Phys.* **1972**, *57*, 2389.

[5] W. Heitler and F. London, *Z. Phys.* **1927**, *44*, 455.

[6] R. F. W. Bader, *Int. J. Quant. Chem.*, **2003**, in press.

[7] a) R. F. W. Bader in *Atoms in Molecules: A Quantum Theory*, Oxford University Press, Oxford, **1990**; b) P. Popelier in *Atoms in Molecules: An Introduction*, Pearson Education, **2000**.

[8] R. F. W. Bader, R. J. Gillespie, P. J. MacDougall, *J. Am. Chem. Soc.* **1988**, *110*, 7329.

[9] R. J. Gillespie, E. A. Robinson, *Angew. Chem.* **1996**, *108*, 539; *Angew. Chem. Int. Ed. Engl* **1996**, *35*, 495.

[10] R. J. Gillespie, E. A. Robinson, *Inorg. Chem.* **2003**, *47*, 3865.

 © 2003 Wiley-VCH Verlag GmbH & Co. KGaA, Weinheim

Bonding and Geometry

Reply to the Comments of Gillespie and Popelier

*Gernot Frenking**

Keywords:
bond theory · correspondence · density functional calculations · molecular geometry

I want to reply to the two instances where my comments are said to be "unjustified and unfair". This is the case at the end of the paragraph on page 3333, column 2. The authors state that I cited unpublished calculations in my review. This is not true! The calculations I am referring to concern the energies which are necessary to distort BF_3 and BCl_3 from the planar equilibrium geometry to the pyramidal structure in the complexes $F_3B{-}NH_3$ and $Cl_3B{-}NH_3$. Unlike in the 1999 paper by Gillespie and co-workers (*Inorg. Chem.* **1999**, *38*, 4659) who used model structures, the calculations of the real molecules show that the distortion energy for BF_3 is smaller than for BCl_3. This was already published by Politzer and co-workers in 1993 (*Inorg. Chem.* **1993**, *32*, 2622). The latter work was cited in the 1999 paper by Gillespie and co-workers, but apparently this part of the paper has escaped their attention.

The second instance where my comments are called "unjustified and unfair" concerns the explanation of the geometry of CF_3O^- in terms of the LCP model. The significant sentence in the book by Gillespie and Popelier reads (page 205, first paragraph): "Because the CO bond is so short, the CF bonds are necessarily longer than in CF_4." Here the authors take the short C–O bond, which "is not much longer than in methanal" (page 204, second paragraph) as the starting point for an explanation of the geometry of CF_3O^-. I call this deceptive because there is no explanation *why* the C–O bond is so short. The atomic charge of oxygen in CF_3O^- is nearly the same as in CH_3OH.

Furthermore, I must make a comment about my sentence "the mathematical object Ψ is too abstract and too elusive for the human imagination to grasp to allow it to become the focus of orthodox chemistry, which instead strives for pictures that are accessible for the human senses" because it was cited in a way which twists my intention in the book review. The meaning of this sentence is not something which must be admitted, but which has to be recognized as a fundamental perception about the material world at the molecular scale, which is the very object of chemistry. The wavefunction Ψ, which is fundamental for our science, is a mathematical object which is not accessible to human senses. Many chemists have problems with recognizing this. Chemistry has a long history of using pictures and models which are attempts to use human imagination for chemical objects. However, the perceptivity of the human senses is restricted in time and space. The scientific discovery that the laws of electrostatic force in the microscopic range are fundamentally different from classical laws and, therefore, are not accessible to human senses, has come as a shock not only to scientists. Chemists have for a long time ignored the revolution which came with quantum theory, because the heuristic models of human imagination had proven very successful as an ordering scheme and a predictive tool for synthetic chemistry. Organic chemists eventually accepted the wave function as a helpful quantity because the important class of pericyclic reactions could only be explained with MO theoretical arguments using the symmetry of Ψ. To recognize symmetry it is necessary to know the *sign* of the wave function. However, the sign and thereby the symmetry is lost when the product $\Psi\Psi^*$ is formed, which after integration yields the electron density ρ! This is one reason why Ψ is more fundamental than ρ which is *not* open to dispute.

Roald Hoffmann has shown that approximate orbital models, even as simple as EHT, may be used to understand chemical reactions and molecular structures which were totally incomprehensible for classical bonding models. With the sentence "in our opinion the electron density which is an easily understandable property of a molecule, that can be obtained directly from the wavefunction, is much more useful for understanding chemical bonding and molecular geometry than its wavefunction", the authors use the easiness of understanding as the reason for choosing ρ as a basis for bonding models. This is misleading, because it ignores the progress in the understanding of chemical bonding that has been gained by quantum chemistry in the last decades which showed that Ψ is the basis for a true understanding of molecular electronic structure.

I see no point to continue arguing about the examples presented in the reply. I encourage interested readers to study the book by Gillespie and Popelier together with my review and then to make their own judgement. There is no reason for me to change anything that I wrote.

[*] Prof. Dr. G. Frenking
Fachbereich Chemie
Philipps-Universität Marburg
Hans-Meerwein-Strasse
35043 Marburg (Germany)
Fax: (+49) 6421-282-5566
E-mail: frenking@chemie.uni-marburg.de

DOI: 10.1002/anie.200320070
© 2003 Wiley-VCH Verlag GmbH & Co. KGaA, Weinheim

Immobilized Biocatalysts

Immobilizing Enzymes: How to Create More Suitable Biocatalysts

*Uwe T. Bornscheuer**

Keywords:
biotransformations · enzyme catalysis · immobilization · lipase · magnetic nanoparticles

Enzymes are versatile biocatalysts and find increasing application in many areas, including organic syntheses. The major advantages of using enymes in biocatalytic transformations are their chemo-, regio-, and stereospecificity as well as the mild reaction conditions that can be used.[1] However, even when an enzyme is identified as being useful for a given reaction, its application is often hampered by its lack of long-term stability under process conditions, and also by difficulties in recovery and recycling. These problems can be overcome by immobilization, which provides the following advantages:

- enhanced stability,
- repeated or continuous use,
- easy separation from the reaction mixture,
- possible modulation of the catalytic properties,
- prevention of protein contamination in the product,
- easier prevention of microbial contaminations.

Since the first uses of biocatalysts in organic synthesis dating back almost a century, researchers have tried to identify methods for linking an enzyme to a carrier. Numerous examples of a broad range of enzymes and reaction systems (both aqueous systems and organic solvents) have been documented in the literature.[2] Although this reflects the importance of biocatalysis, it also exemplifies that a general, broadly applicable method for enzyme immobilization still needs to be discovered. The most frequently used immobilization techniques fall into four categories:

- noncovalent adsorption or deposition,
- covalent attachment,
- entrapment in a polymeric gel, membrane, or capsule,
- cross-linking of an enzyme.

All these approaches are a compromise between maintaining high catalytic activity while achieving the advantages of immobilization. Two recent trends are based on 1) the use of new reagents and/or carriers and 2) approaches that take into account the increasing knowledge of enzyme structure and mechanism.

Reetz et al. described in 1995 that the activity of lipases can be enhanced up to 100-fold by immobilization in sol–gels.[3] Cross-linked enzyme crystals (CLECs)[4] were reported to give an increase in enantioselectivity relative to the native enzyme,[5] but this was mostly attributed to the removal of a less-selective isoenzyme during CLEC preparation. Since crystallization of proteins is not an easy task, cross-linked enzyme aggregates (CLEA), which are obtained by precipitation of proteins followed by cross-linking with glutaraldehyde, might represent an easy alternative. The CLEA from pencillin acylase had the same activity as a CLEC in the synthesis of ampicillin, but the cross-linked aggregate also catalyzed the reaction in a broad range of organic solvents.[6]

A promising combination of easy separation and high stability has been reported for a lipase immobilized on magnetic γ-Fe_2O_3 nanoparticles.[7] The use of magnetic particles is not new,[8] but Ulman and co-workers were able to produce nanoparticles with an average size of 20($\pm$10) nm (instead of the usual 75–100 μm), which were then covalently linked, after thiophene-functionalization, to a lipase from *Candida rugosa*. The resulting biocatalyst exhibited significantly higher stability (over a period of almost one month) than the native enzyme in the hydrolysis of *p*-nitrophenyl butyrate (Figure 1). Moreover, the immobilized enzyme can be easily separated from the reaction mixture by application of a magnetic field, which either holds the immobilized enzyme in place or removes it, as the nanoparticles show very high magnetization values.

The increasing knowledge of enzyme structures and mechanism should also enable more controlled immobilizations. For example, lipase from *Pseudomonas fluorescens* was immobilized on four different carriers.[9] The native enzyme and two carrier-linked lipase preparations showed no or only modest changes in activity and enantioselectivity in the kinetic resolution of a racemic carboxylic acid ethyl ester. However, two immobilizates exhibited substantially altered properties (Table 1). Specific activity was increased sevenfold and enantioselectivity increased from $E = 7$ to $E = 86$ for the lipase immobilized on decaoctyl-sepharose. The authors claim that, during this (also much more rapid) immobilization procedure, the lipase underwent a conformational change from the closed to an open structure. In this process, a hydrophobic "lid", which is known to be present in most lipases, moves aside as a result of an interfacial activation caused by the car-

[*] Prof. Dr. U. T. Bornscheuer
Institut für Chemie und Biochemie
Technische Chemie & Biotechnologie
Ernst-Moritz-Arndt-Universität Greifswald
Soldmannstrasse 16
17487 Greifswald (Germany)
Fax: (+49) 3834-86-4346
E-mail:
uwe.bornscheuer@uni-greifswald.de

 © 2003 Wiley-VCH Verlag GmbH & Co. KGaA, Weinheim DOI: 10.1002/anie.200301664

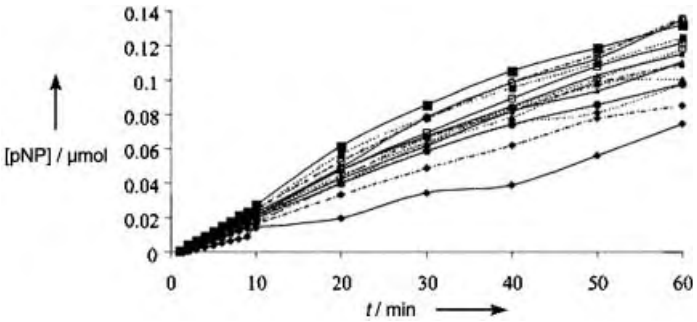
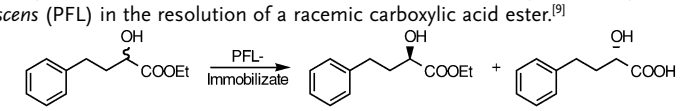


Figure 1. Stability of lipase from *Candida rugosa* immobilized on γ-Fe_2O_3 nanoparticles during the hydrolysis of *p*-nitrophenyl butyrate.[7] The concentration–time profiles (pNP = *p*-nitrophenol), which were recorded between 1 (□) and 27 days (◆, bottom curve), clearly shows the higher stability of the immobilized lipase. Reproduced with permission from the American Chemical Society.

Table 1: Comparison of different "controlled" immobilization techniques for a lipase from *Ps. fluorescens* (PFL) in the resolution of a racemic carboxylic acid ester.[9]



Carrier	Activity [U mg^{-1}][a]	Enantiomeric excess[b] [%]	Enantioselectivity
– (native)	0.5	59	7
dextran-agarose	0.45	58	6.9
glyoxyl-agarose	0.35	74	20
IHA-octyl-agarose[c]	3.5	92	79
IHA-decaoctyl-sepharose[c]	3.4	92.5	86

[a] µmol of substrate hydrolyzed per minute per mg of immobilized protein. [b] Enantiomeric excess of the remaining (*R*)-ester. [c] IHA = interfacial hydrophobic adsorption.

rier and immobilization procedure and provides enhanced access of the substrate to the active site residues. With a similar strategy, the same research group also reported the modulation of the properties of penicillin acylases from three different species, which also undergo conformational changes upon binding of the acyl donor substrate.[10]

In the future, information derived from protein sequences, 3D-structures, and reaction mechanism should be further combined with the properties of carriers (functional groups, hydrophobicity, magnetic properties) and physical/chemical methods in order to produce a directed immobilization strategy.

[1] a) H. E. Schoemaker, D. Mink, M. Wubbolts, *Science* **2003**, *299*, 1694–1697; b) A. Schmid, J. S. Dordick, B. Hauer, A. Kiener, M. Wubbolts, B. Witholt, *Nature* **2001**, *409*, 258–268; c) K. Faber, *Biotransformations in Organic Chemistry*, 4th ed., Springer, Berlin, **2000**; d) U. T. Bornscheuer, R. J. Kazlauskas, *Hydrolases in Organic Synthesis—Regio- and Stereoselective Biotransformations*, Wiley-VCH, Weinheim, **1999**.

[2] a) T. Boller, C. Meier, S. Menzler, *Org. Process Res. Dev.* **2002**, *6*, 509–519; b) J. Lalonde, A. Margolin in *Enzyme Catalysis in Organic Synthesis, Vol. 2* (Eds.: K. Drauz, H. Waldmann), Wiley-VCH, Weinheim, **2002**, pp. 163–184; this review also contains a broad list of further literature about enzyme immobilization.

[3] a) M. Reetz, A. Zonta, J. Simpelkamp, *Angew. Chem.* **1995**, *107*, 373–376; *Angew. Chem. Int. Ed. Engl.* **1995**, *34*, 301–303; b) M. T. Reetz, P. Tielmann, W. Wiesenhöfer, W. Könen, A. Zonta, *Adv. Synth. Catal.* **2003**, *345*, 717–728.

[4] a) N. Khalaf, C. P. Govardhan, J. J. Lalonde, R. A. Persichetti, Y. F. Wang, A. L. Margolin, *J. Am. Chem. Soc.* **1996**, *118*, 5494–5495; b) T. Zelinski, H. Waldmann, *Angew. Chem.* **1997**, *109*, 746–748; *Angew. Chem. Int. Ed. Engl.* **1997**, *36*, 722–724.

[5] J. J. Lalonde, C. Govardhan, N. Khalaf, A. G. Martinez, K. Visuri, A. L. Margolin, *J. Am. Chem. Soc.* **1995**, *117*, 6845–6852.

[6] L. Cao, F. van Rantwijk, R. A. Sheldon, *Org. Lett.* **2000**, *2*, 1361–1364.

[7] A. Dyal, K. Loos, M. Noto, S. W. Chang, C. Spagnoli, K. V. P. M. Shafi, A. Ulman, M. Cowman, R. A. Gross, *J. Am. Chem. Soc.* **2003**, *125*, 1684–1685.

[8] a) L. Cao, U. T. Bornscheuer, R. D. Schmid, *J. Mol. Catal. B* **1999**, *6*, 279–285; b) R. F. H. Dekker, *Appl. Biochem. Biotechnol.* **1989**, *22*, 289–310.

[9] G. Fernández-Lafuente, M. Terreni, C. Mateo, A. Bastida, R. Fernández-Lafuente, P. Dalmases, J. Huguet, J. M. Guisan, *Enzyme Microb. Technol.* **2001**, *28*, 389–396.

[10] a) M. Terreni, G. Pagani, D. Ubiali, R. Fernández-Lafuente, C. Mateo, J. M. Guisan, *Bioorg. Med. Chem. Lett.* **2001**, *11*, 2429–2432; b) S. Rocchietti, A. S. V. Urrutia, M. Pregnolato, A. Tagliani, J. M. Guisan, R. Fernández-Lafuente, M. Terreni, *Enzyme Microb. Technol.* **2002**, *31*, 88–93.

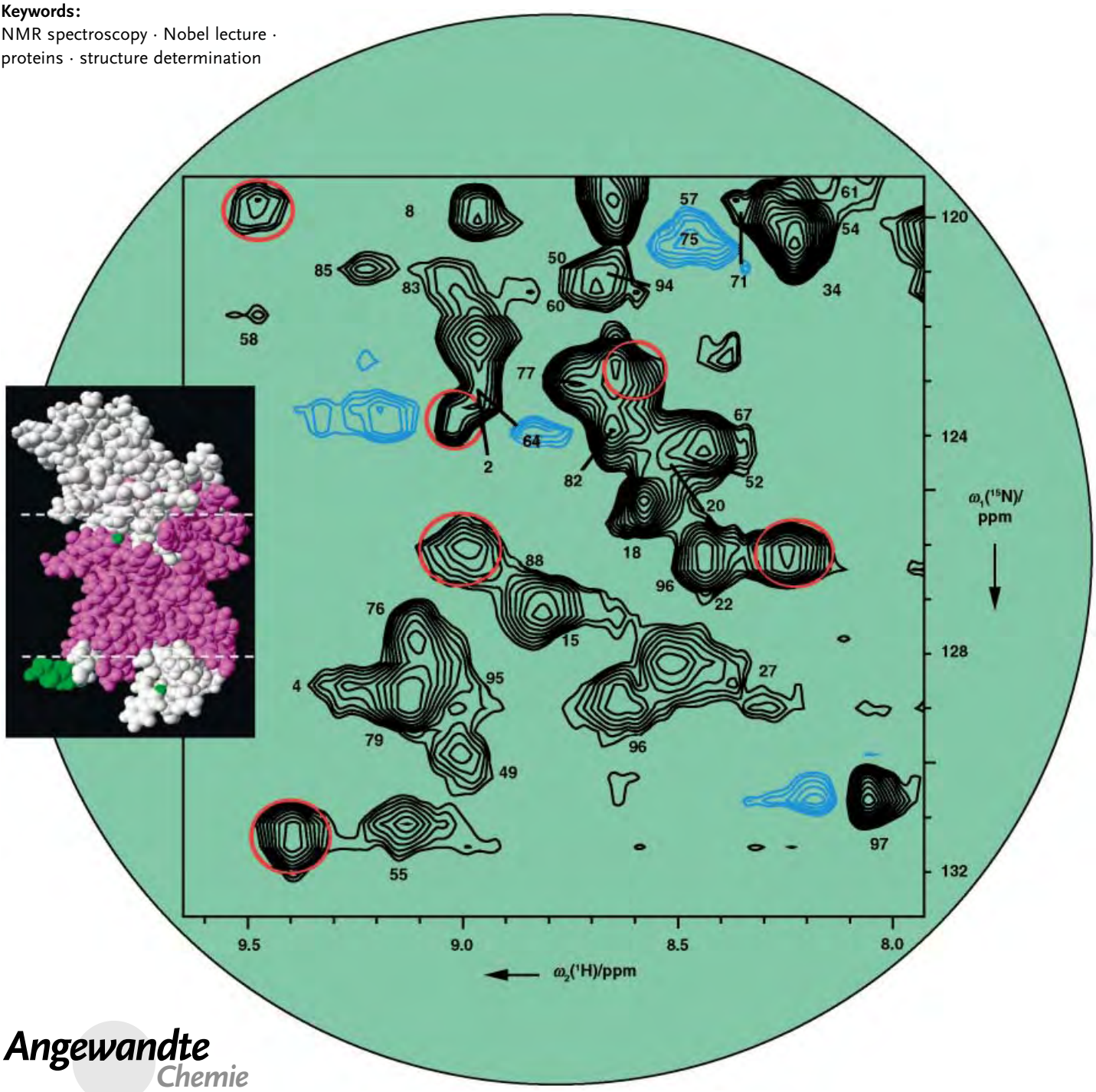
 © 2003 Wiley-VCH Verlag GmbH & Co. KGaA, Weinheim

NMR of Biomacromolecules

NMR Studies of Structure and Function of Biological Macromolecules (Nobel Lecture)**

*Kurt Wüthrich**

Keywords:
NMR spectroscopy · Nobel lecture · proteins · structure determination



© 2003 Wiley-VCH Verlag GmbH & Co. KGaA, Weinheim
DOI: 10.1002/anie.200300595

Angewandte Chemie

From the Contents

1. Introduction	*3347*
2. NMR Spectra of Proteins in Solution	*3348*
3. The Way to NMR Structures of Proteins	*3351*
4. NMR in Structural Biology	*3356*
5. Outlook to NMR Applications in Structural and Functional Proteomics	*3358*

Biographical Note

I was born in Aarberg, Switzerland, on October 4, 1938, and during my childhood I lived in the small town of Lyss in the Berner Seeland. At the time this was a rural area of farmland, forests, and rivers. The roots of the Wüthrich family are in an even more rural, mountainous area, the farming village of Trub in the Emmental near Bern. My mother's family owned the restaurant "Bären" and a bakery in Lyss. My grandfather, Otto Kuchen, enjoyed fishing and hunting, and his jugged hare dish was a widely known fall season delicacy at the "Bären". My interests during childhood were largely influenced by our living in an old farmhouse, where my second grandfather, Jakob Wüthrich, had been a farmer. Although my father, Herrmann Wüthrich, took up an occupation as an accountant, he remained very much attached to his upbringings and our family produced a wide range of farming goods. My mother, Gertrud Wüthrich-Kuchen was the true center of our family life. In addition to raising me and my two younger sisters, Elisabeth and Ruth, she did marvelous things in the kitchen, tended our big garden, raised fowl, and was involved in various activities in the community.



My intense contacts with the rural environment of plants and animals awakened my interest in natural science at an early age. In particular, I acquired a thorough knowledge of the behavior of all sorts of water animals, mostly through observations made while enjoying all aspects of work and fun with a private trout river. On rare occasions I still enjoy fishing trips, and am a member of the Mercury Bay Game Fishing Club in Whitianga, New Zealand, which lists Ernest Hemingway and Zane Grey among its all-time membership. With regard to my professional life, I had set my mind on becoming a forest engineer. Although I subsequently changed my mind in this regard, I still enjoy tending the family forest, which now



With my parents, Herrmann and Gertrud Wüthrich-Kuchen, and my two sisters, Elisabeth and Ruth, in the garden of our home in Lyss, Switzerland, 1944.



At the Mercury Bay Game Fishing Club in Whitianga, New Zealand, 1987.

[*] Prof. Dr. K. Wüthrich
Institut für Molekularbiologie
Eidgenössische Technische Hochschule Zürich
8093 Zürich (Switzerland)
Fax: (+41) 1 633 11 51
E-mail: kurt.wuthrich@mol.biol.ethz.ch
and
The Scripps Research Institute
10550 North Torrey Pines Road, La Jolla, CA 92037 (USA)

[**] Copyright© The Nobel Foundation 2002. We thank the Nobel Foundation, Stockholm, for permission to print this lecture.

 DOI: 10.1002/anie.200300595 © 2003 Wiley-VCH Verlag GmbH & Co. KGaA, Weinheim

contains trees that were planted by three generations of our family, starting with my grandfather.

My formal training toward an academic profession started in 1952, when I transferred from the village school in Lyss to the Gymnasium in the nearby "bilingue" city of Biel/Bienne. During the Gymnasium years my interests widened beyond forestry and fishing. We had the good fortune that our science and language teachers were either former university professors, who had left their academic positions elsewhere in Europe during the Second World War and found a haven in Biel, or followed the then common practice of using a teaching assignment at Gymnasium level as a stepping-stone for an academic career. At age 14 to 18 we were a group of seven students specializing in natural sciences who were thus trained in mathematics and physics at university level, and I happily accepted the challenge. According to my mother, it was during those years that I got used to working through the nights. Another focus was the French language, French literature, and French theatre and movies, which was largely motivated by the fact that the composition of our class as well as our teachers represented the bilingual character of Biel/Bienne. The Gymnasium Biel was informally attached to the Swiss Federal School of Sports and Gymnastics in nearby Magglingen, and thus my interest in competitive sports was awakened. These three areas all play an important role in my life up to the present days. Physics and mathematics are key activities in my professional life, professional visits in Paris and "les provinces" are combined with the sampling of French food, wine, and culture, and I not only obtained the "Eidgenössisches Turn- und Sportlehrerdiplom" (Swiss Federal Gymnastics and Sports Instructor Degree) as one of my University degrees, but also played in a competitive soccer league well beyond the age of 50.

By now I can look back on 40 years of intense involvement with techniques referred to as magnetic resonance spectroscopy. At the outset in 1962 and throughout my graduate studies there was electron paramagnetic resonance (EPR spectroscopy). EPR was complemented during my postdoctoral training from 1965 to 1967 by nuclear magnetic resonance (NMR) spectroscopy applied to chemical physics projects, and since the fall of 1967 I have used NMR for studies of biological macromolecules. From there it was a sinuous avenue that led by 1984 to the NMR method for protein structure determination in solution. Our results were occasionally met with doubts and disbelief, so that considerable moral strength and perseverance were at times called for.

During my student years from 1957 to 1962, NMR spectroscopy was just being introduced as an analytical tool in chemistry, molecular biology was not yet established as an independent discipline, and the initial three-dimensional protein crystal structures at atomic resolution were just emerging. My education at the University of Bern could thus not possibly cover the areas of our current research. The faculty and the student classes in Bern were small in numbers, with three physics students and seven chemistry students starting in 1957. From my curriculum in chemistry, physics, and mathematics, I best remember intense work in linear algebra, classical mechanics, chemical thermodynamics, physical chemistry of synthetic polymers, and preparative biochemistry of proteins and nucleic acids. This combination turned out to be an excellent foundation for my later scientific activities. The last two years of formal education, from 1962 to 1964, were spent at the University of Basel, majoring in sports and obtaining a Ph.D. in chemistry. Studying sports included about 25 weekly hours of intense physical exercise as well as premedical courses in human anatomy and physiology. Combined with experience gained from observations made on myself in the pursuit of competitive sports, this provided an additional dimension to my education. The subject of my Ph.D. thesis in inorganic chemistry with Professor Silvio Fallab was the catalytic activity of copper compounds in autoxidation reactions, and for this project the availability of a state-of-the-art EPR spectrometer in the Physics Institute was a great opportunity.



As a postdoctoral fellow in Berkeley, 1966.

Studying natural sciences has always been a lot of fun for me, but nonetheless my mind was quite solidly set on a career as a high-school teacher with a heavy involvement in sports. In parallel to my studies in natural sciences, I extensively yielded to what I thought to be my vocation. Thus, during the years 1957–1962, I spent part of each winter as a ski instructor in Swiss mountain resorts. From 1959 to 1965, I had part-time jobs in high schools, first teaching physics at the Kantonsschule Solothurn, then chemistry at the Gymnasium Biel, and finally gymnastics at the Mädchengymnasium in Basel. These teaching assignments also had an important impact on my personal life: In 1961, while on my job as a ski instructor in the resort town of Saanenmöser in the Berner Oberland, I met my wife, Marianne Briner, who at the time was an elementary school teacher. We were married in 1963, and Marianne then joined me in studying sports at the University of Basel, graduating with the "Eidgenössisches Turn- und Sportlehrerdiplom" and specializing in modern dance. After the graduate student and postdoctoral years we started



With my wife Marianne, son Bernhard, and daughter Karin in front of our apartment building in Greifensee, Switzerland, 1972.

 © 2003 Wiley-VCH Verlag GmbH & Co. KGaA, Weinheim



Professor Robert E. Connick in my office at the ETH Zürich, 1981.



With, from left to right, Karin, Marianne, and Bernhard in the desert near Tucson, AZ, USA, 1984.

a family, with our son Bernhard Andrew being born in 1968 in Berkeley Heights, NJ, USA, and our daughter Karin Lynn joining us in 1970 in Greifensee near Zürich, Switzerland.

After finishing my graduate studies I spent another year in Basel concentrating on EPR studies of metal complexes in solution. In the spring of 1965 we moved to the USA, where I joined Professor Robert E. Connick at the University of California, Berkeley, for postdoctoral training. We used NMR spin relaxation measurements of ^{17}O, ^{2}H, and ^{1}H in addition to EPR for studies of the hydration of metal ions and metal complexes. The Berkeley period was devoted to intensive work on the theory of nuclear spin relaxation, group theory, and quantum mechanics, which was motivated by Bob Connick's weekly group seminar, a graduate course on Group Theory and Quantum Mechanics by Michael Tinkham, and an intense collaboration with another Swiss postdoc, Alex von Zelewsky, who soon thereafter accepted the chair of inorganic chemistry at the University of Fribourg in Switzerland. Over the years, Marianne and I returned at regular intervals to Berkeley to renew the friendships of the 1960s and revive fond memories.

In October 1967 I joined the Biophysics Department of Dr. Robert G. Shulman at Bell Telephone Laboratories in Murray Hill, New Jersey. I was given responsibility for the maintenance of one of the first superconducting high-resolution NMR spectrometers, which operated at a proton resonance frequency of 220 MHz, and I was otherwise free to use this instrument for research on protein structure and function. Due to my background, my interest was focused on metal centers rather than on polypeptide chains, and all my initial projects in high-resolution NMR had to do with hemoproteins. Using blood sampled from my arm in the first aid station, a Japanese colleague at Bell Laboratories, Dr. Tetsuo Yamane, prepared "hemoglobin (KW)", and within a few months we found entirely new avenues of deriving information on structure–function correlations from the NMR spectra of hemoglobin and other hemoproteins. These projects were a lucky choice: with the limited sensitivity and spectral resolution of the instrumentation available in 1968, the special spectral properties of hemoproteins were a great asset for successful NMR applications. Many years later, the unique NMR spectral features that enabled the early work with these metalloproteins had an important role in various aspects of the development of the NMR method for three-dimensional protein structure determination.

In October 1969 I returned to Switzerland to join the ETH Zürich. From the start I was equally well equipped with NMR and EPR instrumentation as previously at Bell Telephone Laboratories, and during the following 32 years the ETH provided us in regular



Visiting the University of California, Berkeley, 1997. Dudley Herschbach happened to visit on the same day. Lunch at "Chez Panisse" was running late, so our host, Alex Pines, carried the desserts along to the seminar room.

intervals with the most advanced NMR equipment. Until 1975 I was working with a small group of students, a chemical engineer, Rudolf Baumann, who has stayed with me throughout all these years, and a postdoctoral associate with a physics Ph.D. in solid state EPR, Dr. Regula Keller, who pursued highly successful research with hemoproteins from 1970 to 1982. In 1973, Gerhard Wagner decided to do his graduate work with me. Gerhard then stayed with the group until 1987, pursuing a classical European academic career with Habilitation before settling as a Professor at Harvard Medical School. Being able to keep outstanding junior scientists as research associates over extended periods of time was a special privilege enjoyed by senior faculty in the traditional European system, and the continued presence of Rudolf, Regula, and Gerhard during most of my initial 15 years in Zürich was a key factor for success with our research program.

In Zürich, we continued research on hemoproteins with the use of NMR and EPR spectroscopy, where the biochemical work was mostly done by groups outside of the ETH who joined us for collaborative projects, and the spectroscopic work was done by Regula Keller, myself, and a succession of graduate students. In addition, we started a program of systematic studies on the application of NMR techniques to polypeptides and small proteins.

 © 2003 Wiley-VCH Verlag GmbH & Co. KGaA, Weinheim

Spirits were kept high by successful studies of cyclic peptides in collaboration with the Head of the Institute of Molecular Biology and Biophysics, Prof. Robert Schwyzer, the observation of unexpectedly well-resolved and long-lived NMR lines of amide protons in the small protein basic pancreatic trypsin inhibitor (BPTI), and the discovery of ring flips in BPTI. On the main line of research, which was to develop a method for protein structure determination in solution, there was only little progress. In 1975, in an attempt to survey the state of the field of NMR spectroscopy with biological macromolecules, I wrote the monograph *NMR in Biological Research: Peptides and Proteins*. There were two principal conclusions from this venture that would greatly affect the continuation of our work plan. First, I fully realized that we had been extremely fortunate in choosing hemoproteins as a focus for our early NMR efforts. Second, it became clear that attempts of the early 1970s to derive de novo three-dimensional protein structures from conformation-dependent proton chemical shifts was not a promising approach, independent of whether these shifts were caused by intrinsic or extrinsic diamagnetic or paramagnetic probes. We thus had to look for novel avenues for NMR structure determination, where hemoproteins with their unique NMR spectral properties could be an ideal testing ground for new ideas.

Shortly after I had learned my lessons from writing the 1976 monograph, the conditions under which I could pursue my work evolved in quite important ways. After working for more than 5 years with a small group of students and research associates from the environs of Zürich, and being able to spend long hours of my own time at the bench and on the NMR spectrometers, I found myself suddenly surrounded by more than 20 postdoctoral fellows and students from all over the world. At around the same time, I also started to travel quite extensively in all parts of the world, with a first visit to India at the end of 1974, and a first round-the-world trip including stops in the USA and in Japan in the fall of 1975. The visits to India and Japan resulted in new, lasting friendships with local colleagues, and also in attracting a number of most talented postdoctoral fellows to Zürich. Ever since, professional travel has become an important part of my activities. Over the years this also included visiting faculty appointments at the University of California, Berkeley, Cornell University in Ithaca, NY, Johns Hopkins University in Baltimore, MD, the California Institute of Technology in Pasadena, CA, the Scripps Research Institute in La Jolla, CA, RIKEN in Tokyo, Japan, and the University of Edinburgh, UK. Spending part of my time in these places of highest standards added greatly to my quality of life as well as to the progress of our research.

The international aspect of my activities received a special boost in 1975, when—out of the blue—I was elected to membership in the Council of the International Union of Pure and Applied Biophysics (IUPAB). There was little work involved in this assignment, but in 1978 my IUPAB affiliation changed to being its Secretary General, and with this I also became a member of the General Committee of the International Council of Scientific Unions (ICSU) and of the ICSU Standing Committee on the Free Circulation of Scientists. During the six-year term as Secretary General the demands on my time were thus quite heavy. Fortunately, Marianne agreed to run the IUPAB office. This made things easier, since she would travel with me and we dealt with the IUPAB business in makeshift offices temporarily installed in hotels all around the world. The sunny side was that I got to know many prominent scientists, whose names I had previously mostly known from textbooks. For example, structural biology was represented in the IUPAB Council from 1978–1981 by Britton Chance, Henryk Eisenberg, David Phillips, Frederic Richards, and Akiyoshi Wada, a true center of excellence! In the business meetings as well as in the social gatherings, we spent much of our time discussing the latest research advances long before they appeared in print. There was a particularly close collaboration with the IUPAB Presidents during my tenure as Secretary General, Professor Setsuro Ebashi and Professor Richard Keynes. Richard Keynes is a great-grandson of Charles Darwin. During IUPAB-related joint travel in Europe and the Far East in 1982/83, I listened to a more and more enjoyable but seemingly endless series of presentations of his Darwin Lecture commemorating the 100th anniversary of Darwin's death; in return, Richard lived through a heavy dose of biomolecular NMR spectroscopy.

Through my association with ICSU and IUPAB, I also became involved in entirely novel business. Most notable in hindsight were negotiations during the period 1980–1983 about joint adherence of China and Taiwan in international science organizations. We eventually defined terms and conditions for adherence to IUPAB of both "The Biophysical Society of China located in Beijing, China" and "The Chinese Biophysical Society located in Taipei, China". This involved extensive, highly formal correspondence, as well as visits and personal negotiations with Government and Academy officials in both countries. I also participated in IUPAB and ICSU programs of support for scientists in developing countries, and I organized summer schools and symposia in Africa, the Far East, and Latin America. This all greatly influenced my outlook on the world. Although each year the IUPAB-related activities and my research-related travel kept me out of my laboratory for several months, the effect on our research was overall highly beneficial. As a bonus, I



The President and the Secretary General of the IUPAB with their wives during a diplomatic mission in China, 1983. President Professor Richard Keynes and Ann Keynes are on the left and right, respectively.



At dinner during an ICSU General Committee meeting in Munich, Germany, 1985. To my left is Professor Jorge Allende from Chile, to my right is Professor Raymondo Villegas from Venezuela.

 © 2003 Wiley-VCH Verlag GmbH & Co. KGaA, Weinheim



Addressing the audience during the opening session of an IUPAB/ICSU/UNESCO-sponsored "Winter School on Magnetic Resonance in Biology and Medicine" in Cairo, Egypt, 1986. To my left is Professor I. El Gohari, who has over the years been the Egyptian delegate to numerous IUPAB functions.



With Professor Chen-Lu Tsou, enjoying the beautiful scenery of Wuxi, China, during an IUPAB/ICSU-sponsored Summer School on Biophysics, 1992.



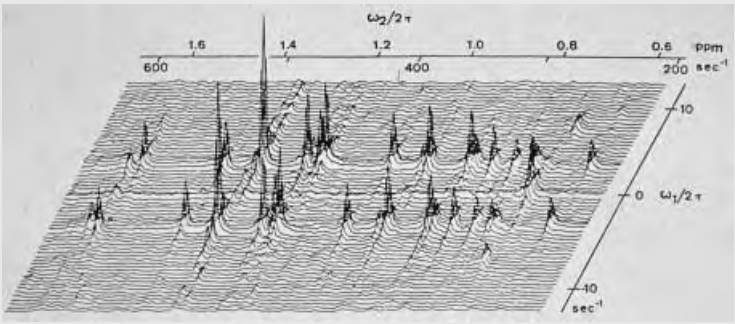
A dinner party during a visit with Professor Setsuro Ebashi (second from the right) in Okasaki, Japan, 1996. Mrs. Ebashi is next to Marianne, and Kuniaki Nagayama, who started 2D NMR with proteins as a postdoctoral fellow with Richard Ernst and myself in the late 1970s, is on the left wing.

gained experience in directing a research group at a distance, and my junior associates could test their own initiatives during my absences.

With all the new talent assembled in my group by 1976, we started to develop new NMR experiments and novel algorithms for the structural interpretation of NMR data, which eventually resulted in the NMR method for protein structure determination. This included the identification of the nuclear Overhauser effect (NOE) as a NMR parameter that can be related in an unambiguous way to three-dimensional macromolecular structures. We made use of the outstanding resolution of parts of the hemoprotein NMR spectra for calibrating NOE distance measurements with the then-available one-dimensional (1D) NMR techniques. In addition to Regula Keller, Sidney Gordon, a sabbatical visitor, made key contributions with the introduction of the 1D transient NOE experiment. Subsequently, the NOE had a key role in the approach used for obtaining sequence-specific assignments of the many hundred to several thousand NMR lines in a protein. The sequential assignment strategy was initially implemented by Gerhard Wagner and a diploma student, Andreas Dubs, using 1D NOE and spin-decoupling experiments. In parallel with the 1D NMR investigations on NOEs and NMR assignment in proteins, the development of two-dimensional (2D) NMR techniques for macromolecular studies had been started in 1976 as a joint project with Professor Richard R. Ernst (Nobel Prize in Chemistry, 1991). In 1977 the first 2D NMR spectrum of a protein was recorded, and by 1980 we had assembled four 2D NMR experiments that allowed for the initial protein structure determinations: COSY (2D correlated spectroscopy), SECSY (2D spin-echo correlated spectroscopy), FOCSY (2D foldover-corrected correlated spectroscopy), and NOESY (2D nuclear Overhauser enhancement spectroscopy). It was a lot of fun at the time to decide on these acronyms! Soon my group started to use 2D NMR experiments in daily practice, and the experience from more than a decade of one-dimensional NMR spectroscopy with proteins was happily and profitably married with the new potentialities of 2D NMR.

By 1982, complete sequence-specific assignments had been obtained for a small protein, BPTI, and for the polypeptide hormone glucagon bound to lipid micelles. This was published in a series of four papers in 1982. Although the first one of these papers already outlines the presently used protocol for protein structure determination by NMR, it took two more years of intense work on metric matrix distance geometry algorithms and their implementation in efficient software packages before the first NMR structure determination of a globular protein, bull seminal protease inhibitor (BUSI), could be completed. A large number of brilliant junior scientists working in my group from 1976 to 1985 contributed directly or indirectly to this result: Gerhard Wagner was involved in each step of the project; Kuniaki Nagayama and Peter Bachmann devised the first generation of 2D NMR experiments for studies of biological macromolecules and wrote the software needed to handle such data with the then-available limited computational facilities; Anil Kumar recorded the first 2D NOESY experiment with a protein; Gerhard Wider made key contributions to 2D NMR spectroscopy and to the sequential assignment method; Werner Braun, Martin Billeter, and Timothy Havel started a tradition in my laboratory of theoretical work on the structural interpretation of NMR data; Peter Strop prepared BUSI and worked on its resonance assignments; finally, Michael Williamson and Timothy Havel actually solved the structure of BUSI. They all, and many additional students and

 © 2003 Wiley-VCH Verlag GmbH & Co. KGaA, Weinheim



The first two-dimensional ^{1}H NMR spectrum of a protein, a "2D J-resolved spectrum", recorded by Kuniaki Nagayama, 1977.

postdoctoral associates from the "heroic period" 1976–1985 have in the meantime started highly successful independent academic careers.

The completion of the first NMR structure of a protein brought new, unexpected challenges. When I presented the structure of BUSI in some lectures in the spring of 1984, the reaction was one of disbelief and suggestions that our structure must have been modeled after the crystal structure of a homologous protein. Apparently the structural biology community had thoroughly adjusted to the role of NMR as a method that could provide some exotic supplementary data, but which would not be suitable for de novo structure determination at atomic resolution. The criticism raised had two major consequences. The first one resulted from a discussion with Robert Huber (Nobel Prize in Chemistry, 1988), after a seminar in Munich, on May 14, 1984. Robert proposed to settle the matter by independently solving a new protein structure in his laboratory by X-ray crystallography and in my laboratory by NMR. For this purpose, each one of us received an ample supply of the α-amylase inhibitor Tendamistat from Hoechst AG. Virtually identical three-dimensional structures of Tendamistat were obtained by NMR in solution and by X-ray diffraction in single crystals, which settled matters once and for all. This was particularly comforting in the context of the fact that the subsequently solved NMR structure of metallothionein was completely different from an independently solved metallothionein crystal structure. (It took six years before the crystal structure was redetermined and found to coincide with the NMR structure!).

The second consequence was that I asked for a sabbatical leave and ended up in Wengen, a beautiful mountain resort in the Berner Oberland. This was possible because I was also finishing my 6-year term as the Secretary General of IUPAB in the summer of 1984. Considering the critical reaction to the initial NMR structure determinations, I felt that it was important to document our work in a complete and detailed fashion. I thus had good reasons to honor my commitment of writing a monograph on the Baker Lectures, which I had delivered in 1983 at Cornell University. As I spent much of the time alone in Wengen, with my family joining me for weekends and vacation periods, work progressed well. The book *NMR of Proteins and Nucleic Acids* covers primarily work in my research group during the period 1977–1984. It also turned out that directing my research group at a distance was surprisingly successful, and since the manuscripts were typed in Zürich from my hand-written notes, it helped that even ordinary mail was still reliably delivered within one day within Switzerland. It was therefore an easy decision for me to extend the stay in Wengen from the originally planned 6 months to 18 months. Besides the deskwork, important occupations in Wengen were skiing in the winter, and jogging and mountain climbing in the summer. According to my diaries I did not miss a single day of skiing from December 1, 1984 to April 10, 1985. This made up for having stayed away from the ski slopes during the 14 years from 1971 to 1984 because of my other professional activities. I also returned to the skiing outstation of the Federal Sports School in Mürren for a much-needed overhaul of my skiing technique, and participated in the organization of the famous Lauberhorn ski race in Wengen.

In the spring of 1986, after a second winter of skiing in Wengen, I had thoroughly cleaned up the backlog of unpublished material, in addition to having finished work on the Baker Lectures monograph. Protein structure determination by NMR had by then found its believers, as documented by the fact that the first printing of my new book was sold out within a few weeks. For us a new chapter had to be opened, and we established contacts with biochemists and molecular biologists for the real test of the NMR technique in applications to biologically interesting systems. By 1990, a collaboration with Professor Walter Gehring of the Biocenter at the University of Basel yielded structure determinations of the *Antennapedia* homeodomain and its complex with the operator DNA. Using this structure as a platform, additional NMR experiments provided entirely novel insights into the role of hydration water for specific DNA recognition. A NMR structure determination of the cyclophilin A–cyclosporin A complex was pursued as a joint project with two former graduate students, Hans Senn and Hans Widmer, and their research team at Sandoz AG. It had immediate practical impact, since the structure of the bound



Tim Havel and Mike Williamson in front of a computer displaying the three-dimensional structure of the protein BUSI that we had just solved, 1984.



View from my office in our home in Wengen, Switzerland, during my first-ever sabbatical, 1984–1986.

 © 2003 Wiley-VCH Verlag GmbH & Co. KGaA, Weinheim

immunosuppressant turned out to be very different from the only other structural information available at the time, that is, crystal and NMR structures of free cyclosporin A. It was, for all involved, a completely unexpected and for many reasons surprising result!

In yet another exciting collaboration, with Professor Rudi Glockshuber at the ETH Zürich, we completed a structure determination for the C-terminal half of the mouse prion protein in April 1996, barely 10 days after the BSE-crisis in Great Britain broke into the open. With this timing, the prion protein structure had high visibility also in the popular media. In 1997 we succeeded in characterizing the structure of the intact prion protein, and found that the N-terminal half of the molecule forms a highly flexible, extended tail. The prion protein thus presented a striking illustration of the unique power of NMR to characterize partially structured polypeptide chains. Others among the more than 70 protein structure determinations completed in my laboratory functionally relate to enzymology, toxicology, chaperone-mediated protein folding, and intercellular signaling.

The biological and biomedical projects pursued during the past 16 years with the use of the NMR technique have added and still add greatly to the quality of my professional life. In these endeavors, the quite extreme specialization needed to maintain a high standard of structure determination breaks open in that I learn about an ever-increasing range of biological systems and biomedical problems. I feel very fortunate that my field of specialization thus leads me to an education in biology from the real experts, who sometimes even tend to consider me as one of their own.

1. Introduction

Nuclear magnetic resonance (NMR) spectroscopy is unique among the methods available for three-dimensional structure determination of proteins and nucleic acids at atomic resolution, since the NMR data can be recorded in solution. Considering that body fluids such as blood, stomach liquid, and saliva are protein solutions where these molecules perform their physiological functions, knowledge of the molecular structures in solution is highly relevant. In the NMR experiments, solution conditions such as the temperature, pH, and salt concentration can be adjusted so as to closely mimic a physiological fluid. Conversely, the solutions may also be changed to quite extreme nonphysiological conditions, for example, for studies of protein denaturation. Furthermore, in addition to protein structure determination, NMR applications include investigations of dynamic features of the molecular structures, as well as studies of structural, thermodynamic, and kinetic aspects of interactions between proteins and other solution components, which may either be other macromolecules or low-molecular-weight ligands. Again, for these supplementary data it is of keen interest that they can be measured directly in solution.

The NMR structure of the *Antennapedia* homeodomain (Figure 1) illustrates one of the exciting features of being able to perform structural studies in solution. The polypeptide chain in this protein is only partially folded, with both chain ends showing pronounced disorder.[1] In the complex with its operator DNA (Figure 2) the *N*-terminal chain end is located in the minor groove of the DNA, where it adopts a well-defined structure.[2] This mode of intermolecular recognition illustrates the functional importance of partially structured polypeptide chains. Mammalian prion proteins are an even more striking example of partial polypeptide folding, since the three-dimensional structure of the benign cellular form (PrP^C) includes a flexibly disordered 100-residue tail linked to the N-terminal end of a globular domain (Figure 3).[3] Considering that the mechanism of transformation of PrP^C into the aggregated, disease-related form of mammalian prion



Figure 1. NMR structure of the *Antennapedia* homeodomain. A bundle of 20 superimposed conformers represents the polypeptide backbone. For the polypeptide segment 7–59, the tight fit of the bundle indicates that the structure is defined with high precision, whereas the two chain ends are disordered.

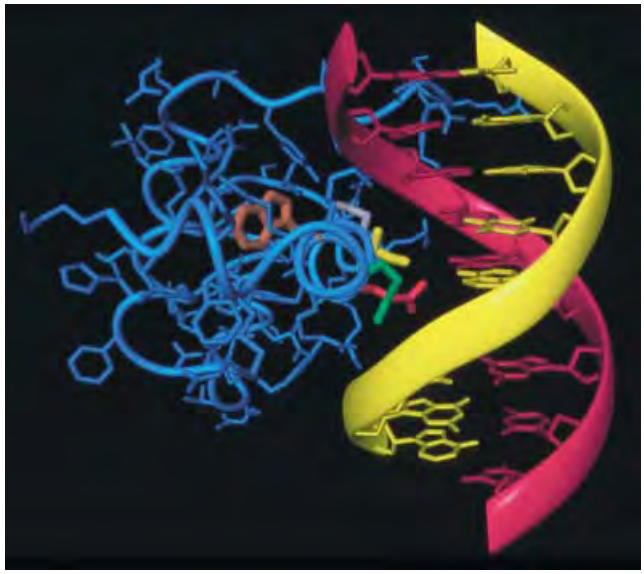


Figure 2. NMR structure of the complex formed between the *Antennapedia* homeodomain (blue, with functionally important residues in red, yellow, green, and brown and its operator DNA (yellow and red).[2]

© 2003 Wiley-VCH Verlag GmbH & Co. KGaA, Weinheim

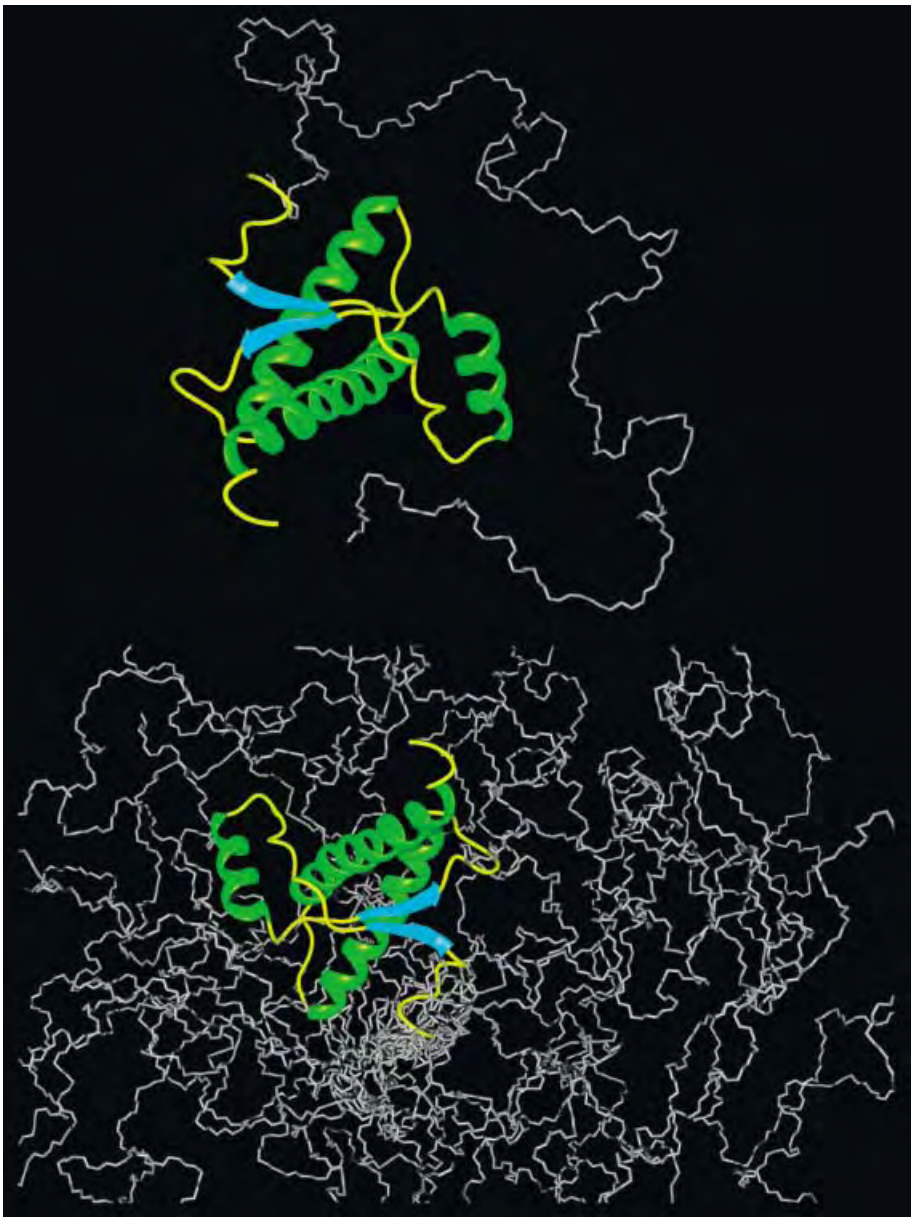


Figure 3. Top: NMR structure of the bovine prion protein. In the C-terminal globular domain of residues 126–230, α helices are green, an antiparallel β sheet is blue, and nonregular secondary structure is yellow; the "unstructured" N-terminal tail of residues 23–125 is white. Bottom: Visual impression of the variation of the bovine prion protein structure during a time period of about 1 ns. The superposition of 20 snapshots illustrates that the globular domain maintains its mean geometry, whereas the tail undergoes large-scale changes with time.

proteins is still subject to speculation, the observation of this flexible tail has been highly intriguing.

Partially folded polypeptide chains are usually difficult to crystallize. Furthermore, if crystals can be obtained, the chain segments that are disordered in solution will either be ordered by intermolecular contacts in the crystal lattice, or they will not be visible by diffraction methods. As a consequence, NMR has in many cases been the only method capable of providing structural information on partially folded polypeptides. Although a standard protocol for NMR structure determination provides a static picture of the unstructured chain segments (see Figures 1 and 3),[4] additional NMR experiments can provide information on the frequencies of the rate processes that mediate transitions between discrete states of the molecule within the conformation space spanned by the static bundle of NMR conformers.[5,6]

The ability of NMR techniques to characterize macromolecular structures and their intermolecular interactions with high spatial and temporal resolution has long attracted keen interest. This article reports on experience gained with NMR studies of proteins in my laboratory during the past 35 years.[7]

2. NMR Spectra of Proteins in Solution

When I joined the field of biomacromolecular NMR spectroscopy in 1967, important qualitative NMR features of amino acids and proteins had already been noted and tentatively rationalized.[8–12] Most important, it had been well documented that the spectrum of a globular protein is more complex than the sum of the NMR lines from the constituent amino acid residues in the polypetide chain (Figure 4a), and the differences between the ^{1}H NMR spectra of folded and unfolded (random coil (rc)) forms of a polypeptide chain had been tentatively explained by different interactions with the solvent (Figure 4b). The spectral analysis was primarily focused on the positions of the individual NMR lines in the ^{1}H NMR spectrum, as given by the chemical shift, δ, in parts per million (ppm) relative to a reference compound (Figure 4a). Although the chemical shift is primarily determined by the covalent structure of the amino acid residue, it can also be significantly affected by the interactions with the solvent. Therefore, the exclusion of the solvent water from the interior of a globular protein (Figure 4b) causes the chemical shifts of the core residues to be different from those of the water-exposed amino acid residues, so that even NMR lines originating from multiple residues of the same amino acid type can be distinguished. This conformation-dependent chemical shift dispersion was found to be sufficiently large to enable ^{1}H NMR studies of protein denaturation (Figure 5).[12] This then indicated the exciting prospect of using NMR for detailed studies of protein folding, and in particular for distinguishing between two-state and multiple-state folding and unfolding transitions. For me, the observations and ideas illustrated by Figures 4 and 5 also showed that one would need the ability of resolving and analyzing highly complex NMR spectra (upper trace in

 © 2003 Wiley-VCH Verlag GmbH & Co. KGaA, Weinheim

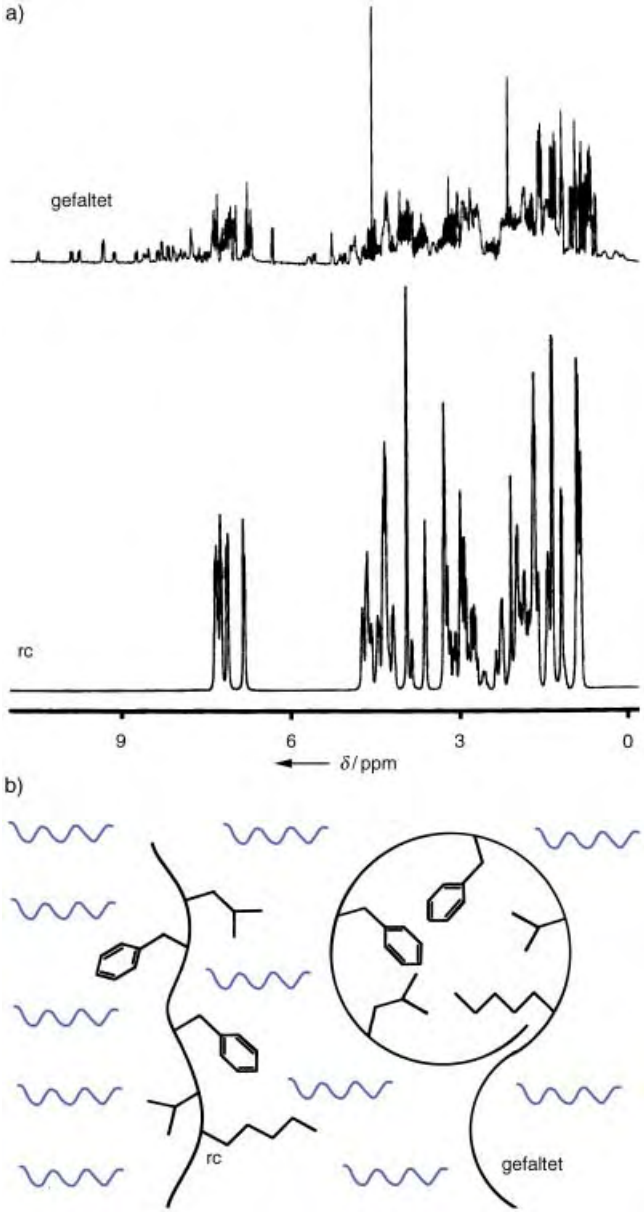


Figure 4. a) One-dimensional (1D) ^{1}H NMR spectra of the small protein bovine pancreatic trypsin inhibitor (BPTI, $M \approx 6000$). Top: Experimental spectrum of folded, active BPTI in a freshly prepared ^2H_2O solution. Bottom: Simulated spectrum for the unfolded, random coil form of the BPTI polypeptide chain. B) The solvent (blue) has free access to all parts of a random coil polypeptide chain (rc), whereas it is excluded from the core of a folded globular protein.

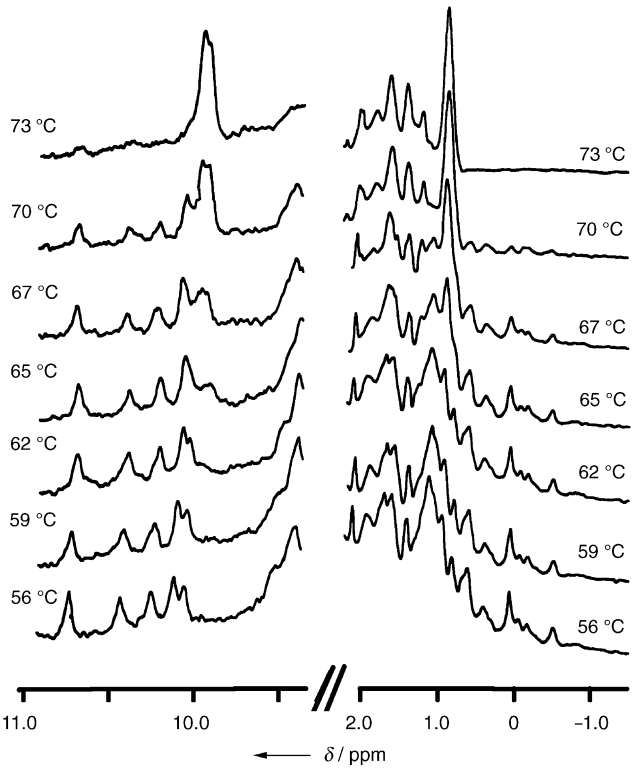


Figure 5. Downfield and upfield regions of 1D ^{1}H NMR spectra of the protein lysozyme at different temperatures, reflecting the transition from the folded form at 56 °C to the random coil form of the polypeptide chain at 73 °C (220 MHz, H_2O solution)[12].

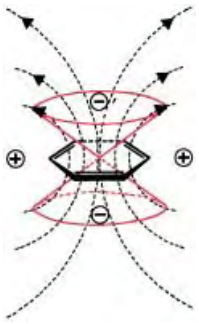


Figure 6. Local "ring-current field" around aromatic rings in solution induced by an external, static magnetic field. The shape of the ring current field is indicated by the red double-cone and by broken magnetic-field lines. The minus sign indicates that the NMR lines of hydrogen atoms located inside the cone in the three-dimensional protein structure are shifted upfield (to the right in the spectra of Figure 4a), whereas for atoms outside of the cone the shifts are downfield.

Figure 4a) in order to obtain information about physiologically active, folded forms of proteins. This was a clearly defined problem that appeared sufficiently challenging to be attractive for my own research.

In attempts at rationalizing in more detail the observations of Figure 4a and Figure 5, it had been suggested that local magnetic fields generated by ring currents in the aromatic amino acid side chains (Figure 6) should cause outstandingly large conformation-dependent chemical-shift changes of hydrogen atoms located near the rings in the three-dimensional protein structure. This was qualitatively confirmed by comparison of the largest observed deviations from random coil chemical shifts[4] in hen egg white lysozyme (Figure 5) with calculations of the ring-current shifts based on the then-available low-resolution crystal structure of this protein.[12] It had also been pointed out that hemoproteins could be expected to have particularly large ring-current shifts for hydrogen atoms located near the heme groups (Figure 7).[10,12]

 © 2003 Wiley-VCH Verlag GmbH & Co. KGaA, Weinheim

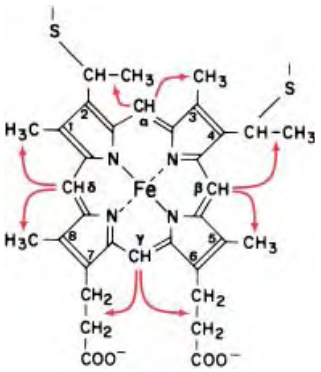


Figure 7. Chemical structure of heme *c*, which is the prosthetic group in cytochromes *c*. The red arrows connect groups of hydrogen atoms in the covalent structure of heme *c* that are separated by a sufficiently short distance to be connected by nuclear Overhauser effects (NOE).

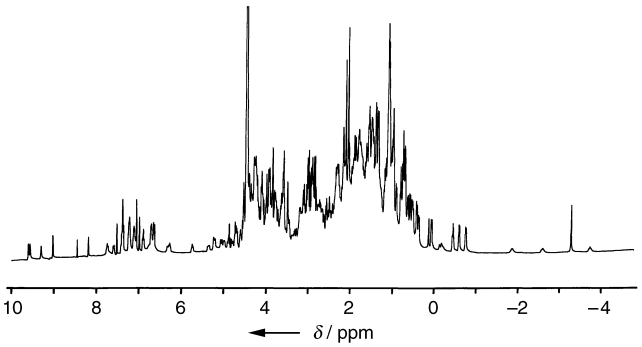


Figure 8. 1D ^{1}H NMR spectrum (360 MHz, 52 °C, solvent ^2H_2O) of horse ferrocytochrome *c* ($M \approx 12000$).

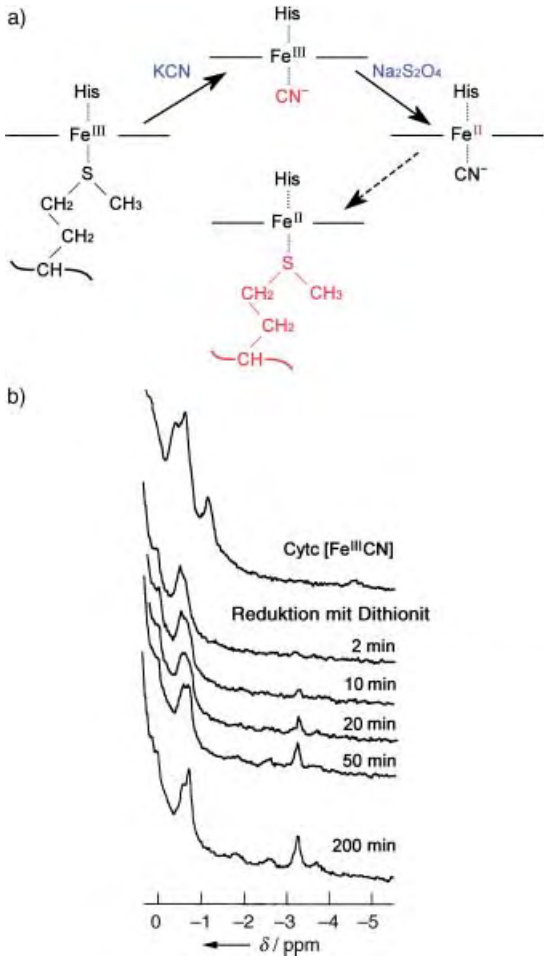


Figure 9. a) Three chemical reaction steps with cytochrome *c* that were used to identify methionine as one of the axial ligands of the heme iron.[13] The roman numerals indicate the oxidation state of the heme iron, and His stands for the amino acid histidine. The solid and broken arrows indicate rapid and slow reaction steps, respectively. Black: heme iron with ligands, where the horizontal line through Fe represents a side view of the heme *c* ring (see Figure 7); blue: chemicals added to the protein solution; red: new structural features resulting from the preceding reaction. b) Changes with time in the 1D ^{1}H NMR spectrum of cytochrome *c* after reducing the ferric cyanide complex with dithionite (220 MHz, 9 °C, solvent ^2H_2O).

For my start in the field of NMR with proteins, the prediction of unique, large heme ring-current shifts seemed to be an attractive feature of hemoproteins, and the presence of the heme iron (Figure 7) was appealing in view of my background in inorganic chemistry. As an additional advantage, low-resolution crystal structures for several hemoproteins were already available in 1967. It turned out that for several years nearly all my research projects were focused on the heme iron and its coordinatively linked ligands, and on the nonbonding interactions of the heme groups with their immediate environment in the hemoproteins. As anticipated, the large heme ring-current field generates a small number of well-separated resonance lines in the spectra of folded, globular hemoproteins (Figure 8). For the paramagnetic states of hemoproteins, additional well-resolved lines result from interactions with the unpaired electrons of the heme iron. Although they represented less than 3% of all the hydrogen atoms in any given hemoprotein, the well-resolved resonances were of crucial importance, because these lines could be selectively irradiated in 1D ^{1}H NMR experiments. For example, performing some simple ligand exchange and redox reactions with cytochrome *c* resulted in the identification of one of the axial ligands bound to the heme iron, which had not been seen in the low-resolution X-ray crystal structure available in 1969 (Figure 9).

The experiments in Figure 9a[13] started with the oxidized form of cytochrome *c*. As was then learned through this study (see below), ferricytochrome *c* contains a methionine side chain in one of the axial heme iron coordination sites. Upon addition of KCN to the protein solution, this methionine is replaced in the binding site on the heme iron by a cyanide ion, and therefore moves out of the heme ring-current field. The completion of this reaction can readily be monitored, since different patterns of well-resolved resonance lines are present in the ^{1}H NMR spectra of ferricytochrome *c* and its cyanide complex.[13] After reduction of the heme iron to the ferrous state, the cyanide complex is thermodynamically less stable than the native form of cytochrome *c*, and in a slow reaction the cyanide in the axial coordination site of the heme iron is again replaced with the natural methionine ligand. The return of the axial methionine into the heme ring-current field was

 © 2003 Wiley-VCH Verlag GmbH & Co. KGaA, Weinheim

monitored in real time (Figure 9b) by the appearance of its typical high-field lines in the ^{1}H NMR spectrum (see Figure 8). This experiment resulted in the identification of the nature of this axial ligand in the native, active form of cytochrome *c*, and further yielded information on the relative thermodynamic stabilities of the four different structures in Figure 9a.

As a sideline, comparison of the Figures 8 and 9b also illustrates the influence of various experimental factors on the appearance of the NMR spectra. The higher resonance frequency and the high temperature used in the experiment of Figure 8, which was recorded around 1980 with Fourier transform spectroscopy, resulted in narrower and more clearly separated peaks in the region 0 to −5 ppm than the experiment in Figure 9b, which was recorded in 1968 with continuous-wave NMR spectroscopy at low temperature.

Other early experiments based on the observation of well-resolved resonances in the ^{1}H NMR spectra of hemoproteins resulted in the characterization of conformation changes during the oxygenation of myoglobin and hemoglobin,[14,15] and in detailed characterization of the electronic structure of the heme groups in different classes of hemoproteins.[16–18]

3. The Way to NMR Structures of Proteins

Around 1970 there was a lot of enthusiasm in my laboratory and elsewhere about the success of experiments of the types illustrated by Figures 4–9. During the following years, however, there was little further progress toward an NMR method for de novo structure determination of proteins. In hindsight this can readily be rationalized: Early successful structural interpretations of NMR data invariably supplemented a previously known low-resolution X-ray crystal structure of the same protein. In spite of the high symmetry of the ring-current fields (Figure 6) and other sources of local conformation-dependent chemical shifts, including natural paramagnetic centers and extrinsic paramagnetic shift reagents,[17,19] the observed chemical shifts could thus in some instances yield exciting new information. In a de novo protein structure determination, however, the high symmetry of the local magnetic fields would lead to ambiguities in the structural interpretation of the resulting chemical shifts. Different approaches were therefore called for, and eventually a NMR method for protein structure determination could be based on the following four principal elements:

3.1 Measurement of NOE Upper Distance Limits as Conformational Constraints

Nuclear Overhauser effects (NOEs) are due to dipolar interactions between different nuclei. The intensity of the NOE is related to the product of the inverse sixth power of the internuclear distance and a correlation function, $f(\tau_c)$, which describes the modulation of the dipole–dipole coupling by stochastic rate processes, with an effective correlation time τ_c [Eq. (1)].

$$\mathrm{NOE} \propto \frac{1}{\langle r \rangle^6} f(\tau_c) \qquad (1)$$

Although the NOE is a common phenomenon for all combinations of closely spaced nuclear spins, NOEs between pairs of hydrogen atoms are of prime interest for structural studies. A ^{1}H–^{1}H NOE is related to the through-space distance between a pair of atoms that are either not at all linked by covalent bonds (intermolecular NOE), or that may be far apart in the amino acid sequence of a polypeptide chain. ^{1}H–^{1}H NOEs can be observed in double-irradiation 1D NMR experiments as the fractional change in intensity of an NMR line that results from preirradiation of another resonance (Figure 10). Although NOE distance measurements had successfully been used for studies of small organic molecules,[20] including oligopeptides,[21] and observation of NOEs in proteins had also been reported,[22,23] it was not clear whether the desired distance information could actually be obtained for proteins.[20,24,25] This uncertainty arose because the Brownian motions of large structures in solution are slow, with long effective correlation times, τ_c, for this stochastic process, and proteins contain a dense network of hydrogen atoms. With the combination of these two features, spin diffusion could partially or fully deteriorate distance measurements based on ^{1}H–^{1}H NOE experiments.[24–28]

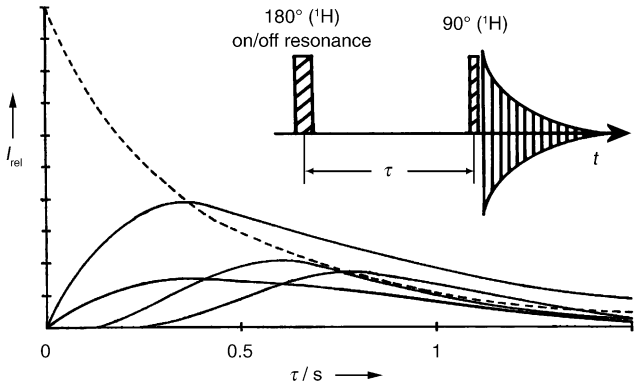


Figure 10. NOE buildup curves observed with 1D transient [^{1}H,^{1}H]-NOE measurements.[26] The relative intensities, I_{rel}, of the preirradiated resonance line (broken curve) and of the lines experiencing NOEs (solid curves) are plotted versus the duration of the mixing period, τ. The experimental scheme used to record transient NOE spectra (inset in the upper right) includes a selective 180° radio-frequency pulse applied to the "pre-irradiated" ^{1}H NMR line and a nonselective 90° pulse applied to the entire ^{1}H NMR spectrum. The two pulses are separated by the mixing period, τ, and followed by signal acquisition. When working with the crowded spectra of proteins, one records the difference between two spectra obtained with the preirradiation 180° (^{1}H)-pulse applied on- and off-resonance.

In the solution NMR experiments discussed here, spin diffusion arises as a consequence of the dependence of the NOE on the inverse sixth power of the internuclear distance, since magnetization transfer between two spins through multiple short steps may be more efficient than a one-step transfer over the longer, direct distance (Figure 11). We used 1D transient NOE-difference experiments (inset in

 © 2003 Wiley-VCH Verlag GmbH & Co. KGaA, Weinheim

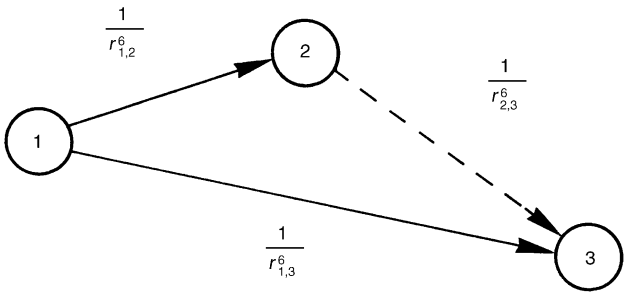


Figure 11. Spin diffusion: Transfer of magnetization between two hydrogen atoms 1 and 3 in the presence of additional hydrogen atoms goes through two competing pathways: the direct NOE across the distance $r_{1,3}$ and two- or multiple-step spin diffusion via intervening hydrogen atoms.

Figure 10)[26] and 1D truncated-driven NOE-difference experiments[27] to record NOE buildup curves (Figure 10), which then provided a basis for ^{1}H–^{1}H distance measurements in macromolecules. These studies showed that even more favorable conditions for NOE distance measurements can be found in macromolecules, which have long effective correlation times for the modulation of dipole–dipole couplings, than in low-molecular-weight compounds, for which the condition of extreme motional narrowing applies.[24,28]

Analysis of ^{1}H–^{1}H NOE buildup curves recorded with 1D transient NOE experiments (Figure 10) is based on the consideration that during the early phase of the mixing period, direct magnetization transfer from spin 1 to spin 3 (Figure 11) will result in a linear increase of the magnetization on spin 3 with time. In contrast, transfer to atom 3 via an intermediate step through atom 2 will have a lag period, even though for long mixing periods, τ, the extent of the magnetization transfer by such spin diffusion may for individual pairs of hydrogen atoms exceed that of the direct transfer (Figure 10). Corresponding considerations apply for the analysis of NOE buildup curves recorded with truncated-driven NOE experiments.[27] With proper selection of the duration of the mixing period, one can thus measure highly selective ^{1}H–^{1}H NOEs between distinct pairs of hydrogen atoms, or groups of chemical-shift-equivalent hydrogen atoms in proteins in solution.

There is a second criterion that needs to be satisfied for obtaining selective NOEs with 1D NMR experiments, that is, at least one of the two lines that are connected by the NOE must be sufficiently well resolved (i.e., separated from all other lines in the spectrum) to enable selective radio-frequency preirradiation (inset in Figure 10). The previously discussed well-resolved lines in the ^{1}H NMR spectrum of ferrocytochrome *c* (Figure 8) thus had again an important role in enabling us to study the spin physics in the interior of this globular protein with 1D ^{1}H NMR experiments, as well as to obtain novel structural information. Figure 12 shows a series of highly selective 1D truncated-driven NOE measurements, which were used to determine ^{1}H NMR assignments for the heme group in a *c*-type cytochrome (see Figure 7).[29]

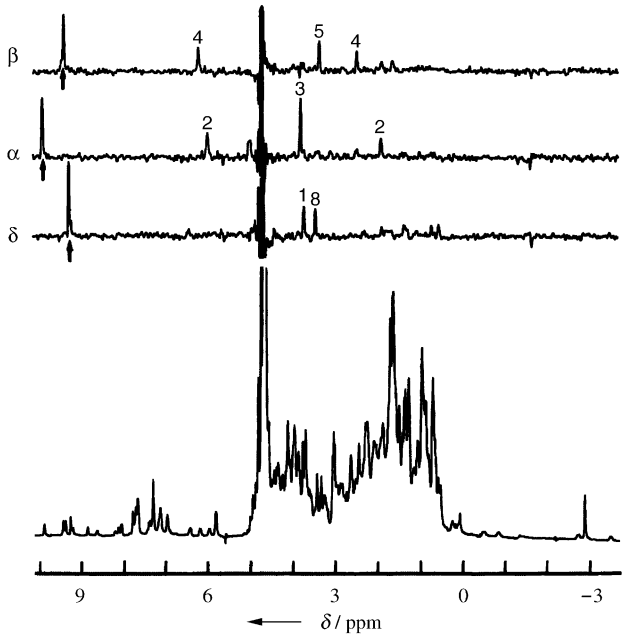


Figure 12. ^{1}H NMR assignments for the heme group of a *c*-type cytochrome using ^{1}H–^{1}H NOEs (see Figure 7). Bottom trace: 1D ^{1}H NMR spectrum of ferrocytochrome *c*-551 from *Pseudomonas aeruginosa* ($M \approx 12000$). Upper traces: three 1D truncated-driven NOE-difference spectra obtained with selective preirradiation (indicated by arrows) on the hydrogen atoms β, α, and δ (360 MHz, 35 °C, ^2H_2O solution). The NOE peaks are identified with numbers indicating the substituents attached to the corresponding porphyrin ring carbons (see Figure 7).

3.2 Sequence-Specific Resonance Assignments

Similar to the situation in heme groups (Figure 7), there are closely spaced pairs of hydrogen atoms in neighboring residues of a polypeptide chain (Figure 13). These can be connected by the observation of sequential NOEs. Figure 13 illustrates that NOE-based ^{1}H NMR assignments for a polypeptide chain can conceptually be considered as a two-step process. Each amino acid residue represents a spin system,[4] that is, it consists of an array of hydrogen atoms, including an amide proton (H^N), an α-proton (H^α), and the side-chain protons, which can be connected by steps over three or less

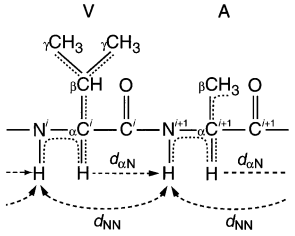


Figure 13. Sequential ^{1}H NMR assignment of proteins. The drawing shows the chemical structure of a valine–alanine (V–A) dipeptide segment in a polypeptide chain. The dotted lines connect groups of hydrogen atoms that are separated by at most three chemical bonds and can therefore be connected using scalar spin–spin couplings. The broken arrows link pairs of hydrogen atoms in neighboring amino acid residues that are separated by short through-space distances, $d_{\alpha N}$ and d_{NN}, and can therefore be connected by "sequential NOEs".

 © 2003 Wiley-VCH Verlag GmbH & Co. KGaA, Weinheim

covalent bonds through the observation of scalar spin–spin (through-bond) couplings (see reference [4] for the exceptions represented by proline and the aromatic side chains). In contrast, hydrogen atoms located in sequentially neighboring amino acid residues are separated by at least four covalent bonds. Pairs of neighboring residues in the sequence can therefore only be connected via NOEs manifesting short through-space distances, such as $d_{\alpha N}$ and d_{NN}. Suitable combinations of intraresidual ^1H–^1H connectivities established by scalar spin–spin couplings, and interresidue connectivities established by sequential NOEs enable progressive resonance assignments while "walking along the polypeptide backbone".

In other words, the spin systems of two neighboring residues can be connected by the intervening H^α–H^N or H^N–H^N sequential NOE connectivities (Figure 13). 1D double-resonance experiments with selective irradiation of the well-resolved amide proton resonances between 8 and 10 ppm in folded BPTI (Figure 4a) thus yielded assignments for most of the residues in the regular secondary structure elements (Figure 14).[30] Further assignments were not possible, because the other regions of the polypeptide chain were not represented by well-separated ^1H NMR lines that could have been selectively irradiated in 1D NMR experiments.

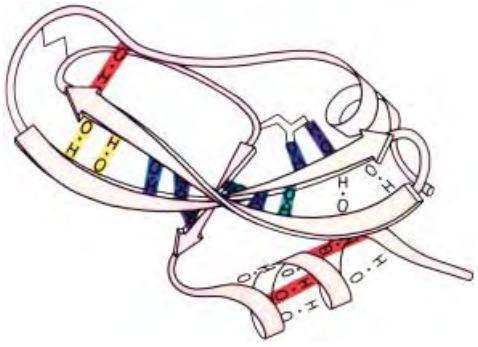


Figure 14. Sequence-specific resonance assignments for BPTI that were obtained using 1D ^1H NMR experiments.[30] The polypeptide backbone is shown, and the assigned residues are identified by indication of hydrogen bonds with their amide protons (the color code indicates variable exchange rates of the amide protons with the solvent; drawing by Jane Richardson, 1980).

3.3 Two-Dimensional (2D) NMR

With the introduction of 2D NMR experiments, and subsequently 3D and 4D NMR experiments, NMR studies of biological macromolecules evolved from intellectually stimulating science to a practical approach for protein structure determination. The foundations of multidimensional NMR have been presented in the Nobel Lecture by Richard R. Ernst.[31] Here, I only want to comment on two crucial consequences of multidimensional NMR for studies of proteins. First, 2D NMR enables the recording of selective interactions between pairs of hydrogen atoms, or groups of chemical-shift-equivalent hydrogen atoms, without selective irradiation of individual resonance lines. It thus enables a detailed analysis of the entire ^1H NMR spectrum of a protein, which contrasts with the 1D NMR situation of being limited to using only a small number of resolved lines at the periphery of the spectrum. Second, the dispersion of the resonances in a two-dimensional frequency plane affords greatly improved separation of the individual peaks. For example, in Figure 15

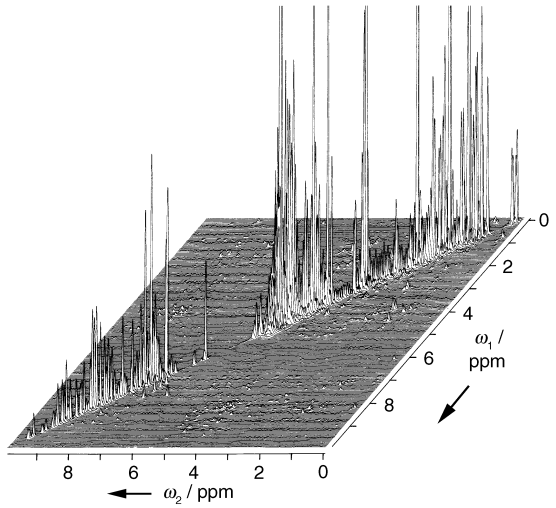


Figure 15. Two-dimensional (2D) [^1H,^1H]-NOE spectroscopy ([^1H,^1H]-NOESY). A stacked plot representation of a spectrum of the small protein bull seminal proteinase inhibitor IIA (BUSI IIA, $M \approx 6000$) is shown (500 MHz, 45 °C, H_2O solution).

the intense lines on the diagonal from the lower left to the upper right correspond to the 1D NMR spectrum, and the weak cross-peaks in the plane outside of the diagonal manifest selective NOEs between pairs of hydrogen atoms, which are represented in the NMR spectrum by two distinct (but not necessarily resolved) chemical shift positions along the diagonal.

The greatly improved separation of the individual cross-peaks is best seen in contour plots of 2D NMR spectra (Figure 16), which is the presentation used for detailed analysis. The 1D decoupling experiments for the identification of scalar spin–spin couplings were thus replaced by 2D correlation experiments, such as COSY, SECSY, and FOCSY, and the 1D NOE-difference experiments were replaced by 2D [^1H,^1H]-NOESY, which yielded similar NOE buildup curves for each NOESY cross-peak (Figure 17) as the 1D transient NOE technique (Figure 10).[4,32,33] Using these 2D ^1H NMR experiments, complete sequence-specific resonance assignments could be obtained for the protein BPTI (Figure 18).[34]

The NOESY–COSY connectivity diagram in Figure 19[4,35] makes use of the fact that standard 2D [^1H,^1H]-COSY and 2D [^1H,^1H]-NOESY spectra are symmetrical with respect to the diagonal peaks. Combining the upper left half of a NOESY spectrum with the lower right half of a COSY spectrum therefore enables a straightforward visualization of assignments by a succession of $d_{\alpha N}$ sequential NOEs and intraresidual H^N–H^α scalar coupling connectivities. The data were recorded in a freshly prepared solution of BPTI in ^2H_2O, where only the resonances of the slowly

 © 2003 Wiley-VCH Verlag GmbH & Co. KGaA, Weinheim

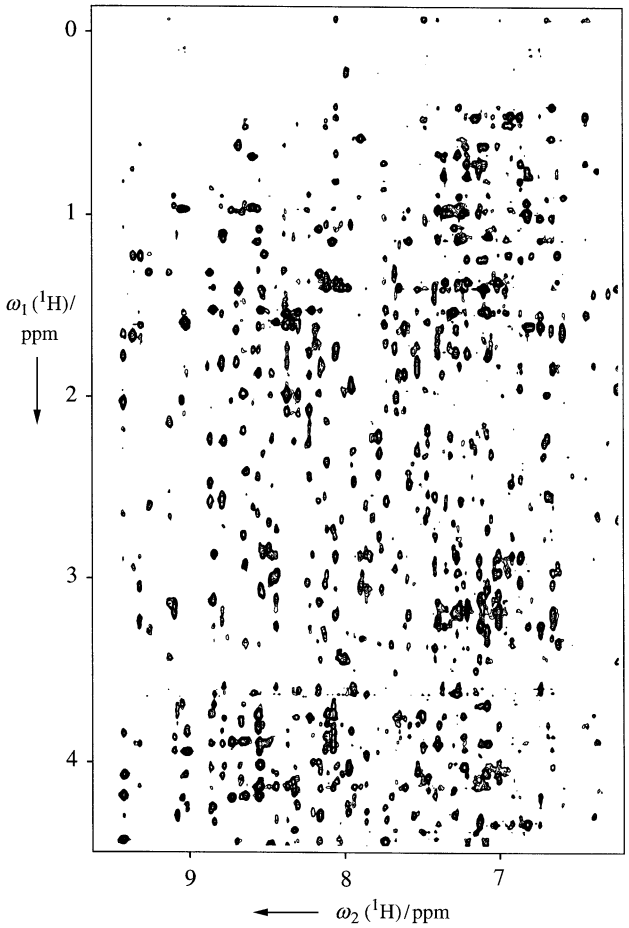


Figure 16. 2D [^{1}H,^{1}H]-NOESY spectrum of the plant pathogenesis-related protein P14A ($M \approx 15000$). A contour plot of the spectral region $\omega_1(^1H) = 0$–4.3 ppm, $\omega_2(^1H) = 6.3$–9.5 ppm (750 MHz, 30 °C, H_2O solution) is shown.

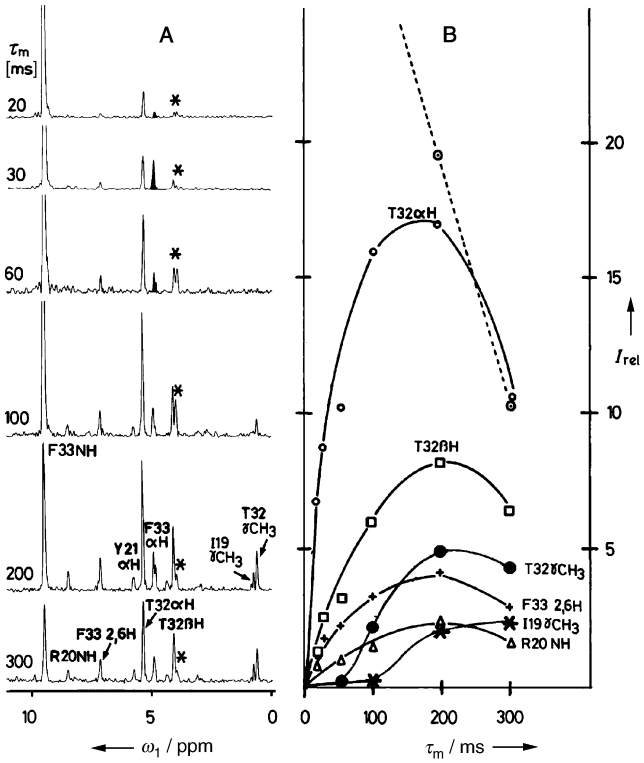


Figure 17. Measurement of NOE buildup curves using 2D [^{1}H,^{1}H]-NOESY experiments. A) Six NOESY spectra of BPTI recorded with different mixing times, τ_m. The same 1D cross-section along the ω_1 frequency axis through the diagonal peak of the Phe 33 amide proton is plotted for each spectrum. B) NOE buildup curves obtained from the analysis of the data in (A); same presentation as in Figure 10, with the relative intensities of the NOESY cross-peaks plotted versus the mixing time, τ_m, and the broken line representing the decay of the magnetization on the diagonal peak of the Phe 33 amide proton.

exchanging amide protons are seen.[35] The assignments start with the COSY cross-peak identified by a black square and, as indicated by the arrows, go clockwise to the sequentially preceding isoleucine residue, and counterclockwise to a sequence of four residues. It is customary that the data leading to the ^{1}H NMR assignments of a protein are collected in a plot versus the amino acid sequence (Figure 20). The figure shows that most of the sequential connectivities are independently documented by two or three different sequential NOEs,[4,36] and that possible remaining gaps in the assignment pathway are readily recognized in this presentation.

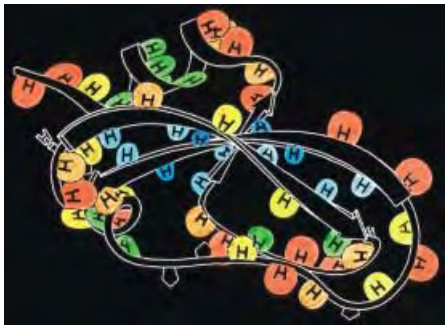


Figure 18. Complete sequence-specific resonance assignments for BPTI obtained using 2D NMR experiments.[34] Each assigned residue is identified by a colored patch around the amide proton (see also the legend to Figure 14; drawing by Jane Richardson, 1982).

3.4. Structural Interpretation of NOE Distance Constraints.

A polypeptide chain with 100 amino acid residues has a length of about 400 Å, whereas NOE-observable distances are shorter than about 5 Å. Observation of a NOE between a pair of hydrogen atoms with assigned chemical shift positions therefore enforces the formation of a ringlike structure (Figure 21). A successful structure determination generates three-dimensional arrangements of the polypeptide chain that simultaneously contain all the small and large circular structures imposed by the ensemble of all NOESY cross-peaks.

Partial structure determination has been obtained by an empirical approach for the identification of regular secondary structures in polypeptide chains, which relies on recognizing distinct patterns of NOEs.[4,37] For example, in Figure 20 a

 © 2003 Wiley-VCH Verlag GmbH & Co. KGaA, Weinheim

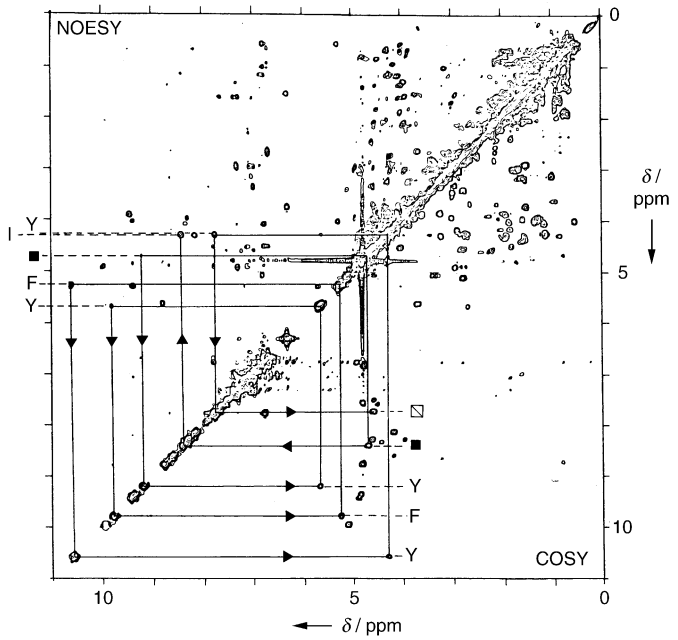


Figure 19. NOESY–COSY connectivity diagram for sequential ^{1}H NMR assignments, using the $d_{\alpha N}$ sequential NOEs. The data were recorded with BPTI in ^2H_2O solution (see text).

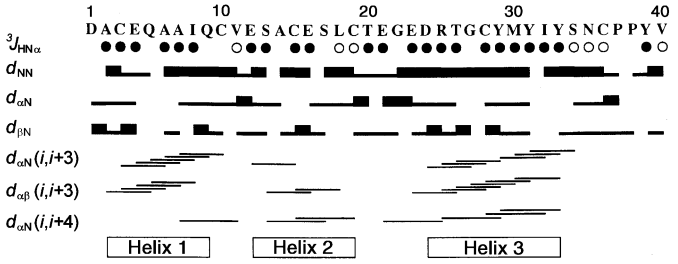


Figure 20. Standard presentation of ^{1}H NMR data leading to sequence-specific resonance assignments and the identification of regular secondary structures in proteins. Experimental data plotted versus the amino acid sequence are shown for the small pheromone protein Er-1 from *Euplotes raikovii* ($M \approx 4500$). $^3J_{HN\alpha}$ are scalar spin–spin coupling constants, with small and big values indicated by filled and empty circles, respectively. d_{NN}, $d_{\alpha N}$ and $d_{\beta N}$ are distances manifested in sequential NOEs, and strong and weak sequential NOEs are indicated by a thick or a thin line, respectively. Small values of the distances $d_{\alpha N}(i,i+3)$, $d_{\alpha\beta}(i,i+3)$, and $d_{\alpha N}(i,i+4)$ are observed by medium-range NOEs linking the given atom types between residues spaced as indicated in the parentheses and by the short horizontal lines. The locations of three α helices are indicated at the bottom.

succession of strong sequential d_{NN} NOEs in combination with the observation of medium-range NOEs in the same polypeptide segment identifies three α-helical structures, which are independently also indicated by successions of small values for the scalar spin–spin couplings $^3J_{HN\alpha}$.[4,38]

For the calculation of complete three-dimensional protein structures from NMR data,[39] it was quite clear from the outset that an input of quantitative NOE distance measurements would be difficult to obtain. The observed NOEs depend on the proton–proton distance, *r*, as well as on the effective rotational correlation times, τ_c [Eq. (1)]. Since for

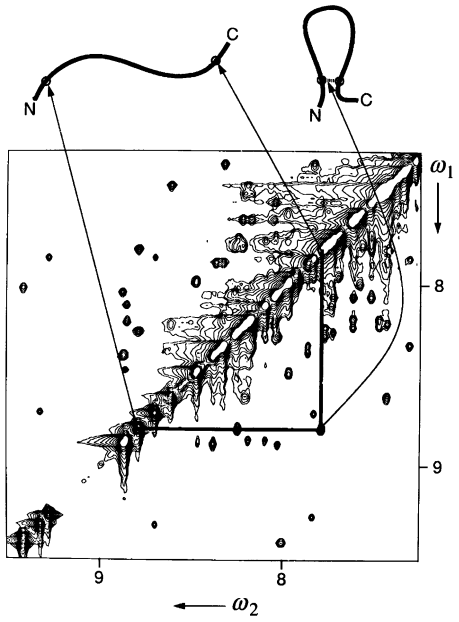


Figure 21. Scheme indicating the relations between an experimental 2D [^{1}H,^{1}H]-NOESY spectrum, a polypeptide with the chain ends indicated by N and C, sequence-specific assignments for two hydrogen atoms in the polypeptide chain indicated by circles, and the NOE upper distance constraint derived from the NOESY cross-peak connecting the chemical shift positions of two assigned hydrogen atoms (see text).

each pair of hydrogen atoms the effective τ_c-value is governed not only by the overall rotational molecular tumbling (Brownian motions), which depends on the size and shape of the protein as well as on the viscosity of the solvent, but can also be affected by intramolecular motions, $f(\tau_c)$ may vary for different pairs of hydrogen atoms in a protein molecule. Additional ambiguities could arise from partial quenching of individual ^{1}H–^{1}H NOEs by competitive spin-relaxation processes, for example, spin diffusion (Figure 11), chemical or conformational exchange, and interactions with other nuclear or electronic spins. Furthermore, as a result of rapid intramolecular mobility, a given NOE may be the result of sampling over a range of distances between the two hydrogen atoms of interest.[40]

In view of these intrinsic limitations for efficient quantitative NOE distance measurements, we decided to use a constant value of the correlation function, $f(\tau_c)$ [Eq. (1)], for all ^{1}H–^{1}H combinations in a protein, and to derive only upper limits on the ^{1}H–^{1}H distances from the NOE measurements. In practice, the input for a structure calculation then consists of allowed distance ranges, which are bounded by a NOE upper limit of 3.0–5.0 Å, depending on the intensity of the NOE, and a lower limit of 2.0 Å, which represents the sum of the van der Waals radii of the two NOE-connected hydrogen atoms. Although each individual entry in the input data thus has only limited precision, this procedure is robust and can conceptually account for the influence of intramolecular mobility in most of the situations that are commonly expected for the structured parts of globular proteins.

For the initial globular protein structure calculations from NMR data (Figure 22), we used a metric matrix distance

 © 2003 Wiley-VCH Verlag GmbH & Co. KGaA, Weinheim

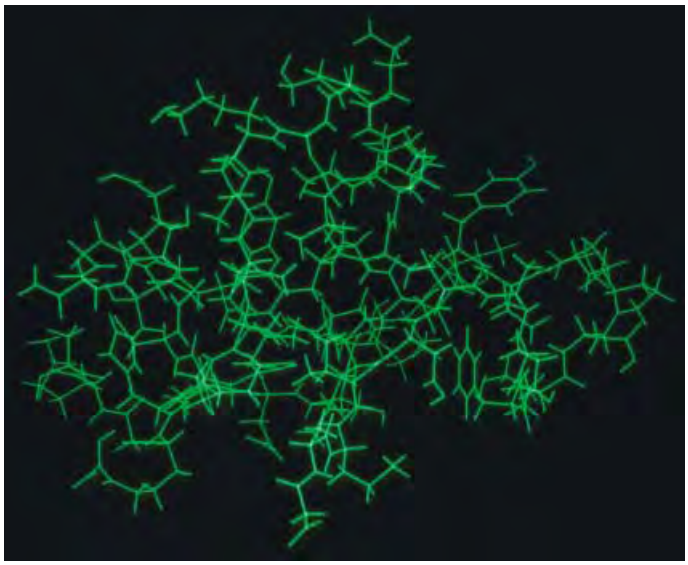


Figure 22. NMR structure of BUSI IIA.[43]

geometry algorithm to search for molecular geometries that are consistent with the ensemble of all experimentally determined NOE distance constraints.[41–43] Each such calculation ends with the minimization of an error function, and the residual error function value represents a straightforward measure for the success of having found a molecular geometry that satisfies the experimental input data. In view of the aforementioned distance-range format of the input, it is further of keen interest to evaluate the uniqueness of the calculated structure. To this end, the structure calculation is repeated with identical input data but different boundary conditions, and the uniqueness of the resulting NMR structure is judged from the tightness of the fit among the resulting ensemble of conformers. Typically, about 100 conformers are generated, and a subgroup of the 20 conformers with the smallest residual error function values is selected to represent the NMR structure of the protein. The average of the pairwise root-mean-square distances (RMSD) calculated for this bundle of conformers (Figure 1) is then taken as a measure for the precision of the structure determination. Visually, a tight fit of the bundle of conformers indicates regions where the structure is defined with high precision by the NMR data, whereas structurally disordered polypeptide segments show a large dispersion among the members of the bundle, as exemplified by the two chain ends of the *Antennapedia* homeodomain in Figure 1. In the absence of long-range NOE distance constraints, a properly functioning algorithm for the structure calculation will sample essentially all of the conformation space that is accessible with the given length of the polypeptide chain, as exemplified by the unstructured tail of the bovine prion protein in Figure 3 (bottom).

4. NMR in Structural Biology

4.1 Standard Protocol for NMR Structure Determination of Biological Macromolecules

The protocol for NMR structure determination includes the preparation of a homogeneous protein solution, the recording and handling of the NMR data sets, and the structural interpretation of the NMR data (Table 1). The techniques used in 1984 for the structure determination of bull seminal proteinase inhibitor IIA are listed in Table 1; the four steps of the structural interpretation (III in Table 1) were performed separately, although the result of the first round of constraint collection and structure calculation was subsequently used for additional checks on the sequence-specific resonance assignments as well as on the collection of conformational constraints. Since 1984, the protocol outlined in Table 1 has been used in over 3000 NMR structure determinations of proteins and nucleic acids, and greatly improved experimental techniques have been incorporated into this general scheme.

Table 1: Standard protocol for NMR structure determination of proteins.

Step[a]		BUSI IIA[b]
I	Sample preparation	Protein isolated from natural source; natural isotope distribution; 16 mM solutions in H_2O and in ^2H_2O
II	NMR spectroscopy	2D ^{1}H NMR
IIIa	Resonance assignments	Sequential NOEs
IIIb	Conformational constraints	[^{1}H,^{1}H]-NOEs, $^3J_{HN\alpha}$, $^3J_{\alpha\beta}$
IIIc	Structure calculation	Metric matrix distance geometry
IIId	Structure refinement	Restrained energy minimization

[a] The structural interpretation of the NMR data, step III, is somewhat arbitrarily divided up into four steps; in practice, one goes through multiple cycles of collection of conformational constraints (IIIb) and structure calculation (IIIc), and the completion of the sequence-specific assignments (IIIa) as well as the structure refinement (IIId) may also be part of this iterative approach. [b] This column lists the techniques used in the first structure determination of a globular protein in 1984.[43]

Major advances in the experimental techniques for NMR structure determination were spurred on by the introduction of methods for the production of recombinant proteins labeled with stable isotopes, in particular ^{13}C, ^{15}N, and ^{2}H.[44,45] For example, this opened the way for efficient use of heteronuclear NMR techniques with proteins, such as 3D [^{1}H,^{13}C,^{15}N]-triple resonance experiments, 3D ^{13}C- or ^{15}N-resolved [^{1}H,^{1}H]-NOESY (Figure 23),[46,47] and the use of heteronuclear filters.[48] Important advances have also been made with the methods of structure calculation, where the cpu time needed for the calculation of a small protein structure has been reduced from about one day in 1984[41,42] to a few seconds.[49] Currently, intense work is focused on the automation and combined execution of the individual steps in

 © 2003 Wiley-VCH Verlag GmbH & Co. KGaA, Weinheim

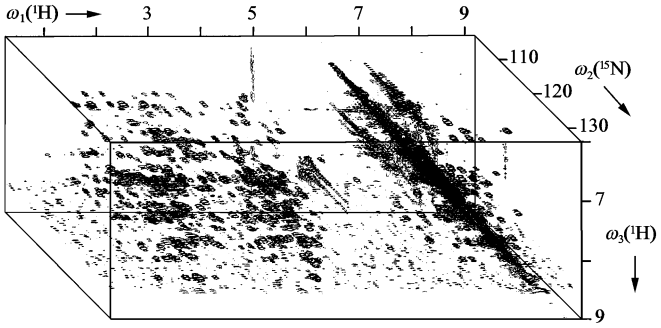


Figure 23. Three-dimensional (3D) ^{15}N-resolved [^{1}H,^{1}H]-NOESY spectrum (600 MHz, 28 °C, H_2O solution) of the DNA-binding domain of the P22 c2 repressor ($M \approx 10000$, uniformly ^{15}N-labeled).

the structural interpretation of the NMR data.[50,51] It is beyond the scope of this article to present in detail the wide range of beautiful novel experimental approaches developed by the community of macromolecular NMR spectroscopists during the past 15 years, which now enable studies with ever more complex systems (Figures 1–3).

4.2 Globular Protein Structures in Solution

The static picture of a protein molecule obtained from the standard protocol for structure determination (Table 1) typically shows variable precision of the structure determination along the polypeptide chain, as manifested by the variations in the closeness of the fit among the bundle of conformers used to represent the NMR structure (Figure 1). Even in proteins where the entire polypeptide chain is part of the global fold, increased disorder is observed toward the periphery of the surface side chains (Figure 24). This pronounced surface disorder, which typically also involves the ends of the polypeptide chain, is in most instances the only significant difference between corresponding globular protein structures in single crystals and in solution.[5] In part the increased disorder in solution arises because of a scarcity of packing constraints, when compared with the protein core, and a concomitant scarcity of NOE distance constraints. With the additional use of NMR spin-relaxation measurements,[24,28,33,52] one can distinguish between static disorder, which would then presumably arise from the scarcity of constraints, and dynamic disorder, with intramolecular motions on the nanosecond and sub-nanosecond time scale. Overall, quite independent of the dynamics issue, the observation of partially folded polypeptide chains in solution (Figures 1, 3 (bottom), and 24) is important complementary information to the data that can be obtained by studies in crystals. It is also the main reason why the quality of a NMR structure determination is not usually characterized by a single, global parameter.[4–6]

An important extension of the characterization of proteins in solution resulted from high-resolution NMR studies of protein hydration. Thereby the location of hydration waters is determined by the observation of NOEs between water protons and hydrogen atoms of the polypeptide chain.[53] Because of the dependence of the NOE on the inverse sixth power of the ^{1}H–^{1}H distance, only one layer of hydration water molecules is observed (Figure 25). For the hydration studies, the dependence of the NOE intensity on the correlation function describing the stochastic modulation of the dipole–dipole coupling between the interacting protons [Eq. (1)] has a key role. The value of $f(\tau_c)$ may be governed either by the Brownian rotational tumbling of the hydrated protein molecule, or by interruption of the dipolar interaction through translational diffusion of the water molecules relative to the protein surface, whichever is faster. On this basis it could be established that surface hydration of peptides and proteins is characterized by very short residence times of the water molecules in the hydration sites, in the range from about 20 to 300 picoseconds at 10 °C. This result presents an intuitive rationale for the generally observed dynamic disorder of the protein surface structure (Figure 24), and

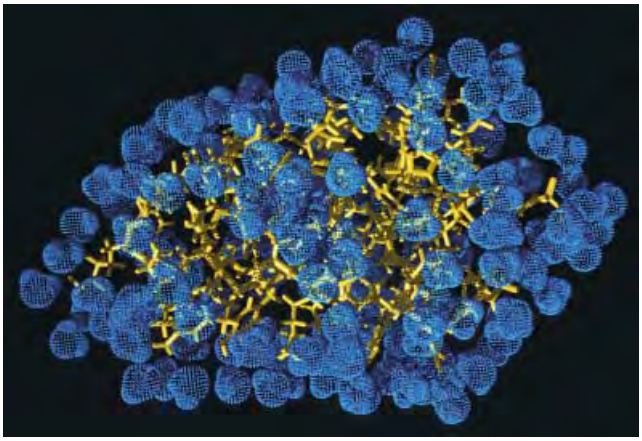


Figure 25. Molecular model of hydrated BPTI in H_2O solution. The drawing shows an all-heavy-atom-presentation of one of the conformers in Figure 24 (yellow) covered with a layer of hydration water molecules (dotted blue spheres).

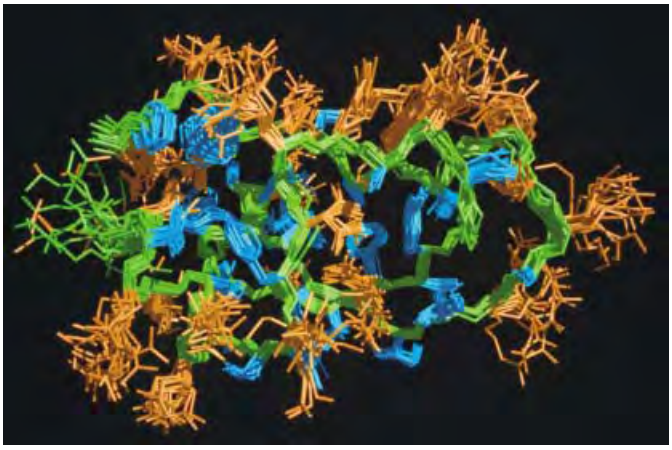


Figure 24. NMR structure of BPTI represented by a bundle of 20 conformers superimposed for best fit of the polypeptide backbone. The polypeptide backbone is green, core side-chains are blue, and solvent-accessible surface side chains are red.

© 2003 Wiley-VCH Verlag GmbH & Co. KGaA, Weinheim

indicates that the dehydration of the polypeptide surface will hardly ever be a rate-limiting step either in protein folding or in intermolecular interactions with proteins.

The BPTI crystal structure contains four interior hydration water molecules. These are an integral part of the molecular architecture and are inaccessible to the solvent in a rigid model of the three-dimensional structure (Figure 26).

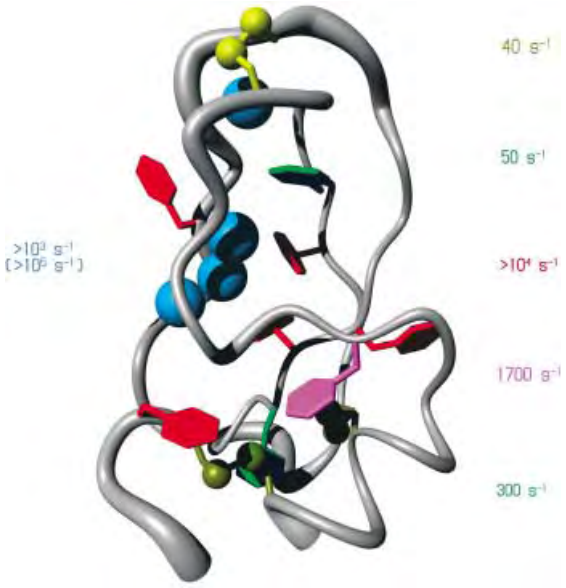


Figure 26. Intramolecular rate processes in BPTI. The polypeptide backbone is represented by a grey spline function through the α carbon positions, with the thickness of the line representing the spread of the bundle of 20 conformers in Figure 24. Individual rate processes and their frequencies are indicated with the following color code: green, magenta, and red: ring flips of phenylalanine and tyrosine; yellow: exchange between the *R* and *S* chiral forms of the disulfide bond at the top; cyan: interior hydration water molecules with indication of the exchange rates with the bulk water.

The chemical-shift dispersion anticipated for these four water molecules on the basis of the considerations in Figures 4–6 was not observed. This degeneracy of the chemical shifts of bound water and bulk water was found to be due to rapid exchange of water molecules in and out of the protein molecule, with an upper limit on the life-time of about 1 millisecond (see reference[53]; as indicated in Figure 26 by the number in parentheses, the actual life times for individual waters may be significantly shorter). Rapid exchange of interior hydration water molecules appears to be a general property of globular proteins, and was also observed for water molecules located at protein–DNA interfaces, for example, in the DNA complex with the *Antennapedia* homeodomain.

Another intriguing NMR observation of internal protein mobility are the 180° ring-flipping motions of phenylalanine and tyrosine.[54] Observation of these ring flips on the millisecond to microsecond timescale (Figure 26) was a genuine surprise for the following reasons: In the refined X-ray crystal structure of BPTI reported in 1975, the aromatic rings of phenylalanine and tyrosine are among the best-defined side chains, with the smallest temperature factors. In each ring the relative values of the temperature factors for the individual atoms increase toward the periphery, so that the largest positional uncertainty is indicated for the peripheral ζ-carbon atom on the symmetry axis through the C^{β}–C^{γ} bond, rather than for the four δ- and ε-ring carbon atoms, which undergo extensive movements during the ring flips. Theoretical studies then resolved this apparent contradiction: The crystallographic temperature factors sample multiple rotation states about the C^{α}–C^{β} bond, but they do not manifest the ring flips because the populations of all non-equilibrium rotational states about the C^{β}–C^{γ} bond are vanishingly small. Although the flipping motions about the C^{β}–C^{γ} bond have low frequencies (Figure 26), they are very rapid 180° rotations connecting two indistinguishable equilibrium orientations of the ring.

Similar to the exchange of internal hydration waters, the ring-flip phenomenon is a general feature of globular proteins, manifesting ubiquitous low-frequency internal motions that have activation energies of 60–100 kJ mol^{-1}, amplitudes larger than 1 Å, activation volumes of about 50 Å^3, and involve concerted displacement of numerous groups of atoms. Combined with sequence-specific NMR assignments, these experiments provide high spatio-temporal resolution for the description of rate processes in proteins. In Figure 26, this is illustrated by a mapping of the frequencies for ring flips and water exchange onto the NMR structure of BPTI.

In addition to the ring flips and the exchange of internal hydration water molecules, Figure 26 includes data on the exchange of a disulfide bond between the *R* and *S* chiral states. In contrast to the other two phenomena, this rate process connects two different molecular structures.

Although all the data collected in Figure 26 have been known for more than a decade, and some of them for nearly three decades, no widely accepted functional interpretation of these low-frequency motional processes has been advanced. The same holds for the conformational equilibria manifested by the protection factors governing the amide proton exchange rates in folded proteins (Figures 14 and 18). Quite possibly these NMR measurements are ahead of their times, and represent a source for future novel insights into structure–function correlations in proteins.

5. Outlook to NMR Applications in Structural and Functional Proteomics

With the availability of a rapidly increasing number of completely sequenced genomes, new challenges arise for the methods used for three-dimensional structure determination. On the one hand, "structural genomics" initiatives in several leading research centers focus on the development of technology for high-throughput structure determination to generate a comprehensive atlas of protein folds, so that remaining gaps could be filled by structure prediction methods. There is clearly a lot of room to further enhance the efficiency of each step of the NMR structure determination procedure (Table 1). On the other hand, we face the situation that newly determined protein structures should

 © 2003 Wiley-VCH Verlag GmbH & Co. KGaA, Weinheim

enable us to predict novel functions, whereas in classical structural biology one encounters more typically the challenge of rationalizing known functions on the basis of the three-dimensional structure. This section describes some recent work in our laboratory that may eventually contribute to future strategies for the discovery of new physiological functions from molecular structure data.

It has been widely recognized that supplementing the determination of new protein folds with data on intermolecular interactions may provide a key for the identification of unknown gene functions. Since efficient use of conventional NMR spectroscopy in solution had been limited to particle sizes with molecular weights up to about 30000 Da (Figure 27, left), a new challenge for solution NMR techniques then arose from the fact that the supramolecular structures resulting from interactions of two or several proteins, or of other macromolecular components, tend to have high molecular weights. Although a 30000-Dalton size limit allowed work with a large pool of physiologically interesting proteins, it was hardly compatible with extensive use of NMR for studies of such supramolecular structures. For example, this size limit would severely narrow down the range of potential receptor systems accessible to NMR in drug discovery projects,[55,56] restrict studies of protein–nucleic acid complexes (Figure 2) to a small number of systems with modest size, and prevent the use of solution NMR for studies of membrane proteins, since these have to be reconstituted and solubilized in mixed micelles with surfactants or lipids (Figure 27, right).

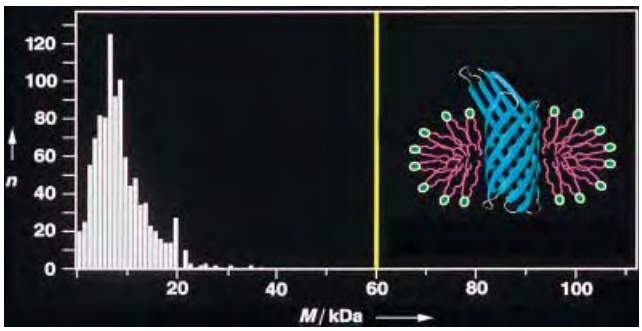


Figure 27. NMR structure determination and molecular weight. The horizontal axis covers the molecular weight range 0–110000 Da. The left side shows the molecular weight distribution of the NMR structures in the protein databank (December 2000). On the right, the structure of the protein OmpX from *E. coli* ($M \approx 18000$) in DHPC micelles ($M \approx 70000$ for the mixed micelles) indicates along the horizontal axis the approximate molecular weight range for NMR structure determination of mixed micelles with membrane proteins that is presently accessible with the NMR techniques of Figures 28–30.

A few years ago this limitation was successfully challenged, since the size range for applications of solution NMR techniques could be significantly extended through the introduction of transverse relaxation-optimized spectroscopy (TROSY).[57] As an illustration, Figure 28 shows a [^{15}N,^{1}H]-TROSY correlation spectrum of a membrane protein reconstituted in detergent micelles. Sharp, well-separated peaks are obtained in spite of the large size of the mixed micelles (Figure 27, right). With the use of the TROSY principle, the more complex NMR experiments needed for a structure determination with [^{2}H,^{13}C,^{15}N]-labeled proteins can also be obtained with high quality,[58] so that solution NMR can now be used for de novo membrane protein structure determination.[59]

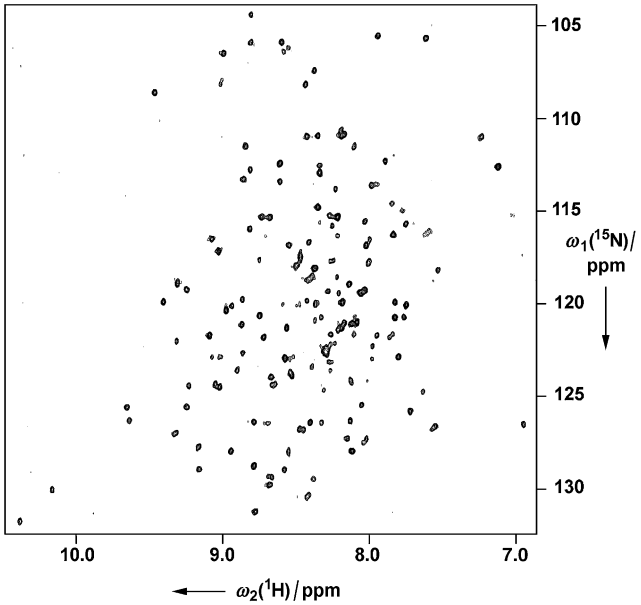


Figure 28. Transverse relaxation-optimized [^{15}N,^{1}H]-correlation spectroscopy (TROSY). A spectrum of the uniformly ^{2}H- and ^{15}N-labelled membrane protein OmpX reconstituted in DHPC micelles is shown (750 MHz, 30 °C, H_2O solution).

The improved quality of the NMR spectra of large structures with the use of TROSY can be qualitatively rationalized by the following considerations. As has previously been indicated in the discussion on NOEs [Section 3.1, Eq. (1)], the appearance of solution NMR spectra is intimately related to the effective correlation time, τ_c, which characterizes the thermal motions of the molecule considered. The increase of the τ_c values in larger structures results in line broadening due to rapid transverse spin relaxation. For example, if the spectrum of Figure 28 had been recorded with conventional NMR techniques, most of the resonance lines would not be individually resolved due to severe line broadening, and one would have experienced a severe loss of sensitivity for detection of the NMR signals. The reduced sensitivity can be readily appreciated by examination of the free induction decays (FID) in the time domain data. Figure 29 shows that rapid loss of magnetization in a conventional NMR experiment with a large structure can be slowed down by the use of TROSY, which corresponds to the reduction of the line width in the frequency domain spectrum.

The impact on the sensitivity is visualized in Figure 30 with a simplified scheme for a 2D correlation experiment, which includes two magnetization transfer periods, and the evolution and acquisition periods. During evolution and acquisition, the system is not subjected to external perturbations, and loss of magnetization occurs at a rate determined by the transverse relaxation time. It is readily apparent that rapid loss of magnetization in a conventional NMR experiment

 © 2003 Wiley-VCH Verlag GmbH & Co. KGaA, Weinheim

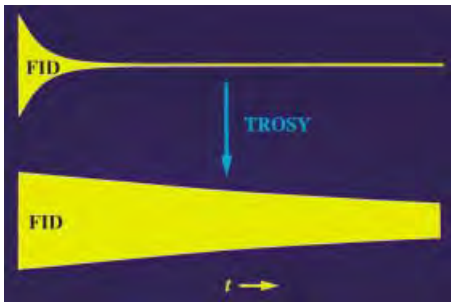


Figure 29. Schematic drawing of the free induction decay (FID) for a large protein with and without the use of TROSY. The period covered along the time axis is of the order of 100 ms. The FID represents the primary recording of the NMR data in the time domain, from which the frequency domain spectrum (for example, Figures 15, 16, and 28) is obtained by Fourier transformation.[31,33]

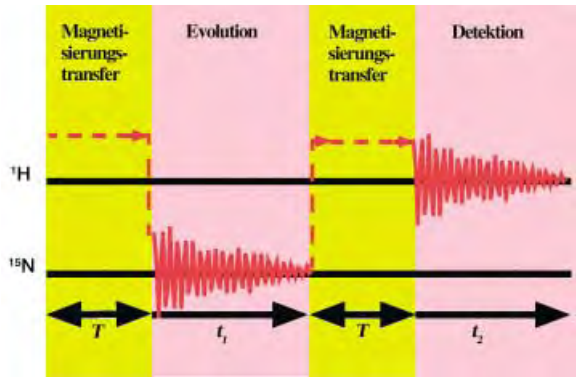


Figure 30. Basic features of a 2D [^{15}N,^{1}H]-correlation experiment. On the left, ^{1}H and ^{15}N indicate radio-frequency channels for irradiation of these isotopes. Yellow shading identifies the $^1H \rightarrow {}^{15}N$ and $^{15}N \rightarrow {}^1H$ magnetization transfer periods, T, and pink shading the evolution and acquisition periods, t_1 and t_2, respectively. During t_1 and t_2 the decay of the magnetization (FID) is schematically indicated. The overall duration of the experiment, $2T+t_1+t_2$, can be of the order of 10 to 1000 milliseconds, depending on the size of the structure studied and the intended purpose of the measurement.

(upper trace in Figure 29) leads to weak or even vanishing signal intensity at the end of the evolution period, and accordingly the sensitivity for detection of the signal during the acquisition period is very low. In contrast, one can obtain much improved sensitivity with the use of TROSY (lower trace in Figure 29), since plenty of signal intensity will be preserved at the end of the evolution period, and the signal can be recorded with high signal-to-noise ratio during a large portion of the acquisition period. Following such considerations for minimizing the loss of magnetization during all four time periods indicated in Figure 30, and with additional optimization of the magnetization transfer techniques,[60] solution NMR spectra have by now been recorded for structures with molecular weights up to 870000. In the spectrum of the co-chaperonin GroES bound to the chaperonin GroEL (Figure 31), resonance lines that provided novel information on structural and dynamic features of the GroES–GroEL interface are colored in red and blue.[61]

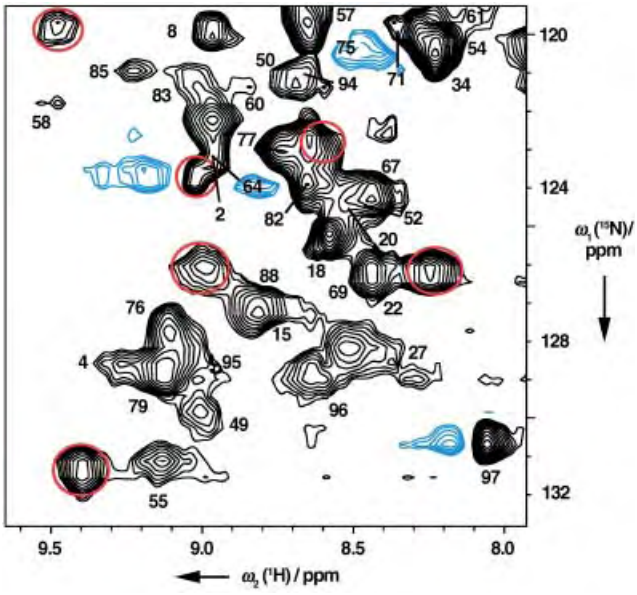


Figure 31. [^{15}N,^{1}H]-Correlation spectrum of the co-chaperonin GroES ($M \approx 70000$) bound to the chaperonin GroEL ($M \approx 800000$). The spectrum was recorded with a [^{15}N,^{1}H]-CRIPT-TROSY experiment.[60,61] The red and blue coloring is explained in the text.

The principal contributions to the rate of transverse spin-relaxation can be traced to two different types of interactions, that is, dipole–dipole coupling of the observed spin with other nearby spins and chemical-shift anisotropy (CSA).[28] These interactions are modulated by the stochastic rotational motions in solution, and as a consequence the rate of transverse relaxation increases for larger structures with slower Brownian motions. TROSY exploits constructive interference between the two relaxation mechanisms, and actually uses CSA relaxation at high fields to cancel the dipolar relaxation.[57] In this way the appearance of the NMR spectrum is effectively uncoupled from the Brownian motions, which then enables the recording of solution NMR spectra with large structures.

It remains to be seen how these new NMR techniques will be employed most profitably in the future. Intriguing possibilities include that NMR can now be employed in drug discovery projects with very large receptors.[55,56] Combined with suitable isotope-labelling strategies, TROSY-based NMR techniques have also been shown to provide a powerful approach for investigations of intermolecular interactions in supramolecular structures with two or several macromolecular components.[62,63] In these applications, a detailed structural interpretation of the NMR data will in most instances be dependent on the availability of an independently determined atomic-resolution structure for one or multiple components, which may have been obtained either by NMR in solution or by diffraction methods in single crystals. Applications of the new NMR techniques for de novo determination of large structures appears to be particularly attractive for, but not limited to, nucleic acid–protein complexes and small membrane proteins reconstituted in soluble detergent or lipid micelles.

 © 2003 Wiley-VCH Verlag GmbH & Co. KGaA, Weinheim

The characterization of a membrane protein structure has also been extended to include the detergents in the mixed micelles (Figure 32),[64] since the areas of the protein surface in contact with the detergent molecules could be delineated

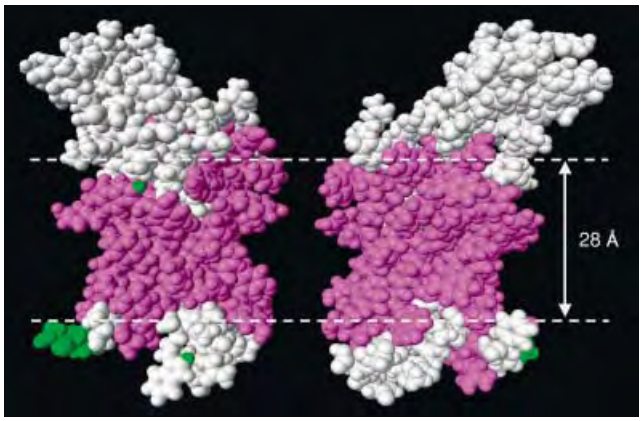


Figure 32. NMR structure of the membrane protein OmpX reconstituted in DHPC micelles. Front and back views of a space-filling model of OmpX are shown, with pink and green coloring identifying the surface area of the protein that is in contact with DHPC molecules in the mixed micelles. The two broken horizontal lines indicate the thickness of the lipid phase in the *E. coli* cell membrane.

by the observation of intermolecular NOEs between hydrogen atoms of the protein and the detergent. In these particular mixed micelles this surface area is virtually identical to the protein surface in contact with the lipid phase in the biological membrane. Since this leaves both ends of the β barrel of OmpX freely accessible to the aqueous solvent, this reconstitution system should also be suitable for functional studies of the membrane protein with NMR.

This last section of my presentation certainly indicates only a narrow range of potential further developments of solution NMR techniques and their applications in structural biology and structural proteomics. I look forward with great expectations to the future evolution of this awesome and beautiful technique, which has given me so many years of joy and excitement in studies of the molecules of life.

From 1970 through 2002, 229 students, postdoctoral research associates, and technical and administrative staff worked with me at the ETH Zürich. I am deeply indebted to all of them for their enthusiasm and dedication, which resulted in the work summarized in this article. Their names and individual contributions can be found in the reference list. Although human minds stand behind all progress in science, the success of our research projects also depended critically on financial resources. I would like to acknowledge the ETH Zürich, the Swiss National Science Foundation, the Kommission für Technologie und Innovation (KTI), Bruker-Biospin AG, and the Scripps Research Institute in La Jolla, CA, USA, for their support.

Received: March 19, 2003 [A595]

[1] "The Structure of the *Antennapedia* Homeodomain Determined by NMR Spectroscopy in Solution: Comparison with Prokaryotic Repressors": Y. Q. Qian, M. Billeter, G. Otting, M. Müller, W. J. Gehring, K. Wüthrich, *Cell* **1989**, *59*, 573 – 580.
[2] "Protein–DNA Contacts in the Structure of a Homeodomain–DNA Complex Determined by Nuclear Magnetic Resonance Spectroscopy in Solution": G. Otting, Y. Q. Qian, M. Billeter, M. Müller, M. Affolter, W. J. Gehring, K. Wüthrich, *EMBO J.* **1990**, *9*, 3085 – 3092.
[3] "NMR Structure of the Bovine Prion Protein": F. Lopez Garcia, R. Zahn, R. Riek, K. Wüthrich, *Proc. Natl. Acad. Sci. USA* **2000**, *97*, 8334 – 8399.
[4] K. Wüthrich, *NMR of Proteins and Nucleic Acids*, Wiley, New York, **1986**.
[5] "NMR—This Other Method for Protein and Nucleic Acid Structure Determination": K. Wüthrich, *Acta Crystallogr. Sect. D* **1995**, *51*, 249 – 270.
[6] K. Wüthrich, *NMR in Structural Biology: A Collection of Papers by Kurt Wüthrich*, World Scientific, Singapore, **1995**.
[7] "The Way to NMR Structures of Proteins": K. Wüthrich, *Nat. Struct. Biol* **2001**, *8*, 923 – 925.
[8] "Nuclear Magnetic Resonance Spectra of Proteins": M. Saunders, A. Wishnia, *Ann. N. Y. Acad. Sci.* **1958**, *70*, 870 – 874.
[9] "Proton Magnetic Resonance Spectra of Amino Acids": O. Jardetzky, C. D. Jardetzky, *J. Biol. Chem.* **1958**, *233*, 383 – 387.
[10] "Nuclear Magnetic Resonance Studies of Proteins": A. Kowalsky, *J. Biol. Chem.* **1962**, *237*, 1807 – 1819.
[11] "Proton Magnetic Resonance Spectra of Some Proteins": M. Mandel, *J. Biol. Chem.* **1965**, *240*, 1586 – 1592.
[12] "Manifestations of the Tertiary Structures of Proteins in High-Frequency Nuclear Magnetic Resonance": C. C. McDonald, W. D. Phillips, *J. Am. Chem. Soc.* **1967**, *89*, 6332 – 6341.
[13] "High Resolution Proton Nuclear Magnetic Resonance Spectroscopy of Cytochrome *c*": K. Wüthrich, *Proc. Natl. Acad. Sci. USA* **1969**, *63*, 1071 – 1078.
[14] "The Absence of "Heme–Heme" Interactions in Hemoglobin": R. G. Shulman, S. Ogawa, K. Wüthrich, T. Yamane, J. Peisach, W. E. Blumberg, *Science* **1969**, *165*, 251 – 257.
[15] "NMR Studies of Hemoglobins VI: Heme Proton Spectra of Human Deoxyhemoglobins and Their Relevance to the Nature of Co-operative Oxygenation of Haemoglobin": D. G. Davis, T. R. Lindstrom, N. H. Mock, J. J. Baldassare, S. Charache, R. T. Jones, C. Ho, *J. Mol. Biol.* **1971**, *60*, 101 – 111.
[16] "Paramagnetic Proton NMR Shifts of Metmyoglobin, Methemoglobin, and Hemin Derivatives": R. J. Kurland, D. G. Davis, C. Ho, *J. Am. Chem. Soc.* **1968**, *90*, 2700 – 2701.
[17] "Structural Studies of Hemes and Hemoproteins by Nuclear Magnetic Resonance Spectroscopy": K. Wüthrich, *Struct. Bonding (Berlin)* **1970**, *8*, 53 – 121.
[18] "Electronic Structure of Cyanide Complexes of Hemes and Heme Proteins": R. G. Shulman, S. H. Glarum, M. Karplus, *J. Mol. Biol.* **1971**, *57*, 93 – 115.
[19] K. Wüthrich, *NMR in Biological Research: Peptides and Proteins*, North Holland, Amsterdam, **1976**.
[20] J. H. Noggle, R. E. Schirmer, *The Nuclear Overhauser Effect*, Academic Press, New York, **1971**.
[21] "Homonuclear INDOR Spectroscopy as a Means of Simplifying and Analyzing Proton Magnetic Resonance Spectra of Peptides and as a Basis for Determining Secondary and Tertiary Conformations of Complex Peptides": W. A. Gibbons, H. Alms, R. S. Bockman, H. R. Wyssbrod, *Biochemistry* **1972**, *11*, 1721 – 1725.
[22] "Double Resonance NMR Observation of Electron Exchange Between Ferri- and Ferrocytochrome *c*": R. K. Gupta, A. G. Redfield, *Science* **1970**, *169*, 1204 – 1206.

 © 2003 Wiley-VCH Verlag GmbH & Co. KGaA, Weinheim

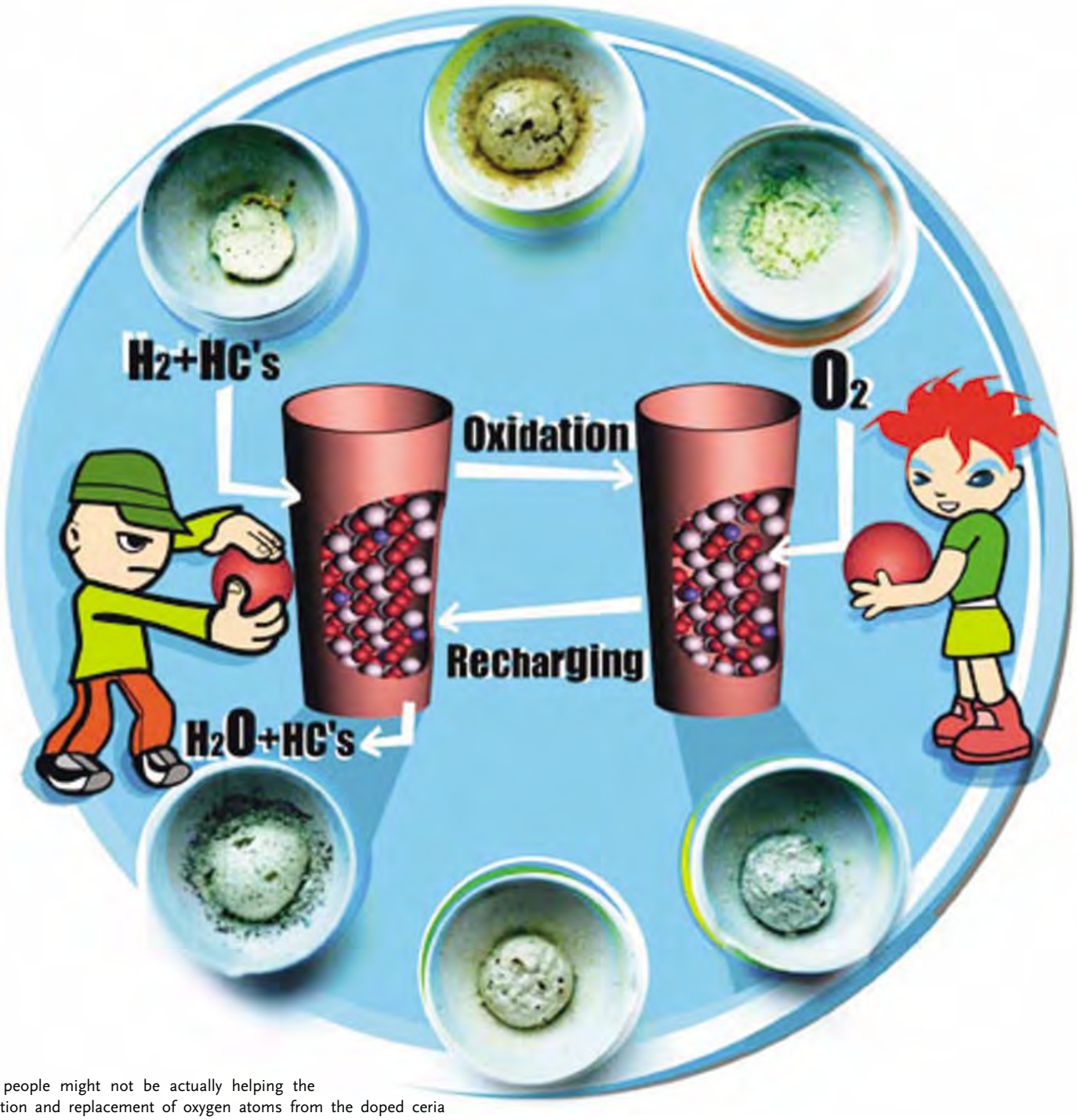
[23] "Negative Nuclear Overhauser Effects as Probes of Macromolecular Structure": P. Balaram, A. A. Bothner-By, J. Dadok, *J. Am. Chem. Soc.* **1972**, *94*, 4015 – 4017.
[24] "Relaxation Processes in a System of Two Spins": I. Solomon, *Phys. Rev.* **1955**, *99*, 559 – 565..
[25] "Proton Magnetic Relaxation and Spin Diffusion in Proteins": A. Kalk, H. J. C. Berendsen, *J. Magn. Reson.* **1976**, *24*, 343 – 366.
[26] "Transient Proton–Proton Overhauser Effects in Horse Ferrocytochrome *c*": S. L. Gordon, K. Wüthrich, *J. Am. Chem. Soc.* **1978**, *100*, 7094 – 7096.
[27] "Truncated Driven Nuclear Overhauser Effect (TOE): a New Technique for Studies of Selective ^{1}H–^{1}H Overhauser Effects in the Presence of Spin Diffusion": G. Wagner, K. Wüthrich, *J. Magn. Reson.* **1979**, *33*, 675 – 680.
[28] A. Abragam, *Principles of Nuclear Magnetism*, Clarendon Press, Oxford, **1961**.
[29] "Evolutionary Change of the Heme *c* Electronic Structure: Ferricytochrome *c*-551 from *Pseudomonas Aeruginosa* and Horse Heart Ferricytochrome *c*": R. M. Keller, K. Wüthrich, *Biochem. Biophys. Res. Commun.* **1978**, *83*, 1132 – 1139.
[30] "Individual Assignments of Amide Proton Resonances in the Proton NMR Spectrum of the Basic Pancreatic Trypsin Inhibitor": A. Dubs, G. Wagner, K. Wüthrich, *Biochim. Biophys. Acta* **1979**, *577*, 177 – 194.
[31] "Nuclear Magnetic Resonance Fourier Transform Spectroscopy": R. R. Ernst, *Angew. Chem.* **1992**, *104*, 817 – 836; *Angew. Chem. Int. Ed. Engl.* **1992**, *31*, 805 – 823.
[32] "Homonuclear Two-Dimensional ^{1}H NMR of Proteins: Experimental Procedures": G. Wider, S. Macura, A. Kumar, R. R. Ernst, K. Wüthrich, *J. Magn. Reson.* **1984**, *56*, 207 – 234.
[33] R. R. Ernst, G. Bodenhausen, A. Wokaun, *Principles of Nuclear Magnetic Resonance in One and Two Dimensions*, Oxford University Press, Oxford, **1987**.
[34] "Sequential Resonance Assignments in Protein ^{1}H Nuclear Magnetic Resonance Spectra: Basic Pancreatic Trypsin Inhibitor": G. Wagner, K. Wüthrich, *J. Mol. Biol.* **1982**, *155*, 347 – 366.
[35] "Systematic Application of Two-Dimensional ^{1}H Nuclear Magnetic Resonance Techniques for Studies of Proteins 2: Combined Use of Correlated Spectroscopy and Nuclear Overhauser Spectroscopy for Sequential Assignments of Backbone Resonances and Elucidation of Polypeptide Secondary Structures": G. Wagner, Anil-Kumar, K. Wüthrich, *Eur. J. Biochem.* **1981**, *114*, 375 – 384.
[36] "Sequential Resonance Assignments in Protein ^{1}H Nuclear Magnetic Resonance Spectra: Computation of Sterically Allowed Proton–Proton Distances and Statistical Analysis of Proton–Proton Distances in Single Crystal Protein Conformations": M. Billeter, W. Braun, K. Wüthrich, *J. Mol. Biol.* **1982**, *155*, 321 – 346.
[37] "Polypeptide Secondary Structure Determination by Nuclear Magnetic Resonance Observation of Short Proton–Proton Distances": K. Wüthrich, M. Billeter, W. Braun, *J. Mol. Biol.* **1984**, *180*, 715 – 740.
[38] "Calibration of the Angular Dependence of the Amide Proton–C^α Proton Coupling Constants, $^3J_{HN\alpha}$, in a Globular Protein: Use of $^3J_{HN\alpha}$ for Identification of Helical Secondary Structure": A. Pardi, M. Billeter, K. Wüthrich, *J. Mol. Biol.* **1984**, *180*, 741 – 751.
[39] "Sequential Resonance Assignments as a Basis for Determination of Spatial Protein Structures by High Resolution Proton Nuclear Magnetic Resonance": K. Wüthrich, G. Wider, G. Wagner, W. Braun, *J. Mol. Biol.* **1982**, *155*, 311 – 319.
[40] "Combined Use of Proton–Proton Overhauser Enhancements and a Distance Geometry Algorithm for Determination of Polypeptide Conformations: Application to Micelle-Bound Glucagon": W. Braun, C. Bösch, L. R. Brown, N. Gō, K. Wüthrich, *Biochim. Biophys. Acta* **1981**, *667*, 377 – 396.
[41] "A Distance Geometry Program for Determining the Structures of Small Proteins and Other Macromolecules from Nuclear Magnetic Resonance Measurements of Intramolecular ^{1}H–^{1}H Proximities in Solution": T. F. Havel, K. Wüthrich, *Bull. Math. Biol.* **1984**, *46*, 673 – 698.
[42] "An Evaluation of the Combined Use of Nuclear Magnetic Resonance and Distance Geometry for the Determination of Protein Conformations in Solution": T. F. Havel, K. Wüthrich, *J. Mol. Biol.* **1985**, *182*, 281 – 294.
[43] "Solution Conformation of Proteinase Inhibitor IIA from Bull Seminal Plasma by ^{1}H Nuclear Magnetic Resonance and Distance Geometry": M. P. Williamson, T. F. Havel, K. Wüthrich, *J. Mol. Biol.* **1985**, *182*, 295 – 315.
[44] "Prospects for NMR of Large Proteins": G. Wagner, *J. Biomol. NMR* **1993**, *3*, 375 – 385.
[45] "Solution NMR Spectroscopy Beyond 25 kDa": L. E. Kay, K. H. Gardner, *Curr. Opin. Struct. Biol.* **1997**, *7*, 564 – 570.
[46] "Methodological Advances in Protein NMR": A. Bax, S. Grzesiek, *Acc. Chem. Res.* **1993**, *26*, 131 – 138.
[47] "Technical Aspects of NMR Spectroscopy with Biological Macromolecules and Studies of Hydration in Solution": G. Wider, *Prog. Nucl. Magn. Reson. Spectrosc.* **1998**, *32*, 193 – 275.
[48] "Heteronuclear Filters in Two-Dimensional [^{1}H,^{1}H]-NMR Spectroscopy: Combined Use with Isotope Labelling for Studies of Macromolecular Conformation and Intermolecular Interactions": G. Otting, K. Wüthrich, *Q. Rev. Biophys.* **1990**, *23*, 39 – 96.
[49] "Structure Calculation of Biological Macromolecules from NMR Data": P. Güntert, *Q. Rev. Biophys.* **1998**, *31*, 145 – 237. .
[50] "Automated Analysis of NMR Assignments and Structures for Proteins": H. N. B. Moseley, G. T. Montelione, *Curr. Opin. Struct. Biol.* **1999**, *9*, 635 – 642.
[51] "Protein NMR Structure Determination with Automated NOE Identification in the NOESY Spectra Using the New Software ATNOS": T. Herrmann, P. Güntert, K. Wüthrich, *J. Biomol. NMR* **2002**, *24*, 171 – 189.
[52] "Semi-Classical Nuclear Spin Relaxation Theory Revisited for Use with Biological Macromolecules": P. Luginbühl, K. Wüthrich, *Prog. Nucl. Magn. Reson. Spectr.* **2002**, *40*, 199 – 247.
[53] "Protein Hydration in Aqueous Solution": G. Otting, E. Liepinsh, K. Wüthrich, *Science* **1991**, *254*, 974 – 980.
[54] "NMR Investigations of the Dynamics of the Aromatic Amino Acid Residues in the Basic Pancreatic Trypsin Inhibitor": K. Wüthrich, G. Wagner, *FEBS Lett.* **1975**, *50*, 265 – 268.
[55] "Discovering High-Affinity Ligands for Proteins: SAR by NMR": S. B. Shuker, P. J. Hajduk, R. P. Meadows, S. W. Fesik, *Science* **1996**, *274*, 1531 – 1534.
[56] "NMR in Drug Discovery": M. Pellecchia, D. S. Sem, K. Wüthrich, *Nat. Rev. Drug Discovery* **2002**, *1*, 211 – 219.
[57] "Attenuated T_2 Relaxation by Mutual Cancellation of Dipole–Dipole Coupling and Chemical Shift Anisotropy Indicates an Avenue to NMR Structures of Very Large Biological Macromolecules in Solution": K. Pervushin, R. Riek, G. Wider, K. Wüthrich, *Proc. Natl. Acad. Sci. USA* **1997**, *94*, 12366 – 12371.
[58] "TROSY in Triple-Resonance Experiments: New Perspectives for Sequential NMR Assignment of Large Proteins": M. Salzmann, K. Pervushin, G. Wider, H. Senn, K. Wüthrich, *Proc. Natl. Acad. Sci. USA* **1998**, *95*, 13585 – 13590.
[59] "Solution NMR Studies of the Integral Membrane Proteins OmpX and OmpA from *Escherichia coli*": C. Fernández, C. Hilty, S. Bonjour, K. Adeishvili, K. Pervushin, K. Wüthrich, *FEBS Lett.* **2001**, *504*, 173 – 178.
[60] "Polarization Transfer by Cross-Correlated Relaxation in Solution NMR with Very Large Molecules": R. Riek, G. Wider, K. Pervushin, K. Wüthrich, *Proc. Natl. Acad. Sci. USA* **1999**, *96*, 4918 – 4923.
[61] "NMR Analysis of a 900 K GroEL–GroES Complex": J. Fiaux, E. Bertelsen, A. Horwich, K. Wüthrich, *Nature* **2002**, *418*, 207 – 211.

 © 2003 Wiley-VCH Verlag GmbH & Co. KGaA, Weinheim

[62] "Pilus Chaperone FimC–Adhesin FimH Interactions Mapped by TROSY-NMR": M. Pellecchia, P. Sebbel, U. Hermanns, K. Wüthrich, R. Glockshuber, *Nat. Struct. Biol.* **1999**, *6*, 336–339.
[63] "TROSY-NMR Reveals Interaction between ERp57 and the Tip of the Calreticulin P-Domain": E. M. Frickel, R. Riek, I. Jelesarov, A. Helenius, K. Wüthrich, L. Ellgaard, *Proc. Natl. Acad. Sci. USA* **2002**, *99*, 1954–1959.
[64] "Lipid–Protein Interactions in DHPC Micelles Containing the Integral Membrane Protein OmpX Investigated by NMR Spectroscopy": C. Fernández, C. Hilty, G. Wider, K. Wüthrich, *Proc. Natl. Acad. Sci. USA* **2002**, *99*, 13533–13537.

 © 2003 Wiley-VCH Verlag GmbH & Co. KGaA, Weinheim

Communications



Little people might not be actually helping the extraction and replacement of oxygen atoms from the doped ceria lattice, but these mixed metal oxides are excellent reservoirs for selective Mars–van Krevelen hydrogen oxidation. $Ce_{0.9}W_{0.1}O_y$ is used to burn hydrogen (97% selectivity and 0% coking) from a hydrogen/ethane/ethylene mixture. For more information see the Communication by G. Rothenberg et al. on the following pages.

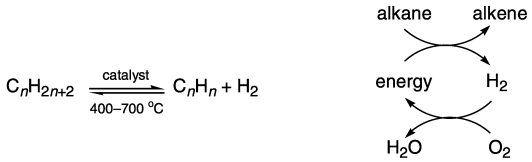
DOI: 10.1002/anie.200351545
© 2003 Wiley-VCH Verlag GmbH & Co. KGaA, Weinheim

Clean Hydrogen Oxidation

Solvent-Free Synthesis of Rechargeable Solid Oxygen Reservoirs for Clean Hydrogen Oxidation**

Gadi Rothenberg, E. A. (Bart) de Graaf, and Alfred Bliek*

Industrial dehydrogenation of alkanes to alkenes is a huge commercial process,[1,2] that nonetheless suffers from unfavorable thermodynamics. It is an equilibrium that unfortunately favors the reactants and consumes expensive energy (Scheme 1, left). In principle, a closed cycle can be envisaged



Scheme 1. Dehydrogenation equilibrium (left) and catalytic cycle for oxidative dehydrogenation (right).

where this energy is supplied by combustion of the hydrogen by-product, also shifting the equilibrium to the desired side (Scheme 1, right). Recent studies by Grasselli and co-workers,[3–5] Lin et al.,[6] and our own studies[7] showed that this selective oxidation of H_2 in the presence of alkanes at 500–700 °C is possible by using supported oxides of p-block metals as catalysts. The problem is, however, that most of these supported metals melt below the reaction temperature, so when the metal oxide is reduced to metal(0) it liquefies, causing sintering and deactivation.

Cerium oxide and ceria-based mixed metal oxides ($Ce_xM_{1-x}O_y$) are known as versatile solid oxygen exchangers. The redox cycle $Ce^{3+} \rightleftharpoons Ce^{4+} + e^-$ facilitates oxygen storage and release from the fluorite lattice. This makes them ideal for direct oxidation applications, such as automotive three-way catalysis[8] and hydrocarbon fuel cells.[9,10] The selectivity of pure CeO_2 in hydrogen oxidation is poor, but the redox chemistry of doped cerium oxides is sensitive to crystal structure defects[11] and may be tuned, in principle, by substituting some Ce ions with ions of different size and/or charge. With this in mind, we searched for doping elements that will give stable rechargeable "oxygen reservoirs" for selective hydrogen oxidation. As Zr enhances ceria stability and Pb increases its selectivity, groups IIIB–VIB and IIIA–VA were a logical starting point. Herein we report the parallel synthesis of a set of ten bimetallic cerium oxides of Bi, La, In, Mo, Pb, Sn, V, W, Y, and Zr (catalysts **1**–**10**, respectively), and study their application in clean hydrogen oxidation. Cerium tungsten oxide ($Ce_{0.9}W_{0.1}O_y$) is discovered to be an excellent hydrogen oxidation catalyst, with practically zero coking levels, good thermal stability, and selectivity $> 97\,\%$.

Single-phase mixed metal oxides can be prepared by precipitation,[12,13] sol–gel methods,[14] or combustion of glycine[15] or citric acid[16] in concentrated HNO_3. We needed a fast and simple protocol to produce catalyst samples in parallel on a 5–10 gram scale. For this, we modified the method reported by Inomata and co-workers.[17] We used no solvents, and instead synthesized the mixed metal oxides directly by boiling ground mixtures[18] of the solid nitrate precursors under vacuum, followed by calcination (for full experimental details see Supporting Information).

The catalysts were tested in a cyclic redox reaction setup with a feed stream simulating the effluent at the end of the ethane dehydrogenation process (20 % v/v C_2H_6, 20 % C_2H_4, 5 % H_2, and balance He). In a simplified description of the system, the hydrogen in the feed reacts in each cycle with some of the lattice oxygen atoms, leaving vacancies in the lattice (Figure 1 C). These vacancies are then refilled by an O_2 stream (Figure 1 B).

Each reaction was repeated 19 times at 600 °C to examine the rechargeability and stability of the materials. Table 1 gives the key surface parameters, the average activity (as % of available oxygen), and the selectivity towards hydrogen oxidation for catalysts **1**–**10**. The absolute amount of O atoms available after each recharging is shown in

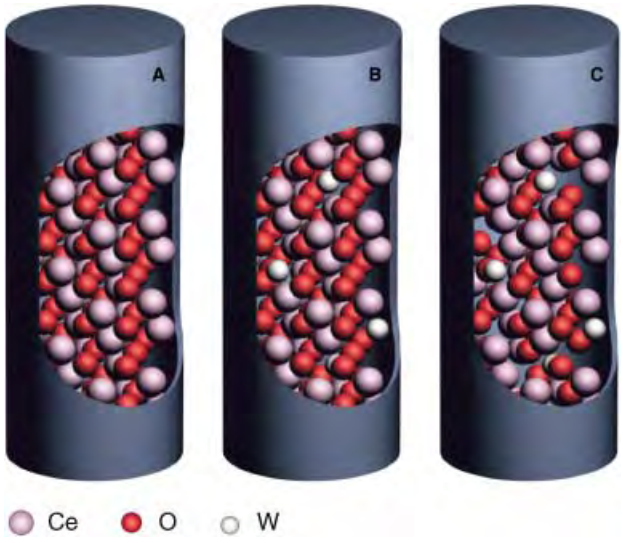


Figure 1. Schematic drawn to scale showing the fluorite structure of pure CeO_2 (A), and the vacancies present in the doped $Ce_{0.9}W_{0.1}O_y$ reservoirs when fully charged (B) and after releasing 30 % of its oxygen atoms (C).

[*] Dr. G. Rothenberg, E. A. de Graaf, Prof. Dr. A. Bliek
Chemical Engineering Department
University of Amsterdam
Nieuwe Achtergracht 166, 1018 WV Amsterdam (The Netherlands)
Fax: (+31) 20-525-5604
E-mail: gadi@science.uva.nl

[**] We thank Dr. E. Eiser for XRD measurements, M. Mittelmeijer-Hazeleger for surface characterization, and A. Rothenburg and M. Schenk for artwork.

Supporting information for this article is available on the WWW under http://www.angewandte.org or from the author.

 © 2003 Wiley-VCH Verlag GmbH & Co. KGaA, Weinheim DOI: 10.1002/anie.200351545

Table 1: Characteristics and performance of the oxygen reservoirs.

Entry	Catalyst/composition	Surface area [$m^2 g^{-1}$]	Pore volume [$mL g^{-1}$]	Pore diameter [nm]	Average activity[a] [%]	Selectivity[b] [%]
1	**1**/$Ce_{0.9}Bi_{0.1}$	44.7	0.15	6.0	33	15
2	**2**/$Ce_{0.9}In_{0.1}$	69.9	0.25	11.5	35	24
3	**3**/$Ce_{0.9}La_{0.1}$	55.0	0.20	13.3	44	34
4	**4**/$Ce_{0.9}Mo_{0.1}$	12.5	0.06	19.0	11	18
5	**5**/$Ce_{0.9}Pb_{0.1}$	33.0	0.14	7.2	29	11
6	**6**/$Ce_{0.9}Sn_{0.1}$	64.5	0.22	9.2	16	75
7	**7**/$Ce_{0.9}V_{0.1}$	26.4	0.10	9.5	28	10
8	**8**/$Ce_{0.9}W_{0.1}$	35.7	0.14	14.0	23	97[c]
9	**9**/$Ce_{0.9}Y_{0.1}$	42.2	0.10	17.6	22	<2
10	**10**/$Ce_{0.9}Zr_{0.1}$	71.2	0.23	9.4	39	35

[a] Mol% fraction of lattice oxygen atoms available for oxidation, compared to the theoretical limit when all the cerium ions are reduced to Ce^{3+}. The values given are the average of 19 repeated experiments, the distribution is ± 3%. [b] Mol% O_2 used to burn H_2 at 600°C, determined by the amount of H_2O detected by GC and selective MS. The values given are the average of triplicate experiments. [c] Six repeated experiments gave 97, 98, 97, 95, 98, and 97%.

We show here that metal-doped cerium oxide can be easily synthesized in parallel and make stable and selective solid oxygen reservoirs. These reservoirs can be recharged many times without losing their activity. Further work will focus on elucidating the reaction mechanism, and especially on understanding the influence of the different dopants and their oxidation states on the redox chemistry of the ceria lattice.[22] At this stage, we venture only to say that the fact that lattice oxygen atoms are used in the oxidation phase and not O_2 may explain the high selectivity towards

Figure 2. The most active combinations are **3**, **10**, and **2**, but it is the high selectivity of CeW **8** that triumphs: over 97% of its oxygen uptake is used to oxidize hydrogen (compare entries 2, 3, 10, with 8 in Table 1).

Coking is a thorny problem in industrial catalysis. In conventional catalytic dehydrogenation (e.g. with Pt-Sn/Al_2O_3) the coke is usually burned off the catalyst to regenerate it and the excess heat is "paid" towards the endothermic equilibrium.[19] However, in oxidative dehydrogenation this energy is not needed. In this case, the coking of the catalyst after the oxygen has been consumed from the lattice can cause severe heat excess problems. Figure 3 shows that catalyst **8** is exceptionally inert towards coke formation, with total coke levels below the GC detection limit (<0.5%). Note that **4** also gives low coking levels (although the selectivity to hydrogen oxidation is poor), in agreement with earlier results reported for molybdenum oxides.[5]

The advantage of these materials over the silica-supported metal oxides[7] is that the catalyst remains a solid, with no liquid phase forming in the reactor even at 600°C. The stable hydrogen uptake in repeated experiments (Figure 2) is a further indication that these materials do not sinter during the reduction step. This compensates for the moderate surface area of these materials compared to silica and alumina (Table 1). Powder X-ray diffraction spectra confirm that homogeneous solid solutions are formed. Only one crystalline phase is observed, and the original cubic fluorite structure is retained when 10% of the Ce ions are replaced (at these low doping values, no appreciable peak shifts are expected[20,21]). However, although the structure is retained the doping ions will create stress in the lattice and possibly ease the transport of oxygen atoms through interstitial sites. In some cases, charge vacancies will also be created (though not for Zr), thus enabling the transfer of O-atoms through ion-vacancy mechanisms.

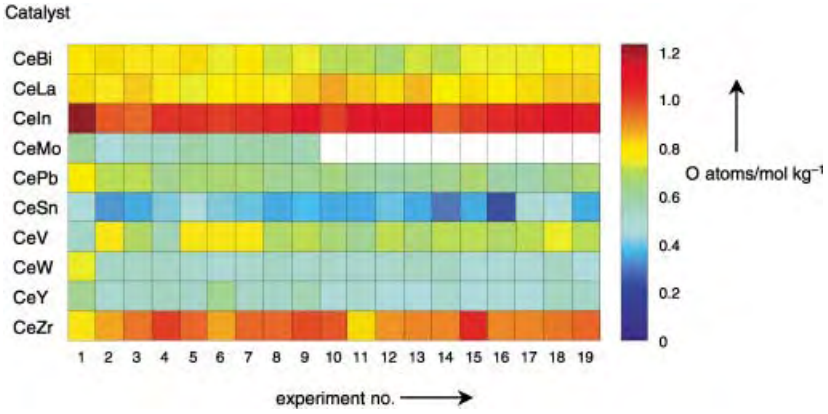


Figure 2. Absolute amount of oxygen atoms (in mol kg^{-1}) available after each recharging of the bimetallic oxide catalysts (white = n/a).

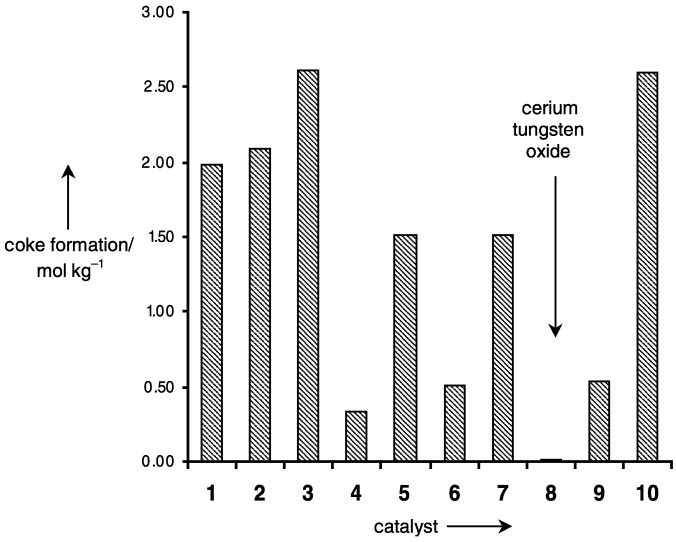


Figure 3. Average amount coke formed (in mol kg^{-1}) on catalysts **1**–**10** after the available oxygen has been consumed. Values are the average of 19 experiments, with a dispersion of ± 2%.

 © 2003 Wiley-VCH Verlag GmbH & Co. KGaA, Weinheim

hydrogen oxidation. It may be that H_2 molecules diffuse into the lattice,[23] where the bulky alkanes and alkenes cannot enter. Another possibility is that H_2 reacts much faster with O atoms that migrate to the surface. Future work will include transient kinetic measurements to gain further understanding into this interesting system.

Detailed experimental procedures for the synthesis of catalysts **1**–**10**, for performing the hydrogen oxidation experiments, and details of the powder XRD measurements are found in the Supporting Information.

Received: April 1, 2003 [Z51545]

Keywords: cerium · dehydrogenation · green chemistry · heterogeneous catalysis · oxidation

[1] D. Richards, *Chem. Mark. Rep.* **2001**, *259*, 7.
[2] J. Baker, *Eur. Chem. News* **1999**, 18.
[3] R. K. Grasselli, D. L. Stern, J. G. Tsikoyiannis, *Appl. Catal. A* **1999**, *189*, 9.
[4] R. K. Grasselli, D. L. Stern, J. G. Tsikoyiannis, *Appl. Catal. A* **1999**, *189*, 1.
[5] J. G. Tsikoyiannis, D. L. Stern, R. K. Grasselli, *J. Catal.* **1999**, *184*, 77.
[6] C.-H. Lin, K.-C. Lee, B.-Z. Wan, *Appl. Catal. A* **1997**, *164*, 59.
[7] L. M. van der Zande, E. A. de Graaf, G. Rothenberg, *Adv. Synth. Catal.* **2002**, *344*, 884.
[8] J. Kašpar, P. Fornasiero, M. Graziani, *Catal. Today* **1999**, *50*, 285.
[9] S. D. Park, J. M. Vohs, R. J. Gorte, *Nature* **2000**, *404*, 265.
[10] E. P. Murray, T. Tsai, S. A. Barnett, *Nature* **1999**, *400*, 649.
[11] A. E. C. Palmqvist, M. Wirde, U. Gelius, M. Muhammed, *Nanostruct. Mater.* **1999**, *11*, 995.
[12] R. Sasikala, N. M. Gupta, S. K. Kulshreshtha, *Catal. Lett.* **2001**, *71*, 69.
[13] Y. Zhang, S. Andersson, M. Muhammed, *Appl. Catal., B,* **1995**, *6*, 325.
[14] C. Agrafiotis, A. Tsetsekou, C. J. Stournaras, A. Julbe, L. Dalmazio, C. Guizard, *J. Eur. Ceram. Soc.* **2002**, *22*, 15.
[15] R. R. Peng, C. R. Xia, Q. X. Fu, G. Y. Meng, D. K. Peng, *Mater. Lett.* **2002**, *56*, 1043.
[16] R. E. Juárez, D. G. Lamas, G. E. Lascalea, N. E. Walsöe de Reca, *J. Eur. Ceram. Soc.* **2000**, *20*, 133.
[17] G. S. Li, R. L. Smith, H. Inomata, *J. Am. Chem. Soc.* **2001**, *123*, 11091.
[18] G. Rothenberg, A. P. Downie, C. L. Raston, J. L. Scott, *J. Am. Chem. Soc.* **2001**, *123*, 8701.
[19] M. Larsson, M. Hulten, E. A. Blekkan, B. Andersson, *J. Catal.* **1996**, *164*, 44.
[20] D. J. Kim, *J. Am. Ceram. Soc.* **1989**, *72*, 1415.
[21] M. Mogensen, N. M. Sammes, G. A. Tompsett, *Solid State Ionics* **2000**, *129*, 63.
[22] S. de Carolis, J. L. Pascual, L. G. M. Pettersson, M. Baudin, M. Wojcik, K. Hermansson, A. E. C. Palmqvist, M. Muhammed, *J. Phys. Chem. B* **1999**, *103*, 7627.
[23] G. Wrobel, C. Lamonier, A. Bennani, A. Dhuysser, A. Aboukais, *J. Chem. Soc. Faraday Trans.* **1996**, *92*, 2001.

 © 2003 Wiley-VCH Verlag GmbH & Co. KGaA, Weinheim

Self-Assembling Circuits

Plasticity in Self-Assembly: Templating Generates Functionally Different Circuits from a Single Precursor**

*Mila Boncheva, Rosaria Ferrigno, Derek A. Bruzewicz, and George M. Whitesides**

The fabrication of microelectronic circuits now follows a strict, deterministic, top-down plan, and relies on the massive parallelism of photolithography to produce multiple replicates of a device.[1] Neural circuits follow an adaptive, bottom-up plan, and assemble themselves of individual components—cells—following a combination of internal program and external guidance.[2] The work we report herein is an initial step towards a strategy for the fabrication of electrical circuits that also relies on a combination of self-assembly and external guidance. We demonstrate the self-assembly of mm-sized components into 3D aggregates that have structures and patterns of electrical connections determined by the shape of a template—that is, by the geometry of the volume in which the self-assembly proceeds. The components carry light-emitting diodes (LEDs), used as surrogates for more complex microelectronic devices, connected to solder-covered pads. The solder connecting these components—when liquid—acts through capillary interactions to drive the self-assembly of the components, and—when solid—establishes electrical and mechanical connections between selected LEDs. Self-assembly in containers of different shape generates topologically different 3D structures—helices, zigzags, and combinations of the two; these structures have different patterns of electrical connections among the LEDs.

Self-assembly[3,4] based on capillary interactions between solder drops has been used to generate aggregates having a single structure and function.[5] Templating has also been used to bring designed asymmetry to self-assembled aggregates.[6–10] In this work we use templating to control the pattern of electrically functional connections among self-assembled components. Our strategy is to use components that—in the absence of restrictions imposed by a template—self-assemble with equal probability into two different configurations; each of these configurations generates a distinct set of electrical connections between the components. The geometry of the volume available for self-assembly templates the 3D structure of the aggregates, and thus determines the

[*] Prof. Dr. G. M. Whitesides, Dr. M. Boncheva, Dr. R. Ferrigno, D. A. Bruzewicz
Department of Chemistry and Chemical Biology
Harvard University
Cambridge, MA 02138 (USA)
Fax: (+1) 617-495-9857
E-mail: gwhitesides@gmwgroup.harvard.edu

[**] This work was supported by the NSF (CHE-0101432) and DARPA. R.F. is grateful to the Swiss National Science Foundation for post-doctoral fellowship.

Supporting information for this article is available on the WWW under http://www.angewandte.org or from the author.

 © 2003 Wiley-VCH Verlag GmbH & Co. KGaA, Weinheim DOI: 10.1002/anie.200351533

patterns of electrical connections formed between the components.

A key issue was to design, and to develop a practical procedure to fabricate, the required components (Figure 1; details of the procedure can be found in the Supplemental Information). Briefly, we defined planar patterns of pads and wires on copper-polyimide composite material by using photolithography (Figure 1 a). We applied manually thermocurable, electrically conducting adhesive to selected pads. Folding of the flexible substrate positioned the copper pads and wires in three dimensions (Figure 1 b, c). Curing the components at a temperature above the glass transition temperature of the polyimide consolidated the four-layered, folded structures into rigid, rhomboid components, and simultaneously solidified the electrically conducting adhesive (Figure 1 d). This strategy for the fabrication of the components allowed us to establish electrical connections in three dimensions by using standard photolithography to pattern planar substrates.[11]

We manually soldered two different LEDs—red and green—onto contact pads on each side of the components, and dip-coated the copper pads with solder ($T_m = 70\,°C$) (Figure 1 e, f). The pairs of identical LEDs on opposite sides of each component were electrically connected in series, and shared a common cathode—that is, the circular central pad δ (Figure 1 g). The components were suspended in dilute aqueous acetic acid (pH 3–4),[12] and heated to a temperature above the melting point of the solder ($\approx 80\,°C$). Rotation of the vessel containing the components caused them to collide with one another and with the walls of the container; capillary interactions between the drops of molten solder caused self-assembly.[5,13]

Each component could interact with, and connect to, two other components. In previous work on patterned self-assembly, the design of the interacting patterns was focused on achieving unique orientational selectivity during self-assembly.[14,15] Here, the threefold symmetry of the patterns of solder could, in principle, allow for three relative orientations in which all pads of solder carried by two components are fully aligned (Figure 2 a). One of these three orientations,

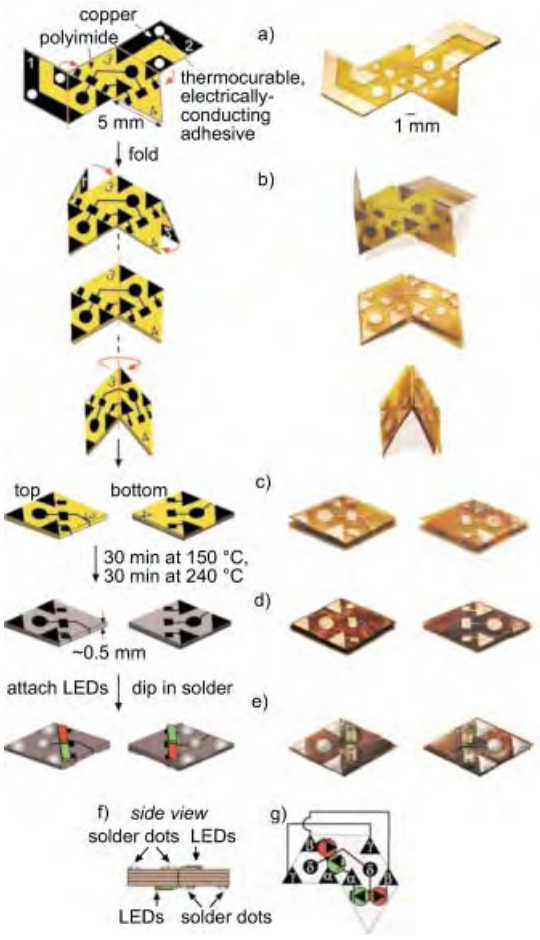


Figure 1. Procedure used for the fabrication of the components. a) Planar patterns of pads and wires were defined on a flexible copper–polyimide composite by using photolithography and wet etching. b) Folding of these patterns resulted in rhomboid structures (c). d) Thermal curing consolidated the four-layer structure. e) LEDs were soldered manually onto the contact pads, and the remaining copper pads were dip-coated with solder. f) Side view of a component after folding and internal interconnection. The thickness is drawn out of scale to emphasize the four-layer structure. g) Scheme describing the electrical connections between pads of solder and LEDs on both sides of one component. The anodes of the green LEDs were connected to pads α, and those of the red LEDs to pads β. Electrical connections (shown as thick solid lines) between symmetrical pads on both sides (β–β and γ–γ) were established by the electrically conducting adhesive.

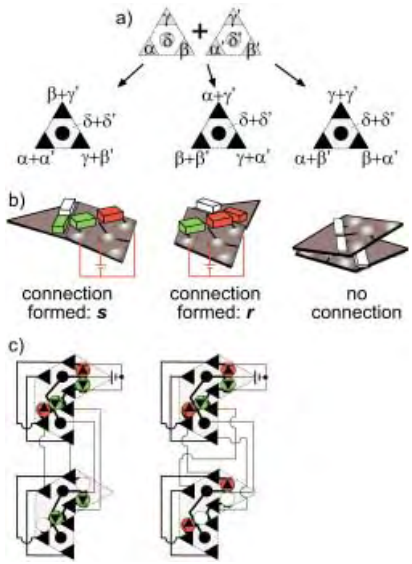


Figure 2. Configuration of the components in an aggregate and pattern of electrical connections formed between the LEDs. a) Two patterns of solder pads (indicated with α, β, γ, and δ on one component, and α′, β′, γ′, and δ′ on another one) can, in principle, overlap completely in three indistinguishable orientations. b) When attached to components, the same pattern of solder pads can overlap completely in only two orientations, *r* or *s*. c) Circuit diagrams describing the electrical connections formed between two components assembled in two different relative orientations, *s* and *r*, after connecting to a battery. Thick lines indicate the electrical connections existing prior to binding of the components, and thin lines indicate the connections formed during binding. The LEDs connected in electrical circuit are shown in their respective color (red or green), and those not included in the circuit are shown in white.

 © 2003 Wiley-VCH Verlag GmbH & Co. KGaA, Weinheim

however, was sterically excluded by the interaction of the multilayer plate of one component with the LEDs on the second (Figure 2b, right). The components could interact in two distinct configurations, *r* and *s* (Figure 2b, left and middle). In both configurations, the overlapping circular central pads (δ and δ′) of adjacent components connect the cathodes of all LEDs in an aggregate in series. In configuration *s*, overlapping peripheral pads α and α′ connect in series the anodes of the green LEDs, and in configuration *r*, overlapping peripheral pads β and β′ connect in series the anodes of the red LEDs. Thus, the different relative orientation of the components results in the formation of electrical circuits that include different LEDs (Figure 2c). When two components connected in configuration *s*, on one component both the green and the red LEDs lighted, and on the second one, only the green LEDs lighted; when the components were connected in configuration *r*, on one component both the green and the red LEDs lighted, and on the second one, only the red LEDs lighted.

When we allowed the self-assembly to proceed in a spherical container or in a cylindrical container with a diameter of ≥ 50 mm, both *r* and *s* connections formed with equal probability. The size of the container, and thus the volume available for self-assembly, imposed no geometric constraint on the shape of the aggregates formed; shearing forces favored irregular aggregates with aspect ratio ≈ 1.

When we allowed self-assembly to proceed in a cylindrical container with a diameter of 8 mm and a volume of ≈ 2 mL that rotated along its principal axis, alternating *r* and *s* connections formed between the components (Figure 3a). The resulting aggregates had a zigzag shape and width of 4.5 mm; no other arrangement of components could fit in the restricted volume available.

When we allowed the self-assembly to proceed in a container with a diameter of 12 mm and a volume of ≈ 2.6 mL that rotated about an axis normal to its own, the restricted volume available for self-assembly of the components geometrically excluded the formation of aggregates with randomly mixed *r* and *s* connections. Zigzag aggregates containing alternating *r* and *s* connections had a high aspect ratio and were, thus, susceptible to disruption by shearing and broke. The geometry of the container favored formation of aggregates containing only *r* or only *s* connections, that is, left-handed or right-handed helices (Figure 3b). The two types of helix initially formed with equal probability, but one type of chirality dominated at the conclusion of the assembly.

Aggregates containing both zigzag and helical regions assembled in a container comprising two cylindrical regions of different width (Figure 3c). The components contained in the narrow portion of the container assembled into a zigzag, and the components contained in the wider portion assembled into a helix. The formation of the two aggregates proceeded independently. The two regions of the container were orthogonal to each other, and the two segments eventually combined into a single, asymmetrical aggregate.

When cooled, the solder drops solidified, bridged the components, and provided both mechanical stability and electrical connectivity. After self-assembly, we connected the aggregates to a power source. The pattern of electrical

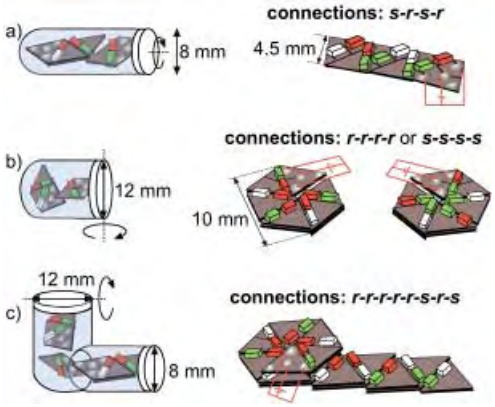


Figure 3. Design of the self-assembling system. The different shapes of the containers in which self-assembly was performed (left) templated formation of aggregates of different geometry (right): a) zigzag, b) left- or right-handed helices, and c) a combination of a zigzag and a helix.

connections that had formed during the assembly was apparent from the pattern of illuminated LEDs. As expected, in aggregates of different geometry the sequence of illuminated LEDs followed different patterns: in zigzag aggregates, (red + green)–(green)–(green)–(red + green)–(red)–(red)–etc. (Figure 4a); in left-handed helical aggregates, (red + green)–(red)–(red + green)–(red)–etc. (Figure 4b); in right-handed helical aggregates, (red + green)–(green)–(red + green)–(green)–etc. (Figure 4c); in aggregates combining helical and zigzag regions, the pattern was a combina-

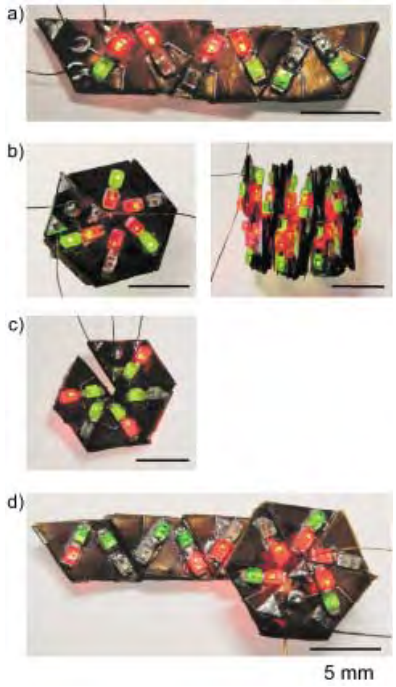


Figure 4. Photographs of self-assembled aggregates shaped as a) a zigzag, b) a left-handed helix shown in top (left) and side (right) views, c) a right-handed helix and d) a combination of a right-handed helix and a zigzag, after connecting to a battery.

 © 2003 Wiley-VCH Verlag GmbH & Co. KGaA, Weinheim

tion of the characteristic patterns for a helix and a zigzag (Figure 4d).

This work demonstrates the use of a macroscopic variable—the geometry of the vessel, and thereby the space available for self-assembly—to direct the self-assembly of a single kind of component in distinct patterns of electrical connections. The work establishes that, in principle, multiple functions can be derived from the same set of components by controlling the shape of the space available for self-assembly. Such external means of control over functional connectivity within self-assembled aggregates might be especially important when the components used to build the aggregates are small, and, therefore, difficult to manipulate by using established pick-and-place fabrication strategies.[16]

To achieve a high volumetric density of functional components in self-assembled aggregates, the components must be smaller than those used in this work. The strategy we used for the fabrication of the components—a combination of photolithography and folding—allows (in principle) the scaling of the components to micrometer sizes: conventional 2D photolithography can be used to fabricate and pattern planar precursors, which can then spontaneously fold into 3D shapes.[5,17,18]

The principle of the design that we describe can be used to develop functional, self-assembled systems in which one set of components—carrying functional elements, for example, microelectronic devices—can be combined into any of several functionally different circuits. This strategy reduces the need to fabricate a different set of components for every new pattern of connections. In our experience, the fabrication of the individual components is the most difficult problem when designing functional, self-assembling systems.

Received: March 31, 2003 [Z51533]

Keywords: capillary forces · microelectronics · self-assembly · templating

[1] S. A. Campbell, *The Science and Engineering of Microelectronic Fabrication*, 2nd ed., Oxford University Press, New York, **2001**.
[2] P. Kostyuk, *Plasticity in Nerve Cell Function*, Oxford University Press, Oxford, UK, **1998**.
[3] G. M. Whitesides, M. Boncheva, *Proc. Natl. Acad. Sci. USA* **2002**, *99*, 4769.
[4] G. M. Whitesides, B. Grzybowski, *Science* **2002**, *295*, 2418.
[5] R. R. A. Syms, E. M. Yeatman, V. M. Bright, G. M. Whitesides, *J. Microelectromech. Syst.* **2003**, in press.
[6] W. T. S. Huck, J. Tien, G. M. Whitesides, *J. Am. Chem. Soc.* **1998**, *120*, 8267.
[7] T. D. Clark, R. Ferrigno, J. Tien, K. Paul, G. M. Whitesides, *J. Am. Chem. Soc.* **2002**, *124*, 5419.
[8] Y. Yin, Y. Lu, B. Gates, Y. Xia, *J. Am. Chem. Soc.* **2001**, *123*, 8718.
[9] O. D. Velev, K. Furusawa, K. Nagayama, *Langmuir* **1996**, *12*, 2374.
[10] A. D. Dinsmore, M. F. Hsu, M. G. Nikolaides, M. Marquez, A. R. Bausch, D. A. Weitz, *Science* **2002**, *298*, 1006.
[11] This procedure is similar to that used for the fabrication of folded stacked-chip packages and multichip modules commercialized respectively by Tessera Technologies, Inc. (http://www.tessera.com) and Valtronic SA (http://www.valtronic.ch).
[12] The acetic medium was necessary to remove oxides that form in water on the surfaces covered with solder.
[13] K. F. Harsh, V. M. Bright, Y. C. Lee, *Sens. Actuators A* **1999**, *77*, 237.
[14] X. Xiong, Y. Hanein, W. Wang, D. T. Schwartz, K. F. Boehringer in *Transducers'01*, Munich, Germany, **2001**, p. 1040.
[15] U. Srinivasan, D. Liepmann, R. T. Howe, *J. Microelectromech. Syst.* **2001**, *10*, 17.
[16] K. F. Boehringer, R. S. Fearing, K. Y. Goldberg in *The Handbook of Industrial Robotics*, 2nd ed. (Ed.: S. Nof), Wiley, New York, **1999**, p. 1045.
[17] D. H. Gracias, V. Kavthekar, J. C. Love, K. E. Paul, G. M. Whitesides, *Adv. Mater.* **2002**, *14*, 235.
[18] E. Smela, O. Inganäs, I. Lundstrom, *Science* **1995**, *268*, 1735.

 © 2003 Wiley-VCH Verlag GmbH & Co. KGaA, Weinheim

[70]Fullerene-Based Photovoltaics

Efficient Methano[70]fullerene/MDMO-PPV Bulk Heterojunction Photovoltaic Cells**

Martijn M. Wienk, Jan M. Kroon, Wiljan J. H. Verhees, Joop Knol, Jan C. Hummelen,* Paul A. van Hal, and René A. J. Janssen**

The widespread use of solar cells as a renewable source of energy is seriously held back by the high cost of the existing crystalline silicon-based technology. The prospect of cheap reel-to-reel processing makes organic semiconducting mate-

[*] Dr. J. M. Kroon, Dr. M. M. Wienk,[+] W. J. H. Verhees
Energy Research Centre of the Netherlands (ECN), Solar Energy
P.O. Box 1, 1755 ZG Petten (The Netherlands)
Fax: (+31) 224-56-8214
E-mail: j.kroon@ecn.nl

Prof. Dr. J. C. Hummelen, Dr. J. Knol
Stratingh Institute and MSC
University of Groningen
Nijenborgh 4, 9747 AG Groningen (The Netherlands)
Fax: (+31) 50-363-8751
E-mail: j.c.hummelen@chem.rug.nl

Prof. Dr. R. A. J. Janssen, Dr. P. A. van Hal
Laboratory of Macromolecular and Organic Chemistry
Eindhoven University of Technology
P.O. Box 513, 5600 MB Eindhoven (The Netherlands)
Fax: (+31) 40-245-1036
E-mail: r.a.j.janssen@tue.nl

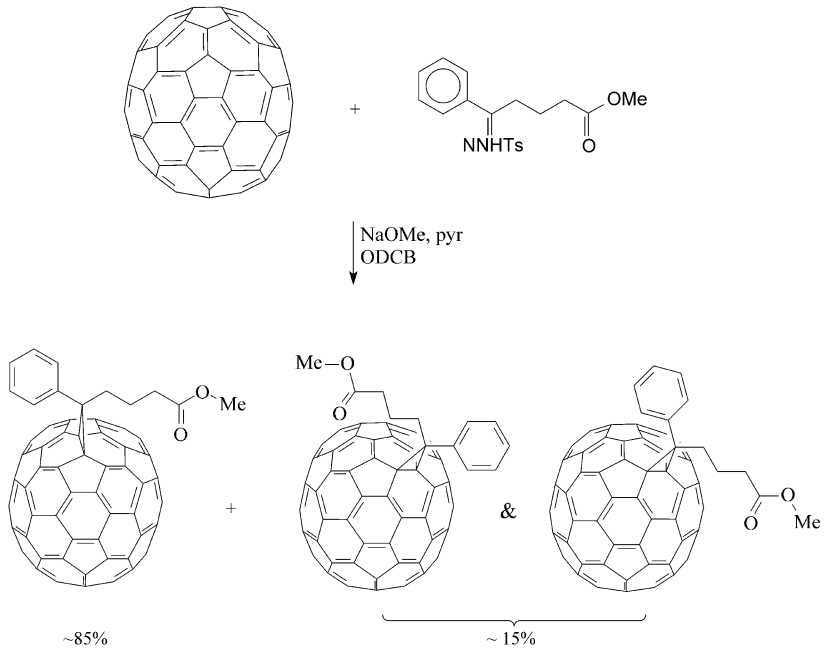
[+] Present address: Dutch Polymer Institute
Laboratory of Macromolecular and Organic Chemistry
Eindhoven University of Technology
P.O. Box 513, 5600 MB Eindhoven (The Netherlands)

[**] We thank Sjoerd Veenstra (ECN) for useful discussions, Pascal Jonkheijm (Eindhoven University) for AFM measurements, Jörgen Sweelssen (TNO Industries, Eindhoven) for the polymer synthesis and Patrick van't Hof and Jan Alma (Groningen University) for repeating the [70]PCBM synthesis. These investigations were financially supported by the Dutch Ministries of EZ, O&W, and VROM through the EET program (EETK97115).

Supporting information for this article is available on the WWW under http://www.angewandte.org or from the author.

 DOI: 10.1002/anie.200351647 © 2003 Wiley-VCH Verlag GmbH & Co. KGaA, Weinheim

rials interesting alternatives for the future generation of photovoltaic devices.[1–5] Organic solar cells that have received considerable attention are of the so-called polymer/fullerene bulk heterojunction type.[6–8] Until now, the photoactive layer of these devices routinely consists of a mixture of a π-conjugated polymer acting as electron donor, and a soluble [60]fullerene derivative, methano[60]fullerene [6,6]-phenyl C_{61} butyric acid methyl ester ([60]PCBM) as electron acceptor.[9] Optimized internal quantum efficiencies (IQE = fraction of absorbed photons converted to electric current) close to 100% have been reported,[7] which demonstrates that very efficient charge generation and collection can be achieved. Therefore, the current densities, which are still low compared to inorganic semiconductor devices, are mainly limited by incomplete utilization of the incident light, because of a poor match between the absorption spectrum of the materials and the solar emission spectrum. The polymers only absorb light at wavelengths less than 650 nm, but more importantly, [60]PCBM, which amounts to at least 75% of the photoactive layer, has a very low absorption coefficient in the visible region of the spectrum. The low absorption of C_{60} derivatives can be attributed to a high degree of symmetry, making the lowest-energy transitions formally dipole forbidden. Therefore, when the C_{60} moiety of [60]PCBM is replaced by a less symmetrical fullerene, these transitions will become allowed and a dramatic increase in light absorption is expected.[10] Herein, we report on a bulk heterojunction photovoltaic cell in which an isomeric mixture of C_{70} derivatives is used as an electron acceptor in combination with poly(2-methoxy-5-{3′,7′-dimethyloctyloxy}-*p*-phenylene vinylene) (MDMO-PPV). [70]PCBM (for instance, in this case a mixture of isomeric [6,6]-phenyl C_{71} butyric acid methyl esters) is the higher fullerene analogue of [60]PCBM, and displays improved light absorption in the visible region. Consequently, when this material is used in a photovoltaic cell instead of [60]PCBM, 50% higher current densities are obtained. The overall power-conversion efficiency η, measured under standard test conditions (AM1.5 (AM = air mass), 1000 W m^{-2}, 25 °C), amounts to 3.0%.



Scheme 1. Synthesis of [70]PCBM. At the bottom, the structures of the chiral α-type isomer (left) and the two possible achiral β-type isomers (right). Ts = toluene-4-sulfonyl.

The synthesis of [70]PCBM was performed in an analogous procedure to that described earlier for [60]PCBM (Scheme 1).[9] However, 1,3-dipolar addition to C_{70} leads to a mixture of regioisomers.[11] The ^{1}H NMR spectrum of the monoadduct fraction ("[70]PCBM"), isolated from the higher adducts and unreacted C_{70} by column chromatography, reveals signals for methoxy groups (ratio ≈ 7:85:8) at δ = 3.48, 3.65, and 3.72 ppm, respectively, which indicates the presence of three isomers. Since the ^{13}C NMR spectrum for typical parts of the molecule (i.e., the phenyl ring, the butyric acid, and methyl ester moieties) does not display multiple resonances, it is concluded that the minor isomers are not visible, due to their relatively low concentration. We therefore attribute all visible ^{13}C resonances to the major isomer. More than 60 resonances for the fullerene carbon atoms are observed, clearly indicating the chirality of the isomer. Based on this observation and on the basis of the known reactivity of C_{70}, we conclude that the major isomer is the "α type"[11] compound formed by 1,3-dipolar addition (with subsequent loss of nitrogen with isomerization to [5,6] fulleroid(s), and followed by back-isomerization to the [6,6]methano[70]fullerene) to the most "polar" double bond (the C(8)-C(25) bond),[12] yielding a chiral derivative. Most likely, the two minor isomers are the achiral stereoisomeric "β type" addends, in which the addend is bound to the C(9)-C(10) double bond (the most "polar" C=C bond in the C_{70} skeleton, after the C(8)-C(25) bond).

The UV/Vis absorption of the [70]PCBM mixture is shown in Figure 1, together with that of [60]PCBM. The significantly higher absorption coefficient in the visible region is most relevant for the application in photodiodes, photodetectors, and photovoltaics. The [70]PCBM mixture is readily soluble in common solvents.

The photoinduced electron transfer from dialkoxy-PPV to fullerenes in the solid state that occurs after excitation of the polymer is well documented and was shown to occur within 40 fs.[13,14] From the spectral response[6] of [60]PCBM:MDMO-PPV photovoltaic cells at wavelengths greater than 600 nm, where the fullerene is excited exclusively, it can be inferred that excitation of the fullerene also contributes to the photocurrent generation, but comparatively little is known about this process. For mixed [70]PCBM:MDMO-PPV (4:1, w/w) films, spin coated from chlorobenzene on a quartz substrate, near steady-state photoinduced absorption (PIA) measurements (performed at 80 K in a nitrogen atmosphere) give direct spectral evidence for photoinduced charge separation, not only upon

 © 2003 Wiley-VCH Verlag GmbH & Co. KGaA, Weinheim

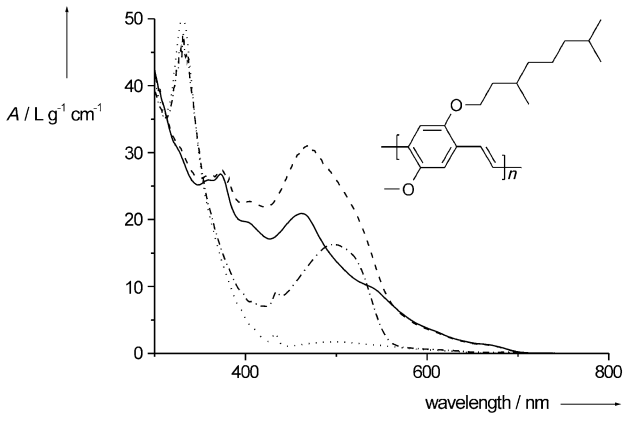


Figure 1. UV/Vis spectra of [70]PCBM (——) and [60]PCBM (••••), both in toluene. To illustrate the contribution of MDMO-PPV to the absorption, the (normalized) spectra of [70]PCBM:MDMO-PPV (4:1, w/w; -----) and [60]PCBM:MDMO-PPV (4:1, w/w; –•–•), also in toluene, are also represented. The inset shows the structure of MDMO-PPV.

excitation of the polymer, but also after selective excitation of [70]PCBM at 630 nm. The PIA spectra measured after excitation at 488 and 630 nm exactly coincide (Figure 2a), and display two absorptions at 0.40 and 1.35 eV—characteristic for cation radicals on MDMO-PPV—and a bleaching signal at 2.25 eV of the MDMO-PPV ground state. The kinetics of charge generation were examined with pump-probe spectroscopy in the sub-picosecond time domain (Figure 2b) by tracing the intensity of the PIA signal of the high-energy cation radical absorption of the MDMO-PPV at 970 nm (1.28 eV). Excitation at 510 nm results in the rise of this band within 500 fs (resolution of the set-up), consistent with ultrafast measurements reported previously.[13,14] Selective excitation of [70]PCBM in the mixture at 660 nm also leads to a rise time within 500 fs. This demonstrates that photoinduced electron transfer from the MDMO-PPV to [70]PCBM is a sub-picosecond reaction, irrespective of which chromophore is excited.

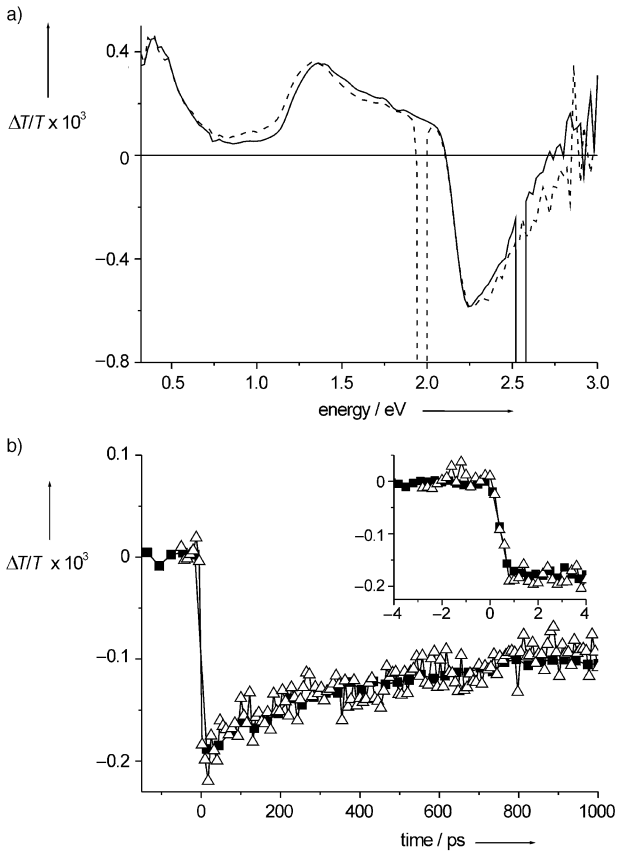


Figure 2. a) Normalized photoinduced absorption spectra of [70]PCBM:MDMO-PPV (4:1 w/w) on quartz after excitation at 488 nm (——) and 630 nm (-----); b) differential transmission dynamics of [70]PCBM:MDMO-PPV (4:1 w/w) on glass after excitation at 510 (△) and 660 nm (■), respectively.

The efficiency of charge generation was examined by steady-state and time-resolved photoluminescence (PL) measurements. Because the ultrafast charge transfer deactivates the excited state before luminescence can occur, a decrease in PL signal of the [70]PCBM:MDMO-PPV mixtures with respect to the pristine materials is expected. As is the case for [60]PCBM:MDMO-PPV mixtures,[15] the MDMO-PPV emission, observed at 570 nm after excitation at 488 nm, is almost completely quenched, which indicates near quantitative charge generation upon polymer excitation. This polymer PL quenching occurs for all [70]PCBM:MDMO-PPV films, spin cast from several different solvents. On the other hand, quenching of the [70]PCBM emission at 720 nm greatly depends on the processing solvent. When chlorobenzene is used, only 30% of the PL is quenched, whereas 60% and over 95% quenching occurs for films from *o*-xylene and *o*-dichlorobenzene (ODCB), respectively. This solvent dependence is also reflected in time-resolved photoluminescence measurements (Figure 3a). The decay kinetics of the fullerene emission at 720 nm of the [70]PCBM:MDMO-PPV (4:1 w/w) mixture, spun from chlorobenzene, hardly differs from that shown by the pristine fullerene. In contrast, for mixtures spin coated from *o*-xylene and especially from ODCB, significantly shorter lifetimes are observed.

The dramatic differences in PL quenching, and the associated charge-generation efficiency is explained by changes in the morphology of the films due to the processing solvent. It has been shown that different solvents can result in distinctly different efficiencies for fullerene:PPV photovoltaic cells as a result of changed morphologies.[6] Tapping-mode atomic force microscopy (AFM) was employed to gain insight into the structure of the different [70]PCBM:MDMO-PPV mixtures. The topography images reveal a very rough surface (root-mean-square (rms) roughness = 12 nm) for films from chlorobenzene and lateral structures with diameters between one and three micrometers, suggesting demixing of the polymer and methano[70]fullerene on a very large scale (Figure 3b). Films from *o*-xylene are smoother (rms roughness = 7 nm) and the apparent domains somewhat smaller but only the films from ODCB are really smooth (rms roughness = 1 nm) with lateral features well under one micrometer.

The very coarse demixing observed by AFM explains the poor PL quenching of the [70]PCBM:MDMO-PPV films processed from chlorobenzene and *o*-xylene. When pure

 © 2003 Wiley-VCH Verlag GmbH & Co. KGaA, Weinheim

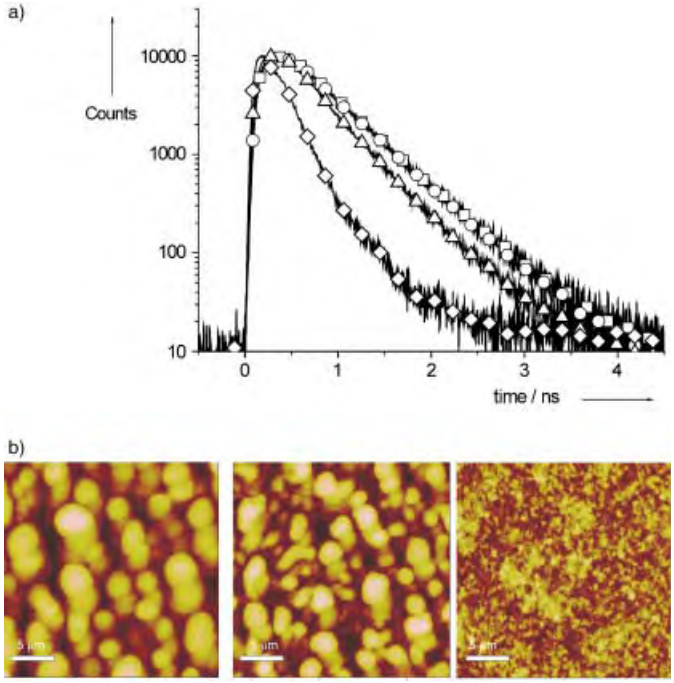


Figure 3. a) Photoluminescence decay of the fullerene emission of [70]PCBM:MDMO-PPV (4:1 w/w) blends at 720 nm on glass, spin coated from chlorobenzene (○), *o*-xylene (△), and ODCB (◇). The PL decay of a pristine [70]PCBM film (□) is also shown; b) AFM tapping-mode height images of [70]PCBM:MDMO-PPV (4:1 w/w) blends on glass, spin coated from chlorobenzene (left, *z* range = 86 nm, rms roughness = 12 nm), *o*-xylene (center, *z* range = 37 nm, rms roughness = 7 nm), and ODCB (right, *z* range = 8.2 nm, rms roughness = 1.0 nm).

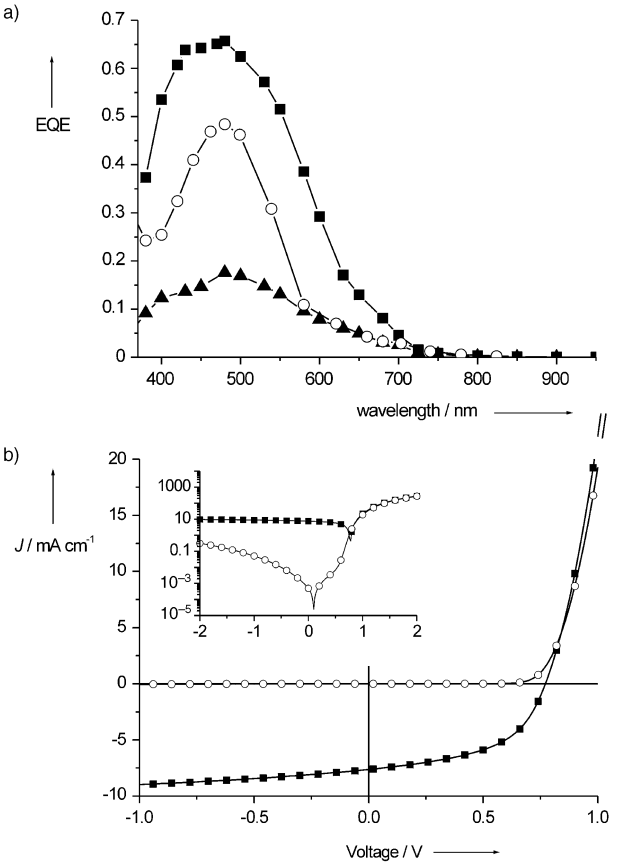


Figure 4. Photovoltaic properties of an ITO/PEDOT-PSS/fullerene:MDMO-PPV/LiF/Al device with an active area of 0.1 cm^2. a) External quantum efficiency (EQE) of [70]PCBM:MDMO-PPV cells, spin coated from chlorobenzene (▲) and ODCB (■), and of [60]PCBM:MDMO-PPV devices spin coated from chlorobenzene (○); b) current–voltage characteristics of [70]PCBM:MDMO-PPV devices, spin coated from ODCB, in the dark (○) and under illumination (AM1.5, 1000 $W m^{-2}$; ■). The inset shows the dark and illuminated *I*/*V* curves in a semilogarithmic plot.

methanofullerene phases are present with a radius larger than the exciton diffusion length, part of the excitons do not reach the fullerene/polymer interface. Consequently, charge transfer cannot occur and the excitation will decay (partly) radiatively. The observation that the MDMO-PPV emission is completely quenched, irrespective of the processing solvent, suggests that in all cases some fullerene is present in the polymer-rich phase, which deactivates the MDMO-PPV excited state.

The large solvent-induced morphology differences are also reflected by the photovoltaic behavior of the [70]PCBM:MDMO-PPV films. Photovoltaic cells were made by sandwiching the photoactive mixture, consisting of [70]PCBM and MDMO-PPV in a 4.6:1 (w/w) ratio,[16] between charge-selective electrodes. ITO/PEDOT:PSS (ITO: indium tin oxide; PEDOT: poly(3,4-ethylenedioxythiophene; PSS: poly(styrene sulfonate) was used as a transparent, high-work-function electrode to collect the holes, and LiF/Al[17,18] as low-work-function electrode for electron collection. The external quantum efficiency (EQE; that is, the fraction of incident photons converted into electric current) of a device spin-coated from chlorobenzene does not exceed 0.2 (Figure 4a), and thus remains much lower than the EQE of corresponding [60]PCBM:MDMO-PPV cells (usually between 0.5–0.55). This can be rationalized by the incomplete charge generation after [70]PCBM excitation that result from the large methano[70]fullerene domains. On the other hand, the EQE of a photovoltaic device processed from ODCB is much higher, with a maximum value of 0.66 at 480 nm. This value is higher than that of an optimized [60]PCBM:MDMO-PPV cell and, as a result of the increased absorption by [70]PCBM, the spectral response is significantly broader as well. Integration of this spectral response with the tabulated AM1.5G spectrum, normalized to 1000 $W m^{-2}$, renders an expected value of 7.9 $mA cm^{-2}$ for the short-circuit current (I_{sc}) under illumination with the solar spectrum. This value corresponds very well to the $I_{sc} = 7.6\ mA cm^{-2}$ obtained by current–voltage measurements (Figure 4b) carried out under a solar simulator according to standard test conditions (AM1.5, 1000 $W m^{-2}$; 25 °C; correction for spectral mismatch[19]). A value of $I_{sc} = 7.6\ mA cm^{-2}$ for the [70]PCBM:MDMO-PPV devices means an increase of over 50% with respect to an optimized [60]PCBM:MDMO-PPV cell. On the other hand, the open-circuit voltage V_{oc} of 0.77 V and a fill factor (*FF*) of 0.51 are somewhat lower for the [70]PCBM:MDMO-PPV devices,[20] resulting in an overall power-conversion efficiency (η) of 3.0%.

 © 2003 Wiley-VCH Verlag GmbH & Co. KGaA, Weinheim

Experimental Section

MDMO-PPV and [70]PCBM were synthesized according to known procedures.[9,21] Details about the [70]PCBM synthesis and characterization are given in the Supporting Information.

Absorption spectra were recorded on a PerkinElmer Lambda 40 spectrometer. Near-steady-state and sub-picosecond transient photoinduced absorption spectroscopy measurements were performed using equipment described previously.[22] Fluorescence spectra were recorded on an Edinburgh Instruments F920. Time-correlated single-photon-counting fluorescence studies were performed on an Edinburgh Instruments LifeSpec-PS spectrometer by photoexcitation at 400 nm and recording at 720 nm. AFM images were recorded on glass substrates with a Nanoscope Digital D3000 AFM operating under ambient conditions in tapping mode. Microfabricated silicon cantilevers (FESP) were used with a spring constant of 1–5 $N\,m^{-1}$.

The photovoltaic devices were prepared by spin coating EL-grade PEDOT:PSS (Bayer AG) onto pre-cleaned, patterned indium tin oxide substrates (14 Ω per square). The photoactive layer was deposited by spin coating from the appropriate solvent. The counter-electrode of LiF (1 nm) and aluminum (100 nm) was deposited by vacuum evaporation at 10^{-6} mbar. The active area of the cell was 0.1 cm^2.

Spectral response measurements were performed using a 12 V/50 W halogen lamp as light source and 22 interference filters as a monochromator. Measurements were carried out without bias illumination with respect to a calibrated Si solar cell. The experiments were carried out in a nitrogen-filled glove box to prevent degradation of the device by water or oxygen, which is commonly observed for polymer devices. Current voltage measurements were performed on devices encapsulated by araldite (Ciba)/aluminum foil under a Spectrolab ZT-10 solar simulator outside the glove box, using a Keithley SMU 2400 source meter. A polycrystalline silicon solar cell, calibrated at PTB, Braunschweig (Germany), was used as reference cell. Efficiencies were determined according to international standard norms (ASTM, IEC).[23]

Received: April 14, 2003 [Z51647]

Keywords: charge transfer · fullerenes · polymers · solar cells · time-resolved spectroscopy

[1] G. Yu, J. Gao, J. C. Hummelen, F. Wudl, A. J. Heeger, *Science* **1995**, *270*, 1789–1791.
[2] W. U. Huynh, J. J. Dittmer, A. P. Alivisatos, *Science* **2002**, *295*, 2425–2427.
[3] P. Peumans, S. R. Forrest, *Appl. Phys. Lett.* **2001**, *79*, 126–128.
[4] M. Gangstrom, K. Petrisch, A. C. Arias, A. Lux, M. R. Andersson, R. H. Friend, *Nature* **1998**, *395*, 257–260.
[5] J. Nelson, *Curr. Opin. Solid State Mater. Sci.* **2002**, *6*, 87–95.
[6] S. E. Shaheen, C. J. Brabec, N. S. Sariciftci, F. Padinger, T. Fromherz, J. C. Hummelen, *Appl. Phys. Lett.* **2001**, *78*, 841–843.
[7] P. Schilinsky, C. Waldauf, C. J. Brabec, *Appl. Phys. Lett.* **2002**, *81*, 3885–3887.
[8] F. Padinger, R. S. Rittberger, N. S. Sariciftci, *Adv. Funct. Mater.* **2003**, *13*, 85–88.
[9] J. C. Hummelen, B. W. Knight, F. LePeq, F. Wudl, J. Yao, C. L. Wilkins, *J. Org. Chem.* **1995**, *60*, 532–538.
[10] J. W. Arbogast, C. S. Foote, *J. Am. Chem. Soc.* **1991**, *113*, 8886–8889.
[11] For a review on the reactivity of C_{70}, see: C. Thilgen, F. Diederich, *Top. Curr. Chem.* **1999**, *199*, 135–171.
[12] W. H. Powell, F. Cozzi, G. P. Moss, C. Thilgen, R. J.-R. Hwu, A. Yerin, *Pure Appl. Chem.* **2002**, *74*, 629–695. The IUPAC name for the major [70]PCBM isomer is: methyl 5-(3′*H*-cyclopropa[8,25](C70-*D*5h(6))[5,6]fullerenyl)-5-phenylpentanoate.
[13] C. J. Brabec, G. Zerza, G. Cerullo, S. De Sivestri, S. Luzatti, J. C. Hummelen, S. N. Sariciftci, *Chem. Phys. Lett.* **2001**, *340*, 232–236.
[14] B. Kraabel, D. McBranch, N. S. Sariciftci, D. Moses, A. J. Heeger, *Phys. Rev. B* **1994**, *50*, 18543–18552.
[15] N. S. Sariciftci, L. Smilowitz, A. J. Heeger, F. Wudl, *Science* **1992**, *258*, 1474–1475.
[16] Photovoltaic cells were prepared with different [70]PCBM:MDMO-PPV weight ratios, ranging from 2:1 to 5:1.
[17] C. J. Brabec, S. E. Shaheen, C. Winder, N. S. Sariciftci, P. Denk, *Appl. Phys. Lett.* **2002**, *80*, 1288–1290.
[18] L. S. Hung, C. W. Tang, M. G. Mason, *Appl. Phys. Lett.* **1997**, *70*, 152–155.
[19] J. M. Kroon, M. M. Wienk, W. J. H. Verhees, J. C. Hummelen, *Thin Solid Films* **2002**, *403–404*, 223–228.
[20] A lower value of V_{oc} may be due to a lower reduction potential of the electron acceptor: C. J. Brabec, A. Cravino, D. Meissner, N. S. Sariciftci, T. Fromherz, M. T. Rispens, L. Sanchez, J. C. Hummelen, *Adv. Funct. Mater.* **2001**, *11*, 374–380. However, the reduction potentials of [60]PCBM and [70]PCBM are identical (not shown). Therefore, we attribute the reduced V_{oc} value to recombination losses. The lower *FF* value is related to a higher series resistance over the device.
[21] F. Louwet, D. Vanderzande, J. Gelan, J. Mullens, *Macromolecules* **1995**, *28*, 1330–1331.
[22] P. A. Van Hal, E. H. A. Beckers, S. C. J. Meskers, R. A. J. Janssen, B. Jousselme, P. Blanchard, J. Roncali, *Chem. Eur. J.* **2002**, *8*, 5415–5429.
[23] P. M. Sommeling, H. C. Rieffe, J. A. M. Van Roosmalen, A. Schönecker, J. M. Kroon, J. A. Wienke, A. Hinsch, *Sol. Energy Mater. Sol. Cells* **2000**, *62*, 399–410.

 © 2003 Wiley-VCH Verlag GmbH & Co. KGaA, Weinheim

Corannulene Complexes

Transition-Metal Complexes of an Open Geodesic Polyarene**

Marina A. Petrukhina, Kristian W. Andreini, James Mack, and Lawrence T. Scott*

Scarcely half a year after the first isolation of solid C_{60},[1] transition-metal complexes of fullerenes began appearing on the rapidly growing list of novel derivatives.[2] At almost the

[*] Prof. Dr. M. A. Petrukhina, K. W. Andreini
Department of Chemistry
University at Albany, State University of New York
Albany, NY 12222 (USA)
Fax: (+1) 518-442-3462
E-mail: marina@albany.edu
Dr. J. Mack, Prof. Dr. L. T. Scott
Department of Chemistry
Merkert Chemistry Center, Boston College
Chestnut Hill, MA 02167–3860 (USA)

[**] The University at Albany, SUNY, has supported this work through an FRAP-2002 award and start-up funds. M.A.P. also thanks the National Science Foundation for the CCD X-ray diffractometer (NSF-01300985) and Dr. E. Dikarev for assistance with the X-ray experiments. Additional support of this work by the Department of Energy and the National Science Foundation is gratefully acknowledged.

 DOI: 10.1002/anie.200351403 © 2003 Wiley-VCH Verlag GmbH & Co. KGaA, Weinheim

same time, a surge of interest in bowl-shaped "fullerene fragments" spawned parallel efforts to prepare transition-metal complexes of open geodesic polyarenes. The intriguing question regarding the preference for metal binding to the concave surface versus the convex surface was first addressed computationally by Faust and Vollhardt,[3] and has been revisited more recently by others.[4, 5] Experimental evidence to support or refute these predictions has, until now, eluded investigators.[6]

Corannulene (Figure 1), the smallest geodesic polyarene ($C_{20}H_{10}$), has previously been found to form a very weak [(η^6-corannulene)Ru(C_5Me_5)] cationic π complex that can be

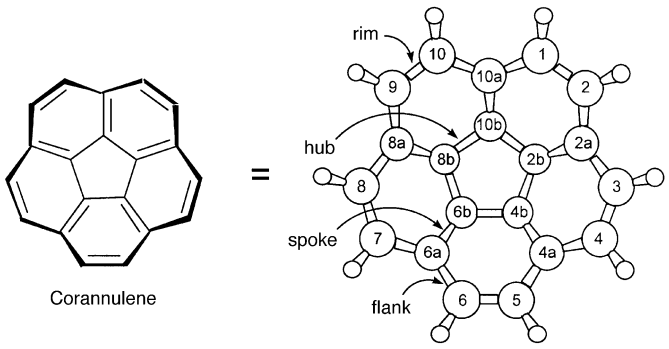


Figure 1. Corannulene structure and atom numbering. There are four types of C–C bonds: rim, hub, spoke, and flank.

characterized in solution by spectroscopic methods.[4b] Unfortunately, its lability precluded crystallographic analysis that would establish whether the metal binds to the concave surface or the convex surface of the hydrocarbon. In the gas phase, corannulene forms both 1:1 and 2:1 cationic complexes with iron ({(corannulene)Fe^+} and {(corannulene)$_2Fe^+$}, respectively).[7] Ligand attachment studies with the 1:1 complex point to η^4 binding of the corannulene with iron; however, the facial preference of the metal is again undetermined. Attempts to prepare the π complex of the C_3-symmetric "semibuckminsterfullerene" [{η^2-Pt(PPh_3)$_2$}{$C_{30}H_{12}$}] by treatment with [Pt(C_2H_4)(PPh_3)$_2$] did not follow the same course as with C_{60}, but led instead to oxidative addition of a strained aryl–aryl C–C bond to the metal center, yielding an η^2-coordinated σ-bonded {Pt(PPh_3)$_2$} complex.[8] Herein we report the first two X-ray crystal structures of transition metal complexes of a geodesic polyarene, namely, corannulene. These new complexes also represent the first η^2-coordinated π complexes of a hydrocarbon in this class. As many as three metal atoms are seen to form a complex with a single corannulene, and π bonding occurs on both the convex and the concave surface.

To prepare these new complexes, we relied on the recently introduced solvent-free synthesis strategy that has proven so successful for the preparation of other polycyclic aromatic hydrocarbon (PAH) complexes of dirhodium(II) tetrakis(trifluoroacetate), [$Rh_2(O_2CCF_3)_4$].[9] Studies to date with planar PAHs have revealed the interesting trend that η^2 metal coordination is site-selective and is correlated with the π-bond order of the C=C bonds, as determined by simple Hückel calculations. This makes the selected dirhodium complex a very sensitive electrophilic probe to test donor properties of the coordinatively more interesting nonplanar aromatic systems.

Corannulene was synthesized according to our three-step procedure,[10] and [$Rh_2(O_2CCF_3)_4$] was prepared in a form containing no additional ligands.[11] Synthesis of the complexes was accomplished by sublimation-deposition reactions of the volatile, complementary donor and acceptor partners. Two new products [[$Rh_2(O_2CCF_3)_4$]$_m$·($C_{20}H_{10}$)$_n$] (m:n = 1:1 (**1**) and 3:2 (**2**)) were isolated from two separate reactions performed at 160 °C.[12] The composition of the products was controlled by varying the reagent ratios in the solid state. An excess of ligand in the solid-state mixture (Rh_2:L ≈ 1:2) favored formation of product **1**, which was isolated in the form of green needle-shaped crystals in yields of 15–20 %. On the other hand, an excess of the dimetal complex (Rh_2:L ≈ 3:1) resulted in deposition of dark-green blocks of **2** in yields of 30–35 %. Crystals of both products **1** and **2** were prepared separately under controlled reaction conditions; they have distinctly different colors and shapes. Both products are relatively stable in air at room temperature but are sensitive to moisture; this behavior is typical for analogous donor–acceptor adducts with planar PAHs. When crystals of **1** or **2** are dissolved in acetone, the complexes undergo ligand exchange and release free corannulene, as confirmed by ^{1}H NMR spectroscopy.

X-ray diffraction studies of the crystals of compounds **1** and **2**[13] have revealed two unique structural motifs built on weak η^2 coordination. Compound **1** is a one-dimensional (1D) polymer consisting of alternating dirhodium units and corannulene molecules (Figure 2). Two crystallographically independent rhodium atoms of the dimetal unit each have bonding contacts with two carbon atoms. Rh1 approaches the ligand from the convex (*exo*) side of the corannulene moiety, while Rh2 binds from the concave (*endo*) side. Both rhodium centers interact with the rim C=C bonds of the ligand in an η^2 coordination mode. There is a significant difference between the two Rh–C bond lengths (0.225 Å) for the Rh1

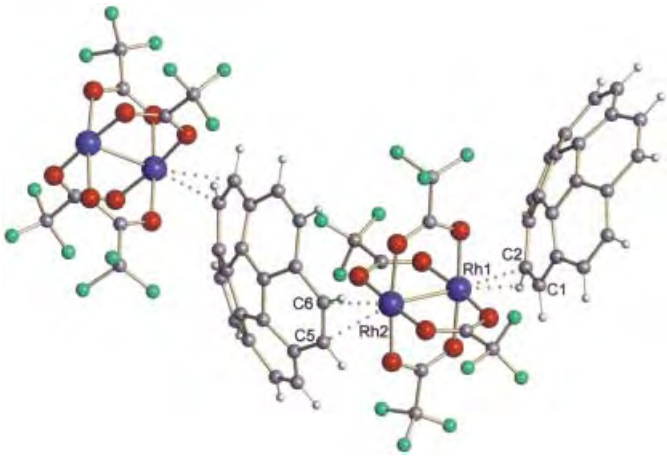


Figure 2. A fragment of a 1D infinite chain in **1**. Rh1-C1 2.756(4), Rh1-C2 2.531(4), Rh2-C5 2.595(4), Rh2-C6 2.564(4) Å.

 © 2003 Wiley-VCH Verlag GmbH & Co. KGaA, Weinheim

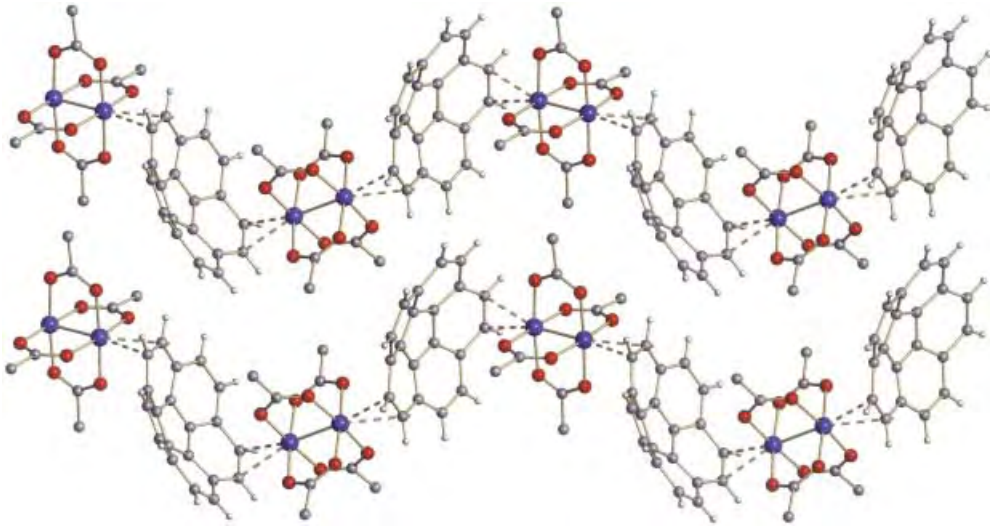


Figure 3. Crystal packing in **1**; Rh blue, O red, C gray, H light gray; fluorine atoms are are omitted for clarity.

atom (*exo* coordination), while there is only a difference of 0.031 Å for the contacts with the Rh2 center (*endo* coordination). The average Rh–C separation is also slightly longer for the rhodium atom that approaches corannulene from the convex side (2.643(4) Å for Rh1; 2.580(4) Å for Rh2). There are no close interactions between the 1D zigzag chains in the crystal structure of **1** (Figure 3).

Compound **2** has an infinite 2D layered network consisting of giant hexagonal cells built of six dimetal units and six corannulene molecules (Figure 4). Each corannulene molecule is coordinated to three dimetal units; two from the convex side and one from the concave side (Figure 5). As in **1**, only rim carbon atoms of the ligand are involved in coordination to the rhodium atoms. All three linear dirhodium units use both axial positions for coordination, with each rhodium center binding two carbon atoms of a corannulene (η^2 coordination mode). For the three crystallographically independent rhodium atoms in the asymmetric unit (Rh1, Rh2, and Rh3), the Rh–C bond lengths are averaged to

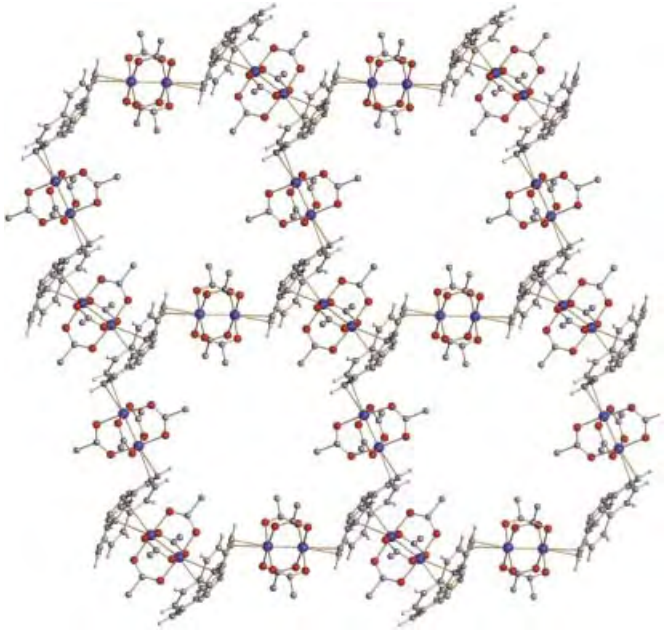


Figure 4. A fragment of a 2D infinite layer in **2**; Rh blue, O red, C gray, H light gray; fluorine atoms are omitted for clarity.

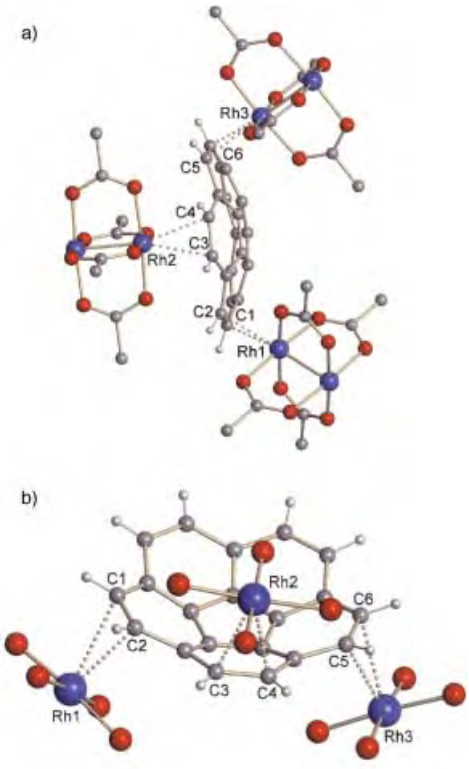


Figure 5. a) A side view of a corannulene molecule in **2** coordinated to three dimetal units. Rh1-C1 2.775(3), Rh1-C2 2.496(3), Rh2-C3 2.565(3), Rh2-C4 2.575(4), Rh3-C5 2.477(3), and Rh3-C6 2.618(3) Å; b) a front view of corannulene showing the six coordinating carbon atoms.

 © 2003 Wiley-VCH Verlag GmbH & Co. KGaA, Weinheim

2.636(3), 2.570(3), and 2.548(3) Å, respectively, with the differences between the two Rh–C bonds for each rhodium atom being 0.279, 0.010, and 0.141 Å, respectively. Again, a significant difference is observed for two Rh–C separations with metal atoms that approach the curved surface of corannulene from the convex side (Rh1 and Rh3).

It is informative to compare the structural characteristics of corannulene in complexes **1** and **2** with those of the "free" $C_{20}H_{10}$ polyarene molecule obtained at −70 °C.[14] This comparison (Table 1) reveals that the metal–π interaction is very weak and does not perturb the structure of the corannulene molecule significantly. Only a slight elongation of the rim C=C bond occurs upon coordination (0.009 Å in **1** and 0.018 Å in **2**), while other geometric characteristics of corannulene in the complexed and uncomplexed forms remain very similar. For example, the sum of the bond angles at the carbon atoms of the complexed rim C=C bonds in corannulene are essentially identical to those of the uncomplexed rim C=C bonds; they all fall in the range 359–360°. Thus, there is no detectable pyramidalization of carbon atoms upon complexation. The characteristics of the dimetal core in both complexes are quite typical for donor–acceptor adducts with weakly bound π-donor ligands.

Table 1: Geometric characteristics of corannulene in the free and coordinated forms

C–C Type	Corannulene (−70 °C)[14a]	**1**	**2**	C=C π-bond order[14b]
hub	1.413(2)	1.413(6)	1.415(4)	0.27
spoke	1.391(4)	1.375(6)	1.371(4)	0.46
flank	1.440(2)	1.447(6)	1.445(5)	0.27
rim(free)	1.402(5)	1.387(6)	1.379(5)	0.73
rim(coordinated)	–	1.396(6)	1.397(4)	–

The observed coordination of electrophilic Rh^{II} centers exclusively at the rim C=C bonds of corannulene in both **1** and **2** is surprising in light of the high kinetic preference shown by other electrophilic species for attack at the radial C=C bonds of corannulene (for example, dihalocarbenes (:CX_2); X = Cl, Br, and I)[15,16] and at the hub carbon atoms (for example, CCl_3, $CHCl_2$, and *i*Pr cations).[16,17] On the other hand, complexation of planar PAHs by $[Rh_2(O_2CCF_3)_4]$ is invariably seen at the rim where η^2-type bonding occurs at the C=C sites with the highest π-bond order.[9] In this connection, a simple analysis of the eleven canonical resonance structures of corannulene indicates a significantly higher Pauling π-bond order for the rim than for the radial C=C bonds (Table 1).[14b]

It is noteworthy that every corannulene unit in both the 1D (**1**) and the 2D (**2**) organometallic networks has one $[Rh_2(O_2CCF_3)_4]$ unit complexed to the concave surface. Baldridge and co-workers calculated that the $[Ru(C_5Me_5)]$ cation should show a preference of about 6 kcal mol^{-1} for complexation to the convex surface of corannulene, whereas Frash et al. calculated a 3 kcal mol^{-1} preference for complexation of Li^+ ions to the convex surface.[4] With $[Rh_2(O_2CCF_3)_4]$, on the other hand, DFT calculations predict a slight preference for complexation to the concave surface of corannulene (approximately 2 kcal mol^{-1}).[18] This result conforms to the view that the electrostatic potential of geodesic polyarenes is more negative on the concave surface than on the convex surface[19] and that $[Rh_2(O_2CCF_3)_4]$ is an exquisite probe for sites of high electron density. Steric hindrance precludes the coordination of two $[Rh_2(O_2CCF_3)_4]$ units to the concave surface of corannulene and presumably directs the two $[Rh_2(O_2CCF_3)_4]$ units on the convex surface in **2** to distal, rather than adjacent rings. It is not obvious, however, why the *endo* $[Rh_2(O_2CCF_3)_4]$ unit in **2** then complexes to the ring between these two, rather than to one of the less congested rings.

With this designed synthesis of corannulene-based organometallic networks we have demonstrated the potential of the gas-phase deposition technique for the coordination of curved surface geodesic polyarenes. This approach readily afforded transition-metal complexes of corannulene in crystalline forms suitable for structural characterization for the first time. Other geodesic polyarenes are currently being examined under similar experimental conditions.

Received: March 14, 2003 [Z51403]

Keywords: aromaticity · carboxylates · corannulene · pi interactions · rhodium · structure elucidation

[1] W. Krätschmer, L. D. Lamb, K. Fostiropoulos, D. R. Huffman, *Nature* **1990**, *347*, 354.
[2] a) P. J. Fagan, J. C. Calabrese, B. Malone, *Science* **1991**, *252*, 1160; b) P. J. Fagan, J. C. Calabrese, B. Malone, *Acc. Chem. Res.* **1992**, *25*, 134, and references therein.
[3] R. Faust, K. P. C. Vollhardt, *J. Chem. Soc. Chem. Commun.* **1993**, 1471.
[4] a) A. Sygula, P. W. Rabideau, *J. Chem. Soc. Chem. Commun.* **1994**, 2271; b) T. J. Seiders, K. K. Baldridge, J. M. O'Connor, J. S. Siegel, *J. Am. Chem. Soc.* **1997**, *119*, 4781; c) M. V. Frash, A. C. Hopkinson, D. K. Böhme, *J. Am. Chem. Soc.* **2001**, *123*, 6687; d) R. C. Dunbar, *J. Phys. Chem. A* **2002**, *106*, 9809.
[5] For calculations on metal complexes of partially hydrogenated geodesic polyarenes, see: a) A. L. Chistyakov, I. V. Stankevich, N. P. Gambaryan, *Russ. Chem. Bull.* **1995**, *44*, 855; b) A. L. Chistyakov, I. V. Stankevich, *Russ. Chem. Bull.* **1999**, *48*, 1628; c) A. L. Chistyakov, I. V. Stankevich, *Russ. Chem. Bull.* **2002**, *51*, 230.
[6] For structural characterization of a zirconium complex of partially hydrogenated corannulene, see: a) R. M. Chin, M. S. Jarosh, J. D. Russell, R. J. Lachicotte, *Organometallics* **2002**, *21*, 2027; Another η^6 complex of corannulene has recently been reported, but again no X-ray structure could be obtained: b) C. A. Alvarez, R. J. Angelici, A. Sygula, R. Sygula, P. W. Rabideau, *Organometallics* **2003**, *22*, 624.
[7] D. Caraiman, G. K. Koyanagi, L. T. Scott, D. V. Preda, D. K. Böhme, *J. Am. Chem. Soc.* **2001**, *123*, 8573.
[8] R. M. Shaltout, R. Sygula, A. Sygula, F. R. Fronczek, G. G. Stanley, P. W. Rabideau, *J. Am. Chem. Soc.* **1998**, *120*, 835.
[9] F. A. Cotton, E. V. Dikarev, M. A. Petrukhina, *J. Am. Chem. Soc.* **2001**, *123*, 11655.
[10] L. T. Scott, P.-C. Cheng, M. M. Hashemi, M. S. Bratcher, D. T. Meyer, H. B. Warren, *J. Am. Chem. Soc.* **1997**, *119*, 10963.
[11] F. A Cotton, E. V. Dikarev, X. Feng, *Inorg. Chim. Acta* **1995**, *237*, 19.

 © 2003 Wiley-VCH Verlag GmbH & Co. KGaA, Weinheim

[12] Synthesis of **1** and **2**: Mixtures of $[Rh_2(O_2CCF_3)_4]$ with corannulene were sealed under vacuum in two separate small glass ampoules. The ratio of the dirhodium complex (0.020 g, 0.030 mmol) to the ligand (0.014 g, 0.056 mmol) was ca. 1:2 in the synthesis of **1**. This ratio in the synthesis of **2** was ca. 2.7:1 (dirhodium complex (0.035 g, 0.053 mmol); corannulene (0.005 g, 0.020 mmol)). The ampoules were placed in electric furnaces that had a small temperature gradient along the length of the tube. The temperature was set at 160 °C in both cases. In three days, crystals of **1** and **2** were deposited in the middle or coldest parts of the ampoules where the temperature was a few degrees below 160 °C. **1**: Yield ca. 15–20 %; IR (KBr): 3067(w), 3041(w), 1664(s), 1464(w), 1441(w), 1402(w), 1349(w), 1314(w), 1225(s), 1194(s), 1170(s), 863(m), 856(m), 785(m), 740(s), 677(m), 663(m) cm^{-1}. **2**: Yield ca. 30–35 %; IR (KBr): 3061(w), 3041(w), 1664(s), 1463(w), 1439(w), 1401(w), 1318(w), 1230(s), 1196(s), 1165(s), 866(s), 788(m), 742(s), 671(m) cm^{-1}. ^1H NMR (200 MHz, $[D_6]$acetone, 22 °C): $\delta = 7.94$ ppm (s).

[13] X-ray crystal data for **1**: $Rh_2C_{28}F_{12}O_8H_{10}$, $M_r = 908.18$, green needle, $0.25 \times 0.07 \times 0.05$ mm, monoclinic, space group $C2/c$, $a = 34.767(2)$, $b = 8.9125(6)$, $c = 18.9825(12)$ Å, $\beta = 104.0530(10)°$, $V = 5705.9(6)$ Å^3, $Z = 8$, $T = 173(2)$ K, $\rho_{calcd} = 2.114$ g cm^{-3}, $2\theta_{max} = 56.38°$. For **2**: $Rh_6C_{64}F_{36}O_{24}H_{20}$, $M_r = 2474.26$, dark-green block, $0.14 \times 0.09 \times 0.08$ mm, triclinic, space group $P\bar{1}$, $a = 11.2082(7)$, $b = 12.8271(8)$, $c = 13.3417(8)$ Å, $\alpha = 94.7400(10)$, $\beta = 96.5280(10)$, $\gamma = 92.9660(10)°$, $V = 1895.5(2)$ Å^3, $Z = 1$, $T = 173(2)$ K, $\rho_{calcd} = 2.168$ g cm^{-3}, $2\theta_{max} = 56.54°$. Bruker SMART APEX CCD diffractometer, $Mo_{K\alpha}$ radiation ($\lambda = 0.71073$ Å). The structures were solved by direct methods and refined using the Bruker SHELXTL (Version 6.1) Software Package. Data were corrected for absorption effects using the empirical methods SADABS (min./max. apparent transmission are 0.7390/0.9384 and 0.8237/0.8934 for **1** and **2**, respectively. All non-hydrogen atoms were refined anisotropically except the disordered fluorine atoms. All H-atoms of corannulene were found in the difference Fourier map and refined independently. The fluorine atoms of some CF_3 groups were disordered over two or three different rotational orientations. This disorder was modeled individually in each case. For **1**, full-matrix refinement on F^2 converged at $R1 = 0.0433$ and $wR2 = 0.1114$ for 494 parameters and 5799 reflections with $I > 2\sigma(I)$ ($R1 = 0.0489$, $wR2 = 0.1164$ for 6572 unique reflections) and a goodness-of-fit of 1.055. For **2**, full-matrix refinement on F^2 converged at $R1 = 0.0285$ and $wR2 = 0.0705$ for 644 parameters and 7607 reflections with $I > 2\sigma(I)$ ($R1 = 0.0330$, $wR2 = 0.0734$ for 8556 unique reflections) and a goodness-of-fit of 1.046. CCDC-201188 and -201189 contain the supplementary crystallographic data for structures **1** and **2**. These data can be obtained free of charge via www.ccdc.cam.ac.uk/conts/retreiving.html (or from the Cambridge Crystallographic Data Centre, 12, Union Road, Cambridge, CB2 1EZ, UK; fax (+44)1223–336–033; or deposit@ccdc.cam.ac.uk).

[14] a) J. C. Hanson, C. E. Nordman, *Acta Crystallogr. Sect. B* **1976**, 1147; For a recent gas-phase molecular structure of corannulene determined by electron diffraction, see: b) L. Hedberg, K. Hedberg, P.-C. Cheng, L. T. Scott. *J. Phys. Chem. A* **2000**, *104*, 7689.

[15] D. V. Preda, L. T. Scott, *Tetrahedron Lett.* **2000**, *41*, 9633.

[16] D. V. Preda, Ph. D. dissertation, Boston College, **2001**.

[17] L. T. Scott, H. E. Bronstein, D. V. Preda, R. B. M. Ansems, M. S. Bratcher, S. Hagen, *Pure Appl. Chem.* **1999**, *71*, 209.

[18] Our calculations were performed at the B3LYP/3-21G* level of theory, with an $[(ethylene)Rh_2(O_2CCF_3)_4]$ unit as the electrophile, using the Spartan suite of programs (Wavefunction Inc., Irvine, CA). Higher level basis sets (e.g., 6-31G*) do not have orbitals for rhodium in Spartan. Note that these calculations probe the intrinsic interaction of only a single corannulene molecule with a single dirhodium unit in the gas phase; no attempt was made to assess the influence of the extended network in the crystal.

[19] F.-G. Klärner, J. Panitzky, D. Preda, L. T. Scott, *J. Mol. Model.* **2000**, *6*, 318.

 © 2003 Wiley-VCH Verlag GmbH & Co. KGaA, Weinheim

Polyrotaxanes

Rotaxane Building Blocks bearing Blocked Isocyanate Stoppers: Polyrotaxanes through Post-Assembly Chain Extension**

Timothy J. Kidd, Ton J. A. Loontjens, David A. Leigh,* and Jenny K. Y. Wong*

Given the high cost of introducing new chemical building blocks, an important challenge for the development of new functional polymers is to try to assemble existing cheap monomeric building blocks in new ways, by using novel types of molecular-level architectures to improve characteristics and provide "added value". For instance, it is thought that by incorporating rotaxanes into macromolecules,[1] some of the properties seen for rotaxanes in solution (that is, the ability to switch, shuttle, or alter shape[2]) could be transferred across to the solid state where easier handling and processibility might provide the basis for new types of "smart" materials and/or molecular-based devices.[3] However, relatively few strategies for polyrotaxane synthesis are suitable for making mechanically interlocked derivatives of commercial polymers on a practical scale.[1] Herein we report the convenient synthesis and polymerization (to give main-chain, side-chain, and cross-linked network polyrotaxane architectures) of cheap and readily obtainable rotaxane monomers (**3**–**5**) stoppered by bulky, blocked (i.e., masked) isocyanate groups. Blocked isocyanates are widely used in commercial heat-curable systems (e.g., powder coatings and heat-setting adhesives)

[*] Dr. T. J. A. Loontjens, Dr. T. J. Kidd
DSM Research
P.O. Box 18, 6160 MD Geleen (The Netherlands)
Fax: (+31) 46-476-3949
E-mail: ton.loontjens@dsm.com
Prof. Dr. D. A. Leigh, Dr. J. K. Y. Wong
School of Chemistry
The University of Edinburgh, The King's Buildings
West Mains Road, Edinburgh EH9 3JJ (UK)
Fax: (+44) 131-667-9085
E-mail: david.leigh@ed.ac.uk

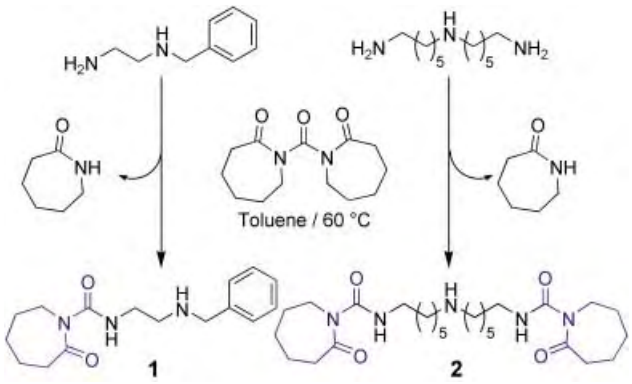
[**] This work was carried out as part of the European Training and Mobility of Researchers (TMR) European Network the Development of Rotaxane-based Unconventional Materials (contract no. ERBFMRXCT970097). D.A.L. is an EPSRC Advanced Research Fellow (AF/982324).

Supporting information for this article is available on the WWW under http://www.angewandte.org or from the author.

 DOI: 10.1002/anie.200351458 © 2003 Wiley-VCH Verlag GmbH & Co. KGaA, Weinheim

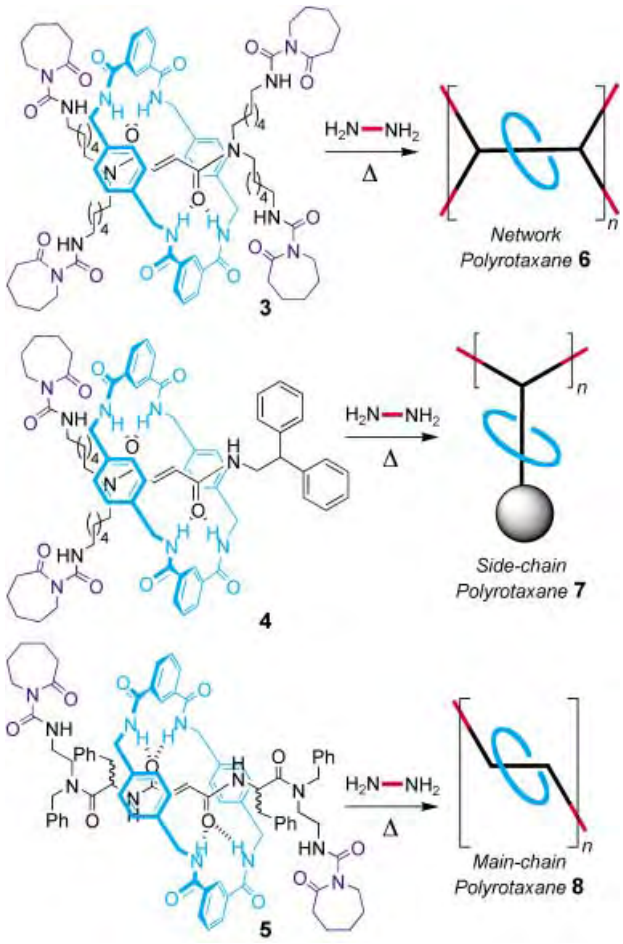
because of their relative stability at ambient temperatures compared to conventional isocyanates.[4] At elevated temperatures (> 150 °C), however, they react rapidly with amino or hydroxy difunctional comonomers to produce polyureas and polyurethanes. Blocked isocyanate rotaxane derivatives can thus act as cheap and readily accessible building blocks for polyrotaxane topological analogues of a wide range of commercial polymer systems.[5] We illustrate this versatility by synthesizing three different polyrotaxane topologies (**6**–**8**) using monomeric rotaxane building blocks **3**–**5** and a single, standard α,ω-amino-terminated polyether. In addition to providing a simple and practical route to a variety of mechanically interlocked architectures, the macrocycle is not able to dissociate from the growing polymer chain during the synthesis, and therefore the degree of macrocycle threading in the final product can be controlled with great precision.[6]

A procedure was recently discovered[7] in which blocked isocyanates can be formed in near-quantitative yields from amines and carbonyl biscaprolactam (CBC). During this reaction, one of the two caprolactam rings in CBC is selectively replaced by an amine forming a blocked isocyanate. The reaction exhibits exquisite selectivity for primary over secondary amines; in molecules containing both functional-group types the primary amine reacts exclusively at temperatures less than 100 °C, leaving the secondary amine available for further elaboration. The synthesis of stoppers containing one (**1**) or two (**2**) caprolactam-blocked isocyanate groups was thus achieved by reacting CBC with either *N*-benzylethylenediamine or bis(hexamethylene)triamine, respectively (Scheme 1). The free secondary amine moiety



Scheme 1. The synthesis of bulky stopper groups **1** and **2** containing caprolactam-blocked isocyanates from the selective reaction of a di- or triamine with carbonyl biscaprolactam.

was then used to attach the polymerizable stopper to a suitable template for rotaxane formation. We chose the fumaramide group, which directs the five component assembly of benzylic amide macrocycle-containing rotaxanes from isophthaloyl dichloride and *p*-xylylenediamine in high efficiency.[8] This modular approach allowed us to attach different combinations of stoppers **1** and **2** onto the monomeric thread to produce rotaxane monomers (**3**–**5**) which, upon reaction with the suitable bisamine comonomer Jeffamine, produced



Scheme 2. The polymerization of monomer rotaxanes containing caprolactam-blocked isocyanate stopper groups (**3**–**5**) leading to cross-linked (**6**), linear side-chain (**7**), and linear main-chain (**8**) polyrotaxane topologies.

polyrotaxanes of different topologies (Scheme 2).[9] The blocked isocyanate rotaxane building blocks proved stable for several months (at least) at room temperature.

The rotaxane comonomers were synthesized through treatment of the blocked isocyanate threads with *p*-xylylenediamine and isophthaloyl dichloride ($CHCl_3$, Et_3N, 2 h, high dilution) to give rotaxanes **3**–**5** in 70, 70, and 45% yield, respectively. In each case, crystals suitable for investigation by X-ray crystallography were obtained through slow diffusion of diethyl ether into a solution of the rotaxane in chloroform. The crystal structures (Figure 1) confirm the interlocked architectures and the unhindered environment of the blocked isocyanates for further chain extension.[10]

Rotaxane building block **5**, comprised of two mono-blocked isocyanate stopper groups **1** (one each side of the fumaramide template), incorporated an additional phenylalanine residue to prevent dethreading of the macrocycle during polymerization.[11] In all cases, the rotaxane building blocks were obtained as colorless powders with melting points in the range 155–170 °C, facilitating handling and storage, consistent with other blocked isocyanate systems used in commercial heat-curable systems.

 © 2003 Wiley-VCH Verlag GmbH & Co. KGaA, Weinheim

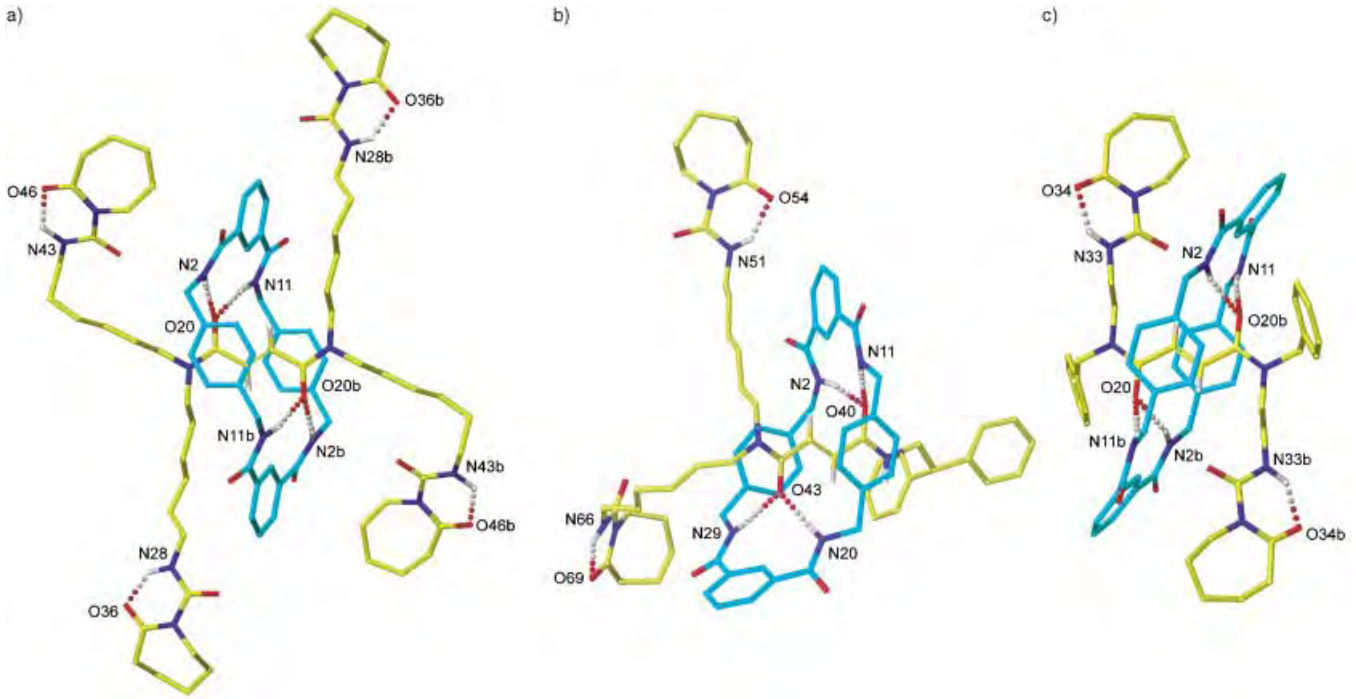


Figure 1. The solid-state structures of a) **3**, b) **4**, and c) a derivative of **5**, as determined by X-ray crystallography. Carbon (macrocyclic rings), light blue; carbon (threads), yellow; oxygen, red; nitrogen, dark blue. Non-amide or alkene hydrogen atoms have been removed for clarity. Hydrogen-bond distances [Å]: a) O20-HN2/O20b-HN2b 2.35, O20-HN11/O20b-HN11b 2.13, O36-HN28/O36b-HN28b 1.77, O46-HN43/O46b-HN43b 1.67; b) O40-HN2 2.12, O40-HN11 2.30, O43-HN20 2.14, O43-HN29 2.25, O54-HN51 1.83, O69-HN66 2.00; c) O20-HN2b/O20b-HN2 2.18, O20-HN11b/O20b-HN11 2.48, O34-HN33/O34b-HN33b 1.86. Hydrogen bond angles [°]: a) O20-HN2/O20b-HN2b 162.0, O20-HN11/O20b-HN11b 171.1, O36-HN28/O36b-HN28b 151.1, O46-HN43/O46b-HN43b 136.5; b) O40-HN2 165.4, O40-HN11 177.1, O43-HN20 169.5, O43-HN29 173.9, O54-HN51 141.7, O69-HN66 138.4; c) O20-HN2b/O20b-HN2 171.5, O20-HN11b/O20b-HN11 164.8, O34-HN33/O34b-HN33b 137.7.[10]

The bulk polymerizations of rotaxanes **3**–**5** were performed by heating a stoichiometric mixture of rotaxane and comonomer at 175 °C for 1 hr under a nitrogen atmosphere. The comonomer (Jeffamine D400) is an amino-terminated polyether with an average molecular weight of 400 g mol^{-1} that is used in a variety of commercial polyurethanes and polyureas. The flexible polyether chains generally afford materials with low glass-transition temperatures (T_g) and should thus allow for mobility of the rotaxane units at ambient temperatures and conditions. In addition, linear polyethers are generally soluble in solvents suitable for ^{1}H NMR spectroscopy and size exclusion chromatography (SEC), which make the resulting polyrotaxanes easy to characterize.

Reaction of the tetrablocked isocyanate rotaxane **3** with two equivalents of difunctional comonomer at 175 °C produced a cross-linked material which proved insoluble in common organic solvents. ^{1}H NMR spectra of a swollen sample of polyrotaxane **6** in $CDCl_3$, however, confirmed that the rotaxane building blocks remained intact during the polymerization process (Figure 2). Repeated extraction of the polymer with solvents that dissolve both monomers did not result in the leaching out of any unreacted material, which verified that the rotaxane units form an integral part of the network polymer. Dynamic mechanical testing (DMTA) measurements on a thin film of polyrotaxane gave a plateau modulus of 10^6 Pa, which confirmed that the material is a stable cross-linked rubberlike polymer. Stress–strain experiments on the polyrotaxane film gave an elongation-at-break value of $>100\,\%$, further confirming the rubbery nature of the material.

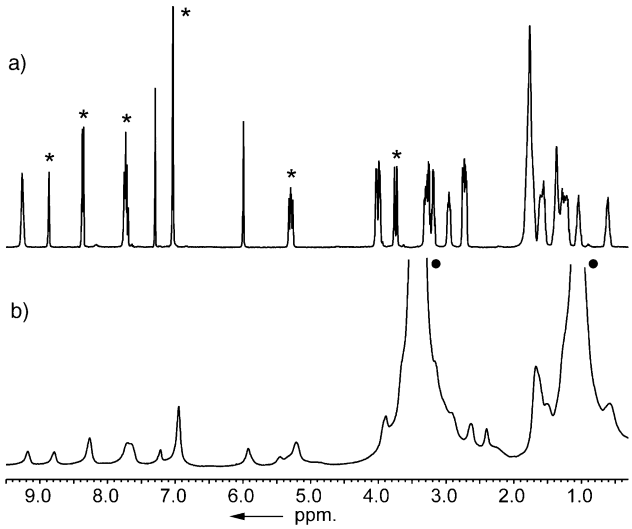


Figure 2. ^{1}H NMR spectra (300 MHz, $CDCl_3$, 298 K) of a) rotaxane monomer **3** and b) a swollen sample of the corresponding cross-linked network polyrotaxane **6** (* denotes macrocyclic protons; ● denotes Jeffamine protons in the polymer).

 © 2003 Wiley-VCH Verlag GmbH & Co. KGaA, Weinheim

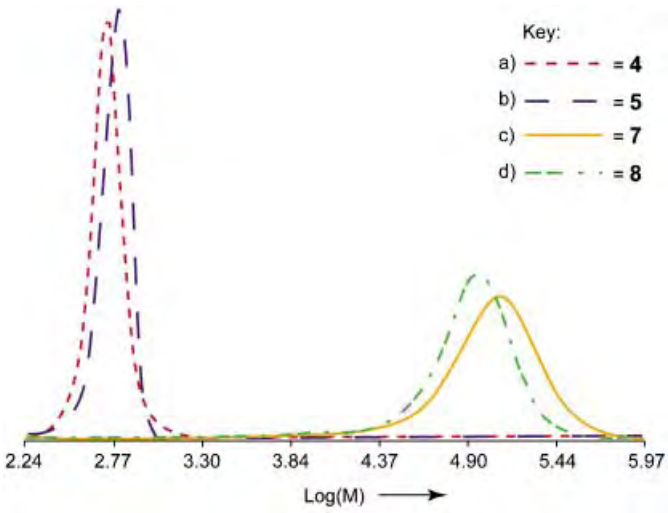


Figure 3. Size exclusion chromatogram of a) pure rotaxane monomer **4**, b) pure rotaxane monomer **5**, c) polyrotaxane **7** from the reaction between **4** and Jeffamine D400, and d) polyrotaxane **8** from the reaction between **5** and Jeffamine D400.

After treatment with one equivalent of Jeffamine D400 comonomer for one hour at 175 °C, rotaxanes **4** and **5** produced polymers with molecular weights (M_w) of 165 kg mol^{-1} ($M_w/M_n = 1.9$) and 86 kg mol^{-1} ($M_w/M_n = 1.6$), respectively (Figure 3), which corresponds to the linear side-chain polyrotaxane **7** (possessing, on average, 96 rotaxane units per polymer chain) and the linear main-chain polyrotaxane **8** (with an average of 46 rotaxane units per polymer chain), respectively.[12] ^{1}H NMR spectroscopy again confirmed the 1:1 ratio of macrocycle:Jeffamine repeat units. Initial studies have shown that there are clear differences in the properties (solubility, mechanical, photochemical, and so forth) of the various polyrotaxane architectures and the corresponding polythreads. Further studies are ongoing and will be reported elsewhere.

In conclusion, a simple, versatile route to polyrotaxanes with a variety of topologies is available through the synthesis and subsequent polymerization of readily accessible, stable, rotaxane monomers containing bulky, blocked isocyanate stopper groups. These monomeric [2]rotaxanes represent a new kind of functional-chain extender that is wholly compatible with methodologies currently used to make a range of commercial polymers and could thus lead to the facile incorporation of a number of rotaxane systems into materials where the effects of the mechanical bond could be tested and realistically exploited. In principle, this system can also be applied to the modular generation of rotaxane-based polymeric materials or "devices" in which individual components can be introduced in different combinations through "bottom-up" processing.

Received: March 24, 2003 [Z51458]
Published online: July 3, 2003

Keywords: polymers · polyrotaxanes · rotaxanes · template synthesis

[1] a) H. W. Gibson, M. C. Bheda, P. T. Engen, *Prog. Polym. Sci.* **1994**, *19*, 843–945; b) H. W. Gibson in *Large Ring Molecules* (Ed.: J. A. Semlyen), Wiley, New York, **1996**, pp. 191–262; c) A. Harada, *Acta Polym.* **1998**, *49*, 3–17; d) H. W. Gibson, C. Gong in *Molecular Catenanes, Rotaxanes and Knots* (Eds.: J.-P. Sauvage, C. Dietrich-Buchecker), VCH, Weinheim, **1999**, pp. 277–321; e) F. M. Raymo, J. F. Stoddart, *Chem. Rev.* **1999**, *99*, 1643–1663.

[2] a) R. A. Bissell, E. Córdova, A. E. Kaifer, J. F. Stoddart, *Nature* **1994**, *369*, 133–137; b) M.-V. Martinez-Diaz, N. Spencer, J. F. Stoddart, *Angew. Chem.* **1997**, *109*, 1991–1994; *Angew. Chem. Int. Ed. Engl.* **1997**, *36*, 1904–1907; c) L. Raehm, J.-M. Kern, J.-P. Sauvage, *Chem. Eur. J.* **1999**, *5*, 3310–3317; d) W. Clegg, C. Gimenez-Saiz, D. A. Leigh, A. Murphy, A. M. Z. Slawin, S. J. Teat, *J. Am. Chem. Soc.* **1999**, *121*, 4124–4129; e) A. M. Brouwer, C. Frochot, F. G. Gatti, D. A. Leigh, L. Mottier, F. Paolucci, S. Roffia, G. W. H. Wurpel, *Science* **2001**, *291*, 2124–2128; f) M. C. Jimenez-Molero, C. Dietrich-Buchecker, J.-P. Sauvage, *Chem. Eur. J.* **2002**, *8*, 1456–1466; g) Y. Luo, C. P. Collier, J. O. Jeppesen, K. A. Nielsen, E. Delonno, G. Ho, J. Perkins, H. R. Tseng, T. Yamamoto, J. F. Stoddart, J. R. Heath, *ChemPhysChem* **2002**, *3*, 519–525; h) C. A. Stanier, S. J. Alderman, T. D. W. Claridge, H. L. Anderson, *Angew. Chem.* **2002**, *114*, 1847–1850; *Angew. Chem. Int. Ed.* **2002**, *41*, 1769–1772; For recent accounts from the UCLA and Strasbourg groups, see: i) A. R. Pease, J. O. Jeppesen, J. F. Stoddart, Y. Luo, C. P. Collier, J. R. Heath, *Acc. Chem. Res.* **2001**, *34*, 433–444; j) J. P. Collin, C. Dietrich-Buchecker, P. Gavina, M. C. Jimenez-Molero, J.-P. Sauvage, *Acc. Chem. Res.* **2001**, *34*, 477–487.

[3] a) V. Balzani, A. Credi, F. M. Raymo, J. F. Stoddart, *Angew. Chem.* **2000**, *112*, 3484–3530; *Angew. Chem. Int. Ed.* **2000**, *39*, 3349–3391; b) Special issue on *Molecular Machines*, *Acc. Chem. Res.* **2001**, *34*, 409–522; c) "Molecular Machines and Motors": *Struct. Bonding (Berlin) Vol. 99*, **2001**.

[4] D. A. Wicks, Z. W. Wicks, Jr., *Prog. Org. Coat.* **1999**, *36*, 148–172, and references therein.

[5] For other examples of post-assembly elaboration of rotaxanes, see: a) M. P. L. Werts, M. van der Boogaard, G. Hadziioannou, G. M. Tsivgoulis, *Chem. Commun.* **1999**, 623–624; b) S. J. Rowan, S. J. Cantrill, J. F. Stoddart, A. J. P. White, D. J. Williams, *Org. Lett.* **2000**, *2*, 759–762; c) S. J. Rowan, J. F. Stoddart, *J. Am. Chem. Soc.* **2000**, *122*, 164–165; d) D. W. Zehnder, D. B. Smithrud, *Org. Lett.* **2001**, *3*, 2485–2487; e) S.-H. Chiu, S. J. Rowan, S. J. Cantrill, J. F. Stoddart, A. J. P. White, D. J. Williams, *Chem. Eur. J.* **2002**, *8*, 5170–5183; f) S.-H. Chiu, S. J. Rowan, S. J. Cantrill, L. Ridvan, P. R. Ashton, R. L. Garrell, J. F. Stoddart, *Tetrahedron* **2002**, *58*, 807–814.

[6] Other approaches for controlling the macrocycle:thread repeat-unit stoichiometry in polyrotaxanes include a) the polymerization of monomer threads containing bulky blocking groups [I. Yamaguchi, K. Osakada, T. Yamamoto, *J. Am. Chem. Soc.* **1996**, *118*, 1811–1812; C. Gong, T. E. Glass, H. W. Gibson, *Macromolecules* **1998**, *31*, 308–313; C. Gong, H. W. Gibson, *Angew. Chem.* **1997**, *109*, 2426–2428; *Angew. Chem. Int. Ed. Engl.* **1997**, *36*, 2331–2333; M. B. Steinbrunn, G. Wenz, *Angew. Chem.* **1996**, *108*, 2274–2277; *Angew. Chem. Int. Ed. Engl.* **1996**, *35*, 2139–2141] and/or initiators [H. W. Gibson, P. T. Engen, S. H. Lee, *Polymer* **1999**, *40*, 1823–1832] in the presence of a macrocycle; b) the formation of a pseudorotaxane coordination polymer [D. Whang, Y.-M. Yeon, J. Heo, K. Kim, *J. Am. Chem. Soc.* **1996**, *118*, 11333–11334; D. Whang, K. Kim, *J. Am. Chem. Soc.* **1997**, *119*, 451–452; E. Lee, J. Heo, K. Kim, *Angew. Chem.* **2000**, *112*, 2814–2819; *Angew. Chem. Int. Ed.* **2000**, *39*, 2699–2701]; and c) the catalytic polymerization of monomer threads where the threaded macrocycle itself acts as the catalyst to polymer formation [D. Tuncel, J. H. G. Steinke, *Chem. Commun.* **1999**, 1509–1510].

 © 2003 Wiley-VCH Verlag GmbH & Co. KGaA, Weinheim

[7] J. A. Loontjens, B. J. M. Plum (DSM), WO patent 00/17169, **2000**.
[8] a) F. G. Gatti, D. A. Leigh, S. A. Nepogodiev, A. M. Z. Slawin, S. J. Teat, J. K. Y. Wong, *J. Am. Chem. Soc.* **2001**, *123*, 5983–5989; b) F. G. Gatti, S. Leòn, J. K. Y. Wong, G. Bottari, A. Altieri, M. A. Farran Morales, S. J. Teat, C. Frochot, D. A. Leigh, A. M. Brouwer, F. Zerbetto, *Proc. Natl. Acad. Sci. USA* **2003**, *100*, 10–14.
[9] Full details of the experimental procedures can be found in the Supporting Information.
[10] Detailed crystallographic data for these compounds is reported in the Supporting Information.
[11] A rotaxane similar to **5** but without the extra phenylalanine residues (Figure 1c) was synthesized through condensation of two equivalents of stopper **1** with fumaroyl chloride. Subsequent polymerization of this rotaxane monomer resulted in the dethreading of the macrocycle from the polymer as a result of the loss of the bulky caprolactam blocking group during chain extension.
[12] The calculated degree of polymerization was based on the SEC-determined average molecular weights of Jeffamine D400 and rotaxane monomers.

 © 2003 Wiley-VCH Verlag GmbH & Co. KGaA, Weinheim

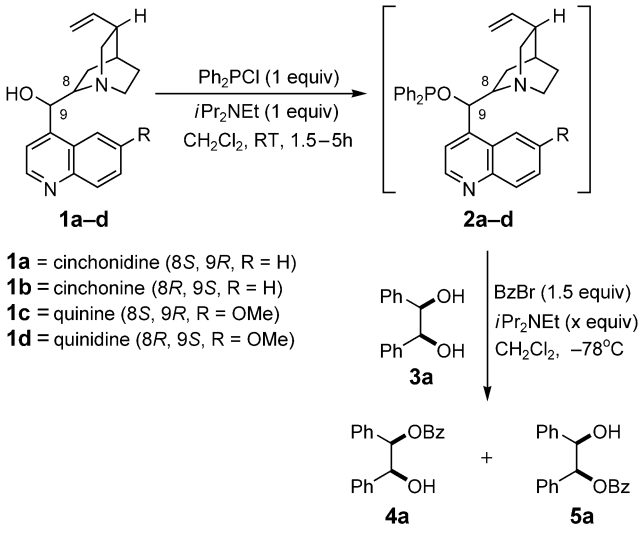
Desymmetrizing meso*-Diols*

Asymmetric Desymmetrization of *meso*-1,2-Diols by Phosphinite Derivatives of Cinchona Alkaloids**

Shinya Mizuta, Mikito Sadamori, Tetsuya Fujimoto, and Iwao Yamamoto*

The asymmetric desymmetrization of *meso*-diols is an important and powerful methodology for obtaining optically active substances. Numerous methods for the asymmetric desymmetrization of *meso*-diols have already been developed,[1] but only a few examples of the catalytic and direct asymmetric desymmetrization reaction of *meso*-diols have been reported.[2,3c] As an efficient catalyst for the stereoselective monoacylation of *meso*-diols, we proposed a bifunctional catalyst containing a Lewis-basic trivalent phosphorus center[3] and a Brønsted-basic tertiary amino group. If these functional groups act cooperatively to activate an acylating reagent and trap a proton in the monoacylating reaction, a more effective and stereoselective desymmetrization reaction may be accomplished. On the basis of this working hypothesis we designed phosphinites derived from cinchona alkaloids as the optimal catalyst. Although phosphinite and phosphite derivatives of cinchona alkaloids have been utilized as chiral ligands in asymmetric metal complexes[4] and intermediates for the synthesis of chiral phosphanes,[5] they have not been employed as catalysts for asymmetric reactions. Herein we report the asymmetric monoacylation of *meso*-1,2-diols with high yield and with high enantioselectivity using phosphinite derivatives of cinchona alkaloids.

A phosphinite derivative generated in situ from the reaction of chlorodiphenylphosphane with cinchonidine in the presence of Hünig's base was added to the benzoylation reaction of *meso*-hydrobenzoin with benzoyl bromide (Scheme 1). As a result, the corresponding monobenzoylated diol **4a** was obtained as the major isomer in 34% yield and 74% *ee* (Table 1, entry 1). Moreover, the addition of one equivalent of Hünig's base to the acylation reaction improved the yield of the product without reducing the enantioselectivity (Table 1, entry 2). The asymmetric desymmetrization of *meso*-hydrobenzoin with other cinchona alkaloids (cincho-



Scheme 1. Generation of the catalyst and desymmetrization of *meso*-hydrobenzoin. Bz = benzoyl, RT = room temperature.

Table 1: Asymmetric monobenzoylation of *meso*-hydrobenzoin in the presence of phosphinite compounds derived from cinchona alkaloids (see Scheme 1).

Entry	Alkaloid	Hünig's base [equiv]	*t* [h]	Major product	Yield [%][a]	*ee* [%][b]
1	**1a**	0	24	**4a**	34	74
2	**1a**	1	24	**4a**[c]	83	78
3	**1b**	1	1.5	**5a**	99	82
4	**1c**	1	3.5	**4a**	58	22
5	**1d**	1	3.5	**5a**	59	29

[a] Yield of isolated product. [b] Determined by chiral HPLC analysis or by the analysis of the corresponding Mosher's ester. [c] $[\alpha]_D^{24} = +28.7°$ ($c = 1.0$, $CHCl_3$, lit: $[\alpha]_D^{25} = -21.0°$ for the corresponding enantiomer **5a** at 64% *ee*).[2b]

[*] Dr. T. Fujimoto, S. Mizuta, M. Sadamori, Prof. Dr. I. Yamamoto
Department of Functional Polymer Science
Shinshu University
Tokida Ueda 386-8567 (Japan)
Fax: (+81) 268-21-5494
E-mail: tfujimo@giptc.shinshu-u.ac.jp

[**] This work was partly supported by The 21st Century COE Program of The Ministry of Education, Culture, Sports, Science, and Technology, Japan. We are also grateful to Kanto Chemical Co., Inc. for a gift of reagents and solvents.

Supporting information for this article is available on the WWW under http://www.angewandte.org or from the author.

 DOI: 10.1002/anie.200250719 © 2003 Wiley-VCH Verlag GmbH & Co. KGaA, Weinheim

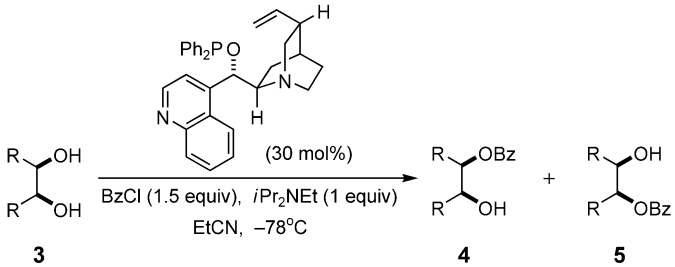
nine, quinine, quinidine) was also examined under the reaction conditions similar to those described for cinchonidine. In particular, when cinchonine, the diastereomer of cinchonidine, was employed, the corresponding enantiomeric monobenzoylated diol **5a** was obtained in nearly quantitative yield and 82% *ee* (Table 1, entry 3).

In order to optimize the reaction conditions for the desymmetrization with the phosphinite derivative of cinchonine, the reactions were conducted in different media and with various acylating reagents (Table 2). The dichloromethane solvent employed for the generation of the phosphinite derivative was removed by evaporation, and the benzoylation was carried out in propionitrile to afford the product with a higher enantioselectivity (Table 2, entry 6). When benzoyl chloride was used as the acylation reagent, an enantioselectivity of 91% ee was accomplished (Table 2, entry 7). In contrast the reactions using benzoic anhydride and pivaloyl chloride resulted in lower yields or no reaction (Table 2, entries 9 and 10).

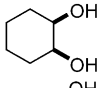
We also attempted the reaction using other cinchonidine derivatives in which the hydroxy group is protected by treatment with benzoyl chloride, pivaloyl chloride, diphenylacetyl chloride, or diphenylphosphinic chloride in place of chlorodiphenylphosphane. However, a racemic product was obtained in low yield for all cases. Consequently, the trivalent phosphinite group in the cinchonidine-based catalyst appears to play an important role in the asymmetric monobenzoylation reaction of *meso*-hydrobenzoin. Although the isolation of the pure phosphinite derivative of the cinchona alkaloid was difficult because trivalent phosphinite is susceptible to oxidation, the phosphinite derivative could be isolated as a mixture with the corresponding phosphinate.[6] The mixture of the phosphinite and phosphinate (ca. 85:15) from cinchonine was adapted for the asymmetric monobenzoylation to provide the monoacylated diol in almost quantitative yield and 91% *ee*. Moreover, the reaction in the presence of a catalytic amount (30 mol%) of the phosphinite as a mixture (containg about 15% phosphinate) afforded the corresponding monoacylated diol in 98% yield and 91% *ee* (Table 3, entry 1). Under the same reaction conditions, other *meso*-1,2-diols containg cyclic or acyclic diols were also monoacylated in good enatioselectivities (Table 3, entries 2–5).[7]

In conclusion, the phosphinite compound derived from cinchonine was found to be an effective desymmetrization catalyst for *meso*-1,2-diols. Further studies will focus on the mechanism of the catalysis and the wide array of applications for various phosphinite catalysts.

Table 3: Catalytic asymmetric acylation of *meso*-1,2-diols with the phosphinite compound derived from cinchonine.

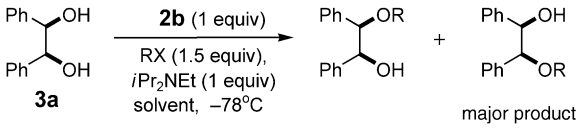


3 **4** **5**

Entry	*meso*-Diol	*t* [h]	Major product	Yield [%][a]	*ee* [%][b]
1		1.5	**5**	98	91
2		4	**4**	99	86
3		3.5	**4**	80	93
4		6	**4**	85	94
5		4.5	ND[c]	80	76

[a] Yield of isolated product. [b] Determined by chiral HPLC analysis. [c] Not determined.

Table 2: Effects of various solvents and acylation reagents on the asymmetric desymmetrization of *meso*-hydrobenzoin.



Entry	Solvent	*t* [h]	RX	Yield [%][a]	*ee* [%][b]
1	CH_2Cl_2	1.5	BzBr	99	82
2	toluene	3	BzBr	58	68
3	THF	2	BzBr	28	74
4	$CHCl_3$[c]	3	BzBr	15	65
5	MeCN[d]	1	BzBr	94	78
6	EtCN	0.5	BzBr	95	88
7	EtCN	1	BzCl	95	91
8	EtCN	2.5	*o*-MeC_6H_4COCl[e]	36	76
9	EtCN	6.5	$(PhCO)_2O$	17	4
10	EtCN	3	*t*BuCOCl	NR[f]	–

[a] Yield of isolated product. [b] Determined by chiral HPLC analysis. [c] $CHCl_3$ was also employed in the preparation of the phosphinite derivative. [d] Reaction was conducted at 0°C. [e] Absolute configuration of the major product was not determined. [f] No reaction.

Experimental Section

General procedure for the desymmetrization of *meso*-hydrobenzoin using the phosphinite compounds generated in situ (Table 2): To a suspension of cinchonine (294 mg, 1 mmol) in CH_2Cl_2 (5 mL) under an argon atmosphere were added dropwise Hünig's base (129 mg, 1 mmol) and chlorodiphenylphosphane (180 μL, 1 mmol). After the resulting solution had been stirred at room temperature for 1.5 h, the solvent was removed under reduced pressure. EtCN (5 mL) and *meso*-hydrobenzoin (214 mg, 1 mmol) were added to the residue, and Hünig's base (129 mg, 1 mmol) and benzoyl chloride (174 μL, 1.5 mmol) were added dropwise to the solution at −78°C. The mixture was stirred for 1.5 h and quenched with water. The resulting solution was

 © 2003 Wiley-VCH Verlag GmbH & Co. KGaA, Weinheim

extracted with CH_2Cl_2, and the combined organic layers were washed with brine, dried over Na_2SO_4, and concentrated under reduced pressure. The crude product was purified by flash chromatography on silica gel using hexane/ethyl acetate 3:1 as the eluent to give the desired monoester as a white solid (302 mg, 95%). HPLC analysis (AD-H, hexane/*i*PrOH 70:30): 91% *ee*.

Preparation of the phosphinite compound derived from cinchonine: A solution of triethylamine (1.01 g, 10 mmol) in THF (2 mL) and a solution of chlorodiphenylphosphane (1.10 g, 5 mmol) in THF (2 mL) were added consecutively and dropwise to a suspension of cinchonine (1.47 g, 5 mmol) in THF (10 mL) under an argon atmosphere. The mixture was stirred at room temperature for 1.5 h, then the solvent was removed under reduced pressure. Water was added to the residue, and the resulting solution was extracted with CH_2Cl_2. The combined organic layers were washed with water, dried over Na_2SO_4, and concentrated under reduced pressure. The residual crude product was purified by flash column chromatography on basic alumina using hexane/ethyl acetate 4:1 as the eluent to give the phosphinite derivative containing the phosphinate (ca. 15%) as a white amorphous solid (1.48 g, 62%). Spectroscopic data for the phosphinite in the mixture: ^{1}H NMR (400 MHz, $CDCl_3$, TMS as an internal standard.): $\delta = 1.48$–1.59 (m, 3H), 1.78 (br s, 1H), 1.93–1.98 (m, 1H), 2.16–2.22 (m, 1H), 2.59–2.79 (m, 3H), 2.84–2.90 (m, 1H), 3.30 (br s, 1H), 4.99–5.06 (m, 2H), 5.57 (br s, 1H), 5.88–5.96 (m, 1H), 7.10–7.23 (m, 5H), 7.33–7.40 (m, 4H), 7.42–7.56 (m, 3H), 7.63–7.67 (m, 1H), 8.07 (d, $J = 7.8$ Hz, 1H), 8.14 (d, $J = 7.6$ Hz, 1H), 8.75 ppm (d, $J = 4.5$ Hz, 1H); ^{31}P NMR (162 MHz, $CDCl_3$, 85% H_3PO_4 as an external standard.): $\delta = 115.44$ ppm (33.1 for the phosphinate); HRMS calcd for $C_{31}H_{31}N_2OP$: 478.2174, found: 478.2202.

General procedure for the catalytic desymmetrization of *meso*-1,2-diols (Table 3): Hünig's base (129 mg, 1 mmol) and benzoyl chloride (174 μL, 1.5 mmol) were added to a solution of the phosphinite compound (167 mg, 0.3 mmol) and *meso*-hydrobenzoin (214 mg, 1 mmol) in EtCN (5 mL) at −78 °C under an argon atmosphere. The reaction mixture was stirred at −78 °C for 1.5 h then quenched with water. The resulting solution was extracted with CH_2Cl_2, and the combined organic layers were washed with brine, dried over Na_2SO_4, and concentrated under reduced pressure. The residue was purified by flash chromatography on silica gel using hexane/ethyl acetate 3:1 as the eluent to give the desired monoester as a white solid (313 mg, 98%). HPLC analysis: 91% *ee*.

Received: December 6, 2002 [Z50719]

Keywords: alkaloids · asymmetric catalysis · desymmetrization · diols · phosphorus

[1] M. C. Willis, *J. Chem. Soc. Perkin Trans. 1* **1999**, 1765–1784.

[2] a) T. Oriyama, K. Imai, T. Sano, T. Hosoya, *Tetrahedron Lett.* **1998**, *39*, 3529–3532; b) T. Oriyama, K. Imai, T. Hosoya, T. Sano, *Tetrahedron Lett.* **1998**, *39*, 397–400; c) T. Oriyama, H. Taguchi, D. Terakado, T. Sano, *Chem. Lett.* **2002**, 26–27; d) Y. Matsumura, T. Maki, S. Murakami, O. Onomura, *J. Am. Chem. Soc.* **2003**, *125*, 2052–2053; e) B. M. Trost, T. Mino, *J. Am. Chem. Soc.* **2003**, *125*, 2410–2411.

[3] Phosphane derivatives have been reported to be efficient catalysts for nucleophilic acylations: a) E. Vedejs, S. T. Diver, *J. Am. Chem. Soc.* **1993**, *115*, 3358–3359; b) E. Vedejs, N. S. Bennett, L. M. Conn, S. T. Diver, M. Gingras, S. Lin, P. A. Oliver, M. J. Peterson, *J. Org. Chem.* **1993**, *58*, 7286–7288; for asymmetric desymmetrization of diols using chiral phosphanes, see: c) E. Vedejs, O. Daugulis, S. T. Diver, *J. Org. Chem.* **1996**, *61*, 430–431.

[4] a) W. Chodkiewicz, D. Jore, W. Wodzki, *Tetrahedron Lett.* **1979**, 1069–1072; b) J. F. Peyronel, J. C. Fiaud, H. B. Kagan, *J. Chem. Res. Synop.* **1980**, 320; c) Y. Vannoorenberghe, G. Buono, *Tetrahedron Lett.* **1988**, *29*, 3235–3238; d) A. M. Gazaliev, S. N. Balitskii, S. D. Fazylov, R. Z. Kasenov, *Zh. Obshch. Khim.* **1991**, *61*, 2365–2366; e) E. E. Nifant'ev, M. K. Grachev, L. K. Vasyanina, *Zh. Obshch. Khim.* **1993**, *63*, 575–582; f) K. N. Gavrilov, I. S. Mikhel', *Zh. Neorg. Khim.* **1994**, *39*, 107–108; g) K. N. Gavrilov, I. S. Mikhel', F. M. Ovsyannikov, A. T. Shuvaev, T. A. Lyubeznova, *Zh. Neorg. Khim.* **1994**, *39*, 933–937; h) K. N. Gavrilov, I. S. Mikhel', G. I. Timofeeva, F. M. Ovsyannikov, A. T. Shuvaev, T. A. Lyubeznova, *Zh. Neorg. Khim.* **1995**, *40*, 954–960; i) K. N. Gavrilov, D. V. Lechkin, L. A. Lopanova, G. I. Timofeeva, *Koord. Khim.* **1996**, *22*, 472–480; j) K. N. Gavrilov, I. S. Mikhel', D. V. Lechkin, G. I. Timofeeva, *Phosphorus Sulfur Silicon* **1996**, *108*, 285–287; k) K. N. Gavrilov, I. S. Mikhel', *Zh. Neorg. Khim.* **1996**, *41*, 83–89.

[5] a) W. Chodkiewicz, D. Jore, A. Pierrat, W. Wodzki, *J. Organomet. Chem.* **1979**, *174*, C21-C23; b) W. Chodkiewicz, *J. Organomet. Chem.* **1979**, *184*, C61-C63; c) W. Chodkiewicz, *J. Organomet. Chem.* **1980**, *194*, C25-C28; d) W. Chodkiewicz, *J. Organomet. Chem.* **1984**, *273*, C55-C56.

[6] The ratio of the phosphinite and the corresponding phosphinate was estimated from the ^{31}P NMR spectrum in which the peaks of the phosphinite and the phosphinate derivatives appear at $\delta =$ 115.4 and $\delta = 33.1$ ppm, respectively.

[7] When less than 30 mol% of the catalyst was used, the yields and enantioselectivities of the monoacylated products decreased except for the reaction of *meso*-hydrobenzoin (90% yield, 92% *ee* with 10 mol% catalyst).

 © 2003 Wiley-VCH Verlag GmbH & Co. KGaA, Weinheim

Metal-Ion Induced Isomerization

First Observation of Alkali Metal Ion Induced *Trans–Cis* Isomerization of Palladium(II) Phosphane Complexes Containing Crown Ether Moieties**

Vivian Wing-Wah Yam, Xiao-Xia Lu, and Chi-Chiu Ko*

There has been growing interest in the design of allosteric host molecules that can efficiently transmit the information associated with the binding of an ion or molecule to another

[*] Prof. Dr. V. W.-W. Yam, Dr. X.-X. Lu, C.-C. Ko
Department of Chemistry, and
Open Laboratory of Chemical Biology of the Institute of Molecular Technology for Drug Discovery and Synthesis
The University of Hong Kong
Pokfulam Road, Hong Kong (P. R. China)
Fax: (+852) 2857-1586
E-mail: wwyam@hku.hk

[**] V.W.-W.Y. acknowledges support from The University of Hong Kong and the University Grants Committee Area of Excellence Scheme and the receipt of a Croucher Senior Research Fellowship (2000–2001) from the Croucher Foundation. C.-C.K. acknowledges the receipt of a Croucher Scholarship from the Croucher Foundation and a Li Po Chun Postgraduate Scholarship from the Li Po Chun Charitable Fund. The work has been supported by a grant from the Research Grants Council of the Hong Kong SAR, China (Project No. HKU 7120/02P). Dr. K. Lau and Dr. K. K. Cheung are gratefully acknowledged for developing the computer program for iterative fits and for solving the X-ray crystal structures, respectively.

Supporting information for this article is available on the WWW under http://www.angewandte.org or from the author.

 DOI: 10.1002/anie.200351178 © 2003 Wiley-VCH Verlag GmbH & Co. KGaA, Weinheim

binding site through structural changes induced on binding.[1,2] Such allosteric binding behavior not only serves as a means to control the binding or release of ions or molecules, but also provides a new strategy for the design and construction of molecular-switching devices. Although *trans–cis* thermal and photoisomerization reactions are well-known[3,4] and numerous works on photoinduced ion binding have appeared in the literature,[3] there have been no reports of metal-ion-induced or -assisted isomerization reactions brought about by allosteric interactions. In this regard, we were interested in investigating the possibility of using metal-ion complexation and allosteric interactions to induce isomerization processes. Herein, we report the unprecedented *trans–cis* isomerization of dichloropalladium(II) phosphanylcrown complexes that is induced by the binding of alkali-metal ions, as evidenced by UV/Vis, ^{1}H NMR, and ^{31}P NMR spectroscopy as well as ESI-MS, and represents a novel type of allosteric host that is the first of its kind.

The reaction of $[PdX_2(PhCN)_2]$ with two equivalents of PPh_2-benzo[15]-crown-5 (PPh_2(B15C5)) or PPh_2-benzo[18]crown-6 (PPh_2(B18C6)) in benzene, by using a modification of literature procedures,[5] produced $[PdX_2\{PPh_2(B15C5)\}_2]$ (X = Cl, **1**;[6] Br, **2**; I, **3**) and $[PdCl_2\{PPh_2(B18C6)\}_2]$ (**4**).[5] The identities of **1**–**4** have been confirmed by ^{1}H, ^{13}C{^{1}H}, and ^{31}P{^{1}H} NMR spectroscopic analysis, positive-ion FAB mass spectrometry, and satisfactory elemental analyses. The crystal structures of **1** and **2** have also been established as having a *trans* configuration by X-ray crystallographic analysis.[7]

Although the complexes exist as *trans* isomers in CD_2Cl_2, dissolution of these complexes in mixed solution of CD_3CN and CD_2Cl_2 (9:1 v/v) results in an equilibrium between the *cis* and *trans* isomers, with the *trans* form being the majority species. For example, a solution of **1** in CD_3CN/CD_2Cl_2 (9:1 v/v) shows two singlets in the ^{31}P NMR spectra (one at $\delta = 24.02$ ppm and one at $\delta = 33.26$ ppm) with an integral ratio of 3.57:1 which are ascribed to the *trans* and *cis* isomers of **1**, respectively. This assignment is consistent with the similar chemical shifts commonly observed in other related $[PdX_2L_2]$ systems (L = monodentate phosphane ligand).[8] The assignment is further supported by an increase in the intensity of the signal corresponding to the *cis* isomer at $\delta =$ 33.26 upon irradiation at $\lambda = 256$ nm of a solution of **1** at −10 °C. This increase is commonly observed in the photoisomerization of *trans*-$[PdX_2L_2]$ systems.[9]

The electronic absorption spectra of solutions of **1**–**4** in CH_3CN showed high-energy bands at about 270–300 nm which are assigned as intraligand (IL) and metal-perturbed IL transitions of the phosphane ligand. The low-energy absorption bands at about 350–430 nm (with extinction coefficients of the order of 10^4 dm^3 mol^{-1} cm^{-1}), which are strongly dependent on the nature of the halides (λ_{abs}: **1**(354 nm) < **2**(374 nm) < **3**(426 nm)), were tentatively assigned as ligand-to-metal charge-transfer (p_π(X)→4d(Pd); X = Cl, Br, I) transitions.

The addition of alkali-metal ions to a solution of **1** in CH_3CN/CH_2Cl_2 (9:1 v/v, 0.1 mol dm^{-3} nBu$_4$NPF$_6$) resulted in changes in the UV/Vis spectrum with well-defined isosbestic points (Figure 1). Similar spectral changes were not observed in a control experiment using a crown-free analogue $[PdCl_2\{PPh_2\{3,4\text{-}(OMe)_2C_6H_3\}\}_2]$ (**5**), which indicates that these changes can be ascribed to the binding of the cations

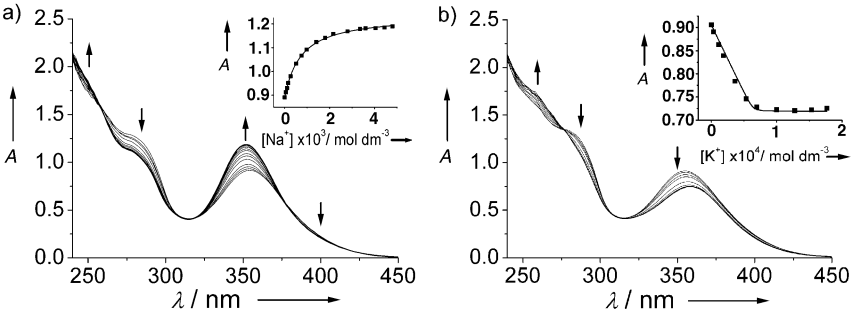


Figure 1. UV/Vis spectral changes of **1** upon addition of various concentrations of: a) $NaClO_4$ and b) KPF_6 in CH_3CN/CH_2Cl_2 (9:1 v/v, 0.1 mol dm^{-3} nBu$_4$NPF$_6$). Insert: absorbance at 355 nm (■) as a function of the concentration of Na^+ or K^+ ions with theoretical fits.

to the polyether cavity. It is interesting to note that addition of $NaClO_4$ to a solution of **1** (6.4×10^{-5} mol dm^{-3}) in CH_3CN/CH_2Cl_2 (9:1 v/v, 0.1 mol dm^{-3} nBu$_4$NPF$_6$) resulted in an increase in the absorbance and a small blue shift in the absorption energy of the low-energy band, which reached saturation at about 2.2×10^{-3} mol dm^{-3} (Figure 1 a). However, a decrease in the absorbance and a small red shift of the band were observed upon addition of KPF_6, which reached saturation at about 6.6×10^{-5} mol dm^{-3} (Figure 1 b). The UV/Vis spectral changes upon addition of other alkali-metal salts such as $LiClO_4$ to a solution of **1** are similar to that of $NaClO_4$, whereas $RbClO_4$ and $CsClO_4$ showed similar changes as KPF_6. The inserts in Figure 1 show the titration curves of **1** with $NaClO_4$ and KPF_6 together with their theoretical fits to the equation for the formation of a 1:1 adduct.[10] Stoichiometry studies indicate that **1** forms 1:1 complexes with both Na^+ and K^+ ions under the conditions studied. Addition of K^+ ions (up to a concentration of 3×10^{-4} mol dm^{-3}) to **4** gave a similar UV/Vis spectral change as that for **1** upon the addition of Li^+ and Na^+ ions, whereas addition of Cs^+ ions to **4** gave a similar spectral change as that observed for **1** upon addition of K^+ ions, that is, a decrease in the absorbance and a small red shift in the low-energy absorption band, which reached saturation at about 7.9×10^{-5} mol dm^{-3}.

Both ^{1}H and ^{31}P NMR studies were undertaken to rationalize these findings. Coordination of alkali-metal ions to both **1** and **4** was signified by downfield shifts of the crown ether protons. Interestingly, signals corresponding to the protons of *cis*-**1** initially shifted downfield upon titration with $NaClO_4$ at low concentrations, which gradually disappeared altogether upon addition of a large excess of $NaClO_4$ (ca. 500-fold), while addition of even a small amount of KPF_6 (< 1-fold)

 © 2003 Wiley-VCH Verlag GmbH & Co. KGaA, Weinheim

resulted in the growth of proton signals corresponding to the *cis* isomer. A more noticeable change could be observed in the ^{31}P NMR titration experiments of **1** with $NaClO_4$ and KPF_6. Figure 2 shows the changes in the ^{31}P NMR spectra of a solution of **1** in CD_3CN/CD_2Cl_2 (9:1 v/v) upon complexation of Na^+ (Figure 2a) and K^+ ions (Figure 2b). Addition of

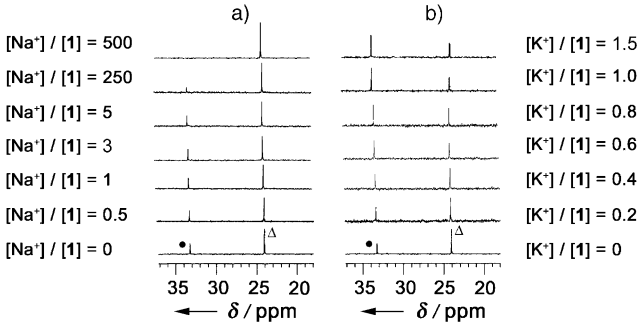
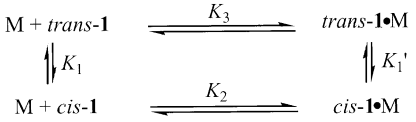


Figure 2. ^{31}P NMR (162 MHz) spectral changes of **1** (1.0×10^{-3} mol dm^{-3}) upon addition of a) $NaClO_4$ and b) KPF_6 in CD_3CN/CD_2Cl_2 (9:1 v/v) at 298 K, with signals corresponding to the *cis* (●) and *trans* (△) isomers indicated.

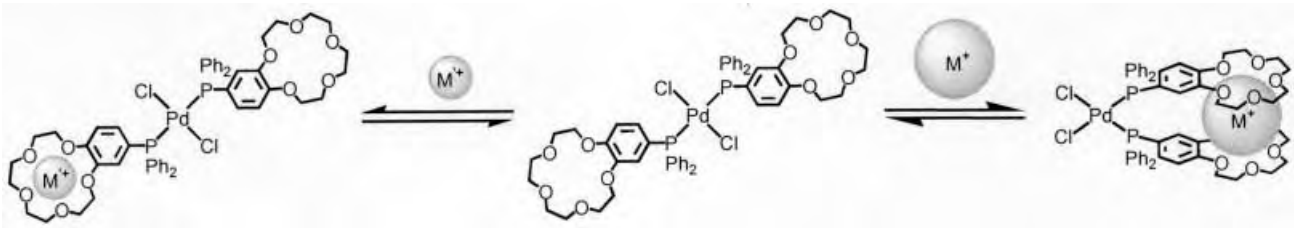
Na^+ ions initially gave rise to a slight downfield shift of the ^{31}P NMR signal, which is typical for the binding of a metal ion to the crown cavity. However, the addition of an excess of Na^+ ions (ca. 500-fold) resulted in the ^{31}P signal corresponding to the *cis* isomer at $\delta = 33.26$ disappearing, and leaving behind only the signal corresponding to the *trans* isomer. The addition of K^+ ions to **1**, in contrast, immediately gave rise to an increase in the population of the *cis* isomer, with the *cis* form becoming the predominant species as the K^+ concentration increased until saturation was reached at a $[K^+]$:[**1**] ratio of approximately unity. Similar findings were not observed in the control experiment with the crown-free analogue **5** under the same conditions, which supports the importance of the crown moieties in the specific association of the metal ions. We believe that the addition of K^+ ions, which are too large to fit into the cavity size of the benzo[15]crown-5 moiety in **1** resulted in the *trans* to *cis* isomerization of the palladium(II) complex, while addition of Na^+ ions in large excess would favor the formation of the *trans* isomer (Scheme 1). In general, benzo[15]crown-5 derivatives tend to form 2:1 (crown ether ring/metal ions) sandwich-type complexes with metal ions that are slightly greater in size than the crown ether cavity, that is, K^+, Rb^+, and Cs^+, with K^+ ions giving the best fit. Such intramolecular sandwich or tweezer binding modes in **1** would favor the conversion into the *cis* configuration, in which the two crown ether rings within the same molecule of **1** would bind to one metal ion. On the other hand, the binding of Li^+ and Na^+ ions into the cavity of benzo[15]crown-5 from solutions at high ion concentrations would favor the formation of the *trans* isomer as a consequence of electrostatic interactions arising from the binding of two metal ions to a molecule of **1**. Similarly, addition of K^+ ions, which could fit into the cavity of benzo[18]crown-6, to a solution of **4** would give rise to the formation of the *trans* isomer at high concentrations of K^+ ions, while Cs^+ ions should favor the formation of the *cis* form for a sandwich-type of binding, even at low concentrations.

The $\log K$ values obtained from the UV/Vis spectrophotometric methods at low to moderate concentrations of Na^+ and K^+ ions, that is, under the conditions for formation of a 1:1 adduct, are 3.88 ± 0.02 for **1** with Na^+ and 4.36 ± 0.03 for **4** with K^+ ions. The close agreement of the experimental data with the theoretical fits confirms the formation of a 1:1 adduct. However, a conversion of the *trans*-**1** isomer into the *cis*-**1** form occurred in the case of the binding of K^+ ions to **1**, as indicated by ^{31}P NMR spectroscopic studies (Figure 2b). The presence of both the *trans*-**1** and *cis*-**1** isomers would require a description involving at least four species in equilibrium[11] (Scheme 2), assuming that only 1:1 **1**·M adducts are formed under the conditions studied.[12] Detailed treatment of the ^{31}P NMR data according to Scheme 2 gave K_1, K_2, and K_3 values of 0.38 ± 0.01, $1.01 \times 10^6 \pm 25\,000$ and $2.55 \times 10^5 \pm 6300\ \text{M}^{-1}$, respectively. The close resemblance of the experimental data to the theoretical fits confirmed the complexation stoichiometry of the K^+ ions to **1** to be 1:1 and, thus, confirmed the validity of Scheme 2. An overall equilibrium constant $\log K$ of 5.59 ± 0.02 was obtained for the process M+*trans*-**1**⇔*cis*-**1**·M, where $K = K_1K_2$. This result is in close agreement with a $\log K$ value of 5.26 ± 0.1 determined by UV/Vis spectrophotometry.



Scheme 2. Proposed binding equilibria between **1** and K^+ ions.

Results from the ESI mass spectrometric measurements provided direct evidence for supporting this hypothesis. In the case of **1**, only the $\{\mathbf{1}\cdot K\}^+$ adduct was observed, irrespective of the concentration of K^+ ions used, while for **4**, only $\{\mathbf{4}\cdot K\}^+$ was



Scheme 1. Schematic representation of the *trans–cis* isomerization in the presence of different metal ions.

 © 2003 Wiley-VCH Verlag GmbH & Co. KGaA, Weinheim

observed at low to moderate concentrations of K^+ ions, but both the $\{\mathbf{4}\cdot K\}^+$ and $\{\mathbf{4}\cdot K_2PF_6\}^+$ ions were observed in the positive ESI-mass spectra at high concentrations of K^+ ions. Other alkali-metal ions were also examined: Only $\{\mathbf{1}\cdot M\}^+$ and $\{\mathbf{4}\cdot M\}^+$ adducts were observed at low to moderate concentrations of Li^+ and Na^+ ions, however, at high metal-ion concentrations, a small amount of the 1:2 bound adducts $\{\mathbf{1}\cdot M_2ClO_4\}^+$ and $\{\mathbf{4}\cdot M_2ClO_4\}^+$ adducts were also observed. In the case of Cs^+, however, only $\{\mathbf{1}\cdot Cs\}^+$ and $\{\mathbf{4}\cdot Cs\}^+$ appeared irrespective of the concentration of Cs^+ ions used. Similarly, for Rb^+ ions, only the $\{\mathbf{1}\cdot Rb\}^+$ adduct was observed with **1** while both $\{\mathbf{4}\cdot Rb\}^+$ and $\{\mathbf{4}\cdot Rb_2ClO_4\}^+$ ions were found with **4** at high concentrations of Rb^+ ions. In addition, **1** was found to be the most selective towards the binding of K^+ ions, while a selective preference for the binding of Cs^+ ions was observed for **4**. A likely explanation for this unprecedented ion-induced or -assisted isomerization reaction is that metal ions which are too large to fit into the size of the crown ether cavity tend to form intramolecular sandwich/tweezer complexes with the bis(crown) unit and this provides the driving force for the isomerization of the *trans* to the *cis* isomer.

In summary, the present bis(crown)-containing $[PdX_2L_2]$ system represents the first demonstration of a metal-ion-induced switching of the *trans–cis* isomerization, which may find interesting applications in the design of ion-controlled switching devices.

Received: February 13, 2003
Revised: May 26, 2003 [Z51178]

Keywords: alkali metals · crown compounds · host–guest systems · isomerization · palladium

[1] a) M. Takeuchi, M. Ikeda, A. Sugasaki, S. Shinkai, *Acc. Chem. Res.* **2001**, *34*, 865; b) R. Heck, F. Dumarcay, A. Marsura, *Chem. Eur. J.* **2002**, *8*, 2438; c) T. Nabeshima, Y. Yoshihira, T. Saiki, S. Akine, E. Horn, *J. Am. Chem. Soc.* **2003**, *125*, 28.

[2] a) J. Rebek, Jr., *Acc. Chem. Res.* **1984**, *17*, 258; b) T. G. Traylor, M. J. Mitchell, J. P. Ciconene, S. Nelson, *J. Am. Chem. Soc.* **1982**, *104*, 4986; c) I. Tabushi, T. Sasaki, *J. Am. Chem. Soc.* **1983**, *105*, 2901.

[3] a) H. L. Ammon, S. K. Bhattacharjee, S. Shinkai, Y. Honda, *J. Am. Chem. Soc.* **1984**, *106*, 262; b) S. Shinkai, T. Nakaji, T. Ogawa, K. Shigematsu, O. Manabe, *J. Am. Chem. Soc.* **1981**, *103*, 111; c) K. Kimura, R. Mizutani, M. Yokoyama, R. Arakawa, G. Matsubayashi, M. Okamoto, H. Doe, *J. Am. Chem. Soc.* **1997**, *119*, 2062.

[4] a) V. W. W. Yam, V. C. Y. Lau, K. K. Cheung, *J. Chem. Soc. Chem. Commun.* **1995**, 259; b) V. W. W. Yam, V. C. Y. Lau, L. X. Wu, *J. Chem. Soc. Dalton Trans.* **1998**, 1461; c) V. W. W. Yam, Y. Yang, J. X. Zhang, B. W. K. Chu, N. Y. Zhu, *Organometallics* **2001**, *20*, 4911.

[5] J. Tsuji, K. Ohno, *J. Am. Chem. Soc.* **1968**, *90*, 94.

[6] T. Okano, M. Iwahara, H. Konishi, J. Kiji, *J. Organomet. Chem.* **1988**, *346*, 267.

[7] See Supporting Information for perspective drawings and crystal structure data of **1** and **2**.

[8] J. A. Rahn, M. S. Holt, J. H. Nelson, *Polyhedron* **1989**, *8*, 897.

[9] N. W. Alcock, T. J. Kemp, F. L. Wimmer, *J. Chem. Soc. Dalton Trans.* **1981**, 635.

[10] J. Bourson, J. Pouget, B. Valeur, *J. Phys. Chem.* **1993**, *97*, 4552.

[11] See supporting information for detailed derivation and fitting procedure.

[12] Although ESI-MS could not differentiate between the formation of a 1:1 complex from a 2:2 complex, we believe that under the experimental conditions employed, in which the concentration of **1** is about 6×10^{-5} mol dm^{-3}, the formation of a 2:2 complex is unlikely. In addition, the formation of a 2:2 complex might also be entropically disadvantageous.

 © 2003 Wiley-VCH Verlag GmbH & Co. KGaA, Weinheim

Solvent-Driven Helix Equilibria

Quantitative Correlation of Solvent Polarity with the α-/3_{10}-Helix Equilibrium: A Heptapeptide Behaves as a Solvent-Driven Molecular Spring**

Paolo Pengo, Lucia Pasquato, Stefano Moro, Alessandro Brigo, Federico Fogolari, Quirinus B. Broxterman, Bernard Kaptein, and Paolo Scrimin**

A considerable amount of converging evidence indicates that the 3_{10}-helical conformation is a thermodynamic intermediate in α-helix folding.[1–3] The two helices differ for the relative position of the C=O and NH groups involved in hydrogen-

[*] Prof. Dr. L. Pasquato[+]
CNR IMT, Padova Section
via Marzolo, 1–35131 Padova (Italy)
Prof. Dr. P. Scrimin, Dr. P. Pengo
Department of Organic Chemistry and
CNR IMT, Padova Section
University of Padova
via Marzolo, 1-35131 Padova (Italy)
Fax: (+39) 049-827-5239
E-mail: paolo.scrimin@unipd.it
Dr. S. Moro, A. Brigo
Department of Pharmaceutical Sciences
University of Padova, via Marzolo, 15-35131 Padova (Italy)
Dr. F. Fogolari
Scientific and Technological Department
University of Verona
Strada Le Grazie, 15—Cà Vignal, 37134 Verona (Italy)
Dr. Q. B. Broxterman, Dr. B. Kaptein
DSM Research
DFC Advanced Synthesis and Catalysis
6160 MD Geleen (The Netherlands)
[+] Current address: University of Trieste
Department of Chemical Sciences
via L. Giorgieri, 1-34127 Trieste (Italy)
Fax: (+39) 040-558-3903
E-mail: pasquato@dschsun3.univ.trieste.it

[**] This work was funded by the Ministry of University and Research (PRIN 2000, grant MM03194891); P.P. thanks the University of Padova for a Young Researcher grant. We thank Prof. C. Toniolo (University of Padova) for fruitful discussions.

Supporting information for this article is available on the WWW under http://www.angewandte.org or from the author.

 © 2003 Wiley-VCH Verlag GmbH & Co. KGaA, Weinheim DOI: 10.1002/anie.200351015

bond formation ($i \leftarrow i+3$ and $i \leftarrow i+4$ in 3_{10} and α helices, respectively). Consequently the helical pitch is different (5.7 and 6.3 Å for the α and 3_{10} helix, respectively) and the relative position of functional groups in the lateral chains varies when switching from one conformation to the other.[4] The number and intrinsic energy content of the individual hydrogen bonds, as well as the interaction between the functional groups in the lateral chains and the surrounding environment, are among the parameters that account for the stabilization of one or the other of the two conformations. In proteins the α helix largely prevails,[3] but the two conformations appear equally probable as the length of the peptide becomes shorter.[3a] Experimental as well as theoretical studies on the $\alpha/3_{10}$ equilibrium have not yet provided conclusive information on the parameters that favor one or other conformation;[5] these studies have focused on the polarity of the solvent,[6] the temperature,[7] and the formation of aggregates.[8]

We present here the outstanding case of a peptide made up of seven amino acids that is not only highly folded but also shows the unique property that the type of helical conformation adopted is dependent on the polarity of the solvent. The peptide sequence Ac-[Aib-L-(αMe)Val-Aib]$_2$-L-His-NH$_2$ (**1**) comprises six C^{α}-tetrasubstituted amino acids (four achiral Aib, α-aminoisobutyric acid amino acid, and two chiral (αMe)Val, C^{α}-methylvaline) and one histidine.[9] We have selected these noncoded amino acids because they are known to induce helical conformations even in very short oligomers[10] as a result of the conformational constraint imposed by the substituents at the α carbon atom. The conformational stability that **1** shares with other oligopeptides composed of similar C^{α}-tetrasubstituted amino acids renders **1** an excellent probe for testing the parameters that affects its conformation. The surrounding environment (namely, the solvent) is, clearly, one of the most important of these parameters.[6] For this reason we have studied the conformation of **1** by circular dichroism (CD) in a series of solvents of different polarity (Figure 1). These spectra show a striking dependence on the nature of the solvent. Thus, in methanol (MeOH) or isopropanol (*i*PrOH) the spectrum signature is that of a right-handed 3_{10} helix:[8,11,12] the spctrum shows a negative Cotton band centered at about 208 nm ($\pi \rightarrow \pi^*$) with a shoulder at 222 nm ($n \rightarrow \pi^*$, $\theta_{222}/\theta_{208}$ ca. 0.3/1).[13] In hexafluoroisopropanol (HFIP), however, the $n \rightarrow \pi^*$ band becomes dominant and the $\theta_{222}/\theta_{208}$ ratio is 1.4:1. Although this ratio is typically reported to be close to 1/1 for α-helical polypeptides, recent results by Kemp et al.[14] have shown that it may become as large as 1.3:1–1.4:1. This phenomenon has been attributed to the formation of very short hydrogen bonds.[15] Thus, it can be safely stated that **1** prevailingly adopts a α-helical conformation in HFIP. The series of spectra shown in Figure 1 hence indicates that **1** converts from a 3_{10}-helical conformation in *i*PrOH into an α-helical one in HFIP. The interconversion does not show any kinetic dependence[8,16] and occurs instantaneously and reversibly upon dissolution of **1** in the appropriate solvent (Figure 1, inset).

We have used the E_T^N polarity scale introduced by Reichardt and Dimroth[18] to correlate the position of the α-/3_{10}-helix equilibrium with a parameter describing the property of the solvent. This scale correlates linearly the

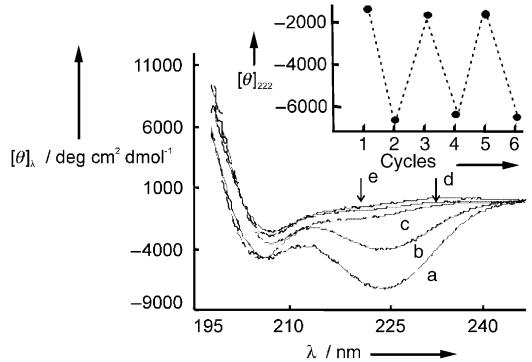


Figure 1. CD spectra of peptide **1** in the 200–250 nm region and in different solvents (a: HFIP; b: TFE; c: MeOH; d: EtOH; e: *i*PrOH). The concentration of **1** was 1 mM.[17] Inset: Change in the ellipticity at 222 nm on repeated cycles of dissolution in *i*PrOH (odd numbers) and HFIP (even numbers) followed, each time, by drying.

Gibbs free energy (ΔG^0) of reaction equilibria with the polarity of the solvent, and has been successfully applied also for predicting solvent effects on reaction rates, solute-solvent interactions, and spectra absorptions. A plot of the mean residue molar ellipticity at the wavelength of the two $\pi \rightarrow \pi^*$ and $n \rightarrow \pi^*$ transitions (208.5 and 222 nm, respectively) against E_T^N reveals the profiles shown in Figure 2 a.

We were able to obtain values for the equilibrium constants ($K_{\alpha/3_{10}}$) in each solvent by using the experimental $[\theta]_\lambda$ value at these two wavelengths in the different solvents (see Supporting Information for the details). Furthermore, by applying the Reichardt and Dimroth approach to the α-/3_{10}-

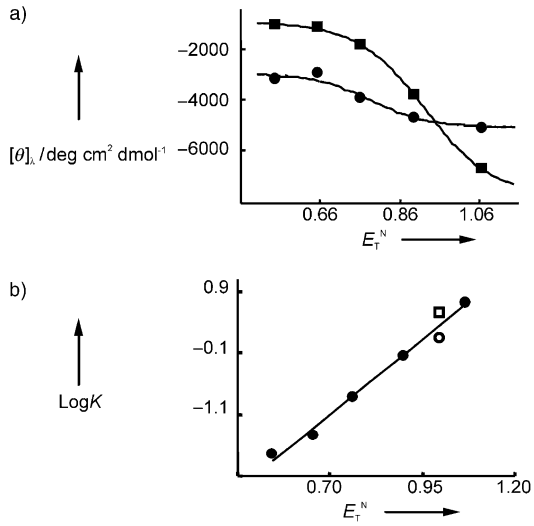


Figure 2. a) Plot of the mean residue ellipticity of peptide **1** at 208.5 (circles) and 222 nm (squares) as a function of the empirical solvent polarity parameter E_T^N. The solid lines represent the best fitting of the points (see Supporting Information for details). b) Linear correlation between the α-/3_{10}-helix equilibrium constants ($\log K_{\alpha/3_{10}}$) and E_T^N. The correlation coefficient is >0.99. Open symbols are the extrapolated values for water from water/MeOH (square) and water/*i*PrOH (circle) mixtures. The linear correlation was performed omitting these two points.

 © 2003 Wiley-VCH Verlag GmbH & Co. KGaA, Weinheim

helix equilibrium, we could fit the experimental points and obtained the two curves shown in Figure 2a. These calculations require that the peptide is mostly folded (as indicated by all experimental evidences (CD and NMR spectroscopy) as well as calculations (see below)) or that the random-coil fraction, if any, does not change as **1** switches from one helix to the other.[19] A plot of $\log K_{\alpha/3_{10}}$ against E_T^N provides the excellent linear free energy correlation shown in Figure 2b. These results suggest that in the case of peptide **1** the α- to 3_{10}-helix equilibrium is governed by the polarity of the solvent, and by increasing E_T^N from 0.546 (*i*PrOH) to 1.068 (HFIP) the $\alpha/3_{10}$-helix ratio changes from 2:98 to 85:15.

In the set of solvents considered, there is the notable absence of water, the typical natural solvent. The reason for this is that **1** is sparingly soluble in this solvent. To overcome this problem we have examined solvent mixtures of different water/alcohol composition using *i*PrOH and MeOH as cosolvents and extrapolated the data to 100% water. The dependence of the α-/3_{10}-helix equilibrium from the solvent composition with both alcohols gives double straight lines with break points at low alcohol:water ratios (at a mole fraction of 0.1 and 0.2 of *i*PrOH and MeOH, respectively, see Supporting Information), as reported for equilibria involving other species.[20] This behavior is likely a consequence of molecular segregation of the alcohol[21] with selective solvation[22] of the peptide. The extrapolation places the $\log K_{\alpha/3_{10}}$ value, as indicated in Figure 2b (open symbols), in fairly good accord with the value expected for the $E_T^N = 1$ of water. Thus, the prevailing conformer in water is the α helix, similar to the situation in 2,2,2-trifluoroethanol (TFE) and HIFP, and there is no evidence of any "structuring effect" of peptide **1** by the fluorinated alcohols,[23,24] clearly because the peptide is already folded in a helical conformation.

Further support for this finding comes from molecular dynamics (MD) simulations in explicit water, a tool that has proven to be quite useful for studying the process of reversible peptide folding. In the case of **1**, we have explored the conformational evolution of the peptide starting from both the α and 3_{10} helix canonical states. All simulations were carried out by using the CHARMm 27 suite,[25] at 300 K and using the explicit TIP3P model for water.[26,27] They show that the helical structure is stable for extended periods on the nanosecond time scale (average root-mean-square deviation, (RMSD) = 0.98 Å), on the basis of the secondary structure analysis implemented by the program MOLMOL.[28] Hydrogen-bonding distance matrix and Ramachandran plots of all seven residues are consistent with a stable α-helical conformation (data not shown). In addition, the 3_{10}-helical conformation does not seem to be thermodynamically stable in the aqueous medium and, in fact, a 3_{10}- to α-helical transition occurs during the first 40 ps of equilibration of the dynamic run (Figure 3a) and evidenced by analyzing the RMSD value during the dynamics run (average RMSD = 2.75 Å). After the 3_{10}- to α-helical transition, the helical structure is stable for extended periods on the nanosecond time scale (Figure 3a, inset). Consistently, hydrogen-bonding-distance matrix and Ramachandran plots are coherent with this observation. This fact further supports the clear preference for the α-helical conformation in water with a shift of the

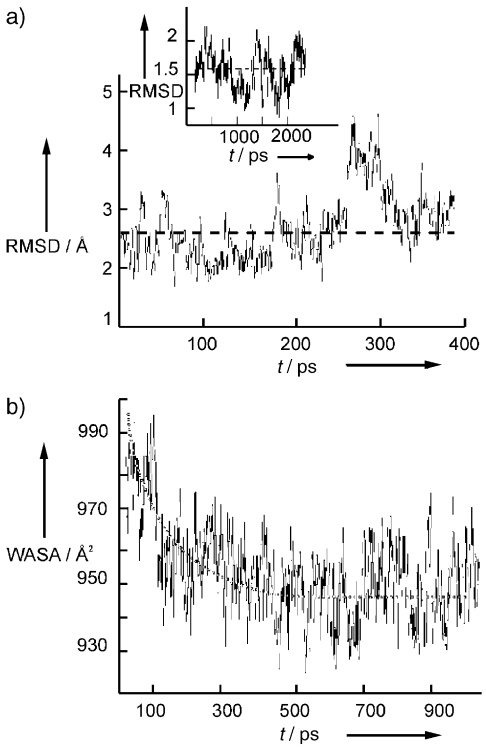


Figure 3. a) Backbone atom positional root-mean-square deviation (RMSD) of peptide **1** for all residues starting from the 3_{10}-helical conformation during the first 400 ps and the following 3000 ps (inset). Dashed lines correspond to the average RMSD with reference to the 3_{10}-helical conformation and the α-helical one, respectively. b) Variation of the calculated water-accessible surface area (WASA) of peptide **1** during the dynamic simulation.

C=O···HN hydrogen bonds from $i \leftarrow i+3$ to $i \leftarrow i+4$, as expected for a 3_{10}- to α-helix transition.

As a result of the way in which the E_T^N values[18] are determined, they reflect all the nonspecific intermolecular forces between solvent and solute molecules occurring in the process, particularly the H-bonding or hydrophobic interactions, but they do not provide any information on the prevailing driving force for the shift of the equilibrium. In particular, when the 3_{10} helix is converted into a α helix the maximum number of intramolecular hydrogen bonds in sequence **1** decreases by one unit (from 6 to 5) while the number of relative interactions between the lateral chains of the amino acids changes because of the decrease in the pitch of the helix. Careful examination of the water-accessible surface area in the MD simulations during the helix conversion reveals that this parameter decreases significantly (Figure 3b). Accordingly, the calculations suggest that a major contribution to the conformational change in aqueous solution is hydrophobic in nature. This result means also that the lateral chains of amino acids in the *i*- and $i+4$-positions in the sequence get closer and interact less with the solvent. Indeed, the peptide shortens from 17 to 15 Å in the course of the transition (Figure 4), thus behaving like a molecular spring whose length and pitch are controlled by the polarity of the solvent. Thus the toothed sawlike profile of the graph in the inset of Figure 1 in fact shows the fully reversible process

 © 2003 Wiley-VCH Verlag GmbH & Co. KGaA, Weinheim

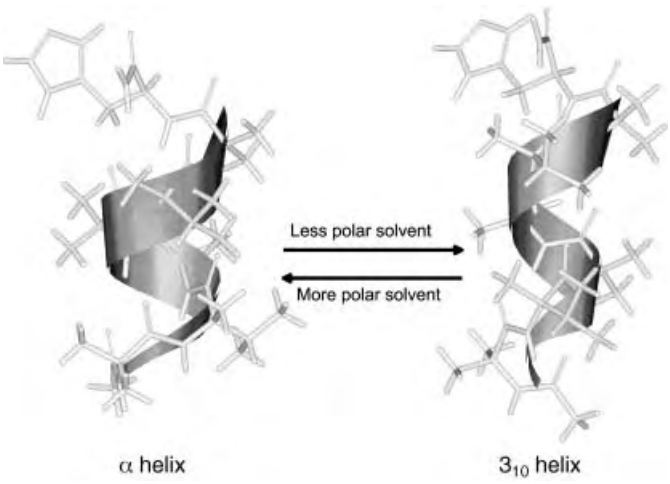


Figure 4. Representation of peptide **1** in its two helical conformations in equilibrium according to the polarity of the solvent. The two helices are shown with the canonical dihedral angles ($\phi = -63°$, $\psi = -41°$ for the α helix and $\phi = -60°$, $\psi = -30°$ for the 3_{10} helix).

of stretching and compressing of the molecular spring represented by peptide **1**.

In conclusion, we have discovered an acylated heptapeptide amide comprising six C^{α}-tetrasubstituted amino acids and one histidine group that adopts two helical conformations according to the polarity of the solvent: a α or 3_{10} helix in higher or lower polarity solvents, respectively. We were able to correlate the position of the α-/3_{10}-helix equilibrium with the empirical solvent polarity parameter E_T^N and also able to show that hydrophobic interactions between the side arms of the amino acids provide a major driving force for the stabilization of the α helix in aqueous solution. As shown by the molecular calculations, switching from one conformation to the other elongates (3_{10} helix) or shortens (α helix) the peptide, thus it behaves like a solvent-driven molecular spring.

Since, in converting the peptide from the 3_{10}- into a α-helical conformation, we trade an intramolecular hydrogen bond for a discrete decrease in the solvent-exposed hydrophobic surface, these data indicate that, by keeping the hydrophobic contribution of each individual amino acid in the folded oligopeptides constant, longer sequenches will prevailing adopt a α-helical conformation in water while shorter ones will favor 3_{10} helices. This finding is in full accord with results found by other research groups.[29,30]

Experimental Section

Synthesis: Peptide **1** was synthesized by solution methods using the acylfluoride to activate the carboxylate group in the coupling process up to the tripeptide z-Aib-L-(αMe)Val-AibO*t*Bu. This was subsequently dimerized to the hexapeptide, z-[Aib-L-(αMe)Val-Aib]$_2$-OtBu, by converting the carboxylate into the oxazolone and treating it with the free amine. His-NH_2 was eventually connected (3-(3-dimethylaminopropyl)-1-ethylcarbodiimide/7-aza-1-hydroxy-1*H*-benzotriazole (EDC/HOAt)) to the hexapeptide to obtain the final protected heptapeptide. Conversion into **1** was performed following standard protocols.

CD studies: The CD spectra of peptide **1** were recorded on a Jasco model J-715 dichrograph by using cylindrical, fused-quartz cells of 1- or 0.1-mm path lengths. The data are expressed in terms of mean residue molar ellipticity (eight amide bonds). The accuracy of the concentrations of the peptide stock solutions were determined by quantitative amino acid analysis.

Calculations: Molecular dynamics simulations were performed using SGI workstations and Intel PIV PCs computers as platforms. Ideal α-helix ($\phi = -63°$, $\psi = -41°$) and 3_{10}-helix ($\phi = -60°$, $\psi = -30°$) conformations for the sequence Ac-[Aib-L-(αMe)Val-Aib]$_2$-L-His-NH_2 (peptide **1**) were constructed by using the BUILD molecular editor module implemented in CHARMm 27. An equilibrated box of solvent was stacked around the α-helix conformation to form a cubic box with 3.5-nm sides. By contrast, the 3_{10}-helix conformation was placed in a slightly longer box (4.0-nm sides) of water to accommodate the longer peptide. Both conformations were introduced into the corresponding boxes, and all water molecules with any atom within 0.28 nm of the peptide were removed. The conformational behavior of the peptide was calculated by using the program CHARMm and the CHARMm 27 force field. The TIP3P water model was used for the solvent. A dielectric permittivity ($\varepsilon = 1$) was assumed and the van der Waals interactions were cut off at 0.8 nm. The SHAKE algorithm[31] (tolerance 0.0005 Å) was applied to all bonds, a 2-fs time step was used, and a temperature of 300 K was maintained through Berendsen temperature coupling. The water-accessible surface area was calculated by using the Molecular Operating Environment (MOE, ver.2002.03).[32]

Received: January 24, 2003
Revised: April 23, 2003 [Z51015]

Keywords: circular dichroism · helical structures · peptides · solvent effects

[1] F. B. Scheinerman, C. L. Brooks III, *J. Am. Chem. Soc.* **1995**, *117*, 10098.
[2] H. W. Long, R. Tycko, *J. Am. Chem. Soc.* **1998**, *120*, 7039.
[3] a) G. L. Millhauser, *Biochemistry* **1995**, *34*, 3873; b) D. J. Barlow, J. M. Thornton, *J. Mol. Biol.* **1988**, *201*, 601.
[4] C. Toniolo, E. Benedetti, *Trends Biochem. Sci.* **1991**, *16*, 350.
[5] K. A. Bolin, G. L. Millhauser, *Acc. Chem. Res.* **1999**, *32*, 1027.
[6] a) M. L. Smythe, S. E. Huston, G. R. Marshall, *J. Am. Chem. Soc.* **1995**, *117*, 5445; b) T. S. Yokum, T. J. Gauthier, R. P. Hammer, M. L. McLaughlin, *J. Am. Chem. Soc.* **1997**, *119*, 1167; c) I. A. Topol, S. K. Burt, E. Deretey, T.-H. Tang, A. Perczel, A. Rashin, I. G. Csizmadia, *J. Am. Chem. Soc.* **2001**, *123*, 6054.
[7] G. Hungerford, M. Martinez-Insua, D. J. S. Birch, B. D. Moore, *Angew. Chem.* **1996**, *108*, 356; *Angew. Chem. Int. Ed. Engl.* **1996**, *35*, 326.
[8] G. Yoder, A. Polese, R. A. G. D. Silva, F. Formaggio, M. Crisma, Q. B. Broxterman, J. Kamphuis, C. Toniolo, T. A. Keiderling, *J. Am. Chem. Soc.* **1997**, *119*, 10278.
[9] Histidine has been introduced for the catalysis of transacylation reactions; see P. Pengo, Q. B. Broxterman, B. Kaptein, L. Pasquato, P. Scrimin, *Langmuir* **2003**, *19*, 2521.
[10] a) C. Toniolo, M. Crisma, F. Formaggio, G. Valle, G. Cavicchioni, G. Précigoux, A. Aubry, J. Kamphuis, *Biopolymers* **1993**, *33*, 1061; b) C. Toniolo, M. Crisma, F. Formaggio, C. Peggion, *Biopolymers* **2001**, *60*, 396.
[11] C. Toniolo, A. Polese, F. Formaggio, M. Crisma, J. Kamphuis, *J. Am. Chem. Soc.* **1996**, *118*, 2744.
[12] F. Formaggio, M. Crisma, P. Rossi, P. Scrimin, B. Kaptein, Q. B. Broxterman, J. Kamphuis, C. Toniolo, *Chem. Eur. J.* **2000**, *6*, 4498.

 © 2003 Wiley-VCH Verlag GmbH & Co. KGaA, Weinheim

[13] Further support for a highly structured conformation in methanol comes from the ROESY NMR spectrum which shows strong intensities of the cross-peaks, thus highlighting the connectivities between the NH(i) and NH($i+1$) protons in the sequence (see the Supporting Information).
[14] a) P. Wallimann, R. J. Kennedy, D. S. Kemp, *Angew. Chem.* **1999**, *111*, 1377; *Angew. Chem. Int. Ed.* **1999**, *38*, 1290; b) P. Wallimann, R. J. Kennedy, J. S. Miller, W. Shalongo, D. S. Kemp *J. Am. Chem. Soc.* **2003**, *125*, 1203.
[15] Z. Dang, J. D. Hirst, *Angew. Chem.* **2001**, *113*, 3731; *Angew. Chem. Int. Ed.* **2001**, *40*, 3619.
[16] S. Mammi, M. Rainaldi, M. Bellanda, E. Schievano, E. Peggion, Q. B. Broxterman, F. Formaggio, M. Crisma, C. Toniolo, *J. Am. Chem. Soc.* **2000**, *122*, 11735.
[17] Note that the mean residue ellipticity does not change in the concentration interval 1–0.02 mM, which suggests the absence of any aggregation phenomenon at the operational concentration. We have also established that the His residue does not affect the CD spectrum significantly.
[18] a) C. Reichardt, K. Dimroth, *Fortschr. Chem. Forsch.* **1968**, *11*, 1; b) C. Reichardt, *Solvents and Solvent Effects in Organic Chemistry*, VCH, Weinheim, **1988**.
[19] By applying the conventional criteria for the determination of the helicity of polypeptides containing natural, *chiral* amino acids, (α helix, see ref. [14]) or unnatural, *chiral* C^{α}-tetrasubstituted amino acids (3_{10} helix, see refs. [11] and [12]), the helical content of **1** would be as low as 30%. We think that this number underestimates the real value of the helicity. Interestingly the peptide converts, upon heating, from an α into a 3_{10} helix (from 4 to 65°C, TFE) but remains in the 3_{10}-helical conformation (from 4 to 54°C, methanol) with no evidence of random-coil formation.
[20] H. Langhals, *Angew. Chem.* **1982**, *94*, 739; *Angew. Chem. Int. Ed. Engl.* **1982**, *21*, 724.
[21] S. Dixit, J. Crain, W. C. K. Poon, J. L. Finney, A. K. Soper, *Nature* **2002**, *416*, 829.
[22] A. Bagno, M. Campulla, M. Pirana, G. Scorrano, S. Stiz, *Chem. Eur. J.* **1999**, *5*, 1291.
[23] A. Cammers-Goodwin, T. J. Allen, S. L. Oslick, K. F. McClure, J. H. Lee, D. S. Kemp, *J. Am. Chem. Soc.* **1996**, *118*, 3082.
[24] D.-P. Hong, M. Hoshino, R. Kuboi, Y. Goto, *J. Am. Chem. Soc.* **1999**, *121*, 8427.
[25] B. R. Brooks, R. E. Bruccoleri, B. D. Olafson, D. J. States, S. Swaminathan, M. Karplus, *J. Comput. Chem.* **1983**, *4*, 187.
[26] W. L. Jorgensen, J. Chandrasekhar, J. D. Madura, R. W. Impey, M. L. Klein, *J. Chem. Phys.* **1983**, *79*, 926.
[27] E. Neria, S. Fischer, M. Karplus, *J. Chem. Phys.* **1996**, *105*, 1902.
[28] R. Koradi, M. Billeter, K. Wüthrich, *J. Mol. Graphics* **1996**, *14*, 51.
[29] I. L. Karle, P. Balaram, *Biochemistry* **1990**, *29*, 6747.
[30] a) P. Hanson, G. Martinez, G. Millhauser, F. Formaggio, M. Crisma, C. Toniolo, C. Vita, *J. Am. Chem. Soc.* **1996**, *118*, 271; b) P. Hanson, G. Millhauser, F. Formaggio, M. Crisma, C. Toniolo, *J. Am. Chem. Soc.* **1996**, *118*, 7618.
[31] J. P. Ryckaert, G. Ciccitti, H. J. C. Berendsen, *J. Comput. Phys.* **1977**, *23*, 327.
[32] Molecular Operating Environment (MOE 2002.03), Chemical Computing Group, Inc, 1255 University St., Suite 1600, Montreal, Quebec, Canada, H3B 3X3.

 © 2003 Wiley-VCH Verlag GmbH & Co. KGaA, Weinheim

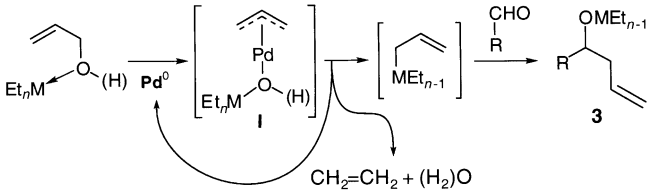
Allylation of Aliphatic Aldehydes

Pd-Catalyzed Nucleophilic Alkylation of Aliphatic Aldehydes with Allyl Alcohols: Allyl, 2-Tetrahydrofuryl, and 2-Tetrahydropyranyl Ethers as Useful C_3, C_4, and C_5 Sources**

*Masanari Kimura, Masamichi Shimizu, Kazufumi Shibata, Minoru Tazoe, and Yoshinao Tamaru**

The allylation of aldehydes at both the carbonyl carbon atom and at the carbon atom α to the carbonyl group is among the most fundamental and useful methods for elaborating molecules. These reactions, in general, have been performed by using the activated forms of allyl alcohols, such as carboxylic acid esters and other organic and inorganic acid esters. A possible reason why allyl halides have been used most widely for alkylation is because of their ready conversion into a variety of allylmetallic species (Metal = Mg, Li, Si, Sn, etc.).

Recently, we disclosed that nucleophilic alkylation of an aromatic aldehyde can be successfully performed by using allyl alcohol itself. This is possible by virtue of the ability of palladium(0) species to catalytically activate allyl alcohol as its π-allylpalladium species in the presence of Et_3B through an allyl–ethyl exchange reaction between the π-allylpalladium and Et_3B species (Scheme 1).[1]



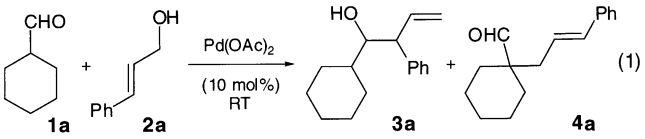
Scheme 1. Pd-catalyzed alkylation of aliphatic aldehydes ($Et_nM = Et_3B$ or Et_2Zn). For the reaction with Et_2Zn, the hydrogen atom(s) in parenthesis should be either ignored or replaced with Zn^{II} arising as a result of the hydrolysis of Et_2Zn.

Unfortunately, the reaction is not applicable to aliphatic aldehydes; aliphatic aldehydes undergo competitive nucleophilic and electrophilic alkylations under similar conditions. For example, the reaction of cyclohexanecarboxaldehyde (**1a**) and cinnamyl alcohol (**2a**) provided a mixture of **3a** and **4a** in almost equal amounts [Eq. 1 and Table 1, entry 1]. The nucleophilic alkylation giving rise to **3a** could be obviated by

[*] Prof. Dr. Y. Tamaru, Dr. M. Kimura, M. Shimizu, Dr. K. Shibata, M. Tazoe
Department of Applied Chemistry
Faculty of Engineering
Nagasaki University
1–14 Bunkyo, Nagasaki 852–8521 (Japan)
Fax: (+81) 95-819-2677
E-mail: tamaru@net.nagasaki-u.ac.jp

[**] We thank the Ministry of Education, Science, Sports, and Culture of the Japanese Government for financial support.

 © 2003 Wiley-VCH Verlag GmbH & Co. KGaA, Weinheim DOI: 10.1002/anie.200351182



(1)

Table 1: Effects of organometallic compounds and ligands (**1a** = 1.1 mmol, **2a** = 1.0 mmol) in the Pd-catalyzed ambiphilic allylation of aliphatic aldehydes with allyl alcohols.

Entry	RM[a] (equiv)	Phosphane (equiv)	Solvent (mL)	Time [h]	% isolated **3a**[b]	**4a**
1	Et_3B (2.4)	PPh_3 (0.2)	THF (5.0)	4	39	30[c]
2	Et_2Zn (3.6)	PPh_3 (0.2)	THF (5.0)	30[d]	18	0
3	Et_2Zn (3.6)	PBu_3 (0.2)	THF (5.0)	10	53	0
4	Et_2Zn (3.6)	PBu_3 (0.2)	tol[e] (0.5)	30	79	0[c]
5	Et_2Zn (3.6)	PBu_3 (0.4)	tol[e] (0.5)	6	75	0

[a] A 1 M solution of Et_2Zn or Et_3B in *n*-hexane was used. [b] *syn*:*anti* = 1:14 to ca. 1:18. [c] 1,4-Diphenyl-1,5-hexadiene was obtained in 20% (entry 1) and 3% yields (entry 3). [d] 45% Conversion. tol = toluene.

using LiCl and Et_3N as additives. This resulted in the selective α-alkylation of aliphatic aldehydes to give **4a**.[2]

Here we report that nucleophilic alkylation of aliphatic aldehydes with allyl alcohols proceeds selectively just by substituting Et_3B for Et_2Zn.[3]

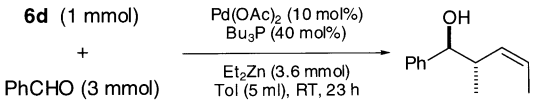
Our working hypothesis (Scheme 1)[2] suggested that organometallic species of higher migratory aptitude might promote the allyl–alkyl exchange process more readily and hence facilitate generation of an allylmetal species. Accordingly, we reexamined the reaction of **1a** and **2a** (Table 1) using Et_2Zn in place of Et_3B. As was expected, **4a** was not produced at all; however, the reaction was very sluggish and provided the expected **3a,** albeit in low yield (Table 1, entry 2). Application of nBu_3P, in place of Ph_3P, dramatically increased the yield of **3a** and the reaction rate (entry 3, Table 1). Interestingly, nonpolar solvents seem to give the best results (Table 1, entries 4 and 5). The solvent system in these reactions is rather unique: it consists of toluene (0.5 mL) and *n*-hexane (3.6 mL) for a 1 mmol scale reaction. The amount of toluene is set to make the initial reaction mixture homogeneous at 0°C (Scheme 2, see also the Experimental Section).

The utility and generality of the present nucleophilic alkylation of aliphatic aldehydes with allyl alcohols are apparent from the results summarized in Scheme 2. The diastereoselectivity found for the reactions carried out with cinnamyl alcohol is modest and seems to depend on the steric bulk of the alkyl chain of the aldehydes and ranges from *syn*:*anti* = 1:18 (cyclo-$C_6H_{11}CHO$) to 1:2 (*n*-$C_5H_{11}CHO$). It is worth noting that, despite in situ formation of zinc alkoxides, no aldol-, Cannizzaro-, or Tischchenko-type products were detected at all in these reactions.

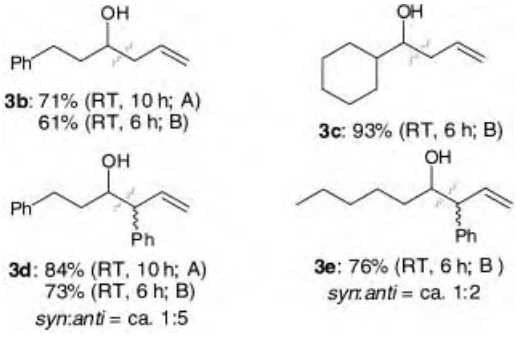
We envisaged that the reaction conditions that were successful for the activation of allyl alcohols should be applicable to the activation of allyl ethers because an ether group is a much better leaving group than a hydroxy group.[4] Indeed, allyl 2-tetrahydrofuryl (THF) ethers **5** and allyl 2-tetrahydropyranyl (THP) ethers **6**[5] turned out to readily effect nucleophilic allylation of ω-formylalkanolates formed in situ to furnish 1,4-dihydroxy-6-heptenes **7** and 1,5-dihydroxy-7-octenes **8**, respectively, in excellent yields (Table 2).[6] Except for highly branched allylic substrates, most of the reactions were completed within a few hours at room temperature.

The regioselectivity is in accord with that displayed by structurally fluctuant allylmetallic species of main-group elements, which give rise exclusively to the most highly branched isomers. In particular, the clean transformation of **6e** to **8e** and **6f** to **8f** is notable. These observations suggest that allylzinc species are reactive intermediates in these reactions. However, the poor stereoselectivity of **8d** (Table 2, entry 6) is quite different from that reported previously by us; the allylation of aldehydes by umpolung of 1,3-dimethylallyl benzoates provides *Z-anti* adducts exclusively.[7]

We thus examined the reaction of **6d** in the presence of three equivalents of benzaldehyde under otherwise identical conditions and found that (*Z*)-*anti*-2-methyl-1-phenyl-3-pentenol (**3f**) was produced exclusively in excellent yield [Eq. 2].



(2)



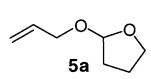
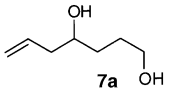
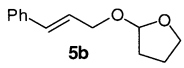
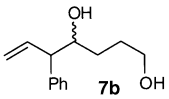
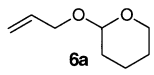
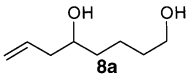
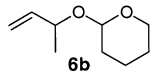
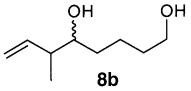
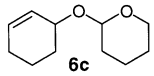
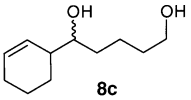
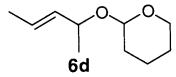
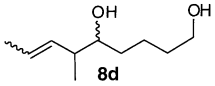
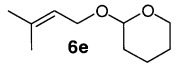
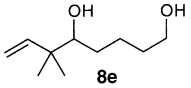
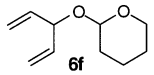
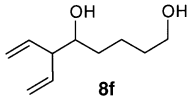
Scheme 2. Nucleophilic allylation of aliphatic aldehydes undertaken using conditions A (Table 1, entry 3) and/or B (Table 1, entry 5).

This result clearly indicates that allylzinc species generated from different sources (benzoate and **6d**) are identical and react with benzaldehyde via a transition state **II** (Scheme 3). The methyl group α to the Zn atom occupies a quasi-axial position in this six-membered chairlike transition state so as to minimize the steric repulsion with the two ligands on the Zn^{II} center. Thus, a quasi-equatorial conformation of the methyl group γ to the Zn^{II} center is rendered the most likely one.[8]

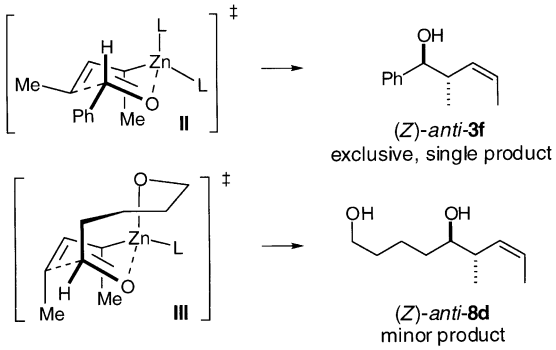
The poor stereoselectivity of **8d** may be attributed to the formation of a cyclic zinc ω-formylalkanolate species through coordination of the aldehyde oxygen atom to the Zn^{II} center, which makes approach of the aldehyde with its substituent in

 © 2003 Wiley-VCH Verlag GmbH & Co. KGaA, Weinheim

Table 2: Pd-catalyzed, Et_2Zn-promoted alkylation of hemiacetals generated from allyl 2-THF **5** and allyl 2-tetrahydropyran (THP) ethers **6**.[a]

Entry	Allyl ether	Reaction time [h]	Product	Yield (diastereomer ratio)
1	 **5a**	1	 **7a**	87
2	 **5b**	1	 **7b**	88 (*syn*/*anti* = 1:3)
3	 **6a**	2	 **8a**	91
4	 **6b**	0.5	 **8b**	97 (*syn*/*anti* = 1:2)
5	 **6c**	17	 **8c**	78 (1:2)[b]
6	 **6d**	27	 **8d**	89 (*Z*:*E*:*E* = 2:1.5:1)[b]
7	 **6e**	9	 **8e**	73
8	 **6f**	1	 **8f**	92

[a] Reaction conditions: **5** or **6** (1 mmol), $Pd(OAc)_2$ (0.1 mmol), $P(n\text{Bu})_3$ (0.4 mmol), and Et_2Zn (3.6 mmol, 1 M *n*-hexane) in toluene (0.5 mL) at room temperature under N_2. [b] The stereochemistry (*syn* or *anti*) is unknown.



Scheme 3. Transition states **II** and **III** leading to *Z*-anti isomers in the reactions of benzaldehydes and ω-formylalkanolates, respectively, with 1,3-dimethylallylzinc.

a quasi-equatorial position impossible. For example, transition state **III**, which leads to a *Z-anti* isomer, apparently suffers from 1,3-diaxial Me···Me repulsion and is unfavorable.

The allyl,[9] 2-tetrahydrofuryl, and 2-tetrahydropyranyl groups have been recognized as useful protecting groups of hydroxy groups.[10] They can be easily introduced and removed selectively under a wide variety of mild conditions, under which other functional groups remain intact. In contrast, the results in Table 2 indicate that these protecting groups could be utilized as useful C_3, C_4, and C_5 sources and provide unsaturated diols **7** and **8**, which are of significant importance as synthetic intermediates.

In conclusion, we have shown that allyl alcohols and their 2-THF and 2-THP ether derivatives are good substrates for performing the nucleophilic allylation of aliphatic aldehydes. The reaction proceeds at room temperature in the presence of a catalytic amount of a Pd^0 species and a stoichiometric amount of Et_2Zn. The reaction contrasts the electrophilic allylation at the α-position of aliphatic aldehydes, which proceeds in the presence of a catalytic amount of a Pd^0 species and a stoichiometric amount of Et_3B together with Et_3N and LiCl.[2]

Further studies to demonstrate the utility of the present umpolung methodology are in progress, for example, modification of carbohydrates that possess five- and six-membered hemiacetal structures such as **5** and **6** as a common structural motif.

Experimental Section

General procedure (Table 2, entry 3): Diethylzinc (3.2 mmol, 1.0 M *n*-hexane solution) and **6a** (142.2 mg, 1.0 mmol) were added successively by syringe to a homogeneous solution of $Pd(OAc)_2$ (22.6 mg, 0.1 mmol) and $n\text{Bu}_3\text{P}$ (80.9 mg, 0.4 mmol) in toluene (0.5 mL, dried over Na/benzophenone ketyl) at 0 °C under N_2. After completion of the addition, the mixture was allowed to warm to room temperature and stirred for an additional 2 h, during which time a copious amount of a white precipitate appeared and the reaction mixture became sludgy. The mixture was diluted with EtOAc and washed with HCl (0.2 M), sat. $NaHCO_3$, and brine and then the organic phase was dried ($MgSO_4$) and concentrated in vacuo to give a yellow oil, which was purified by column chromatography over silica gel (AcOEt/hexane, 1/4 v/v) to give **8a** (230.6 mg, 91 %, $R_f = 0.48$; AcOEt/hexane, 1/4 v/v). **8a**: IR (neat) $\tilde{\nu} = 3331$ (s), 3076 (m), 1641 (m), 1435 (m), 1340 (m), 914 (m) cm^{-1}; ^1H NMR (400 MHz, $CDCl_3$, tetramethylsilane (TMS)) $\delta = 1.40$–1.64 (m, 6H), 2.17 (dt, $J = 14.1$, 7.3 Hz, 1H), 2.29 (br dt, $J = 14.1$, 7.3 Hz, 1H), 2.55 (br s, 2H), 3.64 (m, 1H), 3.63 (t, $J = 6.2$ Hz, 2H), 5.11 (d, $J = 11.7$ Hz, 1H), 5.12 (dm, $J = 15.8$ Hz, 1H), 5.83 ppm (ddt, $J = 15.8$, 11.7, 7.7 Hz 1H); ^{13}C NMR (100 MHz, $CDCl_3$, tetramethylsilane) $\delta = 21.8$, 32.4, 36.3, 42.0, 62.3, 70.7, 117.6, 135.0 ppm; HRMS calcd for $C_8H_{16}O_2$: 144.1150; found *m*/*z* (relative intensity): 144.1098 (1), 126 (4), 116 (2), 71(100).

Received: February 13, 2003 [Z51182]

Keywords: aliphatic aldehydes · allyl alcohols · allylation · palladium · zinc

[1] M. Kimura, T. Tomizawa, Y. Horino, S. Tanaka, Y. Tamaru, *Tetrahedron Lett.* **2000**, *41*, 3627.

 © 2003 Wiley-VCH Verlag GmbH & Co. KGaA, Weinheim

[2] M. Kimura, Y. Horino, S. Mukai, S. Tanaka, Y. Tamaru, *J. Am. Chem. Soc.* **2001**, *123*, 10401.
[3] For the use of allyl alcohols as nucleophiles, see a) Y. Masuyama in *Advances in Metal-Organic Chemistry, JAI, Vol. 3*, **1994**, pp. 255–303; b) S. Araki, T. Kamei, T. Hirashita, H. Yamamura, M. Kawai, *Org. Lett.* **2000**, *2*, 847.
[4] We have already shown with one example that an allyl ether is capable of effecting the nucleophilic allylation of benzaldehyde, albeit in modest yields, when being exposed to a Pd–Et_3B catalytic system: M. Kimura, I. Kiyama, T. Tomizawa, Y. Horino, S. Tanaka, Y. Tamaru, *Tetrahedron Lett.* **1999**, *40*, 6795.
[5] The ethers **5** and **6** were obtained in quantitative yield according to a standard procedure (acid-catalyzed addition of allyl alcohols to dihydrofuran and dihydropyran, respectively). All reagents were commercially available and used as received.
[6] For the nucleophilic activation of allyl ethers by Mn, see a) T. Nishikawa, T. Nakamura, H. Kakiya, H. Yorimitsu, H. Shinokubo, K. Oshima, *Tetrahedron Lett.* **1999**, *40*, 6613; by Zr, see b) Y. Hanzawa, K. Kiyono, N. Tanaka, T. Taguchi, *Tetrahedron Lett.* **1997**, *38*, 4615, and references therein.
[7] Y. Tamaru, A. Tanaka, K. Yasui, S. Goto, S. Tanaka, *Angew. Chem.* **1995**, *107*, 862; *Angew. Chem. Int. Ed. Engl.* **1995**, *34*, 787.
[8] The diastereomeric structures and the ratios of **7b** and **8b** were determined unequivocally by 400 MHz ^{1}H NMR spectroscopy on the basis of the coupling constants between the C5-H and C6-H protons of 5,6-disubstituted 2,2-dimethyl-1,3-dioxanes derived from **7b** and **8b** by: a) benzoylation of the primary alcohol, b) ozonolysis, followed by reduction with $NaBH_4$, and c) acetonization with excess 2,2-dimethoxypropane/cat. TsOH.
[9] T. Taniguchi, K. Ogasawara, *Angew. Chem.* **1998**, *110*, 1137; *Angew. Chem. Int. Ed.* **1998**, *37*, 1136.
[10] T. W. Green, P. G. M. Wuts in *Protective Groups in Organic Synthesis*, Wiley, **1999**.

 © 2003 Wiley-VCH Verlag GmbH & Co. KGaA, Weinheim

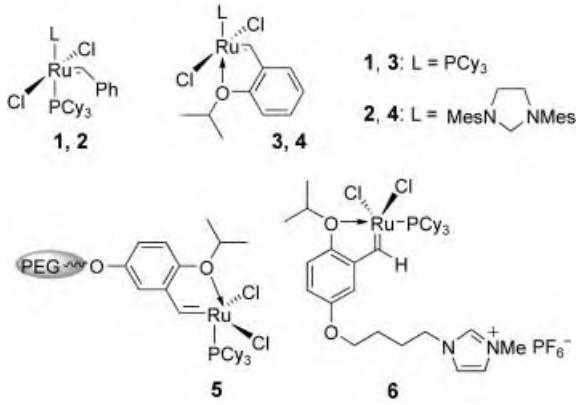
Olefin Metathesis in Ionic Liquids

Olefin Metathesis in the Ionic Liquid 1-Butyl-3-methylimidazolium Hexafluorophosphate Using a Recyclable Ru Catalyst: Remarkable Effect of a Designer Ionic Tag**

Qingwei Yao and Yiliang Zhang*

Environmental concern associated with chemical synthesis has posed stringent and compeling demands for greener processes, and the development of cost-effective and environmentally benign catalytic systems has become one of the main themes of contemporary synthetic chemistry.[1] In this context, efficient recycling and subsequent reuse of homogeneous catalysts are of prime importance.[2] The recently emerged room-temperature ionic liquids hold great potential in meeting these demands, as evidenced by their increasing popularity as innovative and environmentally benign reaction media as well as their use as new vehicles for the immobilization of transition-metal-based catalysts.[3]

The spectacular recent success of olefin metathesis[4] catalyzed by metal–carbene complexes stems largely from the availability of several well-defined catalysts, most notably, the Grubbs-type ruthenium alkylidenes **1**[5] and **2**.[6] Another major advance in this area is the discovery by Hoveyda and co-workers[7] of the recyclable Ru catalysts **3** (Cy = cyclohexyl) and **4** (Mes = mesityl = 2,4,6-trimethylphenyl). We[8] and other research groups[9] have established that various polymeric and solid supports can be used to immobilize these catalysts, as exemplified by the poly(ethylene glycol)-bound catalyst **5** (PEG = poly(ethylene glycol)). Herein, we report our success in the development of Ru complex **6** that features a designer ionic tag incorporated in catalyst **3**. This catalyst can be repeatedly recycled and reused as a highly active catalyst for the ring-closing metathesis (RCM) of various diene and enyne substrates in a minimally ionic solvent system (1-butyl-3-methylimidazolium hexafluorophosphate ([Bmim]PF_6)[10]/CH_2Cl_2, 1:9 v/v) without significant loss of its activity.



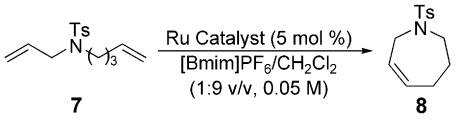
Several Ru carbene complexes, including **1** and **2**, have been shown to be catalytically active for olefin metathesis in room-temperature ionic liquids, but their catalytic reactivity rapidly vanished in subsequent recycling runs and reuse.[11] We suspected that the rapid deactivation of the Ru catalysts might have been caused by the highly ionic nature of the solvents used, and we elected to re-examine the behavior of catalysts **1** and **3** in the RCM of the test diene **7** (Ts = toluene-4-sulfonyl) using a mixture of the ionic liquid [Bmim]PF_6 and CH_2Cl_2 (1:9 v/v) as the solvent (Table 1). Although the RCM of **7** proceeded uneventfully in the first run, as indicted by the clean and quantitative formation of the cyclized product **8** with either **1** or **3**, subsequent reuse of the catalysts recovered from the ionic liquid layer[12] resulted in a dramatic decrease in the conversion of **7**. While the poor recyclability of catalyst

[*] Prof. Dr. Q. Yao, Y. Zhang
Department of Chemistry and Biochemistry
The Michael Faraday Laboratories
Northern Illinois University
DeKalb, IL 60115-2862 (USA)
Fax: (+1) 815-753-4802
E-mail: qyao@niu.edu

[**] This work was supported by grants from the National Institutes of Health (GM63522) and the Petroleum Research Fund, administered by the American Chemical Society (36466-G1).

 DOI: 10.1002/anie.200351222 © 2003 Wiley-VCH Verlag GmbH & Co. KGaA, Weinheim

Table 1: Recycling and reuse of Ru catalysts **1** and **3** in the ring-closing metathesis of diene **7**.[a]



	Catalyst **1**			Catalyst **3**		
Cycle	1	2	3	1	2	3
reaction time [h]	3	3	6	3	3	6
conversion [%][b]	>98	54	41	>98	75	37

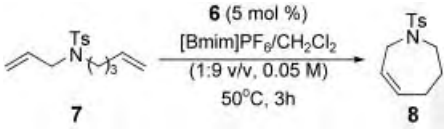
[a] All reactions were performed with 0.5 mmol of the substrate in the solvent system $[Bmim]PF_6/CH_2Cl_2$ (1:9 v/v, 10 mL) at 50°C under an Ar atmosphere. [b] Determined by ^1H NMR spectroscopy at 500 MHz.

1 could be attributed to its known liability toward decomposition, failure to efficiently recover the more robust catalyst **3** indeed pointed to a limitation in using $[Bmim]PF_6$ as an effective means to immobilize Ru catalysts.[13]

It became apparent that an enhancement in the partitioning of the Ru catalyst in the ionic liquid would ultimately be required. We further reasoned that incorporation of an ionic tag mirroring the structural motif of the ionic liquid would best meet such a requirement. To this end, ligand **13** was designed, and synthesized as shown in Scheme 1. The preparation of **13** commenced from the hydroxy-functionalized isopropoxystyrene **9**,[8] which was previously used in the synthesis of PEG-bound catalyst **5**. Alkylation of **9** with 1-chloro-4-iodobutane under standard conditions gave chloride **10**. Reaction of **10** with imidazole in the presence of NaH yielded **11** which was subsequently methylated with iodomethane to give the imidazolium iodide **12**. Anion exchange of iodide **12** with $AgPF_6$ furnished the imidazolium hexafluorophosphate **13**.[14,15] Treatment of **13** with the Grubbs catalyst **1** (first with 1.0 equiv of **1** followed by a second portion of 0.5 equiv of **1**) in the presence of CuCl in CH_2Cl_2 at 50°C, as described by Hoveyda and co-workers,[7b] resulted in complete exchange of the styrene group to deliver the air-stable brownish powder **6**,[16] which was fully characterized by ^1H and ^{13}C NMR spectroscopy as well as by elemental analysis.

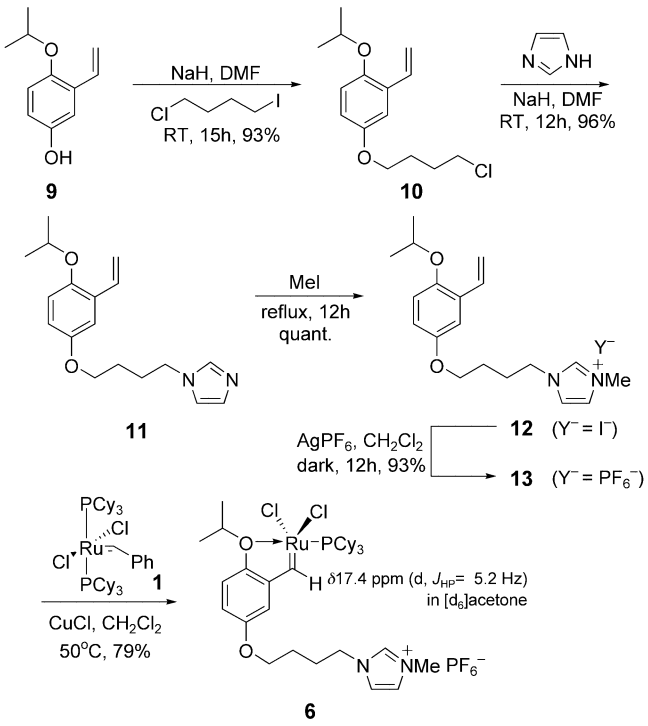
Catalyst **6** was then evaluated for its performance toward the RCM of diene **7** under the same conditions as used for catalysts **1** and **3**. As shown in Table 2, this simple ligand modification resulted in a vast improvement over both catalysts **1** and **3**. Catalyst **6** can be recycled and reused at least 10 times with only a very slight decrease in reactivity after each run. It should be noted that the recycling of both the catalyst and the ionic liquid can simply be carried out in the air by first removing the more volatile CH_2Cl_2 under vacuum followed by extraction of the product with diethyl ether.

Table 2: Recycling and reuse of Ru catalyst **6** in the ring-closing metathesis of diene **7**.[a]



Cycle	1	2	3	4	5	6	7	8	9	10
conversion [%][b]	>98	>98	97	96	95	94	92	92	91	90

[a] The reactions were performed with 0.5 mmol of the substrate in the solvent system $[Bmim]PF_6/CH_2Cl_2$ (1:9 v/v, 10 mL) at 50°C under an Ar atmosphere. [b] Determined by ^1H NMR spectroscopy at 500 MHz .

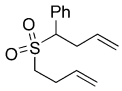
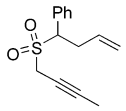
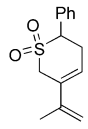


Scheme 1. Preparation of Ru carbene complex **6**.

Having established the superior recyclability and reusability of **6**, we next examined a variety of other representative RCM substrates that lead to the formation of various carbocyclic as well as nitrogen-, oxygen-, and sulfur-containing heterocyclic compounds (Table 3). The benchmark diene substrate toluenesulfonamide **14** cyclized cleanly with high conversion under conditions similar to those used for the metathesis of **7** (entries 1 and 2). Use of a reduced amount (2.5 mol%) of the catalyst relative to the substrate also led to high conversion, even at room temperature (entry 3). The recycled catalyst/ionic liquid from the reaction of **14** was subsequently used for the metathesis of a second substrate (**16**; entry 4). The crude reaction product from **16** consists of only the cyclized product **17** and recovered **16** devoid of any detectable amount of the product from the previous reaction, thus demonstrating the practical advantage of the sequential use of a recyclable and reusable catalyst. Similarly, another batch of catalyst **6** was used to catalyze the RCM of diene **18**

 © 2003 Wiley-VCH Verlag GmbH & Co. KGaA, Weinheim

Table 3: Ring-closing metathesis catalyzed by Ru complex **6** in $[Bmim]PF_6/CH_2Cl_2$.[a]

Entry	Substrate (conc)	Product	Catalyst [mol%]	Conditions	Conversion [%][b] (yield [%][c])
1	 (0.05 M)		5	50 °C, 3 h	98 (95)
2	(0.05 M)		5	50 °C, 3 h	97 (94)
3[d]	(0.1 M)		2.5	RT, 12 h	> 98 (96)
	14	**15**			
4[d]			2.5	50 °C, 4 h	95 (89)
	16[e]	**17**[e]			
1	 (0.05 M)		5	50 °C, 3 h	98 (90)
2	(0.05 M)		5	50 °C, 3 h	96 (89)
	18[e]	**19**[e]			
3[g]	 (0.02 M)		5	50 °C, 6 h	92 (70)
	20[f]	**21**[f]			
4	 (0.05 M)		5	50 °C, 6 h	78 (72)
	22[f]	**23**[f]			
5	 (0.05 M)		5	50 °C, 4 h	87 (83)
	16[e]	**17**[e]			

[a] Unless otherwise indicated, all reactions were performed under the following standard conditions: 0.5 mmol of substrate in the solvent system $[Bmim]PF_6/CH_2Cl_2$ (1:9 v/v, 10 mL) under an Ar atmosphere at the indicated temperature. [b] Determined by ^1H NMR spectroscopy at 500 MHz. [c] Yield of pure product after chromatography on silica gel. [d] Performed with 1.0 mmol of substrate. [e] Ref. [8]. [f] Ref. [17]. [g] Performed with 0.5 mmol of substrate in the solvent system $[Bmim]PF_6/CH_2Cl_2$ (1:24 v/v, 25 mL). Bz = benzyl.

to deliver the dihydropyran **19** for two runs with essentially equal efficacy. The recovered catalyst was then reused consecutively in the RCM of another three different substrates, each giving high yields of the respective product, without any replenishment of either the catalyst or the ionic liquid. It is noteworthy that the catalyst remained highly active (entry 5) even after being recovered from an enyne metathesis (entry 4),[17] which generates a hindered and stabilized Ru–vinylalkylidene intermediate rather than the more reactive Ru–methylidene species as in the case of the RCM of terminal dienes. Catalyst regeneration from the former intermediate would be expected to be more difficult.[18,19]

In conclusion, we have presented evidence that a task-specific modification of the bidentate ligand in **3** brings about an immense improvement in its performance as a recyclable catalyst for olefin metathesis in an ionic liquid. Given the ever-growing interest in the development of catalytic systems suitable for organic synthesis in ionic liquids, the phase-tagging strategy described here could, in principle, be applied to the immobilization of other transition-metal-based catalysts. Application of the phase-tagging ligand **13** to the immobilization of the more-powerful second-generation Grubbs catalyst **2** is currently underway in our laboratory.

Experimental Section

Ring-closing metathesis of diene **7** and general procedure for the recycling and reuse of Ru catalyst **6** and ionic liquid $[Bmim]PF_6$: A 25-mL oven-dried round-bottom flask equipped with a reflux condenser was charged with **6** (22.4 mg, 0.025 mmol). The flask was evacuated and filled with Ar. The ionic liquid $[Bmim]PF_6$ (1 mL) was then added and the flask was degassed 3 times by first evacuation and then filling with Ar. Diene **7** (140 mg, 0.50 mmol) was then added in anhydrous CH_2Cl_2 (9 mL). The flask was then heated to gentle reflux (bath temperature 45–50 °C) for 3 h. After cooling the reaction mixture to room temperature, it was concentrated under vacuum to remove the cosolvent CH_2Cl_2 and extracted with anhydrous diethyl ether (3×5 mL). The combined ether extracts were evaporated to give 125 mg of a crude reaction product. Examination of this crude reaction mixture by 500 MHz ^1H NMR spectroscopy revealed complete conversion of **7** and the clean formation of the cyclized product **8**. The ionic layer was dried on the vacuum line prior to its reuse in a subsequent run as described below.

A second run of the metathesis of **7** using the recycled catalyst and ionic liquid was conducted in exactly the same way as described for the first cycle, and resulted in the clean formation of **8** and complete conversion of **7**. This reaction was repeated eight more times, each time using the catalyst and ionic liquid recovered from a previous cycle. The results are listed in Table 2.

Received: February 19, 2003
Revised: May 12, 2003 [Z51222]

Keywords: carbene complexes · homogeneous catalysis · ionic liquids · metathesis · ruthenium

[1] For selected recent reviews and monographs on green chemistry, see a) "Green Chemistry: Designing Chemistry for the Environment": *ACS Symp. Ser.* **1996**, *626*; b) *Green Chemistry: Theory and Practice* (Eds.: P. T. Anastas, J. Warner), Oxford University Press, New York, **1998**; c) *Green Chemistry: Frontiers in Benign Chemical Syntheses and Processes* (Eds.: P. T. Anastas, T. C. Williamson), Oxford University Press, New York, **1999**.

[2] For general discussions on homogeneous catalysts and their heterogenization, see a) *Applied Homogeneous Catalysis with Organometallic Compounds* (Eds.: B. Cornil, W. A. Hermann)

 © 2003 Wiley-VCH Verlag GmbH & Co. KGaA, Weinheim

Wiley-VCH, Weiheim, **1996**, chap. 3.1; b) *Chiral Catalyst Immobilization and Recycling* (Eds.: D. E. De Vos, I. F. J. Vankelecom, P. A. Jacobs), Wiley-VCH, Weiheim, **2000**; c) N. E. Leadbeater, M. Marco, *Chem. Rev.* **2002**, *102*, 3217.

[3] Selected recent reviews on ionic liquids and their application in transition-metal-catalyzed reactions: a) T. Welton, *Chem. Rev.* **1999**, *99*, 2071; b) P. Wasserscheid, W. Keim, *Angew. Chem.* **2000**, *112*, 3926; *Angew. Chem. Int. Ed.* **2000**, *39*, 3772; c) R. Sheldon, *Chem. Commun.* **2001**, 2399; d) J. Dupont, R. F. de Souza, P. A. Suarez, *Chem. Rev.* **2002**, *102*, 3667.

[4] Selected reviews on olefin metathesis: a) M. Schuster, S. Blechert, *Angew. Chem.* **1997**, *109*, 2124; *Angew. Chem. Int. Ed. Engl.* **1997**, *36*, 2036; b) S. K. Armstrong, *J. Chem. Soc. Perkin Trans. 1* **1998**, 371; c) R. H. Grubbs, S. Chang, *Tetrahedron* **1998**, *54*, 4413; d) A. Fürstner, *Angew. Chem.* **2000**, *112*, 3140; *Angew. Chem. Int. Ed.* **2000**, *39*, 3012; e) T. M. Trnka, R. H. Grubbs, *Acc. Chem. Res.* **2001**, *34*, 18.

[5] P. Schwab, R. H. Grubbs, J. W. Ziller, *J. Am. Chem. Soc.* **1996**, *118*, 100.

[6] a) M. Scholl, S. Ding, C. W. Lee, R. H. Grubbs, *Org. Lett.* **1999**, *1*, 953; for related catalysts, see b) M. Scholl, T. M. Trnka, J. P. Morgan, R. H. Grubbs, *Tetrahedron Lett.* **1999**, *40*, 2247; c) J. Huang, E. D. Stevens, S. P. Nolan, J. F. Petersen, *J. Am. Chem. Soc.* **1999**, *121*, 2674.

[7] a) J. S. Kingsbury, J. P. A. Harrity, P. J. Bonitatebus, A. H. Hoveyda, *J. Am. Chem. Soc.* **1999**, *121*, 791; b) S. B. Garber, J. S. Kingsbury, B. L. Gray, A. H. Hoveyda, *J. Am. Chem. Soc.* **2000**, *122*, 8168; for related catalysts, see c) H. Wakamatsu, S. Blechert, *Angew. Chem.* **2002**, *114*, 832; *Angew. Chem. Int. Ed.* **2002**, *41*, 794; d) H. Wakamatsu, S. Blechert, *Angew. Chem.* **2002**, *114*, 2509; *Angew. Chem. Int. Ed.* **2002**, *41*, 2403; e) K. Crela, S. Harutyunyan, A. Michrowska, *Angew. Chem.* **2002**, *114*, 4210; *Angew. Chem. Int. Ed.* **2002**, *41*, 4038.

[8] Q. Yao, *Angew. Chem.* **2000**, *112,* 4060; *Angew. Chem. Int. Ed.* **2000**, *39,* 3896.

[9] a) S. T. Nguyen, R. H. Grubbs, *J. Organomet. Chem.* **1995**, *497*, 195; b) M. Ahmed, A. G. M. Barrett, D. C. Braddock, S. M. Cramp, P. A. Procopiou, *Tetrahedron Lett.* **1999**, *40,* 8657; c) M. Ahmed, T. Arnauld, A. G. M. Barrett, D. C. Braddock, P. A. Procopiou, *Synlett* **2000**, 1007; d) S. C. Schürer, S. Gessler, N. Buschmann, S. Blechert, *Angew. Chem.* **2000**, *112,* 4062; *Angew. Chem. Int. Ed.* **2000**, *39,* 3898; e) L. Jafarpour, S. P. Nolan, *Org. Lett.* **2000**, *2,* 4075; f) J. Dowden, J. Savovic, *Chem. Commun.* **2001**, 37; g) M. Mayr, B. Mayr, M. R. Buchmeiser, *Angew. Chem.* **2001**, *113*, 3957; *Angew. Chem. Int. Ed.* **2001**, *40*, 3839; h) J. S. Kingsbury, S. B. Garber, J. M. Giftos, B. L. Gray, M. M. Okamoto, R. A. Farrer, J. T. Fourkas, A. H. Hoveyda, *Angew. Chem.* **2001**, *113*, 4381; *Angew. Chem. Int. Ed.* **2001**, *40*, 4251; i) S. Randl, N. Buschmann, S. J. Connon, S. Blechert, *Synlett* **2001**, *10*, 1547; j) L. Jafarpour, M. P. Heck, C. Baylon, H. L. Lee, C. Mioskowski, S. P. Nolan, *Organometallics* **2002**, *21,* 671; k) S. J. Connon, A. M. Dunne, S. Blechert, *Angew. Chem.* **2002**, *114,* 3835; *Angew. Chem. Int. Ed.* **2002**, *41,* 3989; l) K. Crela, M. Tryznowski, M. Bieniek, *Tetrahedron Lett.* **2002**, *43*, 9055; m) S. Gibson, V. M. Swamy, *Adv. Synth. Catal.* **2002**, *344*, 619; n) M. Mayr, M. R. Buchmeiser, K. Wurst, *Adv. Synth. Catal.* **2002**, *344*, 712.

[10] [Bmim]PF_6 can either be purchased from Acros Organics at a relatively low cost or readily made in large quantities by simple procedures.

[11] a) R. C. Buijsman, E. van Vuuren, J. G. Sterrenburg, *Org. Lett.* **2001**, *3*, 3785; b) D. Semeril, H. Olivier-Bourbigou, C. Bruneau, P. H. Dixneuf, *Chem. Commun.* **2002**, 146; c) K. G. Mayo, E. H. Nearhoof, J. J. Kiddle, *Org. Lett.* **2002**, *4*, 1567; d) S. Csihony, C. Fischmeister, C. Bruneau, I. T. Horvath, P. H. Dixneuf, *New J. Chem.* **2002**, *26*, 1667.

[12] [Bmim]PF_6 is essentially nonvolatile and almost completely insoluble in nonpolar solvents such as hexane and diethyl ether. The ionic liquid layer can be readily separated from the reaction mixture by removing the cosolvent CH_2Cl_2 under vacuum first, followed by extraction of the product and any starting material with diethyl ether.

[13] While the poor recyclability of **3** could be attributed in part to the deactivation of the catalytically active Ru–methylidene intermediate formed in the initial turnover, we believe that the diminished activity of the recovered catalyst in the ionic liquid layer is largely due to the extraction of **3** into the diethyl ether layer. To probe this possibility, a solution of *N*-tosyldiallylamine in [Bmim]PF_6/CH_2Cl_2 (1:9 v/v, 0.05 M) was treated with 5 mol% of **3** at 50 °C for 2 h. After separation of the crude reaction product from the ionic liquid layer, ^{1}H NMR analysis revealed a complete conversion of the diene and the presence of catalyst **3** (as evidenced by its carbene signal at $\delta = 17.4$ ppm) in the crude reaction mixture. The crude reaction mixture was then dissolved in CH_2Cl_2 and recharged with another portion of the diene. After heating the reaction mixture to reflux for 2 h, it was analyzed by ^{1}H NMR spectroscopy, which indicated a 98% conversion of the diene. A similar reaction was performed using the recovered ionic liquid. Only 22% of the added diene was found to be converted into the cyclized product.

[14] NMR data of **13**: ^{1}H NMR (500 MHz, $CDCl_3$): $\delta = 8.48$ (s, 1H), 7.24 (d, $J = 17.5$ Hz, 2H), 7.03–6.98 (m, 2H), 6.82 (d, $J = 8.8$ Hz, 1H), 6.73 (dd, $J = 3.2$, 8.8 Hz, 1H), 5.72 (d, $J = 17.9$ Hz, 1H), 5.24 (d, $J = 11.4$ Hz, 1H), 4.37 (hept, $J = 6.1$ Hz, 1H), 4.20 (t, $J = 7.4$ Hz, 2H), 3.94 (t, $J = 5.9$ Hz, 2H), 3.85 (s, 3H), 2.05 (quint, $J = 7.4$ Hz, 2H), 1.74–1.80 (m, 2H), 1.30 ppm (d, $J = 6.1$ Hz, 6H); ^{13}C NMR (125 MHz, $CDCl_3$): $\delta = 152.9$, 149.6, 136.0, 131.6, 129.2, 123.5, 122.0, 117.1, 114.8, 114.4, 111.9, 72.3, 67.4, 49.8, 36.2, 27.0, 25.8, 22.2 ppm.

[15] The presence of free iodide in the reaction media may adversely effect the activity of Grubbs-type Ru catalysts as a result of potential ligand exchange, see a) E. L. Dias, S. T. Nguyen, R. H. Grubbs, *J. Am. Chem. Soc.* **1997**, *119*, 3887; b) M. S. Sanford, J. A. Love, R. H. Grubbs, *J. Am. Chem. Soc.* **2001**, *123,* 6543.

[16] Data of **6**: ^{1}H NMR (500 MHz, [D_6]acetone): $\delta = 17.37$ (d, $J = 5.2$ Hz, 1H), 9.06 (s, 1H), 7.83 (s, 1H), 7.73 (s, 1H), 7.42 (d, $J = 2.7$ Hz, 2H), 7.30 (dd, $J = 2.8$, 9.1 Hz, 1H), 7.24 (d, $J = 9.1$ Hz, 1H), 5.30 (hept, $J = 6.0$ Hz, 1H), 4.51 (t, $J = 7.3$ Hz, 2H), 4.13 (t, $J = 6.0$ Hz, 2H), 4.07 (s, 3H), 2.41 (m, 3H), 2.22–1.26 (m, 34H), 1.75 ppm (d, $J = 6.2$ Hz, 6H); ^{13}C NMR (125 MHz, [D_6]acetone): $\delta = 154.5$, 147.1, 144.2, 137.0, 124.0, 122.6, 115.4, 113.8, 107.3, 75.2, 67.8, 49.5, 36.0, 35.4 (d, $J_{CP} = 25.3$ Hz), 29.8, 27.5 (d, $J_{CP} = 10.1$ Hz), 27.0, 26.1, 25.7, 21.5 ppm; elemental analysis (%) calcd for $C_{36}H_{58}Cl_2F_6N_2O_2P_2Ru$: C 48.11, H 6.50, N 3.12; found: C 48.09, H 6.45, N 3.05.

[17] Q. Yao, *Org. Lett.* **2002**, *4*, 428.

[18] Q. Yao, *Org. Lett.* **2001**, *3*, 2069.

[19] M. Mori, N. Sakakibara, A. Kinoshita, *J. Org. Chem.* **1998**, *63*, 6082.

 © 2003 Wiley-VCH Verlag GmbH & Co. KGaA, Weinheim

Hydroboration Reagents

Di(isopropylprenyl)borane: A New Hydroboration Reagent for the Synthesis of Alkyl and Alkenyl Boronic Acids

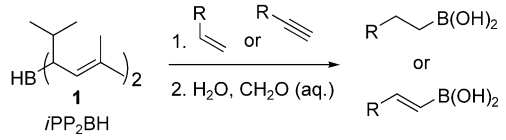
*Alexey V. Kalinin, Stefan Scherer, and Victor Snieckus**

*Dedicated to Professor H. C. Brown***

The discovery of the hydroboration reaction by Brown and Subba Rao almost 50 years ago[1] launched the era of organoborane chemistry, which today constitutes a conventional component of synthetic organic chemistry[2] sustained by the availability of organoboranes either commercially or prepared by reliable protocols.[2,3] The significance of organoboron compounds in synthesis surged when Suzuki and Miyaura discovered the transition-metal-catalyzed cross-coupling reaction,[4] which more recently has seen explosive growth, particularly in industrial practice.[5] The current high activity in this area is evidenced by the further development of cross-coupling reactions of organoboron compounds for C–C[4–6] and C–heteroatom bond formation,[7] C–H insertion,[8] allylic substitution,[9] Diels–Alder and dipolar cycloaddition,[10] and 1,2-/1,4-addition processes.[11] Consequently, the quest for new reagents and procedures for the preparation of organoboronic acids and their derivatives is a continuing necessity.

Herein we report the development and synthetic utility of di(isopropylprenyl)borane (**1**, *i*PP_2BH), a new organoborane reagent that is generated in situ and that provides rapid access to alkyl and alkenyl boronic acids and their derivatives conveniently, economically, and under mild conditions (Scheme 1).

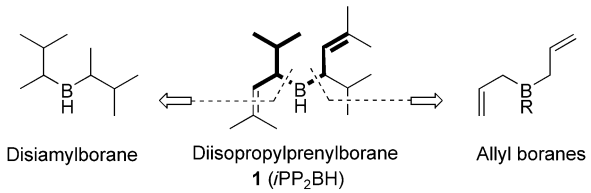
Detailed studies by Brown and co-workers[12] and Mikhailov et al.[13] showed that although hydroboration of conjugated dienes with borane is a complex process that gives rise



Scheme 1. General hydroboration process with **1**.

[*] Dr. A. V. Kalinin
Department of Chemistry, University of Waterloo
Waterloo, Ontario, 2NL 3G1 (Canada)
Dr. S. Scherer
Clariant GmbH, Division LSE, BU Pharmaceuticals
65 926 Frankfurt am Main (Germany)
Prof. Dr. V. Snieckus
Department of Chemistry, Queens University
Kingston, Ontario, K7L 3N6 (Canada)
Fax: (+1) 613-533-6089
E-mail: snieckus@chem.queensu.ca

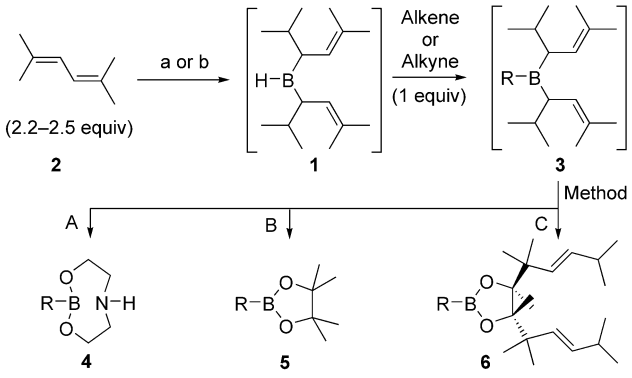
[**] This communication is in celebration of 91 years and with admiration and appreciation of the "from little acorns to tall trees" growth of his borane chemistry



Scheme 2. Amalgamation of two classes of borane reagents in **1**. R = alkyl, alkenyl.

to mixtures of products, application of 9-BBN results in highly selective reactions in certain cases. Of particular interest, 1:1 hydroboration of 2,5-dimethylhexa-2,4-diene (**2**, Scheme 3) with 9-BBN leads to the anti-Markovnikov monohydroboration product in 90% yield.[14] Based on these studies, we postulated that the reaction of borane with slightly more than 2 equivalents of **2** would mainly lead, by double anti-Markovnikov hydroboration, to **1**, which was expected to exhibit hydroboration selectivity resembling that of disiamylborane,[2,15] reactivity towards carbonyls similar to that of allyl boranes,[3,16] and facile hydrolysis in protic media[17] (Scheme 2). Consequently, we envisaged that **1** could serve as a valuable hydroboration reagent, allowing conversion of the product boranes into the corresponding boronic acids under mild conditions similar to those used for the hydrolysis of catechol-[18] and dihaloboranes,[19] without the need for the standard strong oxidizing reagents.[2,20]

In pursuit of results to support this idea, we found that the addition of dimethyl sulfate to a mixture of diene **2** and $NaBH_4$ in diglyme[21] at 0–5 °C was accompanied by intensive gas evolution followed by the formation of a substantial amount of a colorless precipitate upon ageing of the mixture (3 h/0 °C). The precipitate was rapidly consumed in an exothermic reaction with phenylacetylene, leading to the presumed formation of borane **3a** (Scheme 3, R = PhCH=CH). Treatment of the reaction mixture with water and an aqueous



Scheme 3. General protocol for the hydroboration of alkenes/alkynes with **1**. Reagents and conditions: a) $NaBH_4$ (1 equiv), $(MeO)_2SO_2$ (1 equiv), diglyme, 0–5 °C, 3 h; b) BH_3·THF (1 M, 1 equiv), THF, 0–5 °C, 3 h. Method A: H_2O quench, 30 min, room temperature; then aqueous CH_2O (1 equiv), 24 h, room temperature; then $(HOCH_2CH_2)_2NH$ (1.1 equiv). Method B: H_2O quench, 30 min, room temperature; then aqueous CH_2O (1 equiv), 1 h, room temperature; then $HOCMe_2CMe_2OH$ (1.1 equiv), 24 h, room temperature. Method C: MeC(O)C(O)Me (1.1 equiv), 12 h, room temperature. R = alkyl or alkenyl; diglyme = $(MeOCH_2CH_2)_2O$.

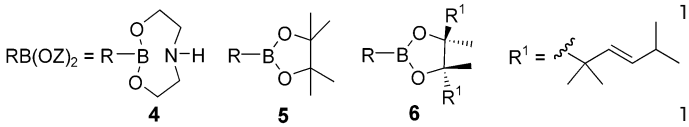
 DOI: 10.1002/anie.200351312 © 2003 Wiley-VCH Verlag GmbH & Co. KGaA, Weinheim

solution of formaldehyde followed by addition of diethanolamine led to the isolation of the corresponding adduct of styrylboronic acid **4a** (R = PhCH=CH) in 77% yield (method A, Scheme 3).[22]

When pinacol was added instead of diethanolamine, the corresponding borolane **5a** was isolated in 83% yield and > 99:1 anti-Markovnikov regioselectivity (GC/MS analysis of the crude mixture; method B, Scheme 3) together with the alcohol **7** (see Scheme 4).[23] Similar results were observed when commercial BH_3·THF complex in THF was used (Table 1, entry 1), but in a homogeneous reaction.

For both procedures involving $NaBH_4$ or BH_3·THF, the results may be rationalized by invoking the formation of **3**,

Table 1: Synthesis of $RB(OZ)_2$ by hydroboration of alkynes/alkenes with **1**.[a]



4 **5** **6**

Entry	R		$NaBH_4$ Selectivity	$NaBH_4$ Yield [%]	BH_3·THF Selectivity	BH_3·THF Yield [%]
1	Ph	**4a**		77		
		5a	99:1		99:1	83
		6a		72		
2	*p*-Tol	**4b**	99:1	74	99:1	70
3	Ph, Ph	**4c**		66		81
			100		100	
		6c				69
4	TMS	**5d**				62[b]
			96:4		84:16	
		6d		59		
5	Ph	**5e**	83			
				70	–	–
	Ph	**5f**	17			
6	EtO, EtO	**5g**	98:2	61	98:2	55
7	*n*-C_6H_{13}	**5h**	96:4	67	99:1	59
8	Ph, (3)	**5i**	97:3	73	98:2	72
9	AcO	**5j**	93:7	55	93:7	41
10[c]	HO	**5k**	–	–	99:1	63
11	*n*Pr, *n*Pr	**4l**	> 99	68	> 99	71

Table 1: (Continued)

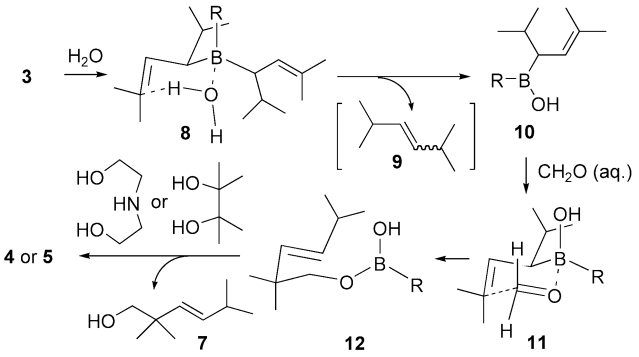
Entry	R		$NaBH_4$ Selectivity	$NaBH_4$ Yield [%]	BH_3·THF Selectivity	BH_3·THF Yield [%]
12	N	**4m**		67		
		5m	> 99		> 99	74
		6m				86
13	O, O, O	**5n**	> 99	77	> 99	72
14	O	**6o**	98:2	73	–	–
15	TMS	**4p**		55		
			> 99		> 99	
		5p				68
16	Ph, Ph	**4q**	–	–	> 99	47
17	EtO, EtO	**5r**	99:1	63	99:1	59
18	Ph	**4s**				67
			98:2		97:3	
		5s		71		
19		**4t**		48		43
			91:9		96:4	
		5t				61

[a] Yields are for purified materials (recrystallized, distilled, or, for **6c** and **6m**, after column chromatography) and are not optimized. Selectivities were determined by GC and GC–MS analysis of the crude reaction mixtures: an aliquot of the reaction mixture was worked up according to method B by preparing the borolane derivative **5**. [b] Yield is for the mixture of α and β isomers; the yield of 98% pure (GC) **5d** (α isomer) is 42%. [c] *O*-TMS-propargyl alcohol was used as the starting material.

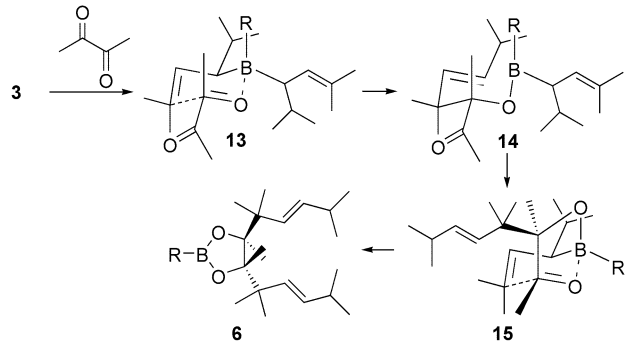
which as expected for allyl boranes,[17] undergoes rapid protonolysis via intermediate **8** to liberate alkene **9**[24] and yield the borinic acid **10** (Scheme 4). Reaction of **10** with formaldehyde leads to **12** via intermediate **11**. Hemiborate **12** is then esterified with diethanolamine (method A) or pinacol (method B) to afford derivatives **4** and **5**, respectively, and alcohol **7** (Scheme 4).

As chemical proof for the formation of **3** and therefore, by implication, of **1**, repetition of the model hydroboration experiment of phenylacetylene with biacetyl (1.1 equiv) as the quenching reagent gave complex borolane **6a** (R = PhCH=CH) in 72% yield as a single isomer, as judged from the ^{1}H NMR spectrum (olefinic $^3J = 18.4$ Hz, C_2 symmetry). The formation of **6** (Scheme 5) may be rationalized by the transition state **13**, which is predisposed for the formation of *trans* olefin **14**. Intramolecular boron–carbonyl coordination leads to the intermediate **15**, in which repulsion between the bulky side chains is minimized by adapting a pseudo-*trans* borolane stereochemistry. Terminal collapse of **15** affords the C_2-symmetrical *trans* borolane **6** with *trans* stereochemistry in both side chains.

 © 2003 Wiley-VCH Verlag GmbH & Co. KGaA, Weinheim



Scheme 4. Proposed hydrolysis and oxidation steps of **3** to products **4** or **5** and **7** (methods A and B).



Scheme 5. Proposed mechanism for the double oxidation of **3** by biacetyl to form **6** (method C).

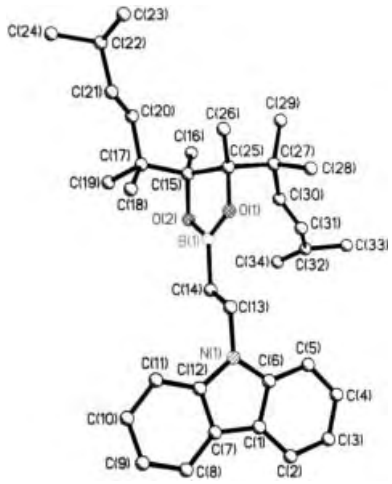
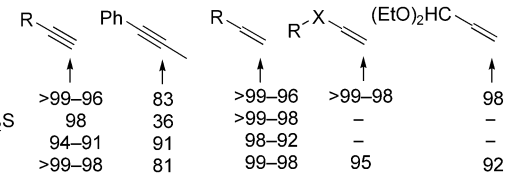


Figure 1. X-ray crystal structure of **6m** at the 50% probability level. Hydrogen atoms have been omitted for clarity.



iPP_2BH	>99–96	83	>99–96	>99–98	98
$Hal_2BH{\cdot}Me_2S$	98	36	>99–98	–	–
CthBH	94–91	91	98–92	–	–
Sia_2BH	>99–98	81	99–98	95	92

Figure 2. General trends in hydroboration with diisopropylprenylborane (*i*PP_2BH), dihaloborane complexes ($Hal_2BH{\cdot}Me_2S$), catecholborane (CthBH), and disiamylborane (Sia_2BH). R = *n*-alkyl, Ph; Hal = Cl, Br; X = O, Si.

In view of the C_2 symmetry of **6**, the stereochemistry of the borolane could not be confirmed by NMR spectroscopic analysis. Fortunately, suitable crystals of **6m** (see Table 1, entry 12) were obtained and X-ray crystallographic analysis established the *trans* stereochemistry of both the borolane ring and of the alkenyl chains (Figure 1).[25] This result infers its derivation from the parent **3** and strongly suggests that **1** is the main product from the reaction of diene **2** with borane.

To explore the scope and limitations of the new boronic acid synthesis, representative examples of alkenes and alkynes were treated with **1** and the results are summarized in Table 1. Several pertinent conclusions may be drawn: a) hydroboration of terminal and symmetrical alkynes and alkenes proceeds in a highly selective anti-Markovnikov fashion (except Table 1, entry 5); b) both sources of borane furnish hydroborated products with comparable regioselectivity (except Table 1, entries 4 and 19); c) derivatives **4**, **5**, and **6** (Scheme 3) are obtained in modest to good yields by using conventional isolation techniques (distillation or crystallization) and in up to 86% yield by using column chromatography (Table 1, entry 12); d) sterically hindered alkenes are less reactive under the tested conditions as reflected in the modest yields of the final products (Table 1, entries 16 and 19). Although direct hydroboration of α,β-unsaturated esters (acrylates and cinnamates) was unsuccessful, these compounds were readily accessed from their protected precursors (Table 1, entries 6 and 17).[26]

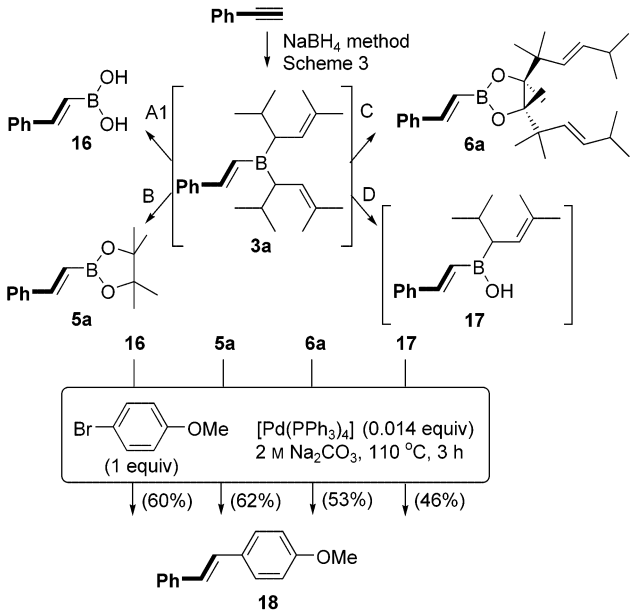
The generally high hydroboration regioselectivities of *i*PP_2BH compare favorably with those observed for CthBH[18] and $Hal_2BH{\cdot}Me_2S$,[19] the commonly used reagents to produce the corresponding boronic acids under hydrolytic, nonoxidative conditions (Figure 2). The similar selectivities achieved with *i*PP_2BH (**1**) and Sia_2BH[2,15] may be attributed to their comparable steric demand (see Scheme 2).

As a logical extension of the new hydroboration procedure, the development of a sequential, "one-pot" hydroboration/Suzuki–Miyaura cross-coupling protocol was realized (Scheme 6). In all experiments, borane **3a**, generated in situ from $NaBH_4$, was coupled with 4-bromoanisole under identical conditions. However, the hydrolysis–oxidation protocol (methods A1, B, C, and D) prior to the cross-coupling step was varied for **3a**.

Thus application of methods A1 and B to **3a** led to the intermediate styrylboronic acid (**16**) and pinacolate **5a**, respectively, which upon coupling with 4-bromoanisole, afforded styrene **18** in virtually identical yields (60% and 62%). Borolane **6a** was found to be a less effective coupling partner, yielding **18** in 53% yield (method C). Interestingly, cross-coupling of the borinic acid **17**, a proposed intermediate in the hydrolysis of **3a**, also gave **18** but in a slightly lower yield (46%, method D).

In conclusion, a new and general reagent for the hydroboration of alkenes and alkynes, *i*PP_2BH (**1**), conveniently prepared in situ by reaction of borane with 2,5-dimethylhexa-2,4-diene (**2**), has been uncovered. Advantageous workup protocols allow rapid access to alkyl and alkenyl boronic acids and their derivatives under mild conditions. Extension to a successful "one-pot" hydroboration/Suzuki–Miyaura cross-

 © 2003 Wiley-VCH Verlag GmbH & Co. KGaA, Weinheim



Scheme 6. One-pot hydroboration/Suzuki–Miyaura cross-coupling protocol. Method A1: similar to method A, but without addition of $(HOCH_2CH_2)_2NH$. Method D: H_2O quench, 1 h, room temperature. Yields are for recrystallized material and are not optimized.

coupling protocol and perusal of the current state of organoboron chemistry[2–4] hold promise for further application of these findings in organic synthesis.

Experimental Section

General procedure (**4a**): Under an argon atmosphere, a flame-dried flask was charged with $NaBH_4$ (757 mg, 20 mmol), **2** (7.1 mL, 50 mmol), and anhydrous diglyme (20 mL), and the resulting mixture was cooled in an ice bath. $(MeO)_2SO_2$ (1.9 mL, 20 mmol) was added to the stirred mixture over ~1 h while maintaining the temperature below 5 °C. The addition was accompanied by an intensive gas evolution and homogeneity of the reaction mixture. The mixture was aged, with stirring, for 3 h at 0 °C, resulting in the gradual formation of a new thick suspension, to which phenylacetylene (2.2 mL, 20 mmol) was added slowly (~20 min) while maintaining the temperature below 5 °C. The resulting mixture was stirred for 1 h at 0 °C, slowly quenched with H_2O (3 mL) (additional gas evolution), stirred for 30 min at room temperature, and treated with a solution of formaldehyde (1.5 mL, 20 mmol, aq 37 wt% solution) in a single addition. The resulting exothermic reaction was compensated by application of an ambient-temperature bath. The reaction mixture was stirred for 24 h at room temperature and diluted with EtOAc (40 mL). After separation of layers, the organic phase was dried (Na_2SO_4), transferred into a flask containing diethanolamine (2.31 g, 22 mmol), and the combined mixture was evaporated under vacuum (25 Torr, then 0.5 Torr, heating bath at 50 then 80 °C). The resulting solid residue was recrystallized from MeCN to give **4a** (3.34 g, 15.38 mmol, 77% yield) as colorless needles. M.p. 197–199 °C (MeCN); IR (KBr): $\tilde{\nu}$ = 3000 (br), 1622, 1598, 1573, 1494, 1469, 1454, 1277, 1242, 1206 cm^{-1}; ^1H NMR (400 MHz, [D_6]DMSO): $\delta = 7.36$ (d, 2H, $J = 7.8$ Hz), 7.27 (t, 2H, $J = 7.5$ Hz), 7.15 (t, 1H, $J = 7.4$ Hz), 6.84 (br s, 1H), 6.66 (d, 1H, $J = 18.1$ Hz), 6.24 (d, 1H, $J = 18.1$ Hz), 3.81–3.73 (m, 2H), 3.71–3.64 (m, 2H), 3.08–2.99 (m, 2H), 2.26–2.70 ppm (m, 2H); ^{13}C NMR (100 MHz, [D_6]DMSO): $\delta = 139.4$, 136.1, 135.1 (br), 128.4, 126.5, 125.7, 62.5, 50.4 ppm; MS (EI): *m*/*z* (%): 217 (M^+, 1), 187 (9), 186 (100), 185 (8), 130 (7), 129 (9), 114 (87), 103 (25), 77 (15); elemental analysis calcd for $C_{12}H_{16}BNO_2$: C 66.40, H 7.43, N 6.45; found: C 66.36, H 7.35, N 6.45.

General Procedure (**6m**): Under an argon atmosphere, a flame-dried flask was charged with a solution of **2** (8.10 mL, 56.92 mmol) in THF (8 mL). The solution was cooled in an ice bath, and BH_3·THF solution (1M, 26 mL) was added while maintaining the reaction temperature below 5 °C. The resulting solution was aged, with stirring, for 3 h at 0 °C, and then treated with a solution of 9-vinylcarbazole (5.00 g, 25.87 mmol) in THF (15 mL) while maintaining the temperature below 5 °C. The reaction mixture was allowed to warm to room temperature, stirred for 2 h, cooled in an ice bath, and slowly quenched with 2,3-butanedione (2.72 mL, 31.04 mmol). The reaction was stirred for 1 h, warmed to room temperature, and stirred for an additional 12 h. Concentration under vacuum and purification by flash column chromatography (silica gel, eluent: EtOAc/hexanes) gave **6m** (11.38 g, 22.16 mmol, 86%) as a colorless glass, which slowly crystallized on standing. M.p. 79–81 °C (MeCN); IR (KBr): $\tilde{\nu} = 2959$, 1630, 1598, 1485, 1464, 1453, 1380, 1347, 1325, 1237, 1081 cm^{-1}; ^1H NMR (400 MHz, $CDCl_3$): $\delta = 8.12$ (d, 2H, $J = 7.7$ Hz), 7.51–7.45 (m, 4H), 7.25 (ddd, 2H, $J = 7.9$, 6.0, 2.2 Hz), 5.63 (dd, 2H, $J = 15.8$, 1.1 Hz), 5.36 (dd, 2H, $J = 15.8$, 6.6 Hz), 4.59–4.46 (m, 2H), 2.35–2.25 (m, 2H), 1.57–1.51 (m, 2H), 1.51 (s, 6H), 1.13 (s, 6H), 1.11 (s, 6H), 1.02 (d, 6H, $J = 6.8$ Hz), 1.01 ppm (d, 6H, $J = 6.8$ Hz); ^{13}C NMR (100 MHz, $CDCl_3$): $\delta = 139.9$, 134.3, 134.2, 125.5, 122.9, 120.3, 118.6, 108.7, 92.4, 45.7, 38.8, 31.5, 25.8, 25.5, 22.6, 22.5, 18.7, 11.5 ppm (br); MS (EI): *m*/*z* (%): 514 (M^++1, 8), 513 (M^+, 20), 293 (17), 292 (62), 291 (25), 181 (12), 180 (44), 112 (16), 111 (100); HRMS (EI): calcd for $C_{34}H_{48}BNO_2$: 513.3778; found: 513.3784.

Received: March 3, 2003 [Z51312]

Keywords: boranes · cross-coupling · homogeneous catalysis · hydroboration

[1] H. C. Brown, B. C. Subba Rao, *J. Am. Chem. Soc.* **1956**, *78*, 5694–5695.

[2] H. C. Brown, *Organic Syntheses via Boranes*, Wiley, New York, **1975**; B. M. Mikhailov, Yu. N. Bubnov, *Organoboron Compounds in Organic Synthesis*, Harwood Academic Science Publishers, Amsterdam, **1984**; A. Pelter, K. Smith, H. C. Brown, *Borane Reagents*, Academic Press, New York, **1988**; D. S. Matteson, *Stereodirected Synthesis with Organoboranes*, Springer, New York, **1995**; M. Zaidlewicz, *Methods of Organic Chemistry (Houben-Weyl), 4th ed. 1952–, Vol. E21d*, **1995**, pp. 4396–4420; "Organoboranes for Syntheses": *ACS Symp. Ser.* **2001**, *783*.

[3] P. V. Ramachandran, *Aldrichimica Acta* **2002**, *35*, 23–35, and references therein.

[4] N. Miyaura, A. Suzuki, *J. Chem. Soc. Chem. Commun.* **1979**, 866–867; in an issue dedicated to 30 years of cross-coupling chemistry: N. Miyaura, *J. Organomet. Chem.* **2002**, *653*, 54–57.

[5] M. F. Lipton, M. A. Mauragis, M. T. Maloney, M. F. Veley, D. W. VanderBor, J. J. Newby, R. B. Appell, E. D. Daugs, *Org. Proc. Res. Dev.* **2003**, *7*, 385–392; N. Yasuda, *J. Organomet. Chem.* **2002**, *653*, 279–287; Y. Urawa, H. Naka, M. Miyazawa, S. Souda, K. Ogura, *J. Organomet. Chem.* **2002**, *653*, 269–278; Z. Xu, J. Singh, M. D. Schwinden, B. Zheng, T. P. Kissick, B. Patel, M. J. Humora, F. Quiroz, L. Dong, D.-M. Hsieh, J. E. Heikes, M. Pudipeddi, M. D. Lindrud, S. K. Srivastava, D. R. Kronenthal, R. H. Mueller, *Org. Process Res. Dev.* **2002**, *6*, 323–328; for a review on the use of boronic acids in protection and catalysis, see: P. Duggan, E. M. Tyndall, *J. Chem. Soc. Perkin Trans. 1* **2002**, 1325–1339; N. Yasuda, M. A. Huffman, G.-J. Ho, L. C. Xavier, C. Yang, K. M. Emerson, F.-R. Tsay, Y. Li, M. H. Kress, D. L. Rieger, S. Karady, P. Sohar, N. L. Abramson, A. E. DeCamp,

 © 2003 Wiley-VCH Verlag GmbH & Co. KGaA, Weinheim

D. J. Mathre, A. W. Douglas, U.-H. Dolling, E. J. J. Grabowski, P. J. Reider, *J. Org. Chem.* **1998**, *63,* 5438–5446.

[6] N. Miyaura, A. Suzuki, *Chem. Rev.* **1995**, *95*, 2457–2483; A. Suzuki in *Metal-Catalyzed Cross-Coupling Reactions* (Eds.: F. Diederich, P. J. Stang), Wiley-VCH, Weinheim, **1998**, pp. 49–97; A. Suzuki, *J. Organomet. Chem.* **2002**, *653*, 83–90; N. Miyaura, *Top. Curr. Chem.* **2002**, *219*, 11–59; K. Fagnou, M. Lautens, *Chem. Rev.* **2003**, *103*, 169–196; G. W. Kabalka, G. Dong, B. Venkataiah, *Org. Lett.* **2003**, *5*, 893–895; G. A. Molander, M. R. Rivero, *Org. Lett.* **2002**, *4*, 107–109; J. H. Kirchhoff, C. Dai, G. C. Fu, *Angew. Chem.* **2002**, *114*, 2025–2027; *Angew. Chem. Int. Ed.* **2002**, *41*, 1945–1947; J. H. Kirchhoff, M. R. Netherton, I. D. Hills, G. C. Fu, *J. Am. Chem. Soc.* **2002**, *124*, 13662–13663; N. Kataoka, Q. Shelby, J. P. Stambuli, J. F. Hartwig, *J. Org. Chem.* **2002**, *67*, 5553–5566; J. Yin, M. P. Rainka, X.-X. Zhang, S. L. Buchwald, *J. Am. Chem. Soc.* **2002**, *124*, 1162–1163; C. Bolm, J. P. Hildebrand, K. Muñiz, N. Hermanns, *Angew. Chem.* **2001**, *113*, 3382–3407; *Angew. Chem. Int. Ed.* **2001**, *40*, 3284–3308; S. R. Chemler, D. Trauner, S. J. Danishefsky, *Angew. Chem.* **2001**, *113*, 4676–4701; *Angew. Chem. Int. Ed.* **2001**, *40*, 4544–4568.

[7] R. B. Bedford, C. S. J. Cazin, S. J. Coles, T. Gelbrich, P. N. Horton, M. B. Hursthouse, M. E. Light, *Organometallics* **2003**, *22,* 987–999; N. R. Anastasi, K. M. Waltz, W. L. Weerakoon, J. F. Hartwig, *Organometallics* **2003**, *22,* 365–369, and references therein; D. E. Portlock, R. Ostaszewski, D. Naskar, L. West, *Tetrahedron Lett.* **2003**, *44*, 603–605; P. Y. S. Lam, D. Bonne, G. Vincent, C. G. Clark, A. P. Combs, *Tetrahedron Lett.* **2003**, *44*, 1691–1694, and references therein; G. W. Kabalka, S. K. Guchhait, *Org. Lett.* **2003**, *5*, 729–731; G. W. Kabalka, B. Venkataiah, *Tetrahedron Lett.* **2002**, *43*, 3703–3705; G. K. S. Prakash, M. Mandal, S. Schweizer, N. A. Petasis, G. A. Olah, *J. Org. Chem.* **2002**, *67*, 3718–3723; D. A. Evans, J. L. Katz, G. S. Peterson, T. Hintermann, *J. Am. Chem. Soc.* **2001**, *123,* 12411–12413; C. P. Decicco, Y. Song, D. A. Evans, *Org. Lett.* **2001**, *3*, 1029–1032; J. C. Antilla, S. L. Buchwald, *Org. Lett.* **2001**, *3*, 2077–2079; T. Ishiyama, N. Miyaura, *J. Organomet. Chem.* **2000**, *611*, 392–402, and references therein; M. Murata, T. Oyama, S. Watanabe, Y. Masuda, *J. Org. Chem.* **2000**, *65*, 164–168.

[8] C. E. Webster, Y. Fan, M. B. Hall, D. Kunz, J. F. Hartwig, *J. Am. Chem. Soc.* **2003**, *125*, 858–859; T. Ishiyama, J. Takagi, K. Ishida, N. Miyaura, N. R. Anastasi, J. F. Hartwig, *J. Am. Chem. Soc.* **2002**, *124*, 390–391, and references therein; M. K. Tse, J.-Y. Cho, M. R. Smith III, *Org. Lett.* **2001**, *3*, 2831–2833.

[9] J. Ramnauth, O. Poulin, S. Rakhit, S. P. Maddaford, *Org. Lett.* **2001**, *3*, 2013–2015; T. Ishiyama, T.-a. Ahiko, N. Miyaura, *Tetrahedron Lett.* **1996**, *37*, 6889–6892.

[10] G. C. Micalizio, S. L. Schreiber, *Angew. Chem.* **2002**, *114*, 160–162; *Angew. Chem. Int. Ed.* **2002**, *41*, 152–154; A. Rastelli, R. Gandolfi, M. Sarzi-Amade, B. Carboni, *J. Org. Chem.* **2001**, *66*, 2449–2458, and references therein; S. C. Pellegrinet, M. A. Silva, J. M. Goodman, *J. Am. Chem. Soc.* **2001**, *123*, 8832–8837; R. P. Litvinovskaya, V. A. Khripach, *Russ. Chem. Rev.* **2001**, *79*, 405–424; J. Renaud, C.-D. Graf, L. Oberer, *Angew. Chem.* **2000**, *112*, 3231–3234; *Angew. Chem. Int. Ed.* **2000**, *39*, 3101–3104; C. D. Davies, S. P. Marsden, E. Stokes, *Tetrahedron Lett.* **2000**, *41*, 4229–4233; R. A. Batey, A. N. Thadani, A. J. Lough, *J. Am. Chem. Soc.* **1999**, *121*, 450–451.

[11] J.-G. Boiteau, R. Imbos, A. J. Minnaard, B. L. Feringa, *Org. Lett.* **2003**, *5*, 681–684; D. F. Cauble, J. D. Gipson, M. J. Krische, *J. Am. Chem. Soc.* **2003**, *125*, 1110–1111; C. Bolm, J. Rudolph, *J. Am. Chem. Soc.* **2002**, *124*, 14850–14851; K. Yoshida, M. Ogasawara, T. Hayashi, *J. Am. Chem. Soc.* **2002**, *124*, 10984–10985; T. Hayashi, M. Takahashi, Y. Takaya, M. Ogasawara, *J. Am. Chem. Soc.* **2002**, *124*, 5052–5058; M. Kuriyama, K. Nagai, K.-i. Yamada, Y. Miwa, T. Taga, K. Tomioka, *J. Am. Chem. Soc.* **2002**, *124*, 8932–8939; M. Pucheault, S. Darses, J.-P. Genet, *Eur. J. Org. Chem.* **2002**, 3552–3557; M. Lautens, C. Dockendorff, K. Fagnou, A. Malicki, *Org. Lett.* **2002**, *4*, 1311–1314; for recent reviews, see: G. Alvaro, D. Savoia, *Synlett* **2002**, 651–673; A. Alexakis, C. Benhaim, *Eur. J. Org. Chem.* **2002**, 3221–3226; N. Krause, Hoffmann-Röder, *Synthesis* **2001**, 171–196; T. Hayashi, *Synlett* **2001**, 879–887; M. P. Sibi, S. Manyem, *Tetrahedron* **2000**, *56*, 8033–8061; S. Kobayashi, H. Ishitani, *Chem. Rev.* **1999**, *99*, 1069–1094; R. Bloch, *Chem. Rev.* **1998**, *98*, 1407–1438; D. Enders, U. Reinhold, *Tetrahedron: Asymmetry* **1997**, *8*, 1895–1946.

[12] H. C. Brown, E. Negishi, *Pure Appl. Chem.* **1972**, *29*, 527–545, and references therein; G. W. Kramer, H. C. Brown, *J. Organomet. Chem.* **1977**, *132*, 9–27; H. C. Brown, E.-i. Negishi, *Tetrahedron* **1977**, *33*, 2331–2357.

[13] B. M. Mikhailov, A. Ya. Bezmenov, L. S. Vasil'ev, V. G. Kiselev, *Dokl. Akad. Nauk SSSR* **1964**, *155*, 141; A. Ya. Bezmenov, L. S. Vasil'ev, B. M. Mikhailov, *Izv. Akad. Nauk SSSR Ser. Khim.* **1965**, 2111; B. M. Mikhailov, *Organomet. Chem. Rev. Sect. A* **1972**, *8*, 1–65.

[14] H. C. Brown, R. Liotta, G. W. Kramer, *J. Org. Chem.* **1978**, *43*, 1058–1063; also see M. Zaidlewicz, J. Meller, *Tetrahedron Lett.* **1997**, *38*, 7279–7282.

[15] H. C. Brown, G. Zweifel, *J. Am. Chem. Soc.* **1961**, *83*, 3834–3840; G. Zweifel, G. M. Clark, N. L. Polston, *J. Am. Chem. Soc.* **1971**, *93*, 3395–3399; H. C. Brown, G. Zweifel, *J. Am. Chem. Soc.* **1961**, *83*, 1241–1246; J. A. Soderquist, A. Hassner, *J. Organomet. Chem.* **1978**, *156*, C12-C16; H. C. Brown, J. Chen, *J. Org. Chem.* **1981**, *46*, 3978–3988; *Encyclopedia of Reagents for Organic Synthesis* (Ed.: L. A. Paquette), Wiley, Chichester, **1995**, pp. 2295–2298.

[16] B. M. Mikhailov, Yu. N. Bubnov, *Izv. Akad. Nauk SSSR Ser. Khim.* **1964**, 1874; P. Y. Yamamoto, N. Asao, *Chem. Rev.* **1993**, *93*, 2207–2293; R. Hoffmann, J. Krüger, D. Brückner, *New J. Chem.* **2001**, *25*, 102–107; J. W. J. Kennedy, D. G. Hall, *J. Am. Chem. Soc.* **2002**, *124*, 898–899; Y. Yamamoto, M. Takahashi, N. Miyaura, *Synlett* **2002**, 128–130; M. C. Kozlowski, S. P. Waters, J. W. Skudlarek, C. A. Evans, *Org. Lett.* **2002**, *4*, 4391–4393; Y. Yamamoto, K. Kurihara, A. Yamada, M. Takahashi, Y. Takahashi, N. Miyaura, *Tetrahedron* **2003**, *59*, 537–542.

[17] The ease of hydrolysis of simple allyl boranes diminishes with increasing substitution of double bond: triallylborane reacts rapidly with alcohols at room temperature with formation of allylboronic anhydride after distillation under vacuum: B. M. Mikhailov, F. B. Tutorskaya, *Dokl. Akad. Nauk SSSR* **1958**, 479; tricrotylborane reacts with methanol at room temperature to give dicrotylmethoxyborane (hydrolysis of only one organic residue on the boron center); to cleave the second crotyl residue, heating in methanol is required: B. M. Mikhailov, V. F. Pozdnev, *Izv. Akad. Nauk SSSR Ser. Khim.* **1964**, 1477.

[18] H. C. Brown, S. K. Gupta, *J. Am. Chem. Soc.* **1975**, *97*, 5249–5255; *Encyclopedia of Reagents for Organic Synthesis* (Ed.: L. A. Paquette), Wiley, Chichester, **1995**, pp. 1017–1020.

[19] H. C. Brown, N. G. Bhat, V. Somayaji, *Organometallics* **1983**, *2*, 1311–1316; H. C. Brown, U. S. Racherla, *J. Org. Chem.* **1986**, *51*, 895–897; H. C. Brown, J. B. Campbell, Jr., *J. Org. Chem.* **1980**, *45*, 389–395; *Encyclopedia of Reagents for Organic Synthesis* (Ed.: L. A. Paquette), Wiley, Chichester, **1995**, pp. 1548–1552 and 1689–1690.

[20] R. Köster in *Methods of Organic Chemistry (Houben-Weyl), 4th ed. 1952–, Vol. 13/3a*, **1982**, pp. 489–853.

[21] The well-documented reduction of halides, sulfonates, and sulfates with sodium borohydride proceeds well in polar aprotic solvents such as diglyme or dimethyl sulfoxide with the generation of an equimolar amount of borane. This consideration led to the development of protocols with borane being scavenged in situ by the present alkene, thus resulting in a hydroboration reaction in situ: H. C. Brown, P. Tierney, *J. Am. Chem. Soc.* **1958**, *80*, 1552–1558; H. C. Brown, K. J. Murray, L. J.

 © 2003 Wiley-VCH Verlag GmbH & Co. KGaA, Weinheim

Murray, J. A. Snover, G. Zweifel, *J. Am. Chem. Soc.* **1960**, *82*, 4233–4241; H. M. Bell, C. W. Vanderslice, A. Spehar, *J. Org. Chem.* **1969**, *34*, 3923–3926; S. Krishnamurthy, H. C. Brown, *J. Org. Chem.* **1980**, *45*, 849–856; *Encyclopedia of Reagents for Organic Synthesis* (Ed.: L. A. Paquette), Wiley, Chichester, **1995**, pp. 4522–4528.

[22] Unlike boronic acids, the corresponding diethanolamine adducts are highly stable, conveniently handled and purified compounds: K. Smith, J. B. Leach, *Organometallic Compounds of Boron*, Chapman and Hall, New York, **1985**; see also: M. Gravel, K. A. Thompson, M. Zak, C. Berube, D. G. Hall, *J. Org. Chem.* **2002**, *67*, 3–15; C. N. Farthing, S. P. Marsden, *Tetrahedron Lett.* **2000**, *41*, 4235–4238; K. A. Thompson, D. G. Hall, *Chem. Commun.* **2000**, 2379–2380.

[23] For experimental details, see Supporting Information.

[24] Experiments to isolate **9** were not conducted (see reference [17]).

[25] CCDC 193654 contains the supplementary crystallographic data for this paper. These data can be obtained free of charge via www.ccdc.cam.ac.uk/conts/retrieving.html (or from the Cambridge Crystallographic Data Centre, 12 Union Road, Cambridge CB21EZ, UK; fax: (+44)1223-336-033; or deposit@ccdc.cam.ac.uk).

[26] E. Jehanno, M. Vaultier, *Tetrahedron Lett.* **1995**, *36*, 4439–4442; J. Tailor, D. G. Hall, *Org. Lett.* **2000**, *2*, 3715–3718.

 © 2003 Wiley-VCH Verlag GmbH & Co. KGaA, Weinheim

Functionalizing Polyoxotungstates

Highly Efficient Peptide Bond Formation to Functionalized Wells-Dawson-Type Polyoxotungstates**

Sébastian Bareyt, Stergios Piligkos, Bernold Hasenknopf, Pierre Gouzerh, Emmanuel Lacôte, Serge Thorimbert, and Max Malacria**

Polyoxometalates (POMs) are a large family of metal-oxygen clusters of the early transition metals in high oxidation states, most commonly V^V, Mo^{VI}, and W^{VI}.[1,2] Their diversity in structure and composition allows a wide versatility in terms of shape, polarity, redox potentials, surface charge distribution, and acidity. The last twenty years have witnessed a growing interest in the biological properties of POMs and their potential applications in medicine.[3] POMs exhibit antiviral—notably anti HIV[4,5]—as well as antitumor[6,7] and antibiotic[8,9] activities. Nonetheless, progress along these lines has been quite slow because of the low physiological stability of most POMs. Only a few POMs were reported with enhanced hydrolytic stability.[4,10,11] An original approach is the encapsulation of POMs in starch nanoparticles.[6]

The introduction of organic groups into the POM framework could greatly increase the number of compounds available for screening, together with a potential modulation of essential features, such as stability, bioavailability, and recognition.[3] While there is a significant amount of work on hybrid POMs,[12–14] there have been only scattered reports of the reactivity of the side chain of such functionalized POMs.[15–17] Many of these organically derivatized POMs are unstable in water. Starting from hydrolytically more stable cyclopentadienyltitanium substituted POMs,[11,18] Keana reported the preparation and reactivity of derivatives with various functional groups.[19–21] We decided to reexamine the heteropolytungstates $[\alpha_2\text{-}P_2W_{17}O_{61}(SnR)]^{7-}$ reported by Pope and co-workers,[22,23] with an alkyltin group in place of the more fragile CpTi-moiety. These heteropolytungstate compounds have promising antitumor activities,[24] but the organic groups that were introduced were very simple and did not allow further functionalization.[18,22,24]

It is important to have access to a wide variety of organic groups on the POM to meet specific requirements in biological applications. Different groups will enable the POM, for instance, to cross a membrane or to reach a specific receptor depending on their precise nature. We report herein our first findings on a flexible synthetic approach.

To obtain polyanions of the type $[\alpha_2\text{-}P_2W_{17}O_{61}(SnR)]^{7-}$ with different R groups, one can treat different $RSnCl_3$ with $[\alpha_2\text{-}P_2W_{17}O_{61}]^{10-}$.[22,24] This strategy suffers from the incompatibility of the trichlorotin moiety with most organic functions, and the scarce versatility it allows. To prepare a functionalized POM useful as a scaffold for many applications, we decided to graft a pendant carboxylic acid onto a POM (Scheme 1), because it would allow peptide or ester coupling reactions, which are compatible with most bioactive compounds.

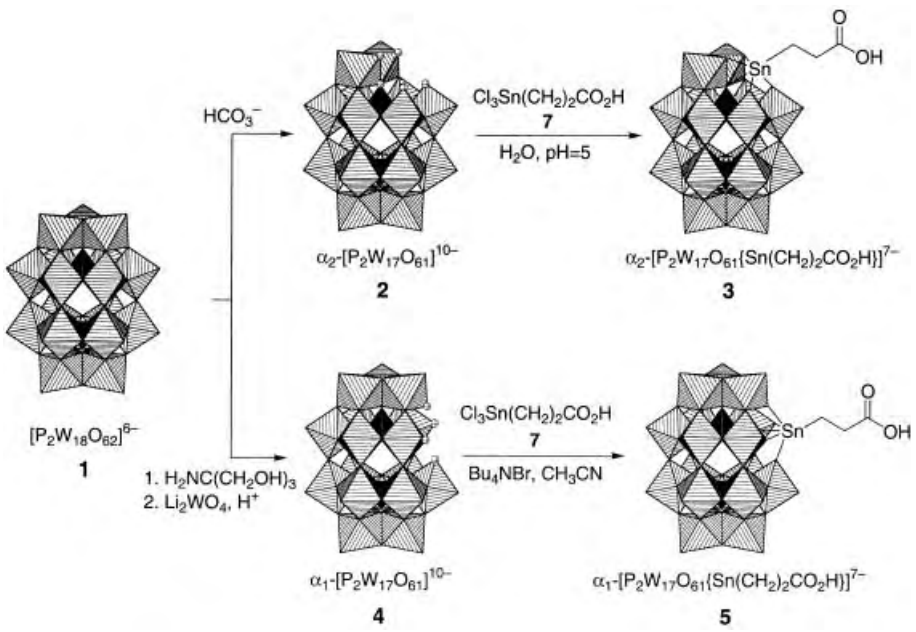
The treatment of a buffered aqueous solution of $K_{10}[\alpha_2\text{-}P_2W_{17}O_{61}]$ **2**[25] with $Cl_3Sn(CH_2)_2CO_2H$ **7**[26] yielded a new anion which was precipitated by the addition of nBu$_4$NBr. The IR spectrum shows the vibrational bands arising from the Wells-Dawson structure without the typical splitting of the P–O stretching vibration in the lacunary compound,[27] thus indicating that the lacuna is filled. ^{31}P NMR analysis showed the presence of a single product with two nonequivalent phosphorous atoms ($\delta = -12.7$ and -9.65 ppm). The high-frequency resonance consists of a single line flanked by a pair of satellites arising from unresolved coupling with ^{117}Sn and ^{119}Sn ($J = 27.5$ Hz). Consequently, the tin atom is bound to the phosphate group. ^{1}H NMR confirms the presence of the side chain, thus showing unambiguously that we succeeded in preparing $[\alpha_2\text{-}P_2W_{17}O_{61}\{Sn(CH_2)_2CO_2H\}]^{7-}$ **3**, the starting compound for a new family of functionalized clusters.

[*] Prof. M. Malacria, Dr. E. Lacôte, Dr. S. Thorimbert
Laboratoire de Chimie Organique, UMR 7611 CNRS
Université Pierre et Marie Curie
4, Place Jussieu, 75252 Paris cedex 05 (France)
Fax: (+33) 144277360
E-mail: malacria@ccr.jussieu.fr
Dr. B. Hasenknopf, S. Bareyt, S. Piligkos, Prof. P. Gouzerh
Laboratoire de Chimie Inorganique et Matériaux Moléculaires
UMR 7071 CNRS, Université Pierre et Marie Curie
4, Place Jussieu, 75252 Paris cedex 05 (France)
Fax: (+33) 144273841

[**] We gratefully acknowledge financial support from UPMC and CNRS. S.B. thanks Prof. G. Béréziat and the Ministère de la Jeunesse, de L'Education Nationale et de la Recherche for a fellowship.

Supporting information for this article is available on the WWW under http://www.angewandte.org or from the author.

 © 2003 Wiley-VCH Verlag GmbH & Co. KGaA, Weinheim DOI: 10.1002/anie.200351346



Scheme 1. Preparation of functionalized Wells-Dawson polyoxotungstates.

With this compound in hand, we endeavored to prepare the functionalized α_1-isomer **5**. Contrary to the α_2 isomer, the α_1 isomer is chiral and could be of great interest for the study of POM/receptor interactions.[4,28] The lacunary compound **4** isomerizes in aqueous solution.[29] For this reason, the reaction of **4** with **7** under the conditions established for the α_2 isomer gave low yields in **5**. We therefore developed a new synthesis in acetonitrile under phase transfer conditions to obtain **5** in 95% yield. To the best of our knowledge, this polyanion is the first example of a Wells-Dawson structure having an organic side chain in the α_1 position.

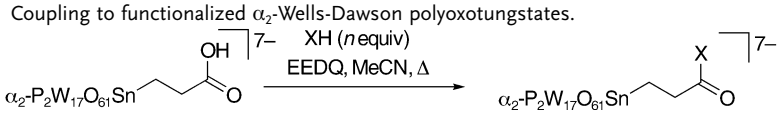
As our objective was to use the POM's "arm" as a linker, we sought conditions that would enable us to attach various molecules to the acid moiety. This task implies finding particularly efficient conditions—POMs with different side chains are almost impossible to separate—without creating cationic byproducts leading to scrambling of the counterions, which causes solubility and purity problems. Eventually, we were able to optimize the EEDQ-mediated coupling.[30] The only by-products are ethanol and quinoline, which can be easily removed (Table 1).

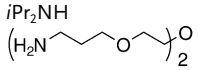
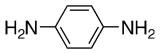
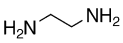
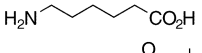
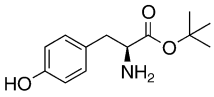
All reactions were carried out in refluxing acetonitrile. Primary and secondary amines led to the corresponding amides in high yields (Table 1, entries 1–3). Entry 3 shows that the reaction is sensitive to steric hindrance, as expected. With the intention of attaching POMs to the C terminus of peptides, it might become useful to have N-terminal scaffolds. Reactions of diamines, whether dialkyl or diaryl, proved surprisingly much more difficult (Table 1, entries 4–6) requiring longer reaction times to produce the aminoamides. However, no other POM was formed. When ethylenediamine was used (entry 6), the reaction never reached completion: at about 80% conversion, degradation occurred rapidly. Acid, ester and phenol functions were tolerated (Table 1, entries 7 and 8). It should be noted that simple α-aminoacids failed to give any amide (no conversion), while C protection of tyrosine triggered a nearly quantitative reaction (entry 8). This is probably due to the low solubility of the aminoacids under the reaction conditions. Lastly, esters could also be prepared. The reaction of **3** with benzyl alcohol (BnOH) gave **6h** in 86% yield. Coupling reactions with **5** proceeded similarly, but were accompanied by degradation. For instance, the reaction with benzylamine led to 50% of the desired amide accompanied by several derivatives of the α_2 isomer (among which 20% of **6a**).

Finally, we had to show that the functionalization of the side chain did not affect the hydrolytic stability of the polyanion. For this purpose, we selected **6a**, which was made water soluble by the exchange of $n\mathrm{Bu_4N^+}$ with $\mathrm{Na^+}$. A saturated solution in physiological serum was monitored by ^{31}P NMR. No decomposition occurred at RT during ten days, and degradation did not exceed 12% at 37 °C after two days.

In conclusion, we have demonstrated that we could prepare both $[\alpha_1\text{-}P_2W_{17}O_{61}\{Sn(CH_2)_2CO_2H\}]^{7-}$ and $[\alpha_2\text{-}P_2W_{17}O_{61}\{Sn(CH_2)_2CO_2H\}]^{7-}$, and also further make derivatives of the α_2 series by attaching organic molecules to the

Table 1: Coupling to functionalized α_2-Wells-Dawson polyoxotungstates.



Entry	XH	*n*	*t* [h]	Product, yield [%]
1	$BnNH_2$	3	4	**6a**, 86
2	Bn_2NH	2	8	**6b**, 90
3	iPr_2NH	3	12	**6c**, 80
4		6	140	**6d**, 70
5		6	120	**6e**, 66
6		7	120	–[a]
7		3	36	**6f**, 50
8		3	36	**6g**, 90
9	BnOH	2	12	**6h**, 86

[a] Maximum conversion was 80%. Rapid degradation followed. EEDQ = 2-ethoxy-1-ethoxycarbonyl-1,2-dihydroquinoline.

 © 2003 Wiley-VCH Verlag GmbH & Co. KGaA, Weinheim

arm. Work to determine the scope and limitation of our method is in progress. These results, as well as the behavior of POMs attached to bioactive compounds such as penicillin, will be reported in due course.

Received: March 7, 2003 [Z51346]

Keywords: amides · organic-inorganic hybrid composites · polyoxometalates · stannanes · tungsten

[1] M. T. Pope, A. Müller, *Polyoxometalate Chemistry: From Topology via Self-Assembly to Applications*, Kluwer Academic, Dordrecht, **2001**.
[2] M. T. Pope, *Heteropoly and Isopoly Oxometalates*, Springer, Berlin, **1983**.
[3] J. T. Rhule, C. L. Hill, D. A. Judd, R. F. Schinazi, *Chem. Rev.* **1998**, *98*, 327–357.
[4] D. A. Judd, J. H. Nettles, N. Nevins, J. P. Snyder, D. C. Liotta, J. Tang, J. Ermolieff, R. F. Schinazi, C. L. Hill, *J. Am. Chem. Soc.* **2001**, *123*, 886–897.
[5] M. Witvrouw, H. Weigold, C. Pannecouque, D. Schols, E. De Clercq, G. Holan, *J. Med. Chem.* **2000**, *43*, 778–783.
[6] X. Wang, J. Liu, M. T. Pope, *J. Chem. Soc. Dalton Trans.* **2003**, 957–960.
[7] X.-H. Wang, J.-F. Liu, Y.-G. Chen, Q. Liu, J.-T. Liu, M. T. Pope, *J. Chem. Soc. Dalton Trans.* **2000**, 1139–1142.
[8] N. Fukuda, T. Yamase, Y. Tajima, *Biol. Pharm. Bull.* **1999**, *22*, 463–470.
[9] T. Yamase, N. Fukuda, Y. Tajima, *Biol. Pharm. Bull.* **1996**, *19*, 459–465.
[10] Y. Hou, C. L. Hill, *J. Am. Chem. Soc.* **1993**, *115*, 11823–11830.
[11] R. K. C. Ho, W. G. Klemperer, *J. Am. Chem. Soc.* **1978**, *100*, 6772–6774.
[12] P. Gouzerh, A. Proust, *Chem. Rev.* **1998**, *98*, 77–111.
[13] B. Hasenknopf, R. Delmont, P. Herson, P. Gouzerh, *Eur. J. Inorg. Chem.* **2002**, 1081–1087.
[14] U. Kortz, M. G. Savelieff, F. Y. A. Ghali, L. M. Khalil, S. A. Maalouf, D. I. Sinno, *Angew. Chem.* **2002**, *114*, 4246–4249; *Angew. Chem. Int. Ed.* **2002**, *41*, 4070–4073.
[15] B. Xu, Y. Wei, C. L. Barnes, Z. Peng, *Angew. Chem.* **2001**, *113*, 2353–2356, *Angew. Chem. Int. Ed.* **2001**, *40*, 2290–2292.
[16] X. Wei, M. H. Dickman, M. T. Pope, *J. Am. Chem. Soc.* **1998**, *120*, 10254–10255.
[17] P. R. Marcoux, B. Hasenknopf, J. Vaissermann, P. Gouzerh, *Eur. J. Inorg. Chem.* **2003**, in press.
[18] W. H. Knoth, *J. Am. Chem. Soc.* **1979**, *101*, 759–760.
[19] J. F. W. Keana, M. D. Ogan, *J. Am. Chem. Soc.* **1986**, *108*, 7951–7957.
[20] J. F. W. Keana, M. D. Ogan, Y. Lu, M. Beer, J. Varkey, *J. Am. Chem. Soc.* **1986**, *108*, 7957–7963.
[21] S. X. Cai, Y. Wu, J. F. W. Keana, *New J. Chem.* **1993**, *17*, 325–329.
[22] F. Zonnevijlle, M. T. Pope, *J. Am. Chem. Soc.* **1979**, *101*, 2731–2732.
[23] G. S. Chorghade, M. T. Pope, *J. Am. Chem. Soc.* **1987**, *109*, 5134–5138.
[24] X.-H. Wang, J.-F. Liu, *J. Coord. Chem.* **2000**, *51*, 73–82.
[25] R. Contant, *Inorg. Synth.* **1990**, *27*, 104–111.
[26] R. E. Hutton, J. W. Burley, V. Oakes, *J. Organomet. Chem.* **1978**, *156*, 369–382.
[27] See Supplementary Material for analytical data of compounds **3, 5, 6a–h**.
[28] M. Sadakane, M. H. Dickman, M. T. Pope, *Inorg. Chem.* **2001**, *40*, 2715–2719.
[29] R. Contant, J.-P. Ciabrini, *J. Chem. Res. Synop.* **1977**, 222.
[30] B. Belleau, G. Malek, *J. Am. Chem. Soc.* **1968**, *90*, 1651–1652.

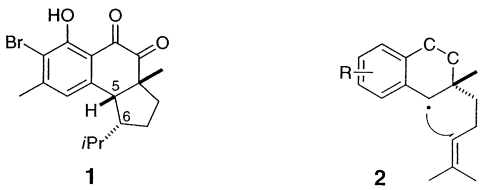
 © 2003 Wiley-VCH Verlag GmbH & Co. KGaA, Weinheim

Natural Product Synthesis

Stereospecific Total Synthesis of the Antiviral Agent Hamigeran B—Use of Large Silyl Groups to Enforce Facial Selectivity and to Suppress Hydrogenolysis**

Derrick L. J. Clive and Jian Wang*

We report the stereospecific synthesis of hamigeran B (**1**, Scheme 1), which is an important member of a group of related compounds isolated[1] from a marine sponge. Hamigeran B has been found to have strong in vitro activity against



Scheme 1. Hamigeran B (**1**) and the radical cyclization of **2**.

polio and herpes viruses but little cytotoxicity.[1] The compound presents a number of constructional problems, and the significant biological properties enhance the potential value of work on its synthesis. One route to hamigeran B and several congeners has been reported.[2] We aimed to deal only with the synthesis of hamigeran B itself and to do so in a stereospecific manner.

The most obvious synthetic difficulty resides in the stereochemistry at C6 (see **1**), as the bulky isopropyl group extends into the more hindered concave face of the structure. This orientation probably disqualifies methods that rely on stereochemical equilibration at C6. Likewise, radical cyclization (see **2**), which is a powerful method for making [4.3.0] bicyclic structures with *cis* ring fusion, does not[3] generate the correct stereochemistry at C6 because the required transition state is destabilized by steric interactions engendered by the isopropylidene group. Further synthetic analysis, as well as experimental work, suggested that double-bond reduction (Scheme 2, **3**→**4**), possibly directed by a suitably placed substituent, would merit detailed investigation. We recognized, however, that the double bond in **3**, being tetrasubstituted, might be resistant to hydrogenation.[4] Also, examination of Dreiding models exposed another potential difficulty: it was not obvious from the shape of **3** whether

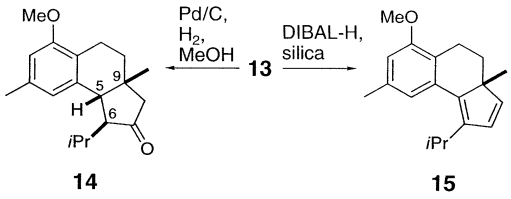
[*] Prof. Dr. D. L. J. Clive, J. Wang
Chemistry Department
University of Alberta
Edmonton, Alberta, T6G 2G2 (Canada)
Fax: (+1) 780-492-8231
E-mail: derrick.clive@ualberta.ca

[**] We thank NSERC for financial support, Dr. R. McDonald (X-Ray Crystallography Laboratory) for crystal-structure determinations, and Professor S. Bergens and S. Fletcher for valuable advice.

 © 2003 Wiley-VCH Verlag GmbH & Co. KGaA, Weinheim DOI: 10.1002/anie.200351519



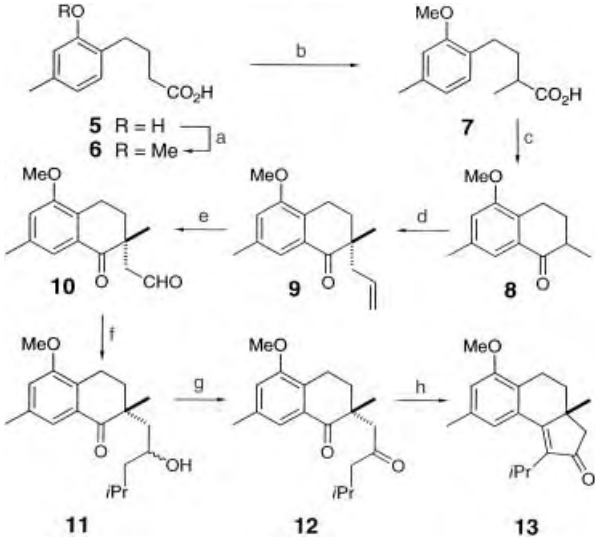
Scheme 2. Key transformation in the synthesis of hamigeran B (**1**).



Scheme 4. Some transformations of enone **13**. DIBAL-H = diisobutylaluminum hydride.

hydrogenation would occur preferentially from the α or β face. Nonetheless, we decided to examine the approach shown in Scheme 2, and we were eventually able, through the temporary introduction of additional steric factors, to develop it into a powerful approach for solving the stereochemical problems inherent in the convex shape and substitution pattern of hamigeran B.

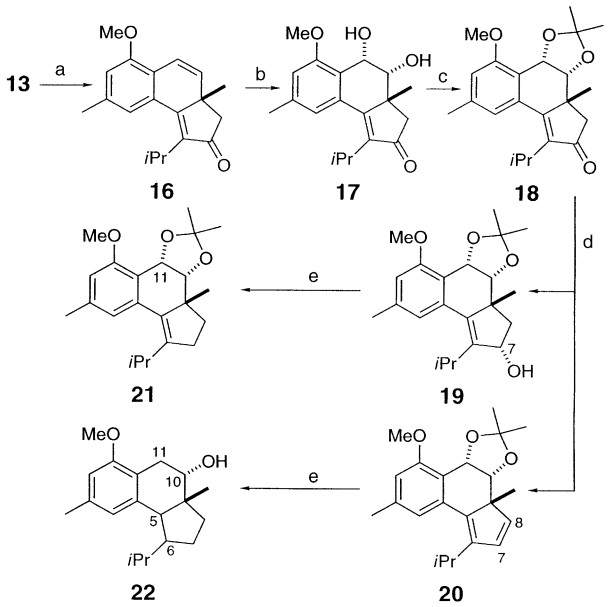
The phenolic carboxylic acid **5** (Scheme 3), easily prepared from *m*-cresol by Friedel–Crafts acylation with succinic anhydride[5] followed by Clemmensen reduction,[6] was



Scheme 3. Preparation of the key intermediate **13**. Reagents and conditions: a) Me_2SO_4, aqueous NaOH, reflux, 12 h, 67% from *m*-cresol; b) LDA, THF, HMPA, −78°C, MeI, 96%; c) $POCl_3$, $Cl_2CHCHCl_2$, reflux, 5 h, 83%; d) LDA, THF, −78°C, allyl bromide, 91%; e) OsO_4, $NaIO_4$, dioxane/water 3:1, 3.5 h, 76%; f) *i*BuMgCl, Et_2O, −78°C, 89%; g) PCC, CH_2Cl_2, 3.5 h, 87%; h) aqueous EtOH, NaOH, reflux, 36 h, 98%. HMPA = hexamethylphosphoric triamide, LDA = lithium diisopropylamide, PCC = pyridinium chlorochromate.

treated with Me_2SO_4 under alkaline conditions (**5**→**6**),[5] and then methylated[7] at the position α to the carboxy group. Cyclization, by treatment with $POCl_3$ (**7**→**8**[7]), and allylation gave the substituted tetralone **9**. Double-bond cleavage (**9**→**10**) and exposure to *i*BuMgCl at low temperature then led to keto alcohols **11**, and oxidation afforded the corresponding diketone **12**. This was cyclized under basic conditions in good yield to produce our first key intermediate, **13**.

Hydrogenation of **13** over Pd/C in MeOH (H_2, 345 kPa) gave the crystalline ketone **14** (Scheme 4) as the major product[8] (52% yield), which has the undesired β stereochemistry at C6, as determined by X-ray analysis. On the assumption that the desired α stereochemistry was generated initially but that the product underwent carbonyl-mediated epimerization, we attempted to reduce ketone **13** to the corresponding allylic alcohol in order to remove that possibility. Treatment of **13** with $NaBH_4$ and $CeCl_3{\cdot}7H_20$, was unsuccessful, as the compound reacted much too slowly, but reaction with DIBAL-H (0°C to room temperature) was rapid. However, the resulting allylic alcohol is very sensitive, and exposure to silica gel during flash chromatography caused dehydration, so that the material isolated (98%) was the diene **15** (Scheme 4). Hydrogenation of this diene (Pd/C, H_2, 345 kPa, MeOH) did saturate the two double bonds, but an inseparable mixture (ca. 1:1 in some experiments) of stereoisomers was formed. We attributed this result to a lack of facial selectivity, and so we decided to introduce a bulky group to block the α face of ketone **13**. To this end, the ketone was dehydrogenated with DDQ (Scheme 5, **13**→**16**). Dihydroxylation (**16**→**17**) with OsO_4 and NMO occurred *anti* to the adjacent methyl substituent, as desired, and the stage was now set to mask the hydroxy groups with a bulky substituent, so as to direct subsequent hydrogenation exclusively to the opposite face.

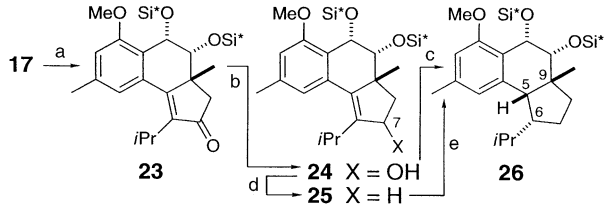


Scheme 5. Reagents and conditions: a) DDQ, dioxane, reflux, 8.5 h, 78%; b) OsO_4, NMO, CCl_4/water/*t*BuOH/acetone 5:1:4:6, 13 h, 98%; c) $Me_2C(OMe)_2$, TsOH·pyridine, acetone, 4 h, 88%; d) DIBAL-H, CH_2Cl_2, 0°C, 8 h, 54% of **19**, 23% of **20**; e) Pd/C, H_2, 345 kPa, MeOH. DDQ = 2,3-dichloro-5,6-dicyano-1,4-benzoquinone, NMO = 5-methylmorpholine *N*-oxide, Ts = toluene-4-sulfonyl.

 © 2003 Wiley-VCH Verlag GmbH & Co. KGaA, Weinheim

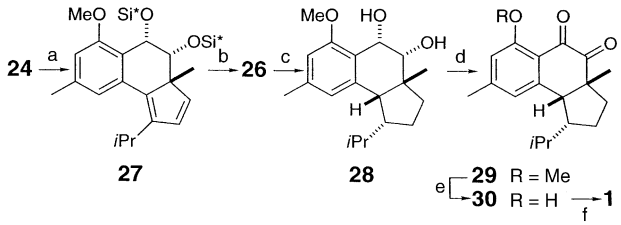
Conversion of diol **17** into ketal **18** was achieved by standard procedures, and the carbonyl group was then reduced with DIBAL-H to give a 2.3:1 mixture of allylic alcohol **19** (tentative stereochemistry shown at C7[9]) and diene **20**. Hydrogenation of **19** gave **21** and a mixture of substances lacking a benzylic oxygen at C11 (absence of ^{1}H NMR signals at $\delta \approx 5$ ppm for the benzylic CH–O). With short reaction times (1 h) **21** was the major product (ca. 80% yield). Only the C7–C8 double bond of diene **20** was reduced when we used Rh/Al_2O_3 (H_2, 4826 kPa, 50 °C, MeOH), Wilkinson's catalyst (H_2, 2758 kPa, MeOH, 50 °C), or Raney 2800 Ni (Aldrich; 7929 kPa, 60 °C, MeOH). Hydrogenation of **20** gave **22** (92% yield, stereochemistry at C5 and C6 not established, Scheme 5). Olefin **21** did not react in refluxing THF with BH_3 or 9-borabicyclo[3.3.1]nonane (9-BBN). Our failure to effect hydroboration and the finding that hydrogenolysis occurred at C11 in experiments with Pd/C caused us to modify the route in a small but effective way.

With the aim of avoiding hydrogenolysis of the C11 oxygen, we decided to protect the hydroxy groups of diol **17** with substituents having sufficient bulk to hinder coordination[10,11] of the benzylic oxygen to the catalyst surface, and so we silylated the hydroxy group with tBuMe$_2$SiOSO$_2$CF$_3$ (Scheme 6, **17**→**23**). DIBAL-H reduction gave an allylic



Scheme 6. Reagents and conditions: a) tBuMe$_2$SiOSO$_2$CF$_3$, CH$_2$Cl$_2$, 2,6-lutidine, 6 h, 84%; b) DIBAL-H, CH$_2$Cl$_2$, 0 °C to room temperature, 10 h, 94%; c) Pd/C, H_2, 345 kPa, MeOH, 18%; d) Pd/C, H_2, 345 kPa, MeOH, 35%; e) Pd/C, H_2, 345 kPa, MeOH, 93%. Si* = SitBuMe$_2$.

alcohol (**23**→**24**, stereochemistry at C7 not determined). Hydrogenation of **24** provided the desired product **26** but in low yield (18%). When the reaction time was only 6.5 h, one of the products was monoene **25** (35%), and this compound could be hydrogenated in high yield to give the desired **26**. These observations showed that the hydroxy group of **24** had a deleterious effect on the outcome of our hydrogenation experiments. Accordingly, we dehydrated allylic alcohol **24** to give the corresponding diene **27** (Scheme 7). Elimination of the intermediate mesylate is slow and required higher temperatures, but the diene, once formed, was very well-behaved and could be reduced to **26** with the required relative stereochemistry at the three contiguous asymmetric centers, C5, C6, and C9. Compound **26** is crystalline, but the crystals were unsuitable for X-ray analysis. However, desilylation (Scheme 7, **26**→**28**), which required unusually harsh conditions but worked efficiently, gave a nicely crystalline diol, whose structure was determined by X-ray analysis. Diol oxidation (**28**→**29**) was easily performed under Swern conditions, and the next task was to remove the *O*-methyl group of **29**. This was done in 78% yield by treatment with LiCl in



Scheme 7. Reagents and conditions: a) MsCl, Et_3N, ClCH$_2$CH$_2$Cl, room temperature for 30 min, then reflux for 8 h, 80%; b) Pd/C, H_2, 269 kPa, 1:1 MeOH/hexane, 36 h, 85%; c) Bu_4NF, THF, reflux, 24 h, 95%; d) (COCl)$_2$, DMSO, Et_3N, −78 °C, 1 h, room temperature, 2 h, 92%; e) LiCl, DMF, reflux, 20 h, 78%; f) NBS, iPr$_2$NH, CH$_2$Cl$_2$, 3 h, 94%. Si* = SitBuMe$_2$. DMSO = dimethyl sulfoxide, Ms = methanesulfonyl, NBS = *N*-bromosuccinimide.

refluxing DMF (**29**→**30**);[13] other standard reagents (BBr_3, $AlCl_3$, Me_3SiI) destroyed the starting methyl ether. Finally, bromination of **30** with NBS in the presence of iPr$_2$NH, a reagent system known to favor *ortho* bromination of phenols,[14] gave hamigeran B (**1**) in 94% yield. The ^{1}H and ^{13}C NMR, FTIR, and MS characteristics of our synthetic material match those reported[1] for the natural product.

The special features of this synthesis are the use of very simple reactions—a fact which should make the route amenable to scale-up, the application of steric factors to ensure facial selectivity, and the protection against hydrogenolysis[15] that is afforded by the bulky tBuMe$_2$Si groups.

Received: March 31, 2003 [Z51519]

Keywords: hamigeran B · hydrogenolysis · natural products · silyl groups · total synthesis

[1] K. D. Wellington, R. C. Cambie, P. S. Rutledge, P. R. Bergquist, *J. Nat. Prod.* **2000**, *63*, 79–85.
[2] a) K. C. Nicolaou, D. Gray, J. Tae, *Angew. Chem.* **2001**, *113*, 3787–3790; *Angew. Chem. Int. Ed.* **2001**, *40*, 3675–3678; b) K. C. Nicolaou, D. Gray, J. Tae, *Angew. Chem.* **2001**, *113*, 3791–3795; *Angew. Chem. Int. Ed.* **2001**, *40*, 3679–3683.
[3] J. Wang, unpublished observations.
[4] a) M. Freifelder, *Catalytic Hydrogenation in Organic Synthesis. Procedures and Commentary*, Wiley, New York, **1978**, p. 15; b) P. N. Rylander, *Catalytic Hydrogenation over Platinum Metals*, Academic Press, New York, **1967**, p. 91; c) Examples of hydrogenation of tetrasubstituted double bonds conjugated with benzene rings are known (Beilstein database); see, especially: A. C. G. Gray, H. Hart, *J. Am. Chem. Soc.* **1968**, *90*, 2569–2578.
[5] R. G. Cooke, H. Dowd, *Aust. J. Chem.* **1953**, *6*, 53–57.
[6] G. L. Martin, *J. Am. Chem. Soc.* **1936**, *58*, 1438–1442.
[7] Cf.L. Ruzicka, H. Hösli, K. Hofmann, *Helv. Chim. Acta* **1936**, *19*, 370–377.
[8] Another stereoisomer was formed for which no NOE was observed between H5 and the methyl group at C9.
[9] Based on observation of NOE effects.
[10] Cf. M. J. Gaunt, J. Yu, J. B. Spencer, *J. Org. Chem.* **1998**, *63*, 4172–4173.
[11] It is believed that hydrogenolysis is facilitated by development of a partial positive charge on the benzylic carbon (see ref. [10]); siloxy groups are not as effective at stabilizing an adjacent positive charge as alkoxy groups (see ref. [12]).

 © 2003 Wiley-VCH Verlag GmbH & Co. KGaA, Weinheim

[12] E. Colvin, *Silicon in Organic Synthesis*, Butterworths, London, **1981**, p. 12.
[13] A. M. Bernard, M. R. Ghiani, P. P. Piras, A. Rivoldini, *Synthesis* **1987**, 287–288.
[14] a) S. Fujisaki, H. Eguchi, A. Omura, A. Okamoto, A. Nishida, *Bull. Chem. Soc. Jpn.* **1993**, *66*, 1576–1579; b) K. Krohn, S. Bernhard, U. Flörke, N. Hayat, *J. Org. Chem.* **2000**, *65*, 3218–3222.
[15] Examples of the following have been reported (without comment): A benzylic *tert*-butyldimethylsilyl ether survives hydrogenation of disubstituted (e.g. ref. [16]) and trisubstituted (ref. [2a]) double bonds. A tertiary benzylic trimethylsilyl ether survives hydrogenation of a tetrasubstituted double bond (ref. [17]).
[16] a) T. J. Connoly, T. Durst, *Tetrahedron* **1997**, *53*, 15969–15982; b) C. R. Mateus, W. P. Almeida, F. Coelho, *Tetrahedron Lett.* **2000**, *41*, 2533–2536.
[17] B. M. Trost, P. D. Greenspan, B. V. Yang, M. G. Saulnier, *J. Am. Chem. Soc.* **1990**, *112*, 9022–9024.

 © 2003 Wiley-VCH Verlag GmbH & Co. KGaA, Weinheim

Aminoglycoside Mimetics

Design and Synthesis of Paromomycin-Related Heterocycle-Substituted Aminoglycoside Mimetics Based on a Mass Spectrometry RNA-Binding Assay**

Yili Ding, Steven A. Hofstadler, Eric E. Swayze, Lisa Risen, and Richard H. Griffey*

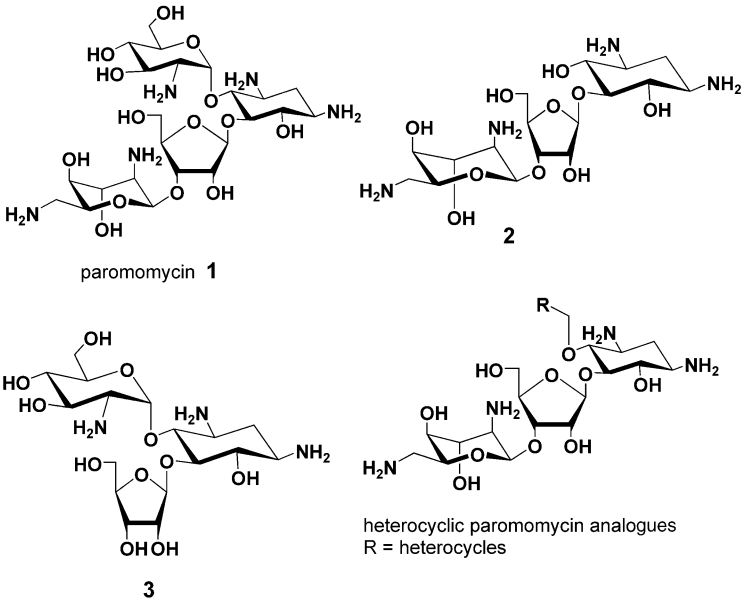
The family of aminoglycosides, which includes neomycin, paromomycin (**1**), lividomycin, kanamycin, and gentamicin, is a very potent group of bactericidal compounds that bind to the RNA of the small ribosomal subunit.[1] This bactericidal action is mediated by binding of the compound to the bacterial RNA in a way that leads to misreading of the genetic code.[2] The decoding region of the 16S ribosomal RNA contains a smaller subdomain (16S) that folds and retains the key structural features of the full-length RNA.[3] This "A-site" subdomain binds aminoglycosides at the same location as the intact rRNA.

ESIMS was used to determine solution-phase dissociation constants of RNA–ligand complexes based on gas-phase measurements of the ratio of free and bound RNA target. ESIMS was also used to determine the location of ligand binding on the RNA and to determine the specificity for 16S and 18S rRNA.[4,5] Paromomycin exhibited an excellent binding affinity and specificity for 16S rRNA in this assay.[6] Therefore, we used MS to carry out structure–activity relationship (SAR) studies to determine how the structure of the aminoglycosides affects their binding activities. Based on these results, paromomycin mimetics were designed and synthesized as new bactericidal compounds.

It has been estimated that over a half of all therapeutic agents consist of heterocyclic compounds. The heterocyclic ring system in many cases comprises the very core of the active moiety or pharmacophore. Therefore, heterocycle-substituted aminoglycoside mimetics may be ideal therapeutic agents.

To determine which rings of paromomycin are important in its 16S rRNA-binding activity, paromomycin (**1**), 5-(β-D-neobisamine)-2-deoxystreptamine (**2**), and 6′-hydroxyribostamycin (**3**) were used as standards[7] to compare their binding affinities in an MS-based RNA-binding assay. In the ESIMS RNA-binding assay, compound **2** exhibited a better binding activity than **3**, which indicated that the D ring of paromomycin may be more important than its A ring for the 16S rRNA-binding activity and specificity.[8] Based on this observation, paromomycin derivatives in which the A ring was replaced with a range of heterocycles were chosen as synthetic targets (Scheme 1).

Owing to the complex nature of the target compounds, it is impractical to prepare them individually for biological activity screening.[9] However, by using MS to study the SAR, we could first screen the 4-heterocycle-substituted 2-deoxystreptamine derivatives, determine which motif has better binding properties, and then design and prepare the target



Scheme 1. Structures of paromomycin (**1**), 5-(β-D-neobisamine)-2-deoxystreptamine (**2**), 6′-hydroxyribostamycin (**3**), and the 4-heterocycle-substituted substituted paromomycin mimetics.

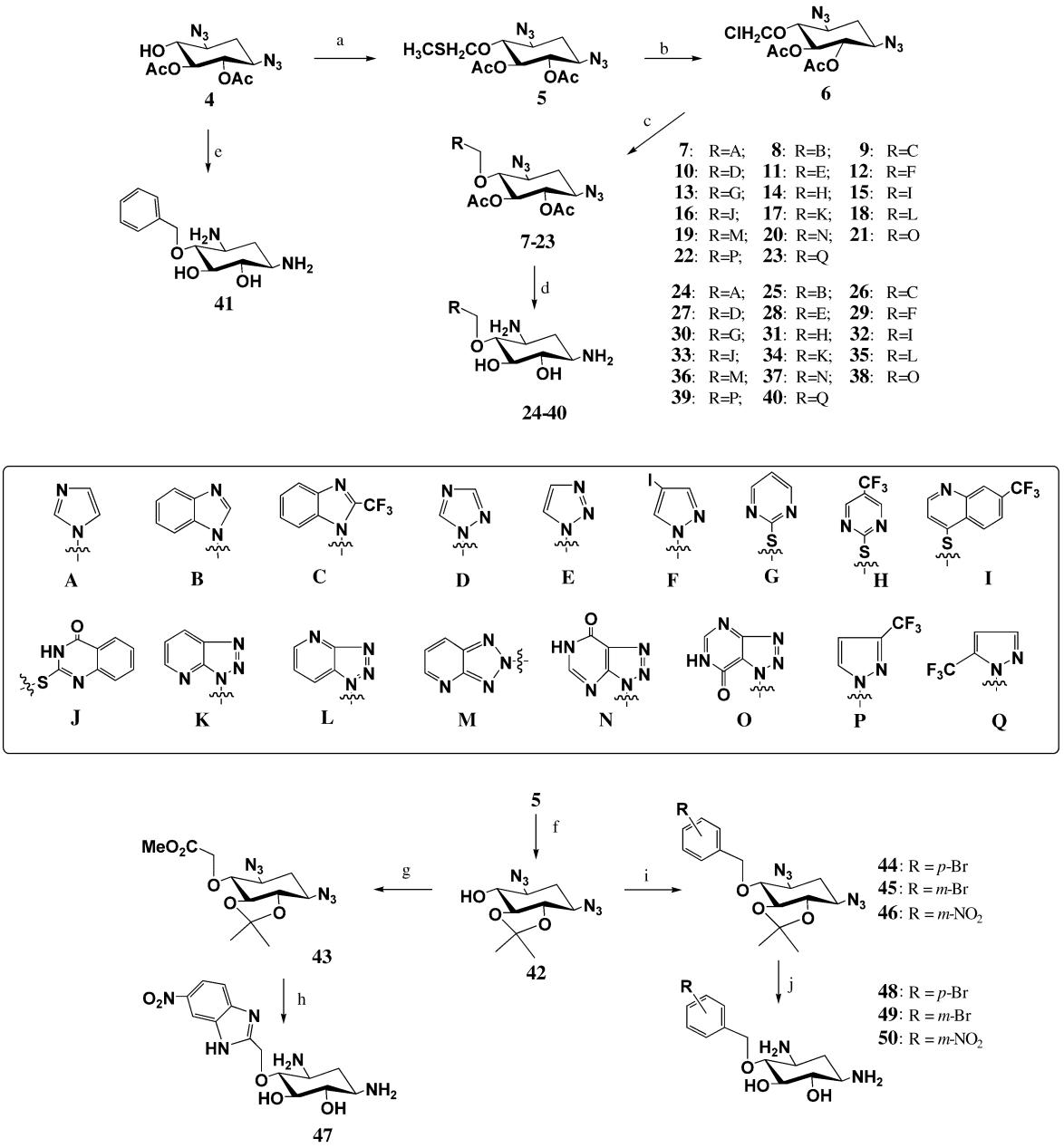
[*] Dr. Y. Ding
Ribapharm
3300 Hyland Avenue, Costa Mesa, CA 92626 (USA)
Fax: (+1) 714-641-7222
E-mail: yding@icnpharm.com
Dr. S. A. Hofstadler, Dr. E. E. Swayze, L. Risen, Dr. R. H. Griffey
Ibis Therapeutics, Isis Pharmaceuticals, Inc.
2292 Faraday Avenue, Carlsbad, CA 92008-7208 (USA)

[**] We thank Mr. Patrick Wheeler for NMR spectroscopic assistance. We are grateful to the DARPA for support of this research work through grant N65236-99-1-5419.

 DOI: 10.1002/anie.200351354 © 2003 Wiley-VCH Verlag GmbH & Co. KGaA, Weinheim

compounds. A concise synthetic strategy for these derivatives is summarized in Scheme 2. The hydroxy group of 5,6-di-*O*-acetylated diazido-2-deoxystreptamine (**4**), which was obtained from the selective enzymatic deacetylation of tri-*O*-acetyl diazido-2-deoxystreptamine,[10] was protected as an MTM ether through a Pummerer rearrangement[11] to give compound **5**. Treatment of **5** with excess SO_2Cl_2 in CH_2Cl_2 gave **6**, which was used as the core starting material for the parallel synthesis.

Compound **6** was coupled with different nucleophilic reagents to afford the corresponding 4-heterocycle-substituted 2-deoxystreptamine derivatives **7**–**23** in satisfactory



Scheme 2. Synthesis of 2-deoxystreptamine derivatives with heterocyclic substituents at C4: a) DMSO (30 equiv), Ac_2O (15 equiv), AcOH (5 equiv), 24 h, 78%; b) SO_2Cl_2 (6 equiv), CH_2Cl_2, room temperature, 30 min, 100%; c) **A**H–**Q**H (1.5 equiv), NaH (1.7 equiv), CH_3CN/DMF, room temperature, 2 h; then **6** (1 equiv), 76–97%; d) 1) NaOMe (0.1 equiv), MeOH, room temperature, 4 h; 2) Me_3P/THF (8 equiv), H_2O/THF (1:1), 10 h, 56–75%; e) 1) benzyl 2,2,2-trichloroacetimidate (4 equiv), TfOH (2 equiv), CH_2Cl_2, room temperature, 5 h; 2) NaOM/MeOH (0.1 M), 4 h; 3) Me_3P/THF (8 equiv), H_2O, room temperature, 10 h, 62%; f) 1) NaOMe/MeOH (0.5 M), 10 h; 2) 2,2-dimethoxypropane, TsOH, room temperature, 10 h; 3) K_2CO_3 (5 equiv), MeI (5 equiv), CH_3COCH_3/H_2O (5:1), 75 °C, 15 h, 23%; g) $BrCH_2CO_2Me$ (2.0 equiv), NaH (2.2 equiv), CH_3CN, room temperature, 4 h, 75%; h) 1) CH_3CO_2H/H_2O (80%), 75 °C, 3 h; 2) NaOH/MeOH/H_2O, room temperature, 5 h; 3) 4-nitro-1,2-phenylenediamine (4 equiv), HCl/H_2O (4 N), 95 °C, 4 h; 4) Me_3P/THF (8 equiv), H_2O/THF (1:1), 10 h, 39%; i) NaH (1.3 equiv), RBnBr (1.2 equiv), room temperature, 4 h, 75–85%; j) 1) CH_3CO_2H/H_2O (80%), 75 °C, 3 h; 2) Me_3P/THF (8 equiv), H_2O/THF, room temperature, 10 h, 55–65%. DMF = *N*,*N*-dimethylformamide, Tf = trifluoromethanesulfonyl, Ts = *p*-toluenesulfonic acid.

 © 2003 Wiley-VCH Verlag GmbH & Co. KGaA, Weinheim

yields.[12] Deprotection and reduction of **7**–**23** gave the derivatives **24**–**40**, respectively. Direct alkylation of **4** with benzyl 2,2,2-trichloroacetimidate followed by deprotection gave the 4-benzyl-2-deoxystreptamine derivative **41**. Deacetylation of compound **5** with methanolic sodium methoxide was followed by protection of the free hydroxy groups as an isopropylidene. Subsequent cleavage of the MTM ether group afforded the product **42**. Alkylation of compound **42** with $BrCH_2CO_2Me$, *o*-BrBnBr, *p*-BrBnBr, and *o*-NO_2BnBr under basic conditions yielded 4-alkylated 2-deoxystreptamine derivatives **43**–**46**. Treatment of **43** with NaOMe/MeOH/H_2O followed by condensation with 3-nitrophenylenediamine (Philips reaction)[13] and subsequent deprotection gave the 4-benzimidazolyl-2-deoxystreptamine derivative **47**. Deprotection of **44**–**46** provided derivatives **48**–**50**, respectively.

The ESIMS RNA-binding assay was then used to evaluate the binding affinities of compounds **24**–**40** and **47**–**50** for a 27-mer RNA representing the 16S A site. The compounds were screened against the 16S A site at equal concentrations in separate experiments. [(7-Trifluoromethyl)-4-quinolinyl]sulfanyl-2-deoxystreptamine (**32**) showed better binding affinity (68 μM) than other 4-heterocycle-substituted 2-deoxystreptamine derivatives.[14]

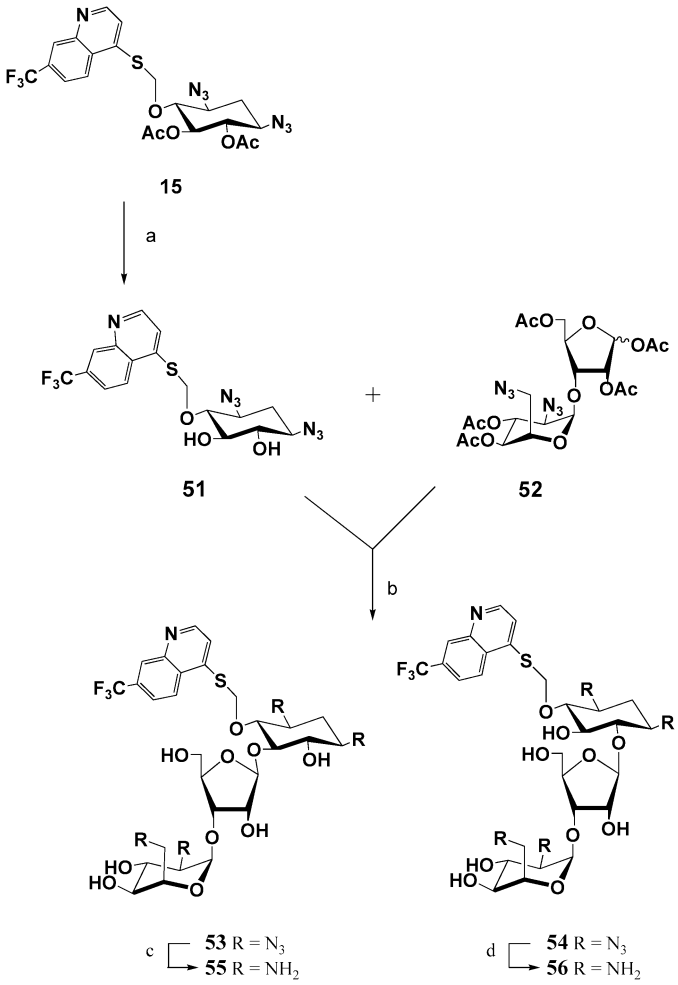
Based on this result, the paromomycin mimetic in which the A ring is replaced with heterocycle **I** was selected as the target. Its concise synthesis is summarized in Scheme 3. Treatment of **15** with methanolic sodium methoxide gave the product **51**. The glycosylation donor **52** was obtained from the acidic hydrolysis of neomycin B in three steps,[7] which is a more simple and effective method than the total synthesis approach. The glycosylation reaction between **51** and C,D-ring donor **52** was performed in CH_2Cl_2 in the presence of TMSOTf. After deacetylation, the desired product **53** was isolated as a minor product and **54** was isolated as the major product. Reduction of the azido groups of **53** with Me_3P/NaOH/THF/H_2O gave the final target **55**. By using a similar method, **54** was converted into **56**.[15]

The ESIMS RNA-binding assay was used to evaluate the binding activity of **55**. This aminoglycoside mimetic exhibited good RNA-binding activity ($K_d < 1$ μM).[16] Its K_d value is higher than that of paromomycin (110 nM), but lower than those of apramycin (2 μM), bekanamycin (2 μM), and tobramycin (2 μM).[4–6]

Compound **55** was tested in a coupled bacterial transcription/translation assay in which the ability of a compound to inhibit either the transcription of a DNA template into mRNA or the subsequent translation of this mRNA into functional luciferase protein is evaluated. Compound **55** inhibited this coupled assay with an IC_{50} of 2 μM, and was shown to have a minimum inhibitory concentration (MIC) of 3 μM against a gram-negative *E. coli* strain (ATCC 25922).

In summary, we used MS to study SAR and were able to design heterocyclic aminoglycoside mimetics more efficiently. A concise synthesis route was used to prepare heterocyclic paromomycin mimetics from neomycin B. The use of this strategy to synthesize more heterocyclic aminoglycoside mimetics will be reported in due course.

Received: March 7, 2003 [Z51354]



Scheme 3. Synthesis of **55** and **56**: a) NaOMe/MeOH (0.5 M), room temperature, 10 h, 85%; b) 1) **51** (1 equiv), **52** (2 equiv), molecular sieves (4 Å), TMSOTf (1 equiv), 4 h; 2) NaOMe/MeOH (0.5 M), 2 h, 10% (**53**), 31% (**54**); c) Me_3P/THF (8 equiv), THF/H_2O (2:1), 10 h, 46%; d) Me_3P/THF (8 equiv), THF/H_2O (2:1), 10 h, 52%. TMS = trimethylsilyl.

Keywords: aminoglycosides · antibiotics · heterocycles · mass spectrometry · synthesis design

[1] T. K. Stage, K. J. Hertel, O. C. Uhlenbeck, *RNA* **1995**, *1*, 95.
[2] B. D. Davis, L. Chen, P. C. Tai, *Proc. Natl. Acad. Sci. USA* **1986**, *83*, 6164.
[3] P. Purohit, S. Stern, *Nature* **1994**, *370*, 659.
[4] S. A. Hofstadler, K. A. Sannes-Lowery, S. T. Crooke, D. J. Ecker, H. Sasmor, S. Manalili, R. H. Griffey, *Anal. Chem.* **1999**, *71*, 3436.
[5] K. A. Sannes-Lowery, R. H. Griffey, S. A. Hofstadler, *Anal. Biochem.* **2000**, *2*, 264.
[6] R. H. Griffey, S. A. Hofstadler, K. A. Sannes-Lowery, D. J. Ecker, S. T. Crooke, *Proc. Natl. Acad. Sci. USA* **1999**, *96*, 10129.
[7] Y. L. Ding, E. E. Swayze, S. A. Hofstadler, R. H. Griffey, *Tetrahedron Lett.* **2000**, *41*, 4049.
[8] The MS RNA-binding data were obtained from the assay described in reference [4]; paromomycin (**1**): $K_d = 0.11$ μM, **2**: $K_d = 80$ μM, **3**: $K_d > 80$ μM.
[9] T. Usui, S. Umezawa, *Carbohydr. Res.* **1988**, *174*, 133.

 © 2003 Wiley-VCH Verlag GmbH & Co. KGaA, Weinheim

[10] W. A. Greenberg, E. S. Priestley, P. S. Sears, P. B. Alper, C. Rosenbohm, M. Hendrix, S. C. Hung, C. H. Wong, *J. Am. Chem. Soc.* **1999**, *121*, 6818.
[11] E. J. Corey, P. H. Hua, B. C. Pan, S. P. Seitz, *J. Am. Chem. Soc.* **1982**, *104*, 6818.
[12] Y. L. Ding, S. A. Hofstadler, E. E. Swayze, R. H. Griffey, *Org. Lett.* **2001**, *3*, 1621.
[13] M. A. Phillips, *J. Chem. Soc.* **1930**, 1409.
[14] The MS RNA-binding data were obtained from the assay described in reference [4], and neamine was used as the standard compound. Some of the MS RNA-binding data were reported in reference [12].
[15] Selected data: **53**: ^{1}H NMR (400 MHz, CD_3OD): $\delta = 5.69$ (d, 1H, $J = 12.4$ Hz), 5.55 (d, 1H, $J = 12.4$ Hz), 5.16 (d, 1H, $J = 2.0$ Hz), 5.12 ppm (d, 1H, $J = 5.2$ Hz); **54**: ^{1}H NMR (400 MHz, CD_3OD): $\delta = 5.82$ (d, 1H, $J = 12.4$ Hz), 5.49 (d, 1H, $J = 12.4$ Hz), 5.37 (d, 1H, $J = 2.0$ Hz), 5.04 ppm (d, 1H, $J = 1.6$ Hz); **55**. ^{1}H NMR (400 MHz, D_2O): $\delta = 5.67$ (d, 1H, $J = 12.4$ Hz), 5.45 (d, 1H, $J = 10.8$ Hz), 5.16 (s, 1H), 5.07 ppm (s, 1H); **56**: ^{1}H NMR (400 MHz, D_2O): $\delta = 5.51$ (d, 1H, $J = 12.0$ Hz), 5.31 (d, 1H, $J = 12.4$ Hz), 5.20 (s, 1H), 4.72 ppm (d, 1H, $J = 7.6$ Hz).
[16] The MS RNA-binding data were obtained from the assay described in reference [4], and paromomycin was used as the standard compound.

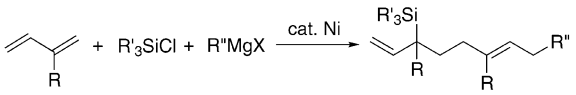
 © 2003 Wiley-VCH Verlag GmbH & Co. KGaA, Weinheim

Carbosilylation-Dimerization

Nickel-Catalyzed Dimerization and Carbosilylation of 1,3-Butadienes with Chlorosilanes and Grignard Reagents**

*Jun Terao, Akihiro Oda, Aki Ikumi, Akifumi Nakamura, Hitoshi Kuniyasu, and Nobuaki Kambe**

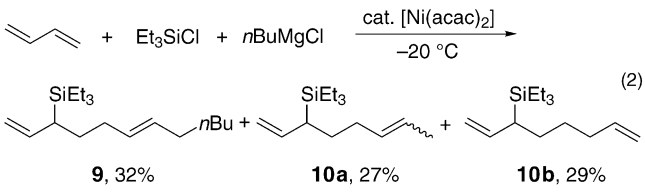
Ni^0 reacts with 1,3-butadienes to form octadienediyl–nickel complexes, which play an important role as key intermediates in the oligomerization of butadienes.[1,2] This reaction demonstrates extreme synthetic utility as a straightforward method for the formation of C_8 building blocks in organic synthesis. The cycloaddition of butadienes is one of the most successful transformations of this type.[1d,3] However, many attempts toward the synthesis of functionalized oligomers (i.e. telomerization) by using Ni catalysts resulted in the formation of mixtures of products.[1b,4] We have recently developed new methods for the regioselective addition of silicon and/or carbon functionalities to alkenes or dienes in the presence of early-transition-metal catalysts, such as zirconium complexes[5] and titanium complexes.[6] During the course of these studies, we found that Ni catalyzes the dimerization and carbosilylation of butadienes in the presence of chlorosilanes and Grignard reagents to give rise to 1,6-dienes with high regio- and stereoselectivity [Eq. (1)].



(1)

When a catalytic amount of $[Ni(acac)_2]$ (0.05 mmol; acac = acetylacetone) was added to a solution of isoprene (2 mmol), chlorotriethylsilane (1 mmol), and *n*BuMgCl (1.2 mmol) in THF (1.3 mL) at −20 °C, and the resulting mixture was stirred for a further 18 hours at the same temperature, compound **1**, with Et_3Si and *n*Bu groups at positions 3 and 8 of its dimerized isoprene skeleton, was isolated in 87 % yield (*E*/*Z* = 76:24) from the crude mixture by HPLC, with $CHCl_3$ as the eluent (Table 1, entry 1). No regioisomers of **1** were formed in the reaction. When $NiCl_2$ and $[Ni(cod)_2]$ (cod = 1,5-cyclooctadiene) were used as catalysts, **1** was obtained in yields of 78 and 80 %, respectively, but no reaction took place in the presence of nickel catalysts with phosphane ligands, such as $[(PPh_3)_2NiCl_2]$, $[(dppe)NiCl_2]$ (dppe = ethane-1,2-diylbis(diphenylphosphane), or $[(dppp)NiCl_2]$ (dppp = propane-1,3-diylbis(diphenylphosphane), under identical conditions. This reaction also proceeded efficiently when a phenyl-substituted chlorosilane (Table 1, entries 2, 6, and 7) and/or a secondary alkyl Grignard reagent (Table 1, entries 2, 3, and 5) were used. The use of a cyclohexyl Grignard reagent with isoprene led to the formation of only the *E* isomer of the product (Table 1, entry 3). The reaction of 2-nonyl-1,3-butadiene with Et_3SiCl and *i*BuMgCl gave a mixture of stereoisomers **8** in a 40:60 ratio and 42 % yield (Table 1, entry 8).

When unsubstituted 1,3-butadiene was used, the coupling products were obtained not only regioselectively but also stereoselectively in all cases examined (Table 1, entries 4–7). A phenyl and a vinyl Grignard reagent could also be used to prepare the allyl arene **6** and the triene **7**, respectively, in good yields (Table 1, entries 6 and 7). However, the reaction of a primary alkyl Grignard reagent gave the desired product **9** in only moderate yield (32 %), along with the hydrosilylated products **10a** and **10b** in 27 and 29 % yields, respectively [Eq. (2)]. The desired product was not obtained when



(2)

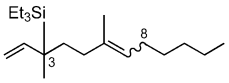
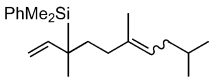
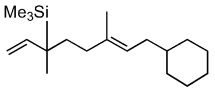
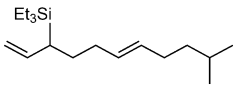
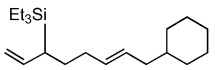
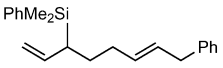
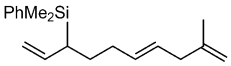
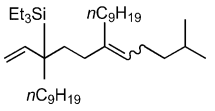
[*] Prof. Dr. N. Kambe, Dr. J. Terao, A. Oda, A. Ikumi, A. Nakamura, Dr. H. Kuniyasu
Department of Molecular Chemistry and Frontier Research Center
Graduate School of Engineering, Osaka University
Suita, Osaka 565-0871 (Japan)
Fax: (+81) 6-6879-7390
E-mail: kambe@chem.eng.osaka-u.ac.jp

[**] This research was supported financially through a grant from the Ministry of Education, Culture, Sports, Science, and Technology of Japan and by the JSPS COE program. We thank the Instrumental Analysis Center, Faculty of Engineering, Osaka University for MS and HRMS measurements as well as elemental analyses.

Supporting information for this article is available on the WWW under http://www.angewandte.org or from the author.

 © 2003 Wiley-VCH Verlag GmbH & Co. KGaA, Weinheim DOI: 10.1002/anie.200351579

Table 1: Ni-catalyzed regioselective coupling of 1,3-dienes with Grignard reagents and chlorosilanes.[a]

Entry	Diene	R′$_3$SiCl	R″MgX	Product		Yield [%][b]	E/Z[c]
1		Et_3SiCl	*n*BuMgCl		**1**	87	76:24
2		$PhMe_2SiCl$	*i*PrMgCl		**2**	86	92:8
3		Me_3SiCl	*c*-C_6H_{11}MgCl		**3**	84	100:0
4		Et_3SiCl	*i*BuMgCl		**4**	78	100:0
5		Et_3SiCl	*c*-C_6H_{11}MgCl		**5**	93	100:0
6		$PhMe_2SiCl$	PhMgBr		**6**	78	100:0
7		$PhMe_2SiCl$			**7**	76	100:0
8		Et_3SiCl	*i*BuMgCl		**8**	42	40:60[d]

[a] For experimental details, see Supporting Information. [b] Yields of isolated products. [c] Determined by GC. [d] Ratio of the stereoisomers: their stereochemistry was not assigned.

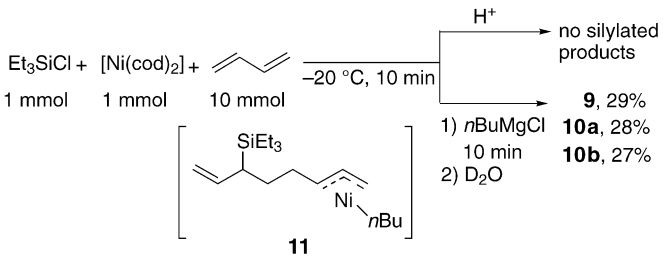
These results suggest that Grignard reagents do, in fact, promote the C–Si bond-forming step. The fact that the hydrosilylated products **10a** and **10b** did not contain deuterium may suggest that a hydrogen atom of the butyl group of the Grignard reagent was transferred to **10a** and **10b**. The formation of the coupling product **9** and hydrosilylated products **10a** and **10b** can be rationalized by assuming a common intermediate **11**, the reaction of which leads to **9** through reductive elimination of the allyl and *n*Bu groups or to **10a** and **10b** through β-hydrogen elimination. This β-hydrogen-elimination process may be disfavored when isoprene (Table 1, entry 1) or *i*BuMgCl (Table 1, entry 4) is used, because of steric reasons, thus resulting in the selective formation of coupling products **1** and **4**, respectively.

We then tested the reaction in the presence of a primary alkyl Grignard reagent with no β-hydrogen atom. The reaction of 1,3-butadiene with Et_3SiCl and $PhMe_2CCH_2MgCl$ afforded the expected coupling product **13** in 26% yield along with cyclized compound **14** (39%; Scheme 2). The latter compound might be formed via **16**, generated by insertion of the terminal carbon–carbon double bond into the allyl–nickel bond of **15**, as reductive elimination from **15** to give **13** is probably retarded because of steric reasons.

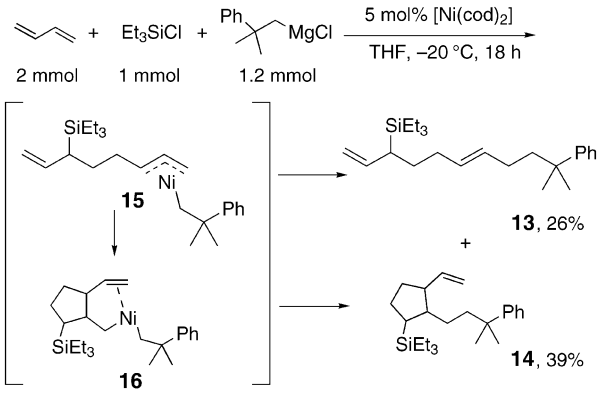
MeMgCl[7] or *t*BuMgCl was used. Under identical conditions, 2,3-dimethyl-1,3-butadiene and 1,4-diphenyl-1,3-butadiene did not react.

We carried out several control experiments to prove the reaction pathway and product selectivity. For example, Et_3SiCl, a stoichiometric amount of [Ni(cod)$_2$], and excess 1,3-butadiene (10 equiv) were stirred as a solution in THF for 10 min at −20 °C. The reaction was quenched with HCl (1N, 1.5 mL), and analysis of the mixture by NMR spectroscopy and GC–MS showed no evidence for the formation of silylated products. However, when 1 equivalent of *n*BuMgCl was added to the reaction mixture prior to quenching with D_2O, a mixture of the monosilylated compounds **9**, **10a**, and **10b** (Scheme 1) was obtained in a similar total yield and ratio to those shown in Equation 2.

A plausible reaction pathway, which takes into account the above evidence, is shown in Scheme 3. The reaction of [Ni(acac)$_2$] with a Grignard reagent affords Ni^0 (**17**), which reacts with butadiene and a Grignard reagent to give η^1,η^3-octadienediyl–nickelate complex **19**[8] via η^3,η^3-octadienediyl–

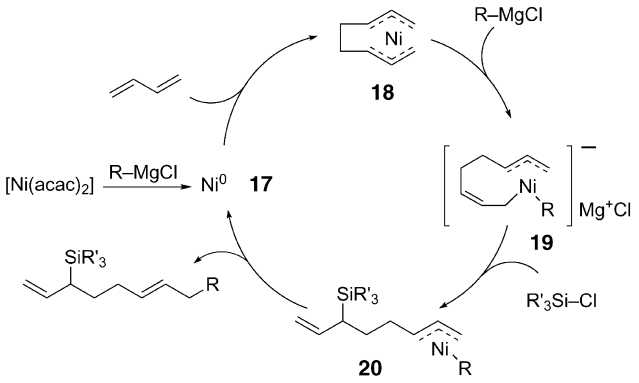


Scheme 1. Significance of the Grignard reagent: Treatment of 1,3-butadiene with Et_3SiCl and [Ni(cod)] in the presence and in the absence of *n*BuMgCl.



Scheme 2. Reaction of a primary alkyl Grignard reagent that bears no β-hydrogen atom.

 © 2003 Wiley-VCH Verlag GmbH & Co. KGaA, Weinheim



Scheme 3. A plausible reaction pathway.

nickel complex **18** or its η^1,η^3 isomer.[9a] Complex **19** then reacts with a chlorosilane at the γ allylic carbon atom to form an allyl complex **20**.[9] The subsequent reductive elimination of **20** affords the coupling product and regenerates **17** to complete the catalytic cycle.

In conclusion, a new method for the highly regioselective nickel-catalyzed four-component coupling[10] of two diene molecules, a chlorosilane, and a Grignard reagent has been developed. This reaction affords 1,6-dienes with an allyl silane unit[11] under mild conditions and, when unsubstituted 1,3-butadiene is used, proceeds stereoselectively to produce only *trans* olefins. This study provides the first example of a C–Si bond-forming reaction that involves chlorosilanes and is catalyzed by a late transition metal.[12]

Experimental Section

5: A solution of Et_3SiCl (152 mg, 1.0 mmol) and a catalytic amount of $[Ni(acac)_2]$ (12 mg, 0.05 mmol) in THF (1.2 mL) was cooled to −78 °C, and 1,3-butadiene (45 mL at 20 °C under 1 atm, 2.0 mmol) was added through a syringe. *c*-$C_6H_{11}MgCl$ (2 M in Et_2O, 0.6 mL, 1.2 mmol) was then added at the same temperature and the mixture was warmed to −20 °C and stirred for a further 18 h. The reaction was quenched with HCl (1 N), and the mixture was extracted with diethyl ether to afford the yellow crude product, which was purified by HPLC to give **5** (292 mg, 93 %). IR (neat): $\tilde{\nu}$ = 2920, 2875, 2851, 1625, 968, 894, 730, 696 cm^{-1}; ^1H NMR (400 MHz, $CDCl_3$, 25 °C): δ = 5.62 (dt, J = 17.1, 10.0 Hz, 1H), 5.41–5.26 (m, 2H), 4.86 (dd, J = 10.0, 1.7 Hz, 1H), 4.82 (d, J = 17.1 Hz, 1H), 2.17–2.08 (m, 1H), 1.92–1.82 (m, 3H), 1.75–1.62 (m, 6H), 1.47 (dt, J = 6.1, 7.8 Hz, 2H), 1.26–1.07 (m, 4H), 0.94 (t, J = 8.4 Hz, 9H), 0.92–0.82 (m, 2H), 0.54 ppm (q, J = 8.4 Hz, 6H); ^{13}C NMR (100 MHz, $CDCl_3$, 25 °C): δ = 140.2, 130.9, 129.1, 111.8, 40.8, 38.3, 33.3, 33.2, 32.2, 31.4, 28.8, 26.8, 26.5, 7.8, 2.4 ppm; MS (EI): *m/z* (%): 306 (0.1), 277 (7), 169 (18), 115 (100), 87 (58), 59 (47); HRMS (*m/z*): calcd for $C_{20}H_{38}Si$ (M^+): 306.2743, found 306.2745; elemental analysis: calcd for $C_{20}H_{38}Si$: C 78.35, H 12.49; found: C 78.19, H 12.57.

Received: April 4, 2003 [Z51579]

Keywords: dienes · Grignard reagents · multicomponent reactions · nickel · silanes

[1] a) P. W. Jolly, G. Wilke, *The Organic Chemistry of Nickel*, Academic Press, New York, **1975**; b) W. Keim, A. Behr, M. Röper in *Comprehensive Organometallic Chemistry, Vol. 8* (Eds.: E. W. Abel, F. G. A. Stone, G. Wilkinson), Pergamon, Oxford, **1982**, pp. 371–462; c) W. Keim, *Angew. Chem.* **1990**, *102*, 251–260; *Angew. Chem. Int. Ed. Engl.* **1990**, *29*, 235–244; d) M. Lautens, W. Klute, W. Tam, *Chem. Rev.* **1996**, *96*, 49–92.

[2] We recently reported that octadienediyl–nickel complexes show unique catalytic activity in $C(sp^3)$–$C(sp^3)$ coupling reactions of alkyl halides with RMgX: J. Terao, H. Watanabe, A. Ikumi, H. Kuniyasu, N. Kambe, *J. Am. Chem. Soc.* **2002**, *124*, 4222–4223; J. Terao, A. Ikumi, H. Kumiyasu, N. Kambe, *J. Am. Chem. Soc.* **2003**, *125*, 5646–5647.

[3] S. McN. Sieburth, N. T. Cunard, *Tetrahedron* **1996**, *52*, 6251–6282.

[4] For a Ni-catalyzed reaction of 1,3-butadiene with Me_2Zn and a ketone, see: a) M. Kimura, S. Matsuo, K. Shibata, Y. Tamaru, *Angew. Chem.* **1999**, *111*, 3586–3589; *Angew. Chem. Int. Ed.* **1999**, *38*, 3386–3388; for reviews of Pd-catalyzed reactions, see: b) J. Tsuji, *Palladium Reagents and Catalysts*, Wiley, Chichester, **1995**, pp. 422–449; c) F. Bouachir, P. Grenouillet, D. Neibecker, J. Poirier, I. Tkatchenko, *J. Organomet. Chem.* **1998**, *569*, 203–215.

[5] a) J. Terao, K. Torii, K. Saito, N. Kambe, A. Baba, N. Sonoda, *Angew. Chem.* **1998**, *110*, 2798–2801; *Angew. Chem. Int. Ed.* **1998**, *37*, 2653–2656; b) J. Terao, T. Watanabe, K. Saito, N. Kambe, N. Sonoda, *Tetrahedron Lett.* **1998**, *39*, 9201–9204.

[6] a) J. Terao, K. Saito, S. Nii, N. Kambe, N. Sonoda, *J. Am. Chem. Soc.* **1998**, *120*, 11822–11823; b) S. Nii, J. Terao, N. Kambe, *J. Org. Chem.* **2000**, *65*, 5291–5297.

[7] Direct reaction with the chlorosilane predominated.

[8] For a similar η^1,η^3-octadienediyl–nickelate complex reported for Li, see: S. Hole, P. W. Jolly, R. Mynott, R. Salz, *Z. Naturforsch. B* **1982**, *37*, 675–676.

[9] a) An η^1,η^3-octadienediyl–nickel complex reacts with H^+ at the γ allylic carbon: R. Benn, B. Büssemeier, S. Holle, P. W. Jolly, R. Mynott, I. Tkatchenko, G. Wilke, *J. Organomet. Chem.* **1985**, *279*, 63–86; b) an η^1,η^3-octadienediyl–palladium complex also reacts with Me_2HSiCl at the γ position: P. W. Jolly, R. Mynott, B. Raspel, K.-P. Schick, *Organometallics* **1986**, *5*, 473–481; c) an η^1-allyl–palladium complex reacts with electrophiles at the γ position: H. Kurosawa, A. Urabe, K. Miki, N. Kasai, *Organometallics* **1986**, *5*, 2002–2008.

[10] For recent reviews of Ni-catalyzed multicomponent coupling reactions, see: a) J. Montgomery, *Acc. Chem. Res.* **2000**, *33*, 467–473; b) S. Ikeda, *Acc. Chem. Res.* **2000**, *33*, 511–519.

[11] Allyl silanes play an important role in organic synthesis as useful intermediates in a number of synthetic transformations; see: T.-Y. Luh, S.-T. Liu in *The Chemistry of Organic Silicon Compounds, Vol. 2* (Eds.: S. Patai, Z. Rappoport), Wiley, Chichester, **1998**, pp. 1793–1868.

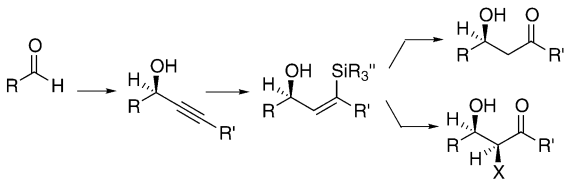
[12] The oxidative addition of chlorosilanes to late transition metals tends to be sluggish as a result of the strong Si–Cl bond energy; see: H. Yamashita, M. Tanaka, M. Goto, *Organometallics* **1997**, *16*, 4696–4704, and references therein; for the Zr-catalyzed silylation of olefins with chlorosilanes, see reference [5a].

 © 2003 Wiley-VCH Verlag GmbH & Co. KGaA, Weinheim

Regioselective Hydrosilylation

Regioselective Hydrosilylation of Propargylic Alcohols: An Aldol Surrogate**

Barry M. Trost, Zachary T. Ball, and Thomas Jöge*

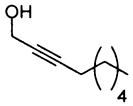
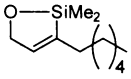
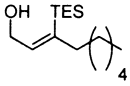
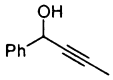
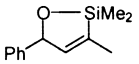
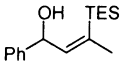
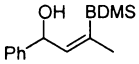
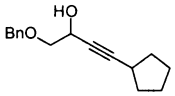
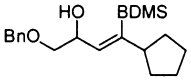
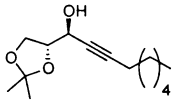
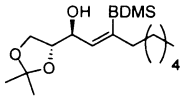
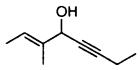
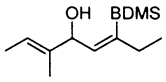
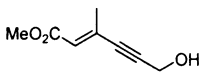
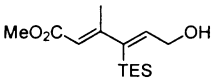
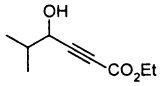
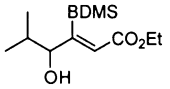


(1)

The aldol reaction has emerged as one of the most powerful ways to assemble complex targets with high stereochemical control in both a relative and an absolute sense. Despite the tremendous successes, deficiencies exist. As aldol adducts are prone to further reactions such as elimination, further substitution at the α-carbon becomes difficult.[1] Asymmetric additions of methyl alkyl ketones have been very limited.[2] Propargylic alcohols can become surrogates for aldols provided that a chemo- and regioselective introduction of a carbonyl group at the alkyne carbon β to the alcohol can be performed. The asymmetric access[3,4] to propargylic alcohols makes this approach an attractive alternative to the asymmetric aldol reaction. Although the direct hydration of a propargylic alcohol is a potentially attractive solution, the difficulty of obtaining regioselectivity as well as of avoiding elimination of the hydroxy ketone product under generally acidic hydration conditions led us to another approach.[5] As outlined in Equation 1, we chose to pursue selective incorporation of a vinyl C–Si bond, which can serve as a versatile ketone precursor.

During the course of our studies of the ruthenium-catalyzed hydrosilylation of alkynes,[6] our attention was drawn to the regioselective hydrosilylation of internal alkynes.[7,8] For some systems the regioselectivity could be simply resolved by tethering the silyl group, wherein a most interesting *endo*-selective intramolecular hydrosilylation occurred.[8a] Unfortunately, such a strategy failed with propargyl alcohols. We, therefore, hoped to harness the electronic bias—or perhaps catalyst ligation—of unprotected propargylic alcohols to effect regiochemical and geometrical selectivity in ruthenium-catalyzed *trans* hydrosilylation using $[Cp^*Ru(NCCH_3)_3]^+PF_6^-$ (**1**, $Cp^* = C_5Me_5$).

Table 1: Hydrosilylation of propargylic alcohols catalyzed by **1**.[a]

Entry	Alkyne	Silane[b]	**1** [mol%]	Major product	Yield,[c] sel.[d]
1[e]		A	2.5		30%,[f] n.d.
2[e]		B	1.0		99%, 13:1
3[e]		A	3.0		73%,[f] 5:1
4[e]		B	2.0		91%, 20:1
5		C	2.0		91%,[f] 14:1
6[e]		C	3.0		96%, 9:1
7		C	4.0		8%, 6:1
8		C	2.0		65%,[f] 5:1
9		B	5.0		63%[f] (84),[g] >20:1
10		C	2.0		83%,[f] 8:1

[a] All reactions were performed with 1.2 equiv silane in acetone from 0°C to room temperature and were complete within 30 min unless otherwise indicated. [b] A = $Me_2(EtO)SiH$, B = Et_3SiH (TES-H), C = $BzMe_2Si$-H (BDMS-H). [c] Yield of both isomers isolated except where indicated. [d] Regiochemistry of silane addition from NMR spectrum of the crude product. [e] Performed with 2.5 equiv silane in CH_2Cl_2. [f] Yield of pure major isomer isolated. [g] Numbers in parenthesis refer to yields based on recovered starting material.

[*] Prof. Dr. B. M. Trost, Z. T. Ball, T. Jöge
Department of Chemistry
Stanford University
Stanford, CA 94305-5080 (USA)
Fax: (+1) 650-725-0002
E-mail: bmtrost@stanford.edu

[**] We thank the National Science Foundation and the National Institutes of Health, General Medical Science (GM-13598), for their generous support of our programs. Z.T.B. is a Stanford Graduate Fellow. Mass spectra were provided by the Mass Spectrometry Regional Center of the University of California–San Francisco supported by the NIH Division of Research Resources.

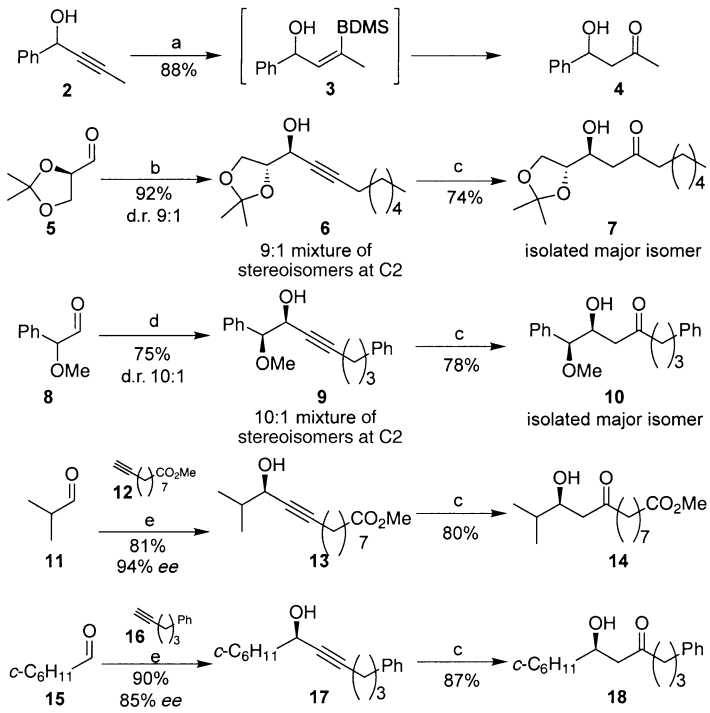
Initial experiments with $(EtO)_3SiH$ and 2-nonyn-1-ol catalyzed by complex **1** produced only extensive decomposition. On the other hand, the reaction of monoalkoxysilane $Me_2(EtO)SiH$ (Table 1, entry 1) gave the β-silyl compound, but mediocre selectivity and poor product stability led to yields of only about 30%. A bulkier secondary alcohol greatly improved product stability, and the desired vinylsilane was isolated in respectable yield (entry 3). A switch to triethylsilane (TES-H) improved the situation dramatically, and the

 DOI: 10.1002/anie.200351587 © 2003 Wiley-VCH Verlag GmbH & Co. KGaA, Weinheim

desired vinylsilanes could be produced in excellent yield with synthetically useful regioselectivity without any product stability issues (entries 2 and 4). In this and in all cases, only the *Z* products of *trans* addition are observed for the two regioisomers.

Although for some subsequent applications triethylvinylsilanes are suitable, we sought a silane that would maintain this clean reactivity and still permit a wide variety of subsequent operations. In our hands, the optimal choice was benzyldimethylsilane (BDMS-H), which we found to react in a manner very similar to triethylsilane, requiring only slightly higher catalyst loadings (generally 2–4%). The propargylic alcohol substrate itself also displays some unique reactivity. Conjugated alkene units and nearby double bonds lead to generally inferior results in the hydrosilylation reaction with **1**, but the substrates in entries 8 and 9 show meaningful reactivity. Entry 10 demonstrates that propargylic alcohols do not overcome the preference for silylation β to conjugated carbonyl groups, and the vinylsilane of opposite regiochemistry is obtained.

Having achieved selective formation of the necessary vinylsilanes, we sought to, first, unmask the ketone through oxidation and, second, utilize the vinylsilane as a handle for functionalization at the α-carbon atom. A key question becomes the fate of the presumed initial oxidation product. Since oxidation of the BDMS group of β-silyl allylic alcohols produces the enol of a β-hydroxy ketone, dehydration may accompany the unmasking.[9] Gratifyingly, elimination did not compete when methanolic basic hydrogen peroxide was used after initial debenzylation with tetrabutylammonium fluoride (TBAF, Scheme 1).[10] In this case, BDMS oxidation was compatible with our hydrosilylation conditions and could be performed directly as a one-pot operation to afford regioselective hydrolysis of the alkyne, whereby **4** was obtained directly from **2** in 88% yield.



Scheme 1. Hydrosilylation–oxidation protocol for propargylic alcohols. a) 1. BDMS-H, 5% **1**, CH_2Cl_2, 0°C to RT, 2. TBAF, then H_2O_2, MeOH, $KHCO_3$; b) octyne, *n*BuLi, $(iPrO)_3TiCl$, −78°C, then **5**; c) 1. BDMS-H, cat. **1** (2% for **9**, **13**, **17**; 3% for **6**), acetone, 0°C to RT, 2. TBAF, then H_2O_2, MeOH, $KHCO_3$; d) 5-phenyl-1-pentyne, *n*BuLi, $ZnBr_2$, −78°C, then **8**; e) 0.20 equiv $Zn(OTf)_2$, 0.22 equiv (+)-*N*-methylephedrine, Et_3N, PhMe, 60°C. RT = room temperature.

The net diasteroselective aldol requires a diastereoselective addition of an acetylide ion to a chiral aldehyde. Thus, a Felkin–Anh addition of a titanium acetylide complex[11] converts aldehyde **5** into the *anti* adduct **6** with a diastereomer ratio of 9:1. On the other hand, a chelation-controlled addition to the α-alkoxy aldehyde **8** using zinc bromide[12] provides the *syn* adduct **9** (10:1 d.r.). In both cases one-pot hydrosilylation followed by oxidation unmasks the aldol adducts **7** and **10**. Chiral propargylic alcohols can be synthesized readily by the asymmetric hydrogenation of ketones or addition to aldehydes.[3,4] Addition to aldehydes **11** and **15** produced their respective alcohols **13** and **17** in 94% and 85% *ee*, respectively.[4] One-pot hydrosilylation/oxidative desilylation gave the corresponding aldols **14** and **18** in high enantioselectivity in a two-pot sequence.

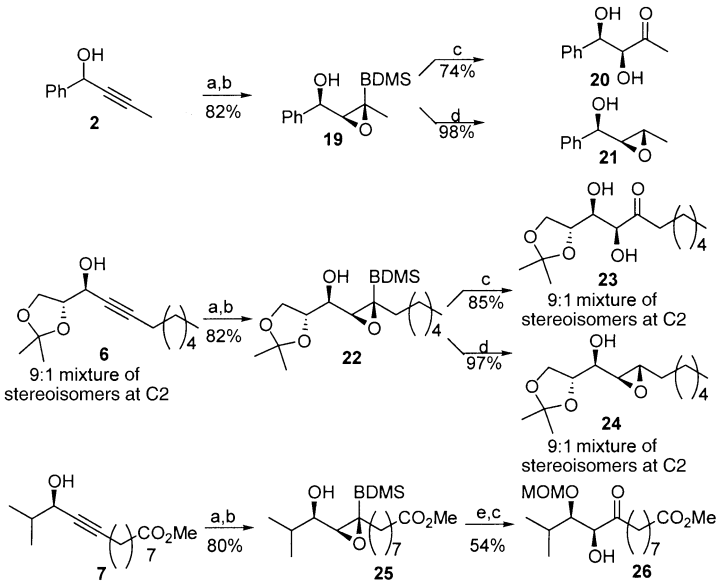
Additional complexity can be introduced through epoxidation of the vinylsilane. The bulky (*Z*)-silyl group serves as an excellent diastereocontrol element to provide *syn*-epoxides for what is otherwise a challenging class for diastereoselective epoxidation (Scheme 2).[13] Protodesilylation of **19** and **22** provides the respective *syn*-epoxy alcohols **21** and **24** with high efficiency and with a facial selectivity of >20:1. Owing to the BDMS group, oxidation provides α,β-dihydroxyketones **20** and **23** of defined relative and absolute stereochemistry.[14] The added alkyne unit functions as a hydroxymethyl ketone equivalent, and the hydroxy and ketone groups are unmasked simultaneously. Attempts to carry out this process in one or two pots without purification of the intermediates resulted in significantly lower yields. Since the amount of TBAF in the oxidation step is crucial to good yields, the epoxide was best fully purified prior to oxidation. Finally, differentiated diols could be produced by protection of the alcohol prior to epoxidation, though in this case the oxidation (**25**→**26**) was less efficient and accompanied by significant protodesilylation, which accounts for the lower yield of **26.**

The regioselective hydrosilylation presented here allows for the selective functionalization of propargylic alcohols. Focusing on oxidative pathways, we show that the alkyne added can serve as a methyl ketone enolate or hydroxymethyl–ketone–enolate equivalent.

Experimental Section

Typical procedure for the hydrosilylation of propargylic alcohols: Preparation of vinylsilane **3**: 1-Phenyl-2-propyn-1-ol (500 mg, 3.42 mmol) and benzyldimethylsilane (0.591 mL, 4.10 mmol) were taken up in acetone (7.0 mL) under Ar at 0°C. Solid **1** (35 mg,

 © 2003 Wiley-VCH Verlag GmbH & Co. KGaA, Weinheim



Scheme 2. Elaboration of silanes by diastereoselective epoxidation. a) BDMS-H, 2% **1**, acetone, 0°C to RT; b) *m*CPBA, CH_2Cl_2, 0°C; c) 1 equiv TBAF, THF, −10°C, then H_2O_2, MeOH, $KHCO_3$, RT; d) TBAF, DMF, RT; e) MOM-Cl, pyr., DCM, 0°C to RT. DCM = dichloromethane, *m*CPBA = *m*-chloroperbenzoic acid, MOM = methoxymethyl, pyr. = pyridine.

0.069 mmol) was added, and the solution was allowed to warm to room temperature and stirred for 30 min. The crude reaction mixture was concentrated directly under reduced pressure and applied to a silica gel column (eluent: petroleum ether/diethyl ether 6:1). The minor olefin regioisomers could be separated to afford the desired vinylsilane (920 mg, 91% yield).

Typical procedure for the one-pot hydrosilylation/oxidation to afford β-hydroxy ketones: Preparation of ketone **18**: To a solution of propargylic alcohol **17** (118 mg, 0.40 mmol) and benzyldimethylsilane (83 μL, 0.48 mmol) in acetone (0.8 mL) was added solid **1** (4.0 mg, 0.008 mmol) at 0°C. The solution was allowed to warm to room temperature and stirred for 30 min. The solution was cooled again to 0°C and treated with THF (1.0 mL) followed by TBAF (0.48 mL, 0.58 mmol, 1M in THF). The reaction mixture was stirred for 15 min, then 30% aqueous H_2O_2 (1.9 mL, 10.7 mmol), MeOH (0.7 mL), and $KHCO_3$ (176 mg, 1.76 mmol) were added sequentially. The reaction mixture was allowed to warm to room temperature and stirred for 18 h. Water (20 mL) was added and the mixture extracted with ethyl acetate (3 × 15 mL). The combined organic layers were washed with saturated aqueous $Na_2S_2O_3$ (10 mL) and dried over Na_2SO_4. The crude product was applied to a silica gel column (eluent: petroleum ether/ethyl acetate/methanol 80:20:1 then 70:30:1) to afford the desired hydroxyketone as a clear, colorless oil (97 mg, 78% yield).

Typical procedure for the production of dihydroxyketones: preparation of ketone **20**: Vinylsilane **3** (650 mg, 2.19 mmol) was taken up in CH_2Cl_2 (20 mL) and treated with *m*CPBA (662 mg, 3.07 mmol assuming 80% purity) at 0°C. After the reaction mixture had been stirred 14 h, saturated aqueous sodium bicarbonate (10 mL) and solid $Na_2S_2O_3$ (ca. 2 g) were added. The mixture was extracted with ether (3 × 30 mL), and the combined organic layers were dried over Na_2SO_4 and concentrated under reduced pressure. Silica gel chromatography (eluent: petroleum ether/ethyl acetate/methanol 100:10:1) afforded the desired epoxyalcohol as a single isomer (615 mg, 90% yield). Epoxysilane **19** (59 mg, 0.19 mmol) was taken up in THF (0.6 mL) under Ar at 0°C. TBAF (0.19 mL, 0.19 mmol, 1.0M in THF) was added dropwise, and after 5 min, methanol (0.60 mL) and $KHCO_3$ (60 mg, 0.60 mmol) were added, followed by 30% aqueous H_2O_2 (0.20 mL). The mixture was then allowed to warm to room temperature. After 14 h, saturated aqueous sodium bicarbonate (3 mL) was added and the mixture extracted with ether (3 × 10 mL). The combined organic layers were dried over $MgSO_4$ and concentrated in vacuo. Purification on a silica gel column (eluent: petroleum ether/ethyl acetate 4:1 then 1:1) afforded the desired diol as a viscous gum (25.1 mg, 74% yield).

Received: April 7, 2003 [Z51587]

Keywords: aldol products · asymmetric synthesis · hydrosilylation · organosilanes · ruthenium catalysis

[1] G. Frater, W. Guenther, U. Mueller, *Helv. Chim. Acta* **1989**, *72*, 1846.

[2] For approaches to asymmetric aldol reactions of methyl alkyl ketones see: a) R. T. Ruck, E. N. Jacobsen, *J. Am. Chem. Soc.* **2002**, *124*, 2882; b) S. E. Denmark, R. A. Stavenger, *J. Am. Chem. Soc.* **2000**, *122*, 8837; c) N. Yoshikawa, Y. M. A. Yamada, J. Das, H. Sasai, M. Shibasaki, *J. Am. Chem. Soc.* **1999**, *121*, 468; d) A. Yanagisawa, Y. Matsumoto, H. Nakashima, K. Asakawa, H. Yamamoto, *J. Am. Chem. Soc.* **1997**, *119*, 9319; e) E. M. Carreira, W. Lee, R. A. Singer, *J. Am. Chem. Soc.* **1995**, *117*, 3649; f) K. Mikami, S. Matsukawa, *J. Am. Chem. Soc.* **1993**, *115*, 7039; g) E. J. Corey, C. L. Cywin, T. D. Roper, *Tetrahedron Lett.* **1992**, *33*, 6907; for reviews see h) E. M. Carreira, in *Catalytic Asymmetric Synthesis, 2nd Ed.* (Ed: I. Ojima), Wiley-VCH, New York, **2000**, Ch. 8-2; i) B. List, *Tetrahedron* **2002**, *58*, 5573; j) S. G. Nelson, *Tetrahedron: Asymmetry* **1998**, *9*, 357.

[3] T. Ohkuma, M. Kitamura, R. Noyori, in *Catalytic Asymmetric Synthesis 2nd Ed.* (Ed: I. Ojima), Wiley-VCH, New York, **2000**, Ch. 1.

[4] a) D. E. Frantz, R. Fassler, E. M. Carreira, *J. Am. Chem. Soc.* **2000**, *122*, 1806–1807; b) N. K. Anand, E. M. Carreira, *J. Am. Chem. Soc.* **2001**, *123*, 9687–9688; c) D. Boyall, D. E. Frantz, E. M. Carreira, *Org. Lett.* **2002**, *4*, 2605–2606.

[5] For a recent example of catalyzed alkyne hydration see a) E. Mizushima, K. Sato, T. Hayashi, M. Tanaka, *Angew. Chem. Int. Ed.* **2002**, *41*, 4563; b) E. Mizushima, K. Sato, T. Hayashi, *Angew. Chem.* **2002**, *114*, 4745.

[6] a) B. M. Trost, Z. T. Ball, T. Joege, *J. Am. Chem. Soc.* **2002**, *124*, 7922–7923; b) B. M. Trost, Z. T. Ball, *J. Am. Chem. Soc.* **2001**, *123*, 12726–12727.

[7] Intermolecular hydrosilylation of internal alkynes: a) G. A. Molander, W. H. Retsch, *Organometallics* **1995**, *14*, 4570–4575; for instances of selective hydrosilylation of propargylic alcohols: b) D. Humiliere, S. Thorimbert, M. Malacria, *Synlett* **1998**, 1255; c) M. Isobe, R. Nishizawa, T. Nishikawa, K. Yoza, *Tetrahedron Lett.* **1999**, *40*, 6927–6932; d) K. Kahle, P. J. Murphy, J. Scott, R. Tamagni, *J. Chem. Soc. Perkin Trans. 1* **1997**, 997–999; e) P. J. Murphy, J. L. Spencer, G. Procter, *Tetrahedron Lett.* **1990**, *31*, 1051–1054.

[8] Intramolecular hydrosilylation: a) B. M. Trost, Z. T. Ball, *J. Am. Chem. Soc.* **2003**, *125*, 30–31; b) S. E. Denmark, S. Pan, *Org. Lett.* **2002**, *4*, 4163–4166; c) J. A. Marshall, M. M Yanik, *Org. Lett.* **2000**, *2*, 2173–2175; d) K. Tamao, K. Maeda, T. Tanaka, Y. Ito, *Tetrahedron Lett.* **1988**, *29*, 6955–6956.

[9] The intramolecular hydrosilylation of homopropargylic alcohols has also been used to create β-hydroxy ketones. In that case elimination from the initial enol is not possible, and the

 © 2003 Wiley-VCH Verlag GmbH & Co. KGaA, Weinheim

vinylsilane intermediate does not allow functionalization at the α-carbon. See refs. [8c,d].
[10] K. Miura, T. Hondo, T. Takahashi, A. Hosomi, *Tetrahedron Lett.* **2000**, *41*, 2129–2132; K. Miura, T. Hondo, T. Nakagawa, T. Takahashi, A. Hosomi, *Org. Lett.* **2000**, *2*, 385–388.
[11] M. Shimizu, M. Kawamoto, Y. Niwa, *Chem. Commun.* **1999**, 1151–1152.
[12] K. T. Mead, *Tetrahedron Lett.* **1987**, *28*, 1019–1022.
[13] H. Tomioka, T. Suzuki, K. Oshima, H. Nozaki, *Tetrahedron Lett.* **1982**, *23*, 3387–3390; I. Hasan, Y. Kishi, *Tetrahedron Lett.* **1980**, *21*, 4229–4232.
[14] For a report on the oxidation of α,β-epoxysilanes: K. Tamao, K. Maeda, *Tetrahedron Lett.* **1986**, *27*, 65–68.

 © 2003 Wiley-VCH Verlag GmbH & Co. KGaA, Weinheim

Natural Product Analogues

Synthetic Studies on Thiostrepton: Construction of Thiostrepton Analogues with the Thiazoline-Containing Macrocycle**

K. C. Nicolaou, Marta Nevalainen, Mark Zak, Stephan Bulat, Marco Bella, and Brian S. Safina*

Thiostrepton (**1**, Scheme 1)[1] is a highly complex thiopeptide antibiotic endowed with an unusual molecular architecture and a mode of action that involves RNA binding. As part of our program directed towards the total synthesis of this unique natural product, we have already reported synthetic approaches to both its dehydropiperidine domain[2] and its segment corresponding to the quinaldic acid macrocycle.[3] Herein we disclose further advances that pave the way for an eventual total synthesis of **1** and its analogues by addressing the remaining challenges posed by the imposing and sensitive structure of the molecule. Specifically, we describe: 1) the construction of the thiazoline **7** and thiazole **8** fragments, 2) the synthesis of the dehydropyrrolidine isomer **4** of the dehydropiperidine domain and its 5*S*,6*S* diastereoisomer **4′**, and 3) the assembly of these fragments into thiostrepton analogues **2** and **3**, which lack only the quinaldic acid macrocycle and differ from thiostrepton (**1**) at the imine-containing ring core (Scheme 1).

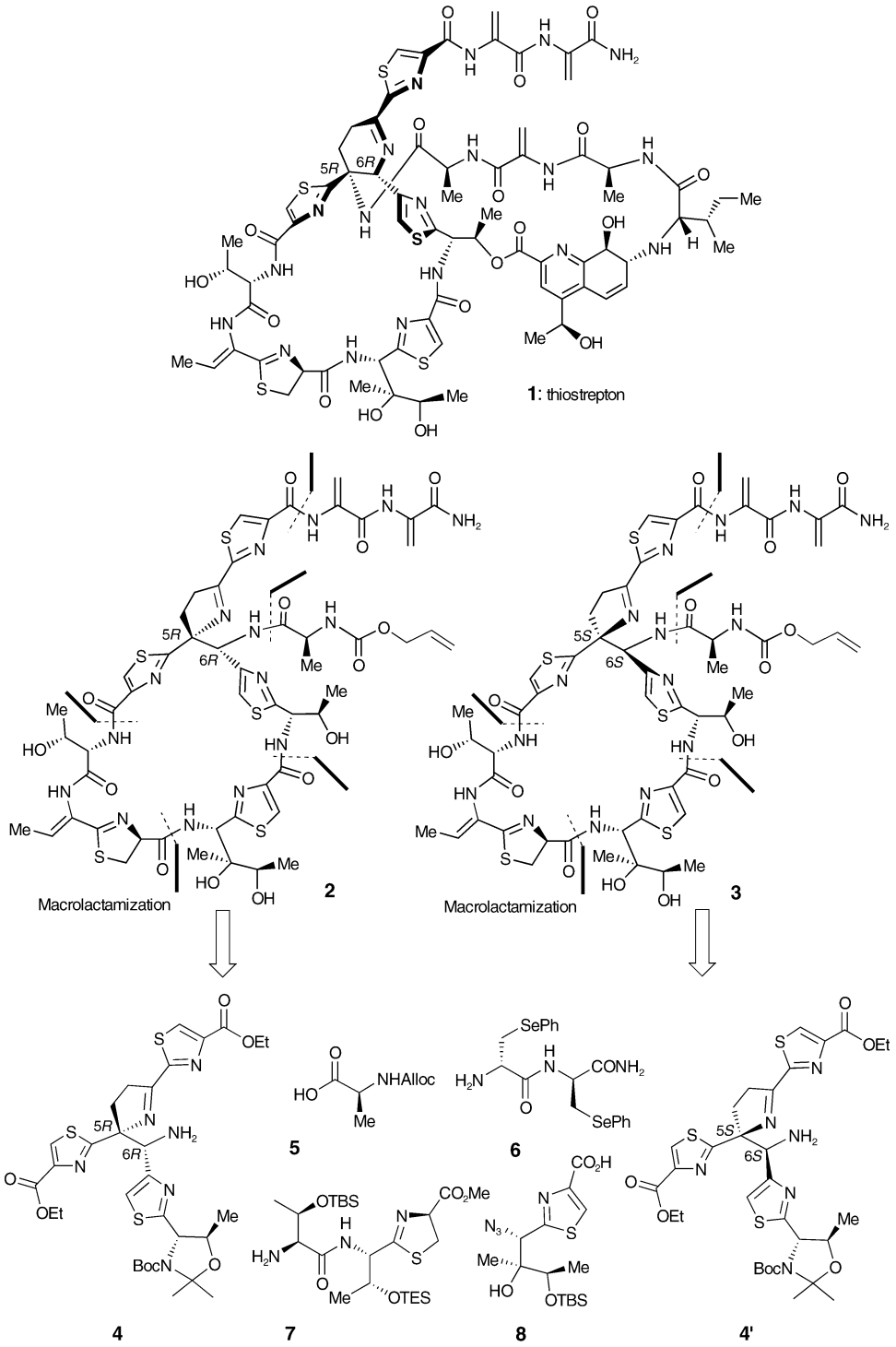
We begin with our previously reported[2] biomimetically inspired aza-Diels–Alder dimerization, which delivered the dehydropiperidine domain **9** (5*R*,6*R*-diastereoisomer, Scheme 2) as a 1:1 mixture with its 5*S*,6*S*-diastereoisomer **9′** (not shown). In solution, these dehydropiperidine compounds (**9** and **9′**) rearrange into their dehydropyrrolidine counterparts **4** and **4′**, respectively, reaching an equilibrium via aminal **10** and **10′**.[4] The six-membered ring imine **9** (and **9′**) can be selectively reduced with $NaCNBH_3$ under acidic conditions over its five-membered counterpart (**4** and **4′**), presumably due to less steric hindrance around the C=N bond, to render diamine **11** (and **11′**), as we already reported.[2] However, under standard amide bond-forming conditions (EDC, HOAt) with alloc-L-Ala-OH (**5**, Scheme 1), the five-membered ring imine **4** (and **4′**) is selectively captured, leading to compound **13** (and **13′**), obtained as a mixture of 5*R*,6*R*- and 5*S*,6*S*-diastereoisomers, which were chromatographically separated (72% combined yield). On the other hand, diamine **11** (and **11′**) can also be coupled with alloc-L-Ala-OH (**5**) (HOAt, HATU, $EtNiPr_2$) predominantly at the primary amine site (2:1 ratio of regioisomers) yielding, upon oxidation with *t*BuOCl and base-induced elimination of HCl from the resulting chloroamine, the dehydropiperidine peptide **12** (and **12′**) in 21% overall yield (from **9** and **9′**). While attempting to optimize this route to **12** (and **12′**), we opted to construct analogues **2** and **3** utilizing the more available dehydropyrrolidine intermediates **13** and **13′** with the dual aim of scouting the ground for the total synthesis of thiostrepton (**1**) and to produce novel thiostrepton analogues for biological evaluation.

With ample quantities of the central core **13** and its 5*S*,6*S* diastereoisomer (**13′**) in hand, we proceeded to construct the remaining key building blocks **6**–**8** (Scheme 1). Scheme 3 outlines the synthesis of the thiazole amino acid equivalent **8**, starting from angelic acid methyl ester (**14**). Thus, sequential conversion of commercially available **14** into its acid **15** (90% yield), acid chloride **16**, and (−)-menthyl ester **17** (70% over two steps) allowed a diastereoselective dihydroxylation with AD-mix-β and $MeSO_2NH_2$, leading to diol **18**[5] (90% yield, d.r. 90:10). The latter compound, **18**, was further protected as acetonide **19** (100% yield) and then reduced with DIBAL-H (90%) to alcohol **20**. In a remarkable one-pot sequence, alcohol **20** was oxidized with DMP; the aldehyde obtained in this manner was engaged in situ with benzylamine in the presence of $Yb(OTf)_3$[6] and molecular sieves (4 Å), and the resulting imine was treated with trimethylsilyl cyanide[7] to furnish Strecker addition product **21** in 90% overall yield. To our delight, not only did this sequence produce virtually a single stereoisomer (d.r. > 95:5 according to ^1H NMR spec-

[*] Prof. Dr. K. C. Nicolaou, Dr. M. Nevalainen, M. Zak, Dr. S. Bulat, Dr. M. Bella, B. S. Safina
Department of Chemistry and
The Skaggs Institute for Chemical Biology
The Scripps Research Institute
10550 North Torrey Pines Road, La Jolla, CA 92037 (USA)
Fax: (+1) 858-784-2469
E-mail: kcn@scripps.edu
and
Department of Chemistry and Biochemistry
University of California, San Diego
9500 Gilman Drive, La Jolla, CA 92093 (USA)

[**] We thank Dr. D. H. Huang, Dr. G. Siuzdak, and Dr. R. Chadha for NMR spectroscopic, mass spectrometric, and X-ray crystallographic assistance, respectively. Financial support for this work was provided by The Skaggs Institute for Chemical Biology, the National Institutes of Health (USA), fellowships from The Academy of Finland (to M.N.), The Skaggs Institute for Research (to M.Z.), and Bayer AG (to S.B.), and grants from Abbott, Amgen, ArrayBiopharma, Boehringer-Ingelheim, Glaxo, Hoffmann-LaRoche, DuPont, Merck, Novartis, Pfizer, and Schering Plough.

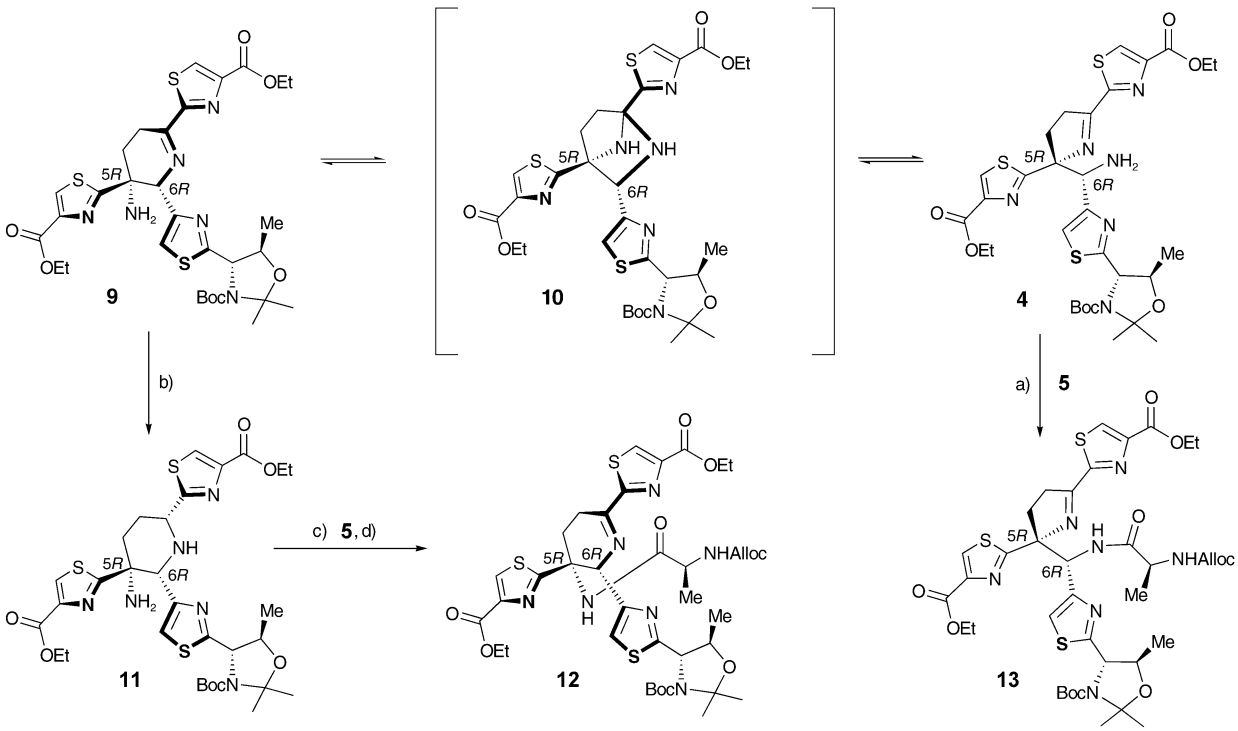
 © 2003 Wiley-VCH Verlag GmbH & Co. KGaA, Weinheim DOI: 10.1002/anie.200351745



Scheme 1. Structures of thiostrepton (**1**) and analogues **2** and **3**, and retrosynthetic analysis of the latter two compounds to building blocks **4**–**8** and **4′**. Alloc = allyloxycarbonyl; Boc = *tert*-butoxycarbonyl; TBS = *tert*-butyldimethylsilyl; TES = triethylsilyl.

troscopic analysis), but, also, the obtained material possessed the correct stereochemistry, as proven by X-ray crystallographic analysis of a subsequent intermediate (i.e. **25**, see ORTEP drawing, Scheme 3). Hydrogenolysis of the benzyl group of **21** in the presence of $(Boc)_2O$ led to Boc derivative **22** in 75% yield. Treatment of **22** with H_2S in the presence of Et_3N in a sealed tube afforded thioamide **23** (90%), which was then treated with ethyl bromopyruvate under standard Hantzsch conditions[8] to afford thiazole **24** in 82% yield. For reasons of protecting-group compatibility in subsequent steps, we moved to modify the diol and amine functionalities within the latter substrate by first removing the groups guarding

 © 2003 Wiley-VCH Verlag GmbH & Co. KGaA, Weinheim



Scheme 2. Construction of dehydropiperidine and dehydropyrrolidine systems **12** and **13**. Reagents and conditions: a) 1) Alloc-L-Ala-OH (**5**) (1.2 equiv), HOAt (1.3 equiv), EDC (1.3 equiv), DMF, 25 °C, 12 h; 2) separation of diastereomers (silica gel, Et_2O/toluene (60–80%), then EtOAc/hexane(90%)), 72% combined yield; b) $NaCNBH_3$ (2.0 equiv), AcOH/EtOH (1:4), 0 °C, 1 h, 50%; c) Alloc-L-Ala-OH (**5**) (1.1 equiv), HOAt (1.1 equiv), HATU (1.1 equiv), $EtNiPr_2$ (3.0 equiv), DMF, 25 °C, 2 h, 60%; d) *t*BuOCl (1.2 equiv), THF, −78 °C, 0.5 h, 4-DMAP (0.2 equiv), Et_3N (2.0 equiv), 25 °C, 10 min, 70%. HATU = *O*-(7-azabenzotriazol-1-yl)-*N*,*N*,*N*′,*N*′-tetramethyluronium hexafluorophosphate; EDC = 1-ethyl-(3-dimethylaminopropyl)carbodiimide hydrochloride; DMF = *N*,*N*-dimethylformamide; 4-DMAP = 4-dimethylaminopyridine; HOAt = 1-hydroxy-7-azabenzotriazole. Compounds **4**, **9**–**13** are accompanied (ca. 1:1) by their 5*S*,6*S* diastereoisomers (**4**′, **9**′–**13**′, respectively, structures not shown).

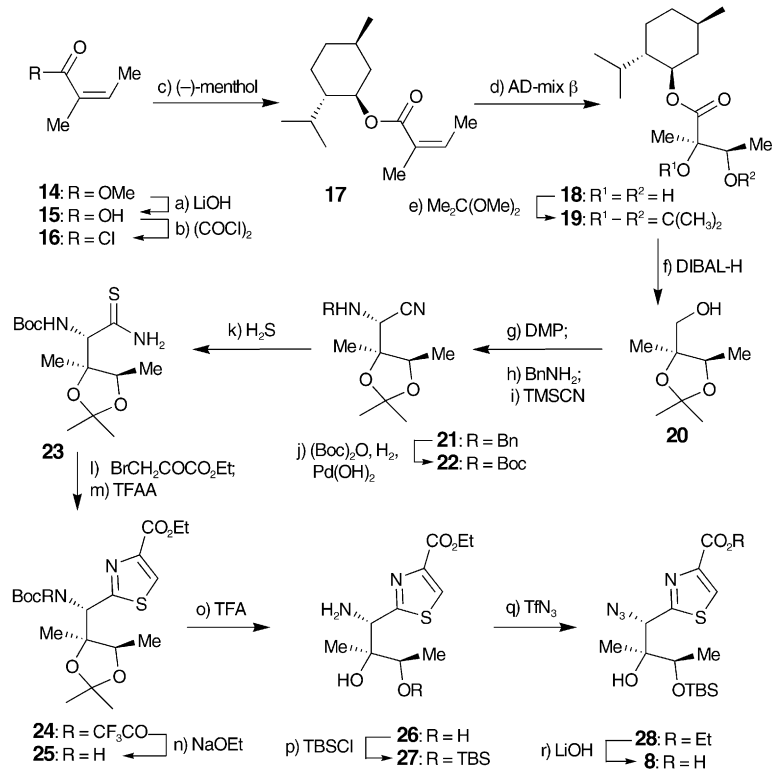
them and then remasking them in a different way. Thus, **24** was exposed to NaOEt in ethanol, furnishing the crystalline derivative **25** by removal of the trifluoroacetate group in quantitative yield. The latter compound (**25**) was then treated with TFA to furnish amino diol **26**, which was selectively converted into monosilyl ether **27** by reaction with TBSCl in the presence of Et_3N (81% yield over two steps). Finally, conversion of the amine within **27** into the corresponding azide (**28**) through the diazo-transfer procedure,[9] followed by basic hydrolysis of the ethyl ester, afforded the targeted building block **8** in 78% overall yield.

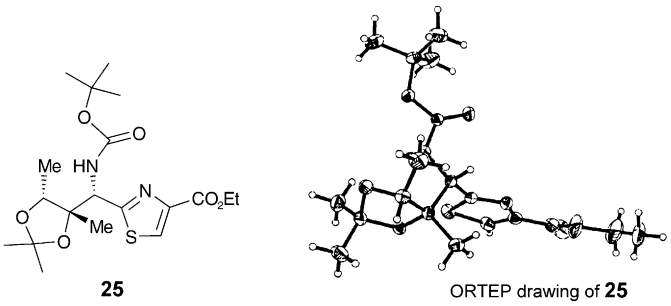
The synthesis of thiazoline moiety **7**, a structural element unique to thiostrepton—the other peptide antibiotics of the same family contain a thiazole instead—was carried out as summarized in Scheme 4 (p. 3422). Coupling of commercially available Fmoc-threonine (**29**) with D-serine methyl ester under standard conditions (EDC, HOBt, Et_3N) gave dipeptide **30** in 70% yield. Silylation of both hydroxy groups of **30** (81% yield), followed by thiocarbonylation with Lawesson's reagent, gave thioamide **32** (79% yield) via bis-TES-derivative **31**. The next requisite amino acid equivalent, compound **37**, was prepared from TBS-protected Boc-L-threonine methyl ester (**34**)[10] by first removing the Boc group with TFA, and then converting the corresponding primary amine of **35** into an azide functionality through the above-mentioned diazo-transfer procedure to provide **36** (72% over two steps). Hydrolysis of the ester provided acid **37** (93% yield), which was then coupled under standard conditions (HATU, HOAt, Et_3N) with amine **33** generated from its Fmoc derivative **32** through the action of Et_2NH to afford tripeptide surrogate **38** (75% from **32**). The primary TES group of **38** was selectively cleaved with THF/AcOH/H_2O (3:1:1) at 25 °C to furnish alcohol **39**, which upon exposure to DAST[11] led smoothly to the expected thiazoline **40** (90% yield). The final step required to complete the synthesis of **7** was the Staudinger reaction[12] of the azide to form the amino group, a transformation smoothly effected with trimethylphosphane and water (92% yield).

Scheme 5 (p. 3422) depicts the synthesis of the dipeptide equivalent to the top side chain of thiostrepton, bisseleno dipeptide **6**. This intermediate was synthesized from known L-serine derivative **41**[13] by first generating the amino selenoamide **43** (via **42**) and then coupling the two (**41** and **43**) under the influence of EDC and HOBt (58% over two steps), followed by removal of the remaining Boc group with TFA (95% yield).

The assembly of the targeted thiostrepton analogue **2** from the five-membered ring imine core **13** and the described

 © 2003 Wiley-VCH Verlag GmbH & Co. KGaA, Weinheim





Scheme 3. Synthesis of thiazole amino acid equivalent **8**. Reagents and conditions: a) LiOH (0.7 equiv), $MeOH/H_2O$ (1:1), reflux, 4 h, 90%; b) KOH (1.0 equiv), $(COCl)_2$ (5.0 equiv), Et_2O, DMF (cat.), 2 h; c) (−)-menthol (0.7 equiv), Et_2O, 25 °C, 48 h, 70% (two steps); d) AD-mix-β (1.5 equiv), $MeSO_2NH_2$ (1.0 equiv), *t*BuOH/H_2O (1:1), 0 °C, 24 h, 90%, 90:10 d.r.; e) $Me_2C(OMe)_2$ (22.0 equiv), TsOH (0.05 equiv), 25 °C, 1 h, 100%; f) DIBAL-H (2.0 equiv), CH_2Cl_2, −78 °C, 2 h, 90%; g) DMP (1.1 equiv), $NaHCO_3$ (2.0 equiv), CH_2Cl_2, 25 °C, 3 h; h) $BnNH_2$ (1.2 equiv), $Yb(OTf)_3$ (0.2 equiv), molecular sieves (4 Å), CH_2Cl_2, 25 °C, 2 h; i) TMSCN (2.5 equiv), CH_2Cl_2, 25 °C, 3 h, 90% (three steps), >95:5 d.r.; j) $(Boc)_2O$ (1.1 equiv), EtOAc, 20% Pd/$Pd(OH)_2$ (0.2 equiv), H_2, 25 °C, 12 h, 75%; k) H_2S, Et_3N/EtOH/pyridine (1.7:1.7:1), sealed tube, 25 °C, 12 h, 90%; l) $BrCH_2COCO_2Et$ (3.0 equiv), $NaHCO_3$ (8.0 equiv), DME, 25 °C, 24 h, 82%; m) TFAA (4.0 equiv), pyridine (9.0 equiv), 0 °C, 1 h, 82% (two steps); n) NaOEt (1.0 equiv), EtOH, 0 °C, 1 h, 100%; o) TFA/EtOH/CH_2Cl_2 (1:1:1), 0–25 °C, 4 h; p) TBSCl (2.2 equiv), Et_3N (3.0 equiv), CH_2Cl_2, 0–25 °C, 12 h, 81% (two steps); q) TfN_3 (3.0 equiv), Et_3N (3.0 equiv), $CuSO_4$ (0.05 equiv), MeOH/H_2O/CH_2Cl_2 (3.3:1:1), 25 °C, 12 h, 82%; r) LiOH (3.0 equiv), THF/H_2O (1:1), 0 °C, 2 h, 95%. DMP = Dess–Martin periodinane; DIBAL-H = diisobutylaluminum hydride; TMS = trimethylsilyl; DME = ethylene glycol dimethyl ether; TFAA = trifluoroacetic anhydride; TFA = trifluoroacetic acid; Ts = *p*-toluenesulfonyl; Tf = trifluoromethanesulfonyl.

building blocks **6**–**8** proceeded as shown in Scheme 6 (p. 3423). Thus, the less polar isomer **13** (5*R*,6*R*) was treated with TFA/CH_2Cl_2 (1:1) to afford amino alcohol **45** while its more polar diastereoisomer **13′** (5*S*,6*S*, not shown) led, under the same conditions, to the corresponding amino alcohol **45′** (5*S*,6*S*, see Figure 1). Crystallization experiments with these diastereoisomers provided a crystalline derivative of the more polar compound (**45′**) with L-tartaric acid, whose X-ray crystallographic analysis revealed its absolute configuration (see ORTEP drawing, Figure 1), and, by extension, that of diastereoisomer **45**. Amino alcohol **45** was then coupled with thiazole amino diol **8** in the presence of HATU and HOAt to afford peptide **46** (65% yield over two steps, Scheme 6). The next problematic issue in the sequence was the differentiation between the two ethyl esters within compound **46**. As a result of the conjugation of one of the thiazole moieties with the imine functionality of **46**, we expected the ester on that thiazole to be more electron-deficient, and, therefore, more prone to hydrolysis. Gratifyingly, we found that, indeed, treatment of the latter compound, **46**, with 1 equivalent of lithium hydroxide in a 3:1:1 mixture of THF/EtOH/H_2O generated, regioselectively, a single carboxylic acid in 52% yield (plus 28% recovered starting material). More significantly,

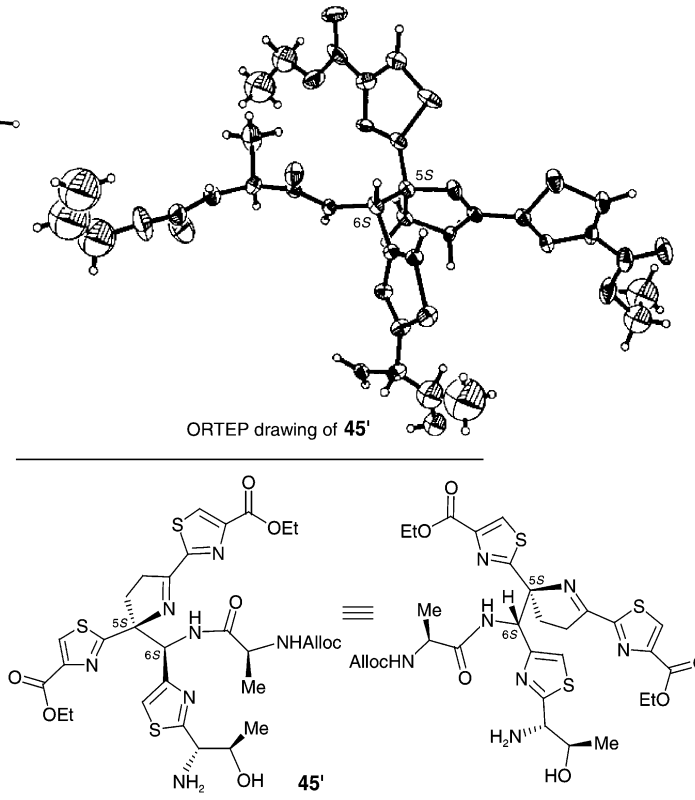
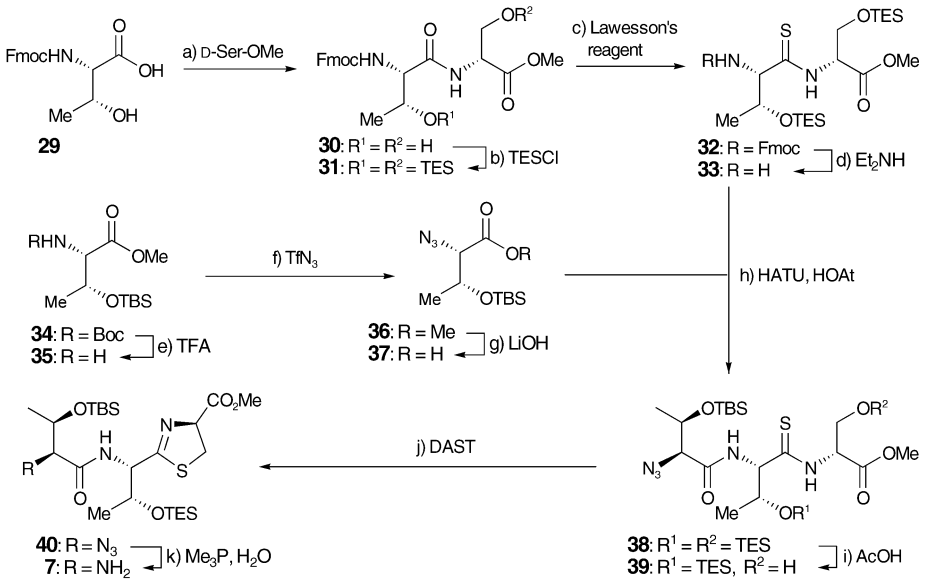
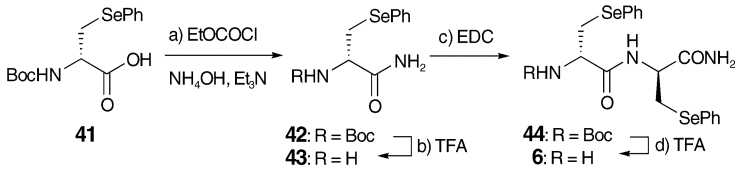


Figure 1. ORTEP drawing of **45′** (4*S*,5*S*) obtained by X-ray crystallographic analysis of its 1:1 salt with L-tartaric acid (L-tartaric acid not shown).

 © 2003 Wiley-VCH Verlag GmbH & Co. KGaA, Weinheim



Scheme 4. Synthesis of thiazoline moiety **7**. Reagents and conditions: a) D-Ser-OMe·HCl (1.0 equiv), Et_3N (3.0 equiv), HOBt (1.2 equiv), EDC (1.2 equiv), CH_2Cl_2, 25 °C, 2 h, 70%; b) TESCl (2.2 equiv), imidazole (3.0 equiv), CH_2Cl_2, 25 °C, 12 h, 81%; c) Lawesson's reagent (0.55 equiv), benzene, reflux, 2 h, 79%; d) Et_2NH (6.5 equiv), DMF, 25 °C; e) TFA/CH_2Cl_2 (1:1), 25 °C, 2 h; f) TfN_3 (3.0 equiv), Et_3N (3.0 equiv), $CuSO_4$ (0.05 equiv), MeOH/H_2O/CH_2Cl_2 (3.3:1:1), 25 °C, 14 h, 72% (two steps); g) LiOH (1.0 equiv), THF/H_2O (1:1), 0 °C, 3 h, 93%; h) HATU (1.1 equiv), HOAt (1.1 equiv), Et_3N (2.0 equiv), DMF, 25 °C, 12 h, 75% (two steps from 32); i) THF/AcOH/H_2O (3:1:1), 25 °C, 12 h, 75% (based on 35% recovered **38**); j) DAST (1.2 equiv), CH_2Cl_2, −78 °C, 20 min, 90%; k) Me_3P (3.0 equiv), THF/H_2O (20:1), 0 °C, 1 h, 92%. HOBt = 1-hydroxybenzotriazole hydrate; DAST = diethylaminosulfur trifluoride; Fmoc = fluorenylmethoxycarbonyl.

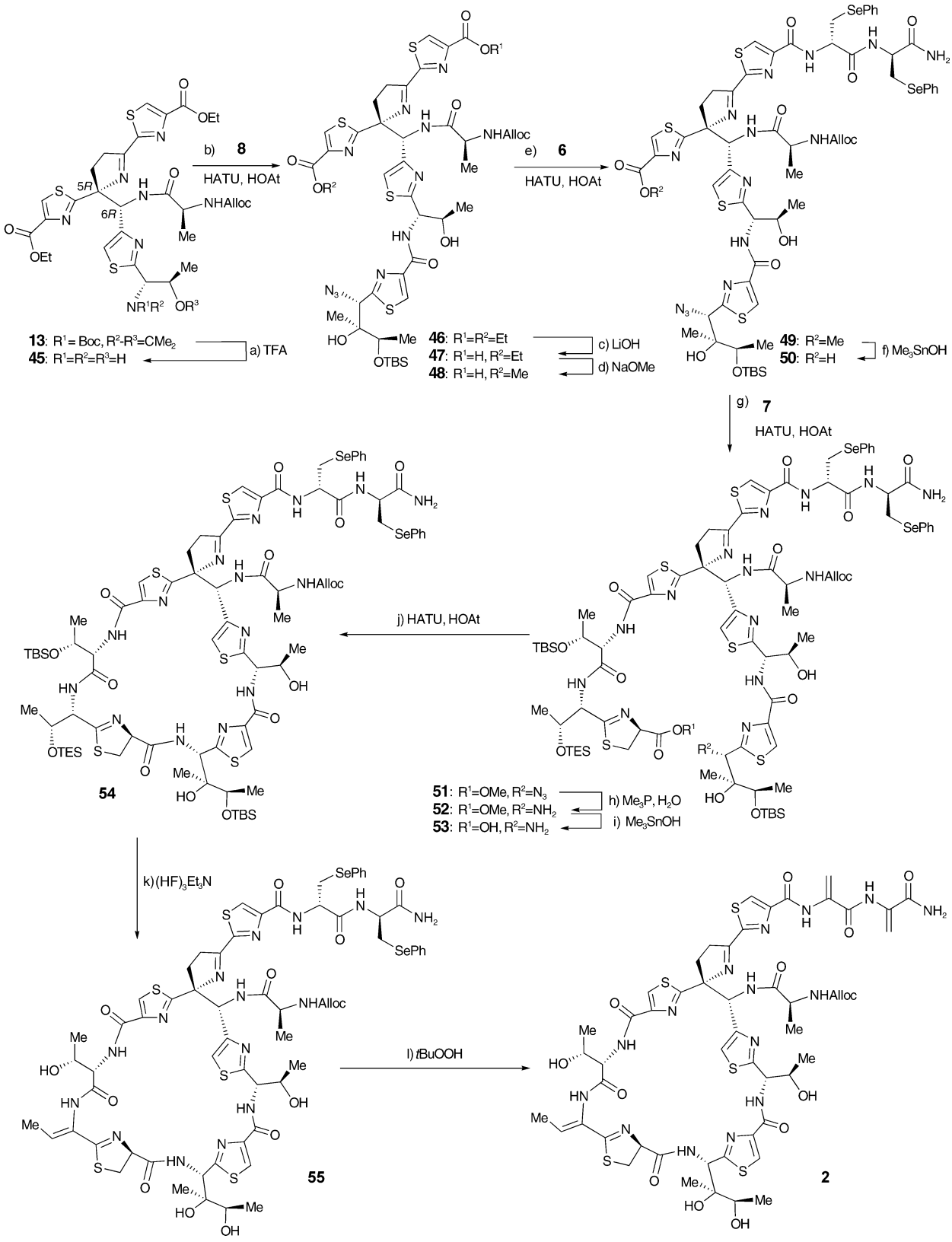


Scheme 5. Synthesis of side-chain precursor **6**. Reagents and conditions: a) ethyl chloroformate (1.05 equiv), NH_4OH (30 equiv), $EtNiPr_2$ (1.05 equiv), THF, 0–25 °C, 1 h, 89%; b) TFA/CH_2Cl_2 (1:1), 0 °C, 1 h; c) **41**, HOBt (1.1 equiv), EDC (1.1 equiv), $EtNiPr_2$ (1.5 equiv), DMF, 25 °C, 5 h, 58% (two steps); d) TFA, CH_2Cl_2 (1:1), 0 °C, 1 h, 95%.

HOAt) to afford product **51** in 75% yield. The obligatory low-temperature conditions employed in this coupling reaction were necessary to avoid premature elimination of the OTES group, which would lead to the conjugated thiazoline system (see structure **2**). Subsequent Staudinger reduction of the azide group within **51** (Me_3P, H_2O), followed by Me_3SnOH-induced methyl ester hydrolysis, led to amino acid **53** via amino ester **52**. Remarkably, the stereochemical integrity of the sensitive thiazoline moiety was preserved in the hydrolysis,[14] suggesting that this Me_3SnOH-mediated non-acidolytic and non-nucleophilic hydrolysis[15] could be a general mild method for the benign cleavage of esters within labile substrates. The key macrolactamization of amino acid **53** was smoothly effected by exposure to HATU and HOAt (0.3 mM concentration), leading to macrolactam **54** in 51% overall yield from **51**. Critically, exposure of **54** to $3\,HF{\cdot}Et_3N$ in THF at room temperature resulted in the cleavage of the two TBS groups, with concomitant base-promoted antiperiplanar elimination of the OTES moiety, furnishing the desired conjugated thiazoline system **55**.[16] Finally, the choice of the PhSe groups as potential progenitors of the olefinic bonds of the top side chain of the targeted molecule paid dividends in that treatment of the bisseleno derivative **55** with *t*BuOOH at ambient temperature resulted in the smooth formation of the five-membered imine analogue **2** of thiostrepton (**1**), lacking only the macrocycle that contains the quinaldic acid group. It should be stressed that the introduction of the last two double bonds into thiostrepton-like structures was proven to be a real challenge owing to the unusual sensitivity of the resulting dehydroamino acids.[17] Thiostrepton analogue **3** (Scheme 1) was synthesized from **4′** via **45′** by an analogous route to that described for **2**, and in similar yields (see Table 1).

Preliminary biological screening[18] with **2** and **3** indicated the lack of any significant antibacterial activity as compared to **1**, suggesting, perhaps, the importance of both the six-membered ring imine and the quinaldic acid motifs of thiostrepton for the recognition of its biological targets.

extensive NMR studies revealed that carboxylic acid **47** was, in fact, the product of this hydrolysis reaction. The remaining ethyl ester of compound **47** was then transesterified to a methyl ester (MeONa/MeOH, 90% yield), and the carboxylic acid function of resulting **48** was coupled to side-chain precursor **6** (HATU, HOAt) to afford tetrapeptide **49** in 83% yield. The inserted transesterification step was necessary to avoid subsequent complications that arose when attempts were made to hydrolyze the more robust ethyl ester, leading to elimination of the rather labile PhSe residues and side reactions thereof. In contrast, the methyl ester of **49** could be cleaved with trimethyltin hydroxide in refluxing dichloroethane (85% yield), conditions which avoided the loss of the selenium moieties otherwise observed in the presence of other reagents, that is, lithium hydroxide. The resulting acid **50** was then coupled to thiazoline segment **7** at 0 °C (HATU,



Scheme 6. Synthesis of the thiazoline macrocyclic system **2**. Reagents and conditions: a) TFA/CH_2Cl_2 (1:1), 25 °C, 2 h; b) **8** (1.0 equiv), $EtNiPr_2$ (3.0 equiv), HOAt (1.1 equiv), HATU (1.1 equiv), DMF, 25 °C, 12 h, 65% (two steps); c) LiOH (1.0 equiv), $THF/EtOH/H_2O$ (3:1:1), 0 °C, 1.5 h, 52% (28% recovered **46**); d) NaOMe (2.0 equiv), MeOH, 0 °C, 1 h, 90%; e) **6** (1.1 equiv), HOAt (1.2 equiv), HATU (1.2 equiv), DMF, 25 °C, 5 h, 83%; f) Me_3SnOH (13.0 equiv), 1,2-dichloroethane, reflux, 4 h, 85%; g) **7** (1.1 equiv), HOAt (1.2 equiv), HATU (1.2 equiv), DMF, 0 °C, 15 min, 75%; h) Me_3P (3.0 equiv), THF/H_2O (20:1), 0 °C, 30 min; i) Me_3SnOH (10.0 equiv), reflux, 1 h; j) HOAt (4.0 equiv), HATU (4.0 equiv), DMF (0.3 mM), 25 °C, 12 h, 51% (three steps); k) $(HF)_3 \cdot Et_3N$ (30.0 equiv), THF, 25 °C, 48 h, 50%; l) *t*BuOOH (5 M in decane, 20.0 equiv), CH_2Cl_2, 25 °C, 3 h, 60%.

 © 2003 Wiley-VCH Verlag GmbH & Co. KGaA, Weinheim

Table 1: Selected data for compounds **2** and **3**.

2: $R_f = 0.32$ (silica gel, CH_2Cl_2/MeOH, 9:1); $[\alpha]_D^{20} = -104.7$ ($c = 0.20$, MeOH); IR (film): $\tilde{\nu}_{max} = 3350, 2927, 2857, 1653, 1512, 1482, 1089, 1059\ cm^{-1}$; ^1H NMR (600 MHz, CD_3OD, 45 °C): $\delta = 8.52$ (s, 1 H), 8.19 (s, 1 H), 8.08 (s, 1 H), 7.44 (s, 1 H), 6.63 (q, $J = 7.0$ Hz, 1 H), 6.47, (d, $J = 1.5$ Hz, 1 H), 6.21 (d, $J = 1.0$ Hz, 1 H), 5.98 (br s, 1 H), 5.85 (br s, 1 H), 5.70 (d, $J = 1.5$ Hz, 1 H), 5.69 (d, $J = 1.0$ Hz, 1 H), 5.51 (s, 1 H), 5.24 (br d, $J = 17.0$ Hz, 1 H), 5.19 (t, $J = 9.2$ Hz, 1 H), 5.13 (br d, $J = 11.0$ Hz, 1 H), 5.09 (d, $J = 4.0$ Hz, 1 H), 4.47–4.41 (m, 3 H), 4.19–4.15 (m, 1 H), 4.13 (q, $J = 7.0$ Hz, 1 H), 3.81 (br d, $J = 10.6$ Hz, 1 H), 3.70 (dd, $J = 9.7$, 1.8 Hz, 1 H), 3.48 (dd, $J = 8.8$, 2.6 Hz, 1 H), 2.85 (quintet, $J = 7.4$ Hz, 1 H), 2.62 (dt, $J = 8.3$, 3.0 Hz, 1 H), 1.82 (d, $J = 7.0$ Hz, 3 H), 1.32 (d, $J = 6.6$ Hz, 3 H), 1.25 (d, $J = 7.5$ Hz, 3 H), 1.24 (s, 3 H), 1.21 (d, $J = 6.6$ Hz, 3 H), 1.05 ppm (d, $J = 6.1$ Hz, 3 H); ^{13}C NMR (125 MHz, CD_3OD, 45 °C): $\delta = 175.4, 173.8, 171.8, 171.5, 169.9, 168.3, 164.6, 164.2, 163.9, 163.4, 161.2, 153.5, 152.2, 150.7, 149.6, 136.4, 136.1, 136.0, 134.4, 130.9, 125.6, 119.3, 117.9, 107.2, 106.1, 102.5, 88.0, 80.14, 76.9, 71.3, 71.0, 69.8, 69.5, 66.9, 59.4, 58.1, 57.5, 37.5, 36.9, 33.7, 30.8, 30.4, 20.9, 19.8, 19.4, 17.5, 14.5$ ppm; HRMS (MALDI): calcd for $C_{52}H_{61}N_{15}O_{14}S_5$ [M+H$^+$]: 1280.3199; found: 1280.3184

3: $R_f = 0.32$ (silica gel, CH_2Cl_2/MeOH, 9:1); $[\alpha]_D^{20} = +98.5$ ($c = 0.55$, MeOH); IR (film): $\tilde{\nu}_{max} = 3375, 2913, 2853, 1658, 1643, 1449, 1249, 1061, 733\ cm^{-1}$; ^1H NMR (600 MHz, CD_3OD, 45 °C): $\delta = 8.51$ (s, 1 H), 8.21 (s, 1 H), 8.12 (s, 1 H), 7.34 (br s, 1 H), 6.61 (q, $J = 7.0$ Hz, 1 H), 6.49, (d, $J = 1.5$ Hz, 1 H), 6.20 (d, $J = 1.5$ Hz, 1 H), 5.86–5.78 (br s, 2 H), 5.71–5.69 (m, 2 H), 5.54 (br s, 1 H), 5.23–5.19 (m, 3 H), 5.09 (b, 1 H). 4.48–4.42 (m, 3 H), 4.38–4.32 (m, 3 H), 4.19–4.16 (m, 1 H), 3.90 (q, $J = 6.6$ Hz, 1 H), 3.65 (t, $J = 10.7$ Hz, 1 H), 3.45 (dd, $J = 8.8$, 2.2 Hz, 1 H), 3.21–3.18 (m, 1 H), 2.59 (dt, $J = 8.3$, 3.1 Hz, 1 H), 1.80 (d, $J = 7.0$ Hz, 3 H), 1.39 (s, 3 H), 1.33–1.31 (m, 6 H), 1.24–1.22 ppm (m, 6 H); ^{13}C NMR (150 MHz, CD_3OD, 45 °C): $\delta = 175.3, 174.8, 174.0, 173.6, 172.0, 171.7, 170.9, 168.3, 164.6, 164.2, 163.7, 161.2, 152.2, 150.6, 149.9, 136.6, 136.4, 136.2, 130.8, 130.2, 119.1, 117.9, 107.3, 106.0, 87.8, 80.1, 76.8, 70.7, 69.8, 69.2, 66.8, 60.2, 59.1, 58.1, 58.0, 37.2, 37.0, 26.4, 20.7, 20.6, 19.5, 18.7, 17.6, 14.6$ ppm; HRMS (MALDI): calcd for $C_{52}H_{61}N_{15}O_{14}S_5$ [M+H$^+$]: 1280.3199; found: 1280.3197

Within the described chemistry may lie clues for both the successful total synthesis of thiostrepton (**1**) and the design of bioactive analogues of this intriguing natural product.

Received: April 24, 2003 [Z51745]

Keywords: amino acids · antibiotics · macrocycles · natural products · thiazolines

[1] Isolation: a) J. F. Pagano, M. J. Weinstein, H. A. Stout, R. Donovick, *Antibiot. Annu.* **1955–1956**, 554–559; b) J. Vandeputte, J. D. Dutcher, *Antibiot. Annu.* **1955–1956**, 560–561; c) B. A. Steinberg, W. P. Jambor, L. O. Suydam, *Antibiot. Annu.* **1955–1956**, 562–565; structure determination: d) C. S. Bond, M. P. Shaw, M. S. Alphey, W. N. Hunter, *Acta Crystallogr. Sect. D* **2001**, *D57*, 755–758; e) B. Anderson, D. C. Hodgkin, M. A. Viswamitra, *Nature* **1970**, *225*, 233–235.

[2] K. C. Nicolaou, M. Nevalainen, B. S. Safina, M. Zak, S. Bulat, *Angew. Chem.* **2002**, *114*, 2021–2025; *Angew. Chem. Int. Ed.* **2002**, *41*, 1941–1945.

[3] K. C. Nicolaou, B. S. Safina, C. Funke, M. Zak, F. J. Zécri, *Angew. Chem.* **2002**, *114*, 2017–2020; *Angew. Chem. Int. Ed.* **2002**, *41*, 1937–1940.

[4] S. Higashibayashi, K. Hashimoto, M. Nakata, *Tetrahedron Lett.* **2002**, *43*, 105–110.

[5] J. M. Torres-Valencia, C. M. Cerda-García-Rojas, P. Joseph-Nathan, *Tetrahedron: Asymmetry* **1998**, *9*, 757–764.

[6] S. Kobayashi, H. Ishitani, M. Ueno, *Synlett* **1997**, 115–116.

[7] C. Cativiela, M. D. Díaz-de-Villegas, J. A. Gálvez, *Tetrahedron Lett.* **1995**, *36*, 2859–2860.

[8] C. Holzapfel, G. J. Pettit, *J. Org. Chem.* **1985**, *50*, 2323–2327.

[9] a) P. T. Nyffeler, C.-H. Liang, K. M. Koeller, C.-H. Wong, *J. Am. Chem. Soc.* **2002**, *124*, 10773–10778; b) P. B. Alper, S.-C. Hung, C.-H. Wong, *Tetrahedron Lett.* **1996**, *37*, 6029–6032.

[10] J. C. Muir, G. Pattenden, R. M. Thomas, *Synthesis* **1998**, 613–618.

[11] P. Lafargue, P. Guenot, J.-P. Lellouche, *Synlett* **1995**, 171–172.

[12] F. Bravo, Y. Díaz, S. Castillón, *Tetrahedron: Asymmetry* **2001**, *12*, 1635–1643.

[13] N. M. Okeley, Y. Zhu, W. A. van der Donk, *Org. Lett.* **2000**, *2*, 3603–3606.

[14] Thiazolines are readily epimerizable substrates, see, for instance: P. Wipf, P. C. Fritch, *Tetrahedron Lett.* **1994**, *35*, 5397–5400.

[15] Although transesterifications from methyl esters to tin esters with Me_3SnOH are known (for a review, see: O. A. Mascaretti, R. L. E. Furlan, C. J. Salomon, E. G. Mata, *Phosphorus Sulfur Silicon Relat. Elem.* **1999**, *150–151*, 89–97), only one application of this method has been reported dealing with the cleavage of benzyl esters: R. L. E. Furlan, E. G. Mata, O. A. Mascaretti, C. Pena, M. P. Coba, *Tetrahedron* **1998**, *54*, 13023–13034.

[16] The corresponding *Z*-conjugated thiazole system of micrococcin P_1 was prepared by stereospecific elimination of the activated hydroxy group: a) F. Yokokawa, T. Shioiri, *Tetrahedron Lett.* **2002**, *43*, 8679–8682; b) M. A. Ciufolini, Y.-C. Shen, *Org. Lett.* **1999**, *1*, 1843–1846.

[17] P. M. T. Ferreira, H. L. S. Maia, L. S. Monteiro, J. Sacramento, *J. Chem. Soc. Perkin Trans. 1* **1999**, 3697–3703.

[18] Minimum inhibitory concentration (MIC) assays were performed with the following bacteria: methicillin-resistant *Staphylococcus aureus* (MRSA) (ATCC 33591), vancomycin-resistant *Enterococcus faecium* (VRE) (ATCC 700221), *Pseudomonas aeruginosa* (PA) (27853), *Escherichia coli* (EC1) (ATCC 700336), *Escherichia coli* (EC2) (ATCC 29425). We thank Dr. J. Fletcher and Dr. R. Ghadiri for these experiments.

 © 2003 Wiley-VCH Verlag GmbH & Co. KGaA, Weinheim

Element Mass Spectrometry

Sulfur as the Key Element for Quantitative Protein Analysis by Capillary Liquid Chromatography Coupled to Element Mass Spectrometry**

*Mathias Wind, Ansgar Wegener, Andreas Eisenmenger, Roland Kellner, and Wolf D. Lehmann**

Quantitative analysis of proteins from (sub)picomolar complex solutions is required to answer the questions raised in many current projects in the life sciences. This challenging task is often hampered by low absolute (submicrogram) sample amounts or by incompatibility between the sample matrix and the analytical method. The classical method for amino acid analysis requires a sensitivity-enhancing modification reaction for the amino acids to be detected.[1,2] Quantification of the relative abundance of identical peptides or proteins in two samples of different biological origin can be achieved by the isotope-coded affinity tag (ICAT) methodology;[3] however, absolute quantification is not possible.

The coupling of capillary liquid chromatography (μLC) with element mass spectrometry (inductively coupled plasma mass spectrometry, ICP-MS) is introduced in this study as a method for quantifying peptides and proteins. Two kinds of analytical information can be extracted from these measurements: first, characterization of the species in terms of its LC retention time, and second, partial information on the elemental composition of the analyte, which has quantitative quality.[4,5] The analyte can be characterized in more detail by applying an additional technique, HPLC-ESI-MS. By combined application of both direct coupling methods peptides and proteins can be both sequenced and quantified.

High-resolution ICP-MS instruments are normally used for the analysis of metals; however, they are also suitable for the specific and quantitative determination of S, Se, I, and P. Among these elements sulfur is of particular interest due to its occurrence in two amino acids, cysteine and methionine. Cys and Met occur with a cumulative abundance of about 5% in natural peptides, so that on a statistical basis at least one sulfur-containing amino acid is expected to occur in every polypeptide exceeding a length of twenty amino acids. Thus, direct detection of sulfur by element mass spectrometry[4,6] represents a widely applicable quantification method for peptides and proteins. In ICP-MS the response is directly correlated to the absolute amount of an element introduced and it is not dependent on the structure of the analyte.

Here we demonstrate the concept of protein quantification by μLC-ICP-MS and sulfur detection by using insulin ($M_w = 5800$ Da, six cysteine residues per molecule) as a model analyte. For the absolute quantification of this peptide a defined amount of an internal standard is added; we selected thiamin (one sulfur atom per molecule). To establish reproducible analytical conditions analyte and standard were coinjected (5.6-fold molar excess of thiamin over insulin), and isocratic elution was performed to eliminate matrix effects on the ICP-MS response. The elution of sulfur-containing analytes was recorded online with selective ^{32}S detection.

Figure 1a displays the chromatographic separation of insulin and thiamin from three subsequent injections, selected from a larger set of analytical runs (injection times are marked with arrows). By measuring the ratio of the signal

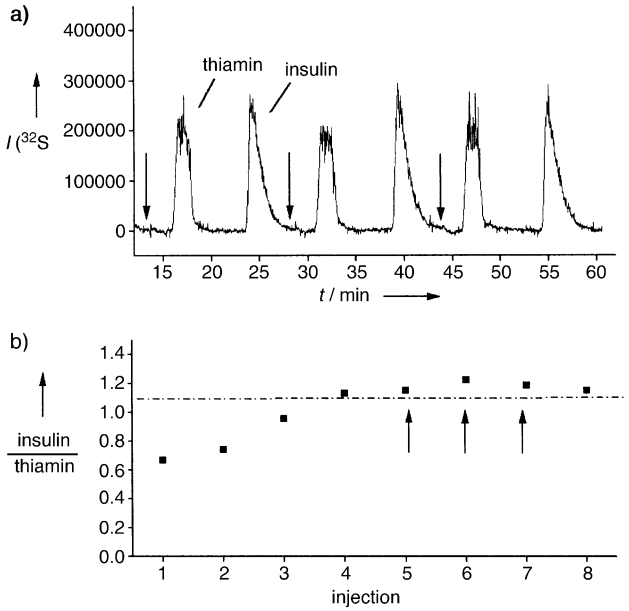


Figure 1. Quantification of insulin (six sulfur atoms per molecule) by μLC-ICP-MS and ^{32}S detection. Internal standard: thiamin (one sulfur atom per molecule). a) RP-LC-ICP-MS with isocratic elution. The sample injections marked with an arrow correspond to the marked data points in part b. b) Peak area ratio insulin/thiamin. The calculated value is marked with a dashed line.

integrals from analyte and standard, the sulfur content in the analyte can be quantified; the ratio extracted from eight consecutive injections is shown in Figure 1b. At the start of the series of analyses a saturation of adsorptive sites is observed, and from the fourth injection onwards the peak area ratios approach a constant value of about 1.15. Systematic error is avoided by selecting isocratic elution conditions. The stable status of the μLC-ICP-MS system reached after the third injection is reflected by a good reproducibility of the data, which show a relative standard deviation of 5%. The experimental ratio differs only slightly (<10%) from the

[*] Prof. Dr. W. D. Lehmann, Dr. M. Wind, Dr. A. Eisenmenger
Zentrale Spektroskopie
Deutsches Krebsforschungszentrum (DKFZ)
Im Neuenheimer Feld 280, 69120 Heidelberg (Germany)
Fax: (+49) 6221-42-4554
E-mail: wolf.lehmann@dkfz-heidelberg.de
Dr. A. Wegener, Dr. R. Kellner
Global Technologies TRB, Merck KGaA
64271 Darmstadt (Germany)

[**] We are indebted to Dr. K. Sauber (Aventis Pharma) for valuable discussions and for a sample of human insulin.

Supporting information for this article is available on the WWW under http://www.angewandte.org or from the author.

 DOI: 10.1002/anie.200250547 © 2003 Wiley-VCH Verlag GmbH & Co. KGaA, Weinheim

calculated value of 1.07, resulting in an insulin concentration which is too high by 7%. A direct peptide quantification with comparable error, which is also independent of the amino acid composition, cannot be achieved by other current analytical methods.

Besides absolute peptide quantification, relative quantifications can also be performed by μLC-ICP-MS, which may be used, for example, to monitor an enzymatic reaction. As an example for such an application we selected the proteolytic cleavage of a mixture of two recombinant protein domains. The two functional domains of the bacterial chemotaxis protein cheA,[7] cheA-H (3-137) and cheA-C (257-513), were synthesized by overexpression in *E. coli* according to the method of Levit et al.[8] These domains were expressed as fusion proteins with the affinity tags 6xHis (cheA-H) and streptag (cheA-C) and isolated with a purity >95%. For the quantitative analysis in this study a mixture consisting of 90% cheA-H and 10% cheA-C was digested with trypsin. The resulting peptide fragments were separated by μLC and analyzed directly by mass spectrometry. The elution of sulfur-containing peptides can be recognized by ^{32}S detection with ICP-MS (Figure 2a).

For peptide identification, an aliquot of the sample was analyzed under identical conditions by μLC-ESI-MS and detection of positive ions. The corresponding base peak chromatogram is shown in Figure 2b. The sequences of the identified tryptic peptides and the quantitative analyses are summarized in Table 1. In a complete tryptic digest of a protein all tryptic peptides are expected to occur in equimolar amounts. The quantitative evaluation of the ^{32}S trace (Table 1 and Figure 2a) is in good agreement with this consideration.

The integrated peak areas of the ^{32}S ICP signals show an average value of 2.8 per sulfur atom with a maximum deviation of 0.4. As expected, the peak integrals for the tryptic peptides of cheA-C are smaller by about one order of magnitude (Table 1, ICP integrals). Concomitantly, the relative fluctuations of the integral values of cheA-C are

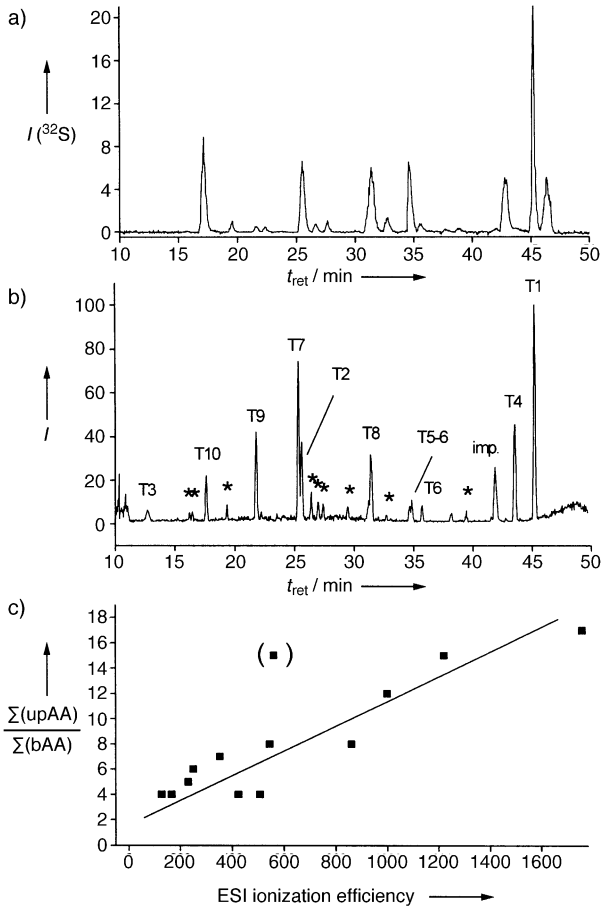


Figure 2. Tryptic digest of a mixture containing 90% cheA-H and 10% cheA-C. a) μLC-ICP-MS of this digest with ^{32}S detection. b) μLC-ESI-MS of the same digest displayed as base peak chromatogram. Tryptic fragments of cheA-C are marked with an asterisk, those of cheA-H have T labels. c) Correlation of the ESI ionization efficiency with the ratio calculated from the number of nonpolar residues divided by the number of basic residues in the corresponding peptide ($R = 0.94$, the data point in brackets was not included).

Table 1: Sequences, ICP-MS signal intensities, ESI-MS signal intensities (sum of all charge states), ESI ionization efficiencies, and properties of the peptides analyzed.

t_{ret} [min]	Sequence	Protein	Intensities			Peptide composition		
			ICP integral	ESI integral	ionization efficiency	basic/ acidic	unpolar	polar
17.1	GETPSA**M**R	cheA-H; T10	3.17	406	128	1/1	4	2
19.5	**M**GGHVEIQSK	cheA-C; T26	0.29	67	231	1/1	5	2
21.6	?		0.18					
22.4	GVG**M**DVVK	cheA-C; T23	0.16	40	250	1/1	6	0
25.5	DI**M**QEQLDAYK	cheA-H; T7	2.67	1133	424	1/3	4	3
26.6	DLQESV**M**SIR	cheA-C; T7	0.26	147	565	1/2	4	5
27.6	SSELDPVNHGDLITS**M**GQLQR	cheA-C; T5	0.29	250	862	1/3	8	7
31.3	QSQEPDAASFDYI**C**QALR	cheA-H; T8	3.23	1138	352	1/3	7	7
32.7	NSVGNLILSAEHQGGNI**C**IEVTDDGAGLNR	cheA-C; T19	0.57	696	1221	1/4	15	14
34.6	RGE**M**QLNTDIINLFLETK	cheA-H; T5-6	2.42	405	167	2/3	8	5
35.5	GE**M**QLNTDIINLFLETK	cheA-H; T6	0.33	180	545	1/3	8	5
37.7	?		0.08					
38.8	VDQLINLVGELVITQS**M**LAQR	cheA-C; T4	0.13	130	1000	1/2	12	6
42.8	GGAGTFGFSVLQETTHL**M**ENLLDEAR	cheA-H; T4	2.81	1575	560	1/3	15	6
45.2	**M**DISSFYQTFFDEADELLAD**M**EQHLLVLQPEAPDAER	cheA-H; T1	5.31/2	4670	1759	1/10	17	7
46.4	?		2.61					

[a] Sulfur-containing amino acids are printed in bold.

 © 2003 Wiley-VCH Verlag GmbH & Co. KGaA, Weinheim

significantly larger (0.13 to 0.57) than those of the cheA-H signals. Reduced cleavage efficiency may be responsible for the relatively small ICP peak areas of cheA-C T4 (0.13) and cheA-C T23 (0.16). Incomplete cleavage by trypsin has been described for the occurrence of basic[9] or acidic[10] residues directly adjacent to arginine or lysine. Incorrectly high ICP peak areas (e.g. cheA-C T19) may be caused by the occurrence of incomplete or nontryptic cleavage products of the main component cheA-H.

If the ^{32}S ICP peak integrals are considered an absolute measure for the amount of a peptide, the peak areas of the corresponding molecular ions observed in the LC-ESI-MS run provide information about the relative ionization efficiency of individual peptides. To obtain a measure for the ionization efficiency (Table 1), the peak areas (sum of all charge states) in the LC-ESI-MS (Figure 2b) were normalized by the corresponding areas of the ^{32}S ICP-MS run (Figure 2a). These lead to the following conclusions on the correlation between peptide composition and ionization efficiency: 1) The ionization efficiency increases with increasing peptide size and with increasing number of nonpolar residues (upAA). 2) The ionization efficiency is reduced by basic residues (bAA) (for example, T6/T5-6). 3) Acidic residues do not affect the ionization efficiency. If the ratio Σ(upAA)/Σ(bAA) is plotted against the electrospray ionization efficiency, a linear correlation is obtained (Figure 2c). Only one peptide (cheA-H T4) is does not fit to this correlation, exhibiting an "incorrectly low" electrospray ionization efficiency. In principle, this correlation is in agreement with the ion evaporation model[11] of electrospray ionization, which explains the preferential ionization of nonpolar analytes by their enrichment on the droplet surface, from where they are preferentially ionized.[12–14]

The experimental data in this study show that element mass spectrometry with ^{32}S detection is suited for quantitative trace analysis of sulfur-containing peptides and proteins. The simultaneous determination of ^{32}S und ^{31}P by ICP-MS has been demonstrated for the determination of the phosphorylation degree of phosphoproteins.[4] When one considers the impact of quantitative data in proteomic analysis and the few methods currently available for this task, this new combination of element and electrospray mass spectrometry has great potential in this area.

Experimental Section

Columns: peptides: 300 μm × 25 cm, insulin: 300 μm × 12.5 cm both packed with Vydac C_{18}, 5 μm 300 Å. Eluents: A: water, 0.065% TFA (trifluoroacetic acid), B: 80% acetonitrile, 0.05% TFA. Gradient for peptide analysis: 5 min 7% B, 5–50 min 7–100% B; insulin analysis: isocratic 36.8% B. Column temperature stabilized at 25°C.

The sample solution for insulin analysis contained 6 μM human insulin (100 Units mL^{-1}, Aventis Pharma), 33.6 μM thiamin in 0.1% TFA. A 5-μL injection contains (180 pmol sulfur from insulin, 168 pmol sulfur from thiamin); calculated ratio based on ^{32}S content: 1.07; experimental ratio: 1.15 (5% RSD).

The expression constructs of the domains cheA-H und cheA-C of the *E. coli* chemotaxis protein (SwissProt Accession No. P07363) were prepared from PCR products of the corresponding gene according to Levit et al.;[8] the sequences encoding for 6xHis and streptagII, respectively, were fused to their 3′-ends. The expression constructs contain the sequences 3-137 (H-domain) and 257-513 (C-domain) of P07363 (see also Supporting Information). The expression system pASK75 (IBA, Göttingen, Germany) in *E. coli* W3110 was used. The following affinity matrices were used for protein purification: NiNTA (Qiagen, Hilden, Germany) for cheA-H-His and streptactin (IBA, Göttingen) for cheA-C-strep.

Element mass spectrometry was performed using a sector-field ICP instrument type Element 2 (ThermoFinnigan, Bremen, Germany). Medium resolution: 4000, scan time: 1.7 s, scan window: 100 mDa. For the μLC-ESI-MS analyses a tandem mass spectrometer type Q-Tof 2 (Micromass, Manchester, UK) was used. All MS analyses were conducted in the positive-ion mode. The raw data were integrated with the software package Origin 5.0.

The limit (signal-to-noise ratio 3:1) for the ^{32}S detection for peptides was estimated for peptides to 10 pmol and for proteins to 25 pmol. The dynamic range of the quantification method appears to be limited by the chromatographic properties of the individual analytes rather than by the ICP-MS detection method.

Received: November 14, 2002 [Z50547]

Keywords: analytical chemistry · electrospray ionization · mass spectrometry · peptides · proteins

[1] M. Weiss, M. Manneberg, J.-F. Juranville, H.-W. Lahm, M. Fountoulakis, *J. Chromatogr. A* **1998**, *795*, 263–275.
[2] R. Kellner, H. E. Meyer, F. Lottspeich in *Microcharacterization of Proteins*, Wiley-VCH, Weinheim, **1999**, pp. 119–140.
[3] S. P. Gygi, B. Rist, S. A. Gerber, F. Turecek, M. H. Gelb, R. Aebersold, *Nat. Biotechnol.* **1999**, *17*, 994–999.
[4] M. Wind, H. Wesch, W. D. Lehmann, *Anal. Chem.* **2001**, *73*, 3006–3010.
[5] M. Wind, M. Edler, N. Jakubowski, M. Linscheid, H. Wesch, W. D. Lehmann, *Anal. Chem.* **2001**, *73*, 29–35.
[6] E. Svantesson, J. Pettersson, K. E. Markides, *J. Anal. At. Spectrom.* **2002**, *17*, 491–496.
[7] A. M. Bilwes, L. A. Alex, B. R. Crane, M. I. Simon, *Cell* **1999**, *96*, 131–141.
[8] M. Levit, Y. Liu, M. Surette, J. Stock, *J. Biol. Chem.* **1996**, *271*, 32057–32063.
[9] B. Keil, *Specificity of Proteolysis*, Springer, Berlin, **1992**, p. 335.
[10] B. Thiede, S. Lamer, J. Mattow, F. Siejak, C. Dimmler, T. Rudel, P. R. Jungblut, *Rapid Commun. Mass Spectrom.* **2000**, *14*, 496–502.
[11] B. A. Thomson, J. V. Iribarne, *J. Chem. Phys.* **1979**, *71*, 4451–4463.
[12] N. B. Cech, J. R. Krone, C. G. Enke, *Anal. Chem.* **2001**, *73*, 208–213.
[13] N. B. Cech, C. G. Enke, *Anal. Chem.* **2000**, *72*, 2717–2723.
[14] K. Tang, R. D. Smith, *J. Am. Soc. Mass Spectrom.* **2001**, *12*, 343–347.

 © 2003 Wiley-VCH Verlag GmbH & Co. KGaA, Weinheim

Electrodeposition of Nanocrystals

Electrodeposition of Nanocrystalline Metals and Alloys from Ionic Liquids

Frank Endres, Mirko Bukowski, Rolf Hempelmann,* and Harald Natter*

By definition ionic liquids are molten salts with a melting point below 100 °C. In general, they are composed of organic cations, such as substituted imidazolium ions or tetraalkylammonium ions, and of inorganic or organic anions, such as $AlCl_4^-$, PF_6^-, BF_4^-, $CF_3SO_3^-$, and $(CF_3SO_2)_2N^-$. Liquids based on substituted imidazolium ions and anions of the latter type show an extraordinarily high chemical and thermal stability as well as wide electrochemical windows. Furthermore they have very low vapor pressures, even at temperatures as high as 300 °C. These properties have lead to a great interest in technical and organic chemistry,[1] particularly with regard to "green chemistry".[2] A lot of different systems have been reported in the literature,[3] and the general trend nowadays is to make hydrophobic ionic liquids that can be handled under air.

Ionic liquids are also of great interest for electrochemical purposes because they have wide electrochemical windows that can reach values of more than 6 volts, depending on the substrate.[3] Thus, they allow access to elements and compounds, especially to less-noble nanocrystalline materials that otherwise cannot be electrodeposited from aqueous or organic solutions. For example, the liquid 1-butyl-3-methylimidazolium hexafluorophosphate has an electrochemical window of slightly more than 4 volts on Au(111), and this value is more than three times that of water. It was shown recently that the semiconductor germanium can be electrodeposited in intrinsic form with such a liquid and that, depending on the bath composition and the electrochemical parameters, Ge(111) bilayers as well as stable Ge nanocrystals can be obtained.[4,5] Ionic liquids based on $AlCl_3$ and organic halides, such as substituted imidazolium ions—which were used for the studies presented here—are ideally suited for the electrodeposition of Al and its alloys. A general overview on the electrodeposition of metals and semiconductors from ionic liquids is reported in Ref. [6].

Nanoscale semiconductors and metals are of great interest for nanotechnology. The band gap of nanoscale semiconductors is a function of the particle size, and normally the band gap increases with decreasing particle size.[7] The hardness of nanocrystalline metals is found to increase with decreasing particle size, which is explained by the increased fraction of atoms located at the grain boundaries; furthermore it is found that the corrosion resistance often gets better for nanocrystalline metals.[8] As an example, nanocrystalline Ni[9] as well as Au, Cu, Ag, and Fe nanomaterials have been made by electrochemical means. Adjusting the hardness of a material simply by varying the grain size opens up many interesting perspectives for technical applications: nanocrystalline Ni is used as a hard coating material to achieve the high hardness and strength of steel without the usual corrosion problems, and nanocrystalline Co can replace the more expensive titanium.

Electrochemistry is a powerful tool for making nanocrystalline materials because the grain size can be adjusted by varying the electrochemical parameters such as overvoltage, current density, pulse parameters in pulsed electrodeposition, bath composition, and temperature.[10] Thus, tailored materials are in principle accessible by simple electrochemical procedures. However, detailed studies on this topic have hitherto only been performed in aqueous solutions where such a procedure is limited to elements that are more noble than hydrogen. Herein we present a novel procedure by which bulk nanocrystalline metals and alloys can be electrodeposited from ionic liquids. For the first time we report on the nanocrystalline electrodeposition of Al, Fe, and an Al-Mn alloy as well as on nanocrystalline Pd. Nanocrystalline noble metals are interesting as catalysts, for example, in low-temperature fuel cells, as a result of their high surface to volume ratio.

Figure 1 shows the XRD pattern of microcrystalline and nanocrystalline Al. The former was made electrochemically in a Lewis acidic ionic liquid based on $AlCl_3$ and 1-ethyl-3-methylimidazolium chloride ($[EMIm]^+Cl^-$) under galvanostatic conditions (55 mol % $AlCl_3$, $I = 54\ mA\,cm^{-2}$, on glassy carbon), while the latter was made under quite similar conditions (55 mol % $AlCl_3$, $I = 16.67\ mA\,cm^{-2}$, on glassy carbon), but with nicotinic acid as an organic additive.[11] Without this additive, pulsed electrodeposition by galvano-

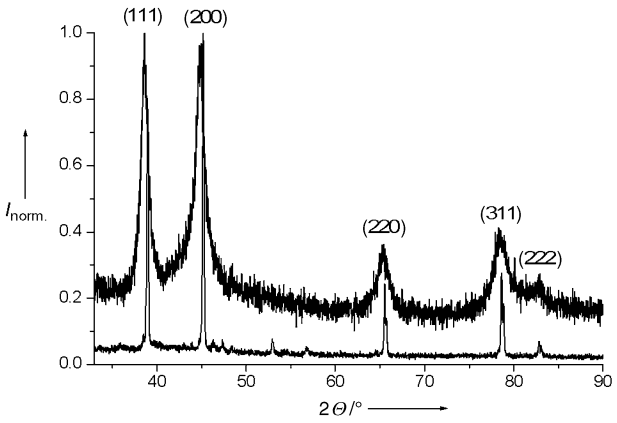


Figure 1. Upper curve: XRD pattern of nanocrystalline Al with a grain size of 12 ± 1 nm prepared from $AlCl_3/[BMIm]^+Cl^-$ (55/45 mol %). Lower curve: Microcrystalline reference sample.

[*] Prof. Dr. F. Endres
FB Physik, Metallurgie und Werkstoffwissenschaften
Technische Universität Clausthal
38678 Clausthal-Zellerfeld (Germany)
Fax: (+49) 5323-72-2460
E-mail: frank.endres@tu-clausthal.de
Prof. Dr. R. Hempelmann, Dipl.-Chem. M. Bukowski, Dr. H. Natter
FR 8.13 Physikalische Chemie
Universität des Saarlandes
66123 Saarbrücken (Germany)
Fax: (+49) 681-302-4759
E-mail: r.hempelmann@mx.uni-saarland.de

 © 2003 Wiley-VCH Verlag GmbH & Co. KGaA, Weinheim DOI: 10.1002/anie.200350912

static or potentiostatic electrodeposition methods gave crystal sizes above 100 nm. It is evident that the full-width at half-maximum height of all the peaks in Figure 1 is much wider in the case of the nanocrystalline sample than in the microcrystalline sample. It has been known for a long time that this peak width can be used in the Scherrer equation to determine the average grain size.[12] For this sample we obtained an average grain size of 14.0 ± 0.3 nm.

Whereas Scherrer analysis only gives an average value for the grain size, the Warren–Averbach procedure also allows the logarithmic normal distribution to be determined by evaluating the complete peak shape.[13,14] It was demonstrated in the literature that a logarithmic normal distribution function accurately describes the size distribution of emulsions,[15] dust particles,[16] sols,[17] and nanocrystalline metals such as Pd.[18] Therefore, a logarithmic normal distribution is also assumed for the samples investigated, and a Warren–Averbach analysis was performed for the harmonic (111) and (222) peaks. A volume-averaged grain size of 12 ± 1 nm is obtained for the nanocrystalline Al sample. The respective logarithmic normal distribution is shown in Figure 2 together with a histogram of the crystal size obtained from TEM measurements (determined from 400 nanoparticles) and a logarithmic normal distribution of the TEM data. We see, that the sizes range from about 5 to 20 nm, with most of them in the range between 8 and 10 nm. It is not surprising that there is a slight deviation between the results from XRD (Warren–Averbach analysis) and TEM (inset in Figure 2). TEM generally yields larger "particle sizes" for face-centered cubic (fcc) metals (such as Pd or Al) because stacking faults readily occur in the (111) direction of a fcc structure. The stacking faults terminate the coherency of the lattice plane sequence for which XRD is sensitive.

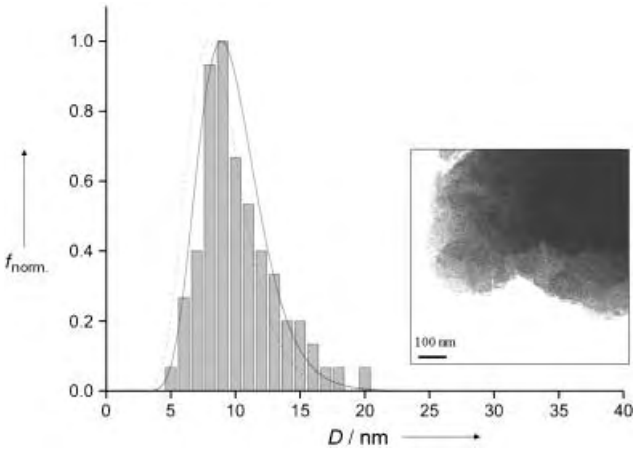


Figure 2. Comparison between the size distribution f of Al nanoparticles (12 ± 1 nm) obtained from the TEM picture (inset), a logarithmic normal fit to these TEM data (solid line; $\sigma = 1.3$, $\mu = 9.5$), and the distribution function obtained from the Warren–Averbach analysis (dashed line; $\sigma = 1.3$, $\mu = 8.5$).

Our results nicely show that grain sizes below 10 nm can be obtained by simple electrodeposition under galvanostatic conditions. Further results show that bulk samples composed of a narrow size distribution of nanocrystals with average sizes ranging from 10 to 100 nm can be obtained by varying the bath composition and the electrochemical parameters.[19] In general, bigger grains are expected to form when lower current densities and lower overvoltages are used; this observation is in qualitative accordance with the electrochemical version of the Kelvin equation.[20] Preliminary results on the hardness of our nanocrystalline Al deposits show that an improvement of between 50 and 150% can be achieved relative to the microcrystalline sample.

It is also possible to deposit several aluminum alloys from ionic liquids based on $AlCl_3$.[6] Of particular interest are electrochemically made Al-Mn alloys,[21] which are widely used in the automobile industry for lightweight construction. For the present study we have attempted to make nanocrystalline Al_xMn_y alloys electrochemically by adding $MnCl_2$ ($3.2\ mmol\,L^{-1}$) and 2 weight% of nicotinic acid to a Lewis acidic liquid (as described above). The deposition was performed by using a current density of $I = 0.5\ mA\,cm^{-2}$ on glassy carbon. Figure 3 shows the XRD pattern of a typical deposit indicating the dominant Bragg peaks for the single-phase alloy (Al-Mn 1:1[22]); in some samples we also find weak signals resulting from Mn and Al. This result implies that a material was obtained that was mainly composed of the Al-Mn alloy with small amounts of Al and Mn in the deposit (up to a maximum of 5%). Further structural studies on these co-deposits are currently under progress. The average grain size of 26 ± 1 nm results from a Scherrer analysis of the Al-Mn Bragg peaks.

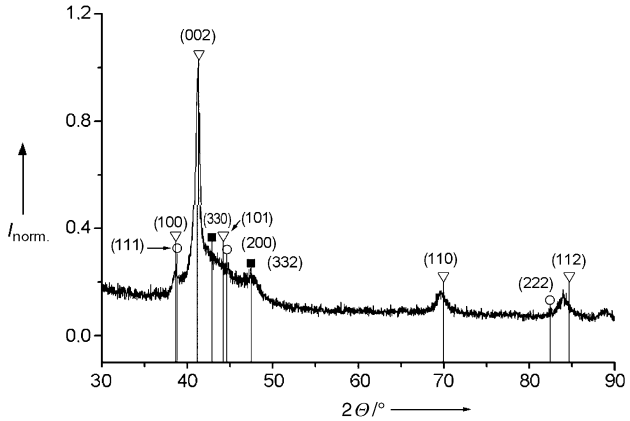


Figure 3. XRD pattern of an electrochemically made sample which is mainly composed of a nanocrystalline Al-Mn alloy with an average grain size of 26 ± 1 nm. Triangles: Al-Mn, circles: Al, squares: Mn.

Nanocrystalline Fe was also obtained by galvanostatic plating ($5\ mA\,cm^{-2}$) from a Lewis acidic ionic liquid of $[BMIm]^+Cl^-$ and $AlCl_3$ (63 mol% $AlCl_3$, $4.3\ mmol\,L^{-1}$ anhydrous $FeCl_3$, 2 weight% of nicotinic acid). Scherrer analysis of the XRD data gives an average grain size of 64 ± 1 nm. Fe-Al alloys as well as Fe-Al co-deposits can also be obtained with higher overvoltages for the electrodeposition.

Finally we report on the electrodeposition of nanocrystalline palladium deposits from a Lewis basic ionic liquid (44 mol% $AlCl_3$, 56 mol% $[BMIm]^+Cl^-$, 2 weight% nicotinic

 © 2003 Wiley-VCH Verlag GmbH & Co. KGaA, Weinheim

acid) using a Pd counter electrode and a current density of $I = 0.66\ mA\,cm^{-2}$. A 1-mm thick microcrystalline copper plate was used as the substrate and the liquid was heated up to 100 °C during electrodeposition. Under these conditions we obtained Pd nanocrystals with an average grain size of 13 ± 1 nm. An advantage over aqueous solutions is that hydrogen evolution does not occur in ionic liquids. In aqueous solutions this side reaction is hard to control and leads to hydrogen adsorption by Pd. Porous and brittle deposits are usually the result. Defect-free nanocrystalline Pd foils would be of great interest for Pd diffusion membranes and for hydrogen purification.

We have shown for the first time that nanocrystalline metals and alloys can be made in ionic liquids by electrochemical means. As a consequence of their wide electrochemical windows, elements can be obtained that otherwise cannot be electrodeposited from aqueous or organic solutions. The grain sizes can be adjusted by varying the bath compositions and the electrochemical parameters. Bulk samples with average grain sizes down to 10 nm can be made by simple electrodeposition. Of particular interest for materials science are studies on the hardness and the corrosion resistance of such nanocrystalline samples.

Experimental Section

The nanocrystalline samples were deposited in a glove box under nitrogen (H_2O and O_2 below 2 ppm). The organic salts ($[EMIm]^+Cl^-$ or $[BMIm]^+Cl^-$) were dried for several days under vacuum at about 50 °C. After careful mixing of the organic component with $AlCl_3$ (Fluka, puriss p. a.), the obtained ionic liquid was put under vacuum for several hours, with stirring, to remove any residual HCl. The electrodes were dipped into the melt and fixed. The working electrodes were either glassy carbon, copper, or aluminum.

To prepare the alloys the appropriate metal halides were added. The depositions were carried out under galvanostatic conditions with current densities between 0.25 and 54 $mA\,cm^{-2}$, with or without nicotinic acid (as indicated). All experiments were done at room temperature except those for the palladium depositions, which were performed at 80–150 °C. The deposits generally had thicknesses between 0.1 and 1 mm.

The X-ray diffraction experiments were carried out with a Siemens D500 diffractometer. Warren–Averbach analysis was done by using our own computer-based fitting program.[14]

Received: January 9, 2003
Revised: April 30, 2003 [Z50912]

Keywords: aluminum · electrodeposition · ionic liquids · metals · nanotechnology

[1] a) P. Wasserscheid, W. Keim, *Angew. Chem.* **2000**, *112, 3*927–3945, *Angew. Chem. Int. Ed.* **2000**, *39*, 3773–3789; b) *Ionic liquids in synthesis*, (Eds.: P. Wasserscheid, T. Welton), Wiley-VCH, Weinheim, **2002**.
[2] M.J. Earle, K. R. Seddon, Pure *Appl. Chem.* **2000**, *72*, 1391–1398.
[3] R. Hagiwara, Y. Ito, *J. Fluorine Chem.* **2000**, *105*, 221–227.
[4] F. Endres, C. Schrodt, *Phys. Chem. Chem. Phys.* **2000**, *2*, 5517–5520.
[5] F. Endres, Sh. Zein El Abedin, *Chem. Commun.* **2002**, 892–893.
[6] F. Endres, *ChemPhysChem* **2002**, *3*, 144–154.
[7] T. Trindade, P. O'Brien, N. L. Pickett, *Chem. Mater.* **2001**, *13*, 3843–3858.
[8] a) D. G. Morris, *Mater. Sci.* **1998**, 269–272, 11–13; b) D. G. Morris in *Mechanical Behaviour of Nanostructured Materials*, Trans Tech, Aedermannsdorf, Switzerland, **1998**.
[9] C. Cheung, F. Djuanda, U. Erb, *Nanostruct. Mater.* **1995**, *5*, 513–523.
[10] *Theory and Practice of Pulse Plating*, (Eds.:J.-C. Puippe, F. Leaman), American Electroplaters and Surface Finishers Society, Orlando, **1986**.
[11] M. Bukowski, F. Endres, R. Hempelmann, H. Natter, *Ger. Offen* **2002**, DE 101 08 893.0.
[12] P. Scherrer, *Göttinger Nachrichten* **1918**, *2*, 98–100.
[13] C. E. Krill, R. Birringer, *Phil. Mag. A* **1998**, *77*, 621–640.
[14] H. Natter, M. Schmelzer, M.-S. Löffler, C. E. Krill, A. Fitch, R. Hempelmann, *J. Phys. Chem. B* **2000**, *104*, 2467–2476.
[15] F. Grum, D. J. Paine, J. L. Simonds, *J. Opt. Soc. Am.* **1971**, *61*, 70–78.
[16] P. Drinker, *J. Ind. Hyg. Toxicol.* **1925**, *7*, 305–311.
[17] E. J. Meehan, W. H. Beattie, *J. Phys. Chem.* **1960**, *64*, 1006–1016.
[18] C. G. Granqvist, R. A. Buhrman, *J. Appl. Phys.* **1976**, *47*, 2200–2219.
[19] M. Bukowski, F. Endres, R. Hempelmann, H. Natter, unpublished results.
[20] E. Budevski, G. Staikov, W. J. Lorenz in *Electrochemical Phase Formation and Growth*, VCH, Weinheim, **1996**.
[21] J. C. Li, S. H. Nan, Q. Jiang, *Surf. Coat. Technol.* **1998**, *106*, 135–139.
[22] a) H. Kono, *J. Pharm. Belg.J. Phys. Soc. Japan* **1958**, *13*, 1444–1451; b) JCPDS No. 11–0416.

 © 2003 Wiley-VCH Verlag GmbH & Co. KGaA, Weinheim

C–H Activation in Ca Complexes

Intramolecular C–H Activation in Alkaline-Earth Metal Complexes**

*Sjoerd Harder**

In the last decade the number of σ- and π-bonded organometallic complexes of the heavier alkaline-earth metals (Ca, Sr, Ba) has increased tremendously. Although studies on the reactivities of this group of organometallic compounds are still scarce, it is clear that they are more than just "heavy

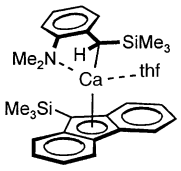
[*] Priv.-Doz. Dr. S. Harder
Fachbereich Chemie, Universität Konstanz
Postfach 5560, M738, 78457 Konstanz (Germany)
Fax: (+49) 7531-883137
E-mail: harder@chemie.uni-konstanz.de

[**] This work was generously supported by the Deutsche Forschungsgemeinschaft and BASF-AG (Ludwigshafen, Germany). Prof. Dr. H.-H. Brintzinger (Universität Konstanz) is kindly acknowledged for stimulating discussions. I also would like to thank Dr. M. H. Prosenc and the Rechenzentrum Hamburg for "long-distance" CPU time.

Supporting information for this article is available on the WWW under http://www.angewandte.org or from the author.

 © 2003 Wiley-VCH Verlag GmbH & Co. KGaA, Weinheim DOI: 10.1002/anie.200351055

Grignard complexes".[1–3] Their structural and chemical behavior has often been compared to that of early d-block and especially lanthanide organometallic compounds.[4] The herein described observation of C–H activation in a benzylcalcium complex represents another analogy between the chemistry of alkaline-earth and early d- and f-block metals.



1

We recently introduced the heteroleptic benzylcalcium compound **1** as an initiator for the living syndiotactic polymerization of styrene.[5] In order to improve the syndioselectivity we are currently varying the spectator ligand. The success of the β-diketiminate (nacnac) ligand in polymerization catalysis[6] prompted us to explore its use in heteroleptic benzylcalcium initiators.

Heteroleptic alkaline-earth complexes can be prepared by ligand-exchange between two homoleptic compounds: $R_2M + R'_2M \rightleftarrows 2\,RMR'$.[7] Such Schlenk equilibria are controlled by steric as well as electronic effects (for **1** the Schlenk equilibrium is completely on the side of the heteroleptic complex).[5] On the basis of the steric bulk of the dipp-nacnac ligand (dipp = *N*,*N*′-bis(2,6-diisopropylphenyl)), we anticipated the Schlenk equilibrium between complex **2** and the sterically crowded [Ca(dipp-nacnac)$_2$] (**3**) to be on the side of the heteroleptic complex (Scheme 1). However, at ambient temperature a mixture of **2** and **3** showed no ligand exchange at all. Structural analyses of **3** showed that this complex is effectively stabilized by C–H···π interactions between isopropyl groups and aryl rings.[8] These stabilizing interactions might be responsible for the unexpected behavior of **3** in ligand-exchange reactions. When the reaction mixture of **2** and **3** was heated at 50 °C, the heteroleptic species **4**[9] formed first. One day later large light-yellow crystalline blocks precipitated, which crystal structure analysis revealed to be the dimeric calcium complex **5** with bridging dipp-nacnac dianions (Scheme 1). This complex was formed by deprotonation of a methyl group in the backbone of the anionic dipp-nacnac ligand by the benzyl anion.

The crystal structure of the centrosymmetric dimer **5** (Figure 1) shows a dipp-nacnac ligand in an unusual N,N-*trans* conformation. The dianionic ligand coordinates to two different Ca^{2+} ions in unequal modes. At first sight it seems to serve as an 1-azapentadienyl ligand as well as an 1-azaallyl ligand (Figure 2). The coordination sphere of calcium is completed with one thf ligand.

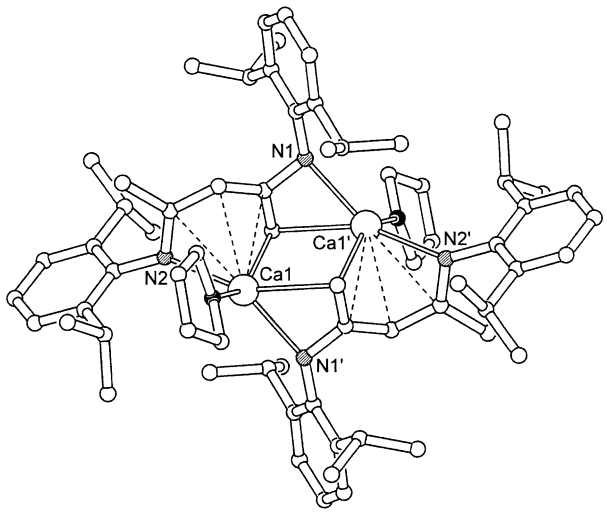


Figure 1. Crystal structure of dimer **5**.

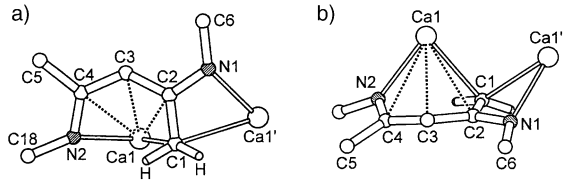
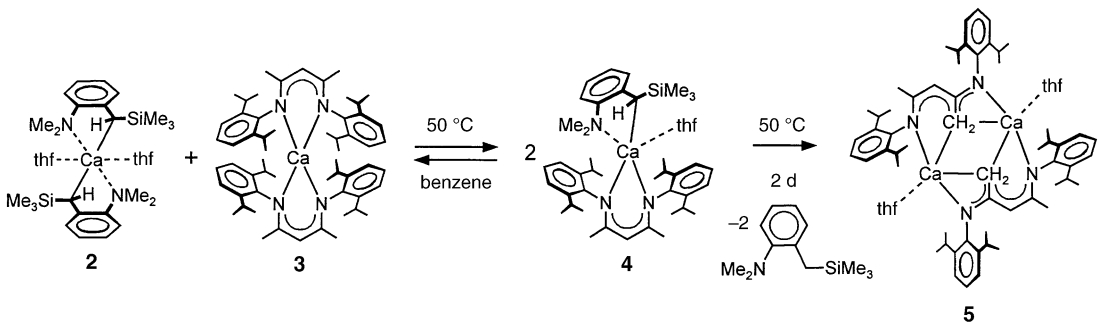


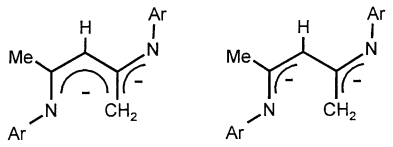
Figure 2. Two views of the partial structure of the nacnac^{2-} ion in **5**. Only the hydrogen atoms at C1 are shown. Selected bond lengths [Å]: Ca1-C1 2.594(3), Ca1-C2 2.824(2), Ca1-C3 2.777(3), Ca1-C4 2.832(4), Ca1-N2 2.418(2), Ca1′-C1 2.662(3), Ca1′-C2 2.793(2), Ca1′-N1 2.361(2), C1-C2 1.418(4), C2-C3 1.447(3), C2-N1 1.364(3), C3-C4 1.404(3), C4-N2 1.340(3).

Although complexes with azaallyl ligands are well-precedented,[10] the structural information on azapentadienyl–metal coordination is rather scarce.[11] The 2,4-disubstituted azapentadienyl moiety in **5** deviates significantly from planarity (Figure 2b). Average and maximum deviations from the least-squares plane N1-C1-C2-C3-C4-C5-N2 are 0.132 Å and 0.233 Å, respectively. Similar deviations have been observed in the monoanionic dipp-nacnac ligand.[8] The bond lengths within the dipp-nacnac^{2-} framework, however, suggest an electronic situation different from that in **6**. The long C2–C3 bond (1.447(3) Å) indicates that the ligand should not be regarded as a delocalized eight-electron azapentadienyl/azaallyl dianion, but rather as a combination



Scheme 1. Ligand exchange between **2** and **3** to give heteroleptic complex **4** and formation of dimer **5**.

 © 2003 Wiley-VCH Verlag GmbH & Co. KGaA, Weinheim



of two four-electron azaallyl anions linked by the C2–C3 bond (**7**). Both 2-substituted azaallyl substructures, N1/C1/C2/C3 and N2/C3/C4/C5, are largely planar and are tilted with respect to each other around the long C2–C3 bond with an interplanar angle of 20.6(2)°. The C–C and C–N distances within the azaallyl units compare very well to those observed in a homoleptic [Mg(azaallyl)$_2$] complex (d(C–C) = 1.406(6) Å, d(C–N) = 1.347(5) Å).[10b] The aryl substituents on N are turned slightly out of the azaallyl planes, as is often observed in this class of ligands. The carbon atoms that bridge the Ca^{2+} ions display hybdridization between sp^2 and sp^3 (the sum of the valence angles is 345(1)°).

Geometry optimization of a nacnac^{2-} model ion by ab initio methods[12] results in a planar structure (Figure 3) in which most bond lengths compare well to those in the crystal

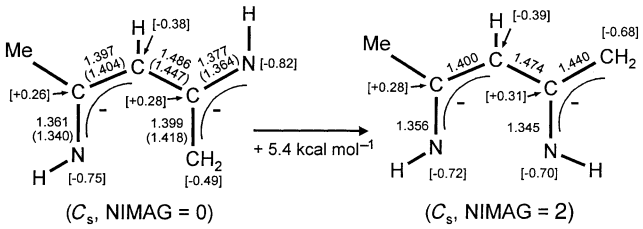
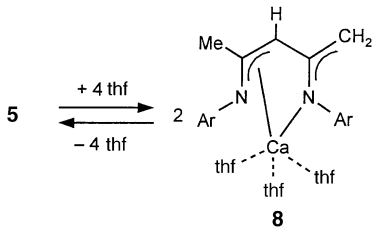


Figure 3. MP2/6-31+G*-optimized structures of the nacnac^{2-} ion. NIMAG = Number of imaginary frequencies. The N,N-*trans*-conformation (left) corresponds to the energy minimum (NIMAG = 0). Values in parentheses are the bond lengths [Å] in the crystal structure. Values in square brackets are the group charges (sum of the charges of the heavy atom and the attached hydrogen atoms; NPA method).

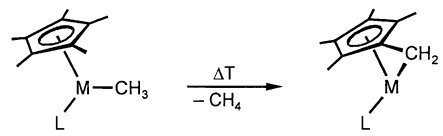
structure. Only the C–C bond connecting the azaallyl units appears longer in the calculated structure of the free nacnac^{2-} ion. The N,N-*trans* conformation is 5.4 kcal mol^{-1} lower in energy than the planar N,N-*cis* conformation. This is presumably due to electrostatic repulsion between the negatively charged nitrogen atoms, which bear most of the negative charge.

The extremely air-sensitive complex **5** is insoluble in aromatic solvents but dissolves slightly in THF. The ^{1}H NMR spectrum of a freshly prepared solution of **5** in [D$_8$]THF shows slow conversion of one (dipp-nacnac)Ca species into another; equilibrium is reached after 24 h. All NMR data point to an equilibrium between species containing the N,N-*trans* and N,N-*cis* conformations,[13] which is strongly temperature- and concentration-dependent (see Experimental Section). It is therefore likely that the dimer **5** is in equilibrium with a monomeric complex **8** in N,N-*cis* conformation (Scheme 2).[14] The preference for the N,N-*cis* conformation in **8** could be due to the advantageous bridging of Ca^{2+} between the most electronegative nitrogen atoms.

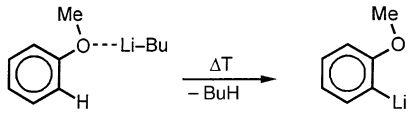


Scheme 2. Equilibrium between dimer **5** and monomer **8** in THF. Ar = 2,6-diisopropylphenyl.

The deprotonation reaction described in Scheme 1 can be classified as an intramolecular C–H activation or cyclometalation, a reaction type that is common for early transition-metal complexes.[15] The formation of "tuck-in" complexes (Scheme 3) are the best documented examples of intramolecular C–H activation and are well-known for metal complexes of groups 3b (including the lanthanides),[15c,d] 4b,[15e–g] and 5b.[15h] However, the reaction in Scheme 1 can also be described as a directed metalation reaction. The *ortho*-directed lithiation of methoxybenzene[16] (Scheme 4) is an example of regioselective deprotonation via an intermediate coordination complex. Such complex-induced proximity effects (CIPEs) are widely used in stereo- and regioselective organic syntheses.[17] The unique position of calcium between the alkali metals and the early transition metals apparently allows a comparison of its chemistry to that of both groups. The fact that intramolecular C–H activation was initially termed *ortho*-metalation[15a,b] illustrates its relation to *ortho*-directed lithiation.



Scheme 3. Formation of "tuck-in" complexes.



Scheme 4. *ortho*-Directed lithiation of methoxybenzene.

It should be stressed, however, that the second deprotonation of the negatively charged dipp-nacnac ligand in good yield (61%) is an unusual reaction.[18] Whereas, twofold deprotonation of the acetylacetonato ligand (acac) is well-known,[19] attempted double deprotonation of dipp-nacnacH with four equivalents (a threefold excess!) of the superbase mixture *n*BuLi/KO*t*Bu in THF and a subsequent quench with deuterated methanol resulted only in limited deuteration of the methyl group (< 5%).[20] Also, reaction of (*o*-Me$_2$N-C$_6$H$_4$)CHSiMe$_3$$^-K^+$ with dipp-nacnac$^-$K$^+$ does not result in formation of the dipp-nacnac^{2-} ion. For these reasons the

 © 2003 Wiley-VCH Verlag GmbH & Co. KGaA, Weinheim

expression C–H activation for the reaction in Scheme 1 is certainly not out of place.

The observation of C-H activation in benzylcalcium complexes is another pillar in the bridge that closes the gap between the chemistry of alkaline-earth and *d*(*f*)-block metals.

Experimental Section

Crystalline $[Ca\{(o\text{-}Me_2N\text{-}C_6H_4)CHSiMe_3\}_2(thf)_2]$[5a] (**2**, 3.70 g, 6.19 mmol) and $[Ca(dipp\text{-}nacnac)_2]$[8] (**3**, 5.30 g, 6.06 mmol) were dissolved in benzene (35 mL) and heated at 50 °C. After one night at this temperature light-yellow crystals of **5** started to form. Large crystalline blocks of **5** were isolated after a reaction time of two days: 3.98 g, 3.77 mmol, 61 %. The reaction also proceeds at room temperature (the formation of crystals starts after one month).

^{1}H NMR (600 MHz, [D$_8$]THF, 20 °C). Dimer **5** with an N,N-*trans* conformation: $\delta = 0.91$ (d, $^3J(H,H) = 6.8$ Hz, 3H; *i*Pr-Me), 0.96 (d, $^3J(H,H) = 6.9$ Hz, 3H; *i*Pr-Me), 1.07 (d, $^3J(H,H) = 6.9$ Hz, 3H; *i*Pr-Me), 1.11 (d, $^3J(H,H) = 6.7$ Hz, 3H; *i*Pr-Me), 1.13 (d, $^3J(H,H) = 6.8$ Hz, 3H; *i*Pr-Me), 1.19 (d, $^3J(H,H) = 6.9$ Hz, 3H; *i*Pr-Me), 1.20 (d, $^3J(H,H) = 6.8$ Hz, 3H; *i*Pr-Me), 1.21 (d, $^3J(H,H) = 6.7$ Hz, 3H; *i*Pr-Me), 1.49 (s, 3H; Me_{C5}), 1.77 (m, thf), 2.06 (dd, $^2J(H,H) = 4.7$ Hz and $^4J(H,H) = 1.3$ Hz, 1H; CH_2), 3.09 (h, $^3J(H,H) = 6.8$ Hz, 1H; *i*Pr-CH), 3.23 (h, $^3J(H,H) = 6.7$ Hz, 1H; *i*Pr-CH), 3.46 (h, $^3J(H,H) = 6.9$ Hz, 1H; *i*Pr-CH), 3.52 (h, $^3J(H,H) = 6.8$ Hz, 1H; *i*Pr-CH), 3.58 (m, thf), 4.03 (d, $^2J(H,H) = 4.7$ Hz, 1H; CH_2), 4.11 (d, $^4J(H,H) = 1.3$ Hz, 1H; CH_{C3}), 6.69–7.12 ppm (m, 6H; aryl). Monomer **8** with an N,N-*cis* conformation: $\delta = 1.11$ (d br, $^3J(H,H) = 6.8$ Hz, 6H; *i*Pr-Me), 1.16 (d br, $^3J(H,H) = 6.9$ Hz, 6H; *i*Pr-Me), 1.21 (d br, $^3J(H,H) = 6.8$ Hz, 6H; *i*Pr-Me), 1.27 (d br, $^3J(H,H) = 6.8$ Hz, 6H; *i*Pr-Me), 1.55 (s, 3H; Me_{C5}), 1.77 (m, thf), 2.04 (d, $^2J(H,H) = 2.9$ Hz, 1H; CH_2), 2.83 (d, $^2J(H,H) = 2.9$ Hz, 1H; CH_2), 3.58 (m, thf), 3.68 (h br, $^3J(H,H) = 6.9$ Hz, 2H; *i*Pr-CH), 3.76 (h br, $^3J(H,H) = 6.8$ Hz, 2H; *i*Pr-CH), 4.77 (s, 1H; CH_{C3}), 6.69–7.12 ppm (m, 6H; aryl). The N,N-*trans*/N,N-*cis* ratio in a 0.028 M solution of **5** in THF at 20 °C is 35:65 (66:34 at 60 °C; at this temperature no coalescence of the CH_2 signals is observed, indicating slow rotation around the C–CH_2 bond). This ratio is also concentration dependent: a 0.014 M solution at 20 °C shows a ratio of 19:81.

Crystal structure determination of **5**:[21] Measurement on an Enraf Nonius CAD4, $T = -120$ °C, $Mo_{K\alpha}$, $2\theta_{max} = 52.2°$, 6149 independent reflections, 3912 reflections observed with $I > 2\sigma(I)$. Crystal data: orthorhombic, space group *Pbca*, $a = 13.6171(9)$, $b = 21.2667(19)$, $c = 21.4561(17)$ Å, $V = 6213.5(8)$ Å^3, $C_{66}H_{96}Ca_2N_4O_2$, $M_r = 1057.63$, $Z = 4$, $R1 = 0.0507$, $wR2 = 0.1386$, GOF = 1.00, $\rho_{max} = 0.40$ e Å^{-3}, $\rho_{min} = -0.32$ e Å^{-3}, $\mu = 0.228$ mm^{-1} (no absorption correction applied). The CH_2 hydrogens were observed and refined freely. CCDC-200810 contains the supplementary crystallographic data for this paper. These data can be obtained free of charge via www.ccdc.cam.ac.uk/conts/retrieving.html (or from the Cambridge Crystallographic Data Centre, 12, Union Road, Cambridge CB2 1EZ, UK; fax: (+44) 1223-336-033; or deposit@ccdc.cam.ac.uk).

Received: January 30, 2003 [Z51055]

Keywords: alkaline-earth metals · calcium · carbanions · C–H activation · cyclometalation

[1] D. J. Burkey, T. P. Hanusa, *Comments Inorg. Chem.* **1995**, *17*, 41.
[2] Reviews: a) T. P. Hanusa, *Coord. Chem. Rev.* **2000**, *210*, 329; b) J. S. Alexander, K. Ruhlandt-Senge, *Eur. J. Inorg. Chem.* **2002**, 2761.
[3] a) A. Yanagisawa, S. Habaue, K. Yasue, H. Yamamoto, *J. Am. Chem. Soc.* **1994**, *116*, 6130; b) M. L. Hays, T. P. Hanusa, *Tetrahedron Lett.* **1995**, *36*, 2435; c) K. Ruhlandt-Senge, J. S. Alexander, *Angew. Chem.* **2001**, *113*, 2732; *Angew. Chem. Int. Ed.* **2001**, *40*, 2658.
[4] a) R. A. Williams, T. P. Hanusa, J. C. Huffman, *Organometallics* **1990**, *9*, 1128; b) R. A. Williams, T. P. Hanusa, J. C. Huffman, *J. Am. Chem. Soc.* **1990**, *112*, 2454; c) M. Rieckhoff, U. Pieper, D. Stalke, F. T. Edelmann, *Angew. Chem.* **1993**, *105*, 1102; *Angew. Chem. Int. Ed. Engl.* **1993**, *32*, 1079; d) D. Stalke, *Angew. Chem.* **1994**, *106*, 2256; *Angew. Chem. Int. Ed. Engl.* **1994**, *33*, 2168; e) K. Izod, W. Clegg, S. T. Liddle, *Organometallics* **2000**, *19*, 3640; f) V. Knapp, G. Müller, *Angew. Chem.* **2001**, *113*, 187; *Angew. Chem. Int. Ed.* **2001**, *40*, 183.
[5] S. Harder, F. Feil, A. Weeber, *Organometallics* **2001**, *20*, 1044;b) S. Harder, F. Feil, K. Knoll, *Angew. Chem.* **2001**, *113*, 4391; *Angew. Chem. Int. Ed.* **2001**, *40*, 4261.
[6] a) W.-K. Kim, M. J. Fevola, L. M. Liable-Sands, A. L. Rheingold, K. H. Theopold, *Organometallics* **1998**, *17*, 4541; b) P. H. M. Budzelaar, A. B. van Oort, A. G. Orpen, *Eur. J. Inorg. Chem.* **1998**, 1485; c) C. E. Radzewich, I. A. Guzei, R. F. Jordan, *J. Am. Chem. Soc.* **1999**, *121*, 8673; d) J. Prust, A. Stasch, W. Zheng, H. W. Roesky, E. Alexopoulos, I. Usón, D. Böhler, T. Schuchardt, *Organometallics* **2001**, *20*, 3825; e) V. C. Gibson, J. A. Segal, A. J. P. White, D. J. Williams, *J. Am. Chem. Soc.* **2000**, *122*, 7120; f) M. H. Chisholm, J. C. Huffman, K. Phomphrai, *J. Chem. Soc. Dalton Trans.* **2001**, 222; g) B. M. Chamberlain, M. Cheng, D. R. Moore, T. M. Ovitt, E. B. Lobkovsky, G. W. Coates, *J. Am. Chem. Soc.* **2001**, *123*, 3229.
[7] a) K. F. Tesh, D. J. Burkey, T. P. Hanusa, *J. Am. Chem. Soc.* **1994**, *116*, 2409; b) D. J. Burkey, E. K. Alexander, T. P. Hanusa, *Organometallics* **1994**, *13*, 2773.
[8] S. Harder, *Organometallics*, **2002**, *21,* 3782.
[9] The ^{1}H NMR spectrum of the reaction mixture shows the homoleptic species **2** and **3**, as well as a new species (**4**) which contains the $(o\text{-}Me_2N\text{-}C_6H_4)CHSiMe_3^-$ ion and the dipp-nacnac ligand and could not be isolated.
[10] a) Review: M. F. Lappert, D.-S. Liu, *J. Organomet. Chem.* **1995**, *500*, 203; b) C. F. Caro, P. B. Hitchcock, M. F. Lappert, *Chem. Commun.* **1999**, 1433; c) W. P. Leung, H. Cheng, D.-S. Liu, Q.-G. Wang, T. C. W. Mak, *Organometallics* **2000**, *19*, 3001.
[11] a) J. R. Bleeke, S. T. Luaders, K. D. Robinson, *Organometallics* **1994**, *13*, 1592; b) J. A. Gutierret, M. E. N. Clemente, M. A. Paz-Sandoval, A. M. Arif, R. D. Ernst, *Organometallics* **1999**, *18*, 1068.
[12] MP2/6-31 + G*-optimized structures with energies corrected for zero-point vibrations: E(N,N-*trans*) = −303.533785 Hartree, E(N,N-*cis*) = −303.525245 Hartree. Gaussian 98 (Revision A.7), M. J. Frisch, G. W. Trucks, H. B. Schlegel, G. E. Scuseria, M. A. Robb, J. R. Cheeseman, V. G. Zakrzewski, J. A. Montgomery, R. E. Stratmann, J. C. Burant, S. Dapprich, J. M. Millam, A. D. Daniels, K. N. Kudin, M. C. Strain, O. Farkas, J. Tomasi, V. Barone, M. Cossi, R. Cammi, B. Mennucci, C. Pomelli, C. Adamo, S. Clifford, J. Ochterski, G. A. Petersson, P. Y. Ayala, Q. Cui, K. Morokuma, D. K. Malick, A. D. Rabuck, K. Raghavachari, J. B. Foresman, J. Cioslowski, J. V. Ortiz, B. B. Stefanov, G. Liu, A. Liashenko, P. Piskorz, I. Komaromi, R. Gomperts, R. L. Martin, D. J. Fox, T. Keith, M. A. Al-Laham, C. Y. Peng, A. Nanayakkara, C. Gonzalez, M. Challacombe, P. M. W. Gill, B. G. Johnson, W. Chen, M. W. Wong, J. L. Andres, M. Head-Gordon, E. S. Replogle, J. A. Pople, Gaussian, Inc., Pittsburgh, PA, **1998**.
[13] All signals were assigned by means of two-dimensional NMR spectroscopic methods. The existence of the N,N-*cis* conformer was proven by the presence of a strong NOE signal between the CH proton in the nacnac bridge and one of the protons in the CH_2^- group. The N,N-*trans* conformer does not show this NOE signal. The latter species shows a long-range ^4J(H,H) coupling of

 © 2003 Wiley-VCH Verlag GmbH & Co. KGaA, Weinheim

1.3 Hz between the CH proton in the nacnac bridge and one of the protons in the CH_2^- group. This is typical for H-C-C-C-H substructures with a W geometry.

[14] An increase in temperature shifts the equilibrium to **5**, the side with the least solvation and highest entropy. A decrease in the concentration shifts the equilibrium to the least aggregated species, that is, monomer **8**.

[15] a) Review: I. P. Rothwell, *Polyhedron* **1985**, *4*, 177; b) M. I. Bruce, *Angew. Chem.* **1977**, *89*, 75; *Angew. Chem. Int. Ed. Engl.* **1977**, *16*, 73; c) M. E. Thompson, J. E. Bercaw, *Pure Appl. Chem.* **1984**, *56*, 1; d) W. J. Evans, T. A. Ulibarri, J. W. Ziller, *Organometallics* **1991**, *10*, 134; e) J. E. Bercaw, R. H. Marvich, L. G. Bell, H.-H. Brintzinger, *J. Am. Chem. Soc.* **1972**, *94*, 1219; f) J. W. Pattiasina, C. E. Hissink, J. L. de Boer, A. Meetsma, J. H. Teuben, *J. Am. Chem. Soc.* **1985**, *107*, 7758; g) A. R. Bulls, W. P. Schaefer, M. Serfas, J. E. Bercaw, *Organometallics* **1987**, *6*, 1219; h) P. N. Riley, J. R. Parker, P. E. Fanwick, I. P. Rothwell, *Organometallics* **1999**, *18*, 3579.

[16] W. Bauer, P. von R. Schleyer, *J. Am. Chem. Soc.* **1989**, *111*, 7191.

[17] a) P. Beak, A. I. Meyers, *Acc. Chem. Res.* **1986**, *19*, 356; b) G. W. Klumpp, *Recl. Trav. Chim. Pays-Bas* **1986**, *105*, 1; c) V. Snieckus, *Chem. Rev.* **1990**, *90*, 879.

[18] To date, two examples of attack at a nacnac ligand have been published. a) Cycloaddition of ethylene to a nacnac ligand: C. E. Radzewich, M. P. Coles, R. F. Jordan, *J. Am. Chem. Soc.* **1998**, *120*, 9384; b) Intramolecular C–H activation of the *N*-aryl *ortho* proton in a $[Zr(nacnac)(CH_2Ph)_3]$ complex has been reported: B. Qian, W. J. Scanlon IV, M. R. Smith III, D. H. Motry, *Organometallics* **1999**, *18*, 1693.

[19] a) J. von Seyerl, G. Huttner, K. Krüger, *Z. Naturforsch. B* **1980**, *35*, 1552; b) W. Clegg, L. Horsburgh, R. E. Mulvey, M. J. Ross, *Angew. Chem.* **1995**, *107*, 1353; *Angew. Chem. Int. Ed. Engl.* **1995**, *34*, 1233.

[20] The reaction mixture was concentrated to dryness, CD_3OD was added, and the sample was analyzed immediately by ^1H NMR spectroscopy. Only traces of CH_2D could be detected, whereas a quench of **5** with CD_3OD shows the expected 1:1 ratio of CH_3/CH_2D. The NMR spectra must be measured immediately after quenching, because under basic conditions dipp-nacnac in CD_3OD is slowly deuterated in the Me groups.

[21] A. L. Spek, PLATON, A Multipurpose Crystallographic Tool, Universiteit Utrecht, Utrecht, Nederland, **2000**.

 © 2003 Wiley-VCH Verlag GmbH & Co. KGaA, Weinheim

Sudden-Polarization Effects

The Sudden-Polarization Effect and its Role in the Ultrafast Photochemistry of Ethene**

*Alexandra Viel, Robert P. Krawczyk, Uwe Manthe, and Wolfgang Domcke**

The term "sudden polarization", which describes the charge separation in excited singlet states of twisted polyenes, especially of ethene, was introduced in the mid-1970s by Salem.[1] The ionic character and the easy polarizability of these valence excited states of alkenes upon a small perturbation was pointed out as early as 1971 by Wulfman and Kumei.[2] Bonačić-Koutecký et al.,[3] in the mid-1970s, were the first to perform an ab initio study of the charge separation in 90°-twisted ethene as a function of an internal perturbation: the one-sided pyramidalization of a CH_2 group (D_{2d} geometry). To our knowledge, all the following studies of the sudden-polarization effect of ethene considered only one-sided pyramidalization.[4–8] We discuss here the effects of one-sided scissoring as another internal perturbation and show that the transfer of electronic charge between the CH_2 groups is first order, whereas the effect is second order in pyramidalization. Moreover, we show that the one-sided scissoring mode plays an essential role in the nonadiabatic photochemistry of ethene.

The sudden-polarization effect can be understood as the direct consequence of a small dissymmetry of the molecule. Ethene has a planar geometry in the ground state, and belongs to the symmetry group D_{2h}. In this group, the delocalized molecular orbitals, π and π^*, are b_{3u} and b_{2g} symmetric, respectively (within Mulliken's axis definition[9]). The three relevant valence states[9] N (π^2), V ($\pi\pi^*$), and Z (π^{*2}) thus have A_g, B_{1u}, and A_g symmetry, respectively. In the planar geometry, the singly excited state lies energetically well below the doubly excited state. The symmetry is lowered to D_2 upon torsion of the CH_2 groups around the C–C bond. The $\pi(\pi^*)$ orbitals transform as $b_3(b_2)$. In this group, both π and π^* belong to the e representation. In this particular geometry, any linear combination of the π and π^* orbitals is acceptable, in particular the orbitals ϕ_r and ϕ_l which are localized on the "right" and "left" CH_2 groups, respectively. Since the two CH_2 groups are rigorously symmetry equivalent, the molecular orbitals have to reproduce a zero dipole moment. The symmetrized linear combinations $\phi_r^2-\phi_l^2$ and $\phi_r^2+\phi_l^2$, which have B_2 and A_1 symmetry, respec-

[*] Prof. Dr. W. Domcke, A. Viel, R. P. Krawczyk, Priv.-Doz. Dr. U. Manthe
Institut für Physikalische und Theoretische Chemie
Technische Universität München
85747 Garching (Germany)
Fax: (+49) 89-89-28-91-36-22
E-mail: wolfgang.domcke@ch.tum.de

[**] A.V. acknowledges financial support from a Marie Curie fellowship from the European Community program (Improving Human Research Potential and the Socio-economic Knowledge Base, no. HPMFCT-2000-00840). U.M. and W.D. acknowledge financial support from the Deutsche Forschungsgemeinschaft.

 © 2003 Wiley-VCH Verlag GmbH & Co. KGaA, Weinheim DOI: 10.1002/anie.200351193

tively, are acceptable solutions. They correspond to two excited states, V and Z, which do not have to be degenerate by symmetry. They are nevertheless close in energy, with the Z state being approximately 0.1 eV below the V state.[6] The potential-energy functions of the V and Z states cross at a torsion coordinate of $\varphi \approx 82°$,[6,10] since the Z state is much higher in energy than the V state in a planar geometry. This crossing turns into a conical intersection if symmetry-breaking coordinates are considered.

If, for some reason, one side of the molecule is distinguished, an asymmetry of the electronic wave functions results, which leads to charge separation.[11] As a consequence of the small overlap between the orbitals on the "left" and "right" sides and the small energy difference between the V and Z states of D_{2d} ethene, the localization of the charge is pronounced, even for small perturbations. Both one-sided pyramidalization as well as one-sided scissoring lower the D_{2d} symmetry of perpendicular ethene to C_s and C_{2v}, respectively, which breaks the left-right symmetry and induces a nonzero dipole moment. The dipole moment is a measure of the non-adiabatic coupling strength and is related to the steepness of the cone of the conical intersection.

The complexity of the electronic structure of the excited states of ethene (resulting from pronounced valence–Rydberg mixing and strong multireference character of the electronic wave functions[12–15]) means that the ab initio determination of the energies and dipole moments of the three lowest valence states is not an easy task, and has been the subject of many publications.[3,5–7,11] Figure 1 shows the dipole moment μ_z of the V and Z states obtained at the CASSCF level with a cc-pVTZ basis set[16] as a function of one-sided pyramidalization ϑ (Figure 1 a) and one-sided scissoring α (Figure 1 b) for $\varphi =$ 90°. The "upward" and "downward" pyramidalizations are symmetry-equivalent, while the reduction and enlargement of the HCH angles relative to the ground state are not. In the case of the single-sided pyramidalization, any physical observable must be an even function for small changes in ϑ, while in the case of the one-sided scissoring it must depend linearly on small displacements of α. In Figure 1 a, the quadratic dependence of the dipole monent μ_z on ϑ can be clearly seen. Figure 1 b shows clearly the corresponding linear dependence of μ_z on the one-sided scissoring α. For both curves, the beginning of saturation (visible by the change of slope) occurs at around $\mu_z = 1$ au, which corresponds to $\vartheta \simeq$ 20° and $\alpha - \alpha_0 \simeq 10°$. $\alpha_0 = 117.3°$ is the HCH angle in the ground state of ethene.

The linear dependence of μ_z on α, versus a quadratic dependence of μ_z on ϑ, makes the polarization induced by one-sided scissoring more pronounced than that induced by one-sided pyramidalization for small distortions. The slope of $\mu_z(\alpha)$ is even larger for $\varphi \simeq 82°$, as one expects from the smaller energy difference between the V and Z states at this torsional angle. The magnitude of the dipole moment in the saturation region is very similar for both distortions: $\mu =$ 1.4 au for $\vartheta = 60°$, $\mu = 1.2$ au for $\alpha - \alpha_0 = 30°$.

The direction of the polarization induced by the scissoring motion is correctly predicted by an electronic pair repulsion model. The ab initio calculations for the (lower) Z state show a positive charge at the CH_2 group with the smaller scissoring angle. At the D_{2d} geometry, the H atoms of one CH_2 group are located in the same plane as the 2p orbital of a carbon atom of the other CH_2 group. Thus, electronic repulsion is minimized if the scissoring angle of the CH_2 group opposite to the negatively charged carbon atom is reduced.

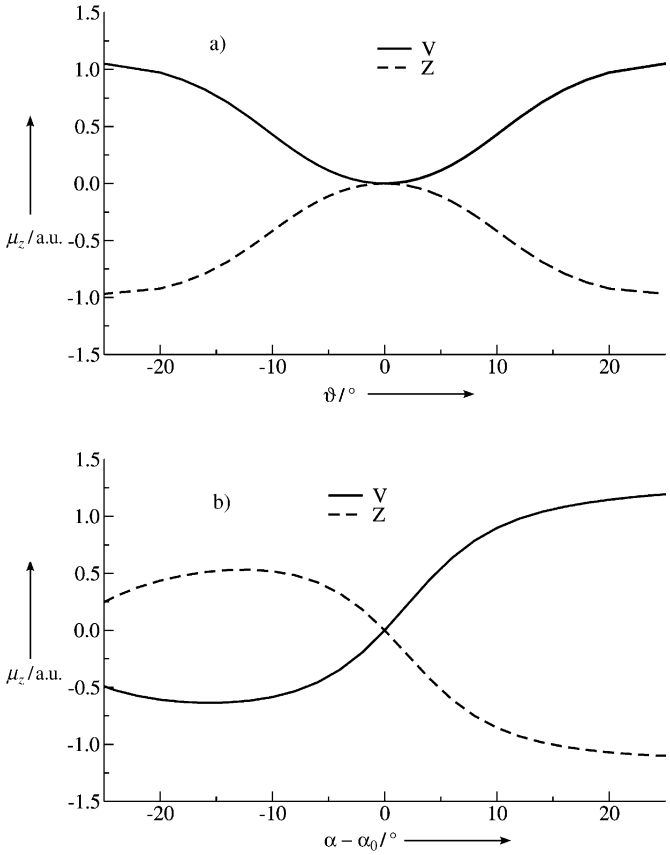


Figure 1. Dipole moment (in atomic units, ea_0) along the C–C bond for the V and Z states for $\varphi = 90°$ as a function of pyramidalization (a) and scissoring (b).

The sudden-polarization effect implies a pronounced modification of the electronic wave functions by a small perturbation of the symmetry. This rapid change of the electronic structure in response to small nuclear deformations implies a strong non-adiabatic coupling between the two excited states for near-perpendicular (D_{2d}) geometries.[17] The effect of this coupling on the nonradiative decay of the V state has been investigated by two-dimensional wave-packet propagations of the photoinduced nuclear motion on the non-adiabatically coupled potential-energy surfaces of the three valence-type singlet states. A diabatic representation of the N, V, and Z states, including 6 of the 12 vibrational degrees of freedom, has been developed recently based on accurate ab initio data (CASPT2).[18] In this model, the diabatic V and Z states are coupled linearly by the antisymmetric scissoring mode and quadratically by the pyramidalization.

The impact of the sudden-polarization effect on the photochemical dynamics has been demonstrated by performing two calculations—one with one-sided scissoring and the other with one-sided pyramidalization, both indicating the

 © 2003 Wiley-VCH Verlag GmbH & Co. KGaA, Weinheim

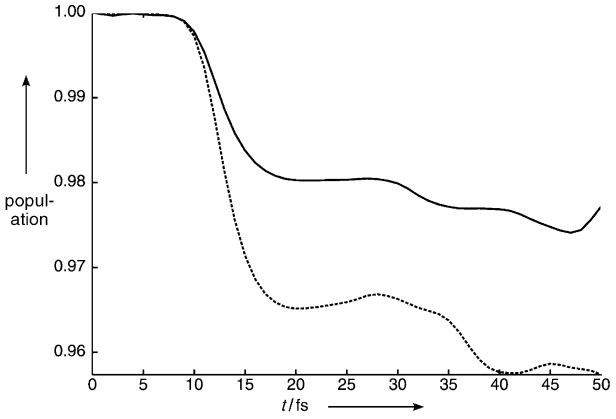


Figure 2. Time evolution of the population probability of the V state for a φ,ϑ (full line) and a φ,α (dotted line) wave-packet propagation, respectively.

torsion. All other coordinates have been kept frozen at their ground-state equilibrium values. Figure 2 shows the time evolution of the population probability of the initially ($t=0$) prepared diabatic $\pi\pi^*$ state (in D_2 symmetry this corresponds to the V state) during the first 50 fs. After vertical electronic excitation from the N to the V state, the population probability stays close to unity during the first 7 fs. After this period, the population decreases in both calculations—this corresponds to a transfer of population between the two excited adiabatic states—but the drop of the population is nearly twice as large in the φ,α calculation than in the φ,ϑ calculation. The initial 7 fs correspond to the time which the torsional wave packet, initially located at the planar geometry, needs to reach the D_{2d} geometry and thus the region of strong non-adiabatic coupling between the V and Z states. The coupling between the V and Z states is more efficient in the φ,α case than in the φ,ϑ case, which reflects the fact that the vibronic coupling is linear in the former case, but quadratic in the latter case.

To conclude, we have shown that the sudden polarization in D_{2d} ethene is first order in the one-sided scissors deformation, and second order in the one-sided pyramidalization. Although it has been emphasized in the literature that *any* geometrical distortion breaking the D_{2d} symmetry will produce a charge separation, the distinguished role of the one-sided scissoring has not been recognized. Following the initial work of Bonačić-Koutecký et al.[3], all subsequent studies have focused on the pyramidalization. The relevance of the first-order vibronic coupling between the V and Z states by the scissors coordinate for the photoinduced dynamics of ethene has been demonstrated by quantum wave-packet calculations. These calculations reveal that the linear coupling between the V and Z states by the scissoring mode provides a substantially faster flow of the electronic population probability out of the initially prepared V state than the quadratic coupling by the pyramidalization mode.

Received: February 17, 2003
Revised: April 24, 2003 [Z51193]

Keywords: ethene · photochemistry · polarization effects · theoretical chemistry

[1] L. Salem, *Science* **1976**, *191*, 822.
[2] C. E. Wulfman, S. Kumei, *Science* **1971**, *172*, 1061.
[3] V. Bonačić-Koutecký, P. Bruckmann, P. Hiberty, J. Koutecký, C. Leforestier, L. Salem, *Angew. Chem.* **1975**, *87*, 599; *Angew. Chem. Int. Ed. Engl.* **1975**, *14*, 575.
[4] G. Berthier, B. Levy, L. Praud, *Gazz. Chim. Ital.* **1978**, *108*, 377.
[5] B. R. Brooks, H. F. Schaefer III, *J. Am. Chem. Soc.* **1979**, *101*, 307.
[6] R. J. Buenker, V. Bonačić-Koutecký, L. Pogliani, *J. Chem. Phys.* **1980**, *73*, 1836.
[7] I. D. Petsalakis, G. Theodorakopoulos, C. A. Nicolaides, R. J. Buenker, S. D. Peyerimhoff, *J. Chem. Phys.* **1984**, *81*, 3161.
[8] S. El-Taher, R. H. Hilal, T. A. Albright, *Int. J. Quantum Chem.* **2001**, *82*, 245.
[9] A. J. Merer, R. S. Mulliken, *Chem. Rev.* **1969**, *69*, 639.
[10] I. Ohmine, *J. Chem. Phys.* **1985**, *83*, 2348.
[11] L. Salem, *Acc. Chem. Res.* **1979**, *12*, 87.
[12] M. Ben-Nun, T. J. Martínez, *Chem. Phys.* **2000**, *259*, 237.
[13] V. Molina, M. Merchán, B. O. Roos, P.-A. Malmqvist, *Phys. Chem. Chem. Phys.* **2000**, *2*, 2211.
[14] S. Krebs, R. J. Buenker, *J. Chem. Phys.* **1997**, *106*, 7208.
[15] T. Müller, M. Dallos, H. Lischka, *J. Chem. Phys.* **1999**, *110*, 7176.
[16] T. H. Dunning, *J. Chem. Phys.* **1989**, *90*, 1007.
[17] G. Orlandi, P. Palmieri, G. Poggi, *Chem. Phys. Lett.* **1979**, *68*, 251.
[18] R. P. Krawczyk, A. Viel, U. Manthe, W. Domcke, *J. Chem. Phys.* **2003**, in press.

 © 2003 Wiley-VCH Verlag GmbH & Co. KGaA, Weinheim

Cover Picture



Zoltan Takats, Sergio C. Nanita, and R. Graham Cooks*

In the beginning the origin of life involved a series of homochiral chemical reactions. Some of these may have involved serine and its homochiral octamer, as shown. Many of these reactions occur in a chirally selective fashion. The chiral exchange reactions favor the enantiomers present in modern life (L-amino acids, D-sugars). More information on the homochiral serine octamer and its role in the prebiotic mechanisms that led to the origin of life are given by R. G. Cooks et al. on page 3521 ff.

Contents

Angewandte EarlyView

The following articles are available online (in Wiley Interscience). You can find them at www.angewandte.org, under Full Text, Forthcoming Articles.

R. R. Davda, J. A. Dumesic:*
Catalytic Reforming of Oxygenated Hydrocarbons for Hydrogen with Low Levels of Carbon Monoxide
DOI: 10.1002/anie.200351664
Published online: June 20, 2003

I. D. Hills, G. C. Fu:*
Catalytic Enantioselective Synthesis of Oxindoles and Benzofuranones that Bear a Quaternary Stereocenter
DOI: 10.1002/anie.200351666
Published online: July 3, 2003

K. C. Nicolaou, Y. Li, N. Uesaka, T. V. Koftis, S. Vyskocil, T. Ling, M. Govindasamy, W. Qian, F. Bernal, D. Y.-K. Chen:*
Total Synthesis of the Proposed Azaspiracid-1 Structure, Part 1: Construction of the Enantiomerically Pure C1–C20, C21–C27, and C28–C40 Fragments
DOI: 10.1002/anie.200351825
Published online: July 17, 2003

K. C. Nicolaou, D. Y.-K. Chen, Y. Li, W. Qian, T. Ling, S. Vyskocil, T. V. Koftis, M. Govindasamy, N. Uesaka:*
Total Synthesis of the Proposed Azaspiracid-1 Structure, Part 2: Coupling of the C1–C20, C21–C27, and C28–C40 Fragments and Completion of the Synthesis
DOI: 10.1002/anie.200351826
Published online: July 17, 2003

Articles judged by the referees or the editior as being either very important or very urgent are immediately edited, proof-read, and electronically published once the manuscript has arrived in the editiorial office in final form. As long as there is no page number available these articles should be cited in the following manner:

Author(s) *Angew. Chem. Int. Ed.*, online publication date, DOI.

News

Organic Chemistry: Awards for Corey, Breslow and Gleiter ——— **3454**

Web Sites

http://spectra.galactic.com ——— **3455** A Database Query Need Not Be Expensive *Christoph Bonauer, Burkhard König*

Books

Late Transition Metal Polymerization Catalysis ——— **3456** Bernhard Rieger, Lisa Saunders Baugh, Smita Kacker, Susanne Striegler *reviewed by B. Drießen-Hölscher*

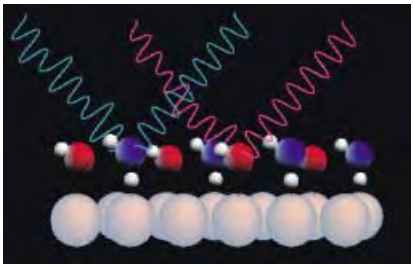
Analysing Gene Expression ——— **3457** Stefan Lorkowski, Paul Cullen *reviewed by S. Brakmann*

Highlights

Water Adsorption and Structure

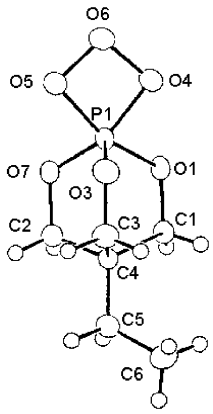
R. Ludwig* ——— **3458 – 3460**

How Does Water Bind to Metal Surfaces: Hydrogen Atoms Up or Hydrogen Atoms Down?



A flat ice structure is formed by water molecules absorbed on the metal surfaces of Pt(111) (see picture). In contrast to conventional wisdom, the structure of water in the first layer is not buckled. Instead all water molecules bind directly to the metal surface (through Pt—O and Pt—HO interactions) and to each other through hydrogen bonds without dissociation.

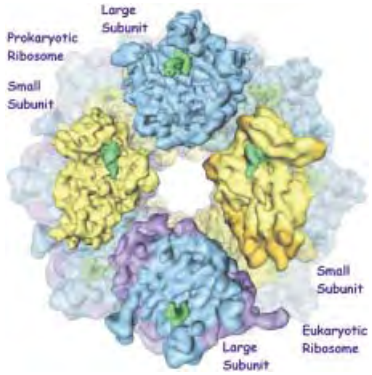
The question of the structure of phosphite ozonides was recently unequivically answered: It contains a four-membered PO_3 ring (see molecular structure). In a further highlight of phosphorus–oxygen chemistry, the synthesis of the first phosphorus(v) oxide ozonide, P_4O_{18}, was synthesized by the low-temperature reaction of P_4O_6 with ozone in dichloromethane.



Phosphorus Ozonides

T. M. Klapötke* _____ **3461 – 3462**

P_4O_{18}—The First Binary Phosphorus Oxide Ozonide



One for all: Ribosomes are the translation machines of the cell which convert genetic information into protein structure in the same manner in all animals. Recent crystallographic and cryo-electron microscopic reconstructions of ribosomes have revolutionized our understanding of the translation process. The superposed illustration shows the impressive structural similarity of prokaryotic and eukaryotic ribosomes.

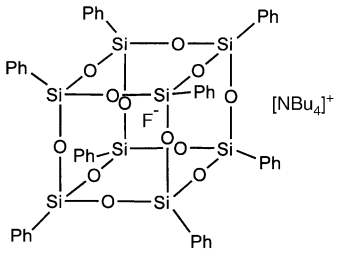
Reviews

Ribosome Structure and Translation

D. N. Wilson,
K. H. Nierhaus* _____ **3464 – 3486**

The Ribosome through the Looking Glass

Taming the caged ion: The X-ray crystal structure of an octaphenyl octasilsesquioxane cage that encapsulates a fluoride ion is presented (see picture). The extent of the Si–F interaction is low, which causes the cage geometry to not change significantly from that of a normal T8 structure. The crystal structure and the NMR data suggest the fluoride ion is essentially "naked".



Communications

Fluoride Ions in Cage Structures

A. R. Bassindale,* M. Pourny, P. G. Taylor,* M. B. Hursthouse,
M. E. Light _____ **3488 – 3490**

Fluoride-Ion Encapsulation within a Silsesquioxane Cage

For the USA and Canada:
ANGEWANDTE CHEMIE International Edition (ISSN 1433-7851) is published weekly by Wiley-VCH PO Box 191161, D 69451 Weinheim, Germany. Air freight and mailing in the USA by Publications Expediting Inc. 200 Meacham Ave., Elmont, NY 11003. Periodicals postage paid at Jamaica NY 11431. US POSTMASTER: send address changes to *Angewandte Chemie*, Wiley-VCH, 111 River Street, Hoboken, NJ 07030. Annual institutional subscription price for institutions: Europe € 2998.00/3148.00. Outside Europe US$ 3718.00/3904.00 (valid for print or electronic/print and electronic delivery); for individuals who are personal members of a national chemical society, or whose institution already subscribes, or who are retired or self-employed consultants, print only (including postage and handling charges): Europe € 248.00/Outside Europe US$ 348.00.

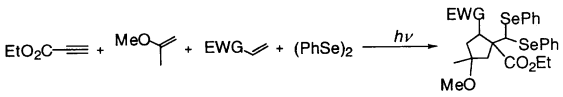
 © 2003 Wiley-VCH Verlag GmbH & Co. KGaA, Weinheim

Contents

Domino Radical Reactions

K. Tsuchii, M. Doi, T. Hirao, A. Ogawa* ——— 3490 – 3493

Highly Selective Sequential Addition and Cyclization Reactions Involving Diphenyl Diselenide, an Alkyne, and Alkenes under Visible-Light Irradiation



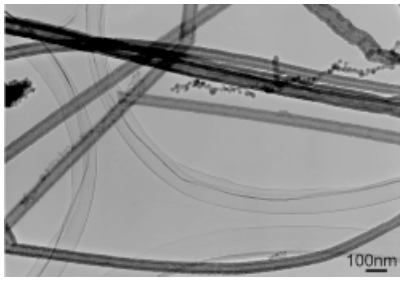
A four-component radical coupling of diphenyl diselenide, an alkyne, and two olefins to form substituted cyclopentanes in good yields is described (see scheme). This selective sequential addition and cyclization is facilitated by the rate of carbon-radical trapping by diphenyl diselenide, appropriate for this transformation, and the efficiency of the 5-*exo* cyclization. EWG = electron-withdrawing group.

Gallium Nitride Nanotubes

J. Hu,* Y. Bando, D. Golberg, Q. Liu ——— 3493 – 3497

Gallium Nitride Nanotubes by the Conversion of Gallium Oxide Nanotubes

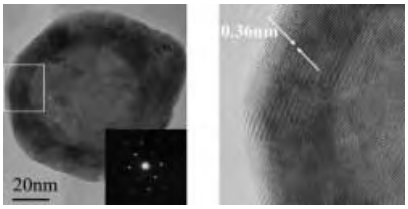
The future technology of blue lasers and optical communication, and is likely to be based on GaN. The creation of crystalline GaN nanotubes in bulk has been achieved by a two-stage process based on the well-controllable amorphous gallium oxide (Ga_2O) nanotube conversion. The as-synthesized GaN nanotubes have fairly uniform diameters of ≈80 nm, wall thicknesses of ≈20 nm, and lengths of up to several tens of micrometers.



Inorganic Fullerene Nanoparticles

X. Wang, Y. Li* ——— 3497 – 3500

Fullerene-Like Rare-Earth Nanoparticles



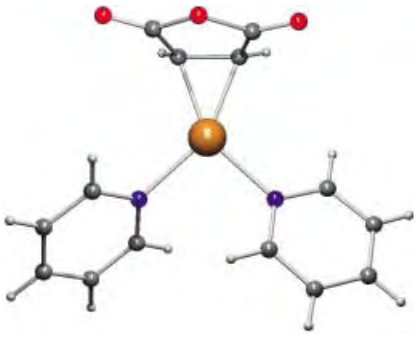
A low-temperature hydrothermal synthesis has been employed to prepare the title materials in the form of their fluorides and hydroxides. Electron microscopy reveals their hollow and closed-cage structures (see HRTEM image). Such nanostructures can be expected to bring forth new opportunities in important research and application fields, such as biological labeling, luminescence, and catalysis.

Zero-Valent Palladium Complexes

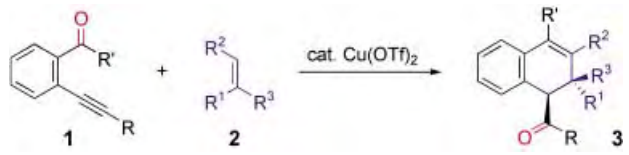
A. M. Kluwer, C. J. Elsevier,* M. Bühl, M. Lutz, A. L. Spek ——— 3501 – 3504

Zero-Valent Palladium Complexes with Monodentate Nitrogen σ-Donor Ligands

The facile synthesis and isolation of the stable zero-valent complexes $[Pd(L)_2(\text{maleic anhydride})]$ with σ-donor N ligands (L = ammonia, aniline, diethylamine, and pyridine) is remarkable in light of the fact that according to the HSAB principle, low-valent palladium compounds with donor groups such as simple amines should be difficult to prepare. The X-ray crystal structure of the pyridine complex is shown (Pd gold, O orange, N blue).



 © 2003 Wiley-VCH Verlag GmbH & Co. KGaA, Weinheim



The [4+2] cycloaddition reaction between *o*-alkynyl(oxo)benzene **1** and olefins **2** in the presence of a catalytic amount of $Cu(OTf)_2$ afforded 1,2-dihydronaphthalene derivatives **3** bearing an oxo function at the 1-position. The reaction proceeds most probably through the formation of benzo[*c*]pyrylium cupric ate complex.

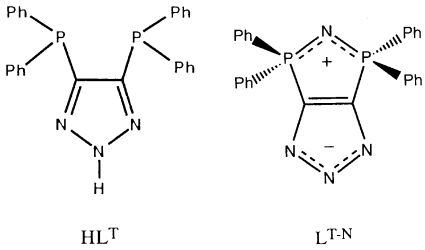
[4+2] Cycloadditions

N. Asao,* T. Kasahara, Y. Yamamoto* ——— **3504–3506**

Functionalized 1,2-Dihydronaphthalenes from the $Cu(OTf)_2$-Catalyzed [4+2] Cycloaddition of *o*-Alkynyl(oxo)benzenes with Alkenes

---

Towards a new family of ligands: The synthesis of the ligand HL^T (depicted left) is described. Although HL^T appears to be a simple chelating diphosphane, the tiazole proton can be removed with a base to produce an anionic diphosphane. Thus HL^T can chelate in two modes: as a neutral rigid diphosphane, or as an anionic rigid diphosphane. Furthermore, HL^T reacts in an unprecedented fashion with Me_3SiN_3 to give $L^{T\text{-}N}$ (depicted right).

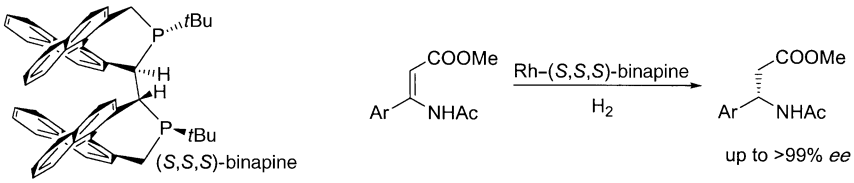


Bis(diphenylphosphanyl) Ligands

S. Trofimenko,* A. L. Rheingold, C. D. Incarvito ——— **3506–3509**

4,5-Bis(diphenylphosphanyl)-1,2,3-triazole and Its Conversion to 1,1,3,3,-Tetraphenyl-1,3-diphospha-2,4,5,6-tetraazapentalene

---



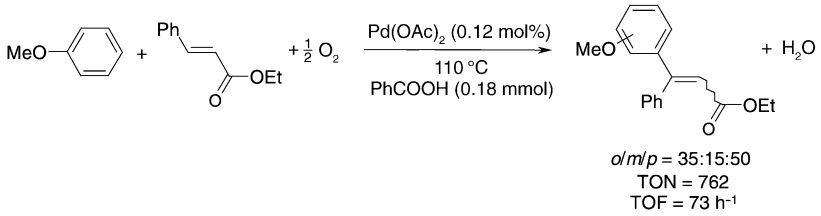
Excellent enantioselectivities and reactivities were observed in the hydrogenation of a variety of methyl (*Z*)-β-aryl-β-(acetylamino)acrylates in the presence of a rhodium catalyst with the chiral ligand binapine (see scheme). This bisbinaphthophosphepine ligand has stereogenic phosphorus centers and shows promise as a powerful ligand for application in the synthesis of chiral β-aryl-β-amino acids by asymmetric hydrogenation.

Asymmetric Hydrogenation

W. Tang, W. Wang, Y. Chi, X. Zhang* ——— **3509–3511**

A Bisphosphepine Ligand with Stereogenic Phosphorus Centers for the Practical Synthesis of β-Aryl-β-Amino Acids by Asymmetric Hydrogenation

---



A 100% carbon-efficient, halide- and solvent-free alternative for the synthesis of Heck-type products is the direct oxidative coupling of arenes with olefins, catalyzed by $Pd(OAc)_2$ under oxygen (see scheme). The reactions can be performed under mild conditions, and water is the only by-product. (TON = turnover number, TOF = turnover frequency.)

Green C-C Coupling Reactions

M. Dams, D. E. De Vos, S. Celen, P. A. Jacobs* ——— **3512–3515**

Toward Waste-Free Production of Heck Products with a Catalytic Palladium System under Oxygen

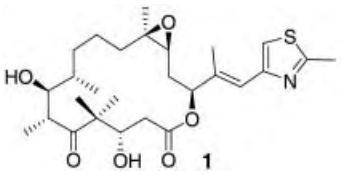
 © 2003 Wiley-VCH Verlag GmbH & Co. KGaA, Weinheim

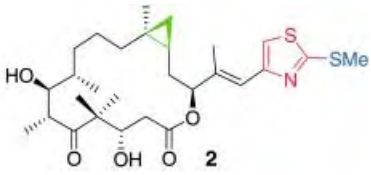
Contents

Epothilone Analogues

K. C. Nicolaou,* P. K. Sasmal, G. Rassias, M. V. Reddy, K.-H. Altmann, M. Wartmann, A. O'Brate, P. Giannakakou . **3515 – 3520**

Design, Synthesis, and Biological Properties of Highly Potent Epothilone B Analogues



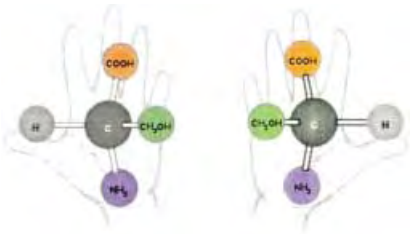


A number of rationally designed epoxide and cyclopropane epothilone B (**1**) analogues with substituted side chains were prepared and their biological activities were evaluated against a series of human cancer cell lines. The cyclopropane analogue **2** with a methylsulfanylthiazole ring stands out as the most potent compound and is sixfold more active than **1**. The methylsulfanyl group enhances the potency of these compounds.

The Prebiotic Role of Serine

Z. Takats, S. C. Nanita, R. G. Cooks* ——— **3521 – 3523**

Serine Octamer Reactions: Indicators of Prebiotic Relevance



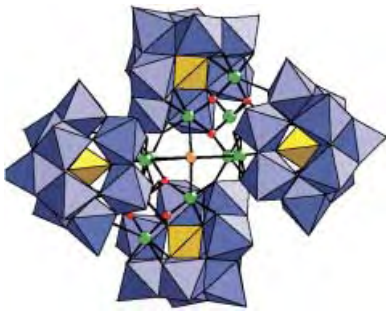
The earliest molecule of life? Chirally selective reactions relevant to the origin of homochiral life are undergone by serine. Chiral exchange between serine, glyceraldehyde, and glucose occurs, favoring the enantiomers (L-serine, D-sugars) present in modern living systems (see picture).

Polyoxometalates

P. Mialane,* A. Dolbecq, J. Marrot, E. Rivière, F. Sécheresse —— **3523 – 3526**

A Supramolecular Tetradecanuclear Copper(II) Polyoxotungstate

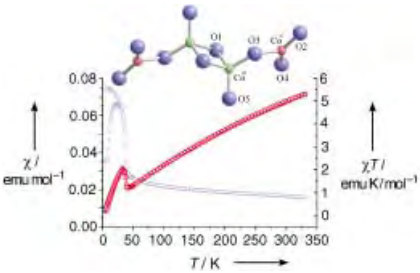
Four $\{SiW_9O_{34}\}$ units enclose a 14 Cu^{II} cluster obtained through halide supramolecular assembly, leading to the polyanion containing the highest number of divalent metal cations (see picture; W blue, Si yellow, Br orange, Cu green, O red).



Mixed-Valent Oligooxocobaltates

M. Sofin, H.-U. Güdel, R. Bircher, E.-M. Peters, M. Jansen* —— **3527 – 3529**

$Na_{10}Co_4O_{10}$, an Oligooxocobaltate(II, III) with Unusual Magnetic Properties



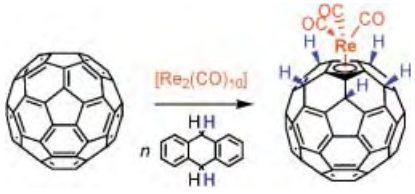
The novel mixed-valent oligooxocobaltate can be synthesized through a direct reaction by the azide/nitrate route. The magnetic properties of the compound are characterized by the strongly distinct hierarchy in the magnetic exchange interactions within the complex anion (see picture).

Hydrogenation of Fullerenes

M. Toganoh, Y. Matsuo, E. Nakamura* ——— **3530 – 3532**

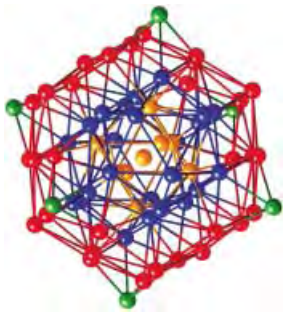
Rhenium-Templated Regioselective Polyhydrogenation Reaction of [60]Fullerene

Functionalizing fullerenes: The first regioselective polyhydrogenation of [60]fullerene has been achieved. Upon treatment of [60]fullerene or its derivative with 9,10-dihydroanthracene in the presence of $[Re_2(CO)_{10}]$, transfer hydrometallation reaction takes place to give a polyhydrogenation product (see scheme). The reaction provided a pathway to a



variety of metal η^5 complexes of hydrofullerenes.

© 2003 Wiley-VCH Verlag GmbH & Co. KGaA, Weinheim



The nanosized icosahedral-based cluster $[Pd_{69}(CO)_{36}(PEt_3)_{18}]$ (see picture) exhibits two new salient stereochemical features: 1) a linear face-condensation of three centered icosahedra that gives rise to a linear face-sharing Pd_{33}-centered triicosahedron, and 2) a hexagonal-shaped Pd_{30} tube formed by cyclic *trans* edge-sharing of six Pd_7-centered hexagons (host), inside of which resides the linear triicosahedron (permanent guest).

Palladium–Carbonyl Clusters

N. T. Tran, L. F. Dahl* ——— **3533 – 3537**

Nanosized $[Pd_{69}(CO)_{36}(PEt_3)_{18}]$: Metal-Core Geometry Containing a Linear Assembly of Three Face-Sharing Centered Pd_{33} Icosahedra Inside of a Hexagonal-Shaped Pd_{30} Tube

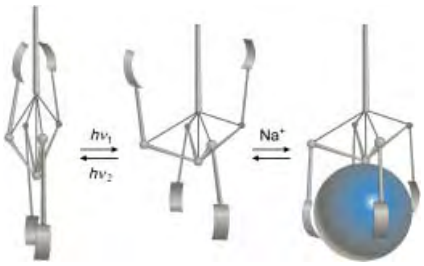
Giving color to data recording: Upon irradiation with selected wavelengths of light the hexane solution of a fused dithienylethene derivative changes from colorless to yellow, green, black, or blue depending on the wavelength, and irradiation time (see picture). This could be a landmark in the development of new data recording materials.



Multicolor Photochromism

K. Higashiguchi, K. Matsuda, M. Irie* ——— **3537 – 3540**

Photochromic Reaction of a Fused Dithienylethene: Multicolor Photochromism



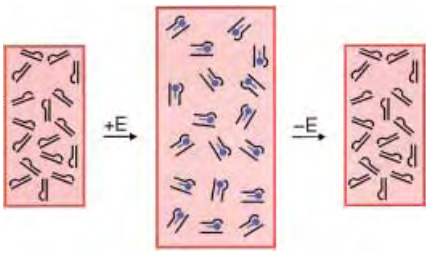
A molecular grapple with four clamping arms constructed from the quadricyclane⇄norbornadiene system can be controlled with light of two different wavelengths (see picture). In the presence of Na^+ the open structure (middle) drops all arms and forms a stable complex (right). All three states of the "molecular grapple" were confirmed by X-ray analysis.

Photoinduced Na^+ Coordination

T. Winkler, I. Dix, P. G. Jones, R. Herges* ——— **3541 – 3544**

Synthesis, Structure, and Complexation Properties of Amide-Substituted Derivatives of Norbornadiene and Quadricyclane

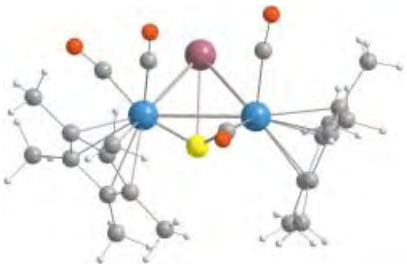
Action and reaction: Implementation of molecular recognition centers into flexible elastomers allows selective recognition processes to be translated into fully reversible macroscopic motions for the first time (see scheme). The expansion and contraction of the polymers depends both on the effector binding energy and the pH value.



Chemically Induced Shape Change

H.-J. Schneider,* L. Tianjun, N. Lomadze ——— **3544 – 3546**

Molecular Recognition in a Supramolecular Polymer System Translated into Mechanical Motion



NO as a η^2-bridging ligand is not known, but $[SbS]^+$, the first diatomic ligand from Group 15 and Group 16 elements Sb and S, adopts a bridging position between two $\{Cp^*(CO)_2Mo\}$ fragments (see structure blue Mo, yellow S, brown Sb, C gray). This $\mu,\eta^{2:2}$-bridging ligand is highly sensitive to steric influences.

Mo Complexes with SbS Ligands

H. Brunner, M. M. Kubicki, A. Lange, J. Wachter,* E. Vigier, M. Zabel ——— **3547 – 3549**

$\mu,\eta^{2:2}$-SbS: An Antimony-Containing Heterodiatomic Ligand from Group 15 and 16 Elements

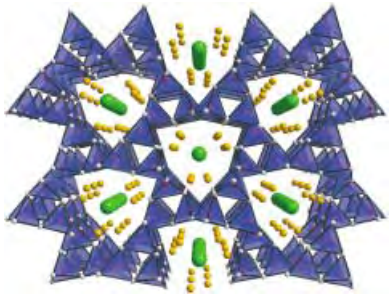
 © 2003 Wiley-VCH Verlag GmbH & Co. KGaA, Weinheim

Contents

Oxonitridophosphate Structures

S. Correll, O. Oeckler,* N. Stock, W. Schnick* ——— **3549 – 3552**

$Li_xH_{12-x-y+z}[P_{12}O_yN_{24-y}]Cl_z$—An Oxonitridophosphate with a Zeolitelike Framework Structure Composed of 3-Rings



New network: A framework topology that has not been observed previously was discovered in oxonitridophosphates. The structural characterization by X-ray single-crystal structure analysis shows that the network is composed of corner-sharing $P(O,N)_4$-tetrahedra forming 12-ring channels.

Communications labeled with this symbol have been judged by two referees as being "very important papers".

The publication of Communications labeled with this symbol has been accelerated because of their topical or highly competitive nature.

Deadline for recruitment adverts

35/2003	August 22	Publication date:	September 15
36/2003	August 29	Publication date:	September 22

Angewandte Chemie International Edition
Advertising Sales Department:
Marion Schulz
Phone: 0 62 01 – 60 65 65
Fax: 0 62 01 – 60 65 50
E-Mail: MSchulz@wiley-vch.de

Place an advert in the printed version and have it made available online for 1 month, free of charge!

Service

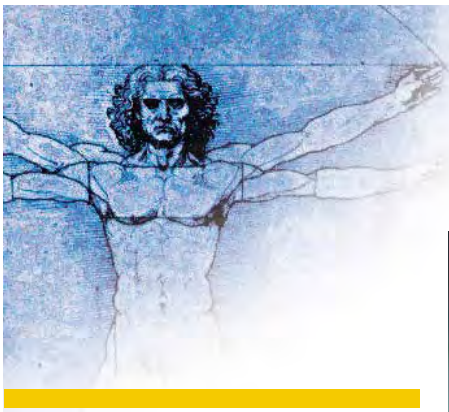
Keywords ——— *3554*

Authors ——— *3555*

Angewandte's Sister Journals ——— *3556 – 3557*

Vacancies ——— *3453*

Preview ——— *3559*



E. J. Corey Receives Priestley Medal

The American Chemical Society (ACS) awards the Priestley Medal annually. Previous recipients include such well-known scientists as Peter Debye, Linus Pauling, and Roald Hoffmann. Now Elias J. Corey, a professor at Harvard University who was awarded the Nobel Prize for Chemistry in 1990,[1] will receive this prestigious award for his outstanding services to chemistry.



E. J. Corey

Corey completed his chemistry studies under the supervision of John C. Sheehan in 1951 with a PhD on synthetic penicillin from the Massachusetts Institute of Technology, and then joined faculty at the University of Illinois in Urbana–Champaign (USA). In 1959 he took up a position at Harvard University. The contributions made by Corey during his career have shaped organic synthesis. His approaches to the logical planning of synthesis,[2] especially with the development of retrosynthetic analysis, have advanced this discipline conceptually. His research group has always chosen ambitious targets in their work on the synthesis of biologically active natural products. Earlier these included the prostaglandins, whereas today the focus is on substances of marine origin. This work has led time and time again to improvements in methodology, for example, in the catalytic, enantioselective construction of molecules with quaternary carbon centers [3a] or in the Diels–Alder reaction.[3b] Corey is also a member of the Academic Advisory Board of *Advanced Synthesis and Catalysis*.

Welch Award to R. Breslow

The Welch Foundation in Houston (Texas, USA) is a private Foundation for the promotion of basic research. The Robert A. Welch Award in Chemistry, with a monetary value of US$ 300 000, is awarded annually by the Foundation. The winner of this Award for 2003 is Ronald Breslow, a professor at Columbia University in New York.



R. Breslow

Breslow studied chemistry at Harvard University and under the guidance of Robert B. Woodward completed his PhD in organic chemistry there in 1955. Following a postdoctoral year in Cambridge (UK) in the research group of Lord Todd he moved to Columbia University. Breslow is the recipient of numerous awards, including the Arthur C. Cope Award in 1987 and the Priestley Medal of the ACS in 1999. He was President of the ACS in 1996.

His research group studies novel molecules with interesting electronic properties. For example, they were the first to synthesize the cyclopropenyl cation: the simplest aromatic system. Furthermore, Breslow introduced the concept of antiaromaticity.[4] He also makes important contributions in the area of biomimetic chemistry [5], especially in the mimicking of enzymatic reactions, often with the aim of discovering new cancer treatments.

R. Gleiter Honored

Rolf Gleiter, a professor in organic chemistry at the Universität Heidelberg (Germany), has been awarded an honorary doctorate from the Russian Academy of Sciences and been made an Honorary Professor at Lomonosov University in Moscow because of his services to chemistry.



R. Gleiter

Gleiter studied chemistry at the Universität Stuttgart (Germany) and completed his PhD there in 1964 under the supervision of Franz Effenberger, with a thesis on "Electrophilic Reactions of Cumulene Systems with C–C Double Bonds". After postdoctoral stays in the research groups of Paul von Ragué Schleyer in Princeton and of Roald Hoffmann in Ithaca, NY (USA), he completed his habilitation in 1972 with Edgar Heilbronner at the Universität Basel (Switzerland). In 1973 he moved to the Technische Hochschule Darmstadt (Germany), before taking up his current position in Heidelberg in 1979.

Gleiter's research interests are focused on the development of simple models to aid understanding of the reactivity of molecules. With this aim he tries to establish relationships between the electronic structure of organic compounds and their properties in the ground and excited states. The model systems under investigation include phanes and electron-rich alkynes. Examples of his most recent work can be read about in a recently published Concept article on tube-shaped supramolecular structures, which happens to be the 200th article in this section in *Chemistry—A European Journal*.[6]

Gleiter is the recipient of various awards, including the Max Planck Research Award in 1991 and the Adolf von Baeyer Medal of the Gesellschaft Deutscher Chemiker (German Chemical Society) in 1994. He is a member of the Advisory Board of the *European Journal of Organic Chemistry*.

[1] E. J. Corey, *Angew. Chem.* **1991**, *103*, 469; *Angew. Chem. Int. Ed. Engl.* **1991**, *30*, 455.

[2] E. J. Corey, X.-M. Cheng, *The Logic of Chemical Synthesis*, John Wiley and Sons, New York, **1995**.

[3] a) E. J. Corey, A. Guzman-Perez, *Angew. Chem.* **1998**, *110*, 402; *Angew. Chem. Int. Ed.* **1998**, *37*, 388; b) E. J. Corey, *Angew. Chem.* **2002**, *114*, 1724; *Angew. Chem. Int. Ed.* **2002**, *41*, 1650.

[4] R. Breslow, *Angew. Chem.* **1968**, *80*, 573; *Angew. Chem. Int. Ed. Engl.* **1968**, *7*, 565.

[5] R. Breslow, *Chem. Rec.* **2001**, *1*, 3.

[6] R. Gleiter, D. B. Werz, B. J. Rausch, *Chem. Eur. J.* **2003**, *9*, 2676.

 © 2003 Wiley-VCH Verlag GmbH & Co. KGaA, Weinheim



A Database Query Need Not Be Expensive

What does the mass spectrum of 1-nitrocyclohexene look like? Where exactly are the IR absorption bands for benzaldehyde? Is my UV spectrum that of the *ortho*- or the *meta*-disubstituted benzene derivative? Until recently, one had to go to the library and search through thick spectrum indexes to answer such questions. These days one can search online databases. Unfortunately, the two largest and most widely used databases for organic-chemistry research, Beilstein and Chemical Abstract Service, do not (yet?) offer spectra or a direct link to online spectra databases. This gap is filled by other service providers such as Thermo Galactic, whose online database offers access to 26000 spectra for substances from a wide palette of substance classes, including active ingredients, standard chemicals, polymers, and many more. The range of spectroscopic methods covered is just as comprehensive: mass spectrometry, FTIR, Raman, UV/Vis, emission, and NMR spectroscopy.

Access to Thermo Galactic is not only free, but also simple and convenient. All functions offered are immediately available after registration (Figure 1). In addition to the standard search parameters: molecular formula, substance name and name fragments, CAS number, and molecular weight, there is a very useful option, whereby the user's own spectra can be compared with those in the database. The user's spectrum is uploaded to the server (common export formats and many specific data formats of the instrument manufacturers are supported), after which the user can check the spectrum again, before the search algorithm is selected and the comparison begins. A list of hits is displayed in decreasing order with respect to how well they match the user's spectrum. When a substance from this list of hits is selected, a list of available spectra for this substance is shown (Figure 2). These spectra are available with Gif- or Java-based viewing options, and can also be printed in Gif format. Further information such as measurement details or the origin of the data, if known, is also provided.

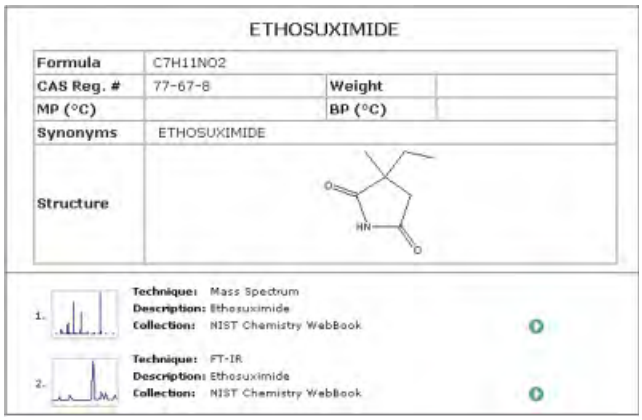


Figure 2. Search result from the database.

The origin of the data is manifold. Compilations of spectra from a few universities such as Notre Dame and Pacific Lutheran University as well as from other organizations such as the US National Institute of Standards and Technology (NIST)[1] are integrated into the database. The spectra of individual users are also added to the database. A special function is offered that aids in the addition of spectra and additional information to the system. However, the data is neither appraised nor edited by Thermo Galactic. All spectra are derived directly from raw data. Therefore some errors, such as an incorrect structural formula, are possible. Other system-orientated errors also sometimes occur. For example, at times links to the spectra from the substance list are temporarily unavailable.

The design of the website is appealing and clear, and it is reduced to only the essential functions. Superfluous advertising and pop-up windows fortunately do not feature. Only a few very small, discreet advertisements appear.

If the available data is used critically, this internet site is very useful for time-saving web research. The database is an excellent resource for researchers who wish to quickly find a spectrum of a postulated by-product for comparison, as well as for those teaching or studying the spectroscopic analysis of organic substances. Through this site and other web-based databases (for example, SDBS[2] with over 30000 substances and a comprehensive NMR compilation), the scope for free database research is becoming sufficiently comprehensive.

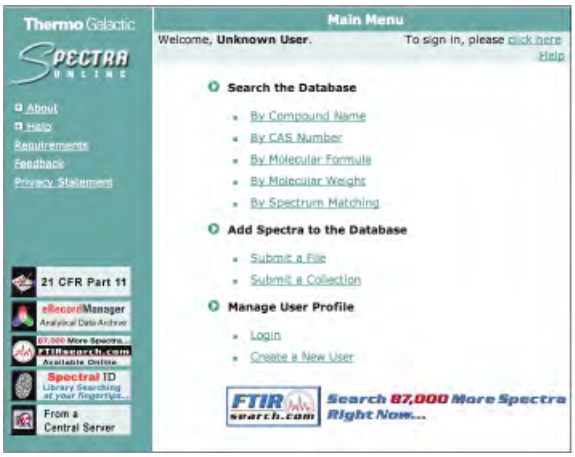


Figure 1. After registration all Thermo Galactic database functions are fully available.

Christoph Bonauer, Burkhard König
Universität Regensburg

[1] D. Schröder, *Angew. Chem.* **2001**, *113*, 4647; *Angew. Chem. Int. Ed.* **2001**, *40*, 4515.
[2] http://www.aist.go.jp/RIODB/SDBS/menu-e.html.

For more information visit
http://spectra.galactic.com/
or contact
science@galactic.com

© 2003 Wiley-VCH Verlag GmbH & Co. KGaA, Weinheim

Water Adsorption and Structure

How Does Water Bind to Metal Surfaces: Hydrogen Atoms Up or Hydrogen Atoms Down?

*Ralf Ludwig**

Keywords:
surface chemistry · water chemistry · X-ray spectroscopy

For a quarter of a century, the water–metal interaction has been one of the most studied adsorption phenomena of modern surface science.[1,2] The adsorption of water molecules on the flat, close-packed surfaces of metals was thought to be simple and well understood. The structure of water on metal surfaces has traditionally been considered a buckled bilayer where every second water molecule binds to the metal. The first layer partially covers the metal surface and binds through the lone electron pairs of the oxygen atoms, whereas the second layer attaches to the water molecules by hydrogen bonds.

Ogasawara et al.[3] now have combined soft X-ray spectroscopy and density functional theory (DFT) calculations to show, that on the (111) surface of platinum, half of the water molecules of the first layer bind through their lone pairs, but the other half bind to the metal surface through their hydrogen atoms. The result is that water molecules form a plane of "flat ice" on a platinum surface. The presence of metal–hydrogen bonds of water molecules, in the absence of free hydroxide ions, challenges current models of water adsorption on metals. This finding may help to better understand processes such as corrosion and the photodissociation of water. The detailed knowledge of water–metal interaction also provides further understanding of electrical potentials and catalysis. Platinum is a common catalyst for the formation of water from hydrogen and oxygen, the key reaction in hydrogen fuel cells.

Though water adsorption on single-crystal precious-metal surfaces has been the focus of many investigations, experiment and theory have yet to produce a consistent picture of the water–metal interface. Experiments appear consistent with the notion that the water molecules first deposited on Ru(0001) arrange in a bilayer such as those that stack to form hexagonal ice (ice I_h), the naturally occurring ice crystal at ambient pressure.[4] In this structure (see Figure 1), the oxygen atoms lie in two planes separated by 0.96 Å. Both hydrogen atoms of the low-lying oxygen atoms form hydrogen bonds to the neighboring water molecules; the upper water molecules have one O–H bond oriented along the surface normal (H-up) and contribute one hydrogen atom to the hydrogen-bonding network. Thus, the principle formation of water structures on metal surfaces was thought to follow the Bernal–Fowler–Pauling rules for the bonding and structure of ice modified by some constraints owing to the water–metal interface.[5,6] Such a bilayer structure estimates a vertical displacement of 0.96 Å but a much smaller value (0.15 Å) was found by a low-energy electron diffraction (LEED) study of water on Ru(0001) by Held and Menzel.[7]

There has been some evidence that a flat two-dimensional hexagonal hydrogen-bonded network is more likely. A first interpretation was given by Feibelman using DFT calculations.[8] He argued that a partial dissociation of water would lead to a near-planar, hexagonal mixed network of water and hydroxide ions. To achieve such a favorable interaction the nonbonding proton pointing towards the substrate needed to be removed. With this atom absent, the oxygen $2p_z$ orbital is a high-energy orbital, unless the oxygen moves closer to the substrate where it can hybridize with ruthenium orbitals. On the other hand on most hexagonally close-packed surfaces, water does not dissociate. Photoemission data supported nondissociative adsorption on Ni(111), Cu(111),

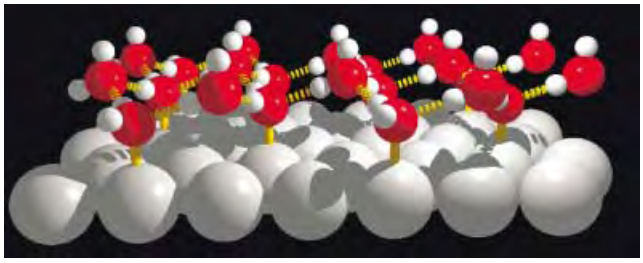


Figure 1. The old standard model for water adsorbed on a metal surface: In a water bilayer the molecules are arranged in the hexagonal phase of ice (I_h). In the first layer the water molecules bind directly to the metal substrate by an oxygen lone-pair orbital, whereas in the next layer they are attached to neighboring molecules by hydrogen bonds and one O–H bond points away from the surface.

[*] Priv.-Doz. Dr. R. Ludwig
Physikalische Chemie, Fachbereich Chemie
Universität Dortmund
Otto-Hahn-Strasse 6, 44221 Dortmund (Germany)
Fax: (+49) 231-755-3937
E-mail: ludwig@pc2a.chemie.uni-dortmund.de

 © 2003 Wiley-VCH Verlag GmbH & Co. KGaA, Weinheim DOI: 10.1002/anie.200301658

and Pt(111).[9] Up to this point, two scenarios were possible: A buckled ice-like layer built upon neutral water molecules or a flat two-dimensional hexagonal hydrogen-bonded network consisting of a mixture of water and hydroxide ions. Thus a flat water structure could be found but required the assumption of dissociated water molecules.

Ogasawara et al.[3] have studied the water bilayer structure on Pt(111) with an array of X-ray spectroscopy methods in combination with DFT calculations. They used X-ray photoelectron spectroscopy (XPS) to address the coordination of atoms to the surface, X-ray absorption spectroscopy (XAS) to determine the orientation of the O–H bonds with respect to the surface, and X-ray emission spectroscopy (XES) together with DFT calculations to explain the detailed bonding mechanism. That the DFT calculations yield reliable results which allow a comparison with measured X-ray spectra can be attributed to the usage of gradient-corrected exchange and correlation functionals throughout.

In the following we will trace this procedure step by step. First, XPS provides information about the bonding state of adsorbate and substrate atoms. From the measurements Ogasawara et al. found consistency with the non-dissociated model and, through the surface core-level shift, could determine the number of water molecules coordinated to surface platinum atoms.[10] Their estimation gives that 2/3 of the surface platinum atoms are coordinated to water molecules which corresponds to the saturation coverage of a water layer on Pt(111). Thus, it could be concluded that all the water molecules are coordinated to surface metal atoms and that such a high surface coordination is in contradiction to the "bilayer structure". These experimental findings were supported by a theoretical geometry optimization also leading to a flat ice layer on the platinum surface. In such a structure each water molecule has three hydrogen bonds that are involved in the hydrogen-bond network. The open question whether the uncoordinated water O–H bond points away (H-up) or towards (H-down) the metal surface could be answered by XAS which allows the local unoccupied orbitals to be selectively probed in different orientations. The oxygen K-edge spectra were calculated for both scenarios: H-up and H-down. Comparison with XAS data, clearly indicated that the chemical shifts[*] of the oxygen 1s orbital is in agreement with the H-down model leading to the flat water structure with O–H bonds pointing to the platinum surface as given in Figure 2. This finding is in nice agreement with results from vibrational spectroscopy. Any interaction between the O–H bonds and the substrate leads to weaker and elongated O–H bonds and thus to a redshift in the infrared spectrum.[11] Additionally the measured intensities indicated only a minor contribution of H-up species.

At this point the structure of water on a platinum surface appears to be clarified. But by using XES and DFT methods Ogasawara et al. addressed some details of the mechanism of the bonding between the water OH group and the surface. The occupied electronic states of the adsorbate layer can be considered in an atom-specific way. The interaction of the oxygen lone-pair orbital of the Pt–O bond with the substrate d band will result in bonding and antibonding contributions. A molecular orbital (MO) analysis of the computed XES spectrum shows the repulsive character of the Pt–O bonding (see the charge-density difference plot (Figure 3, left). The charge density decreases along the bond, through this charge polarization the Pauli repulsion between the lone-pair orbital and the platinum d orbital is minimized. For Pt–HO bonding an increase of charge density between the H and Pt atoms (electron pairing) from the bonding combination and a decrease in charge density on the H atom along the O–H bond from the nonbonding combination can be observed (Figure 3, right). Clearly the Pt–HO bonding leads to the formation of a Pt–H bond along with the weakening of the water internal O–H bond.

This beautiful combination of X-ray spectroscopy and DFT calculations shows that water on Pt(111) forms flat

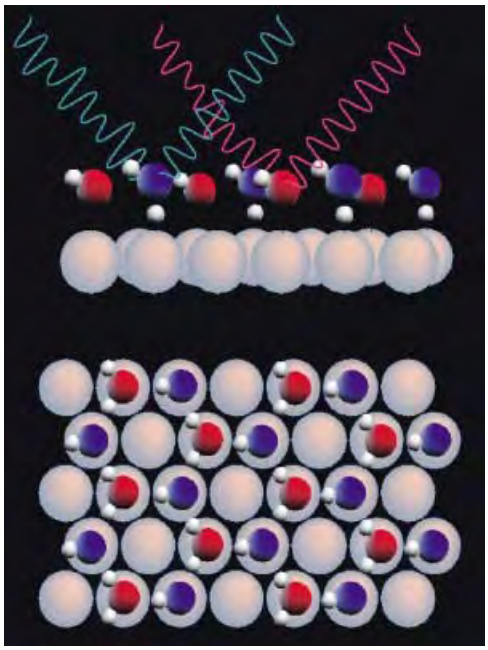


Figure 2. The flat ice structure on Pt(111) metal surfaces. The red spheres represent oxygen atoms in Pt–O bonding water molecules and the blue spheres represent oxygen atoms in Pt–HO bonding water molecules. The thickness of this flat layer is only 0.15 Å (courtesy of A. Nilsson).

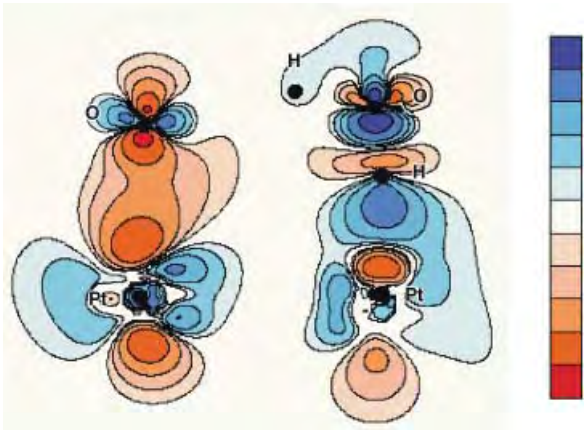


Figure 3. Charge-density differences plots for Pt–O (left) and Pt–HO (right) bonding species; red indicates a decrease in charge density, blue indicates an increased charge density (courtesy of A. Nilsson).

[*] In X-ray photoelectron spectroscopy (XPS) the "chemical shift" is a measure for the shift in the binding energies of the core electrons as function of chemical environment.

© 2003 Wiley-VCH Verlag GmbH & Co. KGaA, Weinheim

ice and that there is both oxygen and hydrogen bonding to the surface. The M–HO bonding results from the balance between M–H bond formation and O–H bond weakening. Thus, water on the Pt(111) surface forms a neutral layer whereas water on a Ru(0001) surface, which has a higher proton affinity, forms a partially dissociated layer as shown by Feibelman.[6]

[1] P. A. Thiel, T. E. Madey, *Surf. Sci. Rep.* **1987**, *7*, 211 – 385.
[2] M. A. Henderson, *Surf. Sci. Rep.* **2002**, *46*, 1 – 308.
[3] H. Ogasawara, B. Brena, D. Nordlund, M. Nyberg, A. Pelmenschikov, L. G. M. Pettersson, A. Nilsson, *Phys. Rev. Lett.* **2002**, *89*, 276102.
[4] D. L. Doering, T. E. Madey, *Surf. Sci.* **1982**, *123*, 305 – 337.
[5] J. D. Bernal, R. H. Fowler, *J. Chem. Phys.* **1933**, *1*, 515 – 548.
[6] L. Pauling, *J. Am. Chem. Soc.* **1935**, *57*, 2680 – 2684.
[7] G. Held, D. Menzel, *Surf. Sci.* **1994**, *316*, 92 – 102.
[8] P. J. Feibelman, *Science* **2002**, *295*, 99 – 102.
[9] W. Ranke, *Surf. Sci.* **1989**, *209*, 57 – 76.
[10] O. Björneholm, A. Nilsson, H. Tillborg, P. Bennich, A. Sandell, B. Hernnäs, C. Puglia, M. Mårtensson, *Surf. Sci.* **1994**, *315*, L983-L989.
[11] H. Ogasawara, J. Yoshinobu, M. Kawai, *Chem. Phys. Lett.* **1994**, *231*, 188 – 192.

 © 2003 Wiley-VCH Verlag GmbH & Co. KGaA, Weinheim

Phosphorus Ozonides

P_4O_{18}—The First Binary Phosphorus Oxide Ozonide**

*Thomas M. Klapötke**

Keywords:
ozonides · phosphite ozonides · phosphorus oxide ozonides · singlet oxygen

It was reported as early as 1961 that ozone reacts with the esters of *ortho*-phosphoric acid ($(RO)_3P$) at low temperatures to form thermolabile ozonide products of the type $(RO)_3PO_3$, which were classified as phosphite ozonides [Eq. (1)].[1] These phosphite ozonides were shown to decompose to yield the corresponding stable phosphates and singlet oxygen ($^1O_2$), and are very convenient precursors for the generation of $^1O_2$ [Eq. (2)].

$$(RO)_3P + O_3 \rightarrow (RO)_3PO_3 \quad (1)$$

$$(RO)_3PO_3 \rightarrow (RO)_3PO + {}^1O_2 \quad (2)$$

However, it was not until very recently that Dimitrov and Seppelt were able for the first time to unequivocally answer the question as to whether these ozonides definitely contained a four-membered PO_3 ring.[2] Crystal-structure analysis of $C_2H_5C(CH_2O)_3PO_3$ showed that this ozonide does in fact contain a symmetric, almost planar, four-membered PO_3 ring (Figure 1).

Despite the knowledge and the recent structural characterization of $C_2H_5C(CH_2O)_3PO_3$, there have been no sound reports regarding binary phosphorus oxide ozonides containing a PO_3 unit. However, in 2003 Meisel and co-workers applied the synthetic strategy of making organic phosphite ozonides to the synthesis of inorganic phosphorus oxide ozonides.[3] Quite recently, the low-temperature reaction of P_4O_6 with ozone in CH_2Cl_2, as well as the formation [Eq. (3)] and subsequent structural characterization of the tetraozonide P_4O_{18} was reported.[3]

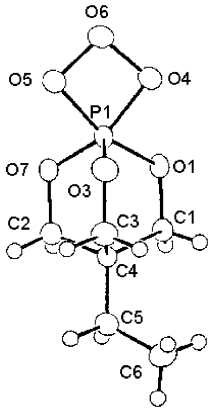


Figure 1. Molecular structure of the first structurally characterized phosphite ozonide $C_2H_5C(CH_2O)_3PO_3$.[2]

$$P_4O_6 + 4\,O_3 \rightarrow P_4O_{18} \quad (3)$$

This novel phosphorus oxide ozonide P_4O_{18} can be regarded as the [1+3] cycloaddition product of phosphorus(III) oxide and ozone. The tetraozonide P_4O_{18} can be isolated at −78 °C as a white powder which slowly decomposes at temperatures above −35 °C in CH_2Cl_2 solution with elimination of oxygen. However, the neat material tends to decompose explosively upon warming.

The structure of P_4O_{18} is (as are the structures of P_4O_6 and P_4O_{10}) based on a P_4 tetrahedron. Every P atom is coordinated with five O atoms in a distorted quadratic pyramidal arrangement. Similar to the above mentioned phosphite ozonide $C_2H_5C(CH_2O)_3PO_3$, the P_4O_{18} molecule also contains four four-membered PO_3 rings and can therefore be regarded as a covalent phosphorus(V) oxide ozonide (Figure 2).

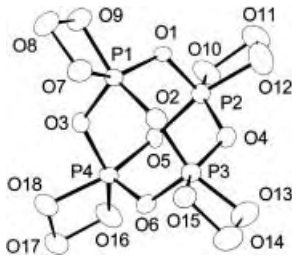


Figure 2. Molecular structure of the first binary phosphorus oxide ozonide P_4O_{18}.[3]

Not only is the synthesis of the first binary phosphorus oxide ozonide by Meisel and co-workers highly interesting in its own right, but the decomposition of the P_4O_{18} molecule is also of great interest. P_4O_{18} liberates oxygen in a controlled reaction in solution or suspension above −35 °C, and forms the thermodynamically favorable P_4O_{10} and singlet oxygen [Eq. (4)]. Reaction (4) is thermodynamically allowed, with $\Delta H = -26.9$ kcal mol^{-1} (MPW1PW91/cc-pVDZ).[4]

$$P_4O_{18} \rightarrow P_4O_{10} + 4\,{}^1O_2 \quad (4)$$

The most intense band in the low-temperature (−80 °C) Raman spectrum of P_4O_{18} at 901 cm^{-1} corresponds to an asymmetric O-O-O stretch of the PO_3 ring. This value was also calculated to be the most intense Raman-active band (970 cm^{-1} at the MPW1PW91/cc-pvDZ level of theory). This band was shown to decrease significantly in intensity at −30 °C and indicates the loss of dioxygen from the PO_3 unit.

Since the generation of singlet oxygen ($^1O_2$) by direct electronic excitation

[*] Prof. Dr. T. M. Klapötke
Department Chemie
Ludwig-Maximilians-Universität München
Butenandtstrasse 5–13 (D)
81377 München (Germany)
Fax: (+49) 89-2180-77492
E-mail: tmk@cup.uni-muenchen.de

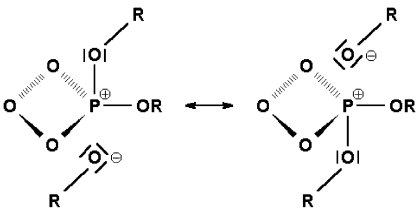
[**] This work was supported by the Fonds der Chemischen Industrie. The author thanks Mrs. C. Nowak for her help with the diagrams and Dr. R. D. Harcourt for many inspired discussions.

DOI: 10.1002/anie.200301663
© 2003 Wiley-VCH Verlag GmbH & Co. KGaA, Weinheim

of the triplet ground state ($^3O_2$) is spin forbidden, singlet oxygen is usually prepared either 1) by chemical reactions that form intermediates which spontaneously eliminate $^1O_2$, or 2) from compounds which decompose to give $^1O_2$. The most well-known example of the latter method is the reaction of basic hydrogen peroxide (BHP) with Cl_2[5] or the above-mentioned decomposition of phosphite ozonides.[1,6] Further work has to be carried out to evaluate the suitability of using P_4O_{18} as a potential source of singlet oxygen. In this context, the very recent report by Alfano and Christe on the first feasible production of $^1O_2$ from a gas–solid reaction should be mentioned [Eq. (5)].[7]

$$Na_2O_2 + 2\,HCl \rightarrow H_2O + 2\,NaCl + 1/2\,{}^1O_2 \qquad (5)$$

Equally interesting is the structure and bonding in the P_4O_{18} molecule which contains four essentially equivalent (approximate D_2 symmetry) hypercoordinate P atoms. Similar to the phosphite ozonide $C_2H_5C(CH_2O)_3PO_3$,[2] the P atom in the P_4O_{18} molecule forms a distorted square pyramid arrangement with the O atoms, with the apical P–O bonds being slightly shorter (1.59 Å) than the four basal P–O bonds (1.63–1.65 Å). The O–O bond lengths in the covalently bound ozonide ligands correspond to typical O–O single bonds (1.45 Å).[3] Since bonding-wise the model compound $(HO)_3PO_3$ (see resonance structures) with a five-coordinate phosphorus atom can best be described as a molecule with an axial 3-center-4-electron bonding unit (see for example, ref. [8]), the possibility exists that at least one 3-center-4-electron bonding unit also exists in P_4O_{18} (O···P···O) and is associated with each P atom. Further theoretical studies are needed to fully understand the structure and bonding in this highly interesting phosphorus oxide ozonide molecule.



[1] Q. E. Thompson, *J. Am. Chem. Soc.* **1961**, *83*, 846–851.

[2] A. Dimitrov, K. Seppelt, *Eur. J. Inorg. Chem.* **2001**, 1929–1932.

[3] A. Dimitrov, B. Ziemer, W.-D. Hunnius, M. Meisel, *Angew. Chem.* **2003**, *115*, 2588–2590; *Angew. Chem. Int. Ed.* **2003**, *42*, 2484–2486.

[4] MPW1PW91/cc-pVTZ: P_4O_{18}, $E = -2718.676900$ au, zpe = 50.2 kcal mol^{-1}; P_4O_{10}, $E = -2117.805845$ au, zpe = 31.9 kcal mol^{-1}; $^1O_2$ ($^1\Delta$), $E = -150.228341$ au, zpe = 2.4 kcal mol^{-1}.

[5] a) A. U. Kahn, M. Kasha, *J. Chem. Phys.* **1963**, *39*, 2105; b) E. McKeown, W. A. Waters, *J. Chem. Soc. B* **1966**, 1040.

[6] N. J. Turro, V. Ramamurthy, K.-C. Liu, A. Krebs, R. Kemper, *J. Am. Chem. Soc.* **1976**, *98*, 6758–6761.

[7] A. J. Alfano, K. O. Christe, *Angew. Chem.* **2002**, *114*, 3386–3388; *Angew. Chem. Int. Ed.* **2002**, *41*, 3252–3254.

[8] a) "Qualitative Valence Bond Descriptions of Electron-Rich Molecules": R. D. Harcourt, *Lect. Notes Chem.* **1982**, *30*; b) R. D. Harcourt in *Quantum Chemical Methods in Main Group Chemistry* (Eds.: T. M. Klapötke, A. Schulz), Wiley, Chichester, **1998**, pp. 217–253; and references therein; c) R. D. Harcourt, *Eur. J. Inorg. Chem.* **2000**, 1901.

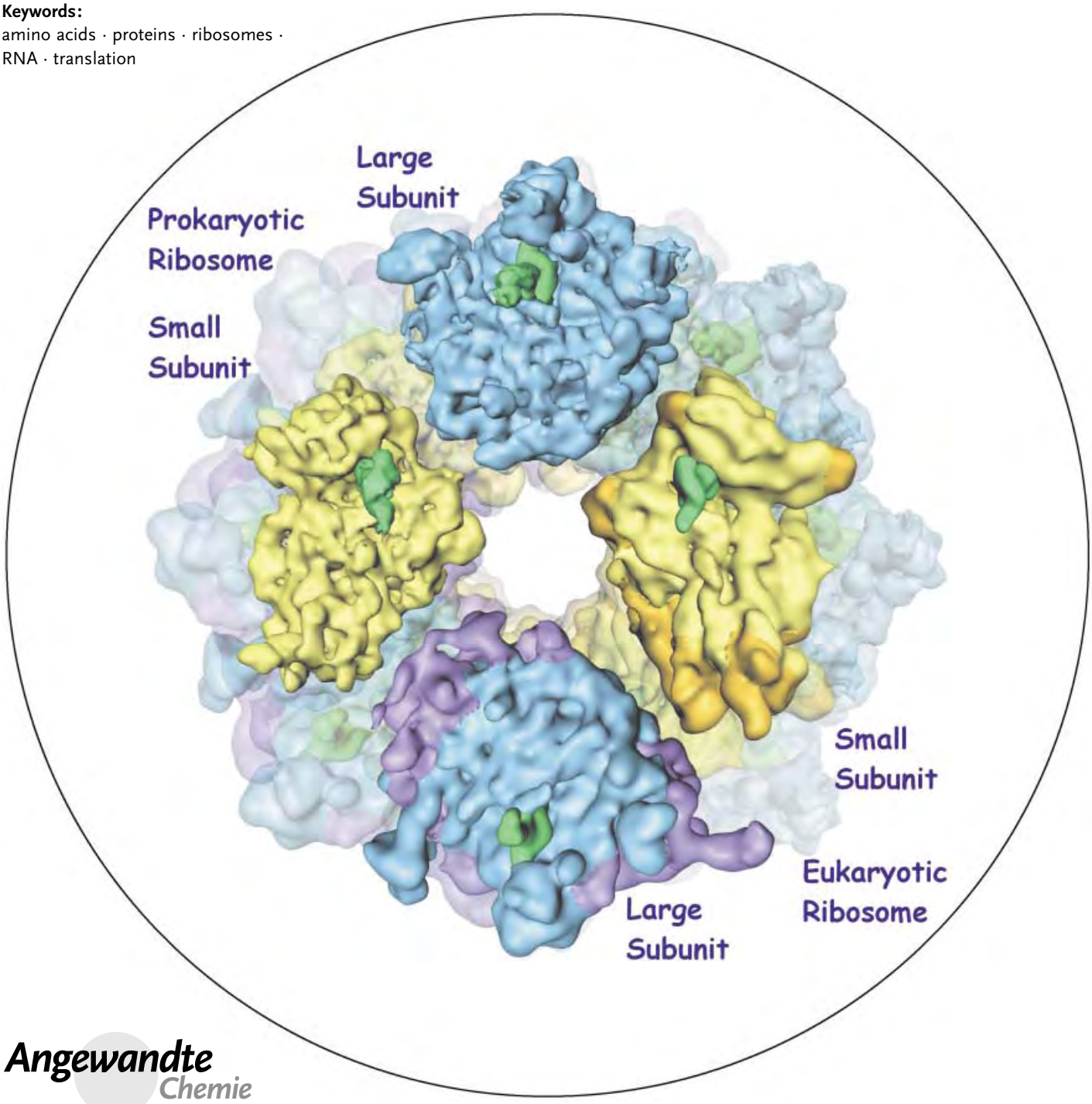
 © 2003 Wiley-VCH Verlag GmbH & Co. KGaA, Weinheim

Ribosome Structure and Translation

The Ribosome through the Looking Glass

*Daniel N. Wilson and Knud H. Nierhaus**

Keywords:
amino acids · proteins · ribosomes · RNA · translation



 © 2003 Wiley-VCH Verlag GmbH & Co. KGaA, Weinheim DOI: 10.1002/anie.200200544

Angewandte Chemie

For almost 20 years crystallographers have sought to solve the structure of the ribosome, the largest and most complicated RNA–protein complex in the cell. All ribosomes are composed of a large and small subunit which for the humble bacterial ribosome comprise more than 4000 ribonucleotides, 54 different proteins, and have a molecular mass totaling over 2.5 million Daltons. The past few years have seen the resolution of structures at the atomic level for both large and small subunits and of the complete 70S ribosome from Thermus thermophilus *at a resolution of 5.5-Å. Soaking of small ligands (such as antibiotics, substrate analogues, and small translational factors) into the crystals of the subunits has revolutionized our understanding of the central functions of the ribosome. Coupled with the power of cryo-electron microscopic studies of translation complexes, a collection of snap-shots is accumulating, which can be assembled to create a likely motion picture of the bacterial ribosome during translation. Recent analyses show yeast ribosomes have a remarkable structural similarity to bacterial ribosomes. This Review aims to follow the bacterial ribosome through each sequential "frame" of the translation cycle, emphasizing at each point the features that are found in all organisms.*

From the Contents

1. The Wonders of the Translational World 3465

2. The Path of the tRNA through the Ribosome 3468

3. Summary and Outlook 3483

1. The Wonders of the Translational World

The ribosome is a translator. It uses the information contained in messenger RNA (mRNA) to produce the corresponding sequence of amino acids, thus linking the worlds of nucleic acids (DNA and RNA) and proteins. It does this by providing the platform on which each codon of the mRNA is matched with the amino acid it encodes. The physical link between the worlds of RNA and protein is the pool of transfer RNAs (tRNAs). One end of each tRNA species, the anticodon, is complementary to the codon of the mRNA while the other end, termed the CCA end, is covalently attached to the amino acid specific for that codon. The correct aminoacylation of tRNAs with the appropriate amino acid is equally important for ensuring the fidelity of translation. This task is performed by synthetases, such that for each of the 20 amino acids there is a correponding synthetase, which recognizes on the one hand the amino acids and on the other hand all tRNAs which decode this amino acid. The job of every ribosome is to ensure that the mRNA is read in the correct frame and that each tRNA faithfully follows the code. The ribosome performs this process with amazing accuracy and at high speed: 10–20 amino acids are incorporated per second into the growing nascent chain, with only one error in every 3000 codons deciphered. To understand how the ribosome achieves this feat, an understanding of the overall structure of the ribosome will be necessary.

1.1. Common Structural Features of the Ribosome

All ribosomes are composed of two subunits of unequal size. Bacterial ribosomes have a relative sedimentation rate of 70S and can be separated into a large 50S subunit and a small 30S subunit. Eukaryotic ribosomes are larger: *Saccharomyces cerevisiae* (yeast) ribosomes, for example, sediment at 80S and are separable into 60S and 40S subunits. Each subunit of a ribosome is a ribonucleoprotein particle. In the eubacteria *Escherichia coli* one third of the mass of a ribosome consists of protein and the other two thirds of ribosomal RNA (rRNA): The 50S subunit contains both a 5S (120 nucleotides) and a 23S rRNA (about 2900 nucleotides), while the 30S subunit contains a single 16S rRNA (approximately 1500 nucleotides). The protein fraction consists of 21 different proteins in the small subunit and 33 proteins in the large subunit. Eukaryotic ribosomes have longer rRNAs (because of the insertion of additional sequences at specific regions termed expansion sequences (ESs)), an additional rRNA, and 20–30 extra ribosomal proteins, which together account for the 30% increase in size relative to *E. coli* ribosomes.

The overall three-dimensional shapes of the 70S ribosome and its component subunits have been characterized by a variety of electron microscopy techniques since the 1980s. The small subunit was described anthropomorphically with a head, connected by a neck to a body with a shoulder and a platform (Figure 1a). The large subunit presents a more compact structure consisting of a rounded base with three protuberances, termed the L1, central protuberance, and the L7/L12 stalk (Figure 1b). A vast improvement in the resolution was achieved by the introduction of single-particle

[*] Prof. Dr. K. H. Nierhaus, Dr. D. N. Wilson
Max-Planck-Institut für molekulare Genetik
Ihnestrasse 73, 14195 Berlin (Germany)
Fax: (+49) 30-8413-1594
E-mail: nierhaus@molgen.mpg.de

 DOI: 10.1002/anie.200200544 © 2003 Wiley-VCH Verlag GmbH & Co. KGaA, Weinheim

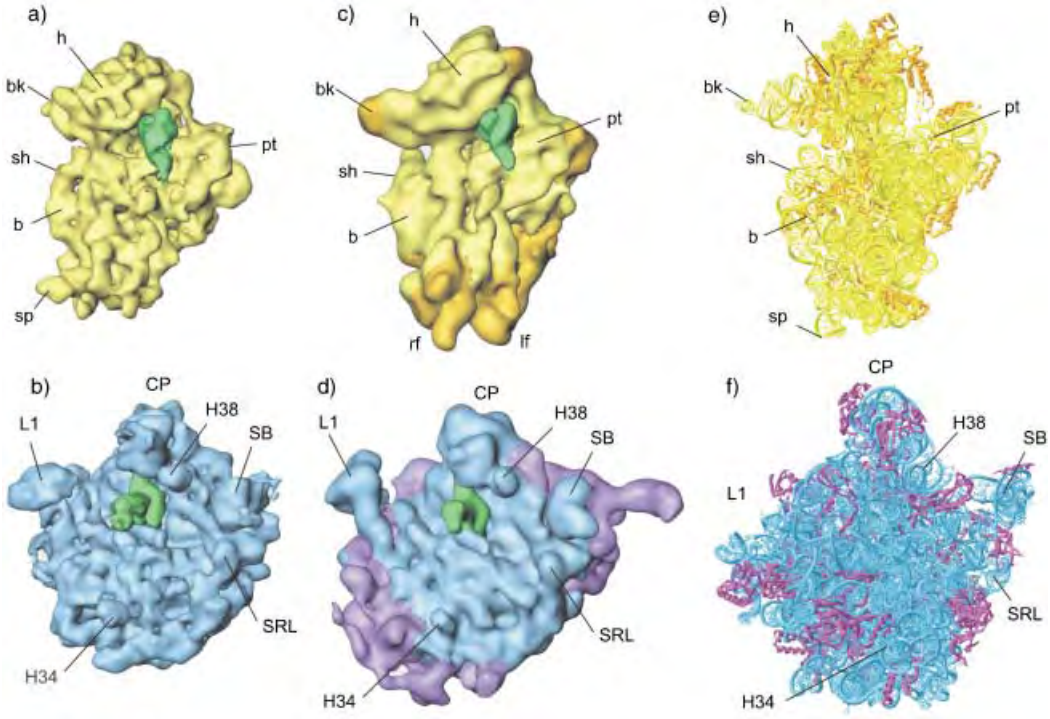
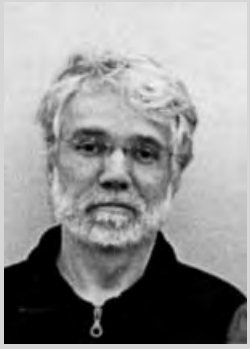


Figure 1. Comparison of the small and large ribosomal subunit from bacteria with those of a lower eukaryote. Cryo-electron microscopic reconstructions of the small (a) and large subunit (b) of the bacteria *Escherichia coli* are compared with the small (c) and large subunit (d) of the yeast *Saccharomyces cerevisiae* and the recent high-resolution crystal structures for the small subunit from the bacteria *Thermus thermophilus* (e) and large subunit from the archeon *Haloarcula marismortui* (f). All subunits are viewed from the interface side with the P-tRNA present in the cryo-EM reconstructions (green). Additional masses within the yeast 80S ribosome compared with that of a bacterial ribosome are shown in dark yellow (40S subunit) and purple (60S subunit). Landmarks of the small subunits include: b, body; bk, beak; h, head; lf, left foot; rf, right foot; pt, platform; sh, shoulder; and sp, spur. Landmarks for the large subunit: CP, central protuberance; L1, L1 protuberance; SB, stalk base; St, L7/L12 stalk; H34, helix 34; H38, helix 38; and SRL, sarcin–ricin loop. Cryo-EM images adapted from Spahn et al.[3]

reconstruction of cryo-electron microscopy images.[1] The general structural features of the ribosome remained at higher resolution, but more detailed structural features appeared, such as the beak and toe or spur on the 30S subunit.

More recently, cryo-EM analysis has been used to examine eukaryotic ribosomes and subunits.[2–5] These reconstructions show that despite the extra size, yeast and mammalian ribosomes show extensive structural similarity with their bacterial counterparts (Figure 1c and d). The differences, which stem principally from additional rRNA and proteins in the eukaryote ribosome (shaded darker in Figure 1c and d), are located predominantly in the surfaces of the subunits exposed to the cytoplasm and not to the intersubunit surface where the subunits interact with one another. Another feature of all ribosomes is a tunnel that traverses the large subunit; it starts at the peptidyltransferase (PTF) center at the interface and exits at the base or cytoplasm side of the large subunit. The growing polypeptide chain is believed to travel through the tunnel before exiting into the cytosol of the cell. The tunnel has a length of approximately 100 Å and can house between 30 and 50 amino acid residues of the growing polypeptide chain.

In the case of proteins that are targeted to organelles and cell compartments, such as the endoplasmic reticulum, chloroplasts, or mitochondria, the ribosome must dock with a pore or protein-conducting channel on the surface of the



Knud H. Nierhaus studied medicine and completed his thesis with Prof. Klaus Betke in Tübingen. In 1968 he joined the MPI für Molekulare Genetik in Berlin, where he currently leads a research group studying different aspects of translation. He is "außerplanmäßiger Professor" at the TU, Berlin and "adjunct Professor" at the Moscow State University. His main achievements include: the development of a method to degrade the large subunit from E. coli ribosomes and the detection of a third tRNA binding site on the ribosome.



Daniel N. Wilson studied Biochemistry and Molecular Biology at Victoria University, Wellington, New Zealand. He carried out his PhD in the laboratory of Prof. Warren Tate in the Biochemistry Department at the University of Otago, Dunedin, New Zealand. In his thesis he focused on the mechanisms of translational termination and recoding events. Following completion of his studies in 1999, he was awarded an Alexander von Humboldt and currently works in the laboratory of Prof. Nierhaus at the MPI für Molekulare Genetik in Berlin.

 © 2003 Wiley-VCH Verlag GmbH & Co. KGaA, Weinheim

organellar membrane, through which the nascent chain is cotranslationally exported. Such a complex from yeast, namely the 80S ribosomes of *S. cerevisiae* bound to the Sec61 pore protein, a protein involved in protein transport into the endoplasmic reticulum, has been analyzed by cryo-EM. The results of these studies show that the funnel-shaped pore sits directly over the exit of the tunnel,[4–6] thus supporting the role of the tunnel as the conduit for the nascent chain.

The presence of the tunnel in ribosomes of all organisms implies its importance, yet its function still remains speculative. The tunnel has been proposed to provide an environment suitable for the early stages of protein folding or to simply protect the nascent chain from proteases until sufficient amino acids have been synthesized to enable secondary structure formation. Recently, a more active role for the tunnel has been proposed, based on the observation of sequence-specific recognition by ribosomal components of nascent oligopeptides within the tunnel, which were shown to influence both protein elongation and translation termination (reviewed by Tenson and Ehrenberg).[7]

1.2. The Ribosome up Close

The last few years have seen the arrival of high-resolution crystal structures of the small subunit from the thermophilic bacterium *Thermus thermophilus* (3 Å; Figure 1e),[8,9] the large subunit from the archaebacterium *Haloarcula marismortui* (2.4 Å; Figure 1f),[10] and also more recently the large subunit from the mesophilic eubacterium *Deinococcus radiodurans* (3.1 Å).[11] A number of excellent reviews followed shortly after, in which the implications of these structures were discussed in regard to our extensive knowledge of the functional aspects of protein synthesis.[12,13]

With the arrival of high-resolution subunit structures, it was now possible to correlate the low-resolution features with particular rRNA helices and/or ribosomal proteins. For example, the beak of the small subunit consists exclusively of helix h33, the spur of h6, and the central protuberance is made up of the 5S rRNA, part of 23S rRNA, as well as ribosomal proteins L5, L18, L25, and L33. A more detailed analysis of the subunit structures reveals an immediately discernible difference in the overall assignment of the domains of the rRNA secondary structure relative to the tertiary domains: In the 30S subunit, the rRNA can be simply divided into tertiary domains, with each domain corresponding with a structural landmark of the 30S subunit; for example, the 5′-domain of the 16S RNA forms the body from the toe to the shoulder, the middle domain forms the platform, and the large 3′-domain the head, and finally the small 3′-domain runs down the intersubunit surface of the 30S subunit. In contrast, rRNA in the 50S subunit has a much more compact interwoven secondary structure, perhaps suggesting that the 50S subunit is older in evolutionary terms, and has had more time to evolve such a complex organization of the domain[14] and/or that the 30S subunit requires more flexibility to perform its function.

With the crystal structures of the ribosomal subunits came 20 new and complete structures for both small[8] and large[10] subunits of ribosomal proteins. A special feature of many of these ribosomal proteins is the presence of a globular domain, which is usually bound to the surface of the subunit, as well as a long filamentous extension, which penetrates deep into the center of the ribosome, the ribosomal RNA core. Ribosomal proteins are commonly found bound to junctions between rRNA helices, thereby often connecting different domains. A comprehensive analysis of the protein–rRNA interactions in the small (30S) subunit revealed that the globular proteins tend to bind early in the assembly process whereas the proteins with long extensions assemble later.[15]

Perhaps one of the biggest surprises from the crystal structures was that, despite a tenfold increase in the amount of RNA structure known, almost all of the secondary structure motifs had been seen before, which suggests that the number of motifs is limited. A common feature of the ribosome is the highly helical nature of the rRNA. Regions that were predicted to be single-stranded loop regions actually appear as slightly irregular double-stranded extensions of neighboring helices in the crystal structure. Furthermore, helical regions stack end-to-end to form long quasi-continuous helical structures. The proportion of adenine residues is significantly underrepresented within these helical or paired regions (Table 1).[16] The significance, both functional and structural, of these residues is evident from the participation of adenine residues in the so-called "A-minor" motif, a recurring feature of the ribosome which is important in the stabilization of the rRNA tertiary structure.[17] In general, the A-minor motif constitutes an interaction between an adenine residue and the minor groove of an rRNA helix and is not limited to ribosome structures, and have been observed previously in *Tetrahymena* and hepatitis delta virus ribozymes.[18] Four variations in this motif have been identified in the ribosome,[17] two of which, type I and II, play a crucial role in ribosome function by being involved in both decoding and formation of a peptide bond. Since the adenine residues involved at both of these sites are universally conserved, the implication is that the mechanisms of decoding and formation of a peptide bond are also conserved between prokaryotes and eukaryotes. The details of these interactions are discussed more thoroughly in Sections 2.2.2 and 2.3.2, respectively.

Table 1: Frequency and distribution for each ribonucleotide within bacterial 16S and 23S rRNAs secondary structure models.[a]

Nucleotide	G	C	A	U
overall frequency	31.4	22.4	25.7	20.5
distribution within helical regions	36.6		14.5	
frequency within unpaired regions		12.5	42.6	
distribution within unpaired regions	30.1	22.3	66.2	41.5
unpaired/paired ratio	0.43/1	0.29/1	1.96/1	0.71/1

[a] Data sourced from Gutell et al.[16]

 © 2003 Wiley-VCH Verlag GmbH & Co. KGaA, Weinheim

2. The Path of the tRNA through the Ribosome

The "decoding site" is located on the small subunit. This is the site where the codons of the mRNA are recognized and deciphered by the complementary anticodon of the tRNA. There are three sites on the ribosome that tRNAs can occupy (A, P, and E; Figure 2). The A site is where the aminoacyl tRNA (aa-tRNA) binds, according to the codon displayed at this site. It is the aa-tRNA that brings in the new amino acid to extend the growing polypeptide chain. The P site is where the peptidyl-tRNA is bound before formation of the peptide bond. This is the tRNA carrying the nascent polypeptide chain. The E site is the exit site for the deacylated or uncharged tRNA. The tRNAs move through each of the sites sequentially during translation, starting at the A site and passing through the P site to the E site, before leaving the ribosome. The exception is the binding of the very first tRNA (the initiator tRNA), which binds directly to the P site (Figure 2a).

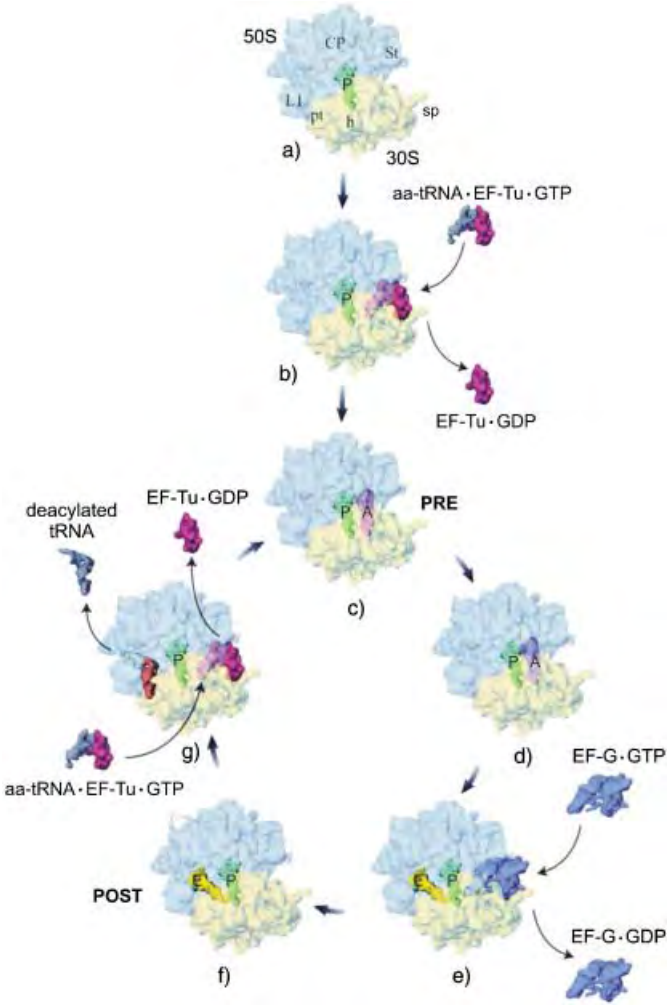


Figure 2. Overview of the translation cycle. Multiple cryo-electron microscopic studies have determined the binding positions of the tRNA and elongation factor on the 70S ribosome during different stages of the elongation cycle (see Ref. [19] and references therein). The small 30S subunit is in yellow, the 50S large subunit in blue. The positions of the ribosomal elongations factors have been overlaid onto a 3D map of the ribosome at a resolution of 11.5 Å to generate a schematic overview of the elongation cycle, the details of which are provided in the text. Adapted from Agrawal et al.[19]

Initiator tRNAs decode the start codon, usually AUG, and carry the amino acid formylmethionine in bacteria or methionine in eukaryotes (including archaea). The codon following the start codon is displayed at the A site and dictates which aa-tRNA will now bind (Figure 2b). The aa-tRNAs are delivered to the A site in the form of a ternary complex consisting of an elongation factor (EF-Tu in bacteria and EF1α in eukaryotes), GTP, and the aa-tRNA. After GTP hydrolysis, EF-Tu·GDP is released from the ribosome and the aa-tRNA docks into the A site (Figure 2c). The formation of a peptide bond involves the transfer of the peptidyl moiety of the P-tRNA to the aminoacyl moiety of the A-tRNA: It is noteworthy that the whole polypeptide chain is added to the new amino acid rather than the addition of the new amino acid to the chain. Formation of peptide bonds occurs on the large subunit at the PTF center. The formation of the peptide bond had no significant change in the positions of the two tRNAs (Figure 2d), although the P site now contains an uncharged tRNA and the A site contains a peptidyl-tRNA.

Transfer of the A- and P-tRNAs to the P and E sites is termed translocation and is mediated by a second elongation factor (EF-G in bacteria (Figure 2e) and EF2 in eukaryotes). In simple terms, the role of the elongation factors is to accelerate the elongation cycle to the rate of 50 msec per elongation cycle in vivo. The rate without elongation factors is about four orders of magnitude slower[20] because of the high energy barrier (120 kJ mol^{-1}) that separates the pre- and posttranslocational states (Figure 2c and f, respectively) in the *E. coli* ribosomes.[21] Translocation places the deacylated tRNA at the E site and peptidyl-tRNA at the P site, thus freeing the A site for the binding of the next aa-tRNA (Figure 2f). Binding of the next A-tRNA releases the E-tRNA (Figure 2g) and so the cycle repeats (that is, back to Figure 2c) until a stop codon appears in the A site. At this point protein termination factors release the completed polypeptide and dissociate the ribosome into subunits in preparation for the next round of translation.

2.1. Initiation of Protein Synthesis: Subunit Association and Intersubunit Bridges

The translation of functionally active protein requires that mRNA be positioned on the 30S subunit such that the start codon will be read first and in the correct frame. Initiation at a codon before or after the start codon would produce either an extended or truncated protein, either of which may be inactive. The placement of the start codon must also be precise: As codons are composed of three nucleotides, this opens the possibility of initiating translation in an incorrect frame through selection of the incorrect first nucleotide of the codon. Thus, the precision and specificity of the initiation phase is crucial for cell viability.

How does the ribosome select the correct start codon and ensure the specificity of the interaction with the initiating tRNA? In fact, there is no single answer to this question, since

 © 2003 Wiley-VCH Verlag GmbH & Co. KGaA, Weinheim

there are so many exceptions to the rule. In general, however, the positioning of the mRNA utilizes the untranslated region (UTR) upstream of the start codon, which directs placement of the mRNA on the small subunit. In bacteria, the mechanism is relatively simple and involves a stretch of nucleotides (the Shine–Dalgarno (SD) sequence) that interacts with a complementary sequence within the 3′ end of the 16S rRNA (the anti-SD sequence). This interaction was directly visualized recently in the Fourier difference maps between empty 70S ribosomes and those carrying mRNAs.[22]

The situation is much more complex in eukaryotes because of the increased regulatory mechanisms operating on translation. In most cases, the 5′-end of eukaryotic mRNAs are modified with a guanine "cap" structure. This cap structure is recognized by specific initiation factors, which direct binding of both the mRNA and the initiator Met-tRNA to the 40S subunit. The mRNA is then "scanned" downstream (in the 3′ direction) until the first AUG start codon is found. The large 60S subunit can now bind and protein synthesis commences. In certain cases, the UTRs contain complex secondary structures, which are recognized and bound by large heteromeric protein complexes. Some of these protein factors interact directly with the 40S subunit to mediate mRNA positioning (reviewed recently by Pestova and et al.).[23]

Despite these differences between translation initiation in bacteria and eukaryotes, a number of distinct similarities are also emerging.[24] For example, formation of initiation complexes in both prokaryotes and eukaryotes involves the binding of the mRNA and initiator tRNA to the small subunit, such that the initiator tRNA is present at the P site of the small subunit. This is a unique situation as all subsequent aa-tRNAs that participate in translation will enter the ribosome through the A site. As discussed in Section 2.2.2, it is the codon–anticodon interactions at the A site that are monitored carefully by the ribosomes to ensure translational fidelity. Initiation, by allowing direct P-site binding, bypasses this important "monitoring" step.

How then does the ribosome ensure that the correct tRNA binds the start codon and that the start codon is placed exactly at the P site? A number of specialist initiation factors have evolved to ensure the fidelity of P-site binding during initiation. In bacteria, this process is mediated by three initiation factors, IF1, IF2, and IF3 (reviewed by Gualerzi and et al.).[25] The only ribosome complexes with protein translation factors that have been solved so far are those with initiation factors IF1 and a domain of IF3.[26,27]

IF3, which may be the first initiation factor to bind to the 30S subunit, displays dual functions. Firstly, by acting as an anti-association factor, it prevents formation of the 70S ribosome by prohibiting association of the 30S subunit with 50S subunits. Secondly, it plays an important role in codon–anticodon discrimination in the P site. IF3 is composed of two domains separated by a long lysine-rich linker. The C-terminal domain (CTD) is sufficient for ribosome binding and fulfills the first function of the factor, while the N-terminal domain (NTD) has been implicated in the second function. The crystal structure of the CTD on the 30S subunit has been solved, which allowed the NTD to be docked into the structure.[27] The binding site of the CTD of IF3 suggests that the anti-association function of this domain operates through conformational changes, not through direct steric obstruction as previously thought. Furthermore, the NTD is proposed to monitor correct codon–anticodon interactions at the P site, not through a direct interaction, but through space restrictions, such that only correct binding orientations are possible.[27]

Recently, footprinting experiments using IF3 led to a contradictory model for IF3 binding on the 30S subunit which suggested the CTD of IF3 does in fact prevent subunit association directly.[28] This result raises the question of whether IF3 has two binding sites on the 30S subunit: perhaps one associated with initiation, thus checking the codon–anticodon interaction, and the other during ribosome disassembly.

Despite the single unequivocal binding site of IF1 on the ribosome, it's exact function still remains a mystery. The small size of IF1 (less than 10 kDa) allowed the factor to be soaked into crystals of the 30S subunit.[26] IF1 was found to bind in the A site which suggested that it helps prevent premature binding of the A site to the initiator tRNA. It was however shown that factor-free 30S subunits bind tRNA exclusively at the P site in the presence of a suitable mRNA,[29] so this additional verification seems unnecessary. The binding of IF1 induces long-range conformational changes within the intersubunit surface, particularly within the helix h44 of the 30S subunit, which together with IF3 may promote association of the subunit.[26] Bacterial IF2 binds specifically to initiator tRNAs and directs them to the 30S subunit. Delivery of the initiator tRNA by IF2 is enhanced by IF1. Interestingly, the central region of eukaryotic translation initiation factor eIF1A forms a so-called "OB fold", as seen for IF1, and thus may bind in an analogous fashion to the A site of the 40S subunit.[30] Homologues to IF2 have been found in eukaryotes and archaea, eIF5B and aIF5B, respectively, and have been shown to interact directly with eIF1A (see the review by Pestova et al.[23]). The complex containing the 40S subunit, the initiator tRNA, initiation factors, and the mRNA with the AUG codon at the P site is called the 43S pre-initiation complex. Association of this pre-initiation complex with the 60S subunit is stimulated by eIF5B. It is likely that the association of the small and large subunit results in conformational change that stimulates hydrolysis of GTP by IF2 or eIF5B and subsequently their release from the ribosome.

A number of contact points between the small and large subunit have been identified in the bacterial 70S ribosome, which are termed intersubunit bridges (Figure 3a and b).[31,32] The functional importance of these intersubunit bridges is emphasized by identification of corresponding bridges in the eukaryotic 80S ribosome (yeast; Figure 3c and d).[3] As well as being important for association of the ribosomal subunits, these bridges probably play an important role in movement of the tRNAs through the ribosome (see Section 2.4) and in signaling between the decoding center on the small subunit and the PTF center on the large subunit. Closer inspection of the bridges within bacterial and yeast ribosomes reveals that many of the bridges, namely B2a, B3, B5a, and B5b, involve

 © 2003 Wiley-VCH Verlag GmbH & Co. KGaA, Weinheim

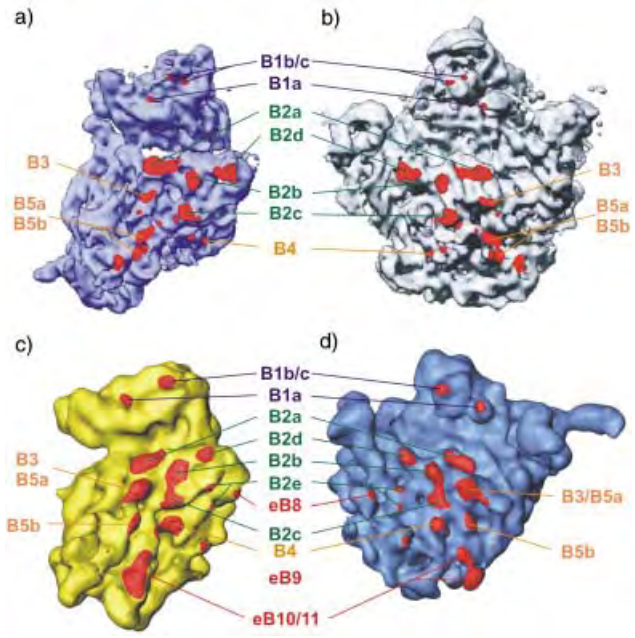


Figure 3. Comparison of bridging positions between the subunits of the bacteria and yeast ribosomes. a, b) The 30S (blue) and 50S (gray) ribosomal subunits of *Thermus thermophilus* are shown from their intersubunit sides. The bridges are marked in red and are annotated according to the nomenclature from Gabashvili et al.[31] Bridges B1, B2, and B3–5 are labeled in blue, green, and orange, respectively. The figure was adapted from Cate et al.[32] c, d): The 40S (yellow) and 60S (blue) ribosomal subunits of *Saccharomyces cerevisiae* are shown from the interface side. The bridges are labeled in red. Those common to *T. thermophilus* are labeled in blue (B1), green (B2), and orange (B3–B5), while additional intersubunit connections in the yeast ribosome are labeled eB8–eB11 in red. Note that bridges B6 and B7 are not included for simplicity. Adapted from Spahn et al.[3]

contacts with h44, a helix of the 30S subunit intimately involved in decoding.

2.2. The A Site: Decoding, Mimicry, and Antibiotic Interaction

With the exception of initiation, the ribosomal A site is the entry point for charged aa-tRNAs. Here the ribosome must determine whether the incoming tRNA is correct with respect to the codon of the A site or not, that is, whether it should be accepted into the A site or rejected. The molecular details of this "decision" have been recently revealed and confirm a 20-year-old hypothesis.[33a] The A site also contributes to the binding site of the elongation factors. During each stage of protein synthesis—initiation, elongation, and termination—translation factors interact with the ribosomal A site. Structures for a number of these translation factors have been determined. Regions of these structures display an overall similarity with one another, but more specifically they exhibit a remarkable similarity with the dimensions of a tRNA, the "true" substrate of the A site. This phenomenon, in which a protein factor mimics the A-tRNA substrate, is an example of molecular mimicry—a reoccurring theme in the translation (see the review by Nissen et al.[34]) that may well have been overextrapolated. As yet there are no ribosome crystal complexes with elongation or termination factors. The reason for this is probably that the large size of the translation factors (40–80 kDa) prohibits the use of simple soaking experiments and instead requires more complex cocrystallization experiments. Thus, most of the structural information for these complexes comes from cryo-EM studies. In contrast, the soaking of small ligands, such as antibiotics, into the ribosome crystals has been very successful. The decoding site is the target for a number of potent translation inhibitors. The structures of antibiotics, such as tetracycline, paromomycin, streptomycin, hygromycin, and spectinomycin, have been solved to atomic resolution in a complex with the 30S subunit.

2.2.1. The Universal Problem of Aminoacyl-tRNA Selection

Following dissociation of the initiation factors, the ribosome is now primed with an aa-tRNA bound at the P site. The codon displayed in the vacant A site is specific for a single species of tRNA that has a perfectly complementary anticodon, the cognate tRNA. However, there are many other tRNA competitors that can interfere with this selection process: 41 tRNAs with different anticodons exist in the bacterium *Escherichia coli* and even more in the eukaryotic cell. To complicate matters further, three to five or six of these tRNAs (near-cognate tRNAs) will have an anticodon similar to the cognate tRNA. The remaining 90% have a dissimilar anticodon and are termed noncognate tRNAs. The problem is compounded further when one considers that the aa-tRNAs are delivered in the form of a ternary complex, that is, in a complex with the elongation factor EF-Tu and GTP. The ribosome must therefore discriminate between relatively large ternary complexes (72 kDa), which present multiple potential interaction sites to the ribosome, on the basis of a small discrimination area, the anticodon (1 kDa).

The ratio of the large surface area and the small discrimination surface defines the corresponding energy ratio: binding is dominated by a relatively large free energy, with only a tiny fraction corresponding to the discrimination energy. The unusual molecular selection problem of the ribosome consists of the fact that a large part of the binding energy of the 41 different ternary complexes (*E. coli*) is identical, and thus the discrimination is based on the tiny fraction corresponding to the discrimination energy. The discrimination potential of the discrimination energy can only be reached under equilibrium conditions. In this case where the binding energy is relatively large, the equilibrium can only be reached after long time periods—in other words, this process must be slow to be accurate.

Since we know that protein synthesis is a relatively fast *and* accurate process, the ribosome must overcome this hurdle. But how? A model has been proposed which overcomes this problem by simply dividing the occupation at site A into two distinct events: a decoding step followed by an accommodation step (see the review in Ref. [35]). During the initial decoding step, the A site is in a low affinity state, which reduces interaction of the ternary complex to codon–anticodon interactions, thus excluding general contacts of the tRNA and elongation factor. By restricting the binding

 © 2003 Wiley-VCH Verlag GmbH & Co. KGaA, Weinheim

surface of the ternary complex to the discriminating feature, that is, the anticodon, the binding energy is both small and approximately equivalent to the discrimination energy. Since the binding energy is small, equilibrium can be rapidly attained, thus ensuring that the efficiency of the reaction is retained. The second step, accommodation in the A site, requires release of the aa-tRNA from the ternary complex. This step utilizes the nondiscriminatory binding energy to dock the tRNA precisely into the A site and the attached aminoacyl residue into the PTF center on the 50S subunit in preparation for formation of a peptide bond. As we will see later, accommodation of the aa-tRNA in the A site is accompanied by release of the E-tRNA. Evidently, this second step of A-site binding involves gross conformational changes within the ribosome[21] and thus can be thought of as a relatively slow process relative to the decoding step. A-site binding occurs through a coupled reaction system consisting of a fast initial or decoding step and a slow accommodation step. This has the important consequence that the initial reaction operates at equilibrium even when under steady-state conditions. The complete process—the fast decoding step with a subsequent slower accommodation step—results in the discriminatory potential of codon–anticodon interactions being efficient and the rate of proton synthesis high.

Recently, the first step of A-site binding (low affinity A site) was visualized by cryo-EM analysis of ternary complexes stalled the A site with the antibiotic kirromycin.[36,37] Although kirromycin allows GTP hydrolysis of EF-Tu, it inhibits the associated conformational changes in EF-Tu that are necessary for dissociation from the ribosome. The cryo-EM reconstructions suggest that the anticodon stem loop (ASL) of the tRNA is kinked to allow codon–anticodon interaction, and thus overcomes the unfavorable incoming angle of the tRNA to the A site as dictated by the ternary complex (see Figure 2b).[36]

As already indicated, the accommodation of an aa-tRNA into the A site involves the dissociation of EF-Tu·GDP from the ribosome, a process which is coupled with the hydrolysis of GTP. It is interesting to note that in *E. coli* up to two GTPs are hydrolyzed during the incorporation of cognate-tRNAs and up to six GTPs during the incorporation of near-cognate-tRNAs, whereas noncognate-tRNAs do not trigger EF-Tu-dependent GTP hydrolysis at all.[38] This observation adds further weight to the argument that the tRNA discrimination is governed predominantly by anticodon–codon interactions during the initial binding step. The next question is: How are the cognate and near-cognate tRNAs discriminated? This is a question that can now be answered at the molecular level, as is discussed in the next section.

2.2.2. *Decoding of Aminoacyl-tRNAs*

A model for the discrimination between cognate and near-cognate aa-tRNAs was proposed by Potapov about 20 years ago.[33a] According to this model, the decoding center of the ribosome recognizes the anticodon–codon duplex, in particular, sensing the stereochemical correctness of the partial Watson–Crick base pairing and the positioning of the phosphate–sugar backbone within this structure. A test of this hypothesis was performed with an mRNA that carried a DNA codon at one of the three ribosomal sites.[33b] If the stability of the base pairs, that is, the hydrogen bonds between codon–anticodon bases of the Watson–Crick base pairs, is the sole requirement for the recognition step, then a 2′-deoxy base in the codon should not affect the decoding process. If, however, the stereochemical correctness of the base pairing is tested, that is, including the positioning of the sugar group, then a 2′-deoxy base should impair the decoding process. It was found that a deoxycodon at the A site was disastrous for tRNA binding at this site, whereas a deoxycodon at the P site had no effect on tRNA binding to the P site. This result was in agreement with earlier data showing that DNA could not perform the same function as an mRNA (see Potapov et al.[33b] and references therein).

Recently, the components of the ribosome directly involved in decoding were identified by crystallography at a resolution of 3.1 Å.[39] The crystal packing of the 30S subunit of *Thermus thermophilus* showed that the spur (h6) of one subunit was placed fortuitously into the P site of another, thus mimicking the anticodon stem loop of a P-tRNA. Another surprise was that the base-pairing partner to the P-tRNA mimic was the 3′-end of the 16S rRNA, which extended into the decoding center by folding back upon itself. This situation, with the P site filled, enabled Ramakrishnan and co-workers to then soak an ASL fragment (ASL-tRNA) and a complementary mRNA fragment into these crystals to study aa-tRNA decoding.[39]

The binding of mRNA and cognate aa-tRNA induces two major rearrangements within the ribosomal decoding center: the universally conserved residues A1492 and A1493 flip out of the internal loop of h44, while the universally conserved base G530 switches from a *syn* to an *anti* conformation. Through this process A1493 recognizes the minor groove of the first base pair of the codon–anticodon helix in the A site. The first base pair between ASL-tRNA and the mRNA consists of position A36 and U1 in Figure 4a, respectively, and recognition takes place through a type I A-minor motif. Three hydrogen bonds are formed between A1493 and the first position of the codon–anticodon duplex (two with the 2′-OH groups of A36 and U1 and another with the O2 of U1). It is noteworthy that the third hydrogen bond is not sequence-specific as might be expected, since the O2 position of the pyrimidines and the N3 position of purines occupy equivalent positions in the minor groove of a double helix and both are hydrogen-bond acceptors.

The second base pair (A35-U2) is also monitored by 2′-OH interactions, but this time by two bases, namely A1492 and G530 (this type II A-minor interaction is seen in Figure 4b). A1492 and G530 are locked in position by secondary interactions with protein S12 (serine 50) and another universally conserved residue C518. Thus, it seems that the monitoring of the middle base pair of a codon–anticodon duplex is more rigid than the first base pair. This finding fits well with the observation that the middle base pair plays the most important role in coding an amino acid, followed by the first base pair. In contrast, the third position is less rigorously monitored and plays no role in the decoding of mRNA information. This less rigorous checking of the third

 © 2003 Wiley-VCH Verlag GmbH & Co. KGaA, Weinheim

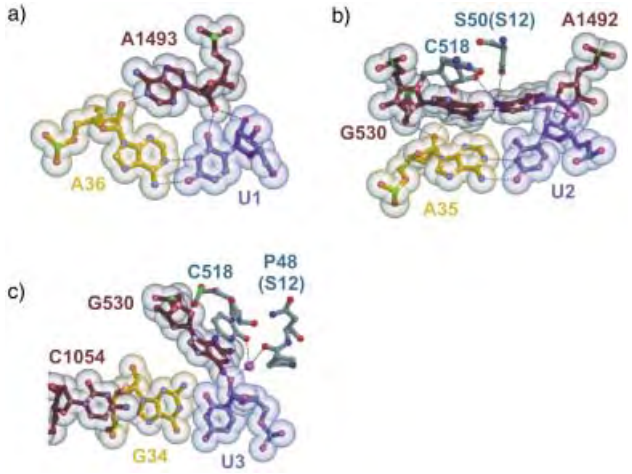


Figure 4. The principles of decoding in the A site of the ribosome. a) The first base pair of a codon–anticodon interaction (position 1) exemplifies a Type I A-minor motif: A1493 binds to the minor groove of the A36-U1 base pair through H bonds (dotted lines). b) Position 2 illustrates a type II A-minor motif: A1492 and G530 act in tandem to recognize the stereochemical correctness of the A35-U2 base pair using H bonds. c) The third (or wobble) base pair (G34-U3) is less rigorously monitored. C1054 stacks against G34 while U3 interacts directly with G530 and indirectly with C518 and proline 48 of S12 through a magnesium ion (magenta). All nucleotides involved in monitoring positions 1 and 2 are universally conserved. Adapted from Ogle et al.[39]

position allows latitude for wobble interactions (Figure 4c). This is evident in the third base pair (G34-U3) where the minor groove remains exposed, despite direct interactions with C1054 and G530 and indirect metal-mediated interactions with C518 and proline 48 of the ribosomal protein S12. Taken together, these results clearly confirm the Potapov hypothesis and explain how decoding operates through the recognition of the correct stereochemistry of the A-form codon–anticodon duplex. Furthermore, since the ribosomal components involved are universally conserved, this suggests that the mechanism of decoding is likely to be similar for all ribosomes.

Prior to the Potapov hypothesis, it had been proposed that the ribosome utilized a "proofreading mechanism" to improve the accuracy of translation.[40,41] This mechanism was suggested to operate by re-selection of the correct substrate during a so-called "discarding step", after the initial binding of the A-tRNA. Since re-selection is dependent upon release of the tRNA from EF-Tu and is accompanied by GTP cleavage, the GTP consumption for the incorporation of a cognate and near-cognate amino acid provides a measure of the power of proofreading. Insofar as the crystal structure of EF-Tu and the ribosome are concerned, the proofreading mechanism does not have its own active center; instead it can be described in terms of a kinetic effect that occurs after the release of the binary complex EF-Tu·GDP.[42] Thus, a simple model for kinetic proofreading is the following: The binding energy during the decoding step (first step of A-site binding, see Section 2.2.1) is lower for the near-cognate aa-tRNA than for the cognate one, therefore, the probability of triggering the gross-conformational change required for A-site accommodation of the aa-tRNA (second step of A-site binding) is lower than for the near-cognate. This in turn prolongs the resting time of the near-cognate aa-tRNA at the low-affinity A site and provides an additional chance for the near-cognate aa-tRNA to fall off the low-affinity A site.[43] Re-binding of this near-cognate aa-tRNA is unlikely in the presence of competing ternary complexes that have an affinity two to three orders of magnitude higher for the A site than the naked aa-tRNA.[44]

The importance of the proofreading step can be quantitatively determined by taking advantage of the fact that the proofreading mechanism requires EF-Tu-dependent GTP hydrolysis. The accuracy of aa-tRNA selection in the presence of EF-Tu and a noncleavable GTP analogue was determined to be 1:1000,[45] an accuracy only a factor of 3 lower than that seen in vivo (1:3000). The same threefold difference was also determined for the GTP consumption per incorporation of cognate versus near-cognate amino acids.[38] Thus, it is clear that the significant contribution to the accuracy of translation (1000-fold) lies within the stereochemical monitoring of the codon–anticodon duplex by the ribosome—as predicted by Potapov—and that the "proofreading mechanism" plays only a minor role in improving the accuracy. This view was qualitatively confirmed by direct measurement of the discrimination power of the initial binding without proofreading, where the binding of cognate and near-cognate ASL-tRNA fragments to the A site of 70S ribosomes were compared. The accuracy was found to be between 1:350 to 1:500, further emphasizing that the "lion's share" of the ribosomal accuracy is carried by the initial binding.[46]

2.2.3. *Mimicry at the Ribosomal A Site*

The A site is not restricted to binding tRNAs exclusively. During the various stages of the elongation cycle a number of translational factors interact at the A site. The first structures determined for these translational factors were those of the translational factors EF-G[47,48] and EF-Tu.[49,50] Interestingly, the structure of the latter, in the form of a ternary complex EF-Tu·GTP·tRNA,[51] had a striking similarity to that of EF-G·GDP, such that domains 3–5 of EF-G closely mimic the tRNA in the ternary complex (Figure 5a and b; see the review by Nissen et al.[34]). This observation suggested that the binding pocket of the A site constrains the translational factors binding there to conform to a tRNA-like shape. In the past few years, structures for various termination factors, also thought to interact with the A site, have generally supported this concept. The recent structures of the ribosome recycling factor (RRF) perhaps presented the most convincing tRNA mimic, exhibiting a similar "L" shape and dimensions as a tRNA (Figure 5c).[53] Although the structures of the bacterial RF2 factor (Figure 5d)[56] and eukaryotic human eRF1[57] factor deviate significantly from the simple tRNA structure, they do reveal overall domain arrangements that were proposed to span the ribosome in an analogous fashion to tRNA: One domain extends into the decoding site of the small subunit and another reaches towards the PTC on the large subunit. However, a recent study has contradicted these results: Cryo-EM microscopy analyses of the termination

 © 2003 Wiley-VCH Verlag GmbH & Co. KGaA, Weinheim

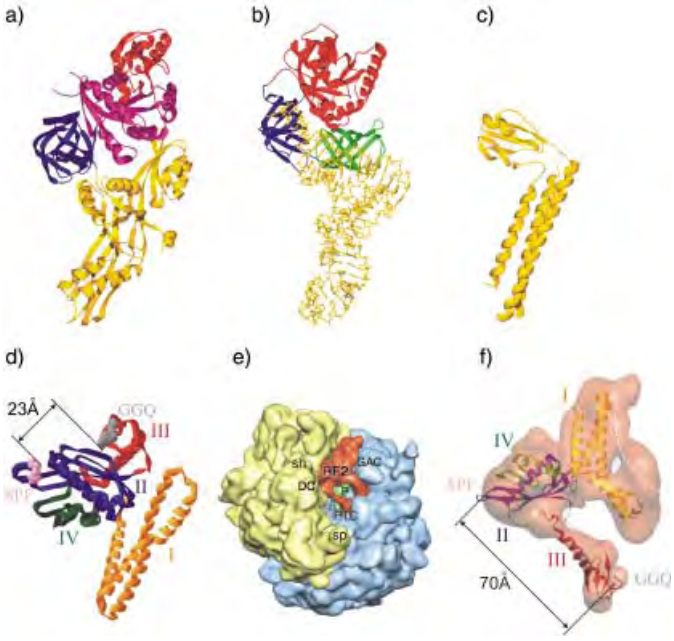


Figure 5. Molecular mimicry of tRNAs by translation factors. Comparison of the crystal structures for a) EF-G·GDP with domains 3–5 in gold (pdb1fmn),[52] b) EF-Tu·GTP·tRNA (pdb1ttt),[51] c) (pdb1eh1),[54] and d) RF2 (pdb1gqe).[56] e) Cryo-EM reconstruction of RF2 (red) bound to the 70S ribosome of *E. coli* (30S in yellow and 50S in blue). DC: decoding center, GAC: GTPase-associated center, P: P-site tRNA, PTC: peptidyltransferase center. f) Modeling of the RF2 crystal structure into the electron density of RF2 seen in (e). In (d) and (f) the Roman numerals indicate the RF2 domains which are colored accordingly, and the GGQ and SPF motifs are indicated in gray and pink, respectively. The dashed white line delineates the RF2 electron density from the ribosome electron density. The pictures of the crystal structures were generated with Swisspdb viewer[55] and rendered with POVRAY. Cryo-EM data adapted from Rawat et al.[59]

complex of RF2 bound to the ribosome revealed that RF2 undergoes dramatic rearrangement upon ribosome binding (Figure 5e).[58,59] This conformational change was not totally unexpected since two regions within the protein factor, the so called "tripeptide anticodon" and the GGQ motif were only 23 Å apart in the solution structure of RF2 (Figure 5d). Since these regions had been associated with decoding of the stop codon and hydrolysis at the PTF center, respectively, they would need to be separated by about 70 Å to make the appropriate interactions (Figure 5f).[58,59]

The structural mimicry of a tRNA by RRF was also brought into doubt when hydroxyl radical probing experiments suggested that the RRF is oriented upside down on the ribosome when the structural similarities with a tRNA were considered.[60] Confirmation of this orientation, however, awaits cryo-EM analysis of the ribosomal RRF complexes. Whether RRF undergoes similar structural rearrangements as seen for RF2 seems unlikely, but it is clear that functional, rather than structural mimicry, is a more appropriate term in this case: After release of the polypeptide chain by the termination release factors, the RRF binds the ribosome and is involved in dissociating the ribosome into subunits, thus recycling them for the next round of translation. This process is mediated by EF-G, which has been proposed to translocate RRF from the A to the P site, thus simulating its tRNA translocative role during elongation.[61]

Mimicry of RNA by a protein may be a more common feature in ribosomes than first realized. Organellar ribosomes generally have shorter rRNA components than *E. coli*. Recent analyses of the chloroplast and mitochondrial ribosome components suggests that these rRNA losses are compensated for by both increases in size of the ribosomal protein homologues and the presence of additional organelle-specific ribosomal proteins.[62] Mitochondria represent an extreme example in that the protein component of the ribosomes represents two-thirds of the mass (instead of one-third as in *E. coli* ribosomes). The rRNA that remains consists predominantly of universally conserved residues that are located at the active centers of the ribosome, that is, the decoding center on the 30S subunit and the PTF center on the large subunit,[63] thus reinforcing the importance of these regions.

2.2.4. *Antibiotic Antagonists of A Site Decoding*

To date, the structures of seven antibiotics, namely tetracycline, paromomycin, spectinomycin, streptomycin, pactamycin, hygromycin B, and edeine, have been solved in complexes with the 30S subunit.[27,39,64,65] Although the primary binding sites of these antibiotic are distinct from one another, they all target functionally important regions of the 30S subunit, mainly rRNA-rich regions associated with tRNA interaction or movement through the ribosome. Here we will focus our attention on tetracycline and paromomycin, both being antibiotics that bind within the decoding site.

Independent studies identified two common tetracycline binding sites on the 30S subunit (Figure 6a).[27,65] In both

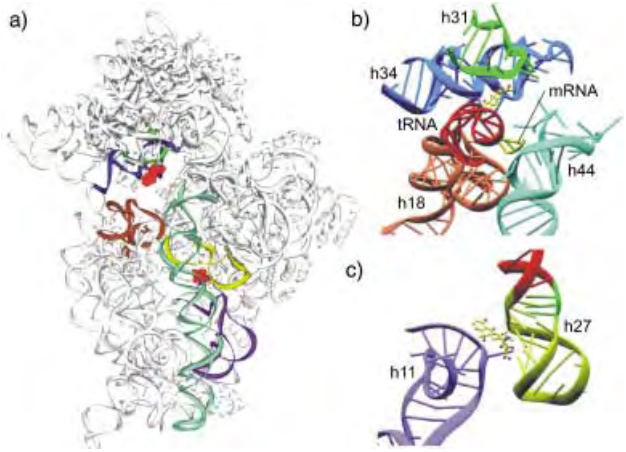


Figure 6. Binding of tetracycline (Tet) to the 30S subunit of *T. thermophilus*. a) Overview of the primary and secondary Tet binding sites (red). b) Close-up view of the primary binding site, with the position of the A-site tRNA (red) and mRNA (yellow). Helix 18 (brown), h31 (green), h34 (blue), and h44 (cyan) are represented in ribbon format. c) The secondary binding site includes h11 (purple) and h27 (yellow). The switch described in the text involves interconversion between the base-pair configuration from red to green. Figure (a) was generated from pdb file 1HNW using Swisspdb viewer[55] and rendered with POVRAY. Figures (b) and (c) are adapted from Brodersen et al.[65]

 © 2003 Wiley-VCH Verlag GmbH & Co. KGaA, Weinheim

cases, the site with the highest occupancy, which is located in a crevice between the head and shoulder of the 30S subunit, was taken to be the primary binding site (Figure 6b). In this position, tetracyclin, which has a system of four fused rings, interact predominately with the 16S rRNA through the oxygen atoms located along one side of the molecule. The oxygen atoms form hydrogen bonds with the exposed sugar phosphate backbone of helix h34. Thus, the hydrophilic side of the tetracycline interacts with the 16S RNA while the hydrophobic side is sited in the lumen of the A site. This is surprising since interaction between two molecules is usually through their hydrophobic regions. The primary binding site of tetracyclin can be expected to overlap with the position of the A site tRNA, and thus the mechanism of action of tetracycline most probably results from a direct inhibition of aa-tRNA during the accommodation step of A-site binding. For two reasons it seems unlikely that the initial binding of the aa-tRNA would be affected: 1) the tetracyline binding site is located on the opposite side of the tRNA from the site of initial anticodon–codon interaction, 2) during the delivery of aa-tRNA to the A site, the anticodon- stem loop of the aa-tRNA of EF-Tu was kinked and presented at an angle,[36,37] which would be predicted to initially avoid contact with the bound tetracycline.[27,65] This is in line with the observation that tetracycline does not inhibit the EF-Tu-dependent GTPase hydrolysis,[66] a step that occurs *after* the initial binding of the ternary complex. The rRNA bases of the primary binding site of tetracycline are poorly conserved between prokaryotes and eukaryotes, and its universal mode of action can be explained since the interaction of tetracyclin is almost exclusively made with the sugar–phosphate backbone. In contrast, the binding sites of pactamycin, edeine, and hygromycin B are highly conserved, and in these cases the main interactions are with the conserved bases.

The secondary binding site of tetracyclin is sandwiched between h11 and h27 in the body of the 30S subunit (Figure 6c). Although h27 has been proposed as a conformation switch modulating the translational fidelity of base pairs in *E. coli*,[67] it seems unlikely that this secondary site plays a role in tetracyclin inhibition. The protein Tet(O) removes tetracycline from the ribosome and thus mediates resistance against this drug. Probing experiments with dimethyl sulfate (DMS) in the presence of Tet(O) demonstrated that tetracycline was removed from the primary rather than from the secondary binding site.[68]

The aminoglycoside paromomycin is well known for increasing the rate of translational misreading. The binding site for paromomycin, determined at a resolution of 3 Å, was observed to involve contacts exclusively with h44 of the 16S rRNA.[39,64] Paromomycin binding induces the universally conserved residues A1492 and A1493 to flip out of h44 in a fashion reminiscent of that observed during the binding of aa-tRNA to the A site. This conformational change is brought about by the insertion of one of the four rings (ring I) of paromomycin into h44. In this position, ring I mimics a nucleotide base: it stacks with G1491 and hydrogen bonds with A1408. The stability of this conformation is further reinforced by hydrogen-bonding interactions between ring I and the backbone of the flipped out A1493. Significantly, rings I and II of paromomycin are found in a number of other aminoglycosides, such as the antibiotics neomycin, gentamycin, and kanamycin families, which suggests that misreading by these antibiotics operates through a similar mechanism.

As we have seen in Section 2.2.2, the formation of appropriate codon–anticodon interactions is monitored by the formation of A-minor interactions between A1492 and A1493 with the codon–anticodon helix. Presumably the energy required to flip out A1492 and A1493 during decoding is compensated for by interactions established with the codon–anticodon helix, thus stabilizing this conformation. In the presence of near-cognate tRNA, the prediction is that these compensatory interactions are not sufficient to stabilize the flipping out of A1492 and A1493, and thus accommodation of the A site does not occur. However, in the presence of paromomycin, the normally uncompensated losses of energy are absorbed by the paromomycin that has already induced A1492 and A1493 to flip out and stabilized them in this open conformation. The outcome is that a near-cognate tRNA becomes fully accommodated into the A site in the presence of paromomycin and thus results in mis-incorporation of an amino acid.

2.3. The P Site and the Peptidyltransferase Center

Historically, much controversy has surrounded the question regarding the catalytic "heart" of the ribosome, the peptidyltransferase (PTF) center. Specifically, the questions posed related to whether this active site was predominantly protein or rRNA. The answers to these questions arrived with the X-ray structure of the 50S subunit, in particular the 50S subunit complexed with a transition intermediate of the PTF reaction.[69] The location of the transition intermediate immediately suggested that, in fact, the catalytic center of the ribosome is exclusively composed of RNA. Furthermore, analyses of the residues within proximity to the CCA end analogues of the tRNA led to the proposal of an acid–base catalysis mechanism for the PTF reaction involving the universally conserved A2451—a proposal that came under immediate attack from a number of research groups who presented biochemical and genetic data to the contrary.[70–72] The ongoing debate as to the exact catalytic contribution of the ribosome and the residues involved is the topic of a recent review.[73] Thus, within a short space of time the debate had moved from whether or not RNA or a protein constituted the catalytic domain, onto more detailed mechanistic questions.

In Section 2.3.1 we analyze the interactions of the peptidyl-tRNA at the P site—certainly the tRNA binding site on which most information from different species has been gathered—and illustrate the universal features. The mechanism of PTF is examined in Section 2.3.2, with particular focus on how the ribosome assists or catalyzes the transfer of the growing polypeptide chain from the P-tRNA to A-tRNA. The extreme conservation of residues within the PTF center suggests that the mechanism of PTF is universally conserved. Finally, the PTF center and its immediate vicinity are the target for a number of antibiotics, the structures of some clinically important examples of which, such as chlor-

 © 2003 Wiley-VCH Verlag GmbH & Co. KGaA, Weinheim

amphenicol, clindamycin, and a number of macrolides, have been solved in complexes with the 50S subunit.[11,74] These structures provide not only an insight into the mechanism of antibiotic inhibition and ribosome function, but may pave the way for the design of specific antibiotics to combat the increase in antibiotic-resistant bacteria.[75]

2.3.1. *Peptidyl-tRNA Contacts at the P Site of the Ribosome*

In the past, the tRNA positions on the ribosome were studied using a large number of biochemical approaches that have identified a number of rRNA nucleotides that are associated with each tRNA site (see Table 3 in Ref. [13]). After a crystal structure of the *Thermus thermophilus* 70S ribosome in complex with three tRNAs was solved with a resolution of 5.5 Å,[76] it became clear that the identified residues either directly contact the tRNA or their altered modification pattern could be explained by conformational changes within binding regions. An excellent example illustrating this correlation is the analysis of cleavage patterns from ribosome-bound phosphorothioated tRNAs.[77] The contact patterns suggested that only 15% of the P-tRNA (nucleotides 29–43, which comprise the anticodon loop and two adjacent stem base pairs) interact with the 30S subunit while the remaining 85% is in contact with the 50S subunit (Figure 7). The fact that the protection patterns cover the entire tRNA again dispels the earlier assumptions that tRNAs bind the ribosome using only their extremities, that is, through anticodon–codon interactions in the small subunit and the CCA end in the large subunit. Furthermore, the ribosome contacts all three tRNAs at universally conserved parts of their structure.[76,77] Phosphorothioate protection studies have also suggested a conformational change of the P-tRNA upon binding to the ribosome.[79] Such a change is evident for the P-tRNA in the 70S/$tRNA_3$ crystal structure, where the P-tRNA is slightly kinked around the junction of the D loop and anticodon stem.[76] A similar conformational change was necessary to dock the crystal structure for the yeast $tRNA^{Phe}$ into the P-site electron density during the cryo-EM reconstruction of a complex of P-tRNA bound to the 80S subunit of a yeast.[3]

We have chosen to analyze P-tRNA binding interactions with the yeast ribosome[3] in detail because of the availability of data, with a view to highlight the conservation in the interaction. A comparison of the contacts between rRNA and the P-tRNA in both bacteria and yeast (Table 2) illustrates the similarity in the contacts.[3,32] The P-tRNA is fixed very tightly on the bacterial 30S subunit through approximately six interactions with the rRNA (a–f in Figure 8a). The codon–anticodon duplex in the P site is positioned in the major groove of the noncanonical helical structure at the base of h44 and is fixed with a number of "ribosomal fingers" mainly to the sugar–phosphate backbone.[32] A similar position for the P-tRNA and arrangement of contacts is also observed for the yeast ribosome (Figure 8b). Two of the rRNA interactions with the P-tRNA in

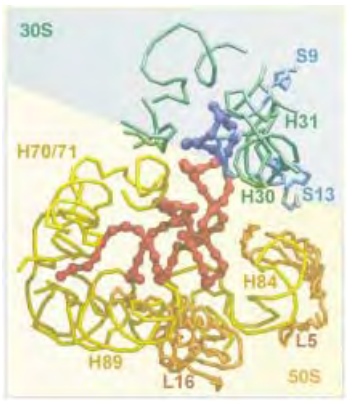


Figure 7. P-tRNA contacts with the 70S ribosome. The region of the P-tRNA that makes contact with the 30S subunit (15%) and the 50S subunit (85%) are shown in blue and red, respectively.[77] The ribosomal components within a 10-Å radius of the P-tRNA are indicated for the 30S subunit (rRNA: green, proteins: cyan), and for the 50S subunit (rRNA: yellow, proteins: orange). H: helices of the tRNA, S and L: proteins of the small and large subunits, respectively. The figure was generated from pdb files 1GIX/1GIY[76] using the program RASMOL[78] and rendered with POVRAY.

Table 2: Comparison of ribosomal intersubunit bridge components between the bacteria *Thermus thermophilus*[32] and the yeast *Saccharomyces cerevisiae*.[3]

Subunit	tRNA position[a]	Ribosomal component (*T. thermophilus*)	rRNA contact (*T. thermophilus*)	Ribosomal component (*S. cerevisiae*)	rRNA contact (*S. cerevisiae*)
small	28	16S h30	1229		
	29/30	16S h30	1229	18S h30	1229/1230
	32			RpS16	Tyr141/ Arg142
	34	16S h31	966	18S h31	966
	35	S9	Arg128		
	36	S13	116–120		
	38 (39)	16S h24	790	(18S h24)	(790)
	(40) 41	(16S h42)	(1339)	18S h43	1338
	(41) 42	(16S h42)	(1338)	18S h43	1339
large	2			RpL10	Lys101
	3	23S H80	2255–2256	25S H80	2285
	4			25S H80	2286
	11–13 (12–13)	(23S H69)	(1908–1909)	25S H69	1908–1910
	14			25S H69	1924
	25–26	23S H69	1922–1923		
	51/52/63			RpL10	Arg24
	56 (56–57)	(RpL5)	(55–66)	RpL11	Tyr51
	71–72			25S H93	2594
	73 (75)	23S H93	(2602)	25S H93	2602
	74/76	23S P loop/L90–93	2252/2585		

[a] tRNA positions from yeast cryo-EM analysis are approximate because of limitations in the resolution.

 © 2003 Wiley-VCH Verlag GmbH & Co. KGaA, Weinheim

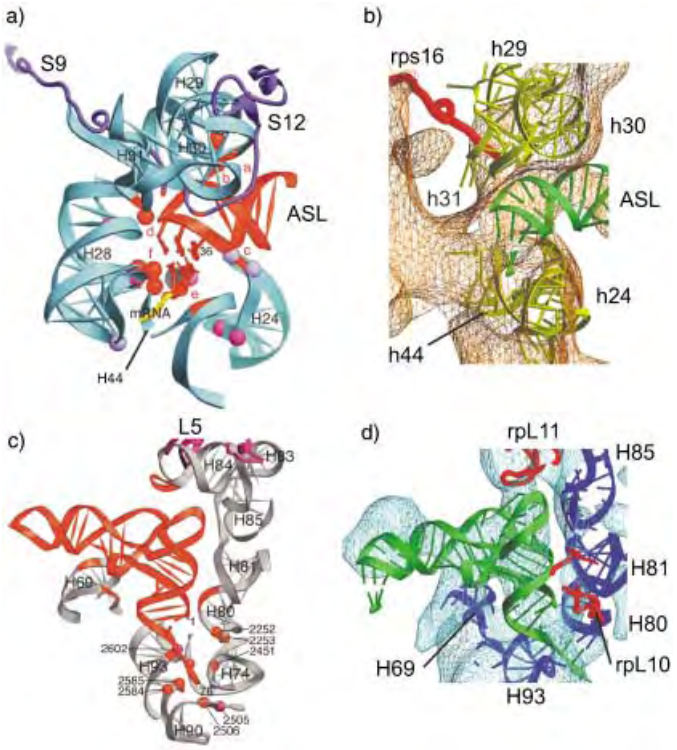


Figure 8. Details of P-tRNA interactions with the small and large subunit of *Thermus thermophilus* and *Saccharomyces cerevisiae* ribosomes. The P-tRNA (red) contacts made with the 30S (a) and 50S (c) subunits from *T. thermophilus* are similar to those made by the P-tRNA (green) with the 40S (b) and 60S (d) subunits from *S. cerevisiae*. The small subunit rRNA is colored cyan (a) or yellow (b), while the ribosomal proteins are colored either purple (a) or red (b). The large subunit rRNA is colored gray (c) or blue (d), while the ribosomal proteins are colored magenta (c) or red (d). The spheres in (a) and (c) represent rRNA bases that are protected from chemical probes upon tRNA binding. In (a) the six ribosomal fingers that hold the anti-codon stem–loop (ASL) in place are indicated by a–f. The figure is adapted from Yusupov et al.[76] and Spahn et al.[3]

Thermus thermophilus are strengthened by interaction with C-terminal ends of ribosomal proteins S9 and S13. The C-terminal end of S9 is highly conserved and contains a universally conserved arginine residue that appears to contact the phosphate group of position 35 in the anticodon loop of the P-tRNA. Again, a similar interaction is seen in yeast with rpS16, the homologue of bacterial S9. In contrast, rpS18, the homologue of S13, does not have a corresponding C-terminal sequence and, on the basis of its position in the 80S ribosome, is probably not involved in P-tRNA fixation. Interaction between the large subunit and the P-tRNA also involves contacts between H69 and the D loop, while the T loop contacts rpL11 in eukaryotes and the homologue L5 in bacteria (Table 2 and Figure 8c and d). Interestingly, both these ribosomal components are involved in the formation of bridges between subunits, which suggests they may play a dynamic role in translation, for example, translocation of the tRNAs (see Section 2.4.2). Although the single-stranded CCA end of the P-tRNA is not resolved in the 80S complex, its position in the crystal structure suggests there is interaction within the PTF center. This is evident from the proximity of the CCA end to base 2602 in the yeast ribosome complex, which in the bacterial ribosome complex contacts position 75, the penultimate base of the CCA end of the P-tRNA.

It is clear from the multiple tRNA contact points with the ribosome that positioning of the tRNA involves a complex network of interactions. The distinct similarity in the arrangement and make-up of the ribosomal components that interact with a P-tRNA, despite the billions of years separating yeasts and eubacteria, suggests an important role for these components during translation. Accurate positioning of tRNAs is essential for ribosomal function. As seen in Section 2.2, the process of decoding is governed by the stereochemical arrangement of the tRNAs relative to the mRNA and the ribosome. Many of the contact points are components of intersubunit bridges, which suggests that these interactions not only "lock" the tRNA in position but may be involved in transporting it through the ribosome (see Section 2.4). Furthermore, tight fixation of both A- and P-tRNAs may be the prerequisite for efficient formation of the peptide bond, as will be described in the following section.

2.3.2. *The Ribosome is a Ribozyme*

The PTF reaction is the central enzymatic activity of the large subunit. It occurs when a pretranslocational (PRE) state is reached, that is, when a peptidyl-tRNA is located in the P site and an aa-tRNA is in the A site. The two L-shaped tRNAs at the P and A sites form an angle of about 40°,[19,76,80] while the acceptor stems of both tRNAs are parallel to each other, such that they can move in a translational movement relative to each other. In contrast, the CCA ends of both tRNAs at the PTF center have rotation symmetry, being arranged at an angle of approximately 180° to each other. The twist needed to accomplish this rotation occurs almost entirely between nucleotides 72 and 74 of the tRNA.[81] Recently, this rotational symmetry of the A- and P-tRNA CCA ends was shown to be complemented by two sets of PTF nucleotides surrounding each of the CCA ends that are also related by a rotational symmetry.[82] This ribosomal structure might play an essential role in guiding the CCA ends during translocation from the A and P sites to the P and E sites, respectively.

During PTF the α-amino group of the A-tRNA attacks the carbonyl group of the peptidyl residue of the P-tRNA, which is linked through an ester bond to the tRNA moiety. This results in the formation of a tetrahedral intermediate, which leads to formation of a peptidyl bond. As a result, the aa-tRNA becomes a peptidyl-tRNA extended by one aminoacyl residue, and the former peptidyl-tRNA is stripped of the peptidyl residue to become a deacylated tRNA (Figure 9).

A long-standing debate within the field of translation concerned whether, or not, the PTF reaction was catalyzed by proteins or rRNA. This question was answered with the identification of the PTF center. A putative transition state analogue of the PTF reaction was soaked into crystals of the 50S subunit from *Haloarcula marismortui*.[69] This analogue (the so-called Yarus inhibitor) is a mimic of the CCA end of a P-tRNA attached to puromycin in the A site (Figure 9), and is a strong competitive inhibitor of the A site substrate.[84] The

 © 2003 Wiley-VCH Verlag GmbH & Co. KGaA, Weinheim

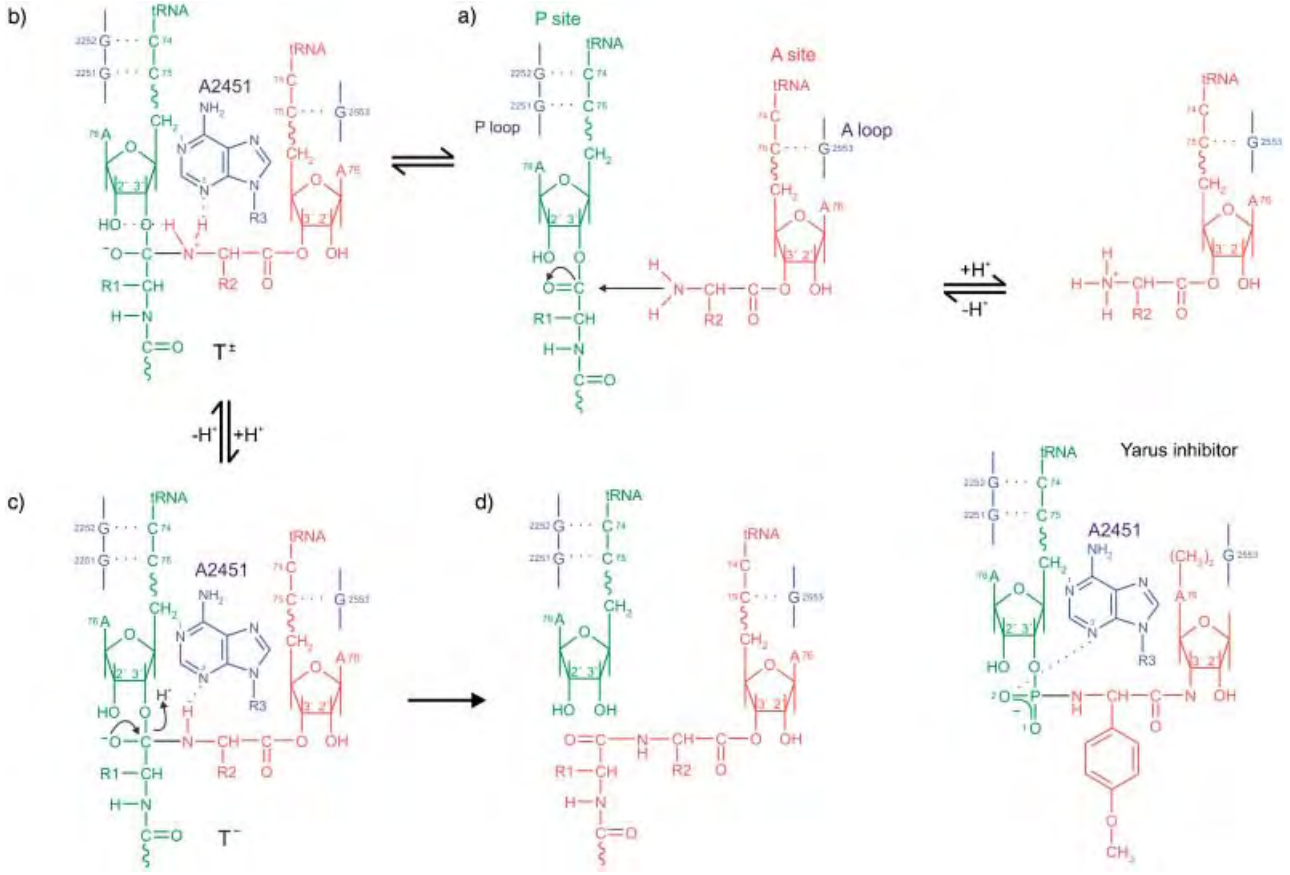


Figure 9. The peptidyltransferase reaction. The picture bottom right shows the Yarus inhibitor CCdAp-puromycin (CCdApPmn) that was used to identify the PTF center of the ribosome. The interactions of the Yarus inhibitor with the rRNA were deduced from the 50S crystal structure of *H. marismortui* ribosomes after soaking the inhibitor into the crystals. It was concluded that the protonated N3 atom of A2451 makes a H bridge to the O2 atom that was thought to mark the position of the oxyanion of the tetrahedral intermediate formed during peptide-bond formation[69] (see the schematic representation in step b). The figure shows the four possible steps of peptide-bond formation according to recent crystallographic and biochemical data.[69,73,81,85] The essential features are: a) C74 and C75 of the P-site tRNA (green) form a Watson–Crick base pair with G2252 and G2251, respectively, of the P loop (blue). Likewise, C75 from the A-site substrate (red) forms a Watson–Crick base pair with G2553 (A loop). The α-amino function of the A-site aa-tRNA is an ammonium ion at pH 7.[83] b) Deprotonation of the ammonium ion triggers the nucleophilic attack of the α-amino function on the carbonyl group of the P site substrate, which results in the tetrahedral intermediate $T^{\pm}$. The secondary NH_2 group forms a hydrogen bond with the N3 atom of A2451 and a second with either the 2′OH group of the A76 ribose at the P site (shown here) or alternatively with the 2′OH group of A2451. The oxyanion of the tetrahedral intermediate points away from the N3-A2451[81] and thus cannot, in contrast to the previous proposal, form a H bridge.[69] c) Further deprotonation of the secondary α-NH_2 group leads to the tetrahedral intermediate T^- and the PTF reaction is completed by an elimination step (d). The peptidyl residue is linked to the aminoacyl-tRNA at the A site through a peptide bond.

region bound by the inhibitor is densely packed with highly conserved bases of the 23S rRNA, mainly derived from the so-called PTF ring of domain V. Although there are 15 proteins that interact with domain V of the 23S rRNA, only the extensions of proteins L2, L3, L4, and L10e come within 20 Å of the active site (Figure 10). The fact that the active center of the ribosome is made exclusively from RNA means that the ribosome is a true ribozyme.

The debate has now turned to whether the PTF reaction simply utilizes a physical principle or whether an additional chemical principle also applies, that is, whether besides the accurate stereochemical arrangement of the substrate (physical principle), a chemical principal, such as a general acid–base catalysis, is also involved.

The universally conserved residue A2451 of domain V is the nearest base to the transition analogue (Figure 9). It was thought to be a good candidate for a general acid–base catalyst, since its N3 atom is about 3 Å from the oxygen atom and 4 Å from the nitrogen atom of the phosphoamide in the Yarus inhibitor (Figure 11 a). This proposal was strengthened when the pK_a value of the A2451 residue was found to be abnormally high at neutral pH ($pK_a = 7$), which is six pH units higher than expected.[71,85] This property is essential for acid–base catalysis, as it allows for easy donation and withdrawal of a proton from the α-amino group of the aa-tRNA at the A site. According to the same model,[69] protonation of A2451 would also allow formation of a hydrogen bond with the carbonyl oxyanion of the tetrahedral transition state analogue (Figure 9). However, modification of position 2451 with dimethyl sulfate showed that pH dependence was only displayed by inactive ribosomes, not by the active ribosomes.[86] Several research groups reported

 © 2003 Wiley-VCH Verlag GmbH & Co. KGaA, Weinheim

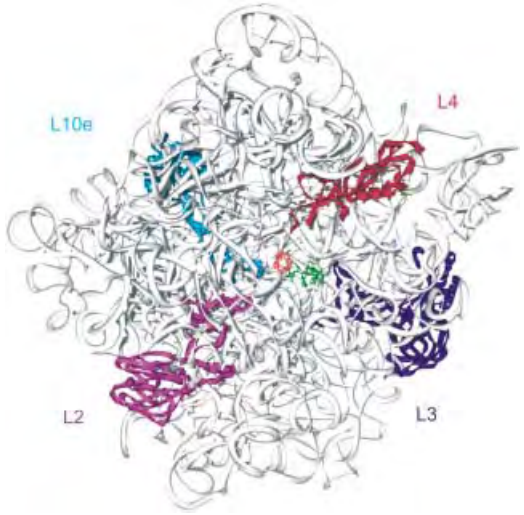


Figure 10. The A- and P-site products (red and green, respectively), bound at the peptidyltransferase center of the 50S subunit. The proteins that reach within about 20 Å of the PTF center include proteins L2 (purple), L3 (blue), L4 (red), and L10e (cyan). This figure was generated from pdb file 1KQS[87] using Swisspdb viewer[55] and rendered with POVRAY.

shortly after that A2451 was not essential for formation of the peptide bond, since ribosomes bearing mutations at position 2451 exhibited only modest (2- to 14-fold) decreases in the rate of peptidyl transfer[72] and were instead shown to be defective in substrate binding.[70]

The next step in the elucidation of the PTF reaction was identifying the position of the products and was obtained by soaking A- and P-site substrates into enzymatically active *H. marismortui* 50S crystals.[87] The structure determined to a resolution of 2.4–3.0 Å was that after formation of the peptide bond but before translocation, and showed that the deacylated CCA bound to the P site had its 3′OH group in proximity to the N3 atom of A2451 (Figure 11 b).[87]

Evidence followed, however, that A2451 was not involved in stabilizing the transition-state analogue: If the oxyanion of the tetrahedral intermediate is hydrogen bonded to the N3 atom of A2451, then this N3 atom must be protonated at around pH 7 and therefore should loose its proton at pH > 7.3. In this case, one would expect the affinity of the Yarus inhibitor to be strongly pH-dependent, since the hydrogen bond would contribute significantly (up to three orders of magnitude) to the affinity. To test this hypothesis, Strobel and co-workers determined the affinity of the Yarus inhibitor for the 50S subunit between pH 5 and 8.5, and found that it remained unchanged.[85] This result is inconsistent with the idea that the oxyanion is stabilized by a hydrogen bond to the N3 atom of A2451. The same conclusion was drawn by subsequent crystallographic studies showing that the oxyanion of the tetrahedral intermediate points away from the N3 atom of A2451, thus excluding the possibility of the formation of a hydrogen bond between these two atoms.[81]

Furthermore, the Yarus inhibitor is not an honest mimic of the transition state. The distance between the O2 atom of the Yarus inhibitor and the C2′ atom of the deoxy-A76 (dA76) ribose at the P site is only 2.8 Å (arrowed in Figure 11 a). A

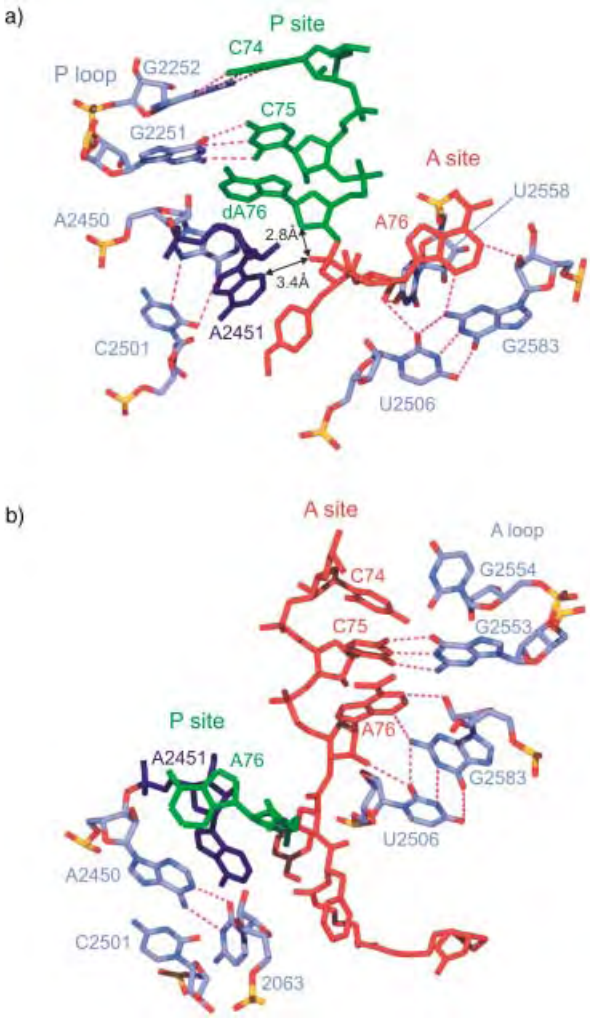


Figure 11. Tight fixation of the CCA ends of the P- (green) and A-tRNAs (red) observed in the 50S subunit from *H. marismortui* in a complex with a) the Yarus inhibitor and b) the products following formation of the peptide bond. The N3 atom of A2451 (dark blue) is 3.4 Å from the O2 atom of the Yarus inhibitor (see also Figure 9). The same O2 atom is only 2.8 Å from the 2′-deoxy position of A76 (arrowed). Selected rRNA residues of domain V of the 23S rRNA are colored light blue, including the A- and P-loop bases that participate in fixation of the CCA ends of the A and P sites (*E. coli* numbering). In (b) C74 and C75 of the P site have been omitted for clarity. Dashes indicate hydrogen bonding and rRNA nucleotides use the following color scheme: O red, P yellow, N blue, C dark blue. Figures (a) and (b) were generated from pdb files 1FFZ[69] and 1KQS,[87] respectively, using Swisspdb viewer[55] and rendered with POVRAY.

physiologically P-site substrate contains a 2′OH group at this C2′ atom which is essential for formation of a peptide bond[88] and would sterically clash with the O2 atom of the Yarus inhibitor positioned as observed in the crystal. The essential nature of this 2′-OH group might be explained by the observation that the α-NH_2 group of the A site possibly forms a hydrogen bond with this 2′-OH group (illustrated in Figure 9 b).

The general base catalysis debate flared up again when Rodnina and co-workers presented evidence that formation of a peptide bond depends on two ionizable groups, one with a

 © 2003 Wiley-VCH Verlag GmbH & Co. KGaA, Weinheim

pK_a value of 6.9 and the other with a pK_a value of 7.5.[89] The former value was shown to be associated with the α-NH_2 group of puromycin used in the kinetic experiments, while the latter value seemed to be associated with the ribosome. The ionizable group seemed to belong to A2451, since the formation of a peptide bond was about 130 times slower than normal when catalyzed by a ribosome bearing an A2451U mutation, and had lost the pH dependence. However, an alternative explanation suggested by the authors was that the protonated group is part of the A2450:C2063 base pair lying directly behind A2451 (shown in Figure 11b). In this case, the ionizable group would be the N1 atom of A2450. Although a distance of 7 Å from the N1 atom to the α-NH_2 group is too long for hydrogen transfer, a postulated conformational change of the PTF center might bring A2450 within range.[89] The assumption of conformational changes again increases the number of possible candidates that might play a role in the kind of chemical catalysis that is advocated here. We note that evidence was presented that His 229 of protein L2 might also be involved in this catalysis,[90] although current atom maps place this residue more than 20 Å away from the tetrahedral intermediate of the transition state.

At the moment it can be said that a direct role of A2451 in a general acid–base catalysis can hardly be reconciled with the observation that A2451 in active ribosomes, in contrast to inactive ribosomes, does not contain a titratable group at this pK_a value.[86]

In fact, the ribosome need not use any direct chemical involvement in the catalysis of the PTF reaction, such as the formation of a transient covalent interaction between the substrate (tRNAs) and the enzyme (the ribosome, or more specifically in this case the rRNA). The template model predicts that tight stereochemical arrangement of substrates relative to one another would be sufficient to provide the dramatic acceleration of the reaction rate needed for the formation of a peptide bond (see the review in Ref. [91]). In this case the role of A2451 would be to remove a proton from the free nucleophilic α-NH_2 group of the A-site substrate or form a hydrogen bond with the α-NH_2 group, thus promoting formation of a peptide bond through proper positioning of the NH_2 group. The reaction scheme would be something like that presented in Figure 9 and described in more detail in the corresponding legend.

Tight fixation of the CCA ends of the P- and A-tRNAs is exactly what is observed both in the analogue-soaked 50S crystal structure (Figure 11a) and the products containing a peptide bond following soaking of the A- and P-site substrates (Figure 11b). The CCA end is locked into position in the P site by formation of two Watson–Crick base pairs (C74 and C75 with G2252 and G2251, respectively). A76 stacks on the ribose of A2451 (shown clearly in Figure 11b). The CCA end of the aa-tRNA in the A site is fixed by: 1) Watson–Crick base pairing between C75 and G2553, 2) a type-I A-minor motif between A76 and the G2583-U2506 base pair, and 3) an additional hydrogen-bonding interaction between the 2′-OH group of A76 and U2585. Tight fixation of the CCA ends of both A- and P-tRNAs at the PTF center underlines the importance of the (purely physical) template model in formation of a peptide bond, namely, that precise stereochemical fixation is predominantly responsible for the enormous acceleration of the reaction. The rate of formation of a peptide bond on the ribosome at about 50 s^{-1} was estimated to be approximately a factor of 10^5 faster than the uncatalyzed reaction (the rate in the absence of ribosomes).[91] The ribosomal PTF reaction without chemical catalysis (that is, when the ionizable group of the ribosome is protonated at pH < 7) occurs with a rate of about 0.5 s^{-1},[89] which is still more than 1000 times faster than the uncatalyzed reaction. If this estimation is correct then the purely physical mode of peptide-bond formation (the exact stereochemical arrangement of the reactants) represents approximately 90% of the reaction rate, with the catalytic component making up the remaining 10%.

2.3.3. *Antibiotic Action on the 50S Subunit*

The functional importance of rRNA at the ribosome active centers is reiterated by the sites of interaction of a variety of clinically relevant antibiotics, such as chloramphenicol (Cam) and clindamycin, which inhibit PTF activity.[11] Cam is well-known as an specific bacterial inhibitor of the CCA-aa end of an A-site tRNA[92] but does not inhibit the CCA fixation of a P-site tRNA.[93] The binding site of Cam was determined to a resolution of 3.5 Å by soaking the antibiotic into crystals of the 50S subunit of *D. radiodurans* and shown to involve interaction with seven nucleotides within the PTF center.[11] A number of these interactions are indirect as they are mediated through putative Mg^{2+} ions. Since moieties important for the antibiotic action of Cam constitute these interactions, this result suggests that the presence of the ions are of extreme importance for antibiotic binding and PTF inhibition. The position of the "tail" of Cam within the PTF center is such that it reaches towards, and may even displace, the CCA end of the A-site tRNA. This observation is in agreement with the result that although tRNAs can bind in the presence of Cam, they cannot undergo formation of a peptide bond, probably because the CCA-aa end of the A-site tRNA is displaced from the correct position. Cam inhibition in vitro is dependent on the nature of the peptidyl residue and the A-site substrate. In particular, Cam is a less effective inhibitor against aromatic amino acids such as phenylalanine. This leads to the conclusion that these amino acids can actually displace Cam during formation of the peptide bond by competing with the phenyl group of the drug for binding. The major overlap between Cam and an amino acid in the A-site tRNA lends credence to the idea that Cam operates predominantly by displacing the aminoacyl residue of the A-site tRNA, which probably indirectly displaces the CCA end.

In contrast with chloramphenicol, the binding site determined for the lincosamide clindamycin spans between both the A and P sites at the PTF center.[11] The majority of the interactions involve hydrogen bonds between hydroxy groups on the sugar moiety and bases within the PTF center; these contacts are in agreement with most of the available mutation resistance data. The proline group of clindamycin overlaps with the position of the phenyl group of Cam, which is in line

 © 2003 Wiley-VCH Verlag GmbH & Co. KGaA, Weinheim

with the A-site nature of clindamycin inhibition. The C8′ atom on the proline moiety of clindamycin comes within 2.5 Å of the N3 atom of C2452 and is thus in proximity to a P-site-bound tRNA. Thus, the binding position of clindamycin traverses both the A and P sites, and would be expected to disturb the positioning of amino acid moieties at both sites.

The positions of no less than seven distinct members of the macrolide family of antibiotics have been solved in complexes with the 50S subunit.[11,74] This large family of antibiotics can be divided into three classes on the basis of the size of the lactone ring. Erythromycin and two erythromycin derivatives (clarithromycin and roxithromycin) are representatives of the 14-membered-ring class, all of which have been solved in complexes with the 50S subunit of *D. radiodurans*.[11] From the two larger 15- and 16-membered classes, the binding sites of azithromycin, spiramycin, tylosin, and carbomycin A have been solved in complexes with the 50S subunit from *H. marismortui*.[74]

The binding positions determined for these macrolides are generally in good agreement with one another, located within the polypeptide tunnel in proximity to the PTF center. In this position, the macrolides would be expected to block the tunnel, thus preventing passage of the nascent polypeptide chain (Figure 12). This proposal can be reconciled with the observation that macrolides cannot inhibit actively translating ribosomes, since the presence of the polypeptide chain in the tunnel precludes the macrolide from binding. Ribosomes prebound with macrolides are able to synthesize oligopeptides up to five amino acids in length, depending on the macrolide present. Since the lactone ring of the bound macrolides are positioned in the tunnel such that the sugar extensions from the C5 position extend towards the PTF center, the length of the side chain dictates the number of peptide bonds that can be formed; for example, tri- or tetrapeptides can be formed in the presence of erythromycin, which has a monosaccharide at the C5 position, whereas only dipeptides are formed in the presence of tylosin and spiramycin, which bear C5-disaccharides. Carbomycin A, which has an additional isobutyrate group on the disaccharide, even prevents formation of the first peptide bond. The isobutyrate group of carbomycin A reaches so far into the PTF center that it occupies the position that the amino acid moiety of the A-site substrate would normally occupy.[74] The direct interaction of the macrolides with position 2058 makes it easy to understand how modifications and mutations at this position in *E. coli* provide resistance to this class of antibiotics. In contrast, erythromycin (or its derivatives) and azithromycin make no direct contact with ribosomal proteins L4 or L22, which suggests that the mutations within these proteins that confer resistance must do so indirectly through conformational changes of the 23S rRNA.

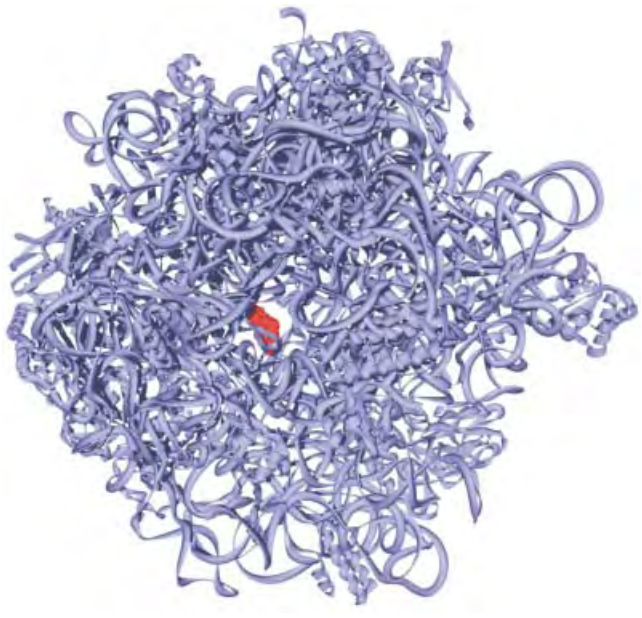


Figure 12. The macrolide carbomycin A bound in the tunnel of the *H. marismortui* 50S subunit. The rRNA and proteins are represented as violet ribbons and carbomycin A as a red space-filling model. The 50S subunit is viewed from the cytoplasmic side (backside) looking up the tunnel to the PTF center. This figure was created from pdb file 1K8A[74] using Swiss-pdb viewer[55] and rendered with POVRAY.

A further interesting discovery was the formation of a reversible covalent bond between the acetaldehyde substituent at position C6 of the 16-membered ring macrolides and the N6 atom of A2062 (*E. coli*).[74] The formation of this carbinolamine is specific for the 16-membered group, since the smaller macrolides do not contain a corresponding aldehyde functional group. Lastly, it is important to note that although the overall binding sites for each macrolide are in general agreement between the two studies discussed here, there are some significant differences in the orientation and conformation of the lactone ring and cladinose sugar moiety of the macrolides bound on the ribosome. In one study interaction with the tunnel wall is made through the hydrophobic face of the lactone ring, whereas in the other interaction is made through a series of hydrogen bonds. Whether these discrepancies arise because of differences in interpretation, differential binding to ribosomes from particular species, or actual differences in the binding of the macrolides themselves is unclear. The last possibility would be surprising since azithromycin and erythromycin differ only by the absence of a ketone oxygen atom and the addition of methyl nitrogen atom. Re-analysis of these structures and the duplication of identical antibiotics for each ribosome species should resolve this problem.

2.4. P- and A-tRNA Translocation within the Ribosome

The position of the tRNAs remains unchanged after formation of the peptide bond. This has been demonstrated by cryo-EM analyses of *E. coli* ribosome complexes[19] and most strikingly by soaking A- and P-site substrates into active 50S *H. marismortui* crystals and solving the structure of the reaction products.[87] After formation of the peptide bond the ribosome must transfer the products—the peptidyl-tRNA in the A site and deacylated tRNA in the P site to the P and E sites, respectively—thus, shifting the ribosome from the pre- to the posttranslational state (Figure 2c and 2f respectively). This process is termed translocation. It must be extremely accurate at both ends of the tRNA molecule: The anticodon–

 © 2003 Wiley-VCH Verlag GmbH & Co. KGaA, Weinheim

codon complex must be moved exactly 10 Å (the length of one codon), longer or shorter movements would result in the ribosome losing the reading frame. At the other end of the A-site peptidyl-tRNA, the CCA end must also be moved precisely into the P site so as to set up the next PTF reaction with the incoming aa-tRNA. Incorrect placement of the peptidyl-tRNA at the P site could be disastrous for the formation of a peptide bond and result in the abortion of translation.

Ribosomes have an innate translocase activity, but it is more than one order of magnitude slower than that of the EF-G-catalyzed reaction.[94] This observation implies that the structures necessary to move the tRNAs reside in the ribosome and that the role of EF-G/EF2 is to reduce the activation energy barrier that separates the two sets of tRNA positions (A plus P and P plus E). Important questions remaining unanswered are: How does EF-G/EF2 mediate translocation and which ribosomal components are involved in the transfer of the tRNAs?

2.4.1. *Conservation in the Binding Site of Elongation Factor-G*

The crystal structure of EF-G has been solved in the absence of the nucleotide[48] and in the complex with GDP (Figure 5a).[47] The GTP form is the active one, which binds to the ribosome and triggers translocation. Hydrolysis of GTP inactivates EF-G and dissociates it from the ribosome (see the review by Kaziro).[95] EF-G belongs to the same subfamily of G proteins as IF2, RF3, and EF-Tu, the latter of which has been crystallized in both GTP (active) and GDP (inactive) forms which exhibit large domain shifts relative to one another.[50]

Cryo-EM reconstructions of EF-G bound to bacterial 70S ribosomes at a resolution of 17.5–20 Å[96–98] and EF2 to eukaryotic 80S ribosomes at 17.5 A resolution[99] show similar binding sites for both factors (Figure 13a and b). Antibiotics were used to trap the elongation factor on the ribosome in these complexes. EF-G was trapped on the 70S ribosome using the antibiotic fusidic acid. This fixation allows translocation and GTP hydrolysis, but blocks the switch into the GDP conformer of the factor, thus preventing dissociation from the ribosome. The eukaryotic eEF2 was locked onto the yeast ribosome using the antifungal sordarin, which is thought to function analogously to fusidic acid.[99] The complex was formed with a typical pretranslational state, that is, A- and P-tRNAs were present. As expected, the tRNAs were translocated to the P and E sites, but of special interest is that the tip, domain IV, of EF-G was shown to occupy the position of the A site. Similarly, EF2 in the EF2–ribosome complex also occupied the A site and came very close to the position of the P-tRNA (Figure 13c and d). EF-G-mediated translocation is also possible in the presence of nonhydrolyzable GTP analogues, such as GDPNP, which suggests that binding of EF-G alone is sufficient for translocation and that hydrolysis is necessary for the conformational change and release of EF-G·GDP.[95]

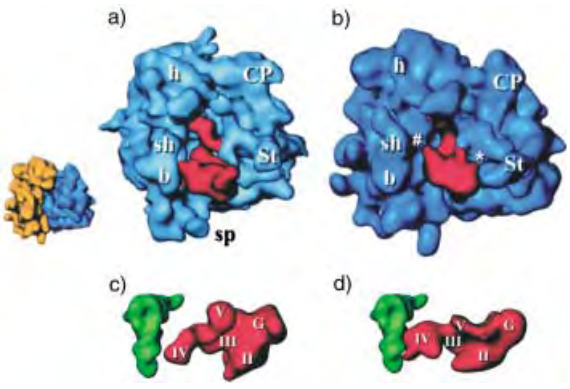


Figure 13. Comparison of cryo-electron microscopic analyses of the EF-G·70S complex from *E. coli* (a) and the EF2·80S complex from *S. cerevisiae* (b); the small subunit is on the left side and the large subunit on the right. The same orientation is seen on the left of an empty 80S ribosome (yellow: 40S, blue 60S). The relative arrangements of EF-G and P-tRNA (c) and EF2 (red) and P-tRNA (d) are illustrated. The abbreviations of the features are as in Figure 1, while roman numerals on EF-G and EF2 refer to the domains of these factors. The figure was modified from Gomez-Lorenzo et al.[99]

For classical G proteins, a GTPase-activating protein (GAP) stimulates the G-protein-mediated hydrolysis of GTP. In the case of EF-G/EF2, the GAP is provided by components of the ribosome. There are certainly gross changes visible upon the binding of each elongation factor to the ribosome. One of the most striking changes is seen within the "stalk" region; there is no electron density for this region in the empty 70S and 80S ribosomes but becomes ordered upon EF-G/EF2 binding,[96,97,99] which supports its universal role in factor binding. Perhaps the best candidates for the GAP role are a region of the 23S rRNA termed the sarcin–ricin loop (SRL) and the pentameric stalk complex of the ribosomal proteins L10·$(L7/L12)_4$. The SRL is so named because cleavage after G2661 of the bacterial 23S rRNA within this region by α-sarcin inhibits all activities dependent on the elongation factor.[100] Similar effects are seen after removing the neighboring base A2660 (*E. coli* nomenclature) in the 26S rRNA of yeast by the *N*-glycosidase activity of the ricin A-chain.[101] Furthermore, this region contains the longest (12 nucleotides) universally conserved stretch of rRNA, which underlines its functional importance.

Recently, hybrid ribosomes were constructed in which the proteins at the GTPase center from *E. coli* (L7/L12 and L10) were replaced with their eukaryotic counterparts from rat P1/P2 and P0, respectively.[102] Both the in vitro translation and GTPase activity of the resultant hybrid ribosomes was strictly dependent on the presence of the eukaryotic elongation factors, EF2 and EF1a. This result reflects not only the specificity of the interaction between the stalk proteins and the elongation factors from each species, but also the importance of the stalk proteins in mediating elongation factor GTPase activity.

The ribosomal protein L11 (and associated L11 binding site on the 23S rRNA) is often considered as a candidate for taking over the function of the GAP. This is because mutations in both L11 and its binding site on the 23S rRNA can confer resistance against the antibiotic thiostrepton, a potent inhibitor of EF-G- and EF-Tu-dependent GTPase activities.[103] However, the direct involvement of L11 in the

 © 2003 Wiley-VCH Verlag GmbH & Co. KGaA, Weinheim

factor-dependent GTPase is not very likely, since mutants lacking L11 are viable, although extremely compromised,[104] and the IF-2-dependent GTPase is stimulated rather than blocked by thiostrepton.[105] Furthermore, replacement of either the L10·$(L7/L12)_4$ complex or L11 with the equivalent rat protein showed that the P0·$(P1{\cdot}P2)_2$ complex, but not the eukaryotic counterpart to L11 (RL12), was responsible for factor specificity and associated GTPase dependence, although addition of L11 or RL12 did stimulate protein synthesis significantly.[102] Thus, the role of L11 is unclear. L11 is in any case in proximity to the elongation factors: Cryo-EM analyses of EF-G bound to 70S ribosomes revealed that the N-terminal domain of L11 is shifted upon binding of EF-G so as to form an arclike connection with the G domain of EF-G.[106] This arclike connection is also observed in the EF2–80S complex although it is broader and fused to a greater extent.[99] Thus it seems likely that EF-G binding stimulates conformational changes in the ribosome, probably through the L10·$(L7/L12)_4$ complex, which triggers translocation of the A- and P-tRNAs. The question remaining is how are the tRNAs actually moved?

2.4.2. Dynamics within the Ribosome

In the α-ε model for translocation a moveable domain within the ribosome is hypothesized to carry the A- and P-tRNAs during translocation (see the review in Ref. [107]). Evidence for this model comes from testing the accessibility of phosphate groups on the tRNAs in the pre- and post-translational states. The essential observation was that the protection patterns of A- and P-tRNAs differ from one another, but the corresponding tRNAs exhibit the same protection patterns in the pre- and the posttranslational states. This observation suggests that distinct ribosomal components are involved in carrying the tRNAs from the pre- to the posttranslational state. There are a number of candidates that may play a role in the translocation of the tRNAs or even constitute portions of the moveable domains.

Distinct regions within the crystal structures are disordered, which most likely reflects the flexibility of these components. A classic example is the stalk region, which, as already mentioned, only becomes ordered upon binding of the elongation factor. Another is the L1 region, the flexibility of which may regulate release of E-tRNA (see Section 2.5). There are also certain structures that become either ordered or rearranged upon association of the subunit. Most of these elements are constituents of the bridges between the subunits. One striking example is the universally conserved helix H69 in domain IV of the larger RNA subunit. H69 is the major element of bridge B2a, the largest inter-subunit bridge (see Figure 3), and is disordered in the structure of the 50S subunit of *H. marismortui*, but ordered in the 50S subunit of *D. radiodurans*. Comparison of the latter structure with the 70S structure of *T. thermophilus* shows that H69 swings out towards h44, another very flexible element, upon association. In this extended conformation H69 would be predicted to make contact with both A and P tRNAs.[108] Another element that is not fully resolved in either of the 50S structures is H38 of domain II, a constituent of bridge B1a and often called the "A-site finger" because it contacts the A site of tRNA. As previously mentioned, both B1a and B2a bridge elements have corresponding counterparts within the 80S yeast ribosome, thus strengthening their candidacy for a role in translocation.

2.5. The E Site and Translational Fidelity

2.5.1. Discovery of a Third Universal tRNA Binding Site on Ribosomes

Despite identification of the E site in bacterial ribosomes in the early 1980s,[109,110] it is only in recent years that it has appeared in some textbooks. The E site has also been discovered in archea[111] and in eukaryotes, both yeast[112] and mammals,[113] which suggests that it is a universal feature of ribosomes. The E site is specific for deacylated tRNA and will not bind peptidyl- or aminoacyl-tRNAs. This result is in accordance with the idea that the E site only accepts the deacylated tRNA from the P site following transfer of the nascent chain to the A-tRNA. At least part of the controversy over the existence of the E site stems from its instability under certain buffer conditions (see the review in Ref. [107]). Stable binding in the E site has been shown to be dependent on physiological buffer conditions, such as in the presence of a low magnesium concentration (3–6 mM) and polyamines. Nonphysiological buffer conditions dissociate the E-tRNA, as nicely illustrated by the visualization of tRNAs in posttranslational complexes under different buffer conditions using cryo-EM.[114,115] Under nonphysiological conditions, the E-tRNA electron density was lost from the E site itself and extra electron density appeared contacting the L1 stalk (the E2 site). It was thought that this position might reflect the path of a tRNA that has left the E site as it dissociates from the ribosome and that the very flexible L1 stalk might play a role in dissociating the E-tRNA from the ribosome. This idea has gained recent support from a comparison of the crystal structure of the *D. radiodurans* 50S subunit with the *T. thermophilus* 70S structure, where the position of the L1 arm differs by 30° (Figure 14). In the latter structure, the L1 arm is closed and contacts the elbow of the E-tRNA, which prevents its release from the ribosome. In contrast, the L1 arm in the *D. radiodurans* structure is open, which may serve to release the E-tRNA during translation.[108] In fact, this mechanism may be universal. In yeast, there is an enormous 70 Å difference in the position of the L1 stalk in the P-tRNA-bound 80S ribosome (pseudo-pretranslational state) and a stalled translating ribosome (artificially induced posttranslational state).[3,4] In light of the conformational flexibility of the L1 stalk (see below), the E2 electron density may not even represent a tRNA, which may have totally dissociated from the ribosome; instead it may merely reflect a buffer-induced conformational change within the L1 region.

The existence of the E site was also confirmed by the presence of three tRNAs in the crystal structure of the 70S subunit of *T. thermophilus*.[76] The E-tRNA results predominantly from the presence of endogenous E-tRNA that co-purified with the ribosomes, thus illustrating the stability of the binding despite the lengthy purification procedure. The

 © 2003 Wiley-VCH Verlag GmbH & Co. KGaA, Weinheim

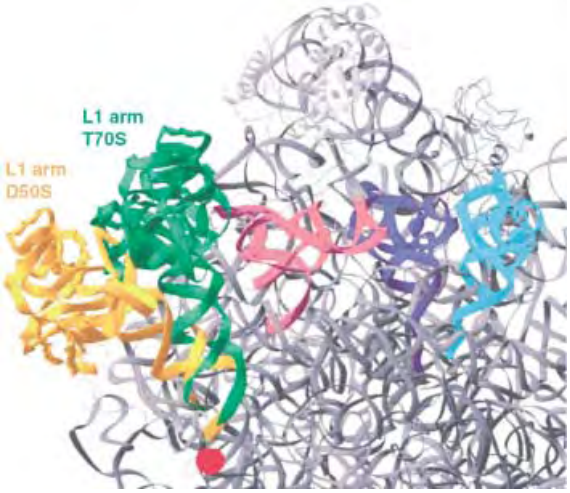


Figure 14. Movement of the L1 arm. A region of the crystal structure of the *D. radiodurans* 50S subunit (D50S) showing the 23S rRNA (gray) with the L1 arm highlighted (yellow). The position of the L1 arm in the crystal structure of the *T. thermophilus* 70S subunit (T50S) is superimposed (green) with the putative pivot point for the L1 arm and is marked with a red dot. The positions of the A- (cyan), P- (blue), and E-tRNAs (pink) are included, with the anticodon arms pointing out of the plane of the paper. Adapted from Harms et al.[108]

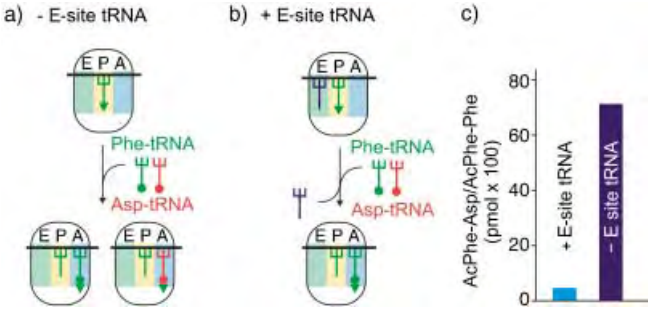


Figure 15. The role of the E site in the accuracy of decoding. Ribosome complexes were prepared using poly(U)-mRNA where the P site was occupied with AcPhe-tRNA. A-site binding of cognate Phe-tRNA (codon UUU) and noncognate Asp-tRNA (codon GAC/U) was performed in the absence (a) or presence (b) of an E-tRNA. Binding of the Phe-tRNA or Asp-tRNAs to the A site was monitored by measuring the formation of the dipeptides AcPhe-Phe or AcPhe-Asp, respectively (c). Both AcPhe-Phe and AcPhe-Asp were formed in the absence of E-tRNA, which indicates that erroneous incorporation of Asp-tRNA at the A site occurred, while normal amounts of AcPhe-Phe with background levels of AcPhe-Asp were formed in the presence of E-tRNA, thus indicating that the cognate Phe-tRNA predominantly bound the A site. Data taken from Geigenmüller et al.[117]

existence of the E site is finally being accepted, but its importance has yet to be fully recognized.

2.5.2. *Importance of the E-Site: Fidelity and Reading Frame Maintenance*

The fact that the E site has been discovered in the ribosomes of both prokaryotes and eukaryotes suggests that it should play an important role during translation. The presence of a deacylated tRNA at the E site has been shown to modulate aa-tRNA selection at the A site (see the review in Ref. [116]). In particular, an occupied E site induces a low affinity A site, such that interaction of the ternary complex is dictated by anticodon interactions. This allows only cognate and near-cognate tRNAs to bind, thus eliminating 90% of the competing noncognate tRNAs (the importance of this was discussed in Section 2.2.1). In contrast, when the E-tRNA is absent, the A site has high affinity, which permits interaction of all tRNAs, including the erroneous incorporation of noncognate tRNAs. These two situations have been demonstrated in vitro.[117] Simply, in the presence of P-tRNA alone, both noncognate Asp-tRNA and cognate Phe-tRNA could bind to an A site UUU codon (Figure 15a), but in the presence of an E-tRNA (and P-tRNA), only the cognate Phe-tRNA could bind the A site (Figure 15b and c). Binding of the A-tRNA releases the E-tRNA from the E site, so that at any one time during translation, except during the first decoding step, there are never more than two tRNAs present on the ribosome. Furthermore, the E-tRNA must be cognate to the E site codon, as a near-cognate E-tRNA could not prevent erroneous incorporation of the Asp-tRNA.[117] It is significant that a cognate tRNA must be present at the E site; this observation indicates that codon–anticodon interactions at the E site is the signal that tells the ribosome to adopt the posttranslational state and display a low affinity A site. Further evidence for anticodon–codon interactions at the E site comes from the *gag-pol* recoding site of HIV-1. Ribosomes recode this site using a posttranslocational slippage mechanism, that is, slippage into the -1 reading frame occurs after translocation, where both P- and E-tRNAs slip simultaneously in the -1 direction.[118] Another recoding site illustrating the importance of the E site is the $+1$ frameshifting site of the termination factor RF2. At codon position 26 within the RF2 mRNA a $+1$ frameshift is required to avoid an internal UGA stop. This internal stop codon is specifically recognized by the RF2 protein and thus provides an autoregulatory mechanism, such that when RF2 protein levels are high in the cell, RF2 termination at the frameshift is favored and a truncated and inactive RF2 protein is produced which is rapidly degraded. When RF2 levels are low in the cell, termination loses out to frameshifting and the full-length active RF2 protein is produced. One important feature that stimulates frameshifting in this case is an upstream Shine–Dalgarno (SD) type sequence that interacts with a complementary anti-SD sequence within the 16S rRNA of the 30S subunit. Interestingly, the SD-anti-SD interaction includes the first position of the E-site codon. Recently it could be demonstrated that formation of the SD-anti-SD duplex displaces the E-tRNA from the ribosome and by doing so promotes frameshifting.[119] Thus the implication is that the presence of the E-tRNA at the E site is necessary for maintaining the correct reading frame during translation.

3. Summary and Outlook

Although we have taken a huge leap forward during the past years in our understanding of ribosome structure and

 © 2003 Wiley-VCH Verlag GmbH & Co. KGaA, Weinheim

function, there is still much that eludes researchers. While some of these questions remain fundamental to the process of translation, for example, those pertaining to the mechanism of peptidyltransferase, translocation, or the role of the tunnel, there are many questions that are perhaps more peripheral, being associated with translational regulation. This is particularly true in the case of eukaryotic translation, with its multitude of factors, additional ribosomal proteins, and rRNA expansion elements. Some of the answers to these questions will arrive with higher resolution structures of ribosomal complexes and translational intermediates. As high-resolution structures are dependent on the production of diffracting crystals it is hard to predict with any certainty the time scale for the preparation of eukaryotic ribosome crystals or prokaryotic ribosome complexes, such as pre- and posttranslocational states, or with large translational factors bound. Unfortunately, these are static structures but the ribosome is a highly dynamic machine, therefore, dissection of its mechanism will require a concerted approach from many different angles, both biochemical and biophysical. Given that protein synthesis is fundamental to all life forms and provides such insight into general molecular interactions, surely the pursuit for further knowledge must be one worth striving for!

Abbreviations

A site	aminoacyl(aa)-tRNA site
A-tRNA	tRNA in the A site
CTD	carboxy-terminal domain
E site, exit site, specific for deacylated tRNA	
E-tRNA	tRNA at the E site
GAP	GTPase activating protein
NTD	amino-terminal domain
P site	peptidyl-tRNA site before peptide-bond formation
P-tRNA	tRNA at the P site
POST	posttranslocational state
PRE	pretranslocational state
PTF	peptidyltransferase
SD	Shine–Dalgarno
SRL	sarcin–ricin loop
UTR	untranslated region of an mRNA

We would like to thank Christian Spahn for supplying high-resolution images of Figure 1 a–d, 3 b, 8 b and d, Özlem Tastan for kindly providing Figure 7, and Meredith Ross, Oliver Vesper, and Sean Connell for critical reading of the Manuscript. D.N.W. would like to thank the Alexander von Humboldt foundation for support. K.H.N. acknowledges the support of the Deutsche Forschungsgemeinschaft (Ni174/8-2 and Ni174/-9-2).

Received: July 23, 2002 [A544]

[1] J. Frank, *Bioessays* **2001**, *23*, 725 – 732.
[2] P. Dube, M. Wieske, H. Stark, M. Schatz, J. Stahl, F. Zemlin, G. Lutsch, M. van Heel, *Structure* **1998**, *6*, 389 – 399.
[3] C. M. Spahn, R. Beckmann, N. Eswar, P. A. Penczek, A. Sali, G. Blobel, J. Frank, *Cell* **2001**, *107*, 373 – 386.
[4] R. Beckmann, C. M. Spahn, N. Eswar, J. Helmers, P. A. Penczek, A. Sali, J. Frank, G. Blobel, *Cell* **2001**, *107*, 361 – 372.
[5] a) D. G. Morgan, J. F. Menetret, A. Neuhof, T. A. Rapoport, C. W. Akey, *J. Mol. Biol.* **2002**, *324*, 871 – 886; b) J. F. Menetret, A. Neuhof, D. G. Morgan, K. Plath, M. Radermacher, T. A. Rapoport, C. W. Akey, *Mol. Cell* **2000**, *6*, 1219 – 1232.
[6] R. Beckmann, D. Bubeck, R. Grassucci, P. Penczek, A. Verschoor, G. Blobel, J. Frank, *Science* **1997**, *278*, 2123 – 2126.
[7] T. Tenson, M. Ehrenberg, *Cell* **2002**, *108*, 591 – 594.
[8] B. T. Wimberly, D. E. Brodersen, W. M. Clemons, R. J. Morgan-Warren, A. P. Carter, C. Vonrhein, T. Hartsch, V. Ramakrishnan, *Nature* **2000**, *407*, 327 – 339.
[9] F. Schluenzen, A. Tocilj, R. Zarivach, J. Harms, M. Gluehmann, D. Janell, A. Bashan, H. Bartels, I. Agmon, F. Franceschi, A. Yonath, *Cell* **2000**, *102*, 615 – 623.
[10] N. Ban, P. Nissen, J. Hansen, P. B. Moore, T. A. Steitz, *Science* **2000**, *289*, 905 – 920.
[11] F. Schlünzen, R. Zarivach, J. Harms, A. Bashan, A. Tocilj, R. Albrecht, A. Yonath, F. Franceschi, *Nature* **2001**, *413*, 814 – 821.
[12] a) V. Ramakrishnan, *Cell* **2002**, *108*, 557 – 572; b) P. B. Moore, T. A. Steitz, *Nature* **2002**, *418*, 229 – 235; c) A. Yonath, *Annu. Rev. Biophys. Biomol. Struct.* **2002**, *31*, 257 – 273.
[13] D. N. Wilson, G. Blaha, S. R. Connell, P. V. Ivanov, H. Jenke, U. Stelzl, Y. Teraoka, K. H. Nierhaus, *Curr. Protein Pept. Sci.* **2002**, *3*, 1 – 53.
[14] P. Schimmel, B. Henderson, *Proc. Natl. Acad. Sci. USA* **1994**, *91*, 11 283 – 11 286.
[15] D. E. Brodersen, W. M. Clemons, Jr., A. P. Carter, B. T. Wimberly, V. Ramakrishnan, *J. Mol. Biol.* **2002**, *316*, 725 – 768.
[16] R. R. Gutell, J. J. Cannone, Z. Shang, Y. Du, M. J. Serra, *J. Mol. Biol.* **2000**, *304*, 335 – 354.
[17] P. Nissen, J. A. Ippolito, N. Ban, P. B. Moore, T. A. Steitz, *Proc. Natl. Acad. Sci. USA* **2001**, *98*, 4899 – 4903.
[18] a) J. H. Cate, A. R. Gooding, E. Podell, K. H. Zhou, B. L. Golden, C. E. Kundrot, T. R. Cech, J. A. Doudna, *Science* **1996**, *273*, 1678 – 1685; b) A. R. Ferre-D'Amare, K. Zhou, J. A. Doudna, *Nature* **1998**, *395*, 567 – 574.
[19] R. K. Agrawal, C. M. T. Spahn, P. Penczek, R. A. Grassucci, K. H. Nierhaus, J. Frank, *J. Cell Biol.* **2000**, *150*, 447 – 459.
[20] L. P. Gavrilova, O. E. Kostiashkina, V. E. Koteliansky, N. M. Rutkevitch, A. S. Spirin, *J. Mol. Biol.* **1976**, *101*, 537 – 552.
[21] S. Schilling-Bartetzko, A. Bartetzko, K. H. Nierhaus, *J. Biol. Chem.* **1992**, *267*, 4703 – 4712.
[22] G. Z. Yusupova, M. M. Yusupov, J. H. Cate, H. F. Noller, *Cell* **2001**, *106*, 233 – 241.
[23] T. V. Pestova, V. G. Kolupaeva, I. B. Lomakin, E. V. Pilipenko, I. N. Shatsky, V. I. Agol, C. U. T. Hellen, *Proc. Natl. Acad. Sci. USA* **2001**, *98*, 7029 – 7036.
[24] A. Roll-Mecak, B. S. Shin, T. E. Dever, S. K. Burley, *Trends Biochem. Sci.* **2001**, *26*, 705 – 709.
[25] C. Gualerzi, L. Brandi, E. Caserta, A. La teana, R. Spurio, J. Tomsic, C. Pon in *The ribosome. structure, function, antibiotics, and cellular interactions* (Eds.: R. A. Garrett, S. R. Douthwaite, A. Liljas, A. T. Matheson, P. B. Moore, H. F. Noller), American Society for Microbiology, Washington, DC, **2000**, pp. 477 – 494.
[26] A. P. Carter, W. M. Clemons, Jr., D. E. Brodersen, R. J. Morgan-Warren, T. Hartsch, B. T. Wimberly, V. Ramakrishnan, *Science* **2001**, *291*, 498 – 501.
[27] M. Pioletti, F. Schlunzen, J. Harms, R. Zarivach, M. Gluhmann, H. Avila, A. Bashan, H. Bartels, T. Auerbach, C. Jacobi, T.

 © 2003 Wiley-VCH Verlag GmbH & Co. KGaA, Weinheim

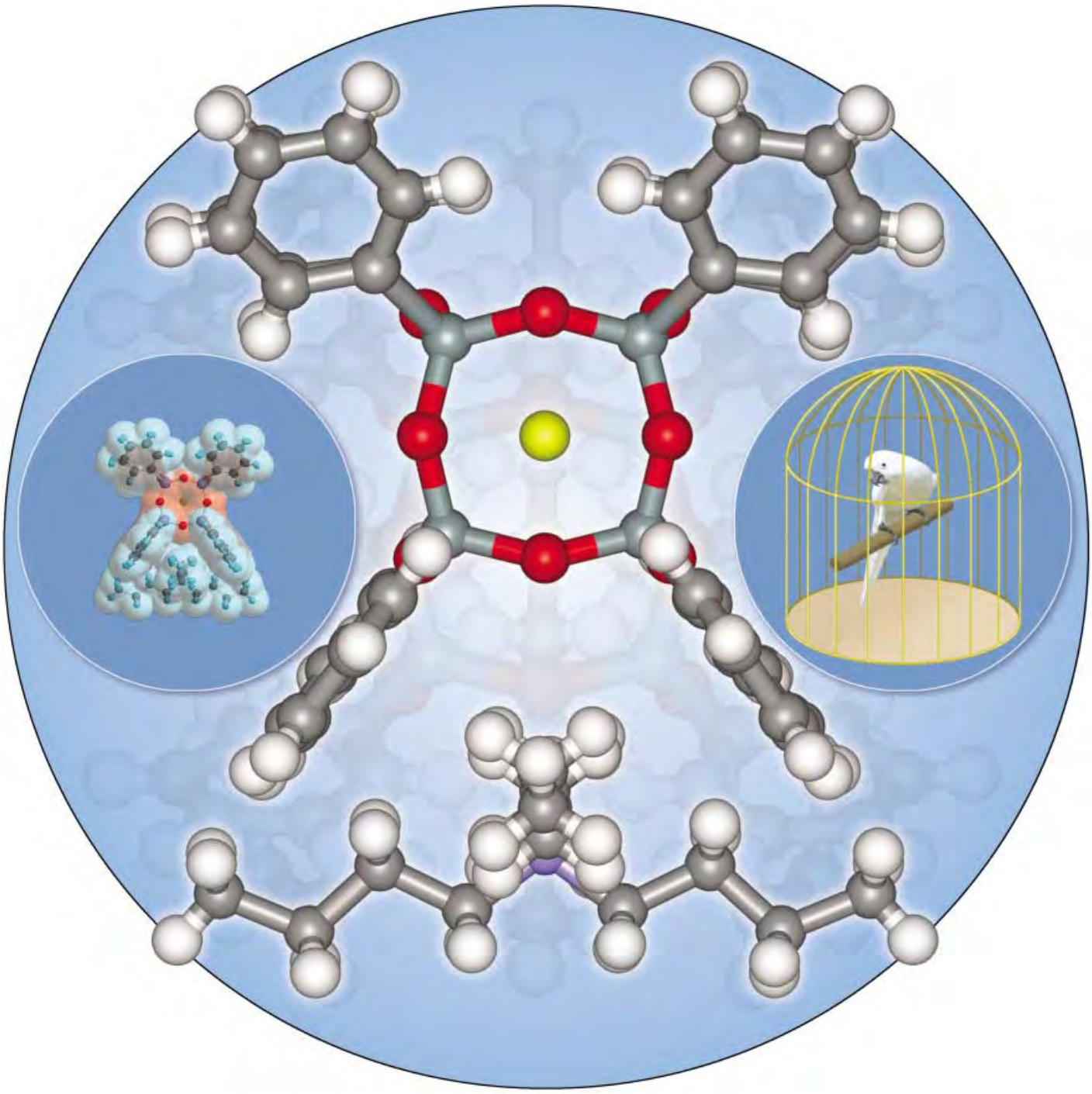
Hartsch, A. Yonath, F. Franceschi, *EMBO J.* **2001**, *20*, 1829 – 1839.
[28] A. Dallas, H. F. Noller, *Mol. Cell* **2001**, *8*, 855 – 864.
[29] A. Gnirke, K. H. Nierhaus, *J. Biol. Chem.* **1986**, *261*, 14506 – 14514.
[30] A. Roll-Mecak, C. Cao, T. E. Dever, S. K. Burley, *Cell* **2000**, *103*, 781 – 792.
[31] I. S. Gabashvili, R. K. Agrawal, C. M. T. Spahn, R. A. Grassucci, D. I. Svergun, J. Frank, P. Penczek, *Cell* **2000**, *100*, 537 – 549.
[32] J. H. Cate, M. M. Yusupov, G. Z. Yusupova, T. N. Earnest, H. F. Noller, *Science* **1999**, *285*, 2095 – 2104.
[33] a) A. P. Potapov, *FEBS Lett.* **1982**, *146*, 28 – 33; b) A. P. Potapov, F. J. Triana-Alonso, K. H. Nierhaus, *J. Biol. Chem.* **1995**, *270*, 17680 – 17684.
[34] P. Nissen, M. Kjeldgaard, J. Nyborg, *EMBO J.* **2000**, *19*, 489 – 495.
[35] K. H. Nierhaus, *Mol. Microbiol.* **1993**, *9*, 661 – 669.
[36] M. Valle, J. Sengupta, N. K. Swami, R. A. Grassucci, N. Burkhardt, K. H. Nierhaus, R. K. Agrawal, J. Frank, *EMBO J.* **2002**, *21*, 3557 – 3567.
[37] H. Stark, M. V. Rodnina, H. J. Wieden, F. Zemlin, W. Wintermeyer, M. Van Heel, *Nat. Struct. Biol.* **2002**, *15*, 15 – 20.
[38] A. Weijland, A. Parmeggiani, *Science* **1993**, *259*, 1311 – 1314.
[39] J. M. Ogle, D. E. Brodersen, W. M. Clemons, Jr, M. J. Tarry, A. P. Carter, V. Ramakrishnan, *Science* **2001**, *292*, 897 – 902.
[40] J. J. Hopfield, *Proc. Natl. Acad. Sci. USA* **1974**, *71*, 4135 – 4139.
[41] J. Ninio, *Biochimie* **1975**, *57*, 587 – 595.
[42] M. Ehrenberg, D. Andersson, K. Mohman, P. Jelenc, T. Ruusala, C. G. Kurland in *Structure, function and genetics of ribosomes* (Eds.: B. Hardesty, G. Kramer), Springer, New York, **1986**, pp. 573 – 585.
[43] M. V. Rodnina, T. Daviter, K. Gromadski, W. Wintermeyer, *Biochimie* **2002**, *84*, 745 – 754.
[44] S. Schilling-Bartetzko, F. Franceschi, H. Sternbach, K. H. Nierhaus, *J. Biol. Chem.* **1992**, *267*, 4693 – 4702.
[45] A. M. Karim, R. C. Thompson, *J. Biol. Chem.* **1986**, *261*, 3238 – 3243.
[46] J. M. Ogle, F. V. Murphy, M. J. Tarry, V. Ramakrishnan, *Cell* **2002**, *111*, 721 – 732.
[47] J. Czworkowski, J. Wang, T. A. Seitz, P. B. Moore, *EMBO J.* **1994**, *13*, 3661 – 3668.
[48] A. Aevarsson, E. Brazhnikov, M. Garber, J. Zheltonosova, Y. Chirgadze, S. Alkaradaghi, L. A. Svensson, A. Liljas, *EMBO J.* **1994**, *13*, 3669 – 3677.
[49] M. Kjeldgaard, J. Nyborg, *J. Mol. Biol.* **1992**, *223*, 721 – 742.
[50] H. Berchtold, L. Reshetnikova, C. O. A. Reiser, N. K. Schirmer, M. Sprinzl, R. Hilgenfeld, *Nature* **1993**, *365*, 126 – 132.
[51] P. Nissen, M. Kjeldgaard, S. Thirup, G. Polekhina, L. Reshetnikova, B. F. C. Clark, J. Nyborg, *Science* **1995**, *270*, 1464 – 1472.
[52] M. Laurberg, O. Kristensen, K. Martemyanov, A. T. Gudkov, I. Nagaev, D. Hughes, A. Liljas, *J. Mol. Biol.* **2000**, *303*, 593 – 603.
[53] a) M. Selmer, S. Al-Karadaghi, G. Hirakawa, A. Kaji, A. Liljas, *Science* **1999**, *286*, 2349 – 2352; b) K. K. Kim, K. Min, S. W. Suh, *EMBO J.* **2000**, *19*, 2362 – 2370; c) T. Yoshida, S. Uchiyama, H. Nakano, H. Kashimori, H. Kijima, T. Ohshima, Y. Saihara, T. Ishino, H. Shimahara, K. Yokose, T. Ohkubo, A. Kaji, Y. Kobayashi, *Biochemistry* **2001**, *40*, 2387 – 2396.
[54] T. Toyoda, O. F. Tin, K. Ito, T. Fujiwara, T. Kumasaka, M. Yamamoto, M. B. Garber, Y. Nakamura, *RNA* **2000**, *6*, 1432 – 1444.
[55] N. Guex, M. C. Peitsch, *Electrophoresis* **1997**, *18*, 2714 – 2723.
[56] B. Vestergaard, L. Van, G. Andersen, J. Nyborg, R. Buckingham, M. Kjeldgaard, *Mol. Cell* **2001**, *8*, 1375 – 1382.
[57] H. Song, P. Mugnier, A. Das, H. Webb, D. Evans, M. Tuite, B. Hemmings, D. Barford, *Cell* **2000**, *100*, 311 – 321.
[58] B. P. Klaholz, T. Pape, A. V. Zavialov, A. G. Myasnikov, E. V. Orlova, B. Vestergaard, M. Ehrenberg, M. Van Heel, *Nature* **2003**, *421*, 90 – 94.
[59] U. B. Rawat, A. V. Zavialov, J. Sengupta, M. Valle, R. A. Grassucci, J. Linde, B. Vestergaard, M. Ehrenberg, J. Frank, *Nature* **2003**, *421*, 87 – 90.
[60] L. Lancaster, M. C. Kiel, A. Kaji, H. F. Noller, *Cell* **2002**, *111*, 129 – 140.
[61] G. Hirokawa, M. C. Kiel, A. Muto, M. Selmer, V. S. Raj, A. Liljas, K. Igarashi, H. Kaji, A. Kaji, *EMBO J.* **2002**, *21*, 2272 – 2281.
[62] a) K. Yamaguchi, K. von Knoblauch, A. R. Subramanian, *J. Biol. Chem.* **2000**, *275*, 28455 – 28465; b) K. Yamaguchi, A. R. Subramanian, *J. Biol. Chem.* **2000**, *275*, 28466 – 28482; c) T. Suzuki, M. Terasaki, C. Takemoto-Hori, T. Hanada, T. Ueda, A. Wada, K. Watanabe, *J. Biol. Chem.* **2001**, *276*, 33181 – 33195; d) E. C. Koc, W. Burkhart, K. Blackburn, M. B. Moyer, D. M. Schlatzer, A. Moseley, L. Spremulli, *J. Biol. Chem.* **2001**, *276*, 43958 – 43969; e) E. C. Koc, W. Burkhart, K. Blackburn, A. Moseley, L. Spremulli, *J. Biol. Chem.* **2001**, *276*, 19363 – 19374.
[63] J. A. Mears, J. J. Cannone, S. M. Stagg, R. R. Gutell, R. K. Agrawal, S. C. Harvey, *J. Mol. Biol.* **2002**, *321*, 215 – 234.
[64] A. P. Carter, W. M. Clemons, D. E. Brodersen, R. J. Morgan-Warren, B. T. Wimberly, V. Ramakrishnan, *Nature* **2000**, *407*, 340 – 348.
[65] D. E. Brodersen, W. M. Clemons, A. P. Carter, R. J. Morgan-Warren, B. T. Wimberly, V. Ramakrishnan, *Cell* **2000**, *103*, 1143 – 1154.
[66] J. Gordon, *J. Biol. Chem.* **1969**, *244*, 5680 – 5686.
[67] J. S. Lodmell, A. E. Dahlberg, *Science* **1997**, *277*, 1262 – 1267.
[68] S. R. Connell, C. A. Trieber, U. Stelzl, E. Einfeldt, D. E. Taylor, K. H. Nierhaus, *Mol. Microbiol.* **2002**, *45*, 1463 – 1472.
[69] P. Nissen, J. Hansen, N. Ban, P. B. Moore, T. A. Steitz, *Science* **2000**, *289*, 920 – 930.
[70] N. Polacek, M. Gaynor, A. Yassin, A. S. Mankin, *Nature* **2001**, *411*, 498 – 501.
[71] G. W. Muth, L. Ortoleva-Donnelly, S. A. Strobel, *Science* **2000**, *289*, 947 – 950.
[72] J. Thompson, D. F. Kim, M. O'Connor, K. R. Lieberman, M. A. Bayfield, S. T. Gregory, R. Green, H. F. Noller, A. E. Dahlberg, *Proc. Natl. Acad. Sci. USA* **2001**, *98*, 9002 – 9007.
[73] R. Green, J. R. Lorsch, *Cell* **2002**, *110*, 665 – 668.
[74] J. L. Hansen, J. A. Ippolito, N. Ban, P. Nissen, P. B. Moore, T. A. Steitz, *Mol. Cell* **2002**, *10*, 117 – 128.
[75] D. Knowles, N. Foloppe, N. Matassova, A. Murchie, *Curr. Opin. Pharmacol.* **2002**, *2*, 501.
[76] M. M. Yusupov, G. Z. Yusupova, A. Baucom, K. Lieberman, T. N. Earnest, J. H. Cate, H. F. Noller, *Science* **2001**, *292*, 883 – 896.
[77] M. A. Schäfer, A. O. Tastan, S. Patzke, G. Blaha, C. M. Spahn, D. N. Wilson, K. H. Nierhaus, *J. Biol. Chem.* **2002**, *277*, 19095 – 19105.
[78] R. A. Sayle, E. J. Milner-White, *Trends Biochem. Sci.* **1995**, *20*, 374.
[79] M. Dabrowski, C. M. T. Spahn, K. H. Nierhaus, *EMBO J.* **1995**, *14*, 4872 – 4882.
[80] K. H. Nierhaus, J. Wadzack, N. Burkhardt, R. Jünemann, W. Meerwinck, R. Willumeit, H. B. Stuhrmann, *Proc. Natl. Acad. Sci. USA* **1998**, *95*, 945 – 950.
[81] J. L. Hansen, T. M. Schmeing, P. B. Moore, T. A. Steitz, *Proc. Natl. Acad. Sci. USA* **2002**, *99*, 11670 – 11675.
[82] A. Bashan, I. Agmon, R. Zarivach, F. Schluenzen, J. Harms, R. Berisio, H. Bartels, F. Franceschi, T. Auerbach, H. A. Hansen, E. Kossoy, M. Kessler, A. Yonath, *Mol. Cell* **2003**, *11*, 91 – 102.
[83] J. M. Berg, J. R. Lorsch, *Science* **2001**, *291*, 203.
[84] M. Welch, J. Chastang, M. Yarus, *Biochemistry* **1995**, *34*, 385 – 390.

 © 2003 Wiley-VCH Verlag GmbH & Co. KGaA, Weinheim

[85] K. M. Parnell, A. Seila, S. A. Strobel, *Proc. Natl. Acad. Sci. USA* **2002**, *99*, 11658 – 11663.
[86] M. A. Bayfield, A. E. Dahlberg, U. Schulmeister, S. Dorner, A. Barta, *Proc. Natl. Acad. Sci. USA* **2001**, *98*, 10096 – 10101.
[87] T. M. Schmeing, A. C. Seila, J. L. Hansen, B. Freeborn, J. K. Soukup, S. A. Scaringe, S. A. Strobel, P. B. Moore, T. A. Steitz, *Nat. Struct. Biol.* **2002**, *9*, 225 – 230.
[88] K. Quiggle, G. Kumar, T. W. Ott, E. K. Ryu, S. Chladek, *Biochemistry* **1981**, *20*, 3480 – 3485.
[89] V. I. Katunin, G. W. Muth, S. A. Strobel, W. Wintermeyer, M. V. Rodnina, *Mol. Cell* **2002**, *10*, 339 – 346.
[90] G. Diedrich, C. M. T. Spahn, U. Stelzl, M. A. Schäfer, T. Wooten, D. E. Bocharov, B. S. Cooperman, R. R. Traut, K. H. Nierhaus, *EMBO J.* **2000**, *19*, 5241 – 5250.
[91] K. H. Nierhaus, H. Schulze, B. S. Cooperman, *Biochem. Int.* **1980**, *1*, 185 – 192.
[92] M. L. Celma, R. E. Monro, D. Vazquez, *FEBS Lett.* **1971**, *13*, 247 – 251.
[93] B. Ulbrich, G. Mertens, K. H. Nierhaus, *Arch. Biochem. Biophys.* **1978**, *190*, 149 – 154.
[94] K. Bergemann, K. H. Nierhaus, *J. Biol. Chem.* **1983**, *258*, 15105 – 15113.
[95] Y. Kaziro, *Biochim. Biophys. Acta* **1978**, *505*, 95 – 127.
[96] R. Agrawal, P. Penczek, R. Grassucci, J. Frank, *Proc. Natl. Acad. Sci. USA* **1998**, *95*, 6134 – 6138.
[97] R. K. Agrawal, A. B. Heagle, P. Penczek, R. A. Grassucci, J. Frank, *Nat. Struct. Biol.* **1999**, *6*, 643 – 647.
[98] H. Stark, M. V. Rodnina, H. J. Wieden, M. van Heel, W. Wintermeyer, *Cell* **2000**, *100*, 301 – 309.
[99] M. G. Gomez-Lorenzo, C. M. T. Spahn, R. K. Agrawal, R. A. Grassucci, P. Penczek, K. Chakraburtty, J. P. G. Ballesta, J. L. Lavandera, J. F. Garcia-Bustos, J. Frank, *EMBO J.* **2000**, *19*, 2710 – 2718.
[100] T. P. Hausner, J. Atmadja, K. H. Nierhaus, *Biochimie* **1987**, *69*, 911 – 923.
[101] Y. Endo, K. Tsurugi, *J. Biol. Chem.* **1987**, *262*, 8128 – 8130.
[102] T. Uchiumi, S. Honma, T. Nomura, E. R. Dabbs, A. Hachimori, *J. Biol. Chem.* **2002**, *277*, 3857 – 3862.
[103] E. Cundliffe in *The ribosome: structure, function and evolution* (Eds.: W. E. Hill, A. Dahlberg, R. A. Garrett, P. B. Moore, D. Schlessinger, J. R. Warners), American Society for Microbiology, Washington, DC, **1990**, pp. 479 – 490.
[104] G. Stöffler, E. Cundliffe, M. Stöffle-Meilicke, E. R. Dabbs, *J. Biol. Chem.* **1980**, *255*, 10517 – 10522.
[105] D. M. Cameron, J. Thompson, P. E. March, A. E. Dahlberg, *J. Mol. Biol.* **2002**, *319*, 27 – 35.
[106] R. K. Agrawal, J. Linde, J. Sengupta, K. H. Nierhaus, J. Frank, *J. Mol. Biol.* **2001**, *311*, 777 – 787.
[107] K. H. Nierhaus, C. M. T. Spahn, N. Burkhardt, M. Dabrowski, G. Diedrich, E. Einfeldt, D. Kamp, V. Marquez, S. Patzke, M. A. Schäfer, U. Stelzl, G. Blaha, R. Willumeit, H. B. Stuhrmann in *The ribosome. structure, function, antibiotics, and cellular interactions* (Eds.: R. A. Garrett, S. R. Douthwaite, A. Liljas, A. T. Matheson, P. B. Moore, H. F. Noller), American Society for Microbiology, Washington, DC, **2000**, pp. 319 – 335.
[108] J. Harms, F. Schluenzen, R. Zarivach, A. Bashan, S. Gat, I. Agmon, H. Bartels, F. Franceschi, A. Yonath, *Cell* **2001**, *107*, 679 – 688.
[109] H.-J. Rheinberger, K. H. Nierhaus, *Biochem. Int.* **1980**, *1*, 297 – 303.
[110] H.-J. Rheinberger, H. Sternbach, K. H. Nierhaus, *Proc. Natl. Acad. Sci. USA* **1981**, *78*, 5310 – 5314.
[111] H. Saruyama, K. H. Nierhaus, *Mol. Gen. Genet.* **1986**, *204*, 221 – 228.
[112] F. Triana, K. Nierhaus, K. Chakraburtty, *Biochem. Mol. Biol. Int.* **1994**, *33*, 909 – 915.
[113] A. V. Elskaya, G. V. Ovcharenko, S. S. Palchevskii, Z. M. Petrushenko, F. J. Triana-Alonso, K. H. Nierhaus, *Biochemistry* **1997**, *36*, 10492 – 10497.
[114] R. K. Agrawal, P. Penczek, R. A. Grassucci, N. Burkhardt, K. H. Nierhaus, J. Frank, *J. Biol. Chem.* **1999**, *274*, 8723 – 8729.
[115] G. Blaha, U. Stelzl, C. M. T. Spahn, R. K. Agrawal, J. Frank, K. H. Nierhaus, *Methods Enzymol.* **2000**, *317*, 292 – 309.
[116] K. H. Nierhaus, *Biochemistry* **1990**, *29*, 4997 – 5008.
[117] U. Geigenmüller, K. H. Nierhaus, *EMBO J.* **1990**, *9*, 4527 – 4533.
[118] J. A. Horsfield, D. N. Wilson, S. A. Mannering, F. M. Adamski, W. P. Tate, *Nucleic Acids Res.* **1995**, *23*, 1487 – 1494.
[119] V. Marquez, D. N. Wilson, F. Triana-Alonso, W. Tate, K. H. Nierhaus, unpublished results

 © 2003 Wiley-VCH Verlag GmbH & Co. KGaA, Weinheim

Communications



The encapsulation of a fluoride ion in an octaphenylsilsesquioxane cage is described by A. Bassindale, P. G. Taylor, and co-workers on the following pages. Viewed from above, the fluoride ion is shown to reside at the center of the cage, rather like the bird depicted; a tetrabutylammonium counterion is located between the phenyl groups of the cage.

DOI: 10.1002/anie.200351249
© 2003 Wiley-VCH Verlag GmbH & Co. KGaA, Weinheim

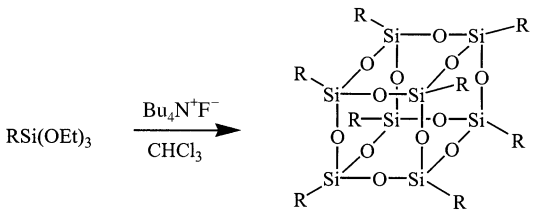
Fluoride Ions in Cage Structures

Fluoride-Ion Encapsulation within a Silsesquioxane Cage

Alan R. Bassindale, Manuel Pourny, Peter G. Taylor,* Michael B. Hursthouse, and Mark E. Light*

Octaspherosilicate structures have found use as scaffolds for dendrimer synthesis,[1–4] as models for aluminosilicate structures,[5] and as supports for organometallic catalysts.[6–8] Space-filling models of such cages suggest there is a void at the center of the cube, but that it is questionable whether it could be filled by an atomic species. Päch and Stosser have shown that γ-irradiation of octaalkyl octasilsesquioxane or octatrialkyl siloxyoctasilsesquioxane leads to hydrogen-encapsulated T8 or Q8 cages.[9] ESR spectroscopy confirmed that the hydrogen originated from the organic substituents of the cage.

We have recently developed a high-yield route to T8 cages based on the reaction of tetrabutylammonium fluoride with trialkoxysilanes (Scheme 1).[10] However, we have found that



Scheme 1.

if instead of precipitating the cage by the addition of acetone the solvent is removed, then concentrating the quantity of tetrabutylammonium fluoride with the cage leads to a new cage structure. For example, the reaction of phenyltriethoxysilane with a 5% solution of tetrabutylammonium fluoride in tetrahydrofuran, followed by removal of the solvent, gives a powder that can be purified by addition of chloroform leaving a white solid that is soluble in acetone. The solubility of this compound confirms that it is not phenyl T8.[11] The ^{1}H NMR spectrum shows that each phenyl T8 cage is accompanied by one tetrabutylammonium cation. The ^{29}Si NMR spectrum confirms the presence of the T8 cage and that the signal is shifted upfield by 0.9 ppm from octaphenyl octasilsesquioxane to $\delta = -80.6$ ppm, which suggests that the cage has been modified in some way. Negative-ion FAB mass spectrometry gives a single peak at $m/z = 1051.2$, with an isotope pattern corresponding to $C_{48}H_{40}Si_8O_{12}F$. These results suggest that a T8 cage associated with a fluoride ion was formed, which was confirmed by single-crystal X-ray crystallography after recrystallization from acetone. Figure 1 shows an ORTEP diagram of the crystal structure, in which the fluoride ion is essentially at the center of the cage.[12]

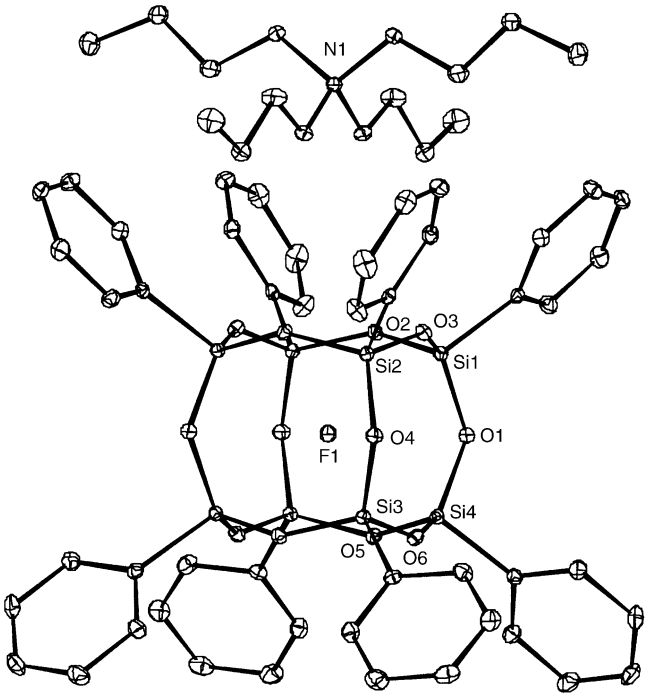


Figure 1. ORTEP representation of tetrabutylammonium octaphenyl octasilsesquioxane fluoride. Selected bond lengths [Å] and angles [°] are given in Table 1.

The cages are packed together in horizontal layers with the tetrabutylammonium ions interleaved between the layers. The phenyl groups are aligned so that the butyl groups of the counterions lie in a cleft formed by the aromatic rings. This means that each cage has a tetrabutylammonium ion on two opposing faces.

Table 1 compares selected bond lengths and bond angles of the fluoride-encapsulated cage with those of the published phenyl T8 cage.[11] This reveals that the presence of the fluoride ion makes very little difference to the structure. The mean separation between the silicon atoms on opposite vertices of the cube is slightly shorter in the fluoride-encapsulated cage (5.306 Å) than in the free structure (5.381 Å) suggesting a small interaction of the fluoride ion with each of the eight silicon atoms. The Si···F separation in the fluoride cage is 2.65 Å, which is much longer than that of a full Si–F covalent bond (1.709 Å) or the Si–F bond length in a typical pentavalent species (1.675 Å).[13] The level of the fluorine–silicon interaction can be estimated by the size of the upfield shift in the ^{29}Si NMR spectrum, which at 0.9 ppm is relatively small compared to the difference between a tetracoordinate silicon atom and the corresponding pentacoordinate silicon center associated with a fluoride ion ($\delta =$

[*] Prof. A. R. Bassindale, Dr. P. G. Taylor, M. Pourny
Department of Chemistry, Open University
Walton Hall, Milton Keynes, MK7 6AA (UK)
Fax: (+44) 1908-858327
E-mail: A.Bassindale@open.ac.uk
P.G.Taylor@open.ac.uk
Prof. M. B. Hursthouse, Dr. M. E. Light
EPSRC National Crystallography Service
University of Southampton
Highfield, Southampton, SO17 1BJ (UK)

 © 2003 Wiley-VCH Verlag GmbH & Co. KGaA, Weinheim DOI: 10.1002/anie.200351249

Table 1: Selected bond lengths [Å] and angles [°] of the phenyl T8 fluoride-encapsulated cage and the phenyl T8 cage.

	Phenyl-T8 fluoride cage	Phenyl-T8
Bond lengths [Å]		
Si(1)–O(1)	1.6224	1.613
Si(1)–O(2)	1.6213	1.607
Si(1)–O(3)	1.6284	1.614
Average Si–O bond length [Å]	1.625	1.612
Bond angles [°]		
O(4)-Si(1)-O(2)	112.98	109.9
O(4)-Si(1)-O(3)	113.55	109.1
O(2)-Si(1)-O(3)	112.40	108.0
Average O-Si-O angle [°]	112.98	109.0
Si(1)-O(1)-Si(4)	141.11	144.6
Si(1)-O(2)-Si(2)	143.36	151.4
Si(2)-O(3)-Si(1)	139.11	151.4
Average Si-O-Si angle [°]	141.19	149.2

63 ppm).[13] The absence of any measurable Si–F coupling also confirms the low degree of silicon–fluoride interaction.

The mean separation between the oxygen atoms on opposite edges of the cube is slightly longer in the fluoride-encapsulated cage (5.413 Å) than in the free structure (5.396 or 5.176 Å), which suggests that the oxygen atoms are repelled by the fluoride ions. Comparison of the bond angles in Table 1 also confirms a general pulling together of the silicon atoms and pushing apart of the oxygen atoms. Closer examination of the position of the fluoride ion suggests that within experimental error it is slightly off center. This almost certainly reflects the slightly staggered packing of the cages.

The ability of fluorine atoms to cause supramolecular self-assembly and be involved in host–guest complexation has been extensively reviewed by Roesky and Haiduc, who provide evidence that fluorine can behave as a mono-, di-, tri-, or tetracoordinating species.[14] Whilst the Si–F interaction is small in the encapsulated cage, it is difficult to imagine that the fluoride ion is randomly placed in the center of the cage. Thus we are forced to conclude that in these octasilsesquioxane cages the fluorine atom is octacoordinated, as has recently been observed by Morris et al.[15] Refluxing the fluoride-ion cage in a range of solvents does not lead to the loss of the fluoride ion; this indicates that the faces of the silsesquioxane cage cannot provide a sufficiently large opening for the fluoride ion to pass through. This suggests that the fluoride ion must be acting as a template for formation of the cage and that once inside, it can only escape when the cage is broken down. Such a templating role for the fluoride ion has been proposed in molecular sieve synthesis, and Roesky et al.[16] and Mason et al.[17] have attempted to encapsulate a fluoride ion in alumino- and gallophosphonate models of the double four-ring (D4R) cage without success. However, Morris et al. have successfully used a hydrothermal synthesis involving HF to prepare the germanium oxide D4R cage containing a fluoride ion.[15] Preparations using tetrabutylammonium chloride show no evidence for encapsulation, and indeed no cage formation. This reflects the key role played by the fluoride ion as a base catalyst,[10] and the precise match between the size of the fluoride ion and the unoccupied space at the center of the cage.

Since the fluoride ion only coordinates with the silicon atoms to a small extent, it is essentially a naked fluoride ion. The ^{19}F NMR spectrum shows a sharp peak at $\delta = -26.4$ ppm, which is one of the highest frequencies recorded for a fluoride salt. The chemical shifts recorded for tetrabutylammonium fluoride are highly variable, ranging from $\delta = -73$ to -146 ppm depending upon solvent coordination and hydrogen bonding, particularly with moisture in the solvent. "Anhydrous" tetrabutylammonium fluoride has a chemical shift of $\delta = -73$ ppm.[18] The solid-state ^{19}F NMR spectrum is identical to that found in solution, which suggests that once inside the cage, the chemical shift of the fluoride ion is not greatly affected by its immediate environment. Recently, we reported that the change in the ^{19}F NMR chemical shift with the extent of Si–F bond breaking in pentacoordinate silicon complexes suggests that a value of about $\delta = -26$ ppm is in keeping with that expected for a naked fluoride ion.[19] Caullet et al. have reported the preparation of an octadecasil zeolite containing a fluoride ion in the D4R cage.[20] Whilst there is no detailed structural information reported, the solid-state ^{19}F NMR shows a peak at $\delta = -38$ ppm. The Si–F coordination is expected to be greater in these silicate structures since there is a Si–O bond apical to the fluoride ion, and thus the peak in the ^{19}F NMR spectrum should be shifted to a lower frequency compared to a naked fluoride ion. The ^{19}F chemical shift of a fluoride ion encapsulated in a D4R alumino- or gallophosphate cage in molecular sieves are observed further downfield at $\delta = -69$ to -95 ppm,[21–23] although the ^{19}F chemical shift of the fluoride ion encapsulated in the germanium oxide D4R cage occurs at $\delta = -15$ ppm.[15]

In conclusion, we have prepared the first fluoride ion to have been encapsulated in a silsesquioxane cage. The X-ray crystal structure and NMR data suggest very little F–Si coordination, such that the fluoride ion essentially resembles a naked fluoride ion. We are at present preparing other T8 cages containing a fluoride ion, but with different organic substituents on the silicon atoms. We are also exploring the novel properties of these molecular anions.

Experimental Section

Tetrabutylammonium octaphenyl octasilsesquioxane fluoride: Tetrabutylammonium fluoride (1M solution in THF, 2.5 cm^3 , with 5% water) was added to phenyl triethoxysilane (1.02 g, 4.2 mmol) dissolved in dry THF (20 cm^3). The mixture was stirred at room temperature for 24 h and a yellow viscous liquid obtained after removal of the solvent. Dry chloroform (10 cm^3) was added, and a white powder was obtained after filtration. Recrystallization from acetone afforded colorless crystals (1.25 g, 46%). ^{1}H NMR (300 MHz, [D$_6$]acetone, TMS): $\delta = 7.81$–7.78 (dd, $^3J(H_2,H_1) = 2.0$ Hz, $^3J(H_2,H_3) = 1.1$ Hz, 2H; *m*-CH), 7.79 (t, $^3J(H_3,H_2) = 1.1$ Hz, 1H; *p*-CH), 7.29 (d, $^3J(H_1,H_2) = 2.0$ Hz, 2H; *o*-CH), 3.39–3.34 (t, $^3J(H_4,H_5) = 8.26$ Hz, 2H; N-CH$_2$), 1.75–1.85 (quintuplet, $^3J(H_5,H_4) = 8.26$ Hz, $^3J(H_5,H_6) = 7.33$ Hz, 2H; CH$_2$), 1.36–1.48 (m, 2H; CH$_2$), 0.95–0.99 ppm (t, $^3J(H_7,H_6) = 7.54$ Hz, 3H, CH$_3$); ^{13}C NMR (75.5 MHz, [D$_6$]acetone, TMS): $\delta = 138.4$ (*p*-C), 134.9 (*m*-C), 129.7 (*i*-C), 128.1 (*o*-C), 49.8 (N-C), 24.3 (CH$_2$), 20.3 (CH$_2$), 13.8 ppm

 © 2003 Wiley-VCH Verlag GmbH & Co. KGaA, Weinheim

(CH_3); ^{19}F NMR (376 MHz, $CDCl_3$): $\delta = -26.4$ ppm; ^{29}Si NMR (79.30 MHz, $CDCl_3$, TMS): $\delta = -80.6$ ppm; IR (KBr disc): $\tilde{\nu} = 3085$ ($\nu_{C\text{-}H}$), 2990 ($\nu_{C\text{-}H}$), 2935 ($\nu_{C\text{-}H}$), 1410 (m), 1120 ($\nu_{as(Si\text{-}O\text{-}Si)}$), 1050, 1000, 750, 700, 510 ($\nu_{s(Si\text{-}O\text{-}Si)}$), 410 cm^{-1} ($\delta_{(O\text{-}Si\text{-}O)}$); MS (MALDI-TOF): *m*/*z* (%): 1294.5 [M^-], 1052.5 (35) [$M^- - C_{16}H_{36}N$], 1034 (100) [$M^- - C_{16}H_{36}NF$], 242.3 (99) [$C_{16}H_{36}N^-$], 19 [F^-].

Received: February 24, 2003 [Z51249]

Keywords: anions · cage compounds · fluorides · silicon ligands · silicon

[1] F. J. Feher, K. D. Wyndham, *Chem. Commun.* **1998**, 323.
[2] P. A. Jaffres, R. E. Morris, *J. Chem. Soc. Dalton Trans.* **1998**, 2767.
[3] T. Matsuo, K. Uchida, A. Sekiguchi, *Chem. Commun.* **1999**, 1799.
[4] I. M. Saez, J. W. Goodby, *Liq. Cryst.* **1999**, *26*, 1101.
[5] F. J. Feher, K. J. Weller, *Organometallics* **1990**, *9*, 2638.
[6] F. J. Feher, *J. Am. Chem. Soc.* **1986**, *108*, 3850.
[7] F. J. Feher, R. L. Blanski, *J. Chem. Soc. Chem. Commun.* **1990**, 1614.
[8] F. J. Feher, R. L. Blanski, *Makromol. Chem. Macromol. Symp.* **1993**, *66*, 95.
[9] M. Päch, R. Stosser, *J. Phys. Chem. A* **1997**, *101*, 8360.
[10] A. R. Bassindale, P. G. Taylor, Y. Yang, Z. Liu, *J. Chem. Soc. Dalton. Trans.* **2003**, in press.
[11] M. A. Hossain, M. B. Hursthouse, K. M. A. Malik, *Acta Crystallogr. Sect. B* **1979**, *35*, 2258.
[12] Cell dimensions and intensity data were recorded using a Bruker Nonius KappaCCD area detector at the window of a molybdenum rotating anode generator following standard procedures. Crystal data: $C_{64}H_{76}NO_{12}FSi_8$, $M_W = 1294.98$, $T = 120(2)$ K, monoclinic, space group *C*2/*c*, $a = 23.8267(4)$, $b = 12.9976(3)$, $c = 22.1794(5)$ Å, $\beta = 108.1550(12)°$, $V = 6526.8(2)$ $Å^3$, $\rho_{calcd} = 1.318$ $g\,cm^{-3}$, $\mu = 0.228$ mm^{-1}, $Z = 4$, reflections collected: 16965, independent reflections: 5719 ($R_{int} = 0.0555$), final *R* indices [$I > 2\sigma I$]: $R1 = 0.0397$, $wR2 = 0.1050$, *R* indices (all data): $R1 = 0.0560$, $wR2 = 0.1134$. CCDC-203187 contains the supplementary crystallographic data for this paper. These data can be obtained free of charge via www.ccdc.cam.ac.uk/conts/retrieving.html (or from the Cambridge Crystallographic Data Centre, 12, Union Road, Cambridge CB21EZ, UK; fax: (+44) 1223-336-033; or deposit@ccdc.cam.ac.uk).
[13] A. R. Bassindale, D. J. Parker, P. G. Taylor, N. Auner, B. Herrschaft, *J. Organomet. Chem.* **2003**, *667*, 66.
[14] H. W. Roesky, I. Haiduc, *J. Chem. Soc. Dalton Trans.* **1999**, 2249.
[15] L. A. Villaescusa, P. Lightfoot, R. E. Morris, *Chem. Commun.* **2002**, 2220.
[16] Y. Yang, J. Pinkas, M. Shafer, H. W. Roesky, *Angew. Chem.* **1998**, *110*, 2795; *Angew. Chem. Int. Ed.* **1998**, *37*, 2650.
[17] M. R. Mason, A. M. Perkins, R. M. Matthews, J. D. Fisher, M. S. Mashuta, A. Vij, *Inorg. Chem.* **1998**, *37*, 3734.
[18] R. D. Chambers, W. K. Gray, G. Sandford, J. F. S. Vaughan, *J. Fluorine Chem.* **1999**, *94*, 213.
[19] A. R. Bassindale, Y. I. Baukov, M. Borbaruah, S. J. Glynn, V. V. Negrebetsky, D. J. Parker, P. G. Taylor, R. Turtle, *J. Organomet. Chem.* **2003**, *669*, 154.
[20] P. Caullet, J. L. Guth, J. Hazm, J. M. Lamblin, H. Gies, *Eur. J. Solid State Inorg. Chem.* **1991**. *28*, 345.
[21] P. Reinert, B. Marler, J. Patarin, *Chem. Commun.* **1998**, 1769.
[22] L. Schreyeck, F. D'agosto, J. Stumbe, P. Caulet, J. C. Mougenel, *Chem. Commun.* **1997**, 1241.
[23] A. Matijasic, J.-L. Paillaud, J. Patarin, *J. Mater. Chem.* **2000**, *10*, 1345.

 © 2003 Wiley-VCH Verlag GmbH & Co. KGaA, Weinheim

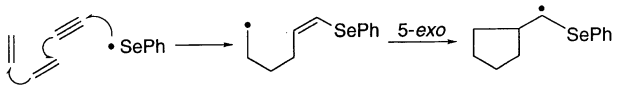
Domino Radical Reactions

Highly Selective Sequential Addition and Cyclization Reactions Involving Diphenyl Diselenide, an Alkyne, and Alkenes under Visible-Light Irradiation**

*Kaname Tsuchii, Mikio Doi, Toshikazu Hirao, and Akiya Ogawa**

Dedicated to Professor Noboru Sonoda on the occasion of his 70th birthday

The development of highly selective carbon–carbon bond-forming reactions with the simultaneous introduction of heteroatom functional groups is of great importance in organic synthesis. A variety of compounds with carbon–carbon unsaturation can be utilized for this purpose.[1] However, the use of several such unsaturated compounds together in a radical reaction usually results in their polymerization. In contrast, we have discovered that the addition of diphenyl diselenide, which has an appropriate carbon-radical-capturing ability,[2] depresses the undesired polymerization and makes it possible to carry out a highly selective sequential addition of $(PhSe)_2$ to unsaturated compounds.[3] Herein, we report a novel four-component coupling of an alkyne, two olefin molecules, and diphenyl diselenide, which proceeds through selective bond formation to connect these four molecules, and a subsequent 5-*exo* cyclization, as depicted in Scheme 1.



Scheme 1. Sequential addition and cyclization strategy.

We started our study of this type of reaction by examining the combination of alkynes that bear an electron-withdrawing group with alkenes that bear an electron-donating group.[4] When a mixture of ethyl propiolate (**1**), *n*-butyl vinyl ether

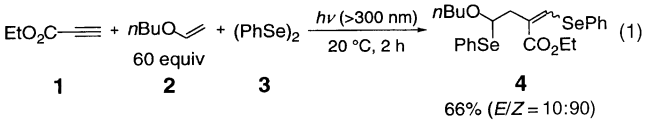
[*] Prof. A. Ogawa, K. Tsuchii
Department of Chemistry, Faculty of Science
Nara Women's University
Kitauoyanishi-machi, Nara 630–8506 (Japan)
Fax: (+81) 742-20-3979
E-mail: a.ogawa@cc.nara-wu.ac.jp
M. Doi, Prof. T. Hirao
Department of Applied Chemistry, Faculty of Engineering
Osaka University

[**] This research was supported by a Grant-in-Aid for Scientific Research on Priority Areas (A) (No. 14044063) "Exploitation of Multi-Element Cyclic Molecules" from the Ministry of Education, Culture, Sports, Science, and Technology, Japan.

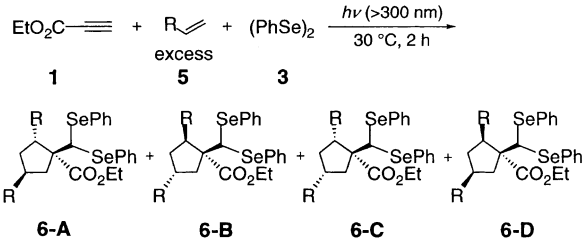
Supporting information for this article, including full procedures and characterization data, is available on the WWW under http://www.angewandte.org or from the author.

 © 2003 Wiley-VCH Verlag GmbH & Co. KGaA, Weinheim DOI: 10.1002/anie.200250790

(**2**), and diphenyl diselenide (**3**) was irradiated through pyrex with a tungsten lamp ($h\nu > 300$ nm) in the absence of solvent, none of the desired sequential addition and cyclization product was formed, and instead the corresponding three-component coupling product **4** was formed selectively, as shown in Equation (1).[3]



Surprisingly, however, when an electron-deficient alkene was employed for this reaction instead of *n*-butyl vinyl ether, the desired sequential addition and 5-*exo* radical cyclization took place selectively. For example, the reaction of *tert*-butyl acrylate (**5a**) under the same conditions provided **6a** in 61% yield (Scheme 2 and Table 1, entry 1),[5] along with small



Scheme 2. Synthesis of substituted cyclopentanes from ethyl propiolate, an alkene, and $(PhSe)_2$ through sequential radical addition and cyclization.

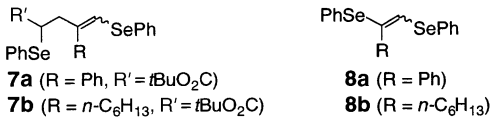
Table 1: Sequential addition and cyclization reactions of ethyl propiolate, alkenes, and $(PhSe)_2$.[a]

Entry	**6**	R	Yield [%][b]	**A/B/C/D**
1	**a**	$tBuO_2C$	61	72:11:11:6
2	**b**	MeO_2C	49	79:21:0:0
3	**c**	NC	41	18:14:60:8
4	**d**	Me(O)C	58	71:16:7:6

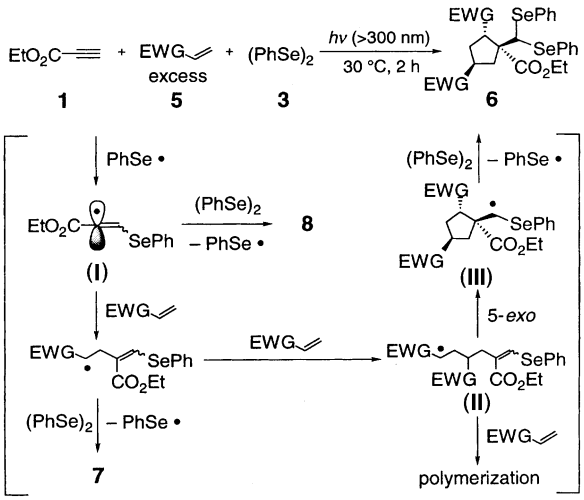
[a] Reaction conditions: ethyl propiolate (0.20 mmol), $(PhSe)_2$ (1 equiv), alkene (40–60 equiv), 30 °C, $h\nu$: tungsten lamp (500 W, pyrex). [b] Yield of isolated products.

amounts of by-products, such as the corresponding acyclic three-component coupling product and the adduct of $(PhSe)_2$ with **1**. The use of $(PhS)_2$ in place of $(PhSe)_2$ under similar reaction conditions led to the polymerization of the olefins and did not provide the desired sequential addition and cyclization product, which is probably a result of the poor carbon-radical-capturing ability of $(PhS)_2$. On the other hand, when $(PhTe)_2$ was used, most of the starting ethyl propiolate (**1**) was recovered, which is probably a result of the lower reactivity of the phenyltelluro radical (PhTe·) toward unsaturated bonds. When a similar reaction was conducted in the presence of nBu_3SnH as a mediator, most of the starting ethyl propiolate (**1**) was also recovered.[6] Thus, the appropriate carbon-radical-trapping ability of $(PhSe)_2$ facilitates its selective sequential addition and cyclization with an alkyne and two olefin molecules.[7]

Methyl acrylate, acrylonitrile, and methyl vinyl ketone can be employed for this sequential addition and cyclization reaction (Table 1). However, when alkynes without an electron-withdrawing group were used in place of ethyl propiolate, the desired product was obtained in very poor yield. For example, the main products isolated from the reactions of phenylacetylene and 1-octyne were the corresponding three-component coupling products (**7a** and **7b**, respectively) and bisselenation products (**8a** and **8b**, respectively).



A possible mechanistic pathway is shown in Scheme 3: 1) Upon irradiation with light of wavelength over 300 nm, diphenyl diselenide (**3**; $\lambda_{max} = 330$ nm) undergoes homolytic



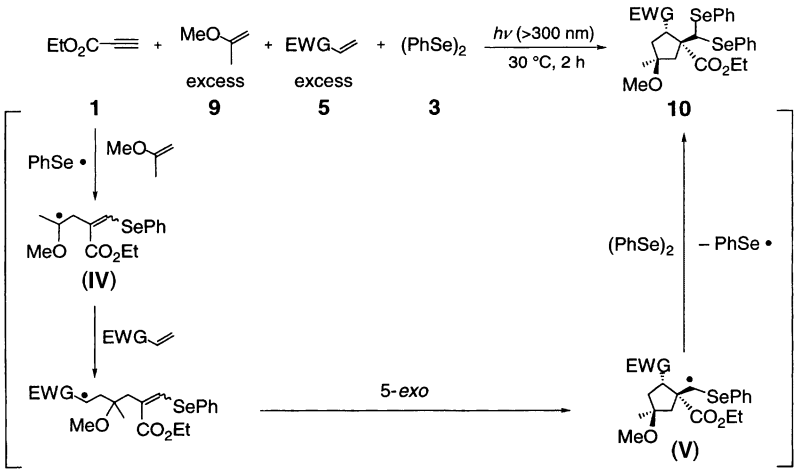
Scheme 3. Proposed mechanism for the formation of cyclopentanes **6** (and by-products) through sequential radical addition and cyclization; EWG = electron-withdrawing group.

dissociation to generate PhSe·,[8] which adds to ethyl propiolate (**1**) selectively to form the β-phenylseleno-substituted vinylic radical **I**;[9,10] 2) the vinylic radical **I** reacts with two olefin molecules to produce the secondary alkyl radical **II**; 3) the radical intermediate **II** cyclizes in a 5-*exo* manner to give the α-seleno radical **III**, which in turn undergoes an S_H2 reaction with $(PhSe)_2$ to provide **6**.

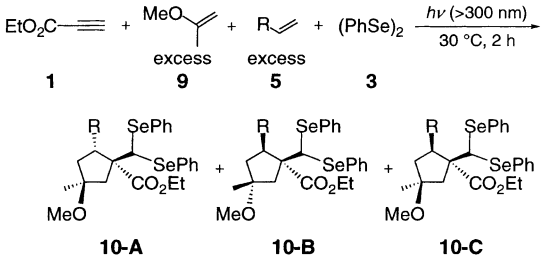
We next examined the four-component coupling reaction in the presence of two types of olefin: an olefin with an electron-withdrawing group and an olefin with an electron-donating group. When the reaction of diphenyl diselenide (**3**) with ethyl propiolate (**1**) and a large excess of both *tert*-butyl acrylate (**5a**) and 2-methoxypropene (**9**) was performed in the

 © 2003 Wiley-VCH Verlag GmbH & Co. KGaA, Weinheim

absence of solvent, sequential addition of the diselenide to the alkyne, of the resulting intermediate to the electron-rich olefin **9**, and of the next intermediate to the electron-poor olefin (**5a**), followed by a 5-*exo* radical cyclization, took place to provide the corresponding cyclic four-component coupling product **10a** in good yield (Scheme 4 and Table 2, entry 1).[11] Small amounts of by-products, such as the corresponding acyclic three-component coupling product and the adduct of $(PhSe)_2$ with the alkyne, were also formed. Similar conditions can be employed with methyl acrylate, acrylonitrile, and methyl vinyl ketone as the electron-deficient alkenes, and the corresponding cyclic four-component coupling products are obtained selectively in good yields (Table 2, entries 2–4). In the case of acrylonitrile, the desired four-component coupling reaction proceeds successfully to give the corresponding five-membered-ring product in 76% yield (Table 2, entry 3).



Scheme 5. Proposed mechanism for the formation of cyclopentanes **10** through sequential radical addition and cyclization.



Scheme 4. Four-component coupling of ethyl propiolate, 2-methoxypropene, a second alkene, and $(PhSe)_2$.

Table 2: Four-component coupling of ethyl propiolate, 2-methoxypropene, a second alkene, and $(PhSe)_2$.[a]

Entry	**10**	R	Yield [%][b]	**A/B/C**
1	**a**	$tBuO_2C$	47	81:19:0
2	**b**	MeO_2C	47	43:37:20
3	**c**	NC	76	60:14:26
4	**d**	Me(O)C	41	72:24:4

[a] Reaction conditions: ethyl propiolate (0.20 mmol), $(PhSe)_2$ (1 equiv), 2-methoxypropene (10–30 equiv), $RCH{=}CH_2$ (10–30 equiv), *hν*: tungsten lamp (500 W, pyrex). [b] Yield of isolated products.

The formation of **10** may be explained by the following proposed mechanism (see Scheme 5): 1) PhSe·, generated from $(PhSe)_2$ by irradiation with light of wavelength over 300 nm, adds to ethyl propiolate (**1**) selectively to form the β-phenylseleno-substituted vinylic radical **I**; 2) the vinylic radical **I** reacts with an electron-rich olefin preferentially to produce the α-methoxyl radical **IV**; 3) the radical intermediate **IV** reacts with an electron-poor olefin and then cyclizes to provide the α-seleno radical **V**, which is trapped with $(PhSe)_2$ to yield the cyclic four-component coupling product **10**, with regeneration of PhSe·.

In summary, diphenyl diselenide has proved to be an excellent mediator for highly selective sequential bond formation between unsaturated compounds. The rate of carbon-radical-capturing by $(PhSe)_2$, appropriate for these transformations, combined with the efficiency of the 5-*exo* radical cyclization, prevent the undesired potential polymerization and make it possible to carry out four-component coupling reactions of unsaturated compounds and $(PhSe)_2$.

Experimental Section

Representative procedure: Ethyl propiolate (19.6 mg, 0.20 mmol), 2-methoxypropene (389 mg, 5.4 mmol), and acrylonitrile (106 mg, 2.0 mmol) were placed in a pyrex glass tube (10 mm × 75 mm) under a N_2 atmosphere. The mixture was irradiated with a tungsten lamp (500 W) at 30 °C for 2 h, and diphenyl diselenide (62.4 mg, 0.20 mmol in total) was added in eight portions during the irradiation.[12] When the reaction was complete, the purification of the products was performed on a recycling preparative HPLC instrument (Japan Analytical Industry Co. Ltd., Model LC-908) equipped with JAIGEL-1H and -2H columns, with $CHCl_3$ as the eluent, to yield **10c** (76%) as a stereoisomeric mixture (60:26:14). The stereochemistry of the diastereoisomers of **10c** was determined by NOE experiments.

10c: Pale yellow oil; ^{1}H NMR (major isomer; 300 MHz, $CDCl_3$, 25 °C, TMS): $\delta = 1.29$ (s, 3H; CH_3), 1.34 (t, $^3J(H,H) = 7.2$ Hz, 3H; $CH_3CH_2O_2C$), 1.95 (dd, $^3J(H,H) = 12.6$ Hz, $^2J(H,H) = 13.2$ Hz, 1H; CCH_2CH), 2.30 (ddd, $^4J(H,H) = 2.1$ Hz, $^3J(H,H) = 6.3$ Hz, $^2J(H,H) = 13.2$ Hz, 1H; CCH_2CH), 2.32 (dd, $^4J(H,H) = 2.1$ Hz, $^2J(H, H) = 14.7$ Hz, 1H; CCH_2C), 2.42 (d, $^2J(H,H) = 14.7$ Hz, 1H; CCH_2C), 2.90 (s, 3H; CH_3O), 3.50 (dd, $^3J(H,H) = 6.3$, 12.6 Hz, 1H; NCCH), 4.16–4.34 (m, 2H; $CH_3CH_2O_2C$), 4.58 (s, 1H; $(PhSe)_2CH$), 7.15–7.31 (m, 6H; Ph), 7.43–7.46 ppm (m, 4H; Ph); ^{13}C NMR (major isomer; 75 MHz, $CDCl_3$, 25 °C, TMS): $\delta = 13.9, 21.0, 38.6, 42.4, 45.6, 49.1, 54.7, 62.5, 64.6, 82.3, 119.6, 128.2, 128.3, 129.3, 134.2, 134.8, 172.2$ ppm; IR (NaCl): $\tilde{\nu} = 2977, 2245$ (C≡N), 1718 (C=O), 1578, 1478, 1439, 1369, 860, 746, 690 cm^{-1}; HRMS (*m*/*z*): calcd for $C_{24}H_{27}NO_3Se_2$: 537.0322; found: 537.0311; elemental analysis: calcd for $C_{24}H_{27}NO_3Se_2$: C 53.84, H 5.08, N 2.62; found: C 53.50, H 5.00, N 2.85.

Received: December 17, 2002
Revised: April 11, 2003 [Z50790]

 © 2003 Wiley-VCH Verlag GmbH & Co. KGaA, Weinheim

Keywords: alkenes · alkynes · cyclizations · domino reactions · radicals

[1] *Radicals in Organic Synthesis, Vol. 1* and *2*, (Eds.: P. Renaud, M. P. Sibi), VCH, Weinheim, **2001**.
[2] The rate constant for the S_H2 reaction of the 5-hexenyl radical with $(PhSe)_2$ is $1.2 \times 10^7\ M^{-1}s^{-1}$: a) G. A. Russell, H. Tashtoush, *J. Am. Chem. Soc.* **1983**, *105,* 1398–1399; b) M. J. Perkins, E. S. Turner, *J. Chem. Soc. Chem. Commun.* **1981**, 139–140.
[3] a) A. Ogawa, M. Doi, K. Tsuchii, T. Hirao, *Tetrahedron Lett.* **2001**, *42*, 2317–2319; b) A. Ogawa, I. Ogawa, N. Sonoda, *J. Org. Chem.* **2000**, *65*, 7682–7685; c) A. Ogawa, M. Doi, I. Ogawa, T. Hirao, *Angew. Chem.* **1999**, *111*, 2066–2069; *Angew. Chem. Int. Ed.* **1999**, *38*, 2027–2029.
[4] B. Giese, *Angew. Chem.* **1983**, *95*, 771–782; *Angew. Chem. Int. Ed. Engl.* **1983**, *22*, 753–764.
[5] The stereochemistry of the sequential addition and cyclization products was determined by NOE experiments (see Supporting Information).
[6] E. Lee, C. U. Hur, Y. H. Rhee, Y. C. Park, S. Y. Kim, *J. Chem. Soc. Chem. Commun.* **1993**, 1466–1468.
[7] The use of $(p\text{-}CF_3\text{-}C_6H_4Se)_2$ and $(MeSe)_2$ in place of $(PhSe)_2$ led to the successful formation of the corresponding four-component coupling products. However, when $(PhCH_2Se)_2$ was used none of the desired four-component coupling products were obtained, probably because of C–Se bond cleavage in $(PhCH_2Se)_2$.
[8] U. Schmidt, A. Müller, K. Markau, *Chem. Ber.* **1964**, *97*, 405–414.
[9] For the radical addition of $(PhSe)_2$ to alkynes, see: a) T. G. Back, M. V. Krishna, *J. Org. Chem.* **1988**, *53*, 2533–2536; b) A. Ogawa, H. Yokoyama, K. Yokoyama, T. Masawaki, N. Kambe, N. Sonoda, *J. Org. Chem.* **1991**, *56,* 5721–5723; c) A. Ogawa, N. Takami, M. Sekiguchi, H. Yokoyama, H. Kuniyasu, I. Ryu, N. Sonoda, *Chem. Lett.* **1991**, 2241–2242.
[10] In general, vinyl radicals are believed to be a stereoisomeric mixture of σ radicals that are in rapid equilibrium: a) R. W. Fessenden, R. H. Schuler, *J. Chem. Phys.* **1963**, *39*, 2147–2195. In contrast, α-aryl-substituted vinylic radicals are thought to be π radicals: b) L. A. Singer, J. Chen, *Tetrahedron Lett.* **1969**, *10*, 4849–4854. The corresponding radical species derived from ethyl propiolate is thought to be a vinylic π radical: c) C. Galli, A. Guarnieri, H. Koch, P. Mencarelli, Z. Rappoport, *J. Org. Chem.* **1997**, *62*, 4072–4077; d) H. Rubin, H. Fischer, *Helv. Chim. Acta* **1996**, *79*, 1670–1682; e) J. O. Metzger, M. Blumenstein, *Chem. Ber.* **1993**, *126*, 2493–2499.
[11] The stereochemistry of the four-component coupling products was determined by NOE experiments (see Supporting Information).
[12] The four-component coupling of ethyl propiolate (**1**) with olefins **5** and **9** and $(PhSe)_2$ described requires the use of excess amounts of the olefins. When the molar ratio of **5** to **1** or **9** to **1** was decreased, the yield of the four-component coupling product also decreased, and the adduct of $(PhSe)_2$ with **1** was formed as a by-product.

 © 2003 Wiley-VCH Verlag GmbH & Co. KGaA, Weinheim

Gallium Nitride Nanotubes

Gallium Nitride Nanotubes by the Conversion of Gallium Oxide Nanotubes**

Junqing Hu, Yoshio Bando, Dmitri Golberg, and Quanlin Liu*

Gallium nitride (GaN), an important semiconductor having a wide direct band gap (3.39 eV at room temperature), is potentially useful in a blue and ultraviolet light emitter, and in high temperature/high power electronic devices.[1] The future of full-colored, flat panel displays, blue lasers, and optical communication is likely to be based on GaN.[2] Nanotubular structures have brought enormous breakthroughs in modern science and technology, including electronics, mechanics, physics, and chemistry.[3] There have been many studies that have focused on compounds characterized by layered structures, for example, graphite,[4] boron nitride,[5] and metal disulfides (MoS_2, WS_2, TiS_2, ZrS_2, and HfS_2).[6] Recent reports indicated that under appropriate experimental conditions, geometrically closed, concentric tubes could be constructed from nonlayered structural materials. Thus far, there has been great progress in the development of new nanotubes; nanotubes of metal oxides (TiO_2,[6] Ga_2O_3, In_2O_3,[8] ZnO,[9] and Al_2O_3[10]), sulfides (CdS and CdSe),[11] and elemental metallic Te,[12] and others [13] were reported.

Along with the development of nanotechnology, 1D structural GaN may find wider applications in many fields. Thus, considerable efforts have been made to fabricate GaN nanowires or nanorods by several routes, such as template-induced growth,[14] metal-catalyzed assisted laser ablation,[15] hot filament vapor–liquid–solid growth,[16] and gallium oxide reacted with ammonia.[17] Although GaN nanotubes were observed in the preparation of GaN nanowires,[18] the synthesis of GaN nanotubes in bulk have not been realized experimentally. Herein we report the growth of GaN nanotubes in bulk by a two-stage process based on a well-controllable conversion of amorphous gallium oxide (Ga_2O) nanotubes.

A dark (or black) material was collected from the C fiber thermo-insulting layer of the induction furnace, in which the deposition temperature was measured to be $\approx$700–800 °C. The yield of the product was estimated to be $\approx$4–5.0 %, based on the amount of the Ga_2O_3 starting material. The phase

[*] Dr. J. Hu, Dr. Y. Bando, Dr. D. Golberg, Dr. Q. Liu[+]
Advanced Materials Laboratory
National Institute for Materials Science (NIMS)
Namiki 1-1, Tsukuba, Ibaraki 305-0044 (Japan)
Fax: (+81) 298-51-6280
E-mail: hu.junqing@nims.go.jp

[+] Permanent address: Institute of Physics and Center for Condensed Matter Physics
Chinese Academy of Science
Beijing 100080 (China)

[**] This work was supported by the Japan Society for the Promotion of Science (JSPS) Fellowship at the National Institute for Materials Science, Tsukuba, Japan.

 DOI: 10.1002/anie.200351001 © 2003 Wiley-VCH Verlag GmbH & Co. KGaA, Weinheim

composition and structure of the as-synthesized product were examined by powder XRD (Figure 1a). All of the strong reflection peaks of the XRD pattern can be readily indexed to hexagonal Wurtzite-structured GaN with lattice constants $a =$ 3.185 Å and $c = 5.177$ Å (the standard values from JCPDS

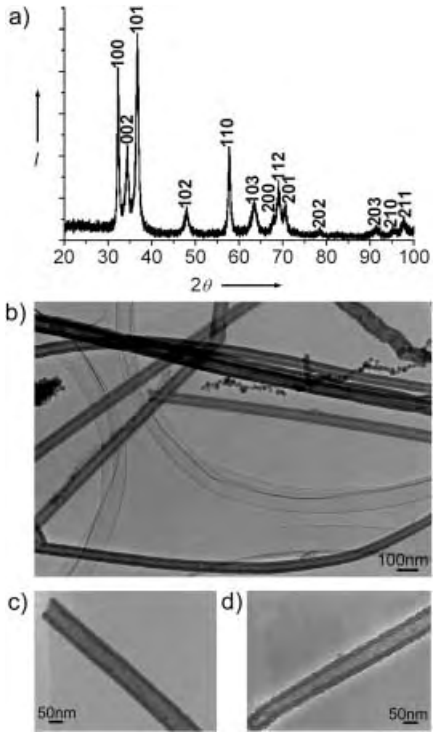


Figure 1. a) An XRD pattern recorded from as-grown GaN nanotubes. b) A typical TEM image of synthesized GaN nanotubes. TEM images showing: c) an open and d) a closed end of GaN nanotubes.

(02–1078): $a = 3.186$ Å and $c = 5.177$ Å), comparable to the literature values for hexagonal GaN.[19] No peaks associated with the other crystalline forms of the gallium oxides can be detected in the pattern. These results suggest that the as-synthesized product contains virtually only one crystalline phase of GaN and the other crystalline phases are below the detection limit (≈5%). The components of Ga and N and the impurities for the sample were further determined by elemental analyses. The amounts (wt%) of Ga and N are 76.80 and 13.40, respectively (calcd for $GaN_{1.00}$:Ga 83.27, N 16.73). This result gives the overall ratio of gallium to nitrogen of 1:0.87 (i.e., not 1:1), which suggests either a gallium-enrichment or nitrogen-deficiency in the synthesized sample. The impurities were (wt%) C 2.1, O 5.0, and the overall metallic elements (such as In, Cu, Zn, Al, Si), 2.7. The black of the synthesized GaN samples is attributed to carbon impurities (from the furnace) and from gallium enrichment (pure h-GaN is pale yellow; the effect of gallium enrichment on the color of the GaN nanocrystals has been demonstrated).[20] The morphology of as-synthesized GaN product was analyzed by transmission electron microscope (TEM; Figure 1b). The clear contrast observed along the lengths of the GaN wirelike product suggests the a tubular structure (the outer part is darker than the inner part). Most of the synthesized GaN nanotubes are straight, although a small quantity are twisted or curved. Typically, the lengths of the GaN nanotubes can reach ≈10 μm. Each tube has a uniform outer diameter and wall thickness (typically ≈80 nm and ≈20 nm, respectively) along its entire length. The TEM images in Figure 1c reveal that some ends of the GaN nanotubes are open and some are closed.

Figure 2a shows a high-magnification TEM image of a segment of a single straight GaN nanotube. A high-resolution TEM image (Figure 2b) of the GaN nanotube wall reveals

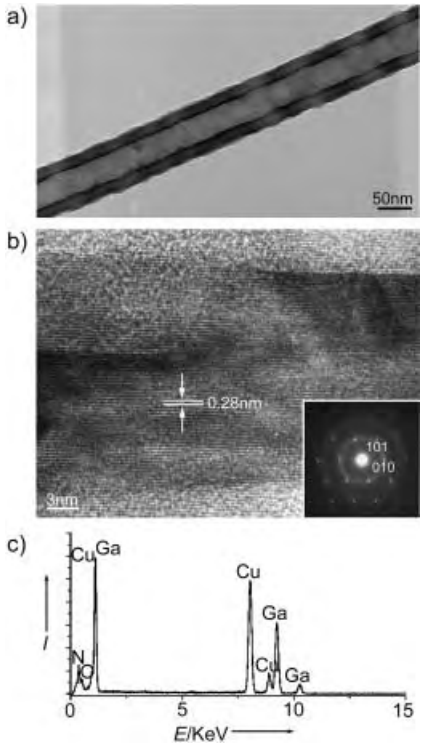


Figure 2. a) A high-magnification TEM image showing a segment of a single straight GaN nanotube. b) A high-resolution TEM image of the GaN nanotube wall as in Figure 2a (lower right inset depicts a corresponding ED pattern). c) An EDS spectrum taken from a single GaN tube.

that the tube is characteristic of a single-crystal. Detailed analysis on the lattice fringes gives an inter-planar spacing of 0.28 nm, which matches well the (101) plane separation of the standard bulk GaN. The lower right inset in Figure 2b depicts the corresponding selected area electron diffraction (ED) pattern; this shows that the brightest diffraction spots can be precisely indexed as the $[10\bar{1}]$ zone axis of hexagonal GaN crystal, whereas the weak diffraction rings may originate from GaN nanocrystallites attached to the tube surface. The phase composition of an individual nanotube was further confirmed by X-ray energy dispersion spectrometry (EDS). The spectrum shown in Figure 2c was recorded from the single GaN tube as in Figure 2a. It reveals the presence of only Ga and N in the nanotubes (Cu signals originate from the TEM grid) with an approximate atomic ratio of 1.00:0.94. A relatively weak oxygen peak in the spectrum probably originates from

 © 2003 Wiley-VCH Verlag GmbH & Co. KGaA, Weinheim

unavoidable surface-oxidation and/or surface-adsorption of oxygen on to the tubes arising from exposure to air during sample processing.

Figure 3 shows a room temperature cathodoluminescence spectrum from the synthesized GaN nanotubes. It is clear that one broad emission peak around 505 nm, which is known as the green band, is detected. Compared with the cathodoluminescence behavior (often a yellow band at 550 nm is observed) of the bulk GaN,[21] the peak position of the grown GaN nanotubes displays a blueshift of ≈40 nm, which may be attributed to some intrinsic point defects,[22] such as Ga vacancies, to impurities, such as oxygen or carbon,[23] or to complexes of intrinsic defects and impurities.[24] In addition, one weak peak at ≈370 nm also is detected in this spectrum, which originates from the near band-edge emission.

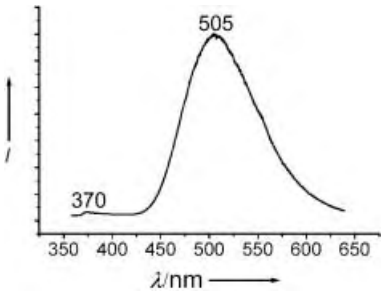


Figure 3. A room temperature cathodoluminescence spectrum of the grown GaN nanotubes.

The reaction of Ga_2O_3 with C (coming from the C crucible) at a synthesis temperature of ≈1250 °C and with pure N_2 as the carrier gas was carried out. The product was examined by using TEM (equipped with a Gatan holder and a twin heating system; Figure 4a and 4b), ED (Figure 4c), and EDS (Figure 4d). These results reveal that the reaction produced amorphous Ga_2O nanotubes (EDS analysis reveals the presence of Ga and O in the tube with an approximate atomic ratio of 2.20:1.00), which were either completely hollow throughout their lengths, or partially filled with Ga.

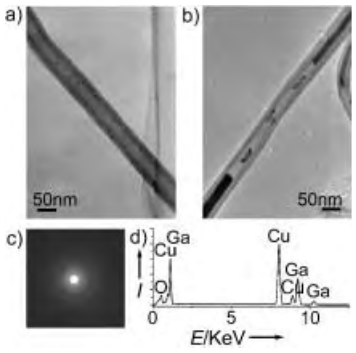


Figure 4. Either hollow a) or partially Ga-filled b) amorphous Ga_2O nanotubes from the reaction of Ga_2O_3 with C at high temperature. c) An ED pattern and (d) an EDS spectrum of the amorphous Ga_2O nanotube as in (a), respectively.

The expansion behavior of a nanoscale liquid Ga column inside an amorphous Ga_2O nanotube has been investigated by TEM, and was demonstrated in carbon nanotubes.[25]. Gaseous Ga_2O forms from the reaction of Ga_2O_3 with C at this reaction temperature: [Eq.(1)][14,16,26]

$$Ga_2O_3 + 2\,C \rightarrow Ga_2O + 2\,CO \quad (1)$$

The formed Ga_2O vapor can be readily transported to the deposition zone by the carrier gas (N_2), and Ga_2O nanotubes forms by a vapor–solid growth mechanism.[27] Meanwhile, the Ga_2O vapor will also react with CO at a desired temperature: [Eq.(2)][25b]

$$2\,Ga_2O + 4\,CO \rightarrow 4\,Ga + C + 3\,CO_2 \quad (2)$$

which will result in liquid Ga filling the Ga_2O nanotubes. Considering the formation of amorphous Ga_2O nanotubes, we speculate that these nanotubes might be converted (or act as a template, thus spatially confining the reaction) into GaN nanotubes through the reaction of Ga_2O with NH_3 at the desired reaction temperature. The reaction can be expressed as: [Eq.(3)]

$$Ga_2O\ (\text{nanotubes}) + 2\,NH_3 \rightarrow 2\,GaN\ (\text{nanotubes}) + H_2O + 2\,H_2 \quad (3)$$

For the synthesis of crystalline GaN nanotubes by the above conversion reaction, a two-stage process was applied by controlling the processing temperature and the carrier gas. In the first stage, a pure N_2 flow was introduced through the quartz tube at a flow rate of 80 sccm (standard cubic centimeter per minute) and at the ambient pressure of the furnace tube. The reactant, Ga_2O_3, was heated to 1250 °C and maintained at this temperature for 1.5 h. The amorphous Ga_2O nanotubes grew at a low temperature, estimated to be around 700 °C. In the second stage, the pure N_2 flow was switched to a pure NH_3 flow with the same flow rate and at ambient pressure in the tube. The furnace was further heated to 1400 °C and kept at this temperature for 1 hour. We speculate that during this stage a significant part of the liquid Ga evaporates out of the Ga_2O nanotube because of the higher reaction temperature. These formed Ga_2O nanotubes serve as energetically favorable sites and enhance NH_3 adsorption on their outer and inner walls (due to the high surface area of these tubes). The reaction shown in Equation (3) may start from the surfaces of the Ga_2O nanotubes, which are thus converted in situ into GaN nanotubes. Therefore, we believe that during the conversion process the formed Ga_2O nanotubes not only are used as a precursor (or an intermediate) but also as a template for confining the reaction in a local space around the nanotubes, which is similar to the synthesis of carbide nanorods with confining reactions by converting carbon nanotubes,[28] except that in present case the Ga_2O nanotubes and GaN nanotubes are both produced from the powdered Ga_2O_3 starting material. The detailed growth mechanisms of Ga_2O nanotubes and GaN nanotubes, however, are not fully understood, and require more systematic investigations.

In summary, GaN nanotubes can be prepared in bulk by a controllable two-stage process that involves the conversion of

 © 2003 Wiley-VCH Verlag GmbH & Co. KGaA, Weinheim

Ga_2O nanotubes. An investigation of the properties of the GaN nanotubes synthesized by this route is in progress.

Experimental Section

The amorphous Ga_2O and crystalline GaN nanotubes were synthesized in a vertical induction furnace, as described in detail elsewhere.[29] Briefly, the furnace consists of a fused-quartz tube (50 cm in length, 12 cm in outer diameter, and 0.25 cm in wall thickness) and an induction-heated cylinder (25 cm in length, 4.5 cm in outer diameter, and 3.5 cm in inner diameter) made of a high purity graphite coated with a C fiber thermo-insulating layer. The inductively heated cylinder has one inlet C pipe and outlet C pipe on its top and base, respectively. A graphite crucible containing Ga_2O_3 powder (2.0 g, 99.9 %, Sigma-Aldrich) was placed at the center cylinder zone. After evacuation of the quartz tube to $\approx$1–2 Torr, a two-stage process by controlling the processing temperature and carrier gas was performed as follows: First, a pure N_2 flow was kept introducing through the quartz tube at a flow rate of 80 sccm and the ambient pressure in the tube, and the starting material Ga_2O_3 was heated to and maintained at 1250 °C for 1.5 h. Next, the pure N_2 flow was switched to a pure NH_3 flow with the same flow rate and at the ambient pressure in the tube. The furnace was further heated to and kept at 1400 °C for 1 hour. During the reaction process, an optical pyrometer with an estimated accuracy of $\pm$10 °C was used to monitor the synthesis temperature or deposition temperature. After the reaction was terminated and the furnace cooled to the room temperature, the black resulting product was collected from C fiber thermal insulating layer for characterization using X-ray powder diffractometer (XRD; RINT 2200) with $Cu_{K\alpha}$ radiation and high-resolution transmission electron microscopy (HRTEM; JEM-3000F) with an X-ray energy dispersive spectrometer (EDS). Elemental analyses were performed on a TC-436 (LECO Co., USA) and a CS-444 LS (LECO Co. USA) element simultaneous analytical determinator and an IRIS Advantage ICAP (Nippon Jarrell Ash Co., Ltd., Japan) spectrophotometer. The cathodoluminescence spectra were measured at room temperature in a spectral range of 300–800 nm by using a He–Cd laser with a wavelength of 325 nm as the excitation source.

Received: January 22, 2003
Revised: May 23, 2003 [Z51001]

Keywords: · gallium · nanotechnology · nanotubes · nitrides

[1] a) J. C. Zolper, R. J. Shul, A. G. Baca, R. G. Wilson, S. Pearton, R. A. Stall, *Appl. Phys. Lett.* **1996**, *68*, 2273; b) Q. Chen, M. A. Khan, J. W. Wang, C. J. Sun, M. S. Shur, H. Park, *Appl. Phys. Lett.* **1996**, *69*, 794.

[2] a) S. Nakamura, *Science* **1998**, *281*, 956; b) F. A. Ponce, D. P. Bour, *Nature* **1997**, *386*, 351.

[3] a) M. Harada, M. Adachi, *Adv. Mater.* **2002**, *12*, 839; b) G. Seifert, H. Terrones, M. Terrones, G. Jungnickel, T. Frauenheim, *Phys. Rev. Lett.* **2000**, *85*, 146; c) C. N. R. Rao, M. Nath, *J. Chem. Soc. Dalton. Trans.* **2003**, 1.

[4] See, for example: a) M. T. Woodside, P. L. McEuen, *Science* **2002**, *296*, 1098; b) S. G. Lemay, J. W. Janssen, M. van den Hout, M. Mooij, M. J. Bronikowski, P. A. Willis, R. E. Smalley, L. P. Kouwenhoven, C. Dekker, *Nature* **2001**, *412*, 617; c) M. S. Fuhrer, J. Nygard, L. Shih, M. Forero, Y. G. Yoon, M. S. C. Mazzoni, H. J. Choi, J. Ihm, S. G. Louie, A. Zettl, P. L. McEuen, *Science* **2000**, *288*, 494; d) K. Tsukagoshi, B. W. Alphenaar, H. Ago, *Nature* **1999**, *401*, 572; e) S. S. Wong, E. Joselevich, A. T. Woolley, C. L. Cheung, C. M. Lieber, *Nature* **1998**, *394*, 52; f) S. Iijima, T. Ichihashi, *Nature* **1993**, *363*, 603.

[5] a) E. J. Mele, P. Kral, *Phys. Rev. Lett.* **2002**, *88*, 056803; b) S. S. Alexandre, M. S. C. Mazzoni, H. Chacham, *Appl. Phys. Lett.* **1999**, *75*, 61; c) N. G. Chopra, R. J. Luyken, K. Cherrey, V. H. Crespi, M. L. Cohen, S. G. Louie, A. Zettl, *Science* **1995**, *269*, 966; d) E. J. M. Hamilton, S. E. Dolan, C. E. Mann, H. O. Colijin, C. A. McDonald, *Science* **1993**, *260*, 659.

[6] a) R. Tenne, L. Margulis, M. Genut, G. Hodes, *Nature* **1992**, *360*, 444; b) Y. Feldman, E. Wasserman, D. J. Srolovitch, R. Tenne, *Science* **1995**, *267*, 222; c) R. Tenne, M. Homyonfer, Y. Feldman, *Chem. Mater.* **1998**, *10*, 3225; d) P. J. F. Harris, *Carbon Nanotubes and Related Structures*, Cambridge University Press, Cambridge, **1999**; e) M. Nath, A. Govindaraj, C. N. R. Rao, *Adv. Mater.* **2001**, *13*, 283; f) M. Nath, C. N. R. Rao, *Angew. Chem.* **2002**, *114*, 3601; *Angew. Chem. Int. Ed.* **2002**, *41*, 3451.

[7] a) J. H. Jung, H. Kobayashi, K. J. C. van Bommel, S. Shinkai, T. Shimizu, *Chem. Mater.* **2002**, *14*, 1445; b) G. H. Du, Q. Chen, R. C. Che, Z. Y. Yuan, L. M. Peng, *Appl. Phys. Lett.* **2001**, *79*, 3702; c) T. Kasuga, M. Hiramatsu, A. Hoson, T. Sekino, K. Niihara, *Langmuir* **1998**, *14*, 3160; d) P. Hoyer, *Langmuir* **1996**, *12*, 1411.

[8] B. Cheng, E. T. Samulski, *J. Mater. Chem.* **2001**, *11*, 2901.

[9] a) J. J. Wu, S. C. Liu, C. T. Wu, K. H. Chen, L. C. Chen, *Appl. Phys. Lett.* **2002**, *81*, 1312; b) J. Q. Hu, Q. Li, X. M. Meng, C. S. Lee, S. T. Lee, *Chem. Mater.* **2003**, *15*, 305.

[10] L. Pu, X. Bao, J. P. Zou, D. Feng, *Angew. Chem.* **2001**, *113*, 1538; *Angew. Chem. Int. Ed.* **2001**, *40*, 1490.

[11] a) Y. J. Xiong, Y. Xie, J. Yang, R. Zhang, C. Z. Wu, G. A. Du, *J. Mater. Chem.* **2002**, *12*, 3712; b) C. N. R. Rao, A. Govindaraj, F. L. Deepak, N. A. Gunari, M. Nath, *Appl. Phys. Lett.* **2001**, *78*, 1853.

[12] M. S. Mo, J. H. Zeng, X. M. Liu, W. C. Yu, S. Y. Zhang, Y. T. Qian, *Adv. Mater.* **2002**, *14*, 1658.

[13] a) C. R. Martin, *Science* **1994**, *266*, 1961; b) P. M. Ajayan, O. Stephan, P. Redlich, C. Colliex, *Nature* **1995**, *375*, 564; c) O. G. Schmidt, K. Ebert, *Nature*, **2001**, *410*, 168; d) J. She, J. J. Niu, X. Y. Ma, J. Xu, X. B. Zhang, Q. Yang, D. Yang, *Adv. Mater.* **2002**, *14*, 1219.

[14] a) W. Q. Han, S. S. Fan, Q. Q. Li, Y. D. Hu, *Science* **1997**, *277*, 1287; b) G. S. Cheng, L. D. Zhang, Y. Zhu, G. T. Fei, L. Li, C. M. Mo, Y. Q. Mao, *Appl. Phys. Lett.* **1999**, *75*, 2455.

[15] X. F. Duan, C. M. Lieber, *J. Am. Chem. Soc.* **2000**, *122*, 188.

[16] H. Y. Peng, X. T. Zhou, N. Wang, Y. F. Zheng, L. S. Liao, W. S. Shi, C. S. Lee, S. T. Lee, *Chem. Phys. Lett.* **2000**, *327*, 263.

[17] a) C. C. Chen, C. C. Yeh, *Adv. Mater.* **2000**, *12*, 738; b) X. L. Chen, J. Y. Li, Y. G. Cao, Y. C. Lan, H. Li, M. He, C. Y. Wang, Z. Zhang, Z. Y. Qiao, *Adv. Mater.* **2000**, *12*, 1432; c) M. Q. He, I. Minus, P. Z. Zhou, S. N. Mohammed, J. B. Halpern, R. Jacobs, W. L. Sarney, L. Salamanca-Riba, R. D. Vispute, *Appl. Phys. Lett.* **2000**, *77*, 3731.

[18] a) F. L. Deepak, A. Govindaraj, C. N. R. Rao, *J. Nanosci. Nanotechnol.* **2001**, *1*, 303; b) M. Q. He, I. Minus, P. Z. Zhou, S. N. Mohammed, J. B. Halpern, R. Jacobs, W. L. Sarney, L. Salamanca-Riba, R. D. Vispute, *Appl. Phys. Lett.* **2000**, *77*, 3731.

[19] a) Y. Xie, Y. T. Qian, W. Z. Wang, S. Y. Zhang, Y. H. Zhang, *Science* **1996**, *272*,1926; b) J. B. Wiley, R. B. Kaner, *Science* **1992**, *255*, 1093.

[20] a) J. -W, Hwang, S. A. Hanson, D. Britton, J. F. Evans, K. F. Jensen, W. L. Gladfelter, *Chem. Mater.* **1990**, *2*, 342; b) J.-W. Hwang, J. P. Campbell, J. Kozubowski, S. A. Hanson, J. F. Evans, W. L. Gladfelter, *Chem. Mater.* **1995**, *7*, 517; c) A. C. Frank, R. A. Fischer, *Adv. Mater.* **1998**, *10*, 961.

[21] a) H. Lei, H. S. Leipner, J. Schreiber, J. L. Weyher, T. Wosinski, I. Grzegory, *J. Appl. Phys.* **2002**, *92*, 6666; b) Y.-H. Cho, H. M. Kim, T. W. Kang, J. J. Song, W. Yang, *Appl. Phys. Lett.* **2002**, *80*, 1141.

[22] a) L. W. Tu, Y. C. Lee, S. J. Chen, I. Lo, D. Stocker, E. F. Schubert, *Appl. Phys. Lett.* **1998**, *73*, 2802; b) H. Siegle, P.

 © 2003 Wiley-VCH Verlag GmbH & Co. KGaA, Weinheim

Thurian, L. Eckey, A. Hoffman, C. Thomsen, B. K. Meyer, H. Amano, I. Akasaki, T. Detchprohm, K. Hiramatsu, *Appl. Phys. Lett.* **1996**, *68*,1265; c) P. Perlin, T. Suski, H. Teiseyre, M. Leszcynsky, I. Grzegory, J. Jun, S. Porowski, P. Boguslawski, J. Bernholc, J. C. Chervin, A. Polian, T. D. Moustakas, *Phys. Rev. Lett.* **1995**, *75*, 296.

[23] a) J. Neugebauer, C. G. Van de Walle, *Appl. Phys. Lett.* **1996**, *69*, 503; b) C. Wetzel, T. Suski, J. W. Ager, E. R. Weber, E. E. Haller, S. Fischer, B. K. Meyer, P. Perlin, *Phys. Rev. Lett.* **1997**, *78*, 3923.

[24] G. Salviati, M. Albrecht, C. Zanotti-Fregonara, N. Armani, M. Mayer, Y. Shreter, M. Guzzi, Yu. V. Melnik, K. Vassilevski, V. A. Dmitriev, H. P. Strunk, *Phys. Status Solidi A* **1999**, *171*, 325.

[25] a) Y. H. Gao, Y. Bando, *Nature* **2002**, *415*, 599; b) Y. H. Gao, Y. Bando, *Appl. Phys. Lett.* **2002**, *81*, 3966.

[26] G. Gundiah, A. Govindaraj, C. N. R. Rao, *Chem. Phys. Lett.* **2002**, *351*, 189.

[27] G. W. Sears, *Acta Metall.* **1956**, *3*, 268.

[28] a) E. W. Wong, B. W. Maynor, L. D. Burns, C. M. Lieber, *Chem. Mater.* **1996**, *8*, 2041; b) H. J. Dai, E. W. Wong, Y. Z. Lu, S. S. Fan, C. M. Lieber, *Nature* **1995**, *375*, 769.

[29] a) D. Golberg, Y. Bando, L. Bourgeois, K. Kurashima, T. Sato, *Carbon* **2000**, *38*, 2017; b) D. Golberg, Y. Bando, W. Q. Han, K. Kurashima, T. Sato, *Chem. Phys. Lett.* **1999**, *308*, 337; c) W. Q. Han, Y. Bando, K. Kurashima, T. Sato, *Appl. Phys. Lett.* **1998**, *73*, 3085.

 © 2003 Wiley-VCH Verlag GmbH & Co. KGaA, Weinheim

Inorganic Fullerene Nanoparticles

Fullerene-Like Rare-Earth Nanoparticles**

*Xun Wang and Yadong Li**

The landmark discovery of the fullerenes[1] has led to the development of thermodynamically stable forms of carbon whose dimensions are reduced to the nanoscale.[1–2] As an analogue to these novel structures, the concept of inorganic fullerene-like (IF) nanostructures has been initially described and confirmed by Tenne and co-workers.[3–6] Stimulated by the novel properties of fullerenes,[7–8] these IF nanoparticles can be expected to open new avenues in the solid-state chemistry of inorganic compounds and offer new opportunities for the application of such nanostructures in the emerging field of nanotechnology, as well as in numerous other areas.[9–12] However, up to now, only a limited number of IF nanoparticles have been successfully prepared from their corresponding layered inorganic compounds, such as WS_2,[3] MoS_2,[5] $NiCl_2$,[6] $CdCl_2$,[13] Tl_2O,[14] NbS_2,[15] and ReS_2.[16] The synthesis of novel IF nanoparticles remains as a challenging task for the years to come. Herein we report the synthesis of rare-earth fluoride and hydroxide IF nanoparticles using a low-temperature hydrothermal synthetic procedure.

In contrast to nanotubes, the formation of IF particles requires folding in all directions, and thus involves higher elastic strain.[9–10] Generally, the synthesis of inorganic fullerene-like particles does not need a catalyst, but usually requires relatively high temperatures.[9] The techniques by which the high temperatures have been achieved includes furnaces,[3,5,6,16] laser vaporization,[1] sonolysis,[14] electron and ion-beam heating,[13] and heating by an STM tip.[17] In this paper, a rational hydrothermal synthetic procedure has been successfully developed to prepare rare-earth IF hollow nanoparticles at low temperatures (80–180 °C), which may suggest a route for the future exploration of synthetic procedures to new IF nanostructures. It is also worthy to note that the fluorides and hydroxides of IF nanotructures have been obtained for the first time; previously, this has been limited to chloride and chalcogenides over the past decade. In addition, the novel properties of rare-earth compounds[18] makes them rather appealing for practical applications in, for example, luminescence, catalysis, and biological fields.

Our synthesis is based on a facile hydrothermal method. A typical synthesis involves the preparation of colloidal fluoride precipitates and/or mixtures of rare-earth oxides and water, which is then treated at a designated temperature under hydrothermal conditions.

The phase purity of the samples has been characterized on a Bruker D8-Advance X-ray powder diffractometer with $Cu_{K\alpha}$ radiation ($\lambda = 1.5418$ Å). Under the adopted conditions, the obtained LaF_3, PrF_3, NdF_3, and SmF_3 IF nanostructures all have hexagonal structures while YF_3 has an orthorhombic structure (Figure 1 d). As an example, Figure 1 a–c shows typical reflection patterns of LaF_3 IF nanoparticles obtained at a temperature of 120, 140, and 180 °C, respectively, which

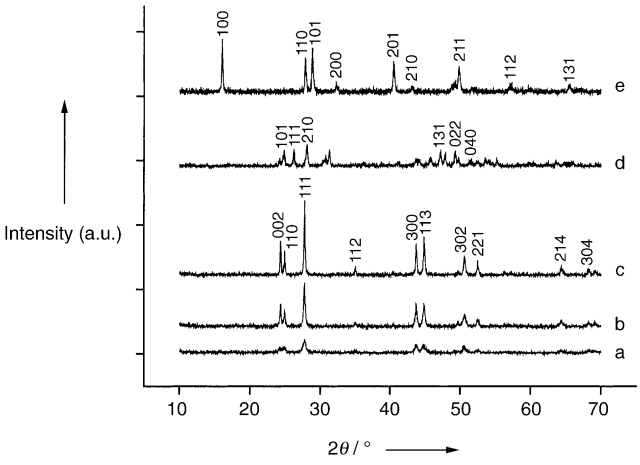


Figure 1. XRD patterns of a) LaF_3 IF nanoparticles (120 °C, La^{3+}:NH_4F = 1:3, pH 4–5); b) LaF_3 IF nanoparticles (140 °C, La^{3+}:NH_4F = 1:3, pH 4–5); c) LaF_3 IF nanoparticles (180 °C, La^{3+}:NH_4F = 1:3, pH 4–5); d) YF_3 IF nanoparticles (180 °C, Y^{3+}:NH_4F = 1:3, pH 4–5); e) $Nd(OH)_3$ nanotubes and IF nanoparticles (140 °C).

[*] Prof. Dr. Y. Li, X. Wang
Department of Chemistry
Tsinghua University
Beijing, 100084 (P. R. China)
Fax: (+86) 10-6278-8765
E-mail: ydli@tsinghua.edu.cn

[**] This work was supported by the NSFC (20025102, 50028201, 20151001), the Foundation for the Author of National Excellent Doctoral Dissertation of P. R. China, and the State Key Project of Fundamental Research for nanomaterials and nanostructures.

 DOI: 10.1002/anie.200351006 © 2003 Wiley-VCH Verlag GmbH & Co. KGaA, Weinheim

can be readily indexed to that of the hexagonal phase of LaF_3 (JCPDS no. 72–1435) with lattice constants $a = 7.163$ and $c = 7.329$ Å. With decreasing hydrothermal temperature, the peaks have been apparently broadened (Figure 1a), which indicates smaller crystal sizes. It seems that the formation of IF nanoparticles is closely related to the hexagonal structures of the corresponding samples, since comparatively fewer IF nanoparticles have been observed in the samples of orthorhombic YF_3 and no IF nanostructures observed in the orthorhombic samples of other LnF_3 (Ln = Eu, Gd, Tb, Dy, Ho, Er, Tm, Yb, and Lu) under our experimental conditions. Similar to the fluorides, most of the hydroxide IF nanoparticles that have been examined possess hexagonal structures, which also coincides well with that of rare-earth hydroxide nanowires and nanotubes.[19–20] As an example, Figure 1e shows the diffraction pattern for $Nd(OH)_3$, which can be readily indexed to that of the hexagonal structure of $Nd(OH)_3$ (JCPDS no. 83-2035) with lattice constants $a = 6.418$ and $c = 3.743$ Å. A thorough XRD characterization indicates that pure phase of the rare-earth fluorides and hydroxides could be obtained under the reported experimental conditions.

Transmission electron microscopy (TEM) provides further insight into the morphology and microstructural details of the rare-earth-based series of IF nanostructures. Figures 2–4 shows typical images of these rare-earth compounds IF

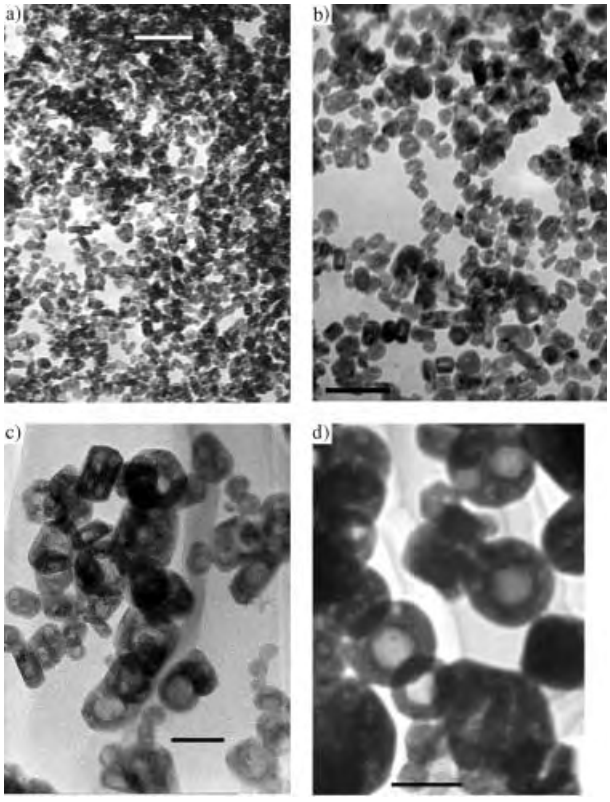


Figure 2. TEM images of a) LaF_3 IF nanoparticles (120 °C, La^{3+}:NH_4F = 1:3, pH 4–5); b) LaF_3 nanoparticles (140 °C, La^{3+}:NH_4F = 1:3, pH 4–5); c) LaF_3 nanoparticles (180 °C, La^{3+}:NH_4F = 1:3, pH 4–5); d) LaF_3 nanoparticles (180 °C, La^{3+}:NH_4F = 1:9, pH 4–5).

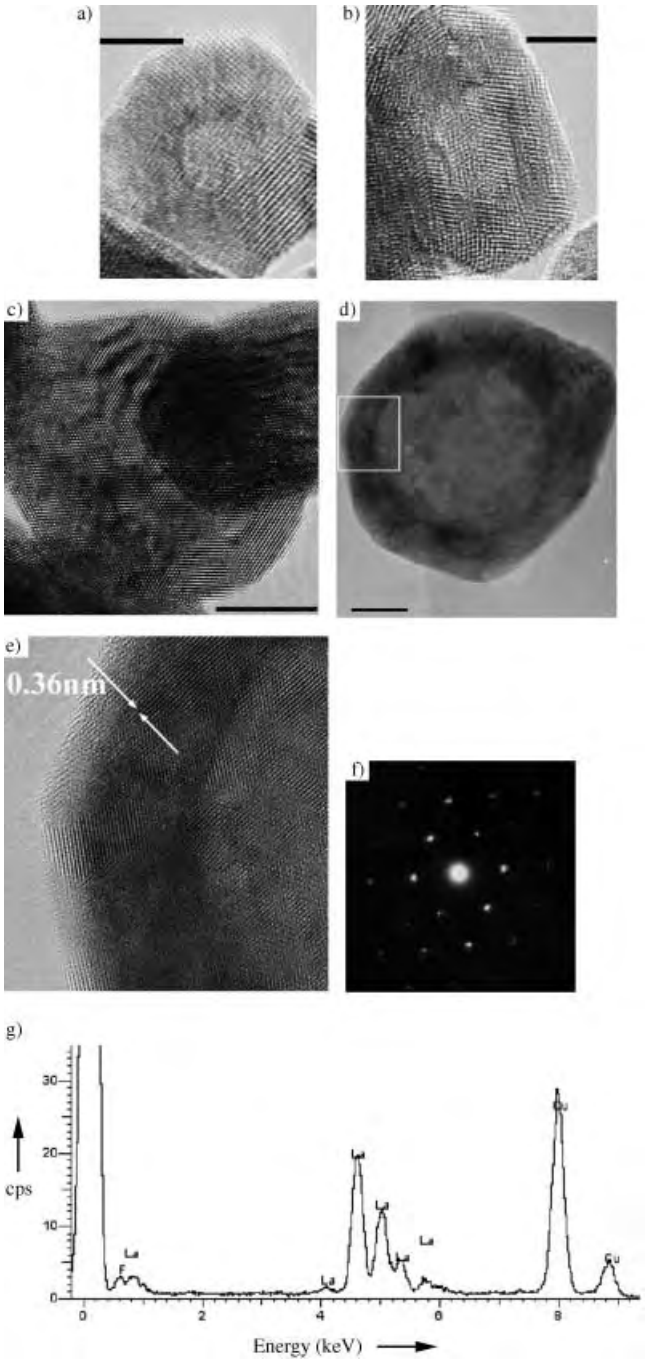


Figure 3. HRTEM images of a) an individual IF nanoparticle with diameter ≈10 nm; b) an individual polyhedral IF nanoparticle; c) an individual IF nanoparticle with diameter ≈30 nm; d) an individual IF nanoparticle with diameter ≈90 nm; e) Magnification of the square section shown in d); f) electron diffraction pattern of the IF nanoparticle in d); g) EDS analysis of the IF nanoparticle in d).

nanoparticles, from which it can be seen that most of the samples dispersed on the copper TEM grids have hollow-sphere morphologies.

The sizes of these IF nanoparticles are flexible to some extent; temperature and molar ratio have been found to be responsible for the size and shape control of these nanostructures. As shown in Figure 2c and d, the size of the LaF_3

 © 2003 Wiley-VCH Verlag GmbH & Co. KGaA, Weinheim

nanoparicles shrinks from approximately 100 to 30 nm when the molar ratio (La^{3+}:F^-) changes from 1:9 to 1:3. Temperature also plays an important role in determining the sizes of these IF nanostructures. Figure 2a shows that the average diameters of the LaF_3 obtained at 120°C are approximately 10 nm, while at higher temperatures (140°C and 180°C), the average sizes increase to 20–40 and 30–50 nm, respectively.

Similar IF structures and size-control phenomena have been observed in the samples of PrF_3, NdF_3, and SmF_3, however, comparatively fewer IF nanoparticles have been observed in the samples of YF_3, perhaps due to its orthorhombic structure.

High-resolution (HR)TEM analysis provides more detailed structural information on these IF nanostructures, and a series of HRTEM images of LaF_3 nanoparticles with diameters ranging from 10 to 100 nm have been provided as further evidence for the formation of rare-earth fluoride IF nanostructures. Figure 3d shows an individual close-caged particle with a diameter of approximately 90 nm. Higher magnification shows that its wall contains about forty layers (Figure 3e). The interlayer distance is calculated to be approximately 0.36 nm (the separation between (002) planes). Electron diffraction (ED) analysis (Figure 3f) taken from this hollow nanoparticle has revealed its single-crystalline nature, and indicates that the nanoparticles have hexagonal symmetry. Energy-dispersive spectroscopy (EDS) of this nanoparticle indicates that it contains only La and F (Figure 3g). IF nanostructures of LaF_3 with different shapes and sizes have been shown in Figure 3a–c, from which the close-caged structures of these nanoparticles can be clearly discerned.

IF nanostructures have also been discovered in our rare-earth hydroxide samples. In contrast to the fluoride IF nanoparticles, the hydroxide nanoparticles usually coexist with nanotubes in the final product (for example in, $Y(OH)_3$, $Sm(OH)_3$, $Eu(OH)_3$, $Gd(OH)_3$, $Tb(OH)_3$, $Dy(OH)_3$, $Ho(OH)_3$, and $Er(OH)_3$). Figure 4 shows HRTEM images of an individual $Eu(OH)_3$ IF nanoparticle. The interlayer distances of the IF particles are approximately 0.364 nm (close to the lattice constant along the *c* axis of the $Eu(OH)_3$ structure). This value is in good agreement with that of the nanotubes obtained by another precipitation method.[20]

The hollow-sphere nature of these samples has been further confirmed through Brunauer–Emmett–Teller (BET) analysis. Nitrogen adsorption/desorption isotherms and corresponding Barrett–Joyner–Halenda (BJH) pore-size distribution plots for samples of PrF_3 IF nanoparticles are shown in Figure 5. The isotherms can be categorized as type IV with a distinct hysteresis loop observed in the range of 0.6–1.0 P/P_0 (Figure 5a) for the samples at 120°C, and 0.8–1.0 P/P_0 (Figure 5b) for the samples at 180°C. The BET surface area for samples prepared at 180°C (average diameters: 30–50 nm) and 120°C (average diameters: about 10 nm) were 23.56 and 58.03 $m^2 g^{-1}$, respectively; these values are much larger than the calculated value for monodisperse PrF_3 spherical nanoparticles (43.92, 21.96, 14,64, 10.98, and 8.78 $m^2 g^{-1}$ for spherical particles with diameters of 10, 20, 30, 40, and 50 nm, respectively; density of a single crystal of $PrF_3 = 6.83\ g\,cm^{-3}$) that are not hollow. The BJH calculations for the pore-size distribution based on desorption data reveal

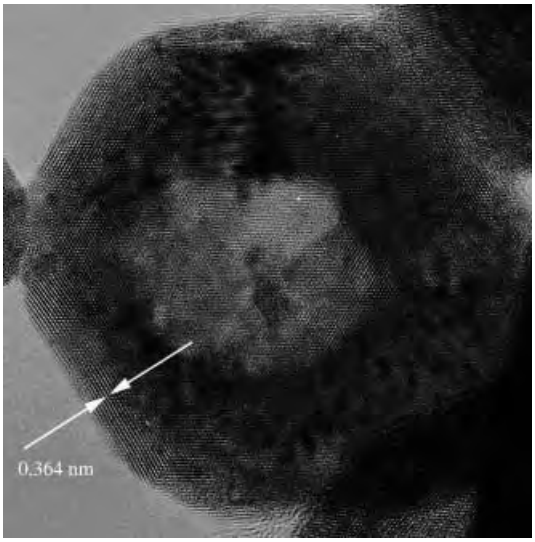


Figure 4. HRTEM image of an individual $Eu(OH)_3$ IF nanoparticle with diameter ≈45 nm.

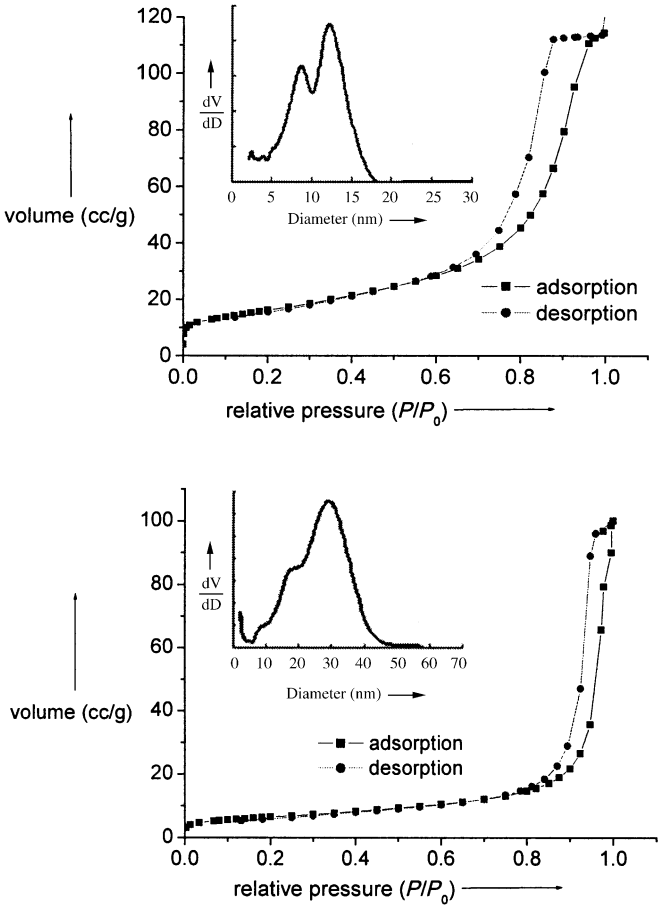


Figure 5. a) N_2 adsorption/desorption isotherm of PrF_3 IF nanoparticles (120°C, Pr^{3+}:$F^- = 1:3$); inset, pore-size distribution curve obtained from the desorption data; b) N_2 adsorption/desorption isotherm of PrF_3 IF nanoparticles (180°C, Pr^{3+}:$F^- = 1:3$); inset, pore-size distribution curve obtained from the desorption data.

 © 2003 Wiley-VCH Verlag GmbH & Co. KGaA, Weinheim

a bimodal distribution for the 120 °C samples centered at 8.5 and 12 nm (Figure 5a, inset), and a distribution for the 180 °C samples centered at 30 nm (Figure 5b, inset), which coincides with the XRD and TEM results of the samples.

Compared with the reported IF nanostructures, rare-earth fluorides and hydroxides have no typical layer structures. However, it seems that the closed-cage structures are also thermodynamically stable for these fluorides and hydroxides. Based on our experimental results, single-crystal nanotubes of rare-earth hydroxides have been successfully obtained,[20] which have shown the possibility of hydroxides forming closed-cage structures. Meanwhile, in the process of studying the formation mechanism of rare-earth hydroxides nanowires, we have observed the wide existence of lamellar structures.[19] Similar two-dimensional (2D) growth phenomena have also been observed in the formation process of fluoride nanostructures. Therefore, we believe that the rare-earth fluorides and hydroxides may not be regarded as typical 3D compounds, and may be the structural intermediates between 3D and 2D structures. However, a clear explanation of the structural rational of these IF nanostructures may need a thorough theoretical and structural investigation.

In this paper, based on a low-temperature hydrothermal method, a series of rare-earth fluoride and hydroxide IF nanoparticles have been successfully synthesized, which have greatly extended the scope of IF nanostructures. Meanwhile, this facile procedure can be easily adjusted for the large-scale synthesis of rare-earth IF nanoparticles. Also, the studies have illustrated the potential of this solution-based route for the synthesis of IF nanostructures in the low-temperature range, especially for the layered hydroxides. We believe that the synthesis and the subsequent properties obtained from these IF structures will offer many opportunities in a number of areas.

Experimental Section

Synthesis of LnF_3 IF nanoparticles: In a typical synthesis, Ln_2O_3 (Y_2O_3, La_2O_3, Pr_2O_3, Nd_2O_3, Sm_2O_3; 0.4 g) was first dissolved in 10% nitric acid, then mixed with another solution containing NH_4F (molar ratio, $Ln^{3+}:F^- = 1:3$) to form colloidal precipitates. 10% KOH (or NaOH) was then added to adjust the system to pH 4–5. The obtained colloidal precipitate was transferred to a 40-mL autoclave, sealed, and maintained at 80–180 °C for 12–24 h; the autoclave was then allowed to cool to room temperature. The precipitate was then filtered, washed with water to remove ions possibly remnant in the final products, and dried at 80 °C in air. Following the above procedures, IF nanoparticles of LaF_3, PrF_3, NdF_3, SmF_3 and YF_3 could be easily obtained. In order to obtain IF nanostructures with different sizes, factors such as molar ratio and temperature have been varied during the experimental process. The functionalization process could also be easily carried out by dissolving the corresponding rare-earth oxides with target ions or atoms.

Synthesis of $Ln(OH)_3$ IF nanoparticles: In a typical synthesis, rare-earth oxide powders (La_2O_3, Pr_6O_{11}, Nd_2O_3, Sm_2O_3, Eu_2O_3, Gd_2O_3, Tb_4O_7, Dy_2O_3, Ho_2O_3, Er_2O_3, Y_2O_3; 0.4 g) were dispersed into distilled water (30 ml), then sealed in a 40-mL autoclave and hydrothermally treated at 140–180 °C for 24 h.

Characterization: The obtained sample was characterized on a Bruker D8-Advance X-ray powder diffractometer with $Cu_{K\alpha}$ radiation ($\lambda = 1.5418$ Å). The size and morphology of the IF nanoparticles were determined at 200 kV by a Hitachi H-800 transmission electron microscope (TEM) and a JEOL JEM-2010F high-resolution transmission electron microscope.

Received: January 23, 2003 [Z51006]

Keywords: fluorides · fullerenes · hydroxides · nanostructures · rare-earth metals

[1] H. W. Kroto, J. R. Heath, S. C. O'Brien, R. F. Curl, R. E. Smalley, *Nature* **1985**, *318*, 162–163.
[2] S. Iijima, *Nature* **1991**, *354*, 56–58.
[3] R. Tenne, L. Margulis, M. Genut, G. Hodes, *Nature* **1992**, *360*, 444–446.
[4] L. Margulis, G. Salltra, R. Tenne, M. Tallanker, *Nature* **1993**, *365*, 113–114.
[5] Y. Feldman, E. Wasserman, D. J. Srolovitz, R. Tenne, *Science* **1995**, *267*, 222–225.
[6] Y. R. Hacohen, E. Grunbaum, R. Tenne, J. Sloan, J. L. Hutchison, *Nature* **1998**, *395*, 336–337.
[7] M. Prato, M. Maggini, *Acc. Chem. Res.* **1998**, *31*, 519–526.
[8] A. L. Balch, M. M. Olmstead, *Chem. Rev.* **1998**, *98*, 2123–2165.
[9] R. Tenne, *Prog. Inorg. Chem.* **2001**, *50*, 269–315.
[10] R. Tenne, *Chem. Eur. J.* **2002**, *8*, 5297–5304.
[11] G. L. Frey, S. Elani, M. Homyonfer, Y. Feldman, R. Tenne, *Phys. Rev. B* **1998**, *57*, 6668–6671.
[12] M. Chowalla, G. A. J. Amaratunga, *Nature* **2000**, *407*, 164–167.
[13] R. Popovitz-Biro, A. Twersky, Y. R. Hacohen, R. Tenne, *Isr. J. Chem.* **2001**, *41*, 7–14.
[14] S. Avivi, Y. Mastai, A. Gedanken, *J. Am. Chem. Soc.* **2000**, *122*, 4331–4334.
[15] C. Schuffenhauer, R. Popovitz-Biro, R. Tenne, *J. Mater. Chem.* **2002**, *12*, 1587–1591.
[16] K. S. Coleman, J. Sloan, N. A. Hanson, G. Brown, G. P. Clancy, M. Terrones, H. Terrones, M. L. H. Green, *J. Am. Chem. Soc.* **2002**, *124*, 11580–11581.
[17] M. Homyonfer, Y. Mastai, M. Hershfinkel, V. Volterra, J. L. Hutchison, R. Tenne, *J. Am. Chem. Soc.* **1996**, *118*, 7804–7808.
[18] G. X. Xu, *Rare Earths*, 2nd ed., Metallurgical Industry Press, Beijing, **1995**.
[19] X. Wang, Y. D. Li, *Angew. Chem.* **2002**, *114*, 4984–4987; *Angew. Chem. Int. Ed.* **2002**, *41*, 4790–4793.
[20] "Rare earth compound nanotubes": X. Wang, Y. D. Li, unpublished results.

 © 2003 Wiley-VCH Verlag GmbH & Co. KGaA, Weinheim

Zero-Valent Palladium Complexes

Zero-Valent Palladium Complexes with Monodentate Nitrogen σ-Donor Ligands**

Alexander M. Kluwer, Cornelis J. Elsevier, Michael Bühl, Martin Lutz, and Anthony L. Spek*

Compared to the large number of known, well-characterized zero-valent [bis(phosphanyl)palladium(alkene)] complexes **A**,[1] the number of [Pd^0(η^2-alkene)] complexes that contain nitrogen ligands is very limited.[2] Moreover, only complexes containing bidentate ligands that display both σ-donor and π-acceptor properties are known. Thus far, zero-valent palladium–alkene complexes **B** that contain simple monodentate



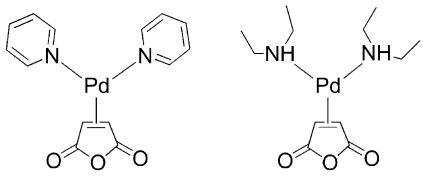
A **B**

nitrogen ligands have not been isolated and characterized. The elusiveness of zero-valent palladium complexes containing ligands that only behave as σ donors has been attributed to the alleged instability of such compounds, which arises from the combination of a soft, low-valent metal center and a hard nitrogen donor atom.[3] In contrast, Ni^0 complexes with one simple N-donor ligand are formed already with ethene as the coligand (e.g. [(L)Ni(C_2H_4)$_2$] (L = NH_3, pyridine, etc.)[4] and related bisamine complexes [$(L)_2$Ni(C_2H_4)], when the strength of coordination of the N ligands is increased by steric effects.[5] Zero-valent palladium compounds are generally either formed in situ by reduction of a suitable palladium(II) compound, or by starting from a zero-valent palladium complex with labile ligands.

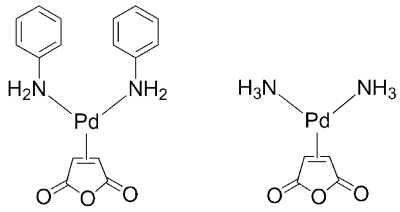
Pörschke and co-workers described the synthesis and use of "naked palladium" complexes, which contain coordination-labile 1,6-diene and other {L–Pd^0} fragments as highly reactive building units.[6] It was shown that the homoleptic dinuclear [Pd_2(1,6-diene)$_3$] and [Pt_2(1,6-diene)$_3$] complexes are very useful starting materials for preparing mononuclear complexes of the general formula [L–M(1,6-diene)] (L = phosphane, phosphite, or nitrile). However, by using this route, the authors did not succeed in preparing similar complexes based on ligands with strong σ-donor character, such as pyridine or an amine.

We now report the synthesis and characterization of several unprecedented Pd^0 compounds with monodentate N ligands as well as an X-ray structure of one such compound, [$Pd(py)_2$(ma)] (py = pyridine, ma = maleic anhydride). For the synthesis of the new Pd^0 compounds [$Pd(L)_2$(ma)], and [Pd(L′)(ma)] in which L′ is a bidentate N ligand, we used [Pd(nbd)(ma)] (nbd = norbornadiene)[7] as a versatile precursor. Dibenzylideneacetone (dba) complexes are not very suitable in this case, as dba is nonvolatile and difficult to separate from many Pd^0 compounds, especially those that are labile. [Pd(nbd)(ma)] is one of the few zero-valent palladium precursors containing volatile, readily dissociating ligands, that can be stored and used at room temperature (similar to some of the dinuclear 1,6-diene complexes[6]) and can even be handled in air for a short time without decomposition. By this new route one can readily prepare a number of zero-valent palladium complexes of the generic formula [$Pd(L)_2$(ma)] (L = pyridine, amine, aniline, or ammonia).

We prepared [Pd(nbd)(ma)][7] by a modified literature procedure (THF was used as the solvent instead of acetone) and found that decomposition to palladium black was appreciably reduced. Next, the zero-valent [$Pd(L)_2$(ma)] complexes **1**–**4** were prepared in typical yields of 65–70% by substitution of the norbornadiene ligand in [Pd(nbd)(ma)] by an excess of the monodentate nitrogen ligand in THF. Importantly, isolation of the product was carried out quickly to prevent undesired side reactions such as decomposition to palladium black. The products **1**–**4** were isolated as yellow



1 **2**



3 **4**

[*] Prof. Dr. C. J. Elsevier, A. M. Kluwer
Institute of Molecular Chemistry, Universiteit van Amsterdam
Nieuwe Achtergracht 166, 1018 WV Amsterdam (The Netherlands)
Fax: (+31) 20-525-6456
E-mail: elsevier@science.uva.nl
Priv.-Doz. Dr. M. Bühl
Max-Planck-Institut für Kohlenforschung
Kaiser-Wilhelm-Platz 1, 45470 Mülheim an der Ruhr (Germany)
Dr. M. Lutz, Prof. Dr. A. L. Spek
Bijvoet Center for Biomolecular Research
Vakgroep Kristal- en Struktuurchemie, Utrecht University
Padualaan 8, 3584 CH Utrecht (The Netherlands)

[**] This work was supported in part (A.M.K., A.L.S., M.L.) by The Netherlands Foundation for Chemical Sciences (CW) with financial aid from the Netherlands Organization for Scientific Research (NWO). M.B. thanks Walter Thiel and the Deutsche Forschungsgemeinschaft for continuous support. The authors thank Prof. Dr. K.-R. Pörschke (Max-Planck-Institut für Kohlenforschung, Mülheim a/d Ruhr, Germany) for carefully reading the manuscript and for several useful suggestions.

 DOI: 10.1002/anie.200351189 © 2003 Wiley-VCH Verlag GmbH & Co. KGaA, Weinheim

crystalline solids, which are stable at room temperature for days in a closed vessel.

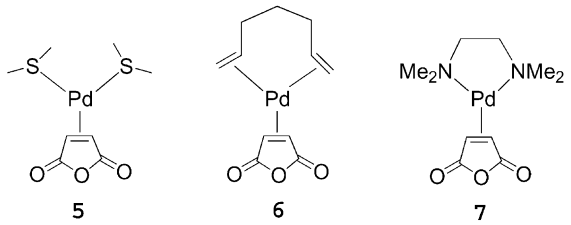
The isolated products were characterized by ^{1}H, ^{13}C NMR, and IR spectroscopy and by exact mass determination. From the NMR spectra, the coordination-induced shifts (CIS) of the signals for the protons of maleic anhydride, $\Delta\delta(H) = -3.44$ ppm for **1** to -3.87 ppm for **4** and for the coordinated carbon atoms $\Delta\delta(C) = -92.32$ ppm for **1** and -74.35 ppm for **4**, are indicative of a highly electron-rich Pd^0 center.

We also carried out several calculations at the BP86/ECP1 level[8] to assess the stabilities of a number of selected $[Pd^0(L)_2(alkene)]$ compounds in terms of the driving force for their formation from the corresponding tris(alkene) model complexes [Eq. (1)].

$$[Pd(C_2H_4)_2(alkene)] + 2\,L \rightarrow [Pd(L)_2(alkene)] + 2\,C_2H_4 \qquad (1)$$

These calculations revealed that when one electron-deficient alkene is coordinated to Pd, the Gibbs free energy ΔG^{298} of this process is only slightly positive or even negative (Table 1). Such thermo-neutral Pd^0–alkene complexes ($\Delta G^{298} \approx 0$) can, in principle, be synthesized if an appropriate kinetic route is chosen. In such a case, the starting compound should contain highly labile ligands, which can be readily displaced in solution to form the desired complex. Calculated thermodynamic data (BP86/ECP1 level) of several relevant compounds are collected in Table 1. The ΔG^{298} values calculated for the $[Pd(L)_2(ethene)]$ complexes are all positive, suggesting that compounds of this type are likely to be unstable under standard conditions and should not be formed from precursors with simple, unactivated olefins. Substitution of ethene by maleic anhydride as the alkene ligand leads to a decrease in the ΔG^{298} values by approximately 40 kJ mol^{-1}. The $[Pd(py)_2(ma)]$ complex (**1**) still has a positive ΔG^{298} value, consistent with the limited stability of this compound at ambient temperature and pressure. Comparing, for instance, entries 1 and 4 (or 10 and 13), the chelate effect (bipyridine vs. pyridine) is clearly reflected in the calculated values of enthalpies (ΔH^{298}) relative to Gibbs free energies (ΔG^{298}), and gives rise to a further stabilization by up to 40 kJ mol^{-1}.

Furthermore, the bis(dimethylsulfide) complex $[Pd(Me_2S)_2(ma)]$ (**5**) as well as the chelate compounds [Pd(1,6-heptadiene)(ma)] (**6**) and [Pd(tmeda)(ma)] (**7**) were prepared following the same synthetic route. The monodentate dialkyl sulfide complex can be isolated, even though the somewhat lower stability of the resulting complexes could have been expected based on the calculations (see Table 1, entry 16). Of course, the calculated ΔG^{298} values for compounds with mono- and bidentate phosphane as well as with bidentate N ligands are negative (see Table 1, entries 14, 15, and 18); in particular, the stabilization for PMe_3 is large. However, the latter complexes can also be obtained by using more conventional starting materials.



5 **6** **7**

Crystals of **1** were obtained by crystallization from pyridine/THF/diethyl ether.[9] The molecular structure of compound **1** with the adopted atom numbering is presented in Figure 1. The structure of **1** shows that the palladium centre

Table 1: Calculated (BP86/ECP1 level) energies, enthalpies, and free energies for the formation of $[Pd^0(L)_2(\eta^2\text{-alkene})]$ complexes according to Equation (1).[a]

Entry	Alkene	$(L)_2$	δE [kJ mol^{-1}]	ΔH^{298} [kJ mol^{-1}]	ΔG^{298} [kJ mol^{-1}]
1	C_2H_4	$(py)_2$	57.9	56.0	52.7
2		$(NH_3)_2$	50.0	47.8	32.1
3		$(NHMe_2)_2$	69.1	69.9	61.3
4		bipy	75.7	67.9	19.8
5		tmeda	79.5	74.9	35.6
6		dab	61.4	54.3	8.4
7		$(SMe_2)_2$	59.7	57.7	49.5
8		C_7H_{12}	14.3	7.9	−23.1
9		PMe_3	−31.6	−33.3	−41.0
10	ma	$(py)_2$	11.9	10.5	11.9
11		$(NH_3)_2$	1.7	4.9	−11.4
12		$(NHMe_2)_2$	16.6	18.8	19.3
13		bipy	36.1	28.8	−14.3
14		tmeda	30.1	26.2	−10.5
15		dab	37.9	31.0	−11.6
16		$(SMe_2)_2$	17.5	15.9	17.4
17		C_7H_{12}	9.2	2.3	−26.6
18		PMe_3	−78.9	−79.6	−77.5

[a] ma = maleic anhydride, bipy = 2,2′-bipyridine, tmeda = tetramethylethylenediamine, dab = 1,4-diazabutadiene.

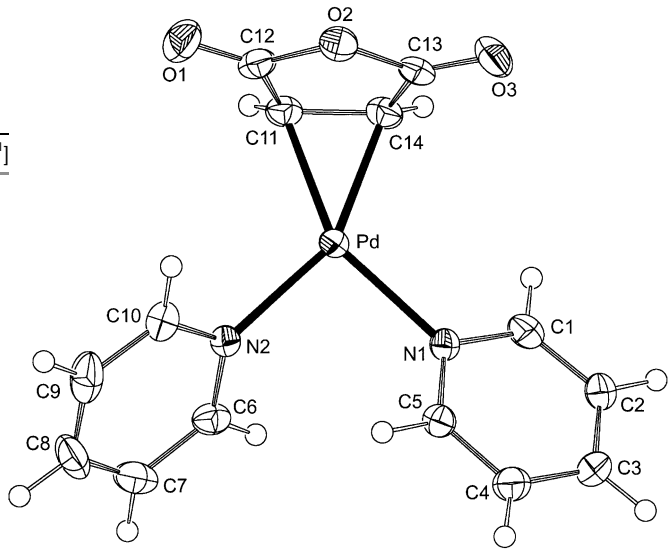


Figure 1. Displacement ellipsoid plot (50% probability level) of compound **1**. Selected distances [Å] and angles [°]: Pd-N1 2.1472(19), Pd-N2 2.1462(18), Pd-C11 2.068(2), Pd-C14 2.062(2), C11-C14 1.430(3), C11-Pd-C14 40.51(10), N1-Pd-N2 94.44(7), C11-Pd-N1 151.96(9), C14-Pd-N2 153.81(8), C11-Pd-N2 113.32(9), C14-Pd-N1 111.73(8), Pd-C11-C12 108.29(17), Pd-C14-C13 105.07(17).

 © 2003 Wiley-VCH Verlag GmbH & Co. KGaA, Weinheim

is trigonal planar, as expected for zero-valent complexes of the type $[M(L)_2(alkene)]$ (M = Pd, Pt). The dihedral angle between the least-squared planes N1/N2/Pd and C11/C14/Pd is 4.74(16)° and thus the complex is slightly distorted from planarity. The Pd–N interatomic distances observed for compound **1** are equal within standard deviation and amount to 2.1472(19) and 2.1462(19) Å, slightly smaller than the BP86/ECP1-optimized values (2.162 and 2.160 Å). The alkene bond length C11=C14 is 1.430(3) Å and is 0.098(3) Å longer than in the free alkene, which is slightly longer than the C=C bond lengthening in the previously reported [Pd(*o*,*o*′-*i*Pr$_2$C$_6$H$_3$-bian)(ma)] (bian = bisiminoacenaphthene) of 1.408(11) Å and [Pd(R′N-SR)(ma)] (R′N-SR = 2-methyl(sulfanylmethyl)pyridine) of 1.413(5) Å.[2d,13,14] The maleic anhydride moiety forms a typical angle of 78.16(16)° with the C11/C14/Pd plane. The other distances in the coordinated maleic anhydride part are similar to the reported complexes and the free molecule.

In summary, the first zero-valent complexes $[Pd(L)_2(ma)]$ with σ-donor N ligands (L = ammonia, aniline, diethylamine, pyridine) have been synthesized and isolated. These $[Pd(L)_2(ma)]$ complexes are stable at room temperature for days and are useful as catalyst precursors.[15]

Experimental Section

General procedure: To a mixture of dry THF (10 mL) and the appropriate N ligand (5 mL) was added solid [(η^2,η^2-nbd)(η^2-ma)Pd^0] (0.15 g, 0.5 mmol). In the case of ammonia, 3–4 mL was condensed at −70 °C, to which cold THF (10 mL) was slowly added, followed by the Pd^0 complex as above. After complete dissolution of the latter, the solution was filtered through Celite and washed with THF (2 × 5 mL). Diethyl ether (15 mL) was then added to the solution, after which the products were obtained as yellow microcrystalline solids in a typical yield of 65%. Selected data: **1**: ^{1}H NMR (500 MHz, [D$_6$]acetone, 25 °C, TMS): δ = 8.58 (m, 4H; py-2-H), 7.97 (m, 2H; py-4-H), 7.54 (m, 4H; py-3-H), 3.9 ppm (br, 2H; C=CH); ^{13}C NMR (125 MHz, [D$_6$]acetone, 25 °C, TMS): δ = 151.68 (py-C2), 137.70 (py-C4), 125.40 (py-C3), 39.80 ppm (CH), (C=O not observed); IR (THF): $\tilde{\nu}$ = 1780, 1726 cm^{-1} (C=O). **2**: ^{1}H NMR (500 MHz, CD_2Cl_2, 25 °C, TMS): δ = 3.5 (br, 2H; C=CH), 2.7 (br, 8H; CH_2), 1.3 ppm (br, 12H; CH_3); ^{13}C NMR (125 MHz, [D$_6$]acetone, 25 °C, TMS): δ = 171.9 (C=O), 48.0 (C=C), 38.3 (CH_2), 15.1 ppm (CH_3); IR (THF): $\tilde{\nu}$ = 1793, 1726 cm^{-1} (C=O). **3**: ^{1}H NMR (500 MHz, [D$_6$]acetone, 25 °C, TMS): δ = 7.06 (t, J = 8.0 Hz, 4H; ArH), 6.68 (d, J = 7.5 Hz, 4H; ArH), 6.59 (t, J = 7.5 Hz, 2H; ArH), 4.59 (br, 2H; C=CH), 2.81 ppm (s, 4H; NH_2); HRMS: calcd for $C_{16}H_{17}N_2O_3Pd$: 391.0281; found 391.0233. **4**: ^{1}H NMR (500 MHz, [D$_6$]acetone, 25 °C, TMS): δ = 3.47 (s, 2H; C=CH), 3.57 ppm (s, 6H; NH_3); ^{13}C NMR (125 MHz, [D$_6$]acetone, 25 °C, TMS): δ = 177.70 (C=O), 62.77 ppm (C=C). **5**: ^{1}H NMR (500 MHz, [D$_6$]acetone, 25 °C, TMS): δ = 4.1 (br, 2H; C=CH), 2.4 ppm (s, 12H). **6**: ^{1}H NMR (500 MHz, [D$_8$]THF, 25 °C, TMS): δ = 4.98 (s, 2H), 4.76 (m, 4H), 3.98 (br, 2H), 3.86 (br, 2H; C=CH), 2.02 (br, 2H), 1.75 (s, 2H), 0.92 ppm (br, 2H); ^{13}C NMR (125 MHz, [D$_8$]THF, 25 °C, TMS): δ = 168.31 (C=O), 99.96, 73.91, 60.73, 31.29, 30.89 ppm. **7**: ^{1}H NMR (500 MHz, CD_2Cl_2, 25 °C, TMS): δ = 3.55 (s, 2H; C=CH), 2.73 (s, 6H; NMe), 2.72 (s, 6H; NMe), 2.5 ppm (m, 4H; CH_2CH_2); ^{13}C NMR (125 MHz, CD_2Cl_2, 25 °C, TMS): δ = 172.22 (C=O), 59.94 (C=C), 50.64 (CH_3), 50.14(CH_3), 39.54 ppm (CH_2).

Received: February 17, 2003 [Z51189]

Keywords: coordination compounds · density functional calculations · donor–acceptor systems · N ligands · palladium

[1] a) D. Choueiry, E.-i. Negishi in *Handbook of Organopalladium Chemistry for Organic Synthesis, Vol. 1* (Ed.: E. I. Negishi), Wiley, New York, **2002**, pp. 47–65; b) P. M. Maitlis, *The Organic Chemistry of Palladium, Vol. 1*, Academic Press, New York, **1971**, pp. 106–144.

[2] a) F. Ozawa, T. Ito, Y. Nakamura, A. Yamamoto, *J. Organomet. Chem.* **1979**, *168*, 375–391; b) K. J. Cavell, D. J. Stufkens, K. Vrieze, *Inorg. Chim. Acta*, **1980**, *47*, 67; c) C. Borriello, M. L. Ferrara, I. Orabona, A. Panunzi, F. Ruffo, *J. Chem. Soc. Dalton Trans.* **2000**, 2545–2550; d) L. Canovese, F. Visentin, G. Chessa, P. Uguagliati, A. Dolmella, *J. Organomet. Chem.* **2000**, *601*, 1–15.

[3] a) R. G. Pearson, *J. Am. Chem. Soc.* **1963**, *85*, 3533; b) R. G. Pearson, *Hard and Soft Acids and Bases*, Dowden, Hutchinson & Ross Inc., Stroudsburg, PA, **1973**.

[4] W. Kaschube, K.-R. Pörschke, W. Bonrath, C. Krüger, G. Wilke, *Angew. Chem.* **1989**, *101*, 790–791; *Angew. Chem. Int. Ed. Engl.* **1989**, *28*, 772–773.

[5] K.-J. Haack, R. Goddard, K.-R. Pörschke, *J. Am. Chem. Soc.* **1997**, *119*, 7992–7999.

[6] J. Krause, G. Cestaric, K.-J. Haack, K. Seevogel, W. Storm, K.-R. Pörschke, *J. Am. Chem. Soc.* **1999**, *121*, 9807–9823.

[7] K. Itoh, F. Ueda, K. Hirai, Y. Ishii, *Chem. Lett.* **1977**, 877–880.

[8] Geometries were fully optimized using the gradient-corrected density functional according to A. D. Becke, *Phys. Rev. A* **1988**, *38*, 3098–3100, J. P. Perdew, *Phys. Rev. B* **1986**, *33*, 8822–8824, J. P. Perdew, *Phys. Rev. B* **1986**, *34*, 7406, the Stuttgart–Dresden relativistic effective core potential for Pd (D. Andrae, U. Häußermann, M. Dolg, H. Stoll, H. Preuß, *Theor. Chim. Acta* **1990**, *77*, 123–141), and standard 6-31G* basis for all other atoms. All optimized structures were characterized as minima by calculation of the harmonic vibrational frequencies, which were also used to evaluate zero-point, enthalpic, and entropic corrections. For a recent review concerning theoretical studies in palladium and platinum molecular chemistry, see: A. Dedieu, *Chem. Rev.* **2000**, *100*, 543–600.

[9] $C_{14}H_{12}N_2O_3Pd$, F_w = 362.66, yellow needle, 0.48 × 0.12 × 0.09 mm^3, orthorhombic, *Pbca* (no. 61), a = 8.1477(1), b = 16.0499(3), c = 20.5190(4) Å, V = 2683.27(8) Å^3, Z = 8, ρ_x = 1.795 g cm^{-3}, μ = 1.391 mm^{-1}; 19822 reflections were measured on a Nonius KappaCCD diffractometer with rotating anode (λ = 0.71073 Å) at a temperature of 150(2) K up to a resolution of $(\sin\theta/\lambda)_{max}$ = 0.65 Å^{-1}; 3073 reflections were unique (R_{int} = 0.051); an absorption correction based on multiple measured reflections was applied (0.77–0.91 transmission); the structure was solved with direct methods (SIR-97[10]) and refined with SHELXL-97[11] against F^2 of all reflections; non-hydrogen atoms were refined freely with anisotropic displacement parameters; H atoms of the maleic anhydride ligand were refined freely with isotropic displacement parameters; H atoms of the pyridine ligands were refined as rigid groups; 189 refined parameters, no restraints; R values ($I > 2\sigma(I)$): $R1$ = 0.0262, $wR2$ = 0.0579; R values (all reflections): $R1$ = 0.0429, $wR2$ = 0.0634; GoF = 1.025; residual electron density between −0.48 and 0.63 e Å^{-3}; molecular illustration, structure checking, and calculations were performed with the PLATON package.[12] CCDC-201446 contains the supplementary crystallographic data for this paper. These data can be obtained free of charge via www.ccdc.cam.ac.uk/conts/retrieving.html (or from the Cambridge Crystallographic Data Centre, 12 Union Road, Cambridge CB2 1EZ, UK; fax: (+44) 1223-336-033; or deposit@ccdc.cam.ac.uk).

 © 2003 Wiley-VCH Verlag GmbH & Co. KGaA, Weinheim

[10] A. Altomare, M. C. Burla, M. Camalli, G. L. Cascarano, C. Giacovazzo, A. Guagliardi, A. G. G. Moliterni, G. Polidori, R. Spagna, *J. Appl. Crystallogr.* **1999**, *32*, 115 – 119.
[11] G. M. Sheldrick, SHELXL-97. Program for crystal structure refinement, University of Göttingen, Göttingen (Germany), **1997**.
[12] a) A. L. Spek, PLATON, A multipurpose crystallographic tool, Utrecht University, The Netherlands, **2002**; b) A. L. Spek, *J. Appl. Cryst.* **2003**, *36*, 7 – 13.
[13] R. van Asselt, C. J. Elsevier, W. J. J. Smeets, A. L. Spek, *Inorg. Chem.* **1994**, *33*, 1521 – 1531.
[14] a) The room-temperature X-ray crystal structure of free maleic anhydride has led to discussions in the literature about the C=C distance in maleic anhydride: R. E. Marsh, E. Ubell, H. E. Wilcox, *Acta Crystallogr.* **1962**, *15*, 35 – 41; b) a neutron diffraction study improved the precision of the results, but was also performed at room temperature: S. F. Parker, C. C. Wilson, J. Tomkinson, D. A. Keen, K. Shankland, A. J. Ramirez-Cuesta, P. C. H. Mitchell, A. J. Florence, N. Shankland, *J. Phys. Chem. A* **2001**, *105*, 3064 – 3070; c) This prompted us to perform a low-temperature X-ray diffraction study of the free maleic anhydride, which showed that the C=C bond length was 1.3322(9) Å: M. Lutz, *Acta Crystallogr. Sect. E* **2001**, *57*, o1136-o1138.
[15] A. M. Kluwer, J. W. Sprengers, C. J. Elsevier, unpublished results.

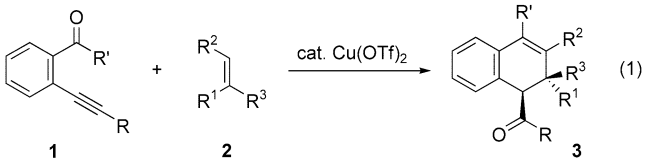
 © 2003 Wiley-VCH Verlag GmbH & Co. KGaA, Weinheim

[4 + 2] Cycloadditions

Functionalized 1,2-Dihydronaphthalenes from the $Cu(OTf)_2$-Catalyzed [4+2] Cycloaddition of *o*-Alkynyl(oxo)benzenes with Alkenes**

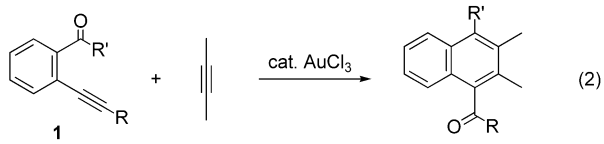
Naoki Asao, Taisuke Kasahara, and Yoshinori Yamamoto**

As dihydronaphthalene derivatives are useful starting materials for the synthesis of biologically active cyclic molecules, numerous synthetic approaches to these compounds have been reported. Among them, the dearomatization of naphthalene derivatives by the nucleophilic addition of certain organometallic reagents is one of the most useful and convenient methods.[1–6] However, to enhance the electrophilicity of naphthalene derivatives, the presence of electron-withdrawing groups such as oxazolino and imino groups on the naphthalene ring is required. A drawback of the nucleophilic-addition method is the difficulty in application to a wide range of substrates. In this contribution we report an unprecedented $Cu(OTf)_2$-catalyzed cycloaddition between *o*-(alkynyl)benzaldehydes (or *o*-(alkynyl)phenyl ketones) **1** and olefins **2**, which affords 1,2-dihydronaphthalene derivatives **3** bearing a ketone function at the 1-position [Eq. (1)].



(1)

We recently reported that the $AuCl_3$-catalyzed reaction of *o*-(alkynyl)benzaldehydes with alkynes produces the [4+2] benzannulation products, naphthalene derivatives, in good to high yields [Eq. (2)].[7] We thought that if we could use



(2)

alkenes, instead of alkynes, dehydronaphthalene derivatives would be obtained, and the scope of [4+2] cycloaddition would be expanded greatly. The reaction of *o*-(phenylethynyl)benzaldehyde (**1a**, R = Ph, R′ = H) with 1.2 equiv styrene (**2a**, R^1 = Ph, R^2 = H, R^3 = H) in the presence of 10 mol% $AuCl_3$ in THF at 90 °C for 20 h gave 1-benzoyloxy-2-phenyl-1,2-dihydronaphthalene (**3a**) in 25% yield (Table 1, entry 1). The stereochemical relationship between benzoyl group and phenyl group was *trans*. To improve the yield of **3a**, we examined several other Lewis acids. Although the CuOTf-catalyzed reaction gave **3a** in 51% yield, the *cis* isomer of **3a** was also produced in 20% yield (entry 2). When the reaction was carried out with $Cu(OTf)_2$ as the catalyst, the yield of **1a** increased dramatically up to 96% without the formation of the *cis* isomer (entry 3). Besides THF, other solvents such as 1,2-dimethoxyethane and 1,4-dioxane could be used for the present reaction (entries 4 and 5). However, less polar solvents such as toluene and 1,2-dichloroethane gave **3a** in lower yields (entries 6 and 7).

We next examined the $Cu(OTf)_2$-catalyzed reaction of aldehydes and ketones **1b–e** with olefins **2a–k** (Table 2). The

Table 1: The Lewis acid catalyzed reaction of *o*-(phenylethynyl)benzaldehyde (**1a**) with styrene (**2a**) to give **3a** (R = R^1 = Ph, R′ = R^2 = R^3 = H).[a]

Entry	Catalyst	Solvent	Conditions	Yield of **3a** [%][b]
1	$AuCl_3$	THF	90 °C, 20 h	25
2	CuOTf	THF	80 °C, 15 h	51[c]
3	$Cu(OTf)_2$	THF	80 °C, 10 h	96
4	$Cu(OTf)_2$	$(CH_2OMe)_2$	80 °C, 10 h	92
5	$Cu(OTf)_2$	1,4-dioxane	80 °C, 10 h	90
6	$Cu(OTf)_2$	toluene	80 °C, 15 h	62
7	$Cu(OTf)_2$	$(CH_2Cl)_2$	60 °C, 3 h	72

[a] The reaction was carried out with **1a** (1 equiv) and **2a** (1.2 equiv) in the presence of the Lewis acid (10 mol%). [b] Yield of isolated product. [c] The *cis* isomer of **3a** was obtained in 20% yield.

[*] Assoc. Prof. Dr. N. Asao, Prof. Dr. Y. Yamamoto, T. Kasahara
Department of Chemistry
Graduate School of Science
Tohoku University
Sendai 980-8578 (Japan)
Fax: (+81) 22-217-6784
E-mail: asao@mail.cc.tohoku.ac.jp
yoshi@yamamoto1.chem.tohoku.ac.jp

[**] OTf = Trifluoromethylsulfonate.

 © 2003 Wiley-VCH Verlag GmbH & Co. KGaA, Weinheim DOI: 10.1002/anie.200351390

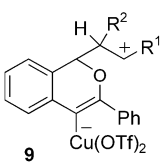
Table 2: The $Cu(OTf)_2$-catalyzed reaction of **1** with olefins **2** to give products **3**.[a]

Entry	1	R	R′	2	R^1	R^2	R^3	3	R	R′	R^1	R^2	R^3	Yield [%][b]
1	**1b**	Bu	H	**2a**	Ph	H	H	**3b**	Bu	H	Ph	H	H	56
2	**1c**	H	H	**2a**	Ph	H	H	**3c**	H	H	Ph	H	H	49
3	**1d**	Ph	Ph	**2a**	Ph	H	H	**3d**	Ph	Ph	Ph	H	H	86
4	**1e**	Ph	Me	**2a**	Ph	H	H	**3e**	Ph	Me	Ph	H	H	26
5	**1e**	Ph	Me	**2a**	Ph	H	H	**3e**	Ph	Me	Ph	H	H	51[c]
6	**1a**	Ph	H	**2b**	*p*-MeC_6H_4	H	H	**3f**	Ph	H	*p*-MeC_6H_4	H	H	98
7	**1a**	Ph	H	**2c**	*p*-$CF_3C_6H_4$	H	H	**3g**	Ph	H	*p*-$CF_3C_6H_4$	H	H	82
8	**1a**	Ph	H	**2d**	2-naphthyl	H	H	**3h**	Ph	H	2-naphthyl	H	H	56
9	**1a**	Ph	H	**2d**	2-naphthyl	H	H	**3h**	Ph	H	2-naphthyl	H	H	90[c]
10	**1a**	Ph	H	**2e**	C_4H_9	H	H	**3i**	Ph	H	C_4H_9	H	H	90
11	**1a**	Ph	H	**2f**	-$(CH_2)_6$-		H	**3j**	Ph	H	-$(CH_2)_6$-		H	44
12	**1a**	Ph	H	**2f**	-$(CH_2)_6$-		H	**3j**	Ph	H	-$(CH_2)_6$-		H	75[c]
13	**1a**	Ph	H	**2g**	Ph	H	Ph	**3k**	Ph	H	Ph	H	Ph	88
14	**1a**	Ph	H	**2h**	Ph	H	Me	**3l**	Ph	H	Ph	H	Me	76
15	**1a**	Ph	H	**2i**	H	Me	Ph	**3m**	Ph	H	Ph	Me	H	65
16	**1a**	Ph	H	**2j**	Ph	Me	H	**3m**	Ph	H	Ph	Me	H	62
17	**1a**	Ph	H	**2k**	Me	Me	Me	**3n**	Ph	H	Me	Me	Me	67

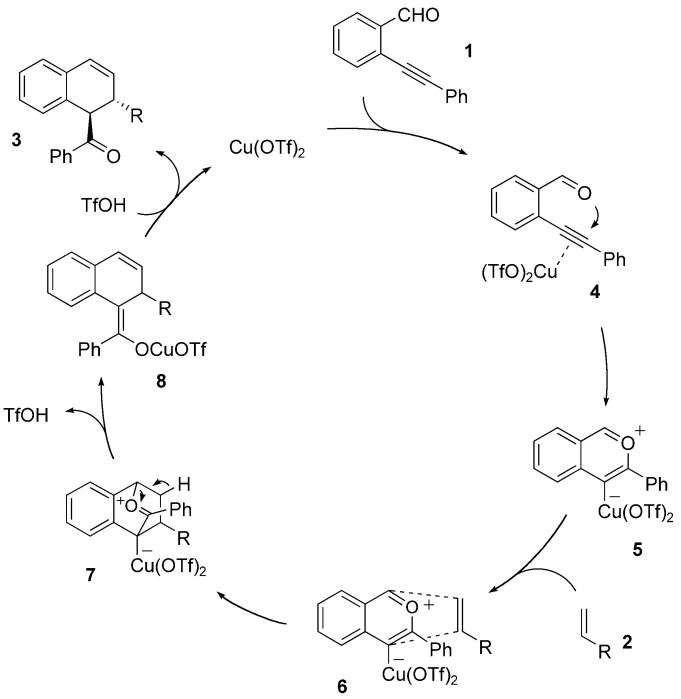
[a] The reaction was carried out with **1** (1 equiv) and **2** (1.2 equiv) in the presence of $Cu(OTf)_2$ (10 mol%) in THF at 80°C unless otherwise noted. [b] Yield of isolated product. [c] The reaction was performed in the presence of 10 mol% CF_3CO_2H as an additive.

reaction of **1b**, bearing a hexynyl group at the *ortho* position, with **2a** gave **3b** in 56% yield (entry 1). The dihydronaphthalene derivative **3c** bearing a formyl substituent was prepared by the reaction of **1c**, which has a terminal alkyne (R = H), with styrene (**2a**) (entry 2). The substrate with a ketone function (**1d**, R′ = Ph) can be used for the present reaction, and **3d** was obtained in a high yield (entry 3). Although the reaction of **1e**, which has an acyl group, with **2a** afforded **3f** in low yield (entry 4), the yield was increased up to 51% when the reaction was carried out in the presence of 10 mol% CF_3CO_2H (entry 5). Not only styrene (**2a**) but also the mono-, di-, and trisubstituted olefins **2b–k** could be employed in the present reaction, and the corresponding products were obtained in good to high yields (entries 6–17). In entries 9 and 12, the yields of **3h** and **3j** were increased by addition of a catalytic amount of CF_3CO_2H.

A plausible mechanism for the present reaction is shown in Scheme 1. The coordination of the triple bond of **1** to $Cu(OTf)_2$ enhances the electrophilicity of the alkyne, and the subsequent nucleophilic attack (as shown in **4**) of the carbonyl oxygen atom on the electron-deficient alkyne forms the cupric ate complex **5**. The Diels–Alder reaction of **5** with olefin **2** gives the intermediate **7** through **6**. Due to the instability of **7**, the cleavage of the carbon–oxygen bond followed by elimination of proton occurs to give the copper enolate **8** and TfOH. Protonation of **8** by TfOH gives **3**, and the copper catalyst is regenerated. In all cases with $Cu(OTf)_2$ as a catalyst, the *trans* isomer was obtained as the sole product. When the *cis* isomer of **3a** was treated with a catalytic amount of $Cu(OTf)_2$ in THF at 80°C, the isomerization to the *trans* isomer **3a** occurred. This result clearly shows that the exclusive formation of the *trans* products is due to their thermodynamic stabilities. The regioselective formation of **3** in the [4+2] cycloaddition [Eq. (1)] is accounted for by considering a carbocation intermediate **9** on the way from **6** to **7**. In the reaction with olefins bearing aryl groups (entries 1–9), the carbocation **9** stabilized by neighboring aryl groups (R^1 = aryl) is preferable to the alternative regioisomeric carbocation in which R^2 is adjacent to the carbocation. In the reaction of hexene (entry 10) the formation of **9** with a butyl group at R^1 is preferred owing to its electron-donating effect.



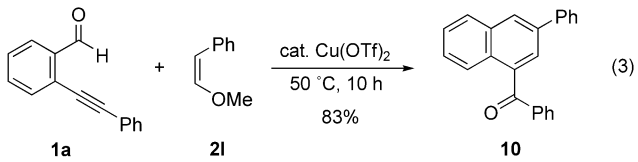
9



Scheme 1. Plausible reaction mechanism.

Interestingly, the reaction of **1a** with β-methoxy-styrene **2l** did not give the corresponding 1,2-dihydronaphthalene but afforded the naphthalene derivative **10** in 83% yield [Eq. (3)]. Perhaps the expected [4+2] cycloaddition took place in a similar way as mentioned above, and the resulting 2-

 © 2003 Wiley-VCH Verlag GmbH & Co. KGaA, Weinheim



methoxydehydronaphthalene underwent elimination of methanol to give **10**.

A novel and efficient synthetic method for 1,2-dihydronaphthalenes has been developed. We are now at a position to synthesize regioselectively functionalized 1,2-dihydronaphthalene derivatives starting from *o*-(alkynyl)benzaldehydes and *o*-(alkynyl)aryl ketones. Further studies to elucidate the mechanism of this novel reaction and to extend the scope of its synthetic utility are in progress in our laboratory.

Experimental Section

Typical experimental procedure: Synthesis of **3a**: To a solution of $Cu(OTf)_2$ (18.0 mg, 10 mol%) in THF (2 mL) were added **1a** (103 mg, 0.5 mmol) and **2a** (0.07 mL, 0.6 mmol) successively at room temperature under Ar atmosphere. The resulting mixture was stirred at 80°C for 10 h and then cooled to room temperature. A saturated aqueous solution of NH_4Cl was added, and the mixture was extracted with ether three times. The combined extracts were washed with brine, dried over $MgSO_4$, and concentrated to dryness to leave the crude product, which was purified by silica gel column chromatography using hexane/EtOAc (8:1) as the eluent to give **3a** (149 mg, 0.48 mmol) in 96% yield.

Received: March 13, 2003 [Z51390]

Keywords: cycloaddition · dihydronaphthalene · Lewis acids

[1] For reviews, see: A. R. Pape, K. P. Kaliappan, E. P. Kündig, *Chem. Rev.* **2000**, *100*, 2917–2940.
[2] D. J. Rawson, A. I. Meyers, *J. Org. Chem.* **1991**, *56*, 2292–2294.
[3] a) A. I. Meyers, J. D. Brown, *Tetrahedron Lett.* **1987**, *28*, 5279–5282; b) A. I. Meyers, K. A. Lutomski, D. Laucher, *Tetrahedron* **1988**, *44*, 3107–3118.
[4] D. Amurrio, K. Khan, E. P. Kündig, *J. Org. Chem.* **1996**, *61*, 2258–2259, and references therein.
[5] A. Ahmed, J. Clayden, M. Rowley, *Chem. Commun.* **1998**, 297–298.
[6] a) K. Tomioka, M. Shindo, K. Koga, *Tetrahedron Lett.* **1990**, *31*, 1739–1740; b) K. Tomioka, I. Inoue, M. Shindo, K. Koga, *Tetrahedron Lett.* **1990**, *31*, 6681–6684; c) M. Shindo, K. Koga, Y. Asano, K. Tomioka, *Tetrahedron* **1999**, *55*, 4955–4968; d) K. Tomioka, M. Shindo, K. Koga, *J. Am. Chem. Soc.* **1989**, *111*, 8266–8268.
[7] N. Asao, K. Takahashi, S. Lee, T. Kasahara, Y. Yamamoto, *J. Am. Chem. Soc.* **2002**, *124*, 12650–12651.

 © 2003 Wiley-VCH Verlag GmbH & Co. KGaA, Weinheim

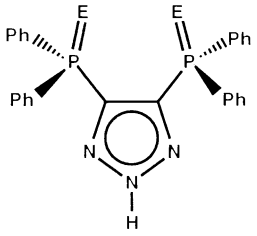
Bis(diphenylphosphanyl) Ligands

4,5-Bis(diphenylphosphanyl)-1,2,3-triazole and Its Conversion to 1,1,3,3,-Tetraphenyl-1,3-diphospha-2,4,5,6-tetraazapentalene

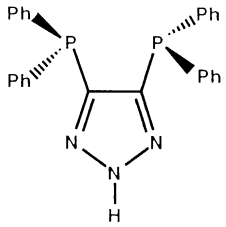
Swiatoslaw Trofimenko, Arnold L. Rheingold, and Christopher D. Incarvito*

The novel ligand system, based on the anion of a 4,5-bis(diphenylphosphanyl)-1,2,3-triazole core, which may contain substituents, such as O, S, Se, NR or NAr, on the two phosphorus atoms, was reported for the case where the substituent was O.[1] This ligand was capable of coordinating in two different ways forming either a five- (O,N) or a seven-membered (O,O) chelate ring, depending on the chelated metal. More recently, the related $(L^{T\text{-}S2})^-$ ligand and some of its complexes were also described.[2] This general ligand type is abbreviated as $(L^{T\text{-}E2})^-$ in its anionic form, or as the free acid $HL^{T\text{-}E2}$, **1**, in which E is the particular heteroatom substituent on phosphorus, with HL^T being the abbreviation for the core molecule, the hitherto unknown 4,5-bis(diphenylphosphanyl)-1,2,3-triazole.[3]

Herein we report a) the synthesis of HL^T, **2**, the core molecule of the whole $HL^{T\text{-}E2}$ system, by deselenation of $HL^{T\text{-}Se2}$, and b) an unprecedented reaction of **2** with Me_3SiN_3, in the course of which **2** is transformed into the novel heterocycle, 1,1,3,3-tetraphenyl-1,3-diphospha-2,4,5,6-tetraazapentalene, **3**.



$HL^{T\text{-}E2}$ = **1**



HL^T = **2**

The reaction of $Ph_2PC{\equiv}CPPh_2$ with selenium formed the known diselenated derivative $Ph_2P(Se)C{\equiv}CP(Se)Ph_2$,[4,5] which reacted with NaN_3 to produce the sodium salt of the ligand, $NaL^{T\text{-}Se2}$, and this on acidification yielded the free acid, $HL^{T\text{-}Se2}$. The NaN_3 reaction required heating, and longer reaction times, than in the case of the oxo- and thio- analogues of $Ph_2P(Se)C{\equiv}CP(Se)Ph_2$, commensurate with the lower electron withdrawing power of the $-PPh_2{=}Se$ substituents in

[*] Dr. S. Trofimenko, Prof. Dr. A. L. Rheingold, C. D. Incarvito
Department of Chemistry and Biochemistry
The University of Delaware
Newark, DE 19716 (USA)
Fax: (+1) 302-831-6335
E-mail: trofimen@udel.edu

 © 2003 Wiley-VCH Verlag GmbH & Co. KGaA, Weinheim DOI: 10.1002/anie.200351437

the series $-PPh_2{=}O > -PPh_2{=}S > -PPh_2{=}Se$ and, consequently, decreased activation of the triple bond. The new ligand was characterized as the triethylammonium salt, $HNEt_3L^{T\text{-}Se2}$, and its structure was determined by X-ray crystallography[6] and found to be similar to the previously reported $HNEt_3L^{T\text{-}S2}$.[3]

The free acid itself, $HL^{T\text{-}Se2}$ was an important starting material in the synthesis of the core heterocycle **2** [Eq. (1)].

$$HL^{T\text{-}Se2} + 2\,P(OEt)_3 \rightarrow \mathbf{2} + 2\,Se{=}P(OEt)_3 \quad (1)$$

Treatment of $HL^{T\text{-}Se2}$ with $P(OEt)_3$ at room temperature resulted in double deselenation and the formation of HL^T, **2**, in good yield.[7] The related compounds $HL^{T\text{-}S2}$ and $HL^{T\text{-}O2}$ failed to react with $P(OEt)_3$ at room temperature, and under conditions designed to force the reaction gave rise only to 1N- and 2N-ethylated derivatives. The core molecule, **2**, has been structurally characterized (Figure 1). Its molecular dimensions in the triazole ring are similar to those found in $HL^{T\text{-}O2}$ and $HL^{T\text{-}S2}$ with the nonbonding distance between the two P atoms being 3.488 Å.

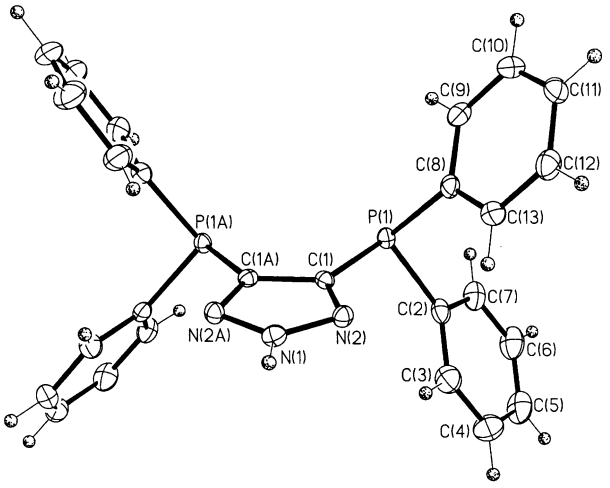
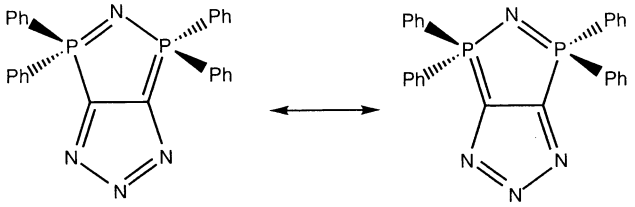


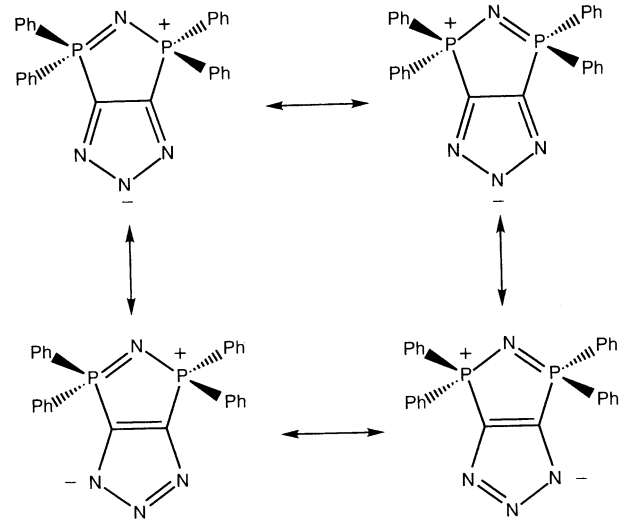
Figure 1. The X-ray crystal structure of HL^T, **2**. Selected bond distances [Å] and angles [°]: P(1)–C(1) 1.820(3); P(1)–C(8) 1.827(2); P(1)–C(2) 1.84393); C(1A)-C(1)-P(1) 124.95(9); C(1)-C(1A)-P(1A) 124.2(5).

Although, at first glance, **2** may be regarded as a simple chelating diphosphane, it has the special feature of containing the triazole proton, which upon removal by base will produce a chelating anionic diphosphane capable of forming neutral bisdiphosphane complexes $M[L^T]_2$ with divalent metals, and thus obviating the need for a counterion, ubiquitous in complexes with analogous neutral vicinal diphosphanes. Thus, **2** can chelate in two modes: as a neutral rigid diphosphane, or as an anionic rigid diphosphane, in each case forming identical five-membered chelate rings of C_{2v} symmetry. Both, the neutral HL^T and the anionic $(L^T)^-$ ligands are isoelctronic and isostructural. Such anionic chelating diphosphanes are unknown, although chelating diphosphanes forming six-membered rings as, for instance, $[Ph_2B(CH_2PPh_2)_2]^-$ and $[PhB(CH_2PPh_2)_3]^-$ were reported.[8,9]

Compound **2** underwent an unprecedented "pseudo-Staudinger" reaction with Me_3SiN_3. Instead of the expected 1,2,3-triazole, which contains two $-PPh_2(=NSiMe_3)$ substituents in the 4,5-positions, as is typical in the reaction of various diphosphane species with Me_3SiN_3,[10,11] we obtained a product that melts at high temperature, **3**, which was stable to air and moisture unlike the very sensitive known $RPPh_2(=NSiMe_3)$ compounds.[12] Compound **3** also contained no $SiMe_3$ signals in the proton NMR spectrum, while its ^{31}P NMR had a single peak at $\delta = 22.3$ ppm, a region more characteristic of phosphorus(v) compounds. For instance, the ^{31}P resonances for $Et_3NH[L^{T\text{-}E2}]$ compounds were $\delta =$ 19.2 ppm (E = O), 32.6 (E = S) and 22.2 ppm (E = Se), while HL^T had its ^{31}P resonance at $\delta = -36.1$ ppm. Structural characterization by X-ray crystallography showed **3** to be a novel molecule, 1,1,3,3-tetraphenyl-1,3-diphospha-2,4,5,6-tetraazapentalene, which belongs to the class of polyazapentalenes. Polyazapentalenes are known to be very stable due to the multiplicity of charge-separated zwitterionic forms that they can adopt,[13] and this seems to be the first example of a polyazapentalene containing phosphorus atoms incorporated into the pentalene ring system. In compound **3**, abbreviated as $L^{T\text{-}N}$, one can write canonical structures with alternating single and double bonds, in which both phosphorus atoms are in their highest, pentavalent oxidation state, as shown below.

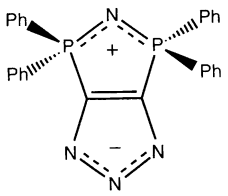


One can also write numerous charge-separated structures:



As in all these charge-separated descriptions of the molecule the positive charge resides in the diphospha portion of the pentalene molecule, and the negative charge is

 © 2003 Wiley-VCH Verlag GmbH & Co. KGaA, Weinheim



3 = $L^{T\text{-}N}$

distributed on the nitrogen atoms of the triazole-derived part, it might be appropriate to write the structure of **3** in delocalized zwitterionic form. Several simple cyclic salts, containing within a five-membered ring the moiety $[-P(Ph_2)P{=}N{-}P(Ph)_2{-}]^+$, associated with a separate bromide anion, were reported.[14]

The structure of **3** (Figure 2) is a molecule with C_{2v} symmetry, both phosphorus atoms being in identical environments. In agreement with this observation, the two equal P–N distances of 1.62 Å fell between the typical P=N and P–N values (1.59 and 1.68 Å, respectively), but closer to a P=N double bond. The triazolyl N(1)-N(2) and N(2)-N(3) bonds were slightly longer in **3** than in **2** (1.35 versus 1.33 Å), while the triazolyl C–N and C–C bonds lengths were essentially the same in **2** and **3** (1.35 and 1.40 Å, respectively). The linking of the two phosphorus atoms in **3** by the bridging nitrogen resulted in the shortening of the nonbonded P···P distance by 0.8 Å (2.696 Å in **3** versus 3.488 Å in **2**).

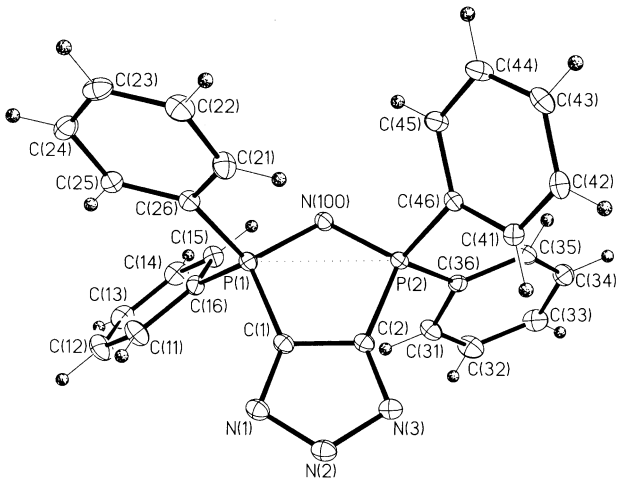


Figure 2. The X-ray crystal structure of L^{T-N}, **3**. Selected distances [Å] and angles [°]: P(1)–N(100) 1.6147(13); P(2)–N(100) 1.6101(13); P(1)–C(1) 1.7809(15); P(2)–C(2) 1.7779(15); C(1)–C(2) 1.394(2); N(100)-P(1)-C(1) 101.78(7); N(100)-P(2)-C(2) 101.75(7); P(1)-N(100)-P(2) 113.32(8).

Whatever the reaction mechanism of **2** with Me_3SiN_3 may be, the driving force for the formation of **3** appears to be the oxidation of both P atoms to the pentavalent state and the formation of the resonance-stabilized novel heterocycle, since in numerous other reactions of chelating diphosphanes with Me_3SiN_3 such oxidative bridging of the two phosphorus atoms was never observed. This net transfer of a single bridging nitrogen atom by Me_3SiN_3 in this "pseudo-Staudinger" reaction appears to be truly unprecedented.

In summary, we have prepared the selenium analogue of the known $(L^{T\text{-}O2})^-$ and $(L^{T\text{-}S2})^-$ ligands, $(L^{T\text{-}Se2})^-$, and converted its free acid to the core molecule of the whole $HL^{T\text{-}E2}$ ligand system, HL^T, **2**. We have also shown that **2** reacts in unprecedented fashion with Me_3SiN_3, and is transformed into the stable novel heterocycle, 1,1,3,3-tetraphenyl-1,3-diphospha-2,4,5,6-tetraazapentalene, **3**. Various aspects of the coordination chemistry of the new ligands $(L^{T\text{-}Se2})^-$, $(L^T)^-$ and HL^T, are being investigated and will be reported in due course.

Experimental Section

All NMR spectra were determined in [D]chloroform, and the IR spectra in KBr. The deselenation reaction of $HL^{T\text{-}Se2}$ and the reaction of HL^T with Me_3SiN_3 were carried out under nitrogen. Each of the products described was air-stable at ambient temperature.

$HNEt_3L^{T\text{-}Se2}$: A stirred slurry of $Ph_2P(Se)C{\equiv}CP(Se)Ph_2$ (19 g, 34 mol) and NaN_3 (2.5 g, 39 mol) in DMF (200 mL) was stirred and heated to 100 °C for until most of the NaN_3 had dissolved. The solution was decanted from a small amount of undissolved NaN_3, and poured slowly into HCl (1 L, 4 M). The precipitated crude $HL^{T\text{-}Se2}$ was separated by filtration off and dried (yield 19.5 g, 96 %), and was used without further purification for the subsequent formation of **2**. $HNEt_3L^{T\text{-}Se2}$ was obtained by stirring a sample of $HL^{T\text{-}Se2}$ in methanol with excess triethylamine, followed by evaporation of this solution, and recrystallization of the product from acetonitrile. M.p. 196–198 °C, decomp; IR: $\tilde{\nu}$ = 3048 (m), 2975 (m), 2621 (m), 2478 (m), 2358 (m), 1479 (s), 1436 (s), 1096 (s), 755 (s), 692 (s), 593 (s), 564 (s), 525 cm^{-1} (s). ^1H NMR: δ = 7.63 (m, 8H, phenyl), 7.26 (m, 4H, phenyl), 7.16 (8H, phenyl), 3.00 (quartet, 6H, CH_2), 1.01 ppm (t, 9H, Me). ^{31}P NMR: δ = 22.2 ppm, $J(^{31}P\text{-}^{77}Se)$ 361 Hz. Elemental analysis calcd (%) for $C_{32}H_{36}N_4P_2Se_2$: C 55.2, H 5.17, N 8.05; found: C 55.0, H 5.09, N 8.00.

2: An excess of $P(OEt)_3$ was added to a stirred slurry of $HL^{T\text{-}Se2}$ (41.0 g, 68.9 mmol) in 100 mL chloroform, whereupon the solid dissolved within a few minutes. After 2 h the volatiles were removed by distillation, ultimately under high vacuum, and the crude **2** thus obtained (yield 29.8 g, 83.3 %), was recrystallized from acetonitrile; m.p. 137–138 °C; IR: $\tilde{\nu}$ = 3175 (b), 3067 (s), 2998 (m), 1476 (s), 1430 (s), 1365 (m), 1092 (s), 1069 (s), 746 (vs), 692 (center of triplet, vs), 505 cm^{-1} (s). ^1H NMR: δ = 7.28 ppm (unresolved m, phenyl); ^{31}P: δ = −36.1 ppm. Elemental analysis calcd (%) for $C_{26}H_{21}N_3P_2$: C 71.4, H 4.81, N 9.69; found: C 71.5, H 4.97, N 9.55 %.

3: A mixture of **2** (12.8 g, 0.03 mol) and Me_3SiN_3 (10 mL, 0.08 mol) in 20 mL toluene was refluxed for 3 h, then the volatiles were removed by distillation, ultimately under high vacuum. The residue was washed with toluene/heptane and isolated by filtration. Crude **3** (yield 10.2 g, 77 %) was recrystallized from acetonitrile; m.p. 234–235 °C; IR: $\tilde{\nu}$ = 3051 (s), 1557 (w), 1478 (m), 1434 (s), 1299 (m), 1118 (s), 746 (s), 727 (s), 697 (s), 570 (s), 509 cm^{-1} (s). ^1H NMR: δ = 7.45 (four symmetrical m, 8H, *o*-H), 7.51 (m, 4H, *p*-H), 7.87 ppm (m, 8H, *m*-H); ^{31}P NMR: δ = 22.3 ppm. Elemental analysis calcd (%) for $C_{26}H_{20}N_4P_2$: C 69.3, H 4.44, N 12.4; found C 69.5, H 4.53, N 12.2 %.

Crystal data for **2** and **3**: All data were collected by using Bruker CCD-equipped diffractometers, $Mo_{K\alpha}$ radiation. For $C_{26}H_{21}N_3P_2$ (**2**), monoclinic, *C*2/*c*, a = 16.3997(13), b = 6.3423(5), c = 22.3242(18) Å, β = 104.5810(10)°, V = 2247.2(3) Å^3, Z = 4, Z' = 1, T = 173 K, ρ_{calc} = 1.293 Mg m^{-3}. Of 4424 data collected, 1968 were independent. $R(F)$ = 5.38 %, $wR(F^2)$ = 14.61 %. There are two orientations for the molecule in an 83/17 ratio that are inversionally related. For $C_{26}H_{20}N_4P_2C{\cdot}0.5\,CH_3CN$ (**3**), monoclinic, $P2_1/c$, a = 18.6594(11), b = 13.9544(8), c = 18.4924(11) Å, β = 102.7540(10)°, V = 4696.3(5) Å3, Z = 8, Z' = 2, T = 153 K, ρ_{calc} = 1.336 Mg m^{-3}. The asymmetric unit contains two molecules of **3** and a molecule of acetonitrile disordered over two sites in approximately equal distribution. Of 53 778 data collected, 11 234 were independent. $R(F)$ = 4.58 %, $wR(F^2)$ = 13.65 %. For both molecules, all non-hydrogen atoms were refined with anisotropic thermal parameters and hydrogen atoms were treated as idealized contributions. All software is contained in libraries distrib-

 © 2003 Wiley-VCH Verlag GmbH & Co. KGaA, Weinheim

uted by Bruker AXS (Madison, WI). CCDC-179388 (**2**) and CCDC-179389 (**3**) contain the supplementary crystallographic data for this paper. These data can be obtained free of charge via www.ccdc.cam.ac.uk/conts/retrieving.html (or from the Cambridge Crystallographic Data Centre, 12, Union Road, Cambridge CB2 1EZ, UK; fax: (+44) 1223-336-033; or deposit@ccdc.cam.ac.uk).

Received: March 18, 2003 [Z51437]

Keywords: · ligand design · N,P ligands · zwitterions

[1] A. L. Rheingold, L. M. Liable-Sands, S. Trofimenko, *Angew. Chem.* **2000**, *112*, 3459; *Angew. Chem. Int. Ed.* **2000**, *39*, 3321.
[2] A. L. Rheingold, L. M. Liable-Sands, S. Trofimenko, *Inorg. Chim. Acta* **2002**, *330*, 38.
[3] If the phosphorus substituents E are non-identical, the abbreviation is $[L^{T\text{-}E,E'}]^-$.
[4] D. M. Anderson, P. B. Hitchcock, M. F. Lappert, *J. Organomet. Chem.* **1989**, *363*, C-7.
[5] I. J. Colquhoun, W. McFarlane, *J. Chem. Soc. Dalton Trans.* **1982**, 1915.
[6] S. Trofimenko, A. L. Rheingold, unpublished results.
[7] Similar deselenations of Ph_3PSe with $P(OEt)_3$ were reported recently. M. Bollmark, J. Stawinski, *Chem. Commun.* **2001**, 771.
[8] J. C. Thomas, J. C. Peters, *J. Am. Chem. Soc.* **2001**, *123*, 5100.
[9] a) J. C. Peters, J. D. Feldman,, T. D. Tilley, *J. Am. Chem. Soc.* **1999**, *121*, 9871; b) A. A. Barney, A. F. Heyduk, D. G. Nocera, *Chem. Commun.* **1999**, 2379; c) I. R. Shapiro, D. M. Jenkins, J. C. Thomas, M. W. Day, J. C. Peters, *Chem. Commun.* **2001**, 2152.
[10] a) R. G. Cavell, R. P. K. Babu. A. Kasani, R. McDonald, *J. Am. Chem. Soc.* **1999**, *121*, 5805; b) C. M. Ong, D. W. Stephan, *J. Am. Chem. Soc.* **1999**, *121*, 2939; c) A. Kasani, R. McDonald, R. G. Cavell, *Organometallics* **1999**, *18*, 3775; d) R. P. K. Babu. R. McDonald, S. A. Decker, M. Klobukowski, R. G. Cavell, *Organometallics* **1999**, *18*, 4226; e) R. P. K. Babu, K. Aparna, R. McDonald, R. G. Cavell, *Inorg. Chem.* **2000**, *39*, 4981; f) R. P. K. Babu, K. Aparna, R. McDonald, R. G. Cavell, *Organometallics* **2001**, *20*, 1451.
[11] Analogous reactions with *p*-tolyl azide, formed −P=N-(*p*-tolyl) species. a) P. Imhoff, R. van Asselt, J. M. Ernsting, K. Vrieze, C. J. Elsevier, W. J. J. Smeets, A. L. Spek, A. P. M. Kentgens, *Organometallics* **1993**, *12*, 1523; b) M. W. Avis, K. Vrieze, H. Kooijman, N. Veldman, A. L. Spek, C. L. Elsevier, *Inorg. Chem.* **1995**, *34*, 4092; c) M. W. Avis, C. J. Elsevier, N. Veldman, H. Kooijman, A. L. Spek, *Inorg. Chem.* **1996**, *35*, 1518.
[12] V. R. Appel, I. Ruppert, *Z. Anorg. Allg. Chem.* **1974**, *406,* 131.
[13] a) R. A. Carboni, J. E. Castle, *J. Am. Chem. Soc.* **1962**, *84*, 2453; b) R. Pfleger, E. Garthe, K. Rauer, *Chem. Ber.* **1963**, *96*, 1827; c) B. M. Lynch, T.-T. Young, *J. Heterocycl. Chem.* **1965**, *2*, 218.
[14] A. Schmidpeter, K. Polborn, *Heteroat. Chem.* **1997**, *8*, 347.

 © 2003 Wiley-VCH Verlag GmbH & Co. KGaA, Weinheim

Asymmetric Hydrogenation

A Bisphosphepine Ligand with Stereogenic Phosphorus Centers for the Practical Synthesis of β-Aryl-β-Amino Acids by Asymmetric Hydrogenation**

*Wenjun Tang, Weimin Wang, Yongxiang Chi, and Xumu Zhang**

Enantiomerically pure β-amino acids are important chiral building blocks for the synthesis of β-peptides, β-lactam antibiotics, and many other important chiral drugs.[1] Although chiral β-amino acids have been synthesized through several stoichiometric and catalytic methods,[2] an efficient and practical synthetic method is still needed. The Rh-[3] or Ru-catalyzed[4] asymmetric hydrogenation of β-(acylamino)-acrylic acid derivatives to make chiral β-amino acids has recently attracted much attention. Although many Rh[3] and Ru[4a,c] complexes with chiral phosphane ligands exhibited high enantioselectivities in the hydrogenation of β-alkyl-β-(acylamino)acrylic acid derivatives, the asymmetric hydrogenation of β-aryl-β-(acylamino)acrylic acid derivatives has met with much less success. Heller and co-workers recently reported that the use of a Rh–Et–ferrotane catalyst can give rise to *ee* values of over 99% in the asymmetric hydrogenation of a set of (*E*)-β-aryl-β-(acylamino)acrylic acid derivatives.[3b] However, the preparation of (*E*)-β-aryl-β-(acylamino)acrylic acid derivatives requires their separation from the corresponding thermodynamically more stable *Z* isomers, and low yields are generally observed.[3b] On the other hand, (*Z*)-β-aryl-β-(acylamino)acrylic acid derivatives can be preferentially formed over their *E* isomers under suitable conditions, and high yields for the synthesis of *Z* substrates are attainable.[4b] A highly enantioselective asymmetric hydrogenation of (*Z*)-β-aryl-β-(acylamino)acrylic acid derivatives would allow the practical synthesis of chiral β-aryl-β-amino acids. In previous work we developed a set of Ru–*o*-binapo complexes,[4b] which gave rise to *ee* values of up to 99% in the asymmetric hydrogenation of (*Z*)-β-aryl-β-(acylamino)acrylic acid derivatives.[5] However, the reactivities of the Ru complexes were moderate. A Rh–TangPhos catalyst promoted both high enantioselectivities (up to 98.5% *ee*) and high reactivities in the hydrogenation of a series of *Z* substrates, with the exception of those with *ortho*-substituted β-aryl groups.[3e] Herein we present a new chiral catalyst for the hydrogenation of (*Z*)-β-aryl-β-(acylamino)-acrylic acid derivatives. The Rh complex of the chiral bisphosphepine ligand **1** (abbreviated as (*S*,*S*,*S*)-binapine),

[*] Prof. X. Zhang, W. Tang, Dr. W. Wang, Dr. Y. Chi
Department of Chemistry, The Pennsylvania State University
University Park, PA 16802 (USA)
Fax: (+1) 814-863-8403
E-mail: xumu@chem.psu.edu

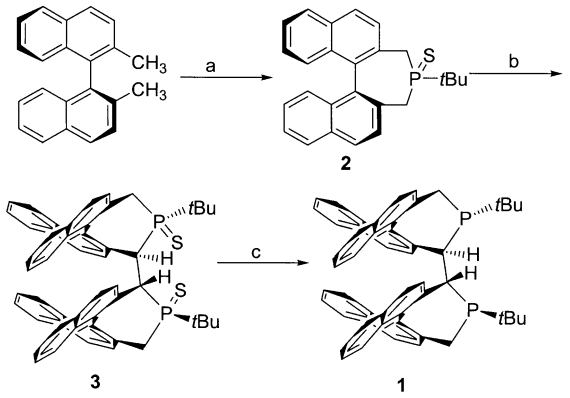
[**] This work was supported by the National Institute of Health.

Supporting information for this article is available on the WWW under http://www.angewandte.org or from the author.

 DOI: 10.1002/anie.200351465 © 2003 Wiley-VCH Verlag GmbH & Co. KGaA, Weinheim

which has stereogenic phosphorus centers, promoted excellent enantioselectivities and reactivities in the asymmetric hydrogenation of a wide range of (*Z*)-β-aryl-β-(acylamino)-acrylic acid derivatives.

Ligand design has played a pivotal role in the development of new efficient metal-catalyzed asymmetric reactions. We recently reported an efficient chiral bisphospholane ligand, TangPhos, with stereogenic P centers, for the asymmetric hydrogenation of various functionalized olefins.[6] In our ongoing efforts toward the development of efficient chiral bisphosphane ligands, we have designed a more rigid chiral bisbinaphthophosphepine ligand, binapine, for use in asymmetric hydrogenation. The structure of ligand **1** not only contains diaxial chirality but also has stereogenic P and C centers. To our knowledge, no chiral bisbinaphthophosphepine ligands with stereogenic P centers have been reported previously.[7] The synthesis of ligand **1** is straightforward (Scheme 1). Double metalation of enantiomerically pure (*S*)-2,2′-dimethylbinaphthyl with *n*BuLi/TMEDA followed by

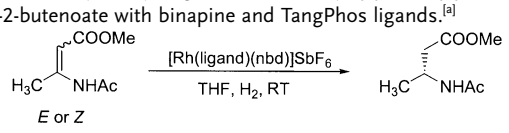


Scheme 1. Synthesis of ligand **1**: a) 1) *n*BuLi, TMEDA, Et_2O; 2) *t*BuPCl$_2$, S, THF, 61%; b) *t*BuLi, TMEDA, HMPA/THF, $CuCl_2$, 25%; c) Si_2Cl_6, benzene, 90%. HMPA = hexamethyl phosphoramide, TMEDA = *N*,*N*,*N*′,*N*′-tetramethylethylenediamine.

reaction with *t*BuPCl$_2$ and sulfur provided the binaphthophosphepine sulfide **2** in 61% yield.[7c,d] Deprotonation of **2** with *t*BuLi/TMEDA at −78°C in HMPA/THF followed by coupling mediated by $CuCl_2$ yielded **3** as a single isomer in 25% yield, along with recovered starting material **2** (50%). The absolute configuration of **3** was confirmed by its X-ray crystallographic structure.[8] Desulfurization of **3** with hexachlorodisilane[6a] in benzene provided ligand **1** in 90% yield. In its solid state this electron-rich bisphosphane is remarkably insensitive to air. No oxidation product was observed after exposure of the ligand to air for several days. Both isomers of binapine can be synthesized by this simple synthetic route.

Ligand **1** was then used in the Rh-catalyzed hydrogenation of β-(acylamino)acrylic acids. The cationic Rh complex [Rh(**1**)(nbd)]SbF_6 (nbd = 3,5-norbornadiene) was prepared and used directly for the hydrogenation of both the *E* and *Z* isomers of methyl 3-acetamido-2-butenoate (Table 1). In contrast to the Rh–TangPhos catalyst, which promoted the formation of the hydrogenation products from both the *E* and the *Z* substrates with high enantioselectivities, the use of the

Table 1: Rh-catalyzed hydrogenation of methyl (*E*)- and (*Z*)-3-acetylamino-2-butenoate with binapine and TangPhos ligands.[a]

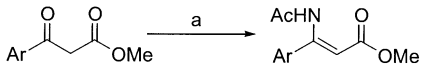


Ligand	Bite angle of Rh complex [°][b]	*ee* [%] from *E* isomer	*ee* [%] from *Z* isomer
(*S*,*S*,*R*,*R*)-TangPhos	75.1	99.6	98.5
1	77.4	32.7	99.2

[a] The absolute configurations of the products were determined as *R* by comparison of their optical rotation data with reported values. The reactions were carried out at room temperature under H_2 (20 psi (138 kPa)) in THF for 24 h. Substrate/[Rh(ligand)nbd]SbF_6 = 100:1. The *ee* values were determined by GC on a chiral phase (Chiralselect 1000 column). [b] Molecular simulations were performed on a CaChe model with MM2 calculations; see Supporting Information for further details.

Rh–binapine catalyst led to superior enantioselectivity for the hydrogenation of the *Z* substrate. However, a low *ee* value was observed for the hydrogenation of the *E* isomer. Molecular simulation on a CaChe model showed that the Rh–binapine complex has a larger P–Rh–P angle (bite angle) than the Rh–TangPhos complex. This difference leads to a sterically more hindered chiral environment in the Rh–binapine complex.

Many chiral β-aryl-β-amino acids are important intermediates for drug synthesis.[9] As a series of (*Z*)-β-aryl-β-(acylamino)acrylic acid derivatives can be obtained in moderate to high yields through the amination of aryl β-keto esters with NH_4OAc, followed by acetylation with acetic anhydride and pyridine at reflux (Scheme 2),[10] the highly

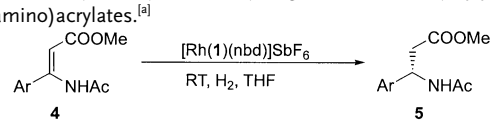


Scheme 2. Synthesis of methyl (*Z*)-β-aryl-β-(acetylamino)acrylates: a) 1) NH_4OAc, CH_3OH; 2) Ac_2O, pyridine, THF, reflux, 50–70% yield of isolated products.

enantioselective hydrogenation of (*Z*)-β-aryl-β-(acylamino)-acrylic acid derivatives could provide a practical method for the synthesis of chiral β-aryl-β-amino acids. We therefore used binapine in the Rh-catalyzed asymmetric hydrogenation of a series of methyl (*Z*)-β-aryl-β-(acetylamino)acrylates. As shown in Table 2, a wide array of chiral β-aryl-β-amino acid derivatives was obtained with *ee* values of over 99%, regardless of the electronic properties of the aryl group on the substrate **4**. Excellent enantioselectivities were also observed in the hydrogenation of substrates with *ortho*-substituted β-aryl groups (Table 2, entries 8 and 9), in contrast to the moderate *ee* values observed when a Rh–TangPhos catalyst was used.[3e] Excellent enantioselectivity was also observed in the hydrogenation of a substrate containing a heteroaryl group. In the presence of HBF_4,[11] the hydrogenation of methyl (*Z*)-β-(3-pyridyl)-β-(acetylamino)acrylate provided the chiral β-(3-pyridyl)-β-amino acid derivative **5j** with 96% *ee* (Table 2, entry 10). **5j** is a key component for the synthesis of the GP IIb/IIIa antagonist RWJ-53308.[9b,c] To further test the catalytic efficiency of the Rh–binapine

 © 2003 Wiley-VCH Verlag GmbH & Co. KGaA, Weinheim

Table 2: Rh-catalyzed asymmetric hydrogenation of methyl (*Z*)-β-aryl-β-(acetylamino)acrylates.[a]



Entry	Ar (**4**)	*ee* [%] (**5**)
1	Ph (**a**)	>99 (**a**)
2	*p*-F-Ph (**b**)	>99 (**b**)
3	*p*-Cl-Ph (**c**)	>99 (**c**)
4	*p*-Br-Ph (**d**)	99 (**d**)
5	*p*-Me-Ph (**e**)	>99 (**e**)
6	*p*-MeO-Ph (**f**)	>99 (**f**)
7[b]	*p*-BnO-Ph (**g**)	>99 (**g**)
8	*o*-Me-Ph (**h**)	>99 (**h**)
9	*o*-MeO-Ph (**i**)	99 (**i**)
10[c]	3-pyridyl (**j**)	96 (**j**)

[a] The reactions were carried out at room temperature under H_2 (20 psi (138 kPa)) in THF for 24 h unless otherwise specified. Substrate/[Rh(**1**)(nbd)]SbF_6 = 100:1. The absolute configurations of the products were determined as *S* by comparison of their optical rotation data with reported values. The *ee* values were determined by GC on a chiral phase (Chiralselect 1000 column), unless otherwise specified. [b] The *ee* value was determined by HPLC on a chiral phase ((*S*,*S*)-Whelk-01 column). [c] The hydrogenation was conducted in MeOH in the presence of HBF_4 (1.5 equiv) under H_2 (20 psi (138 kPa)).

catalyst for the asymmetric hydrogenation of β-aryl-β-(acetylamino)acrylates, substrate **4g** was subjected to hydrogenation in the presence of less [Rh(**1**)(nbd)]SbF_6 catalyst (0.1 mol%), and the chiral product **5g** was obtained in quantitative yield and with 99% *ee*.

In conclusion, we have developed a new chiral bisphosphepine ligand with stereogenic phosphorus centers for the asymmetric hydrogenation of (*Z*)-β-(acylamino)acrylic acid derivatives. Excellent enantioselectivities and reactivities were observed in the hydrogenation of a wide array of (*Z*)-β-aryl-β-(acylamino)acrylic acid derivatives. As the substrates for the asymmmetric hydrogenation can be prepared readily, the new ligand binapine provides an efficient method for the practical synthesis of chiral β-aryl-β-amino acids.[12]

Received: March 24, 2003 [Z51465]

Keywords: asymmetric synthesis · hydrogenation · ligand design · P ligands · rhodium

[1] a) The Chemistry and Biology of β-Amino Acids (Ed.: W. J. Hoekstra), *Curr. Med. Chem.* **1999**, *6*, 905–1004; b) S. H. Gellman, *Acc. Chem. Res.* **1998**, *31*, 173–180; c) *Enantioselective Synthesis of* β*-Amino Acids* (Ed.: E. Juaristi), Wiley-VCH, New York, **1997**; d) D. C. Cole, *Tetrahedron* **1994**, *50*, 9517–9582; e) D. Guenard, R. Guritte-Voegelein, P. Potier, *Acc. Chem. Res.* **1993**, *26*, 160–167.

[2] a) T. P. Tang, J. A. Ellman, *J. Org. Chem.* **1999**, *64*, 12–13; b) M. P. Sibi, J. J. Shay, M. Liu, C. P. Jasperse, *J. Am. Chem. Soc.* **1998**, *120*, 6615–6616; c) S. Kobayashi, H. Ishitani, M. Ueno, *J. Am. Chem. Soc.* **1998**, *120*, 431–432; d) S.-K. Chung, T.-H. Jeong, D.-H. Kang, *Tetrahedron: Asymmetry* **1997**, *8*, 5–9; e) F. Dumas, B. Mezrhab, J. d'Angelo, C. Riche, A. Chiaroni, *J. Org. Chem.* **1996**, *61*, 2293–2304; f) F. A. Davis, J. M. Szewczyk, R. E. Reddy, *J. Org. Chem.* **1996**, *61*, 2222–2225; g) D. Enders, H. Wahl, W. Bettray, *Angew. Chem.* **1995**, *107*, 527–529; *Angew. Chem. Int. Ed. Engl.* **1995**, *34*, 455–457.

[3] a) J. Holz, A. Monsees, H. Jiao, J. You, I. V. Komarov, C. Fischer, K. Drauz, A. Börner, *J. Org. Chem.* **2003**, *68*, 1701–1707; b) J. You, H.-J. Drexler, S. Zhang, C. Fischer, D. Heller, *Angew. Chem.* **2003**, *115*, 942–945; *Angew. Chem. Int. Ed.* **2003**, *42*, 913–916; c) D. Peña, A. Minnaard, J. G. de Vries, B. L. Feringa, *J. Am. Chem. Soc.* **2002**, *124*, 1452–1453; d) D. Heller, H.-J. Drexler, J. You, W. Baumann, K. Drauz, H.-P. Krimmer, A. Börner, *Chem. Eur. J.* **2002**, *8*, 5196–5203; e) W. Tang, X. Zhang, *Org. Lett.* **2002**, *4*, 4159–4161; f) S. Lee, Y. J. Zhang, *Org. Lett.* **2002**, *4*, 2429–2431; g) D. Heller, H.-J. Drexler, A. Spannenberg, B. Heller, J. You, W. Baumann, *Angew. Chem.* **2002**, *114*, 814–817; *Angew. Chem. Int. Ed.* **2002**, *41*, 777–780; h) D. Heller, J. Holz, H.-J. Drexler, J. Lang, K. Drauz, H.-P. Krimmer, A. Börner, *J. Org. Chem.* **2001**, *66*, 6816–6817; i) M. Yasutake, I. D. Gridnev, N. Higashi, T. Imamoto, *Org. Lett.* **2001**, *3*, 1701–1704; j) G. Zhu, Z. Chen, X. Zhang, *J. Org. Chem.* **1999**, *64*, 6907–6910.

[4] a) J. Wu, X. Chen, R. Guo, C.-H. Yeung, A. S. C. Chan, *J. Org. Chem.* **2003**, *68*, 2490–2493; b) Y.-G. Zhou, W. Tang, W.-B. Wang, W. Li, X. Zhang, *J. Am. Chem. Soc.* **2002**, *124*, 4952–4953; c) W. D. Lubell, M. Kitamura, R. Noyori, *Tetrahedron: Asymmetry* **1991**, *2*, 543–554.

[5] As Heller et. al pointed out in reference [3b], the "*E*/*Z* isomeric mixtures of β-aryl-β-(acylamino)acrylates" referred to in references [4b] and [3e] were actually mixtures of (*Z*)-β-aryl-β-(acylamino)acrylates and (*Z*)-diacetylated products. The authors have corroborated the mischaracterization.

[6] a) W. Tang, X. Zhang, *Angew. Chem.* **2002**, *114*, 1682–1684; *Angew. Chem. Int. Ed.* **2002**, *41*, 1612–1614; b) W. Tang, L. Duan, X. Zhang, *Org. Lett.* **2003**, *5*, 205–207.

[7] Several binaphthophosphepine ligands in which the P atoms are not stereogenic centers have been reported; see: a) D. Xiao, Z. Zhang, X. Zhang, *Org. Lett.* **1999**, *1*, 1679–1681; b) D. Xiao, X. Zhang, *Angew. Chem.* **2001**, *113*, 3533–3536; *Angew. Chem. Int. Ed.* **2001**, *40*, 3425–3428; c) Y. Chi, X. Zhang, *Tetrahedron Lett.* **2002**, *43*, 4849–4852; d) K. Junge, G. Oehme, A. Monsees, T. Riermeier, U. Dingerdissen, M. Beller, *Tetrahedron Lett.* **2002**, *43*, 4977–4980.

[8] CCDC-204741 contains the supplementary crystallographic data for this paper. These data can be obtained free of charge via www.ccdc.cam.ac.uk/conts/retrieving.html (or from the Cambridge Crystallographic Data Centre, 12 Union Road, Cambridge CB21EZ, UK; fax: (+44)1223-336-033; or depost@ccdc.cam.ac.uk). We thank Dr. H. Yennawar for solving the crystal structure.

[9] a) G. Beck, *Synlett* **2002**, 837–850; b) H. Boesch, S. Cesco-Cancian, L. R. Hecker, W. J. Hoekstra, M. Justus, C. A. Maryanoff, L. Scott, R. D. Shah, G. Solms, K. L. Sorgi, S. M. Stefanick, U. Thurnheer, F. J. Villani, Jr., D. G. Walker, *Org. Process Res. Dev.* **2001**, *5*, 23–27; c) H. M. Zhong, J. H. Cohen, A. F. Abdel-Magid, B. D. Kenney, C. A. Maryanoff, R. D. Shah, F. J. Villani, Jr., F. Zhang, X. Zhang, *Tetrahedron Lett.* **1999**, *40*, 7721–7725; d) B. B. Shankar, M. P. Kirkup, S. W. McCombie, J. W. Clader, A. K. Ganguly, *Tetrahedron Lett.* **1996**, *37*, 4095–4098.

[10] See Supporting Information for details.

[11] No reaction was observed in the absence of acid. HBF_4 was used to protonate the pyridine nitrogen atom. A similar strategy was applied in the hydrogenation of pyridyl α-dehydroamino acid derivatives; see: C. Döbler, H.-J. Kreuzfeld, M. Michalik, H. W. Krause, *Tetrahedron: Asymmetry* **1996**, *7*, 117–125.

[12] The Supporting Information includes procedures for the synthesis of and analytical data for binapine, procedures for the synthesis of substrates, hydrogenation procedures, information on molecular simulation, and the X-ray crystal structure of **3**.

 © 2003 Wiley-VCH Verlag GmbH & Co. KGaA, Weinheim

Green C-C Coupling Reactions

Toward Waste-Free Production of Heck Products with a Catalytic Palladium System under Oxygen**

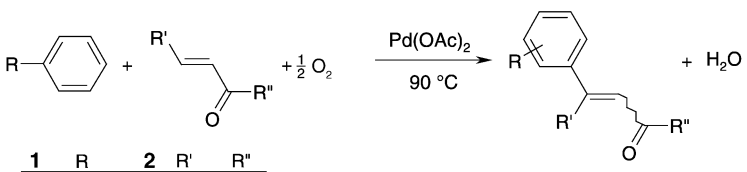
*Mieke Dams, Dirk E. De Vos, Sofie Celen, and Pierre A. Jacobs**

The sp^2–sp^2 coupling of an aromatic ring with an alkene is one of the key transformations catalyzed by Pd. This reaction was pioneered by Heck and Mizoroki and has undergone a lot of progress since that time, but it still suffers from one major drawback, namely the production of salt waste.[1] Indeed, the use of halogenated aromatic compounds requires the use of stoichiometric amounts of base for Pd^0 regeneration, which leads to the formation of large quantities of halide salt by-products, especially in large-scale processes. To circumvent these problems, aromatic carboxylic acid anhydrides and esters have been used by de Vries and co-workers[2] and Gooßen et al.,[3] respectively, as sources of the aryl component in the $PdCl_2$-catalyzed sp^2–sp^2 coupling. When benzoic anhydride is used as the arylating reagent, the benzoic acid produced as a side product can be recycled to the anhydride by dehydration;[2] when an activated *p*-nitrophenyl ester is used, the nitrophenol produced can be esterified to give the starting ester by reaction with the appropriate carboxylic acid.[3] Although CO and H_2O are the only by-products, these reactions still have the disadvantages that they require high temperatures (160 °C), two separate steps, and a minimum concentration of alkali-metal halides for moderate catalyst activity (maximum TON (total turnover number = moles of coupling product per mole of Pd) of 400–150).

Herein we propose a 100% carbon-efficient and halide-free alternative for the synthesis of Heck-coupling products, which involves the direct Pd-catalyzed coupling of arenes with olefins (Scheme 1). Pd^0 intermediates can be reoxidized to active Pd^{II} species under an appropriate pressure of O_2. As no reactive substituents are required on the arene, water is the only by-product. The reactions can be performed under mild conditions, for example at 90 °C and under O_2 (0.8 MPa), have a high turnover frequency, and do not require a solvent or a halide promoter.

Only a few methods exist for the transition-metal-catalyzed reaction of an arene with an olefin through direct C–H bond activation.[4] These include the chelation-assisted alkylation of aromatic ketones mediated by Ru or Rh,[5–6] the hydroarylation of alkenes or alkynes with Ir or Pd,[7–8] and the arylation of an olefin with Rh,[9] Ru,[10] or Pd.[8c,11] This last type of catalytic coupling reaction requires an oxidant.[10,11] As dioxygen is the cheapest available oxidant, we attempted in an initial experiment to couple toluene (**1b**) with ethyl *trans*-cinnamate (**2b**) in the presence of $Pd(OAc)_2$ (1 mol%) and $Mn(OAc)_3$ (4 mol%) under O_2 at 90 °C in neat toluene. Surprisingly, the arylation product **3e** was obtained in 91% yield, together with the diarylated product ethyl 3-phenyl-2,3-ditolyl-propenoate (1.7%).[12] By contrast, when the reaction was carried out under the classical conditions for such Pd-catalyzed coupling reactions, namely in a mixture of acetic acid and acetic anhydride, **3e** was obtained in only 2.5% yield, along with an equimolar amount of the by-product benzyl acetate, formed by the acetoxylation of toluene.[13,14] Thus, in acetic acid only low reactivity and a selectivity of 50% were observed, whereas under solvent-free conditions the reaction proceeded to high conversion with high selectivity.

This first experiment showed convincingly that O_2 can be used for Pd^0 reoxidation instead of, for example, *t*BuOOH, which has been recognized until now as the most effective oxidant for a Fujiwara coupling reaction.[15] Just as observed for oxidative phenol carbonylation[16] or the Wacker olefin oxidation,[17] the electron transfer from Pd^0 to O_2 may be accelerated by cocatalysts. Over 15 transition-metal salts were



1	R
a	H
b	Me
c	OMe

2	R'	R"
a	H	OBu
b	Ph	OEt
c	Ph	Me

3	R	R'	R"
a	H	H	OBu
b	H	Ph	OEt
c	H	Ph	Me
d	Me	H	OBu
e	Me	Ph	OEt
f	Me	Ph	Me
g	OMe	H	OBu
h	OMe	Ph	OEt
i	OMe	Ph	Me

Scheme 1. Pd-catalyzed oxidative coupling of an arene with an olefin under O_2.

[*] Prof. P. A. Jacobs, M. Dams, Prof. D. E. De Vos, S. Celen
Centre for Surface Chemistry and Catalysis, K. U. Leuven
Kasteelpark Arenberg 23, 3001 Leuven (Belgium)
Fax: (+32) 16-321-998
E-mail: pierre.jacobs@agr.kuleuven.ac.be

[**] This work was supported by the Belgian Federal Government within the framework of an IAP program for supramolecular catalysis. M.D. is a research assistant of FWO (Belgium).

screened in the reaction of anisole (**1c**) with ethyl *trans*-cinnamate (**2b**). Acetate complexes appear to be more effective than acetylacetonate complexes. Nearly full conversion of the cinnamate occurred in the presence of Co^{II}, Fe^{II}, Mn^{II}, and Mn^{III} acetates, of which the Mn^{II} and Mn^{III} acetates gave the best results (see Table 1, entries 1–3). Remarkably, the reaction reached completion even in the absence of a cocatalyst (Table 1, entry 4), and the same was

 © 2003 Wiley-VCH Verlag GmbH & Co. KGaA, Weinheim DOI: 10.1002/anie.200351524

Table 1: Optimization of the coupling of anisole (**1c**) with ethyl *trans*-cinnamate (**2b**).[a]

Entry	Additive (mmol)	t_1 [h]	Conv. [%][b]	t_2 [h]	Conv. [%][c]	TON	Max. TOF [h^{-1}]
1	$Mn(acac)_2$ (0.06)			22	0.9	0.9	0.2
2	$Co(OAc)_2 \cdot 4H_2O$ (0.06)	[d]		22	83	87	3.7
3	$Mn(OAc)_3 \cdot 2H_2O$ (0.06)	[e]		22	99	100	7.6
4	-	[d]		22	94	96	4.3
5	$Mn(OAc)_3 \cdot 2H_2O$ (0.12)	5	17	25	97	99	4.4
6[f]	$Mn(OAc)_3 \cdot 2H_2O$ (0.12)	4	11	26	92	93	3.5
7[g]	$Mn(OAc)_3 \cdot 2H_2O$ (0.12)	3.5	6	20	71	73	3.6
8	PhCOOH (0.6)	6.2	83	25	98	97	13.4
9	4-*i*Pr-C_6H_4COOH (0.6)	8.5	27	25	49	50	3.3
10	3-Cl-C_6H_4COOH (0.6)	6	40	24	50	51	8.9
11[h]	PhCOOH (0.18)	6.6	27	23	96	174	7.5
12[i]	PhCOOH (0.18)	8	66	24	90	**762**	**73**

[a] Reaction conditions, unless otherwise indicated: **1c** (4 mL, 37 mmol), **2b** (3 mmol), 90 °C, O_2 (0.8 MPa), and $Pd(OAc)_2$ (1 mol% with respect to **2b**). [b] Conversion of **2b** after t_1. [c] Conversion of **2b** after t_2. [d] Induction period: 2.5 h. [e] Induction period: <1 h. [f] O_2: 0.4 MPa. [g] O_2: 1.6 MPa. [h] $Pd(OAc)_2$: 0.55 mol%. [i] $Pd(OAc)_2$: 0.12 mol%, 110 °C.

observed for arylations of butyl acrylate and ethyl cinnamate with benzene or toluene. In the absence of a cocatalyst there is an induction period, but not when hydrated $Mn(OAc)_3$ is present (Figure 1). This induction period can also be eliminated by the addition of water (0.6 mmol; Figure 1). All these elements indicate that the metal salts do not necessarily intervene in a rate-determining Pd^0 reoxidation; rather, both water and the hydrated acetate salts appear to facilitate the formation of a suitable catalytically active Pd^{II} species in the initial phase of the reaction.

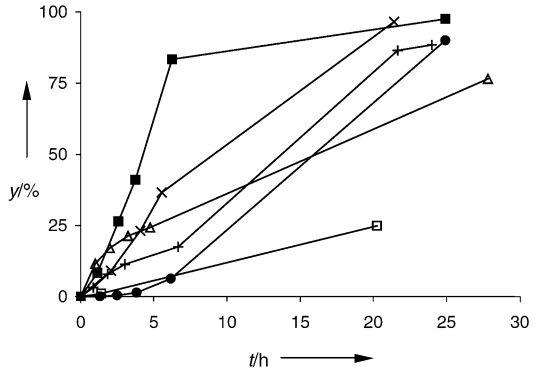


Figure 1. The conversion *y* of **2b** as a function of time: a) no additive (●); b) $Mn(OAc)_3 \cdot 2H_2O$ (2 mol%; ×); c) water (0.6 mmol; +); d) benzoic acid (0.6 mmol; ■), e) trifluoroacetic acid (0.6 mmol; △); f) hexanoic acid (0.6 mmol; □). Other reaction conditions: **1c** (4 mL, 37 mmol), **2b** (3 mmol), $Pd(OAc)_2$ (1 mol% with respect to **2b**), O_2 (0.8 MPa), 90 °C.

Earlier work on aromatic C–H activation suggests that Pd can break the C–H bond by electrophilic aromatic substitution to form an arene–Pd^{II} complex. As high reactivity has been ascribed to highly electrophilic Pd^{II} species such as $Pd(OOCCF_3)^+$,[8c] over 20 different acids were tested as additives in the $Pd(OAc)_2$-catalyzed coupling of ethyl *trans*-cinnamate (**2b**) with neat anisole (**1c**). The effect of the acids largely depends on their structure, substitution pattern, and solubility. Excellent results were obtained with benzoic acid (Table 1, entry 8), and to a lesser extent with *p*- and *o*-toluic acid. These acids eliminate the induction period and the conversion of the cinnamate proceeds about four times faster than in the absence of an additive (Figure 1). ^1H NMR spectroscopic experiments in [D_6]benzene indicated that under these conditions the acetate ligands are displaced and a Pd–benzoate species is formed.[18] Neither electron-donating nor electron-withdrawing groups on the benzoic acid improve the catalyst efficiency (Table 1, entries 9 and 10). With some aliphatic acids, such as acetic, trifluoroacetic, and hexanoic acids, the reaction does not reach completion, in contrast with the acid-free reaction (Figure 1). The unique accelerating effect of benzoic acid on the Pd catalysis appears to be generally true for these coupling reactions, for example, for those of anisole (**1c**) and toluene (**1b**) with butyl acrylate (**2a**), ethyl *trans*-cinnamate (**2b**), and *trans*-4-phenyl-3-buten-2-one (**2c**) (Table 2). In all these reactions, high rates were observed without an induction period.

Several reaction parameters, such as O_2 pressure, reaction volume, and concentration of benzoic acid were optimized for the Pd-catalyzed coupling of anisole with ethyl *trans*-cinnamate. For 4 mL of anisole, 0.8 MPa of O_2 appears to be optimal. When the pressure is too high, lower catalytic activity is observed (Table 1, entries 5–7). A sixfold excess of PhCOOH with respect to Pd^{2+} is sufficient to promote high reaction rates. Under these conditions, the Pd concentration could be reduced to 0.12 mol% at 110 °C (Table 1, entries 11 and 12) with complete conversion to ethyl 3-anisyl-3-phenylpropenoate (**3h**) maintained, which corresponds to a total turnover number (TON) of 762. The maximum turnover frequency (TOF = moles of coupling product per mole of $Pd(OAc)_2$ per hour) was 73 h^{-1}. To our knowledge, these are the highest TON and TOF values described for such oxidative coupling reactions.[19]

Although the Pd/PhCOOH catalyst gives rise to selectivities of over 95% in these coupling reactions, several regioisomers are formed under the solvent-free conditions with anisole and toluene (Table 2).[20] The Pd catalyst attacks all aromatic C–H bonds, with attack at the *para* position of anisole favored over the *ortho* and, to a greater extent, *meta* positions. On the other hand, when toluene is used as the arylating agent, more of the *meta* isomer is formed than the *ortho* isomer. Such data suggest that the first step in the catalytic cycle may not correspond to a classical electrophilic aromatic substitution, as such reactions heavily favor *ortho* and *para* substitution.[21]

As the reaction mixture contains a 12–15-fold excess of the arene, the olefin can be arylated once, twice, or possibly even three times. The selectivity for these multiply arylated

 © 2003 Wiley-VCH Verlag GmbH & Co. KGaA, Weinheim

Table 2: Influence of the cocatalyst $Mn(OAc)_3 \cdot 2H_2O$ and the additive benzoic acid on the induction period and the catalyst activity in the oxidative coupling of arenes and olefins.[a]

Entry	1	2	Additive	t_1 [h]	Conv. [%][b]	t_2 [h]	Conv. [%][c]	Sel. [%][d]	*o*/*m*/*p*[e]
1	**c**	**b**	–	6	10	22.5	94	100:0	38:14:48
2	**c**	**b**	$Mn(OAc)_3$ (2 mol%)	3.5	18	21.5	99	86:14	37:16:47
3	**c**	**b**	PhCOOH (0.6 mmol)	6.2	83	25	98	100:0	32:15:53
4	**c**	**a**	–	6.5	12	25.2	75	100:0:0	45:55[f]
5	**c**	**a**	$Mn(OAc)_3$ (2 mol%)	5.5	26	22.7	93	25:75:0	44:56[f]
6	**c**	**a**	PhCOOH (0.6 mmol)	8.2	74	30	96	91:9:0	43:57[f]
7	**c**	**c**	–	8	6	96	14	100:0	34:13:53
8	**c**	**c**	$Mn(OAc)_3$ (2 mol%)	25	31	168	87	100:0	35:12:53
9	**c**	**c**	PhCOOH (0.6 mmol)	8.2	25	120	99	100:0	33:17:50
10	**b**	**b**	PhCOOH (0.6 mmol)	4.5	12	21.5	89	85:15	30:40:30
11	**b**	**a**	PhCOOH (0.6 mmol)	7.5	76	24.5	96	15:85:0[g]	24:36:40
12	**b**	**c**	PhCOOH (0.6 mmol)	7.5	14	118	97	n.d.[h]	n.d.[h]
13	**a**	**b**	$Mn(OAc)_3$ (4 mol%)	90	97			95:5	–
14	**a**	**a**	–	24	56			99:1:0	–
15	**a**	**a**	–	47	**98**			**89**:11:0	–
16	**a**	**a**	–	76	**97**			37:**63**:0	–
17	**a**	**a**	–	165	**98**			7:18:**75**	–
18	**a**	**c**	$Mn(OAc)_3$ (4 mol%)	77	99			100:0	–

[a] Reaction conditions: arene (4 mL, 37–45 mmol), olefin (3 mmol), $Pd(OAc)_2$ (1 mol%), O_2 (0.8 Mpa), 90°C. All organic products were isolated and characterized by GC–MS, as well as ^1H and ^{13}C NMR spectroscopy. [b] Conversion of the olefin after t_1. [c] Conversion of the olefin after t_2. [d] Selectivity for the 1:1 arene–olefin, 2:1 arene–olefin, and possibly 3:1 arene–olefin adducts after t_2. [e] Selectivity for the *ortho*, *meta*, and *para* adduct after t_2. [f] The *ortho* and *meta* isomers could not be separated by GC. [g] After 7.5 h the selectivity for the monoarylated product was 90%. [h] Not determined.

olefins can be tuned. By stopping the reaction at appropriate times, one may obtain a high yield of the mono-, di-, or even triarylated product. The clean consecutive coupling process is illustrated in Table 2 (entries 14–17) for the reaction of benzene with butyl acrylate. Similar double or triple couplings are feasible with, for example, anisole and toluene.

In the catalytic Pd/O_2 system described above, the reactivity of the aromatic compounds decreases in the following order: anisole > toluene > benzene > acetophenone and chlorobenzene. Thus, the activation of an aromatic C–H bond by Pd is facilitated by electron-donating groups. The trends are less clear for the olefinic component. Unsaturated esters such as acrylates and cinnamates react smoothly. Steric hindrance may explain the sometimes lower reactivity of ethyl *trans*-cinnamate in comparison with butyl acrylate. The unsaturated ketone *trans*-4-phenyl-3-buten-2-one also undergoes complete conversion, but only when a metal cocatalyst or benzoic acid is used (Table 2, entries 7–9, 12, and 18). Furthermore, simple olefins such as styrene and 1-octene can also be oxidatively coupled to arenes. In these reactions styrene is more reactive than 1-octene.

To gain deeper mechanistic insight, oxidative couplings of ethyl *trans*-cinnamate were performed with toluene and $[D_8]$toluene under the conditions described in Table 2, and the kinetic isotope effect (KIE) was determined. The rates considered are derived from the maximal slopes on the conversion curve, that is, after the induction time. With only 1 mol% of $Pd(OAc)_2$, the v_H/v_D ratio was 2.6. When benzoic acid was added, the v_H/v_D ratio decreased to 2.1. This indicates that C–H activation by Pd^{II} is a slow step in the catalytic cycle rather than Pd^0 regeneration, at least in the oxidative coupling of toluene with ethyl *trans*-cinnamate under oxygen. The accelerating effect of benzoic acid, together with the relative reactivity of several arenes as described earlier, suggest the reaction may occur through an electrophilic attack on the aromatic compound, which was also the first step in the mechanism originally proposed by Fujiwara.[11f] The rather high fraction of *meta* products formed in some cases indicates that the Pd species might not be of a purely electrophilic nature. Besides the catalytically active Pd^{II} species, the catalytic cycle probably also involves a Pd^0 intermediate. Indeed, under standard conditions (see Table 2), in the presence of PhCOOH (0.18 mmol), bromobenzene does not only undergo oxidative coupling with ethyl cinnamate, but a stoichiometric amount (with respect to the catalyst: 0.03 mmol) of the Heck product is also formed, probably through oxidative addition of the C–Br bond to Pd^0.

In conclusion, we have presented a 100% carbon-efficient, halide- and solvent-free system for the oxidative arylation of olefins, with water as the only by-product. No organic oxidants or electron-transfer mediators are required, the Pd/benzoic acid catalyst appears to be infinitely stable, and both the TON and the TOF are far higher than those observed previously in similar reactions. This work therefore presents a significant step toward waste-free Heck reactions.

Received: March 31, 2003 [Z51524]

Keywords: C–C coupling · green chemistry · homogeneous catalysis · oxygen · palladium

[1] a) R. F. Heck, *Acc. Chem. Res.* **1979**, *12*, 146; b) A. de Meijere, F. E. Meyer, *Angew. Chem.* **1994**, *106*, 2473; *Angew. Chem. Int. Ed. Engl.* **1994**, *33*, 2379; c) W. Cabri, I. Candiani, *Acc. Chem. Res.* **1995**, *28*, 2; d) I. P. Beletskaya, A. V. Cheprakov, *Chem. Rev.* **2000**, *100*, 3009; e) A. Biffis, M. Zecca, M. Basato, *J. Mol. Catal. A* **2001**, *173*, 249.

[2] M. S. Stephan, A. J. J. M. Teunissen, G. K. M. Verzijl, J. G. de Vries, *Angew. Chem.* **1998**, *110*, 688; *Angew. Chem. Int. Ed.* **1998**, *37*, 662.

[3] L. J. Gooßen, J. Paetzold, *Angew. Chem.* **2002**, *114*, 1285; *Angew. Chem. Int. Ed.* **2002**, *41*, 1237.

[4] V. Ritleng, C. Sirlin, M. Pfeffer, *Chem. Rev.* **2002**, *102*, 1731.

[5] S. Murai, F. Kakiuchi, S. Sekine, Y. Tanaka, A. Kamatani, M. Sonoda, N. Chatani, *Nature* **1993**, *366*, 529.

[6] Y. G. Lim, J. S. Han, S. S. Yang, J. H. Chun, *Tetrahedron Lett.* **2001**, *42*, 4853.

[7] T. Matsumoto, D. J. Taube, R. A. Periana, H. Taube, H. Yoshida, *J. Am. Chem. Soc.* **2000**, *122*, 7414.

 © 2003 Wiley-VCH Verlag GmbH & Co. KGaA, Weinheim

[8] a) C. Jia, W. Lu, J. Oyamada, T. Kitamura, K. Matsuda, M. Irie, Y. Fujiwara, *J. Am. Chem. Soc.* **2000**, *122*, 7252; b) C. Jia, D. Piao, J. Oyamada, W. Lu, T. Kitamura, Y. Fujiwara, *Science* **2000**, *287*, 1992; c) C. Jia, T. Kitamura, Y. Fujiwara, *Acc. Chem. Res.* **2001**, *34*, 633.

[9] K. Sasaki, T. Sakakura, Y. Tokunaga, K. Wada, M. Tanaka, *Chem. Lett.* **1988**, 685.

[10] H. Weissman, X. Song, D. Milstein, *J. Am. Chem. Soc.* **2001**, *123*, 337.

[11] a) Y. Fujiwara, I. Moritani, S. Danno, R. Asano, S. Teranishi, *J. Am. Chem. Soc.* **1969**, *91*, 7166; b) R. Asano, I. Moritani, Y. Fujiwara, S. Teranishi, *J. Chem. Soc. Chem. Commun.* **1970**, 1293; c) R. S. Shue, *J. Chem. Soc. Chem. Commun.* **1971**, 1510; d) R. S. Shue, *J. Catal.* **1972**, *26*, 112; e) J. Tsuji, H. Nagashima, *Tetrahedron* **1984**, *40*, 2699; f) C. Jia, W. Lu, T. Kitamura, Y. Fujiwara, *Org. Lett.* **1999**, *1*, 2097; g) T. Yokota, M. Tani, S. Sakaguchi, Y. Ishii, *J. Am. Chem. Soc.* **2003**, *125*, 1476.

[12] Reaction conditions: toluene/ethyl *trans*-cinnamate = 12.5:1, neat, 90 h; ratio of isomers of **3e**: *o*/*m*/*p* = 29:41:30.

[13] Reaction conditions: toluene/ethyl *trans*-cinnamate = 5:1, HOAc (3 mL), Ac_2O (1 mL), 70 h; ratio of isomers of **3e**: *o*/*m*/*p* = 25:36:39.

[14] E. Benazzi, C. J. Cameron, H. Mimoun, *J. Mol. Catal.* **1991**, *69*, 299.

[15] For the oxidative coupling of ethyl cinnamate (30 mmol) with benzene (150 mmol), catalyzed by $Pd(OAc)_2$ (0.06 mmol) and benzoquinone (0.9 mmol) in the presence of *t*BuOOH (60 mmol), in HOAc/Ac_2O (30 mL/7 mL) at 90 °C, Fujiwara obtained ethyl 3-phenylcinnamate in 56 % yield in 15 h with a TON value of 280.[11f]

[16] A. Vavasori, L. Toniolo, *J. Mol. Catal. A* **1999**, *139*, 109; b) A. Vavasori, L. Toniolo, *J. Mol. Catal. A* **1999**, *149*, 321; c) A. Vavasori, L. Toniolo, *J. Mol. Catal. A* **2000**, *151*, 37.

[17] J. W. Francis, P. M. Henry, *J. Mol. Catal. A* **1995**, *99*, 77.

[18] When $Pd(OAc)_2$ (0.01 mmol) and benzoic acid (0.20 mmol) were heated to 90 °C in [D_6]benzene (1 mL), complete exchange of the acetate and benzoate ligands was observed by ^{1}H NMR spectroscopy (300 MHz); new peaks were observed at δ = 7.95 ppm (d; *o*-Ar-H, $Pd(OBz)_2$) and at δ = 6.71 ppm (m; *m*- and *p*-Ar-H, $Pd(OBz)_2$).

[19] When the oxidative coupling of benzene (30 mmol) with ethyl acrylate (1.5 mmol) was performed in propionic acid (5 mL) at 90 °C, catalyzed by a mixture of $Pd(OAc)_2$ (0.1 mmol), $H_7PMo_8V_4O_{40}$ (0.02 mmol), acetylacetone (0.1 mmol), and NaOAc (0.08 mmol) under O_2 (1 atm), Ishii and co-workers obtained a TON value of 12.6 within 3 h.[11g]

[20] The *ortho, meta*, and *para* isomers of **3d**–**3i** were prepared by Heck reactions of the corresponding iodotoluenes and iodoanisoles.

[21] See, for example: R. M. Roberts, *Friedel–Crafts Alkylation Chemistry: A Century of Discovery*, Marcel Dekker, New York, **1984**.

 © 2003 Wiley-VCH Verlag GmbH & Co. KGaA, Weinheim

Epothilone Analogues

Design, Synthesis, and Biological Properties of Highly Potent Epothilone B Analogues**

K. C. Nicolaou, Pradip K. Sasmal, Gerasimos Rassias, Mali Venkat Reddy, Karl-Heinz Altmann, Markus Wartmann, Aurora O'Brate, and Paraskevi Giannakakou*

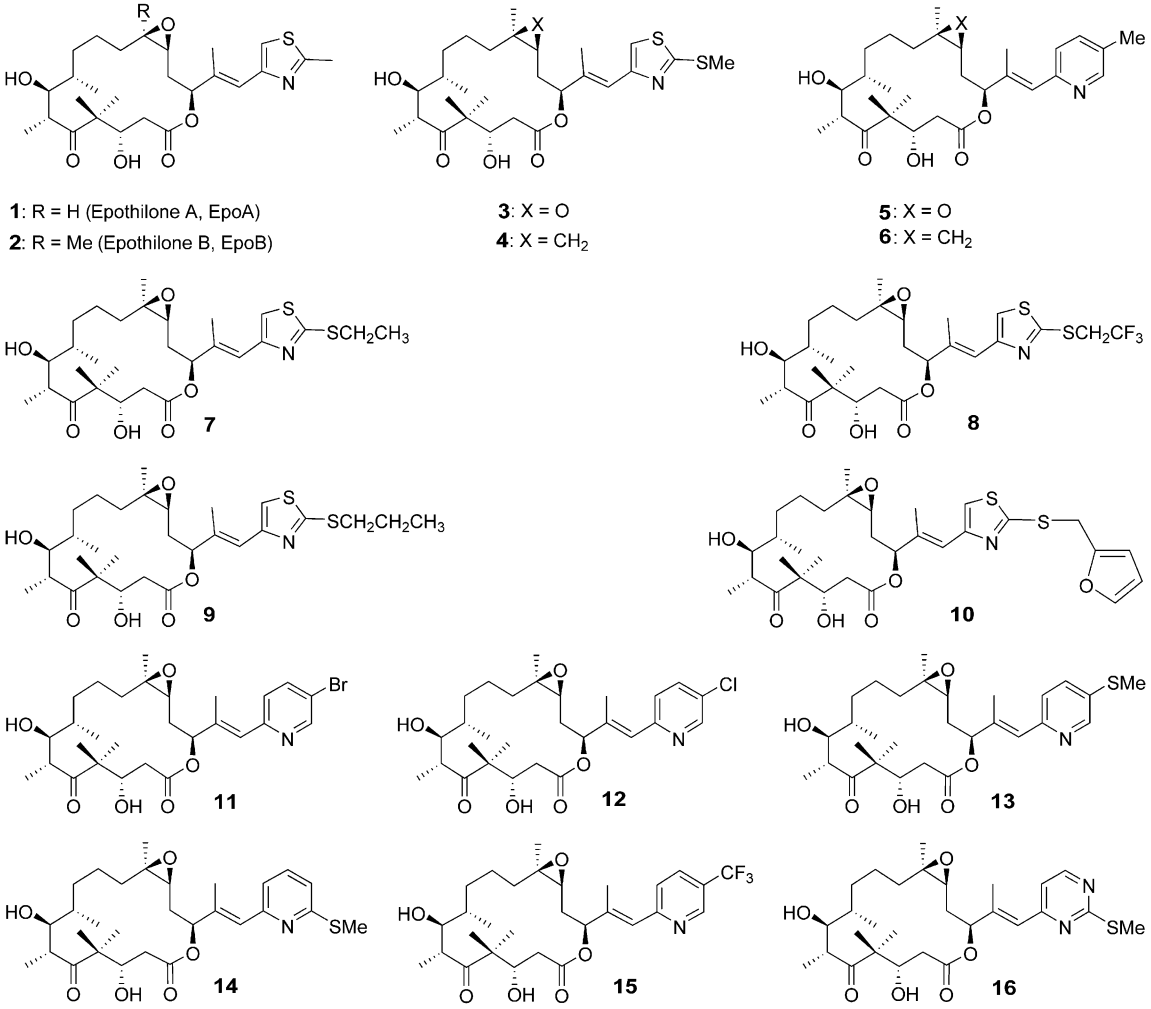
Owing to their potent cytotoxicity against tumor cells, including taxol (paclitaxel)-resistant cell lines, the epothilones (for example, epothilone A (**1**) and epothilone B (**2**))[1] continue to be the focus of intense chemical, biological, and clinical research efforts around the world.[2,3] Following the findings that cyclopropane-,[4] methylsulfanylthiazole-,[2d,5] and pyridine-[6]containing epothilone B derivatives (e.g. **3**[5a] and **5**,[6]) exhibit outstanding biological profiles as potential antitumor agents, we directed our attention toward the synthesis and evaluation of a small designed library of epothilone B analogues whose members are characterized by such structural motifs. Herein we report the details of these synthetic and biological investigations, which culminated in the discovery of 12,13-*cis*-cyclopropane methylsulfanyl epothilone B (**4**) as an extremely potent epothilone B analogue.

The design of the present focused epothilone library was based on the current knowledge of structure–activity relationships (SAR), specifically the facts that: 1) epothilone B (**2**) is considerably more potent than epothilone A (**1**), 2) a methylsulfanyl replacement for the methyl group on the thiazole moiety enhances the potency,[2d,5] 3) a heterocycle (e.g. pyridine)[6] replacement for the thiazole ring needs to maintain the proper position (adjacent to the point of

[*] Prof. Dr. K. C. Nicolaou, Dr. P. K. Sasmal, Dr. G. Rassias, Dr. M. V. Reddy
Department of Chemistry and
The Skaggs Institute for Chemical Biology
The Scripps Research Institute
10550 North Torrey Pines Road, La Jolla, CA 92037 (USA)
Fax: (+1) 858-784-2469
E-mail: kcn@scripps.edu
and
Department of Chemistry and Biochemistry
University of California, San Diego
9500 Gilman Drive, La Jolla, California 92093 (USA)
Dr. K.-H. Altmann
Corporate Research, Novartis Pharma AG
4002 Basel (Switzerland)
Dr. M. Wartmann
Oncology Business Unit, Novartis Pharma AG
4002 Basel (Switzerland)
A. O'Brate, Dr. P. Giannakakou
Winship Cancer Institute, Emory University School of Medicine
Atlanta, GA 30322 (USA)

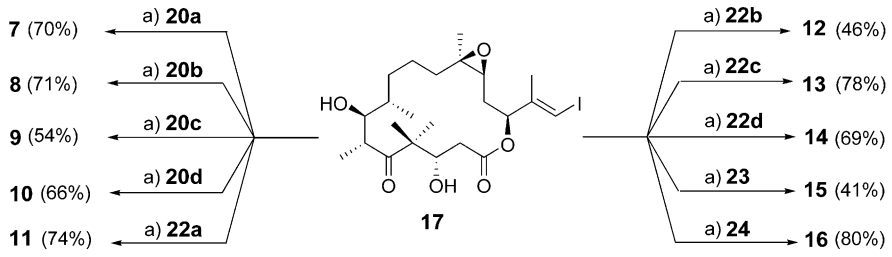
[**] We thank Dr. D. H. Huang and Dr. G. Siuzdak for NMR spectroscopic and mass spectrometric assistance, respectively. Financial support for this work was provided by The Skaggs Institute for Chemical Biology, the National Institutes of Health (USA), and Novartis Pharma.

 DOI: 10.1002/anie.200351819 © 2003 Wiley-VCH Verlag GmbH & Co. KGaA, Weinheim



attachment to the mainframe) for the nitrogen for biological activity, and 4) a cyclopropane ring can replace the epoxide moiety without loss of activity.[4] From these considerations, epothilones **4**, **6**, and **7**–**16** were considered as prime candidates for chemical synthesis and biological evaluation.

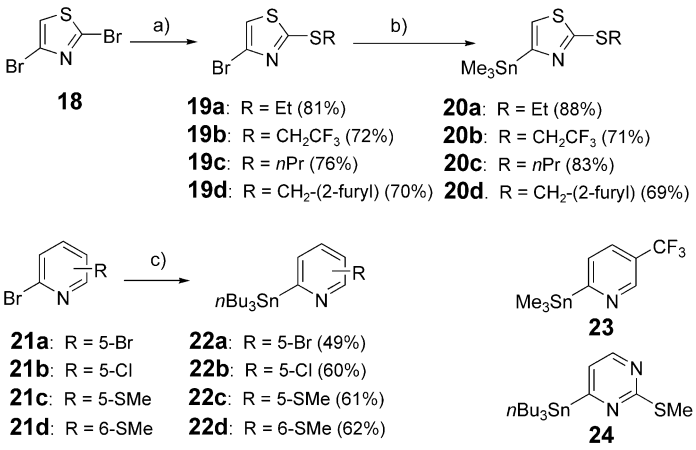
The designed epothilone analogues **7**–**16** were synthesized in a convergent manner from vinyl iodide **17**[7] and the corresponding aromatic stannanes as shown in Scheme 1. A Stille-type coupling of **17** with the appropriate stannanes **20a**–**d**, **22a**–**d**, **23**, and **24** (Scheme 2) was carried out in the presence of $[PdCl_2(MeCN)_2]$, CuI, and $AsPh_3$ in DMF at ambient temperature, leading directly to the desired epothilones **7**–**16** in the indicated yields. The required aromatic stannanes were prepared as summarized in Scheme 2. Thus, for the thiazole compounds **20a**–**d**, the commercially available 2,4-dibromothiazole (**18**) was treated with the corresponding thiol in the presence of NaH, leading first to the intermediate sulfides **19a**–**d** through replacement of the more reactive 2-bromide substituent. Subsequent coupling of these substrates with $Me_3SnSnMe_3$ in the presence of $[Pd(PPh_3)_4]$ in toluene at 100 °C then gave the desired products **20a**–**d** by reaction of the second bromide residue. The pyridyl stannanes **22a**–**d** were similarly synthesized from the readily available 2-bromopyridines **21a**,**b**,[8] **c**,[5a] and **d**,[9] respectively, through a metal–halogen exchange (*n*BuLi) followed by quenching of the resulting 2-lithio derivatives[10] with nBu_3SnCl. Stannanes **23**[11] and **24**[12] were prepared from the respective halides according to the literature procedures.



Scheme 1. Synthesis of **7**–**16**. Reagents and conditions: a) $[PdCl_2(MeCN)_2]$ (0.5 equiv), CuI (2.0 equiv), $AsPh_3$ (1.0 equiv), **20a**–**d**, **22a**–**d**, **23**–**24** (2.5 equiv), DMF, 25 °C, 1–3 h, 41–80%. DMF = *N*,*N*-dimethylformamide.

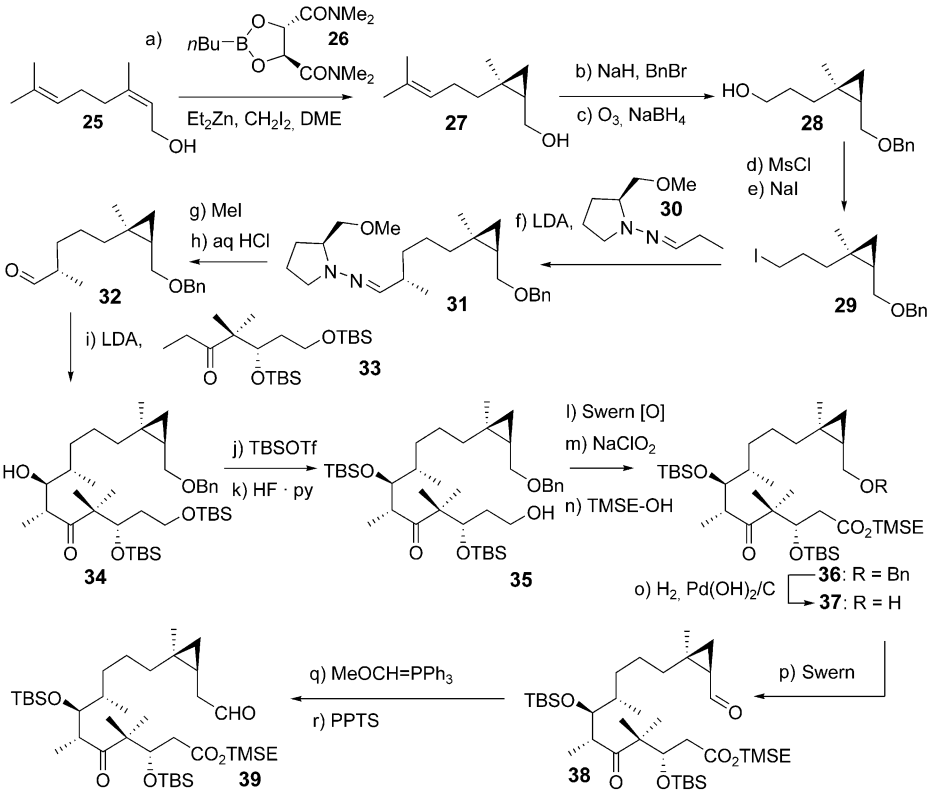
The synthesis of cyclopropane epothilones **4** and **6** required the key aldehyde **39**, which was constructed from nerol (**25**) as shown in Scheme 3. Thus, Charrette asymmetric cyclopropanation[4a,5a,13] of **25** in the presence of

 © 2003 Wiley-VCH Verlag GmbH & Co. KGaA, Weinheim



Scheme 2. Preparation of **20a–d** and **22a–d**. Reagents and conditions: a) NaH (3.0 equiv), RSH (3.0 equiv), *i*PrOH, 25 °C, 24 h, 70–81 %; b) $(Me_3Sn)_2$ (5.0–10.0 equiv), $[Pd(PPh_3)_4]$ (5 mol %), toluene, 100 °C, 1–3 h, 71–88 %; c) *n*BuLi (1.1 equiv), diethyl ether, −78 °C, 1 h; then nBu_3SnCl (1.2 equiv), −78→25 °C, 1 h, 49–62 %.

ligand **26** furnished cyclopropane alcohol **27** in 80 % yield and 95 % *ee*. The hydroxy group in **27** was protected as a benzyl ether (NaH, BnBr, 100 %) and the resulting product was subjected to ozonolysis (O_3, then $NaBH_4$), leading to primary alcohol **28** (83 % yield). This alcohol was converted into the corresponding iodide **29** through mesylation (MsCl, Et_3N) and subsequent displacement of the intermediate mesylate with NaI (91 % overall yield). Alkylation of (−)-SAMP hydrazone **30** with iodide **29** according to the procedure of Enders[14] under the influence of LDA proceeded smoothly to afford hydrazone **31** (87 % yield), whose cleavage (MeI, then aqueous HCl) led to aldehyde **32** (91 % yield). The crucial aldol reaction between ketone **33**[15] and aldehyde **32** in the presence of LDA proceeded smoothly and stereoselectively in THF/Et_2O (1:1) at −78 °C to afford the desired hydroxy ketone **34** in 80 % yield (d.r. > 14:1). Protection of the secondary alcohol in **34** as a silyl ether (TBSOTf, 2,6-lutidine) followed by selective removal of the primary TBS group (HF·py) furnished primary



Scheme 3. Construction of **39**. Reagents and conditions: a) 80 % yield, 95 % *ee*;[4a,5a,13] b) NaH (1.5 equiv), BnBr (1.2 equiv), DMF, 0→25 °C, 12 h, 100 %; c) O_3, CH_2Cl_2/MeOH (4:1), −78 °C; then $NaBH_4$ (3.0 equiv), −78→25 °C, 1 h, 83 %; d) MsCl (1.3 equiv), Et_3N (1.5 equiv), CH_2Cl_2, 25 °C, 1 h; e) NaI (3.0 equiv), acetone, 25 °C, 12 h (91 % for two steps); f) LDA (1.4 equiv), **30** (1.3 equiv), THF, 0 °C, 6 h; then **29**, −98→−10 °C, 14 h, 87 %; g) MeI, reflux, 3 h; h) HCl (3 N)/pentane (1:1), 25 °C, 3 h (91 % for two steps); i) LDA (2.4 equiv), **33** (2.3 equiv), THF/Et_2O (1:1), −78 °C, 1 h; then −40 °C, 0.5 h; then **32** at −78 °C, 5 min, 80 %; j) TBSOTf (1.5 equiv), 2,6-lutidine (2.0 equiv), CH_2Cl_2, −20 °C, 1 h; k) HF·py (1.8 mL mmol^{-1}), pyridine/THF (1:2), 0 °C, 8 h (86 % for two steps); l) $(COCl)_2$ (1.2 equiv), DMSO (2.0 equiv), CH_2Cl_2, −78 °C, 5 min; then **35** (1.0 equiv), 20 min; then Et_3N (3.0 equiv), −78→0 °C; m) $NaClO_2$ (5.0 equiv), NaH_2PO_4 (3.0 equiv), 2-methyl-2-butene (75 equiv), *t*BuOH/THF/H_2O (4:2:1), 25 °C, 1 h; n) TMSE-OH (4.0 equiv), EDC (1.5 equiv), DMAP (0.1 equiv), DMF, 25 °C, 12 h (73 % for three steps); o) $Pd(OH)_2$/C (10 wt %; 10 %), H_2, EtOH/EtOAc (1:1), 25 °C, 2 h, 89 %; p) $(COCl)_2$ (1.2 equiv), DMSO (2.0 equiv), CH_2Cl_2, −78 °C, 5 min; then **37** (1.0 equiv), 20 min; then Et_3N (3.0 equiv), −78→0 °C, 99 %; q) $MeOCH_2PPh_3Cl$ (3.0 equiv), *n*BuLi (2.8 equiv), THF, 0 °C, 1 h; then **38**, −78→0 °C, 2 h, 79 %; r) PPTS (10.0 equiv), dioxane/water (9:1), 70 °C, 12 h, 81 %. Bn = benzyl, Ms = methanesulfonyl, LDA = lithium diisopropyl amide, TBS = *tert*-butyldimethylsilyl, Tf = trifluoromethanesulfonyl, py = pyridine, DMSO = dimethyl sulfoxide, TMSE = 2-(trimethylsilyl)ethyl, EDC = 1-(3-dimethylaminopropyl)-3-ethylcarbodiimide, DMAP = 4-dimethylaminopyridine, PPTS = pyridinium *para*-toluene sulfonate.

 © 2003 Wiley-VCH Verlag GmbH & Co. KGaA, Weinheim

alcohol **35** (86% overall yield). The latter compound was then oxidized, and the resulting carboxylic acid was protected as a TMSE ester to afford **36** in 73% overall yield. Hydrogenolysis of the benzyl group within **36** (H_2, 10% $Pd(OH)_2/C$) led to alcohol **37** (89% yield). Swern oxidation of **37** led to the corresponding aldehyde **38** (99% yield). Homologation of **38** through Wittig olefination ($MeOCH_2PPh_3Cl$, *n*BuLi, 79% yield) followed by acid hydrolysis (PPTS, 81% yield) of the resulting enol ether led to the targeted aldehyde **39**.

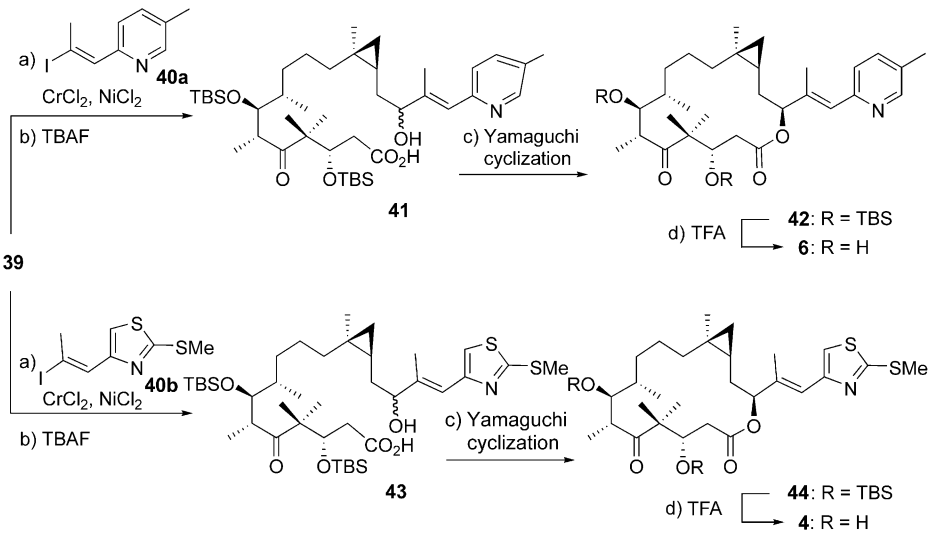
Following on our previously developed strategy[4a] toward epothilone analogues, we subjected aldehyde **39** to a Nozaki–Hiyama–Kishi coupling[16] reaction with vinyl iodides **40a**[4a] and **40b**[5a] followed by treatment with TBAF to afford the corresponding secondary alcohols **41** and **43** as mixtures (ca. 1:1) of the two epimers (at C15) in an unoptimized combined yield of 42–45% (Scheme 4). These mixtures were then cyclized under Yamaguchi conditions[17] (2,4,6-trichlorobenzoyl chloride, Et_3N, DMAP, toluene, 0→75 °C) to afford the desired 15*S* 16-membered lactones **42** (33% yield) and **44** (32% yield) together with their 15*R* epimers (ca. 1:1 ratio, chromatographically separated, silica gel).[18] Finally the TBS groups were removed from **42** and **44** by the action of TFA, leading to epothilones **6** (48% yield) and **4** (Table 1, 71% yield) (unoptimized yields) as shown in Scheme 4.

The biological activities of the synthesized epothilones were evaluated through cell-growth-inhibition assays (cytotoxicity assays). Cytotoxicity was first evaluated in a set of ovarian carcinoma cell lines, including a parental cell line (lA9) and three drug-resistant cell lines, namely the taxol-resistant cell lines lA9/PTX10 and lA9/PTX22[19] and the epothilone-resistant cell line 1A9/A8.[20] These resistant cell lines harbor distinct acquired β-tubulin mutations that affect drug–tubulin interaction and result in impaired taxane and epothilone-driven tubulin polymerization. The results of these biological investigations are summarized in Table 2. Further cytotoxicity studies were carried out on a set of human epidermoid cancer cell lines, including a parent cell line (KB-31) and a taxol-resistant (due to Pgp overexpression) cell line (KB-8511). The results of these studies are summarized in Table 3.

Table 1: Selected data for **4**.

4: $R_f = 0.19$ (silica gel, EtOAc/hexanes 3:7); $[\alpha]_D^{20} = -19.3$ ($c = 0.14$, CH_2Cl_2); IR (film): $\tilde{\nu}_{max} = 3484$ br, 2932, 1729, 1459, 1375, 1249, 1043, 982, 733 cm^{-1}; ^1H NMR (400 MHz, $CDCl_3$): $\delta = 6.97$ (s, 1H), 6.47 (s, 1H), 5.25 (dd, $J = 7.1$, 5.7 Hz, 1H), 4.04 (dd, $J = 8.1$, 3.0 Hz, 1H), 3.91 (dd, $J = 4.1$, 4.1 Hz, 1H), 3.23 (m, 1H), 2.69 (s, 3H), 2.52 (dd, $J = 14.9$, 8.4 Hz, 1H), 2.46 (dd, $J = 14.9$, 2.6 Hz, 1H), 2.11 (s, 3H), 2.04 (dd, $J = 14.5$, 4.0 Hz, 1H), 1.72–1.66 (m, 1H), 1.62–1.44 (m, 4H), 1.36 (s, 3H), 1.35–1.22 (m, 2H), 1.17 (d, $J = 7.5$ Hz, 3H), 1.16 (s, 3H), 1.15–1.04 (m, 1H), 0.99 (d, $J = 7.0$ Hz, 3H), 0.97 (s, 3H), 0.48 (m, 1H), 0.40 (dd, $J = 8.8$, 3.9 Hz, 1H), −0.11 ppm (br t, $J = 4.6$ Hz, 1H); ^{13}C NMR (100 MHz, $CDCl_3$): $\delta = 221.5$, 171.1, 165.7, 152.9, 138.6, 120.1, 116.2, 82.0, 73.8, 73.2, 52.0, 42.9, 39.4, 36.5, 35.0, 33.2, 31.6, 24.6, 23.5, 22.54, 22.49, 21.1, 20.8, 19.4, 17.4, 16.8, 15.0, 13.2 ppm; FTMS (MALDI): *m/z* calcd for $C_{28}H_{44}NO_5S_2$: 538.2655, found: 538.2632 [MH^+]

There is a general agreement in the relative potency of the substituted epothilone B analogues against the 1A9 human ovarian and the KB-31 human epidermoid cancer cells. Collectively, the results of these cytotoxicity assays revealed interesting information in terms of structure–activity relationships within the epothilone family. First, compounds **4** and **6**, in which the C12–C13 epoxide moiety is replaced by a cyclopropane ring, are the two most potent compounds of all the epothilone B analogues presented herein. This result reaffirms that the C12–C13 epoxide moiety is not necessary for biological activity, as previously noted.[4] Compound **4** is six times more active than the parent epothilone B (**2**) against the 1A9 human ovarian carcinoma cells (Table 2), which further confirms that the replacement of the methyl group on the thiazole side chain with a methylsulfanyl group leads to increased activity. This result is in agreement with our previous data on a similar substitution in epothilone B without replacement of the C12–C13 epoxide (i.e. compound **3**).[5a] The latter compound (**3**) was about twice as active as the parent epothilone B, whereas compound **4** is sixfold more potent than epothilone B. This result makes compound **4** the most active epothilone B analogue against the 1A9 cell line synthesized to date and suggests that replacement of the epoxide by a cyclopropane moiety together with the replacement of the methyl substituent on the thiazole moiety with a methylsulfanyl group act synergistically, leading to the observed enhancement of biological activity. Interestingly, substitution of the methyl group of the thiazole ring with



Scheme 4. Synthesis of **4** and **6**. Reagents and conditions: a) $CrCl_2$ (10.0 equiv), $NiCl_2$ (0.2 equiv), 4-*t*BuPy (30 equiv), **40a** or **40b** (3.0 equiv), DMSO, 25 °C, 24 h; b) TBAF (2.0 equiv), THF, 25 °C, 2 h, 42% yield for two steps (**41**) or 45% yield for two steps (**43**); c) Et_3N (6.0 equiv), 2,4,6-trichlorobenzoyl chloride (2.4 equiv), **41** or **43**, THF, 0 °C, 1 h; then DMAP (2.2 equiv), toluene, 75 °C, 3 h, 33% (**42**) or 32% (**44**); d) TFA/CH_2Cl_2 (20% v/v), 25 °C, 3 h, 48% (**6**) or 71% (**4**). TBAF = tetra-*n*-butylammonium fluoride, TFA = trifloroacetic acid.

 © 2003 Wiley-VCH Verlag GmbH & Co. KGaA, Weinheim

Table 2: Cytotoxicity of epothilones **4**, **6**, and **8**–**16** against 1A9 human carcinoma cells and β-tubulin mutant cell lines selected with taxol or epothilone A.[a]

Compound	Cell Line						
	1A9	A8		PTX10		PTX22	
	IC_{50}	IC_{50}	RR	IC_{50}	RR	IC_{50}	RR
taxol	3.0 ± 0.4	10.1 ± 2.9	3.3	89.7 ± 9.0	29.5	53.4 ± 26.5	17.6
EpoA	2.4 ± 0.6	91.0 ± 10.0	38.7	34.2 ± 2.0	14.5	8.7 ± 2.2	3.7
EpoB	0.6 ± 0.3	6.5 ± 0.9	10.7	3.1 ± 0.5	5.2	0.8 ± 0.5	1.3
3[b]	0.17 ± 0.8	1.3 ± 0.65	7.6	0.26 ± 0.11	1.5	0.25 ± 0.17	1.5
4	0.1 ± 0.0	2.4 ± 1.1	23.5	0.7 ± 0.3	6.5	0.6 ± 0.5	5.9
6	0.3 ± 0.1	10.4 ± 2.4	41.4	3.3 ± 1.2	13.2	1.3 ± 1.1	5.3
8	3.5 ± 0.7	18.4 ± 1.4	5.3	16.1 ± 2.1	4.6	3.8 ± 0.3	1.1
9	4.4 ± 2.4	42.9 ± 5.1	9.7	24.7 ± 4.9	5.6	5.2 ± 0.8	1.2
10	2.1 ± 0.8	16.0 ± 5.5	7.6	9.8 ± 1.4	4.7	2.9 ± 1.3	1.4
11	0.7 ± 0.2	11.1 ± 1.0	16.6	3.9 ± 0.4	5.8	0.3 ± 0.1	0.5
12	3.2 ± 0.1	31.9 ± 3.1	10.0	16.1 ± 4.1	5.1	3.2 ± 0.3	1.0
13	0.4 ± 0.1	11.6 ± 6.7	31.7	3.9 ± 1.1	10.5	2.1 ± 1.9	5.8
14	3.3 ± 0.2	27.7 ± 3.2	8.3	12.2 ± 7.4	3.7	6.6 ± 2.6	2.0
15	4.3 ± 0.4	83.0 ± 2.0	19.2	65.3 ± 11.9	15.1	9.6 ± 1.3	2.2
16	8.6 ± 1.2	32.3 ± 2.7	3.8	42.9 ± 10.3	5.0	9.6 ± 1.0	1.1

[a] The antiproliferative effects of the tested compounds against the parental 1A9 and the taxol- and epothilone-selected drug-resistant clones (PTX10, PTX22, and A8, respectively) were assessed in a 72 h growth-inhibition assay using the SRB (sulforhodamine-B) assay.[22] IC_{50} values for each compound are given in nM and represent the mean of three independent experiments ± standard error of the mean. Relative resistance (RR) is calculated as an IC_{50} value for each resistant subline divided by that for the parental cell line (1A9). [b] Results taken from ref. [5a].

Table 3: Cytotoxicity (IC_{50}) of selected epothilones against the human epidermoid cell lines KB-31 and KB-8511.[a]

Compound	KB-31	KB-8511
EpoB[b]	0.19	0.12
3[b]	0.11	0.07
4	0.20	0.12
6	0.44	0.29
8	3.04	2.67
9	10.0	6.73
10	1.16	1.28
11	0.72	0.55
13	0.54	0.41
14	4.87	3.24
15	8.38	7.37
16	9.01	11.65

[a] The antiproliferative effects of the tested compounds were assessed in two human epidermoid cancer cell lines, including a parent cell line (KB-31) and a taxol-resistant (due to Pgp-overexpression) cell line (KB-8511). IC_{50} values are given in nM. [b] Results taken from ref. [5a].

larger moieties (compounds **7**–**10**)[21] led to diminished biological activity relative to epothilone B (Tables 2 and 3).

Among the epothilone B analogues with a side chain at C5 of the pyridine substituent, **11**–**13** and **15**, the methylsulfanyl analogue **13** is the most potent, followed by the bromo-substituted derivative **11** and the chloro-substituted system **12**. When the methylsulfanyl group is relocated from C5 of the pyridine ring (**13**) to C6 (**14**), loss of activity occurs as the IC_{50} value drops from 0.4 nM (for **13**) to 3.3 nM (for **14**) (Table 2). Furthermore, replacement of the methylsulfanyl group at the C5 of the pyridine ring (**13**) with a trifloromethyl group (**15**) results in a tenfold loss of activity. Finally, the least active of the synthesized epothilone B analogues is compound **16** in which a pyrimidine side chain with a methylsulfanyl substituent has replaced the thiazole side chain of the parent compound.

Varying degrees of cross-resistance are obtained with the substituted epothilone B analogues against the taxol- and epothilone-resistant human ovarian carcinoma sublines (Table 2) ranging from 3- to 41-fold. These results suggest that the location of the tubulin mutations in these lines affects differentially the binding of each of the analogues to tubulin. Moreover, and in agreement with the original observations with the naturally occurring epothilones A and B, none of the epothilone B analogues tested herein appears to be a good substrate for the drug-efflux pump P-glycoprotein (Pgp). This is evident by the lack of cross-resistance of each of these analogues to the Pgp-expressing cell line KB-8511 (Table 3). In contrast, we have previously shown that taxol—a known Pgp substrate—was 214-fold less active against KB-8511 cells than against their parent counterpart, non-Pgp-expressing KB-31 cells.[5a]

In conclusion, we have constructed a number of rationally designed epoxide and cyclopropane epothilone B analogues with substituted side chains and evaluated their biological activities against a series of human cancer cell lines. Among the several bioactive analogues, the novel cyclopropyl epothilone B analogue **4** with a methylsulfanyl thiazole ring stands out as the most potent. This compound is six times more active than the naturally occurring epothilone B (**2**) and appears to be, together with its oxygen counterpart **3**, the most potent epothilone B analogue synthesized to date. Our previous structure–activity relationship studies,[2c,4b,5a] together with the data presented herein, reconfirm that the epoxide oxygen atom is not required for biological activity within this class of small molecules and that the lipophilic methylsulfanyl group on the thiazole moiety considerably enhances the potency of these compounds. As epothilone **4** lacks the relatively reactive epoxide function of **2** and **3**, it may prove to be advantageous over the latter compounds with regard to stability and side effects and, therefore, may present a unique opportunity for clinical development.[23]

Received: May 6, 2003 [Z51819]

Keywords: antitumor agents · epothilones · structure–activity relationships · sulfur · total synthesis

[1] G. Höfle, N. Bedorf, H. Steinmetz, D. Schomburg, K. Gerth, H. Reichenbach, *Angew. Chem.* **1996**, *108*, 1671 – 1673; *Angew. Chem. Int. Ed. Engl.* **1996**, *35*, 1567 – 1569.

 © 2003 Wiley-VCH Verlag GmbH & Co. KGaA, Weinheim

[2] For selected reviews on the chemistry and biology of the epothilones, see: a) K.-H. Altmann, *Mini-Rev. Med. Chem.* **2003**, *3*, 149 – 158; b) R. Altaha, T. Fojo, E. Reed, J. Abraham, *Curr. Pharm. Des.* **2002**, *8*, 1707 – 1712; c) K. C. Nicolaou, A. Ritzén, K. Namato, *Chem. Commun.* **2001**, 1523 – 1535; d) K. C. Nicolaou, F. Roschangar, D. Vourloumis, *Angew. Chem.* **1998**, *110*, 2120 – 2153; *Angew. Chem. Int. Ed.* **1998**, *37*, 2014 – 2045.

[3] For recent total syntheses of epothilones and their analogues see: reviews (reference [2]) and a) A. Rivkin, F. Yoshimura, A. E. Gabarda, T.-C. Chou, H. Dong, W. P. Tong, S. J. Danishefsky, *J. Am. Chem. Soc.* **2003**, *125*, 2899 – 2901; b) R. E. Taylor, Y. Chen, A. Beatty, *J. Am. Chem. Soc.* **2003**, *125*, 26 – 27; c) K.-H. Altmann, G. Bold, G. Caravatti, D. Denni, A. Flörsheimer, A. Schmidt, G. Rihs, M. Wartmann, *Helv. Chim. Acta* **2002**, *85*, 4086 – 4110; d) J. Sun, S. C. Sinha, *Angew. Chem.* **2002**, *114*, 1439 – 1441; *Angew. Chem. Int. Ed.* **2002**, *41*, 1381 – 1383; e) Z.-Y. Liu, Z.-C. Chen, C.-Z. Yu, R.-F. Wang, R.-Z. Zhang, C.-S. Huang, Z. Yan, D.-R. Cao, J.-B. Sun, G. Li, *Chem. Eur. J.* **2002**, *8*, 3747 – 3756; f) A. Regueiro-Ren, R. M. Borzilleri, X. Zheng, S.-H. Kim, J. A. Johnson, C. R. Fairchild, F. Y. F. Lee, B. H. Long, G. D. Vite, *Org. Lett.* **2001**, *3*, 2693 – 2696; g) N. Martin, E. J. Thomas, *Tetrahedron Lett.* **2001**, *42*, 8373 – 8377; h) M. Valluri, R. M. Hindupur, B. Panicker, G. Labadie, J.-C. Jung, M. A. Avery, *Org. Lett.* **2001**, *3*, 3607 – 3609; i) C. B. Lee, Z. Wu, F. Zhang, M. D. Chappell, S. J. Stachel, T.-C. Chou, Y. Guan, S. J. Danishefsky, *J. Am. Chem. Soc.* **2001**, *123*, 5249 – 5259; j) H. J. Martin, P. Pojarliev, H. Kahlig, J. Mulzer, *Chem. Eur. J.* **2001**, *7*, 2261 – 2271; k) R. E. Taylor, Y. Chen, *Org. Lett.* **2001**, *3*, 2221 – 2224; l) J. D. White, R. G. Carter, K. F. Sundermann, M. Wartmann, *J. Am. Chem. Soc.* **2001**, *123*, 5407 – 5413; m) B. Zhu, J. S. Panek, *Eur. J. Org. Chem.* **2001**, *9*, 1701 – 1714; n) A. Fürstner, C. Mathes, C. W. Lehmann, *Chem. Eur. J.* **2001**, *7*, 5299 – 5317.

[4] a) K. C. Nicolaou, K. Namoto, A. Ritzén, T. Ulven, M. Shoji, J. Li, G. D'Amico, D. Liotta, C. T. French, M. Wartmann, K.-H. Altmann, P. Giannakakou, *J. Am. Chem. Soc.* **2001**, *123*, 9313 – 9323; b) K. C. Nicolaou, C. Namoto, J. Li, A. Ritzén, T. Ulven, M. Shoji, D. Zaharevitz, R. Gussio, D. L. Sackett, R. D. Ward, A. Hensler, T. Fojo, P. Giannakakou, *ChemBioChem* **2001**, *2*, 69 – 75; c) J. A. Johnson, S.-H. Kim, M. Bifano, J. DiMarco, C. Fairchild, J. Gougoutas, F. Lee, B. Long, J. Tokarski, G. D. Vite, *Org. Lett.* **2000**, *2*, 1537 – 1540.

[5] a) K. C. Nicolaou, A. Ritzén, K. Namoto, R. M. Buey, J. F. Díaz, J. M. Andreu, M. Wartmann, K.-H. Altmann, A. O'Brate, *Tetrahedron* **2002**, *58*, 6413 – 6432; b) K. C. Nicolaou, Y. He, F. Roschangar, N. P. King, D. Vourloumis, T. Li, *Angew. Chem.* **1998**, *110*, 89 – 92; *Angew. Chem. Int. Ed.* **1998**, *37*, 84 – 87.

[6] K. C. Nicolaou, R. Scarpelli, B. Bollbuck, B. Werschkun, M. M. A. Pereira, M. Wartmann, K.-H. Altmann, D. Zaharevitz, R. Gussio, P. Giannakakou, *Chem. Biol.* **2000**, *7*, 593 – 599.

[7] K. C. Nicolaou, D. Hepworth, N. P. King, M. R. V. Finlay, R. Scarpelli, M. M. A. Pereira, B. Bollbuck, A. Bigot, B. Werschkun, N. Winssinger, *Chem. Eur. J.* **2000**, *6*, 2783 – 2800.

[8] N. Virgilio, *J. Org. Chem.* **1973**, *38*, 2660 – 2664.

[9] L. Testaferri, M. Tiecco, M. Tingoli, D. Bartoli, A. Massoli, *Tetrahedron* **1985**, *41*, 1373 – 1384.

[10] H. Gilman, W. A. Grerory, S. M. Spatz, *J. Org. Chem.* **1951**, *16*, 1788 – 1791.

[11] K. Dinnell, G. G. Chicchi, M. J. Dhar, J. M. Elliott, G. J. Hollingworth, M. M. Kurtz, M. P. Ridgill, W. Rycroft, K.-L. Tsao, A. R. Williams, C. J. Swain, *Bioorg. Med. Chem. Lett.* **2001**, *11*, 1237 – 1240.

[12] S. Jessie, U. Kjell, *Tetrahedron* **1994**, *50*, 275 – 284.

[13] A. B. Charette, H. Juteau, H. Lebel, C. Molinaro, *J. Am. Chem. Soc.* **1998**, *120*, 11 943 – 11 952.

[14] a) D. Enders in *Asymmetric Synthesis, Vol. 3* (Eds.: J. D. Morrison, J. W. Scott), Elsevier, Orlando, FL, **1984**, pp. 275 – 339; b) D. Enders, M. Klatt, *Synthesis* **1996**, 1403 – 1418.

[15] K. C. Nicolaou, S. Ninkovic, F. Sarabia, D. Vourloumis, Y. He, H. Vallberg, M. R. V. Finlay, Z. Yang, *J. Am. Chem. Soc.* **1997**, *119*, 7974 – 7991.

[16] a) K. Takai, T. Kitamura, T. Kuroda, T. Hiyama, H. Nozaki, *Tetrahedron Lett.* **1983**, *24*, 5281 – 5284; b) H. Jin, J. Uenishi, W. J. Christ, Y. Kishi, *J. Am. Chem. Soc.* **1986**, *108*, 5644 – 5646.

[17] a) J. Inanaga, K. Hirata, H. Saeki, T. Katsuki, M. Yamaguchi, *Bull. Chem. Soc. Jpn.* **1979**, *52*, 1989 – 1993; b) J. Mulzer, P. A. Mareski, J. Bushmann, P. Luger, *Synthesis* **1992**, 215 – 228.

[18] Based on our previous experience,[5a] we assumed that the desired 15*S* macrolactones (**42** and **44**) eluted after their less polar 15*R* epimers, an assumption verified by their biological activities.

[19] P. Giannakakou, D. L. Sackett, Y.-K. Kang, Z. Zhan, J. T. M. Buters, T. Fojo, M. S. Poruchynsky, *J. Biol. Chem.* **1997**, *272*, 17 118 – 17 125.

[20] P. Giannakakou, R. Gussio, E. Nogales, K. H. Downing, D. Zaharevitz, B. Bollbuck, G. Poy, D. Sackett, K. C. Nicolaou, T. Fojo, *Proc. Natl. Acad. Sci. USA* **2000**, *97*, 2904 – 2909.

[21] The IC_{50} value for compound **7** was found to be 2.5 nM against the 1A9 cell line.

[22] P. Skehan, R. Storeng, D. Scudiero, A. Monks, J. McMahon, D. Vistica, J. T. Warren, H. Bokesch, S. Kenney, M. R. Boyd, *J. Natl. Cancer Inst.* **1990**, *82*, 1107 – 1112.

[23] Note added in proof: After submission of this manuscript, a related article on epothilone analogues was published: F. Yoshimura, A. Rivkin, A. E. Gabarda, T.-C. Chou, H. Dong, G. Sukenick, F. F. Morel, R. E. Taylor, S. J. Danishefsky, *Angew. Chem.* **2003**, *115*, 2622 – 2625; *Angew. Chem. Int. Ed.*, **2003**, *42*, 2518 – 2521. See also: T. Carlomagno, M. J. J. Blommers, J. Meiler, W. Jahnke, T. Schupp, F. Petersen, D. Schinzer, K.-H. Altmann, C. Griesinger, *Angew. Chem.* **2003**, *115*, 2615 – 2619; *Angew. Chem. Int. Ed.*, **2003**, *42*, 2511 – 2515; T. Carlomagno, V. M. Sanchez, M. J. J. Blommers, C. Griesinger, *Angew. Chem.* **2003**, *115*, 2619 – 2621; *Angew. Chem. Int. Ed.*, **2003**, *42*, 2515 – 2517; R. I. Storer, T. Takemoto, P. S. Jackson, S. V. Ley, *Angew. Chem.* **2003**, *115*, 2625 – 2629; *Angew. Chem. Int. Ed.*, **2003**, *42*, 2521 – 2525.

 © 2003 Wiley-VCH Verlag GmbH & Co. KGaA, Weinheim

The Prebiotic Role of Serine

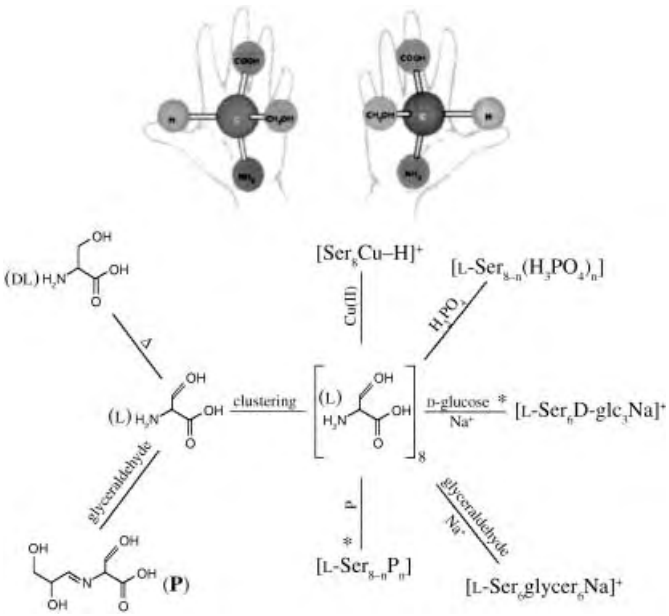
Serine Octamer Reactions: Indicators of Prebiotic Relevance**

*Zoltan Takats, Sergio C. Nanita, and R. Graham Cooks**

Herein we explore the hypothesis[1,2] that serine played an important role in the prebiotic chemistry that led to living organisms. The principal tool used in this study is sonic-spray ionization (SSI),[3,4] a mild method that facilitates investigation of chemical species present in concentrated aqueous solutions.[5,6] It has been reported that serine, alone among the common α amino acids, forms homochiral magic-number clusters.[1,2,7–9] These clusters incorporate other amino acids of like chirality by substitution for serine[10,11] and they are capable of aggregation.[8] These facts allow a prebiotic scenario in which serine clusters were involved in chiral accumulation and in transmission of chirality to other amino acids. We now report observations that suggest unique connections between serine and other compounds of fundamental importance to biochemistry, including glyceraldehyde, glucose, phosphoric acid, and some transition-metal ions. We also suggest a reaction that might have been the locus for symmetry-breaking in serine.

Serine, the putative product of the reaction between the interstellar molecules glycine and formaldehyde,[12,13] is one of the primitive amino acids.[14] It has not been reported in interstellar space but has been identified in meteorites.[15] Both the strong preference for homochirality and the stability of the magic-number cluster set serine apart from other amino acids.[16,17] Herein we report new experimental facts (Scheme 1) that confirm the uniqueness of serine: 1) Serine clusters with glyceraldehyde, undergo chiro-selective reactions involving the octamer, 2) it forms a chirally dependent magic-number cluster with glucose, 3) it incorporates H_3PO_4 into its homochiral octamer, 4) the magic-number octamer is cationized by Cu^{II} ions, while other-magic number clusters of serine are observed with Fe^{II} and Fe^{III} ions. In all these instances serine reacts uniquely compared to other representative amino acids. Finally, 5) serine is amongst the most easily racemized α amino acids.

The recently proposed mechanism for chiral transfer from serine to other amino acids[10] stimulated the search for a chemical connection between the L-serine and D-sugars of living organisms. The interactions of serine with glyceraldehyde, the simplest aldose, were examined. The two compounds undergo a condensation reaction when a neutral aqueous mixture is heated at approximately 75 °C for 14 h, forming a Schiff base. The SSI mass spectrum shows this serine–glyceraldehyde dehydration product to substitute for one or two serines in the octamer, in a similar fashion to that seen for mixtures of serine with α amino acids.[10,11] Remarkably, substitution into the serine octamer is chirally selective, as confirmed by using purified[18] D-glyceraldehyde and recording the SSI mass spectrum. The L-serine octamer incorporates the condensation product of L-serine and D-glyceraldehyde (8% relative abundance for one substitution, 3% for two) whereas no reaction was detectable for the D-serine/D-glyceraldehyde pair. Other amino acids undergo the same reaction with glyceraldehyde to form analogous Schiff base products. Remarkably, serine and threonine were found to be the only amino acids to incorporate the glyceraldehyde dehydration product into a magic-number cluster (the octamers). It is noteworthy that the chiral selection matches that seen in biological systems (L-amino acids and D-sugars).



Scheme 1. Reactions of serine and its octamer; * chiro-selective reactions, **P** = serine/glyceraldehyde condensation reaction product.

Under the mild conditions of the SSI process, a solution containing L-serine and DL-glyceraldehyde (Sigma, St. Louis, MO; solid, 90% + purity) exhibits only one prominent product, a pronounced magic-number cluster, $[Ser_6Glyc_6Na]^+$ (m/z 1193). Tandem mass-spectrometry experiments show that $[Ser_6Glyc_6Na]^+$ fragments by loss of $C_6H_{12}O_6$ units which suggests that glyceraldehyde is present in the form of a dimer (hexose or an isomer) in the cluster.[19] Evidence for the structural assignment and information on chiral control of the reaction was obtained by performing experiments with hexose/serine mixtures. The SSI mass spectrum of a L-serine/D-glucose mixture (Figure 1) shows a remarkable magic-number cluster, nominally the same ion seen with glyceraldehyde. MS/MS experiments showed that analogously to the cluster with glyceraldehyde, the loss of one hexose molecule (m/z 1013) yields the dominant fragment. The strong but incomplete chiral preference for the L-serine/

[*] Prof. R. G. Cooks, Dr. Z. Takats, S. C. Nanita
Department of Chemistry
Purdue University
560 Oval Drive, West Lafayette, IN 47907 (USA)
Fax: (+1) 765-4949-421
E-mail: cooks@purdue.edu

[**] This work was supported by the National Science Foundation (CHE 97-32670) and by the U.S. Department of Energy, Office of Basic Energy Sciences (DE-FG02-94ER14470). We thank Jeffrey Patrick (Eli Lilly Co.) for helpful discussions.

 DOI: 10.1002/anie.200351210 © 2003 Wiley-VCH Verlag GmbH & Co. KGaA, Weinheim

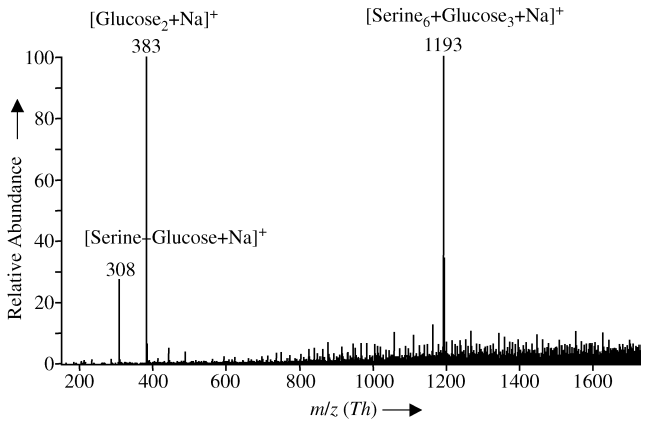


Figure 1. Magic-number cluster at m/z 1193 corresponding to $[Ser_6Glc_3Na]^+$ in the SSI mass spectrum of a L-serine /D-glucose mixture.

D-glucose and D-serine/L-glucose combinations over the homoclusters is evident in both tandem and single-stage mass spectra (Figure 2). Isotopic effects can be ruled out since data taken with 2,3,3-[D_3]-L-serine confirmed the chiral preference. In contrast, magic-number heteroclusters (amino acid/hexose) were not observed for other common amino acids, with the exception of threonine, which behaves similarly to serine.

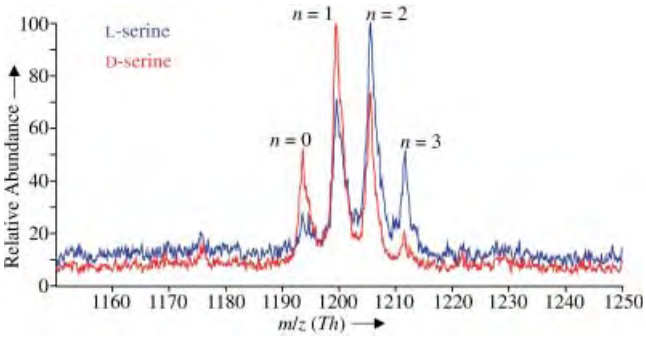


Figure 2. SSI mass spectra for serine/glucose nonameric cluster ions showing the preferential formation of the D-glucose/L-serine and L-glucose/D-serine pairs over their L/L and D/D counterparts using isotopic labeling. Blue: SSI-MS of a solution containing L-serine (5.0 mM), L-glucose (2.5 mM), and D-glucose-U-$^{13}C_6$ (2.5 mM). Red: D-serine (5.0 mM), L-glucose (2.5 mM), and D-glucose-U-$^{13}C_6$ (2.5 mM), where n is the number of D-glucose-U-$^{13}C_6$ in the cluster $[Ser_6Glc_3Na]^+$.

Further tests of the hypothesis that serine played a unique role in prebiotic chemistry involved examining its reactions with phosphoric acid and transition-metal ions. Phosphoric acid incorporates readily into serine clusters by substituting for serine; it gives a series of ions $[Ser_{8-n}+(H_3PO_4)_n+H]^+$,($n=1$–3). Sulfuric acid, by contrast, was not incorporated into clusters of serine under analogous conditions. With other natural amino acids, only single incorporations of phosphoric acid occurred into statistically distributed amino acid clusters, without preferred magic-number effects. The unusual stability of the serine octamer is further indicated by the fact that Cu^{II}, Fe^{II}, and Fe^{III} readily cationize serine clusters. For Cu^{II}, deprotonation is needed for charge balance and Cu^{II} chloride yields the octamer $[Ser_8+Cu\text{-}H]^+$ as well as the analogous tetrameric complex. As expected, Fe^{II} behaves analogously but it also yields an abundant intact adduct $[Ser_{10}+Fe]^{2+}$. Other amino acids generally form dimeric or trimeric clusters with transition-metal ions.

Serine was found to racemize under mild conditions at pH ≈ 6, as shown by a study of 2,3,3-[D_3]-L-serine. An aqueous solution heated in a sealed ampoule showed that the 2,3,3-[D_3]-L-serine was converted into [D_2]-DL-serine. This is evident from the ESI mass spectra in Figure 3, which shows

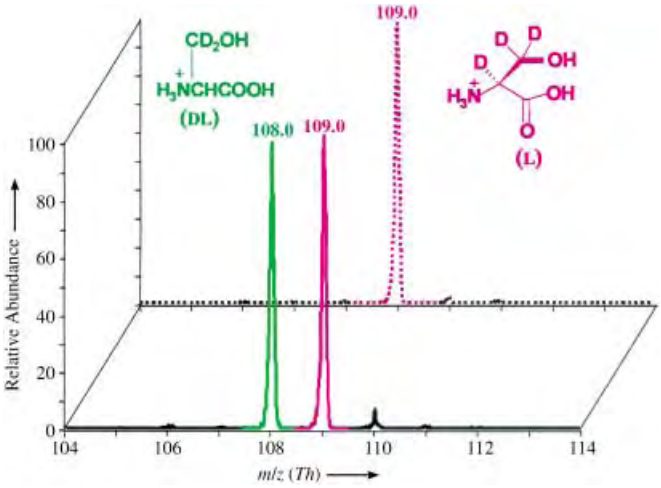


Figure 3. ESI mass spectra of 2,3,3-[D_3]-L-serine reference solution (-----; before heating) and a solution of 2,3,3-[D_3]-L-serine after heating for 30 h at approximately 160 °C (solid line). Approximately half of the L-serine (——) has racemized (DL, ——), as indicated by the final composition of the sample, about 25 % D- and 75 % L-serine.

peaks arising from the protonated form of 3,3-[D_2]-DL-serine at m/z 108 and the remaining protonated 2,3,3-[D_3]-L-serine at m/z 109. At shorter times or lower temperatures, conversion was less complete. Confirmation that the product was racemic [D_2]-serine was obtained by performing chiral analysis by tandem mass spectrometry[20] and by polarimetry on a L-serine solution heated at 160 °C for 30 h. These experiments showed 24 ± 6 % conversion into D-serine, in agreement with the data of Figure 3. Aspartic acid and threonine were also racemized relatively easily, for example L-threonine showed the formation of 10 ± 3 % of D-threonine under identical conditions. The facile racemization of serine has been previously reported.[21,22] It could be the result of dehydration of the hydroxy group with loss of the hydrogen at the α carbon and formation of a vinylic group. The influence of an external chiral agent upon such a low-energy equilibrium process might have resulted in a preference for D- or L-serine, so allowing symmetry breaking.

Significant features related to modern biochemical systems are displayed uniquely by serine. The other amino acids examined fail to show these types of reactions or do so to a smaller extent and without the tell-tale chiral preferences.

 © 2003 Wiley-VCH Verlag GmbH & Co. KGaA, Weinheim

Serine might have separated into its homochiral forms in the course of forming the octamer and its higher clusters in concentrated aqueous solutions; this might then have served as a site for essential prebiotic reactions, which include the binding of C_3 sugars and their dimerization, uptake of phosphoric acid in a form suited to controlled phosphorylation, and transition-metal-ion binding and oxidation. The facile racemization of serine offers a specific chemical process in the context of which symmetry breaking might have occurred.

Received: February 18, 2003 [Z51210]

Keywords: amino acids · chemical evolution · chirality · mass spectrometry · serine

[1] R. G. Cooks, D. Zhang, K. J. Koch, F. C. Gozzo, M. N. Eberlin, *Anal. Chem.* **2001**, *73*, 3646 – 3655.
[2] R. Hodyss, R. R. Julian, J. L. Beauchamp, *Chirality* **2001**, *13*, 703 – 706.
[3] A. Hirabayashi, M. Sakairi, H. Koizumi, *Anal. Chem.* **1994**, *66*, 4557 – 4559.
[4] A. Hirabayashi, M. Sakairi, H. Koizumi, *Anal. Chem.* **1995**, *67*, 2878 – 2882.
[5] J. M. Daniel, S. D. Friess, S. Rajagopalan, S. Wendt, R. Zenobi, *Int. J. Mass Spectrom.* **2002**, *216*, 1 – 27.
[6] S. A. Hofstadler, R. H. Griffey, *Chem. Rev.* **2001**, *101*, 377 – 390.
[7] A. E. Counterman, D. E. Clemmer, *J. Phys. Chem. B* **2001**, *105*, 8092 – 8096.
[8] K. J. Koch, F. C. Gozzo, D. Zhang, M. N. Eberlin, R. G. Cooks, *Chem. Commun.* **2001**, *18*, 1854 – 1855.
[9] R. R. Julian, R. Hodyss, B. Kinnear, M. Jarrold, J. L. Beauchamp, *J. Phys. Chem. B* **2002**, *106*, 1219 – 1228.
[10] K. J. Koch, F. C. Gozzo, S. C. Nanita, Z. Takats, M. N. Eberlin, R. G. Cooks, *Angew. Chem.* **2002**, *114*, 1797 – 1800; *Angew. Chem. Int. Ed.* **2002**, *41*, 1721 – 1724.
[11] Z. Takats, S. C. Nanita, G. Schlosser, K. Vekey, R. G. Cooks, *Anal. Chem.* **2003**, *75*, 1514 – 1523.
[12] K. Kubota, K. J. Yokozeki, *J. Ferment. Bioeng.* **1989**, *67*, 387 – 390.
[13] H. Maeda, K. Takata, A. Toyoda, T. Niitsu, M. Iwakura, K. J. Shibata, *J. Ferment. Bioeng.* **1997**, *83*, 113 – 115.
[14] T. H. Jukes, *Biochem. Biophys. Res. Commun.* **1967**, *27*, 573 – 578.
[15] J. L. Bada, D. P. Galvin, G. D. McDonald, L. Becker, *Science* **1998**, *279*, 362 – 365.
[16] C. A. Schalley, P. Weis, *Int. J. Mass Spectrom.* **2002**, *221*, 9 – 19.
[17] D. Zhang, K. J. Koch, W. A. Tao, R. G. Cooks, *Proceedings of the 48th ASMS conference*, Long Beach, CA, **2000**.
[18] A concentrated aqueous solution of D-glyceraldehyde, 80% in H_2O, was purchased from Lancaster Synthesis Inc., Windham, NH; and recrystallized from water/methanol 1:1 (two times).
[19] A. Wohl, C. Neuberg, *Ber. Dtsch. Chem. Ges.* **1900**, *33*, 3095.
[20] W. A. Tao, D. Zhang, E. J. Nikolaev, R. G. Cooks, *J. Am. Chem. Soc.* **2000**, *122*, 10598 – 10609.
[21] D. E. Schwass, J. W. Finley, *J. Agric. Food Chem.* **1984**, *32*, 1377 – 1382.
[22] G. Nouadje, M. Nertz, F. Courderc, *J. Chromatogr. A* **1995**, *716*, 331 – 334.

 © 2003 Wiley-VCH Verlag GmbH & Co. KGaA, Weinheim

Polyoxometalates

A Supramolecular Tetradecanuclear Copper(II) Polyoxotungstate

Pierre Mialane, Anne Dolbecq, Jérôme Marrot, Eric Rivière, and Francis Sécheresse*

Polyoxometalates (POMs) can be perceived as discrete fragments of extended metal oxide lattices.[1] They continue to attract much attention with respect to their widespread applications.[2] To date, the two most studied POM types have been the so-called Keggin and Dawson–Wells families, which can be formulated $[XM_{12}O_{40}]^{n-}$ and $[X_2M_{18}O_{62}]^{n-}$ ($X = P^{V}$, Si^{IV}; $M = W^{VI,V}$, $Mo^{VI,V}$, $V^{IV,V}$) respectively. These species are diamagnetic when the metals M are in their highest oxidation state. Mono, di and trivacant species of the Keggin type polyoxotungstates can be easily prepared,[3] and then act as nucleophilic ligands for transition-metal (TM) or rare-earth cations. Such inclusions can then lead to the formation of magnetic clusters. Trivacant POMs are the best candidates to obtain compounds with the largest number of interacting magnetic cations. Recently, compounds with a number (from one to nine) of paramagnetic TM centers of the first row ranging were reported.[4] Among the numerous complexes reported to date, the most often encountered contain three or four M^{II} or M^{III} centers. Trimeric M^{II} or M^{III} compounds consist of either complexes in which the TM centers complete the free sites of the POMs to form $[XW_9O_{37}M_3(H_2O)_3]^{n-}$ ($X = Si^{IV}$, $M = Cr^{III}$, Co^{II}, Ni^{II}, Cu^{II}),[5] or sandwich complexes of general formula $[(XW_9O_m)_2M_3(H_2O)_3]^{n-}$ ($m = 37$, $X = P^{V}$, $M = Mn^{II}$, Fe^{II}, Ni^{II}, Cu^{II}, Zn^{II}; $m = 33$, $X = As^{III}$, $M = Mn^{II}$, Ni^{II}, Cu^{II}).[6] Similarly, complexes containing four paramagnetic TM centers have been characterized: the $[H_2PW_9O_{34}Ni_4(OH)_3(H_2O)_6]^{2-}$ POM, in which a nickel cubane caps the $\{PW_9O_{34}\}$ entity,[7] and the sandwich complexes $[(XW_9O_{34})_2M_4(H_2O)_2]^{n-}$ ($X = P^{V}$, $M = Mn^{II,III}$, $Fe^{II,III}$, Co^{II}, Ni^{II}, Cu^{II}, Zn^{II}; $X = Si^{IV}$, $M = Cr^{III}$, Mn^{II}, Cu^{II}, Zn^{II}).[8] In 1995, the hexameric Cr^{III} complex $[\{SiW_9O_{34}Cr_3(OH)_3\}_2(OH)_3]^{11-}$ was isolated,[9] and finally, Clemente-Juan et al. reported in 1999 the nonanuclear Ni^{II} complex $[(PW_9O_{34}Ni_3)_3(H_2O)_6(HPO_4)_2(OH)_3]^{16-}$.[10] An increase in the number of magnetic centers encapsulated in diamagnetic polyoxometalate matrices remains a challenge. We report herein the characterization of tetradecanuclear Cu^{II} com-

[*] Dr. P. Mialane, Dr. A. Dolbecq, Dr. J. Marrot, Prof. Dr. F. Sécheresse
Institut Lavoisier, IREM, UMR 8637
Université de Versailles Saint-Quentin
45 Avenue des Etats-Unis, 78035 Versailles (France)
Fax: (+33) 1-39-25-43-81
E-mail: mialane@chimie.uvsq.fr
Dr. E. Rivière
Laboratoire de Chimie Inorganique, URA CNRS 420
Institut de Chimie Moléculaire d'Orsay
Université Paris-Sud
91405 Orsay (France)

Supporting information for this article is available on the WWW under http://www.angewandte.org or from the author.

 DOI: 10.1002/anie.200351486 © 2003 Wiley-VCH Verlag GmbH & Co. KGaA, Weinheim

pounds, constructed through supramolecular assembly: $Na_{19}K_4[(SiW_9O_{34})(SiW_9O_{33}(OH))(Cu(OH))_6Cu]_2X{\cdot}nH_2O$ (X = Cl, $n = 160$ **2Cl** ; X = Cl, $n = 90$ $\mathbf{2Cl_{dhyd}}$; X = Br, $n = 160$ **2Br** ; X = Br, $n = 90$ $\mathbf{2Br_{dhyd}}$; $\mathbf{2Cl_{dhyd}}$ and $\mathbf{2Br_{hdyd}}$ are the dehydrated forms of **2Cl** and **2Br**, respectively).

These compounds represent, to the best of our knowledge, the molecular POMs with the greatest number of di or trivalent TM ions of the first row.

Compounds **2Cl** and **2Br** were synthesized in good yield starting from the same crude precursor **1**. Compound **1** is an azido complex of general formula $H_5K_6[(SiW_9O_{37})Cu_3N_3]{\cdot}19H_2O$ obtained by mixing in water at room temperature stoichiometric amounts of $[A,\alpha\text{-}SiW_9O_{34}]^{10-}$, $CuCl_2$, and NaN_3. The addition of an excess of azide has no influence on the composition of the final product. The IR spectrum of the product shows the presence of two single bands relative to the $\tilde{\nu}_{as(N=N)}$ vibration at 2082 and 1282 cm^{-1}, thus indicating that the azido group acts as an end-on bridging ligand.[11] Huge efforts were made to obtain single crystals of this compound suitable for X-Ray diffraction without success. A solution of **1** dissolved in molar NaCl or NaBr aqueous media turns from yellow to green upon heating, and crystals of **2Cl** or **2Br,** respectively, appear after cooling to room temperature within minutes. This phenomenon was not observed when the precursor was dissolved in a 1M NaF solution, and reduction followed by the decomposition of the POM occurs when a NaI solution was used. Similarly, the dissolution in nonhalide sodium salt solutions (Na_2SO_4, Na_2SO_3, $NaNO_3$) did not lead to the formation of the expected Cu^{II} complex, and compound **1** was systematically recovered. Even if **2Cl** or **2Br** do not contain any azido ligand, its presence during the synthetic process seems crucial since it has not been possible to obtain the title compound in absence of this reactant. The role of this bridging ligand remains unclear. Sodium azide may act as a base, as a preassembling agent, or may simply favor the crystallization process.

Single-crystal X-ray diffraction analyses were performed on compounds **2Cl** and **2Br**.[12] The protonated oxo bridges were localized by valence bound summations.[13] Complex **2Cl** is formed from two $[(SiW_9O_{34})(Cu(OH))_3]^{7-}$ subunits (denoted $\{Cu_3\}$), and two $[(SiW_9O_{33}(OH))(Cu(OH))_3Cu]^{4-}$ subunits (denoted $\{Cu_4\}$; Figure 1). Each subunit contains a Cu^{II} center in a square pyramidal environment, the remaining Cu^{II} centers are in a highly distorted octahedral geometry. Within the tetradecanuclear Cu^{II} subunit, the four divalent metals capping the $[SiW_9O_{34}]^{10-}$ entity form a distorted trigonal pyramid. Connections between the subunits inside the tetradecanuclear Cu^{II} complex occur a) between one Cu^{II} cation of each subunit and an oxygen atom of an adjacent subunit (Figure 1a), and b) through bridging OH ligands shared by the copper centers (Figure 2). Finally, a Cl^- anion is locked in the center of the cluster, surrounded by six Cu^{II} cations with long Cu–Cl distances ($d_{Cu-Cl} = 2.834(11)$–$3.003(11)$ Å). Compound **2Cl** approaches C_2 symmetry. The C_2 pseudo-axis passes through the chloride anion and is associated with the plane defined by the four Cu^{II} centers of two $\{Cu_4\}$ units linked to the central halide. Assembly of trivacant POMs through Y^{III}[14] or Nb^{V}[15] centers leading to diamagnetic tetrameric species were recently reported. The

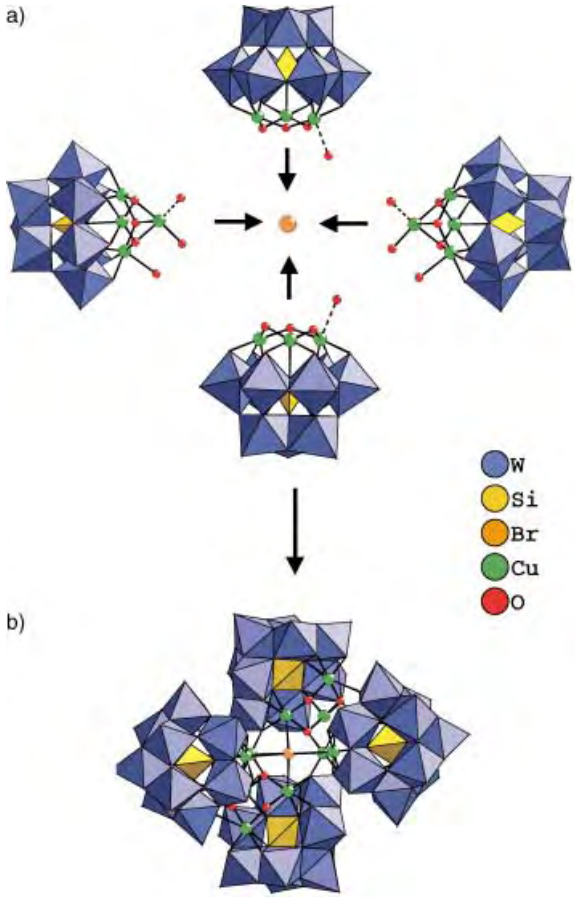


Figure 1. Polyhedral representation showing a) the four building blocks constituting the tetradecanuclear Cu^{II} cluster b) complex $[\{(SiW_9O_{34})\{SiW_9O_{33}(OH)\}(Cu(OH))_6Cu\}_2X]^{23-}$ (X = Cl in **2Cl**; X = Br in **2Br,** depicted). Bounds between Cu^{II} centers and oxygen atoms from another $\{SiW_9O_{34}\}$ subunit are shown as dashed lines.

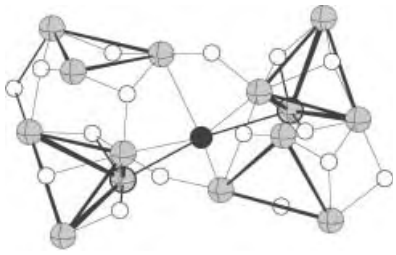


Figure 2. Ball-and-stick structural representation of the $\{Cu_{14}\}$ cluster. Cu = Gray crosshatched circles, O = white circles, X = black circles, (X = Cl in **2Cl**; X = Br in **2Br**). For clarity, only oxygen atoms linking the Cu^{II} ions are represented. Edges of the $\{Cu_3\}$ and $\{Cu_4\}$ sub-units are shown as bold lines.

connecting modes inside the yttrium, niobium and copper tetramers are radically different. In the first case, a $[Y_8W_7O_{30}]^{6+}$ cluster connects the subunits, while a $Nb_4O_6^{8-}$ unit ensures the connection in the second case. In **2Cl**, the formation of the high nuclearity cluster is driven by supramolecular assembly around a templating halide. The structure of **2Br** is similar to that of **2Cl**, the Br^- replacing the Cl^- ion,

 © 2003 Wiley-VCH Verlag GmbH & Co. KGaA, Weinheim

with, as expected, longer metal–halide distances (d_{Cu-Br} = 2.918(15)–3.071(9) Å).

The well defined experimental X-ray diffraction powder pattern performed in air on crystals of **2Cl** is not similar to the simulated powder pattern calculated from the data obtained by single-crystal analysis performed on the same compound in a Lindeman tube. Complexes **2Cl** and **2Br** are highly hydrated; exposure to air of these compounds lead to a spontaneous loss of water molecules of crystallization. Single-crystal X-ray diffraction analysis was performed on a dehydrated crystal of **2Cl** (i.e. $\mathbf{2Cl_{dhyd}}$). Surprisingly, despite the poor quality of the crystal, it has been possible to refine the diffraction data to obtain an acceptable structural model for $\mathbf{2Cl_{dhyd}}$,[12] thus showing that dehydration lead to a large compression along the *a* axis of the lattice (Figure 3).[16] Simulated and experimental powder patterns of $\mathbf{2Cl_{dhyd}}$ are in good agreement. Even in the dehydrated form, the magnetic clusters are well isolated from each other in $\mathbf{2Cl_{dhyd}}$, with the shortest Cu–Cu distances of 7.439 Å (d_{Cu-Cu} = 9.119 Å in **2Cl**).

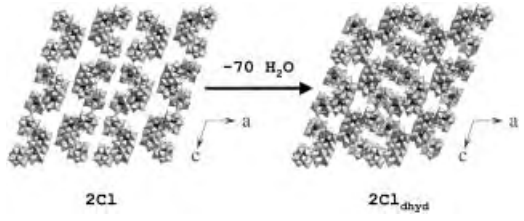


Figure 3. Polyhedral representation of **2Cl** and $\mathbf{2Cl_{dhyd}}$ showing the contraction of the *a* axis when dehydration occurs.

The magnetic behavior of a microcrystalline sample of compound $\mathbf{2Br_{dhyd}}$ has been studied in the range of 2 to 300 K, and the result is shown in Figure 4 under the form $\chi_M T$ versus T (χ_M = molar magnetic susceptibility). Due to the topological complexity of the $\{Cu_{14}\}$ cluster, it is not possible to fit the magnetic behavior of $\mathbf{2Br_{dhyd}}$ with a current theory. Indeed, by using reasonable approximations, up to nine exchange parameters would be required.[17] Nevertheless, the continuous decrease of the $\chi_M T = f(T)$ curve and the $\chi_M T$ value at 300 K ($\chi_M T$ = 4.33 $cm^3 mol^{-1}$ K for a calculated $\chi_M T$ value of 5.79 $K cm^3 mol^{-1}$ for fourteen noninteracting $S = {}^1/_2$ centers assuming g = 2.1; S = spin angular momentum, g = Landé factor) clearly indicates that antiferromagnetic interactions are predominant in $2Br_{dhyd}$. The magnetization study at 2 K showed that M tends to a value of 3 MB at high field (M = magnetization). As a half-spin ground state is excluded, this indicates that excited states are populated at 2 K. In the absence of data at very low temperature, the strong decrease observed under 4 K (Figure 4, inset) cannot be interpreted unambiguously. It can be attributed to the presence of a singlet ground state, but also to a triplet, the decrease being then a consequence of the zero-field splitting effect on the S = 1 state.

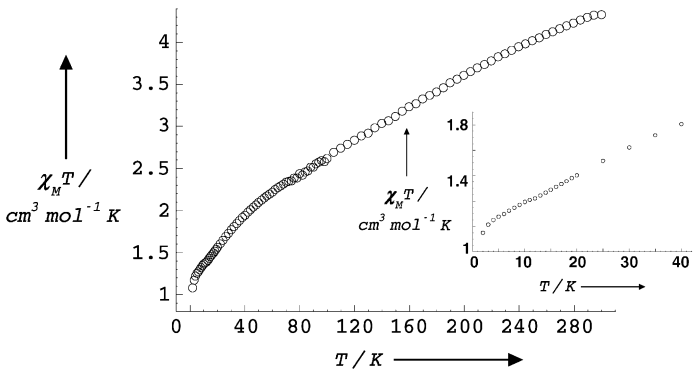


Figure 4. Thermal dependence of $\chi_M T$ for $\mathbf{2Br_{dhyd}}$ a) in the 2–300 K range, (B = 10 kG) b) in the 2–40 K range (B = 1 kG) (inset).

In conclusion, tetradecanuclear Cu^{II} polyoxometalates have been synthesized and characterized. The role of the N_3^- ligand during the synthetic process is not clearly understood but seems crucial. Structural characterization of azido–POM complexes must be performed. The recrystallization of the POM in high halide concentration allowed the formation of a supramolecular assembly. Now, it has to be checked whether the synthetic strategy described herein can be extended to other divalent metals and/or trivacant POMs systems. This work is in progress.

Experimental Section

1: A sample of $Na_{10}[A,\alpha\text{-}SiW_9O_{34}]\cdot 20H_2O$[3] (2.8 g, 1 mmol) was dissolved at room temperature in stirring water (40 mL) by adding solid $CuCl_2\cdot 2H_2O$ (0.5 g, 3 mmol). After 5 minutes, NaN_3 (0.2 g, 3 mmol) in water (20 mL) was added dropwise to the reaction mixture, and the green solution turned instantaneously to yellow. Solid potassium chloride (1.5 g, 20 mmol) was then added. After 2 h, the resulting yellow precipitate was filtered, washed with a KCl solution (20 mL, 1M), dried with ethanol and diethyl ether. Yield: 2.4 g (80%, based on Cu). Elemental analysis calcd (%) for $H_5K_6[(SiW_9O_{37})Cu_3N_3]\cdot 19H_2O$: W 54.41, Cu 6.27, K 7.71, N 1.38; found: W 55.11, Cu 6.11, K 7.56, N 1.58, Na 0.08. IR (KBr pellet): $\tilde{\nu}$ = 2082(s), 1282(w), 1001(m), 940(s), 905(s), 887(s), 783(s), 682(s), 548(m), 527(m), 364(m), 328(m)cm^{-1}. UV/Vis (H_2O): $\lambda_{max}(\varepsilon)$ = 747 (90).

2Cl and **2Br**: Compound **1** (0.3 g) was dissolved in a hot (80°C) aqueous solution of NaCl (1M, 5 mL). The green solution was cooled down to room temperature, and after one hour, large and long green needles of **2Cl** were obtained. Isolation of the product by filtration led to the dehydrated complex $\mathbf{2Cl_{dhyd}}$. Yield: 190 mg, 55% based on Cu. IR (KBr pellet): $\tilde{\nu}$ = 1006(m), 943(s), 910(s), 894(s), 774(s), 735(s), 670(s), 525(m), 357(m) cm^{-1}. UV/Vis (NaCl 1M): $\lambda_{max}(\varepsilon)$ = 757 (310). Elemental analysis calcd (%) for $H_{194}ClCu_{14}W_{36}O_{238}Si_4Na_{19}K_4$: W 54.09, Cu 7.27, Na 3.76, K 0.96, Cl 0.29; found: W 53.98, Cu 7.32, Na 4.08, K 1.26, Cl 0.55.

2Br and $\mathbf{2Br_{dhyd}}$ were obtained following the procedure described for **2Cl** and $\mathbf{2Cl_{dhyd}}$ in the same yield, but dissolving **1** in a 1M NaBr solution instead of a 1M NaCl solution. Infrared and UV/Vis spectra are similar to that found for compound $\mathbf{2Cl_{dhyd}}$. Elemental analysis calcd (%) for $H_{194}BrCu_{14}W_{36}O_{238}Si_4Na_{19}K_4$: W 53.83, Cu 7.24, Na 3.55, K 1.27, Br 0.65; found: W 53.53, Cu 7.26, Na 3.78, K 1.57, Br 1.06.

X-ray powder diffraction data were collected in air on a Siemens D5000 diffractometer (Cu Kα radiation).

TGA was carried out on compounds $\mathbf{2Cl_{dhyd}}$ and $\mathbf{2Br_{dhyd}}$ under nitrogen flow (60 mL min^{-1}) with a Perkin-Elmer electrobalance TGA-7 at a heating rate of 1°C min^{-1} up to 600°C, confirming the degree of hydration of these compounds.

Magnetic susceptibility measurements were carried out with a Quantum Design SQUID Magnetometer with an applied

 © 2003 Wiley-VCH Verlag GmbH & Co. KGaA, Weinheim

field of 1000 and 10000 G. The independence of the susceptibility value with respect to the applied field was checked at room temperature. The susceptibility data were corrected from the diamagnetic contributions of $\mathbf{2Br_{dhyd}}$ as deduced by using Pascal's constant tables. The $M = f(B)$ curve at 2 K is given as supplementary material.

Received: March 26, 2003 [Z51486]

Keywords: copper · magnetism · polyanions · solid-state structures · tungsten

[1] Special issue on Polyoxometalates, (Guest Ed.: C. Hill), *Chem. Rev.* **1998**, *98*, 1.
[2] *Polyoxometalates: From Platonic solid to Anti-Retroviral Activity*, (Eds.: M. T. Pope, A. Müller), Kluwer Academic Publishers, Dordrecht, **1994**.
[3] *Inorganic Syntheses, Vol. 27* (Ed.: A. P. Ginsbergh), Wiley, New York, **1990**.
[4] J. M. Clemente-Juan, E. Coronado, *Coord. Chem. Rev.* **1999**, *193–195*, 361.
[5] J. Liu, F. Ortega, P. Sethuraman, D. E. Katsoulis, C. E. Costello, M. T. Pope, *J. Chem. Soc. Dalton Trans.* **1992**, 1901.
[6] a) W. H. Knoth, P. J. Domaille, R. D. Farlee, *Organometallics* **1985**, *4*, 62; b) W. H. Knoth, P. J. Domaille, R. L. Harlow, *Inorg. Chem.* **1986**, *25*, 1577; c) F. Robert, M. Leyrie, G. Hervé, *Acta Cryst.* **1982**, *B38*, 358; d) P. Mialane, J. Marrot, E. Rivière, J. Nebout, G. Hervé, *Inorg. Chem.* **2001**, *40*, 44; e) U. Kortz, N. K. Al-Kassem, M. G. Savelieff, N. A. Al Kadi, M. Sadakane, *Inorg. Chem.* **2001**, *40*, 4742.
[7] U. Kortz, A. Tezé, G. Hervé, *Inorg. Chem.* **1999**, *38*, 2038.
[8] a) T. J. R. Weakley, H. T. Evans, J. S. Showell, G. F. Tourné, C. M. Tourné, *J. Chem. Soc. Dalton Trans.* **1973**, 139; b) H. T. Evans, C. M. Tourné, G. F. Tourné, T. J. R. Weakley, *J. Chem. Soc. Dalton Trans.* **1986**, 2699; c) R. G. Finke, M. W. Droege, P. J. Domaille, *Inorg. Chem.* **1987**, *26*, 3886; d) T. J. R. Weakley, R. G. Finke, *Inorg. Chem.* **1990**, *29*, 1235; e) C. J. Gómez-García, E. Coronado, P. Gómez-Romero, N. Casañ-Pastor, *Inorg. Chem.* **1993**, *32*, 3378; f) C. J. Gómez-García, J. J. Borrás-Almenar, E. Coronado, L. Ouahab, *Inorg. Chem.* **1994**, *33*, 4016; g) X. Y. Zhang, Q. Chen, D. C. Duncan, R. J. Lachiotte, C. L. Hill, *Inorg. Chem.* **1997**, *36*, 4381; h) X. Y. Zhang, G. B. Jameson, C. J. O'Connor, M. T. Pope, *Polyhedron* **1996**, *15*, 917; i) U. Kortz, S. Isber, M. H. Dickman, D. Ravot, *Inorg. Chem.* **2000**, *39*, 2915.
[9] K. Wassermann, R. Palm, H.-J. Lunk, J. Fuchs, N. Steinfeldt, R. Stösser, *Inorg. Chem.* **1995**, *34*, 5029.
[10] J. M. Clemente-Juan, E. Coronado, J. R. Galán-Mascarós, C. J. Gómez-García, *Inorg. Chem.* **1999**, *38*, 55.
[11] See for example A. Escuer, M. A. S. Goher, F. A. Mautner, R. Vicente, *Inorg. Chem.* **2000**, *39*, 2107.
[12] Crystal data and structure refinements for **2Cl**: a large green needle ($0.35 \times 0.15 \times 0.07$ mm) was analyzed with a Siemens SMART three-circle diffractometer equipped with a CCD bidimensional detector with $Mo_{K\alpha}$ monochromatized radiation ($\lambda = 0.71073$ Å). Monoclinic, space group $C2/c$, $a = 63.5191(16)$ Å, $b = 18.5238(5)$ Å, $c = 41.1156(10)$ Å, $\beta = 107.395(1)°$, $V = 46165.2(2)$ Å^3, $Z = 8$, $\rho_{calc} = 3.273$ g cm^{-3}, $\mu(Mo_{K\alpha}) = 19.353$ mm^{-1}, $F(000) = 39920$, 100177 reflections measured, of which 32701 were independent, 2343 refined parameters, $R_1 = 0.0772$, $wR_2 = 0.1863$. Crystal data and structure refinements for **2Br**: a green large needle crystal ($0.25 \times 0.08 \times 0.06$ mm) was analysed. Monoclinic, space group $C2/c$, $a = 63.4405(9)$ Å, $b = 18.4975(4)$ Å, $c = 41.3627(9)$ Å, $\beta = 107.514(1)°$, $V = 46288.6(16)$ Å^3, $Z = 8$, $\rho_{calc} = 3.270$ g cm^{-3}, $\mu(Mo_{K\alpha}) = 19.462$ mm^{-1}, $F(000) = 39968$, 103640 reflections measured, of which 33148 were independent, 2379 refined parameters, $R_1 = 0.0649$, $wR_2 = 0.1443$. Crystal data and structure refinements for $\mathbf{2Cl_{dhyd}}$: a green large needle crystal ($0.440 \times 0.08 \times 0.04$ mm) was analyzed. Monoclinic, space group $C2/c$, $a = 52.5809(10)$, $b = 18.2519(2)$, $c = 39.89370(10)$ Å, $\beta = 110.35(1)°$, $V = 35897.6(8)$ Å^3, $Z = 8$, $\rho_{calc} = 3.805$ g cm^{-3}, $\mu(Mo_{K\alpha}) = 24.748$ mm^{-1}, $F(000) = 35612$, 80012 reflections measured, of which 25916 were independent, 1135 refined parameters, $R = 0.1816$, $wR_2 = 0.4297$. For **2Cl, 2Br** and $\mathbf{2Cl_{dhyd}}$, data reduction was performed with the SAINT software. The absorption correction was based on multiple and symmetry-equivalent reflections in the data set by using the SADABS program based on the method of Blessing. The structures were solved by direct methods and refined by full-matrix least-squares by using the SHELX-TL package. Crystallographic data for the structure reported in this paper have been deposited at the Fachinformationszentrum Karlsruhe, 76344 Eggenstein-Leopoldshafen, Germany (fax: (+49) 7247-808-666; e-mail: crysdata@fiz-karlsruhe.de), on quoting the depository number numbers CSD-413064 (**2Cl**) and -413063 (**2Br**).
[13] N. E. Brese, M. O'Keeffe *Acta Crystallogr., Sect. B* **1991**, *47*, 192.
[14] R. C. Howell, F. G. Perez, S. Jain, W. DeW. Horrocks Jr. , A. L. Rheingold, L. C. Francesconi, *Angew. Chem.* **2001**, *113*, 4155; *Angew. Chem. Int. Ed.* **2001**, *40*, 4031.
[15] G.-S. Kim, H. Zeng, D. Vanderveer, C. L. Hill, *Angew. Chem.* **1999**, *111*, 3413; *Angew. Chem. Int. Ed.* **1999**, *38*, 3205.
[16] The number of crystallization water molecules have been determined for **2Cl** by considering the difference in cell volume between **2Cl** and $\mathbf{2Cl_{dhyd}}$.
[17] Considering the overall pseudo C_2 symmetry of the magnetic cluster, $\{Cu_{14}\}$ can be viewed as the adjunction of two $\{Cu_7\}$ clusters, formed by a $\{Cu_4\}$ and a $\{Cu_3\}$ subunits. If only one J constant can be considered for the modeling of the magnetic interactions inside the $\{Cu_3\}$ part, four are needed for the $\{Cu_4\}$ subunit. Three additional exchange parameters have to be considered for taking into account the interaction between the $\{Cu_3\}$ and the $\{Cu_4\}$ subunits. Finally, another J constant is needed, related to the interaction between the $\{Cu_7\}$ parts.

 © 2003 Wiley-VCH Verlag GmbH & Co. KGaA, Weinheim

Mixed-Valent Oligooxocobaltates

$Na_{10}Co_4O_{10}$, an Oligooxocobaltate(II, III) with Unusual Magnetic Properties**

*Mikhail Sofin, Hans-Ulrich Güdel, Roland Bircher, Eva-Maria Peters, and Martin Jansen**

The study of magnetic clusters of transition-metal ions is a very active area of research. There are two independent driving forces: one is based on the unusual behavior of so-called spin-ladder compounds, such as $KCuCl_3$ or $Sr_{14}Cu_{24}O_{41}$, which result from an interplay of strong and weak intra and interdimer interactions, respectively.[1,2] The dominant antiferromagnetic coupling within the dimers leads to a singlet ground state and a triplet excited state. Singlet–triplet excitations become delocalized, thus leading to dispersion, by the presence of weak interdimer interactions. The application of an external magnetic field leads to a crossing of the $M_s = -1$ component of the triplet with the singlet state ($M_s =$ electron spin angular momentum), thus creating a quantum critical point. The other driving force is based on the observation, about 10 years ago, of slow magnetic relaxation in molecular spin clusters.[3] These so-called single molecule magnets (SMM) constitute a very interesting class of materials. Besides the slow relaxation of the magnetization, they exhibit quantum tunneling phenomena at low temperatures. Typical SMM are composed of 3d transition-metal ions and organic or inorganic bridging and coordinating ligands.

Alkalioxometallates of the transition elements can consist of oligomeric complex oxoanions which contain magnetic centers of diverse spin moments. Unlike molecular spin clusters the oligomeric complexes in these compounds are not magnetically shielded from each other, and we can expect an interesting interplay of intra and intercluster interactions leading to novel magnetic properties. Such compounds are only accessible through conventional solid-state reactions, in general, and this high-temperature route lacks sufficient control for a directed synthesis of a targeted compound. In particular, fixing mixed valence states of the transition element components is an intricate task. As a rather efficient approach to overcoming such difficulties, we have developed the azide/nitrate route.[4] In this route, all starting materials used are solid, and the composition of the product, including the oxygen content, can be fixed by weighing out the respective alkali azide, nitrate (or nitrite), and transition metal oxide in appropriate ratios. By employing this technique, we synthesized the new mixed valent, oligomeric oxocobaltate $Na_{10}Co_4O_{10}$.

Thoroughly ground starting materials were reacted in a specially designed vessel,[4b] according to Equation (1).

$$76\,NaN_3 + 14\,NaNO_3 + 12\,Co_3O_4 \rightarrow 9\,Na_{10}Co_4O_{10} + 121\,N_2 \qquad (1)$$

The as-obtained single-phase samples are sensitive to air, and are black. They decompose at 600 °C, leaving CoO and $NaCoO_2$ as the only solid residues.

X-ray single crystal structure analysis[5] reveals a novel tetrameric oxoanion to be the prominent structural feature (Figure 1). Two edge sharing tetrahedra form the central unit, to which two CoO_3 triangles are attached by sharing a vertex with each one of the two tetrahedra. An inversion center is located at the middle of the edge common to the tetrahedra. The threefold triangular planar coordination, which is the one strongly preferred by Co^{2+} in alkali oxocobaltates (II),[6] justifies the assignment of the oxidation state of +2 of cobalt to this unit. This interpretation is backed by the Co–O bondlengths which, on average, agree well with data reported in the literature.[6] As a consequence Co^{3+} is assigned to the tetrahedral sites. This is rare, but not without precedent. We are aware of five examples: $RbCoO_2$,[7] β-$KCoO_2$,[8] Na_5CoO_4,[9] $Li_3Na_2CoO_4$[10] and $K_5CoW_{12}O_{40}\cdot 20\,H_2O$[11] are known to contain Co^{3+} in a tetrahedral coordination. Again, the bond lengths observed comply with published data,[9,10] and with the sums of the respective ionic radii.[12] Considering the Co–O separations in detail, one notices significant variations, thus reflecting strong disturbances of the ideal geometries of the coordination polyhedra (Figure 1). However, all deviations can be understood in terms of the different functionalities of the oxygen atoms involved. As a rule, edges shared by two polyhedra are contracted, while the centering cations repel each other. Furthermore, the distances from cobalt centers to bridging ligands are longer than those to terminal ones. With these qualitative rules in mind, the distances Co^{3+}–O1 (common edge) as well as Co^{2+}–O3 (bridging oxygen) being longest, and Co^{3+}–O5, Co^{2+}–O2 and Co^{2+}–O4 (all terminal) being shortest, appear reasonable.

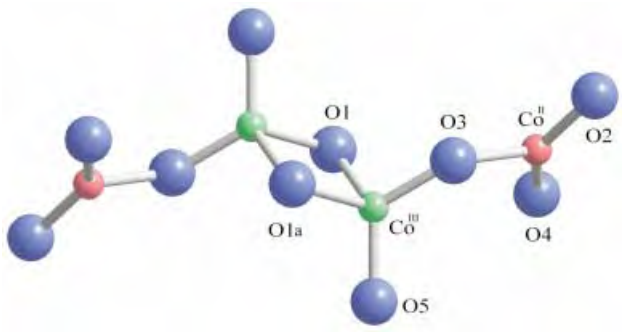


Figure 1. Crystal structure of the $Co_4O_{10}^{10-}$ anion. Bond lengths (Å): Co^{II}–O2 1.798, Co^{II}–O3 1.958, Co^{II}–O4 1.802, Co^{III}–O1 1.927, Co^{II}–O1a 1.951, Co^{II}–O3 1.823, Co^{II}–O5 1.777. Angles (°): Co^{II}-O3-Co^{III}: 124°, Co^{III}-O1-Co^{III}: 92°.

[*] Prof. Dr. M. Jansen, Dipl.-Chem. M. Sofin, E.-M. Peters
Max-Planck-Institut für Festkörperforschung
Heisenbergstrasse 1, 70569 Stuttgart (Germany)
Fax: (+49) 711-689-1502
E-mail: m.jansen@fkf.mpg.de
Prof. Dr. H.-U. Güdel, Dipl.-Chem. R. Bircher
Department of Chemistry and Biochemistry
University of Bern
Freiestrasse 3, 3000 Bern 9 (Switzerland)

[**] We thank E. Brücher und Dr. R. K. Kremer for carrying out the magnetic measurements

 DOI: 10.1002/anie.200351506 © 2003 Wiley-VCH Verlag GmbH & Co. KGaA, Weinheim

Also, the O-Co^{3+}-O angles varying from 88.4° to 118.8° are consistent with this view. The complex anions are "isolated" from each other by sodium ions which on their part have irregular oxygen coordination numbers ranging from 4 to 6 with bond lengths from 2.32 to 2.97 Å (Figure 2), which is again in the expected range.

The magnetic properties of $Na_{10}Co_4O_{10}$, represented as χ versus T and χT versus T, are shown in Figure 3 (χ = magnetic susceptibility). The behavior is most unusual, with a very low χT value of 5.4 emu K per Co_4 unit at 330 K and a sharp increase of χ around 40 K. Below 35 K the zero-field cooled and field-cooled data diverge, which indicates the onset of magnetic order. We can clearly distinguish two different temperature regimes reflecting different magnitudes of exchange interactions. The smooth part of the curve obtained between 330 K and 50 K is characteristic of dominant antiferromagnetic (AF) interactions within the cluster. The discontinuity at 38 K is attributed to cooperative intercluster interactions. Both, the increase and the divergence of χ, point to a magnetic ordering with a nonvanishing magnetic moment.

We can identify and roughly quantify the dominant exchange coupling by comparing the present results with magnetic data obtained for systems containing the constituents of our cluster as isolated units. From the data on Na_4CoO_3[13] for Co^{2+} in triangular oxo coordination, we deduce a χT value of 2 emu K per Co^{2+}, which is essentially independent on T between 300 K and 100 K. Figure 4 shows a comparison of χT versus T values of the title compound and $Na_6Co_2O_6$.[14] The latter was prepared by a similar route to $Na_{10}Co_4O_{10}$, and the crystal structure reveals the presence of dimers of tetrahedrally coordinated Co^{3+} ions sharing an edge, that is, exactly the inner part of the tetramer. The χT values in Figure 4 are given per $Co_4O_{10}^{10-}$ tetramer and $Co_2O_6^{6-}$ dimer, respectively. The two compounds have distinctly different magnetic properties. The dimer χT values are significantly higher and essentially temperature independent between 300 K and 100 K. We conclude that in our Co_4 cluster, showing Co^{2+}–Co^{3+} and Co^{3+}–Co^{3+} separation of 3.33 Å and 2.78 Å respectively, there are dominant antiferromagnetic interactions between the terminal Co^{2+} ions and their nearest Co^{3+} neighbors. These significantly reduce χT from about 12 to 5.4 emu K per tetramer at 330 K and lead to the observed continuous decrease down to about 50 K. We use the simplest possible model to obtain an estimate of this coupling strength. The magnetic moments of Co^{2+} and Co^{3+} are assumed isotropic with $S = 3/2$ and $S = 2$ values, respectively (S = spin angular momentum). The Co^{2+}–Co^{3+} interactions are expressed in terms of a Heisenberg exchange Hamiltonian: [Eq. (2)]

$$\mathscr{H} = -2J(\vec{S}_1\,\vec{S}_2 + \vec{S}_3\,\vec{S}_4) \qquad (2)$$

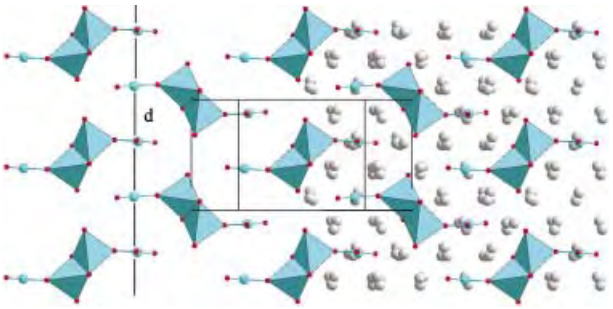


Figure 2. Crystal structure of $Na_{10}Co_4O_{10}$. Viewed along $\bar{4}01$. Co_4O_{10}-clusters are given in cyan with oxygen atoms in red (for detailed structure of the oxoanion see Figure 1). Sodium atoms (gray balls) are drawn only on the right hand part. The dashed line corresponds to a possible interaction pathway between clusters (with Co^{II}-Co^{II} distances $d = 4.1$ Å) leading to cooperative effects below 38 K.

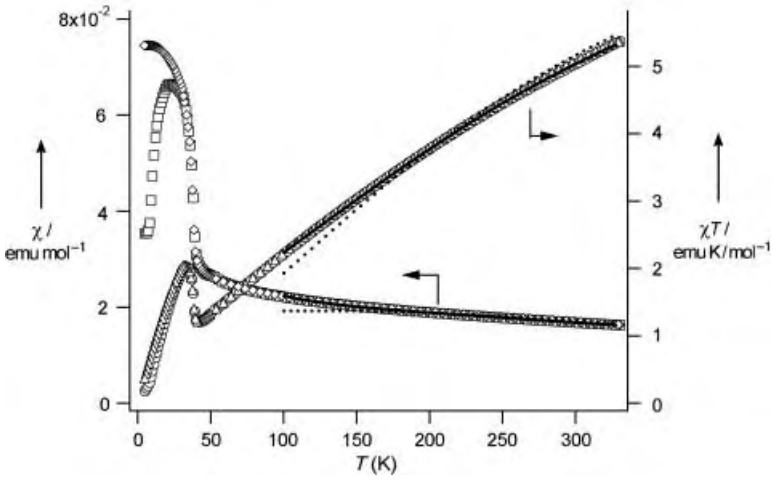


Figure 3. Magnetic susceptibility of $Na_{10}Co_4O_{10}$ represented as χ versus T and χT verus T. The applied field was 1 Tesla, and ZFC (□, ○) and FC (◇, △) refer to zero-field cooled and field-cooled, respectively. The dotted and full lines correspond to least-squares fits using equation (1) and the van Vleck equation. Dotted lines: $g_{Co^{2+}} = g_{Co^{3+}}$ set to 2.0, best fit $2J = -70$ cm^{-1}. Full lines: Best fit with $g_{Co^{2+}} = 1.71$, $g_{Co^{3+}} = 2.15$, $2J = -81$ cm^{-1}.

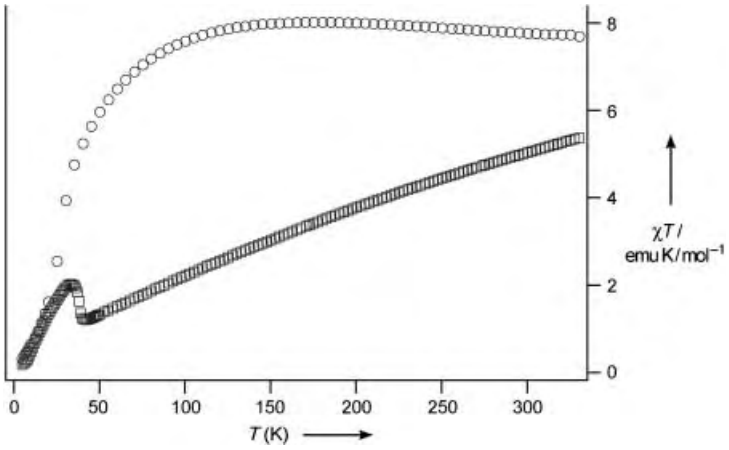


Figure 4. Magnetic susceptibility of $Na_{10}Co_4O_{10}$ (□) and $Na_6Co_2O_6$ (○) represented as χT per tetramer and dimer, respectively, versus T. The applied field was 1 Tesla.

 © 2003 Wiley-VCH Verlag GmbH & Co. KGaA, Weinheim

in which $S_1 = S_4 = 3/2$ and $S_2 = S_3 = 2$, and the Co^{3+}–Co^{3+} interaction is neglected (J = spin coupling constant). A least-squares fit of χT calculated on the basis of Equation (2) and the van Vleck equation[15] with $g = 2.0$ ($g = g$-factor) for all the ions to the data between 330 K and 100 K yields $2J = -70\ cm^{-1}$ and the broken line in Figure 3. The full line corresponds to a fit with the g values as additional fit parameters: $g_1 = g_4 = 1.71$, $g_2 = g_3 = 2.15$ and $2J = -81\ cm^{-1}$. Considering the very approximate character of our model the fits are surprisingly good. Anisotropy, which is expected to be important for both Co^{2+} and Co^{3+} in distorted triangular and T_d coordination, respectively, does not significantly affect the magnetic properties above 100 K.

The dominant antiferromagnetic Co^{2+}–Co^{3+} interaction with $2J = -81\ cm^{-1}$ is due to the superexchange through the oxygen ion. The Co^{3+} lies approximately in the triangular plane of the Co^{2+} coordination, and the Co^{2+}-O-Co^{3+} angle is 124°. The planar Co^{2+} coordination forces two unpaired electrons into the coordination plane. They will have significant overlap with oxygen 2s and 2p orbitals. On the Co^{3+} side all the t_2 orbitals are singly occupied in tetrahedral coordination. As a result of the overlap with the oxygen orbitals some spin density will be transferred also from Co^{3+} to oxygen. The situation thus bears some resemblance with dihydroxo-bridged Cu^{2+} dimers, in which the relevant orbital interactions occur in the Cu^{2+}-O-Cu^{2+} plane.[16] In these, the sign and the magnitude of J is a function of the angle at the bridging oxygen, and for an angle of 124° it is strongly antiferromagnetic. The interaction between the central Co^{3+} ions is much weaker, and we attribute this mainly to the much smaller Co^{3+}-O-Co^{3+} angle of 92°, which leads to a cancellation of ferro and antiferromagnetic contributions to J within Co^{3+}–O/O–Co^{3+} plane. This view is supported by comparison with $Na_6Co_2O_6$ where for a virtually identical geometry there is no manifestation of magnetic interactions down to about 100 K.

At 50 K in $Na_{10}Co_4O_{10}$ we thus have two strongly AF coupled Co^{2+}–Co^{3+} dimers, each with a $S = 1/2$ ground state. The coupling between these dimers is weak and cannot be quantified because of the onset of the ferromagnetic order at 38 K. This cooperative effect results from intercluster interactions. An inspection of the crystal structure (Figure 2) reveals unusually short Co^{2+}–Co^{2+} distances of $d = 4.1$ Å along the b axis between neighboring clusters, which may act as interaction pathways. From the small value of the ordered moment $M = 0.13\ \mu_B$ per Co_4 at 10 K the order is more likely canted antiferromagnetic rather than ferromagnetic.

In conclusion, the unusual new structure of the title compound is accompanied by unusual magnetic properties. We can clearly determine a hierarchy of exchange effects. A strong antiferromagnetic intracluster exchange interaction between Co^{2+} and Co^{3+} ions dominates the high T magnetic behavior. Below 38 K cooperative effects become important. As a consequence, the intracluster Co^{3+}–Co^{3+} coupling and the intercluster interactions cannot be separated.

Experimental Section

Starting materials for the preparation of $Na_{10}Co_4O_{10}$ were NaN_3 (Sigma, 99.5%), $NaNO_3$ (Aldrich, 99%) and activated Co_3O_4. Cobalt oxide was prepared by heating $Co(C_2O_4)\cdot 2H_2O$ (Alfa, Reagent Grade) in a stream of oxygen at 375 °C for 24 h. Precursors (NaN_3, $NaNO_3$ and Co_3O_4) were mixed in the required ratio according to Equation (1), ground in a ball mill, pressed in pellets under 10^5 N, dried under vacuum (10^{-3} mbar) at 150 °C for 12 h, and placed under argon in a tightly closed steel container provided with a silver inlay.[4b] In a flow of dry argon the following temperature treatment was applied: 25→260 °C (100 K h^{-1}); 260→380 °C (5 K h^{-1}); 380–500 °C (20 K h^{-1}) followed by subsequent annealing for 50 h at 500 °C. The obtained black powder is very sensitive to air and moisture and all following manipulation were performed in an inert atmosphere of purified argon.

Single crystals were grown by subsequent annealing of the as-prepared powder at 500 °C for 2000 h in silver crucibles, which were sealed in glass ampoules under dry argon.

Magnetic measurements were performed on a SQUID-Magnetometer (MPMS 5.5, Quantum Design) between 2 and 330 K in a magnetic field up to 5 T.

Received: March 27, 2003 [Z51506]

Keywords: cobalt · crystal structure · magnetic properties · mixed-valent compounds · oxo ligands

[1] N. Cavadini, C. Rüegg, A. Furrer, H. U. Güdel, K. Krämer, H. Mutka, P. Vorderwisch, *Phys. Rev. B* **2002**, *65*, 132415.
[2] G. Blumberg, P. Littlewood, A. Gozar, B. S. Dennis, N. Motoyama, H. Eisaki, S. Uchida, *Science* **2002**, *297*, 584.
[3] A. Caneschi, D. Gatteschi, R. Sessoli, A. L. Barra, L. C. Brunel, M. Guillot, *J. Am. Chem. Soc.* **1991**, *113*, 5873.
[4] a) D. Trinschek, M. Jansen, *Angew. Chem.* **1999**, *111*, 234; *Angew. Chem. Int. Ed.* **1999**, *38*, 133; b) M. Sofin, E. M. Peters, M. Jansen, *Z. Anorg. Allg. Chem.* **2002**, *628*, 2691.
[5] Crystal data: monoclinic, *C*2/*c* (No. 15), $Z = 4$, $a = 14.9061(4)$, $b = 8{,}1008(2)$, $c = 11.4233(3)$ Å, $\beta = 104.6102(9)°$, $M_r = 625.62$, $\rho = 3.11$, Single crystal X-ray structure determination: intensities were measured at 293 K with graphite-monochromatized $Mo_{K\alpha}$ radiation ($\lambda = 0.71069$ Å) on a Bruker AXS Diffraktometer with APEX Smart CCD; 3510 independent reflections (13458 total measured) were analysed by direct method. The refinement by full-matrix least squares gave final values $R_1(\text{all}) = 0.0294$, $R_w(\text{all}) = 0.0689$. Further details on the crystal structure investigations may be obtained from the Fachinformationszentrum Karlsruhe, 76344 Eggenstein-Leopoldshafen, Germany (fax: (+49) 7247-808-666; e-mail: crysdata@fiz-karlsruhe.de), on quoting the depository number CSD-413025.
[6] W. Burow, R. Hoppe, *Z. Anorg. Allg. Chem.* **1979**, *459*, 79; M. G. Barker, G. A. Fairhall, *J. Chem. Res. Synop.* **1979**, 371; W. Burow, R. Hoppe, *Z. Anorg. Allg. Chem.* **1980**, *467*, 158; F. Bernhardt, R. Hoppe, *Z. Anorg. Allg. Chem.* **1993**, *619*, 1807; R. Hoppe, J. Birx, *Z. Anorg. Allg. Chem.* **1988**, *557*, 171; J. Birx, R. Hoppe, *Z. Anorg. Allg. Chem.* **1990**, *591*, 67; J. Birx, R. Hoppe, *Z. Anorg. Allg. Chem.* **1990**, *588*, 7; F. Bernhardt, R. Hoppe, *Z. Anorg. Allg. Chem.* **1994**, *620*, 586.
[7] M. Jansen, R. Hoppe, *Z. Anorg. Allg. Chem.* **1975**, *417*, 31.
[8] C. Delmas, C. Fouassier, P. Hagenmuller, *J. Solid State Chem.* **1975**, *13*, 165.
[9] W. Burow, R. Hoppe, *Naturwissenschaften* **1980**, *67*, 192.
[10] J. Birx, R. Hoppe, *Z. Anorg. Allg. Chem.* **1991**, *597*, 19.
[11] L. C. Baker, T. P. McCutchean, *J. Am. Chem. Soc.* **1956**, *78*, 4503.
[12] R. D. Shannon, *Acta Crystallogr. Sect. A* **1976**, *32*, 751.
[13] A. Möller, *Chem. Mater.* **1998**, *10*, 3196.
[14] M. Sofin, E. M. Peters, M. Jansen, unpublished results.
[15] R. L. Carlin, *Magnetochemistry*, Springer, New York, **1986**.
[16] O. Kahn, *Molecular Magnetism*, VCH Publishers, New York, **1993**, p. 160.

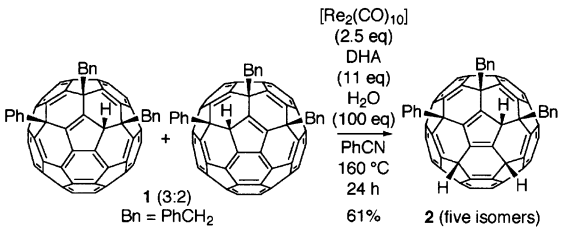
 © 2003 Wiley-VCH Verlag GmbH & Co. KGaA, Weinheim

Hydrogenation of Fullerenes

Rhenium-Templated Regioselective Polyhydrogenation Reaction of [60]Fullerene**

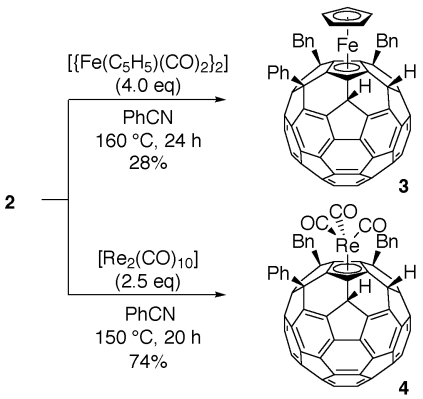
*Motoki Toganoh, Yutaka Matsuo, and Eiichi Nakamura**

With the progress of the science of fullerenes, regioselective polyfunctionalization reactions have acquired a unique importance in the development of new research areas.[1] Owing to the isotropic structure of [60]fullerene, regiocontrol of polyfunctionalization is a fundamental problem, on which considerable effort has been expended to provide useful solutions to the synthesis of polyalkylated fullerene molecules.[2] On the other hand, in spite of a significant number of synthetic routes and suggested utilities in materials applications,[3] polyhydrogenated fullerenes can still only be produced as a mixture of many compounds owing to the lack of control of both the regioselectivity and the number of hydrogen atoms delivered to the fullerene molecule.[4] Herein we report a new class of polyhydrogenation method, a rhenium-templated transfer hydrogenation from 9,10-dihydroanthracene (DHA) to [60]fullerene or its derivatives. The reaction of a [60]fullerene adduct **1** with DHA in the presence of $[Re_2(CO)_{10}]$ and water affords cyclopentadiene **2** [Eq. (1)],



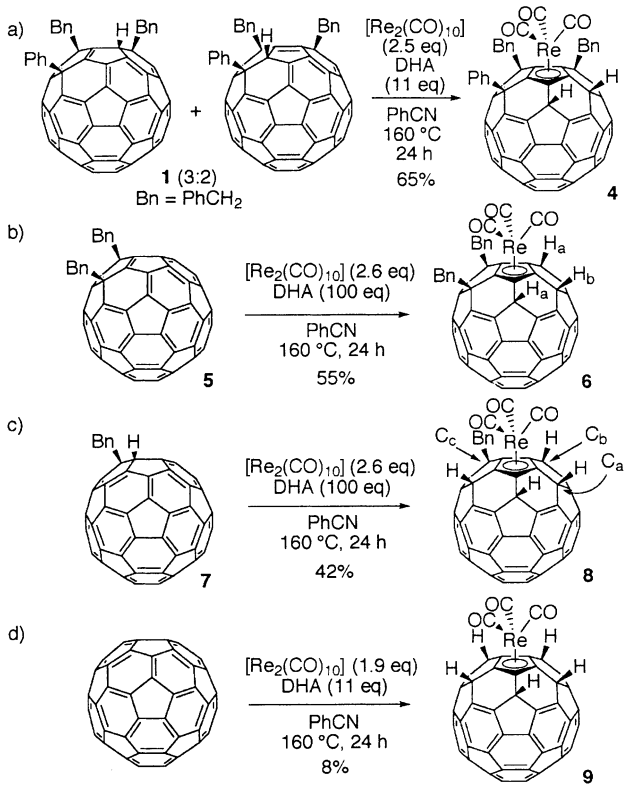
(1)

which can be converted into the corresponding metal complexes, such as an iron(II) complex **3** and a rhenium(I) complex **4** (Scheme 1). The reaction with the rhenium cluster under anhydrous conditions, on the other hand, results in hydrometallation reaction that affords a variety of the η^5-Re hydrofullerene complexes (**4**, **6**, **8**, and **9**, Scheme 2). The new hydrogenation/hydrometallation can also be described as a transfer hydrogenation reaction (see below) and represents the first method for completely regiocontrolled delivery of hydrogen atoms to a fullerene molecule.[5]



Scheme 1. Preparation of metal η^5 complexes by C–H bond activation.

The hydrogenation reaction is illustrated for the reaction of the fullerene tri-adduct $C_{60}(H)(PhCH_2)_2(Ph)$[6] (**1**) (a near 3:2 mixture of regioisomers as to the position of the hydrogen atom as shown in Equation (1)) with DHA (11 equiv) in the presence of $[Re_2(CO)_{10}]$ (2.5 equiv) and H_2O (100 equiv) in PhCN at 160 °C for 24 h [Eq. (1)]. The dihydrogenation product $C_{60}(H)_3(PhCH_2)_2(Ph)$ (**2**) was obtained in 61 % yield (obtained as a regio-mixture as to the position of the



Scheme 2. Hydrometallation reaction affording rhenium-hydrofullerene complexes.

[*] Prof. Dr. E. Nakamura, Dr. M. Toganoh, Dr. Y. Matsuo
Department of Chemistry
The University of Tokyo
Bunkyo-ku, Tokyo 113-0033 (Japan)
Fax: (+81) 3-5800-6889
E-mail: nakamura@chem.s.u-tokyo.ac.jp

[**] This study was supported by a grant-in-aid for Scientific Research (Specially Promoted Research) and by the 21st Century COE Program for Frontiers in Fundamental Chemistry from the Ministry of Education, Culture, Sports, Science and Technology. M.T. thanks the Japan Society for Promotion of Science for a predoctoral fellowship. Generous supply of [60]fullerene from Frontier Carbon Corporation is gratefully acknowledged.

Supporting information (experimental details) for this article is available on the WWW under http://www.angewandte.org or from the author.

 © 2003 Wiley-VCH Verlag GmbH & Co. KGaA, Weinheim DOI: 10.1002/anie.200351722

cyclopentadienyl hydrogen atom; all yields reported herein are based on the fullerene compound). The assigned structure rests on the ^{1}H NMR and mass spectra, and was subsequently confirmed by the single-crystal X-ray analysis of its rhenium derivative **4** (see below).

The cyclopentadiene **2** was readily converted into the corresponding η^5-Fe and η^5-Re complexes through C–H bond activation (Scheme 1).[7] Upon heating of **2** with $[\{(\eta\text{-}C_5H_5)Fe(CO)_2\}_2]$ (4.0 equiv) in PhCN at 160 °C for 24 h, **2** afforded $[(\eta\text{-}C_5H_5)Fe\{C_{60}(H)_2(PhCH_2)_2(Ph)\}]$ (**3**) in 28% yield. Similarly, treatment of **2** with $[Re_2(CO)_{10}]$ (2.5 equiv) gave $[Re(CO)_3\{C_{60}(H)_2(PhCH_2)_2(Ph)\}]$ (**4**) in 74% yield. The rhenium η^5-complex **4** showed IR (2024 and 1939 cm^{-1}), mass atmospheric pressure chemical ionization (APCI) sepctra ($[M^+]$ 1252), and NMR spectra consistent with the assigned structure. The two protons attached to the fullerene skeleton appear as doublet signals at $\delta = 5.32$ and 5.51 ppm, which are coupled with each other with $^5J_{HH} = 2.8$ Hz. In the ^{13}C NMR spectrum the signals of the two carbon atoms attached to these protons (both at $\delta = 44.35$ ppm) show the same $^1J_{CH}$ value of 145 Hz, which indicates 29% s character[8] (that is $sp^{2.4}$) of these "sp^3" carbon atoms.[9]

Unambiguous structure determination of **4** was by X-ray crystallographic analysis of a single crystal (Figure 1), obtained by slow diffusion of hexane to a CS_2 solution of

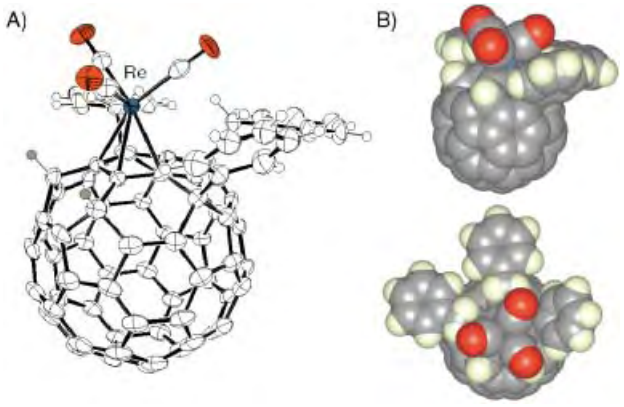


Figure 1. Molecular structure of the hydrofullerene rhenium complex **4**. A) ORTEP drawing with thermal ellipsoids at 30% probability. The CS_2 molecule found in the unit cell was omitted for clarity. B) Space-filling models.

4.[10] The X-ray data clearly indicates that cyclopentadienyl rhenium moiety is surrounded by five sp^3 carbon centers (rather than sp^2 centers) as in the penta-alkylated [60]fullerene metal η^5-complexes reported previously.[7,11] The geometry around the rhenium center is similar to that of $[(\eta\text{-}C_5H_5)Re(CO)_3]$,[12] as the three phenyl rings bound to the fullerene core in **4** point away from the metal center to minimize steric interaction with the carbonyl ligands.

The rhenium-templated polyhydrogenation under anhydrous conditions provides a direct entry to a variety of rhenium η^5-complexes of hydrofullerenes (Scheme 2). Treatment of **1** with DHA (11 equiv) and $[Re_2(CO)_{10}]$ (2.5 equiv) at 160 °C for 24 h in anhydrous PhCN directly afforded the rhenium complex **4** in 65% yield (Scheme 2a).[13] Similarly, the reaction of a dialkyl fullerene $C_{60}(PhCH_2)_2$ (**5**)[14] with DHA and $[Re_2(CO)_{10}]$ afforded a trihydrogenation product $[Re(CO)_3\{C_{60}(H)_3(PhCH_2)_2\}]$ (**6**) in 55% yield (Scheme 2b). The molecular weight determined from the mass spectrum (APCI, $[M^-]$ 1176) is consistent with the assigned structure. The IR (2020 and 1924 cm^{-1}) and NMR spectra are similar to those of **4**. For instance, the protons H_a and H_b are coupled to the neighboring sp^3 carbon atoms with $^1J_{CH} = 144$ Hz and 145 Hz, respectively. We therefore assigned the cyclopentadienyl rhenium structure **6** to the product. In the same manner, the reaction of a monoalkyl fullerene $C_{60}(H)(PhCH_2)$[15] (**7**) under the same conditions afforded a tetrahydrogenation product $[Re(CO)_3\{C_{60}(H)_4(PhCH_2)\}]$ (**8**) in 42% yield (Scheme 2c). The ^{13}C NMR signals indicated the presence of only three kinds of sp^3 fullerene carbon atoms ($C_a = 44.19$ ppm, $C_b = 44.56$ ppm, and $C_c = 55.77$ ppm), which indicates C_s symmetry on the NMR time scale (supported also by the ^{1}H NMR spectrum). Carbon atoms C_a and C_b have $^1J_{CH} = 145$ Hz. Mass (APCI, $[M^-]$ 1086) and IR spectra (2020, 1922 cm^{-1}) are also consistent with its structure.

Finally, the reaction of [60]fullerene with DHA and $[Re_2(CO)_{10}]$ afforded the hydrometallated product **9** albeit in low yield (Scheme 2d). The compound **9** had mass (APCI $[M^-]$ 996), IR (2017, 1921, and 1901 cm^{-1}) and NMR spectra consistent with the assigned structure. The ^{1}H NMR spectrum has only one singlet signal at $\delta = 5.23$ ppm, and the ^{13}C NMR spectrum has only nine signals (indicating C_{5v} symmetry on the NMR time scale) namely, those of an sp^3 ($\delta = 44.73$ ppm, $^1J_{CH} = 145$ Hz), an sp^2 cyclopentadienide ($\delta = 102.97$ ppm), a carbonyl carbon atom ($\delta = 190.64$ ppm), and six sp^2 carbon atoms assigned to the remaining carbon atoms of the fullerene core.

All the reactions described above proceeded cleanly and gave exclusively one regioisomer of the desired hydrogenation product, accompanied only by Diels–Alder adducts between the starting fullerene compound and anthracene (dehydrogenation product of DHA),[16] as well as recovered starting fullerene compound.[17] The solvent PhCN was uniquely effective among the variety of aromatic and other high-boiling-point solvents used. Simple polyhydrogenation products other than **2** have not been obtained to date in synthetically significant yields, this is due to the instability of such polyhydrogenated products towards oxygen and light.[5] On the other hand, the metal complexes **3**, **4**, **6**, **8**, and **9** are very stable.

The mechanism of the present reaction remains unclear. There are nonetheless pieces of experimental information that give some insight into the reaction pathway. First, consumption of [60]fullerene by reaction with DHA in the presence of $[Re_2(CO)_{10}]$ is much faster than in its absence, and, under the latter conditions, the reaction produced a mixture of various hydrogenated products, of which $C_{60}(H)_{36}$ was predominant.[4] Second, the reaction of $[Re_2(CO)_{10}]$ (2.8 equiv) with $C_{60}(H)_{36}$ (prepared by the reaction with DHA and which is thus contaminated with various other hydrogenated products) at 160 °C in PhCN did not give **9** but only produced [60]fullerene. Therefore, hydrofullerenes such as $C_{60}(H)_{36}$ are unlikely to be involved in the reaction

 © 2003 Wiley-VCH Verlag GmbH & Co. KGaA, Weinheim

pathway. Third, the reaction of a deuterated compound [D]**1** (C_{60}(D)($PhCH_2$)$_2$(Ph), >99% D) with DHA (10 equiv) and [$Re_2(CO)_{10}$] (2.5 equiv) at 160 °C in PhCN for 24 h afforded a deuterated product [D]**4** ([Re(CO)$_3${C_{60}(H)(D)($PhCH_2$)$_2$-(Ph)}) in 17% yield and its diprotio compound **4** in 43% yield. It is thus likely that the cyclopentadienyl C–D bond cleavage occurred first to generate a {Re-D} intermediate (transfer deuteration), which delivers the deuterium atom back to the periphery of the cylopentadienyl moiety. Similar C–H bond activation may also be involved in the reaction of **7**. Finally, the rhenium complex **4** could not be converted into the metal-free compound **2** under the wet conditions where **2** was obtained, which suggests that **2** was not formed via **4** in Equation (1).

In summary, we have developed a new transfer hydrogenation reaction to introduce hydrogen atoms regioselectively to [60]fullerene and its derivatives. The reaction under anhydrous conditions provides a flexible method for the synthesis of the η^5-metal complexes of a variety of hydrofullerenes, while the reaction under wet conditions has proven to be effective for the synthesis of the trihydro compound **2**. In contrast to the known polyhydrogenation reactions that invariably produce mixtures of products,[5,18] the control of both the regioselectivity and the numbers of hydrogen atoms is remarkably high. The η^5-structures of the metal complexes[7,11] reported herein are the first examples of such hydrofullerenes. The similarity of the regioselectivity of the formation of **4**, **6**, **8**, and **9** to that of the regioselective polyalkylation reported previously[2b,19] suggests certain mechanistic kinship among these reactions, for example, an electron-transfer mechanism. We anticipate that the hydrofullerene metal complexes will serve as useful molecules in materials chemistry and catalysis.[1,3,20]

Received: April 23, 2003 [Z51722]
Published online: July 11, 2003

Keywords: cyclopentadienyl ligands · fullerenes · hydrogenation · hydrometallation · rhenium

[1] a) S. Zhou, C. Burger, B. Chu, M. Sawamura, N. Nagahama, M. Toganoh, U. E. Hackler, H. Isobe, E. Nakamura, *Science* **2001**, *291*, 1944; b) M. Sawamura, K. Kawai, Y. Matsuo, K. Kanie, T. Kato, E. Nakamura, *Nature* **2002**, *419*, 702.

[2] a) F. Diederich, R. Kessinger, *Acc. Chem. Res.* **1999**, *32*, 537; b) E. Nakamura, M. Sawamura, *Pure Appl. Chem.* **2001**, *73*, 355; c) H. Isobe, N. Tomita, E. Nakamura, *Org. Lett.* **2000**, *2*, 3663; d) E. Nakamura, K. Tahara, Y. Matsuo, M. Sawamura, *J. Am. Chem. Soc.* **2003**, *125*, 2834.

[3] a) R. O. Loutfy, E. M. Wexler, W. Li in *Perspectives of Fullerene Nanotechnology* (Ed: E. Osawa), Kluwer Academic Publishers, Dordrecht, **2002**, p. 281; b) R. O. Loutfy, S. Katagiri in *Perspectives of Fullerene Nanotechnology* (Ed: E. Osawa), Kluwer Academic Publishers, Dordrecht, **2002**, p. 357.

[4] a) J. Nossal, R. K. Saini, A. K. Sadana, H. F. Bettinger, L. B. Alemany, G. E. Scuseria, W. E. Billups, M. Saunders, A. Khong, R. Weisemann, *J. Am. Chem. Soc.* **2001**, *123*, 8482; b) C. Ruechard, M. Gerst, J. Ebenhoch, H. D. Beckhaus, E. E. B. Campbell, R. Tellgmann, H. Schwarz, T. Weiske, S. Pitter, *Angew. Chem.* **1993**, *105*, 609; *Angew. Chem. Int. Ed. Engl.* **1993**, *32*, 584.

[5] a) J. Nossal, R. K. Saini, L. B. Alemany, M. Meier, W. E. Billups, *Eur. J. Org. Chem.* **2001**, 4167; b) M. S. Meier, H. P. Spielmann, R. C. Bergosh, M. E. Gallagher, M. A. Hamon, B. R. Weedon, *Carbon* **2000**, *38*, 1535.

[6] M. Sawamura, M. Toganoh, K. Suzuki, A. Hirai, H. Iikura, E. Nakamura, *Org. Lett.* **2000**, *2*, 1919.

[7] M. Sawamura, Y. Kuninobu, M. Toganoh, Y. Matsuo, M. Yamanaka, E. Nakamura, *J. Am. Chem. Soc.* **2002**, *124*, 9354.

[8] a) N. Muller, D. E. Pritchard, *J. Chem. Phys.* **1959**, *31*, 768; b) N. Muller, D. E. Pritchard, *J. Chem. Phys.* **1959**, *31*, 1471.

[9] P. R. Surján, *J. Mol. Struct. (THEOCHEM)* **1995**, *338*, 215.

[10] Crystal data for **4**: monoclinic space group $P2_1/m$ (No. 11), a = 10.5820(3), b = 19.9100(7), c = 11.8540(4) Å, β = 91.044(2)°, V = 2497.1(1) Å^3, T = 193(2) K, R_1 = 0.070 (all data), wR_2 = 0.203 (all data), GOF (F^2) = 1.12. CCDC-208938 (**4**) contains the supplementary crystallographic data for this paper. These data can be obtained free of charge via www.ccdc.cam.ac.uk/conts/retrieving.html (or from the Cambridge Crystallographic Data Centre, 12 Union Road, Cambridge CB2 1EZ, UK; fax: (+44) 1223-336-033; or deposit@ccdc.cam.ac.uk).

[11] a) M. Sawamura, H. Iikura, E. Nakamura, *J. Am. Chem. Soc.* **1996**, *118*, 12850; b) M. Sawamura, Y. Kuninobu, E. Nakamura, *J. Am. Chem. Soc.* **2000**, *122*, 12407; c) Y. Matsuo, E. Nakamura, *Organometallics* **2003**, *22*, 2554.

[12] P. J. Fitzpatrick, Y. L. Page, I. S. Butler, *Acta Crystallogr. Sect. B* **1981**, *37*, 1052.

[13] Water content of the solvent was determined by Karl-Fisher moisture titrator to be less than 30 ppm.

[14] R. Subramanian, M. Kadish, M. N. Vijayashree, X. Gao, M. T. Jones, M. D. Miller, K. L. Krause, T. Suenobu, S. Fukuzumi, *J. Phys. Chem.* **1996**, *100*, 16327.

[15] A. Hirsch, T. Grösser, A. Skiebe, A. Soi, *Chem. Ber.* **1993**, *126*, 1061.

[16] M. Tsuda, T. Ishida, T. Nogami, S. Kurono, M. Ohashi, *J. Chem. Soc. Chem. Commun.* **1993**, 1296.

[17] The reactions under photochemical conditions gave the numerous products see S. Zhang, T. L. Brown, Y. Du, J. R. Shapley, *J. Am. Chem. Soc.* **1993**, *115*, 6705.

[18] a) W. E. Billups, W. Luo, A. Gonzalez, D. Arguello, L. B. Alemany, T. Marriott, M. Saunders, H. A. Jiménez-Vázquez, A. Khong, *Tetrahedron Lett.* **1997**, *38*, 171; b) S. Ballenweg, R. Gleiter, W. Krätschmer, *Tetrahedron Lett.* **1993**, *34*, 3737; c) M. S. Meier, P. S. Corbin, V. K. Vance, M. Clayton, M. Mollman, *Tetrahedron Lett.* **1994**, *35*, 5789.

[19] a) M. Sawamura, H. Iikura, T. Ohama, U. E. Hackler, E. Nakamura, *J. Organomet. Chem.* **2000**, *599*, 32; b) M. Sawamura, M. Toganoh, Y. Kuninobu, S. Kato, E. Nakamura, *Chem. Lett.* **2000**, 270; c) M. Sawamura, N. Nagahama, M. Toganoh, E. Nakamura, *J. Organomet. Chem.* **2002**, *652*, 31; d) M. Sawamura, H. Iikura, A. Hirai, E. Nakamura, *J. Am. Chem. Soc.* **1998**, *120*, 8285; e) M. Sawamura, M. Toganoh, H. Iikura, Y. Matsuo, A. Hirai, E. Nakamura, *J. Mater. Chem.* **2002**, *12*, 2109.

[20] a) C. P. Casey, *Science* **1993**, *259*, 1552; b) H. Chen, J. F. Hartwig, *Angew. Chem.* **1999**, *111*, 3597; *Angew. Chem. Int. Ed.* **1999**, *38*, 3391.

 © 2003 Wiley-VCH Verlag GmbH & Co. KGaA, Weinheim

Palladium–Carbonyl Clusters

Nanosized $[Pd_{69}(CO)_{36}(PEt_3)_{18}]$: Metal-Core Geometry Containing a Linear Assembly of Three Face-Sharing Centered Pd_{33} Icosahedra Inside of a Hexagonal-Shaped Pd_{30} Tube**

*Nguyet T. Tran and Lawrence F. Dahl**

Dedicated to Professor Boon Teo on the occasion of his 55th birthday

Palladium possesses exceptional versatility as a unique transition metal in forming an unparalleled assembly of highly condensed carbonyl–phosphane clusters containing either ccp-, mixed ccp/hcp-, or icosahedral-based metal-core architectures. Examples of high-nuclearity homopalladium clusters (that is, clusters arbitrarily designated by us to possess at least ten metal-core atoms with direct metal–metal bonding) with ccp or mixed ccp/hcp layer-stacking geometries include $[Pd_{10}(CO)_{12}(PR_3)_6]$ (R = *n*Bu,[1] Et[1a,2]) with a Pd_{10} tetracapped octahedron, $[Pd_{12}(CO)_{12}(PR_3)_6]$ (R = *n*Bu,[3] Ph[4]) with a Pd_{12} hexacapped octahedron, $[Pd_{23}(CO)_{22}(PEt_3)_{10}]$[5] and $[Pd_{23}(CO)_{20}(PEt_3)_{10}]$[6] with a centered hexacapped cuboctahedral Pd_{19} kernel,[5–8] and $[Pd_{30}(CO)_{26}(PEt_3)_{10}]$ and $[Pd_{54}(CO)_{40}(PEt_3)_{14}]$ with interpenetrating ("twinned-core") cuboctahedral Pd_{20} kernels.[9] High-nuclearity homopalladium clusters built on centered icosahedral frameworks are illustrated by $[Pd_{16}(CO)_{13}(PR_3)_9]$ (R = Me,[10] Et[11]) with a single Pd_{13}-centered icosahedron, and $[Pd_{34}(CO)_{24}(PEt_3)_{12}]$ with four interpenetrating Pd_{26}-centered icosahedra.[6,12] $[Pd_{35}(CO)_{23}(PMe_3)_{15}]$[10] and $[Pd_{39}(CO)_{23}(PMe_3)_{16}]$[10] each contain a face-fused Pd_{23}-centered biicosahedron with linear (D_{3h}) and bent (C_{2v}) geometries, respectively; the D_{3h} central Pd_{29} polyhedron of the Pd_{35} core ideally conforms to five interpenetrating centered icosahedra.[10] $[Pd_{59}(CO)_{32}(PMe_3)_{21}]$[10,13] has two Pd_{13}-centered icosahedra that are indirectly connected through *trans* double-face sharing with an inner face-fused Pd_9 bioctahedron. The unique nanosized $[Pd_{145}(CO)_x(PEt_3)_{30}]$ cluster (with $x \approx 60$) contains a capped three-shell 145-atom metal core that closely conforms to I_h icosahedral symmetry.[14]

Herein we report the preparation, isolation, and structural determination of another type of nanosized icosahedral-based cluster, $[Pd_{69}(CO)_{36}(PEt_3)_{18}]$ (**1**), which has two new important stereochemical features: 1) a linear face-condensation of three centered icosahedra that gives rise to a linear face-sharing Pd_{33}-centered triicosahedron, and 2) a hexagonal-shaped Pd_{30} tube formed by cyclic *trans* edge-sharing of six Pd_7-centered hexagons (host), inside of which resides the linear triicosahedron (guest).

It is particularly noteworthy that this face-condensed icosahedral growth pattern in **1** is completely different from the general vertex-sharing growth sequence of the extraordinary centered polyicosahedral Au/Ag and Au/Ag/M halide phosphane supraclusters (where M = Ni, Pd, Pt are centered M atoms) proposed by Teo, Zhang, and co-workers[15] (see below). In addition, the well-defined stoichiometries and widely diversified but precise geometries of **1** and other homopalladium carbonyl phosphane clusters have especially important stereochemical implications concerning multitwinned structures and growth patterns of much larger ligated and nonligated palladium nanoparticles, and hence are of relevance in nanotechnology.

Compound **1** was obtained in moderate yields ($\approx 50\%$) from a reproducible (optimized) synthesis involving the use of the preformed tetracapped octahedral $[Pd_{10}(CO)_{12}(PEt_3)_6]$.[16] Its composition as well as its atomic arrangement were unequivocally established from low-temperature CCD X-ray diffractometry studies[17,18] of two different crystal forms obtained from related reactions: one being trigonal (**1**) and the other triclinic (**1a**) with each molecule having crystallographic $\bar{3}$ (C_{3i}) and $\bar{1}$ (C_i) site symmetry, respectively. The molecular geometries of **1** and **1a** obtained from their well-refined crystal structures are nearly identical.

The configuration of **1** given in Figure 1 consists of a Pd_{69} core composed of the central Pd_{33} triicosahedron with its central icosahedron completely enclosed by a hexagonal-shaped Pd_{30} cylindrical cavity along with six additional square-capping Pd atoms. The Pd_{69} core geometry has crystallographic $\bar{3}$ symmetry but ideally conforms to a D_{3d} geometry.

The linear Pd_{33} triicosahedron arises from face-sharing of the three centered icosahedra on centrosymmetrically opposite faces of the middle centered icosahedron. This imposes a linear D_{3d} geometry with the crystallographic $\bar{3}$ (S_6) axis passing through the three centered atoms and four midpoints of the two face-fused triangular faces and the two opposite triangular faces of the two outer icosahedra. Each of the two outer icosahedra is also linked to the middle one by three additional intericosahedral bonding connections that result from three threefold-related pairs of corresponding Pd(cage) atoms (namely, Pd(4) and Pd(5)) at a distance of 2.834(2) Å (shown as red links in Figure 1a). The D_{3h} linear face-sharing Pd_{23} biicosahedral fragment in the Pd_{35} core of $[Pd_{35}(CO)_{23}(PMe_3)_{15}]$ similarly possesses three threefold-related intericosahedal Pd–Pd interactions (mean: 2.98 Å; range: 2.941(4)–3.020(4) Å), whereas the C_{2v} bent face-sharing Pd_{23} biicosahedral fragment in the Pd_{39} core of $[Pd_{39}(CO)_{23}(PMe_3)_{16}]$ is additionally connected by only two intericosahedral bonding links (namely, two at 2.954(4) Å, with a third nonbonding connectivity at 4.029(5) Å).[19]

Large dispersions of 0.3–0.4 Å in individual Pd–Pd connectivities are observed for each mean separation, other than those for the centered icosahedral radial distances, which

[*] Prof. Dr. L. F. Dahl, Dr. N. T. Tran
Department of Chemistry
University of Wisconsin-Madison
1101 University Avenue, Madison, WI 53706 (USA)
Fax: (+1) 608-262-6143
E-mail: dahl@chem.wisc.edu

[**] This research was supported by the National Science Foundation. Color figures were prepared with Crystal Maker, Interactive Crystallography (version 5; David C. Palmer, P.O. Box 183, Bicester, Oxfordshire, OX26 3TA (UK)). We are indebted to Dr. Ilia Guzei (UW-Madison) for helpful crystallographic advice.

 DOI: 10.1002/anie.200351738 © 2003 Wiley-VCH Verlag GmbH & Co. KGaA, Weinheim

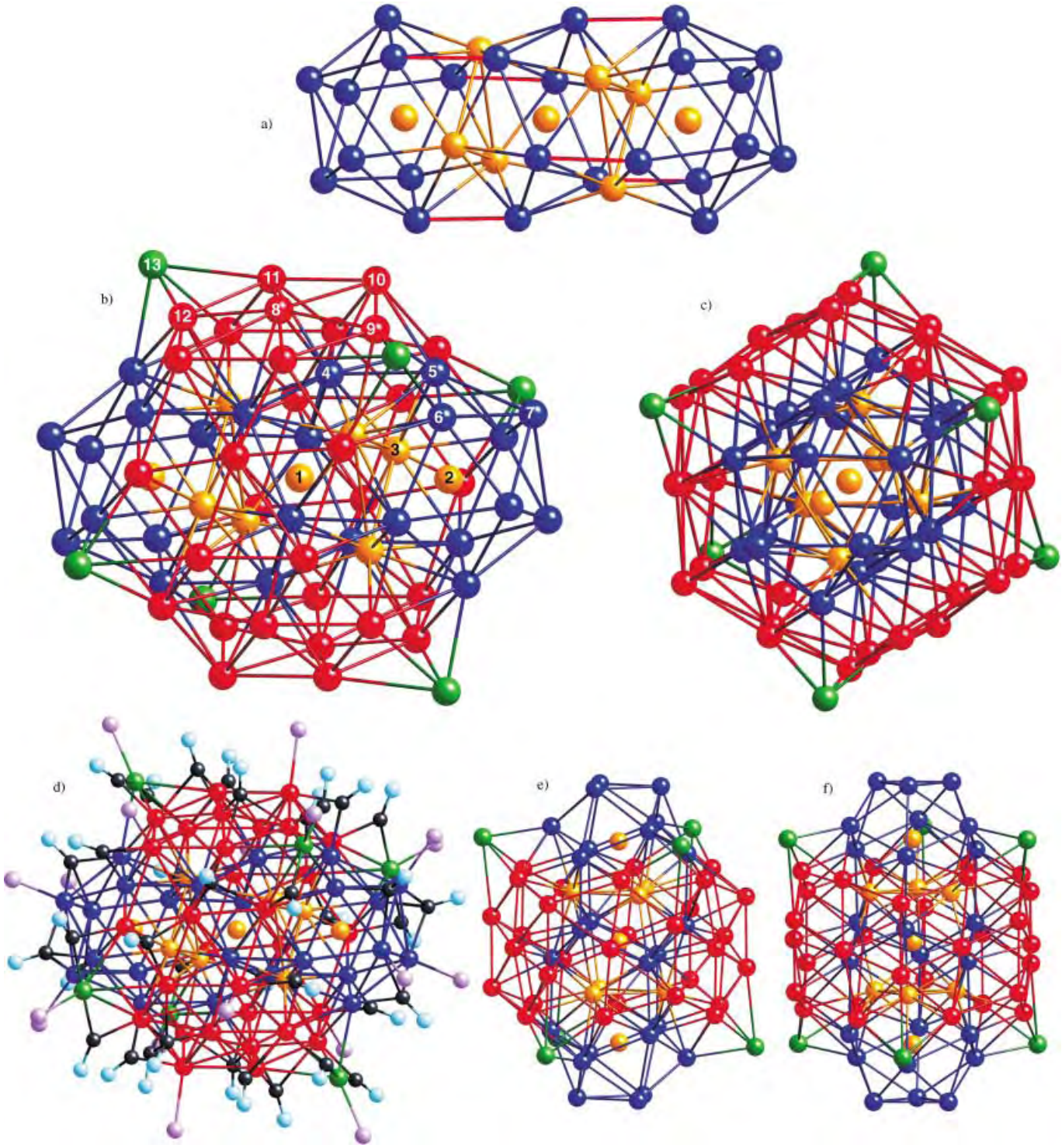


Figure 1. The anatomy of nanosized icosahedral-based $[Pd_{69}(CO)_{36}(PEt_3)_{18}]$ (**1**), with crystallographic $\bar{3}$ (C_{3i}) and pseudo $\bar{3}2/m$ (D_{3d}) symmetry: a) 33-atom core of the linear face-sharing Pd_{33} triicosahedron formed by face-condensation of two outer centered icosahedra on centrosymmetrically opposite triangular faces of the inner centered icosahedron. The three centered and six face-fused atoms are colored gold; b) and c) side and near-front views, respectively, of the entire Pd_{69} core (with numbering scheme for Pd atoms shown in b)). Its formal construction may be described as a Pd_{33} triicosahedron (guest) residing inside a hexagonal-shaped Pd_{30} tube (host; shown in red) with six symmetry-equivalent atoms (green) each asymmetrically capping a square-bonding polygon formed from one atom (blue) of the triicosahedron and three atoms (red) of the encapsulating host; d) entire structure of **1** displaying the geometrical disposition of 18 PEt_3 ligands (without ethyl substituents) and 18 doubly and 18 triply bridging CO ligands; e) front view of one of three pseudohorizontal twofold axes in the Pd_{69} core with centrosymmetric D_{3d} geometry. Each of the three pseudohorizontal twofold axes, which are normal to the principal $\bar{3}$ axis (that is, a combined threefold and inversion center), passes through the centered Pd(1) atom of the middle icosahedron and the centered atoms of two opposite Pd_7-centered hexagons; f) another front view (after counterclockwise rotation of **1** by 30° about the vertically oriented $\bar{3}$ axis) of one of three vertical σ_d mirror planes that bisect pairs of the three horizontal twofold axes in the Pd_{69} core.

 © 2003 Wiley-VCH Verlag GmbH & Co. KGaA, Weinheim

agree within 0.04 Å. Similar large dispersions in Pd–Pd connectivities are found in the other previously mentioned icosahedral-based homopalladium carbonyl–phosphane clusters. Nevertheless, the different bonding Pd–Pd mean separations in **1** are within 0.1 Å of those found in ccp Pd metal (2.751 Å).[19]

For the middle icosahedron of **1**, the mean radial distance of 2.68 Å (range: 2.657(1)–2.702(1) Å) from the central Pd(1) atom to the 12 Pd(cage) atoms is significantly shorter than the mean tangential distance of 2.82 Å (range: 2.657(1)–3.127(2) Å) corresponding to the 30 icosahedral edges of the 12 Pd(cage) atoms. Similarly, for the two symmetry-equivalent outer icosahedra, the corresponding radial and tangential mean separations are 2.72 Å (range: 2.702(2)–2.730(2) Å) and 2.86 Å (range: 2.725(2)–3.127(2) Å), respectively. These observed radial compressions of 5.0% (i.e., [(2.82–2.68) Å/2.82 Å] × 100) and 4.9% (i.e., [(2.86–2.72) Å/2.86 Å] × 100) are identical with the predicted value of approximately 5% for a geometrically regular centered icosahedron[20] and furthermore are completely consistent with experimental values determined for Pd_{13}-centered icosahedra in the previously mentioned Pd_{16}, Pd_{35}, Pd_{39}, Pd_{59}, and Pd_{145} clusters.

The hexagonal-shaped Pd_{30} tube that surrounds the middle icosahedron of the linear face-sharing triicosahedron can be viewed as a cyclic *trans* edge-sharing of six Pd_7-centered hexagons. The Pd–Pd bonding connectivities within the independent Pd(8)-centered hexagon vary considerably, but their mean separations of 2.84 Å (range: 2.697(2)–3.150(2) Å) for the radial Pd(8)–Pd(edge) separations and 2.83 Å (range: 2.743(2)–3.018(2) Å) for the tangential Pd(edge)–Pd(edge) separations are virtually identical. The independent Pd(8)-centered atom is displaced by 0.29 Å from the mean plane of six hexagon atoms in the outward direction away from the Pd_{33} triicosahedral guest. The average diameter of this cylinder-like Pd_{30} tube is approximately 0.86 nm, based upon the distance of 0.92 nm between centrosymmetrically opposite Pd(8)-centered atoms minus 0.06 nm for the net perpendicular displacements of two Pd(8) atoms out of their mean Pd_6 hexagons.

The middle icosahedron of the linear face-condensed Pd_{33} triicosahedron fills the cylindrical cavity of the hexagonal-shaped Pd_{30} tube. Its encapsulation by this tube can be considered as a guest–host model that is fully bonded in this case (that is, a *permanent* guest). Each centered hexagon forms 14 Pd–Pd bonding connectivities with the icosahedral fragment, with a mean length of 2.79 Å (range: 2.627(2)–2.911(2) Å). The number of bonding interactions of each atom of the independent Pd_7-centered hexagon to the triicosahedron varies from one to three.

The resulting Pd_{63} guest–host composite of the Pd_{69} core of **1** is completed by six additional Pd atoms that cap the six bonding square polygons formed between the Pd_{33} triicosahedron and the hexagonal-shaped Pd_{30} tube. The capping Pd atoms are each asymmetrically coordinated to its bonding square Pd_4 base with three short Pd–Pd connectivities that range from 2.723(2) to 2.764(2) Å and one long connectivity of 3.151(2) Å; an analogous asymmetry of one long and three much shorter Pd–Pd connectivities for tetracapping Pd atoms is observed in $[Pd_{23}(CO)_{20}(PEt_3)_8]$.[6b,21]

Compound **1** has 15 interior Pd(i) atoms, consisting of the entire 13-atom middle centered icosahedron and the two centered Pd atoms of the two outer centered icosahedra, and 54 surface Pd(s) atoms. Nanosized diameters of the ellipsoidal-shaped Pd_{69} core are 1.35 nm between the two centrosymmetrically opposite square-capping Pd atoms, 1.24 nm between two opposite outermost icosahedral triangular faces of the triicosahedron, and 0.92 nm between two centered Pd atoms of two opposite centered hexagons.

Compound **1** is stabilized by 18 PEt_3 ligands, together with 18 doubly and 18 asymmetrically coordinated (two shorter/one longer) triply bridging CO ligands.[22] The 18 PEt_3 ligands are each attached to the six Pd atoms of the two outer triangular faces of the triicosahedron, to the six square-capping Pd atoms, and to the six Pd(edge) atoms of the six centered hexagons that are not basal atoms connected to the six square-capping Pd atoms. It is noteworthy that each square-capping Pd atom has two doubly bridging CO ligands that are linked on the two opposite short Pd(axial)–Pd(basal) edges.

A comparison of the face-condensation mode of formation of the centered Pd_{33} triicosahedral guest in **1** with the entirely different vertex-sharing growth-pattern of centered polyicosahedral Au/Ag and Au/Ag/M halide phosphane supraclusters (M = Ni, Pd, Pt) is informative. These remarkable coinage-metal polyicosahedral clusters were prepared, isolated, and structurally/theoretically analyzed by Teo, Zhang, and co-workers[15] who formulated a vertex-sharing sequence of modular centered icosahedral building blocks to account for the generation of known and proposed polyicosahedral geometries containing up to 13 icosahedra (that is, an icosahedron of 12 icosahedra). Known examples include a crystallographically analyzed 36-atom centered triicosahedral Au/Ag phosphane/chloride cluster consisting of three Au-centered icosahedra sharing three vertices in a cyclic array.[23] This particular $Au_{18}Ag_{18}$ triicosahedron was found to contain two additional exopolyhedral Ag atoms. In striking contrast, the *trans* face-fused centered triicosahedron in **1** has 33 rather than 36 metal atoms. The face-condensation of centered icosahedra to give the centered Pd_{23} biicosahedral fragment in both the Pd_{35} and Pd_{39} clusters and the centered Pd_{33} triicosahedron in **1** would suggest that face-sharing of centered icosahedra may be considered as another possible growth process in the formation of the unligated and ligated nanoparticles. It is apparent that the existence of different kinds of ligated icosahedral-based metal clusters greatly depends upon the cohesive energies and relative electronegativities of the metal atoms and the electronic/steric effects of their ligands, as well as the reaction boundary conditions.

Received: April 24, 2003 [Z51738]
Published online: July 11, 2003

Keywords: carbonyl ligands · cluster compounds · palladium · phosphane ligands · structure elucidation

[1] a) E. G. Mednikov, N. K. Eremenko, *Izv. Akad. Nauk SSSR Ser. Khim.* **1982**, 2540; [*Russ. Chem. Bull.* **1982**, *31*, 2240 (*Engl.*

 © 2003 Wiley-VCH Verlag GmbH & Co. KGaA, Weinheim

Trans.)]; b) E. G. Mednikov, N. K. Eremenko, Yu. L. Slovokhotov, Yu. T. Struchkov, S. P. Gubin, *J. Organomet. Chem.* **1983**, *258*, 247.
[2] D. M. P. Mingos, C. M. Hill, *Croat. Chem. Acta* **1995**, *68*, 745.
[3] E. G. Mednikov, Yu. T. Struchkov, Yu. L. Slovokhotov, *J. Organomet. Chem.* **1998**, *566*, 15.
[4] M. Kawano, J. W. Bacon, C. F. Campana, B. E. Winger, J. D. Dudeck, S. A. Sirchio, S. L. Scruggs, U. Geiser, L. F. Dahl, *Inorg. Chem.* **2001**, *40*, 2554.
[5] E. G. Mednikov, N. K. Eremenko, Yu. L. Slovokhotov, Yu. T. Struchkov, *J. Organomet. Chem.* **1986**, *301*, C35; E. G. Mednikov, *Metalloorg. Khim.* **1991**, *4*, 885; [*Organomet. Chem. USSR* **1991**, *4*, 433 (*Engl. Trans.*)].
[6] a) J. Wittayakun, N. T. Tran, D. R. Powell, L. F. Dahl, unpublished results; b) E. G. Mednikov, S. A. Ivanov, J. Wittayakun, L. F. Dahl, *J. Chem. Soc. Dalton Trans.* **2003**, 1686.
[7] Reactions by Wittayakun et al.[6a] of the $[Pd_{13}Ni_{13}(CO)_{34}]^{4-}$ tetraanion[8] with PEt_3 in the presence of acid afforded $[Pd_{23}(CO)_{20}(PEt_3)_{10}]$, which has the same Pd_{23} geometry as that previously reported for $[Pd_{23}(CO)_{22}(PEt_3)_{10}]$[5] but with two fewer CO ligands. A comparative qualitative molecular analysis[6a] favors the existence of both clusters, which have different crystal forms.[6]
[8] N. T. Tran, M. Kawano, D. R. Powell, L. F. Dahl, *J. Chem. Soc. Dalton Trans.* **2000**, 4138.
[9] E. G. Mednikov, S. A. Ivanov, L. F. Dahl, *Angew. Chem.* **2003**, *115*, 337; *Angew. Chem. Int. Ed.* **2003**, *42*, 323.
[10] N. T. Tran, M. Kawano, L. F. Dahl, *J. Chem. Soc. Dalton Trans.* **2001**, 2731.
[11] E. G. Mednikov, Yu. L. Slovokhotov, Yu. T. Struchkov, *Metalloorg. Khim.* **1991**, *4*, 123; [*Organomet. Chem. USSR* **1991**, *4*, 65 (*Engl. Trans.*)].
[12] E. G. Mednikov, N. I. Kanteeva, *Izv. Akad. Nauk SSSR Ser. Khim.* **1995**, 167; [*Russ. Chem. Bull.* **1995**, *44*, 163 (*Engl. Trans*)].
[13] N. T. Tran, M. Kawano, D. R. Powell, L. F. Dahl, *J. Am. Chem. Soc.* **1998**, *120*, 10986.
[14] N. T. Tran, D. R. Powell, L. F. Dahl, *Angew. Chem.* **2000**, *112*, 4287; *Angew. Chem. Int. Ed.* **2000**, *39*, 4121.
[15] a) B. K. Teo, H. Zhang, X. Shi, *J. Am. Chem. Soc.* **1990**, *112*, 8552; b) B. K. Teo, H. Zhang, *Proc. Natl. Acad. Sci. USA* **1991**, *88*, 5067, and references therein; c) B. K. Teo, H. Zhang, *Coord. Chem. Rev.* **1995**, *143*, 611; d) H. Zhang, B. K. Teo, *Inorg. Chim. Acta* **1997**, *265*, 213; e) B. K. Teo, A. Strizhev, R. Elber, H. Zhang, *Inorg. Chem.* **1998**, *37*, 2482.
[16] Reactions were carried out under an inert atmosphere by standard Schlenk techniques. All solvents were thoroughly purged with N_2 before use. $[Pd_{10}(CO)_{12}(PEt_3)_6]$ was prepared by using the Mednikov procedure[1a], and then used as a precursor. In a typical reaction, $Me_3NO{\cdot}2H_2O$ (0.089 g, 0.80 mmol) and NaOH (≈1.0 g, pellet form) were stirred in DMF (20 mL)at 50 °C for about 1 h (in order to form a saturated NaOH solution). Then a suspension of $[Pd_{10}(CO)_{12}(PEt_3)_6]$ (0.211 g, 0.10 mmol) in DMF (10 mL) was quickly transferred to the Me_3NO/NaOH solution. The reaction was performed at 50 °C for one day. The resulting black reaction solution was filtered into PPh_4Cl (≈1.0 g), and then degassed distilled water (150 mL) was added to the ice-cooled solution in order to precipitate out a black solid (that is, the use of ionic PPh_4Cl enabled the formation of a precipitate instead of a colloidal suspension). The precipitate was filtered and washed several times with methanol, after which it was extracted first with CH_3CN and then with THF. Solvent removal from the CH_3CN extract afforded approximately 0.08 g of **1** as the major product (yield ≈50% based upon $[Pd_{10}(CO)_{12}(PEt_3)_6]$). IR spectra of **1** exhibit carbonyl bands at 1855(s) and 1830(sh) in Nujol and 1869(s) and 1826(sh) cm^{-1} in THF. The triclinic crystal form, **1a**, was subsequently obtained as a very minor product (a few crystals) from the similar reaction of $[Pd_{10}(CO)_{12}(PEt_3)_6]$ with NaOH in DMF (but without $Me_3NO{\cdot}2H_2O$) at room temperature for one day.
[17] Crystallographic data are given for the trigonal (**1**) and triclinic (**1a**) crystal forms of $[Pd_{69}(CO)_{36}(PEt_3)_{18}]$. Compound **1** was crystallized by slow diffusion of a diisopropyl ether layer and then a hexane layer over a concentrated THF solution at room temperature, while **1a** was crystallized as a minor product (that was isolated from the CH_3CN extract) by slow diffusion of a diisopropyl ether layer over a concentrated THF solution at room temperature. Black block-shaped crystals of dimensions $0.13\times0.18\times0.24\ mm^3$ for **1** and $0.05\times0.11\times0.28\ mm^3$ for **1a** were used for X-ray data collections. Intensity data were collected for **1** and **1a** at −173(2) °C via a Bruker SMART CCD 1000 area detector system mounted on a Bruker Platform diffractometer with graphite-monochromated $Mo_{K\alpha}$ radiation ($\lambda=0.71073$ Å) from a standard sealed-tube generator. An empirical absorption correction (SADABS) was applied to each data set. Structural determinations were obtained by use of direct methods followed by successive Fourier difference maps. Least-square refinements (based on F^2) were carried out with SHELXTL.[18] $[Pd_{69}(CO)_{36}(PEt_3)_{18}]$ (**1**): trigonal; $R\bar{3}c$; $a=b=18.961(1)$, $c=115.164(15)$ Å, $\alpha=\beta=90$, $\gamma=120°$, $V=35{,}856(6)$ Å^3; $Z=6$; $\rho_{calcd}=2.911\ Mg\,m^{-3}$. 68873 data collected via 0.3 ω scans (60 s/frame) over a 2θ range 4.24–46.60°. Least-squares refinement (411 parameters/276 restraints) on 5452 independent merged reflections ($R_{int}=0.037$) converged at $\omega R_2(F^2)=0.150$ for all data; $R_1(F)=0.053$ for 4981 observed data ($I>2\sigma(I)$). Compound **1** has crystallographic $\bar{3}$ site symmetry, such that the asymmetric part is comprised of 13 Pd atoms, six CO ligands, and three $P(C_2H_5)_3$ ligands. Of the 13 independent Pd atoms, Pd(1) is located at the $\bar{3}$ site, Pd(2) is located on the threefold axis, while the other 11 Pd atoms are in general positions. One oxygen atom of a bridging carbonyl group was disordered at two sites (namely, O(6)/O(6′) with refined occupancies of 0.66/0.34). One independent P atom was disordered at two sites (namely, P(1)/P(1′) with refined occupancies of 0.56/0.44); disordered ethyl carbon atoms attached to P(1)/P(1′) were refined isotropically. Ethyl carbon atoms coordinated to P(2) were refined isotropically in two different orientations. Non-hydrogen atoms were refined anisotropically except for all carbon atoms of the two disordered phosphane groups, as stated above. Restraints were applied to the positional and displacement parameters of the ethyl carbon atoms in order to achieve convergence. $[Pd_{69}(CO)_{36}(PEt_3)_{18}]$ (**1a**): triclinic; $P\bar{1}$; $a=19.103(2)$, $b=19.246(2)$, $c=21.854(2)$ Å, $\alpha=64.877(1)$, $\beta=75.099(2)$, $\gamma=61.913(1)°$, $V=6401.4(11)$ Å^3; $Z=1$; $\rho_{calcd}=2.718\ Mg\,m^{-3}$. 45722 data collected via 0.3 ω scans (120 s/frame) over a 2θ range 4.34–50.00°. Least-squares refinement (1218 parameters/1463 restraints) on 21861 independent merged reflections ($R_{int}=0.039$) converged at $\omega R_2(F^2)=0.130$ for all data; $R_1(F)=0.055$ for 16565 observed data ($I>2\sigma(I)$). Compound **1a** has crystallographic $\bar{1}$ site symmetry, such that the asymmetric part is comprised of 35 Pd atoms, 18 CO ligands, and nine $P(C_2H_5)_3$ ligands. One independent carbonyl ligand is disordered at two orientations (namely, CO(12)/CO(12′) with refined occupancies of 0.59/0.41). All carbon atoms of one independent phosphane ligand are disordered (occupancies of 0.49/0.51). Non-hydrogen atoms were refined anisotropically except for all carbon atoms of the disordered phosphane ligand. Restraints were applied to the positional and displacement parameters of the ethyl carbon atoms in order to achieve convergence. CCDC-208518 (**1**) and -208519 (**1a**) contain the supplementary crystallographic data for this paper. These data can be obtained free of charge via www.ccdc.cam.ac.uk/conts/retrieving.html (or from the Cambridge Crystallographic Data

 © 2003 Wiley-VCH Verlag GmbH & Co. KGaA, Weinheim

Centre, 12, Union Road, Cambridge CB21EZ, UK; fax: (+44) 1223-336-033; or deposit@ccdc.cam.ac.uk).
[18] All software and sources of the scattering factors are contained in the SHELXTL (version 5.1) program library (G. Sheldrick, Bruker Analytical X-Ray Systems, Madison, WI).
[19] J. Donohue, *The Structures of the Elements*, Wiley, New York, **1974**, p. 236.
[20] a) A. L. Mackay, *Acta Crystallogr.* **1962**, *15*, 916; b) S. Ino, *J. Phys. Soc. Jpn.* **1966**, *21*, 346; c) J. Farges, M. F. de Feraudy, B. Raoult, G. Torchet, *Acta Crystallogr. Sect. A* **1982**, *38*, 656.
[21] a) E. G. Mednikov, N. K. Eremenko, Yu. L. Slovokhotov, Yu. T. Struchkov, *Zh. Vses. Khim. O-va. im. D. I. Mendeleeva* **1987**, *32*, 101 (in Russian); b) E. G. Mednikov, *Izv. Akad. Nauk SSSR Ser. Khim.* **1993**, 1299; [*Russ. Chem. Bull.* **1993**, *42*, 1242 (Engl. Trans.)].
[22] In contrast to **1**, six out of 18 triply bridging CO ligands in **1** are doubly bridging in **1a** with the longest connectivity being nonbonding (> 2.5 Å).
[23] a) B. K. Teo, M. Hong, H. Zhang, D. Huang, X. Shi, *J. Chem. Soc. Chem. Commun.* **1988**, 204; b) B. K. Teo, H. Zhang, X. Shi, *J. Am. Chem. Soc.* **1990**, *112*, 8552.

 © 2003 Wiley-VCH Verlag GmbH & Co. KGaA, Weinheim

Multicolor Photochromism

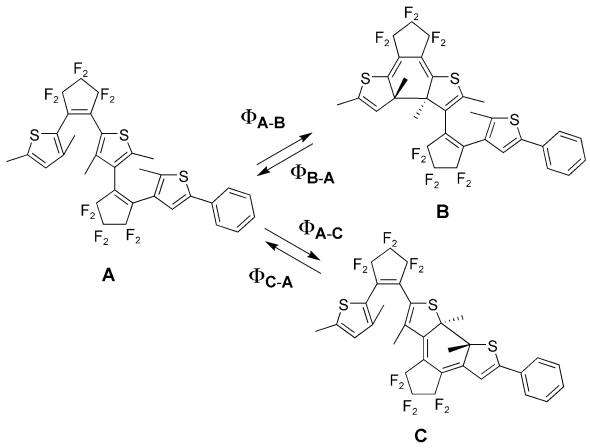
Photochromic Reaction of a Fused Dithienylethene: Multicolor Photochromism**

*Kenji Higashiguchi, Kenji Matsuda, and Masahiro Irie**

Photochromic compounds, which change their color upon irradiation with light of the appropriate wavelength, have attracted increasing attention because of the potential application to optical memory media and switching devices.[1] Diarylethenes with heterocyclic aryl groups are the most promising candidates for practical applications[2] because of their high fatigue resistance and thermal stability.[3]

Multicolor photochromism is useful for optoelectronic devices such as multifrequency optical memories and displays. Multicolor systems can be obtained by mixing photochromic compounds with different colors in solutions,[4a] in polymer matrices,[4b] and in single crystals.[4c] Herein, we took the approach to incorporate two photochromic units in one-molecule.[5,6] Some advantages of a one-molecule system over mixed systems include the high resolution available arising from local homogeneity, long-term storage stability, and applications to multi-frequency single-molecular memories.[7]

In an attempt to obtain a molecule that shows a distinct multicolor change, we have designed the nonsymmetric molecule, **A** (Scheme 1). Compound **A** has two types of dithienylethene moieties, bis(2-thienyl) and bis(3-thienyl)-ethene, with one thiophene ring in common. The closed-ring isomers of bis(2-thienyl)ethenes have their absorption maxima at shorter wavelength than those of bis(3-thienyl)-ethenes.[8] The bis(3-thienyl)ethene moiety in **A** has an extra phenyl ring, which further shifts the maximum.



Scheme 1. Photoreaction of the fused dithienylethene **A**, **B**, and **C**.

A was synthesized by the reaction of 3-(2,3,3,4,4,5,5-heptafluorocyclopent-1-en-1-yl)-2-methyl-5-phenylthiophene with lithiated 1-(3,5-dimethyl-2-thienyl)-2-(4-bromo-3,5-dimethyl-2-thienyl)perfluorocyclopentene. The structure of **A** was confirmed by mass spectroscopy, NMR spectroscopy, elemental analysis and X-ray crystallographic analysis (Figure 1).[9]

A solution of **A** in hexane turned yellow then green upon irradiation with light of 365 nm, as shown in Figure 2. Upon further irradiation with light of 313 nm, the solution turned black. When the solution was exposed simultaneously to UV (313 nm) and blue (436 nm) light, it turned blue (Figure 2, sample 5). The solution turned yellow (Figure 2, sample 2), when it was irradiated with UV (313 nm) and yellow ($\lambda >$ 500 nm) light. From this experiment it is inferred that the color change originates from two kinds of colored species.

The two colored species were isolated by HPLC. The molecular structure of the two species were determined by absorption and NMR spectroscopy[10] to be the closed-ring isomer of bis(2-thienyl)ethene moiety (**B**; Scheme 1) and bis(3-thienyl)ethene moiety (**C**; Scheme 1), which are yellow and blue, respectively. Figure 3 shows the spectra of the open-ring isomer **A** and the isolated closed-ring isomers **B** and **C**. The absorption peak of **B** is located at the absorption valley of **C**. Both **B** and **C** converted back into **A** by irradiation with visible light ($\lambda > 450$ nm). Formation of the closed-ring isomer, in which both dithienylethene units are in the

[*] Prof. M. Irie, Dr. K. Higashiguchi, Dr. K. Matsuda
Department of Chemistry and Biochemistry
Graduate School of Engineering
Kyushu University
6-10-1 Hakozaki, Higashi-ku, Fukuoka, 812-8581 (Japan)
Fax: (+81) 92-642-3568
E-mail: irie@cstf.kyushu-u.ac.jp

[**] The present work is supported by Grant-in-Aids for Scientific Research (No. 15105006) and the 21 st Century COE Program from the Ministry of Education, Culture, Sports, Science and Technology of Japan. The measurement of NMR was made using JEOL GSX400 spectrometer (400 MHz) at the Center of Advanced Instrumental Analysis, Kyushu University.

Supporting information for this article is available on the WWW under http://www.angewandte.org or from the author.

 DOI: 10.1002/anie.200351751 © 2003 Wiley-VCH Verlag GmbH & Co. KGaA, Weinheim

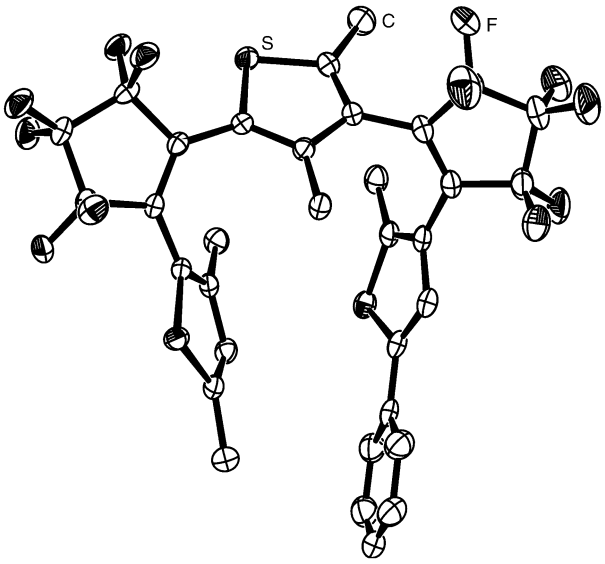


Figure 1. ORTEP drawing of open-ring isomer **A** (ellipsoids set at the 50% probability level). Hydrogen atoms were omitted for clarity.



Figure 2. Color changes of **A** in hexane solution upon irradiation with 365 nm and 313 nm light. Sample 1: initial state; samples 2 and 3: upon irradiation with 365 nm light; sample 4: upon further irradiation with 313 nm light; sample 5: upon irradiation with 313 and 436 nm light.

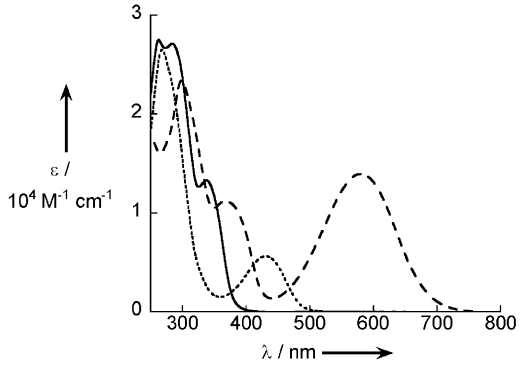


Figure 3. Absorption spectra of **A** (——), **B** (••••), and **C** (-----) in hexane.

closed-ring form, was not discerned. This result is in agreement with the observation for symmetric dimers.[5a,c] Formation of both **B** and **C** upon irradiation with 313–365 nm light indicates that excited energy transfer to the bis(2-thienyl)-ethene unit with lower energy is not efficient. The energy transfer is considered to be less favorable because of non-coplanarity of the three thiophene rings, as shown in Figure 1.

A hexane solution containing **A** was irradiated with 334 nm light, and the concentration changes of **A**, **B**, and **C** were monitored by HPLC (Figure 4). At the initial stage of

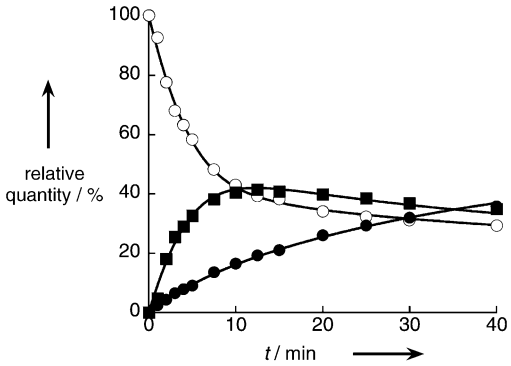


Figure 4. Decay of **A** (open circles) and formation of **B** (filled boxes) and **C** (filled circles) upon irradiation with 334 nm light. The solid lines were least square fitting of the concentration of **A**, **B**, and **C**.

the photoirradiation, the formation of **B** was about four times faster than that of **C**. In the photostationary state, however, the amount of **C** was about 1.4 times larger than that of **B**. The time course of formation of **B** and **C** was analyzed based on Scheme 1, Equations (1)–(9).

$$\frac{dC_A}{dt} = (-k_{A-B}\,C_A + k_{B-A}\,C_B - k_{A-C}\,C_A + k_{C-A}\,C_C)\,F \quad (1)$$

$$\frac{dC_B}{dt} = (k_{A-B}\,C_A - k_{B-A}\,C_B)\,F \quad (2)$$

$$\frac{dC_C}{dt} = (k_{A-C}\,C_A - k_{C-A}\,C_C)\,F \quad (3)$$

$$F = \frac{1-10^{-A}}{A} \quad (4)$$

$$A = \varepsilon_A\,C_A + \varepsilon_B\,C_B + \varepsilon_C\,C_C \quad (5)$$

$$k_{A-B} = \varepsilon_A\,\Phi_{A-B}\,I_0 \quad (6)$$

$$k_{B-A} = \varepsilon_B\,\Phi_{B-A}\,I_0 \quad (7)$$

$$k_{A-C} = \varepsilon_A\,\Phi_{A-C}\,I_0 \quad (8)$$

$$k_{C-A} = \varepsilon_C\,\Phi_{C-A}\,I_0 \quad (9)$$

In these differential equations, I_0 is the intensity of light and Φ_{A-B}, Φ_{B-A}, Φ_{A-C}, and Φ_{C-A} are reaction quantum yields of **A** to **B**, **B** to **A**, **A** to **C**, and **C** to **A**, respectively. ε_A, ε_B, and ε_C are molar absorption coefficients of **A**, **B**, and **C** at the irradiation wavelength (334 nm). C_A, C_B, and C_C are the concentrations of **A**, **B**, and **C**.

 © 2003 Wiley-VCH Verlag GmbH & Co. KGaA, Weinheim

These differential equations were numerically solved and the results were fitted to the experimental data shown in Figure 4; the best-fit curves are shown as solid lines. The parameters used are as follows; $\varepsilon_{\mathbf{A}} = 1.3 \times 10^4\,\text{M}^{-1}\,\text{cm}^{-1}$, $\varepsilon_{\mathbf{B}} = 3.1 \times 10^3\,\text{M}^{-1}\,\text{cm}^{-1}$, $\varepsilon_{\mathbf{C}} = 1.3 \times 10^4\,\text{M}^{-1}\,\text{cm}^{-1}$ (at 334 nm). The ratio of $\Phi_{\mathbf{A-B}}$:$\Phi_{\mathbf{B-A}}$:$\Phi_{\mathbf{A-C}}$:$\Phi_{\mathbf{C-A}}$ was calculated to be 11:44:2.5:1.0.

The quantum yields of cycloreversion reactions of **B** and **C** to **A**, $\Phi_{\mathbf{B-A}}$ and $\Phi_{\mathbf{C-A}}$ were measured in hexane by irradiating the sample with visible light at each absorption maximum. $\Phi_{\mathbf{B-A}}$ and $\Phi_{\mathbf{C-A}}$ were found to be 0.57 and 0.013, respectively, and this ratio (44:1) agrees well with the ratio obtained from the above simulation (44:1). The quantum yields of the cyclization reactions of **A** to **B** and **A** to **C**, $\Phi_{\mathbf{A-B}}$ and $\Phi_{\mathbf{A-C}}$ were found to be 0.14 and 0.032, respectively. The quantum yields are summarized in Table 1. The difference in the cyclization quantum yields ($\Phi_{\mathbf{A-B}} > \Phi_{\mathbf{A-C}}$) favors the formation of **B** and the difference in the cycloreversion quantum yields ($\Phi_{\mathbf{B-A}} \gg \Phi_{\mathbf{C-A}}$) leads to a higher yield of **C** at the photostationary state.

Table 1: Photoreaction quantum yields of the fused dithienylethene.

$\Phi_{\mathbf{A-B}}$	$\Phi_{\mathbf{B-A}}$	$\Phi_{\mathbf{A-C}}$	$\Phi_{\mathbf{C-A}}$
0.14	0.57	0.032	0.013

Irradiation of the black solution with visible light of $\lambda >$ 580 nm led to the disappearance of **C** only, and the solution turned yellow because only **C** absorbs in that region of the visible spectrum. On the other hand, upon irradiation of the black solution with visible light of $\lambda > 420$ nm, the solution turned blue because the cycloreversion quantum yield of **B** is much larger than that of **C**. Upon irradiation with light of 436 nm, the blue color scarcely bleached (Figure 2). The colors completely disappeared when the sample was exposed continuously to visible light of $\lambda > 420$ nm.

In conclusion, we have developed a new fused dithienylethene derivative **A** and studied its novel photochromic performance. Different colors can be obtained by irradiating **A** with different wavelengths and for different periods of time. This phenomenon is characteristic of fused diarylethenes.

Experimental Section

Hexane of spectroscopic grade was distilled before use. Absorption spectra in a solution were measured with a Hitachi U-3500 absorption spectrophotometer. Photoirradiation was carried out by using a USHIO USH-500D 500 W high-pressure mercury lamp as the light source. Monochromatic light was obtained by passing the light through a Ritsu MC-20L monochromator.

Quantum yields for cycloreversion reactions were determined with monochromatic light of a Xe lamp at each absorption maximum of the samples and references. Colored hexane solutions of 1,2-bis(3,5-dimethyl-2-thienyl)perfluorocyclopentene[8] and 1,2-bis(2-methylbenzothiophene-3-yl)perfluorocyclopentene[11] were used as the reference.

Synthesis and characterization of the compounds: ^{1}H NMR spectrum was recorded on a JEOL GSX400 spectrometer (400 MHz). Tetramethylsilane (TMS) was used as an internal standard. Mass spectrum was taken with a Shimadzu GCMS-QP5050A (EI) and a JOEL JMS-GC mate II (FAB). The melting point was measured using a Laboratory Devices MEL-TEMP II.

1-(3,5-dimethyl-2-thienyl)-2-(4-bromo-3,5-dimethyl-2-thienyl)-perfluorocyclopentene was synthesized as follows: Br_2 (0.73 g, 0.23 mL, 4.3 mmol) was added to a solution of bis(3,5-dimethyl-2-thienyl)perfluorocyclopentene[8] (1.59 g, 4.0 mmol) and $FeCl_3$ (13 mg, 0.08 mmol, 2 mol %) in $CHCl_3$ (6.4 mL) at less than 5 °C under an Ar atmosphere. After the mixture was stirred for 1 h at 0 °C, aqueous $Na_2S_2O_3$ was added to the reaction mixture and extracted with $CHCl_3$, washed with brine, dried over $MgSO_4$, and concentrated. Column chromatography (silica, hexane) gave 1-(3,5-dimethyl-2-thienyl)-2-(4-bromo-3,5-dimethyl-2-thienyl)perfluorocyclopentene (1.0 g, 53 %): mp 81.1–82.0 °C; ^{1}H NMR (200 MHz, $CDCl_3$): $\delta = 1.73$ (3H, s); 1.75 (3H, s); 2.43 (3H, s); 2.45 (3H, s); 6.53 ppm (1H, s); MS *m*/*z* [M^+] 474. Elemental analysis calcd (%) for $C_{17}H_{13}BrF_6S_2$: C 42.96, H 2.76; found: C 43.08, H 2.73.

Fused dithienylethene **A** was synthesized as follows: A solution of *t*BuLi in hexane (1.51M, 0.49 mL) was added dropwise to a solution of 1-(3,5-dimethyl-2-thienyl)-2-(4-bromo-3,5-dimethyl-2-thienyl)perfluorocyclopentene (0.16 g, 0.33 mmol) in dry ether (3 mL) at less than −95 °C under an Ar atmosphere. After the mixture was stirred for 5 min at this temperature, 3-(2,3,3,4,4,5,5-heptafluorocyclopent-1-en-1-yl)-2-methy-5-phenylthiophene[12] (0.12 g, 0.33 mmol) in THF (2 mL) was added dropwise. The reaction mixture was allowed to warm up to room temperature. Aqueous NH_4Cl was added to the reaction mixture, which was extracted by ether, washed with water, dried over $MgSO_4$ and concentrated. Column chromatography (silica, hexane) gave **A** (0.031 g, 12 %). mp 132.0–132.7 °C; ^{1}H NMR (400 MHz, $CDCl_3$): $\delta = 1.37$ (3H, s), 1.43 (3H, s), 2.10 (3H, s), 2.14 (3H, s), 2.42 (3H, s), 6.25 (1H, s), 7.02 (1H, s), 7.3–7.6 ppm (5H, m); FAB HRMS (*m*/*z*) [M]$^+$ calcd for $C_{33}H_{22}F_{12}S_3$: 742.0692; found: 742.0686. Elemental analysis calcd (%) for $C_{33}H_{22}F_{12}S_3$: C 53.37, H 2.99; found: C 53.67, H 3.02.

Closed-ring isomers of the fused dithienylethene, **B** and **C**, were isolated by passing a photoirradiated solution containing **A**, **B**, and **C** through HPLC. ^{1}H NMR (400 MHz, $CDCl_3$) data for **B**: $\delta = 0.86$ (2.1H, s), 1.02 (0.9H, s), 1.55 (0.9H, s), 1.60 (2.1H, s), 2.00 (2.1H, s), 2.00 (0.9H, s), 2.07 (0.9H, s), 2.08 (2.1H, s), 2.42 (0.9H, s), 2.51 (2.1H, s), 5.25 (0.7H, s), 5.34 (0.3H, s), 6.84 (0.3H, s), 6.97 (0.7H, s), 7.3–7.5 ppm (5H, m); $\lambda_{max} = 431$ nm ($\varepsilon = 5.6 \times 10^3\,\text{M}^{-1}\,\text{cm}^{-1}$);[13a] for **C**: ^{1}H NMR (400 MHz, $CDCl_3$): $\delta = 1.59$ (3H, s), 2.15 (3H, s), 2.17 (3H, s), 2.17 (3H, s), 2.48 (3H, s), 6.66 (1H, s), 6.69 (1H, s), 7.4–7.6 ppm (5H, m); $\lambda_{max} = 580$ nm ($\varepsilon = 1.4 \times 10^4\,\text{M}^{-1}\,\text{cm}^{-1}$).[13b]

Received: April 25, 2003 [Z51751]

Keywords: conjugation · fused-ring systems · photochromism · sulfur heterocycles · UV/Vis spectroscopy

[1] a) *Molecular Switches* (Ed.: B. L. Feringa), Wiley-VCH, Weinheim, **2001**; b) G. H. Brown, *Photochromism*, Wiley-Interscience, New York, **1971**; c) H. Dürr, H. Bouas-Laurent, *Photochromism, Molecules and Systems*, Elsevier, Amsterdam, **1990**; d) "Recent Progress on Photochromic Dyes": H. G. Heller in *Chemistry of Functional Dyes, Vol. 1* (Eds.: Z. Yoshida, T. Kitao), Mita, Tokyo, **1989**, pp. 267–279.

[2] a) C. B. McArdle, *Applied Photochromic Polymer Systems*, Blackie, Glasgow, **1992**; b) J. C. Crano, R. J. Guglielmetti, *Organic Photochromic and Thermochromic Compounds*, Plenum, New York, **1999**.

[3] M. Irie, K. Uchida, *Bull. Chem. Soc. Jpn.* **1998**, *71*, 985–996.

[4] a) G. M. Tsivgoulis, J.-M. Lehn, *Adv. Mater.* **1997**, *9*, 627–630; b) A. Fernández-Acebes, J.-M. Lehn, *Adv. Mater.* **1999**, *11*, 910–

 © 2003 Wiley-VCH Verlag GmbH & Co. KGaA, Weinheim

913; c) M. Morimoto, S. Kobatake, M. Irie, *Adv. Mater.* **2002**, *14*, 1027 – 1029.
[5] a) A. Peters, N. R. Branda, *Adv. Mater. Opt. Electron.* **2000**, *10*, 245 – 249; b) K. Matsuda, M. Irie, *J. Am. Chem. Soc.* **2001**, *123*, 9896 – 9897; c) T. Kaieda, S. Kobatake, H. Miyasaka, M. Murakami, N. Iwai, Y. Nagata, A. Itaya, M. Irie, *J. Am. Chem. Soc.* **2002**, *124*, 2015 – 2024.
[6] K. Higashiguchi, K. Matsuda, M. Matsuo, T. Yamada, M. Irie, *J. Photochem. Photobiol. A* **2002**, *152*, 141 – 146.
[7] M. Irie, T. Fukaminato, T. Sasaki, N. Tamai, T. Kawai, *Nature* **2002**, *420*, 759 – 760.
[8] K. Uchida, M. Irie, *Chem. Lett.* **1995**, 969 – 970.
[9] Crystallographic data for **A**: $C_{33}H_{22}F_{12}S_3$, $M_r = 742.69$, Monoclinic $P2_1/c$, $a = 14.707(2)$ Å, $b = 13.373(2)$ Å, $c = 17.198(3)$ Å, $\beta = 111.617(2)°$, $V = 3144.4(9)$ Å^3, $Z = 4$, $R_1 = 0.0438$ ($I > 2\sigma$), $wR_2 = 0.1040$ (all data). CCDC 207125 contains the supplementary crystallographic data for this paper. These data can be obtained free of charge via www.ccdc.cam.ac.uk/conts/retrieving.html (or from the Cambridge Crystallographic Data Centre, 12, Union Road, Cambridge CB2 1EZ, UK; fax: (+44) 1223-336-033; or deposit@ccdc.cam.ac.uk).
[10] ^{1}H NMR measurement revealed that the proton at 4-position of 3,5-dimethyl-2-thienyl group shifts from $\delta = 6.23$ to 5.26 ppm in the yellow product and the proton at 4-position of 2-methyl-5-phenyl-3-thienyl group shifts from $\delta = 7.01$ to 6.68 ppm in the blue one.
[11] K. Uchida, E. Tsuchida, Y. Aoi, S. Nakamura, M. Irie, *Chem. Lett.* **1999**, 63 – 64.
[12] T. Kodani, K. Matsuda, T. Yamada, S. Kobatake, M. Irie, *J. Am. Chem. Soc.* **2000**, *122*, 9631 – 9637.
[13] a) Spectral data for closed-ring isomer of 1,2-bis(3,5-dimethyl-2-thienyl)perfluorocyclo-pentene: $\lambda_{max} = 425$ nm ($\varepsilon = 5.8 \times 10^3\,\text{M}^{-1}\,\text{cm}^{-1}$);[8] b) for closed-ring isomer of 1,2-bis(2-methyl-5-phenyl-3-thienyl)perfluorocyclopentene: $\lambda_{max} = 575$ nm ($\varepsilon = 1.2 \times 10^4\,\text{M}^{-1}\,\text{cm}^{-1}$).[14]
[14] M. Irie, T. Lifka, K. Uchida, S. Kobatake, Y. Shindo, *Chem. Commun.* **1999**, 747 – 748.

 © 2003 Wiley-VCH Verlag GmbH & Co. KGaA, Weinheim

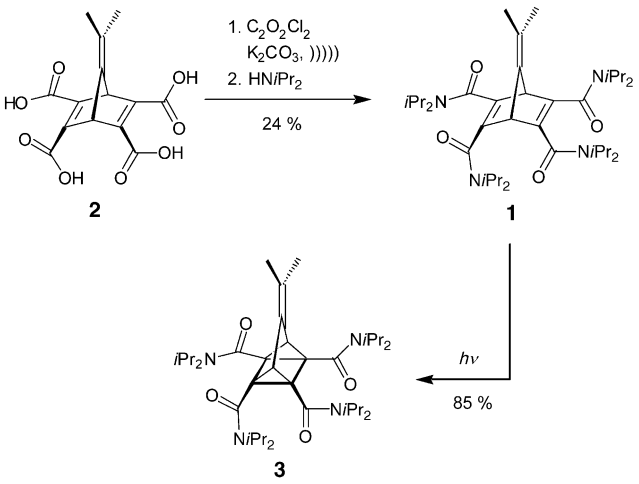
Photoinduced Na^+ Coordination

Synthesis, Structure, and Complexation Properties of Amide-Substituted Derivatives of Norbornadiene and Quadricyclane

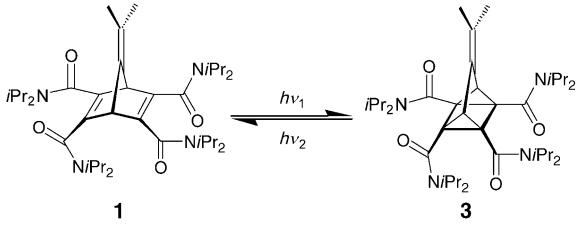
*Torsten Winkler, Ina Dix, Peter G. Jones, and Rainer Herges**

The indirect coupling of external energy sources (e.g. light, redox and proton gradients, and exergonic reactions) to molecular switches[1] to drive a function is one of the most interesting problems in supramolecular chemistry. To our knowledge, light-driven, carrier-mediated, active transport through a membrane against a concentration gradient has not yet been achieved. To this end, we developed a photoswitchable ligand[2] based on the known norbornadiene⇄quadricyclane isomerization.[3] Quadricyclanes with electron-donating substitutents on the cyclobutane ring isomerize to the norbornadienes with a concerted "grapplelike" motion, which can be used to bind or release guests (cations). The main advantage of these compounds is the large reisomerization energy. More than 20 kcal mol^{-1} are released in forming the norbornadiene, which makes the switching process almost independent of the presence of a guest ion. Additional prerequisites for the application of this photosystem as an active ion carrier are the high lipophilicity of the ligand, a considerable difference in the complexation energy of the two isomers, and the high yields of the switching process. Amide substituents are promising for this photoswitchable system because they can act as chromophores for effective photoisomerization and are also efficient donor ligands for alkali-metal cations.[4] In this context calixarene derivatives[5] (some of them even conformationally switchable[6]) have been studied.

Norbornadiene tetramide **1** was prepared from the corresponding tetracarboxylic acid **2** (Scheme 1). After generation of the acid chloride in situ by chlorination with oxalyl dichloride, the reaction mixture was treated directly with diisopropylamine. Quadricyclane tetramide **3** was synthesized photochemically from **1**. According to the ^{1}H NMR spectra, this conversion—a photochemical [2 + 2] cycloaddition—was almost quantitative (> 95 %, 85 % yield after purification by chromatography); side products were not detected. The cycloaddition proceeds with the same efficiency in the presence of Na^+ ions under the same conditions. The reverse reaction (**3**→**1**, Scheme 2) was achieved with UV light of shorter wavelength (mercury low-pressure lamp, quartz filter) with a yield of 50 % (photostationary equilibrium). Upon prolonged irradiation the elimination of propene (Norrish Type-II reaction) was observed as a minor side reaction.



Scheme 1. Synthesis of norbornadiene and quadricyclanediisopropyl tetramides **1** and **3** from tetracarboxylic acid **2**.)))) = ultrasonic radiation.



Scheme 2. Photoinduced interconversion of norbornadiene tetraamide **1** and quadricyclane tetramide **3**.

In view of the complexation of metal cations, the spatial arrangement of the substituents and the size of the cavity they form is particularly interesting. The structures of tetramides **1** and **3** were elucidated by X-ray analysis. The symmetry of norbornadiene tetramide **1** is lowered to C_2, and quadricyclane tetramide **3** exhibits a similar, approximately C_2-symmetrical structure. For steric reasons two carbonyl oxygen atoms diagonal to each other point toward the center of the cavity and the other two point outward. Consequently the bulky diisopropyl groups assume a sterically favorable alternating orientation (Figure 1, top). The distance between the two oxygen atoms pointing towards the interior is 5.66 Å in **1** and 5.53 Å in **3**. In addition, the crystal of norbornadiene tetramide **1** contains disordered solvent molecules (diethyl ether or pentane).

[*] Prof. Dr. R. Herges, Dr. T. Winkler
Institut für Organische Chemie
Christian-Albrechts-Universität Kiel
Otto Hahn-Platz 4, 24098 Kiel (Germany)
Fax: (+49) 431-880-1558
E-mail: rherges@oc.uni-kiel.de
I. Dix
Institut für Organische Chemie
Technische Universität Braunschweig
Hagenring 30, 38106 Braunschweig (Germany)
Prof. Dr. P. G. Jones
Institut für Anorganische und Analytische Chemie
Technischen Universität Braunschweig
Hagenring 30, 38106 Braunschweig (Germany)

Supporting information for this article is available on the WWW under http://www.angewandte.org or from the author.

 DOI: 10.1002/anie.200350959 © 2003 Wiley-VCH Verlag GmbH & Co. KGaA, Weinheim

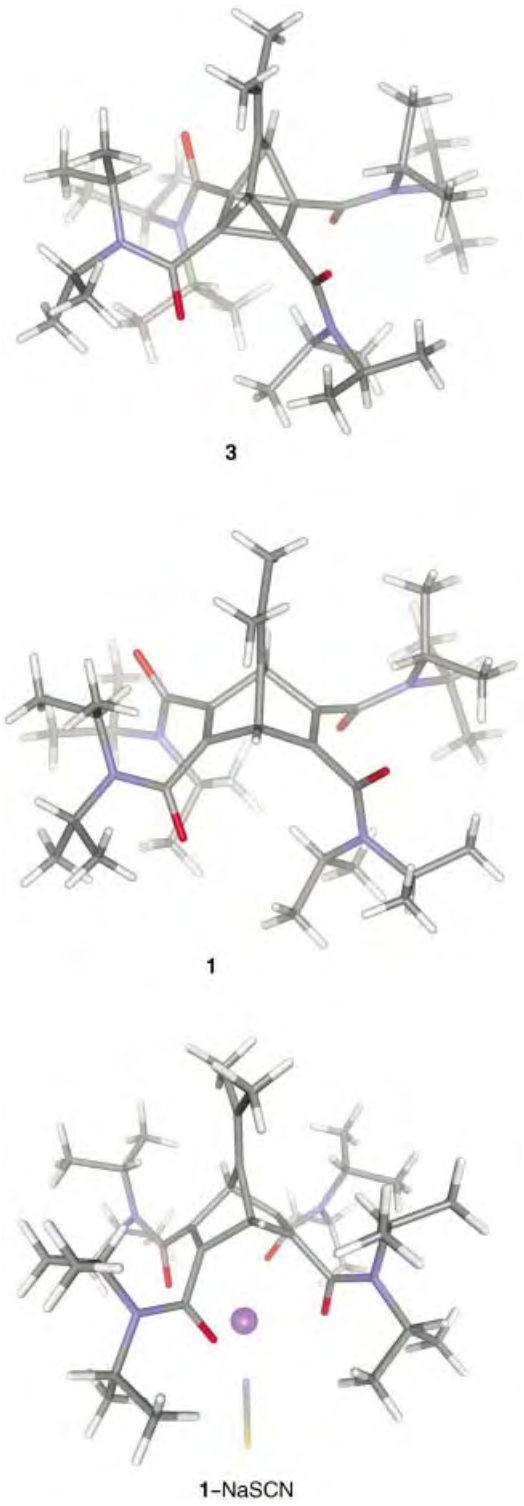


Figure 1. Crystal structures of tetramides **3** and **1** and the complex [**1**-NaSCN].

Can **1** assume a conformation in which all four carbonyl oxygen atoms are available for coordination to a suitable cation? This question was answered by the X-ray structure analysis of a sodium complex of norbornadiene **1** (Figure 1, bottom). In contrast to the arrangement in the free ligand all four carbonyl oxygen atoms in [**1**-NaSCN] point into the cavity and coordinate the Na^+ ion. The Na^+ ion in this complex has the coordination number 5 and nearly square-pyramidal coordination geometry. The symmetry of the complex is C_2; the thiocyanate ion, the Na^+ ion, and the two carbon atoms of the isopropyl group lie exactly on the C_2 axis. The distances between the oxygen atoms and the Na^+ ion are 2.40 and 2.49 Å, that between the Na^+ ion and the nitrogen atom of the thiocyanate is 2.32 Å; the O-Na-O angles between the diagonally facing oxygen atoms are 135.1 and 142.3°. The four carbonyl oxygen atoms almost exactly define a plane, which is located 0.44 Å above the Na^+ ion.

The complexation properties of the quadricyclane and norbornadiene tetramides were investigated by the picrate extraction method. A solution of the ligand in chloroform was used to extract the yellow alkali-metal picrates (Li^+Pic^-, Na^+Pic^-, K^+Pic^-, and Cs^+Pic^-) from an aqueous solution. UV/Vis spectroscopy was used for quantification. The extraction constant K_{ex} and the association constant K_{ass} were determined according to the method of Cram et al. [7] This method was also used to investigate the complexation properties of ether-substituted quadricyclane und norbornadiene derivatives.[8] The K_{ex} and K_{ass} values for norbornadiene tetramide **1** are always higher than those for quadricyclane tetramide **3** (Table 1). In the experiments with **3** the association constants increase with decreasing ion radius. In contrast, norbornadiene **1** binds most strongly to Na^+, indicating a cavity of a defined size. For Li^+ the association constants of **1** and **3** are almost identical, whereas the values for Na^+ coordination are distinctly different (Figure 2).

Table 1: Extraction constants K_{ex} and association constants K_{ass} for the complexation of alkali-metal cations by **1** and **3** in chloroform.

Cation	K_{ex} [L^{-2} mol^{-2}] quadricyclane **3**	K_{ex} [L^{-2} mol^{-2}] norbornadiene **1**	K_{ass} [L^{-1} mol^{-1}] quadricyclane **3**	K_{ass} [L^{-1} mol^{-1}] norbornadiene **1**
Li^+	13.90 ± 0.54	14.06 ± 0.38	9786.80 ± 281.04	9899.50 ± 172.16
Na^+	8.57 ± 0.25	23.31 ± 1.07	4925.86 ± 120.74	13394.15 ± 425.35
K^+	5.13 ± 0.32	6.22 ± 0.16	2013.43 ± 83.45	2440.01 ± 41.26
Cs^+	6.87 ± 0.25	18.54 ± 0.46	1040.72 ± 30.50	2809.50 ± 52.01

The size selectivity of the tertiary amides **1** and **3** in the coordination of alkali-metal ions is opposite to that of the

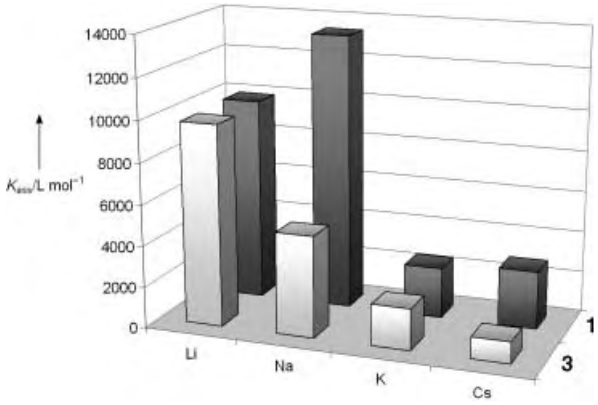
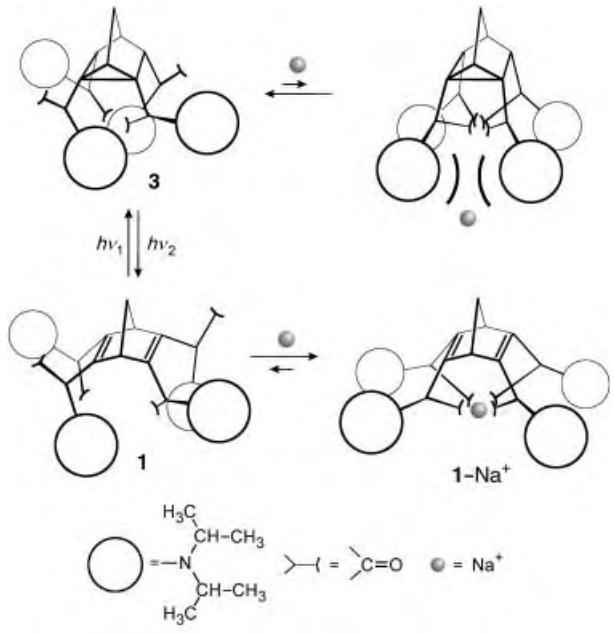


Figure 2. Association constants K_{ass} for the complexation of alkali-metal ions by the tetramides **1** and **3** in chloroform.

 © 2003 Wiley-VCH Verlag GmbH & Co. KGaA, Weinheim

ether-substituted norbornadienes and quadricyclanes.[8] The association constants of the "open" form (norbornadiene) are larger than those of the "closed" isomer (quadricyclane). Apparently the cavity of quadricyclane **3** is too small for binding cations larger than Li^+. Moreover, the conformation necessary for the complexation of a cation, in which all four carbonyl oxygen atoms point towards the center of the cavity and the bulky isopropyl groups are directed outwards, is less favorable in the quadricyclane than in the norbonadiene (Scheme 3).



Scheme 3. Representation of the switching and complexation processes of **1** and **3**. The isopropyl groups are not shown for clarity. The convergent orientation of all four carbonyl groups for the complexation of Na^+ in the interior of the ligand is more strongly hindered by the bulky isopropyl groups in the quadricyclane **3** than in the norbornadiene **1**. Moreover, the cavity in the quadricyclane **3** is considerably smaller.

Experimental Section

1: Compound **2** (750 mg, 2.44 mmol) and potassium carbonate (3.00 g, 21.73 mmol) were suspended in anhydrous dichloromethane (25 mL) and cooled to 0 °C with ice and water in an ultrasound bath. Upon sonification oxalyl dichloride (0.9 mL, 10.39 mmol) and then dimethylformamide (2–3 drops) were added with a syringe. There was a strong generation of gas in the cloudy mixture which ceased after about an hour. A solid precipitated from the clear supernatant yellow–green solution. Diisopropyl amine (5.0 mL, 48.42 mmol) was added with a syringe to the solution of the acid chloride. A fine, colorless precipitate formed thereafter. The mixture was stirred for another 2 h and allowed to warm to room temperature. The precipitate was filtered off and the filtrate was concentrated in vacuo. The crude product was purified by column chromatography (silica gel, cyclohexane/ethyl acetate 1:1, $R_f = 0.60$). Yield: 380 mg (0.59 mmol, 24 %); m.p.: 212 °C; ^{1}H NMR ($CDCl_3$): $\delta = 4.15$ (s, 2H, 1,4-H), 3.89 (sept, $^3J(H,H) = 6.6$ Hz, 4H, 11-H), 3.40 (sept, $^3J(H,H) = 6.8$ Hz, 4H, 11-H), 1.55 (s, 6H, 9-H), 1.44 (d, $^3J(H,H) = 6.8$ Hz, 12H, 12-H), 1.40 (d, $^3J(H,H) = 6.8$ Hz, 12H, 12-H), 1.15 (d, $^3J(H,H) = 6.9$ Hz, 12H, 12-H), 1.13 ppm (d, $^3J(H,H) = 6.9$ Hz, 12H, 12-H); ^{13}C NMR ($CDCl_3$): $\delta = 166.50$ (C_q, C-10), 162.14 (C_q, C-7), 144.01 (C_q, C-2,3,5,6), 98.31 (C_q, C-8), 56.30 (CH, C-1,4), 50.50, 45.48 (CH, C-11), 21.30, 21.02, 20.66, 20.26 (CH_3, C-12) 18.37 ppm (CH_3, C-9); MS (EI, 70 eV): m/z(%) = 640 (25) [M^+], 541 (50), 498 (15), 442 (28), 413 (52), 355 (20), 313 (19), 260 (55), 218 (25), 176 (20), 158 (42), 100 (75), 86 (28), 58 (12), 43 (100); IR (KBr): $\tilde{\nu} = 2961$ (s), 2932 (m), 1628 (ss), 1440 (s), 1371 (m), 1344 (s), 1329 (s), 1208 (m), 1156 (w), 1136 (w), 1037 (m), 815 (w), 781 (w), 610 (w), 570 cm^{-1} (w); HRMS: $C_{38}H_{64}N_4O_4$; calcd for [M^+]: 640.4927, found: 640.4913 ± 3 ppm; UV/Vis (CH_2Cl_2): λ_{max} (ε) = 250 nm (sh, 11965), 285 nm (sh, 2680 L mol^{-1} cm^{-1}); elemental analysis calcd (%) for $C_{38}H_{64}N_4O_4$: C 71.21, H 10.06, N 8.74; found: C 71.31, H 10.20, N 8.76 %.

3: Compound **1** (150 mg, 0.23 mmol) was dissolved in anhydrous THF (~5 mL). The solution was pipetted into five NMR tubes (normal glass) and irradiated with a mercury high-pressure lamp (150 W, Pyrex filter) for 2 h in an ice bath. The solvent was removed in vacuo, and the remaining starting material was separated by flash column chromatography (silca gel, cyclohexane/ethyl acetate 3:1, $R_f = 0.27$). The colorless solid was dried in high vacuum. Yield: 125 mg (0.20 mmol, 85 %); m.p.: > 200 °C (decomp.); ^{1}H NMR ($CDCl_3$): $\delta = 4.09$ (br, 4H, 11-H), 3.38 (sept, $^3J(H,H) = 6.8$ Hz, 4H, 11-H), 2.69 (s, 2H, 2,4-H), 1,97 (s, 6H, 9-H), 1.39 (d, $^3J(H,H) = 6.8$ Hz, 12H, 12-H), 1.36 (d, $^3J(H,H) = 6.8$ Hz, 12H, 12-H), 1.29 (br, 12H, 12-H), 1.11 ppm (d, $^3J(H,H) = 6.3$ Hz, 12H, 12-H). ^{13}C NMR ($CDCl_3$): $\delta = 164.24$ (C_q, C = O), 133.06 (C_q, C-8), 126.72 (C_q, C-3), 49.57, 47.54 (C_q, C-1,5,6,7), 46.02 (CH, C-1,4), 37.97 (CH, C-11), 22.58 (CH_3, C-9), 21.53, 20.66, 20.57, 20.43 ppm (CH_3, C-12); MS (EI, 70 eV): m/z(%) = 640 (15) [M^+], 597 (9), 541 (29), 496 (33), 442 (19), 413 (45), 355 (26), 313 (17), 270 (22), 260 (52), 218 (26), 158 (44), 100 (100), 72 (68); IR (KBr): $\tilde{\nu} = 3447$ (br), 2965 (s), 1638 (ss), 1438 (s), 1374 (m), 1325 (s), 1215 (m), 1038 cm^{-1} (m); UV/Vis (EtOH): λ (ε) = 207 nm (29047 L mol cm^{-1}); HRMS: calcd for $C_{38}H_{64}N_4O_4$: [M^+]: 640.49276, found 640.49250 ± 3 ppm.

Reisomerization **3**→**1**: A solution of **3** (20 mg, 0.03 mmol) in anhydrous THF (1 mL) was irradiated in an NMR tube (normal glass) with a low-pressure mercury lamp (15 W, quartz filter) for 4 h. According to the ^{1}H NMR spectrum ($CDCl_3$), the conversion to **1** was 50 %. Upon prolonged irradiation (8 h) the norbornadiene/quadricyclane ratio does not change. However, small amounts (< 10 %) of 7-isopropylidenenorborna-2,5-diene-2,3,5,6-tetracarboxylic acid tetrakis(isopropyl amide) were observed.

Received: January 16, 2003 [Z50959]

Keywords: amide ligands · association constants · photochemistry · sodium · valence isomerization

[1] a) S. Shinkai in *Comprehensive Supramolecular Chemistry, Vol. 1* (Eds.: J. L. Atwood, J. E. D. Davies, D. D. MacNicol, F. Vögtle), Elsevier, New York, **1996**, pp. 671–700; b) B. E. Feringa in *Molecular Switches*, Wiley-VCH, Weinheim, **2001**.

[2] Reviews: a) K. Hirao, A. Yamashida, O. Yonemitsu in *Carbocyclic Cage Compounds* (Eds.: E. Osawa, O. Yonemitsu), VCH, **1992**, pp. 383-399; see also b) K. Maruyama, H. Tamiaki, S. Kawabata, *Chem. Lett.* **1984**, 743–746; c) K. Maruyama, H. Tamiaki, T. Yanai, *Bull. Chem. Soc. Jpn.* **1985**, *58*, 781–782; d) K. Maruyama, H. Tamiaki, *J. Org. Chem.* **1986**, *51*, 602–606; e) K. Maruyama, H. Tamaki, S. Kawabata, *J. Chem. Soc. Perkin Trans. 2*, **1986**, 543–549; f) K. Maruyama, H. Tamaki, *J. Org. Chem.* **1987**, *52*, 3967–3970; g) G. Kaupp, H. Prinzbach, *Justus Liebigs Ann. Chem.* **1969**, *725*, 52–63; h) S. Sakai, K. Ohkubo, F. Fujiwara, A. Ohyoshi, *J. Mol. Catal.* **1982**, *16*, 181; i) K. Hirao, A. Yamashita, A. Ando, T. Hamada, O. Yonemitsu, *J. Chem. Soc. Perkin. Trans 1.* **1988**, 2913–2916; j) K. Hirao, A. Ando, T. Hamada, O. Yonemitsu, *J. Chem. Soc. Chem. Commun.* **1984**, 300–302; k) C. Kutal, *J. Chem. Educ.* **1983**, *60*, 882–887; l) H. Meier, *Photochemie I* in Houben-Weyl, *Methoden der Organ-*

 © 2003 Wiley-VCH Verlag GmbH & Co. KGaA, Weinheim

ischen Chemie, Vol. IV/5a, Thieme Verlag, Stuttgart, **1975**, pp. 222–261.

[3] a) R. Herges, W. Reif, *Chem. Ber.* **1994**, *127*, 1143 – 1145; b) R. Herges, W. Reif, *Liebigs Ann.* **1996**, 761 – 768; c) F. Starck, P. G. Jones, R. Herges, *Eur. J. Org. Chem.* **1998**, 2533 – 2539; d) R. Herges, F. Starck, T. Winkler, M. Schmittel, *Chem. Eur. J.* **1999**, *5*, 2965 – 2969.

[4] a) L. J. Govenlock, J. A. K. Howard, J. M. Moloney, D. Parker, R. D. Peacock, G. Siligardi, *J. Chem. Soc. Perkin Trans. 2* **1999**, 2415; b) F. Zamora, P. Amo-Ochoa, B. Fischer, A. Schimanski, B. Lippert, *Angew. Chem. Int. Ed.* **1999**, *38*, 2274; c) L. Frkanec, A. Visnjevac, B. Kojic-Prodic, M. Zinic, *Chem. Eur. J.* **2000**, *6*, 442; d) H. Tsukube, Y. Mitsutani, S. Shinoda, M. Tadokoro, K. Hori, *Tetrahedron Lett.* **1997**, *38*, 5021; e) H. Tsukube, Y. Mitsutani, S. Shinoda, T. Okazaki, M. Tadokoro, K. Hori, *Inorg. Chem.* **1999**, *38*, 3506; f) P. D. Beer, P. A. Gale, Z. Chen, M. G. B. Drew, J. A. Heath, M. I. Ogden, H. R. Powell, *Inorg. Chem.* **1997**, *36*, 5880; g) I. L. Karle, *Biochemistry* **1974**, *13*, 2155; h) R. S. Dickins, J. A. K. Howard, J. M. Moloney, D. Parker, R. D. Peacock, G. Siligardi, *Chem. Commun.* **1997**, *1747*; i) R. S. Dickins, J. A. K. Howard, C. L. Maupin, J. M. Moloney, D. Parker, R. D. Peacock, J. P. Riehl, G. Siligardi, *New J. Chem.* **1998**, *22*, 891.

[5] a) M. A. McKervey, M. J. Schwing-Weill, F. Arnaud-Neu in *Comprehensive Supramolecular Chemistry, Vol. 1* (Eds.: J. L. Atwood, J. E. D. Davies, D. D. MacNicol, F. Vögtle), Elsevier, New York, **1996**, pp. 537 – 603; b) A. Casnati, S. Barboso, H. Rouquette, M. J. Schwing-Weill, F. Arnaud-Neu, J. F. Dozol, R. Ungaro, *J. Am. Chem. Soc.* **2001**, *123*, 12182 – 12190; c) A. Casnati, L. Baldini, N. Pelizzi, K. Rissanen, F. Ugozzoli, R. Ungaro, *J. Chem. Soc. Dalton Trans.* **2000**, 3411 – 3415; d) F. Arnand-Neu, S. Barboso, A. Casnati, A. Pinalli, M. J. Schwing-Weill, R. Ungaro, *New J. Chem.* **2000**, *24*, 967 – 972; e) E. Pinkhassik, I. Stibor, A. Casnati, R. Ungaro, *J. Org. Chem.* **1997**, *62*, 8654 – 8659.

[6] P. J. Skinner, A. G. Cheetham, A. Beeby, V. Gramlich, F. Diederich, *Helv. Chim. Acta* **2001**, *84*, 2146 – 2153.

[7] a) J. M. Timko, S. S. Moore, D. M. Walba, P. C. Hiberty, D. J. Cram, *J. Am. Chem. Soc.* **1977**, *99*, 4207 – 4219; b) S. S. Moore, T. L. Tarnowski, M. Newcomb, D. J. Cram, *J. Am. Chem. Soc.* **1977**, *99*, 6398 – 6405.

[8] R. Herges, T. Winkler, *Eur. J. Org. Chem.* **2001**, 4419 – 4422.

 © 2003 Wiley-VCH Verlag GmbH & Co. KGaA, Weinheim

Chemically Induced Shape Change

Molecular Recognition in a Supramolecular Polymer System Translated into Mechanical Motion**

Hans-Jörg Schneider, Liu Tianjun, and Nino Lomadze*

Until now, molecular recognition in supramolecular chemistry has been observed without the possibility of transmitting the molecular event directly into a macroscopic motion. We report here on a new principle of flexible polymers with incorporated recognition sites which exhibit mechanical motions of up to 100% and more (natural muscles change their length at most by 30%) as specific response to different guest compounds. The material also exhibits a very symmetric expansion response to the pH value of the medium, with a minimum in the neutral region. Possible applications include in actuators, sensors, process control, and in particular drug-release systems.

In natural organs, such as muscles, macroscopic movements are initiated by the uptake of compounds such as adenosine 5′-triphosphate (ATP). The artificial muscles and related systems, such as microcapsules, which were prepared previously rely mostly on electric stimulation, photochemical activation, temperature changes, and differences in pH values.[1–4] Ingenious systems based on natural fibers, such as collagen, were devised in the 1960s which exhibit mechanical motions on interaction with salts.[5] The intriguing so-called molecular machines developed recently operate in solution without macroscopic mechanical action.[6]

Our new strategy is based on the incorporation of supramolecular recognition sites into elastic polymers. The acceptor units and their environment can be designed to lead to conformational and dimensional changes by uptake or release of ligands from or to the surrounding aqueous medium, as well as by pH changes. The aim is to obtain polymers which exhibit macroscopically tractable large motions in analogy to natural vessels or muscles through the selective formation of supramolecular complexes.

As a first step towards preparing solid polymers exhibiting chemically induced mechanical motions we synthesized suitable precursers by the reaction of poly(methyl methylacrylate) with diethylenetriamine and various amounts of long-chain alkyl amines. Ion pairing and/or the formation of hydrogen bonds between polyamines and carboxylates or nucleotides have been shown to be the basis of many efficient host compounds in solution.[7] Lipophilic interactions with the

[*] Prof. H.-J. Schneider, L. Tianjun, N. Lomadze
FR Organische Chemie
Universität des Saarlandes
and
Institut für Neue Materialien
66041 Saarbrücken (Germany)
Fax: (+49) 681-302-4105
E-mail: ch12hs@rz.uni-sb.de

[**] L.T. thanks the Alexander von Humboldt foundation for a stipend.

 © 2003 Wiley-VCH Verlag GmbH & Co. KGaA, Weinheim DOI: 10.1002/anie.200219965

alkyl chains in the polymers lead to additional binding and selectivity. The elastic and transparent films of the polymer were preconditioned in buffer solutions and cut into small pieces. Changes in the size were measured upon addition of different compounds and at different pH values.

The changes in the dimensions are completely reversible and are relatively fast, although no attempts have so far been made to further accelerate the velocity. As illustrated in Figure 1, the observed polymer expansion follows clean first-order kinetics. The half-life times $t_{1/2}$ for 50% expansion, for

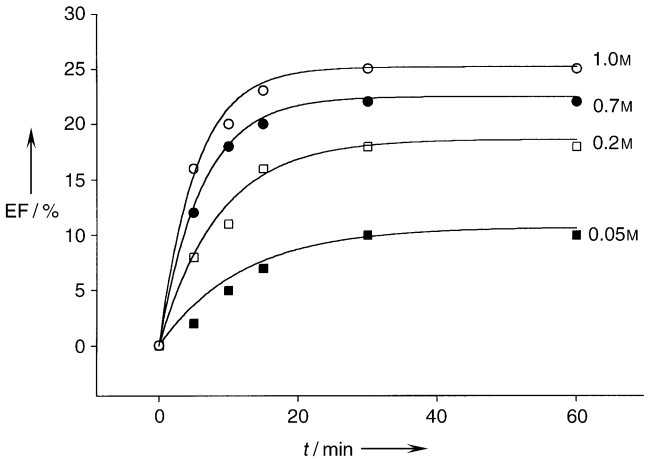


Figure 1. Expansion kinetics with AMP (at concentrations shown) at pH 6.8 in 0.05 M sodium phosphate buffer; a nonlinear fit to a first order equation is shown. EF = expansion factor.

example, in the presence of 0.05 M adenosine 5′-monophosphate (AMP) is usually only a few minutes. The uptake of compounds such as 2-naphthoic acid or AMP can be measured by UV/Vis spectroscopy as a depletion of its concentration in the supernatant solution; the absorption also follows first-order kinetics and shows $t_{1/2}$ values which are 50–70% smaller than the mechanical expansion.

The large pH effect on the polymer expansion (Figure 2) can be ascribed, in an analogous manner to

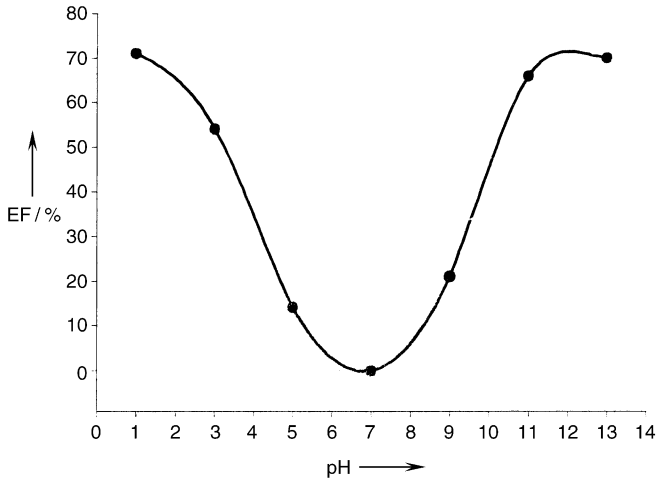
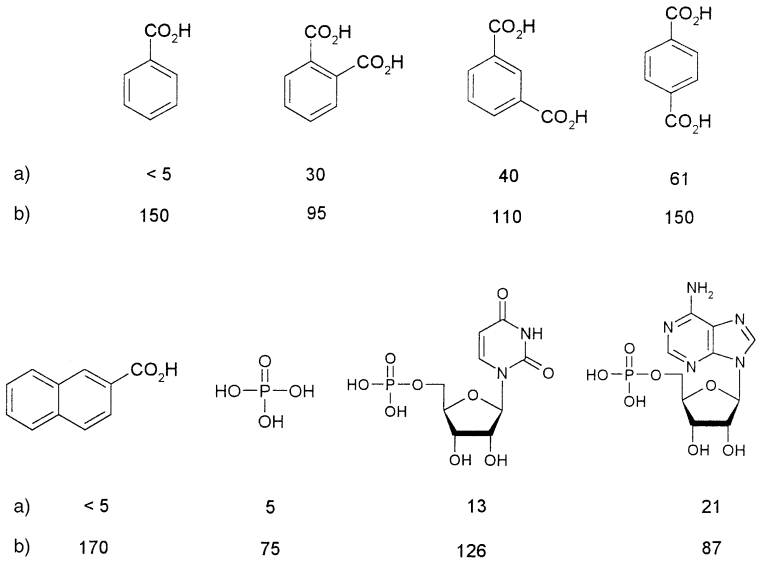


Figure 2. Expansion factors as a function of pH (0.05 M phosphate buffer without host compounds).

viscosity changes in polyelectrolytes,[1] to conformational changes of the polyamine. In the neutral pH region the polyamines are only partially protonated and, therefore, are more closely packed than at lower pH values where the many positively charged nitrogen atoms repel each other within and between the chains. At high pH values the amines become free and can form extended chains with less hydrogen-bonding interactions between them, which results again in a less-dense packing. This argument can also explain the striking observation that the expansion factors exerted by the added ligands are much larger at high pH values (see below). The pH-induced dimensional changes also follow a first-order rate law with half-life times of around five minutes; these values are only slightly decreased at pH 1 or pH 13.

Several measurements at pH 7 show significant selectivity with respect to the effector compound structures (Scheme 1). Inorganic phosphate ions produce very small changes in the



Scheme 1. Different effector substances with typical expansion factors (in %): a) 0.1 M effector, pH 7.0, 0.02 M phosphate buffer; b) 0.1 M effector with added 0.1 M NaOH and 0.05 M phosphate buffer.

dimensions compared to, for example, AMP, benzoic acid, and 2-naphthoic acid. A remarkable selectivity is visible in the changes observed with the three isomeric benzene dicarboxylic acids, which are already active at low concentrations. Although the nucleobase is larger in AMP than in uridine 5′-monophosphate (UMP) there is a larger expansion with UMP (Scheme 1). These examples demonstrate that the polymer expansion is not simply a function of the size of the added compound, but of specific binding energies and conformational changes.

The addition of bases increases the expansion dramatically. Thus, the combined effect of NaOH and AMP can produce an elongation of the polymer of about 150%. If one subtracts the effect of the base alone (which at pH 11 is 66%), the expansion observed with, for example, 0.05 M AMP alone increases to 84% (150–66), while the size increases by 20% at pH 7. Similar results are found on addition of benzoic acid or

 © 2003 Wiley-VCH Verlag GmbH & Co. KGaA, Weinheim

nucleotides (Scheme 1). The kinetics of expansion, for example, with AMP at high pH values remain very similar to those obtained under physiological conditions.

The *contraction* of the polymer (Figure 3) also follows first order kinetics and is again relatively fast, with a $t_{1/2}$ value of about 5 min. The contraction can be achieved simply by

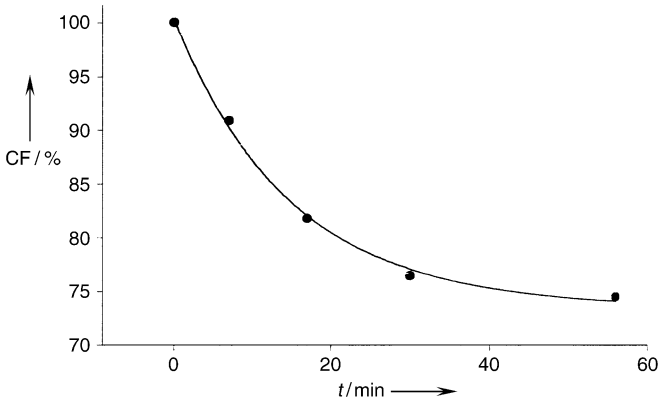


Figure 3. First-order contraction kinetics of a film loaded with AMP at pH 7.0. CF = contraction factor.

providing a ligand-free medium outside the polymer, provided there is a sufficiently large concentration gradient. Similar to expansion, there is a hysteresis if one compares the kinetics of desorption of the effector from the loaded polymers. This process can be followed spectroscopically under stirring of the solution (Figure 4). The desorption of the ligands from the polymer is almost as fast as the absorption process, whereas the contraction is about twice as slow. The observed hysteresis between the uptake or release of effector molecules and the accompanying macroscopic expansions and contractions indicates that conformational reorganization of the polymer network is the rate-determining step of the mechanical movements under the applied conditions.

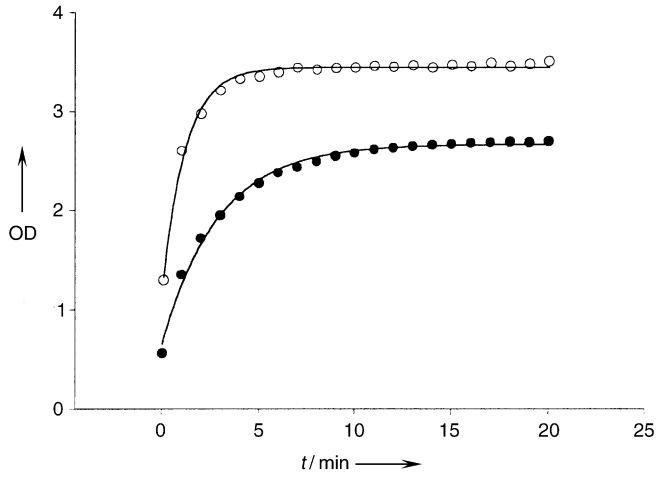


Figure 4. First-order desorption kinetics of fims loaded with AMP (filled circles) and 2-naphthoic acid (open circles); the curves are first order; UV/Vis detection with stirring at pH 7.0. OD = optical density.

The polyamine binding sites used in this study are acceptor units with a relatively broad binding spectrum that is dominated by ion paring, hydrogen bonds, and lipophilic interactions. Higher selectivities will be reached with such polymers by incorporating some of the many specific host structures which have already been developed by synthetic supramolecular chemistry for use in solution.

Polymers which exhibit mechanically tractable motions at specific effector concentrations and pH values have great potential for many applications. Besides sensors, these include artificial muscles, mechanical actuators, process and flow control,[8] and in particular new drug-release systems.[4,9] In contrast to other systems,[10] such devices would need no external controlling machinery, which usually also requires the use of external voltage supplies.[11]

Received: August 14, 2002
Delayed at authors's request [Z19965]

Keywords: actuators · chemomechanics · molecular recognition · polymers · supramolecular chemistry

[1] W. Kuhn, B. Hargitay, A. Katchalsky, H. Eisenberg, *Nature* **1950**, *165*, 514–516, and references therein.
[2] Y. Osada, H. Okuzaki, H. Hori, *Nature* **1992**, *355*, 242–244.
[3] Recent references on polymer-based actuators: *Polymers, Sensors, Actuators* (Eds.: Y. Osada, D. E. De Rossi), Springer, Berlin, **2000**.
[4] J. Kopecek, *Nature* **2002**, *417*, 388–391; N. A. Peppas, Y. Huang, M. Torres-Lugo, J. H. Ward, J. Zhang, *Annu. Rev. Biomed. Eng.* **2000**, *2*, 9–29, and references therein.
[5] M. V. Sussman, A. Katchalsky, *Science* **1970**, *167*, 45–47; I. Z. Steinberg, A. Oplatka, A. Katchalsky, *Nature* **1966**, *210*, 568–571.
[6] See, for example, J. F. Stoddart, *Acc. Chem. Res.* **2001**, *34*, 410–411; V. Balzani, A. Credi, M. Venturi, *Proc. Natl. Acad. Sci. USA* **2002**, *99*, 4814–4817; V. Balzani, A. Credi, F. M. Raymo, J. F. Stoddart, *Angew. Chem.* **2000**, *112*, 3484–3530; *Angew. Chem. Int. Ed.* **2000**, *39*, 3348–3391; J. P. Collin, C. Dietrich-Buchecker, P. Gavina, M. C. Jimenez-Molero, J.-P. Sauvage, *Acc. Chem. Res.* **2001**, *34*, 477–487; B. X. Colasson, C. Dietrich-Buchecker, M. C. Jimenez-Molero, J.-P. Sauvage, *J. Phys. Org. Chem.* **2002**, *15*, 476–483.
[7] See, for example, H.-J. Schneider, A. Yatsimirski, *Principles and Methods in Supramolecular Chemistry,* Wiley, New York, **2000**; J. W. Steed, J. L. Atwood, *Supramolecular Chemistry*, Wiley, New York, **2000**.
[8] For related devices see, for example, K. F. Arndt, D. Kuckling, A. Richter, *Polym. Adv. Technol.* **2000**, *11*, 496–505.
[9] Reviews: N. A. Peppas, *Curr. Opin. Colloid Interface Sci.* **1997**, *2*, 531–537; Y. Qiu, K. Park, *Adv. Drug Delivery Rev.* **2001**, *53*, 321–339; Y. Luo, G. D. Prestwich, *Expert Opin. Ther. Pat.* **2001**, *11*, 1395–1410.
[10] See, for example, L. M. Low, S. Seetharaman, K. Q. He, M. J. Madou, *Sens. Actuators B* **2000**, *67*, 149–160.
[11] Patent applied by instrAction GmbH, Ludwigshafen (www.instraction.de).

 © 2003 Wiley-VCH Verlag GmbH & Co. KGaA, Weinheim

Mo Complexes with SbS Ligands

$\mu,\eta^{2:2}$-SbS: An Antimony-Containing Heterodiatomic Ligand from Group 15 and 16 Elements**

Henri Brunner, Marek M. Kubicki, Andreas Lange, Joachim Wachter, Estelle Vigier, and Manfred Zabel*

NO is a ubiquitous heterodiatomic EX molecule (E = Group 15 element, X = Group 16 element).[1] While its higher congeners NS, PO, and PS are of more or less exotic character in the free state, they attract considerable interest from a theoretical point of view or as versatile ligands in coordination chemistry.[2] Only a few complexes are known with AsS[3] and AsSe[4] ligands. Their ability to use π bonding orbitals for bridging dimetal units in a $\mu,\eta^{2:2}$ coordination mode along with a pronounced dimerization tendency through the unpaired electron (π*-HOMO) make them ideal candidates for the construction of mixed-ligand triple-decker complexes.[4] Herein we report the synthesis and characterization of a dimolybdenum complex bearing the hitherto unknown $\mu,\eta^{2:2}$-SbS ligand.

Potential Sb/S building blocks, such as $[\psi\text{-SbS}_3]^{3-}$ and $[SbS_4]^{3-}$ units, exist in numerous solid-state compounds.[5] A recent and promising strategy for the synthesis of transition-metal complexes with mixed EX ligands is the metathesis reaction of organometallic halides with salts containing E/X anions, for example, K_3AsS_3[6–8] and $K_2As_4Se_6$,[8]. Soluble anions containing antimony, such as $[Sb_4S_6]^{2-}$ or $[Sb_{12}Se_{20}]^{4-}$, are known.[9] A more suitable candidate may be K_3SbS_3, which we synthesized by the reaction of Sb_2S_3 with K/S_8 in liquid NH_3 in analogy to the formation of K_3AsS_3.[10]

The reaction of $[Cp^*Mo(CO)_3Cl]$ ($Cp^* = C_5Me_5$) with 0.5 equivalents of K_3SbS_3 in boiling acetone gave, after chromatography on silica gel, a dark red compound analyzing as $[Cp^*_2Mo_2(CO)_4SbS]Cl$ (**1**-Cl) in 17 % yield. As by-products complexes $[Cp^*_2Mo_3(CO)_3(\mu_2\text{-}CO)(\mu_2\text{-}Cl)_2(\mu_3\text{-}S)]$[11] and various isomers of $[Cp^*_2Mo_2(S)_{4-n}O_n]$ ($n = 1, 2$)[12] have been identified. The presence of oxygen (IR: $\tilde{\nu}(Mo{=}O) = 900$, 890 cm^{-1}) in the latter compounds indicates a certain lability of the Mo–Sb bonds formed towards residual moisture or air. The ESI mass spectrum of **1**-Cl shows the peaks for the parent ion $\mathbf{1}^+$ without chlorine. Subsequent reaction of **1**-Cl with NH_4PF_6 in H_2O/EtOH gave the red-brown salt $[Cp^*_2Mo_2(CO)_4SbS][PF_6]$ (**1**-PF_6). Its composition was confirmed by mass spectroscopy, elemental analyses and, after recrystallization from THF, by single-crystal X-ray diffraction analysis. The new compounds are soluble in THF, acetone, and $CHCl_3$. Their solutions are slightly air-sensitive.

IR spectra reveal four bands for **1**-Cl between 2009 and 1850 cm^{-1}, and three bands (one of which is broad and not well resolved) for **1**-PF_6. The bands may be attributed to terminal CO groups with the exception of the low-energy absorption which may be assigned to a semibridging CO ligand. The ^1H NMR spectra of **1**-Cl and **1**-PF_6 only contain one signal each for the methyl groups. As these signals remain invariant down to −90 °C, the Cp* ligands are equivalent in solution.

A crystal structure determination was carried out for **1**-PF_6.[13] The asymmetric unit contains two independent cations and two PF_6^- ions. The central structural feature of the cation is a $\{Mo_2SbS\}$ tetrahedron that is integrated into a $\{Cp^*_2Mo_2(CO)_4\}$ framework (Figure 1). This means that the

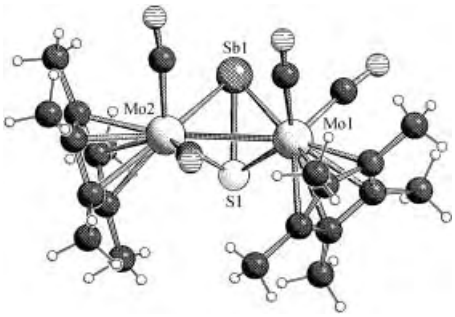


Figure 1. Molecular structure of the cation in **1**-PF_6. Selected interatomic distances [Å] and angles [°] of one of the two independent cations in the asymmetric unit: Mo1-Mo2 3.119(1), Mo1-Sb1 2.844(1), Mo1-S1 2.441(2), Mo2-Sb1 2.776(1), Mo2-S1 2.475(2), Sb1-S1 2.436(1); Mo1-Sb1-Mo2 67.4(1), Mo1-S1-Mo2 78.8(1).

title compound contains an unprecedented heterodiatomic $\mu,\eta^{2:2}$-SbS ligand. Removal of the π* (HOMO) electron from the hypothetical SbS molecule formally leads to the four-electron π-donor $[SbS]^+$ ion, which forms a complex of pseudotetrahedral geometry with the metal centers. Thus, **1**-PF_6 is an extension of the series of $[Cp_2Mo_2(CO)_4E_2]$ complexes with side-on coordinated Group 15 elements (E = P, As, Sb, Bi)[14] to mixed EX ligands. The observed mean Sb–S bond length of 2.430(1) Å fits well with Sb–S separations in coordination compounds, which usually lie between 2.38 and 2.60 Å.[5b,15]

An analysis of the bonding patterns in **1**-PF_6 and in hypothetical free SbS has been carried out by means of DFT (B3LYP) calculations with the pseudopotential basis set LanL2DZ.[16] The optimized bond lengths decrease along the series of free $[SbS]^-$, SbS, and $[SbS]^+$ molecules from 2.447, to 2.327 to 2.240 Å, respectively. Owing to a rather high difference of absolute electronegativities of Sb and S atoms (4.85 and 6.22, respectively)[17] all the molecular orbitals are strongly polarized. For example, in the $[SbS]^+$ ion the sulfur atomic orbitals contribute some 70 % to the bonding σ and π(p) molecular orbitals, whereas in the antibonding molecular orbitals the antimony contribution is predominant.

[*] Dr. J. Wachter, Prof. Dr. H. Brunner, A. Lange, Dr. M. Zabel
Institut für Anorganische Chemie
Universität Regensburg
93040 Regensburg (Germany)
Fax: (+49) 941-943-4439
E-mail: joachim.wachter@chemie.uni-regensburg.de
Prof. Dr. M. M. Kubicki, E. Vigier
Laboratoire de Synthèse et d'Electrosynthèse Organométalliques
Université de Bourgogne
21100 Dijon (France)

[**] We thank the Deutsche Forschungsgemeinschaft for financial support.

 DOI: 10.1002/anie.200350931 © 2003 Wiley-VCH Verlag GmbH & Co. KGaA, Weinheim

The geometry of the cation $\mathbf{1}^+$ has been optimized starting from mean parameters from the X-ray analysis. The calculated structure agrees fairly well with experimental data (d(Mo-Mo) = 3.172 (calcd) vs. 3.130 (mean, exp) Å; d(Sb-S) = 2.523 (calcd) vs. 2.430 Å (exp, overestimated by some 0.09 Å); torsion angle Sb-S/Mo-Mo = 89.3 (calcd) vs. 87.9° (exp)). All four π bonding and antibonding molecular orbitals of the $[SbS]^+$ ion participate in filled molecular orbitals of $\mathbf{1}^+$ through their interactions with suitable π and δ combinations of the Mo_2 fragment. However, we were intrigued by the absence of Sb atomic orbitals in the HOMO of $\mathbf{1}^+$ (which is the minimum-energy optimized state $\mathbf{1a}^+$ in Figure 2a). Consequently, we optimized $\mathbf{1}^+$ constrained to C_s symmetry with a Sb–S/Mo–Mo torsion angle of 90° ($\mathbf{1b}^+$), which is a transition state with a total energy only 0.016 eV (0.37 kcal mol^{-1}) higher than for $\mathbf{1a}^+$. The calculated Mo–Mo (3.324 Å) and Sb–S (2.554 Å) bond lengths for $\mathbf{1b}^+$ are longer than in $\mathbf{1a}^+$ and the energies of frontier orbitals are higher. Moreover, the shapes of some frontier orbitals are highly modified. In particular, the HOMO of $\mathbf{1b}^+$ is destabilized by 0.18 eV, but contrary to $\mathbf{1a}^+$ it has a significant contribution from the Sb atom (Figure 2b). Consequently, the nature of bonding in the ion $\mathbf{1}^+$, which contains the $\{Mo_2SbS\}$ pseudotetrahedral fragment, is very sensitive towards small energy and geometry changes. It is worth noting, that the slight deformation of the cation from ideal C_s symmetry observed in the crystal structure, is not a packing effect, but is an intrinsic electronic property of $\mathbf{1}^+$.

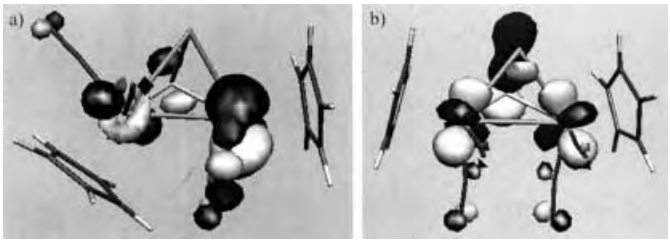


Figure 2. Shapes of the HOMOs in $\mathbf{1}^+$. a) Optimized structure $\mathbf{1a}^+$ ($E = -9.81$ eV, $E_{tot} = -990.786$ eV), b) transition state $\mathbf{1b}^+$ ($E = -9.63$ eV, $E_{tot} = -990.770$ eV).

The ion $\mathbf{1}^+$ is formally isoelectronic[18] with the $[Fe_2(CO)_6(\mu\text{-AsS})]^-$ ion.[3] For this complex an $[AsS]^{3-}$ ligand has been proposed. DFT calculations of the electron rich $[AsS]^{3-}$ ion show it to has a very short life-time.[19] We also calculated the geometrically optimized electronic structure of the $[Fe_2(CO)_6(\mu\text{-AsS})]^-$ ion.[20] In this ion the HOMO consists of the bent Fe–Fe bond, while its LUMO is an Fe–Fe σ* antibonding interaction slightly stabilized with the sulfur lone pair. Taking into account the X-ray data (d(Fe-Fe) = 2.598(1), d(As-S) = 2.227(2) Å in the disordered bridge)[3] together with the optimized structure[20] the $[Fe_2(CO)_6(\mu\text{-AsS})]^-$ ion is best described as an association of $[AsS]^-$ with the $\{Fe_2(CO)_6\}$ fragment.

In contrast, in the molybdenum complex $\mathbf{1}^+$ the metal–metal bond is found in HOMO-1 molecular orbital. The HOMO (as discussed above) is an elusive function of a′ symmetry which in the symmetrical transition state C_s (Figure 2b) has contributions from Sb–S in-plane π bonding, together with σ* Sb–S antibonding and δ Mo–Mo bonding contributions. The LUMO in $\mathbf{1}^+$ of a″ symmetry is roughly the Mo–Mo σ* antibonding orbital.

In conclusion, the nature of frontier valence molecular orbitals in both isoelectronic AsS- and SbS-containing complexes depends on the nature of bridging and metallic atoms. Even if there are some formal electronic analogies between the iron and molybdenum complexes, there is no common model for the bonding therein.

Experimental Section

1-Cl: A mixture of [Cp*Mo(CO)$_3$Cl] (750 mg, 2.14 mmol), K_3SbS_3 (360 mg, 1.07 mmol) and acetone (50 mL) was stirred for 16 h under reflux. The mixture was cooled to room temperature and then solid material was removed by filtration. After concentration of the filtrate the brown residue was dissolved in toluene. Chromatography on SiO_2 (activity II–III, column 15 × 3 cm) with toluene and then toluene/acetone (5:1) gave successively four faint brown and yellow colored bands. These contain $[Cp^*_2Mo_2(S)_{4-n}O_n]$ ($n = 1, 2$) isomers in very low yields. A blue-green band (10 mg) was identified as $[Cp^*_2Mo_3(CO)_3(\mu_2\text{-CO})(\mu_2\text{-Cl})_2(\mu_3\text{-S})]$.[11] Finally, an intense brown-red band was isolated that contained 140 mg (0.18 mmol, 17%) of **1**-Cl. Recrystallization of [**1**]Cl from toluene/pentane (9:4) gave dark red prisms. Elemental analysis (%) calcd for $C_{24}H_{30}ClMo_2O_4SSb$ (763.66): C 37.75, H 3.96, S 4.20; found: C 38.11, H 4.02, S 4.30. ESI-MS (CH_2Cl_2): m/z 728.0 ($M^+ - Cl$) (simulated 728). IR (KBr): $\tilde{\nu}$(CO) = 2009 (vs), 1958 (s), 1877 (vs), 1850 cm^{-1} (s). ^{1}H NMR (400 MHz, C_6D_6): $\delta = 1.65$ ppm (s).

1-PF_6: The solutions of **1**-Cl (160 mg, 0.21 mmol) in EtOH (19 mL) and NH_4PF_6 (68 mg, 0.42 mmol) in water (15 mL) were combined to give a red-brown precipitate, which was collected by filtration and washed with water (20 mL) and then diethyl ether (3 × 2 mL). The dried residue was dissolved in acetone and insoluble material was removed by filtration. After evaporation of the solvent **1**-PF_6 was obtained in 57% yield. **1**-PF_6 was recrystallized from THF. Elemental analysis (%) calcd for $C_{24}H_{30}F_6Mo_2O_4PSSb \cdot 1.5\,C_4H_8O$ (873.17): C 36.72, H 4.31, S 3.27; found: C 36.59, H 4.22, S 3.64. ESI-MS (CH_2Cl_2): m/z 727.9 [$M^+ - [PF_6]$]. IR (KBr): $\tilde{\nu}$(CO) = 2007 (s), 1959 (m), 1885 cm^{-1} (s, br); $\tilde{\nu}(PF_6) = 865$ (m), 844 (vs), 560 cm^{-1} (m). ^{1}H NMR (400 MHz, C_6D_6): $\delta = 1.66$ ppm (s).

Received: January 14, 2003
Revised: April 10, 2003 [Z50931]

Keywords: antimony · hetroatomic ligands · molybdenum · structure elucidation · sulfur

[1] a) W. A. Herrmann, *Angew. Chem.* **1991**, *103*, 835–836; *Angew. Chem. Int. Ed. Engl.* **1991**, *30*, 818–819; b) F. Murad, *Angew. Chem.* **1999**, *111*, 1976–1989; *Angew. Chem. Int. Ed.* **1999**, *38*, 1856–1868.
[2] a) J. Wachter, *Angew. Chem.* **1998**, *110*, 782–800; *Angew. Chem. Int. Ed.* **1998**, *37*, 750–768; b) L. Sedes, J. H. Yamamoto, L. Brissieux, B. T. Herenberg, K. A. Udachin, A. J. Carty, *Inorg. Chem.* **2001**, *40*, 6731–6736.
[3] B. K. Das, M. G. Kanatzidis, *Inorg. Chem.* **1995**, *34*, 6505–6508.

 © 2003 Wiley-VCH Verlag GmbH & Co. KGaA, Weinheim

[4] O. Blacque, H. Brunner, M. M. Kubicki, F. Leis, D. Lucas, Y. Mugnier, B. Nuber, J. Wachter, *Chem. Eur. J.* **2001**, *7*, 1342 – 1349.

[5] Surveys on ternary and quaternary thioantimonates are given in a) G. W. Drake, J. W. Kolis, *Coord. Chem. Rev.* **1994**, *137*, 131 – 178; b) R. Stähler, W. Bensch, *Eur. J. Inorg. Chem.* **2001**, 3073 – 3078.

[6] G. A. Zank, T. B. Rauchfuss, S. R. Wilson, A. L. Rheingold, *J. Am. Chem. Soc.* **1984**, *106*, 7621 – 7623.

[7] H. Brunner, F. Leis, J. Wachter, M. Zabel, *J. Organomet. Chem.* **2001**, *627*, 139 – 143.

[8] H. Brunner, F. Leis, J. Wachter, M. Zabel, *J. Organomet. Chem.* **2001**, *628*, 39 – 45.

[9] a) T. M. Martin, G. L. Schimek, W. T. Pennington, J. W. Kolis, *J. Chem. Soc. Dalton Trans.* **1995**, 501 – 502; b) T. M. Martin, P. T. Wood, J. W. Kolis, *Inorg. Chem.* **1994**, *33*, 1587 – 1588.

[10] M. G. Kanatzidis, J.-H. Chou, *J. Solid State Chem.* **1996**, *127*, 186 – 201.

[11] A Lange, J. Wachter, M. Zabel, unpublished results.

[12] H. Brunner, H. Kauermann, J. Pfauntsch, J. Wachter, J. H. Enemark, C. G. Young, *J. Organomet. Chem.* **1987**, *331*, 45 – 52.

[13] Crystal structure analyses: **1**-PF_6·1.5 C_4H_8O: Dark red crystals, $0.48 \times 0.20 \times 0.04$ mm^3, monoclinic, $P2_1/c$, $a = 22.174(1)$, $b = 25.472(1)$, $c = 13.251(1)$ Å, $\beta = 103.81(1)°$. $V = 7268.0(7)$ Å^3, $Z = 8$, $\rho_{calcd} = 1.794$ g cm^{-3}, $\theta = 2.05$–$25.93°$, $\mu = 1.59$ mm^{-1}, 62352 measured reflections, 14052 independent reflections ($R_{int} = 0.0475$), 11021 observed reflections ($I > 2\sigma(I)$), 838 refined parameters, $R1 = 0.0282$, $wR2 = 0.0687$, residual electron density 1.074/−0.469 e Å^{-3}. Data were collected on a STOE-IPDS diffractometer ($Mo_{K\alpha}$ radiation) at 173 K. The structure was solved by direct methods using SIR97 and refined against F^2 (SHELXL-97) with all reflections. CCDC-200715 (**1**-PF_6) contains the supplementary crystallographic data for this paper. These data can be obtained free of charge via www.ccdc.cam.ac.uk/conts/retrieving.html (or from the Cambridge Crystallographic Data Centre, 12 Union Road, Cambridge CB2 1EZ, UK; fax: (+44) 1223-336-033; or deposit@ccdc.cam.ac.uk).

[14] a) O. J. Scherer, *Angew. Chem.* **1990**, *102*, 1137 – 1155; *Angew. Chem. Int. Ed. Engl.* **1990**, *29*, 1104 – 1122; b) J. R. Harper, A. L. Rheingold, *J. Organomet. Chem.* **1990**, *390*, C36 – C38; c) W. Clegg, N. A. Compton, R. J. Errington, G. A. Fisher, N. C. Norman, T. B. Marder *J. Chem. Soc. Dalton Trans.* **1991**, 2887 – 2895; d) J. E. Davies, L. C. Kerr, M. Mays, P. R. Raithby, P. K. Tompkin, A. D. Woods, *Angew. Chem.* **1998**, *110*, 1473 – 1475; *Angew. Chem. Int. Ed.* **1998**, *37*, 1428 – 1429.

[15] N. Korber, F. Richter, *Helv. Chim. Acta* **2001**, *84*, 2368 – 2372.

[16] Gaussian 98 (Revision A.7), M. J. Frisch, G. W. Trucks, H. B. Schlegel, G. E. Scuseria, M. A. Robb, J. R. Cheeseman, V. G. Zakrzewski, J. A. Montgomery, R. E. Stratmann, J. C. Burant, S. Dapprich, J. M. Millam, A. D. Daniels, K. N. Kudin, M. C. Strain, O. Farkas, J. Tomasi, V. Barone, M. Cossi, R. Cammi, B. Mennucci, C. Pomelli, C. Adamo, S. Clifford, J. Ochterski, G. A. Petersson, P. Y. Ayala, Q. Cui, K. Morokuma, D. K. Malick, A. D. Rabuck, K. Raghavachari, J. B. Foresman, J. Cioslowski, J. V. Ortiz, B. B. Stefanov, G. Liu, A. Liashenko, P. Piskorz, I. Komaromi, R. Gomperts, R. L. Martin, D. J. Fox, T. Keith, M. A. Al-Laham, C. Y. Peng, A. Nanayakkara, C. Gonzalez, M. Challacombe, P. M. W. Gill, B. G. Johnson, W. Chen, M. W. Wong, J. L. Andres, M. Head-Gordon, E. S. Replogle, J. A. Pople, Gaussian, Inc., Pittsburgh, PA, **1998**.

[17] R. G. Pearson, *Inorg. Chem.* **1988**, *27*, 734 – 740.

[18] Following the Wade–Mingos rules (K. Wade, *Adv. Inorg. Chem. Radiochem.* **1976**, *18*, 1 – 66; D. M. P. Mingos, R. L. Johnston, *Struct. Bonding (Berlin)* **1987**, *68*, 29 – 87) $[Fe_2(CO)_6(\mu\text{-AsS})]^-$ and $\mathbf{1}^+$ are of the *nido* trigonal-bipyramidal structural type (12 electrons or 6 skeletal electron pairs (SEPs)). The atomically vacant (vertex) site is occupied by the electrons of the bent metal–metal bond.

[19] Optimized separations (B3LYPLanL2DZ) for $[AsS]^+$, AsS, and $[AsS]^-$ are 2.056, 2.153, and 2.283 Å, respectively, while for $[AsS]^{3-}$ the As–S bond is broken. At a lower level of theory (PM3, B3LYPSTO-3G) $[AsS]^{3-}$ could be optimized, but with a very long (≈ 2.55 Å) bond.

[20] Calculated (B3LYPLanL2DZ) distances for $[Fe_2(CO)_6(\mu\text{-AsS})]^-$: d(Fe-Fe) = 2.578, d(As-S) = 2.391 Å.

 © 2003 Wiley-VCH Verlag GmbH & Co. KGaA, Weinheim

Oxonitridophosphate Structures

$Li_xH_{12-x-y+z}[P_{12}O_yN_{24-y}]Cl_z$—An Oxonitridophosphate with a Zeolitelike Framework Structure Composed of 3-Rings**

Sascha Correll, Oliver Oeckler, Norbert Stock, and Wolfgang Schnick**

Phosphorus oxide nitride (PON) as well as HPN_2 are isoelectronic with SiO_2. The network is made up of corner-linked $P(O,N)_4$ tetrahedra and crystallizes with structures similar to known polymorphs of SiO_2.[1] The partial substitution of silicon by aluminum in silicates allows a considerable variation of the framework charge. This led to a large class of compounds, the aluminosilicates, which were the first group of materials to be recognized for their nanoporosity.[2]

The formal exchange of silicon by phosphorus and the total or partial substitution of oxygen by nitrogen led to nitrido- and oxonitridophosphates, whose framework charge can be adjusted by variation of the O/N ratio. In contrast to oxygen, nitrogen can bridge two ($N^{[2]}$) as well as three ($N^{[3]}$) tetrahedral centers, thus leading to an extension of the structural possibilities. Therefore, a larger structural variety with respect to cage structures and pore sizes is expected in (oxo-)nitridophosphates than in aluminosilicates.

The total exchange of the bridging oxygen atoms by nitrogen atoms in zeolitelike structures has been demonstrated by the synthesis of $Zn_7P_{12}N_{24}Cl_2$. This nitridophosphate crystallizes in the sodalite structure type.[3] The partial substitution of oxygen by nitrogen[4] recently led to the analogous oxonitridophosphate $M_{8-x}H_x[P_{12}N_{18}O_6]X_2$ (M =

[*] Prof. Dr. W. Schnick, S. Correll, Dr. N. Stock
Department Chemie der Ludwig-Maximilians-Universität
Butenandtstrasse 5–13, 81377 München (Germany)
Fax: (+49) 89-2180-77440
E-mail: wolfgang.schnick@uni-muenchen.de
Dr. O. Oeckler
Max-Planck-Institut für Festkörperforschung
Heisenbergstrasse 1, 70569 Stuttgart (Germany)
E-mail: oliver.oeckler@gmx.de

[**] The authors thank Prof. Dr. Arndt Simon and Viola Duppel, Max-Planck-Institut für Festkörperforschung, Stuttgart, for recording transmission electron diffraction patterns. This work was supported by the Fonds der Chemischen Industrie and the DFG.

 DOI: 10.1002/anie.200351372 © 2003 Wiley-VCH Verlag GmbH & Co. KGaA, Weinheim

Cu, Li; X = Cl, Br, I).[5] The structures of these compounds were determined from X-ray powder diffraction data. However, no framework structures containing larger pores were observed in this class of compounds. With $Li_xH_{12-x-y+z}[P_{12}O_yN_{24-y}]Cl_z$ (**1**) we have been able for the first time to synthesize a zeolitelike oxonitridophosphate[6] containing large 12-ring channels and to determine its structure from single-crystal X-ray diffraction data. The framework structure is composed of corner-linked tetrahedra, which form $P_3(O,N)_9$ 3-rings as FBUs (fundamental building units).[7] To date, no similar topology has been experimentally observed in zeolites.[8]

Pure **1** was synthesized by heating a mixture of $Li_2S/HPN_2/OP(NH_2)_3/LiCl$ or $Li_2O/SP(NH_2)_3/LiCl$ in sealed silica ampoules at 700 °C for 3 days. Single-phase products containing suitable single crystals (40–80 μm) for X-ray crystal-structure determination were also obtained from the $Li_2S/SP(NH_2)_3/OP(NH_2)_3/NH_4Cl$ system [Eq. (1)].

$$\begin{gathered} \tfrac{1}{2}x\,Li_2S + y\,OP(NH_2)_3 + (12-y)\,SP(NH_2)_3 + z\,NH_4Cl \\ 700\,^{\circ}C \downarrow \qquad (1) \\ Li_xH_{12-x-y+z}[P_{12}O_yN_{24-y}]Cl_z + (12+\tfrac{1}{2}x-y)\,H_2S + (12+y+z)\,NH_3 \\ \text{with } 6 \le x \le 9,\ 2 \le y \le 4 \text{ and } 2 \le z \le 3. \end{gathered}$$

The crystal structure was elucidated from single-crystal X-ray diffraction experiments.[9] The indexing of the reflections initially led to a hexagonal unit cell with $a = 1641(1)$ and $c = 475(1)$ pm. However, no trigonal or hexagonal space group could be identified unambiguously based on the reflection conditions. Nevertheless, the best structure solution was obtained in the space group $P31c$, although the data set contained reflections that violated the reflection conditions of the c glide plane. The subsequent structure refinement led to unreasonable thermal parameters for the phosphorus atoms in the direction of the trigonal axis and to split positions for the nitrogen and oxygen atoms. The detailed analysis of the sections of the reciprocal space calculated from imaging plate data showed systematic absences in the $hk0$ plane (according to the trigonal system) that were not in agreement with reflection conditions possible in the trigonal or hexagonal crystal systems. Only the assumption of a partial pseudomerohedral triple twinning of index 2 with a smaller orthorhombic unit cell ($a = 475.3(1)$, $b = 1420.8(3)$, $c = 820.3(2)$ pm) could explain the diffraction patterns, and the structure was successfully refined in the space group $Pna2_1$. The pseudosymmetry is also manifested in the broadening of some reflections in the X-ray powder-diffraction pattern of a single-phase sample (Figure 1).[10] Furthermore, electron-diffraction experiments[11] revealed varying diffraction patterns from different areas of crystallites, which were only shifted but not tilted during the experiment (Figure 2). These diffraction patterns could be indexed by using the orthorhombic unit cell and assuming the presence of a triply twinned crystallite. The absence of an inversion center was confirmed by second harmonic generation (SHG) measurements.[12] The oxygen and nitrogen atoms could not be differentiated based on the X-ray crystallographic data. The approximate composition of the single crystals was determined by energy-dispersive X-ray (EDX) analysis[13] and confirmed by chemical elemental analysis (see Experimental Section).

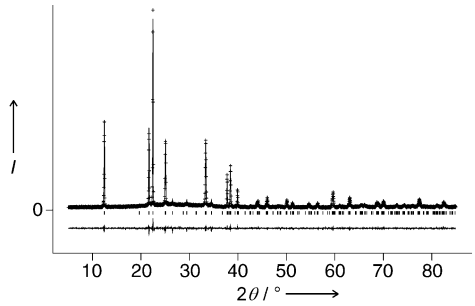


Figure 1. Observed (crosses) and calculated (line) X-ray powder diffraction pattern as well as the difference profile of the LeBail fit of a pure sample of **1**. Allowed peak positions are marked by vertical lines.

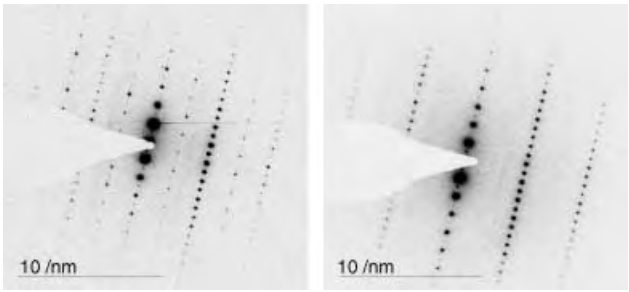


Figure 2. Electron diffraction images at different positions of a triply twinned crystallite of **1** (view along the zone axis [111] with respect to the measured hexagonal cell).

Solid **1** is composed of a network of all-side corner-sharing $P(O,N)_4$ tetrahedra with a topology previously not observed.[14] According to the formula $^3_\infty[(P^{[4]}{}_{12}O^{[2]}{}_yN^{[2]}{}_{24-y})^{(12-y)-}]$,[15] all oxygen and nitrogen atoms bridge two phosphorus atoms. The $P(O,N)_4$ tetrahedra form 3-rings, which constitute the FBU (Figure 3a). Each FBU is connected along [100] through three (O,N)-P-(O,N) bridges; the resulting zigzag chains contain 6-rings (Figure 3b). The chains of 3-rings are connected to a 3D PON framework in the b,c plane. Thus 12-ring channels that contain Cl^- ions in their centers are formed along [100] (Figure 3c). The Li^+ ions occupy the inner walls of these channels and are tetrahedrally surrounded by one Cl^- ion and three O or N atoms. The partial occupancy of the Li positions, which was found by elemental analysis as well as by structure refinement, is compensated by substitution with hydrogen atoms. Solid-state NMR spectroscopic investigations[16] showed that the hydrogen atoms are covalently bound to the nitrogen atoms, which results in compensation of the charge. These imido groups were unequivocally confirmed by IR and Raman spectroscopy.[17]

The Cl^- ions in the channels occupy the preferred positions close to $x = 0$ and $x = \frac{1}{2}$ only with a certain probability. Sections of the electron-density distribution obtained from difference Fourier synthesis perpendicular to

 © 2003 Wiley-VCH Verlag GmbH & Co. KGaA, Weinheim

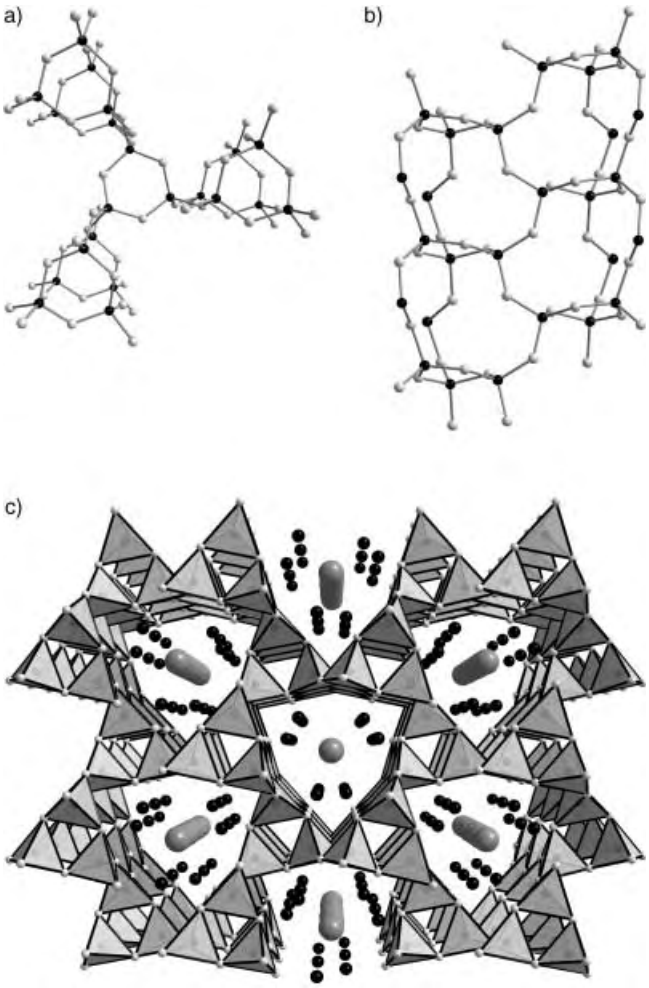


Figure 3. a) Assembly of the $P_3(O,N)_9$ 3-rings, the FBUs, in **1**. P: black; O/N: light gray; view along [100]. b) Linkage of the FBUs along [100] through three (O,N)-P-(O,N) bridging units. Thus, chains of 6-rings are formed. View along [001]. c) Crystal structure of **1**. Chains of 3-rings are connected to a 3D PON framework in the *b*,*c* plane. Thus, 12-ring channels are formed. $[P(O,N)_4]$: gray polyedra, O/N: light gray, Cl^-: dark gray, Li^+: black, view along [100].

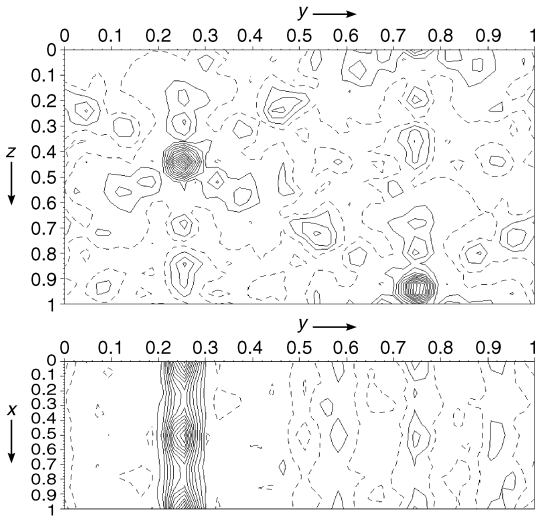


Figure 4. Projection of the electron-density distribution along [100] calculated by difference Fourier synthesis (top) and a section at $z = 0.44$, view along [001] (bottom), after refinement of the PON framework. The Cl^- ions are located in the center of the channels along [100] with a higher probability at the positions close to $x = 0$ and $x = {}^1/_2$.

[001] through the center of the channels show blurred electron density along the channels with maxima at the preferred positions mentioned above (Figure 4). This implies the partial occupancy of the Cl^- ions. Full occupancy of the preferred Cl positions would lead to neighboring Cl–Cl contacts of 223 pm, which is clearly below the sum of the ionic radii (334 pm). On the other hand, as the Cl^- ions presumably dictate the structure, an ordered occupancy of every second position would lead to a Cl^- content that is too small for the stabilization of the network. We have not yet been able to exchange the Cl^- or Li^+ ions with ions of similar size, for example, F^-, Br^-, and Mg^{2+}, in aqueous solution. Nevertheless, Cl^- can be partially replaced by Br^- if the synthesis is carried out in the presence of NH_4Br. A free diameter of the channels of 352 pm is observed, and the framework density is 21.7 T/(1000 Å^3), which is the upper limit observed in oxidic zeolites.[8] Many of the X-ray and electron-diffraction investigations of **1**, and especially those of Br^--containing compounds, led to diffuse diffraction patterns in the higher-order sections of the reciprocal space perpendicular to the pseudo-trigonal axis (Figure 5). The crystal structure of these single crystals could only be refined satisfactorily by assuming a

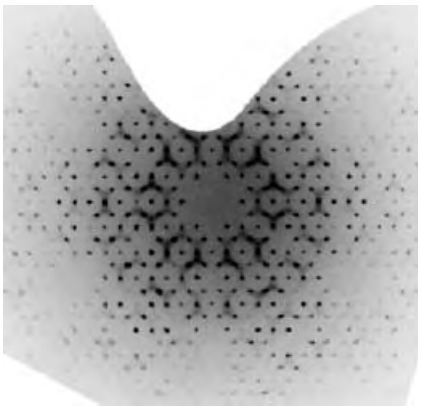


Figure 5. (3*kl*) section of the reciprocal space of **1** containing small amounts of Br^-, calculated from imaging-plate data. Diffuse scattering in the shape of honeycombs is observed in all sections with $h > 0$.

disorder in addition to the triple twinning. Furthermore, split positions had to be introduced for the PON tetrahedral framework for the phosphorus and nitrogen/oxygen atoms, as was previously necessary for the refinement of the structural model in the incorrect space group *P*31*c*. Apparently there are regions in the crystal where the size of the triple-twin domains is below the coherence length of the X-rays. These are better described by a disorder model. In most cases these regions amount to less than 10 % of the crystal. These crystals and crystallites thus contain both large domains, which can be covered by a triple domain refinement, and smaller domains,

 © 2003 Wiley-VCH Verlag GmbH & Co. KGaA, Weinheim

which cannot be resolved by the coherent X-ray beam. Therefore, the latter appear as an averaged structure by taking into account only the Bragg intensities. The boundary of the domains are responsible for the diffuse scattering that is observed in the sections perpendicular to [100] and leads to a honeycomb-like arrangement (for example, Figure 5 shows the (3*kl*) section). From this we can assume the presence of a disordered rod packing. Accordingly, the small domains act as "microfibers" of the structure that build up the crystals/crystallites in an irregular arrangement.

Experimental Section

Typical procedure: Li_2S (15.9 mg, 0.347 mmol; Alfa Aesar, 99.9 %), $SP(NH_2)_3$ (82.5 mg, 0.742 mmol; synthesized according to reference [18]), $OP(NH_2)_3$ (21.9 mg, 0.231 mmol; synthesized according to reference [19]), and NH_4Cl (13.0 mg, 0.243 mmol; Fluka, puriss. p.a.) were thoroughly mixed in a glove box and transferred into a silica ampoule (wall thickness 2 mm, inner diameter 11 mm). The sealed, evacuated ampoule (length 100 mm), was heated to 200 °C (1 °C min^{-1}), and the temperature was maintained for 24 h. The ampoule was then heated to 700 °C (1 °C min^{-1}), kept at that temperature for 48 h, and then cooled down to room temperature (1 °C min^{-1}). Excess NH_4Cl and $(NH_4)_2S$, which were formed during the reaction, sublimed at the upper end of the ampoule. The samples were washed with water to remove further impurities. EDX investigations[13] showed a ratio P/Cl ≈ 5:1. To ensure the purity of the sample, chemical analyses were performed in the microanalytical laboratory Pascher, Remagen. For the reaction mentioned above the following composition was observed: $Li_8H_{4.5}[P_{12}O_2N_{22}]Cl_{2.5}$.

Received: March 11, 2003 [Z51372]

Keywords: oxonitridophosphates · phosphorus · solid-state structures · structure elucidation · zeolite analogues

[1] a) L. Boukbir, R. Marchand, Y. Laurent, P. Bacher, G. Roult, *Ann. Chim.* **1989**, *14*, 475 – 481; b) J.-M. Léger, J. Haines, L. S. De Oliveira, C. Chateau, A. Le Sauze, R. Marchand, S. Hull, *J. Phys. Chem. Solids* **1999**, *60*, 145 – 152; c) C. Chateau, J. Haines, J.-M. Léger, A. Le Sauze, R. Marchand, *Am. Mineral.* **1999**, *84*, 207 – 210; d) J. Haines, C. Chateau, J.-M. Léger, A. Le Sauze, N. Diot, R. Marchand, S. Hull, *Acta Crystallogr. Sect. B.* **1999**, *55*, 677 – 682.

[2] a) A. K. Cheetham, G. Férey, T. Loiseau, *Angew. Chem.* **1999**, *111*, 3466 – 3492; *Angew. Chem. Int. Ed.* **1999**, *38*, 3268 – 3292; b) G. Férey, A. K. Cheetham, *Science* **1999**, *283*, 1125 – 1126; c) M. E. Davis, *Chem. Eur. J.* **1997**, *3*, 1745 – 1750.

[3] W. Schnick, J. Lücke, *Angew. Chem.* **1992**, *104*, 208 – 209; *Angew. Chem. Int. Ed. Engl.* **1992**, *31*, 213 – 215.

[4] R. Marchand, W. Schnick, N. Stock, *Adv. Inorg. Chem.* **2000**, *50*, 193 – 233.

[5] N. Stock, E. Irran, W. Schnick, *Chem. Eur. J.* **1998**, *4*, 1822 – 1828.

[6] N. Stock, PhD thesis, Universität Bayreuth (Germany), **1998**.

[7] a) L. B. McCusker, F. Liebau, G. Engelhardt, *Pure Appl. Chem.* **2001**, *73*, 381 – 394; b) L. B. McCusker, F. Liebau, G. Engelhardt, *Microporous Mesoporous Mater.* **2003**, *58*, 3 – 13.

[8] C. Baerlocher, W. M. Meier, D. H. Olson, *Atlas of Zeolite Framework Types*, 5th ed., Elsevier, Amsterdam, **2001**; http://www.iza-structure.org/databases/

[9] X-ray single-crystal structure determination: Stoe IPDS II diffractometer, $Mo_{K\alpha}$ (71.073 pm), $2\theta_{max} = 56.5°$; crystal ($80 \times 50 \times 40\ \mu m^3$) without any diffuse scattering, orthorhombic, space group $Pna2_1$ (no. 33), $a = 475.3(1)$, $b = 1420.8(3)$, $c = 820.3(2)$ pm, $V = 554.0(2) \times 10^6$ pm^3, $Z = 1$, least-squares refinement on F^2 (G. M. Sheldrick, SHELXL 97 program for the refinement of crystal structures, University of Göttingen, Göttingen (Germany), **1997**); R_1 ($I \geq 2\sigma(I)$) = 0.051 for 5929 reflections, wR_2 (all data) = 0.127 for 7595 reflections and 108 parameters; residual electron density (max./min.) = 0.637/−0.550 e Å^{-3}, all O and N positions were refined as N atoms, H atoms were not observed in the difference Fourier synthesis. Further details on the crystal structure investigations are available from the Fachinformationszentrum Karlsruhe, 76344 Eggenstein-Leopoldshafen, Germany (fax: (+49) 7247-808-666; e-mail: crysdata@fiz-karlsruhe.de), on quoting the depository number CSD-391 200.

[10] The diffraction pattern was recorded on a Stoe Stadi P powder diffractometer ($Cu_{K\alpha 1}$, $\lambda = 154.05$ pm).

[11] Electron-diffraction experiments were performed on a Philips CM30 ST electron microscope (300 kV, LaB_6-cathode).

[12] The authors thank Prof. Dr. Alois Seilmeier and Petra Lehmeier, Lehrstuhl Experimentalphysik III der Universität Bayreuth, for the SHG measurements.

[13] EDX analyses were performed on a JSM 6500F (Jeol, USA) scanning electron microscope.

[14] Although the topology of the framework was not previously observed experimentally, their existence, in principle, had been predicted: M. O'Keeffe, *Acta Crystallogr. Sect. A* **1992**, *48*, 670 – 673. We thank Dr. R. Bell, Royal Institution of Great Britain, London, for this information.

[15] The extensive crystal-chemical formula according to F. Liebau (F. Liebau, *Micropor. Mesopor. Mater.* **2003**, *58*, 15 – 72) has to be set up as follows: $_g|Li_xCl_z|_1\ _h[P_{12}{}^{V[4][1;4]}O_y{}^{[2]}N_{12+x-z}{}^{[2]}\text{-}(NH)_{12-x-y+z}{}^{[2]}]_1\ _h${3/**FR**: ***uB***, 3, 1, 0; ***uB***, 3, 1}$_p${1/[$6^1$$12^2$]^1[100]: 12**R** (3.55 × 3.60), (3.52 × 3.52 × ∞); 2; 46.22**}** **(**O/*Pna*2_1/4.75, 14.21, 8.20/554**)**.

[16] S. Correll, O. Oeckler, N. Stock, J. Senker, W. Schnick, unpublished results.

[17] IR and Raman spectroscopic investigations were performed on a Bruker IFS 66v/S FTIR spectrometer equipped with a FRA 106/S Raman module.

[18] W. Schnick, *Z. Naturforsch. B* **1989**, *44*, 942 – 945.

[19] R. Klement, O. Koch, *Chem. Ber.* **1954**, *87*, 333 – 340.

 © 2003 Wiley-VCH Verlag GmbH & Co. KGaA, Weinheim